



2018

9th International Conference on
Fibre-Reinforced Polymer (FRP)
Composites
in Civil Engineering (CICE 2018),
PARIS 17-19 JULY 2018

CICE
2018

Part 1



Edited by :
FERRIER Emmanuel
BENZARTI Karim
CARON Jean-François



A warm welcome to Paris for CICE 2018 !

Fiber Reinforced Polymers (FRP) composites have emerged over the past two decades as practical materials for civil engineering applications. The wide utilization of FRPs has increased significantly in recent years offering us new ways, both for strengthening of existing structures and for new construction. The rapid increase in the use of FRP composites in civil engineering can be attributed to continuing reductions in material costs, more comprehensive knowledge of the fundamental properties of composites, which has enabled more realistic reduced safety factors, and to the numerous advantages of FRPs as compared with conventional materials such as concrete and steel.

The CICE conference series (International Conference on FRP Composites in Civil Engineering) started in 2001 in Hong Kong and became the official conference series of the International Institute for FRP in Construction, IIFC (www.iifc-hq.org) in 2003. Since then, this major event in the field of FRPs has travelled around the world, with stopovers in Australia (Adelaide 2004), USA (Miami 2006), Switzerland (Zurich 2008), China (Beijing 2010 and Hong-Kong 2016), Italy (Rome 2012) and Canada (Vancouver 2014).

It is a great privilege to host CICE in France this year, in the beautiful city of Paris. The conference is co-organized by IFSTTAR (French Institute of Science and Technology for Transport, Development and Networks), Ecole des Ponts ParisTech and University Claude Bernard LYON 1, and it is hosted at the campus of Paris-Est University in Marne-la-Vallée.

The scientific program of CICE 2018 includes a total of 288 papers from some 40 countries. It has been tailored to reflect the wide spectrum of topics shared by the scientific community, with an emphasis on advanced research and future trends related to FRP strengthening and structural applications, which constitutes the highlight of the CICE conference series. Besides, the program encompasses other hot topics, such as new materials like fiber reinforced cementitious matrix (FRCM) composites or bio-based composites, or more practical issues related to field applications and design guidelines.

We are very confident that CICE 2018, like previous conferences, will provide an international forum where researchers, civil engineers, practitioners and industrial partners will have the opportunity to share their latest advances and open new perspectives for future collaborative projects.

Alongside this enriching technical program, exciting social events will bring a “French touch” to the conference. Delegates and their accompanying persons will enjoy a refreshing cocktail at the first floor of the Eiffel Tower during the welcome reception, and the conference dinner cruise over the river Seine will offer the possibility to taste a gourmet menu while admiring some of the most beautiful monuments of Paris.

Finally, the co-chairs would like to warmly thank all the persons which were involved in the conference organization. First, we are very thankful to all authors who have contributed to the conference by submitting high quality papers. Special thanks are then expressed to the members of the International Scientific Committee who carefully reviewed the papers, and whose input and advice were highly valuable. We are also very grateful to the members of the local organization committee, academic staff and students, who donated their time and contributed to the success of CICE 2018.

The support from the exhibitors and the industrial/institutional sponsors is of course acknowledged and highly appreciated.

We do not forget to acknowledge our academic institutions, IFSTTAR, Ecole des Ponts ParisTech and University Lyon1 (Cellule Congrès) for providing assistance and conference facilities.



**9th International Conference on Fibre-Reinforced Polymer (FRP) Composites
in Civil Engineering (CICE 2018), PARIS 17-19 JULY 2018**

The 9th International Conference on Fibre-Reinforced Polymer (FRP Composites in Civil Engineering (CICE 2018) have been financially support by several companies and institute.

Their support makes our events extra special for attendees. We appreciate their interest in IIFC's vision and are grateful for their support. CICE 2018 Conference wouldn't be possible without the support of our sponsors.



METTLER TOLEDO



Conference Co-Chairs:

Emmanuel FERRIER

Professor at Lyon 1 University

Laboratory of Composite Materials for Construction



Karim BENZARTI

Senior Researcher at IFSTTAR

Department for Materials & Structures



Jean-François CARON

Senior Researcher and Professor

Ecole des Ponts ParisTech.



Local organizing Committee :

Laurent Michel, Associate Professor (Université Lyon 1),

Marc Quiertant, Senior Researchers (IFSTTAR),

Gilles Foret, Professor (Ecole des Ponts ParisTech),

Arthur Lebée and **Loannis Stéfanou**, Researchers (Ecole des Ponts ParisTech)

Sylvain Chataigner, Researcher (IFSTTAR)

Amen Agbossou, Université Savoie

Monssef Drissi Habti, IFSTTAR

International Scientific Committee:

AL-MAHAIDI Riadh	ARAVINTHAN Thiru	BAI Yu
BAKIS Charles E	BANK Lawrence C.	BENMOKRANE Brahim
BENZARTI Karim	BISBY Luke	BUDELMANN Harald
BURGOYNE Chris	BUYUKOZTURK Oral	CAI Steve C.S.
CARON Jean François	CASAS Joan R.	CHEN Guang-Ming
CHEN Jian-Fei	CHENG Li-Juan	CORREIA J. R.
DA SILVA Manuel	DAI Jian-Guo	DARBY Antony
DAWOOD Mina	DE LORENZIS Laura	DRISSI HABTI Monssef
EID Rami	EI-HACHA Raafat	FAM Amir
FENG Peng	FERNANDO D.	FERRIER Emmanuel
FOSTER Stephen	FRANCOIS Raoul G.	GENTRY Russell
GRACE Nabil F.	GREEN Mark F	GREMAL Hughes
GRIFFITH Michael	GUADAGNINI Maurizio	HARIK Issam E.
HARRIES Kent A.	IBELL Tim	ILKI Alper
KANAKUBO Toshiyuki	KARBHARI Vistasp M.	KELLER Thomas
KIM Jimmy	KODUR Venkatesh	KOTYNIA Renata
LAM Lik	LEES Janet	LEUNG Christopher K.Y.
LI Hui	LI Li-Juan	LI Rong
LIU Wei-Qing	LOPEZ Maria	LU Yi-Yan
MA Zhongguo John	MATSUMOTO T.	MATTA Fabio
MEIER Urs	MIRMIRAN Amir	MONTI Giorgio
MOSALAM Khalid M.	MOTAVALLI Masoud	NANNI Antonio
OZBAKKALOGLU T.	PARK Younghwan	PELLEGRINO Carlo
PULIDO, M Dolores	RABINOVITCH Oded	RIZKALLA Sami H.
RTEIL Ahmad	SAVOIA Marco	SCHMIDT Jacob W.
SENA-CRUZ José	SERACINO Rudolf	SHEIKH Shamim A.
SMITH Scott T.	STRATFORD Tim	TAN Kiang Hwee
TAYLOR Susan	TENG Jin-Guang	TRIANAFILLOU T.C.
UEDA Tamon	WAN Bao-Lin	WANG Jia-Lai
WANG Xin	WANG Yuan-Feng	WU Gang
WU Yu-Fei	WU Zhi-Shen	XIAN Gui-Jun
XIAO Yan	XUE Wei-Chen	YANG Yong-Xin
YAO Jian	YE Lie-Ping	YU Tao
YUE Qing-Rui	ZHAO Xiao-Ling	ZHOU Li Min

TABLE OF CONTENTS

Keynotes	19
TECHNICAL SPECIFICITIES WHEN DESIGNING WITH COMPOSITE MATERIALS – CASE OF BUILDING AND ARCHITECTURE.....	20
Samuel Durand ¹	
DEVELOPMENT OF UK GUIDANCE FOR DESIGNERS OF FRP BRIDGES.....	22
N.Farmer	
OPPORTUNITIES FOR RECYCLING AND REUSE OF FRP COMPOSITES FOR CONSTRUCTION IN A CIRCULAR ECONOMY	30
Lawrence C. Bank	
RECENT DEVELOPMENTS ON FRP REBARS AS INTERNAL REINFORCEMENT IN CONCRETE STRUCTURES AND FIELD APPLICATIONS.....	31
Brahim Benmokrane and Hamdy M. Mohamed	
HYBRID FRP-CONCRETE-STEEL TUBULAR MEMBERS	39
Tao Yu	
STRUCTURAL BEHAVIOR OF FRP-REINFORCED GEOPOLYMER CONCRETE SANDWICH WALL PANELS FOR PREFABRICATED CONSTRUCTION	48
Jian-Guo DAI* and Jun-Qi HUANG	
Composite Materials	56
FATIGUE AND DURABILITY OF LAMINATED CARBON FIBRE REINFORCED POLYMER STRAPS FOR BRIDGE SUSPENDERS.....	57
F. Baschnagel ¹ , G. P. Terrasi ^{1,2} , Z. Triantafyllidis ² and U. Meier ³	
GLASS–GFRP HYBRIDS: FROM BRITTLE GLASS TO DUCTILE AND HIGH STRENGTH STRUCTURAL GLASS	66
M. Achintha ^{1*} , B. Balan ¹ , M. Bessonov ¹ , T. Zirbo ¹ and J. Kanvar ¹	
INFLUENCE OF CURING CONDITIONS ON THE MECHANICAL BEHAVIOR OF GLUED JOINTS OF CARBON FIBER REINFORCED POLYMER COMPOSITE/CONCRETE.....	74
A. T. Lee ¹ , M. Michel ¹ , E. Ferrier ¹	
BEHAVIOR OF CFRP STRANDS EXPOSED TO SEVERE ENVIRONMENTAL CONDITIONS.....	82
Omar Khalafalla ¹ , Sami Rizkalla ¹ , Adel ElSafty ² , Mohammad Pour-Ghaz ¹	
INCREASING THE MECHANICAL EFFICIENCY OF PIN-LOADED STRAPS USING THE SLING ANCHORAGE METHOD	89
B. Zwingmann ¹ , Y. Liu ² , M. Schlaich ² and S. Janetzko ³	

ENVIRONMENTAL DURABILITY OF HAND-LAYUP CARBON/EPOXY COMPOSITES INTENDED FOR STRENGTHENING OF CONCRETE STRUCTURES.....	96
Wendlamita Zombré ¹ , Robert Chlela ² , Marie Michel ¹ , Julien Mercier ³ , Karim Benzarti ² , Laurence Curtill	
ASTM SPECIFICATION FOR GLASS-FIBER REINFORCED POLYMER BARS FOR CONCRETE REINFORCEMENT.....	105
R. Gentry ¹ and C. E. Bakis ²	
EFFECT OF INTERNAL MOISTURE CONTENT ON THE TG VALUES OF CFRP RODS	112
Eleni Toumpanaki ¹ , Janet M. Lees ² , Michel Barbezat ³ and Giovanni P. Terrasi ⁴	
HYBRID POLYMER COMPOSITES: A REVIEW.....	119
H. Nguyen ¹ and W. Zatar ²	
RELAXATION OF FRP MATERIALS – ISSUE OVERVIEW IN THE AVAILABLE LITERATURE, CODES AND GUIDELINES	127
M. Przygocka ¹ , R. Kotynia ²	
EVOLUTION OF THE TENSILE RESPONSE OF UNIDIRECTIONAL HYBRID FRP LAMINATES FABRICATED BY HAND LAY-UP METHOD: EXPERIMENTAL AND ANALYTIC ASSESSMENT	135
Filipe Ribeiro ¹ , José Sena-Cruz ² , Eduardo Júlio ¹ , Fernando G. Branco ³ , Fernando Castro ⁴	
NOVEL CAPACITIVE CFRP SENSOR FOR STRUCTURAL HEALTH MONITORING	143
J. Yan ¹ , S. Hassan ¹ , A. Chen ¹ and S. Laflamme ¹	
SHEAR TESTING OF DIFFERENT TYPE AND SIZE OF GFRP REINFORCING BARS	150
A.S. Genikomsou ¹ , G.P. Balomenos ² and M.A. Polak ³	
SALT WATER AND ALKALINE ATTACK ON GFRP REBARS	156
Miguel M. Estêvão ¹ , Manuel A. G. Silva ² , Fernando F. S. Pinho ³	
BEHAVIOUR OF GFRP BARS IN SEAWATER-CONTAMINATED CONCRETE SUBJECTED TO SUSTAINED LOADING.....	164
H. El-Hassan ¹ , T. El-Maaddawy ¹ and A. Al-Sallamin ¹	
EFFECTS OF FIBER ARCHITECTURE ON FLEXURE PROPERTIES OF PULTRUDED GFRP PLATES AND SECTIONS	171
Tianqiao Liu ¹ , Kent A. Harries ^{1,2} and Qi Guo ¹	
EMBEDDED PIEZO MICRO-PATCHES FOR CURE MONITORING OF FIBER-REINFORCED EPOXY IN CIVIL ENGINEERING REPAIRS	177
Olivier Bareille ¹ , Michelle Salvia ¹ , Mingfa Zhang ¹ , Fernanda Benezra-Maia ²	
DYNAMIC TENSILE PROPERTIES OF POLYETHYLENE TEREPHTHALATE FIBER BUNDLE WITH LARGE DEFORMABILITY	183
Y.L. Bai ¹ , Z.W Yan ¹ , J. G. Dai ² , D. J. Zhu ³ , Q Han ¹ , X.L. Du ¹	
INTERFACIAL ADHESION STUDY ON EPOXY PREPREG MODIFIED WITH HIGH POLYCARBONATE) LOADING.....	187

Utai Meekum* and Waree Wangkheeree

TWO-DIMENSIONAL DELAMINATION IN GFRP LAMINATES : EXPERIMENTAL INVESTIGATION	198
A. Cameselle-Molares ¹ , A.P. Vassilopoulos ¹ , T. Keller ¹	
PREDICTION OF TENSILE STRENGTH OF FRP CABLE CONSIDERING RANDOM STRENGTH DISTRIBUTION	206
Z. Q. Peng ¹ , L. N. Ding ² , X. Wang ¹ and Z. S. Wu ¹	
<i>Eco composite or bio sourced composite</i>	213
EMPIRICAL DESIGN EQUATION TO PREDICT THE AXIAL LOAD CAPACITY OF SANDWICH PANELS WITH FLAX FRP SKINS	214
M. Noël ¹ and A. Fam ²	
FATIGUE PERFORMANCE OF BIORESIN GLASS FIBRE REINFORCED POLYMERS	222
A. Watfa ¹ , M. F. Green ² and A. Fam ²	
ILLUMINATED BIOBASED SANDWICH FACADE WITH NATURAL FIBRE REINFORCED POLYMER AND CARDBOARD CORE	229
Carolyn Petzoldt ¹ , Ralf Gliniorz ¹ , Andreas Ehrlich ¹ , Sandra Gelbrich ¹ , Lothar Kroll ¹	
EFFECTS OF CNF CONTENT ON MECHANICAL PROPERTIES OF FLAX FIBER REINFORCED NANOCOMPOSITES	236
Y. Wang ¹ , B. Wan ² and X. Yin ³	
HYGROTHERMAL AGEING OF FLAX FIBRE REINFORCED COMPOSITES INTENDED FOR THE STRENGTHENING OF CONCRETE STRUCTURES	242
R. Chlela ¹ , W. Zombré ² , M. Quiertant ³ , L. Curtil ² , and K. Benzarti ¹	
PHYSICAL AND MECHANICAL CHARACTERIZATION OF NATURAL FIBRES AND FABRICS AS REINFORCEMENT FOR COMPOSITE SYSTEMS	250
G. Ferrara ¹ , B. Coppola ² , L. Di Maio ² , E. Martinelli ³	
BASALT, FLAX AND HYBRID FABRICS REINFORCED EPOXY COMPOSITES TO REPAIR CONCRETE STRUCTURES	258
C. Lacoste ¹ and A. Bergeret ¹	
BIOBASED EPOXY NETWORKS FOR CIVIL ENGINEERING APPLICATIONS	264
J. Galy, A. Viretto	
<i>FRC and cement based composite materials</i>	270
A MULTISCALE APPROACH FOR TEXTILE REINFORCED CONCRETE (TRC): ILLUSTRATION ON TRC SANDWICH PANELS	271
Z.I.Djamai ¹ , A.Si Larbi ¹ , F.Salvatore ¹ , M. El Mankibi ¹	
BOND BEHAVIOR OF BASALT TEXTILE GRID IN UHDC	277
Jiafei Jiang ¹ , Xiangxiang Dou ² , Jiangtao Yu ² , Haibei Xiong ²	

SINGLE FIBRE-TO-MORTAR BOND CHARACTERIZATION IN TRM COMPOSITES	284
Bahman Ghiassi ¹ , Ali Dalalbashi ² , Daniel V. Oliveira ²	
STRAIN AND CRACK DETECTION IN EXPERIMENTAL TESTS ON TEXTILE REINFORCED MORTAR COMPOSITES	290
M. Tekieli ¹ , S. De Santis ² , G. de Felice ² , L. Hojdys ¹ , P. Krajewski ¹ , A. Kwiecień ¹ and F. Roscini ²	
MECHANICAL CHARACTERIZATION OF MULTI-PLY STEEL REINFORCED GROUT COMPOSITES FOR THE STRENGTHENING OF CONCRETE STRUCTURES	298
Georgia E. Thermou ^{1,2} , Gianmarco de Felice ³ , Stefano De Santis ³ , Sultan Alotaibi ¹ , Francesca Roscini ³ , Iman Hajirasouliha ¹ , Maurizio Guadagnini ¹	
INFLUENCE OF PRE-IMPREGNATION PROCESS ON MECHANICAL PERFORMANCE OF GLASS/ETTRINGITIC MATRIX COMPOSITE	306
O. Homoro, M. Michel, E. Lanoye and T.N. Baranger	
APPLICATION OF A TRILINEAR BOND-SLIP MODEL TO FRCM-CONCRETE JOINTS.....	314
Xingxing Zou ¹ , Lesley H. Sneed ² , Tommaso D’Antino ³ , Christian Carloni ⁴	
DURABILITY OF TEXTILE REINFORCED MORTAR (TRM) SYSTEMS	322
Francesca Giulia Carozzi ^{1*} , Pierluigi Colombi ¹ , Tommaso D’Antino ¹ , Carlo Poggi ¹	
STUDY OF THE MATRIX-FIBER BOND BEHAVIOR OF CARBON AND GLASS FRCM COMPOSITES	330
L. H. Sneed ¹ , T. D’Antino ² , J.H. Gonzalez-Libreros ³ , C. Carloni ⁴ , C. Pellegrino ³	
NUMERICAL ANALYSIS OF PBO FRCM-CONCRETE JOINTS	338
Tommaso D’Antino ¹ , Lesley H. Sneed ² , Christian Carloni ³ , Carlo Pellegrino ⁴	
Bond	344
MODE II INTERFACE CONSTITUTIVE LAW FOR CONCRETE SUBSTRATES STRENGTHENED WITH STEEL REINFORCED POLYMERS	345
F. Ascione ¹ , M. Lamberti ² , A. Napoli ³ , A.G. Razaqpur ⁴ , R. Realfonzo ⁵	
FRP-TO-CONCRETE DEBONDING - GLOBAL AND LOCAL BOND BEHAVIOUR.....	353
M. Breveglieri ^{1*} , A. Hosseini ^{1,2} and C. Czaderski ¹	
BOND BEHAVIOR OF PRE-CURED CFRP STRIPS TO CONCRETE USING EXTERNALLY BONDED REINFORCEMENT ON GROOVE (EBROG) METHOD	361
Niloufar Moshiri 1,2, Davood Mostofinejad 1, Amir Tajmir-Riahi 1	
BOND RESISTANCE OF A SINGLE GROOVE IN EBROG METHOD TO ATTACH CFRP SHEETS ON CONCRETE.....	368
Amir Tajmir-Riahi 1, Davood Mostofinejad 1, Niloufar Moshiri 1,2	
WIDTH EFFECT OF INTERFACIAL BOND	374
Yu-Fei Wu 1, Jian-Ping Lin 2, Liang He 3	
THE BOND BEHAVIOR OF SRP-TO-CONCRETE SYSTEM IN FIELD ENVIRONMENT	382

Wei Wang ¹ , John J. Myers ¹	
ATOMISTIC INVESTIGATION ON INTERFACIAL DETERIORATION OF EPOXY-BONDED INTERFACE UNDER HYGROTHERMAL ENVIRONMENT	388
Chao Wu, Ruidong Wu, Lik-ho Tam *	
EXPERIMENTAL STUDY OF CFRP-TO-CONCRETE BONDED JOINTS UNDER FATIGUE LOADING	396
Hao Zhou, Van Thuan Nguyen, Dilum Fernando	
FLEXURAL STRENGTHENING OF PRE-CRACKED RC BEAMS USING SIDE NSM CFRP BARS: AN EXPERIMENTAL INVESTIGATION	404
Thanongsak Imjai ¹ , Udomvit Chaisakulkiet ² and Reyes Garcia ³	
ANALYSES ON THE BOND TRANSFER BETWEEN FRP COMPOSITES AND OTHER STRUCTURAL MATERIALS	412
H. Biscaia ¹ , C. Chastre ² , J. Cardoso ³ and N. Franco ⁴	
COHESIVE ZONE MODELLING OF A PRESTRESSED NON-MECHANICAL CFRP ANCHORAGE SUBJECTED TO FREEZE-THAW CYCLES.....	420
Y.E. Harmanci ^{1,2} , E. Zile ³ , J. Michels ⁴ and E. Chatzi ¹	
INFLUENCE OF VARIOUS PROCESS PARAMETERS ON THE MECHANICAL PERFORMANCE OF CFRP/CONCRETE ADHESIVE BOND	427
Karim Benzarti ¹ , Nicolas Roche ² , Corentin Le Roy ³ , Jeremy Roth ³ , André Flety ³ , Christophe Aubagnac ³	
<i>Composite Structures</i>	436
EXPERIMENTAL AND ANALYTICAL STUDY OF GFRP AND UFC COMPOSITE BEAMS.....	437
I. S. K. Wijayawardane ¹ and H. Mutsuyoshi ²	
FLEXURAL BEHAVIOUR OF AN INNOVATIVE CONNECTION FOR STRUCTURAL SANDWICH PANELS	445
R. Lameiras ¹ , J. Barros ² , I.B. Valente ² and M. Azenha ²	
LONG-TIME BEHAVIOUR OF GFRP/CONCRETE HYBRID STRUCTURES	452
Ibrahim Alachek ¹ , Nadège Reboul ¹ , Bruno Jurkiewicz ¹	
THE BEHAVIOUR OF DUCTILE LINK SLAB DESIGNED WITH FRP REINFORCED ECC	460
Y. Zheng ¹ , L.P Xia ¹ L.F. Zhang ¹ and J.B. Yang ¹	
LARGE-SCALE SLENDER HYBRID FRP-CONCRETE-STEEL DOUBLE SKIN TUBULAR COLUMNS SUBJECTED TO ECCENTRIC COMPRESSION.....	468
P. Xie ^{1,2} , T. Jiang ³ and J.G. Teng ^{2,*}	
HOW MUCH DAMAGE CAN FRP TUBE TOLERATE IN CFFT?	476
Chenxi Lu ¹ , James St. Onge ² and Amir Fam ³	
AXIAL COMPRESSIVE BEHAVIOUR OF COMPOSITE TUBES WITH DIFFERENT GROUT INFILLS	484
Ali A. Mohammed ^{1,2} , Allan C. Manalo ¹ , Ginghis B. Maranan ³ , Yan Zhuge ⁴ and John Pettigrew ⁵	

AXIAL COMPRESSION BENDING INTERACTION BEHAVIOUR OF HYBRID FRP STRENGTHENED RC COLUMN ELEMENTS	492
M. Chellapandian 1, S. Suriya Prakash 2 and Akanshu Sharma 3	
EXPERIMENTAL INVESTIGATION OF A NEW BEAM-COLUMN CONNECTION FOR CONCRETE-FILLED FRP TUBES (CFFTS)	500
Ahmed M. Ali ¹ , Radhouane Masmoudi ²	
MOMENT-CURVATURE CHARACTERISTICS OF STEEL AND CFRP REINFORCED CFFT COLUMNS: EXPERIMENTAL AND THEORETICAL STUDY	508
Maha Hussein Abdallah ¹ , Hamdy M. Mohamed ² , Radhouane Masmoudi ³ , Ahmed Moussa ⁴	
BEHAVIOUR OF CONCRETE SANDWICH WALL PANELS IN FLEXURE USING A NOVEL GFRP SHEAR CONNECTOR.....	513
Debrup Dutta ¹ , Amir Fam ²	
DOUBLY-CURVED SANDWICH PANELS WITH UHPC-FACINGS	520
A. Stark ^{1*} , C. Knorrek ¹ , S. Perse ¹	
BEHAVIOR OF GFRP WALL PANEL WITH INTERNAL TUNED LIQUID COLUMN DAMPER	528
H. Wu ¹ , A. Chen ² and S. Laflamme ³	
<i>Timber and FRP</i>	534
MECHANICAL BEHAVIOR OF HYBRIDAL FLOOR PANELS TO TIMBER COLUMNS JOINTS.....	535
M. Titirla 1, L. Michel 1 and E. Ferrier 1	
BOND ANALYSIS OF BASALT FIBRE REINFORCED POLYMER (BFRP) BARS AND TIMBER BEAMS UNDER AXIAL LOADING.....	543
D. Walline 1 and A. Rteil 2	
COMPRESSIVE BEHAVIOR OF MEDIUM STRENGTH CIRCULAR GLUE LAMINATED TIMBER COLUMNS JACKETED WITH FRP SHEETS.....	551
O. A. Sisman 1, A. Isikara 2, E. Binbir 3 and A. Ilki 4	
WIDTH EFFECT OF FRP EXTERNALLY BONDED TO TIMBER	558
Abbas Vahedian ¹ , Dr Rijun Shrestha ¹ , Prof Keith Crews ¹	
<i>All FRP Structures</i>	566
MONOTONIC AND CYCLIC QUASI-STATIC SWAY TESTS ON PULTRUDED GFRP PLANE FRAMES	575
MF Sá ¹ , D Martins ¹ , JA Gonilha ¹ , JR Correia ¹ , JP Firmo ¹ , JG Ferreira ¹	
EXPERIMENTAL INVESTIGATION ON FLANGE LOCAL BUCKLING OF PULTRUDED GFRP BOX-SECTION UNDER FLEXURE.....	591
Tianqiao Liu ¹ and Kent A. Harries ^{1,2}	
BEHAVIOR OF GFRP WALL PANEL WITH INTERNAL TUNED LIQUID COLUMN DAMPER	598

H. Wu 1, A. Chen 2 and S. Laflamme 3	
EFFECTS OF HOLE GEOMETRY AND BOLT TIGHTENING ON CREEP BEHAVIOR OF PIN-BEARING PULTRUDED FRP CONNECTIONS	604
D.W. Scott 1 and J. Anwar 2	
LONG-TERM DESIGN OF GFRP-PUR WEB-CORE SANDWICH STRUCTURES.....	612
S. Yanes-Armas 1, J. De Castro 1, T. Keller 1	
MULTI-OBJECTIVE OPTIMIZATION OF A COMPOSITE SANDWICH PANEL FLOOR SYSTEM FOR BUILDING REHABILITATION.....	621
M. Garrido ¹ , J. F. A. Madeira ^{2,3} , M. Proença ¹ and J. R. Correia ¹	
DEVELOPMENT OF A SNAP-FIT CONNECTION SYSTEM BETWEEN PULTRUDED GFRP SANDWICH PANELS FOR BUILDING FLOORS.....	631
M. Proença 1, M. Garrido 1 and J. R. Correia 1	
FORM-FINDING AND STRUCTURAL DESIGN OF AN ARCHITECTURAL SCENERY WITH ALL GFRP FREE-FORM FACADE.....	640
Y. Zhao ¹ , X. Jiang ¹ , Q. Zhang ¹ and Q. Wang ¹	
MONOTONIC AND CYCLIC BEHAVIOUR OF BEAM-TO-COLUMN BOLTED METALLIC-CUFF JOINTS BETWEEN PULTRUDED GFRP PROFILES	648
David Martins 1, João Azevedo1, José A. Gonilha 1, João R. Correia 1, Mario Arruda 1 and Nuno Silvestre 2	
INDENTATION AND IMPACT BEHAVIOUR OF GFRP COMPOSITE SANDWICH PANELS FOR CIVIL ENGINEERING STRUCTURAL APPLICATIONS.....	657
R. Teixeira 1, M. Garrido 1, M. Proença 1, J. R. Correia 1 and L.S. Sutherland 2	
EXPERIMENTAL STUDY ON SHEAR PROPERTIES OF GFRP CHANNEL MEMBER	666
Y. Wang 1, H. Nakamura ² , Y. Ishii 3, Y. Inari 4, H. Nakai 5 and M. Nishida 6	
DIC STRAIN FIELD MEASUREMENT OF FRP PLATES WITH AND WITHOUT HOLES	675
B.C. McCoy 1, R. Seracino 2, G.W. Lucier 2, T.W. Langerhans 3	
LOCAL BUCKLING OF PULTRUDED GFRP I-SECTION SUBJECT TO BENDING	680
Everton Souza1, Janine Vieira 2, Daniel Cardoso1	
ADAPTIVE REUSE OF FRP COMPOSITE WIND TURBINE BLADES FOR CIVIL INFRASTRUCTURE CONSTRUCTION	692
R. Gentry 1, L. Bank 2, J. F. Chen 3, F. Arias 2, and T. Al-Haddad 1	
DESCRIPTION & MATERIAL FACTOR OF FRP IN THE STANDARD SPECIFICATION FOR HYBRID STRUCTURES 2014 BY JSCE	699
I. Nishizaki ¹ , H. Nakamura ² , Y. Kitane ³ , T. Matsumoto ⁴ , K. Hashimoto ⁵ and A. Kobayashi ⁶	
FIBER MODEL ANALYSIS ON THE FLEXURAL BEHAVIORS OF CFRP BOX BEAMS	706
T. Matsumoto 1 and M. Nasu 2	

PREDICTION OF THE WEB CRUSHING CAPACITY OF PULTRUDED GFRP I SECTIONS UNDER TRANSVERSE LOADING	712
Xi-Dong Wu 1, Chao Wu 1, *	
FLEXURAL BEHAVIOR OF PRE-CRACKED FRP BEAMS STRENGTHENED WITH CARBON FIBER LAMINATES	721
Himanshu Chawla ¹ and Shamsheer Bahadur Singh ²	
EXPERIMENTAL STUDY ON THE WEB CRIPPLING BEHAVIOR OF PULTRUDED GFRP CHANNEL SECTIONS	728
Li-Teng Zhang ¹ , Xi-Dong Wu ¹ and Chao Wu ¹ ,*	
SHAKING TABLE TEST ON CFRP CABLE DOME STRUCTURE.....	736
W. H. Qin ^{1,2} , Z. Xi ^{1,2} , Y.J. Li ¹ , Z. C. Zhang ¹ and X. Zhang ¹	
SPLICE CONNECTION FOR TUBULAR FRP COLUMN MEMBERS	745
C. Qiu ¹ , Y. Bai ²	
BRIDGE PARADIS NORWAY: DESIGN AND ENGINEERING OF A 42M SPAN FULL FRP FOOTBRIDGE	750
Liesbeth Tromp ¹ , Kees van IJselmuiden ² , Stian Persson ³	
FALCON – A MULTI-DISCIPLINARY EFFORT TO PROMOTE FRP BRIDGES IN SWEDEN	758
Reza Haghani ¹ , Erik Olsson ^{1,2}	
TOWARDS A STRUCTURAL EUROCODE FOR FRP STRUCTURES: THE ROLE OF CEN/TC 250	768
L. Ascione ¹	
ELASTIC GRID SHELL IN COMPOSITE MATERIALS: SOME RECENT DEVELOPMENTS	776
Jean-François Caron, Olivier Baverel, Lionel du Peloux, Cyril Douthe , Pierre Cuvilliers, R.Leroy	
<i>RC structures internally reinforced by FRP bars</i>	784
IMPROVEMENT OF MECHANICAL SHEAR RESISTANCE OF HIGH MODULUS CFRP ROD WITH GFRP RIBS	785
Hiroaki Hasegawa ¹ , Nobuhiro Hisabe ¹ , Yoshiki Onari ² and Isamu Yoshitake ²	
SERVICEABILITY AND MOMENT REDISTRIBUTION OF CONTINUOUS CONCRETE ELEMENTS REINFORCED WITH STEEL-BASALT BARS.....	794
M. Akiel ¹ , T. El-Maaddawy ² and A. El Refai ³	
NUMERICAL MODELING OF THE INTERACTION BETWEEN GFRP REINFORCEMENT AND HIGH STRENGTH CONCRETE DURING HYDRATION PROCESS	802
S. Kammoun ^{1,2} , A. Sdiri ¹ and A. Daoud ^{1,3}	
PARAMETRIC STUDY ON BOND OF GFRP BARS IN ALKALI ACTIVATED CEMENT CONCRETE .	811
B. H. Tekle *, A. Khennane * and O. Kayali *	
BOND STRENGTH OF POST-INSTALLED GFRP BARS IN BEAM-COLUMN CONNECTIONS.....	820
Muhammad Shahraiz Bajwa ^{1,3} , Benjamin Z. Dymond ¹ , Rania Al-Hammoud ²	

EXPERIMENTAL INVESTIGATION OF GEOPOLYMER CONCRETE BEAMS WITH RECTANGULAR GFRP SPIRAL REINFORCEMENT	829
G.B. Maranan 1, A.C. Manalo 2, T.W. Krishna 2 and B. Benmokrane 3	
BEHAVIOUR OF CONCRETE DEEP BEAMS REINFORCED WITH GFRP HEADED-END BARS.....	836
A.M. Mohamed1 and E. F. El-Salakawy2	
INFLUENCE OF DIFFERENT APPROACHES ON DESIGN, DESIGN VALUES AND GENERAL SAFETY FOR INTERNAL FRP REINFORCEMENT	843
André Weber1, Faustin Gauffillet,2	
CONTRIBUTION OF SHEAR TRANSFER MECHANISMS AND STRENGTH OF GFRP REINFORCED CONCRETE BEAMS	851
D. D. E. Pacheco 1, D. C. T. Cardoso 1 and M. Noël 2	
A REVIEW ON EXPERIMENTAL DEFLECTIONS IN FRP RC FLEXURAL MEMBERS	860
C. Barris ¹ , A. Bover ² , J. Gómez ² and L. Torres ²	
NUMERICAL SIMULATION OF SHEAR FAILURE IN SCALED GFRP REINFORCED CONCRETE BEAMS WITHOUT STIRRUPS	869
S. Khodaie 1 and F. Matta 2	
EFFECT OF HIGH TEMPERATURES ON THE BOND PERFORMANCE OF GFRP BARS TO CONCRETE	878
Inês C. Rosa1, João P. Firmo1,2, Luís Granadeiro1, João R. Correia1	
SHEAR TESTS ON GFRP REINFORCED CONCRETE BEAMS USING DIGITAL IMAGE CORRELATION SYSTEM	887
M. Kaszubska 1, R. Kotynia 1, D. Szczech1, M. Urbaniak2	
TESTS ON GFRP REINFORCED CONCRETE CLOSING JOINTS	896
Nader Sleiman 1 and Maria Anna Polak 2	
EFFECT OF SURFACE TREATMENT AND TEST CONFIGURATION ON BOND BEHAVIOUR OF GFRP REBARS.....	905
Ondrej Janus1, Frantisek Girgle2, Vojtech Kostiha2, Petr Stepanek2	
PERFORMANCE STUDY OF A POST-TENSIONED CONCRETE SLAB STRENGTHENED WITH CFRP USING 24 HR AND CYCLIC LOAD TESTING.....	915
Thanongsak Imjai 1, Surin Sutthiprapa 1 Burachat Chatveera 2 and Udomvit Chaisakulkiet 3	
SHRINKAGE BEHAVIOUR OF FIBRE REINFORCED POLYMER GRID REINFORCED INFRA-LIGHTWEIGHT CONCRETE	923
Y. Liu 1, A. Goldack 1, M. Schlaich 1 and A. Hückler 1	
BOND EVALUATION OF GFRP REINFORCING BARS EMBEDDED IN CONCRETE UNDER AGGRESSIVE ENVIRONMENTS	931
A. Ruiz Empananza ¹ , F. De Caso Y Basalo ² , R. Kampmann ³ and A. Nanni ⁴	

EXPERIMENTAL STUDY OF CONCRETE BEAMS REINFORCED WITH HYBRID (SFCB AND BFRP) BARS.....	938
Yang yang1, and Gang Wu2	
BEHAVIOUR OF PRECAST SEGMENTAL CONCRETE BEAMS PRESTRESSED WITH CFRP TENDONS	945
T. M. Pham*, T. D. Le and H. Hao	
STUDIES ON DESIGN AND CONSTRUCTION MONITORING OF PRECAST CONCRERE MUNICIPAL TUNNEL REINFORCED WITH GFRP BARS.....	954
X. Hu 1, W.C. Xue 1, F. Peng1 and T. Liu 1	
EXPERIMENTAL STUDY ON THE BOND BEHAVIOR BETWEEN FRP REBARS AND CONCRETE ..	961
A. Rolland 1, K. Benzarti 2, M. Quiertant 3, P. Argoul 3, S. Chataigner 4 and A. Khadour 5	
FLEXURAL BEHAVIOUR OF BFRP REINFORCED BEAMS WITH PRESTRESSED REINFORCEMENT	969
M. Mirshekari 1, T. Donchev 1 and D. Petkova 1	
EXPERIMENTAL INVESTIGATION ON FLEXURAL BEHAVIOR OF UHPC PANELS REINFORCED WITH FRP BARS	975
Jiaxing Chen1, Zhi Fang 1,2	
AXIAL PERFORMANCE CAPACITY OF HOLLOW CONCRETE COLUMNS REINFORCED WITH GFRP BARS.....	984
Omar S. AlAjarmeh1, Allan Manalo 1, Warna Karunasena1, Brahim Benmokrane2	
PERFORMANCE OF GFRP IN BALCONY SLAB THERMAL BREAKS	991
Sarah Boila1, David Kuhn 2, Kevin Knight 3, John Wells 4, Dagmar Svecova1	
LOAD DEFLECTION BEHAVIOUR OF SELF-CONSOLIDATING CONCRETE BEAMS PRESTRESSED WITH CFRP BARS.....	- 999 -
S. Krem 1, K. Soudki 2	
BOND BEHAVIOUR BETWEEN GFRP RODS AND CONCRETE PRODUCED WITH SEAWATER: AN EXPERIMENTAL RESEARCH.....	1007
José Sena-Cruz 1, Eduardo Pereira 1, Néilson Freitas 1, Emanuel Pereira 1 and Sérgio Soares 1	
FLEXURAL BEHAVIOR OF PULTRUDED GLASS FIBER-REINFORCED POLYMER DISTRIBUTION POLES	1015
Omar I. Abdelkarim1, Jose Manuel Guerrero2, Hamdy M. Mohamed3, Brahim Benmokrane4	
TECHNICAL STANDARDS FOR DEBONDING IN FRP-CONCRETE SYSTEMS: AN EXPERIMENTAL CONTRIBUTION FOR BASALT-FRP.....	1022
Elisabetta Monaldo 1, Francesca Nerilli 1 and Giuseppe Vairo 2	
GFRP STRAND PROTOTYPE: EXPERIMENTAL INVESTIGATION AND TECHNOLOGY READINESS	1030

Marco Rossini 1,*, Pedro Jalles 1, Gabriele Balconi 2 and Antonio Nanni 1

BEHAVIOR OF GFRP REINFORCED CONCRETE UNDER FLEXION: EXPERIMENTAL TESTS ON REAL
SCALE SLABS 1038

M. Arduini 1 and G. Balconi 2

A CONSISTENT DESIGN CONCEPT FOR BOLTED CONNECTIONS AND APPLICATION TO INDUSTRIAL
STRUCTURES.....1044

Matthias Oppe,, J Toby Mottram, Jan Knippers, Knippers



*9th International Conference on Fibre-Reinforced Polymer (FRP) Composites
in Civil Engineering (CICE 2018), PARIS 17-19 JULY 2018*

Keynotes

TECHNICAL SPECIFICITIES WHEN DESIGNING WITH COMPOSITE MATERIALS – CASE OF BUILDING AND ARCHITECTURE

Samuel Durand1
1 : MECA Design Office
12 rue du chapeau rouge
F- 44000 NANTES
samuel.durand@cluster-meca.fr

composite materials in architecture and building are nowadays frequently used. in addition to the recurrent lightening and excellent resistance to environmental conditions, composite materials can lead to new shapes and architectural details in building and construction (millennium dome à london, 2000; princess nora university dome, riyadh, 2010, roof of h.h.r., 2014 in jeddah and mecca, domes escor in paris, 2015).

from a design office point of view, cladding, envelopes, roofs or structural elements made of composite materials have their own specificities, making them specific to their counterparts in concrete, steel or wood. a poor knowledge of the specificities of composite materials can lead to a non-optimized design also called "black metal".



fig. 1. toiture h.h.r. à jeddah, water tests

composite materials are partially covered by standards or regulations for building as for eurocodes types. standardization work is on going [2] to reduce this lack. the design of composite material parts must at least take into account some specificities such as orthotropy, creep behavior, the influence of humidity and temperature on mechanical characteristics and fracture modes that can sometimes be fragile (fiber breaks, delaminations), or progressive (inter-fiber or resin damage). the safety factors must be adapted to the failure mode and the manufacturing process.

the designer must also in early project phases, choose from many manufacturing methods (pultrusion, wet molding, infusion, prepreg, ...). surface aspect, appearance, mechanical performance and ultimately cost are strongly related to the limits and possibilities of the manufacturing process. the work on the optimization of tools must be carried out in parallel with the first budget estimates.

fire resistance and performance are a key element to specify in the case of composite materials. thermosetting resins commonly used (polyester, vinylester, epoxy) are combustible and flammable. the addition of flame retardant fillers and an intumescent gelcoat may be necessary to achieve a minimum fire performance but the

implementation of these resins then becomes more difficult. advances are expected on the development of fire-resistant resins suitable for implementation by the infusion process.



fig. 2. dômes cscor -paris before lifting

références

- [1] durand s. billaudeau e., lubineau g. « design analysis of grp panels for the roof of the haramain high speed railway jeddah station». international conference on sandwich structures, icss10, nantes, 2012.
- [2] ascione l. tromp liesbeth « development of the eurocode, frp technical report wg4 frp structures». composite in construction, compic2015, amsterdam, 2015.
- [3] caron jf. « matériaux composites pour la construction: état de l'art et spécificités». séminaire amac, aussois, 2011.

biographie

samuel durand is the co-creator of the design office meca, specialized in innovative structures for building and construction. since 2006, meca has been involved in many composite materials projects, in france and abroad (rehabilitation of esiee in noisy le grand 2007, roof of multimodal exchange center at saint nazaire 2010, roofs of h.h.r. train stations 2012-2014 in jeddah and mecca, domes cscor in paris, 2015, ...).



DEVELOPMENT OF UK GUIDANCE FOR DESIGNERS OF FRP BRIDGES

N.Farmer

Executive Director, Tony Gee and Partners LLP Esher, Surrey, UK

ABSTRACT

A team of design and construction practitioners, with assistance from academia, has been producing guidance for clients and their designers, and for suppliers who would like to procure FRP bridges, but need reassurance that those involved in the process can be guided by an engineering reference document that is accepted as state-of-the-art by experts in this specialist field. Publication of the guidance document is being progressed by the Construction Sector Group of the Trade Association Composites UK and is due for publication in 2018. The paper explains why the guidance is required and introduces each chapter by highlighting key recommendations in the guidance. To give context to the guidance, case studies will be given in the paper to illustrate the types of FRP bridges already designed and constructed in the UK.

KEYWORDS

FRP, guidance for designers, bridges, structural, processing, inspection, repair.

BACKGROUND – WHY GUIDANCE IS REQUIRED

The first Fibre Reinforced Polymer (FRP) bridge in the UK was installed in 1992, at Aberfeldy in Scotland (Figure 1). Since then more than 30 FRP bridges have been executed in the country. However, no national or international design standards for FRP bridges have been produced (Mottram 2017) that are directly suitable for use in the UK, and there is a relatively poor knowledge of FRP materials and structures generally amongst clients, designers and contractors. On a technical level many designers are not aware of the differences in designing FRP bridges, compared to traditional bridges, or have sufficient knowledge of the wide variety of FRP materials and components available to enable them to select the most appropriate types for a particular application.

Some bridge owners have expressed concern that their traditional supply chain will need guidance to help them understand the construction, inspection and maintenance requirements for FRP bridges and there are differences in the procurement approach compared to traditional bridges. For example, there may be elements of design by the FRP bridge supplier and other elements may be supplied only.

Against this background, in 2011 an ad hoc working group of clients, designers, specialist contractors, suppliers and academics got together and decided to produce a document that brings together best practice design guidance. As all parties were giving their time voluntarily progress was rather slow and completely stalled from time-to-time. However, with the Construction Sector Group of Composites UK, the UK's trade association for the polymeric composites industry, becoming involved in 2016, final editing before publication took place up to February 2018. The ad hoc group is convened by Professor Toby Mottram of Warwick University, who is also a member of CEN/TC250 WG4 that is working towards production of a structural Eurocode for FRP.

The document provides guidance to designers, but is not a design guide in the fashion of a national or international standard, such as we have with the Eurocode suite.



Figure 1: Aberfeldy Footbridge



DOCUMENT STRUCTURE

The guidance document is structured under the following chapters and this paper elaborates on the contents and features of each of these in turn:

Introduction

Background to FRP bridges

Conceptual design

Material types, composite processing and properties

Structural design

Execution of FRP bridges

Long-term inspection, monitoring and maintenance

Sustainability

Summary and recommendations

Appendices: i) UK FRP bridges case studies and ii) Approval in Principle document

It is highly likely that users of the guidance will not be familiar with design using FRP materials, shapes and systems, and, therefore, the document contains a comprehensive glossary of terminology. The introduction in Chapter 1 includes a flow chart that guides the reader through the complete FRP bridge design, procurement, construction and certification processes, including advice on inspection, monitoring and maintenance requirements.

Those not familiar with the key benefits of FRP over traditional materials are enlightened in Chapter 2 by the first section on Background to FRP Bridges together with a history of FRP bridges in the UK, asset management considerations, an honest assessment of the advantages and disadvantages of these structural engineering materials before concluding with a section on lessons learnt from five UK bridge applications.

CONCEPTUAL DESIGN CONSIDERATIONS

The first action in the design flow chart asks the question “Is an FRP structure appropriate and sustainable? To assist the designer in answering this question reference is made in Chapter 3 to the information in Chapters 2 and 8, drawing upon the experiences of previously constructed FRP bridges and research and development work into the sustainability credentials of the materials used in similar FRP structures around the world. This includes comparative Life Cycle Assessments and material impacts for bridges constructed from FRPs and traditional materials such as steel, concrete, timber and aluminium.

Having decided that FRP is appropriate for a particular bridging application the designer has to decide what form of bridge is suitable? Section 1 of Chapter 3 gives some general advice to help determine which structural configuration is appropriate and to consider how the elements will be joined together. In particular will they be adhesively bonded or fastened with connectors, and will the design need to be assisted by testing, a topic that is covered in sub-section 5.1.12. With continuing developments in constituent materials, material strength theory and analysis methods, composite processing and fabrication methods, a section on Future Innovations in Chapter 3 informs the reader on some of the areas where research is being undertaken and may come to market during the lifespan of the guidance document.

The basic requirements of the design, including the principal dimensions, are determined following the guidance given in Chapters 4 to 7 of the document and requirements for durability are reproduced from the JRC Science and Policy Report by Ascione et al. (2016). Having reached this stage in the design process, the selection of appropriate FRP materials for preliminary design is comprehensively covered in Chapter 4, and after some preliminary analysis and stress checks, which are covered in sections 5.2 to 5.4, the design may need to be modified until, by a process of iteration, the conceptual design is established and details of the superstructure design can be developed.

MATERIAL TYPES, COMPOSITE PROCESSING AND PROPERTIES

Chapter 4 of the document is an essential read for those designers, and others, who are unfamiliar with FRP materials, which is a significant part of the target readership. The wide array of choices available can be overwhelming for those used to designing with traditional bridge construction materials. The guidance explains in simple terms what constitutes a fibre reinforced polymeric composite material, before giving detailed resin and matrix property guidance for comparing polyester, vinylester, epoxy, and speciality resin systems used in bridge FRPs, such as phenolic and acrylic resins. This Chapter explains that mechanical properties are influenced by strength and stiffness of fibre type, interface/interphase bond between fibres and matrix, volume fraction in FRP materials and individual layers and orientation of fibre types of which glass, carbon and aramid are most likely to be used in bridge construction. Guidance is given on the properties of each fibre type and the forms of fibre reinforcements and core materials are described in sufficient detail to inform the selection of the most appropriate materials for a particular bridge project application.

A basic introduction to composite material processing methods is given including for spray lay-up, wet or hand lay-up, vacuum bagging, filament winding, pultrusion, pulwinding, resin transfer moulding and proprietary moulding techniques (Figure 2). It is important to understand that mechanical properties are unknown until the composite processing of the component has been completed.

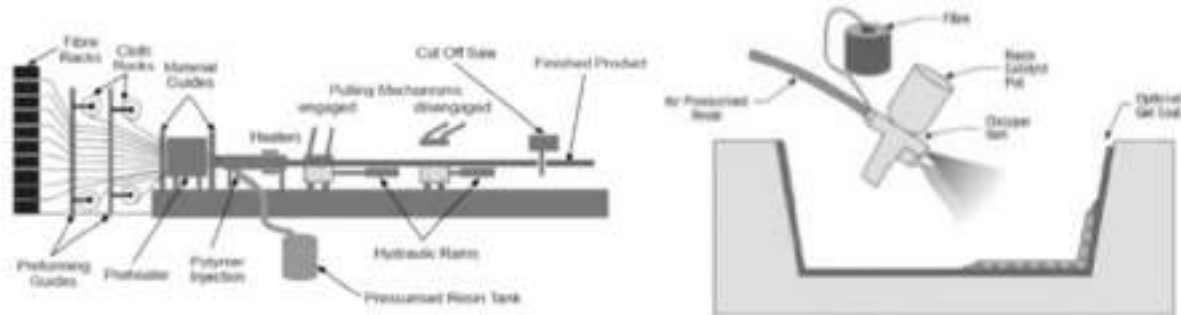


Figure 2: Examples of Processing Methods – Pultrusion and spray lay-up

A sub-section on adhesives for bonded connections gives the types and characteristics of epoxies, toughened epoxies, polyurethanes, urethane methacrylates (acrylics), together with factors to be considered in their selection. The derivation of mechanical properties is extensively covered, including noting that composite material properties can be derived using theoretical approaches, such as micromechanical modelling or lamination theory using individual fibre and matrix constituent test results. Alternatively, the designer is informed that mechanical properties can be determined by individual laminae testing aided by lamination theory for panels and laminates, or whole laminates and panels can be tested. By choosing the later approach the partial factors are their lowest on the resistance side of the design equation; this approach is for the most economical use of the FRP material(s).

Core materials and components produced in a factory in a continuous and repeatable way, together with moulded components, are given separate consideration in terms of the determination of mechanical properties to be used for structural engineering design purposes. The important topics of durability, galvanic corrosion, UV Protection, fire performance and potential effects of vandalism are also covered in Chapter 4 of the guidance document.

STRUCTURAL DESIGN

The adopted basis of design is as in Eurocode standard BS EN 1990:2002 for a design working life of between 60 to 120 years. The design must be robust in case of accidental damage. These requirements will be familiar to all bridge designers operating in the UK and many others throughout Europe. The partial factors for loading are generally as in the UK version of the Eurocode BS EN 1991, but additional factors have been proposed for FRP self-weight (Figure 3). Similarly, partial factors for resistance of the FRP materials are given as suggested by Ascione et al. (2016).

Action	γ (Set A)		γ (Set B)		γ (Set C)	
	Superior value	Inferior value	Superior value	Inferior value	Superior value	Inferior value
FRP self-weight	1.05	0.95	1.2	0.95	1	1

Figure 3: Partial Factors for FRP self-weight

Section 5.2 is dedicated to structural analysis, recognising that the elastic, but non-ductile behaviour differs from that of reinforced concrete and steel, which are more commonly used in the construction of traditional bridges. The anisotropic or orthotropic nature of FRPs and the importance of shear deformation and dynamic effects are highlighted, and guidance given on idealisation of the structure and Finite Element Analysis (FEA), including second-order effects and material geometric and property imperfections (Figure 4).

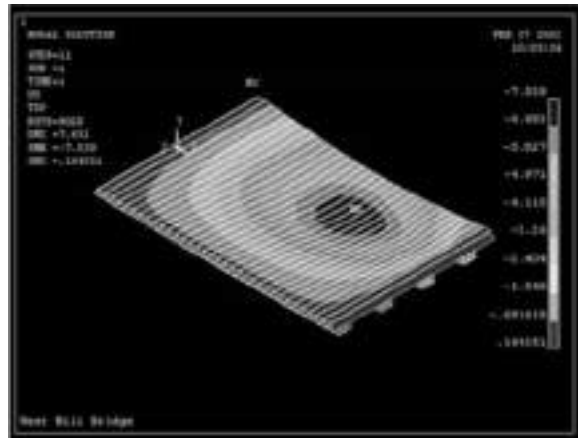


Figure 4: Finite Element Analysis of FRP structures

Design for the ultimate limit state for pultruded FRP members, FRP laminates and sandwich panels are comprehensively covered including beam, panel and core failure modes. Fatigue, particularly under local wheel loading, is an important consideration and the document advises on susceptible locations and strain limits to avoid degradation of an FRP bridge deck.

Design for serviceability limit state considerations includes limiting deflections under live loading to $\text{span}/300$ or a greater value if non-brittle finishes are on the bridge deck. Vibrations are limited to the values in BS EN 1991-2 rather than 5HZ in BD90 (Anonymous 2005), a standard document in the UK's Design Manual for Roads and Bridges. To prevent resin micro-cracking under frequent actions, strains are limited to between 0.2-0.4% depending on the resin matrix type. The effects of temperature changes on the performance of the bridge and its properties are constantly highlighted throughout the guide.

The guide deals comprehensively with connections and joints, covering the various types of connections and the design approaches for both bolted, bonded and hybrid configurations.

Reference is made in Appendix i to various case studies as listed on the Composites UK database. The following five examples in the UK each represent one particular aspect of design:

- West Mill Bridge – wheel loading
- Standen Hey Overbridge – bonded pultruded sections
- Dawlish Station Footbridge - durability
- Bradkirk Footbridge – vibration from train buffeting
- Launders Aqueduct – trestle supports and a water-retaining deck

West Mill Bridge was the first FRP public highway bridge in the UK and was installed in 2002, Luke et al. (2002). The 10 m span bridge crosses a river in Oxfordshire and comprises a bespoke pultruded FRP deck supported on FRP box-shaped beams manufactured by a combination of pultrusion shapes and resin infused carbon fibre reinforced polymer plates. For the 225 mm deep deck a new bespoke shape for road decking was pultruded, and it is today the Fiberline Composites A/S product FBD600 Asset Bridge Deck (2016). The deck was extensively tested under simulated wheel loading as part of an EU funded research project. The surfacing installed was a polymer concrete of a thickness varying between 30mm to 90mm. In 2010 cracking was observed in the polymer concrete surfacing and as a result of the surfacing defects, wear to the top surface of the GFRP sections was evident, (potentially from abrasion). In localised areas, two of the box sections suffered mechanical damage. The stiffness of surfacing system, when compared to the flexibility of deck and lack of adhesive bond, may have resulted in some of the observed problems with the FRP. The addition of a flat plate bonded to the top of pultruded FBD 600 sections has been proved by researchers at the University of Bristol to provide enhanced wheel load distribution characteristics and this enabled local repairs to be carried out to prolong the service life of the road bridge.

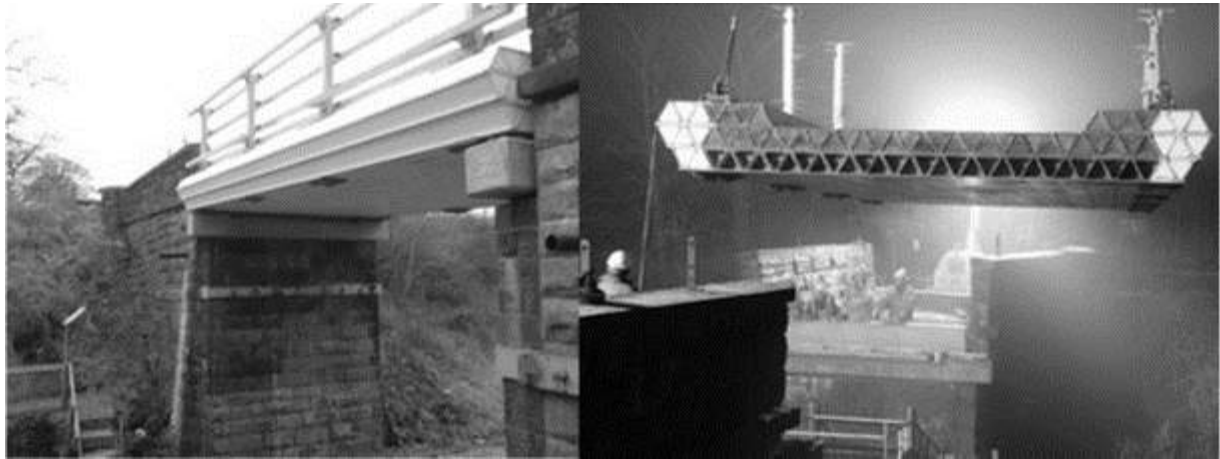


Figure 5: Standen Hey Bridge

Standen Hey Bridge, seen in Figure 5, installed near Clitheroe in 2007, spans 10 m over a railway near Blackburn. It provides local farm access, Dawson and Farmer (2009). This project also used the FBD600 Asset Bridge Deck units as per the deck for the West Mill Bridge, but further minimised weight by using up to three bonded layers of the Asset modules spanning longitudinally, effectively forming a voided deck. A similar concept was used in 2005 for a 6 m span FRP road bridge in Klipphausen, Germany, but only using a single layer of the Asset deck. The deck modules were bonded together with a two part cold-cured epoxy adhesive applied by handheld trowels.

The replacement of Dawlish footbridge in 2012, Kendall et al. (2012), is an example of combined use of pultruded shapes and moulded FRP components. This all-FRP footbridge replaced a badly corroded Grade II listed Victorian metallic footbridge, and was chosen for maximum durability in the very severe coastal environment. Being so close to the sea, in stormy conditions the bridge is drenched by the spray from breaking waves and blasted by wind-born sand from the beach. The 17.5m long bridge form comprised U-frame girders with a glass FRP roof and stairs. Grading II listing necessitated that the new bridge be as identical as practical to the old metallic bridge including features such as dome-headed bolts to replicate rivets. On 5 February 2014 a severe storm hit the south coast of the UK and destroyed large sections of the adjacent railway and severely damaged the station. The FRP footbridge was completely undamaged, demonstrating the excellent durability characteristics of the materials (Figure 6).



Figure 6: Dawlish Station Footbridge



Bradkirk Footbridge consists of two 12m spans, plus staircases constructed using moulded glass/epoxy fibre-reinforced plastic (FRP) material over a major railway line. The lightweight nature of FRP materials, made the dynamic effects of train buffeting of footbridges a consideration during the design of the structure and onsite-measured vibration data was subsequently compared with FEA numerical results. It was found that at the low speed of trains measured (112 km/h), there was no adverse effect on the structure and the structure was found to have a high fundamental natural frequency. There was also a good correlation between the data measured on the bridge and the FEA and theoretical predictions of natural frequencies, Santos and Mohan (2011).

Launders Aqueduct reconstruction in rural Oxfordshire, successfully achieved Network Rail's first use of FRP materials to replace a steel aqueduct over the deep Ardley railway cutting. The innovative design adopted FRP materials for the troughed deck profile and the independent water-tight liner, to provide a durable and low maintenance replacement for the aqueduct. The designed solution and methods also mitigated the impact of the works upon the cutting, which was imperative due to location within a designated site of special scientific interest. The existing steel structure was replaced with a new aqueduct deck of a similar length and configuration, across three spans and supported onto new pier trestles. The new deck and trestles were manufactured using pultruded shapes. The trestles were fabricated as single units, each weighing around half a tonne, and the deck was delivered to site in three sections which were then spliced together into a single 7 tonne superstructure of 35m length.

EXECUTION OF FRP BRIDGES

Chapter 6 describes examples of good practice identified from several of the sources which are referenced in the document, but should not be used directly as part of a contract specification for procurement of an FRP component. The guidance is very clear in highlighting that FRP bridges are not like other bridges and states that "Given the specialist nature of the fabrication and installation of an FRP structure, both on and off site, it is recommended that these activities are carried out by a specialist contractor and operatives with demonstrable experience and training in the installation of structural FRPs or equivalents."

Fabrication advice covers identification and control of materials, dimensional tolerances and working lines, preparation of materials, laminating, bonding and connections, cleaning, sealing and coating, repair procedures, handling and storage. A short section on Installation covers the method of assembly and possible need for appropriate temporary supports. Quality control is a vitally important part of the execution of the works and best practice advice includes testing to ensure conformance to design and specifications, material inspection, fabrication and installation inspection.

Certification of design and construction processes will usually follow those specified by a particular bridge owner. But "experience in the UK, Farmer et al. (2006), has shown that FRP bridge projects are successful when their designer teams have a role in the inspection and monitoring works during the fabrication and installation phases, and the designs are subjected to independent checking by other suitably experienced professional engineers." Load testing is sometimes beneficial to validate the designs of components or sometimes complete structures and reference is also made to sub-section 5.1.12 on Design Assisted by Testing.

LONG-TERM INSPECTION, MONITORING AND MAINTENANCE

Chapter 7 considers asset management in relation to the particular characteristics of FRPs to ensure that the bridge can perform its purpose throughout its design working life.

To facilitate long-term monitoring of in-service performance, the guidance suggests that separate samples of the FRP materials, sourced from a bridge's components, be stored indoors and tested at a later date. The purpose being to establish a benchmark for future visual or acoustic inspections. Other samples may be stored at the bridge site to avoid the need to take samples from the bridge components during its lifetime. Installation of Structural Health Monitoring (SHM) sensor systems is encouraged, particularly if they can be installed during the construction stage rather than reactively when, say, a defect is suspected.

The guide recommends that visual inspections are routinely undertaken every one or two years, during which the surface of the laminate should be inspected for damage or discolouration along with other aspects listed in the guidance. Movement surveys are suggested if there are concerns about the bridge behaviour and dynamic testing can be useful, provided that a benchmark survey has been undertaken shortly after construction for comparative purposes. Detailed surveys are recommended every 6 years. These should be more rigorous and may involve Non-Destructive Evaluation (NDE). If hidden damage such as dis-bonds is suspected (Figure 6), a special inspection is recommended, and may include NDE techniques such as:

Enhanced visual inspection;
Acoustic impact testing;
Transient thermography;
Laser shearography;
Ultrasonic testing;
Radiography.

A table in the guidance identifies what defects each of these techniques can detect.

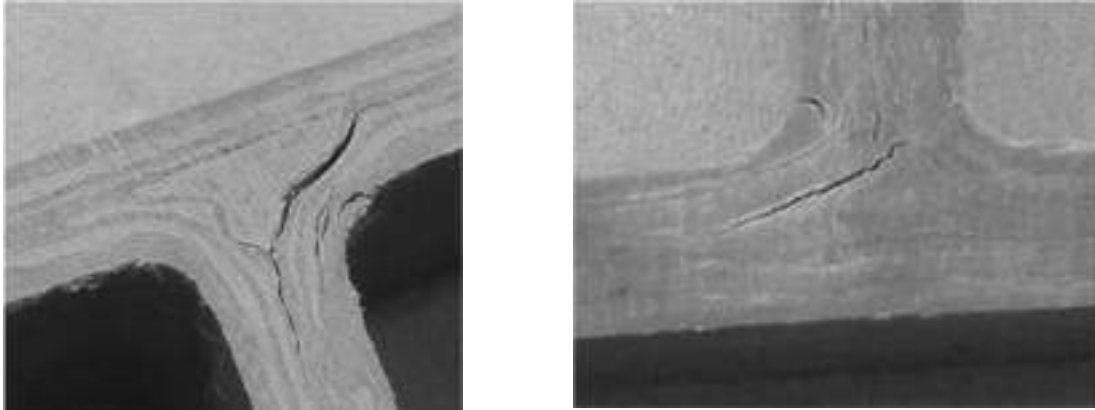


Figure 7: Internal delamination of web-flange junctions

MAINTENANCE AND REPAIRS – REPAIR PROCESSES

While FRP components are expected to be durable, a programme of routine maintenance, such as cleaning, is recommended. Where repairs are necessary, it is good practice to have warning signs installed on or alongside the bridge instructing personnel to seek specific guidance before any work is carried out on the FRP bridge. Once the root cause of any damage has been determined, the guidance refers the reader to a variety of other documents that provide guidance of the repair techniques that can be considered. Health and safety information shall be included in a Health and Safety File as is the legal requirement in the UK.

SUSTAINABILITY

In Chapter 8 the sustainability credentials of FRP materials for bridge engineering are introduced by comparing attributes of several structural materials through case studies. It is recognized that products made of FRP materials can offer significant environmental benefits because of a positive combination of low mass, favourable mechanical properties and resistance to corrosion. One major benefit of reduced structural weight is that it enables faster installation and reduced impacts, such as from highway diversions or rail line closures. This is also the case for life cycle maintenance activities where the inherent durability of FRPs results in lower impacts during the operational phase.

This chapter ends with four sections to further support the sustainability credentials, by introducing essential information on: FRP material impacts; the end-of-life options for FRP; some empirical guidance on the environmental impact of FRP bridges; the overall sustainability of FRP materials in terms of economics, environment and society.

SUMMARY AND RECOMMENDATIONS

The guidance document concludes with a summary of the current position of FRP bridges in the market and makes some specific recommendations to ensure that those involved in this field address twenty one different considerations when designing with these materials. The guidance document is due to be published by the UK construction research association CIRIA during 2018 and the expectation of the ad hoc working group who wrote it is that it will help promote best practice and accelerate development of the FRP bridges market.

ACKNOWLEDGMENTS

The author wishes to acknowledge the assistance of Professor J. Toby Mottram of The University of Warwick, UK, in reviewing this paper and his suggestions with regard to content.



REFERENCES

- Anonymous (2005). Design of FRP Bridges and Highway Structures, Design Manual for Roads and Bridges. Vol. 1 Highway Structures: Approval Procedures and General Design, Section 3 General Design, Part 17, Design Manual for Roads and Bridges, BD 90/05. The Highways Agency, Scottish Executive, Welsh Assembly Government (Llywodraeth Cynulliad Cymru), The Department for Regional Development Northern Ireland.
- L. Ascione, J-F. Caron, P. Godonou, K. van IJselmuiden, J. Knippers, T. Mottram, M. Oppe, M., Gantriis Sorensen, J. Taby L. Tromp (2016). "Prospect for New Guidance in the Design of FRP," Support to the implementation and further development of the Eurocodes. JRC Science for Policy Report, Policy Framework Existing Regulations and Standards, Prospect for CEN Guidance, European Commission, Joint Research Centre Institute for the Protection and Security of the Citizen, JRC 99714, EUR 27666 EN, European Union, Luxembourg, p. 171.
- D. Dawson, N. Farmer (2009). "Replacement FRP Bridge Deck for Vehicle Loading," Proceedings of the Institution of Civil Engineers: Engineering and Computational Mechanics, 162(3), 141-144.
- N. Farmer, I. Smith, S. Luke, L. Canning, B. Bell and B. Cox. (2006). "A Strategic Partnership Approach to FRP Strengthening of UK Railway Bridges," in Proceedings First International Conference on Advances in Bridge Engineering; Bridges — Past, Present and Future, Brunel University, Brunel University Press, UK, Vol. 1, 259-269.
- D. Kendall, I. Smith, C. Young, W. Gough, A. Cross (2012). "Dawlish FRP Footbridge — The First FRP Bridge at a UK Railway Station," FRP Bridges Conference 2012, London, September 2012, NetComposites Ltd., UK.
- S. Luke, L. Canning, S. Collins, E. Knudsen, P. Brown, B. Taljsten, I. Olofsson (2002). "The Development of an Advanced Composite Bridge Decking System - Project ASSET," Structural Engineering International, 12(2), 76-79.
- J.T. Mottram (2017) "Fibre reinforced polymer structures: Design guidance or guidance for designers," in Proceedings Eighth International Conference on Advanced Composites in Construction (ACIC 2017), NetComposites Ltd., Chesterfield, UK, 17-22.
- F. M. dos Santos, M. Mohan (2011). "Train Buffeting Measurements on a Fibre-Reinforced Plastic Composite Footbridge": Available from: <https://www.researchgate.net/publication/233701939>.



OPPORTUNITIES FOR RECYCLING AND REUSE OF FRP COMPOSITES FOR CONSTRUCTION IN A CIRCULAR ECONOMY

Lawrence C. Bank
City University of New York

ABSTRACT

Sustainability and green engineering have evolved into a more comprehensive framework known as the Circular Economy. The importance to this shift in thinking to the FRP composites for construction industry will be discussed. The aerospace and automotive sectors of the composites industry are moving rapidly to embrace the circular economy concepts such as design for reuse, adaptability, modularity, recycling, reclamation, life cycle assessment, materials flow analysis and industrial ecology. Current major projects in Europe and the US will be reviewed. Examples of materials testing and concepts from an ongoing NSF funded US/Ireland/Northern Ireland Tripartite research project on the reuse of glass/polymer wind turbine blades will be presented.



RECENT DEVELOPMENTS ON FRP REBARS AS INTERNAL REINFORCEMENT IN CONCRETE STRUCTURES AND FIELD APPLICATIONS

Brahim Benmokrane and Hamdy M. Mohamed

Department of Civil Engineering, Faculty of Engineering, University of Sherbrooke, QC, Canada.

(Corresponding author: Brahim.Benmokrane@usherbrooke.ca)

ABSTRACT

In the last decade, there has been a rapid increase in using noncorrosive fiber-reinforced polymers (FRP) reinforcing composite bars for concrete structures due to enhanced properties and cost-effectiveness. The FRP bars have been used extensively in different applications such as bridges, parking garages, water tanks, tunnels and marine structures in which the corrosion of steel reinforcement has typically led to significant deterioration and rehabilitation needs. Many significant developments from the manufacturer, various researchers and Design Codes along with numerous successful installations have led to a much higher comfort level and exponential use with designers and owners. After years of investigation and implementations, public agencies and regulatory authorities in North America has now included FRP as a premium corrosion resistant reinforcing material in its corrosion protection policy. Currently, AASHTO LRFD Bridge Design Specifications and the Canadian Highway Bridge Design Code contain design provisions for the design of concrete bridge members reinforced with FRP bars. As a result, well over 500 bridges across Canada and USA have been designed and constructed using FRP bars. This paper presents a summary and overview of different recent field applications of FRP bars in different types of civil engineering concrete infrastructures.

KEYWORD

Fields applications and case studies; Structure; FRP internal reinforcement.

INTRODUCTION

Electrochemical corrosion of steel is a major cause of the deterioration of the civil engineering infrastructure. It is becoming a principal challenge for the construction industry world-wide. An effective solution to this problem is the use of corrosion resistant materials, such as high-performance fiber-reinforced polymer (FRP) composites, (Benmokrane et al. 2007; Mohamed and Benmokrane 2014; Guerin et al. 2018; Hadhood et al. 2018). The applications of FRP reinforcements in the last 10 years have been approved that the cutting-edge technology has emerged as one of the most cost-effective alternative solutions compared to the traditional solutions. The use of concrete structures reinforced with FRP composite materials has been growing to overcome the common problems caused by corrosion of steel reinforcement. The climatic conditions where large amounts of salts are used for ice removal during winter months may contribute to accelerating the corrosion process. These conditions normally accelerate the need for costly repairs and may lead to catastrophic failure. Known to be corrosion resistant, FRP bars provide a great alternative to steel reinforcement. FRP materials in general offer many advantages over the conventional steel, including one quarter to one fifth the density of steel, no corrosion even in harsh chemical environments, neutrality to electrical and magnetic disturbances, and greater tensile strength than steel (Benmokrane et al. 2017 and 2016; Hadhood et al. 2017; Ali et al. 2017).

The objective of this paper is to show that FRP bar is on its way toward gaining widespread acceptance worldwide. Clearly, the most tangible successes are in the area of highway reinforced concrete bridges, parking garages, tunnelling and marine structures in which the corrosion resistance of FRP reinforcements as well as their installation flexibility are taken advantage of. In the following sections, development of codes and guidelines, recent field applications of FRP bars in bridges, tunnels, parking garages and water storage tank are presented.

DESIGN CODES AND GUIDELINES

A number of committees from professional organizations around the world have addressed the use of FRP bars in civil structures. These have published several guidelines and/or standards relevant to FRP as primary reinforcement for structural concrete. The recommendations ruling the design of FRP RC structures currently available are mainly given in the form of modifications to existing steel RC codes of practice, which predominantly use the limit state design approach. Such modifications consist of basic principles, strongly influenced by the



mechanical properties of FRP reinforcement, and empirical equations based on experimental investigations on FRP RC elements.

In North American, several codes and design guidelines for concrete structures reinforced with FRP bars have been published from 2000 to 2018. In 2000, the Canadian Highway Bridge Design Code (CHBDC) [CAN/CSAS6-00, (CSA 2000)] has been introduced including Section 16 on using FRP composite bars as reinforcement for concrete bridges (slabs, girders, and barrier walls). Design manual (ISIS-M03-2001) for reinforcing concrete structures with FRP was presented by the Canadian Network of Centers of Excellence on Intelligent Sensing for Innovative Structures (ISIS). In 2002, CAN/CSA-S806-02 has been published by the Canadian Standards Association (CSA 2002) for design and construction of building components with FRP bars.

The American Concrete Institute (ACI) introduced the first, second, third, and fourth guideline (ACI 440.1R) for the design and construction of concrete reinforced with FRP bars in 2001, 2003, 2006, and 2015, respectively. In 2009 the American Association of State Highway and Transportation Officials (AASHTO) published its first edition (AASHTO LRFD Bridge Design Specifications 2009), respectively. As a result of the valuable, enormous and great research efforts on different types of FRP-reinforced concrete structures in worldwide during the last decade, the aforesaid North American codes and design guidelines have been updated and modified to encourage the construction industry to use FRP materials [CAN/CSAS6-14; CAN/CSA-S806-12; ACI 440.1R-15]. Nowadays, great efforts from the international research committees to release the new developed issue of CSA S6, ACI 440-H Code and ASHTOO LRFD to be published in 2019.

Nowadays, the CAN/CSA-S806-12 (2012) is the most recently issued Canadian guidelines on the design and construction of building components with FRP. The CSA S806 has been completely revised. Many of its provisions have been improved based on the latest research results and experience in the field. The CSA S806-12 contains new provisions on: punching shear at slab-column connections with or without moment transfer, confinement of columns by FRP internal ties or hoops, design of FRP reinforced member for combined effects of shear, torsion and bending, reinforcement development length and detailing, strut and tie model for deep beams, corbels and brackets, shear strengthening of reinforced concrete members by externally bonded reinforcement, and FRP retrofit of reinforced concrete members for enhanced seismic resistance. The new standard covers all the basic design requirements for FRP reinforced and retrofitted structures.

In addition to the design of concrete elements reinforced or prestressed with FRP, the guidelines also include information about characterization tests for FRP internal reinforcement. As for the predominant mode of failure, the CSA S806-12 remarks that “all FRP reinforced concrete sections shall be designed in such a way that failure of the section is initiated by crushing of the concrete in the compression zone”. In this code, new design equations are included for design punching shear capacity of FRP-RC flat slab. Also, it is of interest to mention that this code permits of using FRP bars in columns and compression members.

In order to establish stringent guidelines and values for FRP manufacturers and quality control mechanisms for owners to ensure a high comfort level of product supplied, ISIS Canada together with the manufacturer had initiated the “Specifications for product certification of FRP’s as internal reinforcement in concrete structures”. (ISIS Canada Corporation 2006) This document was the basis for the new Standard CSA S-807-10 on Specification for Fibre Reinforced Polymer (FRP). This Standard covers the manufacturing process requirements of fibre-reinforced polymer (FRP) bars or bars that are part of a grid for use in non-prestressed internal reinforcement of concrete components of structures (e.g., bridges, buildings, and marine structures). The FRP bars are classified on the basis of their fibres, strength, stiffness, and durability. Only FRP bars made with aramid, carbon, or glass fibres are considered in this Standard. New edition of this standard has been updated and included with basalt-FRP (BFRP) bars to be published in 2018.

RECENT FIELD APPLICATIONS

Highway Bridge Structures

Corrosion of steel reinforcing bars stands out as a significant factor limiting the life expectancy of reinforced concrete infrastructure worldwide. In North America in particular, the corrosion of steel reinforcement in concrete bridges subjected to deicing salts and/or aggressive environments constitutes the major cause of structure deterioration, leading to costly repairs and rehabilitation as well as a significant reduction in service life. According to the 2013 *Report Card for America’s Infrastructure* findings, ASCE, nearly one-tenth of the 607,380 bridges in the National Bridge Inventory were classified as structurally deficient. Of this total, over 235,000 are conventional reinforced concrete and 108,000 were built with prestressed concrete (NACE International). The report further



states that \$76 billion are needed for deficient bridges across the United States for maintenance and capital costs for concrete bridge decks and for their concrete substructures. In addition, the United States Federal Highway Administration (FHWA) estimates that eliminating the nation's bridge deficient backlog by 2028 would require an investment of \$20.5 billion annually because of corroded steel and steel reinforcement. The report also states that "the nation's 66,749 structurally deficient bridges make up one-third of the total bridge decking area in the United States, showing that those bridges that remain classified as structurally deficient are significant in size and length, while the bridges that are being repaired are smaller in scale." Problems related to expansive corrosion could be resolved by protecting the steel reinforcing bars from corrosion-causing agents or by using noncorrosive materials such as fiber-reinforced-polymer (FRP) bars. Therefore, since the late 1990s, the Structures Division of the MT at different provinces has been interested in building more durable bridges with an extended service life of 75–150 years. For example, the MT at Québec (MTQ), Canada has carried out, in collaboration with the University of Sherbrooke, (Sherbrooke, Québec), several research projects utilizing the straight and bent non-corrodible FRP rebar in concrete deck slabs and bridge barriers (Mohamed et al. 2014; Ahmed et al. 2014; Mohamed and Benmokrane 2014). The use of FRP bars as reinforcement for concrete bridge provides a potential for increased service life and economic and environmental benefits.

In the last ten years, the FRP bars have been used successfully in hundreds bridge structures across Canada and USA, see Figure 1 (a and b). These bridges were designed using the Canadian Highway Bridge Design Code or the AASHTO LRFD Bridge Design Guide Specifications for GFRP-Reinforced Concrete Bridge Decks and Traffic Railings. Straight and bent FRP bars (carbon or glass) were used mainly as internal reinforcement for the deck slab and/or for the concrete barriers and girders of these bridges. In general, all the bridges that included with FRP reinforcements though the ten years ago are girder-type with main girders made of either steel or prestressed concrete. The main girders are simply supported over spans ranging from 20.0 to 90.0 m. The deck is a 200 to 260 mm thickness concrete slab continuous over spans of 2.30 to 4.0 m. Most of these bridges have been reinforced with the glass FRP bars as a result of their relatively low cost compared to other types of FRPs (carbon and aramid). The FRP bars were used mainly as reinforcement to the deck slabs, barriers and girders.

Recently, the GFRP bars have been used as the main reinforcement in the deck slab of cable stayed bridges, Nipigon River Bridge, ON, Canada. The Nipigon River Bridge spans the Nipigon River in Nipigon, Ontario on Highway 11/17. A new four lane cable stayed bridge is replacing the old two lanes, four span plate girder structures. The new bridge includes cable-supported spans of 112.8 m and 139 m. The 36.2 m wide deck is comprised of concrete deck panels totally reinforced with GFRP bars and supported on transverse steel beams. The objectives were to implement FRP bars in RC cable stayed bridge to overcome the steel expansive-corrosion issues and related deterioration problems; to assess the in-service performance of the FRP-RC bridge deck slab after several years of operation; and to design durable and maintenance-free concrete for cable stayed bridge. The deck slab was design to sustain significant axial compression force resulted from the cables and bending moment as resulted from the live and dead loads (Mohamed and Benmokrane 2012).



(a) bridge deck slab, 410 overpass bridge Qc (2012) (b) cable stayed bridge, Nipigon River Bridge, ON (2016)

Figure 1- Recent FRP-reinforced concrete bridges

Water Tanks

Reinforced concrete (RC) tanks have been used for water and wastewater storage and treatment for decades. Design of these tanks requires attention not only to strength requirements, but also to crack control and durability. RC water treatment plant structures are subject to severely corrosive environments as a result of using the chlorine to treat the wastewater before it is released. So, the challenge for the structural engineer and municipalities is to design these structures using noncorrosive fibre-reinforced polymers (FRP) reinforcing bars. The first worldwide concrete chlorination water treatment tank totally reinforced with FRP bars was designed in 2010 and the construction started and finished in 2012. The project is located in Thetford Mines city, Quebec, Canada and it is

considered as one component of water treatment plant for municipality. The volume capacity of the tank is 4500 m³, and it has the dimensions 30.0 m wide, 30.0 m length and 5.0 m wall height. The design of the tank was made according to CAN/CSA-S806-02, Design and Construction of Building Components with Fibre-Reinforced-Polymers. The tank is well instrumented at critical locations for strain data collection with fiber-optic sensors. Figure 2. shows the FRP bar reinforcements in the vertical walls and overview of the complemented FRP tank. The field test results under actual service conditions for the strain behavior in the FRP bars at different location in the tank are indicated a significant value less the 1.0 % of the ultimate strain. In conclusion, the construction procedure, serviceability performance under real service conditions (water and earth pressure), and monitoring results of the FRP-reinforced walls and slabs of the tank, in terms of strain, cracking and deflection were very conservative and satisfactory when compared with the serviceability requirements and strength needed.



Figure 2- FRP-reinforced concrete tank, Qc, Canada.

GFRP Soft Eyes in Tunnels

Building tunnels with Tunnel Boring Machines (TBM) is today state of the art in different ground conditions. Launching and receiving the TBM in shafts and station boxes has in earlier years required a considerable construction effort (Ali et al. 2016; Hadhood et al. 2016; Afifi et al. 2014). Breaking through the steel reinforced walls of the excavation shaft with a TBM required extensive measurements and preparation works, (Mohamed and Benmokrane 2015; Schürch and Jost 2006). FRP is an anisotropic composite material with a high tensile strength in axial direction and a high resistance against corrosion. The anisotropy of the material is quite advantageous at excavation pits for the starting and finishing processes at automated excavation like tunnel boring machine (TBM) and Pipe jacking. Therefore, using FRP bars in reinforced walls and piles of the excavation shaft allows the designer and contractor today to find innovative solutions for the well-known situation and save time and costs on site. Soft-Eyes consist usually of bore piles or diaphragm walls which are locally reinforced with GFRP bars and stirrups. The sections below and above the tunnel opening are reinforced steel bars. Depending on the designer and contractors preferences full rectangular sections are built out of GFRP bars or the fibre reinforcement follows more closely the tunnel section resulting in a circular arrangement of the GFRP links and similar adjustments for the vertical bars. Building the corresponding reinforcement cages out of GFRP bars on site requires the same working procedures as for an equal steel cage, see Figure 3. Recently, GFRP bars have been used in different tunnel projects in Canada (South Tunnels, Keele Station, Hwy 407 Station-TTC Subway North Tunnels and Eglinton Crosstown LRT: Toronto, ON). Whereas, GFRP bars were used to reinforce GFRP cages up to 19.0 m long (diameters ranged from 600 to 1100 mm). Highest grade 60 GPa 32.0 m vertical bars were used with #5 (16.0 m) 50 GPa continuous spirals with 150 mm pitch, (Mohamed and Benmokrane 2015).



Figure 3- GFRP reinforcement for soft-eyes

Precast Bridge-Piles

Traditional pile materials for bridge foundations and waterfront structures include steel, concrete, and timber. These pile materials have limited service life and high maintenance costs when used in harsh marine environments due to corrosion. Estimates indicate that the United States spends billions of dollars annually to repair and replace bridge substructures such as pier columns (\$2 billion), and marine piling systems (\$1 billion) (NACE International). Problems related to expansive corrosion could be resolved by using noncorrosive materials such as FRP bars. Recent demonstrated field study included the design analysis, construction details, driving test procedures, and results of the field dynamic driving test of two precast GFRP RC piles. The two piles were square in section (24 x 24 Inch) and had a length of 60 ft, see Figure 4. The two piles were longitudinally and transversally reinforced with GFRP bars and ties. Goble's equations were used to design and estimate the tensile stresses in pile during driving and location of the critical section along the pile. The two designed GFRP RC piles were fabricated at Gate Precast Company, at the Jacksonville, Florida. Piles were then unmolded and transferred to the driving location (Arthur Drive Bridge project site in Lynn Haven, Panama City, Florida). Pile driving and testing were performed with a Vulcan 512 single-acting air hammer (12 kips ram weight, fitted with mechanism that allowed for reportedly 3 and 5 feet stroke heights). The pile-driving analyzer (PDA) system was used to monitor the two piles during driving operations. Field driving observation and results indicated that no pile damage occurred during the installation. GFRP spirals were successfully confined the concrete core of the two piles and prevented the cover spalling during the driving. The maximum tensile and compressive stresses measured in the piles were well within the allowable design limits (Mohamed and Benmokrane 2017).



Figure 4- GFRP pile cage and installation

Parking Garages

The need for sustainable structures has motivated the Public Works and Government Services Canada (PWGSC) in the use of FRP rebar as internal reinforcement in concrete infrastructure applications. One of the most important successful applications is using FRP rebar in reinforcing the parking garage. An agreement between PWGSC and the University of Sherbrooke was reached to reconstruct the interior structural slabs of the Laurier-Taché parking garage (Hull, Quebec) using carbon and glass FRP rebar. The design was made according to CAN/CSA-S806-02. This project allows direct field assessment and long-term monitoring of FRP composite bars in a structure subjected to harsh environmental and loading conditions. In 2010, the new large parking garage (La Chancelière parking garage, area 3000 m²) in Quebec City was designed and constructed using the FRP rebar. This design was made according to the CAN/CSA-S413-07 for parking structures and CAN/CSA-S806-02 [13] for design and



construction of building components with fibre reinforced polymers. The two-way flat slabs of La Chancelière had maximum span of about 9.0 m. The thickness of the slabs was 250 mm which increased to 355 mm over the columns through the drop panels. The increased thickness over the columns was devoted to satisfy the punching stresses around the columns' area. The punching strength of the two way slabs were verified using the new punching equations that are being incorporated in the new version of the S806 Standards, Benmokrane et al. 2012).

Continuously reinforced concrete pavement with GFRP bars

Continuously reinforced-concrete-pavement (CRCP) designs are premium pavement designs often used for heavily trafficked roadways and urban corridors. Although CRCP typically is an effective, long-lasting pavement design, it can develop performance problems when the aggregate-interlock load transfer at the transverse cracks has degraded. The prevalence of wide cracks in CRCP has frequently been associated with ruptured steel reinforcement and significant levels of corrosion. This has generated recent interest in identifying new reinforcing materials that can prevent or minimize corrosion-related issues in CRCP. Glass-fiber-reinforced-polymer (GFRP) bars are one product being investigated for use in CRCP instead of conventional steel bars.

Since the early 1990s, the Ministry of Transportation of Quebec (MTQ) has renewed emphasis on building long-lasting concrete pavements suited to local traffic and climatic conditions. In 2000, these efforts led to the construction of Canada's first roadway with continuously reinforced concrete pavement (CRCP). Five years later, however, concerns were raised about the long-term performance of CRCP, as portions of this initial installation were found to have insufficient cover over the bars and core samples showed that the longitudinal reinforcement was corroding at transverse cracks (Thébeau 2006). These observations, coupled with the knowledge that up to 60 tonnes (65 tons) of salt per year can be spread on a 1 km (0.6 mile) long stretch of a two-lane pavement in Montréal (nearly three times the amount of salt used on roads in the State of Illinois), led the MTQ to select galvanized steel as the standard reinforcement for subsequent CRCP projects and to continue investigating other systems with enhanced corrosion resistance. As part of these investigations, the MTQ and the University of Sherbrooke has been studying the use of glass-fiber-reinforced-polymer (GFRP) bars for CRCP since 2006. In September 2006, a 150 m long section of eastbound Highway 40 (Montréal) was selected as a demonstration project (Benmokrane et al. 2008). Through the initial 18 months of pavement life, the maximum measured strain value in the reinforcement was 0.0041. This is within the design limit recommended in ACI 440.1R-06. In February 2008, the measured results showed that the average crack spacing varied between 1.5 and 4 m in most CRCP-GFRP slabs. In addition, the average crack width varied between 0.7 and 0.9 mm, which is less than the AASHTO design limit of 1.0 mm (Benmokrane et al. 2008). In September 2013, it was decided to use GFRP bars in one of Quebec's CRCP highways (300 m long). A stretch of test pavement has since been constructed on westbound Highway 40 in Montreal. The project is located on eastbound Highway 40 in Montréal, QC, and presents a collaboration between the Ministry of Transportation of Quebec (MTQ) and the University of Sherbrooke. A variety of sensors were installed in this project to monitor the early-age behavior and the effects of repeated traffic loads and environmental conditions on the performance of CRCP slab. The test slab was 315 mm (12.4 in.) thick with a GFRP reinforcement ratio of 1.2%. The reinforcement ratio for steel bars in the CRCP steel-reinforced slab is 0.1% for transverse rebar and 0.74% for longitudinal bar, see Figure 5. According to observations at 16 months, the crack spacing and crack width in the steel-reinforced CRCP test section were larger than those of the GFRP-reinforced CRCP section. The field performance of the GFRP CRCP appeared satisfactory, particularly because the crack widths satisfied the AASHTO limiting criterion for crack width as ≤ 1 mm (0.04 in.), which is essential in maintaining pavement integrity by securing adequate aggregate interlock at the crack. Data from this experimental phase will allow for finite-element modeling of the CRCP-GFRP slab.



Figure 5- GFRP bar placement in center lane in Highway 40 (Montréal)-2013



CONCLUSIONS

The observations and the outcomes from the different field applications reported in this paper can be summarized into the following: corrosion resistance is without a doubt the main motive and attraction to use FRP over steel. Application of FRP reinforcement in different structures has been proved to be very successful to date. From the construction point of view, it was felt by the construction personnel that the lightweight of the FRP reinforcements were easy to handle and place during construction. Concrete bridges, water tank, soft eye-tunnel application, bridge piles, parking garage structures and continuously reinforced-concrete-pavement provide an excellent application for the use of FRP in new construction.

ACKNOWLEDGEMENTS

The authors would like to thank and express their sincere appreciation to the NSERC–Canada Research Chair and Industrial Research Chair group (Canada Research Chair in Advanced Composite Materials for Civil Structures & NSERC Research Chair in Innovative FRP Reinforcement for Concrete Infrastructure) at Department of Civil Engineering, Faculty of Engineering, University of Sherbrooke, QC, Canada, for providing technical data along with numerous testing and reports on FRP reinforcement for concrete infrastructure.

REFERENCES

- Afifi, M.Z., Mohamed, H.M., and Benmokrane, B. (2014). "Strength and Axial Behavior of Circular Concrete Columns Reinforced with CFRP Bars and Spirals." *J. Compos. Constr.*, Volume 18, Issue 2, 10.1061/(ASCE)CC.1943-5614.0000430, 04013035.
- Ahmed, E., Settecesi, F., and Benmokrane, B. (2014). "Construction and Testing of GFRP Steel Hybrid-Reinforced Concrete Bridge-Deck Slabs of Sainte-Catherine Overpass Bridges." *J. Bridge Eng.*, 19(6), 04014011.
- Ali, A.H., Mohamed, H.M., and Benmokrane, B. (2017). "Shear Strength of Circular Concrete Beams Reinforced with Glass-FRP Bars and Spirals" *ACI Structural Journal*, V. 114, No. 1, January-February 2017, P. 39-49.
- Ali, A.H., Mohamed, H.M., and Benmokrane, B. (2016). "Shear Behavior of Circular Concrete Members Reinforced with GFRP Bars and Spirals at Shear Span-to-Depth Ratios between 1.5 and 3.0." *J. Compos. Constr.*, 10.1061/(ASCE)CC.1943-5614.0000707, 04016055.
- American Concrete Institute (ACI). (2001; 2003; 2006). *Guide for the design and construction of concrete reinforced with FRP bars*, ACI 440.1R-01;03; 06; 15, Farmington Hills, Mich.
- American Concrete Institute (ACI). (2004). *Guide test methods for fiber reinforced polymers (FRPs) for reinforcing or strengthening concrete structures*, ACI 440.3R-04, Farmington Hills, Mich.
- Benmokrane, B., Ahmed, E., Dulude, C., and Boucher, E. (2012) "Design, Construction, and Monitoring OF the First Worldwide Two-Way Flat Slab Parking Garage Reinforced with GFRP Bars." 6th International Conference on *FRP Composites in Civil Engineering*. CD proceeding, CICE 2012, Rome, Italy.
- Benmokrane, B., Ali, A.H., Mohamed, H.M., Elsafty, A., and Malano, A. (2017). "Laboratory Assessment and Durability Performance of Vinyl-Ester, Polyester, and Epoxy Glass-FRP Bars for Concrete Structures," *Journal Composites Part B.*, Elsevier, Volume 114, 1 April 2017, Pages 163-174.
- Benmokrane, B., Eisa, M., El-Gamal, S., Thébeau, D., and El-Salakawy, E., (2008) "Pavement system suiting local conditions: Quebec studies continuously reinforced concrete pavement with glass fiber-reinforced polymer bars" *ACI Concrete international* / November 2008 pp. 34-39.
- Benmokrane, B., El-Salakawy, E., El-Ragaby, A., and El-Gamal, S. (2007). *Performance Evaluation of Innovative Concrete Bridge Deck Slabs Reinforced with Fibre- Reinforced Polymer Bars*. *Can Jour of Civil Eng.*, 34(3): 298–310.
- Benmokrane, B., Robert, M., Mohamed, H.M., Ali, A., and Cousin, P. (2016). "Durability Assessment of Glass FRP Solid and Tubular Bars (Rock Bolts) for Ground Control of the Jurong Rock Caverns in Singapore." *ASCE Journal of Composites for Construction*, 10.1061/(ASCE)CC.1943-5614.0000775.
- Canadian Standard Association (CSA). (2006). *Canadian Highway Bridge Design Code*. CAN/CSA S6-06, Rexdale, Ontario, Canada, 788.
- Canadian Standards Association (2010). *CAN/CSA S807-10 "Specification for fibre-reinforced polymers*, Canadian Standards Association, Rexdale, Ontario, Canada, 44 p.
- Canadian Standards Association (CSA). (2000). "Canadian highway bridge design code." CAN/CSA-S6-00, Rexdale, Toronto.
- Canadian Standards Association (CSA). (2002-12). "Design and construction of building components with fiber reinforced polymers." CAN/CSAS806-02, Rexdale, Toronto.
- Canadian Standards Association (CSA). (2006-Edition 2010). "Canadian highway bridge design code—Section 16, updated version for public review." CAN/CSA-S6-06, Rexdale, Toronto.
- Guerin, M., Mohamed, H.M., Benmokrane, B., Nanni, A., and Shield, C. (2018). "Eccentric Behavior of Full-Scale Concrete Columns Reinforced with GFRP Bars and Ties." *ACI Structural Journal*, V. 115, No. 2, Page 489-499.
- Hadhood, A., Mohamed, H.M., and Benmokrane, B. (2016). "Experimental Study of Circular High-Strength Concrete Columns Reinforced with GFRP Bars and Spirals under Concentric and Eccentric Loading." *J. Compos. Constr.*, 10.1061/(ASCE)CC.1943-5614.0000734, 04016078.



**9th International Conference on Fibre-Reinforced Polymer (FRP) Composites
in Civil Engineering (CICE 2018), PARIS 17-19 JULY 2018**

- Hadhood, A., Mohamed, H.M., and Benmokrane, B. (2017). "Failure Envelope of Circular Concrete Columns Reinforced with GFRP Bars and Spirals" *ACI Structural Journal*, Vol. 114, Issue. 6, (Nov/Dec 2017): 1417-1428.
- ISIS Canada (2001; 2006; 2007). "Reinforcing concrete structures with fiber reinforced polymers." ISIS-M03-2001; 2006; 2007, The Canadian Network of Centers of Excellence on Intelligent Sensing for Innovative Structures, Univ. of Winnipeg, Manitoba, Canada.
- Marc Schürch and Peter Jost (2006) "GFRP Soft-Eye for TBM Breakthrough: Possibilities with a Modern Construction Material." International Symposium on Underground Excavation and Tunnelling 2-4 February 2006, Bangkok, Thailand.
- Mohamed, H.M., Afifi, M., and Benmokrane, B. (2014). "Performance Evaluation of Concrete Columns Reinforced Longitudinally with FRP Bars and Confined with FRP Hoops and Spirals under Axial Load." *J. Bridge Eng.*, 19(7), 04014020.
- Mohamed, H.M., Ali, A.H., and Benmokrane, B. (2016). "Behaviour of Circular Concrete Members reinforced with Carbon-FRP Bars and Spirals under Shear." *ASCE Journal of Composites for Construction*, 10.1061/(ASCE)CC.1943-5614.0000746 , 04016090.
- Mohamed, H.M., and Benmokrane, B. (2017). "Dynamic Driving Test of Prestressed/Precast Concrete Bridge Piles" University of Sherbrooke, Technical Report, submitted to MTQ, Canada and FDOT, US.
- Mohamed, H.M., and Benmokrane, B. (2014). "Design and Performance of Reinforced Concrete Water Chlorination Tank Totally Reinforced with GFRP Bars." *ASCE J. Compos. Constr.*, 18(1), 05013001-1 – 05013001-11.
- NACE International. "Corrosion Costs and Preventive Strategies in the United States" Publication No. FHWA-RD-01-156, National Association for Corrosion Engineers, (www.nace.org).
- Pultrall Inc, 2016, "Composite Reinforcing Rods Technical Data Sheet." Thetford Mines, Canada, www.pultrall.com



HYBRID FRP-CONCRETE-STEEL TUBULAR MEMBERS

Tao Yu

University of Wollongong, Australia. Email: taoy@uow.edu.au

ABSTRACT

Hybrid fibre-reinforced polymer (FRP)-concrete-steel (FCS) tubular members are an emerging type of structural members. These hybrid members involve the use of an external FRP tube as a confining device and a corrosion-resistant skin, a concrete infill, and encased steel reinforcement of various forms (e.g. steel bars, a steel section, or a steel tube). In such members, the FRP tube is generally designed to possess only a small axial stiffness so that its confinement effectiveness on the concrete is not compromised by buckling due to substantial axial compressive stresses, while the potential buckling of steel reinforcement is well restrained by the confined concrete, leading to excellent structural performance. This paper offers an overview of existing research on hybrid FCS tubular members before providing a summary of several novel forms of such members recently developed at the University of Wollongong.

KEYWORDS

FRP, concrete, steel, hybrid members, tubular members, confinement.

INTRODUCTION

Fibre-reinforced polymer (FRP) composites have emerged rapidly as durable structural materials in recent years. One of the most important applications of FRP is as a confining material for concrete (e.g. Teng and Lam 2004; Yu and Teng 2011). With the confinement of FRP, both the strength and ductility of concrete can be significantly enhanced (Teng and Lam 2004). The use of FRP confinement was initially explored in the strengthening or seismic retrofit of reinforced concrete columns, and more recently for new construction (Teng et al. 2007).

Hybrid FRP-concrete-steel (FCS) tubular members are an emerging type of structural members, in which an external FRP tube is used as a confining device and a corrosion-resistant skin (Yu et al. 2017a). In these hybrid members, the FRP tube is generally designed to possess only a small axial stiffness so that its confinement effectiveness on the concrete is not compromised by buckling due to substantial axial compressive stresses, while steel of various forms is encased in the concrete to serve as ductile longitudinal reinforcement. The potential buckling of steel reinforcement is well restrained by the confined concrete in such members, so that high-strength steel (HSS) can be effectively used with their high yield stress being fully exploited (Yu et al. 2017a). Hybrid FCS tubular members generally have the following advantages: (1) excellent durability because of the use of a durable external FRP tube; (2) excellent ductility as the concrete and the steel is effectively confined by the FRP tube; (3) elimination of the need for formwork. Because of their superior corrosion resistance, hybrid FCS members are desirable for use in outdoor structures such as bridges and coastal structures that are likely to be exposed to a harsh environment. In those applications, the hybrid members can be used as compression members such as bridge piers, piles and various towers (e.g. wind turbine towers), or flexural members such as bridge girders. When used with HSS, hybrid FCS members are also a desirable option for columns in tall buildings where their reduced cross-section size leads to enlarged usable floor areas. Connections of hybrid FCS members to the beams and the foundations can generally be achieved in a way similar to conventional connection technology for composite steel-concrete members, noting that the FRP tube may be locally discontinued in the longitudinal direction as it is mainly used to provide resistance in the hoop direction only.

Extensive recent research has been conducted on various forms of hybrid FCS tubular members, covering various aspects of their structural behavior. In the following sections, this paper first presents an overview of existing research on hybrid FCS tubular members, and then focuses on several novel forms of such members recently developed by the author's group.

EXISTING RESEARCH ON HYBRID FCS TUBULAR MEMBERS

The hybrid FCS tubular members that have been studied can generally be categorized into four types: (a) concrete-filled FRP tubes (CFFTs) with individual steel bars/plates (e.g. Figure 1a) (Yu and Teng 2011; Yu et al. 2017a); (b) CFFTs with an encased steel section, such as a steel open section (Figure 1b) (Karimi et al. 2011a; Yu et al. 2016a), or a steel tube (Figure 1c) (Teng et al. 2018); (c) hybrid FRP-concrete-steel double-skin tubular members

(DSTMs) (Figure 1d) (Teng et al. 2007; Yu et al. 2010a); and (d) FRP-confined concrete-filled steel tubes (CCFTs) (Figure 1e) (Xiao 2004; Yu et al. 2016b).

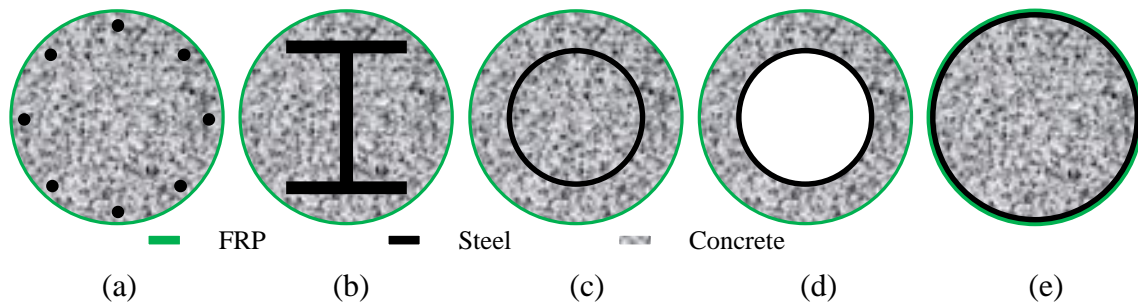


Figure 1. Various forms of hybrid FCS tubular members

Concrete-Filled FRP Tube (CFFT) with Individual Steel Bars/Plates

CFFTs are a popular form of structural members which were first developed in the 1990s (Mirmiran and Shahawy 1997). When there is no steel reinforcement in a CFFT, the FRP tube needs to have significant stiffness and strength in the longitudinal direction to resist bending. In such cases, the tensile failure of the FRP tube in the longitudinal direction can be rather brittle and should generally be avoided in the design (Yu and Teng 2011). Therefore, a natural alternative is to provide ductile longitudinal steel reinforcement in a CFFT so that the brittle failure mode of the member can be avoided, and that a thin (and thus cheap) FRP tube with mainly fibres close to the hoop direction can be used; such an FRP tube is referred to as an FRP confining tube. Yu and Teng (2011) provides a summary of the design provisions for CFFTs with steel bars (Figure 1a) given in the relevant Chinese national standard (GB50608 2011), which were developed on the basis of available research published in the open literature as well as the work undertaken by them.

More recently, Yu et al. (2017a) proposed the use of multiple HSS plates as longitudinal reinforcement in an FRP confining tube filled with concrete. The use of steel plates instead of steel bars allows a larger steel reinforcement ratio without introducing difficulties in casting concrete. Another important novel aspect of CFFTs with HSS plates is that no welding is involved to fabricate steel sections, reducing the fabrication and transportation cost; it also obviates the perceived difficulties with welding HSS among the structural engineering profession. In such a column, the individual steel plates may be connected to each other at discrete locations by angle brackets, which also serve as shear connectors between the steel plates and concrete for improved composite action. The use of multiple separate steel plates also allows the configurations of the steel plates to be optimized for particular applications, which may not be in the shape of traditional sections such as I-section (e.g. a number of steel plates can be used to form a polygonal shape). Yu et al. (2017a) conducted a series of tests on CFFTs with multiple steel plates involving 13 specimens tested under concentric or eccentric compression. The test results demonstrated that the concrete in the tested specimens was very effectively confined, and that buckling of all the steel plates was completely prevented by the encasing concrete up to and beyond the rupture of the FRP tubes, leading to full structural utilization of the construction materials and very ductile column responses.

Concrete-Filled FRP Tube (CFFT) with Steel Section

CFFTs with an open steel section (e.g. I-section) (Figure 1b) are also referred to as FRP-confined concrete-encased steel composite columns (FCSCs) (Yu et al. 2016a). The concept of such hybrid members appears to be first explored by Liu et al. (2005) as a rehabilitation technique for existing steel columns. Karimi et al. (2011a, 2011b) conducted experimental studies on the compressive behavior of CFFTs with a steel I-section either using pre-fabricated FRP tubes for circular columns or FRP wraps for rectangular columns. Zakaib and Fam (2012) conducted an experimental study on the flexural performance of FCSCs with pre-fabricated FRP tubes. These studies have generally demonstrated the good performance including excellent ductility of the hybrid members. More recently, the author's group conducted a combined experimental and theoretical study on the behaviour of both circular and square CFFTs with a steel I-section under eccentric compression (Yu et al. 2016a), and explored the use of a large rupture strain FRP tube for such hybrid members (Huang et al. 2016). Huang et al. (2016) suggested that the encased steel section provided additional confinement to the concrete in the hybrid members, leading to further enhanced strength and ductility of the confined concrete.

CFFTs with an encased steel tube (Figure 1c) was proposed by Teng et al. (2018) who termed such members hybrid double-tube concrete columns. Teng et al. (2018) presented an experimental study on CFFTs with a circular



HSS tube after explaining the concept of such hybrid members. Teng et al.'s (2018) experimental results showed that the HSS tube was prevented from buckling and, importantly, provided significant confining pressure to the core concrete due to its high yield stress, leading to excellent structural performance.

Hybrid Double-Skin Tubular Member (DSTM)

Hybrid DSTMs (Figure 1d) was first proposed some 15 years ago (Teng et al. 2004, 2007) and have since attracted extensive research attention. The inner void in hybrid DSTMs reduces the self-weight of the members without significantly affecting the flexural rigidity of the section and allows the easy passage of service ducts (Teng et al. 2007). A large number of studies have been conducted on hybrid DSTMs as columns, which have demonstrated their excellent performance under various loading scenarios including concentric monotonic compression (e.g. Wong et al. 2008; Fanggi and Ozbakkaloglu 2013; Yu et al. 2017b) or cyclic compression (e.g. Yu et al. 2012; Abdelkarim and ElGawady 2016), eccentric compression (Yu et al. 2010b), cyclic lateral loading (e.g. Han et al. 2010; Zhang et al. 2015), as well as impact loading (Wang et al. 2015a). A number of theoretical studies have also been conducted (e.g. Yu et al. 2010a; Talaetaba et al. 2015). In addition, a simple design approach for circular hybrid DSTMs as columns has also been developed and has been adopted by the relevant Chinese national standard (GB50608 2011).

The use of hybrid DSTMs as flexural members (beams) has also been investigated by a number of existing studies (Yu et al. 2006; Idris and Ozbakkaloglu 2015; Zhao et al. 2016), which have demonstrated the ample ductility of such flexural members. In such applications, the inner steel tube is typically shifted towards the tension side, and shear connectors welded on the steel tube are generally needed to enhance the composite action between the concrete and the steel tube (Zhao et al. 2016).

More recently, a novel arch-bridge system based on the hybrid DSTM concept was developed (Jiang et al. 2016; De Waal et al. 2018). The novel bridge system allows more durable and faster construction than traditional arch bridges and has been demonstrated by experimental tests to possess excellent structural performance.

FRP-Confined Concrete-Filled Steel Tube (CCFT)

The concept of CCFT (Figure 1e) was first proposed by Xiao (2004) as a variation of concrete-filled steel tubular columns. In a CCFT, the FRP confining tube restrains the outward buckling of the steel tube and provides additional confinement to the concrete; such an FRP tube may only be needed at the end portions of the column where the bending moment is the largest (Xiao 2004). Following Xiao's initial work, a number of studies have been conducted by Xiao's group as well as other researchers on various aspects of CCFTs. These include studies on the monotonic compressive behaviour (e.g. Hu et al. 2011; Abdalla et al. 2013; Li et al. 2018), cyclic compressive behaviour (Yu et al. 2014), flexural behaviour (Wang et al. 2015b), seismic behaviour (Cai et al. 2016; Yu et al. 2016b), impact behaviour (e.g. Alam et al. 2015) as well as theoretical modelling (Teng et al. 2013; Dong et al. 2016).

RECENT DEVELOPMENT AT UNIVERSITY OF WOLLONGONG

At the University of Wollongong (UOW), a large amount of work has been conducted on hybrid FCS tubular members and intensive research is continuing. In this section, the latest advances of the ongoing research programme at UOW are briefly presented, covering three novel forms recently developed: (1) FRP-confined concrete-encased cross-shaped steel columns; (2) hybrid FCS multi-tube concrete columns; (3) hybrid DSTMs with a rib-stiffened steel inner tube.

FRP-Confined Concrete-Encased Cross-Shaped Steel Columns

It is well known that the effectiveness of confinement is much more pronounced in circular columns than in square columns (Teng and Lam 2004). FRP-confined concrete-encased cross-shaped steel columns (FCCSCs) are proposed particularly for use as square columns subjected to comparable loads in the two lateral directions. The unique feature of FCCSCs is the use of a cross-shaped steel section within a square FRP outer tube (Figure 2). The cross-shaped steel section serves as ductile longitudinal reinforcement to resist bending in the two lateral directions; it also allows the concrete in FCCSCs to be effectively confined despite the square shape of the column: the existence of two pairs of steel flanges connected by the webs provides additional confinement which is particularly important to the regions that are otherwise not effectively confined (i.e. the regions close to the four flat sides). Compared with normal square CCFTs, in which the confinement is quite non-uniform and the concretes close to the flat sides are not effectively confined, finite element modeling by the author's group has shown that the concrete in FCCSCs is subjected to a much more uniformly-distributed confining pressure (Figure 3).

Huang et al. (2017) conducted a series of axial compression tests on stub column specimens of FCCSCs as well as other similar column forms including square and circular CFFTs. The test results confirmed that the concrete in FCCSCs is very well confined; compared with the concrete in square CFFTs (Figure 4a) and even that in circular CFFTs (Figure 4b), the concrete in FCCSCs has a much larger ultimate axial strain and a larger compressive strength, when the same FRP tube is used (Huang et al. 2017).

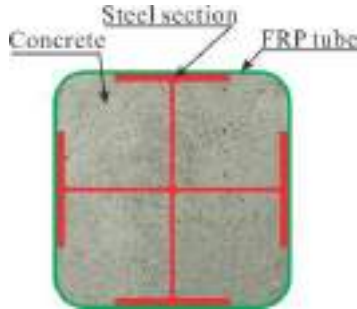
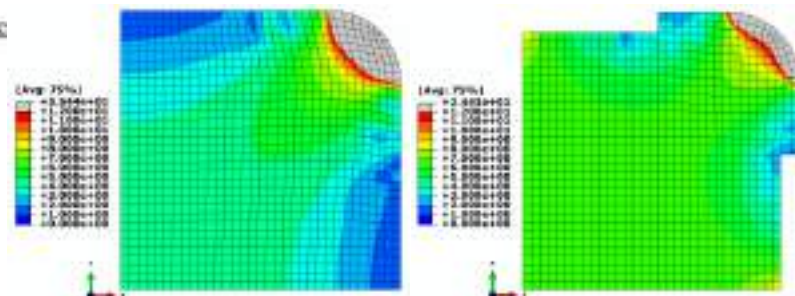


Figure 2. Cross-section of FCCSCs



(a) Square CFFT (b) FCCSC
Figure 3. Distribution of effective confining pressure (in MPa)

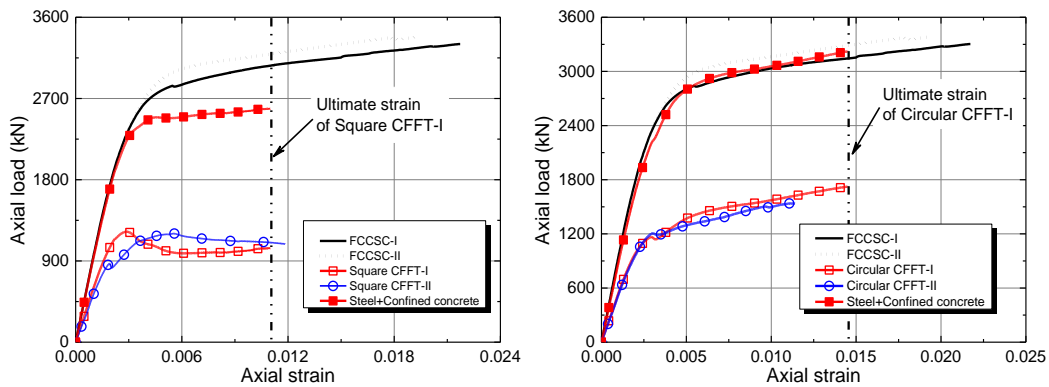


Figure 4. Comparison between FCCSCs and CFFTs

More recently, the author's group completed a series of compression tests to investigate the behavior of slender FCCSCs, and to clarify the effects of load eccentricity and slenderness ratio. A total of 12 specimens, each with a cross section of 200 mm x 200 mm, were tested (Figure 5), covering three column heights (i.e. 1000 mm, 1600 mm and 2400 mm) and three load eccentricities (i.e. 0, 35 mm and 70 mm).

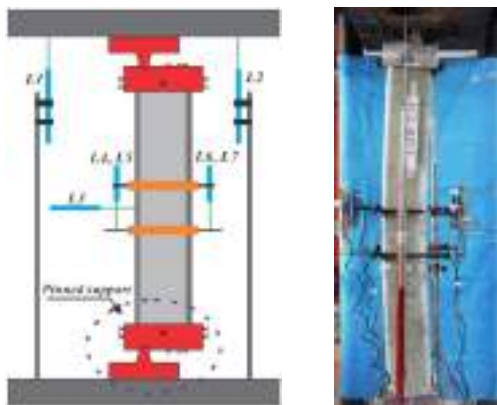


Figure 5. Test set-up for slender FCCSCs

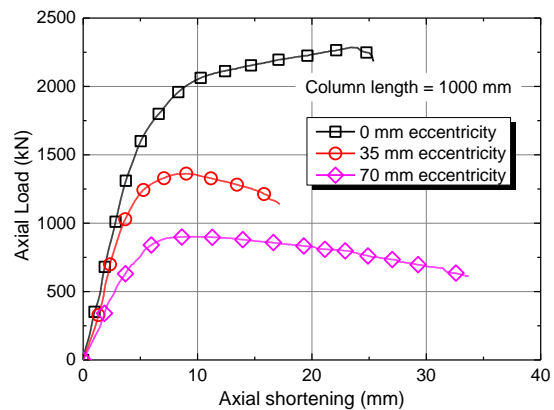


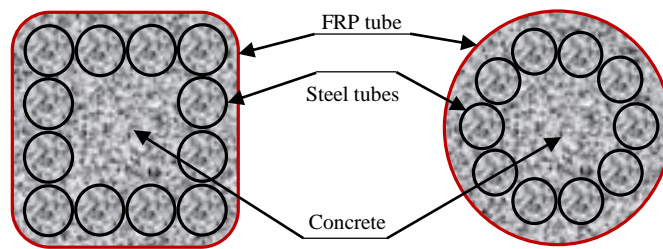
Figure 6. Axial load-shortening curves

Figure 6 show the axial load-shortening behavior of three FCCSC specimens subjected to three different load eccentricities, respectively. All the curves in Figure 6 are terminated at a point when rupture of the FRP outer tube occurred. As expected, the load capacity of FCCSCs decreased with the load eccentricity. It is evident from Figure

6 that all the tested specimens exhibited good ductility. It is also worth noting that buckling of the steel section was completely prevented in all the columns before the rupture of the FRP tube.

Hybrid FCS Multi-Tube Concrete Columns

Hybrid FCS multi-tube concrete columns (MTCCs) are a new form of hybrid FCS members developed by the author's group (Yu et al. 2017c). An MTCC (Figure 7) comprises an external FRP tube and a number of internal steel tubes, with the space inside all the tubes filled with concrete. The internal steel tubes are typically circular and of standard sizes as readily found in the market; they provide the ductile longitudinal reinforcement needed by the column and effectively confine the infilled concrete. The individual steel tubes can be connected to each other by steel angle brackets or steel bars to facilitate their placement inside the FRP tube prior to the casting of concrete. The use of small steel tubes of standard sizes eliminates the difficulties associated with the manufacturing, transportation and installation of large steel tubes; the tubes are also highly effective in confining the concrete inside these tubes because of their circular shape. Furthermore, these steel tubes with the concrete infill form a stiff "wall" to confine the concrete surrounded by them (see Figure 7).



(a) Square MTCCs

(b) Circular MTCCs

Figure 7. Typical cross-sections of MTCCs

The author's group has conducted two series of axial compression tests on circular MTCCs (Yu et al. 2017c) and square MTCCs (Chan et al. 2018), respectively. The test results showed that no buckling of the steel tubes, even those in square MTCCs, occurred before the rupture of the FRP tube (Figure 8). It is also found that, because of the additional confinement from the steel tubes, the lateral expansion of concrete at a given axial strain is much less than that of the concrete in a CFFT with the same FRP tube. As a result, MTCCs generally have a much larger ultimate axial strain than the corresponding CFFTs (Figure 9).

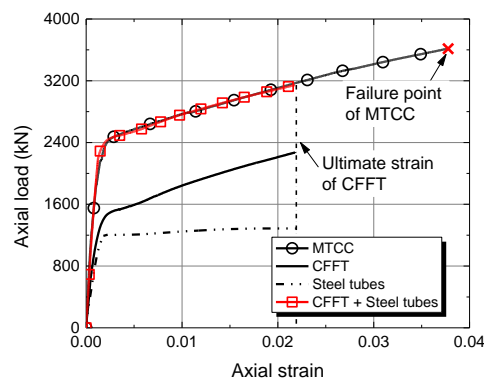
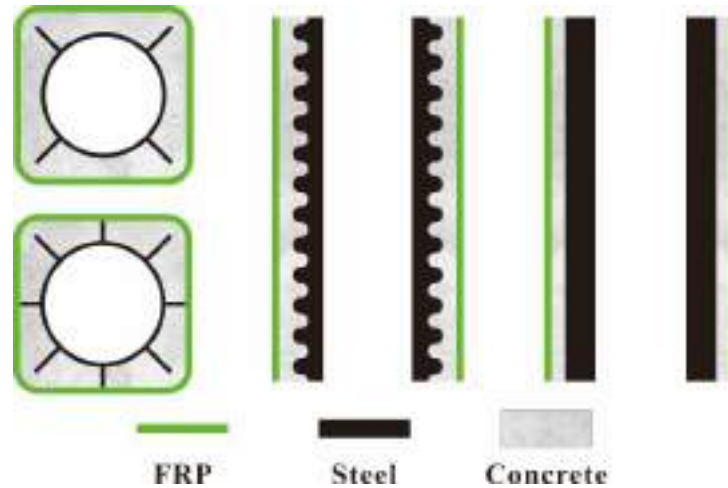


Figure 8. Steel tubes in an MTCC after test Figure 9. Typical comparison between CFFTs and MTCCs

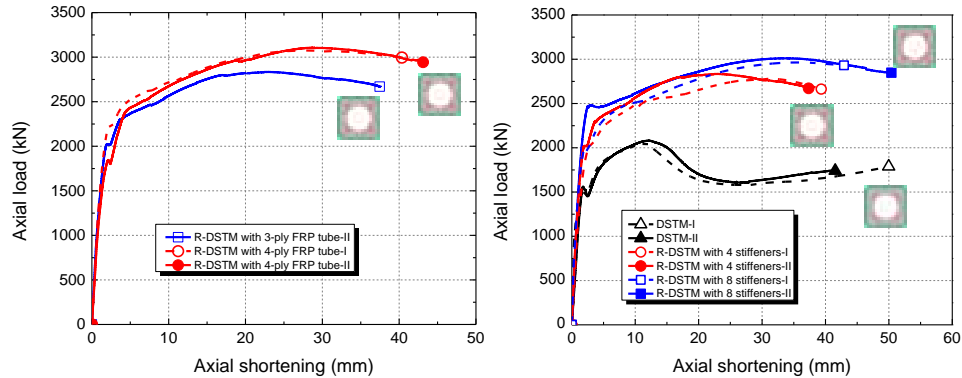
Hybrid DSTMs with Rib-Stiffened Steel Inner Tube

In hybrid DSTMs (Figure 1d), the outward buckling of the steel inner tube is constrained by the FRP-confined concrete, but it can still buckle inwards. Such inward buckling generally does not have a significant effect on the behaviour of circular hybrid DSTMs (Wong et al. 2008), but can be severe in square/rectangular hybrid DSTMs in which the confinement is non-uniform (Cavill and Yu 2014). Even for the circular hybrid DSTMs, the inward buckling can become significant when a relatively thin steel tube is used and/or when an FRP tube with a large rupture strain is used (Yu et al. 2017b). On the other hand, existing research (e.g. Yu et al. 2006; Zhao et al. 2016) has shown that in situations where flexural loading dominates, shear connectors between the concrete and the steel tube are generally needed to enhance the composite action between the two in a hybrid DSTM. Against this

background, a variation of hybrid DSTMs, namely, hybrid DSTMs with a rib-stiffened steel tube (referred to as hybrid R-DSTMs hereafter), was recently developed at UOW (Peng et al. 2017). In such a member, the inner steel tube is stiffened with a number of vertical rib stiffeners (Figure 10a), which can be in the form of flat bars or wave-shape plates with varying widths along the longitudinal direction (Figure 10b). For a square hybrid DSTM, stiffeners generally need to be (at least partially) placed at the corner regions (Figure 10a) where lateral pressure from the concrete to the steel tube is the largest and local buckling of the steel tube is most likely to occur. The stiffeners, with properly selected widths, may also serve as spacers to facilitate the positioning of the two tubes (i.e. FRP tube and steel tube) in hybrid DSTMs during the construction process.



(a) Cross sections (b) Vertical sections
Figure 10. Details of hybrid R-DSTMs



(a) Effect of FRP thickness (b) Effect of stiffener configuration
Figure 11. Axial load-shortening behavior of hybrid R-DSTMs

Peng et al. (2017) presented an experimental program which demonstrated the effectiveness of rib stiffeners in significantly delaying buckling of the steel inner tube in square hybrid DSTMs. In their study, Peng et al. (2017) examined the effect of FRP thickness (Figure 11a), and also compared the performance of hybrid DSTMs with a four-stiffener steel tube and those with an eight-stiffener steel tube, respectively (Figure 11b). It was shown that the use of a larger number of thin ribs is more effective than that of a smaller number of thick ribs with the same amount of rib material (Figure 11b).

CONCLUSIONS

This paper has discussed the rationale and advantages of an emerging type of structural members, namely, hybrid FCS tubular members. This paper has also provided a brief summary of existing research on hybrid FCS tubular members, and outlined the current research on three novel forms of such members recently developed by the author's research group at UOW. Hybrid FCS tubular members, because of their excellent durability and ductility, have a great potential for use in harsh environments and/or seismic regions. The combination of three construction materials (i.e. FRP, steel and concrete) in a structural member also offers ample opportunities for innovation



towards various optimized systems for different applications. Future research is needed to explore the development of structural systems based on hybrid FCS tubular members and to realize the full potential of the hybrid members by practical applications in such systems.

ACKNOWLEDGMENTS

The author is grateful for the financial support received from the Australian Government through the Australian Research Council's Discovery Projects funding scheme (project ID: DP170102992) and the Australian Research Council Industrial Transformation Research Hub for nanoscience based construction material manufacturing (IH150100006). The author would also like to thank Prof Jin-Guang Teng and A/Prof Lip Teh for their valuable suggestions, and his research students Messrs Le Huang, Chunwa Chan and Kaidi Peng for their assistance in preparing the paper.

REFERENCES

- S. Abdalla, F. Abed, and M. AlHamaydeh (2013). "Behavior of CFSTs and CCFSTs under quasi-static axial compression", *Journal of Constructional Steel Research*, 90, 235-244.
- O.I. Abdelkarim, and M.A. ElGawady (2016). "Behavior of hollow FRP-concrete-steel columns under static cyclic axial compressive loading", *Engineering Structures*, 123, 77-88.
- M.I. Alam, S. Fawzia, and X. Liu (2015). "Effect of bond length on the behaviour of CFRP strengthened concrete-filled steel tubes under transverse impact", *Composite Structures*, 132, 898-914.
- Z. Cai, D. Wang, S.T. Smith, and Z. Wang (2016). "Experimental investigation on the seismic performance of GFRP-wrapped thin-walled steel tube confined RC columns", *Engineering Structures*, 110, 269-280.
- G. Cavill, and T. Yu (2014). "Rectangular hybrid FRP-concrete-steel double-skin tubular columns: stub column tests", *Proceedings, 23th Australian Conference on the Mechanics of Structures and Materials (ACMSM23)*, 9-12 December, Byron Bay, Australia.
- C. Chan, T. Yu, and S.S. Zhang (2018). "Compressive behaviour of square FRP-concrete-steel hybrid multi-tube concrete columns", *Advances in Structural Engineering*, 21(8), 1162-1172.
- L. De Waal, S. Jiang, S.R. Hislop-Lynch, D. Fernando, S. Ahn, J.G. Teng, P. Rodman and P. Burnton (2018). "Novel bridge system for durable, low-cost and rapid construction", *Wibe Prize Paper*.
- C.X. Dong, A.K.H. Kwan and J.C.M. Ho (2016). "Axial and lateral stress-strain model for concrete-filled steel tubes with FRP jackets", *Engineering Structures*, 126, 365-378.
- B.A.L. Fanggi, and T. Ozbakkaloglu (2013). "Compressive behavior of aramid FRP-HSC-steel double-skin tubular columns", *Construction and Building Materials*, 48, 554-565.
- GB 50608 (2011). "Technical Code for Infrastructure Application of FRP Composite", China Planning Press, Beijing, China. (in Chinese)
- L.H. Han, Z. Tao, F.Y. Liao and Y. Xu (2010). "Tests on cyclic performance of FRP-concrete-steel double-skin tubular columns", *Thin-Walled Structures*, 48(6), 430-439.
- Y.M. Hu, T. Yu and J.G. Teng (2011). "FRP-confined circular concrete-filled thin steel tubes under axial compression", *Journal of Composites for Construction*, 15(5), 850-860.
- L. Huang, T. Yu, S.S. Zhang and Z.Y. Wang (2017). "FRP-confined concrete-encased cross-shaped steel columns: Concept and behaviour", *Engineering Structures*, 152, 348-358.
- L. Huang, S.S. Zhang, T. Yu and Z.Y. Wang (2016). "Concrete-encased steel columns confined with large rupture strain FRP composites: axial compression tests", *Proceedings, 24th Australian Conference on the Mechanics of Structures and Materials (ACMSM24)*, 6-9 December, Perth, Australia.
- Y. Idris and T. Ozbakkaloglu (2015). "Flexural behavior of FRP-HSC-steel double skin tubular beams under reversed-cyclic loading", *Thin-Walled Structures*, 87, 89-101.
- S. Jiang, D. Fernando, J.G. Teng, M. Heitzmann, and G. Angliss (2016). "Experimental behaviour of hybrid FRP-concrete-steel double-skin tubular arches", *Proceedings, 8th International Conference on Fibre-Reinforced Polymer (FRP) Composites in Civil Engineering, Hong Kong, China*.
- K. Karimi, W.W. El-Dakhkhni and M.J. Tait (2011a). "Behavior of slender steel-concrete composite columns wrapped with FRP jackets", *Journal of Performance of Constructed Facilities*, 26(5), 590-599.
- K. Karimi, M.J. Tait and W.W. El-Dakhkhni (2011b). "Testing and modeling of a novel FRP-encased steel-concrete composite column", *Composite Structures*, 93(5), 1463-1473.



- N. Li, Y. Lu, S. Li and L. Liu (2018). "Slenderness effects on concrete-filled steel tube columns confined with CFRP", *Journal of Constructional Steel Research*, 143, 110-118.
- X. Liu, A. Nanni and P.F. Silva (2005). "Rehabilitation of compression steel members using FRP pipes filled with non-expansive and expansive light-weight concrete", *Advances in Structural Engineering*, 8(2), 129-142.
- A. Mirmiran and M. Shahawy (1997). "Behavior of concrete columns confined by fiber composites", *Journal of structural engineering*, 123(5), 583-590.
- K. Peng, T. Yu and M. Hadi (2017). "Compression tests on square hybrid FRP-concrete-steel tubular columns with a rib-stiffened steel inner tube", *Proceedings, 6th Asia-Pacific Conference on FRP in Structures (APFIS)*, 19-21 July, Singapore.
- S.B. Talaeitaba, M. Halabian and M.E. Torki (2015). "Nonlinear behavior of FRP-reinforced concrete-filled double-skin tubular columns using finite element analysis", *Thin-Walled Structures*, 95, 389-407.
- J.G. Teng and L. Lam (2004). "Behavior and modeling of fiber reinforced polymer-confined concrete", *Journal of structural engineering*, 130(11), 1713-1723.
- J.G. Teng, T. Yu and Y.L. Wong (2004). "Behaviour of hybrid FRP-concrete-steel double-skin tubular columns", *Proceedings, 2nd International Conference on FRP Composites in Civil Engineering*, December 8-10, Adelaide, Australia, 811-818.
- J.G. Teng, T. Yu, Y.L. Wong and S.L. Dong (2007). "Hybrid FRP-concrete-steel tubular columns: concept and behavior", *Construction and building materials*, 21(4), 846-854.
- J.G. Teng, Y.M. Hu and T. Yu (2013). "Stress-strain model for concrete in FRP-confined steel tubular columns", *Engineering structures*, 49, 156-167.
- J.G. Teng, Z. Wang, T. Yu, Y. Zhao and L.J. Li (2018). "Double-tube concrete columns with a high-strength internal steel tube: Concept and behaviour under axial compression", *Advances in Structural Engineering*, 1369433217746838.
- R. Wang, L.H. Han and Z. Tao (2015a). "Behavior of FRP-concrete-steel double skin tubular members under lateral impact: experimental study", *Thin-Walled Structures*, 95, 363-373.
- Q.L. Wang, J. Li, Y.B. Shao and W.J. Zhao (2015b). "Flexural performances of square concrete filled CFRP-steel tubes (S-CF-CFRP-ST)", *Advances in Structural Engineering*, 18(8), 1319-1344.
- Y.L. Wong, T. Yu, J.G. Teng and S.L. Dong (2008). "Behavior of FRP-confined concrete in annular section columns", *Composites Part B: Engineering*, 39(3), 451-466.
- Y. Xiao (2004). "Applications of FRP composites in concrete columns", *Advances in Structural Engineering*, 7(4), 335-343.
- T. Yu and J.G. Teng (2011). "Design of concrete-filled FRP tubular columns: provisions in the Chinese technical code for infrastructure application of FRP composites", *Journal of Composites for Construction*, 15(3), 451-461.
- T. Yu, Y.L. Wong, J.G. Teng, S.L. Dong and E.S. Lam (2006). "Flexural behavior of hybrid FRP-concrete-steel double-skin tubular members", *Journal of Composites for Construction*, 10(5), 443-452.
- T. Yu, J.G. Teng and Y.L. Wong (2010a). "Stress-strain behavior of concrete in hybrid double-skin tubular columns", *Journal of Structural Engineering*, ASCE, 136(4), 379-389.
- T. Yu, Y.L. Wong and J.G. Teng (2010b). "Behavior of hybrid FRP-concrete-steel double-skin tubular columns subjected to eccentric compression", *Advances in Structural Engineering*, 13(5), 961-974.
- T. Yu, B. Zhang, Y.B. Cao and J.G. Teng (2012). "Behavior of hybrid FRP-concrete-steel double-skin tubular columns subjected to cyclic axial compression", *Thin-walled structures*, 61, 196-203.
- T. Yu, Y.M. Hu and J.G. Teng (2014). "FRP-confined circular concrete-filled steel tubular columns under cyclic axial compression", *Journal of Constructional Steel Research*, 94, 33-48.
- T. Yu, G. Lin and S.S. Zhang (2016a). "Compressive behavior of FRP-confined concrete-encased steel columns", *Composite Structures*, 154, 493-506.
- T. Yu, Y.M. Hu and J.G. Teng (2016b). "Cyclic lateral response of FRP-confined circular concrete-filled steel tubular columns", *Journal of Constructional Steel Research*, 124, 12-22.
- T. Yu, L. Teh and M.N. Hadi (2017a). "High-strength steel plates in hybrid fiber-reinforced polymer-concrete-steel columns: Concept and behavior", *Advances in Structural Engineering*, 20(5), 797-811.
- T. Yu, S.S. Zhang, L. Huang and C. Chan (2017b). "Compressive behavior of hybrid double-skin tubular columns with a large rupture strain FRP tube", *Composite Structures*, 171, 10-18.
- T. Yu, C. Chan, L. Teh, and J.G. Teng (2017c). "Hybrid FRP-Concrete-Steel Multitube Concrete Columns: Concept and Behavior", *Journal of Composites for Construction*, 21(6), 04017044.



**9th International Conference on Fibre-Reinforced Polymer (FRP) Composites
in Civil Engineering (CICE 2018), PARIS 17-19 JULY 2018**

- S. Zakaib and A. Fam (2012). "Flexural performance and moment connection of concrete-filled GFRP tube-encased steel I-sections", *Journal of Composites for Construction*, 16, 604-13.
- B. Zhang, J.G. Teng and T. Yu (2015). "Experimental behavior of hybrid FRP-concrete-steel double-skin tubular columns under combined axial compression and cyclic lateral loading", *Engineering Structures*, 99, 214-231.
- J.L. Zhao, J.G. Teng, T. Yu and L.J. Li (2016). "Behavior of large-scale hybrid FRP-concrete-steel double-skin tubular beams with shear connectors", *Journal of Composites for Construction*, 20(5), 04016015.



STRUCTURAL BEHAVIOR OF FRP-REINFORCED GEOPOLYMER CONCRETE SANDWICH WALL PANELS FOR PREFABRICATED CONSTRUCTION

Jian-Guo DAI* and Jun-Qi HUANG

Department of Civil and Environmental Engineering, The Hong Kong Polytechnic University, Hong Kong, China.

Email: cejgdai@polyu.edu.hk

ABSTRACT

Prefabricated concrete sandwich panels (PCSPs) consist of two concrete wythes and a thermal insulation layer between them. They have great potential to be used for prefabricated building construction. This paper experimentally studies the development of a new PCSP system. The two exterior wythes are made of FRP-reinforced geopolymer concrete while FRP tubular connectors are used to realize the composite action. The reported tests include: (1) the structural performance of FRP tubular connectors; (2) the structural performance of steel and BFRP rebar reinforced geopolymer concrete one-way slabs; (3) the structural performance of the formed sandwich wall panels subjected to out-of-plane loading. Due to its green feature and its structural efficiency, the developed PCSP system may find wide applications in prefabricated construction which is popular in Hong Kong and the rest of China.

KEYWORDS

FRP; geopolymer concrete; sandwich wall panel; connector

INTRODUCTION

Prefabricated concrete sandwich panels (PCSPs) have been widely used as the facade wall, the load-bearing wall and the floor slab in practical engineering. They consist of inner and outer reinforced concrete (RC) wythes, a layer of core insulation and connectors penetrating through the insulation. Based on the stiffness and the resistance provided by the connectors, the PCSPs are divided into fully composite, partially composite and non-composite types (PCI Committee, 1997). Traditionally, concrete block and steel bent-up bars (e.g., steel trusses) were used as the connector. They provided a high composite action but due to the higher thermal conductivity of steel and concrete, thermal bridge could occur. This issue could reduce the thermal efficiency of the whole panel. Therefore, recently fiber reinforced polymers (FRPs) were used as the connectors due to their high strength and low thermal conductivity (Salmon et al., 1997). Considerable work has been conducted to study the effect of various FRP one-way connectors (i.e. designed to transfer one-way shear force) on the structural performance of the formed PCSPs (Chen et al., 2015; Choi et al., 2015; Frankl et al., 2011; Kazem et al., 2015; Kim et al., 2015; Pantelides et al., 2008). However, several problems still exist: (1) the issue of how the section parameters influence the plate-type FRP connector's performance remains unknown. Also, there is no information on FRP connectors designed for transferring two-way shear force (i.e., two-way connector); and (2) very limited research has been conducted on the behavior of PCSP with different concrete materials and reinforcement types used for the wythes (Tomlinson and Fam, 2015a and 2015b).

In this paper, a new PCSP system is proposed. The new PCSP has two exterior wythes made of FRP-reinforced geopolymer concrete. Also, it has a developed two-way FRP connector (hexagonal tube connector) to link the exterior wythes. The geopolymer concrete adopts an inorganic binder called "geopolymer cement" (Davidovits, 1991), which is produced through alkaline activation of industrial by-product (e.g. slag and fly ash). A total of four experimental programmes are presented here: (1) In-plane direct shear test on proposed one- and two-way glass FRP (GFRP) connectors. This test is used to study the effect of section parameter and loading direction on the connector's performance; (2) Out-of-plane loading test on steel rebar reinforced geopolymer and ordinary Portland cement (OPC) concrete one-way slabs. This test is for comparing the out-of-plane flexural behaviors of the two mentioned cases; (3) Out-of-plane loading test on basalt FRP (BFRP) rebar reinforced geopolymer concrete one-way slabs. This test is designed for evaluating the out-of-plane shear behavior; and (4) Out-of-plane loading test on precast geopolymer concrete sandwich panel (PGCSP). This part is used to study the effect of different parameters such as connector type, rebar type, reinforcement ratio and connector spacing on the out-of-plane flexural behavior. The reported tests provide a valuable measure for the design of new PCSP system.

PERFORMANCE OF THE PROPOSED GFRP CONNECTORS

Details of the proposed connectors

Figures 1(a)-(c) show the three kinds of GFRP connector and their connection details in PCSPs. The flat and corrugated plate connectors were mainly proposed as one-way connectors. The flat plate connector is a typical plate-type connector that may fail in out-of-plane buckling, especially when the GFRP laminate thickness is small. To delay or avoid buckling, a corrugated plate GFRP connector was also explored (Figure 1(b)). The hexagonal tube GFRP connector was mainly proposed as a two-way connector. Compared with a solid section, the tubular section is expected to be optimal because it may provide improved bending/transverse stiffness when the connectors are subjected to flexure/shear in PCSPs. Considering its manufacturing convenience and structural efficiency, a GFRP tube with a hexagonal section is first proposed in this study. For all of the connectors, a reliable anchorage system was achieved by penetrating the reinforcing bars in the two wythes through the predrilled holes at the top and the bottom of each connector.

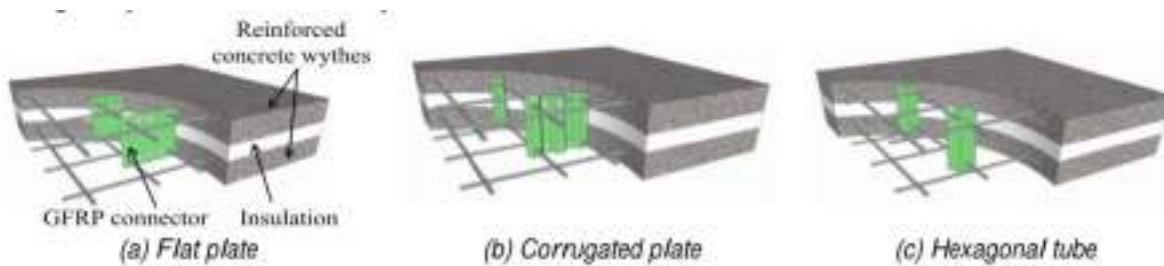


Figure 1: PCSP with the proposed connector

Test specimens

Twenty-four specimens were tested under in-plane direct shear. Two identical specimens were tested for each combination of test parameters to evaluate the performance of the connectors. For the flat and corrugated plate connectors, test parameters are the projected lengths of 100 and 160 mm and the thickness of glass fiber sheets two and four plies. For the hexagonal tube connector, the test parameters are shear force direction i.e. X and Y directions in Figure 2(c) and the thickness of fiber sheets. Figures 2(a)-(c) show the configuration and shear force directions of the connectors.

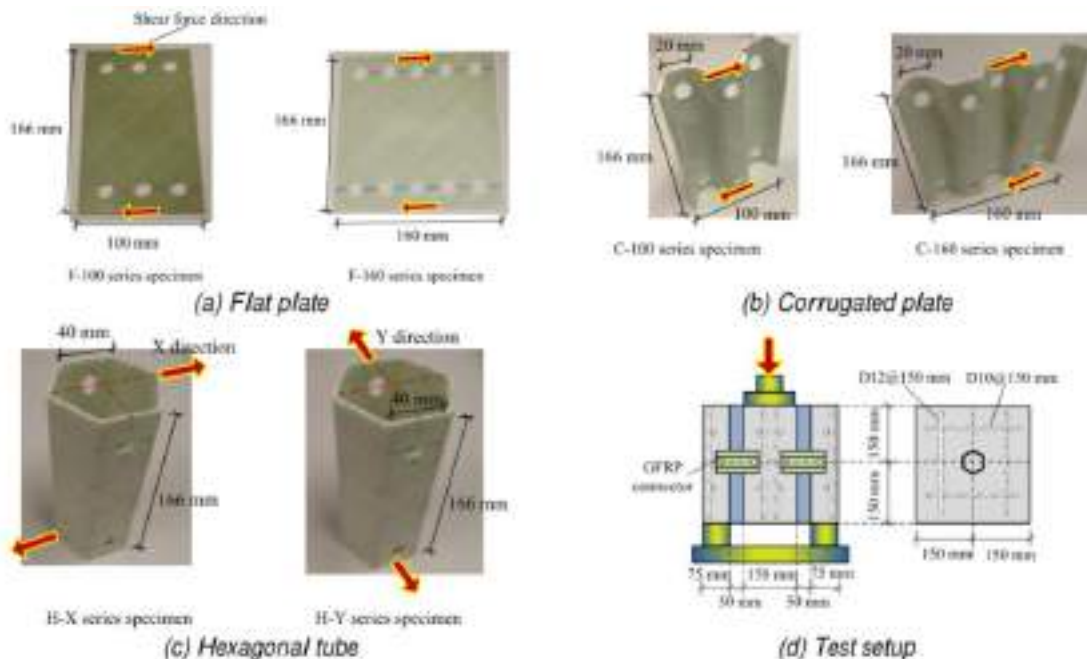


Figure 2: Geometry of proposed GFRP connectors and test setup

All specimens are named as T-S-P-1&2. “T” refers to the connector type (symbolized as “F,” “C,” and “H” for the flat plate, corrugated plate, and hexagonal tube connector, respectively); “S” refers to the projected length (symbolized as “100” and “160” mm) and the shear force direction (symbolized as “X” and “Y”) for the one- and two-way connectors, respectively; and “P” refers to the thickness of the GFRP laminate (symbolized as “2” or “4” plies). The dimension of specimens were 400×300×300 mm (length×width×height), representing two back-to-back sandwich panels. Figure 2(d) shows the details of specimens geometry. In the specimens, extruded polystyrene (XPS) foam with a smooth surface condition was used as the insulation layer. To measure the relative slip between the core concrete wythes and the two outer concrete wythes, linear variable differential transformers (LVDTs) were placed at the front and back of each concrete wythe. The load was applied in a displacement-controlled manner. The loading rate was 1 mm/min. A load cell was placed at the top center of the core concrete wythe to measure the load.

Test Results

Figure 3 shows the shear force vs. relative slip relationship for all specimens. For proposed GFRP connectors under the shear, it is shown that the behaviour is initially linear until the peak force (i.e. P_f in figure 3) and after that, a progressive failure occurs. For the flat and corrugated plate connectors, similar shear resistance and initial secant stiffness are observed. Nevertheless, according to Figure 3(a) and (b) for a thin GFRP laminate (i.e., two plies), the flat plate connector exhibits less ductility than the corrugated one. This is caused by the premature out-of-plane buckling of the laminate. Based on Figure 3(c) and (d), increasing the GFRP laminate thickness can avoid such buckling and therefore ductility is improved. The hexagonal tube connector performed similarly along two orthogonal directions (Figure 3(e) and (f)). This indicates that hexagonal tube connector is potentially suitable for use in PCSPs as a two-way connector.

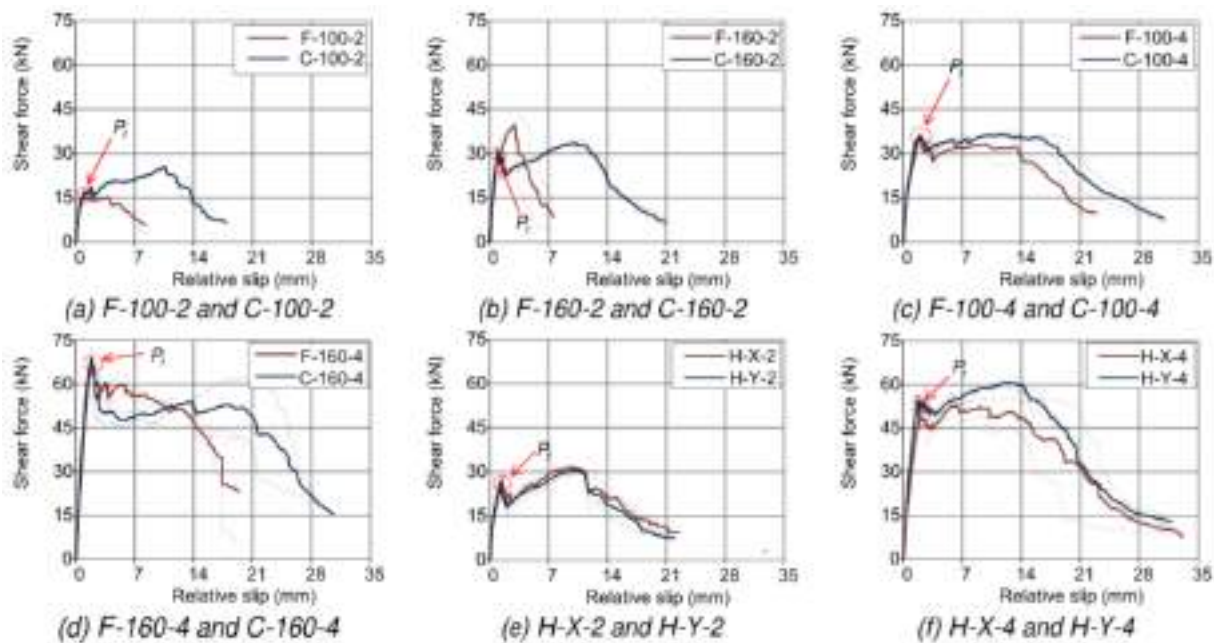
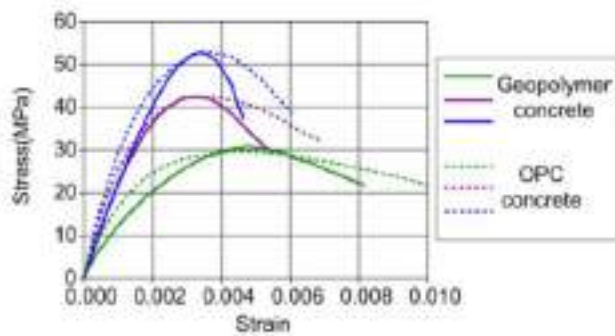


Figure 3: Shear force vs. relative slip relationships of the test specimens

FLEXURAL BEHAVIOR OF STEEL REBAR REINFORCED GEOPOLYMER CONCRETE ONE-WAY SLABS

Test specimens

Twelve steel rebar reinforced concrete one-way slab specimens were fabricated and tested. Size of the specimens was 2100×500×120 mm (length×width×depth). Six of them were fabricated by the geopolymer concrete. As shown in Figure 4(a) three levels of concrete compressive strength i.e. 30, 40 and 50 MPa were used. Also, two adopted reinforcement ratios were 0.82% and 1.20%. The mentioned reinforcement ratios were achieved by changing longitudinal rebar diameter i.e. 10 and 12 mm. The other six slab specimens were made by OPC concrete counterparts. The specimens are named in the form of T-D-C. “T” refers to the concrete type (symbolized as “GCS” and “OCS” for geopolymer and OPC concrete slab, respectively); “D” refers to the diameter of longitudinal rebar (symbolized as “10” and “12” mm); and “C” refers to the concrete compressive strength (symbolized as “30”, “40” and “50” MPa). The flexural behavior of the specimens was studied by four points bending test. The length of shear span and constant moment zone were 640 mm. Figure 4(b) shows the test setup. The deflection was measured at the mid-span and at the loading points by means of LVDTs. The load was applied by the hydraulic jack (Figure 4(b)).



(a) Concrete stress-strain relationship

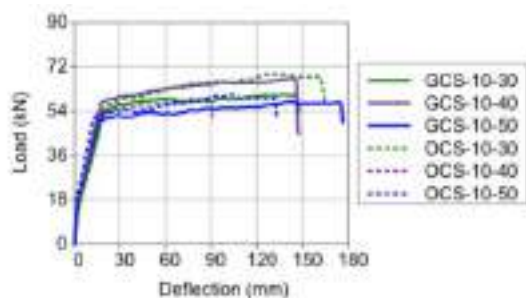


(b) Test setup

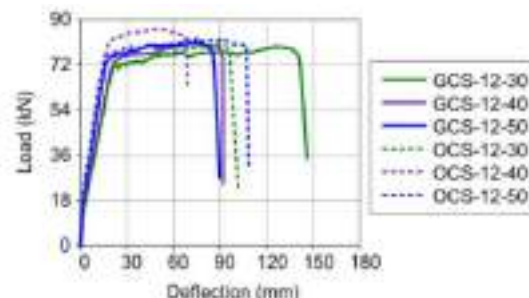
Figure 4: Concrete stress-strain relationship and test setup of the reinforced concrete one-way slab

Test results

Figure 5 shows the load vs. mid-span deflection relationship for all specimens. It seems that the initial and the post-cracking stiffness, cracking load, yielding load and load carrying capacity are similar for both cases i.e. the GCS specimens and the OCS counterparts. The failure mode and crack pattern of GCS-12-50 and OCS-12-50 are shown in Figure 6(a) and (b), respectively. Both of them have experienced a crushing failure at the top surface of the constant moment zone. Therefore it is concluded that the steel rebar reinforced geopolymer concrete one-way slabs had similar flexural behavior compared to the OPC concrete counterparts.



(a) GCS-10 and OCS-10 specimens



(b) GCS-12 and OCS-12 specimens

Figure 5: Load vs. mid-span deflection relationship of the test steel rebar reinforced one-way slab specimens

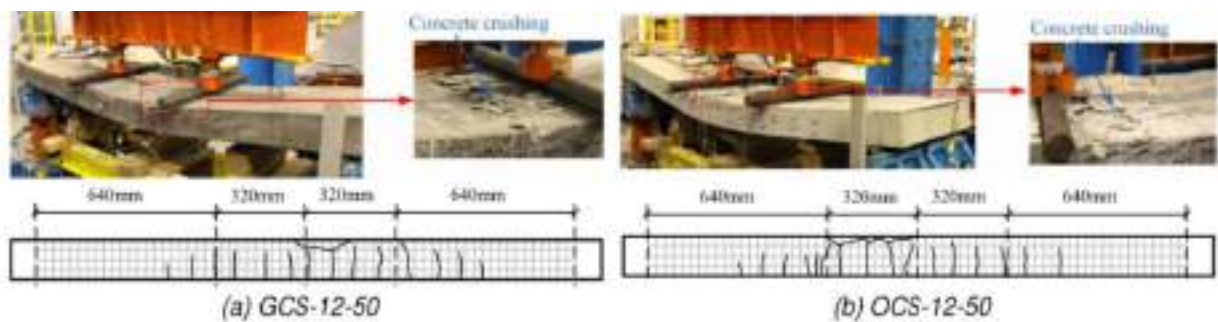


Figure 6: Failure mode and crack pattern of GCS-12-50 and OCS-12-50

SHEAR BEHAVIOR OF BFRP REBAR REINFORCED GEOPOLYMER CONCRETE ONE-WAY SLAB

Test specimens

Six BFRP rebar reinforced geopolymer concrete one-way slab specimens, were fabricated and tested. The size of specimens was 2100×500×120 mm (length×width×depth). As shown in Figure 7(a) the test parameters are the concrete compressive strength i.e. 30, 40 and 50 MPa and reinforcement ratios i.e. 1.20% and 2.18%. Different reinforcement ratios were achieved by changing longitudinal rebar diameter (12 and 16 mm). The out-of-plane shear behavior of the specimens was studied by four points bending test. The specimens were named as GCS-R-C. “R” refers to the longitudinal reinforcement type (symbolized as “B12” and “B16”, for longitudinal BFRP rebar diameter of 12 and 16 mm, respectively); and “C” refers to concrete compressive strength (symbolized as “30”, “40” and “50” MPa). The test setup details are the same as Figure 4(b).

Test results

For all BFRP rebar reinforced geopolymer concrete one-way slab specimens a shear-compression failure was observed. Figure 7(b) shows the load vs. mid-span deflection relationship of the specimens. It is clear that the load carrying capacity of all specimens is between 90.6-96.9 kN. Also, it is shown that the post-cracking stiffness is enhanced by increasing the reinforcement ratio. The failure mode and crack pattern of GCS-B12-30 and GCS-B16-30 are shown in Figure 8(a) and (b), respectively. It is shown that the slab with lower reinforcement ratio maintained a proper integrity at the failure stage. But for the slab with higher reinforcement ratio, the splitting of the concrete cover occurred.

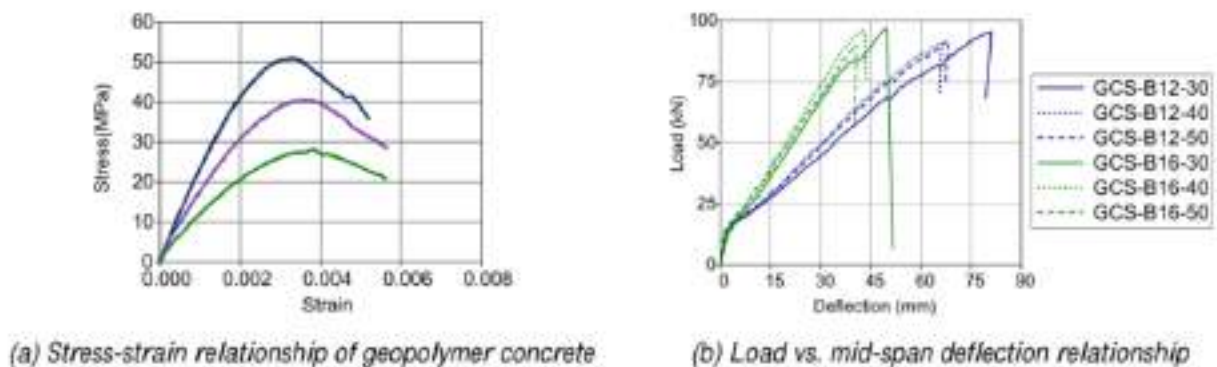


Figure 7: Geopolymer concrete stress-strain relationship and load vs. mid-span deflection relationship of the BFRP rebar reinforced one-way slab specimens

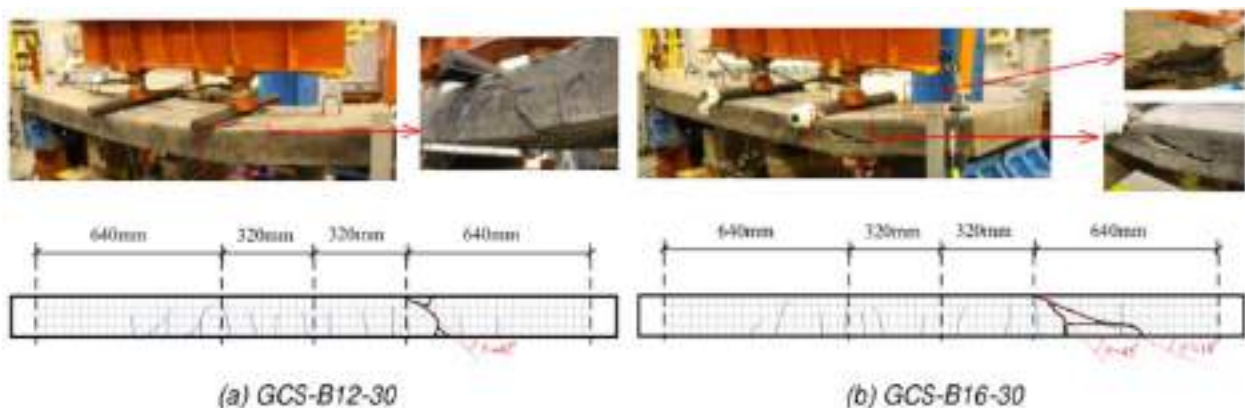


Figure 8: Failure mode and crack pattern of GCS-B12-30 and GCS-B16-30

FLEXURAL BEHAVIOR OF PGCSP ENABLED WITH GFRP CONNECTOR

Test specimens

Eight PGCSP specimens were fabricated and tested. The test specimen was a longitudinal unit of the sandwich wall panel with one column of the GFRP connectors. The size of all specimens was 2340×300×200 mm (length×width×thickness). The thickness of outer concrete wythes was 75 mm and the thickness of core XPS insulation was 50 mm. Parameters investigated consisted of connector type (commercial plate-type and hexagonal tube connector), connector spacing (300 mm and 525 mm), rebar type (BFRP and steel rebar) and reinforcement ratio (0.30% and 0.43%). Different reinforcement ratios were achieved by changing longitudinal rebar diameter (10 and 12 mm). Figure 9(a) shows the comparison of the shear force vs. relative slip relationship between the two adopted connectors. It is shown that the hexagonal tube connector presented a higher initial stiffness and shear resistance than those of the commercial plate-type connector. The specimen was named in the form of C-S-T-R. “C” refers to the connector type (symbolized as “P” and “H” for commercial plate-type the hexagonal tube GFRP, respectively); “S” refers to the connector spacing (symbolized as “300” and “525” mm); “T” refers to the reinforcement type (symbolized as “S” and “B” for steel and BFRP rebar, respectively); and “R” refers to the longitudinal rebar diameter (symbolized as “10” and “12” mm).

The flexural behavior of the specimens was evaluated by four points bending test. The length of the constant moment zone and the shear span were 600 and 770 mm, respectively. LVDTs were used for measuring the deflection at the mid-span and at the loading points. The load was applied by a hydraulic jack (Figure 9(b)).

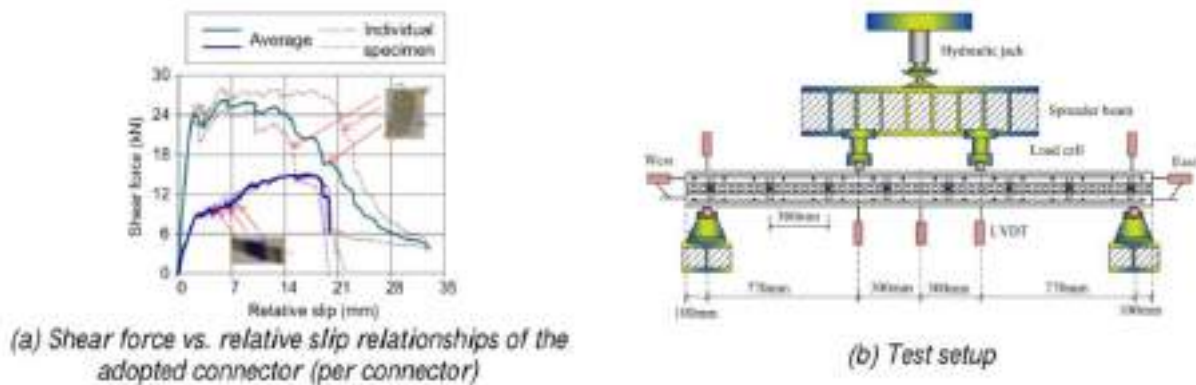


Figure 9: Shear force vs. relative slip relationships of the adopted connectors and test setup

Test results

Load vs. mid-span deflection relationships of the PGCSP specimens are shown in Figure 10(a). The following results are observed: (1) For BFRP rebar reinforced specimens the post-cracking stiffness and the load carrying capacity are lower than those of steel rebar reinforced counterparts; (2) based on the comparison of the four P series specimens, the load carrying capacity increases by increasing the reinforcement ratio; (3) By using hexagonal tube connector, the post-cracking stiffness and load carrying capacity of the PGCSP were significantly higher than those with commercial plate-type connector. This is observed by comparing the curves of P-300-S-12 and P-300-B-12 with those of H-300-S-12 and H-300-B-12; (4) based on the results of four H series specimens, it is observed that the post-cracking stiffness and load carrying capacity of the PGCSP can be enhanced by decreasing the connector spacing.

The connectors at the failure stage are shown in Figure 10(b). Also, the failure mode and crack pattern of P-300-B-12 and H-300-B-12 are depicted in Figure 11. The figures reveal that the failure mode of the P series was governed by the connector failure. However, in the H series, marginal damage in GFRP was observed, and the failure mode was governed by the localized concrete shear failure (Figure 11(b)).

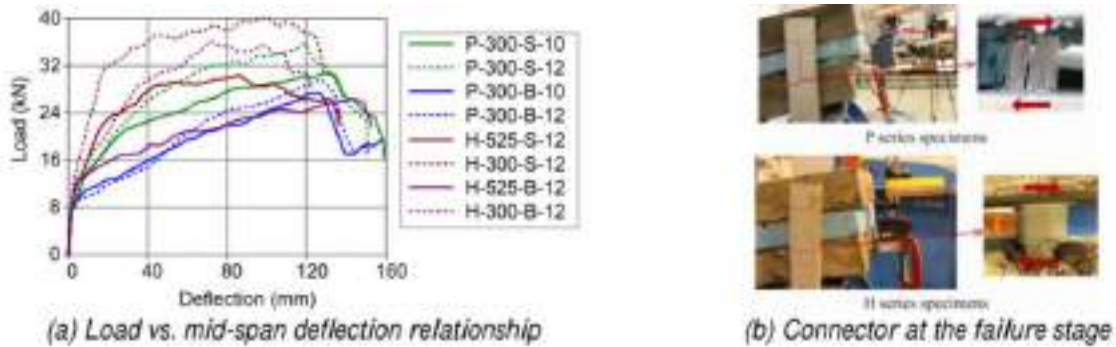


Figure 10: Load vs. mid-span deflection relationship of the PGCSP specimens and the connector at the failure stage

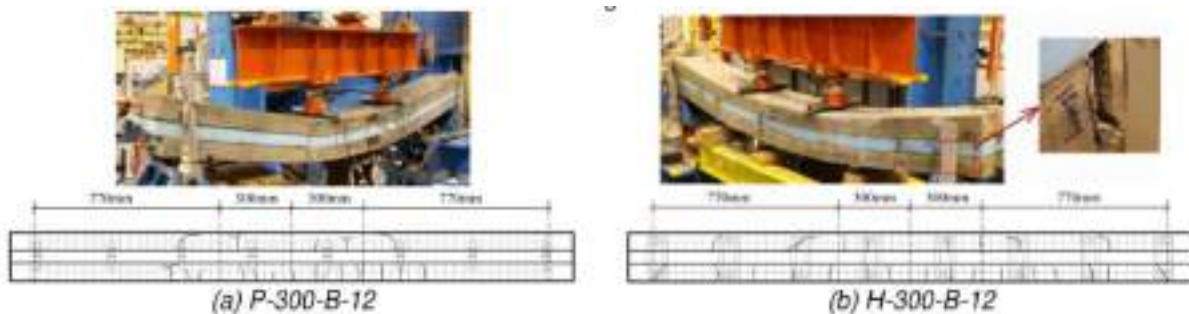


Figure 11: Crack pattern and the failure mode of P-300-B-12 and H-300-B-12

CONCLUSIONS

This paper proposed a new type of PCSP system in which the two outer wythes were BFRP rebar reinforced geopolymer concrete and they were linked by the GFRP hexagonal tube connectors. The four conducted experimental programmes were: (1) In-plane direct shear test of three proposed GFRP connectors; (2) Out-of-plane loading test of steel rebar reinforced geopolymer and OPC concrete one-way slabs; (3) Out-of-plane loading test of BFRP rebar reinforced geopolymer concrete one-way slabs; and (4) Out-of-plane loading test of PGCSP. The following conclusions were drawn based on the tests:

The proposed hexagonal tube connector has a potential to be used as the two-way connector in PCSP. The steel rebar reinforced geopolymer concrete one-way slabs have a similar flexural behavior compared with that of the OPC counterparts. The test BFRP rebar reinforced geopolymer concrete one-way slabs could maintain a similar shear strength with the change of geopolymer concrete strength (30-50 MPa) and reinforcement ratio (1.20%-2.18%). Using the proposed hexagonal tube connector could increase the post-cracking stiffness and load-carrying capacity of the PGCSP compared to using the commercial plate-type connector. This emphasizes the potential of the new type of PCSP system in practical engineering applications.

ACKNOWLEDGMENTS

The authors are grateful for the financial support received from the National Key Research Program of China (Grant No: 2017YFC0703002), the Construction Industry Council, Hong Kong SAR (Project code: K-ZJK2), and the National Science Foundation of China (NSFC) Project No. 51478406. They are also grateful for the help provided by the Industrial Center at The Hong Kong Polytechnic University in manufacturing the GFRP connector.

REFERENCES



**9th International Conference on Fibre-Reinforced Polymer (FRP)
Composites
in Civil Engineering (CICE 2018), PARIS 17-19 JULY
2018**

- Chen, A., Norris, T. G., Hopkins, P. M., Yossef, M., (2015). "Experimental investigation and finite element analysis of flexural behavior of insulated concrete sandwich panels with FRP plate shear connectors", *Engineering Structures*, 98, 95-108.
- Choi, I., Kim, J., Kim, H. R., (2015). "Composite behavior of insulated concrete sandwich wall panels subjected to wind pressure and suction", *Materials*, 8(3), 1264-1282.
- Davidovits, J., (1991). "Geopolymers: inorganic polymeric new materials", *Journal of Thermal Analysis and calorimetry*, 37(8), 1633-1656.
- Frankl, B. A., Lucier, G. W., Hassan, T. K., Rizkalla, S. H., (2011). "Behavior of precast, prestressed concrete sandwich wall panels reinforced with CFRP shear grid", *PCI journal*, 56(2), 42-54.
- Kazem, H., Bunn, W. G., Seliem, H. M., Rizkalla, S. H., Gleich, H., (2015). "Durability and long term behavior of FRP/foam shear transfer mechanism for concrete sandwich panels", *Construction and Building Materials*, 98, 722-734.
- Kim, J., You, Y. C., (2015). "Composite behavior of a novel insulated concrete sandwich wall panel reinforced with GFRP shear grids: effects of insulation types", *Materials*, 8(3), 899-913.
- PCI Committee., (1997). "Precast concrete sandwich wall panels: state of the art of precast/prestressed sandwich wall panels", *PCI Journal*, 42(2), 92-133.
- Pantelides, C. P., Surapaneni, R., Reaveley, L. D., (2008). "Structural performance of hybrid GFRP/steel concrete sandwich panels", *Journal of Composites for Construction*, 12(5), 570-576.
- Salmon, D. C., Einea, A., Tadros, M. K., Culp, T. D., (1997). "Full scale testing of precast concrete sandwich panels", *ACI Structural Journal*, 94, 239-247.
- Tomlinson, D., Fam, A., (2015a). "Combined Loading Behavior of Basalt FRP-Reinforced Precast Concrete Insulated Partially-Composite Walls", *Journal of Composites for Construction*, 20(3), 04015060.
- Tomlinson, D., Fam, A., (2015b). "Flexural behavior of precast concrete sandwich wall panels with basalt-FRP and steel reinforcement", *PCI Journal*, 60, 51-71.



*9th International Conference on Fibre-Reinforced Polymer (FRP) Composites
in Civil Engineering (CICE 2018), PARIS 17-19 JULY 2018*

Composite Materials



FATIGUE AND DURABILITY OF LAMINATED CARBON FIBRE REINFORCED POLYMER STRAPS FOR BRIDGE SUSPENDERS

F. Baschnagel¹, G. P. Terrasi^{1,2}, Z. Triantafyllidis² and U. Meier³

¹ *Empa, Mechanical Systems Engineering Lab, Überlandstrasse 129, 8600 Dübendorf, Switzerland, Email: fabio.baschnagel@empa.ch*

² *Institute for Infrastructure and Environment, The University of Edinburgh, Edinburgh, UK*

³ *Director Emeritus, Empa, Überlandstrasse 129, 8600 Dübendorf, Switzerland.*

ABSTRACT

Steel cables and suspenders in bridges are at high risk of corrosion-fatigue and in some cases of fretting-fatigue in their anchorages. These factors greatly limit the service stresses of a specific cable system and involve expensive corrosion and fretting protection measures. In order to investigate these limitations, the fretting fatigue behaviour of novel pin-loaded carbon fibre reinforced polymer (CFRP) straps was studied as models for corrosion resistant suspenders of half-through arch bridges. Two types of straps were tested: small model straps and large full-scale straps. In a first phase, 15 fully laminated and carbon pin-loaded CFRP model straps were subjected to an ultimate tensile strength test. Thereafter, and in order to assess the durability, 29 model straps were subjected to a fretting fatigue test, which was successfully passed by ten. An S-N curve was generated for a load ratio of 0.1 and a frequency of 10 Hz, showing a fatigue limit of the straps around the epoxy matrix fatigue limit strain, corresponding to nearly half the ultimate tensile strength of the straps. The fatigue limit was defined as 3 million load cycles ($N = 3 \times 10^6$), but tests were even conducted up to $N = 11 \times 10^6$. In a second phase, one full-scale strap was tested for its ultimate tensile strength and two full-scale straps were fatigue tested. In all tests, catastrophic failure of the straps was initiated in their vertex areas. The influence of the fatigue testing on the residual mechanical properties was also assessed for both strap types and although fretting fatigue represents an important limitation for laminated CFRP straps, it could be shown that the investigated CFRP tension members can compete with the well-established steel suspenders.

KEYWORDS

New composite materials, systems and strengthening techniques, fatigue, characterization of FRP and FRC materials/systems, durability, long-term performance, CFRP tensile elements, bridge suspenders.

INTRODUCTION

By weighing six times less than comparable steel tension members, CFRP tension members are of growing importance in the sailing and construction industry (Dawson, 2015), where they are starting to replace steel members that are prone to environmental influences such as salt water, which can cause stress corrosion. However, CFRPs are not unaffected by environmental influences either and in applications such as suspenders used for half-through arch bridges, dynamic fatigue is highly relevant as well (Gao et al., 2013). In the present study, the fretting of the contacting surfaces further increases the material degradation, as shown in Friedrich et al. (1987) and Schulte et al. (1987; 1988). Compared to isotropic materials such as metals, ceramics or polymers, the damage modes and crack propagation are much more complex in CFRPs and depend on a variety of factors. Nevertheless, Reifsnider and Highsmith (1981) characterized the fatigue behaviour of multiaxial fibre reinforced composites (FRPs) in a general way and divided it into three stages. In the first stage, the damage develops at a very rapid rate within the first 10%–15% of the laminate's life. In this stage, the major damage mode is matrix cracking in the laminae with the most off-axis fibre orientation. This intralaminar matrix cracking between the fibres reaches uniform saturation spacing at the end of stage I, called characteristic damage state (CDS). In stage II, comprising 70%–80% of the fatigue life, damage is still initiated and the already existing damages continue to grow, but at a much slower rate, until the laminate is severely damaged and then enters stage III, where the damage process is accelerated again until final failure of the laminate.

For purely unidirectional (UD) CFRP laminates, the situation is different, as no off-axis plies are present. However, since carbon fibres show excellent fatigue behaviour (Morgan, 2005), the matrix and its interaction with the fibres remains the limiting factor in the fatigue life of the composite material (Curtis, 1982; 1986; 1987). Based on this idea, Talreja (1981) introduced a fatigue life diagram in which he suggests that the fatigue life of a unidirectionally reinforced polymer is governed by the composite's quasi-static fracture strain and the matrix fatigue limit strain.



Given the insensitiveness of the fibres to fatigue and neglecting possible fretting, no damage progression takes place in the composite below the epoxy matrix fatigue limit strain of $\varepsilon_{mf} = 0.6\%$ (Dharan, 1975). In the presence of fretting, (Friedrich et al. 1987 and Schulte et al. 1987; 1988) could show how an increased normal contact force leads to a more pronounced decrease in fatigue strength and that the influence of the contact force increases if the contacting ply is oriented in the primary loading direction. This is also the case in the examined CFRP straps and the goal of this study was to investigate the fretting fatigue behaviour of said straps in order to improve the durability of existing CFRP tension members.

METHOD OF SOLUTION

Materials and Manufacturing

The materials used for the production of the carbon fibre/epoxy (CF-EP, unidirectional) prepreg were a XB3515/Aradur[®] 5021 matrix system by Huntsman (2012) and intermediate modulus IMS60 carbon fibres by Toho Tenax[®] (2017), with a reported Young's modulus of 290 GPa and tensile strength of 5'600 MPa. The prepreg tapes with nominal widths of 9, 12 and 50 mm were produced by Carbo-Link AG in Fehraltorf, Switzerland with a reported fibre volume content (V_f) of $62\% \pm 2\%$. The laminate average experimental tensile strength was $2'567 \pm 58$ MPa with a longitudinal (fibre parallel) elastic modulus E_{11} of 168 ± 6.6 GPa and an average ultimate tensile strain ε_{11u} of $1.52\% \pm 0.23\%$. Investigations on the laminate quality of the hand laminated model straps revealed an average V_f of 66% and a void content of less than 1%. The pultruded T300 CF-EP pins (Figure 1a) used for the loading of the model straps had a V_f of 60–65%. The model straps had a thickness t of 1 mm, a shaft length L of 250 mm, a width w of 12 mm or 9 mm, depending on the prepreg tape used, and an inner radius r of 10 mm (Figure 1b). The full-scale strap specimens were manufactured from the 50 mm wide tape by winding it around two 60 mm wide titanium connector eyes ($d_i = 90$ mm, $d_o = 180$ mm) to a final thickness of 10 mm (Figure 1c). The three straps (Strap A-C) had a length of 3'012 mm, 3'015 mm and 3'017 mm and a free-length circular cross-sectional area of 871 mm², 860 mm² and 845 mm², respectively.

Experimental Setup

Model Straps

Figure 1a and Figure 1b illustrate the test setup of a model strap and pin in the testing machine. The ultimate tensile strength (σ_{UTS}) and fretting fatigue tests on the model straps were conducted on a servo-hydraulic testing machine (type 1251, Instron[®], Norwood, MA, USA). The tensile strength tests were performed under displacement-control at a cross-head speed of 2 mm/min. The corresponding fatigue tests were performed under load-control at a frequency f of 10 Hz and a load ratio R of 0.1. The pultruded CFRP pin is placed in a fork-like steel adapter that is screwed to the cross-head of the testing machine. Figure 1a also shows the type K thermocouple that was glued to the outside of the straps during the fatigue tests in order to monitor the temperature development in the critical (vertex) area. It was important to assess temperature increases, e.g. from hysteretic heating at high test frequencies or due to fretting, because they can reduce the fatigue performance of a composite structure. Whenever a narrow strap was tested, thin copper washers were placed on both sides of the strap to ensure the lateral support of the strap, which is reported to reduce stress concentrations (Schürmann, 2007).

Full-Scale Straps

The full-scale straps were tested on an in-house testing machine containing an Amsler P960 pulsator. The titanium connectors of the full-scale straps were mounted on a metal bolt with an intermediate plain bearing brush, see Figure 1c. The quasi-static tensile strength test of Strap C was performed under force-control at 90 kN/min. Strap A was fatigue tested at a frequency of 4.2 Hz and $R = 0.2$ for 800'000 load cycles and additional 11.6 Mio load cycles at a load ratio of 0.42. The corresponding upper stress levels (σ_u) were 660 MPa and 530 MPa, respectively. Strap B was fatigue tested at a load ratio of 0.42 and a frequency f of 4.2 Hz for 11.3 Mio load cycles at an upper stress level σ_u of 537 MPa.

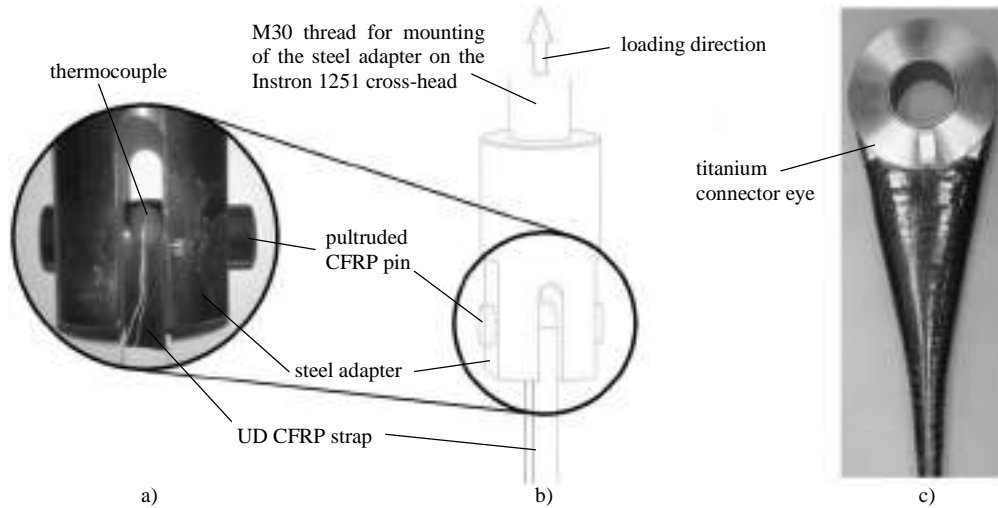


Figure 1: Test setup for model straps (details 1a and 1b) and full-scale strap before testing (detail 1c).

RESULTS AND DISCUSSIONS

Quasi-Static-Behaviour

Prior to the fretting fatigue tests, fifteen model straps and one full-scale strap were tested for their ultimate tensile strength. The results of the quasi-static tensile tests performed on the ten wide (12 mm) and five narrow (9 mm) model straps and the full-scale Strap C are shown in Table 1. Two different types of model straps were tested since the 12 mm wide straps often required a lateral machining of the straps in order to fit into the adapter. The 9 mm model straps, on the contrary, did not require this kind of invasive post-processing which was suspected to negatively influence the mechanical performance of the straps. However, Baschnagel et al. (2016) found no significant influence of the machining on the mechanical properties but found a lower standard deviation (SD) for the non-machined straps. The low tensile strength of the model straps can be explained with the presence of wavy fibres and, as will be shown later, stress concentrations of up to 1.3 in their vertex areas.

Table 1: Average quasi-static tensile strength and stiffness of pristine wide (12 mm) and narrow (9 mm) model straps and quasi-static tensile strength of full-scale Strap C. The fibre parallel elastic modulus E_{11} (GPa) of the model straps was measured with strain gauges (E_{11_SG}) and a linear encoder (E_{11_LE}). The listed composite strains at failure ε_{cf} (%) were measured with the strain gauges.

strap	$\sigma_{UTS,P}$	E_{11_SG}	E_{11_LE}	ε_{cf}
wide	1'653±123	177.8±8.6	177.5±9.8	0.99±0.04
narrow	1'714±55	174.4±1.1	166.2±6.2	1.00±0.05
full-scale	2'124	-	-	-

Fretting Fatigue

S-N Curve

Figure 2 shows the S-N curve obtained from the fretting fatigue testing of 12 mm wide pin-loaded model straps (circular markers). A strap was defined to have reached the fatigue limit once it endured more than 3 million load cycles. In order to confirm this, one model strap was tested for 11'089'000 load cycles at the fatigue limit stress (750 MPa) without failure. The two full-scale straps were also tested for over 11 Mio load cycles but, as stated above, at a different load ratio. For the sake of completeness, the full-scale strap tests are also given in Figure 2 (square markers). Markers containing a cross indicate failed straps.

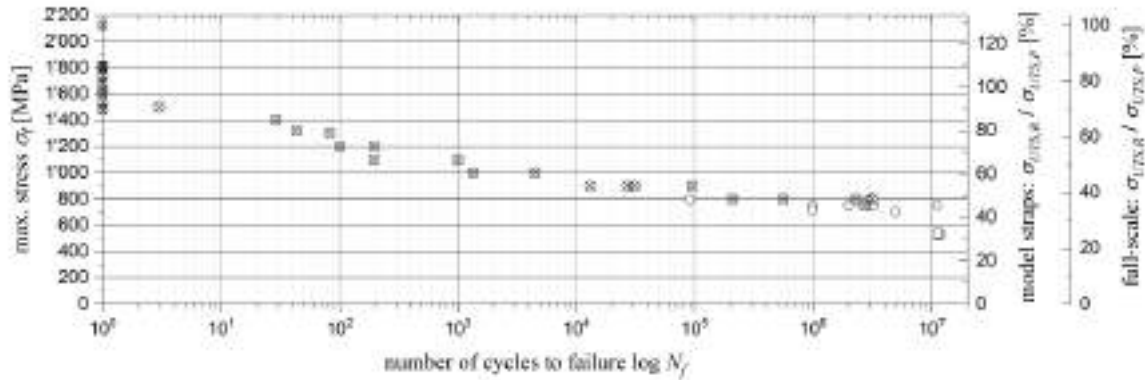


Figure 2: S-N curve of the 12 mm wide model straps (circular markers), listing the upper stress level (σ_u) as a function of endured load cycles at failure (N_f). Complementary the results of the full-scale strap tests (at a different R) are also given (square markers).

Residual Properties

The residual mechanical properties of straps tested without failure after 1, 2, 3 and 11 million load cycles were tested in quasi-static tensile tests until failure. The test setup was the same as for the pristine straps and the obtained results are given in Table 2.

Table 2: Average residual strength ($\sigma_{UTS,R}$) and stiffness properties of 12 mm (wide) model straps after 1, 2, 3 and 11 million load cycles at an upper stress level (σ_u) of 720–750 MPa and residual strength of full-scale straps after 11 million load cycles at $\sigma_u = 530$ -537 MPa. The fibre parallel elastic modulus E_{11} of the model straps was calculated from linear encoder measurements ($E_{11,LE}$).

strap	$\sigma_{UTS,R}$	$E_{11,LE}$	$\sigma_{UTS,R}/\sigma_{UTS,P}$
wide	1'620±65	165.9±4.0	98.0 %
full-scale	1'491±79	-	70.2 %

Comparing the residual moduli of the model straps tested for $N \geq 1 \times 10^6$ to the average modulus of the pristine straps reveals a slight stiffness reduction over time of up to 10%. The ultimate tensile strength of the model straps on the other hand is hardly affected by the fretting fatigue loading. Furthermore, the standard deviation (SD) is much lower in the fatigue tested model straps. First signs of (further) damage occurred only after the straps had reached approximately 80% of their ultimate tensile strength. In pristine model straps, first signs of damage were observed just above 50% of their ultimate tensile strength. Due to the low number of test specimens and the slightly varying testing parameters, the residual strength measurements of the full-scale straps show a higher SD. They also suffer from a more pronounced strength decrease which could be related to the harder connector material (see Friedrich et al. (1987) and Schulte et al. (1987; 1988)) in combination with a larger contacting surface.

Damage Modes

The damage modes of all fretting fatigue tested model straps were similar. First, visible damage always occurred in the form of delamination of the inner- and outermost layers in the shaft with the overlapping plies. The delaminations started at the free ends of the tape and propagated along the shaft until they stopped in the vertex area. Another damage mode was longitudinal matrix cracking. This damage mode occurred solely in the inner- and outermost plies and did not propagate over the vertex areas of the model straps either. However, none of the above failure mechanisms could be directly attributed to a certain stress level during testing. The failure of all straps was initiated in the vertex areas and led to fibre bursting in one or both shafts. Failure of the full-scale Strap C occurred in a similar way, whilst the fatigue tested full-scale straps showed no signs of fibre bursting in the shaft but rather fibre parallel matrix cracking.

Fretting Behaviour

The fretting behaviour of the contacting surfaces was investigated differently for the two types of straps. By placing a transparent adhesive tape on the model strap and CFRP pin surfaces just after testing, the fretting products of these tests could be investigated. The tapes were placed on a sheet of paper and investigated under an optical microscope (ZEISS Axioplan in reflected-light mode). Figure 3 shows two representative pictures of a strap and a pin. Clearly visible are the carbon fibre particle accumulations just outside the vertex area of the strap. In accordance with Schulte et al. (1987) and Cirino et al. (1988a; 1988b), the main damage mode observed on the strap (sliding of the contacting surface in fibre direction) was fibre thinning, resulting in small carbon particles. The fretting products on the pin on the other hand consist mostly of short, broken and pulled-out carbon fibres with parts of neat resin still attached to the fibres. This is also reported by Cirino et al. (1988a; 1988b), Sung and Suh (1979), Winistoerfer (1999) and Schön (2004) to be typical for sliding perpendicular to the fibres. Clear signs of a homogeneous graphite particle film covering the contact area that might act as a lubricant were not detected. However, the graphite particle aggregations just outside the vertex areas of the strap suggest a particle transport from the fretting areas to the free surfaces of the shaft. This would require that the particles do build, at some point, an intermediate film between the pin and the strap which would contribute to a reduction of the coefficient of friction.

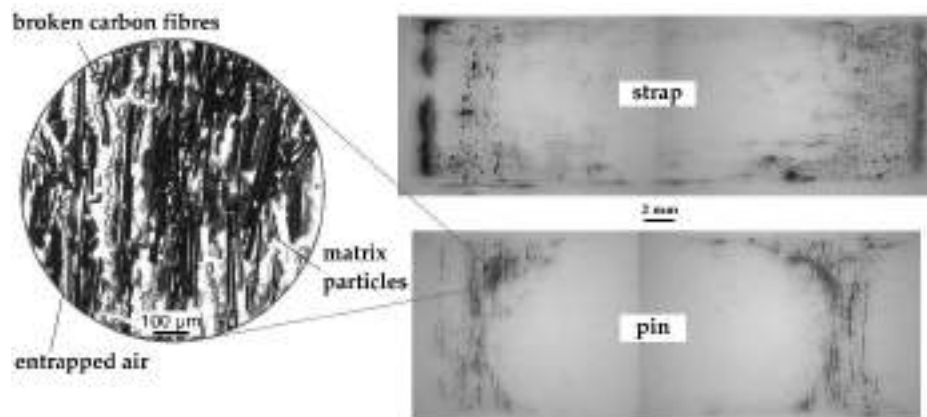


Figure 3: Fretting products of a model strap after 30'000 load cycles (top) and a pin after $N = 1$ Mio (bottom). Both images show fretting products from tests conducted at an upper load level of 720 MPa.

The contacting surfaces of the full-scale straps were investigated under a scanning electron microscope (SEM, FEI ESEM XL30). Figure 4 shows three pictures of typical surface conditions after testing. Figure 4c shows the surface of Strap C in contact with the titanium connector eye in the vertex area. As the strap was not exposed to fatigue testing, the fibres (dark) are still well embedded in the intact matrix (light) and show no signs of fibre thinning. In the regions close to the top (crown) where the relative movement between strap and connector eye is relatively small, the surface of the fatigue tested Strap A was similar. Further away from the top (crown) of the strap, see Figure 4b, the fibres are still intact, but the matrix suffered from the small relative movement between the strap and the connector eye. This matrix deterioration is even more pronounced in the vertex areas of fatigue tested straps, Figure 4a, where the fibres are not visibly embedded in the matrix anymore. The fibre parallel fretting also caused fibre thinning (Figure 4a) and the fretting products agglomerate and cover the fibres (Figure 4a). These particle agglomerations consist of compressed fretting products with particle diameters of 30-100 nm.

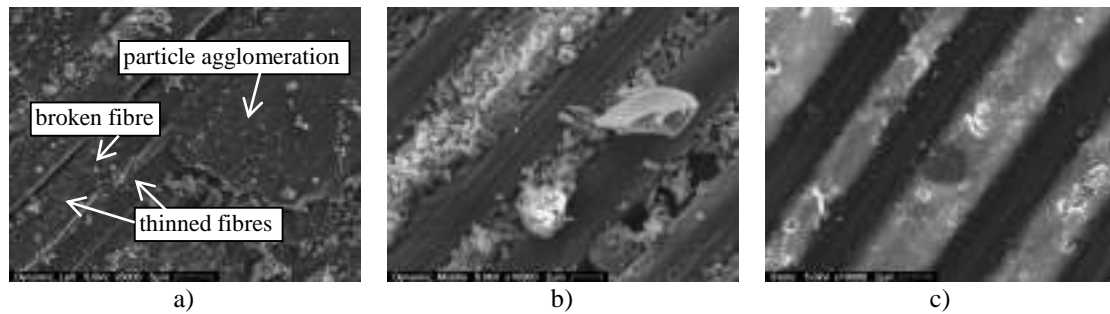


Figure 4: Typical SEM pictures of the full-scale strap surfaces in contact with the titanium connector eye. The pictures were taken in the vertex area of Strap A, Figure 4a, close to the top (crown) area of Strap A, Figure 4b, and in the vertex area of Strap C, Figure 4c, after failure of the straps.

Temperature

Due to the high testing frequencies, the temperature on the outside of the straps was monitored during all fatigue tests. The thermocouples on the outside of the model straps measured a significant initial temperature increase with a peak within the first 10^4 load cycles for all straps. After this peak, the temperature decreases and levels out before increasing again prior to failure of the strap. As the initial peaks never exceeded $65\text{ }^\circ\text{C}$, which is far below the glass transition temperature ($T_g = 140\text{ }^\circ\text{C}$) of the CFRP, and the considered laminate is thin, these temperature increases can be considered non-critical. The temperature measurements on the outside of the full-scale Strap A revealed a maximum temperature of $80\text{ }^\circ\text{C}$ after 2×10^4 load cycles. As the temperature did not decrease within the subsequent $5'000$ load cycles and with a laminate thickness of 10 mm , it had to be assumed that the temperature inside the laminate was even higher. Consequently, the test was paused and σ_u was reduced from 660 MPa to 530 MPa . After these adjustments, the temperature didn't exceed $50\text{ }^\circ\text{C}$, which was also the maximum temperature measured on Strap B.

Numerical Modelling

The analytical model presented in Schürmann (2007) predicts a fibre parallel stress concentration in the vertex area of pin-loaded model straps of 1.1 for the geometry, lateral support and material properties investigated in this study. This value is too low to explain the obtained experimental results. In order to investigate this mismatch, a Finite Element Analysis (FEA) of the pin-strap contact problem under quasi-static tensile loading was conducted in the commercial FEA Software Abaqus/Standard 6.14 (Dassault Systèmes Simulia Corp., Providence, RI, USA). With the help of the FEA, the influence of the coefficient of friction (*cof*), the upper tensile load, the pin diameter and the strap thickness on the stress distribution in the strap and the relative slip between pin and strap could be investigated. Figure 5 shows the resulting stresses in the vertex area of a 12 mm wide and 1 mm thick strap with an inner radius of 10 mm that was subjected to a pin displacement of 1.05 mm ($1'250\text{ MPa}$ shaft-stress). The displacement of the pin causes a bending moment in the vertex area of the strap (bottom right picture) and the resultant significant stress concentrations in fibre direction ($\sigma_1 = \sigma_t$) become clearly visible in the top left picture. Furthermore, the profile of the normal stresses in the strap ($\sigma_3 = \sigma_r$, bottom left) is similar to the wear pattern observed under the microscope, shown in Figure 3.

The obtained results of an increasing stress concentration of σ_1 with decreasing inner radius and/or increasing strap thickness are consistent with the literature (Schürmann, 2007). However, with the help of the FEA it could be shown how the analytical model presented in Schürmann (2007) underestimates the stress concentrations in the innermost plies. This is due to the fact that it does not consider secondary effects such as the bending moment in the vertex area that further increases the local stresses in the innermost plies, leading to σ_1 stress concentrations in the vertex area of factor 1.3.

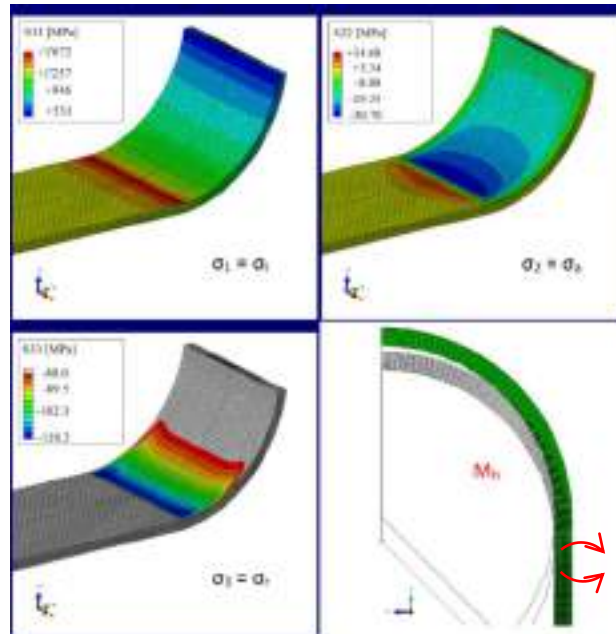


Figure 5: Stress distribution in the vertex area of a 12 mm wide and 1 mm thick strap in contact with an analytical rigid pin ($\text{cof} = 0.5$).

CONCLUSIONS

The fretting fatigue behaviour of pin-loaded CFRP straps under tensile loading was presented in this study. The investigated straps had been subjected to ultimate tensile strength and fretting fatigue tests up to 11×10^6 load cycles. A total number of 31 straps, 29 wide model straps (12 mm) and two full-scale straps, were subjected to fretting fatigue loading. The results were used to generate an S–N curve. The following conclusions can be drawn on the basis of the study described in this paper:

- The pin-loaded model CFRP straps showed a fatigue limit stress of 750 MPa, which corresponds to 45% of their pristine ultimate tensile strength. The fatigue limit was defined to be reached once a strap endured more than 3×10^6 load cycles, and one model strap was tested without failure for 11.09×10^6 load cycles to confirm this.
- The experimentally determined fatigue limit of the model straps corresponds to the matrix fatigue limit strain of 0.6%, which is reported by Talreja (1981) to be the ultimate lower bound for a UD fibre reinforced composite fatigue limit.
- Clear signs of a graphite film acting as lubricant between pin and strap were not found. However, the carbon fibre particle accumulations just outside the vertex area of the inner strap surface require a transport of these particles from the fretting areas to the outside. This in turn means that a particle film is present at some point and presumably contributes to a reduction of the coefficient of friction.
- The pristine full-scale strap showed a significantly higher ultimate tensile stress than the model straps. This might be attributed to the connector eye with an improved geometry, mitigating the stress concentrations in the vertex areas.
- The two full-scale straps were fatigue tested below the matrix fatigue limit strain and did not fail ($N \geq 11 \times 10^6$). This corroborates the above findings for the model straps.
- The fretting of the straps on their respective connector leads to a decrease in residual tensile strength. This effect was more pronounced in the full-scale straps. A possible reason might be the harder connector material and larger contact area, leading to a stronger material deterioration in the CFRP strap.
- Although the fretting behaviour of the presented straps needs to be investigated further, it was shown that pin-loaded CFRP straps can achieve considerable fatigue loading endurance and thus can be a highly competitive alternative to traditional steel tension members.



ACKNOWLEDGMENTS

The authors would like to thank the whole Mechanical Systems Engineering Laboratory at Empa Dübendorf. Special thanks go to Andreas Brunner, Christian Affolter and Daniel Völki. Further thanks go to Christian Loosli, Gerald Kress and Paolo Ermanni from the Laboratory of Composite Materials and Adaptive Structures at ETH Zürich.

REFERENCES

- Baschnagel, F., Rohr, V. & Terrasi, G. (2016). "Fretting Fatigue Behaviour of Pin-Loaded Thermoset Carbon-Fibre-Reinforced Polymer (CFRP) Straps", *Polymers*, 8(4), pp. 124.
- Cirino, M., Friedrich, K. & Pipes, R. B. (1988a). "The effect of fiber orientation on the abrasive wear behavior of polymer composite materials", *Wear*, 121(2), pp. 127-141.
- Cirino, M., Friedrich, K. & Pipes, R. B. (1988b). "Evaluation of polymer composites for sliding and abrasive wear applications", *Composites*, 19(5), pp. 383-392.
- Curtis, P. T. (1982). "RAE Technical Report TR82031". RAE (now DRA), Farnborough, UK.
- Curtis, P. T. (1986). "An investigation of the mechanical properties of improved carbon fibre materials", RAE Technical Report TR86021. RAE (now DRA), Farnborough, UK.
- Curtis, P. T. (1987). "A review of the fatigue of composite materials", RAE Technical Report TR87031. RAE (now DRA), Farnborough, UK.
- Dawson, D. (2015). "Yachtbuilding composites: Rigged for success", *CompositesWorld*. March 2015, Volume 1, No.3. Gardner Business Media. Cincinnati, OH, USA. pp. 60-65.
- Dharan, C. K. H. (1975). "Fatigue Failure Mechanisms in a Unidirectionally Reinforced Composite Material", In: Hancock, J. (ed.), *Fatigue of Composite Materials*, ASTM STP 569. American Society for Testing and Materials, West Conshohocken, PA, USA.
- Friedrich, K., Kutter, S. & Schulte, K. (1987). "Fretting fatigue studies on carbon fibre/epoxy resin laminates: I—design of a fretting fatigue test apparatus", *Composites Science and Technology*, 30(1), pp. 19-34.
- Gao, J., Chen, C. M., Winistörfer, A. & Meier, U. (2013). "Proposal for the application of carbon fiber reinforced polymers (CFRP) for suspenders of arch bridges in China", Second Conference on Smart Monitoring, Assessment and Rehabilitation of Civil Structures, 9-11 September 2013 Istanbul, Turkey.
- Huntsman Advanced Materials GmbH (2012). *Selector guide for composite resin systems* [Online]. Basel, Switzerland. Available: http://www.huntsman.com/advanced_materials/Media%20Library/global/files/EUR_Composites%20-%20Composite%20Resin_Araldite_Epoxy_RTm.pdf [Accessed 30/11/2017].
- Morgan, P. (2005). "Carbon Fibers and Their Composites". CRC Press, Boca Raton, FL, USA.
- Reifsnider, K. L. & Highsmith, A. L. (1981). "Characteristic damage states: A new approach to representing fatigue damage in composite materials", In: Sherratt, F. & Sturgeon, J. B. (eds.), *Materials, Experimentation and Design in Fatigue*. Westbury House, Guildford, UK.
- Schön, J. (2004). "Coefficient of friction for aluminum in contact with a carbon fiber epoxy composite", *Tribology International*, 37(5), pp. 395-404.
- Schulte, K., Friedrich, K. & Kutter, S. (1987). "Fretting fatigue studies of carbon fibre/epoxy resin laminates. Part II: Effects of a fretting component on fatigue life", *Composites Science and Technology*, 30(3), pp. 203-219.
- Schulte, K., Friedrich, K. & Kutter, S. (1988). "Fretting fatigue studies on carbon fibre/epoxy resin laminates: III—Microscopy of fretting fatigue failure mechanisms", *Composites Science and Technology*, 33(3), pp. 155-176.
- Schürmann, H. (2007). "Konstruieren mit Faser-Kunststoff-Verbunden". Springer, Berlin, Germany.
- Sung, N.-H. & Suh, N. P. (1979). "Effect of fiber orientation on friction and wear of fiber reinforced polymeric composites", *Wear*, 53(1), pp. 129-141.



**9th International Conference on Fibre-Reinforced Polymer (FRP)
Composites
in Civil Engineering (CICE 2018), PARIS 17-19 JULY
2018**

Talreja, R. (1981). "Fatigue of composite materials: damage mechanisms and fatigue-life diagrams", *Proceedings of the Royal Society of London. A. Mathematical and Physical Sciences*, 378(1775), pp. 461-475.

Toho Tenax Europe GmbH (2017). *Product Datasheet (EU): Tenax Filament Yarn - Version 24, 2017-05-08* [Online]. Wuppertal, Germany. Available:
https://www.tohotenax.com/fileadmin/PDF/Datenbl%C3%A4tter_en/Filament_Produktprogramm_v24_2017-05-08_En_eu.pdf [Accessed 15/12/2017].

Winistoerfer, A. (1999). *Development of Non-Laminated Advanced Composite Straps for Civil Engineering Applications*. PhD Thesis, University of Warwick, Warwick, United Kingdom.



GLASS-GFRP HYBRIDS: FROM BRITTLE GLASS TO DUCTILE AND HIGH STRENGTH STRUCTURAL GLASS

M. Achintha ^{1*}, B. Balan ¹, M. Bessonov ¹, T. Zirbo ¹ and J. Kanvar ¹

¹ Faculty of Engineering and the Environment, University of Southampton, Southampton, SO17 1BJ, UK

*Email: Mithila.Achintha@soton.ac.uk

ABSTRACT

This paper presents selected findings from a research programme that aimed to exploit the use of adhesively-bonded Glass Fibre Reinforced Polymer (GFRP) laminates as a mean of improving strength and ductility of glass structural elements. In the first half of the paper, using the results of an experimental investigation of the load response and failure behaviour of annealed glass beams reinforced with GFRP laminates, it is shown that the load resistance and the ductility of the glass beams can be enhanced. In the latter half of the paper, it is shown that the stress concentration geometries and bolted joints in annealed glass can sustain greater loads with greater ductility, even after microcracks formed, if the glass is reinforced with adhesively-bonded GFRP laminates.

KEYWORDS

Bending, Ductility, GFRP, Glass, Joints, Reinforcement, Strength.

INTRODUCTION

Due to the distinctive combination of fascinating physical and chemical properties together with recent advances in glass technologies such as low emissivity, solar control, smart glass, etc., it is envisaged that glass will have an increased and central role in future energy-efficient buildings. In order to make buildings more energy efficient using glass, it will be required to use glass as a load bearing construction material (e.g. facades, beams, columns, floors). The exploitation of full potential of glass for delivering energy efficient buildings is currently being held back by brittle material behaviour and the relatively low tensile strength (compared to metals). The tensile strength of basic float glass (also known as annealed glass) is about 40 MPa (IStructE, 2014). The presence of surface flaws and other stress concentration features can further reduce the actual tensile strength of glass. Tempered glass (also known as toughened glass), which is produced by heating up annealed glass up to a high temperature and then rapidly cooled, has a surface compressive pre-stress (i.e. residual stress) of magnitude of 80–150 MPa (IStructE, 2014). Owing to the higher apparent tensile strength, tempered glass can be potentially used in load bearing structures. However, tempered glass display a poor failure behaviour, similar to that in annealed glass, with no residual load capacity after the initiation of a critical crack/defect.

The brittle material behaviour of glass means the design and construction of connections in glass pose major challenges. Mechanical fixings such as clamps and bolted joints are used in contemporary glass designs in order to fix glass panels together or to fix them into a sub-frame support structure. Surface flaws and the consequent stress concentrations cause by drilling holes and the inevitably present localised stress concentrations in the vicinities of mechanical joints significantly weaken glass exactly at locations where glass is subjected to greater stresses. Despite isolating hard materials from glass via the use of softer materials such as plastic and rubber, all of which redistribute stresses to a certain extent, the mechanical fixings methods are not effective in transferring loads through glass. Usually, only the toughened glass can be used with mechanical fixings. Despite the higher cost and additional difficulties due to improper surfaces, toughened glass has poor failure behaviour and low degrees of toughening around bolt holes (Nielsen, et al. 2009). Although adhesive bonding offers the potential to be an attractive alternative to mechanical joints, the use of adhesives in structural glazing has not been fully proven. In particular, the durability and the long-term structural behaviour of adhesive joints are not fully understood and largely considered to be unreliable.

This paper shows a few selected applications of the use of Glass Fibre Reinforced Polymer (GFRP) as a mean of overcoming inherent structural deficiencies in annealed glass when used as a construction material. Four applications are discussed: (1) as a mean of improving ductility of annealed glass beams; (2) use of a prestressed GFRP interlayer as a mean of improving the strength of annealed glass beams; (3) as a mean of improving strength and ductility of stress concentration features in glass; and (4) as a reinforcement in bolted joints in annealed glass. The results show that bonded GFRPs can potentially be used to increase the apparent tensile strength of glass as well as to increase the ductility of glass structures.

REINFORCED GLASS BEAMS

The use of reinforcing materials has potential to improve the post-fracture behaviour of glass structures. For example, commercially available laminated glass where one or more thin PolyVinylButyral (PVB) or ionomer interlayers are bonded in-between laminated glass sheets has relatively safer failure characteristics compared to monolithic annealed/tempered glass. When a laminated glass sheet fails, the interlayer absorbs the energy, and the interlayer also has potential to hold broken glass pieces. This behaviour ensures some post-breakage load resistance, and eliminates a complete failure of the glass sheets. Despite the potential of laminated glass ensuring a safe failure behaviour, the low stiffness and the low strength of the thin interlayers mean careful designs are required in order to ensure an adequate ductility. Cutting, drilling holes etc. on sites without damaging the original laminated glass is difficult. This limitation together with the higher cost compared to monolithic glass hamper the exploitation of full potential of laminated glass in complex building geometries. On the other hand, the use of relatively stronger (in tension) and stiffer reinforcing materials in glass, similar to the concept of using of steel reinforcement bars in concrete beams, has potential develop a new form of reinforced glass which will have greater post-breakage resistance and ductility.

Adhesively-bonded or mechanically-connected additional material, such as steel (e.g. Louter et al., 2012), timber (e.g. Blyberg et al., 2014), and Fibre Reinforced Polymer (FRP) (Achintha and Balan, 2017) have been investigated in the literature as a mean of reinforcing glass beams. The results reported in the literature suggest, after glass has failed in tension, the reinforcement and the compressive stresses can keep the broken glass pieces locked in place whilst the reinforcement resisting the tension in the post-cracked regime of the glass beams. This behaviour ensured an ability to resist load beyond the peak load, thereby enabling a notable post-fracture resistance and stability in the beams. Research investigations show a better ductility in reinforced annealed glass beams compared to that in reinforced tempered glass beams (Louter et al., 2012). This is because annealed glass shatters into large pieces, unlike in tempered glass, in which cracks progress rapidly causing complete fragmentation of small dice. Detailed reviews of types of reinforced glass beams investigated in the literature can be found in Martens et al. (2014), Bos (2009) and Correia et al. (2011).

ANNEALED GLASS BEAMS REINFORCED WITH GFRP INTERLAYER

Owing to high strength, lightweight and semi-transparent characteristics of GFRPs are attractive for reinforcing glass. In most GFRP reinforced glass beams reported in the literature, the GFRP was embed in composites sections of 'I', 'T', 'H' and box profiles. Various forms of GFRP were used in these studies; for example, adhesively bonded GFRP rods (e.g. Louter, 2010) and GFRP pultruded profiles (e.g. Correia et al., 2011, Speranzini and Agnetti, 2014) were the most commonly used GFRP systems. The GFRP reinforced beams demonstrated significant post-fracture resistance and ductility compared to unreinforced annealed and tempered glass beams (Martens et al., 2014). However, despite the favourable post-breakage load resistance, the final failure of the beams were still sudden and explosive due to debonding of the adhesively bonded GFRP from the glass and/or due to glass failure. Some of the GFRP reinforced glass beams also failed due to instability in the lateral direction.

In the present study, a simple arrangement of double layer annealed glass beams reinforced with an adhesively bonded GFRP interlayer (Figure 1) subject to minor axis bending was investigated. This arrangement provides the flexibility required to use GFRP reinforced glass in a range of geometries, including areas around joints and fixtures where greater strengths and ductility are required. As can be noted from the results presented in this paper, the minor axis bending arrangement also eliminated lateral instability failure commonly observed in the beams tested in the studies reported in the literature.



Figure 1: Two-layer annealed glass beam with an adhesively bonded GFRP interlayer

Fabrication of GFRP Reinforced Annealed Glass Beams

10 mm thick annealed glass sheets purchased from a commercial supplier and cut in to dimensions of 600 mm x 40 mm were used in the present study to make glass beams. The GFRP laminate that used to reinforce the glass beams were fabricated by impregnating unidirectional ‘E-glass’ dry fibre sheets using a commercially available epoxy resin by means of a hand lay-up method. The average thickness of the final cured GFRP laminate was ~1.35 mm. The fibre volume fraction of the GFRP was calculated to be ~33%, and the Young’s modulus and the Poisson ratio of the GFRP were 450 MPa, 24.5 GPa and 0.10 respectively (Achintha and Balan, 2017). The length and the width of the GFRP reinforcement layer was taken to be the same as that of the glass beams. The GFRP was bonded as an interlayer between two glass beams by using structural epoxy adhesive, “Araldite2020” (Araldite2020, 2015). In order to bond the GFRP onto glass sheets, an adhesive layer of ~0.1 mm thick was uniformly spread over one surface of each glass sheet, and then placed the GFRP strip on the top of one glass surface. The second glass sheet was then placed on the top of the GFRP, and a good bond was ensured by applying a small pressure on glass sheets. The beams were then first cured inside an autoclave at temperature of 40°C and atmospheric pressure for 24 hours, followed by further six days of curing under ambient conditions.

Beam Tests, Load Response and Failure Behaviour

The beams were tested in four-point bending with a constant moment zone of 400 mm long and two equal shear spans of 50 mm (Figure 2), displacement controlled and at a slow displacement rate representing a static loading scenario. For brevity, only the results of one beam specimen are presented in this paper. Detailed results of other beams tested in the present study, including beams made from glass sheets of different thickness are presented in Achintha and Balan (2017).



Figure 2: Four-point bending test of glass beams

Figure 3a shows the load–midspan deflection relationship of the GFRP reinforced double layer annealed glass beam. In order to compare the load response and the failure behaviour of the reinforced glass beam, the results of a single-layer and an adhesively-bonded double-layer (i.e. without GFRP reinforcement) glass beams are also shown in the figure. As can be seen from the figure, until the formation of the first major crack, the reinforced beams showed linear behaviour, similar to other types of beams. Although the other beams failed in a brittle manner at the peak load, the reinforced glass beam continued to carry the load after the peak load where a major crack caused a fracture of the bottom (i.e. tension) glass sheet. After the attainment of the maximum load (5600 N), the load resistance of the reinforced beam dropped by ~65%, to 1960 N due to the failure of the bottom glass sheet. However, the presence of the GFRP layer prevented a complete failure.

Figure 3b shows the final crack pattern of the reinforced beam: a distributed cracks throughout the top (i.e. compression) glass layer. The figure also shows that the GFRP held the cracked glass pieces together despite the continuous cracking during the post-breakage regime. This behaviour contributed to maintain a notable bending stiffness in the beam in the post-breakage regime. The ‘ductility index’, may be defined as the ratio of the additional midspan deflection after the peak load to that at the peak load. This suggests the ductility index of reinforced beams is over 500%, and this can be compared with the zero ductility index of single and unreinforced double-layer beams.

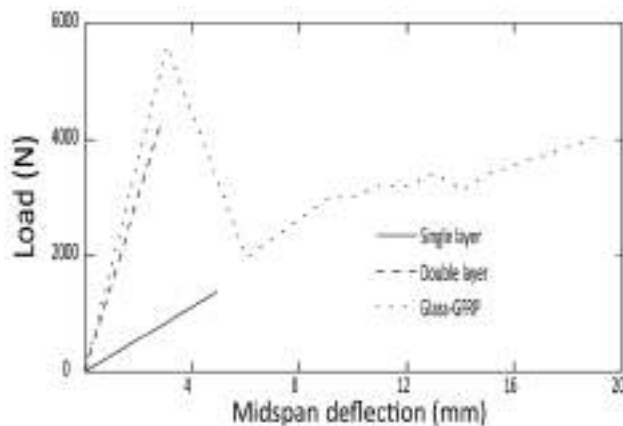


Figure 3a: Load–midspan deflection relationships of the beams



Figure 3b: Final cracking state of the GFRP reinforced glass beam

PRESTRESSED GLASS BEAMS

The results presented in the previous section suggest that the use of GFRP as a reinforcement has potential to ensure a safe post-breakage behaviour in annealed glass beams. However, despite the notable ductility showed by GFRP reinforced annealed glass beams, the GFRP reinforcement cannot increase the tensile strength of glass where fracture initiated due to a critical surface flaw in the tension side (i.e. bottom glass sheet). Since glass is strong in compression, a surface compressive prestress has potential to improve the apparent tensile strength. However, although commercially available toughened glass possess a compressive prestress in the surface regions, the balancing tensile stress in the mid-thickness region (Balan and Achintha, 2015) mean they will break in to small pieces - a behaviour which is not desirable from a structural point of view.

The potential for extending the previous work of reinforcing annealed glass beams with GFRP interlayer by introducing an adhesively bonded pre-tensioned GFRP interlayer was explored in the present study. Unlike in tempered glass where the prestress level cannot be chosen at the sites, by choosing the right force, a desirable compressive prestress in the glass beams which is tailored for the design requirements of the beam can be achieved.

Fabrication of Prestressed GFRP Reinforced Annealed Glass Beams

6 mm thick annealed glass and the GFRP laminate and the adhesive used in the earlier study of GFRP reinforced annealed beams were used here. However, prior to bonding the GFRP onto the glass sheets, the GFRP sheet was tensioned using a hydraulic test machine. Once the tension force in the GFRP had reached a prescribed value, the load was hold until the glass beams were bonded to the either side of the prestressed GFRP. The beams were then cured in the same way as that of previous glass beams with unprestressed GFRP interlayer. End-clamps connections were used to maintain the prestress force in the GFRP until the full curing of the glass–GFRP adhesive bond. A schematic representation of the fabrication process is depicted in Figure 4.

Initial Compressive Prestress in Glass Beams

Once the end clamps were released after the full curing of the glass–GFRP adhesive bond, the stresses present in the glass sheets were measured using a polariscope, SCALP-05 (SCALP, 2015). SCALP-05 instrument uses glass birefringence that changes the polarisation of an input laser beam, and the consequent variation in the intensity (optical retardation) of the scattered light to determine the stress in glass. The use of SCALP-05 to measure initial stresses in glass is presented in Achintha and Balan (2015). The results suggests that the prestressed GFRP interlayer caused a largely uniform (along the thickness of the beam) compressive stress of ~7 MPa in the glass.

Load Response and Failure Behaviour

The prestressed glass beams were tested in the same way as earlier GFRP reinforced beams. Figure 5 presents the load–midspan deflection relationships of the pre-stressed beam and that of an equivalent unprestressed GFRP reinforced glass beam. Similar to the unprestressed beam, the prestressed beam showed a largely linear behaviour until the formation of the first major crack, and followed by a notable post-breakage load carrying behaviour. The peak load of the prestressed beam was determined to be 2200 N. This suggest ~18% increase compared to that of the unprestressed beam (1870 N). The results suggest an increase in the apparent tensile strength resulted in an increase in the peak load of the prestressed beam compared to the unprestressed beam. The prestressed beam displayed a notable ductility, similar to that of the unprestressed reinforced glass beam. The relatively high flexural stiffness of the prestressed beam just after the peak load may be attributed to less cracking occurred in the beam owing to the compression caused by the GFRP. However, as can be seen from Figure 5, with the increase of the damage the flexural stiffness of the prestressed beams approached that of the unprestressed beam.

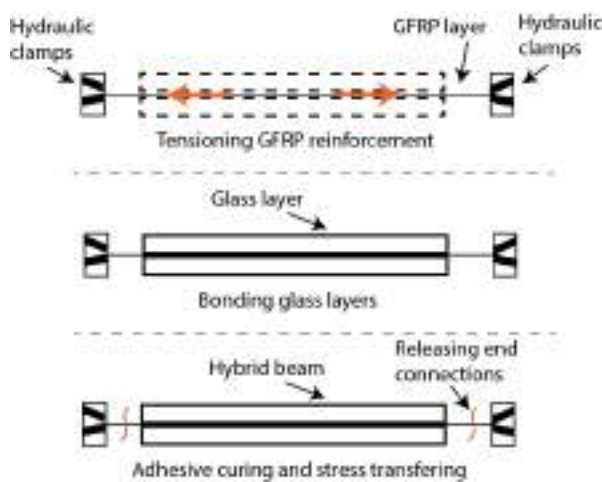


Figure 4: A schematic representation of the fabrication of GFRP prestressed glass beams

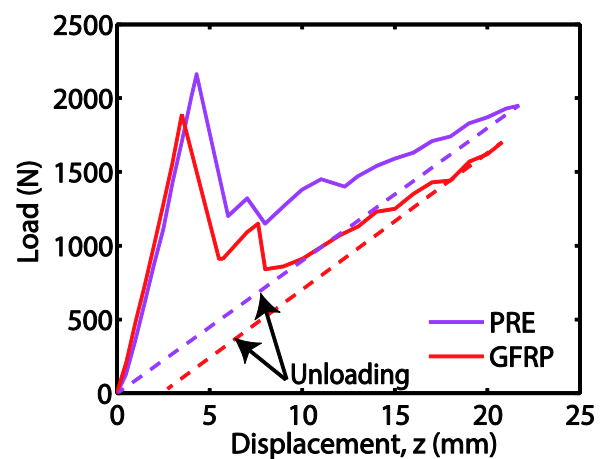


Figure 5: Load–midspan deflection relationships of the reinforced and prestressed glass beams

STRENGTHENING STRESS CONCENTRATIONS FEATURES IN ANNEALED GLASS

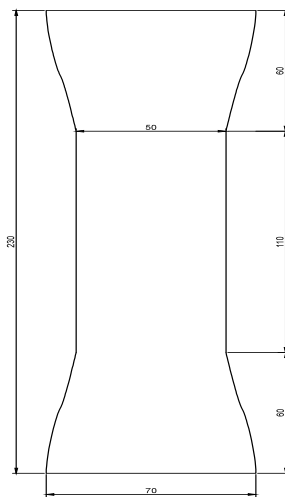
Due to the brittle material behaviour of glass, the stress concentration features pose a major challenge when designing and constructing glass structures. The potential for using adhesively bonded GFRP laminates to strengthen stress concentration zones in glass was experimentally investigated using open-hole annealed glass tensile test specimens.

Test Specimens

A dogbone shape was chosen as the test specimen geometry of the tensile test specimens (Figure 5a). The thickness of the glass was 4 mm and the width and the length of the central part of the test specimen was 50 mm and 110 mm respectively. A 10 mm diameter central hole was drilled using a diamond drilling tool. The efficacy of strengthening was investigated by strengthening the test specimen using GFRP strips. The same GFRP laminate used in the earlier works of the present study was used to strengthen the vicinity of the hole. Two GFRP strips of 50 mm x 20 mm were bonded on each surface of the glass adjacent to the edge of the hole along the loading direction using “Araldite2020”. The reinforced test specimens and the reference unstrengthened specimens were tested in uniaxial tension representing a static loading scenario.

Results

Details of the full experimental programme, including the results of all test specimens tested in the present study can be found in Bessonov (2016). For brevity, only the load–displacement relationships of one strengthened and one reference specimens are shown in Figure 5b. The reference unreinforced specimen failed in a brittle manner across the hole at applied load 2960 kN. In the reinforced specimen, the GFRP strips bridged the cracks those developed around the hole. The results shown in Figure 5b suggest the formation of multiple cracks, consequently resulting in a notable ductility before the final failure. The failure load of 5260 N of this test specimen is 78% higher than that of the reference specimen.



(all dimensions in millimetres)

Figure 5a: Dimensions of the test specimen

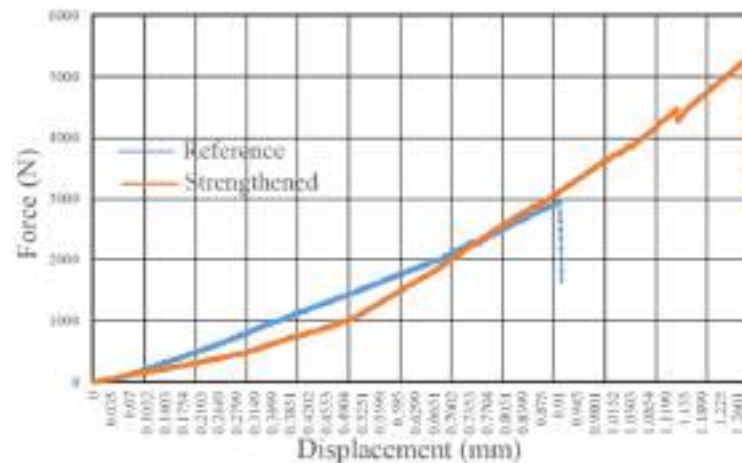


Figure 5b: Applied load–displacement relationship of the reinforced and the reference tensile test specimens

GFRP REINFORCED BOLTED JOINTS IN ANNEALED GLASS

The potential of adhesively bonded GFRP for enhancing strength and ductility of stress concentration features in annealed glass was extended in order to experimentally investigate the efficacy of strengthening bolted joints.

Test Specimens

100 mm x 250 mm pieces of 6 mm thick annealed glass was used in the experimental investigation (Figure 6). Two 11 mm diameter holes were drilled at each end of the test specimen. Cutting the glass specimens in to the required size and drilling of the holes were done by a commercial supplier. All edges, including inside of the bolt holes were polished. At each end of the glass piece, a 100 mm x 60 mm GFRP strip, made from the same GFRP laminate used in the earlier works of the present study was bonded to two glass pieces using “Araldite2020”. 11 mm diameter holes were also drilled on the GFRP and ensured that the holes in the GFRP and the glass were perfectly aligned. The specimens were cured in the same way as the reinforced glass beams described in the first half of this paper. After curing, the GFRP reinforced glass test specimen was connected to aluminium plates using M10 bolts (Figure 6). EPDM rubber was used to avoid direct contact between the glass and the bolts. The aluminium sheets were then connected to a thicker aluminium sheet, which was then used as the fixing grip to the test machine (Figure 6). The test specimens were tested in tension under a displacement rate representative of a static load scenario. The load response and the failure behaviour of the reinforced bolted joints were compared with that of an equivalent glass assembly, but without GFRP reinforcement.

Results

Figure 7 shows the typical failure observed in the GFRP strengthened and reference (i.e. unreinforced) test specimens. As expected, in all test specimens the failure occurred in glass in the vicinity of the bolted joint. The applied load–axial displacement (measured at the mid-length region of the test specimen) relationships of one reinforced and one reference test specimen are shown in Figure 8. As can be noted from the figure, both specimens showed a largely linear response. In the reference test specimen, one glass sheet was failed first causing a little drop in the load resistance. Although the other glass sheet then started to carry the load, it also failed soon after the failure of the first one. The specimen was failed in a brittle manner where glass failed completely throughout the cross section of the joint (Figure 7a) at applied load 3800 N. The strengthened joint did not fail instantaneously, and as can be seen in Figure 7b, also no complete failure occurred across the joint. The GFRP held the broken glass pieces together and also contributed to carry the after the glass started to crack. The peak load of the strengthened joint was 9360 N, ~150% higher compared to the reference specimen. The figure also shows the strengthened joint resisted some load beyond the peak load. The results suggest the GFRP interlayer prevented complete failure of the glass in the vicinity of the bolts and also contributed to carrying the load in the post-cracked regime.



Figure 6: Test arrangement of bolted joints in glass



Figure 7: Failure of the: (a) unreinforced;
reinforced joints

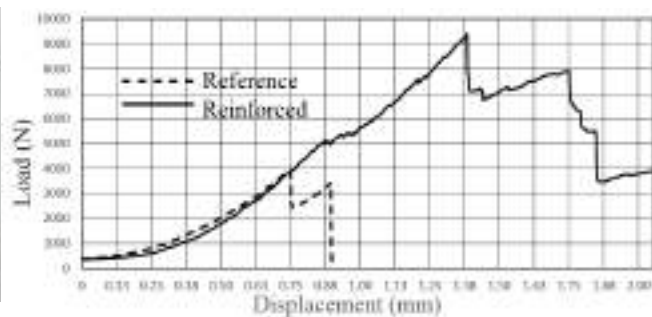


Figure 8: Load–midspan displacement of the reinforced and unreinforced bolted joints

CONCLUSIONS

The experimental results presented in this papers show that:



- the use of an adhesively-bonded GFRP interlayer can improve the ductility of annealed glass beams;
- the mechanical prestressing using a pretensioned GFRP reinforcement has potential to improve the apparent tensile strength of annealed glass beams;
- externally-bonded GFRP laminates has potential to strengthen stress concentration features in annealed glass;
- the use of an adhesively bonded GFRP laminate improved the strength and ductility of bolted joints in annealed glass.

ACKNOWLEDGEMENTS

Funding received from IStructE Research Award (2012) and IStructE MSc Grants 2015/16 and 2016/17 are greatly acknowledged.

REFERENCES

- M. Achintha, B. Balan (2017). "Characterisation of the mechanical behaviour of annealed glass-GFRP hybrid beams", *Construction and Building Materials*, 147, 174-184.
- M. Achintha, B. Balan (2015). An experimentally validated contour method/ eigenstrains hybrid model to incorporate residual stresses in glass structural designs", *The Journal of Strain Analysis for Engineering Design*, 50, 614-627.
- Araldite2020 Product Sheet (2015). Huntsman Advanced Materials, Basel, Switzerland, 2015.
- B. Balan, M. Achintha (2015). "Assessment of stresses in float and tempered glass using eigenstrains", *Experimental Mechanics*, 55, 1301-1315.
- M. Bessonov (2016). Strengthening joints in glass with bonded GFRP strips, MSc thesis, University of Southampton, Southampton, UK.
- L. Blyberg, M. Lang, K. Lundstedt, M. Schander, E. Serrano, M. Silfverhiek, C. Stalhandske (2014). "Glass, timber and adhesive joints – innovative load bearing building component", *Construction and Building Materials*, 55, 470-478.
- F.P. Bos (2009). Safety Concepts in Structural Glass Engineering. PhD thesis, TU Delft, The Netherlands.
- J.R. Correia, L. Valarinho, A. Branco (2011). "Post-cracking strength and ductility of glass-GFRP composites beams", *Composites Structures*, 93, 2299-2309.
- IStructE (2014). Structural use of glass in buildings. 2nd ed., The Institution of Structural Engineers, London, UK, 2014.
- C. Louter, J. Belis, F. Veer, J.P. Lebet (2012). "Structural response of SG-laminated reinforced glass beams; experimental investigations on the effect of glass type, reinforcement percentage and beam size", *Engineering Structures*, 36, 292-301.
- C. Louter (2010). "Structural Glass Beams with Embedded Glass Fibre Reinforcement", *Challenging Glass 2 – Conference on Architectural and Structural Applications of Glass*, Netherlands.
- K. Martens, R. Caspeele, J. Bellis (2015). "Development of composite glass beams – a review", *Engineering Structures*, 101, 1-15.
- J.H. Nielsen, J.F. Olesen, P.N. Poulsen, and H. Stang (2010). "Simulation of residual stresses at holes in tempered glass: a parametric study", *Materials and Structures*, 2010, 43(7), 947-961.
- SCALP Instruction Manual, ver. 5.0 (2015), GlassStress Ltd., Tallinn, Estonia.
- E. Speranzini, S. Agnetti (2014). "Strengthening of glass beams with steel reinforced polymer", *Composites Part B: Engineering*, 67, 280-289.



INFLUENCE OF CURING CONDITIONS ON THE MECHANICAL BEHAVIOR OF GLUED JOINTS OF CARBON FIBER REINFORCED POLYMER COMPOSITE/CONCRETE

A. T. Lee¹, M. Michel¹, E. Ferrier¹

¹ LMC², University Lyon1, France, Email: marie.michel@univ-lyon1.fr

ABSTRACT

Polymeric adhesives are widely used in the case of the bonding of CFRPs on concrete structure. Indeed, structural reinforcement by FRP is a very efficient method thanks to the high mechanical characteristics of the FRP and to the implementation methods which make it possible to reduce work times and are applied with various temperature conditions on site. Working on site assumes that the conditions for implementation are highly dependent on climatic conditions. In fact, the resins used are cold-curing epoxy and so their mechanical and physical properties are temperature and humidity dependent. This paper presents an experimental study to highlight the impact of the application temperature on the behavior of composite reinforcement. The objective is to analyze the mechanical and physical behavior of epoxy polymers used for reinforcement by measuring on one hand the mechanical properties of composite adhesion on concrete support by means of a double-shear and pull-out test and on the other hand, glass transition temperatures T_g . The T_g measurements are carried out by DSC and TMA. Double shear tests results consist on establishing the local composite to concrete shear laws of adhesive joints according to the nature of the polymers and the curing conditions. The tests make it possible to determine the bonding lengths (L_e) and to evaluate the influence of the curing conditions on the value of this length. The physical measurements of T_g support the study by specifying the influence of the curing conditions on these properties.

KEYWORDS

All FRP and smart FRP structures; Experimental study; Characterization of FRP and FRC materials/systems; Bond and interfacial stresses; Glass transition; curing

INTRODUCTION

The external bonded reinforced composites materials are widely used nowadays in civil engineering for structural reinforcement and building repairs. Indeed, composites present generally more elevated mechanical properties than steel, their light weight, their durability, their non-corrosive characteristic and easy transportation to building site are also taken into account. Carbon fibers are commercially applied in building reinforcement thanks to their high stiffness (Young's modulus varies from 200 GPa to 750 GPa) and their elevated strength (failure stress varies from 1,5 GPa to 6 GPa). Several kinds of fibers have also been used for many properties' requirements such as glass fibers (failure deformation up to 5%) or natural-based fibers (low environmental impact for sustainable development).

The composites' mechanical properties depend not only on fibers' characteristics but also on matrix ones. For thermoset resins like epoxy, their physical and mechanical properties change according to curing conditions. Benedetti & al., 2015 investigated the evolution of E-modulus and pull-out force of epoxy resin for NSM-CFRP systems at different curing temperature (20°C, 30°C, 40°C). In order to accelerate curing process, the composites can be exposed to elevated temperature in an autoclave. Michels & al., 2015 compared the glass transition temperature (T_g), measured by the DMA, of resin specimens depending on curing conditions. The authors divided two kinds of specimens: the ones that are cured at room temperature and the others that are cured at elevated temperature process. The T_g increases consistently with curing temperature due to the cross-linkage, the T_g depends on following external factors: product type, maximum curing temperature, specimen age, heating rate, etc. If many studies deal with the influence of high curing temperature on evolution of T_g , only a few researches, (Savvilotidou & al, 2017), (Moussa & al, 2012), have studied the influence of low temperatures on T_g and consequently on mechanical properties of epoxy. These studies only deal with the properties of the matrix and not the composite FRP as a reinforcement of concrete structure.

In this study, four commercial adhesives are retained, samples were cured isothermally at different temperatures (5°C, 10°C, 20°C, 40°C) for different time periods (7 and 14 days) to reproduce very variable environmental conditions such as a onsite applications in different season time. The objective of this investigation is to study not only the influence of curing conditions to the mechanical and physical properties of the epoxy resin but also the mechanical behaviour of the joint adhesive bonded CFRP-concrete.

METHOD OF SOLUTION

Four structural cold-curing epoxy adhesives from four manufacturers were investigated. The properties of each adhesive are given in Table 1 according to manufacturer. The epoxy system is mixed at room temperature respecting ratio by weight of the respective constituents (resin and hardener). All these adhesives are used to impregnate the FRP fabrics used to strengthen existing concrete or steel structures. Sanding the concrete surface is done before FRP bonding.

Table 1: Adhesive used in the study*

Adhesive	manufacturer	type	density (kg/m ³)	mixing ratio	DPU (min)	Tg (°C)
Resin 1	A	epoxy	-	2.5:1	100-130	80-86
Resin 2	B	epoxy	1300	04:01	90 (10°C) ; 30 (35°C)	>40
Resin 3	C	epoxy	1150	2.33:1	45	53.5
Resin 4	D	epoxy	-	2.33:1	80	64

* according to manufacturer

Specimens of each resin are preserved in four storage chambers, each storage chamber has one of the following curing temperatures: 5°C, 10°C, 20°C and 40°C, for 14 days of curing time. After 14 days, all remaining specimens are preserved at room temperature (Figure 1). So as to evaluate the physical properties (Tg) and the mechanical properties (stiffness, strength, normal adhesive ability, shear adhesive ability and mechanical behavior of the bonded joint in shear) test were carried out after 7, 14, 21, 28, and 42 days.

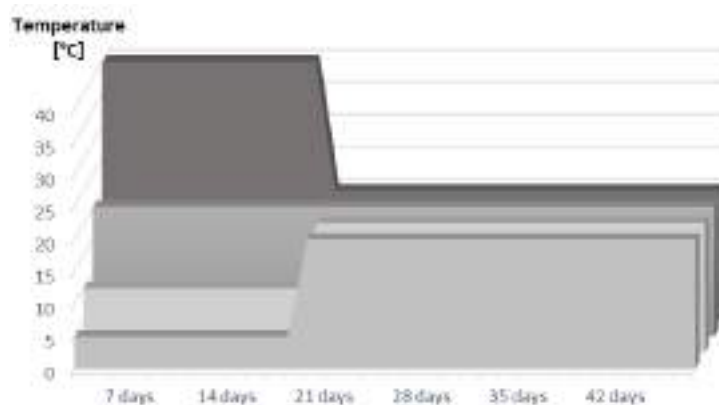


Figure 1: Curing temperatures for the experimental campaign

Glass transition temperatures Tg

The determination of the glass transition temperature Tg is an usual method to describe curing propagation and link it to mechanical properties: as curing advances, the molecular network mobility decreases and the Tg increases (Moussa & al, 2012-2). By definition, glass transition temperature Tg is defined as the point approximately at the middle of the temperature range in which the glass transition occurs.

Glass transition is usually investigated by Differential Scanning Calorimetry (DSC). In this paper, another thermal analysis technique is used: thermomechanical analysis (TMA). Both DSC and TMA, since there are two different testing methods, provide slightly different results for identical curing conditions.

- A Mettler Toledo TMA/SDTA 1 IC/600 instrument was used for the thermomechanical analysis equipped with a quartz glass probe with a ball point of 3mm. Samples of size $5 \times 5 \times 2 \text{ mm}^3$ were subjected to a constant force of 0.02N, under nitrogen purge, with a flow rate of 20 mL/min, while the temperature increased from 5°C to 150°C with a heating rate of $10^\circ\text{C}/\text{min}$.

The glass transition temperature obtained by thermodilatometry (TMA) $T_{g\text{TMA}}$ is defined as the intersection of the tangents to the length / temperature curve before and after the glass transition phase according to the standards ASTM E 1545-00 and ISO 11359-2 (Figure 2 a)).

- The experiments were performed with a Mettler Toledo TGA-DSC3+ differential scanning calorimeter. Epoxy samples of between 10 to 15 mg were placed in an aluminium pan covered with a lid. An empty aluminium pan was used as a reference during every scan. Each DSC experiment was done under nitrogen purge, with a flow rate of 20 mL/min, while the temperature increased from 5°C to 150°C with a heating rate of $10^\circ\text{C}/\text{min}$. Data acquisition was performed using the accompanying software (STARe). Tg is observed as an endothermic stepwise change in the DSC heat flow. Three values, shown in figure 2 b) and according to the standards ASTM E 1356 and NF EN 12614, were considered for the glass transition temperature: $T_{g\text{ONSET}}$ is defined as the temperature corresponding to the intersection of tangents from the baseline and initial slope of the step, $T_{g\text{MIDPOINT}}$ the middle of the step measured as half the step height, $T_{g\text{INFLECTIONPOINT}}$ the inflection point of the step.

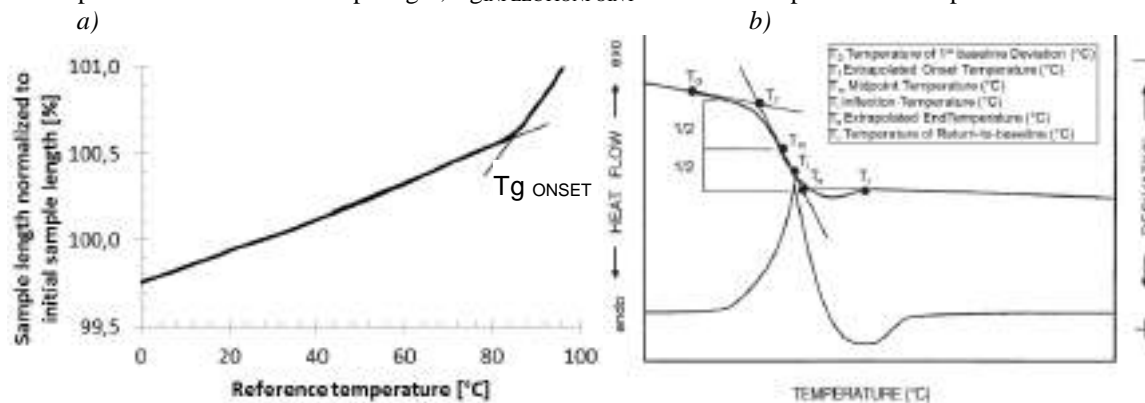


Figure 2: Illustration of TMA and DSC responses
a) Evolution of the length with increasing temperature by TMA;
b) Evolution of heat flow with increasing temperature by DSC (ASTM E 1356)

Mechanical properties

- With tensile test made on a dog-bone shape sample according to the standard NF EN ISO 527-1 (Figure 3), two mechanical properties of epoxy are investigated: the Young modulus and the tensile strength. The tensile load, increase at a speed of 1mm/min, the loading is control in displacement. The strain at the middle of the specimen is measured by a strain gage, which has a resistance of 120 Ohms. The Young modulus is determined by the slope of the stress-strain curve and the strength calculate with the ultimate load and measured width (15 mm) and thickness of specimens. 5 specimens are tested for each set of specimens.

- The adhesive strength is measured by a pull-out test done on cylinder specimen with a diameter of 50 mm according to French standard P18-852. Once the FRP cured, a core drill is used to core the concrete as shown on the figure 6. Then, aluminum disc is stuck to the FRP and after 24h, dynamometer is used applying direct tension to the aluminium disc at the rate of 0.06 MPa/s. The value and kind of failure are the main obtained parameter. 5 specimens are tested for each set of specimen. All four polymer was used with the same carbon fibers sheets. The carbon is a UD textile with a weight by square meter of $300 \text{ g}/\text{m}^2$.

- Double shear test allows studying the mechanical behaviour of the joint CFRP - concrete and the adhesion ability of the resin according to the curing conditions. The tests are performed on a universal tensile machine Zwick 1475 at a cross-head speed of 1 mm/min until failure. The dimensions of a test specimen are presented in the Figure 3.

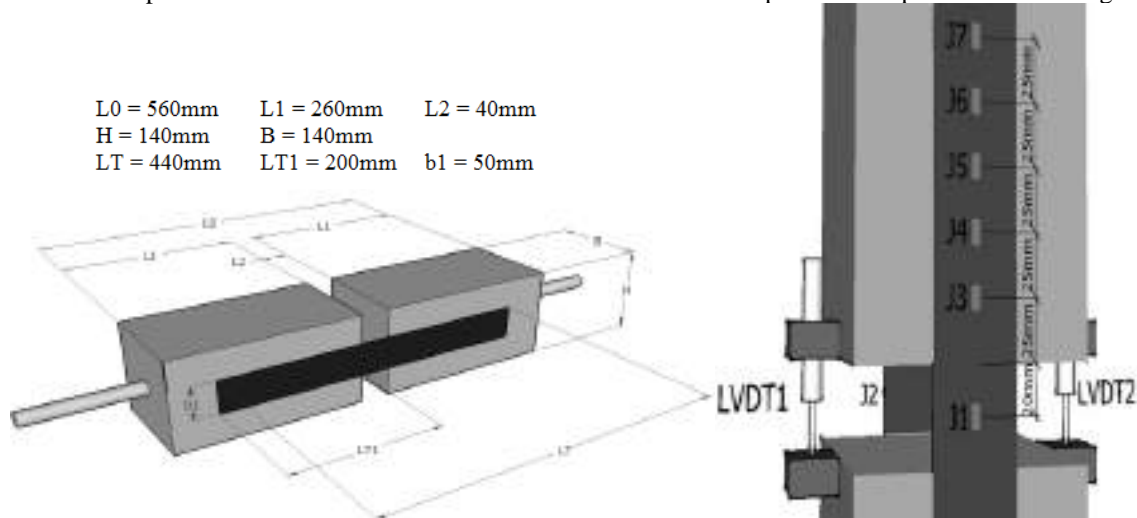


Figure 3: Shear test specimen and its dimensions

The relative distance between the 2 concrete blocks is recorded by the LVDT. During the test, 2 LVDT are set up at two opposite sides. The average value given by LVDT gives the relative distance between the two concrete blocks (ΔL_1).

The strain gages (J1 to J7) are bonded along composite strip in order to get the strain of the studied points of the joint. The gages layout is presented in figure 4. The gages used in this test have a length of 10mm and the maximum captured strain worth 1.5%. Two gages called J1 and J2 bonded to 2 opposite sides in the middle of the composite strip allow to calculate the lengthening of the composite during the loading state. ε_1 and ε_2 are respectively the strain recorded by the first gage and the second gage, the lengthening of composite (ΔL_2) during the loading is written :

$$\frac{\Delta L_2}{L_0} = \varepsilon \Rightarrow \Delta L_2 = \frac{\varepsilon_1 + \varepsilon_2}{2} \times L_0$$

with: L_0 the initial length (initial distance between the 2 concrete blocks)

The total spacing of the concrete blocks (ΔL_1) is due to the lengthening of composite (ΔL_2) during the loading state and the slip of the resin (ΔL). The slip of the joint can be determined by the data given by the LVDT and strain gages: $\Delta L = \Delta L_1 - \Delta L_2$.

The other gages are distributed along composite strip (from J3 to J7). The distance between 2 consecutive gages is 25 mm. The determination of the strain throughout the joint enables to determine the effective bond length (the length of transfer of load). The effective zone of anchoring is the zone in which almost all of local shear stress of the adhesive bonded joint is distributed.

RESULTS AND DISCUSSIONS

Glass transition temperatures T_g

T_g is determined by two different devices. The first one determines T_g by observing the profile of the heat flow during the change of state, the other identifies T_g by benefitting the CTE at the time of transition. The objective of this part is to find the correlation between several notions of T_g , determined by the DSC and T_g measured by the TMA.

In an experimental way, T_g measured by the TMA having the nearest value with T_g inflection point measured by the DSC. For example, for resin 4, heatflow and T_g at 28 days of cure at various curing temperatures are respectively presented in the Figure 4 and in the Figure 5. Theoretically, T_g inflection point, measured by DSC test, means the temperature of transition where the speed of variation of calorific flow according to the temperature is maximum. In this case, since the first heating run is represented in the Figure 4,

Furthermore, T_g measured by the TMA is the temperature where the increasing rate of CTE is in transition. At the time of the transition, the polymer strongly absorbs energy for the endothermic process, that involves a considerable change of the mechanical properties, of which the thermal dilation coefficient.

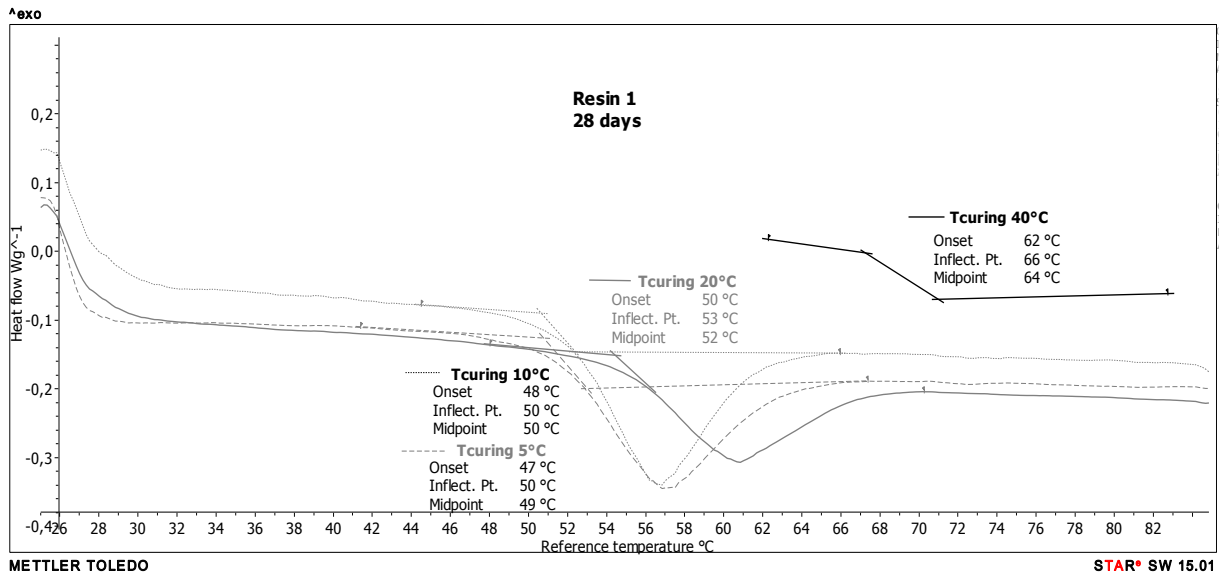


Figure 4: Heatflow as fonction of reference temperature at 28 days with different curing temperature for the resin 1

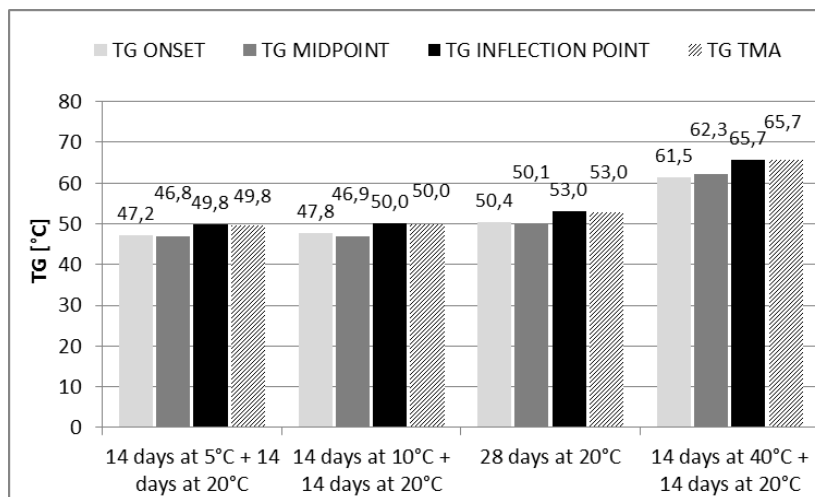


Figure 5: Glass transition temperature T_g evaluated with DSC and TMA for the resin 1

In Figure 6, the T_g Inflection Point is used to draw the evolution curve of the glass transition temperature T_g for the 4 resins with the time and according to curing conditions. For all the studied resins, no results have been obtained at 5°C and 7 days of curing because the samples do not receive sufficiently energy to activate the chemical reaction for cross-linking. After 14 days of cure at 5°C and 10°C, some resins (resin1 and resin2) are not cured yet ($T_g < 30^\circ\text{C}$) while the two other resins (resin3 and resin4) are cured ($T_g > 30^\circ\text{C}$). That involves a conclusion that the minimum curing time at low temperature ($T_{\text{cure}} \leq 10^\circ\text{C}$) of various resins is different. For the category “low curing temperature” (when T_{cure} does not exceed 10°C), there is an increase of T_g in time: the minimum required curing time at 5°C and 10°C is higher than 2 weeks (Figure 5). For the categories “medium and high curing temperatures” (respectively T_{cure} at 20°C and 40°C), there is the stabilization of T_g over time from the seventh day. This phenomenon can be explained by the cross-linking of the epoxy resin in ambient temperature. The higher the ambient temperature is, the more the chemical reaction between the epoxide group and the amine group in the

resin occurs. That involves an evolution of T_g according to the curing temperature: B. Ellis (1993) explains the reaction rate decelerates and becomes diffusion-controlled when curing temperature is lower than T_g . Furthermore F. Lapique (2002) suggests that with curing temperature lower than T_g , the adhesive is not fully cured and the evolution of T_g reaches a plateau-like regime as early as 7 days.

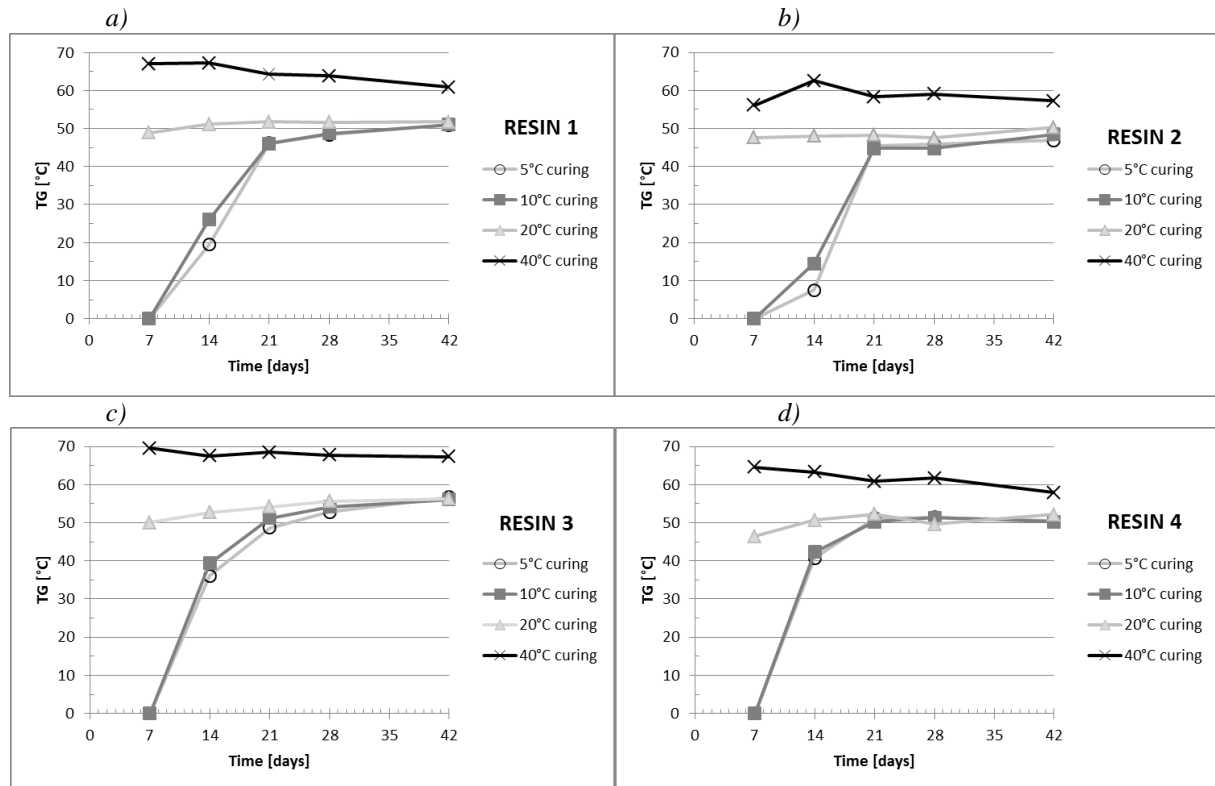


Figure 5: Evolution of the glass transition temperature T_g with the time and according to curing conditions
a) resin 1; b) resin 2; c) resin 3; d) resin 4

Mechanical properties

Results from tensile tests, presented in the Table 2, concern the evolution of the Young's Modulus and the strength through time and different curing conditions. Three samples are tested for each curing condition and time. After 14 days at 5°C and 10°C, no resin is strong enough to be demoulded and tested. After 21 days, only resins 2, 3 and 4 can be tested. This faster kinetics of rise in strength of resins 2, 3 and 4 is in agreement with the evolution of T_g presented in Figure 5c and 5d. Whatever the resin considered, after 28 days, strength increase with curing temperature. The development of the epoxy E-moduli obtained through tensile tests is also presented in Table 2. As regard at the Young's Modulus, no obvious conclusion can be drawn. Indeed, as shown by (M. Savvilotidou & al (2017)), E-modulus essentially increases in the first 20 days and ((Benedetti & al., 2015)) highlighted only a slight increase of the elastic modulus with the curing temperature (20°C, 30°C, 40°C) at 144h.

Table 2: Young's Modulus and strength evolution through curing conditions and time

Curing temperature [°C]	Age [days]	resin 1		resin 2		resin 3		resin 4	
		strength [MPa]	Modulus [MPa]						
5°C	21	-	-	47.2	2691	20.4	3133	23.8	2975
5°C	28	13.3	3288	41.7	2807	27.1	3479	19.4	3062
10°C	21	-	-	53.3	2492	25.7	3443	22.7	2520
10°C	28	23.2	2436	52	2656	34.0	3411	21.4	3143

20°C	14	16.6	3047	52.6	2695	36.2	3317	24.4	3227
20°C	28	31.9	2977	53.7	2752	44.2	3405	25.7	3301
40°C	14	31.5	2811	60.0	2734	41.7	3351	20.9	2849
40°C	28	44.3	2888	57.3	2906	55.9	2646	29	3055

For the adhesion of CFRP and concrete, the results obtained with the pull-out test in all the curing conditions give an identical failure mode: failure in the concrete support (Figure 6). It is possible to outline that for the studied curing conditions (temperature varying between 10°C and 40°C for 14 days and 28 days), the adherence ability of the resin is guaranteed, and with a cohesive failure mode at the composite to concrete interface.

Furthermore, the tensile strength of the concrete, obtained by a splitting (Brazilian) test, is: $f_{ctm}=2.62$ MPa, this result is closed to those measured by the adhesive test, which varies between 2.47 MPa and 2.80 MPa on average.

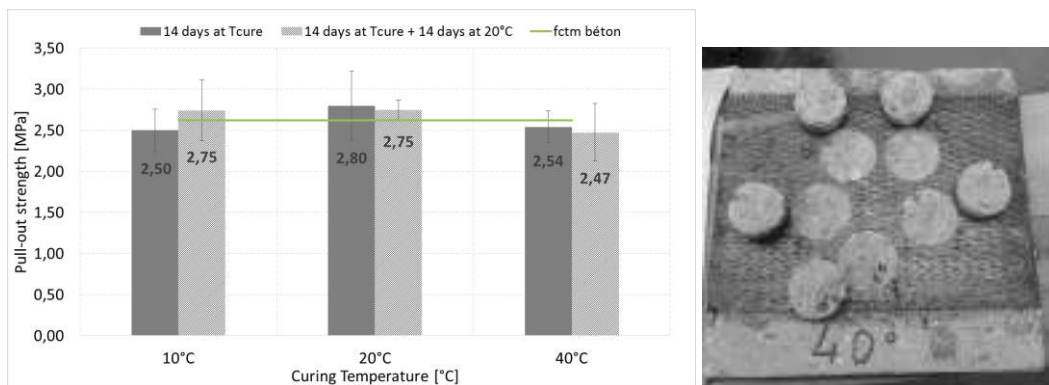


Figure 6: Pull out strength at different curing temperatures and failure mode

Figure 7 presents some of the results obtained with the double shear test: for a load level of 20kN the evolution of local strain along the bonded joint. After 14 days of curing, it is obvious that the curing temperature influences the mechanical behaviour of the joint. First of all, the local strain which represents the stiffness of the joint is higher when the curing temperature is high, as shown by (Caggiano & Schicchi, 2015). It is obvious to conclude that the joint is less stiff if it is exposed to high curing temperature (40°C). So the effective bond length L_e increases with the curing temperature as Figure 7a shows: L_e is around 75mm at 10°C and 20°C, but the value reaches 125mm at 40°C. It is important to note that even if local strain is dependent of the curing temperature at 14 days, failure occurs in the concrete layer in all conditions. After 28 days, whatever curing temperature, the strain distribution along the bonding length is similar. We can conclude that the bond length L_e , around 75mm, is lower overall at 28 days in comparison with the value obtained at 14 days (Figure 7b).

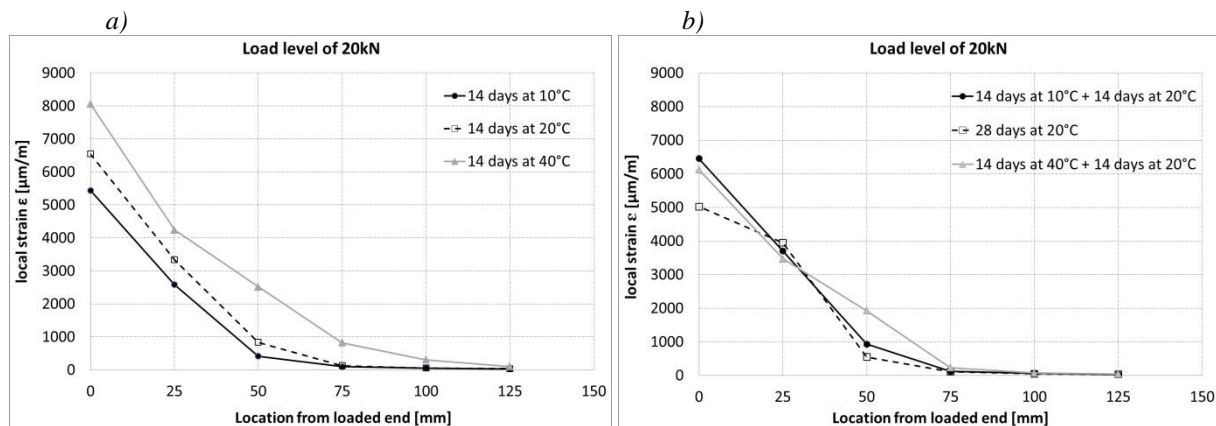


Figure 7: Evolution of local strain in function of the location from the loaded end for a load level of 20kN
a) at 14 days; b) at 28 days



CONCLUSIONS

Based on the results presented in this paper, the following conclusions can be drawn with regard to the resins cured at low temperatures:

- The glass transition temperature T_g measured by the TMA having the nearest value with T_g inflection point measured by the DSC.
- at low temperature ($T_{cure} \leq 10^\circ\text{C}$), kinetics of evolution of the T_g is different according to the resins up to 14 days.
- Evolution of the T_g according time and curing temperature is in agreement with the evolution of tensile strength. Indeed, the molecular network mobility, which is dependent on curing time and curing temperature, guides the evolution of T_g and so on the evolution of mechanical properties. More precisely, a greater degree of cross-linking, obtained at high curing temperature (40°C), provides a more complete reaction ($T_{g_t_{cure}=40^\circ\text{C}} > t_{g_t_{cure}=20^\circ\text{C}}$) and consequently an improvement of mechanical properties (tensile strength).
- A major application of the cold-curing resin studied in this paper is to bond CFRP strips and sheets to a concrete or metallic substrate. With the basic test of pull-out, whatever the resin used, failure occurs on concrete. That shows that the CFRP-concrete interface is not the weak link. The bonding ability, highlighted by the bond length L_e obtained with the double shear test, increases with the curing temperature up to 14 days. However, after 28 days, the bond length L_e is similar and equal to 75mm whatever the curing temperature.

REFERENCES

- A. Benedetti, P. Fernandes, J.L. Granja & al. (2016) "Influence of temperature on the curing of an epoxy adhesive and its influence on bond behaviour of NSM-CFRP systems". *Compos. Part B Eng*, 89, 219–229.
- A. Caggiano, D. S. Schicchi (2015) "A thermos-mechanical interface model for stimulating the bond behavior of FRP strips glued to concrete substrates exposed to elevated temperature". *Engineering Structures*, 83, 243-251
- B. Ellis (1993) "Chemistry and technology of epoxy resins". Chapman & Hall
- F. Lapique, K. Redford (2002). "Curing effect on viscosity and mechanical properties of a commercial epoxy resin adhesive". *Int. Journal of Adhesion & Adhesives*, 22, 337-346
- J. Michels, R. Widmann, C. Czaderski & al. (2015). "Glass transition evaluation of commercially available epoxy resins used for civil engineering applications". *Compos. Part B*, 77, 484–493.
- O. Moussa, A. Vassilopoulos, T. Keller (2012). "Effects of low-temperature curing on physical behaviour of cold-curing epoxy adhesive in bridge construction". *Int. Journal of Adh. & Adhesives* (32), 15-22
- O. Moussa, A. Vassilopoulos, T. Keller (2012(2)). "Experimental DSC-based method to determine glass transition temperature during curing of structural adhesives". *Construction and building materials*, 28, 263-268
- M. Savvilitidou, A.P. Vassilopoulos, M. Frigione, T. Keller (2017). "Effects of aging in dry environment on physical and mechanical properties of a cold-curing structural epoxy adhesive for bridge". *Construction and building Materials* (140), 552-561



BEHAVIOR OF CFRP STRANDS EXPOSED TO SEVERE ENVIRONMENTAL CONDITIONS

Omar Khalafalla¹, Sami Rizkalla¹, Adel ElSafty², Mohammad Pour-Ghaz¹

¹ North Carolina State University, Department of Civil, Construction and Environmental Engineering, USA.

² University of North Florida, College of Computing, Engineering and Construction, USA.

ABSTRACT

Fiber reinforced polymer materials are becoming widely used as a primary reinforcement for concrete structures due to their high strength and non-corroding characteristic, therefore, providing an alternative to steel reinforcement. Degradation of FRP mechanical properties may occur due to environmental factors such as moisture and alkalinity or physical effects such as sustained loading and fatigue. The synergistic effects of environmental and mechanical loading has not been thoroughly studied which lead to a conservative design process. Understanding the synergistic effects on the degradation of FRP leads to a more economic design and a better prediction of the long-term performance of concrete structures.

This paper describes a comprehensive research undertaken to study the durability of CFRP prestressing strands used for concrete bridge girders. The main objective of this research is to understand the effect of severe environmental exposure and sustained loads on the mechanical properties of CFRP prestressing strands. The first part of this research focuses on quantifying the possible degradation of CFRP strands under simultaneous sustained loading and exposure to high alkali solution at elevated temperature. The second part, examines the structural performance of CFRP strands used as pretensioning strands in reinforced concrete beams. The third part, focuses on understanding the durability of constituent materials of CFRP strands.

KEYWORDS

Carbon Fiber Reinforced Polymer, Composites, Durability, Prestressed Concrete, Sustained load effects.

1. INTRODUCTION

Fiber Reinforced Polymer (FRP) materials are currently used in many civil infrastructure, especially in certain corrosive environments where steel members rapidly degrade. While it is understood that the degradation of FRP mechanical properties may occur due to the exposure of FRP composites to environmental factors such as moisture, alkalinity, fire and/or physical effects such as sustained loading and fatigue (Buck et al. 1998, Chen et al. 2007, Karbhari 2007, Pour-Ghaz et al. 2016), the synergistic effect of environmental conditioning and sustained loading has not been thoroughly studied. This lack of research on synergistic effects has led to a very conservative design process. Therefore, studying the simultaneous effect of environmental conditioning and sustained loading on the durability of FRP can potentially lead to more economic design, a more accurate prediction of the long-term performance, enhanced safety, and sustainability of structures.

The research presented in this paper focuses on studying the possible degradation of Carbon FRP (CFRP) prestressing strands due to exposure to environmental conditions and sustained loading. The type of CFRP strands used in this research was Carbon Fiber Composite Cable (CFCC), which is comprised of PAN (polyacrylonitrile) based continuous carbon fibers, epoxy resins acting as adhesive material and a protective wrapping material which include polyester fibers. The general properties of CFCC resemble those of CFRP but CFCC has the same 7-wire configuration similar to the standard steel prestressing strands. Figure 1 shows a cross-sectional view of CFCC and steel prestressing strands. CFCC has many advantages in comparison to conventional steel such as high tensile strength, high tensile elastic modulus, high acid and alkali resistance, lightweight, superior tensile fatigue performance, and flexibility (Enomoto and Ushijima 2012).

CFRP as prestressing strands in concrete girders has been used in several highway bridges (Rizkalla and Tadros 1994, Grace et al. 2002). However, a few research works have studied the long-term behavior of CFRP prestressing strands. Abdelrahman et al. (1996) examined the fatigue behavior of concrete beams pretensioned with CFRP tendons under static and cyclic loading and concluded that the concrete beams failed at a much higher load than expected due to the conservative underestimation of ultimate strength of the CFRP tendons. In addition, the capacity of concrete beams tested after being subjected to 2 million cycles of fatigue loading was very close

to those tested under static loading. Mertol et al. (2007) conducted a study to investigate the durability and fatigue behavior of high strength concrete beams prestressed with CFRP bars. The study concluded that the beams prestressed with CFRP bars exhibited higher strength than beams prestressed with steel wires and the cyclic loading had no major effect on either of the beam types. Recently, a study was conducted by Benmokrane et al. (2015) on the long term durability of CFCC. The study concluded that the average tensile strength and average elastic modulus were reduced by a small percentage.



Figure 1: Cross-section of CFCC strand (left) and prestressing steel strand (right)

2. SCOPE OF THE RESEARCH

The main objective of this research program was to study the combined effects of sustained loading and severe environmental exposure on the durability of CFCC. The study included a comprehensive experimental program consisting of three tasks to study the overall material behavior in concrete and the behavior of the constituent materials independently. The first task of the experimental program focused on examining any possible degradation in the mechanical properties of CFCC under simultaneous sustained loading and exposure to alkaline solution at an elevated temperature. The second task examined the durability of CFCC used as pretensioning strands in reinforced concrete beams. The third task of the experimental program aimed at studying and testing the constituent materials of CFCC.

2.1. Degradation of CFCC strands

To determine the possible degradation of the CFCC mechanical properties as a result of exposure to simultaneous sustained loading and high alkali environment, the mechanical properties of CFCC was evaluated after exposure for 3,000 and 7,000 hours at an elevated temperature. The high alkali environment simulated the concrete pore solution and the elevated temperature was used to accelerate the aging process. The CFCC strands were tensioned inside a steel truss to a load equivalent to 65% of their guaranteed ultimate strength. A total of four steel trusses were fabricated, each truss held 4 CFCC strands of length 6.1 m (20 ft.). The tensioned CFCC strands were placed in a PVC tube filled with alkaline solution. In addition, two steel trusses were thermally isolated using insulating foam and four heating mats were placed along the length of the trusses to increase the temperature to 55 °C (130 °F). Figure 2 shows a photograph of a steel truss with four CFCC strands tensioned, two of which are placed in PVC tubes and filled with alkaline solution. Upon completion of the exposure duration, the sustained load was released and each CFCC strands was cut into 1.3-m (4.25-ft) long specimens and anchored from both ends using steel tubes and epoxy to test their residual tensile capacity. The test setup was designed so that all the replicates for a given condition were prepared from the same CFCC strand, ensuring that they are subjected to the same environmental and mechanical loading.



Figure 2: Steel truss with 4 tensioned CFCC strands

CFCC specimens were tested in tension (Figure 3), upon completion of the exposure to evaluate any possible degradation in their mechanical properties. Table 1 presents the effect of each parameter on the tensile strength of CFCC after 3,000 and 7,000 hours of conditioning including the coefficient of variations. Results indicate that the maximum reduction in the tensile strength of the strands after 7,000 hours of conditioning was 5%. This reduction is within the coefficient of variation range, and therefore, the research clearly indicates that the severe environmental conditioning has no effect on the tensile strength of the CFCC Strands.

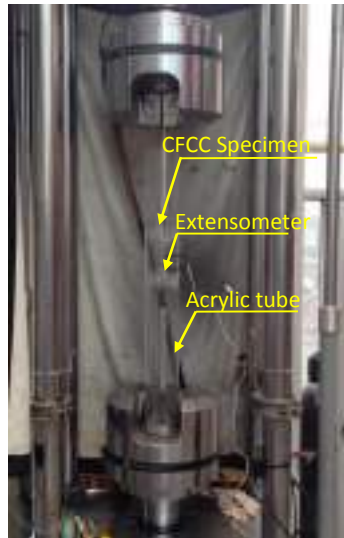


Figure 3: Tensile testing of CFCC specimen.

Table1: Effect of exposure parameters on the tensile strength of CFCC after 3,000 and 7,000 hours.

Parameter	3,000 hours results		7,000 hours results	
	Change in Avg. Tensile Strength	Coefficient of Variation	Change in Avg. Tensile Strength	Coefficient of Variation
Control specimens	N/A	1.8%	N/A	1.8%
Sustained Load	No effect	1.9%	-1.1%	2.3%
Alkaline Solution	- 1.5%	2.3%	-4.9%	2.0%
High Temperature	+ 0.2%	1.7%	-1.5%	2.7%
Sustained Load and Alkaline Sol.	- 2.7%	1.5%	-1.9%	1.4%
Sustained Load and High Temp.	+1.1%	3.2%	+0.9%	0.7%
High Temp. and Alkaline Sol.	-3.6%	2.3%	-2.4%	2.0%
Load, Alkaline Sol. & High Temp.	-3.0%	3.4%	-0.9%	3.5%

2.2. Durability of Concrete beams prestressed with CFCC strands

A total of 12 prestressed concrete beams were tested during this research. Eight beams were placed in two tanks and subjected to wet and dry cycles of saltwater, which simulated the aggressive exposure to seawater and also mimicked the environmental condition of Florida State. The accelerated aging process was facilitated by applying a sustained load to induce cracking in the beams. The sustained load was equivalent to 50 percent of the flexural capacity of the beam. Two control beams were tested at the beginning of the experimental program to determine the flexural capacity of the beams. In addition, two beams were subjected to sustained load only and tested at the end of the exposure duration, in order to exclude the aging effect of concrete from the effect of exposure to saltwater cycles.

In order to evaluate any degradation in the CFCC, the concrete beams were designed to fail by rupture of strands before crushing of concrete. The guaranteed mechanical properties of CFCC, provided by Tokyo Rope Company, were used in the design process. It should be noted that the ultimate strength is significantly higher than the guaranteed strength reported by the manufacturer. All twelve beams had the same geometrical

configuration and cross-sectional dimensions as shown in Figure 4. Each concrete beam was prestressed with two 15.2 mm (0.6 inch) diameter CFCC strands to 65% of their guaranteed tensile strength.

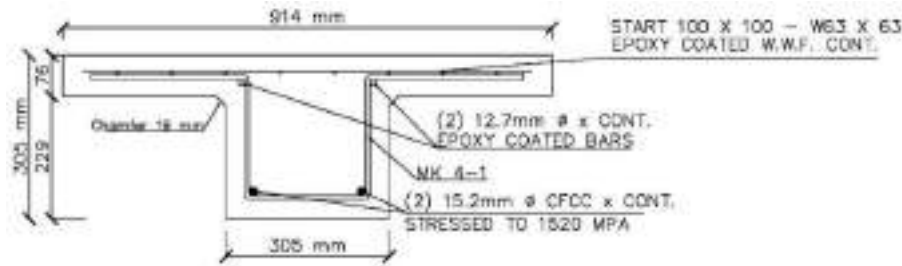


Figure 4: Beam cross-sectional dimensions and reinforcement details.

2.2.1. Conditioning of Beams

Two beams were tested as control specimens and the remaining ten beams were subjected to sustained load equivalent to 50 percent of their flexural capacity in order to induce cracks into the beams and facilitate the aging process. In addition to the sustained load, eight beams were placed in two tanks and subjected to wet and dry cycles of saltwater for 3, 6, 12 and 18 months. The sustained load was applied by tying two beams together at the two ends using high strength stainless steel bars and placing a stainless steel HSS between the two beams at mid span acting as concentrated applied load on the two beams. Figure 5(a) shows two beams subjected to sustained load only and Figure 5(b) shows the remaining 8 beams in the tanks exposed to wet and dry cycles of salt solution and subjected to sustained load. At the end of each exposure period, the beams are tested by monotonically loading in a 3-point bending configuration up to failure to determine the residual strength of the beams prestressed with CFCC.

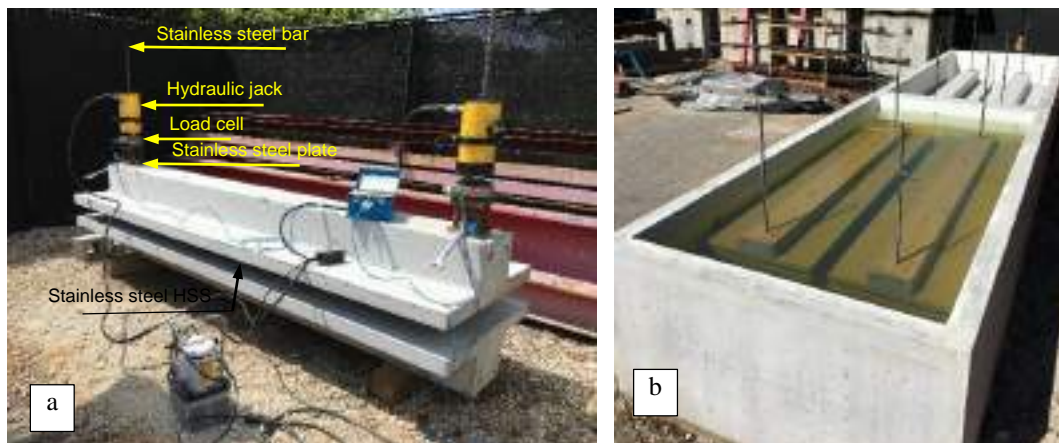


Figure 5: (a) Beams subjected to sustained load only (b) Beams undergoing wet and dry cycles.

2.2.2. Testing of Beams

The concrete beams were tested using a simply supported test setup and monotonic loading up to failure. The load was applied at the mid-span using two 60 tons (120 kips) hydraulic jacks and a spreader beam. Load cells were used to measure the applied load. String potentiometer were used to measure the vertical deflection at mid span. Four linear potentiometers were placed at the ends of each strand to measure any strand slip. Three PI gauges were used to measure concrete strain. All instruments were connected to an electronic data acquisition system to monitor and record the data while testing. Figure 6 shows the test setup used for testing the concrete beams.

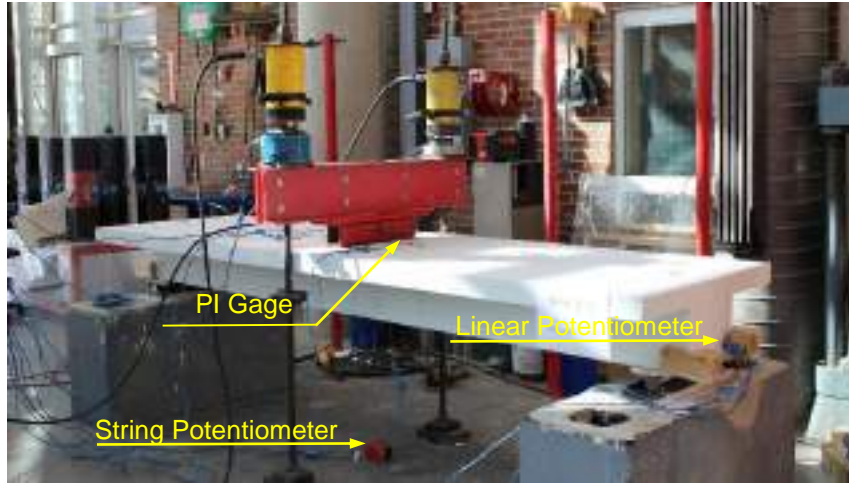


Figure 6: Flexural test of the concrete beams.

2.2.3. Test results of the beams

The behavior of all tested beams was identical having the same load capacity and identical failure due to the rupture of strands. Table 2 presents a summary of the test results in terms of cracking load, failure load and mid span deflection at failure. Figure 7 shows the load deflection curves for all of the tested beams. It should be noted that all beams were loaded monotonically up to failure using load control system, which explains the slight differences in the failure load. It should also be mentioned that if the concrete beams were designed using the guaranteed strength of CFCC, the theoretical failure load would be approximately 30 percent less than the measured failure load as shown in Figure 7 where the dotted line presents the capacity of the beam using the guaranteed strength of CFCC. Based on the measured test results and the observed behavior of all tested beams, it can be concluded that no degradation of the concrete beams prestressed with CFCC was observed after 18 months of exposure to wet and dry cycles of salt solution and sustained load equivalent to 50 percent of the beam's ultimate capacity.

Table 2: Test results of task 2: Concrete beams prestressed with CFCC

Conditioning period		Cracking load KN (kips)	Failure load KN (kips)	Mid span deflection mm (inches)
Control Beams	Beam #1	98 (22)	260 (58.5)	46 (1.8)
	Beam #2		262 (59.0)	53 (2.1)
3 months	Top Beam	Pre cracked	262 (59.0)	-
	Bottom Beam		251 (56.5)	46 (1.8)
6 months	Top Beam		269 (60.5)	51 (2.0)
	Bottom Beam		256 (57.5)	48 (1.9)
12 months	Top Beam		262 (58.9)	48 (1.9)
	Bottom Beam		255 (57.4)	46 (1.8)
18 months	Top Beam		261 (58.6)	46 (1.8)
	Bottom Beam		258 (58.1)	46 (1.8)
18 months (no water cycles)	Top Beam		266 (59.8)	48 (1.9)
	Bottom Beam		253 (56.8)	46 (1.8)

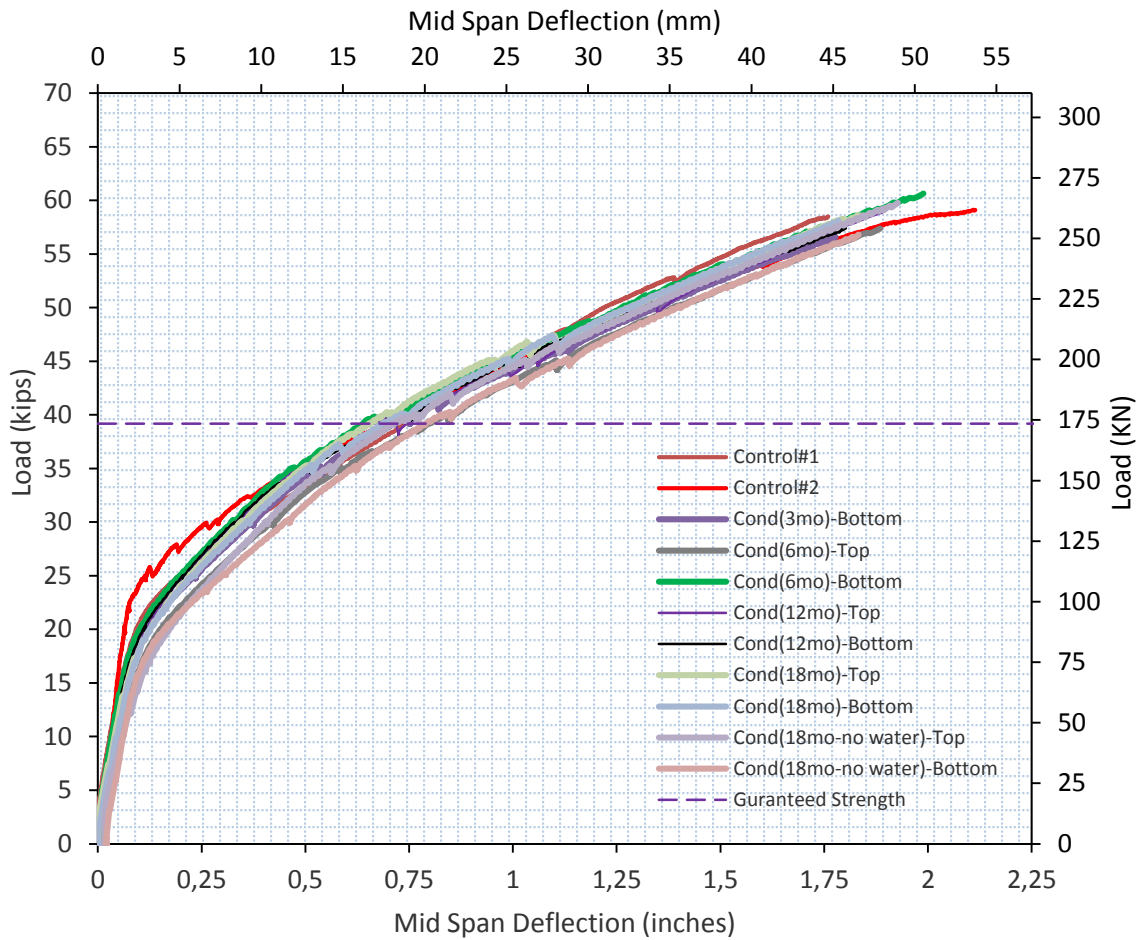


Figure 7: Load-Deflection of all tested beams.

2.3. Degradation of CFCC Constituent Materials

To examine the effect of environmental conditioning on the durability of CFCC constituent materials, carbon fibers and Epoxy coupons were exposed to an alkaline environment at an elevated temperature. Upon completion of the exposure duration, the specimens were tested to determine their mechanical properties as affected by the environmental conditions. Figure 8 shows the tensile testing of (a) carbon fibers and (b) epoxy matrix. Test results of the epoxy specimens indicated a reduction of 10 percent in the average tensile strength after 3,000 hours of conditioning in alkaline solution and exposure to high temperature. However, the test results of the carbon fibers did not show any reduction in the tensile strength after 7,000 hours of exposure.

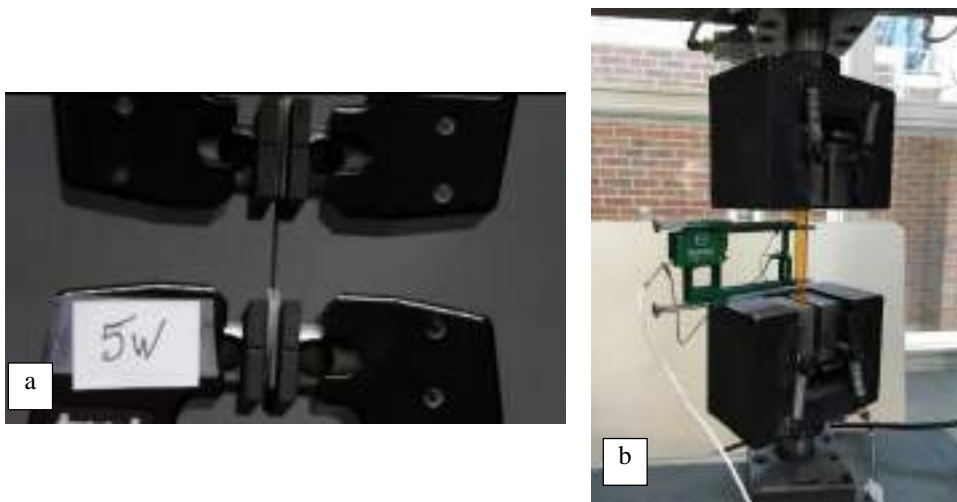


Figure 8: Tensile testing of (a) Carbon Fibers, (b) Epoxy Resin coupons.

3. CONCLUSION

Reported in this paper are the results of a comprehensive study on the simultaneous effect of sustained load combined with environmental conditions on the long-term durability of CFCC. Tests results indicated insignificant changes in the tensile strength of the strands after 7,000 hours of conditioning. The changes were within the coefficient of variation range and therefore, it can be concluded that, conditioning/aging up to 7000 hours, has no effect on the tensile strength of the CFCC Strands. In addition, the performance of CFCC strands used as prestressing strands for reinforced concrete beams was experimentally measured. A total of 12 prestressed concrete T-beams were tested, where 8 beams were subjected to sustained loading to induce cracking and exposed to wetting and drying cycles of saltwater. All beams had the same behavior during testing, same mode failure and failed at the same load level. Based on the test results and the observed behavior of the concrete beams prestressed with CFCC it can be concluded that there was no measured degradation of the CFCC strands up to 18 months of severe environmental exposure.

4. ACKNOWLEDGMENT

The authors would like to acknowledge Florida Department of Transportation for their sponsorship of this research project through the University of North Florida.

5. REFERENCES

- A. A. Abdelrahman, G. Tadros, S. H. Rizkalla. "Test Model for First Canadian Smart Highway Bridge" *ACI Structural Journal* 92.4, 1995, 451-458.
- B. Benmokrane, A. H. Ali, H. M. Mohamed, M. Robert, A. ElSafty. "Durability performance and service life of CFCC tendons exposed to elevated temperature and alkaline environment." *Journal of Composites for Construction* 20.1, 2015, 04015043.
- S.E. Buck, D.W. Lischer, S. Nemat-Nasser. "The Durability of E-Glass/Vinyl Ester Composite Materials Subjected to Environmental Conditioning and Sustained Loading", *Journal of Composite Materials*, 32(9), 1998, 874-892.
- Y. Chen, J. F. Davalos, I. Ray, H. Y. Kim. "Accelerated aging tests for evaluations of durability performance of FRP reinforcing bars for concrete structures" *Composite Structures* 78.1, 2007, 101-111.
- T. Enomoto, N. F. Grace, T. Harada. "Life Extension of Prestressed Concrete Bridges Using CFCC Tendons and Reinforcements" *Proceeding of 6th International Conference on FRP Composites in Civil Engineering (CICE 2012 Rome)*, 13_476. 2012.
- N. F. Grace, F.C. Navarre, R. B. Nacey, W. Bonus, L. Collavino. "Design-Construction of Bridge Street Bridge First CFRP Bridge in the United States *PCI journal*, 47(5), 2002, 20-35.
- V. M. Karbhari. "Durability of composites for civil structural applications", Elsevier, 2007.
- H. C. Mertol, S. Rizkalla, P. Scott, J. M. Lees, R. El-Hacha. "Durability of concrete beams prestressed with CFRP" *Special Session-Subcommittee 440I for FRP Prestressed Concrete in ACI Fall Convention Denver*, 2006.
- M. Pour-Ghaz, B. L. Miller, O. Khalaf Alla, S. Rizkalla, "Do mechanical and environmental loading have a synergistic effect on the degradation of pultruded glass fiber reinforced polymers?" *Composites Part B: Engineering* 106, 2016, 344-355.
- S. H. Rizkalla, G. Tadros. "First smart highway bridge in Canada" *Concrete International* 16.6, 1994, 42-44.



INCREASING THE MECHANICAL EFFICIENCY OF PIN-LOADED STRAPS USING THE SLING ANCHORAGE METHOD

B. Zwingmann¹, Y. Liu², M. Schlaich² and S. Janetzko³

¹ *sbp GmbH, Germany, Email: b.zwingmann@sbp.de*

² *Berlin Institute of Technology, Germany*

³ *SGL Carbon GmbH, Germany*

ABSTRACT

In this paper, the mechanical efficiency of the sling anchorage was predicted using the orthotropic tube model. By applying this model, it was proven that the mechanical efficiency of the sling anchorage is higher than that of the loop anchorage. Analytical analysis showed that the increased cross section reduces the average tension stress providing reserve capacity for additional bending stress. Numerical analysis was used to compare the mechanical behaviour of the loop anchorage and the sling anchorage. The results show that the location of fibre fracture was moved from the inside to the outside of the anchorage. The stress in the sling anchorage was calculated to be significantly lower for the same load. The experimental results showed that the sling anchorage can achieve a mechanical efficiency of 100 %.

KEYWORDS

CFRP, tension member, pin-loaded strap, sling anchorage.

INTRODUCTION

Tension members made out of carbon fibre reinforced polymers (CFRP) have great application potential in civil engineering structures. Anchoring of the carbon fibres at the end of the tension members presents a challenge due to the high tension stress (Schlaich et. al. 2012). The carbon fibres break easily due to additional stresses in the anchorage. The mechanical efficiency η is used to evaluate the performance of anchorages for CFRP tension members by calculating the ratio between the maximum anchored force F_{test} and the design breaking load F_{design} , see equation 1.

$$\eta = \frac{F_{test}}{F_{design}} \quad (1)$$

Pin-loaded straps (see Figure 1a) are tension members with loop anchorages which are commercially successful as high strength but low weight sailing rigs. CFRP pin-loaded straps have been used for the stress ribbon footbridge over the Júcar River (Clemente Ortega et al. 2011), the bowstring-arch bridge at EMPA (Meier et al. 2009) and the stress-ribbon footbridge in Berlin (Schlaich et al. 2007).

The maximum mechanical efficiency of laminated pin-loaded straps is 70 % (Winistörfer 1999) limited by the loop anchorage. Thus, increasing the mechanical efficiency of the anchorage would save approx. 30% of the used CFRP material.

This paper presents a new anchorage for pin-loaded straps called the sling anchorage (Zwingmann 2017). In a sling anchorage, ending carbon fibres are bent and alternately overlapped around a pin. Thus, the cross section at the anchorage is doubled (see Figure 1b) to increase the mechanical efficiency.

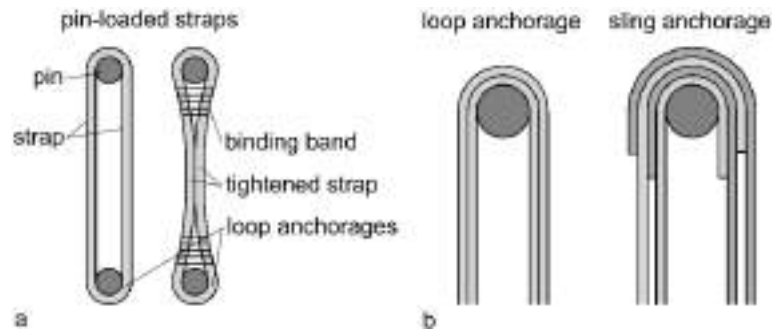


Figure 1: Pin-loaded strap with separated versus tightened strap, b) comparing loop and sling anchorage

METHOD OF SOLUTION

Theory

A pin-loaded strap is a tension member made out of FRP. It consists of two loop anchorages and a strap that can be tightened together, see Figure 1a. The fibre orientation in pin-loaded straps is along the tension member's axis. At the loop anchorages the fibres are orientated tangential to the pin. The mechanical efficiency of the loop anchorage decreases with the R_o/R_i ratio, see Figure 2 and Figure 3.

Figure 1b shows the loop anchorage compared to the sling anchorage. In the loop anchorage all fibres are bent and continue around the pin. Whereas all fibres are bent around the pin in the sling anchorage but end inside the anchorage. The ending fibres of one side overlap alternately with the fibres of the other side of the pin. The cross section of the sling anchorage is twice that of the loop anchorage and of the strap. Therefore, the tension stress is reduced, and its mechanical efficiency is increased.

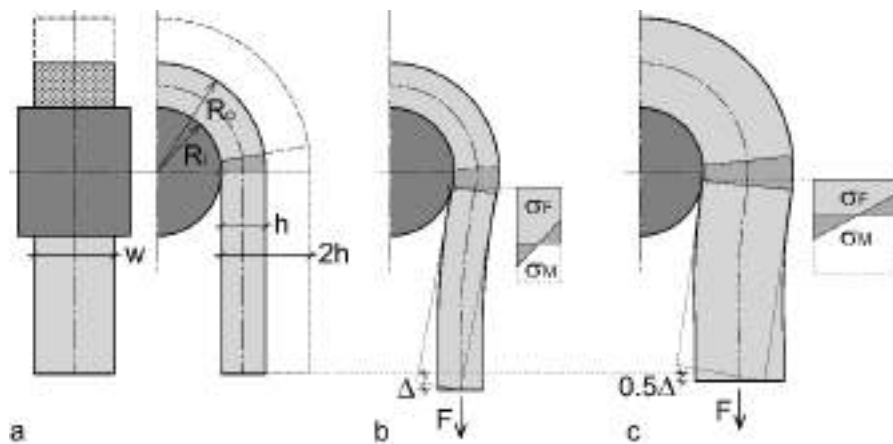


Figure 2: Mechanics of the loop anchorage (Schürmann 2005) and the sling anchorage

Schürmann (2005) explains that the fracture at the detachment point is caused by the stress due to tension and bending. This bending is results from the elastic elongation of the curved strap, see Figures 2a and 2b. The elastic elongation and the bending stiffness of the loop make the strap rotate towards the pin. The tension force then pulls the strap back, which causes bending stress (σ_M) additional to the tension stress (σ_F). The fibres at the inner radius start to break when the stress reaches the tensile strength.

The mechanics of the sling anchorage (Figure 2c) are similar to those of a loop anchorage with doubled thickness h . Therefore, the average tension stress in the sling anchorage caused by the tension force equals to 50 % the tension stress in the loop anchorage. This reduced tension stress can be superimposed with the bending stress without reaching the tension strength.

Having a lower tension stress in the sling anchorage, the elastic elongation is smaller than in the loop anchorage causing a smaller rotation. The bending stress does not change if the thickness is doubled and the rotation is halved

simultaneously. This is shown in equation 2 and 3 using the mechanics of an elastic beam element with rectangular cross section.

$$M = 4 \frac{EI}{L} \varphi = 4 \frac{Ewh^3}{12L} \varphi \quad (2)$$

$$\sigma_M = \frac{Mh}{I \cdot 2} = 2 \frac{E}{L} \cdot h\varphi = 2 \frac{E}{L} \cdot 2h \frac{\varphi}{2} \quad (3)$$

Comparing both stress distributions in Figure 2b and 2c it can be seen that the bending stress σ_M of both anchorages is similar while the tension stress σ_F is much lower in the sling anchorage. Increasing the tension force will cause fibre fracture first at the detachment point of the loop anchorage. Increasing the force will then cause fibre fracture outside the sling anchorage but not at its detachment point.

Mansfield (Mansfield 1983) demonstrated that the maximum tension stress of the loop anchorage depends on the R_o/R_i ratio, see equation 4. He identified the $E_{||}/E_{\perp}$ ratio to determine the peak stress factor $\max(\sigma_{||})/\sigma_F$ which is the ratio between the maximum stress and the mean tension stress and the reciprocal of the mechanical efficiency, see Figure 3.

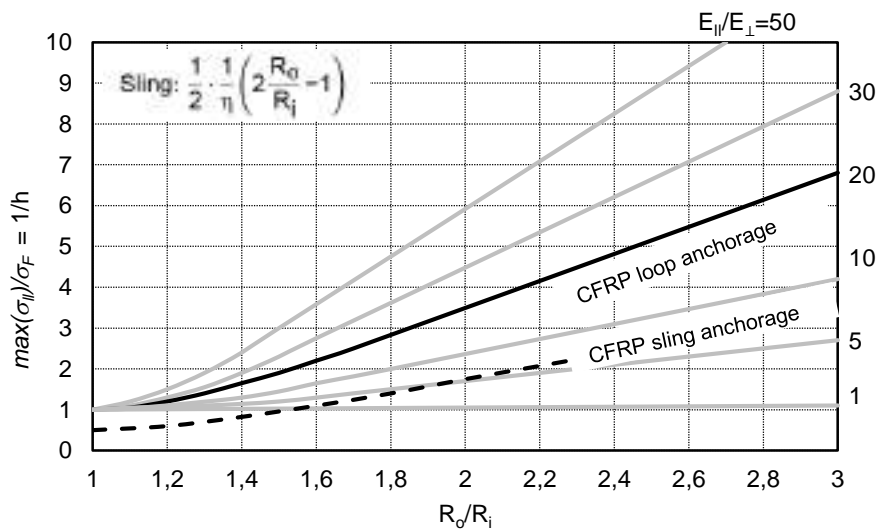


Figure 3: Peak stress factor of loop anchorages for different $E_{||}/E_{\perp}$ ratios depending on the R_o/R_i ratio (Mansfield 1983) and for CFRP sling anchorages

The R_o/R_i ratio for a sling anchorage with the same cross section outside the anchorage was calculated in equation 5. Applying equation 5 to the Mansfield's diagram (dashed line) showed that the peak stress factor for sling anchorages is lower than that for loop anchorages. Additionally, it was lower than 1 (100 % mechanical efficiency) for ratios below 1.5.

$$\frac{R_o^{loop}}{R_i} = \frac{R_i+h}{R_i} = \frac{R_i+R_o-R_i}{R_i} \quad (4)$$

$$\frac{R_o^{sling}}{R_i} = \frac{R_i+2h}{R_i} = \frac{R_i+2R_o-2R_i}{R_i} = \frac{2R_o-R_i}{R_i} = 2 \frac{R_o^{loop}}{R_i} - 1 \quad (5)$$

Figure 4 shows the manufacturing method of sling anchorages. The profiles are divided in two groups and bent alternately around the pin. After bending, all profiles are joint inside the anchorage. For thermosetting matrix glue is used and for thermoplastic matrix the profiles can be welded.



Figure 4: Manufacturing method for the sling anchorage

Experimental Analysis

Sling anchorages were produced using CFRP tapes with thermoplastic matrix (PA 6) and a welding tool, see Figure 5a. The properties of the CFRP tape provided by SGL Group are shown in Table 1. By applying a constant pressure of 20 bar at a temperature of 260 °C the CFRP tapes were welded to become the sling anchorage, see Figure 6b.

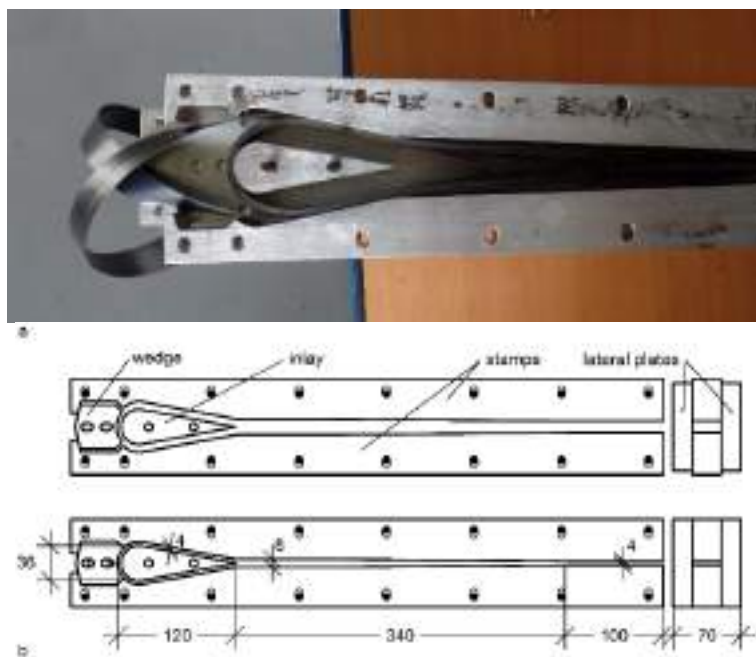


Figure 5: CFRP tapes located inside the welding tool and welding tool dimensions

Table 1: Properties of the CFRP tape (mean values)

Property	Symbol	Unit	Value
Carbon fibre	-	-	CT50-4.0/240-T140
Matrix	-	-	BS3
Fibre content	φ	%	41
Modulus	$E_{ }$	MPa	98000
Modulus	E_{\perp}	MPa	5700
Strength	$R^+_{ }$	MPa	1460
Dimension	$T \times W$	mm ²	1/6 × 30
Weld point	T_{weld}	°C	260

The welding tool consists of aluminium parts (see Figure 5b). Due to slotted holes the stamps can slide towards the central inlay to apply pressure on the CFRP tapes. The wedge moves horizontally due to the vertically movement of the stamps.

The welding tool was used to manufacture six prototypes of sling anchorages with $n = 24$ CFRP tapes. With the cross section the design force was calculated, see equation 6. Since the R_o/R_i ratio is lower than 1.5 (equation 6), the mechanical efficiency of the sling anchorages was assumed to reach 100 %. The design force F_{Design} is given in equation 7.

$$\frac{R_o^{loop}}{R_i} = \frac{R_i+h}{R_i} = \frac{18+4/2}{18} = 1.11 \quad (6)$$

$$F_{design} = nTWR_{\parallel}^+ = 24 \cdot 1/6 \text{ mm} \cdot 30 \text{ mm} \cdot 1460 \text{ MPa} = 175 \text{ kN} \quad (7)$$

The tension test was performed using a universal testing machine with hydraulic gripping device (Figure 6a). The pin ends of the sling anchorages were connected to the universal testing machine using a 36 mm bolt. The binding band was replaced by an aluminium clamp.

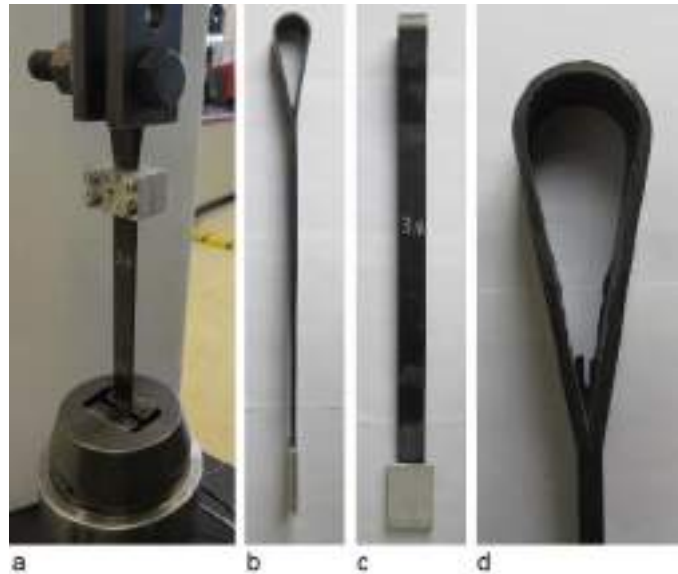


Figure 6: Tension test of sling anchorages

Figures 6b to 6d show a sling anchorage to be tested with milled aluminium plates glued on the clamped end. During test 1, the sling anchorage was pulled out of the aluminium plates. Therefore, all other plates were sand blasted before gluing to increase adhesion. As a result, sling anchorages 2 to 6 failed in fibre fracture mode.

RESULTS AND DISCUSSIONS

Results

The measured breaking load and the mechanical efficiency have been calculated and listed in Table 2. The mechanical efficiency of 100 % was reached by two sling anchorages and the others achieved approx. 90 %.

Table 2: Test results of the sling anchorage tension tests

Parameter	Symbol	Unit	Sling anchorage					
			1	2	3	4	5	6
Measured breaking load	F_{test}	kN	158.5	184.2	154.7	182.9	167.6	159.6
Design breaking load	F_{design}	kN	175.0	175.0	175.0	175.0	190.0	175.0
Mechanical efficiency	η	%	90.6	105.3	88.4	104.5	88.4	91.2

ACKNOWLEDGMENTS

The authors thank SGL Group for funding the research project.

REFERENCES

- L. R. Clemente Ortega, J. Rodado López (2011). "Nueva Pasarela Banda Tesa sobre el río Júcar", *Proceedings of the International Conference on Research in Construction*, Madrid, 17-18 November 2011, A2-04.
- E. H. Mansfield (1983). "Load Transfer from a Pin to a Wound Fibre Composite Strip", *Journal of Composite Materials* 17(5), 414-419.
- U. Meier, R. Brönnimann, R. Widmann, A. U. Winistörfer, P. Irniger (2009). "Bowstring-Arch Bridge made of CFRP, GFRP and Glulam", *Proceedings of the 2nd Asia-Pacific Conference on FRP in Structures (APFIS 2009)*, Seoul, 09-11 December 2009, 557-562.
- M. Schlaich, A. Bleicher (2007). "Spannbandbrücke mit CFK Lamellen", *Bautechnik* 84(5), 311-319.
- M. Schlaich, B. Zwingmann, Y. Liu, R. Goller (2012). "Zugelemente aus CFK und ihre Verankerungen", *Bautechnik* 89(12), 841-850.
- H. Schürmann (2007). "Konstruieren mit Faser-Kunststoff-Verbunden", *Springer*, Heidelberg.
- A. U. Winistörfer (1999). "Development of Non-laminated Advanced Composite Straps for Civil Engineering Applications", Dissertation, University of Warwick.
- B. Zwingmann (2017). "The sling - a loop anchorage made from alternately wrapped carbon fibres for CFRP tension members", Dissertation, Berlin Institute of Technology, <http://dx.doi.org/10.14279/depositonce-6177>.



ENVIRONMENTAL DURABILITY OF HAND-LAYUP CARBON/EPOXY COMPOSITES INTENDED FOR STRENGTHENING OF CONCRETE STRUCTURES

Wendlamita Zombré¹, Robert Chlela², Marie Michel¹, Julien Mercier³, Karim Benzarti², Laurence Curtill

¹ University of Lyon, University Lyon 1, LMC² (EA 7427), France, Email: marie.michel@univ-lyon1.fr

² University Paris-Est, Laboratory Navier (UMR 8205), IFSTTAR, France

³ Freyssinet International, France

ABSTRACT

In the framework of a project funded by the French National Research Agency (ANR), which is called MICRO, a large-scale durability study is currently being conducted on composite materials intended for strengthening applications on building or civil structures. This paper aims at presenting the first results of accelerated ageing tests performed on carbon fiber reinforced polymer (CFRP) laminates made by wet lay-up process, and on CFRP strengthened concrete slabs. The experimental test program consists in subjecting the various specimens (CFRP laminates and strengthened concrete slabs) to six different hydrothermal environments, obtained by combining 3 temperature conditions (25°C, 50°C and 60°C) and 3 relative humidity levels (50%, 75% and 100% RH under total immersion). Mechanical characterizations are periodically carried out on aged specimens to monitor their evolutions in terms of tensile performances and interlaminar shear properties (for CFRP laminates), and in terms of adhesive bond properties (through pull-off tests on concrete/CFRP assemblies). Changes in these performance indicators are then correlated with each other, and with water mass uptake as well. A correlation between water uptake and exposure temperature has been established, revealing the dependence of ageing kinetics upon temperature. It is also showed that when the conditioning temperature is higher than the initial glass transition temperature of the unaged specimens, post cure phenomena occur and lead to an increase in the cohesion of the fiber/matrix interface, together with a slight decrease in the residual performances of the CFRP laminates. In the end, conclusions are drawn regarding links between the selected key performance indicators and mass uptake. Collected data provide a better comprehension on the hydrothermal ageing mechanisms of CFRP laminates and their adhesive bond with concrete, and will be used at a further stage to develop predictive models for reliability and service-life assessment.

KEYWORDS

Strengthening and repair; Durability study; Long-term performance; Mechanical characterization, CFRP Composites; Hydrothermal Ageing.

INTRODUCTION

Building robust models of sustainability requires conducting extensive test programs based on long term exposure and numerous series of tests. To overcome this weakness, optimized strategies have been proposed in the literature, as for instance in (**Fatemi, 2012**). These authors reduce the cost of testing (proportional to the number of products tested and the cumulative test time), while ensuring a sufficient quality level for the resulting estimation. Most often, such an optimization relies on accelerated ageing test protocols.

In general, hydrothermal effects (the combined effects of moisture or humidity and heat) are dominant in the degradation processes of fiber-reinforced polymer (FRP) materials (**Gholami et al., 2013**). Water absorption is also known to affect FRP-to-concrete bond, usually to a greater extent than FRP properties themselves (**Wan and Harries, 2006**).

In the present study, a design of experiments has been proposed, assuming that temperature T and humidity H are the key influencing factors in a civil engineering environment. 3 levels have been considered for each of these factors: 20°C, 40°C and 60°C for T, 50% RH, 75% RH, 100 % RH under immersion for H. Such a design of experiments is based on the Hoke matrix (simplification of a factorial matrix with 3 levels per factor). This type of matrix is built with the minimum number of experiments to perform in order to compute a second-order model. Besides, test methods used in this study to evaluate performance indicators are tensile tests, interlaminar shear

tests and pull off tests, which are very common methods for characterizing mechanical properties of FRP laminates and their bond properties with concrete. Finally, this leads to a consistent database encompassing 18 permutations of test methods and hygrothermal environments.

The first results of this ongoing research program are presented in this paper, with an emphasis on the property evolutions of the CFRP laminates and the CFRP/concrete bond after periods of 3 and 6 months of exposure. These results are discussed in the light of the water uptakes measured for the various tested specimens.

MATERIALS

In this study, a bi-component epoxy resin (Foreva Epx TFC) and bi-directional carbon fiber fabrics (Foreva TFC with a weft to warp weight ratio of 70/30) were provided by Freyssinet International. Composite laminates made of two superimposed plies were manufactured by contact molding (hand lay-up process), using the same protocol recommended for field applications. Mechanical properties claimed by the supplier for the cured adhesive and a CFRP ply (after 7 days cure at 23°C) are shown in Table 1. More information on the constituents is available in Freyssinet International product data sheets.

Table 3: Mechanical properties of materials*

	Foreva Epx TFC	Fabric Foreva TFC	CFRP ply
Ultimate tensile strength	27 ± 3 MPa	4900 MPa	1700 MPa
Tensile strain at failure	1.7 ± 1 %	2,10%	1,62%
Young's modulus E	2.3 ± 0.2 GPa	230 GPa	105 GPa
Linear strength (weft direction)			8,15 kN/cm
Linear strength (wrap direction)			3,50 kN/cm

*As specified on the product data sheet provided by the supplier

The glass transition temperature of the CFRP laminates after initial cure (3 weeks under laboratory conditions at room temperature) was measured by Differential Scanning Calorimetry (DSC) at a heating rate of 10 °C/min, and was equal to 54 ° C. This initial state corresponds to the starting time T0 of the durability test program.

The average volume fraction of fibers of the CFRP laminates was around 30%, as determined from the mass of the composite and the densities of the components. For durability studies, these values are in line with the Canadian technical specification CSA S808-14, which recommends a volume fraction of fibers around 35%.

In addition, CFRP strengthened concrete slab were also prepared according to the hand lay-up method, for the purpose of pull-off tests. A regular concrete was used for the preparation of slabs, with an average compressive strength of 48 MPa, as measured on concrete cylinder 6 months after casting. This value is in agreement with AFGC specification (French Association of Civil Engineering AFGC) which recommends a minimum compressive strength of 40 MPa for concrete used in pull-off specimens.

EXPERIMENTAL PROGRAM

In accordance with the optimized design of experiment that was previously introduced, test specimens were exposed to six different ageing environments (i.e., 6 combinations of temperature and relative humidity, noted Vi with i=1,6) which are summarized in Table 4. These exposures will be maintained up to 24 months.

Ageing effects were assessed using three mechanical performance indicators: tensile properties and interlaminar shear properties of the CFRP laminates, and CFRP/concrete bond properties obtained by pull-off tests.

Tensile and inter-laminar shear (ILS) samples were prepared according to ISO 527 standard and AFGC specifications, respectively (Figure 6). But, to reduce the amount of materials used in the project, the thickness of the specimens was reduced to 2 mm (against 4 mm recommended in the standard). Preliminary tests confirmed that this change did not affect the repeatability of the tests. 4 and 8 samples were respectively cut in the CFRP laminates that were specifically prepared for traction and ILS tests, as shown in Figure 1. Beforehand, in order to reduce the edge effects, the peripheral part (50 mm) of the laminate plates was removed all around.

For all specimens, a curing time of 21 days is respected before starting testing and ageing. During curing time, the laboratory LMC2 storage conditions were typical ambient conditions averaging 20 °C and 45% RH. At this stage of the study, mechanical tests have been completed at T0, and after exposure times of 3 and 6 months.

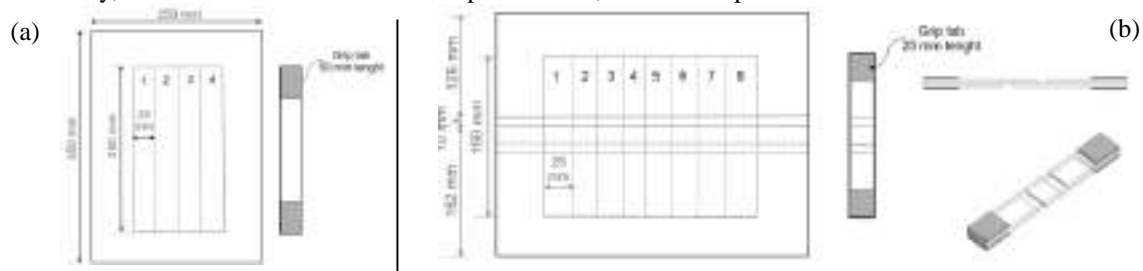


Figure 6: Procedure for cutting samples from the initial CFRP plates: a) tensile samples. b) ILS samples.

The composites laminates made by hand layup process have a thickness / width ratio $<1/100$ (Mercier, 2007) and are stored (or immersed in the case of an environment at 100 RH) vertically in the tanks / climatic chambers in order to favor an optimal 1D moisture diffusion across the thickness. In addition, the tensile and shear plates are stored separately from the strengthened concrete slabs to avoid any interaction of the CFRP laminates with the alkalinity of the concrete specimens.

Aged specimens were tested 2 to 3 days after their removal from the baths / climatic chambers. This time corresponds to the time necessary for the preparation of the samples before the test (cutting of test samples, preparation of the grip tabs, gluing of the gauges). The ageing conditions V1, V2 and V3 are investigated at Ifsttar (Paris, France) while V4, V5 and V6 are done at LMC2 (Lyon France). This implies to make 2 series of tests at T0, one per site for each indicator in order to facilitate the subsequent interpretation of results. The number of samples tested for each type of condition and for each test method is shown in Table 4.

Table 4 : Details of the design of experiments

Information on the experimental matrix				Tensile test			ILS test			Pull -off test		
				Duration								
T °C	RH (%)	conditions	type	T0	3 months	6 months	T0	3 months	6 months	T0	3 months	6 months
≈20	≈ 45	Ambient	V0	56			24			24		
20	50	Enclosure	V1		4	4		8	8		5	5
20	100	in tank	V2		4	4		8	8		5	5
60	50	Enclosure	V3		4	4		8	8		5	5
40	100	in tank	V4		4	4		8	8		5	5
60	75	Enclosure	V5		4	4		8	8		5	5
60	100	in tank	V6		4	4		8	8		5	5

The ageing behavior of composite material subjected to humid environments is known to be dependent on the water concentration in epoxy matrix (Fayolle and Verdu, 2005 ; Sethi and Ray, 2015). For this reason, CFRP laminates were weighed before and after immersion to roughly estimate their water content at the time of their mechanical characterization.

Sorption kinetics and Water uptake of the CFRP laminates

In order to provide a more accurate estimation of the water sorption kinetics, water uptake was monitored on specific small samples stored in the various ageing environments. One CFRP plate molded by hand lay-up was cut into 32 samples of $25 \times 25 \times 2 \text{ mm}^3$, which were evenly distributed in the six ageing conditions. Their mass was systematically measured using a balance of accuracy 0.001g (Mettler Toledo) over a period of 10 days.

Tensile tests

Tensile tests were performed according to ISO 527 and AFGC's recommendations, and allowed to determine the ultimate strength in the longitudinal direction, the modulus of elasticity, and the stress – strain curve. The test was conducted on a 50 kN machine with a displacement control rate of 1mm/min. Electrical resistance strain gages were installed at the middle height of the specimens. Samples that broke in the grip tabs were invalidated.

Interlaminar shear tests (ILS)

ILS tests were carried out according to ASTM D3165 and AFGC's recommendations with slight modifications of the sample geometry (Figure 1). The test was conducted on the same machine than tensile tests, with a displacement control rate of 1mm/min, and allowed to determine the average shear strength.

Pull-off test

These tests were performed on CFRP strengthened slabs according to EN 1542 standard. A partial core was first drilled around the test zone, with an approximate depth of $5 \text{ mm} \pm 2 \text{ mm}$. After 24 hours, a 50 mm diameter aluminum disc was stuck to the test zone using a two-component epoxy (EPONAL 380). Then, 24 hours later, a direct tension was applied to the aluminum disc at a rate of 0.06 MPa/s, using a Proceq DY 216 dynamometer, until failure occurs. This equipment allows to record the peak load and to calculate the bond strength.

RESULTS AND DISCUSSIONS

Kinetics of water sorption

Figure 7 shows the evolutions of the average mass uptakes of the CFRP specimens over a period of 10 days in the various ageing environments V1 to V6. Even though saturation is not reached at the end of the period, some

conclusions can be drawn. In agreement with literature, it is found that the higher the temperature, the higher the sorption kinetics, which confirms an acceleration effect of temperature on the water diffusion phenomena. Furthermore, as the temperature increases, the initial part of the curves becomes less linear, suggesting that Fickian diffusion becomes less dominant and that other mechanisms compete for the transport of moisture. **Robert et al (2010)** have suggested that three different mechanisms may coexist: (1) diffusion of water molecules inside micro-gaps between polymer chains, (2) capillary transport in interfacial regions between fibers and polymer, and (3) transport through micro-cracks formed in the matrix during the manufacture process. Such a deviation from the linear Fickian behaviour is quite obvious for specimens immersed in water at temperatures of 40 and 60°C (in ageing conditions V4 and V5). These specimens may be prone to more extensive swelling compared to samples immersed at 20°C which still exhibit a linear Fickian curve. Such swelling phenomena induced by additional water absorption may damage the CFRP laminate and affect its mechanical properties.

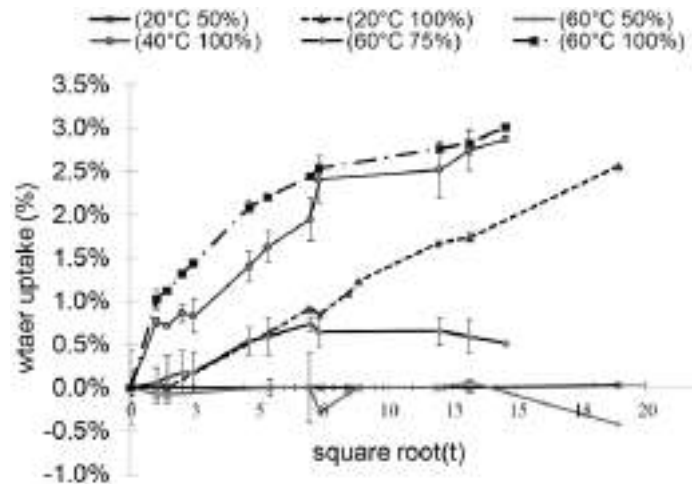


Figure 7 : Evolution of the water uptake for CFRP laminates subjected to the various ageing conditions.

Tensile tests

Table 5 reports the effective ultimate strength σ_u , the effective Young's modulus E and the effective ultimate strain ϵ_u obtained at initial time T_0 , and after 3 and 6 months ageing, which were calculated considering an effective thickness of 0,96 mm conforming to the supplier's recommendation. A slight difference can be observed between the indicator values obtained by the two laboratories at T_0 . The areas of bias, defined as the ratios of LMC2 values to IFSTTAR values, are respectively 0.93, 0.99 and 0.92 for ultimate strength, modulus and ultimate strain. As this bias remains rather limited, the reliability of the test method was not questioned.

The evolutions of these indicators, including water uptake, are shown in figure 3. Except for water absorption, the indicators are all normalized by results obtained at T_0 . The red rectangle represents the reference value at T_0 with its standard deviation. Figure 4 shows typical failure modes for samples tested at T_0 , or after 6 months exposure to V4 (40°C, 100%), V5 (60°C, 75 % RH), and V6 (60°C, 100% RH).

The effective ultimate strength didn't show any degradation after 3 months at 50% RH, whatever the temperature, and a slight increase was even observed. However, complementary physicochemical analyses (which are under progress) are necessary to correlate this slight property enhancement to actual microstructural phenomena occurring in the material. Also, at 60°C and 75% RH, the strength decreases slightly after 3 and 6 months. For immersed composites, there is no significant degradations after 3 months of exposure, excepted at the temperature of 40°C. This observation is in line with the mass uptake of the specimens, as the CFRP plate immersed at 40°C is found to gain much more weight compared to those exposed at 20°C and 60°C.

Regarding the Young's modulus at 3 months, it seems to be affected negatively by high humidity levels, especially at 40°C and 100% RH (figure 3b). After 6 months, a re-increase is observed, but the modulus remains under its initial value at T_0 . These variations seem highly related to the variations of the water content (Figure 3d), which is relevant since water is known to act as a plasticizer of the polymer matrix and the interfacial regions. Specimens stored at 60°C, 50% exhibit the highest modulus, both after 3 and 6 months. This can be explained by a post-cure phenomenon of the polymer matrix (to be confirmed by DSC characterizations). The failure mode at T_0 appears to be the most explosive, with perceptible debonding between fibers and matrix (figure 4). Delamination also occurred in mixed modes. These macroscopic observations suggest that the damage begins through micro-cracks in the matrix which weakens the load transfer process and causes ruin by decohesion at matrix/fiber interfaces. For aged specimens, significant differences are noted between the fracture modes of specimens exposed to V4 (40°C, 100% RH), V5 (60°C, 75 % RH), and V6 (60°C, 100% RH) for 3 and 6 months. At the ageing temperature of 60°C (which is slightly higher than the initial T_g of the matrix), both under immersion or in relative humidity, the

fracture plane of aged samples is sharper and no delamination is observed. This feature is not observed for samples exposed to V4 (40°C, 100% RH) which present a failure very similar to that of specimens tested at T0. This feature suggests a better interfacial cohesion of specimens aged at 60°C, which can be explained by a post-reticulation of the resin at 60°C leading to better fiber/matrix cohesion.

Table 5: Results of tensile tests for the various accelerated ageing conditions and ageing durations.

Ageing conditions	Duration	Tensile properties			Water uptake (%)
		Effective σ_u (MPa)	Effective E (GPa)	Effective ϵ_u (%)	
Baseline LMC2	T0	1424 ± 137	94.1 ± 8.5	1.50 ± 0.05	-
Baseline Ifsttar		1520 ± 146	94.6 ± 6.3	1.62 ± 0.19	-
V1 (20° C, 50% RH)	3 months	1563 ± 74	89.5 ± 5.2	1.77 ± 0.06	negligible
	6 months	1475 ± 120	93.8 ± 9.7	1.58 ± 0.27	negligible
V2(20° C, 100% RH)	3 months	1411 ± 198	81.4 ± 2.4	1.86 ± 0.12	5.4
	6 months	1340 ± 92	80.8 ± 8.1	1.67 ± 0.17	6.2
V3(60° C, 50% RH)	3 months	1635 ± 78	93.4 ± 11.6	1.77 ± 0.23	negligible
	6 months	1558 ± 68	98.4 ± 5.3	1.59 ± 0.14	negligible
V4(40° C, 100% RH)	3 months	933 ± 9.5	67.6 ± 11.2	1.39 ± 0.21	8.5
	6 months	1320 ± 52	79 ± 1.8	1.63	5
V5(60° C, 75% RH)	3 months	1270 ± 81	84.2	1.66	negligible
	6 months	1363 ± 85	83.2 ± 2.7	1.60 ± 0.10	negligible
V6(60° C, 100% RH)	3 months	1285 ± 84	75.6 ± 1.8	1.69 ± 0.07	5.5
	6 months	1285 ± 129	86 ± 1.1	1.66	2.4

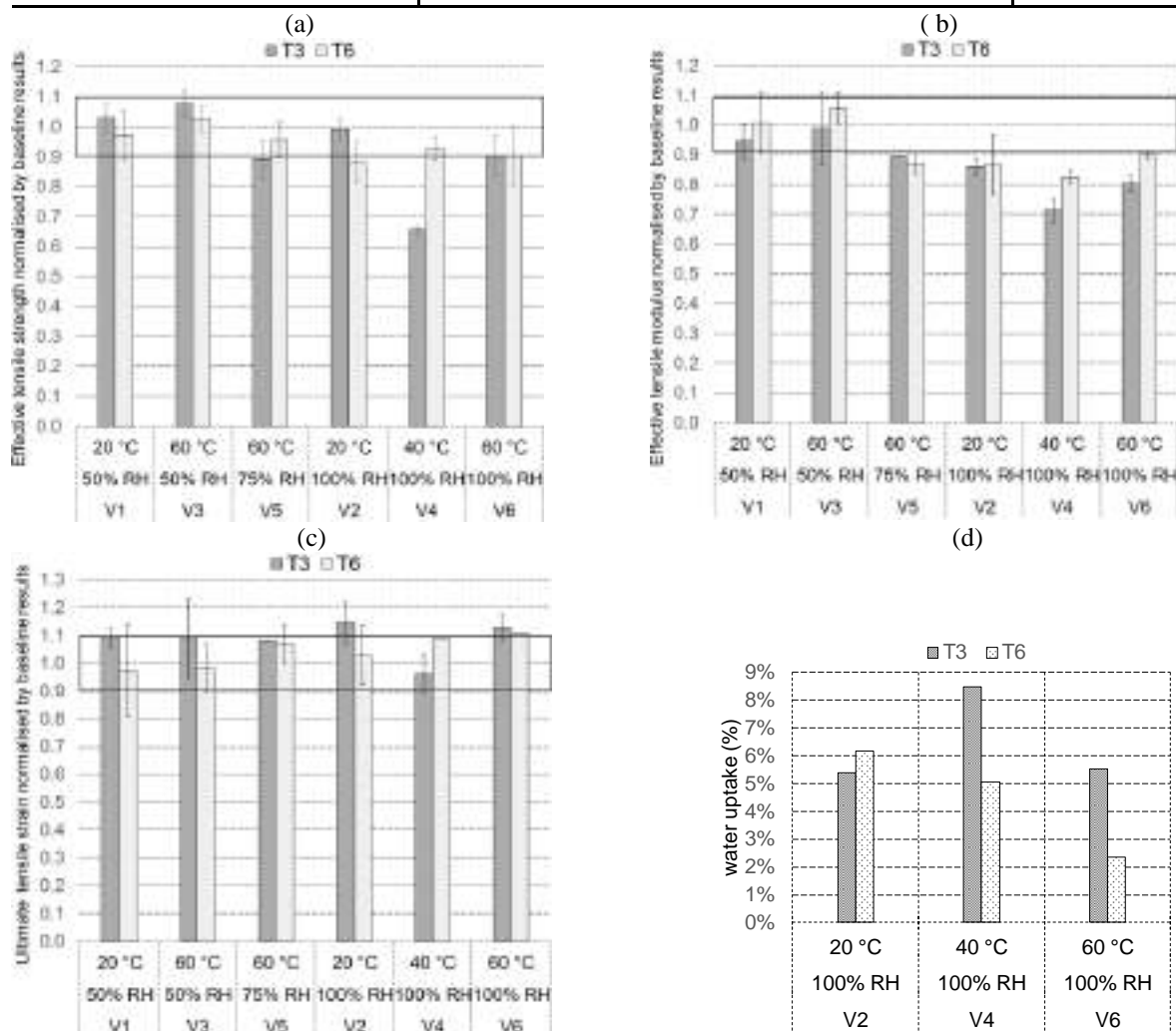


Figure 8 : Evolution of tensile indicators. a) Effective strength. b) Effective modulus. c) Effective ultimate strain. d) Water uptake.



Figure 9 : Typical failure modes of tensile test samples. a) T0, b) V4 6 months, c) V5 6 months d) V6 6 months

Interlaminar shear tests

A maximum coefficient of variation of 15 % was considered for these tests. The area of bias was assumed acceptable (more than 90 %). Results of the tests are summarized in Table 4. Failure occurred by total debonding of the lap joint, as shown in Figure 10. The evolutions of the ILS strength and the mass uptakes after 3 and 6 months exposure are presented in Figure 11. The red rectangle represents the reference value and its standard deviation. Regarding the 3 month-aged specimens, those exposed to immersion conditions at 20°C (V2) and 40°C (V4) exhibit degraded strength values, whereas the other ageing conditions do not show any clear influence. Here again, water sorption seems to be a driving factor, as specimens exposed to V2 and V4 are those showing the highest water uptakes.

Table 6 : Results of interlaminar shear (ILS) tests for the various accelerated ageing conditions and durations.

Ageing conditions	Duration	ILS τ (MPa)	Mass uptake (%)
Baseline LMC2	T0	11.8 ± 1.4	-
Baseline IFSTAR		12.6 ± 1.4	-
V1 (20° C, 50% RH)	3 months	12 ± 1.4	negligible
	6 months	12.8 ± 0.5	negligible
V2 (20° C, 100% RH)	3 months	9.9 ± 1.1	7.2
	6 months	11.2 ± 0.7	3.2
V3 (60° C, 50% RH)	3 months	12.7 ± 1.1	negligible
	6 months	13.7 ± 1	negligible
V4 (40° C, 100% RH)	3 months	10.3 ± 0.8	5.7
	6 months	13.7 ± 1	7.3
V5 (60° C, 75% RH)	3 months	12.3 ± 1.8	negligible
	6 months	13 ± 1.5	negligible
V6 (60° C, 100% RH)	3 months	12 ± 1.3	3.4
	6 months	14.1 ± 2	4.6



Figure 10 : Typical failure of samples after ILS tests.

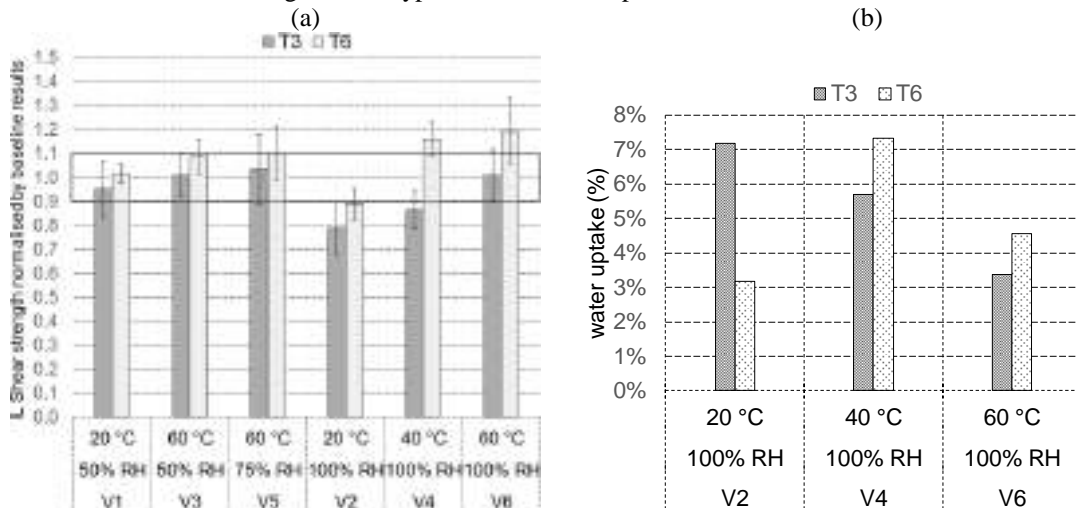


Figure 11 : Results of ILS test. Evolution of a) effective IL strength and b) water uptake.

On the other hand, after 6 months ageing, and without considering the overlap of standard deviations, the ILS strength is found to increase for all ageing conditions, especially for V3 (60°C, 50 % RH), V5 (60°C,75 % RH) and V6 (60°C, 100% RH), as the strength becomes higher than the initial value at T0. This change can be explained by a late post-cure effect caused by keeping the ageing temperature above Tg over a long period.

In the end, regarding specimens exposed to humid ageing, evolutions of ILS strength seem to be controlled by antagonistic phenomena: i) a plasticization process of the matrix and the interfacial areas that induces a decrease in strength, and ii) the post-curing effect that tends to increase this strength value. While plasticization seems to be dominant in a first stage of the ageing process, post-curing becomes more predominant in the long term. This trend, already shown in previous studies (Benzarti et al., 2001; Quiertant et al., 2017) has to be validated by additional DSC investigations (under progress) and upcoming results of ILS tests after 12 and 24 months ageing.

Pull-off tests

Results of pull-off tests are presented in Table 5 and evolution of bond strength is presented in Figure 12a. Various failure modes were obtained depending on the ageing conditions. A concrete cohesive failure (M1) was observed for specimens exposed in the air, while failure of immersed specimens was by debonding of the composite (M3) (Figure 12b), probably due to the degradation of chemical linkages at the concrete/CFRP interface. This latter failure mode is accompanied by a significant reduction in pull-off strength values. Nevertheless, specimens exposed to V6 presents less damage compared to V2, probably due to post-cure effects at 60°C which inhibits degradations.

Table 7 : Results of pull-out tests for each condition and duration.

Ageing conditions	Duration	Bond properties	
		σ_u (MPa)	Failure mode
Baseline LMC2	T0	3.31 ±0.29	M1
Baseline IFSTTAR		4.77 ±0.48	M1
V1 (20° C, 50% RH)	3 months	3.93 ±0.18	M1
	6 months	4.68 ±0.22	M1
V2 (20° C, 100% RH)	3 months	2.02 ±0.18	M3
	6 months	2.10± 0.10	M3
V3 (60° C, 50% RH)	3 months	4.07± 0.32	M1
	6 months	3.86± 0.19	M1
V4 (40° C, 100% RH)	3 months	3.04± 0.44	M3
	6 months	2.13± 0.15	M3
V5 (60° C, 75% RH)	3 months	3.55± 0.30	M1
	6 months	3.72± 0.34	M1
V6 (60° C, 100% RH)	3 months	2.63± 0.29	M3
	6 months	2.93± 0.24	M3

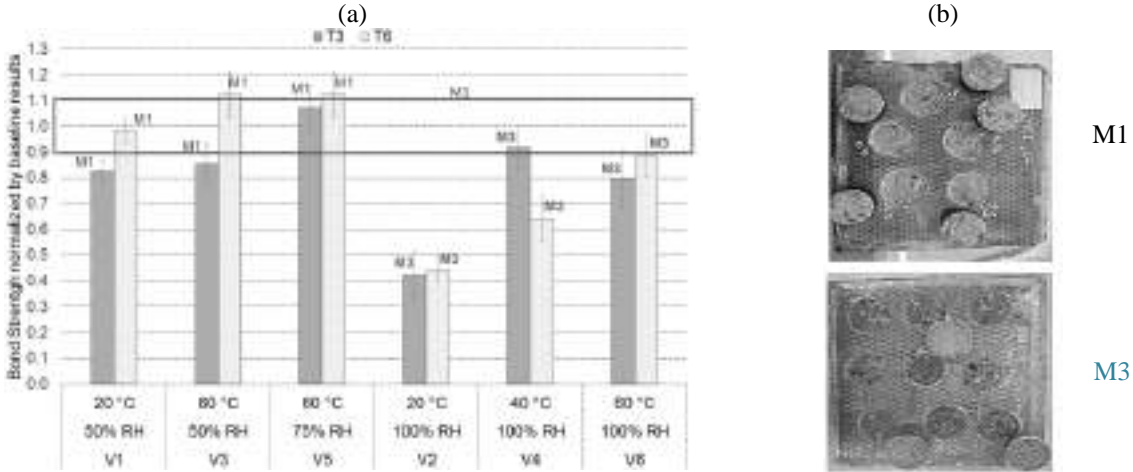


Figure 12 : a) Evolution of the pull-off strength and b) Typical M1 and M3 failure

CONCLUSIONS

This paper has presented the first results of a durability study conducted on CFRP laminates and CFRP strengthened concrete slabs subjected to various accelerated ageing conditions (6 different combinations of temperature and relative humidity). At this stage of the test program, changes in the tensile properties, ILS strength and bond strength have been determined after 3 and 6 months ageing under these various environments.

Despite the dispersion inherent to the test methods, first trends were drawn from these investigations:

- Tensile properties were significantly affected under saturated wet environments (100% RH), especially the longitudinal Young's modulus. The most detrimental ageing condition was V4 (40°C, 100 % RH), which was also correlated to the highest water uptake within the CFRP laminate. Differently a slight increase in tensile properties was noticed over time under V3 condition (50°C, 60% RH), which was ascribed to a post-curing process of the polymer matrix.
- In a same way, the interlaminar (ILS) strength was found very affected after 3 months exposure under immersion conditions (100% RH), especially at temperatures of 20°C and 40°C for which the laminate exhibits the highest water uptakes. Nevertheless, between 3 and 6 months ageing, a re-increase in the ILS was observed for immersed specimens, especially at temperatures of 40°C and 60°C which are relatively close to the Tg of the polymer matrix (around 54°C, as measured by DSC on unaged samples).

These findings suggest that both tensile and ILS properties are controlled by 2 antagonistic phenomena: (i) the plasticization of the polymer matrix / interfacial regions by water, which is dependent on the amount of water absorbed by the material and tends to decrease the mechanical properties; (ii) the post-cure of the polymer network which is mainly dependent on the ageing temperature and its relative value compared to Tg, and which tends to increase the mechanical properties of the laminate. In the present conditions, the plasticization process seems dominant in the first stage of the wet ageing process as the rate of sorption kinetics is maximal, and the post-cure effect becomes more dominant in the long term (after 3 months).

Regarding pull out tests, rupture modes and bond strength were also significantly affected under immersion conditions (100% RH), especially at ambient temperature (20°C). This may be assigned to extensive degradation of the chemical linkages between the CFRP material and the concrete substrate under the action of water molecules. This effect is emphasized at 20°C, because the network remains partially under-cured at this temperature and is thus vulnerable to hydrolysis.

Upcoming tests after ageing periods of 12 and 24 months and complementary microstructural characterizations by DSC and DMA (Dynamic Mechanical Analysis) will provide further evidences of the proposed mechanisms.

ACKNOWLEDGEMENT

Authors wish to acknowledge the National French Research Agency (ANR) for funding the MICRO project (contract ANR-15-C22-0007-04 – “MICRO: Matériaux Innovants Composites pour la Réparation d'Ouvrage”).

REFERENCES

- Benzarti K, Chataigner S., Quiertant M., et al. (2011). “Accelerated ageing behaviour of the adhesive bond between concrete specimens and CFRP overlays”, *Construction and Building Materials*, 25(2),523-538.
- Fatemi S.Z (2012). “Planification des essais accélérés: optimisation, robustesse et analyse”, PhD thesis from Université d'Angers (in French), <https://tel.archives-ouvertes.fr/tel-01004379/document>.
- Fayolle B., J. Verdu. (2005). Vieillissement Physique Des Matériaux Polymères Cor108. *Techniques de l'ingénieur*
- Gholami M, Sam A.R.M., Yatim J.M, Tahir M.M. (2013). “A Review on Steel/CFRP Strengthening Systems Focusing Environmental Performance.” *Construction and building Materials*, 47,301–310.
- Mercier Julien. (2007). “Prise En Compte Du Vieillissement et de l' Endommagement Dans Le Dimensionnement de Structures En Matériaux Composites.” PhD thesis from Ecole nationale Supérieure des Mines Paris (in French), <https://pastel.archives-ouvertes.fr/tel-00156986>.
- Quiertant M., Benzarti K., Schneider J., Landrin F., Landrin M., and Boinski F. (2017). “Effects of Ageing on the Bond Properties of Carbon Fiber Reinforced Polymer/Concrete Adhesive Joints: Investigation Using a Modified Double Shear Test”, *Journal of Testing and Evaluation*, 45(6), 1920-1932.
- Robert M., Roy R., Benmokrane B (2010). “Environmental effects on glass fiber reinforced polypropylene thermoplastic composite laminate for structural applications”, *Polymers and Composites*, 31(4), 604-11.
- Sethi S, Ray BC. (2015). “Environmental Effects on Fibre Reinforced Polymeric Composites: Evolving Reasons

and Remarks on Interfacial Strength and Stability.” *Advances in Colloid and Interface Science* 217. Elsevier ,43–67.

Wan B., Petrou M.F., Harries K.A (2006). “Effect of the presence of water on the durability of bond between CFRP and concrete”, *Journal of Reinforced Plastics Composites*, 25(8), 875–90.



ASTM SPECIFICATION FOR GLASS-FIBER REINFORCED POLYMER BARS FOR CONCRETE REINFORCEMENT

R. Gentry¹ and C. E. Bakis²

¹ Georgia Institute of Technology, School of Architecture, Atlanta, GA 30332 USA
Email: russell.gentry@arch.gatech.edu

² Pennsylvania State University, Engineering Science and Mechanics, University Park, PA 16802 USA

ABSTRACT

A major barrier to the acceptance of FRP composite materials in civil engineering is the lack of standard materials. Non-standard and proprietary materials must be qualified for short- and long-term performance, using test methods and meeting requirements that may also lack standardization. In North America, ASTM D30.10 – Composites for Civil Structures, develops test methods and material standards for FRP materials. This paper reports on the recently approved ASTM Standard for Solid Round Glass FRP Bars for Concrete Reinforcement. The standard covers requirements on constituent materials, bar geometry and testing for physical, mechanical and durability properties. The paper outlines the material specification, introduces the dependent test methods that support the specification, and discusses possible future standardization efforts for FRP bars in ASTM D30.

KEYWORDS

Codes, standards, internal reinforcement, GFRP bar

INTRODUCTION

In civil infrastructure, the progress of FRP composites material development and application has reached the stage where material and product standards are critical to continued market growth (Gutierrez et al. 2007; Stevens et al. 2017). This paper reports on the development of a standard specification for GFRP concrete reinforcements, recently approved by the American Society for Testing and Materials as ASTM D7957/D7957M-17 (ASTM D7957, 2017), Standard Specification for Solid Round Glass Fiber Reinforced Polymer Bars for Concrete Reinforcement.

Producers of infrastructure FRPs seeking independent qualification of their materials have pursued two avenues for acceptance, described here as “open standards” and “product acceptance evaluations”. Open standards are those published by national standards organizations (such as ASTM in the United States) and provide a set of tests and requirements by which any company can produce products meeting the standard. Product acceptance evaluations are given to an individual, often unique, product, which is certified to meet the set of requirements, developed for that product. These requirements are known as acceptance criteria. Organizations developing acceptance criteria include the ICC Evaluation Service in the United States and DIBt in Germany, for example. In general, it is faster to qualify a product using the “product acceptance evaluation” approach, and the first FRP repair materials used commercially in the United States were approved under ICC ES 125 using this approach (Rocca et al. 1997; ICC 2015). The development of consensus-based open standards is generally a much slower process than the development of product acceptance criteria.

Research reports in the early 2000’s highlighted a number of potential market segments for FRP materials, including FRP bridge decks (without concrete), pultruded FRP structures, FRP internally-reinforced concrete, FRP prestressed concrete, and FRP for repair and strengthening (Bakis et al. 2002; Burgoyne and Balafas 2007). Since that time, two market segments—non-prestressed internal concrete reinforcement and externally-bonded repair materials—are driving most of the commercial development of FRP materials in infrastructure. The standardization of test methods, materials and products specifications, and design codes, has been identified as key towards the development of mature markets for these infrastructure materials (Gentry et al. 2011) (Figure 1).

Development of materials specifications in North America has been funded by the Federal Highway Administration in the United States and by the ISIS Research Network and Public Works Canada in Canada. These efforts led to the development of model specifications for FRP materials (Bank et al. 2003) and to the first material specifications for internal concrete reinforcements (ACI 2008; CSA 2015) and for FRP repair materials (ACI 2013). For reinforced concrete structures in the United States, the American Concrete Institute (ACI) typically has jurisdiction over design codes and construction specifications and ASTM has jurisdiction over test

methods and material specifications. In 2005, a working group within ASTM D30 (Composite Materials) was established to transition test methods from ACI to ASTM. This working group within ACI 440K (FRP-Material Characteristics) later became Subcommittee ASTM D30.10 (Composites for Civil Structures). In 2012, the committees began to work on the recently published standard specification that is the focus of this paper. The authors of this paper have been the chairs of ASTM D30.10 and ACI 440K throughout this period of time.

The purpose of this paper is to outline the contents of the D7957/D7957M-17 bar specification (hereafter referred to D7957 for brevity), introduce the dependent test methods that support the specification, and discuss possible future standardization efforts for FRP bars in ASTM D30. The outline of the paper follows the outline of the specification.

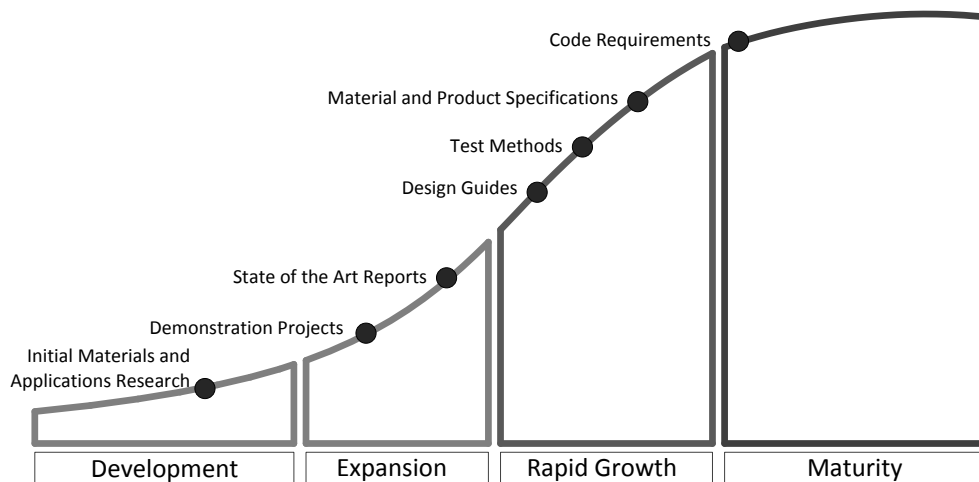


Figure 13: Product Life Cycle for Civil Infrastructure Materials (adapted from Gentry et al. 2011).

SCOPE

ASTM D7957 covers solid, round, GFRP bars provided in cut lengths and bent shapes and having an external surface enhancement for concrete reinforcement. Specifically excluded from the specification are bars made of hybridized load-bearing fibers, bars with no external surface enhancement for bonding with concrete, bars with cross-sectional geometries other than solid and round, and grids and gratings. Inch-pound and SI units are applicable as specifications D7957 and D7957M, respectively.

There is widespread interest on a range of FRP reinforcements that are outside the scope of the standard, including hollow GFRP bars, basalt fiber bars, and bars with non-circular cross sections. D7957 was developed in close coordination with the upcoming ACI design code for GFRP-reinforced concrete, and a decision was taken to limit D7957 to those materials that are widely available from commercial suppliers and that have significant testing data regarding parameters used in the design of reinforced concrete structures, such as bond and anchorage. The new ACI design code will follow D7957. The intent of D7957 and the upcoming ACI design code is not to hinder innovation and the development of new material systems and geometries, but rather to focus the standards and codes on proven materials, geometries, and composites manufacturing techniques. For the bars covered by these documents, there exists almost 25 years of laboratory and field data on strength, serviceability, and durability.

CLASSIFICATION AND GRADES

A central role of a material or product specification is to identify allowable permutations of the types of products covered by the specification. D7957 does not grade the products permitted, as only one material system is allowed: solid, round GFRP bars produced using vinylester resin with a fiber mass content greater than or equal to 70%. By comparison, the Canadian standard, CSA S807-10 (CSA 2015), permits carbon, glass and aramid fibers (but not hybrid fiber systems) with a range of fiber mass fractions. CSA also covers bars made with polyester, vinylester and epoxy resins.

ASTM Committee D30 has chosen to focus on a single product based on coordination with the upcoming ACI code as discussed previously. In addition, we believe that standards play two important market roles: (1) to standardize those products which have demonstrated performance and market acceptance and (2) to clarify, clearly describe (and even limit) the number of products available so as to produce a market for a structural commodity – as has generally happened for other civil infrastructure materials, for example: steel rebar, CMU block, ready-

made concrete, and structural steel shapes. This belief is reinforced by the guidelines for standardization set by ASTM in the Form and Style Manual (ASTM 2017): “Standardization is an inevitable byproduct of most specifications. In some cases it may be the primary function. Standardization involves a deliberate and possibly arbitrary choice of a limited number from the multiplicity of qualities, sizes, compositions, etc., that may be available.”

CONSTITUENT MATERIALS

D7957 is limited to E-glass fibers and vinylester resins as these are the predominant materials in use to-date. Literature on GFRP durability has concluded that typical polyester resin systems do not provide the durability needed for GFRP bars used in conjunction with concrete (Bakis et al. 1998; Gentry et al. 1998; Benmokrane et al. 2002; ACI 2015). Epoxy resin systems are generally used with carbon fibers, are more expensive than vinylesters, and are difficult to pultrude as compared to vinylesters. The standard does not contain prescriptive limits on the use of fillers and additives, but rather provides a list of performance requirements (durability, moisture absorption, glass transition temperature) that preclude the use of inappropriate filler types and amounts.

PROPERTY REQUIREMENTS

The property requirements for bars are broken into four categories: physical properties, which include geometric limits, glass transition temperature, degree of cure, and fiber mass content; mechanical properties, which include tensile, bond, and shear properties; durability properties, which include moisture uptake limitation and alkali resistance; and finally, specific requirements for bent bars. Successful testing of three or more production lots of the bars, according to the test methods and meeting the limits as shown in Table 1, qualifies the bars as meeting the standard. Table 1 refers to mean and guaranteed values, where “mean” is the arithmetic mean of the population sample and “guaranteed” is the mean minus three standard deviations of the sample, as is the custom in US GFRP design guidelines. Ongoing testing of individual bars, selected at random from production lots, according to the methods and meeting the limits shown in Table 2, ensures that ongoing production of bars continues to meet the standards. Tables 1 and 2 refer to Table 3 of D7957 for certain properties, although Table 3 of D7957 is not included in this paper. Tables 1 and 2 have been reproduced here, directly from the standard, with permission from ASTM.

The tests in Table 2 apply for both quality control and certification testing. Though related, the two concepts are different. Quality control is an internal process overseen by the manufacturer, and is completed on every lot of bars produced, to ensure that their production process continues to produce bars meeting the standard. Manufacturers are required to use the tests shown in Table 2, but may also use other tests for quality control. Certification testing is additional testing, often completed by an independent testing lab, which is requested by the purchaser of bars. Certification testing is optional.

Table 1: Property Limits and Test Methods for Qualification^A

Property	Limit	Test Method
Mean Glass Transition Temperature	Midpoint temperature ≥ 100 °C [212 °F]	ASTM E1356
Mean Degree of Cure	≥ 95 %	ASTM E2160
Mean Measured Cross-Sectional Area	Table 3	ASTM D7205/D7205M, subsection 11.2.5.1
Guaranteed ^B Ultimate Tensile Force	Table 3	ASTM D7205/D7205M
Mean Tensile Modulus of Elasticity	$\geq 44,800$ MPa [6 500 000 psi]	ASTM D7205/D7205M
Mean Ultimate Tensile Strain	≥ 1.1 %	ASTM D7205/D7205M
Guaranteed ^B Transverse Shear Strength	≥ 131 MPa [19 000 psi]	ASTM D7617/D7617M
Guaranteed ^B Bond Strength	≥ 7.6 MPa [1100 psi]	ASTM D7913/D7913M
Mean Moisture Absorption to Saturation	≤ 1.0 % to saturation at 50 °C [122 °F]	ASTM D570, subsection 7.4
Mean Alkaline Resistance	≥ 80 % of initial mean ultimate tensile force following 90 days at 60 °C [140 °F]	ASTM D7705/D7705M, Procedure A
Guaranteed ^B Ultimate Tensile Force of Bent Portion of Bar	≥ 60 % of the values in Table 3	ASTM D7914/D7914M

^AFor the determination of the mean and guaranteed properties, at least 24 samples shall be obtained in groups of eight or more from three or more different production lots. The mean and guaranteed properties shall satisfy the limits.

^BGuaranteed property is defined in 3.2.5.

Physical Properties

A key physical property of bars is size. The bar sizes listed in Table 3 of D7957 are mapped to the size of conventional steel reinforcing bars, whose size is dictated by ASTM A615 (2016). The bar sizes range from No.2 (nominally 0.25 in. or 6.3 mm diameter) to No. 10 (nominally 1.27 in. or 32.3 mm diameter). The nominal area of the GFRP bars, determined using immersion testing by ASTM D7205 (2016), subsection 11.2.5.1, is taken to be the same as that of equivalently numbered steel bars, but some modest latitude is given for measured cross-sectional areas due to the variety of ways that adequate bar/concrete bond is assured with surface texturing and supplementary treatments. The bar size requirement is another element of standardization—meaning that only bars that are equivalents to the conventional steel bars are allowed by the standard. This provision is enforced to

promote acceptance of the GFRP bars in the US marketplace, which is accustomed to the bar number nomenclature used for steel reinforcing bars.

Both glass transition temperature (T_g) and degree of cure are required to be measured using ASTM E1356 (2014) and E2160 (2012), respectively. The limits on these properties are set to acknowledge the fact that resin systems with low T_g (when fully cured) or with low degree of cure (relative to the fully cured state) demonstrate durability issues in moist environments. In addition, the minimum T_g is coordinated with fire provisions that are being developed for the ACI design code.

Finally, the physical properties include the minimum fiber mass content for the bars ($\geq 70\%$). This fiber mass content, found using ASTM D2584 (2011) or ASTM D3171 (2015), is used to establish the minimum guaranteed tensile force of each bar size, which, along with the elastic modulus, is a key characteristic used in the design of RC structures with GFRP bars.

Table 2: Property Limits and Test Methods for Quality Control and Certification^{A, B}

Property	Limit	Test Method
Fiber Mass Content	$\geq 70\%$	ASTM D2584 or ASTM D3171
Glass Transition Temperature	Midpoint temperature $\geq 100\text{ }^\circ\text{C}$ [212 $^\circ\text{F}$]	ASTM E1356
Degree of Cure	$\geq 95\%$	ASTM E2160
Measured Cross-Sectional Area	Table 3	ASTM D7205/D7205M, subsection 11.2.5.1
Ultimate Tensile Force	Table 3	ASTM D7205/D7205M
Tensile Modulus of Elasticity	$\geq 44\ 800\ \text{MPa}$ [6 500 000 psi]	ASTM D7205/D7205M
Ultimate Tensile Strain	$\geq 1.1\%$	ASTM D7205/D7205M
Moisture Absorption in 24 h	$\leq 0.25\%$ in 24 h at $50\text{ }^\circ\text{C}$ [122 $^\circ\text{F}$]	ASTM D570, subsection 7.4

^AFor the determination of each of the property limits, five random samples shall be obtained from each production lot. Each individual sample shall satisfy the property limits.

^BFor bent bars, the tests are performed on the straight portion of the bars.

Mechanical Properties

The mechanical properties of the bars include the tensile properties (strength, modulus of elasticity, and ultimate strain), transverse shear strength, and bond strength. For qualification, only the strength limits are expressed in terms of guaranteed values. Tensile strengths are stated in force units, not stress units, as the standard acknowledges that GFRP exhibits a shear lag effect and larger bars have lower effective strengths. The mean modulus and strain limits are constant across all bar sizes: 44.8 GPa (6.5×10^6 psi) and 1.1%, respectively. The tensile properties of the bars are established by ASTM D7205 (2016).

Transverse shear strength and bond strength, which are included only in the qualification requirements, are constant for all bar sizes. These properties are not used directly in design calculations for reinforced concrete members, but are set at appropriate levels to ensure that high quality materials with adequate properties are being delivered according to the standard. The minimum guaranteed transverse shear strength, established by ASTM D7617 (2017) is 131 MPa (19,000 psi). The minimum guaranteed bond strength, established by ASTM D7913 (2014), is 7.6 MPa (1100 psi).

Durability Properties

Durability properties are specified to ensure that the short-term mechanical and physical properties specified by the standard will be maintained at predictable levels during the service life of the bars. The first durability concern deals with moisture uptake, as excess moisture content can lead to plasticization of the polymer matrix and reduced bond between the matrix and glass fibers, along with pitting of the glass fiber and subsequent loss of tensile strength (Gentry et al. 1998). Intrusion of alkaline solutions, from Portland cement concrete porewater, exacerbates the moisture attack on the glass fibers in the bar. A fully-cured bar with low equilibrium moisture uptake has shown to be durable, even in aggressive alkaline environments at elevated temperatures (Robert and Benmokrane 2009).

For product qualification, the standard requires that the equilibrium moisture content of the bar be less than or equal to 1% when conditioned at $50\text{ }^\circ\text{C}$ according to the provisions of ASTM D570 (2010). The standard also requires that bars retain at least 80% of their initial mean ultimate tensile force when conditioned at $60\text{ }^\circ\text{C}$ in an alkaline solution, for 90 days, according to ASTM D7705 (2012). Both of these tests require long durations for completion, and are thus not suitable for quality control or certification testing. Therefore, for quality control or certification testing, a maximum moisture absorption of 0.25% is allowed for bars conditioned at $50\text{ }^\circ\text{C}$ for 24 hours.

Requirements for Bent Bars

FRP bars are bent to provide anchorage to concrete at the termination of bars within reinforced concrete structures. The production of bent FRP bars is of specific concern as, in some cases, straight sections of bars are removed

from the continuous production process and the bends are completed while the resin matrix is in a liquid state. In other cases, the bent bar is produced in a separate molding operation that is distinct from the continuous manufacturing method (usually pultrusion) that produces the straight bar. In addition, because of the inherent orthotropy of the fiber reinforcement, and the complex stress state in the bent bars at the anchorage location, the bend strength of the bars is typically lower than the straight tensile strength.

To accommodate these realities, D7957 provides standard bend diameters, provides lower limits on the strengths of bars at the bend locations, and requires that the straight portion of the bent bar meet the same tensile force and modulus limits as non-bent bars. The strength of bent bars at the bend locations is accomplished using a push-apart test with bars cast in concrete, according to ASTM D7914 (2014), which is an expensive and time-consuming test. Therefore, these tests are completed only for product qualification. For quality control and certification, only the straight portion of the bent bar is required to be tested using ASTM D7205 (2016).

SAMPLING, REJECTION, AND PRODUCT CERTIFICATION

D7957 provides two separate requirements for sampling. For the initial qualification of a bar type and size as meeting the standard, three or more sets of specimens from different production lots, with eight or more samples in each set, are selected for testing. A note in the standard emphasizes the benefit of using larger sample sizes to develop the population statistics for the qualifying material properties. These 24 (or more) samples are tested according to the tests shown in Table 1, and mean and guaranteed properties are calculated for the group of samples. These mean and guaranteed properties must exceed the property limits, also shown in Table 1, for the material to qualify according to the standard.

For ongoing production of bars, quality control and certification testing requires that 5 samples be selected at random from each production lot. Each sample is tested according to the tests shown in Table 2, and each test (individually) must meet the property limits shown in Table 2. If one or more of the samples fails to meet the limits, the entire lot of material is rejected.

MARKINGS AND TRACEABILITY

D7657 requires that bars be indelibly marked at regular intervals along their length with information on the ASTM specification number, the manufacturer's mark, the bar size, and the production lot number. Additional information on bar geometry may be given for bent bars.

FUTURE STANDARDS DEVELOPMENT IN ASTM D30

To promote both innovation and the expansion markets for FRP concrete reinforcements, ASTM D30.10 is preparing additional standard specifications and test methods. It is anticipated that the development of new standard specifications will be accelerated given the precedent set by D7957. Other bar constituents and bar shapes are currently under discussion. Updates to supporting test methods are needed to accommodate such additional bar materials and shapes. Revisions to the suite of bar test methods to uniformly adopt the bar size nomenclature in D7957 will be rolled out in the near future.

The committee also anticipates the development of new test methods focusing on the behavior of bars. Test methods already in draft form include tensile fatigue testing of bars, long-term relaxation of bars, bar anchorage testing, and the testing of bars at deflectors. Finally, the committee has identified a need to detect voids in bars, either directly or through a mechanical property. Testing of bars in a short beam fixture has been cited as one means for detecting voids in bars.

ACKNOWLEDGEMENTS

The authors acknowledge the members of ASTM D30 (Composite Materials) and ACI 440 (Fiber-Reinforced Polymer Reinforcement) for their diligence in the development and balloting of the standard. Tables 1 and 2 from D7957 are reprinted, with permission, from D7957/D7957M-17 Standard Specification for Solid Round Glass Fiber Reinforced Polymer Bars for Concrete Reinforcement, copyright ASTM International, 100 Barr Harbor Drive, West Conshohocken, PA 19428. A copy of the complete standard may be obtained from ASTM, www.astm.org.

REFERENCES

ACI (2008). Specification for Carbon and Glass Fiber-Reinforced Polymer Bar Materials for Concrete Reinforcement, ACI 440.6-08, American Concrete Institute, Farmington Hills, MI, USA.

- ACI (2013). Specification for Carbon and Glass Fiber-Reinforced Polymer Materials Made by Wet Layup for External Strengthening, ACI 440.8-13, American Concrete Institute, Farmington Hills, Michigan, USA.
- ACI (2015). Guide for the Design and Construction of Structural Concrete Reinforced with Fiber-Reinforced Polymer Bars, 440.1R-15, American Concrete Institute, Farmington Hills, MI, USA.
- ASTM (2017). Form and Style for ASTM Standards, ASTM International, West Conshohocken, PA, USA.
- ASTM A615 (2016). Specification for Deformed and Plain Carbon-Steel Bars for Concrete Reinforcement, ASTM A615/A615M-16, ASTM International, West Conshohocken, PA, USA.
- ASTM D570 (2010). Test Method for Water Absorption of Plastics, D570-98(2010)^{e1}, ASTM International, West Conshohocken, PA, USA.
- ASTM D2584 (2011). Test Method for Ignition Loss of Cured Reinforced Resins, ASTM D2584-11, ASTM International, West Conshohocken, PA, USA.
- ASTM D3171 (2015). Test Methods for Constituent Content of Composite Materials, ASTM D3171-15, ASTM International, West Conshohocken, PA, USA.
- ASTM D7205 (2016). Test Method for Tensile Properties of Fiber Reinforced Polymer Matrix Composite Bars, ASTM D7205/D7205M-06(2016), ASTM International, West Conshohocken, PA, USA.
- ASTM D7617 (2017). Test Method for Transverse Shear Strength of Fiber-reinforced Polymer Matrix Composite Bars, ASTM D7617/D7617M-11(2017), ASTM International, West Conshohocken, PA, USA.
- ASTM D7705 (2012). Test Method for Alkali Resistance of Fiber Reinforced Polymer (FRP) Matrix Composite Bars used in Concrete Construction, ASTM D7705/D7705M-12, ASTM International, West Conshohocken, PA, USA.
- ASTM D7913 (2014). Test Method for Bond Strength of Fiber-Reinforced Polymer Matrix Composite Bars to Concrete by Pullout Testing,” ASTM D7913/D7913M-14, ASTM International, West Conshohocken, PA, USA.
- ASTM D7914 (2014). Test Method for Strength of Fiber Reinforced Polymer (FRP) Bent Bars in Bend Locations, ASTM D7914/D7914M-14, ASTM D7913/D7913M-14, ASTM International, West Conshohocken, PA, USA.
- ASTM D7957 (2017). Standard Specification for Solid Round Glass Fiber Reinforced Polymer Bars for Concrete Reinforcement, ASTM D7957/D7957M-17, ASTM International, West Conshohocken, PA, USA.
- ASTM E1356 (2014). Test Method for Assignment of the Glass Transition Temperatures by Differential Scanning Calorimetry, ASTM E1356-08(2014), ASTM International, West Conshohocken, PA, USA.
- ASTM E2160 (2012). Test Method for Heat of Reaction of Thermally Reactive Materials by Differential Scanning Calorimetry, ASTM E2160-04(2012), ASTM International, West Conshohocken, PA, USA.
- Bakis, C. E., A. I. Preimanis, D. Gremel, A. Nanni, (1998) “Effect of resin material on bond and tensile properties of unconditioned and conditioned FRP reinforcement rods.” 1st International Conference on Durability of FRP Composites for Construction, CDCC98, Sherbrooke, Quebec, Canada, 525–533.
- Bakis, C. E., L. C. Bank, V. L. Brown, E. Cosenza, J. F. Davalos, J. J. Lesko, A. Machida, S. H. Rizkalla, Triantafillou, T.C. (2002). “Fiber-reinforced polymer composites for construction - State-of-the-art review,” *Journal of Composites for Construction*, 6(2), 73-87.
- Bank, L. C., T. R. Gentry, B. P. Thompson, J. S. Russell (2003). “A model specification for FRP composites for civil engineering structures,” *Construction and Building Materials*, 17, 405-437.
- Benmokrane, B., P. Wang, T. M. Ton-That, H. Rahman, and J. F. Robert (2002). “Durability of glass fiber-reinforced polymer reinforcing bars in concrete environment,” *Journal of Composites for Construction*, 6(3), 143-153.
- Benmokrane, B., E. El-Salakawy, A. El-Ragaby, T. Lackey (2006). “Designing and testing of concrete bridge decks reinforced with glass FRP bars,” *Journal of Bridge Engineering*, 11(2), 217-229.
- Burgoyne, C., I. Balafas (2007). “Why is FRP not a Financial Success?,” 8th International Symposium on Fiber-Reinforced Polymer Reinforcement for Concrete Structures (FRPRCS-8), University of Patras, Patras, Greece.

CSA (2015). Specification for Fibre-Reinforced Polymers, CSA S807-10 (R2015), CSA Group, Mississauga, Ontario, Canada.

Gentry, T. R., C. Bakis, K. Harries, J. Brown, A. Prota, R. Parretti (2011). "Test method development for infrastructure composites applications," SAMPE Tech 2011 Conference and Exhibition: Developing Scalable Materials and Processes for Our Future, October 17, 2011 - October 20, 2011, Fort Worth, Texas, USA.

Gentry, T. R., L. Bank, A. Barkatt, L. Prian (1998). "Accelerated test methods to determine the long-term behavior of composite highway structures subject to environmental loading," *Journal of Composites Technology and Research*, 20(1), 38-50.

Gutierrez, E., S. Dimova, A. Pinto (2007). Purpose and Justification for New Design Standards Regarding the Use of Fibre-Reinforced Polymer Composites in Civil Engineering, EUR 22864 EN, Joint Research Centre, European Commission, Ispra, Italy.

ICC ES AC125 (2015). Acceptance Criteria for Concrete and Reinforced and Unreinforced Masonry Strengthening using Externally Bonded Fiber-Reinforced Polymer (FRP) Composite Systems, ICC Evaluation Service, Brea, California, USA.

Robert, M, P. Cousin, B. Benmokrane (2009). "Durability of GFRP Reinforcing Bars Embedded in Moist Concrete," *Journal of Composites for Construction*, 13(2), 66-73.

Rocca, S. M. Ekenel, N. Galiati, B. Gerber, T. Alkhrdaji (2011). "Recent revisions to acceptance criteria for concrete and masonry strengthening using externally bonded FRP Systems (AC125)," 10th International Symposium on Fiber Reinforced Polymer Reinforcement for Concrete Structures (FRPRCS-10), Tampa, Florida, USA, April 2-4, 2011.

Stevens, R. P., S. Quinn, R. Veal, S. Gerrard, M. Tsimplis, J. Dulieu-Barton, O. Thomsen (2017). Modernising composite material regulations: A Position Paper. University of Southampton, Southampton, UK.



EFFECT OF INTERNAL MOISTURE CONTENT ON THE T_g VALUES OF CFRP RODS

Eleni Toumpanaki¹, Janet M. Lees², Michel Barbezat³ and Giovanni P. Terrasi⁴

¹Department of Architecture, Centre for Natural Material Innovation, University of Cambridge, 1-5 Scroope Terrace, Cambridge, CB2 1PX, Email: et343@cam.ac.uk

²Engineering Department, University of Cambridge, Trumpington Street, Cambridge, CB2 1PZ, Email: jml2@eng.cam.ac.uk

³Laboratory for Mechanical Systems Engineering, Swiss Federal Laboratories for Materials Science and Technology (EMPA), Überlandstrasse 129, 8600 Dübendorf, Email: michel.barbezat@empa.ch

⁴Laboratory for Mechanical Systems Engineering, Swiss Federal Laboratories for Materials Science and Technology (EMPA), Überlandstrasse 129, 8600 Dübendorf, Email: giovanni.terrasi@empa.ch

ABSTRACT

DMA tests are used for the material characterisation of CFRP tendons for civil engineering applications and to assess the high temperature behavior of CFRP prestressed structures by measuring the glass transition temperature T_g . The glass transition temperature is sensitive to the moisture content of the CFRP tendons and standard test methods (e.g. ASTM D7028 (ASTM 2007)) have not yet qualitatively addressed the effect of small moisture content variations from environmental conditions in the T_g values. The effect of the internal moisture content on the T_g values of two CFRP rods with different diameters and manufacturing process is evaluated. Lab conditioned specimens with varying drying time (9, 15, 36 and 210 days) and thus moisture content are tested to study the effect of small lab conditions variations in the glass transition temperature and the sensitivity of the DMA testing. Exposed specimens at 60°C for roughly 3 years are also investigated to record effect of greater moisture absorption on the T_g values. Two heating runs were conducted for every test to differentiate post-curing effects and mass weight measurements were recorded before and after each heating run. A linear relationship between the mass loss of the specimens due to drying at vacuum and during the heating runs with the glass transition temperature T_g was observed. Post-curing effects could not be clarified even for the dry specimens. The exposed specimens showed a reduction in T_g of 38°C that was reversible after drying. It is recommended that the use of T_g values to infer the degree of curing should be carried out on dry specimens.

KEYWORDS

CFRP, DMA test, Material Characterisation, Environmental Conditions.

INTRODUCTION

Composite materials such as CFRP (Carbon Fibre Reinforced Polymer) rods are increasingly used in structural applications as a proactive measurement against steel corrosion. However, despite being non-corrosive, the structural behavior of CFRPs depends on the performance of the polymer matrix. When exposed to wet environments, the matrix tends to absorb water and consequently swells and plasticizes. The matrix also softens at high temperatures. The softening of the matrix can lead to a degradation of the mechanical properties. Thus the performance of CFRPs is dictated not only by the carbon fibres but also by the chemical stability of the epoxy.

In the civil engineering industry, material characterization methods are being proposed to assess the matrix performance i.e. Interlaminar Shear Test Methods (ILSS), and network structure of composite materials i.e. Differential Scanning Calorimetry (DSC) and Dynamic Mechanical Analysis (DMA). These test methods are well-known in mechanical engineering applications (naval and aeronautical), where FRP laminates are widely used, but are relatively new in the civil engineering field.

DMA tests measure the temperature at which the epoxy in a CFRP tendon moves from a glassy to a rubbery state. This point is termed the glass transition temperature, T_g , and is used to study the high temperature behaviour of CFRP reinforced and prestressed structures and to infer the degree of cross-linking. In a DMA test, the specimen is subjected to a minor sinusoidal oscillation as a function of time and temperature by applying a small sinusoidal force. This force can be applied longitudinally (uniaxial tension or compression), transversally (bending mode) or

in a torsional mode. Dynamic mechanical properties such as the storage modulus, E' , loss modulus, E'' , and loss factor, $\tan\delta = E''/E'$, are derived from DMA tests and different T_g values are obtained from the relevant plots of E' , E'' or $\tan\delta$ vs temperature. The storage modulus E' represents the stiffness of a viscoelastic material and is related to the elastic energy stored during a loading cycle whereas the loss modulus E'' represents the energy lost during a loading cycle. As shown in Figure 1, the $T_{g-onset}$ value is determined from tangent lines associated with the initial slope of the storage modulus (at the point where there is a drop in modulus (2)) and a slope after softening that is extrapolated from the inflection point (1). T_{g-loss} and $T_{g-tan\delta}$ are defined as the temperatures where the peak E'' and $\tan\delta$ values are recorded respectively (see Figure 1). The definition of $T_{g-onset}$ can be subjective as the tangent lines from the inflection point and the initial slope are open to interpretation and it depends if the values are plotted in a linear or a log axis. Therefore, the $T_{g-tan\delta}$ and T_{g-loss} definitions are preferred to deliver a better accuracy and consistency.

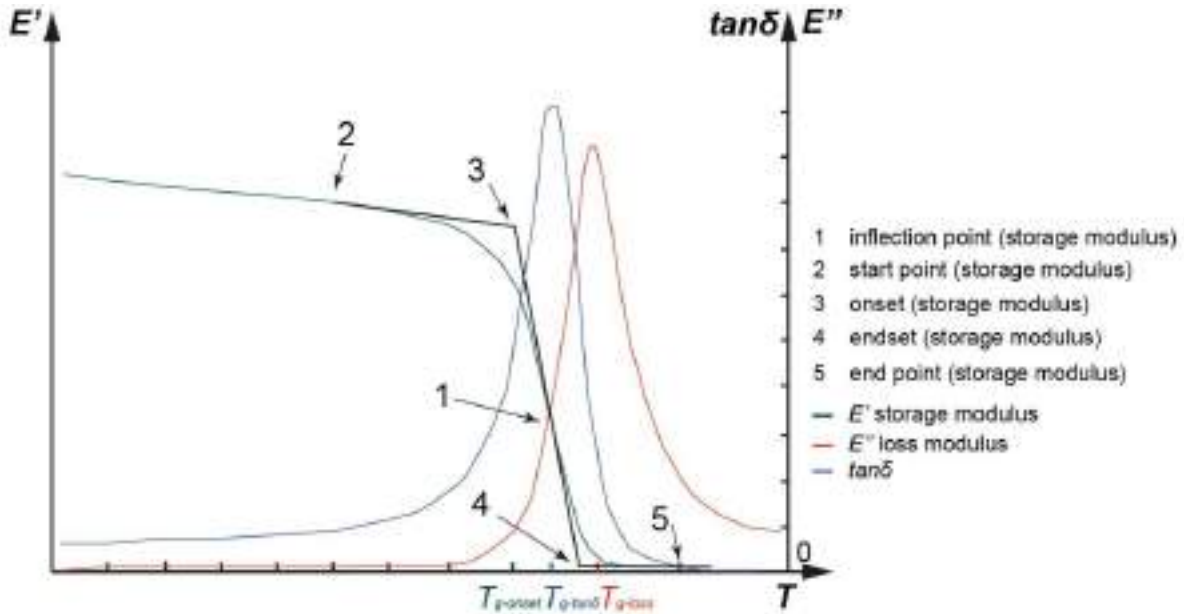


Figure 1: Definitions of glass transition temperature: $T_{g-onset}$, T_{g-loss} and $T_{g-tan\delta}$.

The glass transition temperature is sensitive to the initial moisture content in CFRP tendons. However, standard test methods (e.g. ASTM D7028 (ASTM 2007)) have not yet qualitatively addressed the effect of small moisture content variations due to environmental conditions on measured T_g values. This can lead to variations in the DMA T_g values for the same material when tested in different lab conditions. This is important when DMA tests are being used to infer the level of curing since deviations in the T_g values due to the initial moisture content can lead to erroneous conclusions about the level of crosslinking density in the epoxy of CFRP specimens. A decrease in the T_g value with increasing moisture content has been experimentally recorded (Birger et al. 1989; Nogueira et al. 2000; Chateauinois et al. 1995). It has been suggested that, as a general rule of thumb, a decrease in T_g of around 20°C could be expected for a 1% increase in moisture content (Wright 1981). A drop in T_g values of up to 34°C has been observed for CFRP laminates conditioned in humid air ($RH=95\%$) at 50°C for 960 hr with a 1.7% moisture uptake and a reference T_g value of 135°C (Birger et al. 1989). Similar findings have been reported for GFRP although proved to be reversible after drying of the exposed specimens (Chateauinois et al. 1995, Robert and Benmokrane 2010). However, the reversibility of the plasticising effect is dependent on the epoxy system and irreversible decreases of up to 15°C have been reported elsewhere (Chateauinois et al. 1990). Chateauinois et al. (1995) showed that the width of the $\tan\delta$ plot increases and the $\tan\delta$ value decreases with increasing moisture content. A linearly decreasing relationship between the T_g and mass uptake of GFRP specimens was reported irrespective of the exposure temperature

(range $70-90^\circ\text{C}$). A weight loss of up to 60% of the initial water content for the exposed specimens was recorded when the transition to the rubbery state was achieved and a change in the desorption rate was found analytically. This change in the desorption curve was not clear under high DMA heating rates due to the shorter drying time. Plasticising effects will not be reversible if the CFRP specimens are exposed to high temperatures close to the wet T_g values where additional degradation mechanisms can take place.

The influence of different internal moisture contents on the glass transition temperature of CFRP samples is assessed in this paper by undertaking DMA tests on specimens that have been subjected to different drying regimes. The post-curing effect during a heating run is evaluated. The reversibility of plasticisation effects and irreversible degradation mechanisms are also studied by testing CFRP specimens that have been exposed in water at 60°C for nearly 3 years.

EXPERIMENTAL PROCEDURE

Materials

To study the effect of the internal moisture content on the measured T_g values, two groups of CFRP tendons, groups C and D, were used. The tendons had the same epoxy and carbon fibres but a different diameter, manufacturing process and preconditioning regime. The material properties, as provided by the manufacturer, and main differences between the two tendon groups are summarized in Table 1. Group C tendons were manufactured uncoated for research purposes. The group D tendons were a commercial product and had an outer sand coating layer to improve the bond between the tendon and the concrete. This means that there was an additional in-line production step during pultrusion, where an extra epoxy layer was applied, sand particles were sprayed and further curing followed. All the tendons were produced by the same manufacturer and the core tendon had the same curing regime. The exact details of the curing process are confidential but during the curing process a maximum temperature of 195°C was reached. For comparison purposes, the outer sand coating layer on the group D tendons was gently removed with a blade to avoid misinterpretation of the DMA results due to the additional external resin layer.

Table 1: Material properties of the group C and D CFRP tendons.

SPECIMEN TYPE	C	D
MATRIX/EPOXY HARDENER	EPR 4434/EPH 943	EPR 4434/EPH 943
FIBRES	TENAX UTS 5631	TENAX UTS 5631
VOLUME FRACTION	0.64	0.64
NOMINAL CORE TENDON DIAMETER ¹ (MM)	4.2	5.4
MANUFACTURING PROCESS	UNCOATED	ORIGINALLY SAND COATED
PRE-CONDITIONING	DRIED IN THE OVEN AT 60°C FOR 2 YEARS AND EXPOSED IN WATER AT 60°C FOR ROUGHLY 3 YEARS	STORED IN LAB CONDITIONS
	PREVIOUSLY TESTED IN TORSION	NOT TESTED PREVIOUSLY

Note: ¹ The core tendon diameter is the diameter without the sand coating layer (resin rich layer and sand particles).

Experimental Programme

The group D samples were tested to study the effect of internal moisture content on the T_g values. Therefore, CFRP samples, that had been previously stored in the lab at the University of Cambridge, were dried in a vacuum oven at 80°C for 9, 15, 36 and 210 days and subsequently tested in a DMA machine. Two samples were tested after each drying time and two lab conditioned samples were used as control specimens. Group C samples were used to study the effect of sustained exposure to moisture on the glass transition temperature and thus on the network structure of epoxy. These samples were extracted from a 300 mm long CFRP tendon that was previously tested in torsion within the elastic range (Toumpanaki et al. 2015) after immersion in water at 60°C and no cracking was visually observed. The specimen had been stored in an oven at 60°C for roughly 3 years to

reach a dry condition before exposure in water. The central 200 mm region of the specimen was fully immersed in distilled water whereas the ends of the specimen remained unexposed. One 'dry' control specimen for this group was therefore cut from the unexposed ends. Optical microscopy in group C untested samples showed a significant void content attributed to the manufacturing process. No voids were observed in group D samples. As mentioned in Toumpanaki et al. (2015), the increased number of voids in group C resulted in a higher mass uptake

rate and mass uptake value at saturation leading to a potential greater matrix degradation. Therefore, the contribution of any microcracking from the torsion testing in the moisture absorption was considered negligible.

Two heating runs in the DMA machine were carried out for all samples from both groups. A second heating run was adopted to differentiate between the post-curing effect and the drying effect in terms of any increase in the T_g value. All samples were weighed with a digital balance with a 0.0001g accuracy before and after every heating run.

DMA tests

The glass transition temperature T_g was measured using DMA. The DMA tests (Eplexor 500 from Gabo Qualimeter, Germany) were performed under 3 point bending mode at a 10 Hz frequency and ramp rate of 2°C min from 23–210°C. The maximum load cell capacity in the majority of DMA tests was 150 N. A dynamic amplitude of 0.008% was superposed on a static load of 0.023% flexural strain. All CFRP rod samples from both groups were 50 mm long. For consistency the $T_{g-tan\delta}$ definition was adopted for comparison purposes.

EXPERIMENTAL RESULTS

The glass transition temperature versus mass loss as recorded before and after each heating run for the group D specimens are depicted in Figure 2. All the $T_{g-tan\delta}$ and mass loss values are summarized in Table 2. The notation used is A-#-B-# where the first letter denotes the group D CFRP samples, the first number is the storage days at 80°C in a vacuum (i.e. 0 for the control specimens), the second letter is either ‘a’ or ‘b’ to identify the specimen tested after the same storage conditions, and the number, 1 or 2, is indicative of the 1st or 2nd heating run respectively. The group D lab-conditioned specimens yield an average $T_{g-tan\delta} = 143.5^\circ\text{C}$ and for the ‘dry’ specimens $T_{g-tan\delta} = 171.1^\circ\text{C}$ after the 1st heating run. A maximum increase of 29°C is observed between the lab-conditioned and dried specimens after the second heating run. This was attributed to a –0.68% mass loss due to drying in a vacuum and during DMA testing. The $T_{g-tan\delta}$ values were found to increase linearly with the mass loss according to Eq. 1.

$$T_{g-tan\delta} = -41.47 \Delta M + 140.2 \quad (1)$$

In Figure 2 the $T_{g-tan\delta}$ value is plotted against the mass loss for the group D specimens. A post-curing effect during the 1st and 2nd heating runs cannot be clearly isolated since moisture evaporation is observed during both runs. In the dry specimens desiccated in a vacuum for 210 days, the $T_{g-tan\delta}$ increases by 1.3°C on average after the 2nd heating run and 0.04% moisture evaporation and this change is also consistent with Eq. 1. This suggests that either the CFRP tendons were fully cured or that any potential post-curing effect takes place gradually during the heating runs and so cannot easily be discerned. From Table 2 it is observed that the control specimens and the specimens tested after 9 days have not yet reached the fully dry conditions even after the second heating run. A third heating run could yield even higher $T_{g-tan\delta}$ values associated with moisture evaporation up to –0.68%. Hence, the results from a second heating run to assess the degree of curing in CFRPs should be used with caution since the increases in the $T_{g-tan\delta}$ values can be related to moisture evaporation rather than additional curing effects. It is therefore important to weigh specimens before and after each DMA test to try to differentiate between these two phenomena that influence the glass transition temperature.

The storage modulus E' and $\tan\delta$ values versus temperature curves for one unexposed and two exposed group C specimens are shown in Figure 3. The notation used is A-B-# where the first letter denotes the group C CFRP samples, the second letter is either ‘a’ or ‘b’ for the exposed samples and ‘c’ for the unexposed sample, and the number, 1 or 2, is indicative of the 1st or 2nd heating run respectively. The $T_{g-tan\delta}$ values and mass losses recorded after each heating run are summarised in Table 3. The $T_{g-tan\delta}$ values of the exposed samples in the first run are roughly 38°C lower than the $T_{g-tan\delta}$ of the unexposed sample. The 2nd runs of the exposed samples yield

$T_{g-tan\delta}$ values in the same range as the $T_{g-tan\delta}$ value from the 1st run of the unexposed sample. The moisture induced decrease in $T_{g-tan\delta}$ could be attributed to reversible plasticising moisture effects. Additional degradation mechanisms are not observed and the T_g values of the wet specimens are well above the exposure temperature of 60°C. This is also indicated by the decrease in the width of the $\tan\delta$ plots between the 1st and 2nd runs for the exposed samples. The mass loss recorded after the 1st run is representative of the mass at saturation for the group C CFRP specimens exposed at 60°C (Toumpanaki et al. 2015). The $T_{g-tan\delta}$ value in the second run for the unexposed specimen is 8.6°C higher than the first run and associated with a loss of 0.10% of moisture. This is a

twice the theoretical glass transition temperature change of 4.15°C that would be predicted based on Eq.1 and might indicate that the group C was not fully cured during the manufacturing process.

Table 2: $T_{g-tan\delta}$ and mass loss during the DMA heating runs- Group D experimental series.

	$T_{g-tan\delta}$	ΔM (%) DMA test	before ΔM (%) after 1st run	ΔM (%) after 2nd run
D-0-a-1	143.6	N/A	-0.333	
D-0-a-2	159.8			-0.388
D-0-b-1	143.3	N/A	-0.225	
D-0-b-2	155.9			-0.282
D-9-a-1	157.0	-0.397	-0.397	
D-9-a-2	161.3			-0.452
D-9-b-1	157.9	-0.363	-0.419	
D-9-b-2	160.2			-0.476
D-15-a-1	158.3	-0.385	-0.440	
D-15-a-2	163.0			-0.495
D-15-b-1	159.2	-0.406	-0.746	
D-15-b-2	169.0			-0.848
D-36-a-1	163.2	-0.522	-0.578	
D-36-a-2	167.8			-0.578
D-36-b-1	164.7	-0.512	-0.568	
D-36-b-2	167.8			-0.624
D-210-a-1	171.0	-0.608	-0.631	
D-210-a-2	172.5			-0.675
D-210-b-1	171.2	-0.618	-0.643	
D-210-b-2	172.3			-0.684

Table 3: $T_{g-tan\delta}$ and mass loss during the DMA heating runs-Group C experimental series.

			$T_{g-tan\delta}$	ΔM (%)
Exposed in water at 60°C	C-a-1		115.8	-2.41
	C-a-2		155.9	-0.04
	C-b-1		117	-2.19
	C-b-2		156.2	-0.10
Unexposed at 60°C	C-c-1		154.3	-0.10
	C-c-2		162.9	0.00

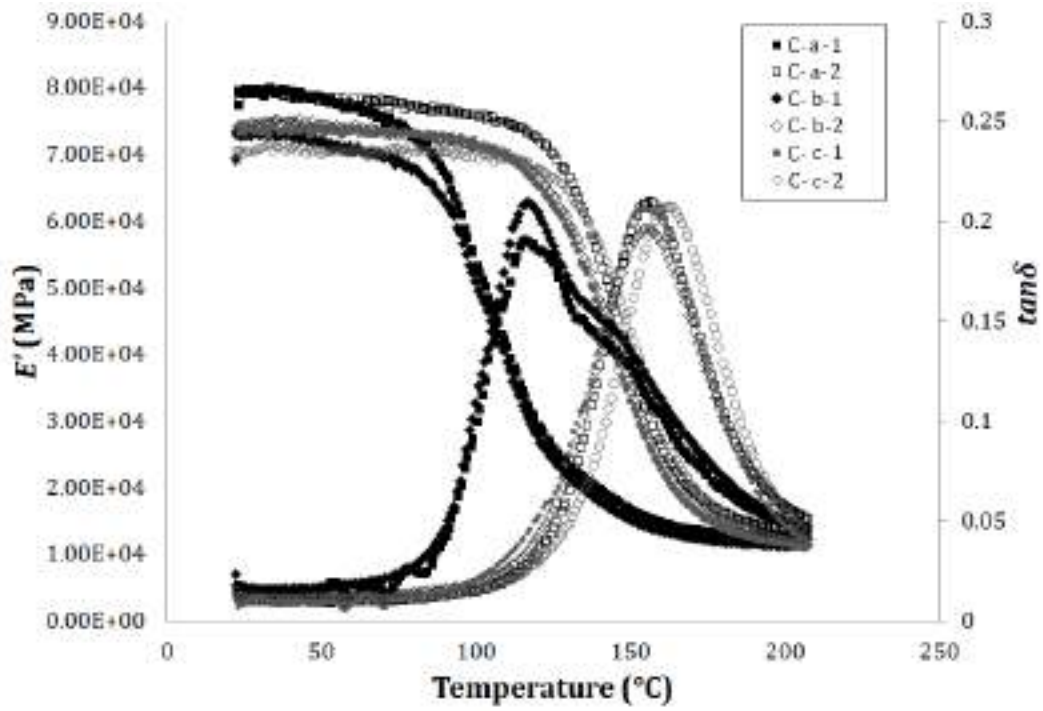


Figure 2: $T_{g-tan\delta}$ versus mass loss ΔM -Group D experimental series.

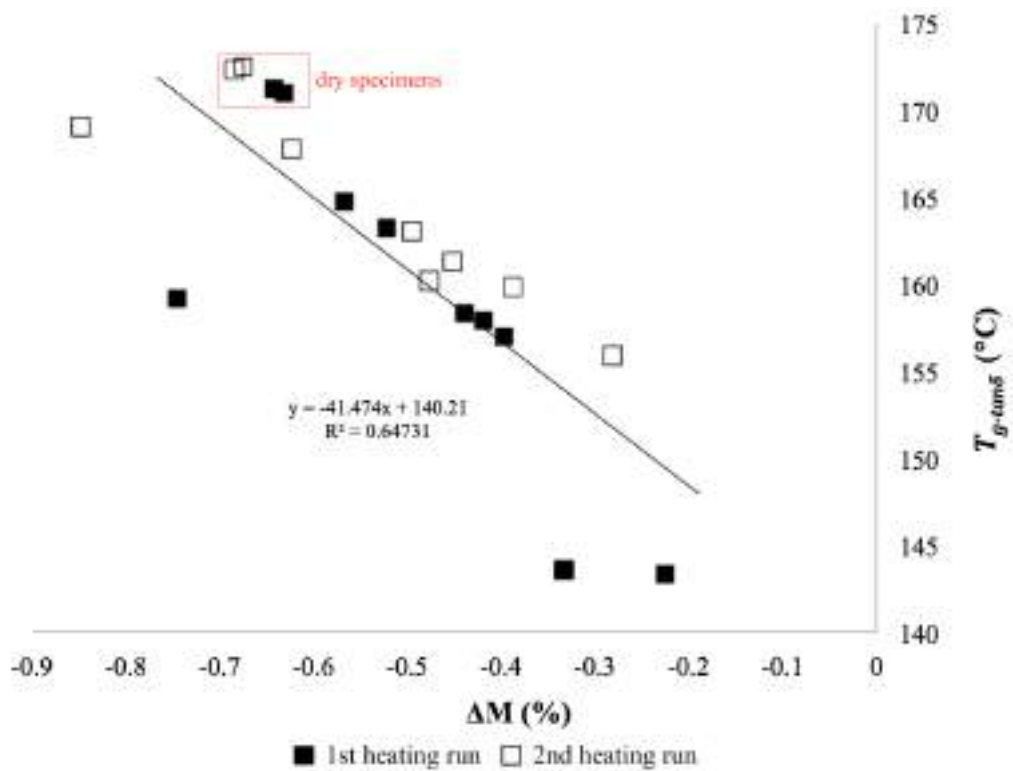


Figure 3: $T_{g-tan\delta}$ versus mass loss ΔM -Group C experimental series.

CONCLUSIONS

1. CFRP samples with an initial moisture content yield lower T_g values.
2. Due to the high temperature applied (up to 210°C), the use of a second heating run to assess the level of crosslinking density in the epoxy of a CFRP specimen should be conducted on dry specimens.
3. Measured T_g values which are up to 38°C lower than that of a dried reference sample are observed for saturated specimens. This could be important for the fire performance of CFRP structures when the CFRP is exposed directly to humid environments e.g. in retrofitting materials, or when encased in a concrete environment with high humidity.
4. For the CFRP samples tested here, the plasticization effects due to exposure to water are reversible upon drying when the highest exposure temperature is well below the wet T_g value of the CFRP material.

ACKNOWLEDGEMENTS

We are grateful to SACAC for their technical and financial support. The financial support from the Onassis Foundation (ET) is also greatly appreciated.

REFERENCES

- ASTM (2007). "Standard Test Method for Glass Transition Temperature (DMA T_g) of Polymer Matrix Composites by Dynamic Mechanical Analysis (DMA)", *ASTM D7028 – 07*, West Conshohocken, PA.
- S. Birger, A. Moshonov, S. Kenig (1989). "The effects of thermal and hygrothermal ageing on the failure mechanisms of graphite-fabric epoxy composites subjected to flexural loading", *Composites*, 20(4), 341–348.
- A. Chateauminois, B. Chabert, J.P. Soulier, L. Vincent (1990). "Long time ageing of glass/epoxy composites", *Proceedings of the International Symposium on Composite Materials with Textile Reinforcement for Use in Building Construction and Related Applications*, Lyon, France, July 16-18.
- A. Chateauminois, B. Chabert, J.P. Soulier, L. Vincent (1995). "Dynamic Mechanical Analysis of Epoxy Composites Plasticised by Water: Artifact and Reality", *Polymer Composites*, 16(4), 288-296.
- P. Nogueira, C. Ramirez, A. Torres, M.J. Abad, J. Cano, J. Lopez, I. Lopez-Bueno, L. Barral (2000). "Effect of Water Sorption on the Structure and Mechanical Properties of an Epoxy Resin System", *Journal of Applied Polymer Science*, 80, 71–80.
- M. Robert, B. Benmokrane (2010). "Effect of aging on bond of GFRP bars embedded in concrete", *Cement and Concrete Composites*, 32(6), 461-467.
- E. Toumpanaki, J. M. Lees, G.P. Terrasi (2015). "Shear Modulus of Cylindrical CFRP Tendons Exposed to Moisture", *Journal of Composites for Construction*, 19(3), 12pp.
- W. W. Wright (1981). "The effect of diffusion of water into epoxy resins and their carbon-fibre reinforced composites", *Composites*, 12(3), 201-205.



HYBRID POLYMER COMPOSITES: A REVIEW

H. Nguyen¹ and W. Zatar²

^{1,2} Marshall University, College of Information Tech. & Eng., United States, Email: nguyenhai@marshall.edu

ABSTRACT

The term “hybrid” is generally understood as an object made from two or more different elements. Hybrid polymer composites are defined as composites consisting of at least two dissimilar materials embedded in either thermosetting or thermoplastic resin matrix. “Synergistic” effect of hybrid composites (defined as the difference between the performance of a fiber in a hybrid composite and in a single fiber composite) has received great attention from researchers and scientists worldwide. Hybrid composites have been widely used for various applications (for example, aerospace, automobile, civil infrastructure, and marine) due to their lightweight and excellent material characteristics. Fibers (in the forms of roving, yarn, woven, etc.) reinforced with polymer matrix are known to result in enhanced mechanical properties of the composites. Synthetic fibers such as carbon, glass, aramid, and basalt are more durable and stronger than most natural fibers. Synthetic-fiber composites have thus been used in high-performance applications such as automotive and aircraft industries. However, there have been limited studies on hybrid synthetic-fiber composites for structural applications. This study sheds some light on a review of hybrid composites with the main emphasis on their mechanical properties (tensile, compressive, and flexural).

KEYWORDS

Hybrid composites; Synthetic fibers; Mechanical properties; Civil applications

INTRODUCTION

Hybrid composite materials (a.k.a. hybrid composites or hybrid materials) are attractive structural materials for the following reasons: (1) They provide designers with the new freedom of tailoring composites and achieving properties that cannot be obtained by binary systems containing one type of fiber dispersed in a matrix; (2) Expensive fibers such as carbon/boron can be partially replaced with less expensive fibers such as glass/Kevlar; and (3) Hybrid composites may potentially achieve a balance of stiffness, strength, and increased elongation to failure. Hybrid composites have also demonstrated lighter weight, reduced notch sensitivity, improved fracture toughness, longer fatigue life, and excellent impact resistance (Chamis and Lark, 1977). Optimizations of composite properties can usually be achieved through a suitable combination of fiber types (Chou and Kelly, 1980). The hybrid composites can be classified as: (1) intraply (intermingled) hybrid, which has more than one type of fiber within a ply; and (2) interply (interlaminated) hybrid, where only one type of fiber is placed in a single ply and then different plies are stacked together to form the laminate. This paper aims at reviewing tensile, compressive, and flexural properties of the latter hybrid composites. Other properties and behavior of the hybrid composite can be found in some references in Table 1.

Table 1 References related to hybrid composites

Description	Reference
Hybrid effect	Hayashi, 1972; Bunsell & Harris, 1974; Phillips, 1976; Aveston & Sillwood, 1976; Zweben, 1977; Ishikawa et al., 1977; Kimura et al., 1977; Marom et al., 1978; Phillips, 1981; Ishikawa & Chou, 1982; Wagner & Marom, 1982; Fukuda & Chou, 1982-1983; Fukuda, 1984; Fukunaga et al., 1984; Fariborz et al., 1985; Peijs & De Kok, 1993; Taketa et al., 2010; Pandya et al., 2011; Dong & Davies, 2012; Mishnaevsky & Dai, 2014; Swolfs et al., 2013, 2015-2016; Wisnom et al., 2016; Iqbal et al., 2017
Tensile behavior	Bunsell & Harris, 1974; Phillips, 1976; Aveston & Sillwood, 1976; Zweben, 1977; Manders & Bader, 1981; Khatri & Koczak, 1996; Taketa et al., 2010
Compressive behavior	Perry & Adams, 1975; Naik et al., 2001; Zhang et al., 2012
Flexural behavior	Giancaspro et al., 2010; Dong et al., 2012; Subagia et al., 2014
Impact and dynamic behavior	Broutman & Rotem, 1975; Xing et al., 1981; Peijs et al., 1990; Imielińska & Guillaumat, 2004; Hosur et al., 2005; Hampson & Moatamedi, 2007; Wang et al., 2008; Sarasini et al., 2013

Fatigue behavior	Fernando et al., 1988; Dickson et al., 1989; Shan & Liao, 2002; Dai & Mishnaevsky, 2014
Creep behavior	Peijs et al., 1993; Maksimov & Plume, 2001
Pseudo-ductility	Czél & Wisnom, 2013; Yu et al., 2015
Thermal behavior	Vanaja & Rao, 2002; Tsai et al., 2009
Erosion wear behavior	Mahapatra & Patnaik, 2009
Review articles	Chamis and Lark, 1977; Summerscales & Short, 1979-1980; Kretsis, 1987; Swolfs et al. (2014)

Tensile Properties of Hybrid Composites

Summerscales and Short (1979-1980), Kretsis (1987), and Swolfs et al. (2014) have reviewed a number of studies on carbon-glass hybrid composites in which a phenomenon termed “synergistic strengthening” or the “hybrid effect” has been identified. This is defined in different ways by different researchers, but the essential observation is that the failure strain of the low-elongation fiber appears to be greater in a hybrid than in an all-carbon fiber composite structure. Observation of the “hybrid effect” is first credited to Hayashi (1972) and has subsequently been reported by several researchers (Table 2). Further list of references regarding the hybrid effect can be found in Table 1.

Bunsell and Harris (1974) experimentally investigated two types of hybrid composites consisting of either unbonded or bonded laminated layers of high-modulus carbon fiber (with low breaking strain) and E-glass fibers, both embedded in an epoxy resin matrix. The behavior of the hybrid composites was predicted and discussed based on Hayashi’s model. As observed by Hayashi (1972), the strain at the point of initial fracture of the carbon fiber component is greater than the breaking strain of the CFRP tested alone, as a result of the residual compressive stress induced in the CFRP during manufacture of the hybrid laminate. The initial fracture occurs at the weakest point of the CFRP layer. Bunsell and Harris (1974) found that, after initial fracture, the well-bonded specimens behaved in a manner quite different the unbonded counterparts. The layers in the unbonded specimens broke independently while bonded specimens failed in a more complex manner. The CFRP layer in the bonded specimen has not broken straight across at one point but has failed in many places over the specimen’s length. When the CFRP layers reach their breaking strain, the unbonded specimens failed in a sudden and brittle manner, which results in a sharp drop in load. On the other hand, in the bonded specimens, the load was distributed over the whole cross-section and the load drop was smaller than that in the unbonded specimens. The bond between layers ensures that the CFRP continues to carry a share of the applied load and to contribute to the overall stiffness of the hybrid.

Phillips (1976) raised three questions pertaining to the hybrid composite: (1) Does it fail when it is supposed to – or later? ; (2) Does it fail in the manner expected – or some other?; and (3) Above all, is the behavior useful – or isn’t it? He has briefly summarized three major aspects of the hybrid composite behavior including tensile stress/strain diagrams, impact strength, and fatigue response. He concluded that the hybrids appear to fail “later” than predicted, in a tough and fatigue resistant manner. Meanwhile, there is no doubt that this behavior is very useful.

Table 2 Results of the “hybrid effect” reported in the literature

Hybrid	Carbon volume fraction, V_f	Hybrid effect (%)	Remarks	References
Carbon/glass	0.25	+45	–	Hayashi (1972)
Carbon/glass	0.47 to 0.5	+42 to +85	All hybrid laminated from preimpregnated fiber material; Epoxy matrix; Multiple fracture failure mode, with delamination between plies of 3-layered sandwich	Bunsell & Harris (1974)
Carbon/glass Carbon/kevlar	0.86 0.82	+12 +14	–	Perry & Adams (1975)
Carbon/glass	0.6	+2 to +20	Unidirectional woven hybrid cloth with tows of glass and carbon alternating in four different carbon ratios (1:1; 1:2; 1:3; and 1:4); vinyl-ester matrix; thermal strains not considered	Phillips (1976)

Carbon/glass	–	+116	Carbon veil is 10 ⁴ filament tow spread to 300 mm width, and combined with 204 filament glass tow in RT curing epoxy	Aveston & Sillwood (1976)
Carbon/kevlar	–	+4	Thornel 300 and Kevlar 49, alternating yarns in preimpregnated fiber material tapes; Differential thermal contractions not significant	Zweben (1977)
AS-carbon/E-glass	0.5	+5 to +13	Thermal contraction differences not considered; Epoxy resin matrix;	Marom et al. (1978)
HTS carbon/E-glass	0.05 to 0.82	+8.7 to +35	High-tensile surface-treated (HTS) carbon fiber	Manders & Bader (1981)
HMS carbon/E-glass	0.05 to 0.5	+6 to +46	High-modulus surface-treated (HMS) carbon fiber	Manders & Bader (1981)
Carbon/HP-PE	–	+1.4 to 19.8	Either surface-untreated or surface-treated high-performance polyethylene (HP-PE) fiber	Peijs & De Kok (1993)
Carbon/ glass	0.56	-17.2 to +90.4	E-glass and T300 carbon	Pendya et al. (2011)
Carbon/glass	0.3 to 0.7	0 to +47.65	S-2 glass and T700S carbon	Dong & Davies (2012)

Aveston and Sillwood (1976) theoretically investigated behavior of a three component hybrid composite consisting of a brittle fiber and a “matrix” made from a binder and less brittle fiber. The theory is tested using a hybrid composite composed of high-modulus carbon and glass fibers, in an epoxy resin matrix. Preliminary test results confirmed that the failure strain of the carbon fibers can be increased to a value of about 1%.

Zweben (1977) presented the statistical analysis for the tensile strength of unidirectional hybrid composite materials consisting of two-dimensional arrays of alternating low elongation (LE) and high elongation (HE) fibers in a common matrix. He found that the theory can explain the “hybrid effect” that has been observed by several researchers: hybrids made by combining HE and LE fibers, such as graphite and glass, often display tensile failure strains greater than those of composites made from the LE fibers. The analysis predicts that the introduction of HE fibers in an LE fiber composite raises the strain level required to propagate fiber breaks because the HE fibers behave like crack arrestors on a micromechanical level.

Manders and Bader (1981) investigated the tensile mechanical properties of hybrid composites fabricated from carbon-glass/epoxy over a range of carbon/glass ratios and states of dispersion of the two phases. The results indicated that the failure strain of the carbon phase increased as the relative proportion of carbon fiber was decreased, and as the carbon fiber was more finely dispersed. This behavior is commonly termed the “hybrid effect”, and failure strain was enhanced up to 50%. They concluded that the laminae of carbon fiber dispersed in the glass fiber phase show a multiple failure mode, and when the constitution is favorable, catastrophic failure does not occur until a considerable number of lamina fractures have accumulated. Failure is thus progressive, and the material is effectively “tougher” than equivalent all-carbon fiber composites. They also proposed the model to explain the hybrid effect based on the statistical strength of the carbon fibers: a lamina or bundle of carbon fibers fails when there is a local critical accumulation of fiber fractures. The model suggests that the critical number of fiber fracture is of the order of 3, and their experimental observations of the failure process support their hypothesis.

Khatri and Koczak (1996) evaluated the tensile behavior of thick-section (16 and 40 plies) hybrid composites with a polyphenylene sulfide (PPS) matrix. The hybrid composites were composed of AS4-graphite and E-glass fibers. The test results showed that the hybridization of AS4-graphite/PPS composites with E-glass resulted in an enhancement of the failure strain and positive hybrid effects of +2% to +8%. The strain enhancement increased with higher fractions of E-glass/PPS. The hybrid effect is due to the crack arresting characteristics of the E-glass fibers. The hybridization of the composites resulted in changes in fracture modes from brittle failure mode of AS4-graphite composites to more ductile hybrid AS4-graphite/E-glass composites (i.e. damage tolerance improved with the addition of E-glass/PPS).

Taketa et al. (2010) explored tensile properties of interply hybrid composites with carbon fiber-reinforced polypropylene (CFRPP) and self-reinforced polypropylene (SRPP). SRPP has an intrinsic behavior of shrinkage under high temperature resulting from hot compaction process of a woven fabric of highly oriented polypropylene. Tensile testing of the hybrid composites revealed a positive hybrid effect of +7% to +18%. The failure strain of the hybrid composites was found to be improved in comparison with CFRPP.

A diagram to predict the tensile strengths of the hybrid composite was proposed by Manders and Bader (1981). Figure 1 exhibits the expected strength of the hybrid composite. The horizontal axis shows the volume fraction of carbon fiber while the vertical axis indicates the mean stress in the hybrid composite. The point A represents the tensile strength of the all-glass composite and the point D represents that of all-carbon composite. It may be

expected that the first failure event will occur in the hybrid when the average strain in the composite exceeds the failure strain of the carbon fiber. This is due to the fact that the carbon fiber has a lower elongation than the glass fiber. The line AD depicts the “rule of mixtures” strength of the composite and the line BD represents the stress in the composite at the failure strain of the carbon fiber. At low volume fraction of the carbon fiber, the glass fibers in the hybrid would be able to carry extra load despite the fracture of the carbon fibers. The line AC is the ultimate strength of the hybrid in this condition. To the left of C (Figure 1), the ultimate strength of the hybrid is determined by the glass fiber (i.e. although the carbon fiber fails at BC, the glass fiber continues to sustain the stress up to AC). To the right of C (Figure 1), the hybrid is expected to fail suddenly right after the carbon fiber fails. Figure 2 shows load versus elongation relationships for these two conditions (the solid line represents the left of C and the dash line represents the right of C). The solid line shows a multiple fracture resulting from several failure events occurring in the carbon fiber. Each failure in the carbon fiber is marked by a load drop. The stiffness reduction after each failure event is observed due to the load transfer from the broken carbon fiber to the unbroken glass fiber. The final failure mode in this case is the catastrophic failure of the glass fiber. On the other hand, the dash line exhibits a single fracture caused by the first failure of the carbon fiber leading to a catastrophic failure of the whole composite. The line ACD in Figure 1, hence, shows the predicted ultimate strength of the hybrid and the line BCD represents the stress at first failure of the carbon fiber. It should be noted that the rule-of-mixtures prediction (the line AD) cannot be used in this case. The hybrid effect is defined as being any observations where the first failure lies above the line BCD or the ultimate strength lies above the line ACD. It is expressed as the percentage increase (change) of the failure strain of the carbon in the hybrid compared with that of an all-carbon composite.

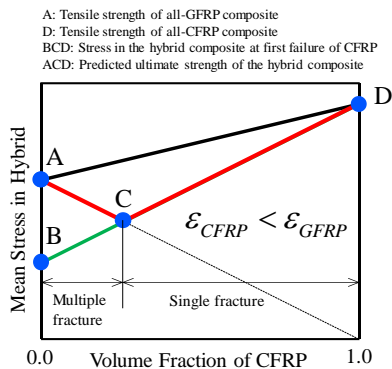


Figure 1: Theoretical strength of glass/carbon fiber hybrid composites

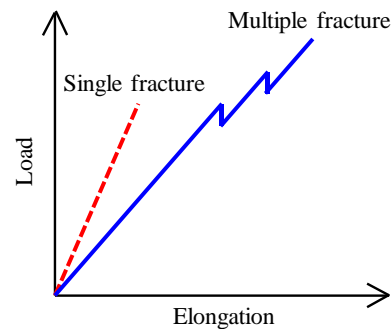


Figure 2: Load-elongation curves

Compressive Properties

Perry and Adams (1975) examined the compressive strength and Charpy impact response of graphite/epoxy hybrid laminates containing discrete plies of unidirectional glass and kevlar-49 (a.k.a. PRD-49) or nylon fibers. They concluded that the combination of material and fiber layup played an importance role in the impact energy absorption capacities of the tested specimens. Young’s modulus in compression was found to double with the addition of only 4.7% of carbon fibers to 50% weight fraction GFRP.

Naik et al. (2001) carried out an experimental study on post impact compressive behavior of hybrid composites consisting of T-300 carbon fiber and E-glass fiber embedded in an epoxy matrix resin. Three hybrid carbon/glass composites with different stacking sequences were prepared. The three symmetrically arranged hybrid $[C_4/G_4]_s$, $[G_4/C_4]_s$, and $[G/C]_{4s}$ were composed of 16 plies of carbon and glass fiber (8 plies for each fiber type). The results showed that the $[C_4/G_4]_s$ hybrid (i.e. carbon-inside/glass-outside clustered hybrid configuration) exhibited higher post impact compressive strength, lower notch sensitivity, and lower transverse displacement compared to the other hybrid configurations.

Zhang et al. (2012) investigated the influences of stacking sequence on the strength of hybrid composites with varying ratios of carbon and glass woven fabric in an epoxy matrix. The test results showed that the hybrid composites with 50% carbon fiber reinforcement exhibited highest compressive strength. The stacking sequence significantly affected the compressive properties of the hybrid. With the same carbon/glass fiber ratio, higher compressive strength and strain were found for the $[C/G/C/G]_s$ composite compared to the $[C_2G_2]_s$ counterpart. The enhanced compressive strength for the alternating stacking sequence may result from the bridging effect of the carbon fiber layer between the failed glass fiber layers.

Flexural Properties

The flexural properties of hybrid composites are more difficult to interpret than the tensile properties as they are highly dependent on the layup (Swolfs et al. 2014). Many researchers have studied the flexural behavior of natural fiber-based hybrid composites. This part of review, however, focuses on hybrid composites with synthetic fibers.

Giancaspro et al. (2010) experimentally investigated the effects of hybrid carbon-glass/geopolymer composites with E-glass composite cores bonded to high-strength carbon fibers. Carbon fibers were bonded to E-glass cores either on only the tension face, on both the tension and compression faces, or dispersed throughout the core in alternating layers to obtain a strong and economical hybrid composite laminate. The results indicated that the hybrid composite laminates with 3k unidirectional carbon tape exhibited 700% flexural capacity improvement compared to all E-glass fiber composite. When the relative amount of carbon fibers in the hybrid composites increased, the likelihood of a compression failure mode also increased. Similar observations were reported by Hai et al. (2010) and Dong et al. (2012).

Dong et al. (2012) evaluated the flexural properties of hybrid T700S carbon/S-2 glass composites in an intraply configuration. Specimens were manufactured by hand lay-up process and tested in the three-point bending scheme in accordance with ASTM D790. The results revealed that the dominant failure mode was compressive failure. Flexural modulus was found to decrease with increasing percentage of S-2 glass fibers. The highest flexural strength was achieved for specimens with 24% S-2 glass fibers. The experimental data showed 3.2% and 8.0% flexural strength improvements when compared to entire glass and carbon composites, respectively. The existence of positive hybrid effects was confirmed by the layerwise finite element modelling, which was successfully used to predict the stress distribution in the hybrid composites.

Subagia et al. (2014) explored the effect of stacking sequence on the flexural properties of the interply hybrid basalt-carbon/epoxy composite. The hybrid composites were composed of four layers of basalt fabrics and six layers of carbon fabrics with different stacking sequences. They were manufactured by vacuum assisted resin transfer molding process and tested under three-point flexural loading conforming to ASTM D790. The fracture surfaces were examined by scanning electron microscopy. The results showed that the primary failure mode was compressive failure, similar to the observations by Dong et al. (2012). The flexural strength and modulus of the hybrid composite laminates were found strongly dependent on the stacking sequence of the reinforcing fibers. Higher flexural strengths and modulus were obtained when carbon fabric was placed at outer layer of the compression side. A more ductile material could be obtained when basalt fabrics are placed at both the compression and tension sides. All the hybrid composites indicated a positive hybridization effect.

In summary, the failure of hybrid composites in tension is found to be non-catastrophic in carbon-rich hybrids and the elongation at first failure is found to be greater than that for the all carbon-fiber composite. Failure of carbon fibers in the hybrid can result in the load being transferred completely to the glass fibers depending on the relative proportions of each fibers in the hybrids. The compressive modulus of glass-rich hybrids is found to be significant higher than that predicted from the single fiber composites. In flexure, the use of the carbon fibers at the outer faces of the hybrid laminates results in higher flexural strength and modulus. The stacking sequence is reported to significantly affect the flexural and compressive properties of the hybrids.

A CASE STUDY OF HYBRID POLYMER COMPOSITES FOR PEDESTRIAN BRIDGE COMPONENTS

Recently, innovative hybrid composite I-shaped girders composed of carbon and glass fibers in a vinylester resin matrix was developed (Figure 3a). The advanced feature of these hybrid I-girders is the optimum use of carbon and glass fibers in the compression and tension flanges to maximize structural performance while reducing the overall cost by using only glass fibers in the web section (Hai et al. 2010).

An extensive research program had been conducted to characterize the behavior of hybrid carbon-glass fiber-reinforced polymer (hereafter called "HFRP") composites (Nguyen et al. 2013-2015). It was found that the developed HFRP I-girders are promising to replace short-span deteriorated pedestrian bridges, especially those exposed to harsh environmental conditions. Additionally, the HFRP girders can provide a competitive and sustainable option for accelerated bridge construction due to their light weight and corrosion-free characteristic. These were proved by the successful application of the HFRP I-girders to a demonstration pedestrian bridge construction in Kure city, Hiroshima prefecture, Japan in 2011 (Figure 3b). The bridge was built to replace an existing deficient steel bridge. The FRP components of the bridge were manufactured and transported to the site for assembly. This bridge consists of two HFRP I-girders topped with a GFRP gratings bridge deck. Each HFRP I-girder was assembled from three HFRP I-section units with two splice connections at quarter locations. The bridge was simply supported with a total length of 12 m and an effective width of 0.75 m. It was exposed to a highly corrosive environment by the ocean. The bridge's condition was periodically assessed by visual inspection.



Figure 3: First hybrid CFRP/GFRP pedestrian bridge in Japan

CONCLUSIONS

This paper throws some light upon hybrid effect of hybrid polymer composites and their civil infrastructure applications. Tensile properties of hybrid polymer composites are well investigated and understood. Hybrid effect of hybrid composites under other loading conditions such as flexural and compression are not well understood and additional works are needed. Carbon-based hybrid composites such as carbon/glass, carbon/Kevlar, and carbon/basalt have found few applications in bridge components. Current advancements and innovations in raw materials and manufacturing technologies have helped reducing the cost of hybrid composites and thus may expand their future applications.

REFERENCES

- Aveston, J., & Kelly, A. (1973). "Theory of multiple fracture of fibrous composites", *Journal of Materials Science*, 8(3), 352-362.
- Aveston, J., & Sillwood, J. M. (1976). "Synergistic fibre strengthening in hybrid composites", *Journal of Materials Science*, 11(10), 1877-1883.
- Aveston, J., & Kelly, A. (1980). "Tensile first cracking strain and strength of hybrid composites and laminates", *Philosophical Transactions of the Royal Society of London A: Mathematical, Physical and Engineering Sciences*, 294(1411), 519-534.
- Broutman, L. J., & Rotem, A. (1975). "Impact strength and toughness of fiber composite materials", In *Foreign object impact damage to composites*. ASTM International.
- Bunsell, A. R., & Harris, B. (1974). "Hybrid carbon and glass fibre composites", *Composites*, 5(4), 157-164.
- Chamis, C. C., & Lark, R. F. (1977). "Hybrid composites – State-of-the-art review: Analysis, Design, Application and Fabrication", *NASA Technical Memorandum*, NASA, TM X-73545.
- Chou, T., & Kelly, A. (1980). "Mechanical properties of composites", *Annual Review of Materials Science*, 10(1), 229-259.
- Czél, G., & Wisnom, M. R. (2013). "Demonstration of pseudo-ductility in high performance glass/epoxy composites by hybridisation with thin-ply carbon prepreg", *Composites Part A: Applied Science and Manufacturing*, 52, 23-30.
- Dai, G., & Mishnaevsky, L. (2014). "Fatigue of hybrid glass/carbon composites: 3D computational studies", *Composites Science and Technology*, 94, 71-79.
- Dickson, R. F., Fernando, G., Adam, T., Reiter, H., & Harris, B. (1989). "Fatigue behaviour of hybrid composites", *Journal of materials science*, 24(1), 227-233.
- Dong, C., & Davies, I. J. (2012). "Optimal design for the flexural behaviour of glass and carbon fibre reinforced polymer hybrid composites", *Materials & Design*, 37, 450-457.
- Dong, C., Ranaweera-Jayawardena, H. A., & Davies, I. J. (2012). "Flexural properties of hybrid composites reinforced by S-2 glass and T700S carbon fibres", *Composites Part B: Engineering*, 43(2), 573-581.
- Fariborz, S. J., Yang, C. L., & Harlow, D. G. (1985). "The tensile behavior of intraply hybrid composites I: Model and simulation", *Journal of Composite Materials*, 19(4), 334-354.
- Fernando, G., Dickson, R. F., Adam, T., Reiter, H., & Harris, B. (1988). "Fatigue behaviour of hybrid composites", *Journal of materials science*, 23(10), 3732-3743.
- Fukuda, H., & Chou, T. W. (1982). "Monte Carlo simulation of the strength of hybrid composites", *Journal of Composite Materials*, 16(5), 371-385.

- Fukuda, H., & Chou, T. W. (1983). "Stress concentrations in a hybrid composite sheet", *Journal of applied mechanics*, 50(4a), 845-848.
- Fukuda, H. (1984). "An advanced theory of the strength of hybrid composites", *Journal of materials science*, 19(3), 974-982.
- Fukunaga, H., Chou, T. W., & Fukuda, H. (1984). "Strength of intermingled hybrid composites", *Journal of reinforced plastics and composites*, 3(2), 145-160.
- Giancaspro, J. W., Papakonstantinou, C. G., & Balaguru, P. N. (2010). "Flexural response of inorganic hybrid composites with E-glass and carbon fibers", *Journal of Engineering Materials and Technology*, 132(2), 021005.
- Hai, N. D., Mutsuyoshi, H., Asamoto, S., & Matsui, T. (2010). "Structural behavior of hybrid FRP composite I-beam", *Construction and Building Materials*, 24(6), 956-969.
- Hampson, P. R., & Moatamedi, M. (2007). "A review of composite structures subjected to dynamic loading", *International journal of crashworthiness*, 12(4), 411-428.
- Hayashi, T. (1972). "Development of new material properties by hybrid composition (1st report)", *Fukugo Zairyo (Composite Materials)*, 1, 18-20.
- Hayashi, T. (1972). "Development of new material properties by hybrid composition (2nd report)", *Fukugo Zairyo (composite materials)*, 1, 21-25.
- Hosur, M. V., Adbullah, M., & Jeelani, S. (2005). "Studies on the low-velocity impact response of woven hybrid composites", *Composite Structures*, 67(3), 253-262.
- Ikbal, M. H., Ahmed, A., Qingtao, W., Shuai, Z., & Wei, L. (2017). "Hybrid composites made of unidirectional T600S carbon and E-glass fabrics under quasi-static loading", *Journal of Industrial Textiles*, 46(7), 1511-1535.
- Imielińska, K., & Guillaumat, L. (2004). "The effect of water immersion ageing on low-velocity impact behaviour of woven aramid-glass fibre/epoxy composites", *Composites Science and Technology*, 64(13), 2271-2278.
- Ishikawa, T., Koyama, K., & Kobayashi, S. (1977). "Elastic moduli of carbon-epoxy composites and carbon fibers", *Journal of Composite Materials*, 11(3), 332-344.
- Ishikawa, T., & Chou, T. W. (1982). "Elastic behavior of woven hybrid composites", *Journal of Composite Materials*, 16(1), 2-19.
- Khatri, S. C., & Koczak, M. J. (1996). Thick-section AS4-graphite/E-glass/PPS hybrid composites: Part I. Tensile behavior. *Composites science and technology*, 56(2), 181-192.
- Kimura, H., Yamaguchi, T., Shiraishi, T., Tsubokawa, M., & Takeuchi, M. (1977). A Study on the Thin Plate with Carbon Fiber Reinforced Hybrid Composite.
- Kretsis, G. (1987). "A review of the tensile, compressive, flexural and shear properties of hybrid fibre-reinforced plastics", *Composites*, 18(1), 13-23.
- Mahapatra, S. S., & Patnaik, A. (2009). "Study on mechanical and erosion wear behavior of hybrid composites using Taguchi experimental design", *Materials & Design*, 30(8), 2791-2801.
- Maksimov, R. D., & Plume, E. (2001). "Long-term creep of hybrid aramid/glass-fiber-reinforced plastics", *Mechanics of composite materials*, 37(4), 271-280.
- Manders, P. W., & Bader, M. G. (1981). "The strength of hybrid glass/carbon fibre composites", *Journal of materials science*, 16(8), 2233-2245.
- Marom, G., Fischer, S., Tuler, F. R., & Wagner, H. D. (1978). "Hybrid effects in composites: conditions for positive or negative effects versus rule-of-mixtures behavior", *Journal of Materials Science*, 13(7), 1419-1426.
- Mishnaevsky, L., & Dai, G. (2014). "Hybrid carbon/glass fiber composites: Micromechanical analysis of structure-damage resistance relationships", *Computational Materials Science*, 81, 630-640.
- Naik, N. K., Ramasimha, R., Arya, H. E. M. E. N. D. R. A., Prabhu, S. V., & ShamaRao, N. (2001). "Impact response and damage tolerance characteristics of glass-carbon/epoxy hybrid composite plates", *Composites Part B: Engineering*, 32(7), 565-574.
- Nguyen, H., Mutsuyoshi, H., and Zatar, W. (2013). "Flexural Behavior of Hybrid Composite Beams", *J Transp Res Board*, 2(2332), 53-63.
- Nguyen, H., Mutsuyoshi, H., and Zatar, W. (2014). "Push-Out Tests for Shear Connections between UHPFRC Slabs and FRP Girder", *Composite Structures*, 118, 528-547.
- Nguyen, H., Zatar, W., & Mutsuyoshi, H. (2014). "Hybrid FRP girders topped with segmental precast concrete slabs for accelerated bridge construction", *J Transp Res Board*, 2(2407), 83-93.
- Nguyen, H., Mutsuyoshi, H., and Zatar, W. (2015). "Hybrid FRP-UHPFRC Composite Girders: Part 1 – Experimental and Numerical Approach", *Composite Structures*, 125, 631-652.
- Nguyen, H., Zatar, W., and Mutsuyoshi, H. (2015). "Hybrid FRP-UHPFRC Composite Girders: Part 2 – Analytical Approach", *Composite Structures*, 125, 653-671.
- Pandya, K. S., Veerajuu, C., & Naik, N. K. (2011). "Hybrid composites made of carbon and glass woven fabrics under quasi-static loading", *Materials & Design*, 32(7), 4094-4099.

- Peijs, A. A. J. M., Venderbosch, R. W., & Lemstra, P. J. (1990). "Hybrid composites based on polyethylene and carbon fibres Part 3: Impact resistant structural composites through damage management", *Composites*, 21(6), 522-530.
- Peijs, A. A. J. M., & De Kok, J. M. M. (1993). "Hybrid composites based on polyethylene and carbon fibres. Part 6: Tensile and fatigue behavior", *Composites*, 24(1), 19-32.
- Peijs, A. A. J. M., Schellens, H. J., & Govaert, L. E. (1993). "Creep behaviour of hybrid composites based on polyethylene and carbon fibres", *Advanced Composites Letters*, 2(6), 201-206.
- Perry, J. L., & Adams, D. F. (1975). "Charpy impact experiments on graphite/epoxy hybrid composites", *Composites*, 6(4), 166-172.
- Phillips, L. N. (1976). "The hybrid effect—does it exist?", *Composites*, 7(1), 7-8.
- Phillips, M. G. (1981). "Composition parameters for hybrid composite materials", *Composites*, 12(2), 113-116.
- Sarasini, F., Tirillò, J., Valente, M., Ferrante, L., Cioffi, S., Iannace, S., & Sorrentino, L. (2013). "Hybrid composites based on aramid and basalt woven fabrics: Impact damage modes and residual flexural properties", *Materials & Design*, 49, 290-302.
- Shan, Y., & Liao, K. (2002). "Environmental fatigue behavior and life prediction of unidirectional glass-carbon/epoxy hybrid composites", *International journal of fatigue*, 24(8), 847-859.
- Short, D., & Summerscales, J. (1979). "Hybrids—a review: Part 1", Techniques, design and construction. *Composites*, 10(4), 215-222.
- Short, D., & Summerscales, J. (1980). "Hybrids—a review: Part 2", Physical properties. *Composites*, 11(1), 33-38.
- Subagia, I. A., Kim, Y., Tijjing, L. D., Kim, C. S., & Shon, H. K. (2014). "Effect of stacking sequence on the flexural properties of hybrid composites reinforced with carbon and basalt fibers", *Composites Part B: Engineering*, 58, 251-258.
- Summerscales, J., & Short, D. (1978). "Carbon fibre and glass fibre hybrid reinforced plastics", *Composites*, 9(3), 157-166.
- Swolfs, Y., Gorbatikh, L., & Verpoest, I. (2013). "Stress concentrations in hybrid unidirectional fibre-reinforced composites with random fibre packings", *Composites Science and Technology*, 85, 10-16.
- Swolfs, Y., Gorbatikh, L., & Verpoest, I. (2014). "Fibre hybridisation in polymer composites: a review", *Composites Part A: Applied Science and Manufacturing*, 67, 181-200.
- Swolfs, Y., McMeeking, R. M., Rajan, V. P., Zok, F. W., Verpoest, I., & Gorbatikh, L. (2015). "Global load-sharing model for unidirectional hybrid fibre-reinforced composites", *Journal of the Mechanics and Physics of Solids*, 84, 380-394.
- Swolfs, Y., Verpoest, I., & Gorbatikh, L. (2016). "Maximising the hybrid effect in unidirectional hybrid composites", *Materials & Design*, 93, 39-45.
- Taketa, I., Ustarroz, J., Gorbatikh, L., Lomov, S. V., & Verpoest, I. (2010). "Interply hybrid composites with carbon fiber reinforced polypropylene and self-reinforced polypropylene", *Composites Part A: Applied Science and Manufacturing*, 41(8), 927-932.
- Tsai, Y. I., Bosze, E. J., Barjasteh, E., & Nutt, S. R. (2009). "Influence of hygrothermal environment on thermal and mechanical properties of carbon fiber/fiberglass hybrid composites", *Composites Science and Technology*, 69(3), 432-437.
- Vanaja, A., & Rao, R. M. V. G. K. (2002). "Fibre fraction effects on thermal degradation behaviour of GFRP, CFRP and hybrid composites", *Journal of reinforced plastics and composites*, 21(15), 1389-1398.
- Wagner, H. D., & Marom, G. (1982). "On composition parameters for hybrid composite materials", *Composites*, 13(1), 18.
- Wang, X., Hu, B., Feng, Y., Liang, F., Mo, J., Xiong, J., & Qiu, Y. (2008). "Low velocity impact properties of 3D woven basalt/aramid hybrid composites", *Composites Science and Technology*, 68(2), 444-450.
- Wisnom, M. R., Czél, G., Swolfs, Y., Jalalvand, M., Gorbatikh, L., & Verpoest, I. (2016). "Hybrid effects in thin ply carbon/glass unidirectional laminates: accurate experimental determination and prediction", *Composites Part A: Applied Science and Manufacturing*, 88, 131-139.
- Xing, J., Hsiao, G. C., & Chou, T. W. (1981). "A dynamic explanation of the hybrid effect", *Journal of Composite Materials*, 15(5), 443-461.
- Yu, H., Longana, M. L., Jalalvand, M., Wisnom, M. R., & Potter, K. D. (2015). "Pseudo-ductility in intermingled carbon/glass hybrid composites with highly aligned discontinuous fibres", *Composites Part A: Applied Science and Manufacturing*, 73, 35-44.
- Zhang, J., Chaisombat, K., He, S., & Wang, C. H. (2012). "Hybrid composite laminates reinforced with glass/carbon woven fabrics for lightweight load bearing structures", *Materials & Design (1980-2015)*, 36, 75-80.
- Zweben, C. (1977). "Tensile strength of hybrid composites", *Journal of materials science*, 12(7), 1325-1337.



RELAXATION OF FRP MATERIALS – ISSUE OVERVIEW IN THE AVAILABLE LITERATURE, CODES AND GUIDELINES

M. Przygocka 1, R. Kotynia 2

¹Lodz University of Technology, Department of Concrete Structures, Poland, Email: martaprzygocka@wp.pl

²Lodz University of Technology, Department of Concrete Structures, Poland

ABSTRACT

Use of the FRP (fiber reinforced polymer) materials for reinforcing and strengthening of RC structures with simultaneous prestress results in the increase of load carrying capacity of RC members and the improvement of serviceability limit state conditions. The prestressing losses should be taken into account in the design of RC structure reinforced or strengthened with pretensioned FRPs. Prestressing losses are the main issue affecting the durability and structure behavior. The general division of prestressing losses distinguishes immediate losses, which appear immediately after the termination of the prestressing and delayed losses increasing with time of occurrence of phenomena that cause them. The immediate prestressing losses are caused by different factors in dependence of the prestressing technique: friction, relaxation of the FRP material, temperature and elastic shortening of concrete. Delayed prestressing losses consists of creep, shrinkage and relaxation. In this paper authors raise the subject of prestressing losses caused by different factors which depend on FRP materials itself and prestressing technique (relaxation of the FRP materials and slip in the anchorage). The overview of experimental tests considering the relaxation of FRP materials in the available literature is presented herein. According to experimental results the relaxation of FRP materials is affected by different factors as insolation, temperature and humidity. The review of test methods for long-term relaxation of FRPs with the description of geometry of samples, anchorage details for different types of tendons (circular, flat), duration of tests and frequency of measurements in available codes and guidelines is also presented.

KEYWORDS

Durability, FRP, long-term performance, prestressing, prestressing losses, relaxation, rheology.

INTRODUCTION

FRP (fiber reinforced polymer) is a type of bi-component material reinforced with unidirectional nonmetallic continuous high-strength fibers (dispersed fraction) embedded in a polymer matrix (continuous fraction). FRP materials demonstrate superiority of the tensile strength and stiffness than other materials. Due to material arrangement (unidirectional fibers) FRP materials are highly anisotropic. Tensile strength of FRP increases with the increase of dispersed fraction in the material volume. Additionally, the relative proportion of fibers affects the density, rate of thermal expansion and elasticity modulus of composite. Physical characteristics of fibers like length and dimension of cross-section significantly affect the strength characteristics of FRP composites. The strength of FRPs is inversely proportional to the fibers diameter. Furthermore, one of the factor influencing the composite characteristics is contact between fractions at the reinforcement and matrix interface. The perfect connection between fractions (excellent adhesion between fibers and matrix) should be pursued in the manufacturing process. The mechanical, physical and chemical characteristics of both fractions, influence the efficiency and durability of fractions connection. Depending on connection between matrix and fibers, the direct and indirect connections could be divided. Direct connection includes mechanical and adhesive conjunctions based on traction on the contact surface of two components. Indirect connections resulting from fabrication a new phase between fibers and matrix – the transition phase. A new phase could be formed by addition a third component or melting one fraction in another. In the manufacturing process, fibers are being covered by chemical compounds with the effect of creating the chemical linking between phases. The transition phase creates chemical bonds with both fibers and matrix..

Particular components of composite material differed in the deformation manner under external loading. The nonmetallic fibers of dispersed phase deformed in linear elastic manner managed by Hook principle. However, polymer matrix deformed both in elastic manner (reversibly) in the early stage of strain and inelastic (irreversible) after exceeding the strain limit value. Due to the fact that composite is made from this two components obtained material evidences viscoelastic characteristics which means that FRP composites are subjected to creep and

relaxation. The FRP viscoelastic properties particularly resulting from great viscoelastic strain of matrix. The behavior of viscoelastic material differs substantially from terms of linear elastic theory (linear stress-strain relationship independent from time) and is characterized by time. The difference in stress – strain relationship curves for further loading and unloading cycles is obtained when comparing the cycle strain of viscoelastic material under external loading which proves the inelastic material behavior. The difference resulting from absorption and dissipation of a portion of energy form as a result of attenuation. Different sources of energy dissipation occurs in fiber composites as viscoelastic nature of matrix, phase between fiber and matrix, damage, viscoplastic absorption and thermo-elastic absorption.

Rheology is the field of science describing the creep phenomena and relaxation and is the study of a materials with both solid and fluid characteristics. Creep phenomena is the time-dependent deformation of a solid material under the influence of permanent stresses in constant temperature. Stress relaxation is the decrease of stress in a material yield to constant loading under constant strain. To describe the deformation and strain of the material depending on time the relation between stresses and their derivatives, strains, speed of strain and time when materials were subjected to external loading referred to as rheological models are used. Rheological models are the combination of three basic perfect bodies which are perfectly elastic body (Hooke), the perfect fluid (Newton's) and perfectly plastic body (St. Venant's). Different creep and relaxation behavior is evident for different types of fibers.

THE RELAXATION LEVEL OF FRP ACCORDING TO CODES

According to the ACI440.4R the relaxation loss (REL) in FRP tendons is the sum of three different causes, namely: relaxation of polymer R_p , straightening of fibers R_s , and relaxation of fibers R_f , expressed as (1):

$$REL = R_p + R_s + R_f \quad (1)$$

Relaxation of polymer R_p appears within the first 24 to 96 hours and is the effect of taking over a portion of loading by matrix which relaxes. Polymer relaxation depends on two characteristics of the tendon: the resin-fiber modular ratio and the volume fraction of fibers in FRP specimen. The relaxation loss is described as follows (2):

$$R_p = n_r \cdot v_r \quad (2)$$

Where:

n_r - the resin-fiber modular ratio

v_r - the volume fraction of resin

The total relaxation of polymer reaches the values in the range within 0.6% to 1.2% of the transfer stress. This relaxation loss can be compensated by overstressing, however this is not recommended due to loss does not occur in the fibers which would be permanently overstressed. The loss caused by straightening of fibers R_s is the result of the not parallel arrangement of fibers in the material volume. When the FRP material is pretensioned the fibers straighten which is considered as relaxation loss. Third source of the relaxation of FRP composites is the relaxation of fibers which is dependent on the fiber type. Carbon fibers are considered to have no relaxation. Aramid materials creep when loaded, and this creep behavior is reflected in its relaxation behavior.

In accordance to the Canadian Code provisions to assess the relaxation of FRP materials for the purpose of design of prestressed concrete structure reinforced or strengthened with FRP materials the following dependences can be used:

$$REL = 0.231 + 0.345 \log(t) \quad \text{for the CFRP} \quad (3)$$

$$REL = 3.38 + 2.88 \log(t) \quad \text{for the AFRP} \quad (4)$$

Where:

t - the time in days.

In Fib Model Code 2010 the relaxation of different types of FRP composites depending on the type of fibers is specified according to Table 1 provided in 3000 hours relaxation tests.

Table 1: Relaxation of FRP according to Fib Model Code 2010

Type of tendon	1000h [%]	50years [%]
GFRP	1.8-2.0	4.0-14.0
CFRP	0.5-1.0	2.0-10.0
AFRP	5.0-8.0	11.0-25.0

Fib Bulletin 40: FRP specifies the relaxation behavior on the basis of experimental investigation described in the literature. According to code the relaxation of FRPs reach values in the ranges of: 2.0% to 3.1% and 18.4% and 23.4% respectively for CFRP and AFRP bars.

Traditional relaxation losses associated with FRP prestressing tendons can be assessed in the same manner as for prestressed steel tendons. The relaxation loss of the prestressed concrete consists of short-term or immediate losses and long-term or time-dependent losses. The initial losses are associated with elastic shortening of concrete ΔF_E , slippage in anchorage ΔF_A , and friction ΔF_{FR} between the CFRP laminate and the surrounding concrete. Time-dependent losses are associated with creep ΔF_{CR} and shrinkage ΔF_{SH} of concrete and relaxation of tendons ΔF_R : The relaxation loss can be expressed as (5):

$$\Delta F = \Delta F_D + \Delta F_A + \Delta F_{FR} + \Delta F_{CR} + \Delta F_{SH} + \Delta F_R \quad (5)$$

TEST METHODS FOR FRP RELAXATION ACCORDING TO CODES AND PROVISIONS

Guidelines ACI 440.3R, JSCE-E 534-1995, ISO 10406-1:201 and CSA S806-02 specifies the assumptions of relaxation tests such as a number and dimensions of samples, anchorage type depending on the geometry of samples (bar or flat laminate), the value of initial pre-tensioning force, duration of test and the intervals between the measurements (if the automatic recording is unavailable). In all codes, after pre-tensioning, the strain should be blocked and maintained for 120s. This time should be deemed to be the test start time. In Table 2 the comparison of test specifications according to different codes is presented. The test samples should consist of test section and anchoring section according to all codes. Type and dimensions of anchors should be adapted to the sample's geometry. Anchoring should be able to transmit axial loads only without transmitting flexural force or torsion and induce the failure in the test section. When sample have failed at the anchoring section or have slipped from the anchorage, the additional sample should be taken.

Table 2: Specification of the relaxation tests according to ACI 440.3R, JSCE-E 534-1995, ISO 10406-1:201 and CSA S806-02.

Code	Number of samples	Length of samples	Length of test section bar	Length of test section flat	Initial pre-tensioning	Minimum period of measurement	intervals between recording of pre-tensioning force
ACI 440.3R	≥ 5	Test section $+2L_a$	100 mm or 40ϕ	According to Tab. 2	70% f_u , or 80% of the million hour creep	1000 hours	Min.: 1, 3, 5, 9, 15, 30, 45. Hours.: 1; 1.5; 2; 4; 10; 24; 48; 72; 96; 120 and every 120
JSCE-E 534-1995	≥ 3	Test section $+2L_a$	100 mm or 40ϕ	2x strand pitch	70% f_u , or 80% of the million hour creep	1000 hours	Min.: 1, 3, 5, 9, 15, 30, 45. Hours.: 1; 1.5; 2; 4; 10; 24; 48; 72; 96; 120 and every 120
ISO 10406-1:2015	≥ 3	Test section $+2L_a$	300 mm or 40ϕ	2x strand pitch	70% f_u	1000 hours	Min.: 1, 3, 5, 9, 15, 30, 45. Hours.: 1; 1.5; 2; 4; 10; 24; 48; 72; 96; 120 and every 120
CSA S806-02	≥ 3	Test section $+2L_a$	40ϕ	According to Tab. 2	75% \pm 2% f_u	1000 hours	Min.: 1, 3, 5, 9, 15, 30, 45. Hours.: 1; 1.5; 2; 4; 10; 24; 48; 72; 96; 120 and every 120

L_a – length of anchoring section; f_u – FRP tensile strength; ϕ – the diameter of circular sample.

Table 3: Recommended width and gauge lengths of flat samples according to ACI 440.3R and to CSA S806-02.

Fiber orientation	Minimum specimen width		Minimum gauge length	
	ACI 440.3R	CSA 806-02	ACI 440.3R	CSA 806-02
[-]	[mm]	[mm]	[mm]	[mm]
0 degree	12.7	12.7	127	127
90 degree	25.4	25.4	127	38
0/90 degree	-	25.4	-	127

STATE OF ART

Wang et al. (2012) carried out an experimental study of flat CFRP samples subjected to sustained loading and flexural tests of RC beams strengthened with pre-tensioned CFRP to investigate long-term prestress losses. The test variables consisted of the pre-tensioning limits and different strengthening ratios. The relaxation tests of three samples under unidirectional tensile test were conducted with different initial loading corresponding to 40, 48, and 56% of the CFRP tensile strength. The CFRP strain was kept constant over a period of 2,500h. According to

test results the decrease of prestressing force in the first 100 hours progress in the nonlinear manner. After this period the linear drop of prestressing force was observed. Nevertheless, the biggest drop of load was observed in the first phase and further decrease was negligible. In Figure 1a the relaxation of samples during entire test period is shown. The remaining ratio of prestress after 2500 hours reached values of 0.978, 0.941 and 0.934 in samples pre-tensioned to 40, 48, and 56%, respectively.

Second part of the experimental program was composed of eight RC beams in total strengthened with CFRP sheets externally bonded to the bottom surface of the specimens. For strengthening the same FRP sheet was used as in the unidirectional tests. Six beams were strengthened with pre-tensioned CFRP sheets from which four were strengthened with one composite layer of 140 mm wide (BPC-30-1, BPC-40-1, BPC-50-1, BPC-60-1) and remaining two were strengthened with two composite layers (BPC-30-2, BPC-30-2a). The pre-tensioning limits of CFRP composites reached values of 30%, 40% , 50% and 60% in case of beams strengthened with one composite layer and 30% in both members strengthened with two composite layers. All members were initially preloaded to the value which represented 63% of flexural capacity due to damage simulation of existing structures. Therefore beams were unloaded and strengthened under dead load only. In all beams, except BPC-30-2a member, the hydraulic jack were kept with applied force for three days which were meant to effectively transfer the prestress to the anchorage and specimen. In specimen BPC-30-2a the prestressing force was immediately released for the purpose of investigation the influence of prestress transfer during epoxy curing on the relaxation loss. The estimated time-dependent loss based on the relaxation tests in specimens in which the adhesive was priming for 72 hours was approximately 2.2%. However, obtained losses reached value of 3.7% in comparison to the initial pre-tensioning load. In the specimen BPC-30-2a where the prestressing force was transferred on the RC beam before resin curing, the loss reached value of 2.3% which was almost identical as predicted value. The higher prestressing loss was caused by creep of resin between concrete and CFRP sheet which was not investigated in the relaxation tests. The resin in specimen BPC-30-2a did not transfer any part of prestressing load, therefore no creep of resin could occur. After all, the total loss of prestressing after 2500 hours was higher in specimen in which transfer of prestress was before the epoxy cuing (20.5%) than in specimens where the resin cured before the transfer (17.9%). The most part of loss was observed in the first 100 hours as obtained in the relaxation tests. The increase of the pre-tensioning level from 40% to 50% of the CFRP tensile strength resulted in the increase of the prestress loss from 2.2% to 6.6% of the initial prestressing load. The prestressing losses are primarily consisting of the initial losses which occurs in the first 72 hours after pre-tensioning. These initial losses are mainly affected by the anchorage slip, creep of hardening matrix in both anchorages and relaxation of FRP composite between anchorages. However, the time dependent losses induced by creep and shrinkage of concrete and relaxation of CFRP are relatively small (from 2.3% to 3.9%). No losses caused by elastic shortening of concrete and friction occurred. The mean values of the strains in the CFRP before and after transferring the prestress force to the anchors and after 2500 h under conditions of no external load are presented in Table 4.

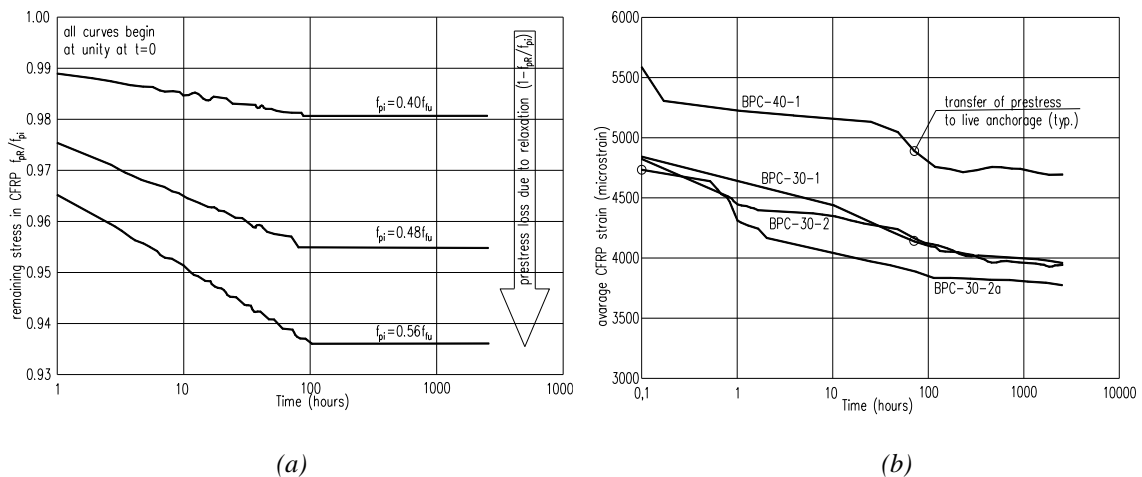


Figure 1. Loss of prestressing force: (a) due to relaxation of CFRP samples depending on pretensioning limit in unidirectional tension test; (b) in strengthened before beam's loading (Wang et al., 2012).

Table 4: Reduction of strain in CFRP (Wang et al., 2012)

Specimen	f_{pi}/f_{pu}	ϵ_f ($\mu\epsilon$)			Strain lost $\Delta\epsilon_f$ [%]		ϵ_a [mm]
		A	B	C	B	C	
BPC-30-1	0.36	4860	4150	3960	14.6	3.9	0.99
BPC-40-1	0.40	5610	4910	4700	12.6	3.6	0.98
BPC-30-2	0.28	4840	4150	3970	14.2	3.7	0.96
BPC-30-2a	0.30	4760	3890	3780	18.2	2.3	1.20

f_{pi} – initial prestress, f_u – CFRP tensile strength, ϵ_a – Anchorage slip, A – stain after pre-tensioning at the moment of anchoring, B – strain of CFRP sheet at releasing the prestressing force (at transfer), C – strain after 2500 hours.

Sasaki and Nishizaki (2012) tested six different types of FRP tendons exposed to different environmental conditions (direct sunlight and sea water) and pre-tensioning limits. Tests included two types of carbon specimens (CFRP), two types of aramid composites (AFRP), one type of glass sample (GFRP) and one type of vinyl tendon (VFRP) which gave 96 samples in total. Carbon and vinyl composites were initially pre-tensioned to $0.8P_u$ and $0.6P_u$ (P_u – FRP tensile strength) while aramid samples were pre-tensioned to $0.75P_u$ and $0.55P_u$. Glass samples were initially loaded to values of $0.4P_u$ and $0.2P_u$. Samples were placed on the deck platform for 17 years, however, part of samples were unloaded and checked after 3 years. After 17 years, the residual tensile force of CFRP and AFRP samples was in the range of 70-80% of initial tensile load in specimens subjected to direct sunlight and 90% and 80% without direct sunlight exposure in CFRP1 and CFRP2, AFRP1-2, respectively. Considering the carbon and aramid samples the loss of prestressing force between 3.5 and 17 years was almost negligible. Figure 2 and Figure 3 illustrate the residual tensile load of CFRP and AFRP tendons with and without direct sunlight exposure after 3.5 and 17 years, respectively. GFRP tendons pre-tensioned to the limit of $0.4P_u$ ruptured due to creep during the test. Although, prestressing load in GFRP samples remained at the level of 90% and 80% in specimens pre-tensioned to $0.2P_u$ of tensile strength respectively without and with sunlight exposure. Residual prestressing load of VFRP samples was less than 50%. The direct sunlight influences the relaxation behavior of CFRP samples causing the increase of the relaxation limit. There was no change in the relaxation of aramid composites regardless of insolation. Samples which were not subjected to direct sunlight, apparent relaxation ratio at 1,000h in $0.7P_u$ tensile loading indicate 5% for CFRP1 and 11-14% for the other cables. The obtained values of relaxation loss after 17 years of exposure for different FRP types were equal to: for CFRP: 10-20% without direct sunlight and 20-30% with direct sunlight, for AFRP: 20-30% irrespective of direct sunlight, for GFRP: around 10% under $0.25P_u$ tensile stress, however, all samples loaded to $0.4P_u$ ruptured by creep behavior and for VFRP: more than 50%.

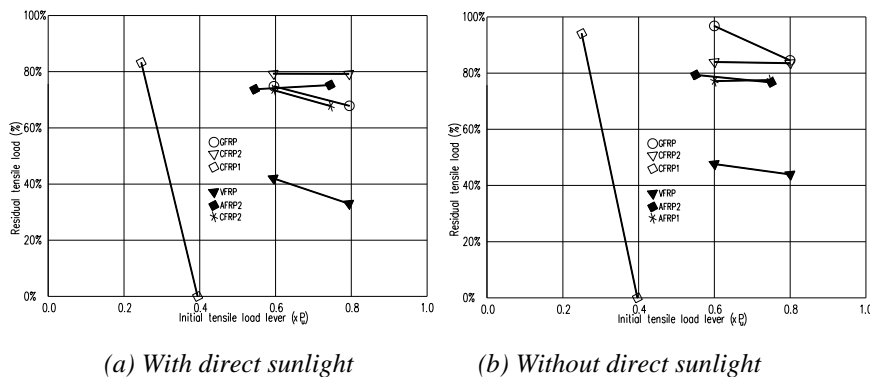


Figure 2. Residual tensile load after 3.5 years exposure (Sasaki and Nishizaki, 2012)

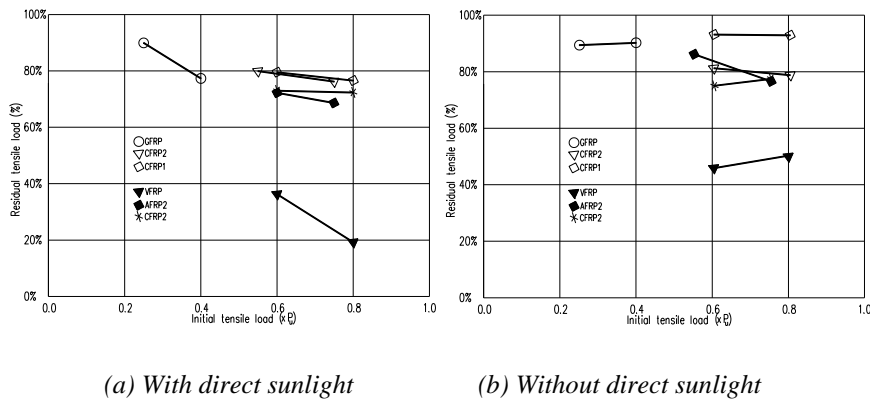


Figure 3. Residual tensile load after 17 years exposure (Sasaki and Nishizaki, 2012)

Shi J. et al. (2016) investigated the behavior of basalt fiber-reinforced polymer tendons subjected to three levels of initial stresses: $0.4f_u$, $0.5f_u$, and $0.6f_u$ (f_u - ultimate strength). Three specimens were tested in each test group. Moreover, the group of tests with the initial pre-tensioning equal to $0.6f_u$ maintained for 3 hours before the proper pre-tensioning (unloading) to the level of $0.5f_u$ was tested. This initial pre-tensioning was described as the optimum treatment of BFRP tendons. The total duration of each relaxation test was 1,000h. The proposed test setup eliminated the impact of slippage at the anchor zone influencing the relaxation value. Results obtained in the tests are presented in Table 5. Relaxation increases with the increase of prestressing load, however during first 10 h the relaxation values for different initial loads have no significant differences. During the stage from 10h to 480 h, the relaxation rates for the initial stress of $0.6f_u$ are significantly greater than those for $0.4f_u$ and $0.5f_u$. At 1,000 h, the relaxation rates obtained in the tests were 4.2%, 5.3%, and 6.4% for stresses of $0.4f_u$, $0.5f_u$, and $0.6f_u$, respectively. All samples behave similarly. From comparison of curves in Figure 4, two different stages of relaxation behavior are visible without distinction of prestressing level. First stage was characterized by rapid decrease of stress, whilst in the second stage the relaxation loss decreased with time. This regularity is caused by straightening of fibres with the viscoelastic deformation of the resin. Visible small fluctuations of the relaxation curves (Figure 4) are the result of changes in the ambient temperature. Samples initially pretensioned and maintained to the value of $0.6f_u$ demonstrated lower decrease of load than without pretensioning treatment.

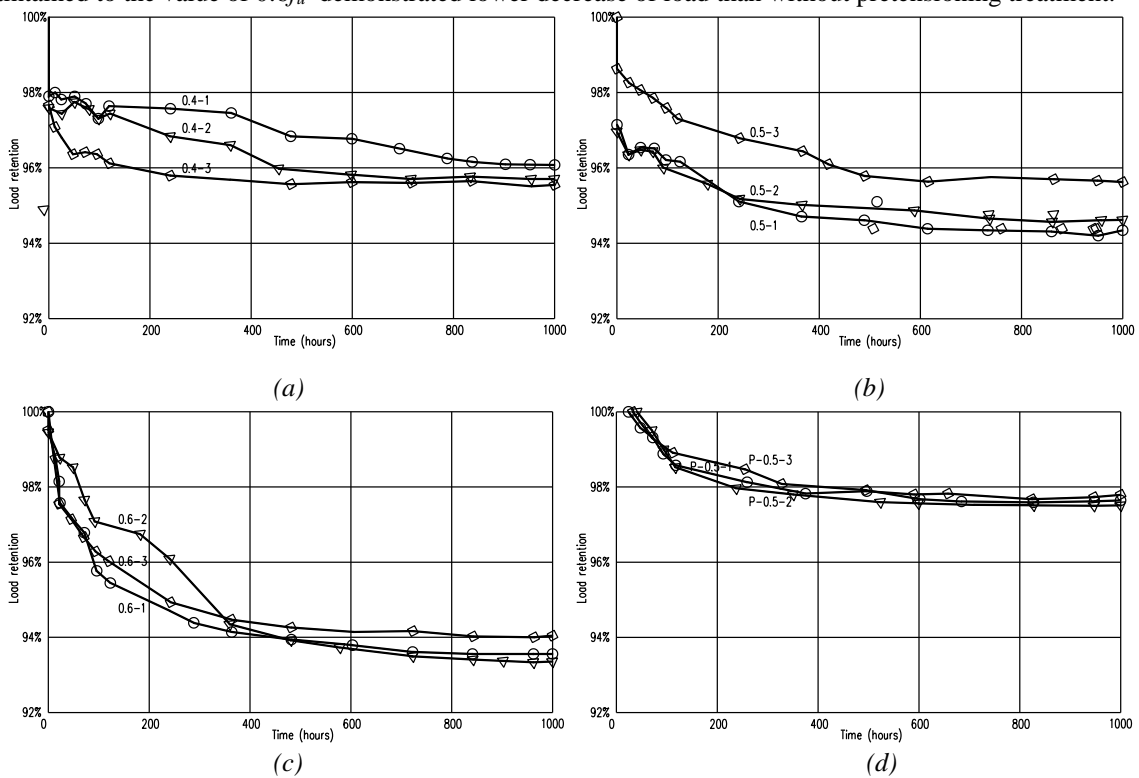


Figure 4. Relaxation curves at the initial stresses of (a) $0.4f_u$; (b) $0.5f_u$; (c) $0.6f_u$; (d) $0.5f_u$ after pretension treatment (Shi et al., 2016)

Table 5: Reduction of strain in CFRP (Shi et al., 2016)

Initial pretensioning	0.4 f_u (600 MPa)			0.5 f_u (750 MPa)			0.6 f_u (900 MPa)		
Sample	1	2	3	1	2	3	1	2	3
Relaxation value (0-1 h) [%]	1.60	1.71	1.57	2.53	1.61	1.00	1.27	1.19	0.89
Relaxation value (1-10 h) [%]	0.79	0.32	1.38	0.86	1.95	1.06	0.76	0.82	0.87
Relaxation value (10-480 h) [%]	1.14	1.98	1.45	2.09	1.55	2.30	4.01	4.16	3.94
Relaxation value (480-1000 h) [%]	0.37	0.27	0.06	0.28	0.37	0.14	0.40	0.53	0.28
Overall relaxation value [%]	3.9	4.3	4.5	5.8	5.5	4.5	6.4	6.7	6.0
Average relaxation value [%]		4.2			5.3			6.4	

Oskouei and Taleie (2010) tested four different test setups, each lasted at least 1000 hours. The aim of the study was to evaluate the relaxation of FRP composites subjected to the uniaxial tension. Two different types of FRP composites were tested: carbon and aramid in the form of dry straight fabrics and pre-cured sheets. The first setup included two carbon samples (SF-C1 and SF-C2) and two aramid samples (SF-A1 and SF-A2) to assess the relaxation of small sheets in the form of straight dry fabrics. Alike, four pre-cured small sheets samples including two carbon fabric specimens (SP-C1 and SP-C2) and two aramid fabric specimens (SP-A1 and SP-A2) were tested in the second setup. The levels of pre-stressing were selected as 20% and 30% of maximum tensile strength for the first and second level of pre-stressing, respectively. The test results except the relaxation loss contained the slip of FRP in the anchorage zone. The most part of relaxation loss occurred within the first hours of the experiment. The amount of stress reduction due to material relaxation for carbon small sheets registered in the tests was higher than 7%. For comparison, 23% of stress reduction was registered in aramid samples. According to test results, the amounts of AFRP relaxation are not dependent upon the pre-stressing level.

Table 6: Relaxation values of aramid and carbon FRPs (Oskouei and Taleie., 2010)

Specimens	Prestressing level	Relaxation after 48h	Relaxation after 1000h
	f_{pi}/f_{pu}	[%]	[%]
SF-A ₁	13.3	12.5	13.6
SF-A ₂	32	8.6	14
SP-A ₁	21	27	35.7
SP-A ₂	32.6	23.4	34
SF-C ₁	18.1	10.3	15.6
SF-C ₂	27.3	15.6	19.2
SP-C ₁	23	13.8	18.8
SP-C ₂	34	19	26.2

f_{pi} – initial prestress, f_u – FRP tensile strength

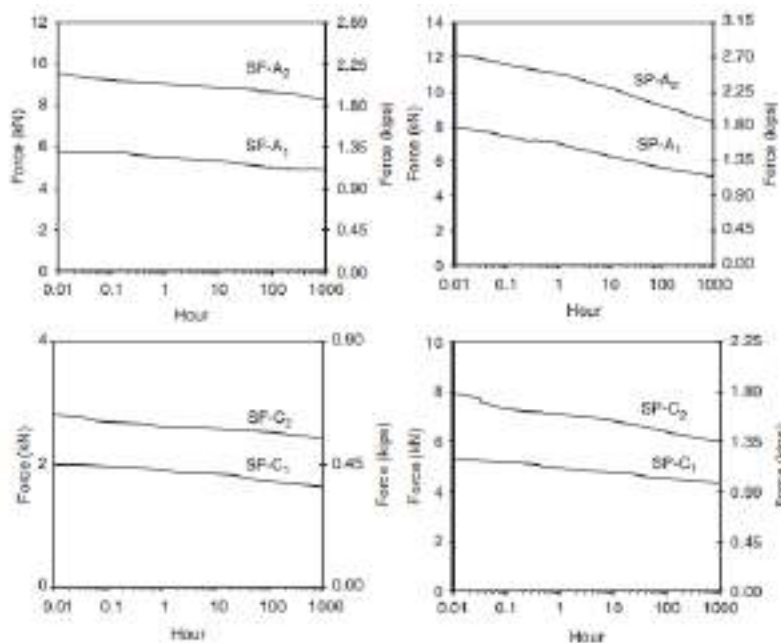


Figure 8. Relaxation of SF and SP samples (Oskouei and Taleie, 2010)

CONCLUSIONS

Prestress losses are affected by different factors as strength properties of used materials, ambient temperature, humidity, UV radiation, bond between the FRP material and RC specimen, type of anchorage and creep of prestressing system. In the described earlier experimental programs two types of tests were conducted: material samples subjected to sustained uniaxial tension (Wang et al., Sasaki and Nishizaki, Shi et al and Oskouei and Taleie) and flexural tests of RC beams strengthened with pre-tensioned FRPs (Wang et al.). Authors considered different types of composites: carbon (Wang et al, Sasaki and Nishizaki, Oskouei and Taleie), aramid (Sasaki and Nishizaki, Oskouei and Taleie), glass (Sasaki and Nishizaki), vinyl (Sasaki and Nishizaki) and basalt (Shi et al.). According to obtained results, the relaxation of FRP materials is affected by the level of pre-tensioning, types of fibers, loading history, environment and size of samples. Different types of fibers exhibit different behavior under sustained loading. Although, carbon fibers reveal negligible viscoelastic behavior, when mix with viscoelastic matrix, they manifest relatively small relaxation. It should be noted that the test results are heavily dependent on temperature. The direct sunlight influences the relaxation behavior of CFRP samples causing the increase of the relaxation limit. This regularity does not concern the AFRP composites, which are resistant for the direct sunlight. Obtained results demonstrated that the increase in the relaxation of FRP composites is directly proportional to the increase in the pre-tensioning limit. However, the relaxation of aramid fibers tends to be independent of the initial applied stress. Considering the carbon and aramid samples the loss of prestressing force between 3.5 and 17 years is almost negligible in the uniaxial tensile tests. Test results indicates that the biggest drop of load was observed in the first 100 hours and further decrease was negligible. The prestress loss progress in the nonlinear manner during this first phase. BFRP tendons are recommended to be applied at an initial stress of $0.5f_u$ after pretension treatment. Samples initially pre-tensioned and maintained to the value of $0.6f_u$ demonstrated lower decrease of load than without pre-tensioning treatment. Tests showed that glass fiber reinforced composites exhibit good relaxation properties at low stress values, however these rods are sensitive to creep. Although direct unidirectional FRP relaxation tests capture the FRP behavior they cannot capture the additional creep and relaxation associated with the adhesive bond line. Prestress losses registered in the RC specimens strengthened with CFRP composites glued to the concrete surface occur in the first 100 hours after pre-tensioning and are negligible thereafter regardless of the initial prestress level. The time dependent prestressing losses in this case are dependent on the relaxation of FRP and creep of the resin as the connection between the composite and concrete. The initial losses could be reduced by bonding the composite to concrete surface before transfer the prestressing force on the RC member for involving the part of composite between the anchorages to transfer the prestressing directly to the member which reduce the slippage in the anchorages.

REFERENCES

- ACI440.4R-04 (2004). "Prestressing Concrete Structures with FRP Tendons, *American Concrete Institute Committee Report*.
- ACI440.3R-12 (2012). "Guide Test Methods for Fiber-Reinforced Polymers (FRPs) for Reinforcing or Strengthening Concrete or Masonry Structures, *American Concrete Institute Committee Report*.
- JSCE-E 534-1995, "Test Method for Long-Time relaxation of continuous fiber reinforcing materials", 102-105.
- ISO 10406-1:2015, "Fibre-reinforced polymer (FRP) reinforcement of concrete – Test Methods – Part 1: FRP bars and grids".
- CSA S806-02, "Design and construction of building components with fibre reinforced polymers".
- I. Sasaki, I. Nishizaki (2012). "Tensile load relaxation of FRP cable system during long-term exposure tests", *Proceedings of 6th International Conference on FRRP, Composites in Civil Engineering (CICE2012)*, June 2012.
- W.-W. Wang, J.-G. Dai, K.A. Harries, Q.-H. Bao (2012). "Prestress losses and Flexural Behavior of Reinforced Concrete Beams Strengthened with Posttensioned CFRP Sheets", *Journal of Composites for Construction*, 207-216.
- J. Shi, X. Wang, H. Huang, Z. Wu (2016). "Relaxation behavior of prestressing basalt fiber-reinforced polymer tendons considering anchorage slippage", *Journal of Composite Materials*, 0(0), 1-10.
- A.V. Oskouei, S.M. Taleie (2010). "Experimental Investigation on Relaxation of Fiber –reinforced Polymer Composites", *Journal of Reinforced Plastics and Composites*, 29, 2705-2718.
- X. Wang, J. Shi, Z. Wu (2016). "Creep strain control by pretension for basalt fiber-reinforced polymer tendon in civil applications", *Mater Des*, 89, 1270-1277.



EVOLUTION OF THE TENSILE RESPONSE OF UNIDIRECTIONAL HYBRID FRP LAMINATES FABRICATED BY HAND LAY-UP METHOD: EXPERIMENTAL AND ANALYTIC ASSESSMENT

Filipe Ribeiro¹, José Sena-Cruz², Eduardo Júlio¹, Fernando G. Branco³, Fernando Castro⁴

¹ CERIS, Instituto Superior Técnico, Universidade de Lisboa, Portugal;

² ISE, Department of Civil Engineering, University of Minho, Portugal; Email: jsena@civil.uminho.pt;

³ ISE, Department of Civil Engineering, University of Coimbra, Coimbra, Portugal;

⁴ CT2M, Department of Mechanical Engineering, University of Minho, Portugal.

ABSTRACT

Hybridisation, i.e., the incorporation of two different types of fibres, namely low strain (LS) and high strain (HS) fibres, within the same polymeric matrix is an established approach to promote the appearance of a gradual and non-fragile tensile failure mode of unidirectional Fibre Reinforced Polymers (FRP). This behaviour is known as pseudo-ductile. In addition, hybridisation can increase the apparent strain at the failure of LS fibres. This phenomenon has been described as “hybrid effect”. In the present work, the tensile behaviour of 10 layer-by-layer unidirectional hybrid combinations has been investigated using both experimental testing and analytical modelling. All the hybrid FRP samples were made through the hand lamination of three different commercially available dry unidirectional fabrics manufactured for civil engineering applications, namely high-modulus (HM) carbon, high-strength carbon and E-glass. For each type, a large number of single fibres were randomly taken from the dry fabrics and tested in tension to define the Weibull distribution parameters. A maximum hybrid effect of circa 28% was achieved, by combining unidirectional fabrics of high-modulus carbon with standard carbon. It was also concluded that combining high-modulus carbon with E-glass can lead to very good pseudo-ductile tensile behaviour. It was demonstrated that global load sharing models can be used to accurately predict the hybrid effect. Finally, the analytical approach adopted in the scope of the present work also allowed the correct prediction of all the failure modes experimentally observed.

KEYWORDS

New composite materials, systems and strengthening techniques; hybrid effect, pseudo-ductility, analytical modelling.

INTRODUCTION

Despite its high mechanical performance, usually unidirectional FRP composites have brittle failures. For this reason, it is not possible to take full advantage of FRP properties, namely the high tensile strength due to conservative design limits (Czél et al. 2017).

The incorporation of two types of fibres, namely low strain (LS) and high strain (HS) fibres, within the same polymeric matrix, designated as hybridisation, is an established approach to achieve the well known hybrid effect and pseudo-ductility (Swolfs, Gorbatikh and Verpoest 2014). The hybrid effect is the increase of the apparent strain at LS fibres failure. In its turn, the pseudo-ductility is the gradual, and thus non-catastrophic, failure mode that has been registered in layer-by-layer configurations (Jalalvand, Czél and Wisnom 2015, Czél et al. 2017). This is due to the load transfer between LS and HS layers, fragmentation (a damage process where multiple fractures take place) of the formers, followed by the stable delamination of the LS layers from the HS layers, close to the LS layer fractures, ending with the failure of the latter (Czél and Wisnom 2013). The latter is one of the most relevant advantage of hybrid composites. However, it is only possible to achieve this behaviour when both the configuration and materials combination are appropriately selected. Please note that the term “pseudo-ductility” is used because it is possible to achieve a flat-topped stress-strain curve in monotonic tensile tests of some unidirectional hybrid FRP composites but the curve is not repeatable on subsequent unloadings/reloadings.

The aim of this research is to investigate the tensile stress–strain responses of 10 different interlayer (layer-by-layer) hybrid composite combinations, made through the hand lay-up method, of 3 different commercially available dry UD fabric materials, namely (i) high-modulus carbon, (ii) standard carbon and (iii) E-glass, in order to evaluate the hybrid effect and to achieve pseudo-ductility, fully exploiting the benefits of hybridisation. It was demonstrated that a progressive damage model can be used to accurately predict the hybrid effect. Finally, the analysis of the obtained experimental results was complemented with analytical modelling based on the approach developed for hybrid composites (Jalalvand et al. 2015).

EXPERIMENTAL PROGRAM

Materials

Commercial dry UD fabrics with similar areal mass of 400 g/m² were used in the present work, namely UD HM carbon (brand name: S&P C-Sheet 640), ST carbon (brand name: S&P C-Sheet 240) and E-glass (brand name: S&P G-sheet E 90/10). For laminating the studied composites an epoxy-based material (brand name: S&P Resin Epoxy 55) was used as matrix. According to the supplier, this epoxy has the following main properties (S&P 2015): (i) a tensile strength of 35.8 MPa; (ii) a strain at the failure of 2.3%; and, (iii) an elastic modulus of 2.6 GPa. In Table 8 the density, areal mass, and thickness properties of the mentioned materials and the respective properties of composite materials determined experimentally are presented.

Table 8 — Properties of the dry fabrics and cured composite materials determined experimentally.

Material ID	Dry fabric			Cured composite properties (Ribeiro et al. 2017)		
	Density [g/m ³]	Areal mass [g/m ²]	Nominal thickness, t_f [mm/layer]	Tensile strength [MPa]	Elastic modulus [GPa]	Failure strain [%]
E-glass (G)	2.60	400	0.154	1671.2	81.6	2.31
ST carbon (C)	1.79	400	0.223	2565.9	231.3	1.09
HM carbon (CHM)	2.10	400	0.190	1749.4	624.1	0.27

The tensile properties of composites were evaluated ignoring the contribution of the resin, considering only the dry fabric thickness (this is a common approach in the case of composites made through the hand lay-up method). This means that tensile strength and consequently the elastic modulus can be slightly overestimated.

Specimen manufacturing and test setup

The hybrid composite laminates were manufactured by hand lay-up method, following the best practices suggested in the guidelines (CNR-DT200 2013). Prior to the manufacturing, dry fabrics were cut into 250 mm × 80 mm² pieces. A Teflon film was used to avoid the adhesion of the produced composite laminate to the rigid base. All the samples were then cured at room temperature (20 ± 0.5°C) for 40 days.

Four specimens of each series were obtained from the laminates produced according to the protocol previously described, using a diamond tipped wheel cutter. Tensile tests were performed according to ISO 527-5:2009 standard (ISO 2009), at room temperature on a universal testing machine (UTM) equipped with a 200 kN load cell (with a linear error less than 0.05% of full scale) and hydraulic grips, as shown in Figure 14(a-b). Aluminium tabs of 50 × 15 mm² were used at each end of the specimen to avoid gripping effects, being the final clean length between tabs equal to 150 mm. A clip gauge with a gauge length of 100 mm (with a linear error, including hysteresis of 0.25%) was used. The specimens were held between grips of the UTM and extended (at a rate of 1 mm/min) up to failure.

Material combinations

Symmetric specimens were adopted to test the hybrid combinations, in order to minimize load eccentricity and differential thermal contraction during the cure of the epoxy resin, ultimately leading to bending-stretching coupling, and thus causing undesirable warping (Summerscales and Short 1978). Furthermore, in a way to try restrict the stress concentrations at the grips, LS layers were sandwiched between HS layers, according to (Wisnom et al. 2016) conclusions.

Hybrid composite combinations of 3 and 5 layers were studied. In total, 10 series were considered. The combinations of 3 symmetrical layers allowed to analyse the following approximate levels of LS fibres vol%: 33% and 66%. In addition, combinations with 5 layers allowed to analyse the following approximate levels of LS fibres vol%: 20%, 40% and 60%. The UD fabrics had slightly different thicknesses and, for this reason, the vol% before mentioned was corrected in the next sections, according to the corresponding thickness layer.

Tensile single fibre test

For each dry fabric, a large number of single fibres (see the details below) were randomly taken from the dry fabrics and tested in tension. The method used follows the guidelines laid down in ASTM D3379-75 for the tensile testing of fibres. The tests were carried out in a Hounsfield H100KS universal testing machine with a maximum load cell capacity of 2.5 N (with an accuracy of ± 0.2% of applied force across load cell force range). Fibres were individually assembled in the tensile jig by means of a paper template with a fixed gauge length of 20 mm, see Figure 14(c-d). Fibre ends were glued to the paper template by an ethyl cyanoacrylate-based adhesive. Then the

tab ends were gripped in the jaws of the machine. The paper template was cut across, so that just the fibre was fixed as a continuous length within the jig, before starting the tensile tests. The measurements were performed at a rate of 1.5 mm/min, until breakage occurred. For each fibre, records of applied load against extension were taken, and using an average mean diameter, determined through the analysis of microscopy images of fibres obtained with SEM, the data were converted to stress against strain.

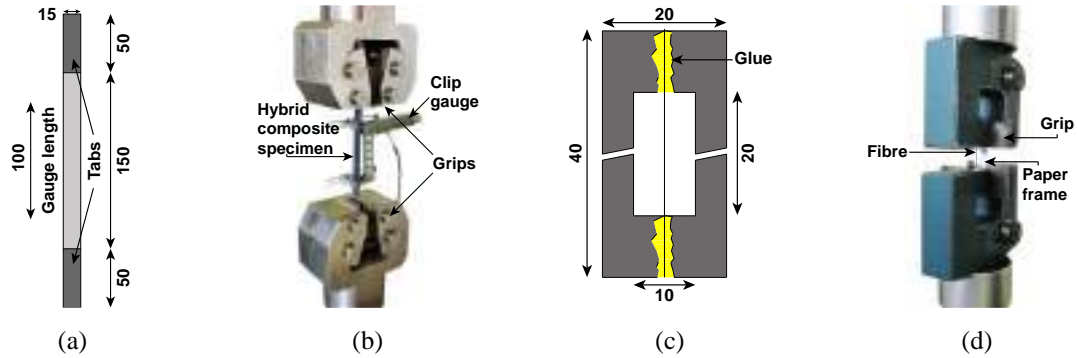


Figure 14: Tensile tests: (a) geometry of composite specimen; (b) illustration of the composite test; (c) geometry of single fibre specimen; (d) illustration of the single fibre test (dimensions in mm).

ANALYTICAL MODELS FOR HYBRID COMPOSITES

Progressive damage model for hybrid composites

In the present work, the Tavares's progressive damage model (PDM) was used to estimate the hybrid effect (Tavares et al. 2016). The PDM is a strength model that assumes that, when a fibre breaks, the load it carried before breaking is shed equally to all other fibres. The strength distribution of fibres was considered in cited PDM by means of Weibull cumulative failure probability distribution:

$$P(\sigma) = 1 - \exp\left(-\left(\frac{L}{L_0}\right)\left(\frac{\sigma}{\sigma_0}\right)^m\right) \quad (1)$$

where L is the characteristic gauge length, L_0 the reference gauge length, σ the fibre strength, σ_0 the Weibull scale parameter and m the Weibull modulus. In this work, the Weibull distribution parameters from single fibre tests were determined by the maximum likelihood method (MLM) (Ambrožič and Gorjan 2011).

The analytical approach proposed (Tavares et al. 2016) assumes as the strain is increased, the fibre fails progressively at randomly positioned flaws producing an increasing number of shorter fragments. The apparent stiffness of the system, matrix and fibre, decreases with the number of fibre breaks due to their loss of ability to carry the load. The number of breaks, $\langle N \rangle$, of a fibre of length L under at a given σ is defined in Equation (1):

$$\langle N \rangle = \frac{L}{L_0} \left(\frac{\sigma}{\sigma_0}\right)^m \quad (2)$$

From the statistic laws, it can be shown that the distance between the two consecutive breaks, x , will follow an exponential law:

$$f(x) = \Lambda e^{-\Lambda x} \quad (3)$$

where Λ is the number of breaks in a fibre per unit length:

$$\Lambda = \frac{\langle N \rangle}{L} = \frac{1}{L_0} \left(\frac{\sigma}{\sigma_0}\right)^m \quad (4)$$

When a fibre breaks, the load carried by the same drops down to zero at the position of the break and the load is transferred by shear between the fibre and the matrix to the fibres in vicinity. This causes a stress redistribution near fibre breaks. The model assumes a linear increase of the axial stress from a fibre break, until a total recovery occur at a certain distance from it. The length of this load recovery region, l_{ex} , is defined as:

$$l_{ex} = \frac{R_f E_f \varepsilon}{\tau} \quad (5)$$

where R_f is the fibre radius, E_f is elastic modulus of fibres, τ the matrix–fibre interfacial shear strength and ε the applied strain.

The average fibre stress along the fibre, σ_m , can be computed by integrating the axial stress over all of the fibre fragments along the fibre length, resulting, after some simplifications (please see the details in (Turon et al. 2005)), in next analytical solution:

$$\sigma_m(\varepsilon) = \left(\frac{1 - e^{-2l_{ex}\Lambda}}{2l_{ex}\Lambda} + \Lambda l_{ex} e^{-\Lambda l_{ex}}\right) E_f \varepsilon \quad (6)$$

Given the tensile responses for the two pure composites using equation (6), the stress-strain response for the hybrid composite can be described simply considering the contribution of two materials, taking into account the vol% of the constituents:

$$\sigma(\varepsilon) = \left(\sum \left(\frac{1-e^{-2l_{ex}\Lambda}}{2l_{ex}\Lambda} + l_{ex}\Lambda e^{-L\Lambda} \right) E_f V_f \right) \varepsilon \quad (7)$$

where V_f is the vol% of each fibre type.

Prediction of stress–strain curves of hybrid composites

For each hybrid composite configuration, three stress levels could be computed (Jalalvand et al. 2015): (i) the stress at which the first crack in the LS material occurs, $\sigma@LF$, (ii) the stress level at which delamination development occurs, $\sigma@del$ and (iii) the stress when the HS material fails, $\sigma@HF$, in accordance with the equations (8) to (10), respectively.

$$\sigma@LF = S_L \frac{\alpha\beta+1}{\alpha(\beta+1)} \quad (8)$$

$$\sigma@del = \frac{1}{1+\beta} \sqrt{\left(\frac{1+\alpha\beta}{\alpha\beta} \right) \left(\frac{2G_{IIC}E_H}{t_H} \right)} \quad (9)$$

$$\sigma@HF = \frac{1}{(1+\beta)} \frac{S_H}{K_t m \sqrt{V}} \quad (10)$$

where S_L is the reference strength of the LS material, α and β are the modulus and thickness ratios of the LS to HS fibre, G_{IIC} is the mode II interlaminar fracture toughness of the interface between LS layers and HS layers of the hybrid composite, E_H the elastic modulus of the HS fibres, t_H is the half thickness of the HS fibre, m_H is the Weibull strength distribution modulus of the HS fibre, S_H is the reference strength of the HS material, K_t is the stress concentration factor in the high strain material and V is the volume of the specimen.

Knowing the magnitude of the three possible stresses it is possible to identify one of the four possible damage modes: (i) premature HS failure, (ii) unstable delamination, (iii) LS layer fragmentation and (iv) LS fragmentation and stable delamination. After the determination of the damage modes, it is possible to plot the tensile stress–strain curve of hybrid FRP, as detailing by (Jalalvand et al. 2015).

In the present work, the length and width of tensile specimens were assumed equal to $L = 150$ mm and $W = 15$ mm, respectively. The ultimate strain of the LS fibres, ε_L , of the different material combinations was assumed to be equal to the experimental values obtained and S_L was computed according to Hooke's law. The interlaminar toughness, G_{IIC} , for the different hybrid interfaces was arbitrated for each combination in way that, in combinations with experimental pseudo-ductile behaviour, the fragmentation & dispersed delamination damage mode was analytical achieved (see Table 10). Weibull modulus of HS fibres was assumed equal to $m_H = 29.3$. The value of the stress concentration factor was assumed constant for all of the specimens, $K_t = 0.97$.

RESULTS AND DISCUSSION

The results of the fibre strength distribution are presented in Table 9 together with the Weibull model results, assuming $L_0=20$ mm and $L=150$ mm. The overall adequacy of the Weibull distribution was evaluated according to the chi-square goodness-of-fit test. It is possible to observe that all of the p -values for these goodness-of-fit statistics are larger than 0.01 implying that the strength follows a Weibull distribution with significant level $>1\%$. During the preparation of tests and the cutting of the paper frame, unlikely some fibres would break, particularly the HM carbon ones. The elimination of the weakest fibres causes deviations from Weibull distribution and underestimates the scatter of strength (which means higher values of m). It is possible to observe in Table 9 that the m value of HM carbon is higher than in other cases. The experience gained in the execution of these tests led to believe that this value is not correct, since it was not possible to test a large number of weak fibres. Assuming an m value equal to the mean of other types of fibres, i.e., $m=2.70$ led to much better adjustment of the hybrid effect predictions. The parameters that define this hypothetical distribution are as well shown in Table 9

Table 9 — Properties of the fibers.

Material ID	R_f [μ m]	E_f [GPa]	L_0 [mm]	L [mm]	N. of tests	σ_0 [MPa]	m	p -value
G	14.98	76.92	20	150	50	5965.90	2.80	0.1455
C	7.88	213.95	20	150	36	9353.44	2.68	0.0267
CHM	11.03	558.07	20	150	26	4559.57	5.51	0.0547
CHM*	11.03	558.07	20	150	-	3208.00	2.70	-

* hypothetical parameters that take account the high fragility of CHM fibres.

Quantitative comparisons between analytical results obtained with PDM and experimental results are presented in Table 10. With the exception of 2 combinations (1G/1CHM/1G/1CHM/1G, 2G/1C/2G) in which the experimental means seem to deviate for some random reason from the trend, the positive hybrid effects were predicted satisfactorily, with relative errors varying between -21.5% and 11.8%. Experimental negative hybrid effects only make sense because the number of layers of LS material is not the same in all hybrid combinations. As is well known, there is a size effect in tensile properties of reinforcing fibre due to the higher probability of finding a cluster of weaker fibre in a larger volume of material (Wisnom et al. 2016). Two or three layers of LS fibres, were used in cases where the hybrid effect was negative. The hybrid effect was computed relatively to the 1 layer non hybrid composite results, for this reason negative hybrid effects are understandable. In any case, in combinations in which the hybrid effect was negative the predictions are very close to zero, what it would be a plausible prediction if the scale effect did not exist.

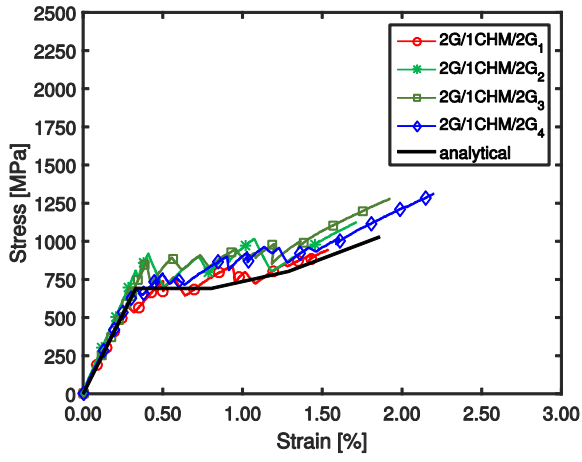
Table 10 — Tensile properties of hybrid FRP composites and hybrid effect prediction.

Material combination	Series ID	Vol. LS fibre [%]	Estimated G_{IIc} [kN/m]	Elastic modulus [GPa] (CoV [%])	Tensile strength [MPa] (CoV [%])	Strain at the failure of LS fibres [%] (CoV [%])	Hybrid effect		
							Experimental [%]	PDM prediction [%]	Relative error [%]
C/G	1C/1G/1C	74.3	1.90	201.7 (9.63)	2176.9 (8.55)	1.04 (1.92)	-4.44	4.00	190.1
	1G/3C/1G	68.5	1.90	202.4 (2.64)	2216.0 (8.77)	1.09 (6.26)	-0.20	5.16	2614.2
	1G/1C/1G/1C/1G	49.1	1.90	148.9 (11.75)	1776.3 (10.55)	1.19 (3.68)	9.15	11.11	-21.5
	1G/1C/1G	42.0	1.90	146.7 (5.92)	1856.0 (5.67)	1.27 (2.72)	16.33	14.47	11.4
	2G/1C/2G	26.6	1.90	110.8 (10.21)	1244.4 (1.74)	1.18 (8.27)	7.33	26.22	-257.9
CHM/G	1CHM/1G/1CHM	71.2	1.46	454.5 (11.95)	1168.9 (19.49)	0.26 (11.66)	-7.07	1.61	122.8
	1G/3CHM/1G	64.9	1.46	439.2 (7.35)	1053.5 (10.14)	0.24 (6.43)	-14.09	2.41	117.2
	1G/1CHM/1G/1C HM/1G	45.1	1.46	318.7 (7.33)	1105.8 (9.18)	0.35 (5.02)	27.66	6.45	76.7
	1G/1CHM/1G	38.2	1.46	252.0 (8.55)	1054.7 (9.11)	0.30 (2.39)	9.97	8.87	11.1
	2G/1CHM/2G	23.6	1.46	214.3 (8.45)	1164.7 (14.47)	0.33 (14.65)	21.94	19.35	11.8

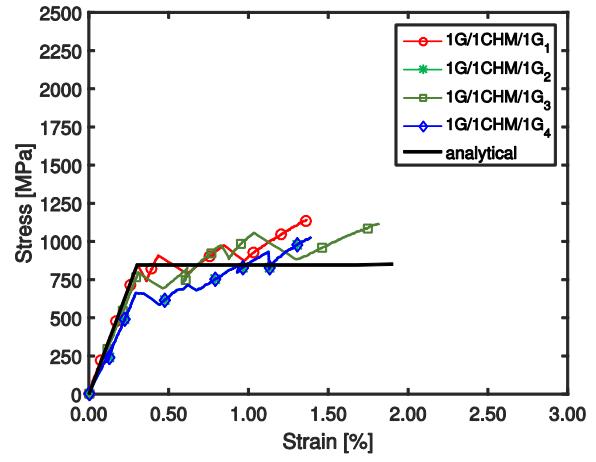
Note: The number before letters in series ID shows the number of layers of each material.

The stress-strain curves are presented in Figure 15 and Figure 16. Analysing the curves, three groups of behaviours can be identified: (i) pseudo-ductile behaviours (In 2G/1CHM/2G and 1G/1CHM/1G combinations) (ii) failure with two peaks (in 1G/1CHM/1G/1CHM/1G and 1G/3CHM/1G combinations), and (iii) premature and abrupt failure of HS fibres (in the remaining cases). In 2G/1CHM/2G and 1G/1CHM/1G combinations, pseudo-ductile tensile responses with multiple fractures were observed. In these combinations, a mean yield stress of 732.6 MPa and 768.2 MPa and mean pseudo-ductile strain of 1.4% and 1.2% were registered, respectively.

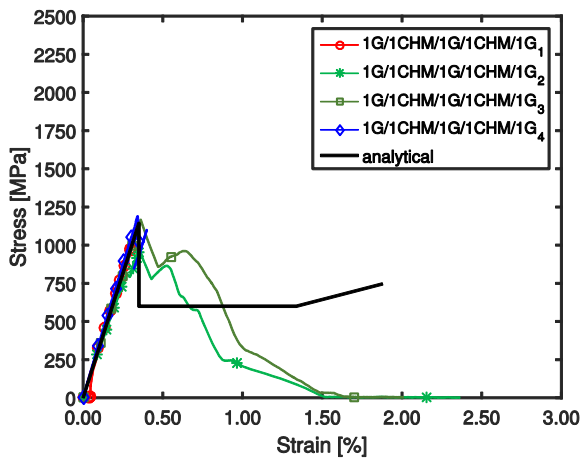
In all cases, it is possible observe that there is a good agreement between predictions and experiments. However, in 1G/1CHM/1G/1CHM/1G and 1G/3CHM/1G series, the model predicted well the catastrophic delamination damage mode, but the prediction of the delamination branch was much higher than the one observed experimentally. This lack of precision is probably related to some overestimation of G_{IIc} in these cases.



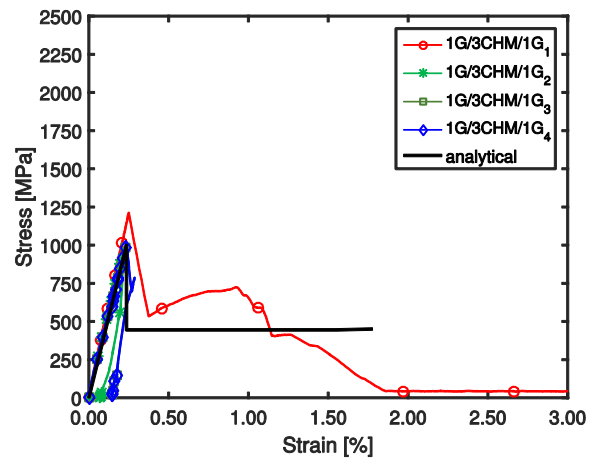
(a)



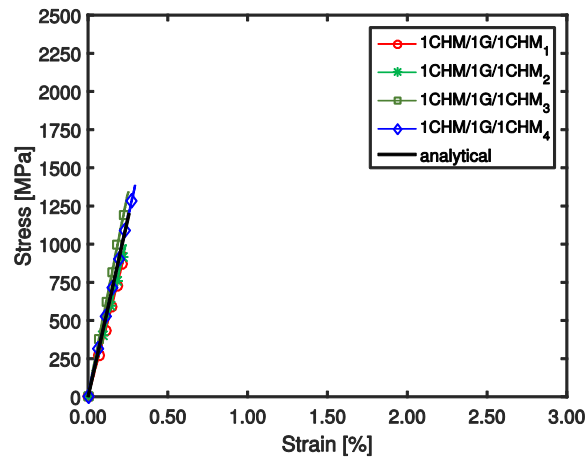
(b)



(c)



(d)



(e)

Figure 15 — Stress–strain curves of CHM/G combinations: experimental versus predicted values.

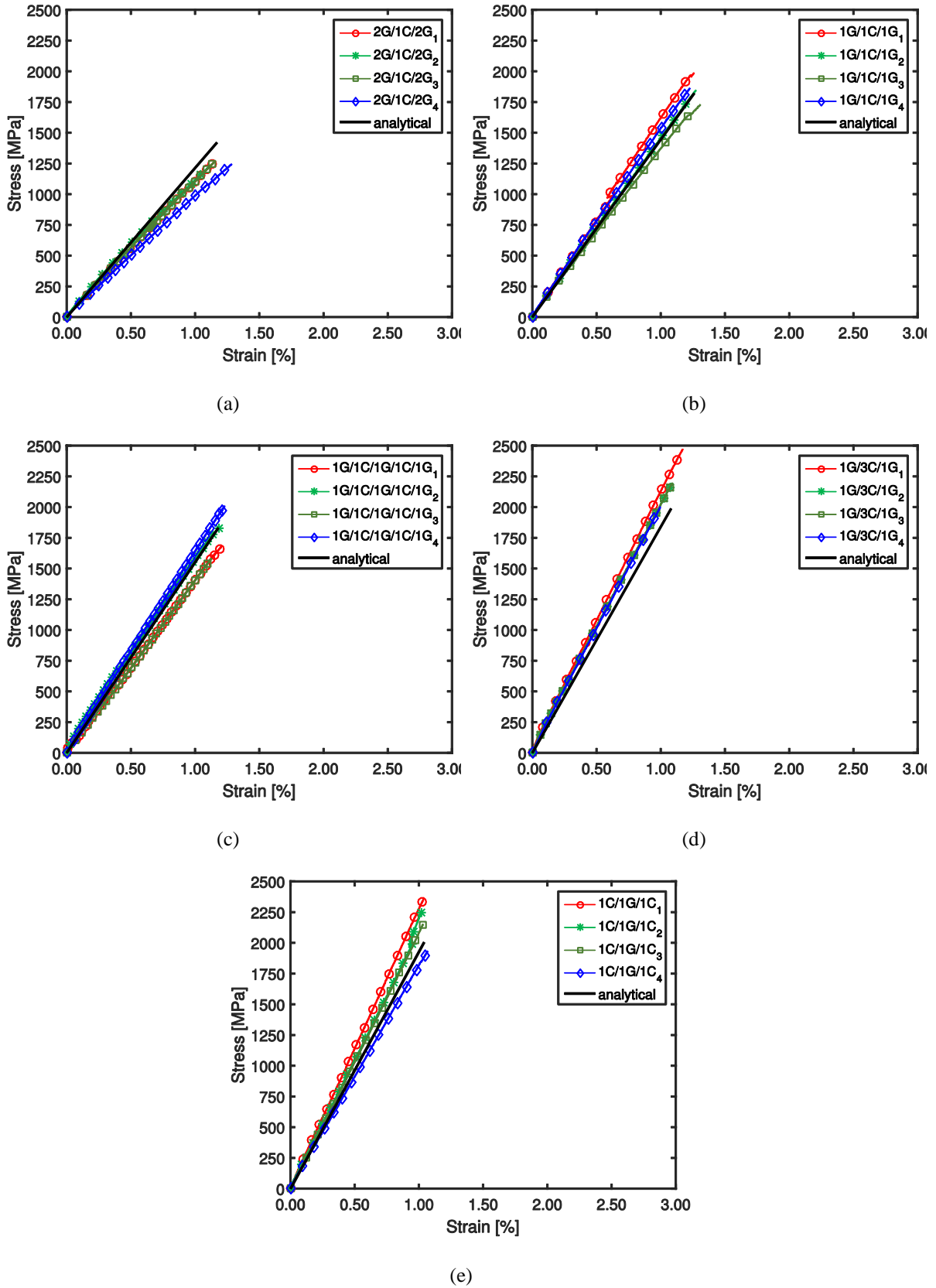


Figure 16 — Stress–strain curves of C/G combinations: experimental versus predicted values.

CONCLUSIONS

The tensile behaviour of several unidirectional layer-by-layer hybrid combinations has been investigated using experimental testing and analytical modelling. All the composites were made through the hand lamination of three different commercially available dry UD fabrics: HM carbon (CHM), ST carbon (C) and E-glass (G).

In the two tested hybrid combinations that included HM carbon as LS material (2G/1CHM/G, 1G/1CHM/1G), pseudo-ductile tensile responses with fragmentation and dispersed delamination were achieved. In these combinations, the mean yield stress varied between 732.6 and 768.2 MPa and the pseudo-ductile strain between 1.2% and 1.4%.

It was demonstrated that PDM is a simple model that if used with care can predict reasonably the hybrid effect. However some limitations should be taken into account. For instances, it does not take into account the real number of fibres leading that scale effects to be ignored. Furthermore, it ignores the dispersion of fibres, which has been shown to be a very important parameter for the hybrid effect. The hybrid effect varied between -14.1% and 27.7%.

The analytical model developed by (Jalalvand et al. 2015) allowed to predict all the failure modes successfully. In this way, the presented work validated the developed model for the set of materials and fabrication method used.

ACKNOWLEDGMENTS

The authors wish to thank to FCT - Portuguese Foundation for Science and Technology and to the Doctoral Program EcoCoRe for supporting the PhD scholarship (PD/BD/52660/2014). Furthermore, this work was partially supported by the following programs: FEDER (European Funds for Regional Development) through the Operational Program for Competitiveness Factors – COMPETE, Operational Program for Competitiveness and Internationalization (POCI) and through FCT under the projects FRPLongDur POCI-01-0145-FEDER-016900 (PTDC/ECM-EST/1282/2014) and POCI-01-0145-FEDER-007633. The authors also like to thank to the company S&P Clever Reinforcement Ibérica, Lda. for the material provided.

REFERENCES

- Ambrožič, M. & L. Gorjan (2011) "Reliability of a Weibull analysis using the maximum-likelihood method". *Journal of materials science*, 46, 1862-1869.
- CNR-DT200 (2013) "Guide for the Design and Construction of Externally Bonded FRP Systems for Strengthening Existing Structures. Advisory Committee on Technical Recommendations for Construction, National Research Council, Rome, Italy".
- Czél, G., M. Jalalvand, M. R. Wisnom & T. Czigány (2017) "Design and characterisation of high performance, pseudo-ductile all-carbon/epoxy unidirectional hybrid composites.". *Composites Part B*, 111 348-356.
- Czél, G. & M. R. Wisnom (2013) "Demonstration of pseudo-ductility in high performance glass/epoxy composites by hybridisation with thin-ply carbon prepreg". *Composites: Part A: Applied Science and Manufacturing*, 52, 23–30.
- ISO (2009) "527-5 Plastics — Determination of tensile properties; Part 5: Test conditions for unidirectional fibre-reinforced plastic composites. EUROPEAN COMMITTEE FOR STANDARDIZATION".
- Jalalvand, M., G. Czél & M. R. Wisnom (2015) "Damage analysis of pseudo-ductile thin-ply UD hybrid composites – A new analytical method". *Composites: Part A*, 69, 83–93.
- Ribeiro, F., J. Sena-Cruz, F. G. Branco & E. Júlio (2017) "Properties of unidirectional hybrid FRP composites fabricated by hand lay-up method for Civil Engineering applications: experimental and analytic assessment". (*submitted to Composites Part A: Applied Science and Manufacturing*).
- S&P (2015) "Technical Data Sheet S&P Resin 55".
- Summerscales, J. & D. Short (1978) "Carbon fibre and glass fibre hybrid reinforced plastics". *Composites*, 9, 157–66.
- Swolfs, Y., L. Gorbatikh & I. Verpoest (2014) "Fibre hybridisation in polymer composites: a review". *Composites Part A: Applied Science and Manufacturing*, 67, 181-200.
- Tavares, R. P., A. R. Melro, M. A. Bessa, A. Turon, W. K. Liu & P. P. Camanho (2016) "Mechanics of hybrid polymer composites: analytical and computational study". *Comput Mech DOI 10.1007/s00466-015-1252-0*.
- Turon, A., J. Costa, P. Maimí, D. Trias & J. A. Mayugo (2005) "A progressive damage model for unidirectional fibre-reinforced composites based on fibre fragmentation. Part I: Formulation.". *Composites Science and Technology*, 65 2039–2048.
- Wisnom, M. R., G. Czél, Y. Swolfs, M. Jalalvand, L. Gorbatikh & I. Verpoest (2016) "Hybrid effects in thin ply carbon/glass unidirectional laminates: Accurate experimental determination and prediction". *Composites: Part A*, 88, 131–139.



NOVEL CAPACITIVE CFRP SENSOR FOR STRUCTURAL HEALTH MONITORING

J. Yan¹, S. Hassan¹, A. Chen¹ and S. Laflamme¹

¹Department of Civil, Construction and Environmental Engineering, Iowa State University, USA
(corresponding author: yanjin@iastate.edu).

ABSTRACT

Carbon Fiber-Reinforced Polymer (CFRP) is widely used in strengthening, rehabilitating and retrofitting of existing structures because of its ease and speed of construction, low maintenance requirement, and high strength-to-weight ratio. The objective of this study is to employ CFRP as a multifunctional material for both strengthening and Structural Health Monitoring (SHM). The authors have developed a capacitive-based CFRP sensor, which consists of two CFRP layers separated by a dielectric layer. Damage can be detected through a variation in the sensor's capacitance provoked by the strain. This design utilizes the advantages of CFRP, including high corrosion resistance, weak thermoelectric behavior, and high electrical conductivity. Such multi-functional CFRP is particularly suitable for applications to civil structures because of its capability to both strengthen and monitor a structure. This paper investigates the use of titania dispersed in the epoxy layer separating the CFRP layers to enhance the strain sensitivity of the sensor. Electromechanical experiments are conducted on tension specimens to demonstrate the capability of utilizing the change in electrical signal to measure strain.

KEYWORDS

All FRP and smart FRP structures; Experimental study; Characterization of FRP and FRC materials/systems.

INTRODUCTION

Carbon Fiber-Reinforced Polymer (CFRP) materials have been widely used for strengthening (Chen and Davalos 2010), rehabilitating and retrofitting (Ray et al. 2010) structures. Over the last decades, Structural Health Monitoring (SHM) using CFRPs has been a subject of increasing interest. For example, CFRPs can be used as a self-sensing material by leveraging the carbon fibers' piezoresistive effect (Abry 1999; Irving 1998; Kaddour 1994; Todoroki 2004). Recent research has used CFRP to produce structural capacitors, whereas strain can be measured as a change in capacitance. Chung and Wang (1999) proposed a capacitor fabricated from semi-conductive carbon fibers and an insulation paper for the dielectric. Luo and Chung (2001) proposed using prepreg CFRP layers as electrodes, also separated by insulation paper, which could provide a capacitance up to 1200 nF/m². Inspired by the promising use of CFRPs as structural capacitors, researchers have focused on the improvement of the capacitance by introducing different separators (O'Brien et al. 2011) and modifying the treatment of surface electrodes (Qian et al. 2013).

The aforementioned studies were mainly focused on enhancing the capacitance of the materials. Limited studies were focused on electromechanical applications. Carlson and Asp (2014) studied the effect of damage on the electrical properties of a structural capacitor that used polyethylene terephthalate (PET) as the dielectric. They reported that the capacitance remained unchanged after significant interlaminar matrix cracking in the CFRP electrodes. Shen and Zhou (2017) discussed that interlaminar damage can instead lead to a reduction in capacitance, and modeled the capacitance as a function of interfacial crack. This behavior is unlike other types of structural capacitors for SHM found in literature (Laflamme et al. 2013), where the capacitance increases following strain.

This study presents a novel capacitive-based CFRP capacitor for SHM. The sensor leverages CFRP to create the conductive plates of the capacitor, separated by an epoxy layer to create the dielectric. The epoxy layer is filled with titania particles to increase the permittivity. The objective is to demonstrate the multifunctional capability of the CFRP materials. The resulting capacitor exhibits an increase in capacitance following strain.

The paper is organized as follows. First, the material properties and fabrication process of the CFRP sensor are presented, followed by a presentation of the sensing principle. Second, the experimental procedures are introduced, and experimental results are presented and discussed. Lastly, the paper is concluded.

BACKGROUND

Sensor Materials

Mbrace® CF 130 fabric and Mbrace® Saturant (BASF Construction Chemicals, LLC - Building Systems) were used to fabricate electrode plates with a unidirectional carbon fiber pattern, with an ultimate tensile strength of 3,800 MPa. The dielectric was fabricated using Mbrace® Saturant filled with PDMS coated titania (TPL inc), a highly permittivity fillers. The mechanical properties of CFRP components are listed in Table 1.

Table 1: Mechanical properties of CFRP components provided from the supplier:

Component	Ultimate Tensile Strength (Mpa)	Young's Modulus (GPa)	Ultimate Rupture Strain
Fiber	4950	-	-
Saturant	55.2	3.034	3.5%
Cured CFRP	3800	227	1.67%

Sensor Fabrication

The capacitive CFRP sensor is composed of two conductive electrodes separated by a dielectric. It is fabricated following two steps:

(1) Fabricate CFRP electrodes plates. The epoxy is first mixed using a mixing machine homogenizer (Figure 1(a)). The uncured saturant is applied onto the fabric and cured using a vacuum bagging process (Figure 1(b)) to obtain good mechanical and electrical properties. To form a better connection to the Data Acquisition (DAQ) for capacitance measurement, two copper tapes with conductive adhesive are attached onto the fabric surface before applying the epoxy. The surface of the copper tape is polished with sand paper after curing. After the electrode plate is cured for 24 hours, plates are cut from the middle section where the thickness is uniform.

(2) Separate the CFRP plates with the dielectric. A separator is made with the same epoxy but filled with 5% titania by weight (Figure 1(c)). The epoxy is applied onto the plates (Figure 1(d)) and let cured using vacuum bagging for 24 hours.

After, the capacitor is cut into 25.4 mm (1 in) wide strips using a table saw. The edges are trimmed to avoid uneven thicknesses. The specimens are further sanded using a sand machine to prevent electrodes from touching at the edge. The finished assembly is illustrated in Figure 2(a).

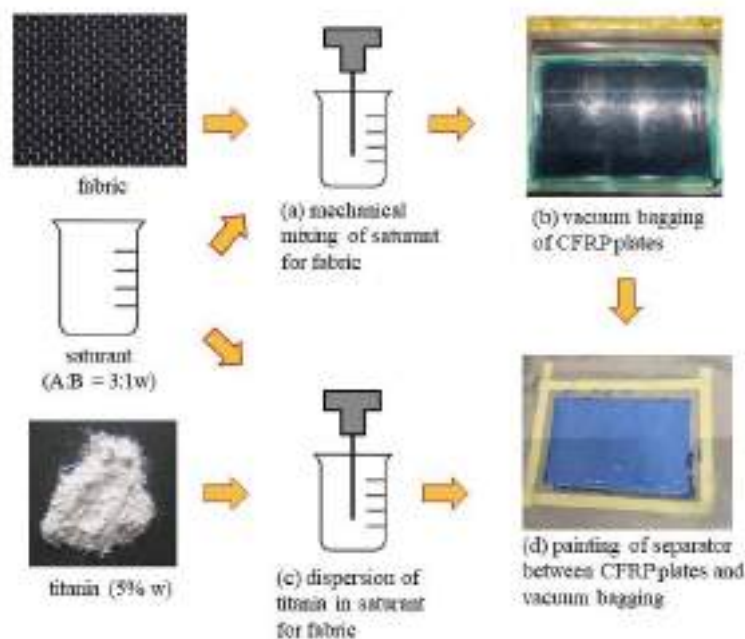


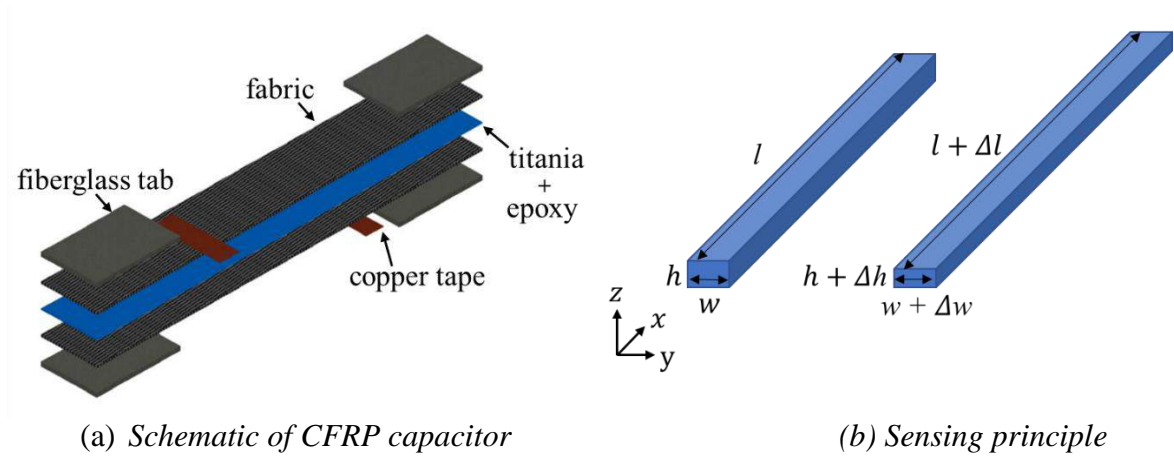
Figure 1: Sensor fabrication process

Sensing Principle

The capacitance, C , of the CFRP capacitor is given by:

$$C = e_0 e_r \frac{A}{h} \quad (1)$$

where e_0 is the vacuum permittivity ($e_0 \approx 8.854 \text{ pF/m}$), e_r is the relative permittivity of the separator, $A = w \cdot l$ the electrode surface area of width of w and length l , and h is the thickness of the dielectric.



(a) Schematic of CFRP capacitor

(b) Sensing principle

Figure 2: Sensing principle

In the coordinate system shown in Figure 2(b), x and y indicate the along fiber and transverse directions, respectively, while z is along the thickness. Assuming that the capacitor is subjected to a unidirectional small strain, the differential of Eq. (1) yields an expression relating strain ε to the relative change in capacitance:

$$\begin{aligned} \frac{\Delta C}{C_0} &= \frac{\Delta l}{l} + \frac{\Delta w}{w} - \frac{\Delta h}{h} \\ &= \varepsilon_x + \varepsilon_y - \varepsilon_z \end{aligned} \quad (2)$$

The CFRP fibers in this study are unidirectional. They are treated as orthotropic, where the properties along fiber differ significantly from those across fiber. Using Hooke's law under plane stress assumption, the out-of-plane strain ε_z and transverse strain ε_y can be written as a function of longitudinal strain ε_x :

$$\varepsilon_y = -\nu_{xy} \varepsilon_x \quad (3)$$

$$\varepsilon_z = -\nu_{xz} \varepsilon_x$$

The Poisson's ratio along the x - y plane ν_{xy} is assumed to be governed solely by the CFRP while the out-of-plane Poisson's ratio ν_{xz} is assumed to be governed solely by the epoxy. It results that, for the sensor subjected to longitudinal strain along fiber, combining Eq. (3) and Eq. (2):

$$\frac{\Delta C}{C_0} = (1 - \nu_{xy} + \nu_{xz}) \varepsilon_x \quad (4)$$

yields an expression for the gauge factor λ :

$$\lambda = \frac{\Delta C}{C_0} / \varepsilon_x = 1 - \nu_{xy} + \nu_{xz} \quad (5)$$

EXPERIMENTAL INVESTIGATION

Experiment Setup and Instrumentation

The experimental setup is shown in Figure 3. The CFRP specimens were 177.8 mm (7 in) long by 25.4 mm (2 in) wide, with thicknesses varying between specimens (reported in Table 2). Fiberglass strips were adhered at the ends of the specimens to insulate the electrode from the hydraulic grip and prevent crushing. A load was applied using a servo-hydraulic MTS machine under displacement control at a loading rate of 2 mm/min. Loads and displacements were acquired from the MTS at a sampling frequency of 10 Hz. CFRP capacitance measurement

was performed using an LCR meter (HP 4284A) under 1 kHz. The thicknesses and electrical properties of the three specimens were measured before initiating tests. Results are listed in Table 2, in which the relative permittivity ϵ_r was back-calculated from the initial geometries. The difference in the relative permittivity values is attributed to the manual fabrication process. Specimen #3 was equipped with a resistive strain gauge (RSG) to obtain an experimental value for the gauge factor. The RSG consisted of a foil gage sampled at 10 Hz using a Vishay Model 5100 B Scanner DAQ.

Table 2: Specimens configuration

Specimen	Thickness (mm)	Initial capacitance (pF)	Relative permittivity (ϵ_r)
# 1	2.64	251.4	16.60
# 2	2.57	266.1	17.10
# 3	2.36	340.8	20.11

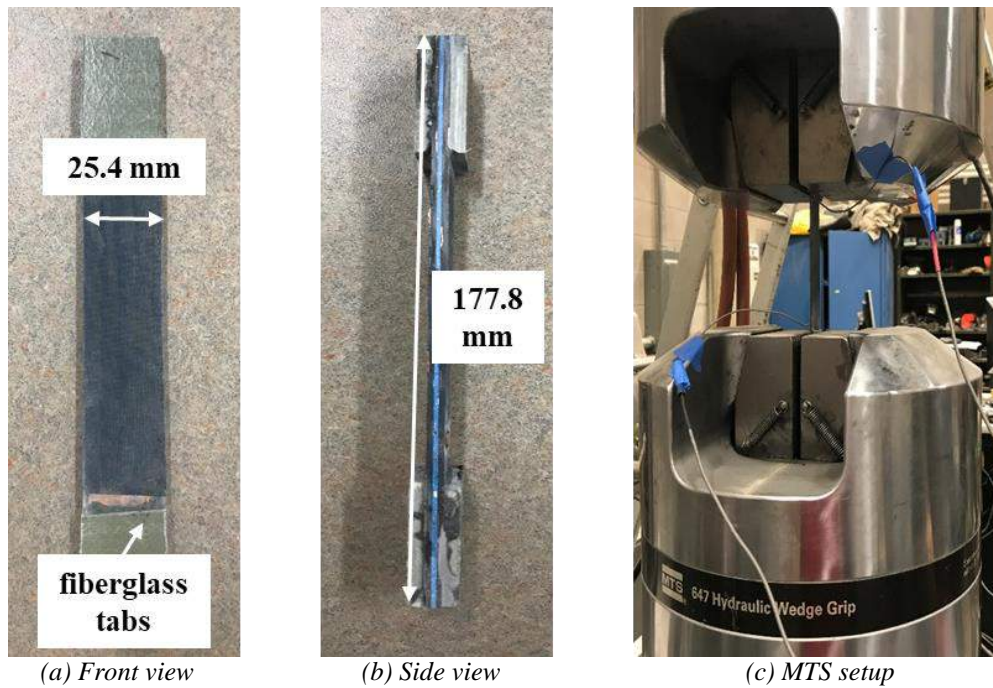


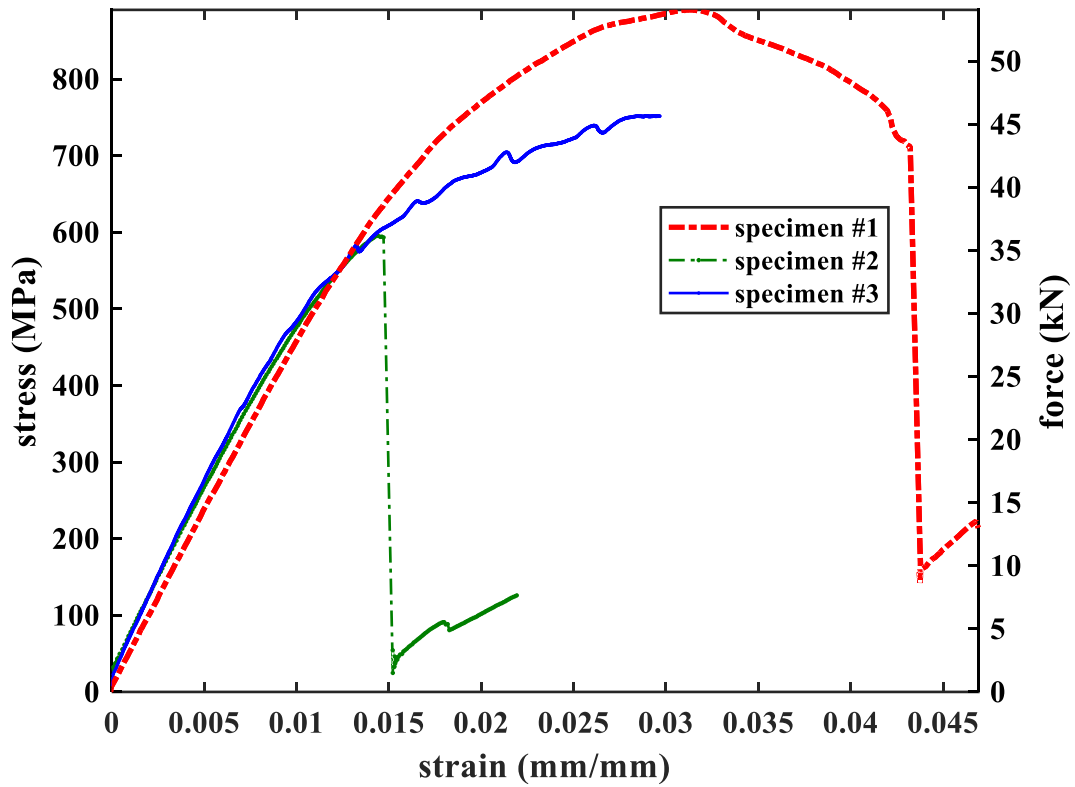
Figure 3: Experimental setup

Results and Discussion

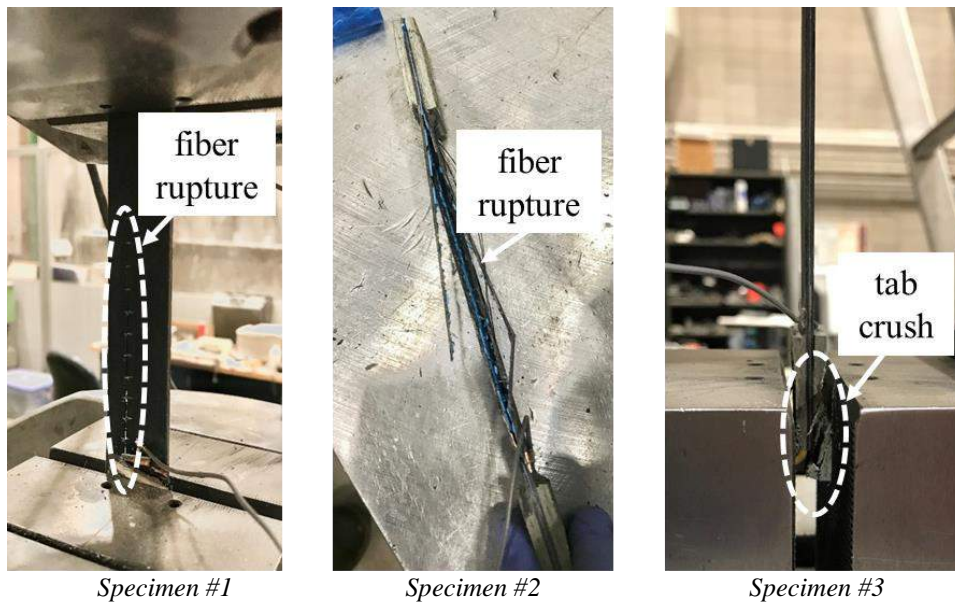
Force/stress-strain curves from the tensile tests are plotted in Figure 4(a). It can be seen from Figure 4(a) that all specimens exhibit a typical linear relationship before they fail or slippage occurs between the end tabs and grip. The experimental Young's modulus of the CFRP-based capacitors are summarized in Table.3. The tensile strength of three specimens average 47.9 GPa, which agrees with typical values for cured CFRP. Figure 4(b) are pictures of the failure modes of the specimens. Specimen #1 and specimen #2 failed from the fracture of the fiber, while the specimen #3 underwent pre-mature crushing of the fiberglass tab. The mechanical properties of specimens are summarized in Table 3. The fracture strain of specimen #1 is higher than the fracture strain of cured epoxy provided by the supplier might be the reason of that the specimen slippage from the grips.

Table 3: Specimens test results

Specimens	Young's Modulus (GPa)	Fracture strain (%)
# 1	45.0	4.4
# 2	45.3	1.5
# 3	53.3	-



(a) Force/stress versus strain curves



(b) Failure modes of the specimens

Figure 4: Test results: (a) force and stress curves; and (b) failure modes

The relative change of the capacitance with respect to the strain back calculated from the MTS displacements are plotted in Figure 5. Results show an increase in capacitance with increasing strain, with the similar slopes among each specimens in the linear range. Specimen #3 exhibits a nonlinear relationship between capacitance and strain beyond approximately 1% strain, which can be attributed to the delamination of CFRP passed this region. This behavior was confirmed by an audible cracking of the specimen during testing, indicating possible delamination of the CFRP.

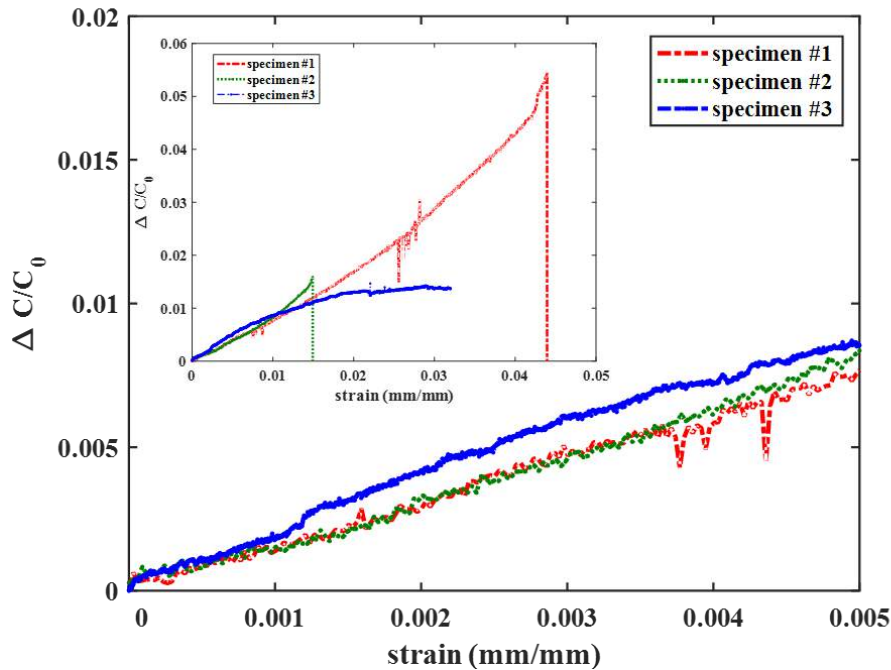


Figure 5: Relative capacitance versus MTS strain

The experimental gauge factor was calculated using the strain values measured directly from the RSG, because the strain back calculated from the MTS displacement values may not reflect the behavior of the specimens accurately enough. Figure 6 plots the relative capacitance versus strain from the RSG for specimen #3 (the only specimen equipped with an RSG) before crushing of the tabs occurred. The linear fit shows a gauge factor of 1.066. Typical Poisson's ratio values ν_{xy} and ν_{xz} for the utilized CFRP and saturant are 0.27 and 0.4, respectively, yielding an analytical gauge factor of approximately 1.13 (Eq. 5). Note that this value has a certain variability due to the unreported value of ν_{xy} from the manufacturer and addition of titania in the saturant. It follows that the experimental gauge factor is in agreement with theory.

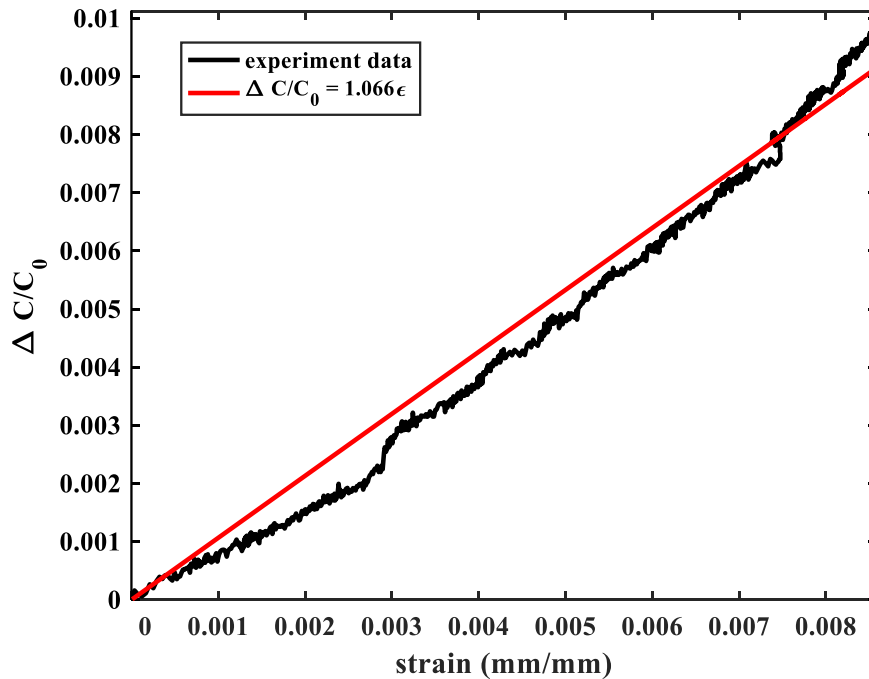


Figure 6: Relative capacitance versus RSG strain, specimen #3

CONCLUSIONS

In this paper, a novel capacitance-based CFRP sensor was proposed. The sensor consists of exterior CFRP plates acting as electrodes separated by a dielectric fabricated using an epoxy filled with titania. To quantify the mechanical and electrical performance of the CFRP sensors, three specimens were fabricated and subjected to unidirectional tensile tests. Experimental results demonstrated that the change in capacitance with respect to strain is positive and linear. However, this linearity is lost when the sensor is damaged. The derived experimental gauge factor of the sensor agreed with theory. The presented results showed the promise of the CFRP sensor at structural health monitoring.

ACKNOWLEDGMENTS

The authors are indebted to Dr. Joseph A. Schaefer from the Department of Aerospace Engineering and to Austin Downey, Douglas Wood, and Owen Steffens from the Department of Civil, Construction, and Environmental Engineering at Iowa State University for their help with the experiments.

REFERENCES

- J.C. Abry, S. Bochart, A. Chateauminois, M. Salvia, G. Giraud (1999). "In situ detection of damage in CFRP laminates by electrical resistance measurements", *Composite Science and Technology*, 59, 925-935
- T. Carlson, L. Asp, (2014). "An experimental study into the effect of damage on the capacitance of structural composite capacitors", *Journal of Multifunctional Composites*, 2 (2)
- A. Chen, J. Davalos (2010). "Strength evaluations of sinusoidal core for FRP sandwich bridge deck panels", *Composite Structures*, 92, 1561-1573
- D. D. L. Chung, S. Wang (1999). "Carbon fiber polymer-matrix structural composite as a semiconductor and concept of optoelectronic and electronic devices made from it", *Smart Materials and Structures*, 8, 161-166
- PE. Irving, C. Thiagarajan (1998). "Fatigue damage characterisation in carbon fibre composite materials using an electrical potential technique", *Smart Materials and Structures*, 7, 456 – 466.
- A. Kaddour, F. Al-Salehi, S. Al-Hassani, M. Hinton (1994). "Electrical resistance measurement technique for detecting failure in CFRP materials at high strain rates", *Composites Science and Technology*, 51, 377–385.
- S. Laflamme, H. Saleem, B. Vasan, R. Geiger, D. Chen, M. Kessler, K. Rajan (2013). "Elastomeric capacitor network for strain sensing over large surfaces", *IEEE/ASME Transactions on Mechatronics*, 18, 1647-1654
- X. Luo, D.D.L. Chung (2001). "Carbon fiber/polymer matrix composites as capacitors" *Composite Science Technology*, 61, 885-888
- D.J. O'Brien, D.M. Baechle, E.D. Wetzel (2011). "Design and performance of multifunctional structural composite capacitors" *Journal of Composite Materials*, 45, 2797-2809
- H. Qian, A. Kucernak, E. Greenhalgh, A. Bismarck, M. Shaffer (2013). "Multifunctional Structural Supercapacitor Composites Based on Carbon Aerogel Modified High Performance Carbon Fiber Fabric", *ACS Applied Materials Interfaces*, 13, 6113–6122
- I. Ray, GC. Parish, JF. Davalos, A. Chen (2010). "Effect of concrete substrate repair methods for beams aged by accelerated corrosion and strengthened with CFRP", *Journal of Aerospace Engineering*, 24, 227-239
- Z. Shen, H. Zhou (2017) "Mechanical and electrical behavior of carbon fiber structural capacitors: Effects of delamination and interlaminar damage", *Composite Structures*, 166, 38-48
- A. Todoroki, J. Yoshida (2004). "Electrical resistance change of unidirectional CFRP due to applied load" *JSME International Journal Series*, 47, 357-364
- Dai J G, Bai Y L, Teng J G. Behavior and modeling of concrete confined with FRP composites of large deformability. *Journal of Composites for Construction*, 2011, 15(6): 963-973



SHEAR TESTING OF DIFFERENT TYPE AND SIZE OF GFRP REINFORCING BARS

A.S. Genikomsou¹, G.P. Balomenos² and M.A. Polak³

¹ Queen's University, Department of Civil Engineering, Kingston, Canada,

Email: aikaterini.genikomsou@queensu.ca

² Rice University, Department of Civil and Environmental Engineering, Houston, USA.

³ University of Waterloo, Department of Civil and Environmental Engineering, Waterloo, Canada.

ABSTRACT

Shear testing of Glass Fiber-Reinforced Polymer (GFRP) reinforcing bars can be considered for material specifications, quality control, quality assurance and structural design purposes. The shear testing procedure requires the cutting blades of the shear device to match exactly the bar's diameter, therefore, for each different bar diameter new blades would have to be manufactured. In this research, a developed device to test GFRP bars in shear is manufactured based on both ASTM D7617 and CSA S806-12 standards. The paper aims to provide information about the significance of shear testing of GFRP bars and the potential outcomes of this type of test. For that purpose, different types of GFRP bars (straight and bent) provided by two different suppliers (sand/ribbed coating), are studied. The conducted tests consider GFRP reinforcing bars with measured diameter 18 mm. Then, the bars are "shaved" using a lathe machine to exclude the external coating and their diameter is reduced to 15.5, 13.5 and 10 mm. The idea of testing GFRP bars with reduced diameter that excludes the effect of the outer treated surface can possibly provide more unbiased information for quality control. Finally, discussion on the failure modes and stiffness is presented for both straight and bent bars.

KEYWORDS

Shear testing; GFRP bars; straight and bent bars; failure modes; bar coating; shear stiffness.

INTRODUCTION

Fiber Reinforced Polymer (FRP) composites have been widely used for structural strengthening and retrofit of existing structures, however they can be also considered as an alternative internal reinforcement for new concrete structures. FRP reinforcing bars consist of high-strength fibers which are impregnated with a resin matrix and provide many advantages such as non-corrosiveness, high tensile strength, fatigue-resistance and light-weight, and can be found in structures exposed to highly corrosive environments (e.g., marine infrastructure). Among other types of FRP reinforcing bars (carbon, aramid, basalt), Glass Fiber Reinforced Polymer (GFRP) bars perform adequately in alkaline environment present in concrete and are economical. In these bars, the glass fibers contribute to the strength and stiffness, while the resin provides the mechanism of load transfer and protection. The composites industry manufactures different types of GFRPs in terms of mechanical properties and external coating. Thus, quality control testing of these GFRP bars is an essential process before using them in structural applications. Among other tests that are required, shear testing seems to be important due to the fact that GFRP bars are often subjected to shear when they are used as bridge barrier connections, stirrups and dowels (Ahmed et al. (2010), Johnson and Sheikh (2016), Shehata et al. (1999), Eddie et al. (2001), Porter (2005)). Shear test provides information for the strength and stiffness of the GFRP bars as they are cut through using a double blade. Gentry (2011) described the ASTM D7617 standard test method to obtain the transverse shear strength of GFRP bars and performed tests on different types of GFRP reinforcing bars. The test results of this study showed that the shear test of GFRP bars is a significant addition to the other test methods.

This study examines two types of GFRP bars with different coating (sand, ribs), which are provided by two different manufacturers. For both types of GFRP bars, straight and the straight portion of bent bars are tested in double shear with the objective to comment on the significance of shear testing results. An intention of this research is to comment on possible changes that can be suggested on the current shear testing procedure. For that purpose, the original bars are "shaved" using a lathe machine excluding their outer treated surface and reducing at the same time their diameter. The idea of reducing the diameter of the GFRP bars derives from the fact that nowadays there are many and different manufacturers that produce bars of varying diameters with different types of coatings. Another reason of considering this technique is that the shear test requires the cutting blades of the device to match exactly the bar diameter. Therefore, for each different bar diameters new blades would have to be manufactured. The reduced diameter that is suggested in study excludes the effect of the outer treated surface and thus the "shaved" bars can possibly provide more unbiased information for quality control allowing for comparison between different manufacturers.

SHEAR TESTING OF GFRP REINFORCING BARS

Description of GFRP bars

The GFRP bars were manufactured by pultrusion and surface treatment, and in this research, were provided by two different companies. Sanded surface GFRP bars are denoted as Type I bars and were provided by company I, while ribbed GFRP bars are denoted as Type II bars and were provided by company II. Figure 1 presents the two different types of straight bars (left part), and the two different types of bent bars (right part). Type I straight bars have a sanded coating, while Type I bent bars have a combination of helical wrapping and sand coating. Type II bars consist of a multitude of continuous fibers, oriented in the direction of the load. The fibers have a diameter of approximately 20 μm and are bonded in a highly durable vinyl-ester (VE) resin matrix. The milled ribs are approximately 1 mm thick increasing by about 2 mm the diameter of the loading carrying core. The outer surface of the bars is coated in an additional layer of VE resin for extra protection. Type II bent bars are produced by bending a specially made polypropylene conduit pipe filled with glass fibers and a vinyl ester epoxy resin into the desired shape. These raw bars are then thermally cured. This procedure allows for a high fiber content and a nearly parallel alignment of the fibers in the bent portion of the bars, resulting in high strength and a modulus of elasticity similar to that of straight bars.

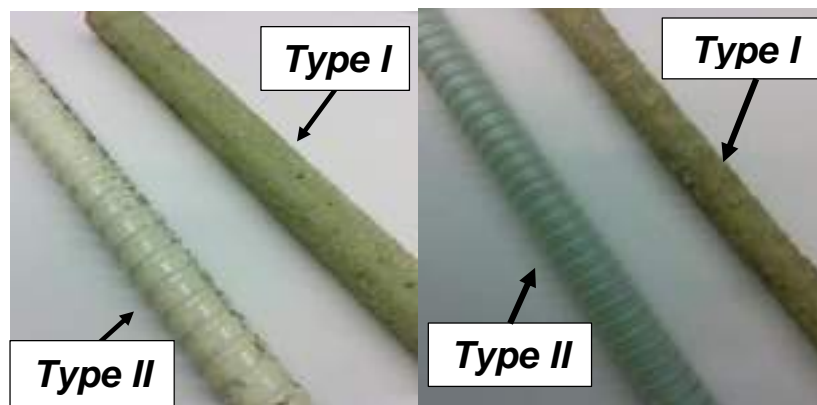


Figure 1: Types of tested GFRP bars: Straight bars (left) and Straight portion of bent bars (right). Type I (surface of sand-Company I), Type II (surface of ribs-Company II).

Shear test

The shear test was conducted according to the ASTM D7617 standard test method and the bars were loaded in transverse shear as a consequence of dowel action in reinforced concrete beams. For each bar diameter, 8 GFRP bars of 300 mm length were tested. The loading rate was such that the shearing stress was increased at a rate of 45 MPa/min. leading to failure after 2 to 5 min. of testing. Each GFRP bar was placed into the shear device and was supported along its length except a part of 25 mm in the center of the length of the bar that was not supported. The load was applied through the upper steel blade (25 mm thick) which was located to fit around the bar. The two lower blades were used in order to support the bar at the two shearing planes in order the bar to fail in double shear. Different sets of cutting blades with diameters 18 mm, 15.5 mm, 13.5 mm, and 10 mm, were manufactured in order to test the bars. The bar's diameter was decreased to the nearest available size of the slot of the blades by "shaving" using a lathe machine.

RESULTS AND DISCUSSIONS

Straight bars

The measured diameter of both types of GFRP bars (Type I-sand coated and Type II-ribbed) found equal to 18 mm. This diameter of the original bars was reduced ("shaved bars") to 15.5 mm, 13.5mm and 10mm. Figure 2 shows the shear stress-strain curves of the straight GFRP bars. The "shaved" bars with the reduced diameters (15.5 mm, 13.5 mm, 10 mm) show similar shear stress and stiffness. As it can be seen in Figure 2a), the original sand coated GFRP bars (Type I) show a greater shear strain deformation and lower shear stiffness before failure compared with the bars that have reduced diameters. However, the maximum shear strength is quite similar for all tested bars. The difference in the stiffness may appear as the effect of the outer coating of the bars. On the other side, by observing the test results of the ribbed GFRP bars (Type II) in Figure 2b), it can be said that both the original ("unshaved") and the bars with the reduced diameters ("shaved") show similar shear stress-strain responses in terms of stiffness and maximum shear stress. Thus, the idea of reducing the diameter of the GFRP bars seems to provide reasonable and consistent results.

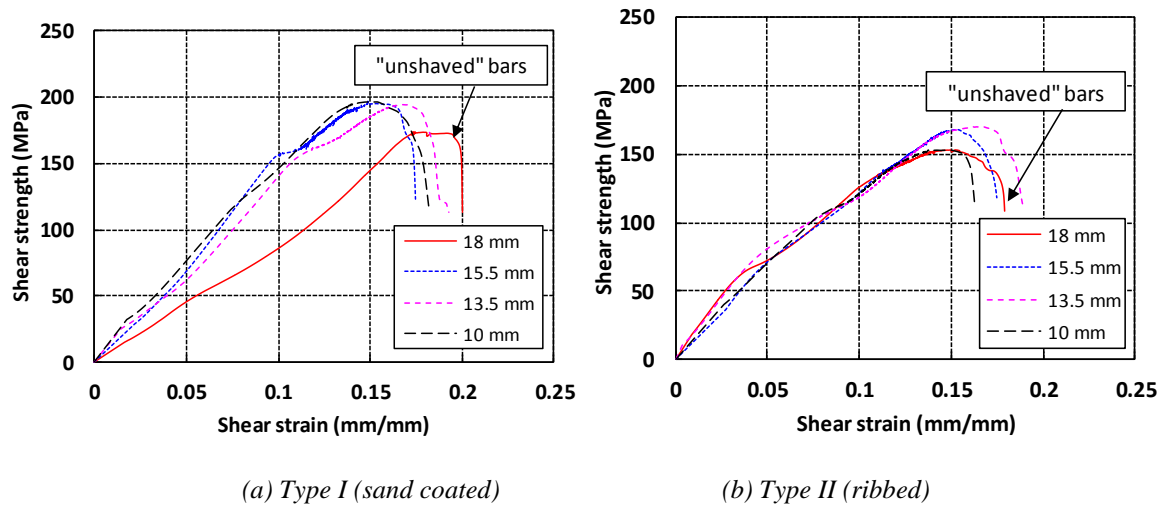


Figure 2: Shear stress-strain curves for straight bars

Bent bars

Then, the straight portion of the bent GFRP bars was tested for both types of bars. Figure 3 shows the test results for the bent GFRP bars. When the diameter of the GFRP bars is reduced, the response of the GFRP bars becomes stiffer and all “shaved” bars appear similar ultimate shear stress and strain. The effect of the outer surface (coating) in both types (sand, ribs) seems to affect the response of the bars in terms of shear stiffness. Both “unshaved” types of bent GFRP bars show a greater shear strain deformation and lower shear stiffness before failure compared to the “shaved” bars. Figure 3b) shows that the “unshaved” ribbed bent GFRP bars experience a higher shear strength compared to the “unshaved” sand coated bent GFRP bars that probably arises from their strong polypropylene conduit pipe outer surface.

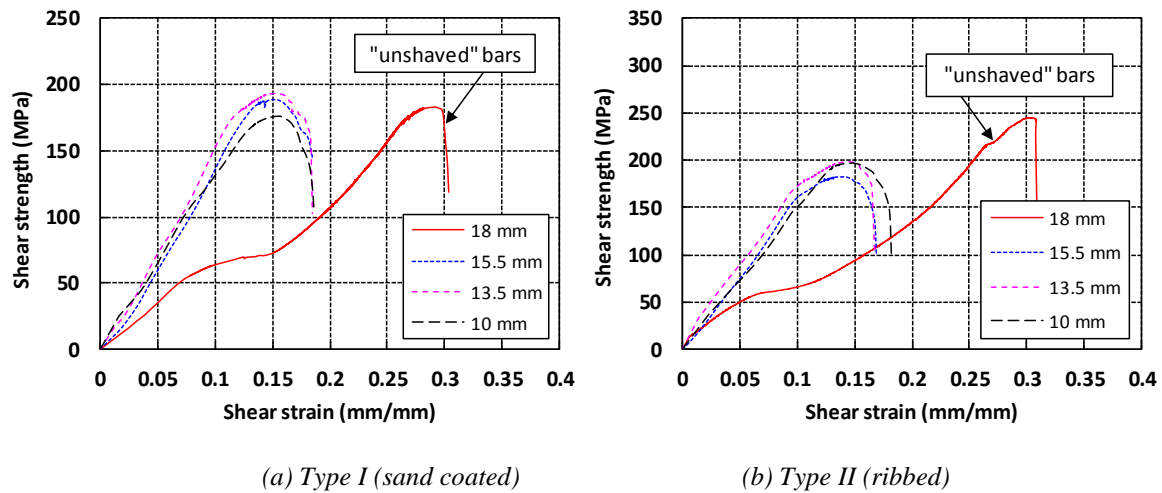


Figure 3: Shear stress-strain curves for bent bars

Failure modes

Two different types of failure were observed from the test results of the original (“unshaved”) straight bars. Figure 4 shows the stress-displacement curve of the two different failure modes of Type II GFRP bars and Figure 5a) presents the failure modes of the same bars. Failure mode I was observed only in few bars, while Failure mode II was observed in the majority of the tested bars. Failure mode I appeared when both shear planes (planes where the blade cuts the bar) failed at the same time, while Failure mode II happened when one shear plane failed first (first peak in stress-displacement curve) and then followed the other (second peak in stress-displacement curve). In Failure mode I, some bars were cut in three pieces and some others were cut in two pieces (one shear plane cut). Similar failure modes were also noticed in Type I GFRP straight bars. Both Type I and Type II “shaved” bars failed in three different types. In all failures, both shear planes failed at the same time, and therefore the stress-displacement curves are similar. Figure 5b) shows the three different failure modes. Failure may occur by

four different ways: by matrix shear failure, by matrix shear failure with fiber debonding, by fiber debonding or by shear rupture of fibers (Agarwal and Broutman, 1990).

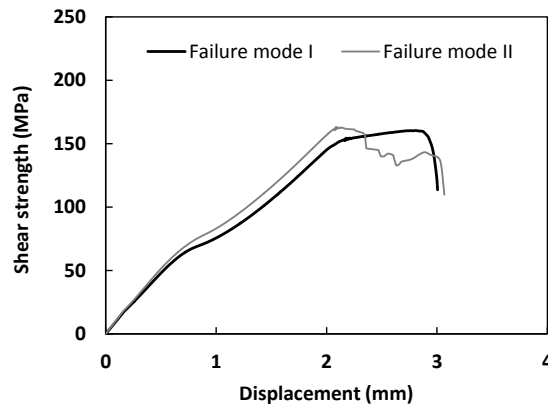


Figure 4: Failure modes (shear stress-displacement curves) of Type II GFRP straight bars

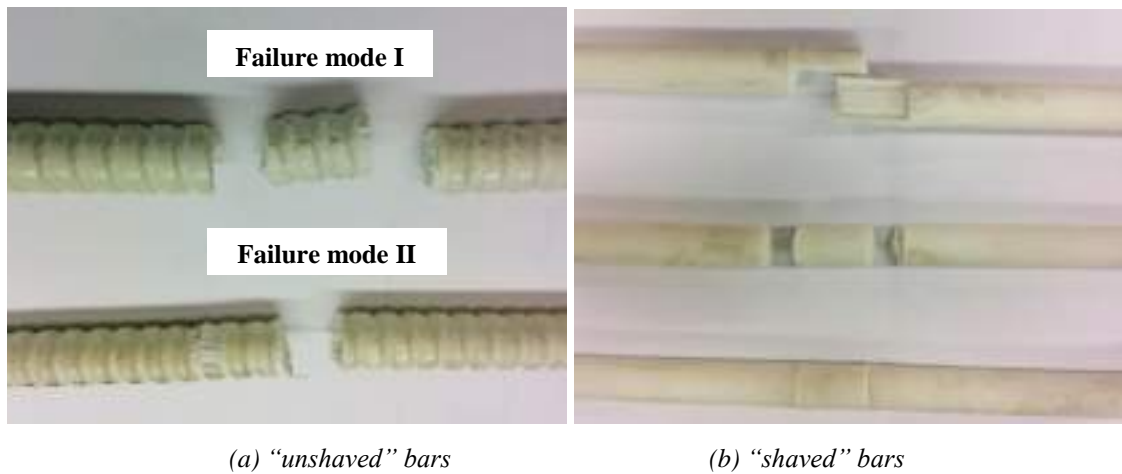


Figure 5: Failure modes (Type II GFRP straight bars)

The two types of bent bars showed different failure modes. Type I “unshaved” bent bars were not cut into pieces at failure as shown in Figure 6. The Type II “unshaved” bent bars failed in the same way as the straight unshaved bars Type I and II, i.e., they were cut into two or three pieces. The “shaved” bent GFRP bars (both Type I and II) failed in a similar manner as the “shaved” straight GFRP bars.



Figure 6: Failure mode of “unshaved” GFRP Type I bent bars

Measure of stiffness

The stress-strain curves of the “unshaved” GFRP can be divided into three sections, i.e., two regions with different shear stiffness, and one region between them that shows a plateau. The stress-strain curves of the “shaved” bars show a different response without the plateau regime. Figure 7 illustrates the measure of stiffness with two regions (H_1 and H_2) and a plateau between them of the “unshaved” GFRP bars, while the “shaved” GFRP bars showed only one measure of stiffness (H). All results for the shear stiffness of the tested bars are presented in Table 1. For each one stress-strain graph of the GFRP bars, the straight portions of the curves are considered to measure the

H_1 , H_2 and H . Then, the mean value of each measure of stiffness for each type of bar was calculated and recorded, considering 8 samples for each diameter of GFRP bars. Initially, only the original “unshaved” bars were tested. It was speculated that H_1 stiffness is based on the resin’s properties, while the H_2 stiffness is linked to the fibers’ properties. The plateau between the two measurements of stiffness appears due to the delamination of the fibers and resin. This concept with the H_1 and H_2 refers to the original GFRP bars.

When the “shaved” bars were tested only one measure of stiffness (H) was noticed. The plateau region between H_1 and H_2 practically disappeared. This could mean that H_1 in the “unshaved” bars, was the result of the blades cutting through the surface finish of the bars and H_2 was then a measure of stiffness reflecting the actual bar quality. The values of stiffness H_2 of the “unshaved” bars seem to be quite close to the stiffness H of the “shaved” bars. The stiffness of the original “unshaved” bent bars is lower than the stiffness of the straight bars and knowing from the manufacturing procedures that bent bars are not as high quality as straight bars, one can speculate that shear stiffness could be an indicator of bars quality. However, it is interesting to note that the stiffness of the “shaved” bent bars is quite similar to the stiffness of the “shaved” straight bars.

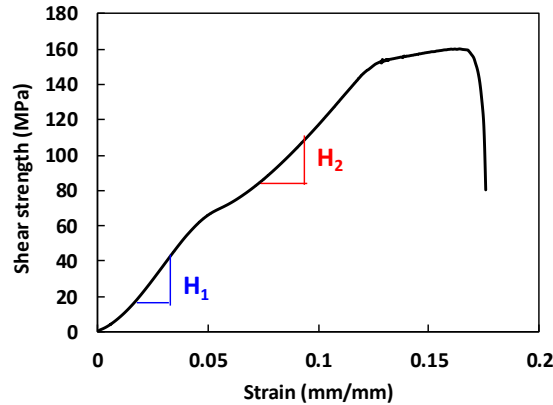


Figure 7: Shear stress-strain curve showing measure of stiffness

Table 1: Measure of stiffness (GPa) of the GFRP bars

Bar diameter	18 mm	15.5mm	13.5mm	10mm	18 mm	15.5mm	13.5mm	10mm		
	H_1	H_2	H	H	H_1	H_2	H	H		
	Straight bars Type I (Number of bars=8)				Straight bars Type II (Number of bars=8)					
Stiffness (GPa)	0.889	1.217	1.450	1.430	1.550	1.500	1.000	1.200	1.223	1.260
	Bent bars Type I (Number of bars=8)				Bent bars Type II (Number of bars=8)					
Stiffness (GPa)	0.667	0.821	1.416	1.433	1.450	1.000	1.228	1.500	1.600	1.423

CONCLUSIONS

The importance of quality control and assurance tests of GFRP reinforcing bars is significant since all manufacturers use different constituent materials, processes and surface treatments. Shear strength is used to determine the dowel strength and the quality of the GFRP bars. In this paper, shear tests were conducted on GFRP reinforcing bars in order to propose a shear testing protocol with the potential objective to reduce the number of cutting blades that are required in the test device. The original GFRP bars were “shaved” in reduced diameters using a lathe machine. The test results examine the shear stress-strain behavior and the measurement of the shear stiffness of the bars.

The “shaved” GFRP bars show similar response despite their type (straight or bent) and despite they were provided by different manufacturers. The “shaved” bars show consistency because their external coating (sand, ribs) was removed and thus the difference in the stress-strain responses in terms of stiffness was minimized. The cost of performing the shear tests can be reduced since specific diameters of cutting blades can be considered and then the bars can be reduced in diameter in order to fit in the available cutting blades. The measure of shear stiffness can provide information about the quality of the bars. Thus, the outcome of testing of GFRP bars in shear should not be only the maximum shear strength of the bars but also the slope of the shear stress-strain curves that can be considered as a measure of shear stiffness of the GFRP bars.

ACKNOWLEDGMENTS

The authors would like to thank the Ministry of Transportation of Ontario (MTO) in Canada for the financial support and Fiberline Composites A/S Inc. Canada and Pultrall Inc. Canada for the specimens.

REFERENCES

- ACI (American Concrete Institute) (2015). Guide for the design and construction of structural concrete reinforced with FRP bars. ACI 440.1R-15, MI, Farmington Hills, USA.
- B.D. Agarwal, L.J. Broutman (1990). "Analysis and Performance of Fiber Composites", Second Edition, Wiley & Sons, New York.
- E.A. Ahmed, E.F. El-Salakawy, B. Benmokrane (2010). "Performance evaluation of glass fiber-reinforced polymer shear reinforcement for concrete beams", *ACI Structural Journal*, 107(1), 53-62.
- ASTM D7617/D7617M-11 (2011). Standard Test Method for Transvers Shear Strength of Fiber – reinforced Polymer Matrix Composite Bars, West Conshohocken, PA, USA.
- B. Benmokrane, P. Wang, T.M. Ton-That, H. Rahman, J.F. Robert (2002). "Durability of glass fiber-reinforced polymer reinforcing bars in concrete environment", *Journal of Composites for Construction*, 6(3), 143-53.
- Canadian Standards Association (CSA) CAN/CSA S806-12 (2012). Design and construction of building components with fibre – reinforced polymers, Rexdale, Ontario, Toronto.
- Canadian Standards Association (CSA) CAN/CSA S807-10 (2010). Specification for fibre reinforced polymers, Rexdale, Ontario, Toronto.
- D. Eddie, A. Shalaby, S. Rizkalla (2001). "Glass fiber-reinforced polymer dowels for concrete pavements", *ACI Structural Journal*, 98(2), 201-206.
- T.R. Gentry (2011). "Transverse shear of GFRP rods: Test method development and potential for durability assessment", 4th International Conference on Durability & Sustainability of Fiber Reinforced Polymer (FRP) Composites for Construction and Rehabilitation.
- D.T. Johnson, S.A. Sheikh (2016). "Experimental Investigation of Glass Fiber-Reinforced Polymer-Reinforced Normal-Strength Concrete Beams", *ACI Structural Journal*, 113(6), 1165-1174.
- M.L. Porter (2005). "Structural Dowel Bar Alternative and Gaps of Knowledge", Proceedings of the Mid-Continent Transportation Research Symposium.
- E. Shehata, R. Morphy, S. Rizkalla (1999). "Fiber reinforced polymer reinforcement for concrete structures", 4th International Symposium on Fiber Reinforced Polymer Reinforcement for Reinforced Concrete Structures (No. SP-188-15)K.F. Nilsson, J.C. Thesken, P. Sindelar, A.E. Giannakopoulos, B. Storakers (2017). "A theoretical and experimental investigation of buckling induced delamination growth", *Journal of the Mechanics and Physics of Solids*, 41(4), 749-782.



SALT WATER AND ALKALINE ATTACK ON GFRP REBARS

Miguel M. Estêvão¹, Manuel A. G. Silva², Fernando F. S. Pinho³

¹Universidade Nova de Lisboa, Faculdade de Ciências e Tecnologia, Portugal;

² Universidade Nova de Lisboa, Faculdade de Ciências e Tecnologia, Portugal Email: mgs@fct.unl.pt;

³ Universidade Nova de Lisboa, CERIS and Faculdade de Ciências e Tecnologia, Portugal

ABSTRACT

The work is focused on environmental degradation of bars of glass fiber reinforced polymers (GFRP) a type of structural reinforcement (fib, 2007) often used in masonry (Tumialan and Nanni, 2002; Mohamed et al. 2012), waterfront structures and bridges (Worner, 2015), and in special cases where steel may cause adverse operational consequences. Uncertainties on service life of those rods under aggressive environmental conditions require further data despite some existing literature on their durability. Those factors motivated an experimental program on the effects of sorption of (i) salt water, with salinity 50g/l, and (ii) an alkaline solution (pH 13.6) on bars of GFRP, including the study of protection given by concrete cover since rods are usually embedded. Diffusion of contaminants was modeled and changes on chemical composition and on the glass transition temperature (T_g) of resin, and on porosimetry of concrete mortar were examined. Redistribution and progressive reduction of the number of larger pores with aging was detected, though causing little effect on porosity, with salt water found more influential than the alkaline solution. Modification of T_g was negligible. Microscopic electronic scanning (SEM) confirmed damage concentration on the matrix, and mostly in the peripheral region of rods. Alterations of proportion of chemical elements were summarized and examined. Interpretation and correlation of data shed light on mechanisms of failure of structural members reinforced with GFRP bars.

KEYWORDS: Strengthening and repair; Experimental study ; FRP internal reinforcement; Durability, long-term performance.

INTRODUCTION

The effects of various environments simulated by saline and alkaline solutions on the durability of GFRP rods have been investigated (Chen, 2005; Tannous and Saadatmanesh, 1998; Micelli and Nanni, 2004). Tests after accelerated aging on which contamination takes place at temperature higher than room temperature (RT) have often been used e.g. (Coomarasamy and Goodman, 1999) to save time and cost. Models based on Fick laws (Gentry et al., 2002) have been assumed by several researchers to analyze the diffusion of solutions in GFRP (Tannous and Saadatmanesh, 1998; Sen et al., 2002; Katsuki and Uomoto, 1996). Dejke used solutions with NaOH, KOH and CaOH to simulate the concentration of chemical elements created by alkaline environments. He immersed both bare and embedded rods in the solution and low concentration of alkali ions was observed by SEM at the periphery of the specimens after 4,600 h of exposure with the alkali solution at a temperature of 60°C It has been reported that alkaline ions can penetrate the GFRP rods, although the resin acts generally as a semipermeable membrane allowing the passage of water molecules but not of alkali ions (Jones, 1998) and some damage could be observed on the surface of the GFRP rods, namely in the resin while the glass fibers appeared to be intact. An estimate of the long-term degradation of GFRP bars based on short time data confirmed that the deterioration of the matrix resin is a major cause of poor behavior especially decreasing bond between fiber and matrix, and adding to the degradation of bond between rods and concrete (Chen et al., 2006). Regarding concrete degradation, studies have shown changes of porosity due to ingress of sulfates and chlorides (Silva Manuel et al., 2017a, 2017b). From the pore size distribution of the contaminated concrete, it was detected a reduction in pore volume and the porosity of concrete after contamination. The likely reason presented was that the crystallized salts and products of reactions between contaminants and concrete remained in the porous structure. Another cause advanced was the formation of microcracks due to pressure on the walls of the voids where crystallization took place, all contributing to changes in the microstructure of concrete that affected the mass transport phenomenon (Silva Manuel et al., 2017a).

Additional data to interpret changes similar to those briefly described above affecting durability were sought for the cases of salt water and an alkaline solution acting on two sets of GFRP rods, one embedded in concrete and the other of bare specimens. The results obtained in an experimental campaign on the effects of sorption of the

two solutions by the rods, including the study of diffusion of the contaminants, modification of porosimetry and porosity of the concrete cover embedment, variation of the glass transition temperature T_g of the resin and SEM images of GFRP samples are briefly presented and discussed below.

EXPERIMENTAL PROGRAM

To simulate field situations where GFRP rods are part of structural reinforcement, cylindrical concrete specimens of 100mm diameter and 400mm long, with GFRP rods of 25mm diameter axially placed were designed, Figure 1. The rods had a vinylester resin, and a weight fiber density of 72% confirmed by calcination. The low permeability concrete with water/cement ratio 0.36 had 430kg of cement mass, per cubic meter, 375kg and 445kg, respectively, of sand 0/2 and 0/4, 455kg and 440kg, respectively, of gravel 6/12.5 and 11/22, 158l of water and 5.2kg of a plastifier. Salt water (50g/l) and an alkaline solution (2.4g/l NaOH plus 19.6 g/l KOH and 2g/l $\text{Ca}(\text{OH})_2$) simulated severe environments, allowed the evaluation of the deterioration of the rod properties by comparing the specimens prior (reference or control) and after immersion. The experimental program consisted on the observation of physical deterioration and measurement of parameters of GFRP rods and concrete using the following techniques:

- Molecular diffusion of the solutions in the GFRP and concrete samples;
- Mercury porosimetry in contaminated concrete samples;
- Scanning electron microscopy (SEM) in contaminated GFRP samples;
- Glass transition temperature (T_g) of resin on GFRP samples.

In terms of porosimetry, samples of concrete were extracted from control specimens and after immersion for 5,800h in each of the solutions, Fig. 2.a). For SEM analyzes, both the bare bars of 25mm diameter and those embedded in concrete cylinders after removal from the mortar, had the faces of cross sections polished, Fig. 2.b). The selected contaminated GFRP rods had been subjected to 4,500 h or 8,400 h of contamination. Short prisms of rectangular cross section were also cut from the rods, to obtain the Glass transition temperature tests (T_g) by Dynamic Mechanical Analysis (DMA, Fig. 2.c)).

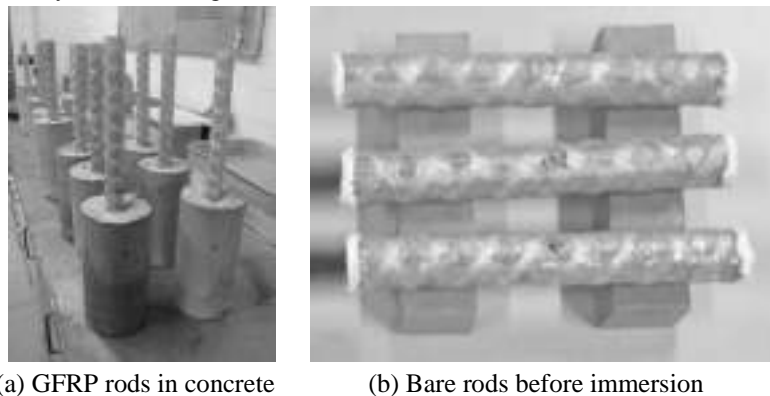


Figure 1 – GFRP rods embedded in concrete (a); and bare rods prior to immersion (b).

The determination of T_g was made with equipment from TA Instruments (model Q800) and the tests had heating ramp from 30°C to 200°C, at a rate of 5°C/min, a frequency 1 Hz and an amplitude of oscillation of 10 μm .

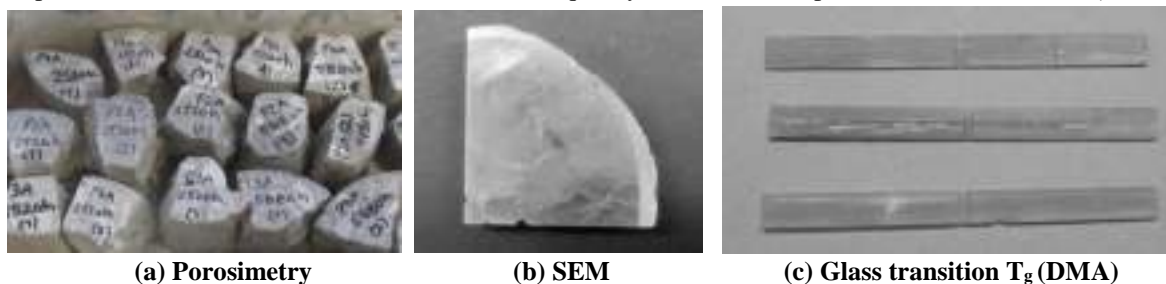


Figure 2 – Samples for porosimetry (a), SEM analyses (b), and T_g ($w=9.7\text{mm}$, $t=3.8\text{mm}$, $L=25.00\text{mm}$) (c).

EXPERIMENTAL RESULTS

Porosity

The porosity of concrete decreased from 10.3% to 9.8 and 8.5%, respectively, after 5,800h of immersion in salt water; while the ion Cl⁻ in the unit volume of concrete increased from 0.03 %, at 0h to 0.38% at 5,800h. The alkaline solution modified the average porosity for the concrete specimens decreased also to 8.5% after 5,800h of contamination.

Mercury porosimetry

Each concrete sample was placed in an accessory recipient, degassed and then immersed in mercury in a Micromeritics Autopore IV 9500. The pore size distribution was obtained from the volume of mercury that was forced into the pores by an applied pressure. Figure 3 shows that the contaminated concrete samples have a higher concentration of pores with a smaller diameter than the reference samples, i.e. the larger pores of the samples were partially occupied by salts resulting contamination by the solutions. The saline environment caused the most noticeable changes on the porosity, namely a decrease of 8% relative to the value in reference samples. The alkaline environment reduced the porosity of the sample by approximately 2%.

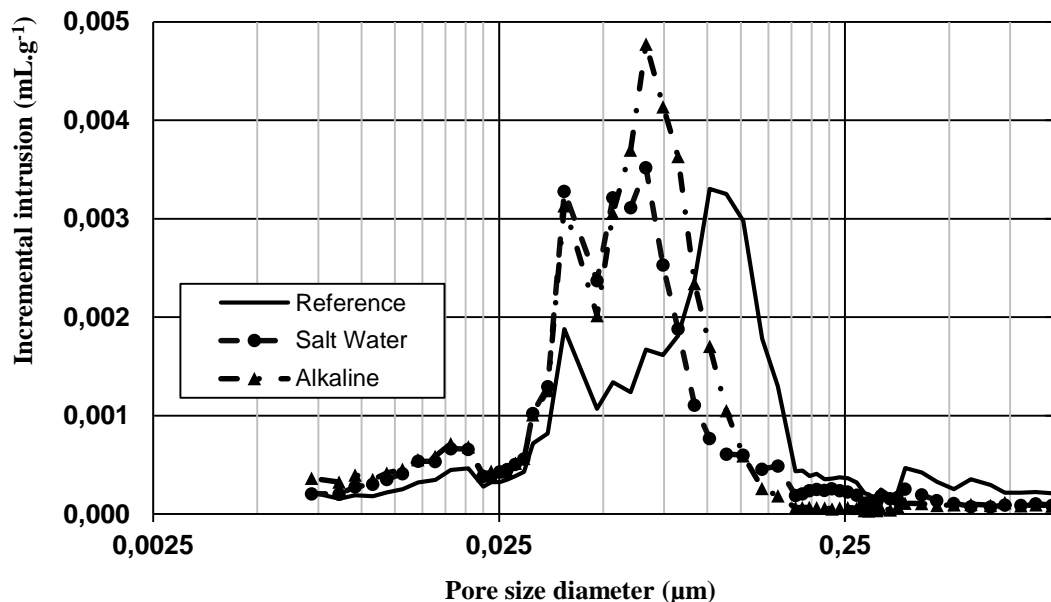
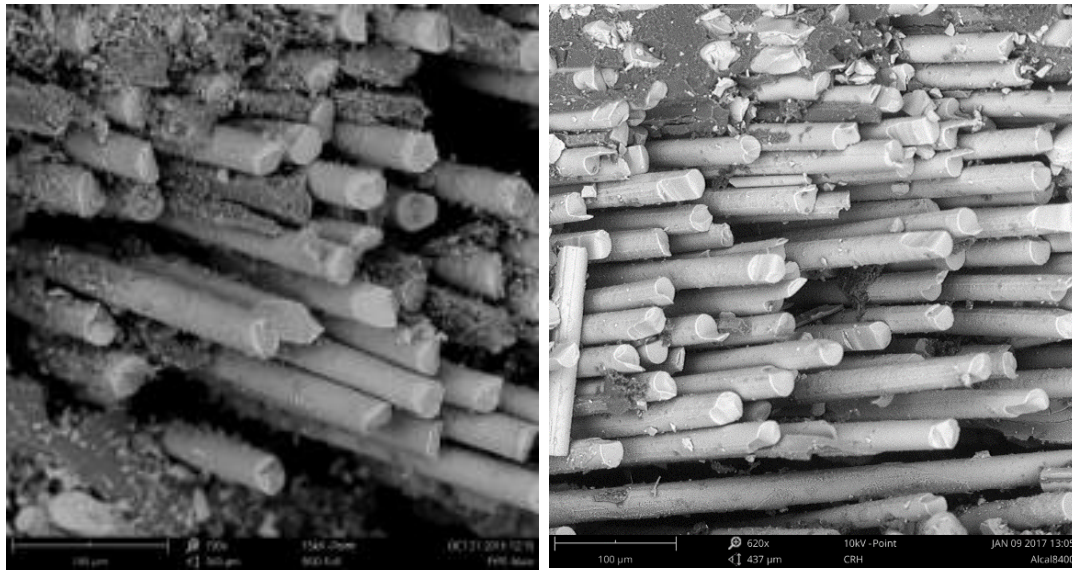


Figure 3 – Comparative pores distribution for concrete at 0h and 5,800h of immersion in salt water (50g/l) and alkaline solutions.

Scanning Electron Microscopy (SEM)

SEM images were captured with a SEM-EDS PRO-X Phenom World equipment. Damage could be better observed on the GFRP samples contaminated by the alkaline solution, and degradation of some fibers and resin could be seen. Figure 4 shows the degradation of the GFRP sample at 4,500 (fractured) and 8,400 h (fractured) at the periphery of the rod section. Small alterations of the glass fiber could be detected. However, there was a significant loss of resin at the periphery of the rods after 8,400h of immersion. In the intermediate phase, at 4,500h, loss of bond between fibers and resin was observed at their interface. In addition, after 4,500 h in the alkaline solution, severe degradation could be seen along the wound spiral of filament used to enhance bond of the rods and mortar.



a) 4,500h (periphery)

b) 8,400h (periphery)

Figure 4 – SEM images of cross sections after 4500h and 8400h immersed in alkaline solution (800x and 600x amplification, respectively)

Through electron beam bombardment of the samples (EDS) coupled with SEM analysis approximate estimates of the composition of the fibers and resin of the GFRP rods after being submerged were attempted, Table 1, despite the localized character of each determination. Data gathered showed very small changes in the fibers for the type and duration of exposure with a slight change in the composition of the glass fibers relative to the reference GFRP sample i.e. a decrease of approximately 1% at the periphery of the rod in the saline environment. The results were essentially non-conclusive in part because a much higher number of spots should have been analyzed and the values found should be averaged. It can be stated that the percent of C increased significantly in all cases, while Ca decreased and SiO₂ showed large decreases especially in the central region. Further data are required to extract conclusions from this type of measurements. The detected variation of values denoted, however, that the resin matrix was significantly affected by the immersion both in salt water and in the alkaline solution as evidenced earlier by SEM images.

The measurements of T_g are summarized in Table 2 and Fig. 5 reproduces a typical tan delta curve found and corresponding to one sample immersed in salt water for 4,436h. The transition vitreous temperature of the vinylester resin resin increased at 4,500h, both for the salt water and the alkaline solution immersion, relative to the non-artificially aged samples, about 5% to 6%, probably because curing of the resin prevailed over the deterioration factors in that period, T_g decaying at 8,400 h due to plasticization and further moisture ingress to a value that was above 3% higher than the value of T_g found prior to immersion. The changes are small and, given the inevitable scattering of the measurements, the contamination was considered to have negligible effects on the glass transition temperature.

Table 1 – Estimated composition of matrix/resin past 5,800h immersion in alkaline solution and salt water, versus values prior to immersion

Comp. ID	Composition by weight (%)					
	0 h		5,800 h			
	Resin		Alkaline Solution		Salt Water	
	Centre	Border	Centre	Border	Centre	Border

SiO₂	39.77	39.45	25.45	31.10	26.83	37.43
Ca	11.14	11.51	6.22	9.40	6.27	10.36
Al₂O₃	11.36	11.38	8.12	9.59	8.98	11.73
C	33.05	32.71	56.68	46.57	52.72	35.93
Mg	1.73	2.06	1.63	1.20	2.21	2.21
Na	-	0.39	0.32	0.36	0.68	0.97
K	-	-	0.16	1.42	0.22	0.40
Cl	2.96	2.25	1.05	0.21	1.70	0.58
S	-	0.28	0.38	0.17	0.41	0.43

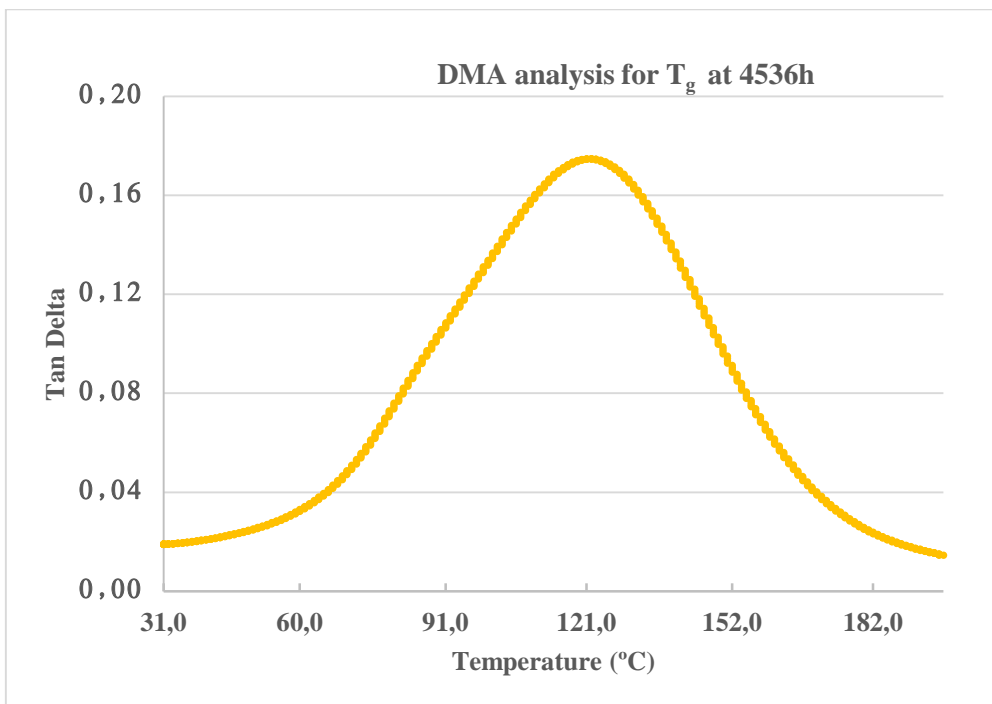


Fig. 5 – Typical tan delta curve for T_g determination. Case of salt water immersion.

Table 2 – Average T_g measurements by the DMA technique

Environment	Exposure Period (h)	T_g (°C)
Reference	0	115.7
Salt water	4,536	122.7
	8,400	119.4
Alkaline	4,536	122.2
	8,400	119.9

Diffusion and gain of mass

Sorption of moisture by GFRP rods may degrade their properties, and more so if diffusion of aggressive solutions takes place. In order to estimate the eventual importance of this factor a study of diffusion was conducted and a brief extract of some of the obtained data summarized graphically below for the two cases of immersion under consideration. At the onset of the experimental study 6 specimens were dried under constant temperature. The gains of mass found in the specimens due to immersion in the solutions were obtained by weighting them, after careful drying their surfaces, and comparing with the value at the previous stage. The average values of the increments normalized by the initial value at the time of immersion are displayed, in percentage, in curves for each solution. Fig. 6 shows the results obtained for specimens of 25mm nominal diameter immersed in the saline solution (50g/l) revealing almost linearity of mass gained versus the square root of elapsed time until a plateau was reached at approximately 1,700h, in agreement with Fick's laws. After 2,500h since the beginning of immersion, sorption restarted to increase due to ingress of material associated with damage and/or communication between voids formerly not linked (Silva, Pinho and Estêvão, 2018).

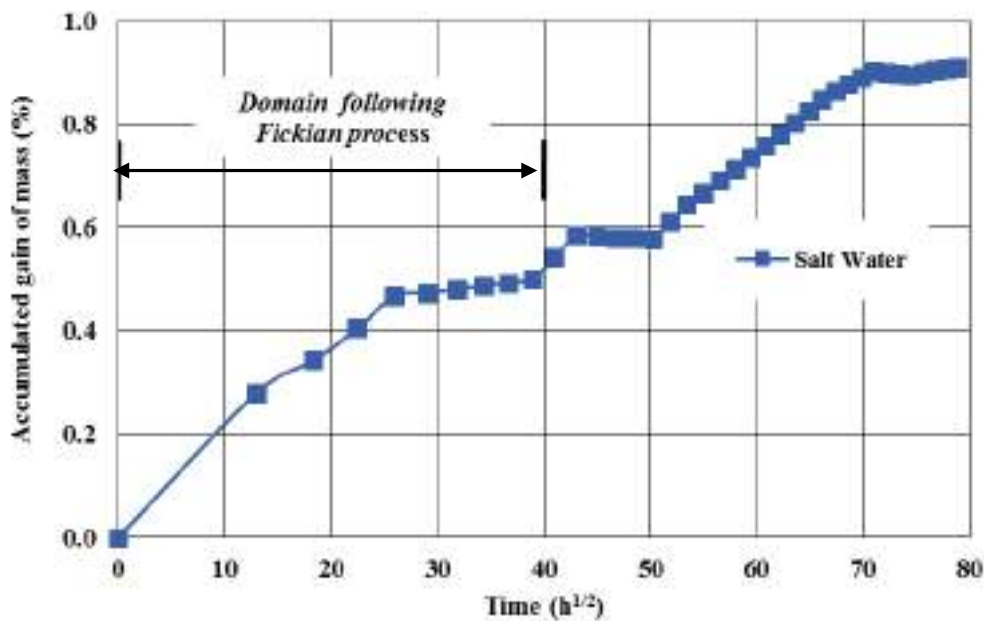


Fig. 6 - Mass gain for bare bars of ϕ 25 mm immersed in salt water, normalized by the initial mass.

Fig. 7 shows the equivalent average curves obtained for immersion of ϕ 25mm rods in the alkaline solution. The GFRP rods ceased the linear growth of added mass much earlier than for salt water, around 200h, displayed a longer plateau and, before 1,600h, showed signs of additional damage, eventually due to water ingressing along the interface fiber/matrix, a process facilitated by some pre-existing longitudinal voids observed in the rods and associated with the pultruding process and randomly present. Past approximately 3,000h, it is seen a reduction of the mass thought to be due to ester hydrolysis and leaching of low weight fragments an aspect referred in the literature (Apicella et al., 1983). It is recalled that higher concentration of the solution leads, in general, to lower gain of mass (Silva and Silva 2007) and in the present study the salt water solution also led to lower values than the less concentrated alkaline solution, in the segment of approximate application of the laws of Ficke.

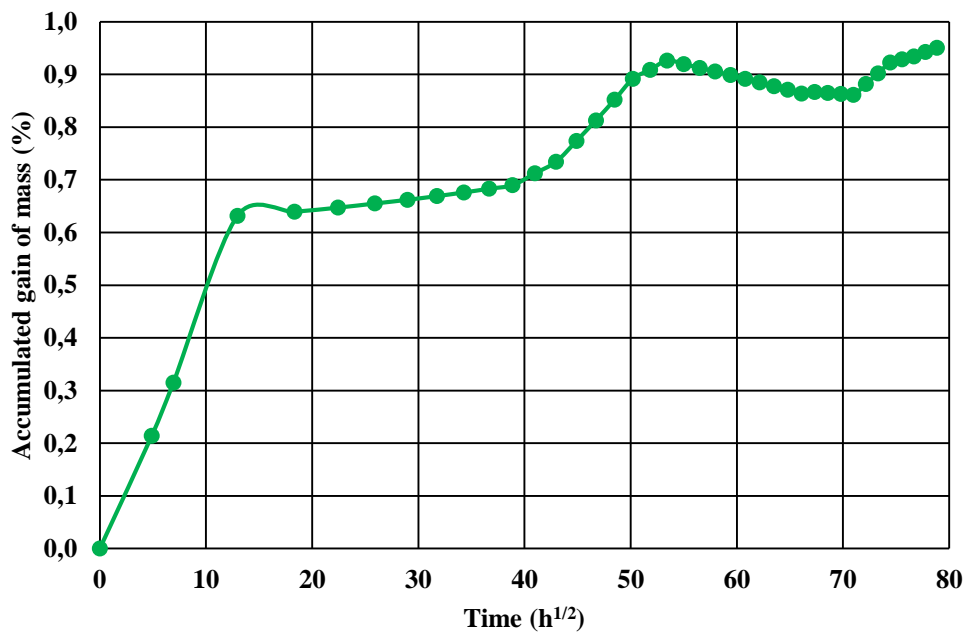


Fig. 7 - Mass gain for bare bars of ϕ 25 mm immersed in alkaline solution, normalized by the initial mass.

CONCLUDING REMARKS

The present work was carried out with the objective of generating further data on the durability of GFRP rods used in construction as part of a MSc thesis (Estêvão, 2017). Techniques from various disciplines were used to detect and interpret the degradation caused by salt water (50g/l salinity) and another solution ((2.4g/l NaOH+19.6 g/l KOH +2g/l Ca(OH)₂) designated as alkaline solution. The following was found:

- There was a small reduction in the porosity of the concrete embedding GFRP rods and a redistribution of the size of those pores after contamination; a progressive reduction in the proportion of the larger pores over time, per unit volume, was observed, in both cases.
- The presence of the ions from the contaminating solutions in the contaminated rods was difficult to detect, due in part to the semi-permeability of the resin more easily penetrated by water molecules.
- Most damage was observed by SEM at in the periphery of the rod cross sections, i.e. along the vicinity of the external surface, more visibly on the resin and on the interface fibers-resin;
- The alkaline environment was more severe than the salt water solution.
- The glass transition temperature of the vinylester resin slightly increased with the contamination
- The experimental curves of mass gain, initially, followed Fickian patterns, but, at later stages, indicated renewed increase of ingress of contaminant associated with inner degradation of the rods.
- The SEM images of samples immersed for approximately 4,500 h showed damage to the resin matrix and the fiber/resin interface, consistent with results of diffusion studies. At 8,400h the data collected did not show much further degradation of the rods when compared with observation after 4,500h.

REFERENCES

- Apicella A, Migliaresi C., Nicolais L., Iaccarino L., Rocco S.. *The water ageing of unsaturated polyester-based composites: influence of resin chemical structure*. Composites. Vol. 14. No 4. (October 1983).
- Chen Yi, Davalos J, Ray I, Kim H. *Accelerated aging tests for evaluations of durability performance of FRP reinforcing bars for concrete structures*, West Virginia University, Morgantown. (2005).

- Chen, Yi, Davalos, Julio F., Ray, Indrajit. "Durability Prediction for GFRP Reinforcing Bars Using Short-Term Data of Accelerated Aging Tests". *Journal of Composites for Construction*, Vol.10, No. 4. (2006).
- Coomarasamy A, Goodman S. *Investigation of the durability characteristics of fiber reinforced plastic (FRP) materials in concrete environment*. *J Thermoplast Compos Mater*, (1999).
- Dejke V. *Durability of FRP Reinforcement in Concrete, Thesis for Licentiate in Engineering*. Chalmers University (2001).
- Estêvão, Miguel M. *Durability of GFRP bars to strengthen concrete structures* (in Portuguese), M Sc Thesis, FCT- Universidade Nova de Lisboa 36-38, (2017).
- fib bulletin 40, Stuttgart, (2007).
- Gentry TR, Bank LC, Thompson BP, Russel JS. *An accelerated-test-based specification for the fiber reinforced plastic for structural systems*. In: *Proceedings of 2nd international conference on durability of fiber reinforced polymer (FRP) composites construction*, Montreal, Canada, 13-24. (2002).
- Jones F. *Designing composites for durability in aqueous and corrosive environments* in *Proceedings of Designing Cost Effective composites*, London, JMechanical Engineers, 65-81, (1998).
- Katsuki F, Uomoto T. *Prediction of deterioration of FRP rods due to alkali attack*. In: *Non-metallic (FRP) reinforcement for concrete structures*, RILEM, London, UK, 82-9 (1996).
- Micelli F, Nanni A. *Durability of FRP rods for concrete structures*. *Construction and Building Mater*, 18(7), 491-503.(2004).
- Mohamed N, Farghaly A, Benmokrane A, Neale K. *Evaluation of a Shear Wall Reinforced with Glass FRP Bars Subjected to Lateral Cyclic Loading*. *APFIS* (2012).
- Sen R, Mullins G, Salem T. *Durability of E-glass/vinylester reinforcement in alkaline solution*. *ACI Structural Journal*, 99(3), 369-375. (2002).
- Silva Manuel A. G., Silva Zenaide C. G. *Degradation of Mechanical Characteristics of Some Polymeric Mortars due to Aging*, Manuel A. G. Silva, Zenaide C. G. Silva, *ACI Materials Journal*, V. 104, No. 4, pp337-343, (July-August 2007).
- Silva, Manuel A G, Cunha, M P, Ramos A M P, Fonseca, B, Pinho F F S *Accelerated action of external sulfate and chloride to study corrosion of tensile steel in reinforced concrete*. *Materiales de Construcción*, Vol. 67, Issue 328. (2017).
- Silva Manuel A G, Pinho Fernando F. S., Estêvão Miguel M. *Effects of sodium chloride and sulfate on GFRP bars*. *ACI Materials Journal*. Accepted. (2018).
- Tannous F, Saadatmanesh H. *Environmental effects on the mechanical properties of E-glass FRP rebars*. *ACI Materials Journal*, 95(2), 87-100. (1998).
- Tumialan J G, Nanni A. *Strengthening of Masonry Walls with FRP Bars*. *Composites Fabricator Magazine*, Arlington, VA. (2002).
- Worner V. *Use of Glass Fibre Reinforced Polymer (GFRP) reinforcing bars for concrete bridge decks*. M Sc thesis, University of Canterbury, NZ. (2015).



BEHAVIOUR OF GFRP BARS IN SEAWATER-CONTAMINATED CONCRETE SUBJECTED TO SUSTAINED LOADING

H. El-Hassan¹, T. El-Maaddawy¹ and A. Al-Sallamin¹

¹ United Arab Emirates University, Department of Civil and Environmental Engineering, Al Ain, United Arab Emirates, Email: helhassan@uaeu.ac.ae

ABSTRACT

In recent years, there has been an increasing interest to replace steel reinforcement in concrete by non-corrosive material to alleviate corrosion-related problems. Glass fiber-reinforced polymer (GFRP) bars are advocated as a potential alternative, owing to their superior physical and mechanical properties. Though, the acceptance of these materials by the construction industry is critically dependent on their long-term performance. This paper investigates the durability behavior of GFRP bars embedded in moist seawater-contaminated concrete under a sustained load of 25% of its ultimate tensile stress. Samples were conditioned for 10 months at temperatures of 20, 40, and 60°C and then retrieved for uniaxial tensile testing. However, GFRP bars conditioned at 60°C experienced creep-rupture during conditioning. As such, tensile strength retentions were measured for non-creep-ruptured bars only as a means to evaluate the long-term durability of GFRP. The microstructure of creep-ruptured specimens was characterized by employing scanning electron microscopy, Fourier transform infrared spectroscopy, and differential scanning calorimetry. Research findings showed that an increase in conditioning temperature from 20 to 40°C led to a decrease in tensile strength retention from 90 to 73% due to accelerated diffusion of water and, consequently, a higher moisture uptake. At a higher conditioning temperature of 60°C, microstructure analysis highlighted development of hydroxyl groups, plasticization and chemical degradation of the matrix, and deterioration of the fiber-matrix interface. In comparison to unloaded, conditioned GFRP samples, the presence of a sustained load promoted tensile strength loss and degradation of GFRP bars. Nevertheless, this detrimental effect was more prominent at elevated temperatures.

KEYWORDS

Durability performance, conditioning, GFRP, tensile strength, microstructure, concrete, sustained load.

INTRODUCTION

Glass fiber-reinforced polymer (GFRP) bars have been advocated as a viable replacement to traditional steel reinforcement. They promise to prolong the service life and reduce maintenance costs in structural systems owing to their non-corrosive behavior, superior performance, and competitive cost. However, recent impediments have hindered their adoption by the construction industry due to their vulnerability to severe environment.

Extensive research has examined the durability performance of GFRP reinforcing bars in concrete by employing accelerated aging tests. The degradation mechanism mainly depended on the conditioning of GFRP bars, but would also intensify under other circumstances. Studies have shown that degradation was promoted when concrete-wrapped GFRP bars were conditioned under a sustained load (Bakis et al., 1998, Bakis et al., 2005). Benmokrane et al. (2002) noted that the degradation was mainly influenced by solution transport through the resin cracks at an increased level of applied stress. Furthermore, Davalos et al. (2012) reported conditioning at 60°C was more critical than applying a sustained load in GFRP bars exposed to concrete for up to 210 days. GFRP samples have also been conditioned for 240 days at temperatures ranging between 23 and 50°C while being preloaded up to 80% of the ultimate tensile strength (UTS) (Robert and Benmokrane, 2010b). Findings showed that the tensile strength was reduced by 11% due to a progressive hydrolysis reaction. Even so, it has been shown that wrapping GFRP bars in concrete and exposing them to harsh environments did not accurately simulate those subject to natural conditioning (Almusallam and Al-Salloum, 2006, Trejo et al., 2011, Robert et al., 2009).

Current studies have reported wide variations in tensile strength reduction of GFRP bars under different exposures and levels of sustained load. Thus, more research is needed to evaluate the long-term performance of GFRP bars in different conditioning environments, including seawater splash. This work aims to provide a better understanding of the behavior of GFRP bars in seawater-contaminated concrete under a sustained load of 25% UTS. Durability performance was assessed based on tensile strength retention. GFRP samples that experienced creep-rupture were examined to correlate any degradation to microstructure changes.

MATERIALS AND METHODS

GFRP test specimens and surrounding concrete

Figure 1 shows the ribbed GFRP bars used in this study. It consisted of high strength continuous glass fibers impregnated in epoxy resin with an inner and outer diameter of 7.2 and 8.0 mm, respectively. The bars had a cross-sectional area of 45.0 mm² (ASTM, 2016) and an ultimate tensile strength of 816 MPa (ASTM, 2016). The respective glass fraction (% , by mass) and void content (% , by volume) were calculated following ASTM D3171 (ASTM, 2015) as 78.0 and 0.10%.



Figure 1: GFRP bar under investigation

GFRP test specimens were cut into 1200 mm lengths and marked into three regions. The middle third was taken as the designated test region with a length of 400 mm, such that it was at least 40 times the bar diameter (ACI 440.3R, 2012). To simulate concrete exposed to seawater in natural field conditions, GFRP bars were covered in a 50 x 50 mm seawater-contaminated concrete. The 400 mm-long end regions of the bars were not wrapped in concrete to avoid any degradation and were used as grips for applying the sustained load. Table 1 presents the mixture proportions of the surrounding concrete. The concrete had a compressive and tensile splitting strength of 40.0 and 3.2 MPa, respectively. Respective results of ultra-pulse velocity, electrical conductivity, and RCPT were 5405 m/s, 8 k Ω .cm, and 2427 Coulombs.

Table 1: Mixture proportions of surrounding concrete

Component	Cement	Crushed stone	Dune sand	Coarse aggregate	Seawater
Weight (kg/m ³)	400	290	290	1160	200

Sustained loading systems

Figure 2 shows the load-magnifying, self-reacting steel frames that served as the loading. Steel end grips, consisting of a steel pipe, 450 mm long, with inner and outer diameters of 25 and 34 mm, respectively, were securely fastened on to the concrete-encased GFRP bars. Steel hooks were then installed on to the end grips and so-produced samples were immersed in water tanks and attached to the steel frames from the hooked ends. The applied sustained load represented 25% of the UTS of three replicate bars. A total of 9 specimens were divided into three groups: 3 samples each placed in the lab at a controlled temperature of 20°C and in heated water tanks at temperatures of 40 and 60°C. These three temperatures were chosen to simulate actual year-round environmental conditions in Dubai, United Arab Emirates. Specimens were left to condition for 10 months and compared to an unconditioned control sample kept at ambient temperature prior to testing. GFRP bars subject to 40 and 60°C experienced creep-rupture and were further evaluated for performance.

Performance evaluation

Due to conditioning, several GFRP bars experienced creep rupture. Their moisture uptake was determined in accordance with ASTM D570 (ASTM, 2010) to assess moisture permeation through the microgaps between polymeric chains, interfacial microcracks at the fiber-matrix transition zone, and matrix microcracks that formed during the compounding process (Abeyasinghe et al., 1982).

The tensile strength of GFRP bars was employed to assess its durability performance. For this test, specimens were extracted from the concrete prisms after removing the end hooks. GFRP bars were then loaded until failure under uniaxial tension in displacement control at a rate of 1.5 mm/min. The tensile load was calculated by dividing the maximum tensile load by the average cross-sectional area of the bar.



Figure 2: Conditioned GFRP test specimens under loading

Microstructure evaluation

Creep-ruptured GFRP reinforcing bars were evaluated for microstructural changes as per the following:

- Scanning electron microscopy (SEM) was employed to examine the changes in microstructure and morphology of control and creep-ruptured, conditioned GFRP samples by using a JEOL-JSM 6390A microscope. Specimens were taken from the middle 100 mm, polished, and sputter coated with a thin 99.9% pure gold layer.
- Fourier transform infrared (FTIR) spectroscopy was conducted using a Varian 3100 FT-IR spectrometer to measure the degradation due to hydrolysis reaction. Specimens were taken from the middle 100 mm of the GFRP bars, pulverized, and interground with potassium bromide (KBr) at a powder:KBr = 1:4, by mass. The mixed powder was studied over 400 to 4000 cm^{-1} at a resolution of 1 cm^{-1} .
- Differential scanning calorimetry (DSC) was performed to determine the glass transition temperature (T_g) as per ASTM E1356 (ASTM, 2008). Powdered specimens, of approximately 10 mg mass, were obtained from the middle 100 mm of the original samples, sealed in aluminum pans, and prepared for analysis. Then, samples were heated from 20 to 225°C at a rate of 5°C/min using a DSC Q2000 calorimeter equipped with a refrigerated cooling system.

RESULTS AND DISCUSSIONS

Moisture uptake

Although GFRP reinforcing bars were concrete-encased, the concrete cracked and allowed passage of water, resulting in the uptake of moisture by the GFRP. The moisture uptake of creep-ruptured GFRP bars under sustained load and conditioning are shown in Table 2. Samples are designated by the notation “XMYC”, where ‘X’ represents the time of rupture in months and ‘Y’ denotes the temperature in degrees Celsius (°C). Results show that conditioning at higher temperatures was more critical than for longer durations, owing to the accelerated diffusion rate of water through microcracks. This is especially clear when comparing 3.8M40C with 2.5M60C. Nevertheless, extended conditioning up to 96 months led to a 64%-increase in moisture absorption.

Table 2: Moisture uptake of GFRP bars conditioned under sustained load

Sample Designation	Conditioning		Moisture absorption (%)
	Duration (months)	Temperature (°C)	
Control	-	Ambient	-
3.8M40C	3.8	40	0.54
2.5M60C	2.5	60	1.19
7.9M60C	7.9	60	1.36
9.6M60C	9.6	60	1.95

Tensile strength

Table 3 summarizes the tensile strengths of concrete-encased GFRP reinforcing bars conditioned under a sustained load. Specimens displayed failure by violent rupture of fibers along with fiber debonding at the fiber-matrix interface. Premature failure at the end grips was not recorded in any of the tested specimens. Even though some specimens experienced creep-rupture, they were still considered in the average strength of the three replicate specimens. In fact, one specimen of those conditioned for 10 months at 40°C failed due to creep-rupture. The

average tensile strength for GFRP 10-40 was thus 395 MPa. This represents a 51.59% loss in strength. However, if the creep-ruptured sample was excluded from the strength calculations, the tensile strength would have been 592 MPa, with a 27.45% loss. All GFRP bars conditioned for 10 months at 60°C experienced creep-rupture. As such, the tensile strength was recorded as 0 MPa. It is clear that higher temperatures accelerate the degradation and result in lower tensile strength.

Table 3: Tensile strength and retention of GFRP bars

Sample Designation	Conditioning		Strength (MPa)	Strength Loss (%)
	Duration (months)	Temperature (°C)		
Control	-	Ambient	816	-
10-20	10	20	733	10.17
10-40	10	40	395	51.59
10-60	10	60	0	100.00

SEM analysis

Scanning electron microscopy was employed to analyze the morphology of creep-ruptures specimens. Figure 3 shows the longitudinal micrographs of GFRP bars under sustained load. After conditioning for 3.8 months at 40°C, a microgap on the range of 2 μm formed at the fiber-matrix interface, as presented in Figure 3(a). This was associated to the propagation of cracks from the matrix to the interface rather than directly into the fiber (Mourad et al., 2010). At higher temperature of 60°C, Figures 3(b-d) show that an increase in conditioning temperature led to a wider gap and weaker fiber-matrix interfacial bond, but did not affect the fiber. Clearly, hydrolysis reaction accelerated in hot environment, leading to matrix disintegration, non-uniform distribution of loads among the fibers, and reduction in tensile strength. Although conditioning-induced separation at the fiber-matrix interface was noted in all samples, it was intensified at higher conditioning temperatures. This indicates the sensitivity of the fiber-matrix interface to degradation at higher conditioning temperatures rather than longer duration.

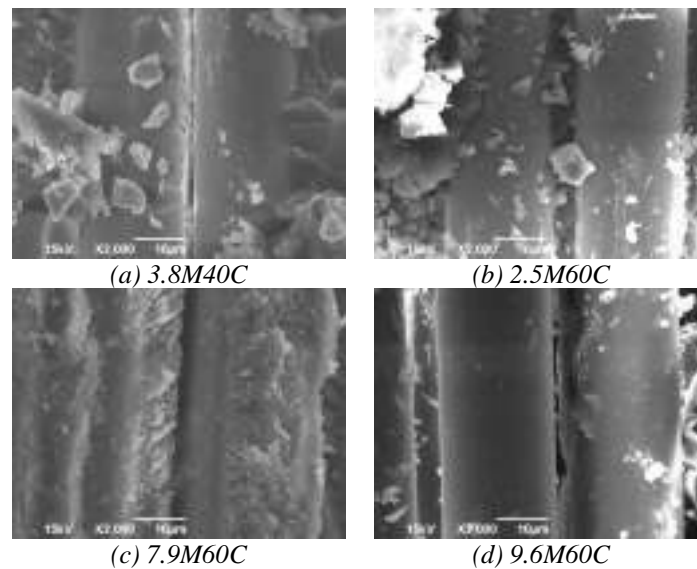


Figure 3: Longitudinal micrographs of GFRP bars conditioned under sustained load

Figure 4 presents the cross-sectional micrographs of GFRP bars subject to sustained load. While samples conditioned at 40°C showed no signs of degradation, circumferential debonding at the fiber-matrix interface particularly at a higher temperature of 60°C. It is clear that elevated temperatures intensify the degradation mechanism. Figures 4(b-d) show that microgaps form within the first 3 months, but widen with prolonged exposure.

FTIR analysis

The degree of hydrolysis reaction was assessed using FTIR spectroscopy. Two spectral regions were mainly examined: 2800–3000 cm⁻¹ and 3200–3600 cm⁻¹, representing carbon-hydrogen (CH) and hydroxyl (OH) groups, respectively. It is worth noting that hydrolysis reaction causes an increase in the infrared band of OH groups, but

does not affect that of CH groups. Based on past research the ratio of maximum peaks in each of OH and CH band was recorded to characterize the relative quantity of hydroxyl groups in samples (Montaigu et al., 2013, Robert and Benmokrane, 2010b, Robert and Benmokrane, 2010a, Robert et al., 2009). Accordingly, higher ratio of OH/CH indicated higher degree of matrix degradation.

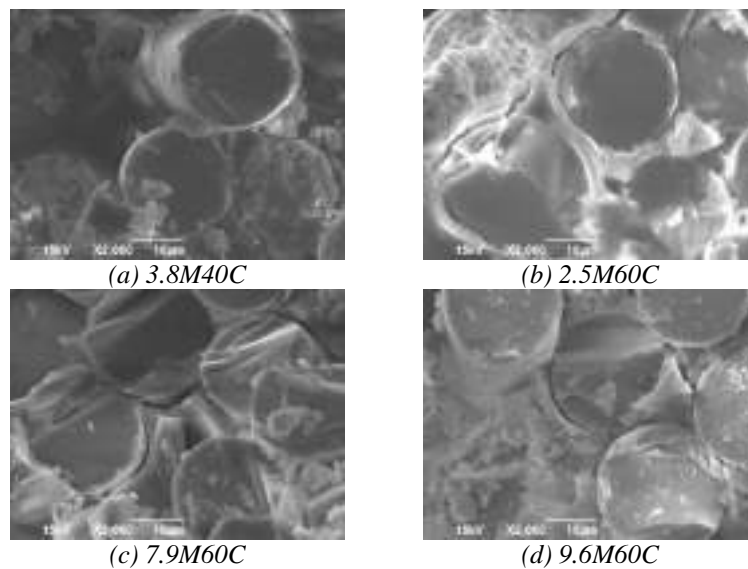


Figure 4: Cross-sectional micrographs of GFRP bars conditioned under sustained load

The band ratios of conditioned and control samples are presented in Table 4. Upon conditioning, an increase in OH/CH ratio was reported, indicating the progression of a hydrolysis reaction. In fact, conditioning for 3.8 months at 40°C increased the OH/CH by 4.4% from 1.07 to 1.12. GFRP bars conditioned for 2.5 months at 60°C resulted in a ratio of 1.22. Although the duration was shorter, the OH/CH was higher than 3.8M40C. This shows that elevated conditioning temperature was more effective in promoting the hydrolysis reaction than prolonged conditioning duration. Nevertheless, extending conditioning to 7.9 and 9.6 months led to further increase in OH/CH. Conditioned GFRP reinforcing bars experienced further development of hydroxyl groups, progression of hydrolysis reaction, weakening of the fiber-matrix interfacial bond, and higher tensile strength reduction.

Table 4: FTIR bands of control and conditioned GFRP samples

Sample Designation	Conditioning		Peaks		OH/CH	Increase (%)*
	Duration (months)	Temperature (°C)	CH	OH		
Control	-	Ambient	3.62	3.88	1.07	-
3.8M40C	3.8	40	4.47	5.00	1.12	4.36
2.5M60C	2.5	60	3.13	3.83	1.22	14.16
7.9M60C	7.9	60	4.92	6.20	1.26	17.57
9.6M60C	9.6	60	6.56	8.33	1.27	18.47

*: percent increase of OH/CH ratio of conditioned GFRP sample compared to that of unconditioned control.

DSC analysis

The glass transition temperature (T_g) of control and creep-ruptured conditioned GFRP bars under sustained load are presented in Table 5. For each sample, two scans were performed: the first scan was to determine the difference between the T_g of control and that of conditioned samples as the decrease in T_g is indicative of plasticization, while the second scan was to investigate the degradation mechanism. After conditioning for 3.8 months at 40°C, a T_g of 95°C was recorded. This represents a 6°C drop compared to that of the unconditioned control sample. Conditioning at elevated temperatures resulted in a further decrease in T_g (90°C). It seems that the microgaps that formed in the matrix microstructure (see SEM analysis) caused debonding at the fiber-matrix interface, thus exposing the polymer matrix to more water/moisture and resulting in higher moisture absorption. Subsequently, the polymer structure was modified and the T_g was reduced.

Samples were re-heated up to 225°C for a second scan. Water evaporation during the second scan reversed the plasticizing effect. As a result, T_g values of conditioned and unconditioned samples were similar. Experimental findings of DSC analysis in Table 5 show that the T_g was unaffected by conditioning during the second scan. This indicates that the polymer matrix was subject to reversible chemical degradation. It is however worth noting that the T_g of GFRP control sample was higher in the second scan due to a post-curing mechanism. Other researchers reported similar findings (Debaiky et al., 2006).

Table 5: Glass transition temperature (T_g) of GFRP bars

Sample Designation	Conditioning		T_g (°C)	
	Duration (months)	Temperature (°C)	1 st Scan	2 nd Scan
Control	-	Ambient	101	106
3.8M40C	3.8	40	95	104
2.5M60C	2.5	60	94	105
7.9M60C	7.9	60	90	105
9.6M60C	9.6	60	90	105

Comparison with unloaded conditioned specimens

Based on previous mechanical performance and microstructure investigation of GFRP reinforcing bars conditioned without a load, a comparison is conducted, including tensile strength retention, moisture absorption, and microstructure changes (El-Hassan et al., 2017). Table 6 shows that GFRP samples conditioned without an applied load could retain up to 98% of initial tensile strength after conditioning. However, the application of a sustained load of 25% UTS decreased the strength retention. GFRP bars conditioned for 10 months at 20, 40, and 60°C under a sustained load could retain 90, 72, and 0% of tensile strength, respectively. In comparison, unloaded specimens could retain 98, 95, and 94%. Although conditioning without a load was detrimental to GFRP durability performance, the application of a sustained load further accelerated the degradation mechanism and reduced the tensile strength. Table 6 also presents the ratio of strength retention loaded to unloaded specimens. This ratio considers creep-ruptured GFRP bars in the calculations. Evidently, elevated conditioning temperatures resulted in a lower ratio. At higher temperatures, unloaded samples experienced a slight reduction in strength retention, while loaded counterparts were much more affected. This implies that degradation intensified when a sustained load was applied at elevated conditioning temperatures.

The moisture absorption of conditioned GFRP samples subject to a sustained load surpassed that of unloaded control specimens (El-Hassan et al., 2017). Even though the same surrounding seawater-contaminated concrete was utilized, applying a load to the GFRP bars resulted in crack formation in the concrete and further exposed the bars to water/moisture. This led to an increase in the absorption. Experimental findings showed that the moisture uptake of loaded specimens ranged between 1.2 to 2 times that of unloaded counterparts. As a result, the degree of hydrolysis reaction was higher, with further development of hydroxyl groups and lower T_g , as evidenced by FTIR and DSC analysis, respectively (El-Hassan et al., 2017).

Table 6: Influence of sustained load on the tensile strength retention of conditioned GFRP samples

Sample Designation	Conditioning		Strength Retention (%)		
	Duration (months)	Temperature (°C)	Sustained Load	No Load	Ratio
10-20	10	20	90	98	0.91
10-40	10	40	72	95	0.76
10-60	10	60	0	94	0.00

CONCLUSIONS

The durability performance of GFRP reinforcing bars subject to conditioning for 10 months at different temperatures and under a sustained load of 25% UTS has been investigated. Based on the results and findings of this work, it was noted that GFRP samples were more susceptible to failure due to creep rupture when conditioned at temperatures exceeding 20°C. Samples that did not experience creep rupture were tested for tensile strength to characterize the durability performance. At higher temperatures, GFRP bars exhibited lower tensile strength retention, owing to higher moisture absorption, diffusion of water, weakening of the fiber-matrix interfacial bond, and development of hydrolysis reaction. Microstructure investigations presented circumferential fiber debonding,

microcrack formation, and production of hydroxyl groups in the polymeric matrix. GFRP bars conditioned at elevated temperatures were more severely degraded compared to those conditioned for longer durations. The application of a sustained load promoted the degradation mechanism of GFRP bars in comparison to unloaded counterparts. However, its effect was intensified when combined with elevated conditioning temperatures.

ACKNOWLEDGMENTS

This project is supported by the United Arab Emirates University (UAEU) under grant number 31N129 and Sultan Qaboos University (SQU) under grant number CL/SQU-UAEU/13/05. The contributions of the UAEU and SQU are greatly appreciated.

REFERENCES

REFERENCES

- Abeyasinghe, H., Edwards, W., Pritchard, G. & Swampillai, G. J. (1982). Degradation of crosslinked resins in water and electrolyte solutions. *Polymer*, 23, 1785-1790.
- ACI 440.3R (2012). Guide test methods for fiber-reinforced polymers (frps) for reinforcing or strengthening concrete structures. Farmington Hills, Michigan: American Concrete Institute.
- Almusallam, T. H. & Al-Salloum, Y. A. (2006). Durability of gfrp rebars in concrete beams under sustained loads at severe environments. *Journal of Composite Materials*, 40, 623-637.
- ASTM (2008). Standard test method for assignment of the glass transition temperatures by differential scanning calorimetry. *E1356*. West Conshohocken, PA: ASTM.
- ASTM (2010). Standard test method for water absorption of plastics. *D570*. West Conshohocken, PA: ASTM.
- ASTM (2015). Standard test methods for constituent content of composite materials. *D3171*. West Conshohocken, PA: ASTM.
- ASTM (2016). Standard test method for tensile properties of fiber reinforced polymer matrix composite bars. *D7205*. West Conshohocken, PA: ASTM International.
- Bakis, C. E., Boothby, T. E., Schaut, R. A. & Pantano, C. G. (2005). Tensile strength of gfrp bars under sustained loading in concrete beams. *ACI Special Publication*, 230, 1429-1446.
- Bakis, C. E., Freimanis, A. J. & Gremel, D. (1998). Effect of resin material on bond and tensile properties of unconditioned and conditioned frp reinforcement rods. *1st International Conference on durability of Fiber Reinforced Polymer (FRP) Composites for Construction*. Sherbrooke, QC, Canada.
- Benmokrane, B., Wang, P., Ton-That, T. M. & Rahman, H. (2002). Durability of glass fiber-reinforced polymer reinforcing bars in concrete environment. *Journal of Composites for Construction*, 6.
- Davalos, J. F., Chen, Y. & Ray, I. (2012). Long-term durability prediction models for gfrp bars in concrete environment. *Journal of Composite Materials*, 46, 1899-1914.
- Debaiky, A., Nkurunziza, G., Benmokrane, B. & Cousin, P. (2006). Residual tensile properties of gfrp reinforcing bars after loading in severe environments. *Journal of Composites for Construction*, 10, 370-380.
- El-Hassan, H., El-Maaddawy, T., Al-Sallamin, A. & Al-Saidy, A. (2017). Performance evaluation and microstructural characterization of gfrp bars in seawater-contaminated concrete. *Construction and Building Materials*, 147, 66-78.
- Montaigu, M., Robert, M., Ahmed, E. A. & Benmokrane, B. (2013). Laboratory characterization and evaluation of durability performance of new polyester and vinylester e-glass gfrp dowels for jointed concrete pavement *Journal of Composites for Construction*, 17, 176-187.
- Mourad, A. H. I., M., A.-M. B., El-Maaddawy, T. & Grami, M. E. (2010). Effect of seawater and warm environment on glass/epoxy and glass/polyurethane composites. *Applied Composite Materials*, 17, 557-573.
- Robert, M. & Benmokrane, B. (2010a). Effect of aging on bond of gfrp bars embedded in concrete. *Cement and Concrete Composites*, 32, 461-467.
- Robert, M. & Benmokrane, B. (2010b). Physical, mechanical, and durability characterization of preloaded gfrp reinforcing bars. *Journal of Composites for Construction*, 14, 368-375.
- Robert, M., Cousin, P. & Benmokrane, B. (2009). Durability of gfrp reinforcing bars embedded in moist concrete. *Journal of Composites for Construction*, 13, 66-73.
- Trejo, D., Gardoni, P. & Joo, K. J. (2011). Long-term performance of glass fiber-reinforced polymer reinforcement embedded in concrete. *Materials Journal*, 108, 605-613.



EFFECTS OF FIBER ARCHITECTURE ON FLEXURE PROPERTIES OF PULTRUDED GFRP PLATES AND SECTIONS

Tianqiao Liu¹, Kent A. Harries^{1,2} and Qi Guo¹

¹University of Pittsburgh, Civil and Environmental Engineering, Pittsburgh, USA (kharries@pitt.edu)

²University of Bath, BRE Centre for Innovative Construction Materials, Bath, UK

ABSTRACT

Flexural properties of pultruded glass fibre reinforced polymer (pGFRP) materials vary considerably and, unlike longitudinal properties, are affected by fibre architecture which, itself, is typically a function of plate thickness. Thin plates may have only a single longitudinal glass roving located near the plate midline while thicker plates will have multiple rovings arranged at a distance from the midline. As a result, thicker plates will be disproportionately stiffer and stronger in their flexural response than thinner plates. While the rule of mixtures is appropriate for assessing axial and shear properties, additional information on the fibre architecture is required to assess flexural properties which the rule of mixtures alone will overestimate. Variation of the location of the roving through the plate thickness will also significantly affect longitudinal flexural properties. Thus the authors argue for a member stiffness approach: determining flexural stiffness as the product of modulus and moment of inertia (EI) rather than determining E and I separately. The paper presents a parametric study of idealised plate geometry that demonstrates the impact of fibre architecture and that the rule of mixtures formulation results in an upper bound solution for stiffness. Subsequent experimental and imaging data is presented that illustrates the significant variation of fibre architecture and its effect on the flexural stiffness of the plate. Conclusions and recommendations are made having direct relevance to ongoing international pGFRP design standards development.

KEYWORDS

All FRP and smart FRP structures; Material Characterization of FRP and FRC materials/systems; Codes, Standards and Design Guidelines; Fiber and Matrix Architecture

NOMENCLATURE

The following nomenclature is adopted in this paper: E_L and E_T are the longitudinal and transverse moduli of elasticity and subindices t , c and f indicate properties obtained from tensile, compressive and flexural tests, respectively. G_{LT} is the in-plane shear modulus.

INTRODUCTION

Pultruded glass fibre reinforced polymer (pGFRP) composite materials are gaining acceptance as a construction material. In order to design with these often highly anisotropic materials, proper material characterisation is required. Design standards (ASCE 2010; EUR 2016) and manufacturer-specific design guides typically specify minimum or “guaranteed” design values for pGFRP which are often considerably lower than material properties obtained from coupon tests. The ratios of longitudinal to transverse moduli (E_L/E_T), longitudinal to shear moduli (E_L/G_{LT}), and longitudinal to flexural moduli (E_L/E_F), also are seen to vary considerably more than design guide values would suggest or permit. These ratios are particularly important for predicting stability (local and global buckling) behaviour. For example, the stability relationships prescribed in EUR 27666 (2016) are limited to $5.9 \leq E_L/G_{LT} \leq 8.3$ while experimental data reported in the available literature varies from 4.1 to 11.5 (Liu et al. 2017). Additionally, these ratios are affected by the nature of the test used to determine the longitudinal modulus, tension or compression (Liu et al. 2017). Perhaps a greater concern may arise if, for instance, only longitudinal properties are measured and standard or default values of other properties are used. Particularly for buckling analyses this may result in non-conservative predictions of design capacity (Liu 2017; Vieira et al. 2017).

Often, simple laminate theory using measured fibre volume ratios is used to assess transverse, flexural and/or shear properties. Agreement with measured longitudinal values is accepted as validation of this approach. This approach, however, is incorrect as it does not account for the anisotropic nature of the glass fibre itself and, as a result, will underestimate off-longitudinal properties (Mallick 2008). More importantly, however, flexural properties of pGFRP materials vary considerably and, unlike longitudinal properties, are affected by through-plate fibre architecture which, itself, is typically a function of plate thickness. Thin plates may have only a single longitudinal glass roving located near the plate midline (neutral axis in flexure) while thicker plates will have

multiple rovings arranged at a distance from the midline. As a result, thicker plates will be disproportionately stiffer and stronger in their flexural response than thinner plates. Essentially, while the rule of mixtures is appropriate for assessing axial properties, additional information on the fibre architecture is required to assess flexural properties. Variation of the location of the roving through the plate thickness will also significantly affect longitudinal flexural properties.

LOCAL COMPRESSION FLANGE BUCKLING

For most practical design scenarios plate flexural behaviour is not required. The exception being in local buckling analysis where, it is argued, plate flexural stiffness should be calculated using the flexural modulus. Due to their low modulus of elasticity and high anisotropy, in addition to the relative slenderness of thin-walled profiles, the performance of pGFRP members is often controlled by a buckling limit state. Proposed equations for calculating the critical longitudinal stress, f_{cr} , in the compression flange of a member subject to axial compression or flexure vary considerably but all take the same general form of a function proportional to $E_L t^3/12$, the flexural stiffness of the buckling flange having thickness t . Reviews of such equations for axial and flexural loaded members can be found in Cardoso (2014) and Liu (2017), respectively. Due to their complexity, and reliance on parameters that also differ for different pGFRP members – most notably the rotational stiffness imparted at flange-web junctions – such equations typically include simplifying empirical elements when translated to design equations (ASCE 2010; EUR 2016). Nonetheless, all known design provisions specify the use of E_{Lc} – the elastic modulus determined from compression tests in the formulation $E_{Lc} t^3/12$.

As will be described below, the ratio of modulus determined from compression and flexural tests, E_{Lf}/E_{Lc} , is less than unity – sometimes significantly so. For this reason, Cardoso (2014) advocated the use of E_{Lf} in his semi-empirical approach to calculating f_{cr} , for local flange buckling of axially loaded pGFRP members, Cardoso et al. (2014 and 2015) demonstrating considerable improvement in predictive capacity using E_{Lf} in short members where flange buckling dominated behaviour and in longer elements where flange and member buckling behaviour interact.

In this work the authors contend that the flexural stiffness, $(EI)_{Lf}$, rather than modulus alone, E_{Lf} , should be used since the former property is a function of plate thickness **and** fibre architecture. Ultimately, buckling behaviour is a function of $(EI)_{Lf}$ rather than E_L or t^3 independently.

COMPARISON OF THEORETICAL FLEXURAL AND AXIAL BEHAVIOURS

The rule of mixtures (Eq. 1) is conventionally used to assess the longitudinal modulus of a uniaxial composite material from its total fibre volume ratio (V_f) and the moduli of its fibre (E_f), continuous strand mat (E_{csm}) and matrix (E_m) constituents:

$$E_L = E_f(1 - \kappa)V_f + E_{csm}\kappa V_f + E_m(1 - V_f) \quad (1)$$

Where E_{csm} is conventionally assumed to be $0.375E_f$ (Krenchel 1964). κ is the proportion of V_f made up of CSM (that is $V_{csm} = \kappa V_f$). κ is relatively large for plates having small thickness and falls for thicker plates. In this theoretical study, values of $\kappa = 0.30, 0.15, 0.10$ and 0.075 are used for plate thickness $t = 3.2, 6.4, 9.6$ and 12.7 mm, respectively. These values result in the same absolute volume of CSM in each plate. In this theoretical illustration, V_f is taken as 0.50 , $E_f = 70$ GPa and $E_m = 3.5$ GPa for all cases. These are typical values for pultruded GFRP materials.

Typically, E_L is multiplied by the gross section area (A_g) or moment of inertia (I_g) in order to determine the axial ($E_L A_g$) or flexural stiffness ($E_L I_g$), respectively. This approach is correct for axial stiffness since all components of the cross section are theoretically subject to uniform axial strain. However when considering the flexural stiffness, the location and relative stiffness of the constituent fibre and matrix effect the stiffness. Indeed, it can be shown that $E_L I_G$ is an upper bound estimate of the actual flexural stiffness.

A simple transformed section treatment of the FRP plate cross section in which the fibre and matrix constituents are modelled discreetly is shown in Figure 1. For simplicity and to maintain a two-component system, the contribution of the CSM is incorporated into the matrix modulus as an effective matrix modulus, E_{meff} .

$$E_{meff} = [0.375E_f\kappa V_f + E_m(1 - V_f)]/[V_f(\kappa - 1) + 1] \quad (2)$$

Four cases are considered as shown in Figure 1. The first case results in an extreme lower bound in estimated flexural stiffness by placing 100% of the fibre content in a single roving located at the neutral axis (mid depth) of the plate. Additional cases consider the fibre volume being broken into 3, 5 or 7 equal rovings. These rovings are placed uniformly through the cross section with one roving at mid depth and the edge of the outermost rovings placed $0.1t$ from the edge of the plate as shown in Figure 1. In pGFRP materials intended for civil engineering applications, those having $t = 3.2$ mm will typically have only a single roving; those having $t = 6.4$ or 9.6 mm typically have 3 or 5 rovings; and those having $t = 12.7$ mm will often have 5 rovings.

It can be inferred from Figure 1 that the calculation of axial stiffness, $E_L A_g$ is identical for all cases. Flexural stiffness, $(EI)_{eff}$, on the other hand is highly dependent on the location of the fibre rovings relative to the neutral axis. Clearly placing as much fibre as possible as far from the neutral axis as possible results in the most efficient section architecture possible. Since an odd number of rovings is most common, three rovings is most efficient.

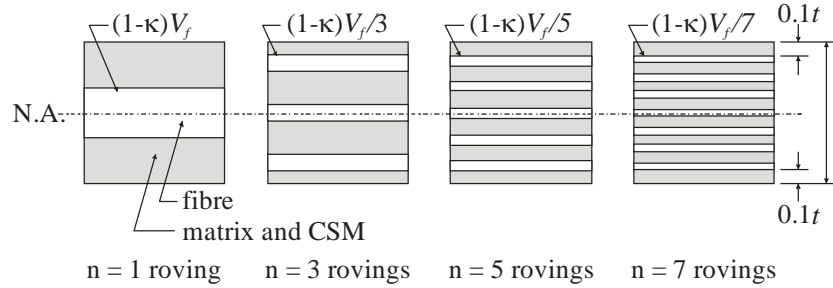


Figure 1: Idealised fibre architecture used for comparison of theoretical stiffness.

Figure 2 shows the results of the theoretical analysis. The resulting effective flexural stiffness for each of the cases shown is normalised by $E_L I_g$ where E_L is determined from the rule of mixtures calculation given by Eq. 1; this is designated $(EI)_{RoM}$. The expected effects of fibre architecture are clear. Single rovings at the neutral axis do not achieve 40% of the theoretical flexural stiffness determined from a rule of mixtures approach. Three equal rovings are most efficient, achieving 85% of the theoretical capacity.

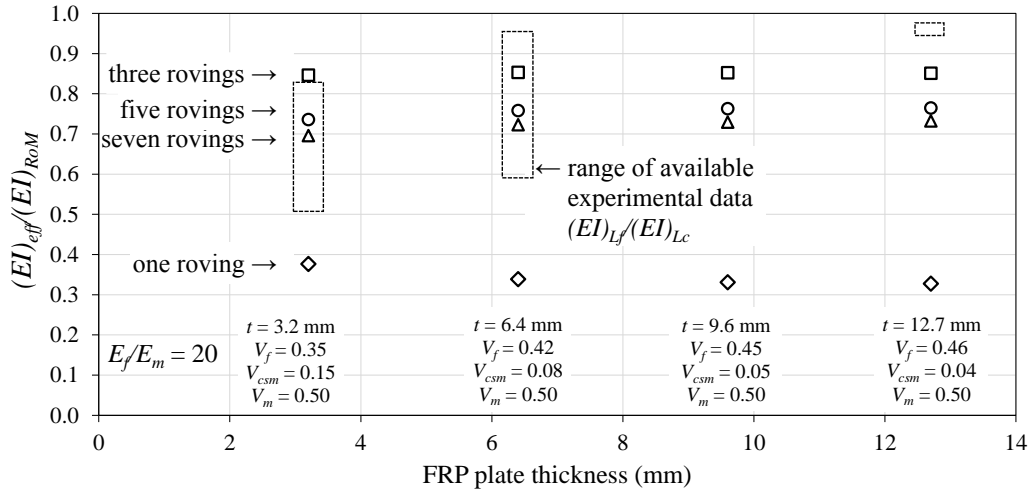


Figure 2: Idealised fibre architecture used for comparison of theoretical stiffness.

EXPERIMENTAL AXIAL AND FLEXURAL BEHAVIOURS

Test specimens were obtained from the flanges of seven different sections and two plate products all supplied by the same manufacturer as summarised in Table 1. In all cases, the compression modulus, E_{Lc} , was obtained from ASTM D695 end loading tests. In the present study, the flexural modulus, E_{Lf} , was obtained from ASTM D7264

four-point bend tests. Previous data reported by Cardoso (2014) obtained flexural modulus from ASTM D790 three-point bend tests. The modular ratios, E_{Lf}/E_{Lc} obtained vary from 0.52 to 0.94 for 3.2 and 6.4 mm plates. For all sections having $t \leq 12.7$ mm, the manufacturer reported values of $E_{Lf}/E_{Lc} = 12400 \text{ MPa}/17200 \text{ MPa} = 0.72$ in this instance. A single series of tests on 12.7 mm plate resulted in an apparent ratio of $E_{Lf}/E_{Lc} = 1.1$, although this is based on tensile, rather than compression properties. The range of observed data is also plotted in Figure 2 and compares reasonably well with the theoretical calculations of flexural stiffness for 3.2 and 6.4 mm pGFRP plate.

It is also seen in Table 1 that the measured plate thickness is typically slightly below the nominal value. This effects the resulting flexural stiffness. Wall thickness in box sections have been seen to vary considerably due (presumably) to misalignment of the pultrusion die. Cardoso (2014) reports 25.4 x 3.2 box sections having one wall only 2.74 mm thick, 86% of nominal. In such a case, the calculated moment of inertia will be 63% of that based on a 3.2 mm wall thickness; effecting buckling capacity accordingly.

Table 1: Experimentally determined compressive and flexural moduli.

	specimens from...	V_f	resin	rovings	image	t_{meas}	t_{meas}/t	E_{Lc}	E_{Lf}	E_{Lf}/E_{Lc}
						mm		MPa (COV)	MPa (COV)	
this study	152 x 152 x 6.4 WF	0.53	PE	3	see 3a	6.17	0.92	31200 (0.09)	18750 (0.10)	0.60
	25 x 3.2 box	0.34	PE	1	see 3b	3.60	1.12	22100 (0.02)	18000 (0.08)	0.81
	76 x 6.4 box	0.50	PE	3 ^a	see 3c	6.55	1.02	31100 (0.04)	27900 (0.11)	0.90
	6.4 mm plate	0.44	PE	3	see 3d	6.27	0.98	$E_{Lc} = 19900$ (0.04)	18800 (0.13)	0.94
	12.7 mm plate	0.41	PE	5	see 3e	12.42	0.98	$E_{Lc} = 21800$ (0.04)	20900 (0.02)	0.96
Cardoso (2014)	25 x 3.2 box	0.38	PE	1	-	3.19	0.99	22100 (0.02)	11500 (0.03)	0.52
	76 x 6.4 box	0.49	PE	3	-	6.23	0.97	31100 (0.04)	25000 (0.12)	0.80
	102 x 102 x 6.4 WF	0.51	VE	1	-	6.34	0.99	25600 (0.18)	21900 (0.06)	0.86
	102 x 102 x 6.4 WF	0.43	PE	3	-	6.23	0.97	25700 (0.09)	19500 (0.01)	0.76

WF = wide flange shape; PE = polyester; VE = vinyl ester

^a3 rovings reported by manufacturer; only two rovings of unequal volume evident in section.

VARIATION OF FIBRE ARCHITECTURE

In addition to variation in plate thickness, fibre architecture varies considerably both across the width and along the length of a plate. This, in turn effects the effective stiffness as shown previously and raises the possibility of local weaknesses that could result in premature buckling initiation.

In this study, a simple method of assessing fibre architecture of specimens is introduced. Instead of complex imaging techniques, digital images of thin sections cut from the end of test specimens are obtained. The thin sections are placed on a mobile telephone screen or similar with a white page showing. The light is easily transmitted through the longitudinal fibre but not the matrix. The resulting images, examples of which are shown in Figure 3, are analysed to determine both fibre content and architecture – the location of the fibre in the cross section. While not the focus of this work, this simple method is proposed to allow the immediate, rapid and economic analysis of specimen fibre architecture.

Figure 3 shows examples of the five specimen types presented in this study (Table 1). The variation in fibre architecture is readily apparent. The 3 rovings shown in Figures 3a are uniform and distributed evenly through the cross section. Based on the observed geometry (Figure 3a), E_{Lf}/E_{Lc} is estimated to be 0.66 using the same assumptions of material properties given in the theoretical analyses presented previously. The experimentally observed ratio was $E_{Lf}/E_{Lc} = 0.60$ (Table 1) having an estimated coefficient of variation, COV = 0.13.

The rovings in Figure 3b and 3d are very intermittent although the fibre rovings are generally located away from the neutral axis and will thus resist flexure in an efficient manner. The material shown in Figure 3c was expected to have three rovings although only two rovings appear to be present. As the two rovings appear to be of unequal volumes, it is suspected that two rovings have been pulled together into one in this instance. The unequal rovings would have the effect of shifting the neutral axis although should lead to relatively efficient section. Based on the observed geometry (Figure 3c), E_{Lf}/E_{Lc} is estimated to be 0.82 using the same assumptions of material properties given in the theoretical analyses presented previously. The experimentally observed ratio was $E_{Lf}/E_{Lc} = 0.90$ (Table 1) having an estimated coefficient of variation, COV = 0.12.

Figure 3e shows the section of a 12.7 mm plate having five rovings. While evenly distributed, the roving volumes vary across the width of the plate. This is believed to be the nature of pultruded plate. The pGFRP plate products shown in Figures 3d and 3e are produced in 1220 mm widths and have a lower fibre volume ratio than comparable pultruded sections. The manufacturer of the materials shown reports $V_f \approx 0.5$ for pultruded shapes having $t \geq 6.4$ mm and $V_f \approx 0.4$ for comparable plates.

photo					
image (fibre rovings shown as white)					
geometry	$t = 6.17$ mm 3 rovings	$t = 3.6$ mm 1 roving	$t = 6.55$ mm 2 unequal rovings	$t = 6.27$ mm 3 rovings	$t = 12.42$ mm 5 rovings
	a) 152 x 152 x 6.4 WF	b) 25 x 3.2 box	c) 76 x 6.4 box	d) 6.4 mm plate	e) 12.7 mm plate

Figure 3: Representative cross sections of flexural test specimens.

CONCLUSIONS AND RECOMMENDATIONS

The data presented in this paper are intended to be representative rather than definitive. Nonetheless, it is shown that apparent longitudinal compression modulus determined from flexural tests, E_{Lf} is less than that determined from compression tests, E_{Lc} . Additionally, the ratio E_{Lf}/E_{Lc} is a function of fibre architecture and is affected by the number of rovings. The rule of mixtures is only able to calculate E_{Lc} , and thus results in an upper bound estimation of E_{Lf} .

The variation in fibre architecture and plate thickness, t , identified strongly supports the use for plate stiffness $(EI)_{Lf}$ in design equations for plate buckling. Current practice (e.g., ASCE 2010, EUR 2016) implies the separate determination of material longitudinal modulus E_{Lc} and the geometric property $t^3/12$. All flexural tests determine $(EI)_{Lf}$ directly from displacement, thus use of this value is not cumbersome in design equations. It is recommended that $E_{Lc}t^3/12$ terms in local buckling equations be treated as an immutable value of stiffness and be determined directly from flexural tests. In local buckling formulations, where $E_{Lc}t^3/12$ cannot be determined explicitly from flexural tests, the value $0.8E_{Lc}t^3/12$ is recommended in which E_{Lc} is the compression modulus determined from compression tests and t is the nominal flange plate thickness. Based on current industry practice, it is recommended that structural load-carrying elements be limited to elements having $t \geq 6.4$ mm having at least 3 rovings.

REFERENCES

American Society of Civil Engineers. (ASCE). (2010). *Pre-Standard for Load and Resistance Factor Design (LRFD) of Pultruded Fiber Reinforced Polymer (FRP) Structures*.

ASTM D695-15 *Standard Test Method for Compressive Properties of Rigid Plastics*.

ASTM D790-17 *Standard Test Methods for Flexural Properties of Unreinforced and Reinforced Plastics and Electrical Insulating Materials*.

ASTM D7264-15 *Standard Test Method for Flexural Properties of Polymer Matrix Composite Materials*.

Cardoso, D., Harries, K.A. and Batista, E. (2014) Closed-Form Equations for Local Buckling of Pultruded Thin-Walled Sections, *Thin-walled Structures*, **79**, pp 16-22.

Cardoso, D., Harries, K.A. and Batista, E. (2015) Compressive Local Buckling of Pultruded GFRP I-Sections: Development and Numerical/Experimental Evaluation of an Explicit Equation, *ASCE Journal of Composites for Construction* **19**(2).

Cardoso, D.T.C. (2014) *Compressive Strength of Pultruded Glass-Fiber Reinforced Polymer (GFRP) Columns*, PhD Dissertation, COPPE, Federal University of Rio de Janeiro.

EUR 27666 (2016) *Prospect for new guidance in the design of FRP* (Ascione L., Caron J.F., Godonou P., van IJselmuiden K., Knippers J., Mottram T., Oppe M., Gantriis Sorensen M., Taby J., and Tromp, L.)

Krenchel H. (1964) *Fibre reinforcement: Theoretical and practical investigations of the elasticity and strength of fibre-reinforced materials*, Copenhagen: Akademisk Forlag; 1964.

Liu, T., Cardoso, D., Vieira, J. and Harries, K.A. (2017) Convenient and Inexpensive Test Methods for Pultruded GFRP Composite Material, *Proceedings of Advanced Composites in Construction (ACIC2017)*, Sheffield, September 2017.

Liu, T. (2017) *Stability Behavior of Pultruded Glass-Fiber Reinforced Polymer I-Sections Subject to Flexure* PhD Dissertation, University of Pittsburgh.

Mallick, P. K. (2008). *Fiber-reinforced composites: materials, manufacturing, and design*, 3rd edition. CRC press.



EMBEDDED PIEZO MICRO-PATCHES FOR CURE MONITORING OF FIBER-REINFORCED EPOXY IN CIVIL ENGINEERING REPAIRS

Olivier Bareille¹, Michelle Salvia¹, Mingfa Zhang¹, Fernanda Benezra-Maia²

¹ Ecole Centrale de Lyon, LTDS CNRS UMR 5513, Université de Lyon, France;

² Federal University of Rio Grande do Sul, Department of Civil Engineering, Brasil

KEYWORDS

All FRP and smart FRP structures; ; Inspection, NDT methods and quality assurance; Characterization of FRP and FRC materials/systems

ABSTRACT:

In recent years high interests of maintenance and repair of civil structures were concentrated on the use of natural fibre or carbon fibre reinforced thermosets as structural component. The thermosets were mainly room temperature curing bio-based epoxies. The properties of the resulting mechanical composites are directly in relation to reinforcement type but also to viscoelastic matrix properties and reinforcement/matrix interactions.

The most important factor which can control the properties of the matrix and of the reinforcement-matrix interface is in particular the cross-linking density resulting from the manufacturing process that is linked to the degree of cure. The cure of a thermoset is a complex process which leads to a three-dimensional macromolecular network. The final morphology of the three-dimensional network, which determines the properties of the material, depends on this transformation. So, there is a growing need for sensors, which provide real-time, in situ monitoring of the manufacturing process. This study, in the frame of a collaborative research (MICRO ANR project), proposes to in-situ follow-up the cure mechanism of an epoxy-amine resin using piezoelectric elements embedded in the composite structure at different locations. The technique used in this work is based on the measurement of the electrical impedance of piezoelectric ceramics. The change in the impedance spectrum which is linked to the changes of matrix viscoelastic properties as cure progressed is used to understand the different steps of the epoxy cure regarding molecular motion, viscosity, density and their consequences on the mechanical properties of the material.

Moreover, after curing, the sensor may be used as damage detector and wear sensor. In order to assess the efficiency of such a system and especially the optimal placement of the set of piezo-patches for both curing observance and health monitoring, tests were performed based on three-point bending measurements and scanning electron microscope.

INTRODUCTION

Thermoset resin based composites are increasingly used as a repair and/or reinforcement method for civil engineering structures structural rehabilitation due to their high specific stiffness and strength and their non-corrosive behaviour especially when reinforced with carbon or natural fibres.

The properties of the resulting mechanical composites are directly in relation to reinforcement type but also to viscoelastic matrix properties and reinforcement/matrix interactions. The most important factor which can control the properties of the matrix and of the reinforcement-matrix interface is in particular the cross-linking density resulting from the manufacturing process that is linked to the degree of cure. The cure of a thermoset is a complex process which leads to a three-dimensional macromolecular network. The final morphology of the three-dimensional network, which determines the properties of the material, depends on this transformation. So, there is a growing need for sensors, which provide real-time, in situ monitoring of the manufacturing process. This study, in the frame of a collaborative research (MICRO ANR project), proposes to in-situ follow-up the cure mechanism of an epoxy-amine resin using piezoelectric elements embedded at different locations in a composite reinforced with flax fibres. The technique used in this work was based on the measurement of the electrical impedance of piezoelectric ceramics. The change in the impedance spectrum which is linked to the changes of matrix viscoelastic properties as cure progressed was used to understand the different steps of the epoxy cure and their consequences on the mechanical properties of the material.

MATERIALS

The thermoset resin system is designed for ambient and low temperature cure. The DGEBA epoxy prepolymer is a low molecular weight “green” epoxy resin made from bio-based epichlorohydrine. The hardener used is Cardolite NX5619 which is a solvent-free, low viscosity phenalkamine curing agent made through the Mannich reaction of cardanol from cashew nuts, formaldehyde, and amines. Resin and hardener were mixed in stoichiometric ratio. The glass transition temperature of the reactive mixture, T_g was -39°C , fairly negative, determined from DSC heat flow curves (midpoint), recorded at a heating rate of 10 K/min (DSC1 device from METTLER-TOLEDO). In this work, the curing was carried out at room temperature (23°C).

The reinforcement is a quasi-unidirectional flax fabric made of untwisted rovings supplied by DEPESTELE Group. The warp ratio is 9/91 and the areal density is 200 g/m².

EXPERIMENTAL

IN SITU MONITORING METHOD

The technique used in this work was based on the measurement of the electrical impedance of piezoelectric PZT ceramic disk embedded in the composite materials. The PZT sensor is 0.2 mm thick disk with a diameter of 7 mm (Figure 1).



Figure 1: Piezoelectric disk [<https://www.steminc.com>]

A first UD fabric layer was arranged on a wooden mould coated with wax (release agent). The resin was then applied by using a squeegee and a paint roller to ensure a good wetting of the reinforcement with the resin and removing excess resin and entrapped air. Once the first layer was fully impregnated the second reinforcement ply in which two piezoelectric disks were placed is applied and impregnated. Figure 2 shows the plate after manufacturing.

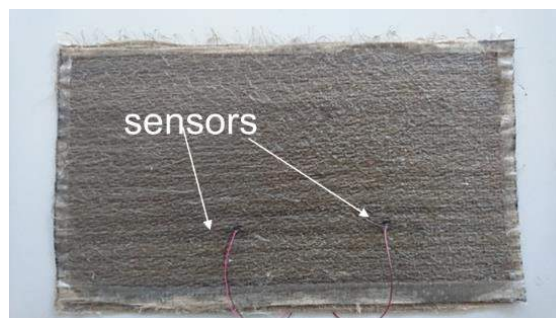


Figure 2: Flax reinforced epoxy composite material with embedded PZT disk

The PZT sensors were connected to an impedance analyser and the impedance was monitored as a function of time at room temperature (RT) at 4 kHz.



DYNAMICAL MECHANICAL ANALYSIS

Dynamical mechanical analysis (DMA) was performed for a better understanding on piezoelectric results. This technique provides convenient and sensitive determination of thermo-mechanical properties of polymers and reinforced polymers at solid or liquid state as a function of frequency and temperature. It consists in either applying a sinusoidal force to a material and measuring the displacement or applying a displacement and measuring the displacement. The displacement is lagged behind the force by a phase angle δ due to the viscoelastic characteristics of the polymers [1]. From the force and displacement measurements the complex stiffness can be deduced, $K^* = K' + j K''$ where K' is the storage stiffness and K'' is the loss stiffness. The loss factor is the ratio of loss stiffness to storage stiffness $\tan \delta = K''/K'$. Knowing the sample geometry either complex tensile (E^*) or shear modulus (G^*) can be obtained depending on the loading mode. This method is particularly appropriate to analyse the relaxation processes ((main or α -) and sub- T_g) of polymer-based materials [2].

DMA can also provide valuable information for monitoring curing progression of thermoset as the material changes from viscous liquid state to infusible cross-linked solid (3D-network) [3-4]. This transformation may involve two main transitions: gelation when the viscous liquid prepolymer is transformed in an infusible, insoluble gel or rubber-like material and vitrification which corresponds to rubber-glass transition. At vitrification the rate of the cure reaction may be reduced due to molecular mobility. This phenomenon occurs only if the reactive mixture is cured at a temperature lower than the infinite glass transition temperature of completely cross-linked system. This occurs when the glass transition temperature (T_g) equals the cure temperature. Gelation is a isoconversion event and therefore it is frequency independent, conversely vitrification which is frequency dependent.

In this study, DMA was performed in the two ways using a DMA50 of 01dB Metravib:

Perpendicular samples (30x10x2 mm³) machined into a rectangular plate cured at room temperature (RT) at various cure times were used to evaluate the complex modulus and the α -relaxation temperature.

Isothermal curing at RT was undertaken on DMA using a resin impregnated flax fabric sample.

EXPERIMENTAL

Thermomechanical analysis of CURED composites

It is well known that the measurement of α -relaxation temperature which is associated to T_g can be used as an accurate indication of cross-link density of a thermosetting. The thermomechanical properties were analysed using DMA on composites after curing at room conditions (23°C, 50% HR) at various cure times (12 hours, 2 and 8 days). Tests were carried out in tension-compression mode at controlled dynamic displacement ($\pm 5 \mu\text{m}$) in the linear viscoelasticity domain within a temperature range of -50 at 150°C (heating rate = 1 K/min) at a constant frequency of 1 Hz.

Typical plots of the storage modulus E' and the loss factor $\tan \delta$ versus temperature were given in Figure 3a and 3b respectively. The onset of the modulus drop and the maximum of $\tan \delta$ were shifted towards high temperatures and the area under the curve of loss factor was reduced with curing time at RT. These features were consistent with a progressive decrease in chain motion due to a degree of crosslink increase with curing time. These Figures show also that the cure rate above 2 days curing was greatly slowed down. Unlike what was usual, the modulus at rubbery plateau increases continuously with temperature in all the cases, even if the amplitude of this phenomenon decreases with curing time. These analyses pointed out that after curing and stabilization 8 days at room temperature a full degree of curing was not achieved. Another temperature sweep was carried out in the RT - 150 °C temperature range on 8 days cured samples which confirmed the non-fully cured state after curing at RT during a little more than one week. Indeed, the α -relaxation increases by about 25°C. Nevertheless, a slight increase in storage rubbery modulus vs temperature occurred again for post-cured samples.

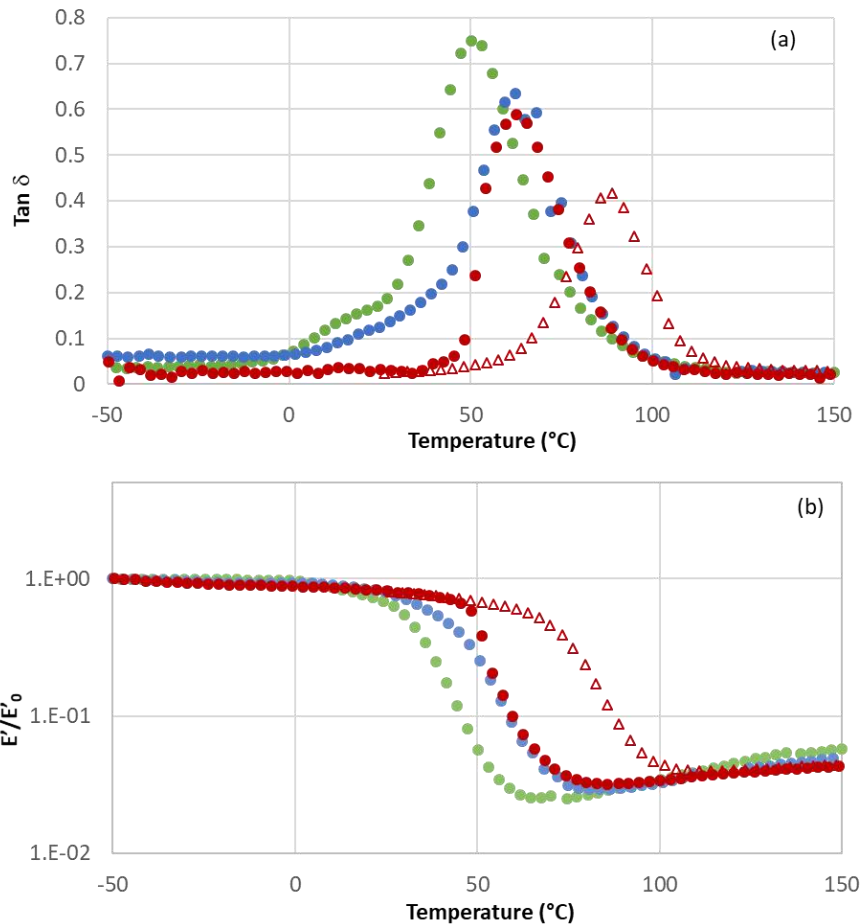


Figure 3: Temperature dependence of (a) $\tan \delta$ and (b) E'/E_0' response at $F=1$ Hz for flax reinforced composites at various curing states: (●) 12 hours; (●) 2 days; (●) 8 days; (▲) 8 days + sweep until 150 $^{\circ}\text{C}$

In situ curing monitoring

Once the impregnation process was completed, the impedance (Z) was monitored at 4 kHz every 10 min at room temperature (23 $^{\circ}\text{C}$). A comparison of normalized change in impedance vs time obtained on two different plates manufactured two weeks apart, shows the high reproducibility that was achieved (Figure 4).

The variation of impedance versus time had a sigmoidal shape. At the very early beginning, a slight increase in impedance appeared. Beyond this lag-time, the impedance increased sharply, then levelled off until it reached a quasi-asymptotic value. There was no obvious definition at which gelation occurred using such measurements. At the very beginning, the thermoset mixture was composed of low-molecular prepolymers. As the reaction proceeded, chain extension occurred to produce relatively high molecular weight reaction products resulting in an increase in impedance. Gelation which corresponded to the first appearance of an infinite cross-linked network was associated in this study to the time at which the first significant increase in stiffness. As mentioned previously, vitrification was associated with the transition from a rubbery modulus to a glassy modulus. Above vitrification, the mobility of the reacting groups was restricted with the reduction of free volume. Thereby, this phenomenon led to an extremely slow reaction, as the reaction became diffusion-controlled. Therefore, vitrification was associated to the instant at which the impedance reached an almost constant value. Beyond, the impedance continued to increase slowly long after the vitrification: the reaction dramatically slowed, since the cure mechanism was controlled by the molecular diffusivity, but did not come to end.

These features were consistent with \square -relaxation results obtained on composites at increasing cure times until about one week and after post-curing. The \square -relaxation temperature can continue to increase long after the vitrification. Nevertheless, the final cross-linking was limited because of the low temperature of cure.

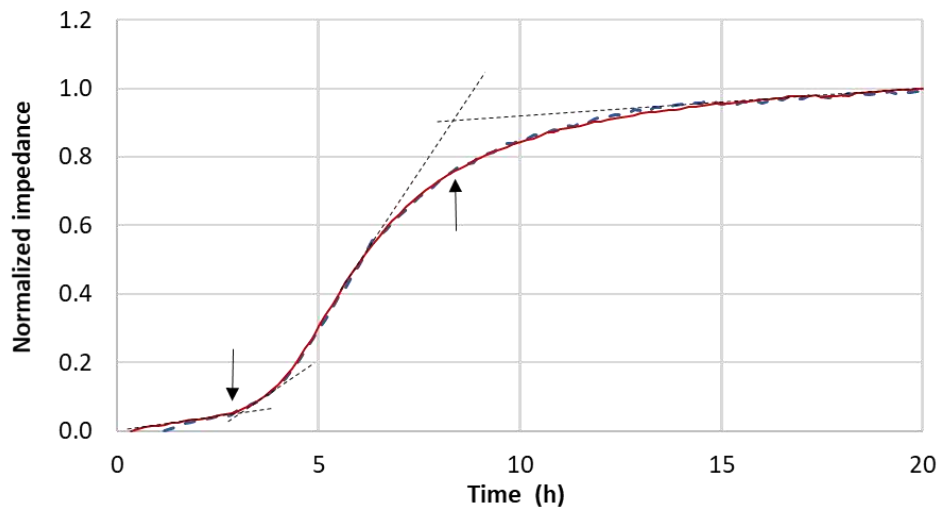


Figure 4: Normalized impedance vs time during cure at RT of two different plates (arrows indicate gelation and vitrification)

Results from impedance correlate with results from DMA tests performed on a sample cut from the flax fabric (22 mm × 13 mm (length and width)) and impregnated by epoxy resin. Test conditions were tension/compression mode at controlled static (5 μ m) and dynamic displacement (± 1 μ m), frequency: 30 Hz and room temperature (Figure 5). The variation of storage stiffness K' versus time showed a similar sigmoidal feature than impedance. Compared to DMA, impedance measurements appeared, in particular, to be more sensitive to changes in properties occurring after the vitrification has occurred when the cure mechanism became controlled by the molecular diffusivity and the crosslinking formation rate was dramatically low. The difference may be due to the fact that for DMA the loading was applied, for practical reasons (correct clamping of the fabric before polymerisation) in the direction of the reinforcement.

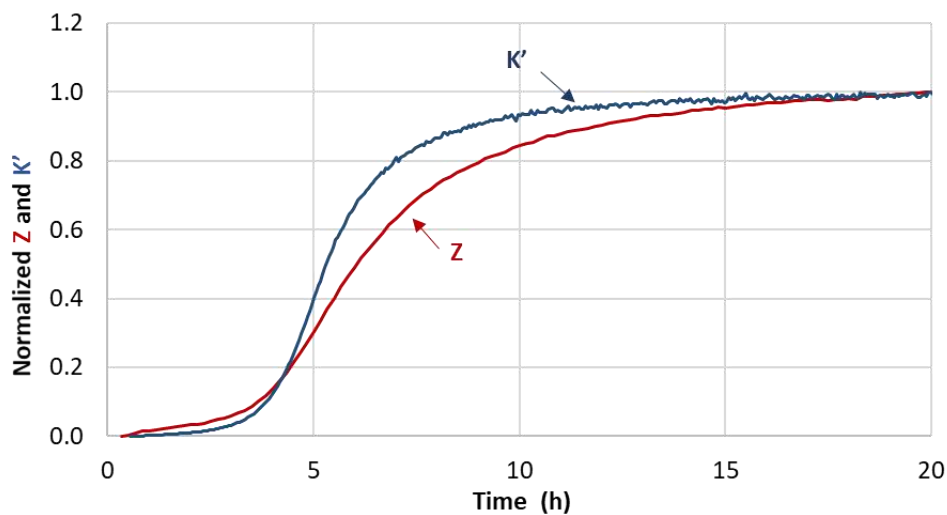


Figure 5: Normalized impedance and storage stiffness vs time during cure at RT



CONCLUSION

The technique used in this work is based on the measurement of the electrical impedance of piezoelectric ceramic micro-patches embedded in a composite material. The change in the impedance spectrum which is linked to the changes of matrix viscoelastic properties as cure progressed was used to understand the different steps of the epoxy matrix cure.

The results showed that the piezoelectric transducers are well suited to in-situ monitor the reaction progress during isothermal curing of a flax reinforced epoxy materials. Tests on moisture effect on natural fibre reinforced epoxy are in progress.

Moreover, after curing, the sensor may be used as damage detector and wear sensor. In order to assess the efficiency of such a system and especially the optimal placement of the set of piezopatches for both curing observance and health monitoring, tests were performed based on three-point bending measurements and scanning electron microscope.

REFERENCES

J. D. Ferry, *Viscoelastic Properties of Polymers*, 3rd Ed, Wiley, New York, 1980.

B. Kechaou, M. Salvia B. Beaugraud, D. Juvé, Z. Fakhfakh and D. Treheux, Mechanical and dielectric characterization of hemp fibre reinforced polypropylene (HFRPP) by dry impregnation process, *eXPRESS Polymer Letters*, **4**, 2010, pp. 171-182 (doi: [10.3144/expresspolymlett.2010.22](https://doi.org/10.3144/expresspolymlett.2010.22)).

C. Billotte, F. M. Bernard and E. Ruiz, Chemical shrinkage and thermomechanical characterization of an epoxy resin during cure by a novel in situ measurement method, *European Polymer Journal*, **49**, 2013, pp. 3548-3560 (doi: [10.1016/j.eurpolymj.2013.07.013](https://doi.org/10.1016/j.eurpolymj.2013.07.013)).

Enns J. and J. Gillham. 1983. "Time-temperature-transformation (TTT) cure diagram: modeling the cure behaviour of thermoset", *Journal of applied polymer science*, **28**: 2567-2591 (doi: [10.1002/app.1983.070280810](https://doi.org/10.1002/app.1983.070280810))



DYNAMIC TENSILE PROPERTIES OF POLYETHYLENE TEREPHTHALATE FIBER BUNDLE WITH LARGE DEFORMABILITY

Y.L. Bai¹, Z.W. Yan¹, J. G. Dai², D. J. Zhu³, Q. Han¹, X.L. Du¹

¹ Key Laboratory of Urban Security and Disaster Engineering of Ministry of Education,
Beijing University of Technology, China.

² Department of Civil and Environmental Engineering,
The Hong Kong Polytechnic University, China.
(corresponding author: cejgdai@polyu.edu.hk.)

³ College of Civil Engineering, Hunan University, China

ABSTRACT

In this paper, strain rate effects on the tensile mechanical properties of Polyethylene Terephthalate (PET) fiber bundles at room temperature were studied. First of all, an MTS load frame together with an Instron drop-weight impact system were used to carry out the tensile test under the quasi-static (1/600s⁻¹) and the dynamic loadings (40, 80, 120 and 160s⁻¹), respectively. The dynamic mechanical properties, consisting of the tensile strength, peak strain, elastic modulus and toughness, were analyzed based on the test data. It was concluded that the tensile strength increases with strain rate while the peak strain and toughness decrease with the strain rate. The initial elastic modulus remains almost unchanged at the low strain rate (no more than 40s⁻¹) and starts to grow when the strain rate is beyond 40s⁻¹. The second-stage elastic modulus rises continuously with the strain rate from 1/600 to 160s⁻¹. Afterwards, the dynamic tensile strength of a PET fiber bundle was statistically analyzed by using the two-parameter Weibull distribution model that can help to quantify the scatter of the dynamic tensile strength. The corresponding parameters can be added into a numerical simulation in future to reflect the different tensile strength caused by defects.

KEYWORDS

Strain rate; Dynamic tensile mechanical properties; Weibull analysis; Polyethylene terephthalate

INTRODUCTION

Fiber reinforced polymer, FRP for short, is a high-performance reinforcing material that consists of reinforced fibers and a matrix according to a certain volumetric proportion. The advantages of light weight and high strength, thermal expansion coefficient similar to concrete, good durability of FRP materials make them extremely attractive for structural retrofit [1]. It is easy to note that structures strengthened with FRP jackets will have opportunities to undertake not only seismic loads, but also blast/impact loads, such as vehicle impacts, terrorist attacks and other dynamic loads during their service life. Therefore, a good understanding of the dynamic mechanical properties of FRPs contributes to reliable strengthening of structures against dynamic loads. The fiber bundle in FRPs, as is known to all, is the main force-bearing element. Understanding of the dynamic mechanical properties of the fiber bundle will help to reveal the failure mechanisms of the corresponding FRP materials and FRP-strengthened structures under dynamic loadings. Against this background, several researches [2, 3] have been conducted on the dynamic mechanical properties of fiber bundles.

Zhu et al. [2] utilized an MTS load frame and a high rate servo-hydraulic system to conduct the quasi-static (4.2×10^{-4} s⁻¹) and dynamic tests (20-100s⁻¹) of a Kevlar 49 single fiber bundle and then found that its tensile strength, toughness, maximum strain and elastic modulus all increased with the increase of strain rate. Ou et al. [3] utilized an Instron drop-weight impact system to investigate the possible strain rate effect on the relevant mechanical properties of glass fiber and found that the tensile strength is increased by 88.0% when the strain rate is increased from 1/600 to 40s⁻¹, which represents a significant strain rate effect.

Recently, a new type of FRP made of polyethylene terephthalate (PET for short) fibers has emerged as an alternative to the traditional FRPs, due to its large rupture strain (more than 5%) [4,5,6,7]. Compared with the conventional FRPs, the large rupture strain FRPs have a lower elastic modulus but are environmentally friendly because they are usually recycled from scrap polymer products (e.g., PET bottles). The LRS FRP has great potential in retrofit applications where large deformability is appreciated (e.g. against seismic or explosive loading). Given that the strain rate between 1-200s⁻¹ occurs commonly in the earthquake and low-speed impact events, it is necessary to study the strain rate effect of PET single fiber within this strain rate range.

The purpose of this paper is to investigate the strain rate effect on the dynamic mechanical properties of the PET single bundle at the intermediate strain rates (40, 80, 120 and 160s⁻¹). The quasi-static test (1/600s⁻¹) was also

conducted for comparison purpose. Then, Weibull distribution model was utilized to quantify the dispersion of tensile strength.

EXPERIMENTAL PROGRAM

To ensure that bundles used in the test have the same cross-sectional area, all specimens with a gauge length of 25 mm were cut from the single long bundle. Thin aluminum sheets with the thickness of 0.2 mm, length of 20 mm and width of 15 mm were roughened the surface and folded along the long side to catch the two ends of each bundle specimen using epoxy resin and then clapped by two toothed steel anchorages. The dimension of the specimens is shown in Fig. 1.

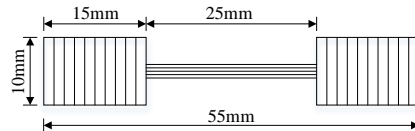


Figure 1: Dimension of tensile specimen

The quasi-static tensile tests were performed on an MTS universal testing machine (C43.304) with the loading capacity from 100 N to 30,000 N and the rate of data sampling up to 1,000 Hz, as shown in Fig. 2(a). The resolution of the controller was 20 bit and a force sensor, whose maximum range is 1,000N, was used with the data acquisition rate of 20 Hz. In this test, the loading speed was set to 2.5 mm per minute for the static loading tests.

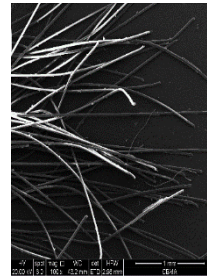


(a)

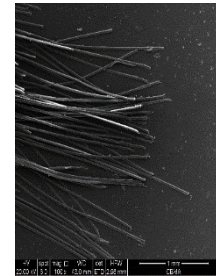


(b)

Figure 2 : (a) MTS universal testing machine; (b) Instron drop-weight impact system



(a)



(b)

Figure 3 : Failure mode at different stain rates: (a) 1/600s⁻¹; (b) 40s⁻¹

The Instron drop-weight impact system (Ceast 9340) was used for dynamic tensile tests, as shown in Fig. 2(b). The drop hammer descends in free fall along the guide rails on both sides. The height of impactor, controlled by its electronic beam positioning system, varies from 0.03 to 1.10 m and the maximum mass of the drop hammer is 37.5 kg so that the maximum impact energy can reach up to 405J. An anti-rebound system was used to avoid the second impact. The specimen was mounted by the upper and lower grips in the environmental chamber that can control the operating temperature. In this test, the initial impact velocity was set as 1, 2, 3 and 4 m/s, respectively.

RESULTS AND DISCUSSION

Failure mode

Figure 3 shows typical failure mode of the ruptured fiber bundles after the test. It can be observed that specimens under quasi-static loading failed in a chaotic manner while specimens under dynamic loading presented a trim fractography. This was mainly attributed to the following factors: the defect of every filament could reach full development at the quasi-static loading while there was no enough time to promote the development of defects of each filament at the higher strain rate so that the failure occurred at the weakest part of the whole.

Stress-strain relation

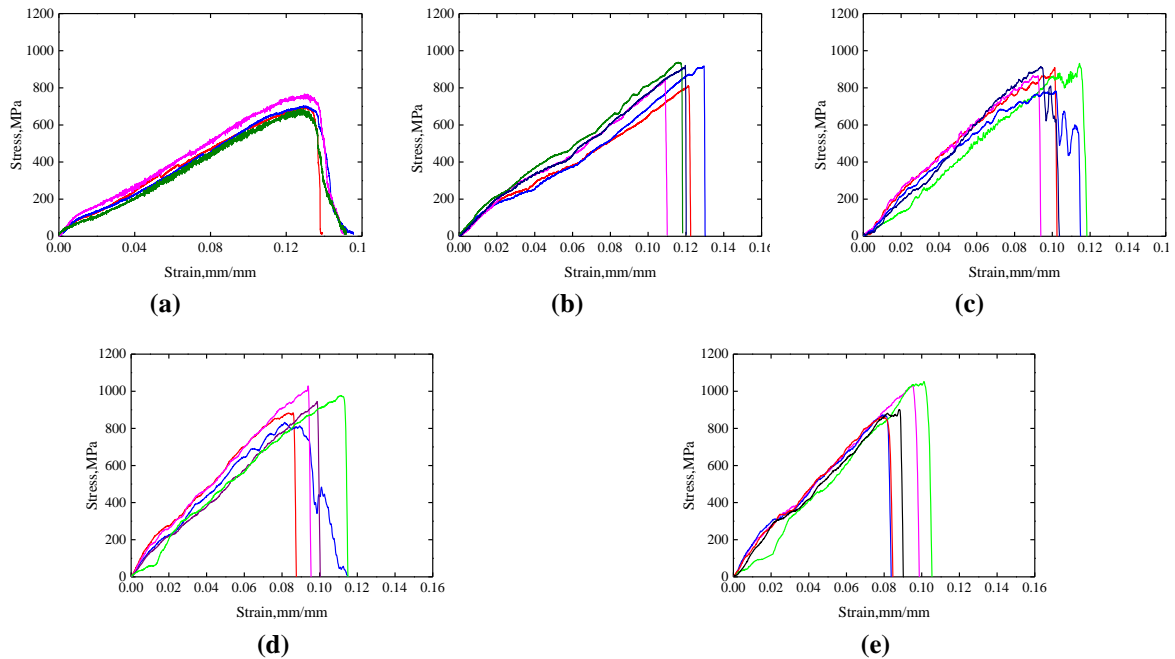


Figure 4 : Stress-strain curves of PET bundles under different strain rates: (a)1/600s-1; (b)40s-1; (c) 80s-1; (d)120s-1; (e)160s-1

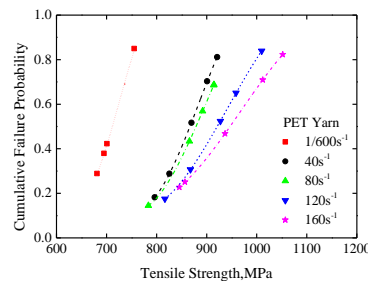


Figure 5 : Cumulative failure probability-tensile strength curves of PET bundles

Figure 4 shows the stress-strain curves of PET fiber bundles under different strain rate. It can be seen that all the curves exhibit a bilinear relationship and the transition points of slopes are within the strain range of 0.015 to 0.018. The fluctuation of curves derived from the quasi-static test is relatively small while curves obtained from the dynamic tests fluctuate obviously, as shown in Fig. 3, which might be caused by the relative vibration between the specimen and the instrument. It is easy to find that the dynamic results behaved more discretely than the quasi-static ones and the stress reduced to zero immediately after the brittle failure. From the Fig. 4, the tensile strength, peak strain, toughness that is defined as the area underneath the stress–strain curves, and elastic modulus can be achieved. The tensile strength was increased by 32.8% from 708.0 ± 32.6 MPa to 940.5 ± 91.7 MPa with the increase of the strain rate from 1/600 to 160s-1. In contrast, the peak strain and toughness were decreased from $13.00 \pm 0.12\%$ to $9.11 \pm 1.06\%$ and from 57.1 ± 4.6 MPa to 46.7 ± 9.6 MPa, respectively, with the corresponding drop of 29.9% and 18.2%. The initial elastic modulus E_1 (i.e., the slope of first part of the stress-strain curve) remained unchanged at the low strain rate (less than 40s-1) but grew up by 61.7% with the strain rate increase from 40 s-1 to 160 s-1. The second-stage elastic modulus E_2 , i.e., the slope of the second part of the stress-strain curve, increased consistently by 85.3% when the strain rate rose from 1/600s-1 to 160s-1.

Weibull analysis

Weibull distribution is a series model based on the theory of the weak ring and relatively a perfect model to describe the distribution of the tensile strength for specimens at different strain rates.

The function of two-parameter Weibull distribution is seen as Eq. (1):

$$F(\sigma) = 1 - \exp\left\{-\left(\frac{\sigma}{\sigma_0}\right)^m\right\} \quad (1)$$



where σ stands for the tensile strength; σ_0 and m are scale and shape parameter, respectively. The expression of cumulative probability density is shown below:

$$F = \frac{i}{N+1} \quad (2)$$

where i is the serial number of current test data. N is the total number of data.

Eq. (3) is thus obtained by substituting Eq. (2) into Eq. (1). Taking double natural logarithm on both sides:

$$Y_i = mX_i - m \ln \sigma_0 \quad (3)$$

where

$$X_i = \ln \sigma \quad (4)$$

$$Y_i = \ln \left\{ -\ln \left(1 - \frac{i}{N+1} \right) \right\} \quad (5)$$

It is easy to find that the correlation coefficient of the regression line is close to 1 so that the Weibull distribution is conformed. The scale and shape parameter can be determined from the slope and intercept of fitting lines. Graphs of the cumulative failure probability versus the tensile strength at different strain rates are shown in Fig. 5 where it is seen that the curve shifts gradually to the high stress region as the strain rate increases. From the 1/600 to the 40 s⁻¹, the shift between two curves is most obvious, implying a conspicuous strain rate effect. In general, the curves are more concentrated on the tensile strength from 800 MPa to 950 MPa, which is considered to be a less sensitive range of strain rate for tensile strength.

Conclusions

In this paper, the tensile mechanical properties of PET single fiber bundle at different strain rates were systematically studied. At room temperature, the tensile strength has a positive correlation with strain rate. However, the ultimate rupture strain and toughness decrease with the increase of the strain rate. The Weibull distribution can somewhat reflect the dispersion of tensile strength at different strain rates.

REFERENCES

- Teng J G, Lam L. Behavior and modeling of fiber reinforced polymer-confined concrete. *Journal of Structural Engineering*, 2004, 130(11): 1713-1723.
- Zhu D, Mobasher B, Erni J, et al. Strain rate and gage length effects on tensile behavior of Kevlar 49 single bundle. *Composites Part A: Applied Science and Manufacturing*, 2012, 43(11): 2021-2029.
- Ou Y, Zhu D, Zhang H, et al. Mechanical characterization of the tensile properties of glass fiber and its reinforced polymer (GFRP) composite under varying strain rates and temperatures. *Polymers*, 2016, 8(5): 196.
- Bai Y L, Dai J G, Ozbakkaloglu T. Cyclic stress-strain model incorporating buckling effect for steel reinforcing bars embedded in FRP-confined concrete. *Composite Structures*, 2017, 182: 54-66.
- Bai Y L, Dai J G, Teng J G. Buckling of steel reinforcing bars in FRP-confined RC columns: An experimental study. *Construction and Building Materials*, 2017, 140: 403-415.
- Bai Y L, Dai J G, Teng J G. Monotonic stress-strain behavior of steel rebars embedded in FRP-confined concrete including buckling. *Journal of Composites for Construction*, 2017, 21(5): 04017043.



INTERFACIAL ADHESION STUDY ON EPOXY PREPREG MODIFIED WITH HIGH POLYCARBONATE) LOADING

Utai Meekum* and Waree Wangkheeree

“Institute of Design Technology, Suranaree University of Technology, Maung, Nakorn Ratchasima, THAILAND

**Corresponding author: umsut@g.sut.ac.th*

ABSTRACT

The interfacial adhesion strength of the in-house prepreg epoxy formulation modified with poly(carbonate)(PC), 50% by mole epoxidized natural rubber(ENR50) and multiwall carbon nanotube(MWCNT) were studied. In the modification of prepreg epoxy matrix formulation with PC at 0 – 80 phr, the interfacial shear strengths showed the tendency to be decreased with increasing the PC loading. The added PC had caused the low surface energy, the constrain in resin infusion/impregnation into fiber due to absolute high viscosity, crack tip sensitive of added PC and inferior in chemical inter locking due to the low network density; retarded by the transesterification and/or cyclization. Those hypothesizes were the main justification for the interfacial strength inferiority. Attempting to enhance the interfacial adhesion by mixing the ENR50 into 30 phr PC modified prepreg epoxy matrix was also found ineffective. The adhesion strength was obviously decreased with increasing the ENR50 loading. The similar hypothesizes with the additional of the rubber phase separation phenomenon were taken for explanation. The interfacial adhesion strength enhancement was achieved by modification the prepreg epoxy formulations by adding MWCNT nanofiller at the concentration not exceed 0.3 phr. The agglomeration of the nanofiller was observed at the critical loading at 0.5 phr. It was suspected for the fiber/matrix adhesion ineffectiveness.

KEYWORDS:

Interfacial shear strength, Prepreg epoxy, Poly(carbonate), Epoxidized rubber and Carbon nanotube.

INTRODUCTION

Carbon fiber reinforced polymer CFRP has been increasingly used in high performance applications such as aerospace, military, automotive and sport industries. One of the major drawback of the epoxy resin is brittle material. Therefore, without scarifying the interfacial adhesion, the toughening of epoxy resin is an important issue for such applications. The modification of epoxy resins to improve the fracture toughness of epoxy resin matrix have been attempted by many methods. Typically, rubbers and engineering thermoplastics toughening have been taken to increasing the fracture toughness of epoxy resin. Elastomer-modified epoxy (EME)/polycarbonate(PC) (EME/PC) binary system and an EME/diglycidyl ether of bisphenol A (DGEBA)/PC (EME/DGEBA/PC) ternary system were examined (Ohsako, Nagura, and Nozue 1993). In the rubber toughening process, Both the Young's modulus and tensile strength of the silicone rubber particle/epoxy resin blends decreased as the volume fraction of the silicone rubber particles was increased. The decreasing became greater at low temperature(Miwa et al. 1995). With the immersing of nanocomposite technology, nanofillers mainly on carbon nanotube(CNT) and graphene, have been considered as ideal reinforcement to improve the mechanical properties of epoxy matrix in CFRP works. In the study on CFRP consisted of traditional carbon fibers and epoxy matrix modified using cup-stacked carbon nanotubes (CSCNTs) in comparison to those CFRP without CSCNTs found that improvement of stiffness and strength and no adverse effects on mechanical properties due to CSCNT dispersion were experimentally verified (Yokozeki et al., 2007).

Interfacial adhesion between fiber and epoxy matrix is a major contribution to the overall mechanical performance of the CFRP. Combination of outstanding adhesive matrix and surface treatment are the main consideration. The effect of processing temperature on interfacial behavior of the carbon fiber composites with epoxy and Bismaleimide (BMI) matrix was studied (Gao et al., 2015). The interfacial interactions of epoxy/CNT nanocomposites by using a molecular modelling approach was conducted. The length of the model CNTs used had a strong influence on the calculated interfacial shear strength. Meanwhile, the influence of the radius and chirality had minor effect (Coto et al., 2013). The experimental studied on mechanical properties and interfacial durability of conventional bisphenol A type epoxy filled with CNT were reported. Mechanical and interfacial



properties of the CNT/epoxy matrix superior to those of the neat epoxy adhesive, especially water resistance (Shin et al., 2017).

In this publication, the interfacial adhesion of the prepreg epoxy modified with high loading of PC, epoxidized rubber and MWCNT nanofiller were explored. The adhesion shear tests were conducted on both autoclaving cured CFRP and GFRP specimen.

EXPERIMENTAL

Materials

The materials used for manufacturing the prepreg epoxy matrix and the CFRP and GFRP samples were classified into three categories; i) epoxy resin system, ii) additive/filler and iii) reinforcements. The commercially available DGEBA based epoxy namely YD127 and YD515, novolac type YDPN631 and aliphatic type reactive diluent RD108 were employed. They were supplied from Aditya Birla Chemicals (Thailand) Ltd. Amine curing agent was comprised of isophorone diamine (IPDA), supplied from BASF (Thailand) Ltd. Triethylenetetramine (TETA), diamio diphenyl sulphone (DDS) and dicyandiamide (DICY) are available from Vantico Co. Ltd. (Thailand). The additive/filler were polycarbonate (PC), Iupillon H-4000, available from Thai Polycarbonate Co. Ltd. (Thailand), 50% by mole epoxidized natural rubber, ENR50, available from SAN THAP International Co. Ltd. (Thailand). Epoxy silane, Silquest®A187, as coupling agent was purchased from Optimal Tech Co. Ltd. (Thailand). The multiwall carbon nanotube (MWCNT) with fiber length of 20 - 50 nm was purchased from Nanogeneration Co., Ltd. (Thailand). The woven fiber reinforcement both glass fiber (GF) and carbon fiber (CF) with the aerial density of 100 g/m² and 160 g/m², respectively, were kindly supplied from Cobra International Co., Ltd. (Thailand). Methyl ethyl ketone (MEK) as typical diluent solvent for the prepreg epoxy formulation was available from Finechem Pty Ltd. (Thailand). The dichloromethane (CH₂Cl₂) purchased from Italmar Co. Ltd. (Thailand) was used as solvent.

Table 1 summarizes the epoxy resin formulation used in this study. Epoxy resin was prepared by mixing the commercial epoxy resins at the assigned weight ratio. In this work, the in house resin formulation was modified with PC, ENR50 and MWCNT, respectively. For the detail preparation was available elsewhere (Meekum and Wangkheeree, 2017).

Table 1. Basic epoxy formulation used for modification

Base Epoxy Resin		Hardener		PC (phr)	ENR50 (phr)	MWCNT (phr)
Ingredients:	(g)	Ingredients:	(g)			
YD 127	48.8	TETA	7.7	Varied	Varied	Varied
YD 515	48.8	RD 108	14.6			
YDPN 631	2.4	IPDA	0.8			
		DDS	0.8			
		BPA	0.4			
		DICY	3.1			
100 g		27.4 g (= phr)				

Test specimen preparation

For each of epoxy resin formulations studied, the GFRP or CFRP prepreg sheet were manufactured by hand lay-up process. The matrix weight fraction in the prepreg was carefully controlled at approx. 40%. Due to the high viscous resin/hardener mixture, the epoxy prepreg was diluted with 30% wt. of MEK solvent. The MEK was removed by evacuating in vacuum oven at 30°C for 15 mins. Then, 2 or 3 layers, depending on the sample requirement, of the prepreg were stacked on the resin releasing cloth. They were cured by autoclaving process at 150°C and at approx. 5.0 bars of consolidate pressure for 1 hour. The tensile and flexural test specimen were obtained by saw cutting and finally post curing at 110°C for 3 hours. The tensile test specimen was tabbed with 3 layers of GFRP.

For the interfacial adhesion test specimen in double lap shear adhesive joints under tension load method, the Type A specimen was employed and prepared, see Fig. 1(a). The middle piece of the test sample was laminated from 3 layers prepreg with the dimension of 65 mm width and 50 mm length. The adherend pieces were made from 2

layers with the same dimension as the middle piece. Similarly, the single lap test sample, see Fig 1(b), was also prepared by using the 2 layers prepreg. The overlap length was approx. 10 mm.

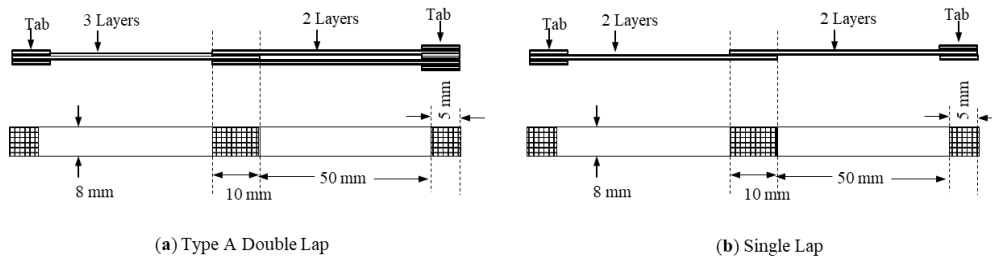


Fig. 1. Form and dimension of (a) double lap and (b) single lap specimen for interfacial adhesion testing.

Standard testing

The mechanical measurement by mean of three point bending flexural and tensile testing were performed in accordance with ASTM D790-10 and ASTM D638, respectively. The universal testing machine (Instron Model 5565, USA) with load cell of 5 kN was employed. The flexural span length at 50 mm and crosshead speed of 15 mm/min were assigned.

In the interfacial adhesion testing, both double and single lap shear adhesive joint by tension loading methods were conducted in accordance with ASTM D1002-10 and ASTM D3528-96, respectively. The Type A sample was employed for the double lap testing. The overlap length for both double and single lap testing was approx. 10 mm. The dimension of both test specimens are indicated in Fig. 1. The adhered surface of CFRP from the interfacial adhesion testing after fail was visually observed by scanning electron microscope (SEM).

RESULTS AND DISCUSSION

Prepreg epoxy formulation modified with PC

Fig. 2 shows the SEM photographs of the woven CF, woven GF, CF filament and GF filament, used in this research work, respectively. It is seen that both CF and GF woven from of the reinforcement fabrics are made from the filament having the diameter approx. at 7-8 and 10-12 μm , respectively. The surface of CF filament is obviously rough. Meanwhile, GF filament shows very smooth surface. Both reinforcement fabrics used in this study was employed without further surface treatment.



Fig. 2. SEM photographs of (a) woven CF, (b) woven GF, (c) Carbon Fiber and (d) Glass Fiber, respectively.

The “double lap” shear adhesive joint testing result derived from both CFRP and GFRP specimen using prepreg epoxy formulation modified with PC at 0 to 80 phr contents are summarized in Table 2. For the interfacial strength data recorded by the “greater than (>)” symbol, it means that there was no broken at “glue line” during the tension testing. Instead, the 2 layers adherend pieces was failed. It was assumed that the adhesion strength at glue line was stronger than the strength of the 2 layers GFRP/CFRP adherend. Therefore, the Loadmax, kN, used for calculating the interfacial shear strength of the epoxy matrix was taken from the load at break of the adherend piece. Then, the symbol of “>” is used to represent the result. Within the standard deviation of testing error, the interfacial shear strengths of epoxy matrix modified with PC shown in Table 2 reveal that they have the tendency to be decreased with increasing the PC loading for both tested on GFRP and CFRP samples. The outcome could be preliminary explained by the surface energy of the modified epoxy matrix. Typically, the surface energy of epoxy and PC is 46.2 and 34.2 mJ/m^2 , respectively (Comyn 1992). Therefore by blending the PC onto epoxy resin, the low surface energy of epoxy/PC matrix would be obtained. Consequently, the resulted shear adhesion strength should be decreased with increasing the PC loading. Not only the surface properties changes but the viscosity



climbing would also be worth to rationalize. By increasing the PC loading in the prepreg epoxy formulation, the viscosity of the resin is dramatically increased. The significant portion of diluent solvent was required in the hand lamination process. It was found that the prepreg was very sticky and excellent for stacking process when PC addition is increased from 0 to 30 phr. At the content beyond 30 phr, upon vacuum drying to remove the diluent solvent, it was found that the prepreg resin became less sticky and turned into soft rubbery “thermoplastic behavior”. At 80 phr of PC, brushing the surface of the prepreg with CH₂Cl₂ during laminate construction was needed. Otherwise, there would be difficult to have the good adhere prepreg laminate for the autoclave curing. With the high viscosity constrain, the resin infusion/impregnation into fiber, especially at the glue line, would be retarded. Consequently, the interfacial shear adhesion would be poor at high PC contents. However in the aspect of lamination process, PC contents up to 30 phr are the most favor formulations because the prepreg sheet derived from such resins are very sticky and easy to use for working with the laminate construction.

Fig. 3(a) to 3(d) show the SEM evidences of the glue line of the CFRP surface obtained from the double lap shear adhesive joints test. At ×5000 magnification, the surface traces due to the CF filament pull-out/delamination are clearly visualized. By using the epoxy prepreg formulation modified by PC at the contents of 10, 30 and 80 phr, they are clearly seen that the CF filament adhere surface become smoother with increasing the PC loading. It suggests lower adhesion strength at higher PC fraction. The SEM evidences are in good agreement and can be used to justify with the interfacial adhesion strength results found above. By closer observation at the matrix cracked phase that lined within the filaments, it is also clearly seen that the rougher crack propagation traces are found at low PC content. On the other hand, smoother cracks are observed at 80 phr PC. It would indicate that the matrix phase become more brittle under shear stress failure at high PC loading. It is well known that PC is one of the very crack tip sensitivity materials. Under the shear adhesive joints testing, the micro crack tips would be instantly generated when the filament is pull-out/delaminated from the matrix. Then, the crack growth propagation would be instantaneously started and failed the matrix phase. According to this phenomenon, low interfacial adhesion strength would be received at high PC loading.

To observe phase morphology of the epoxy prepreg modified with PC by using the SEM examination, the solvent, CH₂Cl₂, etching was performed on the 30 phr PC sample. Fig. 3(b) and 3(d) are glue line surfaces of none-etched and etched surfaces, respectively. On the none-etched surface, no phase separation is observed by SEM analysis. After etching the surface with good solvent, most of the matrix phase is washed away. It is the indication of thermoplastic characteristic. The existing of PC and incomplete crosslink epoxy chains are the most likely suspects. Consequently, it would suggest that the transesterification/cyclization of carbonate groups on PC chain become dominate during the curing reaction of the prepreg epoxy modified with PC at high loading (Li et al. 1996, Li et al. 1997, Li et al. 1997). This phenomenon would inhibit the crosslinking reaction of the epoxy resin. Hence, semi-IPN structure would be formed (Rong and Zeng, 1997). With low crosslink density, the chemical/physical inter locking to the fiber by the network chain would be diminished. Accordingly, the interfacial adhesion strength would be inferior at high PC loading.

Last, but not least, to mention from this study results, the epoxy/fiber surface adhesion strength on CF is always greater than on the GF filament.

Table 2. Summarize the “double lap” interfacial shear strength tested on GFRP and CFRP produced from the epoxy matrix modified with PC.

Sample	PC(phr)	Load _{max} (kN)	Interfacial Shear Strength(MPa)
GFRP	0	1.32±0.18	>7.129±1.116
	10	1.03±0.13	5.995±0.605
	20	1.18±0.28	>4.921.78±1.515
	30	1.32±0.10	>5.010±0.431
	40	1.64±0.29	7.116±0.319
	50	1.14±0.12	5.649±0.545
	80	1.13±0.05	4.070±0.200
CFRP	0	2.72±0.39	>13.094±1.335
	10	2.45±0.16	12.321±0.905
	20	1.80±0.36	9.641±1.307

30	0.70±0.15	3.296±0.717
40	2.07±0.32	9.298±1.420
50	0.79±0.09	3.469±0.386
80	1.91±0.16	6.881±0.656

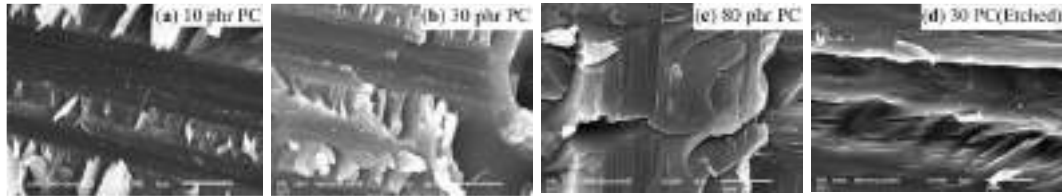


Fig.3. SEM photographs of the glue line at the CFRP adherend

To evaluate the mechanical performance of the GFRP and CFRP manufactured from the prepreg epoxy formulation modified with PC, the tensile and flexural testing were performed on the 2 and 3 layers laminate structures, respectively. The test samples were prepared from the woven fabrics prepreg and cured in autoclaving at the identical conditions applied for the lap joint shear test samples. Test results are summarized in Table 3. The tensile strength and modulus, for both GFRP and CFRP, have the tendency to be marginally decreased with increasing the PC content. Except for at 40 phr PC where the strength and modulus are doubtedly advanced. For the strain at break, it is shown more or less independency to the PC usage. Generally, GFRP has greater strain at break than CFRP. The decreasing in the strength and modulus with increasing the PC content could be explained by low crosslink density of the matrix phase. As mentioned above, at high PC loading, the crosslink reaction is retarded by the transesterification/cyclization of the carbonate group on PC chain. Hence, the “incompletely cured behavior” of epoxy resin would be occurred. Accordingly, the tensile properties of the epoxy matrix become poor. Since the composite structure obey the rule of mixture, at the identical fiber and matrix volume fraction, inferior in the tensile properties of matrix must contribute the negative effect to the final tensile performance of the composite. Also, the tensile performance would further deteriorate with low fiber/matrix interfacial adhesion. For the strain at break, it is mainly controlled by the properties of fiber. Undoubtedly, GF has greater strain at break than CF.

Table 3. Summarize the tensile and flexural properties of GFRP and CFRP produced from PC modified epoxy matrix

Sample	PC (phr)	Tensile Properties				Flexural Properties		
		Strength (MPa)	Stress at break (MPa)	Strain at break (%)	Modulus (GPa)	Strength (MPa)	Modulus (GPa)	Max. Def (mm)
GFRP	0	284.61±27.47	284.61±27.47	4.52±0.46	8.34±0.16	240.55±32.76	7.81±0.93	7.29±0.33
	10	250.28±19.60	250.22±19.67	5.50±0.29	5.97±0.20	174.39±2.33	3.37±1.04	4.62±0.13
	20	249.50±15.68	249.04±16.47	4.04±0.22	8.82±0.38	276.22±15.26	9.87±3.07	9.00±0.35
	30	264.12±16.71	264.12±16.71	4.43±0.32	7.59±0.22	237.96±9.90	11.28±3.53	8.88±0.43
	40	340.34±23.16	340.02±22.78	5.11±0.16	8.89±0.37	228.32±17.44	12.15±1.13	8.97±0.22
	50	224.76±31.57	224.33±32.17	4.59±0.34	6.31±0.91	189.09±6.68	6.65±0.79	5.72±0.47
	80	319.46±9.19	262.34±85.58	5.03±0.48	8.44±0.24	209.79±17.20	7.22±5.75	5.50±0.61
	CFRP	0	321.04±2.13	321.04±2.13	3.22±0.34	13.75±0.46	610.36±28.65	38.38±1.13
10		260.73±2.11	260.73±2.11	2.80±0.03	11.52±0.08	252.95±21.29	29.88±2.37	2.22±0.23
20		257.34±37.74	249.39±48.31	2.86±0.23	11.71±0.59	201.02±14.31	27.04±2.59	2.08±0.29
30		293.37±39.00	293.37±39.00	3.15±0.28	11.23±1.02	182.50±7.37	27.23±0.64	1.87±0.132
40		293.03±30.67	293.03±30.67	3.29±0.45	11.10±0.57	231.11±10.66	32.91±0.62	2.12±0.31
50		231.41±16.74	207.09±47.98	2.81±0.18	10.24±0.34	147.40±4.40	22.86±2.31	2.08±0.12
80		292.82±21.10	283.46±26.99	3.39±0.21	11.78±0.72	345.23±18.61	33.06±0.48	2.87±0.13

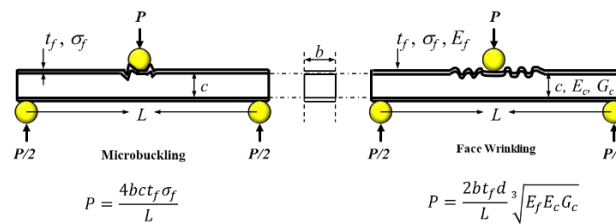


Fig. 4. Proposed failure modes of GFRP/CFRP under three-point bending flexural testing

Unlike the tensile testing, flexural properties under the three point bending load of the 3 layer GFRP and CFRP samples are quite obviously decreased with increasing the PC loading. At the given 3 layers laminate structure test specimen employed this study, it is presumably as the sandwich beam having the identical faces and core thickness. With the sandwich structure having high stiffness core, the failure mode would be either “microbuckling” or “face wrinkling” as shown in Fig. 4 (Craig et al. 2004). Considering the GFRP or CFRP as rigid and brittle faces, the “microbuckling” failure mode is the most favored during the flexural bending test. With the identical sample geometry, the required bending force to fail the sandwich beam specimen depends largely on the compressive strength (σ_f) of the face. This parameter is also directly related to the interfacial adhesive shear strength. Therefore, higher interfacial adhesion shear strength results in greater flexural strength or vice versa.

Prepreg epoxy formulation modified with PC and ENR50

According to the above results, the interfacial shear strength was found to be weakened at high PC loading. However, with the composite manufacturing aspect, it was found that the sticky prepreg was obtained with PC loading up to 30 phr. For the sake of mechanical and processing needs in the composite industries, the epoxy prepreg formulation having the PC loading at 30 phr was considered as the most suitable formulation for further investigation to enhance the interfacial adhesion strength. Addition of 50% by mole epoxidized natural rubber (ENR50) into the epoxy prepreg having 30 phr PC was explored. The prepreg epoxy modified with ENR50 at 0 to 20 phr were prepared by Soxhlet dissolving process. The “single lap” specimen was prepared by autoclaving process and the adhesive joint shear test was performed. The test results are reported in Table 4. The decreasing in the interfacial adhesive shear strength with increasing the ENR50 loading is clearly evidenced for both types of samples, GFRP and CFRP. By adopting the SEM technique to observe the adhesion scenes at CF filament and the matrix glue line, the photos at $\times 1500$ are shown in Fig. 5(a) to 5(d). SEM images reveal that the matrix surface after fiber pull-out/delamination is relatively rough for the prepreg epoxy without ENR50. By increasing the ENR50 to 5 and 20 phr, the smoother surface was observed. Moreover, at 20 phr, the gap between CF filament and the matrix is clearly visualized. Even more, the matrix break-off was also evidence at 20 phr ENR50 loading. The smooth surface due to fiber pull-out/delamination and also the space between fiber and matrix are the indicators for poor adhesion between fiber/matrix/fiber. Consequently, low interfacial adhesive shear strength is resulted under tension shear testing. With the closer observation, in particular at 20 phr ENR50, the rubber phase separation from the epoxy matrix phase is evidenced. This is one of the main causes for weak interfacial adhesion (Tan et al., 2013). Another point worth to be raised is that by increasing the ENR50 concentration in the prepreg epoxy formulation, the surface energy of the rubber modified epoxy resin is lower than the formula without rubber modification (Comyn 1992). As the result, weak fiber/matrix adhesion strength should be obtained. Furthermore, as stated above, the crosslinking reaction of epoxy would be retarded by adding both PC and ENR50. The statement is reinforced by the SEM photo shown in Fig. 5(d). It is the solvent etched surface of the adherend CFRP produced using the prepreg epoxy modified with 30 phr PC and 20 phr ENR50. The trace of CF filament pull-out is become wilder, greater than 10 μm , after undergoing solvent etching. It was caused by the matrix phase dissolving during the etching process. Solvent dissolvable is the common characteristic of non-crosslink chain structure. With this SEM evidence, it means that added ENR50/PC and the existed non-crosslink epoxy chain were dissolved by the etching solvent. With low crosslink density of epoxy matrix, the chemical/physical interlocking arising from the network chain structure would be diminished. With those hypotheses explained; (i) epoxy/ENR50 phase separation, (ii) low surface energy of the prepreg epoxy modified with PC/ENR50 and (iii) low crosslink density due to crosslinking reaction retardation, the inferiority in the interfacial adhesive shear strength of the epoxy prepreg with increasing the ENR50 dosing would be justified. Again, it is worth to mention that, by using the epoxy prepreg

modified with 30 phr PC and ENR50 for manufacturing the fiber reinforced composites, the epoxy/fiber surface adhesion on CF is typically superior to GF.

Table 4. Summarize the “single lap” interfacial adhesion shear strength tested on GFRP and CFRP manufactured from epoxy prepreg matrix modified with PC/ENR50

Sample	PC(phr)	ENR50(phr)	Load _{max} (kN)	Interfacial Shear Strength(MPa)
GFRP	30	0	1.24±0.10	4.135±0.337
		5	0.37±0.14	1.109±0.409
		10	0.51±0.05	0.515±0.054
		15	0.47±0.04	0.470±0.038
		20	0.43±0.04	0.430±0.036
CFRP	30	0	1.52±0.27	5.203±0.787
		5	0.78±0.11	2.842±0.417
		10	0.81±0.17	2.646±0.557
		15	0.58±0.08	2.045±0.311
		20	0.65±0.14	2.225±0.453

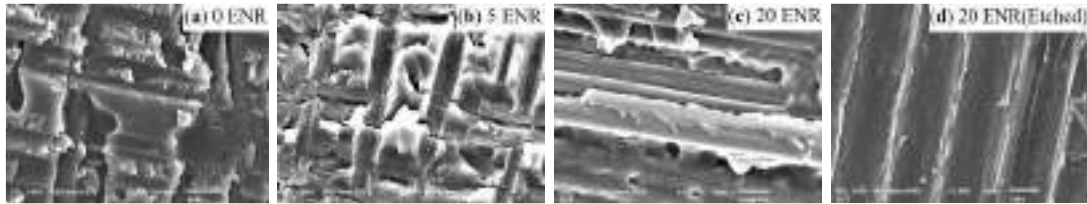


Fig. 5. SEM photographs of CFRP surface at the glue line manufactured from the prepreg epoxy formulation modified with 30 phr PC and ENR50

To evaluate the tensile performance of prepreg epoxy contained 30 phr PC and ENR50, the 2 layers laminate GFRP and CFRP specimen were manufactured by autoclaving process. The tensile properties results are reported in Table 5. On both type of woven fibers, it is noticed that the strength and stress at break of the composites show the decline trend with increasing the rubber content. However, the modulus are almost constant regardless with the rubber loading. The modulus of the composite made from the resin without ENR50 addition is clearly lower than the ones obtained from the ERN50 modified resins. In case of the strain at break, it is noticed that the fiber reinforced composites made from the prepreg epoxy matrix modified with ENR50 are lower than the samples prepared with the resin without rubber addition. Typically, with good fiber/matrix interfacial adhesion, the tensile properties of the fiber reinforced composite is obeyed the rule of mixture; volume fractions(v_i) and modulus of fiber and matrix(E_i). In this study, volume fractions between fiber and matrix of the test samples were identically controlled for every samples. Therefore, the final tensile properties of the composite sample is mainly regulated by the performance of the matrix and the interfacial adhesion between matrix and fiber. With increasing the ENR50 loading from 0 to 20 phr, the rubber phase separation was experienced. Hence, lower in tensile properties of the matrix shall be obtained. Also, from the above interfacial adhesion results, they were reduced at higher ENR50 content. Accordingly, the tensile properties of the GFRP and CFRP manufactured from the prepreg epoxy resin modified with 30 phr PC and ENR50 must be deprived by increasing the epoxidized rubber contents. With inadequate fiber/matrix interfacial adhesion, the tensile strain at break and modulus of the composite sample is mainly regulated by the fiber.

According to the performance outcome found in this study, the prepreg epoxy formation without addition of ENR50 is recommended for the mechanically advantage of the GFRP and CFRP products.

Table 5. Summarize the tensile properties of GFRP and CFRP manufactured from PC/ENR50 modified epoxy matrix

Sample	PC(phr)	ENR50(phr)	Tensile Properties			
			Strength(MPa)	Stress at break(MPa)	Strain at break(%)	Modulus(GPa)
GFRP	30	0	306.14±25.98	306.14±25.98	5.20±0.30	6.44±0.03
		5	281.82±23.34	281.82±23.34	3.70±0.33	9.26±0.25
		10	285.48±6.90	285.48±6.90	4.04±0.25	8.69±0.26



		15	260.85±21.57	260.85±21.57	3.80±0.48	8.45±0.22
		20	285.97±16.75	285.97±16.75	4.35±0.38	8.22±0.63
		0	347.67±36.26	346.46±35.88	3.30±0.46	12.35±0.77
		5	357.86±19.34	357.86±19.34	2.46±0.36	16.70±1.11
CFRP	30	10	248.47±31.52	243.41±28.40	2.09±0.26	16.63±1.03
		15	301.73±19.44	298.08±24.67	2.37±0.17	15.57±0.64
		20	307.32±8.71	306.81±9.43	2.48±0.45	16.88±1.79

Epoxy formulation modified with PC and MWCNT

Conferring to the above discussions, prepreg epoxy resin without PC and ENR50 addition showed the remarkable adhesive strength with GF and CF woven. It also demonstrated the mechanical advantages when employing as the matrix for manufacturing GFRP and CFRP product, respective. However, for the laminate processing aspect, both GF and CF prepregs sheet produced from epoxy formulations loaded with 5 – 30 phr PC demonstrates very good sticky surface touch. This prepreg characteristic is one of the most preferences in composite industries. Therefore, both prepreg epoxy formulations; without and with 30 phr PC, were chosen for further interfacial adhesion enhancement study by adding the multiwall carbon nanotube (MWCNT) filler. The nanofiller loading from 0 to 0.5 phr with respect to the based epoxy ingredient were explored. The GFRP and CFRP “single lap” joint interfacial adhesion shear test samples were prepare by autoclaving process. The adhesion shear strength results are measured and reported in Table 6. On GFRP/CFRP samples using the epoxy resin matrix without PC addition, the interfacial adhesion shear strengths are generally improved when 0.1 to 0.3 phr of MWCNT were added. Exceeding the MWCNT loading above 0.3 phr, the down trend in the adhesion strength is observed. On the 30 phr PC modified epoxy prepreg formulation, the identical trend to those without PC addition is noticed, especially the results tested on the CF surface. In comparison between the prepreg formulation without and with 30 phr PC addition, it is no doubt that, at the same MWCNT loading, the epoxy matrix without PC addition has superb interfacial adhesion shear strength to the matrix modified with 30 phr PC. Moreover, at the given epoxy prepreg formulation and given MWCNT content, it is clearly demonstrated that interfacial surface adhesion on CF is much more superior to the GF. The increasing in the interfacial adhesion shear strength of the prepreg epoxy resin with addition of MWCNT from 0.1 to 0.3 phr could be rationalized through the surface energy enhancement by adding the nanofiller. At very low fraction and with good dispersion of the carbon nanotube filler in the epoxy matrix, the excellent surface adhesion by mean of electrical and/or physical interlocking due to the enhancement of the surface energy must be achieved. Consequently, the interfacial adhesion shear strength must also enhanced. Therefore, the mechanical properties of the fiber reinforced composite manufactured from the MWCNT filled prepreg epoxy must be superior (Nam et al., 2016). Exceeding the critical concentration, the agglomeration of the nanofiller is typically experienced. Hence, the effectiveness of the surface properties enhancement by the added nanofiller would normally be diminished. Accordingly, the interfacial adhesion strength would be declined at above critical concentration. Regarding to the results found in this work, as demonstrated in Table 6, the down trend of the interfacial strength was observed at 0.5 phr MWCNT loading. So, with the result observed it could justify that the agglomeration effect of MWCNT in the prepreg epoxy formulation is occurred when the nanofiller loading exceed 0.5 phr. Further SEM evidence to reinforce this statement will be provided later on.

Table 6. Summarize the “single lap” interfacial adhesion shear strength tested on GFRP and CFRP manufactured from PC/MWCNT modified epoxy matrix

Sample	PC(phr)	MWCNT(phr)	Load _{max} (kN)	Interfacial Shear Strength(MPa)
GFRP	0	0	1.49±0.20	>6.090±0.761
		0.1	1.52±0.08	>6.400±0.327
		0.3	1.65±0.13	>7.610±0.711
		0.5	1.34±0.17	>5.041±0.641
	30	0	1.17±0.09	>5.558±0.376
		0.1	0.82±0.04	4.081±0.219
		0.3	0.85±0.13	4.047±0.595
		0.5	0.73±0.09	3.132±0.416
CFRP	0	0	2.44±0.32	>12.307±1.704
		0.1	2.07±0.50	>9.502±2.197
		0.3	2.64±0.32	>11.104±2.023



	0.5	2.64±0.37	>10.370±1.485
	0	1.35±0.16	6.616±0.765
	0.1	1.71±0.25	7.547±0.962
30	0.3	1.80±0.14	7.861±0.584
	0.5	1.84±0.28	7.234±1.011

Fig. 6(a) and (b) are non-etched and solvent etched SEM photographs of CFRP adherend surfaces at the glue line, respectively. The photos were taken at $\times 50$ magnification. They are made from prepreg epoxy matrix modified with 30 phr PC and without MWCNT addition. It is clearly seen that matrix phase between the CF filaments is dissolved away by the etching solvent. Because the filament peel/pull off traces during the single lap shear test are unmistakably visualized by solvent etching process. The solubility of the matrix is caused by the existing of the soluble PC and also non-crosslinked epoxy chains. As mentioned previously, the crosslink reaction would be retarded by blending PC at high loading into the prepreg epoxy formulation. Hence, the non-crosslinked epoxy chains would be obtained and low network density epoxy matrix would be resulted. This SEM evidence could confirm that the semi-IPN with the thermoplastic characteristic domination matrix could be formed in the cured prepreg epoxy modified with high PC loading (Rong and Zeng, 1997). At $\times 5000$ magnification SEM investigation, Fig. 6(c) to 6(h) reveal the SEM photos of the CFRP adherend surfaces at the glue line. They are made from prepreg epoxy modified with 30 phr PC and 0, 0.3 and 0.5 phr of MWCNT, without and with solvent etching, respectively. On the non-etched surfaces, completely peel/pull off filament traces are observed when 0 and 0.5 phr MWCNT added prepreg epoxy matrix were employed. They are indicated that weak fiber/matrix surface adhesion strength is weaker than the tension force during the adhesion shear testing. Therefore, the fiber filament is pull-out and/or delaminated. On the other hand, with the test sample manufactured from 0.3 phr MWCNT added prepreg epoxy matrix, the broken cured matrix that adhered on the CF filament surface is visualized. It is evidenced that stronger fiber/matrix adhesion than the tension force was constructed. These SEM scenes support the foreseen interfacial adhesion shear strength testing results that the strength was increased with increasing the MWCNT loading up to 0.3 phr. Beyond 0.5 phr loading, the adhesion strength was decreased. MWCNT loading greater than 0.5 phr was assigned as the critical concentration for the agglomeration effect. To justify the presenting of MWCNT agglomeration at high loading, the solvent etching of the CFRP adherend surfaces were performed and examined by SEM technique. The obtained SEM images are shown in Fig. 6(d), 6(f) and 6(h) for the 0, 0.3 and 0.5 phr MWCNT addition, respectively. Without MWCNT addition, cracked and homogenous etched surface is revealed in Fig 6(d). With 0.3 phr loading, Fig. 6(f), the etched surface with cracked traces and the uniform dispersed of ultra tiny particles with the size less than $1 \mu\text{m}$ is evidenced. Finally, on the etched surface of 0.5 phr MWCNT added epoxy matrix, Fig. 6(h), the agglomerated fibril like particle having approx. size of $5 \mu\text{m}$ are presented. From these SEM evidences, the well uniform dispersed and agglomerated particles are suspicious, with highly possibility, as the added MWCNT. With this inclusive SEM evidences, they could point out that the good dispersion of MWCNT in the prepreg epoxy formulation, employed in this study, could be obtained at the concentration not exceed 0.3 phr. At MWCNT loading 0.5 phr and above, the nanofiller agglomeration could be developed. Correspondingly, enhancement in the epoxy/CF adhesion could not be achieved. To obtain good surface property of the prepreg epoxy matrix by adding the MWCNT, concentration less than 0.3 phr would be recommended.

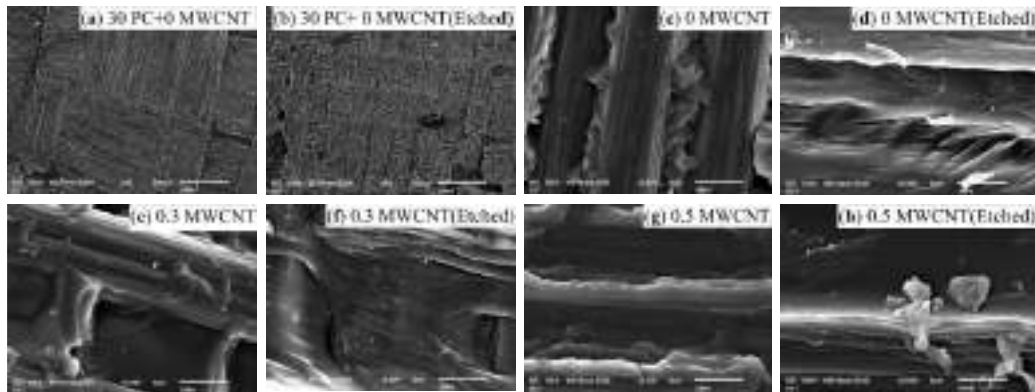


Fig. 6. SEM photographs of CFRP surface at the glue line manufactured from the prepreg epoxy formulation modified with 30 phr PC and MWCNT.

By applying the above MWCNT filled epoxy prepreg formulations for manufacturing the GFRP and CFRP samples, their mechanical performances by mean of tensile and flexural properties are summarized in Table 7. General reviewing, the tensile properties by mean of ultimate strength, stress at break, strain at break and modulus of both GFRP and CFRP samples are in the similar trend to those interfacial adhesion strength results, regardless to the type of prepreg epoxy formulations. They are typically in the upright trend when the MWCNT loading is increased from 0 to 0.3 phr. Then, the reversed trend is observed when the loading reach 0.5 phr. The results also reinforce that adding low concentration of the nanofiller, MWCNT, and with good dispersion with epoxy, it has remarkable effect not only on the interfacial adhesion properties but also on the mechanical properties of the matrix phase. Consequently, the tensile performance is superior by adding the nanofiller (Zhang et al., 2013). In comparison between GFRP and CFRP at the given epoxy formulation and MWCNT content, there is no doubt that CFRP has remarkably superior in the tensile properties to the GFRP. The relationship between flexural performance of the GFRP and CFRP samples with MWCNT are almost in the identical trend to those tensile properties. However, in the flexural properties enhancement by adding the MWCNT, the interfacial shear strength improvement must be the main contribution and also rationalization for explanation. Again, CFRP demonstrates superior in flexural properties to the GFRP sample.

Table 7. Summarize the tensile and flexural properties of GFRP and CFRP manufactured from PC/MWCNT modified epoxy matrix

Sample	PC (phr)	MWCNT (phr)	Layer	Tensile Properties				Flexural Properties		
				Strength (MPa)	Stress at break (MPa)	Strain at break (%)	Modulus (GPa)	Strength (MPa)	Modulus (GPa)	Max. Def. ^a (mm)
GFRP	0	0	2	275.17±11.69	275.17±11.69	4.29±0.25	6.54±0.09	261.10±9.55	85.43±3.82	5.55±0.35
		0.1	2	265.46±19.57	265.46±19.57	4.44±0.13	7.05±0.35	464.95±10.36	118.05±3.72	7.10±0.34
		0.3	2	287.09±26.67	287.09±26.67	4.93±0.28	6.80±0.23	389.36±13.89	86.96±8.23	7.21±0.82
		0.5	2	219.90±27.39	219.90±27.39	3.79±0.25	6.94±0.45	369.48±9.51	93.82±3.96	6.29±0.39
	30	0	2	248.75±22.34	230.69±54.83	4.08±0.23	7.74±0.36	237.96±9.90	16.23±1.88	8.88±0.43
		0.1	2	243.92±36.92	243.92±36.92	3.92±0.47	7.58±0.39	149.30±5.86	41.66±11.84	8.55±0.31
		0.3	2	266.98±43.80	243.92±36.92	4.26±0.56	7.74±0.83	434.95±0.26	112.89±8.09	8.25±0.18
		0.5	2	220.59±27.02	220.59±27.02	3.69±0.42	7.33±0.17	433.78±22.37	94.18±4.73	9.28±0.21
CFRP	0	0	2	309.27±36.07	309.27±36.07	2.84±0.32	13.18±0.21	1015.70±93.53	309.17±23.20	3.63±0.27
		0.1	2	271.57±31.05	271.57±31.05	2.61±0.57	13.06±0.57	673.26±142.00	286.30±43.33	2.56±0.30
		0.3	2	337.01±48.77	271.57±31.05	2.96±0.49	14.61±1.02	978.45±137.01	317.42±19.02	3.44±0.37
		0.5	2	299.87±26.06	299.87±26.06	2.89±0.19	12.66±0.74	951.63±91.00	304.65±11.58	3.67±0.31
	30	0	2	402.79±27.95	402.58±27.76	3.74±0.57	14.77±0.72	821.37±20.58	338.45±15.91	3.42±0.31
		0.1	2	343.15±27.27	343.15±27.27	3.06±0.17	14.92±1.00	907.58±48.49	307.51±1.43	3.08±0.12
		0.3	2	354.40±35.80	354.40±35.80	2.94±0.30	16.56±0.40	1171.40±81.31	389.37±25.52	3.56±0.21
		0.5	2	376.43±6.48	370.80±11.80	3.38±0.36	15.58±0.19	1173.34±19.71	394.29±12.08	3.67±0.12

CONCLUSIONS

By modification the prepreg epoxy matrix formulation with PC, the interfacial shear strengths showed the decreasing trend with increasing the PC loading. Four hypothesizes were gather to explain the interfacial adhesion inferiority with the addition of PC; (i) low surface energy of prepreg epoxy modified with PC, (ii) the resin



infusion/impregnation with fiber was restricted by absolute high viscosity of the epoxy modified PC matrix, (iii) crack tip sensitive of the loaded PC and (iv) diminishing in the chemical/physical network chains interlocking due to the low network density of cured epoxy matrix that was retarded by the transesterification/cyclization reaction. Attempting to enhance the interfacial adhesion by mixing the epoxidized natural rubber, ENR50, into 30 phr PC modified prepreg epoxy matrix was also found ineffective. The adhesion strength was obviously decreased with increasing the ENR50 loading. The similar hypothesizes and also the rubber phase separation phenomenon were taken for explanation. The interfacial adhesion strength enhancement was achieved by adding MWCNT nanofiller into prepreg epoxy formulations at the concentration not greater than 0.3 phr. The agglomeration of the nanofiller was observed at the critical loading which was greater than 0.5 phr.

ACKNOWLEDGMENTS

This work was supported by the Office of Higher Education Commission under the NRU Project of Thailand and patronage under the Institute of Research and Development at Suranaree University of Technology.

REFERENCES

- Comyn, J. (2013). "Contact angles and adhesive bonding." *Int. J. of Adhesion and Adhesives*, 12(3), 145-149.
- Coto, B., Antia, I., Barriga, J., Blanco, M., and Sarasua, J.-R. (2013). "Influence of the geometrical properties of the carbon nanotubes on the interfacial behavior of epoxy/CNT composites: A molecular modelling approach." *Computational Materials Science*, 79, 99-104. doi:10.1016/j.commatsci.2013.05.057
- Craig, A.S. and Norman, A. P. (2004). "Collapse of sandwich beam with composite faces and a foam core, loaded in three-point bending. Part II: Experimental investigation and numerical modelling," *International Journal of Mechanical Sciences* 46, 585-608. DOI: 10.1016/j.ijmecsci.2004.04.004
- Gao, A., Gu, Y., Wu, Q., Yuan, C., Li, M., and Zhang, Z. (2015). "Influence of processing temperature on interfacial behavior of HKT800 carbon fiber with BMI and epoxy matrices." *Chinese Journal of Aeronautics*, 28(4), 1255-1262. doi:10.1016/j.cja.2015.04.003
- Gürkan, İ., and Cebeci, H. (2016). "An approach to identify complex CNT reinforcement effect on the interlaminar shear strength of prepreg composites by Taguchi method." *Composite Structures*, 141, 172-178. doi:10.1016/j.compstruct.2016.01.043
- Horiuchi, S., Street, A. C., Ougizawa, T., and Kitano, T. (1994). "Fracture toughness and morphology study of ternary blends of epoxy, poly(ether sulfone) and acrylonitrile-butadiene rubber." *Polymer*, 35(24), 5283-5292. doi:10.1016/0032-3861(94)90481-2
- Meekum, U., and Wangkheeree, W. (2017). "Designing the Epoxy Adhesive Formulations for Manufacturing Engineered Woods." *BioResources*, 12(2), 3351-3370. doi:10.15376/biores.12.3351-3370
- Miwa, M., Takeno, A., Hara, K., and Watanabe, A. (1995). "Volume fraction and temperature dependence of mechanical properties of silicone rubber particulate/epoxy blends." *Composites*, 26(5), 371-377. doi:10.1016/S0010-4361(06)80136-9
- Nam, T. H., Goto, K., Nakayama, H., Oshima, K., Premalal, V., Shimamura, Y. and Kobayashi, S. (2014). "Effects of stretching on mechanical properties of aligned multi-walled carbon nanotube/epoxy composites." *Composites Part A*, 64, 194-202. doi:10.1016/j.compositesa.2014.05.013
- Ohsako, T., Nagura, K., and Nozue, I. (1993). "Morphologies and tensile properties of elastomer-modified epoxy and polycarbonate blended systems." *Polymer*, 34(24), 5080-5084. doi:10.1016/0032-3861(93)90251-5
- Shin, P.-S., Kwon, D.-J., Kim, J.-H., Lee, S.-I., DeVries, K. L., and Park, J.-M. (2017). "Interfacial properties and water resistance of epoxy and CNT-epoxy adhesives on GFRP composites." *Composites Science and Technology*, 142, 98-106. doi:10.1016/j.compscitech.2017.01.026
- Tan, S. K., Ahmad, S., Chia, C. H., Mamun, A., Heim, H. P. (2013). "A Comparison Study of Liquid Natural Rubber (LNR) and Liquid Epoxidized Natural Rubber (LENR) as the Toughening Agent for Epoxy." *American Journal of Materials Science*, 3(3), 55-61. doi: 10.5923/j.materials.20130303.02
- Yokozeki, T., Iwahori, Y., Ishiwata, S., and Enomoto, K. (2007). "Mechanical properties of CFRP laminates manufactured from unidirectional prepreps using CSCNT-dispersed epoxy." *Composites Part A*, 38(10), 2121-2130. doi:10.1016/j.compositesa.2007.07.002
- Zhang, J., Ju, S., Jiang, D., and Peng, H.-X. (2013). "Reducing dispersity of mechanical properties of carbon fiber/epoxy composites by introducing multi-walled carbon nanotubes." *Composites Part B*, 54, 371-376. doi:10.1016/j.compositesb.2013.05.046



TWO-DIMENSIONAL DELAMINATION IN GFRP LAMINATES : EXPERIMENTAL INVESTIGATION

A. Cameselle-Molares¹, A.P. Vassilopoulos¹, T. Keller¹

¹ Composite Construction Laboratory (CCLab), École Polytechnique Fédérale de Lausanne (EPFL), Bâtiment BP, Station 16, CH-1015 Lausanne, Switzerland

Email: thomas.keller@epfl.ch

ABSTRACT

The 2D delamination behavior of composite laminates under quasi-static out-of-plane opening loading has been experimentally investigated. A new design and experimental set-up for square GFRP/epoxy plates have been developed. A circular embedded pre-crack was introduced in the center and at the midplane of the laminate. To investigate the effect of the fiber architecture on the fracture behavior, three different types of isotropic and orthotropic fabrics were selected. Increasing load-displacement curves were obtained as a result of an increasing crack front length during propagation. During the loading process, stiffening and softening mechanisms were activated. The stretching of the delaminated laminates, in both the radial and circumferential directions, constituted the main stiffening mechanism that appeared and increased as the plate opened. Once the crack started growing, a corresponding softening due to crack propagation occurred together with a secondary stiffening mechanism, fiber-bridging. All these stiffness-related mechanisms were reflected in the compliance.

KEYWORDS

2D delamination; laminates; embedded pre-crack; crack area.

INTRODUCTION

Composite materials such as GFRPs (glass fiber-reinforced polymers) are commonly used for high performance load-bearing structural elements because of their high stiffness- and strength-to-weight ratios and great resistance to environmental impact (e.g. corrosion). The successful use of FRP for primary structural parts depends on its integrity and reliability. Delamination in laminated composites is one of the most common and critical types of damage and due to the significant reduction in the structural load-bearing capacity that it can cause, many investigations have been carried out to characterize the delamination fracture behavior of composite materials. Research efforts and standards (Benzeggagh *et al.*, ASTM D6671/D6671M) have focused on beam-like specimens where the crack propagates with a constant width and thus it is measured only in the longitudinal direction. However, delamination in real structures is not restricted to one direction but spans all around its contour.

The fracture behavior of composite materials is usually characterized by the fracture energy release rate (ERR) and the identification of the critical value beyond which cracks initiate and propagate is of a great importance for the damage-tolerant design of structures. Although delamination may initiate and grow under opening and shear fracture modes (Mode I and Mode II/III respectively) each one of the modes must be investigated independently. In some cases, compressive loads (pure or in bending) can cause laminates with defects or voids to open at these points, being crucial the characterization of the opening fracture behavior. To study the fracture behavior of composites under Mode I, the double cantilever beam is typically employed and the derived fracture values are commonly used for the design of structural elements (Nilsson *et al.*). Nevertheless, many factors affecting the fracture behavior may be missed in such type of experiments, and new fracture experimental designs capable of better approaching reality are needed.

In this paper, the main objective was the experimental investigation of the two-dimensional (2D) delamination behavior in GFRP/epoxy plates and to identify potential differences in the behavior compared to 1D delamination. For that purpose, a novel design and experimental set-up suitable for the investigation of the 2D fracture behavior of laminates with internal circular disbonds, subjected to opening loads, similar to the loads applied in a Mode I DCB specimen, was developed. Similar out-of-plane stresses are likely to appear in real applications such as local face sheet wrinkling in sandwich panels or curved face sheets (also in sandwich panels) with interlaminar defects.

EXPERIMENTAL INVESTIGATION

Material and specimen description

Three different types of glass fiber reinforcements were used to fabricate the laminates: two types of woven fabrics with different proportions of reinforcement in the warp/weft directions (50/50 (W50.50) and 60/40 (W60.40), of 390, 500-g/m² weight respectively); and a long continuous filament mat (CFM) with a weight of 600 g/m² and no binder or stitching. Photos of the different reinforcements are presented in Figure 1. The selected matrix was an epoxy resin (Sika Biresin CR83) intended for infusion techniques.

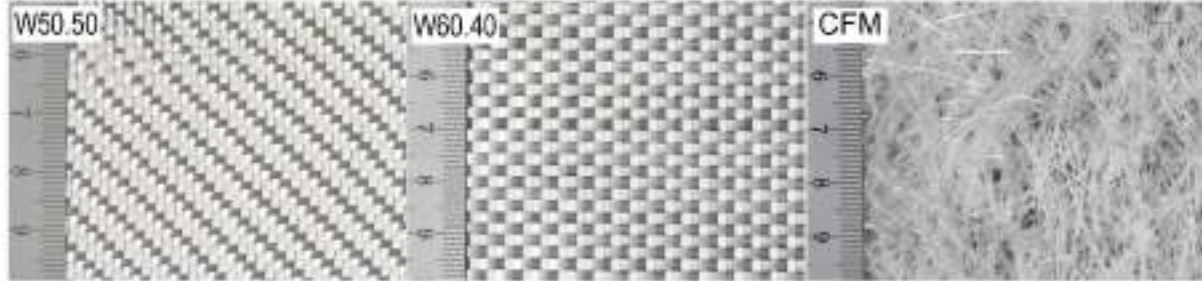


Figure 1: Detail of glass fiber reinforcements used

The experimental program was conducted on six GFRP plates, two for each type of reinforcement. The pairs of plates were labeled accordingly (i.e. W50.50.1/2, W60.40.1/2 and CFM.1/2) and their layup and geometrical description are presented in Table 1.

Table 1: Description of GFRP plates

Plate type	No. of layers	Dimensions (mm, width x height x avg. thickness)
W50.50.1/W50.50.2	8	460x460x3.33/480x480x3.53
W60.40.1/W60.40.2	6	410x410x3.05/410x410x3.06
CFM.1/CFM.2	6	420x420x7.5/420x420x6.99

All the GFRP laminates were symmetric with respect to both the midplane and each of the halves separately. Likewise, they were all fabricated by a vacuum infusion process. The plate configuration is shown in Figure 2. To introduce the load, two stainless steel inserts of 1.2-mm thickness and 100-mm diameter were placed in the center and the midplane of the reinforcements. Between them, a Teflon film of 13- μ m thickness and 180-mm diameter was placed to introduce the pre-crack (see Figure 2). The infusion was performed from side to side of the specimens. The laminates were cured under vacuum for at least 16 hours at room temperature and subsequently, once demolded, they were cured at 70°C for eight hours.

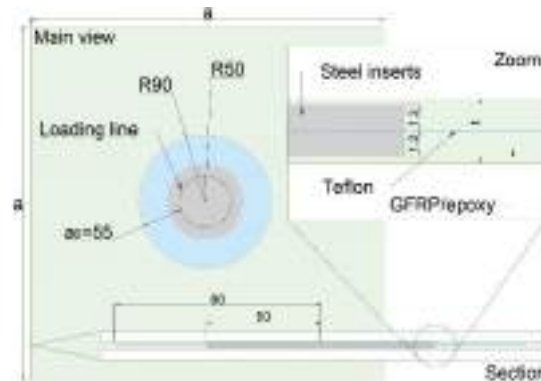


Figure 2: GFRP plate configuration; dimensions in mm

The procedure developed for the introduction of the out-of-plane load into the infused plates is detailed in Figure 3. First, six holes of $\text{Ø}10$ mm were drilled starting from one side of the plate until the midplane, where the diameter was changed to $\text{Ø}6$ mm to complete the hole from the midplane to the other side of the plate. The same procedure was followed on the other side but with an alternated location of the holes (i.e. again six holes but rotated by 30° with respect to the center). All the holes were drilled along the loading line (Figure 2) represented by a

the load started to decrease. For plates CFM, the crack propagation was automatically interrupted by the matrix failure and therefore a sharp decrease in the loads was registered. Only one specimen of each pair of plates is shown in Figure 7. The other specimen of each pair of plates behaved similarly. The initiation points are indicated for all the plates.

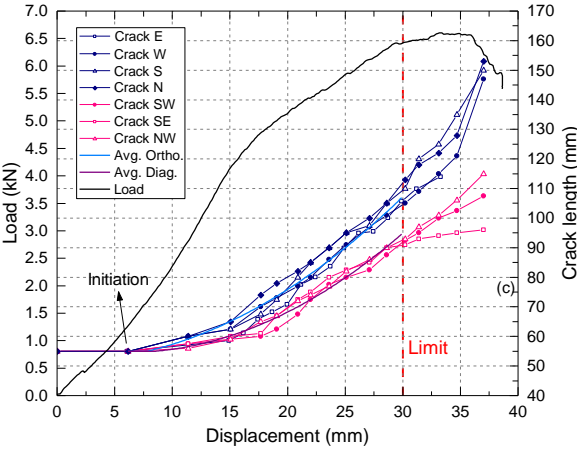


Figure 5: Load and crack lengths vs opening displacement curve of plate W50.50.1

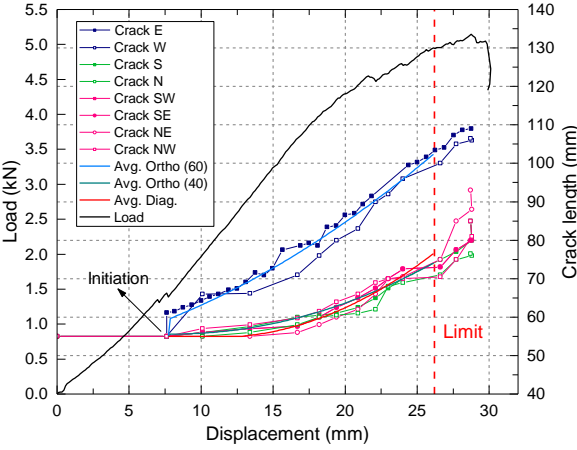


Figure 6: Load and crack lengths vs opening displacement curve of plate W60.40.1

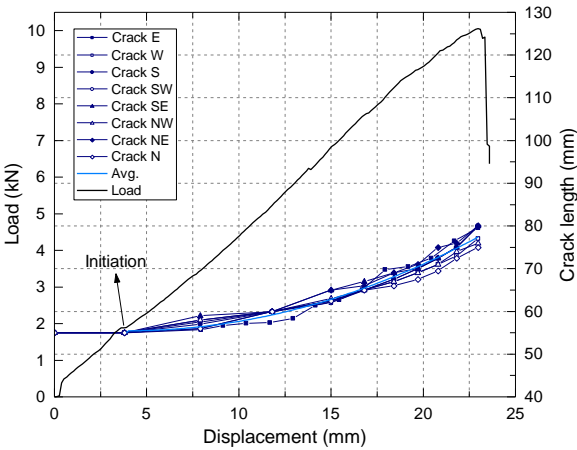


Figure 7: Load and crack lengths vs opening displacement curve of plate CFM.1

As previously mentioned, the vertical displacements on the four corners were recorded by the LVDTs. Different values were recorded depending on the corner for all the plates except for the CFM pair, where the four corners presented approximately the same displacement values. The variation in stiffness and the different distances from the crack tip to the free end depending on the direction of propagation resulted in the recorded boundary behaviors. Initially, the crack propagations were not affected by these boundary displacements and a symmetric and stable propagation could be observed. When the boundary displacements became higher, they started to influence the crack front and the symmetry in the growth was lost (see Figure 8).

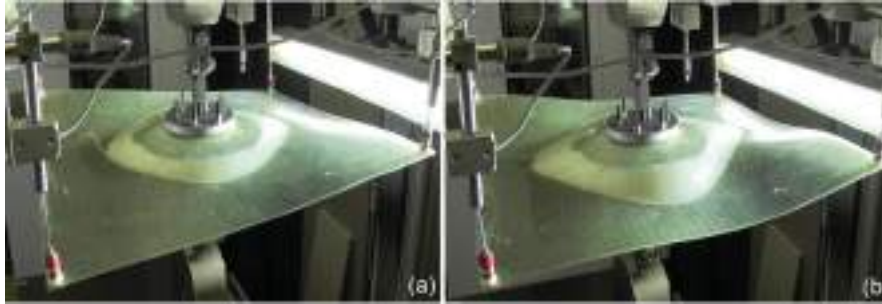


Figure 8: Example of deformation in plate W50.50.1 at (a) limit of symmetric propagation and (b) beyond limit.

The crack lengths vs opening displacement response of the W50.50.1 plate is shown in Figure 5. The blue lines represent the orthogonal directions (i.e. $0/90^\circ$, both equally reinforced in this case) and the magenta lines represent the diagonal directions (i.e. $\pm 45^\circ$). It can be observed that the measured lengths along the diagonal directions remained fairly consistent with each other as well as for the orthogonal directions, indicating a practically symmetric growth of the crack front. The limit of the symmetric behavior corresponded to a 30-mm opening displacement and is marked with a dashed vertical red line. It is evident how the values between the diagonal crack lengths and also between the orthogonal crack lengths began to diverge from this point onwards. Additionally, in order to obtain a continuous evaluation of the crack front, average curves for the orthogonal and diagonal directions were derived by means of parabolic expressions, as shown in Figure 5.

The same representation is shown in Figure 6 for the W60.40.1 plate. Here, the blue lines represent the orthogonal directions with 60% reinforcement, the green lines the orthogonal directions with 40% of reinforcement and the magenta lines the diagonal directions. The corresponding average crack length curves were also plotted for the three groups of directions. The limit of symmetric propagation in this case corresponded to a displacement of 26.2 mm. It can be observed that, as expected, it was along the most reinforced directions (blue lines) that the crack front propagated the furthest. Initially, the propagation along the less reinforced directions was slightly greater than along the diagonals. Once the crack fronts advanced sufficiently further, the behavior was inverted and the propagation along the 40% reinforced directions became smaller (see Figure 6).

The load and crack lengths vs the displacement curves of the CFM.1 plate is presented in Figure 7. Due to the concentric growth of the crack up to the failure of the matrix near the holes, the values of the crack lengths showed the same trend.

Crack propagation patterns

Crack propagation in the W50.50 plates advanced symmetrically to the orthogonal axes up to around 30 mm of propagation in the diagonal directions and 50 mm of propagation in the orthogonal directions in both plates. The shape of the crack front for the last symmetric contour for W50.50.1 is drawn in blue in Figure 9 (a). From this point onwards, the boundary displacements started to affect the specimens' propagation behavior. A similar performance was found for the W60.40 laminates where the crack grew symmetrically to a propagation length of around 45 mm in the orthogonal directions of 60% reinforcement, 15 mm in the orthogonal directions of 40% reinforcement and 20 mm in the diagonal directions. In Figure 9 (b) the shape of the last symmetric crack front for the plate W60.40.1 is also indicated in blue.

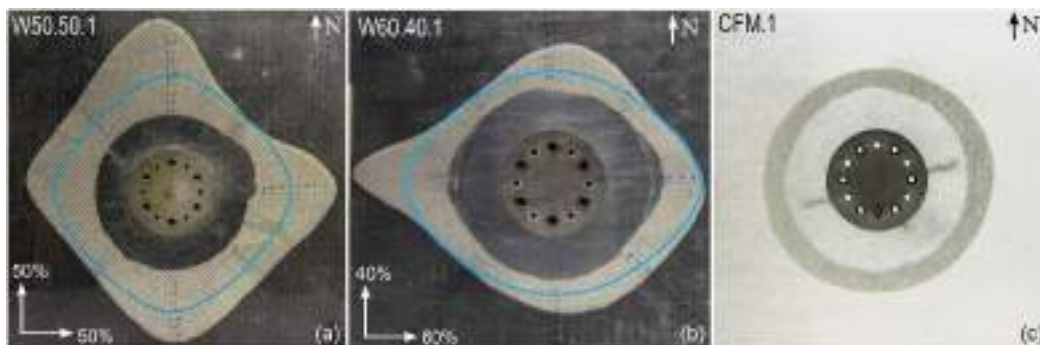


Figure 9: Crack propagation pattern for (a) W50.50.1; (b) W.60.40.1; and (c) CFM.1

For the CFM laminates a concentric circular crack front propagation was observed as expected for an in-plane isotropic reinforcement. A propagation along the entire contour of 22.5 mm for CFM.1 was achieved before failing as a result of matrix failure initiating from the holes (Figure 9 (c)).

The crack initiated and propagated in all of these plates between the adjacent plies of the pre-crack (i.e. the midplane).

Compliance behavior

The experimental values of the crack lengths along the different directions were used to derive the corresponding average curves (see Figures 5-7), providing continuous evaluation of the crack propagation fronts. The area of the crack was calculated for each increment as the area between the obtained crack front and the loading line, as for the standard fracture mechanics experiments. The compliance plotted against the crack area is shown for W50.50, W60.40 and CFM plates in Figure 10 (a, b and c respectively).

Woven laminates W50.50 and W60.40 exhibited comparable behavior, i.e. first a descending branch down to a minimum and then an ascending branch corresponding respectively to a stiffening and subsequent softening of the system (Figure 10 (a,b)). For the CFM plates, a third branch appeared, apart from the descending and ascending parts already described for the previous plates, showing an increase in the compliance during the initial propagation of the crack (Figure 10 (c)).

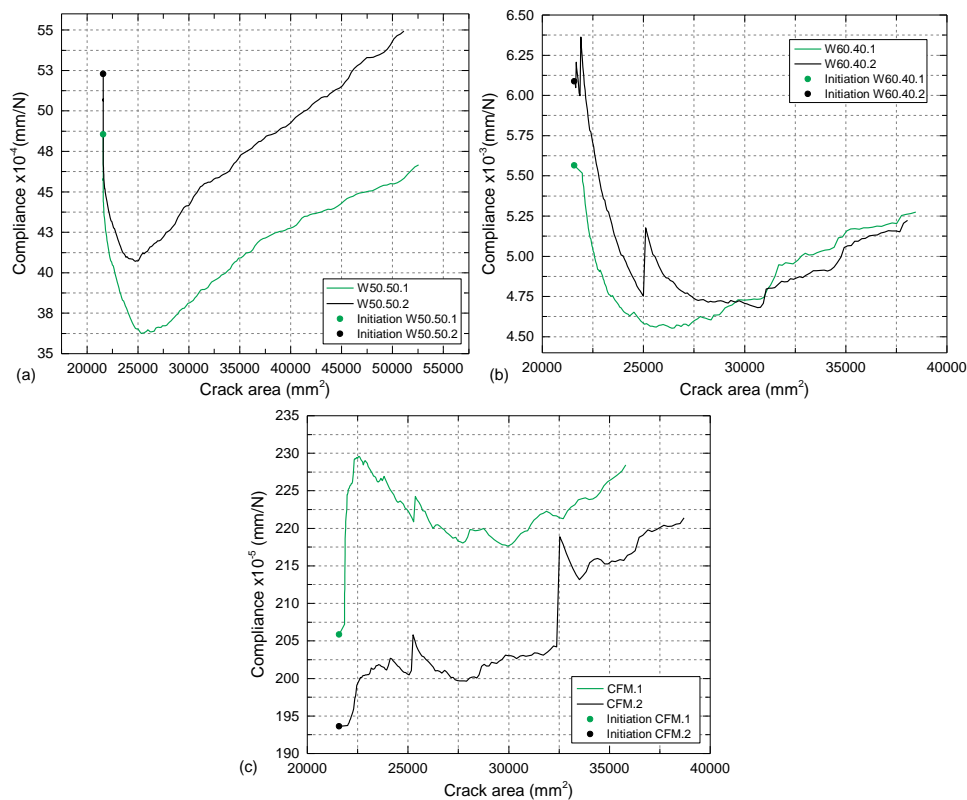


Figure 10: Compliance vs crack area for (a) W50.50; (b) W60.40; and (c) CFM pairs

DISCUSSION

Increasing load behavior

As previously described, a continuously increasing load-opening displacement behavior was monitored from the beginning of all experiments up to the loss of symmetry of propagation or failure, depending on the plate. In contrast to the results shown in this paper, in standard fracture mechanics experiments, the load always decreases once the crack starts to propagate. This contradictory behavior can be understood by comparing how the crack grows in both cases. For standard fracture mechanics experiments the crack area grows proportionally throughout the entire experiment. For the 2D experiments presented here, the crack was embedded in the laminate and consequently, since the crack area started to grow symmetrically with respect to the orthogonal axes, the length of

the crack front increased accordingly. As a result, a disproportionate growth of the crack area occurred, whose increments were higher as the crack advanced, forcing the load to increase to continue the propagation of the crack.

When the boundary displacements started to affect the propagation of the crack, the length of the crack fronts ceased to increase symmetrically. Some of the directions of the crack fronts were constrained by the boundary deformation of the plate and some other directions were favored (see “W” in Figure 9 (b)). This caused a reduction of the crack front length and consequently a decrease in the load (Figures 5 and 6).

Stiffness-related mechanisms

Three different mechanisms affecting the specimens’ stiffness could be distinguished in the experiments: stretching, fiber bridging and crack propagation. When thin beams, plates or shells are subjected to transversal efforts and their boundary conditions are fixed on both sides in such a way that their deformation will cause in-plane tension (called stretching), the structure will become significantly stiffer with increasing deformation. For the specimens investigated here, the boundary conditions caused stretching to become a significant stiffening mechanism. As the crack opened, two curvatures appeared: the radial and the circumferential, see Figure 8. As a result of the geometrical constraints, the plates were therefore subjected to a bi-directional stretching phenomenon. Once the crack started propagating, two additional mechanisms were activated, fiber bridging, as an additional stiffening mechanism, and crack propagation itself as a softening mechanism. The fiber bridging was not measured and due to the nature of the experiment it could not be observed either, but it was expected to exist mainly for the CFM specimens and on a much smaller scale for the rest of the specimens. Typically, for a standard fracture experiment, crack propagation is the dominant mechanism after crack initiation, leading to an upwards behavior of the compliance. On the contrary, for these 2D experiments, the stiffening mechanisms played an important role in the performance of the specimens, prevailing over the softening and thus significantly affecting the results.

Based on the curves presented in Figure 10, an identification of the stiffening and softening regions in both the compliance vs crack curve (shown for W50.50.1, Figure 11 (a)) and load vs displacement curve (shown for both W50.50 specimens, Figure 13 (b)) was carried out for all the plates. Two regions were differentiated on the compliance vs crack area curve. The first region, designated “A”, which spans from crack initiation (“initiation point”) up to a minimum (“transition point”), represents the interval where the stiffening mechanisms (stretching and fiber bridging) prevail over the softening mechanisms (crack propagation), causing the corresponding decrease in compliance. Only when the softening becomes the dominant mechanism, prevailing over the others (at the transition point) does the compliance start to grow, then entering the second region, designated “B” (Figure 11 (a)).

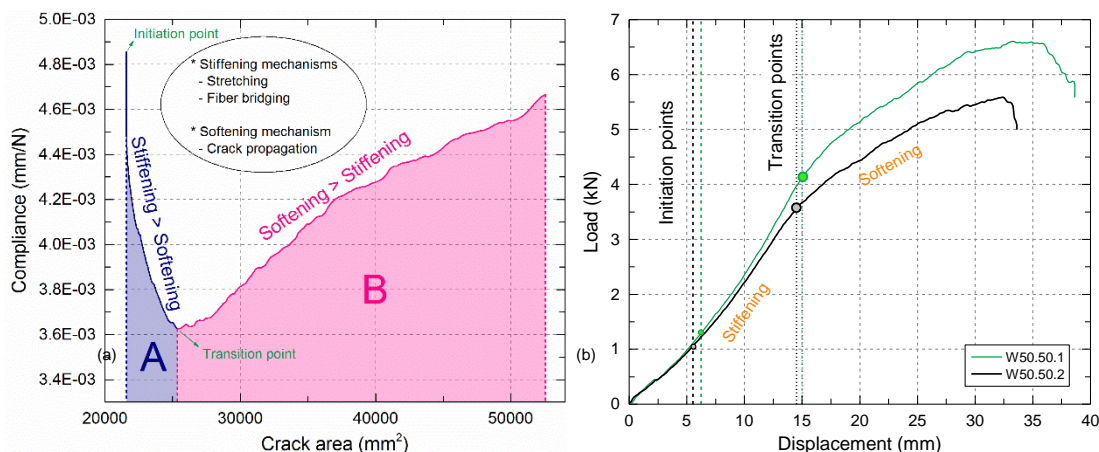


Figure 11: Stiffening and softening regions on W50.50: (a) compliance vs crack area; (b) load vs displacement

The same differentiation procedure in the compliance vs crack curve can be established for the W60.40 and CFM plates by identifying the minimum values as from which the general trend of the compliance increases.

CONCLUSIONS

The 2D delamination behavior of composite laminates with a circular embedded pre-crack under quasi-static out-of-plane loading has been experimentally investigated. The following conclusions were drawn:

1. An experimental design suitable for investigating the 2D propagation of an embedded pre-crack under out-of-plane opening loading was successfully developed.
2. Increasing loads were obtained as a result of a continuously increasing crack front length and a consequently disproportionate increase in the propagation area.
3. As the plates started to deform, stretching stresses appeared in both the radial and circumferential directions as a result of the geometrical constraints. Consequently, the plates were subjected to a dual stiffening effect.
4. Stretching of the specimens and fiber bridging (both stiffening mechanisms) were capable of delaying the general softening of the system that typically occurs once the crack starts to propagate.

ACKNOWLEDGMENTS

The authors wish to acknowledge the support and funding of this research by the Swiss National Science Foundation (Grant No. 200021_156647/1).

REFERENCES

M.L. Benzeggagh, M. Kenane (1996). "Measurement of mixed-mode delamination fracture toughness of unidirectional glass/epoxy composites with mixed-mode bending apparatus", *Composite Science Technology*, 56, 439-449.

ASTM D5528-13: Standard test method for mode I interlaminar fracture toughness for unidirectional fiber-reinforced polymer matrix composites, in Annual book of ASTM standards: adhesive section 15.03.



PREDICTION OF TENSILE STRENGTH OF FRP CABLE CONSIDERING RANDOM STRENGTH DISTRIBUTION

Z. Q. Peng¹, L. N. Ding², X. Wang¹ and Z. S. Wu¹

¹ National and Local Unified Engineering Research Center for Basalt Fiber Production and Application Technology, International Institute for Urban Systems Engineering, Southeast University, Nanjing 210096, China, E-mail: pzq8251228@163.com

² School of Civil Engineering, Nanjing Forestry University, Nanjing 210037, China.

ABSTRACT

Fibre-reinforced polymer (FRP) cables have been developed as advanced materials to substitute steel cables for their light weight, high strength, and high resistance to corrosion. In this paper, a finite element model was established to predict the tensile strength of the cable component FRP tendon considering random strength distribution. The influence of initial curvature of fibre yarns was particularly discussed, and simulated results showed that curvature had neglectable effect on tensile strength but significant influence on coefficient of variation of strength. The predicted ultimate strength and strain of the tendon based on the proposed model achieved good consistency with the experimental results, which provides an efficient method for further study on members and structures regarding FRP cables.

KEYWORDS

FRP cable, tensile strength, random distribution, finite element analysis, initial curvature.

INTRODUCTION

Among various types of FRP composites, cable plays a crucial role for its significant utilization in cable supported structures, for instance, long-span bridge structures, prestressed concrete structures, tension integrity structures, etc. As a unidirectional loading member, high strength of FRP could be fully exerted in form of cable combined with prestressing, while anisotropy of FRP would be evaded.

In the past several decades, the studies refer to FRP cables had emerged continuously, which could be generally divided into three categories: (a) Exploration of behaviour of FRP cables and corresponding methods for improvement. Taking basalt fibre-reinforced polymer (BFRP) cables for instance, researchers (Wang et al. 2013, 2016) had investigated the fatigue and creep behaviour of BFRP tendons, revealing that the creep rupture stress limit for BFRP tendons could be adopted up to 52% of its tensile strength, while the recommendation of a stress range was proposed according to the reliability-based analysis. The degradation of fatigue behaviour of BFRP cables under marine environment had also been studied (Shi et al. 2017). On these bases above, an enhancement for creep behaviour of BFRP tendons through pre-tension had been introduced (Shi et al. 2015). In addition, hybridization was an efficient methodology for improving static and fatigue behaviour of FRP cables (Nageh M. Ali et al 2013); (b) Study of accessory member of FRP cables. The most important accessory member is the anchorage system, which to some extent limits the high strength of FRP cables. Numerous types of anchorage system had been developed in recent decades (Schmidt 2012), which could be divided into bonded anchorage, frictional anchorage, clamping anchorage, etc. Further, a novel anchor toward large-sized FRP cable with multi tendons was proposed with continuous-fibre-reinforced load transfer component (LTC) to overcome shortcomings of conventional anchors (Wang et al. 2015); (c) Investigation of structural behaviour using FRP cables. For FRP cables were application-oriented, plenty of works had been done with respect to FRP cables combined with structures. Antonio Nanni (1992) was one of the pioneers to study the behaviour of pretensioned prestressed concrete members with bonded braided aramid FRP (AFRP) and carbon FRP (CFRP) cables, as well as its anchorage system. T. Katou (1993) also investigated the testing and applications of prestressed concrete beams with CFRP cables. Recently, the durability behaviours of concrete members with different kinds of FRP cables were also addressed (T. Uomoto 2003).

Random analysis is a significant methodology in study of heterogeneous materials. The randomness always includes geometric randomness and property randomness. In terms of geometric randomness, representative volume element (RVE) with suitable boundary conditions was an efficient method to calculate the effective properties of the composites (A.A. Gusev 1997; Ostoja-Starzewski 2006). Meanwhile, Monte Carlo simulation (MCS) and stochastic finite element method (SFEM) were also powerful tools when taking property randomness

into consideration (H.K. Jeong 2000; G. Stefanou 2009). Nevertheless, the vast majority of previous random analysis aimed at FRP laminated plates in field of aerospace, and always needed more cost for calculation. As mentioned above, few of previous works referred to FRP cables itself regarding strength prediction. Zhu et al. (2016) established numerical model to investigate tensile behaviour of Kevlar[®]49 fabric and stress-strain curve was obtained through simulation. However, unlike Kevlar[®]49 fabric, there exists resin in FRP cables which makes situation more complicated. Moreover, in reality, destructive tests for measuring tensile strength of FRP cables may cost much time and expense. Therefore, prediction of tensile strength which gives a reference value with certain reliability becomes quite meaningful.

In this paper, a finite element model based on ANSYS has been established to predict the tensile strength of basalt FRP (which can also be replaced with other kind of FRP) cables considering random strength distribution and initial curvature of fibre yarns. Failure mechanism of FRP cables and pattern of stress-strain relationship can be accurately simulated. The results predicted by this model can be useful for further study on members and structures regarding FRP cables.

CONCEPTUAL MODEL

Basic Assumptions and Model Demonstration

Generally, we consider FRP composites made up of fibres and resin but the microscale size of fibre makes calculation difficult. From another perspective, FRP cables can also be regarded as the combination of continuous impregnated yarns and resin. The impregnated yarns have much less amount than fibres and it is more convenient to test the behaviours of impregnated yarns. The following main assumptions are adopted:

(1) as illustrated in Figure 1, the entire cable is regarded as a “rigid frame” including longitudinal impregnated yarn elements and transverse resin elements. The beam element with circular cross section is applied in all elements. 19 impregnated yarns in plane arrays as shape of hexagon (for the case of 4 mm diameter cable) and the resin elements connect the adjacent impregnated yarn elements.

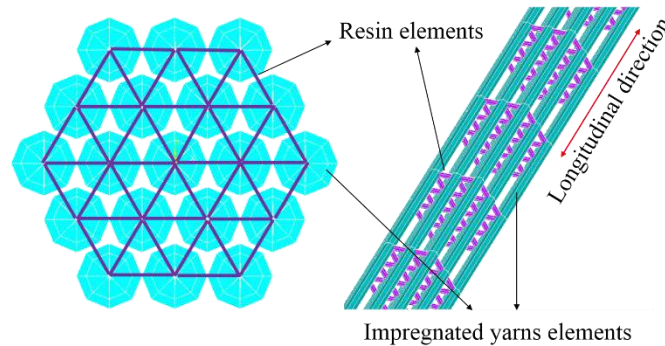


Figure 1: Cross section and 3D patterns of model for the case of 4mm diameter cables

(2) considering relatively low tensile strength and longitudinal elastic modulus of resin, it is treated as making no contribution to tensile strength and longitudinal elastic modulus of entire cable. The transverse resin elements aim at transmitting load between impregnated yarns to simulate ideal bonding perfect among yarns. This assumption can compensate the detrimental influence caused by fabrication error and experimental error.

(3) the tensile strength of impregnated yarn elements and shear strength of resin elements follow two-parameter Weibull distribution. The parameters of them can be obtained from experiments.

(4) the load of each impregnated yarn is uniform.

Random Strength Distribution

It is widely recognized that random mechanical properties are universally existed in materials. Especially in prediction of tensile strength of FRP cable, owing to the weakest element controlling the whole load-carrying capacity of cable, disregard of randomness may lead to deviation of final result. Consequently, the two-parameter Weibull distribution model is introduced to both strength of impregnated yarn and resin elements, which is described as Eq. 1.

$$\begin{aligned}
 P(\sigma) &= 1 - \exp\left[-\left(\frac{\sigma}{\sigma_0}\right)^m\right] \\
 P(\tau) &= 1 - \exp\left[-\left(\frac{\tau}{\tau_0}\right)^n\right]
 \end{aligned}
 \tag{1}$$

where σ and τ are tensile strength of impregnated yarn elements and shear strength of resin elements, respectively. σ_0 and τ_0 are the reference or scaling value related to mean, while m and n are the Weibull modulus or shape parameters.

The parameters in equation (1) can be obtained by statistical analysis of results from mechanical experiments of impregnated yarns and epoxy resin as shown in Table 1.

Table 1 Weibull parameters of impregnated yarns and resin

Item	Scaling value	Shape parameter
Impregnated yarn (1200tex)	2640	18
Epoxy resin	42.88	70

Failure Demonstration

Once one or more impregnated yarn elements achieve their corresponding tensile strength, the cable begins to fail successively with proceeding of loading. The failure diagrams of cable with or without transverse resin elements are described as Figure 2 and Figure 3. Assuming no resin elements in cable, the external longitudinal load is unable to transmit to the other end when failure elements (black elements) occur in impregnated yarns, making entire cable failure occurs immediately. Whereas, when transverse resin elements are taken into consideration, the shear deformation of resin elements makes transmitting external load possible while part of yarn elements fracture, promising entire cable still remain capacity for carrying tensile load. This failure mechanism is beneficial for load carrying and accord with actual situation.

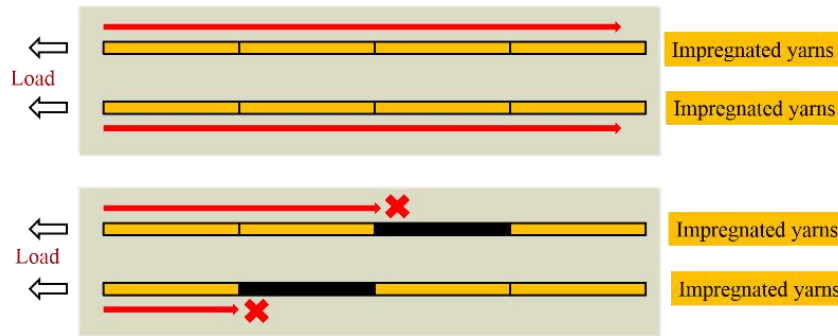


Figure 2: Failure diagram of cable without transverse resin elements

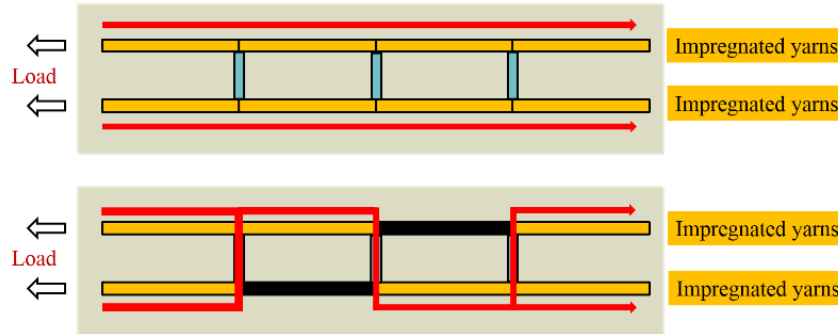


Figure 3: Failure diagram of cable with transverse resin elements

NUMERICAL RESULTS

In order to validate the accuracy of this method, an entire basic model of 4 mm basalt FRP single cable was established, the main parameters of the basic model along with materials are listed in Table 2. The length of yarns elements was set to be 100 mm, while the length of resin elements was 0.8 mm. The equivalent basalt fiber volume fraction was 68%.

Table 2 Main parameters of the basic cable model

Longitudinal length	Diameter of impregnated yarns (1200tex)	Diameter of epoxy resin elements	Spacing of adjacent impregnated yarns axes
1000 mm	0.76 mm	0.2 mm	0.8 mm
Elastic modulus of impregnated yarns	Poisson's ratio of impregnated yarns	Elastic modulus of epoxy resin	Poisson's ratio of epoxy resin
83.9 GPa	0.3	4.2 GPa	0.3

Discussion of Simulated Results

The loading procedure of simulation was controlled by displacement (strain), for which the strain step was set to be 0.001 after elements began to fail. To simulate the failure of fibre and resin, for each step, the elements exceeding their corresponding strength would be differentiated from the whole elements and were to be removed from present model. Termination of calculation was characterized by misconvergence phenomenon of iteration, which indicated that entire model had lost its load-carry capacity. In addition, the damage factor was defined as the proportion of failed elements to all elements. The initial curvature isn't taken into account in this part of discussion.

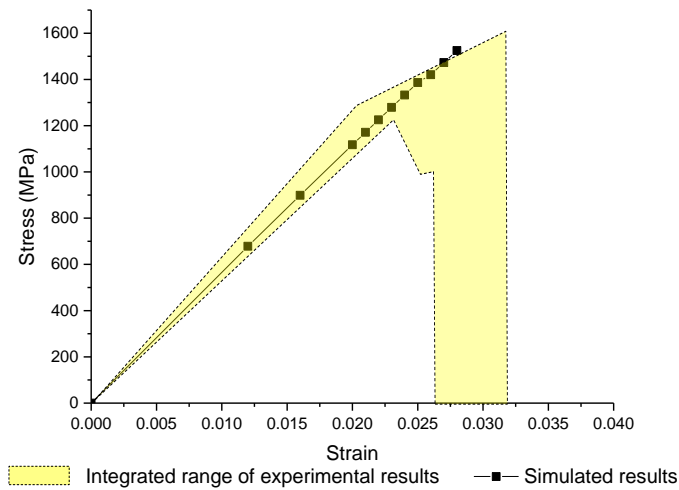


Figure 4: Simulated load-strain curve of FRP cables

Table 3 Results of simulation and experiments

Item	Simulated results (for one combination of random series)	Experimental results (in average)
Ultimate load	19.16kN (0.20%)	19.12kN
Ultimate stress	1525MPa (0.20%)	1521MPa
Elastic Modulus	56.19GPa (7.09%)	52.47GPa
Ultimate strain	2.80% (3.45%)	2.90%

*Figures in the brackets represent relative error of the items.

The elastic modulus is obtained from slope of linear stage of curve.

The Figure 4 and Table 3 show the comparison between simulated stress-strain curve and experimental results. It is noted that the solid curve was generated by one combination of several random strength series. Therefore, in order to obtain results with higher reliability, repeating simulation with more combinations of random series is essential in further study.

The overall trend of simulated curve was congruent with experimental results, which emerged as two stages, elastic linear stage (prior to strain of 0.02) with no element fractured and successive failure stage caused by random strength of elements. In general, the results of simulation were close to experimental results, proving the validation of this model to this aspect. However, the relative error might be caused by inaccuracy of random strength, deviation of volume ratio of fibers and length of elements.

Besides, owing to the scattering of tensile strength of impregnated yarns, the ultimate load (stress) was far below the average tensile strength of impregnated yarns (2640MPa), which indicated that the cable fails without all impregnated yarns exerting its strength. This phenomenon revealed that elements with lower tensile strength controlled the failure of entire cable.

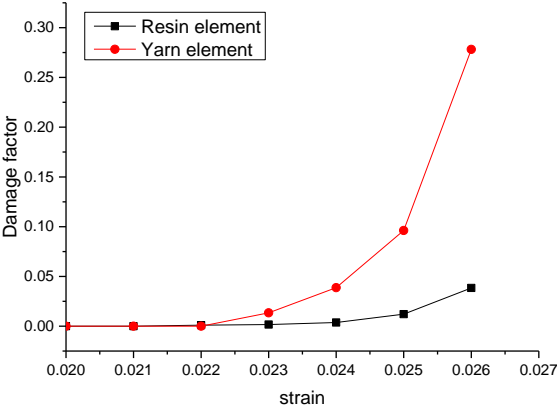


Figure 5: Damage factors of yarn and resin elements with respect to strain

Figure 5 shows the damage factors of yarn and resin elements with respect to strain. While cable destroyed at strain of 0.026, the damage factor of resin element approaching 27.8% was much larger than that of yarn, which was only 3.84%. This phenomenon suggested that although fiber yarn carried vast majority of tensile load, a number of resin also failed under shear deformation caused by failure of fiber yarn. Besides, it is noted that the yarn fractured prior to resin at strain of 0.023, indicating the failure of weak yarn motivated the overall failure of cable.

Consideration of Initial Curvature of Yarns

Initial curvature of yarns may result in uncertain reflection on the tensile behavior of cable, so it is notable to take it into consideration and discuss its effect. However, it is difficult to obtain real configuration of fiber curvature in cable. To simplify this problem, the initial curvature of yarns was regarded as equivalent to fluctuation of coordinates of yarn nodes, which is illustrated in Figure 5. Likewise, with respect to 3D problem, the fluctuation δ was assumed to occur in x or y direction (in plane of cross-section) randomly, the value of which follows normal distribution as $\delta \sim N(\mu, \sigma^2)$, where mean value $\mu = 0$ and standard deviation $\sigma = 0.01$. The positive value of δ represents fluctuating along positive direction of x or y axis.

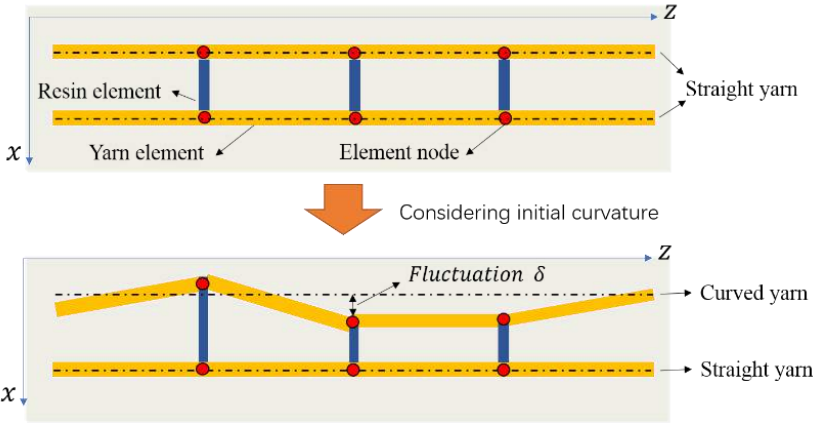


Figure 6: Equivalence of initial curvature of yarns in 2D

Based on displacement controlling mode, the influence of initial curvature is shown in Fig 7, in which each point was generated from 20 simulations due to uncertainty of strength series, from which we could conclude that while initial curvature taken into consideration, regardless of proportion of curved yarns, the average ultimate strength of cable was reduced slightly for around 15 MPa. Nevertheless, the coefficient of variation evidently extended

when curvature occurred, leading to relatively lower design strength of cable. Thus, it is recommended to straighten the yarns (fibers) in the cable to eliminate as much curvature as possible in application.

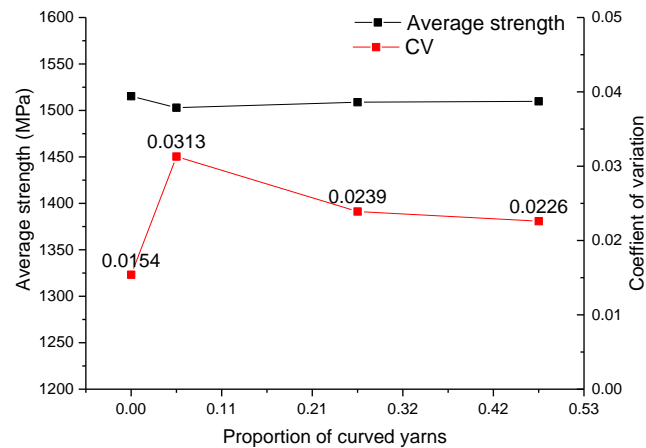


Figure 7: Effect of initial curvature of yarns in static load

CONCLUSIONS

A finite element model based on ANSYS has been established to predict the tensile strength of FRP cables considering random strength distribution. Failure mechanism of FRP cables and stress-strain curve can be simulated with considerable accuracy. The influence of initial curvature of fibre yarns was particularly discussed, and simulated results showed that curvature had neglectable effect on static tensile behaviours of cable but significant effect on CV. The results predicted by this model can be useful for further study on members and structures regarding FRP cables. Optimization of displacement step, comparison of different size of cables, refinement of initial curvature would be emphasized in further study.

ACKNOWLEDGMENT

The authors gratefully acknowledge the financial support provided by the National Key Research and Development Program of China (No. 2017YFC0703000), the National Science Foundation of China (NSFC. 51508277).

REFERENCES

- Ali. N.M, X. Wang and Z.S Wu (2014). "Integrated Performance of FRP Tendons with Fiber Hybridization", *Journal of Composites for Construction*, A4013007.
- Antonio Nanni. et al (1992). "Bond anchorage of pretensioned FRP cable at force release", *J. Struct. Eng.*, 118, 2837-2854.
- A.A Gusev (1997). "Representative volume element size for elastic composites: A numerical study", *Journal of the Mechanics and Physics of Solids*, 45, 1449-1459.
- H.K. Jeong, R.A. Shenoi (2000). "Probabilistic strength analysis of rectangular FRP plates using Monte Carlo simulation", *Computers and Structures*, 76, 219-235.
- Mufti. et al (2007). "Field study of glass-fibre-reinforced polymer durability in concrete", *Canadian Journal of Civil Engineering*, 34, 355-366.
- M. Ostoja-Starzewski (2006). "Material spatial randomness: From statistical to representative volume element", *Probabilistic Engineering Mechanics*, 21, 112-132.
- J.W Schmidt, et al (2012). "Mechanical anchorage of FRP cables-A literature review", *Construction and Building Materials*, 32, 110-121.
- J.Z Shi et al (2017). "Fatigue behavior of basalt fiber-reinforced polymer cables under a marine environment", *Construction and Building Materials*, 137, 46-54.
- J.Z Shi et al (2015). "Creep behavior enhancement of a basalt fiber-reinforced polymer cable", *Construction and Building Materials*, 94, 750-757.

- G. Stefanou (2009). "The stochastic finite element method: past, present and future", *Comput Methods Appl Mech Eng*, 198, 1031–51.
- T. Katou, N. Hayashida (1993). "Testing and Applications of Prestressed Concrete Beams with CFRP Cables", *Fiber-Reinforced-Plastic (FRP) Reinforcement for Concrete Structures*, 249-265.
- T. Uomoto, H. Nakai, H. Sakai, T. Nishimura (2003). "Durability of aramid and carbon frp pc beams under natural and accelerated exposure", *Fibre-Reinforced Polymer Reinforcement for Concrete Structures*, 785-794.
- X. Wang, et al (2014). "Creep behavior of basalt fiber reinforced polymer cables for prestressing application", *Materials & Design*, 59, 558-564.
- X. Wang, et al (2016). "Fatigue Behavior of Basalt Fiber-Reinforced Polymer Cables for Prestressing Applications", *Journal of Composites for Construction*, 20, 04015079
- X. Wang, et al (2015). "A novel anchor method for multi-cable FRP cable: Concept and FE study", *Composite Structures*, 120, 552–564.



*9th International Conference on Fibre-Reinforced Polymer (FRP) Composites
in Civil Engineering (CICE 2018), PARIS 17-19 JULY 2018*

Eco composite or bio sourced composite



EMPIRICAL DESIGN EQUATION TO PREDICT THE AXIAL LOAD CAPACITY OF SANDWICH PANELS WITH FLAX FRP SKINS

M. Noël¹ and A. Fam²

¹ University of Ottawa, Ottawa, Canada, Email: MartinNoel@uOttawa.ca

² Queen's University, Kingston, Canada.

ABSTRACT

A new design approach is presented for predicting the axial strength of flax fiber reinforced polymer (FFRP) sandwich panels which is calibrated using experimental results with consideration of different failure modes including global buckling and localized failures. Use of natural fiber composite materials for construction is rapidly gaining interest in response to the growing need to reduce consumption of non-renewable resources and the embodied energy of buildings and infrastructure to meet sustainability and climate change initiatives. FFRP materials in particular have shown potential as an alternative to glass fiber reinforced polymer (GFRP) composites with similar mechanical properties for structural and semi-structural applications. Lightweight insulated FFRP sandwich panels with polyisocyanurate foam cores present one such application which can be used in rapid modular construction, cladding, or decking. The current study presents a new model for predicting the ultimate axial strength of FFRP sandwich panels which has been calibrated using an experimental study comprised of 87 column specimens having cross-sectional dimensions of 100 x 50 mm that investigated the effects of slenderness ratio (ranging from 22 to 62), FFRP skin thickness (one to five layers corresponding to core-to-skin thicknesses of 15 to 64), and foam core density (ranging from 32 to 96 kg/m³). The preliminary model presented agreed well with experimental results with an experimental-to-predicted ratio of 0.98 and a COV of 0.18. Additional work is needed to apply the model to other FRP skin types and core thicknesses.

KEYWORDS

Flax fiber-reinforced polymers; sandwich panels; axial load capacity; design equation; sustainability; bio-sourced composite materials.

INTRODUCTION

With increasing societal awareness of the importance of sustainability in construction, novel building systems and materials have emerged with lower ecological footprints and improved energy efficiency over their service lives. One highly promising solution utilizes natural flax fiber reinforced polymer (FFRP) sheets bonded to a foam core resulting in a lightweight customizable sandwich panel for cladding and decking applications (CoDyre & Fam 2017).

Whereas the thermal properties of FFRP sandwich panels are primarily governed by the type and thickness of the foam core, which may consist of either conventional or bio-based insulation materials (Carlsson 2011, Sadeghian et al. 2016), the load-bearing capacity depends on composite action between the outer FFRP skins and the inner core. Previous tests have shown that the structural performance of FFRP sandwich panels can be similar to that of sandwich panels made with glass fiber reinforced polymer (GFRP) skins in flexure and axial load capacity with the added advantages of lower density, lower embodied energy, and utilization of renewable materials (Matheson & Fam 2014, Mak et al. 2015, Sadeghian et al. 2016, CoDyre & Fam 2017).

CoDyre & Fam (2017) conducted an experimental study in which 87 FFRP sandwich panel column specimens with cross-sectional dimensions of 100 mm x 50 mm thickness were tested under concentric axial load. The number of FFRP skin layers ranged from one to five, giving core-to-thickness (c/t) ratios of 15 to 64. The height of each specimen ranged from 500 mm to 1500 mm, giving slenderness ratios between 22 and 62. Each panel had a foam core made from polyisocyanurate with different densities ranging from 32 to 96 kg/m³. The test results showed that panels with three FFRP layers showed a similar axial strength to similar sandwich panels with a single GFRP skin layer. Furthermore, the axial load capacity and failure mode were dependent on the number of FFRP layers, foam core density (or more accurately, Young's modulus and shear modulus), and specimen height.

While the experimental test results highlighted the good performance of the sustainable FFRP panels, the study did not explore predictions of their load capacity. The present study explores in more detail an empirical approach to predict the axial load capacity of sandwich panels with FFRP skins.

EXPERIMENTAL PROGRAM

The details of the test program are briefly summarized here. For further information, the reader is directed to the previously published experimental work by CoDyre & Fam (2017).

A unidirectional flax fibre fabric was used for this study with a reported tensile strength of 500 MPa and a Young's modulus of 50 GPa. A two-component high elongation epoxy was used as the saturating resin. Tension and compression tests performed on FFRP coupons produced in the laboratory resulted in the stress-strain curves presented in Figure 1 (Mak et al. 2015). The stress-strain curve in compression is non-linear; the initial Young's modulus is approximately 10 GPa up to a stress of approximately -50 MPa.

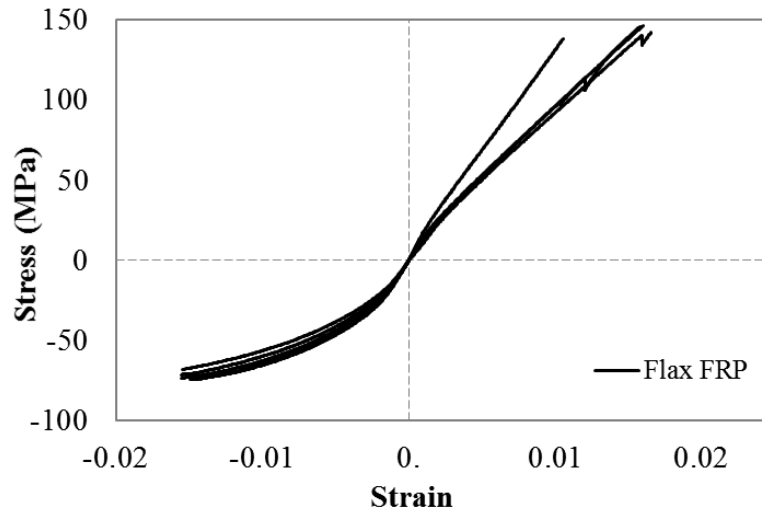


Figure 1: Stress-strain curves for unidirectional FFRP coupons

Three types of rigid closed cell polyisocyanurate foams with a thickness of 50 mm were used for the cores. The reported properties of the various foam insulation types are given in Table 1. Five cubes with dimensions of 50 mm x 50 mm x 50 mm were prepared for each foam type and tested in compression and tension according to ASTM C365 and ASTM C297, respectively. The average results of the cube tests are presented in Table 2.

Table 1: Reported properties of foam insulation

Foam type	Density (kg/m ³)	Parallel shear strength (kPa)	Perpendicular shear strength (kPa)	Parallel shear modulus (MPa)	Perpendicular shear modulus (MPa)	R-value (m ² C/W)
P200	32	151	110	1.52	1.22	1.06
P400	64	379	344	5.86	5.17	1.04
P600	96	585	489	7.23	6.06	0.97

Table 2: Average measured foam mechanical properties (CoDyre & Fam 2016)

Foam type	Compression yield stress (MPa)	Compression elastic modulus (MPa)	Tensile strength (MPa)	Tensile elastic modulus (MPa)
P200	0.209	4.9	0.198	10.1
P400	0.456	12.6	0.317	20.0
P600	0.869	35.1	0.568	59.3

A total of 87 column specimens were fabricated using the three foam types sandwiched between outer skins made of 1, 3 or 5 layers of FFRP applied using a wet-layup method, with average measured single skin thicknesses of 0.78, 2.10, and 3.39 mm, respectively. The column heights were 500, 750, 1000, 1250, or 1500 mm, and were tested under uniaxial compression with both ends pinned. An out-of-straightness analysis confirmed that the test specimens were acceptable for testing. Three replicate samples were tested for each combination of parameters.

ANALYSIS

The design approach presented is an empirically-calibrated model based on the test data obtained by CoDyre & Fam (2017). While the model is based on the results of only one large experimental study, the approach is simple and has the potential to be extended to other configurations and FRP types in the future. Three different failure modes are considered, as described below.

Global buckling

Due to the soft foam core, significant shear deformations can occur under loading which reduces the composite action between the two outer skins, and consequently the buckling failure load. In the case of full composite action (i.e. infinite shear stiffness of the core), the global buckling load is given by the famous Euler equation (Eq. 1):

$$P_E = \frac{\pi^2 E_s I}{L^2} \quad (1)$$

where P_E is the global buckling load, E_s is the elastic modulus of the FFRP skins (the flexural stiffness of the foam is ignored), I is the composite section moment of inertia of the outer FFRP skin system, and L is the effective length of the column.

Considering the other extreme, in which the core is infinitely flexible and no composite action occurs, the buckling load of the sandwich panel would simply be twice that of a single FFRP skin (i.e. replacing the composite section moment of inertia in Eq. 1 with I_s , the moment of inertia of a single skin, and changing P_E to P_{ES} , which is the buckling load for a single skin).

Depending on the column geometry, the fully composite and non-composite global buckling loads may vary by several orders of magnitude, neither of which (in general) are appropriate for predicting the capacity of a soft-core sandwich panel with partial composite action. The level of composite action achieved is a function of the shear stiffness of the foam core (i.e. its shear modulus, G_c), and the relative thickness of the skin and core layers (i.e. t and c , respectively).

Skin wrinkling

In less slender columns, local wrinkling of the skin may result in premature failure before the critical buckling load is reached. In this case, the skin-core interaction may be considered as a beam on elastic foundation (Allen 1969). The critical parameters in this case are assumed to be the thickness of the skin layer (t), the stiffness of the foam and FRP (E_c and E_s , respectively), and the thickness of the core layer (c). Skin wrinkling is a local mode of failure, and is therefore assumed to be independent of the column height.

Crushing

In the case of very short and stiff columns, it may be possible to reach failure by crushing of the FRP skins in compression. In this case, the ultimate axial load capacity is given by Equation 2:

$$P_{crushing} = A_f f_u \quad (2)$$

where $P_{crushing}$ is the ultimate axial load causing skin crushing, A_f is the total cross-sectional area of both skins, and f_u is the ultimate compressive strength of the FFRP.

Empirical model

Excluding the crushing failure mode, which governs only in the case of very short columns and/or with a very stiff core, the response of the sandwich panels under axial loading depends largely on a few main parameters which include the length, L , the stiffness of the core and skin materials (E_s , E_c , G_c), and the cross-sectional geometry (I , c , t). In the current study, the skin material and core thickness were not varied; however, the influence of the other parameters may be observed in the experimental results.

The relative importance of each parameter may be hypothesized with the aim of developing a simple empirical equation that predicts well the axial load capacity of the tested sandwich panels. For example, the column length and core stiffness may be considered to be critical parameters in determining the governing failure mode, as slender columns will tend to fail by global buckling while short columns with soft cores will have more localized failure modes such as skin wrinkling. In the case of buckling failure, the load capacity is inversely proportional to the square of the column length, whereas the column length has no effect on the skin wrinkling strength. Other parameters, i.e. the relative stiffness and thickness of each material, are important for both failure modes.

This concept may be explored further by isolating the effects of each parameter on the experimental results. Figures 2 and 3 show the effect of increasing the number of FRP skin layers and core density for sandwich panel columns of fixed lengths. It can be qualitatively observed, within the range of parameters considered, that the failure load increases with increasing the number of skin layers and increasing core density (which is linked to its core stiffness) regardless of the specimen length.

The data may also be presented for specimens with a fixed core density, as shown in Figures 4 and 5 for increasing number of skin layers and increasing specimen length, respectively. Once again, it can be qualitatively asserted that the failure load increases with increasing skin thickness regardless of core density (Figure 4). However, from Figure 5, it is rather evident that specimen length has a nearly negligible effect on specimens with a low or medium core density, and may be considered to be inversely proportional to the failure load for specimens with a high core density. This is likely attributed to the fact that panels with softer cores are more susceptible to localized failure modes as deduced earlier.

Finally, the results are presented as a function of specimen length and core density for a fixed skin thickness in Figures 6 and 7. Observations of the effect of specimen length for a fixed skin thickness do not show a clear trend, suggesting that the number of FRP layers is not a good indicator of the expected failure mode. Once again, the failure loads were approximately proportional to core density in all cases.

These observations may be used to form the basis for an empirical model to predict the failure load for axially loaded soft-core sandwich panels with FRP skins. Currently, the model is limited to the results of this study and therefore does not account for variations in FRP skin materials, or core thickness. Future work will aim to extend the model to consider these parameters.

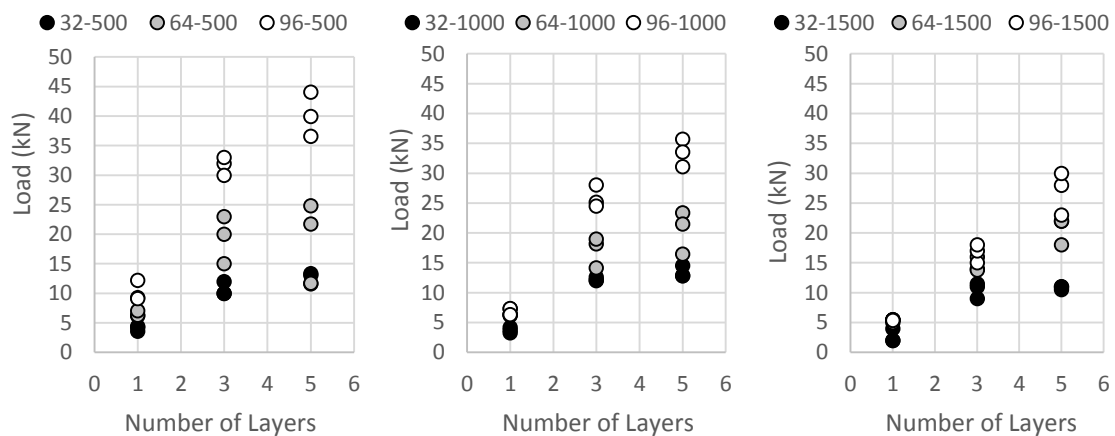


Figure 2: Effect of skin thickness on axial capacity for fixed length columns

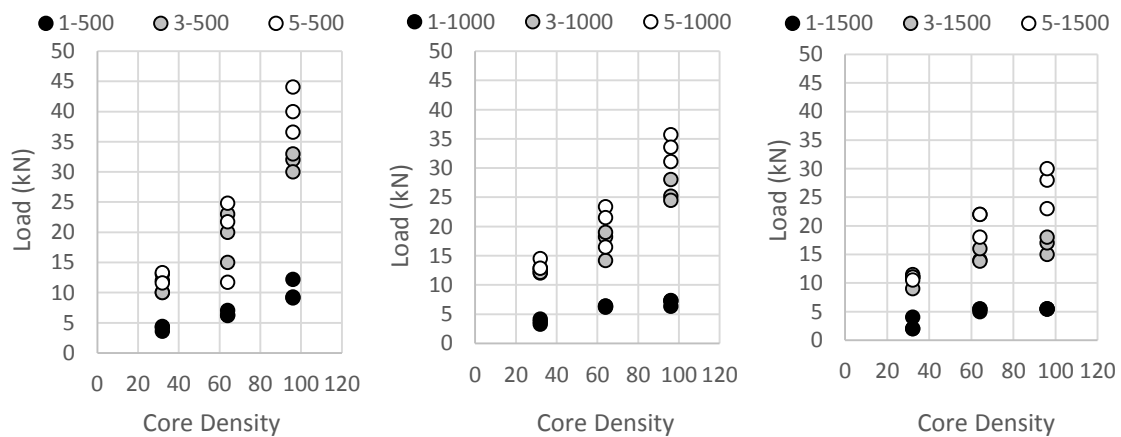


Figure 3: Effect of core stiffness on axial capacity for fixed length columns

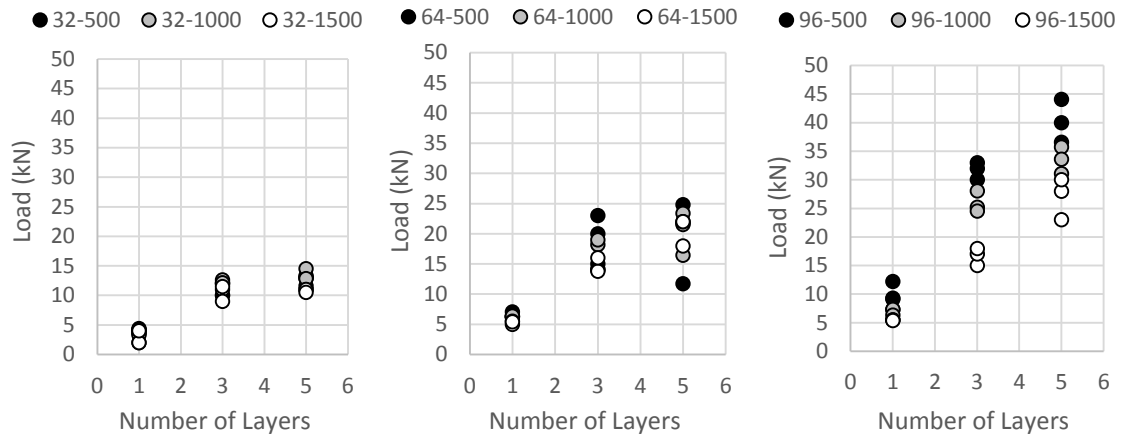


Figure 4: Effect of skin thickness on axial capacity for columns with fixed core stiffness

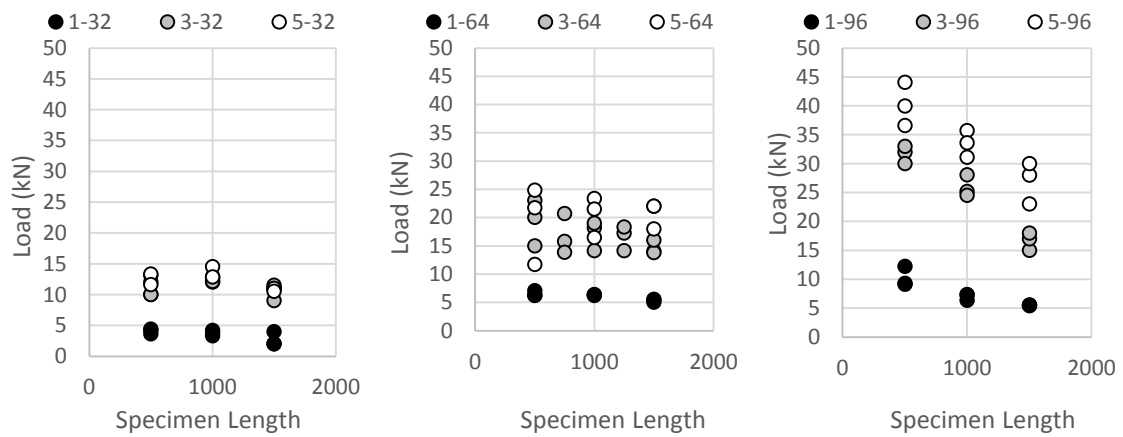


Figure 5: Effect of specimen length on axial capacity for columns with fixed core stiffness

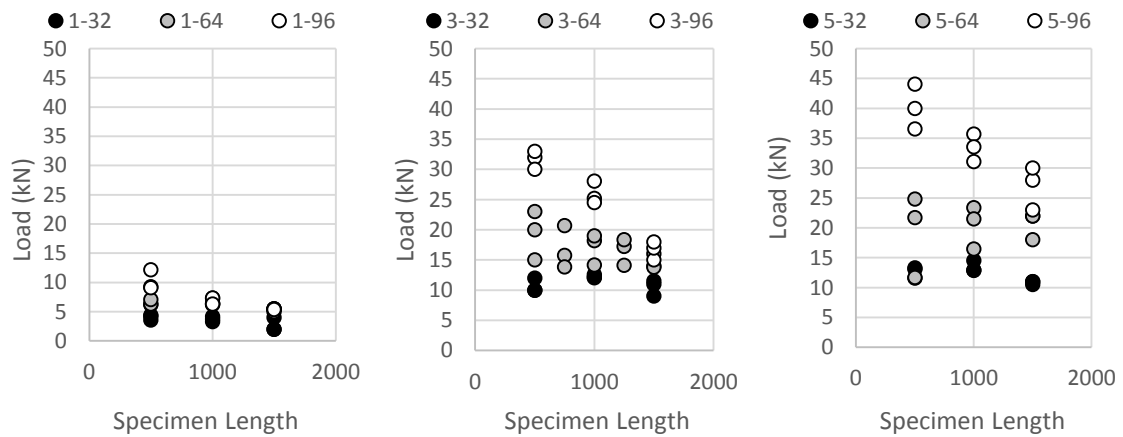


Figure 6: Effect of specimen length on axial capacity for columns with fixed skin thickness

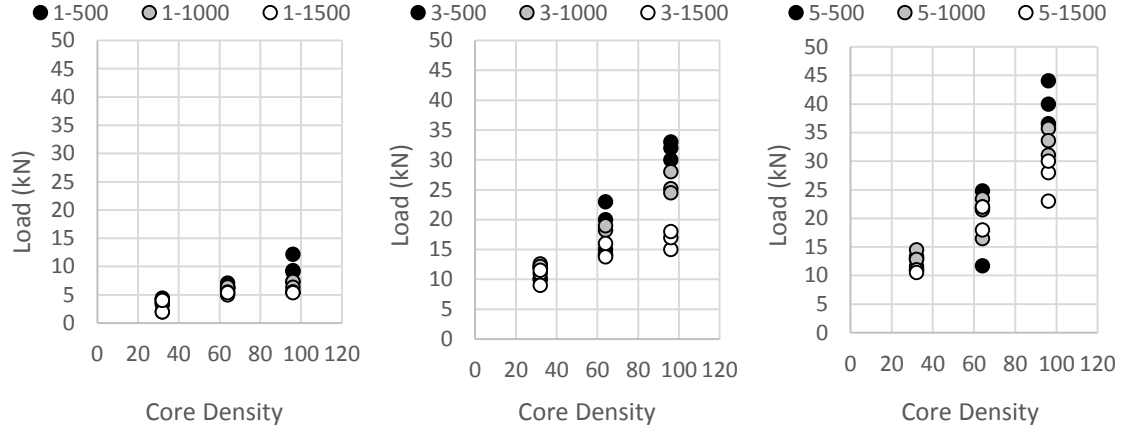


Figure 7: Effect of core stiffness on axial capacity for columns with fixed skin thickness

The proposed simplified model consists of two equations: one for specimens governed by global buckling and hence sensitive to specimen length, and a second equation for specimens expected to fail by local skin wrinkling. (The skin crushing mode was also considered, but was in all cases higher than the predicted strength from the other two failure modes). Based on the observations from the experimental results, the parametric comparisons in Figures 2 through 7, and Equation 1, it is hypothesised that the global failure load is proportional to the Euler buckling load with a modification factor to account for the level of composite action attained as a function of the core shear modulus (G_c), skin thickness (t), and specimen length (L). Similarly, the skin wrinkling capacity is governed by the critical stress level which is a function of the skin thickness (t), skin elastic modulus (E_s), and foam core elastic modulus (E_c).

The dependent relationships relating the skin thickness and foam core stiffness to the axial load capacity are assumed to follow an exponential form (i.e. $y = Ax^B$) where a value of $B=1$ signifies a directly proportional or linear relationship and $B=0$ signifies a negligible effect. The two equations are given in their general forms by Equations 3 and 4:

$$P_{axial} = At^B G_c^C L^D \left(\frac{E_s I}{L^2}\right) \quad (3)$$

$$P_{axial} = A E_s^B E_c^C b t^D \quad (4)$$

The mathematical coefficients A, B, C, and D in Equations 3 and 4 were fitted using a least squares regression analysis (Figure 8) assuming that the minimum value obtained from the two equations will govern the failure mode. The exponent for the skin thickness in Equation 3 was determined to be equal to zero, implying that the effect of the skin thickness is already fully accounted for in the moment of inertia term. The analysis results are given by Equations 5 and 6, which resulted in an average experimental-to-predicted ratio of 0.98 with a COV of 0.18:

$$P_{axial} = \frac{0.27 G_c^{0.34} E_s I}{L^{0.61}} * 10^{-6} \quad (5)$$

$$P_{axial} = 0.27 E_s^{1.24} E_c^{0.60} b t^{0.54} * 10^{-6} \quad (6)$$

where G_c , E_s , and E_c are given in units of MPa, I is given in mm^4 , L , b , and t are given in mm, and the axial load P_{axial} is in units of kN.

It should be noted once again that the effects of variations in FRP skin material and core thickness are not captured by these equations. It is expected that these equations could likely be recalibrated once additional data is added to the dataset to account for these parameters. Furthermore, it should also be mentioned that Equation 5 uses the perpendicular shear modulus of the foam core, G_c , to account for changes in the foam core behaviour, while Equation 6 employs the elastic Young's modulus, E_c . The reason for this is that global buckling failure depends on the magnitude of the shear deformations while the skin wrinkling failure is treated as a beam on elastic foundation.

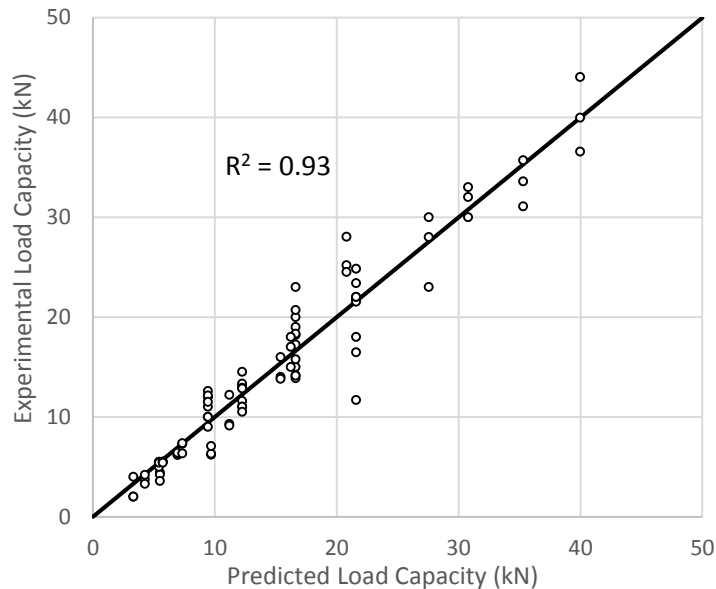


Figure 8: Regression analysis for empirical model calibration

RESULTS & DISCUSSION

The predictions from the empirical model are compared against the experimental data in Figure 9. The axial load capacity of short columns with a single skin layer tended to be over-predicted, but in almost all other cases the predicted results were close to the experimental values. The experimental values in some cases showed considerable scatter, varying in some cases by a factor of 2 or more for the same test parameters. Nevertheless, the empirical model developed shows good potential for use in design once it has been extended to account for FRP type and core thickness.

CONCLUSIONS

This paper presents the preliminary results of the model development for predicting the axial load capacity of FRP sandwich panels with soft foam cores. The following conclusions may be drawn:

The axial failure load of FRP sandwich panels with foam cores increases with increasing FRP skin thickness and increasing foam stiffness. The axial load capacity generally decreases with an increase in effective length only in the case of specimens with a high foam stiffness, as local failures tend to dominate for softer foams.

An empirical model was calibrated using a large number of experimental results, which accounted for different failure modes and the effects of the foam core properties and FRP skin thickness on the level of composite action attained. The empirical model was able to predict the experimental load capacities with an average experimental-to-predicted load ratio of 0.98 and a COV of 0.18.

The empirical model developed has not yet been compared with different types of FRP skin nor variations in the thickness of the foam core. The model will be extended to account for these parameters with additional data.

REFERENCES

- Allen, H. G. (1969). "Analysis And Design Of Structural Sandwich Panels." Pergamon Press, Oxford, U.K.
- Carlsson, L. A. (2011). "Structural and Failure Mechanics of Sandwich Composites." Springer, New York.
- CoDyre, L., & Fam, A. (2017). "Axial Strength of Sandwich Panels of Different Lengths with Natural Flax-Fiber Composite Skins and Different Foam-Core Densities." *Journal of Composites for Construction*, 21(5).
- Mak, K., Fam, A., & MacDougall, C. (2015). Flexural Behavior of Sandwich Panels with Bio-FRP Skins Made of Flax Fibres and Epoxidized Pine-Oil Resin. *J. Compos. Constr.*, 19(6), 13.
- Matheson, H., Fam, A. (2014). "Axial Loading Tests and Simplified Modeling of Sandwich Panels with GFRP Skins and Soft Core at Various Slenderness Ratios." *J. Compos. Constr.*, 19(2), 13.

Sadeghian, P. Hristozov, D. and Wroblewski, L. (2016) "Experimental and analytical behavior of sandwich composite beams: Comparison of natural and synthetic materials", Journal of Sandwich Structures and Materials, DOI: 10.1177/1099636216649891

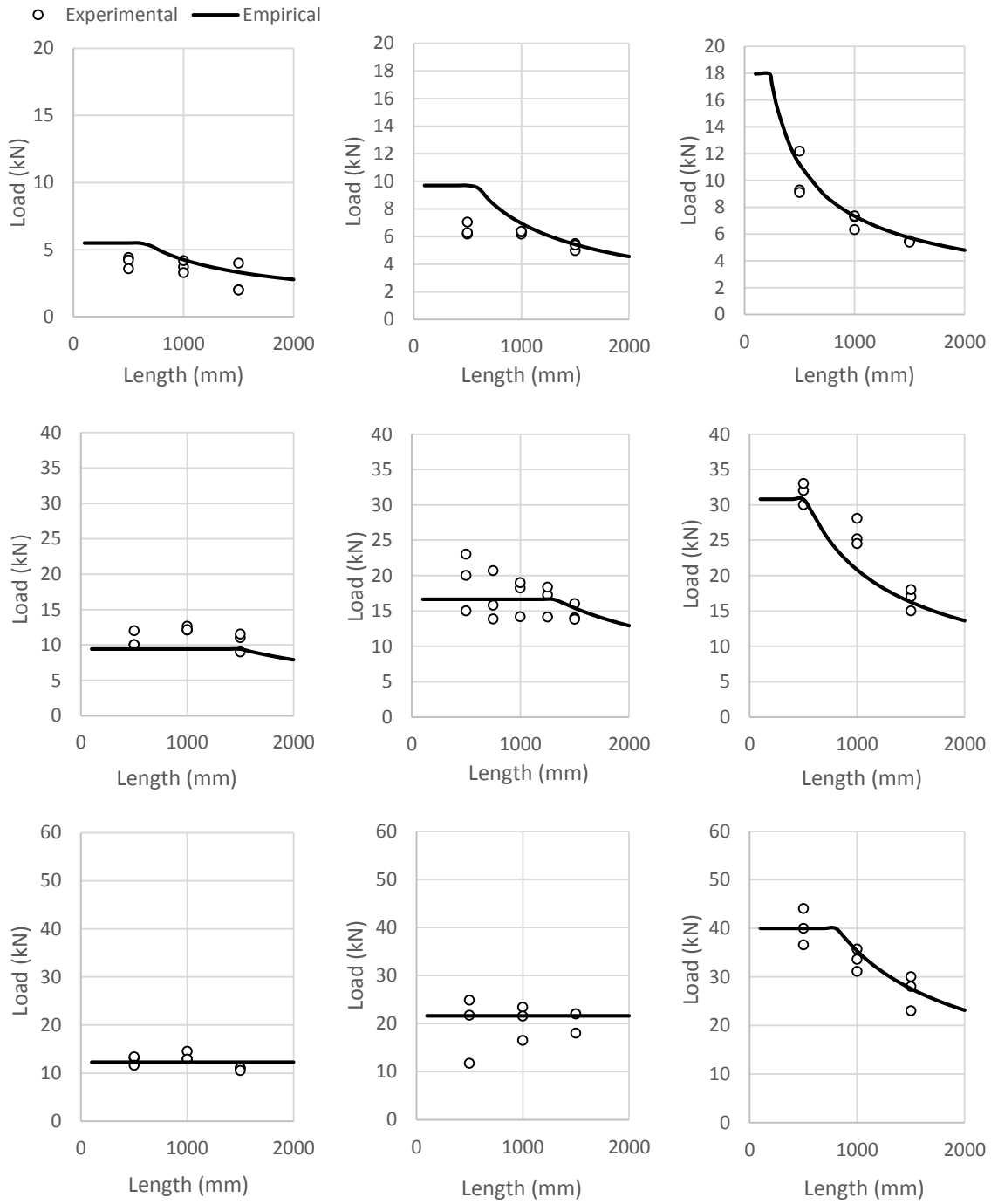


Figure 9: Predicted vs. experimental results. Rows from top to bottom: 1, 3 and 5 FRP layers. Columns from left to right: core density of 32, 64, and 96 kg/m³

Figure 9: Predicted vs. experimental results. Rows from top to bottom: 1, 3 and 5 FRP layers. Columns from left to right: core density of 32, 64, and 96 kg/m³



FATIGUE PERFORMANCE OF BIORESIN GLASS FIBRE REINFORCED POLYMERS

A. Watfa 1, M. F. Green 2 and A. Fam 2

¹ Queen's University, Department of Civil Engineering, Kingston, Canada, Email: 11ahwl@queensu.ca

² Queen's University, Department of Civil Engineering, Kingston, Canada.

ABSTRACT

Fatigue performance of glass fibre reinforced polymers (GFRPs) is critical for applications for wind turbine towers. Substantial experimental fatigue data is available for GFRPs with epoxy, polyester, and vinylester matrices. However, the cyclic behaviour of GFRP with bioresins is a new research area and little information is available. This paper investigates the fatigue behaviour of unidirectional GFRPs fabricated with a bioresin matrix for wind turbine tower applications.

Seventeen single layer GFRP specimens (36 % fibre volume fraction) are subjected to tension-tension cyclic loading of varying loading stress ratio of $R = 0.1$ and $R = 0.5$ in constant amplitude load control with a loading frequency of 2.5 Hz. At least twelve specimens are tested for each loading stress ratio. Additionally, two to three specimens are considered at each maximum stress level for consistency purposes. Stress-life experimental data are obtained for the single layer bioresin GFRPs. The S-N curves show that the tensile strength degradation of the bioresin GFRP is 58% after 10^6 cycles for a stress ratio of 0.5. Two methods for the statistical analysis of unidirectional bioresin GFRP fatigue data and the derivation of reliability-based S-N curves are also presented.

KEYWORDS

All FRP and smart FRP structures; Fatigue ; Durability, Long-term performance; Characterization of FRP and FRC materials/systems; Bioresin; GFRP.

INTRODUCTION

Engineering structures such as bridges and wind turbine blades are required to sustain 10^8 - 10^9 fatigue loading cycles during their operational life (Vassilopoulos and Keller, 2011). Basically, fatigue stresses on wind turbine towers are caused by the blade rotation and wind fluctuation. Every blade rotation is a cycle that causes a small stress change. Consequently, wind turbine towers are subjected to fatigue load cycles during their life, in the magnitude of 10^8 - 10^9 , and these fatigue cycles are associated with long-term stress changes. However, fatigue cycles are interrupted in real life, and it was recently observed that the fatigue life is 1.4 times longer when constant load amplitude was interrupted several times. Consequently, fatigue design should be conservative if continuous fatigue cycling tests are adopted (Vassilopoulos and Keller, 2011).

The prediction of fatigue failure for fibre reinforced polymers (FRPs) is of great importance in the design of composite components used in various engineering applications (Al-Assaf and El Kadi, 2001). However, the behaviour of composite materials subjected to fatigue cycles is less predictable than that for conventional metal materials (Lee et al., 1999). Because of superior mechanical properties, FRPs are used in constructing wind turbine blades with diameters greater than 100 m (Vassilopoulos and Keller, 2011). Significant research efforts have been made to understand the fatigue performance of FRPs. In addition, techniques have been developed to predict the fatigue life of composite materials. Therefore, extensive experimental fatigue data have been derived for such composite materials in several engineering fields such as wind turbine applications (Vassilopoulos and Keller, 2011).

For example, Vassilopoulos and Keller (2011) constructed the S-N curves for polyester GFRP composites of different angle fibre orientations tested in load control with a frequency of 10 Hz. Statistical analysis for all S-N curves was performed. El Kadi and Ellyin (1994) studied the fatigue performance of epoxy GFRP for fibre angle orientation of 0° , 19° , 45° , 71° and 90° under stress ratio of tension-tension cycles ($R = 0, 0.5$) and tension-compression ($R = -1$) where R is the ratio of minimum stress, S_{min} , to maximum stress, S_{max} , in the cycle (i.e., $R = S_{min}/S_{max}$). The strain energy concept was used to develop the failure criterion of the composite GFRP for the different stress ratios. It was concluded that the compressive and tensile stresses do not contribute equally to the damage.

In addition, the selection of loading frequency is of great interest. Hosoi et al. (2010) tested quasi-isotropic carbon FRP laminates having a stacking sequence of $[45^\circ/0^\circ/-45^\circ/90^\circ]_s$ with a loading frequency of 100 Hz. It was found

that the fatigue behaviour was not affected if the temperature of the laminates remained below the glass transition temperature of the examined material. This indicated that it is possible to develop new models based on high cyclic fatigue experimental data. Shuler et al. (1993) studied the influence of loading frequency on the room-temperature fatigue of $0^\circ/90^\circ$ woven-carbon-fibre/ceramic matrix (C_f/SiC -matrix) composite. Tension-tension fatigue tests were conducted under sinusoidal load control at frequencies of 1, 10, and 50 Hz for a stress ratio R (S_{min}/S_{max}) of 0.1. The fatigue life of the carbon fibre/ SiC composites for the various frequencies showed no major difference in the fatigue life corresponding to 1 and 10 Hz. However, the fatigue life was lower for all stresses at 50 Hz. The temperature rise for the fatigue experiments performed at 1, 10, and 50 Hz was investigated. It was observed that the temperature rise as a result of internal frictional heating in the specimens increased as the loading frequency and maximum fatigue stress were increased.

The response of glass FRPs (GFRPs) with conventional resins to cyclic loads have been investigated in the last years due to the remarkable growth of wind energy industry (Vassilopoulos and Keller, 2011). Nonetheless, the fatigue behaviour of bioresin GFRPs is not well defined. Consequently, the main objective of the present study is to assess the fatigue performance of such GFRPs. Cyclic tests have been conducted on unidirectional bioresin GFRP composites under tension-tension loading. The aim of this study is to present a mathematical methodology for predicting fatigue life of bioresin GFRPs.

EXPERIMENTAL PROGRAM

Twenty-four bioresin-based GFRP specimens were fabricated to carry out the experimental research work. The GFRP composites consisted of unidirectional E-glass fibre fabric (Tyfo SEH-51A) and a Super Sap CLR partially bio by 25 % resin that was composed of epoxidized pine oils and produced by Entropy Resins. The manufacturer reported the tensile strength and modulus of the dry glass fibres as 3240 MPa and 72.4 GPa, respectively. The two-part bioresin was mixed with a ratio of 100 parts of component A to 47 parts of component B by weight. The tensile strength and elastic modulus of the bioresin as reported by the manufacturer were 65.5 MPa and 3.0 GPa, respectively.

Unidirectional bioresin glass fibre reinforced polymers (GFRP) specimens of dimensions 25×250 mm were fabricated according to ASTM D3039 guidelines by the wet lay-up technique. The glass fibre fabrics were saturated by pouring and spreading the bioresin on both edges of the fabrics. These saturated fabrics were placed between two smooth and heavy High Density Polyethylene (HDPE) boards for curing. The thicknesses of the GFRP specimens were measured at different locations. These thicknesses of the cured specimens were $1.30 \text{ mm} \pm 0.05 \text{ mm}$. To avoid grip failure, GFRP tabs of length 50 mm and 25 mm width were adhered to the four sides at both ends of the coupons using Sikadur30 viscous epoxy. The fibre volume fraction of the cured specimens was 36 % measured by weights and densities of constituents. All specimens were tested in accordance to ASTM D3479 standards. Therefore, fatigue tests were performed using an Instron 8802 machine under load control at under tension-tension cyclic loadings of $R = 0.1$ and $R = 0.5$. Two to three replicate tests were carried out at several stress levels. All fatigue tests were run at a frequency of 2.5 Hz with constant amplitude sine-wave loading under room temperature laboratory conditions. The test instrumentation and setup are shown in Fig. 1.



Fig. 1: Fatigue test instrumentation and setup of bioresin GFRP specimens using Instron 8802 (a sample specimen at failure is shown)

In addition, the following assumptions were adopted: (1) no void percentage was considered in the specimens, (2) uniaxial stress state was employed, and (3) variable amplitude loading was not considered.

RESULTS AND DISCUSSIONS

Tests were subjected to tensile cycles (tension-tension) of varying stress ratio $R = 0.1$ and $R = 0.5$. At least twelve specimens will be tested at different maximum stress levels. Furthermore, it was recently recommended that three specimens shall be tested at each maximum stress level for consistency purposes (Vassilopoulos and Keller, 2011).

Basquin (1910) stated that a power law is the best mathematical model to describe the stress-life relationship. Additionally, ASTM E739-10 (2015) stated that the stress level must be the independent variable, whereas the corresponding number of cycles to failure must be the dependent one. Consequently, the typical fitted curves are of the form:

$$S_a = S_0 N^{\frac{-1}{k}} \quad (1)$$

where:

S_a = stress amplitude (or stress maximum or stress range), N = number of cycles to failure, and S_0 and k are constants.

Constant amplitude fatigue data are plotted on the S-N plane. The fatigue data have been used for estimation of the derived S-N curve parameters. The stress is based on total area of composite including the resin. The normalized stress-life (S-N) data of the novel material are presented in Fig. 2. The S-N curve for $R = 0.1$ is steeper than the one for $R = 0.5$. The normalized S-N curves revealed that the residual strength of bioresin GFRP was 45.7% and 44.4% of its ultimate tensile strength after half a million cycles for the stress ratios of $R = 0.1$ and $R = 0.5$, respectively.

Based on data available in the literature (Epaarachchi and Clausen, 2003), the S-N curves in Fig. 2 provide evidence for a preliminary finding that the fatigue performance of the bioresin GFRPs is comparable to the fatigue performance of GFRPs with conventional resins.

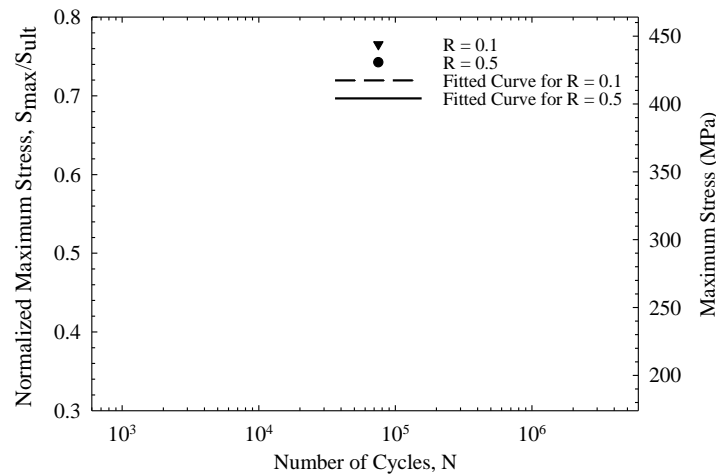


Fig. 2: Normalized stress-life (S-N) curves of the bioresin GFRP under tension-tension fatigue loading

Experimental data obtained from S-N curves under tension-tension cyclic loading can be plotted together in the stress mean-stress amplitude ($S_m - S_a$) plane as radial lines from the origin of the coordination system to form the constant life diagram (CLD). Each line represents a single S-N curve at each R-ratio using the following equation:

$$S_a = \left(\frac{1-R}{1+R} \right) S_m \quad (2)$$

This diagram is intended to represent the S-N curves under different R-ratios from the curves derived experimentally. Constant life (CL) lines can be derived by connecting the points on each S-N curve (radial line) corresponding to the same number of cycles.

It is worth mentioning that the CLD curves converge to the ultimate tensile stress (Vassilopoulos and Keller, 2011). The CLD curves of the unidirectional bioresin GFRPs for $R = 0.1$ and $R = 0.5$ are shown in Fig. 3.

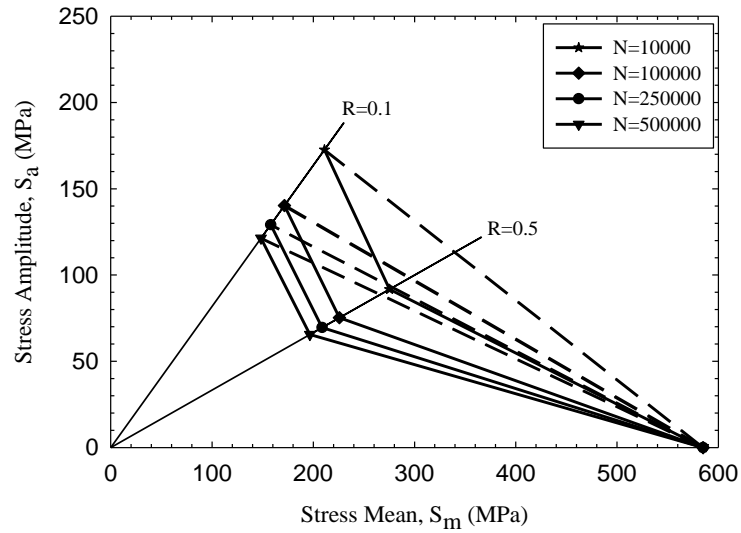


Fig. 3: Constant life diagram (CLD) of unidirectional bioresin GFRP for different loading cycles

It can be seen in Fig. 3 that a direct linear relationship between the ultimate tensile stress and points on $R = 0.1$ would be very unconservative for both low and high cycle fatigue ranges ($N < 500,000$). Consequently, the consideration of two R -ratios in tension-tension fatigue cycles is of great interest to establish the tension-tension CLD of the novel GFRP composite.

The failure modes are shown in Fig. 4 for tension-tension cycles of $R = 0.1$ and $R = 0.5$. The failure of the bioresin-based GFRP specimens starts by damage and cracking of the matrix (or debonding between fibres and matrix) leading to eventual failure of fibres and fibre splitting (Fig. 4). The dominant failure modes in static tension tests are fibre rupture and fibre splitting. The accumulation of matrix cracks during fatigue loading is more noticeable than was observed in static tests (Watfa et al., 2017).

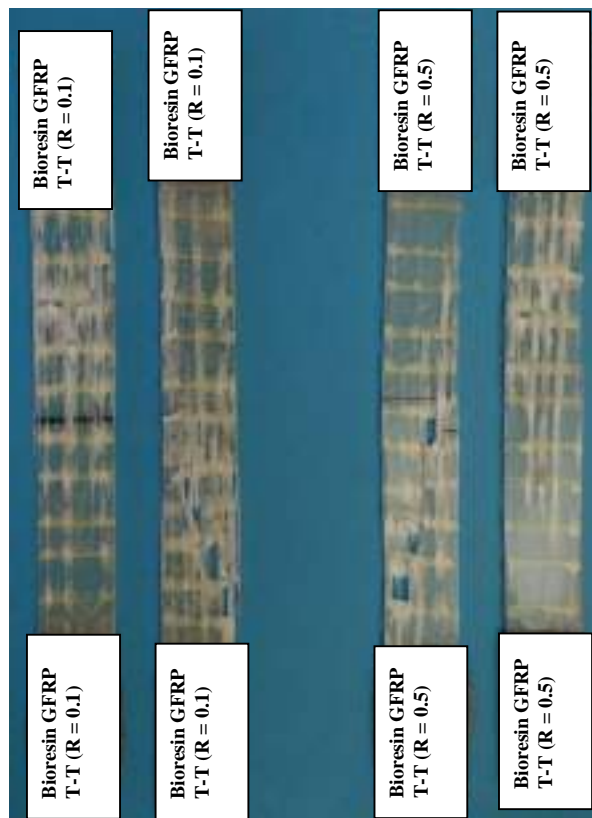


Fig. 4: Failure modes of bioresin GFRP specimens at $R = 0.1$ and $R = 0.5$

In addition, epoxy GFRP specimens (with same fibre volume fraction) will be tested as a part of ongoing research study. The S-N curves of the epoxy GFRPs will be compared to those of the bioresin GFRPs.

STATISTICAL ANALYSIS

Since several factors, such as the nature of fibres and fabrication methods, can often cause defects in the specimens, experimental fatigue data for FRPs often present high scatter (Vassilopoulos and Keller, 2011). Consequently, the fitted S-N curve is not adequate if no information concerning model reliability is provided.

The derivation of S-N curves with high reliability levels is important to be conform to design codes. In addition, the derivation of models to describe the fatigue performance of composite materials with some statistical significance requires a large number of fatigue tests. However, several models have been presented to provide reliability-based S-N curves derived from limited experimental data.

Two models for the statistical analysis of fatigue data of composites and the derivation of reliability-based S-N curves have been considered in this paper: Normal Lifetime Distribution (NLD) and ASTM E739-10 (2015). For a given reliability level (95%) and a coefficient of variation (15%), the NLD method assumes a normal distribution of the lifetime per stress level to estimate the characteristic number of cycles to failure. The S-N curve is derived by fitting the characteristic number of cycles per stress level to the corresponding cyclic stress value, considering the stress parameter as the independent variable. The ASTM E739-10 (reapproved 2015) standard procedure results in an S-N relationship with statistical significance when at least 12 specimens are considered. This method is not suggested for extrapolation outside the available experimental data. The estimated model parameters to represent maximum cyclic stress (S_{max}) are shown in Table 1.

Table 1: Fatigue statistical model parameters

R	Basquin (1910)		NLD		ASTM	
	S_0 (MPa)	$1/k$	S_0 (MPa)	$1/k$	S_0 (MPa)	$1/k$
0.1	878.8	0.090	844.5	0.093	929.4	0.095
0.5	810.2	0.086	713.3	0.078	811.3	0.085

The mathematical representation of the S-N curve and the statistical model curves for stress ratio $R = 0.1$ are illustrated in Fig. 5. Although a small number of experimental data points were used in the statistical analysis for $R = 0.1$, the S-N curve obtained per ASTM-E739 was highly comparable to the S-N curve as per the mathematical power law. The NLD curve is more conservative.

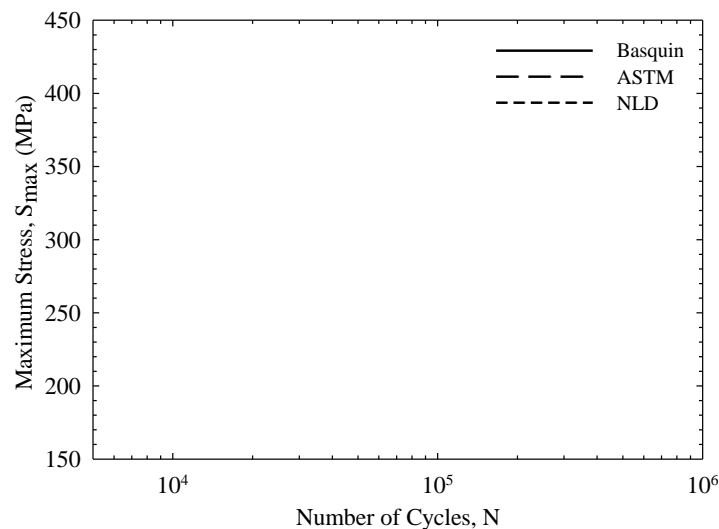


Fig. 5: Reliability-based S-N curves for unidirectional bioresin GFRP, $R = 0.1$

The power function of S-N curve and the statistical model curves for stress ratio $R = 0.5$ are indicated in Fig. 6. Similarly, the ASTM-E739 model curve is in good agreement with the mathematical representation of the S-N curve. However, both of these curves are unconservative for data with an intermediate number of cycles (e.g., N between 10,000 and 100,000). The NLD approach approximates the data in this intermediate range better than the other two models, but is conservative for lower or higher numbers of cycles.

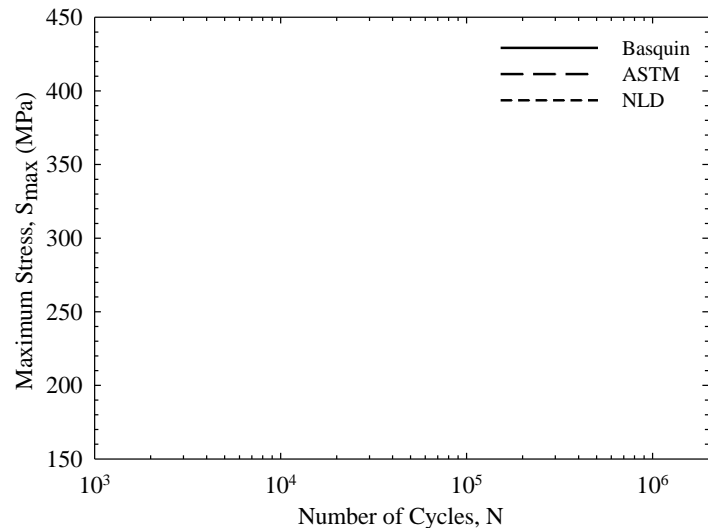


Fig. 6: Reliability-based S-N curves for unidirectional bioresin GFRP, $R = 0.5$

CONCLUSIONS

This research work highlights the results of tension-tension cyclic tests on GFRPs fabricated with a bioresin matrix. A fibre volume fraction of 36 % was considered. The bioresin-based GFRP specimens were tested in constant amplitude load control to failure and S-N curves were established for tension-tension loadings: $R = 0.1$ and $R = 0.5$. The following conclusions were drawn:

1. The residual tensile strength was approximately 45% after half a million cycles for tension-tension stress ratios.
2. Fatigue behaviour of the bioresin GFRPs was comparable to the fatigue behaviour of GFRPs with conventional resins.
3. The statistical model of ASTM E739-10 (2015) showed good agreement with the mathematical representation of S-N curves. This model was less conservative than the NLD approach.

ACKNOWLEDGMENTS

The authors would like to thank the financial support of the NSERC CREATE Sustainable Engineering in Remote Areas (SERA) program. Many thanks go to the technical staff at Queen's University for their assistance.

REFERENCES

- Y. Al-Assaf, H. El Kadi (2001). "Fatigue life prediction of unidirectional glass fiber/epoxy composite laminae using neural networks", *Journal of Composite Structures*, 53(1), 65-71.
- ASTM D3039 (2014). "Standard test method for tensile properties of polymer matrix composite materials", ASTM International.
- ASTM D3479/D3479M12 (2012). "Standard test method for tension-tension fatigue of polymer matrix composite materials", ASTM International.
- ASTM E739-10 (2015). "Standard Practice for Statistical Analysis of Linear or Linearized Stress-Life (S-N) and Strain-Life (ϵ -N) Fatigue Data", ASTM International.
- Basquin OH (1910). "The exponential law of endurance Tests", *Proceedings of ASTM*, Vol. 10, 625-630.
- H. El Kadi, F. Ellyin (1994). "Effect of stress ratio on the fatigue of unidirectional glass fibre/epoxy composite laminae", *Composites*, 25(10), 917-924.
- J.A. Epaarachchi, P.D Clausen (2003). "An empirical model for fatigue behavior prediction of glass fibre-reinforced plastic composites for various stress ratios and test frequencies". *Composites Part A: Applied science and manufacturing*, 34(4), 313-326.
- A. Hosoi, N. Sato, Y. Kusumoto, K. Fujiwara, H. Kawada (2010). "High-cycle fatigue characteristics of quasi-isotropic CFRP laminates over 10^8 cycles (initiation and propagation of delamination considering interaction with transverse cracks)", *International Journal of Fatigue*, 32(1), 29-36.
- J. A. Lee, D. P. Almond, B. Harris (1999). "The use of neural networks for the prediction of fatigue lives of composite materials", *Composites Part A: Applied Science and Manufacturing*, 30(10), 1159-1169.
- S. F. Shuler, J. W. Holmes, X. Wu, D. Roach (1993). "Influence of Loading Frequency on the Room-Temperature Fatigue of a Carbon-Fiber/SiC-Matrix Composite", *Journal of the American Ceramic Society*, 76(9), 2327-2336.

A. P. Vassiloupoulos, T. Keller (2011). "*Fatigue of fiber-reinforced composites*", Springer Science & Business Media.

A. Watfa, A., M.F. Green, A. Fam (2017). "Fibre Reinforced Polymers with Bioresins for Wind Turbine Towers-Material Investigation", *5th International Conference on Durability of Fibre Reinforced Polymer (FRP) Composites for Construction & Rehabilitation of Structures*, Sherbrooke, Canada.



ILLUMINATED BIOBASED SANDWICH FACADE WITH NATURAL FIBRE REINFORCED POLYMER AND CARDBOARD CORE

Carolin Petzoldt¹, Ralf Gliniorz¹, Andreas Ehrlich¹, Sandra Gelbrich¹, Lothar Kroll¹

¹ *Technische Universität Chemnitz, Institute of Lightweight Structure, 09107 Chemnitz, Germany, Email: carolin.petzoldt@mb.tu-chemnitz.de*

ABSTRACT

This paper reports about the development and implementation of a free forming facade system, consisting of biobased sandwich elements. The build-up of the sandwich contains face sheets from natural fibre reinforced polymer (NFRP), using flax fibres and biobased epoxy resin respective pre-accelerated, filled polyester resin with excellent weather resistance and no significant reduction in fire performance, and a stuck cardboard core structure. Furthermore a formwork system was designed enabling biobased sandwich elements to be produced with special needs according to efficiency and architectural design. As a result, the biobased and sustainable sandwich elements exhibit low system weight, high sound reduction and sufficient load capacity for the use as facade elements. Additionally LED-strips were integrated for illuminating the facade elements. Because of the regular pattern of the stuck cardboard core and the translucent face sheet laminates the facade works like a screen on which each created pixel can be controlled in RGB-colours. Therefore an area of 10 m x 5 m biobased sandwich facade with 25 elements is planned as a reference object in Chemnitz (Germany), forming a facade with 100 x 48 pixels. In summary the illuminated biobased sandwich element produced with an efficient technology of production and with the use of renewable resources can replace extensively 3D-formed customary facade systems.

KEYWORDS

Interactive FRP-material; Eco-composite, biobased composite materials; Characterization of FRP materials.

INTRODUCTION

Globally, the growth of population and economy increase the consumption of natural resources and energy from non-renewable materials, like raw oil, natural gas, coal and uranium (Tichelmann et al. 2007). More than 30% of total energy consumption and more than 50% of raw material consumption are used for the construction industry with their emerged buildings (Haase et al. 2011). This aspect has caused growing interests in many countries and international politics for sustainability in the last 20 years. Hence the building envelope as an integral part of buildings and renewable resources have a key role for the implementation of sustainability. So the use of natural fibre reinforcement and biobased materials contribute to the reduction of limited fossil resources and optimize the whole ecological balance sheet and concept of sustainability within the building industry.

In this context fibre reinforced polymer (FRP) composites, consisting of natural fibres and biobased resin systems, are predestined being used in facade elements for buildings. They are ecologically beneficial and energy efficient and are supposed to replace less environmental and petrochemical FRP (Ehrenstein 2006). Current application fields for natural fibre reinforced polymers (NFRP) are for example automotive industry, bio-medicine, packaging industry and building industry (e. g. Mühsig et al. 2007, Türk 2014, Paul 2010). Natural fibres, like domestic flax, hemp or jute have low fibre density and similar specific stiffness compared to glass fibres, what is interesting for the use as fibre reinforcement in lightweight structures and components in the building industry. Furthermore natural fibres have the distinction of a low energy demand of 9.55 MJ/kg (flax fibres) in comparison to glass fibres mats with 54.7 MJ/kg (Holbery and Houston 2006). Moreover the biobased resin component has a significantly reduced carbon footprint of about 40% compared to petrochemical resin systems (embodied energy of 76 MJ/kg) (Sicomini 2017, Howarth et al. 2014).

Research in the fields of innovative facade structures from biobased materials with high potential for lightweight design has been object of scientific and application-oriented efforts (e. g. Köhler 2013, Vermeulen 2013, Li and Knippers 2015). Also the integration of additional functions like the illumination of elements are shown in the development of a smart GFRP honeycomb sandwich for interactive bridges (Rudolph et al. 2016).

Therefore the aim of the project was the development of a free forming facade system from biobased materials and integrated functions (like illuminating the elements) used in the field of modern architecture.

METHOD OF SOLUTION

Materials and Sample Preparation

Figure 1 illustrates the build-up of the biobased sandwich element with two face sheets covering a core component. They are adhered with each other and transmit forces and stresses, like a traditional sandwich element (Gelbrich 2016). The outer face sheet is from NFRP, consisting of a flax fibre reinforcement and biobased resin matrix with a thickness of 4 mm. Therefore two layers of a bidirectional flax fibre woven fabric (surface weight of 400 g/m²) were integrated in an epoxy resin, based on biological components with 56% carbon from vegetable origin. The biobased epoxy resin SR GreenPoxy 56 from Sicomin has a Young's modulus of 3.2 GPa, a tensile strength of 50 MPa, an elongation of break of 1.6% and a glass transition temperature of 53°C. The flax fibre reinforced face sheet laminates show a tensile strength of 67 MPa, a bending strength of 97 MPa and a Young's modulus of 5.6 GPa, based on a calculated fibre volume content of 24 Vol.-%. The inner face sheet consists of two layers bidirectional flax fibre woven fabric and a pre-accelerated, filled polyester resin with excellent weather resistance and no significant reduction in fire performance. The polyester resin CRYSTIC® 356PA from Scott Bader Company Limited has a tensile strength and Young's modulus of 45 MPa and 7.4 GPa. The elongation at break amounts 0.7%.

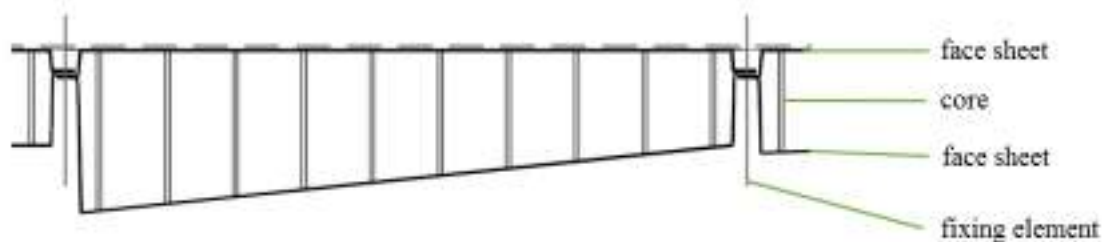


Figure 17: Facade element, horizontally sectional drawing

The used core material was a stuck cardboard structure (Figure 18, b) with advantages such as low weight, resource efficiency, recyclability and the use of recycled material. The cardboard material consists of a BC-flute (combination of fine and medium flute) with a material thickness of 6.91 mm and a surface weight of 1191 g/m². So the cardboard was cut in 2D elements and stuck together to build a 3D core component. The width of the compartments as well as the height of the core component amounted 100 mm to 200 mm.

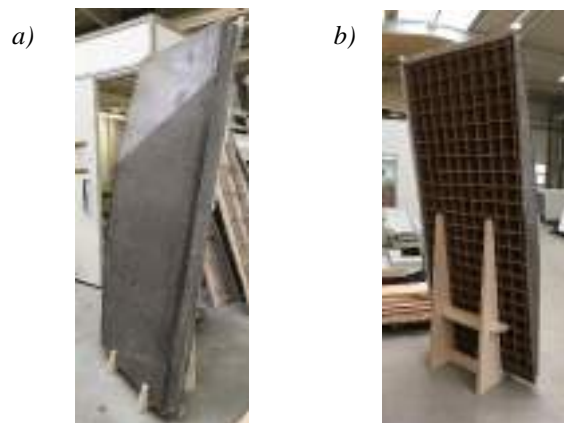


Figure 18: Biobased facade element without second NFRP face sheet laminate (a: front view, b: rear view)

Additional a special coating based on sodium silicate was applied to protect the cardboard material against environmental conditions and to avoid water absorption and inflammability. Several specimens were prepared for the mechanical and physical characterization of the constituent materials and composite material. The

manufacturing process of the face sheet laminates occurred with hand lay-up process. Furthermore the cardboard core was processed “wet-in-wet”.

Characterization

Characterization of NFRP laminates

The NFRP laminates were tested according to water vapour diffusion following DIN EN ISO 12572. The round samples with a diameter of 80 mm were adhered airtight on top of a glass receptacle with the drying agent calcium chloride (CaCl_2) inside (Figure 19, a). With a defined temperature and relative humidity of 23°C and 50 % the water vapour transmission between the surrounding air and the specimen were measured periodically.

Characterization of cardboard core

To validate the cardboard core the flammability and flame dispersion were determined by means of the flammability test apparatus CEAST UL 94, with samples which measured 90 mm × 230 mm based on DIN 4201 class B2 (Figure 19, b). Therefore a flame was applied to the specimen for 15 s. The test was failed, when the flame spread achieved the measuring mark at 190 mm within 20 s.

Furthermore the water absorption was measured by means of the Cobb-Unger test apparatus based on DIN EN ISO 535 (Figure 19, c). The Cobb₆₀ value determines the calculated mass of water, which is absorbed in 60 s from 1 m² cardboard. So the cardboard was clamped into the test apparatus, which was filled with water. After turning the apparatus, the water was applied to the cardboard for 60 s. With the measurement of the cardboard weight before and after the test, the water absorption can be calculated.

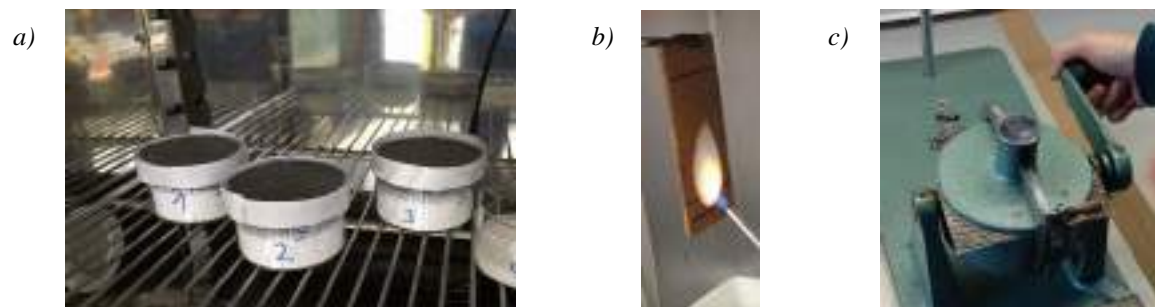


Figure 19: NFRP-samples for water vapour diffusion (a), cardboard sample whilst fire test (b) and Cobb-Unger test apparatus (c)

Characterization of biobased sandwich element

The validation of the biobased sandwich element includes 4-point-bending tests by means of the Toni Technik ToniNorm with samples which measured 1000 mm × 200 mm × 100 mm (length × width × height). The span width set was 900 mm, the upper support distance was 300 mm and the load speed 50 N/s constant.

Furthermore the flammability and flame dispersion were measured, as well as the airborne sound reduction and thermal conductivity. So the airborne sound reduction index was determined by means of the SINUS transmission tube AFD 1200 Acoustic Tube based on DIN EN ISO 717-1. The round samples had a diameter of 40 mm and a height of 100 mm.

In addition to that the heat transition (U value) was tested. Therefore the thermal conductivity of the NFRP laminates were measured by means of thermographic camera FLIR-T62101 of FLIR Systems GmbH. The measurement occurred with relative measurement. The specimen were integrated in an institutes own heat-insulated test frame with dimensions of 500 mm × 500 mm. Two radiant heater with 2000 W each were used as heat source. Hence the average temperature gradient between the irradiated surface and the unirradiated surface was measured with the use of thermographic pictures. In comparison to a reference test, the coefficient of thermal conductivity were determined of the NFRP laminates. Furthermore the U value was calculated based on the measured coefficient of the thermal conductivity, the calculated heat transmission of the materials and the defined heat transmission on the in- and outside of the sandwich element according to DIN EN ISO 6946.

Furthermore the flammability and flame dispersion of the biobased sandwich composite were determined by means of a single burning item test (Figure 20, b) following DIN EN 13823 with samples which consisted of two sample parts arranged like a corner, which measured 500 mm × 155 mm × 1500 mm and 1000 mm × 155 mm × 1500 mm (Figure 20, a). The test specimen have been stored for conditioning until constant mass according to DIN EN 13238-6 prior to testing. The flame with a heat release rate of 30 kW were placed on the inside of the specimen edge (Figure 20, b), consisting of flax fibre reinforced polymer with fire retardant polyester resin. The fire behaviour of the specimen is tested for a period of 20 min. Further determinations according to flammability and

flame dispersion following DIN EN ISO 11925-2 with samples which measured 90 mm × 50 mm × 250 mm and a classification regarding reaction to fire tests based on DIN EN 13501-1 were realized.

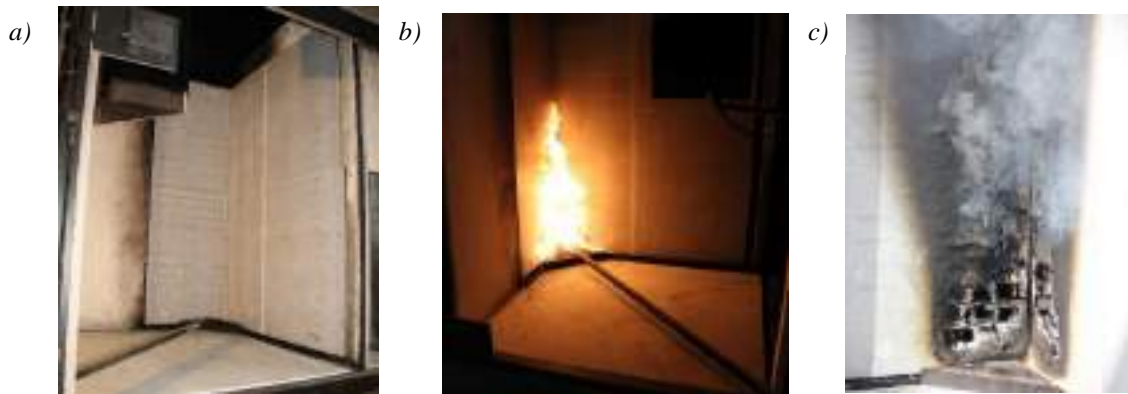


Figure 20: Biobased sandwich element for single burning item test according to DIN EN 13823 (a) with defined flame (b), and smoke formation after single burning item test (c)

Integration of Function and Reference Object

The benefit of the cardboard core consists of sustainability, light weight character and high stiffness. But the unique characteristic is created by the regular pattern of the stuck cardboard structure. They shape square-formed cavities between the translucent face sheets and can so be illuminated as pixels of a matrix screen. With the use of special LED-stripes each resulting pixel is separately activated by a controller and all pixels together form a matrix screen in RGB-colours, which can give out information or advertising (Figure 21, a).

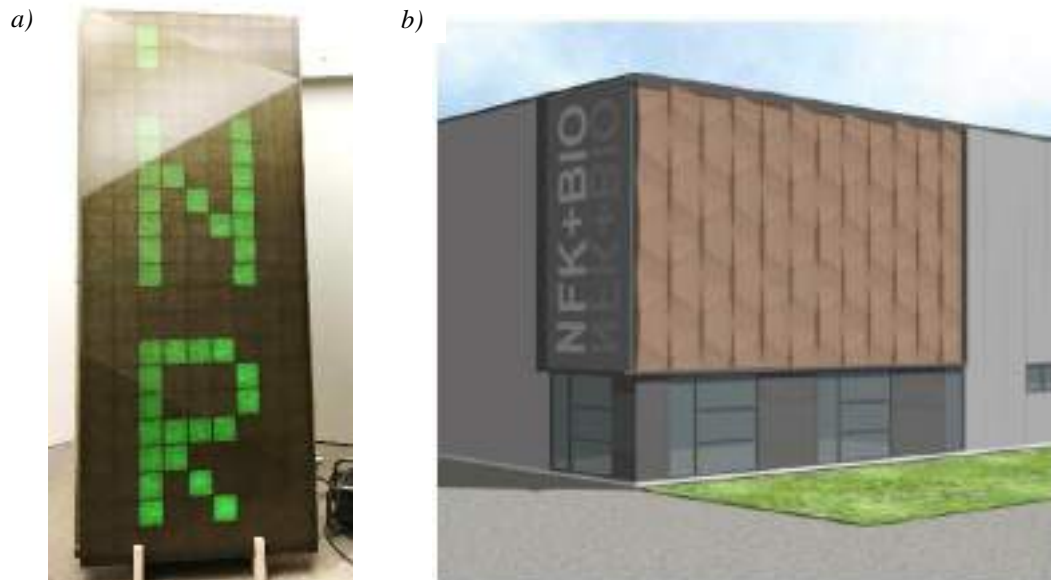


Figure 21: Design of illuminated element (a) and reference object (b)

Based on an architectural design the biobased sandwich elements will be mounted on a production building in Chemnitz, Germany. It replaces a part of a building envelope on an area of 10 m to 5 m (Figure 21, b). With 15.840 LEDs the created screen resolution here is about 100 to 50 pixels. So the 25 extensively 3D-formed elements in parametrical design are manufactured in one formwork with regard to resource efficiency and economical aspects. The biobased sandwich facade will be finished in spring 2018 as reference object.

RESULTS AND DISCUSSIONS

Properties of the NFRP Face Sheets and Cardboard Core

Using a Cobb-Unger test apparatus, water absorption of 58 g/m^2 in 60 s were determined in the coated cardboard core (cardboard without coating: 63 g/m^2). This means the cardboard core still can absorb moisture, which results in a decrease of the mechanical properties. Therefore the cardboard core structure has to be protected by the NFRP sheet laminates. According to that, the water vapour diffusion of the NFRP face sheet laminate was classified as resistant corresponded to class V3 according to DIN EN 1063 with a water vapour transmission rate of $36.1 \text{ mg}/(\text{m}^2 \text{ h})$ after 24 days. So the resistant face sheet laminates, according to water vapour diffusion, showed that the sandwich composite works like a closed system, where moisture almost cannot entry into the composite and into the cardboard structure. So the cardboard core is protected against moisture and ingress of water. With a special clamp-in valve with semipermeable membrane even the surplus moisture inside of the sandwich element can diffuse outside.

Regarding flammability and flame dispersion the coated cardboard core passed all requirements according to class B2 based on DIN 4102 in comparison to an uncoated cardboard core, which failed the test. So when the cardboard core is effected by fire the remained water of the sodium silicate coating is released whilst foam formation. Because of that, the flammability and flame dispersion is handicapped. After flame exposure the cardboard core has a self-extinguished behaviour. Because of that the sodium silicate coating of the cardboard core is imperative.

Furthermore the cardboard core had a determined shear strength of 0.1 MPa and a shear modulus of 7 GPa , which is comparable with traditional PUR-foam sandwich elements (shear strength about 0.2 MPa , shear modulus about 5 GPa).

Properties of the Biobased Sandwich

The biobased sandwich element has a sound reduction index of 42 dB , determined by transfer-matrix method by Song und Bolton (2000) and according to DIN EN ISO 717-1 (Figure 22, a). The significant decrease of the sound reduction index at 500 Hz (Figure 22, a) can be ascribed with coincidence frequency, where the wavelength of the airborne sound correlates with the flexible shaft of the composite. In comparison to traditional sandwich elements for facades (consisting of aluminium face sheets and PUR foam core) with a sound reduction index of about 26 dB , the biobased sandwich composite outdo the requirements for acoustical behaviour.

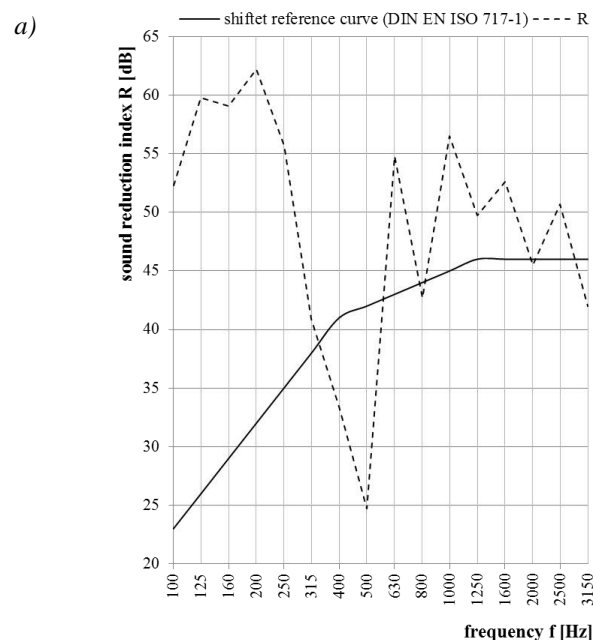


Figure 22: Sound reduction index (R) of biobased sandwich element in dependence of the frequency

Using the thermographic camera, a coefficient of thermal conductivity of $0.063 \text{ W}/(\text{m}\times\text{K})$ was determined for the NFRP laminates. The pursued calculation of the U value according to DIN EN ISO 6946 yielded a thermal transition of the biobased sandwich element of $2.7 \text{ W}/(\text{m}^2\times\text{K})$. This comparatively high U -Value results from missing heat insulation and an air circulation inside the core compartments. For a reduced heat transition the construction of the cardboard core element was adjusted with an additional layer of heat insulation. The integrated

rock wool insulation had a width of 60 mm and a coefficient of thermal conductivity of 0.035 W/(m×K). Hence, the calculated U value was decreased to 0.47 W/(m²×K). Thus, the requirements regarding EnEV (Bundesministerium für Umwelt, Naturschutz und Reaktorsicherheit 2015) in Germany are achieved, which allows a usage for new production buildings according to heat insulation guidelines.

Furthermore the fire behaviour was tested according to DIN EN 13501-1. The average result for the FIGRA_0.2 and FIGRA_0.4 parameter is 88.8 W/s and 87.4 W/s. The total released energy in the first 600 s amounts 5.8 MJ. On the basis of that the biobased sandwich composite is classified as flame retardant and corresponded to class of fire behaviour B – s3 – d0 (according to DIN EN 13501-1), with unlimited smoke production and no flaming droplets. In general this complies the condition for fire behaviour of facade elements on production buildings in Germany.

CONCLUSIONS

At the current stage of development, a biobased sandwich facade element was able to be implemented using renewable resources in lightweight construction method. Arising from the specifications placed on the biobased sandwich element, the following was developed in the context of the presented research: load-bearing NFRP face sheets were assembled, a cardboard core structure with special coating was developed and integrated into the sandwich composite, a formwork system at prototype scale was designed enabling the biobased sandwich elements to be produced with an efficiency- and application-oriented approach and examined in practical investigations. Integrating flax fibres in a biobased epoxy resin generated load-bearing face sheets with a positive effect on water vapour diffusion regarding the core component. The mechanical investigations showed that the core element of the sandwich facade can be made of coated cardboard structure. Proof was also given of fire retardant, resistance of flame dispersion and flaming droplets, as well as good sound reduction. The tests regarding heat insulation and heat transition showed a sufficient U value according to german heat insulation guideline EnEV by adding a rock wool insulation into the sandwich composite. Furthermore, the integration of illumination was achieved, which builds the unique characteristic of the sandwich facades.

This new biobased sandwich facade meets requirements as regards resource efficiency in combination with modern architecture. Especially the use of cardboard and natural fibres for facade elements can be exemplary for following projects to increase the use of renewable raw materials.

ACKNOWLEDGMENTS

We are very grateful to our donor of subsidies "FNR-Fachagentur Nachwachsende Rohstoffe e.V.", BMEL and our associate partners Fiber-Tech Construction GmbH and richter & heß Verpackungsservice GmbH.

REFERENCES

- Bundesministerium für Umwelt, Naturschutz und Reaktorsicherheit (2015). „Energieeinsparverordnung (EnEV)“, www.bmub.bund.de/P3427/; access: 27.11.2017.
- G. W. Ehrenstein (2006). „Faserverbundkunststoffe. Werkstoffe – Verarbeitung – Eigenschaften“.
- S. Gelbrich (2016). „Funktionsintegrative Leichtbaustrukturen für Tragwerke im Bauwesen“, *Universitätsverlag Chemnitz*, ISBN 978-3-96100-005-0.
- W. Haase et al. (2011). „Adaptive textile und folienbasierte Gebäudehüllen“, *Ernst & Sohn Verlag für Architektur und technische Wissenschaften GmbH & Co. KG*, Bautechnik 88, 2, 69-75.
- J. Holbery, D. Houston (2006). “Natural –Fiber-Reinforced Polymer Composites in Automotive Applications”, *The Journal of The Minerals, Metals & Materials Society*, November, 58, 11, 80-86.
- J. Howarth et al. (2014). “Energy intensity and environmental analysis of mechanical recycling of carbon fibre composite”, *Journal of Cleaner Production*, 81, 46-50, ISSN 0959-6526, <https://doi.org/10.1016/j.jclepro.2014.06.023>.
- C. Köhler (2013). “Biobased plastics for exterior facades”, *Bioplastics Magazine*, 8, 12-14.
- J. Li, J. Knippers (2015). “Segmental Timber Plate Shell for the Landesgartenschau Exhibition Hall in Schwäbisch Gmünd the Application of Finger Joints in Plate Structures”, *International Journal of Space Structures*, 30, 2.
- J. Mühsig et al. (2007). „Karosserie aus Naturfasern und Pflanzenöl“, *Kunststoffe*, 3.
- N. Paul (2010). „Spatenstich für ein Bürogebäude der neuen Generation“

E. Rudolph et al. (2016). "Development of a smart GRFP honeycomb sandwich for interactive bridges", In: J.G. Teng, J.G. Dai (Ed.): *Proceedings of the Eight International Conference on Fibre-Reinforced Polymer (FRP) Composites in Civil Engineering (CICE 2016)*, 113, ISBN 978-988-14480-26.

Sicomini (2017). "Lebenszyklusanalyse"; Sicomin Epoxy Systems; https://www.timeout.de/pdf/SR_GP_Greenpoxy%20Lebenszyklus-Analyse_2017_09_04.pdf, access: 17.11.2017.

B. Song, J. Bolton (2000). "A transfer-matrix approach for estimating the characteristics impedance and wave numbers of limp and rigid porous materials", *Journal of the acoustical society of America*, 107, 3.

K. Tichelmann (2007). „Schwerpunkt Nachhaltigkeit – Eigenschaften und Potentiale des Leichtbaus“, *Bau.Genial*.

O. Türk (2014). „Stoffliche Nutzung nachwachsender Rohstoffe: Grundlagen – Werkstoffe – Anwendungen“, *Springer Fachmedien*, ISBN 978-3-8348-1763-1, DOI 10.1007/978-3-8348-2199-7.

M. Vermeulen (2013). "World's first biobased façade"; <http://www.marcovermeulen.nl/projecten/selectie/122/gasontvangststation>; access: 17.11.2017.



EFFECTS OF CNF CONTENT ON MECHANICAL PROPERTIES OF FLAX FIBER REINFORCED NANOCOMPOSITES

Y. Wang¹, B. Wan² and X. Yin³

^{1,3} Dalian University of Technology, School of Civil Engineering, Dalian, China;

² Marquette University, Department of Civil, Construction and Environmental Engineering, Milwaukee, USA.

(corresponding author: baolin.wan@marquette.edu)

ABSTRACT

Flax fibers are widely grown materials which have short growth cycle, low density, high specific strength, and high specific stiffness. Therefore, flax fiber reinforced polymer (FFRP) has potential to replace part of GFRP and CFRP in engineering applications. Adding nanoparticles to epoxy resin matrix can improve the mechanical and thermal properties, and fire resistance of the composite material. In order to study the effect of carbon nanofibers (CNF) on the mechanical properties of epoxy resin and FFRP, different amounts of CNF were dispersed in the epoxy resin matrix by using high-speed mechanical mixing, vacuum and ultrasonic dispersion methods in this study. Direct tensile tests were performed to evaluate the tensile strength, modulus of elasticity and elongation at break of the CNF modified epoxy and the flax fiber reinforced nanocomposites. Scanning electron microscope (SEM) was also used to observe the CNF distribution in the epoxy resin matrix. The test results show that both tensile strength and modulus of elasticity of the nanocomposites increased first and then decreased with the increase of the content of CNF. However, all specimens with CNF had larger tensile strength and modulus of elasticity than those of specimens with pure epoxy resin. The maximum tensile strength and modulus of elasticity happened in the flax fiber reinforced nanocomposite with 0.5% of CNF in epoxy resin by weight. The elongation of the specimens increased continuously with the increase of CNF content. SEM images show that CNF dispersed more uniformly in the specimens with 0.5% of CNF than those with 1.0% of CNF. This is the reason why the mechanical properties of the nanocomposites with 0.5% of CNF were better than those with 1.0% of CNF.

KEYWORDS

Carbon nanofibers (CNF); Flax fiber reinforced polymer (FFRP); Mechanical properties; Nanocomposites; Scanning electron microscope (SEM).

INTRODUCTION

Fiber reinforced polymer (FRP) composite materials with advantages of lightweight, high strength, and excellent durability have been applied as repairing and retrofit purposes for existing structures and as a construction material for new structures (Teng et al. 2002; Karbhari et al. 2003). However, the relatively high cost of glass or carbon fiber FRPs has limited their broad applications. In recent years, natural fibers have been studied to replace glass or carbon fibers in FRP because of their low price and environmentally friendly (Coroller et al. 2013). Flax fibers are widely grown materials which have short growth cycle, low density, high specific strength, and high specific stiffness. Therefore, flax fiber reinforced polymer (FFRP) has potential to replace part of GFRP and CFRP in the application of civil infrastructures. It will contribute to the development of low-carbon buildings and cities to address global warming and promote sustainability of the infrastructures.

Nanoparticles have large surface area and stable structure due to its small-scale structure. They can form strong bond with resin. Therefore, adding nanoparticles to epoxy resin matrix can improve the mechanical and thermal properties, and fire resistance of the composite material (Wang and Pinnavaia 1998; Lagly 1999; Alexander and Dubois 2000; Ray et al. 2006; Khanbabaie et al. 2007). Mahfuz et al. (2004) found that the tensile strength and modulus of elasticity of the composite were increased by 16.9 and 16.37%, respectively, after adding 2% of carbon nanoparticles/whiskers by weight. The addition of small percent of carbon nanotubes (CNT) to the epoxy matrix has a remarkable effect on the mechanical properties (Allaoui et al. 2002). Carbon nanofiber (CNF) has a length in the order of micron while its diameter in the order of nano-meter, which is produced in a similar manner as CNT, but has different geometry from concentric carbon nanotubes. The geometry of CNFs has a unique structure as stacked truncated conical or planar layers along the filament length, which makes them useful as reinforcing fillers in polymeric composites (Choi et al. 2005).

In this research, different amounts of CNF were dispersed in the epoxy resin matrix by using high-speed mechanical mixing, vacuum and ultrasonic dispersion methods. Direct tensile tests were performed to evaluate

the tensile strength, modulus of elasticity and elongation at break of the CNF modified epoxy and the flax fiber reinforced nanocomposites to study the effect of CNF on the mechanical properties of epoxy resin and FFRP. Scanning electron microscope (SEM) was also used to observe the CNF distribution in the epoxy resin matrix.

EXPERIMENTAL WORK

Materials and Specimen Preparation

The epoxy used in this study is a commercially available two-part epoxy (SWANCOR 2511-1A/BS, produced by Shangwei Wind Power Product Co., China). The carbon nanofiber, CNF-24, is PR-24-XT-HHT which is produced by Pyrograf Products Co., USA. The diameter, length and surface area of the CNF are 100 nm, 50-100 μm and 40-50 m^2/g , respectively, provided by the manufacturer. The bi-directional flax fabrics supplied by Changli Textile Company in Harbin, China, was used in this study. The flax fabric has normalized thickness of 0.16 mm and its density is 1.5 g/mm^3 . The manufacturer provided tensile strength and modulus of elasticity of the flax fabric with epoxy in warp direction are 185 MPa and 13.6 GPa, respectively. They are 349 MPa and 19.7 GPa, respectively, in the weft direction. In this study, the specimens were tested in the warp direction.

The nanocomposites with CNF contents of 0%, 0.25%, 0.5%, and 1% of epoxy's weight, respectively, were prepared in this study. At first, a mechanical mixer was used to mix CNF into Part A of the epoxy for 30 minutes at the speed of 2000 r/min. Then it was put into ultrasonic disperser for eight hours. During the dispersion process, the container for the epoxy with CNF was sealed with plastic film and put in water bath with constant temperature of 60 $^{\circ}\text{C}$ to reduce the viscosity of the mixture. After the completion of dispersion, the mixed solution was placed in a vacuum chamber to be evacuated for 30 minutes or until no bubbles coming out. For specimens with CNF content larger than 0.5% by weight (i.e., 1%), acetone was added during mixing to improve the dispersion of the CNF in the epoxy. In order to remove the acetone after the dispersion process was completed, the stirring speed was increased up to 3000 r/min and the mixture was placed in a constant water bath with temperature of 60 $^{\circ}\text{C}$ while mechanical stirring. After the CNF was well mixed into Part A of the epoxy, the curing agent (Part BS) was added into the completely dispersed mixture. The mixture with all components (Part A, CNFs and Part BS) was preliminary stirred with a glass rod and then stirred by the mechanical mixer for five minutes. The mixture was placed into vacuum chamber again to be evacuated for 20 minutes to remove the air which could be trapped into the mixture during the mixing process. To make the specimens of epoxy (Figure 1a) with different amount of CNF, the mixture was poured into forms to cure for 48 hours in room temperature (23 $^{\circ}\text{C}$). The solid specimens were removed from the forms and then cured in an oven with temperature of 80 $^{\circ}\text{C}$ for another 10 hours before they were cooled to room temperature for testing.

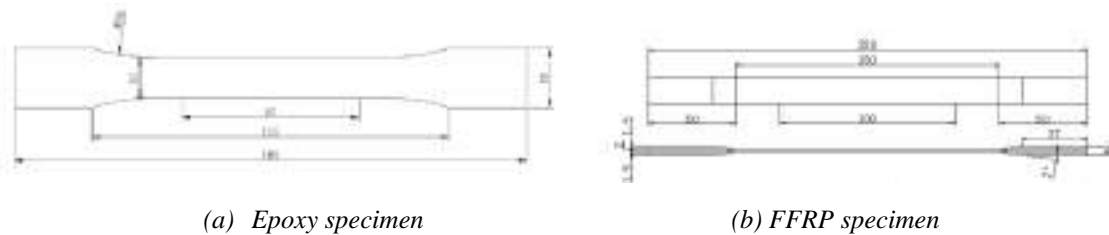


Figure 1: CNF modified epoxy and FFRP specimens for tensile test (unit: mm)

To make the specimens of flax fiber reinforced polymer (FFRP) with different amounts of CNF, the flax fiber fabric was cut to the size of 350 \times 350 mm^2 . A flat glass was used as the form to make flax fiber reinforced nanocomposite specimens. A layer of thin polyester film was placed on the surface of the glass for easily removing the specimen after it was cured. A brush was used to apply a layer of CNF modified epoxy uniformly on the polyester film, and then a piece of flax fiber fabric was placed on top of it. A plastic roller was used to roll the flax fiber fabric back and forth to let it to be completely soaked in the epoxy and to extrude air bubbles. The second layers of epoxy and flax fiber fabric were applied by following the same procedure. Another layer of thin polyester film and another piece of glass were used to cover the top of the specimen. A weight of 30 kg was placed on the top of the glass and it was left for curing for one week in room temperature. The extra fibers at the outside of the specimens were cut by a scissor before they were placed in an oven for curing at the temperature of 60 $^{\circ}\text{C}$ for 24 hours. They were then stored in lab at room temperature for tests. The cured FFRP plates were cut to the size and shape of specimen as shown in Figure 1b by using a stone cutting machine before test.

Mechanical Property Tests

The uniaxial tensile tests were performed by following ASTM D638 specifications. The test was performed by displacement control at the loading rate of 2 mm/min at room temperature. The load was measured by the load cell. An extensometer with gauge length of 50 mm was attached to the middle region of the specimen by rubber bands to measure the strain during the test. An FFRP specimen with CNFs under testing is shown in Figure 2. The load and strain data were recorded by a data acquisition system.



Figure 2: Tensile test of FFRP with CNFs

SEM Examination

It is very difficult to distribute nanofibers uniformly in the epoxy matrix. The properties of the composite with nanoparticles depend not only the properties of the constitutive materials, but also the distribution of the nanoparticles. Small pieces of CNF modified epoxy near the fracture of some tensile specimens were cut for examining the distribution of CNF in the composite material by a scanning electron microscope (SEM). The sample was stuck on a small piece of metal with double-sided conductive tape, and then was sputter-coated with gold prior to SEM investigation.

RESULTS AND DISCUSSIONS

Mechanical Properties of CNF Modified Epoxy

Figure 3 shows the ultimate strength, modulus of elasticity and elongation at break, respectively, of the epoxy specimens with different amounts of CNFs.

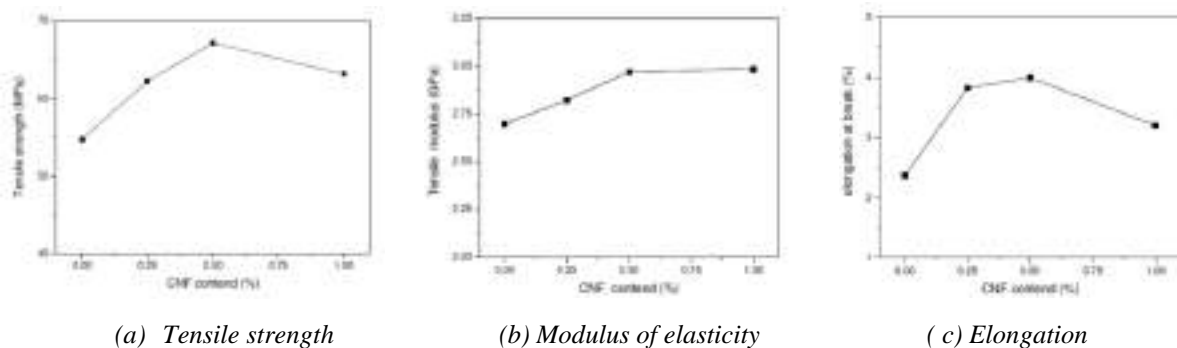


Figure 3: Mechanical properties of epoxy with different amount of CNFs

Figure 3a shows that the tensile strength of the composite increased with the increase of the content of CNFs, then decreased when the amount of CNFs was larger than 0.5% of its weight. However, all specimens with CNFs had higher tensile strength than the pure epoxy specimen. The maximum tensile strength increase was 22.6% when the CNFs content was 0.5% by weight. The modulus of elasticity increased with the increase of CNFs as shown in Figure 3b. The specimens with 0.5% and 1.0% of CNFs had similar modulus of elasticity, which were 10% and 10.37%, respectively, higher than that of pure epoxy specimen. With the increase of the content of CNFs, the elongation at break increased first and then decreased, but still higher than that of the pure epoxy resin as shown

in Figure 3c. The specimens with 0.5% of CNFs had largest elongation, which was 78.1% higher than that of the pure epoxy specimen.

The mechanical properties of epoxy with different amounts of CNFs are summarized in Table 1. It can be seen in the table that adding a small percentage of CNFs in the epoxy resin matrix clearly increases the mechanical properties of the epoxy. This is because the CNFs work with epoxy to resist the load when the CNFs are dispersed evenly into the matrix. There are stable interfaces between the surface of CNFs and the epoxy matrix due to the interaction between the atoms on the CNF surface and the polymer in the matrix. Such stable interface can transfer force well between the two materials, therefore increases the strength of the composite. The increase of modulus of elasticity is due to the higher hardness and stiffness of the CNFs. The toughness of the composite increases when the CNFs are distributed evenly in the matrix. Therefore, the elongation increases. However, when the content of CNFs is high (1.0% in this study), the CNFs may agglomerate and result in voids and bubbles. Therefore, the tensile strength and elongation decrease when too much CNFs are added.

Table 1: Mechanical properties of CNFs reinforced epoxy composites

CNF content (wt.%)	Tensile Strength (MPa)	Gain in strength (%)	Modulus of elasticity (GPa)	Gain in modulus (%)	Elongation at break (%)
0	55	-	2.70	-	2.37
0.25	62	13.66	2.82	4.44	3.82
0.5	67	22.55	2.97	10	3.99
1.0	63	15.32	2.98	10.37	3.20

Mechanical Properties of FFRP with CNF

With the increase of the content of CNFs, both tensile strength and modulus of elasticity of the FFRP nanocomposites increased first and then decreased as shown in Figure 4. However, all FFRP specimens with CNF had larger tensile strength and modulus of elasticity than those of specimens with pure epoxy resin. The maximum tensile strength and modulus of elasticity happened in the flax fiber reinforced nanocomposite with 0.5% of CNF in epoxy resin by weight. Its tensile strength and modulus of elasticity were 11.82% and 25.49%, respectively, higher than those of specimens without CNFs. The elongation of the specimens increased continuously with the increase of CNF content. The elongation of the specimen with 1.0% of CNFs in its epoxy matrix increased 15.76%.

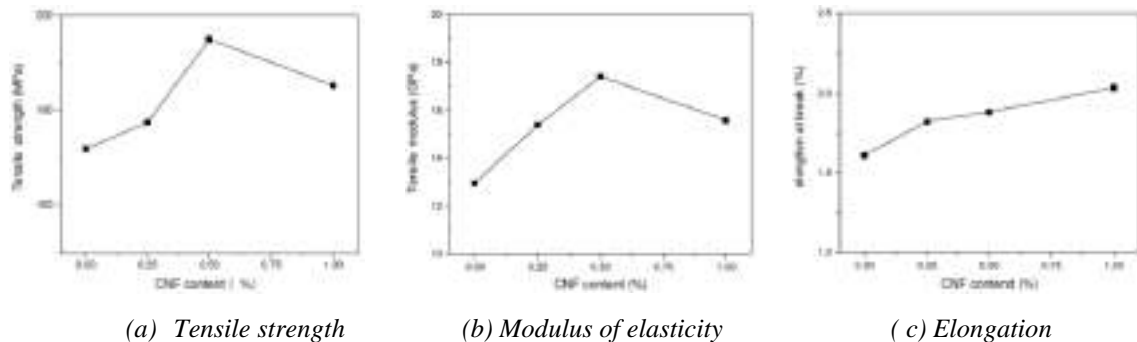


Figure 4: Mechanical properties of FFRP with different contents of CNF.

Table 2 lists the mechanical properties of FFRP with different amounts of CNFs in the epoxy matrix. The strength of the FFRP composite mainly depends on the strength of the flax fibers. Although the tensile strength of the epoxy matrix was increased due to the CNFs, the improvement of the tensile strength of the FFRP composite was not as high as that of the epoxy specimens with same amounts of CNFs.

Table 2: Mechanical properties of FFRP with different amounts of CNFs in the epoxy matrix

CNF content (wt.%)	Tensile Strength (MPa)	Gain in strength (%)	Young's modulus (GPa)	Gain in modulus (%)	Elongation at break (%)
0	172	-	12.98	-	1.71
0.25	177	3.20	15.39	18.57	1.82
0.5	195	13.40	17.42	34.20	1.88
1.0	185	7.72	15.59	20.11	2.03

SEM Images

Figure 5 shows the SEM images of the fracture sections of the epoxy specimens with different amounts of CNFs, which were magnified by 10,000 times. The white lines in the images are the CNFs. Comparing Figures 5b and 5c, it can be seen that CNFs dispersed more uniformly in the specimens with 0.5% of CNFs than those with 1.0% of CNFs. This is the reason why the mechanical properties of the nanocomposites with 0.5% of CNF were better than those with 1.0% of CNF.

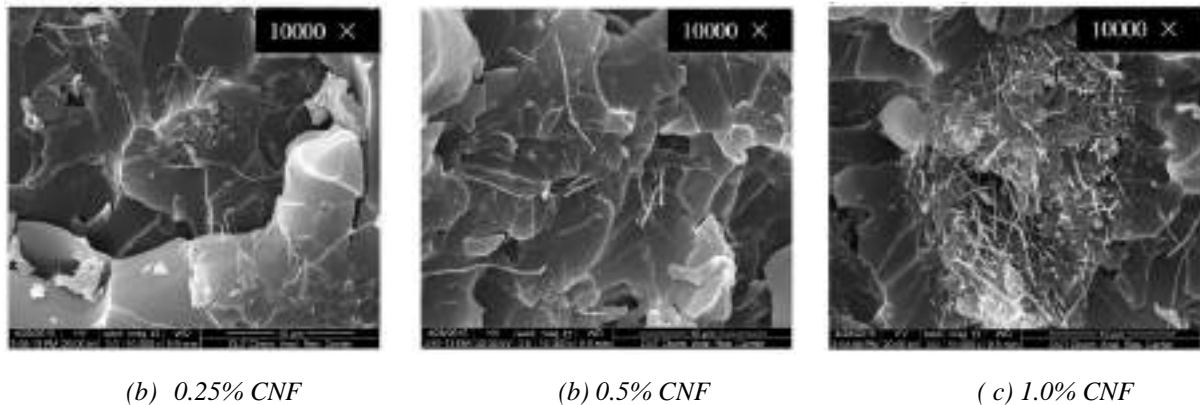


Figure 5: SEM images of the fracture sections of epoxy specimens with different amounts of CNFs (10,000 \times).

CONCLUSIONS

In this study, different amounts of carbon nanofibers (CNFs) were dispersed in the epoxy resin matrix by using high-speed mechanical mixing, vacuum and ultrasonic dispersion methods. Wet-layup method was used to make flax fiber reinforced polymer (FFRP) with different amounts of CNFs in the epoxy matrix. Direct tensile tests were performed to evaluate the mechanical properties of the epoxy and FFRP with CNFs. Scanning electron microscope (SEM) was used to observe the fracture surface of the specimens. Following conclusions can be obtained from this research:

1. With the increase of the content of CNFs, the tensile strength and elongation of the nanocomposites first increased and then decreased, but all higher than those of the pure epoxy specimens. The modulus of elasticity of the epoxy specimens continued to increase with the increase of CNFs. However, the moduli of elasticity of the specimens with 1% and 0.5% of CNFs by weight were very close.
2. The improvement of the tensile strength of the FFRP due to adding CNFs was not as high as that of epoxy specimens. This is because the strength of the FFRP composite mainly depends on the strength of the flax fibers. The maximum tensile strength and modulus of elasticity happened in the flax fiber reinforced nanocomposite with 0.5% of CNF in epoxy resin by weight. The elongation of the specimens increased continuously with the increase of CNF content.
3. SEM images show that CNF dispersed more uniformly in the specimens with 0.5% of CNF than those with 1.0% of CNF. This is the reason why the mechanical properties of the nanocomposites with 0.5% of CNF were better than those with 1.0% of CNF.

ACKNOWLEDGMENTS

The work described in this paper was supported by the National Basic Research Program (973 Program) (Grant No. 2012CB026200) in China, and the Haitian Scholar Program at Dalian University of Technology.

REFERENCES

- M. Alexander and P. Dubois (2000). "Polymer-layered Silicate Nanocomposites: Preparation, Properties and Uses of a New Class of Materials", *Materials Science & Engineering*, 28, 1–63.
- A. Allaoui, S. Bai, H.M. Cheng, and J.B. Bai (2002). "Mechanical and electrical properties of a MWNT/epoxy composite", *Composites Science and Technology*, 62, 1993–1998.

Y.K. Choi, Y. Gotoh, K.I. Sugimoto, S.M. Song, T. Yanagisawa, and M. Endo (2005). "Processing and characterization of epoxy nanocomposites reinforced by cup-stacked carbon nanotubes", *Polymer*, 46(25), 11489–11498.

G. Coroller, A. Lefevre, A.L. Duigou, A. Bourmaud, G. Ausias, T. Gaudry, and C. Baley, (2013). "Effect of flax fibres individualisation on tensile failure of flax/epoxy unidirectional composite", *Composites Part A: Applied Science and Manufacturing*, 51, 62–70.

V.M. Karbhari, J.W. Chin, D. Hunston, and B. Benmokrane (2003). "Durability gap analysis for fiber-reinforced polymer composites in civil infrastructure", *Journal of Composites for Construction*, 7(3), 238–247.

G. Khanbabaie, J. Aalaie, A. Rahmatpour, A. Khoshniyat, and M.A. Gharabadian (2007). "Preparation and Properties of Epoxy-Clay Nanocomposites", *Journal of Macromolecular Science Part B: Physics*, 46(5), 975–986.

G. Lagly (1999). "Introduction: From Clay Mineral-Polymer Interactions to Clay Mineral-Polymer Nanocomposites", *Applied Clay Science*, 15(1), 1-9.

H. Mahfuz, A. Adnan, V.K. Rangari, S. Jeelani, and B. Z. Jang (2004). "Carbon nanoparticles/whiskers reinforced composites and their tensile response", *Composites Part A: Applied Science and Manufacturing*, 35(5), 519 – 527.

D. Ray, S. Sengupta, S.P. Sengupta, A.K. Mohanty, and M. Misra (2006). "Preparation and Properties of Vinyl ester Resin/Clay Nanocomposites", *Macromolecular Materials and Engineering*, 291(12), 1513–1520.

J. Teng, J. Chen, S.T. Smith, and L. Lam (2002). *FRP strengthened RC structures*, Wiley, Chichester, West Sussex, U.K.

Z. Wang and T. Pinnavaia (1998). "Hybrid Organic-Inorganic Nanocomposites: Exfoliation of Magadiite Nanolayers in an Elastomeric Epoxy", *Chemistry of Materials*, 10(7), 1820–1826.



HYGROTHERMAL AGEING OF FLAX FIBRE REINFORCED COMPOSITES INTENDED FOR THE STRENGTHENING OF CONCRETE STRUCTURES

R. Chlela¹, W. Zombré², M. Quiertant³, L. Curtil², and K. Benzarti¹

¹ Université Paris-Est, Laboratoire Navier (UMR 8205), IFSTTAR, France, Email: robert.chlela@ifsttar.fr

² Université Claude Bernard Lyon 1, Laboratory of Composite Materials for Construction (LMC²), France

³ Université Paris-Est, IFSTTAR, MAST-EMGCU, France.

ABSTRACT

The combination of natural fibres and a bio-based matrix to produce environmentally friendly composites for structural strengthening applications in construction has been the subject of a significant amount of research. However, a main drawback of natural fibres is their sensitivity to environmental conditions, which may affect the mechanical properties of both the composite itself and its adhesive bond with the host structure in the long term. The present durability study, conducted in the framework of the MICRO project funded by the French National Research Agency (ANR), aims at investigating the influence of hygrothermal ageing on the mechanical performances of an innovating composite strengthening system based on a bio-epoxy matrix reinforced by flax fibres. The test program consists in subjecting composite laminates and strengthened concrete slabs to accelerated ageing conditions, under six different combinations of temperature and humidity. Aged laminates are then periodically characterized by tensile tests and interlaminar shear tests, while the bond properties of concrete/composite assemblies are assessed by pull-off tests.

This paper presents the first results of this ongoing experimental program which is scheduled over a total period of 2 years. Results are discussed in the light of complementary investigations (monitoring of the water sorption behaviour, microscopic observations, and evaluation of the glass transition temperature by differential scanning calorimetry – DSC) in order to relate the observed performance evolutions to actual microstructural changes or damage processes taking place in the material during ageing.

KEYWORDS

Hygrothermal ageing, flax fibre reinforced polymer composites, bio-based epoxy matrix, tensile test, pull-off test, water sorption.

INTRODUCTION

Throughout the past few decades, composite materials have been proven effective for the rehabilitation and strengthening of concrete structures because of their high mechanical properties to weight ratio. However, considering their energy-consuming fabrication process and the increase of global concerns towards climate change and reduction of carbon emissions, the search for more eco-friendly material makes sense. This consideration has led to the development of bio-composites as a greener alternative to conventional composites, in which synthetic fibres, such as carbon and glass fibres, are replaced by natural fibres such as flax (Yan et al. 2014), hemp (Lu et al. 2011), sisal (Zhao et al. 2014), etc...

On the other hand, with the use of natural fibres, several new durability problems emerge due to the hollow structure and non-homogeneous hydrophilic nature of these fibres, that makes the bio-composite susceptible to extensive moisture absorption. Multiple studies have proven that the mechanical properties of vegetal fibres composites are strongly affected by water absorption (Cuinat-guerraz 2015; Duigou et al. 2009; Hallonet et al. 2016; Rosenboom & Rizkalla 2006; Thuault 2013; Yan et al. 2015; Scida et al. 2013), but until now there is no clear understanding of the coupling effect of temperature and moisture absorption in the ageing behavior of these materials. Therefore, the present study aims at achieving a better understanding of this coupling on the mechanical properties of an innovative bio-composite consisting of a biobased epoxy matrix reinforced by flax fibres.

MATERIALS AND METHODS

Materials and ageing conditions

The unidirectional flax fibre fabrics used in this study were produced by Groupe Depestele, a French natural textile company. The main characteristics of these fabrics are listed in Table 1.

Table 1: Characteristics of the unidirectional flax fabrics LINCORE® FF 200

Characteristics	Value	Unit of measure	Method
Nominal weight	200 ± 4%	g/m ²	UNI 5114
Thickness	250 ± 15%	µm	UNI EN ISO 5084
Nominal construction	<u>Warp</u> <u>Weft</u> 3.7 5.1	threads/cm	UNI EN 1049-2
Weight distribution	91 9	%	-

The epoxy resin (CHS-EPOXY G520) was supplied by Spolchemie, a Czech Republic chemical company known for its green environmental-friendly products. This resin (30% bio-sourced) was mixed with an amine hardener (100% bio-sourced) in stoichiometric proportions. Composite laminates made of two plies of UD flax fabrics were then manually prepared (hand lay-up technique) by impregnating the fabrics with the previous polymer mix. The resulting laminates had a fibre volume fraction of 16%, and were cured in the laboratory conditions (20°C/35-50% RH) for 3 weeks until stabilization of the polymerization process. These specimens were then divided into 6 series that were placed in climatic chambers or in thermo-regulated water tanks (in the case of 100% RH environments), located either at LMC2 Laboratory in Lyon or at Ifsttar in Paris. In total, 6 different combinations of temperature and humidity were selected according a design of experiments based on Hoke's matrix (simplification of a factorial matrix with 3 levels per factor where the factors in our case are the temperature and humidity). These ageing conditions are named V1 to V6 (see details in Table2).

Within the framework of the French National Research Agency (ANR) project called MICRO, it is planned to conduct this durability study over a period of 2 years, however this paper only displays the results of the first 6 months considering that the ageing process is still in progress until 2019.

Table 2: Ageing conditions considered in the optimized design of experiments

Name	Temperature	Humidity	Location
V1	20°C	50% RH (climatic chamber)	Ifsttar
V2	20°C	100% RH (immersion in water)	Ifsttar
V3	60°C	50% RH (climatic chamber)	Ifsttar
V4	40°C	100%RH (immersion in water)	LMC ²
V5	60°C	75% RH (climatic chamber)	LMC ²
V6	60°C	100% RH (immersion in water)	LMC ²

In addition to the previous composite laminates, strengthened concrete slabs were also prepared for the purpose of the adhesive bond characterizations by pull-off tests. Concrete slabs were first prepared using a ready-to-mix commercial mixture of compressive strength 50 MPa at 28 days (see Table 3). The slabs were stored for 90 days before being strengthened with a single ply of UD flax fabric impregnated by the bio-epoxy matrix. As previously, a 3 week cure was respected prior exposure of the test specimens to the various ageing environments.

Table 3: Composition of the concrete mixture

Material	Cement CEM III/B	Sand 0/5	Gravel 10/25	Water
Quantity (kg / m ³)	350	865	1030	145

Kinetics of sorption

In order to evaluate the water sorption kinetics of the Flax Fibre-Reinforced Polymer (FFRP) composite, square samples of 25 x 25 mm² were cut from a 250 x 250 mm² laminate plate.. These samples were also subjected to the various accelerated ageing environments, and were periodically weighted with a Sartorius CP 4235 balance of precision of 0.001 g.

Tensile testing procedure

Direct tensile tests were carried out according to ISO 527 standard and French AFGC standard. The geometry of test specimens (which are made of 2 layers of flax fibre sheets) is presented in Figure 1. In addition, glass fibre composite tabs are glued to each extremity of the specimens using an epoxy adhesive. An Instron 5969 universal testing machine, equipped with a non-contact AVE extensometer, was used to apply the loading speed of 1 mm/min as advised in the standard.

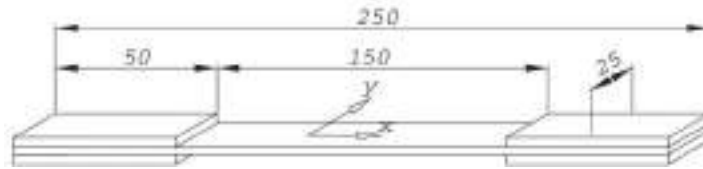


Figure 1: Geometry of the tensile specimens (dimensions in mm)

Pull-off testing procedure

Pull-off tests were carried out according to EN 1542 and AFGC standards. The single layer of FFRP composite reinforcing each concrete slab was first drilled using a cylindrical core drill of diameter 50 mm, until reaching a depth of 4 mm within the concrete substrate. A cylindrical steel disc of diameter 50 mm was then glued to the drilled zone using an epoxy adhesive. Finally, a tensile loading was applied to the disc at constant speed of 0.05 MPa/sec using a Proceq DY-216 dynamometer, until failure occurred. This allowed to determine the peak load, and to further evaluate the pull-off bond strength. The type of failure mode is also an important characteristic.

Microscopic observations

Cross-sections of the aged FFRP composite specimens were polished using a Struers LaboForce 100 device equipped with adequate series of grinding discs. Diamond spray was also used during for achieving a smooth mirror surface. Finally, these polished surfaces were examined using a Zeiss Axio Scope A1 optical microscope.

Determination of the Glass Transition Temperature (T_g)

In order to assess the impact of accelerated ageing on the microstructure of the polymer matrix, characterizations by differential scanning calorimetry (DSC) were performed on small samples (~10 mg) of aged FFRP specimens. These analyses were carried out with a Discovery DSC 250 apparatus from TA Instruments, using a ramp of temperature from -10 to 180°C at a heating rate of 2°C/min, and a superimposed temperature modulation (amplitude of 1.5° with a period of 60s). The glass transition temperature (T_g) was determined from the reversing heat flow thermograms, using the midpoint-by-half-height identification method. 4 analyses were performed for each type ageing condition, to obtain an average value and a standard deviation.

RESULTS AND DISCUSSIONS

Water sorption behaviour

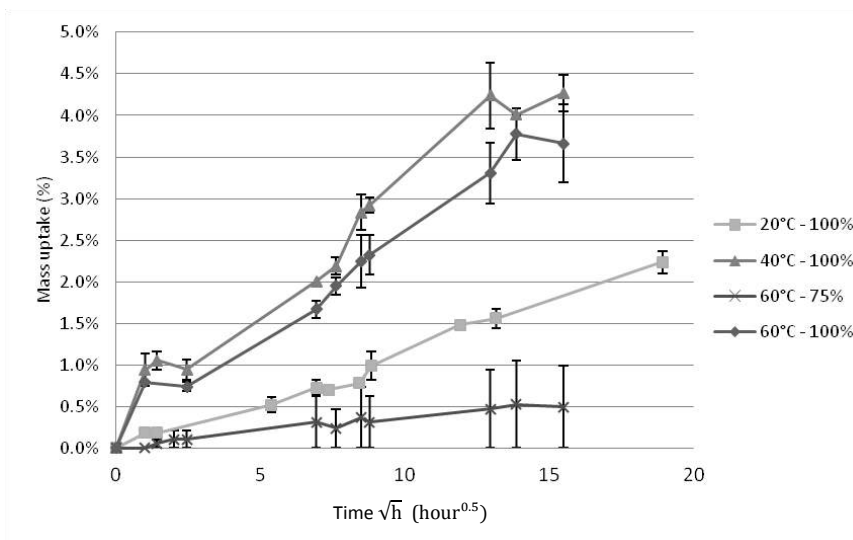


Figure 2: Evolution of the mass uptake of FFRP composites subjected to the various ageing conditions

Figure 2 shows the mass uptake evolution curves for FFRP composites subjected to the different ageing environments, with the exception of conditions at 20°C/50% RH and 60°C/50% RH for which no mass variation was measured. Globally, the initial part of the curve is linear, suggesting that sorption is controlled by a Fickian diffusion process. As expected, relative humidity and temperature play both major roles in the sorption kinetics,

as the slope of the curve increases significantly as one of these two factors is raised. At this stage, one cannot calculate the diffusion coefficients, as water saturation has not been reached. However, large water uptakes (up to 4.5%) were obtained under 100% RH conditions after 12 to 15 days. This result shows that FFRP composites are susceptible to extensive water ingress under wet environments, and water absorption may thus be a leading factor in the degradation of the mechanical performances of both the laminate and its adhesive bond with concrete during wet ageing. This point will be investigated in the next sections.

Microstructural changes

Glass transition temperatures (T_g) measured by DSC on the initial FFRP laminate and on specimens subjected to accelerated ageing in the various environments for periods of 3 and 6 months are shown in Figure 3.

Regarding the unaged laminate, which was cured for 3 weeks at room temperature, a T_g of $(54.9 \pm 0.4)^\circ\text{C}$ was obtained (this reference value is depicted by the red line in Figure 3). For this reference material, the polymerization process didn't reach completion and the corresponding samples remained under-cured.

After 3 months exposure at 20°C under moderate humidity (50% RH), a slight increase in T_g was observed, up to 59°C . Between 3 and 6 months, this value didn't evolve any more, suggesting that the polymer network is stabilized in this condition, but still in an under-cured state.

Exposures for 3 months at 60°C under moderate or intermediate humidity (50% and 75% RH) led to a large increase in T_g up to 82°C , which was assigned to a post-curing process of the polymer matrix. Indeed, this elevated ageing temperature facilitates the diffusion of unreacted monomers and promotes further cross linking of the thermo set network. Between 3 and 6 months in the same conditions, no additional significant evolution of T_g was noticed, suggesting that the network had reached equilibrium (and was possibly fully cured).

Regarding samples immersed at 100% RH for 3 months, T_g was found to increase as the ageing temperature was raised, due to the same post-cure effect. Nevertheless, for a given temperature of 60°C , T_g of immersed samples remained significantly lower compared to that of specimens exposed to moderate or intermediate humidity level (50% and 75% RH). This result suggests that, under wet environment, the evolution of T_g may be controlled by both the post-cure process and the plasticization by water, which have opposite effects.

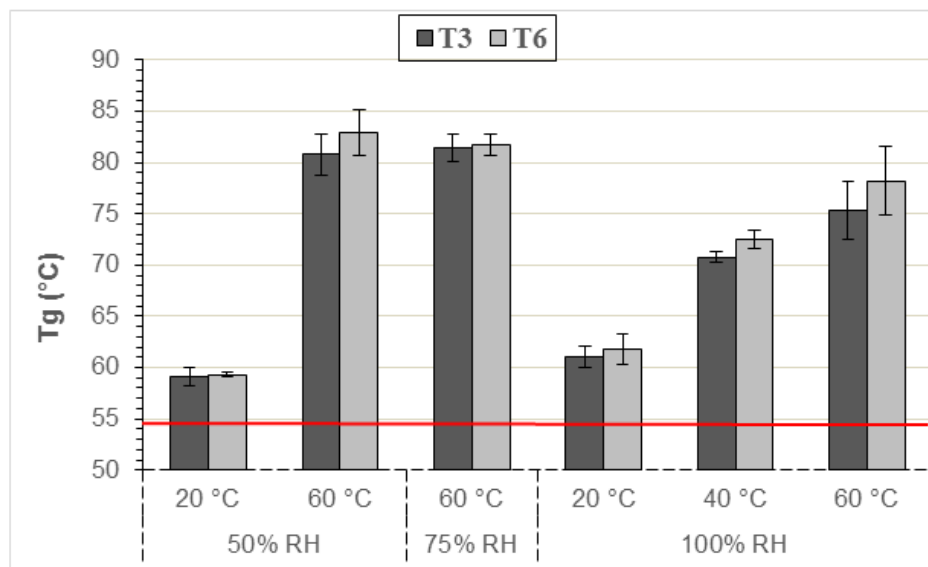


Figure 3: T_g of the FFRP laminates after exposure for 3 and 6 months in the various ageing conditions

Tensile strength of FFRP composites

Figures 4 to 6 reports the tensile properties (strength, modulus and ultimate strain, respectively) that were determined for the unaged FFRP samples and for specimens subjected to ageing periods of 3 and 6 months in the various environments. As mentioned before, this is an inter-laboratory study, and half of the exposure (V1 to V3) and mechanical tests were carried out at Ifsttar, while the other half was performed at LMC2 Laboratory (V4 to V6). Small differences were found on average property values and dispersions obtained in the two laboratories for unaged specimens (Figs 4.a, 5.a and 6.a), since different operators were involved in the tests. Therefore, in order to have a comparable referential, residual tensile properties of aged specimens obtained in each laboratory were normalized by the initial values determined in the same laboratory.

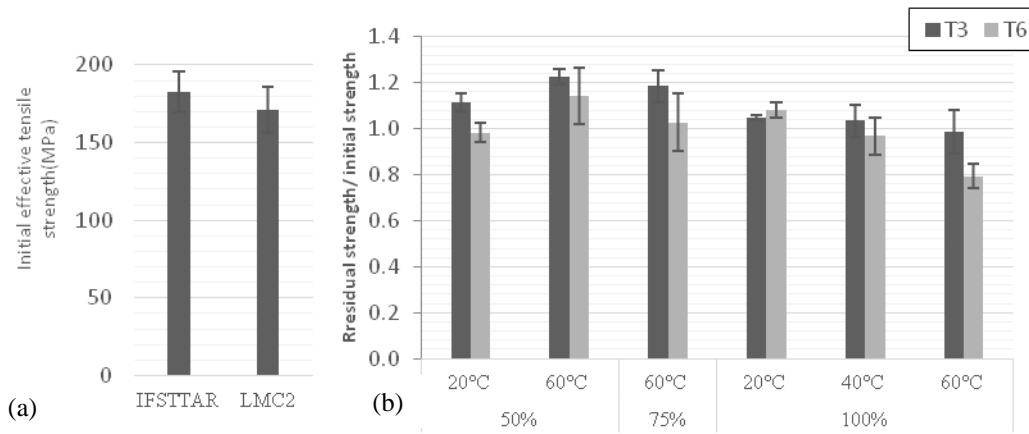


Figure 4: Tensile strength of FFRP composites - (a) value of unaged specimens obtained in the 2 laboratories and (b) residual of specimens that were exposed to the various ageing conditions for 3 and 6 months.

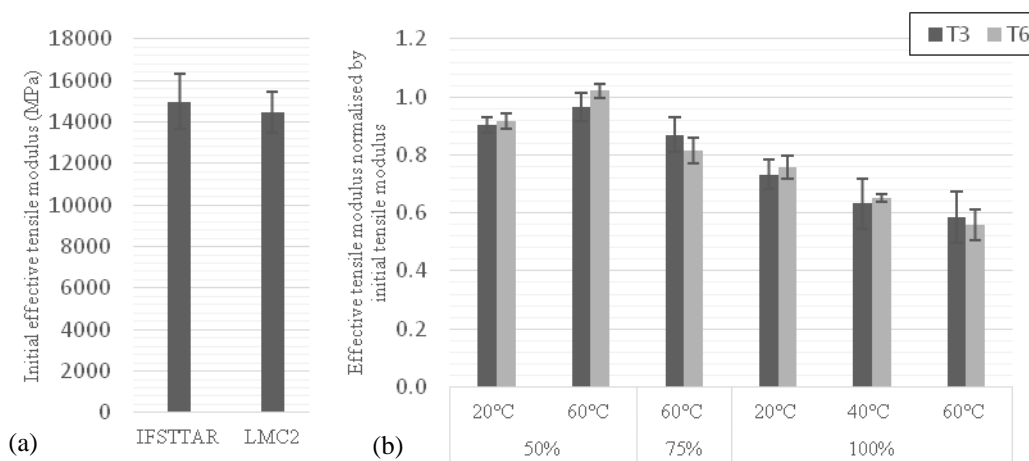


Figure 5: Tensile modulus of FFRP composites - (a) value of unaged specimens obtained in the 2 laboratories and (b) normalized values of specimens exposed to the various ageing conditions for 3 and 6 months.

Regarding the tensile strength (Figure 4), FFRP composites didn't show any degradation after 3 months ageing, and significant increases were even observed for specimens exposed to 50% and 75% RH, especially at the temperature of 60°C, which was explained by the post-curing process of the bio epoxy matrix as previously evidenced by DSC experiments. Between 3 and 6 months ageing, a global decrease in the effective tensile strength was noticed for all specimens. Nevertheless, only the specimen exposed to 60°C/100% RH decreased its strength significantly below the initial value (reduction of 20%, approximately). This may be explained by the extensive water absorption process observed in this specific condition, as shown previously in Figure 2.

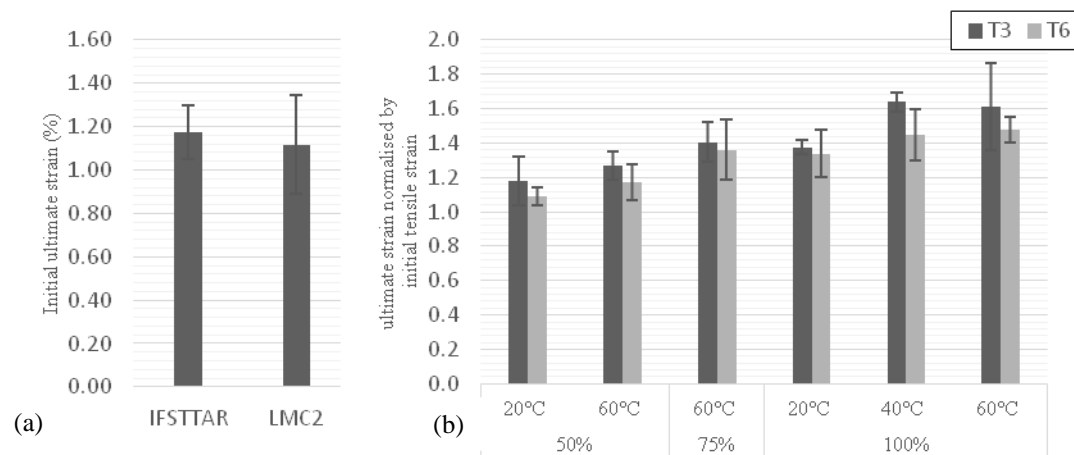


Figure 6: Ultimate Tensile strain of FFRP composites - (a) initial values of unaged specimens obtained in the 2 laboratories and (b) normalized values of samples exposed to the various ageing conditions for 3 and 6 months

Regarding the evolution of the tensile Young's modulus (Figure 5), the increase in humidity is found to degrade significantly the longitudinal stiffness of the FFRP laminates over ageing. This effect is accompanied by an increase in ultimate strain, as shown in Figure 6. These phenomena can be assigned to the plasticization effect induced by water on the bio-epoxy matrix, and to degradations of the fibre/matrix interfacial regions as well. On the other hand, the effect of temperature seems to depend on the level of relative humidity. At low RH values, the tensile modulus is found to increase over ageing as the temperature is raised, but contrariwise, at 100% RH (immersed samples), the modulus decreases when the temperature rises. These trends may relate to the relative effects of post-cure and plasticization phenomena, as post-cure seems predominant at low RH and high temperature, while plasticization becomes dominant at high RH and high temperature. This is consistent with previous observations from the same team in the case of conventional carbon fibre reinforced composites (Benzarti et al 2011; Quertant et al 2017) and is also supported by DSC analyses.

Adhesive bond properties

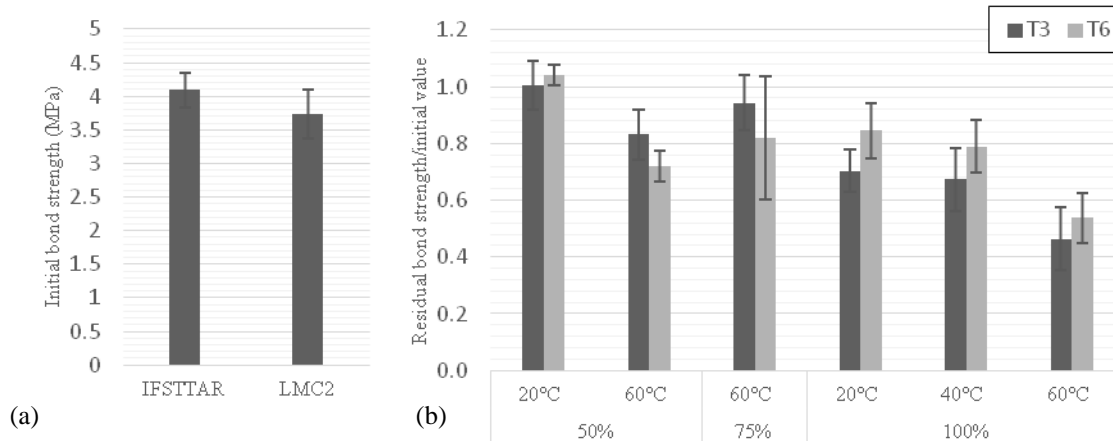


Figure 7: Bond strength between FFRP and concrete - (a) initial values of unaged specimens obtained in the 2 laboratories and (b) normalized values of samples exposed to the various ageing conditions for 3 and 6 months

A slight difference was obtained between initial bond strengths determined at IFSTTAR (4.09 ± 0.25) MPa and at LMC² (3.73 ± 0.36) MPa. It was attributed to the fact that 2 different operators were involved in the sample preparation and test procedure. Therefore, similar to previous tensile tests, results of pull-off tests obtained in each laboratory for aged specimens were normalized by the initial value obtained in the same laboratory.

Figure 7.b displays the residual bond strengths of specimens exposed to the various environments for periods of 3 and 6 months. A significant decrease in bond strength was observed for all specimens, with the exception of those stored at 20°C/50% RH. Moreover, samples exposed to 100% relative humidity were the most affected, with reduction up to 50% in the case of samples subjected to 60°C/100% RH, which is also consistent with the large water uptake evidenced for FFRP composites in these conditions. Such a degradation of the bond strength under wet conditions was accompanied by a change in failure mode, from an initial cohesive concrete failure towards a mixed failure after ageing (both in concrete and by partial peeling of the composite, as shown in Figure 8). This change in failure mode and the reduction in bond strength are both attributed to a weakening of physico-chemical bonds at the concrete/composite interface in the presence of water.

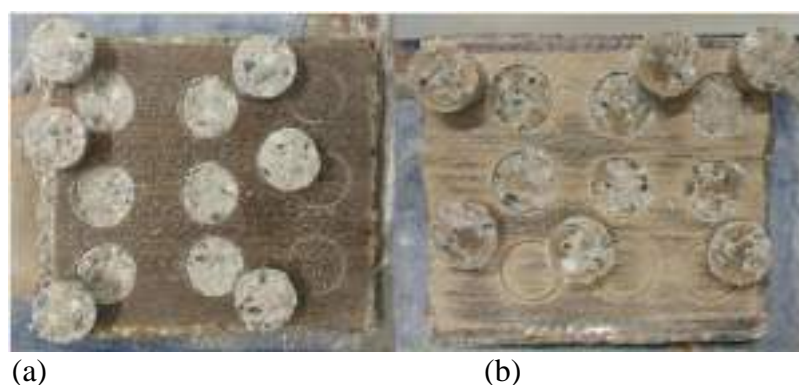


Figure 8: Failure modes after pull-off tests - (a) initial cohesive concrete failure for unaged specimens, and (b) typical mixed failure obtained for specimens subjected to wet ageing at 100% RH.

Microscopic observations

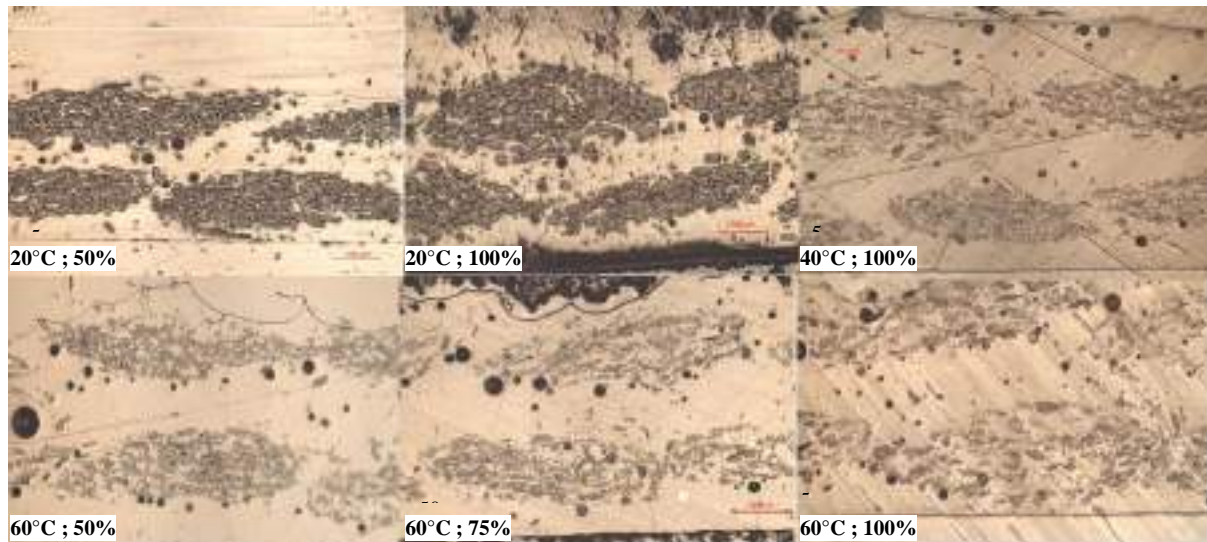


Figure 9: Microscopic observations of polished cross-sections of FFRP laminates subjected to various ageing conditions for 3 months.

Figure 9 displays several images obtained by optical microscopy, showing polished cross-sections of FFRP laminates that had been exposed to the various ageing environments for periods of 3 months. Two main features are revealed by these images:

- A variation of the apparent section of flax fibres can be noticed, depending upon the ageing conditions. An increase in the fibre cross-section is observed for laminates subjected to 20°C/100% compared to those subjected to 20°C/50% RH, which can be assigned to the swelling of flax fibres induced by water absorption. Differently, specimens exposed to elevated temperatures show reduced fibre sections compared to those stored at 20°C, whatever the level of relative humidity. This result is not clearly explained at this stage of the study, but suggests that for FFRP composites immersed at high temperature, the extensive sorption process evidenced in Figure 2 mainly results from water absorption by the polymer matrix and not by the fibres, since the section of these latter is reduced after ageing.
- Besides, a change of color of the flax fibres is observed for FFRP laminates exposed to high temperatures.

Complementary observations are currently being performed by Scanning Electron Microscopy (MEB), in order to provide a better understanding of the previous phenomena.

CONCLUSIONS

This paper has presented the first results of a durability study conducted on FFRP laminates and FFRP strengthened concrete slabs subjected to various accelerated ageing conditions (6 different combinations of temperature and relative humidity). At this stage of the test program, changes in the tensile properties and bond strength have been determined after 3 and 6 months ageing in these environments. Additional characterizations were also carried out to evaluate the water sorption behaviour and microstructural changes in aged laminates.

Water sorption kinetics was directly linked to the level of relative humidity of the ageing environment and was also accelerated by temperature. Micrographic observations showed significant swelling of the flax fibres for specimens immersed at 20°C, but contrarily, a reduction of the fibre section was noticed after immersion at 40 and 60°C, suggesting that water sorption occurs mainly within the bio-epoxy matrix in this case.

Tensile tests revealed limited effects of ageing on the effective strength: a slight increase was observed at elevated temperature (60°C) and moderate/intermediate humidity (50 and 75% RH), due to a post-cure effect of the polymer matrix confirmed by DSC analyses. Besides, wet ageing had a negligible effect on strength, with the exception of samples immersed at 60°C which exhibited a strength reduction of about 20%.

Differently, the longitudinal Young's modulus of laminates was significantly affected under wet environments: immersed samples showed substantial degradation of their modulus over time (up to 40% loss for samples subjected to 60°C and 100% RH which had the highest water uptakes). This draws a direct correlation between the water uptake and the rigidity of the FFRP laminate, due to extensive plasticization of the bio-polymer matrix and possible degradation at the fibre/matrix interface..

Finally, a degradation of the bond strength was observed for FFRP reinforced slabs exposed to high RH levels, with a change in the failure modes from a cohesive concrete failure to a mixed failure (concrete + partial peeling of the composite). This result suggested a weakening of physico-chemical bonds at the concrete/FFRP interface.

ACKNOWLEDGMENTS

Authors wish to acknowledge the National French Research Agency (ANR) for funding the MICRO project (contract ANR-15-CE22-0007-04 -“MICRO: Matériaux Innovants Composites pour la Réparation d'Ouvrages”).

REFERENCES

- AFGC 2011. Réparation et renforcement des structures en béton au moyen des matériaux composites - Recommandations provisoires. Association Française de Génie Civil, France, 2011.
- Benzarti, K., Chataigner, S., Quiertant, M., et al., 2011. Accelerated ageing behaviour of the adhesive bond between concrete specimens and CFRP overlays. *Construction and Building Materials*, 25(2), 523-538.
- Cuinat-guerraz, N., Dumont, M.-J., Hubert, P., 2016. Environmental resistance of flax / bio-based epoxy and flax / polyurethane composites manufactured by resin transfer moulding. *Composites Part A*, 88, 140-147.
- Duigou, A. Le, Davies, P. & Baley, C., 2009. Seawater ageing of flax / poly (lactic acid) biocomposites. *Polymer Degradation and Stability*, 94(7), 1151–1162.
- EN 1542. Produits et systèmes pour la protection et la réparation des structures en béton - Méthodes d'essais - Mesurage de l'adhérence par traction directe, Tirage 2 2010-09-01.
- Hallonet, A., Michel, L. & Ferrier, E., 2016. Investigation of the bond behavior of flax FRP strengthened RC structures through double lap shear testing. *Composites Part B*, 100, 247–256.
- ISO 527-4. Détermination des propriétés en traction - Partie 4 : conditions d'essai pour les composites plastiques renforcés de fibres isotropes et orthotropes.
- Lu, N., Jr, R.H.S. & Ferguson, I., 2012. Composition, structure and mechanical properties of hemp fiber reinforced composite with recycled high-density polyethylene matrix. *Journal of Composite Materials*, 46 (16), 1915-1924.
- Quiertant, M., Benzarti, K., Schneider, J., Landrin, F., Landrin, M., and Boinski, F, 2017. Effects of Ageing on the Bond Properties of Carbon Fiber Reinforced Polymer/Concrete Adhesive Joints: Investigation Using a Modified Double Shear Test. *Journal of Testing and Evaluation*, 45(6), 1920-1932.
- Rosenboom, O. & Rizkalla, S., 2006. Behavior of Prestressed Concrete Strengthened with Various CFRP Systems Subjected to Fatigue Loading. *Journal of Composites for Construction*, 10(6), 492–502.
- Scida, D., Assarar, M., Poilâne, C., and Ayad, R., 2013. Influence of hygrothermal ageing on the damage mechanisms of flax-fibre reinforced epoxy composite. *Composites Part B*, 48, 51–58.
- Thuault, A., Eve, S., Blond, D., Bréard, J., Gomina, M., 2014. Effects of the hygrothermal environment on the mechanical properties of flax fibres. *Journal of Composite Materials*, 48(14), 1699-1707.
- Yan, L., Chouw, N. & Jayaraman, K., 2014. Flax fibre and its composites – A review. *Composites Part B*, 56, 296–317.
- Yan, L., Su, S. & Chouw, N., 2015. Microstructure, flexural properties and durability of coir fibre reinforced concrete beams externally strengthened with flax FRP composites. *Composites Part B*, 80, 343–354.
- Zhao, X., Li, R.K.Y. & Bai, S.L., 2014. Mechanical properties of sisal fiber reinforced high density polyethylene composites: Effect of fiber content, interfacial compatibilization, and manufacturing process. *Composites Part A*, 65, 169–174.



PHYSICAL AND MECHANICAL CHARACTERIZATION OF NATURAL FIBRES AND FABRICS AS REINFORCEMENT FOR COMPOSITE SYSTEMS

G. Ferrara¹, B. Coppola², L. Di Maio², E. Martinelli³

¹ Dept. of Civil Engineering, University of Salerno, Italy, Fisciano (SA), Italy

² Dept. of Industrial Engineering, University of Salerno, Italy, Fisciano (SA), Italy

³ Dept. of Civil Engineering, University of Salerno, Italy, Email: e.martinelli@unisa.it

^{1,2,3} Via Giovanni Paolo II, 132 - 84084 Fisciano (SA), Italy

ABSTRACT

In recent years, the increasing interest in environmentally friendly materials has brought the attention of material technologists and civil engineers to natural fibres and their potential use in composite materials. Although several research activities have shown the good mechanical properties of these fibres, their use is still limited due to both the absence of standards and guidelines and some open durability issues highlighted in the literature.

The present work is a contribution to identifying the main physical and mechanical properties of flax fibres and fabrics intended as internal reinforcement in composite materials with mineral matrix. Due to the lack of standardization on vegetal fibres as constituent of building materials, the experimental research moves from characterising the geometry of bundles. The diameter of single yarn and twisted bundles has been measured by means of a large number of measurements obtained by a microscope: specifically, six values have been recorded for each one of thirty specimens. A comparison with a most accurate SEM analysis has been performed as well. Tensile tests on single yarn, double yarn twisted bundle and textile strip specimens have been carried out. Tensile tests on flax textile have been performed after a specific curing period in controlled environment in order to evaluate the durability of the textile and its sensitivity to alkali agents. The results of the experimental activity showed that the diameter values assessed by means of a microscope are affected by the irregularities of the flax bundles, due to their twisted arrangement. Future developments will target the mechanical behaviour of Textile Reinforcing Mortar (TRM) composite systems based on a bidirectional grid fabric made of the aforementioned flax fibres: assessing the potential of these sustainable and reversible composites systems as a technical solution for in seismic strengthening of existing masonry members and structures is the final goal of this research.

KEYWORDS

Strengthening and repair, Experimental study, Eco-composite & bio-sourced composite materials, FRCM and cement composite materials, Flax fibres.

INTRODUCTION

Nowadays, the increasing ecological awareness has resulted in a rising interest for reducing environmental impact due by the construction sector. In fact, the use of more sustainable materials is deserving more and more attention, among the newly available eco-friendly technological solutions. As the production processes of vegetal fibres require low energy, both for processing and transportation, they certainly represent a “green” material. In recent years, several studies have been devoted to the investigation of these materials, describing them as a valid alternative to the most traditional industrial fibres, such as carbon, glass or plastic ones, used in composite applications in construction industry (Faruk et al. 2012).

Natural fibres, such as flax, jute, hemp, sisal, coir, have shown a mechanical performance, in terms of tensile strength and strain, not so different from those exhibited by the most common synthetic fibres (Torgal & Jalali 2011).

Although natural fibres represent a promising reinforcing material in composite systems, their use is still limited by several drawbacks. Firstly, they present an important variability of the mechanical properties due to the non-uniformity of their structure. Many factors, such as humidity content, structure, irregularities, the morphology of the plant, may affect their mechanical, physical and geometrical properties (Codispoti et al. 2015). Secondly, vegetal fibres present durability issues.

Composite materials produced with Ordinary Portland Cement matrix register an important loss of strength due to the fibre mineralization and alkali attack related to the variation of humidity (Toledo Filho et al. 2000). Moreover, the adhesion between natural fibre and cementitious matrices is still an open issue (Ferreira et al, 2016).

That said, further investigations are still needed with the aim to assess the potential of vegetal fibres to be used as internal reinforcement in cementitious composites.

This study aims to analyse both the physical and mechanical properties of flax textile used as reinforcement in cement-based composite systems. Different measurement techniques have been implemented and compared each other in order to assess geometric parameters of the textile. In order to mechanically characterize the textile, tensile tests have been performed on differently sized flax coupons.

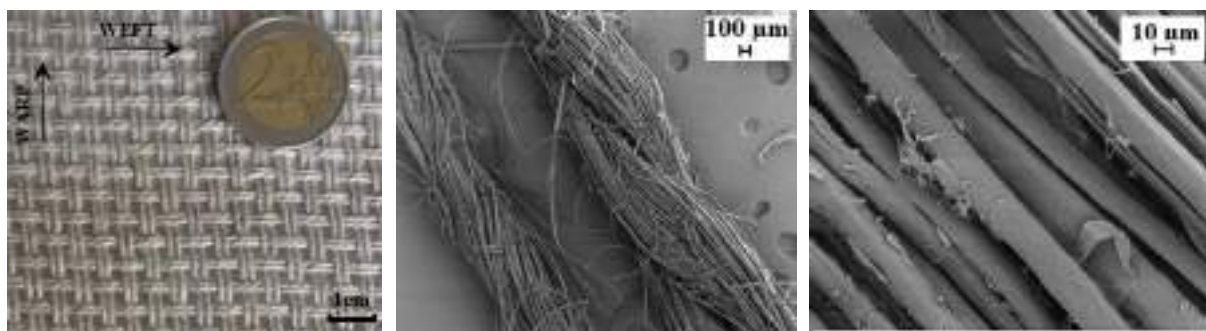
Furthermore, with a view to future applications of the material as reinforcement in cement-based composite systems, the response of flax single bundle coupons subjected to an ageing protocol has been observed, giving information about the durability of the material.

MATERIALS AND METHODS

Materials

The material subject of study is a bi-directional woven flax fabric with plain weave in which the warp and the weft directions are arranged forming a simple cross pattern (Figure 23a).

The fabric is characterized by 4.3 threads per centimetre, each one of them consists of a double-twisted flax yarn (Figure 23b), and each single yarn in turn, at the micro-scale, is composed by vegetal filaments (Figure 23c).



(a) bi-directional arrangement (b) single yarn and double-twisted yarns (c) filaments

Figure 23: Flax fabric arrangement

The relevant physical properties of the flax textile under consideration are the *apparent thread diameter*, the *filament diameter*, the *density* and the *effective area* of the bundles. The apparent diameter of the flax bundles has been evaluated by means of an optical microscope: 15 double-twisted yarn samples 15cm long have been analysed and 6 values of the diameter have been recorded for a total of 90 measurements.

A Scanning Electron Microscope (SEM) analysis has been performed in order to scrutinise the geometric and physical properties at a more detailed scale. The investigation of the SEM image in Figure 23b, representing a double-twisted yarn with a magnification of 50x, shows an apparent diameter of the bundle consistent with the assessment performed by means of the optical microscope.

Four SEM images detecting 4 different samples, with a magnification of 1000, have been investigated providing a geometric identification of the filaments constituting the flax threads by means of 28 measurements (Figure 23c). As shown by the SEM images, due to the presence of voids among the flax filaments, the apparent diameter cannot give an effective value of the cross-section to be used for mechanical investigations. The effective cross-section area of the flax bundle has been obtained by means of indirect measurements. Specifically, the density of five 15 cm long double-twisted flax yarns samples has been assessed by using a hydrostatic balance. As known, the evaluation of the density in water is strongly affected by the presence of voids within the sample.

Therefore, only saturated specimens can give reliable values. In order to make sure having saturated samples, the absorption rate of the fibres has been studied. Five flax threads, having a length of 15 cm, have been weighed and then immersed in deionized water. The weighing of the samples has been repeated at an interval of 1 or 2 days up to the achievement of a negligible weight gain. The water absorption curve, whose values have been obtained by dividing the water weight gain for the initial dry weight, is reported in Figure 24 and shows a water absorption rate equal to 222%, with a coefficient of variation of 19%, achieved in 96 hours.

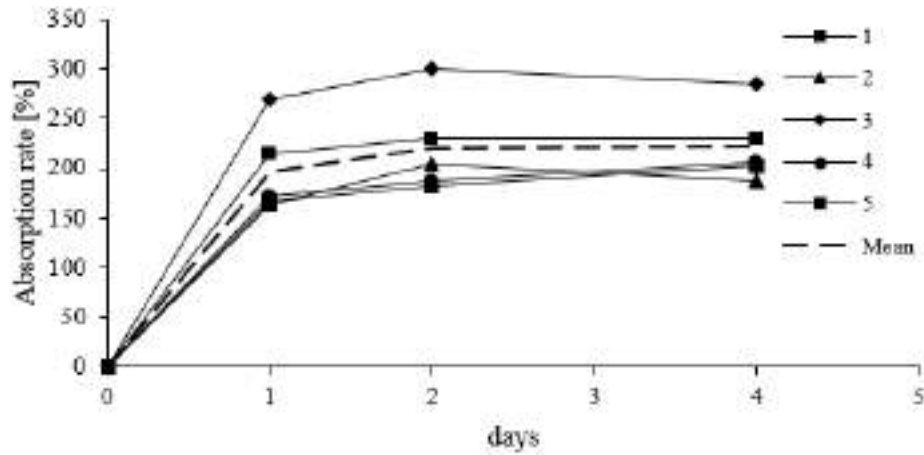


Figure 24: Flax thread water absorption rate

The specific gravity of the 5 flax saturated samples subjected to the water absorption test has been assessed. An indirect estimate approximation of the effective cross-section area has been obtained by dividing the weight of the samples for their density and length. The mean value and its respective coefficient of variation of all the physical properties assessed in this study are reported in Table 11.

Table 11: Physical and mechanical properties of flax fabric

	Mean	Co.V. (%)
filament diameter (μm)	16.78	29.64
density (g/cm^3)	1.19	3.29
linear density (Tex)	302	15.27
n° bundles*/cm	4.3	-
Apparent Diameter* (mm)	0.88	5.27
Effective Area* (mm^2)	0.25	16.62
Young's Modulus* (Gpa)	9.36	10.67
Strain to failure* (%)	3.85	12.94
Tensile strength* (Mpa)	353.72	11.53

*Values refer to flax double twisted yarn samples

Methods

Tensile tests have been performed on different sized flax samples, in order to provide a mechanical characterization of the material and to monitor the variability of the properties of the fabric. The following series of specimens have been considered:

- *Flax-1Y*: it consists of 15 cm long single yarn samples obtained by separating each other the two yarns constituting the main thread of the fabric (Figure 23a);
- *Flax-2Y*: it represents the main thread of the textile, and it is characterised by double-twisted yarns. Specimens having a length of 15 cm have been obtained from the flax roll both in warp and weft directions (Figure 25b);
- *Flax fabric-2cm*: it consists of flax fabric strips 2 cm wide and 15 cm long, characterised by 8 “2Y-threads” (Figure 25c);
- *Flax fabric-6cm*: it consists of flax strips 6 cm wide and 30 cm long, characterised by 24 “2Y-threads” (Figure 25d).

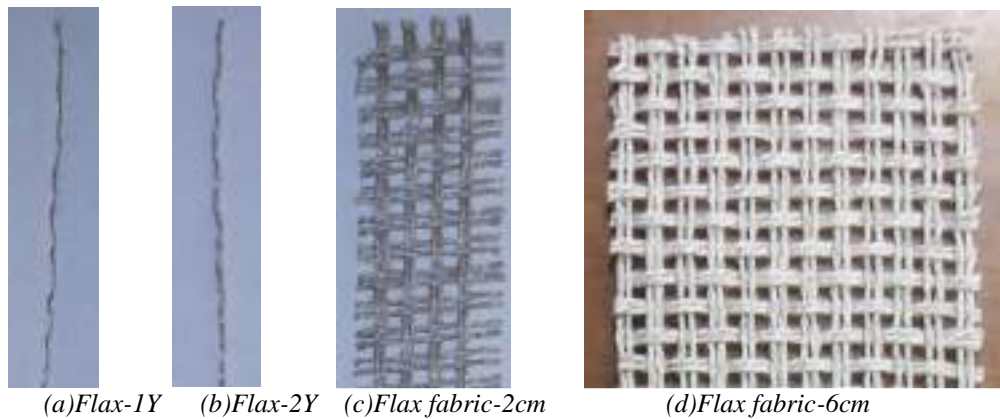


Figure 25: Flax tensile test specimens

The specimens having a length of 15 cm have been tested by using a SANS Universal Testing Machine having a capacity of 10 kN. Tensile tests have been performed by using a 1 kN load cell, with a displacement rate of 4mm/min, adopting a gauge length of 100 mm (Figure 26a).

The mechanical characterization of the “Flax fabric-6cm” specimens has been carried out according to the ISO 13934-1. Tensile tests have been carried out by means of a Zwick Roell Schenck Hydropuls S56, with a maximum capacity of 630 kN. The tests have been executed in displacement control at a rate of 4mm/min and a gauge length of 20 cm. Steel plates have been glued to the specimens ends by means of epoxy resin in order to avoid slipping during the tests (Figure 26b).

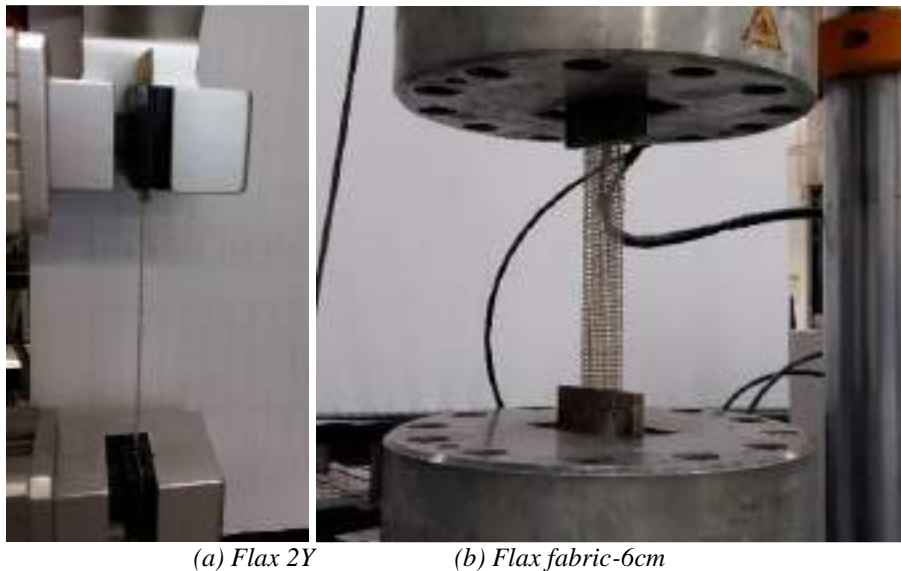


Figure 26: Tensile test on different sized flax samples

The ageing protocol adopted in this study to analyse the durability of the flax textile has been chosen in view of the application of these fibres as reinforcement in cement-based composite systems. According to the AC434-1011-R1, the mechanical properties of the so-called Textile Reinforced Mortar (TRM) composite systems are investigated after conditioning periods in specific water environments (Nobili & Signorini 2017). Depending on the conditioning environment the following series of specimens have been considered:

- *Control*: it is represented by the “Flax-2Y” series in warp direction;
- *W1000*: Flax-2Y specimens have been immersed in deionised water for a period of 1000 h (~42 days);
- *S1000*: Flax-2Y specimens have been immersed for a period of 1000 h (~42 days) in a saline environment consisting of 3.5% weight sodium chloride (NaCl) aqueous solution, that should reproduce the world’s ocean seawater average salinity;
- *Alk1000*: Flax-2Y specimens have been immersed for a period of 1000 h (~42 days) in an alkaline environment with 9.5 PH level, reproduced by adding sodium hydroxide (NaOH) to the deionised water.

RESULTS AND DISCUSSIONS

Table 12 reports the main mechanical properties deriving from the tensile tests performed on different flax samples.

Table 12: Mechanical properties of different sized flax samples

	Director	Number of tests	P_u		f_t		E		ε_u	
			Mean	Co.V.	Mean	Co.V.	Mean	Co.V.	Mean	Co.V.
			(N)	(%)	(MPa)	(%)	(GPa)	(%)	(%)	(%)
Flax-1Y	Weft	15	37.39	15.54	293.40	15.54	11.61	10.03	2.55	9.65
Flax-2Y	Weft	12	87.95	12.75	345.04	12.75	8.53	6.44	4.19	12.37
Flax-2Y	Warp	14	92.05	10.47	361.15	10.47	10.07	6.95	3.56	6.31
Flax fabric-2cm	Weft	14	476.11	8.60	233.49	8.60	4.39	8.40	5.96	9.33
Flax fabric-6cm	Weft	5	1758.81	7.50	287.52	7.50	8.25	9.93	3.61	4.79
Flax fabric-6cm	Warp	5	1743.71	3.91	285.05	3.91	9.81	3.14	2.93	7.66

P_u = Maximum Load; f_t = Tensile Strength; E = Young's Modulus; ε_u = strain at failure

The results are expressed in terms of maximum load, tensile strength, elastic modulus and strain at failure. For each series of values, the coefficient of variation is reported as well. Figure 27 shows the stress-strain curves of Flax fabric-6cm specimens belonging to both the warp and weft directions. The comparison between the two series of specimens shows that the textile is characterized by the same tensile strength in both directions, while a slight change in the Young's Modulus and in the strain at the failure is recorded.

The results represented in Figure 27 fall within the range variation of the same quantities reported in other similar studies already published in the literature (Asprone et al. 2015; Codispoti et al. 2015; Olivito et al. 2014; Pickering et al. 2016).

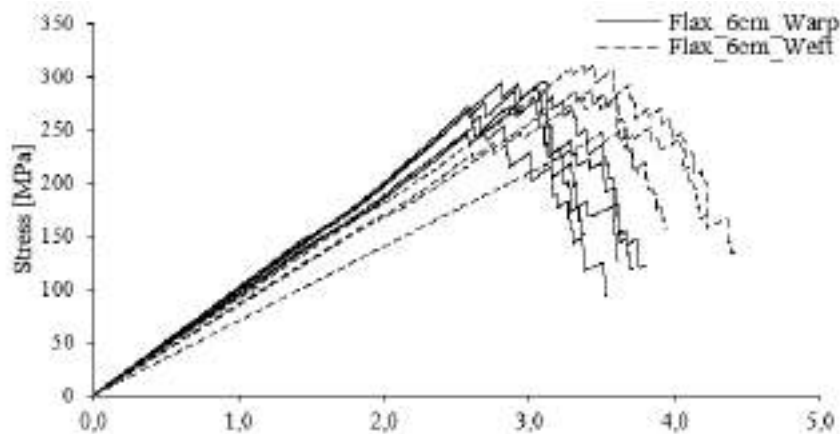


Figure 27: Stress-strain curve of Flax-6cm specimens in warp and weft directions

The main values of the tensile strength referring to the different sized samples are represented in Figure 28. It is clear that the maximum value of the stress is recorded in the double-twisted yarn samples "Flax 2Y". The reduction of the peak stress in the strip samples is due to a non-uniform distribution of the stress among the threads. Figure 28b shows that the main value of the tensile strength of the control series of specimens is even slightly lower than the one recorded in the aged series of specimens. This phenomenon may be attributed to the natural variability of the mechanical properties of the textile.

Table 13 reports the results deriving from the tensile tests of the specimens subjected to the ageing process. It clearly highlights that the adopted ageing and environmental exposure protocol does not result in any reduction of the relevant mechanical property, neither in terms of strength, nor in terms of stiffness. The invariance of mechanical properties after those protocols does not only deal with the average values, as the corresponding Coefficient of Variation is generally about in the order 10%.

The stress-strain curves represented in Figure 29 further confirm this experimental observation.

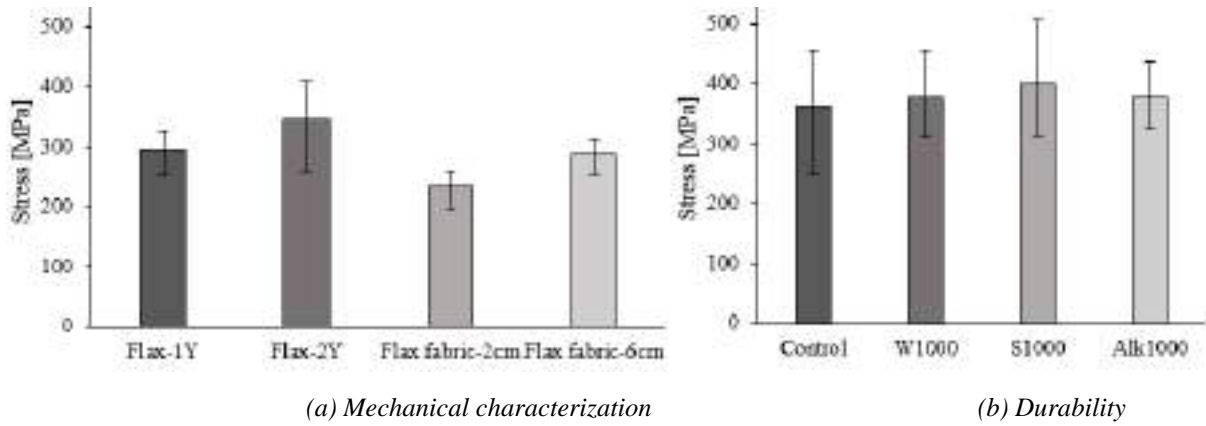


Figure 28: Comparison between the tensile strengths of different series

Table 13: Mechanical properties of samples subjected to the durability protocol

	Ageing environment	Number of tests	P_u		f_t		ε_u	
			Mean (N)	Co.V. (%)	Mean (MPa)	Co.V. (%)	Mean (%)	Co.V. (%)
Flax-Y2	Control	12	92.05	10.47	361.15	10.47	3.56	6.31
Flax-Y2	W1000	12	96.17	10.75	377.30	10.75	4.37	10.63
Flax-Y2	S1000	13	102.27	13.19	401.23	13.19	4.40	6.57
Flax-Y2	Alk1000	13	95.92	8.74	376.34	8.74	4.54	7.10

P_u = Maximum Load; f_t = Tensile Strength; ε_u = strain at failure

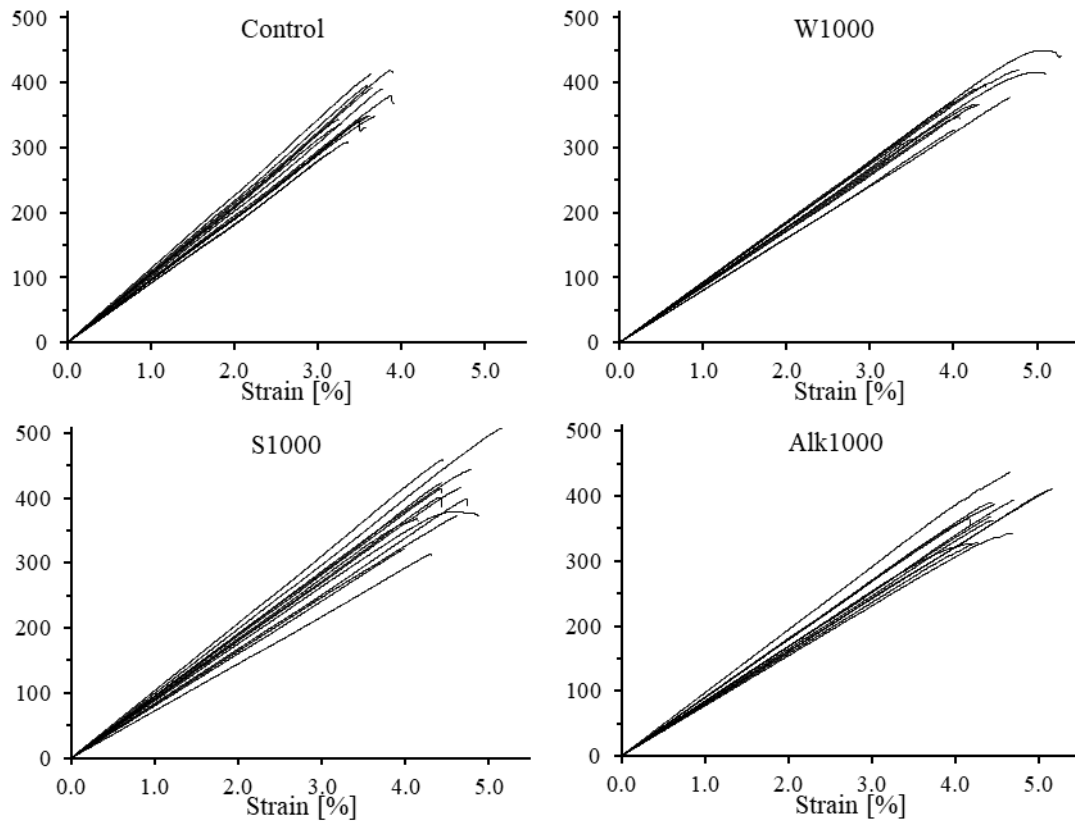


Figure 29: Stress-strain curves of series of specimens subjected to the durability protocol

Finally, the images reported in Figure 30 derive from the SEM analysis and depict the surface of four representative samples of the four series of fibres considered in this study with a magnification of 10000. As can be seen, they do not evidence any relevant damage on the filament surface of the samples subjected to the environmental exposure protocol. This confirms that a period of 1000h under the aforementioned conditions does not affect the mechanical behaviour of the flax fabric under consideration in this study.

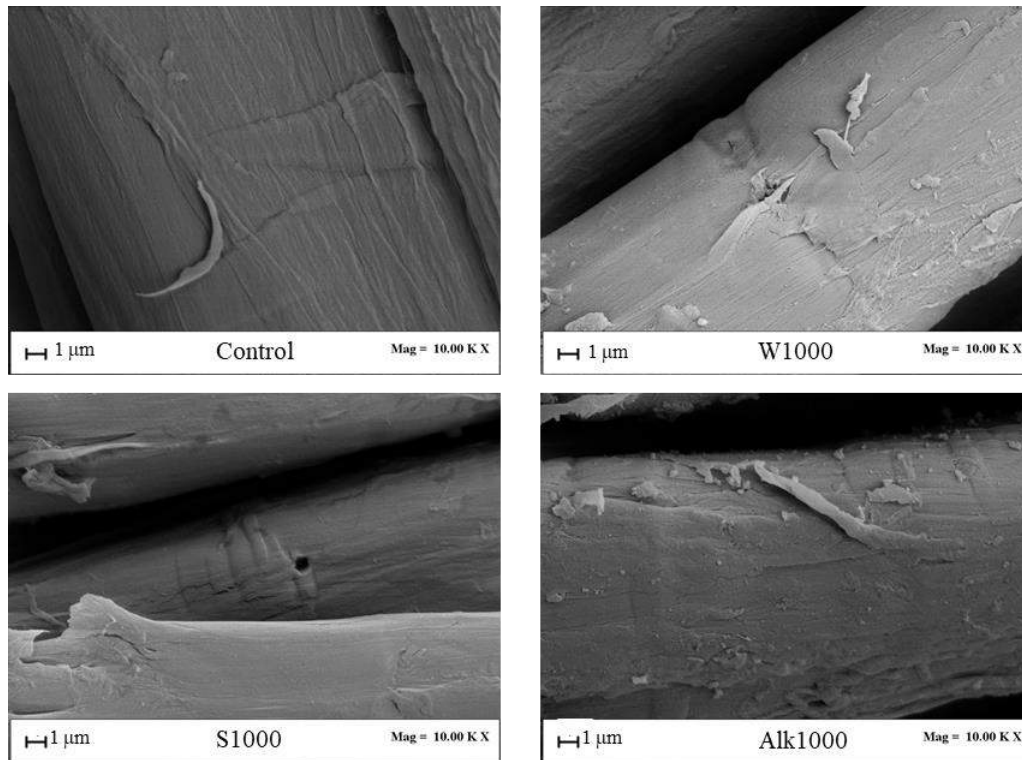


Figure 30: SEM images of samples subjected to the durability protocol

CONCLUSIONS

The experimental study, carried out to mechanically characterise the flax textile and to consider its effectiveness in strengthening composite systems, has led to the following conclusions:

- the geometric investigation by means of an optical microscope cannot provide reliable values to be used for mechanical purposes;
- the main values of the mechanical properties, consisting in a tensile strength of 353.72 MPa, a Young's Modulus of 9.36 GPa, and a strain at the failure of 3.85%, are in line with what is present in the literature;
- the durability protocol chosen is not aggressive enough to trigger the degradation of the natural textile;
- the SEM analysis is an effective technique for both the investigation of the fibres filaments, and the monitoring of the degradation status of the textile.

In order to check the effectiveness of the use of natural fibres, experimental analysis has to be conducted directly on composite systems reinforced by this textile. Moreover, a more challenging durability protocol should be considered with the aim to provide a more representative environmental exposure condition for vegetal fibres under consideration.

ACKNOWLEDGEMENTS

The first Author's Ph.D. scholarship is awarded by the Italian Ministry for Education, University and Research (MUIUR) as part of the programme "Dottorati Innovativi a caratterizzazione industriale" funded by the European Union (Structural Funding ERDF-ESF for "Research and Innovation" 2014-2020), whose financial support is gratefully acknowledged. The authors gratefully acknowledge INNOVATIONS s.r.l. for providing the materials tested in the experimental research presented in this paper.

REFERENCES

- AC 434-1011-R1 (2011). "Acceptance Criteria for Masonry and Concrete Strengthening Using Fiber-reinforced Cementitious Matrix (FRCM) Composite Systems".
- D. Asprone, M. Durante, A. Prota, G. Manfredi (2011). "Potential of structural pozzolanic matrix-hem fiber grid composites", *Construction and Buildings Materials* 25 2867-2874.
- R. Codispoti, D.V. Oliveira, R.S. Olivito, P.B. Lourenco, R. Fanguiero (2015). "Mechanical performance of natural fiber-reinforced composites for the strengthening of masonry", *Composites Part B* 74-83.
- O. Faruk, A.K. Bledzki, H. Fink, M. Sain (2012). "Biocomposites reinforced with natural fibres: 2000-2010", *Prog Polym Sci* 37:1552-96.
- S.R. Ferreira, E. Martinelli, M. Pepe, F. de Andrade Silva, R.D. Toledo Filho (2016), Inverse identification of the bond behavior for jute fibers in cementitious matrix, *Composites Part B: Engineering* 95, 440-452
- ISO 13934-1 (2013). "Textiles-Tensile properties of fabrics- Determination of maximum force and elongation at maximum force using the strip method".
- R.S. Olivito, O.A. Cevallos, A. Carrozzini (2014). "Development of durable cementitious composites using sisal and flax fabric reinforcement of masonry structures", *Materials and Design* 57 258-268.
- K.L. Pickering, M.G. Aruan Efendy, T.M, Le (2016). "A review of recent developments in natural fibres composites and their mechanical performance", *Composites: Part A* 83 98-112.
- R.D. Toledo Filho, K. Scrivener, G.L. England, K. Ghavami (2000). "Durability of alkali sensitive sisal and coconut fibers in cement based composites", *Cement Concr Compos*; 6(22):127-43.
- F.P. Torgal, S. Jalali (2011). "Cementitious building materials reinforced with vegetable fibres: A review", *Constr. Build Mater*; 25(2):575-81.
- A. Nobili, C. Signorini (2017). "On the effect of curing time and environmental exposure on impregnated Carbon Fabric Reinforced Cementitious Matrix (CFRCM) composite with design considerations", *Composites Part B* 112 300-313.



BASALT, FLAX AND HYBRID FABRICS REINFORCED EPOXY COMPOSITES TO REPAIR CONCRETE STRUCTURES

C. Lacoste¹ and A. Bergeret¹

¹ C2MA, IMT Mines Ales, University of Montpellier, Alès, France, Email: clement.lacoste@mines-ales.fr

ABSTRACT

This study is focus on new sources of environmental friendly fabrics in Fiber Reinforced Polymer (FRP): basalt and flax fabrics. An innovative fabric composed of basalt fibers in the wrap direction, and flax fibers in the weft direction was also characterized and presented in this work. The derived hybrid composite shows more equilibrate properties than the unidirectional basalt or flax composite counterpart. However, basalt-epoxy fabrics provide the best tensile strength with a value of 391 MPa. Flax-epoxy composites are instead less resistant and show lower interface adhesion with the matrix. As a consequence, there are more sensitive to water absorbency which can provide a fiber-matrix rupture. Basalt composites appears as promising materials for civil engineering applications.

KEYWORDS

Composite, Fiber Reinforced Polymer, basalt, interface, flax, hybrid composite.

INTRODUCTION

Concrete structures could be modified under various environmental conditions (corrosion, fatigue or exceptional loads) and need to be reinforced to extend their service life. A popular approach has been introduced with Fiber Reinforced Polymer (FRP). The reinforcement of concrete structure is achieved by hand lay-up of more than one layer composite (Marouani et al. 2011). Usually, Carbone Fiber Reinforced Polymer (CFRP) is the first commercial choice according to their high tensile strength and durability. However, considering the need of lowering the delivery and environmental cost of the composite materials, non-conventional innovative materials should be explored.

Strong, lightweight, durable and economically viable fibers are currently required for fabricating the FRP. Basalt fibers are a material of choice and are inorganic fibers with extremely good mechanical properties, high temperature resistance, natural and inexpensive (Dhand et al. 2015). Basalt fibers are obtained after extrusion from basalt-based molten igneous volcanic rock (Banibayat and Patnaik 2014) and have excellent resistant to alkaline attack which make them suitable in contact with concrete. Basalts fibers to reinforced concrete structure were studied by Sim et al. (2005) and authors demonstrate an increase of concrete resistance. Some authors also studied the use of basalt fibers to reinforced polymer. Ary Subagia et al (2014) make basalt/epoxy composites with tourmaline micro/nano particles (0.5-2 wt%) using the vacuum assisted resin transfer molding technique. Laminates showed that the tensile and flexural strength increased by 16% whereas an increase of 27% and 153% was observed for the tensile and flexural modulus respectively.

Lopresto et al. (2011) made two epoxy laminates through vacuum bag method reinforced with E-glass (290 g/m²) or basalt plain (200 g/m²) weave fabrics. The fiber volume fractions were measured in values of 51% and 46% respectively for basalt and glass laminates. The experimental results showed a high performance of the basalt material in terms of young modulus, compressive and bending strength, impact force and energy. Furthermore, the short-beam strength tests confirmed a quite good interfacial adhesion between basalt fibers and epoxy matrix, not worse than the one between E-glass and epoxy matrix.

Dorigato and Pegoretti (2012) compared the quasi static tensile and fatigue properties of epoxy based laminates reinforced with woven fabrics of basalt, E-glass, and carbon fibers with the same areal density (200g/m²). All the laminates were prepared by means of vacuum bagging technique, thus obtaining volume fiber content equal to 63.5%, 56.3%, 61.3% for carbon, glass and basalt reinforced epoxy respectively. The experimental result showed that the basalt fibers laminates present elastic moduli and strength values higher than those of the corresponding laminates reinforced with glass fibers, with tensile strength values near to that of carbon fibers based laminates.

The promising nature, biodegradability, low cost and effective properties of natural fibers like flax fibers could make the microstructure of a flax fiber is extremely complex due to the organization of its structure a different scale and also containing different components in various proportions. The main constituents of a flax fiber consist

of cellulose, hemicellulose, wax, lignin and pectin, in varying quantities. This variety of composition is due to the intra-species variability and the growth conditions of the plant (Yan et al. 2014).

Natural Fiber Reinforced Composite (NFRP) is a prospective candidate for reinforcement in FRP. Lignocellulosic flax fibers are known for their competitive specific mechanical properties despite their low densities. Their use as reinforcement in NFRP has showed a relative fast increase in the recent past and will probably become significant in the next future. Assarar et al. (2011) compared the tensile properties of flax- and glass-fabric reinforced epoxy composites which were fabricated by a hand lay-up process. It was found that the tensile strength of flax composites reached up to 380 MPa, making it close to that of glass-fabric reinforced epoxy composites.

Some authors studied the tensile properties of basalt, flax compared to glass fibers. Their properties are presented in Table 1.

Table 1: Fibers mechanical properties

Fibers	Density (g/cm ³)	Tensile Modulus (MPa)	Tensile strength (MPa)	Strain (%)	Reference
Flax	1.4-1.5	30-70	300-1500	0.8-3.3	Yan et al 2014
Basalt	2.8	89	2800	3.2	Fiore et al. 2011
E-glass	2.6	73	1400-2500	1.8-3.2	Fiore et al. 2011

In the recent past, hybrid composites, i.e. reinforced with at least two different type of fibers/fabrics, received a great attention. Petrucci et al (2012) have made hybrid composites composed of basalt fabrics layers with an external layer in glass, flax, or hemp fabrics by injection molding. The fiber content value was 21% to 23%. The mechanical properties of these materials were higher than flax- or hemp-epoxy composite, but lower than full basalt-epoxy composite.

On the contrary, Fiore et al. (2016) have made basalt-flax epoxy fabrics with an external layer in basalt in order to increase the durability of the laminates. The mechanical properties were increased up to 49% and 71% for and for the flexural modulus and the tensile strength respectively. The water uptake was also reduced (-61%) after 700h in water.

This study is focus on the mechanical characterization of unidirectional fabrics of basalt, flax, and hybrid flax-basalt epoxy composites. The hybrid composite is not composed of laminates with alternative layer of different fabrics, but the fabric is fabricated itself with one type of fibers in the wrap direction, and another in the weft direction. The intrinsic tensile properties were measured in order to evaluate the possibility to use these materials to repair concrete structure. The durability of the composites was also measured after water aging.

MATERIALS AND METHODS

Materials

Unidirectional flax fabric UD23 (200 g/m²) was supplied by Fibres Recherche Developement (FRD, France), basalt fabrics UN350 (350 g/m²) were supplied by Basaltex (Belgium). The hybrid basalt/flax fabric was made by Depestele (France) (260 g/m²). This twill fabric is composed of 50% of basalt fibers by weight and 50% of flax fibers. The two-component epoxy resin, namely InfuGreen 810 resin and SD8822 hardener, was purchased from SICOMIN. The resin is produced with about 38% of carbon from plant origin.

Composites

All the composites investigated were realized using the hand lay-up technique, cured at room temperature (20°C) for 24h and post-cured at 40°C during 24h. The curing cycle condition was chosen in order to obtain the highest tensile modulus according to the technical datasheet of the resin.

Slab of 300 x 200 mm² of each fabric was impregnated by the resin by hand lay-up on each face. The resin was prepared as recommended by Sicomin in the following proportion: (resin:hardener) = (1:0.31).

The target volume fraction of fibers is $v_f = 40\%$. As the density of basalt fibers ($\rho_b = 2.70 \text{ g/cm}^3$) and of flax fibers ($\rho_f = 1.54 \text{ g/cm}^3$) are different, the quantity of resin was determinated to achieve this ratio. The composite weight and density were used to control the ratio with the method described by Petrucci et al (2012). The composites were stored in a climate room at 22°C and relative humidity of 50% during 7 days before being tested. For all tests, samples were done in triplicate. Samples of 250 x 50 mm² were then cut considering the fibres orientation.

Table 2: Basalt, flax, and hybrid epoxy composites parameters

Sample	Fabrics	Tensile test direction/fibers	Fabric weight (g/m ²)
Flax_L	Unidirectional UD23	Parallel	220
Flax_T	Unidirectional UD23	Perpendicular	220
Basalt_L	Unidirectional BAS350	Parallel	350
Basalt_T	Unidirectional BAS350	Perpendicular	350
Hybrid_F	Bi-directional Hybrid F/B	Parallel to flax fibers	260
Hybrid_B	Bi-directional Hybrid F/B	Parallel to basalt fibers	260

The composites obtained are presented in Fig. 1.



Figure 1 : Basalt, Flax and hybrid epoxy composites fabricated by hand lay-up

Tensile tests

Tensile tests were performed with a MTS universal press according to ISO 527 equipped with a 100 kN load cell and self-tightening grips at 1 mm/min. Aluminium heels were then used in order to avoid damaging the composite during the test.

Vibration analysis

From a general point of view, vibration techniques aim to study the dynamic behaviour of a structure using its fundamental natural mode of vibration (Corn et al 2012, Regazzi et al. 2016). In the present study, this technique was expected to evaluate the intrinsic viscoelastic properties of the materials and more particularly their dynamic elastic modulus.

Briefly, samples were set in free end position with a free length of 250 mm. The material was stimulated by a short impulse leading the sample to vibrate. The displacement was recorded by a piezoelectric sensor. The time response was then converted to a frequency response by means of a Fast Fourier Transform. This mode corresponds to the first flexural mode. The frequency is related to the modulus of the material according to Euler-Bernoulli relation:

$$f = \frac{\beta^2}{2\pi L^2} \times \left(\frac{EI}{\rho A}\right)^{0.5} \quad (1)$$

where ρ is the density of the composite, A the surface area, I the inertia, L the length, and β is the frequency parameter which depends on the limit conditions. As the sample is free, the value becomes $\beta = 4,73$.

Determination of the modulus

The modulus of the composite was estimated by two methods:

- a. the first method considers the vibration properties of the composite:

$$E_1 = \frac{\rho A}{I} \left(\frac{2\pi L^2}{\beta^2}\right)^2 \quad (2)$$

- b. the second method is the modulus obtained from the stress (σ) –strain (ε) curves between 0.1 and 0.3% (ISO 2747) of strain on 3 samples:

$$E_2 = \frac{\sigma}{\varepsilon} \quad (3)$$

Water uptake

In order to compare the water uptake of the composites, 3 samples of each composite were periodically removed from the distilled water bath with the range 0-15 days, and weighed with an analytical balance. The absorption of the composites in weight percentage W was calculated as follow:

$$W = \frac{m_t - m_0}{m_0} \times 100 \quad (3)$$

Where m_t is the wet weight at time t and m_0 is the dry weight of the sample.

RESULTS AND DISCUSSIONS

Tensile strength

The tensile strength and the maximal strain are given in Figure 2. Both unidirectional flax and basalt composite have poor tensile strength in the transverse direction compared to the strength along the fibers. The maximum strength was obtained with Basalt_L sample with a value of 391 MPa. The low tensile strength of the Flax-L sample suggests a poor interfacial adhesion between the lignocellulosic fibers and the epoxy matrix. The fiber-matrix interface is indeed known to play a major role in the stress transfer and a good adhesion protect also the composite against water aging by limiting water penetration. The flax-fiber matrix interface must be improved in the future to be used in such application. The hybrid composite shows more equilibrate properties in the both direction even if the tensile strength is still higher when basalt fibers are parallel to the force applied.

Thus, basalt-epoxy composites have more maximal strain values with make then less brittle.

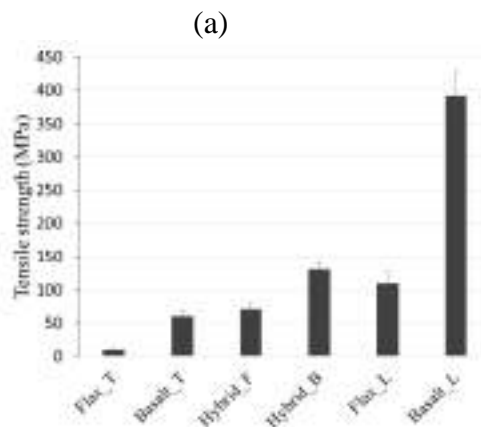


Figure 2a: Tensile strength of the composites

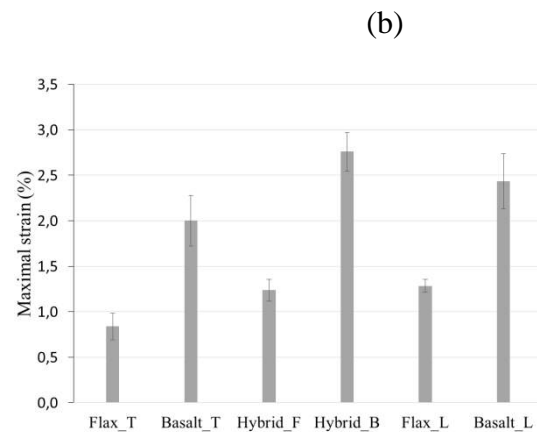


Figure 2b: Maximal strain of the composites

Figure 2: Tensile properties of the flax-, basalt, and hybrid composites

Modulus

The moduli of the composites were calculated with different methods and the results are presented in Fig. 3. Unidirectional composites are more rigid when the force is applied along the fibers direction: Basalt_L has a modulus of 20,2 GPa and Flax_L modulus value is 10.5 GPa. Hybrid composite is less rigid in both direction but its modulus is again more equilibrate with values of 6.1 GPa and 4.7 GPa in the basalt and flax direction respectively.

The method used to determine the modulus is close to the results measured by static tests. This method is advantageous because it is a non-destructive and easy way to estimate with a good correlation the modulus of these type of composites.

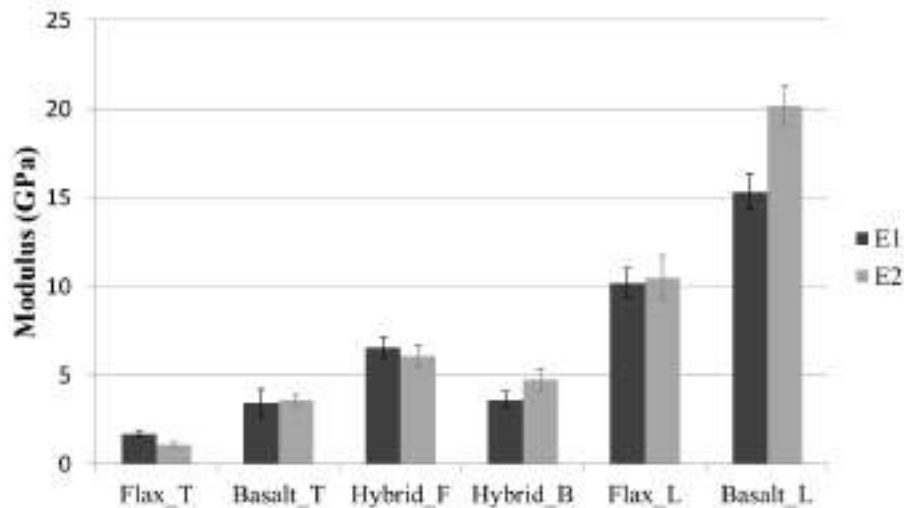


Figure 3: Tensile Moduli (MPa) of the basalt, flax, and hybrid composites measured by vibration analysis (E1) and static tests (E2)

Water uptake

The water uptake percentage of composites vs. aging time is shown in Fig. 4. For every composite, the water absorption quickly increased and reached a plateau after around 2 days. The maximum water absorbed values were of about 10.6% (± 1.1), 13.9% (± 2.2) and 12.1% (± 1.1) for basalt, flax, and hybrid composites respectively. The percentage of water uptake with time is slightly higher for composite containing flax fibers. Flax fibers are indeed known for their hydrophilic properties due to their specific chemical composition and microstructure. More informations can be found in Yan et al. (2014). An increment of the diffusion processes occur since the swelling of hydrophilic flax fibers leads, in turns, to fiber-matrix debonding. This creates voids, which act as a reservoir for moisture.

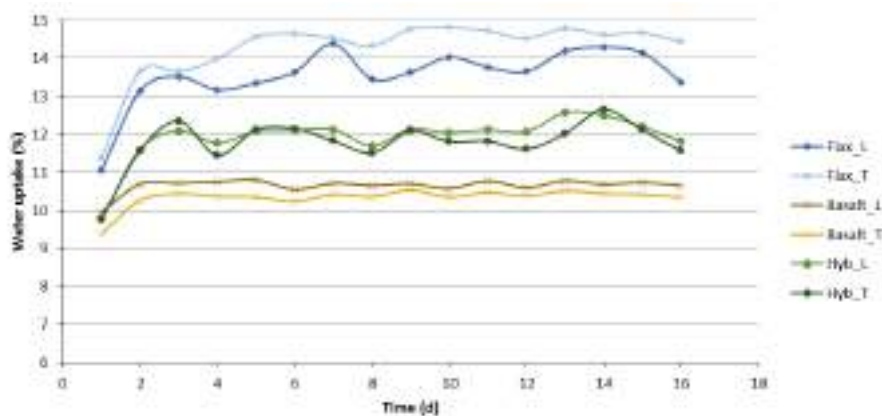


Figure 4: Water uptake (%) in the composites as a function of time

Basalt composites appear as less sensitive to degradation when it is exposed to critical environment conditions. The hybrid composite trend also suggests that basalt fibre improve fibre-matrix interface, i.e. the interfacial voids volume is reduced and prevents water penetration into the composite.

CONCLUSIONS

Three strategies were investigated in this work: flax-, basalt-, and a new hybrid flax-basalt-epoxy composite to study to possible substitution of traditional FRP used to repair concrete structures by these composites. Flax-epoxy composites show relatively low tensile properties due to a poor chemical affinity between fibers and matrix, they are then more sensitive to water absorption with can rapidly damage the material. Hybrid composite has more equilibrate properties than the unidirectional flax or basalt composite, but its tensile strength is still not convenient for such application. However, with a modulus of around 20 GPa and a tensile strength value of 391 MPa, basalt-epoxy composites appears as a good candidate to reinforced or to repair concrete structures even if additional layer(s) of fabrics or using a stronger epoxy resin should be considered in the future to achieve the same level of mechanical performance than CFRP.

ACKNOWLEDGMENTS

The research leading to these results is part of the project ANR MICRO (15-CE22-007) with is a national R&D program funded by the French Research National Agency. All the authors acknowledged the support.

REFERENCES

- M. Assarar, D. Scida, A. El Mahi, C. Poilâne, R. Ayad (2011). « : flax-fibers and glass-fibers », *Materials and Design*, 32, 788-795.
- P. Banibayat, A. Patnaik (2014). “Variability of mechanical properties of basalt fiber reinforced polymer bars manufactured by wet lay-up method”, *Materials and Design*, 56, 898-906.
- S. Corn, J-S. Dupuy, P. Ienny, L. Daridon (2012). “Vibration analysis techniques for detecting filler-matrix decohesion in composites”, *Revue des Composites et des Matériaux Avancés*, 22, 77-90.
- V. Dhand, G. Mittal, K. Yop Rhee, S-J. Park, D. Hui (2015). “A short review on basalt fiber reinforced polymer composites”, *Composites: Part B*, 73, 166-180.
- A. Dorigato, A. Pegoretti (2012). “Fatigue resistance of basalt fibers-reinforced laminates”, *Journal of Composite Materials*, 46, 1773-1785.
- V. Fiore, G. Di Bella, A. Valenza (2011). « Glass-basalt/epoxy hybrid composites for marine applications », *Materials and Design*, 32, 4244-4250.
- V. Fiore, T. Scalici, L. Calabrese, A. Valenza, E. Proverbio (2016). “Effect of external basalt layers on durability behaviour of flax reinforced composites”, *Composites Part B*, 84, 258-265.
- V. Lopresto, C. Leone, ID. Iorio (2011). “Mechanical characterization of basalt fiber reinforced plastic”, *Composites Part B*, 42, 717-723.
- S. Marouani, L. Curtil, P. Hamelin (2012). “Aging of carbon/epoxy and carbon/vinylester composites used in the reinforcement and/or the repair of civil engineering structures”, *Composites: Part B*, 43, 2020-2030.
- R. Petrucci, E. Nisini, D. Ghelli, C. Santulli, D. Puglia, F. Sarasini, G. Minak, J.M. Kenny (2012). « Mechanical and impact characterization of hybrid composite laminates based on flax, hemp, basalt and glass fibers produced by vacuum infusion », *15th European Conference on Composite Materials*, Italy.
- A. Regazzi, S. Corn, P. Ienny, J-C. Bénézet, A. Bergeret (2016). “Reversible and irreversible changes in physical and mechanical properties of biocomposites during hydrothermal aging”, *Industrial Crops and Products*, 84, 358-365.
- J. Sim, C. Park, DY. Moon (2005). “Characteristics of basalt fiber as a strengthening material for concrete structures”, *Composites Part B*, 36, 504-512.
- IDG. Ary Subagia, LD. Tijing, Y. Kim, CS. Kim, FG-IV. Vista, HK. Shon (2014). “Mechanical performance of multiscale basalt fiber-epoxy laminates containing tourmaline micro/nano particles”, *Composites Part B*, 58, 611-617.
- L. Yan, N. Chouw, K. Javaraman (2014). « Flax fiber and its composites – A review », *Composites Part B*, 56, 296-317.



BIOBASED EPOXY NETWORKS FOR CIVIL ENGINEERING APPLICATIONS

J. Galy, A. Viretto

*Université de Lyon, INSA Lyon, Ingénierie des Matériaux Polymères (IMP-UMR 5223), 17 Avenue Jean Capelle, 69621, Villeurbanne, France,
Email : jocelyne.galy@insa-lyon.fr*

ABSTRACT

In the context of sustainable development, the aim of our study is to develop biobased epoxy matrices as an alternative to the traditional petroleum-based epoxy matrices used in carbon fibre reinforced polymers (CFRP). We focus on two biobased epoxy monomers: a diglycidyl ether of bisphenol A (DGEBA) and a sorbitol polyglycidyl ether (SPGE). These monomers were reacted with a biobased curing agent, a phenalkamine (PhA), derived from cardanol. The reactivity of both systems, DGEBA-PhA and SPGE-PhA, was studied using DSC and rheology. The properties of the networks were characterised via dynamic mechanical analysis and water uptake measurements for networks with partial or full conversion of epoxy groups. The two types of networks were obtained by crosslinking at room temperature or at high temperature, respectively. These biobased formulations were compared to an epoxy model system inspired from a commercial formulation used in civil engineering applications. The results reveal that the two systems are good candidates for the preparation of green composite materials as they meet the requirements necessary for manufacturing composites in civil engineering applications.

KEYWORDS

Epoxy, Biobased matrices, New composite materials.

INTRODUCTION

Composite materials based on carbon fibres and epoxy matrices are used in civil/structural engineering applications including the repair of structurally deficient piping, structural rehabilitation, and the reinforcement of new infrastructures. Current research mainly focusses on the ageing process, and prediction of the lifetime and durability of the repaired structures (Marouani 2012; Cabral-Fonseca 2011; Stewart 2012). However, another avenue of research is to look for biobased composite materials as an alternative to the classical systems that have been and are currently used for the rehabilitation of concrete structures. Properties and costs must rival those of composites with synthetic constituents. To our knowledge this specific application of biobased composites is new and not much considered in the literature (Hallonet 2016; Yan 2013). The work presented in this paper focuses on biobased epoxy matrices, but is part of a much larger research study to develop biobased composite systems, where the use of natural reinforcing fibres such as flax or basalt fibres, instead of glass or carbon fibres, is investigated (Benzarti 2017).

The development of a new epoxy formulation for the repair of civil engineering structures must fulfil strict requirements: the viscosity as well as the reactivity (often expressed in terms of pot-life defined in technical datasheets) must be compatible with a hand lay-up process done under ambient conditions of temperature and humidity, i.e. not in controlled conditions; curing at room temperature in a reasonable time must lead to glassy networks, with a high modulus and low water absorption. In addition, the system must be robust enough to withstand severe conditions of outdoor processing. This is achieved by the appropriate choice of both the epoxy resin and the curing agent. In this paper, we selected two biobased epoxy formulations, one formulated from a biobased diglycidyl ether of bisphenol A (DGEBA, synthesized using biobased epichlorhydrin, itself obtained from bio-derived glycerol) and phenalkamines (PhA) a curing agent derived from cardanol,

(Cardolite 2017), the other from sorbitol polyglycidyl ether (SPGE) and the same PhA. Our study involves the kinetics of the crosslinking reaction and the characterisation of the networks in terms of their thermo-mechanical properties and hygrothermal ageing. Our results are compared to an epoxy model system representative of a commercial formulation used in some civil engineering applications (Brochure Foreva). The objective is to determine if these biobased formulations are good candidates for such applications.

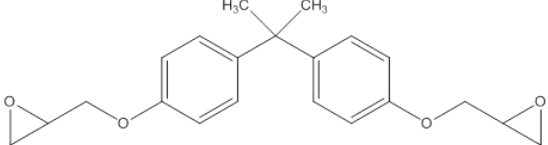
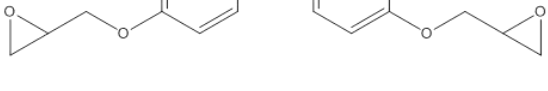
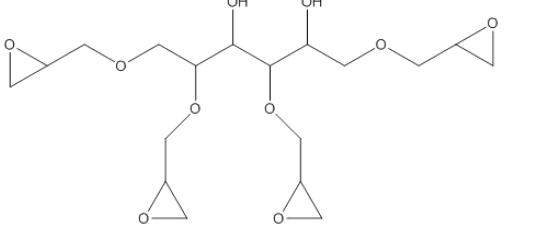
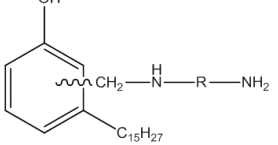
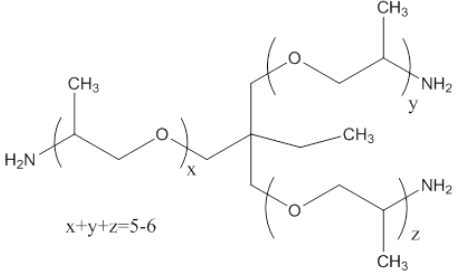
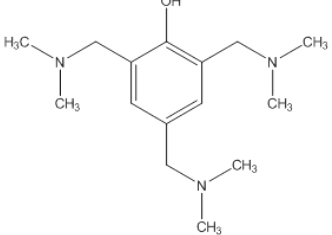
MATERIALS AND METHODS

Materials and sample preparation

The model reference system was based on a conventional DGEBA, LY556, cured with Jeffamine T403, both from Huntsman and a catalyst (DMP30). The commercial system was obtained from Freyssinet. Biobased DGEBA was obtained from Spolchemie (CHS-G530). SPGE was obtained from Nagase (Denacol EX-622). A biobased phenalkamine curing agent, with the reference NX5619, was supplied by Cardolite. The simplified chemical structure of the reagents and their characteristics are shown in Table 14.

All compounds used in this work were viscous liquids at room temperature. The epoxy prepolymer was mixed with the curing agent using a high-speed mixer (IGT Testing Systems). The stoichiometric ratio of amino hydrogen to epoxy, a/e , was 1. Afterwards the mixture was degassed under vacuum and transferred into a PTFE-coated aluminium mould. The networks were either cured at room temperature for seven days, or cured for 24 hours at room temperature followed by a post-cure treatment of 2 hours at 120 °C; these two curing cycles were named as RT and RT-HT, respectively.

Table 14: Simplified chemical structures of the epoxy monomers and curing agents (EEW: epoxy equivalent weight (g/eq), AHEW: amino hydrogen equivalent weight (g/eq))

Reference	Structure	EE (g/eq)	AHEW (g/eq)	Viscosity (Pa.s)
DGEBA LY556		188	/	10-12
DGEBA CHS-G530		184	/	9
SPGE Denacol EX622		181		11.8
Phenalkamine NX5619		/	104	0.425
Jeffamine T403		/	81	0.07
DMP30		/	/	0.2

Network formation and characterization

Differential scanning calorimetry (DSC) was used to monitor the non-isothermal curing reaction. A Q10 instrument (TA Instruments) was used at a heating rate of 10 °C/min from -70 °C to 250 °C to measure the glass transition temperature of the unreacted system, T_{g0} ; the enthalpy of reaction, ΔH , and the temperature at the peak maximum, T_{max} . The glass transition temperature, T_g , of the networks cured according to our curing cycles defined above was taken at the onset point, in the same heating conditions.

Rheological properties were measured using an Ares G2 Rheometer from TA Instruments, at 40 °C. The reactive mixture was placed between parallel plates with a 25 mm diameter and a gap of approximately 1 mm. Multi-frequency sweeps were performed and the complex viscosity, G^* , and G'' were recorded. The gel time was determined according to the Winter – Chambon criterion that implies the independence of the loss factor, $\tan\delta = G''/G'$, as a function of frequency (Winter 1986).

Dynamic mechanical analysis in tension mode was carried out using a Mettler Toledo DMA/STDA 861e instrument, in order to determine the storage (E') and loss (E'') moduli, as well as $\tan\delta$ as a function of temperature. Samples (10.5 x 5 x 1 mm³) were heated from -20 °C to 150 °C at a heating rate of 3 °C/min. The frequency was 1 Hz and the static force was equal to 3 N.

Water uptake experiments were performed by first taking initial mass of the sample, W_0 , prior to immersion in a distilled water bath at room temperature. At periodic intervals, the samples were removed and weighed, W_t , and then replaced in the water bath. The relative water uptake, M_t , was calculated according to

$$M_t = \frac{W_t - W_0}{W_0} * 100 (\%).$$
 The sample dimensions were 1 x 5 x 30 mm³.

RESULTS AND DISCUSSIONS

Model reference systems

Commercial epoxy formulations commonly used for infrastructure repair are very complex two-component systems (Brochure Foreva): generally part A (resin) is composed of a mixture of epoxy monomers, among them DGEBA, and fillers, Part B (hardener) is composed of mixture of room temperature curing agents and catalysts. We identified that a formulation based on a classical DGEBA resin (LY 556 or similar), Jeffamine T403 hardener (43 phr) and DMP30 (4 phr) as catalyst is a good model of a commercial system as shown in Figure 31 where the reactivity of both systems are compared by DSC. Both systems react in the same temperature range, with a peak maximum temperature equal to 117°C; the lowest enthalpy of reaction, ΔH , observed in the commercial formulation is due to the presence of a high amount of fillers (~25 wt%). After RT curing cycle, a glass transition temperature close to 50°C was found for the commercial network and 62°C for the model network, typical values for epoxy networks cured at room temperature.

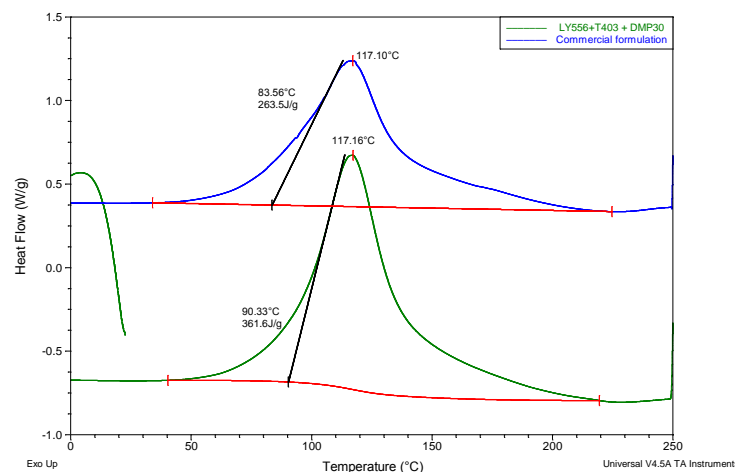


Figure 31 DSC thermograms of the commercial (blue curve) and epoxy model systems (green curve).

Biobased systems

Matrix viscosity is an important parameter that is directly relevant to the process of making the composite material. In civil engineering applications, wet hand lay-up is one of the preferred processes. It is therefore important to investigate the rheological behaviour of biobased epoxy systems to determine if they can be adapted to the process. The variation of the viscosity of the biobased epoxy systems as a function of the reaction time at 40 °C is plotted in Figure 32. It can be seen that the initial viscosity is around 2–3 Pa.s for both systems. This low viscosity is

compatible with hand lay-up processes. The systems show no significant increase in viscosity over 90 min for the DGEBA-PhA and 55 min for the SPGE-PhA, at 40 °C. The gel times at 40 °C were determined from multi-frequency experiments. The DGEBA-PhA formulation has a longer gel time than the SPGE-PhA formulation — 140 min and 57 min, respectively (Table 15). The shorter gel time of the SPGE-PhA system is due to the functionality of the SPGE prepolymer, which is greater than two; and also to the presence of numerous hydroxyl groups which catalyse the epoxy-amine reaction (Chrysanthos 2013). At 40 °C the pot-life is long enough to allow the manufacture of composites. This temperature represents somewhat extreme temperature conditions that may nonetheless be experienced during infrastructure repair.

The two biobased systems were analysed using nonisothermal DSC, and the obtained thermograms are shown in Figure 32. The crosslinking reactions occur in the same temperature range as the model and commercial formulations. Table 15 shows the glass transition temperatures of the unreacted systems (T_{g0}), the peak maximum temperatures (T_{max}), the total heat of reaction (ΔH), and the glass transition temperatures obtained after room temperature curing (T_{gx}). The initial glass transition temperatures, T_{g0} , and the beginning of the reaction are almost the same for both systems. SPGE-PhA showed a lower temperature peak compared with the DGEBA-PhA system; this is an indication that the SPGE-PhA system has a slightly higher reactivity, ascribed to the catalyst effect of hydroxyl groups. The enthalpy of reaction of the SPGE-PhA system is significantly lower than that of the DGEBA-PhA system, while the EEW values for the two epoxy prepolymers are similar. A similar result has also been observed by Chrysanthos et al. using isophorone diamine as the curing agent. This lower enthalpy of reaction is a sign that the epoxy-amine reaction is not complete, and some oxirane functionalities are very likely hindered

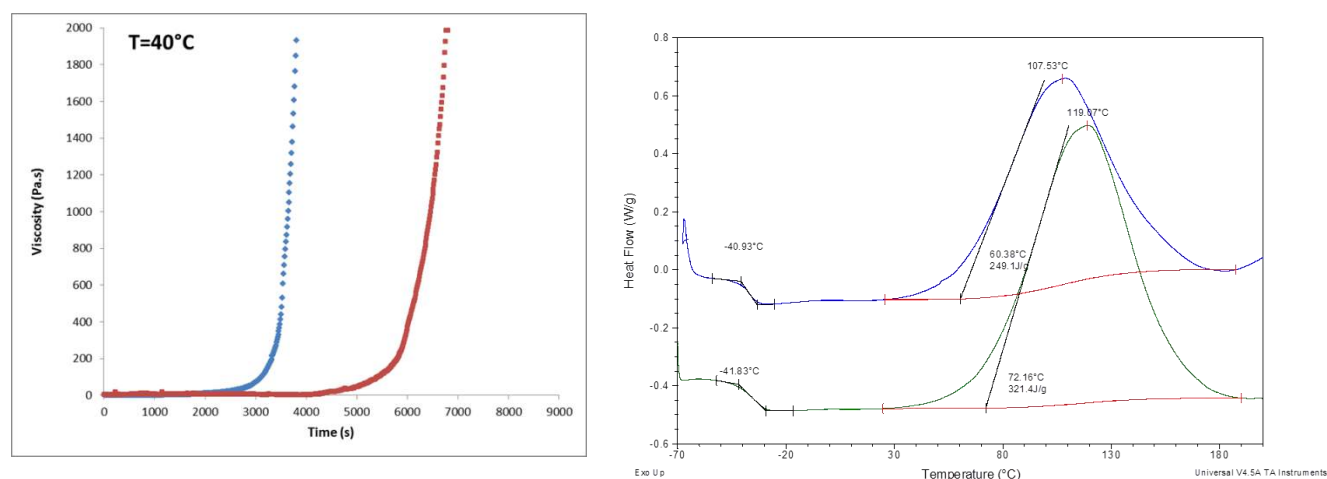


Figure 32: Comparison of the reactivity of biobased formulations – Left: Viscosity as a function of time at 40 °C, measured at 5 Hz between parallel plates: ■: DGEBA – PhA, ◆: SPGE – PhA; Right: DSC Thermograms of biobased DGEBA-PhA (green curve) and SPGE-PhA (blue curve).

Table 15: Curing behaviour results for the two biobased epoxy systems (pot life at 40 °C (time after which viscosity started to increase), gel times at 40 °C, DSC results and glass transition temperature after RT curing cycle.

System	Pot life (min)	Gel time (min)	T_{g0} (°C)	T_{max} (°C)	ΔH_r (J/g)	T_{gx} (°C)
DGEBA + PhA	90	140	-35	119	320	54
SPGE + PhA	55	57	-37	107	250	40

Network properties

The thermo-mechanical properties of the materials were evaluated by means of dynamic mechanical analysis. Figure 33 shows the temperature dependence of E' and $\tan\delta$ for the two biobased networks either partially cured at room temperature (RT) or fully cured after a post-curing cycle at 120 °C (RT-HT). Table 16 summarises the main parameters calculated from these curves.

Partially cured networks: obviously, the main transition (related to the glass transition), α , is higher for the DGEBA-based network with $T\alpha = 61$ °C compared with $T\alpha = 46$ °C for the SPGE-based network. This difference, also seen by DSC (Table 15) is explained by the fact that DGEBA has an aromatic structure and SPGE has an aliphatic structure. The two networks have a similar modulus, ~3 GPa, at low temperature (-10°C). However, the decrease in the modulus in the glassy state until the glass transition is more pronounced for the SPGE-PhA network

compared with the modulus of the DGEBA-PhA network which is nearly constant. After the glass transition in the rubbery state, the modulus of the SPGE based network is significantly higher than the rubbery modulus of the DGEBA based network, with values of 25 and 8.8 MPa at $T\alpha + 30^\circ\text{C}$, respectively. It is also observed that the rubbery modulus for the DGEBA-PhA network increases continuously as the temperature is increased, while it remains almost constant for the SPGE based network. This means that the DGEBA-PhA network undergoes a post-cure during the DMA experiment. The difference in the rubbery modulus between the two room temperature cured networks is due to the difference in chemical structure of the epoxy prepolymers, which has consequences on the epoxy conversion and on the flexibility and length of the chains between crosslinks. According to the rubber elasticity theory, the average molar mass of the segment between crosslinking points (M_c) can be calculated using the following equation:

$$E' = 3dRT/M_c$$

where E' , d , R , and T are the storage modulus (MPa) at $T\alpha + 30^\circ\text{C}$, the density of the network (g/cm^3 , measured by Archimedes' method in water), the gas constant ($8.314 \text{ J}/\text{mol}\cdot\text{K}$), and the temperature (K), respectively. The calculated values of M_c are presented in Table 16. The shortest value of M_c is obtained for the network based on SPGE.

Fully cured networks: A post-curing cycle of 2 hours at 120°C causes some changes in the networks, which are especially marked for the DGEBA based network (Figure 33). The temperature at the maximum of $\tan\delta$ is increased to 89°C and the rubbery modulus becomes 15.12 MPa at $T\alpha + 30^\circ\text{C}$. The rubbery modulus is thereafter constant with increasing temperature, unlike the case of the room temperature cured network; it is evidence that the network is fully cured. The molar mass between crosslinking points after the post-curing cycle is $740 \text{ g}/\text{mol}$. In the SPGE-PhA network, the changes are less significant: T_{\max} is increased to 50°C , the rubbery modulus becomes 31 MPa at $T\alpha + 30^\circ\text{C}$ and M_c is $347 \text{ g}/\text{mol}$. These changes show that the SPGE-PhA network was not fully cured at room temperature, and the post-curing cycle allowed some of the residual epoxy and amine functions to react. The two fully cured networks exhibit distinct features: the DGEBA-PhA network has a higher glass transition temperature than the SPGE-PhA network, but a lower crosslink density.

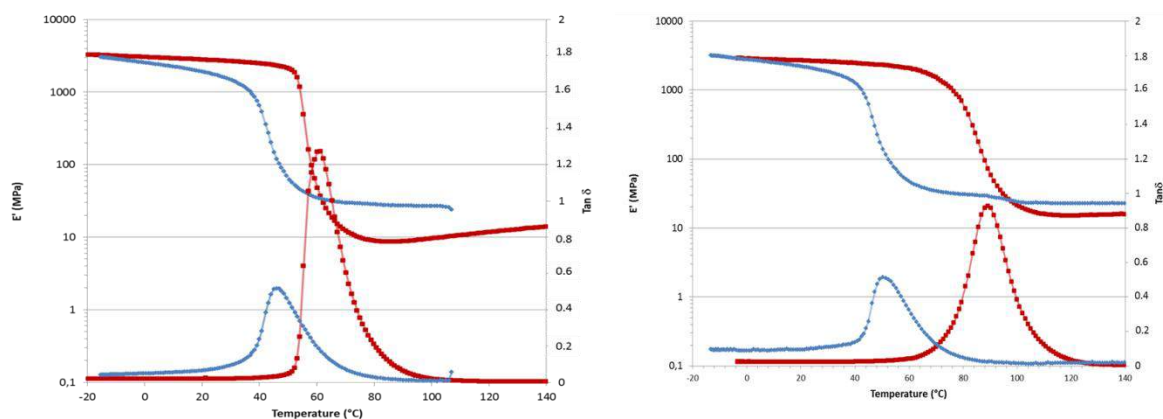


Figure 33: Temperature dependence of E' and $\tan\delta$ for the two biobased networks after RT (left), after RT-HT (right): ■: DGEBA-PhA, ◆: SPGE-PhA.

Water uptake: The percentage of water absorbed at equilibrium by the four networks after immersion in distilled water at room temperature is reported in Table 16. Equilibrium was obtained after 14 days of immersion in water at $23\text{--}24^\circ\text{C}$. Very low values of water uptake are obtained for the DGEBA based networks, less than 1 wt%. The water absorption at equilibrium is independent of the curing cycle: the post-cured and room temperature cured networks show similar values, less than 1 wt%. This result is a very positive point from the perspective of durability. To our knowledge such values are exceptional in epoxy networks synthesised from DGEBA and diamine curing agents. Studies on hygrothermal ageing have evidenced the presence of many factors influencing the diffusion kinetics and the amount of absorbed water at equilibrium in epoxy based resins for example the free volume hole size, the fractional free volume, the chemical structure of the curing agent and the resulting polarity. In general, the use of aliphatic amines leads to networks that have lower water absorption compared with networks obtained from cycloaliphatic or aromatic diamines (Bellenger 1989). The hydrophobic behaviour of our DGEBA based network is due to the structure of the PhA curing agent, which has a long aliphatic side chain on the aromatic ring. A very different behaviour is observed for the SPGE based networks. Higher values of water absorption are reached at equilibrium, 4.80 and 4.51 wt%, for the room temperature and post-cured samples respectively. Such high values are explained by the polarity of the epoxy prepolymer. As mentioned previously SPGE has a large number of hydroxyl groups which makes the compound more hydrophilic than DGEBA. Even if the PhA curing agent

introduces hydrophobicity to the system, it is not sufficient to compensate for the hydrophilic character of the SPGE. Nevertheless, water absorption in the range of 5 wt% is not unusual at all in epoxy networks, especially when aromatic curing agents are used.

Table 16 Thermo-mechanical properties, density (d, measured by Archimedes method) and equilibrium water uptake at 25 °C (Mm) for the biobased networks.

Network / curing cycle	T α (°C)	E' (20°C) (GPa)	E' (T α +30°C) (MPa)	d (g/cm ³)	Mc (g/mol)	Mm (wt%)
DGEBA+PhA / RT	61	2.78	8.8	1.14	1176	0.88
DGEBA+PhA / RT-HT	89	2.70	15.12	1.14	740	0.89
SPGE+PhA / RT	46	1.88	25	1.22	425	4.80
SPGE+PhA / RT-HT	50	2.2	31	1.22	347	4.51

CONCLUSIONS

In this paper, the properties of a commercial epoxy formulation commonly used in civil engineering application and those of a model formulation were presented. These properties give the targets to reach for the development of new epoxy formulations. So, two bio-based epoxy precursors (DGEBA and SPGE) and a bio-based curing agent (PhA), all commercially available, were selected with the aim of developing reactive formulations for the processing of composite materials that could be used for structural strengthening of concrete structures. The initial biobased components used in their synthesis were epichlorhydrin, sorbitol and cardanol, respectively. It was shown that DGEBA-PhA and SPGE-PhA formulations are both compatible in terms of viscosity, pot-life and gel time with the processing conditions for these types of material. However the glass transition temperature of the SPGE-PhA networks is lower than the targeted value of 50°C (after RT), but could be increased by adding rigid comonomers. Properties of DGEBA-PhA networks fit to the expected values, especially water uptake which is exceptionally low, less than 1 wt%. This is very positive for the targeted applications in which the materials involved will be exposed to outdoor environmental conditions, including humidity, water from rain, saline water, etc. It can therefore be concluded from the results obtained in this study that the two biobased epoxy matrices developed can meet the requirements for the manufacture of composite materials under ambient conditions, via a wet hand lay-up process.

ACKNOWLEDGMENTS

Funding for this study was provided by ANR (Agence Nationale de la Recherche) through the contract ANR-15-CE22-0007-04 - "MICRO: Matériaux Innovants Composites pour la Réparation d'Ouvrage".

REFERENCES

- V. Bellenger, J. Verdu, E. Morel (1989). "Structure-properties relationships for densely cross-linked epoxide-amine systems based on epoxide or amine mixtures - Part 2 Water absorption and diffusion," *J. Mater. Sci.*, 24, no. 1, 63–68.
- K. Benzarti, R Chlela, M Quiertant, S Zombre, L Curtil, A Viretto, J Galy (2017). "[Durability of flax/bio-based epoxy frp composites intended for structural strengthening: presentation and first results of the micro project](#)", 15th European-Japanese Symposium on Composite Materials, Imperial College London (UK), 24-25 September. Brochure Foreva solution, http://www.freyssinet.com/freyssinet/wfreyssinet_en.nsf/sb/reparation.
- S. Cabral-Fonseca, J. P. Nunes, M. P. Rodrigues, M. I. Eusébio (2011). "Durability of carbon fibre reinforced polymer laminates used to reinforce concrete structures," *Sci. Eng. Compos. Mater.*, 18, no. 4, 201–207.
- M. Chrysanthos, J. Galy, J. P. Pascault (2013). "Influence of the bio-based epoxy prepolymer structure on network properties," *Macromol. Mater. Eng.*, 298, no. 11, 1209–1219.
- Composites product overview, *Cardolite Corporation*: <http://www.cardolite.com/composites>, February 2017.
- A. Hallonet, L. Michel, E. Ferrier (2016). "Investigation of the bond behaviour of flax FRP strengthened RC structures through double lap shear testing," *Compos. Part B Eng.*, 100, 247–256.
- S. Marouani, L. Curtil, P. Hamelin (2012). "Ageing of carbon/epoxy and carbon/vinylester composites used in the reinforcement and/or the repair of civil engineering structures," *Compos. Part B Eng.*, 43, no. 4, 2020–2030.
- A. Stewart, E. P. Douglas (2012). "Accelerated testing of epoxy-FRP composites for civil infrastructure applications: Property changes and mechanisms of degradation," *Polym. Rev.*, 52, no. 2, 115–141.
- H. H. Winter and F. Chambon (1986). "Analysis of linear viscoelasticity of a crosslinking polymer at the gel point," *J. Rheol.* (N. Y. N. Y.), 30, no. 2, 367–382.
- L. Yan and N. Chouw (2013). "Crashworthiness characteristics of flax fibre reinforced epoxy tubes for energy absorption application," *Mater. Des.*, 51, 629–640.



*9th International Conference on Fibre-Reinforced Polymer (FRP) Composites
in Civil Engineering (CICE 2018), PARIS 17-19 JULY 2018*

FRC and cement based composite materials



A MULTISCALE APPROACH FOR TEXTILE REINFORCED CONCRETE (TRC): ILLUSTRATION ON TRC SANDWICH PANELS.

Z.I.Djamai¹, A.Si Larbi¹, F.Salvatore¹, M. El Mankibi¹

1-Université de Lyon, Ecole Nationale d'Ingénieurs de Saint-Etienne (ENISE), Laboratoire de Tribologie et de Dynamique des Systèmes (LTDS), UMR 5513, 58 rue Jean Parot, 42023 Saint-Etienne Cedex 2, France.

2- Département de Génie Civil et Bâtiment, Ecole Nationale des Travaux Publics de l'Etat (ENTPE), 3 Rue Maurice Audin, 69518 Vaulx-en-Velin, France

ABSTRACT

The present study establishes a numerical strategy for describing the textile /concrete bond behaviour in textile-reinforced concrete (TRC) composites that separates the cohesive and coulomb friction contributions.

The textile -concrete bond approach, validated on an existing pull out test in the literature, has been used to calibrate the textile-concrete bond slip law of an existing TRC tested in tension by an innovative inverse approach thanks to its pull-out mode of failure.

The calibrated bond slip law has been used as an input parameter to produce an enhanced TRC multiscale numerical model that is based on the nonlinear behaviour of its constitutive components (concrete, textile, and textile-concrete bond slip law) and takes into account all the damage mechanisms of TRC, which are mainly characterized by matrix cracking and yarn pull-out .The model has been validated on the basis of the previous TRC experimental tensile test.

3D TRC multiscale finite element approach which involves definition of the textile-concrete interaction bond slip law has been used to evaluate the behavior of a TRC sandwich panel. Accurate results have been achieved with the TRC multiscale approach; furthermore, the experimental mode of failure of the sandwich panel has been captured

KEYWORDS

Composite material, bond behaviour, Numerical modelling method, multiscale, TRC sandwich panel,

INTRODUCTION

The design of TRC structures can be simplified by establishing material models available in commercial finite element software, particularly in the case of accurate simulation of the nonlinear behaviour due to cracking of the matrix and textile-matrix debonding .Actually, the few contributions to TRC modelling focused on the TRC as a composite material with macro stress-strain behavior. Cuypers (2013) [1] uses the ANSYS program (2D element PLANE 82), to model a TRC sandwich panel subjected to a four- point bending test considering TRC as one entity obeying a tri-linear stress- strain relation . Ba Tam Truong (2016) [2] establishes a numerical model of reinforced concrete beams that are repaired with TRC also using a macroscopic constitutive law for the composite TRC identified experimentally. The macro models established for TRC are efficient for establishing a qualitative global behaviour for the composite .However ,they are not always able to take into account the evolution of some local parameters such as the degradation of the bond strength (textile-mortar) due to alkalinity and hydration kinetics as described in Butler (2009) [3] and the degradation of the mechanical characteristics of the textile itself due to an alkali attack .Moreover, they are unsuited for predicting local failure mechanisms within the yarn in the bonding layer and in the cementitious matrix.

For all these reasons, the main objective of this paper is to develop a 3D finite element model that can reproduce either global or local behavior of TRC structures starting from single-yarn pull-out (micro-scale) up to TRC tensile tests (meso-scale) and finishing with a TRC sandwich panel (macro-scale).

MULTISCALE MODELLING APPROACH

1. Micro-scale: numerical modelling of the textile-concrete debonding process

A traction-separation law originally developed to describe the delamination process has been modified to describe the textile-concrete interface debonding process according to the assumption of adhesion (I), damage (II) and friction in the destroyed bond zone (III) (the cohesive-friction contact model), [4] **figure 1**.

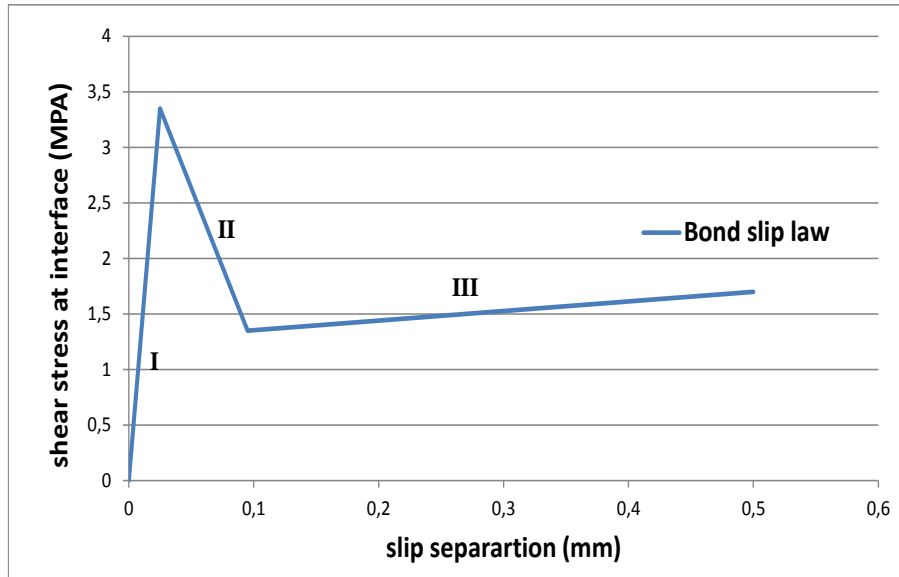


Figure 1: Tri-linear textile concrete bond slip law

Considering the detailed description of the double sided pull out test available in Ortlepp's investigation (2013) [4], the result obtained using the cohesive-friction contact model is compared with data from the pull-out test [4] in terms of force transmitted vs crack opening to verify the relevance of the proposed approach. In the double-sided pull-out test, a TRC sample with a predetermined crack is prepared, such that a yarn embedding length of $L_{E,0}=18$ mm can be gradually pulled out from the concrete-matrix.

the numerical and experimental results are compared in terms of yarn force vs crack opening at the predetermined breaking point location, i.e. F (force) vs w (crack opening) in (figure 2).

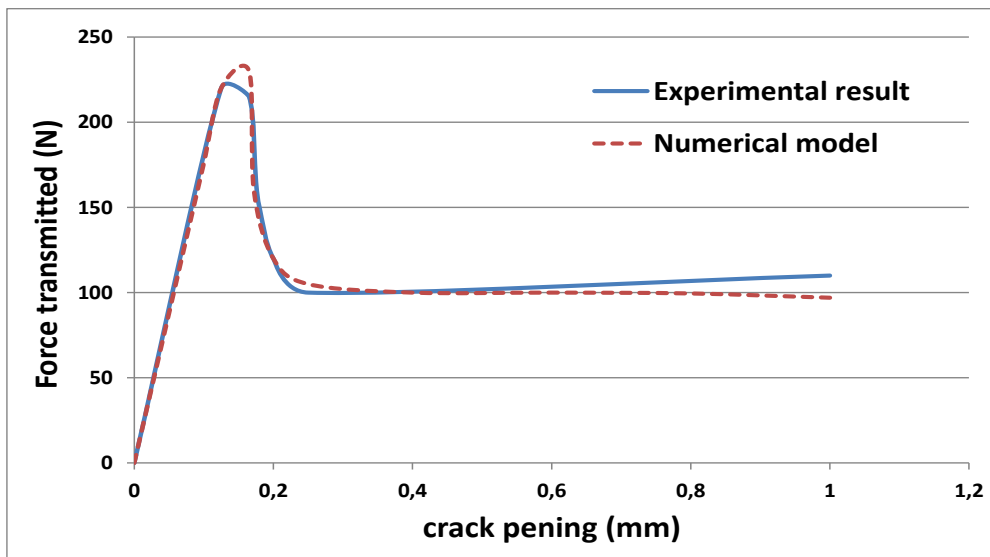


Figure 2: Experimental pull out test vs Numerical model

2. Meso-scale: The enhanced TRC model

In the second part of the present paper, the validated numerical approach describing the textile-concrete debonding process has been used to produce an enhanced TRC model at the meso-scale, taking into account all the possible failure mechanisms of its constitutive materials

To calibrate the textile-concrete bond slip law introduced in the enhanced TRC model, an innovative inverse approach has been investigated; taking advantage of the pull-out mode of failure due to the insufficient clamping length of the TRC specimen tested in tension in Colombo (2013) [5], see global behavior in **figure 3**

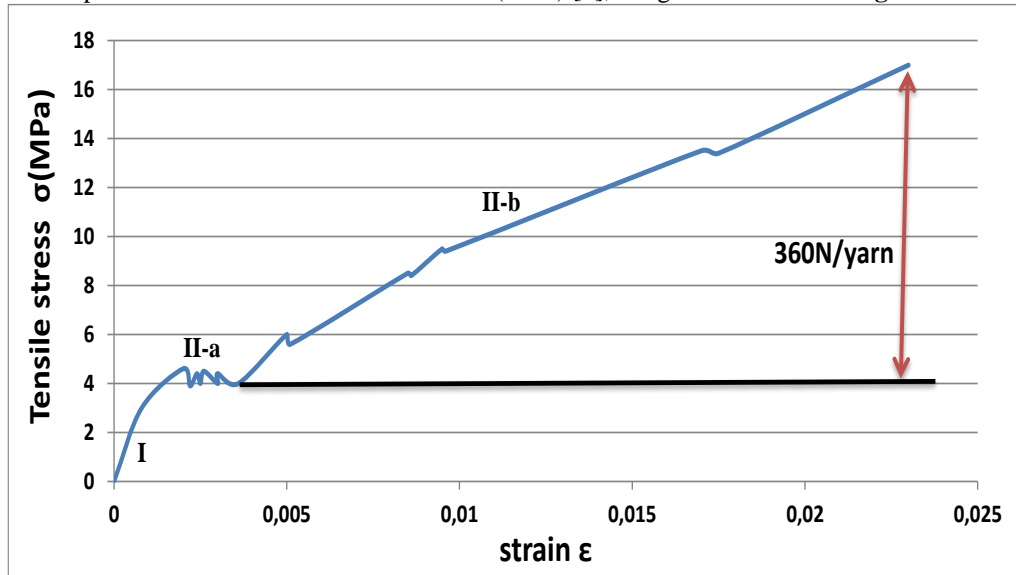


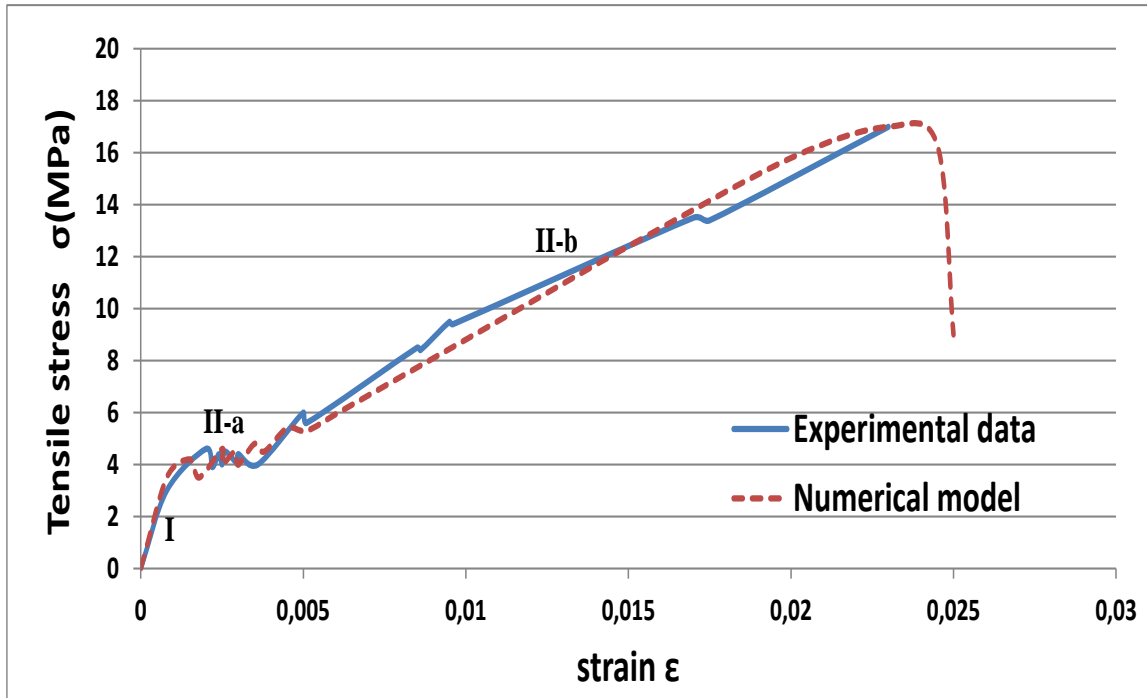
Figure 3: TRC Tensile test behaviour Colombo [6]

From the end of the multicracking step (**II a, figure 3**) to the ultimate failure of the TRC sample, the tensile test [5] can be assimilated to a double-sided pull-out test with a predetermined macro-crack located at the transition between the clamping and the free length and a maximum transmitted load of 360 N per longitudinal yarn (deduced from the $\sigma - \epsilon$ curve); see (**figure 3**).

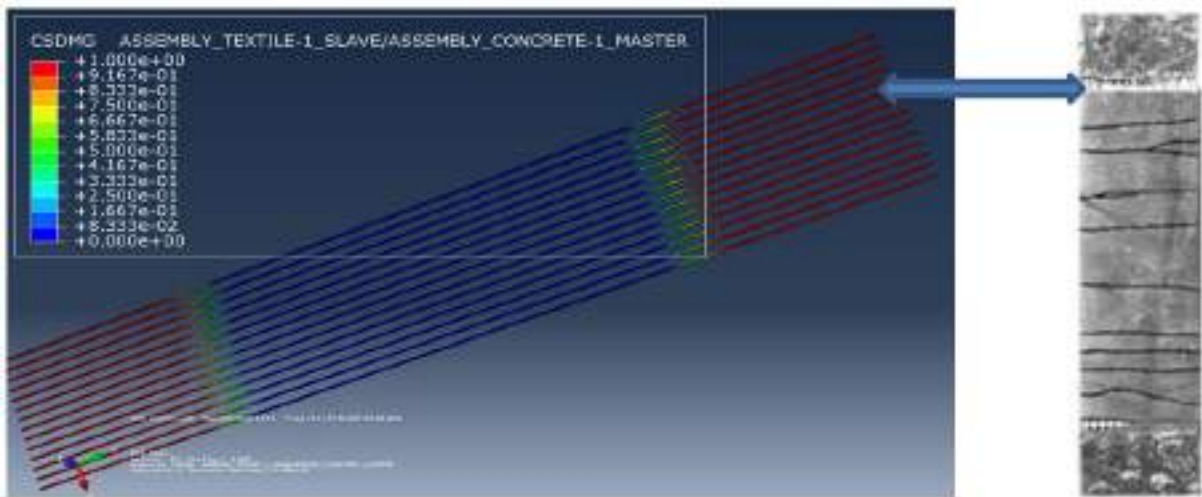
To achieve the evaluation of the bond slip law ($\tau - \delta$), An inverse approach have been used .Only one yarn is modelled. The upper length of adherence (above the breaking zone) corresponds to the real clamping length (55mm), and the lower anchoring length is the remaining free length of 290 mm in the tensile test [5]. The evaluated bond slip law corresponds to a load transmission of 360N per yarn

Once the textile-concrete bond slip law calibrated, it has been integrated as an input parameter to produce an enhanced TRC multiscale model validated on the basis of the TRC experimental tensile test described above. To achieve the construction of the enhanced TRC multiscale model, concrete has been modelled with the 3D C3D8R stress finite element with 14 rectangular holes corresponding to the location of the textile yarns. The coated yarns as 3D C3D8R stress element with a rectangular section area corresponding to the equivalent rounded section to avoid meshing problems and ensure the exact superposition of every two opposite nodes belonging to the master (concrete) and the slave (textile) surfaces .At the interface zone the cohesive friction contact law evaluated above is assumed.

The experimental and numerical TRC model results are compared in terms of stress transmitted to the entire TRC specimen (σ) vs strain ($\epsilon = \frac{\delta}{l}$) in **Figure 4**



(a)



(b)

Figure 4: (a) Experimental vs numerical comparison of TRC global behaviour, (b) TRC mode of failure due to pull out

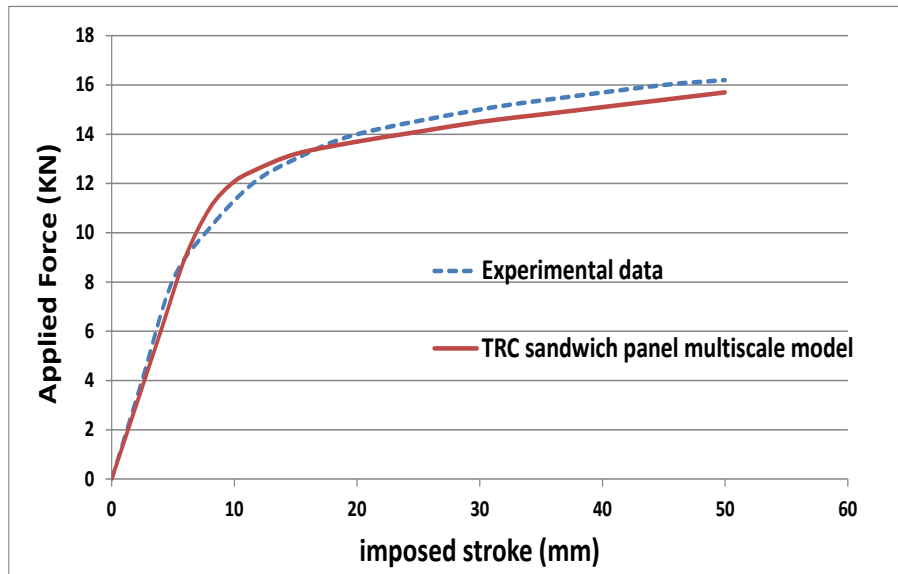
3. Macro-scale: Application to TRC sandwich panel

In this part, the performance of the proposed enhanced TRC multiscale model has been evaluated on reproducing global and local behaviour of a TRC sandwich panel described in Colombo (2015) [6] and tested in four point bending.

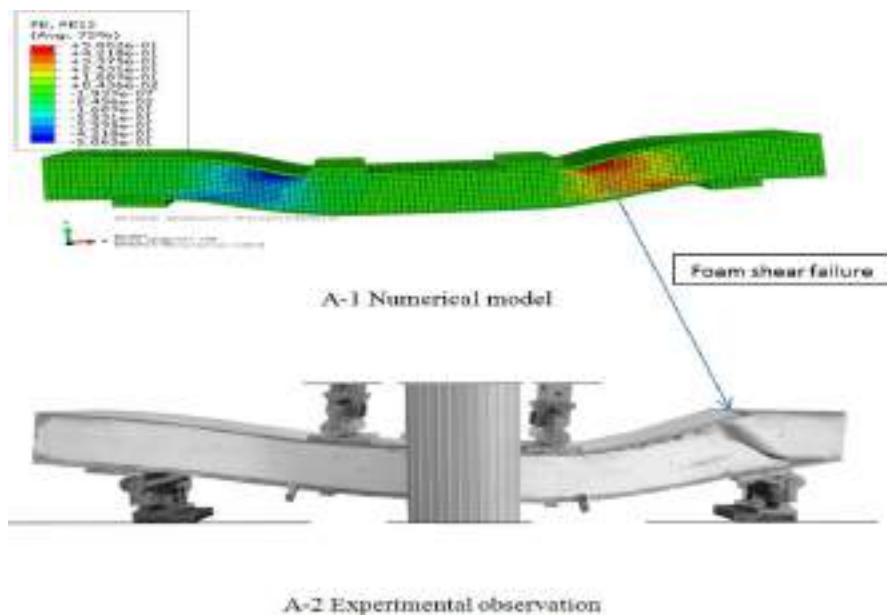
The external TRC sandwich panel consists of two skins made of TRC (10 mm thick, 300mm large, 1200 mm long) and an insulation layer made of expanded polystyrene foam EPS 250 (100 mm thick, 300 mm large), TRC described in [6] to cast the sandwich panel is the same as characterized during the TRC tensile test [5].

3D Finite Element mechanical model of the TRC sandwich panel has been built to reproduce either global or local behaviours observed during the experimental campaign.

In this approach, the polystyrene layer and the steel plates has been modelled as solid homogeneous sections with 8-node linear elements (C3D8R) when TRC layers are considered with the enhanced multiscale approach. Thus, concrete has been modelled with a 3D stress element with rectangular holes corresponding to the location of the textile yarns and with an equivalent rounded area corresponding to the textile used to reinforce TRC skins. At the interface zone, the cohesive contact law determined by the inverse approach (see section 2) has been considered. The crushable foam hardening law has been used to account for the foam hardening. The numerical model and experimental result are compared in terms of force vs imposed stroke in (figure 5)



(a)



(b)

Figure 5 Experimental vs Numerical comparison (a) global behaviour (b) failure mode

A good matching has been achieved between the mechanical model and the experimental investigation. Moreover, the experimental mode of failure (shear failure of the EPS foam) is correctly captured (plastic angular strain at shear failure of the foam exceeded $\gamma \geq 0.5$, see (figure 5)). This can be explained by the fact that the integration of

the concrete – textile interaction law permits the TRC to exhibit its full ductile behaviour and bearing strength capacity which leads to the sudden shear failure of the EPS foam before TRC reaches its ultimate tensile strength.

CONCLUSION

A novel numerical approach (cohesive-friction model) is presented for the textile-concrete debonding process in TRC composites; the proposed model permits the friction phenomena observed in the literature after reaching the overall damage of the cohesive strength to be taken into account. The proposed approach has been validated on the basis of an experimental double-side pull-out test available in the literature

The cohesive-friction bond slip law allowed for creation of an enhanced TRC multiscale model, taking into consideration all the possible mechanisms of failure of its constitutive materials (concrete cracking and concrete-textile debonding) .The model has been validated on the basis of the previous tensile test.

A numerical approach for the TRC sandwich panel has been developed, in which the enhanced TRC model is considered and the concrete-textile bond law is integrated .Although time-consuming, the multiscale TRC sandwich panel model adequately reproduces the experimental results and the mode of failure.

REFERENCE

- [1] H.Cuypers, J.Wastiels (2013) Analysis and verification of the performance of sandwich panels with textile reinforced concrete faces in *Journal of sandwich structures and materials*;5 p589-603
- [2] B.Truong , A. Si Larbi. (2016) Numerical Modelling of reinforced concrete beams repaired by TRC composites in *Composite Structures* ; 152 p779-790.
- [3] M Butler, V .Mechtcherine (2009) Experimental investigations on the durability of fibre–matrix interfaces in textile-reinforced concrete; 31 p221–231 in *Cement & Concrete Composites*
- [4] E.Lorenz , R.Ortlepp (2013) Bond Behavior of Textile Reinforcements - Development of a Pull-Out Test and Modeling of the Respective Bond versus Slip Relation *Proceedings of the RILEM-International Workshop*
- [5] I G.Colombo, A.Magri, G .Zani, M.Di Prisco (2013) Erratum to: Textile Reinforced Concrete: experimental investigation on design parameters in *Materials and Structures*; 46 p1953-1971
- [6] I.Colombo, M. Colombo, M.Di prisco (2015) Bending behavior of Textile Reinforced Concrete sandwich beams in *Construction and Building Materials*;95 p675–685



BOND BEHAVIOR OF BASALT TEXTILE GRID IN UHDCC

Jiafei Jiang¹, Xiangxiang Dou², Jiangtao Yu², Haibei Xiong²

¹ Research Institute of Structural Engineering and Disaster Reduction, Shanghai, China, Email:

jfjiang@tongji.edu.cn

² Shanghai, China; ² Research Institute of Structural Engineering and Disaster Reduction, Shanghai, China

ABSTRACT

Textile reinforced mortar (TRM) is one possible solution to replace the organic binding for the application of fiber reinforced polymer (FRP) in retrofitting. Although it can solve the fire resistance and durability issue from epoxy, but the brittle fracture of the traditional mortar makes great influences on the bond strength transfer between matrix and fiber and subsequently causes a significant decrease on the efficiency of fibers/textiles. A new inorganic composite, textile reinforced ultra high ductility cementitious composite (TR-UHDCC), was proposed to replace the mortar and expected to have an attractive foreground of engineering applications for UHDCC and large rupture strain (LRS) FRP. Fundamentally, the transfer of force from the textile to UHDCC is accomplished through the bond properties which finally affect the tensile behaviour of TR-UHDCC. In this paper, the experimental study is presented, targeting on the basalt textile grid reinforced UHTDCC. The UHDCC was developed by Yu et al (2017), which is PE fiber reinforced cementitious composite and has higher rupture strain before strain-softening than traditional Engineered Cementitious Composite (ECC). The double-sided pull-out test was conducted on 54 specimens. The bond performance is studied with consideration of the bridging effect from the fibers in the matrix. The bond behavior differs with different failure modes, which is related to the embedded length, grid spacing and warp and weft spacing ratio.

KEYWORDS:

New composite materials, systems and strengthening techniques, Experimental study, FRC and cement composite materials, Bond and interfacial stresses.

INTRODUCTION

The development of fiber-reinforced polymer (FRP) retrofitted for reinforced concrete (RC) structures has become an active field of research and engineering practice over the past two decades. This technology provides advantages over the traditional repair materials in terms of arising from excellent corrosion resistance, high strength-to-weight ratio, better mechanical and chemical performance and easier constructability. However, there is still no efficient way to solve the FRP composites associated with organic resin as the bonding adhesive to achieve higher resistance to fire resistance, degradations UV radiations, and durability in moist or dry/wet cycling environments (Lee 2002). Such weaknesses cause a greater safety factor for ultimate strength or a limit state of ultimate load carrying capacity in strengthening buildings exposed to specific environment. To overcome these problems, some researcher made a possible action through replacing organic resins with inorganic matrices to develop new fiber-reinforced inorganic polymer (FRIP) composite systems (Hegger 2006) as follows: (1) dry fiber sheet impregnated with a cementitious material, (2) FRP bars/grids coated with cement mortars and (3) textile reinforced concrete/mortar (TRC/TRM). Many research shows that TRC/TRM has several significant advantages such as producing very thin mortar elements due to there is no risk of corrosion.

Dai (2013) studied three types of cement mortars are employed as matrix materials, and previous research reported that the brittle fracture of the cementitious matrix makes great influences on the bond strength transfer between matrix and fiber and subsequently causes a significant decrease on the effectiveness of fibers/textiles. The reason for the influences is that the outer filaments of fiber bundle are more highly loaded at the matrix cracks and fail earlier, while the core is not able to bear the additional loads after cracking due to the unbalanced distribution. Dai (2009) proposed a new composite system, textile reinforced Engineered Cementitious Composites (TR-ECC), which uses fiber reinforced cementitious composite as matrix material and bonding agent and is proved to be able to postpone the cracking effect on the interaction between textile and matrix. This new system was expected to be an attractive foreground of engineering application for the strain-hardening behavior and multiple cracks behavior of ECC. With the development of ECC, a new composite, ultra high ductility cementitious composite (UHDCC), was developed by Yu et al. (2017). It has improved the rupture strain, which can even reach the ultimate strain of

large rupture strain (LRS) FRP. The supreme ductile behaviour of UHDCC under tension will solve the problem due to the brittleness and have the potential of using LRS FRP. A good composite behavior between the textile and UHDCC depends mainly on the bond performance. The bond properties between textile and concrete/mortar have been studied by many researchers since 1980s, however, the bond properties between textile and UHDCC is a new topic, which will differ from those between textile and concrete/mortar on account of the different mechanical properties between UHDCC and concrete/mortar. Since UHDCC has multi-minor-cracking process during the interaction between grids and UHDCC, the bond-slip reaction will be generated during this stage, in other words, the bond performance of grid yarn in the matrix will combine with the bridge effect from the micro fibers in the matrix. Therefore, in this study, the pull-out tests were performed to study bond properties between textile and UHDCC with consideration of fiber bridge effect. Parameters of the study were the embedded length, grid spacing, and warp and weft spacing ratio.

EXPERIMENTAL PROGRAM

Properties materials

Basalt fibers are characterized by good resistance to low and high temperatures from (-260 to 900°C), vibration resistance, and durability. They are linear elastic up to failure with ultimate strain around 2% (Ludovico 2010), or even 5% (Ates et al. 2017). In this study, three different kinds of basalt textile grids have been used, which have the knitted structure with different grid spacing (Fig. 1 and Table 1). The scanning electron microscopy (SEM) equipment was used to observe the cross section of warp yarns (see Fig.2) to obtain the area. The micro image can also observe the performance of impregnation of the yarns. It shows the best performance of resin impregnation goes for type II and the worst one goes for type III. To obtain the mechanical properties of the textile fabrics used, the coupons of the grids were prepared and tested under uniaxial tension at the constant strain rate of 1×10^{-4} /s. Table 1 presents the basic mechanical properties.

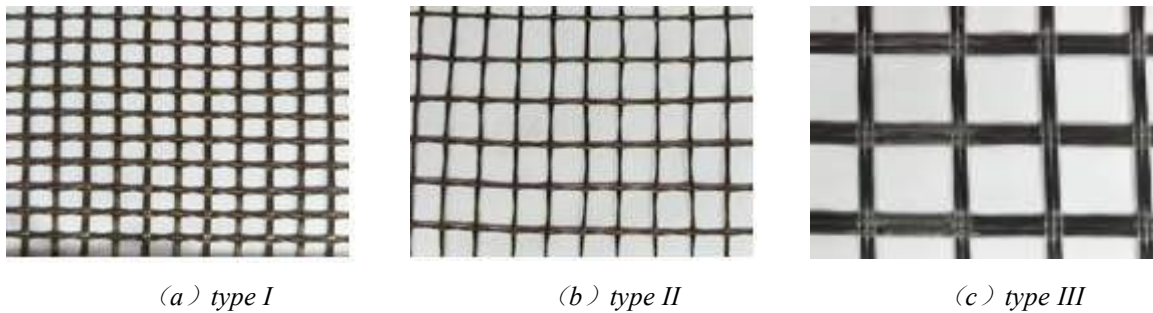


Figure 1: Image of basalt textile grid

Table 1: Tensile properties of basalt textile grid

Type	Grid spacing/mm×mm	Area of warp yarn(mm ²)	F_{max} /kN	Ultimate force per yarn /kN	E /GPa	σ_{max} /MPa	ε /%
I	5×5	0.369	0.934	0.18	30.21	491.2	1.91
II	10×10	0.324	0.688	0.17	30.04	514.9	2.05
III	25×25	3.082	5.253	2.25	28.98	643.4	2.31

Table 2: Mix proportions of UHDCC (g/L)

Water	Cement	Fly ash	Silica powder	PE Fiber	Thickener	Superplasticizer
388.1	593.0	711.6	474.4	19.1	1.2	5.0

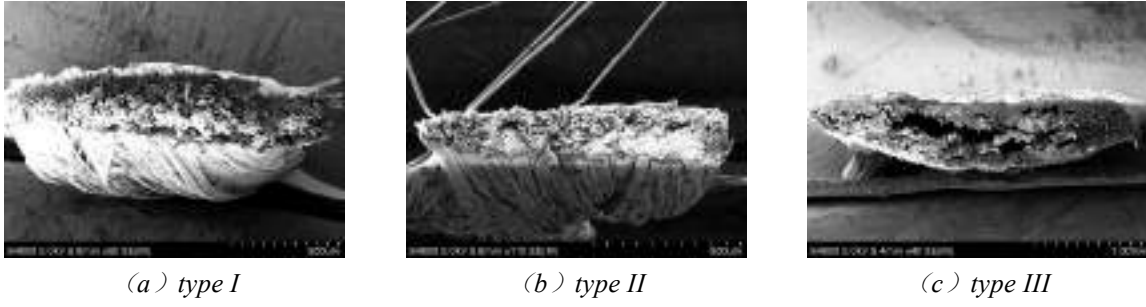


Figure 2: SEM images of basalt warp yarn

To serve as the standard bonding matrix, UHDCC was casted based on the fixed mix-proportion without any variation on the tensile mechanical behavior (Table 2). The fibers used for UHDCC was PE fibers with a length of 18mm and a diameter of $20\mu\text{m}$. The mechanical properties of UHDCC were obtained by the tensile tests on dog-bone-shaped specimens. The results are shown in Table 3.

Table 3: Mechanical properties of UHDCC

Tensile strain capacity (%)	Ultimate tensile strength (MPa)	First cracking strength (MPa)
7.81	4.86	2.13

Details of pull-out specimens

Pull-out tests were performed on the specimens with basalt textile grids embedded in UHDCC with the aim of figuring out the bond-slip behaviour between the grids and UHDCC. At present, the types of test configurations for investigating the pull-out behavior of textile in the cementitious matrix include one-sided and double-sided one can be found in Portal (2014). The double-sided tests have either symmetrical or unsymmetrical anchoring length. The benefit of using unsymmetrical anchoring lengths is that the longer length guarantees the predominant slip deformation coming from the shorter side. The specimen configuration used in this paper was based on the unsymmetrical double-sided test. The key variables for studying the bond behavior are the grid spacing, warp and weft spacing ratio, and embedded length (Fig. 3 and Table 4). Each batch has three identical specimens, and each specimen was cut from a standard plate with dimensions $600\text{mm}\times 400\text{mm}\times 10\text{mm}$. The plates were manufactured according to the following steps: (1) placing a layer of UHDCC with the thickness of 5mm in a mold; (2) putting one layer of basalt grid upon the UHDCC layer; and (3) casting the second layer of UHDCC with the same thickness of 5mm. After one day, the specimen was demolded and cured under standard condition for the remaining 27 days. And then, the specimens for pull-out testing were cut from the plate as shown in Fig. 3. The specific configuration of 1-1 saw cut is to leave one single warp yarn of grid along the loading direction. The edge of the cut was carefully controlled without cutting the fibers of yarn to be pulled. The 2-2 saw cut is through the plate to maintain the embedment length of B. A pair of strips of CFRP sheets was used to join the 2-2 cut.

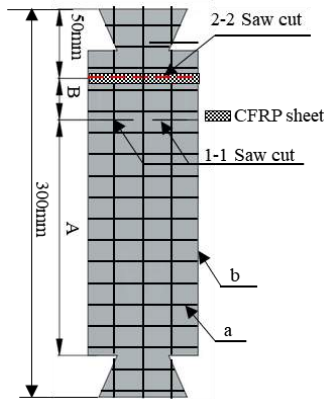


Figure 3: The specimen configuration

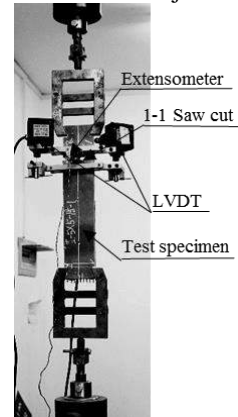


Figure 4: Test setup

Table 4: Details of specimens

Type	a×b/mm ×mm	Warp and weft space ratio, a/b	Embedded length/mm	ID ¹	Failure mode	F_{max}/N	Minimum anchorage length /mm
I	5×5	1	15	I-5×5-15	Pull out	420.7	15~20
			20	I-5×5-20	Grid rupture	547.3	
			25	I-5×5-25		516.7	
	5×10	0.5	10	I-5×10-10	Pull out	614.7	10~15
			15	I-5×10-15	Grid rupture	586.7	
			20	I-5×10-20		500.0	
	5×15	0.3	10	I-5×15-10	Compound mode	614.7	≤10
			15	I-5×15-15	Grid rupture	637.3	
			20	I-5×15-20		839.3	
	10×5	2	10	I-10×5-10	Pull out	482.7	10~15
			15	I-10×5-15	Grid rupture	760.0	
			20	I-10×5-20		729.3	
II	10×10	1	15	II-10×10-15	Pull out	526.7	20~30
			20	II-10×10-20		606.0	
			30	II-10×10-30	Grid rupture	645.3	
III	25×25	1	40	III-25×25-40	Pull out	932.7	≤60
			50	III-25×25-50	Compound mode	879.3	
			60	III-25×25-60		797.3	

Note: 1. Take I-5×5-15 for example, I for the grid type, 5×5 representing grid spacing of a×b in Fig. 2, and 15 denoting the embedded length.

Experimental process and testing results

The test setup is shown in Fig.4. A universal testing machine was used to perform the tests. Tests are conducted at constant displacement rate of 1.0 mm/min. An extensometer was mounted at the opening edges at the loaded end to measure the slip, as deformation in the late stage exceeded the limit of extensometer. Two linear variable displacement transducers (LVDTs) were additionally mounted on two sides of the specimen and attached to two edges of 1-1 saw cut with the enlarged gauge length of 10 mm. The comparison between results of extensometer and LVDTs shows the consistence in the slip deformation record. Therefore, the final recorded deformation data were from the results of LVDTs.

Three failure modes were observed through the pull-out tests: grid rupture (Fig. 5a), pull out (Fig. 5b), and compound mode with both pull out and grid rupture (Fig. 5c). For the grids of type I and type II, the failure mode will change from pull out to grid rupture with the increase of embedded length. The compound mode only occurs in the type III grid which has rather larger cross section of yarn. The minimum embedded length is estimated based on the failure mode (Table 4). The maximum embedded length in the test where it fails in the grid pull-out pattern is deemed as lower boundary value of the minimum anchorage length, and the minimum one in the test where it fails in grid rupture is as the upper boundary value. Generally, the grid with thicker yarns will have larger minimum anchorage length. Surface treatment can be adopted to improve the bond performance of grid with thicker yarns

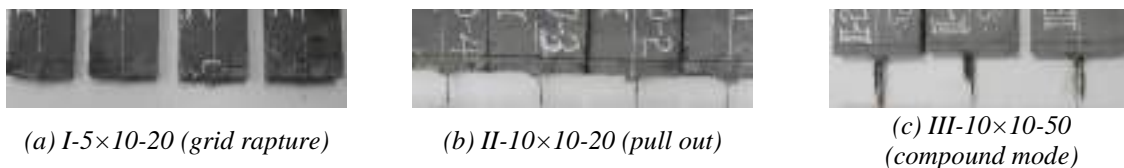


Figure 5: Failure modes

All the force vs. slip curves with pull-out failure modes are illustrated in Fig. 6. At the beginning of the test, the stiffness is bigger due to the chemical cohesive resistance at the interface, similar to the results for TRC/TRM. The curve turns to be fluctuated before reaching maximum force which confirms the bridge effect due to the PE fiber in the remaining matrix attached to the fibers. The bridge effect is terminated when the curves step into softening. The pull-out force gradually decreases with obvious slip developing. Compared with other two types of grids, continuous fluctuation can be observed in the type III grid at post-peak stage. It can be attributed the

configuration of joint. The warp and weft yarn is jointed by the glue and additional threads. It has higher rigidity than that in type I or type II grid where the warp yarn is only restrained by the cross weaving structure of weft yarn (Fig 1). The rigid joint configuration contributes to the additional bond resistance during slipping for type III grid.

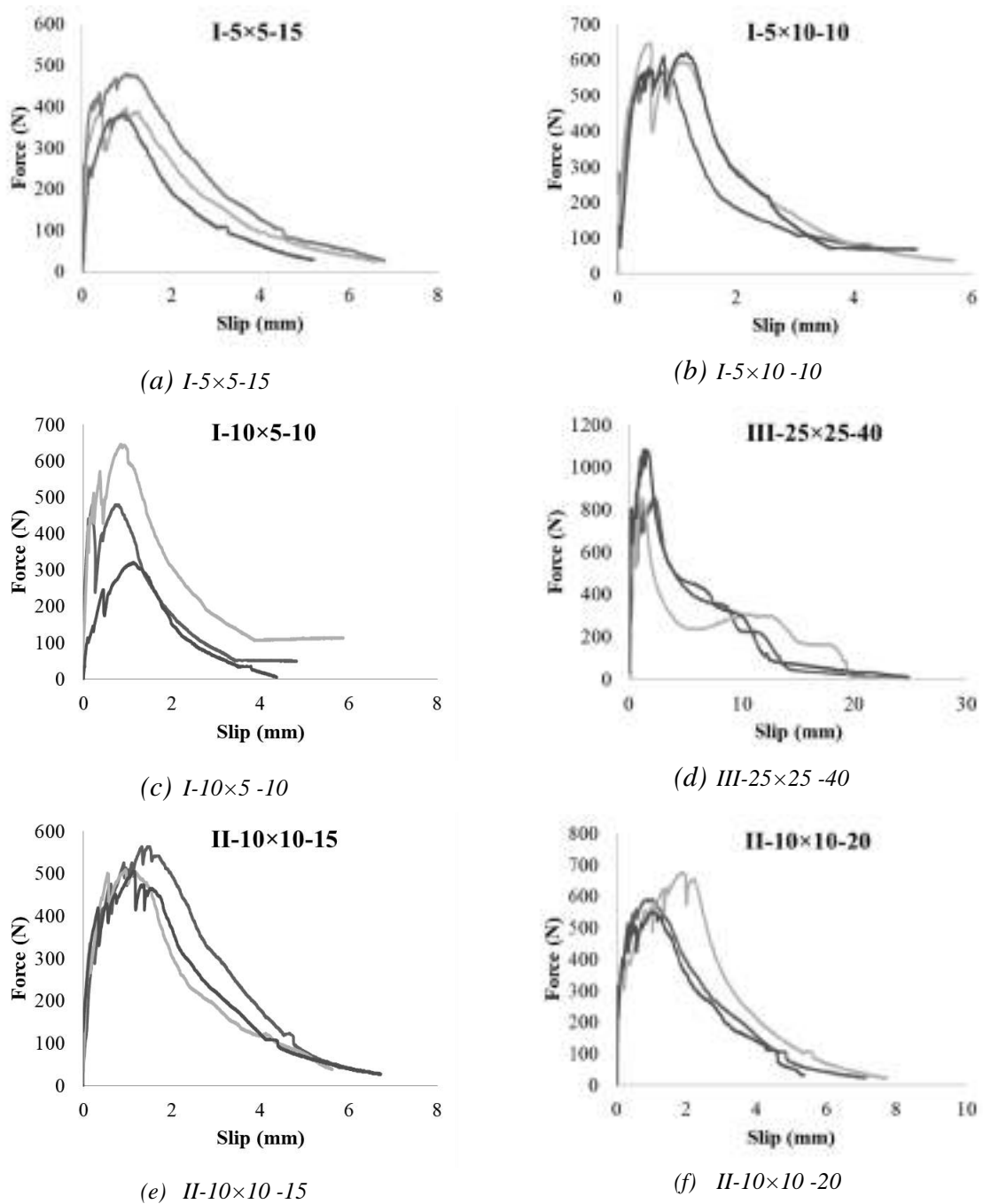


Figure 6: Force vs. slip curves for pull-out failure pattern

To investigate the bond performance due to the dimension of grid spacing, spacing ratio and embedded length, the bond strength, τ_{\max} , is studied with the variation of three variables, listed in Table 4. For the factor of embedded length, it will affect the failure mode as mentioned hereinbefore. It can be observed that τ_{\max} will decrease with the increase of embedded length In Fig. 7a. These test specimens are the original grid pattern manufactured from the factory as shown in Fig. 1. The grid spacing ratio, a/b , is one. It can also be found that the bond strength has no major difference with the increase of grid spacing from 5 mm to 10 mm where the grids have similar cross-section area in the warp yarn. Although the denser grid spacing has its potential of higher confinement along the

anchorage, the fiber reinforced matrix is more difficult to uniformly fill within the space. The non-uniform distribution of the matrix is prone to cause the weft yarn having more flexible space and loose restraint towards the warp yarn. While, when the spacing increases to 25 mm as that in type III grid, the bond strength has been dramatically decreased (Fig. 7a). It shows the smaller grid spacing of grid can exert higher confinement to strengthen the bond performance when the spacing will not affect the uniform distribution of the matrix.

Meanwhile, the effect of spacing ratio, a/b , was investigated by adjusting type I grid spacing in either weft or warp direction. For the same embedded length as 15 mm, four specimens with different grid configuration were compared. As the failure mode for 5×10 , 5×15 and 10×5 pattern is grid rupture, the theoretical pull-out bond strength due to bond performance should be larger than the current value. Therefore, it can be found the increase of grid spacing will increase the bond strength (Fig. 7b). The larger grid space will has more promising effect on the bond performance. It is due to the similar reason for the difference between the 5×5 grid and 10×10 grid. While, we can find the 10×10 grid shows having smaller bond strength compared with the other modified grids. It demonstrates that there exists the optimized spacing in both weft and warp directions for uniformity of the matrix. The optimized spacing may vary with the dimension of micro fibers and workability of UHDC. To compare the bond strength for three modified grids at 10 mm embedded length, it can further concluded that when the spacing in either direction, but especially in the weft direction, turns to be larger than the optimized value, large grid spacing has adverse effect on the bond performance due to weft yarn having loose restraint towards the warp yarn..

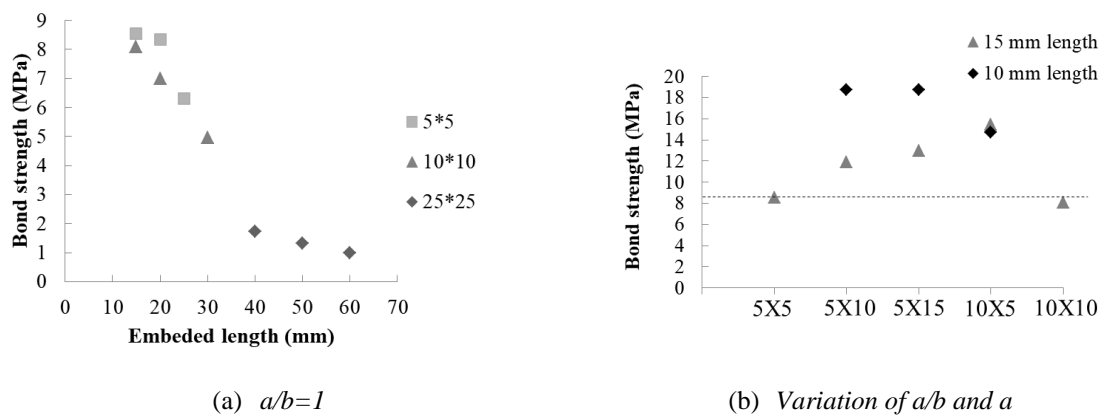


Figure 7: Bond strength

CONCLUSIONS

In this study, the effect of the grid spacing, warp and weft spacing ratio and embedded length was investigated by the pull-out tests for basalt textile grid in the matrix of ultra high ductility cementitious composite (UHDC). It has three different failure modes, including pull-out, grid rupture and the compound mode. The pull-out force vs. slips curve for pull-out failure mode exhibits similar bond performance as the other reinforcements, large hardening stiffness in the beginning and continuous softening curve after reaching the peak value. The specific phenomenon is the fluctuation in the pre-peak which is attributed to the fibers' bridging effect from the UHDC.

The bond strength shows continuous decrease with the increase of embedded length. The grid spacing will have different effect depending on the distribution of UHDC within the grid space and restrain from weft yarns. The results demonstrate that the dense grid spacing will affect the uniform distribution of UHDC so that the restraint from weft yarns towards the warp yarn (pull-out direction) will be weakened. There exists the optimized spacing in both weft and warp direction. When the configuration of grid space meets the optimized condition, the trend of the looser the spacing in the weft the smaller bond strength can be established.

This current study was limited to the basalt textile within the limited grid configuration. Although it has covered the configuration in majority factory products in China, more general conclusion for other configuration of basalt textile grid needs to draw with the assistance of numerical simulation to optimize the better performance when basalt textile grid integrated with UHDC. And it also need further study on the other kinds of fibers bonding performance in UHDC.

ACKNOWLEDGEMENTS

The authors gratefully acknowledge the financial support from the projects 51478362 and 51778461, which are all supported by the National Natural Science Foundation of China and the foundation from International Joint Research Laboratory of Earthquake Engineering (ILEE). This research was also funded from Guangdong Provincial Key Laboratory of Durability for Marine Civil Engineering and the project 2016-KF08 by Shanghai Key Laboratory of Engineering Structure Safety (SRIBS), Shanghai, China.

REFERENCES

- Ates A O, Tore E, Khoshkholghi S, et al (2017). Sprayed Textile Reinforced GFRC for Retrofitting of Sub-Standard Non-Circular Concrete Columns. World Conference on Earthquake Engineering, 16WCEE, 9-13, January, Santiago, Chile.
- Dai, J. G., Wang, B. and Xu, S. L. (2009). Textile Reinforced Engineered Cementitious Composites (TR-ECC) Overlays for the Strengthening of RC Beams. Proceedings of the 2nd Asia-Pacific Conference on FRP in Structures, APFIS-2009, Edited by J. Sim, 9-11, December, Seoul, Korea, pp. 75-81.
- Dai J G, Munir S, Ding Z (2013). "Comparative study of different cement-based inorganic pastes towards the development of FRIP strengthening technology", *Journal of Composites for Construction*, , 18(3): A4013011.
- Hegger J, Will N, Bruckermann O, et al. Load-bearing behavior and simulation of textile reinforced concrete[J]. *Materials and Structures*, 2006, 39(8):765-776.
- Lee H S(2002). "Fire resistance property of RC structure members strengthened with fiber sheet", *Mag. Korean Conc. Inst*, 14(2): 45-50.
- Ludovico M D, Prota A, Manfredi G (2010). "Structural Upgrade Using Basalt Fibers for Concrete Confinement", *Journal of Composites for Construction*, 14(5):541-552.
- Portal, N. W., Perez, I. F., Thrane, L. N., & Lundgren, K. (2014). "Pull-out of textile reinforcement in concrete", *Construction & Building Materials*, 71(71), 63-71.
- Sim, J., Park, C., & Moon, D. Y. (2005). "Characteristics of basalt fiber as a strengthening material for concrete structures", *Composites Part B Engineering*, 36(6), 504-512.
- Yu, K., Wang, Y., Yu, J., & Xu, S. (2017). "A strain-hardening cementitious composites with the tensile capacity up to 8%", *Construction & Building Materials*, 137, 410-419.



SINGLE FIBRE-TO-MORTAR BOND CHARACTERIZATION IN TRM COMPOSITES

Bahman Ghiassi¹, Ali Dalalbashi², Daniel V. Oliveira²

¹ Department of Civil Engineering, Faculty of Engineering, University of Nottingham, Nottingham, United Kingdom, (bahman.ghiassi@nottingham.ac.uk)

² ISE, University of Minho, Department of Civil Engineering, Guimarães, Portugal

ABSTRACT

Textile-reinforced mortars (TRM) have been identified as sustainable materials for externally bonded reinforcement (EBR) of masonry and historical structures. The fibre-to-mortar bond, the TRM-to-masonry bond, and the mechanical properties of the TRM constituents have a fundamental role in the performance of this strengthening technique. Although several studies can be found in the literature with the focus on characterization of the tensile response and TRM-to-masonry bond behaviour, the fibre-to-mortar bond response that plays a critical role in the performance of these systems have received few attention.

This paper, as an step towards addressing the gap in characterization of the fibre-to-mortar bond behaviour, presents an experimental and analytical investigation on the effect of test setup and fiber embedded length on the pull-out response and bond-slip laws in TRM composites. Three different pull-out test setups, consisting of one pull-pull and two pull-push configurations, are developed and investigated for characterization of the single fibre-to-mortar bond behaviour. The experimental and analytical results are discussed and presented and bond-slip laws are extracted for each test setup and embedded length.

KEYWORDS

Strengthening and repair; Experimental study; Bond and interfacial stresses; FRC and cement composite materials; TRM; Pull-out test.

INTRODUCTION

Textile Reinforced Mortars (TRMs) have recently received extensive attention as a sustainable solution for externally bonded reinforcement of masonry and historical structures. TRMs provide several advantages, compared to conventional Fibre Reinforced Polymers (FRPs) including physical and mechanical compatibility with the masonry substrate, acceptable performance under high temperatures and fire exposure, and low installation costs (Ghiassi et al. 2016; Leone et al. 2017; Caggegi et al. 2017; De Stantis et al. 2017).

These composites are made of continuous fibres embedded in an inorganic (cementitious or lime-based) matrix. Cementitious mortars are usually used for application to new buildings or concrete structures and lime-based mortars are suggested for application to existing masonry and historical structures. Several types of fibres including steel, glass, basalt and PBO are available in the market as the reinforcement. The large variety of available fibres and mortar types leads to a wide range of TRMs with different mechanical and physical properties. Mechanical properties of TRMs and TRM-strengthened structural components are strongly dependent on the mortar and fibre properties, the fibre-to-mortar bond behaviour and the TRM-to-masonry bond response (Ghiassi et al. 2016). While several studies can be found in the literature devoted to characterization of mechanical properties of TRMs, e.g. (Larringa et al. 2013; Caggegi et al. 2017; Leone et al. 2017), or to the characterization of TRM-to-masonry bond behaviour, e.g. (Razavizadeh et al. 2014; Ascione et al. 2015), the fibre-to-mortar bond response in these systems has only received a limited attention (Ghiassi et al. 2016). A clear understanding of this mechanism is however critical for fully utilization of this strengthening system and, without any doubt, requires special attention (Ghiassi et al. 2016).

A variety of test methods have been developed in the literature for characterization of the fibre-to-mortar (or matrix) bond behaviour. These include the single fibre pull-out tests in which the load is applied to the fibre and can be generally categorized into pull-push or single-sided (Sahnag et al. 1997; Sueki et al. 2007; Baena et al. 2016) and pull-pull or double-sided (Huang et al. 2016; Li et al. 2018) configurations. While in these test methods the fibre is directly loaded, in other cases the matrix is directly loaded (such as tensile tests on FRPs). Single fibre pull-out tests are generally more suitable for composites made of brittle matrices that show several transverse cracking due to the fibre bridging as is the case of TRMs (Zhandarov and Mader 2005).

It is clear that the choice of a suitable test setup should be based on producing a similar-to-reality stress distribution in the test specimens. This paper presents an experimental investigation on characterization of fibre-to-mortar

interface in TRM composites with the aim of single fibre pull-out tests. Different fibre pull-out configurations, including two pull-push and one pull-pull, are considered to evaluate the differences between obtained experimental results and their effect on the extracted bond-slip laws.

GENERAL DESCRIPTION OF EXPERIMENTAL TESTS

The materials included a unidirectional ultra-high tensile strength steel fibre (with a density of 670 g/m^3 , an effective area of one cord (five filaments) equal to 0.538 mm^2 and the cord diameter of 0.827 mm) as the reinforcing material and a commercially available hydraulic lime based mortar as the matrix. The main materials mechanical properties including the compressive and flexural strength of the mortar and the tensile strength of the steel fibres were characterized following relevant standards and test procedures. The compressive and flexural tests were performed according to ASTM C109 (2005) and EN 1015-11 (1999). Cubic $50 \times 50 \times 50 \text{ mm}^3$ and prismatic $40 \times 40 \times 160 \text{ mm}^3$ specimens were prepared for compressive and flexural tests, respectively. The tests were carried out with a Lloyd testing machine under force-controlled conditions at a rate of 2.5 N/s (for the compressive tests) and 10 N/s (for the flexural tests). The results are presented in Table 1 as the average of five tested specimens. As for the steel fibres, direct tensile tests under displacement controlled conditions and with the rate of 0.3 mm/min were conducted to obtain their tensile strength and elastic modulus. The specimens had a free length of 300 mm and their deformation was measured with a 100 mm clip gauge attached to the centre of the specimens. The results showed an average tensile strength of 3141 [MPa] and elastic modulus of 174.87 [GPa] .

Table 1: Mortar test methods and mechanical properties.

Material	Compressive strength	Flexural strength
Standard	ASTM C109, EN 1015-11	
Specimen	$50 \times 50 \times 50 \text{ mm}^3$	$40 \times 40 \times 160 \text{ mm}^3$
Test speed (load controlled)	2.5 N/s	10 N/s
Mortar (age 60 days)	8.81 (13.80)	2.09 (8.3)

The pull-out tests consisted of a series of single fibre pull-out tests in three different test setups. Two pull-push and one pull-pull test setups were developed for this reason (Fig. 1). The specimens included steel fibres embedded in a hydraulic lime-based mortar with an embedded length of 150 mm . Five specimens were tested in each test setup resulting in a total of 15 pull-out tests.

In the first pull-push configuration (referred as pull-push I), the specimens consisted of single fibres embedded in mortar cylinders with 75 mm diameter and 150 mm length (equal to the fibre embedded length). The tests were performed by blocking the specimens to a rigid frame and pulling the fibres from their free end (Fig. 1a). A servo-hydraulic system with a maximum capacity of 20 kN was used for performing the tests. Aluminum tabs were glued at the fibres' free end to facilitate gripping. The resultant load was measured by the load cell integrated in the testing machine and the slip of the fibre from the mortar was measured by an LVDT mounted on the fibres. A small preload was applied to the fibres to reduce their flexibility and to facilitate attachment of the LVDT to the fibres. As it was not possible to attach the LVDT base in the vicinity of the mortar-to-fibre interface, it was mounted at the distance 20 mm from the mortar surface. The slip was then calculated as the recorded displacements minus the elastic elongation of the unbonded textile.

In the second test setup (referred as pull-push II), the specimens consisted of single fibres embedded in rectangular prism mortar with the dimensions of $150 \times 125 \times 16 \text{ mm}^3$. The free length of the fibres was embedded in an epoxy resin block over a length of 200 mm and with a rectangular cross-sectional area of $10 \times 16 \text{ mm}^2$. This block, also used in Banholzer (2006), facilitates the gripping and the slip measurements in one-sided pull-out tests and protects the fibres from premature failure. Here, a U-shape steel support was used for supporting the specimens (Fig. 1a). A mechanical clamp was used to grip the epoxy resin from the top and two LVDTs were located at both sides of the epoxy block to record the slip.

In the third test setup type (pull-pull), the specimens had a geometry similar to the pull-push II test setup but they were made longer. The specimens are gripped from the bottom with a fixed mechanical gripping system in this case (and therefore the supporting system is not placed on top). Two LVDTs are again mounted on the testing block with the support placed on the mortar edge to measure the slip during the tests.

All the tests were performed under displacement control conditions with reference to the internal LVDT of the system by pulling the fibres with a velocity of 0.3 mm/min .

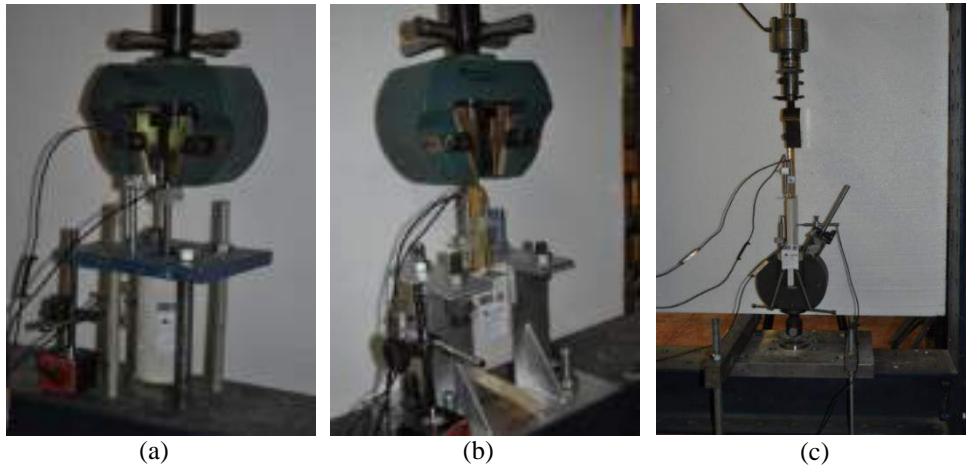


Fig. 1. Test setups and instrumentation used for pull-out tests: (a) pull-push I; (b) pull-push II; (c) pull-pull.

EFFECT OF TEST SETUP

The experimental envelope and average force-slip curves obtained from different test setups are shown in Fig. 2. The differences in the obtained force-slip curves is clear. It also seems that the pull-push I test setup leads to the largest variation in the results compared to the pull-push II and pull-pull tests. This was expected due to the difficulties in exact vertical alignment of the fibres in the cylindrical mortar.

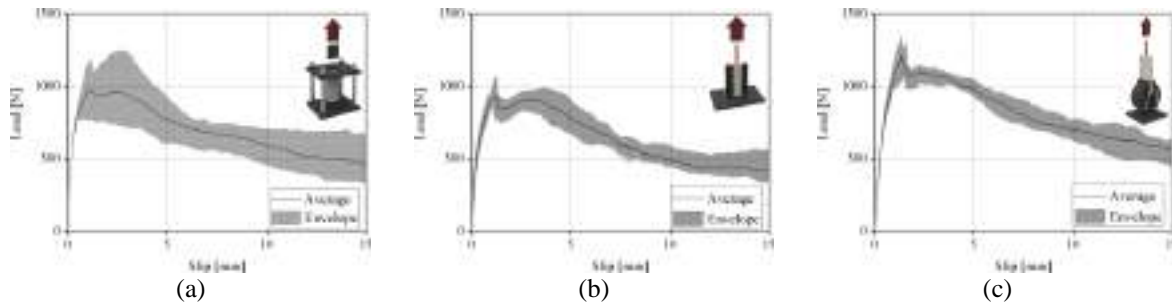


Fig. 2. Envelope load-slip curves for different test setups: (a) pull-push I; (b) pull-push II; (c) pull-pull.

The main outputs of single fibre pull-out tests is the force-slip curves from which the peak load, the slip corresponding to the peak load, the toughness (defined as the area of the force-slip curve until the peak load) and the initial stiffness of the pull-out curve can be extracted. These parameters are obtained from the experimental results and the average values are presented in Table 2. It can be observed that all the extracted parameters are higher in the specimens tested in pull-pull test configuration compared to the specimens tested in pull-push configuration. The reason for this is the differences in the stress distributions in the mortar, fibre and fibre-to-mortar interfaces in these two test setups. The larger initial stiffness of the specimens in pull-push II configuration, compared to pull-push I, clearly shows the effect of embedment of the free fibres in epoxy resin block on slip measurements. In pull-push I test setup, the LVDTs are mounted on the free length of the fibre (at a distance from the mortar edge) and therefore the elastic deformation of the fibre during the tests should be reduced from the measured slip values. This can lead to errors in the slip measurements and therefore increased/decreased stiffness of the elastic region in the force-slip curves. In pull-push II test setup, however, the resin block eliminates this problem. Additionally, no preloading is required in this case for attachment of the LVDTs.

The analytical formulations proposed in (Naaman et al. 1991a; Naaman et al. 1991b) were used for extraction of the bond-slip laws in the pull-pull test configuration. These formulations were modified to consider the pull-push configuration as well. For the details of the formulations and calculations the reader is referred to (Dalalbashi et al. 2018). A detailed discussion on the effect of different input parameters on the analytical bond-slip laws are also provided in this publication. Here, we only present the results obtained from the analytical modelling followed by a consistent use of input values.

It is assumed that the pull-out response consist of three main stages namely: elastic, nonlinear, and dynamic stages (Naaman et al. 1991a; Shannag et al. 1997, Mobasher 2012). The bond-slip is also defined as presented in Fig. 3. The main input values are generally the mechanical properties of fibre and mortar (including the cross section

area and elastic modulus). The analytically obtained parameters of the bond-slip law for each test setup are presented in Table 3. It can be observed that the main differences are found in the stiffness of the bond-slip curves, κ , the frictional stress, τ_f , and the slip corresponding to the initiation of the dynamic stage, S_0 . The obtained bond strength is however similar ranging from 3.18 MPa to 3.2 MPa.

Table 2: Summary of the pull-out tests results (CoVs are presented in parentheses).

Specimen	Peak load [N]	Slip corresponding to peak load [mm]	Toughness until peak load [N.mm]	Initial stiffness [N/mm]
pull-push I	987 (21.8)	0.78 (40.7)	571 (56.5)	1762 (9.9)
pull-push II	992 (9.8)	1.08 (17.6)	730 (23.2)	2772 (18.2)
pull-pull	1245 (12.5)	1.33 (20.8)	1098 (30.8)	2032 (27.3)

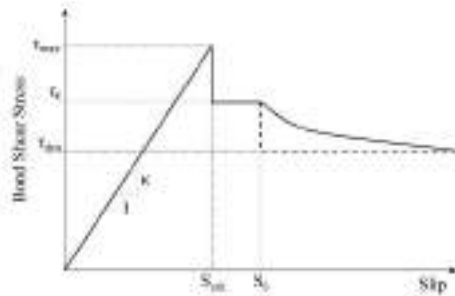


Fig. 3. Considered bond-slip law.

Table 3. Bond-slip law parameters obtained for each test setup.

Specimen	κ [N/mm ³]	τ_f [N/mm ²]	τ_{max} [N/mm ²]	S_0^* [mm]
pull-push I	9.252	2.424	3.18	0.782
pull-push II	41.777	2.499	3.27	1.045
pull-pull	5.408	3.192	3.2	0.804

* S_0 is the slip corresponding to the initiation of the dynamic stage

EFFECT OF BOND LENGTH AND MORTAR TYPE

The effect of fibre embedded length is investigated in this section. For this reason, specimens with different bonded lengths from 100 mm to 150 mm were prepared and tested with the pull-push I test setup. The results presented in the last section showed that the pull-out results in the pull-push I test setup can have similar peak forces but significantly different recorded displacements (slips) and stiffness compared to pull-push II test setup. The tests were performed on steel fibres (with properties presented before) embedded in three different mortars including two commercially available pozzolanic lime-based mortars with similar mechanical properties (denoted as A and B) and a geopolymeric-based mortar with a low mechanical properties (denoted as G) with mechanical properties shown in Table 4. Mortar A (MAPEI Planitop HDM) was a two component mortar prepared by mixing the components with an electric mixer until reaching a consistent paste as proposed in the technical datasheets. Mortar B (BASF ALBARIA STRUTTURA) was a one component mortar prepared by mixing the mortar with water (each 1 kg of mortar with 0.23 liters of water) in an electric mixer. The geopolymeric-based mortar was produced in the laboratory based on activation of alkaline materials rich in silica and alumina. The mortar was obtained by a mixture of sand (1000 gr.), fly ash (280 gr.), sodium hydroxide (144 gr.), sodium silicate (144 gr.), selected based on previous experience of the authors. Five pull-out tests were performed on each bonded length and each mortar type at the age of 60 days and the average results are presented next.

The results were obtained in terms of force-slip curves and failure mode of the specimens. The failure mode of the specimens was slipping of the fiber from the mortar in all bonded lengths and mortar types, with the exception of SRGB specimens with $l_b=200$ mm in which the tensile failure of the fibers occurred. As the tensile strength of the fibers was less than the bond strength in these latter specimens, the SRGB specimens with $l_b=250$ mm were not tested anymore as a similar behavior (failure mode and peak load) was expected.

Table 4. Mechanical properties of mortars used for investigation of the effect of fibre embedded length (CV in round brackets).

Material	Age [days]	$f_{cm-cubic}^*$ [N/mm ²]	$f_{cm-cylinder}$ [N/mm ²]	E_{cm} [kN/mm ²]	f_{tm} [N/mm ²]
Mortar A	30	9.78 (9.7%)	9.85 (13.4%)	-	5.00 (13.7%)
	60	10.73 (6.7%)	10.79 (9.9%)	-	6.71 (20.8%)
	90	13.21 (10.1%)	12.74 (11.8%)	3.25 (14.6%)	6.07 (15.2%)
Mortar B	30	11.60 (13.4%)	12.66 (12.2%)	-	3.32 (5.4%)
	60	14.19 (14.3%)	-	-	3.68 (10.3%)
	90	18.12 (12.8%)	12.42 (15.4%)	14.05 (28.0%)	3.43 (11.2%)
Mortar G	30	4.16 (13.8%)	5.22 (15.7%)	-	1.68 (2.6%)
	60	3.63 (12.2%)	3.50 (21.4%)	-	1.68 (20.0%)
	90	4.19 (13.8%)	6.48 (4.0%)	13.7 (9.35%)	1.23 (16.8%)

* $f_{cm-cubic}$ is the cubic compressive strength; $f_{cm-cylinder}$ is the cylindrical compressive strength; E_{cm} is the compressive elastic modulus; and f_{tm} is the flexural tensile strength.

The average force-slip curves for different bond lengths are compared in Fig. 4. It can be observed that the maximum pull-out force (F_{max}) and the slope of the initial elastic region increase with bond length in all mortar types (until 200 mm bond length). On the other hand, no specific change in the peak slip (S_p) is observable. The peak force in SRGA and SRGG specimens increases only until bond length of 200 mm. This indicates that the effective bond length is in the range of $200\text{ mm} < l_e < 250\text{ mm}$ in these systems. Razavizadeh et al. (2014) also obtained a similar numerical value for the effective bond length in a similar SRG system. On the other hand, the peak force in SRGB specimens increases until fiber tensile rupture at 200 mm bond length. The tensile rupture of the steel fiber in SRGB shows the effective bond length is in the range of $150\text{ mm} < l_e < 200\text{ mm}$. The F_{max} in SRGB specimens is always higher than SRGA which can be attributed to the higher elastic modulus of mortar B and the different bond mechanisms existing in these two systems. On the other hand, the bond strength in SRGG system is comparable to SRGA system, although mortar G has a lower mechanical properties than mortar A.

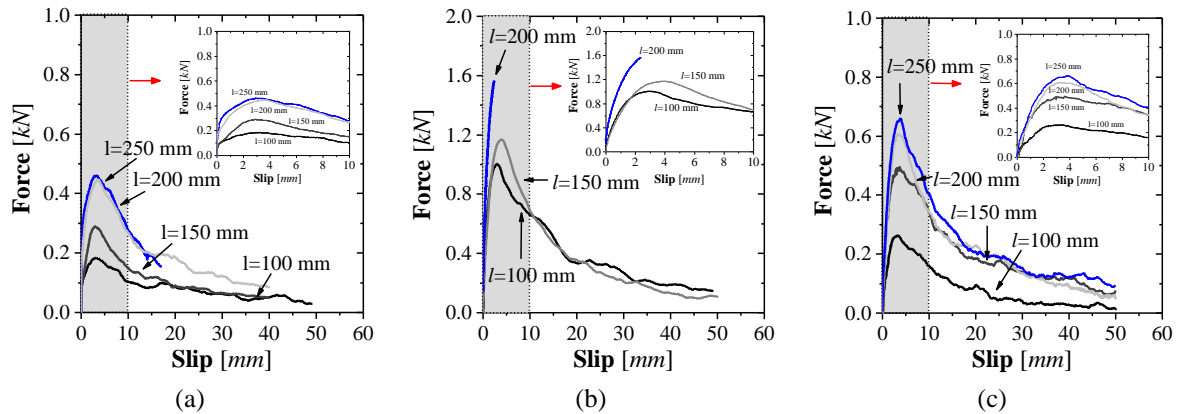


Fig. 4. Effect of fibre embedded length: (a) SRGA; (b) SRGB; (c) SRGG.

CONCLUSIONS

The effect of test setup and embedded bonded length on the fiber-to-mortar bond properties were experimentally evaluated in this study. Two pull-push and one pull-pull test setups were developed. Single fiber pull-out tests were performed on steel based TRM composites with the aim of the developed test setups. The results showed that different test setups can lead to different force-slip curves and consequently bond-slip laws. The main effect of the test setup was on the initial stiffness, frictional stress and the slip corresponding to the initiation of the dynamic stage in the extracted bond-slip laws. The bond strength was, however, found similar in all the test setup. This observation is of critical importance for interpretation and comparison of the experimental results obtained from different test setups and for proposal of reliable constitutive laws. The effect of fibre embedded length was investigated considering three different mortar type and a pull-push test configuration. The results showed the significant effect of mortar properties on the bond response. In general, the pull-push tests seem to be more suitable than pull-pull tests as the possibility of tensile cracking of the mortar at the grips is avoided. At the same time, the pull-push II tests seems to produce more reliable results and are easier to perform and are therefore suggested for further investigations.

ACKNOWLEDGMENTS

The first author acknowledges the financial support of the European Union's Marie Curie Individual Fellowship program under REA grant agreement No. 701531. This work was partly financed by FEDER funds through the Competitiveness Factors Operational Programme (COMPETE) and by national funds through the Foundation for Science and Technology (FCT) within the scope of project POCI-01-0145-FEDER-007633. The support to the second author through grant SFRH/BD/131282/2017 is acknowledged.

REFERENCES

- L. Ascione, G. de Felice, and S. De Santis (2015). "A Qualification Method for Externally Bonded Fibre Reinforced Cementitious Matrix (FRCM) Strengthening Systems." *Composites Part B: Engineering*, 78, 497-506.
- ASTM C109/C109M (2005). Standard Standard Test Method for Compressive Strength of Hydraulic Cement Mortars.
- M. Baena, L. Torres, A. Turon, et al. (2016). "Bond Behaviour between Recycled Aggregate Concrete and Glass Fibre Reinforced Polymer Bars." *Construction and Building Materials*, 106, 449-60.
- B. Banholzer (2006). Bond of a strand in a cementitious matrix. *Mater Struct*, 39, 1015-28.
- BS EN 1015-11 (1999). Methods of Test for Mortar for Masonry. Determination of Flexural and Compressive Strength of Hardened Mortar.
- C. Caggegi, F.G. Carozzi, S. De Santis, et al. (2017). "Experimental Analysis on Tensile and Bond Properties of PBO and Aramid Fabric Reinforced Cementitious Matrix for Strengthening Masonry Structures." *Composites Part B: Engineering*, 127, 175-195.
- A. Dalalbashi, B. Ghiassi, D.V. Oliveira, and A. Freitas. (2018). "Effect of Test Setup on the Fiber-to-Mortar Pull-out Response in TRM Composites: Experimental and Analytical Modeling." *Composites Part B: Engineering*. Under publication.
- B. Ghiassi, D.V. Oliveira, V. Marques, et al. (2016). "Multi-Level Characterization of Steel Reinforced Mortars for Strengthening of Masonry Structures." *Materials & Design*, 110, 903-13.
- L. Huang, Y. Chi, L. Xu, P. Chen, et al. (2016). "Local Bond Performance of Rebar Embedded in Steel-Polypropylene Hybrid Fiber Reinforced Concrete under Monotonic and Cyclic Loading." *Construction and Building Materials*, 103, 77-92.
- P. Larrinaga, C. Chastre, J.T. San-Jose, et al. (2013). "Non-Linear Analytical Model of Composites Based on Basalt Textile Reinforced Mortar under Uniaxial Tension." *Composites Part B: Engineering*, 55, 518-27.
- M. Leone, M.A. Aiello, A. Balsamo, F.G. Carozzi, et al. (2017). "Glass Fabric Reinforced Cementitious Matrix: Tensile Properties and Bond Performance on Masonry Substrate." *Composites Part B: Engineering*, 127, 196-214.
- X. Li, J. Bielak, J. Hegger, et al. (2018). "An Incremental Inverse Analysis Procedure for Identification of Bond-Slip Laws in Composites Applied to Textile Reinforced Concrete." *Composites Part B: Engineering*, 137, 111-22.
- B. Mobasher (2012). *Mechanics of Fiber and Textile Reinforced Cement Composites*. London- New York: Taylor & Francis Group.
- A.E. Naaman, G.G. Namur, J.M. Alwan, et al. (1991a). "Fiber Pullout and Bond Slip. Ii: Experimental Validation." *Journal of Structural Engineering*, 117(9), 2791-2800.
- A.E. Naaman, G.G. Namur, J.M. Alwan, et al. (1991b). "Fiber Pullout and Bond Slip. I: Analytical Study." *Journal of Structural Engineering*, 117 (9), 2769-90.
- A. Razavizadeh, B. Ghiassi, and D.V. Oliveira. (2014). "Bond Behavior of SRG-Strengthened Masonry Units: Testing and Numerical Modeling." *Construction and Building Materials*, 64, 387-97.
- S. De Santis, F. Ceroni, G. de Felice, et al. (2017). "Round Robin Test on Tensile and Bond Behaviour of Steel Reinforced Grout Systems." *Composites Part B: Engineering*, 127: 100-120.
- M.J. Shannag, R. Brincker, W. Hansen. (1997). "Pullout Behavior of Steel Fibers From Cement-Based Composites." *Cement and Concrete Research*, 27(6), 925-36.
- S. Sueki, C. Soranakom, B. Mobasher, et al. (2007). "Pullout-Slip Response of Fabrics Embedded in a Cement Paste Matrix." *Journal of Materials in Civil Engineering*, 19(9), 718-27.
- S. Zhandarov, E. Mäder. (2005). "Characterization of Fiber/matrix Interface Strength: Applicability of Different Tests, Approaches and Parameters." *Composites Science and Technology*, 65(1), 149-60.



STRAIN AND CRACK DETECTION IN EXPERIMENTAL TESTS ON TEXTILE REINFORCED MORTAR COMPOSITES

M. Tekieli¹, S. De Santis², G. de Felice², Ł. Hojdys¹, P. Krajewski¹, A. Kwiecień¹ and F. Roscini²

¹Cracow University of Technology, Faculty of Civil Engineering, Poland, Email: mtekieli@15.pk.edu.pl

²Roma Tre University, Department of Engineering, Italy.

ABSTRACT

This paper presents the application of Digital Image Correlation (DIC) to measure displacements and detect crack pattern in tensile and bond tests on Textile Reinforced Mortar (TRM) composites. DIC is a full-field contactless optical method based on the correlation of the digital images taken during test execution. With respect to conventional methods, it offers the advantageous possibility of selecting several measurement points after the test, is more cost-efficient, does not entail any risks of damage to instrumentation, and is generally less affected by stroke or encumbrance limitations. On the other hand, it detects only the outer surface of the specimen and requires particular care for setup preparation. In this work, two DIC software programs were used and their results were compared to each other as well as to those provided by traditional transducers for mutual validation. The advantages offered by DIC as a tool for improving the mechanical characterization of TRMs and for developing a deeper understanding of their behaviour are discussed together with some of its limitations.

KEYWORDS

Direct tensile tests, shear bond tests, crack pattern, contactless technique, textile reinforced mortar (TRM), fabric reinforced cementitious matrix (FRCM), steel reinforced grout (SRG).

INTRODUCTION

Composite materials are an effective, cost efficient and versatile solution for the reinforcement of existing structures. They comprise unidirectional or multidirectional fabrics, externally bonded by means a (either organic or inorganic) matrix, and have high strength-to-weight ratio. Mortar-based composites, named as textile reinforced mortar (TRM) or fabric reinforced cementitious matrix (FRCM), have been developed to overcome the drawbacks of the polymeric matrices of fibre reinforced polymers (FRP) related to toxicity, fire resistance and possibility of application to historic substrates and uneven or wet surfaces.

The experimental studies carried on TRMs (de Felice et al. 2014, De Santis et al., 2017a, De Santis 2017) highlighted that measuring their mechanical properties with sufficient accuracy may be as crucial as difficult with traditional devices, such as displacement (LVDTs and potentiometers) and strain (extensometers and strain gauges) transducers. In order to overcome these drawbacks, full-field contactless optical techniques have been developed, including Particle Image Velocimetry (PIV) (Callaway et al. 2012), 3D Vision (De Canio et al. 2016) and Digital Image Correlation (DIC) (Sutton et al. 2009). DIC is a full-field optical method for measuring the displacements of the surface of an object, based on the correlation of the digital images taken during test execution. To calculate displacements, a computational grid is defined on the picture or on a portion of it, named Region Of Interest (ROI). The pictures taken before and after deformation are correlated and the points of the grid in the ROI are matched. DIC has been widely used in experimental mechanics (Pan et al. 2009) and also in experiments on composites (Carloni et al. 2013; Ghiassi et al. 2013, 2015, Napoli et al. 2016, Tekieli et al. 2017), but its potential application to the characterization of TRMs has not been fully investigated yet.

In this work, DIC was applied in combination with traditional measurement devices (displacement transducers and extensometers) to tensile and bond tests on TRM reinforcements, comprising different textiles and matrices. Two DIC software programs, namely CivEng Vision (Tekieli et al. 2013, Tekieli et al. 2014, Tekieli et al. 2015) and Ncorr (Blaber et al. 2015), were used and their results were compared to each other as well as to those provided by traditional transducers for mutual validation. The advantages offered by DIC with respect to conventional sensors, as a tool for improving the mechanical characterization of TRMs and for developing a deeper understanding of their behaviour, are discussed together with some of its limitations.

DIRECT TENSILE TESTS

Direct tensile tests were carried out on prismatic TRM specimens (coupons) with 600 mm total length, 50 mm width and 10 mm thickness. Their ends were wrapped with GFRP to ensure uniform load distribution and limit damage to the matrix (De Santis et al. 2017b). Tests were performed with a Universal Testing Machine (Figure 1a). The load was applied under displacement control and recorded by an integrated load cell. Stresses were derived by dividing the load by the cross sectional area of the textile. Global displacements (from end plate to end

plate) were recorded by the LVDT of the testing machine with 10 μm resolution, while local strain measures were acquired by an extensometer with 50 mm gauge length (1 μm resolution). In addition, two displacement transducers of 1 μm resolution were placed on the matrix by means of aluminium plates to measure displacements over a segment of about 250 mm, excluding the gripping areas. Strains were derived by dividing the recorded displacement by the measurement base of the devices, with resulting strain resolution between 4 μm (potentiometers) and 25 μm (LVDT).

In direct tensile tests on TRM composites, the occurrence of cracks may complicate the measurements performed with the transducers placed on the matrix, making displacement/strain data not particularly useful or even unreliable. Moreover, the base length of the device should be large enough to include a sufficient number of cracks, but the exact number and location of cracks is hardly predictable and may vary randomly from test to test, and crack spacing is not even uniform along the specimen. On the other hand, the transducer integrated in the testing machine may overestimate the strain if some sliding occurs in the gripping areas. Finally, strain gauges provide local data that may differ from the overall behaviour of the TRM, require higher efforts (they need to be glued on the textile before the manufacturing of the coupon), complexity (cables may complicate the realization of the specimens and influence cracking), and cost (they are disposable). With the aim of overcoming these drawbacks, DIC was used to measure the displacement field of the surface of the coupons.

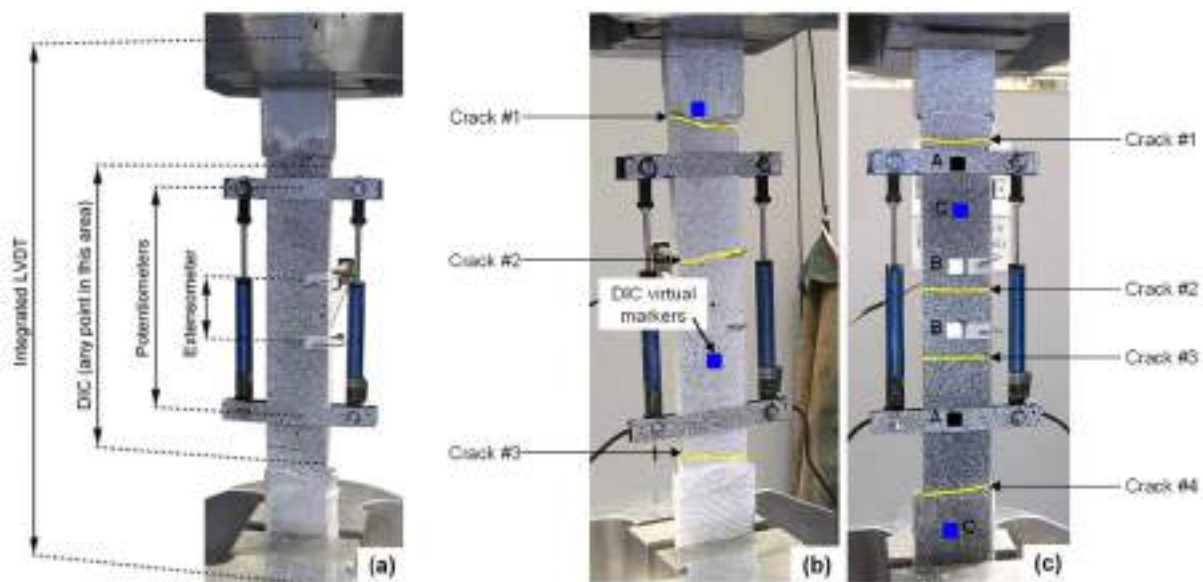


Figure 1: tensile tests on TRM coupons: experimental setups (a) and crack pattern at failure on composites comprising carbon textile and fibre reinforced cement mortar (b) and basalt fabric and lime mortar (c).

Measurement of displacements and strains

Figure 1 shows two specimens comprising carbon textile and fibre reinforced cement mortar (Figure 1b), and basalt fabric and lime mortar (Figure 1c), and test results are represented in terms of stress-strain curves in Figure 2, in which different displacement/strain measurement methods are compared to each other.

In the former test, after the initial stage in which the mortar was uncracked and the stiffness of the composite was very high due to the high stiffness and strength of the mortar in tension, the stress-strain response showed large load drops associated to cracking. The progressive damage development influenced the readings of the instruments, such that their data display a significant mismatch. Three load drops, one per crack, are clearly identifiable in the curve provided by the integrated LVDT, which monitors the whole length of the coupon and is no able to detect sliding in the gripping areas. The first two cracks developed near the GFRP wrapping, whereas the third crack appeared in the middle. This crack was the only one detected by the potentiometers and its occurrence caused a sudden decrease of the measured strain, which however remained smaller than those recorded by the LVDT. Finally, no cracks occurred within the measurement base of the extensometer, which, therefore, provided much lower strain values than the other devices.

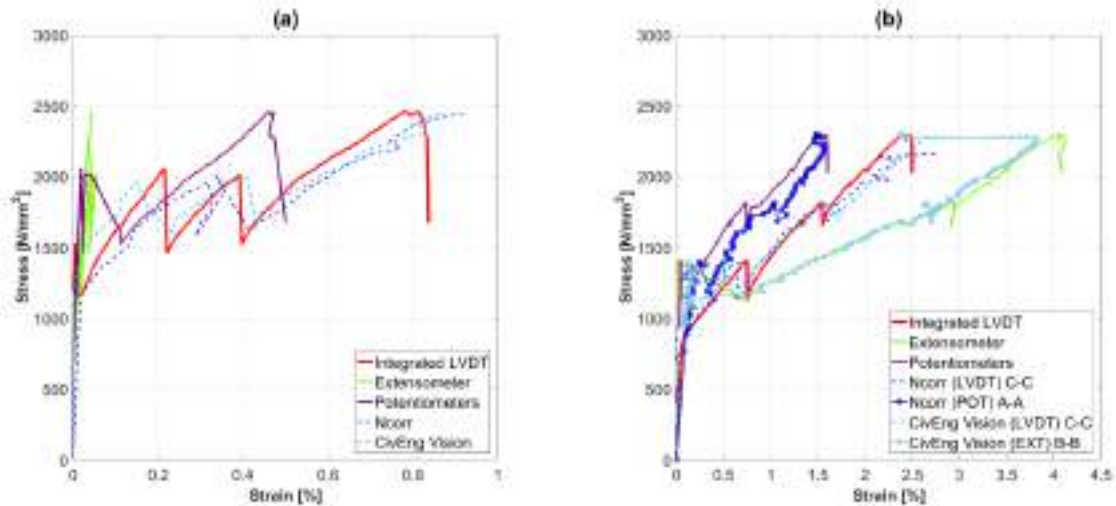


Figure 2: Stress-strain curves provided by different displacement/strain measurement methods in tensile tests on TRMs comprising carbon textile and fibre reinforced cement mortar (a) and basalt fabric and lime mortar (b).

DIC provided the displacement field of the entire surface of the specimen. In order to obtain a strain measure for comparing data with the other methods, two points were selected, one on the reinforcement near the gripping area and another one in the central portion of the specimen, in the middle between two cracks. The choice of the points for strain calculation was based on the following observations of the stress transfer mechanism between textile and matrix (Figure 3). The occurrence of cracks yields a variation of the shear stress distribution at the textile-to-matrix interface and of the axial stress distribution in the textile and in the mortar. In a zone near the crack edge, the textile-to-matrix bond is partially lost and that sliding between textile and mortar appears. At a certain distance, the bond is fully restored, but the textile-to-matrix load transfer has not completely developed yet and a certain relative slip still exists (shear lag zone). Finally, beyond a certain distance from the edge of the crack, there is no slip between textile and matrix and the stress in both of them is constant (Triantafillou 2016). Since DIC only provides information on the outer surface of the coupon, but the response of the composite is generally referred to the textile, the virtual markers should be selected where the textile-to-matrix relative sliding is null and, therefore, the displacement of the matrix corresponds to that of the textile. In principle, this holds in the middle between two cracks due to symmetry, even when the cracks are so close to each other, or the textile-to-matrix bond is so poor, that the zone with uniform stress vanishes.

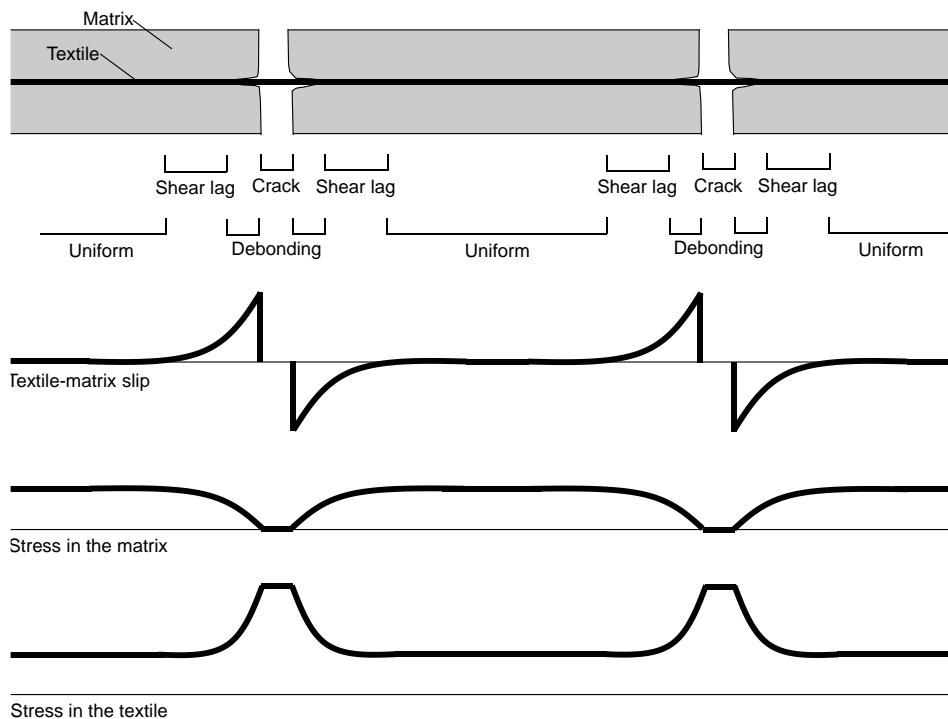


Figure 3: Stress transfer mechanism between textile and matrix: cracked composite specimen, identification of the stress transfer zones, and distribution of textile-to-matrix slip, stress in the matrix and stress in the textile.

The response curves provided by CivEng Vision and Ncorr show two load drops associated to the development of the two cracks in the measurement length (Figure 1b). As a general trend, the strain values agree with those recorded by the LVDT (the Root Mean Square Error between DIC and LVDT was RMSE=0.49% for CivEng Vision software and 0.51% for Ncorr). DIC data are however notably noisier than those of the other devices, especially at the time instants when cracks occurred (Figure 2a).

In the TRM composite with basalt fabric and lime mortar, shown in Figures 1c and 2b, four cracks developed, two near the gripping areas and two in the middle of the specimen. One crack occurred in the measurement base of the extensometer, which, however, overestimated the strain, since the saturation crack spacing (average distance between cracks in the last stage of the test, when the crack pattern was stabilized), equal to 85 mm, was larger than the 50-mm measurement base. Conversely, two cracks were included in the portion of the specimen recorded by the potentiometers, which provided and underestimate of the strain, because their base length of 200 mm was larger than twice the saturation crack spacing. Therefore, neither the portion of the specimen monitored by the extensometer nor that detected by the potentiometers can be considered fully representative of the overall mechanical behavior of the specimen.

Taking advantage of the possibility of selecting the measurement points after the test, two couples of points were used for DIC analyses. In order to validate DIC results, a first analysis was carried out with Ncorr using two points (indicated by letters A in Figure 1b) about 200 mm apart, such that two cracks were included between them. The resulting strain data were comparable to those of the potentiometers with RMSE of 0.22% (Figure 2c). A second analysis was carried out with CivEng Vision taking two points (B) at 50 mm distance and including one crack, leading to a good agreement with results provided by the extensometer (RMSE=0.51%). Finally, an analysis was performed with two points (C), one in the middle between two cracks and one on the lower GFRP reinforcement. This latter measurement base was about 250 mm long and included three cracks. In this case, a very good agreement was found with strain data provided by the integrated LVDT (the RMSE was 0.35% for CivEng Vision and 0.14% for Ncorr).

Detection of crack pattern

The crack pattern (location of cracks, distance between cracks and crack width) and its evolution under increasing load represent important information on the textile-to-matrix load transfer mechanism. Despite DIC assumes that the displacement field is continuous, it can provide information on the crack pattern, as shown in Figure 4, in which the analysis of a TRM comprising a basalt mesh embedded in lime mortar is represented as sake of example. The strain field recorded by DIC (Ncorr) is plotted for subsequent time instants corresponding to 20%, 40%, 60%, 80% and 100% of the maximum stress f_t . Strong concentrations clearly appear near the cracks (Figure 4a). The contour plots provide the location of the cracks and the stage in which they appear, well before they become visible to the naked eye, or even hardly detectable by visual inspection. Conversely, the portions of matrix between two cracks remain undeformed. Note that the strain value provided by DIC within the crack is unreliable. The profiles of the strain and of the displacement were computed along the vertical midline of the specimen, as an average over a 10 mm wide strip widthwise. The former (strain profile) indicates the number and location of cracks, making it possible to compute automatically their number and spacing (Figure 4b). In this case, at the end of the test (100% f_t), 8 cracks were identified, whose distance varied between 16 mm and 48 mm and was, on average, 36 mm. In order to compute the crack width, two points were selected on the two sides of the crack, such that the subsets of pixels around each of them did not cross the crack, not to compromise the reliability of DIC results. Since the portion of the specimen where these two points are located is basically undeformed, their relative displacement reasonably corresponds to the crack width. This latter, for the specimen under consideration, ranged between 0.5 mm to 2.5 mm at the end of the test. Furthermore, at this stage, the sum of the widths of the eight cracks was 9.1 mm, which is in good agreement with the relative displacement between the ends of the specimen. This approach for crack pattern analysis was applied to the direct tensile tests on the TRM composites described previously and shown in Figures 1b (carbon textile and fibre reinforced cement mortar) and 1c (basalt fabric and lime mortar). The occurrence of cracks is associated to the stress drops in the response curves (Figures 5a,b), The evolution of crack width is shown in Figure 5c and in Figure 5d, in which the numbering of the cracks goes from the top to the bottom of the specimen (Figure 1). The plots show that the width of a crack slightly reduced when a new crack formed, due to the stress reduction. For most of the test, all the cracks had a similar width, in the order of 0.8-1 mm for the first test (Figure 5c) and of up to 2 mm for the second test (Figure 5d). Conversely, when approaching the failure, only one crack significantly enlarged, up to a width of about 5 mm, in both specimens, while the width of the other ones remained stable.

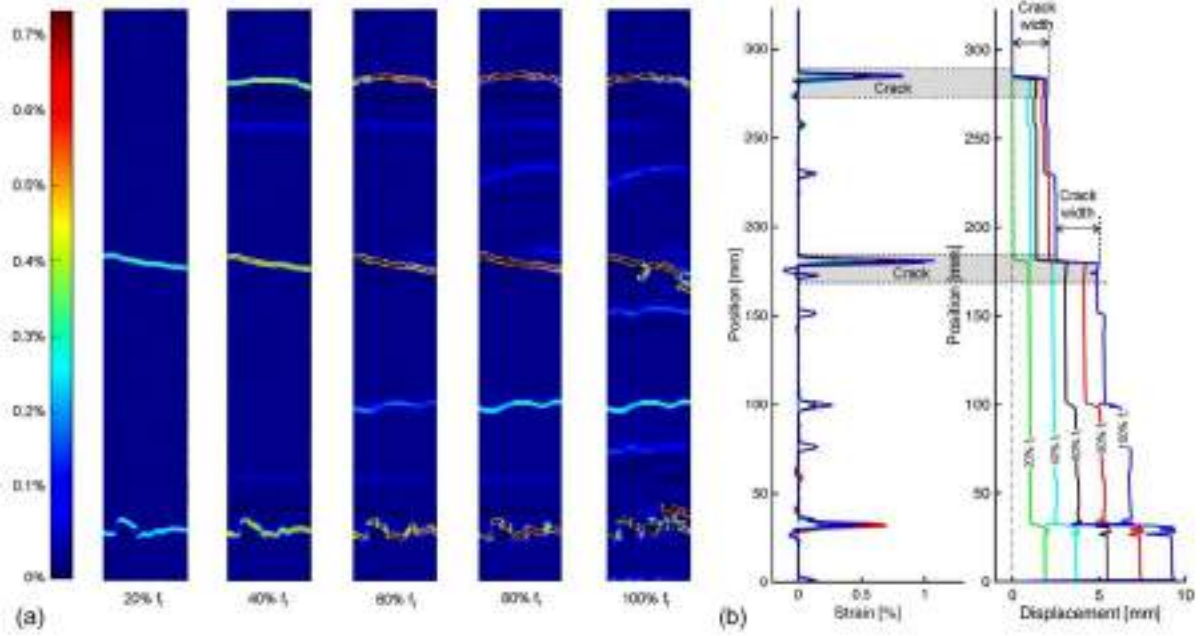


Figure 4: Vertical strain field (a) and vertical strain and displacement profiles along the midline of the specimen for crack pattern detection (b).

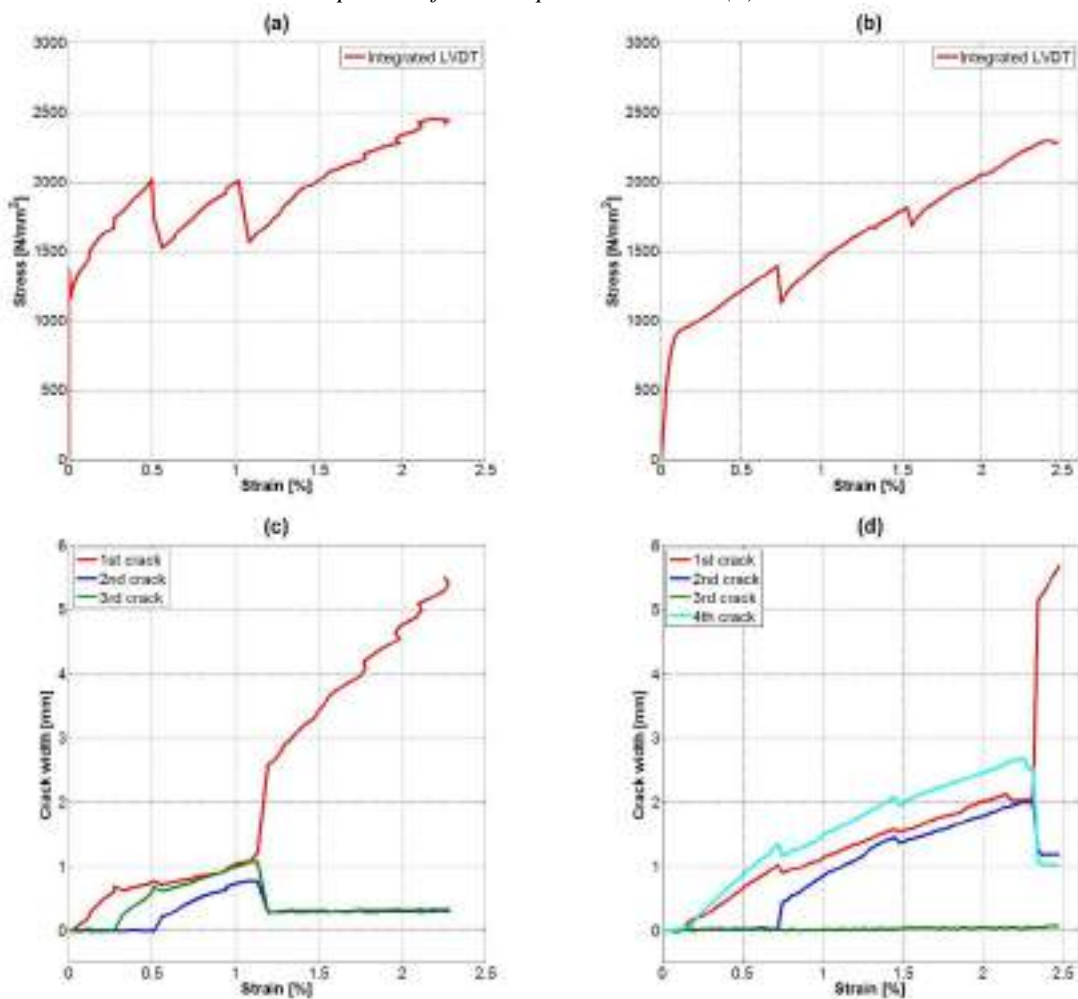


Figure 5: Direct tensile tests on TRM composites comprising carbon textile and fibre reinforced cement mortar (a,c) and basalt fabric and lime mortar (b,d): stress-strain response curve (a,b) and crack width (c,d).

SHEAR BOND TESTS

Single lap shear bond tests were carried out on TRM reinforcements applied to brickwork prisms. The bonded area was 50 mm wide and 200 mm or 260 mm long. The textile was left unbonded for a length of about 500 mm (de Felice et al. 2018). Tests were performed under displacement control using a Universal Testing Machine, provided with a hydraulic actuator. A stiffened steel frame was clamped in the upper wedges of the machine and the specimen was placed in it. The unbonded textile was clamped in the lower wedges (after the application of aluminium tabs to prevent local damage) and pulled from below. The load cell integrated in the testing machine recorded the applied load, providing the maximum load that can be transferred from the structural element to the externally bonded reinforcement. The relative displacement between substrate and reinforcement at the loaded end of the bonded area (slip) was measured by two LVDTs with accuracy of 0.1% of the ± 5 mm full stroke and 1 μ m resolution, which were fixed to the unbonded textile by means of metal plates (Figure 6a).

Measurement of substrate-to-reinforcement relative displacement

DIC was used to measure the slip and to record vertical displacement and strain fields over the bonded area, whose whole surface was selected as ROI. Figure 6b shows the subsets associated to the nodes of the grid for image correlation. Each subset (or virtual marker) had 50×50 pixel size. Some specimens were prepared with a speckle pattern on both the bonded area of reinforcement and substrate, while in other specimens the natural texture of the surface was used without specific preparation. An artificial marker was placed on the unmoving upper steel plate to detect apparent movements of the setup, which are actually caused by movements of the digital camera. The resolution of DIC was in the order of 2 μ m, which is close to that of the LVDTs. In order to measure the slip with DIC, two points were selected on the substrate (one per each side of the reinforcement), near the loaded end of the bonded area. Another point was selected on the metal plate glued to the textile to fix the LVDTs. The plate was provided either with the speckle pattern or with artificial markers.

Figures 6a,b show the load-slip curves of two shear bond tests carried out on a reinforcement comprising a steel textile and a lime-based mortar. In the former (Figure 6a), the displacements measured by the LVDTs were negative in the first phase, due to an out-of-plane rotation of the unbonded textile that was not completely straight under low load values. The measurement provided by DIC exhibited an initial very stiff phase, in which the slip is basically null, followed by an increase after slippage activation. This behaviour detected by DIC appeared more reasonable than that provided by LVDTs and was therefore taken as reference. It is worth noting that this (quantitative) information about the error induced by out-of-plane rotations would not have been available otherwise. The response of another test in which such out-of-plane rotation did not occur is plotted in Figure 6b. In this case, the curve provided by the LVDTs shows a good agreement with those obtained by both CivEng Vision and Ncorr, but DIC data showed higher noise than those of the LVDTs, due to the unavoidable movements of the metal plate fixed to the textile.

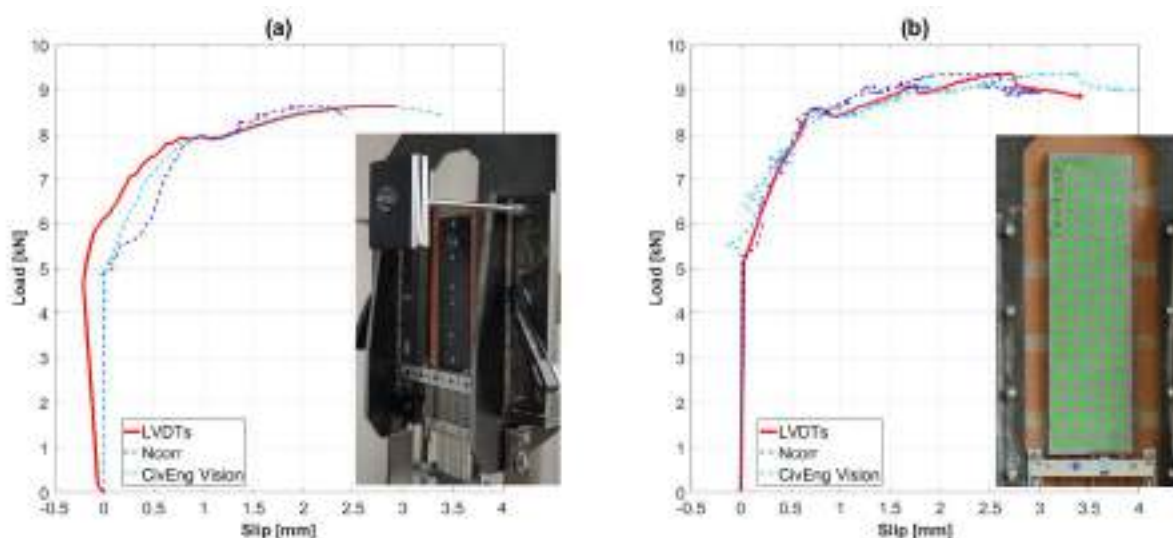


Figure 6: Setups and load-slip curves provided by different measurement methods in shear bond test on masonry substrate with the error induced by out-of-plane rotations on one specimen (a) and without out-of-plane rotations on another specimen (b).

CONCLUSIONS

Digital Image Correlation (DIC) was applied to the mechanical characterization of TRM composites, in combination with displacement transducers and extensometers. DIC measured strains in direct tensile tests and the reinforcement-to-substrate relative displacement in shear bond tests. Two software programs were used and the agreement of their results with those provided by traditional devices validated test outcomes and demonstrated that DIC reliable independently from the specific software used for image processing.

DIC provided additional information that would have been unavailable otherwise. In direct tensile tests, it measured the average strain on the entire length of the specimen excluding the gripping areas, provided occurrence, number, location, width and distance of cracks even before they became visible to the naked eye, and automatically. In bond tests, DIC measured the slip even when LVDTs provided unreliable results.

DIC offers the advantageous possibility of selecting the measurement points after the test based on the crack pattern, so its reliability is not affected by crack location. Furthermore, many virtual markers can be selected, with negligible increase of time and no additional cost. On the other hand, since only the outer surface of the specimen is monitored, no direct information is provided on the textile within the matrix. Therefore, differently from composites with organic matrix, it is not possible to investigate the strain field at the reinforcement-to-substrate interface and to estimate the effective transfer length. Virtual markers need to be selected in middle of two cracks where, due to symmetry, the displacement of matrix and textile coincide.

ACKNOWLEDGMENTS

The industrial partners G&P Intech srl, Kerakoll SpA and Ruredil SpA supplied reinforcements. G. de Felice, S. De Santis and F. Roscini acknowledge the financial support provided by the projects “Innovative materials for interventions in seismic areas” (ReLUIS-DPC, 2017-18) and “Composites with inorganic matrix for sustainable strengthening of architectural heritage” (Italian Ministry for Foreign Affairs, 2017-18, N. PGR00234).

REFERENCES

- S. De Santis, G. de Felice, A. Napoli, R. Realfonzo (2016). “Strengthening of structures with Steel Reinforced Polymers: a state-of-the-art review”, *Composites Part B: Engineering*, V. 104, pp. 87-110.
- A. Kwiecień (2014). “Shear bond of composites-to-brick applied with highly deformable, in relation to resin epoxy, interface materials”, *Materials and Structures*, V. 47, pp. 2005-2020.
- A. Kwiecień, G. de Felice, D.V. Oliveira, B. Zając, A. Bellini, B. Ghiassi, G.P. Lignola, P.B. Lourenço, C. Mazzotti, A. Prota, S. De Santis (2016). “Repair of composite-to-masonry bond using flexible matrix”, *Materials and Structures*, V. 49, No 7, pp. 2563-2580.
- P. Callaway, M. Gilbert, CC. Smith (2012). “Influence of backfill on the capacity of masonry arch bridges”, *Proceedings of the Institution of Civil Engineers: Bridge Engineering*, V. 165, No 3, pp. 147-158.
- G. De Canio, G. de Felice, S. De Santis, A. Giocoli, M. Mongelli, F. Paolacci, I. Roselli (2016). “Passive 3D motion optical data in shaking table tests of a SRG-reinforced masonry wall”, *Earthquakes and Structures*, V. 10, No 1, pp. 53-71.
- M.A. Sutton, J.J. Orteu, H.W. Shreier (2009). “Image correlation for shape, motion and deformation measurements”, Springer: New York, US.
- B. Pan, K. Qian, H. Xie, A. Asundi (2009). “Two-dimensional digital image correlation for in-plane displacement and strain measurement: a review”, *Measurement Science and Technology*, V. 20, No 6, paper 062001.
- C. Carloni, K.V. Subramaniam (2013). “Investigation of sub-critical fatigue crack growth in FRP/concrete cohesive interface using digital image analysis”, *Composites Part B: Engineering*, V. 51, pp. 35-43.
- B. Ghiassi, J. Xavier, D.V. Oliveira, P.B. Lourenço (2013). “Application of Digital Image Correlation in investigating the bond between FRP and masonry”, *Composite Structures*, V. 106, pp. 340-349.
- A. Napoli, G. de Felice, S. De Santis, R. Realfonzo (2016). “Bond behaviour of Steel Reinforced Polymer strengthening systems”, *Composite Structures*, V. 152, pp. 499-515.
- B. Ghiassi, J. Xavier, D.V. Oliveira, A. Kwiecień, P.B. Lourenço, B. Zając (2015). “Evaluation of the bond performance in FRP-brick components re-bonded after initial delamination”, *Composite Structures*, V. 123, pp. 271-281.
- M. Tekieli, S. De Santis, G. de Felice, A. Kwiecień, F. Roscini (2017). “Application of Digital Image Correlation to composite reinforcements testing”, *Composite Structures*, V. 160, pp. 670-688.

- M. Tekieli, M. Słoński (2013). "Application of Monte Carlo filter for computer vision-based Bayesian updating of finite element model", *Mechanics and Control*, V. 32, No 4, pp. 171-177.
- M. Tekieli, M. Słoński (2014). "Particle filtering for computer vision-based identification of frame model parameters", *Computer Assisted Methods in Engineering and Science*, V. 21, pp. 39-48.
- M. Tekieli, M. Słoński (2015). "Digital image correlation and Bayesian filtering in inverse analysis of structures", *Recent advances in civil engineering: computational methods*, V. 481, pp. 111-124.
- J. Blaber, B. Adair, A. Antoniou (2015). "Ncorr: Open-Source 2D Digital Image Correlation Matlab Software", *Experimental Mechanics*, V. 55, No 6, pp. 1105-1122.
- S. De Santis, F. Ceroni, G. de Felice, M. Fagone, B. Ghiassi, A. Kwiecień, G.P. Lignola, M. Morganti, M. Santandrea, M.R. Valluzzi, A. Viskovic (2017a). "Round Robin Test on tensile and bond behaviour of Steel Reinforced Grout systems". *Composites Part B: Engineering*, 2017;127:100-120.
- S. De Santis (2017). "Bond behaviour of Steel Reinforced Grout for the extrados strengthening of masonry vaults". *Construction and Building Materials* 150, 367-382.
- S. De Santis, F.G. Carozzi, G. de Felice, C. Poggi (2017b). "Test methods for Textile Reinforced Mortar systems", *Composites Part B: Engineering*, 127, 121-132.
- A. Napoli, G. de Felice, S. De Santis, R. Realfonzo (2016). "Bond behaviour of Steel Reinforced Polymer strengthening systems", *Composite Structures*, V. 152, pp. 499-515.
- G. de Felice, M.A. Aiello, C. Caggegi, F. Ceroni, S. De Santis, E. Garbin, N. Gattesco, L. Hojdys, P. Krajewski, A. Kwiecień, M. Leone, G.P. Lignola, A. Nanni, C. Mazzotti, D. Oliveira, C.G. Papanicolaou, C. Poggi, T.C. Triantafillou, M.R. Valluzzi, A. Viskovic (2018). "Recommendation of RILEM Technical Committee 250-CSM: Composites for Sustainable Strengthening of Masonry. Test method for the Textile Reinforced Mortar to substrate bond characterization", *Materials and Structures*, to appear.



MECHANICAL CHARACTERIZATION OF MULTI-PLY STEEL REINFORCED GROUT COMPOSITES FOR THE STRENGTHENING OF CONCRETE STRUCTURES

Georgia E. Thermou^{1,2}, Gianmarco de Felice³, Stefano De Santis³, Sultan Alotaibi¹, Francesca Roscini³, Iman Hajirasouliha¹, Maurizio Guadagnini¹

¹The University of Sheffield, Civil and Structural Engineering Department, Sir Frederick Mappin Building Mappin Street, Sheffield, S1 3JD, UK (corresponding author: g.thermou@sheffield.ac.uk); ²Aristotle University of Thessaloniki, Civil Engineering Department, 54124, Thessaloniki, Greece (on leave); ³Roma Tre University, Department of Engineering, Via Vito Volterra 62, 00146 Rome, Italy

ABSTRACT

The use of externally bonded Steel-Reinforced Grout (SRG) composites, comprising Ultra High Tensile Strength Steel (UHTSS) textiles embedded in an inorganic mortar matrix, has been shown to provide an effective and cost-efficient solution for the repair and strengthening of existing structures. Although several studies have been carried out in the last decade to investigate the SRG-to-concrete bond behaviour, most of the existing literature examines the use of systems with a single layer of steel textile and only limited information is available on multi-ply SRG composites, which are often required for applications to large structural elements. This paper presents the preliminary results of an experimental study on SRG systems comprising multiple layers of galvanized UHTSS textiles within a geopolymer mortar. The investigation comprises three stages: 1) direct tensile tests on SRG coupons to characterize the tensile properties of the composite system; 2) lap-splice tests (for overlap length ranging from 100 mm to 300 mm) to develop an improved understanding of the textile-to-textile load transfer capacity; 3) single-lap bond tests to examine the effect on bond behaviour of number of steel textile plies (one, two or three) and steel cord density (4 and 8 cord/in) on concrete substrates. Digital Image Correlation (DIC) was used to obtain full-field displacement measurements and map crack development.

KEYWORDS

New composite materials, systems and strengthening techniques; Experimental study; Bond and interfacial stresses; Bond and interfacial stresses; Steel-Reinforced Grout (SRG); Digital Image Correlation (DIC)

INTRODUCTION

With the passing of the years, structures become deficient during or after their working life as a result of seismic events, changes in codes and in use, continuous deterioration caused by ageing and environmental induced degradation (e.g. De Santis et al. 2017b). In those cases that demolition is not an option due to either the prohibited cost or the cultural and historical significance of the structure, retrofitting is the only solution. Depending on the objectives of retrofitting and the level of intervention, global as well as local intervention methods could be selected (e.g. Thermou et al. 2012).

In the past three decades, the use of Fibre Reinforced Polymers (FRPs) has emerged as one of the most popular local strengthening methods. However, FRPs have shown some drawbacks including high cost, poor fire resistance, lack of vapour permeability, toxic nature of epoxy, incompatibility of resins and substrate, and poor reversibility (e.g. Matana et al. 2005; Huang et al. 2005). Since many of these drawbacks are mainly associated with the use of organic matrix as the bonding material, a new generation of composite systems, named either Fabric Reinforced Cementitious Matrix (FRCM) or Textile Reinforced Mortar (TRM) systems, has been developed where inorganic matrix is used instead (e.g. Huang et al. 2005; Papanicolaou et al. 2008; de Felice et al. 2014).

Experimental studies on the bond behaviour of various FRCM systems have identified the complexity entailed in the shear transfer mechanisms. The failure modes observed in the inorganic-based composite systems are related to the bond strength developed between the composite and the substrate (de Felice et al. 2014; Ascione et al. 2015) as well as to the adhesion between the fabric and the matrix (Donnini et al. 2016).

In case of the Steel-Reinforced Grout (SRG) system, studies on bond behaviour have been conducted for both concrete (Matana et al. 2005; Stievanin et al. 2013; Bencardino et al. 2017) and masonry (de Felice et al. 2014; Razavizadeh et al. 2014; De Santis and de Felice 2015; Ascione et al. 2015; De Santis 2017; De Santis et al. 2017b; Bilotta et al. 2017) substrates. Different parameters were considered in these investigations including bond length (e.g. Matana et al. 2005; De Santis 2017), fabric density (e.g. De Santis et al. 2017b; Bilotta et al. 2017), surface preparation (de Felice et al. 2014; Matana et al. 2005), matrix strength (e.g. Ascione et al. 2015), substrate strength (e.g. De Santis and de Felice 2015) and substrate curvature (e.g. De Santis 2017).

As expected, the bond behaviour of SRGs is quite similar to that of the other FRCMs due to the presence of the inorganic matrix. For the SRG system, the failure modes observed are related to debonding at fabric-matrix interface (e.g. Matana et al. 2005), debonding at substrate-matrix interface with or within a thin layer of substrate (cohesive failure in substrate) (e.g. De Santis and de Felice 2015), detachment of the composite from the substrate (e.g. De Santis and de Felice 2015), slippage of fabric out of the matrix (De Santis et al. 2017) and fabric rupture (tensile failure) (e.g. Bilotta et al. 2017). De Santis and de Felice (2015) attributed the debonding at substrate-matrix interface to the high strength of the matrix applied on a relatively weak substrate. Detachment of the composite from the substrate is mainly associated with short bond (anchorage) lengths. Slippage of fabric out of the matrix is attributed in (De Santis et al. 2017b) to the poor interlocking between the grout and the smooth surface of stainless steel cords and ropes.

Some of the above-mentioned studies suggested an effective bond length ranging from 150 to 300 mm (Matana et al. 2005; De Santis et al. 2017b, Bencardino et al. 2017). The suggested effective bond length on concrete substrates was higher than that on masonry substrates. This might be attributed to the variation in terms of mechanical (e.g. strength) and physical (e.g. porosity) properties between masonry and concrete. The fact that failure in SRG system generally occurs at fabric-matrix interface led to the conclusion that high level of surface preparation other than cleaning may not be required (Matana et al. 2005). All the previous studies related to the bond behaviour of SRG systems focused on the study of single-layered SRG systems.

SRG can be used effectively as externally bonded reinforcement for the flexural strengthening of RC beams and multiple layers of fabric may be required, depending on the target level of performance (Napoli and Realfonzo 2015). To date, there is very limited knowledge on the shear transfer mechanism developed along the multiple layers of the steel fabric and the overall mechanical behaviour of multi-ply SRG composites. This study aims to bridge the gap and build a better understanding of the bond behaviour of multi-ply SRG composites applied to concrete substrates. The tensile behaviour of SRG composite is studied to assess the influence of cracking and the contribution of the grout to the overall composite behaviour (i.e. tension stiffening effect). The stress transfer between different layers of fabric is investigated through lap-splice tests. In a future stage of the study, single-lap shear bond tests will be carried out on multi-ply SRG composites comprising one, two, and three layers of steel fabric of two different densities (4 and 8 cords/in).

MATERIALS

The textile utilized in this study is made of unidirectional Ultra-High Tensile Strength Steel (UHTSS) micro-cords, fixed to a fibreglass micromesh to facilitate installation. Each cord has a diameter of 0.9 mm and is obtained by joining 5 filaments, 3 straight and 2 wrapped with a high torque angle to enhance the interlocking with the mortar (Fig. 1a). Cords have a cross sectional area of 0.11 mm² and are coated with zinc (galvanized) to provide protection against rusting. Two different fabrics were tested, having density of 4 cords/in (1.57 cords/cm; S4) and 8 cords/in (3.15 cords/cm; S8). In the lower density textile (S4), cords are evenly arranged such that the clear spacing between each two cords is 5.45 mm while cords in the latter (S8) are paired such that the clear spacing between each two pairs is 4.55 mm (Fig. 1b). The design thickness of the textiles is 0.169 mm and 0.084 mm and their surface mass density is 1330 and 670 g/m² for S8 and S4 respectively. The UHTSS textiles were embedded in a mineral geo-mortar with a crystalline reaction geo-binder base. The mechanical characteristics of the grout

according to the manufacturer's datasheet (evaluated at 28 days) including compressive strength, tensile strength, and adhesion bond strength are 55 MPa, 10 MPa, and 2 MPa respectively. Grout was mixed with water at a water-to-cement ratio of 1:5.

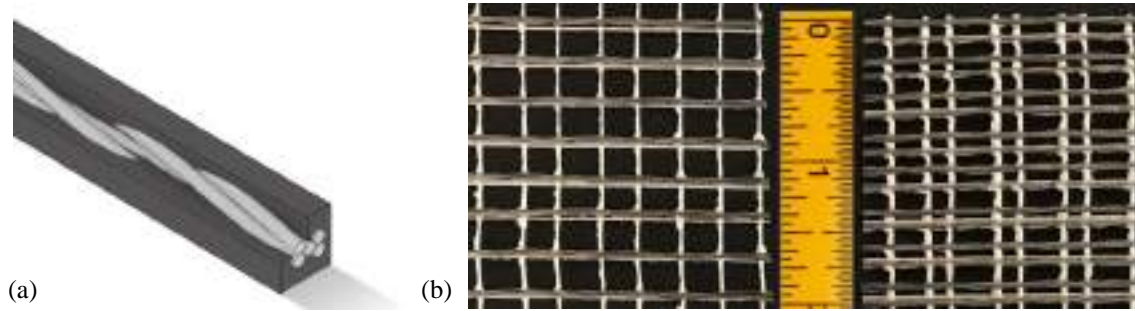


Figure 1: Schematic representation of a single cord embedded in the grout matrix (a) and photographs of the 4 cords/in (left) and 8 cords/in (right) textiles (b)

LAP-SPLICE TESTS

Direct tensile tests

Direct tensile tests were carried out on prismatic specimens (coupons) with 600mm total length, 50mm width and 10mm thickness, comprising a textile strip comprising either 8 cords (in the case of S4 textile) or 16 cords (S8). Coupons were manufactured in Perspex moulds, kept wet for the first 48h, then demoulded and placed in water for 26 days and, finally, stored in the laboratory for at least 7 days before testing. Tests were performed with a 500kN hydraulic universal testing machine under displacement control at 0.01mm/s rate. The specimens were clamped in the wedges of the machine with sufficient gripping pressure to avoid slippage. In order to ensure a proper load transfer and avoid the crushing of the mortar matrix in the gripping areas, the ends of the specimens were wrapped with glass fibre reinforced polymer (GFRP) (De Santis et al. 2017a). The load was recorded by an integrated load cell. Stress (f) was derived by dividing the load by the cross sectional area of the steel textile, equal to 4.27mm² for S4 and to 8.54mm² for S8. Displacements were recorded by two linear potentiometers and the strain (ϵ) was derived as the mean of the displacements recorded by the transducers divided by their gage length (200mm). Digital image correlation (DIC) was also used and images were taken at 5s intervals during test execution with a digital camera mounted on a stiff frame at a distance of 1.1m from the specimen ensuring the parallelism between the surface of the specimen and the sensor. All images were post-processed to derive the displacement field on the whole surface of the coupon. Two points were selected, one in the upper portion and one in the lower portion of the coupon, each of which was in the middle between two cracks, and the strain was calculated as their relative displacement divided by the initial distance (Tekieli et al. 2017). Eight specimens with S4 and eight with S8 were tested. The stress-strain response curves, plotted in Figure 1, exhibit a first linear stage in which the mortar is uncracked, a second stage in which the crack pattern progressively develops, and, finally, a third stage, in which no new cracks appear and failure is attained by the nearly-simultaneous rupture of the steel cords. Such a three-stage behaviour has already been observed on similar SRG composites comprising high-strength cement or geopolymers mortars (De Santis et al. 2017b). The mean values of peak stress (f_t), corresponding strain (ϵ_t), and tensile modulus of elasticity in the uncracked stage (E_t) and in the cracked stage (E_c) are summarised in Table 1, alongwith the corresponding coefficient of variation (in round brackets).

Table 2: Results of direct tensile tests and lap-splice tests: mean values (coefficients of variation in round brackets).

Textile	L' [mm]	Series	f_t [N/mm ²]	ϵ_t [%]	E_t [kN/mm ²]	E_c [kN/mm ²]	s_p [mm]
S4	0 ^(a)	S4-000	3062.1 (1.7%)	2.06 (4.3%)	1713.2 (5.5%)	177.9 (5.6%)	–
	100	S4-100	2394.0 (12.2%)	–	–	–	1.14 (29.5%)
	200	S4-200	2769.9 (5.2%)	–	–	–	2.05 (28.5%)
	300	S4-300	2795.5 (3.8%) ^(b)	–	–	–	2.39 (24.9%)
S8	0 ^(a)	S8-000	3014.7 (2.5%)	2.29 (6.4%)	1688.1 (10.8%)	172.9 (5.8%)	–
	100	S8-100	988.8 (12.2%)	–	–	–	0.41 (29.1%)
	200	S8-200	1193.0 (5.3%)	–	–	–	1.02 (21.2%)
	300	S8-300	1139.6 (5.4%)	–	–	–	1.33 (23.4%)

^(a) Direct tensile tests (no overlap); ^(b) One specimen failed by tensile rupture of the steel cords.

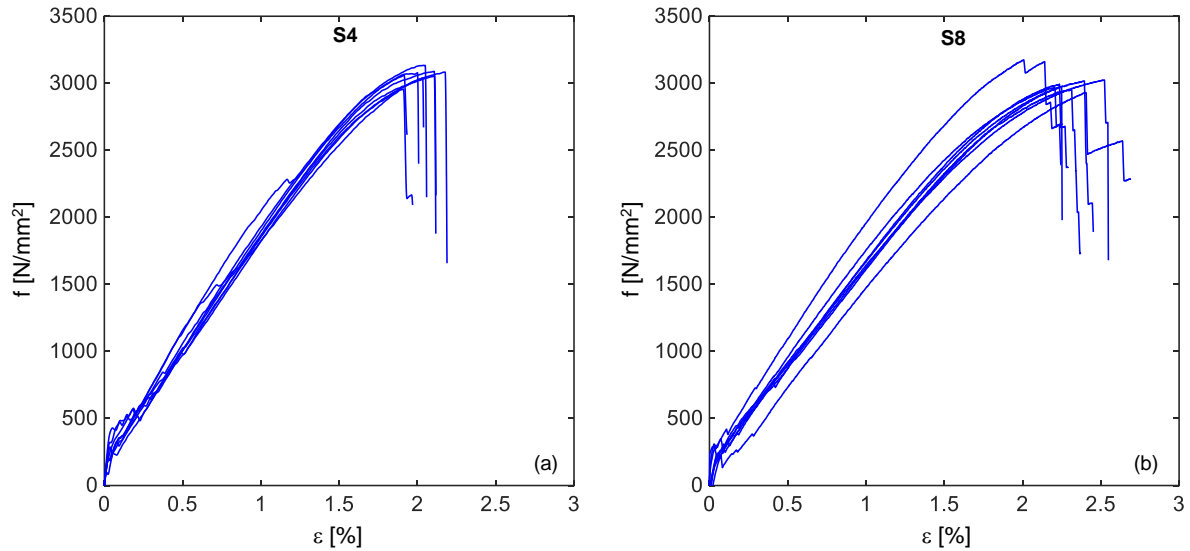


Figure 2: Stress-strain response curves of direct tensile tests on SRG coupons comprising S4 (a) and S8 (b) textiles.

Lap-splice tests

Lap-splice tests were carried out to investigate the textile-to-textile load transfer capacity, which is a key transfer mechanism in multi-ply externally bonded SRG reinforcements and can be limited by the development of interlaminar shear failure between textile layers. Since no attempts of running lap-splice tests on SRG composites have been made so far, the ASTM standard D7616 (ASTM 2017) developed for FRPs was followed. The specimens were similar to those subjected to direct tensile tests. They had 600mm total length, 50mm width and 12mm thickness, were manufactured in the same moulds and underwent the same curing process. In this case, however, the textile strip was not continuous. Two layers were placed on one side, 6mm spaced, and one layer was placed, on the other side, in the middle between them, with an overlap length (L') of 100mm, 200mm or 300mm (Figure 2). The spacing between the plies at the overlap was 3mm. The symmetry with respect to the thickness prevented the occurrence of parasitic bending moments caused by eccentricities during test execution. During manufacturing, particular care was paid to ensure that the textile strips were aligned, that their spacing was constant, and that an adequate amount of mortar passed through the voids between the cords. The ends of the coupons were wrapped with GFRP and tests were performed with the same protocol of direct tensile tests. Five specimens nominally identical were manufactured and tested for each value of L' , for a total of 15 specimens for S4 and 15 for S8.

In the initial phase of the test, the specimens were uncracked. Then, a first (main) transversal crack formed at the end of the overlap, on the side of the single textile layer. From this moment on, the width of this crack increased with the increase of the applied load and other cracks progressively appeared on the portion of the coupon comprising one ply of textile (Figure 3a), whereas the surface of the other portion remained uncracked. A longitudinal crack also appeared, and progressively extended, in the thickness of the coupon along the overlap (Figure 3b). In all specimens, failure occurred by the relative sliding of the textile layers, with the only exception of specimen with S4 textile and 300mm overlap length, in which the cords fractured. Figure 4 shows the stress-slip response curves, the stress (f) being referred to one ply of textile and the slip (s) being the relative displacement between the two portions of coupon separated by the main crack. The slip was measured with DIC using two points that were selected after the end of the test, on the two sides of the main crack. It is worth noting that this would have been unfeasible with conventional measurement devices (displacement transducers) since the crack pattern was unknown a priori. At the attainment of the peak stress, a brittle failure occurred with the shortest overlap length ($L'=100$ mm), whereas a stress quasi-stabilization was observed with $L'=200$ mm and $L'=300$ mm, indicating that the effective transfer length was exceeded. In this case, the increase of slip was associated with the portion of overlap involved in the load transfer process progressively shifting away from the main crack. The values of peak stress (f) attained in lap-splice tests are shown in Figure 5 together with those of direct tensile tests, and are also listed in Table 1 together with the ultimate slip (s_u). With S4 textile, the maximum stress resulted similar to the tensile strength with $L'=200$ mm and $L'=300$ mm, suggesting that the effective transfer length is comprised between 100mm and 200mm. It should be considered that the peak stress in lap-splice tests might be expected to be lower than that of direct tensile tests (in this case, by 9% on average) due to unavoidable misalignments and to the different clamping conditions of the textile on one side (at the overlap), which may cause uneven stress distribution amongst the cords. Much lower stress (on average 37-39% of the tensile strength) was

attained in lap-splice tests with S8, due to its higher density, which resulted in a lower amount of mortar matrix passing through the cords.

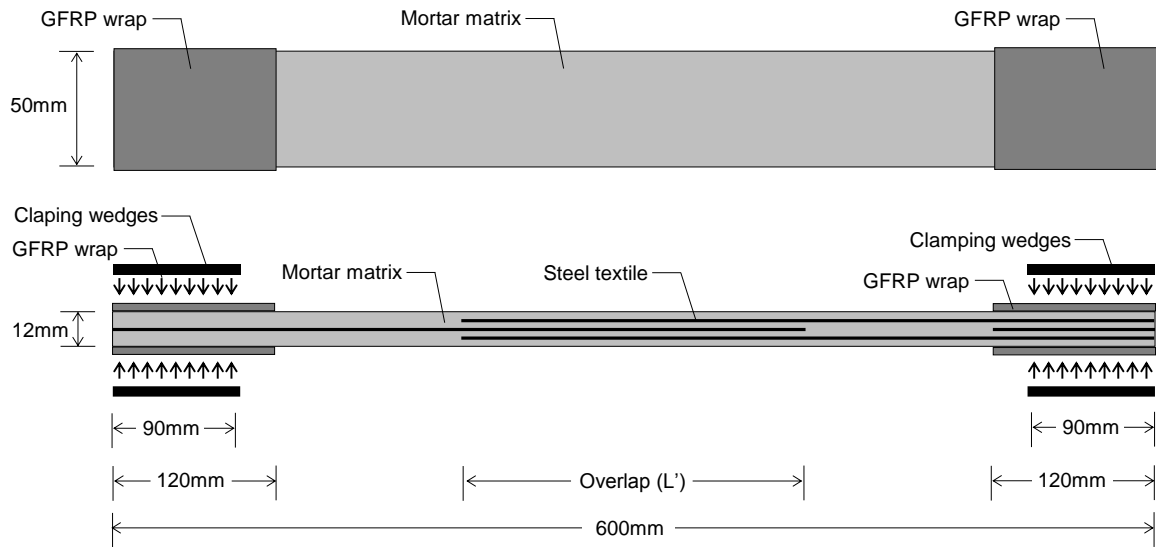


Figure 3: Top and side view of SRG specimens manufactured for lap-splice tests.

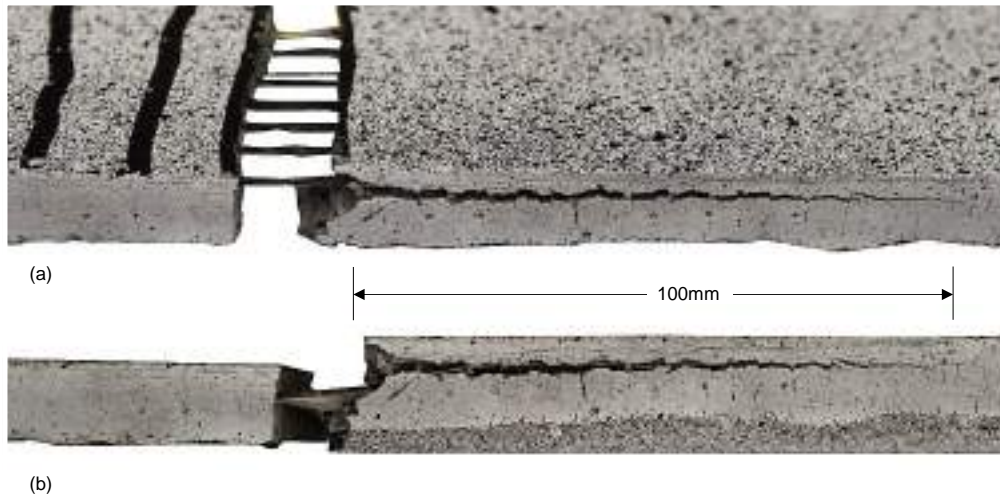


Figure 4: Typical crack pattern observed in lap-splice tests (S4-100-02 specimen).

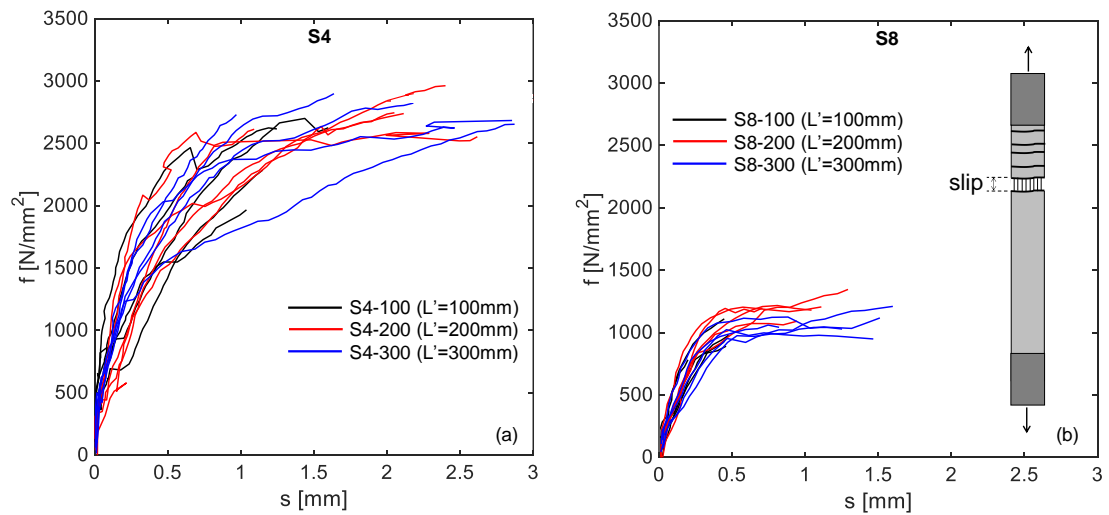


Figure 5: Stress-slip response curves of lap-splice tests on SRG specimens comprising S4 (a) and S8 (b) textiles.

BOND SHEAR TESTS

Specimens details and preparation

A set of 24 unreinforced concrete prisms were cast for the single-lap shear bond tests. The typical concrete prism has a square cross section of 150 mm and a length of 500 mm. The compressive strength ($f_{cm,cube}$) of the concrete prisms used for the single-lap shear bond tests was evaluated by testing six cubes at 28 days and the average value was 27.2 MPa. The concrete substrate was ground to remove the smooth layer and to expose the aggregates (Figure 6a). After the concrete surface was cleaned from the dust, it was saturated with water. Then, the first layer of grout was applied over a length of 300 mm and a width of 100 mm. The SRG composite was terminated 50 mm to the edge of concrete block (the loaded end) to avoid edge-effects. The thickness of the grout layer was kept to approximately 3 mm by using specially designed moulds (Figure 6b). The steel fabric was then placed and gently pressed to ensure good impregnation with grout. Another layer of grout having the same thickness (3 mm) was then applied. This process was repeated for multiple layers. In case of two and three layers, attention was paid to ensure a good alignment between fabric layers. Moulds were removed two days after casting. Then, the specimens were carefully moved and kept in laboratory conditions for at least 28 days. At the far end of the dry steel fabric (gripping area), the steel cords were encapsulated in a two-component epoxy and sandwiched between aluminium plates. For multiple layers, the spacing between different layers of fabric was kept to 3 mm by using similar aluminium plates.

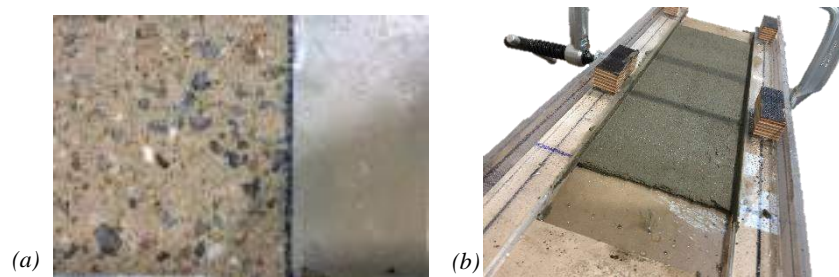


Figure 6: Substrate after preparation (a) and mortar layer and mould used to control the thickness of the SRG (b)

Test setup

The direct single-lap shear bond test setup will be adopted in this phase of testing (Fig. 7). The potential misalignment between the actuator and the SRG composite will be mitigated by: 1) adjusting the position of the specimen within the reaction frame by means of a levelling plate, three levelling bolts and one stabilizer bolt; 2) selecting a free length of the dry fabric that is long enough (400mm) to limit the effect of its inclination. DIC will be used to measure the strain in the composite and gain detail insights into slip, cracking pattern and strain distribution.

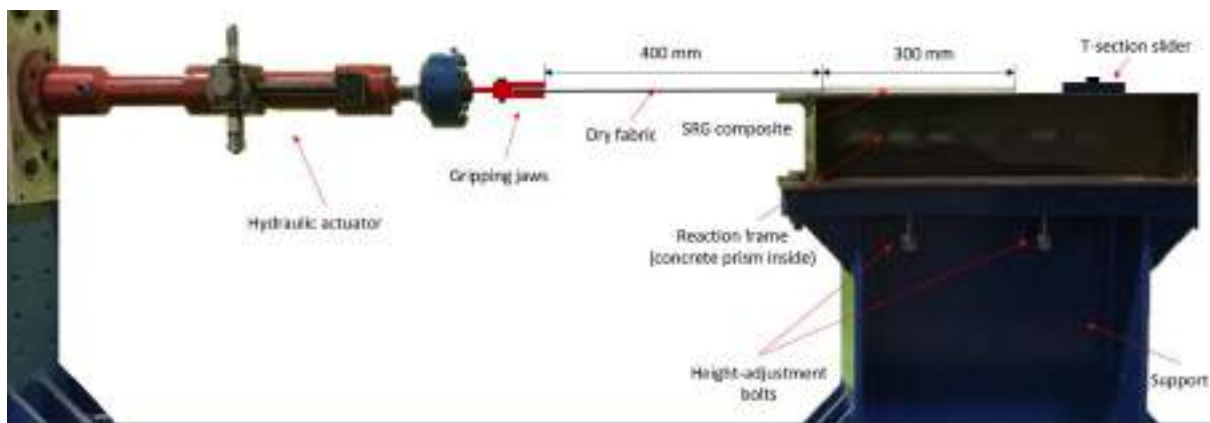


Figure 7: Experimental setup for direct single-lap shear bond tests.

CONCLUSIONS

This paper presented some preliminary results of an experimental study on SRG systems comprising multiple layers of galvanized UHTSS textiles within a geopolymer mortar. The mechanical properties of the SRG system such as the mean values of peak stress and strain, and tensile modulus of elasticity in the uncracked and in the cracked stage were defined by direct tensile tests. Lap-splice tests were carried out and conclusions were drawn about the textile-to-textile load transfer capacity. It was observed that rupture of the steel cords occurred only in the specimens with S4 textile and 300mm overlap length. In all other cases failure occurred by relative sliding of the textile layers. In the case of S4 textile specimens, the effective transfer length was found to be between 100mm and 200mm. The shortest overlap length ($L'=100\text{mm}$) led to brittle failure at the attainment of the peak stress, whereas for the higher overlap lengths examined ($L'=200\text{mm}$ and $L'=300\text{mm}$) a quasi-stabilization was observed. This implies that the increase of slip was associated with the portion of overlap involved in the load transfer process progressively shifting away from the main crack. A third phase of testing is currently underway to examine the effect on SRG-to-concrete bond behaviour of a number of steel textile plies and steel cord density.

ACKNOWLEDGMENTS

Kerakoll S.p.A. is kindly acknowledged for providing the materials. The first author wishes to acknowledge the financial support provided by the European Union's Horizon 2020 research and innovation programme under the Marie Skłodowska-Curie grant agreement No 700863. G. de Felice, S. De Santis and F. Roscini acknowledge the Italian Ministry for Foreign Affairs for cofounding this study within the Research Projects "Composites with inorganic matrix for sustainable strengthening of architectural heritage" Affairs (Year 2017, Grant N. PGR00234).

REFERENCES

- A. Bilotta, F. Ceroni, E. Nigro, M. Pecce (2017). "Experimental tests on FRCM strengthening systems for tuff masonry elements", *Construction and Building Materials*, 138, 114-133
- A. Razavizadeh, B. Ghiassi, D. V. Oliveira (2014). "Bond behaviour of SRG-strengthened masonry units: Testing and numerical modelling", *Construction and Building Materials*, 64, 387-397
- ASTM (2017). "Standard Test Method for Determining Apparent Overlap Splice Shear Strength Properties of Wet Lay-Up Fiber-Reinforced Polymer Matrix Composites Used for Strengthening Civil Structures", D7616M - 11
- E. Stievanin, F. Da Porto, M. Panizza, E. Garbin, C. Modena (2013). "Bond characterization between historical concrete substrate and SRG/SRP strengthening systems", *Proceedings of 5th Int. Conference on Structural Engineering, Mechanics and Computation SEMC2013*, Cape Town, South Africa
- F. Bencardino, A. Condello, A. F. Ashour (2017). "Single-lap shear bond tests on Steel Reinforced Geopolymeric Matrix-concrete joints", *Composites Part B: Engineering*, 110, 62-71
- G.E. Thermou, S.J. Pantazopoulou, A.S. Elnashai (2012). "Global interventions for seismic upgrading of substandard RC buildings", *Journal of Structural Engineering*, ASCE, 138(3), 387-401.
- G. de Felice, S. De Santis, L. Garmendia, B. Ghiassi, P. Larrinaga, P.B. Lourenço, D.V. Oliveira, F. Paolacci, C.G., Papanicolaou (2014) "Mortar-based systems for externally bonded strengthening of masonry. *Materials and Structures*", 47(12), 2021-2037.
- J. Donnini, V. Corinaldesi, A. Nanni (2016). "Mechanical properties of FRCM using carbon fabrics with different coating treatments", *Composites Part B: Engineering*, 88, 220-228
- L. Ascione, G. de Felice, S. De Santis (2015). "A qualification method for externally bonded Fibre Reinforced Cementitious Matrix(FRCM) strengthening systems", *Composites Part B: Engineering*, 78, 497-506
- M. Matana, A. Nanni, L.R. Dharani, P. Silva, G. Tunis (2005). "Bond Performance of steel reinforced polymer and steel reinforced grout", *Proceedings Int. Symp. On bond behaviour of FRP in structures (BBFS)*, Hong Kong, China
- M. Tekieli, S. De Santis, G. de Felice, A. Kwiecień, F. Roscini (2017). "Application of Digital Image Correlation to composite reinforcements testing", *Composite Structures*, 160, 670-688.

- S. De Santis (2017). "Bond behaviour of Steel Reinforced Grout for the extrados strengthening of masonry vaults", *Construction and Building Materials*, 150, 367-382
- S. De Santis, F. Carozzi, G. de Felice, C. Poggi (2017a). "Test methods for Textile Reinforced Mortar systems", *Composites Part B: Engineering*, 127, 121-132.
- S. De Santis, F. Ceroni, G. de Felice, M. Fagone, B. Ghiassi, A. Kwiecień, G. Lignola, M. Morganti, M. Santandrea, M. Valluzzi, A. Viskovic (2017b). "Round Robin Test on tensile and bond behaviour of Steel Reinforced Grout systems", *Composites Part B: Engineering*, 127, 100-120
- S. De Santis, G. de Felice (2015). "Steel reinforced grout systems for the strengthening of masonry structures", *Composite Structures*, 134, 533-548
- X. Huang, V. Birman, A. Nanni, G. Tunis (2005). "Properties and potential for application of steel reinforced polymer and steel reinforced grout composites", *Composites Part B Engineering*, 36 (1), 73-82
- C.G. Papanicolaou, T.C. Trinantafillou, M. Papathanasiou, K. Karlos (2008). "Textile reinforced mortar (TRM) versus FRP as strengthening material of URM walls: out- of- plane cyclic loading", *Materials and Structures*, 41, 1, 143-157.
- A. Napoli, R. Realfonzo (2015) "Reinforced concrete beams strengthened with SRP/SRG systems: Experimental investigation" *Construction and Building Materials*, 93, 654-677.



INFLUENCE OF PRE-IMPREGNATION PROCESS ON MECHANICAL PERFORMANCE OF GLASS/ETTRINGITIC MATRIX COMPOSITE

O. Homoro, M. Michel, E. Lanoye and T.N. Baranger

Université de Lyon, Université Lyon 1, LMC2-EA7427, F-69622 Villeurbanne, France.

Email: Marie.Michel@univ-lyon1.fr, Thouraya.Baranger@univ-lyon1.fr

ABSTRACT

Textile-reinforced concrete (TRC) materials are currently receiving great attention for strengthening or repair of concrete, masonry and wood structures, owing to their many advantages (high tensile strength and pseudo ductile behavior, nontoxicity, availability of raw materials, recyclability, etc.). However, the use of multifilament reinforcements for cements is challenging because the cement particles cannot fully penetrate the space between the inner filaments, which leads to the decrease of the yarn/matrix bond and consequently the mechanical performance of the composite. The objective of this work is to improve this bond by pre-impregnating the glass yarn with mineral powder according to two different processes: Conventional pre-impregnation in a wet way and pre-impregnation in a dry way which is based on the use of an alternating electrostatic field that allows to impregnate powder into yarns. The pullout response of AR glass yarn embedded in ettringitic matrix has been investigated and reported to this study. Three types of specimens have been tested: a dry yarn (D), a yarn pre-impregnated in a wet way (PIW) with matrix particles, and a yarn pre-impregnated in a dry way (PID) with different types of powder. Four embedded lengths have been experimented and their effect on the result is discussed. It was found that pullout behavior is dependent on pre-impregnation method, pre-impregnation powder type and embedded length. The pre-impregnation in wet way was the best process, which improved the mechanical performances especially at small-embedded lengths.

KEYWORDS

Glass multifilament yarns, ettringitic matrix, pre-impregnation, pullout, yarn/matrix bond.

INTRODUCTION

Textile reinforced concrete (TRC) is a composite material consisting of a cement-based matrix with small aggregate grain sizes and high performance continuous multifilament yarns made of alkali-resistant (AR) glass, carbon, polymer, or other materials (Bramshuber 2006). During the last few decades, owing to its excellent mechanical properties and durability, the material is being increasingly used to construct new light structures and to strengthen and repair structural elements made of reinforced concrete or other traditional materials (Lieboldt et al. 2008; Mechtcherine 2013).

Textile fabrics are commonly made of multifilament yarns that are composed of hundreds or thousands of fine-diameter filaments. However, the use of this form of yarn is challenging because of the particulate nature of the cementitious matrix. This consists of relatively large particles ($\sim 5\text{--}70\ \mu\text{m}$ particles) that cannot easily penetrate the spaces between the inner filaments of the bundle (spaces of less than $\sim 5\ \mu\text{m}$). This creates two zones: sleeve zone, in which external filaments are in direct contact with the hydration products of the cement matrix, and core zone, in which internal filaments remain relatively free (Figure 34.a) (Banholzer et al.2006). Consequently, the external filaments which are well bonded to the matrix are fractured during loading, providing high first-crack stress. After the external filaments fail, a telescopic type of pullout is generated (Figure 34.b), in which the core filaments slip against the external filaments increasing the ductility of the composite. They then interact and transfer stresses only through surface contacts between them (Banholzer et al.2006). A composite with a low sleeve/core ratio is characterized by ductile behavior; in contrast, a high sleeve/core ratio can confer high tensile strength with brittle behavior.

Based on the above, to obtain superior performance of multifilament reinforced composite, it is necessary to ensure efficient stress transfer between the cement matrix and the inner filaments by filling the space between the bundle's filaments. The most common way to enhance the loading capacity of bundles within the cement matrix is by coating them with polymers. Many studies have focused on the effects of coating the bundles (Gao et al. 2004; Dvorkin and Peled 2016). Xu et al. (2004) observed improved bond resistance in cement-based composites (pullout tests) by pre-impregnating carbon, aramid and AR glass fabrics with epoxy resin, as compared to non-coated fabrics. However, one limitation of polymer coating is its low bonding with the cement matrix, which causes

delamination of composite (Dvorkin and Peled 2016). Another solution to improve bundle-loading capacity is by filling it with mineral fillers (Dvorkin and Peled 2016; Zamir et al. 2014).

The objective of the current work was to study the pullout behavior of AR glass multifilament yarn embedded in cement matrix and pre-impregnated with different types of powder (mineral and organic powder) according to two different methods: (i) classical wet method and (ii) dry method based on the use of an alternating electrostatic field that allows penetration of powder into yarns. The effect of the embedded length has also been evaluated in this study. Finally, preliminary comparison with simple analytic model followed the experimental study.

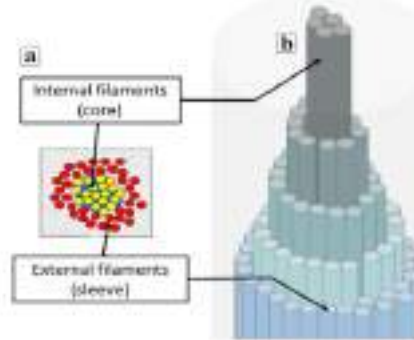


Figure 34. (a) Schematic cross-section of a multifilament yarn embedded in a cement matrix; (b) schematic view of the telescopic pullout under tensile loads (Dvorkin and Peled 2016).

EXPERIMENTAL INVESTIGATION

To investigate the pullout response of the multifilament yarn from cement matrix by observing the effect of embedded length and pre-impregnation using wet and dry methods, one type of AR glass yarn and specific cement matrix K3 has been used. This section describes properties of materials, specimens manufacturing methodology, experimental configurations and test set up.

Materials

The yarn used in this study is a direct roving consisting of continuous AR glass filaments bonded into a single strand and wound onto a bobbin shape. The main characteristics of the yarn are given in Table 17.

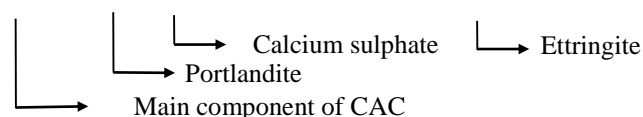
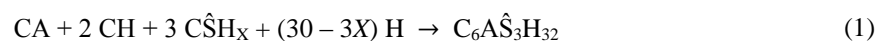
Table 17: Characteristics of the AR glass multi-filaments yarn (supplier's data).

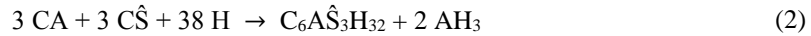
Filament Diameter	Specific Gravity	Linear weight	Tensile Strength	Modulus of elasticity	Softening point
19 μm	2.68 g/cm^3	1200 tex	1700 MPa	72 GPa	860 $^{\circ}\text{C}$

The cement matrix K3 (Ambroise and Michel 2014) used consists of granular skeleton with a particle size of less than 300 μm , an ettringitic binder and an additive system as shown in table 2. The particularity of this composition resides in the nature of binder, which is an ettringitic binder, consisting of calcium aluminate cement (CAC), calcium sulphate and Portland cement. Portland cement is characterized by slow hydration that does not allow to obtain sufficiently short hardening time to demold in few minutes. However, the ettringitic binder is characterized by the fact that its dormant period is reduced to only a few minutes. The main hydrate, ettringite, is formed from the first moments according to equations (1) and (2), which gives the product specific characteristics, namely rapid hardening and rise in strength (Older 2000). Granular skeleton comprises silica, limestone, and silico-aluminous fillers. The additive system consists of setting modifying agents used to adjust pot life and cure time of the grout and an association of rheology agents to ensure fluidity and stability of the matrix.

Table 18: composition of K3 matrix.

Constituents	Masse [g]
Ettringitic binder	268
Granular skeleton	624
Additive system	108
Total solid	1000
Water	240





Specimens preparation

Cylindrical specimens of 34 mm diameter are used in this study, composed of ettringitic matrix, straight yarn which passes through the axis of cylinder, two threaded metal rods of 4 mm diameter and a composite plate glued to the free end of the yarn (Figure 35). The specimens were prepared from PVC molds. Each PVC pipe was placed on a molding plate drilled with 3 circular holes of 4 mm diameter: a hole in the center of the plate allowing the passage of the yarn without filament damage and two other holes for the metal rods making with the central hole a distance corresponding to half the cylinder radius. Glue was applied at the junction of the pipe and the molding plate in order to ensure the sealing after matrix casting. A specific device is used to maintain vertical position of yarn while the casting of matrix. The fresh matrix was then cast into molds that were vibrated to close up the voids. A plastic layers protected specimens' upper surfaces in order to limit drying and premature shrinkage of the upper surface. After 24h, specimens were removed from mold. Then, a composite plate was glued to the free end of the yarn using an epoxy adhesive (EPONAL 380). Specimens were kept at ambient atmosphere and temperature for 6 days, before to be tested. The tests were run until complete failure of specimen.

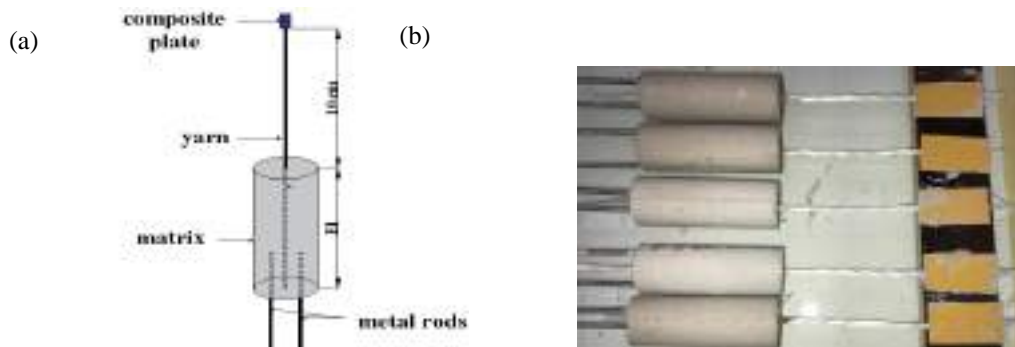


Figure 35: (a) schematic pullout specimen; (b) specimens ready to be tested.

Yarn pre-impregnation method

Before putting it into the mold, the multifilament yarn was pre-impregnated with different types of powder using two different processes:

- Pre-impregnation in wet way: before casting, the yarn was saturated with matrix slurry. This saturation was obtained by manual action on the yarn placed in a slurry batch.
- Pre-impregnation in dry way: this innovative process, which was developed by a French manufacture called Fibroline, allows to impregnate yarns with powder thanks to high intensity alternating electrostatic fields. The technology principle is presented in Figure 36. Five kinds of pre-impregnation powders (mineral and polymer) were mixed with silica filler to ensure their fluidity. The mixture (96% powder + 4% silica filler) was then scattered onto the glass yarn segments. The yarn/powder system was then placed between two dielectrics. A strong alternative electrostatic field is created by the high tension applied to the electrodes. At the end of the treatment, the powder scattered on top of the yarns finds itself inside, few seconds residence time is sufficient, and leads to a homogeneous distribution of the powder inside the yarn segments. Finally, the pre-impregnated yarns were water sprayed before casting matrix.

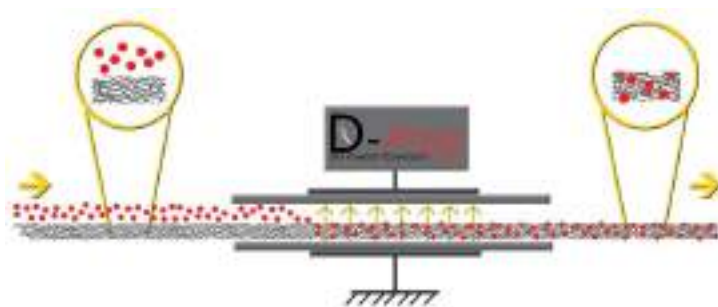


Figure 36: Principle of the Fibroline dry impregnation process.

Experimental configurations

Different pre-treatments were applied to each yarn before putting it into the mold, using wet and dry methods, and different types of powder:

- PIW.K3 : the yarn was pre-impregnated in wet way with the K3 ettringitic matrix;
- PID.B : the yarn was pre-impregnated in dry way with only the binder of K3 matrix;
- PID.B+F : the yarn was pre-impregnated in dry way with the binder and the fillers of K3 matrix;
- PID.K3 : the yarn was pre-impregnated in dry way with the K3 matrix;
- PID.SAC : the yarn was pre-impregnated in dry way with a SAC mono-component binder (sulfo-aluminous cement);
- PID.P : the yarn was pre-impregnated in dry way with polymer powder (polyvinyl acetate).

Hereafter, D denotes air dried yarn at room temperature before casting, the penetration of cement particles into the filaments was restricted.

In order to investigate the effect of embedded length (EI) on the pullout behavior, four embedded lengths: 2, 5, 7, 10 mm were tested in the case of three yarn pre-treatments: D, PIW.K3 and PID.B+F. Table 19 shows the list of specimens.

Table 19: list of specimens.

Configurations	EI = 2 cm		EI = 5 cm	
	Number of tests	Designation	Number of tests	Designation
D	3	EI2.D	5	EI5.D
PIW.K3	4	EI2.PIW.K3	6	EI5.PIW.K3
PID.B	-	-	3	EI5.PID.B
PID.B+F	2	EI2.PID.B+F	4	EI5.PID.B+F
PID.K3	-	-	4	EI5.PID.k3
PID.SAC	-	-	3	EI5. PID.SAC
PID.P	-	-	4	EI5.PID.P

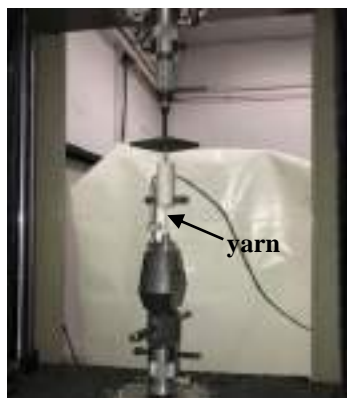
Configurations	EI = 7 cm		EI = 10 cm	
	Number of tests	Designation	Number of tests	Designation
D	5	EI7.D	5	EI10.D
PIW.K3	5	EI7.PIW	6	EI10.PIW.K3
PID.B+F	3	EI7.PID.B+F	-	-

Test set up

The test set up is illustrated in Figure 37(a). It consists of:

- a Zwick/Roell universal testing machine with a force sensor of 65 kN,
- a metal plate connected to the specimen and the testing machine by means of the system described in Figure 37(b).

The free end of yarn was fixed by clamping the composite plate into the lower jaw of the machine. The tests are displacement-controlled by imposing a constant displacement rate equal to 1 mm/min.



(a) (b)
Figure 37: The pullout test set up.

RESULTS AND DISCUSSION

Pullout test results

- Figure 38(a) presents pullout responses of D specimens, in terms of axial force as function of displacement, for embedded lengths ranging from 2 cm to 10 cm. One typical force/displacement curve is shown for each embedded length. All curves started with a linear zone, characterized by a good bond between yarn and matrix, until reaching approximately 70 to 95% of failure load, where the filaments-matrix bonds began to break. This rupture was associated with the tensile rupture of external filaments, which were well impregnated by the cement matrix on the one hand, and the rupture of internal filament-matrix adhesion on the other hand. The successive rupture of these bonds decreased the slope of the ascending part of the curve until reaching the maximal force. The pullout curve is characterized by a descending part, corresponding to a significant drop in loading force. It is accompanied by the rupture of the last bonds, between the filaments and the matrix until reaching a threshold force in the order of 40 N. Once all the filament-matrix bonds were broken, the inner filaments started to slip and transfer the stress only through their contact surface. In this third phase, a very small decrease in the loading force was observed until the specimen failure.
- Figure 38(b) shows pullout curves obtained for PIW.K3 yarn specimens, in the case of the four embedded lengths. For each length only one typical curve is shown. All curves present two different parts. The first one, corresponding to the ascending part of the curve, represents two phenomena: the beginning of the curve describes the loading of all filaments and the ending part, when slope decreases, describes a progressive rupture of filaments until ultimate load. In fact, generally, shortest filaments are loaded first and broken first. Then force was distributed on the remaining filaments, which explains the decrease of the slope. When most of the filaments broke, a sudden drop of the force was observed, characterized by the second part of the curve, the descending one. The rupture of the filament-matrix bonds in this case corresponds only to the tensile rupture of the filaments (Figure 39). No slip of internal filaments was observed as in the case of a D yarn, which means that the yarn-matrix adhesion has been improved by this yarn treatment.

The shape of the pullout curves obtained in the case of a PID yarn for an embedded length of 5 cm varies according to the type of the pre-impregnation powder used. In the case of a PID.B and PID.P yarn, the behavior is similar to that of a PIW.K3 yarn, characterized by a sudden rupture of the specimen. However, in the case of a PID.B+F, PID.K3 and PID.SAC yarn, the behavior is similar to that of a D yarn characterized by a slip of filaments from a force of around 16N.

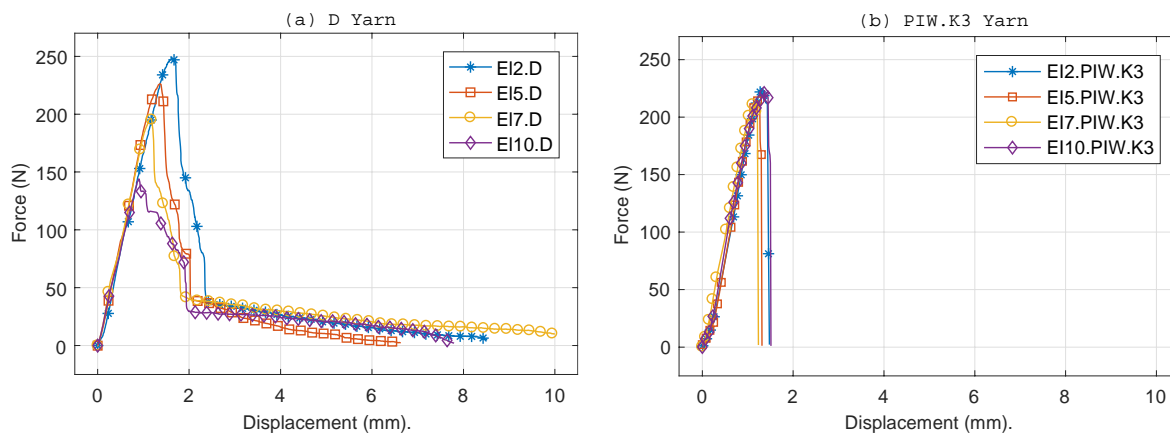


Figure 38: (a) pullout behavior of D composite; (b) PIW.K3 composite at different embedded lengths.

Failure modes

Figure 39 shows the specimens after pullout test. As mentioned above, for a D yarn, the external filaments broke and the inner filaments slipped. This mode of rupture is also observed for a PID.B, PID.B+F and PID.SAC yarn. However, in the case of PIW.K3 yarn, no filament was extracted from the matrix and the rupture of the specimens was associated with the tensile rupture of all filaments (the bond strength became greater than tensile yarn strength).

A total extraction of PID.K3 and PID.P yarn from the matrix was observed accompanied with the rupture of some external filaments. This is due to presence of polymer fillers, which exhibited low bonding with the cement matrices, because of their hydrophobic characteristics.

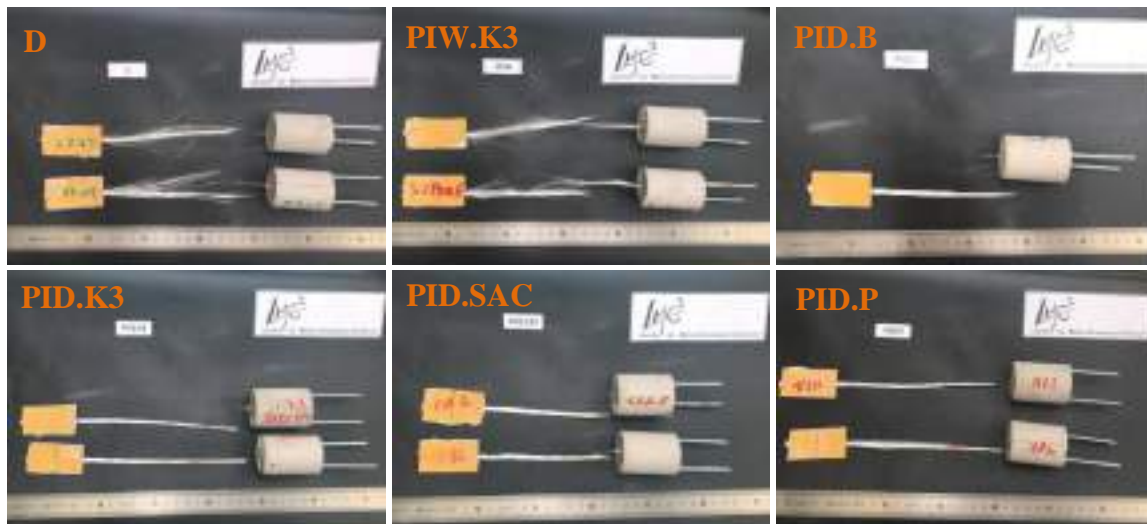


Figure 39: Specimens after pullout test for different configurations ($El = 5$ cm).

Effect of embedded length

The evolution of the maximum force as a function of the embedded length El , for the configurations D, PIW.K3 and PID.B+F is shown in Figure 40(a). In the case of D yarn, the maximum force was strongly dependent on the embedded length. Indeed, the maximal force increased when the embedded length increased, this increase was important when El varied from 2 cm to 5 cm (about 50%), beyond 5 cm, the variation became lower (about 6%). This can be related to the embedded fiber-matrix area, which increased when El increased, i.e., more load is needed to cause debonding as this area increases.

By using the two pre-impregnation methods, the embedded length didn't have a significant effect on the pullout force, if values' fluctuation was taken into account. For the PIW.K3 yarn, this can be explained by the mode of rupture of specimens depending only on the tensile resistant of the yarn that remains constant for all embedded length. This yarn pre-treatment allowed for a good bond resistance greater than the tensile yarn strength. This effect decreased when the embedded length varied from 2 cm to 7 cm. it was in fact an increase in the maximal load of 69% at $El= 2$ cm, 25 % at $El= 5$ cm and 5% at $El= 7$ cm. However, when El reached 10 cm, this pre-treatment had no effect on the force, which was equal to that obtained in the case of a D yarn. In contrast, contrary to what was expected, the dry pre-impregnation not only didn't contribute to the improve of the D yarn force, but it caused a drop of 23% and 37% of the average force for embedded lengths of 5 and 7 cm, respectively. This reduction can be attributed to the nature of the pre-impregnation powder used, or the calendaring of the yarn (before dry impregnation), which reduced the cohesion between the filaments and weakened the yarn, or the saturation of the yarn with the water, which prevented the anchoring of external filaments. These assumptions are under investigation.

Effect of yarn pre-treatment

The effect of pre-impregnation methods and type of pre-impregnation powder used on the pullout force for an embedded length of 5 cm is presented in Figure 40(b). This embedded length was chosen in order to avoid: boundary effects in PID process for short lengths; and yarn's filaments fracture rather than pullout for long lengths. The results reveal that wet pre-impregnation method exhibited the greatest pullout force with a gain of 25% compared to reference specimen (D yarn), due to the good penetrability of cement particles in between the bundle filaments. The dry pre-impregnation method also showed pullout load superior to that of the reference with a gain of approximately 7%, but only when using K3 binder, SAC and polymer fillers as pre-impregnation powder. However, the figure indicates that the PID.B+F and PID.K3 yarns exhibited lower pullout strength than the reference. Thus, for the dry pre-impregnation process, the type of the powder used plays an important role in the pullout strength; the addition of fillers and additives of the K3 matrix had negative effect on matrix-yarn bond due to the particle size. The polymer fillers improved the mechanical strength of the specimen but exhibited low adhesion to the cementitious matrices, which led to a complete extraction of the yarn from matrix.

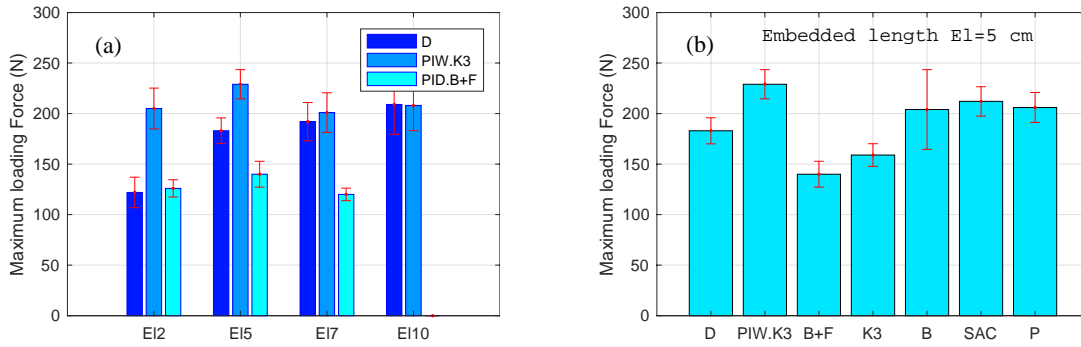


Figure 40: (a) Evolution of the maximal force as a function of embedded length for the configurations: D, PIW.K3 and PID.B+F; (b) Evolution of the maximal force according to the configurations investigated ($E_l=5$ cm).

PRELIMINARY COMPARISON WITH AN ANALYTIC MODEL

In addition to previous experimental studies, a simple analytical model developed by several authors for instance Stang et al. (1996) and Zhang et al. (2014) was considered. Model's parameters have been identified and calibrated with the experimental results, to simulate the pullout behavior of glass yarn embedded into cement matrix. In this model the failure mechanism is analyzed by dividing the pullout curve into three phases: perfect bonding phase, debonding phase and pure friction phase. The slip of the yarn at the interface is considered as the creation of a circumferential interfacial crack. This model is based on three assumptions: the matrix is considered as a rigid body and only the displacement of the yarn to the matrix is studied; the yarn and the matrix are homogeneous, isotropic and linearly elastic; the shear stress τ at the yarn/matrix interface is proportional to the displacement of the yarn in the bonding part ($\tau = k \cdot u$). It reaches its maximal value τ_{max} at the crack tip of the debonding phase and then the debond occurs when $\tau_{max} = \tau_0$. The parameters k and τ_0 are identified from experimental data.

Experiment pullout curves obtained from D yarn embedded into ettringitic matrix for different embedded lengths are used to calibrate the model parameters. Table 20 presents the average values of these parameters. Figure 41 shows the pullout curves from the experiments and the model. It can be observed that the analytic results agree well to the experimental results.

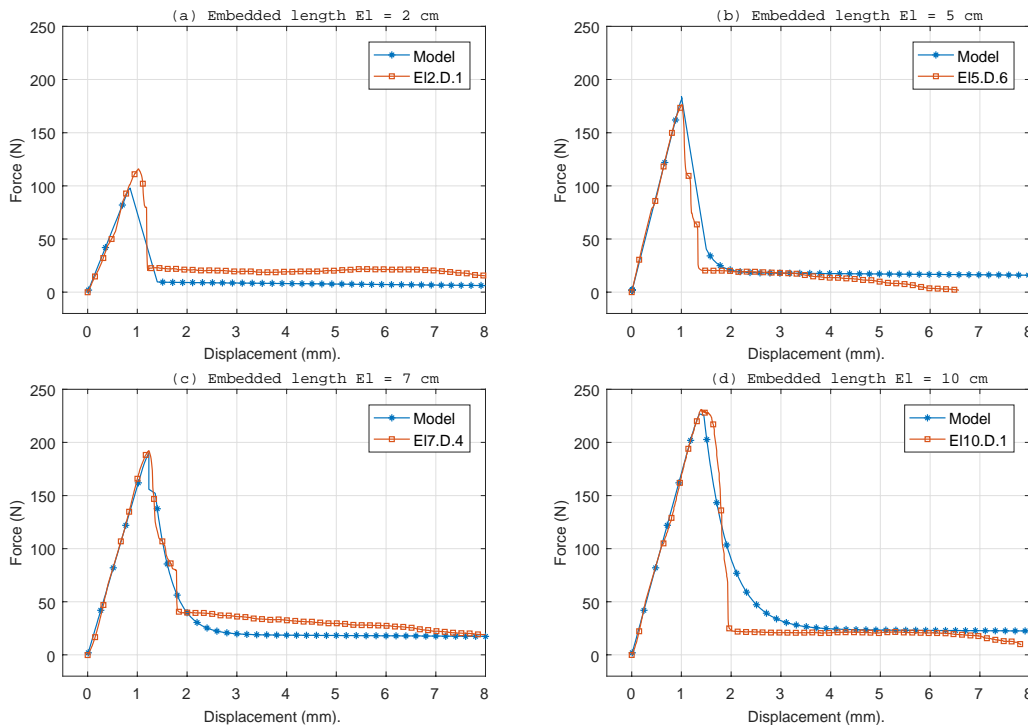


Figure 41: Comparison of analytical and experimental results for different embedded lengths (D yarn).

Table 20: Average values of calibrated model parameters

Parameters	k (MPa/mm)	τ_0 (MPa)	G_c (KJ/m ²)
Average	1.52	1.422	0.003
Coefficient of variation (%)	40	27	0

CONCLUSIONS

The aim of this work was to study the influence of pre-impregnation methods with different types of powder at varying embedded lengths on the pullout behavior of glass yarn embedded into ettringitic matrix. Based on the results and analyses presented in previous sections of this paper, the following conclusions can be drawn:

- The ultimate load of specimens with D yarn increased as the embedded length increased. However, PIW.K3 and PID.B+F yarns pulled out from matrix haven't shown to be sensitive to the embedded length.
- PIW method had positive effect on the pullout strength of D yarn, this effect decreased as the embedded length increased, at $El = 10$ cm, the D and PIW.K3 yarns exhibited the same ultimate pullout load.
- The effect of the PID method depends on the type of pre-impregnation powder used; K3 binder, SAC and polymer fillers have been beneficial for the bond yarn/matrix, allowing a gain in failure load of about 7%, but polymer fillers exhibited poor adhesion to cement matrices, leading to a total extraction of yarn from matrix, which may limit their practical use. By contrast, the PID.B+F and PID.K3 yarns exhibited the worst load carrying capacity. Although the PIW method exhibited the best improvement of the yarn-matrix bond, it is suited only for the manufacturing of simple prefabricated elements, unlike the PID method, which allows to product large-size building elements in site by ensuring a homogenous and controlled distribution of powder into textile in just a few seconds.
- An analytical model was calibrated to predict the pullout behavior of D yarn embedded into cement matrix. The preliminary results obtained were in good agreement with the experimental results.

REFERENCES

- W. Brameshuber (2006). *Report 36: Textile Reinforced Concrete-State-of-the-Art Report of RILEM TC 201-TRC. RILEM publications.*
- M. Lieboldt, M. Butler, V.Mechtcherine (2008). "Application of textile reinforced concrete in prefabrication", *Proceedings of the seventh RILEM international symposium on fibre reinforced concrete: design and applications. RILEM Publications, SARL, 253-562.*
- V. Mechtcherine (2013). "Novel cement-based composites for the strengthening and repair of concrete structures", *Construction and Building Materials, 41,365-373.*
- B. Banholzer, T.Brockmann, W. Brameshuber (2006). "Material and bonding characteristics for dimensioning and modelling of textile reinforced concrete (TRC) elements", *Materials and structures, 39, 749-763.*
- S.L. Gao, E. Mader, R. Plonka(2004). "Coatings for glass fibers in a cementitious matrix", *Acta Materialia, 52, 4745-4755.*
- D. Dvorkin, A. Peled (2016). "Effect of reinforcement with carbon fabrics impregnated with nanoparticles on the tensile behavior of cement-based composites". *Cement and Concrete Research, 85, 28-38.*
- S. Xu, M. Kruger, H.W. Reinhaedt (2004). "Bond characteristics of carbon, alkali resistant glass, and aramid textiles in mortar", *Journal of materials in civil engineering, 16, 356-364.*
- M. Zamir, D. Dvorkin, A. Peled (2014). "Fabric cement-based composites with nanoparticles filler, interfacial characteristics", *3rd International RILEM Conference on Strain Hardening Cementitious Composites (SHCC-3). RILEM Publishers, 171-178.*
- I. Odler (2000). "Cements containing calcium sulfoaluminate", *Special inorganic cements. E & FN Spon, 69-87.*
- Stang H, Li Z, Shah SP (1990). Pullout problem – stress versus fracture mechanical approach. *J Eng Mech – ASCE, 1990;116(10):2136-50.*
- X.B. Zhang, H. Aljewifi, J. Li (2013). "Failure behaviour investigation of continuous yarn reinforced cementitious composites", *Construction and Building Materials, 47 (2013) 456-464.*
- J. Ambroise, M. Michel (2014). "Matrice minérale destinée à la fabrication de composites minces par imprégnation de renforts tissés ou non tissés", *Patent, W02015158891A1.*



APPLICATION OF A TRILINEAR BOND-SLIP MODEL TO FRCM-CONCRETE JOINTS

Xingxing Zou ¹, Lesley H. Sneed ², Tommaso D'Antino ³, Christian Carloni ⁴

¹ Missouri University of Science and Technology, Department of Civil, Architectural and Environmental Engineering, 1401 North Pine Street, Rolla, MO, 65409 USA;

² Missouri University of Science and Technology, Department of Civil, Architectural and Environmental Engineering, 1401 North Pine Street, Rolla, MO, 65409 USA; Email: sneedlh@mst.edu

³ Politecnico di Milano, Department of Architecture, Built Environment, and Construction Engineering, Piazza Leonardo Da Vinci 33, 20133 Milan, Italy;

⁴ University of Bologna, Department of Civil, Chemical, Environmental, and Materials Engineering, Viale Risorgimento 2, 40136 Bologna, Italy

ABSTRACT

This study presents an analytical approach for predicting the load-slip response of fiber reinforced cementitious matrix (FRCM)-concrete joints. The FRCM-concrete interfacial behavior was described with a trilinear cohesive material law consisting of a linear stage, a softening stage, and a friction stage. Accordingly, provided that the bonded length is longer than the composite effective bond length, the full-range applied load-global slip response consists of five stages: an elastic stage, an elastic-softening stage, an elastic-softening-debonding stage, a softening-debonding stage, and finally a fully debonded stage. Closed-form solutions for the applied load-global slip, interfacial shear stress distribution, and longitudinal stress distribution along the composite bonded length were derived. Also, the debonding load, peak load, and the effective bond length were analytically obtained. Results of the analytical model were compared to experimental results of six single-lap shear specimens instrumented with strain gauges mounted to the longitudinal fibers along the composite bonded length.

KEYWORDS

Fiber reinforced cementitious matrix (FRCM) composite, Trilinear bond-slip model, Effective bond length, New composite materials, Systems and strengthening techniques.

INTRODUCTION

A recent innovation for the strengthening of civil structures is the application of externally bonded fiber-reinforced polymer (FRP) composites owing to their high strength-to-weight ratio, good corrosion resistance, and versatility (Teng et al. 2002; Hollaway 2010). However, the use of polymeric matrix as a binding agent makes FRP composites vulnerable to high heat and UV exposure, and difficult to install onto wet surfaces (e.g., Trapko 2013; Raoof and Bournas 2017; Bisby et al. 2017). Fiber reinforced cementitious matrix (FRCM) composites are a new type of composite material that replaces the polymeric matrix used in FRP composites with a cement based matrix and can provide better heat resistance and compatibility with concrete and masonry substrates (D'Antino et al. 2014). Over the past decade, FRCM composites were investigated for strengthening concrete and masonry structures in bending (e.g., D'Ambrisi and Focacci 2011), shear (e.g., Blanksvärd et al. 2009; Azam and Soudki 2014; Gonzalez-Libreros et al. 2017), torsion (e.g., Alabdulhady et al. 2017), and confinement (e.g., Trapko 2013).

The effectiveness of externally bonded FRCM reinforcement depends on the stress-transfer between the composite and the substrate. Therefore, a large number of laboratory experiments have been conducted to investigate the mechanical behavior of FRCM-substrate joints (e.g., D'Antino et al. 2014; Awani et al. 2015; Raoof et al. 2016). It was found that, for the majority of the FRCM specimens, when a single layer of fibers is employed, debonding occurs at the matrix-fiber interface and is characterized by slippage of the fibers with respect to the matrix (D'Ambrisi et al. 2012; D'Antino et al. 2016). Regarding flexural and shear strengthening of structures, debonding of the composite will result in loss of composite action and then trigger member failure (D'Ambrisi and Focacci 2011; Azam and Soudki 2014). Therefore, determining the distribution and development of the interface shear stresses along the composite bonded length is crucial for predicting the ultimate capacity and for achieving an appropriate design of FRCM strengthened structures.

Single- and double-lap shear tests were conducted to determine the matrix-fiber interfacial behavior where discrete shear stress τ -slip s relationships were computed from the axial strain data measured on fiber bundles and then

fitted by different equations. D'Ambrisi et al. (2012) and Focacci et al. (2017) considered different $\tau(s)$ models and applied them to polyparaphenylene benzo-bisoxazole (PBO) FRM-concrete joints. Generally, the models consist of an increasing stage until the shear stress peak value, a decreasing softening stage, and a friction stage with a constant residual shear stress. However, the equations associated with the models proposed can be solved only using iterative methods, i.e., no closed-form solution for the interfacial shear stress and axial stress distribution are available.

Yuan et al. (2004) proposed a closed-form solution to obtain the shear stress, slip, and axial strain of FRP-concrete joints based on a bilinear bond-slip model. However, this bilinear model reproduces the behavior of FRP-concrete joints, i.e., the friction stage in FRM-concrete joints is not considered. A trilinear bond-slip model, which consists of the conventional bilinear model plus an additional branch that represents the non-zero residual shear strength due to friction, could be used to predict the full-range behavior of FRM-substrate joints (Carozzi et al. 2016).

In this paper, a trilinear bond-slip model is employed to describe the behavior of FRM-concrete joints that fail at the matrix-fiber interface. The idealized load response and the analytical model assumptions are first presented. The derivation of the full-range analytical solution is then provided. For each stage, closed-form expressions for the applied load-global (loaded end) slip response, interfacial shear stress distribution, and longitudinal (axial) stress distribution along the composite bonded length are derived. Validation of the solution is carried out with respect to six single-lap shear tests of PBO FRM-concrete joints.

IDEALIZED APPLIED LOAD RESPONSE

It is known that failure of FRM-concrete joints may occur: (a) within the concrete substrate, (b) at the concrete-internal matrix layer interface, (c) at the matrix-fiber interface, or (d) involving a combination of these interfaces (Focacci et al. 2017). This paper focuses on debonding failure at the matrix-fiber interface (i.e. failure mode b), which was observed for the case of FRM composites with different types of fibers including PBO, carbon, and glass (D'Antino et al. 2014, D'Antino et al. 2015a). Since slippage of the fibers relative to the embedding matrix governs this type of debonding failure, the deformation of concrete and matrix can be ignored (Carloni et al. 2014). As a result, the fibers can be assumed to be under uniaxial tension, and a zero-thickness matrix-fiber interface can be adopted.

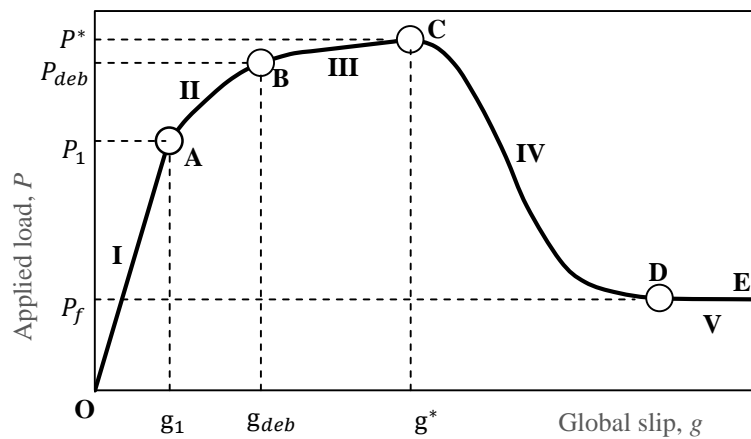


Figure 1: Idealized applied load P -global slip g relationship

Carloni et al. (2014) put forward an idealized load P versus global slip g response for FRM-concrete joints based on results of direct shear tests carried out by controlling the loaded end displacement. A trilinear bond-slip model was employed to reproduce the idealized P - g response by Carozzi et al. (2016). Provided that the bonded length is longer than the composite effective bond length, which is the minimum length needed to fully develop the FRM-substrate joint load carrying capacity (D'Antino et al. 2015b), this trilinear model shows five different stages: elastic, elastic-softening, elastic-softening-debonding, softening-debonding, and fully debonded stages (see Fig. 1, stages I, II, III, IV, and V, respectively). It should be noted that the post-peak behavior determined experimentally and shown in Figure 1, which is characterized by increasing global slip g (i.e., slip at the loaded end), is different from the post-peak behavior determined analytically, where snap-back can be observed (Carozzi et al. 2016). Based on strain compatibility and force equilibrium, closed-form solutions were derived for the load-displacement relationship. For each stage, the distributions of the interfacial shear stress and fiber axial stress can be obtained. Furthermore, the peak load and effective bond length can be computed.

TRILINEAR BOND-SLIP MODEL

In this paper, a trilinear bond-slip model is used to describe the interfacial debonding mechanism between the FRCM composite and substrate. Then, the distributions of the interfacial shear stress and fiber axial stress at each stage, the peak load, and the effective bond length are derived.

The trilinear model is composed of three branches: (i) a linear-elastic branch from the origin to the peak shear stress τ_m , which is associated with a slip s_m ; (ii) a linear softening branch until the shear stress reaches τ_f , which is associated with a slip s_f ; and, (iii) a constant residual shear stress that represents the friction and interlocking mechanism. The trilinear bond-slip model can be expressed as:

$$\tau(s) = \begin{cases} \frac{\tau_m}{s_m} s & , 0 \leq s \leq s_m \\ \tau_m \left[\frac{(s_f - s) + \mu(s - s_m)}{s_f - s_m} \right] & , s_m \leq s \leq s_f \\ \mu \tau_m & , s \geq s_f \end{cases} \quad (1)$$

where μ is defined as the ratio of the residual shear stress τ_f to the peak stress τ_m , i.e., $\tau_f = \mu \tau_m$. It is noted that $\mu = 0$ means that no friction exists after complete debonding of the composite, as is usually assumed for FRP-concrete joints (Lu et al. 2005). The non-zero value of μ is a peculiarity of certain FRCM composites including the PBO FRCM composite in the present study (D'Ambrisi et al. 2012; D'Antino et al. 2016; Focacci et al. 2017).

Assumptions and Governing Equations

The analytical model presented is based on the following assumptions:

- (i) The displacement is the same in each longitudinal fiber yarn across the width of the FRCM composite, and the external applied load is equally distributed among the longitudinal fiber bundles;
- (ii) A linear-elastic constitutive law is used to describe the axial stress-strain behavior of the longitudinal fiber bundles;
- (iii) The matrix-fiber interface can be described as a zero-thickness interface associated with a trilinear bond-slip model given by Eq. 1;
- (iv) The presence and influence of the FRCM transversal fiber bundles is neglected;
- (v) There is no deformation of the matrix and concrete substrate.

Based on the aforementioned assumptions, enforcing the equilibrium of a segment of fiber, the equation governing the problem can be obtained:

$$\frac{d\sigma(y)}{dy} - \frac{\tau(s)}{t_f} = 0 \quad (2)$$

where $\tau(s)$ is the shear stress at the matrix-fiber overall contact interface, t_f is the thickness of the longitudinal fiber bundles, and $\sigma(y)$ is the axial stress in the longitudinal fiber bundles.

Assumption (ii) leads to:

$$\sigma(y) = E_f \varepsilon(y) = E_f \frac{ds(y)}{dy} \quad (3)$$

where E_f is the elastic modulus of the fibers.

Substituting Eq. 3 into Eq. 2, the governing equation can be expressed as:

$$\frac{d^2 s(y)}{dy^2} - \frac{s_f}{\tau_m} \lambda^2 \tau(s) = 0 \quad (4)$$

where:

$$\lambda^2 = \frac{\tau_m}{s_f E_f t_f} \quad (5)$$

The axial stress in Eq. 3 can be rewritten as:

$$\sigma(y) = \frac{\tau_m}{s_f t_f \lambda^2} \frac{ds(y)}{dy} \quad (6)$$

The governing differential Eq. 4 can be solved assuming a bond-slip model and enforcing proper boundary conditions.

Analytical Solution

The shear stress distribution along the axial direction is shown in Figure 2. Under a small applied load level, the entire length of the interface remains elastic (see Figure 2 (b) and segment OA in Figure 1). As the applied load increases, the shear stress attains the peak shear stress at the composite loaded end ($y = \ell$, see Figure 2 (c) and segment AB in Figure 1). As global slip increases, the shear stress starts to decrease at the loaded end, the peak shear stress τ_m is transferred towards the composite free end ($y = 0$), and part of the interface near the loaded end enters the softening stage. With the development of the softening length a , see Figure 2 (d), the applied load P continues to increase because more length of the interface is mobilized to resist the load until debonding initiates (see Figure 2 (e)). As the global slip increases, a debonding branch characterized by a constant residual shear stress commences at the loaded end (see Figure 2 (f) and segment BC in Figure 1). With the development of the debonded length d , see Figure 2 (f), the applied load P continues to increase linearly because of the friction and interlocking contribution. During this stage, the applied load attains the peak load, which is denoted by P^* , see point C in Figure 1. Further increase in the global slip after the peak load is attained determines a decrease in the applied load (softening–debonding stage, segment CD in Figure 1 and Figure 3 (h)). The fully debonded stage starts when the softening zone disappears (point D in Figure 1). In this stage, the applied load is solely provided by the interface friction and interlocking (Figure 2 (i)).

The following steps were followed to solve Eq. 4: (i) definition of the boundary conditions for the specific stage; (ii) substitution of Eq. 1 into Eq. 4; and (iii) solution of the equation defined in (i). The governing equation and solution for each stage are summarized in Table 2.

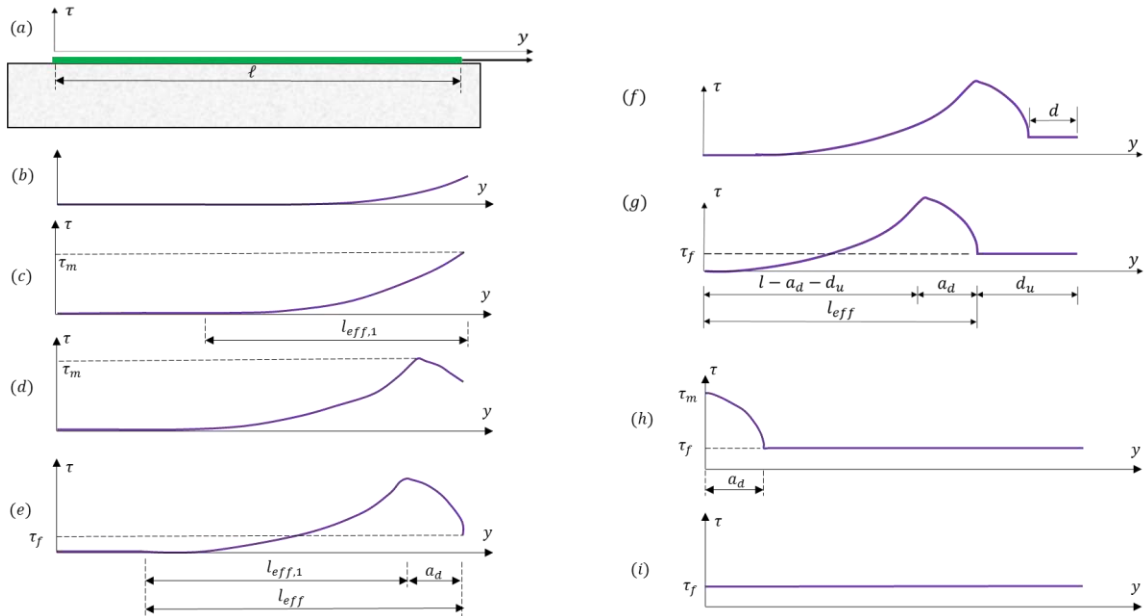


Figure 2: Evolution of interfacial shear stress distribution: (a) schematic side view of single-lap shear test; (b) elastic stage; (c) end of the elastic stage ($P = P_1$); (d) elastic–softening stage; (e) end of the elastic–softening stage ($P = P_{deb}$); (f) elastic–softening–debonding stage; (g) end of the elastic–softening–debonding stage ($P = P^*$); (h) end of the softening–debonding stage; and (i) the fully debonded stage.

Table 1: Solutions for different stages

Stage	Equations and solutions
	$\frac{d^2s(y)}{dy^2} - \lambda_1^2s(y) = 0 \quad (7)$
I	$s(y) = \frac{s_m\lambda_1P \cosh(\lambda_1y)}{\tau_m b_f \sinh(\lambda_1\ell)} \quad (8)$
	$\tau(y) = \frac{\lambda_1P \cosh(\lambda_1y)}{b_f \sinh(\lambda_1\ell)} \quad (8)$
	$\sigma(y) = \frac{P \sinh(\lambda_1y)}{t_f b_f \sinh(\lambda_1\ell)} \quad (9)$
	$\begin{cases} \frac{d^2s(y)}{dy^2} - \lambda_1^2s(y) = 0, (0 \leq s \leq s_m) \\ \frac{d^2s(y)}{dy^2} + \lambda_3^2s(y) = \lambda_2^2(s_f - \mu s_m), (s_m \leq s \leq s_f) \end{cases} \quad (10)$
	Solution for $s_m \leq s \leq s_f$, also $\ell - a \leq y \leq \ell$
II	$s(y) = (s_f - s_m) \left[\frac{\lambda_2}{\lambda_1\omega} \tanh[\lambda_1(\ell - a)] \sin[\lambda_3(y - \ell + a)] - \frac{\cos[\lambda_3(y - \ell + a)]}{1 - \mu} \right] + \frac{s_f - \mu s_m}{1 - \mu} \quad (11)$
	$\tau(y) = -\tau_m \left[\frac{\lambda_3}{\lambda_1} \sin[\lambda_3(y - \ell + a)] \tanh[\lambda_1(\ell - a)] - \cos[\lambda_3(y - \ell + a)] \right] \quad (12)$
	$\sigma(y) = \frac{\tau_m}{t_f \lambda_3} \left[\frac{\lambda_3}{\lambda_1} \cos[\lambda_3(y - \ell + a)] \tanh[\lambda_1(\ell - a)] + \sin[\lambda_3(y - \ell + a)] \right] \quad (13)$
	$\begin{cases} \frac{d^2s(y)}{dy^2} - \lambda_1^2s(y) = 0, (0 \leq s \leq s_m) \\ \frac{d^2s(y)}{dy^2} + \lambda_3^2s(y) = \lambda_2^2(s_f - \mu s_m), (s_m \leq s \leq s_f) \\ \frac{d^2s(y)}{dy^2} = \lambda^2\mu s_f, (s \geq s_f) \end{cases} \quad (14)$
	Solution for $s \geq s_f$, also $l_{eff} \leq y \leq \ell$
III	$s(y) = \frac{s_f}{2} \left\{ 2 + \mu\lambda^2(y - l_{eff})^2 + 2\lambda^2 \left[\frac{\sin(\lambda_3 a_d)}{\lambda_3} + \frac{\cos(\lambda_3 a_d) \tanh(\lambda_1 l_1)}{\lambda_1} \right] (y - l_{eff}) \right\} \quad (15)$
	$\tau(y) = \mu\tau_m \quad (16)$
	$\sigma(y) = \frac{\tau_m}{t_f} \left[\mu(y - l_{eff}) + \frac{\sin(\lambda_3 a_d)}{\lambda_3} + \frac{\cos(\lambda_3 a_d) \tanh(\lambda_1 l_1)}{\lambda_1} \right] \quad (17)$
	$\begin{cases} \frac{d^2s(y)}{dy^2} + \lambda_3^2s(y) = \lambda_2^2(s_f - \mu s_m), (s_m \leq s \leq s_f) \\ \frac{d^2s(y)}{dy^2} = \lambda^2\mu s_f, (s \geq s_f) \end{cases} \quad (18)$
	Solution for $s \geq s_f$, also $a_1 \leq y \leq \ell$
IV	$s(y) = s_f + \frac{s_f}{2} \mu\lambda^2(y - a_1)^2 + \frac{\mu\lambda_2(s_f - s_m)(y - a_1)}{\omega} \tanh(\lambda_3 a_1) \quad (19)$
	$\tau(y) = \mu\tau_m \quad (20)$
	$\sigma(y) = \frac{2\mu\tau_m}{t_f \lambda^2 s_f} \left[\lambda^2 s_f (y - a_1) + \frac{\lambda_2(s_f - s_m)}{\omega} \tanh(\lambda_3 a_1) \right] \quad (21)$
	$\frac{d^2s(y)}{dy^2} = \lambda^2\mu s_f, (s \geq s_f) \quad (22)$
V	$\tau(y) = \mu\tau_m \quad (23)$
	$\sigma(y) = \frac{\mu\tau_m y}{t_f} \quad (24)$

In Table 1, note that a is the softening length for the elastic–softening stage and the elastic–softening–debonding stage (see Figure 2), and a_1 is the softening length for the softening–debonding stage. The following expressions

were used to simplify the equations in Table 1: $\omega = \sqrt{1 - \mu}$, $\lambda_1 = \sqrt{\tau_m / (s_m E_f t_f)}$, $\lambda_2 = \sqrt{\tau_m / [(s_f - s_m) E_f t_f]}$, and $\lambda_3 = \lambda_2 \omega$.

The elastic stage ends when the shear stress reaches the bond shear strength τ_m at a slip of s_m at $y = \ell$ [Figure 2 (c), and point A in Figure 1]. The applied load at the initiation of interface softening (also referred to as the load at the end of the elastic stage) P_1 is:

$$P_1 = (1/\lambda_1)\tau_m b_f \tanh(\lambda_1 \ell) \quad (25)$$

The bonded length needed to provide a total resistance equal to 97% of the applied load for a joint with an infinite bonded length, referred to as the elastic effective bond length $l_{eff,1}$ (Yuan et al. 2004), is:

$$l_{eff,1} = 2/\lambda_1 \quad (26)$$

The debonding load P_{deb} is obtained when $s(\ell) = s_f$ for the elastic–softening stage:

$$P_{deb} = (b_f \tau_m / \lambda_3) [(\lambda_3 / \lambda_1) \cos(\lambda_3 a_d) \tanh[\lambda_1 (\ell - a_d)] + \sin(\lambda_3 a_d)] \quad (27)$$

where a_d is determined by $s(\ell) = s_f$, which gives $a_d = (1/\lambda_3) \arcsin \left[\sqrt{s_f - s_m} \left(\sqrt{s_f - \mu s_m - \mu^2 (s_f - s_m)} - \mu \omega \sqrt{s_m} \right) / (s_f - \mu s_m) \right]$.

It should be noted that a_d does not depend on ℓ , therefore, a_d is a constant length and is determined by the parameters in the trilinear bond-slip model.

An estimation of the effective bond length l_{eff} can be obtained by adding a_d to $l_{eff,1}$:

$$l_{eff} = a_d + l_{eff,1} \quad (28)$$

It should be noted that this formulation is similar the one provided in (Carozzi et al. 2016) and does not always provide a value of effective bond length that is consistent with the value provided by the procedure proposed by D'Antino et al. (2018).

For long bonded lengths, it could be assumed that $\tanh[\lambda_1 (\ell - a_d)] \approx 1$. Then Eq. 27 can be rewritten as:

$$P_{deb} = \frac{b_f \tau_m}{\lambda_3} \left[\frac{\lambda_3}{\lambda_1} \cos(\lambda_3 a_d) + \sin(\lambda_3 a_d) \right] \quad (29)$$

The peak load P^* becomes:

$$P^* = b_f \tau_m \left[\mu d_u + \frac{\sin(\lambda_3 a_d)}{\lambda_3} + \frac{1}{\lambda_1} \cos(\lambda_3 a_d) \tanh(\lambda_1 l_1) \right] \quad (30)$$

where $d_u = \ell - a_d - (1/\lambda_1) \operatorname{arctanh}(\sqrt{1 - \mu / \cos(\lambda_3 a_d)})$.

For long bonded lengths, assuming $\tanh(\lambda_1 l_1) \approx 1$, the difference between the peak load and the debonding load can be expressed as:

$$P^* - P_{deb} = \mu \tau_m b_f d_u \quad (31)$$

Model Validation

In this section, values of the effective bond length, debonding load, and peak load determined from the analytical solution are compared with those determined from experimental results of six single-lap shear tests of PBO FRCM-concrete joints tested by Carloni et al. (2014). The specimens included in the comparison are listed in Table 2, and details of the experimental campaign can be found in D'Antino et al. (2014) and Carloni et al. (2014). A fracture mechanics approach based on the fiber strain profiles obtained from strain gauges mounted to the

central fiber bundle along the composite bonded length was used to determine the effective bond length l_{eff} and the debonding load P_{deb} for each specimen (D'Antino et al. 2014; Carloni et al. 2014). The experimentally determined values are reported with the subscript "e" in Table 2.

To apply the analytical solution, parameters of the $\tau(s)$ relationship associated with the matrix-fiber interface are required. An average $\tau(s)$ relationship was obtained for the six specimens listed in Table 2 by differentiation and integration of the fitted strain profiles for each specimen, and then averaging the values of shear stress corresponding to the same slip value obtained (D'Antino et al. 2018). The resulting average $\tau(s)$ relationship is referred to as CML_0 in (D'Antino et al. 2018), and the fracture energy of the matrix-fiber interface obtained from CML_0 was $G_F = 0.481$ N/mm. The continuous curve given by CML_0 can be approximated as a trilinear model with the same peak shear stress and corresponding slip, and the same fracture energy G_F , which is referred to as CML_3 in (D'Antino et al. 2018). The resulting values of the matrix-fiber interface, considering the total shear stress of two contact surfaces, s_m , s_f , τ_f , and τ_m were 0.18 mm, 1.17 mm, 0.12 MPa, and 1.54 MPa, respectively, and were used to employ the analytical solution in Table 1. The analytically determined values are reported with the subscript "a" in Table 2.

Results in Table 2 show the analytically determined values are in reasonable agreement with the experimentally determined values. The average value of the ratio $l_{eff,a}/l_{eff,e}$ is 0.88 with a CoV of 0.09. The average value of the ratio $P_{deb,a}/P_{deb,e}$ is 1.24 with a CoV of 0.22. The average value of the ratio P_a^*/P_e^* is 1.17 with a CoV of 0.22.

Table 2: Comparison between the analytical solution and experimental results

Specimen	Carloni et al. (2014)			CML_3			Comparison CML_3		
	$l_{eff,e}$ (mm)	$P_{deb,e}$ (kN)	P_e^* (kN)	$l_{eff,a}$ (mm)	$P_{deb,a}$ (kN)	P_a^* (kN)	$\frac{l_{eff,e}}{l_{eff}}$	$\frac{P_{deb,a}}{P_{deb,e}}$	$\frac{P_a^*}{P_e^*}$
DS_330_43_S_2 ^T	280	4.17	5.12	223	4.80	5.12	0.80	1.15	1.00
DS_330_43_S_3 ^T	280	2.71	3.03	223	4.80	5.12	0.80	1.77	1.69
DS_330_60_S_2	225	6.65	7.31	223	6.73	7.17	0.99	1.01	0.98
DS_330_60_S_3	240	5.75	6.55	223	6.73	7.17	0.93	1.17	1.09
DS_450_60_S_1	255	5.70	6.63	223	6.73	7.67	0.87	1.18	1.16
DS_450_60_S_2	255	5.77	6.86	223	6.73	7.67	0.87	1.17	1.12
Average							0.88	1.24	1.17
CoV							0.09	0.22	0.22

CONCLUSIONS

In this paper, a closed-form analytical solution has been presented to predict the entire debonding process of FRCM-concrete joints. To obtain this solution, a trilinear bond-slip model is employed. The solution provides closed-form expressions for the interfacial shear stress distribution and load–displacement response for the different loading stages. As a result, the solution provides a rigorous and complete theoretical basis for understanding the full-range load–displacement behavior of FRCM-concrete joints.

REFERENCES

- M. Y. Alabdulhady, L.H. Sneed, C. Carloni. (2017). Torsional behavior of RC beams strengthened with PBO-FRCM composite—An experimental study. *Engineering Structures*, 136, 393-405.
- O. Awani, A. El Refai, T. El-Maaddawy. (2015). Bond characteristics of carbon fabric-reinforced cementitious matrix in double shear tests. *Construction and Building Materials*, 101, 39-49.
- R. Azam, K. Soudki. (2014). FRCM strengthening of shear-critical RC beams. *Journal of Composites for Construction*, 18(5), 04014012.
- L. Bisby, T. Stratford, C. Hart, S. Farren. (2013). Fire performance of well-anchored TRM, FRCM and FRP flexural strengthening systems. *Advanced Composites in Construction*.
- T. Blanksvärd, B. Täljsten, A. Carolin. (2009). Shear strengthening of concrete structures with the use of mineral-based composites. *Journal of Composites for Construction*, 13(1), 25-34.

- D.A. Bournas, P.V. Lontou, C.G. Papanicolaou, T.C. Triantafillou. (2007). Textile-reinforced mortar versus fiber-reinforced polymer confinement in reinforced concrete columns. *ACI Structural Journal*, 104(6), 740.
- C. Carloni, T. D'Antino, L.H. Sneed, C. Pellegrino. (2014). Role of the matrix layers in the stress-transfer mechanism of FRCM composites bonded to a concrete substrate. *Journal of Engineering Mechanics*, 141(6), 04014165.
- C. Carloni, S. Verre, L.H. Sneed, L. Ombres. (2017). Loading rate effect on the debonding phenomenon in fiber reinforced cementitious matrix-concrete joints. *Composites Part B: Engineering*, 108, 301-314.
- F.G. Carozzi, P. Colombi, G. Fava, C. Poggi. (2016). A cohesive interface crack model for the matrix–textile debonding in FRCM composites. *Composite Structures*, 143, 230-241.
- T. D'Antino, C. Carloni, L.H. Sneed, C. Pellegrino. (2014). Matrix–fiber bond behavior in PBO FRCM composites: A fracture mechanics approach. *Engineering Fracture Mechanics*, 117, 94-111.
- T. D'Antino, C. Pellegrino, C., Carloni, L.H. Sneed, G. Giacomini, G. (2015a). Experimental analysis of the bond behavior of glass, carbon, and steel FRCM composites. *Key Engineering Materials*, 624, 371-378.
- T. D'Antino, L.H. Sneed, C., Carloni, C. Pellegrino. (2015b). Influence of the substrate characteristics on the bond behavior of PBO FRCM-concrete joints. *Construction and Building Materials*, 101, 838-850.
- T. D'Antino, L.H. Sneed, L. H., C. Carloni, C., Pellegrino. (2016). Effect of the inherent eccentricity in single-lap direct-shear tests of PBO FRCM-concrete joints. *Composite Structures*, 142, 117-129.
- T. D'Antino, P. Colombi, C. Carloni, L.H. Sneed. (2018). Estimation of a matrix-fiber interface cohesive material law in FRCM-concrete joints. *Composite Structures*, 193, 103-112.
- A. D'Ambrisi, F. Focacci. (2011). Flexural strengthening of RC beams with cement-based composites. *Journal of Composites for Construction*, 15(5), 707-720.
- A. D'Ambrisi, L. Feo, F. Focacci. (2012). Bond-slip relations for PBO-FRCM materials externally bonded to concrete. *Composites Part B: Engineering*, 43(8), 2938-2949.
- F. Focacci, T. D'Antino, C. Carloni, L.H. Sneed, C. Pellegrino, C. (2017). An indirect method to calibrate the interfacial cohesive material law for FRCM-concrete joints. *Materials and Design*, 128, 206-217.
- J.H. Gonzalez-Libreros, L.H. Sneed, T. D'Antino, C. Pellegrino. (2017). Behavior of RC beams strengthened in shear with FRP and FRCM composites. *Engineering Structures*, 150, 830-842.
- L.C. Hollaway. (2010). A review of the present and future utilisation of FRP composites in the civil infrastructure with reference to their important in-service properties: review article. *Construction and Building Materials*, 24(12):2419–45.
- X.Z. Lu, J.G. Teng, L.P. Ye, J.J. Jiang. (2005). Bond–slip models for FRP sheets/plates bonded to concrete. *Engineering Structures*, 27(6), 920-937.
- S.M. Raoof, L.N. Koutas, D.A. Bournas. (2016). Bond between textile-reinforced mortar (TRM) and concrete substrates: Experimental investigation. *Composites Part B: Engineering*, 98, 350-361.
- S.M. Raoof, D.A. Bournas. (2017). TRM versus FRP in flexural strengthening of RC beams: Behaviour at high temperatures. *Construction and Building Materials*, 154, 424-437.
- J.G. Teng, J.F. Chen, S.T. Smith, L. Lam. FRP-Strengthened RC Structures. UK: John Wiley & Sons; 2002.
- T. Trapko. (2013). The effect of high temperature on the performance of CFRP and FRCM confined concrete elements. *Composites Part B: Engineering*, 54, 138-145.
- H. Yuan, J.G. Teng, R. Seracino, Z.S. Wu, J. Yao. (2004). Full-range behavior of FRP-to-concrete bonded joints. *Engineering Structures*, 26(5), 553-565.



DURABILITY OF TEXTILE REINFORCED MORTAR (TRM) SYSTEMS

Francesca Giulia Carozzi^{1*}, Pierluigi Colombi¹, Tommaso D'Antino¹, Carlo Poggi¹

¹ Politecnico di Milano, Department of Architecture, Built Environment, and Construction Engineering, Milan, Italy, Email: francescagiulia.carozzi@polimi.it

ABSTRACT

Textile Reinforced Mortar (TRM) materials represent an innovative strengthening technique particularly used in the retrofitting of masonry structures. These systems are composed of a fiber net embedded in an inorganic matrix (lime or cementitious mortar) sometimes enriched with short fibers.

The knowledge of the durability of these composite materials is of primary importance in order to calibrate design guidelines and to evaluate the design life of the strengthened structure. In the literature, only few experimental works are available, and only a limited number of systems and aggressive environments are considered.

In this paper, the preliminary results of an ongoing extensive experimental campaign at the Material Testing Laboratory of the Politecnico di Milano are described. A series of TRM (also pre-cracked) coupons were subjected to freeze and thaw cycles. After the conditioning, the samples were subjected to tensile tests and the results were compared with those obtained by tests performed on control specimens. In particular, the slopes of the different phases of the stress-strain curves and the stress reached at the onset of cracking and at collapse are compared. Different materials were analyzed, composed of lime or cementitious mortars and glass, PBO, and carbon fibers. The experimental results obtained and the analysis reported could represent an important contribution in the calibration of environmental coefficient for design procedures.

KEYWORDS

New composite materials, systems and strengthening techniques; Experimental study; Durability; Long-term performance; FRC and cement composite materials; TRM systems

INTRODUCTION

Textile Reinforced Mortar (TRM) materials represent an innovative retrofitting technique frequently used for the reinforcement of masonry elements. These systems are composed of a bare textile made of different fibers (glass, carbon, PBO, steel, basalt) applied with an inorganic matrix that could be a lime or a cementitious mortar, in some cases enriched with short fibers. These materials present many advantages with respect to Fiber Reinforced Polymer (FRP) systems in terms of reversibility, compatibility with masonry substrate, vapour permeability, and resistance to (relatively) high temperature.

Some of the most important issues concerning a retrofitting material applied to a structure are the durability and the resistance of the systems to different aggressive environment. This field should include both the study of the mechanical properties of the reinforcement subjected to artificial aging and the bond properties between the system and the substrate.

A consolidate knowledge [Sciolti et al. (2012); Rivera et al, (2002); Cromwell at al. (2011); Wang et al (2017)] and national guidelines for the evaluation of durability properties of FRP materials are available. However, less attention was devoted in the literature to durability issues of TRM materials.

Most of the research works available in the literature are referred to the exposure of textiles to alkaline environment. This choice is due to the presence of the mortar in which the textile is embedded. In Micelli et al. (2017), an extensive experimental research is described, different types of dry and impregnated fibers were subjected to different ageing protocols in alkaline solution, and then tested under tensile load. The results showed that the cementitious environment results more aggressive respect to the lime one. E-glass and basalt textiles showed a significant decrease of the mechanical properties due to the exposure to alkaline environment, whereas carbon and steel materials showed limited vulnerability to the alkaline environment. A significant deterioration of the E-glass textile subjected to alkaline environment was highlighted also by De Santis et al. (2017), whereas aramid fibers and AR-glass textiles presented a lower decrease of the mechanical properties. This paper demonstrated also that an alkali-resistant coating might be insufficient by itself to ensure the long-term performance of the system. Nobili (2016) tested FRCM systems with glass textiles subjected to saline and alkaline environment. In this case both matrix and textile were influenced by the treatment, the matrix degradation caused a different failure mode that turned from fibers rupture to slippage at the textile-matrix interface. Arboleda et al. (2014) described an experimental study conducted on FRCM materials with PBO and carbon fibers. The samples were subjected to freeze and thaw cycles, seawater, and alkaline environments. The test results were compared

with those obtained by control samples tested at 28 days. The comparison showed that there was no significant degradation and a strength improvement was noted probably due to the continued hydration of the mortar after 28 days.

In this paper, the preliminary results of an ongoing extensive experimental project developed at the Material Testing Laboratory of the Politecnico di Milano are described. The project involves the execution of tensile tests on TRM systems subjected to different artificial ageing treatments, namely sea water, alkaline environment, and freeze and thaw cycles.

EXPERIMENTAL PROGRAM

The TRM systems were subjected to freeze and thaw cycles that simulated an artificial aging. After the treatment, the behaviour of the inorganic matrix, the adhesion properties between mortar and textile and, if present, the damage of the textile were analyzed. The cycles properties were the same described by AC434 and Italian guideline for the qualification of FRP materials: one week at 38 °C and 98% humidity and twenty freeze-thaw cycles consisting of four hours at -18 °C followed by 12 hours at 38 °C and 98% humidity.

Materials

TRM systems composed by different fiber textiles and inorganic matrices were considered. Namely, a PBO and a carbon (C) textile applied with a cementitious matrix and a glass (G) fiber textile applied with a lime mortar were studied.

The PBO textile is unbalanced, with 10 mm and 20 mm spaced yarns in longitudinal and transversal direction, respectively. The nominal thickness in the two fiber directions is 0.046 mm and 0.011 mm, respectively. In Carozzi et al. (2015), a series of tensile tests was performed on PBO dry longitudinal yarns to evaluate the mechanical properties of this material. The average elastic modulus obtained was equal to 216 GPa and the maximum stress, obtained with tests performed on strips, was equal to 3397 MPa.

The carbon textile is a balanced net with yarns disposed in two orthogonal directions at a nominal space of 10 mm. The equivalent thickness is equal to 0.047 mm in both directions. The elastic modulus and tensile strength, obtained in Carozzi et al. (2015), were equal to 203 GPa and 1944 MPa, respectively.

The glass textile is a balanced net with yarns disposed at a nominal space of 20 mm and with an equivalent thickness of 0.048 mm in both directions. The average mechanical properties were described in Carozzi et al. (2018). The tensile strength was equal to 1442 MPa and the elastic modulus was 75.4 GPa. The fiber textiles are represented in Figure 1.

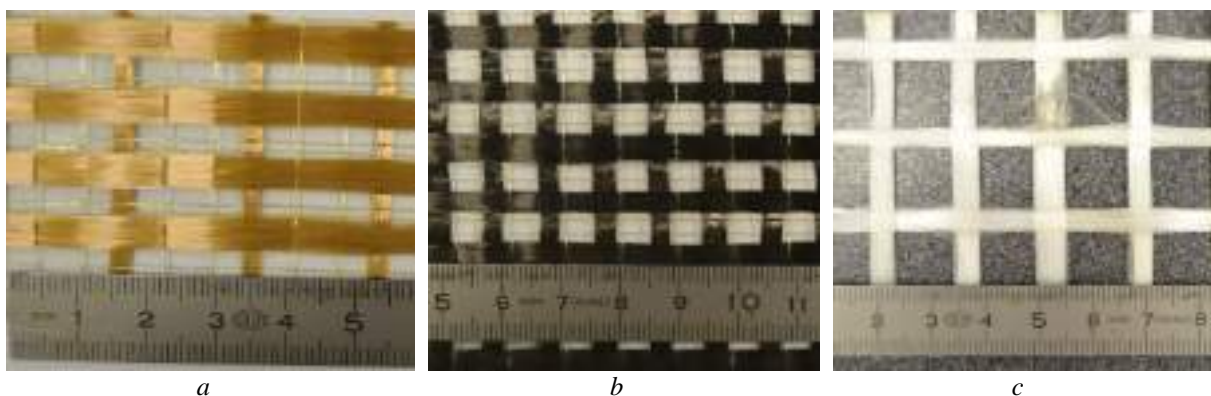


Figure 1: Fiber textiles geometry: a) PBO; b) carbon; c) glass

The samples were composed of two layers of mortar and one layer of textile. The total nominal thickness is equal to 10 mm. The nominal length was 400 mm for all specimens whereas the width was equal to 40 mm, which corresponds to four yarns, for PBO-TRM and C-TRM samples and equal to 50 mm for G-TRM samples, which allowed for including 3 yarns.

For PBO-TRM samples three casting were prepared (namely PBO-TRM_1; PBO-TRM_2; PBO-TRM_3). Both the first and second casting included six specimens, three were subjected to the freeze-thaw cycles and three were tested without any treatment as control specimens. The two groups were tested at the same time, in order to exclude differences in the mechanical properties due to the different age of the inorganic matrix. PBO-TRM_3 specimens were tested after being cured for two years. Some PBO-TRM_3 specimens were tested previously and the results were illustrated in Carozzi et al. (2015). Five samples were pre-cracked before the freeze-thaw cycles. Due to the pre-cracking of the samples, the mortar did not contribute to the specimen initial stiffness (first phase). Therefore, for these specimens the un-cracked phase was not studied and the results obtained were compared with samples tested at a different time. To pre-crack the specimens the samples were subjected to tensile testing until the

complete cracking of the mortar. When the specimens were unloaded the cracks closed, but it is possible to assume that the humidity could easily penetrate and reach the textile.

The TRM systems with carbon textile (C-TRM) were the same investigated in Carozzi et al. (2015) and considered as control specimens. Seven samples were subjected to freeze-thaw cycles and four of them were pre-cracked as previously described. Nine tests were performed on TRM samples with glass textile (G-TRM): four samples were pre-cracked and subjected to the freeze-thaw cycles while five specimens were used as “control”.

In Table 1, the test matrix is showed and the number of tested specimens is reported for each configuration.

Table 1 – Number of samples tested

System	Freeze-thaw cycles		Control (un-cracked)
	un-cracked	Pre-cracked	
PBO-TRM_1	3	-	3
PBO-TRM_2	3	-	3
PBO-TRM_3	-	5	23*
C-TRM	3	4	10*
G-TRM	-	4	5

* described in Carozzi et al. (2015)

Test set-up and instrumentation

The tensile tests were performed according to De Santis et al. (2017). At the extremities of the samples two FRP tabs were bonded to guarantee a homogeneous stresses distribution in the sample and to avoid damage of the mortar in compression when the sample was clamped by the testing machine.

A testing machine with a load capacity of 100 kN was used under displacement control at a rate of 0.2 mm/min up to the beginning of the mortar cracking. After the cracking phase the speed was increased up to 0.5 mm/min. For the pre-cracked samples, the displacement rate was equal to 0.5 mm/min throughout the entire test.

An extensometer with a gauge length equal to 200 mm was applied in the central area of the samples to measure the longitudinal strain during the test. The test set-up is showed in Figure 2.

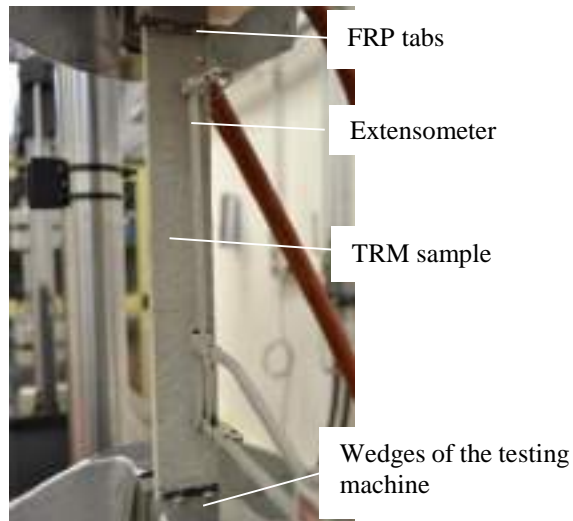


Figure 2 – Test set-up

Experimental results

In this section, the experimental results are shown. The results are described for each material analyzed (PBO-TRM, C-TRM, and G-TRM). Each sample was named cFT/FT_C_textile material_x_y, where “cFT” indicates the samples not subjected to the treatment (control specimen); “FT” indicates the samples subjected to the Freeze-Thaw cycles; “C” indicates the pre-cracked specimens; “x” (if present) indicated the number of the casting and “y” is the progressive number of the samples. Figure 3 shows the observed failure modes that are described in detail for each material.

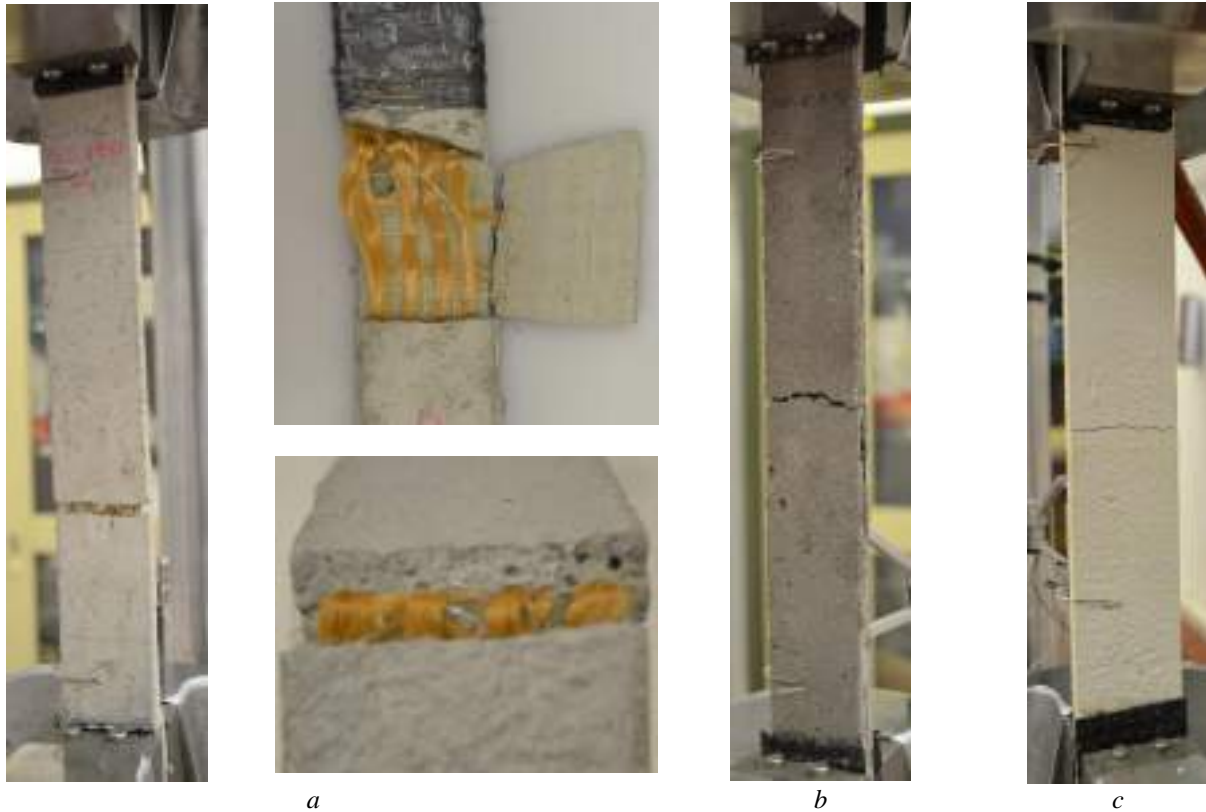


Figure 3: Failure modes of samples subjected to freeze-thaw cycles: a) PBO-TRM; b) C-TRM; c) G-TRM

PBO-TRM

Tensile tests on PBO-TRM_1 and 2 samples showed a tri-linear behaviour. In the first phase the mortar was uncracked and the slope of the stress-strain curve was mostly determined by the elastic modulus of the mortar (first phase). When the mortar tensile strength was reached (point T_1) the stiffness decreased significantly and the mortar cracked in different sections along the length of the sample (second phase). When the mortar was completely cracked the load was totally transferred to the textile and the slope of the stress-strain curve reflected the elastic modulus of the dry textile (third phase).

Table 2 and Figures 4a and 4b show the results and the stress-strain curves of the PBO-TRM_1 and PBO-TRM_2 series. All the parameters were computed with respect to the cross-sectional area of the fibers, except σ_{T1}^* and E_{T1}^* that were referred to the cross-sectional area of the matrix. The comparison between the aged samples and the control ones showed differences in the maximum stress and slope of the first and third phases. The properties of the mortar seem to improve during the freeze-thaw cycles, probably due to the continuous curing. The stress reached at the end of the first phase was equal to 126% of the control one, while the elastic modulus was equal to 114% (PBO-TRM_1) and to 131% (PBO-TRM_2). On the opposite, the ultimate stress and the stiffness of the third phase presented an evident decrement. The ultimate stress was equal to 80% (PBO-TRM_1) and 78% (PBO-TRM_2) of the control one, while the slope was equal to 79% (PBO-TRM_1) and 88% (PBO-TRM_2).

In Figure 3 the failure modes are shown. For all specimens, the matrix cracked in different sections and the collapse was caused by tensile failure of the fibers. The yarns failure was not located in a single section, but the single filaments broke in different points and a complete failure of the textile was not noted. As shown in Figure 3, the matrix was characterized by the presence of macro-pores that might be caused by the freeze-thaw cycles. Moreover, in some cases longitudinal cracks at mortar-textile interface occurred. It is possible to hypothesize that the adhesion between textile and matrix was reduced by the freeze-thaw cycles; and that the textile mechanical properties were affected by the absorption of the water penetrated in the mortar during the treatment.

PBO-TRM_3 was composed of a series of samples that were pre-cracked before being subjected to the freeze-thaw cycles. The results (Figure 4c) were compared with those described in Carozzi et al. (2015). Due to the large variability of these results, Table 2 reports the average, minimum, and the maximum values obtained. The results showed a clear reduction of the textile mechanical properties. The maximum strength was equal to 64% of the corresponding average strength of control specimens, and the slope of the third phase was equal to 93%.

Table 2 – Experimental results: PBO-TRM system

System	Sample	σ_{T1} [MPa]	σ_{T2} [MPa]	σ_u [MPa]	E_1 [GPa]	E_3 [GPa]	σ^*_{T1} [MPa]	E^*_1 [GPa]
PBO-TRM_1	FT_PBO_1_1	566.10	862.27	3540.16	1665	178.84	2.48	7.31
	FT_PBO_1_2	787.84	630.08	2373.85	1969	184.04	3.12	7.79
	FT_PBO_1_3	611.04	897.14	2561.74	1697	157.45	2.50	6.96
	Average	654.99	796.50	2825.25	1777	173.44	2.70	7.35
	cFT_PBO_1_1	481.44	750.66	3539.75	1459	203.55	2.20	6.67
	cFT_PBO_1_2	532.59	595.16	3206.22	1133	199.13	2.24	4.76
	cFT_PBO_1_3	469.83	767.81	3826.55	1879	250.62	1.99	7.95
	Average	494.62	704.55	3524.17	1490	217.77	2.14	6.46
PBO-TRM_2	FT_PBO_2_1	525.30	673.84	2751.37	1319	204.61	1.83	5.56
	FT_PBO_2_2	574.56	694.76	3063.24	2049	188.01	2.31	9.61
	FT_PBO_2_3	640.10	790.60	2538.00	1486	166.67	2.65	7.17
	Average	579.99	719.73	2784.20	1618	186.43	2.27	7.45
	cFT_PBO_2_1	435.39	464.02	3429.36	1431	203.23	2.04	6.71
	cFT_PBO_2_2	491.82	596.13	3991.04	1213	226.29	2.41	5.94
	cFT_PBO_2_3	549.92	960.00	3293.22	1074	204.92	2.63	5.14
	Average	492.38	673.38	3571.19	1239	211.48	2.36	5.93
PBO-TRM_3	FT_C_PBO_3_1	-	-	2328.41	-	206.24	-	-
	FT_C_PBO_3_2	-	-	2315.66	-	153.25	-	-
	FT_C_PBO_3_3	-	-	2011.36	-	211.94	-	-
	FT_C_PBO_3_4	-	-	1930.34	-	246.85	-	-
	FT_C_PBO_3_5	-	-	1984.73	-	185.32	-	-
	Average	-	-	2114.10	-	200.72	-	-
	cFT_PBO_3 Average	890.20	1099.61	3316.41	1181	215.80	3.65	4.84
	cFT_PBO_3 min. value	509.81	551.10	2485.10	902.61	189.24	2.09	3.70
	cFT_PBO_3 max value	1119.52	1640.61	4669.43	1612.84	250.03	5.49	6.64

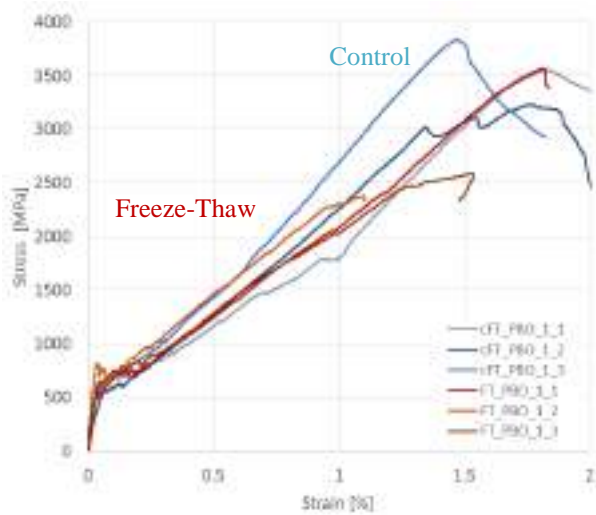


Figure 4a – Stress-strain behaviour: PBO-TRM_1;

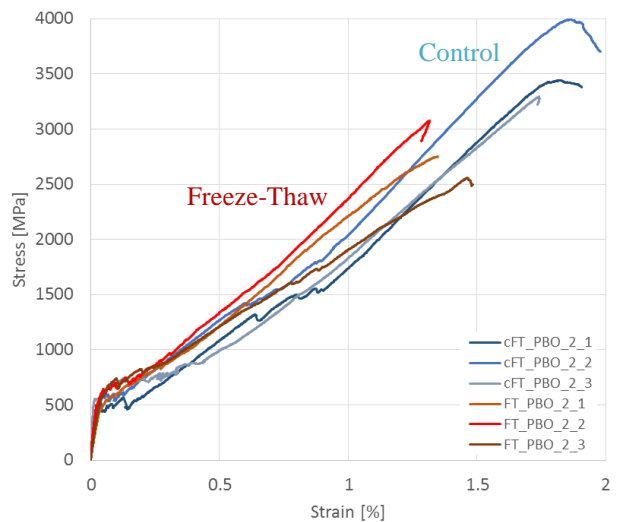


Figure 4b – Stress-strain behaviour: b) PBO-TRM_2;

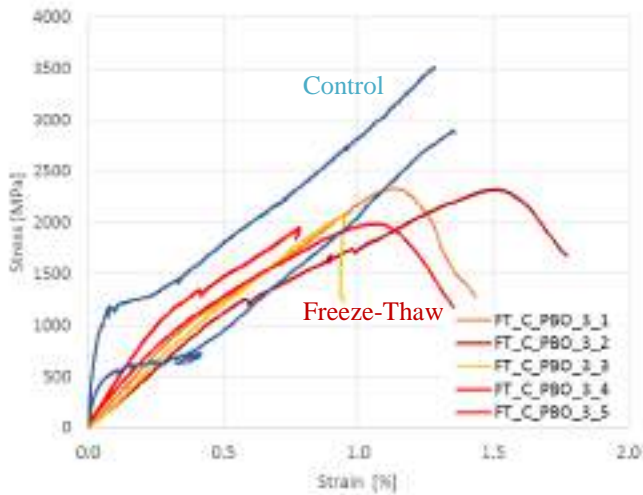


Figure 4c – Stress-strain behaviour: PBO-TRM₃

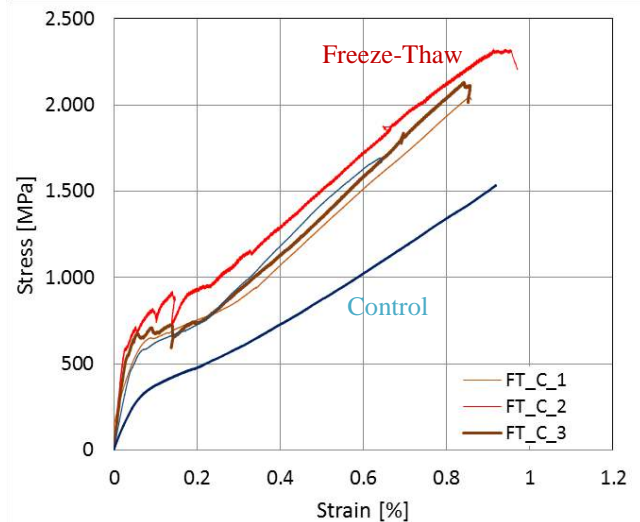


Figure 5 – Stress-strain behaviour: C-TRM

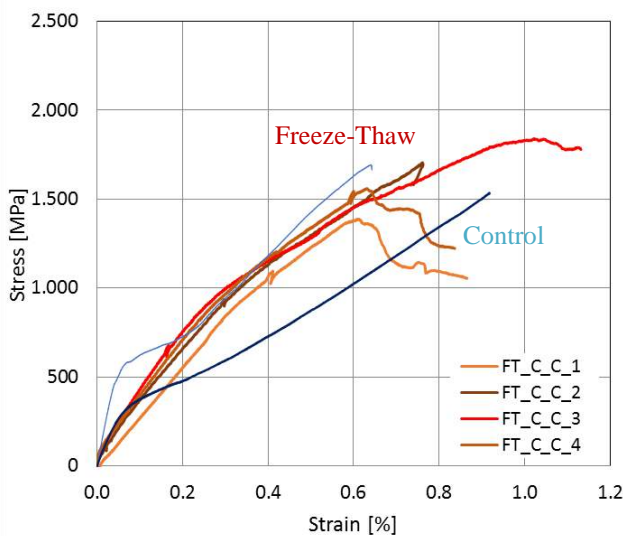


Figure 6 – Stress-strain behaviour: pre-cracked C-TRM

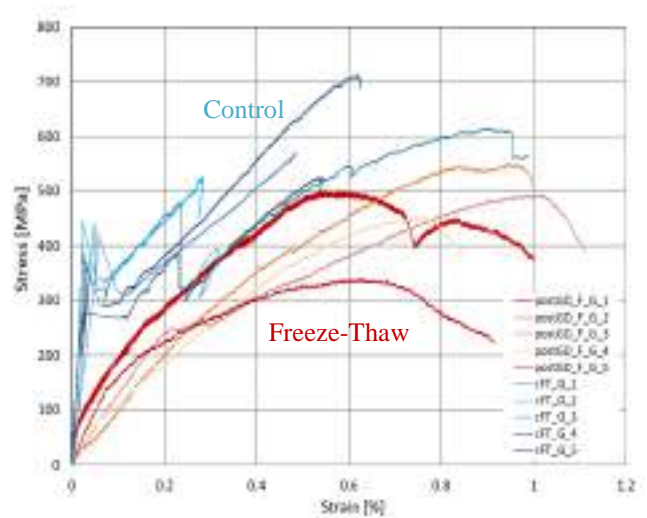


Figure 7 – Stress-strain behaviour: pre-cracked G-TRM

CARBON-TRM

C-TRM specimens presented a tri-linear stress-strain behaviour and a failure mode characterized by homogeneous cracking of the mortar and fibers tensile rupture. Figure 3b shows the typical failure mode.

In Table 3, the results of C-TRM systems are reported. Also in this case the results were compared with the ones described in Carozzi et al. (2015). The three tests performed on aged un-cracked samples showed an improvement of the mechanical properties. The stress reached at the end of the first phase and at collapse were equal to 118% and to 133% of the control ones, respectively. The slopes of the first and third phases were equal to 173% and 105%, respectively. The improvement of the mechanical properties in the first phase was already experienced and described for PBO-TRM specimens (see previous section). The mechanical properties of the third phase showed that the carbon textile was not influenced by the treatment. This phenomenon was verified also in the pre-cracked specimens, even if the slope of the third phase presented a decrement from 186 GPa to 158 GPa, probably due to a decrease of the adhesion properties between mortar and textile. In Figure 5 and Figure 6 the stress-strain curves are reported.

GLASS-TRM

The typical behaviour of G-TRM systems is described in Leone et al. (2017). The tests performed showed a tri-linear stress-strain behaviour in which the second phase was characterized by the opening of a single crack in the

mortar. Only pre-cracked samples were subjected to the ageing treatment, so the comparison with the unconditioned samples is referred only to the maximum load and the stiffness of the third phase. The mechanical properties were affected by the treatment: the ultimate stress and the stiffness of the third phase were equal to 84% and 75% of the control one, respectively. In Table 4 and Figure 7 the parameters obtained and the stress-strain curves are reported. The curves show a last phase with a decreasing stress due to the progressive failure of the glass filaments in the yarns. Figure 3c shows the typical failure mode characterized by the formation of only one crack in the middle of the specimen and by tensile failure of the yarns.

Table 3 – Experimental results: C-TRM system

System	Sample	σ_{T1} [MPa]	σ_{T2} [MPa]	σ_u [MPa]	E_1 [GPa]	E_3 [GPa]	σ_{T1}^* [MPa]	E_1^* [GPa]
C-TRM	FT_C_1	595.21	846.07	2033.47	1178	164.11	2.56	5.07
	FT_C_2	566.05	955.04	2300.48	2264	191.73	2.49	9.96
	FT_C_3	550.12	679.51	2174.21	2391	227.37	2.45	10.68
	Average	570.41	826.69	2169.16	1944.36	194.40	2.50	8.57
	FT_C_C_1	-	-	1705.25	-	166.39	-	-
	FT_C_C_2	-	-	1840.71	-	133.93	-	-
	FT_C_C_3	-	-	1559.49	-	190.44	-	-
	FT_C_C_4	-	-	1388.61	-	142.01	-	-
	Average	-	-	1623.51	-	158.19	-	-
	cFT_C Average	481.72	619.56	1492.02	1102	186.42	2.02	4.96
	cFT_C min. value	332.07	480.00	1031.91	802	136.10	1.39	3.37
	cFT_C max value	614.74	748.90	1994.68	1519	245.04	2.58	6.38

Table 4 - Experimental results: G-TRM system

System	Sample	σ_{T1} [MPa]	σ_{T2} [MPa]	σ_u [MPa]	E_1 [GPa]	E_3 [GPa]	σ_{T1}^* [MPa]	E_1^* [GPa]
G-TRM	FT_C_G_1	-	-	495.86	-	77.32	-	-
	FT_C_G_2	-	-	544.42	-	57.67	-	-
	FT_C_G_3	-	-	490.57	-	45.21	-	-
	FT_C_G_4	-	-	540.16	-	59.07	-	-
	Average	-	-	495.25	-	59.82	-	-
	cFT_G_1	436.92	368.02	609.95	993	76.92	2.42	5.53
	cFT_G_2	404.00	298.15	561.21	1034	69.18	2.01	3.41
	cFT_G_3	369.68	271.02	525.81	1068	85.43	1.93	6.29
	cFT_G_4	386.67	287.74	713.13	1574	78.46	2.12	9.76
	cFT_G_5	439.19	338.06	525.34	1328	86.34	2.41	8.99
	Average	407.29	312.56	587.05	1199	79.27	2.12	6.79

CONCLUSIONS

This paper describes the preliminary results of an extensive experimental campaign performed at the Material Testing Laboratory of the Politecnico di Milano to study the durability properties of different TRM materials and fiber textiles. The TRM systems were composed of PBO, carbon, and glass textiles impregnated with cementitious and lime mortars. The samples were subjected to freeze-thaw cycles and tested in tension to study the effect of ageing on the stress-strain behavior. In particular, the maximum stress and the stiffness of the first and third phases of the stress-strain curves were analyzed.

The treatment caused the absorption of water by the matrix and, during the freeze cycles, the water could freeze and modify the dimensions of the pores in the mortar. The effects of this treatment are related to the chemical properties of the matrix and to the dimensions of the aggregates or of the polymers, if present.

It was shown that the mechanical properties of the mortar increased after the treatment, whereas the fiber properties were reduced by the freeze-thaw cycles. This fiber properties reduction was particularly pronounced for PBO textiles, while carbon fibers were undamaged.

Due to the large variability in the experimental results and to the different aspect that should be considered, the results obtained represent only a first contribution to the study of the durability properties of TRM materials.

The ongoing project includes a large experimental campaign in which both TRM systems and dry textiles will be subjected to different ageing treatments. This project could represent an important contribution to the knowledge of the durability of these materials and to the calibration of environmental reduction factors for guideline procedures for the qualification of these systems.

ACKNOWLEDGMENTS

The research activities were performed at the Material Testing Laboratory of the Politecnico di Milano. The tests were carried out on specimens produced using reinforcing materials and mortars provided by Ruredil S.p.A. and TCS srl. Their support is gratefully acknowledged.

REFERENCES

- AC 434. Proposed acceptance criteria for masonry and concrete strengthening using fiber-reinforced cementitious matrix (FRCM) composite system (2013)
- D. Arboleda, S. Babaeidarabad, C. Hays, A. Nanni (2014). "Durability of Fabric Reinforced Cementitious Matrix (FRCM) composites". CICE 2014, Vancouver, Canada
- F.G. Carozzi, C. Poggi (2015). "Mechanical properties and debonding strength of Fabric Reinforced Cementitious Matrix (FRCM) systems for masonry strengthening. *Composites Part B*, 70: 215-230
- F.G. Carozzi, C. Poggi, E. Bertolesi, G. Milani (2018). Ancient masonry arches and vaults strengthened with TRM, SRG and FRP composites: Experimental evaluation. *Composite Structures*, 187: 466-480
- J.R. Cromwell, K.A. Harries, B.M. Shahrooz (2011) "Environmental durability of externally bonded FRP materials intended for repair of concrete structures". *Construction and Building Materials*, 25: 2528-2539
- S. De Santis, de Felice G. (2015). "Tensile behaviour and durability of mortar based strengthening systems with glass aramid textiles". *Key Engineering Materials*, 624: 346-353
- S. De Santis, F.G. Carozzi, G. de Felice, C. Poggi (2017). "Test methods for Textile Reinforce Mortar systems". *Composite Part B*, 127: 121-132
- Leone, M.A., Aiello, M.A., Balsamo, A., Carozzi, F.G., Ceroni, F., Corradi, M., Gams, M., Garbin, E., Gattesco, N., Krajewski, P., Mazzotti, C., Oliveira, D., Papanicolaou, C., Ranocchiai, G., Roscini, F., Saenger, D. (2017). "Glass fabric reinforced cementitious matrix: Tensile properties and bond performance on masonry substrate". *Composites Part B*, 127: 196-214
- Italian Guide Line: "Linea Guida per la identificazione, la qualificazione ed il controllo di accettazione di compositi fibrorinforzati a matrice polimerica (FRP) da utilizzarsi per il consolidamento strutturale di costruzioni esistenti" Consiglio Superiore dei Lavori Pubblici, 2015
- F. Micelli, M.A. Aiello (2017). Residual tensile strength of dry and impregnated reinforcement fibers after exposure to alkaline environments. *Composites Part B*. Article in Press
- A. Nobili (2016) "Durability assessment of impregnated Glass Fabric Reinforced Cementitious Matrix (GFRCM) composites in the alkaline and saline environments. *Construction and Building Materials*, 105: 465-471
- M.S. Sciolti, M.A. Aiello, M. Frigione (2012). "Influence of water on bond behavior between CFRP sheet and natural calcareous stones", *Composites Part B*, 43: 3329-3250
- J. Rivera, V.M. Karbhari (2002). "Cold-temperature and simultaneous aqueous environment related degradation of carbon/vinylester composites". *Composites Part B*, 33: 17-24
- Z. Wang, X.L. Zhao, R.K. Singh Raman, S. Al-Saadi (2017). "Durability study of interlaminar shear behaviour of basalt, glass and carbon fibre reinforced polymer bars in seawater sea sand and concrete environment. *Construction and Building Materials*, 156: 985-1004



STUDY OF THE MATRIX-FIBER BOND BEHAVIOR OF CARBON AND GLASS FRCM COMPOSITES

L. H. Sneed¹, T. D'Antino², J.H. Gonzalez-Libreros³, C. Carloni⁴, C. Pellegrino³

¹ Missouri University of Science and Technology, Department of Civil, Architectural and Environmental Engineering, 1401 North Pine St., Rolla, MO, 65409 USA, Email: sneedlh@mst.edu

² Politecnico di Milano, Department of Architecture, Built Environment, and Construction Engineering, Piazza Leonardo Da Vinci 33, 20133 Milan, Italy

³ University of Padova, Department of Civil, Environmental, and Architectural Engineering, Via F. Marzolo 9, 35131 Padua, Italy

⁴ University of Bologna, Department of Civil, Chemical, Environmental, and Materials Engineering, Viale Risorgimento 2, 40136 Bologna, Italy

ABSTRACT

Strengthening and retrofitting of existing reinforced concrete (RC) elements have been gaining interest in recent decades. Among the strengthening solutions available, fiber reinforced composites present certain advantages, such as high strength-to-weight ratio and low invasivity, which make them attractive in some applications. In particular, fiber reinforced polymer (FRP) composites have been successfully employed for bending and shear strengthening and for confinement of axially loaded elements, however they suffer from UV degradation, (relatively) high temperature exposure, and cannot be applied onto wet surfaces. To overcome these limitations, which are mostly related to the use of organic binders (usually epoxy resins), a new type of composite comprised of a fiber mesh embedded within an inorganic matrix has recently been developed and is referred to as fiber reinforced cementitious matrix (FRCM) composites. While FRCM composites have proven effective for strengthening RC elements, each specific composite presents a different behavior and needs to be properly characterized. In this paper, the results of single-lap direct-shear tests of carbon and glass FRCM-concrete joints are presented and discussed. Specimens with different composite bonded lengths were tested in an attempt to identify the effective bond length of each composite. The debonding stress experimentally obtained for carbon FRCM composites is also compared with that obtained through a fracture mechanics approach based on fiber strains measured on the same material using strain gauges bonded to the longitudinal fibers.

KEYWORDS

New composite materials, systems and strengthening techniques, Experimental study, characterization of FRCM materials/systems, bond and interfacial stress, FRCM, Effective bonded length.

INTRODUCTION

Studies on the bond behavior of FRP-concrete joints have shown that the effective bond length, l_{eff} , plays a key role on the load-carrying capacity of the system. As defined by Chen and Teng (2001), l_{eff} for FRP composites is the length beyond which an extension of the bonded length cannot increase the load carrying capacity. Therefore, a bonded length equal to or longer than l_{eff} is required to attain the full contribution of the FRP system. Hence, the assessment of the effective bond length is crucial for proper design of FRP-strengthened structures to avoid undesirable debonding failures, and to determine the actual load-carrying capacity of the composite.

For the case of FRCM composites, although research is still scarce, the existence of l_{eff} has also been reported (D'Antino et al. 2014a). According to their results, the relationship between the peak stress σ^* and the composite bonded length ℓ for polyparaphenylene benzobisoxazole (PBO) FRCM-concrete joints is comprised of an initial nonlinear branch for bonded lengths less than (or equal to) l_{eff} and a linearly increasing branch for bonded lengths longer than (or equal to) l_{eff} . When $\ell=l_{eff}$, the peak stress provided by the PBO FRCM-concrete joint is equal to the debonding stress σ_{deb} . It is important to note that for the case of FRCM composites, the increase in σ^* for bonded lengths longer than l_{eff} is associated with the presence of friction (interlocking) between the fibers and the cementitious matrix, which is not present in FRP composites. In fact, for FRP composites, σ^* remains constant after $\ell=l_{eff}$.

For FRP composites, the experimental database collected by D'Antino and Pellegrino (2014b) showed that values of l_{eff} are usually lower than 150 mm. According to the results presented by D'Antino et al. (2014a), a value of $l_{eff} = 260$ mm can be estimated for PBO FRCM-concrete joints, which is considerably higher than that of FRP composites. However, information regarding the value of l_{eff} for FRCM-concrete joints with different types of fibers is limited in the technical literature.

For concrete beam and slab flexural strengthening applications in which the composite is bonded to the flexural tension surface, it can be assumed that the provided bonded lengths will be longer than the effective bond length, and therefore either FRP or FRCM composites should be able to achieve values of peak stress equal to the debonding stress provided that plate end debonding is prevented (D'Antino and Triantafillou 2016). However, for the case of shear strengthening applications in which the composite is bonded to the side faces of the member (and potentially the bottom and/or top surface of the member), the length available to bond the composite is limited by the height (h) of the member, and the debonding stress might not be attained. This implies that to properly design a shear strengthening solution, the relationship between the peak stress in the composite and the bonded length needs to be fully established.

In this paper, the results of 31 single-lap direct-shear tests of carbon and glass FRCM-concrete joints are presented and discussed. The results of specimens with different composite bonded lengths, which were shown in part by D'Antino et al. (2016), were analyzed in an attempt to identify the effective bond length of each composite. The debonding stress experimentally obtained for carbon FRCM composites is also compared with that obtained through a fracture mechanics approach based on fiber strains measured in carbon FRCM-concrete joints with strain gauges applied to the embedded longitudinal fibers.

EXPERIMENTAL CAMPAIGN

Materials

FRCM composite comprised of carbon or glass fibers were investigated in this study. Carbon and glass fibers used in the experimental campaign presented in this paper were provided by a single manufacturer. The carbon fibers were comprised of fiber bundles spaced at 20 mm in the longitudinal and transversal directions with an overall areal weight ratio of 170 g/m². The glass fiber bundles were spaced at 25 mm in the longitudinal and transversal directions with an overall areal weight ratio of 250 g/m². The glass fiber bundles were coated while the carbon bundles did not have a surface treatment. The area of a single fiber bundle (A_b) of carbon and glass fiber, as reported by the manufacturer, were 0.94 mm² and 1.25 mm², respectively. Average values of tensile strength (σ^*) for carbon and glass fibers, performed on single fiber bundles with a length of 500 mm according to ASTM D3039 (2008), were 1260 MPa (4 specimens, CoV=0.033) and 716 MPa (5 specimens, CoV=0.029), respectively.

The carbon and glass FRCM composites were comprised of the same cementitious matrix. Three batches (named batch A, B, and C) were used at different times to cast the FRCM strips. A minimum of three 40 mm x 40 mm x 160 mm samples from each batch were cast and tested according to UNI EN 1015-11 (2007). Batch A had an average flexural strength, f_{flex} , and average compressive strength, r_{cm} , equal to 3.60 MPa and 16.70 MPa, respectively. For batch B, values of f_{flex} and r_{cm} were equal to 4.50 MPa and 17.10 MPa, whereas batch C had $f_{flex} = 3.90$ MPa and $r_{cm} = 11.40$ MPa.

The concrete blocks were made of normalweight concrete. Compressive tests according to UNI EN 12390-3 (2009) were carried out on six 150 mm cubes cast from the same batch used to cast the concrete blocks. The average cubic compressive strength was 59.3 MPa (CoV=0.150).

Experimental set-up

The bond behavior of carbon and glass FRCM-concrete specimens was investigated by means of push-pull single-lap direct-shear tests. A strip of FRCM composite, comprised of one layer of fiber net embedded within two 4 mm thick matrix layers, was applied onto concrete blocks with 125 mm x 125 mm cross-section and 500 mm length (see Figure 1a). The bonded width of the carbon FRCM composite, $b_1=60$ mm, was designed to include three longitudinal fiber bundles and to leave a distance of half the net spacing between the matrix edge and the external fiber bundle edge. For the case of glass FRCM composite, bonded width b_1 was equal to 55 mm, which included three longitudinal fiber bundles and was equal to the width of the fiber net. Four different bonded lengths (ℓ) were adopted (100 mm, 200 mm, 330 mm, and 450 mm). For three specimens, four strain gauges were attached to the central fiber bundle along the composite bonded length.

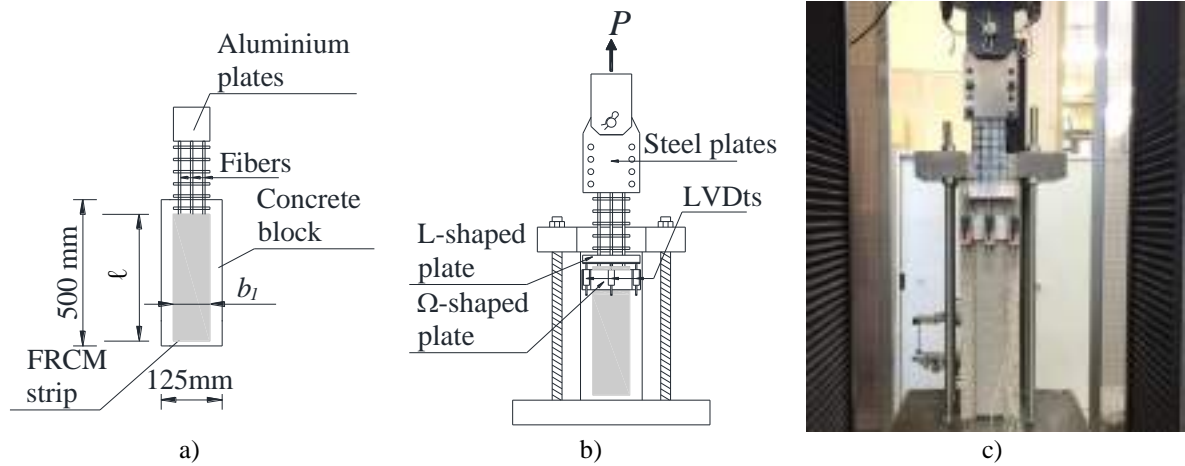


Figure 1: Single-lap direct-shear tests: a) Test specimen; b) Test set-up; c) Photo of specimen DS_CS170BL_450_60_3

The specimens were placed in a steel frame and restrained to avoid rotations and distortions (see Figure 1). The end of the strips were glued between two aluminum plates to avoid slippage of the fiber strip (see Figure 1a). Two through-bolted steel plates connected to the testing machine through a hinge joint were used to clamp the aluminum plates (see Figure 1b). Three LVDTs were mounted on the sides of a Ω -shaped aluminum plate bonded to the concrete block near to the loaded end of the composite (see Figure 1b and c). The LVDTs reacted off of a thin aluminum L-shaped plate bonded to the fibers at the loaded end. The two LVDTs placed on the sides of the Ω -shaped plate were used to measure the displacement of the fibers at the loaded end with respect to the concrete support (see Figure 1b and c). The average displacement measured by the two LVDTs on the sides of the composite corresponds to the global slip g of the textile if the substrate is considered rigid. The displacement measured by the central LVDT was used to control the test and was increased at a constant rate equal to 0.008 mm/s.

Specimens were named following the notation DS_FMK_X_Y_(S)_Z, where F corresponds to the type of fiber (C=carbon, G=glass), M is the type of matrix employed (Matrix S), K indicates the areal weight of the fiber nets in g/m^2 , X is the bonded length ℓ in mm (100 mm, 200 mm, 330 mm, and 450 mm), Y is the bonded width b_1 in mm (60 mm for carbon fibers, and 55 mm for glass fibers), S (if present) indicates that strain gauges were attached to the central fiber bundle, and Z is the specimen number. Seventeen single-lap direct-shear tests were conducted with carbon fibers, whereas 14 were conducted with glass fibers.

RESULTS AND DISCUSSION

Failure mode

For carbon FRCM-concrete joints, the failure was characterized by debonding of the fiber net from the embedding matrix and slippage between the fibers and the matrix. For glass FRCM-concrete joints with bonded length equal to 100 mm, fiber debonding at the matrix-fiber interface was also observed. However, for bonded lengths longer than 100 mm, with the exception of specimen DS_GS25_200_55_3 that showed a behavior similar to that observed for specimens with $\ell=100$ mm, rupture of one or more longitudinal fiber bundles near the loaded end was observed after the peak stress was attained.

Applied stress σ vs. global slip g response

Peak stress values σ^* , computed as $P^*/(nA_b)$, where P^* is the peak applied load and n is the number of longitudinal bundles ($n=3$ for carbon and glass fibers), are reported in Table 1 for each specimen tested. Additionally, the average value of σ^* for specimens with the same characteristics is provided in Table 1. It is highlighted that specimens DS_GS25_100_55_1 and DS_GS25_200_55_1 achieved values of σ^* that were significantly lower than other specimens with the same characteristics and were not used to compute the average value (Avg) of σ^* . In Table 1, the fiber exploitation ratios, calculated as σ^*/σ_t^* , are also included for each specimen.

Table 1: Results of single-lap direct-shear tests

Specimen	σ^* [MPa]	Avg σ^* [MPa]	σ^*/σ_t^*	Specimen	σ^* [MPa]	Avg σ^* [MPa]	σ^*/σ_t^*
DS_CS170BL_100_60_1	270		0.21	DS_CS17BL_450_60_S_3	601		0.48
DS_CS170BL_100_60_2	200	192	0.16	DS_GS250BA_100_55_1+	127		0.18
DS_CS170BL_100_60_3	150		0.12	DS_GS250BA_100_55_2	210	183	0.29
DS_CS170BL_100_60_4	150		0.12	DS_GS250BA_100_55_3	170		
DS_CS170BL_200_60_1	310		0.25	DS_GS250BA_100_55_4	170		0.24
DS_CS170BL_200_60_2	340	307	0.27	DS_GS250BA_200_55_1+	178		0.25
DS_CS170BL_200_60_3	270		0.21	DS_GS250BA_200_55_2	330	317	0.46
DS_CS170BL_330_60_1	560		0.44	DS_GS250BA_200_55_3	280		
DS_CS170BL_330_60_2	560	535	0.44	DS_GS250BA_200_55_4	340		0.47
DS_CS170BL_330_60_3	440		0.35	DS_GS250BA_330_55_1	470		0.66
DS_CS170BL_330_60_4	580		0.46	DS_GS250BA_330_55_2	460	487	0.64
DS_CS170BL_450_60_1	610		0.48	DS_GS250BA_330_55_3	530		
DS_CS170BL_450_60_2	660		0.52	DS_GS250BA_450_55_1	550		0.77
DS_CS170BL_450_60_3	550	619	0.44	DS_GS250BA_450_55_2	550	577	0.77
DS_CS17BL_450_60_S_1	665		0.53	DS_GS250BA_450_55_3	630		
DS_CS17BL_450_60_S_2	630		0.50				

+Results were disregarded for computing the average σ^*

The envelope of the applied stress σ vs. global slip g curves for specimens with carbon and glass fibers and $\ell=100$ mm, 200 mm, 330 mm, and 450 mm are shown in Figure 2a, b, c, and d, respectively. The applied stress σ is computed as $P/(nA_b)$, where P is the applied load, and the other variables were defined previously. It can be seen that for carbon FRCM-concrete joints σ initially increases linearly with the increase of g , which is followed by a non-linear branch until σ^* is attained. After this point, the applied stress decreases to an approximately constant value, which is associated with the friction between the fibers and the cementitious matrix. This behavior resembles the idealized load response proposed by D'Antino et al. (2014a) for specimens with PBO fibers. Specimens equipped with strain gauges are plotted in Figure 2d and showed a behavior consistent with that observed for other specimens with the same bonded length.

For glass FRCM-concrete joints, Figure 2 shows that the load response presents an initial linear behavior followed by a nonlinear branch. However, for specimens with $\ell=100$ mm, a long load plateau is observed after the nonlinear branch. The presence of such plateau indicates that the contribution of friction between fibers and matrix and between fiber filaments to the applied load is higher than the contribution of the matrix-fiber bond. For the specimens with longer bonded lengths, sudden drops in the load response after σ^* is attained were observed. These drops are associated with the rupture of the fiber bundles, as discussed previously.

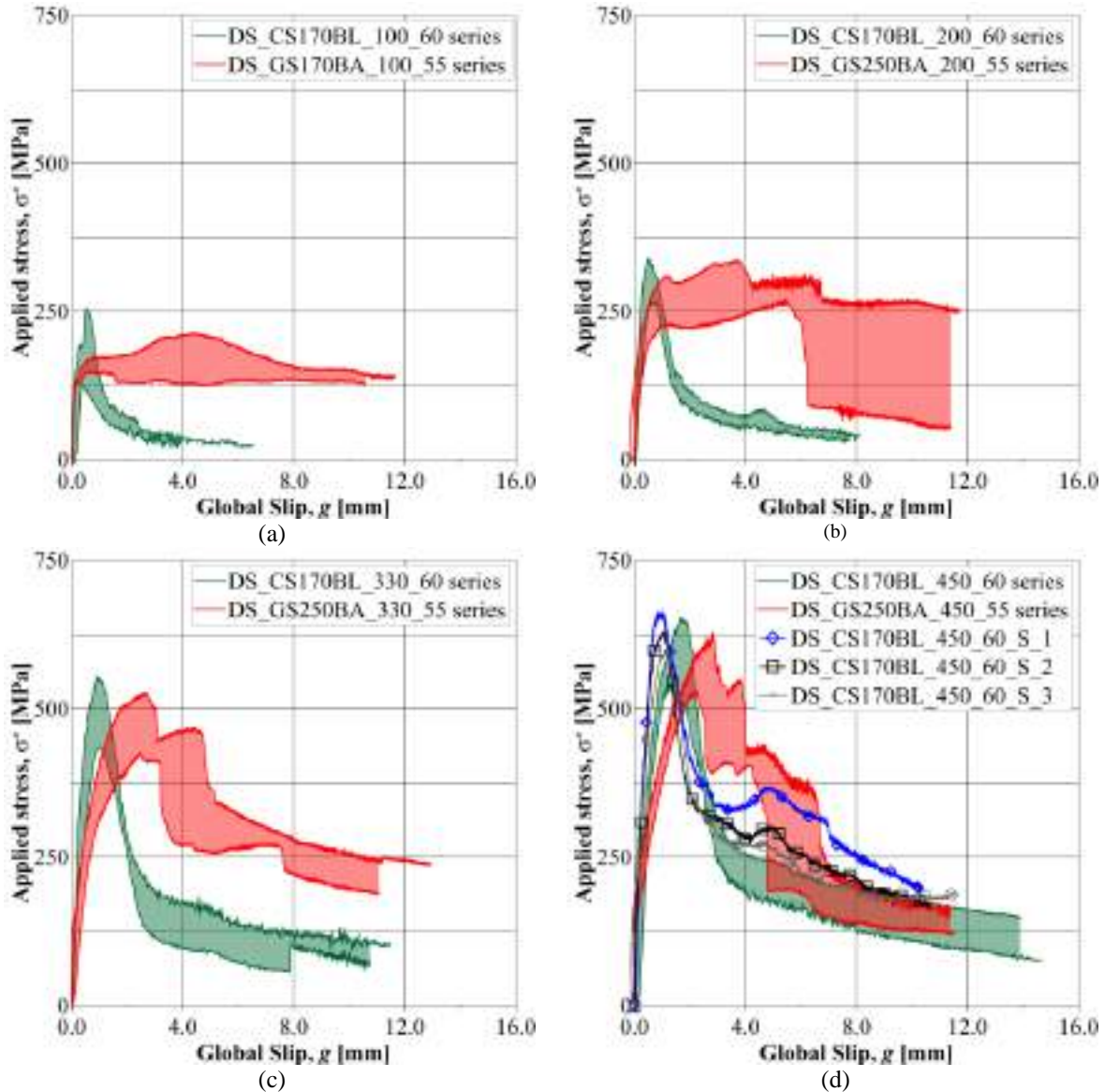


Figure 2: Applied stress, σ^* vs. global slip, g curve for specimens with a) $\ell=100$ mm; b) $\ell=200$ mm, c) $\ell=330$ mm, and d) $\ell=450$ mm

Fiber exploitation ratio

As shown in Table 1, higher fiber exploitation ratios are achieved for specimens with glass fibers, although values of σ^* are similar for both fiber types. In fact, for glass FRCM-concrete joints with $\ell=450$ mm, the average value of σ^*/σ_t^* is 0.81, with a maximum of 0.88 for specimen DS_GS250BA_450_55_3. For carbon FRCM-concrete joints, on the other hand, the average σ^*/σ_t^* for specimens with $\ell=450$ mm is 0.49, which is considerably lower than that observed for glass fibers. The higher fiber exploration ratio obtained for specimens with glass fibers may be associated with the coating of the fiber bundles, which provides a better matrix-fiber bond capacity.

Effective bond length

Results in Table 1 indicate that the peak stress σ^* increases with bonded length ℓ for both types of fiber. Values of σ^* are plotted against ℓ for carbon FRCM-concrete joints in Figure 3a and for glass FRCM-concrete joints in Figure 3b.

For carbon FRCM-concrete joints, lower increase rates of σ^* are achieved for values of ℓ equal to or longer than 330 mm (see Figure 3a). In fact, σ^* for specimens with $\ell=450$ mm is only slightly larger than the peak load for specimens with $\ell=330$ mm (average increase = 11.5%). This suggests that the length needed to fully establish the

stress transfer mechanism (i.e. the effective bond length) is less than 330 mm. However, further tests of FRMC-concrete joints with bonded length between 200 and 330 mm are needed to determine the value of the l_{eff} .

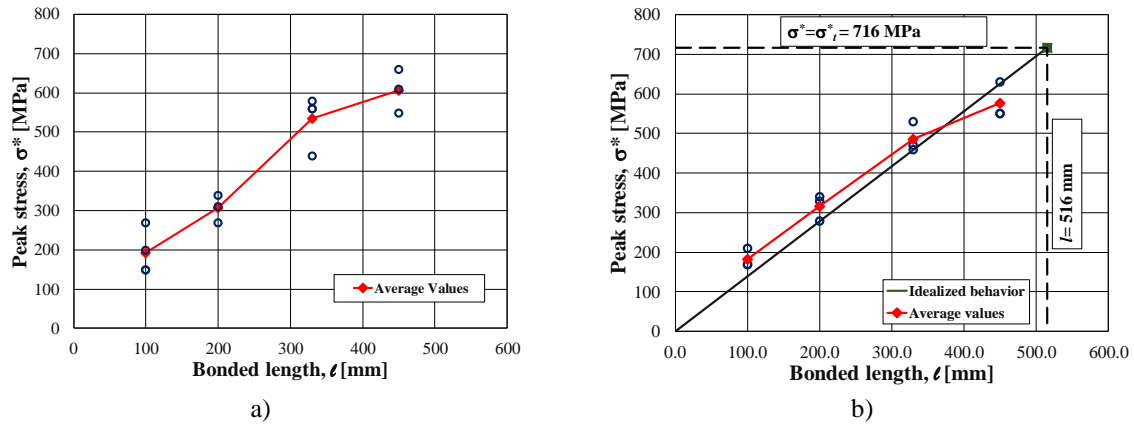


Figure 3: Peak stress σ^* vs. bonded length l for: a) carbon FRMC-concrete joints; b) glass FRMC-concrete joints

For glass FRMC-concrete joints, Figure 3b shows that σ^* increases linearly with respect to l . Considering that the maximum value of σ^* that can be reached by the fibers is equal to the fiber tensile stress (σ_t^*), and assuming a linear behavior of the σ^* vs. l response (see idealized behavior line in Figure 3b), the value of l associated with σ_t^* , i.e. value of l when $\sigma^* = \sigma_t^*$, can be obtained. A value of $l = 516$ mm is computed using the procedure described above. This value of l can be interpreted as an upper bound of the effective bond length for the FRMC composite with glass fibers used in the tests presented in this paper. However, it should be noted that an exploitation ratio equal to 1.0 might not be achieved due to stress concentrations or uneven distribution of stresses in adjacent bundles, which is particularly pronounced for specimens including a limited number of fiber bundles.

Debonding stress

Carbon FRMC-concrete joints described in this paper failed due to debonding at the matrix-fiber interface. After the onset of debonding, the applied stress further increased due to the presence of friction between the matrix and debonded fibers. Enforcing the equilibrium of an infinitesimal segment of fiber embedded into the matrix, a portion of a fiber bundle of infinitesimal length and applying the fracture mechanics approach described by D'Antino et al. (2014a), the longitudinal fiber strain ε can be employed to compute the shear stress τ and corresponding interfacial slip s :

$$\tau = \frac{1}{2} E_f \frac{A_b}{b^*} \frac{d\varepsilon}{dy} \quad (1)$$

$$s = \int_0^l \varepsilon dy \quad (2)$$

where b^* is the width of a single fiber bundle, equal to 5 mm for the carbon fiber net employed, y is the longitudinal coordinate along the bonded length ($y=0$ at the free end), and E_f is the fiber elastic modulus equal to 240 GPa, as declared by the manufacturer (G&P Intech 2016). It should be noted that Eq. 1 takes into account the presence of an internal (toward the concrete support) and an external (toward the external layer of matrix) matrix-fiber interface.

As a first attempt, the strain measured by the strain gauges attached to the central fiber bundle of specimens DS_CS170BL_450_60_S_1, 2, and 3 were differentiated and integrated in a discrete manner (D'Antino et al. 2014a):

$$\tau(y_i) = \frac{1}{4} E_f \frac{A_b}{b^*} [(\varepsilon_{i-1} - \varepsilon_i)(y_{i-1} - y_i) + (\varepsilon_i - \varepsilon_{i+1})(y_i - y_{i+1})] \quad (3)$$

$$s(y_i) = \sum_i^N \frac{1}{2} (\varepsilon_i + \varepsilon_{i+1})(y_i + y_{i+1}) \quad (4)$$

where y_i is the i -th coordinate of the strain gauge, ε_i the corresponding measured strain, and N is the number of strain gauges considered (equal to 4 in this paper). Combining the results of Eqs. 3 and 4 for the same y_i , the shear stress-slip relationship (i.e. cohesive material law, see Focacci et al. 2017) can be obtained. The area beneath the cohesive material law represents the fracture energy G_F of the interface and can be employed to compute the debonding stress σ_{deb} (Carloni et al. 2015):

$$\sigma_{deb} = \sqrt{4E_f \frac{b^*}{A_b} G_F} \quad (5)$$

Eqs. 3 and 4 should be applied to strains measured after the onset of debonding. However, slip of the fibers with respect to the matrix tends to damage the strain gauges, which may provide inaccurate measurements after the onset of debonding. Therefore, three points of the applied stress-global slip response around the assumed debonding stress value of specimens with strain gauges were considered. The strain measured along the bonded length for these three points, named C1, C2, and C3, is depicted in Figure 4a for specimen DS_CS170BL_450_60_S_1. The corresponding cohesive material law obtained by combining results of Eqs. 3 and 4 is depicted in Figure 4b.

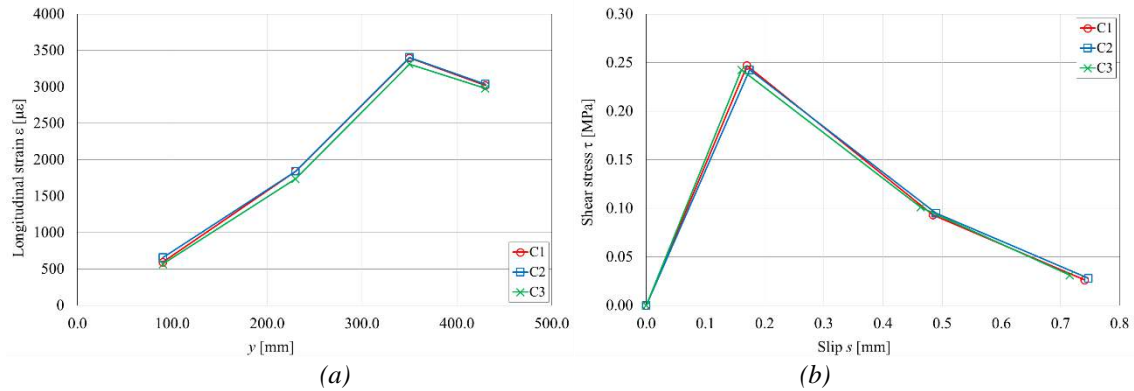


Figure 4: a) Strain measured along the composite bonded length for specimen DS_CS170BL_450_60_S_1; b) shear stress – slip relationship obtained for specimen DS_CS170BL_450_60_S_1

Values of the debonding stress σ_{deb} obtained by Eq. 5 for each applied stress σ considered are reported in Table 2 for the three specimens with strain gauges. Additionally, average values (Avg) of the experimental debonding stress and of the corresponding estimation by Eq. 5 are reported in Table 2. The average results show that the debonding stress obtained by the fracture mechanics approach described above provides a good estimation of the experimental values, with a maximum difference of 21% in the case of specimen DS_CS170BL_450_60_S_3. However, it should be noted that the discrete differentiation and integration of the strain profile (Eqs. 3 and 4) might be strongly affected by the local variation of the strain measured (D'Antino et al. 2014a). Fitting procedures that involve continuous functions may provide more accurate results (Focacci et al. 2017).

Table 2: Debonding stress [MPa] obtained by Eq. 5

Point	DS_CS170BL_450_60_S_1		DS_CS170BL_450_60_S_2		DS_CS170BL_450_60_S_3	
	σ	σ_{deb} (Eq. 5)	σ	σ_{deb} (Eq. 5)	σ	σ_{deb} (Eq. 5)
C1	728	677	652	671	575	726
C2	750	678	651	671	582	743
C3	759	671	658	678	589	746
Avg	746	675	653	673	582	738

CONCLUSIONS

In this paper, the results of 31 single-lap direct-shear tests of carbon and glass FRMC-concrete joints were presented. The main parameter investigated was the composite bonded length. The results obtained allowed for estimating the effective bond length for the glass and carbon FRMC composites studied based on the behavior of the peak stress-bonded length curve provided by the direct-shear tests. Furthermore, three carbon FRMC-concrete joints were equipped with strain gauges attached to the central fiber bundle embedded within the matrix. Applying a fracture mechanics approach, the strain measured were differentiated and integrated in a simple discrete manner

to obtain the cohesive material law associated with the matrix-fiber interface. Finally, the area under the cohesive material law, i.e. the matrix-fiber interface fracture energy, was employed to estimate the debonding stress, which was shown to be similar to the experimentally measured values.

ACKNOWLEDGMENTS

The experimental work presented in this paper was conducted at the University of Padua, Italy. G&P Intech of Altavilla Vicentina, Italy, is gratefully acknowledged for providing the FRCM composite materials.

REFERENCES

ASTM INTERNATIONAL (2008) 'Standard test method for tensile properties of polymer matrix composite materials', ASTM D3039/D3039M-08, West Conshohocken, USA.

C. Carloni, T. D'Antino, L. H. Sneed, C. Pellegrino (2015), "Role of the matrix layers in the stress-transfer mechanism of FRCM composites bonded to a concrete substrate", *Journal of Engineering Mechanics*, 141, 1-10.

J.F. Chen, J.G. Teng (2001). 'Anchorage strength models for FRP and steel plates', *Journal of Structural Engineering*, 127(c), 784-791.

COMITÉ EUROPÉEN DE NORMALIZATION (2009). 'Testing hardened concrete. Compressive strength of test specimens', UNI EN 12390-3, Brussels, Belgium.

COMITÉ EUROPÉEN DE NORMALIZATION (2007). 'Methods of test for mortar for masonry – Part 11: determination of flexural and compressive strength of hardened mortar', UNI EN 1015-11, Brussels, Belgium.

T. D'Antino, C. Carloni, L.H. Sneed, C. Pellegrino (2014a). 'Matrix-fiber bond behavior in PBO FRCM composites: A fracture mechanics approach', *Engineering Fracture Mechanics*, 117, 94-111.

T. D'Antino, C. Pellegrino (2014b). 'Bond between FRP composites and concrete: Assessment of design procedures and analytical models', *Composites Part B: Engineering*, 60, 440-456.

T. D'Antino, T. C. Triantafillou (2016), "Accuracy of design-oriented formulations for evaluating the flexural and shear capacities of FRP-strengthened RC beams", *Structural Concrete*, 17, 425-442.

T. D'Antino, J. Gonzalez-Libreros, C. Pellegrino, C. Carloni, L. H. Sneed (2016), "Experimental investigation of glass and carbon FRCM composite materials applied onto concrete supports", *Applied Mechanics and Materials*, 847, 60-67.

F. Focacci, T. D'Antino, C. Carloni, L.H. Sneed, C. Pellegrino (2017), "An indirect method to calibrate the interfacial cohesive material law for FRCM-concrete joints", *Materials & Design*, 128, 206-217.

G&P Intech. C-SHEET. Tech Datasheets; 2016. <www.gpintech.com> [accessed September 1, 2016].



NUMERICAL ANALYSIS OF PBO FRCM-CONCRETE JOINTS

Tommaso D'Antino¹, Lesley H. Sneed², Christian Carloni³, Carlo Pellegrino⁴

¹ Politecnico di Milano, Department of Architecture, Built Environment, and Construction Engineering, Piazza Leonardo Da Vinci 33, 20133 Milan, Italy, Email: tommaso.dantino@polimi.it

² Missouri University of Science and Technology, Department of Civil, Architectural and Environmental Engineering, 1401 North Pine Street, Rolla, MO, 65409 USA

³ University of Bologna, Department of Civil, Chemical, Environmental, and Materials Engineering, Viale Risorgimento 2, 40136 Bologna, Italy

⁴ University of Padova, Department of Civil, Environmental, and Architectural Engineering, Via F. Marzolo 9, 35131, Padova, Italy

ABSTRACT

The use of fiber reinforced composites for strengthening and retrofitting existing reinforced concrete (RC) structures has been gaining popularity in the last few decades. Fiber reinforced polymer (FRP) composites have been heavily studied and proven successful for bending and shear strengthening of RC beams and slabs and for confining axially loaded RC elements. Recently, fiber reinforced cementitious matrix (FRCM) composites, which are comprised of high-strength fiber net embedded within inorganic matrices, have been proposed as an alternative to FRP composites.

The bond behavior of fiber reinforced cementitious matrix (FRCM) composites applied to concrete elements is investigated in this paper by means of a three-dimensional numerical analysis. The FRCM-concrete joints studied are part of an extensive experimental campaign conducted using the single-lap direct-shear test set-up and include specimens both with and without the external layer of matrix. The input data of the numerical models are obtained applying a fracture mechanics approach that allowed for studying the shear stress – slip relationships that characterize the matrix-fiber interfaces. The load responses and strain profiles obtained from the numerical models of specimens with and without the external matrix layer are compared with the corresponding load responses and strain profiles observed in the experimental tests. A good agreement between the numerical solutions and the experimental results is obtained.

KEYWORDS

New composite materials, systems and strengthening techniques, Material, Bond and interfacial stresses, FRC and cement composite materials, FRCM, Numerical analysis.

INTRODUCTION

In the last few decades the use of high performance composite materials for strengthening and retrofitting existing structures has been gaining increasing popularity in the civil engineering industry. Among them, fiber reinforced polymer (FRP) composites have been largely used for strengthening existing reinforced concrete (RC) structures under bending (e.g. Triantafillou and Plevris 1992), shear (e.g. Pellegrino and Modena 2006), and axial or axial/bending (e.g. Yang et al. 2015) load. FRP composites employ high strength fibers applied onto the element in need of strengthening using an organic matrix. The organic binder, which transfers the tensile stress from the support to the fibers, is responsible for some of the negative attributes reported for FRP composites, such as poor properties when exposed to temperatures close to or higher than the matrix glass transition temperature (Nigro et al. 2014), degradation when exposed to UV radiation, and non-applicability onto wet surfaces. Recently, inorganic matrices have been used to replace organic binders to form high-strength composites that help overcome some of these issues. Fiber reinforced composites that employ cement-based matrices are usually referred to as fiber reinforced cementitious matrix (FRCM) composites. FRCM composites are comprised of high strength fibers organized in discrete bundles to form a net and to improve the matrix-fiber bond. Although various FRCM composites are commercially available, few studies have been carried out to understand their bond behavior. FRCM composites have been shown to be effective in strengthening existing RC and masonry elements in flexure (e.g. D'Ambrisi and Focacci 2011; Ombres 2012; Sneed et al. 2016) and shear (e.g. Blanksvärd et al. 2009; Tzoura and Triantafillou 2014; Gonzalez-Libreros et al. 2017a, 2017b) and to confine axially loaded elements (e.g. Peled 2007; Carloni et al. 2015a). Failure of FRCM-strengthened elements is generally reported to be associated with debonding of the FRCM composite (e.g. Pellegrino and D'Antino 2013; Papanicolau et al. 2007). Debonding may occur at the matrix-fiber interface, at the composite-substrate interface, or within the substrate depending on the materials employed (D'Antino et al. 2015; Focacci et al. 2017) and the strengthening configuration

(Babaeidarabad et al. 2014). A thorough investigation of the bond behavior of FRCM composites must be carried out before a reliable design model can be proposed.

This paper presents a three-dimensional numerical model developed to describe the bond behavior of FRCM-concrete joints. The numerical approach adopted was calibrated on and validated against the experimental results previously obtained by the authors on FRCM-concrete joints tested with a single-lap direct-shear set-up (Sneed et al. 2014; D'Antino et al. 2014; Carloni et al. 2014). The numerical models of two specimens with one layer of fibers and either one or two layers of matrix are shown in this paper. The matrix-fiber interfacial bond behavior was defined in the numerical models using a contact damage cohesive law.

EXPERIMENTAL CAMPAIGN

Test Set-up and Materials

Single-lap direct-shear tests were conducted on FRCM-concrete specimens comprised of one layer of a bidirectional polyparaphenylene benzobisoxazole (PBO) fiber net applied onto the substrate using an inorganic polymer-modified cementitious matrix. The parameters varied were the composite bonded width b_1 and bonded length ℓ . FRCM composite strips were applied on concrete blocks (prisms) with 125 mm \times 125 mm cross-section and 375 mm or 510 mm length. The measured compressive strength of the short (375 mm) and long (510 mm) concrete blocks was 42.5 MPa (CoV=0.013) and 33.5 MPa (CoV=0.085), respectively, whereas the corresponding measured splitting tensile strength was 3.4 MPa (CoV = 0.113) and 3.0 MPa (CoV= 0.042), respectively. The thickness and width of a single PBO fiber bundle were 0.092 mm and 5 mm, respectively. The average measured tensile strength, ultimate strain, and elastic modulus of the PBO fiber were 3014 MPa (CoV = 0.068), 0.0145 (CoV = 0.104), and 206 GPa (CoV = 0.065), respectively. The measured compressive and splitting tensile strength of the matrix were 28.4 MPa (CoV=0.092) and 3.5 MPa (CoV=0.231), respectively. The fiber net was placed on a 4 mm thick (internal) layer of matrix applied on the concrete block. A second 4 mm thick (external) layer of matrix was applied on the fiber net for some specimens, whereas it was omitted for others. Only the formed faces of the block, which were sandblasted before the composite application, were used. The classical push-pull configuration was adopted where the fibers were pulled while the concrete block was restrained (Figures 1a and b).

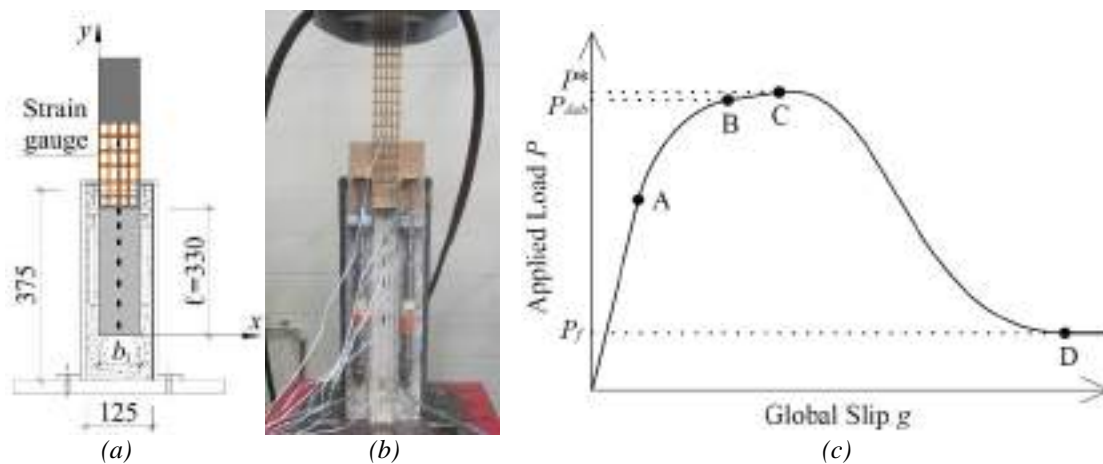


Figure 1: (a) Sketch of the single-lap direct-shear set-up (dimensions in mm). (b) Specimen DS_330_43_L_S_2 before testing (the external matrix layer is omitted in this specimen), (c) Idealized applied load – global slip response (right)

Fibers were embedded within the matrix only along the bonded length, whereas they were left bare outside the bonded length. Tests were conducted in displacement control by increasing the relative displacement between points on the concrete block and on the bare fibers just outside the bonded area, named global slip g , at a rate of 0.00084 mm/s. Further details about test set-up and material properties can be found in Sneed et al. (2014), D'Antino et al. (2014), and Carloni et al. (2014).

Idealized Load Response

The FRCM-concrete joints tested failed due to debonding of the fiber net from the embedding matrix (Sneed et al. 2014). Based on the information inferred from the results of the experimental campaign, the authors put forward the idealized load response of PBO FRCM-concrete joints shown in Figure 1c, which is valid when the bonded length is long enough to allow the full development of the stress-transfer mechanism. After point A of Figure 1c, which is the upper bound of the interface elastic behavior, the applied load response becomes non-linear until the

onset of debonding of the fiber net (point B in Figure 1c). The load value P_{deb} corresponding to the onset of debonding, can be divided by the area of the cross-section of the longitudinal bundles to obtain the debonding stress. After the onset of debonding, the presence of friction (interlocking) between single fiber filaments and between fibers and matrix in the debonded region leads to an increase of the applied load up to the peak load P^* (point C in Figure 1c). Further increase of the global slip after P^* results in a decrease of the applied load until the constant load P_f due to friction is attained (point D in Figure 1c). Test results indicate that the behavior of the idealized load response of Figure 1c is valid for specimens with or without the external matrix layer (Carloni et al. 2014). The bond behavior of the internal matrix layer is different from the bond behavior of the external matrix layer. The stress-transfer mechanism associated with the internal and external matrix-fiber interfaces can be described by the shear stress τ_{zy}^j vs. slip s^j relationship, where the superscript j is equal to i or e to indicate the internal or external matrix layer, respectively. The fracture energy of the interfaces is computed as the area under the $\tau_{zy}^j - s^j$ curves when $0 \leq s^j \leq s_f^j$, s_f^j being the beginning of the plateau associated with friction in the $\tau_{zy} - s$ curve. The strain profiles of specimens equipped with strain gauges mounted to the fibers along the composite bonded length were differentiated and integrated to obtain the $\tau_{zy}^j - s^j$ curves. As a first attempt to determine the $\tau_{zy}^j - s^j$ relationships for specimens with both internal and external layers of matrix, it was assumed that the bond behavior of the internal and external layers of matrix was equal, i.e. $\tau_{zy}^i = \tau_{zy}^e = \tau_{zy}$ and $s^i = s^e = s$ (D'Antino et al. 2014). The same fracture mechanics procedure was used to obtain the $\tau_{zy,L} - s_L$ relationship for specimens without the external matrix layer and equipped with strain gauges. The subscript L indicates that the external matrix layer was omitted (Carloni et al. 2014). Assuming that the interfacial behavior between the internal matrix layer and the fibers is not influenced by the presence of the external matrix layer ($\tau_{zy}^i = \tau_{zy,L}$ and $s^i = s_L$), the ratio between the internal- and external-layer fracture energy was computed from the ratio η_{deb} between the average debonding stress of specimens without and with the external matrix layer. η_{deb} was equal to 0.93, which indicates that the internal matrix layer is responsible for most of the matrix-fiber stress transfer (Carloni et al. 2014).

NUMERICAL MODEL

The bond behavior of both the internal and external matrix-fiber interfaces was numerically modelled using the finite element program Abaqus (Simulia 2010). As a first attempt to simulate the bond behavior of FRCM-concrete joints with and without the external matrix layer, both the PBO fibers and the matrix layers were specified as homogeneous isotropic linear elastic materials. The internal and external matrix-fiber interfaces were modeled by means of a master-slave contact interaction that follows a damage cohesive law. The contact surfaces between the matrix and the sides of the fiber bundle, each having an area equal to 0.092 mm^2 per unit length, were disregarded. The $\tau_{zy} - s$ curves obtained from two experimental tests were employed to determine the input values for the shear stress – slip relationship between the master and slave surfaces. The surface-based cohesive behavior available in Abaqus (Simulia 2010) was used to model the linear elastic branch of the $\tau_{zy} - s$ relationship, whereas the non-linear branch was modeled by introducing a damage variable that simulates the interface degradation. Further details of the numerical approach adopted can be found in Carloni et al. (2015b). Since the experimental investigation of specimens with different bonded widths showed that a global width effect does not exist for the entire composite width (D'Antino et al. 2014), only one fiber bundle was modelled and the results obtained were simply multiplied by the number of bundles present in the corresponding experimental test. The results of three-dimensional numerical modeling of PBO FRCM-concrete that takes into account the presence of different contact interfaces can be found in Carloni et al. (2017).

The experimental results obtained for one specimen with the external matrix layer, namely specimen DS_330_43_S_5 (D'Antino et al. 2014), and one without the external matrix layer, namely specimen DS_330_43_L_S_2 (Carloni et al. 2014), were reproduced numerically in this paper. Both specimens had a composite bonded length and bonded width of 330 mm and 43 mm, respectively, and included 5 longitudinal fiber bundles. Different mesh sizes were employed to study the influence of the model discretization. The mesh size adopted and herein described was found to be appropriate since it provided accurate results with a short solution time. Each matrix layer was discretized into 13212 8-node brick elements with an average edge of 0.4 mm, whereas the fiber bundle was discretized into 19800 8-node brick elements. The geometry of the numerical models DS_330_43_S_5_num and DS_330_43_L_S_2_num, which correspond to specimens DS_330_43_S_5 and DS_330_43_L_S_2, respectively, is shown in Figure 2.

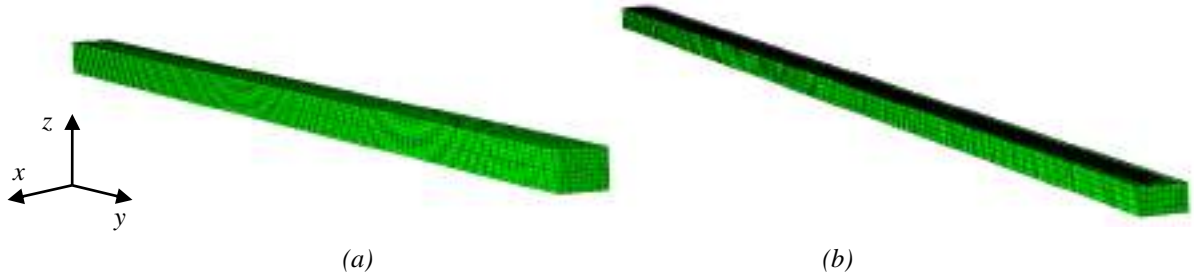


Figure 2: Geometry and mesh of model (a) DS_330_43_S_5_num and (b) DS_330_43_L_S_2

Only the longitudinal fiber bundle was included in the models, whereas the transversal fiber bundles were neglected. Each matrix layer had a length, thickness, and width of 330 mm, 4 mm, and 10 mm, respectively, and was implemented in the numerical model as a continuum body. The width of the matrix layers was equal to the fiber net transversal spacing. The fiber bundle, centered on top of the internal matrix layer, had the same length as the matrix layers and a 0.092 mm-thick \times 5 mm-wide rectangular cross-section. Since the $\tau_{zy} - s$ curves were obtained from the fracture mechanics approach assuming that the matrix deformation is negligible (D'Antino et al. 2014; Carloni et al. 2014), the matrix layers were specified as rigid bodies by setting their elastic modulus equal to 1000 GPa. The elastic modulus of the fibers was 206 GPa, and the value of Poisson's ratio of the matrix and the fibers was 0.2 and 0.3, respectively (Carloni et al. 2015b). The concrete substrate, whose deformation was assumed to be negligible with respect to the matrix and fiber deformation, was not modeled, and the internal matrix layer surface was restrained from any movement. A displacement of 4 mm in the y direction was applied to one end of the fiber bundle and was attained through steps whose amplitude was automatically determined by the software to obtain the most rapid convergence. The $\tau_{zy} - s$ curves obtained from the fracture mechanics approach applied to specimens DS_330_43_S_5, assuming that the internal and external matrix layers have the same behavior, and DS_330_43_L_S_2 were used to determine the parameters needed to define the damage cohesive contact law that controls the master-slave interaction (Carloni et al. 2015b).

DISCUSSION

Figures 3a and 3b show the average $\tau_{zy} - s$ curve obtained from the strain profiles corresponding to five points close to point B (Figure 1c) (D'Antino et al. 2014) of the experimental load response of specimens DS_330_43_S_5 and DS_330_43_L_S_2, respectively. Point B for the two experimental load responses is shown in Figure 4. Figure 3 also plots the $\tau_{zy} - s$ curves used in the numerical model. Point B_num in Figures 4a and b represents the point where the stress transfer is fully established and s attains the value s_f , i.e. the onset of debonding

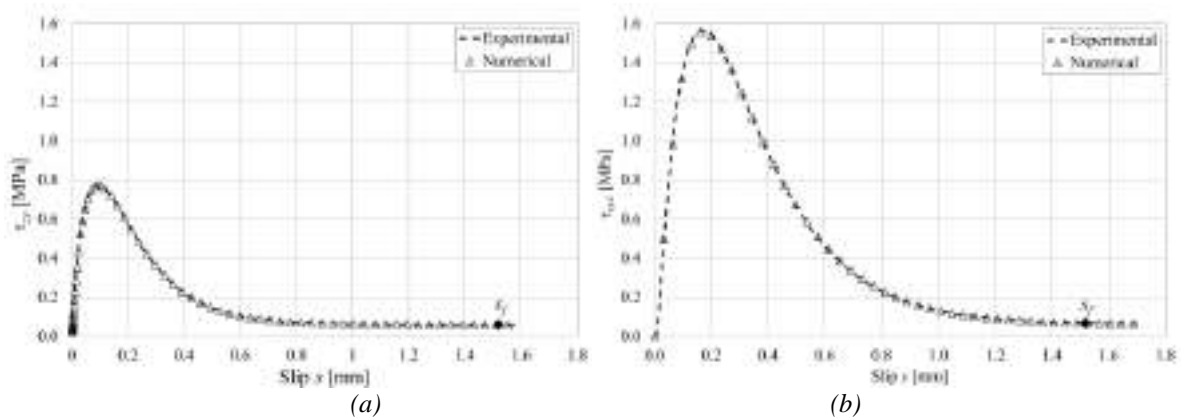


Figure 3: Comparison between experimental and numerical $\tau_{zy} - s$ curves for specimens (a) DS_330_43_S_5 and (b) DS_330_43_L_S_2

Figure 4 shows the comparison between the experimental and numerical load responses of the specimens considered. The results obtained from the numerical models, which were multiplied by the number of fiber bundles included in the specimens, are in good agreement with the experimental results. The decreasing branch of the load response, which in the experimental tests is characterized by a softening behavior, appears to be brittle in the numerical simulation. The post peak behavior of FRCM-concrete joints is indeed characterized by complex phenomena that cannot be captured by a $\tau_{zy} - s$ relationship obtained when the stress-transfer mechanism is fully

established. In addition, the full Newton solution technique employed, which is not able to capture complex non-linear phenomena, affected the numerical post peak response. Numerical and analytical studies of the FRCM-concrete joint bond behavior showed that, when a cohesive material law is adopted, the post-peak behavior should present a snap-back phenomenon (Focacci et al. 2017, Carloni et al. 2017). Using a damage cohesive contact law, the load response can be accurately reproduced up to the peak load, whereas the post-peak behavior observed experimentally cannot be fully reproduced. It should be noted, however, that failure of FRCM strengthened elements is not characterized by a post-peak softening behavior and could be estimated by applying the numerical approach described in this paper.

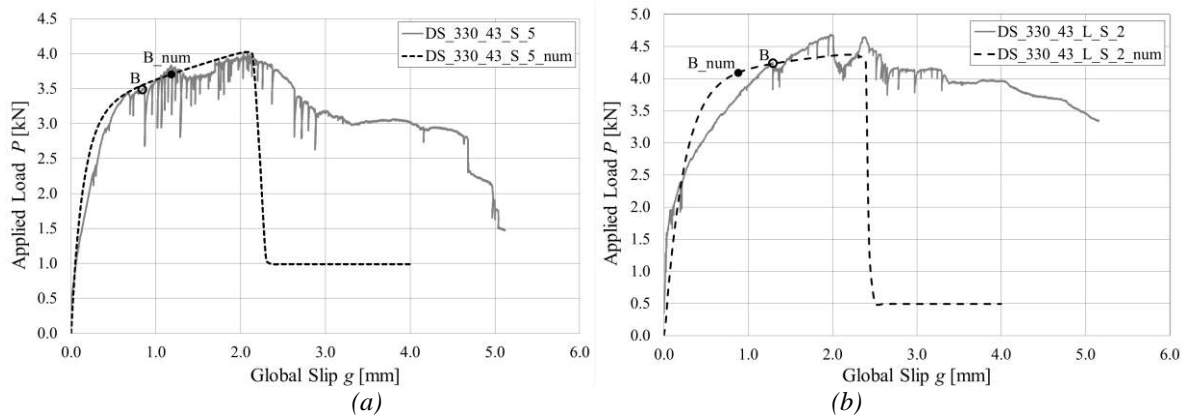


Figure 4: Comparison between the experimental and numerical load responses of specimens (a) DS_330_43_S_5 and (b) DS_330_43_L_S_2

CONCLUSIONS

The stress-transfer mechanism of PBO FRCM-concrete joints was studied in this paper by means of a three-dimensional numerical model implemented in the software Abaqus. The results of two single-lap direct-shear tests conducted on FRCM-concrete joints with one layer of PBO fiber with and without the external matrix layer were simulated. The matrix-fiber interfaces were modeled by means of a cohesive damage law calibrated on the shear stress-slip relationship obtained from experimental strain measurements. The numerical results obtained are in good agreement with the experimental observations and confirm the idealized load response put forward by the authors.

REFERENCES

- S. Babaeidarabad, G. Loreto, A. Nanni (2014). "Flexural strengthening of RC beams with an externally bonded fabric-reinforced cementitious matrix," *Journal of Composites for Construction*, 18(5), DOI: 10.1061/(ASCE)CC.1943-5614.0000473.
- T. Blanksvärd, B. Täljsten, A. Carolin (2009). "Shear strengthening of concrete structures with the use of mineral-based composites", *Journal of Composites for Construction*, 13(1):25-34.
- C. Carloni, T. D'Antino, L.H. Sneed, C. Pellegrino (2014). "Role of the matrix layers in the stress-transfer mechanism of FRCM composites bonded to a concrete substrate," *Journal of Engineering Mechanics*, DOI: 10.1061/(ASCE)EM.1943-7889.0000883.
- C. Carloni, C. Mazzotti, M. Savoia, K.V. Subramaniam (2015a). "Confinement of masonry columns with PBO FRCM composites," *Key Engineering Materials*, 624:644-651.
- C. Carloni, T. D'Antino, L.H. Sneed, C. Pellegrino (2015b). "An investigation of PBO FRCM-Concrete joint behavior using a three-dimensional numerical approach," 15th International Conference on Civil, Structural, and Environmental Engineering Computing, Prague, Czech Republic.
- C. Carloni, T. D'Antino, L. H. Sneed, C. Pellegrino (2017). "Three-dimensional numerical modeling of single-lap direct shear tests of FRCM-concrete joints using a cohesive damaged contact approach", *Journal of Composites for Construction*, DOI: 10.1061/(ASCE)CC.1943-5614.0000827.
- A. D'Ambrisi, F. Focacci (2011). "Flexural strengthening of RC beams with cement based composites," *Journal of Composites for Construction*, 15(2):707-720.
- T. D'Antino, C. Carloni, L.H. Sneed, C. Pellegrino (2014). "Matrix-fiber bond behavior in PBO FRCM composites: A Fracture Mechanics Approach", *Engineering Fracture Mechanics*, 117:94-111.

- T. D'Antino, C. Pellegrino, C. Carloni, L.H. Sneed, G. Giacomini (2015). "Experimental analysis of the bond behavior of glass, carbon, and steel FRCM composites," *Key Engineering Materials*, 624:371-378.
- F. Focacci, T. D'Antino, C. Carloni, L.H. Sneed, C. Pellegrino (2017), "An indirect method to calibrate the interfacial cohesive material law for FRCM-concrete joints", *Materials & Design*, 128, 206-217.
- J. H. Gonzalez-Libreros, L. H. Sneed, T. D'Antino, C. Pellegrino (2017a). "Behavior of RC beams strengthened in shear with FRP and FRCM composites", *Engineering Structures*, 150, 830-842.
- J. H. Gonzalez-Libreros, C. Sabau, L. H. Sneed, C. Pellegrino, G. Sas (2017b). "State of research on shear strengthening of RC beams with FRCM composites", *Construction and Building Materials*, 149, 444-458.
- E. Nigro, G. Cefarelli, A. Bilotta, G. Manfredi, E. Cosenza (2014). "Guidelines for flexural resistance of FRP reinforced concrete slabs and beams in fire," *Composite Part B: Engineering*, 58:103-112.
- L. Ombres (2012). "Debonding Analysis of Reinforced Concrete Beams Strengthened with Fibre Reinforced Cementitious Mortar," *Engineering Fracture Mechanics*, 2012, 81:94-109.
- C.G. Papanicolau, T.C. Triantafillou, M. Papathanasiou, K. Kyriakos (2007). "Textile reinforced mortar (TRM) versus FRP as strengthening material for URM walls: out-of-plane cyclic loading," *Materials and Structures*, 41(1):143-157.
- A. Peled (2007). "Confinement of damaged and nondamaged structural concrete with FRP and TRC sleeves. *Journal of Composites for Construction*," 11(5):514-22.
- C. Pellegrino, T. D'Antino (2013). "Experimental behaviour of existing precast prestressed reinforced concrete elements strengthened with cementitious composites," *Composite Part B: Engineering*, 55:31-40.
- C. Pellegrino, C. Modena (2006). "FRP shear strengthening of RC beams: experimental study and analytical modelling," *ACI Structural Journal*, 103(5):720-728.
- Simulia. Abaqus 6.10 Extended Functionality Online Documentation (generated September 29, 2010).
- L.H. Sneed, T. D'Antino, C. Carloni (2014). "Investigation of bond behavior of PBO fiber-reinforced cementitious matrix composite-concrete interface," *ACI Materials Journal*, 111(5):569-580.
- L. H. Sneed, S. Verre, C. Carloni, L. Ombres (2016), "Flexural behavior of RC beams strengthened with steel-FRCM composite", *Engineering Structures*, 127, 686-699.
- T.C. Triantafillou, N. Plevris (1992). "Strengthening of RC beams with epoxy-bonded fibre-composite materials, *Materials and Structures*, 25:201-211.
- E. Tzoura, T.C. Triantafillou (2014). "Shear strengthening of reinforced concrete T-beams under cyclic loading with TRM or FRP jackets," *Materials and Structures*, DOI 10.1617/s11527-014-0470-9.
- Y. Yang, L.H. Sneed, A. Morgan, M.S. Saiidi, A. Belarbi (2015). "Repair of RC bridge columns with interlocking spirals and fractured longitudinal bars - An experimental study," *Construction and Building Materials*, 78:405-420.



*9th International Conference on Fibre-Reinforced Polymer (FRP) Composites
in Civil Engineering (CICE 2018), PARIS 17-19 JULY 2018*

Bond



MODE II INTERFACE CONSTITUTIVE LAW FOR CONCRETE SUBSTRATES STRENGTHENED WITH STEEL REINFORCED POLYMERS

F. Ascione¹, M. Lamberti², A. Napoli³, A.G. Razaqpur⁴, R. Realfonzo⁵

¹ Dept. of Civil Engineering, University Salerno, Italy, Email: fascione@unisa.it

² Dept. of Civil Engineering, University Salerno, Italy, Email: malamberti@unisa.it

³ Dept. of Civil Engineering, University Salerno, Italy, Email: ananpoli@unisa.it

⁴ College of Env. Science and Eng., Nankai University, Tianjin, China, Email: grazaqpur@nankai.edu.cn

⁵ Dept. of Civil Engineering, University Salerno, Italy, Email: rrealfonzo@unisa.it

ABSTRACT

A new, effective and economical method has been introduced in the literature for the external strengthening of existing reinforced concrete structures, consisting of an innovative composite material using steel wires, in lieu of traditional carbon or glass continuous fibers, embedded in a polymer matrix. The resulting composite is termed Steel Reinforced Polymer (SRP). The SRP can be externally bonded to a substrate via wet lay-up, using either epoxy or polyester resin. To accurately predict the debonding load and the interface mode of failure of SRP strengthened concrete interfaces, a robust local bond-slip model is required. For estimating debonding failure load, some design guidelines specify the mode II fracture energy (G_{II}) as the key material property. For SRP-concrete interfaces the above quantity has not been established yet. Since G_{II} is related to the area under the bond-slip curve of the SRP-concrete interface, knowledge of this curve is necessary. Consequently, here two interface laws are presented and calibrated using results of a previous extensive experimental program on SRP-concrete bonded joints. Specifically, detailed measured axial strain values of the bonded SRP strips are utilized for calibration. The first model entails a bilinear bond-slip relationship and is analogous to the model originally proposed by others for bonded FRP-to-concrete system. The second model, proposed here, comprises a fully nonlinear bond-slip relationship. The results show that the proposed nonlinear bond-slip model provides a more accurate prediction of the maximum shear stress and corresponding slip than the companion bilinear model.

KEYWORDS

Steel Reinforced Polymer (SRP), strengthening techniques, experimental study, local bond-slip model.

INTRODUCTION

In the field of external strengthening and repairing of existing structures made of traditional materials such as concrete and masonry, Fibre Reinforced Polymer (FRP) has attracted a great deal of attention world-wide due to its ease of application, ability to limit the aesthetic impact of the repair work on the original structure, and its adequate reversibility for historical or artistic reasons (Rilem 2016). The growing interest in the development of other similar effective and economical solutions has recently led to the introduction of another innovative composite material that makes use of steel wires in lieu of traditional carbon and glass fibers. It consists of continuous High Tensile Strength Steel (HTSS) micro wires, twisted into small diameter cords or strands that are uniaxially embedded in a polymer matrix to form a unidirectional composite fabric. Similar to FRP laminates, the new steel fabric can be externally bonded to a substrate via wet lay-up using either epoxy or polyester resin. The resulting composite system is termed Steel Reinforced Polymer (SRP). A state-of-the-art review of the experimental research performed on SRP systems applied to concrete members is provided by De Santis et al. (2016).

One of the salient advantages of SRP over FRP is the high stiffness and ductility of steel wires versus glass, aramid or low modulus carbon fibres. Furthermore, if brittle interfacial debonding can be averted, SRP retrofitted structures could exhibit ductile behaviour and higher energy dissipation at failure (Wobbe et al. 2004, Barton et al. 2005, Figeys et al. 2005, Wang et al. 2005, Ceroni et al. 2007, Lopez et al. 2007, Capozucca et al. 2010, Valluzzi et al. 2012, Stievanin et al. 2013, Napoli et al. 2016).

Like the FRP systems, one of the key factors in the design of SRP strengthened structures is knowledge of the behaviour of the interface between SRP and concrete and the corresponding debonding failure modes. The FRP debonding failure can be accurately predicted by employing a proper local bond-slip interface law (Ferracuti et al. 2007, Lu et al. 2005, Monti et al. 2003, Dai et al. 2003, 2005). However, in spite of the great number of experimental, theoretical and numerical studies on this topic, the formulation of an accurate bond-slip interface law is still a topic of research for FRPs and even more so for SRP systems due to paucity of research on the latter system.

Currently, the bilinear shear stress-slip constitutive relation is the most utilized interfacial debonding model. However, the bilinearity assumption does not have a clear physical meaning, for the slope of the softening branch, after the attainment of peak shear stress, is determined via energy consideration alone and this normally overestimates the actual post-peak shear stress. Hence, there is need for an improved law. Accordingly, the writers propose here a non-linear bond-slip law that is calibrated using data obtained by the writers in an extensive series of tests previously reported by Ascione et al. (2017). The results show that the proposed law better predicts experimentally observed FRP/SRP-concrete interfacial bond-slip response than the existing bilinear law.

EXPERIMENTAL PROGRAM

In this study, a database was compiled based on the results of 94 single lap shear tests on SRP strips bonded to concrete prisms by means of a two component epoxy resin. The database includes results of tests performed by the writers as reported by Ascione et al (2017). In these tests, each prism had 200 x 150 mm² cross-section and 400 mm length as depicted in Figure 1. The 28-day standard cylinder concrete compressive strength (f_{cm}) of concrete in the prisms varied from 13 to 26 MPa. Three different strip densities were used, i.e.: low density (LD), medium density (MD) and high density (HD); the key details and mechanical properties of these strips are reported in Table 1, where the symbols γ , $t_f (= A_{cord} \cdot \rho)$, $f_{s,u}$, E_s , and $\epsilon_{s,u}$ designate mass density, equivalent design thickness, average tensile strength, Young's modulus, and ultimate strain, respectively.

Table 21: Properties of dry steel fabric.

Tape density	γ (g/m ²)	t_f (mm)	$f_{s,u}$ (MPa)	E_s (GPa)	$\epsilon_{s,u}$ (%)
Low (LD)	670	0.084	3191.0	182.1	2.19
Medium (MD)	2000	0.254	3085.7	183.4	2.09
High (HD)	3300	0.381	3064.6	182.2	2.09

Furthermore, two different concrete surface finishes (grinded and bush hammered) at the SRP-concrete interface were tested. Finally, in order to evaluate the effective transfer length for a given strip density, five different bonded lengths were experimentally examined (100, 150, 200, 300 and 350 mm).

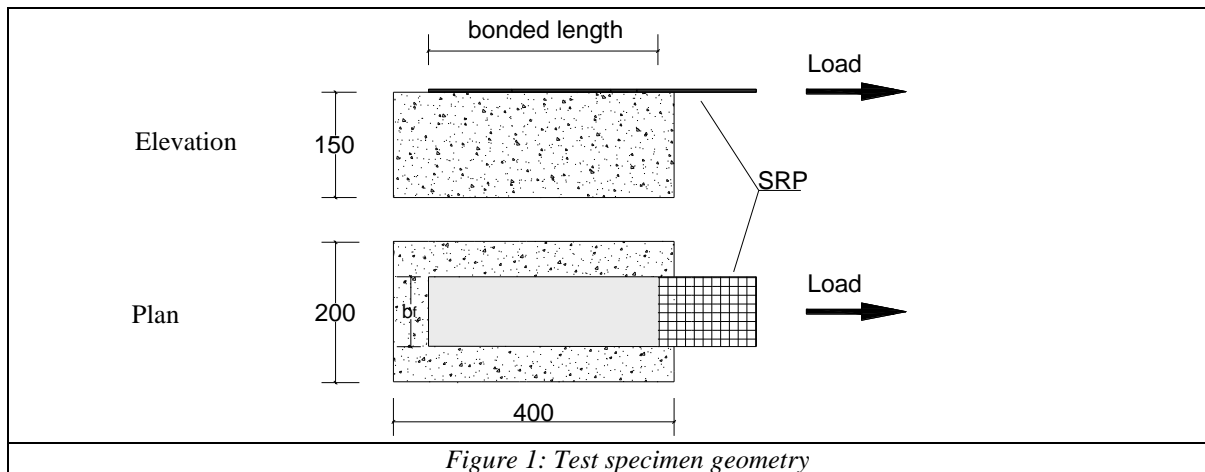


Figure 1: Test specimen geometry

Table 2 provides the main mechanical properties of the matrix (two component epoxy resin) as reported in the technical specifications online by the manufacturer, where the symbols $f_{m,u}$, $\tau_{m,u}$ and $E_{m,c}$ designate the tensile strength, shear strength and secant Young's modulus in compression, respectively (Kerakoll 2017).

Table 2: Properties of epoxy mineral adhesive (Geolite[®] Gel).

$f_{m,u}$ (MPa)	$\tau_{m,u}$ (MPa)	$E_{m,c}$ (MPa)
> 14	> 12	> 5300

Figure 2 schematically illustrates the typical single-lap test set-up. Tests were performed using a Schenck universal testing machine having a hydraulic actuator with 630 kN capacity. Tests were conducted by holding the SRP-concrete block assembly firmly in place between the top and bottom machine platens by means of a stiff

steel jig (frame) while the SRP free end was grabbed by the machine grips and subjected to tension. The tensile force was applied via displacement control at the rate of 0.01 mm/s.

To measure the SRP strip axial displacement and strain, the instrumentation of Figure 2 was used. In particular, the slip at the loaded end was measured in two ways: first, two potentiometers, designated as LDT 1 and LDT 2, were placed to the left and right of the strip to measure its axial displacement at the location of the start of the bonded length; second, the same displacement was also indirectly measured by two non-contact laser sensors, designated as Laser 1 and Laser 2. The overall extension of the loaded end of the strip was monitored via the vertical displacement of the testing machine crosshead.

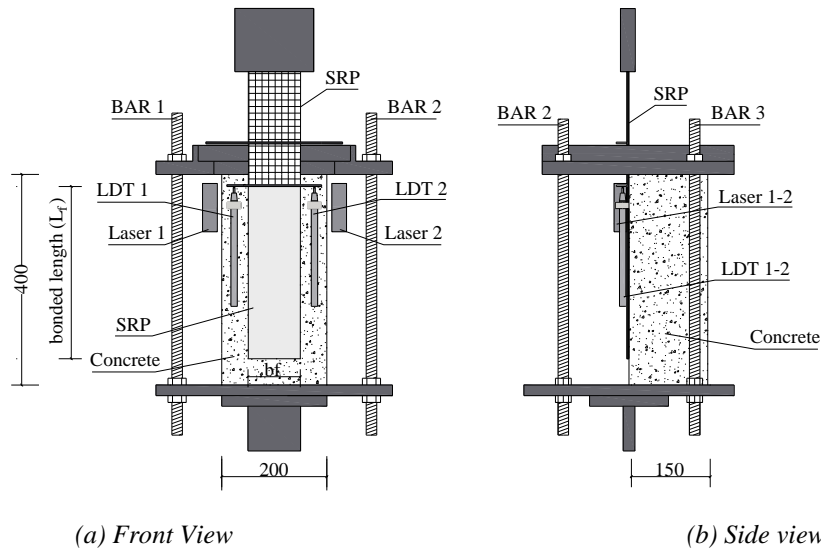


Figure 2: Schematics of the Test Set-up

To measure the SRP strain variation along and across the bonded length, a number of electrical resistance strain gauges were applied on the outer face of its bonded length, with the actual number being made dependent on the considered value of L_f . For the length equal to 300mm, a length relevant to the purpose of the present paper, the strain gauges designation and precise location are depicted in Figure 3.

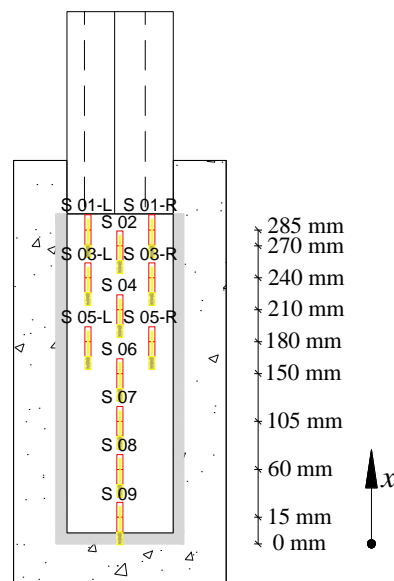


Figure 3: Strain gauge locations on steel strip for a bond length of 300 mm

The aforementioned database is summarized in Tables 3 and 4 for the two different concrete surface finishes mentioned earlier. The symbols F_d and F_{max} represent, respectively, the debonding initiation load and the maximum load resisted by the specimen during the test while s_d and s_{max} , denote the slip values associated with F_d and F_{max} . Finally, s_u , is the slip at failure. The first column in the tables identifies each specimen. The

identification label has the generic form “ x - YD # z ” where: “ x ”, “ YD ” and “ z ” denote, respectively, the SRP provided bonded length in centimeter (30 or 35), SRP density (L = low; M = medium; H = high), and the order of the replicate test specimen for a group of nominally identical specimens tested. Among all experimental data reported by Ascione et al. (2017), related to different bonded lengths, only the values of 300 and 350 mm are here adopted in order to satisfy the assumption of infinite length anchorage as discussed later in this paper.

Table 3: Database of pull tests: grinded surface.

Test	f_{cm} (MPa)	F_d (kN)	F_{max} (kN)	S_d (mm)	S_{max} (mm)	S_u (mm)
30LD#1	22.0	13.57	14.72	0.62	1.92	2.34
30LD#2	29.7	9.36	10.83	0.28	0.78	1.58
30LD#3	29.7	11.15	12.95	0.54	2.13	2.34
30LD#4	28.7	14.50	16.78	0.64	2.45	2.45
30MD#1	22.0	18.47	19.46	0.57	0.95	1.33
30MD#2	22.0	19.24	19.24	0.29	0.29	0.87
30MD#3	22.0	17.50	20.93	0.39	0.97	0.97
30MD#4	28.7	20.02	21.58	0.71	1.34	1.34
30MD#5	24.7	22.06	23.79	0.48	0.88	1.17
30HD#1	22.0	20.95	21.11	0.49	0.51	0.98
30HD#2	29.7	25.33	25.33	0.32	0.32	0.84
30HD#3	29.7	18.50	19.22	–	0.25	1.29
30HD#4	28.7	25.55	26.09	0.06	0.65	0.85
35HD#1	29.7	12.12	16.19	1.06	2.19	2.22
35HD#2	29.7	13.85	16.63	0.80	1.91	1.91
35HD#3	24.7	25.49	32.65	0.30	1.02	1.33
35HD#4	25.0	20.96	22.04	0.33	0.94	1.01

Table 4: Database of pull tests: bush hammered surface.

Test	f_{cm} (MPa)	F_d (kN)	F_{max} (kN)	S_d (mm)	S_m (mm)	S_{um} (mm)
30LD#3	29.7	12.04	14.15	2.02	3.81	3.95
30LD#4	29.7	17.14	17.36	0.60	1.95	2.53
30MD#4	28.7	20.73	21.21	1.41	2.20	2.20
30MD#5	28.7	22.34	22.60	0.54	0.94	1.18
30MD#6	25.0	16.00	16.45	0.56	1.02	1.02
30HD#3	29.7	17.44	22.93	0.49	0.95	0.95
30HD#4	28.7	24.06	28.33	0.28	0.93	0.93
30HD#5	25.0	19.68	20.33	0.76	0.90	0.90
35HD#1	29.7	20.51	30.16	1.09	1.51	1.52
35HD#2	29.7	21.82	21.82	0.48	0.48	1.04
35HD#3	28.7	26.15	27.34	0.65	1.13	1.23

BOND-SLIP EXPERIMENTAL EVALUATION

The strain gauges bonded on the SRP strip allowed for recording the strain distribution along the interface for any displacement level. Using the strain distribution profile, the local bond-slip relation of SRP-concrete interface is evaluated by following the procedure described below.

A reference coordinate system, composed of the centroid O and the axis x , is adopted as depicted in Figure 3. The position of i -th strain gauge is denoted by x_i (with $i = 1, 2, \dots, 9$), while the interval between two consecutive strain gauges is represented by $\Delta x = x_{i+1} - x_i$.

In order to evaluate the local bond-slip relationship some assumptions are made:

- no slip between steel strip and concrete at first strain gauge position ($x = 0$);

- deformation of concrete specimen far from the external cover is negligible compared to the associated steel strip ($\varepsilon_c = 0$);
- linear variation of strain in the SRP strip between two consecutive strain gauges.

The average shear stress per each interval with length Δx can be obtained using the following expression:

$$\tau_{i+1/2} = \frac{E_s t_s (\varepsilon_{i+1} - \varepsilon_i)}{\Delta x} \quad (1)$$

where ε_{i+1} and ε_i are the strain recorded at the $(i+1)$ and i gauges, respectively, while, E_s and t_s are the Young's modulus and the thickness of the SRP strip, respectively.

The average local slip $s_{i+1/2}$, evaluated at midpoint of two consecutive strain gauges is calculated using the following expression:

$$s_{i+1/2} = \frac{s(x_{i+1}) + s(x_i)}{2} \quad (2)$$

where the local slip at point x along the bonded length is evaluated using

$$s(x) = s(x_i) + \frac{(\varepsilon_{i+1} - \varepsilon_i)(x - x_i)^2}{(x_{i+1} - x_i)^2} + \varepsilon_{i+1}(x - x_i) \quad (3)$$

The interfacial fracture energy G_{exp} is based on the evaluation of the integral in Eqn (4), which is obtained generally starting from the constitutive equation of steel ($N_s = E_s A_s \varepsilon_s$) and concrete ($N_c = E_c A_c \varepsilon_c$) and the equilibrium of horizontal forces acting on the SRP

$$G_{\text{exp}} = \int_0^{\infty} \tau(s) ds = \int_0^{L_f} E_s t_s (\varepsilon_s - \varepsilon_c) d\varepsilon_s = \int_0^{L_f} E_s t_s \varepsilon_s d\varepsilon_s = \frac{F_{\text{max}}^2}{2E_s t_s b_s^2} \quad (4)$$

The final results was obtained according to the assumption before introduced ($\varepsilon_c = 0$).

LOCAL BOND-SLIP INTERFACE LAWS AND THEIR CALIBRATION

First the bi-linear interface law, originally proposed by Monti et al. (2003) for the case of FRP-concrete system, is characterized by the following two expressions for the elastic and the softening branch, respectively:

$$\tau(s) = \tau_{\text{max}} \frac{s}{s_{\text{max}}} \quad \text{if } 0 \leq s \leq s_{\text{max}} \quad (5a)$$

$$\tau(s) = \tau_{\text{max}} \frac{s_u - s}{s_u - s_{\text{max}}} \quad \text{if } s_{\text{max}} \leq s \leq s_u \quad (5b)$$

where τ_{max} and s_{max} indicate the maximum shear stress and the corresponding slip, while s_u represents the value of the post peak shear stress slip for which the shear stress becomes equal to zero. For the calibration of this law, the set of unknown parameters is $\{\tau_{\text{max}}, s_{\text{max}}, s_u\}$.

The second interface law, proposed by the writers, is nonlinear for both the ascending and the softening branch. The expression for each branch is shown in the following Eqs (6a) and (6b).

$$\tau(s) = \tau_{\text{max}} \left(\frac{s}{s_{\text{max}}} \right)^\lambda \quad \text{if } 0 \leq s \leq s_{\text{max}} \quad (6a)$$

$$\tau(s) = \tau_{\max} \left(\frac{s_{\max}}{s} \right)^K \text{ if } s_{\max} \leq s \leq s_u \quad (6b)$$

where λ and K are two shape constant parameters. In particular, λ is defined in the range (0,1) while K has to be greater than one. In this case, the set of unknown parameters is $\{\tau_{\max}, s_{\max}, \lambda, K\}$.

The set of unknown parameters for the two interface laws can be found by applying the well-known least square minimization criterion as follows:

$$\min \sum_{i=1}^N \sum_{j=1}^M \left(\tau(s)_{i,j} - \tau(s)_{\text{exp},i,j} \right)^2 \quad (7)$$

In Eqn (7), $\tau(s)$ and $\tau_{\text{exp}}(s)$ represent the numerical and the experimental shear stress, respectively, while N and M represent the total number of experimental test data and the total number of points $\tau(s)$ per each test for a given displacement level, respectively. Specifically, the total number N of test data is equal to seventeen for the grinded surface (Table 3) and eleven for the bush hammered surface (Table 4).

Furthermore, considering that the tests were performed in displacement control at the rate of 0.01 mm/s, every ten seconds (0,1 mm) a point $\tau(s)$ was recorded per each of the eight couples of consecutive strain gauges (Figure 3). For the calibration of both interface laws the following constraint was considered to reduce the number of unknown parameters:

$$G_{\text{exp}} = G_{\text{num}} \quad (8)$$

The experimental fracture energy can be obtained by Eqn (4) while the numerical fracture energy for each interface law can be obtained by the following expression:

$$G_{\text{num}} = \int_0^{\infty} \tau(s) ds \quad (9)$$

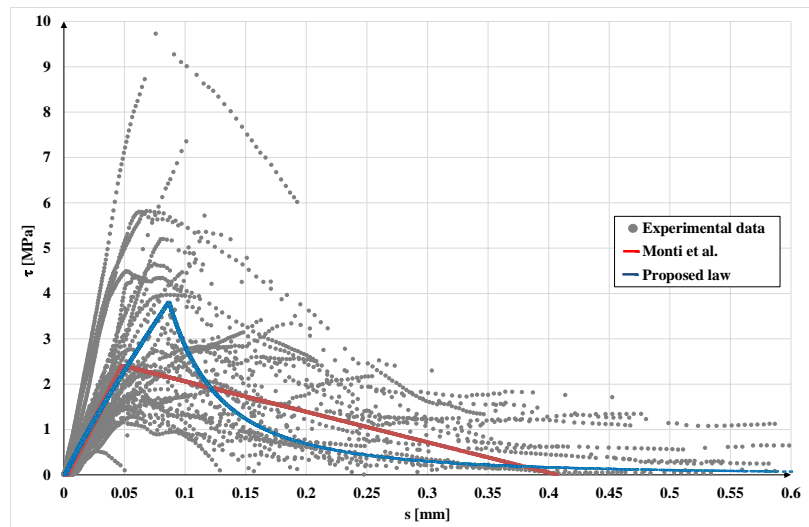
After some algebraic manipulation, one can easily verify that the aforementioned numerical fracture energy for the two interface laws is equal to:

$$G_{\text{num}, \text{Monti et al}} = \frac{\tau_{\max} s_u}{2} \quad (10)$$

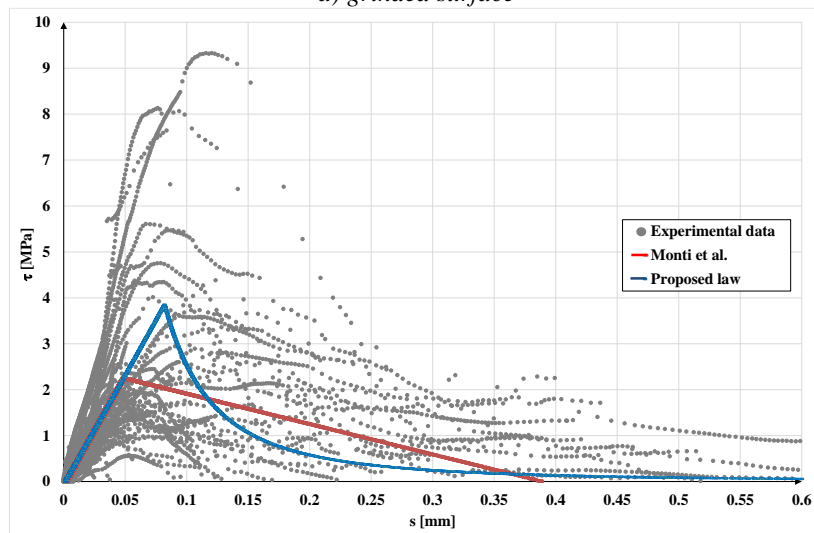
$$G_{\text{num}, \text{proposed}} = \frac{\tau_{\max} s_{\max}}{1 + \lambda} + \frac{\tau_{\max} s_{\max}}{K - 1} \quad (11)$$

For the bilinear and non-linear interface law, respectively, the relative values of the unknown are $\{2.40, 0.05, 0.41\}$ and $\{3.82, 0.09, 0.90, 2.03\}$ for the grinded surface with standard deviation equal to 0.726 and 0.722, respectively, while $\{2.25, 0.05, 0.39\}$ and $\{3.84, 0.08, 1.00, 2.11\}$ for bush hammered surface with standard deviation equal to 0.874 and 0.857, respectively.

The interface laws are depicted in Figure 4 together with the experimental shear stress-slip values. It is worth noting that the bilinear law is in good agreement with the experimental data insofar as the stiffness of the ascending branch is concerned but underestimates the maximum shear stress and consequently the stiffness of the softening branch. On the contrary, the proposed nonlinear interface law compares better with the experimental data in terms of maximum shear stress while the tail of the softening branch seems to underestimate the $\tau(s)$ value. In terms of the elastic shear stiffness, given by the slope of the ascending branch, no significant difference was found between the two laws.



a) grinded surface



b) bush hammered

Figure 4: Bond-slip curve for SRP-concrete interface

CONCLUSIONS

In the present paper a nonlinear bond-slip interface law (model) was introduced to more accurately predict the debonding load and the interface mode of failure for SRP retrofitted concrete prisms. The model parameters were calibrated using a relatively large set of experimental data in conjunction with a least square minimization procedure. The greater accuracy of the nonlinear law, compared to a similarly calibrated typical bilinear law, is demonstrated by the relatively more accurate prediction of the experimental data in terms of maximum shear stress and its corresponding slip while no significant difference is observed between the two laws insofar as the elastic shear stiffness of the interface is concerned.

REFERENCES

- F. Ascione, M. Lamberti, A. Napoli, G. Razaqpur, R. Realfonzo (2017). "An experimental investigation on the bond behavior of steel reinforced polymers on concrete substrate", *Composite Structures*, 181, 58-72.
- B.L. Barton, E. Wobbe, L.R. Dharani, P. Silva, V. Birman, A. Nanni (2005). "Characterization of reinforced concrete beams strengthened by steel reinforced polymer and grout (SRP and SRG) composites", *Mater Science Eng A*, 412, 129-36.
- R. Capozucca (2010). "Experimental FRP/SRP-historic masonry delamination", *Compos Struct*, 92:891-903.

- F. Ceroni, M. Pecce (2007). "Cracking behaviour of RC beams externally strengthened with emerging materials", *Constr Build Mater*, 21(4), 736-745.
- J.G. Dai, T. Ueda (2003). "Bond Stress-Slip Relations for FRP Sheets-Concrete Interfaces", *FRPRCS-6. Conference Proceedings*.
- J.G. Dai, T. Ueda, Y. Sato (2005). "Development of the Nonlinear Bond Stress-Slip Model of Fiber Reinforced Plastics Sheet-Concrete Interfaces with a Simple Method", *J. Compos. Constr.*, 80, 52-62.
- S. De Santis, G. de Felice, A. Napoli, R. Realfonzo (2016). "Strengthening of structures with Steel Reinforced Polymers: a state-of-the-art review", *Composite Part B Eng*, 104, 87-110.
- B. Ferracuti, M. Savoia, C. Mazzotti (2007). "Interface law for FRP-concrete delamination", *Composite Structures*, 80, 523-531.
- W. Figeys, L. Schueremans, K. Brosens, D. Van Gemert (2005). "Strengthening of concrete structures using steel wire reinforcement polymer", *ACI Sp Publ*, 230, 743-62.
- X. Huang, V. Birman, A. Nanni, G. Tunis (2005). "Properties and potential for application of steel reinforced polymer and steel reinforced grout composites", *Compos Part B Eng*, 36, 73-82.
- Kerakoll Spa, web site: <www.kerakoll.com> [accessed Nov 2017].
- A. Lopez, N. Galati, T. Alkhrdaji, A. Nanni (2007). "Strengthening of a reinforced concrete bridge with externally bonded Steel Reinforced Polymer (SRP)", *Compos Part B Eng*, 38, 429-436.
- X.Z. Lu, J.G. Teng, L.P. Ye, J.J. Jiang (2005). "Bond-slip models for FRP sheets/plates bonded to concrete", *Engineering Structures*, 27, 920-937.
- M. Matana, A. Nanni, L.R. Dharani, P. Silva, G. Tunis (2005). "Bond Performance of steel reinforced polymer and steel reinforced grout", *Proceedings Int. Symp. On bond behaviour of FRP in structures (BBFS), Hong Kong, China*.
- G.J. Mitolidis, T.N. Salonikios, A.J. Kappos (2008). "Mechanical and bond characteristics of SRP and CFRP reinforcement: a comparative research", *Open Constr Build Tech J*, 2, 207-216.
- M. Monti, M. Renzelli, P. Luciani (2003). "FRP adhesion in uncracked and cracked concrete zones. In Proc. Of 6th international symposium on FRP reinforcement for concrete structures. Singapore", *World Scientific Publications*, 183-92.
- A. Napoli, G. de Felice, S. De Santis, R. Realfonzo (2016). "Bond behaviour of steel reinforced polymer strengthening systems", *Compos Struct*, 152, 499-515.
- RILEM State-of-the-Art Report (2016). "Design Procedures for the Use of Composites in Strengthening of Reinforced Concrete Structures", *State-of-the-Art Report of the RILEM Technical Committee 234-DUC*.
- E. Stievanin, F. da Porto, M. Panizza, E. Garbin, C. Modena (2013). "Bond characterization between historical concrete substrate and SRG/SRP strengthening systems", *Proceedings of 5th Int. Conf. On structural engineering, mechanics and computation SEMC2013, cape Town, South Africa*.
- M.R. Valluzzi, D.V. Oliveira, A. Caratelli, G. Castori, M. Corradi, G. de Felice (2012). "Round robin test for composite to brick shear bond characterization", *Mater Struct*, 45, 1761-1791.
- E. Wobbe, P. Silva, B.L. Barton, L.R. Dharani, V. Birman, A. Nanni (2004). "Flexural capacity of R/C beams externally bonded with SRP and SRG", *Proceedings of Society for the advancement of material and process engineering Symp., Long Beach, CA, USA*.



FRP-TO-CONCRETE DEBONDING - GLOBAL AND LOCAL BOND BEHAVIOUR

M. Breveglieri ^{1*}, A. Hosseini ^{1,2} and C. Czaderski ¹

¹ Empa, Swiss Federal Laboratories for Materials Science and Technology, Dübendorf

² Resilient Steel Structures Laboratory, EPFL, Lausanne, Switzerland

*Email: matteo.breviglieri@empa.ch

ABSTRACT

FRP (fiber reinforced polymer) strips are used to flexurally strengthen reinforced concrete (RC) beams. The global bond strength namely the maximum transferable bond stress due to the increase of FRP tensile stress in a cracked concrete element (subsequently named as global bond shear stress) is a relevant aspect of flexural strengthening design. The differences between the bond strength in an uncracked concrete (end anchorage) and in a cracked concrete element have been highlighted in the existing literature; however, despite a large number of research works on the simple lap-shear test (local bond shear stress), less effort has been dedicated to investigate and model debonding on a global view. The current version of Swiss code on externally bonded reinforcement (SIA 166-2004) limits the local and global bond strength by means of the shear stresses, $\tau_{f,max}=\tau_{l0}$ and $\tau_{l,lim}$, which are both assumed to be only functions of the concrete tensile strength. Nevertheless, it has been demonstrated in the literature that the maximum interfacial shear stress between two adjacent flexural (or flexural-shear) cracks depends also on the stress level in the FRP (σ_o). In the current paper, the difference between the local and global bond behavior and its debonding processes is explained and discussed with analytical and numerical models.

In analogy to the existing approach developed to study the bond behavior of prestressed carbon fiber reinforced polymer (CFRP) strips during force release, a fracture energy-based model is proposed in the current study to determine the maximum global bond developed in a so-called intermediate crack element (ICE). The proposed model is a function of the FRP tensile stress (σ_o) and assumes a constant shear stress law. It is here demonstrated that the proposed model provides similar results to the more complicated models available in the literature. The main findings are here discussed with the aim to evaluate the feasibility of this new model for a future enhancement of the Swiss code.

KEYWORDS

FRP-Concrete interfacial shear stress, standards, externally bonded reinforcement, flexural strengthening, RC concrete

INTRODUCTION

Local bond behavior

The bond between concrete and FRP is one of the most relevant aspects of the research on composite material for structural strengthening, the shear stress transfer mechanism between the two materials is fundamental for the design of strengthening and retrofitting interventions since debonding failure modes are the most recurrent in both flexural and shear strengthening. FRP bond behavior and resistance highly influence the performance at both serviceability and ultimate limit state of a strengthened RC element. The bond of conventional reinforcement bars embedded in concrete influences the serviceability limit state, i.e. the width and spacing of cracks, tension stiffening, and curvature. At ultimate state, bond influences the strength of end anchorages and lapped joints, and the ultimate rotation capacity of the plastic hinge regions (fib 2013).

FRP bond behavior of Externally Bonded Reinforcement (EBR) is traditionally studied using pull-off (i.e. lap shear test), the FRP is bonded to the concrete surface and loaded from one side, with a force F , (Figure.1a). As the force is applied a slip, Δ , in Section 1 (Figure.1) occurs. The slip is defined as the relative displacement between the FRP and the concrete section. The force-slip behavior represents the behavior of the bonded FRP-concrete system and provides the main information regarding its ultimate strength. However, to have a better understanding of the problem and to develop design criteria it is necessary to use a local bond-slip model. The local bond-slip law describes the local shear stress transfers mechanism at the FRP-concrete interface when the relative longitudinal displacement between the two bonded parts occurs. Some of the bond slip- relationships available in literature are presented in Figure. 1. All these functions provide similar results in terms of force-slip behavior, and a closed form solutions for the differential equation of the bond behavior exists, with the exception of the bilinear bond-slip law. The bilinear model is, however, the most used since in its relative simplicity provides a reasonable physical explanation of the mechanism. The ascending branch simulates the elastic behavior of the interface, while the descending describes the progressive bond degradation. When compared to the local bond slip behavior for embedded steel reinforcement presented in the Model Code (fib 2013), it is possible to notice that

the fracture energy for externally bonded FRP is about ten times smaller. The bond length has a relevant role since the maximum transferable force is reached only if l_b is larger than the effective bond length l_{ba} , which can be defined as the length along which most of the interfacial stress is transferred to the concrete.

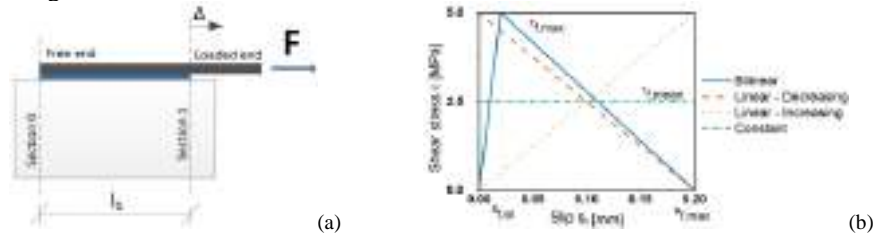


Figure.1 (a) Lap-shear test (b) Bond-slip behavior available in literature for FRP, all the presented models have the same fracture energy (G_f), values assumed as given in Table 1

Figure. 2a shows the theoretical force-slip relationship at the loaded free ends, for a “long bond length” ($l_b > l_{ba}$), under the assumption of bilinear bond-slip local behavior (Figure.1). As the force F is applied, slip at the loaded end and shear stresses, τ , are generated, the stress propagates from the loaded section towards the free end as the imposed force increases. When the maximum force is reached, a further increase of slip does not produce any increase of force. The three-points highlighted in the Figure correspond to (1) end of the elastic phase, at this point the maximum shear stress is reached in Section 1 (Figure 1a) and loaded end slip reaches the value corresponding to the peak of the local bond-slip relationship, (2) point at which the maximum force is reached, at this point the active bond length is “fully mobilised” (Figure 2b) and the maximum slip of the local bond-slip behavior is reached (Figure.2c) (3) point where the force F starts to decrease for further increase of slip. The slip and shear stress can be calculated by solving the differential equations (Czaderski 2012) for the assumed slip, τ - s_f relationship. By integrating τ along the bonded length it is possible to calculate the force F .

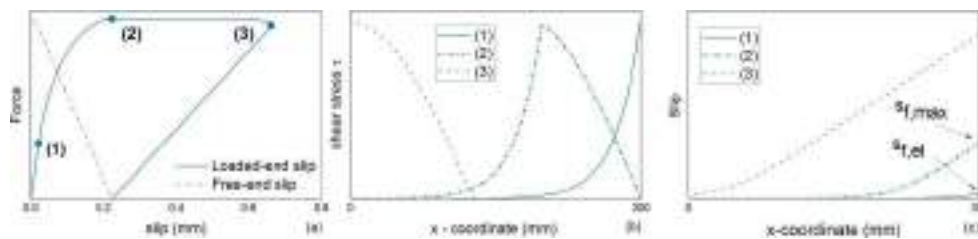


Figure 2: Long bond length: (a) Force-slip, (b) shear-stress (c) slip

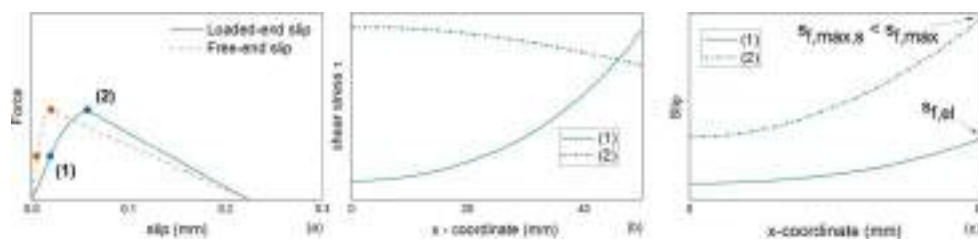


Figure 3: Short bond length: (a) Force-slip (b) shear-stress (c) slip

In case of short bond length ($l_b < l_{ba}$), the global behavior changes significantly (Figure 3). The maximum transferable force is lower, and as the maximum force is reached, it rapidly decreases. In Fig 3b it is possible to notice that the shear-stress curves for the previously defined points are limited by the geometry. Unlike for long bond length, slip occurs at the free end for a small value of force (Fig 3a,c), and the slip at maximum load is $s_{f,max,s}$ is smaller than $s_{f,max}$. If a short bond length is used no information in regards to the length of the active bond length can be obtained. Nevertheless, the short bond length allows, to calculate with approximate accuracy the local bond slip behavior, through a mean shear stress $\tau_{f,m}$, obtained by averaging the force along the bonded area. This approach is adopted by the RILEM (1978) test to estimate the bond strength of embedded reinforcement. In terms of end anchorage design the approach used for conventional reinforcement has not been modified since several years, and in the latest version of the Model Code (fib 2013), is still based on a simple assumption of average stress on the surface of the bar over the bond length l_b . In case of EBR FRP, the “long bond length” is usually adopted as a lap shear test set-up, first for practical reasons related to the experimental testing and second, because for this type of test it is possible to have information on the real active bond length.

Global bond behavior

The global bond shear stress, $\tau_{f,gl}$ is here considered, as the bond stress that exists on a defined length. In Figure 4a the load is transferred from the concrete to the strip over a certain length and not in one point. The global bond stress develops from the beginning of the loading over the fixed length l_l and increases as the load increases. The difference is clear when it is compared to the local bond shear stress, in Figure 4b for the lap-shear test the active bond length increases with a constant bond stress value $\tau_{f,mean}$.

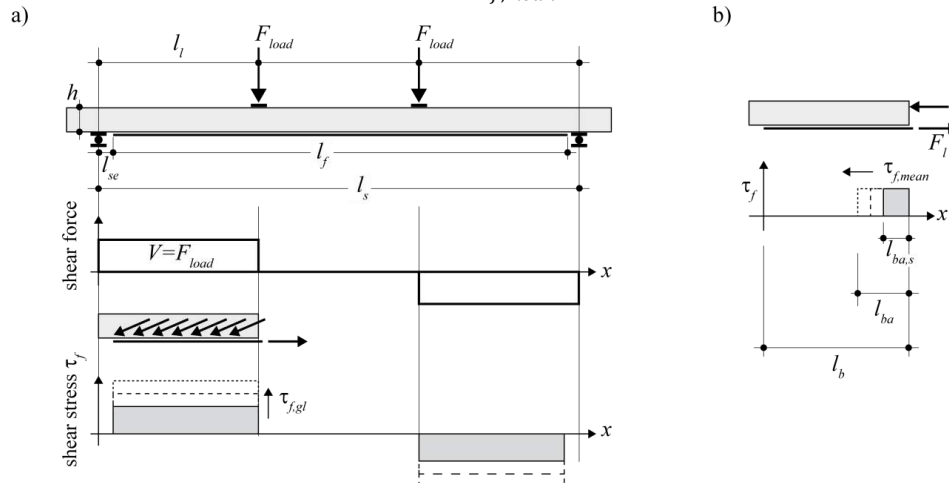


Figure 4. (a) Schematic of a beam with EBR. The load is transferred to the EBR by the global bond shear stress on the complete length of the strip (b) schematic of a lap-shear test with $l_{ba} < l_b$ and of the local bond shear stress. Figure taken from Czaderski (2012).

FLEXURAL STRENGTHENING AND IC DEBONDING

To evaluate the flexural capacity of FRP strengthened RC beams, the SIA (2004) requires the calculation of three debonding failure modes (Figure 5a): (i) *end anchorage (local behavior)*, where it is required to calculate the FRP anchorage force at the flexural crack closest to the point of zero moment, (ii) *high FRP strain*, which limits the FRP strain to 0.8%, so to avoid local debonding due to compatibility problems between strip and concrete at flexural cracks, and (iii) *intermediate crack (IC) debonding*, which limits the global shear stress in cracked elements between two cracks, mode details are provided in the following section. This type of approach is common for many FRP design guidelines (fib 2001, Zilch et al 2014).

IC debonding can be triggered by the high shear stress generated between the cracks, an accurate analysis involves checking that the force change in the FRP can be transferred by bond to the uncracked concrete element. Fig 5b shows a graphical representation of the intermediate crack element (ICE). As load increases forces in the FRP strip ends of the ICE increases, the difference between this two forces: ΔF_f is limited by the bond resistance of the FRP to concrete interface.

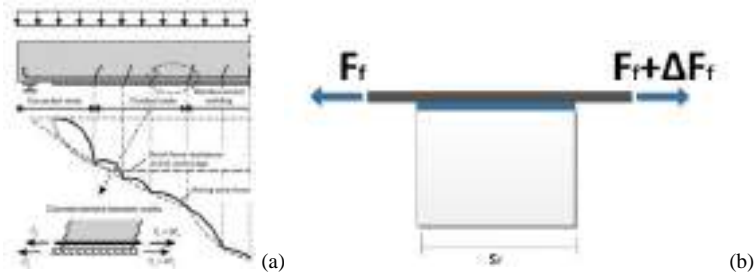


Figure 5: a) Graphical explanation of the difference between end-anchorage and intermediate crack element from (Zilch et al.2014), (b) intermediate crack element (element between two cracks) graphical representation.

SIA 116 model

The Swiss code (SIA 2004) takes into account the IC debonding failure by limiting the shear stress at the concrete FRP interface. The maximum admissible value of shear stress $\tau_{f,lim,s}$ calculated as indicated in Eq.1, has to be larger than the shear stress between the strip and the concrete which can be estimated following Eq.2 where term $\Delta F_f / \Delta x$ express the force change in the FRP in the element of length Δx .

$$\tau_{f,\text{lim}} = 2.5 \cdot \tau_c = 2.5 \cdot 0.3 \sqrt{f_{ck}} \quad \tau_c \cdot \text{from SIA 262 (2013)} \quad (1)$$

$$\tau = \frac{\Delta F_f}{\Delta x \cdot b_f} \quad (2)$$

This approach is rather simple, and one of its major drawbacks lies in estimating the maximum admissible shear stress only as a function of the concrete strength, when it has been demonstrated in literature (fib 2001, Zilch et al 2014) that the force that can be transferred to the concrete is also function of the stress in FRP. In addition, this approach does not consider the crack spacing.

Niedermeier model

An alternative approach has been adopted by the German guidelines (Zilch et al 2014) and the fib bulletin 14 (2001). The current versions of these guidelines are based on the work of Niedermeier (2001). Despite the latest version of the cited norms consider in the so-called “accurate method” the effect of friction and curvature as additional components in the estimation of the IC debonding, in this paper only the basic value of the adhesive bond ΔF_B is here discussed. The model is based on a bilinear shear stress law, and consists in evaluating the admissible force change ΔF_B that can be transferred by bond at the concrete elements between the crack using as a function of the base shear force F_f . ΔF_B is calculated as follows:

$$\Delta F_B = \begin{cases} \Delta F_B^G - \frac{\Delta F_B^G - \Delta F_B^D}{F_B^D} \cdot F_f & \text{for } F_f \leq F_B^D \\ \sqrt{b_f^2 \cdot \tau_{\max} \cdot s_{f,\max} \cdot E_f \cdot t_f + F_f^2} - F_f & \text{for } F_B^D < F_f \leq F_{fu} \end{cases} \quad (3)$$

The model for the bond strength, ΔF_B consists of two sections as shown in Fig 6a. The first part between point G and D ($F_f \leq F_B^D$), characterised by a lower base force F_f , is influenced from the crack distance s_r , and therefore represents the range over which the required transfer length of the bilinear bond stress-slip model is larger than the length of the element between the cracks s_r . The second part of Eq. (3), characterised by a high base force F_f , $F_B^D < F_f \leq F_{fu}$ the bond is not influenced by the crack distance, and additional resisting stress depends only on the bond fracture energy and bond characteristics. The second part of Eq. 3 has been obtained by Niedermeier (2001) through the adoption of the “linear-decreasing” bond-slip relationship presented in Figure 1b. One relevant aspect of the model is the definition of the points G and D. Point G, is characterised by a force base shear force equal to zero which is the end-anchorage loading scenario. The value ΔF_B^G (Point G) calculated as indicated in Eq.4 is a function of the bond strength $f_{bf}(s_r)$, this latter value can be calculated following (Zilch et al 2014)

$$\Delta F_B^G = f_{bf}(s_r) \cdot b_f \cdot t_f \quad (4)$$

Point D, which specify the value of base force F_f , beyond which value the crack spacing, s_r does not influence the strength of the ICE, is calculated using Eq (5).

$$F_B^D = \frac{s_{f,\max} \cdot E_f \cdot b_f \cdot t_f}{s_r} - \tau_{\max} \frac{s_r \cdot b_f}{4} \quad (5)$$

Point D is calculated by assuming constant bond shear stress along the entire length of the ICE, the characteristic bond-slip law is then solved by assuming zero slip at the less stressed crack edge, and maximum slip (of the assumed local bond-slip model) at the most stressed crack end. Under this assumption F_B^D can be calculated as a function of s_r and the bond-slip law parameters. The value of ΔF_B^D required in Eq. (3) is calculated by substituting the value of F_B^D in F_f in the second part of Eq.3. In addition, the model limits the tensile force F_f of the CFRP strip by the value F_{fu} , FRP breaking force.

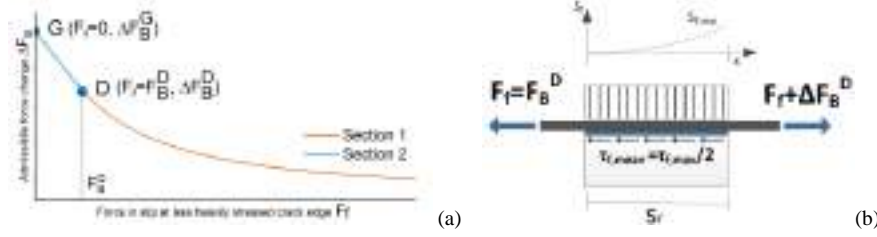


Figure 6 (a) Qualitative representation of the Niedermeier (2001) model, (b) simplified model, adopted by Niedermeier to estimate the value of F_B^D (Point D)

NUMERICAL INVESTIGATION

Finite element model

A simplified finite element model implemented in the FE-software Abaqus (Simulia 2015) is used to understand the shear stress transfer mechanism of an IC element. The model, shown in Figure 7a represents an FRP strip glued to an uncracked concrete element, the strip is pulled from both ends using a different ratio of α , where α represents the ratio between the forces F_2 and F_1 acting at the ends of the model. Both concrete and CFRP elements are here modeled using truss elements, the concrete nodes are fixed in horizontal and vertical direction, meanwhile, the CFRP nodes are fixed only in the vertical direction. The two materials are connected using cohesive surfaces of zero thickness, which means that the vertical coordinates of CFRP and concrete elements are the same. The width of the interface is equal to the CFRP width: 50 mm. It is possible to verify that the stiffness of the concrete does not play a relevant role in the study of the interface (Uлага 2003, Chen et al. 2012).

The cohesive zone model CZM interface is simulated using the bilinear τ -slip relationship (Figure 7b) and considers only the tangential behavior of the interfaces. The model is loaded by increasing the forces F_1 and F_2 and keeping constant the ratio $F_1/F_2 = \alpha$. The material parameters used for the study are presented in Table 1, for this example, a concrete compressive strength f_{ck} of 40 MPa, has been considered. Non-linearity has been considered only at the interface. Values used for the bilinear shear-stress/slip model are the one recommended in (Czaderski 2012). The value of concrete compressive strength is used only to evaluate the properties of the FRP concrete interface. The constitutive model of the interface is able to take into account the damage (Figure 7b). The α values adopted for this study range in between of 1.01 and ∞ . The ∞ corresponds to the pull-off test configuration. Four different crack spacing has been considered in the numerical study, $s_r = 50, 100, 150, 200$ mm.

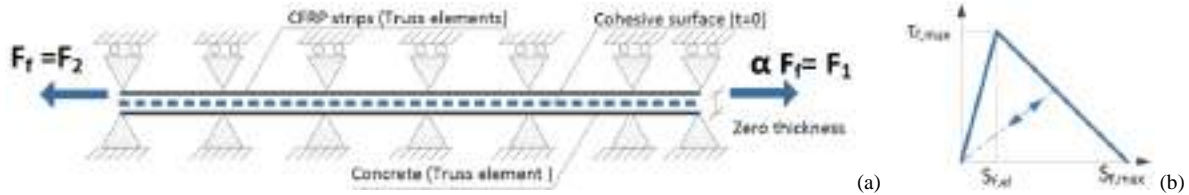


Figure 7: Schematic finite element model (a) shear-stress/slip adopted to simulate the interface behavior.

Table 1: Material parameters used in the numerical study.

CFRP		Interface		Concrete
E_f	170 GPa	$\tau_{f,max}$	5.0 MPa	$f_{ck} = 40$ MPa
b_f	50 mm	$s_{f,el}$	0.02 mm	$d_{max}=32$ mm
t_f	1.2 mm	$s_{f,max}$	0.20 mm	
		G_f	0.5^a N/mm	$a G_f = 0.018 \cdot f_{ck}^{2/3} \cdot d_{max}^{1/4}$ (Czaderski 2012)

Numerical results

The effectiveness of similar numerical approaches has been already demonstrated by (Chen et al. 2012), the model has been validated using the analytical solutions obtained from the differential equations. Figure 8 shows the Force-slip relationship at both ends, for two different crack spacing s_r (50 and 200 mm). The orange curves show the force-slip relationship at the most stressed end for the force $F_1 = \alpha F_2$, and the blue curves show the force -slip relationship at the less stressed end for the Force F_2 . Figure 8 shows the full force slip behavior only for the simulations with α equal to 1.1 and 2.0. For the other values of α only the force-slip values obtained at maximum forces F_1 and F_2 are displayed, these correspond to the orange and blue round markers, for F_1 and F_2 , respectively. For low values of α , high values of forces are observed, this evidence is justified by the fact that small forces ΔF have to be transferred to the concrete to satisfy the equilibrium. It is interesting to remark that $\alpha = 1$ corresponds to the case of an ICE situated in a cross-section with constant bending moment, which implies no force change in the FRP strip and zero global shear stress. For high values of α , the forces are lower because to satisfy the element

equilibrium a high force ΔF has to be transferred to the concrete. In the figure, it is also possible to highlight the different behavior of crack element length, in Figure 8a shows the results in case of a s_r shorter than the effective bond length, whereas Fig 8b shows the results for a higher s_r than l_{ba} .

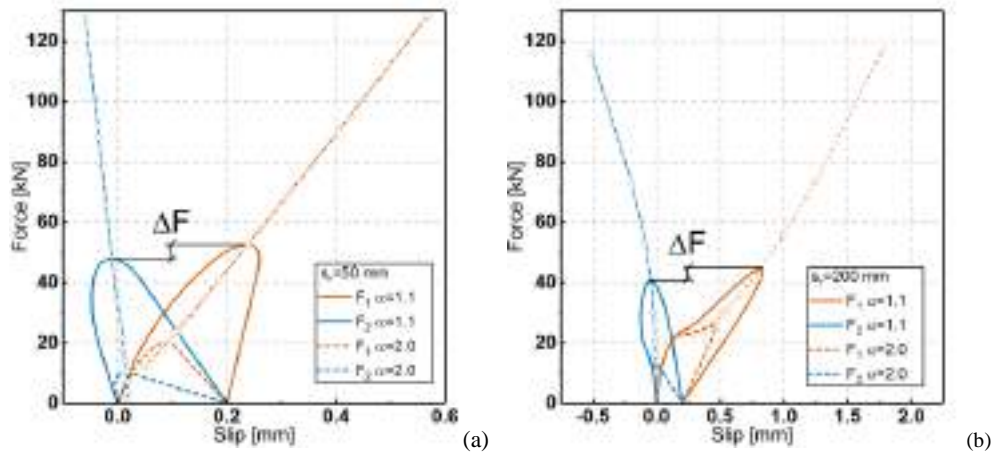


Figure 8: Numerical results for element length (a) $s_r=50\text{mm}$ (b) $s_r=200\text{mm}$.

PROPOSED MODEL

Czaderski (2012) discussed the interaction between the release of a prestress force on one side and a pulling force on the other side of a concrete blocks. It was observed that if the bond length is short, the release of the prestress force on one side interacts with the pulling force on the other side. The anchorage resistance was therefore estimated by assuming a reduced value of fracture energy $G_{f,red}$. A similar approach is here extended to the IC debonding, with the difference that, unlike the prestressed force release case in which the available bond fracture energy is reduced, in the ICE the available fracture energy is increased. The proposed model is based on the constant shear stress bond-slip model shown in Fig 1. The following equations are written under the assumption of intermediate crack element length s_r , smaller than the effective bond length l_{ba} . The value of constant shear stress, $\tau_{f,mean}$ is calculated using Eq. 6, more information about the constant shear stress bond-slip model can be found in Czaderski (2012).

$$\tau_{f,mean} = \tau_{f,max} / 2 \quad (6)$$

The effective bond length is then defined as:

$$l_{ba} = \sqrt{\frac{2s_{f,max} E_f t_f}{\tau_{f,mean}}} \quad (7)$$

Figure 9 shows the interaction between the forces F_1 and F_2 for a short bond length ($s_r < l_{ba}$). Due to the opposite direction of F_1 and F_2 , at force F_2 , less stressed end, correspond negative slip and shear stress, meanwhile at the other end, at the force $F_1 = F_2 + \Delta F$, correspond positive slip and shear stress. Unlike the case of the prestress release and anchorage pulling resistance where the $G_{f,red}$ is calculated by the value of the consumed fracture energy, the contribution of F_2 on the calculation of the F_1 , can be estimated by considering an enhancement of the available fracture energy and can be calculated as $G_{f,a} = G_{f,1} + G_{f,2}$. Under the made assumptions the pulling force of the ICE can be calculated as follows:

$$F_1 = F_2 + \Delta F = b_f \sqrt{2 \cdot (G_{f,1} + G_{f,2}) \cdot E_f t_f} \quad (8)$$

The values of $G_{f,1}$ and $G_{f,2}$ are obtained, form the bond shear stress and slip corresponding to forces F_1 and F_2 as indicated in Figure 9 and can be calculated as indicated in Eq. 9

$$G_{f,1} = \frac{s_r^2 \cdot \tau_{f,mean}^2}{2E_f t_f} \quad G_{f,2} = \frac{F_2^2}{2b_f^2 E_f t_f} \quad (9)$$

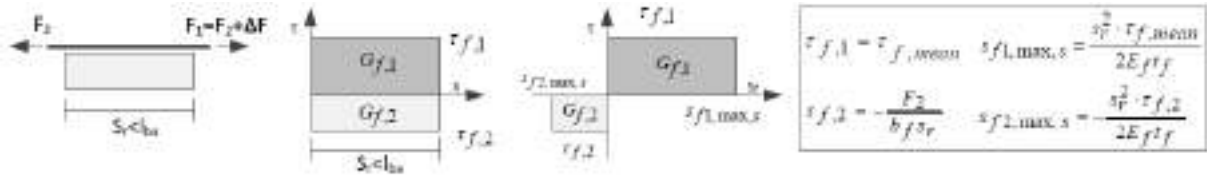


Figure 9: Schematic view of the ICE and the corresponding idealized bond-slip response. Equations used to calculate τ_f and slip $s_{f,max,s}$ corresponding to forces F_1 and F_2 for $s_r < l_{ba}$ (Equations adapted from Czaderski (2012)).

It results that the force F_1 can be calculated as:

$$F_1 = F_2 + \Delta F = \sqrt{F_{IR,s}^2 + F_2^2} \quad (10)$$

Where $F_{IR,s} = \tau_{f,mean} s_r b_f$ is the end-anchorage strength for bond length shorter than the active bond length. Eq.10 is similar to the one used by Czaderski (2012) to evaluate the anchorage pulling resistance after prestress release, but the sign has changed; since the direction of the base force acting on an ICE is opposite to a prestress load. The value of ΔF can be obtained as follows:

$$\Delta F = \sqrt{F_{IR,s}^2 - F_2^2} - F_2 \quad (11)$$

Eq. 11 states the failure envelope of an ICE, i.e. the relationship between a base load level F_2 and additional resisting load ΔF that can be resisted by an ICE prior to failure. This relation has been plotted in Figure 10 for different crack spacing, the obtained equations are extended, with proper changes to $l_b > l_{ba}$. The proposed model is compared with the formulation proposed in Zilch et al.(2014), the SIA 166 (2004) and with the numerical results presented in the previous section.

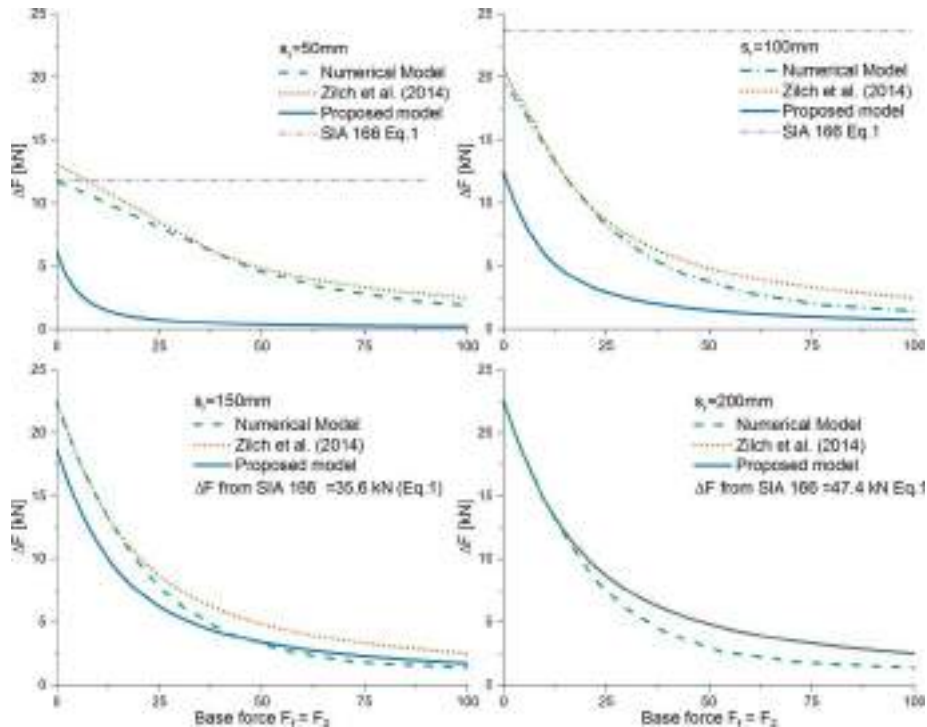


Figure 10: Results obtained using the presented models for the investigated element length s_r

Figure 10 shows that the proposed model is able to catch the behavior of the ICE elements, the value of ΔF decreases as the F_f increase. It can be observed that the difference between the proposed model and the numerical model increases as the cracked element size decrease. This evidence can be mainly explained by the low value of $F_{IR,s}$. The assumed relationship $F_{IR,s} = \tau_{f,mean} s_r b_f$ is very conservative. It can be demonstrated that if $F_{IR,s}$ is calculated as indicated in fib (2001) or Zilch et al. (2014), the difference between the curves for $s_r < l_{ba}$ decrease significantly. This figure also shows that the Zilch model provides accurate solutions for all the investigated bond length. It is interesting to observe that Eq.11 is equal to the second part of Eq.3, the only difference lies in the end

anchorage strength formulation. The main advantage of the proposed approach is its simplicity because the failure envelope can be calculated with only one equation as a function of the end anchorage strength of an element of length s_r . In Fig 10 also the value obtained for the SIA 166 (2004) are displayed, this norm does not take into account the stress state in the FRP, i.e. the base force F_f . Reasonable values are obtained only for the crack spacing of 50 and 100mm, for the remaining spacing the value of ΔF cannot be compared with the other analytical and numerical models (the value has not been plotted only the obtained number is displayed).

CONCLUSIONS AND FUTURE RESEARCH

In this work an analytical model to estimate the FRP intermediate crack debonding strength is proposed and compared with different models available in literature. A simplified numerical model has been developed to study different loading ratios between the forces acting at the loaded ends of an ICE. The numerical results of the bond strength have been used to build failure envelope curves, where the maximum force increment ΔF is expressed as a function of the base force F_f . The failure curves are then used to assess the robustness of analytical models. It was here demonstrated that the analytical models provide similar results, with the exception of the SIA 166 (2004) for large crack spacing. As Czaderski (2012) has experimentally shown, the cracking spacing in the vicinity of the EBR can be very low due to crack branches. The model by Zilch et al. (2014) provides good results when compared to the numerical simulations. The proposed model gives low values of ΔF , mainly for small crack spacing s_r , which, as explained in the paper, is justified by some assumptions made for this simplified model; further work is needed to avoid this drawback.

At the present stage of this research, the model represents a starting point for a wider work dedicated the IC debonding mechanisms. It is the aim of the authors to develop a simple and accurate model for possible future enhancement of the Swiss code.

ACKNOWLEDGMENTS

The financial contribution of the Swiss Road Authorities (FEDRO/ASTRA) within the framework of the project AGB 2016/003.

REFERENCES

- G.M. Chen, J.F. Chen, J.G. Teng (2012) "Behaviour of FRP-to-concrete interfaces between two adjacent cracks: A numerical investigation on the effect of bondline damage". *Construction and Building Materials*;28584-591.
- C. Czaderski (2012) "PhD Thesis No. 20504: Strengthening of reinforced concrete members by prestressed, externally bonded reinforcement with gradient anchorage". Institute of Structural Engineering, ETH Zurich and Empa, Structural Engineering Research Laboratory. 2012, p. 459, <http://dx.doi.org/10.3929/ethz-a-007569614>
- fib (2001) "Externally bonded FRP reinforcement for RC structures – Bulletin 14", International Federation for Structural Concrete (fib), Switzerland. P. 125
- fib (2013) "Model Code for Concrete Structures 2010". International Federation for Structural Concrete (fib), Switzerland. P. 402
- R.P. Niedermeier (2001) "Zugkraftdeckung bei klebarmierten Bauteilen" Phd Thesis Technische Universität München
- RILEM/CEB/FIP (1978) "Bond test for reinforcing steel 2: pullout test. recommendation RC6", Bagneux, France.
- SIA 166 (2004) "Klebebewehrungen (Externally bonded reinforcement)". Schweizerischer Ingenieur- und Architektenverein SIA; 2004.
- SIA 262 (2013) "Betonbau (Concrete structures)". Schweizerischer Ingenieur- und Architektenverein SIA; 2013.
- SIMULIA(2015) "Abaqus Theory Manual", Version 6.16, Dassault Systèmes Simulia Corp.
- T. Ulaga (2003). PhD Thesis ETH No. 15062 in German: Betonbauteile mit Stab- und Lamellenbewehrung: Verbund- und Zuggliedmodellierung (Concrete members with Internal Bar and External Plate Reinforcement: Bond and Tension Chord Modelling). ETH Zürich. p. 161.
- K. Zilch, R. Niedermeier, and Finckh, W. (2014) "DAfStb guideline, in Strengthening of Concrete Structures with Adhesively Bonded Reinforcement: Design and Dimensioning of CFRP Laminates and Steel Plates", Ernst & Sohn.



BOND BEHAVIOR OF PRE-CURED CFRP STRIPS TO CONCRETE USING EXTERNALLY BONDED REINFORCEMENT ON GROOVE (EBROG) METHOD

Niloufar Moshiri 1,2, Davood Mostofinejad 1, Amir Tajmir-Riahi 1

¹ Isfahan University of Technology (IUT), Civil Engineering Department, Isfahan, Iran

² Swiss Federal Laboratories for Materials Science and Technology (Empa)

(Corresponding author: niloufar.moshiri@cv.iut.ac.ir)

ABSTRACT

FRP debonding from concrete substrate may lead to premature failure and diminish the FRP-strengthening performance. Externally Bonded Reinforcement On Groove (EBROG) technique has been presented as a promising substitute to Externally Bonded Reinforcement (EBR) in order to postpone FRP debonding. Eliminating/postponing of debonding of FRP sheets installed through wet layup EBROG was demonstrated in previous studies. In this research, bond behavior of pre-cured CFRP strips with much higher level of stiffness and strength were investigated to examine versatile efficiency of EBROG technique. To do so, 6 specimens were strengthened with EBR and EBROG techniques. Bond resistance and failure modes were experimentally assessed. EBROG method removed the concrete failure and thus, helped the bonded joint to resist higher anchorage resistance. Specimens with two longitudinal grooves in this study experienced a bond resistance twice of those in EBR specimen. In addition, inspecting slip distribution revealed that effective bond length was longer in EBROG method compared to EBR.

KEYWORDS

Strengthening and repair, Experimental study, Bond and interfacial stresses, EBROG method, CFRP strips, DIC, Externally Bonded Reinforcement On Groove.

INTRODUCTION

Fiber-reinforced polymer (FRP) composites have been extensively used in strengthening and retrofitting of reinforced concrete structures. Externally bonded reinforcement (EBR) method is a renowned one utilized in FRP strengthening. However, a major concern regarding the efficiency of FRP strengthening is debonding of FRP from substrate. A great deal of research has been conducted to investigate the bond behavior of FRP to concrete substrate (Chen and Teng 2001, Lu, Teng et al. 2005, Toutanji, Saxena et al. 2007, Czaderski, Soudki et al. 2010, Michels, Zile et al. 2014, Ghorbani, Mostofinejad et al. 2017). Evaluating the stress/strain at which debonding may occur has been subsequently established and some are utilized in design guidelines (International Federation for Structural Concrete 2001, American Concrete Institute (ACI) 2008). As an attempt to postpone FRP debonding, externally bonded reinforcement on groove (EBROG) technique has been proposed as a substitute for EBR (Mostofinejad and Mahmoudabadi 2010). EBROG technique which is a sub-technique of grooving method (GM) was first studied by Mostofinejad and Mahmoodabadi (Mostofinejad and Mahmoudabadi 2010). In a short description, EBROG technique consists of cutting some grooves in the concrete cover, filing them with adhesive and applying FRP sheets on the substrate by adhering them. No other surface preparation is needed prior to FRP installing. Near surface mounted (NSM) is another common technique to bond FRP to concrete substrate (Nordin and Täljsten 2002, Bilotta, Ceroni et al. 2011). In this method, some slits are cut in concrete cover and FRP strips or rods are placed in the slits. In order to clarify the difference between EBROG method and some conventional existing methods, they are schematically demonstrated in Figure 42. It is seen here that EBROG method is different from EBR and NSM which its efficiency on bond behavior of procured FRP strips-to-concrete is experimentally investigated in this paper, and will be analytically studied in future papers.

Mostofinejad and Mahmoodabadi conducted a series of experimental tests for flexural strengthening of beams through EBROG and EBR methods. They demonstrated that using grooving method with longitudinal grooves on the tension face of the beam postponed FRP debonding (Mostofinejad and Mahmoudabadi 2010). Significant increase in load carrying capacity of the strengthened beam was therefore observed compared to the beam

retrofitted through EBR method. Promising results of this new method paved the road to make more studies on it and now, it is still an ongoing research topic. In this regard, bond behavior of FRP composites attached to concrete substrate by means of EBROG method has been investigated partially (Hosseini and Mostofinejad 2013, Hosseini and Mostofinejad 2013, Ghorbani, Mostofinejad et al. 2017). However, there is no study so far on the efficacy of EBROG method when pre-cured strips are used. Maximum load which can be developed in pre-cured strips are much higher than the ones carried by 1 ply of FRP sheets. The capability of EBROG method to transfer such high load level to concrete substrate should be further studied. Present research is thus aimed at investigating the bond behavior of pre-cured CFRP strips attached by means of EBROG method. Bond resistance and failure mode of the joint will be assessed through an experimental program. Moreover, load-slip behavior and slip distribution will be determined through a 2D digital image processing technique.

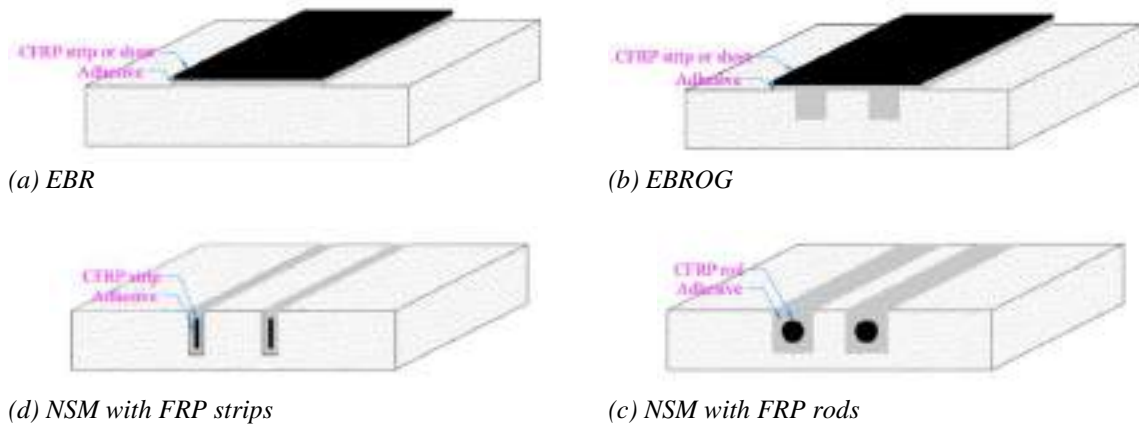


Figure 42: Schematic figure of different bonding techniques

EXPERIMENTAL PROGRAM

Material

Single lap-shear tests were carried out on 6 concrete specimens having cylindrical compressive strength of 38.2 MPa and square cross section of 150×150 mm and length of 350 mm. Unidirectional pre-cured CFRP strips, Sika Carbodur S514, with nominal thickness of 1.4 mm, ultimate tensile strength of 2800 MPa and elastic modulus of 165 GPa was used in this study. Sikadur 31 adhesive with tensile strength of 15-20 MPa and elastic modulus of 4.3 GPa was used to adhere CFRP to concrete. The FRP strip was 50 mm wide, bonded along 245 mm length, starting at a location 55 mm far from the edge of concrete block.

Test Layout

Table 1 describes the test specimen. Reviewing Table 1, it is deduced that label of each specimen starts with the strengthening method used. In series I, labels are in the form of $EBR-n$ or $EBROG-b_g \times h_g-n$ for specimens strengthened through EBR or EBROG method, respectively. Notations b_g and h_g refer to groove width and depth, respectively; and symbol n denotes the order of the repetitive tests (1 or 2). For the sake of simplicity, specimens strengthened through EBR or EBROG method are called EBR joint or EBROG joint hereafter. Single lap-shear tests were carried out by means of a 300-kN hydraulic jack. Tensile load was applied on the FRP strip in displacement-controlled mode with a rate of 2 mm/min. Test setup and instrumentations are illustrated in Figure 43.

Table 1 Test layout

Specimen No.	Specimen label	Strengthening method	Groove width, b_g (mm)	Groove depth, h_g (mm)	P_{max} (kN)	$P_{max,avg}$ (kN)	Increase in $P_{max,avg}$ (%)	STRAIN (‰)	Strain ratio
1	EBR-1	EBR	-	-	25.8	25.0	-	2.2	0.13
2	EBR-2		-	-	24.2			2.1	0.12
3	EBROG-5×5-1	EBROG	5	5	48.0	48.0	94	4.2	0.24
4	EBROG-5×5-2		5	5	33.0*			-	-
5	EBROG-5×10-1	EBROG	5	10	53.7	53.0	112	4.6	0.27
6	EBROG-5×10-2		5	10	52.4			4.5	0.27

*Premature failure in clamps. This result is therefore excluded.



Figure 43: Test instrumentations

Strengthening technique

In order to retrofit the concrete specimen through EBR, surface preparation was conducted as usual, i.e. removing a weak layer of concrete surface by means of a disk grinder. EBROG joints were prepared and strengthened via following steps:

- Two 245 mm long grooves with free distance of 20 mm were cut along the length of the specimen using a circular saw.
- Grooves were then completely filled with epoxy. A layer of epoxy with 1.1 mm thickness was applied on the substrate.
- Subsequently, the FRP strip was cleaned with acetone and attached to the specimen's face.

Deformation Measurement through Digital Image Correlation (DIC)

In order to utilize the image correlation system, a colorful pattern was made on the face of each specimen. To do so, the specimen was first painted in white. Small red, green and blue spots were then produced on the specimen's face by spraying each color on it. Successive digital images taken during the tests were implemented in GeoPIV8 software, a DIC system to calculate full-field displacements. The so called software was developed by White and Take at Cambridge University (2002) was used in this study (White, Take et al. 2003). Further description on the application of digital image analysis techniques in FRP-to-concrete bond tests can be found in Carloni and Subramaniam (Carloni, Subramaniam et al. 2012).

RESULTS AND DISCUSSIONS

Load-slip behavior

Load-slip behaviors of specimens are plotted in Figure 44. Typical bilinear response of EBR joint is observed here. The point in this diagram over which no significant increase in load is observed corresponds to the initiation of debonding. Slip values regarding this stage is around 0.1 mm for EBR specimens. However, EBROG joints did not show a bilinear response. In other words, the slope of load-slip behavior decreases gradually, while load and slip are both increasing up to final stages. It is seen that EBROG joints experienced large slips before debonding initiates and the no further increase in load is observed. It is worth mentioning that specimen EBROG-5×5-2 showed a premature failure when it was slipped in the clamps, and hence, it was excluded from the results.

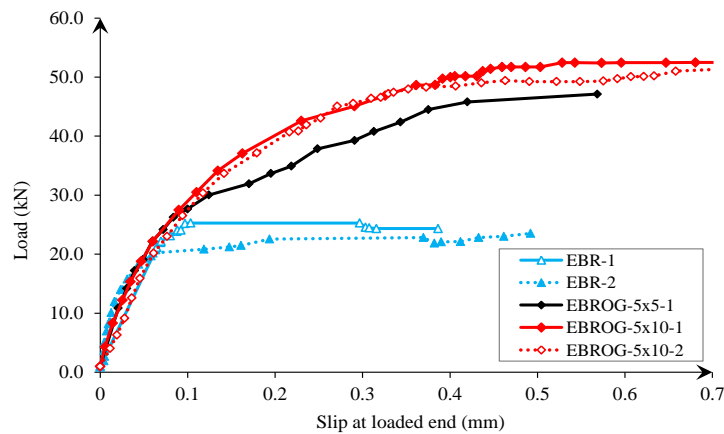


Figure 44: Load-slip behavior

Bond resistance

It can be seen in Table 1 that EBROG method enhanced the bond resistance significantly. Increase of 94% and 112% were observed for specimen EBROG-5×5 and EBROG-5×10, respectively, compared to EBR specimen. It is concluded therefore that EBROG method was highly efficient to improve the anchorage resistance of FRP-to-concrete bonded joints.

Strain Ratio

Strain values developed in the CFRP strip at loaded end were determined by dividing maximum load to the (section area × CFRP stiffness). Table 1 shows the strain values and also their ratio with respect to the ultimate tensile strain of strips. It is observed that strain value for EBR specimen was 2.15‰ on average, while it increased two times for EBROG specimen. Strain exploitation ratios were 0.12, 0.24 and 0.27 for EBR, EBROG-5×5 and EBROG-5×10, respectively.

Slip distribution along the FRP length

Slip distribution along the length of FRP composite is depicted in Figure 45. Numerous diagrams are plotted each for a specific load. By increasing the load level, longer bond length of the strip experienced slips. In order to be able to compare to the slip distribution of different specimens, the load stage corresponds to the initiation of debonding was selected and the slip-distance diagrams were plotted for this stage (Figure 46). It is worth mentioning that slip-distance diagrams are determined for consecutive photos, without distinct load/time increment between them. So, the stage corresponding to initiation of debonding cannot be easily prosecuted from current slip-distance diagrams.

In order to be able to determine the stage of initiation of debonding, load-slip diagrams are taken into account. For EBR specimens, simply the stage where load-slip behavior turns into horizontal (after the ascending branch) is the stage of initiation of debonding. For EBROG specimens, this stage was defined as the one over which no considerable increase in load is observed.

It is seen in Figure 46 that EBROG specimens had larger slip values compared to EBR. In addition, longer bond length of EBROG specimens experienced slips at the initiation of debonding. It is perceived, therefore, that the effective bond length was larger for EBROG method compared to EBR. The average effective bond lengths were 90, 145 and 160 mm for EBR, EBROG-5×5 and EBROG-5×10, respectively. The deeper the grooves were, the larger was the effective bond lengths. It is believed that EBROG method can transfer the interfacial shear stresses to the concrete depth. As the contact area between FRP and concrete is bigger in EBROG compared to EBR, the joint can resist higher loads.

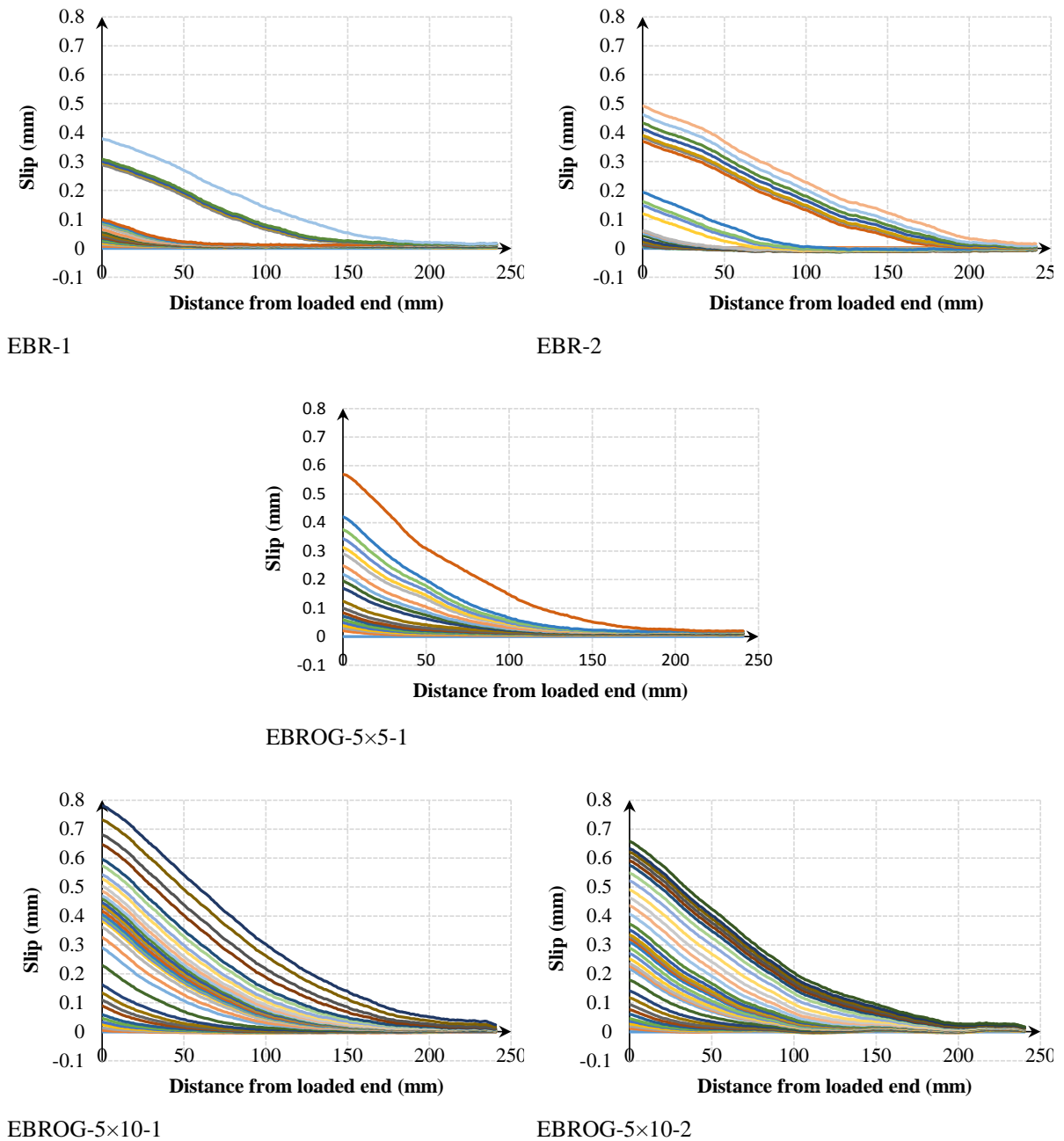


Figure 45: Slip distribution along the FRP length (bond length=240 mm)

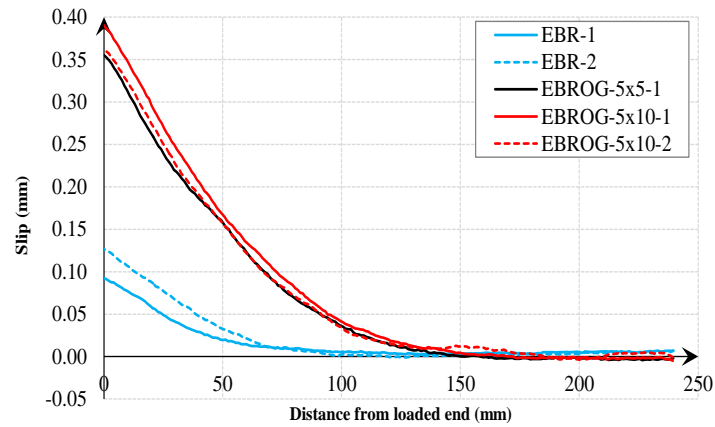


Figure 46: Slip distribution along the FRP length at initiation of debonding (bond length=240 mm)

Failure mode

Debonding occurred in concrete beneath the CFRP strip in EBR specimens. However, in EBROG specimens, cohesive failure occurred in the adhesive layer. Failure mode of different specimens is demonstrated in Figure 47. It means that EBROG method was able to remove the concrete failure and helped the FRP-to-concrete bonded joint to resist higher anchorage resistance.



EBR-1

EBROG-5×5-1

EBROG-5×10-1

Figure 47: Failure modes

CONCLUSIONS

- Bond resistance of EBROG specimens were approximately twice the EBR ones. It means that EBROG technique was capable of improving the bond behavior of FRP-to-concrete when pre-cured FRP strips with high fiber volume fraction were used.
- Load-slip behavior of EBR joints demonstrated a typical bilinear behavior. However, this behavior was not experienced in EBROG joints. They showed an ascending branch up to final stages with a gradually decreasing slope of this diagram.
- The effective bond length was evaluated through slip distribution along the FRP strip. It was shown that in EBROG method the effective bond length was larger compared to EBR.

- Slip distribution along the CFRP strip showed that EBROG method resulted in high slip values at the initiation of debonding, compared to EBR.
- EBROG method helped the joint to remove debonding in concrete. Therefore, it was able to resist higher anchorage force and finally, cohesive failure in the adhesive happened.

REFERENCES

- American Concrete Institute (ACI) (2008). "ACI 440.2R-08, Guide for the design and construction of externally bonded FRP systems for strengthening concrete structures." Farmington Hills, MI.
- Bilotta, A., F. Ceroni, M. Di Ludovico, E. Nigro, M. Pecce and G. Manfredi (2011). "Bond efficiency of EBR and NSM FRP systems for strengthening concrete members." *Journal of Composites for Construction* 15, 757-772.
- Carloni, C., K. V. Subramaniam, M. Savoia and C. Mazzotti (2012). "Experimental determination of FRP–concrete cohesive interface properties under fatigue loading." *Composite Structures* 94, 1288-1296.
- Chen, J. F. and J. G. Teng (2001). "Anchorage strength models for FRP and steel plates bonded to concrete." *Journal of Structural Engineering* 127, 784-791.
- Czaderski, C., K. Soudki and M. Motavalli (2010). "Front and side view image correlation measurements on FRP to concrete pull-off bond tests." *Journal of Composites for Construction* 14, 451-463.
- Ghorbani, M., D. Mostofinejad and A. Hosseini (2017). "Bond Behavior of CFRP Sheets Attached to Concrete through EBR and EBROG Joints Subject to Mixed-Mode I/II Loading." *Journal of Composites for Construction* 21, 04017034.
- Ghorbani, M., D. Mostofinejad and A. Hosseini (2017). "Experimental investigation into bond behavior of FRP-to-concrete under mixed-mode I/II loading." *Construction and Building Materials* 132, 303-312.
- Hosseini, A. and D. Mostofinejad (2013). "Effect of groove characteristics on CFRP-to-concrete bond behavior of EBROG joints: experimental study using particle image velocimetry (PIV)." *Construction and Building Materials* 49, 364-373.
- Hosseini, A. and D. Mostofinejad (2013). "Experimental investigation into bond behavior of CFRP sheets attached to concrete using EBR and EBROG techniques." *Composites Part B: Engineering* 51, 130-139.
- International Federation for Structural Concrete (2001). "fib Bulletin No. 14, Externally bonded FRP reinforcement for RC structures." Lausanne, Switzerland.
- Lu, X., J. Teng, L. Ye and J. Jiang (2005). "Bond–slip models for FRP sheets/plates bonded to concrete." *Engineering structures* 27, 920-937.
- Michels, J., E. Zile, C. Czaderski and M. Motavalli (2014). "Debonding failure mechanisms in prestressed CFRP/epoxy/concrete connections." *Engineering Fracture Mechanics* 132, 16-37.
- Mostofinejad, D. and E. Mahmoudabadi (2010). "Grooving as alternative method of surface preparation to postpone debonding of FRP laminates in concrete beams." *Journal of Composites for Construction* 14, 804-811.
- Nordin, H. and B. Täljsten (2002). Prestressed near surface mounted reinforcement (NSMR) for strengthening concrete beams. FRP Composites in Civil Engineering-CICE 2004: Proceedings of the 2nd International Conference on FRP Composites in Civil Engineering-CICE 2004, 8-10 December 2004, Adelaide, Australia, CRC Press.
- Toutanji, H., P. Saxena, L. Zhao and T. Ooi (2007). "Prediction of interfacial bond failure of FRP–concrete surface." *Journal of composites for construction* 11, 427-436.
- White, D., W. Take and M. Bolton (2003). "Soil deformation measurement using particle image velocimetry (PIV) and photogrammetry." *Geotechnique* 53, 619-632.



BOND RESISTANCE OF A SINGLE GROOVE IN EBROG METHOD TO ATTACH CFRP SHEETS ON CONCRETE

Amir Tajmir-Riahi 1, Davood Mostofinejad 1, Niloufar Moshiri 1,2

¹ *Isfahan University of Technology (IUT), Civil Engineering Department, Isfahan, Iran*

² *Swiss Federal Laboratories for Materials Science and Technology (Empa)*

(Corresponding author: amir.tajmir@yahoo.com)

ABSTRACT

Nowadays the strengthening of existing building in order to ensure proper operation in emergency time is one of the most important construction industry's challenges. Because of composite sheets fast and easy implementation, their very low weight and very high tensile resistance and ability to resist corrosion, FRP composite sheets has become one of the most widespread materials for strengthening of concrete structures. The conventional method for utilizing FRP sheets is externally bonded reinforcement (EBR). The main advantage of EBR technique is facile installation, but premature debonding of FRP sheets has restricted EBR technique. Externally bonded reinforcement on groove (EBROG) method has been proposed as an alternative to EBR method. EBROG in comparison with EBR is capable of postponing/eliminating of debonding phenomenon and the results have been discussed in the literature. In this paper, load carrying capacity of a single groove is experimentally evaluated. To focus on bond resistance of a groove, just one groove with length of 200mm is created in the middle of bond zone. Size effect of grooves is another intention of the current research. To do so, single shear tests were conducted on 8 specimens with dimension of 150×150×350mm that were strengthened with EBR and EBROG. Results showed that the maximum load carried by an EBROG joint is much more than that of the counterpart EBR joint. The bond resistances of a single groove in EBROG joint are also compared in different sizes of grooves. In addition, an innovative method was proposed to evaluate the effective bond length.

KEYWORDS

Strengthening and repair; Experimental study; Bond and interfacial stresses; EBROG method; Size effect, FRP sheet.

INTRODUCTION

Externally bonded reinforcement on groove (EBROG) method was developed to inhibit premature debonding of fiber reinforce polymer (FRP) composites from concrete substrate. EBROG method, as an alternative to conventional externally bonded reinforcement (EBR), showed promising results in postponing FRP debonding for different applications. For instance, flexural and shear strengthening of RC beams, shear retrofit of RC beam-column joints, axial-flexural strengthening of RC columns, and FRP-to-concrete bond behavior were all the topics studied to examine the EBROG method (Mostofinejad and Mahmoudabadi 2010, Hosseini and Mostofinejad 2013, Mostofinejad and Kashani 2013, Moshiri, Hosseini et al. 2015, Mostofinejad and Torabian 2015, Mostofinejad and Akhlaghi 2016, Ghorbani, Mostofinejad et al. 2017). Besides extensive research on EBROG so far, different aspects are still unidentified. Among them is the bond behavior of FRP to concrete substrate using a single line of groove without any interference with adjacent grooves. This study is necessary for proposing design equations to consider the effect of a single groove. Moreover, it was assessed in this paper that to some extent is efficient one longitudinal groove. To do so, single lap shear tests were conducted on 8 concrete blocks strengthened through EBR and EBROG methods. Different dimensions of the groove section were examined. In addition, a new understanding of effective bond length was introduced in this paper and the corresponding values were obtained and compared for different specimens.

EXPERIMENTS

Single lap-shear tests were conducted on 8 concrete blocks with dimensions of 150×150×350 mm and concrete compressive strength of 56 MPa. In order to strengthen the specimens, SikaWrap 230C unidirectional carbon fiber sheets with 48 mm width were used. Thickness, elastic modulus and ultimate tensile strength of fiber sheets were

0.131 mm, 238 GPa and 4300 MPa, respectively. For impregnating the fiber sheets, attaching them to the concrete substrate and filling the grooves in EBROG method, Sikadur 330 epoxy with elastic modulus of 4.5 GPa and ultimate tensile strength of 30 MPa was utilized.

EBR and EBROG methods were used to strengthen the specimens through wet lay-up application. In all eight specimen, a tinny layer of concrete, i.e. dust and dirt, was first removed. EBR strengthening included applying a thin layer of adhesive to the surface, attaching fiber sheets to concrete and impregnating them. To utilize EBROG method, one longitudinal groove with desired dimensions of groove section and a length of 200 mm were cut in concrete substrate. Grooves were then filled completely with epoxy adhesive and fiber sheets were attached on the surface with fibers parallel to the groove longitude. Similar bond length of 200 mm were considered for all specimens. A free 35 mm length were remained unbonded on the pulling side to inhibit stress concentration (Mazzotti, Savoia et al. 2008). Schematic configuration of EBROG specimen is shown in Fig. 1. Seven days curing at room temperature was held for all specimens. A color surface was then applied on the surface of specimen for DIC measurements. To do so, the surface was painted in white and then, red, green and blue spots were randomly sprayed on it to provide a color texture. Therefore, displacement analysis could be executed through an image based analysis, called particle image velocimetry (PIV). GeoPIV8 MATLAB code developed at Cambridge University (White, Take et al. 2003), was utilized to evaluate displacement vectors of center of 128×128-pixels patches. Test instrumentation is depicted in Fig. 2. Specimens were loaded under displacement control mode up to failure with rate of 2 mm/min.

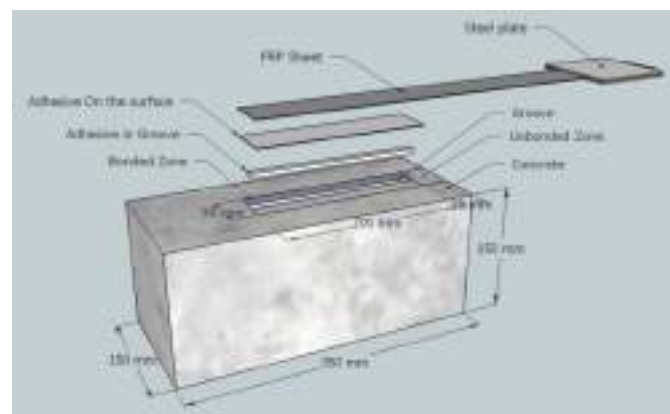


Figure 1: Schematic configuration of EBROG specimen



Figure 2: Test setup

Specimens' details are stated in Table 1. Specimen label starts with the name of strengthening method, i.e. EBR or EBROG. For EBROG specimens, it follows with the groove width (b_g) and depth (h_g), and the ordinal number of repetitive tests (1 or 2), as well. Due to simplicity, specimens strengthened by means of EBR or EBROG method are called EBR joint or EBROG joint, respectively. In addition, results of lap-shear tests are collected in Table 1. Maximum load of each specimen, P_{max} (kN), the average for two similar specimens, $P_{max,avg}$ (kN), increase in maximum load respect to EBR specimen (%), and the effective bond length, l_{eff} , can be seen in Table 1.

Table 1: Test specimens' details

Specimen No.	Specimen label	Strengthening method	Groove width, b_g (mm)	Groove depth, h_g (mm)	P_{max} (kN)	$P_{max,avg}$ (kN)	Increase in $P_{max,avg}$ (%)	l_{eff} (mm)
1	EBR-1	EBR	-	-	7.17	7.31	-	55
2	EBR-2				7.46			50
3	EBROG- b_g5-h_g5-1	EBROG	5	5	9.94	10.40	42.25	38
4	EBROG- b_g5-h_g5-2			5	10.87			38
5	EBROG- b_g5-h_g10-1			10	12.66	32		
6	EBROG- b_g5-h_g10-2			10	11.84	38		
7	EBROG- b_g5-h_g15-1			15	10.86	27		
8	EBROG- b_g5-h_g15-2			15	11.31	27		

RESULTS AND DISCUSSION

Maximum load

It can be seen in Table 1 that the specimens which were strengthened through grooving method resulted in much higher bond resistance terms of maximum carried load. More than 40% increase in anchorage resistance was observed for all grooving methods compared to specimen strengthened with EBR method. It is demonstrated in Table 1 that for a small groove dimension, i.e. depth and width of 5 mm, maximum load was 10.40 kN on average. While, the corresponding EBR specimen showed anchorage load of 7.31 kN, on average. Therefore, 42% enhancement was concluded for specimen with 5×5 mm groove.

In addition, larger groove of 5×10 mm in specimen EBROG-5-10-25 enhanced the anchorage resistance equal to 67% over EBR specimen. However, increasing the depth of the groove to 15 mm did not further increase the maximum load. It seems therefore that there might be an optimized groove dimension over which no additional improvement in maximum load is seen. More studies are thus proposed.

Failure mode

Fig. 3 illustrates the failure mode of specimens at ultimate point. It is obvious that EBR specimens experienced usual debonding failure in which the CFRP, adhesive and a thin layer of concrete detached from substrate. Debonding phenomena occurs in EBROG joints, as well. However, how deep the debonded layer is varies in different specimens. Comparing EBROG specimens in Fig. 3, it can be deduced that the detached layer in specimens with 10mm-depth groove was thicker respect to other EBROG specimens. In other words, deeper layer of concrete was removed in a way that aggregates were easily distinguishable. It means that debonding occurred where strong bond between aggregates existed before debonding. This fact can explain the higher bond resistance of EBROG specimen with 10mm deep groove compared to those with different groove depths.

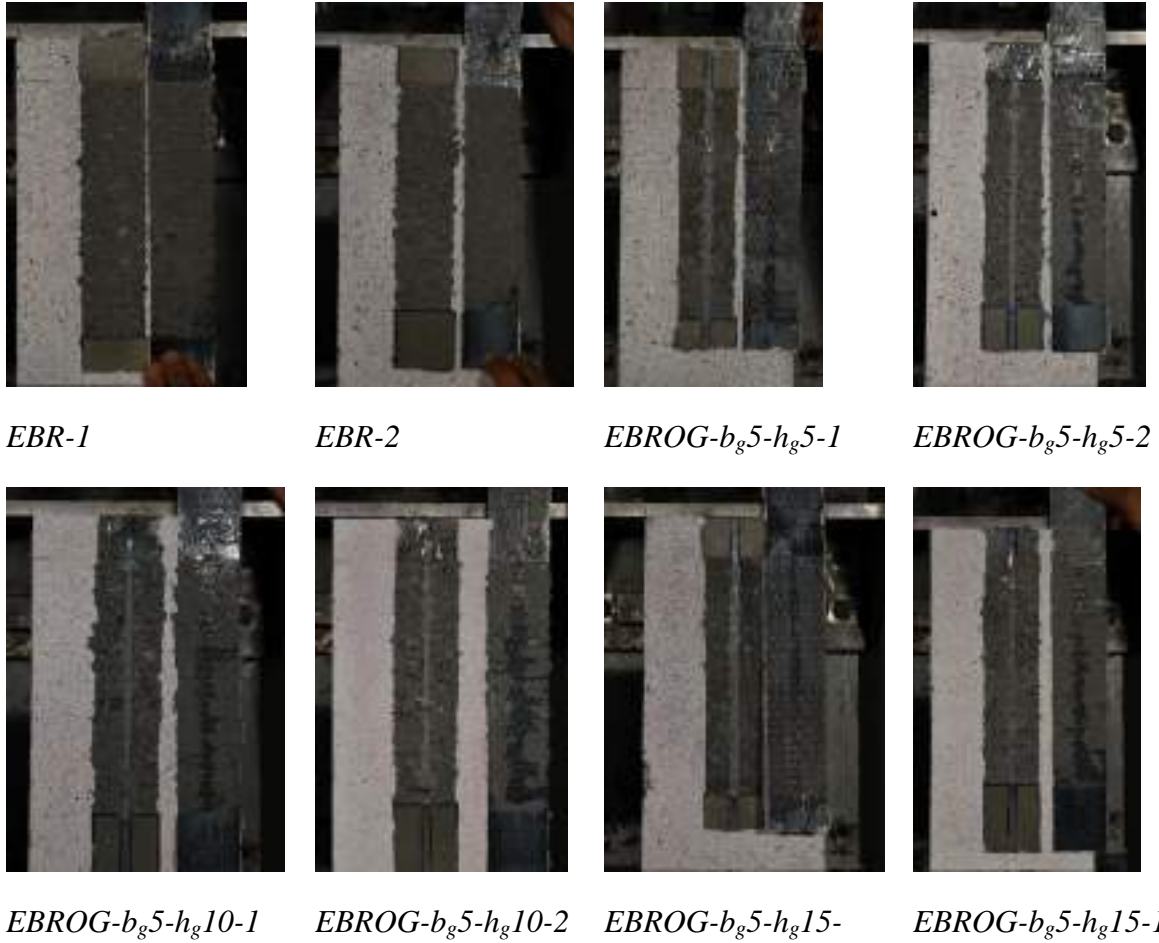
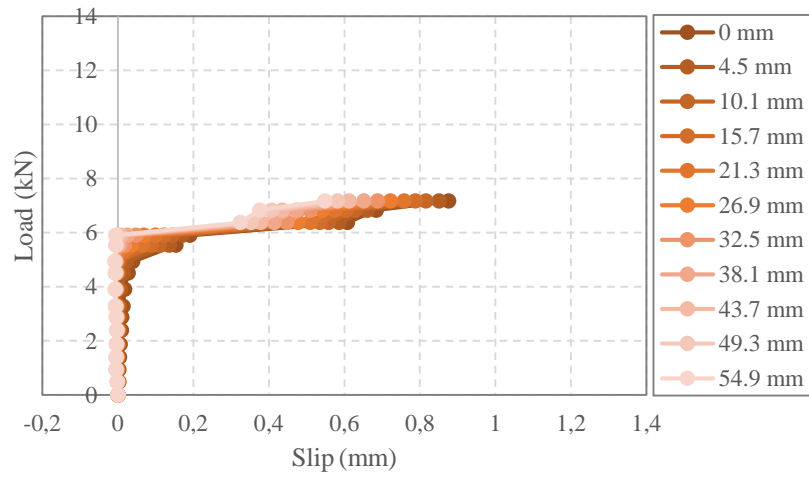


Figure 3: Failure modes of tested specimens

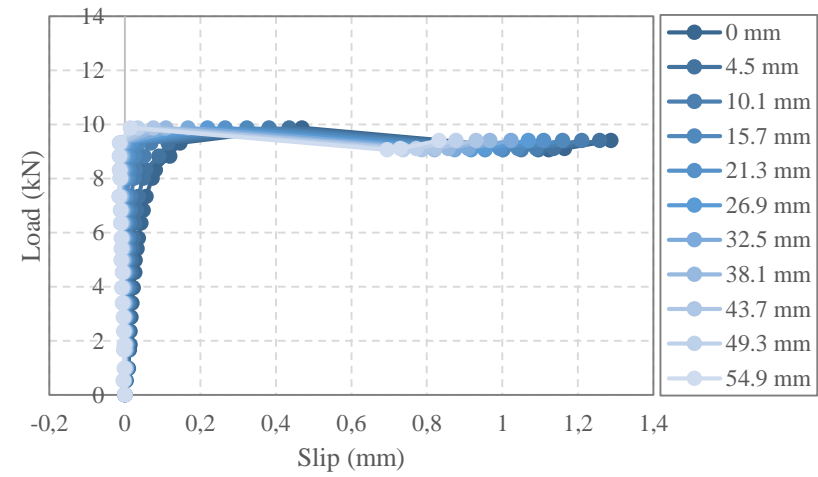
Load-slip behavior along the FRP length

Utilizing an image-based correlation system for evaluating the deformations in this study, provided a new promising diagram from which interesting concepts can be concluded. Load-slip behavior along the length of the FRP is demonstrated in Fig. 4. The inner diagram is the load-slip behavior at the loaded end of the FRP width. Passing across the diagrams outward, the slip is attributed to different sections with spacing of almost 4.5 mm along the FRP length. It is seen that at a certain load level, slip is decreased as moving along the FRP length. There is a section at which the load-slip behavior is almost vertical and stick to the load axis. In other words, no significant slip is understood at this section until initiation of debonding. This reminds the concept of effective bond length. It can be concluded, therefore, that this section is the end of effective bond length. Using this innovative technique, effective bond length was obtained for different specimens and was reported in Table 1 (l_{eff}).

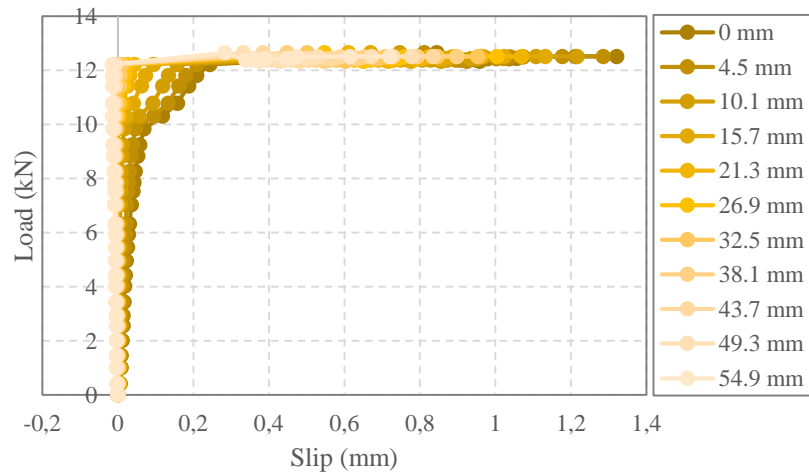
It is demonstrated that l_{eff} was between 50 and 55 mm for EBR specimen while it was calculated much less for EBROG specimens. For example, it was equal to 38, 35 and 27 mm for specimens *EBROG-b_g5-h_g5-1*, *EBROG-b_g5-h_g10* and *EBROG-b_g5-h_g15*, respectively. It is evident that the deeper the groove, the less the effective bond length.



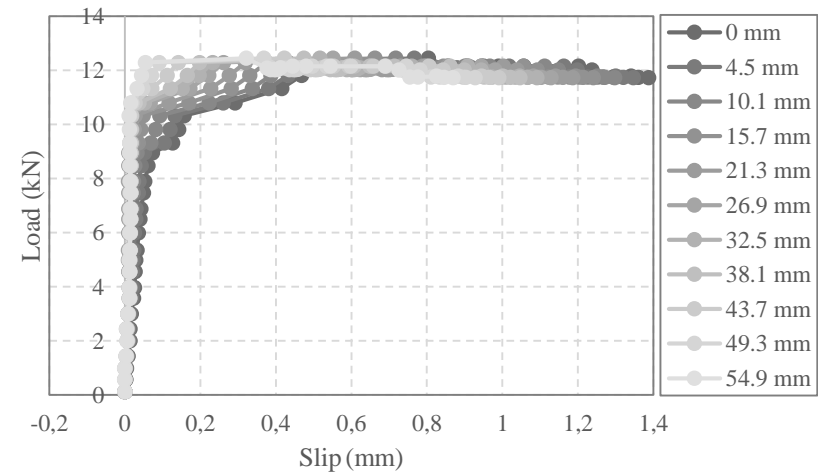
EBR-1



EBROG-b_g5-h_g5-1



EBROG-b_g5-h_g10-1



EBROG-b_g5-h_g15-1

Figure 4: Load-slip behavior along the FRP length

CONCLUSION

- Considering one line of longitudinal groove with small dimensions, i.e. width of 5 mm and depth of 5, 10 and 15 mm, significant improvement in maximum anchorage resistance was observed for EBROG specimens compared to EBR specimens. For instance, using 5×5 mm groove led to 42 percent increase in maximum carried load.
- A creative technique was described to evaluate the effective bond length of specimens by means of load-slip diagrams along the CFRP length. It was shown that EBROG specimens had less effective bond length compared to EBR ones. In these specimens, effective bond length decreased as the groove depth increased.

REFERENCES

- Ghorbani, M., D. Mostofinejad and A. Hosseini (2017). "Bond Behavior of CFRP Sheets Attached to Concrete through EBR and EBROG Joints subject to Mixed-Mode I/II Loading", *Journal of Composites for Construction* 21, 04017034.
- Hosseini, A. and D. Mostofinejad (2013). "Experimental investigation into bond behavior of CFRP sheets attached to concrete using EBR and EBROG techniques", *Composites Part B: Engineering* 51, 130-139.
- Mazzotti, C., M. Savoia and B. Ferracuti (2008). "An experimental study on delamination of FRP plates bonded to concrete", *Construction and Building Materials* 22, 1409-1421.
- Moshiri, N., A. Hosseini and D. Mostofinejad (2015). "Strengthening of RC columns by longitudinal CFRP sheets: Effect of strengthening technique", *Construction and Building Materials* 79, 318-325.
- Mostofinejad, D. and A. Akhlaghi (2016). "Experimental Investigation of the Efficacy of EBROG Method in Seismic Rehabilitation of Deficient Reinforced Concrete Beam–Column Joints Using CFRP Sheets", *Journal of Composites for Construction* 21, 04016116.
- Mostofinejad, D. and A. T. Kashani (2013). "Experimental study on effect of EBR and EBROG methods on debonding of FRP sheets used for shear strengthening of RC beams", *Composites Part B: Engineering* 45, 1704-1713.
- Mostofinejad, D. and E. Mahmoudabadi (2010). "Grooving as alternative method of surface preparation to postpone debonding of FRP laminates in concrete beams", *Journal of Composites for Construction* 14, 804-811.
- Mostofinejad, D. and A. Torabian (2015). "Experimental study of circular RC columns strengthened with longitudinal CFRP composites under eccentric loading: Comparative evaluation of EBR and EBROG methods", *Journal of Composites for Construction* 20, 04015055.
- White, D., W. Take and M. Bolton (2003). "Soil deformation measurement using particle image velocimetry (PIV) and photogrammetry", *Geotechnique* 53, 619-632.



WIDTH EFFECT OF INTERFACIAL BOND

Yu-Fei Wu¹, Jian-Ping Lin², Liang He³

¹ Professor, School of Engineering, RMIT University, Australia
(corresponding author: yufei.wu@rmit.edu.au);

² Lecturer, College of Civil Engineering, Huaqiao University, Xiamen, China;

³ Engineer, Guangzhou Metro Design and Research Institute Corporation Limited, China.

ABSTRACT

The bond properties of an interface in composite structures are generally considered as local mechanical characteristics in extant literature. Through experimental testing, analytical study, and numerical simulation, it is shown in this work that the interfacial bond characteristics are generally size dependent and non-local structural properties. Interfacial shear bond generally involves both Mode II and Mode III fractures. When both fracture modes are involved, the bond characteristics are size dependent. However, when only Mode II fracture is involved, the interfacial bond is size independent. Rational study of the problem indicates that some key and important factors have not been considered in existing models. A more sensible and accurate bond model considering all the key factors and the size effect is developed in this work for externally bonded FRP-to-concrete joints.

KEYWORDS

Interface, bond, size effect, width effect, fracture mode.

INTRODUCTION

Interfacial bonding connects substrates of different materials by adhesion, friction or mechanical interlocking. The stress and strain fields at the bond interface, involving bonding agent and the local vicinity of adjacent substrate materials, are usually much more complicated than those in other parts of a structure. To avoid the complication and facilitate the application of conventional structural theories to such composite structures, a convenient and sensible approach is to lump all additional deformations that cannot be included in conventional structural theory (such as beam theory) into a concentrated displacement at the interface, namely, interfacial slip. The interaction between the substrate materials is subsequently simplified into a resistance to the interfacial slip by a bond-slip relationship which can be identified from bond tests or pull-off tests for a particular type of interfacial joint.

For a joint where a reinforcing material is bonded to substrate, both the deformation of the bonding agent and that of substrate contribute to the interfacial slip. The interfacial shear movement contributed by the deformation in substrate is resisted by not only the substrate material directly below the bonded area, but also that surrounding the boundary of the bond area. When the bond area becomes smaller or approaches zero, the resistance to slip caused by the substrate material directly under the bond area reduces and diminishes and that by the surrounding substrate material increases quickly. Due to this additional restraint from the surrounding material, the bond-slip relationship at the boundary of a bond area is much stiffer than that inside (Zhou et al. 2010). This boundary effect to bond-slip relationship is related to the size of the bond area, and hence, is not local but size dependent. On the other hand, the rigidity of reinforcing material also has a significant effect on the bond-slip relationship.

On a two-dimensional interface such as concrete beams reinforced with externally bonded (EB) steel or fiber-reinforced polymer (FRP) plates, this size effect is referred to as the width effect (Chen and Teng 2001; Dai et al. 2005; Lu et al. 2005; Subramaniam et al. 2007). The interfacial bond properties of such composite beams are affected by the width of the attached plate b_f relative to the width of the beam b_c (Fig. 1). Numerous models have been developed to consider the width effect on bond properties of EB-steel or -FRP reinforced beams (Chen and Teng 2001; Dai et al. 2006; Lu et al. 2005; Niedermeier 2000; Subramaniam et al. 2007; Wu et al. 2009). However, the modeling of the size effect so far is not only significantly scattered compared with test results (Wu and Jiang 2013) but also theoretically flawed. For example, only b_f/b_c is considered in most width effect models. Based on the discussions above, it is clear that more factors affect this width effect.

In this paper, a new approach is used to investigate the width effect. Digital Image Correlation (DIC) was used to capture the strain field of FRP sheet externally bonded to a concrete block. Through rational analytical studies of the measured strain fields and finite element analyses, the width effect is identified and quantified, from which a new width factor model is developed for engineering use.

EXPERIMENTAL TESTS AND RESULTS

Pull-off tests are currently the conventional means for investigating interfacial bond properties. The single pull-off test was adopted in the bond tests in this work (Fig. 1). A total of 65 specimens were tested in the Heavy Structure Testing Laboratory at City University of Hong Kong. The concrete blocks used for the pull-off tests had the dimensions of 150 mm (width) \times 150 mm (depth) \times L_c (length), where $L_c = 300, 450, \text{ or } 600$ mm, for bond lengths of $L = 30-100, 250$ and 400 mm, respectively. Test variables involve concrete strength, including five grades of C20, C30, C40, C50, and C60, the bond length, being 30, 50, 100, 250, and 400 mm, and the rigidity of FRP sheet, with three variations of 1-, 2-, and 3-ply of carbon FRP (CFRP). Tests were conducted under a displacement control mode at a rate of 0.001-0.003 mm/s.

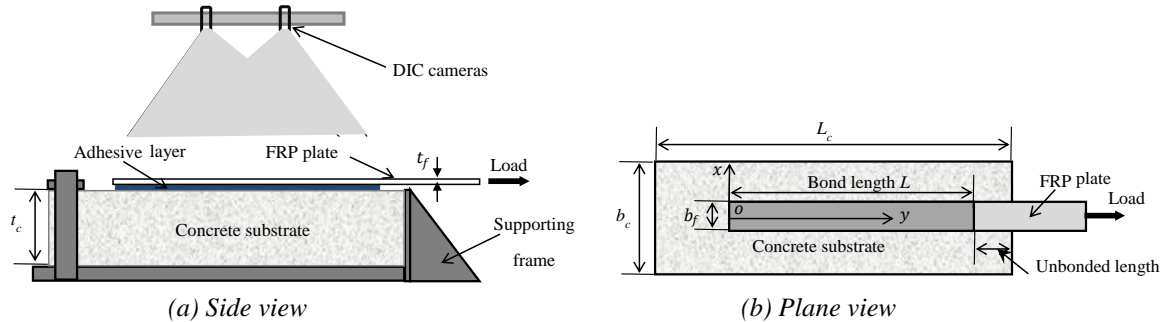


Figure 3: Pull-off test

The displacement and strain fields on the surface of the test specimens were continuously captured by the DIC system. The typical strain distributions of the FRP sheet for specimen C30-250-3 are shown in Fig. 2, where ϵ_{yy} and ϵ_{xy} are the longitudinal and transverse shear strain, respectively. The dashed lines show the boundary of the FRP sheet.

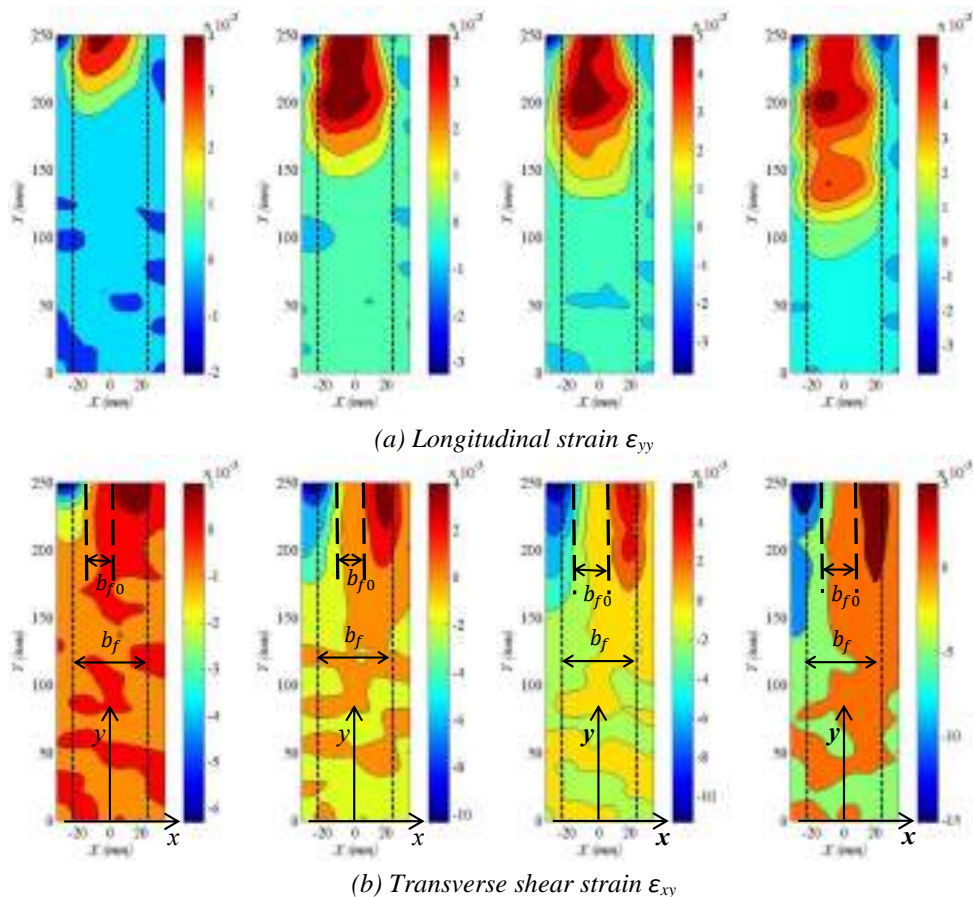


Figure 4: Variation of surface strains captured by DIC

A few typical transverse and longitudinal sections of ϵ_{yy} distributions are shown in Fig. 3. The longitudinal strain distribution can be divided into three regions: (I) unstressed region; (II) stress transfer zone; and (III) fully debonded zone (Fig. 3b). Figure 3a shows that the longitudinal strain for a particular cross-section is not uniform.

This variation in the transverse direction (X direction) is the result of the width effect. In other words, in bond tests when there is no width effect, the longitudinal strain across a cross-section should be uniform.

In the central region, the FRP strain and bond stress across the width direction are essentially uniform; and hence this does not involve the width effect. Thus the bond properties derived from the central region do not involve the width effect. Furthermore, the crack front is perpendicular to the direction of loading in the central region. Based on the definition of fracture mode, interfacial debonding in this region belongs to Mode II fracture. The FRP in the edge regions is subjected to both shear and longitudinal strains. Hence, the interfacial cracking in the edge regions involves Mode III fracture where the transverse shear stress is parallel to the crack front. In other words, debonding in the edge regions is a mix of Mode II and Mode III fractures. This analysis indicates that it is the presence of Mode III fracture that causes the width effect.

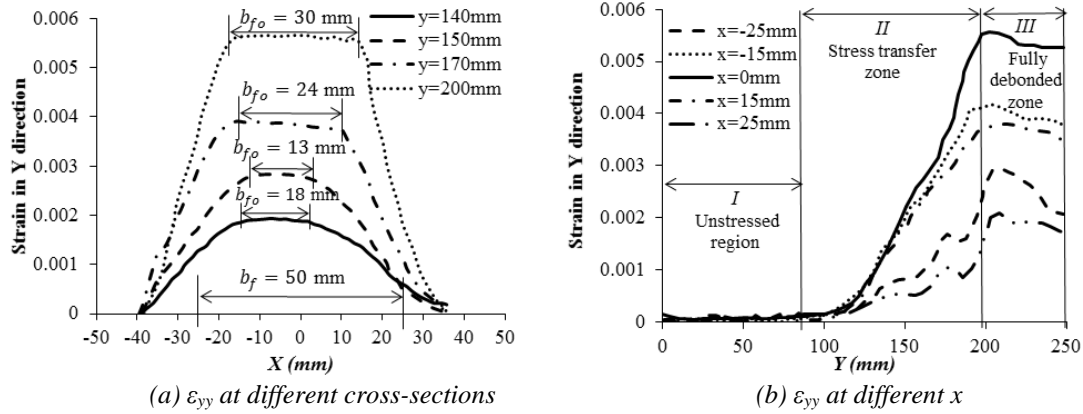


Figure 5: Longitudinal strain distributions of specimen C30-250-3

BOND PROPERTIES UNDER PURE MODE II FRACTURE

The bond stress at a particular location of the interface can be calculated by Eq. (1) (Wu et al. 2012; Yuan et al. 2004):

$$\tau(y) = E_f t_f \frac{\varepsilon(y + \Delta y / 2) - \varepsilon(y - \Delta y / 2)}{\Delta y} \quad (1)$$

where E_f and t_f are the elastic modulus and thickness of the attached sheet, respectively; $\varepsilon(y)$ gives the strain of the attached sheet at location y and Δy is an incremental length used for calculation of bond stress. The FRP strain distribution in the central region is used to calculate bond-slip curves in this section, where only Mode II fracture exists without the width effect. Typical bond-slip curves calculated in this way are shown in Fig. 4 for specimen C30-400-2 at different locations. It can be seen from Fig. 4a that the bond-slip curves at different locations in the central region are similar.

The bond-slip curves calculated from the average strain and slip of the FRP sheet at a cross-section are shown in Fig. 4b. The average bond-slip curves at different cross-sections involve different width effects, and hence, should be different, as illustrated by Fig. 4b. Clearly, the bond-slip curves from the central region, where the fracture mode is pure Mode II, do not involve the width effect, and hence, should be used to calculate the bond-properties.

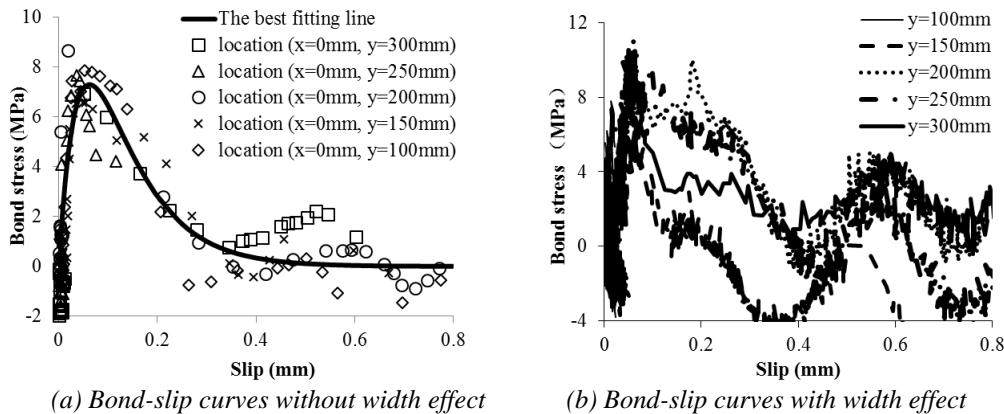


Figure 6: Bond-slip curves of specimen C30-400-2 at different cross-sections

The popular bond-slip model as given by Eq. (2) (Dai et al. 2005; He et al. 2015; Liu and Wu 2012; Zhou et al. 2010) and shown in Fig. 5a is used to derive the interfacial bond parameters herein:

$$\tau(s) = \frac{E_f t_f \alpha}{\beta^2} e^{-s/\alpha} (1 - e^{-s/\alpha}) \quad (2)$$

where α and β are the two parameters that control the amplitude and shape of the bond-slip curve. The corresponding loaded-end slip vs. pull force curve obtained by integration of the bond-slip curve is shown in Fig. 5b.

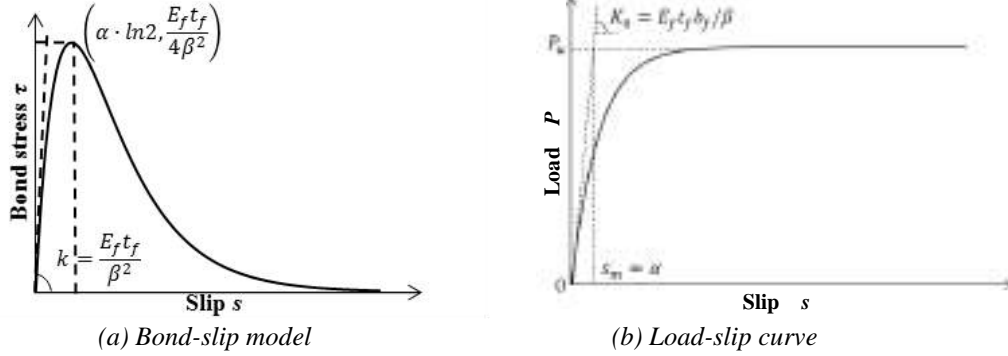


Figure 7: Bond model

Based on the definition of interfacial fracture energy and Eq. (2), one has:

$$G_f = \int_0^{\infty} \tau ds = \frac{E_f t_f \alpha^2}{2\beta^2} \quad (3)$$

The maximum bond stress (peak point in Fig. 5a) can be obtained from $d\tau/ds=0$, which gives

$$\tau_{\max} = \frac{E_f t_f \alpha}{4\beta^2} \quad (\text{when } s = \alpha \times \ln 2) \quad (4)$$

It is analytically concluded by Wu and Jiang (2013) that α is affected only by the local properties of concrete and hence can be expressed as a function of f_{co} , while β is a function of f_{co} , $E_f t_f$ and the width effect. As the bond parameters discussed in this section do not involve the width effect, β is only a function of f_{co} and $E_f t_f$. Therefore, α and β can be expressed by

$$\alpha = A f_{co}^B \quad (5)$$

$$\beta = C f_{co}^D (E_f t_f)^E \quad (6)$$

It is widely accepted in the literature that the interfacial fracture energy and the maximum bond stress are not related to $E_f t_f$ (Bilotta et al. 2011; Dai et al. 2005; Lu et al. 2005; Niedermeier 2000; Pan and Leung 2007). Substituting Eqs. (5) and (6) into Eq. (3) gives $G_f = A^2 f_{co}^{2B-2D} / [2C^2 (E_f t_f)^{2E-1}]$. To ensure G_f is not related to $E_f t_f$, the term $2E-1$ must be equal to 0 which gives $E = 0.5$. The same result of $E = 0.5$ is obtained by substituting Eqs (5) and (6) into Eq. (4).

Using the experimental bond-slip curves of a test specimen as illustrated in Fig. 4a, the values of α and β can be determined by regressing (best matching) Eq. (2) to the test curves. The values of α and β for all test specimens are calculated in this way. Using the values of α and β , coefficients A , B , C and D in Eqs. (5) and (6) can be determined from regression analyses, which gives

$$\alpha = 0.124 f_{co}^{-0.103} \quad (7)$$

$$\beta = 0.174 f_{co}^{-0.205} (E_f t_f)^{0.5} \quad (8)$$

BOND PROPERTIES INVOLVING MODE III FRACTURE

Based on the analytical solution proposed by the authors (He et al. 2015; Wu et al. 2012; Wu and Jiang 2013), the bond strength of the joint with a finite bond length is given by

$$P_u(L) = \kappa_L \cdot P_u(\infty) \quad (9)$$

where $P_u(\infty)$ is the bond strength when the bond length L approaches infinity, or the maximum strength, given by

$$P_u(\infty) = E_f t_f b_f \frac{\alpha}{\beta} \quad (10)$$

and κ_L is a length factor relating the maximum strength $P_u(\infty)$ to the bond strength $P_u(L)$ of a joint with a finite bond length L . A closed form mathematical solution of κ_L has been derived by the authors which can be found in Wu et al. (2012) and He et al. 2015.

Substituting Eq. (3) into Eq. (10) gives Eq. (11), which is identical to the well-known ultimate bond strength model based on fracture mechanics (Dai et al. 2005; Täljsten 1997; Wu et al. 2009).

$$P_u(\infty) = b_f \sqrt{2G_f E_f t_f} \quad (11)$$

However, the analytical solutions of Eqs. (9)-(11) are for 2-D problems that ignore the width effect. The width effect can be catered for by applying a width factor κ_w to Eq. (9), or

$$P_u(L) = E_f t_f b_f \frac{\alpha}{\beta} \kappa_L \kappa_w \quad (12)$$

Based on the discussions earlier, the width factor κ_w equals to 1 when only Mode II fracture is involved at the interface. When Mode III fracture occurs together with Mode II, κ_w is greater than 1 because the fracture energy of Mode III is about two times that of Mode II (Lockner et al. 1991).

Through mathematical study, a simple and sufficiently accurate equation for κ_L can be obtained (He et al. 2015), as given by

$$\kappa_L = \tanh(0.3L / \beta) \quad (13)$$

ANALYSIS OF WIDTH EFFECT

As the edge zone involves the transverse shear strain (Fig. 3) and FRP rigidity affects the transverse shear strain, the width factor should also be a function of the FRP rigidity. As the slip of FRP sheet in the central region is larger than those at the edge regions, the width effect can be visualized as a side-dragging by the concrete outside FRP sheet. The width effect of the FRP-concrete interface is affected by the properties of the substrate material that is related to concrete strength, as well as the rigidity of FRP sheet which affects the shear strain (strain gradient). The side dragging effect should be higher in case of harder materials. Therefore, κ_w should increase when f_{co} increases from this point of view.

On the other hand, the dragging effect is not only related to the strain profile of FRP sheet at a particular cross-section but also related to the longitudinal strain distribution that is reflected by the effective bond length L_e . This can be seen in Fig. 3a where different width effects are shown at different cross-sections. When $E_f t_f$ approaches infinity or f_{co} approaches zero, L_e approaches infinity. This is a two-dimensional side dragging without the three-dimensional dragging effect and hence gives a smaller value of κ_w . From this point of view, κ_w should reduce when $E_f t_f$ increases or f_{co} reduces.

The above conclusions are consistent with those discussed in the introduction. Based on the above arguments, the model of κ_w should take the following form:

$$\kappa_w = 1 + f(f_{co}) \cdot g(E_f t_f) \cdot h(b_f, b_c) \quad (14)$$

where $f(f_{co})$, $g(E_f t_f)$, and $h(b_f, b_c)$ are functions of f_{co} , $E_f t_f$, and FRP and concrete widths, respectively. These functions are to be determined. Eq. (14) satisfies all of the mechanisms discussed above.

NUMERICAL STUDY

Numerical analysis of width effect was also carried out. A three-dimensional concrete prism with a 45 mm thick substrate concrete is adopted in the FE simulation. The geometry of the FE model is similar to that adopted by Lu et al. (2006; 2005) and Tao and Chen (2015). A typical FE mesh for the pull-off test model is shown in Fig. 6. Based on previous works (Lu et al. 2005; Tao and Chen 2015), the size of the smallest element is selected to be 0.5 mm.

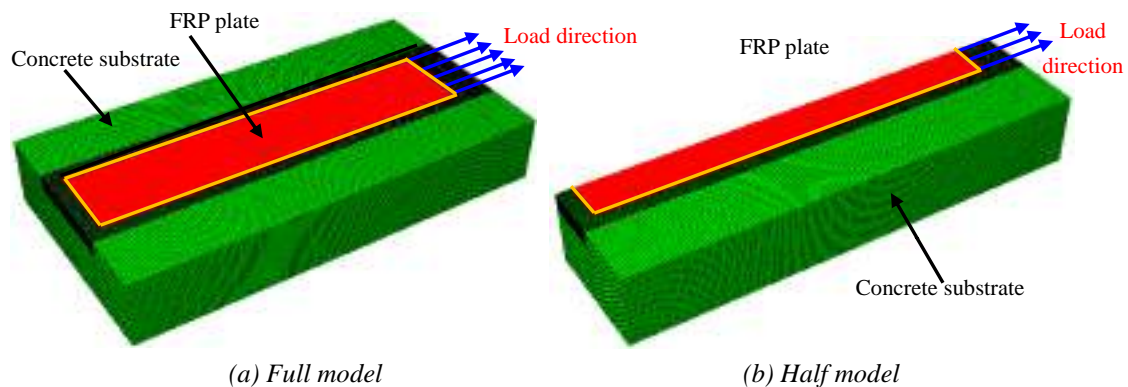


Figure 8: Typical FE mesh

The FRP plate is assumed to be linear-elastic during the whole pull-off process. The nonlinear behavior of concrete can be modeled by the concepts of damage and plasticity (Contrafatto and Cuomo 2006; Yu et al. 2010).

In this study, the concrete is therefore modeled using the concrete damage-plasticity model available in ABAQUS. The constitutive model reported in Chen et al. (2012; 2011) is adopted.

The damage parameter d_c is assumed to be zero before the peak stress, and is given by the following equation after the peak stress for concrete under uniaxial compression (Wu et al. 2014; Yu et al. 2010):

$$d_c = 1 - \sigma_c / f_{co} \quad (15)$$

For concrete under uniaxial tension the damage parameter d_t proposed by Chen et al. (2011) is adopted as follows

$$d_t = w_t / (w_t + h_c \sigma_t / E_0) \quad (16)$$

The concrete and FRP plate are modeled using solid elements and plane elements, respectively. A displacement controlled mode of loading is applied. As the pull-off failure process involves local instability such as concrete cracking and debonding, the solution can be quite unstable if it is treated as a nonlinear static problem (Chen et al. 2012; Chen et al. 2011; Yu and Ruiz 2006). Therefore, a dynamic solution method with explicit time integration is employed for the numerical solution of the FE model in order to overcome convergence difficulty (Chen et al. 2015).

The proposed FE model is used to simulate different pull-off tests reported in the literature where all the necessary material and geometrical properties required are provided. Simulation results of the load versus loaded end slip curves of specimen II-5 in Yao et al. (2005), and specimen C50-250-1 in Wu and Jiang (2013) are shown in Fig. 7. The proposed FE model can capture the general trend of the test results very well. Generally, the simulation results of FRP strain distributions are in close agreement with the test results, which demonstrates the accuracy of the FE model. The development of crack pattern of the concrete substrate for test specimen C50-250-1 in Wu and Jiang (2013) are shown in Fig. 8. The non-uniform crack distributions in the lateral direction in Fig. 8 have been observed and captured in experimental tests (Pellegrino et al. 2008; Salomoni et al. 2011). FE simulation results show that width effect does exist during the pull-off tests.

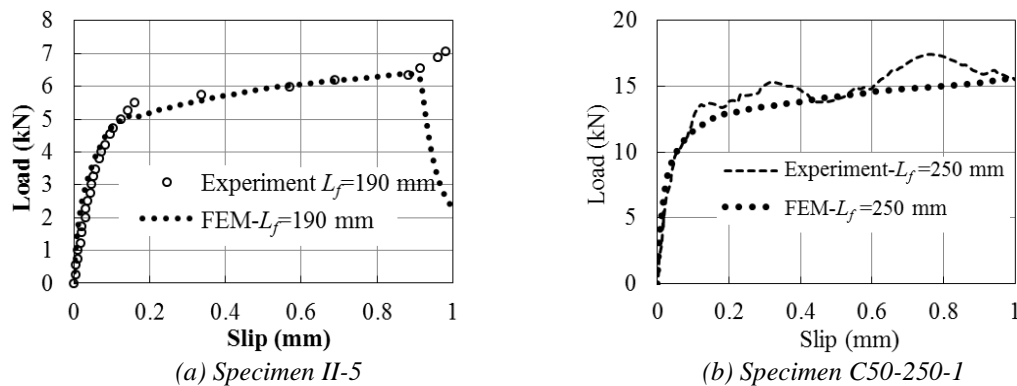


Figure 9. Load-slip curves

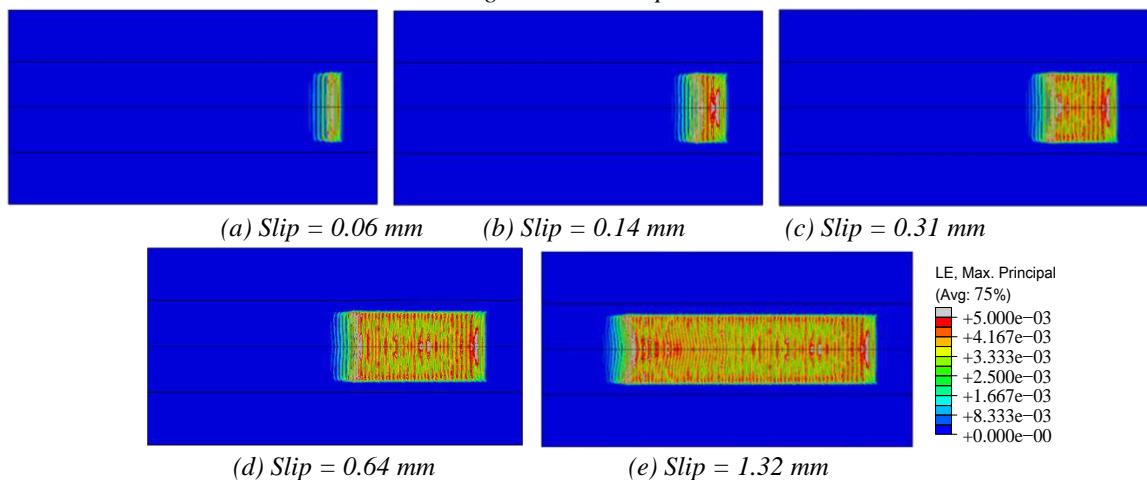


Figure 10: Development of interfacial cracking: numerical simulation

The proposed FE model is then used for the analysis of variation trend of width factor. Numerical results show that, the FRP-to-concrete width factor is not only a function of the FRP-to-concrete width ratio, but also a function of the FRP width. For a constant FRP-to-concrete width ratio, the width factor decreases with an increase of the FRP width. The width factor increases with an increase of concrete strength, while the width factor increases with a decrease of FRP rigidity.

Based on the trend of the effect of key parameters on bond strength obtained from the FEM simulations, the relationship given by Eq. (14) obtained from the analytical study in the previous section is confirmed.

MODELING OF WIDTH EFFECT

Rearranging Eq. (12) gives

$$\kappa_w = \frac{P_u(L)\beta}{E_f t_f b_f \alpha \kappa_L} \quad (17)$$

where P_u denotes the ultimate bond strength of the pull-off test specimen. Test results of $P_u(L)$ are collected from both extant literature and the authors' own tests to form a database for calculation of κ_w . It contains 850 test results of EB-FRP bond tests. The concrete strength, FRP rigidity $E_f t_f$, bond length and the width ratio (b_f/b_c) vary between 18.9 to 75.5 MPa, 8.7 to 360 GPa·mm, 20 to 700 mm, and 0.096 to 1, respectively.

Through regression analyses using the collected database, functions in Eq. (14) are determined to be $f(f_{co}) = f_{co}^{0.385}$, $g(E_f t_f) = 8(E_f t_f)^{-0.25} + 0.01$, and $h(b_f, b_c) = (1 - b_f / b_c)^{0.61} / (1 + 0.01b_f^{1.5})$. Substituting these functions into Eq. (14) gives

$$\kappa_w = 1 + f_{co}^{0.385} \left[8(E_f t_f)^{-0.25} + 0.001 \right] \left(1 - b_f / b_c \right)^{0.61} / \left(1 + 0.01b_f^{1.5} \right) \quad (18)$$

When b_f is equal to b_c , there is no width effect and the width factor is equal to 1.

CONCLUSIONS

The size effect of interfacial bond is investigated through experimental, analytical study, and numerical simulation, in this work. The main findings are summarized as follows:

- Strictly speaking, interfacial bond is size dependent. For one-dimensional members such as beams and columns, the size effect is reflected by the width effect of bond. When only pure Mode II fracture is involved in interfacial bond, there is no width effect. It is the presence of Mode III fracture that causes the width effect.
- The width effect varies along the bond length. In other words, average bond-slip relationship at different cross-sections involves different width effects.
- The width factor is not only a function of the FRP-to-concrete width ratio, but also related to FRP width. The width factor increases with an increase of concrete strength. The FRP rigidity should also be included in the width factor model.
- A new bond strength model involving all above effects are developed for engineering applications.

ACKNOWLEDGMENTS

This work was supported by the National Natural Science Foundation of China (Grant Nos. 51608211), the Provincial Natural Science Foundation of Fujian Province (Grant No. 2017J05083), and the Scientific Research Funds of Huaqiao University (Grant No. 16BS403).

REFERENCES

- A. Bilotta, M. D.Ludovico, E. Nigro (2011). "FRP-to-concrete interface debonding: Experimental calibration of a capacity model." *Composites Part B Engineering*, 42(6), 1539-1553.
- G. M. Chen, J. F. Chen, J. G. Teng (2012). "On the finite element modelling of RC beams shear-strengthened with FRP." *Construction and Building Materials*, 32, 13-26.
- G. M. Chen, J. G. Teng, J. F. Chen, Q. G. Xiao (2015). "Finite element modeling of debonding failures in FRP-strengthened RC beams: A dynamic approach." *Computers & Structures*, 158, 167-183.
- G. M. Chen, J. G. Teng, J. F. Chen, (2011). "Finite-Element Modeling of Intermediate Crack Debonding in FRP-Plated RC Beams." *Journal of Composites for Construction*, 15(3), 339-353.
- J. F. Chen, J. G. Teng (2001). "Anchorage strength models for FRP and steel plates bonded to concrete." *Journal of Structural Engineering*, 127(7), 784-791.
- L. Contrafatto, M. Cuomo (2006). "A framework of elastic - plastic damaging model for concrete under multiaxial stress states." *International Journal of Plasticity*, 22(12), 2272-2300.
- J. Dai, T. Ueda, Y. Sato (2005). "Development of the nonlinear bond stress - slip model of fiber reinforced plastics sheet - concrete interfaces with a simple method." *Journal of Composites for Construction*, 9(1), 52-62.

- J. Dai, T. Ueda, Y. Sato (2006). "Unified Analytical Approaches for Determining Shear Bond Characteristics of FRP-Concrete Interfaces through Pullout Tests." *Journal of Advanced Concrete Technology*, 4(1), 133-145.
- L. He, Y. Wu, Y. Xiao (2015). "Analytical Solution for Externally Bonded Joints Considering Snap-Back." *Journal of Composites for Construction*.
- K. Liu, Y. Wu (2012). "Analytical identification of bond – slip relationship of EB-FRP joints." *Composites Part B: Engineering*, 43(4), 1955-1963.
- D. A. Lockner, J. D. Byerlee, V. Kuksenko, A. Ponomarev, A. Sidorin (1991). "Quasi-static fault growth and shear fracture energy in granite." *Nature*, 350(6313), 39-42.
- X. Z. Lu, J. J. Jiang, J. G. Teng, L. P. Ye (2006). "Finite element simulation of debonding in FRP-to-concrete bonded joints." *Construction and Building Materials*, 20(6), 412-424.
- X. Z. Lu, L. P. Ye, J. G. Teng, J. J. Jiang (2005). "Meso-scale finite element model for FRP sheets/plates bonded to concrete." *Engineering Structures*, 27(4), 564-575.
- R. Niedermeier (2000). "Zugkraftdeckung bei klebarmierten bauteilen (Envelope line of tensile forces while using externally bonded reinforcement)." *TU Munchen (in German)*.
- J. Pan, C. K. Y. Leung (2007). "Effect of concrete composition on FRP/Concrete bond capacity." *Journal of Composites for Construction*, 11(6), 611-618.
- C. Pellegrino, D. Tinazzi, C. Modena (2008). "Experimental Study on Bond Behavior between Concrete and FRP Reinforcement." *Journal of Composites for Construction*, 12(2), 180 - 189.
- V. Salomoni, G. Mazzucco, C. Pellegrino, C. Majorana (2011). "Three-dimensional modelling of bond behaviour between concrete and FRP reinforcement." *Engineering Computations*, 28(1), 5-29.
- K. V. Subramaniam, C. Carloni, L. Nobile (2007). "Width effect in the interface fracture during shear debonding of FRP sheets from concrete." *Engineering Fracture Mechanics*, 74(4), 578-594.
- B. Täljsten (1997). "Defining anchor lengths of steel and CFRP plates bonded to concrete." *International Journal of Adhesion and Adhesives*, 17(4), 319-327.
- Y. Tao, J. F. Chen (2015). "Concrete Damage Plasticity Model for Modeling FRP-to-Concrete Bond Behavior." *Journal of Composites for Construction*, 19(040140261), 1-13.
- Y. Wu, X. Xu, J. Sun, C. Jiang (2012). "Analytical solution for the bond strength of externally bonded reinforcement." *Composite Structures*, 94(11), 3232-3239.
- Y. Wu, Y. Yun, Y. Wei, and Y. Zhou (2014). "Effect of Predamage on the Stress-Strain Relationship of Confined Concrete under Monotonic Loading." *Journal of Structural Engineering*, 140(12), 1-18.
- Y. Wu, C. Jiang (2013). "Quantification of Bond-Slip Relationship for Externally Bonded FRP-to-Concrete Joints." *Journal of Composites for Construction*, 17(5), 673-686.
- Z. Wu, S. M. Islam, H. Said (2009). "A Three-Parameter Bond Strength Model for FRP-Concrete Interface." *Journal of Reinforced Plastics & Composites*, 28(19), 2309-2323.
- J. Yao, J. G. Teng, J. F. Chen (2005). "Experimental study on FRP-to-concrete bonded joints." *Composites Part B: Engineering*, 36(2), 99-113.
- R. C. Yu, G. Ruiz (2006). "Explicit finite element modeling of static crack propagation in reinforced concrete." *International Journal of Fracture*, 141(3-4), 357-372.
- T. Yu, J. G. Teng, Y. L. Wong, S. L. Dong (2010). "Finite element modeling of confined concrete-II: Plastic-damage model." *Engineering Structures*, 32(3), 680-691.
- H. Yuan, J. G. Teng, R. Seracino, Z. S. Wu, J. Yao (2004). "Full-range behavior of FRP-to-concrete bonded joints." *Engineering Structures*, 26(5), 553-565.
- Y. Zhou, Y. Wu, Y. Yun (2010). "Analytical modeling of the bond – slip relationship at FRP-concrete interfaces for adhesively-bonded joints." *Composites Part B: Engineering*, 41(6), 423-433.



THE BOND BEHAVIOR OF SRP-TO-CONCRETE SYSTEM IN FIELD ENVIRONMENT

Wei Wang¹, John J. Myers¹

¹ Missouri University of Science and Technology, Department of Civil, Architectural & Environmental Engineering, MO, USA

ABSTRACT

In this study concrete beams reinforced with a steel reinforced polymer (SRP) strengthening system that were loaded and unloaded were subjected to real-time seasonal weather and solar exposure in Rolla, MO for 12 months. Two types of steel fibers (micro-fine galvanized and micro-fine brass coating steel fibers) were used in this study. A total of 22 SRP specimens, including 12 specimens loaded and 10 specimens unloaded, were maintained in outdoor weather in Rolla, which has moderate UV radiation with various freeze-thaw, and variable temperature and moisture conditions. Flexural bending tests and direct pull-off bond tests were performed to evaluate the long-term bond performance of SRP-to-concrete interfaces. The flexural bending test results illustrated that the bond behavior between SRP and concrete was affected by the harsh environmental conditioning. The results for the pull-off test were scattered. This high variability was related to several issues such as non-homogenous characteristic of the concrete, applied load rate using hand, or the inappropriateness to prepare the specimens.

KEYWORDS

Steel reinforced polymer (SRP), micro-fine galvanized and micro-fine brass coating steel fibers, freeze-thaw, temperature and moisture conditions, flexural bending tests, direct pull-off bond tests.

INTRODUCTION

Currently, there are several composite application technologies to repair and retrofit deficient and aging concrete members in existing buildings and bridges. These technologies involve manual FRP lay-up, pre-cured laminate plates, near surface mounted (NSM) bars, mechanically fastened FRP, and SRP. There is limited available data to exhibit the influence of real-time seasonal weather on the bond performance between SRP strengthening systems and concrete. Deng et al. (2015) evaluated durability performance of concrete beams reinforced with CFRP sheet under real-time weather and solar exposure, and found flexural strengths showed a 45% loss. The failure modes were also changed from substrate to interfacial. Direct pull-off tension strength decreased after 18 months of real-time exposure. Liao and Tsent (1998) reported that cracks occurred when CFRP specimens were exposed to the UV, finally reducing the strength due to stress concentrations.

In order to investigate the effects of field exposure on the bond performance of concrete beams reinforced with SRP, they were subjected to real-time weather and solar exposure in Rolla, MO for 12 months (from October 2015 to September 2016). A total of 22 SRP specimens, including 12 specimens loaded and 10 specimens unloaded, were maintained in outdoor weather in Rolla, which has moderate UV radiation with various freeze-thaw, and variable temperature, and moisture conditions. These SRP specimens were tested in three-point loading. At the same time, direct pull-off tension tests were conducted after 12 months of exposure.

EXPERIMENTAL PROGRAMS

Properties of Materials

In this study, Hardwire® tapes of 5 wires per inch were utilized with 3x2-G Hardwire® (RG, a new galvanized coated wire version) and 3x2 Hardwire® (RNG) applied individually to study the durability performance of concrete members reinforced externally with composite materials made from Hardwire® and epoxy. In addition, Sikadur® 330, which consists of Sikadur® 330 US Part A (component A) and Part B (component B), was used. It was manufactured by Sika Corporation. It is a two-component, solvent-free, moisture-tolerant, high strength, and high modulus structural epoxy adhesive. Plain concrete beams with a compressive strength of 6010 psi (41.4 MPa) were cast. The dimension was 6 in. (width) x 6 in. (height) x 24 in. (length) (152.4 x 152.4 x 609.6 mm).

Preparation of Flexural Bending Specimens

The specimen preparation included two major steps: fabrication of concrete beams and application of SRP laminates.

Fabrication of concrete beams

First, the tension surfaces of concrete beams were ground. All loose particles and other contaminations on the tension side were removed to attain proper surface roughness in order to increase the contact area, obtain an appropriate bond, and improve the mechanical interlock between the concrete and SRP strengthening system. Secondly, a concrete saw was used to make saw cuts with a width of approximately 0.125 in. (3.18 mm) on the tension side of the beam at mid-span. The depth of saw cuts was 2 in. (50.8 mm). This process follows the ACI 440.9R-15 (2015) protocols.

Application of SRP laminates

Two layers of steel laminate strips were utilized with 1 in. (25.4 mm) width for the first ply and 0.75 in. (19.05 mm) width for second ply. The external reinforcement sheet was centered on the tension surface of concrete using Sikadur® 330 epoxy resin. The 12 in. (304.8 mm) long strips had a development length of 6 in. (152.4 mm) on each side of the saw cut based on previous research and ACI 440.9R-15. First of all, the first layer epoxy was applied to the tension surface as the primer, and to cover the voids on the surface of concrete, and first ply steel sheet with dimensions of 12 x 1 in. (304.8 x 25.4 mm) was applied and pressed into the epoxy, then brushed the second layer resin. The second ply steel fibers with dimensions of 12 x 0.75 in. (304.8 x 19.1 mm) were then staggered to apply to first steel ply to decrease the interval between steel fibers, which can increase the tensile strength of the SRP strengthening system, and pressed this steel strip into the epoxy. The air voids contained in the resin were dispersed by using a small steel plate. Finally, the third layer of epoxy was brushed to cover the steel wires completely. Additional epoxy of 0.5 in. (12.7 mm) and 0.25 in. (6.35 mm) was applied to each longitudinal and transverse sides of the SRP, respectively, in order to decrease corrosion of the steel fibers in the epoxy resin, resulting in a total length of 12.5 in. (317.5 mm) and a width of 2 in. (50.8 mm) for the SRP strengthening system.

Fabrication of SRP pull-off specimens

The procedure of preparation of concrete surface was the same as that of the flexural bending specimens. One layer of epoxy was brushed onto the roughened surface, and then a 5.5 x 5.5 in. (140 x 140 mm) steel sheet was applied. The second layer resin was applied to the first ply steel sheet and epoxy. Another 5.0 x 5.0 in. (127 x 127 mm) steel fabric square was performed in the exact same manner as the first steel ply. These two steel squares were also staggered to put together. The air voids inside were dispersed using the same method as that of the preparation of flexural bending specimen. Finally, the third layer of epoxy was applied to cover the two-ply steel fibers completely. RG and RNG steel fibers were used to prepare the SRP specimens, respectively. The surface of SRP was ground to guarantee a flat SRP surface, which makes the surface drill cores easily. A diamond bit was used to drill the cores to separate the adhesion fixture from the surrounding SRP. According to ASTM D7522 (2015), the depth of core drilling into the SRP specimen should be between 0.25 in. (6 mm) and 0.5 in. (12 mm). In this research, the SRP specimen was drilled until ground fine concrete particles extruded from the core drill bit. The depth of the core was consistently around 0.25 in. (6 mm). The aluminium disk (dolly) with a 2 in. (50.8 mm) diameter was bonded to the SRP testing surface.

Sustained Loading

The SRP specimens, including six RG and RNG steel fiber samples, were subjected to real-time seasonal exposure. The ten SRP specimens exposed to field environment were unloaded including five RG and five RNG specimens. Pairs of back-to-back specimens were subjected to the sustained three-point flexural load in the vertical orientation using a spring-loaded fixture. This fixture consisted of clamps that were made of steel plates and beams, long threaded bolts with nuts, and springs, as shown in Figure 1. The spring had a free length of 5 in. (127 mm) and was compressed 0.28 in. (7.1 mm) for 20% of ultimate capacity and 0.56 in. (14.2 mm) for 40% of ultimate load to subject the samples to sustained loads of 700 lb (3.1 kN) and 1,400 lb (6.2 kN), respectively. Throughout the exposure period the spring compression was monitored and adjusted as required to provide a constant sustained load level. In most field applications, structures that will be strengthened are reinforced concrete (RC) structures which include mild steel reinforcement. In the case of older RC highway bridges that require upgrades to meet

today's load rating standards in the United States, a 10% to 20% overall upgrade in capacity is required (i.e. the existing RC capacity plus the addition of the strengthening system). The 20% and 40% sustained load levels selected on the concrete prism specimens in this study, therefore correlate to the upgrade requirement often needed in the field.

Bending tests of six unconditioned RG and RNG specimens were performed to measure the ultimate capacity before the specimens were loaded. Figure 1 details the sustained load frames in an exterior environment.



Figure 1: Spring-loaded fixture and testing samples under the real-time exposure

EXPERIMENTAL RESULTS AND DISCUSSIONS

Flexural Bending Testing (Three-Point Load Testing)

The bond durability between the SRP strengthening system and concrete substrate was evaluated through flexural bending tests. The specimens were loaded by using an MTS 880. Load was applied at a constant rate of 0.005 in./min (0.127 mm/min) to cause the specimens to fail in 9 to 10 minutes. The deflections of both sides at the mid-span of the SRP specimen were measured by using two linear variable displacement transducers (LVDTs) with ± 0.5 in. (12.7 mm). Figure 2 illustrates a typical three-point loading test configuration.



Figure 2. A typical three-point loading test configuration

The typical load-deflection characteristics of the loaded, unloaded, and control RG and RNG specimens are illustrated in Figure 3

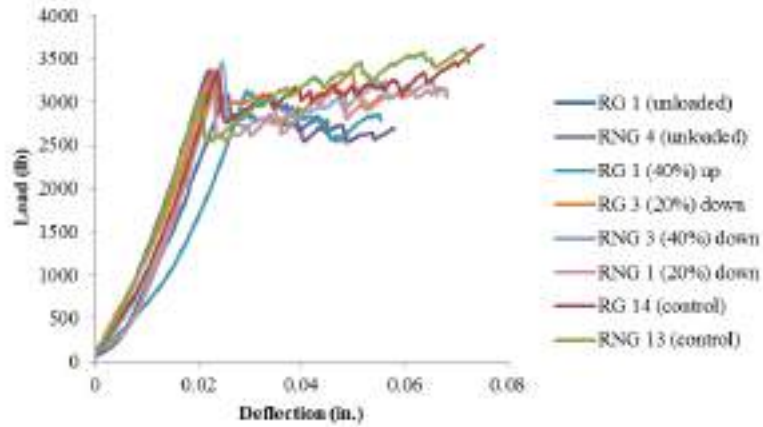


Figure 3: Load-deflection characteristics of the SRP specimens reinforced with galvanized and brass coating steel fibers

The SRP control specimen experienced higher strength and greater ductility than the conditioned specimens that were exposed to field environment. Ultimate ductility of the control specimens was higher than that of the conditioned specimens. It should be noted that a significant decrease occurred in ultimate load capacity of SRP sheet-strengthened specimens after one year of the real-time exposure when compared to the control samples. The average deflection of the control specimens was 0.0706 in. (1.79 mm). The average displacements of the specimens stressed by 40% of the ultimate load, 20% of the ultimate load, and unloaded were 0.0504 in. (1.28 mm), 0.0385 in. (0.98 mm), and 0.0412 in. (1.05 mm), respectively. They decreased by 28.7%, 45.5%, and 41.7% respectively, when compared with that of control specimens. All SRP specimens failed due to the de-bonding between the concrete and the SRP strengthening system. Figures 4 and 5 show the typical failed specimens in this section.



Figure 4: A representative failed conditioned specimen



Figure 5: A representative failed control specimen

No sign of corrosion was observed on the surface of the SRP strengthening system for the exposed specimens. It can be concluded that the epoxy resin utilized in this research exhibited a perfect moisture-tolerant behavior to protect the steel fibers for the period studied. The average percentage of concrete cover area for the control specimens was 31.5%. In contrast to this, the percentages of concrete cover area of loaded (40% and 20%) and unloaded specimens decreased by 60.6%, 24.8%, and 34.3% respectively. According to the ultimate loads of all RG and RNG specimens, a C_E factor of 0.80 for the environmental reduction is suggested in an aggressive

environment with a moderate UV radiation based on the results obtained herein and under other laboratory accelerated environmental testing. This value is based on the relative bond durability of SRP strengthening system studied.

Direct Pull-Off Tests

The bond strength and failure mode were evaluated by direct pull-off test and compared to the results of the flexural bending tests. The specimen preparation was the same as that of the experiment in the environmental chamber. The test setup is illustrated in Figure 6.



Figure 6: The test setup for the pull-off bond test

The bond between concrete and SRP sheet was evaluated by pull-off tensile stresses at failure. The bond strength of these specimens were calculated by using the Eq.1.

$$\sigma = \frac{4F_p}{\pi D^2} \tag{1}$$

where σ is the pull-off bond strength (psi [MPa]), F_p is the pull-off force (lb [N]), and D is the diameter of the loading fixture (in. [mm]). The representative pull-off specimens with discs are illustrated in Figures 7 and 8.



Figure 7: A typical pull-off specimen



Figure 8: A typical control specimen

The average bond stresses, standard deviations, and COVs of conditioned and control RG and RNG specimens are summarized in Table 1.

Table 1: The average bond strength, standard deviation, and COV

SRP specimen	Ave. bond stress psi (MPa)	Standard deviation psi (kPa)	COV (%)
Conditioned RG	344.2 (2.37)	80.5 (555)	23.4
Conditioned RNG	374.4 (2.58)	61.7 (425)	16.5
Control RG	340.9 (2.35)	58.5 (403)	17.2
Control RNG	333.4 (2.30)	43.6 (301)	13.1

High standard deviations and coefficients of variation (COVs) of the control and conditioned specimens are shown in Table 1. All the pull-off test results illustrated a higher COV when compared to that of ASTM C 39 (10%) (2016). There was a large degree of scatter and variation, indicating the variability of this test method. The average bond strength of control RG specimens was almost the same as the results of the control RNG specimens. The average bond stresses of the conditioned specimens were higher than the results of the control specimens.

When considering this test method, not only is the value of the load/bond stress at failure important, but it is also important to understand the failure mode. There are three primary modes of failure that may occur when using the direct pull-off test. This includes 1) failure in the concrete substrate, 2) failure at the interface between the SRP strengthening system or 3) a mixed mode failure that occurs as a combination of 1) and 2). It is also possible that the pull-off test could fail between the pull-off puck and the SRP strengthening system, but this is avoided by using an epoxy that is high strength to prevent this possibility. If the pull-off test fails within the concrete substrate as shown in Figures 7 and 8, this indicates that the bond strength of the SRP system is higher than tensile capacity of the concrete which indicates load is easily transferred between concrete face and strengthening system.

Since both the control and conditioned specimens failed within the concrete substrate, this test was unable to capture and specific degradation within the bonded system. While some degradation may have occurred the failure mode from control to conditioned specimens still occurred within the concrete substrate.

CONCLUSIONS

Test results of three-point loading tests indicated that the externally bonded SRP strengthening systems can capture the durability performance and degradation factors, C_E , can be established for use in design models such as ACI 440.2R. When subjected to real-time weather and solar exposure, the concrete covered areas of the exposed specimens reduced significantly when compared to the counterparts of the control specimens. The degradation should be attributed to loss of adhesion at the bond surface due to the influence of moisture and temperature.

For direct pull-off tests, this study determined a 5.3% (RG specimens) and 13.8% (RNG specimens) tensile strength increase when the specimens were exposed to real-time weather and solar exposure for 12 months. The results of this test exhibited a large degree of scatter and variation, indicating the variability of this test method. Therefore, direct pull-off tests may not be considered as a technology to evaluate the long-term bond performance of SRP-to-concrete systems. However, it may be an effective avenue for installation minimum bond compliance.

REFERENCES

- J. Deng, J.E Tanner, D. Mukai, H.R Hamilton, C.W Dolan (2015). "Durability performance of carbon fiber-reinforced polymer in repair/strengthening of concrete beams", *ACI Material Journal*, 112, 247-257.
- W.B Liau, F.P Tseng (1998). "The effect of long-term ultraviolet light irradiation on polymer matrix composites", *Polym. Compos.*, 19, 440-445.
- ACI Committee 440.9R-15 (2015). "Guide to accelerated conditioning protocols for durability assessment of internal and external fiber reinforced polymer (FRP) reinforcement for concrete", *American Concrete Institute, Farmington Hills*.
- ASTM D30 (2009). "Standard Test Method for Pull-Off Strength for FRP Bonded to Concrete Substrate", *American Society for Testing and Materials*.
- ASTM C39/C39M-16b (2016). "Standard Test Method for Compressive Strength of Cylindrical Concrete Specimens," *American Society for Testing and Materials*.



ATOMISTIC INVESTIGATION ON INTERFACIAL DETERIORATION OF EPOXY-BONDED INTERFACE UNDER HYGROTHERMAL ENVIRONMENT

Chao Wu, Ruidong Wu, Lik-ho Tam *

School of Transportation Science and Engineering, Beihang University, 37 Xueyuan Road, Beijing 100191, China, Email: leo_tam@buaa.edu.cn

ABSTRACT

The fiber reinforced polymer (FRP) has been increasingly used for strengthening concrete infrastructure through external bonding by using epoxy adhesive. The long-term durability of FRP-concrete structure is seriously degraded under hygrothermal environment at high level of temperature and humidity, which is mainly caused by interfacial debonding between concrete and epoxy. The microscopic information on local interfacial deterioration is important for understanding the failure mechanism of epoxy-bonded FRP-concrete structure under hygrothermal environment, which is still lacking at this stage. This paper aims to understand the effect of hygrothermal environment on nanoscale mechanical and interfacial behavior of epoxy-bonded interface by using molecular dynamics simulation. The interface model is conditioned in dry and wet environment at room and elevated temperature. By simulating interfacial debonding process, the structural and mechanical properties of epoxy-bonded interface are examined, which degrades most seriously in wet environment at elevated temperature, resulting in significant decrease of interfacial adhesion. The mechanistic knowledge provided in this paper could contribute to the understanding of environment-affected structural failure of FRP-concrete system from the nanoscale perspective, and it is believed to be applicable to similar FRP-strengthened structure.

KEYWORDS

Epoxy-bonded interface, interfacial integrity, hygrothermal environment, molecular dynamics simulation.

INTRODUCTION

Due to the outstanding properties, including high specific stiffness- and strength-to-weight ratios, good thermal stability, and strong corrosion resistance, fiber reinforced polymer (FRP) has emerged as the viable alternative to metal reinforcement for concrete beam and slab components (Teng et al. 2002; Hollaway 2010). The concrete infrastructure is usually strengthened by external bonding of lightweight FRP laminate in the form of sheet and plate by using epoxy adhesive (Hamilton et al. 2009; Aydin et al. 2016). Previous experimental studies by using short-term tests have shown that the concrete cohesive failure is the major failure mode of epoxy-bonded FRP-concrete structure in dry condition (Büyüköztürk et al. 2004; Gravina et al. 2017). In practice, the structure is often exposed to various environments, which involve large variation in temperature and humidity (Hollaway 2010; Cromwell et al. 2011; Aydin et al. 2016). Due to the existence of epoxy functional groups and molecular-size holes in the system, water molecules could penetrate into epoxy structure and epoxy-bonded interface, and affect the system performance, which are more pronounced at elevated temperature (Zhou and Lucas 1999; Myers et al. 2014). Consequently, the long-term durability of epoxy-bonded FRP-concrete structure is severely affected under hygrothermal environment at high level of temperature and humidity, with the interfacial degradation between concrete and epoxy as the main reason for the system performance loss (Hamilton et al. 2009; Aydin et al. 2016). To understand the failure mechanism of epoxy-bonded FRP-concrete structure under hygrothermal environment, it requires the microscopic information on interfacial deterioration of local epoxy-bonded interface, which is lacking at this stage.

Earlier efforts have been focused on characterizing the relationship between the performance of FRP-concrete structure and the epoxy-bonded interfacial property under environment effect. At macroscale, the bulk epoxy-bonded FRP-concrete beam as shown in Figure 1(a) is usually subjected to accelerated aging test to investigate the interfacial property (Lyons et al. 2002; Au and Büyüköztürk 2006; Lai et al. 2009; Tuakta and Büyüköztürk 2011; Zheng et al. 2015; Qin et al. 2016). Specifically, by carrying out the peel and shear tests on epoxy-bonded carbon FRP (CFRP) strengthened concrete beam, it was observed that after 8-week exposure to 100% relative humidity at 23 °C, there was a 13% loss in the shear fracture toughness as compared to the unexposed specimen, and a more severe degradation of over 50% was seen for specimen conditioned at elevated temperature of 50 °C (Au and Büyüköztürk 2006). To focus on the local interfacial failure process between concrete and epoxy, the sandwiched concrete-epoxy beam specimen is commonly used, as shown in Figure 1(b) (Lau and Büyüköztürk 2010; Namrou and Kim 2016; Amidi and Wang 2017; Zhou et al. 2017). Notably, after conditioned in the water bath up to 10 weeks, the concrete-epoxy beam was measured to have a substantial decrease of about 50% in interface fracture toughness by using the four-point bending test (Lau and Büyüköztürk 2010). Meanwhile, the

shift of failure mode to the interfacial debonding occurred after moisture conditioning at 23 °C for 4 weeks while after moisture conditioning at 50 °C for 2 weeks, which demonstrates the more severe deterioration of epoxy-bonded interface at elevated temperature. From these macroscale experimental studies, it is demonstrated that under hygrothermal environment, the performance of epoxy-bonded FRP-concrete structure is degraded, which is largely resulted from the interfacial debonding between concrete and epoxy. Although the interaction between the epoxy-bonded interface and the moisture plays an important role in the interfacial deterioration, the microscopic interfacial behavior under hygrothermal environment remains unclear, as it is difficult to characterize by using macroscale experimental approach.

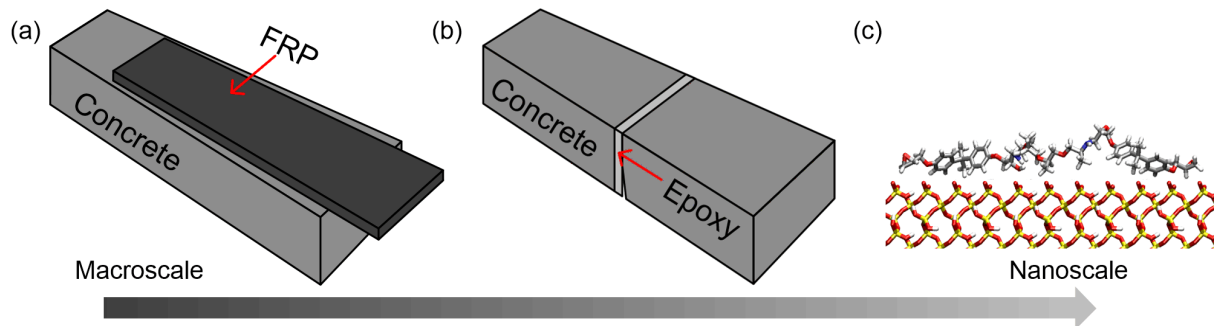


Figure 1: Schematic diagram of epoxy-bonded FRP-concrete structure at different length scales: at macroscale, (a) FRP- concrete beam; and (b) sandwiched concrete-epoxy beam; at nanoscale, (c) molecular interface between silica and epoxy chain, where silica represents the nanoscale model of concrete as it constitutes a large proportion of concrete solid ingredient.

In recent years, molecular dynamics (MD) simulation has been increasingly used in investigating the interfacial integrity of epoxy-bonded interface under humid environment, as it allows high-level control of material microstructure and high fidelity in investigated properties (Büyüköztürk et al. 2011; Gunes et al. 2013; Tam and Lau 2015; Tam et al. 2018). In previous simulation studies, the molecular model of epoxy-silica interface is developed to represent concrete-epoxy interface, as shown in Figure 1(c) (Büyüköztürk et al. 2011; Gunes et al. 2013). Specifically, the silica constituting a large proportion of concrete solid ingredient is chosen as to represent concrete at nanoscale, while a single polymer chain as the basic unit is used as the epoxy model. A large reduction of interfacial adhesion is observed when the interface is fully immersed in water, and the presence of water molecules in epoxy-bonded interface is one of the major reasons for adhesion decrease. By observing simulation process, these studies have provided information about the motion of interface and surrounding solution at molecular level, but the microscopic detail of interaction between epoxy-bonded system and surrounding environment is still largely unknown, particularly for condition at elevated temperature.

The objective of this paper is to probe microscopic interfacial deterioration of epoxy-bonded interface in FRP-concrete structure under hygrothermal environment. The molecular interface model of epoxy-bonded system is constructed by bonding cross-linked epoxy model to the flat substrate representing concrete at nanoscale, which is conditioned in simulated dry and wet environment at room and elevated temperature. The interaction and dynamics of interface and simulated environment under different environmental exposures are studied. The interfacial adhesion is quantified by using steered molecular dynamics (SMD) simulation, which correlates with structural and mechanical behavior of the system under different environments. The simulation results in this study reveal the relationship between interfacial deterioration of epoxy-bonded system and environment exposure, which is of great use in understanding environment-induced interfacial debonding failure of FRP-concrete system at larger length scales. The fundamental understanding of interfacial deterioration forms basis for developing the epoxy and bonded materials with enhanced resistance to environmental degradation.

COMPUTATIONANL METHOD

To investigate microscopic interfacial deterioration, epoxy-bonded system representing local interface between concrete and epoxy is developed, which is conditioned in vacuum and water at temperature of 27 and 50 °C, and the elevated temperature refers to upper bound of service temperature that the concrete suffers during the service life (Mays and Hutchinson 2005). The details of model construction and MD simulation are given as follows.

Force Field and Molecular Model

The consistent valence force field (CVFF) is adopted to characterize the bonded and non-bonded interaction of atoms, which has been extensively used in investigating the epoxy-bonded system, yielding good agreement with theoretical and experimental measurements (Dauber-Osguthorpe et al. 1988; Maple et al. 1988; Büyüköztürk et

al. 2011; Tam and Lau 2015; Jian et al. 2018; Tam et al. 2018). Specifically, for non-bonded interaction, a cutoff distance of 10 Å is used for van der Waals (vdW) and short-range Coulombic interaction, which is a reasonable approximation as the energy and force of these non-bonded interactions are quite small at such distance, while particle-particle particle-mesh solver is used to calculate long-range Coulombic interaction (Hockney and Eastwood 1988). Meanwhile, partial charge of atom is calculated by using bond increment method (Oie et al. 1981). The force field parameters for water molecules are taken from the TIP3P model (Jorgensen et al. 1983). For FRP-concrete structure under environmental exposure, the clear separation between concrete and epoxy is generally observed after interfacial debonding, and structural integrity of bonded materials is preserved (Au and Büyüköztürk 2006; Lai et al. 2009; Lau and Büyüköztürk 2010; Tuakta and Büyüköztürk 2011; Amidi and Wang 2017; Zhou et al. 2017). Therefore, this study focuses on the debonding process where clean interface is formed. The epoxy-bonded system modeled here is shown in Figure 2(a), which consists of cross-linked epoxy molecule bonded with supporting substrate representing the concrete at nanoscale, as referring to the model used in our recent study (Tam et al. 2018). The epoxy molecule is cross-linked from the monomer formed by bisphenol A diglycidyl ether, i.e. the basic structural unit of epoxy adhesive used in FRP-concrete structure. For the concrete, it is a heterogeneous material mainly comprising hydrated cement and aggregate, and among these constituent materials, the silica constitutes a large portion of over 40% by mass (Büyüköztürk et al. 2011). In previous simulation studies, crystalline silica with atomically smooth surface is adopted to represent the concrete in concrete-epoxy bonded system, and the interfacial debonding occurs along the bonded interface, which is in line with experimental observation (Büyüköztürk et al. 2011; Gunes et al. 2013; Jian et al. 2018). In this work, a perfectly smooth implicit wall representing a typical substrate in the bonded material system is used to simulate the silica substrate (Xia et al. 2016; Tam et al. 2018). The energetic wall interacts with the epoxy molecule through the vdW force by using the 12-6 Lennard-Jones (LJ) potential, which keeps the same definition of the vdW potential term as that of CVFF potential. The functional form is shown in Eq 1,

$$U_{LJ}(r) = 4\epsilon_{LJ} \left[\left(\frac{\sigma_{LJ}}{r} \right)^{12} - \left(\frac{\sigma_{LJ}}{r} \right)^6 \right] \quad r \leq r_{cut} \quad (1)$$

where r denotes distance between the wall and the atom, $r_{cut} = 10 \text{ \AA}$ denotes cutoff interaction distance, σ_{LJ} denotes distance at which potential U_{LJ} crosses zero, and ϵ_{LJ} denotes interaction strength of potential well depth. The value of σ_{LJ} equals 4.0 Å, which is close to those of silicon and oxygen atom defined in CVFF potential (Dauber-Osguthorpe et al. 1988; Maple et al. 1988). Meanwhile, the value of ϵ_{LJ} is 3.0 kcal·mol⁻¹, which is chosen so that the surface energy of the energetic wall corresponds to that of atomically smooth silica surface of around 100.0 mJ·m⁻² (Kang et al. 2010; Rimola et al. 2013). The energetic wall is set as parallel to the x - y plane, and epoxy molecule is placed above the wall of 0.5 nm. The periodic boundary conditions are applied in the x - y plane of simulation cell with the dimension of 13.0 nm × 13.0 nm, and non-periodic boundary condition is applied to orthogonal direction of the cell with the dimension of 100.0 nm, so as to create the free surface on top of the epoxy. Given that the dimension of epoxy molecule is 5.9 nm × 5.9 nm × 4.7 nm, the simulation cell is large enough to minimize the interaction between mirrored images (Tam and Lau 2015; Tam et al. 2018). To simulate the wet environment, the simulation cell is filled with water molecules, as shown in Figure 2(b). The water layer has a thickness of around 9.0 nm, which is sufficiently large to eliminate the effect of upper-surface water molecules on the epoxy motion (Tam et al. 2018). Under the applied periodic boundary condition in the x - y plane, the water molecules can move across the cell boundary.

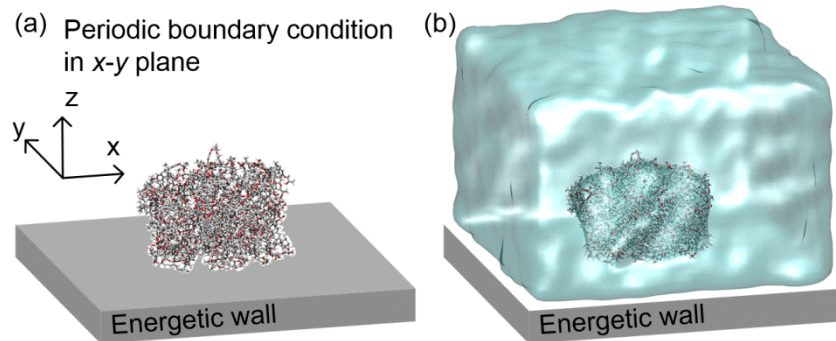


Figure 2: The molecular model of epoxy-bonded system in (a) vacuum and (b) a water box to simulate dry and wet environment. An energetic wall with atomically smooth surface is used to simulate the silica.

Molecular Dynamics Simulation

The structural equilibration and computational adhesion test are carried out in open source code LAMMPS (Plimpton 1995). During equilibration, the epoxy-bonded interface model is equilibrated in vacuum and water at temperature of 27 and 50 °C, respectively. Under each condition, the equilibration process is performed in canonical (NVT) ensemble for 1 ns with a timestep of 1 fs, and Nosé–Hoover thermostat is used for controlling the constant temperature level (Shinoda et al. 2004). The root mean squared displacement (RMSD) of epoxy atom reaches the constant level before the end of equilibration, which indicates that the system is equilibrated adequately. After equilibration, SMD simulation is applied to the equilibrated system to simulate interfacial debonding process under various environment exposures. In the simulation, epoxy molecule is pulled off the fixed wall at a constant pulling rate v . The pulling force, stress, and position of mass center of epoxy molecule are recorded until the final detachment, which are used to analyze the adhesion energy of epoxy-bonded system by using the extended Bell's approach (Büyükoztürk et al. 2011; Tam et al. 2017; Jian et al. 2018; Tam et al. 2018). The procedures for SMD simulation and Bell's analysis are described in our recent study (Tam et al. 2018). In Bell's analysis, the pulling rate v is related to the bonding associated properties according to Eq 2,

$$v = v_0 \exp\left(\frac{f \cdot x_B}{k_B T}\right) \quad (2)$$

where f denotes pulling force, x_B denotes distance between attached state and detached state, k_B is Boltzmann constant, T denotes temperature, and v_0 denotes natural bond breaking speed as defined in Eq 3,

$$v_0 = \omega_0 x_B \exp\left(-\frac{E_B}{k_B T}\right) \quad (3)$$

where ω_0 denotes natural vibration frequency equaling $1 \times 10^{13} \text{ s}^{-1}$, and E_B denotes energy barrier between attached state and detached state, which represents the interfacial adhesion energy. Based on these two equations, the relation between pulling force f and pulling rate v can be expressed as

$$f = \left(\frac{k_B T}{x_B}\right) \ln v - \frac{k_B T \ln v_0}{x_B} = A \cdot \ln v + B \quad (4)$$

According to linear regression analysis of $f-\ln(v/v^*)$ plot, the calculated slope and y-intercept are used to quantify energy barrier E_B . It is noted that v^* equaling $1 \text{ m} \cdot \text{s}^{-1}$ is used for normalization purpose. During debonding process, the pulling rate v varies from 2.5 to 40.0 $\text{m} \cdot \text{s}^{-1}$, which is in slow deformation regime. Therefore, it enables adequate dynamic response of the system and hence, leads to measurement of intrinsic interfacial adhesion energy independent of pulling rate (Tam et al. 2018). During pulling process, the recorded maximum pulling force is taken as the value of f used in Bell's analysis. Three sets of SMD simulation results are carried out under each investigated condition, and the average and standard deviation of energy barrier E_B is reported.

RESULTS AND DISCUSSIONS

The results obtained from MD simulation described in previous section are presented here, including the microscopic detail of interaction between epoxy-bonded system and surrounding environment, and the change in structural, mechanical, and interfacial behavior of the system under hydrothermal environment.

The epoxy molecule possesses two hydrogen bonding sites, i.e. the hydroxyl group and ether oxygen, which can form hydrogen bond (H-bond) with each other and with water. With the variation in temperature and humidity, the molecular interaction of epoxy-bonded system is affected, which is characterized by focusing on the H-bond network of epoxy-bonded system. The H-bond is considered to form if the distance of donor-acceptor oxygen is less than 3.5 Å, and the angle of donor-hydrogen-acceptor is more than 130 °C (Tam et al. 2018). The H-bond is examined from the equilibration trajectory under each investigated condition every 10 ps, and time-averaged value of H-bond number from last 200 ps is shown in Figure 3(a) and 3(b). In wet environment, the H-bond number between epoxy functional groups decreases, implying that the non-bonded interaction of epoxy is affected by surrounding water molecules. Meanwhile, at elevated temperature, the H-bond number formed in epoxy molecule increases slightly in both conditions, which indicates that epoxy molecule reaches a more equilibrium configuration due to the enhanced thermal motion, as demonstrated by the higher MSD level of epoxy atoms as shown in Figure 3(c). At high temperature, as an increased amount of functional groups are involved in epoxy-epoxy H-bond interaction, the number of H-bond between epoxy and water molecule decreases accordingly, as shown in Figure 3(b). Moreover, the epoxy-water H-bond interaction is also interrupted by the accelerated motion of surrounding water molecules as shown in Figure 3(d). The MSD recorded from the first 10 ps simulation is nearly the same and it is not shown here. From the simulation result, it is observed that the molecular interaction of epoxy-bonded system is significantly affected by surrounding environment at high level of temperature and humidity, which could be associated with the interfacial deterioration of the system.

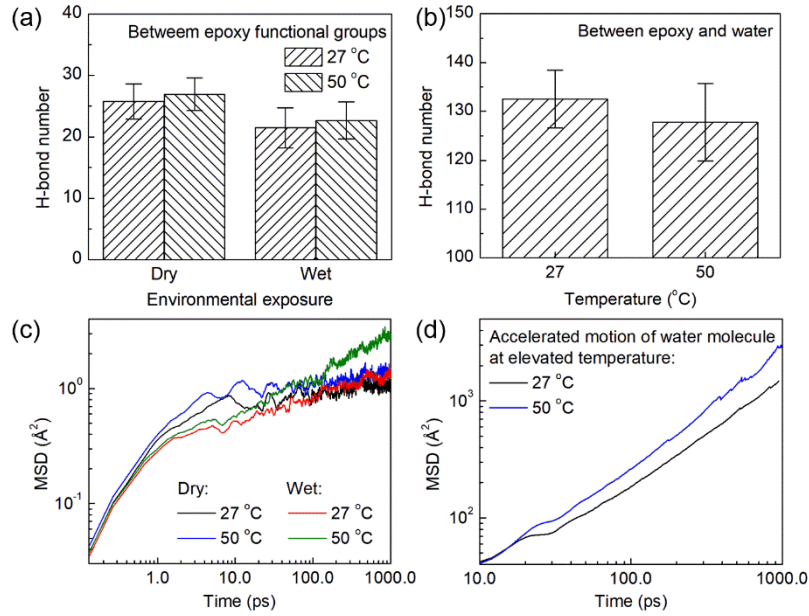


Figure 3: The H-bond number (a) between epoxy functional groups and (b) between epoxy and water molecule; mean squared displacement (MSD) of (c) epoxy and (d) water molecules increases at elevated temperature.

In order to gain insight into property variation of epoxy-bonded system under hygrothermal environment, the molecular structure of epoxy in the bonded interface is firstly characterized. The number density of epoxy molecule along z direction is averaged from last 200 ps equilibration, as shown in Figure 4(a). The cutoff distance of epoxy-wall interaction is 10 \AA from wall surface to the interior of epoxy molecule, and no direct interaction is formed between the wall and epoxy beyond that range. From the figure, a noticeable difference is observed in number density profile within cutoff range of the interaction. Similar to H-bond formation between epoxy functional groups, the level of epoxy number density profile is lower in wet environment, as demonstrated in the enlarged figure, which indicates that the contact of epoxy and wall is weakened by surrounding water molecules. The pronounced peak within this range is an important feature of the change of epoxy structure, and the peak value is shown in Figure 4(b). In dry environment, the peak value is higher at elevated temperature, which implies that the enhanced thermal motion leads to stronger substrate-induced densification effect on epoxy, as similar to the change of H-bond formation of epoxy molecule. Comparatively, there is a decrease of peak value in wet environment at elevated temperature, which indicates the further weakening of epoxy-wall interaction. Under hygrothermal environment, the accelerated motion of water molecule significantly affects the local structure of epoxy thin film.

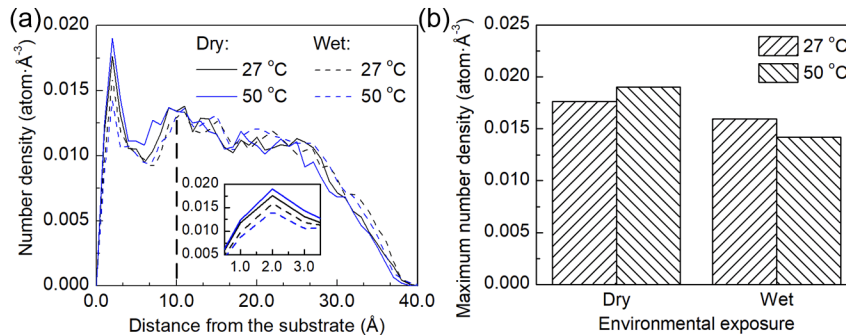


Figure 4: (a) The number density profile of epoxy molecule in dry and wet environment: a densified layer is formed close to the interface; and (b) the maximum number density defined as peak value in interface region.

After characterizing the structure of epoxy molecule, the mechanical response of epoxy-bonded system is examined under each investigated condition. The recorded stress of epoxy molecule during SMD simulation is plotted as function of displacement of its mass center along z direction, as shown in Figure 5(a). Here, the data from the pulling process at rate v of $2.5 \text{ m}\cdot\text{s}^{-1}$ is plotted, as this pulling rate in slow deformation regime enables a more adequate dynamic evolution of the system in response to the applied loading (Tam et al. 2018). The initial

stress starts with the negative value as the epoxy molecule is contracted due to epoxy-wall interaction. At the beginning stage, the steady increase of the stress implies that the epoxy molecule sticks firmly to the wall, and the deformation is mainly within the cross-linked structure. As pulling process continues, there is occasional drop of stress, which is resulted from the detachment of a small portion of epoxy molecule from the wall, as observed from the simulation trajectory. As the major portion of epoxy keeps sticking with the wall, the stress continues to increase until reaching the peak value. After that, the stress starts to decrease as the residual epoxy portion fails to withstand the pulling load and detaches from the wall finally. From the plotted curves, it is observed that the stress level of epoxy-bonded system reduces significantly in wet environment, which agrees very well with the observation of H-bond formation and structural behavior of epoxy molecule, demonstrating the mechanical degradation of epoxy-bonded system as affected by the moisture. In dry environment, though the epoxy molecule achieves a more equilibrium state due to the accelerated motion at elevated temperature, its mechanical response degrades as epoxy molecule generally softens with increasing temperature, as demonstrated by the lower stress level. Similarly, the epoxy-bonded system shows the reduced stress level and reaches the peak stress more easily in wet environment at elevated temperature, which demonstrates that the epoxy-bonded system is most vulnerable to hygrothermal environment. Through examining the stress evolution of epoxy-bonded system, it is clear that the mechanical response of the system is degraded at elevated temperature, with the worst case under hygrothermal environment, which is correlated with the variation in molecular interaction and structural behavior of epoxy-bonded system.

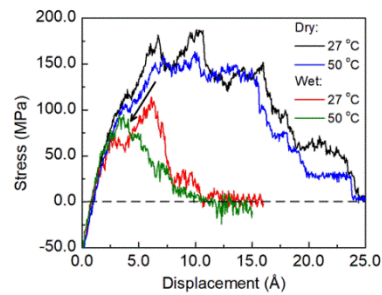


Figure 5: The stress evolution of epoxy during pulling process at a rate of $2.5 \text{ m}\cdot\text{s}^{-1}$ in dry and wet environment.

After learning the structural and mechanical degradation of epoxy-bonded system under hygrothermal environment, the interfacial integrity is further quantified. In Bell's analysis, the calculated coefficient of determination from linear regression analysis of all the $f\cdot\ln(v/v^*)$ plot is over 0.73. The data from one set of SMD simulation under each investigated condition is plotted in Figure 6(a) and 6(b) for dry and wet environment, respectively. According to linear regression result, the adhesion energy of epoxy-bonded system is calculated and summarized in Figure 6(c). The adhesion energy of epoxy-bonded system is lower in wet environment, which confirms the interfacial deterioration of the system under humid environment. The lowest adhesion of epoxy-bonded system is observed under hygrothermal environment with a value of $3.07 \pm 0.01 \text{ kcal}\cdot\text{mol}^{-1}$. The decreasing trend is in good accord with environment-induced performance loss of macroscopic FRP-concrete system, indicating the detrimental effect of hygrothermal environment on interfacial integrity of epoxy-bonded system (Lyons et al. 2002; Au and Büyüköztürk 2006; Lai et al. 2009; Lau and Büyüköztürk 2010; Tuakta and Büyüköztürk 2011; Zheng et al. 2015; Qin et al. 2016). The simulation finding on the interfacial deterioration observed from the MD simulation explains the global behavior of macroscopic FRP-concrete structure, i.e. the change of failure mode to concrete-epoxy interfacial delamination after hygrothermal environmental exposure, which has been observed in a wide range of epoxy-bonded material systems.

By using MD simulation approach, it is shown that the structural, mechanical, and interfacial behavior of epoxy-bonded system is significantly deteriorated under hygrothermal environment. For the system conditioned at elevated temperature, the weakest location is close to the local interface region, as demonstrated by the smallest peak value of epoxy number density close to the interface. Meanwhile, the mechanical behavior of the system is degraded significantly as indicated by the lower stress level. The degradation of structural and mechanical behavior is highly correlated with interfacial deterioration of epoxy-bonded system. The microscopic detail of system behavior enables one to understand the interfacial delamination failure of macroscopic FRP-concrete system under hygrothermal environment. This study reveals the relationship between the epoxy-bonded system and various environmental exposures, which is believed to be applicable to understanding the long-term mechanical behavior of different bonded material systems where the epoxy adhesive is used for bonding dissimilar materials.

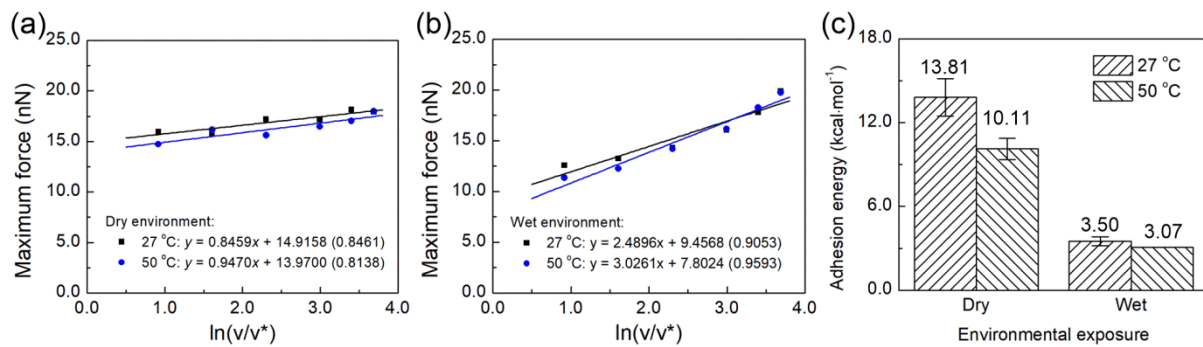


Figure 6: The recorded maximum pulling force as a function of pulling rate v in (a) dry and (b) wet environment, respectively. The calculated coefficient of determination from linear regression analysis is shown in bracket. (c) The adhesion energy of epoxy-bonded system is the lowest under hygrothermal environment.

CONCLUSIONS

In this study, MD simulation is carried out to investigate the interfacial deterioration of epoxy-bonded system under hygrothermal environment. The interface model is constructed and conditioned in simulated dry and wet environment at room and elevated temperature. Under hygrothermal environment, the surrounding water molecules with accelerated motion significantly disrupt epoxy-wall interaction, and weaken the close contact between epoxy and bonded material. Meanwhile, the epoxy molecule shows a degraded mechanical response under pulling load, and detaches easily from the bonded material. With the degraded structural and mechanical behavior, the interfacial integrity of epoxy-bonded system is the worst under hygrothermal environment. In practice, the enhanced moisture motion under hygrothermal environment could accelerate the moisture diffusion and absorption in epoxy-bonded system. In the saturated state of moisture concentration, the local epoxy-bonded interface region is deteriorated significantly, which leads to the interfacial delamination failure of exposed FRP-concrete specimen. The simulation findings provide explanation for experimental observation of interfacial failure at molecular level, and pave the way for advancing the failure analysis via simulation approach.

ACKNOWLEDGMENTS

This work was supported by the National Natural Science Foundation of China (Grant No. 51608020) and by the Thousand Talents Plan (Young Professionals) in China. The support from the China Postdoctoral Science Foundation (Grant No. 2017M620015) was also gratefully acknowledged.

REFERENCES

- S. Amidi, J. Wang (2017). "Direct Measurement of Traction-Separation Law of Concrete-Epoxy Interfaces Subjected to Moisture Attack under Mode-I Loading." *Journal of Composites for Construction*, 21(5), 04017028.
- C. Au, O. Büyüköztürk (2006). "Peel and shear fracture characterization of debonding in FRP plated concrete affected by moisture." *Journal of Composites for Construction*, 10(1), 35-47.
- H. Aydin, R.J. Gravina, P. Visintin (2016). "Durability of Adhesively Bonded FRP-to-Concrete Joints." *Journal of Composites for Construction*, 20(5), 04016016.
- O. Büyüköztürk, M.J. Buehler, D. Lau, C. Tuakta (2011). "Structural solution using molecular dynamics: Fundamentals and a case study of epoxy-silica interface." *International Journal of Solids and Structures*, 48(14), 2131-2140.
- O. Büyüköztürk, O. Gunes, E. Karaca (2004). "Progress on understanding debonding problems in reinforced concrete and steel members strengthened using FRP composites." *Construction and Building Materials*, 18(1), 9-19.
- J.R. Cromwell, K.A. Harries, B.M. Shahrooz (2011). "Environmental durability of externally bonded FRP materials intended for repair of concrete structures." *Construction and Building Materials*, 25(5), 2528-2539.
- P. Dauber-Osguthorpe, V.A. Roberts, D.J. Osguthorpe, J. Wolff, M. Genest, A.T. Hagler (1988). "Structure and energetics of ligand binding to proteins: Escherichia coli dihydrofolate reductase-trimethoprim, a drug-receptor system." *Proteins: Structure, Function, and Bioinformatics*, 4(1), 31-47.
- R.J. Gravina, H. Aydin, P. Visintin (2017). "Extraction and Analysis of Bond-Slip Characteristics in Deteriorated FRP-to-Concrete Joints Using a Mechanics-Based Approach." *Journal of Materials in Civil Engineering*, 29(6), 04017013.

O. Gunes, D. Lau, C. Tuakta, O. Büyüköztürk (2013). "Ductility of FRP–concrete systems: Investigations at different length scales." *Construction and Building Materials*, 49, 915-925.

H.R. Hamilton, B. Benmokrane, C.W. Dolan, M.M. Sprinkel (2009). "Polymer Materials to Enhance Performance of Concrete in Civil Infrastructure." *Polymer Reviews*, 49(1), 1-24.

R.W. Hockney, J.W. Eastwood (1988). *Computer simulation using particles*, CRC Press.

L.C. Hollaway (2010). "A review of the present and future utilisation of FRP composites in the civil infrastructure with reference to their important in-service properties." *Construction and Building Materials*, 24(12), 2419-2445.

W. Jian, L.-h. Tam, D. Lau (2018). "Atomistic study of interfacial creep behavior in epoxy-silica bilayer system." *Composites Part B: Engineering*, 132, 229-236.

W.L. Jorgensen, J. Chandrasekhar, J.D. Madura, R.W. Impey, M.L. Klein (1983). "Comparison of simple potential functions for simulating liquid water." *The Journal of Chemical Physics*, 79(2), 926-935.

J.-H. Kang, K.-S. Kim, K.-W. Kim (2010). "Molecular dynamics study on the effects of stamp shape, adhesive energy, and temperature on the nanoimprint lithography process." *Applied Surface Science*, 257(5), 1562-1572.

W.L. Lai, S.C. Kou, C.S. Poon, W.F. Tsang, C.C. Lai (2009). "Effects of elevated water temperatures on interfacial delaminations, failure modes and shear strength in externally-bonded CFRP-concrete beams using infrared thermography, gray-scale images and direct shear test." *Construction and Building Materials*, 23(10), 3152-3160.

D. Lau, O. Büyüköztürk (2010). "Fracture characterization of concrete/epoxy interface affected by moisture." *Mechanics of Materials*, 42(12), 1031-1042.

J. Lyons, D. Laub, V. Giurgiutiu, M. Petrou, H. Salem (2002). "Effect of Hygrothermal Aging on the Fracture of Composite Overlays on Concrete." *Journal of Reinforced Plastics & Composites*, 21(4), 293-309.

J.R. Maple, U. Dinur, A.T. Hagler (1988). "Derivation of force fields for molecular mechanics and dynamics from ab initio energy surfaces." *Proceedings of the National Academy of Sciences*, 85(15), 5350-5354.

G.C. Mays, A.R. Hutchinson (2005). *Adhesives in civil engineering*, Cambridge University Press.

J.N. Myers, C. Zhang, K.-W. Lee, J. Williamson, Z. Chen (2014). "Hygrothermal Aging Effects on Buried Molecular Structures at Epoxy Interfaces." *Langmuir*, 30(1), 165-171.

A.R. Namrou, Y.J. Kim (2016). "Residual performance of concrete–adhesive interface at elevated temperatures." *Construction and Building Materials*, 105, 113-122.

T. Oie, G.M. Maggiora, R.E. Christoffersen, D.J. Duchamp (1981). "Development of a flexible intra- and intermolecular empirical potential function for large molecular systems." *International Journal of Quantum Chemistry*, 20(S8), 1-47.

S. Plimpton (1995). "Fast parallel algorithms for short-range molecular dynamics." *Journal of Computational Physics*, 117(1), 1-19.

G. Qin, P. Huang, H. Zhou, X. Guo, X. Zheng (2016). "Fatigue and durability behavior of RC beams strengthened with CFRP under hot-wet environment." *Construction and Building Materials*, 111, 735-742.

A. Rimola, D. Costa, M. Sodupe, J.-F. Lambert, P. Ugliengo (2013). "Silica Surface Features and Their Role in the Adsorption of Biomolecules: Computational Modeling and Experiments." *Chemical Reviews*, 113(6), 4216-4313.

W. Shinoda, M. Shiga, M. Mikami (2004). "Rapid estimation of elastic constants by molecular dynamics simulation under constant stress." *Physical Review B*, 69(13), 134103.

L.-h. Tam, C.L. Chow, D. Lau (2018). "Moisture effect on interfacial integrity of epoxy-bonded system: a hierarchical approach." *Nanotechnology*, 29(2), 024001.

L.-h. Tam, D. Lau (2015). "Moisture effect on the mechanical and interfacial properties of epoxy-bonded material system: An atomistic and experimental investigation." *Polymer*, 57, 132-142.

L.-h. Tam, A. Zhou, Z. Yu, Q. Qiu, D. Lau (2017). "Understanding the effect of temperature on the interfacial behavior of CFRP-wood composite via molecular dynamics simulations." *Composites Part B: Engineering*, 109, 227-237.

J.G. Teng, J.F. Chen, S.T. Smith, L. Lam (2002). *FRP: Strengthened RC Structures*. Chichester, West Sussex, England, Wiley-VCH, John Wiley & Sons, Ltd.

C. Tuakta, O. Büyüköztürk (2011). "Deterioration of FRP/concrete bond system under variable moisture conditions quantified by fracture mechanics." *Composites Part B: Engineering*, 42(2), 145-154.

W. Xia, J. Song, D.D. Hsu, S. Keten (2016). "Understanding the Interfacial Mechanical Response of Nanoscale Polymer Thin Films via Nanoindentation." *Macromolecules*, 49(10), 3810-3817.

X. Zheng, P. Huang, G. Chen, X.M. Tan (2015). "Fatigue behavior of FRP–concrete bond under hygrothermal environment." *Construction and Building Materials*, 95, 898-909.

A. Zhou, O. Büyüköztürk, D. Lau (2017). "Debonding of concrete-epoxy interface under the coupled effect of moisture and sustained load." *Cement and Concrete Composites*, 80, 287-297.

J. Zhou, J.P. Lucas (1999). "Hygrothermal effects of epoxy resin. Part I: the nature of water in epoxy." *Polymer*, 40(20), 5505-5512.



EXPERIMENTAL STUDY OF CFRP-TO-CONCRETE BONDED JOINTS UNDER FATIGUE LOADING

Hao Zhou, Van Thuan Nguyen, Dilum Fernando

The University of Queensland, St. Lucia, Brisbane, Australia, Email: dilum.fernando@uq.edu.au

ABSTRACT

Externally bonded (EB) FRP strengthening of reinforced concrete (RC) structures has gained popularity worldwide because of its many advantages compared to conventional strengthening methods. Performance of the structures strengthened using EB FRP laminates depends significantly on the performance of the bonded interface between the FRP and concrete. Therefore, extensive research has been carried out to study the behaviour of FRP-to-concrete bonded joints, and numerous theoretical models have been developed to predict the behaviour of such bonded joints under monotonic loading. However, only limited research efforts have been made on understanding and modelling the behaviour of FRP-to-concrete bonded joints under fatigue cyclic loading. This paper presents the results of an experimental study aimed at investigating the behaviour of FRP-to-concrete bonded joints under fatigue cyclic loading. A customized data acquisition system was developed to capture the axial strains of FRP plate during fatigue cyclic loading. From the test results, it was observed that the loading amplitude, concrete strength and the type of the CFRP plate used significantly affected the failure mode of FRP-to-concrete bonded joints under fatigue cyclic loading.

KEYWORDS

FRP-to-concrete bonded joints, Data acquisition, Fatigue behaviour, Failure mode.

INTRODUCTION

Externally bonded (EB) fibre reinforced polymers (FRP) laminates strengthening has become an increasing popular retrofitting method for reinforcement concrete (RC) structures. In such strengthening system, the effective interfacial shear stress transfer between the retrofitted structure and the FRP laminate is of great importance to achieve a good strengthening performance (Smith and Teng 2002a, b). Therefore, much research has been carried out on understanding and modelling the behaviour of FRP-to-concrete bonded interfaces under interfacial shear loading (Yao *et al.* 2005, Yuan *et al.* 2004, Lu *et al.* 2005). Few researchers have also studied the behaviour of FRP-to-concrete bonded joints under quasi-static cyclic loading (Carrara and De Lorenzis 2015, Zhou and Fernando 2016). Above studies found that the failure of FRP-to-concrete bonded joints typically occur within concrete few millimetres beneath the adhesive-to-concrete interface (Yao *et al.* 2005, Zhou and Fernando 2016). However, when FRP-to-concrete bonded joints were subjected to fatigue cyclic loading, many different failure modes such as adhesion failure at the adhesive-FRP bi-material interface (Carloni and Subramaniam (2013), cohesion failure within concrete (Li *et al.* 2014) may occur. Governing failure will depend on many factors including loading rate, loading amplitude and mechanical properties of each constituent. Li *et al.* (2014) concluded that at a loading rate of 2.5HZ, when cycled at a maximum loading amplitude higher than 70% of the bond strength, cohesion failure within concrete will occur, and in all other cases adhesion failure at the adhesive-FRP bi-material interface will be the governing failure mode. However, the same conclusion could not be achieved through the FRP-to-concrete bonded joints tested at a loading rate of 1HZ (Carloni and Subramaniam 2013). While it is clear that different failure modes are observed in FRP-to-concrete bonded joints under fatigue cyclic loading, and parameters such as type of FRP, type of adhesive, concrete strength, loading rate, loading amplitude, etc. have been found to may affect the failure mode, no clear understanding on the effects of different parameter on the failure of CFRP-to-concrete bonded joints cannot be drawn from the existing test results.

In terms of predicting fatigue life of FRP-to-concrete bonded joints, S-N curves have been proposed based on the experimental results (Ferrier *et al.* 2005, Li *et al.* 2014). However, it is well known that the bond behaviour of FRP-to-concrete bonded joints is dependent on the bond length, with load-deformation curved of such bonded joints with bond lengths longer than effective bond length showing displacement increase without further increase in maximum load (Yuan *et al.* 2004). Considering such behaviour, S-N curves without properly addressing the effect of bond-length appear to be inadequate for predicting the fatigue life of a FRP-to-concrete bonded joint. In addition, fatigue life-of a FRP-to-concrete bonded joint will also dependent on the dominant failure mode, thus any prediction model should also consider the dominant failure mode(s).

Bond-slip curves are commonly used to model the constitutive behaviour of the FRP-to-concrete bonded joints under quasi-static monotonic and cyclic loading (Chen and Teng 2001, Zhou *et al.* 2017). A bond-slip model is often used to represent the relationship between the local interfacial shear stress and the relative slip between the two adherents. However, so far only few experimental studies have been carried out (Zhang 2017, Li *et al.* 2018) on obtaining the bond-slip behaviour of the FRP-to-concrete bonded joints under fatigue cyclic loading. Bond-slip models proposed from those experimental studies (Zhang 2017), did not considered the effect of failure modes, thus not suitable as a general model for predicting the behaviour of FRP-to-concrete bonded joints under fatigue cyclic loading. Carrara and De Lorenzis (2015) proposed a damage plasticity model accounting for the bond-behaviour of FRP-to-concrete bonded joints under both quasi-static cyclic loading and fatigue loading. A key parameter in this theoretical model is the interfacial fracture energy, which is dependent on the failure mode of the bonded joint. Therefore, in order to apply the Carrara and De Lorenzis (2015) model, one must already know the interfacial fracture energy, thus the failure mode.

With the aim of further expanding the understanding of CFRP-to-concrete bond behaviour, especially the failure modes, a series of CFRP-to-concrete single shear pull-off tests under fatigue cyclic loading was conducted at the University of Queensland, Structures Laboratory. This paper presents the details and results of this study. Strain distribution along the bond length during fatigue loading was measured and recorded using a specially designed data acquisition system (DAQ). It was found that the failure mode of the FRP-to-concrete bonded joints under fatigue cyclic loading could change from cohesion failure in concrete to interlamina failure of the CFRP plate or cohesion failure of the adhesive.

MATERIALS AND TESTING METHOD

Specimen Details and Material Characteristics

Single shear pull-off test setup have been used by many researchers to study the behaviour of FRP-to-concrete bonded joints under monotonic loading (Yao *et al.* 2005) as well as fatigue cyclic loading (Li *et al.* 2014, Zhang 2017, Carloni and Subramaniam 2013). In single-shear pull-off test setup, bonded interface is predominantly subjected to interfacial shear stresses, thus adopted in this study. The overall test set-up and specimen detail are given in Figure 1.

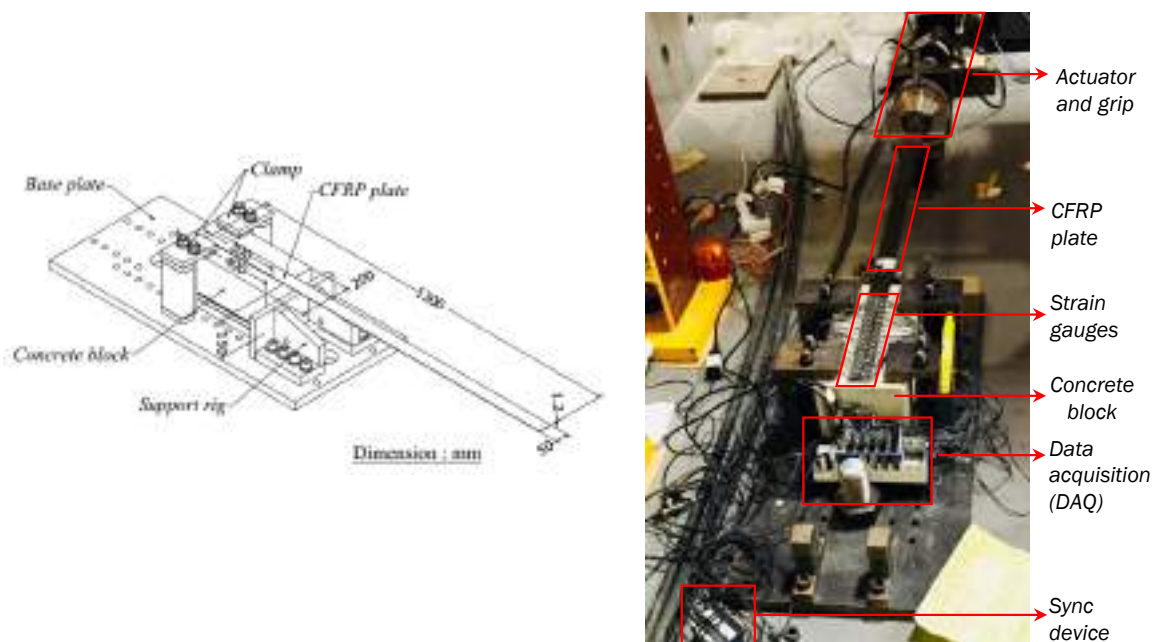


Figure 1: The test set-up of single lap pull-off test

In total seven specimens covering two types of CFRP (160GPa and 180GPa for elastic modulus and 1.4mm and 1.2 mm for the thickness) and concrete with two different average compressive strength (64.4MPa and 49.17MPa) were manufactured and tested. For simplicity, CFRP plates with 160GPa nominal elastic modulus and 1.4mm nominal thickness is denoted as CFRP-I, while CFRP plate with 180GPa nominal elastic modulus and 1.2mm nominal thickness is denoted as CFRP-II. Similarly concrete with average compressive strength 64.4MPa is denoted as CI and concrete with average compressive strength 49.1MPa is denoted as CII. Compressive strengths of CI and CII concrete were obtained using cylinder tests according to AS1012.9:2004 (AS1012.9 2014). Commercially available Sikadur-30 adhesive was used to bond the CFRP plate to the concrete block. A 50mm gap between the front of the bonding area (50×300 or 325 mm) and the supporting edge of the block was provided to

avoid the edge effects (Yao *et al.* 2005, Mazzotti *et al.* 2008). Before bonding, the concrete block was ground with needle gun until the coarse aggregates were exposed and then cleaned with compressed air to remove dust from the ground surface. The CFRP plate was slightly sanded with fine sand paper (180 grit) to remove the loose fibres and oxide layer, followed by further cleaning with acetone (Fernando *et al.* 2013). The thickness of adhesive was controlled to be 1.0mm by placing spacers on both sides of the bonding zone while applying adhesive. The bonded specimen was stored in the laboratory environment for at least two weeks before testing. In the present study, seven samples in total were tested with different loading amplitudes. Loading amplitudes used for each specimen are given in Table 1. Maximum and minimum loading amplitude was determined as a percentage of the bond strength of single-shear pull-off test specimens under monotonic loading reported in Zhou *et al.* (2017). The maximum loading amplitude was varied from 60% to 82% of the bond strength to study the effect of loading amplitude on the debonding rate of the bonded joints. Minimum loading was controlled to ensure CFRP plate will remain under tension during the unloading.

Table 1: Details about tested samples

Sample No.	CFRP	Concrete	No. of loading cycles applied	Load amplitude (Load-carrying capacity)	Fatigue failure mode
1	CFRP I	CI	380850	15-60% and 15-70% (31.1kN)	FRPD
2	CFRP I	CI	120400	15-70% (32.1kN)	CC+ FRPD
3	CFRP I	CI	41300	15-78% (31.1kN)	FRPD
4	CFRP II	CI	65250	15-73% (34.1kN)	CA+AF
5	CFRP II	CII	11900	13-73% (30kN)	CC
6	CFRP I	CII	479900	15-60%, 15-65% and 71% (28.0kN)	FRPD
7	CFRP I	CII	57350	15-75% and 15-82% (28.0kN)	FRPD+CC

Note: FRPD= FRP Delamination; CC=Cohesion Failure in concrete; CA= Cohesion failure in the adhesive; AF= Adhesion Failure

Instrumentation and Test Procedures

To measure the axial strain distribution along the bond length, 20 strain gauges were attached to the CFRP plate at 15mm intervals. Two more strain gauges were attached to the unbonded part of the CFRP plate 50mm away from the support edge of concrete. In order to capture strain distribution along the bonding length during the fatigue cyclic loading, a customized data acquisition system (DAQ) and data sync system were programmed with Labview (Instruments 2017). As shown in Figure 2, force and displacement of the actuator, together with the strain along the bonding length was read by the NI9235 strain gauge module at a sampling rate of 400. Simultaneously, force and displacement were also transmitted from the MTS controller to a customized synchronization software for counting the loading cycles. If the loading cycles reached the predetermined criterions, such as every 50 cycles, a series of synchronized signal consisting of 12 high-voltage (3.2v) pulse in one loading cycle was sent to the synchronizing device and the DAQ. As soon as the DAQ received the high voltage signals, stain readings at these high-voltage moment will be recorded and write to a data file for further processing. Otherwise, the synchronized voltage will remain low and no data will be recorded. The advantage of this system is that strain data can be obtained during the fatigue loading only at specific loading cycles. Therefore, the data volume can be reduced significantly while the accuracy can still be guaranteed. At the same time, strain distribution along the bond length at force-peak and valley of one loading cycle can be captured.

At the beginning of the test, the sample was first monotonically loaded to the upper limit of the fatigue cyclic loading amplitude and then unloaded to the mean value. After that, fatigue cyclic loading at predetermined loading amplitude was applied at 5Hz with force control. During the fatigue cyclic loading, the strain distribution along the bond length was carefully observed. When at least half of the bond length was debonded, the sample was loaded monotonically until failure.

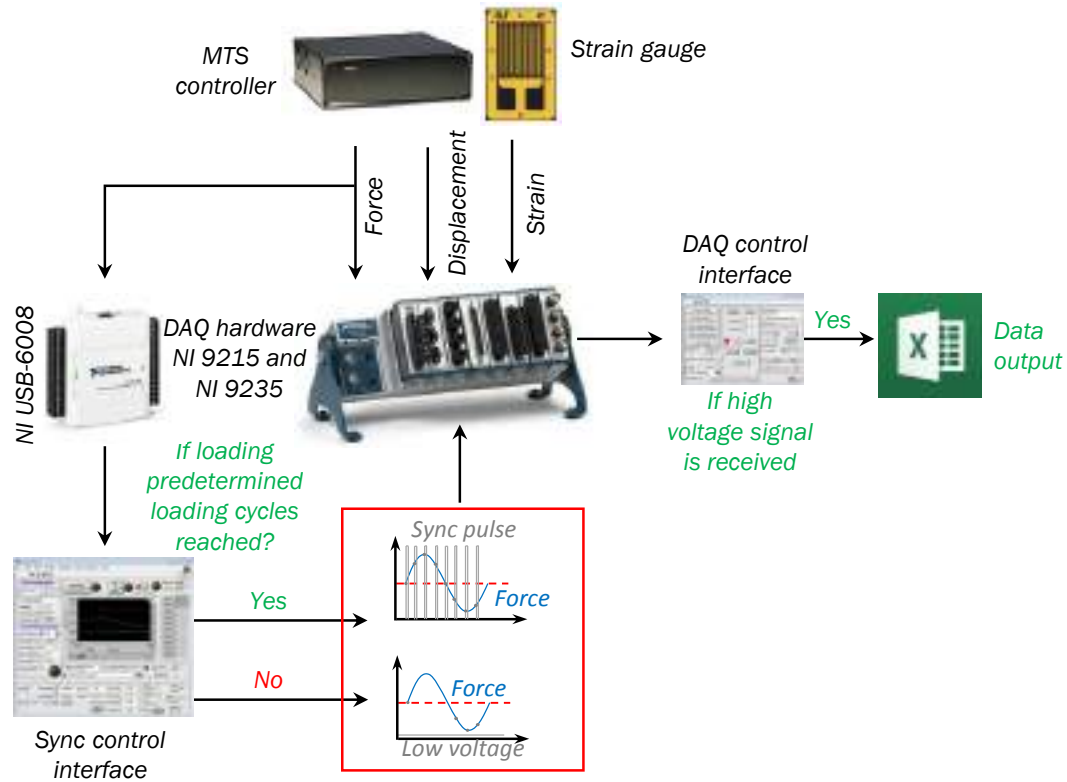


Figure 2: Customized data acquisition system

TEST RESULTS

Failure Mode

Failed samples are shown in Figure 3, while the corresponding failure modes are given in Table 1. In many samples (except for sample 5), different failures such as interlaminar failure of FRP, adhesion failure could be observed. However, final failure of all the specimens were due to cohesion failure within concrete (Table. 1). In all specimens except for specimen 7, interlaminar failure within CFRP was observed towards the far end of the specimens when loaded monotonically. This is also commonly observed in FRP-to-concrete bonded joints under monotonic loading (Yao *et al.* 2005). This failure, which is due to monotonic loading was ignored in specifying the failure modes in Table 1.

Comparing the specimens with CFRP plate I and II, all the specimens with CFRP plate I showed interlaminar failure of the CFRP plate, and specimens with CFRP plate II failed due to either cohesion failure within concrete or adhesion failures within bi-material interfaces and showed no signs of interlaminar failure within the CFRP plate. Two types of pultruded CFRP plates, were obtained from two different manufacturers, which used different types of epoxy resins in manufacturing the CFRP plates. Differences in two CFRP plates were found to be detrimental in controlling the interlaminar failure of the CFRP plate due to fatigue cyclic loading.

In specimens with CFRP plate II, specimen 4 (with concrete CI) failed in adhesion failure of the bi-material interface while specimen 5 (with concrete CII) failed with the cohesion failure within concrete. This clearly demonstrate the effect of concrete strength on the failure mode, with lower strength concrete specimens failing due to cohesion failure within concrete, and increasing the concrete strength resulting in dominant failure changing to adhesion failure within the bi-material interfaces. This effect could not be clearly seen in specimens with CFRP plate I due to the occurrence of interlaminar failure of CFRP plate in all samples. Nevertheless, when comparing samples 6 and 7, it could be seen that the variation of loading amplitudes also had an effect on the failure mode. In specimen 6, failure under fatigue cyclic loading was due to interlaminar failure of CFRP plate. In specimen 7, failure closer to the loaded end initiated as cohesion failure within concrete and changed to interlaminar failure in CFRP plate within a short distance from the loaded end. Once maximum loading amplitude was increased to 82% of the bond strength, failure changed to cohesion failure within concrete. While the current test results indicate that the loading amplitude may have an effect on the failure mode, more test results are necessary to come to a clear conclusion.

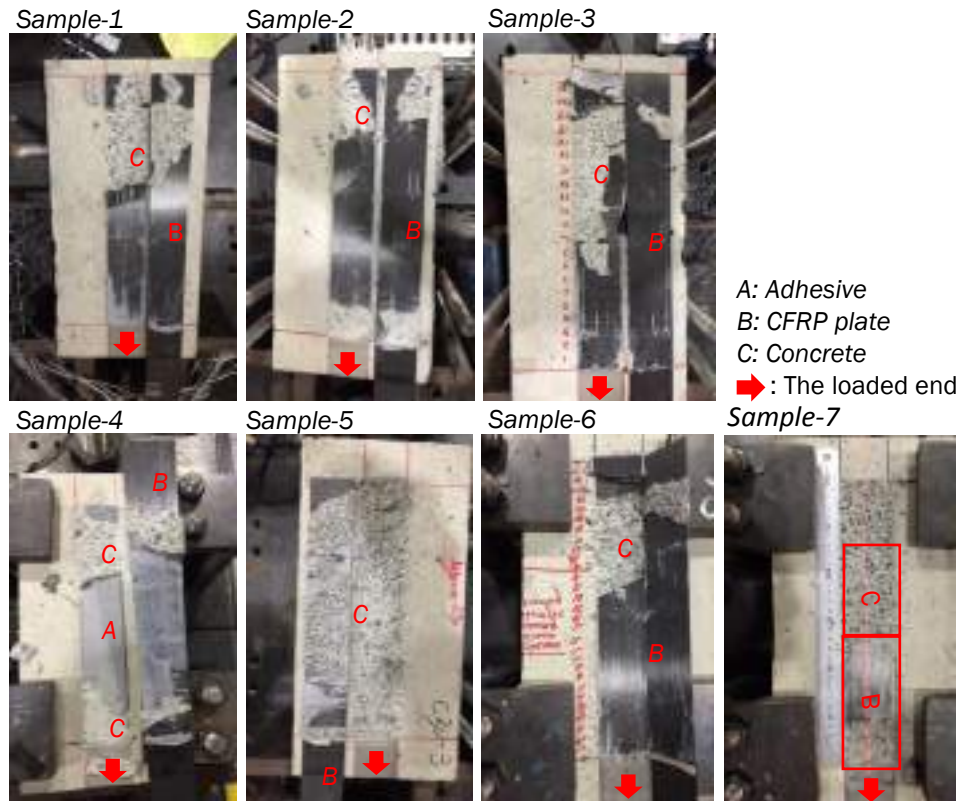


Figure 3: Failed samples

Strain Distribution and Load Displacement Curves

As described in the previous section, the strain distribution along the bonding length was measured and recorded by a customized DAQ system. Figure 4 illustrates the data acquisition in one of the tests. It can be seen that data was recorded every 50 cycles (test was running at 5Hz). In the particular cycle when data was recorded, 12 data points were triggered by a high-voltage signal (Figure 4b). Through this method, the strain distribution along the bond length at maximum and minimum force were captured. The strain distribution along the bond length at force peak and force valley are plotted in Figure 5 at 1st and 41300th loading cycles.

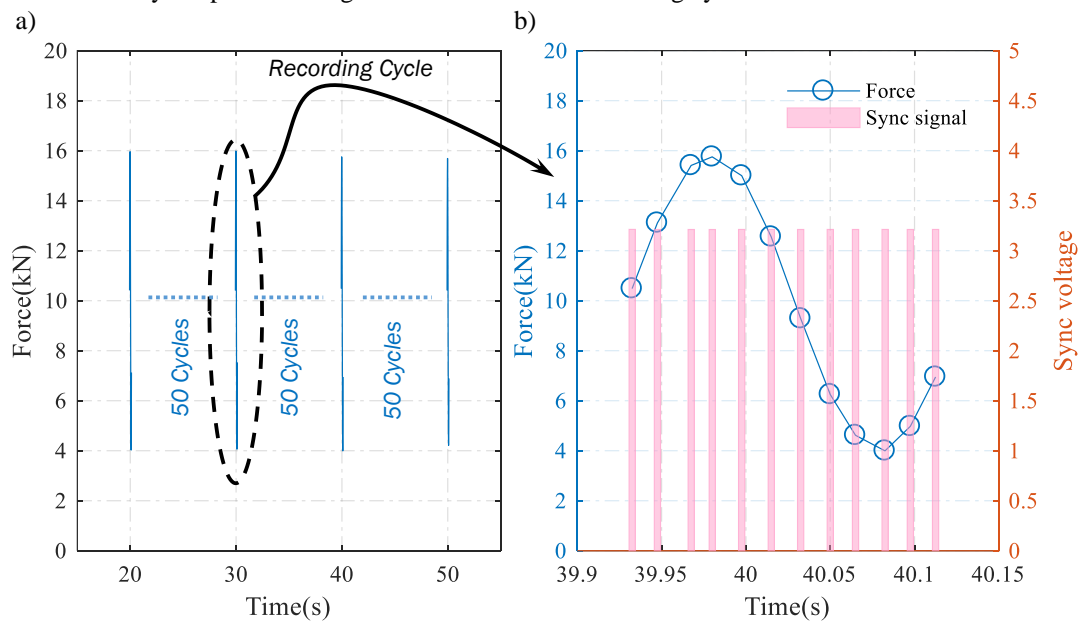


Figure 4: Illustration of data acquisition

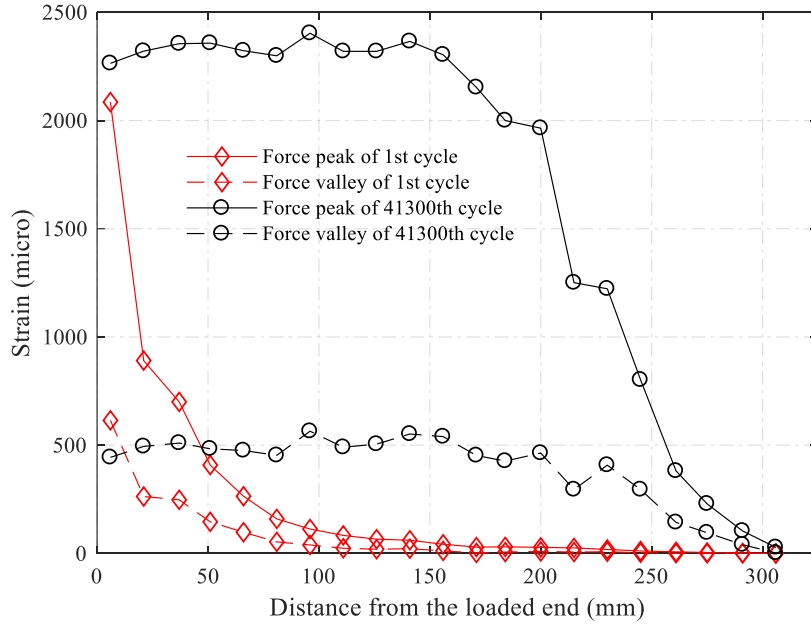


Figure 5: Strain distribution along the bond length at different loading cycles of Sample-3

Since some noise in the strain data was observed, it was necessary to reduce the noise of the strain data to obtain meaningful results. Therefore, the strain distribution was further regressed with the following expression (Carloni and Subramaniam 2013),

$$\varepsilon_x = \varepsilon_0 + \frac{\alpha}{1 + e^{\frac{x-x_0}{\beta}}} \quad (1)$$

Where ε_0 , x_0 , α and β are parameters determined from nonlinear regression analysis of the computed strains. As shown in Figure 6, the fitted strain distribution matches well with tested results.

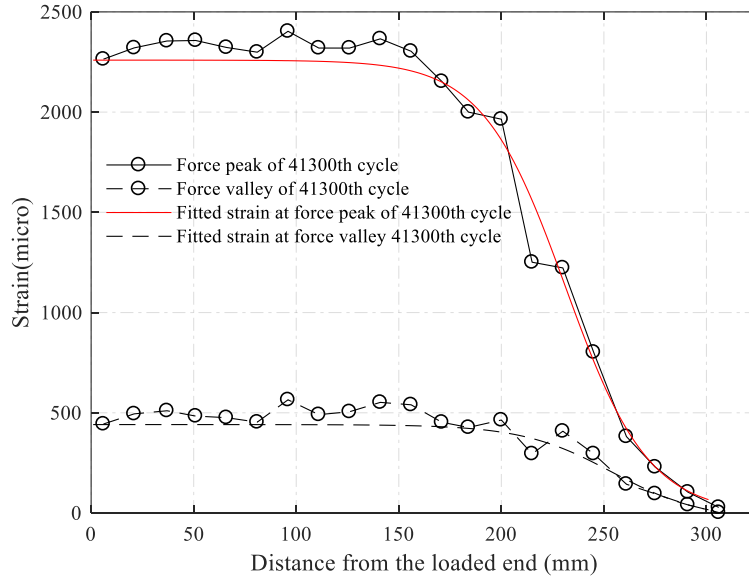


Figure 6: Fitted strain distribution along the bond length at 41300th loading cycle of Sample-3

With fitted strain distribution along the bond length, the slip and shear stress at the loaded end were calculated as follows,

$$\delta_{i/2} = \frac{(\varepsilon_i + \varepsilon_{i+1})}{4}(L_{i+1} - L_i) + \sum_{i=1}^n \frac{(\varepsilon_i + \varepsilon_{i+1})}{2}(L_{i+2} - L_{i+1}) \quad (2)$$

Where ε_i is the strain value at the i th data point extracted from the DIC analysis, counted from the loaded end of the CFRP plate; L_i is the distance of the data point from the loaded end of the CFRP plate; E_p and t_p are the elastic modulus and thickness of the CFRP plate; n is the number of data points counted from the free end of

the CFRP plate to the current calculating point; $\tau_{i/2}$ and $\delta_{i/2}$ are the shear stress and slip at the middle point between the i th and $(i+1)$ th data point. Then the load-displacement at the loaded end was depicted in Figure 7.

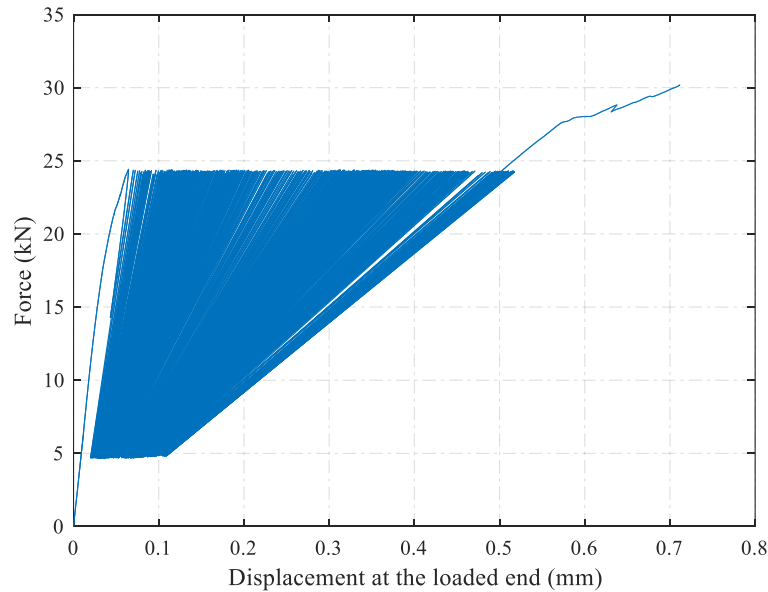


Figure 7: Load-displacement at the loaded end of Sample-3

From Figure 7, it is evident that as the number of fatigue cycles increased, loaded end displacement at the maximum load tends to increase. Also with the increase in number of fatigue cycles, the stiffness of the load-displacement curve decreases. This shows the damage propagation of the bonded interface. This damage propagation also seen in strain distributions (Figure 6), where at 41300th loading cycle, constant strain region closer to the loaded end indicating debonding within the bonded interface.

In the current series of tests, a clear damage propagation in the bonded interface could be seen with the increase in number of fatigue loading cycles. This gradual propagation of damage was observed in all specimens irrespective of the failure mode. However, the interfacial fracture energy is dependent on the failure mode, thus the rate of damage is also dependent on the failure mode. With different specimens showing different failure modes, it is difficult to obtain a general predictive model for damage propagation due to fatigue cyclic loading from the current test results. Data from specimen 5, where failure occurred due to cohesion failure within concrete could be used for developing predictive models for fatigue damage of CFRP-to-concrete bonded joints where failure occurs within concrete. Data from specimens 1, 3 and 6 could be used for developing models for fatigue damage of CFRP-to-concrete bonded joints where failure is due to interlaminar failure of CFRP plate. However, in understanding and modelling fatigue damage of CFRP-to-concrete bonded joints, a better understanding of the factors contributing to changes in failure modes of such bonded joints is necessary. Currently further experiments are being carried out at UQ structures laboratory to better understand the behaviour of CFRP-to-concrete bonded joints and the factors affecting failure modes under fatigue cyclic loading.

CONCLUSIONS

A series of CFRP-to-concrete bonded joint was tested in this present study to investigate the bond behaviour of such bonded joints under fatigue cyclic loading. Specimens tested covered two different CFRP materials, two different concrete strengths, and different loading amplitudes. To measure and record the strain distribution along the bond length during fatigue loading, a customized DAQ system was programmed. Based on the test results, some conclusions can be drawn as follows:

1. The customized DAQ system showed a good performance for recording test data under fatigue loading. Strain distribution at the force-peak and force-valley moment can be captured accurately;
2. Different failure modes can occur for CFRP-to-concrete bonded joints under fatigue loading, compared to cohesion failure in concrete for such bonded joints under monotonic loading;
3. The failure mode of such bonded joints under fatigue loading is sensitive to factors including but not limited to the fatigue performance of different materials in such bonded joints and the load amplitude applied.
4. Evident damage initiation and accumulation under fatigue loading can be observed through the strain distribution along the bond length and the load-displacement curve.

ACKNOWLEDGMENTS

Authors would like to thank technicians at the UQ structures lab for their help in carrying out experimental tests.

REFERENCES

- AS1012.9 (2014). "Methods of testing concrete, Methods 9: Compressive strength tests-Concrete, mortar and grout specimens (AS 1012.9:2014)".
- Carloni, C. and Subramaniam, K. V. (2013). "Investigation of sub-critical fatigue crack growth in FRP/concrete cohesive interface using digital image analysis". *Composites Part B: Engineering*, 51(35-43).
- Carrara, P. and De Lorenzis, L. (2015). "A coupled damage-plasticity model for the cyclic behavior of shear-loaded interfaces". *Journal of the Mechanics and Physics of Solids*, 85(1), 33-53.
- Chen, J. F. and Teng, J. G. (2001). "Anchorage strength models for FRP and steel plates attached to concrete". *Journal of Structural Engineering*, 127(7), 784-791.
- Fernando, D., Teng, J. G., Yu, T. and Zhao, X. L. (2013). "Preparation and Characterization of Steel Surfaces for Adhesive Bonding". *Journal of Composites for Construction*, 17(6).
- Ferrier, E., Bigaud, D., Hamelin, P., Bizindavyi, L. and Neale, K. (2005). "Fatigue of CFRPs externally bonded to concrete". *Materials and structures*, 38(1), 39-46.
- Instruments, N. (2017). "LabVIEW 2017 Help - National Instruments".
- Li, K., Cao, S.-Y. and Wang, X.-L. (2014). "Experimental Study on the Fatigue Endurance of the CFRP-Concrete Interface". *Journal of Composites for Construction*, 19(4), 04014075.
- Li, K., Cao, S., Yang, Y. and Zhu, J. (2018). "Bond-Slip Relationship for CFRP Sheets Externally Bonded to Concrete under Cyclic Loading". *Materials (Basel)*, 11(3).
- Lu, X. Z., Teng, J. G., Ye, L. P. and Jiang, J. J. (2005). "Bond-slip models for FRP sheets/plates bonded to concrete". *Engineering Structures*, 27(6), 920-937.
- Mazzotti, C., Savoia, M. and Ferracuti, B. (2008). "An experimental study on delamination of FRP plates bonded to concrete". *Construction and Building Materials*, 22(7), 1409-1421.
- Smith, S. T. and Teng, J. G. (2002a). "FRP-strengthened RC beams. I: review of debonding strength models". *Engineering Structures*, 24(4), 385-395.
- Smith, S. T. and Teng, J. G. (2002b). "FRP-strengthened RC beams. II: assessment of debonding strength models". *Engineering Structures*, 24(4), 397-417.
- Yao, J., Teng, J. G. and Chen, J. F. (2005). "Experimental study on FRP-to-concrete bonded joints". *Composites Part B: Engineering*, 36(2), 99-113.
- Yuan, H., Teng, J. G., Seracino, R., Wu, Z. S. and Yao, J. (2004). "Full-range behavior of FRP-to-concrete bonded joints". *Engineering Structures*, 26(5), 553-565.
- Zhang, W. (2017). "Prediction of the Bond-Slip Law Between Externally Bonded Concrete Substrates and CFRP Plates Under Fatigue Loading". *International Journal of Civil Engineering*.
- Zhou, H. and Fernando, D. (2016). "Experimental study of the cyclic behaviour of FRP-to-concrete bonded joints". *the 8th International Conference on Fibre-Reinforced Polymer (FRP) Composites in Civil Engineering (CICE 2016)*, 14-16 December 2016, HongKong, China.
- Zhou, H., Fernando, D., Chen, G. and Kitipornchai, S. (2017). "The quasi-static cyclic behaviour of CFRP-to-concrete bonded joints: An experimental study and a damage plasticity model". *Engineering Structures*, 153(43-56).



FLEXURAL STRENGTHENING OF PRE-CRACKED RC BEAMS USING SIDE NSM CFRP BARS: AN EXPERIMENTAL INVESTIGATION

Thanongsak Imjai¹, Udomvit Chaisakulkiet² and Reyes Garcia³

¹Dept. of Civil Engineering, Rajamangala University of Technology Tawan-Ok, Bangkok, Thailand,
Email: thanongsak_im@rmutto.ac.th

²Dept. of Civil Engineering, Rajamangala University of Technology Rattanakosin, Bangkok, Thailand

³Dept. of Civil Engineering, The University of Sheffield, Sheffield, United Kingdom

ABSTRACT

This paper presents the results of an analytical and experimental study on the performance of repaired and strengthened rectangular reinforced concrete (RC) beams using near surface-mounted (NSM) CFRP rods. All beams with NSM strengthening scheme were tested under four-point bending. In Phase 1, one beam was tested up to the load level that induced cracking at service condition, and strengthening using NSM in the second phase and the other two beams were tested up to failure and used as control specimens. In Phase 2, one of the damaged beam was strengthened using side NSM CFRP rod, and then tested again up to failure. The test results indicate that the flexure capacity of a repaired and FRP-NSM strengthened beam increased by up to 40% over the control beam, thus confirming that the strengthening solution was very effective at enhancing the flexural capacity of damaged RC beams. The predictions given by linear cracked sectional analysis match well the deflection response of the NSM strengthened beams but only up to a service load. Moreover, ultimate capacity of NSM strengthened RC section by current design equation gives a good agreement with the experimental results.

KEYWORDS

Strengthening and repair, Structure, Bond and interfacial stresses, Side Near-surface Mounted, SNSM.

INTRODUCTION

The use of NSM FRP reinforcement has been adopted by the construction industry for strengthening of RC structures (Alkhrdaji, and Nanni 2000; Tumialan et al. 2007; Tang et al. 2006) and initial design guidelines have already been published (ACI-440 2017; CCIP-56 2012). The NSM involves the insertion of strengthening strips or rods into pre-cut grooves in concrete cover usually at the bottom side (BNSM) and then filling the grooves with epoxy adhesive (Tang et al. 2006; Parretti, and Nanni 2004; Lorenzis, and Teng 2007). NSM FRPs is an effective rehabilitation solution to strengthen RC structures, as it can enable higher load carrying capacity and ductility than conventional Externally Bonded Reinforcement (EBR). However, the performance of elements strengthened in flexure is still controlled by bond failure between the NSMR system and the concrete substrate. This can reduce both the effectiveness and safety of NSMR systems and should be accounted for in design [8]. Bond tests show the superior bond behaviour of NSM to that of EBR (Hassan and Rizkalla 2003; Hassan and Rizkalla 2004), both in terms of bond performance and post-peak behaviour. NSM exhibits higher bond strength even with short embedment lengths and was also found to superior EBR in terms of debonding load in flexural tests (Tang et al. 2006). The efficiency of flexural strengthened of RC beams with NSM CFRPs were extensively studied (June at al. 2007; El-Hacha and Rizkalla 2004; Castro at al. 2007; Jung at al. 2005; Lorenzis at al. 2002; Mahmoud at al. 2009; Mahmoud at al. 2010; Barros and Fortes 2005; Housen at a. 2015). In most cases, the flexural capacity of strengthen specimens increase between 30-70% compared to their counterpart control specimens and failed by end debonding, critical diagonal crack debonding and concrete cover separation. However, original BNSM system has some restrictions as structural members must have sufficient width for the necessary edge clearance and clear spacing between the adjacent NSM grooves (Lorenzis and Teng 2007). In many cases, the strengthening of a structural element needs to support mechanical and electrical works attached at the bottom side of the member (Housen at a. 2015). In the present study, side pre-cut grooves (SNSM) is introduced to overcome the limitation of BNSM technique in order to examine the flexural performance and enhance the serviceability of the RC beams.

The aim of this experimental work is to experimentally investigate the use of side and bottom NSM CFRP reinforcement in flexural strengthening applications, so as to enable the development of side pre-cut grooves NSM technique where bottom pre-cut grooves for NSM cannot meet serviceability requirement and obstructed by M&E works. To achieve this, SNSM and BNSM-strengthened beams with Carbon rod were tested in flexure. The paper

summarises the main findings of this experimental programme and discusses the effectiveness of existing guidelines at predicting the expected capacity and deflections.

EXPERIMENTAL PROGRAMME

The experimental work involved preparation and testing of three concrete beams reinforced with conventional flexural and shear steel reinforcement. All beams were under-reinforced in flexure. In Phase I of testing, all specimens were tested in four-point bending and one beam was pre-cracked up to the load level that induced the first flexural crack. To examine the effectiveness of BNSM strengthening performance in testing phase I, one beam was strengthened with NSM by adding 1 CFRP rod into the pre-cut groove at the bottom of the beam. To examine the effectiveness of strengthening interventions in testing phase 1, one of the pre-cracked beam was strengthened using SNSM CFRP rods alongside of the beam and re-tested in phase 2.

Design of beam specimens

Table 1 summarises details of the tested beams as well as the parameters examined in this study. The beam specimens had a rectangular cross-section of 150×250 mm and a span length of 2300 mm (see **Table 1**). To promote a flexural dominated behaviour, each beam was subjected to four-point bending with a shear span to effective depth ratio (a/d) equal to 3.68. Two $\phi 12$ mm steel reinforcement ($f_y = 392$ MPa) were used as flexural bottom reinforcement in all of beam specimens, thus leading to a flexural reinforcement ratio $\rho_f = 0.68\%$. The reinforcement in the compression zone (at the shear span zone) of each beam consisted of two $\phi 9$ mm bars ($f_y = 235$ MPa) to support shear links. To prevent shear failure, each shear span was reinforced in shear with 9 mm steel stirrups (two legs) at spacing of 100 mm ($\rho_w = 0.84\%$). In **Table 1**, the beams were identified using one letter (B), followed by the specimen number (1 to 3). In phase 1, beam B1 was used as control specimens and was not repaired or strengthened. Beam B2 was strengthened with near surface-mounted by adding 1 CFRP rod at the bottom (BNSM) of the beam and tested up to failure (**Figure 1**). As for the beam B3 tested in phase 1, this beam was tested up to the load level that the first flexural crack occurs. Beam B3 was then strengthening using near surface-mounted by adding 2 CFRP rods along the side of beam (SNSM) and denoted as “B3S” in phase 2, as shown in **Figure 1**.

Table 1: Characteristics of tested beams and test set-up

Testing phase	Beam reference	NSM details	Damage level (last load reading)
I	B1	-	Up to failure
	B2	BNSM	
	B3	-	1st flexural crack
II	B3S	SNSM	Up to failure

Instrumentation & Test set-up

Material properties

A ready-mix concrete was used to cast the beams. The mix was produced using concrete C25 with 10 mm maximum aggregate size and Ordinary Portland Cement type I. A target slump of 50 mm was specified. The 28-day compressive strength of concrete (f_c) was 30 MPa obtained from 150 mm cubes according to BS EN 12390-3 (2009). The indirect tensile splitting strength ($f_t = 3.1$ MPa) was determined from tests on six 150×300 mm cylinders according to BS EN 12390-6 (2009). The flexural strength ($f_b = 4.1$ MPa) was obtained from four-point bending tests on three prisms of 100×100×500 mm according to BS EN 12390-5 (2009). All cubes, cylinders and prisms were cast at the same time and cured together with the beams. **Table 1** reports the average results and standard deviations for strength from the tests on cylinder and prism control specimens. Sand coated CFRP rod (fibre volume = 68%) with a diameter (ϕ) of 8 mm was used for both bottom and side NSM strengthening configurations. The tensile strength was 2400 MPa, and the modulus of elasticity was 200 GPa with elongation at break = 1.5%. Two-part commercially available epoxy adhesive, Sikadur 30 was used to bond the composite reinforcement to the concrete. Sikadur 30 consists of two parts (A-white : B-black) which were mixed in a ratio of 3:1 until a uniform grey colour was achieved using a rotary mixing tool. The epoxy bond strength for concrete

and steel was 4 and 21 MPa, respectively. Mechanical and physical properties of epoxy adhesive after 7 days, given by the manufacturer is shown in Table 2.

Table 2: Epoxy adhesive for NSM strengthening system

Epoxy adhesive Part A & B		Mechanical properties	MPa
		Compressive strength	95
		Tensile strength	31
		Shear strength	19
		Modulus of elasticity	11,200

Instrumentation and test set up

Four-point bending tests were conducted on three reinforced concrete specimens. All of the beam specimens were tested in two consecutive phases. In Phase 1, unstrengthened beam (B1) and pre-strengthened beams (B2) were tested up to failure whilst beam B3 was tested up to the load level that induced flexural cracking at service load conditions. In Phase 2, pre-cracked beam B3 (denoted by “B3S” in phase 2) was strengthened using NSM without any cracks repairing. The overall deflections were measured at each load increment using three Linear Variable Differential Transducers (LVDTs) located at the mid-span and under the point-loads (Table 1-left). Two additional LVDTs were placed on the top-face of each of the beam supports to calculate net mid-span deflections. Moreover, two LVDTs were also placed at the two ends of the beam to monitor beam horizontal translation.

Repair and Strengthening procedure

In Phase 1, beam B1 was used as controlled specimen and tested up to failure. Beam B2 was pre-strengthened using BNSM by adding 1 CFRP rod at the bottom face of the beam and tested up to failure whereas specimen B3 was loaded in the first phase to produce damage at the service load level (P_{cr}), which induced the first flexural cracks. Pre-cracked beam was then strengthened using SNSM by adding 2 CFRP rods along the side of the beam without repairing cracks that previously developed during the first test (Figure 1-b).



(a) Cleaning the groove with air jet prior applying half-filled with epoxy

(b) Insert the CFRP rod into the groove



(c) Filled the groove level the surface (B3S)



(d) Filled the groove level the surface (B2)

Figure 1: NSM strengthening procedure

ANALYSIS OF THE TEST RESULTS

Capacity and failure behaviour

Table 3 summarises the experimental results in terms of the ultimate load at failure (P_u), ultimate deflection at mid-span (δ_{max}), maximum measured crack width (w_f) and failure mode (SY=steel yielding, CC=concrete

crushing). The values w_f shown in Table 3 were measured at the first cracking load (from B1). All results correspond to the second phase of the experimental programme. In Phase 1, first flexural cracks were observed for all of the beams at the cracking load ($P_{cr} = 16.8$ kN). Initially, small narrow flexural cracks developed within the mid-span and shear span region. Flexural cracks widened and were visible to the naked eye as the load further increased. The maximum load of the beam B1 was 59.5 kN and the mid-span deflection 22.4 mm, and the beam failure was dominated by steel yielding (SY) (i.e. Figure 2a). The specimen with BNSM strengthening (B2) had a similar to beam B1 and failed at 85.3 kN accompanied by concrete crushing (Figure 2b). For the beam B3 tested in phase 1, testing was halted when the cracking load (P_{cr}) reached the predicted value derived from cracked-sectional analysis (CSA). In this case, it was assumed that the cracking load was close to the capacity of the tested beams at service load ($P_{cr} = 16.8$ kN, mid-span deflection = 1.58 mm, see Figure 2c). Specimen B3 was then strengthened using SNSM and tested up to failure in Phase 2. As the load increased, flexural and shear cracks (which developed in Phase 1), propagated and penetrated considerably deeper towards the loading points. The measured ultimate capacity of B3S was failed at 75.1 kN with mid-span deflection = 26 mm. Failure was dominated by concrete crushing (CC) at the top fibre (Figure 2d). Observed crack widths for all of the tested beams ranged from 0.10-0.15 mm at the first cracking load (Table 3).

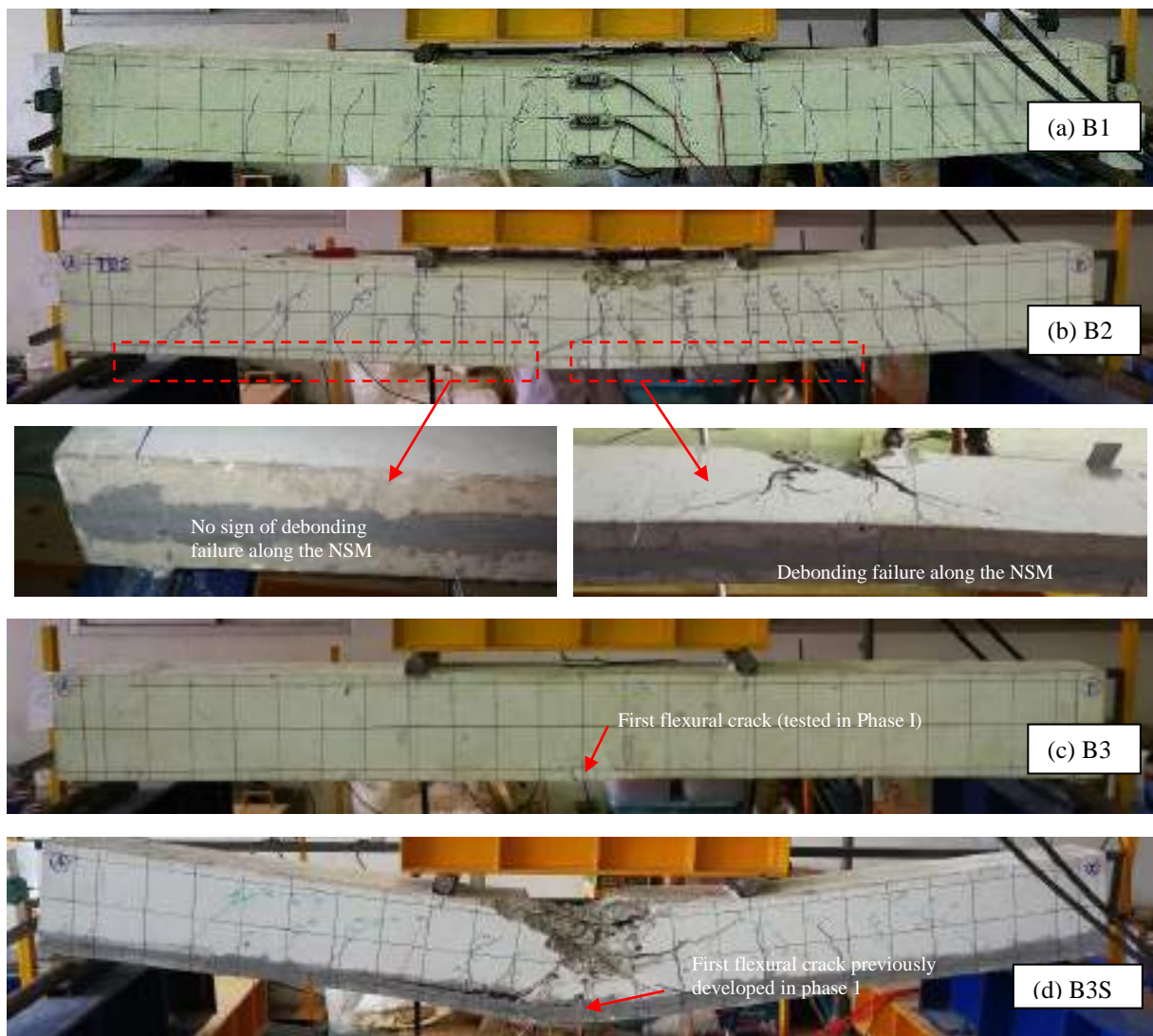


Figure 2: Crack pattern and failure mode of beam specimens

Table 3: Experimental results.

Phase	Beam reference	P_u (kN)	δ_{max} (mm)	w_f (mm) @ P_{cr}	failure mode
I	B1	59.5	22.4	0.15	SY
	B2	85.3	34.5	0.10	CC

	B3	16.8	1.58	0.15	-
II	B3S	75.1	26.0	0.15	CC

Note: P_u is the ultimate load, δ_{max} is the mid-span deflection, SY is steel yielding and CC is concrete crushing, BNSM is the bottom NSM CFRP rod, and SNSM is the side NSM CFRP rod.

Analysis of RC beams strengthened with NSM

The force equilibrium and strain compatibility requirements (Mahmoud et al. 2009) are used to calculate the ultimate load of the unstrengthened and strengthened beams as shown in Figure 3. As expected, failure mode of the strengthened beams are anticipated as the crushing of the concrete in the compressive zone after yielding of the tension steel reinforcement.

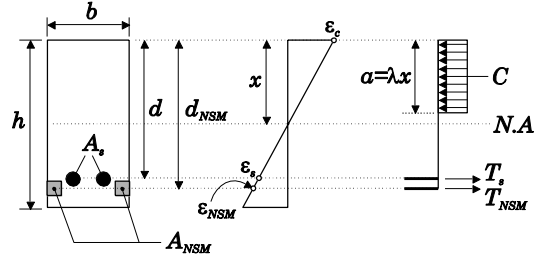


Figure 3: Sectional analysis for RC beam strengthened with NSM.

For equilibrium, the forces C , T_s , and T_{NSM} can be expressed in the following:

$$C = \lambda x \cdot b \cdot f'_c \quad (1)$$

$$T_s = A_s \cdot f_y \quad (2)$$

$$T_{NSM} = A_{NSM} \cdot E_{NSM} \cdot \epsilon_{NSM} \quad (3)$$

According to ACI 440 [4], for $f'_c < 50\text{MPa}$, $\lambda = 0.8$. From Figure 3, strain developed in CFRP rod (ϵ_{NSM}) is a function of concrete strain (ϵ_c) and can be calculated as

$$\epsilon_{NSM} = \epsilon_c \cdot \frac{d_{NSM} - x}{x} \leq \epsilon_{NSMu} \quad (4)$$

Therefore, substituting Eq. (4) into Eq. (3) and the neutral axis (x) can be determined and the ultimate moment of the section (M_u) can be computed as follows:

$$M_u = A_s f_y (d - 0.4x) + A_{NSM} E_{NSM} \epsilon_c \cdot \left[\frac{d_{NSM} - x}{x} \right] \cdot (d - 0.4x) \quad (5)$$

For the beam shown in Table 1-left, the ultimate load (P_u) can be calculated below:

$$P_u = 2M_u / 0.767 \quad (6)$$

Where b is the beam width, h is the beam depth, d is the effective depth of the beam, A_{NSM} is the area of NSM bar, A_s is the area of steel reinforcement in tension, f'_c is the compressive strength of concrete, f_y is the yield strength of steel reinforcement, ϵ_c is the strain of the top fibre of concrete, ϵ_s is the strain in the tension steel, ϵ_{NSM} is the strain in the NSM reinforcement, ϵ_{NSMu} is the ultimate strain in the NSM reinforcement.

Figure 4-left shows a comparison between the experimental and predicted ultimate load of the tested beams. The ratios between experiment (Exp.) and analytical (Analy.) prediction for beam specimens were also presented in Figure 4-right. As seen in the figure, specimens B1 and B2 having Exp/Analy. = 1.28 and 1.10 respectively, yield the conservative prediction (i.e. outside the grey-shaded area). For specimens B3 and B3S, the ratios of Exp/Analy. = 0.95 and 0.96, respectively. The code prediction by ACI 440.2R (2017) showed an overestimated results compared to the experimental values (less than 5%). This is because specimen B3S had several cracks developed previously in phase 1 prior to strengthening work. The pre-cracked beam was strengthened using SNSM without repairing cracks thus causing an overestimated prediction by the code. Both strengthened beam specimens (B2&B3S) failed by concrete crushing mode as a result of an over-reinforced section after adding CFRP rods into the pre-cut grooves. Beam B2 (85 kN) had a higher failure load over B3S (75 kN) because specimen B2 (un-

cracked section) was strengthened prior to testing in phase 1 whereas B3S was pre-cracked in phase I prior to testing up to failure in phase 2.

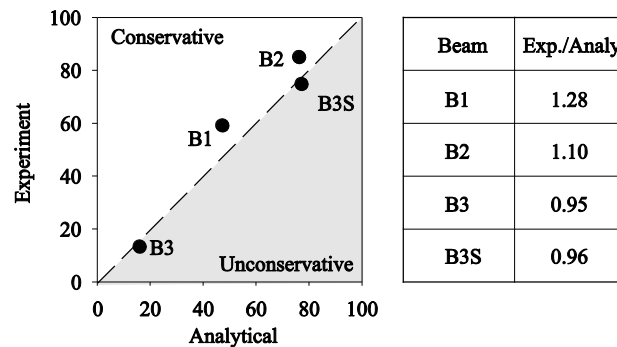


Figure 4: Comparison of experimental and predicted ultimate loads.

Analysis of beam deflection

Figure 5 shows the load-deflection responses for beams B1-B3S with a) only the flexural deflection predictions for unstrengthened beam (B1) calculated according to cracked section analysis (CSA) (i.e. assuming an approach similar to Al-Sunna et al. 2012). It should be noted that the concrete tensile strength used to determine the cracking moment and cracking load was derived from inverse analysis to account indirectly for the variability of concrete, size effects, as well as shrinkage effects on the initial strain state within the element and on the apparent concrete properties (Bischoff 2005). The result indicates that the CSA can predict reasonably well the beam B1 for both first flexural cracking load (i.e. B1 & B3) and failure load (i.e. B1). Overall, the results in Figure 6 indicates that the CSA predict reasonably well the deflections up to (low) loads (i.e. at $P=40$ kN for beam B3S) corresponding to service conditions for the pre-cracked beam B3S tested in phase 2.

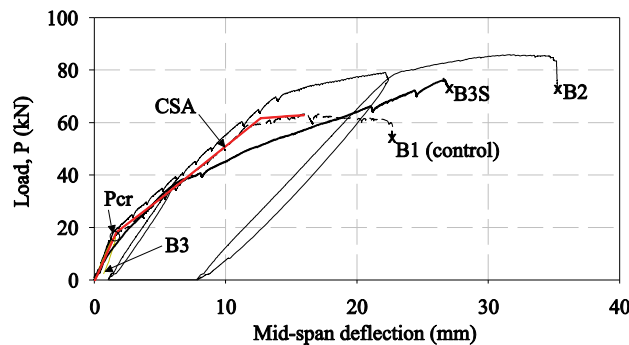


Figure 5: Experimental load-deflection vs. cracked sectional analysis.

As seen in Figure 5, the deflection of strengthened beam specimens can be adequately predicted by equations included in current guidelines but only up to the 30% of maximum loads. At higher load levels, such equations can significantly underestimate deflections by up to 15%. Furthermore, the predictions given by the CSA underestimate considerably deflections at higher loads (i.e. after concrete cracking). Such inconsistencies are due to the formation of shear cracks at higher load levels, which results in an additional component of deformation. This component is referred to as shear crack induced deformation, as reported recently by Imjai et al. (2016). Based on 12 tests from FRP RC beams, the authors reported that the estimated total deflection of strengthened concrete specimens could be significantly improved by adding the component of deflection due to shear action and crack opening to the flexural deflection calculated by existing predictive equations.

Strengthening performance

Figure 6 compares the ultimate loads reached by the tested specimens. It is shown that, for the control specimen B1 was under-reinforced section and failed by steel yielding mode (see Figure 2a). As expected, strengthened beams B2 & B3S had the higher load capacity (85.3 kN and 75.1 kN) as the result of NSM CFRP strengthening and the ultimate capacity of these strengthened beams were limited by concrete crushing failure as shown in Figure

3b,d. It is also interesting to note that the BNSM using 1 CFRP rod enhances the beam capacity by approximately 43% over un-strengthened beam. Moreover and as expected, strengthened beam B2 had higher capacity than B3S due to the higher stiffness of the un-cracked concrete section. Overall, these results indicate that using SNSM for pre-cracked beam can restore flexural capacity of the beam and provided section capacity in of the ultimate load by up to 26% over un-strengthened section.

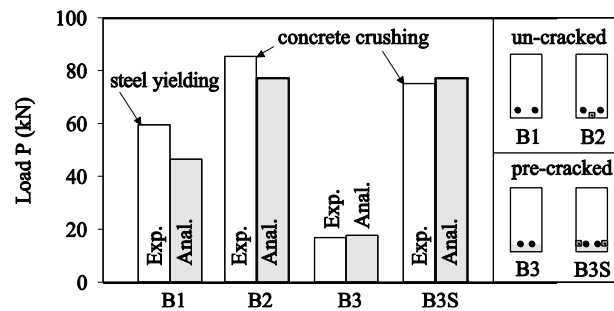


Figure 6: NSM strengthening performance of RC beams.

CONCLUDING REMARKS

The flexural strength, deflection, mode of failure and crack behaviour as well as strengthening performance of the tested beams were analysed. From the study, following conclusions can be drawn:

- The deflection of unstrengthened beam specimens can be adequately predicted by equations included in current guidelines but only up to the 30% of maximum loads. At higher load levels, such equations can significantly underestimate deflections by up to 15% due to shear crack induced deflection.
- Strengthened un-cracked beam by BNSM using 1 CFRP rod enhances the beam capacity by approximately 43% over un-strengthened beam.
- Strengthened pre-cracked beam by SNSM can restore flexural capacity of the beam and provided section capacity in of the ultimate load by up to 26% over un-strengthened counterpart.
- Experiment and analytical analysis showed that ultimate flexural capacity of NSM strengthened beams were limited by concrete crushing failure.
- Had the higher load capacity over un-strengthened section as the result of NSM CFRP strengthening and the ultimate capacity of these strengthened beams were limited by concrete crushing failure
- Ultimate capacity of NSM strengthened RC section by current design equation gives a good agreement with the experimental results.

ACKNOWLEDGMENT

The first author thankfully acknowledge the financial support from the National Research Council of Thailand (Contract No. 560265/2560) and the Rajamangala University of Technology Tawan-Ok. The second author would like to acknowledge the financial support offered by Rajamangala University of Technology Rattanakosin.

REFERENCES

- T. Alkhrdaji, and A. Nanni, "Flexural Strengthening of Bridge Piers Using FRP Composites," ASCE, 2000.
- J. G. Tumialan, M. Vatovec, and P.L. Kelley, "Case Study: Strengthening of Parking Garage Decks with Near-Surface-Mounted CFRP Bars," *Journal of Composites for Construction* 11(5), pp. 523-530, 2007.
- W.C. Tang, R.V. Balendran, A. Nadeem, and H.Y. Leung, "Flexural strengthening of reinforced lightweight polystyrene aggregate concrete beams with near surface mounted GFRP bars," *Build Environ* 41(10), pp. 1381–93, 2006.
- ACI-440-Committee, "Guide for the Design and Construction of Externally Bonded FRP Systems for Strengthening Concrete Structures," Farmington Hills, MI, USA. 2017
- Cement and Concrete Industry Publication, "Technical report No. 55: Design guidance for strengthening concrete structures using fibre composite materials," CCIP-56, 2012.
- R. Parretti, and A. Nanni, "Strengthening of RC members using near-surface mounted FRP composites: design overview," *Advances in Structural Engineering* 7(6). Pp. 469-483, 2004.

- De L. Lorenzis, and J.G. Teng, "Near-surface mounted FRP reinforcement: an emerging technique for strengthening structure," *Composites: Part B*, 38, pp. 119–43, 2007.
- T. Hassan, and S. Rizkalla, "Investigation of Bond in Concrete Structures Strengthened with Near Surface Mounted Carbon Fiber Reinforced Polymer Strips," *Journal of Composites for Construction*, 7(3), pp 248-257, 2003
- T. Hassan, and S. Rizkalla, "Bond mechanism of near surface mounted fibre reinforced polymer bars for flexural strengthening of concrete structures," *ACI Structural Journal*, 101(6), pp. 830–839, 2004.
- W. Jung, J. Park, and Y. Park, "A Study on the Flexural Behavior of Reinforced Concrete Beams Strengthened with NSM Prestressed CFRP Reinforcement," In *Proceedings of the 8th International Symposium on Fiber Reinforced Polymer Reinforcement for Reinforced Concrete Structures (FRPRCS-8)*, July 16–18, 2007. Patras, Greece: University of Patras. CD-ROM.
- R. El-Hacha, and S. H. Rizkalla, "Near Surface Mounted FRP Reinforcements for Flexural Strengthening of Concrete Structures," *ACI Structural Journal*, 101(5), pp. 717–726. 2004.
- E. K. Castro, G. S. Melo, and Y. Nagato, "Flexural Strengthening of RC "T" Beams with Near Surface Mounted (NSM) FRP Reinforcement," In *Proceedings of the 8th International Symposium on Fiber Reinforced Polymer Reinforcement for Reinforced Concrete Structures (FRPRCS-8)*, July 16–18, 2007. Patras, Greece: University of Patras. CD-ROM.
- W.T. Jung, Y.H. Park, J.S. Park, J.Y. Kang, and Y.J. You, "Experimental investigation on flexural behaviour of RC beams strengthened by NSM CFRP reinforcements," *ACI special publication*, 2005.230.
- De Lorenzis L, Micelli F, La Tegola A. Passive and active near surface mounted FRP rods for flexural strengthening of RC beams," In: *Proceedings ICCI-02*, San Francisco (CA), CD-ROM version; 2002.
- A. F. Mahmoud, A. Castel, R. Francois, and C. Tourneur, "Strengthening of RC members with near-surface mounted CFRP rods," *Composite Structures*, 91(2), pp. 138–47, 2009.
- A. F. Mahmoud, A. Castel, R. Francois, and C. Tourneur, "RC beams strengthened with NSM CFRP rods and modeling of peeling-off failure," *Composite Structures*, 92(8), pp. 1920–30, 2010
- J.A.O. Barros, and A.S. Fortes, "Flexural strengthening of concrete beams with CFRP laminates bonded into slits," *Cement Concrete Composites*, 27(4), pp. 471–80, 2005.
- M.D.A. Housen, M.Z. Jumaat, and A.B.M. Saiful Islam, "Side near surface mounted (SNSM) technique for flexural enhancement of RC beams," *Material & Design*, 83, pp. 587-597, 2015
- BS EN 12390-3, "Testing hardened concrete Part 3: Compressive strength of test specimens," British Standards Institution, London, UK, 2009.
- BS EN 12390-5, "Testing hardened concrete Part 5: Flexural strength of test specimens," British Standards Institution, London, UK, 2009.
- BS EN 12390-6. "Testing hardened concrete Part 6: Tensile splitting strength of test specimens," British Standards Institution, London, UK, 2009.
- R. Al-Sunna, K. Pilakoutas, I. Hajirasouliha, M. Guadagnini, "Deflection behaviour of FRP reinforced concrete beams and slabs: an experimental investigation," *Composites Part B: Engineering*, 43, pp. 2125-2134, 2012.
- P.H. Bischoff, "Re-evaluation of deflection prediction for concrete beams reinforced with steel and FRP bars," *Journal of Structural Engineering*, ASCE, 131, pp. 363–374, 2005.
- T. Imjai, M. Guadagnini, R. Garcia, and K. Pilakoutas, "A practical method for determining shear crack induced deformation in FRP RC members," *Engineering Structures*, 126, pp. 253-364, 2016



ANALYSES ON THE BOND TRANSFER BETWEEN FRP COMPOSITES AND OTHER STRUCTURAL MATERIALS

H. Biscaia¹, C. Chastre², J. Cardoso³ and N. Franco⁴

¹ Fluid and Structures Engineering, UNIDEMI, Department of Civil Engineering,
NOVA University of Lisbon, Portugal. Email: hb@fct.unl.pt

² Civil Engineering Research and Innovation for Sustainability, ICIST, Department of Civil Engineering,
NOVA University of Lisbon, Portugal. Email: chastre@fct.unl.pt

³ Fluid and Structures Engineering, UNIDEMI, Department of Mechanical and Industrial Engineering,
NOVA University of Lisbon, Portugal. Email: jbc@fct.unl.pt

⁴ Department of Civil Engineering, NOVA University of Lisbon, Portugal. Email: ni.franco@campus.fct.unl.pt

ABSTRACT

Fibre Reinforced Polymer (FRP) can be used as a strengthening material in several types of structures built with different materials, such as concrete, timber, steel, aluminium or clay masonry. Contrary to fasteners, the bond technique currently used to connect the FRP composites to the substrate avoids stress concentrations. The knowledge on the performance of those bonded joints has been increasing but there are several issues not well understood yet. For instance, it is not clear which interfacial local bond-slip relationship should represent best each type of interface. Such knowledge could be important for distinguishing different bond behaviours that, along with the contribution on to the field of the numerical and/or analytical modelling, will certainly help to identify the main causes for such differences between them all. Furthermore, the case of bonded joints between FRP and masonry clay bricks is now starting their first steps and in this particular case, the actual knowledge needs to be improved in order to increase the heritage building life cycle. Likely to other bonded joints such as FRP/concrete, FRP/masonry joints have been tested under single/double-lap shear conditions as well. These two bonded joints share, at least, one common particularity: both develop cracks when submitted to tensile stresses. Therefore, it is expected that similar interfacial bond-slip relationships may be used in both circumstances. In bonded joints between FRP composites and steel or timber substrates, the cracking phenomenon doesn't arise. However, on FRP/timber interfaces, depending on the type of the timber used or depending on the orientation of the grains throughout the bonded area, the interfacial bond-slip relationship may change. The work herein reported presents a full comparison of bonded joints between FRP composites and other structural materials in which will be used different analytical approaches to model their debonding behaviours. All modelling is based on cohesive bond-slip relationships experimentally obtained from tests carried out by the authors or collected from the literature which have the purpose of locally induce a cohesive rupture within the adhesive.

KEYWORDS

FRP composites; Concrete; Timber; Steel; Masonry; Bond; Closed-form solution; Modelling.

INTRODUCTION

The use of Fibre Reinforced Polymers (FRP) has been seen as a good solution for strengthening existing structures with structural deficiencies. The external strengthening of Reinforced Concrete (RC) structures with FRP composites have been the main focus of several researches, e.g. (Dai *et al.*, 2005; Cornetti *et al.*, 2015; Biscaia *et al.*, 2015; Biscaia *et al.*, 2017a), but other types of structures made with other materials such as steel (Xia and Tend, 2005; Yang *et al.*, 2017), timber (Biscaia *et al.*, 2016a; Biscaia *et al.*, 2017b), masonry clay bricks (Zheng *et al.*, 2012) or even aluminium (Biscaia *et al.*, 2017c) have deserved more recently detailed attention of different researchers. One main issue that have been concerned the scientific community derives precisely from the External Bond Reinforcement (EBR) with FRP composites which prematurely debonds from the substrate quite often at an earlier stage of its ultimate strain. That is why researchers have been dedicated some efforts to propose analytical and/or numerical approaches that could explain properly the full debonding process of adhesively bonded interfaces aiming to suggest, e.g., the FRP strain limit to be considered on these joints. This paper presents a brief series of different closed-form solutions developed by the authors that can predict the bond behaviour of adhesively bonded interfaces accurately. Due to the differences between bonded materials, each interface has a particular local behaviour that was taken into account on each close-form solution. To eliminate the premature failure, an

innovative bonding technique is analytically simulated and the results are also presented for the Carbon (C) FRP-to-concrete and masonry clay bricks interfaces.

BOND-SLIP MODELS OF DIFFERENT BONDED JOINTS

The local bond-slip relationships of CFRP-to-concrete interface, CFRP-to-timber interface and CFRP-to-steel interface were experimentally obtained (see Fig. 1a, 1c-d) from a study carried out by the authors (Biscaia *et al.*, 2015). The results were all obtained from single-lap pull-push tests and the same test setup was used. More detailed descriptions of the test setup configuration used there can be seen elsewhere (Biscaia *et al.*, 2016c). The bond-slip relationship shown in Fig. 1b was obtained the work developed by Zheng *et al.* (2012). The results show clearly that depending on the substrate, the bond-slip relationship presents a different shape. Thus, the similarities observed between the CFRP-to-concrete and CFRP-to-clay masonry interfaces may be justified by the brittleness and crack development within both substrates. However, the combination of masonry clay bricks with low strength with CFRP sheets used by Zheng *et al.* (2012) proportionate a much lower peak bond stress in this interface than that obtained from concrete where CFRP laminates and normal concrete strength were used. In the cases of CFRP-to-steel and CFRP-to-timber interfaces, the bi-linear and tri-linear bond-slip behaviours seems to be the most adequate bond-slip models to represent both interfaces, respectively. Unlike concrete and masonry clay bricks, steel and timber show an important elastic constitutive behaviour which justifies the first elastic stage that ends at a peak bond stress value and it is followed by a linear softening. In the CFRP-to-steel interface the linear softening ends when no more bond stresses can be transferred between materials and the complete debonding begins whereas in the case of the CFRP-to-timber the constant stage can be explained due to the bonded area that mostly covered the sap wood of the timber which is much softer than the grains.

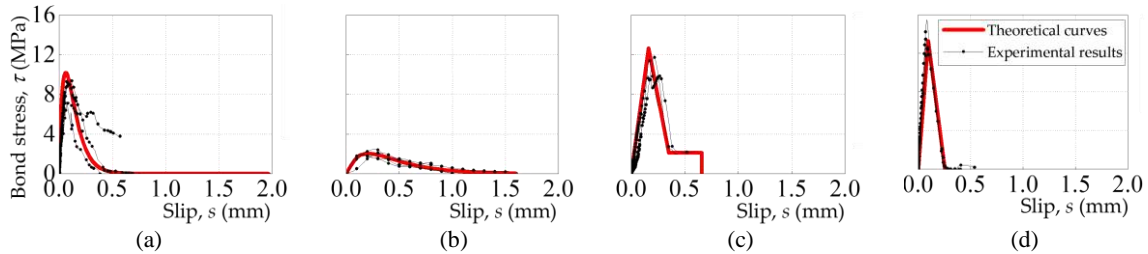


Figure 1: Bond-slip relationships experimentally obtained for different adhesively bonded interfaces: (a) CFRP-to-concrete; (b) CFRP-to-clay masonry; (c) CFRP-to-steel; (d) CFRP-to-timber.

CLOSED-FORM SOLUTIONS

General assumptions

In the following mathematical deductions, the models herein presented lead to closed-form solutions where in each one the following assumptions were taken into account: (i) the strains field in the FRP composite are constant through its width and consequently, the bond stresses are also constant through the width of the FRP; (ii) the cross sectional area of the FRP composite remains unchanged during the full debonding failure process; (iii) although the assumption of an infinite bond length is useful to ensure some mathematical simplifications other cases with a finite bonded length can be also predicted which means that each adhesively bonded length as an effective bond length where beyond which the maximum strength of the interface is always reached; (iv) and the load transmitted to the FRP composite induces only interfacial shear stresses into the adhesively bonded interface, which means that the obtained rupture mode is consistent with the fracture Mode II and therefore, the influence and/or development of peeling stresses within the bonded interfaces are ignored. Additionally to the previous assumptions, it is worth to bear in mind that the presented closed-form solutions in the subsequent subsections aim to simulate the debonding failure process of the single-lap pull-push tests. In such circumstances, for an infinitesimal segment with a length dx , the equilibrium equation that governs the debonding process is (e.g. Dai *et al.*, 2005; Cornetti and Carpinteri, 2011; Biscaia *et al.*, 2013; Biscaia *et al.*, 2014; Biscaia *et al.*, 2016b):

$$\frac{d^2 s(x)}{dx} - \tau(s) \cdot \left(\frac{1}{E_f \cdot t_f} + \frac{b_f}{E_s \cdot b_s \cdot t_s} \right) = 0 \quad (1)$$

where E_f , b_f and t_f are the Young modulus, the width and the thickness of the FRP composite, respectively; E_s , b_s and t_s are the Young modulus, the width and the thickness of the substrate (concrete, steel, timber or masonry clay bricks), respectively; s is the relative displacement (or slip) between bonded materials; x represents the axis parallel to the bond length; and $\tau(s)$ is the local bond-slip relationship of each bonded interface.

CFRP-to-concrete and CFRP-to-masonry clay brick interfaces

For an adhesively bonded interface between an elastic material such as an FRP composite and concrete, the exponential bond-slip model proposed by Dai *et al.* (2005) has been widely used:

$$\tau(s) = 4\tau_{\max} \cdot (e^{-B \cdot s} - e^{-2B \cdot s}) \quad (2)$$

where τ_{\max} is the maximum bond stress developed within the interface; and B is a stiffness index obtained from the experimental strain vs. slip curve. It was already shown by Biscaia *et al.* (2016b) that when Eq. (2) is introduced into Eq. (1) the solution of this 2nd order differential equation is:

$$s(x) = \frac{1}{B} \cdot \ln \left[\frac{e^{(D \cdot x + C_2) \left(B \cdot \sqrt{1 - (1 - e^{-B \cdot s_0})^2} \right)} + 2 + 2 \cdot \sqrt{1 - (1 - e^{-B \cdot s_0})^2}}{2 \cdot \sqrt{1 - (1 - e^{-B \cdot s_0})^2} + 2 \cdot [1 - (1 - e^{-B \cdot s_0})^2]} \right] \quad (3)$$

where s_0 is the slip at the FRP free end; and C_2 is determined from:

$$C_2 = \frac{\ln \left[e^{B \cdot s_0} \cdot \left(2 \cdot \sqrt{1 - (1 - e^{-B \cdot s_0})^2} + 2 \cdot (1 - (1 - e^{-B \cdot s_0})^2) \right) - 2 - 2 \cdot \sqrt{1 - (1 - e^{-B \cdot s_0})^2} \right]}{B \cdot \sqrt{1 - (1 - e^{-B \cdot s_0})^2}} \quad (4)$$

and, for an Externally Bonded Reinforcement (EBR), D is defined as:

$$D = \sqrt{\frac{2G_F}{t_f} \cdot \left(\frac{1}{E_f} + \frac{b_f \cdot t_f}{E_s \cdot t_s \cdot b_s} \right)} \quad (5)$$

where G_F is the Mode II fracture energy released at the end of the debonding process.

CFRP-to-timber interfaces

The interfacial behaviour of the adhesively bond interface between a CFRP composite and a timber substrate can be defined through a tri-linear bond-slip model (Biscaia *et al.*, 2016a). In such case, the bond-slip model will stay defined by a first elastic stage (E), followed by a softening linear stage (S) and with a last constant stage (C). Hence, for the determination of the closed-form solutions of the CFRP-to-steel interface, the following bond-slip model is assumed:

$$\tau(s) = \begin{cases} \frac{\tau_{\max} \cdot s}{s_{\max}} & \text{if } 0 \leq s \leq s_{\max} \text{ (Elastic stage)} \\ \frac{\tau_c - \tau_{\max}}{s_c - s_{\max}} \cdot s + \frac{\tau_{\max} \cdot s_c - \tau_c \cdot s_{\max}}{s_c - s_{\max}} & \text{if } s_{\max} < s \leq s_c \text{ (Softening stage)} \\ \tau_c & \text{if } s_c < s \leq s_{ult} \text{ (Constant stage)} \\ 0 & \text{if } s > s_{ult} \text{ (Debonded stage)} \end{cases} \quad (6)$$

where, τ_c is the constant bond stress; s_{\max} is the slip corresponding to the maximum bond stress; s_c is the slip corresponding to the initiation of the constant bond stress; and s_{ult} is the ultimate slip corresponding to the complete separation between materials, i.e. with no stress transfer. As mentioned before, to make possible ignore the constant stage, constant bond stress is assumed ~ 0 and $s_c \approx s_{ult}$. In these circumstances, the solution of the 2nd order differential equation in (1) should respect the states that the CFRP-to-steel interface is subjected to until its complete failure. Therefore, the bonded interface will undergo through six distinct states: (i) Elastic (E); (ii) Elastic-Softening (E-S); (iii) Elastic-Softening-Constant (E-S-C); (iv) Elastic-Softening-Constant-Debonded (E-S-C-D); (v) Softening-Constant-Debonded (S-C-D); and (vi) Constant-Debonded (C-D). Therefore, the solution for the E state can be obtained by introducing the elastic stage in (6) into Eq. (1) and the slip developed within the interface is (Biscaia *et al.* 2016a):

$$s_E(x) = \frac{P}{\alpha_1 \cdot E_f \cdot b_f \cdot t_f} \cdot \frac{\cosh(\alpha_1 \cdot x)}{\sinh(\alpha_1 \cdot L_b)} \quad (7)$$

where L_b is the bond length; P is the load transmitted to the FRP composite; and

$$\alpha_1^2 = \frac{\tau_{\max}}{s_{\max}} \cdot \left(\frac{1}{E_f \cdot t_f} + \frac{b_f}{E_s \cdot b_s \cdot t_s} \right) \quad (8)$$

The solution for the E-S state leads to two distinct domains where the elastic region is obtained by introducing the elastic stage in (6) into Eq. (1) whereas the softening part is obtained by introducing the softening stage in (6) into the 2nd order differential equation:

$$\frac{d^2 s(x)}{dx^2} + \alpha_2^2 \cdot s = a \cdot \alpha_2^2 \text{ for } s_1 \leq s \leq s_2 \quad (9)$$

where:

$$\alpha_2^2 = \frac{\tau_{\max} - \tau_c}{s_c - s_{\max}} \cdot \left(\frac{1}{E_f \cdot t_f} + \frac{b_f}{E_s \cdot b_s \cdot t_s} \right) \quad (10)$$

$$a = \frac{\tau_{\max} \cdot s_c - \tau_c \cdot s_{\max}}{\tau_{\max} - \tau_c} \quad (11)$$

Thus, using the right boundary conditions (see e.g. Biscaia *et al.*, 2016a), the solution for the E region is:

$$s_E(x) = s_{\max} \cdot \frac{\cosh(\alpha_1 \cdot x)}{\cosh[\alpha_1 \cdot (L_b - L_{s,1})]} \quad (12)$$

where

$$L_{s,1} = -\frac{2}{\alpha_2} \cdot \arctan \left[\frac{\sqrt{(\alpha_1 \cdot s_{\max})^2 + \alpha_2^2 (s_{\max} - a)^2 - \frac{P^2}{(E_f \cdot b_f \cdot t_f)^2} - \alpha_2 \cdot (a - s_{\max})}}{\frac{P}{E_f \cdot b_f \cdot t_f} + \alpha_1 \cdot s_{\max}} \right] \quad (13)$$

The solution for the softened region where $s_{\max} \leq s \leq s_{ult}$, i.e. at $L_b - L_{s,1} \leq x \leq L_b$, is obtained through:

$$s_s(x) = a - \frac{\frac{P}{E_f \cdot b_f \cdot t_f} \cdot \cos[\alpha_2 \cdot (L_{s,1} - L_b + x)] - \alpha_1 \cdot s_{\max} \cdot \cos[\alpha_2 \cdot (L_b - x)] \cdot \tanh[\alpha_1 \cdot (L_b - L_{s,1})]}{\alpha_2 \cdot \sin(\alpha_2 \cdot L_{s,1})} \quad (14)$$

The next state to develop within the bonded interface will be E-S-C state. In this E-S-C state, region closest to the FRP pulled end, the slips are higher than s_c but less than s_{ult} which corresponds to a constant bond stress distribution. Therefore, for each region of the bonded length, the 2nd order differential equation in (1) should be solved for the three first slip ranges defined in (6). Thus, for the particular case of the constant stage, the following 2nd order differential equation should be solved:

$$\frac{d^2 s(x)}{dx^2} = \alpha_3 \quad \text{for } s_c \leq s \leq s_{ult} \quad (15)$$

where:

$$\alpha_3 = \tau_c \cdot \left(\frac{1}{E_f \cdot t_f} + \frac{b_f}{E_s \cdot b_s \cdot t_s} \right) \quad (16)$$

Assuming the boundary conditions of the E-S-C state (Biscaia *et al.*, 2016a), the solutions for the E, S and C stages are, respectively:

$$s_E(x) = s_{\max} \cdot \frac{\cosh(\alpha_1 \cdot x)}{\cosh[\alpha_1 \cdot (L_b - L_{s,1} - L_{c,1})]} \quad (17)$$

$$s_s(x) = a + \frac{\cos[\alpha_2 \cdot (L_{s,1}^{\max} - L_b + L_{c,1} + x)] \cdot (s_c - a)}{\cos(\alpha_2 \cdot L_{s,1}^{\max})} + \frac{\alpha_1 \cdot s_{\max} \cdot \sin[\alpha_2 \cdot (L_b - L_{c,1} - x)] \cdot \tanh[\alpha_1 \cdot (L_{s,1}^{\max} - L_b + L_{c,1})]}{\alpha_2 \cdot \cos(\alpha_2 \cdot L_{s,1}^{\max})} \quad (18)$$

$$s_c(x) = \frac{\alpha_3}{2} x^2 + \left(\frac{P}{E_f \cdot b_f \cdot t_f} - \alpha_3 \cdot L_b \right) \cdot x + s_c - \frac{\alpha_3}{2} \cdot (L_b - L_{c,1})^2 - \left(\frac{P}{E_f \cdot b_f \cdot t_f} - \alpha_3 \cdot L_b \right) \cdot (L_b - L_{c,1}) \quad (19)$$

where

$$L_{c,1} = \frac{\frac{P}{E_f \cdot b_f \cdot t_f} \cdot \cos(\alpha_2 \cdot L_{s,1}^{\max}) - \alpha_1 \cdot s_{\max} - a \cdot \alpha_2 \cdot \sin(\alpha_2 \cdot L_{s,1}^{\max}) + s_c \cdot \alpha_2 \cdot \sin(\alpha_2 \cdot L_{s,1}^{\max})}{\alpha_3 \cdot \cos(\alpha_2 \cdot L_{s,1}^{\max})} \quad (20)$$

The E-S-C-D state begins once the ultimate slip at the FRP pulled end is reached and the bond stress distribution within the interface propagates towards the FRP free end. Therefore, all the equations that can be derived from the E-S-C state still remain valid since L_b is replaced by $L_b - L_d$. However, for the slip distribution at the debonded region of the interface it should be considered always the deformation of the FRP composite:

$$s_D(x) = s_{ult} + \frac{P}{E_f \cdot b_f \cdot t_f} \cdot (x - L_b + L_d) \quad (21)$$

At the end of this state, i.e. when no longer the bond length exhibits an E region and the next state is initiated, the bonded length is:

$$L_b = L_{s,1}^{\max} + L_{c,1}^{\max} + L_d \quad (22)$$

where $L_{s,1}^{\max}$ and $L_{c,1}^{\max}$ are the maximum lengths that limits the softening and the constant regions of the interface determined from Eqs. (13) and (20), respectively. The solutions of the E and S stages of the S-C-D state of the bonded interface can be determined, respectively:

$$s_s(x) = \left[\alpha_3 \cdot (L_{s,2} + L_{c,1}^{\max}) - \alpha_3 \cdot L_{s,2} - \frac{P}{E_f \cdot b_f \cdot t_f} \right] \cdot \frac{\cos(\alpha_2 \cdot x)}{\alpha_2 \cdot \sin(\alpha_2 \cdot L_{s,2})} \quad (23)$$

$$s_c(x) = \frac{\alpha_3}{2} x^2 + \left[\frac{P}{E_f \cdot b_f \cdot t_f} - \alpha_3 \cdot (L_b + L_{c,1}^{\max}) \right] \cdot x + s_c - \frac{\alpha_3 \cdot L_{s,2}^2}{2} - L_{s,2} \cdot \left[\frac{P}{E_f \cdot b_f \cdot t_f} - \alpha_3 \cdot (L_{s,2} + L_{c,1}^{\max}) \right] \quad (24)$$

where

$$L_{s,2} = \frac{1}{\alpha_2} \cdot \arctan \left[\frac{L_{c,1}^{\max} \cdot \alpha_3 - \frac{P}{E_f \cdot b_f \cdot t_f}}{\alpha_2 \cdot (s_c - a)} \right] \quad (25)$$

Finally, the slips developed in the C stage of the C-D state of the bonded interface are determined accordingly to:

$$s_c(x) = \frac{\alpha_3}{2} x^2 + s_{ult} - \frac{\alpha_3 \cdot L_{c,2}^2}{2} \quad (26)$$

where

$$L_{c,2} = \frac{P}{b_f \cdot \tau_c} \quad (27)$$

CFRP-to-steel interfaces

For the CFRP-to-steel interface, a bi-linear bond-slip model seems to fit quite well. So, it is worth to bear in mind that the model already briefly presented for CFRP-to-timber interfaces may be seen as a more generalized solution that can be used for those cases where the interfacial behaviour is more likely to a bi-linear shape. For that purpose it is only needed to assume very small values for the constant stress ($\tau \approx 0$) and $s_c \approx s_{ult}$. Under such conditions, the bond-slip model will have a bi-linear shape with a first elastic stage (E), followed by a softening linear stage (S) where the constant stage (C) can be ignored during the debonding process. Hence, the closed-form solutions of the CFRP-to-timber interface can be used for the CFRP-to-steel interface to describe four distinct states that this bonded interface will undergo through: (i) Elastic (E); (ii) Elastic-Softening (E-S); (iii) Elastic-Softening-Debonded (E-S-D); and (iv) Softening-Debonded (S-D).

THEORETICAL vs. EXPERIMENTAL RESULTS

Properties of materials and bond-slip definitions

The uniaxial compression tests carried out on three samples of plain concrete cubes with face 150×150×150 mm, lead to 22.7 MPa. The timber was identified as being redwood (*Pinus Sylvestris L.*) with a density of 400 kg/m³ with a mean tensile strength of 88.4 MPa and a mean compressive strength of 39.4 MPa. In the case of the steel, it was not possible to test the rectangular hollow sections and thereby it was simple assumed that the Young modulus of the steel is 210 GPa. The CFRP laminate used was the S&P 150/2000 with a cross sectional area of 10×1.4 mm and from the 5 tensile tests carried out, the mean rupture strain is 1.03% (22.93 kN), the mean tensile strength 1,565 MPa and a calculated average Young modulus of 159 GPa. The resin used to bond the CFRP laminates to the substrates was always the same: S&P200 with a mean rupture strain of 0.79%, a mean tensile strength of 29.0 MPa and a calculated Young modulus of 3.65 GPa (e.g. Biscaia *et al.*, 2016c). For the particular CFRP sheets bonded on the masonry clay bricks with 0.167×50 mm (thickness of one layer×width), the tests performed by Zheng *et al.* (2012) lead to a tensile strength of 3,335.6 MPa, a rupture strain of 1.61% and a Young modulus of 242.6 GPa. The bond-slip models used for each adhesively bonded interface are defined as follows: (i) CFRP-to-concrete: $\tau_{\max} = 10.19$ MPa, $B = 10.94$ mm⁻¹, $s_{\max} = 0.063$ mm and $G_F = 1.870$ N/mm; (ii) CFRP-to-timber: $\tau_{\max} = 12.68$ MPa, $s_{\max} = 0.162$ mm; $\tau_c = 2.10$ MPa, $s_c = 0.350$ mm; $s_{ult} = 0.660$ mm and $G_F = 2.84$ N/mm; (iii) CFRP-to-steel: $\tau_{\max} = 13.27$ MPa, $s_{\max} = 0.096$ mm; $s_{ult} = 0.256$ mm and $G_F = 1.699$ N/mm; and (iv) CFRP-to-clay masonry: $\tau_{\max} = 2.03$ MPa, $B = 3.25$ mm⁻¹, $s_{\max} = 0.213$ mm and $G_F = 1.246$ N/mm. The bonded lengths used for each adhesively bonded interface was 300 mm for the CFRP-to-concrete and CFRP-to-clay masonry interface, 280 mm for the CFRP-to-timber interface and 200 mm for the CFRP-to-steel interface. With the

exception of the CFRP-to-clay masonry interface where the authors (Zheng *et al.*, 2012) didn't mention and/or determined the effective bond length of the interface (L_{eff}), i.e. the length beyond which the maximum load transmitted to the CFRP composite cannot increase, the remaining adhesively bonded interfaces have all a bonded length higher than their corresponding the effective bond length. Particularly, the effective bond length of the CFRP-to-concrete, CFRP-to-timber and CFRP-to-steel interfaces are 160 mm, 250 mm and 130 mm, respectively (Biscaia *et al.*, 2016c).

Load-slip behaviour

In Figure 2, the comparison between the theoretical load-slip predictions with the experimental results carried out by Biscaia *et al.* (2016c) and Zheng *et al.* (2012) are shown where the bond-slip models in Figure 1 were considered for the determination of the theoretical predictions. It can be seen that the proposed theoretical predictions are able to estimate, in close agreement, the experimental results.

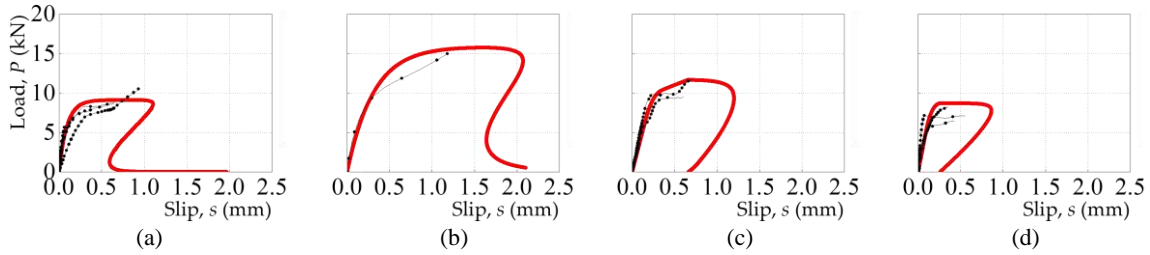


Figure 2: Load-slip behaviour for different adhesively bonded interfaces: (a) CFRP-to-concrete interface; (b) CFRP-to-clay masonry interface; (c) CFRP-to-timber interface; and (d) CFRP-to-steel interface.

Strain distributions

The strain distributions obtained for each adhesively bonded interface are presented in Figure 3. The results shown correspond to the end of the Elastic (E) stage, at the end of the softening (S) stage and somewhere at the debonding process with some unbonded length (D). Additionally, in the case of the CFRP-to-timber interface another curve was added which corresponds to the end of the Constant stage (C). It should be noted also that the D stage was not experimentally obtained for all the interfaces and for that reason no matching is shown in Figure 3. The results show that the strain distribution in the CFRP composite increases at their loaded end and, for the E state, tends to decrease with the distance from the loaded end. In the next state, i.e. Elastic-Softening (E-S), the strain distribution show a sigmoid shape. Naturally, in the case of the CFRP-to-timber interface, the subsequent state (Elastic-Softening-Constant, E-S-C) of the interface, an almost linear strain distribution, can be seen from the limited region that covers the C stage at the CFRP most loaded end. As the debonding initiates to propagate towards the CFRP free end, the strain becomes constant which means that no more bond stresses can be transferred between bonded materials. For the examples presented, the highest strain herein obtained was reached at 0.77% in the CFRP-to-clay masonry interface whereas the lowest one was obtained in the CFRP-to-steel interface with 0.39% followed by the CFRP-to-concrete interface with 0.41%.

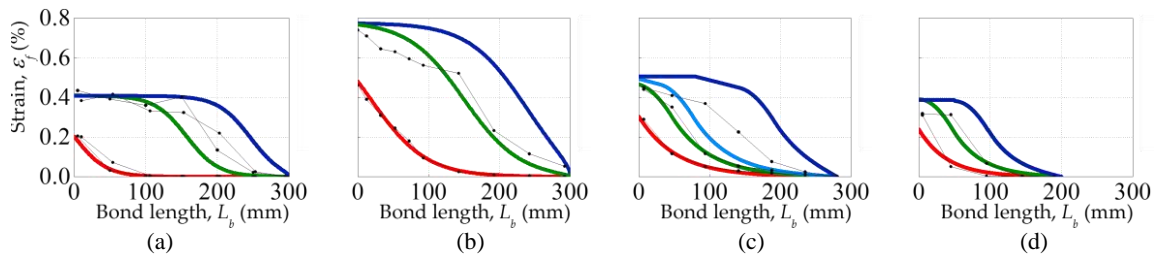


Figure 3: Strain distributions in the CFRP composite: (a) CFRP-to-concrete interface; (b) CFRP-to-clay masonry interface; (c) CFRP-to-timber interface; and (d) CFRP-to-steel interface.

Bond stress distributions

Likely to the same criterion used before, Figure 4 shows the bond stress distribution at the same slip at the CFRP loaded end, i.e. at the end of the E stage, S stage, C stage (only for the CFRP-to-timber interface) and the theoretical results obtained for the D stage. It is also clear from Figure 4 all the state that the adhesively bonded interfaces undergo until their complete debonding. Hence, from the curve that predicts the end of the E state of the interface it can be seen that the maximum bond stress is reached at the CFRP loaded end and then, as the load increases, this maximum value moves towards the CFRP free end which corresponds to the E-S state of the interface. In the particular case of the CFRP-to-timber interface, when the E-S state ends, the E-S-C state develops which is characterized by the constant bond stress that appears at region closest to the CFRP loaded end. The debonding,

when initiated, makes the bond stress distribution to translate from the CFRP loaded end to its free end and when their area is maximized the maximum load transmitted to the CFRP composite is expected to be reached. Consequently, the length that limits these bond stresses also allows the determination of the effective bond length of the adhesively bonded interface.

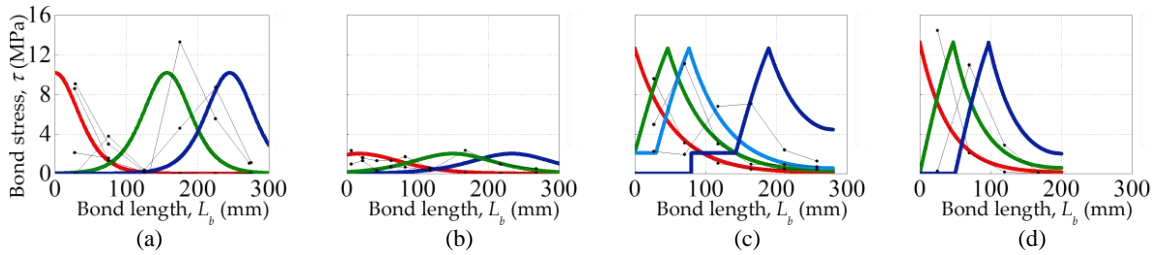


Figure 4: Bond stress distributions within the interface: (a) CFRP-to-concrete interface; (b) CFRP-to-clay masonry interface; (c) CFRP-to-timber interface; and (d) CFRP-to-steel interface.

INFLUENCE OF THE CREAtE STRENGTHENING SYSTEM

To avoid the premature debonding of the CFRP from the substrate at earlier strain, a new strengthening system designated by Continuous Reinforcement Embedded at Ends (CREAtE) was proposed by Rodrigues *et al.* (2016). This technique intends to restrict the slips at the opposite CFRP loaded end by introducing and adhesively anchoring the CFRP free end inside the substrate. This technique doesn't introduces initial strains in the CFRP composite due to the external compression stresses as observed for other conventional techniques, e.g., followed by Biscaia *et al.* (2017b) where a steel plate was attached against CFRP-to-timber interfaces by introducing an external compression stress. Figure 5 shows how the use of this technique can strongly improve the final performance of adhesively bonded interfaces. The results herein shown were obtained from the analytical approach proposed by Biscaia *et al.* (2017a) in which the same exponential bond-slip model previously used for CFRP-to-concrete and masonry clay brick interfaces was used to predict the performance of anchored adhesively bonded interfaces. The results clearly show that the rupture of the CFRP composite can be obtained and it also shows that, unlike the previous unanchored cases, the strains at the opposite side of the CFRP loaded end increase and the length limited by the bond stresses is no longer kept unchanged and it actually tends to decrease due to the zero slip restriction imposed by this innovative strengthening system at $x = 300$ mm.

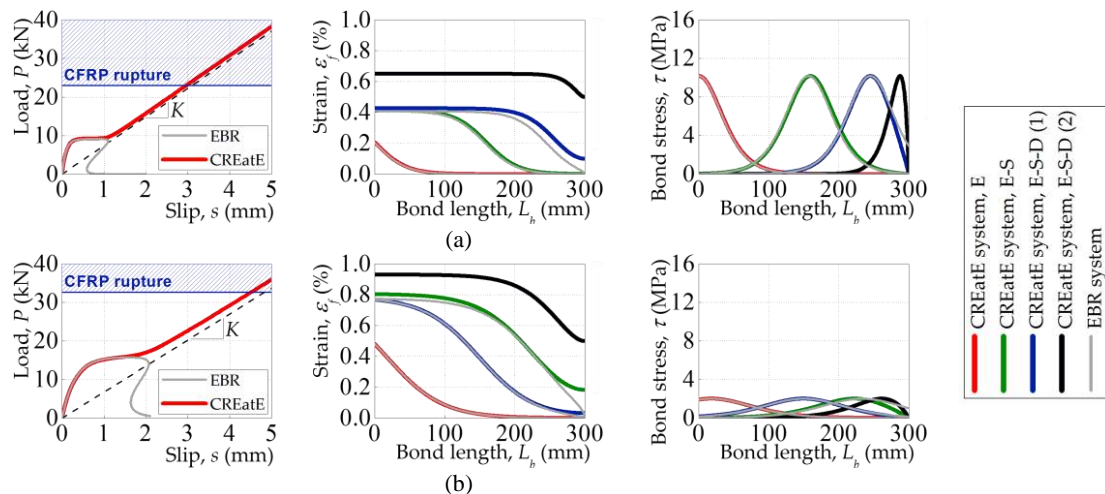


Figure 5: Prediction of the load-slip behaviours for the CREAtE bonding system: (a) CFRP-to-concrete interface; (b) CFRP-to-clay masonry interface.

CONCLUSIONS

This work showed the differences of the interfacial behaviour between different adhesively bonded interfaces. For instance, and due to its brittleness, the interfaces with concrete and the masonry clay bricks had an interfacial behaviour most likely approximated to an exponential bond-slip model whereas the interfaces with steel and timber the bond-slip models were most likely to be approximated to straight lines. Nevertheless, in any of the interfaces herein analysed, all the interfacial behaviours showed a first Elastic stage that ended at a peak bond stress and then, it was followed by a Softening stage. Still, only the CFRP-to-timber interface showed a residual (constant higher than zero) bond stress after the ending of the S stage probably due to the large area bonded on the sap wood of the

timber which is more soft than the grains. The analytical approaches herein presented were also able to predict the experiments accurately showing that the closed-form solutions can be used to estimate the full debonding process of these types of interfaces. Moreover, an innovative strengthening technique (CREatE) that intended to eliminate the premature debonding phenomenon was briefly simulated under a single/double-lap shear test. The results revealed that the performance throughout the bonded length of the anchored interface slightly differs from the unanchored cases and it leads to the rupture of the CFRP composite which attests the effectiveness of this new technique.

ACKNOWLEDGMENTS

The authors gratefully acknowledge the partial financial support provided by the Portuguese Foundation for Science and Technology (FCT) through the strategic project **PEst-OE/EME/UI0667/2014**. The first author would like to express also his gratitude for the research grant SFRH/BPD/111787/2015.

REFERENCES

- C.C. Rodrigues, H. Biscaia, N. Franco, A. Monteiro (2016). "Structural strengthening system with internally anchored reinforcements by adherence", WO 2016005941 (A1), Faculdade de Ciências e Tecnologia, Universidade Nova de Lisboa. Portugal.
- H.C. Biscaia, C. Chastre, C. Silva, N. Franco (2017a). "Mechanical response of anchored FRP bonded joints: A nonlinear analytical approach", *Mechanics of Advanced Materials and Structures*, 25(3), 2018, 238-252.
- H.C. Biscaia, C. Chastre, D. Cruz, A. Viegas (2017b) "Prediction of the interfacial performance of CFRP laminates and old timber bonded joints with different strengthening techniques", *Composites Part B: Engineering*, 108, 2017, 1-17.
- H.C. Biscaia, J. Cardoso, C. Chastre (2017c) "A finite element based analysis of double strap bonded joints with CFRP and aluminium", *Key Engineering Materials*, 754, 237-240.
- H.C. Biscaia, D. Cruz, and C. Chastre (2016a) "Analysis of the debonding process of CFRP-to-timber interfaces", *Construction and Building Materials*, 113, 96-112.
- H.C. Biscaia, I.S. Borba, C. Silva, C. Chastre (2016b). "A nonlinear analytical model to predict the full-range debonding process of FRP-to-parent material interfaces free of any mechanical anchorage devices", *Composite Structures*, 138, 52-63.
- H.C. Biscaia, C. Chastre, I.S. Borba, C. Silva, D. Cruz (2016c). "Experimental evaluation of bonding between CFRP laminates and different structural materials", *Journal of Composites for Construction*, 20(3), 04015070.
- H.C. Biscaia, M.A.G. Silva, C. Chastre (2015). "Factors influencing the performance of externally bonded reinforcement systems of GFRP-to-concrete interfaces", *Materials and Structures*, 48(9), 2961-2981.
- H.C. Biscaia, R. Micaelo, J. Teixeira, C. Chastre (2014). "Delamination process analysis of FRP-to-parent material bonded joints with and without anchorage systems using the Distinct Element Method", *Composite Structures*, 116, 104-119.
- H.C. Biscaia, C. Chastre, M.A.G. Silva (2013). "Modelling GFRP-to-concrete joints with interface finite elements based on the Mohr-Coulomb failure criterion", *Construction and Building Materials*, 47, 261-273.
- J. Dai, T. Ueda, Y. Sato (2005). "Development of the nonlinear bond stress-slip model of fiber reinforced plastics sheet-concrete interfaces with a simple method", *Journal of Composites for Construction*, 9(1), 52-62.
- P. Cornetti, M. Corrado, L.D. Lorenzis, A. Carpinteri (2015). "An analytical cohesive crack modeling approach to the edge debonding failure of FRP-plated beams", *International Journal of Solids and Structures*, 53: 92-106.
- P. Cornetti, A. Carpinteri (2011). "Modelling the FRP-concrete delamination by means of an exponential softening law". *Engineering Structures*, 33(6), 1988-2001.
- S.H. Xia, S.H. and Teng, J.G. (2005). "Behaviour of FRP-to-Steel Bonded Joints", in *e International Symposium on Bond Behaviour of FRP in Structures (BBFS 2005)*.
- Y. Yongming, H.C. Biscaia, C. Chastre, M.A.G. Silva (2017), "Bond characteristics of CFRP-to-steel joints", *Journal of Constructional Steel Research*, 138, 401-419.
- Y. Zheng, Y., Jin-qing, J., Li, L. and Shi-kuan, Y. (2012). Bond-Slip Constitutive Behavior between Fiber-reinforced Polymer and Masonry. *Advanced Materials Research*, 446-449, 3165-3170.



COHESIVE ZONE MODELLING OF A PRESTRESSED NON-MECHANICAL CFRP ANCHORAGE SUBJECTED TO FREEZE-THAW CYCLES

Y.E. Harmanci^{1,2}, E. Zile³, J. Michels⁴ and E. Chatzi¹

¹ Department of Structural Engineering, ETH Zurich, Zurich, Switzerland

² Structural Engineering Research Lab., Empa, Dübendorf, Switzerland

³ Institute for Mechanics of Materials, University of Latvia, Riga, Latvia

⁴ re-fer AG, Brunnen, Switzerland.

ABSTRACT

The application of prestressed carbon fiber reinforced polymers (CFRP) as an externally bonded reinforcement has attracted significant attention due to its well-known advantages both for the ultimate state as well as serviceability conditions. Initially conceptualized by Urs Meier, gradient anchorage offers an alternative to conventional mechanical anchoring techniques purely based on the bond between CFRP-epoxy-concrete. It is achieved by a segment-wise prestressing force release at the strip end after the accelerated curing of epoxy under high temperatures. The long-term behaviour is a significant factor for real-world applications due to the thermal- and moisture sensitive nature of epoxy. Experimentally, it has been observed that FTC causes a reduction in the residual anchorage resistance and deformation capacity of the system. Moreover, the failure mode is switched from a concrete substrate to an epoxy-concrete interface failure. In order to accurately capture the failure mechanisms, a cohesive zone modelling (CZM) approach is herein. Zero-thickness cohesive elements are embedded between each continuum element, and subsequently constitutive traction-separation laws of the concrete substrate and epoxy-concrete interface are introduced. These laws are derived via an inverse analysis relying on experimental observations, obtained via digital image correlation. The CZM approach proves successful in accurately simulating the experimentally observed behaviour based on the provided traction-separation curves.

KEYWORDS

Structural strengthening, numerical modelling, bond and interfacial stresses, prestressed CFRP, durability, freeze-thaw cycles.

INTRODUCTION

Structural strengthening with CFRP has established its place within the engineering community, measuring 30 years of research and industry experience. In terms of flexural strengthening of reinforced concrete beams/slabs, prestressing is gaining popularity since it offers the possibility to exploit the high tensile strength of the material, increasing capacity, reducing deflections and closing cracks previously existing on the structure (Harmanci 2013). End-anchorage of prestressed CFRP systems merits special consideration since concrete cannot carry shear stresses that occur due to high prestressing forces, thereby provoking a premature delamination (Triantafyllou et al. 1992). The current state-of-the art in field applications lies in utilization of metallic end plates bolted to concrete in order to inhibit this premature failure mode, yet non-metallic alternatives have also been investigated (Kim et al. 2008). Contrary to the aforementioned methods, the *gradient anchorage* is a non-mechanical technique developed at Swiss Federal Laboratories for Materials Science and Technology (Empa), which exploits the accelerated curing capability of epoxy under elevated temperatures (Stöcklin and Meier 2003). Section-wise heating followed by a gradual prestress-force-releasing over a predefined end-anchorage length allows the interfacial shear stresses not to exceed the critical delamination thresholds (Michels et al. 2013). Its performance has been verified (Michels et al. 2014a), with further investigations offered on its short-term load carrying mechanisms (Czaderski 2012). Since the anchorage only relies on its constituents (concrete, epoxy, CFRP and their interfaces), and epoxy is known for its temperature and humidity-sensitive features (Benzarti et al. 2011), a long-term investigation of the gradient anchorage is vital in the verification of its stability when exposed to environmental conditions. For this purpose, an experimental series was launched and recently concluded, focusing on the effect of accelerated carbonation and freeze-thaw cycles (FTC) on the residual anchorage resistance. It was observed that carbonation induced an increase (%15) and FTC a decrease (%30) in the anchorage resistance. A shift in the failure mode was observed after FTC, from concrete-cohesive to epoxy-concrete interface failure (Harmanci et al. 2016, 2017a). To the contrary, individual material tests on concrete and epoxy after FTC exhibited no sign of significant deterioration (Harmanci et al. 2017b).

Numerous finite element based techniques have been utilized to model the debonding process based on smeared crack models (Chen et al. 2010), extended finite element method (Benvenuti et al. 2016), and damage models (Benzarti et al. 2011) just to name a few. For this study, a cohesive zone model (CZM) methodology was employed herein relying in use of experimentally derived material parameters offering deeper insights into the debonding process, without necessitating pre-defined crack path. Such an approach was previously employed by Michels et al. (2014b) to simulate short-term debonding failure mechanisms during prestress-force-releasing portion of the gradient anchorage. CZM relies on the traction-separation and shear-slip laws defined within embedded zero-thickness cohesive elements between continuum elements as well as interfaces. Its advantages for quasi-brittle fracture phenomena have been demonstrated previously; interested readers are referred to Elices et al. (2002). The aim of this study is to use the CZM technique to infer more information on the failure mechanisms observed in the experiments after FTC. A particular interest is the interplay of shear stresses induced by prestress-force-releasing and lap-shear testing, since they cannot be measured simultaneously in an experimental setting.

METHODOLOGICAL FRAMEWORK

Experimental Investigation and Results

The experimental investigation comprises prestress-force-release and lap-shear tests on concrete blocks. The prestress-force-releasing is achieved by strip prestressing, gluing and subsequent heating of a single-section anchorage. Heating is completed after 35 minutes and a prestressing force of 8 kN is then released from one end, introducing shear stresses onto the bonded area. Assuming a constant shear stress along the bond length, a prestressing force of 8 kN would correspond to an interfacial shear stress of 1 MPa. A specially designed clamping system holds the prestressing force on the other end, allowing blocks to be placed in the freeze-thaw chamber while maintaining the prestressing force. Blocks are then tested in a conventional lap-shear test with a manually operated hydraulic jack to determine their residual anchorage resistance. Reference specimens are tested two days after releasing, whereas other blocks are transferred to a chamber for subsequent FTC exposure for 120 cycles. Each cycle lasts 12 hours, where maximum/minimum temperatures of +25,-15 are kept constant for 5 hours with 1-hour transition periods in between. Key steps of the experimental procedure are presented in Figure 1. For the uncarbonated FTC case, 3 blocks were successfully prepared and tested. Additionally, concrete prisms with notches were tested in a three point bending test (TPBT) configuration under crack mouth opening displacement (CMOD) control in order to derive the fracture parameters for concrete.

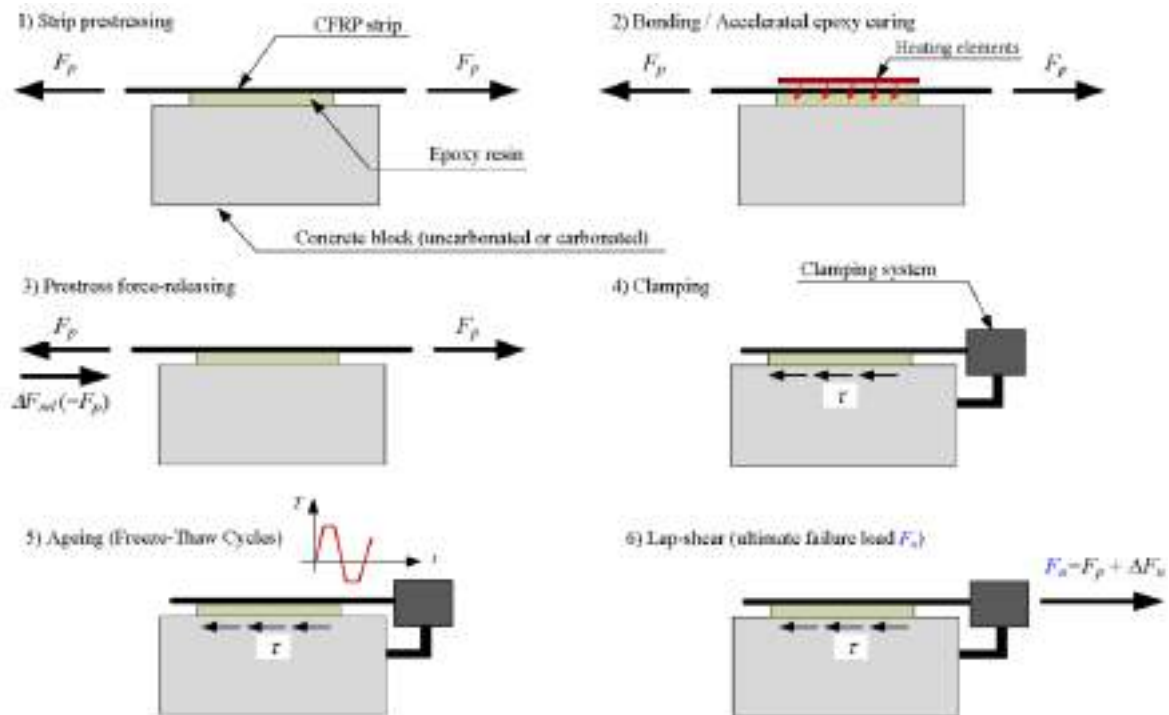


Figure 1: Schematic description of the experimental methodology

Full-field displacements of CFRP and concrete were measured during prestress-force-releasing and lap-shear tests via a commercial 3D-DIC system. The slip is derived from these measurements, as shown in Figure 2, where point A denotes the releasing end of the bond and point B corresponds to the lap-shear end.

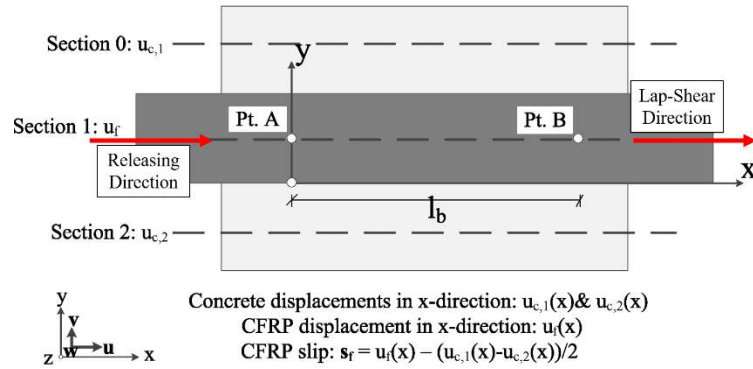


Figure 2: Graphical description of slip derivation.

The load-slip (at point B) behaviour as well as the failure surfaces of reference and uncarbonated FTC (UCFTC) specimens are presented in Figure 3. Based on these results, exposure to FTC induces a reduction of ~30% in the residual anchorage resistance and elastic stiffness of the system. Moreover, maximum slips measured at failure are reduced by 50%, indicating a significant detrimental effect of FTC on the load carrying and deformation capacity of the anchorage. Another consequence of this exposure can be visually noticed in the failure surfaces. The failure mode of the reference case is cohesive through the concrete substrate, whereas after FTC this shifts to an epoxy-concrete interface failure. Possible reasons for this phenomenon are further discussed in Harmanci (2017b).

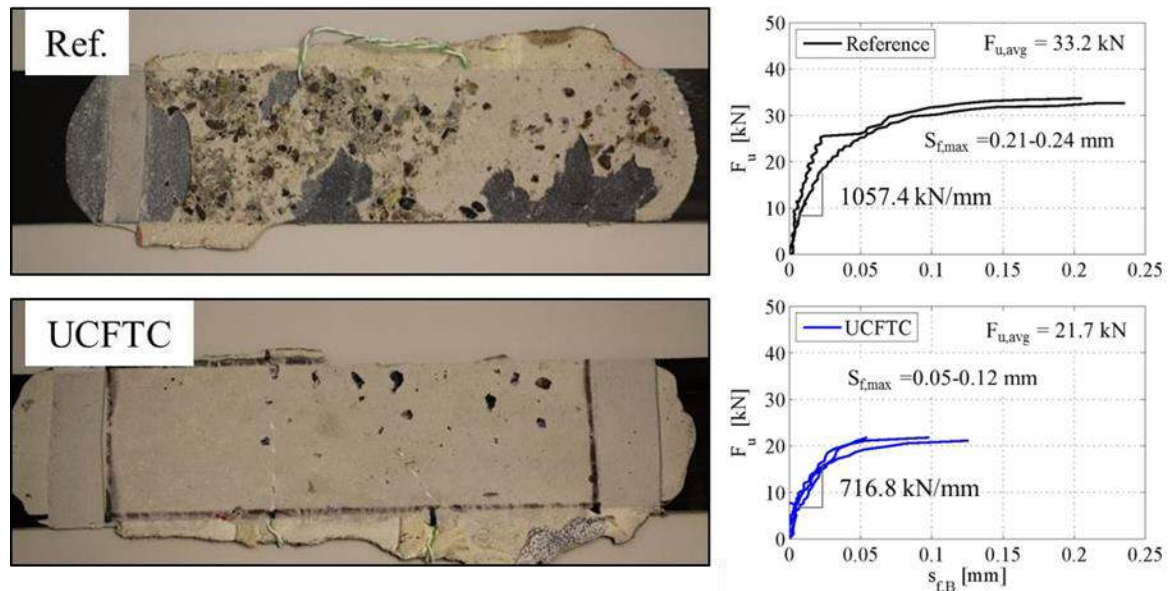


Figure 3: Failure surfaces (left) and load-slip behaviour (right) of reference and UCFTC specimens.

Inverse Modelling Approach

The cohesive zone modelling technique requires traction-separation and shear stress-slip laws of the materials and interfaces for damage initiation and propagation. Slips obtained through 3D-DIC measurements are used for this purpose. Governing shear stress-slip laws of the concrete-epoxy interface are determined by an inverse analysis procedure as described in Martinelli et al. (2011). An optimization problem is constructed by tuning the variables of a bilinear cohesive law and by minimizing the difference between calculated and experimentally observed slips. A reduction of approximately 20% was obtained for the maximum allowable shear stress and the fracture energy decreased considerably, from 590 to 189 Nm^{-1} after FTC. A similar methodology is used for concrete, this time minimizing difference between experimentally obtained and calculated force-CMOD curves (Østergaard, 2003). Contrary to the system-level behaviour, concrete as an isolated material did not suffer significant deterioration from FTC and only a minor reduction in the elastic modulus was observed. Results for the reference and uncarbonated FTC cases are given in Figure 4.

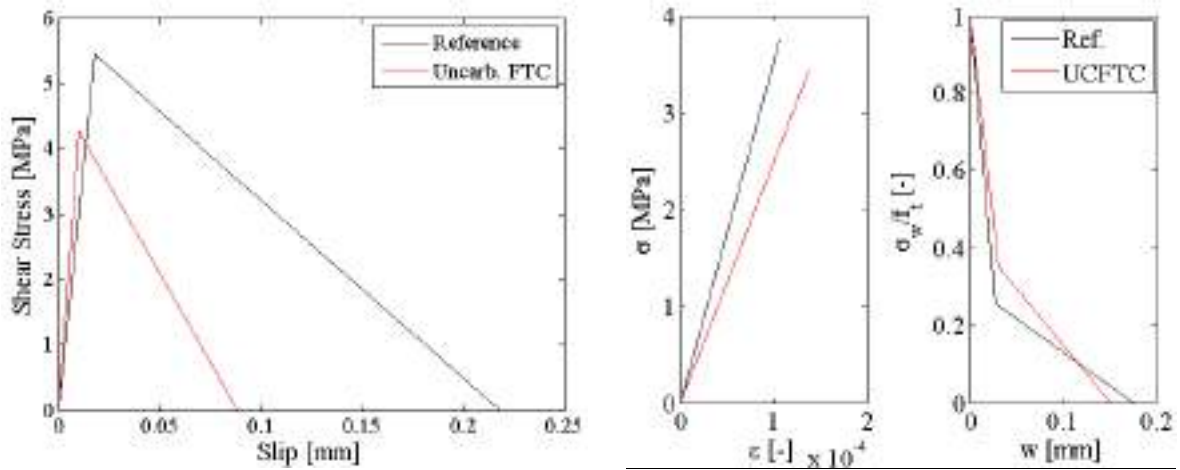


Figure 3: Shear stress-slip laws of the interface (left) and traction-separation laws of concrete (right, elastic and bilinear softening part drawn separately) before and after FTC.

Modelling Approach

A finite-element model was developed in Abaqus 6.14 to recreate the experiments and deliver further information about the failure mechanisms after FTC. As mentioned earlier, the cohesive zone modelling approach is adopted herein due to its ability to handle crack initiation and propagation without the need to predefine a crack as well as its ability to incorporate the fairly large fracture process zone of quasibrittle materials unlike LFM (Elices et al 2002).

The debonding process is extremely rapid, which implies rapid stress redistributions and a highly nonlinear contact problem. An explicit formulation has been chosen to cope with this nonlinearity, utilizing sufficiently small time steps without Newton-Raphson. Only half of the setup is modelled due to the symmetric nature of the problem. CFRP and concrete bulk materials outside the region of interest are modelled with solid C3D8R elements, whereas concrete and epoxy around the bonded region are modelled with tetrahedral C3D4 elements. Zero-thickness COH3D6 cohesive elements were embedded within the concrete substrate and at the epoxy-concrete interface via a Python script (Michels et al. 2014b). Both concrete and the interface rely on a quadratic nominal stress based damage initiation criterion (Eq. 1) and a softening branch with a second degree power-law mode-mixity (Eq. 2).

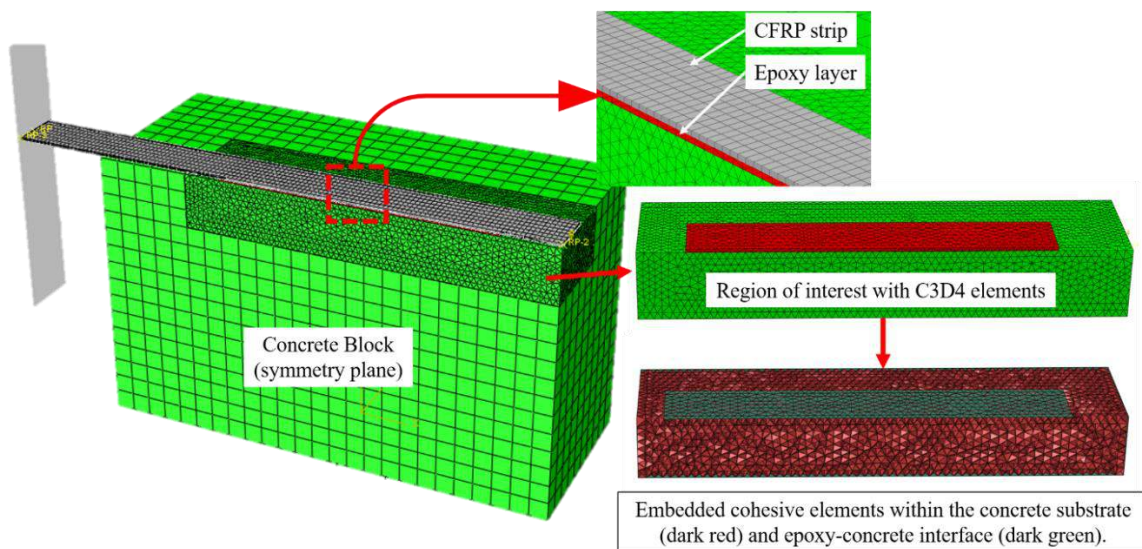


Figure 4: Overview of the FE-model with cohesive elements.

$$\left(\frac{\langle \sigma_n \rangle}{\sigma_n^{\max}}\right)^2 + \left(\frac{\tau_s}{\tau_s^{\max}}\right)^2 + \left(\frac{\tau_t}{\tau_t^{\max}}\right)^2 = 1 \quad (1)$$

$$\left(\frac{G_n}{G_{nc}}\right)^2 + \left(\frac{G_s}{G_{sc}}\right)^2 + \left(\frac{G_t}{G_{tc}}\right)^2 = 1 \quad (2)$$

RESULTS AND DISCUSSIONS

Results obtained from the simulation are compared against experimental observations at two distinct stages, (i) slips along the bond after prestress-force-releasing and (ii) force-slip (at point B, see Figure 2) behaviour of lap-shear tests. The first comparison is presented in Figure 5, which indicates an accurate representation of the slip behaviour when comparing the experimental measurements to the model with average material parameters. Numerous parameters regulate this behaviour, with the epoxy stiffness and the epoxy-concrete interface stiffness at the time of releasing comprising the dominant ones. This is due to the fact that the epoxy layer is only partially cured after exposure to elevated temperatures for accelerated curing.

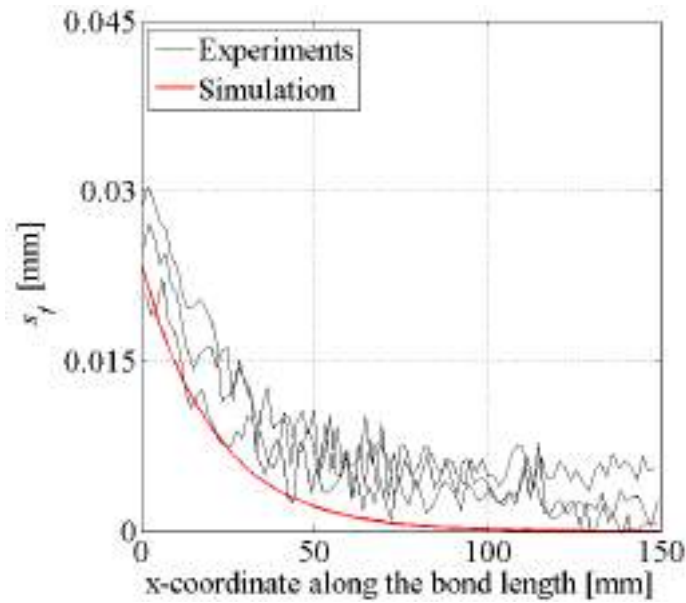


Figure 5: Slip along the bond length during prestress-force-releasing.

A second comparison of the model is made against the applied load-slip curves, where the slip is measured at the loading end of the bond, presented in Figure 6. It is important to note that the presented simulation is offered only until the maximum achieved force level, since this corresponds to the manually controlled loading conditions of the experimental setup. The model was able to accurately reproduce experimental results in terms of residual resistance, maximum slip and initial stiffness. Furthermore, the failure mode was, as expected, through the epoxy-concrete interface.

The primary purpose of this simulation is to provide an aid in understanding the effect of prestress-force-releasing on the overall bond behaviour during lap-shear testing. A series of interfacial shear stresses are provided in Figure 7, after prestress-force-releasing (a), at interface damage initiation and propagation along the bond (b-c), at the maximum achieved load level (d), and at initiation of degradation of the anchorage resistance (e). The applied load is able to further increase when the bond has enough space to dissipate the external energy, but it starts to decrease (and eventually fail) in a displacement controlled environment as soon as both regions coalesce. This is expected, since the released part already “consumed” part of the fracture energy of the interface and additional stresses from lap-shear end cannot be carried as effectively as in unaffected regions. However, this effect occurs only toward the end of the debonding process, which can be considered as a minor influence.

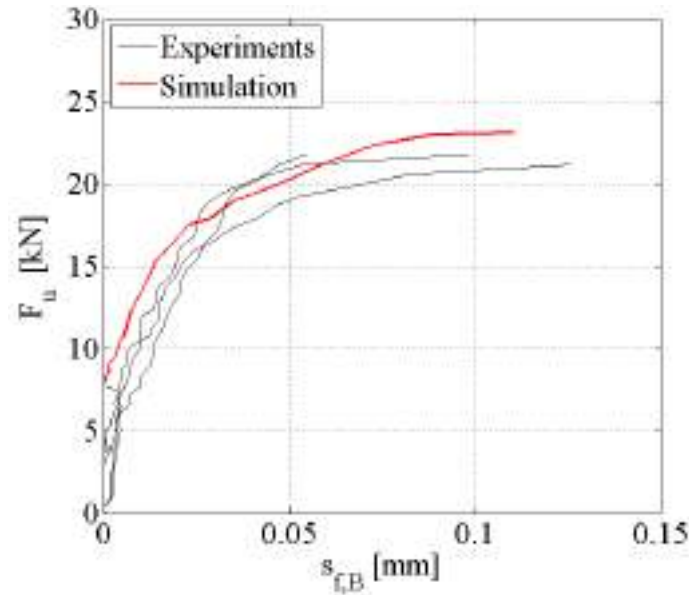


Figure 6: Force-slip comparison of experiments and simulation (Slip measured at the loading end of bond).

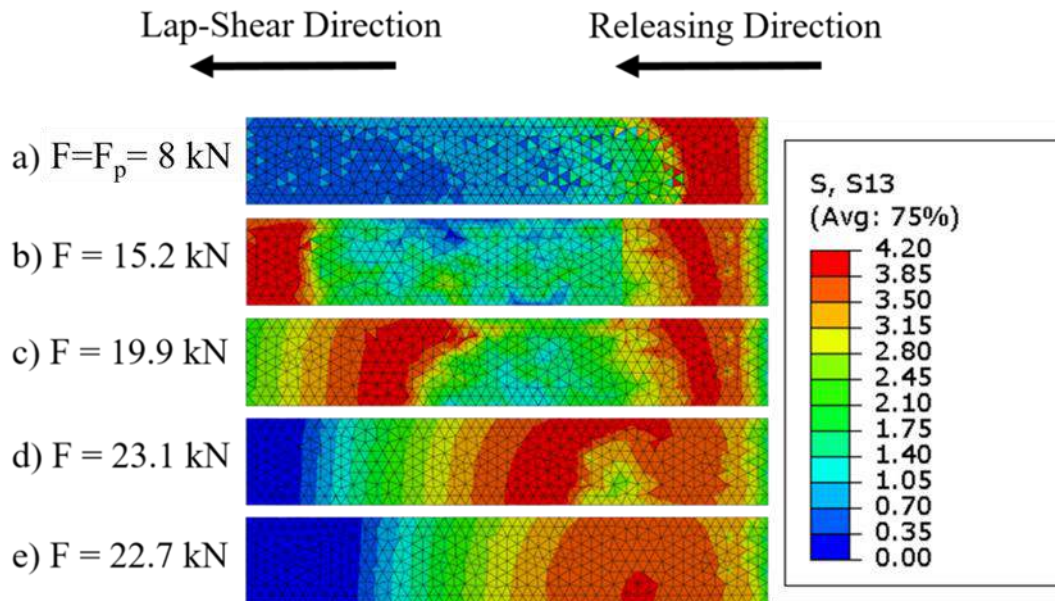


Figure 7: Interfacial shear strains (in MPa) of cohesive elements along the epoxy-concrete interface at various load stages during lap-shear testing.

CONCLUSIONS AND OUTLOOK

The effects of FTC on a non-mechanical prestressed CFRP anchorage were experimentally investigated and material and interface constitutive models were established based on 3D-DIC measurements. Identified material and interface models were implemented within a finite element analysis based on the cohesive zone model methodology to recreate experimental observations and infer more details on the debonding failure mechanisms. First results indicate that both prestress-force-releasing and lap shear tests are simulated accurately, capturing the identical epoxy-concrete interface failure mode. The effect of prestress-force-releasing on the damage evolution process was showcased, yet it was concluded to be a minor influence at this particular load level.

Future efforts will focus on the extension of simulations to evaluate the effect of a wide spectrum of parameters on the residual anchorage resistance, including scenarios where failure occurs through the concrete substrate.

Some of these parameters include, but are not limited to, different prestressing levels, different ageing scenarios such as carbonation and the synergistic action of carbonation and FTC, as well as different material properties.

ACKNOWLEDGMENTS

The authors want to acknowledge the help of the laboratory staff of the Structural Engineering Research Unit at Empa and ETH Zürich. Financial support of the Swiss National Science Foundation (SNSF) for the project No. 124401 is highly appreciated.

REFERENCES

- Benvenuti, E., Orlando, N., Ferretti, D., Tralli, A. (2016). "A new 3D experimentally consistent XFEM to simulate delamination in FRP-reinforced concrete", *Composites Part B: Engineering*, 91, pp.346-360.
- Benzarti, K., Chataigner, S., Quiertant, M., Marty, C., Aubagnac, C. (2011). "Accelerated ageing behaviour of the adhesive bond between concrete specimens and CFRP overlays", *Construction and building materials*, 25(2), pp.523-538.
- Benzarti, K., Freddi, F., Frémond, M. (2011). "A damage model to predict the durability of bonded assemblies. Part I: Debonding behavior of FRP strengthened concrete structures", *Construction and building materials*, 25(2), pp.547-555.
- Chen, G.M., Teng, J.G., Chen, J.F. (2010). "Finite-element modeling of intermediate crack debonding in FRP-plated RC beams", *Journal of composites for construction*, 15(3), pp.339-353.
- Czaderski-Forchmann, C. (2012). "Strengthening of reinforced concrete members by prestressed, externally bonded reinforcement with gradient anchorage", Ph.D. Thesis, ETH Zurich, Zurich, Switzerland.
- Elices, M.G.G.V., Guinea, G.V., Gomez, J., Planas, J. (2002). "The cohesive zone model: advantages, limitations and challenges", *Engineering fracture mechanics*, 69(2), pp.137-163.
- Harmanci, Y.E. (2013). Prestressed CFRP for structural retrofitting - experimental and analytical investigation", M. Sc. thesis, ETH Zürich, Zurich, Switzerland.
- Harmanci, Y.E., Michels, J., Chatzi, E.N. (2016). "Residual Resistance of Non-Mechanical Prestressed CFRP Anchorages Subjected to Environmental Conditions", In *7th International Conference on Advanced Composite Materials in Bridges and Structures (ACMBS-VII)*. Vancouver, Canada
- Harmanci, Y.E., Michels, J., Chatzi, E.N. (2017a). "Behaviour of Prestressed CFRP Anchorages under Freeze-Thaw Cycle Exposure", In *4th Conference on Smart Monitoring, Assessment and Rehabilitation of Civil Structures (SMAR 2017)*. Zurich, Switzerland.
- Harmanci, Y.E., Michels, J., Czaderski, C., Loser, R., Chatzi, E. (2017b). "Long-term residual anchorage resistance of gradient anchorages for prestressed CFRP strips", *Composites Part B: Engineering*, 139, pp.171-184.
- Kim, Y.J., Gordon Wight, R., Green, M.F. (2008). "Flexural strengthening of RC beams with prestressed CFRP sheets: Using nonmetallic anchor systems", *Journal of Composites for Construction*, 12(1), pp.44-52.
- Martinelli, E., Czaderski, C., Motavalli, M. (2011). "Modeling in-plane and out-of-plane displacement fields in pull-off tests on FRP strips", *Engineering Structures*, 33(12), pp.3715-3725.
- Michels, J., Sena-Cruz, J., Czaderski, C., Motavalli, M. (2013). "Structural strengthening with prestressed CFRP strips with gradient anchorage", *Journal of Composites for Construction*, 17(5), pp.651-661.
- Michels, J., Martinelli, E., Czaderski, C., Motavalli, M. (2014a). "Prestressed CFRP strips with gradient anchorage for structural concrete retrofitting: Experiments and numerical modeling", *Polymers*, 6(1), pp.114-131.
- Michels, J., Zile, E., Czaderski, C., Motavalli, M. (2014b). "Debonding failure mechanisms in prestressed CFRP/epoxy/concrete connections", *Engineering Fracture Mechanics*, 132, pp.16-37.
- Østergaard, L. (2003). "Early-Age Fracture Mechanics and Cracking of Concrete: Experiments and Modeling", PhD Thesis, Technical University of Denmark, Lyngby, Denmark.
- Stöcklin, I., Meier, U. (2003). "Strengthening of concrete structures with prestressed and gradually anchored CFRP strips", In *Fibre-Reinforced Polymer Reinforcement for Concrete Structures*, pp. 1321-1330.
- Triantafillou, T. C., Deskovic, N., Deuring, M. (1992). "Strengthening of concrete structures with prestressed fiber reinforced plastic sheets", *ACI Structural Journal*, 89 (3), 235-244.



INFLUENCE OF VARIOUS PROCESS PARAMETERS ON THE MECHANICAL PERFORMANCE OF CFRP/CONCRETE ADHESIVE BOND

Karim Benzarti¹, Nicolas Roche², Corentin Le Roy³, Jeremy Roth³, André Flety³, Christophe Aubagnac³

1 Université Paris-Est, Ecole des Ponts ParisTech, Laboratoire Navier (UMR 8205), France

Email: karim.benzarti@ifsttar.fr

2 EDF, TEGG/SGC, Organic Materials Group, Aix en Provence, France

3 CEREMA, DTerCE/DLA, Autun, France.

ABSTRACT

CFRP are widely used in RC structures reinforcement and retrofitting, a large majority of which are currently applied manually by hand lay-up, leading to various defects in the composite laminate and the adhesive bond depending on the experience of the applicator.

In this experimental study, pultruded CFRP plates were installed on concrete blocks by controlling different parameters of the bonding process, such as viscosity/consistency of the epoxy adhesive, temperature of the concrete substrate, application of a contact pressure during bonding operation or the use of vacuum bagging. The influence of these parameters on various bond characteristics was studied by performing mechanical tests and micrographic observations. Mechanical bond performances were assessed using an instrumented Single Lap Shear (SLS) test setup providing the shear capacity of the assembly. Standard Pull-off tests were also performed.

Besides, the morphology/geometry of the concrete/CFRP adhesive joint (thickness of the joint and penetration depth of the polymer adhesive in the porous concrete substrate) was characterized by optical microscopy, and the influence of the process parameters on these characteristics was discussed. Finally, the possible relationship between morphological characteristics of the adhesive joint and mechanical properties was discussed.

KEYWORDS

CFRP, concrete, adhesive bonding, process parameters, pressure, vacuum bagging, bond performances, morphology of the adhesive joint

INTRODUCTION

Structural rehabilitation or strengthening by externally bonded carbon fiber reinforced polymers (CFRP) composites has become a well-established technique worldwide, which offers an effective solution for extending the service life of ageing / deficient infrastructures. In this context, the main applications are as follows:

- i) flexural strengthening of concrete beams using prefabricated CFRP plates (manufactured by pultrusion), which are bonded directly on the bottom face using a cold curing epoxy adhesive. This latter has usually a pasty and thixotropic texture in order to facilitate installation,
- ii) shear strengthening of beams or other sub-structures by means of carbon fiber fabrics which are impregnated onsite with a medium-viscosity epoxy resin. This latter serves both for the saturation of the fabrics and its attachment to the concrete substrate,
- iii) retrofitting of concrete columns using resin saturated carbon fabrics which are wrapped around the structure.

In most cases, FRP composites (either CFRP plates or saturated fabrics) are applied manually by an operator, using grooved rollers. Unfortunately, the quality of application strongly depends on the operator's dexterity as this method doesn't ensure uniform pressure and generates defects (voids, entrapped air bubbles, varying thickness) both in the laminates and in the adhesive layer. Such defects may cause stress concentrations and consequently lead to delamination at low average stress. The durability and effectiveness of the composite repair in the long term may also be compromised.

In other industrial sectors (aeronautics, automotive), advanced processing methods are routinely used and involve the application of pressure or vacuum assisted impregnation to produce denser FRPs with low defect densities. Recently, few attempts were made for transposing these processes in construction to improve the quality of FRP systems externally bonded to concrete structures (Aguilar, 2009; Hadigheh, 2016). These studies showed that the use of vacuum bagging or the application of external pressure during installation of saturated glass or carbon fabrics can lead to significant improvement of the bond properties (as determined by pull-off or single lap shear tests). However these processes have never been explored in the case of bonded pultruded plates.

In the present study, it is thus proposed to investigate the influence of some process parameters (application of pressure on the adhesive joint during installation, use of vacuum bagging just after installation of the bonded CFRP plate, modulation of the consistency of the polymer adhesive, and elevation of temperature during application) on the bond performances of concrete blocks strengthened by pultruded CFRP plates. In addition the influence of these parameters on the geometrical characteristics of the adhesive joints (thickness of the joint, penetration depth of the adhesive in the porous substrate) is also discussed.

EXPERIMENTAL

Geometry of the test specimens

Specific test specimens were designed for this experimental program (Figure 1), consisting of concrete blocks of dimensions 210 x 410 x 105 mm³ strengthened by bonded CFRP plates; these latter are installed at two different locations of each block, in order to perform two types of mechanical tests on the adhesive joint: one plate at the front part is intended for a single lap-shear test while another plate at the back part is intended for 2 pull-off tests.

Preparation of the CFRP strengthened concrete specimens

Constant parameters of the fabrication

Some parameters were kept constant for the fabrication of all specimens of this study, in particular the preparation of concrete blocks and the type of pultruded CFRP plates used for strengthening concrete elements:

- Concrete blocks were cast from a regular C30/37 formulation, based on a Portland cement (CEM I 52.5N from Calcia Befes) and silico-calcareous aggregates (0/12.5) with a conventional water to cement ratio of 0.5. The compressive strength of concrete at 28 days was 52.5 ± 3.5 MPa. These concrete blocks were stored in the laboratory for 2 years before preparing the CFRP strengthened specimens. At this stage, the total porosity of concrete determined by water saturation was 14.5% and complementary tests using phenolphthaleine indicator showed that surface carbonation of the blocks was negligible. Finally, the upper face of all blocks was abraded using a grinding tool in order to generate an adequate surface roughness, and residual dust was carefully removed by vacuum cleaning,
- Identical CFRP plates (Carbodur[®] S812, provided by Sika France) were used for the preparation of all strengthened specimens. Before application, CFRP plates were carefully degreased using Sikadur[®] cleaner.

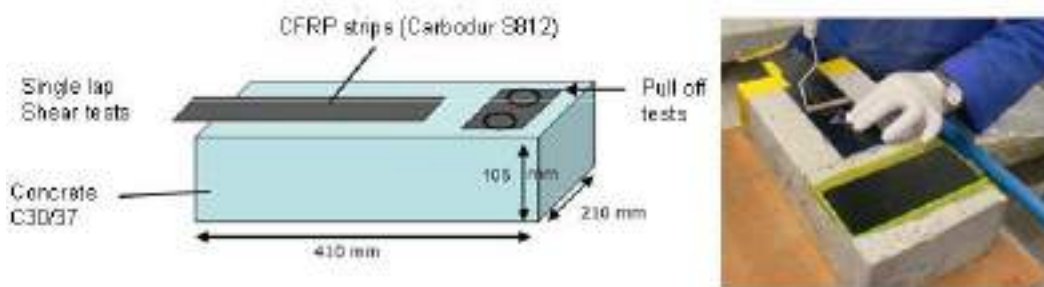


Figure 1: Geometry of the test specimens and detail of the manual installation of CFRP composites.

Variable parameters of the fabrication

Other parameters were varied in order to study their possible influence on the mechanical and physical characteristics of the adhesive bond. In particular, several series of specimens were fabricated considering different viscosities/consistencies of the epoxy adhesive, different methods for the application of the CFRP plate, and different temperatures of the concrete substrate:

- Regarding the polymer adhesive, 3 bi-component epoxy systems were selected which exhibit different consistencies. Sikadur[®]30 is the actual system prescribed by Sika for the bonding of Carbodur[®] CFRP plates, and has a very pasty texture. Sikadur[®]330 is rather prescribed for impregnation and bonding of carbon fiber sheets (Sikawrap[®] fabrics) and has a creamy consistency. Sikadur[®]53 is commonly used as injection grout and exhibits

liquid behavior. The main characteristics of these 3 epoxy systems, as provided by the manufacturer's technical data sheets, are reported in Table 1. After application, the polymer joints were left to cure in the laboratory condition (20°C) for at least 15 days before starting the mechanical tests.

- Different methods were also investigated for the application of the CFRP system on concrete blocks:
 - i) A first series of specimens was prepared manually using a hand roller (Figure 1), as in the field.
 - ii) Alternatively, a metallic frame connected to a hydraulic jack was specially designed and constructed for the present study, which is able to apply a uniform level of pressure over the adhesive joints of three test specimens, simultaneously (Figure 2). The objective is to ensure a compaction of the joint, evacuate air bubbles and force the penetration of the polymer adhesive into the porous structure of the concrete substrate. Thanks to this device, series of specimens were fabricated at pressure levels of 0.3 and 1 bar, which are representative of pressures encountered in two advanced manufacturing processes of composite materials, namely infusion and resin transfer moulding (RTM), respectively.
 - iii) A last setup, inspired from the vacuum bagging process used in the composite industry, was developed in order to bond simultaneously CFRP plates on 3 test bodies (Figure 3). A depression of 1 bar is applied thanks to the hermetic plastic membranes connected to a pneumatic compressor, leading to a confinement of the adhesive joints. Here again, the confinement is expected to compact the joint and force the penetration of the polymer adhesive into the porous concrete substrate.
- The temperature of the concrete substrate was also varied. As an alternative to the laboratory temperature of 20°C set for the other series of test specimens, a single series was prepared by heating the concrete substrate and the polymer adhesive at 40°C before bonding the CFRP plates. This was done for Sikadur®30 adhesive only. It is expected that this elevated temperature reduces the viscosity of the adhesive and facilitates the penetration of the polymer in the porosity of the substrate.

Table 1: Main characteristics of the 3 epoxy adhesives used in this study

	Sikadur®30	Sikadur®330	Sikadur®53
<i>Main application in the field</i>	Bonding of CFRP plates	Impregnation of carbon fabrics	Injection grout
<i>Consistency</i>	Paste	Cream	Liquid
<i>Viscosity (mPa.s)</i>	NA	6000 at 23°C	5800 at 20°C
<i>Young's Modulus (GPa)</i>	11.2	4.5	6.3
<i>Tensile strength (MPa)</i>	26-31	30	30
<i>Shear strength (MPa)</i>	16-19	NA	NA

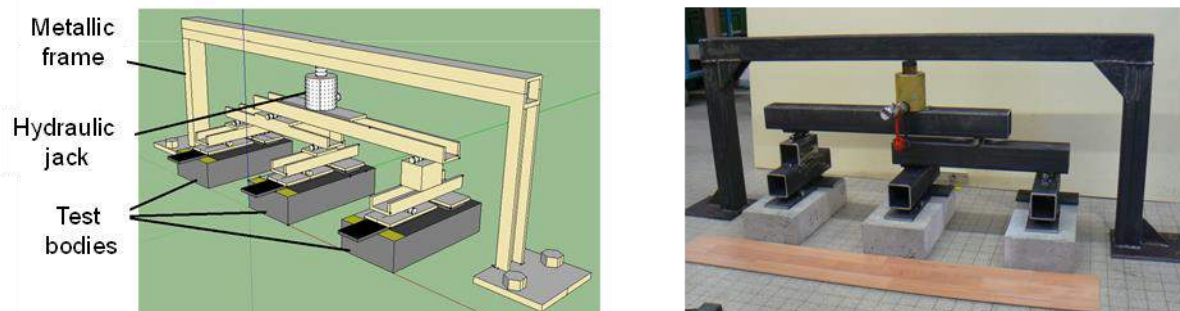


Figure 2: Proposed device for applying a fixed/uniform level of pressure on adhesive joints of 3 test specimens.



Figure 3: Proposed setup for preparing a series of 3 test-specimens by vacuum bagging

The matrix presented in Table 2 summarizes the combinations of variable process parameters that were considered in the fabrication of the different series of CFRP strengthened specimens. As three test bodies were fabricated per series, the total number of specimens was 39.

Table 2: Matrix showing the various series of test specimens fabricated by varying the consistency of the polymer adhesive and the condition of application of the CFRP plate.

	Pasty adhesive (Sikadur®30)	Creamy adhesive (Sikadur®330)	Liquid adhesive (Sikadur®53)
<i>Manual installation</i>	3	3	3
<i>Pressure 0.3 bar</i>	3	3	3
<i>Pressure 1 bar</i>	3	3	3
<i>Vacuum Bag</i>	3	3	3
<i>Manual installation at 40°C</i>	3	-	-

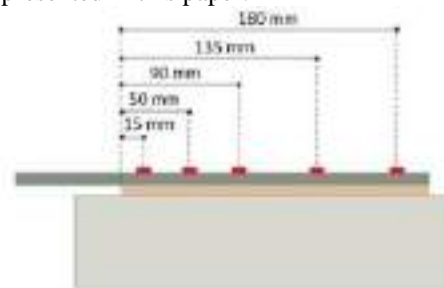
Characterization methods

Pull-off tests were performed on each test specimen according to EN 1542 standard (2 tests per specimen, on the delimited test zone located at the back of the block, as shown in Figure 1). Since there are 3 specimens in each series of the experimental matrix (Table 2), 6 pull-off tests were carried-out per series.

Single lap shear tests were conducted using a hydraulic testing machine which is shown in Figure 4a and described in previous studies (Benzarti 2011; Chataigner 2011). One test is carried out per specimen, hence 3 tests per series. This method provides the ultimate shear capacity of the concrete/CFRP adhesive joint. It is to note that strain gage instrumentation was also used in order to analyze the load transfer mechanism along the lap joint (Figure 4b) and evaluate the effective transfer length, but these data are not presented in this paper.



(a) Picture of the testing machine

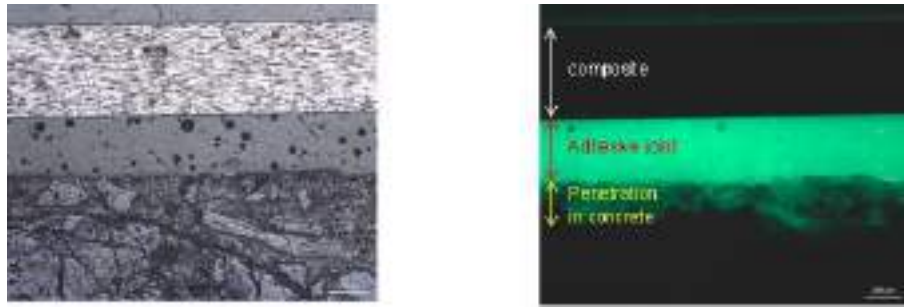


(b) Strain gage instrumentation

Figure 4: Characterization by single-lap shear tests (the bonded length is 200mm for all specimens)

Additional geometrical and morphological characterizations of the adhesive joints were performed by optical microscopy (Zeiss Scope A1 apparatus). Classical observations under visible light (Figure 5.a) allowed measuring the apparent thickness of the adhesive joint, while observations with a fluorescence filter made it possible to assess the average penetration depth of the polymer into the porosity of concrete (Figure 5b). It is to note that a fluorescent dye (Epodye, from Struers) was introduced in the polymer adhesive during preparation. Collected micrographs were analyzed using ZEN software commercialized by Zeiss Instruments.

Complementary analyses were also carried out by Differential Scanning Calorimetry (DSC Q100 from TA instruments) on small fragments taken from the adhesive joints (after mechanical characterization) in order to evaluate the possible influence of the process parameters on the glass transition temperature (T_g) of the adhesive.



(a) Observation under visible light

(b) Observation using a fluorescence filter

Figure 5: Typical cross-section of a concrete/adhesive/composite interface observed by optical microscopy

RESULTS AND DISCUSSIONS

Pull-off tests

Values of pull-off strengths obtained for the various series of CFRP strengthened concrete blocks are reported in Figure 6. All specimens failed by cohesive concrete failure. A significant dispersion can be observed on experimental data, which is an inherent feature of the pull-off test. Considering this dispersion, no clear influence of the installation process and the consistency of the polymer adhesive can be drawn. In this regard, it must be highlighted that the pull-off tests is known to be mainly influenced by concrete properties, since the partial coring around the test zone generates localized stress concentrations within the concrete substrate. Therefore it may not be very sensitive to variations in the adhesive bond properties and it is often recommended to use shear test methods rather than the pull-off test (Benzarti, 2011).

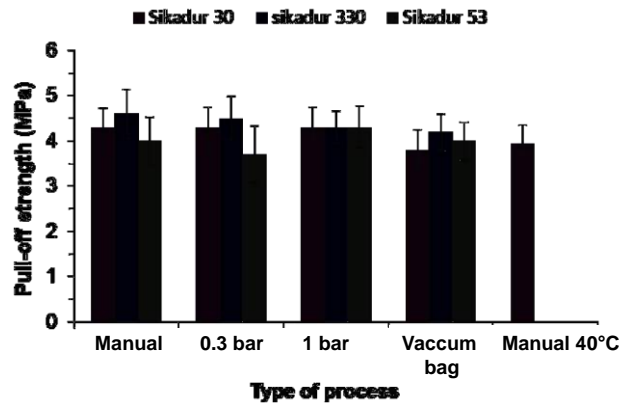


Figure 6: Influence of the resin and the fabrication process on the pull-off strength

Single-lap shear test

Experimental values of the maximum shear capacities are displayed in Figure 7 for the various series of specimens. In addition, typical aspects of the fractured surface are illustrated in Figure 8 and the corresponding failure modes are described in Table 3.

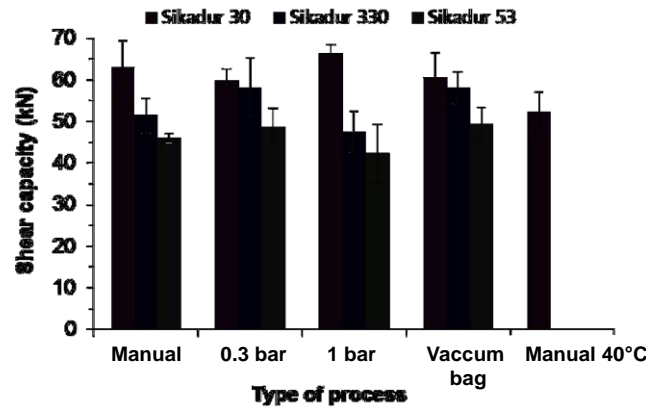


Figure 7: Influence of the resin and the fabrication process on the Shear Capacity

Different *failure modes* are observed on Figure 8 depending on the types of adhesive and processing conditions:

- For specimens based on Sikadur[®]30 and fabricated by manual process (both at 20°C and at 40°C), cohesive concrete failures are obtained. Specimens fabricated under pressure fail by mixed failure mode (cohesive both in concrete and in the polymer adhesive), and the fraction of polymer failure tends to increase with the pressure level. Finally, the vacuum bagging process leads to a very specific failure mode at the interface between the CFRP plate and the polymer joint; it was attributed to a non-homogeneous thickness of the joint (thicker at the center) induced by the confinement of the plastic membrane which impedes the evacuation of the polymer in excess during compaction.
- For specimens based on Sikadur[®]330, mixed failure modes are observed (cohesive failures in concrete and in the polymer adhesive) but the fractions of polymer failure are higher compared to those of Sikadur[®]30 specimens. The vacuum bag process provides again a specific failure at the CFRP/polymer interface.
- All specimens made with Sikadur[®]53, even by vacuum bagging, fail mostly by cohesive concrete failure.

Table 3: Description of the failure modes for the various series of specimens after shear tests

	Sikadur [®] 30	Sikadur [®] 330	Sikadur [®] 53
<i>Manual installation</i>	~95% concrete/5% polymer	~55% concrete/35% polymer	~90% concrete/10% polymer
<i>Pressure 0.3 bars</i>	~70% concrete/30% polymer	~35% concrete/65% polymer	~90% concrete/10% polymer
<i>Pressure 1 bars</i>	~55% concrete/45% polymer	~20% concrete/80% interface concrete	~85% concrete/15% polymer
<i>Vacuum Bag</i>	100% interface CFRP	~15% concrete/85% interface CFRP	~80% concrete/20% polymer
<i>Manual inst. at 40°C</i>	~95% concrete/5% polymer	--	--



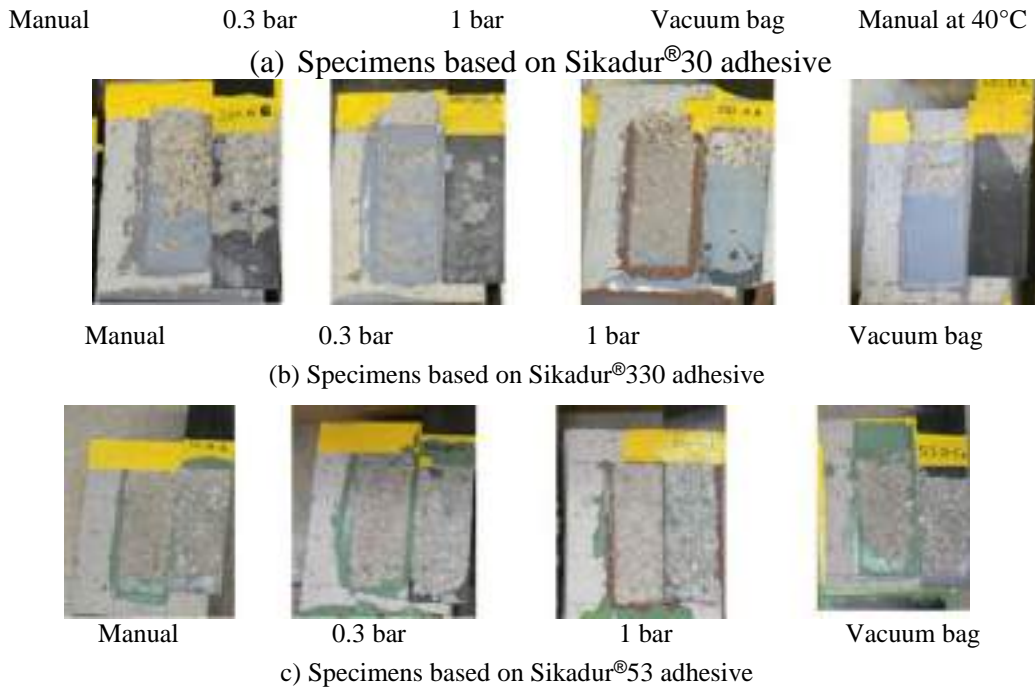


Figure 8: Pictures showing typical failure modes for the various series of specimens after shear tests

Regarding the *shear capacities* (Figure 7), the following trends are observed:

- Considering the dispersion on experimental data, there seems to be only limited influence of the application method for a given type of adhesive. Maybe a slight increase in capacity can be noticed when applying pressure (respectively 1 bar and 0.3 bar) in the case of Sikadur30 and 330. But the most significant trend is the slight decrease in the shear capacity of the specimen processed by manual installation at 40°C (unique series with Sikadur[®]30), compared to that processed manually at 20°C.
- Differently, there is a strong influence of the type of polymer adhesive. Globally, the highest shear capacities are achieved using Sikadur[®]30 (average around 62 kN), which is the system prescribed by the manufacturer for the application of Carbodur plates. Come then the specimens fabricated with Sikadur[®]330 (average shear capacity around 56 kN) and those made with Sikadur[®]53 (average capacity of 47 kN).

Further information (possible variations in the effective transfer length) is expected from the analysis of experimental data provided by strain gage instrumentation during shear tests. This work is currently under way.

Geometrical / morphological characterization of the adhesive joints

Microscopic observations were made on cross-sections of adhesive joints of the various series of specimens, to investigate the influence of the variable process parameters on the geometrical characteristics of the joints, and verify possible correlations between these characteristics and the mechanical properties of the CFRP strengthened concrete blocks.

Figure 9.a displays measured values of the joint thickness, while Figure 9.b shows the values of the average penetration depth of the polymer into the concrete substrate for the various series of specimens.

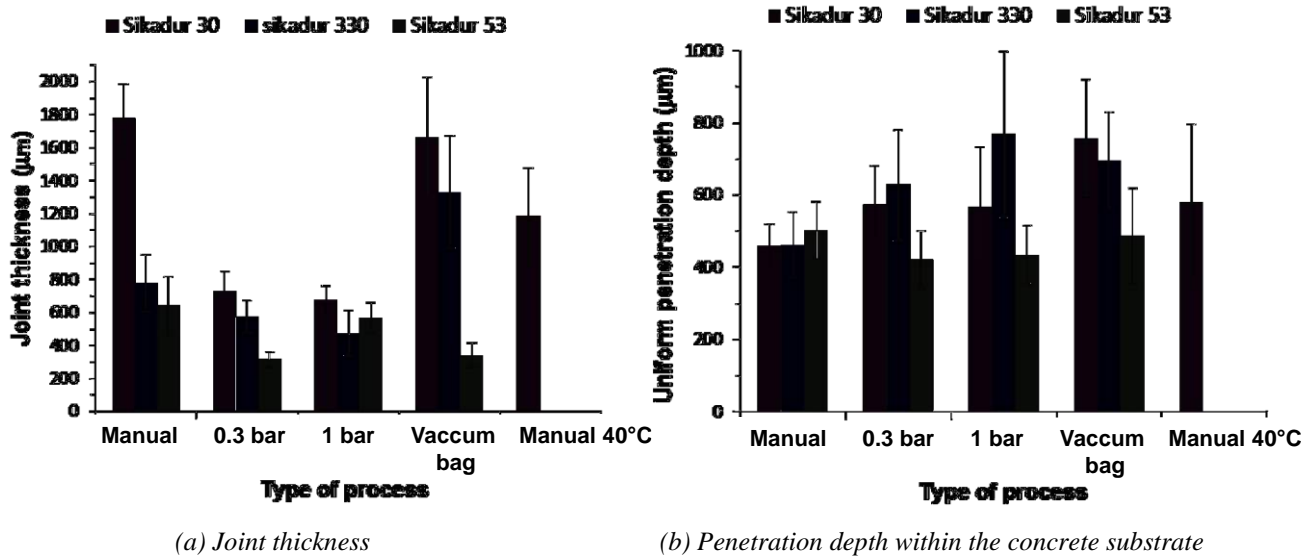


Figure 9: Influence of the resin and the fabrication process on the characteristics of the polymer joint

Regarding the **joint thickness**, results show that the application method plays a very important role, which is moreover dependent on initial rheological properties of the polymer adhesive:

- For the pasty adhesive (Sikadur[®]30), joint thicknesses are much larger than for the 2 other adhesives of lower viscosities, whatever the application method. Indeed, the higher the viscosity, the more difficult the spread of the adhesive towards the exterior of the joint during compaction. With a manual application at 20°C, the thickness of Sikadur[®]30 joint is around 1.8 mm against 0.8 and 0.65 mm for Sikadur[®]330 and 53.
- The application of pressure forces the evacuation of the adhesive in excess and leads to a significant reduction of the joint thickness, especially for the pasty adhesive Sikadur[®]30 but also for the other systems. The 2 pressure levels (0.3 and 1 bar) induce very comparable effects.
- Differently, the vacuum bag method creates a confinement effect which impedes the evacuation of the adhesive outside the joint, at least for the pasty and creamy adhesives for which the joint thickness remains high (1.7 and 1.3 mm, respectively). This confinement has less effect with the liquid adhesive Sikadur[®]53.
- Besides, an increase in temperature during application (comparison of manual installations at 20°C and 40°C with Sikadur[®]30 adhesive) lowers the adhesive viscosity and leads to a reduced joint thickness.

The **penetration depth** is also significantly influenced by the polymer consistency and the type of application:

- For the pasty adhesive (Sikadur[®]30), the penetration depth is around 0.46 mm with the manual process. This is higher than the value of 0.2 mm reported in a previous study in the case of hardened cement paste substrates without aggregates (Djouani, 2001). Furthermore, the penetration depth increases with the application of pressure and becomes maximal with the vacuum bag process (0.76 mm).
- Regarding the creamy epoxy (Sikadur[®]330), the value obtained by manual application is comparable to that of Sikadur[®]30. Nevertheless, the effect of pressure is more pronounced, probably due to the lower viscosity which facilitates penetration in the concrete substrate. Vacuum confinement is also effective.
- For Sikadur[®]53, the penetration depth observed with the manual application is slightly higher (0.5mm), due to the liquid texture. However the application of pressure or the vacuum confinement doesn't modify significantly this value, probably due to a quick evacuation of the liquid adhesive in excess out of the joint.

Discussion on the influence of the process parameters

Previous observations show that process parameters affect the geometrical characteristics of the adhesive joint. The application of pressure or vacuum confinement tends to reduce the joint thickness and forces the penetration of resin in the porosity of the concrete. However, if the adhesive is very liquid (case of Sikadur[®]53), a large amount of polymer is rapidly spread out of the joint, hence reducing the effectiveness of compaction. In this regard, the creamy adhesive (Sikadur[®]330) appears as a good compromise for reaching high penetration depths.

Nevertheless, when comparing these geometrical characteristics of joints (Figure 9) to the mechanical properties determined by shear tests on the various series of specimens (Figure 7), one cannot establish any correlation at this stage. In the end, no clear influence of the process parameters (application method or rheology of the polymer) can be drawn, and the observed variations of the shear capacity (in Figure 7) seem mainly dependent on the intrinsic properties of the crosslinked polymer adhesive (modulus, mechanical properties...). Moreover, the adhesive prescribed by the manufacturer for bonding Carbodur plates is actually the most performant. The analysis of experimental data from strain gage instrumentation may provide additional information very soon.

Glass transition temperatures (T_g) of the adhesive joints

Figure 10 displays values of T_g that were determined by DSC on fragments of adhesive joints for the various series of specimens. Obviously, T_g is little influenced by the process parameters. A small decrease in T_g is only observed for Sikadur[®]53 liquid adhesive in the case of manual application or with a pressure of 0.3 bar.

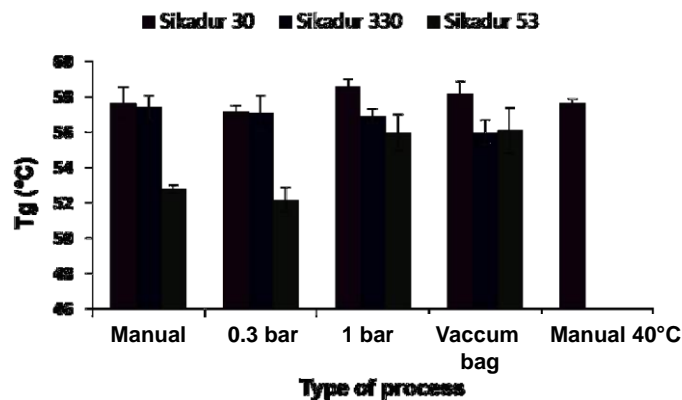


Figure 10: Influence of the resin and the fabrication process on T_g of the polymer joint

CONCLUSIONS

In this paper, the influence of the process parameters (method of application of the CFRP plate on concrete blocks and initial viscosity of the adhesive) on the bond characteristics of the concrete/CFRP interface was investigated. It was found that the application of an external pressure or the use of vacuum bagging didn't modify significantly the pull-off strengths and shear capacities of the bonded assemblies for a given type of adhesive. However, significant variations in shear capacities were observed as a function of the type of adhesive, which seem not correlated to actual geometrical characteristics of the joint (thickness / penetration depth of the polymer in the porous concrete substrate), but may rather relate to the intrinsic characteristics of the crosslinked adhesive (stiffness...) and their repercussion on the load transfer mechanism. On this point, further information is expected from the analysis of strain gage data. The adhesive prescribed by the manufacturer provided the highest shear capacities. Besides, T_g of the adhesive was little affected by the process parameters.

REFERENCES

- S.A. Hadigheh, R.J. Gravina, S. Setunge (2016), "Influence of the Processing Techniques on the Bond Characteristics in EB Joints-Experimental and Analytical Investigations", *J. Compos. Constr.*, 20(3), 04015081
- J. Aguilar, D. Winters, R. Sen et al. (2009), "Improvement in Fiber-Reinforced Polymer-Concrete Bond by External Pressure", *Transportation Research Record*, 2131, 145-154
- K. Benzarti, S. Chataigner, M. Quiertant, C. Marty, C. Aubagnac (2011), "Accelerated ageing behaviour of the adhesive bond between concrete specimens and CFRP overlays", *Constr. Build. Mater.*, 25(2), 523-538.
- S. Chataigner, J.F. Caron, K. Benzarti, M. Quiertant, C. Aubagnac (2011), "Use of a single lap shear test to characterize composite-concrete or composite-steel bonded interfaces", *Constr. Build. Mater.*, 25(2), 468-478.
- F. Djouani et al. (2011), "Cement paste-epoxy adhesive interactions", *Constr. Build. Mater.*, 25(2), 411-42.

Composite Structures



EXPERIMENTAL AND ANALYTICAL STUDY OF GFRP AND UFC COMPOSITE BEAMS

I. S. K. Wijayawardane¹ and H. Mutsuyoshi²

¹ Saitama University, Department of Civil & Environmental Engineering, Saitama and Japan, Email: isuruwijayawardane@gmail.com

² Saitama University, Department of Civil & Environmental Engineering, Saitama and Japan.

ABSTRACT

Glass fiber reinforced polymer (GFRP) and ultra-high strength fiber reinforced concrete (UFC) composite beams are a good alternative for short-span bridge girders located in severe corrosive environments. The outstanding features of GFRP include high corrosion resistance, high fatigue resistance, low density, and high tensile strength. The use of UFC slab on the GFRP I-beams can avoid premature delamination failure and increase both flexural strength and stiffness of the GFRP I-beams. However, the relatively low stiffness of the GFRP I-beams becomes one of the critical design limitation of GFRP bridges. The American Association of State Highway and Transportation Officials (AASHTO) and the Japan Society of Civil Engineers (JSCE) suggest that the deflection limit for pedestrian bridges should be less than $L/500$, where L corresponds to the bridge span. Therefore, it is important to analyze the flexural behavior of GFRP-UFC composite beams prior to their application on a real bridge. This paper describes the analysis of GFRP-UFC composite beams using a simple fiber model, which is economical and less time-consuming. Large-scale four-point bending tests were conducted on GFRP-UFC composite beams having different beam parameters and the experiment results were compared with the fiber model analysis results. The fiber model results were agreed well with the experiment results.

KEYWORDS

Hybrid structures, FRC and cement composite materials, Characterization of FRP and FRC materials/ systems, Fiber model analysis, Flexural behavior, Deflection limit.

INTRODUCTION

The excellent durability, low-weight, high fatigue resistance and high tensile strength of fiber reinforced polymer (FRP) make them suitable for construction of pedestrian bridges (Foster et al. 2000; Hayes et al. 2000). As the FRP has relatively low stiffness and high initial cost compared to prestressed concrete and steel, they are much suitable for short-span bridges. It is more economical to use FRP-concrete composite beams for bridge girders, rather than only the FRP I-beams, because of the elimination of the premature delamination failure of the compression flange (Hai et al. 2010). On the other hand, the structural design of FRP bridges is governed mostly by the deflection limitation due to the relatively low stiffness of FRP composites and the use of concrete can improve the stiffness of the FRP I-beams. According to the American Association of State Highway and Transportation Officials (AASHTO) and the Japan Society of Civil Engineers (JSCE), the deflection limit for pedestrian bridges should be less than $L/500$, where L corresponds to the bridge span (AASHTO 2008; JSCE 2011). Authors developed a composite beam using glass FRP (GFRP) and ultra-high strength fiber reinforced concrete (UFC) and found that the UFC slab significantly improves the stiffness of the GFRP I-beam (Wijayawardane et al. 2014). In GFRP-UFC composite beam, precast UFC slab was fixed to the I-beam using steel bolts and epoxy adhesive. Durability of the GFRP-UFC composite beam was further improved by replacing the steel bolts by FRP bolts.

In this study, the experiments were carried out to investigate the flexural behavior of the GFRP-UFC composite beams. A simple fiber model was used to verify the experiment data and it was used to predict the flexural behavior of real-scale short-span pedestrian bridge girder.

EXPERIMENT METHODOLOGY

Materials

GFRP I-Beam

Pultruded GFRP I-beams consist of glass fibers oriented in the directions of 0° , 90° and $\pm 45^\circ$, GFRP continuous strand mat (CSM) and vinylester resin. In CSM, glass fibers are randomly oriented. Overall length and height of the GFRP I-beam is 3,500 mm and 250 mm respectively. The flange is 14 mm in thickness and 95 mm in width

and the web is 9 mm in thickness. The mechanical properties of the GFRP flanges and GFRP web are shown in Table 22.

UFC has a densely packed microstructure compared to ordinary concrete and hence, it's considered as a durable material compared to reinforced or prestressed concrete. UFC segments used for the GFRP-UFC composite beam were precast and they consisted of steel fibers, premixed cementitious powder (ordinary Portland cement, Silica fume and Ettringite), water, sand and water reducing agent. The high strength steel fibers were of 0.2 mm in diameter and the lengths were 22 mm and 15 mm. Equal amounts of fibers from each length were used for UFC. The tensile strength of steel fibers was 2,000 MPa and they were added at approximately 1.75% volume ratio. The mix proportions of the materials in UFC can be found in Wijayawardane et al. (2016). The size of UFC segments used for this study is 300x95x35 mm. The mechanical properties of the UFC are given in Table 22.

Table 22: Mechanical properties of GFRP flanges, GFRP web and UFC

Property	GFRP Flange	GFRP Web	UFC
Compressive strength (MPa)	252	299	173
Tensile strength (MPa)	448	185	14.3
Young's modulus (GPa)	20.2	17.8	48.6

FRP bolts and epoxy adhesive

FRP bolts and epoxy adhesive were used as a connecting material of UFC segments to the top flange of the GFRP I-beam. The reason for using FRP bolts instead of steel bolts is to improve the corrosion resistance of the GFRP-UFC composite girder in severe environments. Two sizes of FRP bolts (10 mm and 16 mm diameter) were used in this experiment and all the FRP bolts were embedded into the precast UFC segments. Tensile strength and shear strength of the bolts are 160 MPa and 140 MPa, respectively. The shear capacity of the epoxy adhesive is 9.6 MPa.

Test Variables

Beam flexural tests were carried out on five different GFRP-UFC composite beams and the test variables are given in Table 23. The main test variables of the beam test were bolt type, bolt diameter and bolt spacing. Three different bolt types were used in the study, 1) 16 mm diameter FRP threaded bars (no bolt-heads, in beam G10-F16-B4), 2) 16 mm diameter FRP bolts with head (in beams G10-F16-BN4 and G10-F16-BN6), 3) 16 mm diameter steel bolts. In order to check the effect of bolt diameter on the flexural capacity of the composite beam, 10 mm diameter FRP bolts were used in G10-F10-BN6. The beams G10-F16-BN6 and G10-F16-BN4 were used to compare the effect of bolt spacing.

Table 23: Test variables

Specimen name	Bolt type	Bolt spacing (mm)	FRP bolt diameter (mm)	Bolt-head in the UFC
G10-F16-B4	FRP	150	16	No
G10-F10-BN6	FRP	100	10	Yes
G10-F16-BN4	FRP	150	16	Yes
G10-F16-BN6	FRP	100	16	Yes
G10-S16-BN4	Steel	150	16	Yes

Notation G10-X##-BN*
X: Bolt type (F = FRP; S = Steel) ##: Bolt diameter (16 mm or 10 mm)
B: FRP threaded bar BN: Bolt with head (FRP bolt or steel bolt)
*:Number of bolts per UFC segment (4 or 6)

The cross-sectional details of a GFRP-UFC composite beam and the details of four-point bending test set up are shown in Figure 48 and Figure 49, respectively. All the beams had a flexural span and shear spans of 700 mm and 1,250 mm, respectively. As shown in Figure 49, seven strain gauges were attached at the midspan section of the beams and nine GFRP stiffeners were attached to each sides of the composite beam to avoid local buckling. Monotonic load was applied on each specimen by a manually controlled hydraulic jack until the beam failure and at each loading step, the midspan deflection and strain at the midspan section were recorded.

RESULTS AND DISCUSSIONS

There were two main failure patterns in the GFRP-UFC composite beams, shown in Figure 50. A brittle failure was observed in beams having high flexural capacity as well as high stiffness (G10-F16-B4 and G10-F10-BN6) and the cause of failure was crushing of UFC segments in the bending span (Figure 50a). Beams G10-F16-BN4, G10-F16-BN6 and G10-S16-BN4 failed due to crushing of UFC segments, followed by crushing of the GFRP flange and web as shown in Figure 50b.

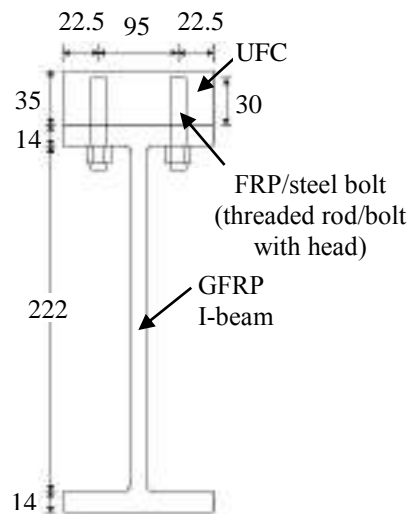


Figure 48: Cross-section of GFRP-UFC composite beam (units in mm)

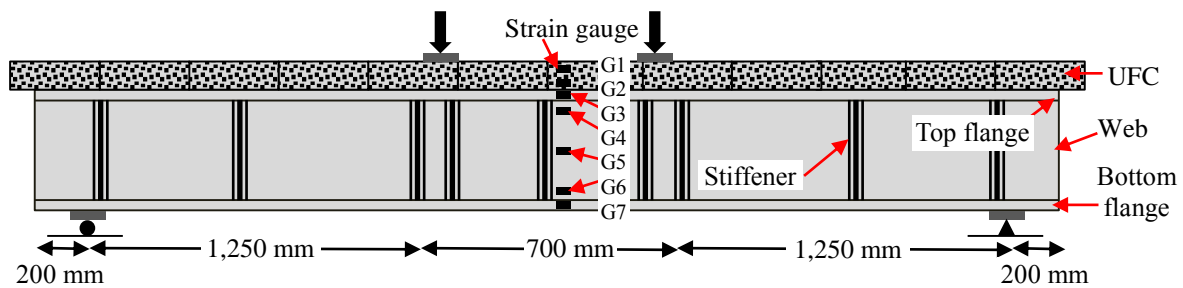


Figure 49: Bending test setup



(a) UFC crushing



(b) Crushing of UFC and GFRP I-beam

Figure 50: Failure patterns of GFRP-UFC composite beams

Figure 51 shows the load-deflection relationship of all specimens. The deflection was measured at the midspan section of beams. Authors conducted four-point bending test on GFRP I-beam and the flexural capacity of the GFRP I-beam without concrete slab was 109 kN (Wijayawardane et al. 2014). This confirms, with the installation of the UFC slab, the flexural capacity of the GFRP I-beam was significantly increased despite the bolt type, bolt spacing and bolt diameter (all specimens in Figure 51 have flexural capacity more than 150 kN). Experiment results show that the beams G10-F16-B4, G10-F10-BN6, G10-F16-BN6, and G10-S16-BN4 have higher flexural

capacities, (approximately 25% to 30%) compared to that of beam G10-F16-BN4 (Figure 51). This concludes that the flexural capacity of the GFRP-UFC composite beams having FRP bolts varies with the availability of the bolt head and the bolt spacing. The beam with least stiffness is G10-F16-BN6 and the main reason for this low stiffness compared to other beams with larger bolt spacing is, when the volume of FRP bolt material (weaker material compared to UFC) becomes larger in the UFC slab, the stiffness of the overall slab decreases. As shown in Figure 51, the beams G10-F10-BN6 (beam with 10 mm diameter FRP bolts) and G10-F16-B4 (beam without FRP bolt-heads) had the highest stiffness because of their FRP bolt content in the UFC slab was lower than other beams. The stiffness and flexural capacity of G10-F10-BN6 and G10-F16-B4 was as good as the stiffness of the GFRP-UFC composite beam with 16 mm diameter steel bolts (G10-S16-BN4).

Figure 52 shows the strain variation across the midspan section in beams G10-F16-B4 (FRP threaded bars) and G10-S16-BN4 (steel bolts). Section depth is the distance to the strain gauge from the bottom of the GFRP-UFC composite beam. It is clear that both beams have almost similar strain variation across the midspan section even though the bolt types are different. The neutral axis of both beams was around 210 mm from the beam bottom. Therefore, the FRP threaded bars can be used for GFRP-UFC composite beams instead of steel bolts and the corrosion resistance of the beam can be improved.

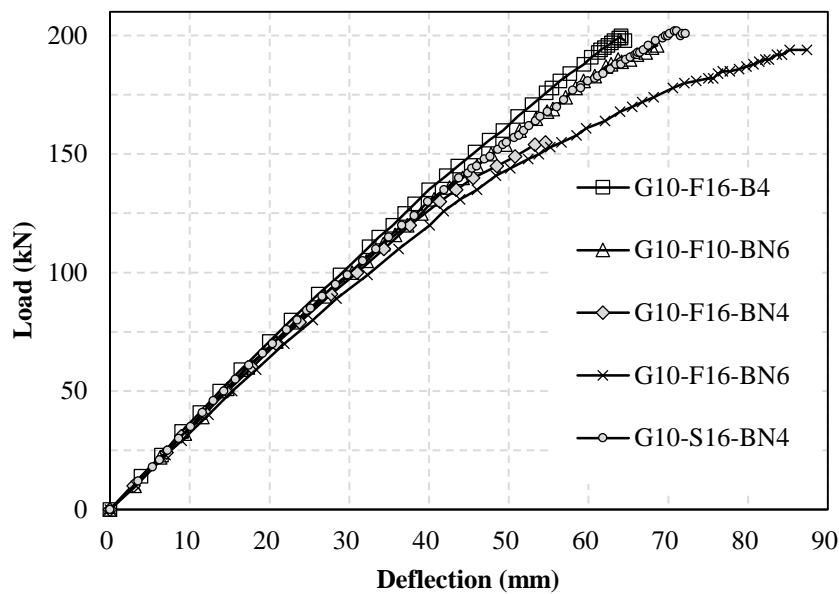


Figure 51: Load-deflection relationship

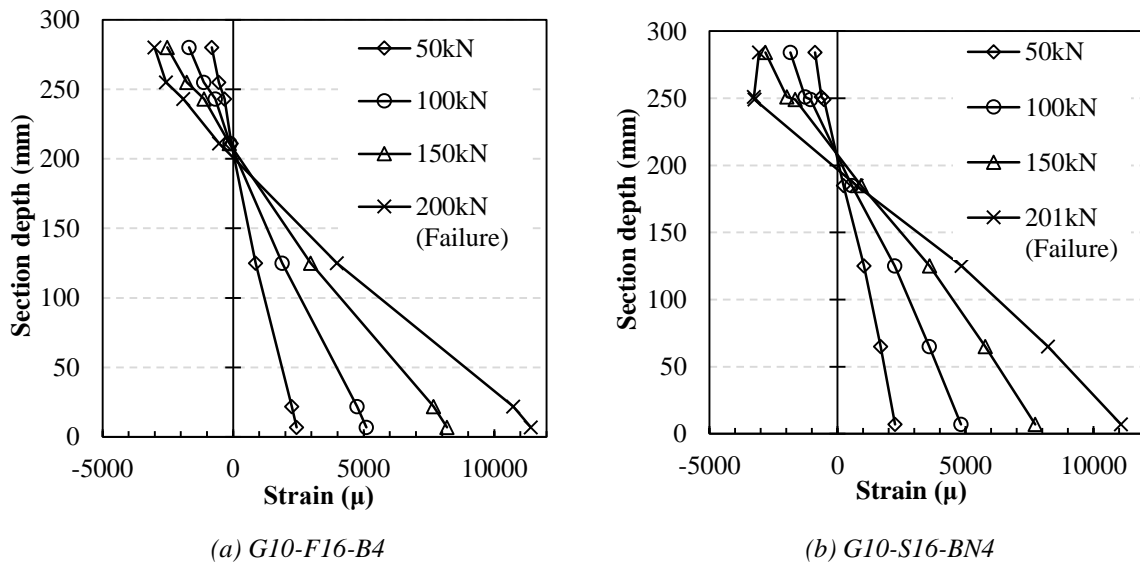


Figure 52: Strain variation across midspan cross-section

FIBER MODEL ANALYSIS (FMA)

The fibre model analysis (FMA) is a one dimensional model and it is comparatively less time-consuming and cost-effective compared to the commercial finite element software packages. It has been used successfully by researchers to analyse the flexural behaviour of FRP-concrete composite beams (Wijayawardane et al. 2016; Manalo and Aravinthan 2012). The flexural behaviour of the GFRP-UFC composite beams was predicted using FMA and verified by the experimental results.

In the FMA, the composite beam is divided into ‘ m ’ longitudinal segments along the span ($m = a + 2b$), in which, ‘ a ’ and ‘ b ’ are the number of longitudinal segments in the midspan and a shear span, respectively. The midspan cross-section is divided into ‘ n ’ discrete horizontal elements. The following assumptions were made in the analysis: 1) GFRP-UFC composite beam behaves under Euler-Bernoulli beam theory; 2) there is full interaction between the UFC segments and the GFRP I-beam top flange until beam failure and hence, there is no slip at the UFC-GFRP interface. Two material models were used for the analysis: 1) UFC bi-linear model proposed by Japan Society of Civil Engineers (JSCE 2004); and 2) GFRP model (developed using material test results).

Initially, the compressive and the tensile strains of top and bottom elements (ε_c and ε_t) at the midspan section are assumed in the fibre model. The average strain at the centre of i^{th} element (ε_i) is given by Eq. 1, where d_i denote the distance to the centroid of the i^{th} element from the beam top (Eq. 2).

$$\varepsilon_i = \varepsilon_c - \frac{d_i(\varepsilon_c + \varepsilon_t)}{h} \quad (1)$$

$$d_i = \frac{h(i - 0.5)}{n} \quad (2)$$

The stress in each element of the GFRP-UFC beam cross-section is calculated using the element strains and the material models corresponding to the beam temperature being considered. The force equilibrium is checked using Eq. 3, where ΣF_c and ΣF_t are the resultant compressive and tensile forces acting on the GFRP-UFC cross-section, respectively.

$$\sum F_c - \sum F_t = 0 \quad (3)$$

If Eq. 3 is not satisfied, an iterative method is used in the fibre model to achieve the force equilibrium. Once force equilibrium is obtained, the resultant moment (M) and the curvature (ϕ) are calculated using Eqs 4 and 5, where, F_i is the element force of the i^{th} element.

$$M = \sum F_i d_i \quad (4)$$

$$\phi = \frac{\varepsilon_c + \varepsilon_t}{h} \quad (5)$$

The average curvature of each section of the longitudinal segments (ϕ_j) is calculated and then the maximum deflection at the midspan (δ_{max}) is calculated according to Eq. 6, where l_j denote the length of the longitudinal segment.

$$\delta_{max} = \sum_{j=1}^{0.5a+b} \phi_j l_j \quad (6)$$

In FMA, loop calculations are carried out by increasing the ε_c and ε_t until the ultimate compressive strain of the UFC is reached.

FMA for GFRP-UFC Composite Beams

The fiber model analysis was carried out for beams G10-F16-B4 and G10-F16-BN4 and the results are shown in Figure 53. The difference between these two beams is, in G10-F16-B4 FRP threaded bars are used whereas in 10-F16-BN4, FRP bolts with heads are used. FMA results of beam G10-F16-B4 showed good agreement with the experiment results. However, in beam G10-F16-BN4, the stiffness of the beam was a little bit over estimated by the FMA. The main reason for this is, in the fiber model analysis, a perfect bond between the UFC and the GFRP I-beam flange is assumed, whereas the test specimens may experience some deformation at the bond interface. According to the analytical results, the difference in failure loads between the analysis and the experiment was less than 5%.

FMA for Real-scale Short-span Pedestrian Bridge Girder

The GFRP-UFC composite beams similar to G10-F16-B4 beam was used to construct short-span pedestrian bridge in Japan. Because of the governing design criteria for FRP composite bridges is the deflection limitation, the GFRP-UFC composite beam’s deflection was checked with the allowable deflection limit ($l/500$) stated by JSCE (2011) and AASHTO (2008). Two GFRP-UFC composite beams (6,000 mm long) were used in the pedestrian bridge and the overall length and width of the bridge is 6,000 mm and 960 mm, respectively. The cross-sectional

dimensions of the GFRP-UFC composite beams are same as in Figure 48, except the GFRP I-beam flange width and the UFC slab width. The flange width is 160 mm and the UFC slab width is 960 mm. The UFC slab is used as the deck of the pedestrian bridge. Figure 54 shows the GFRP-UFC pedestrian bridge in Miyagi prefecture, Japan.

Before construction of the bridge, proposed FMA was used to check the flexural behaviour of a GFRP-UFC composite beam within the serviceability limit state. In this case, half of the bridge was taken into account for calculating the design loads. As recommended by the Japan Highway Association (1979), a 3.5 kN/m² design live load on each GFRP-UFC composite beam and a 5.0 kN/m² design live load on the floor area of the bridge were applied. The allowable deflection limit for the GFRP-UFC composite beam is 12 mm. Figure 55 shows the FMA analysis results of a GFRP-UFC composite beam in the pedestrian bridge within the serviceable limit. The GFRP-UFC composite beam satisfied the design requirement and hence it was used for the pedestrian bridge.

In the pedestrian bridge, there was GFRP used for both handrails and for bracings (Figure 54). Prior to install the bridge on-site, a load test was conducted on the bridge. An eccentric distributed load was applied along the bridge by standing twelve people on the bridge (Figure 56). The load-deflection relationship of the mostly deflected beam is shown in Figure 57. The design load on the bridge was calculated according to the loading suggested by Japan Highway Association (1979) and the allowable deflection of the bridge (12 mm) was checked. In order to determine the maximum deflection at the design load, the load-deflection curve (obtained from the loading test) was extended Figure 57. The calculated maximum deformation was less than the allowable limit.

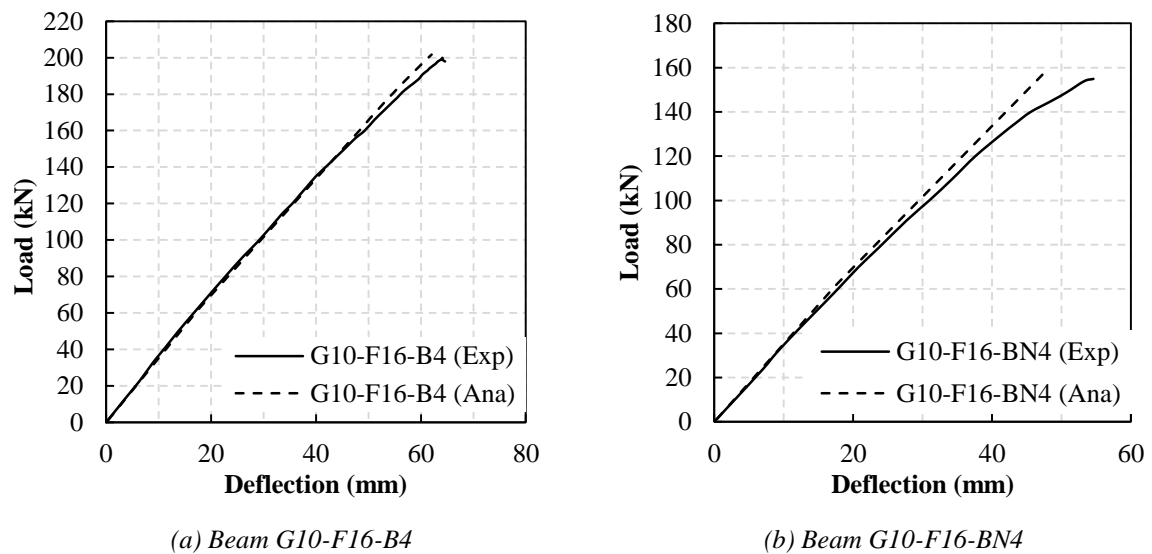


Figure 53: Comparison of load-deflection relationship of FMA and experiment



Figure 54: GFRP-UFC pedestrian bridge, Miyagi prefecture, Japan

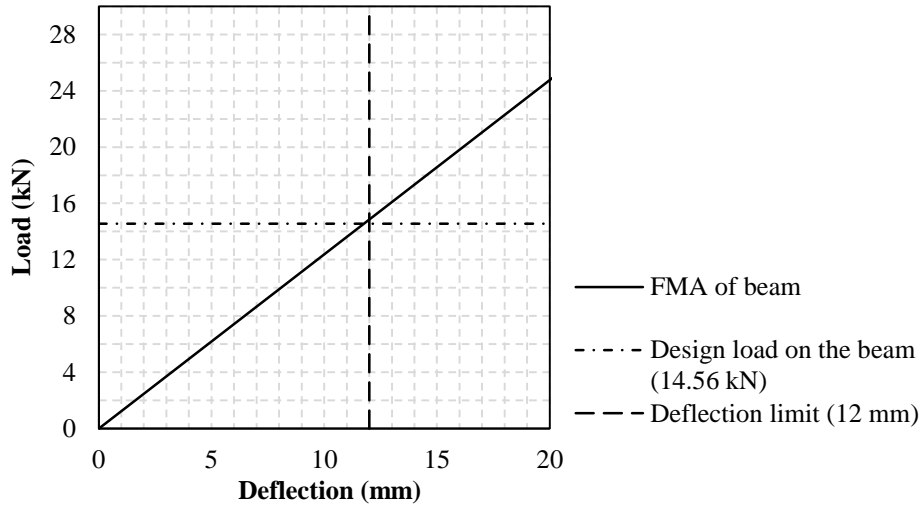


Figure 55: FMA analysis results of a GFRP-UFC composite beam in the pedestrian bridge



Figure 56: Eccentric distributed loading on the bridge

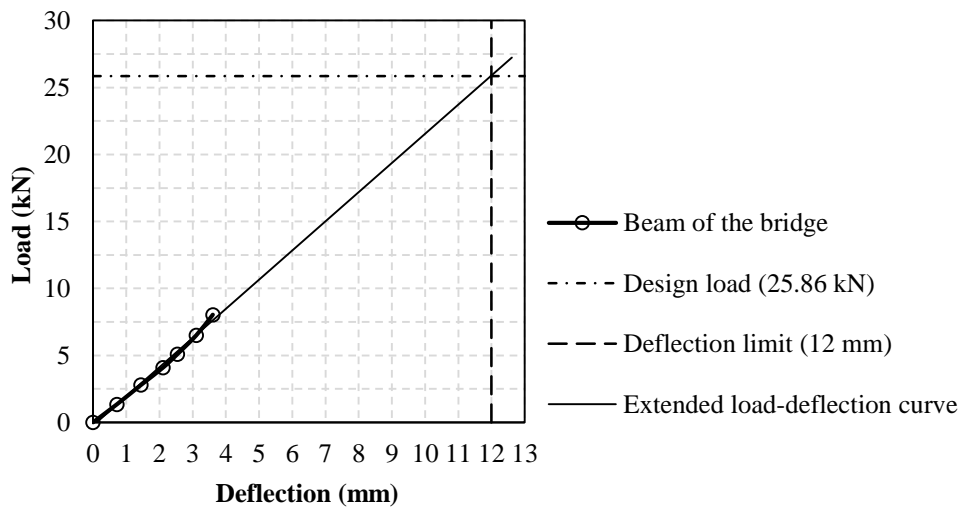


Figure 57: Load-deflection relationship of the pedestrian bridge

CONCLUSIONS

Main conclusions of the study are given below.

- A
- B
- C

ACKNOWLEDGMENTS

Authors would like to thank all members of the FRP research group at Saitama University, who provided support for the successful implementation of the experiments. The authors gratefully acknowledge the financial support of the Japan Ministry of Economy, Trade, and Industry for this research project. They thank the Fukui Fibertech Company for providing FRP materials.

REFERENCES

- AASHTO (2008). Guide specifications for design of FRP pedestrian bridges (1st edition), American Association of State Highway and Transportation Officials (AASHTO), Washington, USA.
- JSCE (2011). Guidelines for Design and Construction of FRP Footbridges, Japan Society of Civil Engineers (in Japanese).
- Foster, D. C., Richards, D., and Bogner, B. R., Design and installation of fiber-reinforced polymer composite bridge, *Journal of Composites for Construction*, 2000, Vol. 41, pp. 33–37.
- Hayes, M. D., Lesko, J. J., Haramis, J., Cousins, T. E., Gomez, J., and Masarelli, P., Laboratory and field testing of composite bridge superstructure, *Journal of Composites for Construction*, 2000, Vol. 43, pp. 120–128.
- Hai, N.D., Mutsuyoshi, H., Asamoto, S. and Matsui, T. (2010). "Structural behavior of hybrid FRP composite I-beam", *Construction and Building Materials*, Vol. 24, No. 6, pp. 956-969.
- JSCE (2004). *Recommendations for Design and Construction of Ultra High Strength Fiber Reinforced Concrete Structures (Vol. 9)*, JSCE Guidelines for Concrete, Japan Society of Civil Engineers Tokyo, Japan, pp. 1-106.
- Manalo, A. and Aravinthan, T. (2012). "Behaviour of glued fibre composite sandwich structure in flexure: Experiment and Fibre Model Analysis", *Materials & Design*, Vol. 39, pp. 458-468.
- Wijayawardane, I.S.K., Mutsuyoshi, H. and Perera, S.V.T.J. (2014). "Innovative composite girders using FRP I-beams and precast UFC slab segments", *Proceedings of 7th International Conference on FRP Composites in Civil Engineering (CICE)*, Vancouver, Canada.
- Japan Highway Association (1979). *Technical Standard for Solid Crossing Facilities* (in Japanese). Japan.



FLEXURAL BEHAVIOUR OF AN INNOVATIVE CONNECTION FOR STRUCTURAL SANDWICH PANELS

R. Lameiras¹, J. Barros², I.B. Valente² and M. Azenha²

¹ University of Brasília – UnB, Campus Darcy Ribeiro, FT-ENC, Brasília, Brazil, email: rmlameiras@unb.br

² University of Minho, Campus de Azurém, Guimarães, Portugal

ABSTRACT

This paper presents the results of an experimental work conducted with composite beam specimens that are part of a series of feasibility studies for a new type of shear connector, called PERFOFRP. The connector is applied in Steel Fibre Reinforced Self-Compacting Concrete (SFRSCC) structural sandwich wall panels. PERFOFRP consisted of a flat Glass Fibre Reinforced Polymer (GFRP) plate with aligned holes evenly distributed along its length. The perforated part of connector is embedded in the outer concrete layers and the connection is materialized by the combined effects of friction/adhesion and mechanical interlock between the perforated laminate and the concrete dowels formed by the concrete that pass through the holes. In previous works, the authors this paper investigated the mechanical behaviour of connections made with PERFOFRP connectors under transversal loads. The flexural behaviour of sandwich panels produced with the PERFOFRP connectors is a subject that has not yet been reported. In such context, this paper pertains to research on the overall mechanical behaviour of the connection under flexure with explicit focus on: failure modes, stiffness and ultimate flexural capacities of composite beams. Further focus is given to the impact of using connectors made with two different types of GFRP laminates on the mechanical behaviour of composite beams.

KEYWORDS

Hybrid structures, Characterization of FRP and FRC materials/systems, Sandwich panel, Connector, PERFOFRP, Flexural behaviour.

INTRODUCTION

A concrete structural sandwich wall, as envisaged here, is basically a three-layered concrete-insulation-concrete panel in which the outer concrete layer usually resists the external horizontal loads (i.e.: wind and mechanical impacts) and the internal concrete layer generally acts together with the external layer to resist the horizontal loads and usually also withstand eventual vertical loads due to the slabs and their use. An essential component of a concrete sandwich panel is the connection between the concrete layers. The connections must be capable to transmit all the stress components between this two concrete layers, where the in-plane shear and the longitudinal stress components are paramount governing design factors.

In the search for improved thermal efficiency of sandwich panels, different types of Fibre-Reinforced Polymer (FRP) connectors have been proposed by several researchers for reinforced/prestressed concrete sandwich panels (Einea, 1992, Salmon et al., 1997, Davies, 2001, Rizkalla et al., 2009, Benayoune et al., 2008, PCI, 2011, Tomlinson, 2015), and some of them are even commercially available (Naito et al., 2012, PCI, 2011).

In 2013, the authors of this paper proposed an innovative sandwich panel consisting on Steel Fibre Reinforced Self-Compacting Concrete (SFRSCC) outer layers connected by Glass Fibre Reinforced Polymer (GFRP) perforated plates, hereinafter referred as PERFOFRP connectors (Lameiras et al., 2013a, Lameiras et al., 2013b, Lameiras et al., 2018). The interest of this innovative connection system lies in two major aspects: first, the GFRP is a material characterized by its relatively low thermal conductivity, avoiding the thermal bridges and, consequently, increasing the thermal efficiency of the sandwich wall panel, and, secondly, the plate geometry of this connector allows for effective and competitive production methods for the prefabrication of sandwich panels of better quality and lower price when compared with the traditional solutions.

This paper reports the results of experimental tests executed to assess the mechanical effectiveness of the connections between PERFOFRP and SFRSCC in loading conditions representative of the real application. For a better understanding of the structural behaviour of the panels, this paper centres efforts for assessing the influence of the use of two distinct types of GFRP on the ductility and strength capacity of connections under flexure.

METHODS

Six composite small scale beam specimens subjected to a symmetrical two-point load were tested at the Laboratory of the Structural Division of the University of Minho. Details about the specimens, materials and experimental procedure are provided in the following sections.

Geometry and Materials

Each specimen consisted of a sandwich beam with length of 1245 mm and rectangular cross-section with overall thickness of 180 mm and width of 200 mm. Each specimen was composed of three layers with 60 mm thickness: the outer layers are made by Steel Fibre Reinforced Self-Compacting Concrete (SFRSCC), while the core layer is constituted by Expanded Polystyrene (EPS). The arrangement of the layers, their thickness and the materials were chosen to be representative of the sandwich wall panels previously optimized through parametric studies based on numerical simulations (Lameiras et al., 2013b). The SFRSCC layers were connected with a continuous PERFOFRP connector positioned in the middle of the beam's cross section along all its length, as shown in Fig. 1.

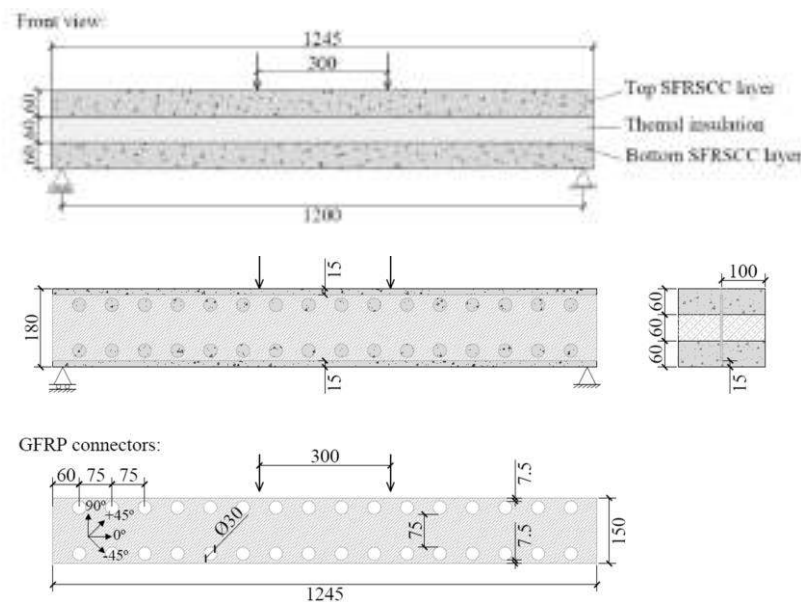


Figure 58: Geometry of test specimen (units in millimetres).

The PERFOFRP connector used in this work was designed to have the same hole diameter (30 mm) and spacing used in the connectors previously tested under pull-out and push-out loads (Lameiras et al., 2018). The diameter of holes (30 mm) and the SFRSCC cover thickness (15 mm) was determined for assuring the passage of the fresh SFRSCC through the holes and the gap between the connector and the formwork, without the occurrence of segregation of aggregates and fibres. This thickness aims to protect the GFRP connector, and also to avoid the formation of a visible line on the external surfaces of the panel coinciding with the location of the connector (due to the different physical properties of GFRP and SFRSCC). Indeed, the occurrence of these lines would have negative impact on the appearance of the panel. The diameter of the holes, as well as the cover thickness of 7.5 mm have taken into account the stress concentration and failure modes observed in the pull-out and push-out tests (Lameiras et al., 2018).

The SFRSCC consisted of ordinary Portland cement (413 kg/m³) type CEM I 42.5 R according to EN 197-1: 2011 (European Committee for Standardization, 2011), fine river sand (233 kg/m³), coarse river sand (700 kg/m³), limestone filler (353 kg/m³), crushed limestone coarse aggregate with 12 mm maximum size (582 kg/m³), water (148 kg/m³), SIKA ViscoCrete 3005 superplasticizer (7.83 kg/m³) and hooked-end steel fibres (60 kg/m³). The steel fibres were characterized by a length (L_f) equal to 35 mm, a diameter (d_f) equal to 0.55 mm, and an aspect ratio ($\lambda_f = L_f/d_f$) of 65. According to the data given by the supplier, their yield stress ranges between 1244 and 1446 MPa. The compressive characteristics of the SFRSCC were determined from seven 150 × 300 mm diameter × height cylinders tested after 31 days of curing. The average compressive strength (f_{cm}) was 45.27 MPa (CoV of 1.0%), obtained following the procedures given in EN 12390-3 (CEN, 2009). An average modulus of elasticity (E_c) of 34.20 GPa (CoV of 1.1%) was obtained. The flexural-tensile behaviour of SFRSCC was obtained from five notched three-point beam tests (3PBTs) performed on prisms of 150 mm square cross section and 600 mm length, following the recommendations of RILEM TC 162-TDF (RILEM TC 162-TDF, 2000) in terms of the loading and casting procedures. From the three point notched beam tests (3PBTs), the following results were determined: limit of proportionality ($f_{ict,L}$); equivalent ($f_{eq,2}$ and $f_{eq,3}$) and residual (f_{Ri} , with $i=1$ to 4) flexural

tensile strength parameters. The f_{R1} , f_{R2} , f_{R3} and f_{R4} is the flexural stress corresponding to the CMOD of 0.5, 1.5, 2.5 and 3.5 mm, respectively, as recommended by the *fib* Model Code. The average values (coefficient of variation; lower bound value determined with 95% of confidence level) obtained for $f_{ct,L}$, $f_{eq,2}$, $f_{eq,3}$, f_{R1} , f_{R2} , f_{R3} , f_{R4} were, respectively, 5.80 MPa (13.3%; 5.13 MPa), 9.62 MPa (12.4%; 8.57 MPa), 8.10 MPa (15.0%; 7.03 MPa), 9.21 MPa (13.8%; 8.10 MPa), 8.11 MPa (15.4%; 7.02 MPa), 6.82 MPa (15.7%; 5.88 MPa) and 4.13 MPa (19.4%; 3.22 MPa).

According to the data supplied by the manufacturer, the EPS adopted in the middle layer, as an insulating material, has an apparent density of 15 kg/m³.

Two different GFRP laminates were adopted for the PERFOFRP connectors. Both were produced by Vacuum Assisted Resin Transfer Moulding (VARTM), and were made by glass fibre reinforcement and polyester resin matrix. The first laminate, hereinafter called CSM, consisted of five layers of Chopped Strand Mat (CSM) with 450 g/m² of E-glass fibres per each layer. This reinforcement is characterized by short length fibres randomly oriented in its plane. The second laminate, MU4, consisted of bi-axial Stitched Roving Fabric (SRF) and unidirectional mat, with their continuous reinforcement arranged on $\pm 45^\circ$ and 0° directions. The average final thickness of laminates was 2.0 mm for CSM and 4.0 mm for MU4 laminates. Fibre contents, by volume, equal to 41 % and 49 % were determined for CSM and MU4 composites, respectively. The tensile properties of the composites were determined from direct tensile tests performed with six specimens of each type, with the loading direction respect to fibre system orientation represented in the inset of Fig. 2, considered 0° . The direct tensile tests followed the procedures described in ASTM D3039 (ASTM, 2008). The engineering tensile stress was assumed as the ratio between the registered load and the average cross-sectional area of specimen, while the engineering axial strain was determined by attaching a clip-gauge transducer with a reference length of 50 mm to the mid-span of specimen. The ultimate tensile stress, the elastic limit stress, the corresponding strains and the tensile modulus of elasticity obtained in these tests are shown in Table 1. The stress–strain curves obtained from tension coupon tests are represented in Fig. 2. The shear properties of CSM laminate were obtained by testing four specimens in a standard Iosipescu apparatus following the procedures described in ASTM D5379 (ASTM, 2012). Average shear strength of 139.60 MPa, ultimate shear strain of 19510 $\mu\epsilon$ and shear modulus of 3.97 GPa were obtained with coefficient of variation of 1.2 %, 16.4 % and 2.5 %, respectively.

Table 24: Relevant results obtained from the direct tensile tests with CSM and MU4 specimens.

FRP	Dir.	Ultimate tensile stress $\sigma_{pt,u}$		Ultimate tensile strain $\epsilon_{pt,u}$		Elastic limit stress $\sigma_{pt,el}$		Elastic limit strain $\epsilon_{pt,el}$		Tensile modulus of elasticity E_{pt}	
		Avg. [MPa]	CoV	Avg. [$\mu\epsilon$]	CoV	Avg. [MPa]	CoV	Avg. [$\mu\epsilon$]	CoV	Avg. [GPa]	CoV
CSM	-	252.54	8.5%	18029	9.8%	252.54	8.5%	18029	9.8%	14.64	7.4%
MU4	$0^\circ/90^\circ$	183.48	8.5%	26788	2.3%	73.44	4.3%	5016	3.8%	16.70	3.0%

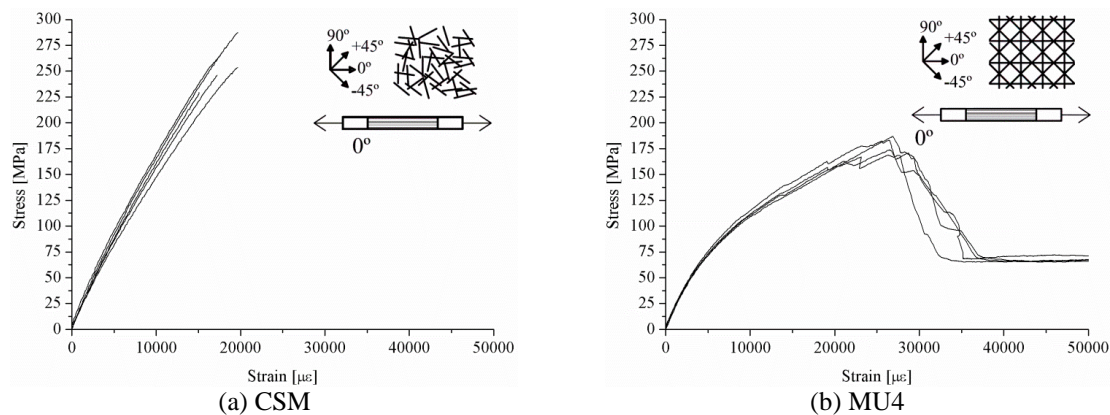


Figure 59: Stress versus strain response obtained in direct tensile tests with specimens representative of PERFOFRP connectors made by different laminates.

Three identical sandwich beams were cast for each type of GFRP used in the PERFOFRP connectors. Initially, the connector was positioned in the middle of each beam. The bottom SFRSCC layer was poured up to the 60 mm

level marked in the wood form. Two EPS blocks with the same length of the beam and 60 mm of thickness were positioned in each side of GFRP connector. The top SFRSCC layer was then poured. All the specimens were covered with plastic foil, and twenty four hours after the casting procedure they were removed from the mould to cure in air until testing. The tests were conducted when the specimens attained an age between 114 and 120 days.

Test setup, instrumentation and test procedure

The beam specimens were tested under the four-point bending loading configuration represented in Fig. 3. The load was applied by a 500 kN hydraulic jack via a load-spreader I-section steel beam and two halves of steel cylinders that were in contact to the top surface along all the width of the beam's cross section. The beams were simply-supported on steel rollers, with a span of 1200 mm. One of the supports had the rotation and sliding released in the direction parallel to the specimen's axis. All the specimens were tested with the beams positioned in the same direction that they were casted, that is, with their rough surface of the top SFRSCC layer upside.

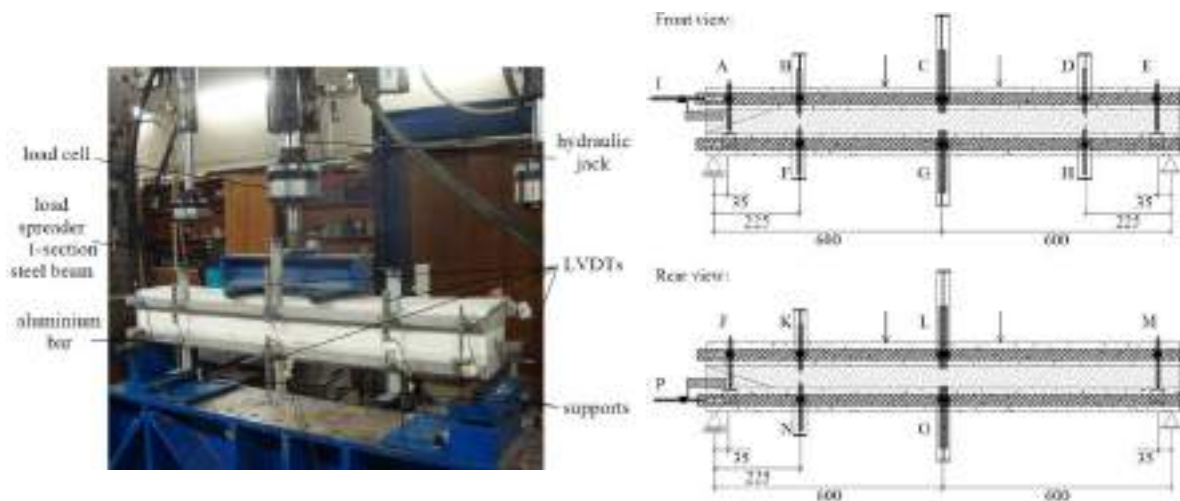


Figure 60: Test setup and instrumentation (units in millimetres).

The load was registered by a 250 kN capacity load cell attached at the extremity of the hydraulic jack (see Fig. 3). The following monitoring system was installed: ten LVDTs for measuring deflections along the beam's span (LVDTs C, G, L and O, with a stroke of ± 50 mm) and at a distance of 225 mm from the supports (B, D, F, H, K and N, with stroke of ± 25 mm). To evaluate possible misalignment of loading application, in the first and second specimens of each series, deflections were obtained in the front and rear sides of beams, as shown in Fig. 3. In the third specimen of each series, deflections were obtained only in the rear side of beam. Deflections were obtained from measurements in the LVDTs fixed to an auxiliary steel bar in order do not include parasitic displacements in measurements (Japan Society of Civil Engineers, 1984). The measurements of deflections of top and bottom SFRSCC layers were made independently. Two LVDTs (stroke of ± 10 mm) were used to measure the end slips (longitudinal direction) between the PERFOFRP and the SFRSCC layers (LVDTs I and P). Four LVDTs (stroke of ± 2.5 mm) were used to measure the relative displacement (i.e.; transversal direction) between the top and bottom SFRSCC layers (LVDTs A, E, J and M). The arrangement of LVDTs is shown in Fig. 3.

A hundred unloading-reloading cycles between 0 to 14 kN were applied at the beginning of testing the third specimen of each series. During the load cycles, the test was load controlled at 1.02 kN/s, and afterwards the test was controlled by deformation at 0.005 mm/s. The loading was conducted until the specimen's load carrying capacity drops at least 50% of its maximum capacity. All measurements made by the load cell and LVDTs were registered continuously along all the test at a rate of 2 Hz.

RESULTS AND DISCUSSION

The experimentally obtained cracking load, maximum applied load and maximum midspan deflection for each specimen are summarized in Table 2. The load-deflection curves are shown in Fig. 4.

Table 25: Cracking load, maximum applied load and midspan deflection corresponding to the maximum applied load.

Specimen Ref.	Cracking load			Maximum applied load			Midspan deflection corresponding to the maximum applied load		
	Value	Avg	CoV	Value	Avg	CoV	Value	Avg	CoV
	[kN]		[%]	[kN]	[%]		[mm]		[%]
CSM 01	15.5			25.4			1.62		
CSM 02	14.3	14.7	5	28.3	26.1	7	1.77	1.6	12
CSM 03	14.2			24.7			1.40		
MU4 01	15.7			32.2			17.33		
MU4 01	15.6	15.6	1	27.9	29.6	8	17.01	16.2	11
MU4 03	15.5			28.8			14.11		

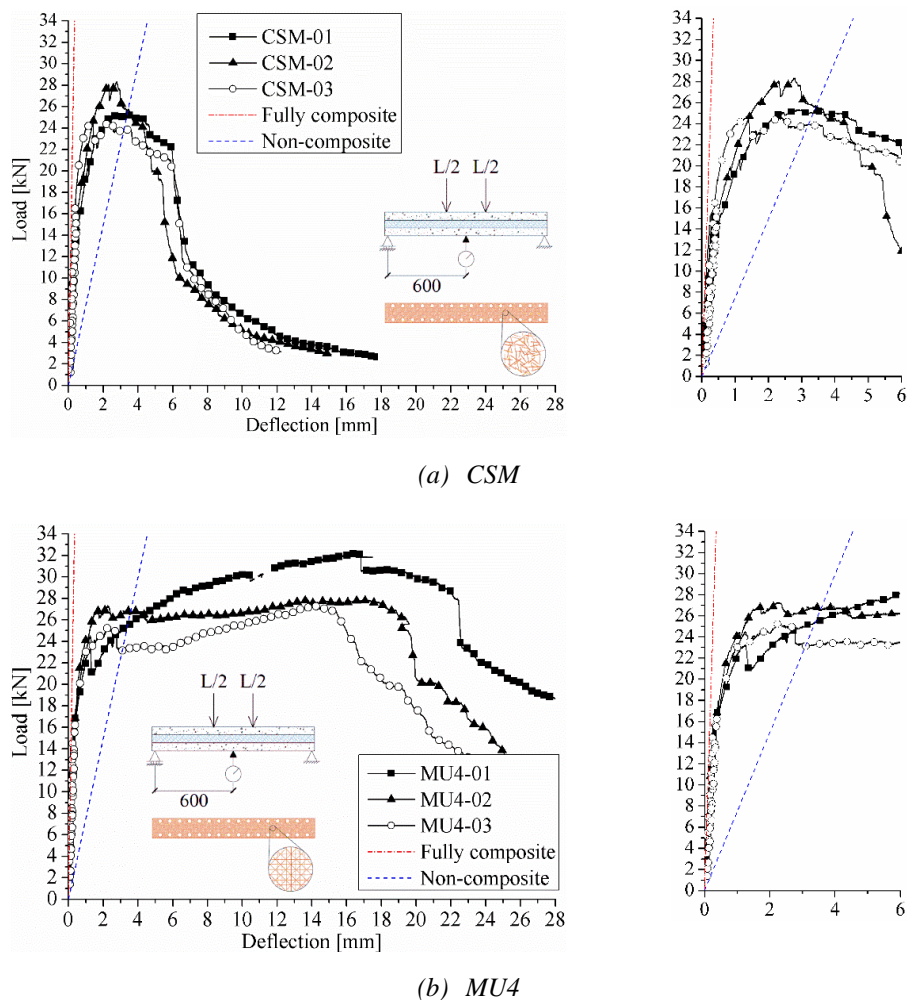


Figure 61: Average load-midspan deflection curves for CSM and MU4 specimens.

The deflections calculated for the upper concrete layer were obtained as the measured deflection diminished by the average vertical displacement recorded in the support ends (recorded in the LVDTs A, E, J and M). All the specimens of each group presented similar experimental responses. In general, the responses are characterized by an initial linear branch until the occurrence of the first crack, after which the initial stiffness of the specimen has decreased. Flexural cracks were first observed at the bottom and front sides of the bottom SFRSCC layer. The average cracking load was 14.7 kN (st. dev. equal to 0.74 kN) and 15.6 kN (st. dev. equal to 0.16 kN) for specimens made with CSM and MU4 laminates, respectively. These cracks progressed transversely

across the underside of the bottom SFRSCC layer, and were located in the “pure” bending zone. Other hairline cracks occurred in the bottom SFRSCC layer within the flexure/shear spans.

At this stage, for CSM specimens, these cracks propagated progressively towards the top of the bottom SFRSCC of sandwich panel. Then, some hairline cracks also appeared in the bottom face of the top SFRSCC layer. The CSM specimens attained an average maximum load of 26.08 kN. For a deflection just after the one corresponding to the peak load a louder sound was heard, and the width of one of the cracks that appeared in the bottom SFRSCC layer started to increase, while the other cracks almost ceased to propagate. Then, the load was decreasing pronouncedly with the increase of the deflection.

For the MU4 specimens, after the cracks in the top SFRSCC layer have formed, a longitudinal crack appeared in the upper surface of the top SFRSCC layer, aligned with the PERFOFRP connector. Subsequently, this longitudinal crack extended over the length of the beam, and the crack opening has increased. Thereafter, new cracks opened in the top SFRSCC layer, and similar to what occurred for the CSM specimen, a loud sound was emitted, and one of the cracks of the bottom SFRSCC layer degenerated in a macro-crack. A more intense cracking and wider cracks were also noticed for the specimens made with MU4 connector. The failure of these specimens occurred after a sequence of louder noises, typical of the failure of the GFRP laminates under direct tension. At this stage the load-carrying capacity of sandwich beam dropped suddenly.

After the tests, the specimens were carefully destroyed in order to extract the connectors and analyse their anchorage conditions. The final aspect of some connectors are shown in Fig. 5. After the observation of the final aspect of connectors, the failure of the sandwich beams was therefore attributed to the rupture of the GFRP connectors caused by the propagation of flexural cracks. Similarly to the behaviour of the composites under direct tensile tests (see Fig. 2), the specimen made with CSM connectors presented a more brittle behaviour when compared to the behaviour of specimens with MU4 laminates. Moreover, the first sound heard during the tests was probably related to the failure of the laminates in the region right below the holes. After this rupture the neutral axis of the beam’s cross section in this region naturally was shifted upward. In the case of MU4 connectors, a new equilibrium was attained because the tensile strength of the laminate, together with the post-cracking residual strength of the SFRSCC, were able to carry the higher load transferred to the connector. Nonetheless, for the specimens made with CSM connectors, the smaller ductility of this type of connector conducted to a more abrupt load decay of the beam just after damage initiation in the connector. Fig. 5 evidences that a “discrete crack” was formed in the CSM connector (localized failure), while a damage zone was developed in the MU4 connector (smeared damage).

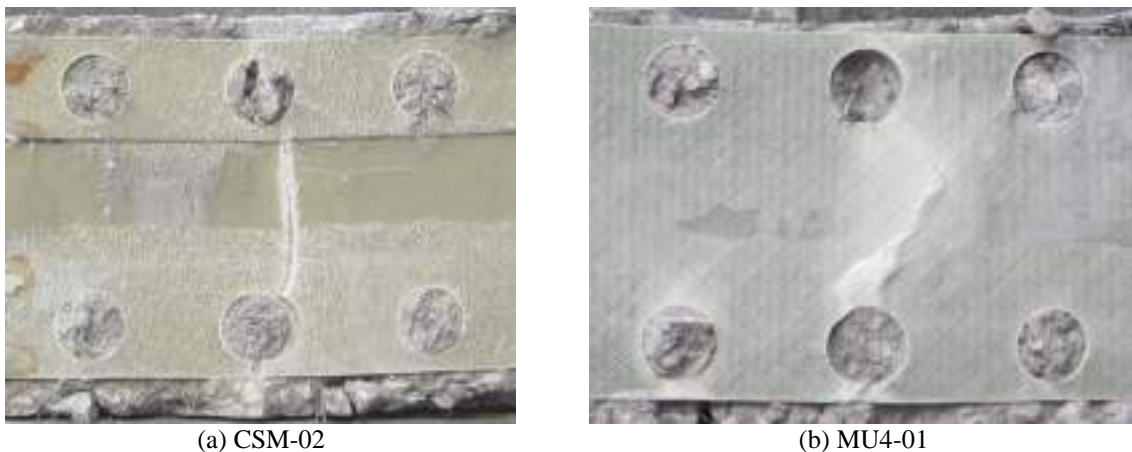


Figure 62: Final aspect of connectors after failure of sandwich beams.

CONCLUSIONS

This paper presented an experimental investigation on the flexural behaviour of connections for sandwich panels containing PERFOFRP connectors and SFRSCC layers. Sandwich beams made with two different types of GFRP connectors (i.e.; CSM and MU4) were tested under four-point bending, and the results were analysed in terms of deflections and failure mechanisms. The main conclusions derived from the experimental investigations are the following ones:

- Independently on the type of laminate used in the connector, the ultimate failure mechanism of the connections under flexure is always associated to the flexural failure of the PERFOFRP connector after an extensive cracking in the SFRSCC layers.
- Although no significant increase on the cracking or ultimate load of the tested sandwich beams were obtained by replacing CSM connector by another stiffer connector, MU4,

the failure mode obtained in the beams made with MU4 laminates was much more ductile.

ACKNOWLEDGMENTS

Authors would like to thank the companies Mota-Engil, Civitest and PIEP. The authors also thank the collaboration of the following companies: Maccaferri for supplying the fibres and BASF for providing the superplasticizer.

REFERENCES

- ASTM 2008. D3039 / D3039M: Tensile properties of polymer matrix composite materials. West Conshohocken, PA: ASTM International.
- ASTM 2012. D5379 - 12: Test method for shear properties of composite materials by the V-notched beam method. West Conshohocken, PA: American Society for Testing and Materials (ASTM).
- BENAYOUNE, A., SAMAD, A. A. A., TRIKHA, D. N., ALI, A. A. A. & ELLINNA, S. H. M. 2008. Flexural behaviour of pre-cast concrete sandwich composite panel – Experimental and theoretical investigations. *Journal of Construction and Building Materials*, 22, 580-592.
- CEN 2009. EN 12390-3. Testing hardened concrete – Part 3: compressive strength of specimens. Lisbon: European Committee for Standardization (CEN).
- DAVIES, J. 2001. *Lightweight sandwich construction*, Wiley-Blackwell.
- EINEA, A. 1992. *Structural and thermal efficiency of precast concrete sandwich panel systems*. Ph.D, University of Nebraska.
- EUROPEAN COMMITTEE FOR STANDARDIZATION 2011. EN 197-1: Cement. Composition, specifications and conformity criteria for common cements.
- JAPAN SOCIETY OF CIVIL ENGINEERS 1984. JSCE-SF4: Method of tests for flexural strength and flexural toughness of steel fibre reinforced concrete. Part III-2 Method of tests for steel fibre reinforced concrete. Concrete library of JSCE.
- LAMEIRAS, R., BARROS, J., AZENHA, M. & VALENTE, I. B. 2013a. Development of sandwich panels combining fibre reinforced concrete layers and fibre reinforced polymer connectors. Part I: conception and pull-out tests. *Composite Structures*, 105, 446-459.
- LAMEIRAS, R., BARROS, J., AZENHA, M. & VALENTE, I. B. 2013b. Development of sandwich panels combining fibre reinforced concrete layers and fibre reinforced polymer connectors. Part II: Evaluation of mechanical behaviour. *Composite Structures*, 105, 460-470.
- LAMEIRAS, R., VALENTE, I. B., BARROS, J. A. O., AZENHA, M. & GONÇALVES, C. 2018. Pull-out behaviour of Glass-Fibre Reinforced Polymer perforated plate connectors embedded in concrete. Part I: Experimental program. *Construction and Building Materials*, 162, 155-169.
- NAITO, C., HOEMANN, J., BEACRAFT, M. & BEWICK, B. 2012. Performance and Characterization of Shear Ties for Use in Insulated Precast Concrete Sandwich Wall Panels. *Journal of Structural Engineering*, 138, 52-61.
- PCI 2011. State-of-the-art of Precast/Prestressed Sandwich Wall Panels (PCI Committee on Precast Sandwich Wall Panels). *Precast/Prestressed Concrete Institute Journal*, 56, 131-175.
- RILEM TC 162-TDF 2000. Bending test. *Materials and Structures*, 33, 3-5.
- RIZKALLA, S., HASSAN, T. & LUCIER, G. 2009. FRP Shear Transfer Mechanism for Precast, Prestressed Concrete Sandwich Load-Bearing Panels.
- SALMON, D. C., EINEA, A., TADROS, M. K. & CULP, T. D. 1997. Full Scale Testing of Precast Concrete Sandwich Panels. *ACI Structural Journal*, 94, 354-362.
- TOMLINSON, D. G. 2015. *Behaviour of partially composite precast concrete sandwich panels under flexural and axial loads*. PhD, Queen's University.



LONG-TIME BEHAVIOUR OF GFRP/CONCRETE HYBRID STRUCTURES

Ibrahim Alachek¹, Nadège Reboul¹, Bruno Jurkiewicz¹

¹Université Claude Bernard Lyon1, Laboratoire des matériaux composites pour la construction LMC², Lyon, France, Email : ibrahim.alachek@univ-lyon1.fr

ABSTRACT

This study presents experimental and numerical investigations about the creep behaviour of a hybrid structure consisting of I-shaped GFRP pultruded profile bonded to a thin deck made of reinforced concrete. The experimental program included flexural creep tests on GFRP I-profiles and on hybrid beams subjected to constant loads equivalent to one-third of their ultimate loads. To assess the influence of environmental conditions on the behaviour and the load-carrying capacity of these beams, other beams were left beside the loaded beams during the test period and they were tested to failure under short term loading at the end of creep tests. The deflections and longitudinal strains over time, at the midspan sections, were measured in natural environmental conditions and recorded for a time duration up to 3500 h. Also, in this study, three-dimensional models based on the linear viscoelastic theory were proposed to study the evolution and distribution of strains and stresses over time for the GFRP and hybrid beams. The results of the sustained-load test show that creep deflection on the order of 33% of the initial static deflection is observed for the hybrid beam after 142 days of loading. It is also found that, for the hybrid beam, the rapid degradation of bond strength, resulted from the combined effect of environmental conditions and applied loading, leads to debonding and subsequently a brutal failure. Furthermore, the finite-element analysis is found to be able to simulate the long-term behaviour of the hybrid beam and help understand the complex changes in the stress state that occur over time. The time-dependent behaviour with the effects of the environmental agents must be considered when designing bonded hybrid structures.

KEYWORDS

Hybrid structures, Creep, Durability, Long-term performance, Bond and interfacial stresses, Glass fibers

INTRODUCTION

Regardless of the polymer nature of the eventual GFRP (Glass Fibre Reinforced Polymer) profile and of the viscoelastic behaviour of concrete (Bažant and Wu 1974), a hybrid beam currently needs to be tested at full-scale under permanent load to validate its structural performance during its service life. This because, till the present time, reasonable doubt exists, in real civil engineering applications such as footbridges, they are not completely sure whether the structural behaviour and performance can remain sufficient to insure the safety of hybrid structures. The available scientific literature consequently does not offer much in the way of information concerning the time-dependent behaviour of GFRP-concrete bonded hybrid beams. There are only two studies reported on the literature about the creep response of GFRP-concrete hybrid structures and in both studies, the hybrid beams were made of GFRP pultrude I-section profiles connected to a thin steel fibre reinforced self-compacting concrete (SFRSCC) slab by M10 steel anchors and a thick epoxy adhesive layer (Mendes et al. 2011; Gonilha et al. 2013). There are not many experimental studies in the area of creep behaviour of hybrid bonded structures. On the contrary, prediction of the deformation and long-term strength of polymeric materials has emerged as an independent scientific endeavour and attracted the interest of many researchers. There have been numerous published studies on the time-dependent behaviour of pultruded GFRP profiles (Mosallam and Bank 1992; Mottram 1993; Sá et al. 2011a, 2011b). In these studies, analytical and numerical methods based on empirical and regressions laws, especially the power laws of Findley were used to predict the creep behaviour of GFRP profiles. The results of proposed models agreed well with experimental data. But, these models cannot be easily extended to the case of numerical methods including finite element. For this reason, numerical approaches with finite element are then required to predict the long-term creep response and to study the strain and shear distribution along the adhesive joint.

Therefore, the purpose of the current paper is to attempt to shed some light on the creep behaviour of GFRP-concrete hybrid bonded structures. To meet this objective, this paper presents experimental and numerical investigations about the creep behaviour of a hybrid structure consisting of I-shaped GFRP pultruded profile bonded to a thin deck made of reinforced concrete. A general step-by-step procedure is proposed to predict the long-term behaviour of beams based on the linear viscoelasticity theory and numerical study is conducted to validate the proposed method.

EXPERIMENTAL PROGRAM

The tests were made to investigate the short- and long-term behaviours of hybrid FRP beams consisting of GFRP pultruded profile and concrete slab. The experimental program consisted of testing five beams: two GFRP beams (Pu3 and Pu4) and 3 GFRP-concrete hybrid beams (PCB1, PCB2, PCB3). All the beams were simply supported on two supports and tested in three-points bending configuration. The load was applied at mid span section to simulate the most severe loading in a proposed application, such as footbridge.

Beams geometry

The hybrid beams consist of GFRP pultruded profiles with a I-shape section bonded to concrete slabs. Figure 63 (a) shows the cross-section of the hybrid beams, which present a total length of 3010 mm and a simply supported span length of 2800 mm as shown in figure 63(b). The glass fibre reinforced polymer beams used in the tests were pultruded I-profiles. The beams were 150 mm in height and 75 mm in width with a thickness of flanges and web of 8 mm. For all the used profiles, reinforced concrete jackets (stiffener) were executed between flanges at the support sections in both sides of the web, with a length of 145 mm, to avoid local web crushing failure.

The concrete slabs have a cross section of $b \times h = 400 \times 60 \text{ mm}^2$. The concrete slabs were reinforced, on the tension zone, longitudinally with $3\text{Ø}7 \text{ mm}$ steel bars and transversally with $\text{Ø}7 \text{ mm}/150 \text{ mm}$ steel bar with a 10-mm cover. The cross-section was chosen based on design equations to benefit from the mechanical properties of each material (the high tensile strength of GFRP and the high compressive strength of concrete) and to prevent the local/global buckling of GFRP profile. The dimensions were then selected to obtain a neutral axis lying in the concrete slab.

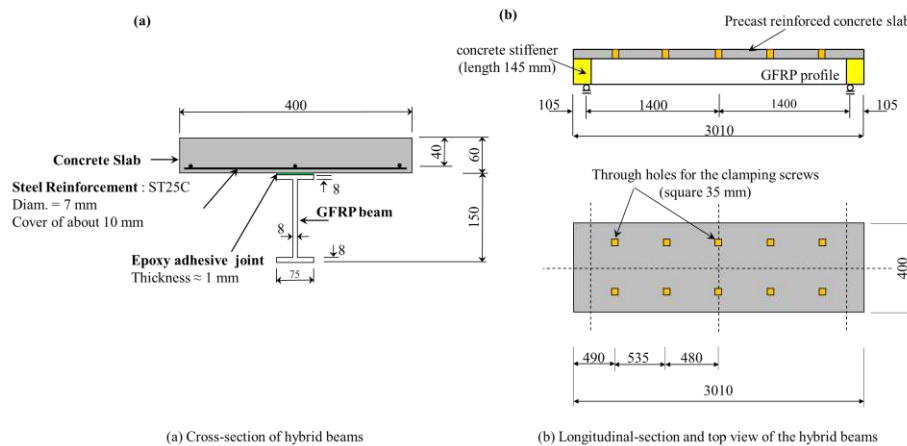


Figure 63 : Hybrid beams geometry (dimensions in mm)

Materials description and characterization tests

The pultruded GFRP profile used in this study was produced by TopGlass and made of E-glass fibres embedded in a polyester matrix. The GFRP profile contained both random continuous filament mat and E-glass roving. The Young's modulus and the tensile strength were measured by testing several rectangular prismatic coupon specimens extracted, in the pultrusion direction, from the flanges and web accordingly to the ISO 527 - 1. Table 26 summarises the results obtained in the GFRP material characterisation tests in this study.

Table 26: Tensile properties of the pultruded GFRP profile obtained from small scale specimens

Property	Test method	Value (C.O.V.)	Unit	
Longitudinal tensile strength		379.7 (9.6%)	MPa	
Flange	ISO 527	Longitudinal tensile modulus	23.9 (10.9%)	
		Strain at failure	15903 (1.3%)	$\mu\text{m.m}^{-1}$
Web	ISO 527	Longitudinal tensile strength	395.3 (12.3%)	
		Longitudinal tensile modulus	25.0 (12.3)	GPa
		Strain at failure	15827 (0.5)	$\mu\text{m.m}^{-1}$

The concrete slabs were fabricated using an artificial Portland cement CEM I 52.5 produced by LAFARGE with a commercial name Durabat X-Trem. Several 100 mm-edge cubes for compression test (for each batch of concrete) and $\text{Ø}160 \times 320 \text{ mm}^2$ cylindrical specimens for splitting test were poured and used to evaluate the mechanical properties at different ages of concrete. The tests were performed according to NF EN 12390 -3 and NF P 18-408. Table 27 presents the results of compression and tensile tests performed on concrete specimens for each hybrid beam. To bond GFRP profile to concrete slab, a two-part resin and hardener thixotropic epoxy adhesive (Sikadur®

- 31 EF) was used. The mechanical properties of adhesive were measured by testing several plates of bulk adhesive instrumented with strain gauges and prepared according to the ISO 527-2. Table 28 summarises the mechanical properties of bulk adhesive specimens for each hybrid beam.

Table 27: Average compressive and tensile strengths of concrete

Hybrid beam	Concrete age (days)	Concrete compressive strength (MPa)	Concrete tensile strength (MPa)
PCB1	88	49,4 ± 6,5	-
	28	45,7 ± 3,4	3,1 ± 0,1
PCB2-3	315 (aged under laboratory conditions)	38,7 ± 4,2	3,3 ± 0,2
	315 (exposed to outdoor conditions)	48,9 ± 3,6	3,4 ± 0,9

Table 28: Average mechanical properties of epoxy adhesive (Sikadur® 31-EF)

Hybrid beam	Specimen age (days)	Ultimate tensile strength (MPa)	Strain at failure ($\mu\text{m.m}^{-1}$)	Young's tensile modulus (MPa)
PCB1	37	10.8 ± 1.2	-	-
PCB2	265	13.2 ± 4.6	-	-
PCB3	266	11.8 ± 3.8	934 ± 468	11749 ± 5224

Static tests (short-term tests)

A hydraulic jack with a capacity of 500 kN and a maximum stroke of 500 mm was used for the statics tests. Steel plate was used to apply the load on the top flange of profile or on the top side of concrete slab to limit the concentration of stresses. A displacement rate of 4 mm.min⁻¹ were used for all tests. The applied loads were measured by load cells within the machine. The longitudinal strain at certain locations on the beam were recorded using electrical resistance strain gages positioned at mid-span. The midspan deflection was measured using a linearly variable differential transformer LVDT.

In the first phase of the experimental program, the beam PCB1 were loaded up to failure with the load at the mid-span position in order to validate the hybrid system, to observe its behaviour and to evaluate its failure load. In the second phase, each hybrid beam was subjected to several load and unload cycles at different load levels (from 10 to 30 kN) to observe the behaviour of the beams and to verify the proper operation of the instrumentation prior to loading the beams to its creep load.

In order to evaluate the full-scale elastic properties of GFRP profiles (flexural and shear moduli), a procedure proposed by Bank (Bank 1989) that simultaneously gives the longitudinal and the shear moduli of GFRP profile from three-point bending tests was applied. A full scale GFRP profile were simply supported on supports with different span lengths (1.4, 2.1 and 2.8 m) and subjected to a three-point bending test under a given applied load (10 kN). A flexural modulus of 29.3 GPa and a shear modulus of 2.26 GPa were obtained.

Creep tests (long-term tests)

The experimental campaign presented herein was performed under outdoor conditions in Villeurbanne (France) which has a moderate climate. For all the beams, the gages were covered with an environmental protection coating to limit the effects of humidity and other environmental factors.

The hybrid beam PCB2 was loaded using 1m³ concrete blocks weighting 2300 kg. This load was approximately one third of the PCB1 beam's failure load. The test was carried out from September 2016 to February 2017. Figure 64(a) shows the details of creep test setup. At 129 days after the concrete pour, the beam PCB2 was loaded while the beam PCB3 was kept unloaded beside the beam PCB2 for the whole duration of the first long-term experiment to measure the effects of shrinkage and ageing on the beam behaviour and on its failure load. The beam PCB3 was subjected to its own self weight during this time period. This creep test was carried out until the failure of PCB2. Moreover, a creep experiment was performed on the GFRP beam "Pu3". The test was carried out from October 2017 and is still continuing. The beam was subjected to a sustained load of 8.88 kN. This load was approximately one third of the initial estimated failure load of GFRP beams. Figure 64(b) shows the details of creep test setup for GFRP beam. Beside Pu3, another GFRP beam Pu4 was left without loading during the test period to evaluate the effects of ageing on the static behaviour of GFRP beams.

The long-term behaviour of these beams was monitored by measuring deflection and strains over time. The deflection of each beam was measured at 100 mm from the midspan section using a digital level "Leica LS15". The gages were read on a manual strain indicator and switching box system "Vishay P-3500". Temperature was recorded with each reading.

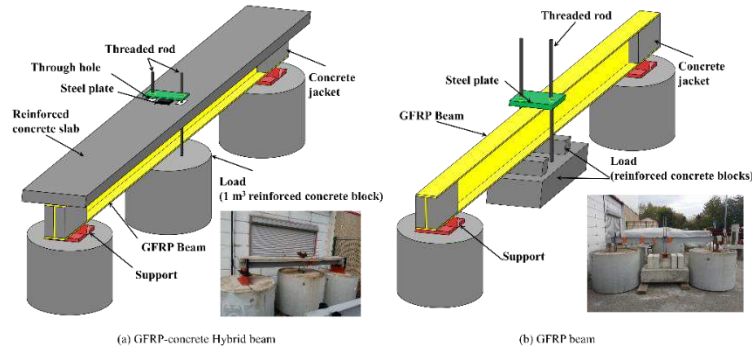


Figure 64: Creep tests set-up

NUMERICAL STUDY AND PREDICTION OF CREEP BEHAVIOUR

Finite element model description

Regarding to desired purpose, meshes should be selected that lead to most precise results so, 3D FE models were generalised by using the finite elements code Cast3M (CEA) and the meshes of both GFRP and hybrid beam models used for the time-dependent simulations are shown in Figure 65. The longitudinal and transversal symmetry simplifications were applied. One quarter of the beams was modelled. The concrete slab and the GFRP beams were modelled by using the massif 4-node tetrahedral elements TET4. The 6-node joint elements (JOI3) were employed to simulate the interface between the top flange and the concrete slab. The GFRP beam model had a total number of 36212 nodes and 119380 TET4 elements whereas the hybrid beam model had 101054 nodes and 456237 elements. The boundary conditions were chosen to represent a similar situation as the tests. The vertical displacement of the GFRP bottom flange at 105 mm from the beam end was restrained (on the right side). The self-weight was applied. External distributed loads were applied in terms of a series of concentrated forces at the nodes located in a surface corresponding to the area of the bearing plate used in the experimental set-up.

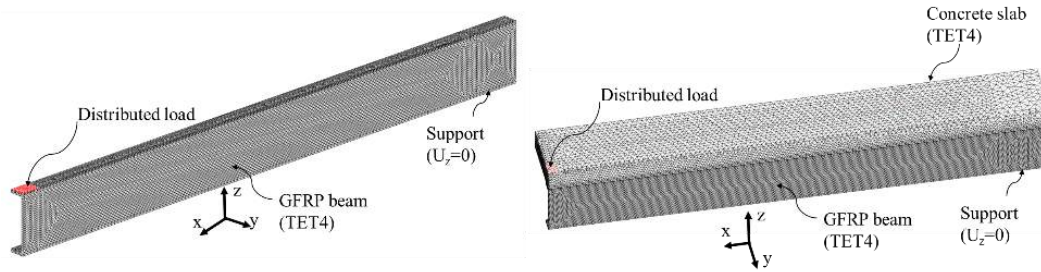


Figure 65: Meshes of finite element models

The concrete and the adhesive were assumed to be elastic and isotropic whereas the GFRP beam is considered as an orthotropic material (Bank 1989; Mottram 1993). The initial elastic material properties used in this simulation were identified based on the experimental results of characterization tests. The long-term behaviour of the materials constituting the cross-section has been considered by means of the theory of linear viscoelasticity. Shrinkage of concrete and thermal strains effects were neglected.

Rheological model: linear viscoelastic constitutive model

In the present study, a Maxwell chain model has been adopted for the linear viscoelastic material behaviour where the creep behaviour is associated to several Maxwell units (spring and dashpot in series) in parallel with a Hooke unit (spring), as shown in Figure 66 (a). For this model, the linear viscoelastic constitutive law can be written in the form of a set of differential equations. For the μ^{th} Maxwell unit, the following differential relation can be written:
$$E_{\mu}(t)\varepsilon^{ve}(t) = \frac{\partial\sigma_{\mu}(t)}{\partial t} + \frac{\sigma_{\mu}(t)}{\tau_{\mu}} \quad (1)$$

where $\varepsilon^{ve}(t)$ is the total viscoelastic strain, $\tau_{\mu} = \frac{\eta_{\mu}(t)}{E_{\mu}(t)}$ is the relaxation time of the μ^{th} Maxwell unit, $\eta_{\mu}(t)$ is the viscosity coefficient of the dashpot in the μ^{th} Maxwell unit, $E_{\mu}(t)$ is the elastic modulus of the spring in the μ^{th} Maxwell unit and $\sigma_{\mu}(t)$ is the hidden stresses in the μ^{th} Maxwell units. In the case of ageing materials such as concrete, E_{μ} and η_{μ} are functions of time whereas for non-ageing materials such as GFRP, E_{μ} and η_{μ} are independent of time.

The numerical solution of differential system (Eq. (1)) can be expressed as an incremental expression for any finite time interval $[t_r, t_r + \Delta t_r]$ by assuming that, for small time steps, $\varepsilon^{ve}(t)$ and $E_\mu(t)$ evolve linearly in the time interval $[t_r, t_r + \Delta t_r]$ (i.e. $\frac{\partial \varepsilon^{ve}(t)}{\partial t} = \frac{\Delta \varepsilon^{ve}(t_r)}{\Delta t_r}$ and $\frac{\partial E_\mu(t)}{\partial t} = \frac{\Delta E_\mu(t_r)}{\Delta t_r} \forall t \in [t_r, t_r + \Delta t_r]$):

$$\sigma_\mu(t_r + \Delta t_r) = \sigma_\mu(t_r) e^{-\frac{\Delta t_r}{\tau_\mu}} + \tau_\mu \frac{\Delta \varepsilon^{ve}(t_r)}{\Delta t_r} \left[\left(E_\mu(t_r + \Delta t_r) - E_\mu(t_r) e^{-\frac{\Delta t_r}{\tau_\mu}} \right) - \tau_\mu \frac{\Delta E_\mu(t_r)}{\Delta t_r} \left(1 - e^{-\frac{\Delta t_r}{\tau_\mu}} \right) \right] \quad (2)$$

The constitutive law can then be turned into an incremental form (Jurkiewicz et al. 1999) on any finite time interval $[t_r, t_r + \Delta t_r]$:

$$\Delta \sigma(t_r) = \sigma^{hist}(t_r) + \Delta \varepsilon^{ve}(t_r) \tilde{E}(t_r) \quad \forall t_r, \Delta t_r \quad (3)$$

where $\sigma^{hist}(t_r)$ is the history term which depends on a set of internal cumulative variables updated after every time interval and can be expressed by Eq. (4) and $\tilde{E}(t_r)$ is a fictitious modulus of elasticity which can be computed by Eq. (5). $\Delta \sigma(t_r)$ and $\Delta \varepsilon^{ve}(t_r)$ are respectively the strain and stress increment over time interval Δt_r .

$$\sigma^{hist}(t_r) = \sum_{\mu=1}^m \sigma_\mu^{hist}(t_r) = \sum_{\mu=1}^m \sigma_\mu(t_r) \left(e^{-\frac{\Delta t_r}{\tau_\mu}} - 1 \right) \quad (4)$$

$$\tilde{E}(t_r) = \left(E_0(t_r) + \frac{\Delta E_0(t_r)}{2} \right) + \sum_{\mu=1}^m \frac{\tau_\mu}{\Delta t_r} \left[E_\mu(t_r) \left(1 - e^{-\frac{\Delta t_r}{\tau_\mu}} \right) - \Delta E_\mu(t_r) \left(1 - \frac{\tau_\mu}{\Delta t_r} \left[1 - e^{-\frac{\Delta t_r}{\tau_\mu}} \right] \right) \right] \quad (5)$$

where $E_0(t_r)$ is the elastic modulus of Hooke unit at t_r and m is the number of Maxwell units

This uniaxial viscoelastic model presented in this paragraph can be easily generalized for a three-dimensional body by considering a Maxwell chain model for each component of the elasticity matrix.

For the concrete slab, the Eurocode 2 model was adopted to describe the rheological behaviour of concrete creep. According to a previous study conducted by Jurkiewicz *et al.* (Jurkiewicz et al. 1999), the viscoelastic behaviour of concrete can be described with a good accuracy by a Maxwell chain model constituted of 4 Maxwell units in parallel with a spring, under the hypothesis of constant Poisson's ratio. To consider the ageing creep behaviour of concrete, the spring and dashpot parameters were identified according to the age of the concrete (age-dependent parameters) (Bažant and Wu 1974; Jurkiewicz et al. 1999).

For the GFRP pultruded beam, the creep behaviour can be described by two independent creep functions: axial and shear creep functions (Bank and Mosallam 1992; Mottram 1993). The longitudinal elastic modulus E_L and longitudinal–transverse shear modulus G_{LT} are only involved in the model to simplify the experimental calibration of viscoelastic constitutive laws. For each function, a Maxwell chain model with 5 branches (spring in parallel with 4 Maxwell units) as that used for concrete, but with non-ageing parameters, was used. The other components of elasticity matrix (Poisson's ratios, transversal moduli) were supposed constant and equal to their initial values. Since no standard creep functions for GFRP materials are available, the Findley's power law was used to identify the creep functions based on the experimental results and the results available in the literature.

In order to identify the parameters for Maxwell chain for the ageing material (concrete) and for the non-ageing material (GFRP), a calibration procedure was written using the Finite Elements code "Cast3m". More details about this procedure and the method used for computing the E_μ -values can be found in the study of Bažant and Wu (Bažant and Wu 1974). After having identified the parameters, the step-by-step procedure has been implemented in Cast3M. Figure 66 (b) shows the algorithm of the complete procedure.

RESULTS AND DISCUSSION

Static tests

The load-displacement curves for the hybrid beams and for the GFRP pultruded profiles are shown in Figure 67. Comparing the behaviour of hybrid beams with that of simple GFRP pultruded profiles, under the same load level (10kN), it can be seen clearly the structural improvements of the GFRP/concrete hybrid solution compared to GFRP profile alone. The bending stiffness EI of hybrid system, calculated using Eq. (6), increased about 417% compared to that of GFRP beams.

$$EI = \frac{1}{\delta_b(L/2)} \left(\frac{1}{48} PL^3 \right) \quad (6)$$

Where P is the applied load, L is the span length and $\delta_b(L/2)$ is the deflection at the middle of span.

Under static load, the five hybrid beams showed an almost linear-elastic response up to 30 kN when the first small transversal cracks appeared in the tension zone of the concrete slab below the loading plate. Beyond this load level, the strain gage located on the bottom side of concrete slab was out of service for most of them.

The hybrid beam PCB1 showed an approximately linear behaviour up to a load of 50 kN after which a non-linearity is observed (Figures 5 and 6(a)). This phase continues up to 70 kN where the crushing of concrete by compression in the top concrete slab started. A few moments later, the profile's top flange suddenly detached from the profile's web at a load of 71 kN, as shown in Figure 69(a). The maximum strains at this stage in the top concrete layer and the bottom GFRP level were 0.37% and 1.04% respectively for a maximum deflection of 52 mm.

The hybrid beam PCB3 was firstly exposed to outdoor exposure for up to 5 months. After ageing, it was loaded up to failure under 3-point bending. PCB3 showed a linear behaviour up to 82 kN where the failure began with

crushing of the concrete top at the midspan. This load corresponds to a maximum deformation in the compressed concrete of 0.4% (Figure 68(b)). Beyond this load level, the behaviour becomes slightly non-linear and at 85 kN, the failure ended by shearing at the junction zone between the profile's top flange and the profile's web, as shown in Figure 69(b). At this failure load, the maximum strains noted are 0.4% in the top concrete and 1.01% in the profile's bottom flange for a maximum deflection of 46.5 mm. The cause of the brittle collapse was supposed to be the increased shear stress which had developed at the web-flange junctions, which maybe have low shear resistance due to the low fibre contents.

For the two tested beams, the interface was visibly intact, and no cracks/separation was observed. The increase in the load carrying capacity of hybrid beam after ageing may be explained by the rigidification process of concrete slab due to post cure of the cement in presence of water. This rigidification process makes the concrete slab more stiffer and more fragile, which induces a decrease in the maximum deflection and an increase in the load carrying capacity.

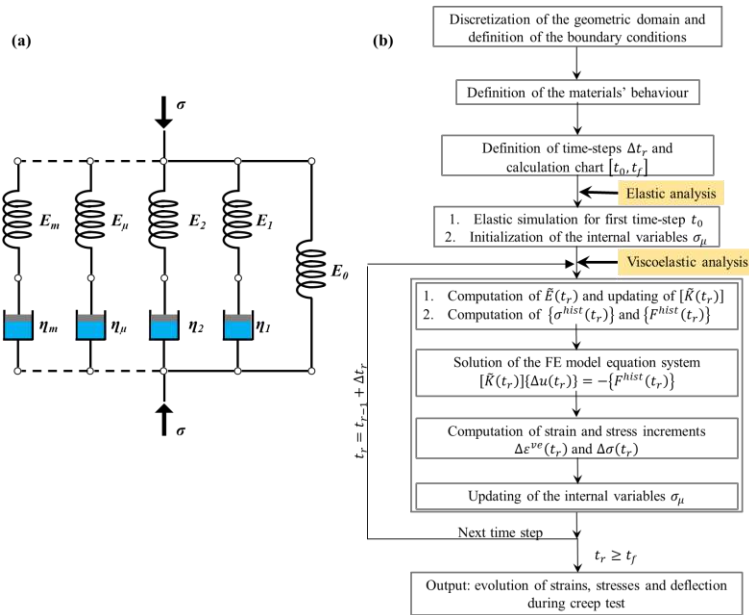


Figure 66: (a) Generalized Maxwell model, (b) Algorithm of the step-by-step procedure implemented in Cast3m

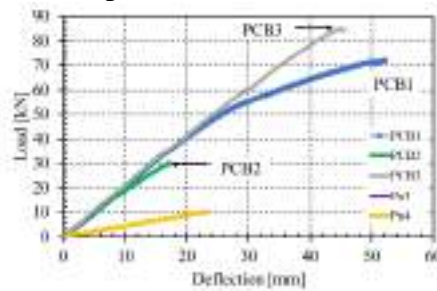


Figure 67: Load deflection response at mid-span section for (hybrid beams and pultruded profiles under static loading

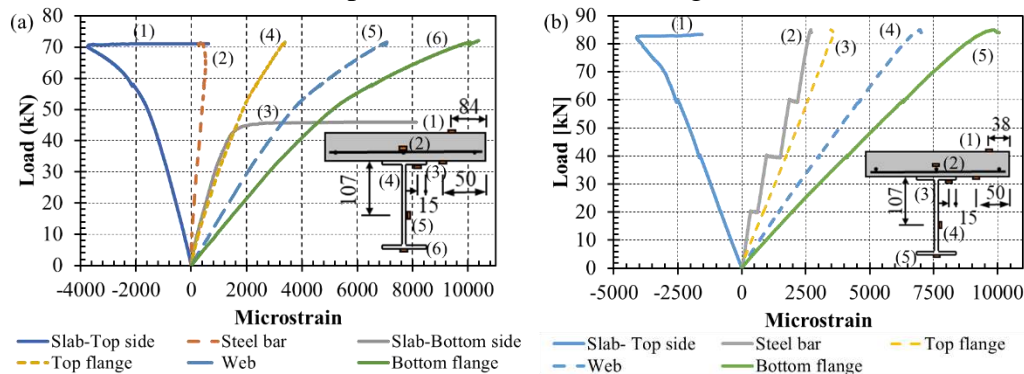


Figure 68: Variation of longitudinal strains at mid span (static test) in function of the applied load for (a) PCB1 and (b) PCB3



Figure 69: Failure mode of hybrid beams PCB1 and PCB3 (static test)

Creep tests

Figure 70 shows the experimental results of creep test performed on the hybrid beam PCB2 and the results predicted using the numerical model. Instantaneous deflection of the beam PCB2 was 12.40 mm. After about 138 days, the failure occurred by shearing the interface between the profile's top flange and the concrete bottom, as shown in Figure 71. This failure mode is an indicative of damage occurring at the interface between concrete and epoxy namely debonding. The diffusion of water through concrete slab leads to an accumulation of water molecules on the adhesive-concrete interface. This accumulation with the presence of alkali ions in the concrete can generate a high osmotic pressure at the interface causing a large degradation of the adhesive/adherent interface which eventually causes failure by decohesion and delamination at this interface. The combined effects of loading (shear stresses) and water diffusion (degradation of joint) may have led to this premature failure of hybrid beam PCB2. At the end of creep test, the deflection due to creep and shrinkage effects reached 4 mm, about 33% of the instantaneous deflection due to the creep load. Comparing the experimental results of creep test with that predicted using the FE model, it can be seen clearly the forecasting performance of the model under study. The deflection and strains in different locations of hybrid beam can be estimated with a reasonable degree of accuracy using the proposed model.

For the second creep test, the mid-span deflection was selected to assess the time-dependent behaviour of the GFRP beam, and its variation with time for GFRP beam Pu3 and for their corresponding numerical model was reported herein as given in Figure 72. The instantaneous deflection of the GFRP beam Pu3 was 18.41 mm. The results of creep test in the case of GFRP beam show a higher dispersion than the results obtained for the hybrid beams. Nevertheless, the general trend of the FEM results is found to be similar to the experimental deflections.

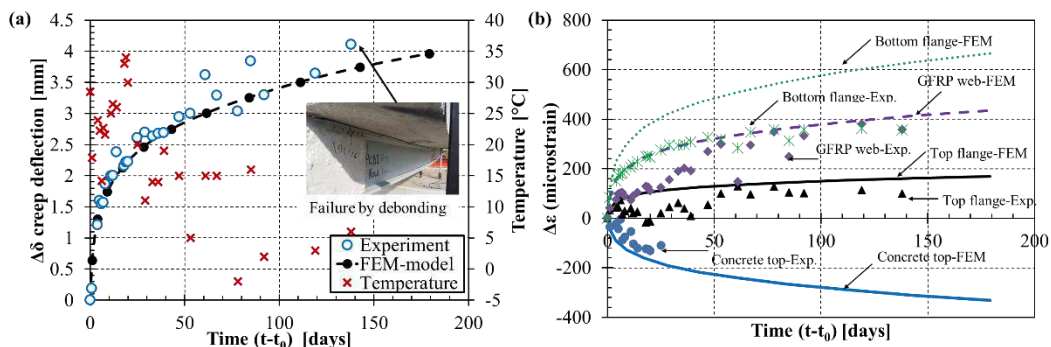


Figure 70: Creep test results for hybrid beam PCB2



Figure 71: Failure mode of hybrid beam PCB2

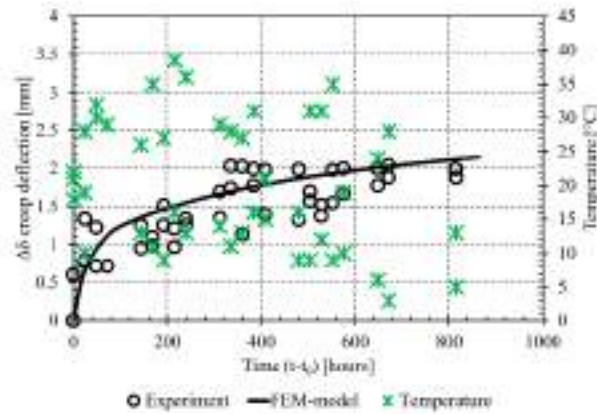


Figure 72: Experimental and numerical evolutions of deflection over time for GFRP profile Pu3

CONCLUSIONS

This paper describes the details of an experimental program intended for investigation of the long-term behaviour of hybrid GFRP pultruded/concrete bonded beams. Total two sets of full scale experiments are reported along with some results collected during the experiments. All experiments showed considerable increase in beam deflection over time due to concrete creep and shrinkage and GFRP creep. Linear viscoelastic models with an incremental procedure were proposed and numerical results compared with experimental ones. The comparison is found to be good.

REFERENCES

- L.C. Bank (1989). "Flexural and shear moduli of full-section fiber reinforced plastic (FRP) pultruded beam", *Journal of Testing and Evaluation*, 17,40-45.
- L. C. Bank, A. S. Mosallam (1992). "Creep and failure of a full-size fiber-reinforced plastic pultruded frame", *Composites Engineering*, 2, 213-227.
- Z.P. Bažant, S.T. Wu (1974). "Rate-type creep law of aging concrete based on Maxwell chain", *Matériaux et Constructions*, 7, 45-60.
- J.A. Gonilha, J.R. Correia, F.A. Branco (2013). "Creep response of GFRP–concrete hybrid structures: Application to a footbridge prototype", *Composites. Part B: Engineering*, 53, 193–206.
- B. Jurkiewicz, J.-F. Destrebecq, A. Vergne (1999). "Incremental analysis of time-dependent effects in composite structures", *Computers and Structures*, 73, 425-435.
- P. J. Mendes, J. A. Barros, J. M. Sena-Cruz, M. Taheri, (2011). "Development of a pedestrian bridge with GFRP profiles and fiber reinforced self-compacting concrete deck", *Composite Structures*, 93, 2969–2982
- J. T. Mottram (1993). "Short- and long-term structural properties of pultruded beam assemblies fabricated using adhesive bonding", *Composite Structures*, 25, 387-395
- M. F. Sá, A. M. Gomes, J. R. Correia, N. Silvestre (2011a). "Creep behavior of pultruded GFRP elements–Part 1: Literature review and experimental study", *Composite Structures*, 93, 2450-2459.
- M. F. Sá, A. M. Gomes, J. R. Correia, N. Silvestre (2011a). "Creep behavior of pultruded GFRP elements – Part 2: Analytical study", *Composite Structures*, 93, 2409–2418.



THE BEHAVIOUR OF DUCTILE LINK SLAB DESIGNED WITH FRP REINFORCED ECC

Y. Zheng¹, L.P Xia¹ L.F. Zhang¹ and J.B. Yang¹

¹ Department of Civil Engineering, Dongguan University of Technology, Email: zhengy@dgut.edu.cn

ABSTRACT

In the multispan deck system, mechanical expansion joints are typically designed and employed to facilitate both rotations and lateral movements between simply supported adjacent bridge spans due to thermal expansions, shrinkage, creep and girder deflections due to service loads. However, it is well reported that the deterioration of mechanical expansion joint components, such as rubber aging and steel corrosion, has been one of the major factors in the deterioration of those bridge structures. A possible approach to solve the durability problem and reduce the high cost of maintenance in expansion joints is the elimination of mechanical deck joints. As a result, continuous and jointless bridge decks have been suggested and proposed. One type of jointless bridge design proposed by a number of researches is the application of link slab elements within bridge deck, which is used to connect the two adjacent simple-span girders. In this paper, a flexible and corrosion-free link slab element by utilizing highly ductile ECC and low stiffness non-corrosive FRP reinforcement is proposed and suggested. The proposed link slab needs to maintain structural integrity and durability while conforming to crack width limitations and having sufficient deformation capacity. In addition, a low stiffness of the link slab element is desired in order for the two adjacent simply supported bridge deck spans, connected by the link slab, to undergo unrestrained deformations. In this study, to verify that the proposed ECC material is able to exhibit the criteria of link slabs in the literatures, a group of ECC specimens were employed and tested under compression, tension and flexure to investigate the material properties. Subsequently, a FRP reinforced ECC slab was used as joint link slab in bridge deck structures and a group of test specimens were conducted, including ECC link slab, ECC link slab reinforced with FRP grid and ECC link slab reinforced with FRP bars. A series of monotonic repeated loading was applied for all the test specimens. The performance is described based on the load-deflection/moment-rotation response, strain development, cracking and energy absorption. The influence of FRP reinforcing materials on the link slab structural performance is presented and discussed. The significant enhancement of deflection capacity and crack with control in ECC link slab reinforced with FRP bars suggest that the use of ductile ECC and low stiffness FRP can be effective in extending the service life of joint-free bridge deck system.

KEYWORDS

Hybrid structures, Experimental study, FRP reinforcement, Durability, Long-term performance, ECC

INTRODUCTION

A majority of high-way bridges are composed of multiple-span steel or prestressed concrete girder simply supported at piers. The girders support cast-in-place or precast concrete decks. In this deck system, mechanical expansion joints are typically designed and employed to facilitate both rotations and lateral movements between simply supported adjacent bridge spans due to thermal expansions, shrinkage, creep and girder deflections due to service loads. In addition, those expansion joints are designed to protect the substructure from exposure to corroding substances by provided watertight seal between the adjacent bridge decks over piers and abutments. However, it is well reported that the mechanical joints are expensive to install and maintain. Deterioration of joint functionality due to debris accumulation can lead to severe damage in the bridge deck and substructure. The durability of girder ends, bearing and supporting structures can be compromised by water leakage and flow of deicing chemicals through the deteriorated joints (Alampalli and Yannotti 1998; Aktan et al. 2002). As a consequence, mechanical expansion joints have been found to have a negative influence on all stages during the service life of bridge structures (Wolde-Tinsae 1987).

A possible approach to solve the durability problem and reduce the high cost of maintenance in expansion joints is the elimination of mechanical deck joints in multispan bridges. As a result, continuous and jointless bridge decks have been suggested and proposed (Burke 2009). One type of jointless bridge design proposed by a number of researches is the application of link slab elements within bridge deck (Kim et al 2004), which is used to connect the two adjacent simple-span girders. Caner and Zia developed the experimental investigations of the structural behaviour of jointless decks and proposed design procedures for the link slab (Caner and Zia 1998). Thereafter, further research reported in the literatures suggested the use of ductile concrete materials known as engineered

cementitious composites (ECC) reinforced with standard steel reinforcement (Au et al. 2013; Lepech and Li 2009; Kim and Li 2004). Subsequently, a field demonstration was carried out by Lepech and Li in the Michigan Department of Transportation (Lepech and Li 2006). As a result of the moment demand and restrictions on the working stress of the reinforcement, which was limited to 40% of the yield strength, the link slab was heavily reinforced and consequently did not behave as a joint. Due to this high reinforcement percentage generally used, the resulting large bending stiffness of the link slab and consequently the negative moment generated in the joint are undesirable effects and deserve additional consideration (Lárusson 2013).

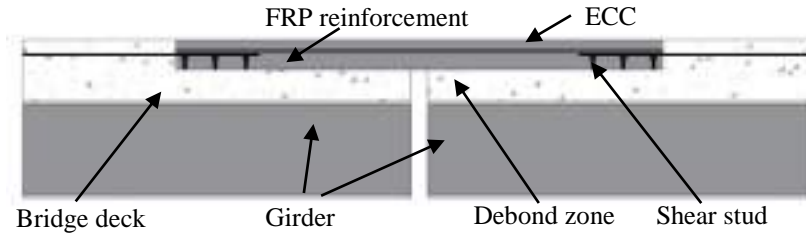


Figure 1 Link slab of ECC reinforced with FRP

Additionally, the corrosion of steel reinforcement embedded inside the link slab could cause the problems of structural deterioration and durability. For more than three decades, it is well reported that one solution to this corrosion problem is the use of alternative materials to steel reinforcement that do not corrode, such as fibre reinforced polymer (FRP) (Bakis et al. 2002; Zheng et al. 2015). In this paper, a flexible and corrosion-free link slab element by utilizing highly ductile ECC and non-corrosive FRP reinforcement is suggested, as shown in Figure 1. The proposed link slab needs to maintain structural integrity and durability while conforming to crack width limitations and having sufficient deformation capacity. In addition, a low stiffness of the link slab element is desired in order for the two adjacent simply supported bridge deck spans, connected by the link slab, to undergo unrestrained deformations. The aim of this research is to test and investigate the behaviour of this novel link slab capable of facilitating relatively large flexural deformations.

EXPERIMENTAL PROGRAMME

Material properties

Table 1: Properties of PVA fiber

Type of fibre	Length /mm	Diameter / μ m	Tensile strength /MPa	Young's modulus /GPa
PVA fibre	12	31	1600	47.29

Table 2: Mix proportion of ECC specimens

Specimen	Binders					Water to binder ratio	Sand to binder ratio	Super-plasticizer (%)	PVA Fibre (%)
	Cement	Fly ash	Lime stone powder	Meta-kaolin	Silica fume				
1	0.4	0.5	0.04	0.04	0.02	0.27	0.36	0.1	2.0

Large scale laboratory testing of ECC link slabs was conducted to investigate the structural performance of ECC link slabs, along with the development of cracking on the tensile face of the ECC link slab (Wang and Li 2007). In order to obtain higher corrosion resistance and durability, polyvinyl alcohol (PVA) fibre was used in this article. The properties of PVA fibre are shown in Table 1. In order to develop new type of anti-cracking technique for ECC link slabs, a new cementitious composite reinforced by a combination of carbon textile and PVA fiber was proposed. CFRP grid and CFRP bars were placed along the direction of principal stress so that the reinforcing effect can be significantly enhanced. The reinforcement ratio of link slabs are 1.4% and 0.154%. Mix proportions were adopted based on the design criteria, as shown in Table 2, based on the property requirements of ECC material for link slabs. At the same time, a control group of concrete was set up. The compressive strength is 35MPa. According to the previous experimental studies (Kim et al. 2004), the link slab is in bending and behaved similar as a flexural component rather than a tension member and the crack at the center of slab did not extend to the bottom face of the slab. In order to analyze the bending performance of link slab, a series of ECC slabs were

designed and tested. The size of ECC slab was determined to be 15mm×100mm×400mm. In the study, a four-point loading test was carried out to investigate the bending behaviour of all the ECC slabs according to the ASTM c1018 (see Fig. 2a). It can be seen that all the ECC specimens achieve strain-hardening and ductile behaviour as shown in Fig.2b. In addition, Fig. 2c illustrates multiple-cracking behaviour in the ECC test slabs.

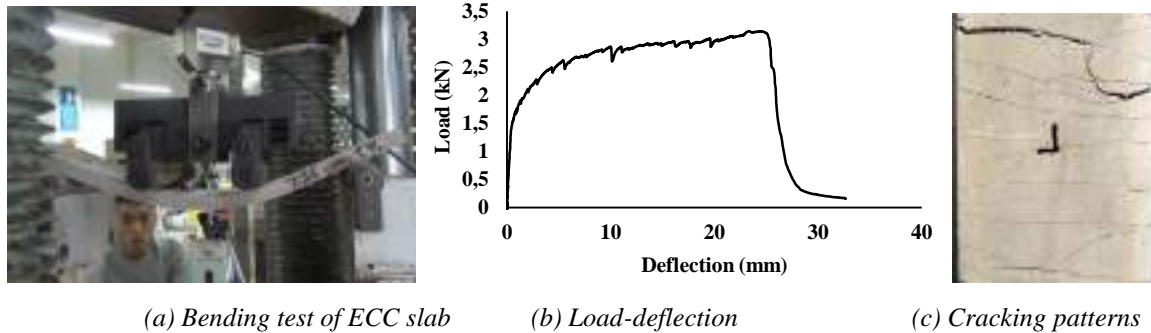


Figure 2: Four-point bending test for ECC specimens

Structural test configuration

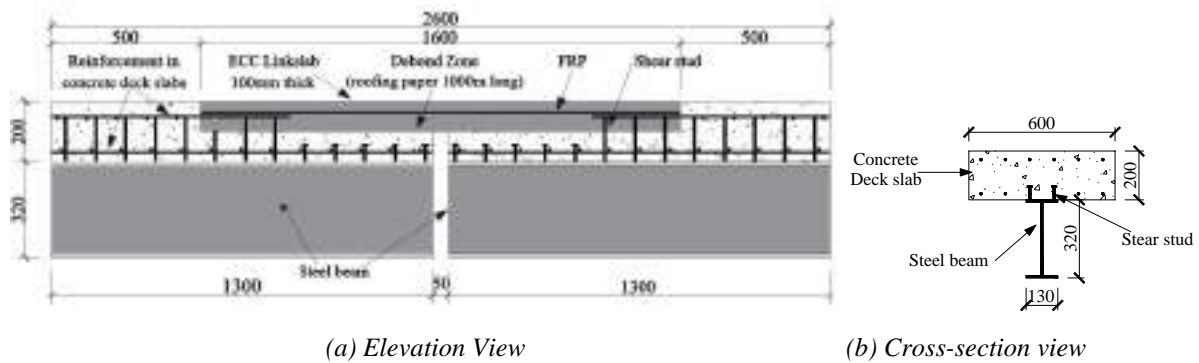
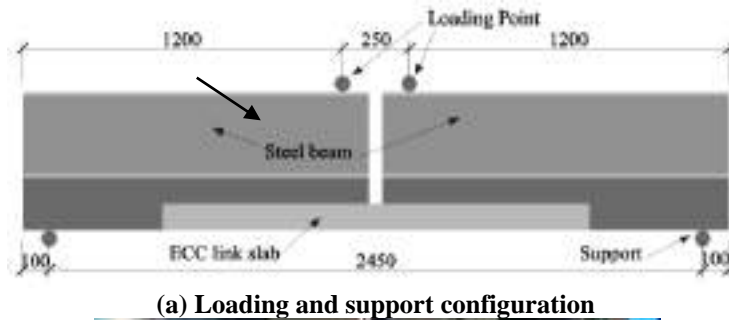


Figure 3: Test model dimension (unit: mm)



(a) Loading and support configuration



(b) Test model

Figure 4: Loading configuration (unit: mm)

In this study, an experimental study was conducted to investigate the structural performance of ECC link slab in bridge deck systems using full scale test models. The main objective of this laboratory tests were: (1) To study the structural behaviour of ECC link slabs under the monotonic cyclic load simulate traffic loading; (2) To study the influence of FRP reinforcing materials on the behaviour of ECC link slabs. Fig. 13 shows the geometry of the test model in this test, which is a single deck system designed in accordance to the design concept by Lepech and

Li (2009) and Kim et al. (2004). It can be seen that the test models consist of steel supporting beam section and a concrete slab section, 600mm wide and 200mm thick. In this experimental test, the concrete strength of deck slabs is 35 N/mm² and the internal reinforcement percentage of deck slab is designed as 0.7%. This concrete deck system corresponds to typical deck slabs in simply supported composite girder bridges with two adjacent 25-meter spans. As shown in Fig. 13, the ECC link slab in all the test models is designed as 1600 mm long and 100 mm thick with the debond zone length of 1000mm, which is equal to 2.5% of both adjacent spans (Lepech and Li 2009). Due to using the FRP reinforcement, the slender depth of ECC link slab (100mm) was used in this test, which is just half of depth of concrete deck slabs. As shown in Figure 4, the inflection points spanning 2450mm were simulated by the pin and roller supports.

As well reported in the publish literature (Lepech and Li 2009), deflection-control method was used in the loading procedure. As shown in Figure 5, all the test specimens are subjected to sequential monotonic cyclic loading up to failure or the rotation angle of 0.04rad, which is around 27 times of maximum rotation angle, θ_{max} (0.00375rad) (Kim et al 2004). When the rotation angel of supporting beams reaches this value (0.04 rad), the experimental test has to be terminated due to the possible collision of the ends of two adjacent beams. In the test process, the applied load, displacements, rotation angles, strains in the FRP reinforcement and ECC link slabs at the midspan were monitored using a data acquisition system. Cracks were marked and crack number is accounted at each loading cycle. Meanwhile, the crack widths were measured using hand held crack gauges.

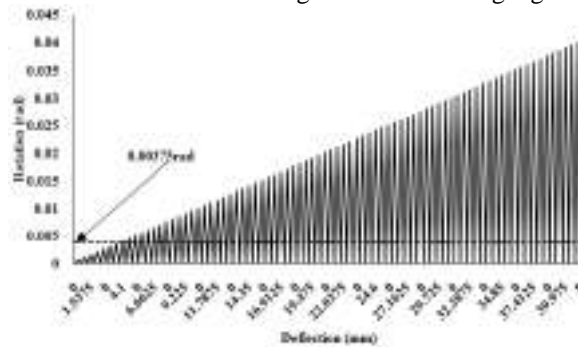
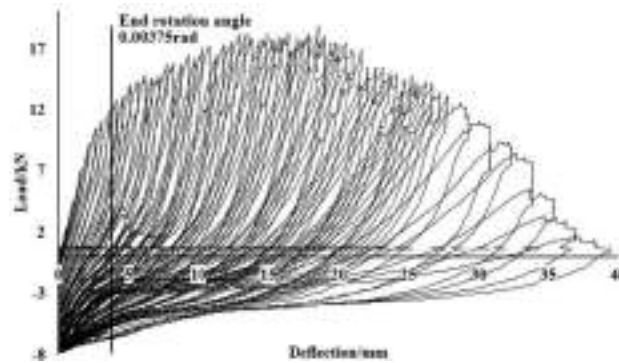
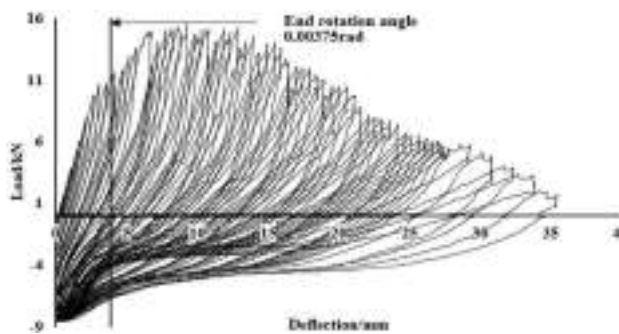


Figure 5: Loading sequence used in this study

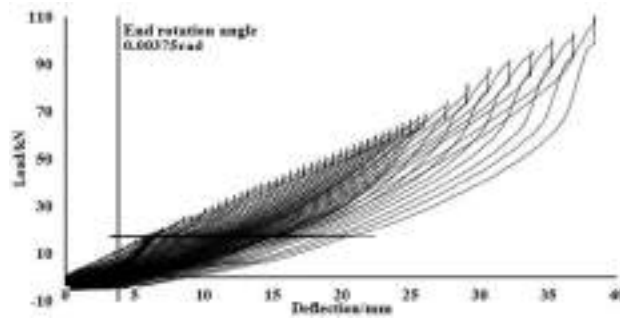
RESULTS AND DISCUSSIONS



(a) Response of load vs. deflection at midspan under monotonic load (Specimen LS1)



(b) Response of load vs. deflection at midspan under monotonic load (Specimen LS2)



(c) Response of load vs. deflection at midspan under monotonic load (Specimen LS3)

Figure 6: Response of load vs. deflection at midspan under monotonic load

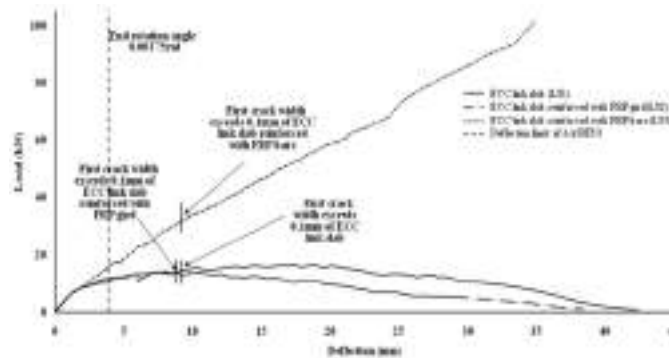
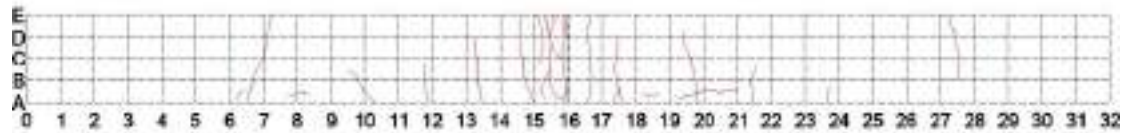


Figure 7: Envelop of load vs. deflection at midspan under monotonic load

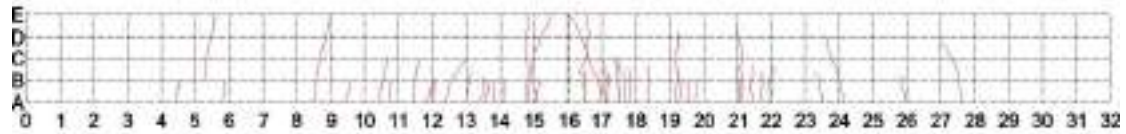
Figure 6 illustrates the responses of load vs. vertical deflection at midspan of ECC link slabs under monotonic cyclic loads. In addition, the relationship of applied load vs. the peak value of deflections in each loading cycle was shown in Figure 7 for further study of this structural performance. Due to the small reinforcement percentage and flexural stiffness of BFRP grid in test specimen LS2, it can be seen that the load-deflection responses in two test specimens coded as LS1 and LS2 are similar. As shown in Figures 6a&b, the elastic response of the link slab reaches approximately 0.0015rad rotation angle of steel beams, before ECC link slabs exhibit plastic deformation when cracks start developing. It can be seen that the structural failure occurs in those two link slabs at the deflection of around 10mm. As shown in Figure 7, the deflection at the crack with of 0.1mm (the crack-width limitation for permeability requirement in AASHTO) is larger than the deflection corresponding to the maximum rotation value in AASHTO (2007). This indicates that the proposed ECC material can satisfy construction application requirement in current design standard. Interestingly, an approximately linear structural response is presented in load vs. deflection behaviour of the link slab reinforced with BFRP bar (test specimen coded as LS3). During all the loading sequences, this test model did not fail in all the test procedure and the experimental test was terminated due to the largest rotation angle of supporting beam (0.04rad). As shown in Figure 7, the elastic structural behaviour can be found in this model even when the rotation of steel supporting beams reaches the maximum angle (0.04rad). Additionally, the bending stiffness of the ECC link slab is increased without any degeneration during all the test loading process. It can be summarised that combination of the ductile behaviour of ECC and similar stiffness of BFRP bars the composite interaction of two materials results in compatible deformations, such as strain compatibility.



(a) Test specimen coded as LS1



(b) Test specimen coded as LS2



(c) Test specimen coded as LS3

Figure 8: Crack patterns through the depth of test link slabs

Table 3: Test results

Test specimen	Reinforcing material	Reinforcement percentage (%)	Crack number	Average crack width (mm)	Variance of crack width	Maximum crack width at deflection limit in AASHTO (mm)
LS1	None	0	35	0.16	0.381	0.1mm
LS2	BFRP grid	0.15%	24	0.14	0.461	0.08mm
LS3	BFRP bar	1.40%	49	0.073	0.049	0.05mm

The results of crack number, average crack width, variance of crack width and maximum crack width at the deflection limit in AASHTO (0.00375rad in rotation of supporting beams) for different test specimens were presented in Table 6. It can be seen that the maximum crack width of ECC link slab of LS1 (0.1mm) when the deflection reaches the limitation in AASHTO (0.00375rad) is larger than the other two slabs reinforced with FRP materials. This reveals that the application of FRP reinforcing materials is beneficial to improve the crack-control ability and anti-permeability in ECC link slabs. The crack patterns through the depths of all the test link slabs are illustrated in Figure 8. It should be noted that cracks developed in the test specimens coded as LS1 and LS2 were similar, which are focused in the area corresponding to the loading zone. Compared to those two link slabs, the cracks distribute more evenly in the ECC link slab reinforced with BFRP bars (LS3) with the smaller value variance of cracks (0.049 in Table 7). As a consequence, more cracks were developed with smaller crack width in the test specimen of LS3 compared to the other two specimens. This strong strain-hardening attribute of ECC with limited crack widths and improved interfacial bonding results in increased durability of the link slab in terms of ECCs ability to maintain structural integrity of the matrix. This attribute of ECC, together with similar stiffness of FRP bar, is essential in order to obtain and maintain strain compatibility at relatively high strain level. Furthermore, some governing factors on crack width development, including reinforcement percentage and diameter of FRP bars, should be investigated in the future study.

A comparison of envelopes of FRP reinforcement strain vs. the deflection and the ECC strain at the corresponding position vs. the deflection are demonstrated in Fig. 25. It can be seen that the strain values of FRP reinforcing materials were almost identical to the ECC strain at the tension face in test specimen coded LS2 before the failure occurred. In the test specimen LS3, the strain values of FRP bars are also close to that of ECC link slab during all the loading sequences. This indicates that the composite interaction by combining two materials of ECC and FRP with similar stiffness results in compatible deformation. This evenly distributed force transfer and compatible deformation behaviour results in lower localised stress, which translates to less deterioration of the interfacial bond between the rebar and the matrix. Finally, this structural performance is beneficial to improve the multiple-cracking behaviour and evenly distribution of cracks, as shown in Figure 7.

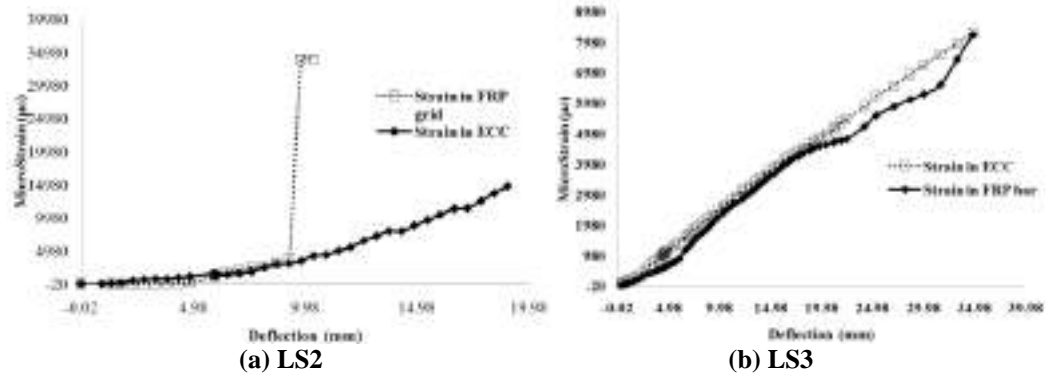


Figure 9: Comparison of strain vs. deflection response in the ECC link slab reinforced with FRP materials

A comparison of envelopes of FRP reinforcement strain vs. the deflection and the ECC strain at the corresponding position vs. the deflection are demonstrated in Figure 9. It can be seen that the strain values of FRP reinforcing materials were almost identical to the ECC strain at the tension face in test specimen coded LS2 before the failure occurred. In the test specimen LS3, the strain values of FRP bars are also close to that of ECC link slab during all the loading sequences. This indicates that the composite interaction by combining two materials of ECC and FRP with similar stiffness results in compatible deformation. This evenly distributed force transfer and compatible deformation behaviour results in lower localised stress, which translates to less deterioration of the interfacial bond between the rebar and the matrix. Finally, this structural performance is beneficial to improve the multiple-cracking behaviour and evenly distribution of cracks, as shown in Figure 8.

CONCLUSIONS

To develop the potential of a flexible and durable link slab in concrete bridge deck system using the combination of ECC material and FRP reinforcing material, an experimental investigation of full scale ECC link slabs under monotonic cyclic loading was performed. The main findings and conclusions from those investigations are summarised as following.

- (1) The test results of the structural experimental investigation of full scale link slabs in deck systems reveal that the structural behaviour of ECC link slab without reinforcement are similar as that of the link slab reinforced with FRP grid, which could be due to the small flexural stiffness of FRP grid and small reinforcement percentage (0.15%). The structural performance of the link slab reinforced with FRP bars is almost elastic during all the loading sequences. This is attributed to the large flexural stiffness and increase in FRP reinforcement percentage (1.4%) .
- (2) This attribute of ECC, together with the similar stiffness of FRP, is essential in order to obtain and maintain strain compatibility at relatively high strain levels. Therefore, the cracks through the depth in the link slab coded as LS3 distributed more evenly compared to those of the link slab without any reinforcement (LS1). This structural performance also results in more significant multi-cracking behaviour and smaller crack widths in the test model of LS3 compared to the other two test models. As a result, the localisation of stress in ECC link slab can be avoided in the test specimen reinforced with FRP bars.
- (3) The use of FRP reinforcement in ECC link slabs enhances elastic loading and unloading and allows for compatible composite deformation behaviour due to the similar stiffness between FRP and ECC materials. In addition, due to the noncorrosive nature of FRP reinforcement combined with the limited crack widths of ECC results in improved corrosion resistance of the suggested link slab in field applications.

ACKNOWLEDGMENTS

The authors wish to express their sincere appreciation of the Guangdong Science and Technology Planning (2016A010103045), the Innovation Research Project by Department of Education of Guangdong Province (2015KTSCX141), the National Science Natural Science Foundation of China (51678149) and Division of Transportation Guangdong Province (2013-02-029) in supporting this research.

REFERENCES

- AASHTO (2002), Standard Specifications for Highway Bridges, 17th edition, American Association of State Highway and Transportation Officials, Washington D.C., 1052p.
- H. Aktan,, Y. Koyuncu, J. Rutyna, T.M. Ahlborn, J.M. Kasper (2002). Causes and cures for prestressed concrete I-beam deterioration. Research report RC-1412. Michigan Department of Transportation. Lansing. Michigan.
- S. Alampalli, and A. P. Yannotti (1998). In-service performance of integral bridges and jointless decks Transportation Research Record, pp. 1-7.
- A. Au, C. Lam, J. Au, B. Tharmabala (2013), Eliminating deck joints using debonded link slabs: research and field tests in Ontario, Journal of Bridge Engineering, ASCE, Vol. 18, No. 8, 768-778
- C. Bakis, L. Bank, V. Brown, E. Cosenza, J. Davalos, J. Lesko, A. Machida, S. Rizkalla, T. Triantafillou (2002). Fiber-reinforced polymer composites for construction—state of the art review. Journal of Composites for Construction, 150TH ANNIVERSARY PAPER, 6(2), p. 73–87.
- Burke, M. J. (2009), Integral and Semi-Integral Bridges, John Wiley & Sons
- Caner A and Zia P (1998). Behavior and design of link slabs for jointless bridge decks[J]. PCI Journal, 43(43):68-81.
- Kim, Y. Y. and Li, V. C. (2004), Fatigue Response of Bridge Deck Link Slabs Designed with Ductile Engineered Cementitious Composite (ECC), Proceedings of International Conference on Concrete under Severe Conditions, Seoul, Korea, pp.832-841.
- Kim, Y. Y., Fischer, G., Li, V. C. (2004), Performance of bridge deck link slabs designed with ductile engineered cementitious composite ACI Structural Journal, American Concrete Institute 101, 792-801
- L. H. Lárusson (2013), Development of flexible link slabs using ductile fiber reinforced concrete, PhD thesis, Technical University of Denmark.
- M. D. Lepech and V. C. Li (2006), Long term durability performance of engineered cementitious composites, Restoration of Buildings And monuments, 12, 119-132
- M. D. Lepech and V. C. Li (2009), Application of ECC for bridge deck link slabs, Materials and Structures, 42, 1185-1195
- S.X. Wang and V. C. Li (2007). Engineered cementitious composites with high-volume fly ash, ACI Materials Journal, Title No.104-M25, 2007.
- A. M. Wolde-Tinsae and J. E. Klinger (1987). Integral bridge design and construction. Report FHWA/MD-87/04. Maryland Department of Transportation.
- Y. Zheng, C.H. Li, J.B. Yang, C. Sun (2015), Influence of arching action on shear behaviour of laterally restrained concrete slabs reinforced with GFRP bars, Composite Structures, Vol. 132, pp.20-34.



LARGE-SCALE SLENDER HYBRID FRP-CONCRETE-STEEL DOUBLE SKIN TUBULAR COLUMNS SUBJECTED TO ECCENTRIC COMPRESSION

P. Xie^{1,2}, T. Jiang³ and J.G. Teng^{2,*}

¹ Department of Civil Engineering, South China Agriculture University, Guangzhou, China;

² Department of Civil and Environmental Engineering, The Hong Kong Polytechnic University, Hong Kong, China, *Email: cejteng@polyu.edu.hk

³ Department of Civil Engineering, Zhejiang University, Hangzhou, China,

KEYWORDS :

Hybrid structures; Experimental study ; Characterization of FRP and FRC materials/systems; Eccentric compression; Slenderness

ABSTRACT

Hybrid FRP-concrete-steel double skin tubular columns (hybrid DSTCs) are a new and promising form of columns that exhibits excellent structural performance and corrosion resistance. Previous studies on hybrid DSTCs have mainly been limited to small-scale specimens and paid limited attention to the behavior of eccentrically-loaded slender hybrid DSTCs. This paper presents the test results of two eccentrically-loaded large-scale hybrid DSTCs, including one short column and one slender column, of a larger test program aimed at investigating the behavior of large-scale slender hybrid DSTCs subjected to eccentric compression. A comparison of test results of the two columns reveals clearly the effect of slenderness on the load-carrying capacity and failure mode of eccentrically-loaded hybrid DSTCs. To capture the effect of slenderness on the behavior of eccentrically-loaded hybrid DSTCs, a theoretical column model, which traces the lateral deflection of columns using the numerical integration method and incorporates an eccentricity-dependent stress-strain model for concrete in hybrid DSTCs, was developed. It is shown that the column model is accurate in predicting the load-carrying capacity of hybrid DSTCs and reasonably accurate in predicting the lateral deflection of hybrid DSTCs.

INTRODUCTION

Hybrid FRP-concrete-steel double skin tubular columns (hybrid DSTCs) are a new form of columns invented by Professor J.G. Teng (Teng *et al.* 2004, 2007). A hybrid DSTC consists of an outer tube made of FRP and an inner tube made of steel, with the annular space in between filled with concrete. This new form of columns has excellent promise for use in situations where ductility and corrosion resistance are of major concern. A large body of research has been conducted on hybrid DSTCs since their invention; however, the existing experimental studies on the static behavior of hybrid DSTCs have mainly been concerned with concentric compression testing of small-scale short specimens with a diameter of 200 mm or less and a height-to-diameter ratio of three or less (e.g., Wong *et al.* 2008; Qian and Liu 2006; Ozbakkaloglu and Fanggi 2014, 2015; Zhang *et al.* 2017). In practice, most columns are larger in size and more slender than those specimens and are subjected to combined compression and bending rather than concentric compression. Therefore, eccentric compression tests on large-scale slender hybrid DSTCs are much needed. To date, only Yao *et al.* (2015) has conducted a series of such tests, in which a total of five hybrid DSTCs of 300 mm in diameter and 1800 mm in height were tested under combinations of three values of load eccentricity (30 mm to 90 mm) and two values of FRP tube thickness (6 mm and 10 mm). A significant deficiency of their tests is that the effect of column slenderness was neither sufficiently well reflected nor properly interpreted as the column height was kept constant.

To better understand the effect of slenderness on the behavior of hybrid DSTCs, the authors carried out a systematic test programme on large-scale slender hybrid DSTCs subjected to eccentric compression, which covered four values of slenderness (a height-to-diameter ratio of 3 to 11), four values of load eccentricity (from 0 mm to 150 mm) and three values of FRP tube thickness (2 mm, 3 mm and 4 mm) (Xie 2018). This paper presents the test results of two columns of that test programme although some of the observations from the entire test programme are also mentioned to help understand the behavior of the two chosen columns. The two chosen columns had the two extreme values of slenderness (height-to-diameter ratio = 3 or 11) examined in the test programme, and their other geometric and material properties were the same. The test results are also compared with a theoretical column model, and the effect of using a different stress-strain model for the confined concrete in the column model is examined in the comparison.

Test Specimens

The two hybrid DSTCs both had a nominal outer diameter (D_o) of 300 mm (excluding the thickness of the GFRP tube which was 3 mm) and were provided with the same steel tube (with an outer diameter of 219 mm and a thickness of 6.12 mm) and filament-wound GFRP tube (with 6 layers of FRP, fiber winding angles of $\pm 80^\circ$ with respect to the longitudinal axis of the tube, and a nominal fiber volume fraction of 55%). Both columns were tested under the same load eccentricity of 50 mm. The two columns are respectively designated as C3 and C11 to indicate their height-to-diameter ratios (L/D_o) of 3 and 11. Self-compacting concrete (SCC) was used to fill the relatively narrow space between the outer FRP tube and the inner steel tube. The SCC had a compressive strength of 51.5 MPa and a corresponding axial strain of 0.00290. The modulus of elasticity and the yield stress of steel tubes were 215.4 GPa and 278.5 MPa, respectively. The hoop modulus of elasticity of the GFRP tubes was found to be 39.62 GPa from material testing.

The layout of strain gauges and LVDTs of Specimen C11 is illustrated in Figure 1. Strain gauges were installed at seven sections (i.e., Sections A, B, C, D, E, F and G) covering the 1800 mm mid-height region of the specimen. The mid-height section (i.e., Section A) was expected to be the most critical section, so it was most densely instrumented with strain gauges: the outer surfaces of the steel tube and the GFRP tube were respectively installed with eight pairs of uni-directional strain gauges (one axial strain gauge and one hoop strain gauge) at 45° apart. In addition, the axial deformation of the 240 mm mid-height region (covering Section A) of the column was measured by four LVDTs (L113 to L116) at 90° apart. For the other six sections, only the strains of the FRP tube were monitored with the number of strain gauge pairs reduced to four for the two outermost sections (Sections F and G, see Figure 1). At each of the seven sections, a horizontal LVDT (L117 to L123) was also installed on the tension side of the column to monitor the lateral deflections of the column. Another four LVDTs (L124 to L127) were employed to monitor the rotations of both ends of the column. For Specimen C3, the instrumentation was similar but the number of sections monitored was reduced to one due to its much smaller height. The end loading assembly, comprising a steel roller rested on a grooved steel plate, was installed on each corbel end to receive the compressive load at the desired eccentricity (50 mm) as shown in Figure 2. The compression tests were conducted using a 10,000 kN servo-hydraulic testing machine under displacement control at a constant axial strain rate of 0.0005/min.

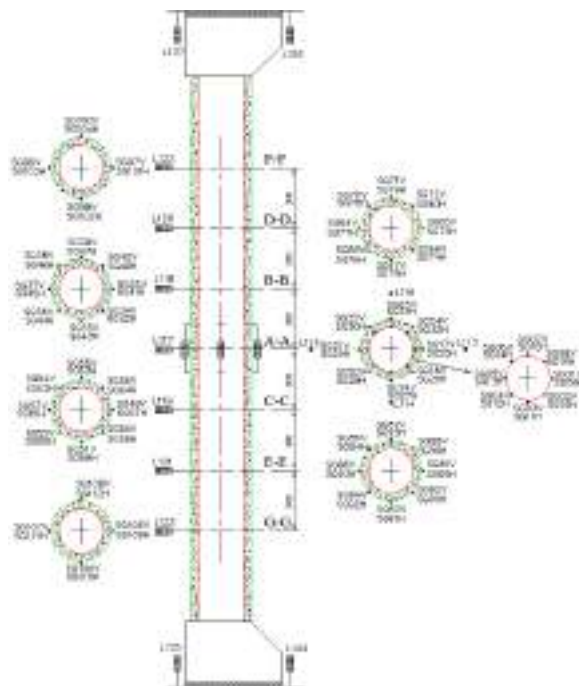


Figure 1 Layout of strain gauges and LVDTs of Specimen C11



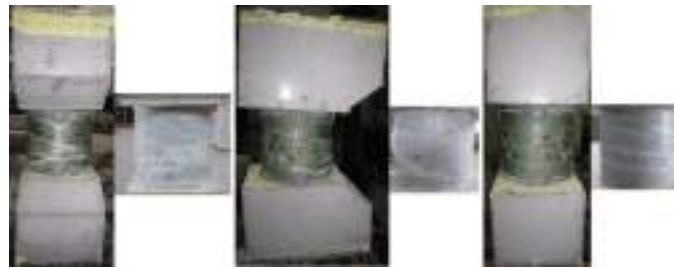
Figure 2 Test setup

Test Results and Discussions

Failure modes

An inspection of the failed column specimens of the test programme revealed two different failure modes: the compression-dominated mode and the flexure-dominated mode. The former failure mode was observed in

relatively short specimens (e.g. Specimen C3) while the latter failure mode was observed in relatively slender specimens (e.g. Specimen C11). The two failure modes are illustrated in Figure 3 using Specimens C3 and C11. For each specimen, Figure 3 shows six photos taken at three different angles for the compression face, the lateral face and the tension face, in sequence from left to right. Each view angle includes two photos: before and after the removal of the outer GFRP tube of the failed specimen. It can be seen that Specimen C3 failed by the hoop tensile rupture of the GFRP tube on the compression side near specimen mid-height due to the dilation of the confined concrete. By contrast, Specimen C11 showed no clear sign of rupture of the GFRP tube until the test was terminated due to excessive lateral deflections; instead, intensive tensile cracks (white stripes) along the fiber directions developed on the tension side of the GFRP tube as a consequence of resin damage due to the development of tensile cracks at the corresponding positions of the concrete. This statement is substantiated by the coincidence of positions of cracks in the GFRP tube and those in the concrete as can be seen in the pair of photos for the tension face. Tensile cracks also developed in Specimen C3, but their intensity and widths were much smaller as the second-order moment induced by the lateral deflection of the specimen was much less significant.



(a) Specimen C3



(b) Specimen C11

Figure 3 Failure modes of eccentrically-loaded hybrid DSTCs

Axial Strain Distributions over Mid-height Section

The distributions of axial strains over the mid-height section of the two specimens are shown in Figure 4, in which the axial strain at the extreme fiber was obtained from the reading of the corresponding axial strain gauge while the axial strain at each of the other positions was taken to be the average reading of the pair of axial strain gauges at the same distance from specimen centerline. In Figure 4, each set of symbols of the same shape represents the

axial strain distribution at a specified axial load level, with the final load level being the peak load of the specimen. The hollow symbols represent the axial strains of the GFRP tube while the solid symbols represent the axial strains of the steel tube. Overall, the axial strains of steel tubes and GFRP tubes are approximately proportional to the distance from the neutral axis, suggesting the general validity of the plane section assumption.

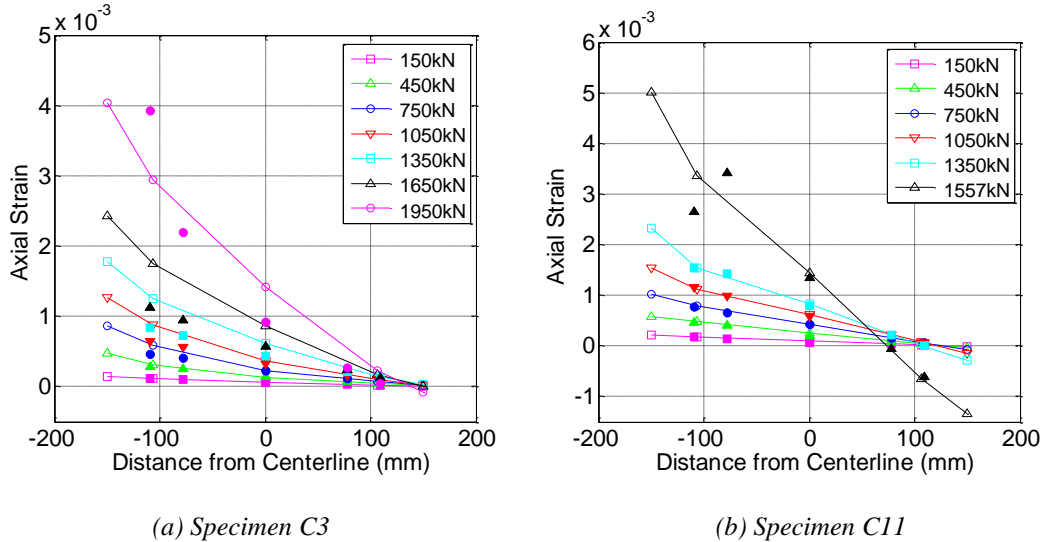


Figure 4 Axial strain distributions in the FRP and the steel tubes at the mid-height section

In addition, a comparison of all column specimens (Xie 2018) showed that the ultimate axial strain at the extreme compression fiber increases with an increase in load eccentricity. This phenomenon is termed the “axial strain enhancement effect” and has also been observed in RC columns (e.g. Scott *et al.* 1982) and FRP-confined RC columns (e.g. Bisby and Ranger 2010). It is believed that this phenomenon can be attributed to the presence of an axial strain gradient due to eccentric compression, which allows the concrete at the more compressed region to dilate towards the less compressed region.

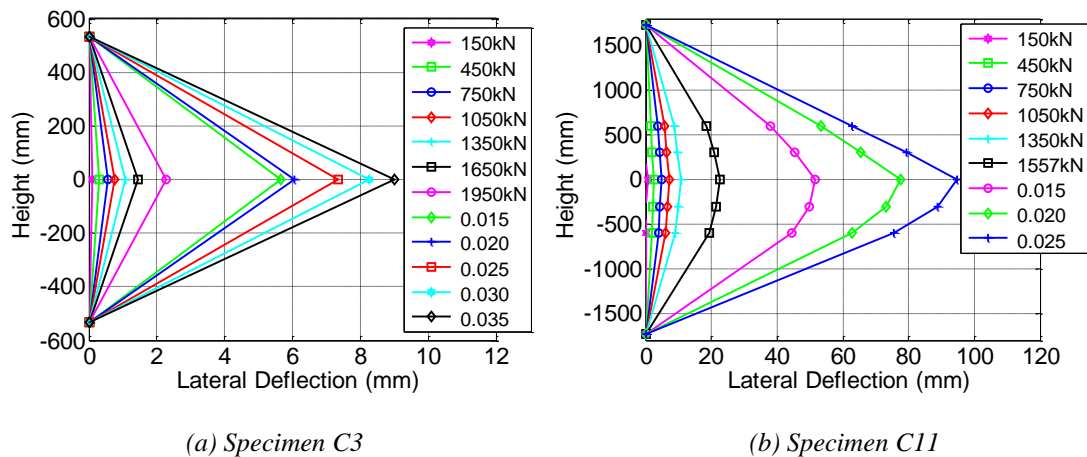


Figure 5 Lateral deflections down the column height

Column Lateral Deflections

The lateral deflections along the height of the two column specimens are shown in Figure 5. The lateral deflections were obtained from the readings of horizontal LVDTs installed at different heights of the specimen. In Figure 5, each curve represents the column lateral deflection profile corresponding to a specific deformation state: before the attainment of peak axial load, the curves are denoted by specific axial load levels; afterwards, the curves are denoted by the axial strain levels of the extreme compression fiber of concrete. It can be seen from the results of Specimen C11 that the lateral deflection profile is nearly symmetrical with respect to column mid-height.

Axial Load-Axial Strain and Axial Load-Lateral Deflection Responses

Figures 6 and 7 show respectively the axial load-axial strain curves for the extreme compression fiber and the axial load-lateral deflection curves for the column mid-height to examine the effect of slenderness on the behavior of hybrid DSTCs. The axial strain at the extreme compression fiber and the lateral deflection at column mid-

height were respectively taken from the readings of the longitudinal LVDT nearest to the extreme compression fiber (i.e., L113 in Figure 1) and the horizontal LVDT at column mid-height (i.e., L117 in Figure 1). As expected, the axial load capacity of the specimen decreases with an increase in slenderness: the axial load capacity of Specimen C11 is only 72% that of Specimens C3. Of the two specimens compared, Specimen C3 suffered material failure while Specimen C11 suffered stability failure, and the shapes of the second segment of the curves are thus ascending and descending respectively. Additionally, the lateral deflection at mid-height at ultimate condition is seen to increase with column slenderness. Each curve in Figures 6 and 7 is marked with a solid dot to indicate the point of ultimate condition. For Specimen C3, the ultimate condition was reached when the FRP tube ruptured. For Specimen C11, the horizontal LVDT at column mid-height was removed shortly before the termination of testing as the lateral deflection there approached the capacity of the LVDT (100 mm). Therefore, for convenience of discussion, the ultimate condition of Specimen C11 is defined as the condition of the column when the horizontal LVDT at column mid-height was removed.

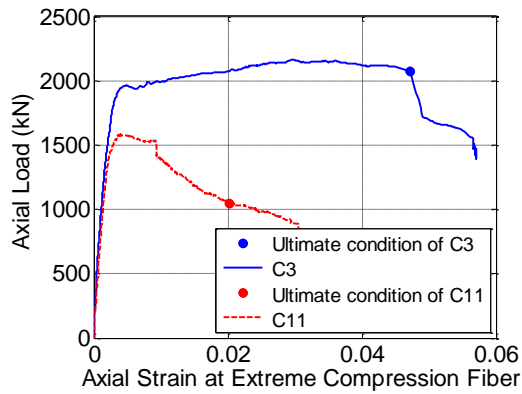


Figure 6 Axial load-axial strain curves for the extreme compression fiber

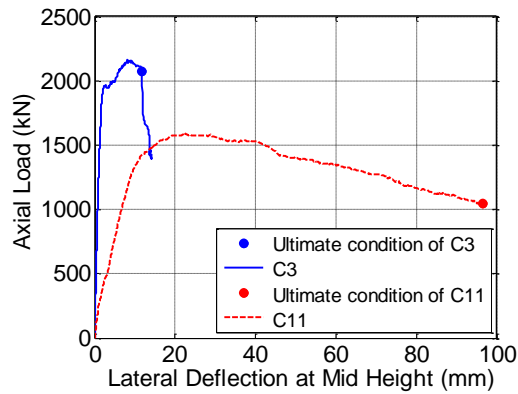


Figure 7 Axial load-lateral deflection curves for column mid-height

Key Test Results

The key test results are summarized in Table 1. In this table, N_{peak} is the peak axial load of a specimen while the other results are all for the ultimate condition. N_u and M_u are respectively the axial load and the bending moment at column mid-height at the ultimate condition. M_u is the sum of the first-order bending moment due to the initial eccentricity (e) and the second-order bending moment caused by the lateral deflection at column mid-height at the ultimate condition (e'_u). $\epsilon_{h,rupt}$ and ϵ_{cu} are respectively the hoop strain of the FRP tube and the corresponding axial strain at the extreme compression fiber at the ultimate condition. $\sigma_{\theta u}$ is the hoop stress of the FRP tube calculated from ϵ_{cu} and $\epsilon_{h,rupt}$ considering the nonlinear biaxial tube behavior using Jones and Nelson's (1975) model (Xie *et al.* 2017). $\epsilon'_{h,rupt}$ is the nominal hoop rupture strain and $= \sigma_{\theta u}/E_{\theta}$, where E_{θ} is the hoop modulus of elasticity of the FRP tube.

Table 1 Key test results of eccentrically-loaded slender DSTCs

Specimen	N_{peak} (kN)	M_u (kN·m)	N_u (kN)	e'_u (mm)	ϵ_{cu}	$\epsilon_{h,rupt}$	$\sigma_{\theta u}$ (MPa)	$\epsilon'_{h,rupt}$
C3	2166	128.1	2076	11.71	0.0472	0.0108	256.3	0.00647
C11	1557	150.1	1025	96.46	0.0203	0.00625	183.4	0.00463

THEORETICAL ANALYSIS

Eccentricity-Dependent (EccD) Stress-Strain Models

Eccentricity-dependent (EccD) stress-strain models for FRP-confined concrete subjected to eccentric compression can be formulated by modifying a concentric-loading stress-strain model known also as an "eccentricity-independent (EccI) stress-strain model". In the modification process, the ratios between the parameters for concentric compression and those for eccentric compression can be directly or indirectly related to the load eccentricity. Lin (2016) developed an EccD stress-strain model for FRP-confined concrete by modifying Teng *et al.*'s (2009) EccI stress-strain model. Yu *et al.* (2010b) proposed an EccD stress-strain model for confined concrete in hybrid DSTCs by modifying a previous EccI stress-strain model developed by the same research group (Yu *et al.* 2010a). The main difference between Yu *et al.*'s EccD model and Lin's EccD model is that the ultimate axial

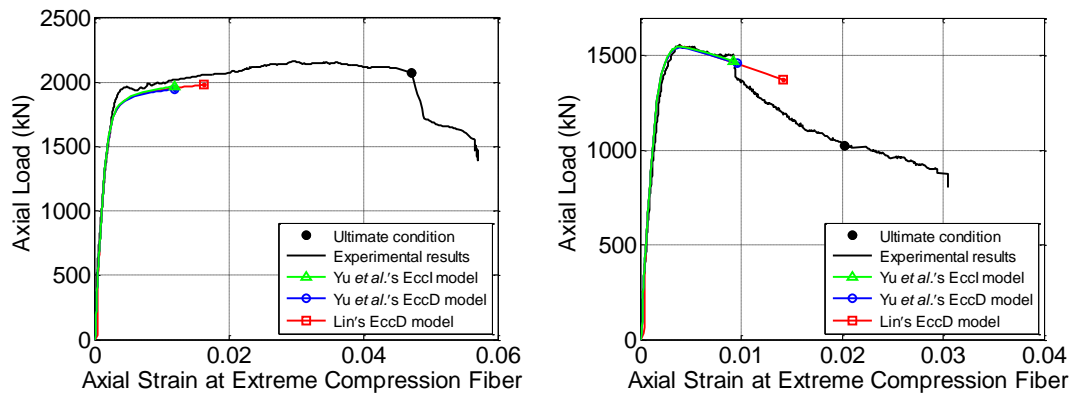
strain (ϵ_{cu}) is eccentricity-independent for the former while ϵ_{cu} increases with the eccentricity for the latter (i.e., axial strain enhancement effect).

Theoretical Column Model

The theoretical column model was modified from Jiang and Teng's (2012) column model for FRP-confined RC columns which can capture the slenderness effect in columns. Jiang and Teng's (2012) column model was built on a general framework in which the lateral deflection of a column is traced using the numerical integration method and Teng *et al.*'s (2009) EccI stress-strain model for FRP-confined concrete is adopted in section analysis for each grid point. In the present column model for slender hybrid DSTCs, the general framework of Jiang and Teng's (2012) column model is retained, but the stress-strain response of the confined concrete in hybrid DSTCs is described by one of the following three stress-strain models: Yu *et al.*'s EccI model, Yu *et al.*'s EccD model and Yu *et al.*'s EccI model modified using the approach of Lin's EccD model (referred to simply as Lin's EccD model). Note that the position of the neutral axis, which varies during the analysis process using Lin's EccD model, should be determined through an iterative process to reach force equilibrium for each axial strain value. It should also be noted that the actual eccentricity is the sum of the initial load eccentricity and the lateral deflection, which varies down the height of the column; that is, in the analysis procedure using Yu *et al.*'s EccD model, the stress-strain curve of concrete to be used for each grid point needs to be updated for each lateral deflection value. The inner steel tube was assumed to have an elastic-perfectly plastic stress-strain behavior in the longitudinal direction, and the effect of its hoop stresses on its longitudinal behavior was ignored. Besides, the direction axial contribution of the GFRP tube to the mechanical resistance of the column was neglected due to its small cross-sectional area. Details of the column model can be found in Xie (2018).

Comparison with Test Results

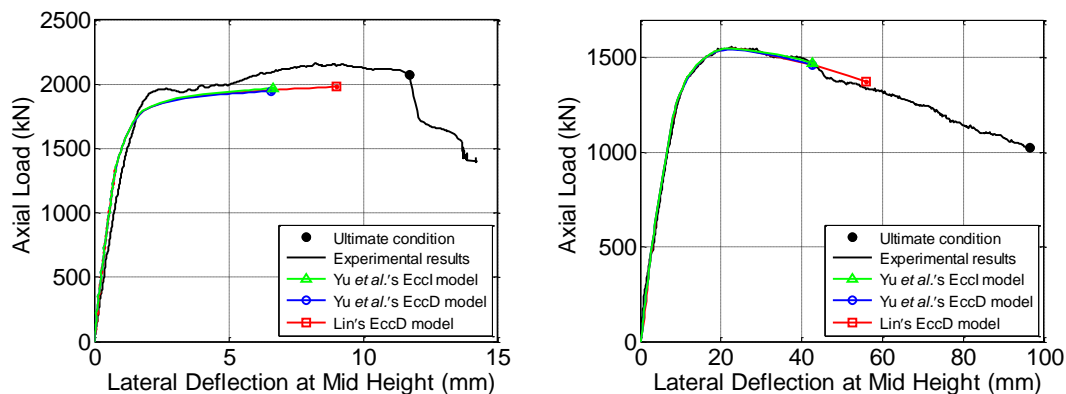
The experimental axial load-axial strain curves for the extreme compression fiber and the experimental axial load-lateral deflection curves for the column mid-height are compared with the predicted curves in Figures 8 and 9, respectively. The predicted curves terminate when the hoop strain at the extreme compression fiber of FRP tube reaches its nominal hoop rupture strain given in Table 1 (i.e., the hoop stress of FRP tube reaches $\sigma_{\theta u}$).



(a) Specimen C3

(b) Specimen C11

Figure 7 Experimental versus predicted axial load-axial strain curves



(a) Specimen C3

(b) Specimen C11

Figure 8 Experimental versus predicted axial load-lateral deflection curves

It can be seen from Figures 8 and 9 that the three stress-strain models all lead to close predictions for the peak axial load. However, the two indicators related to deformability (i.e., axial strain at the extreme compression fiber at the ultimate condition and the corresponding lateral deflection at mid-height), especially the former, are significantly underestimated by the column model regardless of the choice among the three stress-strain models. Of the three models, Lin's EccD model provides relatively close predictions for the two deformability indicators because it considers the axial strain enhancement effect. The underestimation of deformability may be attributed to the incapability of the column model to capture the effect of steel tube local buckling and the likely loss of full composite action in hybrid DSTCs during later stages of loading..

CONCLUSIONS

This paper has presented the test results of two eccentrically-loaded large-scale hybrid DSTCs (including a short column, Specimen C3, and a slender column, Specimen 11) of a test programme aimed at investigating the behavior of large-scale slender hybrid DSTCs subjected to eccentric compression. The following conclusions can be drawn from comparisons of test results between the two columns and comparisons between test results and numerical predictions:

- (1) As the column slenderness increases, the failure mode of hybrid DSTCs changes from one of material failure to one of stability failure. Of the two specimens discussed in the present paper, Specimen 3 reached its ultimate condition when the FRP tube ruptured due to hoop tension generated by the dilation of concrete while the rupture of FRP tube was not observed during the testing of Specimen 11.
- (2) As expected, when a hybrid DSTC becomes more slender, its axial load capacity decreases and its lateral deflection at the ultimate condition increases;
- (3) The theoretical column model predicted the load-carrying capacities of the two columns well but failed to provide accurate predictions for the column mid-height deflection
- (4) The three stress-strain models used in the column model, including Yu *et al.*'s EccI stress-strain model, Yu *et al.*'s EccD stress-strain model and Lin's EccD stress-strain model, all led to reasonably accurate predictions for the axial load capacity of slender hybrid DSTCs. However, they all underestimated the lateral deflection of eccentrically-loaded slender hybrid DSTCs, although Lin's EccD model is significantly more accurate than the other two models in this respect.

ACKNOWLEDGMENTS

The authors are grateful for the financial support from the National Key Research and Development Programme of China (Project No.: 2017YFC0703000) and the National Natural Science Foundation of China (Project No: 51778246).

REFERENCES

- Bisby, L. and Ranger, M. (2010). "Axial-flexural interaction in circular FRP-confined reinforced concrete columns", *Construction and Building Materials*, 24(9), 1672-1681.
- Jiang, T. and Teng, J.G. (2012). "Theoretical model for slender FRP-confined circular RC columns", *Construction and Building Materials*, 32(4), 66-76.
- Lin, G. (2016). *Seismic Performance of FRP-Confined RC Columns: Stress-Strain Models and Numerical Simulation*, Ph.D. thesis, The Hong Kong Polytechnic University, Hong Kong, China.
- Ozbakkaloglu, T. and Fanggi, B. L. (2014). "Axial compressive behavior of FRP-concrete-steel double-skin tubular columns made of normal- and high-strength concrete", *Journal of Composites for Construction*, ASCE, 18(1), 04013027.
- Ozbakkaloglu, T. and Fanggi, B.A.L. (2015). "FRP-HSC-steel composite columns: behavior under monotonic and cyclic axial compression", *Material and Structures*, 48(4), 1075-1093.
- Qian, J.R. and Liu, M.X. (2006). "Experiment of FRP-concrete-steel double-skin tubular long columns under axial compressive load", *Concrete*, 9, 31-34. (in Chinese)

- Scott, B.D., Park, R. and Priestley, M.J.N. (1982). "Stress-strain behavior of concrete confined by overlapping hoops at low and high strain rates", *ACI Journal*, 79(2), 13-27.
- Teng, J.G., Yu, T. and Wong, Y.L. (2004). "Behavior of hybrid FRP-concrete-steel double-skin tubular columns", *Proceedings, Second International Conference on FRP Composites in Civil Engineering*, 8-10 December, Adelaide, Australia, 811-818.
- Teng, J. G., Huang, Y. L., Lam, L. and Ye, L. P. (2007). "Theoretical model for fiber reinforced polymer-confined concrete", *Journal of Composites for Construction*, ASCE, 11(2), 201-210.
- Teng, J.G., Jiang, T., Lam, L. and Luo, Y.Z. (2009). "Refinement of a design-oriented stress-strain model for FRP-confined concrete", *Journal of Composites for Construction*, ASCE, 13(4), 269-278.
- Wong, Y.L., Yu, T., Teng, J.G. and Dong, S.L. (2008). "Behavior of FRP-confined concrete in annular section columns", *Composites Part B-Engineering*, 39(3), 451-466.
- Xie P., Lin G., Teng, J.G. and Yu, T. (2017). "Modelling of concrete-filled FRP tubes considering nonlinear biaxial tube behavior", *Proceedings, 6th Asia-Pacific Conference on FRP in Structures (APFIS 2017)*, 19-21 July, Singapore.
- Xie, P. (2018). *Behavior of Large-Scale Hybrid FRP-Concrete-Steel Double-Skin Tubular Columns Subjected to Concentric and Eccentric Compression*, Ph.D. thesis, The Hong Kong Polytechnic University, Hong Kong, China.
- Yao, J., Jiang, T., Xu, P. and Lu, Z.G. (2015). "Experimental investigation on large-scale slender FRP-concrete-steel double-skin tubular columns subjected to eccentric compression", *Advances in Structural Engineering*, 18(10), 1737-1746.
- Yu, T., Teng, J.G. and Wong, Y.L. (2010a). "Stress-strain behavior of concrete in hybrid double-skin tubular columns", *Journal of Structural Engineering*, ASCE, 136(4), 379-389.
- Yu, T., Wong, Y.L. and Teng, J.G. (2010b). "Behavior of hybrid FRP-concrete-steel double-skin tubular columns subjected to eccentric compression", *Advances in Structural Engineering*, 13(5), 961-974.
- Zhang, B., Teng, J.G. and Yu, T. (2017). "Compressive behavior of double-skin tubular columns with high-strength concrete and a filament-wound FRP tube", *Journal of Composites for Construction*, ASCE, 21(5), 04017029.



HOW MUCH DAMAGE CAN FRP TUBE TOLERATE IN CFFT?

Chenxi Lu ¹, James St. Onge ² and Amir Fam ³

¹ MAsc. Student, Department of Civil Engineering, Queen's University, Canada, Ellis Hall, 58 University Avenue, Kingston, K7L 3N6, Canada, Email: 16cl2@queensu.ca

² PhD. Candidate, Department of Civil Engineering, Queen's University, Canada,

Ellis Hall, 58 University Avenue, Kingston, K7L 3N6, Canada, Email : james.st.onge@queensu.ca

³ Associate Dean of Research and Graduate Studies, Donald and Sarah Munro Chair in Engineering and Applied Science, Professor Department of Civil Engineering, Queen's University, Canada, Ellis Hall, 58 University Avenue, Kingston, K7L 3N6, Canada, Email: amir.fam@queensu.ca.

ABSTRACT

Concrete-filled FRP tube (CFFT) is an attractive system suitable for structural applications such as columns, piles, poles and arches. The tube is a stay-in-place structural form that fully or partially replaces internal reinforcement. Layers or fibres oriented at various directions provide great flexibility and control of the strength and stiffness in the longitudinal and circumferential directions. One vulnerability of the system is that the FRP tube, being external, is exposed. As such, it is possibly vulnerable to accidental or intentional damage. This study is the first of its kind to address this concern. Damage is simulated by a controlled narrow cut of the tube throughout its full thickness. The extent of damage is represented by the length of the cut. The objective is to establish the threshold of damage beyond which significant strength loss of the CFFT member is observed. The findings of the work will help inform important decisions made by engineers, for example shutting down a bridge or a building to remove live loads, or alternatively conducting the repair work while the structure is in service. This paper focuses on flexural performance of damaged CFFTs, while the next phase of the study will focus on axial compression members. Seven CFFT specimens of 113 mm-diameter were fabricated and tested under four-point bending. One CFFT was tested fully intact as a control specimen. The other six CFFTs were cut at mid-span on the tension side to eliminate the primary contributing fibres in tension. Five were cut in the circumferential direction, one in the longitudinal direction and one had a square cut. The length of the cut varies as a percentage of the perimeter of the tube. The results showed that a 3% circumferential cut in tension results in nearly 50% loss of ultimate moment, however, the rate of reduction in strength is much lower at longer length cuts. For the tube used in this study, the critical circumferential cut length that can be sustained by the CFFT was found to be 29% of the tube perimeter, after which the member should be taken out of service.

KEYWORDS

concrete-filled, FRP tube, damage, cut, section loss, flexure

INTRODUCTION

Concrete-filled fibre-reinforced polymer tubes (CFFTs) provide an effective composite system for a number of applications including piles, columns, bridge piers, poles, and highway overhead sign structures (Fam et al. 2003). The fibre-reinforced polymer (FRP) tube provides a concrete reinforcement with a high strength-to-weight ratio and a permanent, non-corrosive formwork. The FRP tube in this system takes place of the traditional steel rebar reinforcement to resist tension and shear, but can also provide concrete confinement (Davol et al. 2001) and increase the ductility of the concrete and result in large energy absorption capacity (Mirmiran et al. 1997). The fibres in the circumferential direction are used to confine the concrete against dilation and the fibres in the axial direction provide the flexural strength and stiffness (Fam et al. 2003). CFFTs have been studied for over twenty years, and it has already been used in a number of existing structures, such as precast piles for Route 40 bridge in Virginia (Fam et al. 2003), the King's Stormwater Bridge and Marine Piles.

With an increasing number of field applications using CFFTs and the availability of the AASHTO Design Guide, concerns have been raised on the capacity of CFFTs subjected to damage. Due to the external nature of the FRP tube, it is easily accessible and could be subjected to vandalism or impact from vehicles. It is now of great importance to determine the damage level a CFFT can sustain before it needs to be taken out of service, especially in a system where there is no internal reinforcement.

EXPERIMENTAL PROGRAM

Testing Overview

The objective of this experimental program was to determine the reduction in the flexural moment capacity of CFFTs which have had their FRP tube damaged. The damage of the FRP tube was simulated by cutting the tube and the parameters of interest in this study include the cut length and orientation. One control and six damaged CFFT specimens were tested in four-point bending.

Materials

FRP tubes

The outer diameter of the tube was 113 mm and the structural wall thickness was 3.6 mm. The length of each specimen was 1152 mm, which was equivalent to 10 tube diameters. Burning-off the epoxy of FRP tube samples in a muffle furnace at 600°C exposed the fibre structure. The laminate structure was [85°/-6°/85°/-6°/85°/-6°/85°/-14°/85°], which is considered a near-cross-ply arrangement where the fibres are predominantly oriented in the longitudinal and hoop directions. The inner most layer was an epoxy rich layer with chopped fibres which is considered a non-structural layer. Coupon test was carried out to test the properties of FRP. According to ASTM D3039, FRP coupons were tested in tension to get the maximum tensile strength using an Instron 8802 testing machine. An extensometer was used to measure the strain as shown in Figure 1. Six coupons were tested and the average values were recorded as the property data. The ultimate longitudinal tensile strength of FRP was 194 MPa. In the elastic region, the Young's modulus was 16.3 GPa.



Figure 1: Coupon Test Setup

Concrete

Normal strength concrete was used in all tested specimens. The concrete infill for these was all taken from the same concrete batch. Three 100 x 200 mm concrete cylinders were tested as per ASTM C39 to determine the concrete compressive strength f'_c . The average compressive strength of the concrete was 29 MPa.

Test Setup

The CFFT specimens were tested in four-point bending. The point load was applied from a Riehle Universal Testing machine with a 900 kN load capacity. The testing machine operated in stroke control at a rate of 1 mm/min. The layout of the test setup and ratio of each span is shown in Figure 2.

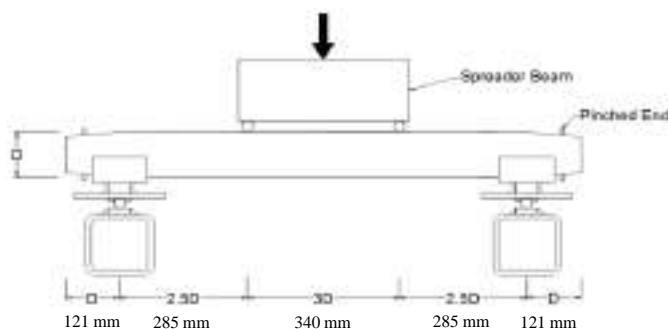


Figure 2: Test Setup Layout

The total span between the centreline of the two supports was 910 mm. The length of the constant moment region was 340 mm, equivalent to three tube diameters. The test setup used a combination of pin supports and sliding plates to ensure the specimens could safely deflect to their full extent, free from any external restraint. All specimens had their FRP tubes pinched at both ends with steel threaded rods before casting. The ends became ovals with a smaller dimension in the vertical direction. The conical end is intended to minimize slip of concrete relative to the tube to achieve full composite behaviour.

Simulated Damage in CFFT Specimens

To simulate the damage of CFFTs, artificial cuts were made using a hand-held rotary tool. The diameter of the cutting bit was 1.07 mm. The length and orientation of each cut differed with each specimen. The error of the cut was within 0.5 mm after measuring the actual cut lengths. All cuts were made symmetrical around the bottom-most fibre in tension, at mid-span. Figure 3 shows a schematic of the under-side of the tubes (in tension) at mid-span, including the various cuts. The first specimen (F1) was the control sample that did not have any damage. The cuts on other six specimens (F2-F7) were all made on the tension side (bottom side during testing) at the mid-span location. The lengths of the cuts were classified as a percentage of the outer perimeter of the FRP tube. Samples F2, F3, F4, and F5 were cut in circumferential direction with lengths of 1%, 3%, 10%, and 20% of the perimeter, corresponding to 3.5 mm, 10.7 mm, 35.5 mm and 71 mm, respectively. Specimen F6 had a cut in the longitudinal direction with a length of 10% of perimeter, equivalent to 35.5 mm. Specimen F7 had a square section of the tube wall removed with the side dimensions being 10% of the perimeter and is equivalent to 35.5x35.5 mm. Figure 4 shows typical fabricated specimens along with typical cuts on the tension side in the longitudinal direction (a), circumferential direction (b), and the square cut (c).

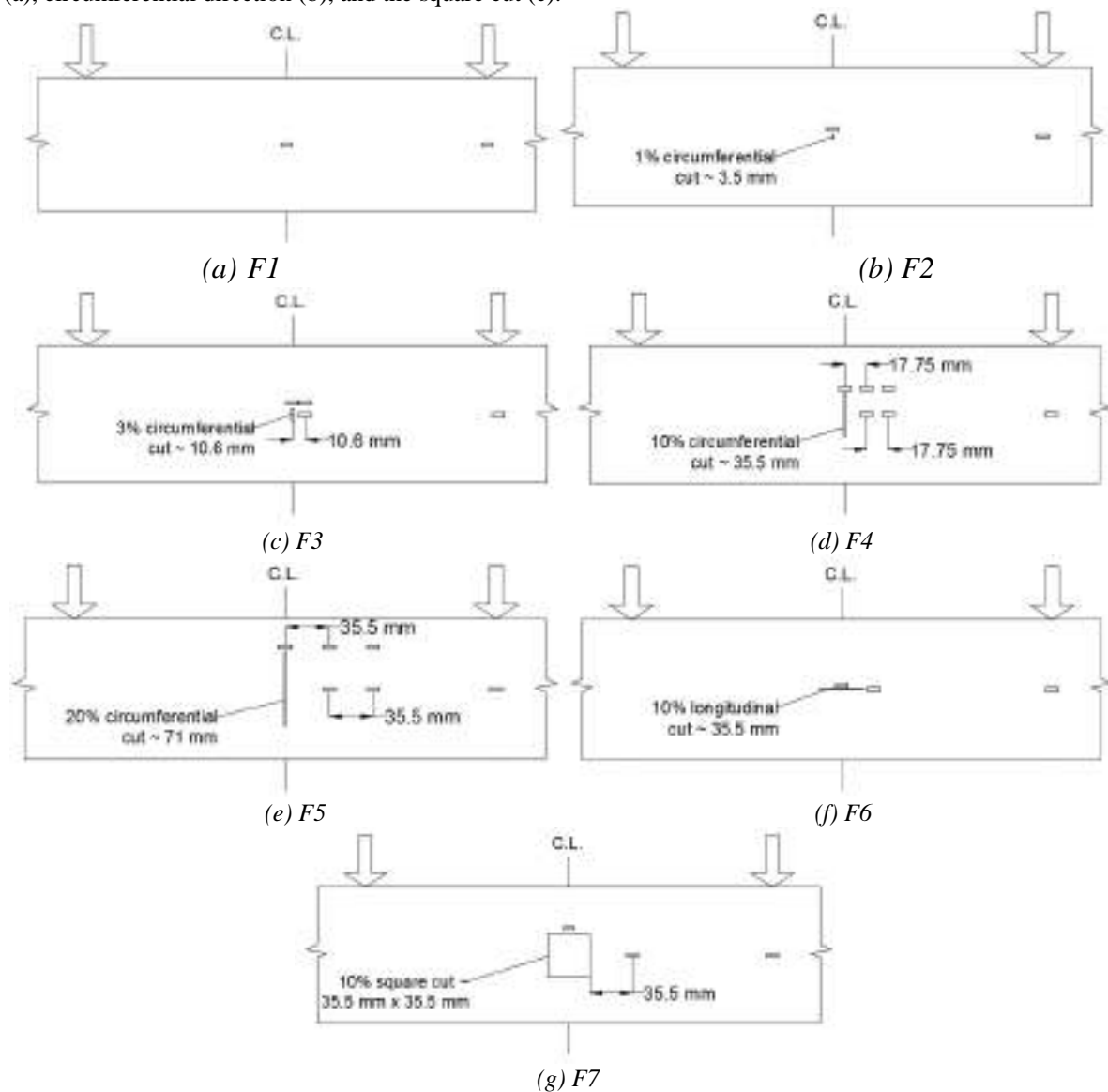


Figure 3: Various Cuts and Strain Gauge Layouts on Tension Side

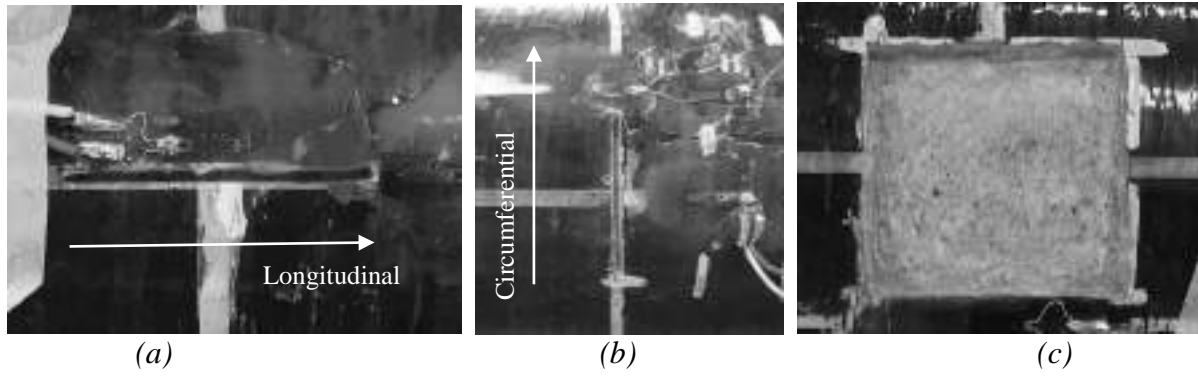


Figure 4: Longitudinal Cut (a), Circumferential Cut (b) and Square Cut (c) on Tension Side

Instrumentation

Strain gauges and linear potentiometers (LPs) were used in each test. Every specimen had a strain gauge at the mid-span on the compression side (top). The locations of strain gauges on the tension side (bottom) were shown in Figure 3. The figures show the spans of the CFFT between two applied point loads. Two LPs were used during each test and placed at the mid-span of the specimen on either side. The LPs measured deflections of the CFFTs from an aluminium bracket that was adhered to the outside of the FRP tube using epoxy. The average deflection value read by the two LPs was recorded as the deflection of the specimen at mid-span.

RESULTS AND DISCUSSIONS

Table 1 shows a summary of test results. The weight of the specimen was 26.5 kg, and the weight of the spreader beam was 20.76 kg. The resulting moment from the dead load of the specimen and the spreader beam was 0.06 kNm. The moment capacity shown in Table 1 was the maximum moment due to the applied load and self-weight. The control specimen (F1) had the largest moment capacity of 11.27 kNm.

Table 1: Summary of Test Results

Specimen	Percentage of Cut (% πD)	Length of Cut (mm)	Direction of cut	Maximum Load (kN)	Maximum Moment (kNm)	Moment capacity (kNm)	Maximum Deflection (mm)
F1	0	0	-	78.65	11.21	11.27	28.73
F2	1	3.5	Circumferential	16.68	7.33	7.39	51.47
F3	3	10.7	Circumferential	40.75	5.81	5.87	12.16
F4	10	35.5	Circumferential	29.89	4.26	4.32	8.68
F5	20	71.0	Circumferential	19.14	2.73	2.79	6.74
F6	10	35.5	Longitudinal	54.44	7.76	7.82	17.73
F7	10	35.5 x 35.5	Square	32.48	4.63	4.69	10.57

Figure 5 demonstrates the relation between the reduction in bending moment capacity and the crack length of the tube in the circumferential direction, based on specimens F1 to F5. Clearly, the moment capacity decreases as the crack length is increased, however, it is not a linear relationship. Initially, at crack length up to 2% of the perimeter a sharp decline in strength, up to 45% is observed. Beyond this, the rate in moment capacity loss is reduced, such that the reduction in strength increases from 45% to 75% as crack length increase from 2% to 20% of the perimeter. This is attributed to the fact that efficiency of fibres vary from maximum at the extreme bottom fiber to zero at neutral axis. As such, loss of fibers near the extreme tension side is more critical than loss of fibers further away from the extreme tension.

Specimens F4, F6 and F7 were used to compare the effect of orientation and configuration of cuts. Circumferential cuts remove the longitudinal fibres, longitudinal cuts remove the circumferential fibres, and a square cut removes both longitudinal and circumferential fibres. The bending moment capacity of the 10% longitudinal cut (F6) and the square cut (F7) specimens were 81% and 9% larger, respectively, than that of the 10% circumferential cut specimen (F4). This is because the longitudinal fibres are more important to flexural strength than circumferential

fibers. The moment capacities of F4 and F7 are fairly close. It can be seen that the addition of the longitudinal cut in F7 had little impact on the strength, which further highlights the importance of the longitudinal fibres. In addition, due to the thickness of the rotary drill bit, sample F6 can be considered effectively as a circumferential cut equivalent to the thickness of the bit of 1.07 mm, which is equivalent to 0.3% of the perimeter and this has led to 30.6% reduction in moment capacity.

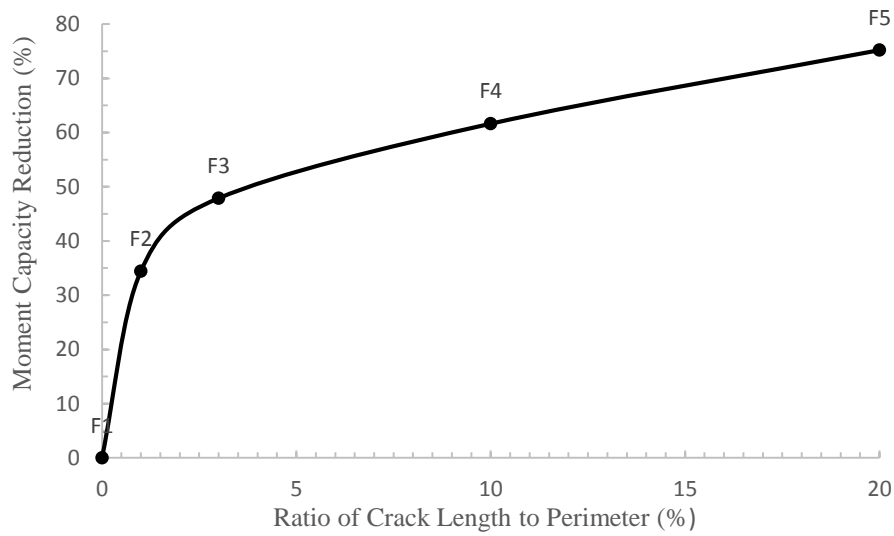


Figure 5: Relation between Moment Capacity and Crack Length

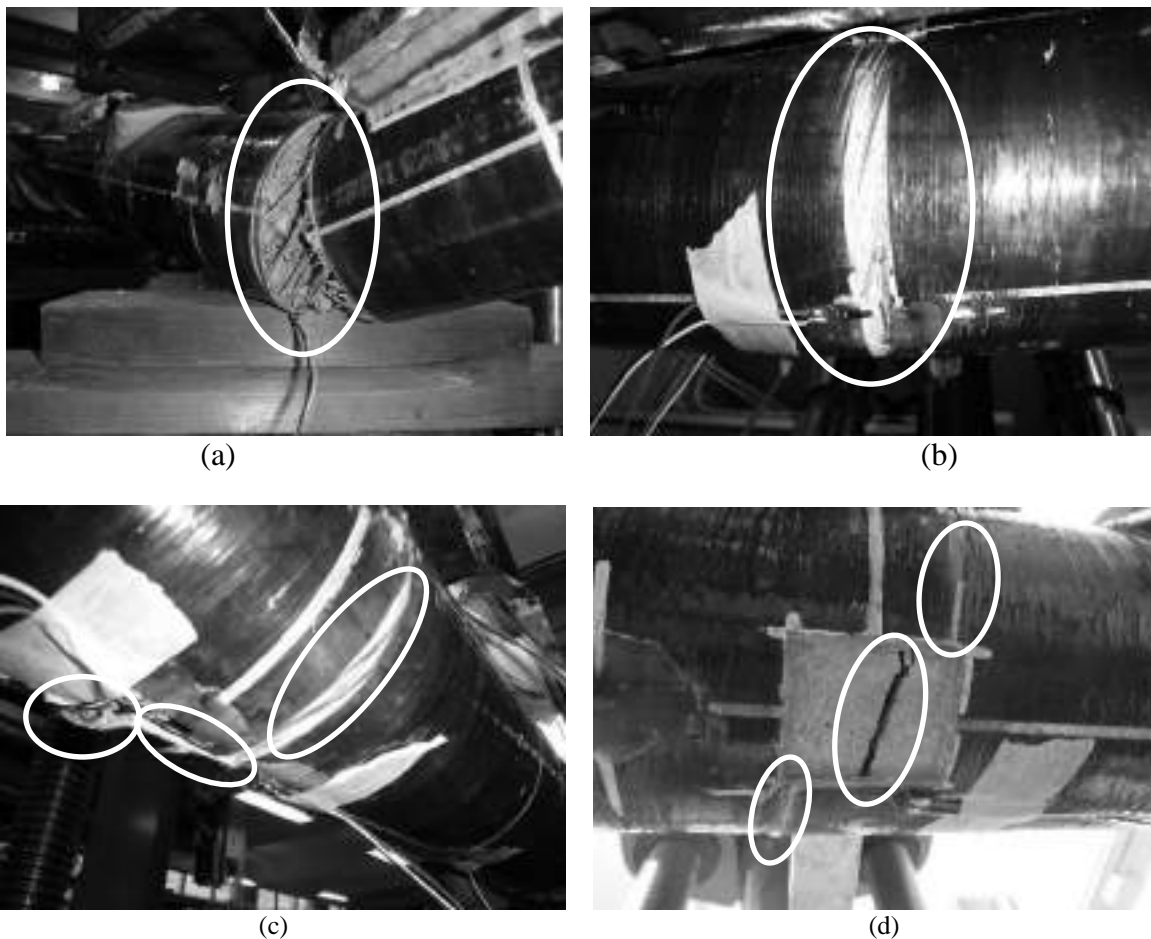


Figure 6: Typical Failure of the Control Specimen F1(a), Specimens with Circumferential Cut, F4(b) Longitudinal Cut, F6 (c), and Square Cut, F7 (d)

All seven specimens failed by tensile rupture of the FRP tube, resulting in complete failure of the CFFT. Figure 6 shows the typical failure of the control specimen F1 (a), specimen with 35.5 mm cut in the circumferential direction of F4 (b), specimen with 35.5 mm cut in the longitudinal direction of F6 (c), and 35.5 mm square cut of F7 (d). All tensile cracks took place from the tip of the cuts and extended parallel to the direction of circumferential fibres.

CASE STUDY

This section attempts to determine the damage tolerance of circumferential cuts for design purposes of CFFTs similar to those tested in this study. In principal, the reduced moment resistance of the damaged CFFT must remain higher than or equal to the demand moment. The demand moment includes two components, namely, dead load moment and live load moment, which are usually available to the designer. However, in this case study the dead load moment is assumed equal to the self-weight of the CFFT and spreader beam, while live load will be establish indirectly, based on two criteria: a) limiting service stress criterion, and b) limiting service deflection criterion. The resulting lower moment will be considered service live load moment.

For the limiting stress criterion, AASHTO CFFT Design Guide specifies that the design ultimate longitudinal tensile strength (f_{ful}) of FRP tube should be reduced from the actual strength established from coupon tests to account for the service environment. For glass fibres, the reduction factor is 0.65. Additionally, the maximum longitudinal tensile stress in the FRP tube under all sustained loads and cyclic loading due to live loads should not exceed 20% of the design ultimate tensile strength (f_{ful}). Therefore, the total service load tensile stress should not exceed 13% of the ultimate tensile strength from coupons. The ultimate tensile strength (f_{ful}^*) of FRP is 164 MPa from coupon tests. The limiting service load design tensile stress is therefore 21.3 MPa. In the elastic region, the Young's Modulus of FRP from coupon tests is 16.3 GPa. Therefore, the maximum design service load strain is 1308 $\mu\epsilon$. Figure 7 shows the relation between moment and strain at mid-span on tension side of specimen F1 due to machine loading (which is live load). Note that dead load moment is only 0.06 kNm and the corresponding strain is only 29 $\mu\epsilon$, which is insignificant in this case. The moment corresponding to 1308 $\mu\epsilon$ is 1.16 kNm, and is considered the service live load based on limiting stress criterion.

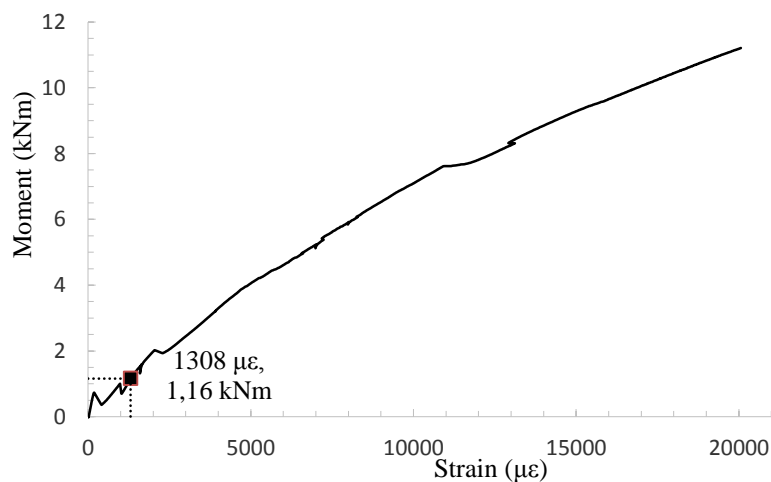


Figure 7: Relation between Moment and Strain at Mid-Span on Tension Side

For the limiting deflection criterion, deflection under live load should not exceed $L/360$, as commonly specified in design codes, where L is the span and is 910 mm. The deflection limit

is then 2.53 mm. Figure 8 shows the relation between moment and deflection due to live load. The corresponding moment is 1.57 kNm and is considered the service live load due to deflection limit criterion.

The lower of the two values, which is 1.16 kNm, is considered the final service live load moment M_{LL} . M_{DL} was 0.06 kNm as indicated earlier. The demand, which is the factored load moment, is then calculated using the combination: $M_f = 1.25M_{DL} + 1.5M_{LL}$, which was 1.815 kNm. This value is far less than the moment resistance M_r of the intact CFFT as measured from control sample F1, which is 11.27 kNm. We may now apply the principal established earlier that the reduced moment resistance of the damaged CFFT must remain higher than or equal to the demand moment M_f . This suggests that the damaged CFFT moment resistance should not be less than 1.815 kNm. This moment represents 16.1% of the full M_r of the intact CFFT. Figure 9 shows the relation between the ultimate moment retention ration and circumferential crack length. The crack length that corresponds to a moment retention ratio of 16.1% is 29.2% of the perimeter. In other words, if a CFFT similar to that tested in this study is used in design and subjected to a damage in the form of a circumferential cut in the tension zone and length of the cut is smaller than or equal to 29% of the perimeter, it could still resist the factored static design load. If the cut is longer than 29% the CFFT does not meet the ultimate strength limit state requirement. It should be noted that this exercise is limited to static loading and the reduced fatigue life under cyclic loading conditions due to a cut, even if it was a very small cut, is beyond the scope of this study.

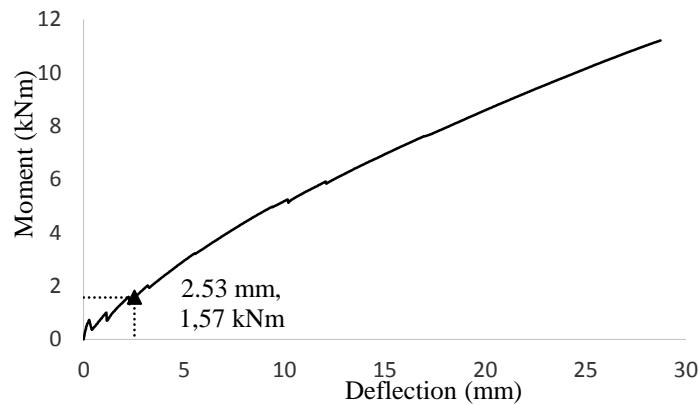


Figure 8: Relation between Moment and Deflection at Mid-Span on Tension Side

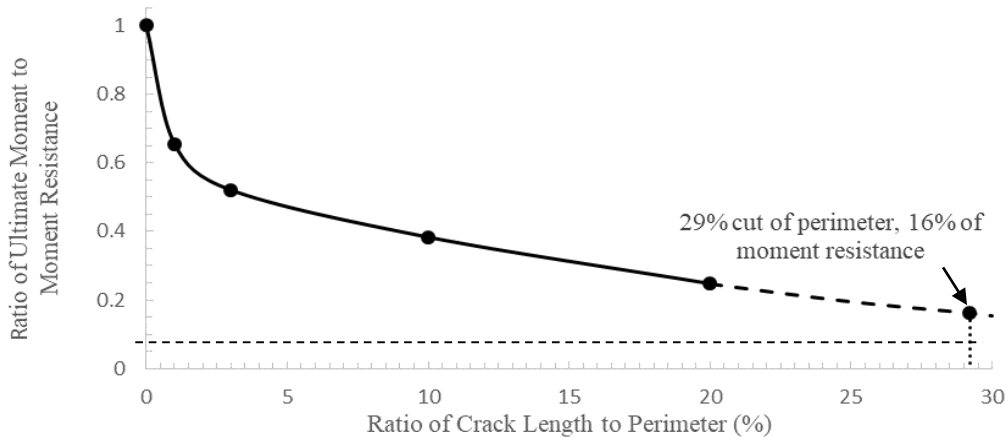


Figure 9: Relation between the Ratio of Ultimate Moment to Moment Resistance and Ratio of Crack Length to Perimeter

CONCLUSIONS

This study addressed a question raised by designers of CFFTs that has never been looked at before: how much damage the FRP tube can take before the CFFT flexural member is considered inadequate to meet the required loading demand? Seven CFFT beam specimens were tested to determine their ultimate moment capacity as it relates to different lengths and configurations of induced full thickness cuts of the tube in the tension side. The following conclusions are drawn:

1. The results showed that the bending moment capacity decreased with an increase in the length of circumferential cuts on the tension side, but not at constant rate. Initially, at crack length up to 2% of the perimeter a sharp decline in strength, up to 45% is observed. Beyond this, the rate in moment capacity loss is reduced, such that the reduction in strength increases from 45% to 75% as crack length increase from 2% to 20% of the perimeter. This is attributed to the fact that loss of fibers near the extreme tension side is more critical than loss of fibers closer to neutral axis.
2. Longitudinal cuts on the tension side are less critical than circumferential cuts for the tube tested in this study.
3. It was found that in a case study representing a field application design, a comparable CFFT to the one tested in this study can tolerate a circumferential cut with a length of up to 29% of the tube perimeter before it has to be taken out of service, provided that the nature of loading is static.

The results presented in this paper only simulated damage on the tension side of CFFTs in flexure, and was a small portion of a larger study currently underway to examine damage of tubes of different laminate structures in both flexure and under axial compression loads.

REFERENCES

- A. Fam, B. Flisak, S. Rizkalla (2003). "Experimental and analytical modeling of concrete-filled Fiber-reinforced polymer tubes subjected to combined bending and axial loads", *Construction and Building Materials*, 17, 501-576.
- A. Fam, S. Rizkalla (2003). "Large scale testing and analysis of hybrid concrete/composite tubes for circular beam-column applications", *Construction and Building Materials*, 17, 507-516.
- A. Davol, R. Burgueño, F. Seible (2001). "Flexural behavior of circular concrete filled FRP shells", *Journal of Structural Engineering*, Volume 127 Issue 7.
- A. Fam, M. Pando, G. Filz, S. Rizkalla (2003). "Precast piles for route 40 bridge in Virginia using concrete filled FRP tubes", *PCI Journal*, 48-3: 32-45.
- A. Mirmiran, M. Shahawy (1997). "Behavior of concrete columns confined by fiber composites", *Journal of Structural Engineering*, Volume 123 Issue 5.
- A. Fam, S. Rizkalla (2002). "Flexural behavior of concrete-filled fiber-reinforced polymer circular tubes", *Journal of Composites for Construction*, Volume 6 Issue 2.
- J. Mitchell, A. Fam (2010). "Tests and analysis of cantilevered GFRP tubular poles with partial concrete filling", *Journal of Composites for Construction*, Volume 14 Issue 1.
- ASTM D3039. "Standard test method for tensile properties of polymer matrix composite materials".
- ASTM C39. "Standard test method for compressive strength of cylindrical concrete specimens".
- AASHTO CFFT Design Guide. "AASHTO LRFD guide specifications for design of concrete-filled FRP tubes", 1st Edition.
- CSA A23.3-14." Design of concrete structures".



AXIAL COMPRESSIVE BEHAVIOUR OF COMPOSITE TUBES WITH DIFFERENT GROUT INFILLS

Ali A. Mohammed^{1,2}, Allan C. Manalo¹, Gingham B. Maranan³, Yan Zhuge⁴ and John Pettigrew⁵

¹Centre for Future Materials (CFM), School of Civil Engineering and Surveying, University of Southern Queensland, Toowoomba 4350, Australia

²Environmental Engineering Department, College of Engineering, The University of Mustansiriya, Baghdad, Iraq

³Civil Engineering, School of Engineering, Faculty of Science and Engineering, University of Waikato, Hamilton 3216, New Zealand

⁴School of Natural & Built Environments, University of South Australia, Adelaide 5001 Australia

⁵Joinlox Pty Ltd, Unit 2, 30 Walker Street, Brisbane, Queensland 4105, Australia

ABSTRACT

This paper investigates the effects of grout infill characteristics on the axial compressive behaviour of glass fibre reinforced polymer (GFRP) tubes to determine the most effective infill for prefabricated composite repair systems. Three different types of grout-infills were considered in this study based on their availability, with taking into consideration the nominal compressive strength and Modulus of Elasticity (MOE). Grout infills made of concrete, cementitious and epoxy grouts with compressive strength ranging from 10 MPa to 70 MPa and MOE ranging from 10 GPa to 35 GPa, respectively, were selected. Characterisation of the compressive properties of these grouts was conducted. These grouts were then filled into 3 mm thick GFRP tubes to investigate the effectiveness of the different grouts in stabilising the composite tubes and effectively utilising its hoop strength. The experimental results showed that the increase of the grout MOE increases the overall stiffness of the filled GFRP tube, while a low compressive strength grout (less than 20 MPa) is more effective than high compressive strength grouts in utilising the GFRP tubes' hoop strength. Moreover, the degree of GFRP tube rupture decreases and becomes less severe and more localised at the upper section of the specimen as the grout compressive strength increases, which tends to suggest that increasing the infill compressive strength decreases the portion of FRP tubes being utilised.

KEYWORDS

Systems and strengthening techniques, FRP tube, Grout-infills Composite jacket.

1 INTRODUCTION

Retrofitting, strengthening, and repairing of aging infrastructures are becoming a major task and complex problem faced by engineers and researchers nowadays. The deficient structures need to be either replaced or retrofitted to maintain their serviceability. In US, Canada, and Europe, it is estimated that more than \$5 billion annually is needed to maintain the RC bridges of each country (Azam et al., 2016). While \$13 billion is the annual bill to the Australian economy due to the corrosion-induced damages, lost production and shutdowns to make repairs (Cassidy et al., 2015). Generally, repairing the existing damaged structures is far more economical than to replace them. Following effective rehabilitation techniques can be economically beneficial by minimizing the off-service time of the structure, and eventually saving a significant amount of resources. Since the traditional rehabilitation techniques, i.e. concrete and steel jacketing, have several drawbacks in terms of weight and the complexity of steel anchorage (Delatte, 2009), the introduction of fibre-reinforced polymer (FRP) composites for strengthening and rehabilitation of civil infrastructure has immediate wide range acceptance. The superior characteristics of this advanced material, such as high strength, corrosion resistance, lightweight, high fatigue resistance, high impact resistance, and durability, enabled it to be successfully utilised for strengthening and repairing damaged concrete and steel structures, especially those that are located in harsh environments such as marine and mining areas (Manalo et al., 2016).

Pre-fabricated composite jackets are becoming increasingly used in repairing structures, especially for under water applications. These composite repair systems are manufactured at specialised plants, thereby achieving high quality and uniformity. In addition, they can be easily installed at site by placing the jacket around the damaged structure and serving as a permanent formwork. Then, an appropriate grout is placed to fill the gap between the jacket and the existing structure. The pre-fabricated FRP jacket provides protective shield and induces lateral confining passive pressure, which eventually strengthens the damaged structure. Lopez-Anido et al. (2005) proposed a repair system utilizing SCRIMP™ FRP shells with two different types of grouting systems, cement-based structural grout and expanding polyurethane chemical grout, to provide protection and structural restoration

for deteriorated wood piles. Vijay et al. (2016) used pre-cured FRP shells for encasing and rehabilitating the water-submerged steel H-piles of a bridge in the USA. The space between the FRP shells and the steel piles was filled with self-consolidating concrete to strengthen and protect the piles from further deterioration. Considering the behaviour of the repair system components, Shamsuddoha (2014) highlighted the effectiveness of using FRP composites and grout infills for steel pipeline repairs. In these applications, the repair systems have been successfully implemented by providing grout infills between the annulus of the existing structure and the prefabricated composite jackets.

The grout infill is the key that controls the effectiveness of the pre-fabricated FRP jacket in repairing damaged structures. It plays a vital role in transferring the stresses between the core structure and the external FRP jacket to develop the composite action (Sum and Leong, 2013). The compressive strength and modulus of elasticity are the two most important mechanical characteristics that affect the grout's functionality in load transfer and effective utilisation of the FRP system (Shamsuddoha, 2014, Mohammed et al., 2018). Sum and Leong (2013) conducted a numerical analysis on a composite sleeve and epoxy grouts over a pipe subjected to internal pressure. The results indicated that a stiffer epoxy grout is preferable because it is more effective in stress transfer and makes the repair system act compositely. The grout is also necessary to assure a full contact between the system components as it provides a smooth bed for the FRP jacket and refill the damaged profile of the existing structure (Shamsuddoha, 2014).

Few studies have used several types of grouts as infill for the pre-fabricated FRP repair system (Lopez-Anido et al., 2005, Vijay et al., 2016); however, these studies did not consider the structural contribution of the grout infills. There is a need therefore to have a better understanding on the mechanical properties of the grout infills and how they affect the stress development on the composite repair system. This study evaluated the properties of three different grout materials and the structural behaviour of a FRP repair system filled with different grouts. The results of this study provide information on the important characteristics of the grouting materials that will be useful to effectively utilise the inherent properties of the pre-fabricated composite repair systems.

2 EXPERIMENTAL PROGRAM

2.1 Material Properties

2.1.1 Infills

Three different types of infills were considered in this study: (1) concrete-grout infill, (2) shrinkage compensating cementitious-grout infill, and (3) epoxy-grout infill. These infills were selected based on their market availability and current industry practice, with taking into consideration the compressive strength and elastic modulus of the infills. For the concrete-grout infill, three different compressive strength grades, i.e. Grade 1, Grade 2 and Grade 3, of commercially available normal concrete with maximum aggregate size of 10 mm were used. The shrinkage-compensating cementitious grout, commercially known as BluCem GP60, was made up of cement powder with 0.3 mm maximum particle size. Its shrinkage-compensating feature allowed the final product to be volumetrically stable during the initial stage of curing and prevented cracking due to plastic shrinkage. Following the mentioned procedure in the technical data sheet, a water-to-cement weight ratio of 0.175 was adopted to obtain a flowable grout that suits filling applications and to prevent the formation of voids. A high strength chemical epoxy grout, commercially named as CHEMRITE® Pad Grout used in this study consisted of two main components; the polyurethane (Part A) and binder (Part B). After the proper mixing of these components, fine graded aggregate used as a filler for epoxy compounds, it was added to the mix to produce the desired grout mortar.

2.1.2 GFRP tubes

Prefabricated glass-fibre-reinforced polymer (GFRP) tubes that were manufactured, using the filament winding method, for this study. Experimental approaches were adopted to ascertain the tensile and compressive properties of the GFRP tubes. The test coupons were cut from the large GFRP laminates, with the same lay-up and composition as the GFRP tubes, using the water jet cutting machine. The results of the material characterisation showed that the GFRP tubes had average tensile strength (f_t) and tensile modulus (E_t) equivalent to 297 MPa and 24 GPa, respectively. The compressive strength (f_c) and compressive modulus (E_c) on the other hand, were equal to 180 MPa and 30 GPa, respectively. Burnout test was also conducted to determine the fibre content ratio and fibre stacking sequence of the GFRP tubes. The test revealed that the GFRP tube material has 67.6% fibre content by weight. Moreover, the GFRP tube had a stacking sequence of $-45^\circ/+45^\circ/-45^\circ/+45^\circ$ with respect to the hoop direction. Such configuration is effective in managing multi-axial stresses and in achieving more ductile behaviour at failure (Parvin and Jamwal, 2006).

2.2 Test Specimens, Test Set-up and Procedure

Three replicates were prepared for each type of specimen, yielding a total of 33 specimens including three (3) hollow GFRP tubes, fifteen (15) infill cylinders and fifteen (15) grout-filled GFRP tubes. The specimens were cured and tested after seven days. Figure 1 shows the geometry and configuration of the tested specimens. The average height (h_i) and diameter (d_i) of the infill cylinders were 200 mm and 100 mm, respectively, while the average thickness (t_g), height (h_g), and internal diameter (d_{gi}) of GFRP tubes were 3, 200 and 100 mm, respectively.

Grades 1, 2, and 3 cylindrical concrete infills were labelled as C1, C2, and C3, respectively, and were collectively labelled as C#. The cylindrical cementitious-grout and epoxy-grout infills were labelled as CG and EG, respectively. The grout-filled GFRP tubes were then identified by adding the prefix G- to the infill label while the hollow GFRP tubes were named as H-Tube. For example, the specimen named as G-EG stands for GFRP tubes filled with epoxy-grout. The concrete-filled GFRP tubes were collectively called as G-C#.

The compression test was conducted in accordance with the ASTM C39/C39M as shown in Figure 1. The specimens were vertically positioned at the centre of the loading plates. The monotonically increasing loads were applied using the 2000 kN SANS servo-hydraulic compression testing machine at a displacement rate of 3.0 mm/min. The machine was equipped with a digital acquisition system that measured and recorded the applied loads and corresponding deformations. The axial and lateral strains were measured using strain gauges (SG) glued longitudinally and transversely at the mid-height of the specimens and were captured using the System 5000 data logger. A calibrated 2000 kN load cell attached to the logger was also used to synchronise the deformation readings obtained from the SANS machine and the strain readings captured from the data logger.

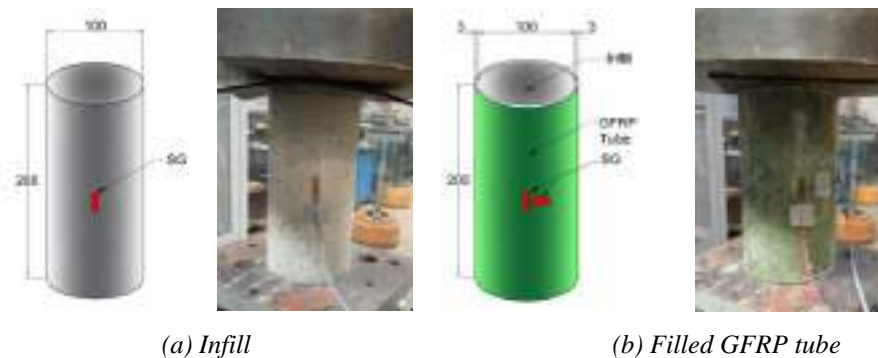


Figure 1. Geometry and configuration of the test specimens and test set-up.

3 RESULTS AND OBSERVATION

3.1 Behaviour of Infill Material

3.1.1 Failure Mode

Figure 2 shows the failure modes of the tested cylindrical infill specimens after the compression test. Visible crushing and cracking were observed at the top section of the concrete and cementitious grout cylinders during the test. As the applied load increased, the cracks spread and propagated downward with increased crushing. At failure, C1 (Figure 2a), C2 (Figure 2b), and C3 (Figure 2c) undergone concrete crushing coupled with the formation of longitudinal cracks throughout the height of each specimen. In general, as the compression strength of concrete increases, the degree of aggregate separation and crushing severity decreases while the width of cracks increases. CG (Figure 2d) exhibited nearly similar failure mode as the concrete specimens, but with a sharp and sudden break in the form of a large vertical crack throughout the height of the cylinder. The failure of EG (Figure 2e), on the other hand, was governed by the combination of cone formation at the bottom and large fracture without crushing at both ends. Interestingly, the same failure pattern was observed by Shamsuddoha (2014), but without the cone formation. This specimen underwent the most violent compression failure among all the other infills, wherein a loud snapping sound was heard at failure.

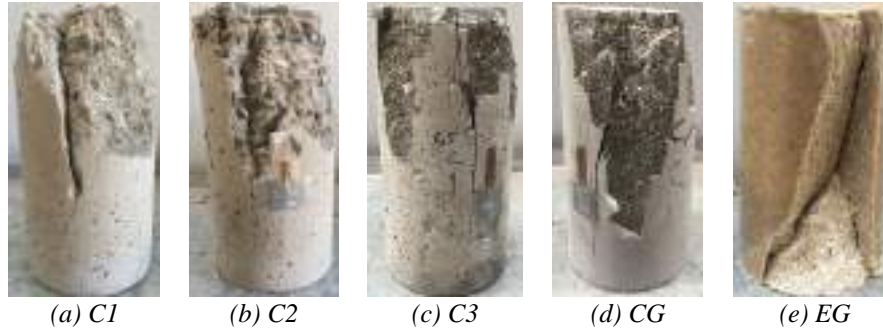


Figure 2. Representative failure modes of the cylindrical infills.

3.1.2 Stress-strain behaviour

Figure 3 presents the typical relationship between the axial stress (σ_c) and the axial strain (ϵ_c) of the tested cylindrical infills. As shown in the figure, C# exhibited a linear elastic behaviour, wherein the load increased rapidly with the deformation. As can be expected, the elastic modulus increases with the compressive strength. A short nonlinear behaviour prior to peak load was observed, owing to the simultaneous crushing and cracking of the specimen. After reaching the maximum load, the load dropped progressively. C3 showed the fastest degradation followed by C2 and C1, respectively. In the case of CG, the axial stress increased rapidly with the axial strain; however, CG did not yield any post-peak response as the curve dropped immediately after failure. The typical stress-strain curve of EG was composed of a short linear segment followed by a long nonlinear segment prior to peak, owing to the high deformability characteristic of the epoxy grout, which was then followed by a short decreasing stress-strain segment.

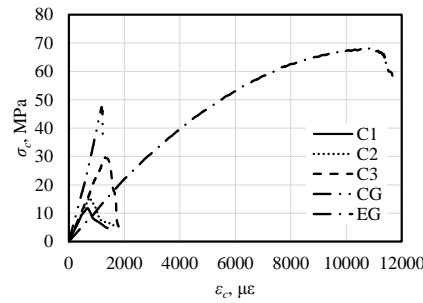


Figure 3. Representative stress-strain (σ_c - ϵ_c) curves of the cylindrical infill materials.

3.1.3 Compressive Strength, Modulus of Elasticity, and Axial Strain at Peak

Table 1 summarises the experimental results obtained from the compression tests of cylindrical infills including the average axial load capacity (P_{iu}), the average peak compressive strength (σ_{iu}) and corresponding standard deviation (s_{iu}), the modulus of elasticity (MOE_i), and the axial strain at peak (ϵ_{iu}). The P_{iu} of C1, C2, and C3 were 99.1 kN, 136.5 kN, and 215.8 kN, respectively, which translate to σ_{iu} of 12.6 MPa, 17.4 MPa, and 27.5 MPa respectively. CG and EG, on the other hand yielded P_{iu} of 378.4 kN and 619.5 kN that were equivalent to σ_{iu} of 48.2 MPa and 78.9 MPa, respectively. The values of s_{iu} ranged from 1.4 MPa to 4.6 MPa, suggesting a good precision among the obtained results. The MOE_i values were taken from the regression analysis of the linear segment of the stress-strain curves. As expected, C3 (26.8 GPa) yielded the highest MOE_i among the concrete infills followed by C2 (19.5 GPa) and C1 (18.4 GPa), respectively. CG exhibited the highest MOE_i (34.3 GPa) among the tested cylindrical infills. Interestingly, the experimental MOE of the concrete-grout and cementitious-grout infills were more or less comparable to the theoretical values obtained from the established empirical formula (Eq. 1) for normal concrete:

$$MOE_i = 4700\sqrt{\sigma_{iu}} \quad (1)$$

Although EG yielded the highest σ_{iu} among infills, it produced the least MOE_i (10 GPa). This value was equivalent to the MOE_i (11 GPa) reported by Shamsuddoha (2014) for epoxy-based grout with relatively similar material composition as the epoxy grout adopted in this study. The magnitude of ϵ_{iu} increases with the compressive strength of the concrete infills, wherein C3 (1312 $\mu\epsilon$) yielded the largest value followed by C2 (755 $\mu\epsilon$) and C1 (662 $\mu\epsilon$), respectively. The ϵ_{iu} of CG and EG, on the other hand, were equivalent to 1178 $\mu\epsilon$ and 10800 $\mu\epsilon$, respectively.

Table 1. Peak axial load, compressive strength and its standard deviation, elastic modulus, and strain at peak of the cylindrical grout infills.

Specimen	P_{iu} , kN	σ_{iu} , MPa	s_i , MPa	MOE_{is} , GPa	ε_{iu} , $\mu\varepsilon$
C1	99.1	12.6	1.4	18.4	662
C2	136.5	17.4	4.4	19.5	755
C3	215.8	27.5	3.1	26.8	1312
CG	378.4	48.2	1.1	34.3	1178
EG	619.5	78.9	4.6	10.0	10800

3.2 Behaviour of hollow and filled GFRP tubes

3.2.1 Failure Mode

Figure 4 shows the typical mode of failure of the hollow and grout-filled GFRP tubes. As shown in Figure 4a, the hollow GFRP tubes underwent localised crushing just below the loading point (end crushing). Then, the damage was transferred axially to the body by forming a large crack with continuous fibre rupture. Sounds of resin cracking and fibres rupturing were heard before the final failure. Filling the GFRP tubes with grout infills, however, modified the failure from axial to hoop failure. For all the grout-filled GFRP tubes, the failure was initiated by the development of cracks and crushing of the core infills. White spots appeared onto the body of the tubes, especially at the potential failure zones due to the tensioning of fibres. The mechanism and extent of fibre rupture, however, were different for each type of grout infill.

G-C# exhibited a failure mode that was characterised by longitudinal cracks perpendicular to the fibre orientation. G-C1 (Figure 4b) exhibited the most violent and most severe degree of failure among the G-C# specimens, owing to the rupture of fibres all throughout its height, followed by G-C2 (Figure 4c) and G-C3 (Figure 4d), respectively, which exhibited local fibre rupture at the top portion. Interestingly, this localised failure was also reported by Vincent and Ozbakkaloglu (2013) for FRP-tube encased specimens. G-CG (Figure 4e) also exhibited similar failure mode as G-C3 specimens but with shorter cracks and less violent failure. On the other hand, more localised failure was observed in G-EG (Figure 4f). An upside down triangle-shaped FRP rupture was observed in the upper part of G-EG, which seems to be a replicate of the top fracture that was observed in CG (Figure 3e).

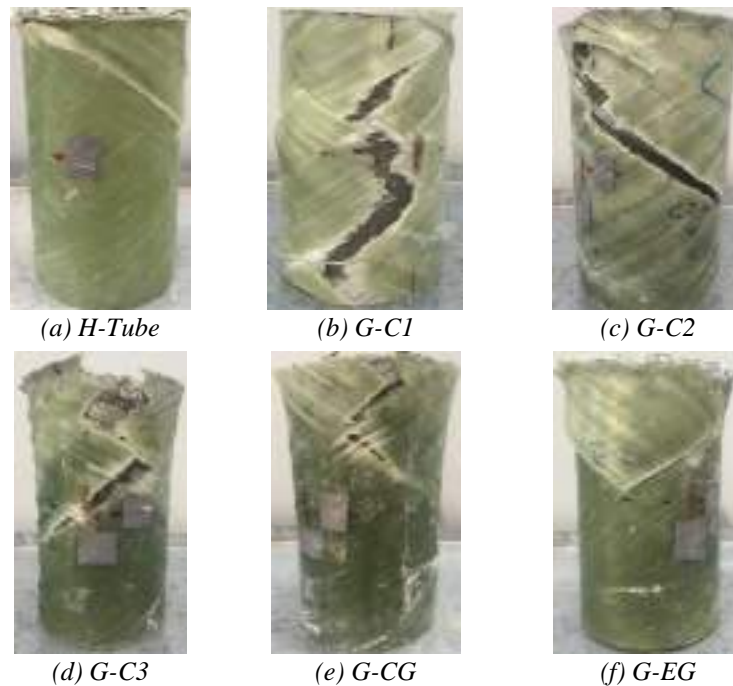


Figure 4. Typical compression failure of hollow and filled GFRP tubes.

3.2.2 Stress-strain Behaviour

Figure 5 shows the representative axial stress-axial strain (σ_c - ε_c) curves of the grout-filled GFRP tubes. The typical σ_c - ε_c behaviour of G-C# specimens was embodied by a monotonically increasing bi-linear curve. It is an increasing type of σ_c - ε_c curve, wherein both the significantly enhanced compressive strength and ultimate strain were reached at the same time (Lam and Teng, 2003). The initial rapidly ascending linear segment represents the elastic region

wherein the axial behaviour of the G-C# was comparable to that of their corresponding infills, which can be expected since the behaviour of the specimen at this stage was governed by the core infills. As long as the axial stress is lower than the compressive strength of the concrete core, the core dilation will be insignificant to activate the passive confinement of the low modulus GFRP tube and hence, will not influence the overall behaviour of the specimen (Berthet et al., 2005, Boumarafi et al., 2015). In fact, negligible hoop strain readings up until an applied stress equivalent to the compressive strength of the infills were recorded during the test as shown in Figure 6. Furthermore, this can be mathematically proven by calculating the axial rigidity (EA) of filled GFRP tube system, wherein the EA of C1, C2, and C3 were equivalent to 97.2%, 97.4% and 97.6% of the overall EA of G-C1, G-C2, and G-C3, respectively, suggesting that more loads were attracted by the infills during the elastic stage. The next segment was represented by another linear segment with a reduced slope (E_2) that embodies the plastic hardening behaviour of the specimens. The infills undergo more severe crushing and cracking that fully activated the passive confinement of the tubes as evidenced by the large amount of strain values obtained along the hoop direction. At this stage, the GFRP tube mainly governed the behaviour of the specimens. The GFRP tubes filled with C1 infill yielded the highest E_2 than those filled with C2 and C3, respectively. The specimens did not show any response after reaching their peaks. A nonlinear behaviour was observed between the two linear segments that indicated the initiation and propagation of concrete crushing and cracking, and the partial activation of the tubes.

The typical σ_c - ϵ_c curve of G-CG specimens, on the other hand, can be categorised as a decreasing type featured by a post-peak descending branch (Lam and Teng, 2003). A slight load drop occurred after the initial peak. This drop marked the transition from linear to nonlinear behaviour and was not observed in concrete infills having compressive strength lower than that of the cementitious-grout infills (48.9 MPa). Vincent and Ozbakkaloglu (2013) reported that this phenomenon happened in specimens filled with high strength and ultra-high strength concrete (59 MPa to 112 MPa) and not in the specimens filled with normal strength concrete (34.8 MPa to 38.0 MPa). However, this phenomenon will start to transpire at a strength ranges from 38.0 MPa to 48.9 MPa. After reaching the peak or the confined compressive strength, a softening segment occurred. At this stage, more severe infill crushing and cracking transpired concomitant with fibre rupture and crushing of matrix of the GFRP tubes. The compressive stress at FRP rupture was higher than that of the compressive strength of the infill, suggesting that CG were still sufficiently confined. Moreover, the σ_c - ϵ_c behaviour of G-EG specimens can be represented by a bilinear curve. The initial linear branch was similar to that of the cylindrical epoxy grouts. The second linear segment tend to show the plateau behaviour of the specimens. A short nonlinear transition zone transpired in between the two segments that marked the beginning of the GFRP tube's confinement.

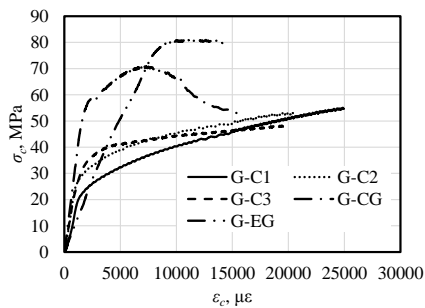


Figure 5. Axial stress-axial strain curves of the grout-filled GFRP tubes.

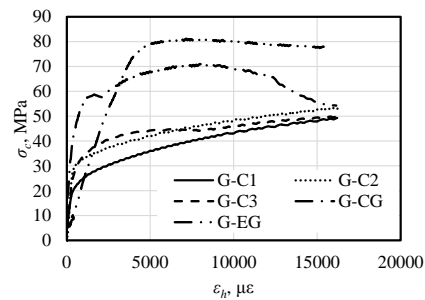


Figure 6. Axial stress-hoop strain curves of the grout-filled GFRP tubes

3.2.3 Ultimate Strength

Table 2 summarises the average peak load (P_{gu}) and the peak stress (σ_{gu}) and corresponding standard deviation (s_g) of the filled GFRP tubes. The P_{gu} and σ_{gu} of G-C1, G-C2, and G-C3 were 692.7 kN and 78.5 MPa, 599.5 kN and 67.9 MPa, and 498.2 kN and 56.5 MPa, respectively. It was obvious from the results that the strength of filled GFRP tubes decreases as the compression strength of the concrete core infill increases. The P_{gu} were 616 kN and 798 kN for G-CG and G-EG, respectively, which are equivalent to σ_{gu} of 78.4 MPa and 101.6 MPa, respectively.

3.2.4 Axial and Hoop Strains

The average axial and hoop strains at peak stress (ϵ_{gu} and ϵ_{hu} , respectively) and at FRP rupture ($\epsilon_{g,rupt}$ and $\epsilon_{h,rupt}$, respectively) in the grout-filled GFRP tubes are also presented in Table 2. G-C1 (24850 $\mu\epsilon$) produced the highest ϵ_{gu} tailed by G-C2 (20900 $\mu\epsilon$) and G-C3 (19780 $\mu\epsilon$), respectively. G-CG yielded the lowest ϵ_{gu} equivalent to 6980 $\mu\epsilon$ and $\epsilon_{g,rupt}$ of 16140 $\mu\epsilon$ while the ϵ_{gu} and $\epsilon_{g,rupt}$ for G-EG were equivalent to 10800 $\mu\epsilon$ and 15390 $\mu\epsilon$, respectively. In the case of concrete-filled GFRP tubes, $\epsilon_{g,rupt}$ and $\epsilon_{h,rupt}$ were equivalent to their ϵ_{gu} and ϵ_{hu} , respectively.

Table 3. Peak axial load, peak axial stress and corresponding standard deviation and strains at rupture of grout-filled GFRP tubes.

Specimen	P_{gu} , kN	σ_{gu} , MPa	s_g , MPa	σ_{gu} / σ_{iu}	ϵ_{gu} $\mu\epsilon$	ϵ_{hu} , $\mu\epsilon$	$\epsilon_{g,rupt}$, $\mu\epsilon$	$\epsilon_{h,rupt}$, $\mu\epsilon$	ϵ_{gu} / ϵ_{iu}	ϵ_l , $\mu\epsilon$	ϵ_{85} , $\mu\epsilon$	μ	U_T , MPa
G-C1	692.7	78.5	11.4	6.2	24850	16200	24850	16200	37.6	4266	24850	5.8	1.01
G-C2	599.5	67.9	5.0	4.1	20900	16230	20900	16230	27.7	3235	20900	6.5	0.88
G-C3	498.2	56.5	3.6	2.2	19780	16170	19780	16170	15.1	2108	19780	9.4	0.83
G-CG	645.1	73.1	0.3	1.6	6980	7990	16116	16140	5.9	2131	10976	5.2	0.93
G-EG	798.5	90.5	7.2	1.3	10800	7170	15200	15390	1.0	9048	10914	1.2	0.84

4 DISCUSSION

4.1 Effect of Concrete Grade on the Behaviour of GFRP Tubes

This section presents the effects of the concrete grade on the behaviour of the GFRP tubes. In general, the amount of stress needed to activate the passive confinement of the GFRP tubes decreases with the compression strength of the concrete. This is attributed to the low compression resistance of C1 infills, which undergone early crushing and cracking at lower applied stress. The advance activation of the passive confinement resulted in the enhancement of the performance of the GFRP tubes. In general, the strength and strain enhancement ratio decrease when the compressive strength of the concrete core infill decreases. This result may be explained by the fact that the concrete brittleness increases with its strength, thereby changing the crack pattern development from heterogenic micro-cracks to localised macro-cracks (Ozbakkaloglu and Akin, 2011). The localised crack pattern limits the stress distribution along and around the GFRP tubes as was apparent in the failure configuration of the specimens. The fibre rupture transpired along the height of G-C1 while those with higher strength concrete (G-C2 and G-C3) experienced local fibre rupture mainly at the upper section of the GFRP tube. Interestingly, the same trend of straight gain was reported by Vincent and Ozbakkaloglu (2013). According to their study, the FRP tube-encased specimens with normal strength concrete yielded the highest strength enhancement ratio followed by the high strength concrete and the ultra-high strength concrete, respectively. Berthet et al. (2005) also reported the same trend, but for specimens with concrete core having compressive strength of 100-200 MPa only. Further studies are recommended to verify these differences.

4.2 Effect of Infill Types on the Behaviour of GFRP Tubes

Different stress-strain behaviour were observed upon filling the GFRP tubes with different types of infills. The concrete-, cementitious-, and epoxy-filled GFRP tubes yielded increasing, decreasing, and plateauing stress-strain curves, respectively. This observation could be attributed to the post-peak response of the infills, wherein the cylindrical concrete infills yielded a degrading stress-strain curves. The cylindrical cementitious grout did not show any post peak response while the cylindrical epoxy grout showed a decreasing post-peak response, but at a faster rate compared to cylindrical concrete infills. The concrete-filled GFRP tubes showed the highest strength and strain enhancement ratios while the epoxy-filled GFRP tubes showed the least. This finding suggested that the epoxy grout was not effectively confined. This can be attributed to the high deformability and insufficient stress absorption of the epoxy grout, which immediately stressed the GFRP tube as soon as the load was applied. Shamsuddoha (2014) reported that, for pipeline repairs using FRP systems, the low stiffness epoxy grout did not absorb the stress from the steel and hence, did not transfer the stress efficiently to the FRP. It is important to note however that the epoxy grouts considered by Shamsuddoha (2014) has a MOE of only up to 10 GPa which is slightly lower than that of the epoxy grouts used in this study. On the other hand, the ductility tend to increase with the concrete compressive strength; however, an opposite trend was found in terms of the energy absorption. Upon using different types of grout infills, no trend was found. This could be expected since each type of infill have different material composition and mechanical properties.

5 CONCLUSIONS

The effects of filling the GFRP tubes with concrete, cementitious and epoxy grouts on the behaviour of a simulated prefabricated composite repair system was investigated in this study. Based on the experimental results, the following conclusions were derived:

- The behaviour of the infill materials was largely dependent on the modulus of elasticity and the compressive strength of the grout infill. High compressive strength and high modulus cementitious and epoxy grouts failed in a more brittle manner than the concrete infill. After the peak load, the concrete-, cementitious-, and epoxy-filled GFRP tubes yielded increasing, decreasing, and plateauing stress-strain curves.
- The type of the grout infill dictated the overall behaviour of the composite repair system. The brittle failure behaviour of the cementitious and epoxy grouts lead to localised failure in the FRP repair system

while the progressive cracking and crushing of the concrete infill resulted in effectively utilising the high strength properties of the composite materials.

- The high compressive strength of the infill material limited its capacity to transfer the stresses uniformly around the tubes due to the increased brittleness. This resulted in the strength and strain enhancement ratios of only 1.3 and 1.0, respectively for the GFRP repair system filled with epoxy grouts but up to 6.2 and 38 times, respectively to the tubes filled with the lowest strength and modulus concrete.

ACKNOWLEDGEMENTS

The authors gratefully acknowledge Joinlox™ Pty. Ltd., Australia for the financial, materials and technical support in conducting this study.

REFERENCES

- R. Azam, A. K. El-Sayed & K. Soudki (2016). "Behaviour of reinforced concrete beams without stirrups subjected to steel reinforcement corrosion". *Journal of Civil Engineering and Management*, 22, 146-153.
- J. Berthet, E. Ferrier & P. Hamelin (2005). "Compressive behavior of concrete externally confined by composite jackets. Part A: experimental study". *Construction and Building Materials*, 19, 223-232.
- A. Boumarafi, A. Abouzied & R. Masmoudi (2015). "Harsh environments effects on the axial behaviour of circular concrete-filled fibre reinforced-polymer (FRP) tubes". *Composites Part B: Engineering*, 83, 81-87.
- M. Cassidy, J. Waldie & S. Palanisamy (2015). "A Method to Estimate the Cost of Corrosion for Australian Defence Force Aircraft".
- N. Delatte (2009). "Failure, distress and repair of concrete structures", Elsevier.
- L. Lam & J. Teng (2003). "Design-oriented stress-strain model for FRP-confined concrete". *Construction and building materials*, 17, 471-489.
- R. Lopez-Anido, A. P. Michael, T. C. Sandford & B. Goodell (2005). "Repair of wood piles using prefabricated fiber-reinforced polymer composite shells". *Journal of performance of constructed facilities*, 19, 78-87.
- A. Manalo, C. Sirimanna, W. Karunasena, L. Mgarva & P. Falzon (2016). "Pre-impregnated carbon fibre reinforced composite system for patch repair of steel I-beams". *Construction and Building Materials*, 105, 365-376.
- A. A. Mohammed, A. C. Manalo, G. B. Maranan, Y. Zhuge & P. V. Vijay (2018). "Comparative study on the behaviour of different infill materials for pre-fabricated fibre composite repair systems". *Construction and Building Materials*, 172, 770-780.
- T. Ozbakkaloglu & E. Akin (2011). "Behavior of FRP-confined normal-and high-strength concrete under cyclic axial compression". *Journal of Composites for Construction*, 16, 451-463.
- A. Parvin & A. S. Jamwal (2006). "Performance of externally FRP reinforced columns for changes in angle and thickness of the wrap and concrete strength". *Composite Structures*, 73, 451-457.
- M. Shamsuddoha. (2014). "Behaviour of Infilled Rehabilitation System with Composites for Steel Pipe". PhD, University of Southern Queensland.
- W. Sum & K. Leong (2013). "Numerical study of annular flaws/defects affecting the integrity of grouted composite sleeve repairs on pipelines". *Journal of Reinforced Plastics and Composites*, 0731684413503721.
- P. Vijay, P. R. Soti, H. V. Gangarao, R. G. Lampo & J. D. Clarkson (2016). "Repair and Strengthening of Submerged Steel Piles Using GFRP Composites". *Journal of Bridge Engineering*, 04016038.
- T. Vincent & T. Ozbakkaloglu (2013). "Influence of concrete strength and confinement method on axial compressive behavior of FRP confined high-and ultra high-strength concrete". *Composites Part B: Engineering*, 50, 413-428.



AXIAL COMPRESSION BENDING INTERACTION BEHAVIOUR OF HYBRID FRP STRENGTHENED RC COLUMN ELEMENTS

M. Chellapandian¹, S. Suriya Prakash² and Akanshu Sharma³

¹ Department of Civil Engineering, IIT Hyderabad, India, Email: ce15resch11005@iith.ac.in

² Department of Civil Engineering, IIT Hyderabad, India, Email: suriyap@iith.ac.in

³ Institute of Construction Materials, TU Stuttgart, Germany, Email: akanshu.sharma@iwb.uni-stuttgart.de

ABSTRACT

Strengthening of reinforced concrete (RC) element is challenging as the efficiency of a particular strengthening scheme may change under different loading conditions. The importance of hybrid Fiber Reinforced Polymer (FRP) strengthening on the behavioral improvement of RC column elements under combined axial and bending loads is investigated. In total, thirty-two RC square elements of dimensions 230 mm (B x D) are cast. The specimens are tested under different uniaxial eccentric (e) compression like (i) axial compression ($e=0$), (ii) low eccentric compression ($e=0.15*D$), (iii) high eccentric compression ($e=0.63*D$) and (iv) pure flexure ($e=\infty$). The specimens are strengthened using (i) Near Surface Mounting (NSM) of CFRP laminates, (ii) External Bonding (EB) of CFRP fabrics and (iii) Hybrid strengthening which uses a combination of NSM and EB technique. Two specimens are tested under each series to ensure the consistency of test results. Axial compression (P) – bending (M) interaction diagram developed from the experimental results revealed that hybrid FRP strengthening resulted in the best performance under all combinations of axial compression and bending loads. EB strengthening which exhibited better performance under axial compression had a reduced improvement under combined bending and compression loads. Moreover, the behavior of NSM strengthened specimens had significant improvement due to presence of bending in the interaction diagram.

KEYWORDS

CFRP, EB Strengthening, Interaction Behavior, NSM Strengthening, Hybrid Strengthening, RC Column Element.

INTRODUCTION

Strengthening of concrete members using FRP composites is commonly adopted for improving the capacity of existing concrete elements. Strengthening of members becomes challenging when there are frequent changes in the loading conditions. Near Surface Mounting (NSM) and External Bonding (EB) are the two different techniques that is commonly used for improving the overall performance of RC elements (Parvin and Wang 2001; Rocca et al. 2008). However, the efficiency of these FRP strengthening technique reduces drastically when there is change in the type of load acting (compression or tension dominant) in the member. External bonding of FRP fabric has been successfully used to improve the capacity of columns that are predominantly subjected to compression behavior (Hadi 2006). Due to the effect of bending moment, the capacity of FRP confined columns reduces drastically (Maaddawy 2009). Near Surface Mounting (NSM) strengthening of RC elements are effective when they are subjected to bending dominant behavior (Barros et al. 2008). However, the overall capacity reduces when the NSM strengthened elements are subjected to axial compression loading owing to buckling dominant failure. Therefore, there is a necessity of finding an improved strengthening technique which is feasible under all combinations of combined compression and bending loads. Hybrid FRP strengthening is one such type where the NSM CFRP laminates is combined with externally confined CFRP fabric (Chellapandian and Prakash 2016; Chellapandian and Prakash 2017; Chellapandian et al. 2017; Jain et al. 2017). The advantage of this innovative approach is the effective confinement of NSM laminates to prevent its buckling failure mode under compression and debonding failure mode under tension enabling it to undergo large deformations before failure. Behavior of hybrid strengthened RC elements on improving the flexural efficiency has been investigated in the past by some researchers (Bournas and Triantafillou 2009; Perrone et al. 2009; Rezazadeh and Barros 2014). However, their efficiency under all combinations of bending and axial compression is not well understood yet. In this study, the experimental behavior of reinforced concrete columns strengthened using Near Surface Mounted (NSM) CFRP laminates, External Bonded (EB) CFRP fabric and their hybrid combinations in improving the overall performance is investigated. Thereafter, an experimental axial load – bending moment interaction diagram is developed for RC columns with different FRP strengthening schemes to show the efficiency of hybrid strengthening under different levels of bending and compression loads.

RESEARCH MOTIVATION AND OBJECTIVES

Though significant amount of research work is available on the behavior of FRP strengthened RC columns, only few studies have focused on hybrid strengthening technique. Moreover, the efficiency of this strengthening scheme under combined bending and compression loading is not well established. This study will help in filling in the existing knowledge gap by investigating the behavior of RC columns strengthened using hybrid FRP technique. The objective of this research is to establish axial – bending interaction behaviour for hybrid FRP strengthened RC columns. To meet the objectives, the columns are tested under (i) axial compression ($e/D=0$), (ii) low eccentric compression ($e/D=0.15$), (iii) high eccentric compression ($e/D=0.63$) and (iv) pure flexure ($e/D=\infty$).

EXPERIMENTAL PROGRAM

General Description:

In this study, thirty-two RC square elements are cast for testing under different loading conditions. The details of experimental program are given in Table 1. The cross sectional dimension of the square column used in this study is 230 mm (Figure 1). The longitudinal reinforcement consists of eight bars of 12 mm diameter ($A_{st} = 904 \text{ mm}^2$). The transverse reinforcement is provided with 10 mm diameter bars at a spacing of 100 mm. The specimens are divided into four categories. Eight control specimens (CP) are tested without FRP strengthening. Eight specimens are strengthened using only NSM CFRP laminates while the other eight specimens are confined with two plies of CFRP fabric. The last series of specimens are strengthened using a hybrid combination of NSM CFRP laminates and EB CFRP fabrics. The details of different types of strengthening are schematically illustrated in Figure 2. Two specimens were tested under each series to understand the consistency of test results. In each series, two specimens are tested under axial compression ($e=0$), low eccentric compression ($e=35 \text{ mm}$), high eccentric compression ($e=145 \text{ mm}$) and pure flexure ($e=\infty$).

Table 1: Test Matrix

Specimen ID	Cross-Sectional Details (mm)			FRP Strengthening Details		Eccentricity Ratio (e/h)
	Breadth	Depth	Test Region	Type	Quantity	
CP-0	230	230	450	--	--	0
CP-35			450			0.15
CP-145			600			0.63
CP-F			1800			∞
NSM-0	230	230	450	CFRP Laminates	8 No's (12.5 mm x 4.2 mm)	0
NSM-35			450			0.15
NSM-145			600			0.63
NSM-F			1800			∞
EB-0	230	230	450	CFRP Fabric	Two Plies (450 mm x 0.2 mm)	0
EB-35			450			0.15
EB-145			600			0.63
EB-F			1800			∞
HYB-0	230	230	450	CFRP Laminates + CFRP Fabric	8 No's (12.5 mm x 4.2 mm) + Two Plies (450 mm x 0.2 mm)	0
HYB-35			450			0.15
HYB-145			600			0.63
HYB-F			1800			∞

***Note:** CP-Control Specimen; NSM – Near Surface Mounting Strengthening; EB – External Bonding Strengthening; HYB-Hybrid Strengthening; 0,35,145 – different eccentricity levels; F-Flexure.

Material Properties:

Concrete

The concrete elements are cast for a design mix of M40 grade (IS 10262-2008). The mix proportions of cement: fine aggregate: coarse aggregate are kept as 1: 2.1 :3.32. A water reducing admixture (1% of the weight of cement) is added for improving the workability of concrete mix. The specimens are water cured for a period of 28 days after which the specimens are strengthened. The average cubic and cylinder strength of the concrete after 28 days of curing are found to be 55 MPa and 40 MPa.

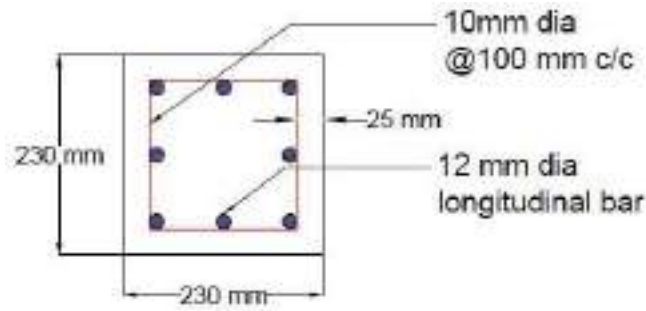


Figure 1: Cross-Sectional Details of Test Specimen

Steel Reinforcement and Fiber Reinforced Polymer:

Eight bars of 12 mm diameter ($A_{st}=904 \text{ mm}^2$) is used as the main reinforcement (Figure 1). 10 mm diameter bars are used as transverse reinforcements at a spacing of 100 mm c/c. Coupon test of steel reinforcements are carried out using a servo controlled tension testing machine. The yield strength and ultimate strain of steel reinforcement are found to be 512 MPa and 7.8%. CFRP laminates are used as FRP reinforcement in NSM strengthening. Pultruded CFRP laminates of size 12.5 mm x 4.2 mm is used in this experimental work. For confinement, unidirectional carbon fabric of 230 GSM and size 450 mm x 0.2 mm is used. The coupon test details of FRP laminates and fabric under tension and compression can be found elsewhere (Chellapandian et al. 2017; Chellapandian and Prakash 2018).

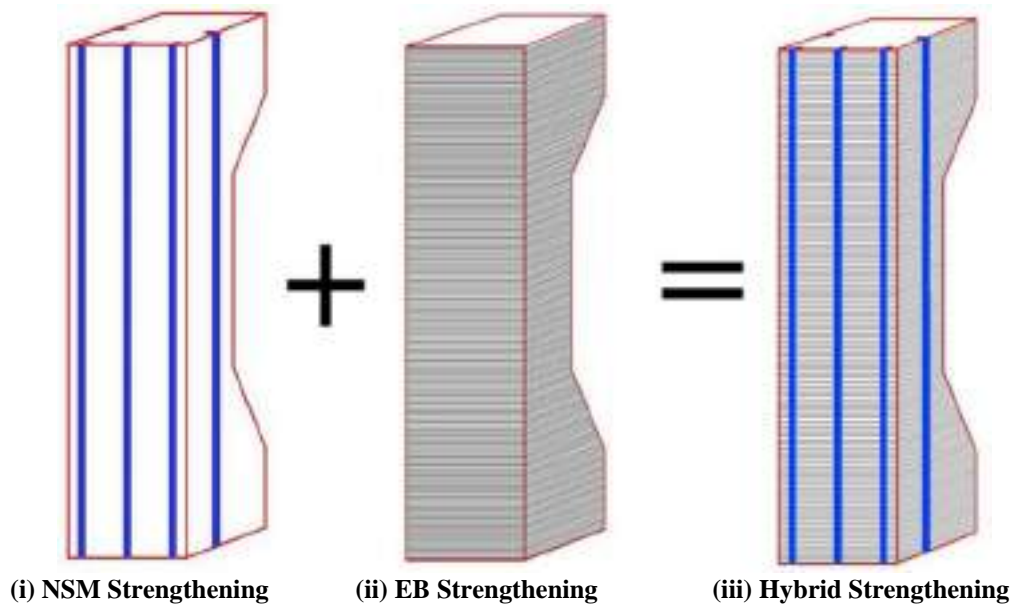


Figure 2: Schematic Representation of Different Types of Strengthening

FRP STRENGTHENING OF CONCRETE ELEMENTS

NSM Strengthening

NSM Strengthening is carried out as per ACI 440.2R-17 provisions. Firstly, the grooves are cut for the dimensions which is not lesser than 1.5 times the dimensions of the CFRP laminates. After grooving, the grooves are thoroughly cleaned with water and then applied with primer. After 24 hours, epoxy is applied on the grooves and the laminates are pressed against them. After 48 hours of minimum curing period, the specimens are tested.

EB Strengthening

EB strengthening is carried out as per ACI 440.2R-17 provisions. In FRP confined specimens of non-circular cross-section, corners are the most critical areas of stress concentration. In this study, the corners are grind to a minimum radius of 15 mm to avoid possible stress concentration (ACI 440.2R-17). After thorough cleaning of surface, primer is applied for better bond efficiency. Thereafter, a two component based epoxy (Base: Hardener=2.6:1) resin is applied for CFRP confinement. Two CFRP plies are applied for providing better confinement effect (Chellapandian et al. 2018).

Hybrid Strengthening

Hybrid strengthening uses a combination of NSM and EB strengthening technique (Figure 2). The important advantage of hybrid technique is that CFRP laminate is allowed to undergo higher strain levels before failure due to effective confinement provided by CFRP Fabric. The hybrid strengthened columns are expected to have a better performance under all combinations of axial compression and bending loads. In hybrid technique, the specimens are first strengthened using NSM strengthening followed by EB confinement.

EXPERIMENTAL SETUP AND INSTRUMENTATION

The schematic representation of test program and instrumentation details are depicted in Figure 3. The specimens are tested under different loading conditions namely (i) pure axial compression ($e=0$), (ii) uniaxial eccentric compression ($e=35\text{mm}$ and 145mm), (iii) four-point bending ($e=\infty$). The columns are tested under axial compression using a servo controlled compression testing machine of 5000 kN capacity. Four Linear Variable Displacement Transducers (LVDTs) of 20 mm stroke are used to measure the surface displacements and strains. Strain gauges of 5 mm gauge length are installed at the mid-span of longitudinal and transverse reinforcements to predict their yielding and ultimate strain levels. For testing the columns under eccentric compression, 3000 kN servo controlled compression testing machine is used. Two LVDTs of 20 mm stroke is used to measure the strain gradient effect due to eccentricity in specimens. Moreover, two LVDTs of 50 mm stroke is used to measure the lateral displacement at mid-span. For testing RC elements under bending, servo controlled universal testing machine of 2000 kN capacity is used. The overall test setup and instrumentation details are provided in Figure 3(iii). Two LVDTs are provided in horizontal direction to measure the curvature profile of the section.

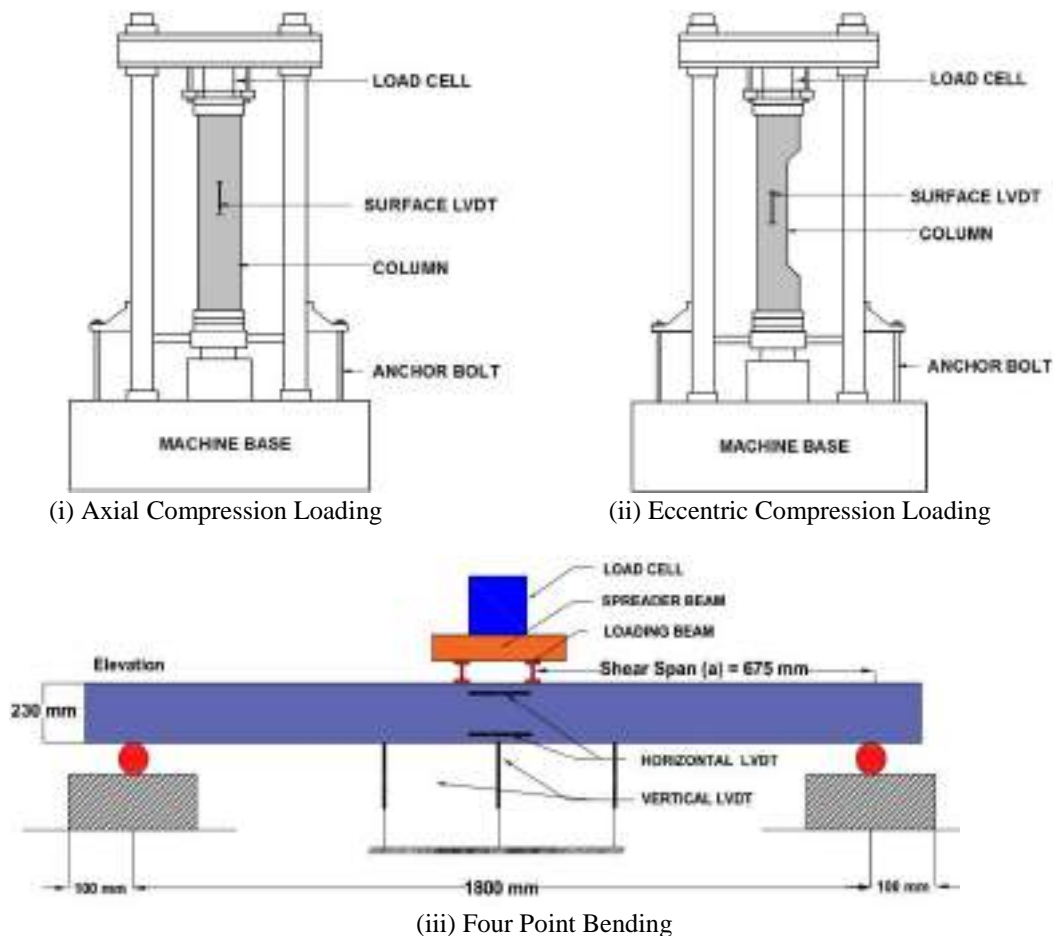


Figure 3: Schematic Representation of Test Setup and Instrumentation under Different Loads

RESULTS AND DISCUSSION:

Load – Displacement Behavior:

The overall load –displacement behavior of specimens tested under different loading conditions with and without FRP strengthening is detailed in Table 2 and depicted in Figure 4. The displacement values represented in Table.2 corresponds to axial displacements of the columns measured in their surface under axial and eccentric compression loading. The displacement mentioned under four-point bending test corresponds to their mid-span deflection.

Table 2: Summary of Test Results

Specimen ID	Yield Displ. (mm)	Peak Load (kN)	Peak Displ. (mm)	Failure Displ. (mm)	Ductility ($\mu=\Delta_u/\Delta_y$)	Increase in Peak load (%)	Increase in Ductility (%)
CP-0	0.35	2148	0.39	1.12	3.20	--	--
CP-35	0.36	1998	0.78	0.89	2.47		
CP-145	0.34	761	0.43	1.78	5.24		
CP-F	9.0	205	24.7	73.5	8.20		
NSM-0	0.39	2319	0.45	1.64	4.21	8.0	31.6
NSM-35	0.26	2303	0.32	1.00	3.87	15.3	55.5
NSM-145	0.18	1063	0.21	0.94	5.22	39.7	-0.38
NSM-F	13.6	433	32.2	39.8	2.96	111.0	-177
EB-0	0.38	2599	0.43	1.41	3.71	20.9	15.9
EB-35	0.28	2530	0.66	0.92	3.29	26.6	36.0
EB-145	0.27	816	0.39	1.85	6.85	7.2	30.7
EB-F	6.50	217	63.4	85.8	13.2	6.0	60.9
HYB-0	0.34	2695	0.51	1.63	4.79	25.6	49.6
HYB-35	0.33	2925	0.46	1.34	4.06	46.4	64.3
HYB-145	0.29	1152	0.48	2.47	8.52	51.4	62.6
HYB-F	13.7	564	35.8	66.0	4.90	174.5	67.4

**Note: Ductility is defined as the ratio of failure displacement (Δ_u) to the yield displacement (Δ_y).

Axial Compression Loading (e=0):

Control specimen (CP-0) had an average peak load of 2148 kN and failure displacement of 1.12 mm. NSM strengthened specimen had improvement in axial load of 8% (2319 kN) and displacement ductility of 31.6% (4.21). NSM strengthened specimens had failure due to excessive spalling of concrete and concrete crushing. EB strengthened specimens had improvement in peak load of 20.9 % (2599 kN) and ductility of 15.9% (3.71). Though EB strengthened specimens had improved peak strength, the failure mode is brittle due to FRP debonding. Hybrid strengthened specimens had better performance with improvement in peak load and ductility of 25.6% and 49.6% respectively. The failure mode is ductile enabling the column specimens to undergo larger concrete strain of 1.3%.

Low Eccentric Compression Loading (e/h=0.15):

Control specimen (CP-35) had peak load and ductility of 1998 kN and 2.47 respectively. The specimen had a sudden brittle failure mode with a reduced strain level when compared to similar specimens under axial load. NSM strengthened specimen had improved peak strength and ductility about 15.3% and 55.5% when compared to similar specimen without strengthening (CP-35). EB strengthened specimens had improvement in peak load and ductility about 26.6% and 36% respectively. The specimens had a brittle failure with first FRP rupture crack in the tension face and FRP debonding in the compression face of the member. Hybrid specimens had improvement in peak load and failure displacement ductility of 46.4% and 64.3% respectively under eccentric compression loading. The specimen had failure at a higher level of axial strain of about 0.008 due to FRP debonding in the compression face.

High Eccentric Compression Loading (e/h=0.63):

The load – displacement behavior of specimens under low eccentric compression is shown in Figure 4 (iii). Due to high level of eccentricity, the capacity of control specimen is reduced to a peak load of 761 kN with the ductility improvement of 5.24. NSM strengthening exhibited nearly 40% improvement in peak load with no ductility improvement. The failure mode is brittle with initial cracking in tension face followed by concrete crushing and laminate rupture in the compression face. EB strengthened specimens showed only marginal improvement in peak load (7.2%) with high ductility of about 31%. The specimen failed in a ductile manner exhibiting larger curvature. Hybrid strengthened specimens (HYB-145) had better performance in terms of both strength and ductility about 51% and 64% respectively. The failure mode is ductile with the failure occurring due to FRP rupture in the compression face.

Pure Flexure using Four Point Bending ($e/h=\infty$):

The control RC elements tested under pure flexure using four-point bending configuration had a ductile behavior. Though EB strengthened specimen had only marginal strength improvement, they failed at a higher displacement ductility of 13.20. NSM strengthened specimen showed 111% improvement in peak load with a brittle failure due to FRP debonding. Hybrid strengthened specimens had good improvement in peak load capacity (174.5%). Though there is no improvement in ductility in hybrid specimens, CFRP laminates are effectively confined from debonding failure and enabling laminates to undergo higher strain before failure.

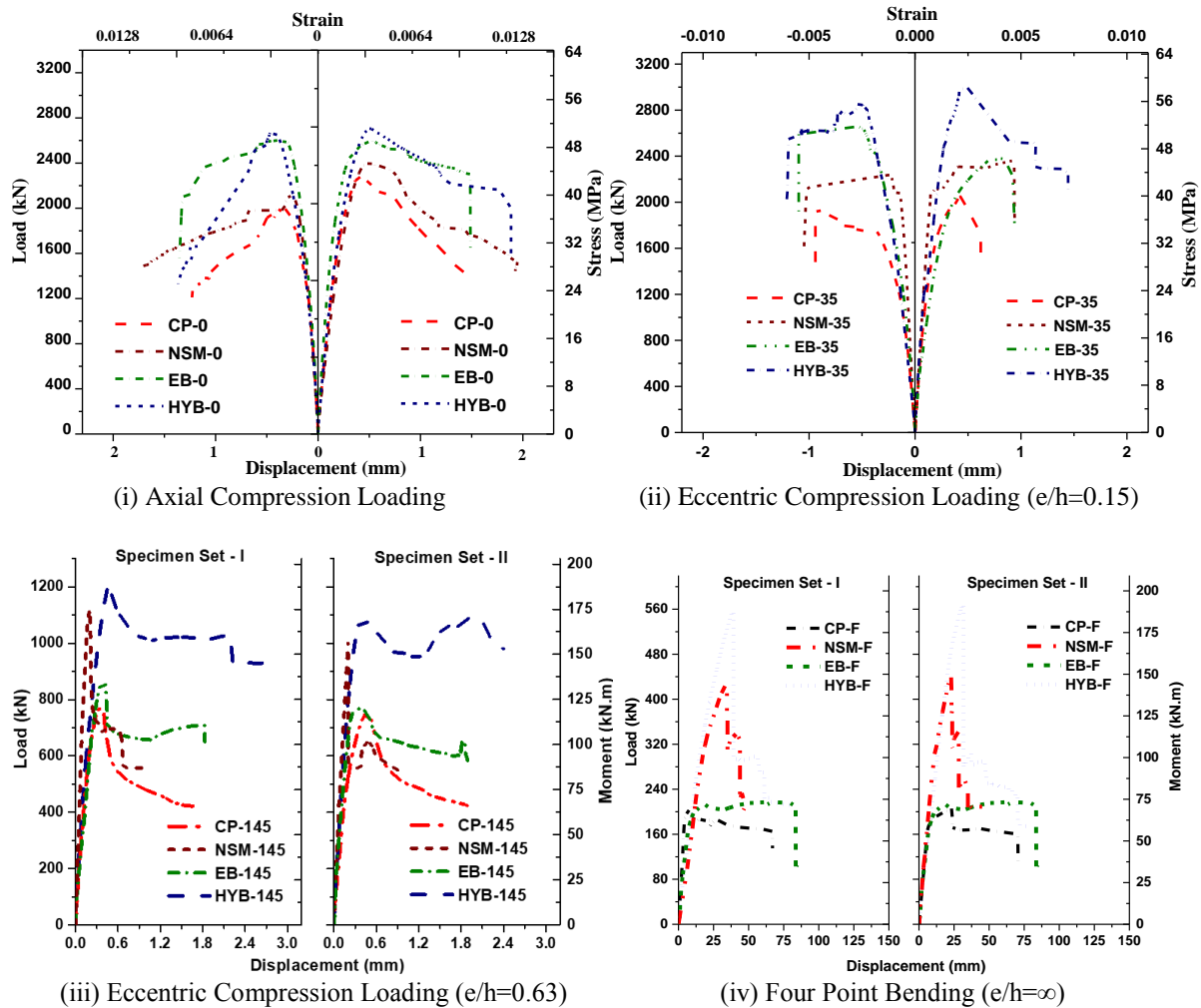


Figure 4: Load – Displacement Behavior of Specimens under Different Loading Conditions

Axial Load – Bending Moment Interaction Diagram:

A normalized axial compression - bending moment interaction diagram is developed for the columns strengthened with different FRP techniques (Figure 5). The values of axial load and moment are normalized as shown in Equations (1) – (2).

$$K_n = \frac{P_n}{(f_c A_g)} \quad \text{----- (1)}$$

$$R_n = \frac{M_n}{(f_c A_g d)} \quad \text{----- (2)}$$

Where, K_n is the normalized axial load, R_n is the normalized bending moment, P_n is the peak load, M_n is the moment corresponding to the peak load, f_c is the cylinder concrete strength, A_g is the gross cross-sectional area and d is the depth of the specimen.

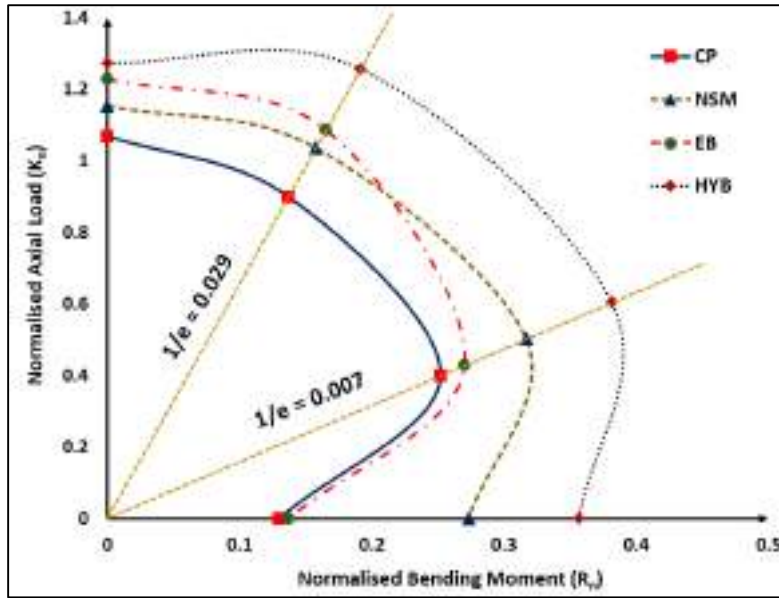


Figure 5: Axial Load – Bending Moment Interaction Diagram for RC Columns

Control specimens had brittle failure when subjected to combined axial compression and bending loads. NSM strengthened specimen had only marginal improvement in axial compression loading. Their efficiency increases once bending starts governing the behavior. EB strengthened specimen with an improved capacity under axial compression reduces once the failure mode is governed by tension. Hybrid strengthened specimens exhibited better overall performance under all combinations of axial and bending loads. Moreover, hybrid specimen witnessed increase in load capacity even in the tension controlled regime of P-M interaction diagram (Figure 5).

CONCLUSIONS

Axial compression – bending moment interaction diagram for square RC elements with and without different FRP strengthening techniques has been developed. In this study, thirty-two RC elements are cast and tested under different loading conditions of axial and bending loads. The following are the major conclusions drawn from this experimental work.

- Concrete columns without any strengthening exhibited brittle failure mode under combined axial and bending load due to concrete crushing in the compression face.
- Though the NSM strengthened specimens had marginal strength improvement under pure axial compression, it exhibited better performance under tension dominant behavior. In addition, these columns failed in brittle mode due to debonding of NSM FRP laminates under tension.
- EB strengthening resulted in good strength and ductility improvement under axial compression. However, it exhibited only marginal improvement in strength under bending dominant behavior.
- Hybrid FRP strengthening resulted in good strength improvement under all combination of bending and axial compression.

ACKNOWLEDGMENTS

This research work was sponsored by “FAST – Center for Sustainable Development” funded by Ministry of Human Resource Development, India. FRP materials required for this research work is supplied by R&M International Pvt. Ltd. and their help is also duly acknowledged. This research work is a joint collaborative effort of IIT Hyderabad, India and University of Stuttgart, Germany. The authors would like to thank their parent organizations for permitting this collaborative effort.

REFERENCES

A. Parvin, W. Wang (2001). “Behavior of FRP jacketed concrete columns under eccentric loading”, *ASCE Journal of Composites for Construction*, 5(3), 146-152.

- S. Rocca, N. Galati, A. Nanni (2008). "Review of design guidelines for FRP confinement of reinforced concrete columns of non-circular cross section.", *ASCE Journal of Composites for Construction*, 12(1), 80-92.
- E.T. Maaddawy (2009). "Strengthening of eccentrically loaded reinforced concrete columns with fiber reinforced polymer wrapping system – experimental investigation and analytical modeling", *Journal of Composites for Construction*, 13(1), 146-152.
- M.N.S. Hadi (2006). "Behavior of FRP wrapped normal strength concrete columns under eccentric loading", *Composite Structures*, 72, 503-511.
- J.A.O. Barros, R.K. Varma, J.M. Sena-Cruz, A.F.M. Azevedo (2008). "Near surface mounted FRP strips for the flexural strengthening of RC columns - experimental and numerical research", *Engineering Structures*, 30(12), 3412-3425.
- D.A. Bournas, T.C. Triantafillou (2009). "Flexural strengthening of RC columns with NSM FRP or stainless steel", *ACI Structural Journal*, 106(4), 495- 505.
- M. Perrone, J.A.O. Barros, A. Aprile (2009). "CFRP based strengthening technique to increase the flexural and energy dissipation capacity of RC columns", *ASCE Journal of Composites for Construction*, 5, 372-383.
- M. Rezazadeh, J.A.O. Barros (2014). "A new hybrid methodology according to NSM CFRP technique for the flexural strengthening of RC beams", *Journal of Reinforced Plastics and Composites*, 33(21), 1993-2009.
- M. Chellapandian, S.S. Prakash (2016). "Behavior of FRP strengthened RC columns under pure Compression – Experimental and Numerical Studies", *Proceedings of Structural Engineering Convention, SERC, Chennai*, 1730-1735.
- M. Chellapandian, S.S. Prakash, A. Sharma (2017). "Strength and ductility of innovative hybrid NSM reinforced and FRP confined short reinforced concrete columns under axial compression", *Composite Structures*, 176, 205-216.
- S. Jain, M. Chellapandian, S.S. Prakash (2017). "Emergency repair of severely damaged reinforced concrete column elements under axial compression: an experimental study", *Construction and Building Materials*, 155, 751-761.
- M. Chellapandian, S.S. Prakash, A. Rajagopal (2018). "Analytical and Finite Element Studies on the behavior of hybrid FRP strengthened RC columns under axial and eccentric compression", *Composite Structures*, 184, 234-248.
- M. Chellapandian, S.S. Prakash (2018). "Rapid repair of severely damaged reinforced concrete columns under combined axial compression and flexure – An experimental study", *Construction and Building Materials*, 173, 368-380.
- M. Chellapandian, S.S. Prakash (2017). "Behavior of hybrid NSM reinforced and externally confined short RC columns under eccentric compression – experimental and numerical studies, *Proceedings of 71st RILEM Week – ICACMS Conference, Chennai*, 2, 519-528.
- Indian Standards 10262 (2009). "Recommended guidelines for concrete mix design", Bureau of Indian Standards, New Delhi.
- ACI 440.2R (American Concrete Institute) (2017). "Guide for the design and construction of externally bonded FRP system for strengthening concrete structures", Farmington Hills, MI.



EXPERIMENTAL INVESTIGATION OF A NEW BEAM-COLUMN CONNECTION FOR CONCRETE-FILLED FRP TUBES (CFFTS)

Ahmed M. Ali ¹, Radhouane Masmoudi ²

¹ Université de Sherbrooke, (J1K 2R1), Canada, PhD Candidate, Email: ahmed.ali3@usherbrooke.ca

² Université de Sherbrooke (J1K 2R1), Canada, Professor, Email: radhouane.masmoudi@usherbrooke.ca

ABSTRACT

Concrete-filled fiber reinforced polymer (FRP) tube (CFFT) is a superior hybrid system regarding to its high performance. Previous research was conducted to study the behavior of CFFTs as column or as beam separately. Very limited data are available about how to connect CFFT beam and column together. This research is presenting a new precast CFFT beam-column connection. The beam tube was a pultruded FRP tube and the column tube was a filament-winding tube. The connection part was consisted of hollow rectangular steel beam welded to a steel-end plate. The beam FRP-tube was filled with normal strength concrete. After concrete hardening, the CFFT beam was embedded into the rectangular steel beam. The void-gap between the steel connection and the CFFT beam was filled with epoxy-grout. The steel-end plate of the steel connection is bolted to the high-stiffness CFFT column using eight high-strength bolts. This CFFT beam-column connection was tested under monotonic loading. The experimental results indicated that the failure occurred on the tension side of the CFFT beam in flexural failure manner. The slippage between the CFFT beam and the grout, as well as between the steel connection and the grout were measured.

KEYWORDS

Fiber-reinforced polymer, Concrete-filled FRP tubes, Precast CFFT connection, Beam-column connection, Monotonic loading, Bond.

INTRODUCTION

CFFTs are considered as superior structural elements because of their high-strength, high-ductility, and their high-resistance to harsh environmental conditions. In addition, the tube itself serves as a permanent lightweight formwork and provides a longitudinal and transverse reinforcement. Several research were conducted to investigate the different behaviour of CFFT members as beam or column individually. Mohamed and Masmoudi (2010) studied the behaviour of the circular CFFT beams and columns. The authors illustrated the benefits of using CFFT as beams and columns in terms of the strength and the ductility. In addition to a theoretical model was presented to design the circular CFFT beams and columns. Ozbakkaloglu et al (2006, 2007, and 2014) studied the behaviour of square and circular CFFT members under cyclic and monotonic loading. Abouzied and Masmoudi (2015, 2017) examined the flexural behaviour of rectangular CFFT beam consequently a theoretical model was developed to analyse and design the rectangular CFFT beams. Limited research were processed to investigate the connection between the CFFT column and the reinforced concrete (RC) footings such as Zhu (2004) and Nelson et al. (2008) and Lai (2010). Zakaib (2011) tried to investigate a moment connection for circular CFFT beams by embedding a steel I-beam into the circular CFFT section to a certain length and the other end of the steel I-beam was welded to steel plate, which was fixed to a rigid steel assembly by four steel anchors to provide the end fixation. Bond between the FRP tube and the concrete is an important factor, which effect on CFFT member behaviour. Belzer et al (2011) investigated the bond effect on rectangular CFFT beams. Ali et al (2017) investigated the effect of the bond on the flexural behaviour of circular CFFT members under cyclic loading. The authors concluded that, the bond has a significant effect on the flexural capacity and the stiffness of the CFFT members. Also using sand coating on the internal surface of the tube improves the bond. Up-to-date the CFFT beam-column connection is considered as a point of lack in this field consequently this research tries to fill research gaps and introduces a new precast CFFT beam-column connection. Achieving a properly CFFT beam-column connection will open the way for CFFT members to propagate widely in the construction field especially in the infrastructural building and residential buildings.

EXPERIMENTAL PROGRAM

Material properties

Two different types of rectangular FRP tubes were used in this experimental program. The beam tube was a pultruded tube with 7.67 mm flange thickness and 6.4 mm web thickness. The Creative Pultrusions Company fabricated this tube from glass fibre (GFRP) and vinyl ester resin. The column tubes was a filament winding tube,

this tube was fabricated in the Composite Material Reinforcement Laboratory of Sherbrooke University. The column tube was manufactured from GFRP and vinyl ester resin with 8.5 mm thickness and stacking sequences of (90/±30/90). Table 1 shows the mechanical properties of the beam tube where b , h , t_f , t_w , E_l , f_{tl} , and f_{cl} are the tube width, tube depth, flange thickness, web thickness, modulus of elasticity, tensile strength, and compressive strength in the longitudinal direction respectively. Normal weight concrete with 35 MPa target compressive strength was used to fill the tubes. The average compressive strength of six cylinders, which were tested on the same day of the connection testing, was 37 MPa. The strength of the high performance epoxy grout after 7 days shown in Table 2. Steel reinforcement bars with 15 mm diameter, modulus of elasticity 200 GPa, and yield stress 440 MPa were used. The steel HSS tube (A500 Grade C) has 254 mm x 152 mm cross section dimensions and 12 mm thickness. The yielding stress of the HSS section and tensile strength are 317 MPa and 427 MPa respectively. The steel HSS tube was welded to a steel plate (44W) with 300 x 400 mm dimensions and 38 mm thickness with 4 holes on each side. The yield strength and the ultimate tensile strength are 300 MPa and 450 MPa respectively. Figure 1 shows the connection details.

Table 1: Tubes mechanical properties

	b (mm)	h (mm)	t_f (mm)	t_w (mm)	E_l (GPa)	f_{tl} (MPa)	f_{cl} (MPa)
Beam tube	102	152.5	7.6	6.4	37.666	450	380

Table 2: Mechanical properties of the epoxy grout

	Compressive modules	Compressive strength	Flexural strength	Tensile Strength	Adhesion to Steel
MPa	3917	103	27	14	17
ASTM Standard	D 695	C 579 B	C 580	C 307	

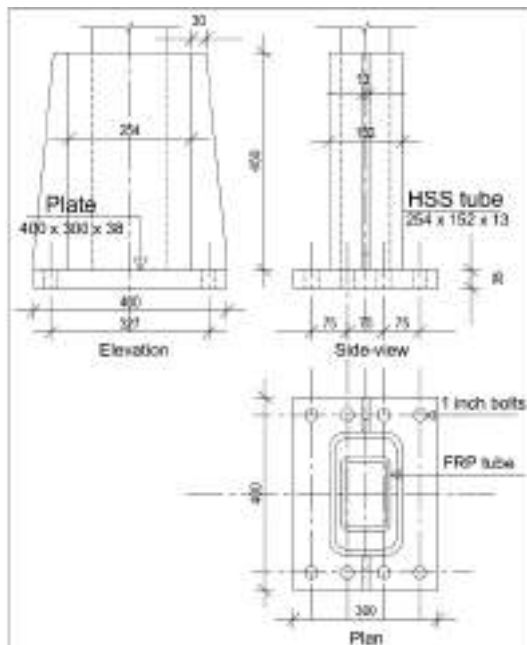


Figure 1: Details of the proposed connection

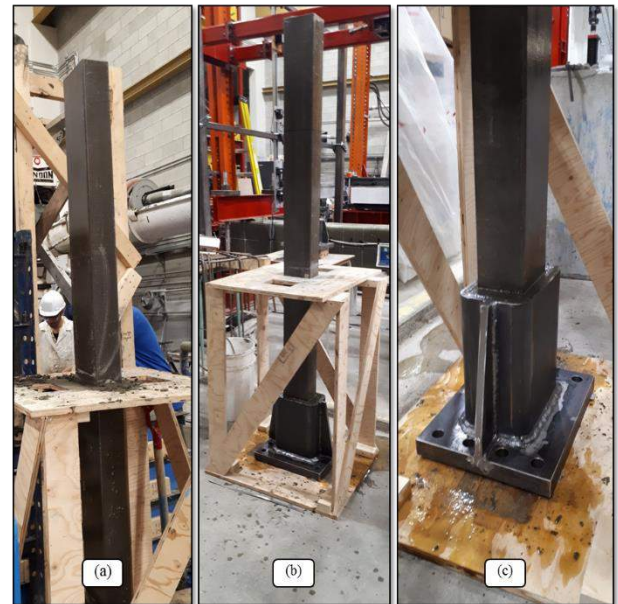


Figure 2: Preparation steps of the CFFT beam, (a): casting of concrete. (b): inserting the GFRP tube in the steel connector. (c): fill the gap between the GFRP tube and the steel tube by the epoxy grout.

Preparation and description of the connection

The interior surface of the FRP beam tube was prepared with sand coating (Ali et al. 2017) then the tube was filled with the concrete without any internal reinforcement. After 14 days, the casted FRP tube was embedded 450 mm into the steel connection. Wood frame was used to insure the verticality and support the beam. The epoxy grout was poured in the space between the steel and the FRP tube. The preparation of the column tube is independent on the beam tube. Wood form was used to guide the driller during the making of the holes on the top and the

bottom flange of the FRP column tube. Steel cage consists of 3M15 in the top and bottom was inserted into the FRP column tube. Eight PVS plastic pipes were inserted on the holes before the casting of the concrete. The two tubes were assembled together using eight anchors with one inch diameter, which bolted to the steel part and passing through the plastic pipes and bolted on another plate from the other side. The length of the CFFT column and the CFFT beam was 3000 mm and 2000 mm respectively. Figure 2 and Figure 3 shows the preparation of the CFFT beam and the CFFT column respectively.

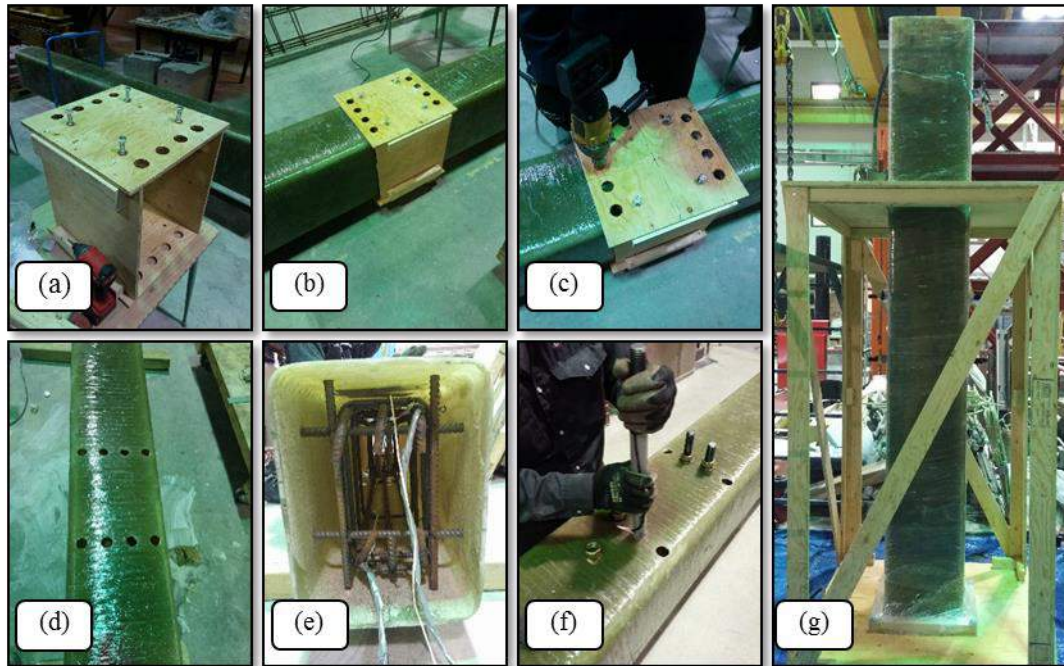


Figure 3: Preparation steps of the CFFT column, (a): wood form with holes. (b): inserting the GFRP tube in the wood form. (c): drilling the holes in the GFRP tube. (d): the GFRP after drilling the holes. (e): inserting of the steel cage. (f): inserting the PVC plastic pipes in the holes. (g): casting the concrete on the GFRP tube.

Test setup and instrumentations

The test setup was established, as shown in Figure 4, the column was positioned horizontally and the beam was positioned vertically. Two steel frames connected together by two rectangular steel beams. Four steel members supported the main frame to prevent any deformation. The rectangular steel beams were used as a lateral guide system. A hydraulic actuator with 500 kN capacity and 500 mm stroke attached to the main frame. The horizontal movement of the column was prevented using steel beam attached to the secondary frame. The shear span of the column was 2500 mm, measured from the centreline of the supporting beams. The clear span of the beam was 1840 mm, measured from the column top surface to the loading level. Displacement control procedure with constant loading rate was applied up to the failure of the specimen.

The displacement of the beam was measured using potentiometers at different height, 495 mm, 571 mm, 648 mm, 800 mm, 1308 mm, and 1840 mm from the column surface. Another four potentiometers were used to measure the deflection of the column. Two potentiometers were used to measure the slippage on the compression and the tension side between the steel tube and the grout. The slippage between the FRP tube and grout measured by two LVDTs, one on the tension side and one on the compression side. Vertical and horizontal electrical strain gauges were used to measure the strain over the FRP tubes and the Steel connector. Figure 5 shows the instrumentation layout.

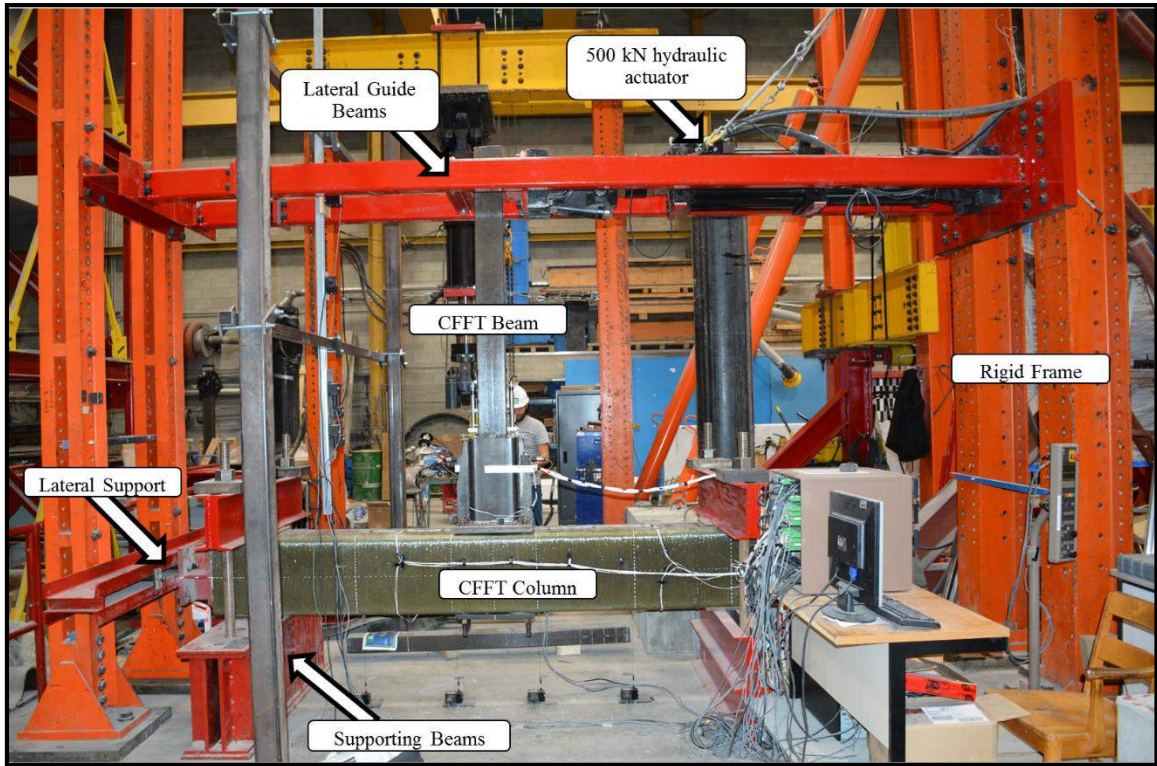


Figure 4: Test setup

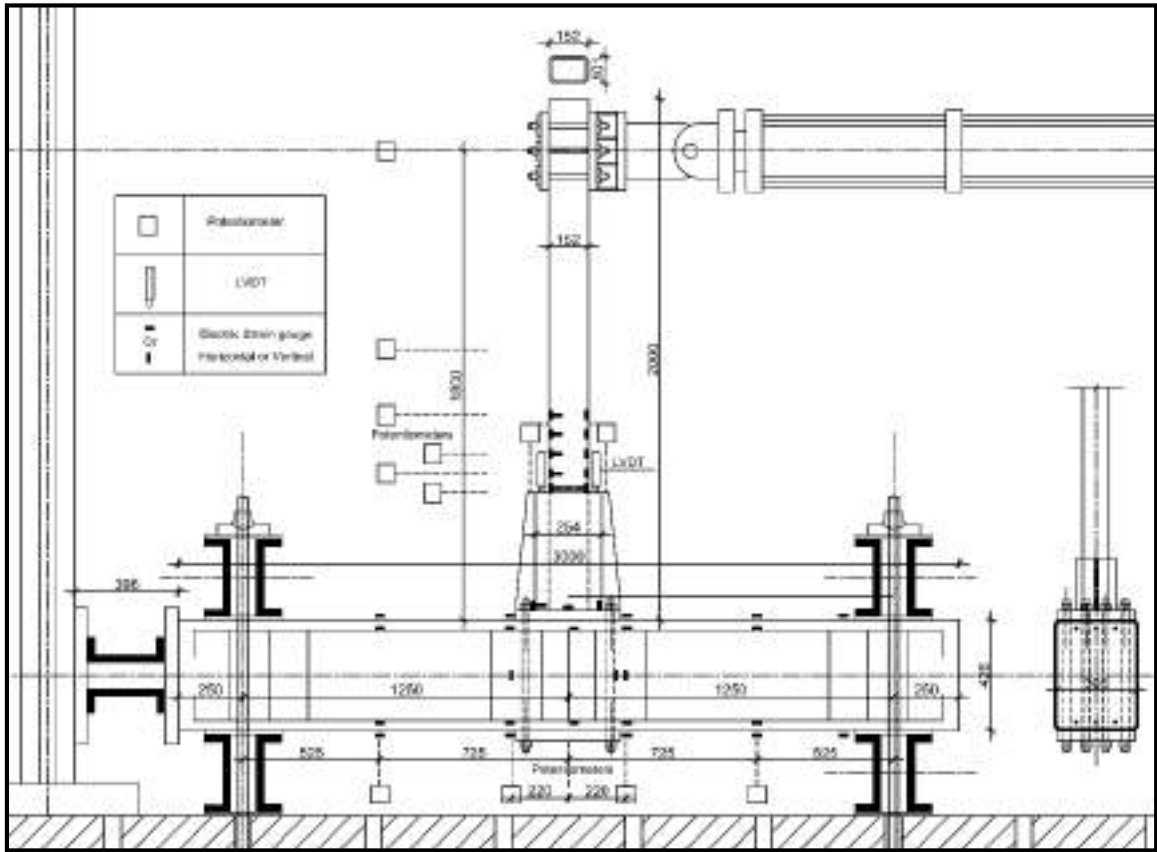


Figure 5: Instrumentation layout

THEORETICAL AND EXPERIMENTAL ANALYSIS.

Test observations and failure mode

As mentioned previously, this research presents a new precast CFFT beam-column connection. It was predicted in the design of the specimen; the failure should be in the connection part between the beam and the steel connector due to the slippage or in the CFFT beam, if the beam reached its flexural strength. It was observed that, the failure of the connection occurred in the CFFT beam in tension failure manner as was expected. Full rupture of the tube occurred suddenly on the beam tension side above the steel connector. It is attributed to the excessive tensile strains and stresses, which applied on the tension side of the tube. Figure 6 shows the failure of the specimen. The load-deflection response of the specimen is shown in Figure 7. The response of the CFFT beam was linear in the beginning of the loading up to the cracking point of the concrete consequently the slope of the curve was decreased but still linear up to the failure of the specimen. The experimental flexural capacity was calculated by multiply the failure load by the distance from the loading point to top surface of the steel connector (1350 mm). The failure load, top displacement, and moment were 48.5 kN, 122.9 mm, and 65.25 kN.m respectively.



Figure 6: Failure model of the CFFT beam-column connection.

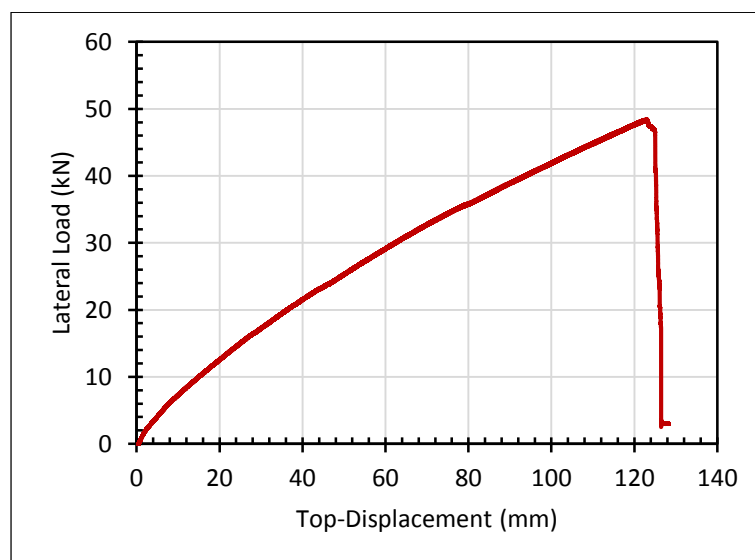


Figure 7: Load-top displacement response

Slippage observations

The slippage between the grout and the CFFT beam was measured using LVDT. Eyes observed no slippage however; the maximum slippage measured at the failure load was less than 1.00 mm. This measurement was occurred due to the excessive tensile strain on this zone. The slippage between the grout and the steel connector was measured by potentiometer. The slippage at the maximum moment was 1.70 mm, Figure 8 represents the moment-slippage response between the grout and the steel connector.

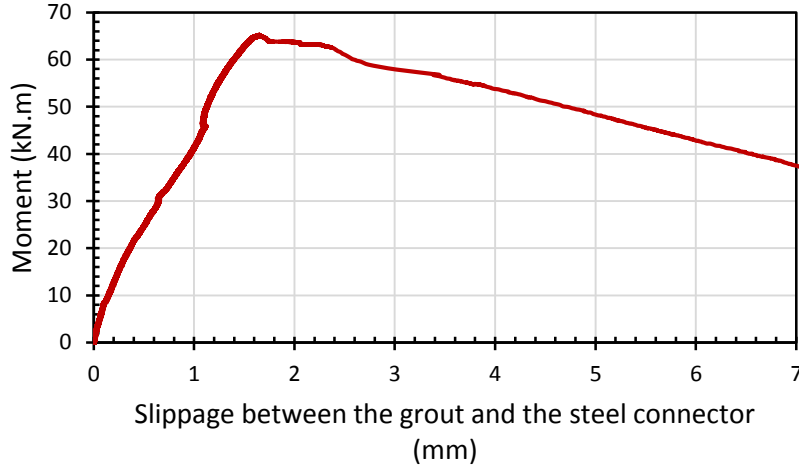


Figure 8: Moment-slippage response

Theoretical model to predict the flexural capacity of the CFFT beam

Based on the fundamentals and the basic assumptions of the flexural design of reinforced concrete section, as shown in Figure 9, theoretical equations were developed to calculate the compression zone depth (c) and the flexural moment (M_{th}) for tension failure mode. The tension forces on the tube can be formulated on two-forces (T_w) and (T_f) act on the tension part of the tube web and flange respectively. The compression forces act on the concrete compression zone and the compression part of the tube web and flange are (C_{con}), (C_w), and (C_f) respectively. The value of the web/flange tube compression/tension force can be calculated by multiply the tube cross-section area of this part by the tube elastic modulus by the strain corresponding to the centroid of this part, as shown in Eqns. 1 to 4. Depending on the rectangular block assumption, the compression concrete force (C_{con}) can be calculated as shown in Eq. 5. The compression zone depth (c) can be calculated from the equilibrium of the section, where the total compression force is equal to the total tension force ($T_{total} = C_{total}$). Equation 6 presents a formula to calculate the compression zone depth (c). The theoretical moment can be calculated according to Eqn. (7).

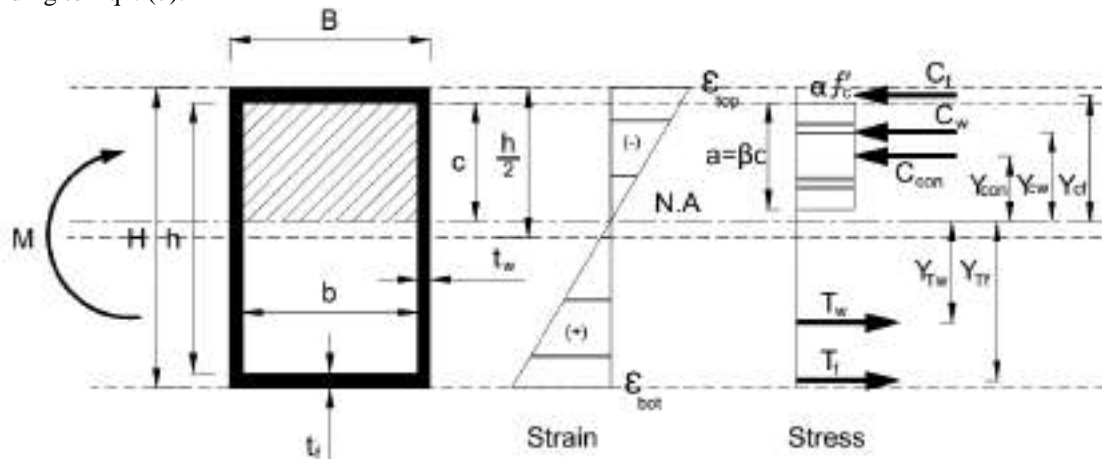


Figure 9: Section analysis of rectangular CFFT member under flexure.

$$T_w = t_w \times E_{tube} \times \left[\frac{(h-c)^2}{H-t_f-c} \right] \epsilon_{bot} \quad (1)$$

$$T_f = B \times t_f \times E_{tube} \times \left[\frac{H-1.5t_f-c}{H-t_f-c} \right] \varepsilon_{bot} \quad (2)$$

$$C_w = t_w \times E_{tube} \times \left[\frac{c^2}{H-t_f-c} \right] \varepsilon_{bot} \quad (3)$$

$$C_f = B \times t_f \times E_{tube} \times \left[\frac{c+0.5t_f}{H-t_f-c} \right] \varepsilon_{bot} \quad (4)$$

$$C_{concrete} = \alpha \times f'_c \times \beta \times c \times b \quad (5)$$

$$c = \left(\frac{H-t_f}{2} \right) + \frac{A f_{tl}}{2 \alpha f'_c \beta b} - 0.5 \sqrt{t_f^2 + H^2 + \frac{2 A f_{tl} t_f}{\alpha f'_c \beta b} - 2 H t_f + \left(\frac{A f_{tl}}{\alpha f'_c \beta b} \right)^2} \quad (6)$$

$$\begin{aligned} M_{th} &= T_w \times Y_{T_w} + T_f \times Y_{T_f} + C_w \times Y_{C_w} + C_f \times Y_{C_f} + C_{con} \times Y_{conc} = \\ &= T_w \left(\frac{2(h-c)}{3} \right) + T_f (H - 1.5t_f - c) + C_w \left(\frac{2c}{3} \right) + C_f \left(c + \frac{t_f}{2} \right) + C_{con} \left(c - \frac{c\beta}{2} \right) \end{aligned} \quad (7)$$

Where H and B are the outer tube depth and width respectively, h and b are the depth and the width of concrete core, A is the cross section area of the tube ($A = HB - hb$), E_{tube} is the modulus of elasticity of the FRP tube in the longitudinal direction, t_f is the thickness of the tube flange, ε_{bot} is the strain of bottom fibre of the tube. The ultimate strain of the FRP tube in the longitudinal direction ε_{fu} is equal to ε_{bot} for the tension failure, f'_c is the concrete compressive strength. According to the ACI 318-14, β and α are parameters defining a rectangular stress block in the concrete equivalent to the nonlinear distribution of stress, ($\beta = 0.85 - \frac{f'_c - 28}{140}$), ($\alpha = 0.85$). The distances from the neutral axis to the forces (T_w), (T_f), (C_{con}), (C_w), and (C_f) are equal to (Y_{T_w}), (Y_{T_f}), ($Y_{C_{con}}$), (Y_{C_w}), and (Y_{C_f}) respectively. The flexural capacity of the CFFT beam according to this theoretical model is equal to 64.00 kN.m.

CONCLUSIONS

The experimental flexural capacity of the CFFT beam is higher than the theoretical calculation by 2% in addition to the flexural failure mode of the specimen. These reasons give a significant indication about the efficiency of the presented CFFT beam-column connection. The embedded length of the CFFT beam into the epoxy grout and the steel connector was sufficient to achieve the flexural strength of the CFFT beam. Design equations of rectangular unreinforced CFFT member for tension failure mode were presented. The optimization of the embedded length of the CFFT beam into the steel connector will be the next step as a future work.

ACKNOWLEDGMENTS

This paper is a part of a research project sponsored by the Natural Sciences and Engineering Research Council of Canada (NSERC). Special thanks to the manufacturer (Creative Pultrusions, PA, USA) for providing pultruded FRP tubes.

REFERENCES

- A. Abouzied et R. Masmoudi (2015). "Structural performance of new fully and partially concrete-filled rectangular FRP-tube beams", *Elsevier, Engineering Structures Journal*. Vol. 101, pp. 652-660.
- A. Abouzied et R. Masmoudi (2017). "Flexural behavior of rectangular FRP-tubes filled with reinforced concrete: Experimental and theoretical studies", *Elsevier, Construction and Building Materials*. Vol. 133, pp. 59-73.
- American Concrete Institute (ACI), (2014). "Building code requirements for structural concrete," ACI-318-14, Detroit, USA.
- A.M. Ali, D. Robillard, R. Masmoudi, I.M. Khan (2017). "Experimental investigation of bond and tube thickness effect on the flexural behavior of concrete-filled FRP tube under lateral cyclic loading", *Elsevier, Journal of King Saud University – Engineering Sciences*.
- B. Belzer, M. Robinson, D. Fick (2013). "Composite action of concrete-filled rectangular GFRP tubes", *ASCE Compos. Construct. J.* 17 (5), pp. 722-731.
- H. M. Mohamed, R. Masmoudi (2010), "Flexural strength and behavior of steel and FRP-reinforced concrete-filled FRP tube beams", *Elsevier, Engineering Structures Journal*. Vol. 32, pp. 3789-3800.

- M. Nelson, Y. C. Lai, and A. Fam (2008) "Moment Connection of Concrete Filled Fiber Reinforced Polymer Tubes by Direct Embedment into Footings", *Advances in Structural Engineering*, 11(5):537-547.
- S. E. Zakaib (2011). "Flexural Performance and Moment Connections of Concrete Filled GFRP Tubes (CFFTs) and CFFT-Encased Steel I-Sections." *M.Sc. Thesis, Queen's University, Kingston, Canada.*
- T. Ozbakkaloglu et M. Saatcioglu (2006). "Seismic behavior of high-strength concrete columns confined by fiber-reinforced polymer tubes". *Journal of Composites for Construction*, Vol. 10, No 6, p. 538-549.
- T. Ozbakkaloglu et M. Saatcioglu (2007). "Seismic performance of square high-strength concrete columns in FRP stay-in-place formwork". *Journal of Structural Engineering*, Vol. 133, No 1, p. 44-56.
- T. Ozbakkaloglu. et Y. Idris (2014). "Seismic Behavior of FRP-High-Strength Concrete-Steel Double-Skin Tubular Columns". *Journal of Structural Engineering*, Vol 140, No 6, p. 04014019 (14 pp.).
- Y. C. Lai (2010). "Moment Connections of Concrete-Filled Fibre Reinforced Polymer Tubes to Reinforced Concrete Footings." *M.Sc. Thesis, Queen's University, Kingston, Canada.*
- Z. Zhu (2004). "Joint Construction and Seismic Performance of Concrete-Filled Fiber Reinforced Polymer Tubes." *PhD. Thesis, North Carolina State University, Raleigh, NC, United states of America.*



MOMENT-CURVATURE CHARACTERISTICS OF STEEL AND CFRP REINFORCED CFFT COLUMNS: EXPERIMENTAL AND THEORETICAL STUDY

Maha Hussein Abdallah¹, Hamdy M. Mohamed², Radhouane Masmoudi³, Ahmed Moussa⁴

1 PhD candidate Department of Civil Engineering, University of Sherbrooke, Quebec, Canada, J1K2R1.

Maha.Abdallah@Usherbrooke.ca

2 Research Associate-Lecturer, Department of Civil Engineering, University of Sherbrooke, Quebec, Canada, J1K2R1. Hamdy.Mohamed@Usherbrooke.ca

3 Professor of Civil Engineering Department of Civil Engineering University of Sherbrooke, Quebec, Canada, J1K2R1, Radhouane.masmoudi@usherbrooke.ca.

4 Professor of Concrete Structures, and former Dean, Helwan University.

Dean of faculty of Engineering, Badr University in Cairo, BUC, E-mail: ahmoussa2@yahoo.com.

ABSTRACT

The paper highlights the investigation of experimental and theoretical moment-curvature relationships for circular steel and carbon-fiber-reinforced polymers (CFRP) reinforced concrete-filled FRP tube (CFFT) columns. To experimentally investigate the moment curvature behavior of circular CFFT columns, Steel reinforced CFFT and CFRP reinforced CFFT columns were tested under eccentric loads. It was found that a nonlinear moment-curvature ($M-\phi$) response was observed regardless the type of reinforcement and the applied eccentricity ratio. A theoretical model based on layer by layer method has been developed to investigate the theoretical behavior of CFFT columns. Material constitutive models of each component of the column have been chosen adequately to insure the accuracy of the developed model. The analytical model has been validated with the experimental results and proved to be an accurate model.

KEYWORD

Concrete, Eccentricity, Columns, Moment-Curvature.

INTRODUCTION:

Concrete-filled fiber-reinforced-polymer (FRP) tubes (CFFTs) provide an innovative alternative system to conventional materials for several structure applications, including structures piles, bridge columns and piers, overhead sign structures, poles, posts, traffic signs, traffic lights, pipes and tunnels, beams, and bridge girders. The concept of CFFT was developed for different purposes including, the development of non-corrosive piles for marine environments to replace the reinforced, prestressed, and concrete-filled steel tube piles (Mirmaran and Shahwy 1996) The concrete filling also significantly enhances the ductility of the system (Mohamed and Masmoudi 2008), therefore, they can be used as bridge columns and piers in seismic zones (Mohamed and Masmoudi 2010,2011). Despite the fact that most of the structure columns under axial loads exhibited to eccentric loads due to unintentional load eccentricities, possible construction error, lateral deformation and buckling phenomenon, limited investigations have been carried on to study the behavior of CFFT columns under eccentric loading (Lillistone et al.(1997), Hadi et al. (2016)). On the other hand, the behavior of FRP bars as longitudinal reinforcement in compression members is still a relevant issue to be addressed and it is not recommended by ACI 440.1R-15 to resist compression stresses. Current guidelines and codes of practice do not recommend the use of FRP bars as internal reinforcement in either compression members or eccentrically-compression loaded members. However, code standards (CAN/CSA S806-12) allow using FRP bars in the compression zone of flexural members, provided that they are neglected in determining the member's axial or flexural strength. In this study, steel reinforced CFFT and CFRP reinforced CFFT columns, were tested under eccentric loads. A theoretical model has been developed for the moment-curvature curve. The analytical models have been validated with the experimental results.

EXPERIMENTAL INVESTIGATION

Materials

Glass-fiber reinforced polymer (GFRP) tubes were used as structural formwork for the CFFT specimens. The GFRP tubes were fabricated using filament winding technique; E-glass fiber and epoxy resin were utilized for manufacturing these tubes. The tubes had a core diameter of 152 mm and a wall thickness of 2.65 mm (6 layers).

The fiber orientations of the tubes were mainly in the hoop direction (± 60 degree with respect to the longitudinal axis). All specimens of this study were constructed using normal concrete strength. Concrete batch was supplied by ready mix concrete supplier. The 28-day average concrete compressive strength was found equal to 30 ± 0.6 . Two types of reinforcing bars were used as longitudinal reinforcement for the CFFT columns; deformed steel bars No. 10 M (11.3 mm nominal diameter) and sand-coated carbon FRP (CFRP) bars No. 3 (9.52 mm nominal diameter). The mechanical properties of the steel bars were obtained from standard tests that were carried out according to ASTM A615/A615M-09, on five specimens for each type of the steel bars. The average values of the yield tensile strength, f_y was 462 with an ultimate tensile strength, f_{su} , 577 MPa. On the other hand, the CFRP bars were manufactured and developed by Pultrall Inc., Quebec, Canada. The bars were made of continuous fiber impregnated in vinylester resin with a fiber content of 73%, using the pultrusion process. The elastic modulus and ultimate tensile strength were 128 GPa and 1431 MPa with an ultimate tensile strain 1.2 ± 0.09 .

Test Specimens

In this study reinforced CFFT columns (2 CFRP reinforced and 2 steel reinforced) were tested under eccentric loading. All specimens were 152 mm in diameter and 912 mm in height. Table 1 summarizes different configurations of the tested specimens. The experimental program was carried out on four reinforced CFFT specimens. The four specimens were included through two series. The tested columns had a circular cross-section of 152 mm diameter. Series No. 1 and 2 present reinforced CFFT columns with a total height 912 mm, reinforced longitudinally with 6 steel or CFRP bars, respectively. The bars were distributed uniformly inside the cross section of the GFRP tube. The bars were fixed at the top and the bottom of the height using two steel stirrups of 3.2 mm diameter, to fix the bars during casting. The distance between the bars and the tubes was 8 mm. A concrete cover of 10 mm was provided between the ends of the longitudinal bars and the end surfaces to avoid the stress concentration at the bars area. Specimens ID were shown in the second column of Table 1, the numbers indicate the eccentricity (e) in mm and the letter S or C refers to the type of internal reinforcement, respectively, steel or CFRP bars. The load eccentricity-to-diameter (e/D) ratios for the reinforced CFFT columns 0.2 and 0.4.

Table 1- Specimens details and summary of test results

Series No.	Specimen ID	(e/D)	Bar type	P_u (kN)	Δ_h (mm)	M_e (kN.m)	M_Δ (kN.m)	M_u (kN.m)	(f'_{cc}/f'_c)
1	S-30	0.2	Steel	620.0	45.5	9.40	18.60	28.00	0.65
	S-60	0.4	Steel	367.0	73.00	4.70	22.02	26.72	0.17
2	C-30	0.2	CFRP	614.5	43.46	8.28	18.44	26.71	0.82
	C-60	0.4	CFRP	375	75.32	5.74	22.50	28.24	0.37

Instrumentation and Test Setup

For the eccentrically loaded CFFT columns, the load was applied with specific eccentricities using specially designed two rigid steel end caps and roller bearing assembly. The two rigid steel end caps were designed and fabricated from high strength steel plates and semicircular section of thicknesses 30 mm and 5 mm, respectively. The steel plates and semicircular section were welded together with outward radiating stiffeners of thickness equal to 25 mm. The CFFT specimens were tested under two variable eccentric loads. Therefore, two lines holes were drilled at the top and bottom surfaces of the steel plate of the two caps at distance 30, 60 mm from the center of specimen's position to fix the roller steel rod. The caps sections were placed over the two ends of the CFFT specimens and clamped together 15 mm with high strength steel bolts. The specimens were tested using a 6,000 kN (1350 kips) capacity FORNEY machine, where the CFFT columns were setup vertically at the center of loading plates of the machine. Figure 1 shows the test setup.

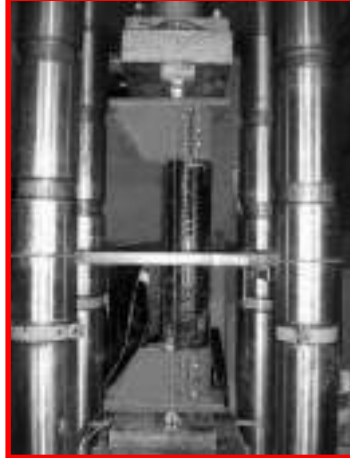


Figure 1-Test set up for eccentric axial load

Experimental moment-curvature for steel and CFRP reinforced CFFT columns

Figures 3 and 4 show the experimental moment-curvature diagrams for series 1 & 2 which were plotted by calculating the curvature ϕ using the following equation:

$$\phi = \frac{|\varepsilon_{tension}| + |\varepsilon_{compression}|}{D_o} \quad (1)$$

Where $\varepsilon_{tension}$ and $\varepsilon_{compression}$ are the compressive and tensile strains measured from the two longitudinal strain gauges installed on the FRP tubes on two opposite sides at the mid height of each column. The midheight moment is calculated as follow;

$$M_u = M_e + M_{\Delta} \quad (2)$$

$$M_e = P_u e \quad (3)$$

$$M_{\Delta} = P_u \Delta \quad (4)$$

Moment-Curvature Analytical Model

Layer by layer numerical integration method was used for creating the analytical moment curvature diagrams for both series Figure (2). Adequate material modeling of different parts of the concrete filled FRP tube columns assures the accuracy of the developed theoretical model. Thus, Lam and Teng (2003) model for confined concrete was chosen to model the stress-strain curve for the circular confined concrete, this model proved to be one of the most accurate model to predict the stress-strain curve for circular confined columns (Ozbakkaloglu (2013), Abdallah et al. (2017)). In this model, they assume that the stress-strain curve of the confined concrete consists of two parts, the first is parabolic, while the second is a straight line. More details of this model can be found in Lam and Teng (2003). For reinforcing steel bars an elastic plastic stress-strain relation was used. For the FRP bars a linear elastic until rupture theory presented by Kobayashi et al. (1995) was used. In addition, for design purpose a reasonable assumption to consider the contribution of FRP bars in tension only while the bars in compression were replaced by the same area of concrete (Zadeh & Nanni (2013)). A linear elastic stress-strain relationship was adopted for FRP tube where the parts above and below the neutral axis are considered effective in resisting the compression and tension forces, respectively (Figure 2). The following steps illustrated the calculation procedure for the theoretical moment curvature as follows;

1. Assume strain of the outermost Concrete fiber (ε_{top});
2. Assume neutral axis depth (C);
3. Calculate the strains ,stresses and accordingly forces in the confined concrete, bars and tube using the material constitutive models;
4. Calculate P_u and M_u ,and calculate the associated eccentricity ($e = \frac{P_u}{M_u}$), if $e = e_{given}$ then the associated curvature can be calculated as follows;

$$\phi = \frac{\varepsilon_{top}}{c} \quad (5)$$

5. If $e \neq e_{given}$, assume new strain value and repeat steps from step number 1.

Consequently, through repeating the previous steps, the complete moment-curvature diagram can be generated by increasing the compressive strain ε_{top} to its ultimate state (ε_{cu}). Figures (3, 4) show that excellent agreement between the experimental and theoretical results occurred and moment capacities were accurately estimated. In addition, regardless the type of reinforcement and the eccentric ratio, all specimens exhibited nonlinear moment-curvature (M- ϕ) responses. The moment-curvature curves mainly consist of 3 zones, the first zone represents the

initial portion of both series of moment-curvature diagrams where they are nearly identical for curvature between 0 and 0.00002 1/mm as the stiffness depends mainly on the initial stiffness of concrete. This zone exhibit small curvatures and the load combination was not large enough to cause concrete cracks, thus the tube confining mechanism was not fully engaged. The second zone is the transition zone between initial concrete stiffness and the confined concrete stiffness, this zone corresponds to curvatures between 0.00002 and 0.000045 1/mm. The third zone is with curvature of 0.000045 1/mm up to failure.

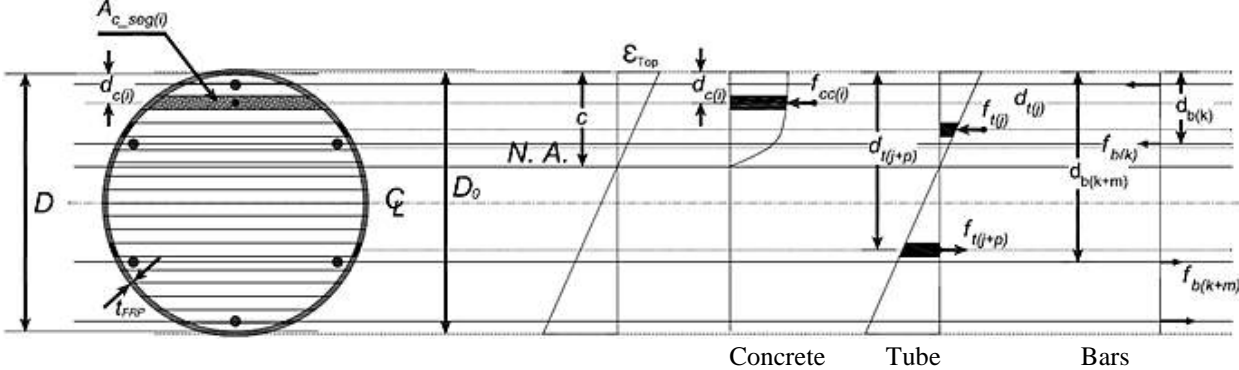


Figure 2- Discretized Section for CFFT Column and its Strain and Stress Profiles

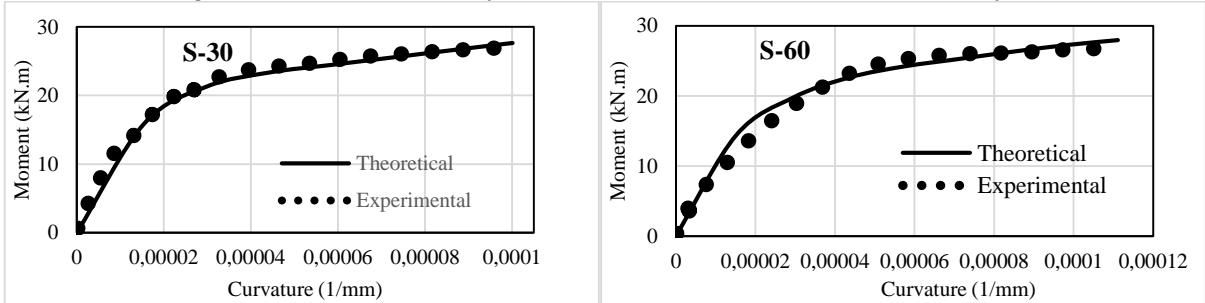


Figure 3- Experimental and Theoretical Moment-Curvature Diagrams for Steel CFFT Columns

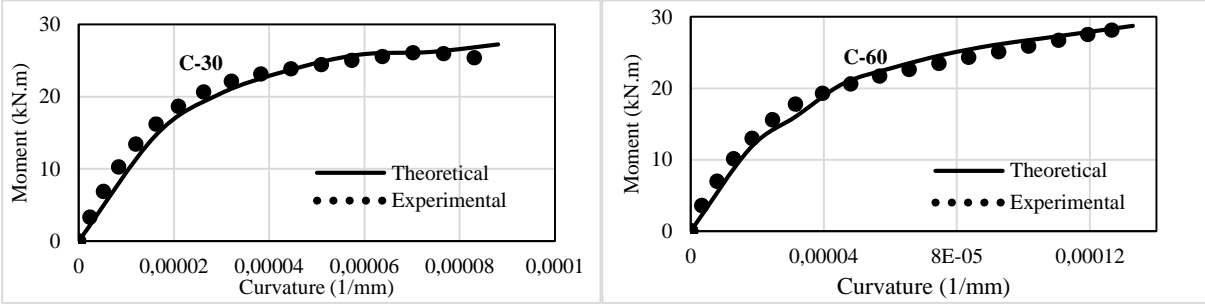


Figure 4- Experimental and Theoretical Moment-Curvature Diagrams for CFRP CFFT Columns

CONCLUSIONS

A total of full scale 4 reinforced CFFT columns were constructed and tested under eccentric compression loads to investigate the behavior of steel and CFRP reinforced CFFT columns. The bending moment curvature behavior was investigated experimentally and analytically for the 4 specimens. The test parameters were the internal reinforcement type and the eccentricity to diameter ratio (e/D). The developed analytical model for computing the moment-curvature diagram based on the layer by layer numerical integration provided accurate predictions compared to the experimental results. It also shows that regardless the type of reinforcement and the eccentric ratio all specimens exhibit nonlinear moment-curvature ($M-\phi$) responses.

REFERNCES

Abdallah , M., Shazly,M., Mohamed, ,H., Masmoudi,R., and Mousa, A. (2017)” Nonlinear finite element analysis of short and long reinforced concrete columns confined with GFRP tubes .” J. Reinf. Plast. Comp., 13:972 – 987.

ACI 440.1R-15. (2015) “Guide for the design and construction of concrete reinforced with FRP bars.” ACI committee 440. Farmington Hills: American Concrete Institute

- ASTM- 2009. "Standard specification for deformed and plain carbon steel bars for concrete reinforcement." A615/A615M-09, West Conshohocken, Pa.
- CAN/CSA S806-12. (2012) "Design and construction of building components with fiber reinforced polymers." Ontario, Canada: Canadian Standards Association.
- Lam, L. Teng, J.G. (2003) "Design-oriented stress–strain model for FRP-confined concrete." *Constr. Build. Mater.* 17(6–7), 471–489.
- Mohamed, H., and Masmoudi, R. (2008) "Compressive Behaviour of Reinforced Concrete Filled FRP Tubes" *ACI Spec Publi (SP), SP-257-6*, pp. 91-109.
- Mohamed H, Abdel-Baky H, Masmoudi R. (2010) "Nonlinear stability analysis of concrete-filled fiber-reinforced polymer-tube columns: experimental and theoretical investigation." *ACI struct J* 2010; 107, 699-708.
- Mohamed H.M. Masmoudi R. (2010) "Axial load capacity of concrete-filled FRP tube columns: Experimental versus Theoretical Predictions." *J. Compos. Constr.* 14(2), 231–243.
- Mohamed, H. Masmoudi, R. (2011) "Deflection prediction of steel and FRP-reinforced concrete-filled FRP tube beams." *J Compos Constr., (ASCE)*, 15(3): 462-472
- Hadi, M.N.S., Khan, Q.S. & Sheikh, M.N.(2016) " Axial and flexural behavior of unreinforced and FRP bar reinforced circular concrete filled FRP tube columns." *Constr. Build. Mater.* , 122, pp.43–53.
- Kobayashi K, Fujisaki T.(1995) "Compressive behavior of FRP reinforcement in non prestressed concrete members in non-metallic (FRP) reinforcement for concrete structures." In: *Proceedings of the second international RILEM symposium* vol. 29. CRC Press; Aug 3. p. 267.
- Lillistone D, Jolly CK.(1997) " Concrete filled fibre reinforced plastic circular columns." In;*Proceedings of Composite construction-conventional and innovative conference, composite construction-Conventional and innovative :759-764.*
- Mirmiran A, Shahawy M. (1996) "Anew concrete-filled hollow FRP composite column." *Compos Part B*;27B:263–8.
- Ozbakkaloglu T. (2013) " Compressive behavior of concrete-filled FRP tube columns: assessment of critical column parameters." *Eng Struct*; 51: 188–199.
- Zadeh, H., and Nanni, A. (2013) "Design of RC columns using glass FRP reinforcement." *J. Compos. Constr.*, 10.1061/ (ASCE) CC.1943- 5614.0000354, 294–304.



BEHAVIOUR OF CONCRETE SANDWICH WALL PANELS IN FLEXURE USING A NOVEL GFRP SHEAR CONNECTOR

Debrup Dutta¹, Amir Fam²

1Queen's University, Department of Civil Engineering, Kingston, Canada (15dd13@queensu.ca)

2Queen's University, Department of Civil Engineering, Kingston, Canada (amir.fam@queensu.ca)

ABSTRACT

This paper investigates the structural behaviour of three half-scale concrete sandwich panels with a new GFRP shear connector, under four-point bending. The connector attempts to maximize the degree of composite action between the two concrete wythes while maintaining a minimal thermal bridging, compared to steel connectors. The overall dimensions of the specimens are 3048 mm x 610 mm x 279 mm. Each concrete wythe is 76 mm thick and are separated by a 127 mm thick Extruded Polystyrene (XPS) foam layer in between the wythes. The GFRP shear connector is a 203 mm deep C-shaped pultruded channel located at mid-width of the specimens and its two flanges are embedded at mid thickness of the concrete wythes. The first specimen was fabricated using a flexural steel reinforcement ratio of 0.34% in its concrete wythes, while the second specimen was fabricated with a steel ratio of 0.68%, with the aim to study the effects of change of reinforcement ratio in the slab system. In both specimens the same GFRP connector, in the form of one continuous GFRP section, was used. The last specimen was fabricated using a conventional steel truss shear connector system with a cross sectional stiffness of the diagonals equivalent to the GFRP C-section and the same steel reinforcement ratio in the wythes as the first specimen. The aim was to compare the two different shear connectors. It was found that the GFRP connector resulted in a flexural strength 2.85 times that of the specimen with steel truss system. Also, doubling the steel reinforcement ratio of the wythe increased flexural capacity by 40% when GFRP connectors were used.

KEYWORDS

Sandwich panels, Composite action, Shear connector, Concrete wythe, Thermal bridging, Pultruded sections.

1. INTRODUCTION

Concrete sandwich panels are conventionally used as exterior walls in multi-unit residential, commercial, and ware house buildings all across North America (Salmon et al. 1994). These wall panels are generally precast and they maybe prestressed to enhance the structural performance of the panels under loading. They are meant to provide excellent thermal insulation and at the same time have adequate structural resistance to external loads like wind load, seismic load and impact damages caused due to forklifts or other heavy machineries in applications like factories or warehouses (PCI 2011).

Concrete sandwich panels generally consist of two layers of concrete, conventionally called as wythes, separated by a layer of insulation foam in the middle. The two concrete layers are generally connected by a shear connector to ensure continuity of the structure. The structural performance of the panels depends highly on the degree of composite action developed because of the shear connector between the two wythes. A panel capable of complete shear transfer between the two concrete wythes is considered to be fully composite. In this case, the strain profile would be a continuous straight line with a constant slope running thorough the entire depth of the panel. In other words, there is full compatibility of strain across the whole cross section (Goudarzi et al. 2016). At any cross-section, plane sections before bending remain plane after bending. This signifies that unit strain above and below the neutral axis are proportional to the distance from the neutral axis. On the other hand, if the shear transfer is negligible, panels are called as non-composite. In this case, each of the concrete wythes resist loads individually. The plane sections remain plane across each of the individual wythes, but not across the cross section of the wall. For walls where shear transfer is in between fully composite and non-composite, they are known as partially composite. It is much more complicated to study the behaviour of partially composite panels compared to their fully composite or non composite counter parts. Arriving at an accurate conclusion regarding the performance of these panels is an arduous challenge. Large scale experiments and complex computer modelling become a necessity (Tomlinson et al. 2014).

Since the initial introduction of sandwich panels in the construction industry, steel and concrete have been widely used as shear connectors to achieve a high degree of composite action with negligible shear deformation in the connectors. But, they are also known to induce thermal bowing and cause significant loss in thermal insulation. For the last couple of decades, researchers have slowly started venturing into the use of fibre reinforced polymer (FRP) connectors as a replacement for steel and concrete, to have better thermal and cost efficiencies.

This experimental study introduces a novel GFRP shear connector with the aim of maximizing composite action. The GFRP connector is a commercially available light weight C-shaped pultruded channel. The flanges are embedded in the wythes, thereby provide additional bond area with concrete. The performance of the GFRP stud has been compared against a conventional steel truss shear connector. The effect of increasing the flexural steel reinforcement ratio of the wythe has also been studied.

2. EXPERIMENTAL PROGRAM

2.1 Test Specimens

For the purpose of investigating the structural behavior of the sandwich panels with the new GFRP shear connector, three half scale specimens each having the dimensions of 3048 mm x 610 mm x 279 mm were fabricated (Figures 1, and 3). Each of the specimens has a 76 mm thick concrete wythe at the top and a 76 mm thick concrete wythe at the bottom. These two layers are separated by a 127 mm inch thick Extruded Polystyrene (XPS) foam in between for thermal insulation. The Styrofoam blocks were completely wrapped in moisture barrier plastic sheets as a bond breaker with concrete, to ensure that shear transfer is only through the GFRP connector. Also, adhesion between insulation and concrete may not be quite reliable at long term under thermal and mechanical loading cycles. Out of the three specimens, two had the GFRP channel connecting the top and bottom wythes. The GFRP connector is a 203 mm deep C-shaped pultruded channel (Figure 3) located at mid-width of the specimen and running throughout the length of the specimen. The third specimen has a conventional steel truss in the form of a W-shape as the shear connector (Figure 4). The cross section of the steel rod, which was bent to form the truss, was chosen in such a way that it has the same diagonal cross-sectional stiffness as the web of the GFRP channel (Figure 5) in the diagonal direction at 45 degrees. The top and the bottom wythes are reinforced using 4 x 4 D4/D4 steel wire meshes, located right above the flanges of the GFRP connector or the truss connector in the top wythe and right beneath them in the bottom wythe.

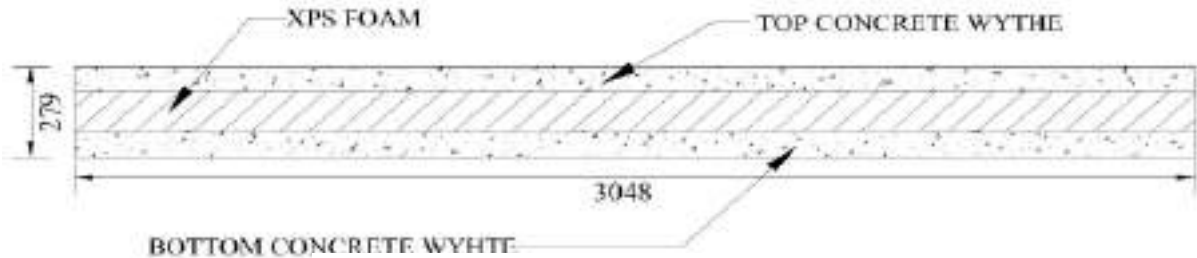


Figure 1: Side view of the specimens (dimensions in mm)

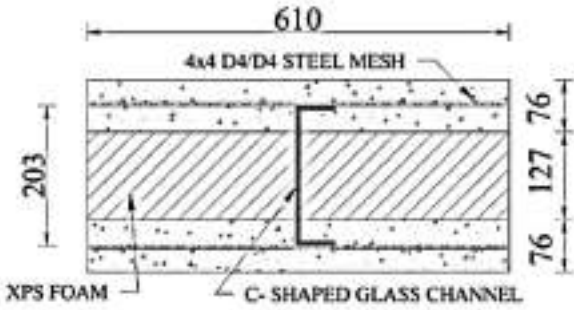


Figure 2: Cross-sectional view of the Specimens (dimensions in mm).

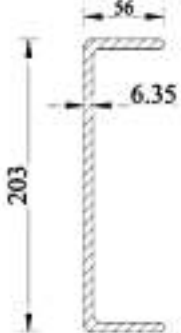


Figure 3: Cross section of the GFRP Shear connector (dimensions in mm).

Table 1 provides a summary of test matrix. *Specimen CR* is considered the control specimen for the study. It has a steel reinforcement ratio in each wythe of 0.34% and a continuous GFRP channel running throughout the length

of the specimen (Figures 1 to 3). The reinforcement ratio is achieved by using size $4 \times 4 \times D4/ D4$ wire mesh in each of the top and bottom wythes, and this ratio is higher than the minimum ratio requirement of 0.1%, recommended by design codes.

Specimen DR has a reinforcement ratio of 0.68%, double the reinforcement ratio of the control specimen (CR), achieved using two layers of the steel mesh in each wythe. The GFRP channel also runs throughout the length of the specimen.

Specimen TR has a conventional steel truss as the shear connector and has the same reinforcement ratio as the control specimen (0.34%). The steel truss was formed by bending a 8 mm diameter smooth steel rod at 45 degrees. The effective height of the truss was 203 mm, equal to the height of the GFRP channel. The truss has an effective length of 3048 mm same as the length of the GFRP channel in the previous specimens (Figure 2-2).

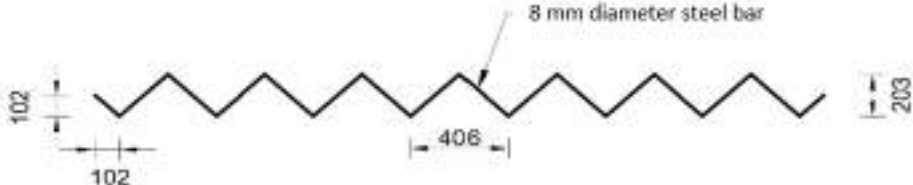


Figure 4: Steel Truss shear connector (dimensions in mm)

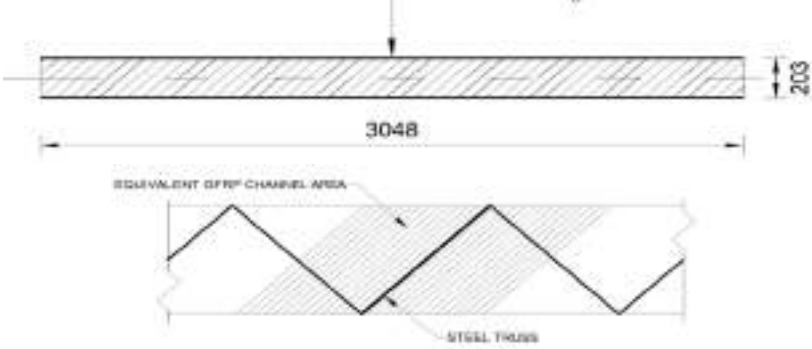


Figure 5: Continuous GFRP connector (dimensions in mm)

Table 1: Test Matrix

Specimen ID	Overall Dimensions			Flexural Reinforcement Material	Flexural Reinforcement Ratio	Shear Connection Type
	Length (mm)	Width (mm)	Thickness (in mm)			
CR	3048	610	279	Steel	0.34%	GFRP Channel
DR	3048	610	279	Steel	0.68%	GFRP Channel
TR	3048	610	279	Steel	0.34%	Steel Truss

2.2 Materials

Concrete: A regular concrete mix of an average 28 day strength of 30 MPa was used. The maximum aggregate size in the mix was 14 mm. Superplasticizer was added in order to make the concrete more workable in between the closely packed components of the panels.

GFRP Shear Connector: The GFRP shear connectors used in the study were cut from commercially available pultruded fibreglass channels. The channel height was 203 mm and the channel thickness was 6.35 mm. The flanges had a width of 56 mm. According to the reported manufacturer data, the minimum flexural strength of the channel is 207 MPa and the Modulus of Elasticity is 17.2 GPa. Because of its light weight (density of around 1830 Kg/m³), the glass shear connector is quite easy to handle and work with (Figure 6). The fibre material has a reported thermal conductivity of 0.58 W(m*K).

Steel for Flexural Reinforcements: The specimens has steel meshes in both wythes. The reinforcement ratios were 0.34% (for specimen CR and TR) and 0.68% for specimen DR, and both ratios were achieved using steel meshes of size $4 \times 4 \times D4/D4$ (Figure 7). For specimen DR, two sheets of steel meshes were tied together to achieve the desired reinforcement ratio of 0.68%.

Styrofoam: The Styrofoam used was XPS and was in accordance to the ASTM C578 standard (Figure 8). It has a reported compressive strength of 0.17 MPa and a density of around 30 kg/m³. The manufacturer reported R-Value

for the Styrofoam sheets varies from 5.6 m²C/W to 6.3 m²C/W depending on the external temperature. The reported flexural strength is 0.3 MPa.

Steel truss connector: The diameter of the steel rod (8 mm) to make the truss shear connector was chosen in such a way, that the sectional stiffness of this smooth circular rod in the direction of its member running diagonally along the depth of the specimen connecting the top and the bottom wythe tie member is equal to the sectional stiffness of the GFRP channel in the same direction. Hence the tributary area of the GFRP channel lying at an angle of 45° with the horizontal, in between the centre points of the two consecutive truss triangles is represented by the diagonal member of the truss connector (Figure 4). The elastic modulus chosen for the GFRP channel was that of the reported manufacturer value in the transverse direction, which is somewhat close to the value at an angle of 45° for pultruded GFRP sections.



Figure 6: Lightweight GFRP connector Figure 7: 4x4 D4/D4 steel wire mesh Figure 8: Extruded Polystyrene sheet

2.3 Fabrication

All specimens were fabricated in the Queen's University structural laboratory. The panels were cast horizontally on a level ground. Wooden formwork was used for the casting. First, the bottom mesh was carefully lowered into the formwork with suitable chairs to maintain the required concrete cover. The GFRP channel is then lowered into the formwork, so that it rests on the bottom mesh (Figure 9). Concrete is then poured into the formwork and levelled off using a wooden jig to maintain a 76 mm thick wythe (Figure 10). After that, the Styrofoam blocks, each of cross-sectional dimensions 305 mm x 127 mm, and 3048 mm long were inserted on either side of the channels (or the truss). The top steel mesh was placed on top of the foam with the required chair size. Concrete was poured and levelled off to make the top wythe thickness equal to 76 mm (Figure 11).



Figure 9: The bottom mesh and GFRP connector before casting bottom wythe of DR specimen

Figure 10: The bottom wythe being levelled off to a thickness of 76 mm in the CR specimen.

Figure 11: The top wythe being cast after the Styrofoam blocks have been inserted in TR specimen.

All the panels were tested in four-point bending with an effective structural span of 2890 mm. The constant moment zone was 500 mm and the constant shear zone was 1195 mm on either side (Figure 12). The load was applied using a stroke control system. An HSS spreader beam was used to distribute the concentrated load onto the two rollers at the loading points. The rollers were placed on top of two steel plates and a thin layer of plaster was applied in between these plates and the top concrete surface, to ensure full contact. The deflection at the mid-span was measured using two linear potentiometers (LPs), placed on either sides of the slabs. The surface strain on the concrete along the depth, in the constant moment zone at mid-span was measured using four 100 mm displacement type strain transducers (PI Gauges). Two PI Gauges were mounted on each wythe. To measure the relative slip at each end of the specimens, LPs were used. Five millimeter long uniaxial strain gauges were installed on the top flange of the GFRP channel at mid-span to measure the strain at the top flange of the channel. Similarly, two uniaxial strain gauges were installed on the inside and the outside of the bottom flange to measure longitudinal

strains. Each of the steel meshes at the top and bottom wythes had a uniaxial strain gauge at their mid-span on the longitudinal bars and midway between the welds on the mesh to measure the longitudinal strains.

3. EXPERIMENTAL RESULTS

Figure 13 shows the load-deflection responses of all three panels while Figure 14 shows the load-slip responses where slip is defined as the relative longitudinal displacement of the two concrete wythes. The bottom wythe in all three specimens cracked throughout the full thickness of the wythe prior to cracking of the top wythe (Figure 15). The cracks are reflected in the drops in the load-deflection curves of the specimens. The cracking loads in each of the wythes for all the specimens is summarized in Table 2. The Canadian building code maximum service and factored wind pressures are 1.37 and 2.9 kPa, respectively (peak 50 year return period). These pressures are equivalent to 1.5 and 3.1 kN of concentrated loads, respectively, for the test setup used based on an equivalent maximum moment. The deflection under the service load of 1.5 kN are well below the deflection limit of $L/360$. Also, the failure loads are all well above the maximum factored load of 3.1 kN.

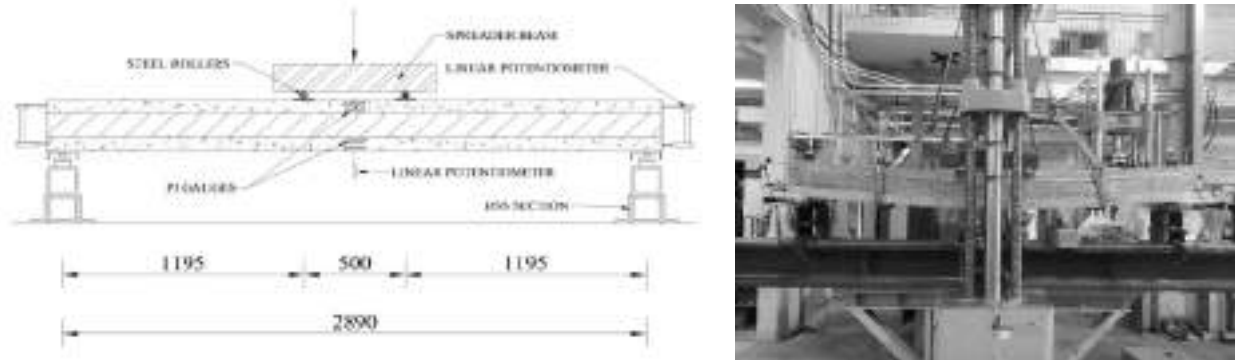


Figure 12: Test setup and instrumentation (dimensions in mm)

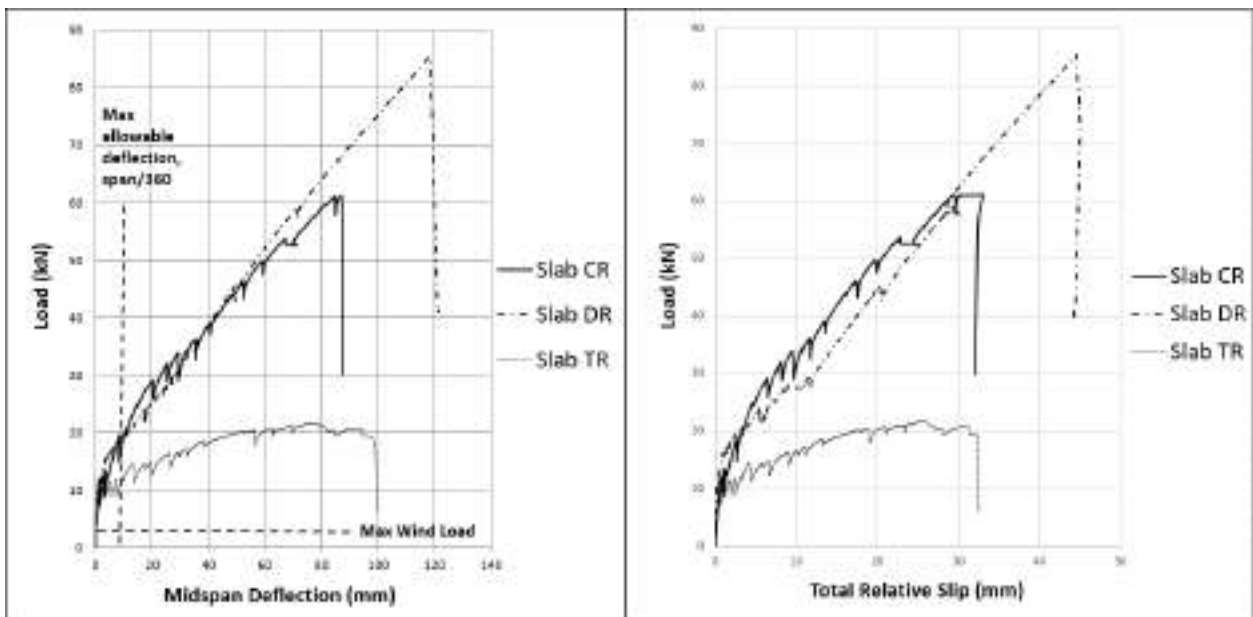


Figure 13: Load vs Midspan deflection responses

Figure 14: Load vs Relative Slip responses

Although the steel truss shear connector had the same diagonal cross sectional stiffness as the web of the GFRP channel as explained before, the peak load reached for specimen TR was considerably lower, only 21.7 kN, compared to the 61 kN reached by control specimen CR with the GFRP channel (Figure 13). This is attributed primarily to the contribution of the GFRP flanges of the C-section inside the wythes to the overall flexural strength. Additionally, the continuous GFRP web also contributes in the longitudinal direction, unlike the discrete diagonal steel members. The stiffness after cracking of the TR specimen was also lower than the other two specimens. The failure mode was governed by the rupture of the steel mesh in the bottom wythe, whereas CR failed by rupture of the GFRP flange in tension.

3.2 Effect of doubling the steel reinforcement ratio

This can be examined by comparing specimen DR with the control specimen CR. Doubling the reinforcement ratio resulted in increasing the ultimate load from 61 kN to 85.3 kN (Figure 13). However, no significant change in

stiffness was observed. The failure mode of this specimen was governed by GFRP failure. As soon as it ruptured in tension, the web crushed inwards making the v-shaped wedge in the channel web (Figure 16).



Figure 15: Cracks in the bottom wythe in case of specimen CR.



Figure 16: GFRP channel rupture in tension in case of specimen DR.

Table 2: Summary of test results.

Specimen ID	Top Wythe cracking load (in kN)	Bottom wythe cracking load (in kN)	Ultimate load (in kN)	Midspan deflection at ultimate (in mm)
CR	14.0	12.4	61.0	87
DR	20.6	15.8	85.3	119
TR	15.1	10.2	21.7	79

3.3 Load-Slip Behavior

The load-Slip curves are plotted in Figure 14. The relative slip between the top and the bottom wythes was of similar magnitudes on either ends for each of the panels, as listed in Table-3. As can be seen from the Figure 14, the load-slip responses for all the three specimens are quite similar with insignificant slip until the first crack in the concrete wythe occurred. After cracking, specimens CR and Dr had somewhat similar rate of slip despite the difference in flexural reinforcement ratio. However, at any given load after cracking, the slip of TR with steel truss connector is significantly higher than that of CR with GFRP channel. This suggests that the GFRP system is more effective in providing a better composite action. At peak loads, the total slip for the control specimen, the double reinforcement and the truss specimens are 45 mm, 33 mm and 26 mm, respectively.

Table 3: Slip values at ultimate load

Specimen ID	Relative Slip at Peak Load, First End (in mm)	Relative Slip at Peak Load, Second End (in mm)	Total Slip at Peak Load (in mm)	Peak Load (in kN)
CR	16.71	16.36	33.07	61.0
DR	21.73	22.82	44.55	85.3
TR	12.94	13.14	26.08	21.7

4. CONCLUSIONS

1. The proposed GFRP C-shaped shear connector provides significantly higher degree of composite action, compared to conventional steel truss connector of equivalent diagonal stiffness. This is evidenced by the remarkably reduced relative slip between the concrete wythes.
2. The panel with GFRP connector achieved 2.8 times higher ultimate load than that with steel truss connector, for the same flexural reinforcement ratio in the wythes of both specimens. This increase is attributed to two factors, namely; the contribution of the GFRP flanges embedded in the wythes, and the enhanced degree of composite action.
3. For panels with GFRP connectors, doubling the longitudinal steel reinforcement ratio in the wythes resulted in a 40% increase in the ultimate load.
4. Failure mode of panels with GFRP connectors was by rupture of the GFRP flange in tension, while that of the panel with steel truss connector was by rupture of the longitudinal steel bars in tension.
5. All panels satisfied serviceability requirement for maximum deflection under service wind load that represents maximum wind in Canada.

5. REFERENCES

- N. Goudarzi, Y. Korany, S. Adeeb, R. Cheng (2016). "Characterization of the shear behavior of Z-shaped steel plate connectors used in insulated concrete panels", *PCI Journal*, March-April, 23-37.
- D.C. Salmon, A. Einea, M.K. Tadros, T.D. Culp (1994). "Full scale testing of precast concrete sandwich panels", *ACI Structural Journal*, 94-S32.
- D. Tomlinson, A. Fam.(2014). "Experimental investigation of precastconcrete insulated sandwich panels with Glass Fiber-Reinforced Polymer shear connectors", *ACI Structural Journal*, 111(3), 596-605.
- PCI Committee on Precast Sandwich Wall Panels, "State of the Art of Precast/Prestressed Concrete Sandwich Wall Panels", *PCI Journal*, Spring 2011.



DOUBLY-CURVED SANDWICH PANELS WITH UHPC-FACINGS

A. Stark^{1*}, C. Knorrek¹, S. Perse¹

¹Institute of Structural Concrete, RWTH Aachen University, Mies-van-der-Rohe-Str. 1, 52074 Aachen, Germany,

* Corresponding author: Email: astark@imb.rwth-aachen.de

ABSTRACT

Sandwich-structured composites represent an efficient method to establish building envelopes which concurrently satisfy several demands. Besides low self-weight with high load-bearing capacity, sandwich panels provide sufficient physical properties, such as heat and sound insulation. In general, sandwich panels for applications in building industry are made of flat or thin profiled metal sheets or thick concrete facings. However, standard elements without additional bearing structures are limited to short spans. In contrast, spatially shaped concrete structures with curved geometry provide high stiffness and load-carrying capacity even for thin elements. The application of curved concrete structures to sandwich panels combines the advantages of both construction methods enabling light elements with long spans and high load-carrying capacities. To realise thin facings in various shapes, high performance cementitious composites are advantageous. Ultra-high performance fibre reinforced concrete (UHPFRC) provides high compressive and tensile strengths with ductile material behaviour. The application of non-corrosive reinforcement, e.g. carbon fibre reinforced polymer (CFRP), allows for filigree concrete elements with a thin concrete cover to only fulfil bond requirements. For sandwich panels with curved facings, new production methods are necessary to account for cross-sections in various shapes as well as high bond strengths between UHPFRC facings and core material.

This paper introduces the basic ideas of doubly-curved concrete sandwich elements for long-span roof structures and the developed production methods.

KEYWORDS

Sandwich constructions, CFRP, UHPFRC, PU, foamed polyurethane, production methods.

INTRODUCTION

The application of sandwich constructions in the building industry has become increasingly important in recent decades. Especially as facade elements or as roof structures, sandwich panels show several advantages compared to standard building methods. Sandwich elements in construction industry generally consist of two outer layers of steel or reinforced concrete and a less stiff core material of e.g. polyurethane. The outer layers primarily carry loads from sandwich action. The steel layers and steel reinforcement in conventional concrete layers are vulnerable to corrosion in humid environments. Hence, for load-bearing structures thick concrete coverings are necessary (EC2 2011; CEB-FIB Model Code-1990 1993; ACI 318-05 2005), which leads to massive elements with high weight. Nevertheless, even thick layers cannot guarantee the corrosion resistance over decades. Reinforcement and prestressing tendons made of carbon-fibre reinforced polymers (CFRP) are corrosion-resistant and show tensile strengths of up to 3000 MPa. This alternative allows for slender structures with high potential for economic savings in terms of materials and transport, as well as reduced time and effort during mounting. Generally, applications for reinforcement meshing or bars, as well as pre-tensioned strands are feasible. Pre-tensioned CFRP reinforcement has been investigated in terms of bond behaviour to concrete and structural performance (e.g. Lu 2000; Soudki 1997; Stark 2013). In addition, the use of ultra-high performance concrete (UHPC) allows a further reduction in the thickness of structures, since UHPC has considerably higher compressive and tensile strength compared to normal concrete.

The load-bearing behaviour of sandwich members is determined by stiffness and strength of concrete facings and core material, as well as the bond strength between concrete and core, which depends on the production method (Shams 2014; Shams 2015). In addition, the core layer serves for thermal and sound insulation. Typically, sandwich panels with concrete facings are assembled using pre-fabricated slabstock foams. Using this standard method, the concrete facings tend to crack from shrinkage. Additionally, placing the slabstock foam into fresh concrete may negatively influence the bond quality between core material and concrete facings. On the one hand, fine dust is covering the cutting edges of slabstock foams and on the other hand, during the assembly, air inclusions may occur when placing the pre-fabricated core material into the fresh concrete (Shams 2015). In order to overcome these issues, i.e. to achieve a homogenous and reliable bond quality, the core made of polyurethane

(PU) is foamed in pack (Shams 2015) between the hardened concrete layers made of UHPC. This prevents unbonded parts in certain areas and makes various shapes of cross-sections possible.

The combination of these innovative concrete elements opens up new possibilities with regard to the architectural design and the load capacity of sandwich constructions. In addition to a high load-carrying capacity, these sandwich constructions fulfil other physical requirements, such as heat and sound insulation, by using polyurethane as the core material between the concrete layers.

MATERIAL CHARACTERIZATION

Ultra-High Performance Concrete

For all test specimens, the same concrete mixture of a fine-grained UHPC with straight steel fibres (Stark 2013) was applied (Table 1). This mixture was developed within the priority programme 1182 of the German Research Foundation. Steel fibres with a length of 9 mm and a diameter of 0.15-0.17 mm (tolerances) were added to the mixture to ensure a satisfactory ductile behaviour and sufficient pouring quality (Hegger 2010). The steel fiber ratio in the mixture was chosen to 0.9 Vol.-%.

Table 1: UHPC Mixture

Material	Quantity [kg/m ³]
Cement Cem I 52,5 R HS-NA	825.0
Silica fume	175.0
Quartz powder W12	200.0
Sand 0.125 – 0.5 mm	975.0
Steel fibres (0.9 Vol.-%)	70.7
Water	175.0
Superplasticizer	27.5

In order to determine the material properties of the applied UHPC mixture, test specimens were produced simultaneously during casting of doubly-curved shells. After 28 days, a uniaxial compression strength of about 175 MPa (cubes, 150x150x150 mm³) and a Young's Modulus of about 45,000 MPa were determined. After one day, i.e. release of prestressing force, the uniaxial compression strength was about 80 MPa and the Young's Modulus was about 32.000 MPa. The flexural tensile strength was determined on prisms (40x40x160 mm³). After 28 days and after one day, 19 MPa and about 9 MPa were observed, respectively. All tests were conducted in accordance with DIN EN 196-1 (2016), DIN EN 206 (2017) and EC2 (2011).

Reinforcement

Carbon-fibre-reinforced polymers (CFRP) consist of carbon fibres, which are bonded and coated with a polymer matrix made of thermosetting or thermoplastics (for example epoxy resin). The high tensile strength and the high corrosion resistance of CFRP prestressing tendons are particularly advantageous for slender concrete constructions and allow low concrete coverings. The Poisson's ratio of CFRP usually varies between 0.02 and 0.27 (FIB Bulletin 40 2017). The thermal expansion in transverse direction is about 10 to 40 times higher than in longitudinal direction (FIB Bulletin 40 2017; ACI 440.4R-04 2004). Experiments at 100°C showed a reduction in ultimate limit strength of 20 to 40 % (FIB Bulletin 40 2017). For the use of CFRP reinforcement, these factors have to be considered.

For the experimental studies, CFRP bars and CFRP seven-wire strands were tested (Tokyo Rope Mfg., Co., Ltd.). To enhance the bond behaviour these CFRP tendons are wrapped with coated carbon fibres. Both types of CFRP reinforcement, used in the experimental study, show a tensile strength of over 2,500 MPa. The properties given by the manufacturer are shown in Table 2.

Table 2: CFRP Material Properties

Designation [-]	Diameter [mm]	Eff. cross-sectional area [mm ²]	Guaranteed capacity [kN]	Young's Modulus [GPa]
● U 5.0Ø	5.0	15.2	38	167
⦿ 1x7 7.5Ø	7.5	31.1	76	155

Core Material

For the experimental studies, a two component polyurethane (PU) core was used, which was foamed in pack between hardened UHPC facings. The mixed PU core has a density of about 90 kg/m^3 . The general manufacturing process is shown schematically in Figure 1. First of all, the concrete facings were cast, which were either reinforced or prestressed with CFRP reinforcement. Afterwards, two hardened concrete facings were placed in a wooden formwork (Figure 1a) and PU two component mixture was filled in between. The formwork was then completely closed. Due to the pressure from expansion of the PU in the closed formwork, the density as well as the homogenous and repeatable bond quality could be controlled.

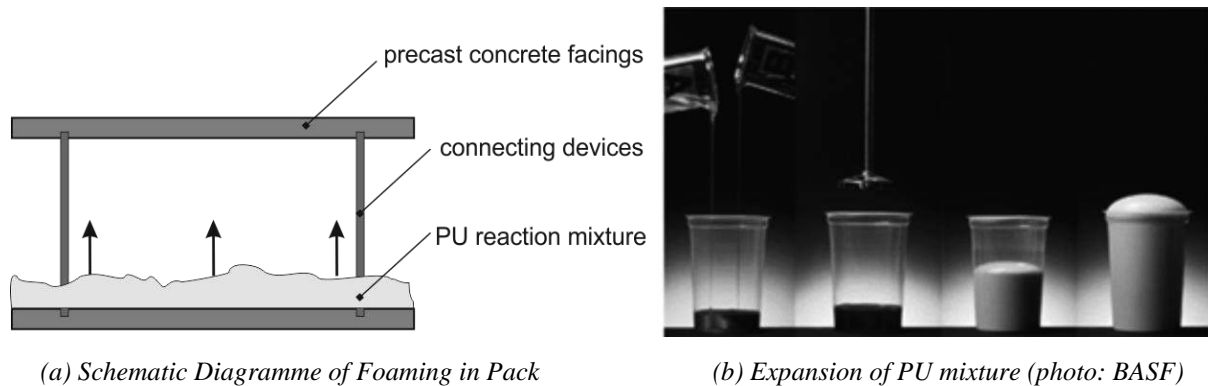


Figure 1: Production method for sandwich panels with hardened concrete facings by foaming in pack of PU mixture (Shams 2015; Stark 2017)

The mechanical properties of the PU foam were determined by tensile, compressive, and shear tests, in accordance with (DIN EN 826 2013; DIN EN 1607 2013; DIN EN 12090 2013). A compressive strength of about 950 kPa with a Young's modulus of 32,000 kPa was determined. The tensile strength was about 580 kPa with a Young's modulus of 45,000 kPa. The shear strength was about 570 kPa with a shear modulus of 11,500 kPa. All results show a relatively low standard deviation of less than 15%.

In addition, small-scale tests on sandwich elements showed high repeatable bond stresses under tensile and shear loading between core foam and UHPC facings. Maximum tensile stresses of 400 kPa and shear stresses of k 400 kPa were derived (Stark 2017). In the future, investigations on the fire resistance and long-term loading have to be conducted. The fire resistance is assumed to be at least comparable to sandwich panels with thin metal facings.

MANUFACTURING PROCESS

Geometry of test specimens

A total of six doubly-curved sandwich elements were produced for the first test series. In addition, six single UHPC shells, i.e. facings, were examined to validate the sandwich effect. The UHPC facings of the sandwich elements were produced with a length of 4.10 m, a width of 0.80 m and a thickness of 0.06 m. The thickness of 0.06 m was derived from tests on the transfer length to provide a crack-free cross-section. The concrete shells were given the form of a double-curved shell with a cantilever in the longitudinal direction of 0.05 m (z^+) and in the transverse direction of 0.10 m (z^-) (Figure 2, (a)). This geometry corresponds to the geometric surface of a hyperbolic paraboloid.

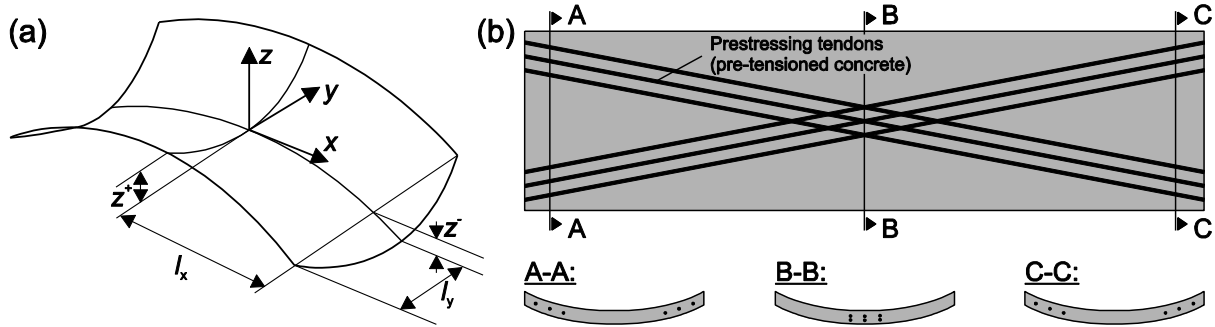


Figure 2: Doubly-Curved Surface (a) and prestressing tendons in doubly-curved concrete shell (b) (Stark 2017)

The shape of a hyperbolic paraboloid (HP) opens up an appealing architectural design and the curved geometry offers a higher stability and load-bearing capacity compared to flat sandwich constructions. Since hyperbolic paraboloids mathematically consist of a family of straight lines, these doubly curved elements were produced as pre-tensioned concrete members. In Figure 2 (b), a schematic example of the arrangement of tendons is shown. For the test specimens, pre-tensioned concrete with CFRP prestressing tendons was utilised. For pre-tensioned concrete UHPC offers the advantage of high strength already after one day of concrete hardening. For doubly-curved single shells as well as sandwich panels, different arrangements of reinforcement and prestressing forces were tested.

Production Method

During the production of the HP single shells, the type of reinforcement and the applied prestressing force were varied. In the case of the HP shells without prestressing, four to six CFRP bars with a diameter of 5.0 mm were used. For pre-stressed HP single shells, four to six seven-wire CFRP strands with a diameter of 7.5 mm were applied. The CFRP bars and strands were arranged as diagonal, straight lines.

The HP shells were cast in a horizontal position to ensure, that the steel fibres in the UHPC mixture were aligned in longitudinal direction during concreting. Hence, the fibres were able to bridge flexural cracks. A closed formwork was set up using the principle of straight but skew lines (Figure 3 (a)). A thin medium density fibreboard (MDF) was placed in strips of 50 mm width on wooden frames. These frames were shaped like the corresponding top or bottom surface at the particular position. Afterwards, a filler was applied on top of the MDF to provide a smooth surface (Figure 3 (b)), which is impermeable to water. The elements were cast upside down to avoid discontinuities from casting at midspan (highest position) of the elements. Therefore, at both ends openings were provided to cast in the UHPFRC. Thus, the resulting discontinuities were placed close to the supports, which did not negatively affect structural performance. The UHPFRC mixture was cast from only one side until the formwork was filled up. Hence, ventilation was guaranteed and smooth surfaces with only small air inclusions were producible.

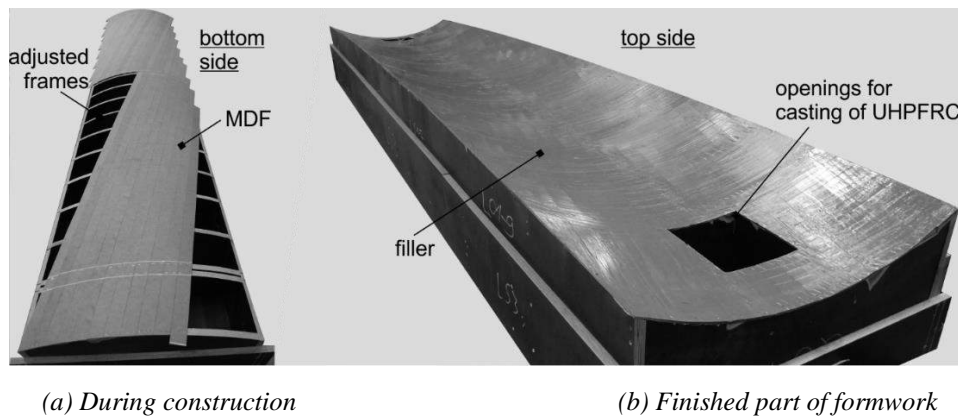


Figure 3: Formwork for doubly curved elements (Stark 2017)

For the investigated doubly curved elements, a standard prestressing bed could not be utilised. Instead, a stiff frame was set up to allow for skew, but linear configuration of reinforcement (Figure 4 (a)). Hollow piston cylinders were applied for jacking at each CFRP tendon. Additionally, adjusting screws were used to ensure correct positions of tendons. The tendons were placed about half the diameter up for one diagonal direction and

down for the other diagonal direction. With this method it was ensured that the tendons did not bend at the crossing points. In case of elements without prestressing, wedge anchors and adjusting screws were applied for straight alignment of the coiled CFRP rebars.

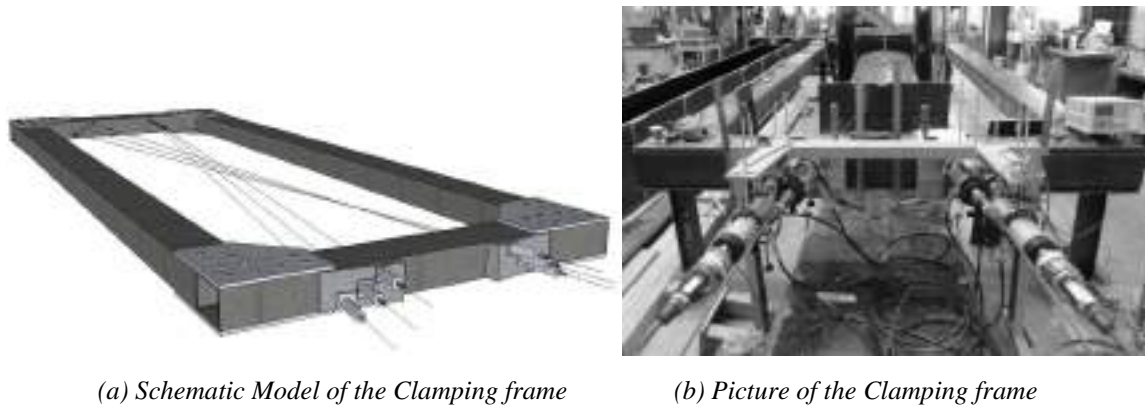


Figure 4: Clamping frame of the HP concrete shell (Stark 2017)

After one day of concrete hardening and stripping of the top side of the formwork, the prestressing forces were released. Afterwards, the elements were turned into final position.

For the core material of sandwich panels, a two component reaction mixture of polyurethane (PU) was applied. Therefore, two hardened UHPC facings were placed into a braced wooden formwork. After weighing the two components for the reaction mixture of PU and preparing of formwork with hardened UHPFRC facings, the PU mixture was poured in (Figure 5). The wooden formwork was closed and a counterweight was applied to withstand the pressure from expansion of the PU mixture. With this method, the core thickness was controlled and a high bond strength was achieved. In this study no shear connectors were applied, i.e. the sandwich moment was carried by the foam only.



Figure 5: Exemplary manufacturing steps for the sandwich shells (Stark 2017)

TESTING METHODS

Structural façade and roof elements are subjected to snow, wind and temperature loads. Concrete members are additionally subjected by creep and shrinkage. For the prediction of the load-bearing capacity of prestressed sandwich elements with foamed cores and UHPFRC facings, experimental and theoretical investigations are necessary.

In Stark (2013), Stark (2014), Shams (2015) small-scale tests were presented. The bond behaviour of CFRP tendons in UHPC were analysed to determine the transfer length and minimum thicknesses of UHPC elements. Small-scale tests on sandwich section under tensile and shear loading, were used to verify the production method of foaming in pack of PU. With the information, flexural tests on doubly-curved sandwich panels were developed.

Flexural Testing of Doubly-Curved Sandwich Elements

For the investigation of the structural performance of doubly-curved sandwich panels, four-point bending tests were conducted. Figure 6 shows the test setup and geometry of HP sandwich panels with spans of 4.0 m.

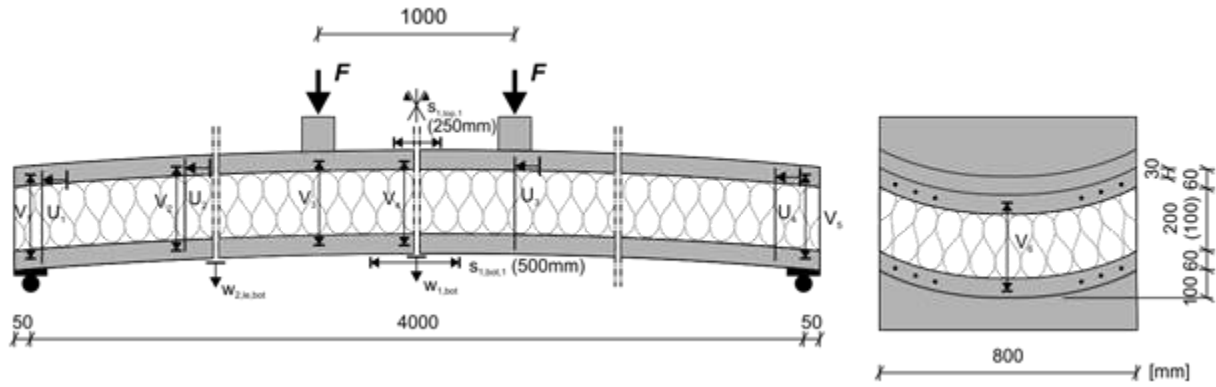


Figure 6: Test setups of bending tests on doubly-curved sandwich elements including measuring technique (Stark 2017)

All UHPC facings were made with a thickness of 60 mm. Types of CFRP reinforcement (bar (B) and seven-wire strand (S)), prestressing of top and bottom layers as well as core height were varied (Table 3).

Table 3: Test Specimens of Flexural Testing

Test [-]	Reinforcement		Prestressing bottom [MPa]	Prestressing top [MPa]	Core height [mm]
	Bottom	Top			
1	6 B	6 B	---	---	200
2	4 W	4 W	675	675	200
3	6 W	6 W	675	675	200
4	6 W	6 B	675	---	200
5	6 W	6 W	1350	675	200
6	6 W	6 B	675	---	100

All test specimens were loaded displacement controlled with 1.0 mm/min. Test load, deflections, core compressions, relative displacements of the UHPC layers and concrete strains were measured continuously during testing.

Discussion of Test Results

At first, doubly curved single elements were tested to investigate the influence of different prestressing forces and reinforcement arrangements. Afterwards, different arrangements of reinforcement and prestressing force were applied to doubly curved sandwich beams. The test results of doubly curved single elements were additionally used as reference to evaluate the sandwich action. At this stage, only the load-midspan deflection responses are compared. In Figure 7(a) the load-deflection response of doubly curved single and sandwich elements with different prestressing forces (six bars or strands) under four-point flexural loading is depicted exemplary for four tests. For sandwich elements with equal prestressing and arrangement of reinforcement, the maximum load was four to five times higher compared to doubly curved single elements. Crack widths remained less than 2.5 mm until 80 % of maximum load for doubly curved single shells and sandwich elements. In Figure 7(b), the crack patterns for elements without prestressing of facings are shown. For single doubly curved elements a compression failure was observed. The failure was induced in the vicinity of the load application at deflection ratios of $L/60$ to $L/40$, depending on the prestressing. In general, it was observed in all tests on doubly curved single elements that with increasing prestressing, the single elements remained longer in the linear-elastic range and achieved higher maximum loads with smaller deflections. The results of flexural tests on sandwich sections showed no increase in test load due to prestressing, but less deflection. The failure of sandwich elements was induced by shear cracks in the core material due to relative slip of the outer UHPFRC layers. Compression failure, as observed for single doubly curved elements, did not occur in tests on sandwich elements, since the UHPFRC shells were not loaded to their full load-bearing capacity. In the case of the sandwich sections, there was never a major failure of the UHPFRC shells, but always a failure of the core material and/or a bond failure. Thus, the bond strength between UHPFRC and core material and the strength of the core material determine the maximum load capacities of the sandwich sections and the prestressing primarily affects their stiffness. Deformations in transverse direction of the elements due to loading were not observed.

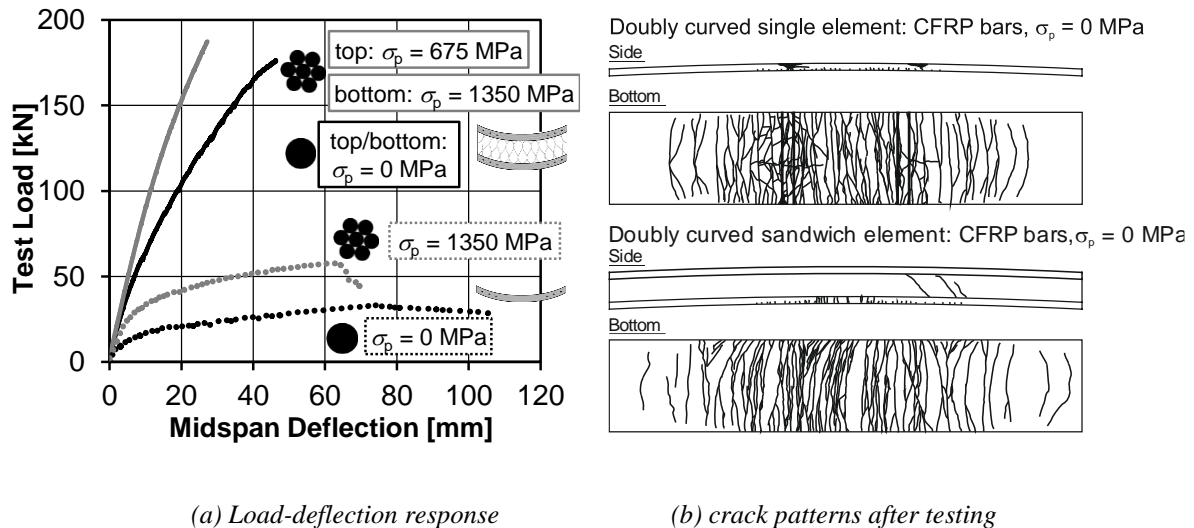


Figure 7: Single doubly curved elements and doubly curved sandwich elements with different prestressing forces

CONCLUSIONS AND OUTLOOK

In this paper, the basic ideas of doubly curved sandwich panels as well as the production methods were presented.

The key conclusions are:

- The developed prestressing frame provided an easy way for pretensioning of CFRP strands.
- Formwork can be provided for doubly curved UHPFRC facings with simple methods
- UHPFRC facings reach superior surface quality without major air pockets
- Fibres in UHPFRC limit crack widths to a few millimetres
- Foaming in pack of polyurethane between hardened concrete facings provides high bond strength
- Compared to single facings, the developed sandwich panels reach about 3-4 times maximum load

For the practical use of the developed sandwich panels, questions regarding shear connectors between the concrete facings, time-dependent behaviour of high performance materials as well as heat and fire resistance need to be investigated closely.

ACKNOWLEDGMENTS

The author gratefully acknowledges the financial support of the German Research Foundation (DFG) within the priority program SPP 1542 (HE 2637/16-2).

REFERENCES

- ACI 318-05/318R-05 (2005). "Building Code Requirements for Structural Concrete and Commentary", *ACI Committee 318, American Concrete Institute*.
- ACI 440.4R-04 (2004). "Prestressing concrete Structures with FRP Tendons", *ACI Committee 440*, (Reapproved 2011).
- CEB-FIB Model Code 1990 (1993). *Thomas Telford Ltd, London*. 1993.
- DIN EN 196-1 (2016). "Method of Testing Cement – Part 1: Determination of Strength", German Version EN 196-1:2016.
- DIN EN 206 (2017). "Concrete - Specification, performance, production and conformity", German Version EN 206:2013+A1:2016.
- DIN EN 826 (2013). "Thermal Insulating Products for Building Applications – Determination of Compression Behavior", German Version EN 826:2013.
- DIN EN 1607 (2013). "Thermal Insulating Products for Building Applications – Determination of Tensile Strength Perpendicular to Faces", German Version EN 1607:2013.

- DIN EN 12090 (2013). “*Thermal Insulating Products for Building Applications – Determination of Shear Behavior*”, German Version EN 12090:2013.
- EC2 (2011). “*Eurocode 2: Design of concrete structures – Part 1-1: General rules and rules for buildings*”, German version EN 1992-1-1:2004 + AC:2010, European committee for standardization (Cen).
- FIB Bulletin 40 (2017) FRP Reinforcement for RC Structures. *Technical Report on the Design and Use of Fibre Reinforced Polymer Reinforcement (FRP) for Reinforced Concrete Structures*.
- Hegger, J.; Bertram, G. (2010). “Verbundverhalten von vorgespannten Litzen in UHPC, Teil 1: Versuche zur Verbundfestigkeit und zur Übertragungslänge” (*Bond Behavior of prestressed Strands in UHPC. Part 1: Tests on Bond Strength and Transfer Length*), *Beton- und Stahlbetonbau (Concrete and Reinforced Concrete Structures)* Volume 105, Issue 6, 2010, pp. 379-389.
- Lu, Z.; Boothby, T.; Bakis, C.; Nanni, A. (2000). “Transfer and Development Lengths of FRP Prestressing Tendons”, *PCI Journal*, March-April 2000, pp. 80-91.
- Shams A., Hegger J. (2014). “Experimental Investigations on TRC sandwich panels with foamed PU cores”, *Proceedings of the 10th fib international PhD Symposium in Civil Engineering*, July 21-23, 2014, Université Laval, Québec, Canada, pp.327-332.
- Shams, A.; Stark, A.; Hoogen, F.; Hegger, J.; Schneider, H. (2015). “Innovative sandwich structures made of high performance concrete and foamed polyurethane”, *Composite Structures*, Vol. 121, March 2015, pp. 271-279.
- Soudki, K.; Green, M.; Clapp, F. (1997). “Transfer Length of Carbon Fiber Rods in Precast Pretensioned Concrete Beams”, *PCI Journal*, September-October 1997, pp. 78-87.
- Stark, A.; Hegger, J. (2013). “Verbundverhalten von CFK-Spannbewehrungen in UHPFRC” (*Bond behavior of pre-tensioned CFRP tendons in UHPFRC*), *Beton- und Stahlbetonbau (Concrete and Reinforced Concrete Structures)*, Volume 108, No 10, 2013, pp. 701-710.
- Stark, A.; Hegger, J. (2014). “Development of CFRP Pre-tensioned Sandwich Panels with Concrete Facings”, *CICE 2014: The 7th International Conference on FRP in Civil Engineering*, Vancouver, Canada, August 20-22, 2014. ISBN 978-1-77136-308-2, p. 210 (full paper on CD-ROM).
- Stark, A. (2017). “Analysis of Prestressed Sandwich Panels with Ultra-High Performance Concrete Facings.” Institute of Structural Concrete, RWTH Aachen University, Doctoral Thesis.



BEHAVIOR OF GFRP WALL PANEL WITH INTERNAL TUNED LIQUID COLUMN DAMPER

H. Wu¹, A. Chen² and S. Laflamme³

¹ Iowa State University. Department of Civil, Construction and Environmental Engineering, USA,
Email: haowuj@iastate.edu;

² Iowa State University. Department of Civil, Construction and Environmental Engineering, USA,
Email: achen@iastate.edu;

³ Iowa State University. Department of Civil, Construction and Environmental Engineering, Department of
Electrical and Computer Engineering, USA, Email: laflamme@iastate.edu.

ABSTRACT

Pultruded Glass Fiber-Reinforced Polymer (GFRP) structures have been increasingly used in buildings and civil infrastructure systems because of their high strength, light weight, durability, and fatigue resistance. However, these structures are elastic and typically have low damping ratio, which limits their capability to dissipate energy during earthquakes. Adding damping mechanisms to GFRP components can improve traditional structures' resistance to lateral loads. This paper studies a cellular GFRP wall panel with an internal liquid flow system, engineered to control a structure's temperature using liquid as thermal exchange. In this study, we further adapt the panel to allow oscillation of water in its internal hollow cells, providing supplemental damping for the GFRP structure during seismic events. Different combinations of water heights and cell openings are evaluated using shaking table tests to study vibration reduction of the GFRP wall panel by leveraging the motion of water. For each combination, the natural frequency of TLCD can be predicted with a simple model. It is found that higher water volume inside the panel can achieve greater mitigation. A Computational Fluid Dynamics (CFD) model is created to study the liquid motion inside the GFRP panel under harmonic ground excitations. Results from the CFD simulation are in good agreement with those from the test.

KEYWORDS

Pultruded GFRP, Seismic resistance, Tuned liquid column damper, CFD simulation.

INTRODUCTION

Pultruded GFRP structures have been widely studied, showing as good alternatives to steel and Reinforced Concrete (RC) solutions due to their high strength-weight ratio, easy installation, and corrosion resistance. Common applications include low-rise buildings, bridge decks, space structures, towers, etc. Static tests demonstrated that GFRP components are viscoelastic and anisotropic (Ascione et al. 2011; Wattick and Chen 2017). Several other researchers studied the dynamic behavior of pultruded GFRP structures. Boscato and Russo (2009) showed that GFRP structures tended to have low frequency and high deformability, which may be leveraged to mitigate seismic loading. While it was discussed that pultruded FRP does not suffer significant degradation after large numbers of cyclic loading (Yang et al. 2009), it was found that GFRP structures have low damping ratios (usually less than 2%), and their performance in dissipating vibration energy was poor (Russo 2012). It follows that the inclusion of damping mechanisms inside pultruded GFRP structures can result in a significant enhancement of their lateral load mitigation performance.

This study focuses on a GFRP panel structure with an internal liquid flow system. This GFRP panel has a cellular section and functions as an exterior structural wall. The internal liquid system is originally intended as a circuit cooling and heating system using liquid as the thermal exchanger to control for a structure's temperature. We propose to leverage the internal liquid flow system to provide supplemental damping capability for the GFRP panel structure. Liquid motion, such as flow through orifices and sharp corners of the internal pipe network, can result in liquid head loss, dissipating kinetic energy. This damping mechanism can be found in some structures in the form of a tuned liquid column damper (TLCD), which is a specialized passive damping device that leverages the liquid's gravity force as the restoring force and generates damping from the head loss around orifices and sharp corners. TLCDs have been effectively used in suppressing the vibration of tall buildings and long bridges under wind or earthquake hazards (Shum et al. 2008; Min et al. 2014). Both design procedures and experimental studies have been conducted on TLCDs (Connor and Laflamme 2014; Di Matteo et al. 2014). More recently, Computational Fluid Dynamics (CFD) method was introduced to validate TLCD numerically (Cammelli et al.

2016). Min et al. (2014) proposed a novel passive TLCD with multiple cells that can be opened or sealed after installation, and provided a methodology to compute the natural frequencies of multi-celled liquid damper system.

This paper first describes a shaking table test on the proposed GFRP panels with an internal TLCD, demonstrating that this damping system can reduce the panel's vibrations under harmonic ground excitations. Next, a simple model is presented to compute the TLCD's natural frequency. Lastly, CFD models are created to simulate the liquid motion and measure the damping forces generated by the internal damper.

SHAKING TABLE TEST

Test setup

The pultruded GFRP panel is a 7-celled geometry with a dimension of 121.1 cm × 61.0 cm × 8.1 cm (height × width × depth), as shown in Fig. 1. The thickness of the outer and inner shells are 0.297 cm and 0.218 cm, respectively. Both in-plane and out-of-plane properties obtained from material tests are summarized in Table 1 (Wu and Chen 2016).

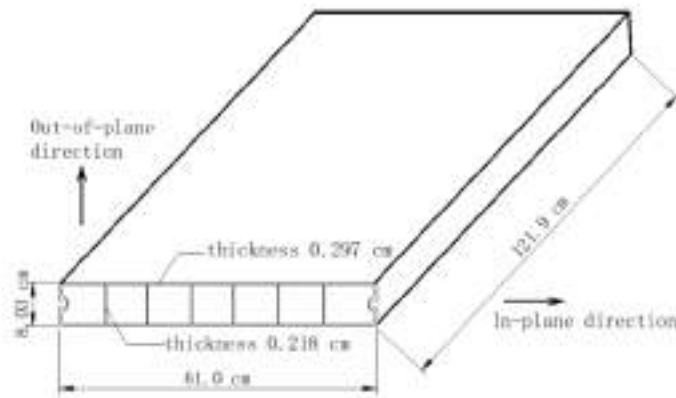


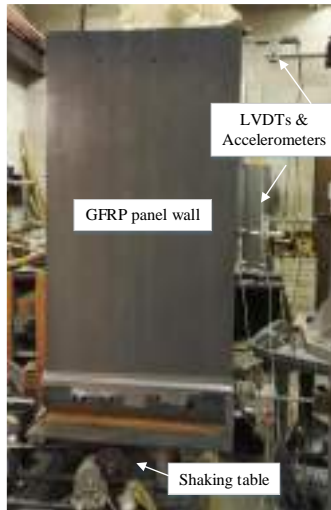
Figure 1 Geometry of the pultruded GFRP panel

Table 1. Material property of pultruded GFRP

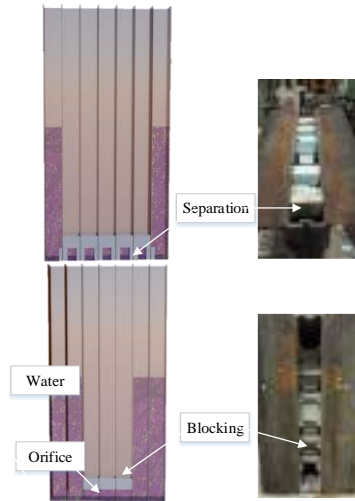
Directions	Elastic modulus	Poisson's ratio	Strength	Moment of Inertia
Out-of-plane	5.52 GPa	0.27	162 MPa	$6.62 \times 10^6 \text{ mm}^4$
In-plane	6.10 GPa	0.27	130 MPa	$1.76 \times 10^8 \text{ mm}^4$

The shaking table test is conducted in the Structural Engineering Research Laboratory at Iowa State University. The test setup is shown in Fig. 2a. A steel block is attached at the top of the GFRP panel to mimic the seismic weight from the dead load and 20% of the snow load. The panel itself is attached to the shaking table by steel bolts and to reproduce a fixed support at the bottom. Harmonic ground excitations generated by the shaking table are recorded by an accelerometer and a Linear Variable Differential Transformer (LVDT) using MEGADAC data acquisition system at a sampling rate of 2000 Hz. Two other accelerometers and LVDTs are installed at the middle and top of the panel to record its acceleration and deformation. The shaking table can generate harmonic ground motions with a frequency ranging from 10 to 60 Hz. Displacement and acceleration of for two harmonic ground motions of different frequencies are shown in Table 2 and Fig. 3. The panel vibration amplitude, which is defined as the difference between the panel's top and bottom displacements, is directly related to the panel deformation.

The interior of the TLCD system is shown in Fig 2b, where 5 cm × 5 cm square orifices are cut at the bottom to allow water to flow freely across all cells. Different numbers of cells are blocked using hard foam to limit water motion in these cells, as illustrated in Fig. 4a. Different water heights are investigated, i.e., 0 cm, 31 cm, 62 cm and 93 cm, as illustrated in Fig. 4b. For each scenario, a companion test is conducted under the water distribution but with the orifices blocked to prevent water motion (Fig.2b). The inclusion of water changes the mass distribution of the panel and increases the lateral inertia force. The research goal of this study is to quantify the vibration reduction provided by the water flow. Comparison of the vibration amplitudes between cases where water flows freely and cases where water motion is blocked can help quantify this damping effect by excluding the effect of increased liquid inertia force from the test results.



(a) GFRP panel mounted on the shaking table

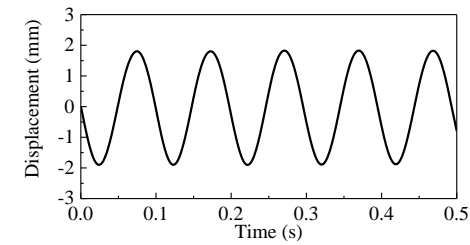


(b) Interior of the multi-celled GFRP wall

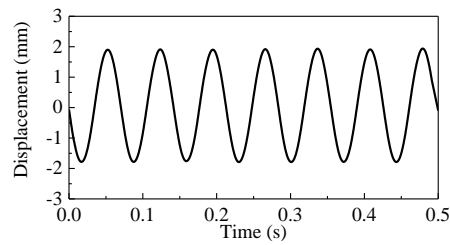
Figure 2 Shaking table test setup

Table 2. Harmonic ground motions of shaking table tests

Ground Motion	Frequency	Max displacement	Max acceleration
1	10.1Hz	1.85 cm	1.4g
2	12.6Hz	1.93 cm	2.5g



(a) Ground motion 1



(b) Ground motion 2

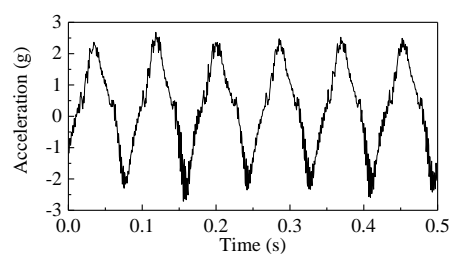
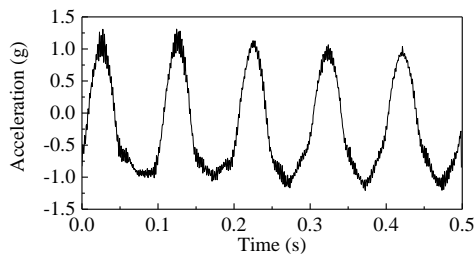
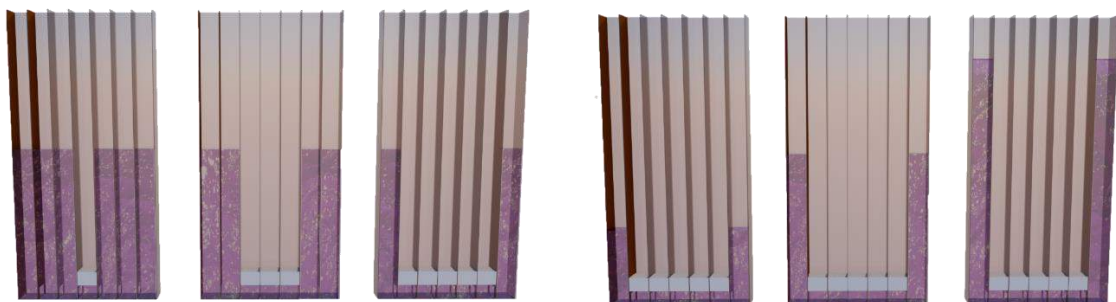


Figure 3 Harmonic ground motions



(a) Different number of cells opened

(b) Different water heights

Figure 4 Different water distribution configurations inside the GFRP panel

Natural frequency of TLCD

Due to the symmetry of water heights and cell openings, the natural frequencies of the TLCD can be estimated using a liquid column vibration absorber (LCVA) model proposed by Hitchcock et al. (1994). An LCVA is a specialized TLCD with unequal horizontal and vertical cross sections. Min et al. (2014) suggested that adjacent cells can be combined by recalculating the effective length from centerlines (Fig. 5):

$$\omega = \frac{1}{2\pi} \sqrt{\frac{2g}{B \cdot A_v / A_h + 2H}} \quad (1)$$

where A_v , A_h are the vertical and horizontal tube cross section areas, respectively, g is the gravitational acceleration, B is the effective length between tube centerlines, and H is the water height. Based on this model the TLCD's natural frequencies under investigation range from 0.457 Hz to 0.716 Hz.

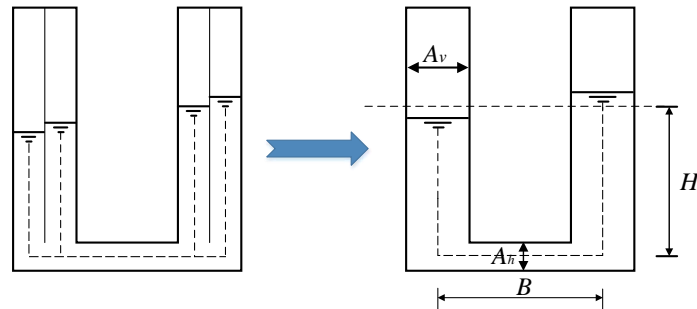


Figure 5 Model used in the computation of natural frequencies

Test results and discussion

The GFRP panel's displacement amplitudes under ground motions 1 and 2 are summarized in Table 3. Since the ground motions are harmonic waves, the vibration amplitude is a good indication of the maximum panel deformation during the shaking table test. The vibration amplitude is larger when more water is included due to the increased inertia force, which offsets the damping effect provided by water head loss. From the test results, it can be observed that in all the cases the GFRP panel's vibration is reduced when water is allowed to flow freely compared to the cases where water flow is blocked, indicating that the TLCD system provides damping. The percentage of the amplitude reduction increases as the cell number increases, but nonlinearly. Increased water height also results in a greater vibration reduction, with the exception that the maximum water height (93 cm) leads to a slightly lower reduction for the 2 and 6 cells cases. This is attributed to the water motion slowing down when the water fills most of the panel. It is noted that the frequency of the generated ground motion is higher than that of the TLCD configurations, which is due to the limitations of shaking table. This test can be viewed as a preliminary test to access the effect of liquid damping on GFRP panels.

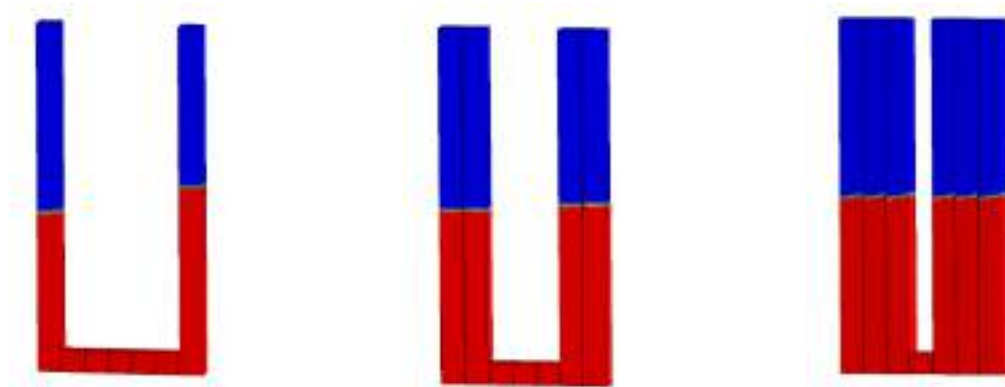
Table 3. Vibration amplitude of GFRP panel (mm)

		Water height	0 cm	31 cm	62 cm	93 cm
Ground motion 1, 2 cells filled	water flow blocked		0.576	0.706	0.770	0.921
	free water flow		0.576	0.680	0.724	0.875
Reduction percentage (%)			0.00	3.75	6.34	5.26
Ground motion 2, 4 cells filled	water flow blocked		1.168	1.372	1.651	2.057
	free water flow		1.168	1.295	1.549	1.880
Reduction percentage (%)			0.00	5.88	6.56	9.46
Ground motion 1, 6 cells filled	water flow blocked		0.584	0.711	0.838	0.965
	free water flow		0.584	0.635	0.660	0.787
Reduction percentage (%)			0.00	12.00	26.92	22.58

CFD SIMULATIONS

In order to better understand the water flow inside the pultruded GFRP panel and the damping performance of the internal TLCD, the liquid motion is simulated using the CFD method in the ANSYS 17.2 Fluent software. The model is solved using a standard $k-\epsilon$ solver, which is widely used to simulate turbulent flow. Figure 6 shows the

water motion under harmonic ground motions when half the panel is filled with water. For the 2 cells case, the water surface fluctuates over a range of 8 cm. The 4 cells case shows a smaller water oscillation amplitude of 3 cm. For the 6 cells case, it is observed that there is not only water flow between different cells, but also water sloshing within each individual cell.



(a) 2 cell, 62 cm water height (b) 4 cell, 62 cm water height (c) 6 cell, 62 cm water height
 Figure 6 CFD simulations of water motion (red represents water)

The CFD method can be used to evaluate the damping capability of TLCDs by computing the total lateral dynamic pressure acting on the GFRP panel. The time series of damping force, plotted in Fig. 7, can be obtained by subtracting the inertia force to the lateral reacting force of the GFRP panel. The magnitudes of the damping forces for the 2 cells, 4 cells and 6 cells are 27 N, 33 N, and 56 N, respectively, corresponding to the amplitude reduction percentage trend from the shaking table test. The damping forces are comparable to the GFRP panel's self-weight and may reduce GFRP structure's vibration during seismic events.

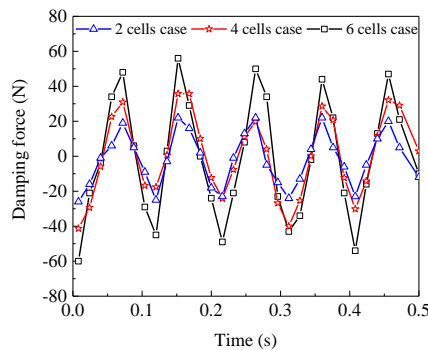


Figure 7 Time series of damping force

CONCLUSION

In this paper, a GFRP panel with an existing internal liquid flow system was adapted into a TLCD system, which can dissipate kinetic energy during seismic events. Shaking table tests were conducted to evaluate the damping effect of the TLCD system. Test results demonstrate that, compared to the cases without water flow, vibrations in the GFRP panel are reduced. This reduction effect generally increases with the water height and number of cells filled with water. CFD models show that the damping forces generated from TLCDs have the same trend as those from the experimental tests, and that their amplitudes are comparable to the GFRP panel's self-weight. The damping mechanism can be a promising technique to promote wider applications of pultruded GFRP structures in seismic regions.

ACKNOWLEDGMENTS

This material is based in part upon work supported by the National Science Foundation under Grant No. CMMI-1562992. Any opinions, findings, and conclusions or recommendations expressed in this material are those of the authors and do not necessarily reflect the views of the National Science Foundation.

REFERENCE

- L. Ascione, V. P. Berardi, A. D'Aponte (2011). "A viscoelastic constitutive law for FRP materials", *International Journal for Computational Methods in Engineering Science and Mechanics*, 12(5), 225-232.
- G. Boscato, S. Russo (2009). "Free vibrations of pultruded FRP elements: Mechanical characterization, analysis, and applications", *Journal of Composites for Construction*, 13(6), 565-574.
- S. Cammelli, Y. F. Li, S. Mijorski (2016). "Mitigation of wind-induced accelerations using Tuned Liquid Column Dampers: Experimental and numerical studies", *Journal of Wind Engineering and Industrial Aerodynamics*, 155, 174-181.
- J. Connor, S. Laflamme (2014). *Structural motion engineering*. New York, Springer.
- A. Di Matteo, F. L. Iacono, G. Navarra, A. Pirrotta (2014). "Experimental validation of a direct pre-design formula for TLCD", *Engineering Structures*, 75, 528-538.
- P. A. Hitchcock, K. C. S. Kwok, R. D. Watkins, B. Samali (1994). "The effectiveness of a multiple liquid column vibration absorber", *Proceedings of the 4th Workshop on Wind Engineering*, Australian Wind Engineering Society, Sydney, 81-86.
- K. W. Min, J. Kim, H. R. Lee (2014). "A design procedure of two-way liquid dampers for attenuation of wind-induced responses of tall buildings", *Journal of Wind Engineering and Industrial Aerodynamics*, 129, 22-30.
- K. W. Min, C. S. Park, J. Kim (2015). "Easy-to-tune reconfigurable liquid column vibration absorbers with multiple cells", *Smart Materials and Structures*, 24(6), 065041.
- S. Russo (2012). "Experimental and finite element analysis of a very large pultruded FRP structure subjected to free vibration", *Composite Structures*, 94(3), 1097-1105.
- K. M. Shum, Y. L. Xu, W. H. Guo (2008). "Wind-induced vibration control of long span cable-stayed bridges using multiple pressurized tuned liquid column dampers", *Journal of wind engineering and industrial aerodynamics*, 96(2), 166-192.
- J. A. Wattick, A. Chen (2017). "Development of a prototype fiber Reinforced Polymer–Concrete Filled wall panel", *Engineering Structures*, 147, 297-308.
- H. Wu, A. Chen (2016). "Seismic Behavior of Glass FRP Wall Panels", 8th International Conference on FRP Composites in Civil Engineering
- X. Yang, Y. Bai, J.L. Luo, X.L. Zhao, F.X. Ding (2016). "Dynamic and fatigue performances of a large-scale space frame assembled using pultruded GFRP composites", *Composite Structures*, 138, 227-236.

Timber and FRP



MECHANICAL BEHAVIOR OF HYBRIDAL FLOOR PANELS TO TIMBER COLUMNS JOINTS

M. Titirla¹, L. Michel¹ and E. Ferrier¹

¹ *Laboratoire des Matériaux Composites pour la Construction, LMC²
Université LYON 1*

82 boulevard Niels BOHR, Site de Villeurbanne DOUA, 69622 VILLEURBANNE Cedex - FRANCE
Emails: magdalini.titirla@univ-lyon1.fr; laurent.michel@univ-lyon1.fr; emmanuel.ferrier@univ-lyon1.fr

ABSTRACT

The aim of the present paper is the experimental investigation of five different types of joints between concrete-timber hybrid panels and timber columns. Each panel consists of Glulam timber and/or Concrete members with timber and concrete beams and concrete cladding. The first connection type incorporates a dowel-type column that jointed to the beam through long bolts, while the second one is a steel plate slotted into the timber beam and timber columns connected to them by means of transverse bolts. The other three connection types are far from the bolted connections, as the third connection type incorporates a steel rebar connection in UHPFRC concrete, the fourth one is made of Carbon FRP rebar in glulam both in the timber and concrete part of the beams, while the fifth one connected by Glass FRP rebar in glulam both. The experimental set-ups of all the connections is subjected to monotonically increasing bending action, and there are conducted at the premises of Laboratory for Composite Materials and Composite Structures of the University Claude Bernard Lyon I.

KEYWORDS

Component models, carbon FRP, glass FPR, joints, timber reinforcement, Hybrid system.

INTRODUCTION

In a more environmentally friendly approach, the use of timber elements in construction is an alternative solution and it is governed by Eurocode 5. However, one of the major problems of timber material is the low value of elastic modulus which can only be countered by having a higher depth significantly limiting the use of the elements. In addition, several solutions have emerged like the strengthening of timber structure by adding specific materials.

Various researchers (Piazza and Ballerini, 2000; Gutkowski et al, 2008) have proposed composite elements as first approach to ensure better performances of timber structure. The idea is to combine wood with other materials. According to Ferrier et al (Ferrier et al, 2014), the development of hybrid systems that focus on the ecology, economy, and performance of the final product is required and it is the next step in civil engineering. Researches in more efficient materials have allowed the recent development of ultra-high performance fiber-reinforced concrete (UHPFRC), which has better properties than ordinary concrete (OC). This hybrid solution shows many advantages, the cross-section can be reduced by decreasing the height of wooden beams and mechanical performance are improved in term of load capacity and stiffness.

Hybrid structural systems that combine materials of complementary properties have the potential to achieve significant levels of efficiency. The main problem remains the connection type of these panels with the facade of the building. Several studies have been carried out regarding the connection of the hybrid construction systems, in which steel and timber are the main structural materials or are joined in order to enhance the load-bearing capacity (Steinberg et al, 2003; Loss et al, 2015; Karagiannis et al, 2017).

This paper deals with the mechanical response of a five new type of hybrid connections between Glulam timber - concrete panels and Glulam timber columns by means of experimental studies. The first connection type incorporates a dowel-type column that jointed to the beam through long bolts, while the second one is a steel plate slotted into the timber beam and timber columns connected to them by means of transverse bolts. The other three connection types are far from the bolted connections, as the third connection type incorporates a steel rebar connection in UHPFRC concrete, the fourth one is by Carbon FRP rebar in glulam both in the timber and concrete part of the beams, while the fifth one is by Glass FRP rebar in glulam both. The experimental set-ups of all the connections is subjected to monotonically increasing bending action, and there are conducted at the premises of Laboratory for Composite Materials and Composite Structures of the University Claude Bernard Lyon I.

BEHAVIOR OF A 3 FLOOR PLANE STRUCTURE WITH CONCRETE-WOOD HYBRID PANELS

Geometry and Loading

The study is based on a three floor plane structure, which is manufactured from the hybrid panels as the floor and the facade of it. Each panel is composed of glued laminated wood beams and / or concrete constituting the floors and wooden beams constituting the supporting framework of the facade elements. The dimensions of the hybrid panels are defined in the project in order to guarantee appropriate implementation and transport conditions. For these reasons, the width of the panels is fixed at 1.20m and the length equal to 7.5m (Augeard et al, 2018), as a result the storey heights and width are equal to 3 and 7.5 m, respectively (Figure 1).

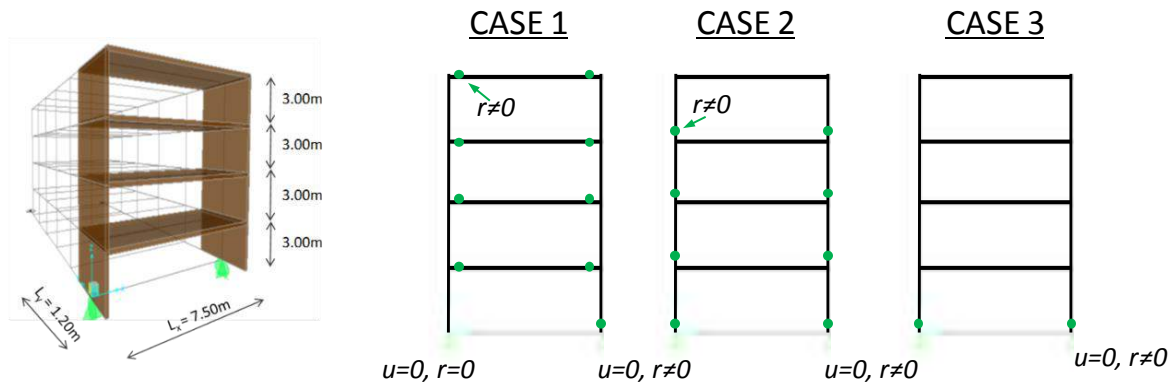


Figure 1: The 3 floor investigated building.

The columns are hinged at their base but capable of carrying moments along the whole height of the building, while beams are i) hinge connected to the columns (case 1) and ii) moment connected to the columns (case 2 and 3). In the second case, each floor is independent with the previous. In order to be the building of the first case isostatic, it was necessary to fixed one column in the ground. The three buildings were modelled and analyzed in SAP 2000 ver. 11.0.3 (Sap200, 2007). The panels and the columns were modelled by frame elements. Gravity load (dead and live loads), snow and wind are assuming on the beams and horizontal wind to the columns, based to European Standard (CEN EN 384:2010). Detailed description of the three cases is given in Table 1, where N is the maximum axial load in the columns, Q is the maximum shear load in the connection, M_c is the maximum bending moment in the connection while M_b is the maximum bending moment in the beam. In addition, U_v is the maximum deflexion in the centre of the beam and U_h is the maximum floor horizontal displacement in the 3rd floor. From the analyzed results (Table 1), we can confirmed that in the case where the beams are shear connected to the columns (case 1) the maximum value of the bending moments are in the connection of the two columns between the floors, while in the case where the beams are moment connected to the columns (case 2 or 3) the maximum values are in the connection of the beam with the columns. In addition, the smaller deflection in the centre of the spam is noticed in the case where the beams are moment connected to the columns (case 2 or 3). The frames (beams of the panel and columns) are designed for the maximum load combination in accordance with the structural Eurocode EC5 in the case of a rigid connection (case 3).

Table 1: Summarised results.

Case	N (kN)	Q (kN)	Mc (kNm)	Mb (kNm)	U_v (mm)	U_h (mm)
1	140.00	54.00	204.00	101.00	180	1445
2	252.00	66.90	149.00	90.60	36	352
3	252.00	71.52	169.00	101.00	33	350

Description of the proposed connections

The present section presents in more detail the innovative connections between the hybrid panels and the wooden columns. Each panel is composed of five glued laminated wood beams and / or concrete constituting the floors and five wooden beams constituting the supporting framework of the facade elements. The columns are rectangular with cross section 90x225mm, while the beams 90x290mm plus 50mm the concrete slab (UHPFRC) that connect the beams (Figure 2). The connection of the wood surface of the beams with the surfaces of the concrete slab is a specific bond technic to allow a perfect adhesion between concrete and wood(Augeard et al,

2018). For test reasons, the junction specimens were first reduced to two beams and tested at a 90° rotation. In this case, the force generating the rotation and / or the moment is applied horizontally (Figure 2), this in order to avoid the effects P-δ of the displacements of the column and to focus our attention only on the connections.

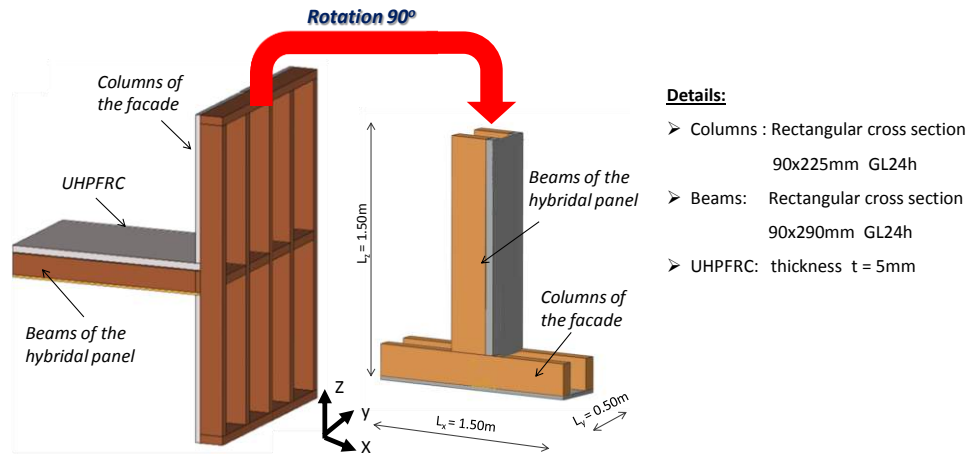


Figure 2. The rotated system

Five different connection types are investigated. All the connections have been designed based to Eurocode in order to support the maximum load combination that calculated in the section 2. The first connection type incorporates a dowel-type column that jointed to the beam through long bolts (Figure 3a), while the second one is a steel plate slotted into the timber beam and timber columns connected to them by means of transverse bolts (Figure 3b). The other three connection types are far from the bolted connections, as the third connection type incorporates a steel rebar connection in UHPFRC concrete (Figure 3c), the fourth one is by Carbon FRP rebar in glulam both in the timber and concrete part of the beams (Figure 3d), while the fifth one is by Glass FRP rebar in glulam (Figure 3e).

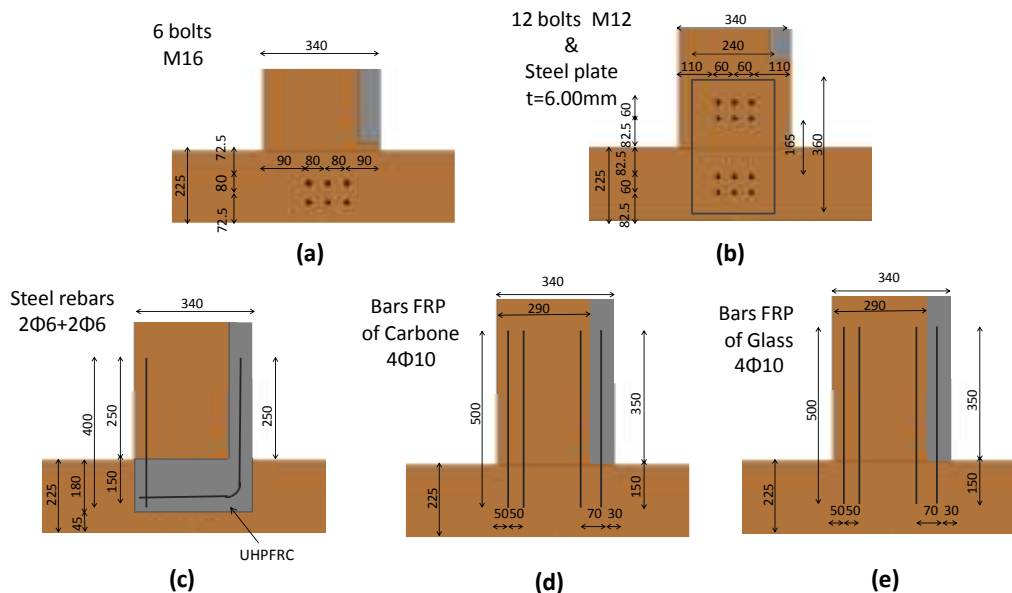


Figure 3. The five proposed connections that experimentally investigated.

EXPERIMENTAL SET UP

Figure 4 shows the experimental set-up used for testing the five innovative moment connections between Hybrid panels and timber columns under bending. A hydraulic actuator operating in displacement control (fixed to a strong wall) was attached to the top of the glulam beam through a specially designed clamping device. The displacement at the top of the beam was increased gradually at a rate of around 4 mm/min until the stroke of the

actuator was reached or until clear connection failure was observed. The load cell incorporated within the actuator was employed to record the applied load at the top of the beam. Eleven Linear Variable Differential Transformers (LVDT) and one Laser were positioned at each specimen, which measure the corresponding displacement at different position in the whole specimen (see Figure 4). All data was recorded and stored in a digital data system via a computer. The fixed position of the column relative to the strong floor was achieved by the help of fixing blocks in both horizontal and vertical directions.

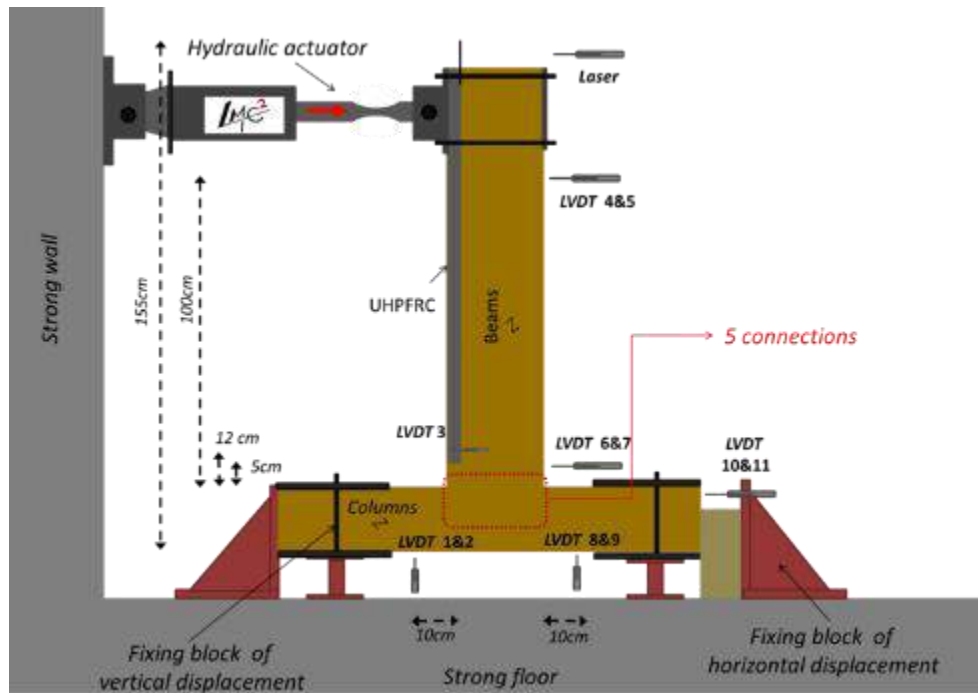


Figure 4. Details of the experimental set up.

RESULTS AND DISCUSSIONS

Stiffness

Figure 5 illustrates the force-displacement diagram at the top of the beam (laser displacement) compared in the five investigated connections. We can notice two different types of response. Connections d and e show a first linear phase with very high stiffness 2.00 kN/mm and 1.45 kN/mm respectively coupled to a high tensile strength of 20.47 kN and 24.06 kN . After the failure of the first bar, the load is reduced. As Carbone is stiffer than the Glass material, we can notice in the connection with the Carbone FRP (connection d) an increase of the connections rigidity equal to 37% regarding the solution with the Glass FRP (connection e) that resulting with reduction of the maximum load equal to 17%. The response of these two connections is like fragile type.

On the other hand, connections a to c show comparable stiffness but do not make it possible to reach high breaking loads without generating large overall displacements. In the case of the solution with bolts (solution a), the limit of elastic behavior is close to 2.3 kN and a second phase of behavior with a stiffness of 0.1 kN/mm allowing to reach a maximum load of 5.12 kN . Compared with the solution with the Carbone FRP, the maximum load of the bolted connection is 4 times smaller and the stiffness almost 10 times smaller. Solution b shows a behavior similar to the configuration a, but with a big slipping at the beginning of the test in the junction between the wood elements and the steel plate, as a result the limit of the elastic behavior is close to 0.9 kN and a second phase of behavior with a stiffness of 0.17 kN/mm allowing to reach a maximum load of 2.75 kN . That means for this kind of connection (bolted with or without steel plate) in order to increase the stiffness and the load, it is necessary the increase of the number of the bolts and the cross section of the beams in order to respect the limits that Eurocode provides.

Last but not least, in the case of solution c, the limit load of elastic behavior is close to 8.25 kN and a breaking load close to 11 kN . In the elastic part, this connection is stiff enough (1.63 kN/mm) but we notice the loosing of interaction between the surface of the UHPFRC and the surface of the timber in load of 8.25 kN (2.5 times smaller than the maximum load of the Carbone FRP connection).

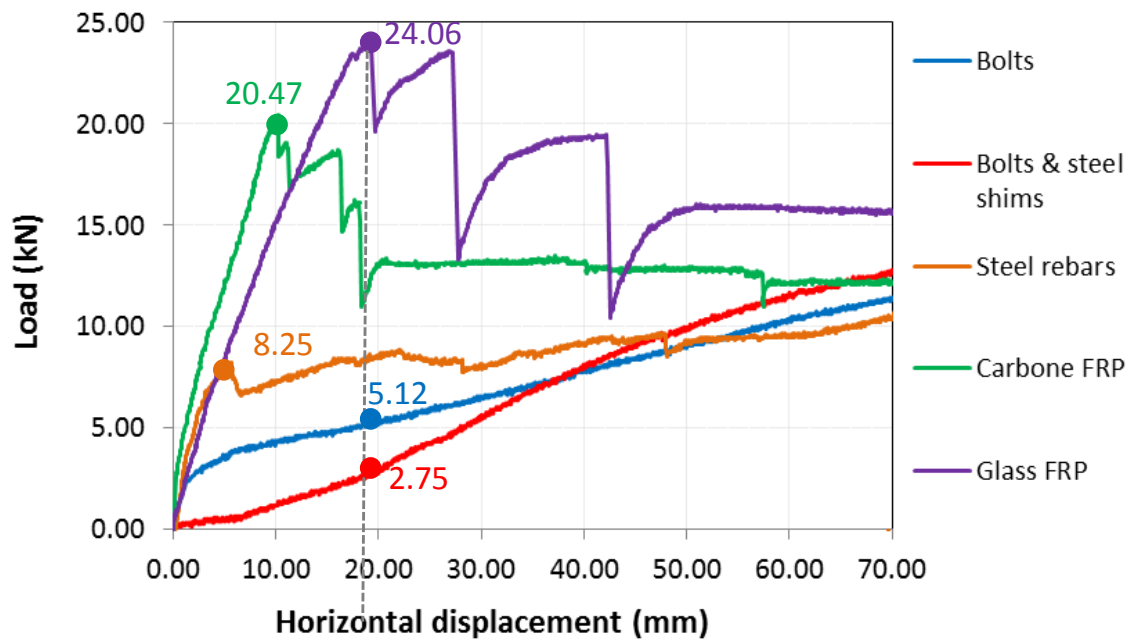


Figure 5. Load vs horizontal displacement at the top of the beam.

Table 1. Summary of the five test specimen connections.

Connection	Stiffness (kN/mm)			Max Force (kN)
	K1	K2	Keff	
a Bolts	2.03	0.14	0.27	5.12
b Bolts and steel plate	0.10	0.17	0.14	2.75
c Steel rebars	1.63	-	1.63	8.25
d Carbone FRP	2.00	-	2.00	20.47
e Glass FRP	1.45	-	1.45	24.06

Type of failure

In the following figures, the type of the failure of each one of the investigated connection is presented. The types of the failure are also different depending on type of the response. The bolted connections (connections a and b) show mixed fractures with changing the shape of the wood holes at the outer holes and with the plasticity of the bolts (Figure 6). In addition, in the connection b (with the 12 bolts of M12 and one steel plate) we can notice the compression of the columns during the rotation of the beam (Figure 7).



Figure 6. Failure of the connection (numbered a) with 6 bolts M16.



Figure 7. Failure of the connection (numbered b) with 12 bolts M12 and one steel plate ($t=6\text{mm}$).

Connection c with the steel bars in the concrete UHPFRC node shows a rupture by detachment of the concrete in the tension zone and an over compression of the concrete part in the opposite zone (Figure 8). Connections d and e exhibit fragile behavior. The configurations with carbon FRP (connection d) and glass FRP (connection e) showed a rupture by the pull out of the bar engraved in the beam transverse to the bars (Figure 9).



Figure 8. Failure of the connection (numbered c) with steel rebar in a UHPFRC part.



Figure 9. Failure of the connections (numbered d & e) with Carbon or Glass FRP.

CONCLUSIONS

This article presents an experimental study of five innovative connections between hybrid floors and timber columns. The first connection type incorporates a dowel-type column that jointed to the beam through long bolts, while the second one is a steel plate slotted into the timber beam and timber columns connected to them by means of transverse bolts. The other three connection types are far from the bolted connections, as the third connection type incorporates a steel rebar connection in UHPFRC concrete, the fourth one is by carbon FRP rebar in glulam both in the timber and concrete part of the beams, while the fifth one is by glass FRP rebar in glulam both.

The experimental tests show that solutions with glued composite bars provide significant loads and stiffness. The last two connections with the FRP bars, provide similar results but not exactly the same due to the young modulus of the two materials (carbon and glass). As carbone is stiffer than the glass material, we can notice in the connection with the carbon FRP (connection d) an increase of the connections rigidity equal to 37% regarding the solution with the glass FRP (connection e) that resulting with reduction of the maximum load equal to 17 %. The solution with the steel bars (connection c), in the elastic part, is stiff enough (1.63 kn/mm) but we notice the loosing of interaction between the surface of the UHPFRC and the surface of the timber in load of 8.25 kN (2.5 times smaller than the maximum load of the carbon FRP connection).

On the other hand, in the bolted connections, the breaking load is reached after a large displacement. As a result, these solutions do not guarantee a recovery of the moments in the junctions without involving strong rotations. Also, for this kind of connection (bolted with or without steel plate) in order to increase the stiffness and the load, it is necessary the increase of the number of the bolts and the cross section of the beams in order to respect the limits that Eurocode provides.

ACKNOWLEDGMENTS

The authors would like to thank the FUI project "HYBRIDAL" for funding the present study. The authors also thank the staff of the Laboratory of Composite Materials for Construction LMC2 (E. Janin and N. Cottet) for their technical support.

REFERENCES

- E. Augeard, L. Michel, E. Ferrier, "Experimental and analytical study of the mechanical behavior of heterogeneous glulam–concrete beams and panels assembled by a specific treatment of wood," (under review)
- Computers and Structures Inc. SAP 2000 nonlinear version 11.0.3 user's reference manual. Berkeley, California; 2007.
- European Committee for Standardization (CEN), EN 12512:2001, Timber structures-test methods-cycling testing of joints made with mechanical fasteners, CEN, Bruxelles, Belgium, 2001.
- European Standard CEN EN 384:2010. Structural timber – determination of characteristic values of mechanical properties and density, Bruxelles, Belgium , 2010.
- EN 1991-1-5:2003. Eurocode 1: actions on structures – Part 1–5: general actions – thermal actions; Bruxelles, Belgium 2003.
- EN 1995-1-1. Eurocode 5: design of timber structures, Part 1–1: general common rules and rules for buildings; Bruxelles, Belgium 2004.
- E. Ferrier, A. Agbossou, L. Michel (2014). "Mechanical behaviour of ultra-high-performance fibrous-concrete wood panels reinforced by FRP bars", *Compos Part B Eng*, 60, 663–72.
- R. Gutkowski, K. Brown, A. Shigidi, J. Natterer (2008). "Laboratory tests of composite woodconcrete beams", *Constr. Build. Mater*, 22 (6), 1059–1066.
- V. Karagiannis, C. Málaga-Chuquitaype, A.Y. Elghazouli (2017). "Behaviour of hybrid timber beam-to-tubular steel column moment connections" *Engineering Structures* ,131, 243–263.
- C. Loss, M. Piazza, R. Zandonini (2015). "Connections for steel-timber hybrid prefabricated buildings. Part II: Innovative modular structures", *Constr. Build. Mater*, 46, 45–67.
- M. Piazza, M. Ballerini (2000). "Experimental and numerical results on timber–concrete composite floors with different connection systems" in: *Proceedings of the World Conference on Timber Engineering (WCTE)*, Whistler, Canada.
- E. Steinberg, R. Selle, T. Faust (2003). "Connectors for timber–lightweight concrete composite structures" *J. Struct. Eng*, 129, 1538–1545.



BOND ANALYSIS OF BASALT FIBRE REINFORCED POLYMER (BFRP) BARS AND TIMBER BEAMS UNDER AXIAL LOADING

D. Walline 1 and A. Rteil 2

¹ *The University of British Columbia, School of Engineering, 3333 University Way, Kelowna, BC, V1V 1V7, Canada, Email: devin.walline@gmail.com*

² *The University of British Columbia, School of Engineering, 3333 University Way, Kelowna, BC, V1V 1V7, Canada, Email: ahmad.rteil@ubc.ca*

ABSTRACT

Flexural reinforcement of damaged or deteriorated timber beam using fibre reinforced polymer (FRP) bars is a potentially attractive solution to extend the service life of aged or historic timber structures. However, to ensure full utilization of the FRP, the bond between the two materials must be strong enough to reach the ultimate strength of the FRP bars. This paper details the investigation of the effects of bar size and bond length on the bond strength of basalt FRP bars and Douglas Fir timber beams under axial loading. A total of 18 double shear specimens were tested. Both parameters were determined to be statistically significant and an empirical model was proposed. From the empirical model, a bonded length of 467 mm and 1938 mm would be required to prompt bar failure for 6 mm and 10 mm bars respectively.

KEYWORDS

Strengthening and repair, experimental study, bond and interfacial stresses, timber beams, development length, fibre reinforced polymer (FRP)

INTRODUCTION

A potential strategy for increasing the strength of existing or new timber members is the incorporation of fibre reinforced polymer (FRP) bars as a reinforcement, like that of steel in reinforced concrete members (Micelli, Scialpi, & La Tegola, 2005). Over the past two decades, engineers have realized the numerous advantages of FRP as a structural material with a significantly high strength to weight ratio and non-corrosive properties. Thus far, most of the research and field application of FRP has been directed at concrete structures (Raftery & Harte, 2011). The few research studies conducted on the use of FRP as reinforcement in structural timber elements have shown that a relatively low reinforcement ratio (~1%) can result in an increase in flexural capacity of up to 63% (Johnsson, Blanksvärd, & Carolin, 2006; Raftery & Kelly, 2015). Bond between timber and FRP is an essential factor. However, most of the research completed on bond to date has used direct pull-out test method which results in an unrealistic stress condition when considering flexural reinforcement. However, in terms of analyzing different parameters and their effects on bond strength, the double shear test allows for a simple and effective procedure. This paper presents an experimental research project conducted to study the effects of bar size and bond length on the bond strength of basalt FRP bars and timber beams under double shear loading.

EXPERIMENTAL INVESTIGATION

The test matrix that was used for this study is detailed in Table 29. Two bar diameters (6 mm and 10 mm) and three bond lengths (100 mm, 200 mm, and 300 mm) were tested in order to define the bond strength vs. bond length relationship. Each of the variations in the test matrix was tested three times to determine the average bond strength. The specimen consisted of two timber sections (Figure 73); the anchor block which was 600 mm in length and the test block which was 400 mm in length. The FRP bars were bonded into a notch cut on both soffits. The notch dimensions were chosen to be a function of the bar diameter. The notches were square shaped with a size approximately equal to two times the bar diameter, resulting in a 12.7 mm and 19.1 mm notch for the 6 mm and 10 mm bars respectively. The FRP bars were bonded in using a two-part structural epoxy, which was recommended for use with FRP and timber.

The anchor portion of the FRP bar had a bonded length of 600 mm, which provided at least two times the bonded length of the test bar. The anchor and test blocks were separated by a distance of 200 mm, which allowed for the test frame to be installed on the inside faces of each block.

Table 29: Test matrix

Specimen ID	Bar Diameter (mm) - d_b	Bond Length (mm) - l_b
D6_L100	6	100
D6_L200	6	200
D6_L300	6	300
D10_L100	10	100
D10_L200	10	200
D10_L300	10	300

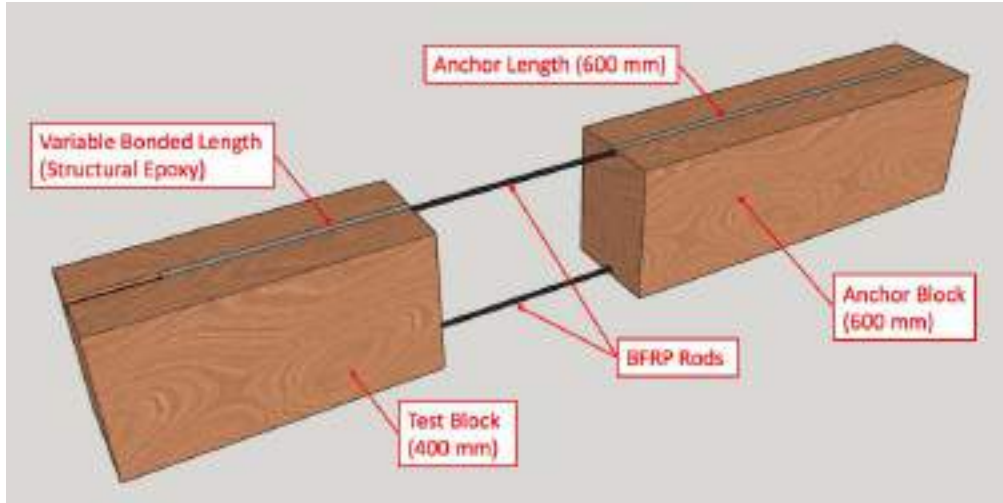


Figure 73: 3D model of double shear specimens

MATERIAL PROPERTIES

Wood

The timber used was a low-grade solid sawn Douglas Fir harvested in British Columbia, Canada. The cross-sectional dimensions were 150 mm x 200 mm and were chosen to replicate a realistic size that one would encounter in a timber building. The average tensile strength was determined to be 41.2 MPa and the average flexural strength was determined to be 31.5 MPa. It was noted during the experimental testing that the quality of timber varied from specimen to specimen, and thus should be considered when analyzing the results.

BFRP Bars

The basalt FRP bars used in this experimental study had a tensile strength of 1230 MPa and modulus of elasticity of 46.6 GPa. The bars surface was sand coated in order to promote a quality bond. As mentioned above, 6 mm and 10 mm bars were used. The basalt material was chosen as sustainable alternative compared to steel, carbon fibre, or glass fibre. The bars used are reported to emit approximately 57.1% of the carbon dioxide emitted during stainless steel bar manufacturing (MagmaTech, 2017).

Epoxy

The epoxy chosen to bond the BFRP bars to the timber was a high modulus, high strength, structural epoxy paste adhesive that is recommended for use with FRP bars and numerous other materials in overhead applications. The two-part system was mixed as per the manufacturer's specifications and applied using plastic spatulas and scrapers. The mechanical properties provided by the manufacturer are given in Table 30.

Table 30: Hardened epoxy specifications (Sika Canada, 2015)

Value (after at least 14 days)	Strength (MPa)
Tensile strength	24.8
Shear strength	15
Bond strength (concrete to steel)	22
Compressive strength	59.3

SPECIMEN PREPARATION

The specimens were prepared as follows: 1) the blocks were cut to the required lengths (400 mm for test block and 600 mm for the anchor block), 2) the appropriately sized notches (12.7 mm and 19.1 mm) were cut into the top and bottom of the beams using a router, a jig, and a rectangular bit, 3) the notches were cleaned out with high pressure air, 4) strain gauges were applied to the BFRP bars at various locations, 5) the BFRP bars were bonded into the notches using the epoxy paste (with a 600 mm bond length on the anchor side and varying bond length on the test side as shown in Table 29).



Figure 74: Double shear specimens following casting

TESTING

The double shear specimens were tested under a constant displacement-controlled loading rate of 2 mm/min using a 500 kN MTS Load Frame (Figure 75). The displacement of the actuator head and the corresponding load were recorded at a rate of 8 measurements per second.

The testing frame consisted of two “T-plates” that were affixed to the top and bottom jaws of the MTS frame. Threaded bars were run for each “T-plate” to a flat pressure plate on the inside of both faces of the double shear specimens. All threaded bars were tightened down with nuts and wrenches.

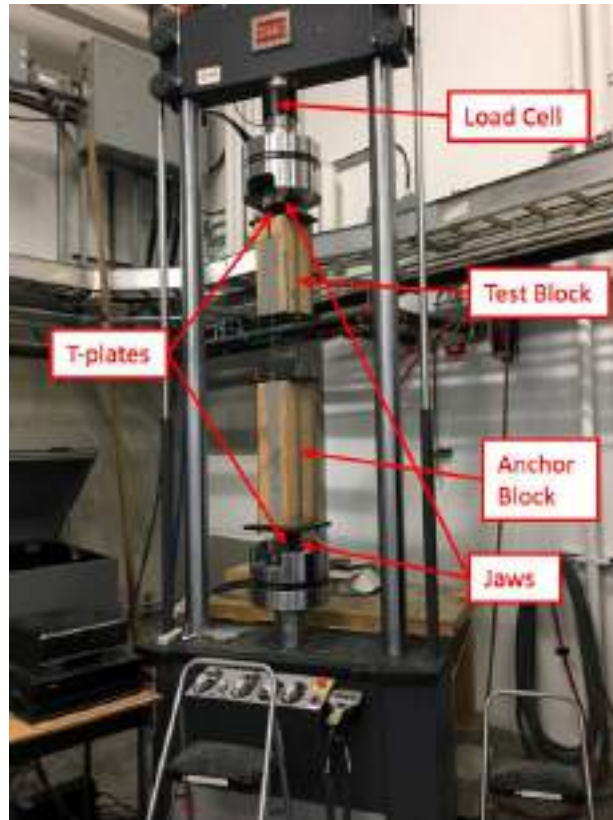


Figure 75: Test setup

Data Acquisition

On one of each set of three repeats, an array of 5 mm strain gauges was applied directly to the BFRP bar prior to being cast into the notch (Figure 76). This allowed for the strain of the BFRP bar to be measured and recorded as the load was applied.

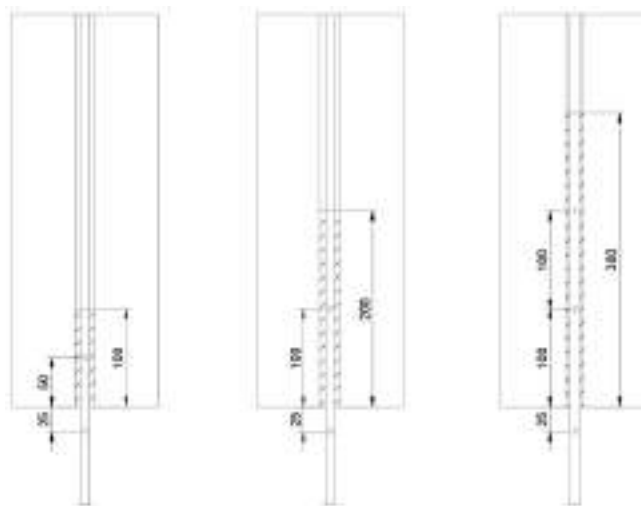


Figure 76: Strain gauge location by bond length

EXPERIMENTAL RESULTS AND DISCUSSION

The results obtained during testing are presented in Table 31. From equilibrium, the maximum load (F_{max}) reported is half of the load at failure that was recorded during testing. The stress (σ) in the bar is calculated as the force divided by the cross-sectional area of the bar. The bond stress between the bar and the epoxy (τ_b) was calculated as the maximum load divided by the surface contact area between the bar and the epoxy. The bond stress between the epoxy and the wood (τ_{ew}) was calculated as the maximum load divided by the area of contact between the epoxy and the wood. Three failure modes were observed during testing: bar pull-out (BP) which is the bar slipping

within the epoxy, timber block shear (TB) which is a block failure of the timber specimen, and timber plug shear (TP) which is a localized plug of timber being pulled out around the bonded length. The three failure modes are shown in Figure 77.

Table 31: Test results

ID	Maximum Load F_{max} (kN)	Tensile Stress σ (MPa)	Bond Stress τ_b (MPa)	Bond Stress τ_{ew} (MPa)	Failure Mode ¹
D6_L100_1	18.4	649.1	9.74	4.82	BP
D6_L100_2	18.0	637.0	9.55	4.73	BP
D6_L100_3	16.8	595.5	8.93	4.42	BP
Average (SD)	17.7 (0.65)	627.2 (22.94)	9.41 (0.34)	4.65 (0.17)	
D6_L200_1	26.9	950.2	7.13	3.53	BP
D6_L200_2	17.5	619.8	4.65	2.30	TB
D6_L200_3	25.1	886.6	6.65	3.29	BP
Average (SD)	23.2 (4.05)	818.9 (143.13)	6.14 (1.07)	3.04 (0.53)	
D6_L300_1	29.5	1044.5	5.22	2.58	TB
D6_L300_2	20.5	723.9	3.62	1.79	BP
D6_L300_3	27.7	980.5	4.90	2.43	BP
Average (SD)	25.9 (3.92)	916.3 (138.54)	4.58 (0.69)	2.27 (0.34)	
D10_L100_1	32.9	418.8	10.47	5.76	TP
D10_L100_2	38.9	495.0	12.38	6.80	BP
D10_L100_3	30.4	386.7	9.67	5.31	BP
Average (SD)	34.1 (3.57)	433.5 (45.43)	10.84 (1.14)	5.96 (0.62)	
D10_L200_1	39.6	504.1	6.30	3.46	TP
D10_L200_2	42.3	538.7	6.73	3.70	BP
D10_L200_3	40.6	516.7	6.46	3.55	BP
Average (SD)	40.8 (1.12)	519.9 (14.3)	6.5 (0.18)	3.57 (0.1)	
D10_L300_1	50.7	645.3	5.38	2.96	TB
D10_L300_2	39.5	502.9	4.19	2.30	TP
D10_L300_3	52.5	668.9	5.57	3.06	BP
Average (SD)	47.6 (5.76)	605.7 (73.3)	5.05 (0.61)	2.77 (0.34)	

¹ BP: Bar Pull-out, TP: Timber Plug Shear, TB: Timber Block Shear



Figure 77: Failure modes

The relative maximum force increase for each bonded length is given in Figure 78. With respect to bonded length, as expected with an increase in bond length comes an increase in maximum force. A 200% and 300% increase in bond length resulted in an average increase of 31% and 46% for 6mm bars and 20% and 40% for 10 mm bars respectively.

The relative maximum force increase for each bar diameter is given in Figure 79. Again, as expected the maximum force for each bonded length increases with bar diameter. For an increase from 6 mm to 10 mm, a relative increase in the maximum force of 92%, 76%, and 84% was observed for a bonded length of 100 mm, 200 mm, and 300 mm respectively.

As for the failure mode, there was no observed trend between bonded length or bar diameter with the failure mode.

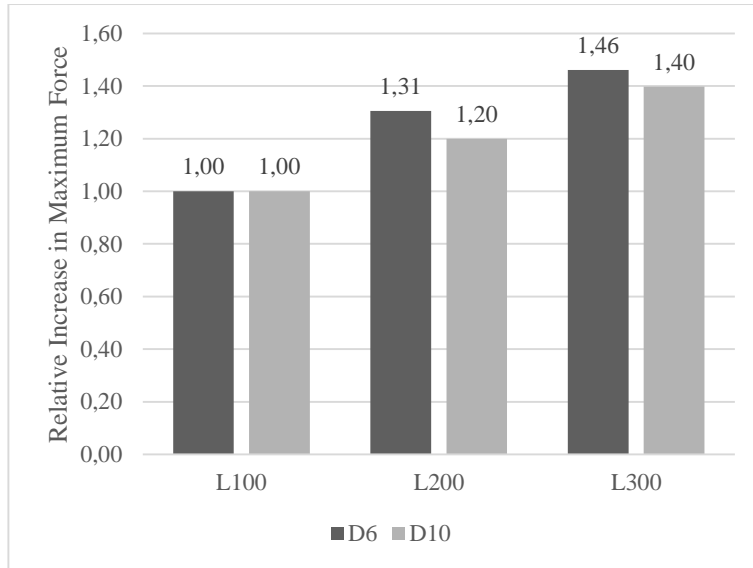


Figure 78: Relative increase in maximum force for bonded length

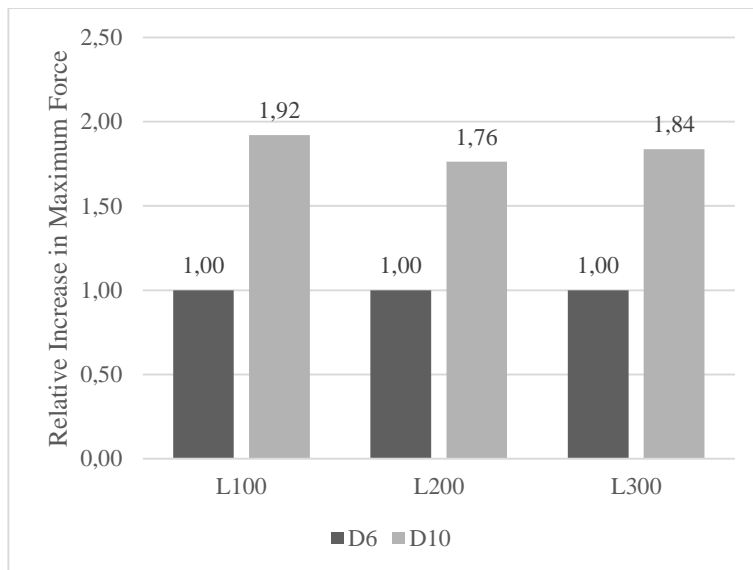


Figure 79: Relative increase in maximum force for bar diameter

Statistical Analysis

A statistical analysis was performed on the data to determine the significance of the variables and to determine the relationship between the significant variables.

First, a two-factor analysis of variance (ANOVA) with replications was conducted considering the bonded length and bar diameter as the input variables and the maximum force as the output value. The confidence level was set at 95% ($\alpha = 0.05$) and the ANOVA results table is given in Table 32. As shown in the results, the bonded length and the bar diameter were both determined to be significant parameters with their p-values being less than 0.05 (α). The interaction between bonded length and bar diameter was determined to be insignificant, with a p-value of 0.59.

Table 32: ANOVA results

<i>Source of Variation</i>	<i>SS</i>	<i>df</i>	<i>MS</i>	<i>F</i>	<i>P-value</i>	<i>F crit</i>	<i>Significant?</i>
Bonded Length	355.0	2	177.49	8.96	0.004	3.885	Yes
Bar Diameter	1548.7	1	1548.73	78.14	0.000	4.747	Yes
Interaction	23.2	2	11.60	0.59	0.572	3.885	No
Within	237.8	12	19.82				
Total	2164.7	17					

The next step taken in the statistical analysis was to explore the relationship between the significant variables (bonded length and bar diameter), by running a regression analysis. The regression analysis allowed for an empirical model to be developed that can quantify the relationship between the significant parameters. The model used to describe the empirical relationship is given in Equation (1). The model chosen had the constant value set to zero, as it is assumed that if the bond length and bar diameter values are zero, the maximum force value is also zero. The results for the regression analysis are given in Table 33 and the model is presented in Equation (2). The adjusted R^2 value was calculated to be 0.912, indicating that the model yields good results. From the regression analysis, Equation (3) was proposed as a simplified form of Equation (2).

$$y = \beta_1 x_1 + \beta_2 x_2 \quad (1)$$

Table 33: Regression results

	Coefficients	Standard Error	t Stat	P-value
Intercept	0	-	-	-
Bond Length	0.033	0.014	2.432	0.027
Bar Diameter	3.211	0.354	9.076	0.000

$$F_{\max} = 0.033 * l_b + 3.211 * d_b \quad (2)$$

$$F_{\max} = l_b / 30 + 3.2 * d_b \quad (3)$$

Where, F_{\max} is the maximum axial force (in kN) that can be exerted on the BFRP bar before it fails in bond, l_b is the bonded length (in mm), and d_b is the diameter of the bar (in mm).

Discussion

For maximum effectiveness of FRP reinforcement in timber structures, the bond must be strong enough to engage the FRP bar to the point of tensile failure. In the case of the basalt FRP bars used in this study, the tensile stress would need to reach 1230 MPa. This translates to an axial load of 34.78 kN and 96.60 kN for the 6 mm and 10 mm bars respectively. In order to determine the bond length required to reach this force, Equation (3) can be rearranged, as shown in Equation (4).

$$l_b = 30 * (F_{\max} - 3.2 * d_b) \quad (4)$$

Solving for the required bonded length leads to 467 mm and 1938 mm for the 6 mm and 10 mm bars respectively. However, when considering the failure modes that were presented in Table 31, timber failure could occur before the bar ruptures. With this proposed equation, it is shown that using smaller diameter bars result in higher tensile stresses in the bars. This means that the FRP can be used in a more efficient manner.

CONCLUSIONS

This paper described an experimental investigation of the bond strength between basalt fibre reinforced polymer (BFRP) bars and douglas fir timber beams, which was undertaken at the University of British Columbia. The bond strength was tested under axial loading using a double shear test setup. A number of conclusions can be made:

- Increasing the bar diameter from 6 mm to 10 mm resulted in an average relative increase in maximum bond strength of 84%.
- Increasing the bonded length from 100 mm to 200 mm and 300 mm resulted in an average relative increase in maximum bond strength of 20% and 40% respectively.
- With the specimens tested, none were able to reach the point of bar tensile failure. The three failure modes included: bar pull-out, timber plug failure, and timber block failure.

- Both bonded length and BFRP bar diameter were statistically significant when considering the bond strength between near surface mounted (NSM) BFRP bars and douglas fir timber beams.
- An equation was proposed to quantify the relationship between bonded length and bar diameter, with respect to bond strength. In order to reach tensile failure, the proposed equation requires a bonded length of 467 mm and 1938 mm for the 6 mm and 10 mm bars respectively.
- According to the proposed equation, smaller diameter bars would be more effective for use as reinforcement in NSM applications for timber beams as the setup results in higher stresses in the smaller bars.

REFERENCES

- Johnsson, H., Blanksvärd, T., & Carolin, A. (2006). Glulam members strengthened by carbon fibre reinforcement. *Materials and Structures*, 40(1), 47–56. <https://doi.org/10.1617/s11527-006-9119-7>
- MagmaTech. (2017). RockBar Product Data Sheet. Retrieved February 23, 2017, from <http://magmaTech.co.uk/downloads/RockBar.pdf>
- Micelli, F., Scialpi, V., & La Tegola, A. (2005). Flexural reinforcement of glulam timber beams and joints with carbon fiber-reinforced polymer rods. *Journal of Composites for Construction*, 9(4), 337–347. [https://doi.org/Doi.10.1061/\(Asce\)1090-0268\(2005\)9:4\(337\)](https://doi.org/Doi.10.1061/(Asce)1090-0268(2005)9:4(337))
- Raftery, G. M., & Harte, A. M. (2011). Low-grade glued laminated timber reinforced with FRP plate. *Composites Part B: Engineering*, 42(4), 724–735. <https://doi.org/10.1016/j.compositesb.2011.01.029>
- Raftery, G. M., & Kelly, F. (2015). Basalt FRP rods for reinforcement and repair of timber. *Composites Part B: Engineering*, 70(1), 9–19. <https://doi.org/10.1016/j.compositesb.2014.10.036>
- Sika Canada. (2015). Sikadur ® 30. Retrieved May 13, 2017, from https://can.sika.com/en/solutions-and-products/document-download/Sikadur_PDS_Alpha.html



COMPRESSIVE BEHAVIOR OF MEDIUM STRENGTH CIRCULAR GLUE LAMINATED TIMBER COLUMNS JACKETED WITH FRP SHEETS

O. A. Sisman 1, A. Isikara 2, E. Binbir 3 and A. Ilki 4

¹ Senior Student, Civil Engineering Faculty, Istanbul Technical University, 34469 Maslak, Istanbul, Turkey

² Master Student, Energy Institute, Istanbul Technical University, 34469 Maslak, Istanbul, Turkey

³ PhD Candidate, Civil Engineering Faculty, Istanbul Technical University, 34469 Maslak, Istanbul, Turkey

⁴ Professor, Civil Engineering Faculty, Istanbul Technical University, 34469 Maslak, Istanbul, Turkey. E-mail: ailki@itu.edu.tr

ABSTRACT

Glue laminated timber (glulam) is an aesthetical, natural, energy saving and sustainable construction material that is a renewable, easily applicable and lightweight alternative in low and medium rise buildings, unlike steel and other reinforced concrete structural elements. In high-rise buildings, however, high strength and ductile columns and long-span beams are required. To meet these requirements, mechanical properties of timber are enhanced by minimizing the effects of initial defects, knots and discontinuities in the wood and protecting against deterioration caused by moisture and weathering that result in splitting, cracks, insect damage and fungal decay. Use of fiber reinforced polymer (FRP) sheets is also among potential promising approaches to improve mechanical performance of timber members. This paper presents compression test results of medium strength circular glulam columns externally jacketed with carbon fiber reinforced polymer (CFRP) sheets to enhance the structural behaviour of timber columns. In the experimental program, 6 reference and 6 externally jacketed circular glulam columns were prepared with three different diameters and tested under uniaxial compression loading. The aim of this research is to investigate the failure modes and to obtain stress-strain relationships of these columns before and after jacketing with CFRP sheets. The external jacketing of glulam columns with CFRP sheets has resulted in significant improvement in deformability. However, in contrast, the confinement effect was not that significant for some strengthened specimens due to the presence of knots at the outer surface. In addition, generally, there was a slight gain in compression strength due to external jacketing as well.

KEYWORDS

CFRP, Compression, Fiber reinforced polymers, Glulam, Timber columns.

INTRODUCTION

Sustainable design concept has progressed very rapidly in the field of civil engineering for the past decade due to increasing ecological impacts of building related activities. According to Intergovernmental Panel on Climate Change (2015), buildings in 2010 are responsible for 32% of aggregate final energy use, 19% of energy-related greenhouse gas emission, 37,5% of fluorinated gases and around one-third of black carbon emission. What is worse is that the emission and related energy use due to the buildings might get doubled or potentially even tripled in the following 40 years. To reduce the negative impacts of construction activities, use of wood-based materials in buildings, due to their low carbon emission and low embodied energy, is accelerating. For instance, medium height timber building constructions have become widespread in Canada and further in Australia, USA and Europe. Furthermore, innovative hybrid timber structures have been developed to provide alternative solutions especially for high-rise buildings (Karacabeyli and Lum 2014; Green and Karsh 2012; SOM 2013).

On the other hand, there are several studies that aim to strengthen the timber structural elements. One approach for strengthening timber members is using fiber reinforced polymer (FRP) composites. Advanced FRP composite usage is a recent strengthening technique speeding up within the construction market. FRP composites have a high strength-to-weight ratio, high durability and corrosion resistance. Being lightweight, they are also easily applicable for any geometry. In order to strengthen and enhance the durability of current and new building members including historical buildings, FRP strengthening techniques have provided effective solutions against structural damages caused by corrosion, cracks, impacts, and earthquakes (Hollaway 2003). One of the pioneering

design guidelines on FRP strengthening techniques for existing timber structures has been published by National Research Council (2007). Use of FRP strengthening techniques on timber building members have led to several new structural solutions: for long-span beams such as glued-laminated timber with FRP shear and flexural reinforcement (Gentry 2011), for slabs such as FRP-glulam slab systems (Jorge et al. 2011), and for connections such as CFRP reinforced bolted glulam beam-column connection (Song et al. 2016). Nevertheless, the studies on FRP strengthening techniques in the case of timber columns are in earlier stages. FRP confinement of massive and cracked timber wood specimens was the focus of previous studies about timber columns (Najm et al. 2007; Zhang et al. 2011). In the study of Najm et al. (2007), FRP confinement of clear poplar wood specimens with 57 mm diameter has resulted in improvements in strength, stiffness, and also ductility. However, FRP confinement of engineering wood products with larger cross-sectional area needs to be investigated further in order to understand the effects of confinement on timber columns with the presence of knots at the outer surface and inner part of the wood. In this paper, it is aimed to assess the possible enhancement in the structural compressive behaviour of glulam columns due to external CFRP jacketing. For the experimental program, 6 reference and 6 externally CFRP jacketed circular glulam columns were prepared with three different diameters. In total, 12 medium strength circular glulam column specimens were tested under uniaxial compression loading and test results are presented based on the damage mechanisms, failure modes and the stress-strain relationship of these columns before and after jacketing with CFRP sheets.

SPECIMENS AND MATERIALS

Glue laminated timber columns made of Norway spruce were GL24h class which is manufactured according to EN 14080 (2013), due to the availability and wide range of usage in Turkish and European construction markets. The column specimens were cut from the same batch and stored in the laboratory of Istanbul Technical University. The test program consists of 6 confined and 6 reference column specimens, in total 12 circular glulam columns, with the diameters of 135, 170 and 195 mm. The height of the specimens was set as two times of each columns' diameter. The average moisture content was 13,5 % at room temperature and the average density was 0,462 g/cm³ with the standard deviation 0,032 g/cm³. Characteristic compressive strength and elastic modulus of the timber columns were respectively 24 MPa and 11,6 GPa. The test specimens are denoted according to their cross-sectional shape (C: Circular), diameter and lastly the number of CFRP plies used for confinement. For example; C-135-1a represents a circular specimen with a diameter of 135 mm, jacketed with 1 ply of CFRP sheets. The mechanical properties of CFRP sheets (339 g/m²) were obtained from the specifications of the manufacturer that they obtained based on coupon tests. The elasticity modulus, tensile strength, maximum elongation and thickness of epoxy-impregnated CFRP sheets were 92,39 GPa, 1400 MPa, 1,5 % and 0,533 mm, respectively.

Before the compression tests, except 6 reference specimens, all specimens were externally wrapped with 1 ply of CFRP sheets in the transverse direction with 0-degree orientation. During the jacketing process of the specimens, column surfaces were prepared by sanding, cleaning, forming one layer of epoxy-polyamine primer and one layer of epoxy putty to avoid forming of voids at the interface. Then, CFRP sheets were bonded on the specimens with epoxy adhesive. Before fully jacketing the specimens with CFRP sheets, the organic matrix was mixed and then cooled down to increase the workable time by slowing the chemical reactions between epoxy system components. Furthermore, the jacketing process was carried out carefully using hand pressure to prevent stress concentrations due to surface roughness and to fit CFRP sheets tightly on the specimens. In order to obtain adequate bonding, an overlap of 150 mm was arranged at the end of the wrap. Additional one layer of CFRP sheets was used to confine the ends of specimens better to force the failure to mid-height of the columns. Finally, all specimens were left to dry for two weeks before the tests.

TEST SETUP

In the experimental program, all specimens were tested under uniaxial compression loading using an Amsler universal testing machine that has 5,000 kN loading capacity. Axial and traverse strains are measured respectively by displacement transducers (LVDT) and surface strain gauges (PL-60) to obtain stress-strain diagrams. The top and bottom surfaces of the specimens were smoothed with a capping compound, used for concrete test specimens, to provide even surfaces while loading. Two different gauge lengths were used in order to measure average axial strains by LVDTs. Four transducers with the gauge length equal to specimen height were placed outside of the specimens with 90 deg intervals around the perimeter. Two transducers with the gauge length equal to half of the specimen height were installed on mid-height of the specimens with 180 deg intervals around the perimeter. In addition, two strain gauges were bonded vertically to measure axial strains at mid-height with 180

deg intervals around the perimeter. Transverse strains were also measured at mid-height with horizontally bonded strain gauges. The test setup of the reference and confined specimens are shown in Figure 1.

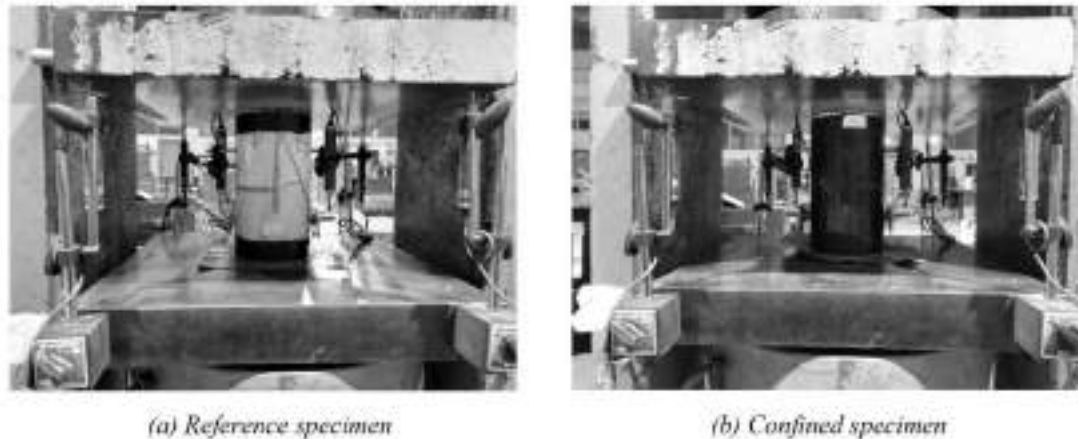
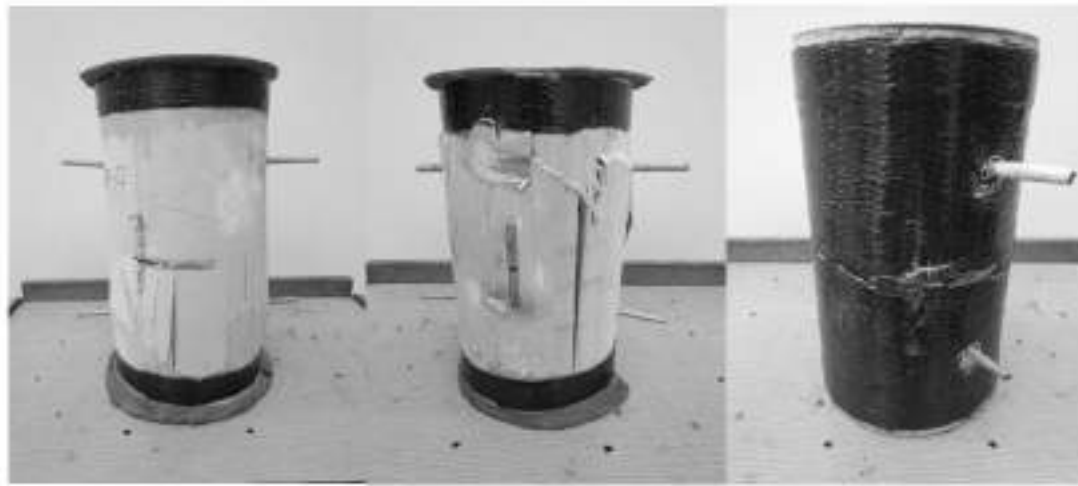


Figure 1: General appearance of the test setup

RESULTS AND DISCUSSIONS

Observed Failure Modes

For the reference specimens, the observed common failure mode was localized compressive failure either at the end or the middle of the samples. Firstly, crushing of timber started with a continuous sound of compression damages when the peak load was reached. Secondly, this was followed with local buckling of wood fibers around the surface. After 85% of the ultimate load was exceeded on the descending branch, circumferential bulging occurred in different parts of the columns (Figure 2a) and tension rupture occurred longitudinally by splitting of timber grains as shown in Figure 2b. For the case of confined timber columns, the observed failure mode was tension ruptures which were propagated vertically in the CFRP jacket at the mid-height of the specimens (Figure 2c). There was not a significant change before the peak load. After the peak load, CFRP jackets suppressed potential damage initiations due to local defects within the timber and limited crack propagation for the specimens C-135-1b, C-170-1a and C-170-1b. CFRP jackets ruptured at about 85% of the peak load at relatively large axial deformations. The fracturing of the CFRP sheets, depending on failure mode of timber, occurred with a dense sound where crushing and buckling of the wood fibers were observed. It demonstrated that the perpendicular-to-grain cracking of timber was successfully restrained by CFRP sheets. For a group of confined specimens, C-135-1a, C-195-1a and C-195-1b, CFRP sheets were ruptured suddenly after the peak load. The fracture of CFRP jacket in the specimen C-195-1b, similar to C-135-1a and C-195-1a, was located at the mid-height where a large knot was pushed toward outside of the jacket (Figure 2d). Even though the CFRP sheets have failed in a brittle manner, the loading was continued until timber itself failed. Therefore, strength loss of these specimens was similar to the reference columns. After the tests, the CFRP jackets of these specimens were removed from timber columns to perform an autopsy. During the autopsy, stress concentrations and local significant residual deformations initiated around the knot were observed as shown in Figure 2e. In addition, all specimens were cut horizontally into several pieces to investigate the inner part of the wood to assess where the failure was initiated. The locations of knots along the failure sections were quite different (Figure 2f): clear wood layer cut from C-195-0a (left), layer cut from C-170-1b with a knot at the inner part (middle), and layer cut from C-195-1b with a knot at the outside surface (right). Most of the specimens underwent asymmetric damages at the weakest layer with defects including the jacketed ones. For the confinement, the adverse effect of large knots especially at the outer surface were more significant compared to small knots at the inner part of the wood. Such relatively large knots particularly close to outer zones apparently caused irregularities, which lead to asymmetric behavior and non-homogeneous deformations resulting in reduced efficiency of FRP jacketing. It should be noted that the specimen C-170-0b, one of the reference specimens, was excluded from the test data base due to incorrect measurements.



(a) Circumferential bulging

(b) Splitting of grains

(c) Tension rupture



(d) Before the autopsy

(e) After the autopsy



(f) Failure sections

Figure 2: Observed failure modes

Effect of Confinement on Stress-Strain Relationships

Elastic modulus, maximum stress and deformability for each specimen were calculated using the compression test results and presented in Table 1. Elastic modulus was calculated as a linear gradient of the stress-strain curve according to the study of Frese et al. (2012). As it can be seen in Table 1 and Figure 3, and as expected, there was not a consistent change in the elastic modulus between the reference and confined specimens. The average strength gains were only 2,08 MPa, 0,63 MPa, and 1,69 MPa in the C-135, C-170 and C-195 series, respectively. These

values correspond to strength enhancements approximately equal to or less than 5%. Deformability was obtained by the ratio of the axial strains corresponding to 85% of the ultimate load on the descending and ascending branches. For all of the specimens, the average axial strains taken from the measurements of two vertical strain gauges and two transducers at the mid-height were used to plot the stress-strain curve before the peak load. After the peak load, the measurements of four displacement transducers measuring the average strain over all height was used since it was not possible use the measurements taken from transducers installed on the specimens and strain gages at mid-height due to local damages of the specimens. The stress-strain relationships of reference and confined specimens are shown in Figure 3 for three series; C-135, C-170, and C-195.

Table 1: Compression test results

Specimens	σ_{max} (MPa)	E_c (MPa)	Deformability
C-135-0a	43,73	11946	4,69
C-135-0b	41,27	12994	3,19
C-135-1a	43,39	12156	4,39
C-135-1b	45,78	14464	8,11
C-170-0a	38,67	12659	3,63
C-170-0b	-	-	-
C-170-1a	39,91	12413	16,38
C-170-1b	38,69	12063	13,39
C-195-0a	42,73	16091	5,21
C-195-0b	39,14	14284	4,62
C-195-1a	42,73	12989	4,31
C-195-1b	42,52	15225	4,64

All of the reference specimens exhibited local compression failure at the peak load. After that, they exhibited a softening behaviour generally with a significant gradual strength loss with increasing axial strains (Figure 3). The best post-peak performance among the reference columns were observed in C-135-0a and C-195-0a specimens in which their failure surfaces were without knots. For a group of the externally jacketed specimens (C-135-1a, C-195-1a, C-195-1b), in contrast to results obtained for clear wood specimens in the study of Najm et al. (2007), no significant improvement of ductility could be obtained with one ply of CFRP jacketing due to stress concentrations around the knots which induced the tension rupture failure of CFRP sheets quite suddenly at around the peak load. However, for other specimens similarly jacketed with one ply of CFRP sheet (C-135-1b, C-170-1a, C-170-1b), the strength was almost constant until considerable axial strains after the peak load and compressive strength could be sustained only with limited degradation until relatively higher axial strains. For instance, the average deformability of confined columns was 4,1 times that of the reference column for the C-170 series. In case of these specimens, CFRP jackets reduced/retarded the adverse effects of local defects and misalignments of wood fibers, leading to enhanced post-peak behaviour of glulam columns. The difference between the post-peak performances of CFRP jacketed specimens can be attributed to the presence and variations of extents of defects of the specimens.

CONCLUSIONS

In this preliminary study, glulam columns with relatively larger cross-sectional areas with respect to previous studies were tested under concentric compression before and after being jacketed with CFRP sheets. The aim of

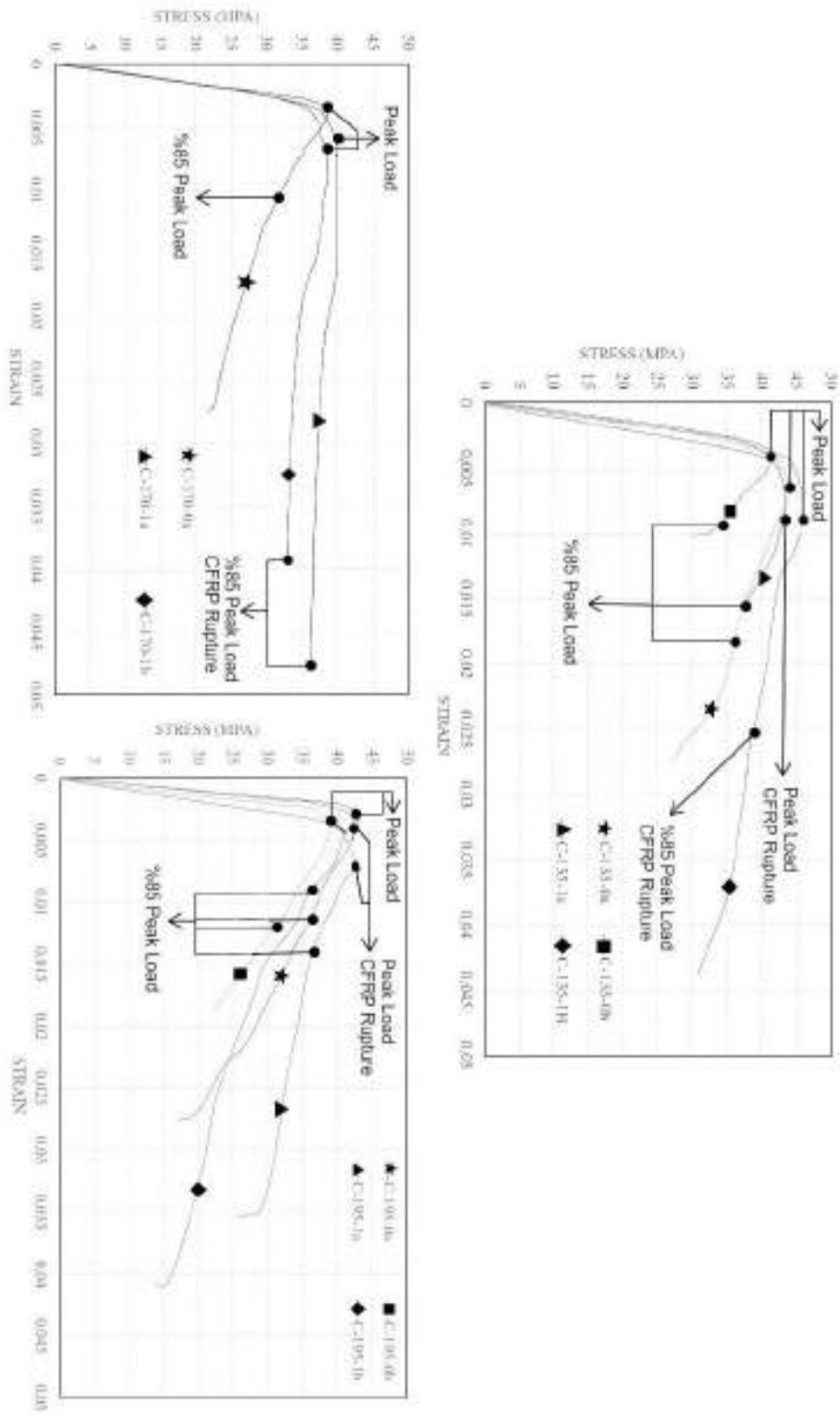


Figure 3: Stress-Strain Relationship of C-135, C-170 and C-195 Series

the study was to better understand the effects of external CFRP jackets on larger timber sections, for some cases with knots on the wood. Although there was a slight gain in strength due to external jacketing, there was no gain in the elastic modulus. CRFP sheets restrained cracking and enlargement of local defects effectively in the inelastic range for a group of externally jacketed specimens. This remarkably improved the deformability of these specimens. However, for some other similar specimens, the positive effect of confinement on deformability was not as pronounced due to the sudden tension rupture of CFRP sheets at around large knots particularly close to outer zones of the wood sections. This demonstrates the vital importance of presence, extent and location of the knots on wood on the confinement effect.

In summary, CFRP jacketing provided a high level of energy absorption by increasing the ultimate axial deformations and providing a better post-peak response for the specimens without knots or with knots at the inner part of wood, whereas improvement was limited on the ultimate axial deformations for similar specimens with large knots on the outer surface.

Obviously, more research is required to confirm the performance of composite columns consisting of glulam and CFRP jackets. In future studies, the effects of stiffness of FRP jackets should also be addressed.

ACKNOWLEDGMENTS

This research project was funded by Dow Aksa and Asmaz Company. Their contributions are greatly appreciated. The authors also wish to thank Dr. C. Demir and Mr. I. H. Sisman for the assistance during the preparation of specimens.

REFERENCES

- EN 14080 (2013). "Timber structures. Glued laminated timber and glued solid timber. Requirements", *European Committee for Standardization*, Bruxelles, Belgium.
- M. Frese, M. Enders-Comberg, H.J Blaß, P. Glos (2012). "Compressive strength of spruce glulam", *European Journal of Wood and Wood Products*, 70(6), 801-809.
- T.R Gentry (2011). "Performance of glued-laminated timbers with FRP shear and flexural reinforcement", *Journal of Composites for Construction*, 15(5), 861-870.
- M. Green, J. Eric Karsh (2012). "Tall Wood. The Case for Tall Wood Buildings. How Mass Timber Offers a safe, economical, and Environmentally Friendly Alternative for Tall Building Structures", *British Columbia*, 1-237.
- L. C Hollaway (2003). "The evolution of the way forward for advanced polymer composites in the civil infrastructure", *Construction and Building Materials*, 17, 365–378.
- Intergovernmental Panel on Climate Change (2015). *Climate change 2014: mitigation of climate change* (Vol. 3). Cambridge University Press.
- M. Jorge, J. M Branco, J. Sena-Cruz, J. A Barros, G. Dalfré (2011). "Response of FRP-glulam slab systems under five-point bending load", *International Conference on Advances in Construction Materials Through Science and Engineering*.
- E. Karacabeyli, C. Lum, eds. (2014). *Technical guide for the design and construction of tall wood buildings in Canada*. Pointe-Claire, QC: FPIinnovations.
- H. Najm, J. Secaras, P. Balaguru (2007). "Compression tests of circular timber column confined with carbon fibers using inorganic matrix", *Journal of Materials in Civil Engineering*, 19(2), 198-204.
- National Research Council (2007). "Guidelines for the design and construction of externally bonded FRP systems for strengthening existing timber structures", *CNR DT 201*, 2005, Rome, Italy.
- X. Song, Y. Ma, X. Gu, M. Wang (2016). "Carbon Fiber-Reinforced Polymer Reinforcement for Rotational Behavior of Bolted Glulam Beam-to-Column Connections", *Journal of Composites for Construction*, 21(3): 04016096.
- SOM (Skidmore, Owings, and Merrill) (2013). *Timber tower research project: Final report*, WoodWorks Education Lab, Chicago.
- W. Zhang, X. Song, X. Gu, H. Tang (2011). "Compressive behavior of longitudinally cracked timber columns retrofitted using FRP sheets", *Journal of Structural Engineering*, 138(1): 90-98.



WIDTH EFFECT OF FRP EXTERNALLY BONDED TO TIMBER

Abbas Vahedian¹, Dr Rijun Shrestha¹, Prof Keith Crews¹

¹ School of Civil and Environmental Engineering, University of Technology, Sydney, Australia (corresponding author: abbas.vahedian@student.uts.edu.au)

ABSTRACT:

Bond mechanism between timber and fibre reinforced polymer (FRP) composites is affected by a number of variables. However, effect of parameters such as bond width, bond length, material properties and geometries on the bond strength is not fully understood. This study investigates the influence of bond width on the bond strength and failure mode of externally bonded FRP-to-timber interface. Pull-out tests on 136 FRP-to-timber joints with different FRP widths were conducted. Results of experimental tests showed that the bond width has significant effect on the bond strength; with the increase of FRP width, the interfacial bond strength increases. In addition, it was observed that the maximum shear stress decreases with the increase of FRP-to-timber width ratio. Furthermore, FRP-to-timber width ratio impacts on the local bond-slip in which slip of the bond reduces when this ratio is increased.

KEYWORD: Bond strength, Width effect, LVL, FRP, Bond-Slip.

INTRODUCTION

In recent years, fibre reinforced polymers (FRPs) have received significant attention by civil engineers as an alternative material for repair and/or strengthening of structures because of their excellent characteristics. FRP is a powerful and viable alternative to steel when considered as a retrofitting material for timber structures. FRPs are light, highly resistant to corrosion, cost effective and have superior strength and stiffness properties and its specific strengths remain high at elevated temperatures (Hollaway 2010; Soleimani 2006). These composites have lately become a mainstream technology for strengthening of infrastructures such as steel, concrete and more recently, timber and masonry structures (Soleimani 2006). As a composite strengthening material, externally bonded (EB) FRP has valuable advantages and in some cases, is the only reasonable and applicable material that can be used for retrofitting, particularly in places where it is impossible to gain access for heavy machinery (Motavalli and Czaderski 2007).

However, one of the most common problems associated with the use the externally bonded FRP sheets is the premature failure due to debonding, which limits the full utilisation of the material strength of the FRP (Khelifa and Celzard 2014; Wu and Hemdan 2005). Debonding has been identified as the single most important failure mechanism of retrofitted beams (Kabir et al. 2016) that occurs at much lower FRP strains than its ultimate strain. Debonding directly impacts the total integrity of structure, with the subsequent outcome that the ultimate capacity and desirable ductility of the structure may not achieved. Therefore, for the safe and economic design of externally bonded FRP systems, particularly when FRP is attached to timber, a sound understanding of the behaviour of FRP-to-timber interfaces needs to be developed and consequently, further understanding of the bond is essential.

The bond mechanism between timber and FRP is relatively complex and is influenced by a number of variables. A number of studies have been carried out experimentally (Cao et al. 2007; Mazzotti et al. 2008) and theoretically (Dai et al. 2006; Ferracuti et al. 2007) to address the behaviour of FRP bonded to concrete substrates. Many studies have been conducted (both theoretically and experimentally) to predict the initiation of debonding in retrofitted concrete beams, and also the ultimate load that the composite layers can resist prior to debonding (Achintha and Burgoyne 2013). However, different failure modes when FRP is externally bonded to timber have not been fully investigated and limited attempts have been made to investigate the bond behaviour of FRP to timber joint (D'Ambrisi et al. 2014) and the developed theories to date mostly cover FRP-to-concrete joint (Chen and Teng 2001; Dai et al. 2005).

Whilst FRP-timber bond behaviour has been previously investigated (Wan 2014) the importance of bond width and FRP-to-substrate ratio which has a major impact on the bond strength of FRP-concrete joint (Chen et al. 2001;

Kim and Harries 2010) has been ignored. Consequently, further understanding of the effectiveness of the bond width is essential. The main intention of the current study is to scrutinise the effect of bond width on the bond strength, bond stress and the local slip of externally bonded FRP to timber. Results of experimental tests showed that the bond width significantly impacts on the bond strength; with the increase of the FRP plate width, the interfacial bond strength increases and interface reaches higher level of load. Conversely, at the same level of applied load, experimental results illustrated that the local slip decreased when wider FRP bonded to timber. In addition, the maximum bond stress decreased with the increase of FRP-to-timber width ratio.

DETAILS OF RESEARCH PROJECT

In total, 136 modified single shear CFRP-to-timber joints were fabricated and tested. Two different types of timber were used, namely Laminated Veneer Lumber (LVL) (using softwood species) and hardwood sawn timber. The LVL samples consisted of 320 and 370 mm long with a 110 mm x 65 mm cross section, and the overall dimension of hardwood samples were 320 mm long x 110 mm wide x 35 mm deep. One and two plies of unidirectional wet-lay up of CFRP (MBRACE™) with the nominal thickness of 0.117 mm were externally bonded with an epoxy base (Sikadur®330) to the timber. The hardwood samples contained bond width of 45 mm and bond lengths of 50 mm, 100 mm, 150 mm and 200 mm. However, in the LVL series, three different bond widths with five different bond lengths (50 mm, 100 mm, 150 mm, 200 mm and 250 mm) have been fabricated and tested. Strain gauges were attached to the CFRP surface to measure the strain variation of the bond during the experiment. Results of LVL series are presented in this study since the widths vary in LVL samples and only one bond width was considered hardwood specimens.

Compressive and tensile tests for timber and tensile tests for FRP coupons were conducted as per the respective standards (ASTM-D3039/D3039M 2014; BS_EN_408 2010) to establish the measure mechanical properties of the timber and FRP. A modified single shear test setup was adopted to accurately monitor bond behaviour of FRP-timber joint as shown in Figure 80. The timber block was restrained in a steel rig and load was applied to the free end of the FRP. The slip between timber and CFRP was measured by one LVDT which was mounted on the surface of timber block. The pull-out tests have been performed using a universal testing machine. More details of the samples tests can be found in the previous studies conducted by the authors (Vahedian et al. 2018).



Figure 80, Test setup and fabricated specimens

EFFECT OF FRP WIDTH ON BONDING STRENGTH

Many factors control the likely occurrence of a debonding failure mode for a FRP strengthened beam. The bond strength is typically defined as the peak load divided by the effective bonded area ($A_{eff} = b_f \times L_{eff}$); where b_f is the width of FRP and L_{eff} is effective bond length. Therefore, bond width and bond length are amongst main parameters

affecting bond strength. The bond length and its influence on the bond strength has been already considered by the authors (Vahedian et al. 2017) and a novel empirical model was derived for the calculation of effective bond length when FRP externally bonded timber joints. In order to monitor the effect of bond width on the bond strength; bond stress; and local slip, three different bond widths namely, 35 mm, 45 mm, and 55 mm have been attached to the surface of LVL as shown in Figure 81. Accordingly, the FRP-to-timber width ratio for these three bond widths are 32%, 41% and 50%. Five specimens were tested for each of the bond widths and selected results are shown Figure 3. Results of experimental tests showed that the bond width significantly impacts on the bond strength; with the increase of the FRP plate width, the interfacial bond strength increases. As shown in Figure 3, the greater the width of FRP plate, the higher the interfacial bond strength of FRP-to-timber for various bond lengths (50 mm, 100 mm, 150 mm and 200 mm). However, this difference is more noticeable for samples with higher FRP-to-timber with ratio (50%). Figure 83 shows the maximum, minimum and average ultimate loads of five specimens in each series under various bond widths and bond lengths. Figure 83c and Figure 83d illustrate that the maximum, minimum and mean loads remained almost constant when the bond length increase from 150mm to 200mm. This condition signifies the concept of effective bond length that there is no benefit in extending the bond length beyond that where there is no increase in the bond strength. Therefore, although increasing bond length increases the area of bond interface, bond strength cannot increase further once the bond length exceeds the effective bond length. On the other hands, the maximum, minimum and average loads increased by around two times when the bond width increased from 35mm to 55mm for all bond lengths. Increasing bond width not only increases the area of the bond interface but also allows the load to be distributed over a larger area resulting in reduced stress concentration. Results obtained from previous work conducted by the authors (Vahedian et al. 2017) showed that the maximum shear stress decreased with the increase of FRP-to-timber width ratio as shown in Figure 84. It is important to note that all bond characteristic and timber type in samples shown in Figure 84 are identical except bond width. This finding is in agreement with the previous studies when the FRP was bonded to concrete (Xu et al. 2015; Ye and Yao 2008). One reason can be highlighted that when FRP-to-timber width ratio is low, the force transfers from the FRP to timber leads to a non-uniform stress distribution across the width of timber leading to fail the interface at lower load level. Furthermore, a smaller FRP width compared to the timber width may result in a higher stress in the bond at failure; directing stress from bonded area to the timber outside of the bonded zone. These findings are consistent with the previous studies conducted by (Xu et al. 2015).

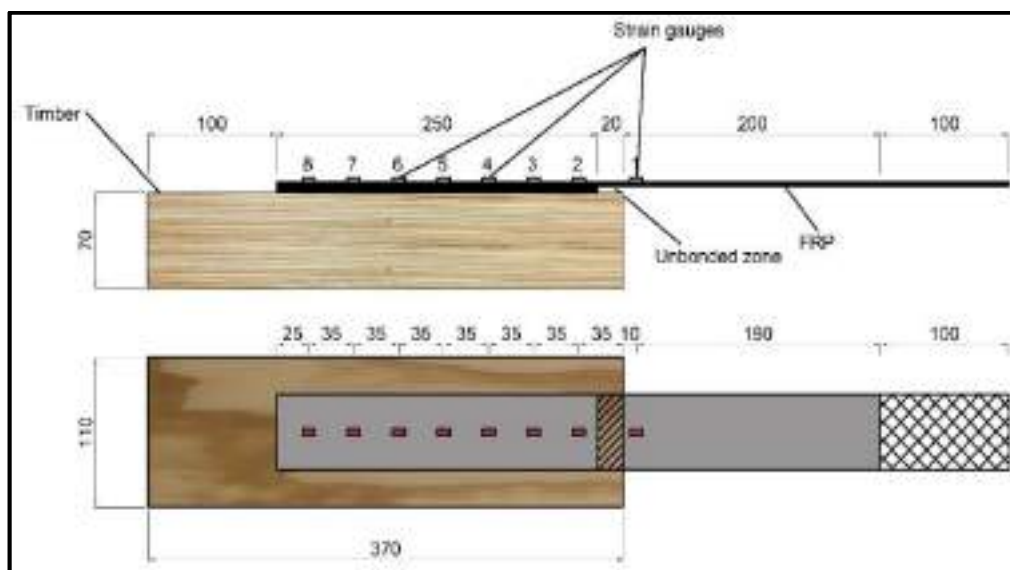


Figure 81, a schematic view of the bond and the strain gauges arrangement

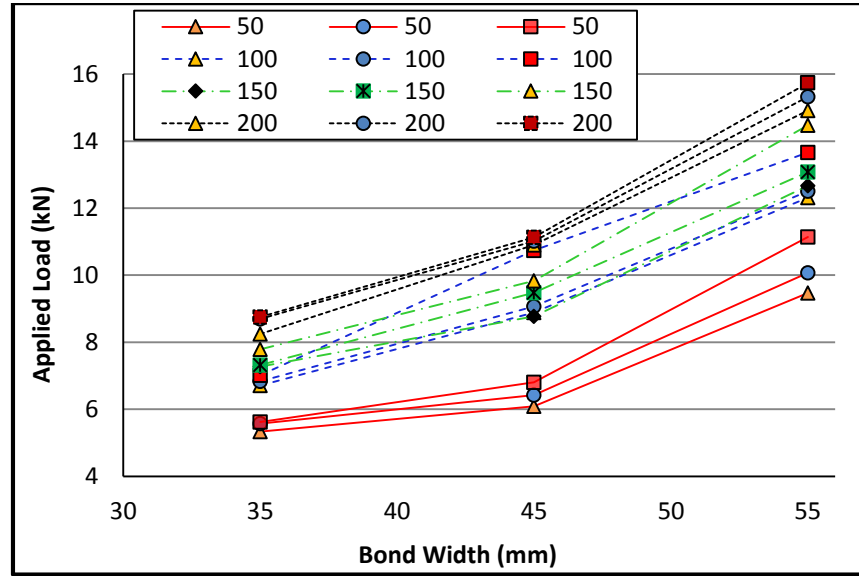


Figure 82, Relationship between applied load and bond width in four different bond lengths

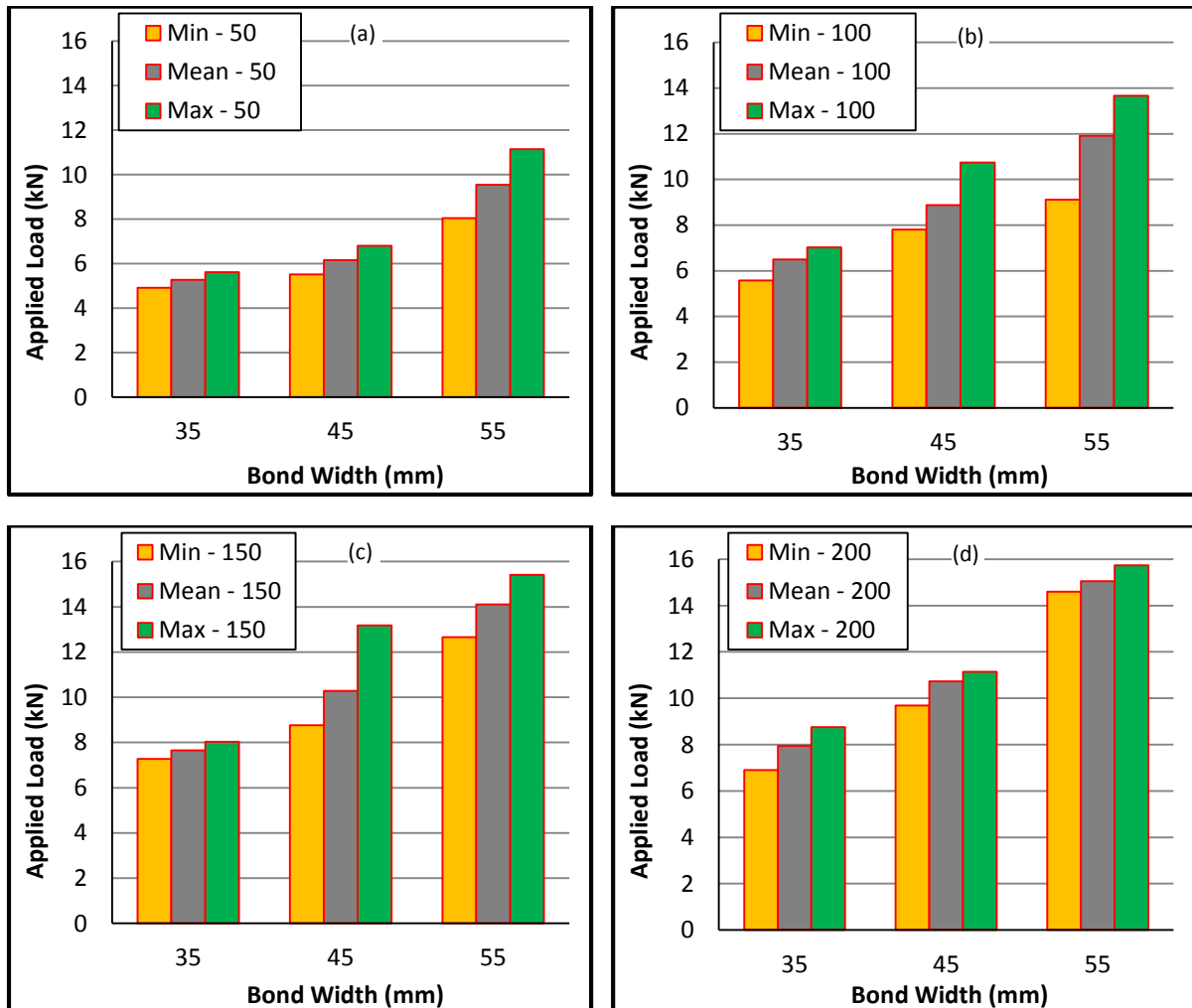


Figure 83, Recorded maximum, minimum and average loads for 35mm, 45mm and 55mm bond widths for four different bond lengths

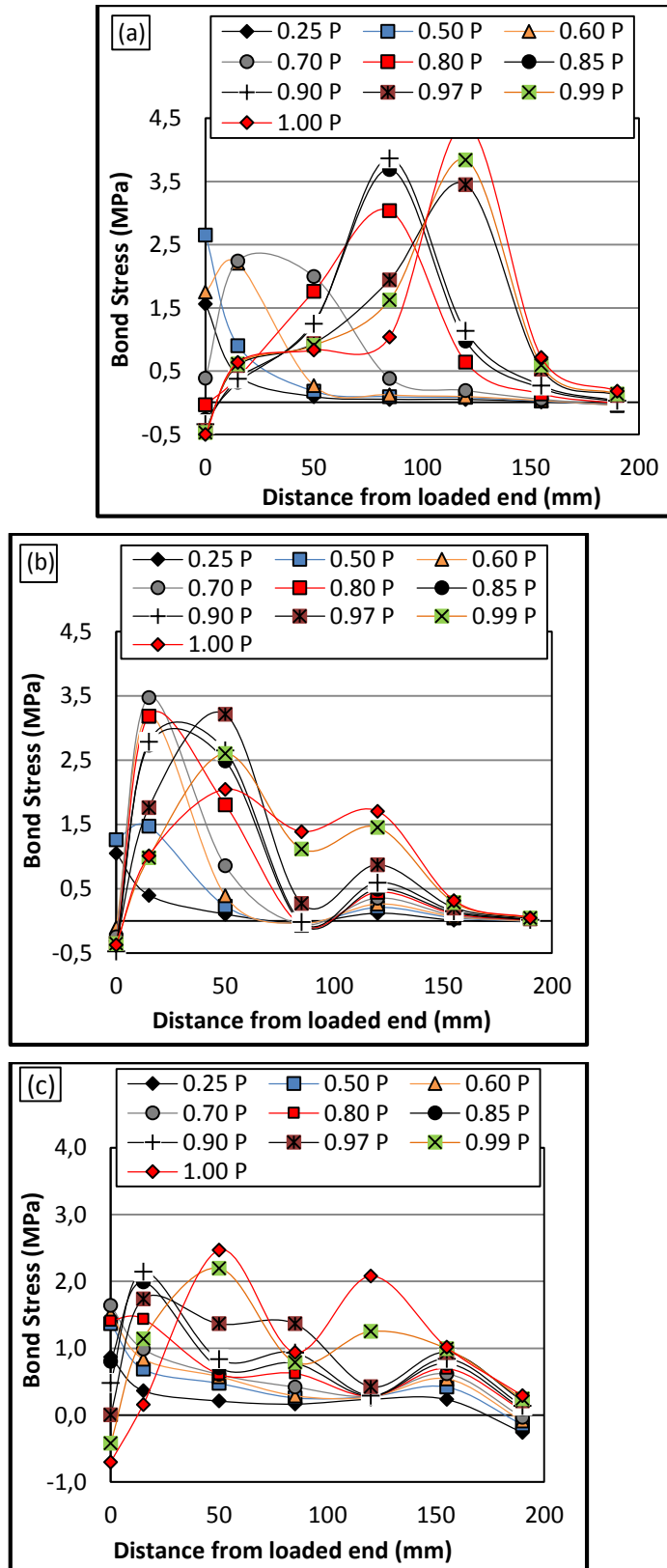


Figure 84, Relationship between bond stress and FRP-to-timber width ratio; (a) 32% LVL 200-35-01-2, (b) 41% LVL 200-45-01-4, and (c) 50% LVL 200-55-01-5

EFFECT OF FRP WIDTH ON LOCAL SLIP

The slip between timber prism and CFRP was measured by a LVDT mounted on the surface of timber block. Figure 6 shows typical stress versus slip curves along bonded length for FRP with 35mm, 45mm and 55mm width; with FRP-to-timber width ratio 32%, 41% and 50%, respectively. The bond lengths of the selected samples shown in Figure 6 are 100mm, 150mm and 200mm. As can be seen, specimens with wider FRP sheet exhibited higher slope in the initial elastic deformation. The slip increases linearly at lower stress in the bond, indicating that there is no interfacial softening or debonding along the interface. However, when the debonding occurs at the FRP-to-timber interface, there is a rapid increase in slip with increasing applied load and then slip tends to plateau until failure. In addition, with the increase of FRP width, the slip is lower at the same stress level, resulting to decrease the ultimate interfacial slip at the bonded joint. In Figure 6 (b), for instance, when the bond stress is around 1.5MPa, the average slips of 0.88mm, 0.76mm and 0.64mm were recorded for specimens where the FRP widths are 35mm, 45mm and 55mm, respectively. Similar trend observed in the other tested series is shown in Figure 6 (a) and Figure 6 (c). This finding is in agreement with the previous studies when the FRP was bonded to concrete (Chen and Pan 2006; Xu et al. 2015; Ye et al. 2008). This phenomenon may be due to distribution of load over a larger area of the bond. When FRP-to-timber width ratio is large enough, a larger area of the bond is active and the stress distributes more uniformly across the width of timber leading to fail the interface at higher load level. Nevertheless, debonding starts when the relative slip between FRP and timber exceeds the ultimate slip. At this point, the ultimate load that can be carried out by FRP plate is attained and simultaneously, the effective bond zone is being shifted towards the free end of the bond. Therefore, the ultimate load (P_u) remains almost constant.

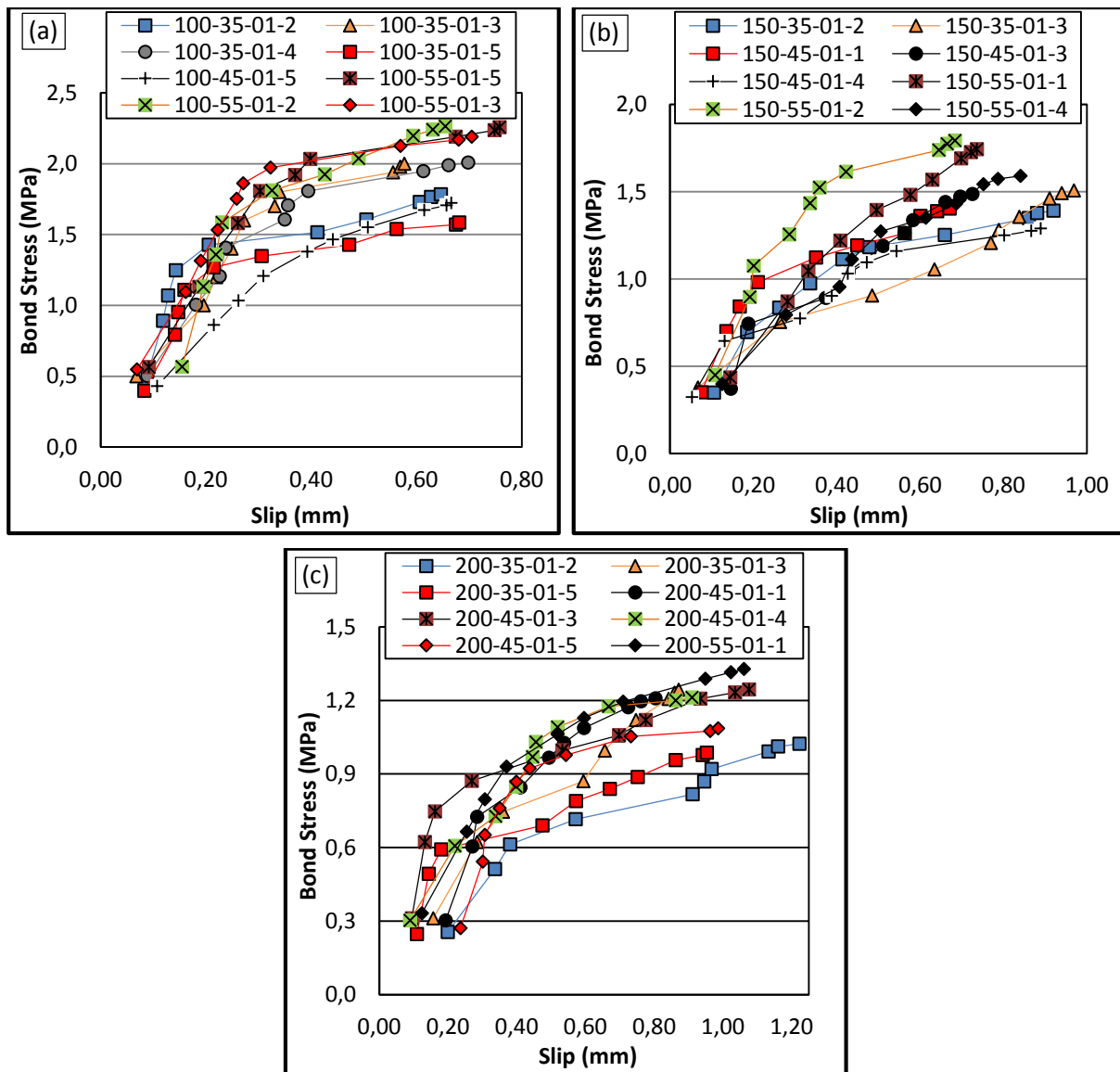




Figure 85, Relationship between local slip and bond width

CONCLUSION:

This paper presents the results of a series of tests for investigating influence of bond width on the bond strength, local slip and bond stress when FRP sheets are externally bonded to timber. It was observed that with increase of FRP plate width, the interfacial bond strength increases whilst the interfacial slip during the softening-debonded stage decreases. The bond strength doubled when the FRP width was increased by about 60%. This is because when FRP width is lower than timber prism, the FRP-timber interface is subjected to higher stress concentration, especially at the edges of FRP. Furthermore, samples with higher FRP-to-timber width ratio exhibited lower slip at the same level of applied load. That is because the interface has a higher effective bonded area that leads to more uniform stress distribution across the width of timber.

ACKNOWLEDGEMENT:

The authors wish to acknowledge the support provided by Australian Government Research Training Program Scholarship. The support of Sika Australia Pty. Ltd., who supplied the materials for this study, is gratefully acknowledged.

REFERENCES:

- Achintha, M. & Burgoyne, C. 2013, 'Fracture energy of the concrete-FRP interface in strengthened beams', *Engineering Fracture Mechanics*, vol. 110, pp. 38-51.
- ASTM-D3039/D3039M 2014, *Standard test method for tensile properties of polymer matrix composite materials*, West Conshohocken, PA, USA,.
- BS_EN_408 2010, *Timber structures - structural timber and glued laminated timber - determination of some physical and mechanical properties*, British Standards Institution, London, UK,.
- Cao, S., Chen, J., Pan, J. & Sun, N. 2007, 'ESPI measurement of bond-slip relationships of FRP-concrete interface', *Journal of Composites for Construction*, vol. 11, no. 2, pp. 149-160.
- Chen, J. & Pan, W. 2006, 'Three dimensional stress distribution in FRP-to-concrete bond test specimens', *Construction and Building Materials*, vol. 20, no. 1, pp. 46-58.
- Chen, J. & Teng, J. 2001, 'Anchorage strength models for FRP and steel plates bonded to concrete', *Journal of Structural Engineering*, vol. 127, no. 7, pp. 784-791.
- D'Ambrisi, A., Focacci, F. & Luciano, R. 2014, 'Experimental investigation on flexural behavior of timber beams repaired with CFRP plates', *Composite Structures*, vol. 108, pp. 720-728.
- Dai, J., Ueda, T. & Sato, Y. 2005, 'Development of the nonlinear bond stress-slip model of fiber reinforced plastics sheet-concrete interfaces with a simple method', *Journal of Composites for Construction*, vol. 9, no. 1, pp. 52-62.
- Dai, J., Ueda, T. & Sato, Y. 2006, 'Unified analytical approaches for determining shear bond characteristics of FRP-concrete interfaces through pullout tests', *Journal of Advanced Concrete Technology*, vol. 4, no. 1, pp. 133-145.
- Ferracuti, B., Savoia, M. & Mazzotti, C. 2007, 'Interface law for FRP-concrete delamination', *Composite structures*, vol. 80, no. 4, pp. 523-531.
- Hollaway, L.C. 2010, 'A review of the present and future utilisation of FRP composites in the civil infrastructure with reference to their important in-service properties', *Construction and Building Materials*, vol. 24, no. 12, pp. 2419-2445.
- Kabir, M.I., Shrestha, R. & Samali, B. 2016, 'Effects of applied environmental conditions on the pull-out strengths of CFRP-concrete bond', *Construction and Building Materials*, vol. 114, pp. 817-830.
- Khelifa, M. & Celzard, A. 2014, 'Numerical analysis of flexural strengthening of timber beams reinforced with CFRP strips', *Composite Structures*, vol. 111, pp. 393-400.
- Kim, Y.J. & Harries, K.A. 2010, 'Modeling of timber beams strengthened with various CFRP composites', *Engineering Structures*, vol. 32, no. 10, pp. 3225-3234.
- Mazzotti, C., Savoia, M. & Ferracuti, B. 2008, 'An experimental study on delamination of FRP plates bonded to concrete', *Construction and Building Materials*, vol. 22, no. 7, pp. 1409-1421.
- Motavalli, M. & Czaderski, C. 2007, 'FRP composites for retrofitting of existing civil structures in Europe: state-of-the-art review', *Proceedings of the American Composites Manufacturers Association 2007*.



- Soleimani, S.M. 2006, 'Sprayed glass fiber reinforced polymers in shear strengthening and enhancement of impact resistance of reinforced concrete beams', The University of British Columbia, Vancouver, Canada.
- Vahedian, A., Shrestha, R. & Crews, K. 2017, 'Effective bond length and bond behaviour of FRP externally bonded to timber', *Construction and Building Materials*, vol. 151, pp. 742-754.
- Vahedian, A., Shrestha, R. & Crews, K. 2018, 'Analysis of externally bonded Carbon Fibre Reinforced Polymers sheet to timber interface', *Composite Structures*, vol. 191.
- Wan, J. 2014, 'An investigation of FRP-to-timber bonded interfaces', The University of Hong Kong Pokfulam, Hong Kong.
- Wu, Z. & Hemdan, S. 2005, 'Debonding in FRP Strengthened Flexural Members with Different Shear-Span Ratios', *Proceeding of the 7th International Symposium on Fiber Reinforced Composite Reinforcement for Concrete Structures*, vol. 1, Michigan, USA, pp. 411-426.
- Xu, T., He, Z., Tang, C., Zhu, W. & Ranjith, P. 2015, 'Finite element analysis of width effect in interface debonding of FRP plate bonded to concrete', *Finite Elements in Analysis and Design*, vol. 93, pp. 30-41.
- Ye, F. & Yao, J. 2008, 'A 3D Finite Element Study on The Effect of FRP Plate Width on Interfacial Stress between FRP and Concrete [J]', *Bulletin of Science and Technology*, vol. 24, no. 6, pp. 853-859.



*9th International Conference on Fibre-Reinforced Polymer (FRP) Composites
in Civil Engineering (CICE 2018), PARIS 17-19 JULY 2018*

All FRP Structures

BRIDGE PARADIS NORWAY: DESIGN AND ENGINEERING OF A 42M SPAN FULL FRP FOOTBRIDGE

Liesbeth Tromp¹, Kees van IJselmuiden², Stian Persson³

¹ Liesbeth.Tromp@RHDHV.com, Royal HaskoningDHV, Infrastructure, Rotterdam, The Netherlands;

² Royal HaskoningDHV, Infrastructure, Amsterdam, The Netherlands; ³ Norwegian Public Roads Administration-Statens vegvesen, Bridge Department Region West, Bergen, Norway;

Keywords : All FRP and smart FRP structures; Case studies ; Codes, standards and design guidelines; Durability, long-term performance

Mini-Symposium: "Full FRP system: design and standard"

ABSTRACT:

This paper presents the engineering story behind the bridge Paradis, Bergen, Norway. It is a full Fiber Reinforced Polymer (FRP) tender design, prepared by Royal HaskoningDHV. The material and detailing have been optimised for the application in the Norwegian wet and cold climate. Statens vegvesen requires a low maintenance solution to minimise life cycle costs and hindrance for traffic on road and rail. The choice for FRP was made to prevent durability issues due to thermal fatigue and salting in winter times.

With its free span of 42m, this bridge is one of the longest spans for bridges in full FRP worldwide. A team of architects and engineers of RoyalHaskoningDHV prepared the design in close cooperation with a multi disciplinary team of the Client, Statens vegvesen. This way of work contributed to the confidence in FRP design and developing design and engineering protocols for FRP structures in Norway. In the design use was made of the latest insights in FRP design, safety concepts and material safety factors. Structural challenges involved connections, stability of FRP members and behaviour of FRP material and connections under sustained loading. This paper presents the interaction of design, material and manufacturing process from an engineering perspective. It describes the results of the structural analysis and highlights the principle of the solutions for reliable and easy to assemble connections.



Figure 86. Bridge Paradis, Bergen, Norway

INTRODUCTION

The design of the FRP bridge at Paradis aims to realise an aesthetically pleasing FRP structure, that is optimised to be cost effective and maximises durability by choice of material, minimising the number of connections and clever detailing. The main motivation for Statens vegvesen to look into FRP structures is the policy emphasising durable infrastructure crossing high traffic roads and railways that minimises demand for periodic maintenance. For lightweight long span bridges human induced vibrations are one of the main design governing parameters. Dynamic analyses formed an important part of the engineering, to determine the level of comfort the pedestrians will experience on the bridge. For this design also buckling is governing, as the design has some long slender members loaded in compression.

Finite element analyses have been carried out to determine the dimensions and the behaviour under among others traffic loads and wind loads, based on analyses including Eigenfrequency analyses and global buckling analyses. In this paper the tender design of the bridge Paradis is described and design choices are explained, relating to aspects of the architecture, structure, material and manufacturing process.



ARCHITECTURE SKETCH

The structure has been designed by RoyalHaskoningDHV architect Joris Smits. Several concepts have been developed, see *Figure 2*. The abutment is located on rocks, which provides an opportunity for clamped supports. However, Statens vegvesen does not prefer clamped supports in this situation, due to the uncertainty in the capacity of the rocks combined with a new type of material.



Figure 87. Architecture sketch Bridge Paradis

Concept 3 was preferred and selected by Statens vegvesen. This structural concept is a faceted arch structure and reminds slightly of the stainless steel truss bridge, which was considered in an earlier design study.

Design for durability

The design is based on Fibre Reinforced Polymer (FRP). Durability is further maximised by the following design measures:

- Selection of vinylester resin, a high grade chemically resistant resin type.
- Application of conservative design factors (conversion factors for wet conditions)
- Design based on high grade manufacturing technique such as vacuum infusion.
- Minimising the number of connections.
- Detailing to minimise moisture or dirt ingress.

The design consists of a profile based upper structure and an integrated monocoque deck. The fiber reinforcement used in the tender design is E-glass. Carbon Fiber reinforcement has been considered in case additional stiffness was needed, but it was found that sufficient stiffness and strength could be realised using standard glass fiber reinforced polymer (GFRP). The design makes use of stainless steel connectors. The foundation is made out of concrete.

Structural principle

The structure acts as an arch structure and has stays supporting the deck. The upper beams are loaded in compression. The stays are FRP tubes and loaded in tension, see *Figure 88*.

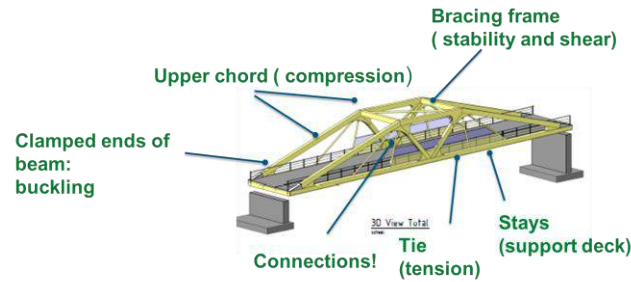


Figure 88. Structural members bridge Paradis

The diagonal beams and transverse beams of the superstructure form a stabilising portal for the top chords, from which the bridge deck is supported.

Dimensions

The global dimensions of the bridge are depicted in Figure 89. Initial calculations on a simplified structure were used to determine the global dimensions. In the materialisation phase the height and cross section of the beams were further adjusted to fit the structural and functional needs.

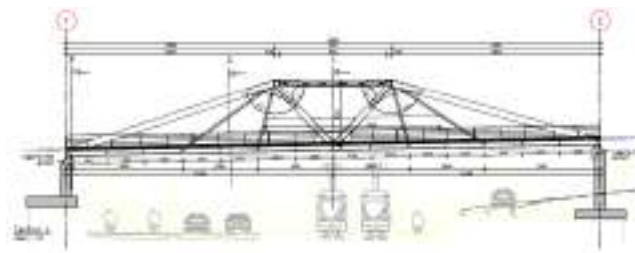


Figure 89. Global dimensions bridge Paradis

The height of the superstructure is 5.5 m. Typical dimensions of the beams of the superstructure are around 0.55 m * 0.50 m.

Connections

The constituting members and connections are seen in Figure 90. The lower chord that functions as the tie has been designed as a continuous member.

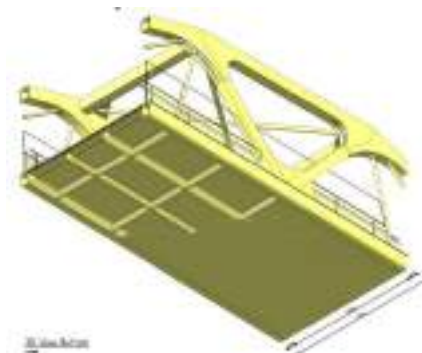


Figure 90. Principle of the connections

Connections of the profiles

The connection of profiles to profiles and the stays to the lower chord have been designed as hybrid bolted and adhesive connections. The adhesive prevents moisture ingress in the bolt holes. Due to the high forces at the location of the bolted connections, the thickness of the laminate must be increased locally. Compressive forces are also transmitted by contact, requiring close tolerances.

In the nodes stainless steel inserts have been applied for ease of assembly and create high strength load transfer in x,y and z-directions, see *Figure 91*. To connect the top chord beams, a stainless steel insert is used. The connection insert consists of a stainless steel web plate welded to tube profiles, see *Figure 91*. Stainless steel is the preferred material for the connectors, because in FRP the connection of the web to the tube is complicated and the strength for an FRP connector will be lower.

The length of the stainless profiles depends on the number of bolts required to transfer the forces. The connection will be a combined adhesive and bolted connection, where each connection type individually will have 100% of the required capacity.

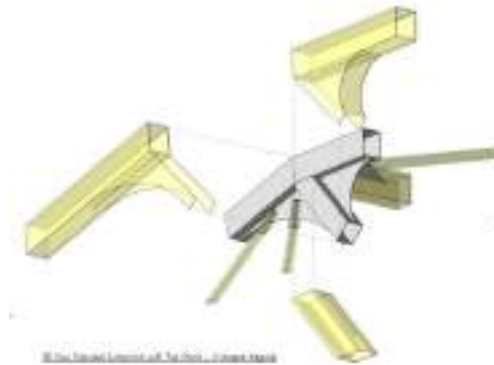


Figure 91. Principle of profile connection

Connections of the deck

The deck sections are built up using prefabricated FRP integrally produced or laminated parts using adhesive and laminated connections. At strategic locations bolted connections and shear studs may be introduced as a structural back up and for reasons of assembly.

Design Standards

The design is elaborated in accordance with the Eurocodes and the Norwegian National annexes. The specific requirements for this design phase have been captured in an AIP (Approval In Principle), which included the Client specific requirements by Statens vegvesen. For the FRP structures use has been made of the CUR96 [1] and Eurocomp Design Code [2]. These codes provide among others FRP specific partial material factors and guidance for the design of connections. Use has been made of latest insights from design guidance development (revision of CUR96, CUR96;2017) and discussions on European level (CEN-TC250 WG4).

Structural analysis

Finite Element software SOFiSTiK version 14.10-30 is used for the analysis of the FRP bridge Paradis structures and the concrete foundation. The software is used for the analysis of the stresses and stability (ULS) and deformations (SLS) of the bridge structure. The design choices are agreed with the technical experts of Statens vegvesen.

FE Model

The model of the bridge structure uses 2D shell elements for the deck structure and 1D beam elements for the superstructure and stays, see *Figure 92*.



Figure 92. FE model bridge Paradis

The bearings are modelled as springs with an infinite stiffness. The spring is connected to a node. Per spring axis a separate spring element has been created. This element is later on used to get the spring force. For the expansion joint a node at deck level is inserted. The translations and movements for this node are used as input for the expansion joint design.

Materials

The materials used In the FE analysis are of type anisotropic GFRP55, a balanced, symmetric lay up of glass fiber reinforced vinyl ester with fibers distribution of [55%/15%/15%/15%] in orientations [0°/90°/45°/-45°] and quasi-isotropic GFRP with distribution of [25%/25%/25%/25%] in orientations [0°/90°/45°/-45°]. The strongest and stiffest direction of the anisotropic material is in line with the local x-axis of the members. The material properties are given in Table 34.

Table 34. Material properties GFRPQI and GFRP55

Property		GFRP QI GFRP Quasi isotropic [0°/90°/45°/-45°] [25%/25%/25%/25%]s	GFRP 55 GFRP anisotropic [0°/90°/45°/-45°] [55%/15%/15%/15%]s
Fiber volume fraction	V_f	50%	50%
Young's modulus in x- direction	E_x [N/mm ²]	18600	25800
Young's modulus in y- direction	E_y [N/mm ²]	18600	15900
In plane shear modulus in xy- direction	G_{xy} [N/mm ²]	7000	5600
Density	ρ [kg/m ³]	1850	1850
Axial strength x- direction	$f_{x,Rk}$ [N/mm ²]	223	310
Axial strength y- direction	$f_{y,Rk}$ [N/mm ²]	223	191
In plane Shear strength xy-direction	$\tau_{xy,Rk}$ [N/mm ²]	112	90
Inter laminar shear strength	$\tau_{ILSS,Rk}$ [N/mm ²]	20	20
Thermal expansion coefficient in x-direction	α_x [mm/(mm·K)]	1.3E-005	1.07 E-005

In the next design phase, further optimisation of the material lay ups is possible. Where more axial stiffness or strength is needed, i.e. in the main members of the superstructure, the percentage of unidirectional fibres can be further increased, or even carbon fibres can be applied in combination with glass fiber reinforcement.

Deformations

The deformations of the bridge under full pedestrian load (5 kN/m²) are seen in Figure 90.

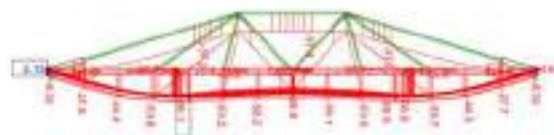


Figure 93. Global deformation [mm]; load 5 kN/m²



The bridge displacement at quarter of the span is larger than at the mid span. The reason for this is that at mid span a stiff V-shaped frame is present and the fact that the outer stay is a less rigid support due to its angle and its slenderness. The deformations are within the opposed limit of $L/350$ under frequent loading conditions (75%), taking into account the applied conversion factors for effects of temperature and moisture effects.

Permanent loads

An important design requirement for Norwegian infrastructure is the ability to resist spike tyres and snow plows, as they are frequently used in winter season. For that reason in the calculations an asphalt layer with an average thickness of app. 50 mm is taken into account. This implies quite high permanent loads, and as FRP is a creep sensitive material the permanent loads are to be considered with the required attention for both deformations as well as strength evaluations. Methods from [1], [2] and [5] were compared and the most conservative factor has been applied in this preliminary stage.

The self weight of the FRP structure is app. 42 tonnes. The estimated weight of asphalt, steel connectors, handrails, etcetera is 45 tonnes! Due to the weight issues in relation to creep and stability, alternative solutions to the asphalt layer will be looked into in the next design phase.

The deformation under permanent load is approximately 44 mm. The forces in the super structure under permanent loads are app. 700 kN (Figure 94). These forces are used for the assessment of the connections. The resulting stresses in the global structure are very low (around 11 MPa) and not critical for the global design.

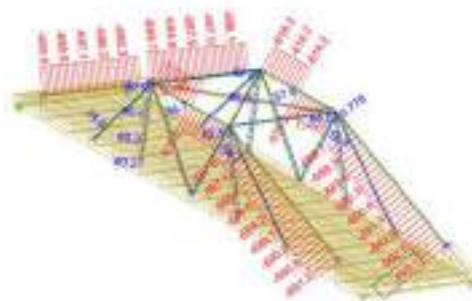


Figure 94. Forces under permanent loads [kN]

Eigenfrequency

For long span footbridges the high strength over stiffness ratio of GFRP means that comfort of the footbridge is an important design criterion. The Eurocode refers to the JRC-technical report on human induced vibrations for footbridges [3], which provides detailed criteria and methods for the analysis. The design requirement prescribes Comfort Class 2 for Traffic Class 3, which implies maximum accelerations of between $0.7 - 1.0 \text{ m/s}^2$ for a pedestrian density of 0.5 person/m^2 .

An important imposed additional requirement, from CUR96, prescribes that between 2.1 Hz – 2.5 Hz the reduction factor Ψ , that takes into account the chances of the occurrence of interlocking, see[3], cannot be taken lower than 0.25, see red line in Figure 95. This restrictive requirement has been added because the accuracy of prediction of eigenfrequency, mass, and changes of mechanical properties over time does not justify the exclusion of interlocking over such a narrow range.

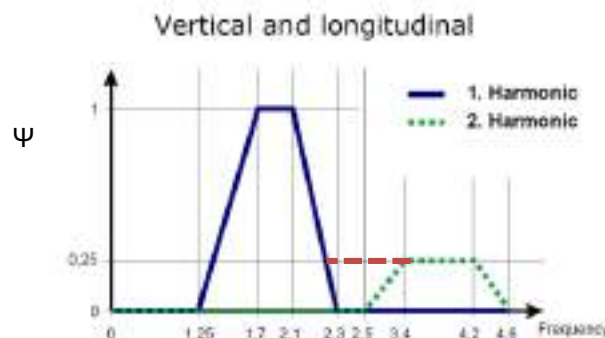


Figure 95. Reduction factor Ψ , [3], with suggested additional restriction (red dashed line)

The first mode for the tender design is a lateral mode: 1.9 Hz. This value is $> 1.2\text{Hz}$ and therefore outside of the critical range for lateral excitation. The first vertical mode including ageing occurs at 2.5 Hz, see Figure 96.



Figure 96. Modal shape of 1st vertical eigenmode

This mode is within the critical range, so a more detailed analysis was performed. Assuming a damping of 1%, the associated maximum vertical acceleration was determined to be $0,2\text{ m/s}^2$. Including the conservatively assumed effects of ageing, the eigenfrequency reduces to 2.1 Hz, and the associated vertical acceleration was determined to be $0,7\text{ m/s}^2$, and thus just within the set acceptable limits. The accelerations are relatively low because of the relatively high modal mass of the vibration mode, with a modal mass factor of 0.8 instead of 0.5. This high modal mass can also be recognised from Figure 93.

The low eigenfrequency is partly due to the contribution of the asphalt. It is recommended to further optimise the design and increase the eigenfrequency. This can be achieved either by reduction of the dead weight, for example by investigating the application of an alternative lighter wear surface, or by increasing the stiffness of the FRP-material.

Stresses

The capacity of FRP for the preliminary design is based on a simplified strain failure criterion with axial failure strain of 1.2% and a shear failure strain of 1.6%. The maximum stress in the global structure is $< 47\text{ N/mm}^2$, and the unity-checks on the stresses are low, < 0.6 . It is concluded that material strength is not governing for the design for the global structure.

Stability

Looking at the structure it can be seen that the long diagonal beams of the super structure are loaded in compression and must be evaluated for stability. Using the FE-model, the resistance against buckling was determined for the structure including buckling. A unity check based on this Eulerian capacity of 0,53 was found for the structure, see Figure 97.



Figure 97. Modal shape of the 1st buckling mode around local y-axis

This includes the conservative reductions to take into account the effect of the climate and ageing, but not the effect of geometric imperfections. To include this effect the reduction factors as described in the revision of [1] have been applied. This method uses the research done on buckling of pultruded profiles [4]. For the interaction between compression and bending moment the formulae according to EN1993-1-1 are used.

The resulting unity check of 0.93 proves that the capacity of the structure is sufficient. Because of the limited experience of the applied reduction factors and the importance of stability of the structure, strong recommendations are made for the evaluation of stability in the next design phase as well as during the realisation phase and the health monitoring of the structure.

It is recommended to increase the resistance of the structure against buckling, especially since these measures will affect both the comfort and the load bearing capacity positively. In addition it is recommended to perform a geometrically non linear buckling analysis with clearly defined and quantified margins on tolerances for



misalignments and other relevant imperfections. This analysis will give the allowable limits for geometric imperfections in the realisation phase. In addition to initial imperfections also creep deformations must be included. Because buckling is the design governing failure mode, these geometrical tolerances must be verified with great attention, and must be addressed with the required priority in quality control procedures.

CONCLUSIONS

In close cooperation with Statens vegvesen the structural design of the bridge at Paradis was developed to meet the architectural design. As a final statement, a 3D printed model was prepared, see Figure 98.

The technical performance of the tender design has been demonstrated to meet all requirements as specified by the Eurocodes and Statens vegvesen. It has therefore been demonstrated that a 42 m footbridge can be realised with a full FRP structure based on glass fiber reinforcement.

Based on the tender design, the design opportunities and aspects that require special attention have been identified. The FRP technical specifications will be prepared in cooperation with the technical specialists of Statens vegvesen. The bridge is put to tender in 2018. When this bridge is built, it will be the first FRP bridge built by the Norwegian Public Roads Administration.



Figure 98. 3D printed model bridge Paradis

REFERENCES

- [1] CUR96, (2003), CUR aanbeveling 96 "Vezelversterkte kunststoffen in bouwkundige en civieltechnische draagconstructies", eerste herziene uitgave.
- [2] Clarke J. L., (1996), "Structural Design of Polymer Composites"; Eurocomp Design Code and Handbook, E&FN Spon.
- [3] JRC, EUR 23984 EN, (2009) "Design of Lightweight Footbridges for Human Induced Vibrations".
- [4] Trumpf H., (2006), "Stabilitätsverhalten ebener Tragwerke aus pultrudierten faserverstärkten Polymerprofilen", Stuttgart, Shaker Verlag, Aachen.
- [5] BÜV-Empfehlung (2010), "Tragende Kunststoffbauteile im Bauwesen [TKB]".



MONOTONIC AND CYCLIC QUASI-STATIC SWAY TESTS ON PULTRUDED GFRP PLANE FRAMES

MF Sá¹, D Martins¹, JA Gonilha¹, JR Correia¹, JP Firmo¹, JG Ferreira¹
¹ CERIS, Instituto Superior Técnico, University of Lisbon, Portugal
(corresponding author: jose.gonilha@tecnico.ulisboa.pt)

ABSTRACT

This paper presents an experimental study on the structural behaviour of pultruded GFRP frames subjected to in-plane horizontal loads. Monotonic and cyclic tests were performed in full-scale plane frames ($\sim 3 \times 3 \text{ m}^2$) comprising GFRP profiles with square tubular cross-section ($120 \times 10 \text{ mm}^2$). The beam-to-column joints consist of a connection system developed earlier by the authors, materialized by internal steel auxiliary parts bolted to the GFRP profiles. To evaluate the influence of non-structural infill walls, the frames were tested (i) with (filled) and (ii) without (unfilled) GFRP sandwich wall panels. In the monotonic tests, as expected, the filled frames presented considerably higher stiffness and strength than the unfilled frames. Conversely, the unfilled frames were able to sustain a higher *drift* than their filled counterparts. In the cyclic tests both series presented *pinching* effects (consistent with the behaviour of the corresponding beam-to-column connections), with the filled frames showing much higher energy dissipation capacity and damping for the same *drift* level. The results obtained in these experiments showed the influence of infill walls in the sway behaviour of GFRP frames, highlighting the importance of duly considering them in the seismic design of GFRP structures.

KEYWORDS

Glass fibre reinforced polymers (GFRP), pultruded plane frames, sway tests, monotonic and cyclic behaviour.

INTRODUCTION

Pultruded glass fibre reinforced polymer (GFRP) profiles are a promising alternative to traditional structural materials, for both new construction and rehabilitation, owing to their high strength, lightness and improved durability. However, their low elastic moduli, brittle behaviour and lack of widely accepted design guidelines have been hindering a widespread use of these advanced composite materials. In particular, the seismic design of GFRP frame structures is underdeveloped, with very few studies having been performed about the influence of the connection technology on the behaviour of GFRP frames under lateral loads (Correia *et al.*, 2015; Na, 2008). The seismic design of these composite structures must also account for the linear-elastic behaviour and lack of (or at least limited) ductility at the material level, as well as the effects of infill walls, since these may have a significant influence on the structural performance of GFRP frames.

The present work was part of the ClickHouse project (Correia *et al.*, 2015), which aimed at developing a prefabricated housing system using composite materials, *cf.* Fig. 1. The main goal of this project was to develop a constructive solution for emergency situations and/or temporary shelters (*e.g.*, construction sites), that should be light and quick/easy to transport, assemble and disassemble while fulfilling applicable structural safety and thermal performance requirements. The structure of the house is composed of pultruded GFRP profiles and the walls, floor and roof are made of sandwich panels with GFRP skins and a polyurethane core. The electrical and water piping networks are included within the sandwich panels. The beam-to-column connection used in the ClickHouse was studied in previous experimental investigations (Martins *et al.*, 2017).

The main objective of the experiments described in the present paper was to characterize the *quasi*-static and hysteretic behaviour of GFRP two-dimensional (2D) frames using those connections, when subjected to monotonic and cyclic loads. Both types of responses were assessed in the sway mode of the non-braced frames subjected to lateral forces. The influence of the infill wall panels on the frame behaviour was also studied, aiming at evaluating a much more realist performance of the 2D frames as part of the three-dimensional house module prototype.

EXPERIMENTAL PROGRAMME

Frame specimens

Two different typologies of 2D GFRP frames were tested under monotonic (M) and cyclic (C) loading: (i) GFRP frames without infill walls; and (ii) GFRP frames with an infill wall made of three 0.96 m wide composite sandwich panels, constituted by polyurethane foam core (density of 40 kg/m^3 , 66 mm thick) enclosed between two 2 mm thick GFRP skins. These frames were labelled as UF-M/C and F-M/C, with U and F standing for unfilled and filled, respectively, and M and C for monotonic and cyclic loading, respectively. Their modular structure comprised two beams and two columns with a square hollow section ($120 \times 10 \text{ mm}^2$), cf. Fig. 2. The tested specimens comprise a plane frame of the full-scale ClickHouse prototype (Correia *et al.*, 2015), whose plan area of each unit module is about $3 \times 3 \text{ m}^2$ (cf. Fig. 1).



Fig. 1: The ClickHouse: architectural design (top) and prototype (bottom).

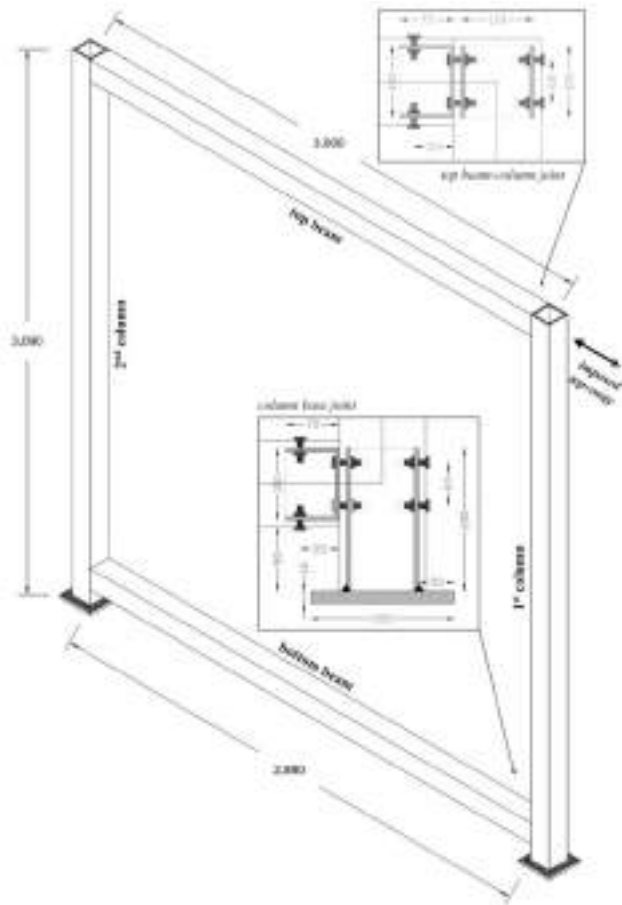


Fig. 2: Frame geometry (in mm) and designations, including details of the connection parts.

In what concerns the beam-to-column connections, both top and bottom joints included steel bolts (M10, Class 8.8) and 3-5 mm thick steel plates; the latter parts (related to the beam connection) were embedded in the cavity of the profiles in a length of about 100 mm – further details can be found in Martins *et al.* (2017). The base connection was materialized by a metallic part that comprised two elements welded together: (i) a bolted tube and (ii) a square plate ($200 \times 16 \text{ mm}^2$), cf. Fig. 2 (details). The connection between the profiles and the sandwich panels was ensured by means of small square tubular ($50 \times 5 \text{ mm}^2$) GFRP profiles, which were bolted and adhesively bonded to the inner face of the main profiles and, in turn, fitted inside the panels' edges based on a *tongue-and-groove* connection system. The vertical link between the wall panels was performed similarly to the referred interlock system, but using two auxiliary square tubular GFRP profiles ($50 \times 5 \text{ mm}^2$), bonded and bolted to each other, that allowed the adjacent panels assembling.

Set-up and instrumentation

Fig. 3 depicts the test setup. Horizontal displacements were imposed at the frames' top beam by a mechanical actuator, with capacity of 1000 kN and stroke of 400 mm, mounted in a reaction wall. The load applied to the frame was measured by a *Novatech* load cell, with capacity of 300 kN, positioned between two cylindrical hinges allowing rotation during the horizontal movement. The steel bases of the frames were connected directly to a rigid foundation beam anchored to the laboratory's strong floor. In order to prevent out-of-plane displacements during the tests a lateral restraint system was applied to the top beam. Fig. 4 outlines the position of the instrumentation used at different frame sections, where (i) Δ_i stands for string pot displacement transducers, (ii) δ_i stands for general displacement transducers, (iii) I_i stands for rotation transducers, and (iv) ε_i stands for strain gauges bonded in the GFRP profiles. Data acquisition was carried out using built-in data loggers from *HBM* and registered at a rate of 5–10 Hz.



Fig. 3: Test set-up (detail of frame fixation in the base).

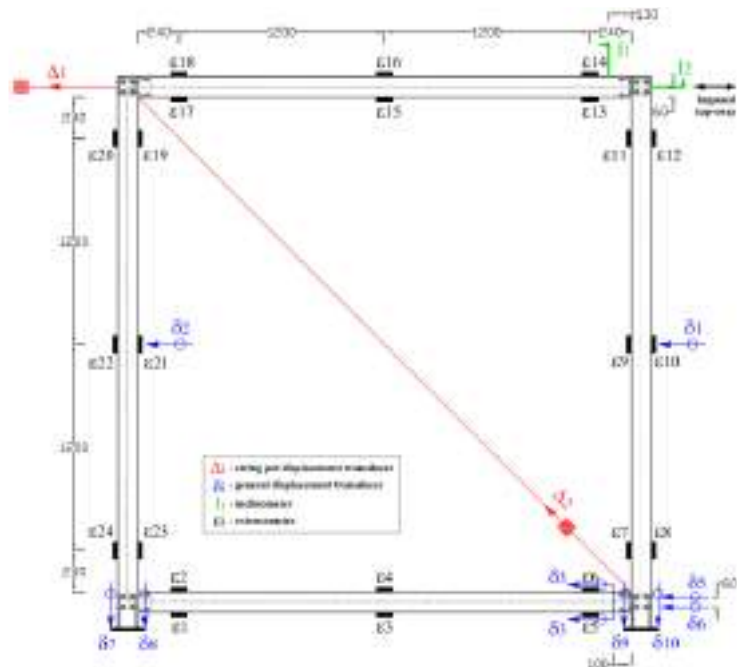


Fig. 4: Instrumentation position (in mm).

Load history protocol

The *top-sway* displacement was imposed by the actuator at an average speed of 15 and 30 mm/min for the monotonic and cyclic tests, respectively. In the monotonic tests the displacement was applied until a maximum force was reached or remained stable, or until the maximum stroke of the actuator (*ca.* 400 mm for the monotonic tests) was reached.

The load history protocol used on both cyclic test series (Fig. 5) was based on the following parameters adapted from the **ECCS Manual (1986)**: (i) proportional limit of elastic range – $\Delta_{1,el}$; (ii) *top-sway* displacement range (eighths and quarters of $\Delta_{1,el}$ up to 100%); and (iii) number of cycles. The proportional limits were established based on the results of the monotonic tests, considering the limits of the linear elastic behaviour, focused on the more representative linear range of the initial response. In general, those limits were associated to a reduction of the initial stiffness, corresponding to the damage initiation. Such behavioural characterization of the GFRP frames cannot be directly related to the procedures for assessing the behaviour of structural steel elements under cyclic loads, due to inherent differences between GFRP material and steel, the latter exhibiting yielding when subjected to ductility demands.

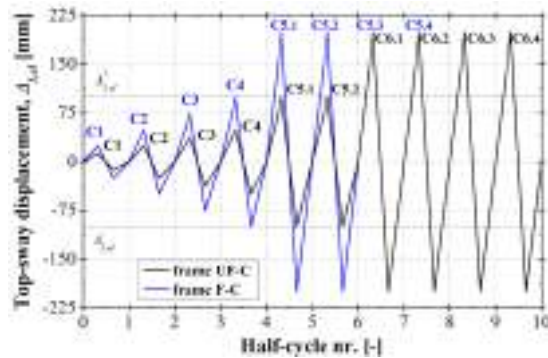


Fig. 5: Load history protocols for the cyclic tests (C_i – cycle's order number i).

The differences between the protocols established for the cyclic tests of frames ($\Delta_{1,el} \approx 100$ mm) was due to the variation of the elastic-to-ultimate limits ratios as defined from the corresponding monotonic responses. Notwithstanding, it should be mentioned that in both tests, the maximum displacements of the final cycles were limited by the stroke capacity of the actuator (± 200 mm). The total duration of each cyclic test was approximately 2 h (at about 30 mm/min), with frames UF-C and F-C being subjected to 8 and 10 cycles, respectively, in that period.

RESULTS AND DISCUSSION

Monotonic test series: UF-M and F-M

The main experimental results obtained from the two monotonic tests are presented in Fig. 6a-b, namely in terms of the following curves: *load vs. top-sway displacement / top-drift*¹ ($F - \Delta_1/SW$), *load vs. diagonal displacement* ($F - \Delta_2$) and *load vs. columns half-height displacement* ($F - \delta_1, \delta_2$).

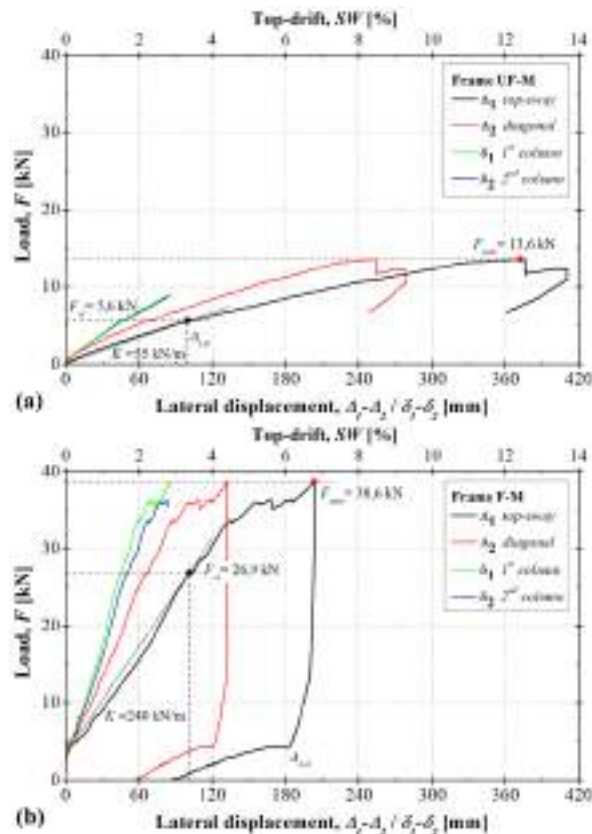


Fig 6: Load vs. monotonic displacements: (a) UF-M frame and (b) F-M frame.

¹ Top-drift: $SW = (\Delta_1/H) \cdot 100\%$, in terms of percentage, assuming column height $H = 3.000$ mm.

Both frames exhibited a roughly linear behaviour up to a certain point, when a short load drop occurred associated to the occurrence of the 1st local failure (F_{el}), with that initial stage being characterized by an approximately constant stiffness (K). The filled frame (F-M) initially presented a very stiff behaviour up to around 4 kN, which may have been due to the initial higher friction of the wall panels. After the initial stage, the frames' response presented gradual stiffness reduction, due to several local failures that developed on the profiles (described ahead) until the maximum load was reached ($F_{max} = 13.6$ kN and $F_{max} = 38.6$ kN for the UF-M and F-M frames, respectively). This peak load corresponded to the following *top-sway* deformations: (a) $\Delta_l = 372$ mm / $SW = 12.4\%$ for the UF-M frame, and (b) $\Delta_l = 204$ mm / $SW = 6.8\%$ for the F-M frame. The deformed configuration of the frames corresponding to their respective F_{max} load is illustrated in Fig. 7; very high lateral deformations are well visible in both frames, including the wall panels of the filled frame (F-M).



Fig 7: Large lateral deformability: (a) UF-M frame ($SW \approx 12\%$) and (b) F-M frame ($SW \approx 7\%$).

When comparing the monotonic responses of the frames, it can be seen that the filled frame presented considerably higher stiffness and strength than the unfilled frame (4.4 and 2.8 times higher, respectively). The very significant performance increase of the F-M frame was due to the transmission of the applied load through the wall panels (which acted as a bracing system, considerably increasing the overall stiffness), thus reducing the frame's deformability. Conversely, the UF-M frame was able to sustain a higher *top-drift* than its filled counterpart.

The damage that occurred on the unfilled frame concentrated essentially in the connections, although compressive cracks appeared first in the web-to-flange junctions of both column bases (Fig. 8a). The damage progression involved several mechanisms, namely: (i) crushing of the top beam against the columns; (ii) widening of the cracks developed initially at the column bases; (iii) compressive and tensile rupture at the lower and upper side of the top joint (*farther w.r.t.* the load application position); and (iv) web-flange junction's separation with rupture and tearing of material along the pultrusion direction (Fig. 8b). After failure developed at the top of the frame, a residual load capacity could still be kept, provided by the bottom (fixed) connections; this residual capacity was kept until a brittle fracture occurred at the *nearest* bottom connection. The final failure mode, shown in Fig. 8c, comprised a combination of the following damage mechanisms on the column: (i) strong flexural cracks in the base; (ii) web-to-flange junction separation; (iii) web *crippling*; and (iv) local crushing and tearing at the upper side of the joint, as a consequence of the beam's penetration into the column.

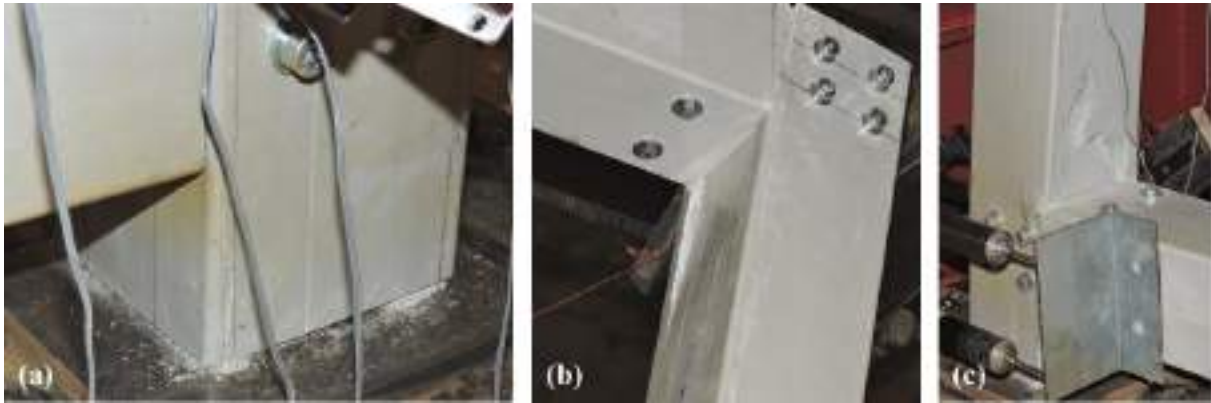


Fig. 8: Damage on the UF-M frame: (a) cracking in junctions, (b) failure in the column top, (c) crushing and tearing.

Regarding the failure of the filled frame, initially some crushing cracks were also observed at both column bases, more exuberant in the 2nd column (*cf.* Fig. 2). The first local failure occurred on the bottom beam due to the penetration of the skin of one wall panel (which, at some point, debonded from the core), with fracture propagation along the contact region. Some other local damages occurred on the panels, *e.g.*, crushing and skin *crippling* at the frame's corner. Then, the top beam also exhibited damage due the above-mentioned mechanisms – panel's penetration into the beam's bottom flange. Several failure modes developed on the small hollow profiles (used for the fitting of the panels) due to the large deflections imposed to the beams, and the magnitude of the damage increased further at the final stages of the test (Fig. 9a). The most prominent damage suffered by those profiles included the debonding from the main GFRP beams and flexural damage with material delamination. Additionally, compressive damage with delamination in the top connection next to the load application section was also observed. Fig. 9b shows the damage at one column base, at the brink of the maximum imposed *top-drift*, highlighting the progressive crushing in the base material and flexural cracking up to the level of the bolts.



Fig. 9: Damage on F-M frame: (a) beam large deflection with panels' penetration and (b) damage at one column base.

Cyclic test series: UF-C and F-C

Fig. 10a-b presents the various lateral displacements hysteresis loops obtained from the two cyclic tests performed: $(F - \Delta_1/SW)$, $(F - \Delta_2)$ and $(F - \delta_1, \delta_2)$; for comparison purposes, these curves are plotted together with the main experimental results $(F - \Delta_1/SW)$ obtained from the corresponding monotonic tests.

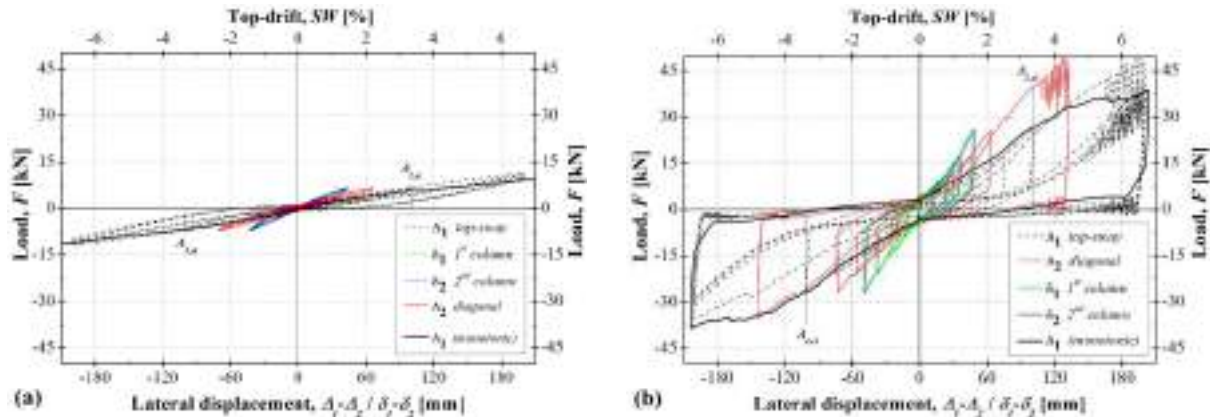


Fig. 10: Load vs. lateral displacements hysteresis loops: (a) UF-C frame and (b) F-C frame.

The unfilled frame exhibited symmetric behaviour with similar load amplitudes in both directions, showing a relatively low energy dissipation² capacity. The hysteresis diagrams indicate that the frame sustained the loading capacity in an elastic-stable behaviour up to the maximum *top-drift* level imposed (*ca.* 7%), with almost negligible load and stiffness degradation. From both (+/-) envelopes, it seems that the stiffness and the elastic limit load were not influenced by the increased cyclic loading. However, within each repeated loading cycle of the final groups (C5 and C6, *cf.* Fig. 5), some constriction can be noted near the central area of the hysteresis loops. This effect – loop’s *pinching* – can be associated to a loss of stiffness and it may be attributed to the opening and closing of the cracks in the GFRP material and to beam-column joints degradation – starting from cycle C5 (unloading branch).

The filled frame exhibited considerably higher energy dissipation capacity and also presented symmetric behaviour, although reaching slightly lower load levels in the negative excursions, mainly during the final cycles. Despite local failures took place, the frame was able to sustain the overall load in a stable manner also up to the maximum *top-drift* ratio imposed (*ca.* 7%), but in this case with strength deterioration and stiffness degradation triggered at the final stages. The hysteresis diagram is characterized by a high initial stiffness (*quasi-rigid* behaviour due to the initial higher friction of the wall panels, as observed in the static test) and an early nonlinear behaviour preceding an increasing stiffness. Some *pinching* effect was also triggered before the elastic limit deformation was achieved (at cycle C3, < 75 mm), corresponding to the first cracks developed in the GFRP material. In the unloading branches, the frame had an immediate loss of strength. This can be associated to the fact that there is no reaction/restriction against the movement of the skins (of the panels) that had penetrated inside the GFRP profiles. In the last group of cycles, both loading/unloading directions present strong *pinching* effects, caused by the excessive crushing of the GFRP material surrounding the connections and also of the webs of the profiles, with consequent opening of the cracks’ width at the final stage. The high stiffness recovery after that large horizontal plateau shows the frame’s ability to internally redistribute stresses after occurrence of extensive local damage. During the last three cycles (C5.2-C5.4), some degradation of this recoverable stiffness was also observed, together with important strength deterioration. These phenomena were absent between the successive cyclic steps, occurring only in the stabilization cycles of the last group.

In addition to the higher initial stiffness and strength ratios achieved, it is clear that the filled frame presented the highest energy dissipation capacity and damping coefficient³ – about 6.0 and 1.8 times higher than the corresponding properties obtained for the unfilled frame, respectively, concerning the same *top-drift* level imposed to both frames (*ca.* 7%). These results highlight the great influence of wall panels on the behaviour of GFRP frames under both monotonic and cyclic loading. When comparing the monotonic and cyclic curves of each frame typology, it seems clear that they are similar in terms of stiffness and elastic limit forces, in particular

² Energy dissipation given by the sum of the areas of the positive and negative half-cycles of the *top-sway* displacement hysteresis loops.

³ Damping coefficient given by the relationship between the energy dissipation and a multiplicative factor (converted in radians, 2π) computed by the absolute maximum values of the force (F) with the respective displacement amplitude (Δ_1).

for the filled frame, whose monotonic response matches the positive hysteretic loops of the cyclic response (more closely than the unfilled frame).

The unfilled frame presented the first signs of damage at the facing flanges of both bases during an imposed displacement of about 73 mm. As observed in the homologous monotonic test, those first damages consisted of small crushing cracks whose dimensions did not significantly increase during the group of two 100 mm cycles (C5). When the last group of cycles was initiated (C6 – above the theoretical $\Delta_{l,el}$ limit), loud cracks were heard followed by a slight load loss. This behaviour was attributed to the crushing of the 1st column (*cf.* Fig. 2) against the top beam, at the top connection, whose steel parts exhibited large rotations. Fig. 11a shows the resulting external damage at the 1st top connection – strong vertical delamination at web-to-flange junction. The vertical cracks initiated in the column bases were increasingly opened during the last two repeated cycles, being then propagated into large cracks along the height of the bottom joints. Fig. 11b shows the flexural cracks in the flanges and the delamination at the web-to-flange junctions of the column base. This damage mode can be associated to the highest *pinching* effect captured in the last loops of Fig. 10a, nevertheless presenting a considerable stiffness recovery during load excursion, which was similar to that of the first hysteretic curves (as no relevant nonlinear regime has been reached).

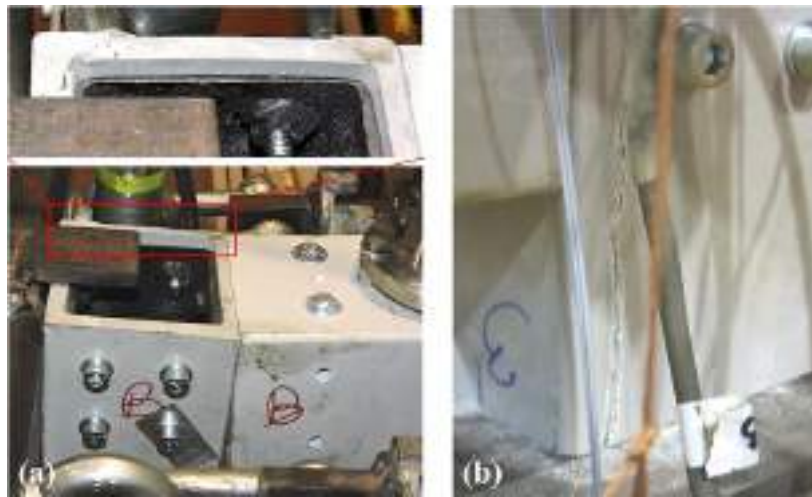


Fig. 11: Damage on the UF-C frame: (a) delamination at the top 1st joint and (b) large cracking at one column base.

Regarding the failure of the filled frame, after cycle C1, soft cracking was heard and attributed to the contact forces of the sandwich panels on the beams' flanges, when the frame/panels started to deflect/distort more significantly. During cycle C3, considerable vertical cracks were then noticed at the bases of both columns, being more meaningful in the 2nd column (*ca.* +62 mm), which corresponded to some initial *pinching* effect. The deflection of the bottom beam increased significantly with the lateral deformation of the frame. As in the corresponding frame under monotonic loading, these deformations culminated on the penetration of the panels (skins) inside the bottom beam, when the *top-drift* was about to reach the reverse cycle C4 (*ca.* -98 mm). Analysing the respective hysteresis loop, a strong *pinching* effect can be depicted, mainly at the negative branch. Due to the large deformation imposed on the bottom beam, a local failure next to its left connection support occurred during cycle C4. Fig. 12 details the failure mode developed, which can be characterized by the rupture of all four web-to-flange junctions in a considerable length. No damage was visually identified on the steel plates of the joint, as well as on the bolts.



Fig. 12: Bottom beam's failure on the F-C frame: (a) front side, (b) back side and (c) bottom side views.

After occurrence of the above described failure modes, the frame continued to deform in a markedly nonlinear manner (approximately bilinear) with stiffness reduction – noticeable *pinching* effect could be identified until maximum load capacity was reached for about 50 kN at the first positive cycle of the final group (C5.1). During this cycle, different types of damage occurred in the entire frame, including: (i) buckling of the panels' skins; (ii) crushing of the top beam against the columns (both sides); (iii) debonding and flexural failure of the auxiliary tubular profiles; (iv) separation of the web-to-flange junctions of the bottom beam on the load application side; and (v) progression of the penetration of the panels' skins at the central zone of the beams. It is worth referring that, at some point in the tests, when the wall panels started to exhibit significant in-plane distortion (buckling), the skins debonded from the core, in the same way as in the corresponding static test. Fig. 13 shows the final damage scenario of the frame's top and bottom parts under large displacements. It can be seen that a quite extensive damage developed within the frame, yet without the occurrence of a (full) collapse.



Fig. 13: Final damage scenario on the F-C frame: (a) top beam, (b) bottom beam with (c) debonding of profiles.

CONCLUSIONS

This paper presented an experimental study about the *quasi*-static behaviour of pultruded GFRP plane frames under monotonic and cyclic loads. Those composites frames were developed to be used in modular house construction for temporary or emergency scenarios. The following main conclusions are drawn:

The frames subjected to monotonic loading exhibited initial linear elastic response followed by a gradual decrease of global stiffness until the maximum top-drift imposed was attained – 12% (ca. 400 mm) on the unfilled frame and 7% (ca. 200 mm) on the filled frame.

The initial stiffness and maximum load of the filled frame were about 4 and 3 times higher, respectively, than those of the unfilled frame and the frames presented similar ratio between elastic limit strength and maximum load for the same top-drift level;

Both types of frames (unfilled and filled) presented stable and quasi-symmetric hysteretic behaviours, in which the stiffness was not markedly influenced by the increased cyclic loading; nevertheless pinching effect was noticed within each repeated loading cycle of the final groups, mainly on the filled frame.

The filled frame exhibited some stiffness degradation and considerable strength deterioration during the last 3-repeated cycles; the high stiffness recovery at this final stage of the cyclic test attested the ability of the infilled GFRP frame to redistribute internal forces after suffering extensive damage.

In addition to the higher stiffness and strength values/ratios achieved consistently on both tests (monotonic and cyclic), the filled frame presented the highest energy dissipation capacity and damping for the same top-drift level imposed (ca. 7%) – respectively, 6.0 and 1.8 times higher compared to the unfilled frame.

Infill walls made of lightweight GFRP sandwich panels had a great influence on the structural performance of GFRP frames under both monotonic and cyclic lateral loading.

ACKNOWLEDGMENTS

The authors wish to thank CERIS for funding this research. The financial support of Agência Nacional da Inovação (ANI, through the funding of project Clickhouse – Project nr. 38967) and Fundação para a Ciência e a Tecnologia (FCT, through the funding of project FRP-Quake PTDC/ECM-EST/6465/2014) is gratefully acknowledged. The third and fifth authors are also grateful to FCT for funding their research through scholarships SFRH/BPD/112216/2015 and SFRH/BPD/108319/2015, respectively.



REFERENCES

J.R. Correia, D. Martins, J.A. Gonilha, J.G. Nascimento, M. Arruda, A. Castelo, F. Branco (2015). “Clickhouse project – an all-composite emergency housing system”. *International Conference on Advances in Composite Materials and Structures (CACMS)*, Istanbul.

Gwang-Seok Na (2008). “Load-displacement behaviour of frame structures composed of FRP composite materials”. PhD Thesis, Georgia Institute of Technology.

D. Martins, M. Proença, J.R. Correia, J. Gonilha, M. Arruda, N. Silvestre (2017). “Development of a novel beam-to-column connection system for pultruded GFRP tubular profiles”, *Composite Structures*, 171:263–276.

ECCS Manual (1986). “Recommended Testing Procedures for Assessing the Behaviour of Structural Steel Elements under Cyclic Loads”. *European Convention for Constructional Steelwork*.



FALCON – A MULTI-DISCIPLINARY EFFORT TO PROMOTE FRP BRIDGES IN SWEDEN

Reza Haghani¹, Erik Olsson^{1,2}

¹ Chalmers University of Technology, Department of Architecture and Civil Engineering, Gothenburg, Sweden;

² ELU Consultants, Gothenburg, Sweden (corresponding author: reza.haghani@chalmers.se).

ABSTRACT

Sweden has a long history in using fiber reinforced polymer (FRP) composites in marine, transportation and energy sectors. However, when it comes to application of composite materials to build bridge structures, it somewhat falls behind.

Despite several advantages that FRP composites offer, such as high specific strength and stiffness, corrosion resistance and light-weight, their infrastructural applications in Sweden have not been fully understood and yet to be realized. The first efforts to use FRP composites for construction of pedestrian bridges started in 2011, however, due to lack of knowledge about the materials and design of composite structures among engineers, they were halted.

To identify the existing gaps and hindrances, a joint effort project called “Falcon” was realized. The main goal of the project was to realize the first FRP pedestrian bridge and pave the way towards widespread infrastructural application of composites. This paper, presents some findings of the project and a brief description of a few pilot projects realized in the country.

KEYWORDS

FRP bridge, design guidelines, procurements.

INTRODUCTION

At the present, sustainable development is an important aspect in many engineering fields. Construction is, of course, not an exception. Aging and overloading of infrastructure in conjunction with lack of proper maintenance have led to “global infrastructure crisis”. Therefore, finding innovative materials and technical solutions to construct infrastructure with longer service life and lower life cycle cost, has been a priority for many bridge authorities and infrastructure owners in European countries, as presented in Mara et al. (2013). In addition, advanced industrialized production as an approach to reduce production cost, is gaining a great deal of interest among industrial communities and engineers. In this respect, off-site manufacturing and on-site assembly is of great importance in bridge construction.

Emergence of fiber reinforced polymer (FRP) composites in construction industry in mid-1970’s, opened up new horizons towards achieving abovementioned goals. FRPs are classified as composite materials and are basically composed of two constituents: reinforcing fibers and a polymeric matrix. Depending on the expected mechanical and durability characteristics, different types of fibers and matrices can be combined. Common FRPs used in construction include carbon, E-glass and aramid fibers. Matrix is often a thermosetting resin such as epoxy or polyester. Lately, natural fibers and bio-based resins have been researched, but due to concerns regarding the long-term performance, and often inferior mechanical properties of bio-based composites, they have not been realized in commercial projects.

The possibility of combining different types of fibers and matrices offers the great advantage of “tailor-ability” in the sense that the “right” constituents can be mixed to get the “right” properties. FRP composites have superior mechanical properties such as very high specific strength and stiffness and very good durability characteristics. The light weight of FRPs is very attractive when it comes to prefabrication, as it provides the possibility for off-site manufacturing and on-site assembly. When compared to other European countries such as UK and Netherlands, infrastructural application of FRPs in Sweden somewhat falls behind.

This paper, presents results of a research project carried with the aim to identify technical and management problems towards widespread application of FRPs as well as activities to facilitate the acceptance of FRP composites as a reliable and cost-effective alternative to traditional building materials such as steel and concrete. Sweden has a long history in using fiber reinforced polymer composites in marine, transportation and energy sectors. Despite the advantages offered by FRPs, the experience and the knowledge among different industries about design and manufacturing of FRP components, FRPs have not yet found their place in Swedish construction sector yet.



PREVIOUS EFFORTS

Structural engineers in Sweden are generally not educated about FRP as a construction material so it is not surprising that there has not been a pull from the construction industry to explore the possibilities provided by FRPs as a building material. The initial efforts were made by the composite industry (especially manufacturers and material providers), searching for new market areas in 2010. Architects also found new opportunities in using the material to create complex geometries and tried to “promote” such solutions. The problem, however, was the lack of knowledge among architects about the material which created unrealistic expectations without considering the technical and practical limitations. The idea of using FRP for building pedestrian bridges in Sweden, initiated in 2013. Two examples of these ideas were Kaponjär bridge (Figure 1) proposed by Ramböll consultants and Architect bridge (Figure 2) by ELU consultants. Even though the concepts were very attractive from architectural point of view, the complexity involved in the design and manufacturing of these concepts, halted both projects. A learned lesson from these failures was that it was the lack of knowledge about the FRP materials in the engineering community and among clients which did not allow the realization of these projects.



Figure 99. Concept of Kaponjär FRP bridge over Rosenlundskanal in Gothenburg. Picture courtesy of Ramböll

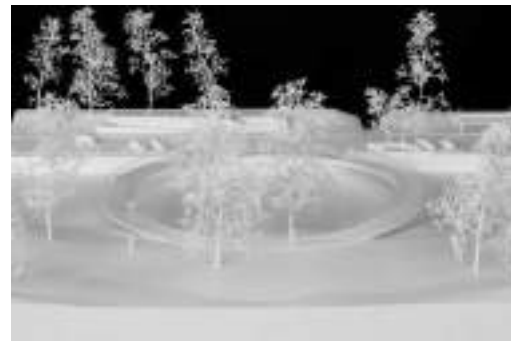


Figure 100. Concept of Architect bridge in Haga area in Gothenburg. Picture courtesy of Erik Andersson Architects

THE FALCON PROJECT: A MULTIDISCIPLINARY EFFORT

It was soon realized that to create the foundation for application of FRPs in bridges, a comprehensive and multidisciplinary work with contribution of all players was needed. In this context, Falcon, “future advanced lightweight construction (2016-2018)”, a joint effort project with total budget of 640 k Euro funded by VINNOVA and co-funded by industrial consortium partners. It is coordinated by Swerea Sicom (a leading Swedish research institute in FRP composites) and was initiated to identify the hindrances towards the infrastructural application of FRP composites and facilitate the acceptance of FRP solutions by paving the way towards realization of the first FRP bridge in Sweden. The project consortium consists of 14 partners from universities, research institutes, bridge designers, manufacturers, material suppliers and clients.

The main objective of the project was to implement the best practice for design and procurement of FRP bridges. In this regard, a draft of “technical client demands” along with a background document were prepared in accordance with Swedish national regulation for design and procurement of bridges. The main aim of these documents was to establish a framework for clients to process innovative technical solutions not covered by Eurocodes within the existing legal boundaries.

THE WAY TOWARDS WIDESPREAD APPLICATION OF FRPS IN SWEDEN

FRP Deck for the bascule road bridge 261

Bridge 261 located in the city of Malmö, is a two-lane bascule steel bridge composed of two supporting side trusses and a steel decking system built in 1953. The orthotropic steel deck in the bridge had dimensions of 8.9m x 32.9m and was degraded due to corrosion over time. Visual inspections also revealed multiple cracks in the asphalt layer, a typical problem due to local bending of the top plate in orthotropic decks, which added to maintenance cost of the bridge, see Figure 3. Therefore, the refurbishment of the bridge was necessary. The client needed a fast assembly solution as the bridge was located on one of the main roads in the city and considerable traffic disruption would have taken place if the bridge had been closed for a long time. It was decided to use FRP solution to accelerate the operation and provide a more durable solution compared to a steel alternative.

Circumstances of the project necessitated using tailor-made FRP sandwich panels. To keep the cost low, glass fibers and polyester matrix were chosen. The design and manufacturing of the deck panels was carried out by the Dutch supplier FiberCore Europe.



Figure 101. Wear of the surface and transverse cracks in the orthotropic steel deck, Photo courtesy of Per Andersson



Figure 102. Cross section of the sandwich panel used as new decking system



Figure 103. Removal of the old steel deck and preparation of the stringers for installation of FRP panels, Photo courtesy of Per Andersson



Figure 104. Installation of FRP deck panels, Photo courtesy of Per Andersson

The deck panels in this project had a height of 105 mm with face sheet thickness of 19mm on the top and 17mm in the bottom, see Figure 4. To avoid on-site joints in the perpendicular to the length direction, two longitudinal panels were manufactured with dimensions of 32.9m x 4.44m with total areas of 292m². The old steel deck was firstly removed from the bridge (Figure 5). In the next step, the holes on the steel girders were prepared by slightly enlarging them. The panels were then placed on the girders and connection were made using hollo-bolts. The project was completed in summer 2016.

FRP deck for rehabilitation of the university bridge

The university bridge in Malmö is a two-span asymmetrical cable-stayed swing bridge with a main span of 25 m and a 15 m long back stay span. The total length of the bridge is ca. 76 m including approach spans. The width of the bridge is 16 m, including 2 lanes of carriageway and 2 lanes for pedestrians and cyclists. The bridge was built in 2004. Already in 2015, signs of deterioration in wooden planks covering the pedestrian lines were observed.



Deformation of the planks had caused uneven surface of the walkway and was a potential threat for the users, see Figure 7.



Figure 105. Deterioration of the wooden planks on sidewalks of the university bridge, Photo courtesy of Per Andersson



Figure 106. FRP panels installed on sidewalks, Photo courtesy of Per Andersson

The municipality of Malmö decided to replace the wooden planks with a more durable alternative. At the same time, there was a need for a lightweight solution not to disturb the balance of the spans as modifying the counterweight was not an option in this project. FRP deck panels with thickness of 65 mm produced by FiberCore Europe were installed on steel stringers spacing at 1.12m. 6 deck panels with width of 3 m were put alongside each other to cover the whole length of the bridge, see Figure 8. The project was completed in 2017.

Pedestrian bridge 254 – The first FRP pedestrian bridge in Sweden

The original bridge 254 in Malmö was a pedestrian timber bridge built in 1981. The bridge had undergone a considerable degradation and was classified as not safe for use. In 2016, the municipality of Malmö decided to replace the bridge. Different alternatives, including full concrete slab and concrete slab on steel girders were studied.



Figure 107. Proof loading of the composite beams during manufacturing, Photo courtesy of Composite Design



Figure 108. Installation of the bridge, Photo courtesy of Composite Design

The results from life cycle cost analyses on different concepts demonstrated that an FRP bridge would be the least expensive choice for this project. Composite Design, a Swedish FRP manufacturing company, took over the project. The superstructure of this bridge consists of seven sandwich beams glued together creating an FRP composite deck. Each beam consists of four smaller beams, laminated together to form a longer beam. The beams



were created using lightweight concrete (Siporex) core wrapped with prepreg carbon fibre fabrics. Each beam was 505 mm wide and 420 mm high and had 11 layers of carbon fiber on the top and bottom with thickness of ca. 0.95 mm for each layer (total skin thickness of ca. 10.5 mm) and 3 layers of carbon fiber on the sides, ca. 2.3 mm.

The FRP bridge is 3.5 m wide, 17.62 m long and has area of 62 m². Each beam was loaded with 4.2 tons at the workshop to check if they fulfill the requirement for stiffness and deformation, see Figure 9. The bridge was installed in March 2017 and the mounting operation took only one hour, Figure 10.

Neptuni Bridge

Neptuni Pedestrian bridge shall be the next FRP bridge project to be started in the beginning of 2018 in city of Malmö, Figure 11. It will have a span of 15 m with variable width from 4.6m in the widest part to 2.4m in the narrowest section, see Figure 12. The main incentive for choosing FRP was the lower life cycle cost of this concept in comparison to steel and concrete alternatives.



Figure 109. Concept of the Neptuni bridge in Malmö, Photo courtesy of municipality of Malmö

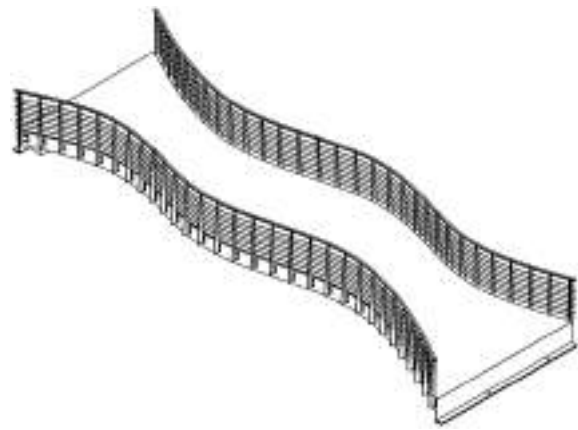


Figure 110. 3D illustration of the Neptuni bridge

SUMMARY AND CONCLUSIONS

FRP composites provide several benefits in bridge construction including: (i) flexibility in geometry and material choice (which of course come at a greater design effort, time and cost), (ii) lightweight, which offers smaller substructure, easier transport, faster installation and, all in all, off-site manufacturing and on-site assembly in addition to better quality, (iii) high specific strength and stiffness as well as good durability leading to resilient structures with large safety margins and low maintenance cost.

This paper presents the latest efforts in Sweden to increase the acceptance of FRP composites as a reliable, cost effective and sustainable building materials by authorities and infrastructure owners. At the present, according to investigations made in Falcon project, a good deal of interest at Swedish Transport Administration and local municipalities to use FRP composites in future bridge projects exists. The main reason is found to be the pressure on infrastructure owners, due to deterioration and consequent large maintenance costs of their assets. Dissemination activities such as demonstrations and workshops arranged in Falcon project, have led to an increased awareness about FRP technology for infrastructural use. Based on the learnings from the outcomes of the project, three main areas for improvement can be speculated:

- **Engineering education:** As mentioned earlier, bridge designers in Sweden, generally have very limited knowledge regarding FRP materials. In authors' view, it is the structural designer's knowledge which determines suitability of FRP for a certain project with specific circumstances in the first place. Providing teaching materials, design examples, coordinated workshops shall be an essential step towards creating the culture of using FRP in infrastructure in Sweden.



- **Lack of design codes and guidelines:** Lack of codes and regulations on design of FRP bridges adds to the difficulty associated with acceptance of FRP as a construction materials by major clients such as Swedish Transport Administration. Public procurement is strictly governed by laws and regulations so, in that sense, there is no difference between procuring a concrete bridge and an FRP bridge. The difficulty lies in technical questions such as reliability, accuracy of design models, durability and maintainability. It is believed that upon release of the “Technical Specifications” for FRP structures, which is under preparation by WG4 in CEN Technical Committee 250 - Structural Eurocodes in 2020, Ascione et al. (2017), a large part of technical and legal issues with acceptance of FRP solutions will be eliminated and new market opportunities for FRP constructions in Sweden will be arisen.
- **Integrated industrial manufacturing:** The level of interest from FRP manufacturers in other engineering disciplines has a direct relationship with the infrastructure market potential and attractiveness. However, FRPs are fundamentally innovative materials. They have not been resulted from improvement or modification of traditional construction materials. The supply chain of FRP structures is completely separated from those being used in civil engineering projects. At the present, there is a good potential interest among FRP manufacturers, especially from marine related, to enter FRP bridge market. However, the relationship between the FRP manufacturers and bridge design offices has not yet been realized. It of great importance for FRP manufacturing industry to comprehend the specific technical demands put by designers for bridge structures as the nature of bridge structures is completely different from types of products they use to deal with. This is mainly due to more serious consequences of failures and stringent legal issues. Manufacturing tolerances, defect sensitivity and transportation handling are three main areas of consideration which need to be improved. This is where the authors believe the role of universities and knowledge-based SMEs to connect the design offices to manufacturers will be pronounced.

Finally, Falcon is evaluated to be a great step forward and, as almost all the pilot FRP projects in Sweden, were initiated, procured and conducted with direct or indirect support of the expert team in the consortium. This support will continue for future projects as the great potential for FRP materials is realized in Sweden by all involved stake holders. A potential that can lead to considerable cost saving, less impact on the environment and creating new job opportunities.

ACKNOWLEDGMENTS

The authors acknowledge Vinnova (Sweden’s government agency for innovation) for financing and Swerea Sicomp for coordinating the Falcon project. We would like thank Mrs. Cecilia Ramberg, the coordinator of the LIGHTer program and Mr. Abbas Khayyami from municipality of Malmö for their interest and continuous support of the project.

REFERENCES

- Mara, V., Haghani, R., Sagemo, A., Storck, L., Nilsson, D., 2013, Comparative Study of Different bridge concepts based on life-cycle cost analysis and life-cycle assessment, Asia Pacific Conference on FRP in Structures (APFIS 2013), Dec 2013, Melbourne, Australia.
- Ascione, L. et al. (2017). “Prospect for New Guidance in the Design of FRP”, *Support to the implementation, harmonization and further developments of the Eurocodes*.



EXPERIMENTAL INVESTIGATION ON FLANGE LOCAL BUCKLING OF PULTRUDED GFRP BOX-SECTION UNDER FLEXURE

Tianqiao Liu¹ and Kent A. Harries^{1,2}

¹University of Pittsburgh, Civil and Environmental Engineering, Pittsburgh, USA (kharries@pitt.edu)

²University of Bath, BRE Centre for Innovative Construction Materials, Bath, UK

ABSTRACT

Flexural stability of various pultruded glass fibre reinforced polymer (pGFRP) profiles, such as I-, C- and box-sections, have been experimentally and analytically investigated in numerous studies in past decades. Flange local buckling (FLB) behaviour of pGFRP box-sections subject to flexure, however, has not been sufficiently studied through practical experiments. Consequently, a lack of data impedes the development and validation of theoretical predictions of the critical FLB behaviour of box-sections. To augment the data for box-sections, an experimental program, consisting of a series of four-point bending tests having various constant moment and shear span lengths, was conducted to investigate the FLB behaviour of pGFRP box-sections having slender flanges subject to flexure. The sections and loading patterns were intentionally selected to promote FLB behaviour. Additionally, in order to accurately evaluate the mechanical properties of the specimens, material characterisation tests were carried out. Experimentally determined critical FLB moments were contrasted with the analytical solution for an infinitely long plate supported at its edges subject to uniform compression. Variations of this solution are used by all known design guides. The lower bound prediction, using measured material properties provided a reasonable and suitably conservative estimate of actual behaviour for the 102 x 152 x 6.4 mm box sections tested.

KEYWORDS

All FRP and smart FRP structures; Experimental Study; Flange Local Buckling

INTRODUCTION

Pultruded glass fibre reinforced polymer (pGFRP) composite materials have been widely used as structural members in various types of civil infrastructures. Due to their low modulus and high anisotropy, pGFRP structural profiles tend to exhibit local and global buckling behaviours prior to achieving the material strength limit state. Flange local buckling (FLB) behaviour of pGFRP I-sections subject to flexure has been identified as a dominant limit state in a number of experimental studies (Barbero et al. 1991; Pecce and Cosenza 2000 and Correia et al. 2011). Bank et al. (1996) identified the importance of the rotational stiffness of flange-web junction (affecting the boundary condition of the flange) on the FLB behaviour of pGFRP I-sections. More recently, Vieira et al. (2017) carried out 62 four-point bending tests on pGFRP I-sections having four different flange slenderness ratios ($b/2t = 12, 10, 8$ and 6) identifying those having $b/2t \geq 8$ as being susceptible to FLB. Through previous studies, it is shown that slender flange plates and poor rotational restraint at flange-web junctions of pGFRP I-sections can result in FLB behaviour and therefore reduced flexural capacity. Given the anisotropy and dimensional constraints of pGFRP, it is evident that wide-flange I-sections are not most efficient pGFRP shape. It is suggested that box-sections – having two supporting edges for the compression flange – are a more efficient pGFRP section for resisting flexure. Despite this, only eight experimental flexural tests on 100 x 100 x 4.3 mm box-sections (Barbero et al. 1991) are found in the literature. These box-sections sections had a flange slenderness ratio, $b/t = 23.2$ and exhibited FLB behaviour. The lack of FLB data on box-sections primarily results from the fact that square pGFRP box-sections [having typical wall thicknesses] simply do not exhibit FLB behaviour prior to achieving their flexural capacity. Nonetheless, there are rectangular pGFRP box-sections available that have sufficiently high flange slenderness [in weak axis flexure] that FLB becomes a dominant ultimate limit state.

Analytical models based on plate theory and the energy method have been proposed to determine the critical FLB moment capacity of pGFRP box-sections (Barbero et al. 1991; Qiao et al. 2001; Kollár 2003; Correia et al. 2011). Existing consensus design guides address FLB of box-sections in variations of the same manner. Each adopts the analytic solution for an infinitely long plate, supported at its transverse edges subject to a uniform compression field. The critical compression stress, f_{cr} , in this case is given by Equation 1 and the critical moment by $M_{cr} = S f_{cr}$ where S is the elastic section modulus of the cross section. Each guideline prescribes different values for α and β .

$$f_{cr} = \frac{\pi^2}{t_f b_f^2} \left[\alpha \sqrt{D_{11}^f D_{22}^f} + \beta (D_{12}^f + 2D_{66}^f) \right] \quad (1)$$



Where D_{ij}^f are the flexural stiffness parameters of the orthotropic flange plate having width b_f and thickness t_f ; $D_{11} = E_L t_f^3 / 12(1 - \nu_{LT} \nu_{TL})$; $D_{22} = E_T t_f^3 / 12(1 - \nu_{LT} \nu_{TL})$; $D_{12} = \nu_{LT} D_{22}$; and $D_{66} = G_{LT} t_f^3 / 12$. The minor Poisson's ratio may be calculated as: $\nu_{TL} = E_T \nu_{LT} / E_L$. E_L and E_T are the longitudinal and transverse moduli of elasticity of the flange plate, respectively.

Setting $\alpha = \beta = 2$ corresponds to the case of a simply supported plate while the case of plate fixed along its transverse edges corresponds to $\alpha = 4.53$ and $\beta = 2.44$. EUR 27666 (2016) reports these values as lower and upper limits of box-section FLB behaviour without additional guidance. The 2010 ASCE Prestandard (ASCE 2010) adopted Kollar's (2003) equations to better define the critical stress between these limits by defining α and β to account for the rotational stiffness of the flange supports. This approach is often considered unnecessarily complex for design equations and design is often conducted using the lower bound case without adjustment. In any case, the design equations promulgated in design guides are based on plate theory solutions and – due to the lack of available data – have not been validated with experimental results. In this work, to augment the data in the field, an experimental program was carried out to investigate the FLB behaviour of pGFRP box-sections; results were compared with Equation 1.

EXPERIMENTAL PROGRAMME

In this work, an experimental program of four-point flexure tests, was conducted on pGFRP box-sections to investigate flange local buckling (FLB) behaviour. In order to have a relatively high flange slenderness and minimize the lateral torsional buckling behaviour, two 102 x 152 x 6.4 mm rectangular box-sections (denoted B1 and B2) were tested in weak-axis flexure. In each beam it was found that the two 152 mm flange plates had considerably different thickness (presumably resulting from a misalignment of the inner and outer pultrusion dies). Thus, the test specimens were further denoted as F1 and F2 to indicate their orientation during testing – whether flange 1 or 2 is the compression flange. The measured cross section geometries of the specimens are shown in Table 1. All tests were conducted in the linear range of the material, permitting each specimen (B1 and B2) to be tested in both orientations (F1 or F2 in compression). Additionally, the specimens were tested over decreasing span lengths. This approach to testing the same specimens multiple times – ensuring only limited elastic buckling – has been demonstrated in previous studies including Vieira et al. (2017).

Table 35: Specimen geometry

Beam Specimen	B1		B2	
nominal designation, $d \times b \times t$	102 x 152 x 6.4 mm			
Compression flange	F1	F2	F1	F2
depth, d	101.5 mm		101.4 mm	
flange width, b	152.3 mm		152.3 mm	
flange thickness, t_f	7.08 mm	6.07 mm	6.98 mm	6.07 mm
b/t_f	21.5	25.1	21.8	25.1
web thickness, t_{w1}	6.25 mm		6.29 mm	
web thickness, t_{w2}	6.74 mm		6.70 mm	

The pGFRP box sections used were fabricated with a fire retardant polyester (PE) resin. The 6.4 mm wall thickness contains three rovings of primary reinforcement and has a fibre volume ratio, $V_f = 0.37$. The experimentally determined material properties of the pGFRP box-sections are given in Table 2. It can be seen that measured properties are all greater than the manufacturer-reported values as well as the minimum requirements prescribed by ASCE (2010). In all subsequent calculations in this work, the measured material properties are used.

In this work, following the test method by Vieira et al. (2017), a 900-kN capacity four-point bending test set-up was used for all specimens, as shown in Figure 1a. Both specimens, B1 and B2, were tested over the span configurations, shown in Table 3. Three electrical resistance strain gages spaced at $b/2 = 75$ mm, centred on the midspan, were installed on the compression flanges of each specimen (Figure 1b). The expected buckling half-wave length for a box-section is b ; therefore this gage arrangement is sufficient to capture buckling behaviour.



Table 2: Material properties of pGFRP box-sections

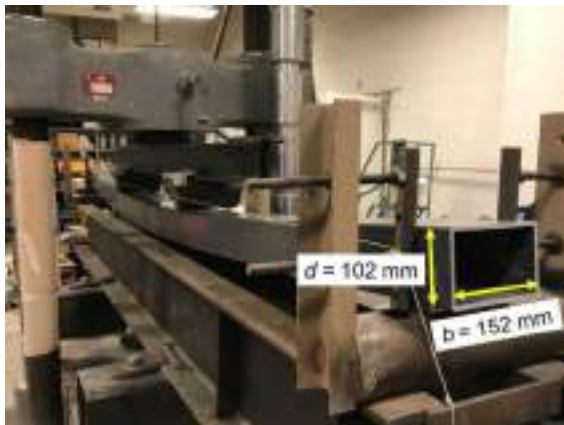
Material property	Test method	Experimentally obtained value (COV)	Manufacturer reported value	ASCE (2010) minimum requirement
		Flange	Flange/Web	Flange/Web
E_{Ll} (MPa)	ASTM D3039	21824 (0.09)	17200	20685
E_{Lc} (MPa)	ASTM D695	21367 (n.a.)	17200	20685
E_T (MPa)	nonstandard ¹	11260 (0.03)	5500	5516
E_{Lf} (MPa)	ASTM D7264	18485 (0.08)	12400	n.a.
G_{LT} (MPa)	ASTM D3518	3399 (0.03)	3100	2758
ν_{LT}	ASTM D3039	0.29 (n.a.)	n.a.	0.30 ²

¹ see Liu et al. (2017)
² in absence of test data, $\nu_{LT} = 0.30$ is permitted by ASCE (2010).

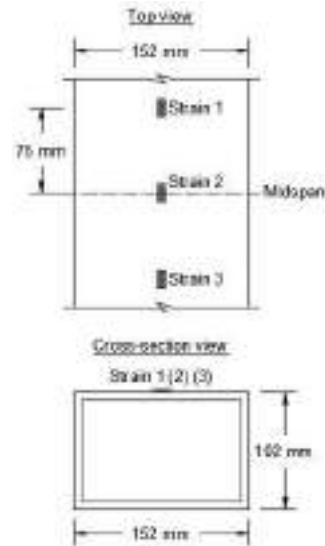
Table 3: Span configurations

Test ¹	shear span (mm)	constant moment region (cmr) (mm)	simple span (mm)	Test set-up
B1-F1-700	750	700	2200	
B1-F1-800	800	800	2400	
B1-F2-700	750	700	2200	
B1-F2-800	800	800	2400	
B2-F1-900	900	900	2700	
B2-F1-1000	850	1000	2700	
B2-F1-1100	800	1100	2700	
B2-F2-900	900	900	2700	
B2-F2-1000	850	1000	2700	
B2-F2-1100	800	1100	2700	

¹test designation: [beam]-[compression flange]-[cmr span]; that is, B1-F1-700 corresponds to beam B1 tested such that flange F1 is in compression over constant moment region of 700 mm.



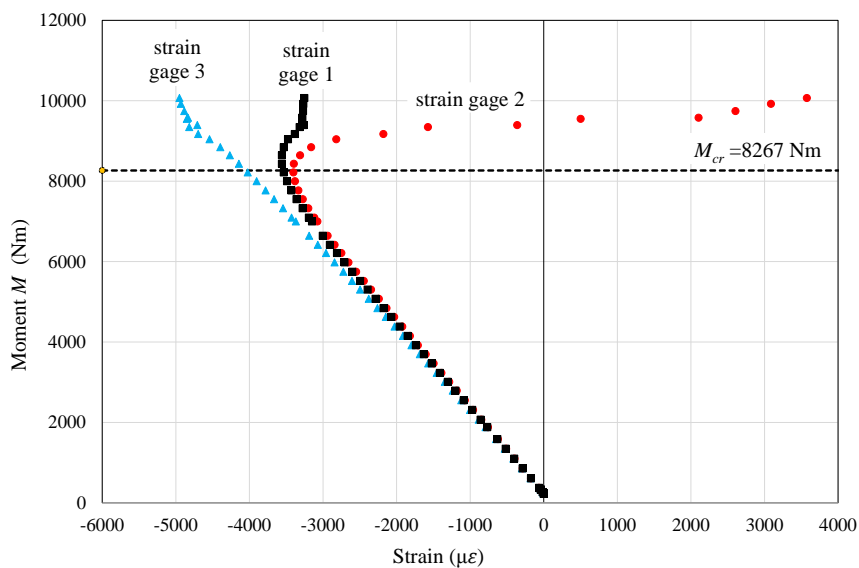
a) Four-point bending test set-up (B2-F2-900 shown)



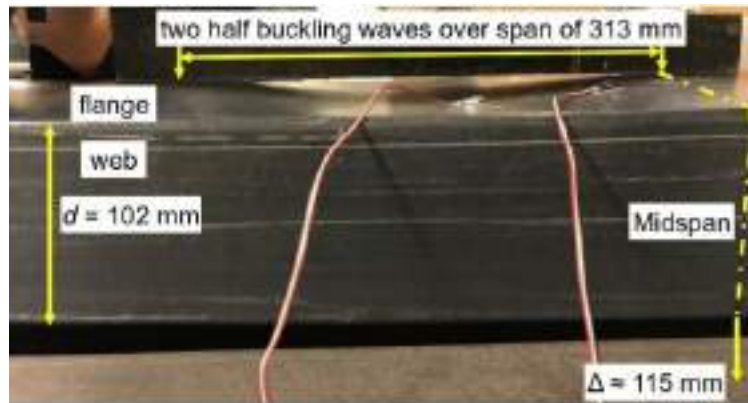
b) Strain gage layout in constant moment region for each test arrangement

Figure 1: Four-point bending test set up and instrumentation.

The moment-strain curves determined during testing were used to determine the critical FLB moments. An example is shown in Figure 2a in which the critical buckling moment, $M_{cr} = 8267$ Nm is determined from the obvious bifurcation of, in this case, strain gage 2. An image of the compression flange of the same specimen is shown in Figure 2b. The flange buckling is readily apparent. Strain gage 2, located at midspan, is clearly located on the tension side of the buckle as indicated by the strains shown in Figure 2a. Additionally, the buckle half-wave length can be determined as twice length between peak amplitudes, in this case 156 mm, very close to the expected value of 152 mm, the box-section flange width. The critical buckling moments for all tests are given in Table 4.



a) moment-strain response; $M_{cr} = 8267$ Nm



b) image of compression flange buckling

Figure 2: Compression flange behaviour of specimen B2-F2-900

COMPARISONS WITH PREDICTED FLB BUCKLING CAPACITY

In Table 4, experimentally determined critical FLB moments were compared with lower ($\alpha = \beta = 2$) and upper ($\alpha = 4.53$ and $\beta = 2.44$) bound predictions given by Equation 1. The lower bound predictions are often used in design. The values between lower and upper bound predictions reflect the rotational stiffness of the flange supports at the web; where the lower bound represents a pinned condition and the upper bound a fixed condition. Kollár (2003) provides a method of calculating the elastic rotational stiffness of the flange-web junctions supporting the box-section compression flange and therefore is thought to represent a more accurate solution. For the box section tested, Kollár's formulation leads to parameters $\alpha = 3.00$ and $\beta = 2.06$ for flange F1 and $\alpha = 3.30$ and $\beta = 2.11$ for flange F2.

In the analytical predictions shown in Table 4 measured geometric and material properties (Tables 1 and 2) are used. For simplicity, the average web thickness, $t_w = 6.50$, was used when required. In all calculations, the longitudinal modulus determined for flexural tests, E_{L_f} , is used to characterise flange buckling behaviour as recommended by Cardoso (2014) in relation to FLB of axially loaded members and Liu (2017) in relation to FLB of members in flexure. The use of E_{L_f} in flange buckling formulations is described at length in Liu et al. (2018).

Table 4: Experimentally and analytically determined critical FLB moments

Test	Experimentally determined critical FLB moments	Analytically determined critical FLB moments					
		lower bound Eq. 1 with $\alpha = \beta = 2$		Kollár (2003) α and β given in text		upper bound Eq. 1 with $\alpha = 4.53$ and $\beta = 2.44$	
		M_{cr} (Nm)	M_{cr} (Nm)	pred/ex p	M_{cr} (Nm)	pred/ex p	M_{cr} (Nm)
B1-F1-700	12558	10634	0.85	13933	1.11	19615	1.56
B1-F1-800	12310	10634	0.86	13933	1.13	19615	1.59
B1-F2-700	9954	7238	0.73	10200	1.02	13351	1.34
B1-F2-800	9207	7238	0.79	10200	1.11	13351	1.45
B2-F1-900	10315	10226	0.99	13490	1.31	18861	1.83
B2-F1-1000	11414	10226	0.90	13490	1.18	18861	1.65
B2-F1-1100	12059	10226	0.85	13490	1.12	18861	1.56
B2-F2-900	8267	7218	0.87	10170	1.23	13313	1.61
B2-F2-1000	7216	7218	1.00	10170	1.41	13313	1.85
B2-F2-1100	7425	7218	0.97	10170	1.37	13313	1.79

As shown in Figure 3, the experimentally obtained results fall between the ideal lower and upper bound predictions and tend to fall closer to the lower bound. The calculation that includes the effect of rotational stiffness of the flange-web junction (Kollár 2003) overestimates the experimentally observed values; although this overestimation falls as the moment span becomes shorter. None of the ideal calculations account for imperfections or variations in geometry or material properties; and thus the over-prediction is not unexpected. Furthermore, the calculation of the flange-web junction rotation stiffness, itself, is ideal and may therefore tend to overestimate this stiffness. Like plate flexural properties (Liu et al. 2018), the rotational stiffness of the flange-web junction will be impacted by the fibre architecture as the fibre rovings transition from flange to web.

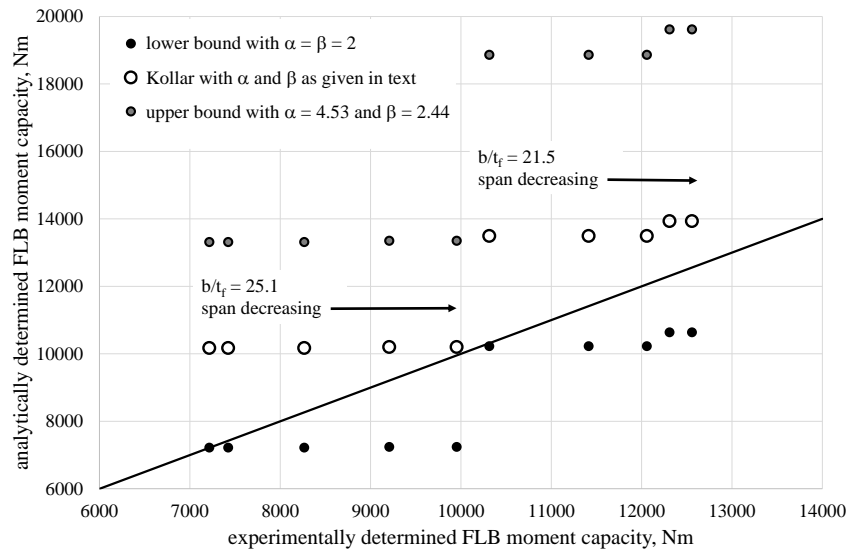


Figure 3: Experimental versus analytically determined FLB moment capacity

The calculations in Table 4 use measured material properties. For design, nominal or manufacturer-reported properties are likely to be used. In this case, using manufacturer-reported properties rather than measured properties (see Table 2) in Equation 1 results in reduction in all predicted values of approximately 40%. While safely conservative, such under prediction of capacity results in inefficient material utilisation.

CONCLUSIONS

In this work, ten four-point bending tests were conducted on pGFRP box-sections. Flange local buckling (FLB) behaviour was observed and critical FLB moments were obtained. Experimental results were compared with the analytical solution for an infinitely long plate supported along its edges subject to a uniform compression stress (Equation 1).

Experimental results fall between lower and upper bound predictions based on ideal sections. The lower bound prediction, using measured material properties provides a reasonable and suitably conservative estimate of actual behaviour for the 102 x 152 x 6.4 mm box sections tested. Using the lower bound prediction – with measured material properties – would appear to incorporate initial imperfections and variations in geometry and material properties. However, universally adopting lower-bound predictions in design may result in variation in the resulting reliability of predictions.

ACKNOWLEDGEMENT

The authors wish to thank Bedford Reinforced Plastics for providing pGFRP materials used in this work.

REFERENCES

American Society of Civil Engineers. (ASCE). (2010). *Pre-Standard for Load and Resistance Factor Design (LRFD) of Pultruded Fiber Reinforced Polymer (FRP) Structures*.



- Barbero, E. J., Fu, S. H., and Raftoyiannis, I. (1991). Ultimate bending strength of composite beams. *ASCE Journal of Materials in Civil Engineering*, **3**(4), 292-306.
- Bank, L. C., Gentry, T. R., and Nadipelli, M. (1996). Local buckling of pultruded FRP beams-analysis and design. *Journal of reinforced plastics and composites*, **15**(3), 283-294.
- Cardoso, D.T.C. (2014) *Compressive Strength of Pultruded Glass-Fiber Reinforced Polymer (GFRP) Columns*, PhD Dissertation, COPPE, Federal University of Rio de Janeiro.
- Correia, J. R., Branco, F. A., Silva, N. M. F., Camotim, D., and Silvestre, N. (2011). First-order, buckling and post-buckling behaviour of GFRP pultruded beams. Part 1: Experimental study. *Computers and Structures*, **89**(21), 2052-2064.
- EUR 27666 (2016) Prospect for new guidance in the design of FRP (Ascione L., Caron J.F., Godonou P., van IJselmuiden K., Knippers J., Mottram T., Oppe M., Gantriis Sorensen M., Taby J., and Tromp, L.)
- Kollár, L. P. (2003). Local buckling of fiber reinforced plastic composite structural members with open and closed cross sections. *ASCE Journal of Structural Engineering*, **129**(11), 1503-1513.
- Li, Z., and Schafer, B.W. (2010) "Buckling analysis of cold-formed steel members with general boundary conditions using CUFSM: conventional and constrained finite strip methods." Proceedings of the 20th Int'l. Spec. Conf. on Cold-Formed Steel Structures, St. Louis, MO. November, 2010.
- Liu, T. (2017). Stability Behavior of Pultruded Glass-Fiber Reinforced Polymer I-Sections Subject to Flexure. Doctoral dissertation, University of Pittsburgh.
- Liu, T., Harries, K.A. and Guo, Q. (2018) Effects of Fiber Architecture on Flexure Properties of Pultruded GFRP Plates and Sections, Proceedings of the 9th International Conference on Fibre-Reinforced Polymer Composites in Construction (CICE 2018), Paris, July 2018.
- Liu, T., Cardoso D. T., Vieira J. D., and Harries K. A. (2017). Convenient and Inexpensive Test Methods for Pultruded GFRP Composite Materials. *Advanced Composites in Construction*. Sheffield, UK, September 2017.
- Pecce, M., and Cosenza, E. (2000). Local buckling curves for the design of FRP profiles. *Thin-walled structures*, **37**(3), 207-222.
- Qiao, P., Davalos, J. F., and Wang, J. (2001). Local buckling of composite FRP shapes by discrete plate analysis. *ASCE Journal of Structural Engineering*, **127**(3), 245-255.
- Vieira, J., Liu, T. and Harries, K.A. (2017) Flexural Stability of Pultruded GFRP I-Sections, ICE Structures and Buildings <http://dx.doi.org/10.1680/jstbu.16.00238>



BEHAVIOR OF GFRP WALL PANEL WITH INTERNAL TUNED LIQUID COLUMN DAMPER

H. Wu¹, A. Chen² and S. Laflamme³

¹ Iowa State University. Department of Civil, Construction and Environmental Engineering, USA,
Email: haowuj@iastate.edu;

² Iowa State University. Department of Civil, Construction and Environmental Engineering, USA,
Email: achen@iastate.edu;

³ Iowa State University. Department of Civil, Construction and Environmental Engineering, Department of
Electrical and Computer Engineering, USA, Email: laflamme@iastate.edu.

ABSTRACT

Pultruded Glass Fiber-Reinforced Polymer (GFRP) structures have been increasingly used in buildings and civil infrastructure systems because of their high strength, light weight, durability, and fatigue resistance. However, these structures are elastic and typically have low damping ratio, which limits their capability to dissipate energy during earthquakes. Adding damping mechanisms to GFRP components can improve traditional structures' resistance to lateral loads. This paper studies a cellular GFRP wall panel with an internal liquid flow system, engineered to control a structure's temperature using liquid as thermal exchange. In this study, we further adapt the panel to allow oscillation of water in its internal hollow cells, providing supplemental damping for the GFRP structure during seismic events. Different combinations of water heights and cell openings are evaluated using shaking table tests to study vibration reduction of the GFRP wall panel by leveraging the motion of water. For each combination, the natural frequency of TLCD can be predicted with a simple model. It is found that higher water volume inside the panel can achieve greater mitigation. A Computational Fluid Dynamics (CFD) model is created to study the liquid motion inside the GFRP panel under harmonic ground excitations. Results from the CFD simulation are in good agreement with those from the test.

KEYWORDS

Pultruded GFRP, Seismic resistance, Tuned liquid column damper, CFD simulation.

INTRODUCTION

Pultruded GFRP structures have been widely studied, showing as good alternatives to steel and Reinforced Concrete (RC) solutions due to their high strength-weight ratio, easy installation, and corrosion resistance. Common applications include low-rise buildings, bridge decks, space structures, towers, etc. Static tests demonstrated that GFRP components are viscoelastic and anisotropic (Ascione et al. 2011; Wattick and Chen 2017). Several other researchers studied the dynamic behavior of pultruded GFRP structures. Boscato and Russo (2009) showed that GFRP structures tended to have low frequency and high deformability, which may be leveraged to mitigate seismic loading. While it was discussed that pultruded FRP does not suffer significant degradation after large numbers of cyclic loading (Yang et al. 2009), it was found that GFRP structures have low damping ratios (usually less than 2%), and their performance in dissipating vibration energy was poor (Russo 2012). It follows that the inclusion of damping mechanisms inside pultruded GFRP structures can result in a significant enhancement of their lateral load mitigation performance.

This study focuses on a GFRP panel structure with an internal liquid flow system. This GFRP panel has a cellular section and functions as an exterior structural wall. The internal liquid system is originally intended as a circuit cooling and heating system using liquid as the thermal exchanger to control for a structure's temperature. We propose to leverage the internal liquid flow system to provide supplemental damping capability for the GFRP panel structure. Liquid motion, such as flow through orifices and sharp corners of the internal pipe network, can result in liquid head loss, dissipating kinetic energy. This damping mechanism can be found in some structures in the form of a tuned liquid column damper (TLCD), which is a specialized passive damping device that leverages the liquid's gravity force as the restoring force and generates damping from the head loss around orifices and sharp corners. TLCDs have been effectively used in suppressing the vibration of tall buildings and long bridges under wind or earthquake hazards (Shum et al. 2008; Min et al. 2014). Both design procedures and experimental studies have been conducted on TLCDs (Connor and Laflamme 2014; Di Matteo et al. 2014). More recently, Computational Fluid Dynamics (CFD) method was introduced to validate TLCD numerically (Cammelli et al.

2016). Min et al. (2014) proposed a novel passive TLCD with multiple cells that can be opened or sealed after installation, and provided a methodology to compute the natural frequencies of multi-celled liquid damper system.

This paper first describes a shaking table test on the proposed GFRP panels with an internal TLCD, demonstrating that this damping system can reduce the panel's vibrations under harmonic ground excitations. Next, a simple model is presented to compute the TLCD's natural frequency. Lastly, CFD models are created to simulate the liquid motion and measure the damping forces generated by the internal damper.

SHAKING TABLE TEST

Test setup

The pultruded GFRP panel is a 7-celled geometry with a dimension of 121.1 cm × 61.0 cm × 8.1 cm (height × width × depth), as shown in Fig. 1. The thickness of the outer and inner shells are 0.297 cm and 0.218 cm, respectively. Both in-plane and out-of-plane properties obtained from material tests are summarized in Table 1 (Wu and Chen 2016).

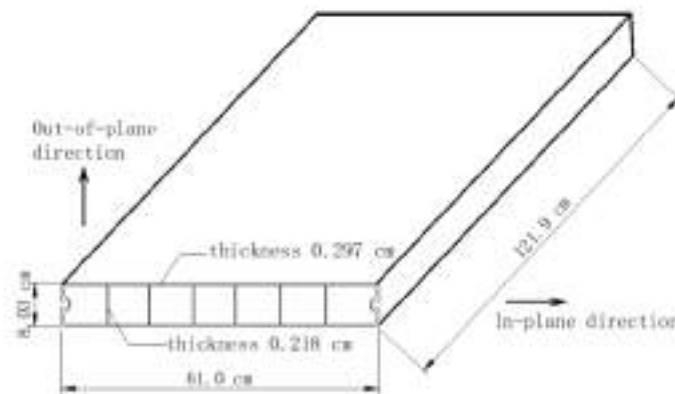


Figure 1 Geometry of the pultruded GFRP panel

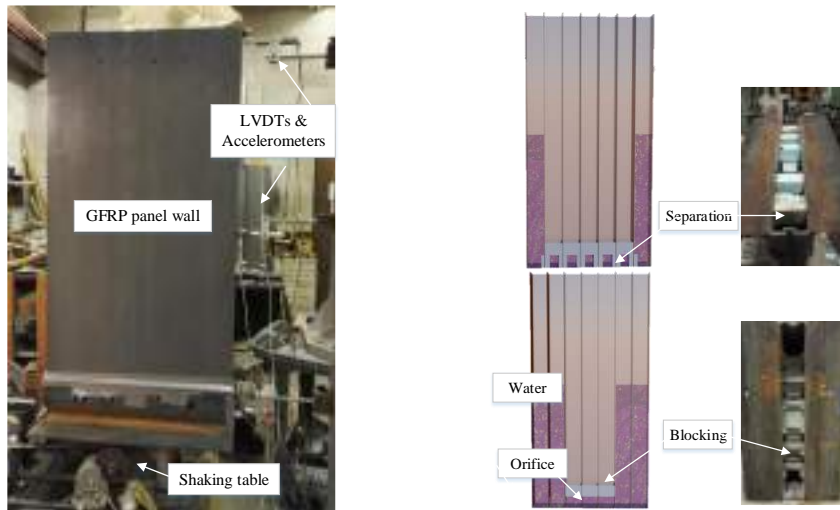
Table 1. Material property of pultruded GFRP

Directions	Elastic modulus	Poisson's ratio	Strength	Moment of Inertia
Out-of-plane	5.52 GPa	0.27	162 MPa	$6.62 \times 10^6 \text{ mm}^4$
In-plane	6.10 GPa	0.27	130 MPa	$1.76 \times 10^8 \text{ mm}^4$

The shaking table test is conducted in the Structural Engineering Research Laboratory at Iowa State University. The test setup is shown in Fig. 2a. A steel block is attached at the top of the GFRP panel to mimic the seismic weight from the dead load and 20% of the snow load. The panel itself is attached to the shaking table by steel bolts and to reproduce a fixed support at the bottom. Harmonic ground excitations generated by the shaking table are recorded by an accelerometer and a Linear Variable Differential Transformer (LVDT) using MEGADAC data acquisition system at a sampling rate of 2000 Hz. Two other accelerometers and LVDTs are installed at the middle and top of the panel to record its acceleration and deformation. The shaking table can generate harmonic ground motions with a frequency ranging from 10 to 60 Hz. Displacement and acceleration of for two harmonic ground motions of different frequencies are shown in Table 2 and Fig. 3. The panel vibration amplitude, which is defined as the difference between the panel's top and bottom displacements, is directly related to the panel deformation.

The interior of the TLCD system is shown in Fig 2b, where 5 cm × 5 cm square orifices are cut at the bottom to allow water to flow freely across all cells. Different numbers of cells are blocked using hard foam to limit water motion in these cells, as illustrated in Fig. 4a. Different water heights are investigated, i.e., 0 cm, 31 cm, 62 cm and 93 cm, as illustrated in Fig. 4b. For each scenario, a companion test is conducted under the water distribution but with the orifices blocked to prevent water motion (Fig.2b). The inclusion of water changes the mass distribution of the panel and increases the lateral inertia force. The research goal of this study is to quantify the vibration reduction provided by the water flow. Comparison of the vibration amplitudes between cases where

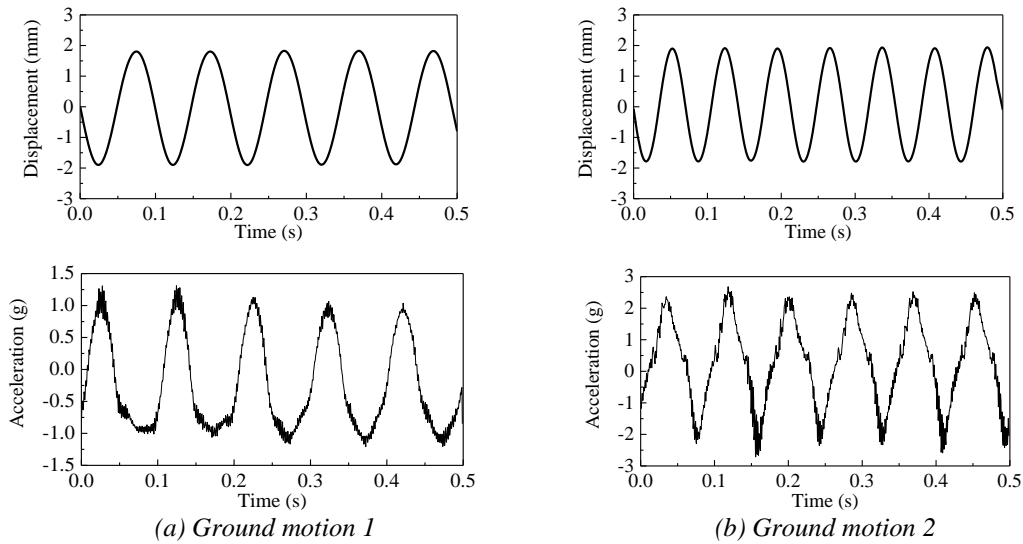
water flows freely and cases where water motion is blocked can help quantify this damping effect by excluding the effect of increased liquid inertia force from the test results.



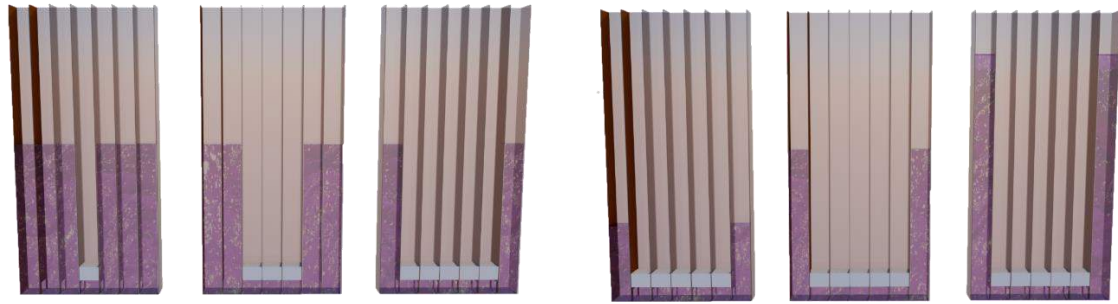
(a) GFRP panel mounted on the shaking table (b) Interior of the multi-celled GFRP wall
Figure 2 Shaking table test setup

Table 2. Harmonic ground motions of shaking table tests

Ground Motion	Frequency	Max displacement	Max acceleration
1	10.1Hz	1.85 cm	1.4g
2	12.6Hz	1.93 cm	2.5g



(a) Ground motion 1 (b) Ground motion 2
Figure 3 Harmonic ground motions



(a) Different number of cells opened (b) Different water heights
Figure 4 Different water distribution configurations inside the GFRP panel

Natural frequency of TLCD

Due to the symmetry of water heights and cell openings, the natural frequencies of the TLCD can be estimated using a liquid column vibration absorber (LCVA) model proposed by Hitchcock et al. (1994). An LCVA is a specialized TLCD with unequal horizontal and vertical cross sections. Min et al. (2014) suggested that adjacent cells can be combined by recalculating the effective length from centerlines (Fig. 5):

$$\omega = \frac{1}{2\pi} \sqrt{\frac{2g}{B \cdot A_v / A_h + 2H}} \quad (1)$$

where A_v , A_h are the vertical and horizontal tube cross section areas, respectively, g is the gravitational acceleration, B is the effective length between tube centerlines, and H is the water height. Based on this model the TLCD's natural frequencies under investigation range from 0.457 Hz to 0.716 Hz.

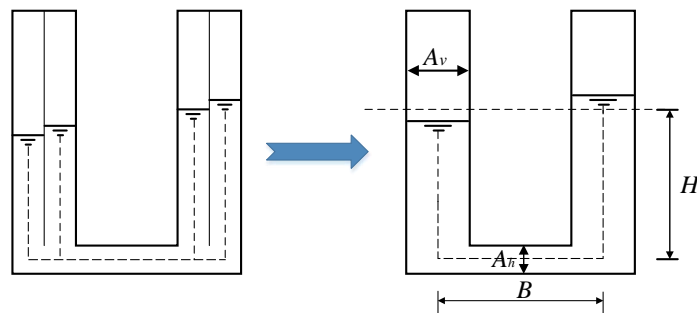


Figure 5 Model used in the computation of natural frequencies

Test results and discussion

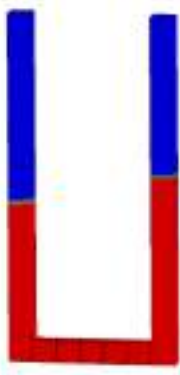
The GFRP panel's displacement amplitudes under ground motions 1 and 2 are summarized in Table 3. Since the ground motions are harmonic waves, the vibration amplitude is a good indication of the maximum panel deformation during the shaking table test. The vibration amplitude is larger when more water is included due to the increased inertia force, which offsets the damping effect provided by water head loss. From the test results, it can be observed that in all the cases the GFRP panel's vibration is reduced when water is allowed to flow freely compared to the cases where water flow is blocked, indicating that the TLCD system provides damping. The percentage of the amplitude reduction increases as the cell number increases, but nonlinearly. Increased water height also results in a greater vibration reduction, with the exception that the maximum water height (93 cm) leads to a slightly lower reduction for the 2 and 6 cells cases. This is attributed to the water motion slowing down when the water fills most of the panel. It is noted that the frequency of the generated ground motion is higher than that of the TLCD configurations, which is due to the limitations of shaking table. This test can be viewed as a preliminary test to access the effect of liquid damping on GFRP panels.

Table 3. Vibration amplitude of GFRP panel (mm)

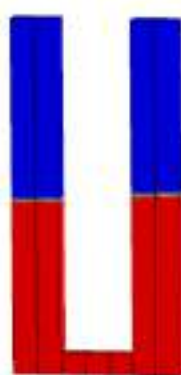
	Water height	0 cm	31 cm	62 cm	93 cm
Ground motion 1, 2 cells filled	water flow blocked	0.576	0.706	0.770	0.921
	free water flow	0.576	0.680	0.724	0.875
Reduction percentage (%)		0.00	3.75	6.34	5.26
Ground motion 2, 4 cells filled	water flow blocked	1.168	1.372	1.651	2.057
	free water flow	1.168	1.295	1.549	1.880
Reduction percentage (%)		0.00	5.88	6.56	9.46
Ground motion 1, 6 cells filled	water flow blocked	0.584	0.711	0.838	0.965
	free water flow	0.584	0.635	0.660	0.787
Reduction percentage (%)		0.00	12.00	26.92	22.58

CFD SIMULATIONS

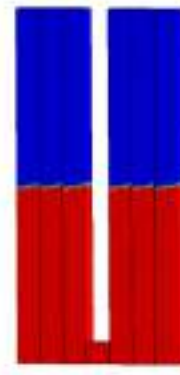
In order to better understand the water flow inside the pultruded GFRP panel and the damping performance of the internal TLCD, the liquid motion is simulated using the CFD method in the ANSYS 17.2 Fluent software. The model is solved using a standard k- ϵ solver, which is widely used to simulate turbulent flow. Figure 6 shows the water motion under harmonic ground motions when half the panel is filled with water. For the 2 cells case, the water surface fluctuates over a range of 8 cm. The 4 cells case shows a smaller water oscillation amplitude of 3 cm. For the 6 cells case, it is observed that there is not only water flow between different cells, but also water sloshing within each individual cell.



(a) 2 cell, 62 cm water height



(b) 4 cell, 62 cm water height



(c) 6 cell, 62 cm water height

Figure 6 CFD simulations of water motion (red represents water)

The CFD method can be used to evaluate the damping capability of TLCDs by computing the total lateral dynamic pressure acting on the GFRP panel. The time series of damping force, plotted in Fig. 7, can be obtained by subtracting the inertia force to the lateral reacting force of the GFRP panel. The magnitudes of the damping forces for the 2 cells, 4 cells and 6 cells are 27 N, 33 N, and 56 N, respectively, corresponding to the amplitude reduction percentage trend from the shaking table test. The damping forces are comparable to the GFRP panel's self-weight and may reduce GFRP structure's vibration during seismic events.

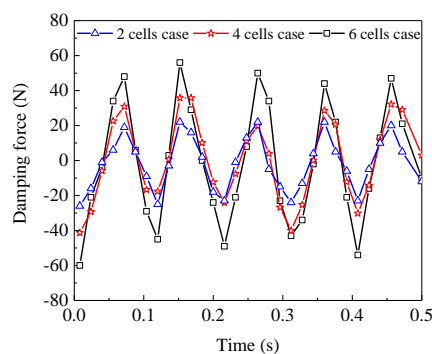


Figure 7 Time series of damping force



CONCLUSION

In this paper, a GFRP panel with an existing internal liquid flow system was adapted into a TLCD system, which can dissipate kinetic energy during seismic events. Shaking table tests were conducted to evaluate the damping effect of the TLCD system. Test results demonstrate that, compared to the cases without water flow, vibrations in the GFRP panel are reduced. This reduction effect generally increases with the water height and number of cells filled with water. CFD models show that the damping forces generated from TLCDs have the same trend as those from the experimental tests, and that their amplitudes are comparable to the GFRP panel's self-weight. The damping mechanism can be a promising technique to promote wider applications of pultruded GFRP structures in seismic regions.

ACKNOWLEDGMENTS

This material is based in part upon work supported by the National Science Foundation under Grant No. CMMI-1562992. Any opinions, findings, and conclusions or recommendations expressed in this material are those of the authors and do not necessarily reflect the views of the National Science Foundation.

REFERENCE

- L. Ascione, V. P. Berardi, A. D'Aponte (2011). "A viscoelastic constitutive law for FRP materials", *International Journal for Computational Methods in Engineering Science and Mechanics*, 12(5), 225-232.
- G. Boscato, S. Russo (2009). "Free vibrations of pultruded FRP elements: Mechanical characterization, analysis, and applications", *Journal of Composites for Construction*, 13(6), 565-574.
- S. Cammelli, Y. F. Li, S. Mijorski (2016). "Mitigation of wind-induced accelerations using Tuned Liquid Column Dampers: Experimental and numerical studies", *Journal of Wind Engineering and Industrial Aerodynamics*, 155, 174-181.
- J. Connor, S. Laflamme (2014). *Structural motion engineering*. New York, Springer.
- A. Di Matteo, F. L. Iacono, G. Navarra, A. Pirrotta (2014). "Experimental validation of a direct pre-design formula for TLCD", *Engineering Structures*, 75, 528-538.
- P. A. Hitchcock, K. C. S. Kwok, R. D. Watkins, B. Samali (1994). "The effectiveness of a multiple liquid column vibration absorber", *Proceedings of the 4th Workshop on Wind Engineering*, Australian Wind Engineering Society, Sydney, 81-86.
- K. W. Min, J. Kim, H. R. Lee (2014). "A design procedure of two-way liquid dampers for attenuation of wind-induced responses of tall buildings", *Journal of Wind Engineering and Industrial Aerodynamics*, 129, 22-30.
- K. W. Min, C. S. Park, J. Kim (2015). "Easy-to-tune reconfigurable liquid column vibration absorbers with multiple cells", *Smart Materials and Structures*, 24(6), 065041.
- S. Russo (2012). "Experimental and finite element analysis of a very large pultruded FRP structure subjected to free vibration", *Composite Structures*, 94(3), 1097-1105.
- K. M. Shum, Y. L. Xu, W. H. Guo (2008). "Wind-induced vibration control of long span cable-stayed bridges using multiple pressurized tuned liquid column dampers", *Journal of wind engineering and industrial aerodynamics*, 96(2), 166-192.
- J. A. Wattick, A. Chen (2017). "Development of a prototype fiber Reinforced Polymer–Concrete Filled wall panel", *Engineering Structures*, 147, 297-308.
- H. Wu, A. Chen (2016). "Seismic Behavior of Glass FRP Wall Panels", 8th International Conference on FRP Composites in Civil Engineering
- X. Yang, Y. Bai, J.L. Luo, X.L. Zhao, F.X. Ding (2016). "Dynamic and fatigue performances of a large-scale space frame assembled using pultruded GFRP composites", *Composite Structures*, 138, 227-236.



EFFECTS OF HOLE GEOMETRY AND BOLT TIGHTENING ON CREEP BEHAVIOR OF PIN-BEARING PULTRUDED FRP CONNECTIONS

D.W. Scott¹ and J. Anwar²

¹ Georgia Institute of Technology, Atlanta, GA, USA, email: dscott@gatech.edu

² National University of Sciences and Technology, School of Civil Engineering, Risalpur, Pakistan

ABSTRACT

This paper presents the results of an experimental investigation into the time-dependent pin-bearing behavior of pultruded E-glass/polyester fiber-reinforced polymer (FRP) composite materials. In this study, long-term pin-bearing strength tests are carried out on single-bolt connections subjected to in-plane loading in tension under a double-lap shear configuration. The connection geometry is selected such that bearing is the predominant failure mode. The time-dependent response of the connection is evaluated at various load levels and lateral applied bolt torques. The time-dependent experiments are carried out for durations of up to 1,000 hours at sustained load levels of 60% and 90% of the characteristic short-term pin-bearing strength. The results indicate that increasing loads and lateral applied torque significantly increase bolt-hole deformations in the system. In addition, apparent increases in short-term pin-bearing strength due to lateral applied torque are lost when the FRP material exhibits viscoelastic behavior under sustained loading.

KEYWORDS

pultrusion, connections, creep, durability, design

INTRODUCTION

Connections in pultruded profiles can generally be divided into three categories: bolted, adhesively-bonded, and combined (bolted and bonded). Bolted connections are often preferred in civil engineering applications because of their practicability, ease of installation in the field, dismantling, and simple inspection procedures. The strength and failure mode(s) of a bolted connection are influenced by a variety of factors, including geometric parameters, environmental conditions, and loading type. As discussed by Mottram and Turvey (2003), the scope of testing required for evaluating the number of connection variables is so large that it may be impractical to carry out. Similarly, the response of bolted connections under sustained loading is a complex phenomenon because of the viscoelastic behavior of many FRP materials.

Pin-bearing strength (R_{br}) is typically computed as the projected area (specimen thickness t times bolt-diameter d) of the bolt bearing multiplied by characteristic pin-bearing strength (F_{θ}^{br}) (ASCE 2010.) By definition, the pin-bearing strength is the mean stress at bearing failure. However, the failure load is defined when the connection has no lateral restraint (Mottram 2009). To show the lack of consistency in measuring the pin-bearing strength, Mottram and Zafari (2011) presented a detailed review of standard test methods. Thoppul et al. (2009) reviewed the mechanics of bolted connections. Recently, Girão Coelho and Mottram (2015) presented a detailed review of the behavior of FRP connections and joints. Previous studies of the effects of lateral applied torque, lateral confinement area, and diameter-to-thickness ratio (d/t) are briefly discussed here because they are pertinent to the present work.

Stewart (1965) established the relationship between lateral torque and bolt tension and found that the torque coefficient was substantially constant at a value of 0.2 for all bolt diameters. Stockdale and Matthews (1976) concluded that bearing failure load was approximately proportional to the ratio of washer outside to inside diameter. Collings (1977) further established the relationship between torque and constraint stress. Kretsis and Matthews (1985) observed that the strength of laterally unrestrained specimens was less than “finger-tight” specimens by 20-30% and the ultimate bearing strength for “finger-tight” bolts decreased considerably as the d/t ratio increased. Abd-El-Naby and Holloway (1993) studied the effects of the area and the material used for clamping on bearing strength and observed that, in general, the strength increased as the confinement area increased. Cooper and Turvey (1995) studied the effect of joint geometry and bolt clamping torque on failure load and observed that as bolt torque increased, the bearing failure load increased significantly. Sun et al. (2002) observed that failure load increased as the size of the clamped area increased. Yuan and Liu (2005) conducted experiments on bolted connections in GFRP flat sheets and concluded that the ultimate load capacity increased as the bolt torque increased. Khashaba et al. (2006) found that the stiffness of the joint increased as the washer size



decreased and the load–displacement plots became increasingly nonlinear. The ASCE Pre-standard (ASCE 2010) specifies that bolts in bearing-type FRP connections need only be tightened to the “snug-tightened” condition. This condition has been defined by researchers as the tightness that exists when all parts in a joint are in firm, but not necessarily continuous contact. To prevent the likelihood of material crushing, the EUROCOMP Design Code and Handbook (Clarke 1996) specifies that the clamping force should not be higher than one-third of the through-thickness crushing strength of the material and in no event higher than 68 MPa. Mottram and Zafari (2011) showed that for a small bolt-hole clearance size, pin-bearing strength decreased by about 15% as the d/t ratio increased.

EXPERIMENTAL PROGRAM

Specimen Details

The pultruded material used in the study consists of e-glass continuous strand mat (CSM), e-glass fiberglass rovings, a synthetic surfacing veil, and an isophthalic polyester resin. Specimens were cut from 101.6 mm square-tube structural elements with a wall thickness of 6.35 mm. To determine the tensile properties, ten tests were conducted in accordance with ASTM D3039-14 (2006). Table 1 lists the mean and characteristic strengths, where F_L^t and E_L^t represent tensile strength and modulus in the longitudinal direction of the FRP, respectively. The Weibull probability distribution was assumed for the population as suggested by Zureick et al. (2006), and characteristic strengths were computed in accordance with ASTM D7290-06 (2011).

Table 1. Tensile properties of the FRP material

Property	F_L^t (MPa)	E_L^t (GPa)
Mean	358	21.8
Characteristic	287	17.6
Standard Deviation (SD)	26	1.3
% COV	7.3	7.0

Short-Term Tests

In the short-term tests, close-fit, single-bolt tension connections were loaded under a double-lap shear configuration. In this study, the “close-fit” condition is defined as a bolt hole with small clearance (≤ 0.3 mm). High-strength steel bolts were used having sufficient shaft lengths such that bolt threads were not in contact with the FRP material. The geometry of the test specimen was selected so that bearing was the expected mode of failure. Tests conducted at various e/d and w/d ratios showed that specimens failed consistently in bearing failure mode at e/d and w/d ratios of 8 and 6 respectively (where e is edge distance, d is bolt diameter, and w is connection width). Figure 1 shows the test setup and Table 2 provides the specimen geometry configuration. Tests were conducted using a computer-controlled hydraulic load actuator; pneumatic grips were used to mitigate slipping and crushing of the test specimen outside of the gage length. The bearing failure load was taken as the maximum load on the load-deflection curve. The effect of the d/t ratio was investigated for two lateral constraint conditions: laterally unrestrained and moderately torqued. In this study a test specimen with a “laterally unrestrained” condition is defined as having no lateral restraint on either side such that the specimen is free to deform laterally. Values representing moderate torque were calculated based on previous work in the literature. For a 6.35 mm diameter bolt, ASTM D5961-10 (2010) specifies a light lateral applied torque value of 2.2 to 3.4 N-m, and Kallmeyer and Stephens (1997) used a value of 5.65 N-m to represent moderate torque. Therefore, a torque value of 5.65 N-m was selected to represent moderate torque for a 6.35 mm diameter bolt. The lateral constraint stress was then computed in accordance with work done by Collings (1997). For an equivalent lateral constraint stress, torque values of 14.90, and 35.33 N-m were then computed to represent moderate torque for 9.53 and 12.7 mm diameter bolts respectively. The torque coefficient k was assumed to be 0.2; other details are given in Table 3.

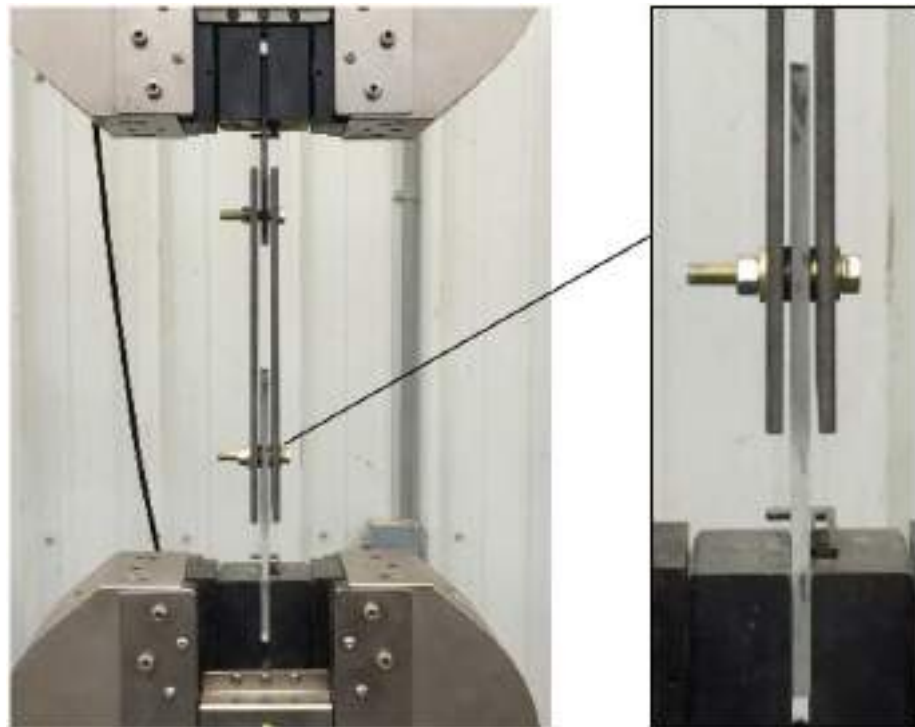


Figure 1. Short-term pin-bearing test arrangement – moderately torqued specimen

Table 2. Specimen geometry - short-term pin-bearing tests

d/t	e (mm)	d (mm)	w (mm)	e/d	w/d
1	50.8	6.35	38.10	8	6
1.5	76.2	9.53	57.15	8	6
2	101.6	12.70	76.20	8	6

Table 3. Moderate torque values for test specimens

d (mm)	Washer size	Torque T (N-m)	Lateral constraint σ_z (MPa)
6.35	$2.2 d$	5.65	36.59
9.53	$2 d$	14.90	36.59
12.7	$2 d$	35.33	36.59

Long-Term Tests

In the long-term tests, bearing deflections were recorded in the FRP material at the pin for time durations of up to 1,000 hours at normal room temperature conditions. Close-fit single-bolt tension connections were tested under a double-lap shear configuration. Axial load was applied to the single-bolt connection using a static lever-arm test setup as shown in Figure 2. Strain gauges were affixed to both sides of a rigid steel plate at the bottom of the fixture to ensure that the test specimen was properly aligned prior to the application of load with no bending along the length of the test specimen. Two precision deflection gauges were affixed to the specimen as shown in Figure 2 for measuring the relative deformation at the bolt-holes. Deflections were recorded every 6 minutes for the first hour, every 15 minutes for the next three hours, every hour for the following 24 hours, and every day thereafter up to 1,000 hours. All the specimens were nominally 6.35 mm thick, 38.1 mm wide, and 406.4 mm long. One hole was drilled 50.8 mm away from both ends of the specimen, achieving d/t , e/d , and w/d ratios of 1, 8, and 6 respectively. For the laterally unrestrained connections, tests were conducted at 60, 90, and 100% of the respective short-term characteristic pin-bearing strength. For the moderately torqued connections, tests were conducted at 60, and 90% of the respective short-term characteristic pin-bearing strength.

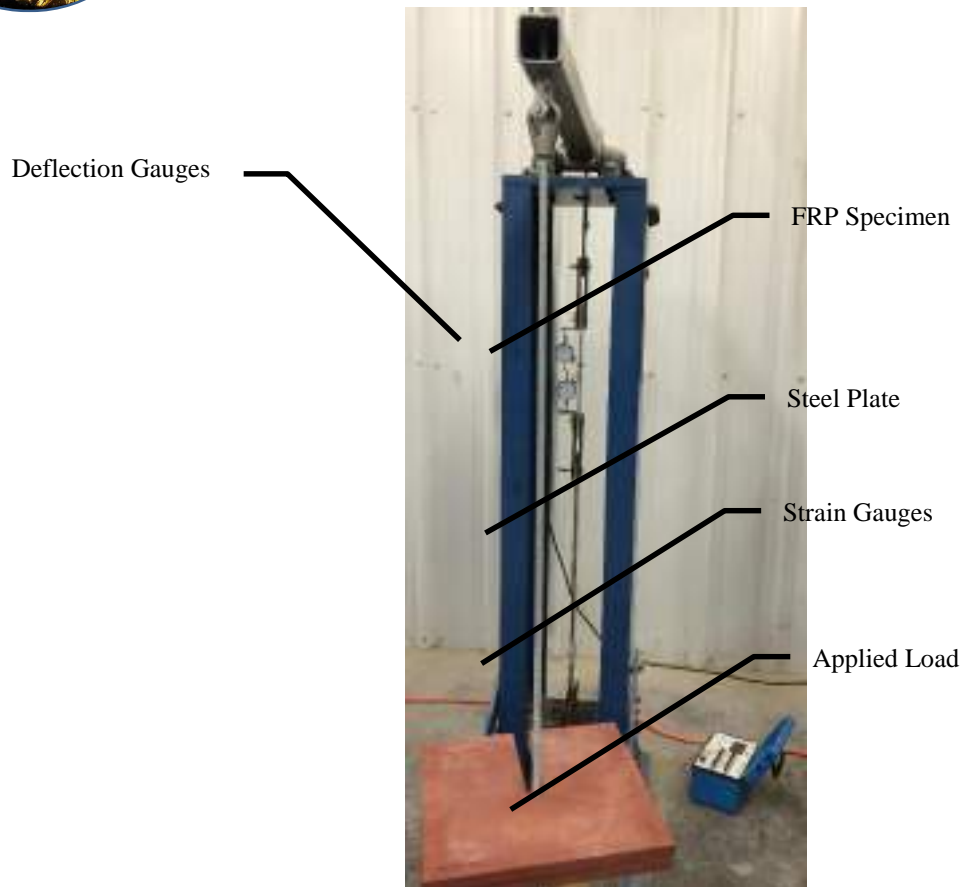


Figure 2. Creep test setup

RESULTS AND DISCUSSION

Short-term Tests

Observations of the laterally unrestrained specimens in the test cases revealed that as the load increased, the bolt shank pressed against the hole and the material in the vicinity of the bolt-hole started to fail. As the material was free to deform laterally, significant bearing damage of the FRP near the bolt-hole was observed, indicating the onset of bearing failure. The behavior of all of the specimens was linear up to the ultimate load, when the load exhibited a sudden significant drop without recovery. All the connections failed in bearing, as intended. The corresponding bearing strength (F_L^{br}) of the connection was calculated by dividing the ultimate load by the initial projected area of the bolt-hole. The results indicate that for a laterally unrestrained connection in this pultruded material, the pin-bearing strength decreases as the d/t ratio increases. In moderately torqued connections, as the specimens were constrained laterally, bearing damage of the material in the vicinity of the loaded pin was suppressed by the washers. This resulted in an increased load carrying capacity and the specimens exhibited bilinear behavior. Initially the connection demonstrated linear response until it exhibited a significant reduction in stiffness as previously observed by Hart-Smith (1987). Cooper and Turvey (2009) defined this point of stiffness reduction as the damage load. In all tested specimens, the second linear region of the load-displacement plot was observed to be comparatively shorter than the first one. The results indicate that for the moderately torqued specimens, no specific relationship can be established between the pin-bearing strength and the d/t ratio. Figure 3 shows the representative load-displacement curves and Table 4 gives a summary of test results.

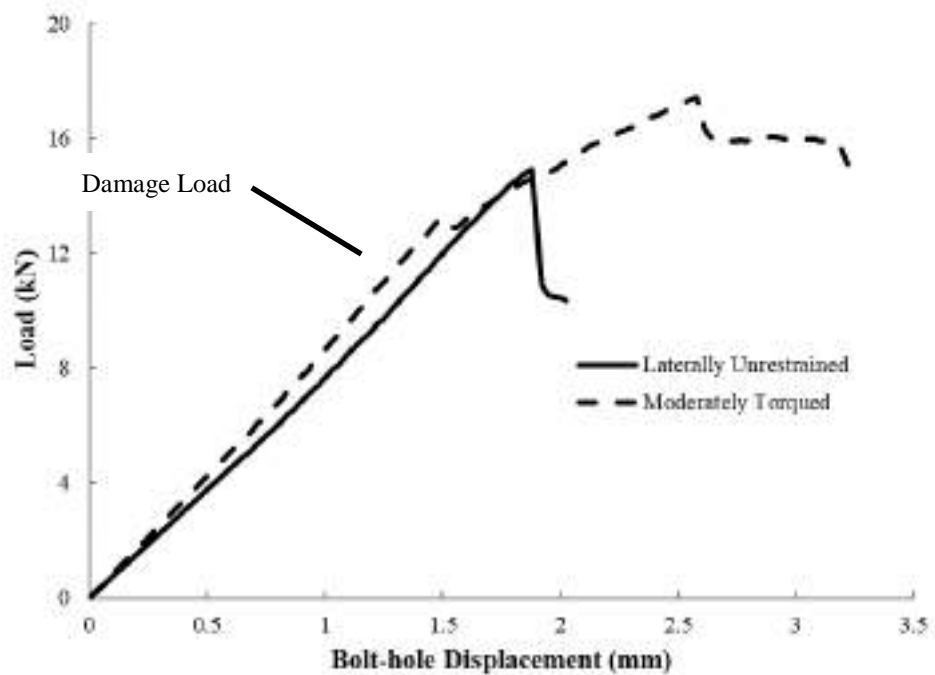


Figure 3. Representative load-deflection curves (specimens with d/t ratio of 1)

Table 4. Short-term pin-bearing tests

d/t	Mean strength (MPa)	SD (MPa)	COV (%)	Characteristic strength (MPa)
Laterally unrestrained specimens				
1	354	22	5.7	299
1.5	313	21	7.6	248
2	257	26	8.5	199
Moderately torqued specimens				
1	430	28	8.2	333
1.5	482	15	3.6	427
2	442	12	2.5	400

Long-term Tests

For laterally unrestrained connections, a total of five tests were conducted at a sustained load level of 100% of the short-term characteristic pin-bearing strength. All those specimens failed prior to the specified duration of 1,000 hours. The specimens failed at various time durations, ranging from 17 minutes to 150 hours. Figure 4 shows a representative test specimen at failure. Creep tests were also conducted at load levels representing 60% and 90% of the characteristic pin-bearing strength. None of those tested specimens failed during the 1,000-hour test duration. Visual examination of the bolt-holes at the end of tests revealed slight bearing damage in the region where the bolt shank was in contact with the FRP material.

For moderately torqued connections, a 5.65 N-m torque was applied using a torque wrench. Washers with an outer diameter of $2.2d$ were used on both sides of the FRP connection. A total of four tests were conducted at a sustained stress level of 90% of the short-term characteristic pin-bearing strength. Three tests failed prior to reaching the specified duration of 1,000 hours. The specimens failed at various time durations of 15, 316, and 575 hours. This observation suggests that the beneficial effect of increased bearing strength achieved by providing lateral restraint is lost or reduced significantly under sustained loading. Also, noticeable bearing damage of the specimen was observed outside the washers where the material was free to deform laterally. Three tests were conducted at a sustained stress level of 60% of the characteristic strength and none of the tested specimens failed during the 1,000-hour test duration. Visual examination of the bolt holes at the end of test did not show any significant damage to the bearing hole.



Figure 4. Representative test specimen at failure – stress level 100% of characteristic strength - laterally unrestrained specimens.

Table 5 shows the results of the creep tests, which shows the normalized creep component of the relative bolt-hole deformation ($\Delta d_{creep}/d$). Figure 5 shows the results of tests under sustained loading, expressed as the mean of the creep component of the relative bolt-hole deformation. The variation in the test data indicates that behavior of the bolt-holes is highly dependent on the specific fiber/matrix composition directly adjacent to the bolt-hole. Since the fiber geometry is not completely uniform in the material, it will certainly influence the viscoelastic response of the material in the vicinity of a connection. Another reason for this variation may be the absence of lateral restraint. Since lateral restraint confines the potential damage area adjacent to the hole, the deformation of the holes with washers under even a small amount of torque is expected to be more uniform over a range of tests.

Table 5. Creep component of the relative bolt-hole deformation

Sustained Load Level (% of Char)	$\Delta d_{creep}/d$ (%)					
	Test 1	Test 2	Test 3	Test 4	Test 5	Test 6
Laterally unrestrained specimens						
60%	0.78	0.72	1.06			
80%	2.92	1.6	1.04	1.24	0.88	0.52
90%	0.96	5.46	1.92			
Moderately torqued specimens						
60%	1.46	2.10	2.00	2.24	1.88	2.60
90%	6.96	6.88				

CONCLUSIONS

The following conclusions may be drawn from the short- and long-term pin-bearing test results.

- 1) For close-fit laterally unrestrained connections, the pin-bearing strength decreases as the d/t ratio increases.
- 2) For a given d/t ratio, an increase in the bolt-hole clearance decreases the pin-bearing strength.
- 3) For the close-fit moderately torqued connection, no significant relationship exists between the pin-bearing strength and the d/t ratio.
- 4) An increase in lateral restraint increases short-term pin-bearing strength significantly.
- 5) The viscoelastic behavior of FRP materials does influence the response of bolted connections under the sustained loading and hence must be accounted for in the design criteria. This viscoelastic behavior becomes more pronounced with the increase in relative stress level.
- 6) The perceived increased bearing strength achieved by providing lateral restraint is lost or reduced significantly under sustained loading.

ACKNOWLEDGMENTS

The authors gratefully acknowledge the technical support and equipment provided by the Georgia Institute of Technology while conducting this investigation. Thanks also to the Strongwell® Corporation for providing the pultruded GFRP profiles used in this research work.

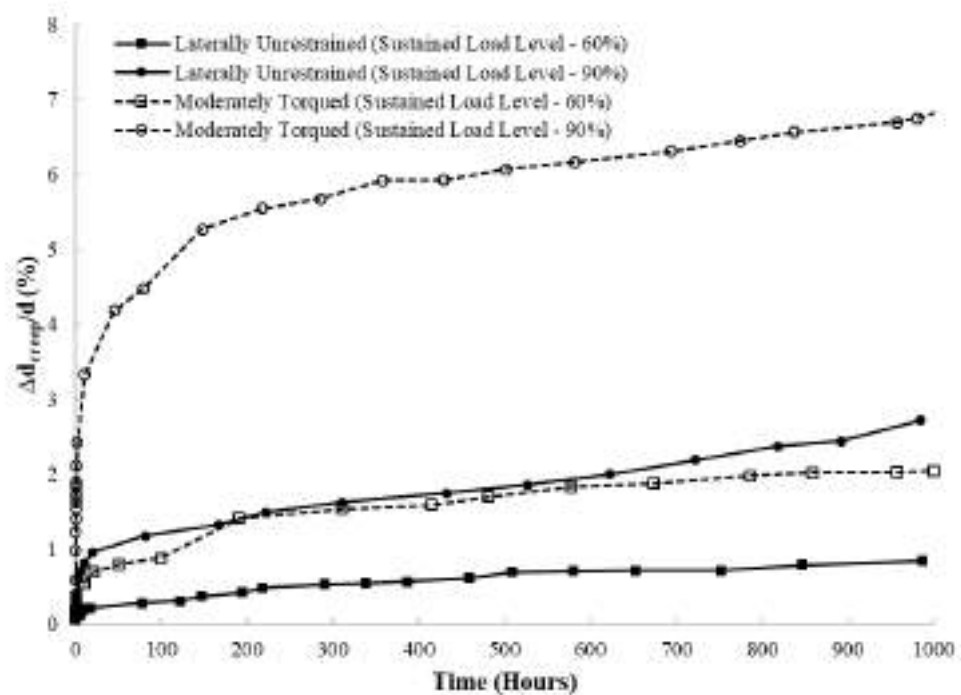


Figure 5. Mean values for creep component of the relative bolt-hole deformation.

REFERENCES

- Abd-El-Naby, S. F. M., and Holloway, L. (1993). "The Experimental Behavior of Bolted Joints in Pultruded Glass/Polyester Material. Part 1: Single-Bolt Joints," *Composites*, 24(7), 531-538.
- American Society of Civil Engineers (ASCE) (2010). *Pre-Standard for Load & Resistance Factor Design (LRFD) of Pultruded Fiber Reinforced Polymer (FRP) Structures (Final)*, American Society of Civil Engineers, Reston, VA.
- ASTM D 5961/D 5961 M-10 (2010). "Standard Test Method for Bearing Response of Polymer Matrix Composite Laminates" ASTM International, West Conshohocken, PA, DOI:10.1520/D5961_D5961M-10.
- ASTM Standard D7290-06 (2011). "Standard Practice for Evaluating Material Property Characteristic Values for Polymeric Composites for Civil Engineering Structural Applications" ASTM International, West Conshohocken, PA, DOI: 10.1520/D7290-06R11.
- ASTM Standard D3039/D3039M-14 (2014). "Standard Test Method for Tensile Properties of Polymer Matrix Composite Materials," ASTM International, West Conshohocken, PA, 2014, DOI 10.1520/D3039_D3039M-14.
- Clarke, J. L. (Ed.) (1996). *Structural Design of Polymer Composites, EUROCOMP Design Code and Handbook*, E&FN Spon, London, UK.
- Collings, T. A. (1977). "The Strength of Bolted Joints in Multidirectional CFRP Laminates," *Composites* 8, 43-54.
- Cooper, C., and Turvey, G. J. (1995). "Effects of Joint Geometry and Bolt Torque on the Structural Performance of Single Bolt Tension Joints in Pultruded GRP Sheet Material," *Composite Structures*, 32, 217-226.
- Girão Coelho, A. M. and Mottram, J. T. (2015). "A Review of the Behaviour and Analysis of Bolted Connections and Joints in Pultruded Fibre Reinforced Polymers," *Materials and Design*, 74, 86-107.
- Hart-Smith, L. J. (1987). "Design and Empirical Analysis of Bolted or Riveted Joints," *Joining Fibre Reinforced Plastics*, Elsevier Applied Science Publishers Ltd., London, UK.



- Kallmeyer, A. R., and Stephens, R. I. (1997). "Creep Elongation of Bolt Holes Subjected to Bearing Loads in a Polymer Matrix Composite Laminate," *Composite Materials: Fatigue and Fracture (Sixth Volume) ASTM STP 1285*, American Society for Testing and Materials, West Conshohocken, PA, 452–467.
- Khashaba, U. A., Sallam, H. E. M., Al-Shorbagy, A. E., and Seif, M. A. (2006). "Effect of Washer Size and Tightening Torque on the Performance of Bolted Joints in Composite Structures," *Composite Structures*, 310-317.
- Kretsis, G. and Matthews, F. L. (1985). "The Strength of Bolted Joints in Glass Fibre/Epoxy Laminates," *Composites*, 16(2), 92-102.
- Mottram, J. T. and Turvey, G. J. (2003). "Physical Test Data for the Appraisal of Design Procedures for Bolted Joints in Pultruded FRP Structural Shapes and Systems," *Progress in Structural Engineering and Materials* 5, 195-222.
- Mottram, J. T. (2009). "Determination of Pin-Bearing Strength for the Design of Bolted Connections with Standard Pultruded Profiles," *Proceedings of the 4th International Conference on Advanced Composites in Construction (ACIC 2009)*, 483-495.
- Mottram, J. T. and Zafari, B. (2011). "Pin-Bearing Strengths for Bolted Connections in Fibre-Reinforced Polymer Structures," *Proceedings of the Institution of Civil Engineers: Structures and Buildings*, 164(5), 291-305.
- Stewart, W. C. (1965). "Bolted Joints," *Metals Engineering Design*, ASME Handbook, 2nd Ed, New York, NY, 328-334.
- Stockdale, J. H., and Matthews, F. L. (1976). "The Effect of Clamping Pressure on Bolt Bearing Loads in Glass Fibre-Reinforced Plastics," *Composites*, 34-38.
- Sun, H. T., Chang, F. K., and Qing, X. (2002). "The Response of Composite Joints with Bolt-Clamping Loads, Part II: Model Verification," *Journal of Composite Materials*, 36(1), 69-92.
- Thoppul, S. D., Finegan, J. and Gibson, R. F. (2009). "Mechanics of Mechanically Fastened Joints in Polymer-Matrix Composite Structures – A Review," *Composites Science and Technology*, 69, 301-329.
- Yuan, R. L., and Liu, C. J. (2000). "Experimental Characterization of FRP Mechanical Connections," *Proceedings of the 3rd International Conference on Advanced Composite Materials in Bridges and Structures (ACMBS-3)*, 103–110.
- Zureick, A., Bennett, R. M., and Ellingwood, B. R. (2006). "Statistical Characterization of Fiber-Reinforced Polymer Composite Material Properties for Structural Design," *ASCE Journal of Structural Engineering* 132(8), 1320-1327.



LONG-TERM DESIGN OF GFRP-PUR WEB-CORE SANDWICH STRUCTURES

S. Yanes-Armas 1, J. De Castro 1, T. Keller 1

¹ Composite Construction Laboratory (CCLab), École Polytechnique Fédérale de Lausanne (EPFL),
Bâtiment BP, Station 16, CH-1015 Lausanne, Switzerland

Email: thomas.keller@epfl.ch

ABSTRACT

The structural behavior of GFRP-polyurethane (PUR) web-core sandwich structures subjected to sustained loading was investigated. The influence of creep on the web-core interaction, i.e. on the shear load distribution and local instability phenomena were analyzed. The effects of applying particular design recommendations on the design were assessed based on the example of a real GFRP-PUR sandwich roof. The design shear resistance of the GFRP webs, their dimensions and governing failure mode significantly depended on the applied recommendation. A design procedure to evaluate the overall shear resistance of the GFRP-PUR core over time, taking into account creep effects, was presented.

KEYWORDS

Sandwich structures, web-core sandwich, creep, polyurethane foam, design guidelines.

INTRODUCTION

Fiber-reinforced polymer (FRP) sandwich structures constitute an efficient, versatile and lightweight structural system suitable for a wide variety of structural applications. Owing to their advantageous properties, their use for civil infrastructure applications, in both the new construction and rehabilitation sectors, is arousing increasing interest. In particular, foam-core-based sandwich structures offer high potential in the building construction domain. The adoption of polymeric foams with low thermal conductivity as core material provides FRP structural sandwich panels with the thermal insulation characteristics required for roof and wall applications. In this respect, rigid polyurethane (PUR) foam is one of the most commonly used core materials. The low stiffness and strength of low-density polymeric foams can limit the structural performance of sandwich constructions – the core may govern both the deformation and load-bearing capacity of the structure. In order to increase the shear stiffness and strength of foam-core sandwich structures, web-core sandwich panels, in which the foam core is reinforced by internal FRP webs or ribs, have been proposed by several authors (Keller et al. 2008, Fam and Sharaf 2010, Correia et al. 2012). The hybrid core of these web-core sandwich panels fulfills similar structural functions to those of a homogeneous core. A key function of the foam core is to laterally stabilize the thin webs, which are sensitive to local instabilities due to in-plane shear stresses, and prevent wrinkling of the compressed face sheet laminates.

FRP sandwich structures employed for civil infrastructure applications may be subjected to high long-term or permanent loads compared to their self-weight, especially when used for roofs and building floors. Furthermore, the working life required of building structures is typically equal to or higher than fifty years. In this context, it is essential that creep be considered in structural design. FRP sandwich panels with polymeric foam cores subjected to sustained loads are prone to creep due to the viscoelastic character of both the foam and the FRP laminates. Thus, creep constitutes a major concern regarding the application of FRP sandwich structures for building construction.

In a previous study, the authors conducted the structural design of a web-core FRP-PUR sandwich roof to replace the existing timber roof of the CLP building in Switzerland (Yanes-Armas and Keller 2016). Two potential construction scenarios differing significantly in the magnitude of the long-term loads were considered: (i) the sandwich finishing surface providing the roof's exterior appearance and no additional construction elements added above; (ii) a sedum green roof installed on the top, see Figure 1. The substantial influence of high permanent loads on the roof solution was shown and highlighted the relevance of considering creep effects in the design of FRP sandwich structures. In this paper, the creep effects on the load-bearing behavior of web-core sandwich structures are analyzed. First, the current structural design approach to take creep effects on PUR foams into account when used as core material of sandwich panels with FRP face sheets is addressed. Subsequently, the structural design aspects affected by the web-core interaction and the influence of creep on local stability phenomena are investigated. The effects of applying particular design recommendations on the resulting design are assessed based

on a case study. Lastly, the shear resistance over time of the hybrid web-core subjected to sustained loading is evaluated.



Figure 1: Rendering of CLP sandwich roof (a) without and (b) with green rooftop.
Architects: J. Brönnimann & P. Gottreux (Vevey, Switzerland).

CREEP OF PUR FOAMS IN STRUCTURAL DESIGN OF SANDWICH PANELS

Several design recommendations or corresponding prospective guidelines – German BÜV (2014), European EUR 27666 (Ascione et al. 2016), Dutch CUR96+ (2012) – are currently available for the structural design of sandwich panels consisting of FRP face sheets and foam core. All these recommendations highlight the relevance of taking creep effects into account in the design. Long-term loading effects are included by applying to the material properties a reducing influence or conversion factor ($A_I / \eta_{cv} / \gamma_{ck}$ in the BÜV / EUR 27666 / CUR96+, respectively). However, among the abovementioned guidelines, only the BÜV provides such influence factors for foams. The A_I influence factor in the BÜV is formulated as $A_I(t) = (A_{I,20I})^T$, where $A_{I,20I}$ is the basic value for A_I after a 20-year loading time and the exponent T is calculated as $T = 0.253 + 0.142 \log(t)$, with t in hours. The $A_{I,20I}$ values for PUR foams are not provided in the BÜV, presumably due to the absence of creep experimental data covering a 20-year period. Instead, A_I reference values for loading times of 1000, 5000 and 10000 h are given and $A_{I,20I}$ can be calculated by using those values conjointly with the aforementioned formulation. Different A_I reference values for stiffness are given depending on the foam density and loading type. The A_I influence factors can be used to obtain the moduli reduction factors, $\chi(t)$, that represent the ratio between the time-dependent modulus ($E(t)$ or $G(t)$ for compression and shear, respectively) and the relevant initial elastic moduli (E_0 or G_0) of the material for a given creep time, as follows: $\chi(t) = 1 / A_I(t)$.

The shear modulus reduction factor $\chi_G(t)$ calculated according to the BÜV for a 50-kg/m³ PUR foam is shown in Figure 2. The $A_I(1000 \text{ h}) = 2.6$, $A_I(5000 \text{ h}) = 3.9$ and $A_I(10000 \text{ h}) = 4.4$ reference values (Table C-1 in the BÜV) and their corresponding loading times were used to calculate $A_{I,20I}$. The resulting $\chi_G(t)$ curves for each calculated $A_{I,20I}$ and for the average, $A_{I,20I}^{av}$, are shown. For a 50-year load duration, considering the reference value corresponding to $A_I(1000 \text{ h})$ results in χ_G values that are 52% and 32% higher than if using the reference value from $A_I(10000 \text{ h})$, or the average $A_{I,20I}^{av}$, respectively. Reliable creep predictions for long-term scenarios may thus need longer experimental times.

The experimental investigation of shear creep conducted by Just (1996) on sandwich panels with a 46-kg/m³ PUR foam core and steel face sheets is the quoted source in the BÜV for the A_I^G values of the 50-kg/m³ foam. The $\chi_G(t)$ curves for the foam investigated by Just (1996) were obtained using the reported creep experimental data and the model proposed by the author to represent the creep factor, based on Findley's law. A comparison of the $\chi_G(t)$ curves obtained by applying the BÜV and those calculated from Just (1996) is shown in Figure 2. The two sets of curves show different trends: the decreasing rate of $\chi_G(t)$ in the curves from Just (1996) is more pronounced with increasing time, whereas it stabilizes for those from the BÜV. As a result, for time periods shorter than approximately 3000 h, the $\chi_G(t)$ values from the BÜV underestimate the experimentally-based values of the reduction factor, by a maximum of 35% after a 24-h loading time for the average curve. For structures where a high ratio of short- to long-term loads applies and the short-term scenario governs the final design, the structure would be overdimensioned. However, for long-term scenarios, the $\chi_G(t)$ values from the BÜV are higher than the



experimentally-based values (up to nearly 70% higher after a 50-year loading time for the average curve). For structures with high permanent loads, this may result in an unconservative design.

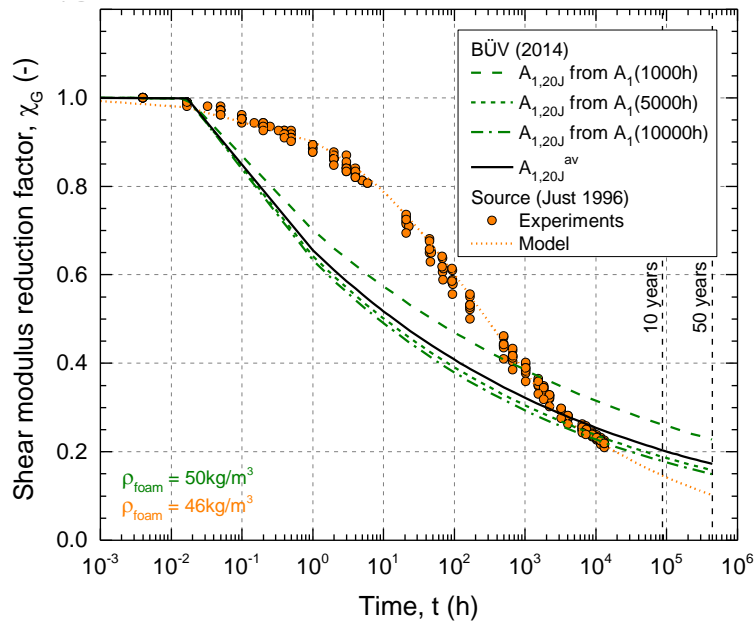


Figure 2: Comparison of shear modulus reduction factor for 50-kg/m³ PUR foam calculated according to BÜV and experimentally determined from Just (1996)

TIME-DEPENDENT BEHAVIOR OF WEB-CORE SANDWICH PANELS

The shear forces applied to a sandwich panel are borne by the core material(s) or system. In web-core sandwich panels whose core is composed of PUR foam and FRP webs or ribs, the applied shear force is distributed between both elements of the hybrid core according to their shear stiffnesses. Given the viscoelastic behavior of both the PUR foam and the FRP laminates, sustained loading results in a reduction of the shear stiffness of both core constituents with increasing loading time. Since the PUR foam and FRP laminates exhibit different creep behavior, their individual contributions to the total shear stiffness of the hybrid core and therefore the distribution of shear forces between the FRP webs and the PUR foam are time-dependent. Garrido et al. (2017) proposed formulations to estimate the proportions of shear force borne by the FRP webs (α_w^{GA}) and the PUR foam core (α_c^{GA}) throughout time. These proportions depend on the dimensions of the web and core components, their initial shear moduli and relevant $\chi_G(t)$ factors. In the following, the influence of the selected $\chi_G(t)$ curves to take into account the creep behavior of the PUR foam on the shear distribution is assessed. This is done based on a case study of a web-core sandwich roof composed of a PUR foam core and glass-FRP (GFRP) webs and face sheets (Keller et al. 2008). Subsequently, on the basis of the same case study, the influence of creep on the shear resistance of the web components is evaluated.

Description of Case Study

The GFRP-PUR sandwich roof of the Novartis Campus Main Gate Building is used as case study (Keller et al. 2008). The core of the sandwich structure consists of a PUR foam with three different densities (60, 80 and 145 kg/m³) and mechanical properties. The PUR core is reinforced by an internal grid of orthogonal GFRP webs spaced 925 mm apart. The roof structure can be modeled as a girder grid system of 925-mm-wide (width= b) beams consisting of the upper and lower face sheets as flanges and a hybrid GFRP-web/PUR-foam core. The cross-sectional configuration of the hybrid beam is schematically represented in Figure 3. The following dimensions apply: face sheet thickness $t_{f,bottom} = t_{f,top} = 6-10.5$ mm, web thickness $t_w = 3-9$ mm, sandwich thickness $h_{total} = 70-620$ mm. For the current study, the GFRP-PUR sandwich at the support location, subjected to the maximum shear, was analyzed. The 80-kg/m³ PUR foam was adopted and web dimensions ($t_w \cdot h_w$) of 3.400 and 6.400 mm² were evaluated. The characteristic material properties are given in Table 1.

The shear moduli reduction factors of the GFRP webs ($\chi_{G,w}(t)$) and the PUR foam core ($\chi_{G,c}(t)$) to be applied for the obtaining of α_w^{GA} and α_c^{GA} are shown in Figure 4(a). They were calculated according to the BÜV. Additionally,

in order to assess the influence of the $\chi_{G,c}(t)$ curve selection on the expected shear distribution, the model for the $\chi_{G,c}(t)$ factor given by Garrido et al. (2016) for a 87-kg/m³ foam subjected to shear creep at a temperature of 24°C is also used. The proposed empirical model is based on Findley's power law formulation, which results in different trends with time of $\chi_{G,c}(t)$ compared to the equivalent curves obtained from the BÜV, as highlighted in the previous Section.

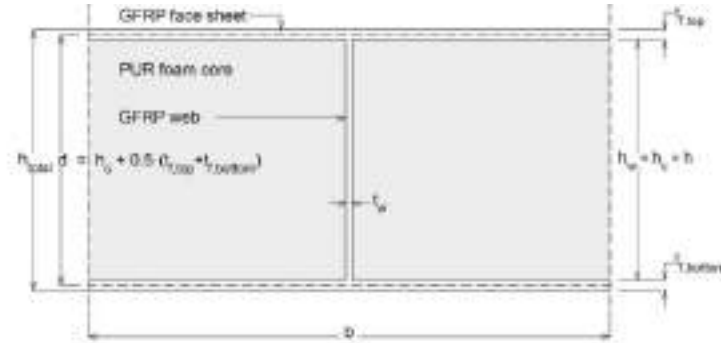


Figure 3: Cross-sectional geometry of web-core sandwich panel (not to scale)

Table 1: Characteristic material properties of GFRP web laminates and PUR foam core (Keller et al. 2008)

Property	GFRP web laminates	PUR foam core
Elastic modulus	$E_{w,k} = 11200$ MPa ^(a)	$E_{c,k} = 25$ MPa
Shear modulus	$G_{w,k} = 3000$ MPa	$G_{c,k} = 10$ MPa
Shear strength	$\tau_{w,k} = 47$ MPa	$\tau_{c,k} = 0.36$ MPa

^(a) Not available in Keller et al. (2008), value for the face sheet laminates

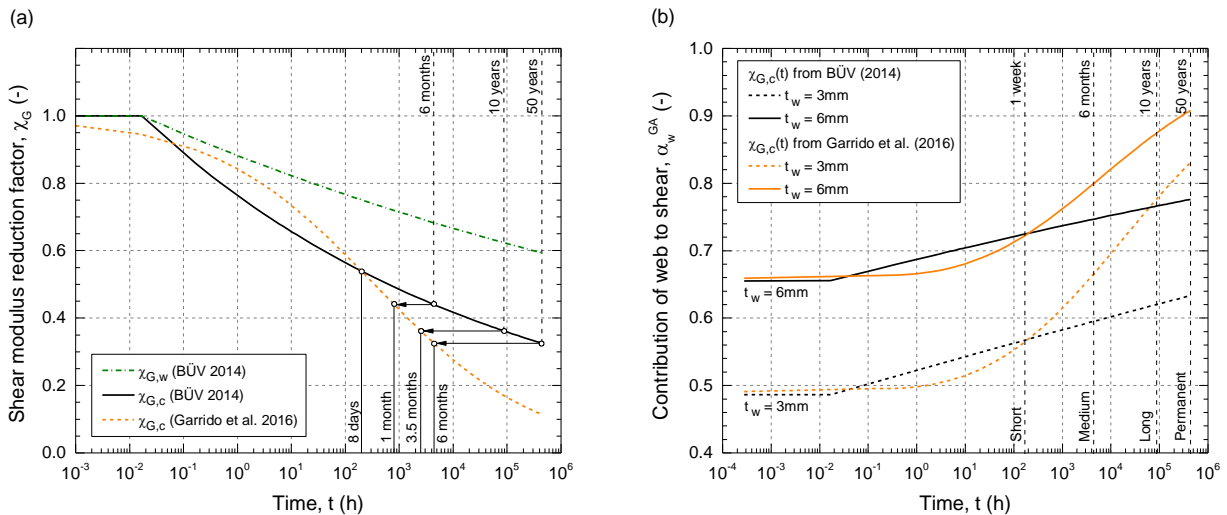


Figure 4: (a) Shear moduli reduction factors for GFRP webs and PUR foam core; (b) Time-dependent contribution of GFRP webs to bearing shear forces

Resulting Time-Dependent Shear Distribution

The resulting contributions of the GFRP webs to bearing the shear forces during time, $\alpha_w^{GA}(t)$, were calculated according to Garrido et al. (2017) using the above-mentioned $\chi_G(t)$ and are shown in Figure 4(b). The calculated proportion of shear force borne by the webs increases with time, indicating that the shear load is partially transferred from the foam core to the webs over time – the PUR foam is more affected by creep than the GFRP laminates and the applicable shear modulus reduction factor is smaller for the former than for the latter, see Figure 4(a). Comparison of the $\alpha_w^{GA}(t)$ curves determined using $\chi_{G,c}(t)$ from the BÜV and from Garrido et al. (2016) shows that for instantaneous loading equal initial $\alpha_{w,0}^{GA}$ values are obtained in both cases – for $t = 0$ the distribution



depends only on the relative area of webs/core and on the initial shear moduli of the components. However, different trends result over time: a linear increase of $\alpha_w^{GA}(t)$ with time (on the logarithmic scale) is obtained using $\chi_{G,c}(t)$ from the BÜV, whereas an increasing rate of $\alpha_w^{GA}(t)$ with time is observed when applying the experimentally-based $\chi_{G,c}(t)$ model from Garrido et al. (2016). The two sets of curves intersect at an approximately 8-day time point – $\chi_{G,c}(199 \text{ h})$ is the same in both cases, see Figure 4(a). As from this point, considering $\chi_{G,c}(t)$ from the BÜV results in significantly smaller $\alpha_w^{GA}(t)$, i.e. in less shear transfer from the core to the webs. The $\chi_{G,c}(t)$ values from the BÜV may therefore result in underestimating the shear force borne by the webs for long-term scenarios. The influence of the $\chi_{G,c}(t)$ curve selection on the expected shear distribution is further analyzed in Yanes-Armas et al. (2017).

Shear Resistance of Webs

The webs of GFRP-PUR web-core sandwich panels are designed to verify the ULS for shear. Additionally, the ULS for local stability (shear wrinkling) has to be verified – local wrinkling instability can limit the shear strength of webs, particularly when a flexible core is used (the lateral support it provides to the web laminates may not be sufficient) or under sustained loading (the stabilizing effect of the foam decreases due to creep). Based on the case study presented in the previous Section, the web components are designed for shear according to three different recommendations: Eurocomp (Clarke 1996), BÜV and EUR 27666. The dissimilarities between them and the effects of selecting a particular recommendation on the resulting designs are discussed.

Table 2: Design shear and shear wrinkling strength equations

	Eurocomp	BÜV	EUR 27666
τ_d	$\frac{\tau_k}{\gamma_m}$	$\frac{\tau_k}{\gamma_M \cdot A^f_{mod}}$	$\eta^f_c \frac{\tau_k}{\gamma_M}$
$\tau_{wr,d}$	$0.5 \cdot \left(\frac{0.50}{\gamma_m} \sqrt[3]{E_{w,k} \cdot E_{c,k} \cdot G_{c,k}} \right)^{(a)}$	$0.5 \cdot \left(0.82 \cdot \sqrt[3]{E_{w,d} \cdot E_{c,d} \cdot G_{c,d}} \right)$	$0.5 \cdot \left(\frac{0.50 \cdot \eta^f_c}{\gamma_{M2}} \sqrt[3]{E_{w,k} \cdot E_{c,k} \cdot G_{c,k}} \right)$

^(a) Not available in Eurocomp; adapted from EUR 27666

All the recommendations provide similar expressions to verify the ULS for shear. The design shear resistance is defined as the product of the shear area, A_w , multiplied by the design shear strength, τ_d . The latter is calculated from the characteristic shear strength, τ_k , by applying the material factors and conversion factors relating to strength, see Table 2. The shear area equals the web cross-sectional area ($A_w = h_w \cdot t_w$) in all cases. The applicable material and conversion factors for the GFRP webs and PUR foams are detailed in Yanes-Armas et al. (2017). None of the recommendations provides expressions to obtain the shear wrinkling strength, $\tau_{wr,d}$, of FRP laminates; however, the design wrinkling strength under uniaxial compression, $\sigma_{wr,d}$, is defined in the BÜV and EUR 27666. A conservative low bound value of the shear wrinkling strength may be estimated from the compressive wrinkling strength as $\tau_{wr,d} = 0.5 \cdot \sigma_{wr,d}$ (Wiedemann 1996). It should be noted that the wrinkling strength depends on the stiffness properties of the FRP webs (E_w) and the PUR foam core (E_c, G_c), see Table 2. The obtaining of the design value differs in the BÜV and EUR 27666. The specific design values of each stiffness property ($E_{w,d}, E_{c,d}, G_{c,d}$) are used in the former, i.e., the different factors for the FRP laminates and PUR foam are considered. On the other hand, the characteristic stiffness properties are used in EUR 27666, and only the FRP factors are applied to the resulting (characteristic) strength. Therefore the absence of material/conversion factors for PUR foams in EUR 27666 does not prevent the wrinkling verification. For the design according to Eurocomp, the shear wrinkling expression provided in Table 2 was adapted from the expression given in EUR 27666.

The design shear and shear wrinkling strengths, τ_d and $\tau_{wr,d}$, over time obtained according to all the recommendations are shown in Figure 5. Different governing failure modes are obtained depending on the selected recommendation: shear for the BÜV and shear wrinkling for Eurocomp and EUR 27666. Moreover, significant differences in the resulting lowest design strengths are observed: 56% between τ_d (BÜV) and $\tau_{wr,d}$ (EUR 27666); 90% between τ_d (BÜV) and $\tau_{wr,d}$ (Eurocomp) for a 50-year loading time.

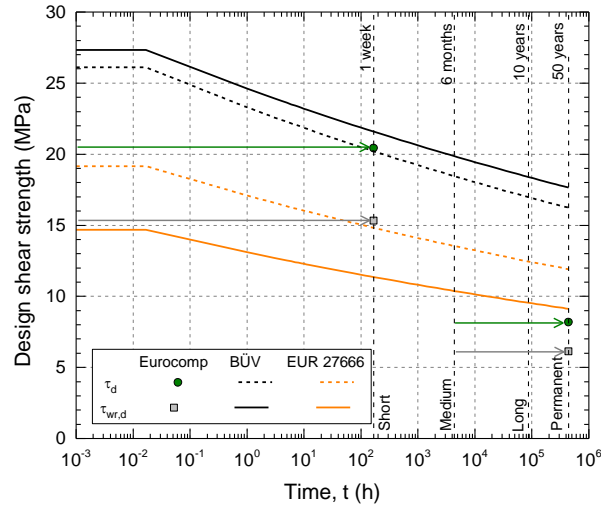


Figure 5: Design shear and shear wrinkling strength of GFRP webs from case study

SHEAR RESISTANCE OF HYBRID FRP-PUR CORE

The shear forces applied to an FRP-PUR web-core sandwich panel are distributed between the web and core components of the hybrid core according to their shear rigidities. The shear resistance of the hybrid core depends therefore on the individual resistances provided by each of them. However, the shear strength and stiffness of each material are differently affected by creep. As a result, the overall shear resistance of the hybrid core considering creep effects cannot be estimated from the addition of the individual resistances over time of its components. In the following, this subject is analyzed on the basis of the case study previously presented.

The shear resistance under sustained loading of a hybrid core consisting of an 80-kg/m³ PUR foam reinforced by GFRP webs spaced at $b = 925$ mm is evaluated. The web thickness of $t_w = 3$ mm is selected (for the sake of simplicity a normalized web area of $a = t_w / b = 0.3\%$). The material properties of the PUR foam core are given in Table 1. For the GFRP webs, slightly different material properties to those presented in Table 1 were considered. The average stiffness properties were estimated from the fiber architecture reported by Keller et al. (2008) by using indicative ply properties provided in EUR 27666 and classical lamination theory (CLT). Average values of $E_{w,m} = 13580$ MPa and $G_{w,m} = 2560$ MPa were obtained. A characteristic shear strength of $\tau_k = 50$ MPa was used. The design was carried out according to the BÜV.

The contributions of the GFRP webs and PUR foam core to bearing the shear forces over time, $\alpha_w^{GA}(t)$ and $\alpha_c^{GA}(t)$ respectively, were calculated as by Garrido et al. (2017) and are shown in Figure 6(a). The design values of the individual shear resistances over time provided by the webs ($V_{Rd,w}$) and foam core ($V_{Rd,c}$) can be obtained as follows:

$$V_{Rd,w}(t) = \tau_{Rd,w}(t) \cdot A_{V,w} = \tau_{Rd,w}(t) \cdot a \cdot b \cdot h \quad (1)$$

$$V_{Rd,c}(t) = \frac{\tau_{Rd,c}(t) \cdot A_{V,c}}{1.5} = \frac{\tau_{Rd,c}(t) \cdot (1-a) \cdot b \cdot h}{1.5} \quad (2)$$

where $\tau_{Rd,w}(t)$ = minimum time-dependent design strength of the GFRP web considering both shear (τ_d) and shear wrinkling ($\tau_{wr,d}$), $\tau_{Rd,c}(t)$ = time-dependent design shear strength of the PUR foam, $A_{V,w}$ = effective shear area of the web, $A_{V,c}$ = effective shear area of the core; a = normalized web area ($a = t_w / b$ for $h_w = h_c$ in Figure 3); the remaining variables are defined as previously.

The resulting design shear resistances normalized per unit area of the hybrid core ($b \cdot h$) are shown in Figure 6(b). Provided that under the shear distribution illustrated in Figure 6(a) failure occurred simultaneously in the web and core components, the design resistance of the hybrid core, $V_{Rd}(t)$, would be given by the addition of the individual shear resistances of the components, i.e. $V_{Rd}(t) = V_{Rd,w}(t) + V_{Rd,c}(t)$. However, since the decrease of the stiffness and strength properties of each material over time due to creep is different, failure will first occur in one of the components, governing the shear capacity of the hybrid core. The design shear resistance of the hybrid core corresponding to web and core failures, $V_{Rd,1}(t)$ and $V_{Rd,2}(t)$ respectively, can be obtained as follows:



$$V_{Rd,1}(t) = \frac{V_{Rd,w}(t)}{\alpha_w^{GA}(t)} \quad (3)$$

$$V_{Rd,2}(t) = \frac{V_{Rd,c}(t)}{\alpha_c^{GA}(t)} \quad (4)$$

The design shear resistance of the hybrid core can therefore be expressed as: $V_{Rd}(t) = \min\{V_{Rd,1}(t), V_{Rd,2}(t)\}$. The normalized shear resistance values corresponding to the addition of $(V_{Rd,w}(t) + V_{Rd,c}(t))$ as well as those resulting from Eqs. 3 and 4 are shown in Figure 6(b). Figure 6(b) shows that considering the summation of the components' individual resistances may result in an unsafe design – for all load durations, either $V_{Rd,1}(t)$ or $V_{Rd,2}(t)$, corresponding to web and core failure, respectively, are smaller than $(V_{Rd,w}(t) + V_{Rd,c}(t))$. For the analyzed case the shear resistance of the hybrid core is governed by core failure for load durations smaller than t_1 ($V_{Rd,2} / bh$, representing core failure, gives the lower envelope for the hybrid core resistance at $t \leq t_1$), whereas for greater load durations the shear resistance of the hybrid core is governed by web failure (at $t \geq t_1$ the lower envelope is given by $V_{Rd,1} / bh$). This can be further illustrated by obtaining the contributions of the GFRP webs and the PUR foam core to the $(V_{Rd,w}(t) + V_{Rd,c}(t))$ addition, denoted as $\alpha_w^{VRd}(t)$ and $\alpha_c^{VRd}(t)$ respectively:

$$\alpha_w^{VRd}(t) = \frac{V_{Rd,w}(t)}{V_{Rd,w}(t) + V_{Rd,c}(t)} \quad (5)$$

$$\alpha_c^{VRd}(t) = \frac{V_{Rd,c}(t)}{V_{Rd,w}(t) + V_{Rd,c}(t)} \quad (6)$$

The obtained values are given in Figure 6(a) together with the shear distribution coefficients. Figure 6(a) shows that the $\alpha^{GA}(t)$ curves intersect the pertinent $\alpha^{VRd}(t)$ curves at a $t = t_1 = 3$ -month loading time, representing the time at which under sustained loading the failure mode of the hybrid core changes from core to web failure – $\alpha_c^{VRd}(t) < \alpha_c^{GA}(t)$ for $t \leq t_1$ and $\alpha_w^{VRd}(t) < \alpha_w^{GA}(t)$ for $t \geq t_1$.

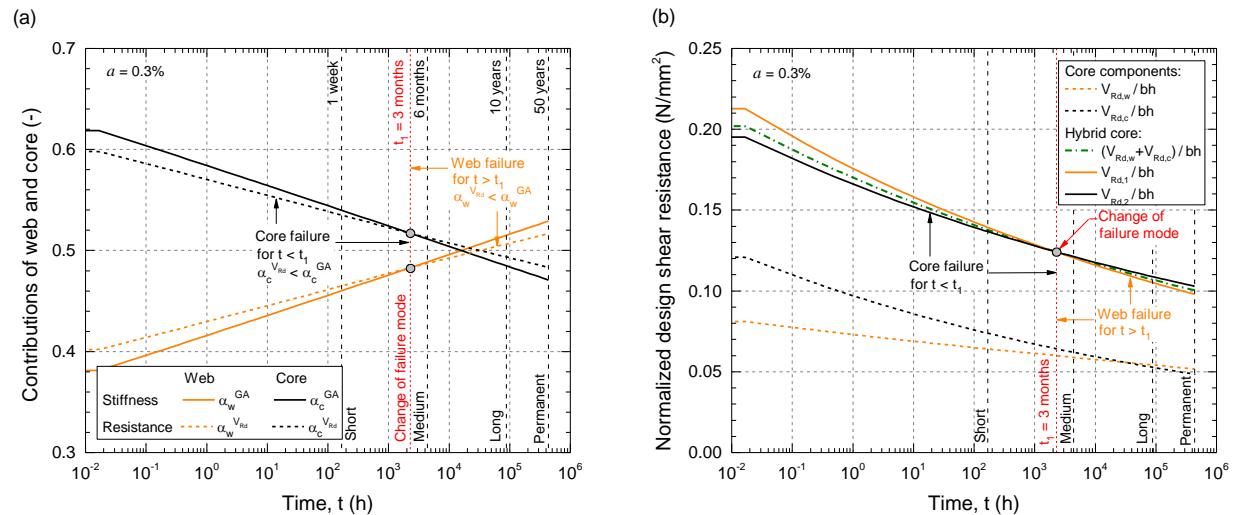


Figure 6: (a) Time-dependent contribution of web-core components to shear stiffness and resistance; (b) Time-dependent normalized shear resistance of hybrid core and individual components from case study

The procedure presented above can be applied to design the web-core dimensions (t_w, b), considering the contributions of both the FRP webs and PUR core to the shear resistance of the hybrid core. The design can be simplified by neglecting the load-bearing capacity of the foam core. A greater t_w value, and therefore higher FRP material consumption, would be however required to fulfill the shear resistance verification.



CONCLUSIONS

The structural design of FRP-PUR web-core sandwich structures subjected to sustained loading was addressed in this study. The time-dependent behavior of web-core sandwich panels, and in particular the aspects influenced by the web-core interaction, were analyzed and the effects of selecting particular guidelines for the design were evaluated. The following main conclusions were drawn:

- (1) Current design recommendations for FRP sandwich structures contain limited or no provisions for the consideration of PUR foam creep behavior in structural design. The comparison of structural designs using proposed creep parameters (BÜV) and equivalent experimental ones shows that the former may result in an unconservative design for long-term sustained loads.
- (2) The design shear resistance of the FRP web laminates, and therefore the web dimensions, depend significantly on the applied design recommendations. Regarding the performed case study, the BÜV provided the least conservative resistance and EUR 27666 the most conservative one, except for permanent loads, for which Eurocomp is more conservative. Different governing failure modes are obtained depending on the applied recommendation.
- (3) The overall shear resistance of the hybrid FRP-web/PUR-foam core under sustained loading depends both on the varying shear stiffness and strength over time of the individual components and its load-bearing capacity is governed either by web or core failure. Considering the summation of the components' individual resistances results in an unsafe design. A straightforward procedure to take this into account was proposed.

REFERENCES

- L. Ascione, J.F. Caron, P. Godonou P, K. Van IJselmuiden, J. Knippers, T. Mottram, et al (2016). "Prospect for new guidance in the design of FRP: Support to the implementation, harmonization and further development of the Eurocodes". Publications Office of the European Union. Report No. EUR 27666 EN.
- Bau-Überwachungsverein (BÜV e.V.) (ed.) (2014). "Tragende Kunststoffbauteile : Entwurf – Bemessung – Konstruktion". Wiesbaden: Springer Vieweg.
- J.L. Clarke (ed.) (1996). "Structural design of polymer composites: Eurocomp design code and handbook". London: E & FN Spon.
- J.R. Correia, M. Garrido, J.A. Gonilha, F.A. Branco and L.G. Reis (2012). "GFRP sandwich panels with PU foam and PP honeycomb cores for civil engineering structural applications: Effects of introducing strengthening ribs", *International Journal of Structural Integrity*, 3, 127–147.
- CUR96+ (2012). "Revised CUR96 FRP composite structures. Draft for updating CUR96:2003". Utrecht: CUR.
- A. Fam, T. Sharaf (2010). "Flexural performance of sandwich panels comprising polyurethane core and GFRP skins and ribs of various configurations", *Composite Structures*, 92, 2927–2935.
- M. Garrido, J.R. Correia, T. Keller (2016). "Effect of service temperature on the shear creep response of rigid polyurethane foam used in composite sandwich floor panels", *Construction and Building Materials*, 118, 235–244.
- M. Garrido, J.R. Correia, T. Keller, S. Cabral-Fonseca (2017). "Creep of sandwich panels with longitudinal reinforcement ribs for civil engineering applications: experiments and composite creep modeling", *Journal of Composites for Construction*, 21, 04016074.
- M. Just (1996). "Abschlußbericht zum AiF-Forschungsvorhaben 10011B. Untersuchungen zum Langzeitverhalten von Sandwichplatten mit CO₂-getriebenen Polyurethan-Schaumstoffkernen". Dresden: IMA Materialforschung und Anwendungstechnik. Report No. B85/4.
- T. Keller, C. Haas, T. Vallée (2008). "Structural concept, design, and experimental verification of a glass fiber-reinforced polymer sandwich roof structure". *Journal of Composites for Construction*, 12, 454–468.



J. Wiedemann (1996). "Leichtbau 1: Elemente". Berlin: Springer.

S. Yanes-Armas, T. Keller (2016). "Structural concept and design of a GFRP-polyurethane sandwich roof structure". In: Proceedings of the Eighth International Conference on Fibre-Reinforced Polymer (FRP) Composites in Civil Engineering (CICE2016), Hong Kong, 1318–1323.

S. Yanes-Armas, J. De Castro, T. Keller (2017). "Long-term design of FRP-PUR web-core sandwich structures in building construction", Composite Structures, 181, 214–228.



MULTI-OBJECTIVE OPTIMIZATION OF A COMPOSITE SANDWICH PANEL FLOOR SYSTEM FOR BUILDING REHABILITATION

M. Garrido ¹, J. F. A. Madeira ^{2,3}, M. Proença ¹ and J. R. Correia ¹

¹ CERIS, Instituto Superior Técnico, Universidade de Lisboa, Portugal, Email:
mario.garrido@tecnico.ulisboa.pt

² IDMEC, Instituto Superior Técnico, Universidade de Lisboa, Portugal

³ Department of Mathematics, ISEL, IPL, Portugal.

ABSTRACT

Composite sandwich panels are being increasingly considered for structural applications in civil engineering. However, their high versatility regarding possible constituent materials and geometrical arrangement translates to a high number of design variables. Additionally, there is a potentially large number of design requirements and objectives related to the panels' functions. This paper presents an optimization study of a composite sandwich panel floor system for use in building rehabilitation. Pultruded multicellular panels with a polyurethane (PUR) foam core and carbon- or glass-fibre reinforced polymer (C/GFRPF) faces and ribs/webs are considered. The Direct MultiSearch (DMS) optimization method is adopted. The panel architecture is defined using 3 geometrical variables and 14 material related variables. In addition, 8 competing objective functions are studied, related to different aspects, such as structural serviceability and resistance, thermal insulation, acoustic performance, cost minimization, and environmental performance. The results are presented in the form of Pareto optimal sets, from which several conclusions are drawn regarding common design-related options. The influence of core material density, number of ribs/webs or the type of fibre reinforcement and its respective layout on the different objective functions is addressed. Optimal solutions for meeting different design purposes are presented, providing useful insights for structural designers and composite sandwich panel manufacturers.

KEYWORDS

Direct MultiSearch (DMS), optimization, sandwich panels, composites, building floors, building rehabilitation.

INTRODUCTION

Composite sandwich panels are being increasingly considered for civil engineering structural applications due to their relatively low weight and high strength and stiffness characteristics. These features make them particularly interesting for weight sensitive applications, such as bridge decks, roof structures, or building floors (Garrido 2016). Sandwich panels offer inherently high versatility, both in terms of possible constituent materials and of geometrical arrangement of those materials (Davies 2001; Zenkert 1997). Additionally, a potentially large number of design requirements and objectives are usually set as a function of the end application of the sandwich panels. In the case of building floors, besides structural serviceability and resistance criteria, aspects such as thermal insulation and acoustic performance must be considered. In addition to these requirements, cost minimization and environmental performance also need to be taken into account. Under this scope, the design of sandwich panels constitutes a problem that is particularly well addressed in the framework of multi-objective optimization.

This paper presents a study concerning the optimization of composite sandwich panels for building floor rehabilitation using the Direct MultiSearch (DMS) method (Custódio *et al.* 2011). Multicellular panels with a polyurethane (PUR) foam core and carbon- and/or glass-fibre reinforced polymer (C/GFRP) faces and ribs/webs are considered. The envisaged production method for the panels is pultrusion, due to its relatively low cost and high production rates when compared to other traditional FRP production methods. The sandwich panel architecture is defined in terms of 3 geometrical variables and 14 material related variables. A total of 8 competing objective functions are considered, related with the different types of requirements mentioned above. The obtained results are presented in the form of Pareto optimal sets, allowing several conclusions to be drawn regarding common design-related options. Optimal solutions for meeting different design purposes (*e.g.*, minimum cost, minimum carbon footprint, thermal or acoustic insulation characteristics) are presented, providing useful insights for structural designers and sandwich panel manufacturers. Ultimately, solutions with a significantly lower cost and carbon footprint when compared to other existing sandwich systems (all fulfilling code requirements in terms of structural safety) are obtained, increasing the economical attractiveness and sustainability of the proposed sandwich panel floor system.

OPTIMIZATION APPROACH

Overview

Figure 1 shows a generic cross-section of the type of sandwich panels considered in this study. Sandwich panels usually comprise two relatively thin and stiff face sheets and a relatively thick and soft core. The typically low stiffness of the core often leads to the panels having a relatively high shear deformability. One of the most effective ways to increase the shear stiffness of sandwich panels is the introduction of longitudinal reinforcement ribs along the edges of the panels and/or webs within the core (Fam and Sharaf 2010), leading to a foam-filled multicellular panel design, as illustrated in Figure 1. Other core reinforcement techniques, such as stitching/Z-pinning or the introduction of 2D/3D trusses, were not considered in this study, given the high labour intensity required for their manufacture and their poor suitability for implementation in a pultrusion process.

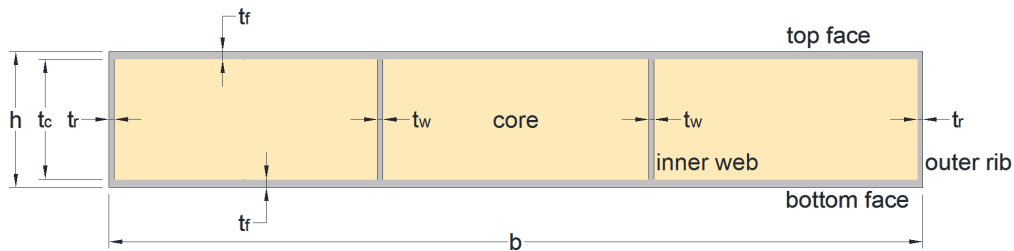


Figure 1: Generic cross-section of the considered sandwich panels

The design and optimization of the panels were carried out considering a fixed span length of 4.0 m, which is commonly found in old masonry buildings (in Portugal and in other European countries). Other cross-sectional and material related features were considered as variables in this study. For the envisaged application in building floors, the sandwich panels must fulfil a series of requirements, mostly related to structural safety and serviceability criteria, but also regarding thermal and acoustic insulation, as well as requirements pertaining to the feasibility of the pultrusion process and the economic competitiveness of the floor solution. The variables and requirements considered in this study, as well as the optimization objectives and algorithm, are detailed in the following sections. The standardized procedures and calculation methods adopted in the sandwich panel design verifications are detailed in Proença *et al.* (2017) and are not reproduced in this paper for the sake of brevity.

Variables

Table 1 presents the variables adopted in this study and their respective variation bounds and steps. The first three variables (X1 to X3) correspond to geometrical parameters used in the definition of the general cross-sectional shape, namely (i) the core thickness (t_c), (ii) the total panel width (b), and (iii) the number of equally spaced inner webs included in the panel (n_w). The remaining variables (X4 to X17) define the materials used in the panels. A discrete variation was adopted for all variables, resulting in a total number of possible combinations of about 3×10^{12} .

The variation interval for the core thickness (50-200 mm) was defined considering the reasonable bounds taking into consideration the type of sandwich panels under study and their application in building floors. It was also deemed desirable to obtain solutions that would not exceed the total thickness of traditional floor solutions for similar spans (~0.15-0.20 m). Regarding the lower bound for the panel width (300 mm), the adopted value was considered as the reasonable minimum width for the floor system. In fact, all panels will need to be connected to the adjacent panels along their edges, and having too narrow panels would increase the number of connection operations, thus negatively affecting the on-site productivity and the economic competitiveness of the solution. The upper bound for the width (600 mm) was defined taking into consideration the volume and weight of the panels, which should not be too high to enable an easy handling and installation by a team of two to four workers.

For the inner webs, a minimum of zero webs and a maximum of three equally spaced webs were considered. The two outer ribs were included by default, *i.e.* when $n_w = 0$ the panel will still have the two longitudinal reinforcements along the outer edges. This was considered for two reasons: (i) the pultrusion process requires the FRP elements to fully envelop the foam core; and (ii) having outer FRP ribs along the panel edges facilitates the execution of panel-to-panel joints during floor assembly, given that bonding the panels directly at the soft foam core would be unadvisable (the resulting bond would be too weak).



Variable X4 corresponds to the core material, for which rigid PUR foams of densities ranging between 35 kg/m^3 and 120 kg/m^3 were considered. The resin system used in the FRP elements is defined in variable X5, for which two different orthophthalic polyester resins were considered, (i) one with low reactivity (LR) and (ii) one with high reactivity (HR). The FRP layup is given by variables X6 to X17, which define the fibre volume content (v_f) of the laminates (variable X6) and fibre layup sequence of the faces (variables X7 to X16) and ribs/webs (X7 to X17). The values taken by variables X7 to X16 correspond to particular types of fibre reinforcement: $X_i=0$ corresponds to a skipped lamina; $X_i=1$ to unidirectional glass fibre roving; $X_i=2$ to unidirectional carbon-fibre tows; and $X_i=3$ to cross-ply woven glass fibre fabrics (other possibilities could have been easily considered). The engineering constants of the FRP laminates were determined using Classical Lamination Theory (CLT).

Table 1: Definition of the adopted variables and their variation range and step

Variable	Description	Range	Step
X1	Thickness of core (t_c) [mm]	50 - 200	5
X2	Total panel width (b) [mm]	300 - 600	10
X3	Number of inner webs (n_w) [-]	0 - 3	1
X4	Core material [-]	1 - 10	1
X5	Resin [-]	1 - 2	1
X6	Fibre volume content (v_f) [-]	0.35 - 0.55	0.05
X7	Face layup (first lamina) [-]	1 - 3	1
X8:X16	Face layup (remaining laminas) [-]	0 - 3	1
X17	No. of laminas in the ribs [-]	1 - 10	1

Requirements

Table 2 presents the 13 requirements (R1 to R13) whose fulfilment was checked in order to assess the viability of the solutions. The first requirement (R1) is a verification of the minimum FRP laminate thickness necessary for the pultrusion process (of this particular type of section), and was carried out for all the laminates in the panels (faces, ribs, webs). Requirements R2 to R8 relate to ultimate limit states verifications, *i.e.*, the assessment of structural safety regarding the main failure modes of sandwich panels in bending. The following two requirements (R9 and R10) concern serviceability limit states verifications, in which the long-term (50-year) deflection of the panels and their natural frequency are checked against their respective allowable limits. The requirement R11 corresponds to the maximum allowable heat transfer coefficient (U-value), which is a measure of the thermal insulation provided by the panels, if they are to be used in the building envelope (in Lisbon). The two remaining requirements (R12 and R13) concern the maximum panel cost per unit area and maximum panel weight, respectively.

Table 2: Solution viability requirements

Requirement	Description	Limit value
R1	Minimum laminate thickness	4 mm
R2	Failure of the faces	-
R3	Wrinkling of the compressed face	-
R4	Shear failure of the core	-
R5	Shear failure of the ribs/webs	-
R6	Compression failure of the ribs/webs and/or core at the supports	-
R7	Rib buckling failure due to in-plane compression	-
R8	Rib buckling failure due to shear	-
R9	Maximum deflection control	8 mm
R10	Minimum undamped natural frequency	5 Hz
R11	Maximum U-value (thermal insulation)	$0.30 \text{ W/m}^2\text{K}$
R12	Maximum panel cost	250 €/m^2
R13	Maximum panel weight	80 kg

A maximum cost requirement (250 €/m^2) was included in order to ensure a minimum economic competitiveness of the optimized solutions. It is worth highlighting that only the cost of materials was considered here; other costs, such as labour, consumables, services, or indirect production costs are not contemplated in this study, owing to



the fact that these will vary to a greater extent between different producers compared to the cost of the panels' constituent materials (thus, considering them would reduce the global relevance of the analysis).

A maximum panel weight requirement was included in agreement with the previously mentioned concern regarding the possibility of the panels being handled and installed manually on-site by a team of two to four workers. The 80 kg limit value corresponds to a load per worker of 20 kg considering a team of four workers. Note that in several urban centre districts, it is often virtually impossible to install a crane in the construction site.

Objective Functions

Eight objective functions (F1 to F8) were used in the multi-objective optimization, as presented in Table 3. These include minimization of panel cost (F1), carbon footprint (F2), panel weight (F3), heat transfer coefficient (thus maximizing thermal insulation, objective function F4), and weighted standardized impact sound pressure level ($L_{nT,w}$, thus maximizing acoustic insulation to impact sounds, objective function F6); additionally, the maximization of weighted standardized level difference ($D_{nT,w}$, relating to the acoustic insulation to airborne sounds, objective function F5) and of the panels' axial stiffness along the longitudinal (F7) and transverse (F8) directions were also pursued. The two last objectives were intended to provide a certain degree of axial stiffness of the panels, which is necessary for the floors to function as a relatively rigid diaphragm; this feature is particularly relevant for resisting and redistributing horizontal loads acting on buildings during earthquakes.

Table 3: Optimization objective functions

Objective	Description	Goal
F1	Total cost per panel area [€/m ²]	Minimize
F2	Carbon footprint per panel area [kgCO ₂ eq/m ²]	Minimize
F3	Panel mass [kg]	Minimize
F4	Heat transfer coefficient [W/(m ² K)]	Minimize
F5	Weighted standardized level difference (airborne sound insulation) [dB]	Maximize
F6	Weighted standardized impact sound pressure level [dB]	Minimize
F7	Axial stiffness per unit width along the longitudinal direction [N/mm]	Maximize
F8	Axial stiffness per unit width along the transverse direction [N/mm]	Maximize

DMS Multi-Objective Optimization Method

The *Direct MultiSearch* (DMS) (Custódio *et al.* 2011) multi-objective optimization (MOO) methodology was adopted in this study. This method is inspired on the search/poll paradigm of direct-search methods of directional type and does not aggregate any of the objective functions, rather using the concept of Pareto dominance to maintain a list of feasible non-dominated solutions. In each iteration, the DMS method updates an iterate list of feasible non-dominated points (instead of updating a single point per iteration). Iteration success is measured by changes in the non-dominated points list. The DMS methodology has been extensively assessed regarding its capability to effectively and robustly obtain Pareto fronts, having been compared to various other solvers with very positive results. The reader is referred to Custódio *et al.* (2011) for a detailed explanation and validation of the DMS method.

RESULTS AND DISCUSSION

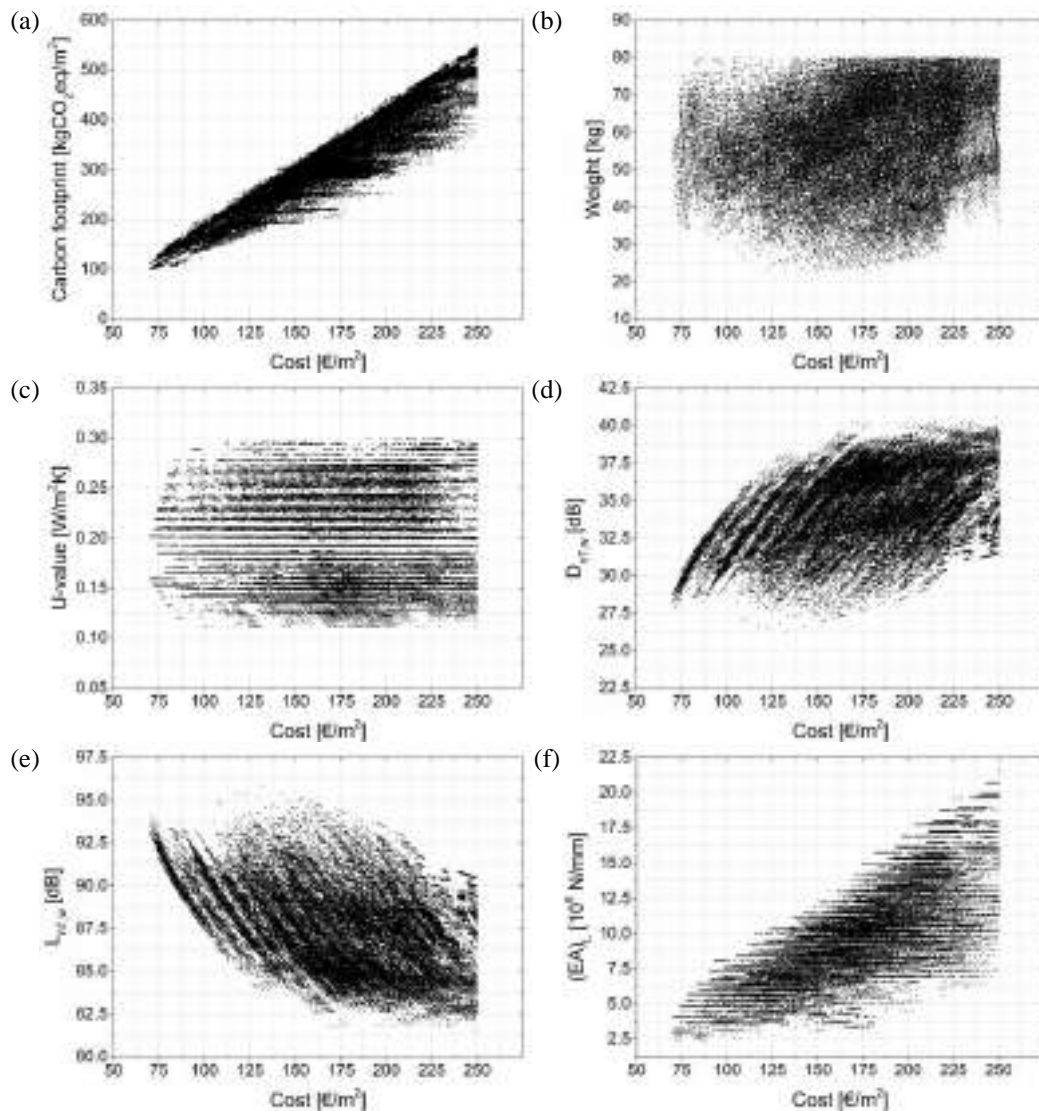
Pareto Optimal Sets

The DMS algorithm yielded a Pareto optimal set composed of 41,760 non-dominated solutions, a number that illustrates the size and complexity of the sandwich panel optimization problem presented here. This 8-dimensional solution set is plotted in Figure 2, projected on the planes that combine the cost (F1) objective function with the remaining objective functions (F2 to F8). From these plots one may analyse and discuss the relationships between the different optimization objectives as considered in this study. As an example, Figure 2-a shows an approximate proportionality between cost and carbon footprint (F2); this proportionality is an expected result considering the materials' unit cost and carbon footprint values provided in Tables 2 to 4. In fact, cost increases are mostly related to the use of higher quantities of material, or improved materials, such as carbon fibres, or heavier cores, which also entail higher carbon footprint values per unit area. In terms of minimum and maximum values obtained for these objective functions, the cost of the non-dominated solutions varied from 61.82 €/m² to 250.00 €/m² (the upper limit value set for this parameter), whereas for the carbon footprint the solutions ranged between 101.88 kgCO₂eq/m² and 547.39 kgCO₂eq/m². It is worth highlighting that all solutions in the Pareto optimal set



fulfil the structural behaviour requirements, and are thus viable options for application in a building floor. The broad range of cost and carbon footprint values that characterise the obtained solutions is illustrative of the complexity and potential for optimization in the current problem.

The relationship between panel cost and panel weight (F3, Figure 2-b) does not follow any specific trend. *A priori*, one could expect higher panel weight to be associated with higher material quantities and densities, which should lead to a relationship of general proportionality between F1 and F3. However, the low weight and high cost of carbon fibre reinforcement contributes to the inverse trend, resulting in the rather high scatter of results plotted in Figure 2-b. A relatively similar dispersion may be observed for the relationship between panel cost and thermal insulation, given by the U-value (F4, Figure 2-c). However, in Figure 2-c there is clear stratification of the solutions along the vertical axis; this results from the discrete variation of the core thickness and density (variables X1 and X4, respectively), which have a dominant effect on the U-value. The weight of the obtained solutions ranged from 23.04 kg to 80.00 kg, while the lowest U-value achieved was 0.11 W/m²K and the highest was 0.30 W/m²K (the maximum values for both parameters corresponded to the upper limits defined for each of these objective functions).



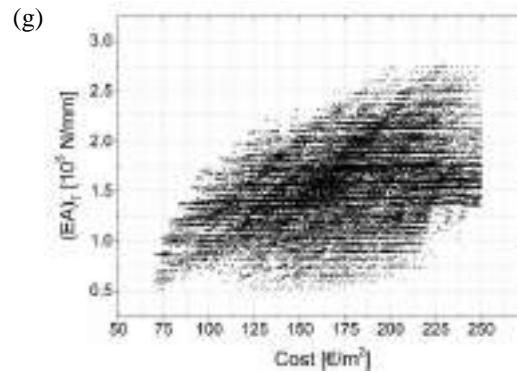


Figure 2: Projection of the Pareto optimal set on the following planes: (a) F1-F2, (b) F1-F3, (c) F1-F4, (d) F1-F5, (e) F1-F6, (f) F1-F7, and (g) F1-F8

The acoustics-related objective functions, namely the weighted standardized level difference (*i.e.*, airborne sound insulation, F5, calculated as $D_{nT,w}$ and plotted in Figure 2-d) and the weighed standardized impact sound pressure level (*i.e.*, impact sound insulation, F6, calculated as $L_{nT,w}$, Figure 2-e), showed comparable relationships with panel cost (taking into account that the former should be maximized and the latter minimized). As expected, the two acoustics parameters are closely related, with increases in $D_{nT,w}$ typically resulting in decreases in $L_{nT,w}$ in a proportional ratio. The single solution with the best acoustic performance (highest $D_{nT,w}$ – 40.49 dB – and lowest $L_{nT,w}$ – 81.55 dB) has a cost of 248.71 €/m² (nearing the maximum value allowed for this objective function). In general, a trend of cost increase with increasing acoustic performance is observed. This stems from the adoption of stiffer and heavier materials, which improve the acoustic insulation characteristics of the panels, but are costlier per unit area of produced panel. The worst performing solution in terms of acoustic insulation was characterised by a $D_{nT,w}$ of 26.21 dB and an $L_{nT,w}$ of 95.75 dB, and a cost of 131.83 €/m².

Regarding the longitudinal and transverse axial stiffness of the panels (objective functions F7 and F8, shown in Figure 2-f and Figure 2-g, respectively), a general trend of increasing cost for higher stiffness values is also observed, which is logical. This behaviour is more marked for the longitudinal axial stiffness, where the stiffer solutions incorporate higher contents of carbon fibre reinforcements. Along the transverse direction, the higher stiffness values are mainly obtained with the incorporation of woven glass fibre fabrics, which have a higher cost per unit area compared to simple unidirectional glass fibre roving. Regarding the minimum and maximum values obtained for these objective functions, the longitudinal axial stiffness of the non-dominated solutions ranged from 2.25×10^5 N/mm to 2.15×10^6 N/mm, while the transverse axial stiffness values varied between 5.13×10^4 N/mm and 2.78×10^5 N/mm. These values compare quite well with axial stiffness values found in typical timber floors (often ranging between 2.5×10^5 N/mm and 1.5×10^6 N/mm along the longitudinal direction, and between 3.0×10^4 N/mm and 1.5×10^5 N/mm along the transverse direction).

Optimal Solutions per Objective Function

The best performing solutions with regard to each individual objective function are illustrated in Figure 3. Along with each solution, its respective objective function values are given (F1 to F8), as well as their geometrical characteristics, the employed materials, and the elasticity constants of the face and rib/web laminates. The laminate layups are given by indicating the sequence of fibre reinforcements adopted, from the outer to the innermost layers, where the symbols “G”, “C”, and “W” correspond to glass fibre roving, carbon fibre tow, and woven glass fibre fabric, respectively. Subscript numbers are used to indicate multiple laminas of the same reinforcement. All laminates were symmetrical, as indicated by the “S” subscript.

Minimum cost per unit area

As expected, in the solution with the lowest cost per unit area the only fibre reinforcement adopted is glass fibre roving, which provides suitable mechanical performance at a relatively low cost. The highest fibre volume fraction allowed is adopted, as well as the resin with higher mechanical properties, resulting in a laminate with relatively high Young’s moduli. However, the absence of fibre reinforcement along the transverse direction may be unfavourable if two-way bending behaviour is required, or when considering connection systems for the panels (not analysed here but possible to consider as an additional requirement). It is interesting to note that a relatively wide panel is obtained (500 mm), presumably optimizing the spacing of the outer ribs, and unlike what one might



expect *a priori* the lightest and less expensive core density (35 kg/m^3) was not used. The limiting factor in the selection of the core density was avoiding the wrinkling failure of the relatively thin (5 mm) top face sheet.

Minimum carbon footprint per unit area

The solution that minimizes the panels' carbon footprint is fairly similar to the one previously described w.r.t. cost minimization. However, slight changes are observed to further reduce the carbon footprint by reducing the quantity of GFRP used in the face sheets (having 4 mm of thickness instead of 5 mm in the faces). These include further increasing the face separation by adopting a higher core thickness, and providing a higher cross-sectional area of the ribs (thus increasing shear stiffness), which in turn enables the panel to be wider.

Minimum panel mass

The solution with the lowest mass, with only 23 kg over an area of 1.24 m^2 ($\sim 0.18 \text{ kN/m}^2$), was achieved by adopting the lowest fibre volume fraction allowed (0.35), unidirectional carbon fibre reinforcement in 4 mm thick faces and ribs, and a core density of 45 kg/m^3 . The lowest core density was not adopted, as in this case it would lead to a "no pass" result in the face wrinkling verification; thus, from a weight minimization standpoint, it was preferable to increase the core density, thus providing a better elastic foundation for the faces, rather than to increase the thickness of the faces. Despite the low quantity of materials in this solution, the use of carbon fibre reinforcement results in a considerable cost increase (+89%) relative to the most economical solution.

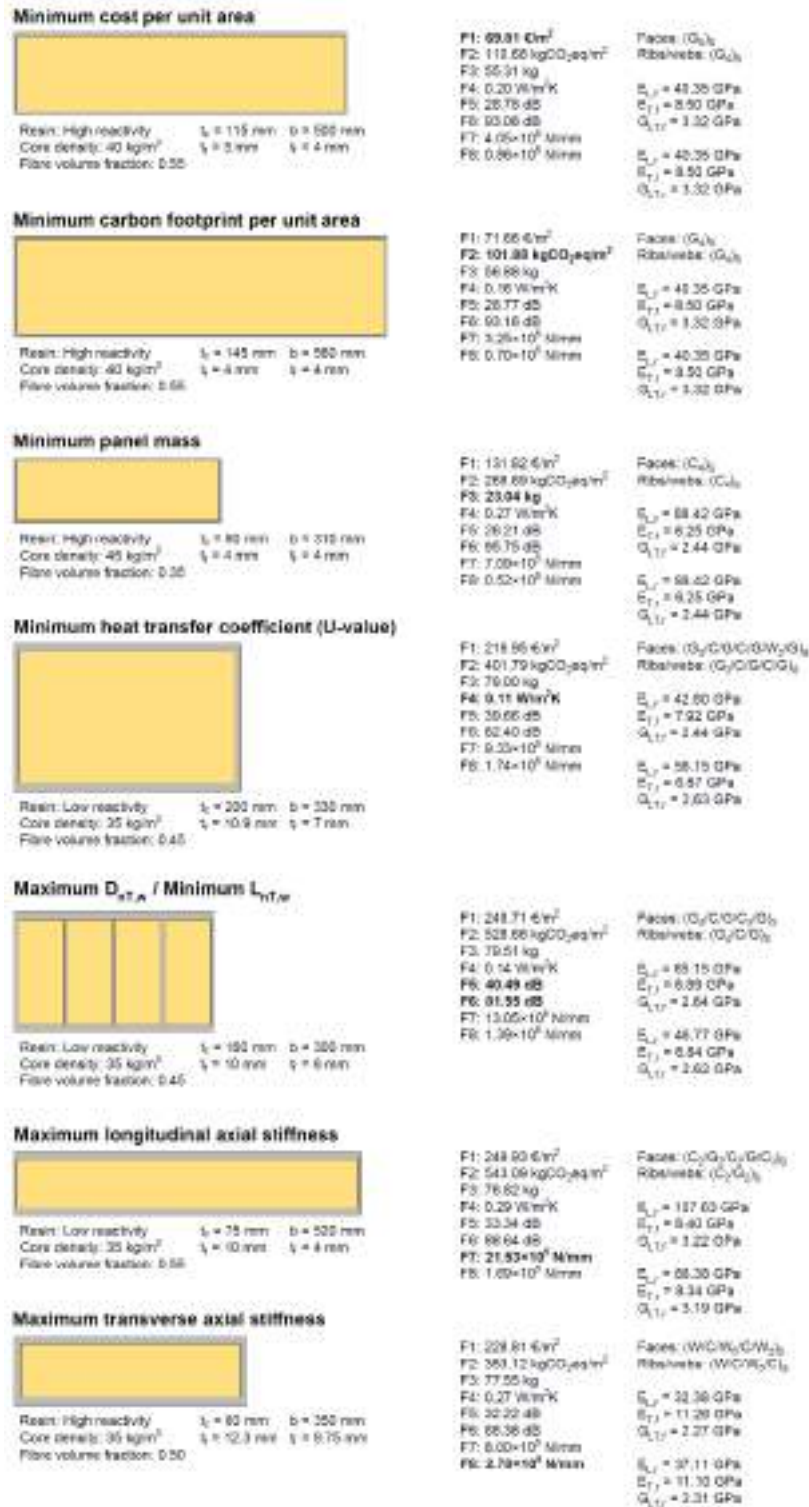


Figure 3: Best performing solutions for each objective function (laminate layup key: G – glass fibre roving; C – carbon fibre tow; W – woven glass fibre fabric; material properties: E_L and E_T refer to elasticity moduli in longitudinal and transverse directions and G_{LTr} to the in-plane shear modulus, with subscripts f and r corresponding to faces and ribs)

*Minimum heat transfer coefficient (U-value)*

As expected, the solution that minimizes the heat transfer coefficient, thus maximizing thermal insulation, is achieved by adopting the lowest possible core density and highest core thickness, as well as relatively thick FRP laminates. However, it is important to bear in mind that all the solutions obtained in this optimization exercise fulfil the most demanding thermal requirements foreseen in the Portuguese legislation.

Maximum $D_{nT,w}$ and minimum $L_{nT,w}$

Regarding acoustic behaviour, the optimization algorithm provided a solution with nearly the highest mass allowed (80 kg), achieved through the adoption of three inner webs (in addition to the two outer ribs), which also significantly increase the stiffness of the panels. This solution provided the best acoustic behaviour for both airborne and impact sounds. A $D_{nT,w}$ value of 40.5 dB was obtained, comparing with a minimum threshold of 50 dB for new construction in Portugal. Regarding $L_{nT,w}$, a value of 81.6 dB was achieved, comparing to a maximum threshold of 60 dB. Such values could still be significantly improved with additional sound insulation measures, such as the adoption of resilient floor coatings and suspended ceilings with adequate anti-vibration fasteners. This would place the sandwich panel floors close to fulfilling the demanding requirements set for new construction, even if their envisaged application is in building rehabilitation (for which such requirements do not apply). It is interesting to note that the best solution was achieved by increasing the mass and stiffness of the FRP laminates rather than of the foam core, for which the lowest density was adopted. This presumably allows for cost savings that outweigh the resulting mass and stiffness increases.

Maximum axial stiffness

For maximum longitudinal axial stiffness, the optimal solution presents relatively thick FRP laminates (10 mm) with unidirectional glass and carbon fibre reinforcements. This also results in a high bending stiffness, which allows the panels to be wide and have relatively narrow ribs, and no webs. In maximizing the transverse axial stiffness, the optimal solution presents mostly woven glass fibre fabric, which has about 46% of fibres oriented along the transverse direction. This results in a lower bending stiffness along the longitudinal direction, which is balanced mainly by decreasing the width of the panel (and consequently the rib spacing) and increasing the thickness of the ribs.

CONCLUSIONS

The design of sandwich panels for structural purposes in civil engineering, illustrated here for the practical case of building floors, is a considerably complex exercise with a high number of design variables and performance requirements. Multi-criteria optimization can be a very useful tool for this purpose, providing helpful insights as to (i) how each variable can be used to achieve the desired performance in the most efficient way, and (ii) how the different performance requirements correlate and effect one another in the final design. It should be noted that a final design decision in such a multi-variable and multi-criteria exercise strongly depends on the subjective valuation that is given to each performance requirement or objective function. For this reason, the authors did not seek to obtain a single optimal solution, rather preferring to analyse the results from a standpoint of Pareto dominance and of the correlations between variables, objective functions, and requirements.

ACKNOWLEDGMENTS

This work was supported by the Portuguese National Innovation Agency (ANI, Project no. 2015/3480).

REFERENCES

- A.L. Custódio, J.F.A Madeira, A.I.F. Vaz AIF, *et al.* (2011). "Direct multisearch for multiobjective optimization", *SIAM Journal on Optimization*, 21(3), 1109–1140.
- J.M. Davies (2001). *Lightweight Sandwich Construction*, Oxford: Blackwell Science, 370 p.
- A. Fam, T. Sharaf (2010). "Flexural performance of sandwich panels comprising polyurethane core and GFRP skins and ribs of various configurations", *Composite Structures*, 92, 2927-2935.
- M. Garrido (2016). *Composite sandwich panels floors for building rehabilitation*, PhD thesis in Civil Engineering, Instituto Superior Técnico, University of Lisbon.



M. Proença, M. Garrido, J.R. Correia, G. Escusa, J. Sena-Cruz, (2017). *Preliminary design of the EasyFloor sandwich panels*, Task 1.1 – Report 1.1, ANI Project (3480) Easyfloor - Development of innovative sandwich panels made of fibre reinforced polymer (FRP) for the rehabilitation of degraded wooden floors of old buildings, Report CERIS DTC 9/2017.

D. Zenkert (1997). *The Handbook of Sandwich Construction*, Worcestershire: Engineering Materials Advisory Services (EMAS), 442 p.



DEVELOPMENT OF A SNAP-FIT CONNECTION SYSTEM BETWEEN PULTRUDED GFRP SANDWICH PANELS FOR BUILDING FLOORS

M. Proença 1, M. Garrido 1 and J. R. Correia 1

¹ CERIS, Instituto Superior Técnico, Universidade de Lisboa, Portugal, Email: mario.garrido@tecnico.ulisboa.pt

ABSTRACT

This study presents the development of a snap-fit connection system to join FRP composite sandwich panels produced by pultrusion. The panels were developed for the replacement of degraded timber floors in old buildings, where restrictions in the available on-site space are often encountered, limiting the maximum size and weight of the sandwich panels. A preliminary design was made and used as baseline for a parametric study on the influence of the joint geometry in the deformability and behaviour of the connection. Finite element (FE) models were developed for this purpose, simulating two connected sandwich panels loaded along their transverse direction. The force required for the assembly of the snap-fit joint taking into account the geometric clearances, and the stresses and strains resulting from the joining operation, were analytically predicted. An FE model of a floor composed of sandwich panels connected using the developed snap-fit system was used to predict the load distribution along the main floor spans, as well as maximum deflections and stress vs. strain profiles in the panels. The parametric study provided a better understanding of the influence of different parameters concerning the snap-fit in the joints' deformability. The study of the assembly forces indicated the advantage of adopting longer latches in order to reduce the mating forces and induced deformations. The results obtained show that those forces should enable the use of only manual labour for the execution of the connections, and that the joints should exhibit sufficient stiffness and strength to guarantee an adequate structural performance of the composite floor, promoting the distribution of loads along the main directions of the sandwich panels.

KEYWORDS

Composite sandwich panels, building floors, connections, snap-fit, finite element modelling, analytical modelling.

INTRODUCTION

The use of fibre reinforced polymer (FRP) sandwich panels in civil engineering structural applications is an interesting and increasingly considered option for various applications, stemming from bridge decks to building floors and roofs. In several cases, sandwich panels are required to cover large construction areas, which, in addition to a relatively underdeveloped connection technology, often leads to the manufacturing of large unwieldy parts. It is thus important to improve the sandwich panel connection technology, developing systems that are logistically easier to handle and faster to install on site, preferably not requiring the use of structural adhesives.

Snap-fit connections are a widely adopted solution in the plastics industry, being used as a simple, quick, and cost-effective solution for parts' assembly (BASF 2007, Bayer 2013, Solvay 2013). However, these connections are mainly used for relatively small and typically non-load bearing parts; adopting such a connection system in civil engineering structural elements is not a trivial transition. Some pultruded multicellular deck panel systems, such as those studied in Sá *et al.* (2017), already comprise snap-fitted panel-to-panel connection systems. These systems were seen to provide significant potential regarding both their mechanical behaviour and ease of installation. This connection design is yet to be adopted in FRP composite sandwich panels and this is the main motivation of the study presented in this paper.

This paper presents the development of a structural snap-fit connection system for panel-to-panel joints between pultruded glass-FRP (GFRP) sandwich panels. After the definition of a baseline design, a parametric study was carried out to determine the influence of various geometrical parameters on the joint's behaviour. For this purpose, finite element (FE) models simulating two connected sandwich panels loaded along their transverse direction were developed. Subsequently, the force required for the assembly of the snap-fit joint taking into account the geometric clearances, and the stresses and strains resulting from the joining operation, were analytically predicted. Finally, a floor composed of sandwich panels connected using the developed snap-fit design was numerically modelled and used to predict the load distribution along the main floor spans, the floor's maximum deflections, and the stress vs. strain profiles in the panels.



BASELINE DESIGN

For the preliminary development of the snap-fit connection system, a panel geometry with total thickness of 110 mm was considered, comprising 5 mm thick faces and 100 mm thick core. A cantilever type of snap-fit was deemed as the most adequate for the envisaged application. Anti-symmetrical panel-to-panel connections were adopted, allowing for a sequential vertical positioning and assembly of the panels - this is a main practical advantage for in situ installation in confined spaces, such as in building applications. Compared to bonded connections, the main potential disadvantage of this system is the higher flexibility of the panel-to-panel joints.

The thickness of the connection elements was set at 5 mm, being equal to the face thickness. The fillet radius used in the preliminary design was 3 mm, following the recommendations of Bayer (2013) regarding the minimum fillet radius of 0.6 times the thickness of the faces. The overhang of the snap-fit latch was considered to have a depth of 1 mm. The role of this overhang is to lock the snap-fit joint and to prevent relative vertical displacements between the panels. The overhang was placed in the mid-height of the snap-fit latch. The entrance side of the overhang has a much milder angle than the retraction side (which has) to reduce the assembly force. For the retraction side, an angle of 90° relative to the cantilever face was adopted in order to ensure interlocking between the connected panels.

The geometry of the baseline snap-fit joint is presented in Figure 111. The geometrical details of the baseline snap-fit joint are the following: (i) 15 mm latch length; (ii) 2° slope of the faces of the joint (corresponding to the outer ribs of the panels); (iii) 5 mm thick latch, and (iv) 5 mm thick recess. At this stage, the existence of two inner ribs and three cells inside the panel was also considered. Clearances of the snap-fit joint were not directly considered in the baseline design, so as to simplify the numerical analyses.



Figure 111: Geometry of the baseline sandwich panel and snap-fit joints (in mm)

PARAMETRIC STUDY

Overview

A parametric study about the influence of the geometrical details of the panel-to-panel connection on the joint's behaviour was performed in what concerns four parameters: (i) the slope of the joint face (i_{jf} , between 0° and 8°); (ii) the length of the snap-fit latch (l_l , between 10 mm and 25 mm); (iii) the thickness of the snap-fit latch (t_l , between 3.5 mm and 7 mm); and (iv) the thickness of the recess of the snap-fit latch (t_r , between 3.5 mm and 7 mm). These variables and their variation are illustrated in Figure 112. The different solutions were analysed regarding their maximum deflections, the gap opening at the bottom (tensioned) snap, and the stresses and strains that develop in the joints.

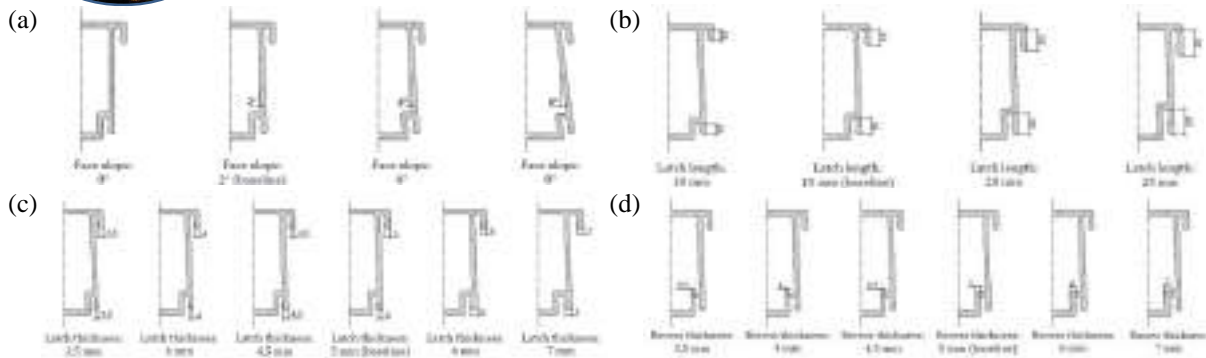


Figure 112: Parametric study variables: (a) slope of the joint face; (b) the length of the snap-fit latch; (c) thickness of the snap-fit latch; and (d) thickness of the recess of the snap-fit latch

The study was performed using the commercial software package *Abaqus/CAE*. Three-dimensional (3D) FE models were developed using solid hexahedral elements (C3D8) for all model parts. In addition to the GFRP faces and snap-fit details, which were modelled as a single part, additional parts were considered for the foam core blocks. The finite element mesh was especially refined in order to adequately predict the local behaviour of the snap-fit joint. A maximum element global size of 2 mm was adopted for the faces, less than half of the GFRP face thickness. The mesh adopted for the baseline case is presented in Figure 113.



Figure 113: FE mesh adopted for the baseline design: (a) general view; and (b) close-up of the snap-fit region

The materials were modelled with linear elastic behaviour; no failure criteria were considered. The following orthotropic material properties were defined for the GFRP laminates: $E_1 = 29.0$ GPa, $E_2 = E_3 = 10.0$ GPa, $G_{12} = G_{13} = G_{23} = 3.0$ GPa, and $\nu_{12} = \nu_{13} = \nu_{23} = 0.3$, where E_i is the Young's modulus along the i direction, G_{ij} is the shear modulus in the ij plane, and ν_{ij} is the Poisson's ratio in the ij plane. For the panel core, typical polyurethane (PUR) foam properties were considered, assuming a density of 100 kg/m^3 with the mechanical properties reported in Garrido (2016); this material was thus modelled as an isotropic material with elasticity modulus (E) of 26.0 MPa, Poisson's ratio (ν) of 0.49 and shear modulus (G) of 8.7 MPa. Steel supports were simulated with $E = 210$ GPa.

The loading was applied to simulate a four-point bending configuration with an overall span of 1.0 m, achieved by transversely connecting two panels. Loading was applied to the model by a set of pressure forces on the top face of the sandwich panels, each of the two surfaces carrying a total load of 500 N distributed over areas of $30 \times 200 \text{ mm}^2$. Simply supported beam boundary conditions were adopted, with a fixed support on one side and a sliding support on the other. A frictionless hard contact was considered in all GFRP-to-GFRP contact surfaces. A surface-to-surface, small-sliding discretization method was chosen. A tie restraint was applied to all steel-to-GFRP contact surfaces (in the supports) and to all GFRP-to-PUR contacts.

Summary of the main results

The parametric study allowed for a better understanding of the joint's behaviour and deformability (Figure 114-a,b). It was possible to conclude that the bottom snap is responsible for most of the deformation of the joint. In the lower snap, the deformation (opening) of the recess is responsible for most of the snap's deformation as it is longer and less restricted than the remaining parts. A thicker recess leads to a stiffer joint with lower stresses, indicating that this parameter should be maximized (within reasonable values). The parameter with the most influence in the stiffness of the joint is the snap-fit latch length, which in turn defines the recess depth. The mid-

span displacement increases significantly with the latch length, suggesting the interest in adopting a minimum latch length.

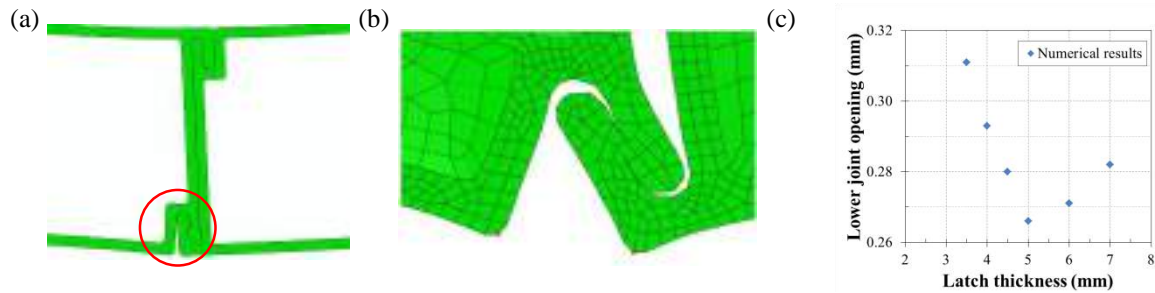


Figure 114: Selected results from parametric study: (a) general view of the joint's deformed shape; (b) close-up of the bottom snap; and (c) plot of joint opening at the bottom face as function of latch thickness

As for the slope of the face of the joint, the results indicated that a vertical face leads to stiffer joints, yet the influence of this parameter on the joint behaviour is relatively low. However, using a slightly sloped face (*e.g.*, with a slope of 2°) together with vertical connection latches should help achieving a better mechanical lock, preventing accidental disassembly of the joint, while resulting in only a minimal stiffness reduction. For the latch thickness parameter, it was concluded that the best solution is to use elements with the same thickness as the recess and the faces of the panel, as this leads to minimal joint opening (as illustrated in Figure 114-c) and deflection.

ASSEMBLY FORCES

Overview

In the parametric study summarized above, the deformability and the stresses of snap-fit joints subjected to transversal flexure were evaluated without considering the mechanics of their assembly process. However, the forces and deformations involved in the assembly procedure are extremely relevant to assess the viability and practicality of using these connections. The evaluation of such parameters was carried out using simplified analytical expressions and numerical models. For this analysis, the force at the tip of the latch and the vertical assembly forces were calculated considering different latch lengths. A study on the effects of clearance size was performed to better understand the relationship between the assembly force, the assembly deformation of the latch, and the locking effect of the snap-fit. Allowable strains were defined for this analysis, ensuring that the assembly procedure does not induce damage in the joint components.

Allowable strains

In order to define allowable strain values, the results of material characterization tests carried out for GFRP laminates, reported in Garrido (2016) and Paiva (2017), were considered. These were defined for compression (ϵ_{al}^-), tension (ϵ_{al}^+), and in-plane shear (γ_{al}), by identifying the points in the respective stress vs. strain curves that corresponded to the occurrence of first damage (typically micro-cracking of the polymer matrix). Table 36 presents the allowable (nominal) strain values adopted, affected by safety factors of 1.0, 1.5, and 2.0. A safety factor of 1.0 results in a strain value leading to damage initiation, whereas with a factor of 2.0 only half of that strain is allowed.

Table 36: Allowable strains for the GFRP laminates

Safety factor [-]	ϵ_{al}^- [$\mu\text{m}/\text{m}$]	ϵ_{al}^+ [$\mu\text{m}/\text{m}$]	γ_{al} [$\mu\text{m}/\text{m}$]
1.0	16,518	32,584	14,612
1.5	11,012	21,722	9,741
2.0	8,259	16,292	7,306



Assembly force calculation

Force at the tip of the latch

The force at the tip of the latch mainly depends on three parameters: (i) the latch length, (ii) the latch thickness, and (iii) the displacement at the tip of the latch required for assembly. Regarding the latch length, an initial assessment showed that for latches of 15 mm or shorter, the required forces were excessively high, rendering such solutions unfeasible from a practical standpoint. Thus, longer latches with lengths of 20, 25 and 30 mm were considered in this part of the study. A constant thickness of 5 mm was considered for all cases. The displacement required for assembly depends on the overhang depth, for which a base value of 1 mm was considered; however, with the need to adopt clearances between parts, such depth has to be reduced. To take this into account, a possible clearance of 0.25 mm was considered, reducing the required displacement at the latch tip to 0.75 mm.

Simple beam theory was used (considering the latch as a cantilever with rectangular cross-section, subjected to a transverse load applied at its tip section) to obtain an approximate estimate of the force at the tip of the latch and the maximum (axial and shear) stresses and strains that develop during the assembly process for the three different latch lengths. The results are presented in Table 37; one may observe that by increasing the latch length from 20 mm to 25 mm, the assembly force at the tip of the latch decreases approximately by a factor of two. For latch lengths of 25 mm and above, the strains at the latch are well within the allowable values, considering a safety factor of 1.5 or 2.0.

Table 37: Forces at the tip of the latch for connection assembly and subsequent axial stresses and strains

Latch length (l) [mm]	F [kN]	σ [MPa]	ε [$\mu\text{m/m}$]	γ [$\mu\text{m/m}$]
20	117.2	140.6	14060	2930
25	60.0	90.0	9000	1518
30	34.7	62.5	6250	868

Vertical assembly force

To calculate the vertical assembly force, a simple wedge model may be used to account for the contact between the faces of the latches in the snap-fit. The wedge slope will be responsible for the conversion of the vertical force applied during assembly into a horizontal force deflecting the tip of the latch. This mating force (W) may be estimated using the following equation (Bayer 2013),

$$W = F \cdot \frac{\mu + \tan(\alpha)}{1 - \mu \cdot \tan(\alpha)} \quad (\text{Eq. 1})$$

where F is the force at the tip of the latch, α is the entrance angle, and μ is the friction coefficient. As there was no specific data available regarding the friction coefficient of the final (as produced) materials, calculations of the mating force were carried out considering two cases: (i) negligible friction ($\mu = 0$), and (ii) friction coefficients of 0.1 or 0.3, which are within the range of values referred in the literature for the contacts between GFRP surfaces (Fernandes 2014). The assembly force was calculated for three different latch lengths (20, 25, and 30 mm), considering a sandwich panel length of 4.0 m (typical in old buildings). The entrance angle (α) is defined by the latch length in the adopted design, with shorter latches having steeper entrance angles. Additionally, estimates of the mating force were calculated for the multicellular pultruded deck panels studied in Sá *et al.* (2017) (the Rigmat SF75H panels produced by Kookmin Composite Infrastructure, Inc.), which had a connection length of 2.5 m. In that study, the panels were connected by snap-fit joints, which were easily assembled by hand. Thus, the mating force estimates for those panels were useful in assessing the validity of the results obtained in the present study, regarding the feasibility of the snap-fit connection system for sandwich panels.

Table 38 presents the most relevant values for the above-mentioned calculations per unit of length of the panels. The forces involved in the assembly of the pultruded sandwich panels with a 20 mm long latch are comparable to the snap-fit system studied by Sá *et al.* (2017), in terms of vertical (mating) assembly force. For longer latch lengths, the mating forces decrease significantly. One can infer that the proposed design is expected to provide greater ease of assembly compared to the snap-fit system for deck panels, even taking into account the higher length of the sandwich panels for building applications compared to the multicellular deck panels for pedestrian

bridges. Nonetheless, the results obtained highlight the significant effect of friction on the mating force that is required to assemble the connections. Such effect is more significant in the connections proposed here due to the lower slope of the entrance side of the latch compared with the deck panels studied by Sá *et al.* (2017), given that a lower entrance angle leads to a higher predominance of friction force in the total mating force.

Table 38: Estimates of mating force (W) per meter of length for sandwich panels with different latch lengths (considering different friction forces) and for the deck panels studied by Sá *et al.* (2017)

Panel	l_l [mm]	α [°]	F [kN]	$W_{\mu=0}$ [kN]	$W_{\mu=0.1}$ [kN]	$W_{\mu=0.3}$ [kN]
Pultruded sandwich panels	20	6	29.3	3.1	6.1	12.3
	25	5	15.0	1.3	2.9	6.0
	30	4	8.7	0.6	1.5	3.3
Deck panels (Sá <i>et al.</i> 2017)	34	14	19.2	4.8	6.9	11.4

FINAL DESIGN AND FLOOR MODEL

Optimized snap-fit joint design

The results from the parametric and assembly force studies were used to refine and optimize the design of the snap-fit joint. In this redesign, the main goal was to increase the ease of assembly and improve the overall joint behaviour. The main changes made to the previous joint design consisted of moving the overhang groove to the tip of the latch, and adopting a progressively reducing cross-sectional thickness in the latch. Compared with the previous design (mid-length overhang groove and constant latch cross-section), this new configuration offers two additional advantages: (i) milder entrance angle, due to a longer entrance side, which reduces the assembly force (mating force), and (ii) reduction of maximum strains at the base of the latch (according to Bayer 2013). The final design is shown in Figure 115, where a 30 mm long latch is represented.

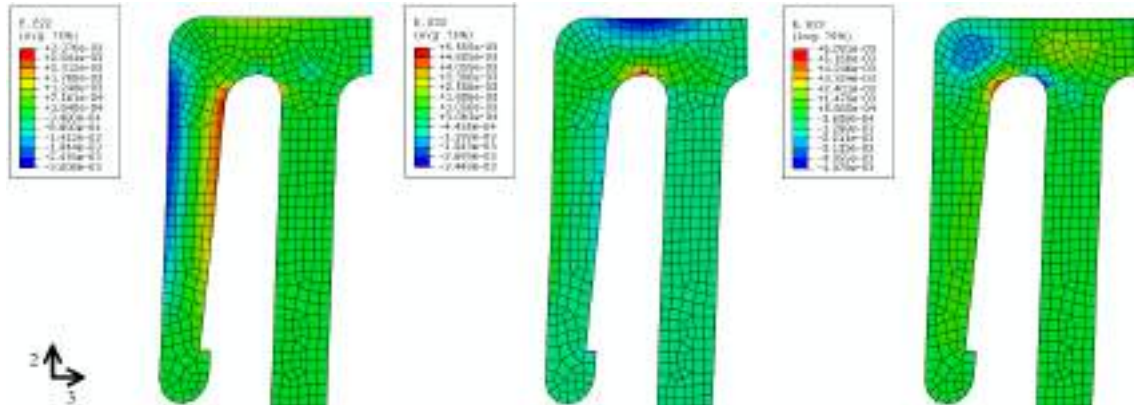


Figure 115: Redesigned snap-fit: FE predictions of strains during joint assembly.

An FE model similar to those of the preliminary study was developed for the optimized design to estimate in further detail (and with higher accuracy) the stresses and strains associated with the assembly process. A clearance of 0.25 mm was now considered, leading to a displacement at the tip of the latch of 0.75 mm in order to overcome the depth of the groove (1.0 mm). Figure 115 presents the strain distributions obtained. As expected, when the latch bends (as a cantilever), (i) axial compressive and tensile stresses develop, respectively, in the outer and inner surfaces, and (ii) shear stresses are maximum at the base of the latch. Both axial and shear strains predicted by the FE models are well below the permissible limits previously defined (*cf.* Table 36). It is worth mentioning that while the maximum axial strains agreed relatively well with the analytically estimated values (Table 37, 30 mm latch), the maximum numerical shear strains were significantly higher than those estimated analytically. These differences are due to the higher accuracy of the FE model in estimating the local stresses and strains for the real geometry of the latch (relatively complex), when compared to the simple cantilever analytical model.



Floor plan analysis

Overview

A numerical study was carried out to assess the global behaviour of a full-scale sandwich panel floor assembled using the developed connection system. Three-dimensional (3D) FE models were developed using the *Abaqus* software to simulate the behaviour of a floor with a square plan (4.50 by 4.50 m²). The main objective was to evaluate the load distribution between the main (longitudinal) and secondary (transverse) spans subjected to uniformly distributed loading. This information will help to estimate the design loads that should be considered along each of those directions when designing floors with the developed snap-fit connections. In that regard, a square floor plan was considered in order to provide an upper limit estimate of the loads carried out along the transverse direction, which in turn will determine the relevant actions for the snap-fit design. This study also aimed at assessing the influence of the snap-fit connection's latch length on that load distribution, given that longer latch lengths generally lead to more flexible connection designs. Two different latch lengths were adopted in this study, 25 mm and 30 mm. The influence of this length on the overall bending behaviour of the sandwich panel floors was investigated by analysing parameters such as the maximum floor deflections, maximum gap opening at the connections, the reaction force distribution, and the axial stresses in the panels' face sheets.

Model description

Symmetry simplifications were adopted along the longitudinal and transverse spans, thus reducing the models' computational effort. From the introduction of the longitudinal symmetry simplification, only half-length of the panels (2.25 m) was explicitly modelled. For the symmetry simplification in the transverse direction, attention was paid to offset the plane of symmetry from the location of the panel-to-panel connections. To do so, models of half-width panels were created and the symmetry simplification was imposed where the mid-width plane of the central sandwich panels would be located. The resulting model layout is depicted in Figure 116-a, where the modelled portion of the floor corresponds to the square area defined by the ABCD vertices, with the AC and AB edges being simply supported. The panels were modelled with longitudinal GFRP ribs along their lateral edges, these being part of the snap-fit connection detail. In addition, two internal GFRP webs were also modelled, for a total of four equally spaced longitudinal GFRP reinforcements (ribs) per panel. The cross-section design adopted and respective dimensions are shown in Figure 116-b.

The GFRP components in each panel were modelled as single parts comprising the faces, ribs, and connection details. Elastic orthotropic material properties were considered for the GFRP laminates. A Young's modulus of 30 GPa was adopted along the main span direction (*i.e.*, aligned with the main fibre reinforcement direction). Along the two directions that are orthogonal to the main span, Young's moduli of 10 GPa were adopted. The values for the shear moduli and Poisson's ratios were set as 3 GPa and 0.3, respectively, independently of the (main) direction/plan considered. The selection of such material constants was carried out considering typical values for the mechanical properties of pultruded GFRP components used in structural applications. For the core material, the mechanical properties of a polyurethane foam which has been extensively characterized at IST were considered (Garrido 2016). This foam has density of 87.4 kg/m³ and shear modulus of 8.7 MPa, and was modelled as an isotropic linear elastic material with Young's modulus of 26.9 MPa and Poisson's ratio of 0.495. For both materials, no failure criteria were adopted. The floor models included two types of interactions between the different model parts: (i) "cohesive behaviour" for the interactions between core blocks and their respective enveloping GFRP parts, and (ii) "tangential-normal behaviour" with friction coefficient of 0.3 for the interactions between different sandwich panels, namely affecting the contacts between the various surfaces of the snap-fitted connections.

(a)

(b)

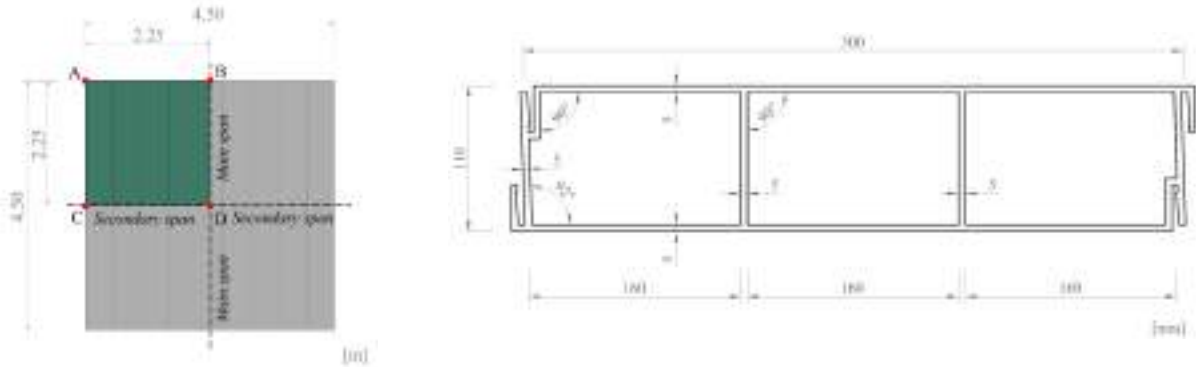


Figure 116: General view of the floor model: (a) plan view, and (b) panel cross-sectional dimensions

Simply supported conditions were adopted along the perimeter of the sandwich panel floors. Uniformly distributed pressure loads were applied to the top face of the floors throughout their entire area. The applied load corresponded to a uniformly distributed load of 1 kN/m². Linear analyses were performed and linear elastic material properties were considered in this study; therefore, results obtained for a unit load were extrapolated for other significant load values (e.g., design loads), provided that these would be within the limits of elastic response.

Main results

The deformed shape of the sandwich panel floors (Figure 117) was generally similar for the two models created (i.e., with different latch lengths). The simulation results indicate a correct functioning of the snap-fit connections. Observing the connection areas in detail, some separation is visible between the bottom faces of adjacent panels, mainly caused by bending in the bottom recess walls, as would be expected for this type of snap-fit connection. The models predicted an approximately reaction force distribution of 75%-25% among the main and secondary spans, respectively, with differences between latch lengths being nearly negligible (around 1%).

The maximum deflection (δ_{max}) values, occurring at the centre of the floors, were slightly higher in the 30 mm latch model. For a unit load, the maximum (elastic) deflection with a 25 mm latch connection was 4.475 mm, comparing to a value of 4.574 mm with a 30 mm latch, a relatively marginal increase of 2.2%. Regarding the gap opening at the connections between adjacent panels (w_s), these values are more significantly affected by the length of the connection latch. The highest differences occur at the connection closest to the supports, where a gap opening of 0.116 mm was predicted in the 25 mm latch model against a value of 0.133 mm in the 30 mm latch model (again, for a unit load). When considering serviceability limit states, such values are considered to be small enough to be easily accommodated by typical flexible (e.g., silicone-based) joint sealants.

Overall, the effects of the latch length on floor behaviour were mostly limited to localised aspects of the connection's behaviour. The global response of the floors, namely regarding their stiffness, were not significantly affected by the latch length for the 25 mm and 30 mm cases investigated here. As such, the selection of a latch length of up to 30 mm should be mainly based on the connection's local performance and behaviour, namely considering aspects related to the required fitting force, admissible fitting strains, and load capacity along the floor's transverse direction (discussed earlier in this paper), among other relevant aspects which may be identified from a more detailed analysis.

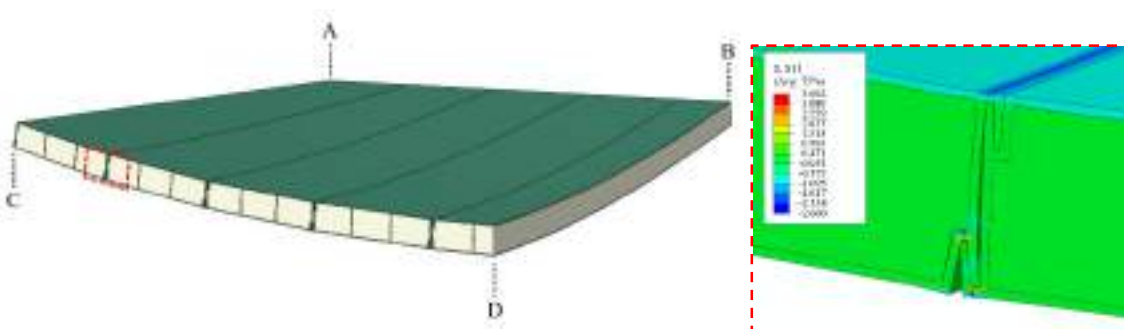


Figure 117: General view of the deformed shape (left) and detail of the deformations and axial stresses in the transverse direction (represented as "S11", in MPa, right) at a snap-fit connection



CONCLUSIONS

This paper presented the development of a snap-fit connection system to join pultruded FRP sandwich panels for the rehabilitation of building floors. The various steps in the development of the snap-fit joints contributed to a better understanding of the influence of several parameters in the joints' behaviour. The lower snap is responsible for most of the joint's deformation, especially due to the deformability of the latch recess, which is higher for longer latches and thinner recess walls. Furthermore, regarding the thickness of the connection elements, it was found that it is preferable to have similar thickness in the recess walls as in the latch. Regarding the slope of the joint face (panel rib), the results indicated that this parameter has little influence on the joint stiffness (for the range of slopes considered). The study of the assembly forces pointed out the advantage of adopting longer latches in order to reduce the mating forces and allowable deformations. The results obtained here show that those forces should enable the use of manual labour only in the assembly of the connections. Furthermore, numerical simulations showed that a floor system comprising the developed snap-fit joint seems to be structurally viable (particularly regarding its deformability, which is a critical factor in overall design), and that such joints are able to transfer a non-negligible portion of the load along the floors' transverse direction, namely ~25% in a square floor plan.

ACKNOWLEDGMENTS

This work was supported by the Portuguese National Innovation Agency (ANI), through Project no. 2015/3480 (EasyFloor), developed in cooperation between CERIS/IST-ULisbon, ALTO Perfis Pultrudidos Lda and Minho University.

REFERENCES

- BASF Corporation (2007). *Snap-fit design manual*, New Jersey, USA.
- Bayer Material Science LLC (2013). *Snap-fit joints for plastics – A design guide*, Pittsburgh, Pennsylvania, USA.
- L. A. Fernandes (2014). *Structural behaviour of GFRP beams subjected to concentrated loads: experimental tests, numerical modeling and analytical study* (in Portuguese). MSc Dissertation in Civil Engineering, Instituto Superior Técnico, Universidade de Lisboa, Portugal.
- M. Garrido (2016). *Composite sandwich panel floors for building rehabilitation*. PhD Thesis in Civil Engineering, Instituto Superior Técnico, Universidade de Lisboa, Portugal.
- J. Paiva (2017). *Comportamento mecânico de ligações coladas em materiais FRP* [Mechanical behaviour of bonded joints in FRP composite materials] (in Portuguese). MSc Dissertation in Civil Engineering, Instituto Superior Técnico, Universidade de Lisboa, Portugal.
- M. F. Sá, A. M. Gomes, J. R. Correia, N. Silvestre (2018). "Flexural behavior of pultruded GFRP deck panels with snap-fit connections", *International Journal of Structural Stability and Dynamics*, Vol. 18, No. 2, 1850019, 2018.
- Solvay Speciality Polymers (2013). *Snap-fit latch design*, Technical Bulletin.



FORM-FINDING AND STRUCTURAL DESIGN OF AN ARCHITECTURAL SCENERY WITH ALL GFRP FREE-FORM FACADE

Y. Zhao ¹, X. Jiang ¹, Q. Zhang ¹ and Q. Wang ¹

¹ College of Civil Engineering, Tongji University, Shanghai, China, Email: jiangxu@tongji.edu.cn

ABSTRACT

With the pursue of architecture artistic effect improving rapidly all around the world, constructions with curved facade were built one after another. This gives a challenge to the construction skills of facade, and also exposes the weakness of traditional materials when applying to curved surface modelling. GFRP (Glass-Fibre-Reinforced Polymer), as an emerging building material, has advantages on plenty of aspects over traditional materials, especial on processability. Thus, it is an extremely ideal free form surface modelling material and possible to provide an excellent solution to curved architecture facade. The architecture schematic design of a sunken plaza covering structure in Fuzhou, China is a sculptural shaped construction similar to three morning glories. The whole design presents an obvious warping shape from the top view, thus its surface is complicated and completely in free form curve. The owners' demand for the final effect of the structure is pretty high, so traditional materials were abandoned since they cannot meet the demand and GFRP are selected as facade material finally. There are three main problems are encountered in detailed designing and processing stage of GFRP: a. processing technology of free-form surface panels for mass production; b. the selection and layout of secondary girders which support panels; c. the connection problem between GFRP panels and secondary girders. The contradiction points and solving process of these three main practical problems are discussed in this paper and solutions are listed, thus similar problems encountered in the future can be further directed.

KEYWORDS

GFRP; Free form curved facade; Processing technology; Secondary girders

INTRODUCTION

In recent years, with the rapid increase in the whole world to pursue the artistic effect of the building structure, structures of curved surface appearance emerge one after another, and the traditional facade materials also exposure more disadvantages when applied to curved facade, thus, it is urgent to develop a new process or new material suitable for special-shaped architecture facade, while GFRP seems to be a potential material.

First of all, the workability of GFRP is excellent, the conventional processing methods include hand lay-up and RTM forming, and with particular thermal property, GFRP processes potential hot working property, such as multi-point forming method might be utilized to process free-form surface, thus it is suitable to process curved panels. In addition, the physical and mechanical properties of GFRP, compared with traditional civil engineering materials, are also advantageous, so in recent years it has made great development in civil engineering area. However, the application of this kind of material is still very limited due to several reasons.

Two north-south symmetry sunken plazas of a constructing commercial centre in Fuzhou, China are designed to be covered by a sculptural shaped construction similar to three morning glories respectively. The overall appearance present an irregular state of free-form surface, which makes its visual impact extremely strong. Meanwhile, the final effect of the owners' demand for the structure are also very high, thus little adjustment can be made to original architecture design. Membrane was first put forward to adopted but at last abandoned for its weld joints and problems of ageing, therefore, the traditional building materials is difficult to meet the requirements, or the cost will be alarming, so new craft has to be found. This structure, as freeform surfaces, is suitable for the application of GFRP panels for form-finding; in addition, as a scenery structure, the safety and comfort of common building structure need not to be taken into account. Coupled with the volume and area of the structure is small, so it is suitable as an attempt to test GFRP if it really an ideal curved facade material. Try to detect the parameters of its properties through actual design, manufacture and construction, and discover and solve the possible problems through this structure.

In this paper, a comprehensive discussion on the major contradictions and solutions for the three major issues of this project are conducted: a. process issues of massive freeform

GFRP panels production; b. secondary girders, which support GFRP panels, designing issues, including the selection of cross section and the layout; c. issues of connection between freeform GFRP panels and secondary girders. These three issues are the major contradictions of design phase, initial production phase and construction phase. This paper elaborates on the solutions of the issues and the main principles of program implementation.

Other detailed problems would be dealt with in the actual work based on the main principles, and provide references for future works.

PROJECT OVERVIEW

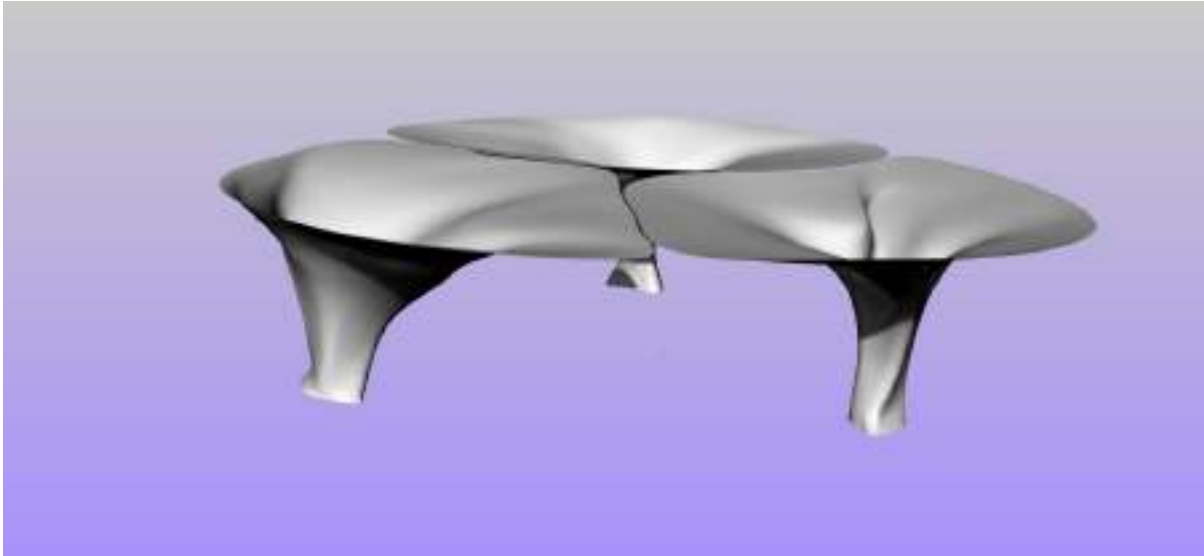


Figure 1: Freeform curved surface

The structure, located in Fuzhou, Fujian Province, China, is still under construction and will be completed by the end of 2017. The architectural design of the structure is shown in Figure 1, the height is 9.8m and it appears as a circle with a 43m diameter in top view, covering a round sunken plaza with a 25m diameter in the middle of morning glories. The entire area is about 1460 square meters, each morning glory is separate from another with a gap in the middle. The entire models are completely free-form surfaces, there is no exactly the same position, and somewhere locally is in a very distorted state. Thus, the structure design is very complicated and the suitable selection of material and structure system is even more important in the very beginning. Due to the owners' requirements of the structure to appear a completely seamless smooth surface state, GFRP is selected as panel material at last. According to the characteristics of GFRP and the requirements of the owners, many targeted refinement programs are designed and experiments are conduct to test its effect.

FREEFORM PANELS PROCESSING TECHNOLOGY

Processing Technology Selection

Considering all the circumstances, the size of each GFRP panels in this project is determined to be about 2m × 2m, and 838 totally different curved panels are divided. The production of massive different curved panels presents a great challenge to processing technology and management. In this paper, the production technology are mainly discussed. The matrix of GFRP panels is epoxy resin and glass fibre cloth is laid in $\pm 45^\circ$ direction. Processing technology has to be determined first, since each panel's shape is unique and has to make a mould for it, the cost of mould is extreme high, thus, has to consider carefully and control, and at last, plastic foam is applied as mould material.

Hand lay-up process and RTM process can be taken to produce GFRP panels, and both of them have advantages suit for this structure and disadvantage that must be considered. The biggest advantage of hand lay-up process is without size and shape constraints, the equipment is simple and investment is small, and this feature is very suitable for the project: large size, bending shape. However, the disadvantages are also obvious. The stability of the product produced by the process is poor, the mechanical properties of the panels are low, and the most important is on the production efficiency, labour intensity and poor sanitary conditions of hand lay-up process. The project schedule is very tight, so this process needs further thought. The other processing method is RTM (resin transfer molding) process. The quality of RTM products is obviously higher than that of hand lay-up process. The fibre content of products is high, sanitary conditions are good in the production process, the pollution is small,



and the key is the high production efficiency. RTM process can also make curved panels, but for the purposes of this project, which is making single curved panel, its applicability is not as good as hand lay-up process.

Therefore, this project involves the trade-off between the two processes. According to the characteristics of the project and the adjustment of the process, the RTM process is adopted in the end, mainly considering the following subjective and objective reasons.

A. Subjective reasons: the panel quality of hand lay-up process depends mainly on the man-made workmanship and other man-made behaviours. But the panels will be connected into a whole surface at last, therefore, the panels need a more consistent quality, while the panels made through RTM possess better quality, and the quality is more consistent and higher yield moreover. In addition hand lay-up process sanitary conditions are poor, workers need to wear adequate protective clothing, but the production time of the project mainly concentrated in the summer, workers are more contradictory for thick working clothes.

B. Objective reasons: the project schedule is very tight, it is necessary to increase productivity, reduce human workload and increase machine work as much as possible. The labor amount of hand lay-up process is too high and efficiency is too low, thus, it is impossible to completed the production in time.

Process Adjustment



Figure2: Single-sided foam male mould

Since the shape of each panel are not the same, each mould could used only twice(two sunken plaza), and therefore need to produce a large amount of moulds, resulting in mould cost is very high and must be controlled. Plastic foam shown in figure 2 is selected to manufacture mould, the advantages and disadvantages of foam are co-exist. Soft foam material can be quickly and accurately carved into the needed shape to improve production efficiency and guarantee the schedule; but the disadvantage is also obvious and need to adjust the panel making process. Foam material makes it different from gel coat painting on conventional mould, so traditional hand lay-up process and RTM process cannot be applied directly and must be adjusted. Considering all the situation, RTM process is adopted but different from the common. Adopt double-side vacuum film, on the top and bottom , and bonded into a bag, and then use the roller to make the wet semi-finished panel and the mould as close as possible. However, GFRP panels produced this way would exist surface flatness problem, so panels need further finishing after resin cured (shown in figure 3), then polish and paint after installation.



Figure 3: Curved GFRP panels

SECONDARY GIRDER DESIGN

Main content of secondary girder design lies in the system selection and arrangement, both of which were associated with GFRP panel division, actually because the panels are connected at the secondary girders and formed into a whole surface, the arrangement of secondary girders is substantially equivalent to the division of the GFRP panels. Therefore, the approximate size of the GFRP panels has to be determined first. According to *Load Code for the Design of Building Structures* (2012), the basic wind pressure is 0.75kN/m^2 , which is much larger since Fuzhou is vulnerable to typhoons in the summer, and because of the opening property of the structure, the wind load must consider wind suction plus wind pressure at the same time, which almost doubles the wind load. There is no stipulation on the maximum deformation of the composite panel in *Technical Code for Building*

Curtain Wall (2012), so refer to other material's stipulation: the maximum deformation is 1/60 of the short side length. Through calculation, the maximum deformation size is about 1/60 when the GFRP board size is around $2\text{m} \times 2\text{m} \times 4\text{mm}$, meanwhile consider the panel processing technology, 2m side length is also a more appropriate size. Therefore, the size of the secondary girder cells is similar to that of the GFRP division, which is around 2m.

In order to fit better with the surface, the secondary girders must be bent and twisted processing and the construction accuracy must be relatively high. Therefore, the precision of secondary girders is very important which must be considered while selecting the cross section and arranging layout. To sum up, there are three points to note:

A. Select welded "T" shaped cross-section to built up secondary girders. Webs and flanges of such cross-section can be bent and twisted respectively and then welded together, thus, much easier to process and ensure accuracy.

B. Try to dispose secondary girders at relatively flat portion. As the curved panels and flat panels production is similar, try to avoid to arrange the secondary girders at large curvature region of the surface. Such arrangement can also simplify processing, and installation at construction site will be more convenient, in addition, the connection between panel and secondary girder is also easier.

C. In order to facilitate the construction, the layout of secondary girder should also be convenient positioning, so try to continuously arranged the secondary girders and reduce the bifurcation, thus, ensure the continuity. Ensure that each flower has a few vertical secondary girders continuous up and down and these can be used as benchmark positioning secondary girders, other vertical secondary girders also try to be continuous. Horizontal secondary girders cannot avoid bending, thus each of them is broken at the joint, so that horizontal secondary girders are short and easy to twist, with less relative error.

Due to the difficulty of high precision control, bolt connection could even be impossible for this structure, since preset bolt holes might be difficult to align considering large error. Thus all secondary girders joint will be welded. Such connection can improve the integrity of whole structure and reduce the relative slip, and eventually reduce the risk of cracking on the girder joint position of painted surface. The final steel secondary girders design is shown in figure 4.

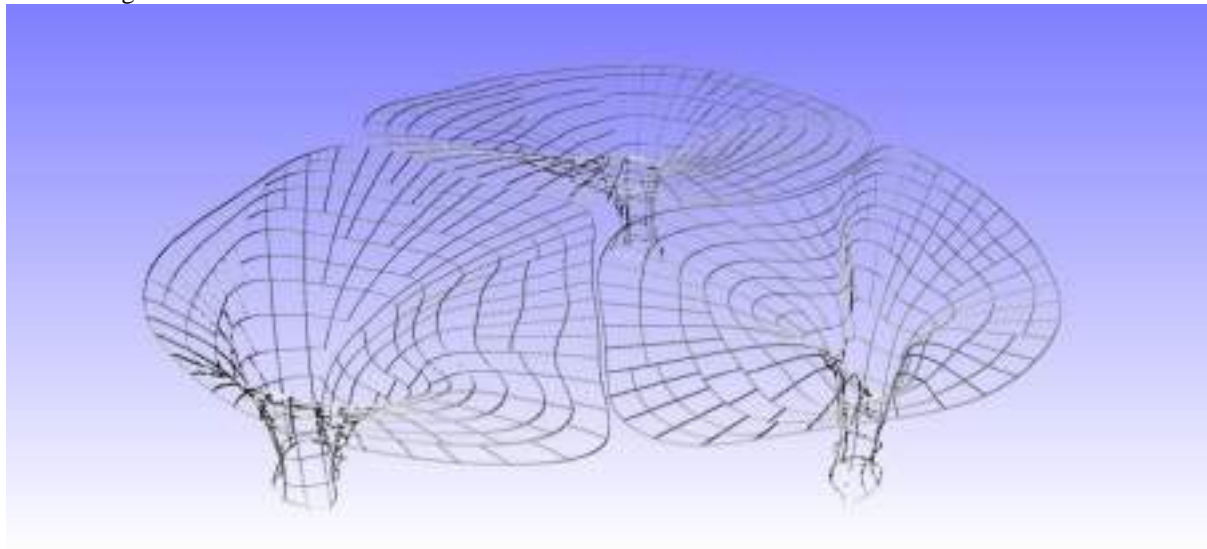


Figure 4: Secondary girders

CONNECTION BETWEEN PANELS AND SECONDARY GIRDERS

The connection between GFRP panels and secondary girders is a essential part of this structure. As a attempt of new material structure, only by ensuring the connection of the structure can the strength, safety and reliability be guaranteed. First thing of the connection issue is to select appropriate connecting form, and then ensure the strength. When determining the connecting form, first it must meet the architectural and structural requirements, and then the feasibility including strength assurance and construction assurance. The effect of this structures' facade requires continuously smooth, thus, seams between panels must be treated to ensure the smooth. Therefore, the panels and secondary girders should be effectively connected to ensure the passing of the load, the seams between panels need to be filled to ensure the entire facade behave as one (Benthem Crouwel Architects 2014).

The matrix of GFRP is epoxy resin, and epoxy system-based structural adhesive is commonly used, so their compatibility would be fine anyway. Therefore select an effective structural adhesive which can ensure two points: gluing GFRP panels and steel secondary girders strongly; fill the seams between panels to make panels work as a whole surface. Since the structural adhesive requires a curing time, the panels and the steel girders require fastening means before adhesive cured, and countersunk rivet is adopted as temporary fastener. Rivet capacity should be neglected when calculating the strength of the connection, thus, rivets can also provide additional strength. So the actual connection between GFRP panels and steel secondary girders is shown as figure 5, this connection is simple and effective, and the feasibility of on-site construction is guaranteed, but still there are points to pay attention when constructing

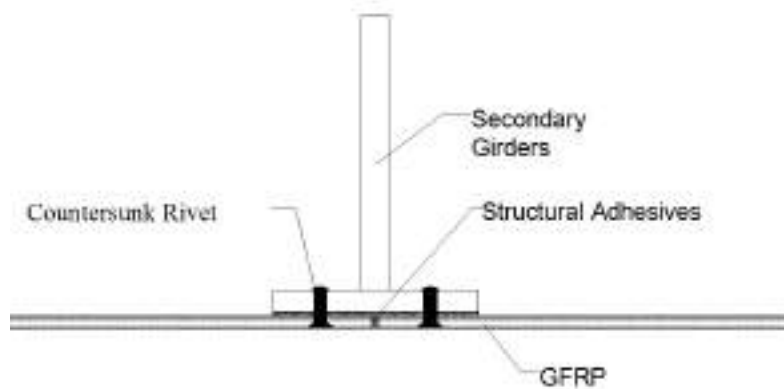


Figure 5: Connection diagram

Connection strength between GFRP panel and steel must be confirmed after setting connection form, so design an simple experiment to test the strength as shown in figure 6. Respectively upper and lower "T" section steel, and a 4mm thick GFRP panel in the middle, use structural adhesive to glue the steel flange and GFRP panel on both sides, which can ensure that the specimen finally destroy at adhesive layer between GFRP panel and steel flange, simple and effective. Prepare specimens according to the actual situation on-site: simple polished flange surface, apply structural glue on two sides of GFRP panel, sandwich the panel between two steel flanges and then fully press two "T" section steels, keep it for 24 hours to guarantee curing completely, finally conduct the experiment on test machine and calculate the tensile strength.

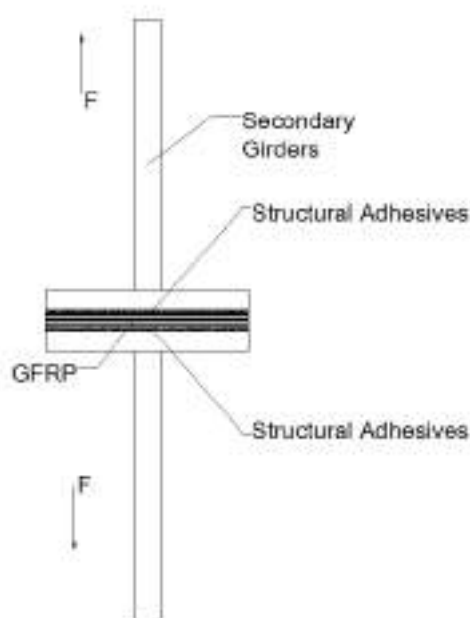


Figure 6: Test specimen and experiment machine



Figure 7: Conducting experiment and destroyed specimen

Table 1: Experiment result

Specimen number	1	2	3	4	5	6
Tension strength/MPa	6.354	7.576	10.461	5.509	6.312	12.302
	Avg.	8.086		Min.	5.509	

It can be seen from the specimen in figure 7 that fracture surface is mainly located at steel corrosion layer, and partially on glued surface of GFRP and structural adhesive. Summarized from Table 1 that the tension strength of all the specimens are more than 5MPa. The GFRP panels and the secondary girders connected on all four sides with a design connection width of 3cm on each side, thus, the tensile strength of 5MPa sufficiently guarantee the connection strength. However, the actual connections' complex stress state required further testing and simulation, in order to provide more accurate guidance to similar connection in the future.

CONCLUSIONS

This project is a new attempt to use GFRP panels for freeform surface finding and forming a smooth, seamless surface as facade. A great deal of problems were encountered during the implementation of the project, and many of the major problems could never be realized without practice. Some of the issues that were thought to be the major ones in the design phase of the project actually become secondary issues, but many unexpected things become tricky. This paper mainly discusses three issues: GFRP freeform panels processing technology, secondary girder design and connection between panels and secondary girders, and introduces the solution adopted in this project. Of course these solutions might not be the most appropriate ones, and there are still many points to be focused on in the actual implementation process, thus, need to be optimized in all aspects, and the research on these aspects will continue to the operational phase of this structure after the construction is completed. It is believed that with continuous improvement, more all GFRP structures will further come into our sight.



REFERENCES

- X. Jing et al. (2012). *Load Code for the Design of Building Structures*.
- K. Zhou et al. (2012). *Technical Code for Building Curtain Wall*.
- Bentham Crowel Architects (2014). "The New Stedelijk Museum Amsterdam", *Architecture Technique*, 7, 84-93.



MONOTONIC AND CYCLIC BEHAVIOUR OF BEAM-TO-COLUMN BOLTED METALLIC-CUFF JOINTS BETWEEN PULTRUDED GFRP PROFILES

David Martins 1, João Azevedo1, José A. Gonilha 1, João R. Correia 1, Mario Arruda 1 and Nuno Silvestre 2

¹ CERIS, Instituto Superior Técnico, University of Lisbon, Portugal, Email: jose.gonilha@tecnico.ulisboa.pt

² IDMEC, Instituto Superior Técnico, University of Lisbon, Portugal

ABSTRACT

Pultruded glass fibre reinforced polymer (GFRP) profiles are a promising alternative to traditional structural materials due to their high strength, light-weight and corrosion resistance. Nevertheless, widespread use has been hindered by their brittle behaviour, low elastic moduli and lack of widely accepted design guidelines. The connection technology for GFRP frame structures, which must account for the linear-elastic behaviour at the material level and has a significant influence on the overall deformability of pultruded GFRP members, is still relatively underdeveloped. This paper presents the development of a novel beam-to-column connection system for GFRP tubular profiles comprising an external thin-sheet metallic cuff tailored to 120 mm square section profiles, being bolted to the beam's (i) webs or (ii) flanges. Such connection aimed at the development of ductile or pseudo-ductile connection systems, envisaging the inelastic energy dissipation under cyclic loads and, thereafter, the development of GFRP frame structures with adequate seismic performance. The experimental programme comprised (i) monotonic and (ii) cyclic tests on these beam-to-column joints. The results show that the metallic cuff is a promising structural solution for GFRP beam-to-column connections, providing an enhanced performance, in terms of strength and stiffness, when compared to other connection systems previously tested. Moreover, the test results show that this connection system provides considerable ductility (monotonic tests) and ability to dissipate energy (cyclic tests), despite the pinching effect. Alongside the experiments, non-linear finite element numerical models were developed to simulate the monotonic tests, providing a good agreement with experimental results.

KEYWORDS

All FRP and smart FRP structures; Experimental study; Seismic applications; Characterization of FRP and FRC materials/systems; Beam-to-column connections.

INTRODUCTION

Pultruded glass fibre reinforced polymer (GFRP) profiles are being increasingly used in civil engineering due to their lightness, strength and non-corrodibility (Correia 2008). One of the major difficulties in the development and design of GFRP frame structures is the connection technology, which initially mimicked bolted steel connection arrangements (Keller 1999). Therefore, those connections (in general, between I-section profiles) consisted of seated GFRP angles bolted to the beam's web and column's flange, and were designed as pinned. However, such technology transfer does not take into account the considerable differences between the materials, in particular the orthotropy, brittle failure and creep susceptibility of the GFRP material. Moreover, designing GFRP structures with pinned connections can be very penalizing in terms of deformations, leading to inefficient and uneconomical profile selections.

Various "improved" connection systems were developed, especially for I-section profiles (*cf.* Mottram and Zheng 1997). These connection systems were deemed to achieve higher rotational stiffness in order to allow the connections to be designed as semi-rigid. However, these systems presented other problems and consequently an efficient way to connect pultruded GFRP profiles has not yet been achieved.

The main motivation of the study presented in this paper was the need to develop a novel connection system between GFRP pultruded tubular profiles, which would present considerable ductility and capacity to dissipate energy, simultaneously guaranteeing an adequate stiffness and resistance of the connection. This connection system, described ahead, comprises a metallic cuff enclosing the beam and column to be connected. To study the behaviour of such novel connection system, full-scale tests were carried out in beam-to-column connections with two alternative bolt configurations subjected two different types of loading: (i) monotonic; and (ii) cyclic. At the same time, non-linear numerical models were developed to simulate the monotonic behaviour of both connection configurations, where a damage propagation model was considered for the GFRP material. A parametric study of

the GFRP fracture energies was performed based on the comparison between the numerical and experimental results, in terms of connections' stiffness, strength and damage/failure modes.

EXPERIMENTAL PROGRAMME

Materials

The GFRP profiles used in the beam-to-column connection tests had a $120 \times 10 \text{ mm}^2$ square tubular cross-section, and were subjected to an extensive experimental characterization, namely regarding: (i) strength (σ_{cu}) and modulus of elasticity (E_c) in compression, in both longitudinal (L) and transverse (T) directions; (ii) longitudinal tensile strength ($\sigma_{tu,L}$), modulus of elasticity ($E_{t,L}$) and Poisson ratio (ν_{LT}); (iii) longitudinal flexural strength ($\sigma_{fu,L}$) and modulus of elasticity ($E_{f,L}$); (iv) interlaminar shear strength (τ_{is}); and (v) in-plane shear strength by means of Iosipescu shear tests (τ_{LT}). The results obtained are summarized in Table 1.

Table 1: GFRP material properties (average \pm standard deviation).

Test	Method	Property	Average \pm St. dev.	Unit
Compression	ASTM-D695	$\sigma_{cu,L}$	435.1 ± 52.6	MPa
		$E_{c,L}$	21.2 ± 3.3	GPa
		$\sigma_{cu,T}$	88.9 ± 16.3	MPa
		$E_{c,T}$	4.8 ± 0.9	GPa
Tension	EN ISO 527	$\sigma_{tu,L}$	326.2 ± 16.8	MPa
		$E_{t,L}$	32.7 ± 3.0	GPa
		ν_{LT}	0.32 ± 0.0	-
Flexure	EN ISO 14125	$\sigma_{fu,L}$	415.1 ± 61.3	MPa
		$E_{f,L}$	24.9 ± 5.8	GPa
Interlaminar shear	ASTM-D2344	τ_{is}	30.6 ± 2.6	GPa
In-plane shear	ASTM-D5379	τ_{LT}	41.4 ± 6.2	GPa

The cuff connectors were made of carbon steel S235 and had a 2 mm thickness, while the rods (bolts) were C18.8. In the future, the proposed connection can be made using stainless steel, in order to enhance the corrosion resistance of the system and, therefore, its durability.

Connection configuration

The beam-to-column connection system developed in this study consists of a steel cuff connection, as illustrated in Figure 3. The geometry of this parts is similar to those of the GFRP connectors proposed by Smith *et al.* 1998 and Sigamsethi *et al.* 2005. This connection configuration intended to transfer moment not only through the bolts, but also by the contact between the profiles and the cuff, thus reducing the typical damage of bolted GFRP connections. Furthermore, in our study the connection was produced with thin steel sheeting (2 mm), bent and welded to create the desired geometry, enclosing the GFRP profile, in order to achieve higher ductility and energy dissipation capacity. Two cuff configurations were considered with a 360 mm height and a 242 mm depth, differing in the positioning of the beam's bolted connection: (i) in the web – configuration W (Figure 1) and (ii) in the flanges – configuration F (Figure 2).

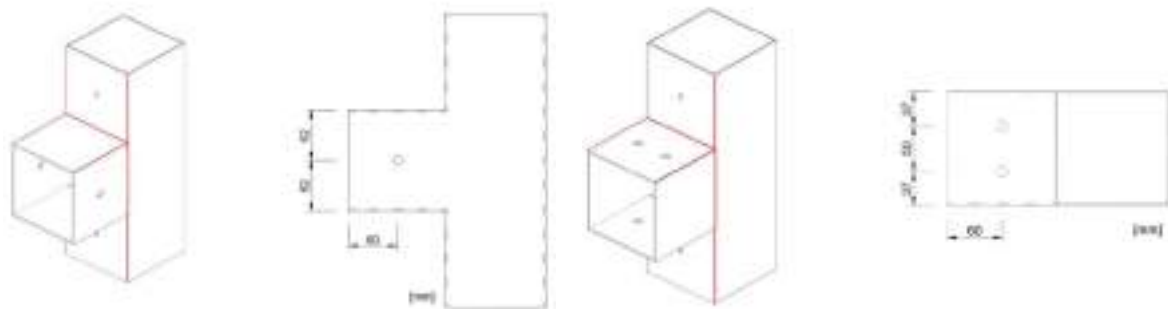


Figure 1: Configuration W: 3D view (welds in red) and side view. Figure 2: Configuration F: 3D (weld in red) and top view.

Setup, instrumentation and procedure

Both monotonic and cyclic tests were performed inside a closed steel frame, using the setup presented in Figure 3. Both column ends were fixed (rotations and displacements prevented) to the steel frame and the lateral edges of the beam tip were prevented to displace laterally with two aluminum cylindrical bars (Figure 3). The load was applied to the beam at a distance of 600 mm from the face of the column flange by an *Enerpac* hydraulic jack, with load capacities of 600 kN and 250 kN, respectively in compression and tension, and a maximum stroke of 250 mm. The applied load was measured by a *TML* load cell with 300 kN of load capacity (both in tension and compression). Ten displacement transducers and two rotation transducers (all from *TML*) were used to measure: (i) the beam's vertical displacements; (ii) the beam's rotation; (iii) the column's rotation, and (iv) the joint's horizontal displacement. The rotation of the beam and column were measured in two distinct ways: with the rotation transducers, measuring the rotations in the steel cuff; and with pairs of displacement transducers, measuring the rotations in the members (in the beam and, in the column, above and below the cuff). Considering that the measurement of the rotation in the members is the most representative of the overall connection's behaviour, the rotations considered were the ones measured with the displacement transducers.



Figure 3: Test setup

The monotonic tests were performed by applying a descending vertical load to the beam until a maximum displacement of ~135 mm was reached; tests were performed under displacement control at an average speed of 60 mm/min. The cyclic tests were conducted based on a displacement protocol defined in ECCS (1986, for the assessment of the cyclic behaviour of steel structures), taking into account the results of monotonic tests; in this case, a maximum displacement of ± 125 mm was set due to the maximum stroke of the hydraulic jack. Three tests were performed for each bolt configuration and type of loading (12 tests in total).

RESULTS AND DISCUSSION

Monotonic tests

Figures 4 and 5 present, respectively, the load vs. vertical displacement curves obtained for all specimens of configurations W and F (bolts in beam's web or flange). Both configurations initially displayed a linear behaviour. For average displacements of ~21 mm for configuration W and ~27 mm for configuration F, the connections started to exhibit non-linear behaviour with progressive stiffness reduction. At some point, all specimens presented failure, followed by a load reduction, which was gradual in some specimens and sudden in others. The single exception was specimen WM3 that never failed (the hydraulic jack reached its maximum stroke).

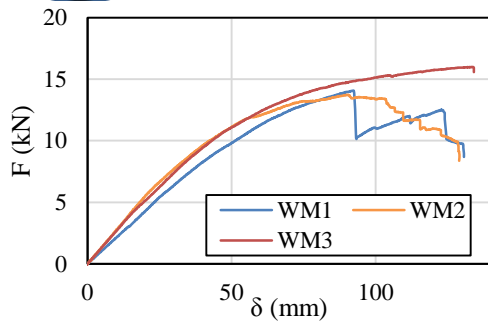


Figure 4: Load vs. vertical displacement (beam tip) of configuration W.

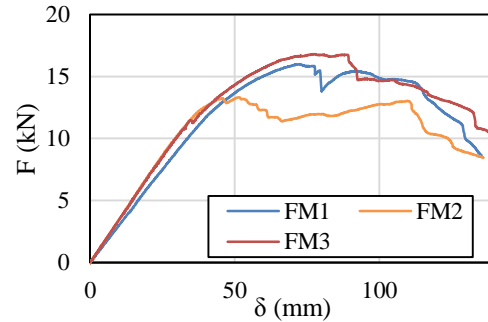


Figure 5: Load vs. vertical displacement (beam tip) of configuration F.

The damage in both configurations was assessed during the tests and after the disassembly of the specimens. The main damage modes in configuration W were: (i) bearing, sometimes followed by shear out, on the web bolt holes of the GFRP beam (Figure 6); (ii) web-flange junction failure of the GFRP beam (typically responsible for the failure of the connections, Figure 6); and (iii) significant yielding of the steel cuff. Configuration F presented the following damage modes: (i) bearing, sometimes followed by shear out, on the top flange bolt holes of the GFRP beam (Figure 7); (ii) web-flange junction failure on the GFRP column; and (iii) failure of the weld that connects the webs of the column and the beam in the steel cuff (typically responsible for the failure of the connections, Figure 8).

Table 2 presents the main values measured in the monotonic tests. In general, configuration F presented better performance than configuration W, with higher values of force-vertical displacement and moment-rotation stiffness (K_δ and K_θ , respectively) and “yield” load (F_y). In terms of strength (F_u) and ductility (C_d), both configurations presented similar values. The latter index was calculated according to one of the methods proposed by Jorissen and Fragiaco (2011) for timber nailed connections (which also comprise brittle and ductile materials, wood and steel, respectively).



Figure 6: WM1 GFRP beam damage.



Figure 7: FM3 GFRP beam damage.



Figure 8: FM3 steel cuff failure.

Table 2: Results of the monotonic tests (average \pm standard deviation)

Configuration	K_δ kN/m	K_θ kNm/rad	F_y kN	F_u kN	δ_y mm	δ_u mm	C_d rad
W	252.0 \pm 33.4	99.3 \pm 13.9	5.3 \pm 0.5	14.6 \pm 1.2	21.4 \pm 3.5	105.4 \pm 24.4	0.81 \pm 0.07
F	330.8 \pm 25.8	138.9 \pm 17.7	8.7 \pm 33.41	15.4 \pm 1.8	26.6 \pm 4.7	67.1 \pm 14.0	0.77 \pm 0.04

Cyclic tests

As mentioned, the cyclic tests were based on ECCS (1986) recommendations; two displacement histories were defined, one for each configuration, based on their “yield” displacements (21 mm and 27 mm for configurations W and F, respectively). All tests were considered valid, with the exception of one of “web” specimens (WC3), which had a defect on the steel cuff.

Figures 9 and 10 present examples of the load vs. vertical displacement curves measured in the cyclic tests for both configurations, comparing also the most representative curves from the monotonic tests for the respective configuration.

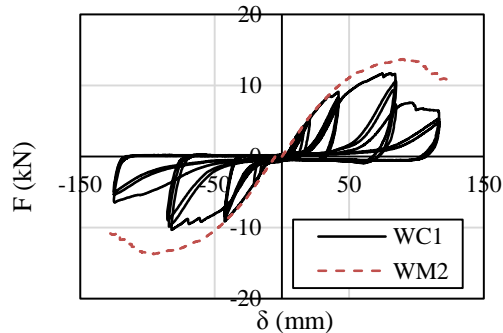


Figure 9: Cyclic test of specimen WC1.

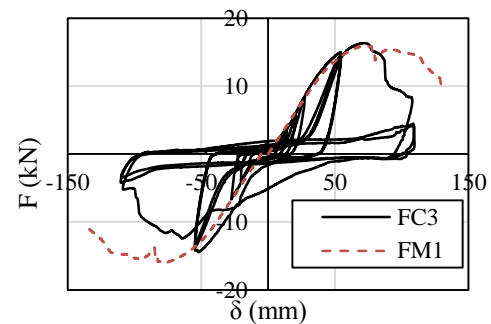


Figure 10: Cyclic test of specimen FC3.

For both configurations, the hysteresis curves presented reasonable symmetry, although this symmetry was lost in configuration F, due to the damage of the steel cuff. Both configurations presented a baseline where the connection did not absorb any load. This baseline was caused by a small clearance in the steel cuff and became larger with the cycles due to the damage progression.

The damage modes were similar to the ones observed in the monotonic tests for both configurations. Additionally, configuration W also presented (i) failure of the weld responsible for the web-flange junction in the steel cuff, (ii) buckling of the beam's webs after the flange-web failure, and (iii) crushing of the beam's corners. Configuration F also presented (i) failure of the weld responsible for the web-flange junction in the steel cuff, and (ii) failure of the weld responsible for the connection between the webs of the beam and the webs of the column in the steel cuff, which occurred not only in the top part of the weld, but also at the bottom part, with those damages eventually merging for larger displacements.

The strength progression at each cycle was also assessed following the recommendations of ECCS (1986), by the resistance ratio (ε), which is given by the ratio between the absolute value of the load at the end of each cycle and the "yield" load attained in the monotonic tests. Figure 11 presents the average strength ratios per cycle for both configurations, *i.e.* the ratio between the maximum force at each cycle and the "yield" force. Both configurations presented an ascending trend until the 5th cycle, in which the "yield" displacement was exceeded. The resistance ratios dropped in the repetitions of the same displacement and rose once more when the displacement was again increased (8th cycle). Thereafter, the resistance dropped in every cycle, for both configurations. On the other hand, Figure 12 presents the average accumulated absorbed energy for both configurations. Configuration F absorbed significantly more energy than configuration W, showing that, despite the moment transfer of the connection relying mostly on the contact between the profiles and the cuff, the bolted configurations also influenced the behaviour of the connection. In conclusion, configuration F presented an overall better performance for cyclic loading.

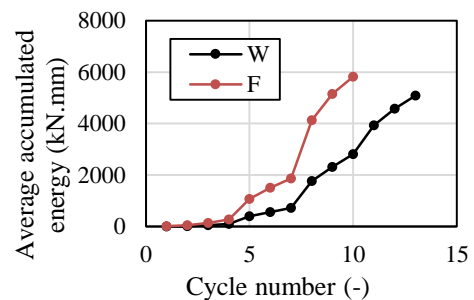
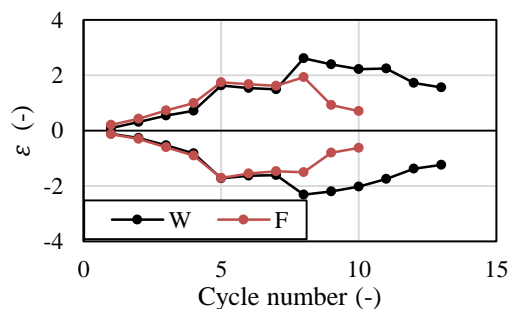


Figure 11: Average resistance ratios per cycle.

Figure 12: Average accumulated absorbed energy.

NUMERICAL ANALYSIS

Model description

The numerical analysis presented herein was made using ABAQUS finite element (FE) commercial package. All the geometrical features of the modelled connection were carefully simulated in accordance to the specimens tested. Since the connection was symmetrical, only half of it was modelled. The analysis performed were static implicit (standard), geometrically linear and physically non-linear (for all materials). The GFRP members were modelled using two different types of FEs: (i) continuum shell (SC8R) elements in the connection area and next to it, namely in a length of 10 mm and 120 mm after the end of the cuff element for the columns and the beams, respectively (*cf.* Figure 13); and (ii) frame (B33) elements, in the regions farther away from the connection. The steel cuff was modelled with continuum shell (SC8R) elements and the bolts with tetrahedral solid elements (C3D4).

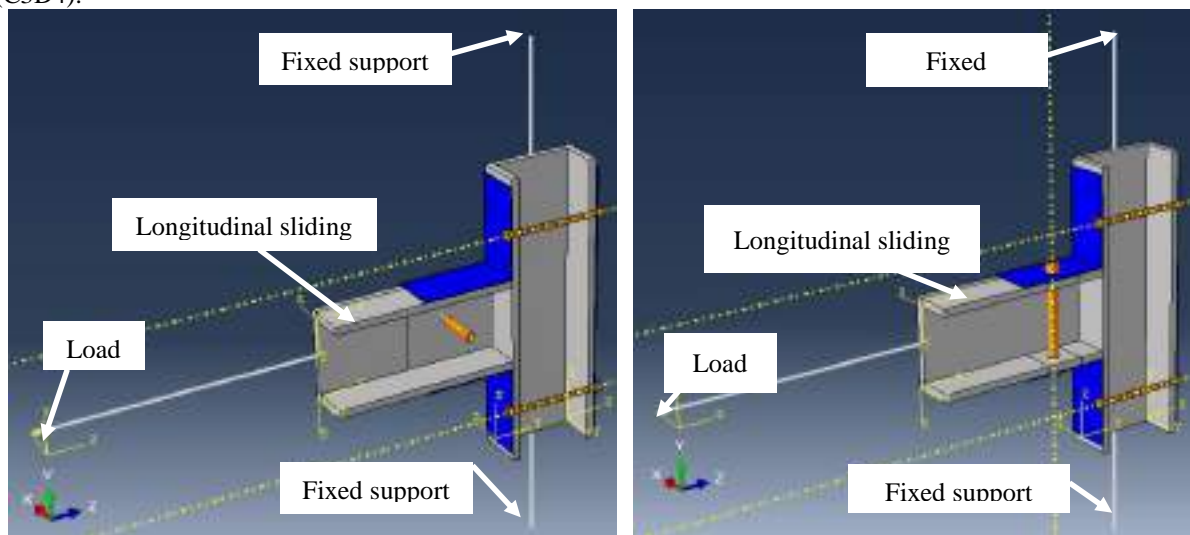


Figure 13: Boundary conditions (*left-W; right-F*).

Boundary conditions

Figure 13 displays the boundary conditions of the numerical models. The load was applied at a distance of 600 mm of the column's facing flange and consisted of a 120 mm imposed displacement. Both column ends were fixed (displacements and rotations restrained) and all the faces coincident with the symmetry plane were modelled with a longitudinal sliding boundary condition, so the symmetry simplification was valid.

Contact and friction formulation

All contacts were modelled as frictionless and with a stiffness of 10,000 MPa/mm, sufficiently rigid to discard their effect on the connection stiffness. The only exception was the contact between the top flanges of the GFRP beam and the cuff, which was modelled with a numerical artificial clearance of 1 mm (to simulate the actual clearance of the steel cuff). Because this clearance brought convergence problems, the stiffness of this contact was changed to 5,000 MPa/mm. Surface-to-surface contact and small-sliding theory were used in all surfaces.

Material modelling

The material properties considered were those derived from the experimental tests (*cf.* section Materials). The GFRP was modelled as orthotropic; the Hashin criterion and the Rotem damage model (included in the software package library) were used to simulate respectively the damage initiation and propagation, based on a bi-linear model defined by means of fracture energies (G_f). Given the uncertainty in the definition of the fracture energies for the different directions (f – fibre and m – matrix) and loads (T – tension and C – compression), a parametric study was performed in order to select the energies that would provide the best fit to the experimental data of both configurations; such study yielded the following values: $G_{f,C} = 5$ N/mm, $G_{f,T} = 50$ N/mm, $G_{m,C} = 100$ N/mm and $G_{m,T} = 150$ N/mm. In order to reduce convergence difficulties in the softening regime, a viscous regularization

scheme was used, causing the tangent stiffness matrix of the softening material to be positive, for sufficiently small time increments. In this case a value of 10^{-5} was used for all the aforementioned damage directions and solicitations. Regarding the steel materials, they were modeled as isotropic with elastoplastic behaviour.

Results and discussion

This section presents the results obtained with the FE models for both configurations. To evaluate the global damage in the GFRP material the DAMAGESHR variable was used, as it includes all damage modes (fibres and matrix, in tension and compression), and the PEEQ variable was used to evaluate the yielding distribution of the steel cuff.

Figure 14 and Figure 15 present the load vs. vertical displacement responses obtained with the numerical models of the monotonic tests, for configurations W and F, respectively. The curves of both configurations initially present two distinct linear branches with different stiffness values. In the first one, the contact between the top flanges of the GFRP beam and the steel cuff was not yet established, so the moment transfer was only due to binary in the bolts. After damage occurred (bearing of the GFRP near the holes), contact was established, allowing the moment to transfer not only through the bolts, but also by contact with the steel cuff. For both configurations, this was followed by a gradual stiffness reduction. Finally, configuration W reached the failure load (F_u), for which the connection experienced a sudden load drop; configuration F did not present such a behaviour, displaying an elastoplastic response.

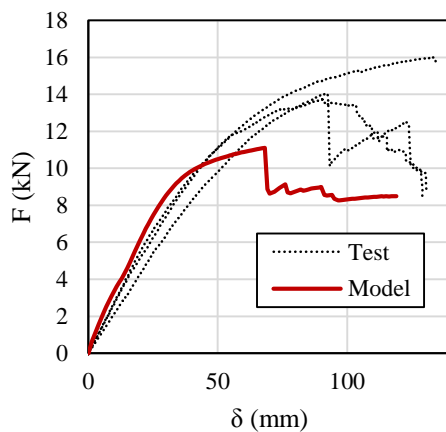


Figure 14: Load vs. vertical displacement curves for configuration W.

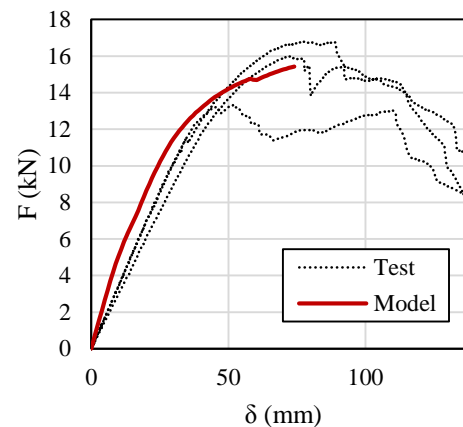


Figure 15: Load vs. vertical displacement curves for configuration F.

Regarding the comparison between numerical and experimental results, in terms of stiffness, initially the numerical results were considerably higher than the experimental ones, but after the contact of the top flanges was established, the values of stiffness presented relatively good agreement (less than 25% of relative difference). Concerning strength, for configuration W the numerical value of maximum load was lower than the experimental one (-23.9%) due to the aforementioned premature damage in the beam's webs, while for configuration F an excellent agreement was obtained (+0.4%, in this configuration the numerical resistance considered corresponded to the maximum load attained, since the model was tending to a constant load value).

Figure 16 presents the final shear damage distribution in the GFRP for both configurations. The numerical model of configuration W (Figure 16-a) provided a similar damage pattern to that observed experimentally, with a crack in the beams' top web-flange junction and another one aligned with the hole. This is similar to the experimental damage, which generally occurred in the web-flange junction, sometimes extending adjacently to the hole (*cf.* Figure 6). The bearing on the hole was also predicted, but without evolving to shear-out. The numerical model of configuration F (Figure 16-b) predicted the bearing on the holes of the beam's top flange, without developing to shear-out either (*cf.* Figure 7), and also the damage in the web-flange junction of the column. These results are consistent with the ones observed experimentally.

Figure 17 presents the yielding of both connections. For connection W (Figure 17-a) the model presented accurate results, with the most plasticized part of the steel cuff being consistent with the one observed in the experiments.

For connection F (Figure 17-b) the results also matched the experiments, with the most plasticized part of the steel cuff corresponding to the one where failure was seen to occur in the tests (*cf.* Figure 8).

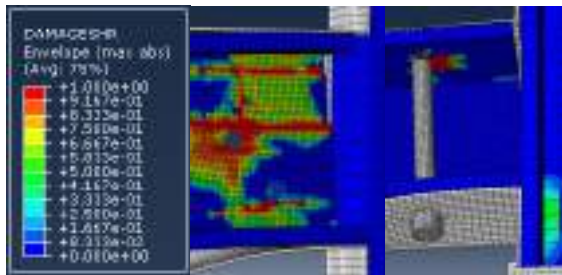


Figure 16: DAMAGESHR in both models (left - W; right-F).

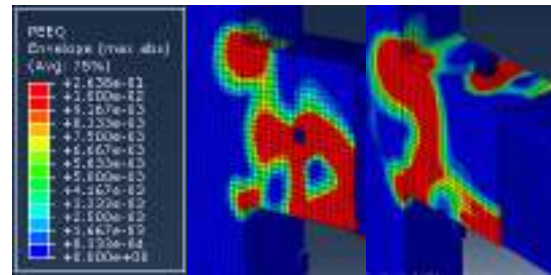


Figure 17: PEEQ in both models (left - W; right-F).

CONCLUSIONS

In the present study, a novel beam-to-column connection system was developed and proved to offer advantages over existing systems. In fact, the system developed presents a good balance between structural performance, ease of fabrication and assembly, and compatibility with other building elements.

The tests on the beam-to-column connections allowed assessing the behaviour of two alternative bolt configurations. In terms of serviceability behaviour under monotonic loading, configuration F presented higher values of stiffness and “yield” load. Nevertheless, both configurations presented similar values of failure load and ductility. Concerning the cyclic behaviour, configuration F also provided better performance, presenting higher values of dissipated energy. Regarding the damage progression, for both types of loads (monotonic and cyclic), the two bolt configurations presented significant damage in the GFRP profiles (especially in the beam), with configuration F presenting more extensive yielding and damage in the steel cuff. Since the steel cuff was produced with a thin steel sheeting (2 mm), it should be noted that the only construction limitations come from the bolt nuts’ position. In this aspect, configuration W presents advantages when compared to configuration F (in terms of compatibility with floor slabs), although the limitations of the latter can be easily overcome.

Regarding the numerical study of the monotonic behaviour of the connections, despite the generally good agreement between the numerical and experimental results, some limitations were identified. It was confirmed that, ideally, the simulation of this kind of structural problems should be conducted resorting not only to the damage initiation criteria of the materials involved, especially the GFRP, but also to the damage progression. Only in this way it is possible to evaluate precisely the performance of the connections, since the use of damage initiation criteria alone does not allow studying their full behavior, providing very conservative strength predictions. While the models were well able to predict the maximum load of configuration F, they underestimated it for configuration W. Despite all this, the overall damage/failure modes were well predicted by the numerical model.

ACKNOWLEDGMENTS

The authors wish to thank CERIS for funding this research. The financial support of Fundação para a Ciência e a Tecnologia (FCT, through the funding of project FRP-Quake PTDC/ECM-EST/6465/2014) is gratefully acknowledged. The third author is also grateful to FCT for funding his research through scholarship SFRH/BPD/112216/2015.

REFERENCES

- J.R. Correia (2008). *GFRP Pultruded Profiles in Civil Engineering: Hybrid Solutions, Bonded Connections and Fire Behaviour*. PhD Thesis in Civil Engineering, IST, UTL.
- ECCS (1986), *Recommended Testing Procedure for Assessing the Behaviour of Structural Steel Elements under Cyclic Loads* (no 45). Brussels: ECCS.



A. Jorissen, M. Fragiaco (2011). "General notes on ductility in timber structures". *Engineering Structures*, 33, 2987–2997.

T. Keller (1999). "Towards structural forms for composite fibre materials". *Structural Engineering International*, 9, 297–300.

J.T. Mottram, Y. Zheng (1997). "State-of-the-art review on the design of beam- to-column connections for pultruded frames", *Composite Structures*, 35(4), 387–401.

S.K. Singamsethi, J.M. LaFave, K.D. Hjelmstad (2005). "Fabrication and testing of cuff connections for GFRP box sections", *Composites for Construction*, 9(6), 536–544.

S.J. Smith, I.D. Parsons, K.D. Hjelmstad (1998). "An experimental study of the behaviour of connection for pultruded GFRP- I beams and rectangular tubes", *Composite Structures*, 42(3), 281–290.



INDENTATION AND IMPACT BEHAVIOUR OF GFRP COMPOSITE SANDWICH PANELS FOR CIVIL ENGINEERING STRUCTURAL APPLICATIONS

R. Teixeira 1, M. Garrido 1, M. Proença 1, J. R. Correia 1 and L.S. Sutherland 2

¹ CERIS, Instituto Superior Técnico, Universidade de Lisboa, Portugal, Email:
mario.garrido@tecnico.ulisboa.pt

² CENTEC, Instituto Superior Técnico, Universidade de Lisboa, Portugal

ABSTRACT

Composite sandwich panels are a promising solution for the rehabilitation of building floors and pedestrian bridges. However, previous studies on relatively thin sandwich panels have pointed out their particular susceptibility to concentrated loads. In this respect, studies developed for relatively thick sandwich panels such as those used in civil engineering structural applications are scarce. The present work presents an experimental, numerical and analytical study of the indentation/punching and perforation behaviour of relatively thick GFRP composite sandwich panels under concentrated loads. In the experimental study, the effects of the indenter geometry (shape and diameter) and of different core materials (PUR and PET foams and balsa wood) on the indentation stiffness, first damage and peak resistances, and energy absorption capacity of the sandwich panels are investigated. The results obtained show that the present type of sandwich panels, despite exhibiting high resistance values, present a relatively low energy absorption capacity up to first damage. Indenter geometry was the most influential parameter for the low-velocity impact behaviour of these thick FRP composite sandwich panels. The indentation stiffness was mainly influenced by the core material, but the effect of this on impact resistance was less marked. Quasi-static tests provided a conservative estimate for the impact behaviour of composite sandwich panels. The numerical study comprised the development of 3D finite element models of the sandwich panels, concluding that the Hashin (failure initiation) criterion gives a very reasonable prediction of the first damage resistance (12% relative difference compared to the test value selected as a case study). For the two analytical models analysed, a parametric study was completed and a new formulation was proposed; the results obtained showed that the models can provide very reasonable predictions of first damage resistance.

KEYWORDS

GFRP composite sandwich panels, foam core, balsa core, quasi-static indentation, low-velocity impact, tests, numerical models, analytical models.

INTRODUCTION

Composite sandwich panels are a promising solution for the rehabilitation of building floors and pedestrian bridges (Garrido 2016). The reduced installation periods, high strength- and stiffness-to-weight ratios and reduced maintenance costs are some of the advantages that explain the increasing interest in this solution as an alternative to traditional materials. However, composite sandwich panels are a relatively recent solution in the construction sector and their widespread use is being limited by, among other factors, the absence of specific regulation and the limited understanding of various aspects of their behaviour. One of such aspects is their resistance to concentrated loads. Previous studies developed on relatively thin composite sandwich panels highlighted their particular susceptibility to concentrated loads (Abrate 1997). The dropping of tools during the installation phase and the action of localised loads during the service stage, caused by furniture (in buildings) or high heels and umbrellas (in footbridges), are examples of events that can cause localized damage with significant detrimental consequences for the behaviour of the sandwich panels.

Previous tests showed that the impact behaviour of composite sandwich panels is strongly dependent on the material properties and on the characteristics of the impact event (namely the indenter geometry and the boundary conditions). The influence of indenter geometry on the impact behaviour of composite sandwich panels was studied by Zhu *et al.* (2006), who performed tests with hemispherical and flat indenters in sandwich panels with an aluminium honeycomb core. As expected, the use of flat indenters led to higher elastic stiffness, and higher first damage and peak resistances. According to the authors this may be explained by the higher stress concentration verified for the hemispherical indenters. The influence of the core material was studied by Atas and Sevim (2010) who tested composite sandwich panels composed of PVC foam (62 kg/m³) and balsa (157 kg/m³) cores at various impact energies. For higher energies matrix and fibre damages at the unimpacted faces were observed. The balsa-cored sandwich panels exhibited higher elastic stiffness and slightly higher strength values



for the perforation of the impacted face. In contrast, for the perforation of the second face higher values were observed for sandwich panels with PVC foam due to densification of the core.

The numerical modelling of the quasi-static behaviour of composite sandwich panels under concentrated loads is often based on user-defined routines with failure initiation simulation of the composite skins using the Hashin criterion together with a damage progression law (Rizov 2006; Foo *et al.* 2008). Good agreement between the experimental data and numerical models has often been achieved but these studies do not consider the types of sandwich panels suitable for civil engineering structural applications. In fact, for applications in civil infrastructure and building construction sandwich panels typically require much thicker face laminates and therefore their behaviour under local and impact loads may not be comparable.

Analytical models predicting the impact behaviour of composite sandwich panels are most often based on Hertzian contact, energy balance and / or spring-mass models (Abrate 1997). However, these models are only capable of describing the elastic phase of the impact behaviour, and become invalid as soon as damage occurs. Analytical models proposed for the prediction of the onset of damage which may be used in the preliminary design of composite sandwich panels are still very scarce; those by Olsson (2002) and Wen *et al.* (1998) are among some of the very few examples available.

In this context, the current paper presents experimental, numerical and analytical studies of the quasi-static indentation and low-velocity impact behaviour of FRP composite sandwich panels for civil engineering structural applications. The Olsson (2002) and Wen *et al.* (1998) predictions of the onset of damage are assessed and a new analytical formula based on the adaptation of Olsson's model is proposed and evaluated.

EXPERIMENTAL PROGRAMME

Objectives and Materials

In order to evaluate the impact behaviour of thick FRP composite sandwich panels three common alternative sandwich cores were tested: (i) rigid polyurethane (PUR) foam; (ii) polyethylene terephthalate (PET) foam; and (iii) end-grained balsa (BAL). The vacuum infused sandwich panels were of total thickness 134 mm, comprising of two 7 mm thick faces separated by a 120 mm thick core. The relevant mechanical and physical properties of the core materials and GFRP laminates are presented in Tables 1 and 2, including their density (ρ), tensile strength (σ_{tu}), compressive strength (σ_{cu}), shear strength (τ_u), tensile elasticity modulus (E_t), shear modulus (G) and Poisson ratios (ν), and where the subscripts L and T refer to the longitudinal and transverse directions. The laminates comprised of unidirectional continuous E-glass fibres with a symmetrical fibre layup of $[0/0/30/-30/90/0]_s$ embedded in an orthophthalic polyester resin.

Table 1: Core material mechanical properties (Garrido 2016)

Material	ρ [kg/m ³]	σ_{tu} [MPa]	σ_{cu} [MPa]	τ_u [MPa]	G [MPa]
PUR foam	87.4	0.68	0.64	0.32	8.7
PET foam	105.4	1.03	1.32	0.94	19.2
Balsa wood	101.4	4.26	5.76	0.93	48.8

Table 2: GFRP laminate mechanical properties (Garrido 2016)

$\sigma_{tu,L}$ [MPa]	$E_{t,L}$ [GPa]	$\sigma_{tu,T}$ [MPa]	$E_{t,T}$ [GPa]	$\sigma_{cu,L}$ [MPa]	$\sigma_{cu,T}$ [MPa]	$\tau_{u,LT}$ [MPa]	G_{LT} [GPa]	ν_{LT} [-]	ν_{TL} [-]	$\tau_{isu,L}$ [MPa]	$\tau_{isu,T}$ [MPa]
437.3	29.4	179.6	15.6	249.8	194.2	49.4	4.1	0.31	0.17	37.1	24.1

Tests Programme and Description

Overview and specimen dimensions

Previous experience has shown that quasi-static tests can be used as a simpler and less resource intensive alternative for predicting the impact response of monolithic laminates (Sutherland and Guedes Soares 2012). Hence, in order to evaluate the use of this approach for sandwich laminates the experimental programme here

included two distinct types of tests, both using the same experimental set-up: (i) quasi-static indentation and (ii) low-velocity impact. Eleven different core material / indenter geometries (hemispherical and flat, each with diameters of 10, 20, and 30 mm) were assessed. Following a preliminary quasi-static indentation assessment, a 200×200 mm² specimen size was selected, except for the PUR specimens tested with 20 mm and 30 mm indenters for which specimens of 300×300 mm² were tested. This ensured that the specimen dimensions were large enough to ensure that global crushing of the core was not an issue, and that only localised damage was induced, thus guaranteeing that the experiments are representative of the impact and indentation phenomena in larger panels.

Quasi-static indentation tests

An *Instron 1343* universal test machine was used for the quasi-static tests. The specimens were fully supported by a rigid 50 mm thick steel plate and a quasi-static (2 mm/min) concentrated load applied at the centre of the sandwich panels (Figure 1-a). In order to validate the specimen geometry by verifying that the panel edges did not deform significantly a video-extensometer (*Sony XCG-5005E* high-definition camera with *Fujinon Fujifilm HF50SA-1* lens) was used to measure the displacements of 15 points marked on one edge face of the panels (Figure 1-b). Two displacement transducers were also used to measure vertical deflections at two different points along the longitudinal and transverse directions.

Low-velocity impact tests

The impact tests were carried out using a *Rosand IFW5* instrumented drop weight machine (Figure 1-c). Fully supported specimens (ensuring comparability with the quasi-static tests) were impacted by a variable mass dropped from a fixed height of 0.75 m. The force was measured by a load cell between the impact mass and the indenter. A metal flag of accurately known height attached to the falling weight gave the incident velocity as it passed through an optical gate, allowing integration of the force time data to give displacement and energy values.

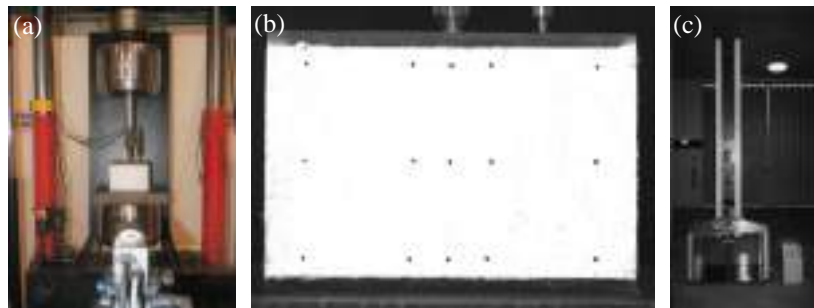


Figure 1: (a) Quasi-static tests setup and instrumentation; (b) target points for monitoring deformations with the video-extensometer; (c) low-velocity impact test machine

EXPERIMENTAL RESULTS AND DISCUSSION

Quasi-static Indentation Tests

Figure 2-a presents the typical load vs. displacement (cross-head displacement given by the test machine) behaviour for one representative specimen (PET foam core) of each indenter shape (hemispherical and flat). For both indenters an initial approximately linear stage was observed, ending as the first visible damage to the specimens occurred. This damage corresponded to stiffness reduction for both types of indenters, with a sudden force drop visible only for the flat indenters. Damage was characterized by the appearance of a region of whitening around the contact area between the indenter and the specimen, which was due to delamination of the face laminate.

After this first damage the load again increased until the onset of the perforation process (represented in the plot by the maximum force), after which a progressive or sudden force decrease was seen for the hemispherical and flat indenters, respectively. These differences in perforation force-deflection behaviour corresponded to the variable contact area of the hemispherical indenters causing progressive damage and shearing of the fibres (Figure 2-b), whereas in contrast the constant contact area of the flat indenters led to sudden shearing of the fibres (Figure 2-c). It should be noted that even in the initial linear stage before any significant damage was observed cracking sounds were audible for loads between 2.8 and 5.0 kN (independent of specimen core material), which was caused by resin matrix micro-cracking. The video-extensometer measurements did not capture any

significant deformation of the lateral faces of the specimens throughout the duration of the experiments, confirming that the adopted specimen geometries were adequate.

Figure 3-a compares the initial linear stage stiffness values by core material and indenter geometry, where it is seen that core material is the most influential factor; a stiffer core material predictably gave a higher indentation stiffness. For a given core material, the indentation stiffness was not significantly affected by indenter geometry and those slight variations observed did not follow any clear trends.

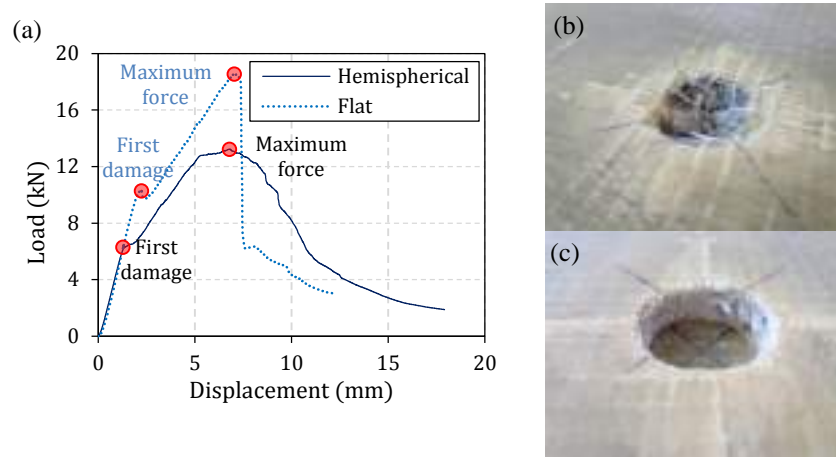


Figure 2: Quasi-static indentation: (a) typical load vs. displacement curves; damage caused by the action of (b) hemispherical and (c) flat indenters

Figures 3-b and 3-c show the effects of core material and indenter geometry on first damage and maximum (perforation) resistances, respectively. No large core material effects were seen, although a slight increase in both initial damage and maximum load (perforation) resistance with core material stiffness is indicated. As expected, for the same indenter type the forces to both first damage and peak load increased with diameter due to a larger force distribution area. This trend was stronger for flat indenters but was also observed for the hemispherical indenters, which may be because the contact areas of hemispherical indenters of different diameters are relatively similar especially at lower loads and deformations.

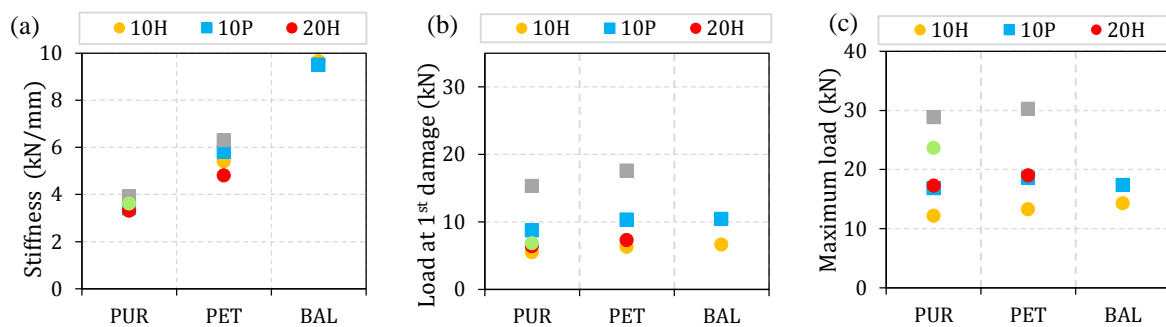


Figure 3: Comparisons for different core materials and indenters of: (a) initial linear stage stiffness, (b) load values at first damage, and (c) maximum load

Figure 4 compares the energy absorbed up to first damage (a), maximum force (b) and total perforation (c) for the various core materials and indenters. ‘Total perforation’ (of the impacted face laminate) is difficult to define in practice, and so for consistency here it was considered to have occurred when the load had reduced to 90% of the full drop from maximum force to final asymptotic post-perforation ‘plateau’ value. For flat indenters a softer core led to an increase in absorbed energy values mainly due to the higher deformations seen compared to panels with stiffer core materials. However, for hemispherical indenters this trend was not always followed.

In general, larger diameters absorbed more energy for a given indenter type, and (as for the above discussed influence of indenter size on first damage and peak loads) this effect was stronger for flat indenters than for

hemispherical ones (Figure 4-a). However, for maximum force (Figure 4-b) and total perforation (Figure 4-c) the hemispherical indenters gave a greater increase in absorbed energy with indenter diameter than did the flat indenters. This may be explained by the different failure modes caused by the two types of indenter, as discussed above).

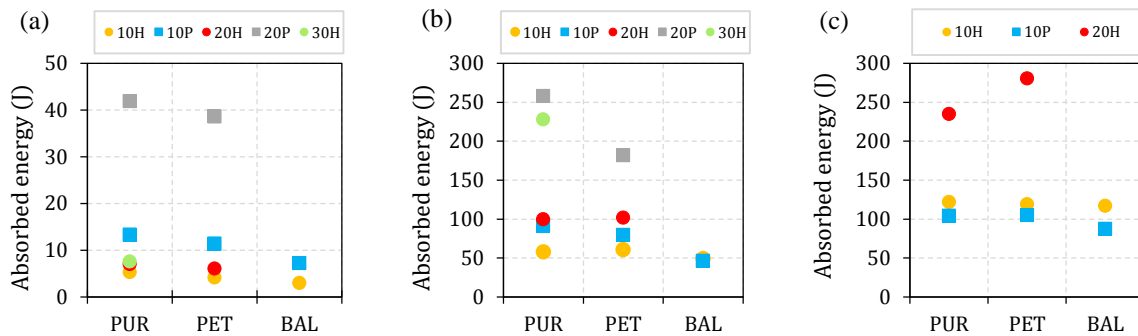


Figure 4: Absorbed energy comparisons for different core materials and indenters to: (a) first damage, (b) maximum force, and (c) total perforation

Low-velocity Impact Tests

Figure 5 compares quasi-static (QS) and impact test results with respect to load-displacement and absorbed energy-displacement curves for the rigid polyurethane (PUR) foam-cored sandwich laminates using 10 mm diameter hemispherical (10H, Figure 5-a) and flat (10P, Figure 5-b) indenters. Generally, quasi-static and impact load-displacement curves are very similar in form. For all specimens and indenters, the resistance to first damage values were very similar for quasi-static and impact tests. Hence the results suggest that quasi-static tests (which are much simpler to carry out than impact tests) may provide cost effective predictions of sandwich panel impact response and the onset of first damage, as was previously found for monolithic laminates (Sutherland and Guedes Soares 2012).

Figure 5-c compares the quasi-static and impact test maximum force values and shows that neither of these were significantly affected by core material. Also, there was no significant difference between static and dynamic maximum force values for the 10 mm hemispherical (10H) indenter. However, for the 20 mm hemispherical (20H) and 10 mm flat (10P) indenters the static maximum strengths were significantly lower (by 62% to 72%) than those achieved in impact tests. Further work would be needed to clarify exactly why this is, but it suggests that the behaviour for indenters with a diameter comparable to the face laminate thickness is not the same as that for larger diameter indenters. In this case, the results suggest that quasi-static testing may provide cost effective, if conservative predictions of the perforation of sandwich panels, again as was previously found for monolithic laminates (Sutherland and Guedes Soares 2012).

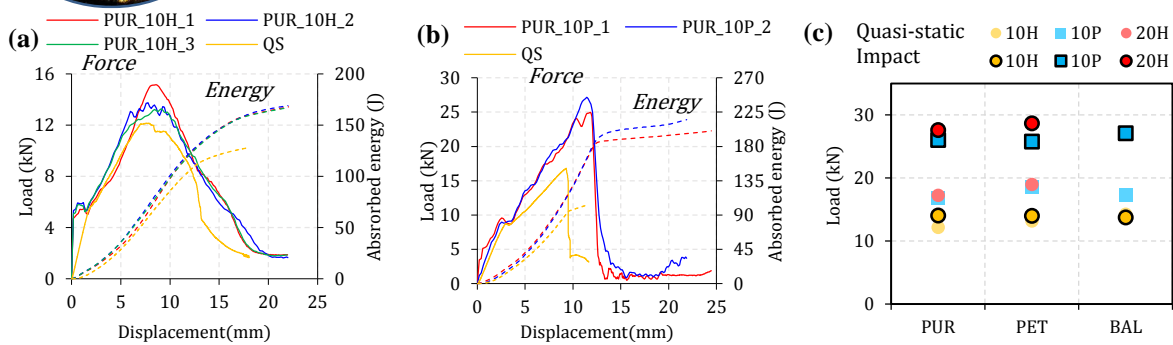


Figure 5: Comparison of quasi-static and impact test results: (a) load-displacement curves for PUR 10H, (b) load-displacement curves for PUR 10P, and (c) maximum strength values.

NUMERICAL STUDY

Objectives

One of the main purposes of the numerical study was to investigate the suitability of conventional FE numerical models to simulate the indentation phenomenon in GFRP composite sandwich panels with relatively thick faces. In particular, the models were expected to replicate the previously presented experimental test results. For this study, in order to simulate the first damage, the Tsai-Hill and the Hashin criteria were considered. Beyond these general goals this study aimed to: (i) evaluate the reliability of the numerical models in predicting the elastic indentation stiffness in composite sandwich panels; and (ii) analyse the stress and strain fields induced by the indentation phenomenon and their relationship with the failure modes observed during the experimental program.

Model Description

In this numerical study, carried out using the commercial software *Abaqus CAE*, the indentation tests performed with flat indenters were simulated. Triangular (S3) *Continuum Shell* elements were used to model the GFRP faces, while solid ten-node tetrahedral elements (C3D10) were used to model the core materials. Figure 6-a presents an example of the geometry of the numerical models developed.

The contacts between all adherent surfaces (face-core interfaces) were modelled using the “cohesive behaviour” option for the interaction properties in ABAQUS/CAE, adopting the package’s default contact enforcement method regarding traction-separation behaviour. Fixed boundary conditions were applied to the lower face. The concentrated load was applied by defining an imposed displacement at a coupled node region representing the flat indenter surface. The material properties obtained in the material characterisation tests (*cf.* Tables 1 and 2) were used as input. For the GFRP face sheets an orthotropic behaviour was considered as well as two damage initiation criteria: Tsai-Hill and Hashin; the latter was associated to the Rotem damage model (included in the package library as a bi-linear model) defined by the following fracture energies (proposed by Nunes *et al.* 2016): $G_{f,t} = 2.4$ N/mm, $G_{f,c} = 5.3$ N/mm, $G_{m,t} = 0.42$ N/mm and $G_{m,c} = 0.95$ N/mm, respectively for longitudinal (fiber, f) tension (t), longitudinal compression (c), transverse (matrix, m) tension and transverse compression. For the simulation of the PUR foam core material a bilinear elastic behaviour was considered with a reduction of 90% in the elastic modulus after exceeding the core failure stress. The modelling options for the remaining core materials are described in detail in Teixeira (2017).

Results and Discussion

Figure 6 plots the numerical model results for one representative case (PUR 10P) according to Tsai-Hill (Figure 6-b) and Hashin (Figure 6-c) criteria. The notable points, marked in the load-displacement curves, represent the initial failure mode considered in each criterion. Regarding the Tsai-Hill index results, note that in the analysis there is no reduction in the elastic stiffness after the first damage. As expected, according to previous numerical studies concerning local loads in GFRP elements (Nunes *et al.* 2016), the Tsai-Hill criterion presents fairly conservative predictions of the first damage force (between 44% to 72% of the experimental values). This may be explained by the fact that Tsai-Hill criterion does not consider the damage propagation and stress redistribution in the material which is particularly important for the action of local loads. As mentioned above, the Hashin model considers four different failure modes (longitudinal tension, longitudinal compression, transverse tension and transverse compression). The simulations stopped at some point of the analyses due to convergence issues and only three failure modes were identified. Considering the order of magnitude associated with the first mode (tension in transverse

direction) it is supposed that this corresponds to the first audible cracking reported in the experimental study. However, it was not possible to correlate the transverse compression failure value with any events observed during the tests. For the last failure mode (tension in the longitudinal direction) predicted by the Hashin criterion a good approximation to the experimental first damage force was observed (88% of the experimental value). Nevertheless, it is important to mention that the Hashin criterion does not consider the delamination phenomenon.

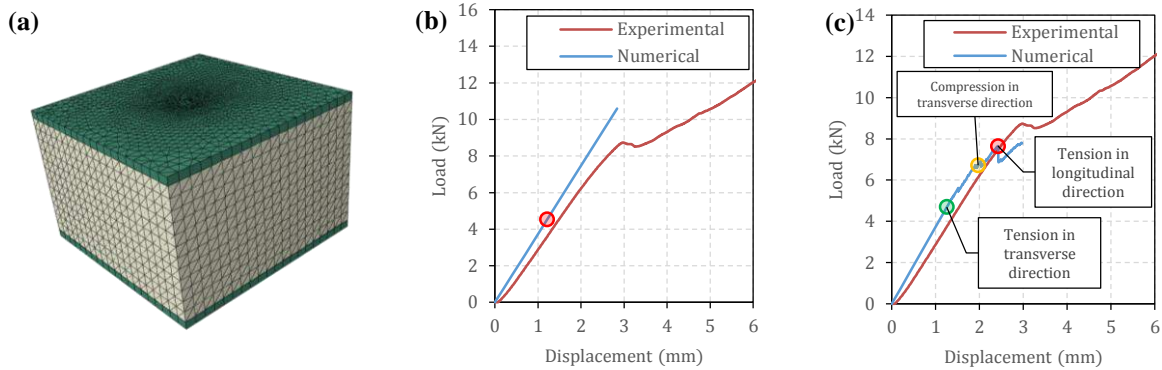


Figure 6: Finite element models: (a) mesh and geometry; (b) results for PUR 10P case using the Tsai-Hill criterion; and (c) results for PUR 10P case using the Hashin criterion

The numerical models were able to simulate the increase in stiffness indentation for sandwich panels with stiffer core materials, namely PET foam and balsa. However, increases of the indenter diameter showed to have a greater impact in the indentation stiffness when compared to experimental results (Teixeira, 2017).

ANALYTICAL STUDY

Objectives

The main objective of the analytical study was to evaluate the suitability of two analytical models available in the literature, as presented and assessed below.

Model description

Wen *et al.* model

Wen *et al.* (1998) proposed an analytical model to simulate the behaviour of composite sandwich panels with thick faces impacted by flat indenters. According to the authors, for thick faces the membrane effect can be neglected. The first damage resistance of the sandwich panels is thus given by,

$$P_f = 2\pi R h \tau_{13} + K_c \pi R^2 q \quad (1)$$

in which R is the indenter radius, h is the face thickness, τ_{13} is the laminate (through-thickness) shear strength, K_c is a constraint factor and q is the core compressive strength. In the previous equation the first term gives the face laminate contribution and the second the core contribution. The constraint factor K_c represents the effect of the surrounding material in the core.

Olsson model

Olsson (2002) proposed an analytical model to simulate the behaviour of composite sandwich panels impacted by hemispherical indenters. According to this model the core contribution to the first delamination is neglected and this is assumed to be dependent only on face laminate parameters; namely the bending stiffness of the faces D_f and the mode II critical strain energy release rate (G_{IIc}), leading to the following expression for the force at first delamination:

$$F_d = \pi \sqrt{\frac{32 D_f G_{IIc}}{3}} \quad (2)$$



A modification to this model was proposed in this study to include the core contribution to the first delamination. A second term similar to that of the formula by Wen *et al.* was added to the Olsson model, giving the following equation:

$$F_d = \pi \sqrt{\frac{32D_f G_{IIc}}{3}} + K_c \pi R^2 q \quad (3)$$

Results and discussion

Wen et al. model

The constraint factor K_c is an empirical parameter. Reference values ($1.7 < K_c < 2.5$) were presented by Reddy *et al.* (1991) for sandwich panels with metallic faces and a foam core. However, these sandwich laminates are very different from those studied here. In order to evaluate the influence of the constraint factor a parametric study was carried out where different values of K_c (ranging from 0 to 4) were considered. For cases with lower stiffness behaviour (PUR 10P, PUR 20P, PET 10P and PET 20P) the core contribution to the first damage was found to be of little relevance, and varying K_c between 0 and 4 resulted in relative differences between predicted values ranging from 2 to 9%. In an analogous comparison for balsa-cores sandwiches the core contribution was considerably more significant with a maximum difference of 17% between the values obtained using a K_c of 0 and then 4. Overall, the model provided reasonably accurate estimates with errors varying between -21% and +13% in relation to the experimental values for the ‘worst case scenarios’ of assuming $K_c = 0$ for PET 10P and $K_c = 4$ for PUR 20P, respectively.

Olsson modified model

Due to the lack of available G_{IIc} values for the face laminates used in this study the direct use of equation (3) was not possible. Hence, in order to evaluate this model for thick composite sandwich panels and to compare it with the original Olsson Model a parametric study was completed varying G_{IIc} between 500 J.m² and 950 J.m². Based on the proposal of Fatt and Park (2001) a $K_c = 2$ value was adopted. For this analysis the variation of K_c with both the indenter diameter and the core material was neglected. The lowest mean squared error between analytical predictions and experimental results was obtained for a value of G_{IIc} of 720 J.m². In order to study the influence of the core, predictions with different K_c values were computed and compared to the experimental results (hence $K_c = 0$ represents the original Olsson model). Using the original Olsson model gives the same predicted values for all of the core / indenter combinations studied, resulting in errors compared to the experimental data of between 23 and 27%. The development of the Olsson model to consider both the effects of core material and indenter diameter resulted in a considerable improvement in predicted values for larger diameters and stiffer sandwich cores with errors with respect to experimental data of between -7 and +10% (assuming $K_c = 2$). Nevertheless, it is worth noting that in these analyses the values of G_{IIc} and K_c were assumed or obtained via curve fitting to the experimental data and values should be obtained in the future using more explicit methods.

CONCLUSIONS

The composite sandwich panels studied resisted perforation well, although relatively low energy levels were required to inflict first damage. Indenter geometry was the most influential parameter for the low-velocity impact behaviour of these thick FRP composite sandwich panels. The indentation stiffness was mainly influenced by the core material, but the effect of this on impact resistance was less marked. Quasi-static tests provided a conservative estimate for the impact behaviour of composite sandwich panels. Regarding numerical modelling, the Hashin criterion coupled with a damage propagation law provided closer predictions for the first damage resistance of the composite sandwich panels when compared to the Tsai-Hill criterion. The analytical models assessed in this paper, including a modified version of Olsson’s model, were able to provide reasonable predictions for the first damage resistance measured in quasi-static tests.

REFERENCES

- S. Abrate (1997). “Localized impact on sandwich structures with laminated facings”, *Applied Mechanics Reviews*, 50(2), 69-82.
- C. Atas, C. Sevim (2010). “On the impact response of sandwich composites with cores of balsa wood and PVC foam”, *Composite Structures*, 93(1), 40–48.



- M. S. H. Fatt, K. S. Park (2001). "Modeling low-velocity impact damage of composite sandwich panels", *Journal of Sandwich Structures and Materials*, 3, 130–168.
- C. C. Foo, G. B. Chai, L. K. Seah (2008). "A model to predict low-velocity impact response and damage in sandwich composites", *Composites Science and Technology*, 68(6), 1348–1356.
- M. Garrido (2016). *Composite sandwich panels floors for building rehabilitation*, PhD thesis in Civil Engineering, Instituto Superior Técnico, University of Lisbon.
- F. Nunes, N. Silvestre, J. R. Correia (2016). "Progressive damage analysis of web-crippling of GFRP pultruded I-sections", *Journal of Composites for Construction*, 04016104 1-13.
- R. Olsson (2002). "Engineering method for prediction of impact response and damage in sandwich panels", *Journal of Sandwich Structures and Materials*, 4(1), 2–29.
- V. I. Rizov (2006). "Non-linear indentation behaviour of foam core sandwich composite materials - A 2D approach", *Computational Materials Science*, 35(2), 107–115.
- H. M. Wen, T. Y. Reddy, S. R. Reid, P. D. Soden (1998). "Indentation, penetration and perforation of composite laminates and sandwich panels under quasi-static and projectile loading", *Key Engineering Materials*, 141-143, 501552.
- T. Reddy, P. Soden, S. Reid, M. Sadighi (1991). "Impact response of thick composite laminates and sandwich panels", Collaborative Research Program on the Cost-Effective Use of Fibre-Reinforced Composite Offshore, Marintech Research, Phase 1, Report No. CP04.
- L. S. Sutherland, C. Guedes Soares (2012). "The use of quasi-static testing to obtain the low-velocity impact damage resistance of marine GRP laminates", *Composites Part B: Engineering*, 43, 1459–1467.
- G. Zhou, M. Hill, J. L. Hookham (2006). "Damage characteristics of composite honeycomb sandwich panels in bending under quasi-static loading", *Journal of Sandwich Structures and Materials*, 8(1), 55-90.
- R. Teixeira (2017). "Low-Velocity Impact Response of GFRP Composite Sandwich Panels: Experimental, Numerical and Analytical Study", Master Dissertation in Civil Engineering, Instituto Superior Técnico, University of Lisbon, 2017.



EXPERIMENTAL STUDY ON SHEAR PROPERTIES OF GFRP CHANNEL

MEMBER

Y. Wang¹, H. Nakamura², Y. Ishii³, Y. Inari⁴, H. Nakai⁵ and M. Nishida⁶

¹ Tokyo Metropolitan University, Department of Civil and Environmental Engineering, Hachioji-shi, Japan

² Tokyo Metropolitan University, Department of Civil and Environmental Engineering, Hachioji-shi, Japan

³ East Nippon Expressway Co., Ltd., Saku-shi, Japan

⁴ Nippon Expressway Research Institute Co., Ltd., Machida-shi, Japan

⁵ Maedakosen Co., Ltd., Chuo-ku, Japan

⁶ Nihon FRP Co., Ltd., Osaka-shi, Japan

ABSTRACT

A pultruded GFRP made of unidirectional material is a typical material for FRP structures, for example, a footbridge, inspection path, hydraulic gate, etc. The properties of tensile, compression and bending have been investigated in pultruded GFRPs. However, the shear properties were not clarified sufficiently, nevertheless shear failures were often observed. In study, shear properties and evaluation method of pultruded GFRP made of unidirectional materials (Channel member; C75) were investigated experimentally. The several shear tests were conducted using the coupon and beam specimens for shear properties. In the V-notched beam method based on ASTM D 5379, it was found that the shear properties were equivalent of the result of the beam test. The short beam specimens were conducted by 3-point bending test. As a result, shear failures occurred in the shear span and shear strength was properly and easily evaluated by short beam test, Therefore, the V-notched beam method was proper method for evaluation of shear properties of pultruded unidirectional GFRP members.

KEYWORDS

GFRP channel member; unidirectional material; shear strength; shear modulus.

INTRODUCTION

Fiber-reinforced polymer is the high-strength and light-weight material and the performance of FRP have been recognized in construction and retrofit applications, specifically in aging, damaged or overloaded structures. However, the application of FRP structures is limited due to the low elastic modulus of FRP structures, and limited information about material properties of FRP and available evaluation method. In order to expand the application of FRP in the future, it is significant to grasp material properties of FRP and evaluation method.

The mechanical properties of FRP for structures have been studied using evaluation methods specified by different industrial standards. Although the strength of FRP has been evaluated by coupon test, the difference between member strength and material strength by coupon test has been often reported. In addition, if the same test specimens are evaluated by different methods, mechanical properties obtained are likely to be different.

On the other hand, test data of mechanical properties such as compression, tension and bending is always accumulated as design documents, but so far study about shear strength is not enough especially to the bending test that shear failure will occur. Therefore, in the study, aimed at GFRP channel member (C75: one direction member), which is frequently-used material, several of coupon tests and bending tests were carried out to investigate shear properties. First, shear modulus of elasticity and shear strength were evaluated by the material test based on ASTM D 5379. Next, in order to study the shear failure resulted from bending test of channel member, 3-point bending test was carried out, and the shear strength of member was also predicted using the material strength by coupon test.

EVALUATION OF SHEAR STRENGTH BY V-NOTCH BEAM METHOD

Test overview

Shear properties of GFRP channel member were investigated by coupon test based on ASTM D 5379, it is called as V-notch beam test in this paper. Figure 1 shows the sampling position of the test specimens, conjugate shear stress theoretically holds for an-isotropic materials like unidirectional materials, though it was written in ASTM book that shear strength was evaluated by 0.2% off-set strength, since there are some unclear reasons, in this study, test specimens collected from the fiber direction and the fiber orthogonal direction were examined. Considering about different fiber contents between center and end of web, five 0° direction pieces named as C75L were picked

out as shown in Figure 1 (a) and six 90° direction pieces named as C75T were picked out by the 75 mm long side as shown in Figure 1 (b).

Figure 2 shows the specimen of V-notch beam method. The tip of the 90° notch was processed into fillet at radius of 1.3 mm. Figure 3 shows the set-up of V-notch beam test. In this test, compressive force was applied by displacement control machine through the jig that shear force acts on the center of the specimen. Loading speed was 1.0mm/min and 2-axes strain gauges were installed in the ±45° directions on the front and back at the center of test specimens.

In this test, shear strength F_u , in-plane shear stress τ_i , in-plane shear strain γ_i and shear modulus of elasticity G_{xy} were calculated by following formulas.

$$F_u = \frac{P_u}{A} \quad (1a)$$

$$\tau_i = \frac{P_i}{A} \quad (1b)$$

$$\gamma_i = |\varepsilon_{+45}| + |\varepsilon_{-45}| \quad (1c)$$

$$G_{12} = \frac{\tau''_{12} - \tau'_{12}}{\gamma''_{12} - \gamma'_{12}} \quad (1d)$$

Where F_u , P_u , A , τ_i and P_i are shear strength (N/mm²), maximum load (N), cross-sectional area of V-notch (mm²), shear stress (N/mm²), load (N). ε_{+45} , ε_{-45} are +45° direction strain, -45° direction strain. γ'_{12} is 1,500×10⁻⁶ and γ''_{12} is 5,500×10⁻⁶. τ'_{12} is shear stress when the strain is γ'_{12} (N/mm²), τ''_{12} is shear stress when the strain is γ''_{12} (N/mm²).

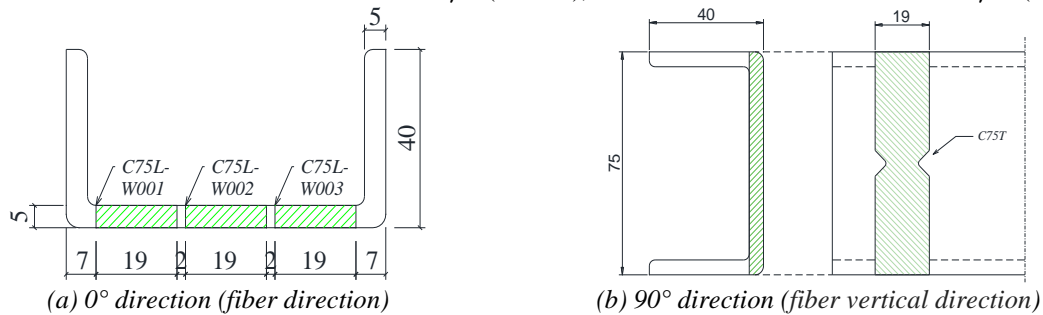


Figure 1: Sampling position in V-notch beam test

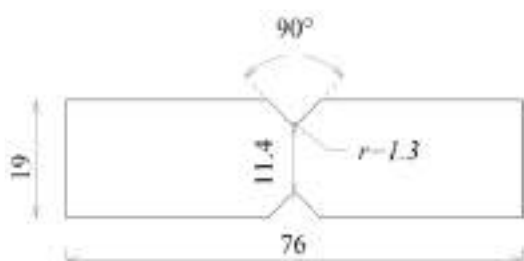


Figure 2: Specimen drawing by V-notch beam method



Figure 3: Test set-up

Evaluation for 0° direction (fiber direction)

Figure 4 shows the relationship between representative shear stress and shear strain (C75L-W003-2). It can be known that linear behavior occurred within the evaluation range about shear modulus of elasticity, however the maximum value of shear stress is indefinite. Figure 5 shows the failure mode. Failure along the direction of loading was observed, but since the shear force was applied at fiber orthogonal direction, it is considered that the 0° direction fiber was bearing the load after shear failure occurred. In the case when the strength cannot be evaluated by the maximum load, as described above, shear strength is evaluated based on the 0.2% strength and the result is as follows.

Table 1 shows the result of V-notch beam test for 0° direction. It can be found that the variation coefficient about the shear modulus of elasticity for each sampling position was as little as 5% or less while the variation coefficient

of all specimens is about 8% and since the shear properties are not same in different collection positions, the variation coefficient about shear strength have the same trend about 6% for all specimens.

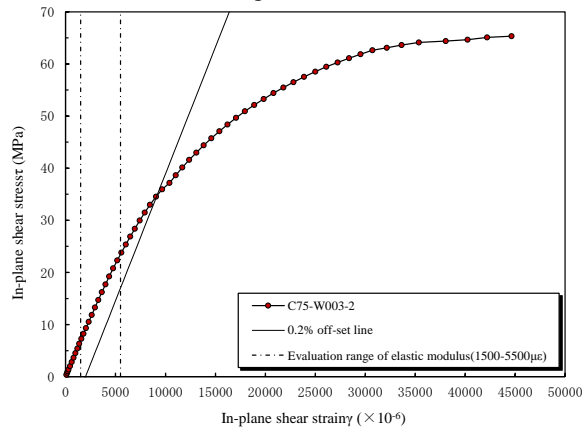


Figure 4: Relationship between shear stress and shear strain in 0° direction

Table 1: Test result of V-notch beam method in 0° direction

Test specimen	Shear modulus of elasticity G_{xy}		Off-set shear strength τ_u	
	Average (kN/mm ²)	Variation coefficient	Average (N/mm ²)	Variation coefficient
C75L-W001	3.91	0.031	37.7	0.065
C75L-W002	3.70	0.046	37.5	0.035
C75L-W003	4.37	0.034	40.7	0.033
C75L(Average)	3.99	0.080	38.6	0.058

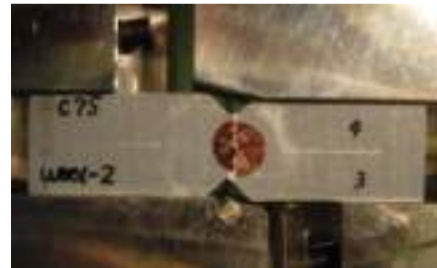


Figure 5: Failure mode in 0° direction

Evaluation for 90° direction (fiber vertical direction)

Figure 6 shows the relationship between shear stress and shear strain for all specimens. It can be seen from the figure that linear behavior occurred within the evaluation range about shear modulus of elasticity and although the maximum load of each test specimen varied, the maximum load has been clearly obtained, which is since the load was applied in parallel direction with fiber, after failure occurred, fiber did not resist load. Figure 7 shows the failure along the direction of shear force.

Table 2 shows the test result of V-notch beam test for 90° direction. It can be seen that the variation coefficient about shear modulus of elasticity is 9% and the variation coefficient of shear strength is about 12% that is higher than the result in 0° direction, which was considered that the drilling accuracy ($r=1.3$ mm) and the finishing around the V-notch was not clean up thoroughly before starting test and it had effects on the strength of specimens for 90° direction. In addition, the average of shear modulus of elasticity is 3.12 kN/mm² and the average of shear strength is 32.5 N/mm², both of them are lower than the results for 0° direction.

Comparing to the under mentioned material properties of GFRP channel member (C75), the shear modulus of elasticity studied by V-notch beam test for 0° direction is higher than the result by 3-point bending test while the shear modulus of elasticity conducted by V-notch beam test for 90° direction is slightly lower than the result by 3-point bending test.

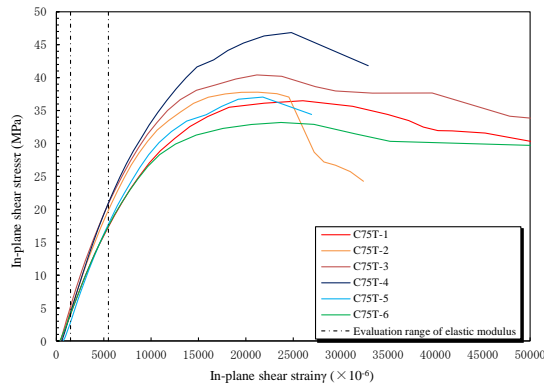


Figure 6: Relationship between shear stress and shear strain for 90° direction

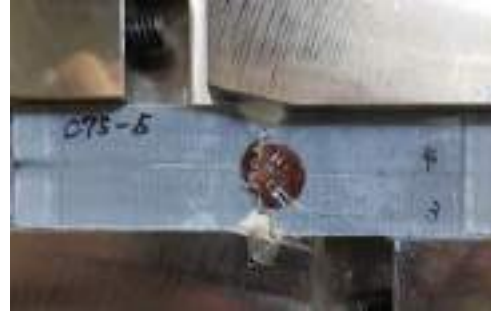


Figure 7: Failure mode in 90° direction

Table 2: Test result of V-notch beam test for 90° direction

Stress concentration factor	Shear modulus of elasticity G_{xy}		Shear strength τ_u		Shear strain at maximum load $\gamma_u (\times 10^{-6})$			
	Average (kN/mm ²)	Variation coefficient	Average (N/mm ²)	Variation coefficient	Minimum value	Maximum value	Average	Variation coefficient
Before correction	3.12	0.088	32.5	0.121	21,161	26,023	23,125	0.088
After correction	3.72		38.8					

Study on shear stress distribution of specimen with notch part

In the V-notch beam method test, although the tip of V notch was processed into the fillet of $r = 1.3$ mm as shown in Figure 2, it is necessary to consider the influence of the shear stress concentration, so stress concentration coefficient was calculated by analysis and attempted to correct the test result.

Figure 8 shows the FE analysis model. Specimens were modeled using thick shell elements by finite element analysis software (Msc Marc 2013). Table 3 shows the material properties of the applied GFRP channel member C75. The elastic modulus E_1 for fiber direction and Poisson's ratio ν_{12} were obtained by conducting the material test based on JIS K 7164 and the shear modulus of elasticity was obtained from the result of the 3-point bending load test described in next Chapter, for other physical property values, assumed value was used. Furthermore, in order to reproduce the effect of the same shearing force as in the test, the same displacement speed was used for loading section. Also, in the fixed part, only one point on the end part was supported by pin while the other parts were supported by rollers.

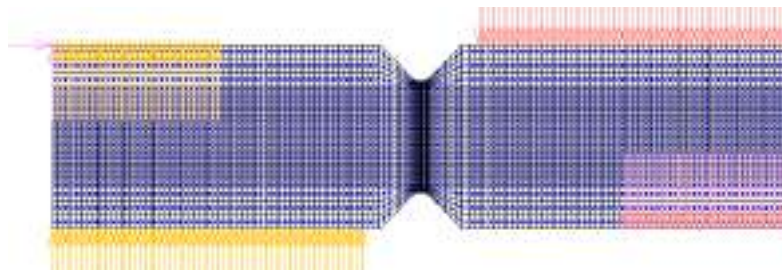


Figure 8: FE analysis model

Table 3: Material properties of GFRP channel member (C75)

Fiber direction elastic modulus E_1 (GPa)	39.5
Elastic modulus for fiber orthogonal direction E_2 (GPa)	4.0
Elastic modulus for plate thickness direction E_3 (GPa)	4.0
In-plane elastic modulus G_{12} (GPa)	3.58
Out-plane elastic modulus G_{23} (GPa)	2.0
Out-plane elastic modulus G_{31} (GPa)	2.0

Poisson's ratio ν_{12}	0.3
Poisson's ratio ν_{23}	0.05
Poisson's ratio ν_{31}	0.05

Figure 9 shows the stress distribution. The analysis values are shown for cases of isotropic and anisotropic. In addition, for rectangular cross section between notches, maximum shear stress and average shear stress calculated by beam theory are also shown in Figure 9. The shear stress was normalized by the average shear stress τ_{mean} of the beam theory. In the V-notch beam method test, both isotropy and anisotropy in the 0° direction and the 90° direction are smaller than the maximum shear stress of the beam theory. The stress concentration coefficient α of shear stress was calculated by the following equation using these analysis values and theoretical values.

$$\alpha = \frac{\tau_{FEA}}{\tau_{mean}} \quad (2)$$

Where α , τ_{FEA} and τ_{mean} are stress concentration coefficient, FE analysis values (N/mm^2), average shear stress (N/mm^2).

Considering the strain gauge length (3 mm) in the coupon test, shear stress by analysis was averaged within the range of the strain gauge length. τ_{mean} is the average shear stress calculated by the equation (1a) in the V-notch beam method test. Table 4 shows the stress concentration coefficient α of the shear stress calculated from equation (2). In the case of isotropy, the shear stress concentration coefficient α is 1.055, which is approximately same to the average shear stress τ_{mean} of the beam theory. In the case of anisotropy, the shear stress concentration coefficients α in the 0° direction and the 90° direction were 0.936 and 1.195, in particular, it was found that there was a difference about 20% in the 90° direction. From this, it can be found that when evaluating the shear stress in the direction of 90° , it is necessary to take shear stress concentration into consideration. For the 0° direction, the value of the stress concentration coefficient is close to 1.0, the analysis value τ_{FEA} of the shear stress is smaller than the average shear stress τ_{mean} of the beam theory and it is evaluated conservatively, so the stress concentration doesn't need to be considered.

Using this identified stress concentration coefficient α , corrected V-notch beam method test result in the 90° direction is shown in Table 4. The elastic coefficient is calculated from the shear strain by test and the shear stress corrected by multiplying α . As shown in Figure 6, the shear stress in the direction of 90° is a nonlinear behavior from the beginning to the maximum value, but in ASTM, shear strength is calculated by the linear equation of the formula (1a), so it can be found that the shear strength can be corrected using the stress concentration coefficient. As shown in Table 2, the shear modulus of elasticity is 3.72 kN/mm^2 , which is nearly same to the shear modulus of elasticity in Table 3. The shear strength is 38.8 N/mm^2 , which was found to be about the same as the off-set shear strength in the 0° direction.

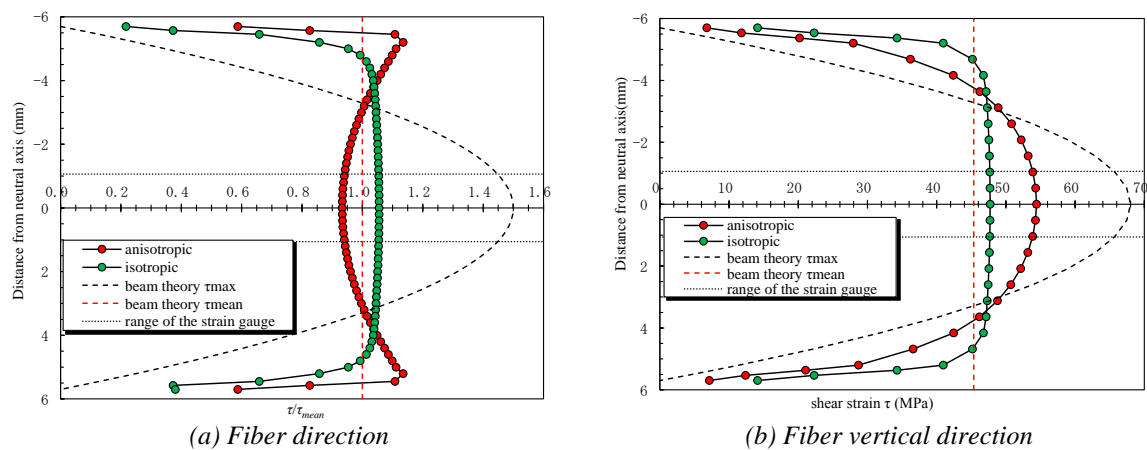


Figure 9: Stress distribution

Table 4: Stress concentration coefficient of shear stress

τ_{FEA}/τ_{mean}	isotropic	anisotropic	
		0° direction	90° direction
	1.055	0.936	1.195

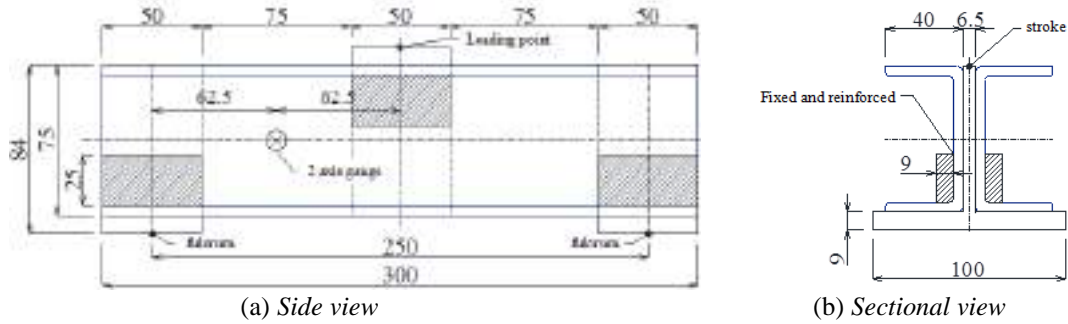


Figure 10: Specimen of 3-point bending load test

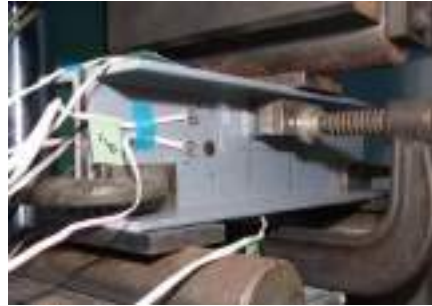


Figure 11: Set-up of 3-point bending test

EVALUATION OF SHEAR STRENGTH BY 3-POINT BENDING TEST

Test method and specimens

Shear properties of GFRP channel member (C75) have been evaluated by 3-point bending test in a short span. Figure 10 shows test specimen of bending test, Figure 11 shows the set-up of 3-point bending test. Using the same cross-sectional shape of channel members, two channel members were fixed to the back-to-back as shown in Figure 10 and 2-axis strain gauges were installed on the front and back of the web center and the center of the shear span in $\pm 45^\circ$ direction. Concentrated load was applied at 1.0 mm/min using hydraulic servo type material testing machine and the shear stress at the center of the web is calculated from the following equations.

$$\tau_{d/2} = \frac{q_{d/2}}{t_w} \quad (3a)$$

$$q_{d/2} = \frac{P}{4} \cdot \frac{1}{2I} \left(bdt_f + \frac{d^2 t_w}{4} \right) \quad (3b)$$

Where $\tau_{d/2}$, $q_{d/2}$, P and I are shear stress at the center of the web (N/mm^2), shear flow in the middle of the web (N/mm), load (N) and moment of inertia (mm^4). b , d , t_f and t_w are flange width (mm), web height (mm), flange thickness (mm), thickness of web (mm), respectively.

In addition, the validity of thin-walled beam theory for isotropy is confirmed by analysis described later. In this test, it is considered that the value of the axial strain did not change and $\pm 45^\circ$ strain is evaluated by rosette analysis. The shear modulus of elasticity was evaluated within the range ($1,500 \times 10^{-6}$ - $5,500 \times 10^{-6}$) in which the linear relationship can be confirmed in accordance with ASTM D 5379.

Test results and discussions

Figure 12 shows the failure mode of 3-point bending test. Figure 13 shows the relationship between shear stress and shear strain. In figure 13, analytical values by finite element analysis (Msc Marc 2013) are also shown, in the analysis model, the material properties in Table 5 were applied using thick shell elements. Figure 13 also shows the result of the V-notch beam method test for the 90° direction corrected by the shear stress concentration coefficient. The figure shows linear behavior in the evaluation range of the shear modulus of elasticity, it is found that the test value and the analysis value are roughly in agreement in the linear region. It is also found that the shear stress gradually approaches a certain value as the strain increases. In each test specimen, some strain gauges failed when the load was closed to the maximum value and strains cannot be measured accurately, but behaviors are similar to the V-notch beam method test in the direction of 90° . Also, it can be known that the maximum load is within the range of the maximum load by the V-notch beam method test. Failure modes are shown in Figure 12, it can be found that all of specimens failed along the fiber orientation at the shear span. Since the failure of C75-SP7 and C75-SP8 occurred at the loading point before the shear failure, it was impossible to obtain appropriate

shear strength. Figure 14 shows the relationship between load and stroke. It is shown that the maximum load was clearly obtained as same as the V-notch beam test for 90° direction. In addition, in this study, it can be seen that the additional deflection due to shear deformation is large and the displacement is significantly different comparing to the displacement based on Bernoulli-Euler beam theory and Timoshenko beam theory. In this test, comparing the test values with the analytical values, when the load is 3kN or less, since

Table 5: Result of 3-point bending test

Test specimens	Shear strength τ_u (N/mm ²)	Shear modulus of elasticity G_{xy} (kN/mm ²)	Maximum load P_{max} (kN)
C75-SP1	40.1	3.50	47.6
C75-SP2	40.8	3.95	48.3
C75-SP3	39.5	3.11	46.8
C75-SP4	41.1	3.11	48.2
C75-SP5	37.5	3.17	44.1
C75-SP6	35.8	3.93	42.2
C75-SP7	-	4.04	-
C75-SP8	-	3.86	-
Average	39.1	3.58	46.2

the influence of the deformation of the jigs at the supported and loading point are relatively large, difference

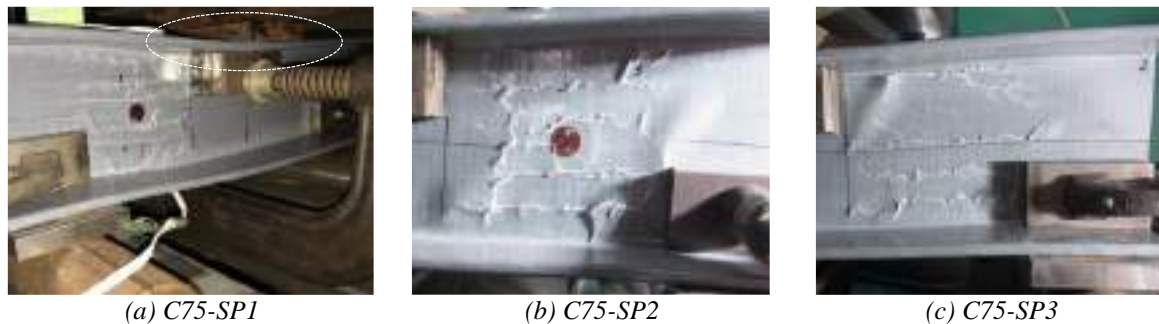


Figure 12: Failure modes of 3-point bending test

occurred, but in the range where the linear behavior is exhibited, the rigidity of the experimental values showed good agreement with analytical values. As shown in Figure 12 (a), it was considered that the reason why the displacement of experimental values are large is the local deformation of the specimens just under the loading point was larger. Although the rigidity of specimens is somewhat different because the test was carried out in different time and jigs were readjusted before and after. Since all specimens have similar shear properties, it can be found that all of the present tests are valid.

Figure 15 shows the shear strain distribution of the central cross section in the shear span. The shear strain of the experimental value was obtained by calculating the slope using the incremental amount of shear strain at $\Delta P = 5\text{kN}$ within the range where the linear relationship can be confirmed and dividing the load by the slope. From the figure, in the case of isotropy, the value of the center position of the web almost agrees with the calculated value by the beam theory. In the case of anisotropy, the difference was larger in the flange part than the calculated value by the beam theory, the analysis value was slightly smaller at the web center position, but its value was about the same as the average of the experimental values. Furthermore, as shown in Figure 13, the shear stress by beam theory almost agrees with the result of the V-notch beam method test within the nonlinear region. From this, it can be found for anisotropic channel member, the shear stress at the web center can be calculated from the beam theory using the elastic modulus E and the shear modulus G . Table 5 shows the result of 3-point bending test. As previously mentioned, shear strength was evaluated in 6 specimens except C75-SP7 and C75-SP8 while the shear modulus of elasticity was evaluated for all specimens. Although there was a slight variation in each specimen about shear strength and shear modulus of elasticity, the average values are 3.58 kN/mm² and 39.1 N/mm² which are higher than the result by the 45° direction tensile test, it is considered that since oriented fibers were cut out in the 45° direction, the failure modes are different. On the other hand, despite the results of shear modulus of elasticity by 0° direction V-notch beam test and 90° direction V-notch beam test corrected by the stress concentration coefficient are a little higher, it can be said that generally agreed to this test owing to the similar jig and the same shear load reproduced.

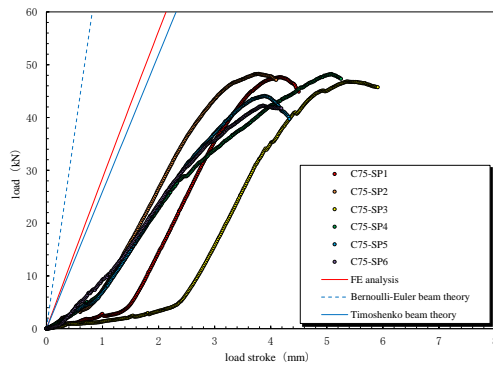
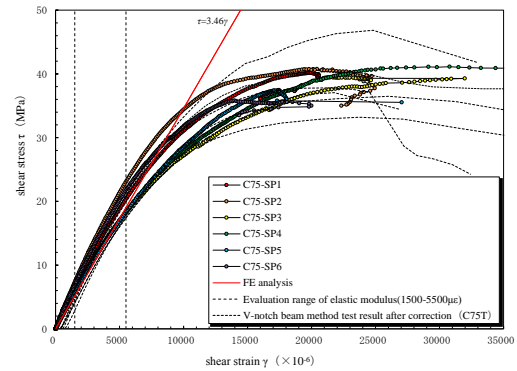


Figure 13: Relationship between shear stress and strain Figure 14: Relationship between load and stroke

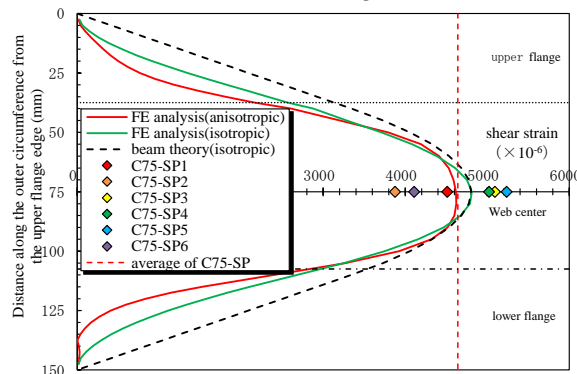


Figure 15: Distribution of shear strain in the central section of the shear span

CONCLUSIONS

In this study, focusing on GFRP channel member (C75) of pultruded unidirectional material widely used for FRP for civil engineering structure, with the aim of studying shear properties and evaluation methods, various of coupon tests and 3-point bending test were carried out. In conclusion, the findings in this paper are summarized as follows:

- (1) In the V-notch beam method test in the 0° direction (fiber direction), the maximum load cannot be clearly obtained so that the shear strength cannot be evaluated, however if it is evaluated by the 0.2% off-set shear strength, the shear strength obtained is close to the result by 3-point bending test.
- (2) In the V-notch beam method test in the 90° direction (fiber orthogonal direction), the maximum load can be clearly obtained and it can be known that both of the shear modulus and the shear strength were lower than the result by the 3-point bending test.
- (3) Considering the shear stress concentration coefficient of the V-notch part calculated from the FE analysis, the results of the shear test in the 90° direction (fiber orthogonal direction) are about the same to the results of the shear test by the 3-point bending load test.
- (4) Shear failure occurred at the shear span by performing a 3-point bending test of a specimen with two grooved members fixed on the back. It can be found that the shear property of the channel members can be evaluated simply.



From the above, the shear properties of the unidirectional GFRP channel members (C75) could be evaluated by the V-notch beam method test. In particular, it was confirmed that the shear modulus and shear strength of the beam member can be roughly evaluated from the shear test results in the 90° direction (fiber orthogonal direction) considering the stress concentration of the shear stress.

Although the shear strength evaluation method for GFRP channel member (C75) of pultruded unidirectional material have been studied, in order to correspond to actual structures, it is necessary to consider the shear properties when shear force and axial force act at the same time, further, the bending test applying compression, tensile axial force is planned to carry out.

REFERENCES

- Committee on hybrid structure (2011). "Guidelines for design and construction of FRP footbridges", Hybrid structure series 04, *Japan Society of Civil Engineer*. [in Japanese]
- Committee on structural engineering (2004). "FRP Bridges -Technologies and their future", Structural Engineering Series 14, *Japan Society of Civil Engineer*. [in Japanese]
- Committee on hybrid structure (2014). "Guidelines for design and construction of FRP hydraulic gate, Hybrid structure series 06, *Japan Society of Civil Engineer*. [in Japanese]
- Committee on hybrid structure (2015a). "Basic design data of FRP members for civil engineering structure", Hybrid structure report 11, *Japan Society of Civil Engineer*. [in Japanese]
- Committee on hybrid structure (2015b). Standard Specifications for Hybrid Structures 2014. [in Japanese]
- Y. Ishii, K. Kozumi, H. Nakamura, Y. Furuya, H. Nakai and M. Nishida (2016). "Study on serviceability and load carrying capacity in bridge inspection path using GFRP trussed girder", *Journal of Japan Society of Civil Engineers*, Ser. A1 (Structural Engineering & Earthquake Engineering (SE/EE)), Vol.72, No.5, pp.II_33-II_45. [in Japanese]
- JIS K 7019 (1999). "Fiber-reinforced plastic composites—Determination of the in-plane shearstress/shear strain response, including the in-plane shear modulus and strength, by the $\pm 45^\circ$ tension test method". [in Japanese]
- ASTM D5379/D5379M-12 (2012). "Standard Test Method for Shear Properties of Composite Materials by the V-Notched Beam Method".
- The Japan Reinforced Plastics Society (2016). "Basics of FRP", Corona Publishing. [in Japanese]
- Y. Kitayama, K. Maeda, H. Nakamura, T. Watanabe (2011). "Design and Serviceability of Slab Type Footbridge Using GFRP Pultrusion Profiles, *Journal of Japan Society of Civil Engineers*, Ser. A1 (Structural Engineering & Earthquake Engineering (SE/EE)), Vol.67, No.2, pp.258-271. [in Japanese]
- F. Nishino (1984). "Mechanics of continuum (II)", *Civil Engineering Series 6*, Shokokusha Publishing, 102-104. [in Japanese]



DIC STRAIN FIELD MEASUREMENT OF FRP PLATES WITH AND WITHOUT HOLES

B.C. McCoy 1, R. Seracino 2, G.W. Lucier 2, T.W. Langerhans 3

¹NC State University, Dept. of Civil, Construction, and Environmental Engineering, Raleigh, NC 27695
Email: bcmccoy@ncsu.edu

²NC State University, Dept. of Civil, Construction, and Environmental Engineering, Raleigh, NC 27695

³United States Military Academy, Dept. of Civil and Mechanical Engineering, West Point, NY 10996

ABSTRACT:

This paper examines the results of material testing of hybrid glass/carbon fiber reinforced polymer (FRP) plates for use in mechanically fastened applications. The small-scale material tests were conducted in three phases: 1) uniaxial tension without holes, 2) uniaxial tension with open holes, and 3) uniaxial tension with bolted connections. In all three phases of testing, Digital Image Correlation (DIC) was used to obtain continuous strain data, showing holistic strain field development through failure. The high-resolution strain data provides detailed information for the design of an efficient hole pattern in Mechanically Fastened-Fiber Reinforced Polymer (MF-FRP) plates. The tests presented here are an initial phase of a larger project that aims to employ prestressed MF-FRP plates as a repair for deteriorated prestressed hollow-core bridge slabs. Candidate slabs are those that have exposed tendons such that the bridges are typically load posted. It is proposed that the use of a prestressed MF-FRP repair will restore lost performance until replacement can be scheduled in a way that is cost effective, rapid, and enables periodic inspection over the lifespan of the short-term repair – prior to scheduled superstructure replacement. The use of prestressed MF-FRP in this application will eliminate the need for an adhesive bond and QA/QC concerns that are often associated with externally bonded FRP.

KEYWORDS:

Strengthening and Repair, Material, Digital Image Correlation, Mechanically Fastened-FRP.

INTRODUCTION:

Prestressed concrete beams of various shapes and forms are among the common bridge superstructure systems currently in service in North Carolina and across the United States. Many such bridges are in varying states of distress and require retrofit to extend their useful service life prior to complete superstructure replacement. Saliem et al. (2014) conducted a study for the North Carolina Department of Transportation (NCDOT) to quantify the deterioration of a specific bridge that was load posted by the NCDOT and needed either replacement or repair to remove or increase the posted load limit. Other research conducted by Shapack et al. (2016) and Van Brunt et al. (2016) presented similar findings with respect to deteriorated cored slabs. The findings in these earlier NCDOT projects form the basis of a current NCDOT project to develop a retrofit solution for deteriorated hollow-core bridge slabs located in aggressive coastal environments of North Carolina. The retrofit solution desired by the NCDOT is rapidly installed and easily inspected with minimal impacts on traffic, cost effective, and sufficient for the desired 3- to 5-year repair life span until superstructure replacement is scheduled.

BACKGROUND:

Strengthening of reinforced concrete bridge decks and girders to increase the Federal Highway Administration (FHWA) load rating using Mechanically Fastened-Fiber Reinforced Polymer (MF-FRP) was the subject of earlier research projects (Bank et al, 2002; Lamanna et al, 2004a and 2004b), which focus on various types of fasteners, and the interactions between the concrete and fasteners at various loads. Additional experimental projects for the Wisconsin DOT and Missouri DOT which examined the increased load rating and construction procedures required to strengthen reinforced concrete bridge decks using MF-FRP plates were presented by Bank (2004). Ebead and Saeed (2014) examined the behavior of reinforced concrete beams strengthened with externally bonded FRP, MF-FRP, and hybrid solutions that use both external bonding and mechanical fasteners. The research presented concludes that MF-FRP carries increased shear stress across the interface between the FRP and reinforced concrete beam when compared to externally bonded techniques – a desirable effect for the prestressed applications to be examined in this project. Further, Elsayed et al. (2009) examined two types of mechanical



fasteners and compared the performance to external bonding alone for FRP strengthening of concrete elements. The results of the study concluded that a sufficient number and proper spacing of fasteners enables a significantly higher load in MF-FRP plates compared to externally bonded FRP plates, with pure rupture and debonding failure modes, respectively.

While studies suggest that hybrid systems provide the greatest stress transfer across the interfacial zone between FRP and concrete (Ebead and Saeed, 2014), installation time constraints, impacts on traffic, maintenance and inspection procedures, and the associated costs with each, support a proposed bridge retrofit solution which excludes external bonding and focuses on mechanical fastening methods only.

The research presented in this paper serves as the initial series of small-scale material testing conducted during the first phase of an NCDOT project to examine the application of prestressed MF-FRP plates as a repair solution for deteriorated prestressed hollow-cored slabs. The small-scale material testing phase of the project includes examination of hybrid glass/carbon FRP plates (Figure 1) in pure tension with and without holes using digital image correlation (DIC) techniques to develop a continuous strain field of the specimen throughout the test. The strain field allows visualization of the disturbed region that develops around holes, and informs the researcher on the distribution of longitudinal strain, development of shear strain, and hole spacing in the plate for placement of mechanical fasteners which enable development of the MF-FRP plate capability. Subsequent small-scale material tests, beyond the scope of this paper, will use DIC techniques to examine bearing effects between the selected mechanical fastener and the FRP plate, anchorage pattern and number of fasteners required to develop the required prestress force in each FRP plate, and sustained loading effects on the interaction between the FRP plate and anchorage mechanism which fastens the prestressed FRP plate to the concrete substrate.



Figure 1: FRP plate sample examined in this study

METHODOLOGY:

Number of replicates for each test condition:

Because the use of prestressed MF-FRP to restore lost performance of deteriorated hollow-cored slabs is extremely limited and not well-known, the authors desired a result which could be statistically quantified at the 90% confidence level (or higher) with a 5% limit of error (e). The confidence level (CL) for a desired test result can be calculated in terms of the material's coefficient of variation (CV) and a sufficient number of sample tests using either a student-t distribution (fewer than 30 tests), or a standard normal distribution (greater than 30 tests). For the purposes of this study, a student-t distribution was used to determine the number of specimens (n) required for each test to achieve the desired 90% CL. The sample size required to achieve the desired 90% CL with 5% limit of error can be calculated using:

$$n = \left(1.7 \frac{CV}{e}\right)^2 \tag{1}$$

where e is typically taken as half of $1 - CL$, and 1.7 is the approximate value for $t_{0.95,df=n-1}$, the critical value taken from a student-t distribution.

Material test data from the manufacturer was used to determine the CV for the material for various types of behavior – pure tension, open hole tension, and bolt bearing. The material test data available for the FRP used in this study included the mean value for each set of material tests and the design value, which is published as three standard deviations below the mean in accordance with ACI 440.2R (2008). Therefore, the standard deviation for each test was determined using:

$$S_{test} = \frac{\text{mean value} - \text{design value}}{3} \tag{2}$$



A universal testing machine (UTM) with an 890 kN +/- 0.25% capacity load cell was used to conduct a series of tension tests using four different hole patterns – no holes, single hole, 4 holes 2-by-2, and 4 holes staggered. Statistical analysis of the results presented later in this paper refers to each test variation as a treatment to be consistent with terminology used in statistical modeling. For each 4-hole treatment, two transverse spacing distances were examined creating a total of six tension test treatments. Figure 2 shows each test treatment configuration and corresponding specimen identification referenced in the test matrix (Table 3). Each tension test treatment contains at least the minimum number of replicates to achieve the 90% CL. The ASTM that applies to each test is also noted in Table 3.

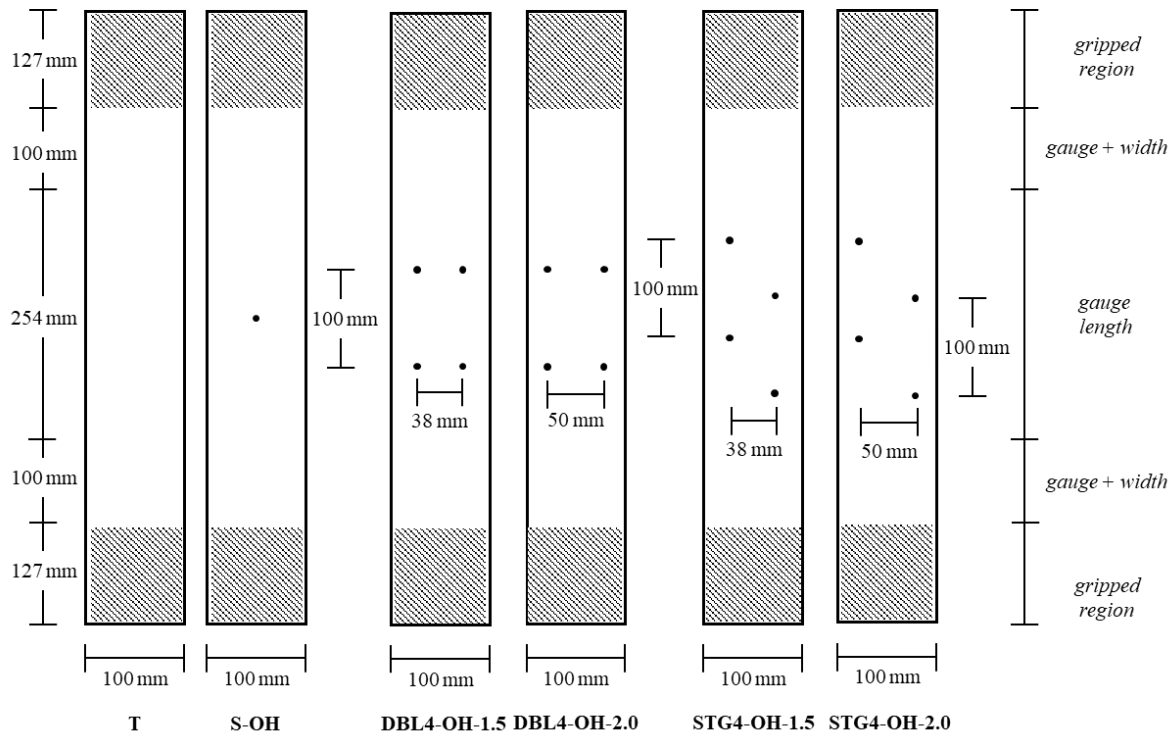


Figure 2: Test treatment configurations with specimen identification

Each specimen was cut from one of three rolls of FRP material using a standard wet-saw. An equal number of specimens from each roll was taken for each treatment group to ensure variation between rolls was reflected in each sample set. Prior to painting and applying the DIC speckle pattern, 14.3 mm holes were drilled in the samples using a tungsten carbide hole saw per the dimensions in Figure 2, and measurements were taken using a digital caliper (0.025 mm precision) to record the actual thickness, width, and hole diameter for each individual specimen.

Universal Testing Machine tension test set-up:

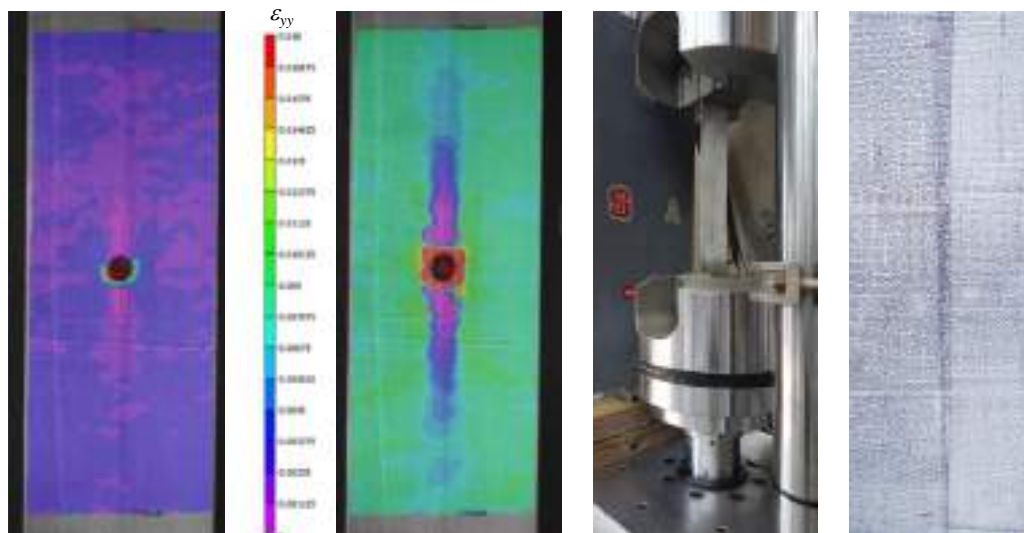
Tensile forces in the UTM were transferred to the test specimen through 127 mm by 127 mm knurled, steel wedge grips. Care was taken to ensure each specimen was plumb with the axis of the UTM to minimize eccentric load effects. Tests were also conducted to determine if the wedge grips of the UTM required modification, or if tabs were needed on the FRP material to properly grip each specimen such that rupture in the FRP occurred before any premature failure at the grips. It was determined that the wedge grips alone were sufficient to develop rupture in the FRP without slipping between the steel grips and the FRP plate. An example test set-up with the FRP specimen gripped in the UTM and applied speckle pattern applied is shown in Figures 3c and 3d, respectively.

Tension tests without holes (specimens T-1 through T-8) were conducted in accordance with ASTM D3039 (2014). Each test specimen had a nominal thickness of 3.18 mm and nominal width of 100 mm. Actual thickness and width were recorded for each specimen prior to testing. Total specimen length (Figure 2) was determined using a 254 mm gauge length, plus 200 mm (2 x width), plus 254 mm (127 mm for each grip) as specified in ASTM D3039 (2014). Each specimen was loaded under displacement control with a constant rate of 1.25 mm/min., and load-displacement data was recorded in addition to the DIC strain data for each test. Tests were conducted until rupture, and each failure mode was recorded in accordance with ASTM D3039 (2014) failure codes.

Table 3: Test Matrix

Specimen ID	No. of Specimens	Treatment Description	ASTM
T	8	No holes	D3039
S-OH	6	Single open hole centered in gauge length	D5766 ¹
DBL4-OH-1.5	6	4 open holes; 2-by-2; 38-mm transverse spacing; 100-mm longitudinal spacing	D5766 ¹
DBL4-OH-2.0	6	4 open holes; 2-by-2; 50-mm transverse spacing; 100-mm longitudinal spacing	D5766 ¹
STG4-OH-1.5	6	4 open holes; staggered with 50-mm offset; 38-mm transverse spacing; 100-mm longitudinal spacing	D5766 ¹
STG4-OH-2.0	6	4 open holes; staggered with 50-mm offset; 50-mm transverse spacing; 100-mm longitudinal spacing	D5766 ¹

¹ASTM D5766 specifies a single hole with $w/D=6$; test was adapted to accommodate desired $w/D=2.25$ and multiple holes.



(a) ϵ_{yy} at low tensile load (b) ϵ_{yy} after longitudinal splitting (c) UTM setup (d) DIC speckle pattern
Figure 3: Example DIC results and test setup

RESULTS AND DISCUSSION:

Summary results for all tests are presented in Table 4.

Tension with no holes:

A total of eight (8) individual replicates were tested in the pure tension - no holes condition. The material CV for pure tension is 8.28% (considered the population CV for this study) per the manufacturer's data presented in Table 1. Therefore, using Eq. 1, a 90% CL with a 5% limit of error is achieved with a sample size of 8. The mean peak load for the 8 tests was 340 kN, and the mean peak stress for the sample set was 1014 MPa with a sample CV of 3.97% based on recorded peak stresses. All 8 specimens failed with explosive rupture in the middle region of the gauge length (XGM in accordance with ASTM D3039, 2014). The manufacturer's data provides a mean peak stress of 852 MPa (Table 1) – 18.9% lower than the peak stress from the sample set. This difference is more than double the population CV value, indicating a significant discrepancy between the sample set tested in this study and the manufacturer's data. It is difficult to determine the source of this difference, but it is likely due to differences in testing procedures and specimen preparation. The manufacturer material testing for tension was conducted using ASTM D638 (2014), a specification for testing plastic polymers, whereas the standard applied to the tension tests conducted in this study is ASTM D3039 (2014), a specification for testing polymer matrix composite materials such as the FRP used in the study. The significant difference between ASTM D638 (2014)



and ASTM D3039 (2014) is the use of reduced cross-section specimens in ASTM D638 (2014). The authors believe this to be the probable source of the mean peak stress and CV differences. A reduced cross-section for the non-homogeneous FRP plate tested in this study would produce variable results which are dependent upon the carbon fiber content remaining after the cross-section reduction is applied to each specimen. It is worth noting a 3.99% CV, assuming this is representative of the true population CV, yields an actual CL = 99% with $n = 8$ (Table 4). However, without further testing to determine the true CV for the FRP material in tension, the assumed population CV of 8.28% is sufficient to report a mean peak load at the 90% CL.

Table 4: Summary Test Results

Specimen ID	No. of Specimens	Mean Peak Load (kN)	Mean Peak Stress ² (MPa)	Sample Peak Stress Standard Deviation (MPa)	Sample Peak Stress CV (%)	CL based on Sample CV (%)	Population Peak Stress (MPa)	Population Peak Stress CV (%)	CL based on Population CV (%)
T	8	340	1013	40.4	3.99	99	854	8.28	90
S-OH	6	296	1040	42.2	4.06	96	652 ²	5.56	97
DBL4-OH-1.5	6	229	944	30.0	3.18	97	NA	5.56 ¹	97
DBL4-OH-2.0	6	233	909	44.5	4.89	95	NA	5.56 ¹	97
STG4-OH-1.5	5	234	958	15.6	1.63	99	NA	5.56 ¹	93
STG4-OH-2.0	5	228	937	12.6	1.35	99	NA	5.56 ¹	93

¹ Multiple hole CV values are assumed to follow single hole testing values;

² ASTM D5766 stress calculation uses gross sectional area, sample peak stress is calculated using net sectional area.

Tension with holes:

Single hole condition:

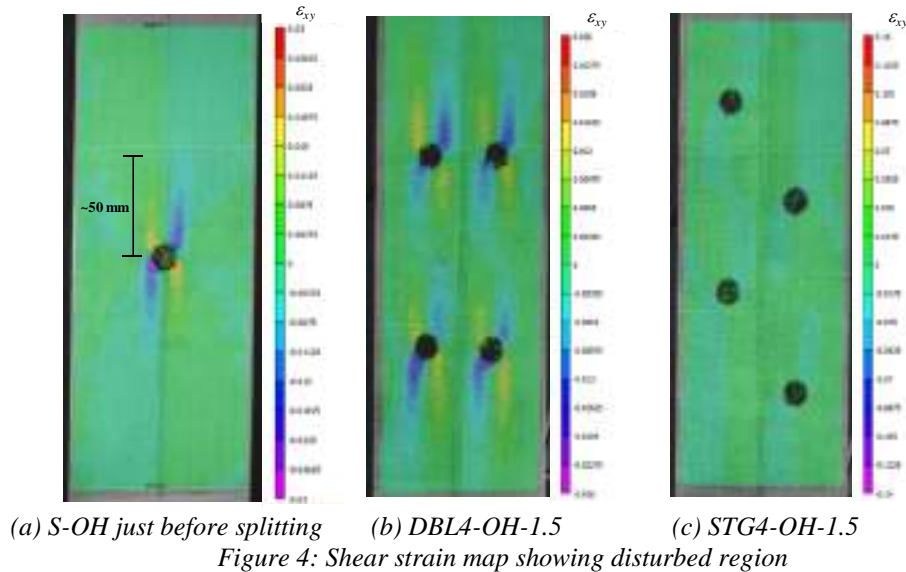
Six (6) total specimens were tested in the single open-hole condition providing a 97% CL with 5% limit of error base on the CV determined from the manufacturer testing. The test procedure was adapted from ASTM D5677 which specifies a specimen-width-to-diameter-ratio equal to 6 ($w/D = 6$). The desired w/D ratio in this study is 7.1 to incorporate a 14.3 mm hole diameter to accommodate a 12.7 mm diameter fastener. The stress calculation using ASTM D5677 uses the gross cross-sectional area of the test specimen whereas the stress calculation used in this study uses the net cross-sectional area. The mean peak load for the single hole test condition was 299 kN and the mean peak stress using the net cross-sectional area was 1040 MPa. The mean peak stress reported by the manufacturer using $w/D = 6$ and the gross cross-sectional area is 652 MPa. The calculated mean peak stress using the manufacturer test data and the net cross-sectional area is 786 MPa. The mean peak stress for the sample set in this study and the manufacturer test data differs by 32.4 % of the manufacturer mean peak stress using the net cross-sectional area. This difference is likely due to the non-homogeneity of the material and amount of carbon fiber included in the net cross-section for each test specimen – lower peak stress results with less carbon fiber in the cross section. All 6 specimens failed in longitudinal shear throughout the gauge length (SGM in accordance with ASTM D3039 (2014)).

The DIC shear strain results show the development of the disturbed region above and below the hole (Figure 4a) just before splitting is approximately 50 mm. Therefore, the longitudinal spacing between holes for multiple hole test conditions is taken as 100 mm (Figure 2) to minimize possible interaction between disturbed regions.

2-by-2 and staggered hole conditions:

Two (2) transverse spacing distances were tested for each of the 2-by-2 (DBL4) and staggered (STG4) hole spacing conditions: 1) 38 mm and 2) 50 mm (shown in Figure 2). The mean peak stress for each of the four treatments is 910 MPa, 945 MPa, 958 MPa, and 938 MPa for DBL4-OH-1.5, DBL4-OH-2.0, STG4-OH-1.5, and STG4-OH-2.0, respectively (Table 4). Six (6) replicates were tested for each of the 4 treatments; however, one of the STG4 replicates slipped in the grips during testing, creating an outlier result. Therefore, for the STG4 treatment group, only 5 tests were considered in the analysis of the results to eliminate the effects of the slip that occurred during one test. All specimens in both the DBL4 and STG4 test treatments experienced SGM failure modes in the same manner as the single open hole treatment groups.

Figure 4 shows the DIC shear strain results for both the DBL4-OH-1.5 and the STG4-OH-1.5 test treatments just prior to longitudinal splitting. The load is approximately 170 kN for each image in Figure 4. The 100 mm longitudinal spacing between holes is shown in the images to be sufficient to minimize the interaction of shear strain between each hole.



Analysis of Variance (ANOVA) Results:

A Multi-Factor Analysis of Variance (ANOVA) test was conducted to determine if there is a statistically significant difference between the DBL4, STG4, 38 mm and 50 mm treatments. The following null (H_0) and alternate (H_a) hypotheses were tested:

$$H_{0A}: \alpha_1 = \alpha_2 = 0 \quad \text{and} \quad H_{0B}: \beta_1 = \beta_2 = 0 \quad (3a)$$

and

$$H_{aA}: \text{at least one } \alpha_i \neq 0 \quad \text{and} \quad H_{aB}: \text{at least one } \beta_i \neq 0 \quad (3b)$$

where α_i is the effect of the hole pattern treatment (DBL4 or STG4) on the mean peak load and β_i is the effect of the transverse spacing treatment (1.5 or 2.0) on the mean peak load.

The results of the multi-factor ANOVA are shown in Table 5. When tested at the 95% CL ($\alpha = 0.05$) the P-value for α_i is 0.443 (Table 5) and the P-value for β_i is 0.855, therefore, we fail to reject both null hypotheses. This failure to reject both null hypotheses means there is no statistically significant difference (at the 95% CL) between the effects of both the hole pattern (STG4 or DBL4) and the transverse spacing (38 mm or 50 mm) on the mean peak load for each test.

Table 5: Multi-Factor ANOVA results

Source of Variation	SS	df	MS	F	P-value	F crit
Hole Pattern	22.532	10	2.253	1.097	0.443063	2.97824
Transverse Spacing	0.0718	1	0.072	0.035	0.855383	4.9646
Error	20.534	10	2.053			
Total	43.137	21				

The results of the ANOVA are consistent with the manner in which the FRP test specimens carry load in the pure tension tests conducted in this study. The tensile forces are carried in the longitudinal carbon fibers of the FRP plate (shown in Figure 1), and therefore the staggered nature of the STG4 treatment does not change the manner in which the longitudinal fibers carry load that is applied in the same direction as the carbon fibers. For the same reason, the transverse spacing between the holes does not affect the capacity of FRP plate in axial tension.

CONCLUSIONS:



The following conclusions can be made from the study presented in this paper:

- 1) DIC is a useful and independently sufficient technique for determining localized strain and presenting a global strain map to visualize loading effects during testing;
- 2) when established coefficients of variance are available for a given material and loading condition statistically significant results can be achieved with a reasonable number of replicates;
- 3) there is no statistically significant difference on the mean peak load between the 2-by-2 and staggered hole patterns; and
- 4) the consistency between the 2-by-2 and staggered treatment groups is controlled by longitudinal shear failure which occurs in the transverse glass fibers of the hybrid glass/carbon FRP plate examined in this study.

REFERENCES:

- ACI 440.2R (2008). "Guide for the Design and Construction of Externally Bonded FRP Systems for Strengthening Concrete Structures." American Concrete Institute, Farmington Hills, MI, 76.
- ASTM D3039. (2014). "Standard Test Method for Tensile Properties of Polymer Matrix Composite Materials." ASTM International, West Conshohocken, PA, 13.
- ASTM D5766. (2011). "Standard Test Method for Open-Hole Tensile Strength of Polymer Matrix Composite Laminates." ASTM International, West Conshohocken, PA, 7.
- ASTM D638. (2014). "Standard Test Method for Tensile Properties of Plastics." ASTM International, West Conshohocken, PA, 17.
- Bank, L. C. (2004). "Mechanically-fastened FRP (MF-FRP) – a viable alternative for strengthening RC members." *FRP Composites in Civil Engineering – CICE 2004*, R. Seracino (ed.), Taylor and Francis Group, London, 3-15.
- Bank, L. C., Lamanna, A. J., Ray, J. C., and Velazquez, G. I. (2002). "Rapid strengthening of reinforced concrete beams with mechanically fastened, fiber-reinforced polymeric composite strips." *Rep No. ERDC/GSL TR-02-4*, U.S. Army Corps of Engineers Engineer Research and Development Center, Vicksburg, MS, 99.
- Bomarito, G. F., Hochhalter, J. D., Ruggles, T. J., and Cannon, A. H. (2017). "Increasing accuracy and precision of digital image correlation through pattern optimization." *Optics and Lasers in Engineering*, 91, 73-85.
- Ebead, U., and Saeed, H. (2014). "Flexural and Interfacial Behavior of Externally Bonded/Mechanically Fastened Fiber-Reinforced Polymer-Strengthened Reinforced Concrete Beams." *ACI Structural Journal; Farmington Hills*, 111(4), 741-751.
- Elsayed, W. E., Ebead, U. A., and Neale, K. W. (2009). "Studies on Mechanically Fastened Fiber-Reinforced Polymer Strengthening Systems." *ACI Structural Journal; Farmington Hills*, 106(1), 49-59.
- Hoult, N. A., Take, W. A., Lee, C., and Dutton, M. (2013). "Experimental accuracy of two-dimensional strain measurements using Digital Image Correlation." *Engineering Structures*, 46, doi: 10.1016/j.engstruct.2012.08.018.
- Lamanna, A. J., Bank, L. C., and Borowicz, D. T. (2004a). "Mechanically Fastened FRP Strengthening of Large Scale RC Bridge T Beams." *Advances in Structural Engineering*, 7(6), 525-538.
- Lamanna, A. J., Bank, L. C., and Scott, D. W. (2004b). "Flexural Strengthening of Reinforced Concrete Beams by Mechanically Attaching Fiber-Reinforced Polymer Strips." *Journal of Composites for Construction*, 8(3), 203-210.
- Seliem, H., Lucier, G., Seracino, R. (2014). "Structural Assessment and Repair of Deteriorated Exterior Precast Prestressed Concrete Channel Girders." *Technical Report No. RD-14-03*, North Carolina Department of Transportation, March, 43.
- Shapack, G., Seracino, R., Lucier, G., and Rizkalla, S. (2016). "CFRP Strands in Prestressed Cored Slab Units." *Technical Report No. FHWA/NC/2014-09*, North Carolina Department of Transportation, February, 133.
- Strongwell (2016) "SAFSTRIP® Fiber Reinforced Strengthening Strip." Online at www.strongwell.com [accessed 11/13/2017].



Van Brunt, Z., Seracino, R., Lucier, G., and Pour-Ghaz, M. (2016). "Assessment of Deteriorated Cored Slabs: Bridges No. 150035 and 150039." *Technical Report No. FHWA/NC/2014.35*, North Carolina Department of Transportation, February, 233.

Xie, H., and Kang, Y. (2015). "Digital image correlation technique." *Optics and Lasers in Engineering*, 65, doi: 10.1016/j.optlaseng.2014.07.010.



LOCAL BUCKLING OF PULTRUDED GFRP I-SECTION SUBJECT TO BENDING

Everton Souza¹, Janine Vieira ², Daniel Cardoso¹

¹ Pontifical Catholic University of Rio de Janeiro, Department of Civil and Environmental Engineering, Rio de Janeiro, Brazil;

² Fluminense Federal University, Department of Civil Engineering, Niteroi, Brazil. (corresponding author: janinedv@id.uff.br)

ABSTRACT:

The use of pultruded glass fiber reinforced polymer (pGFRP) has increased significantly in the last few years, especially in aggressive environments. The structural performance of pGFRP members is strongly dependent on their buckling behavior, because of the association of low elastic properties and relatively thin-walled sections adopted. The aim of this study is to present the results of an ongoing experimental work focused on evaluating the local buckling behavior of GFRP I-beams subject to 4-point bending tests. Lateral deflections were measured with displacement transducers and the curvature at compression flange during loading was measured with back-to-back strain gages. A finite element model using actual material properties and bracing conditions was adopted to ensure behavior governed by local buckling and to determine critical bending moment. The influence of web-to-flange rotational stiffness on the behaviour is discussed and, finally, experimental critical loads obtained using Southwell and Koiter techniques are compared to those obtained using analytical expressions recently proposed in literature and to computational analysis.

KEYWORDS

Glass fiber reinforced polymer (GFRP), local buckling, flexural tests, rotational stiffness.

INTRODUCTION

Pultruded glass fiber-reinforced polymer (pGFRP) members had their first applications in aerospace industry followed by oil and automotive industries. In the last years, the use of pGFRP increased in structural engineering because of its good performance in aggressive environments and high tensile and compressive strengths (parallel to fiber direction), comparable with steel. However, the association of the low modulus of elasticity in the longitudinal direction - about 1/8 that of steel - to the relatively thin-walled sections adopted and high material anisotropy makes pGFRP members susceptible to instability problems and significant interaction between local and global buckling modes (Cardoso et al., 2015)

Several authors have dedicated efforts to study local buckling behavior of pGFRP members subject to compression with different cross-sections (e.g. Tomblin and Barbero, 1994; Turvey and Zhang, 2006a; Cardoso et al., 2015). However, only a few have been exclusively dedicated to experimentally the local buckling in bending. In the early 1990's, Barbero et al. (1991) conducted a series of tests in pGFRP beams subject to bending. Specimens were laterally braced at mid-span and the authors observed that failure by local buckling governed the behavior. Bank et al. (1994) performed four-point bending tests in beams designed to fail in local buckling and reported typical failure mode by tearing along the web-flange junction at the constant-moment region. Later, Bank et al. (1995) reviewed experimental data of three beams and proposed an appropriate technique to determine the critical load accounting for the non-linear behavior and avoiding overestimated results. Finite element method (FEM) analyses were also carried out to show that anisotropy and inhomogeneity of pultruded material may affect significantly local buckling behavior. Recently, Vieira et al. (2017) reported the results of an experimental study aiming to investigate the flexural behavior of GFRP beams for a variety of section geometries and spans. The work showed different buckling modes and the experimental results were compared with those obtained using design methods available in standard under development (ASCE, 2010, EUR27666, 2016) as well as to the equation proposed by Kollar (2013) and to Finite Strip Method (FSM). According to the authors, the design methods were found to be conservative. It is also worth reporting the interesting study carried out by Kubiak et al. (2016) in non-pultruded composite channel sections. To ensure local buckling due to 'pure' flexure, i.e. avoiding influence of shear in the buckling mode, rigid blocks were adopted at the shear spans and, to account for the non-hyperbolic load-deflection behavior, experimental critical loads were obtained using Koiter's technique.



Several closed form equations to calculate the critical load for different loading conditions are available in literature (e.g. Kollar, 2003, Mottram, 2004, Ascione et al., 2016, Cardoso and Vieira, 2017). Kollar (2003), for instance, presented explicit expressions considering the cross-section comprised of orthotropic plates with rotationally restrained edges. The method allows considering different cross-sections and loading conditions and has been validated for I-sections, resulting in its inclusion in the latest versions of standards under development. Closed form equations for I-section beams subject to pure bending are also presented by Ascione et al. (2016) and Cardoso and Vieira (2017). In these works, equations were obtained using energy methods along with assumed approximate buckled shapes and good results were obtained when compared to numerical methods. Approaches considering interaction between flange and web lead to superior agreement and will soon prevail over the simple but old-fashioned approach where web-to-flange junction is assumed as hinged. Another important parameter is the flexibility of the flange-to-web junction (e.g. Turvey and Zhang, 2006b). To date, there is no explicit equation accounting for this flexibility, although significant reduction in critical loads has been reported in literature (Ascione et al., 2013).

The flexural performance of pGFRP is dependent on its buckling behavior. Due to its orthotropic properties, formulations proposed for isotropic materials on instability studies give unreliable results. The aim of this paper is to present results of an ongoing research on flexural behavior of pultruded GFRP I-sections. Results from tests on I-sections having flange-to-web width ratio equal to 1.0 are reported and compared to those obtained using finite element method (FEM) and analytical expressions proposed Cardoso and Vieira (2017), as well as by EUR 27666 (2016) and ASCE (2010). The influence of the flexibility of the web-to-flange junction is also discussed.

EXPERIMENTAL PROGRAM

Material Characterization

The wide flange pultruded profiles with section depth, d , equal to flange width, b_f , used in this study were made with vinyl ester resin and E-glass fiber. In order to obtain the relevant properties of the material, specimens were extracted from flanges and web and mechanical characterization was carried out. The average values (and COV in parentheses) of the experimental mechanical properties as well as those reported by the manufacturer are presented in Table 1. It is important to mention that all moduli in flexure are related to the bending of constituent walls and that the transverse modulus, $E_{T,f}$, was determined with a non-standard test since the geometry of the pultruded profile did not allow extraction of specimens with standards dimensions. Figure 1 shows the tests performed for mechanical characterization of the pultruded material.

Table 1: Mechanical properties of GFRP profiles, in MPa.

Mechanical properties	Test method	Experimental values (COV)		Manufacturer reported
		Flange	Web	
Longitudinal modulus in tension, $E_{L,t}$	ISO 527-4	32653 (0.11)	26350 (0.03)	17260
Longitudinal modulus in compression, $E_{L,c}$	ASTM D6641	30401 (0.17)	28328 (0.09)	-
Longitudinal modulus in flexure, $E_{L,f}$	ISO 14125	19854 (0.25)	17425 (0.01)	10984
Transverse modulus in flexure, $E_{T,f}$	non-standard	7867 (0.05)	-	5492
Shear modulus, G_{LT}	ASTM D5379	2298 (0.42)	2374 (0.11)	-
Longitudinal strength in tension, $F_{L,t}$	ISO 527-4	425 (0.04)	330 (0.15)	287
Longitudinal strength in compression, $F_{L,c}$	ASTM D6641	275 (0.05)	370 (0.15)	287
Longitudinal strength in flexure, $F_{L,f}$	ISO 14125	470 (0.09)	477 (0.04)	287

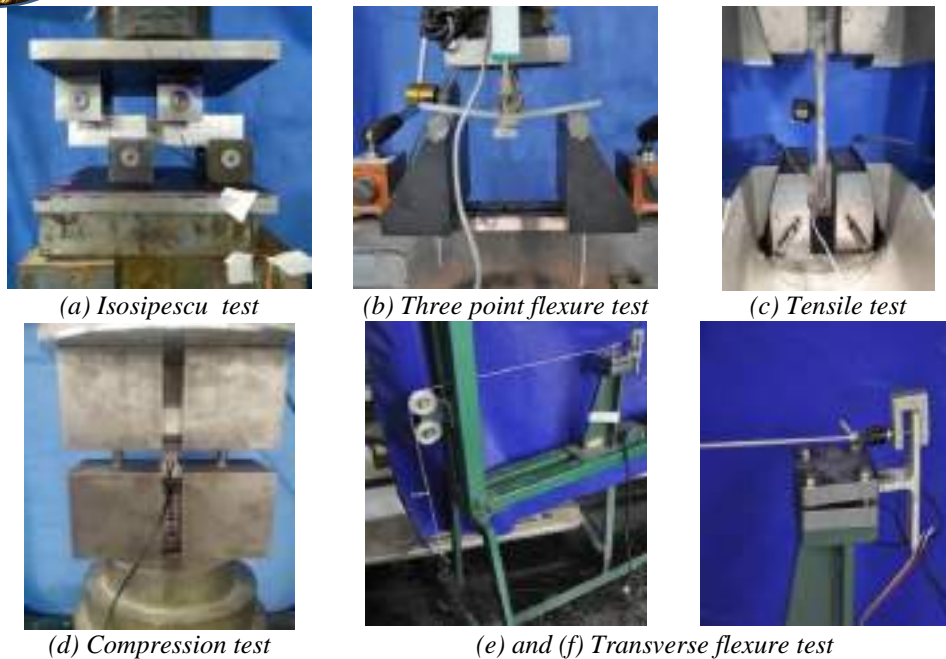


Figure 1: Mechanical characterizations tests

Rotational spring constant (k_0)

It has been shown in literature that the rotational stiffness of the web-to-flange junction may affect significantly the critical load and buckling mode (Turvey and Zhang, 2006b, Ascione et al., 2013). In this work, an experimental characterization of the rotational spring constant was carried out. Three ‘tee’ specimens 85-mm wide extracted from the pultruded profiles were used. The flange of the specimen was clamped at a test frame using rigid aluminum bars to ensure no displacement and steel plates were attached to the web to assure negligible plate bending during the tests. To measure the lateral displacement, a displacement transducer was placed at the free end of the ‘tee’ stem, in the direction of applied load. The load was applied using dead weights and was incremented manually. Figure 2 shows the set-up adopted for the experimental test. The average value for k_0 obtained was 10085 N.mm/mm/rad.

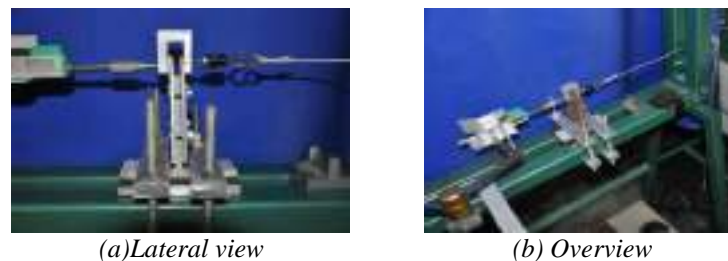


Figure 2: Set-up for the rotational stiffness test

Flange Local Buckling (FLB) – Four-point bending test

For the flange local buckling (FLB) investigation, three I-sections with nominal dimensions 102 x 102 x 6 mm ($d \times b_f \times t$, where t is the uniform thickness) with a flange slenderness, $b_f/2t$, of 8.5 were tested. Four-point bending tests over a span of 1100 mm consisting of two 310-mm shear spans and a 480-mm constant moment region were carried out. In all tests, lateral supports were provided near supports and loading points to prevent lateral torsional buckling (LTB) and distortion. For this purpose, steel plates coated with teflon to avoid the friction between the profile and the plates were used. A narrow neoprene layer was used at the loading points to concentrate loads over web, i.e. without introducing transverse flexure on flanges. To monitor the onset and development of FLB, back-to-back strain gages were applied to both tips of the compression flange, at the middle of the constant moment region. Draw-wire transducers were used to measure the vertical deflection and the lateral displacement of the

beam at mid-span. All the tests were carried out using a 1000 kN capacity servo-hydraulic MTS actuator with a displacement control of 0.6 mm/min up to failure. Figure 3 shows the setup for the flexural tests.

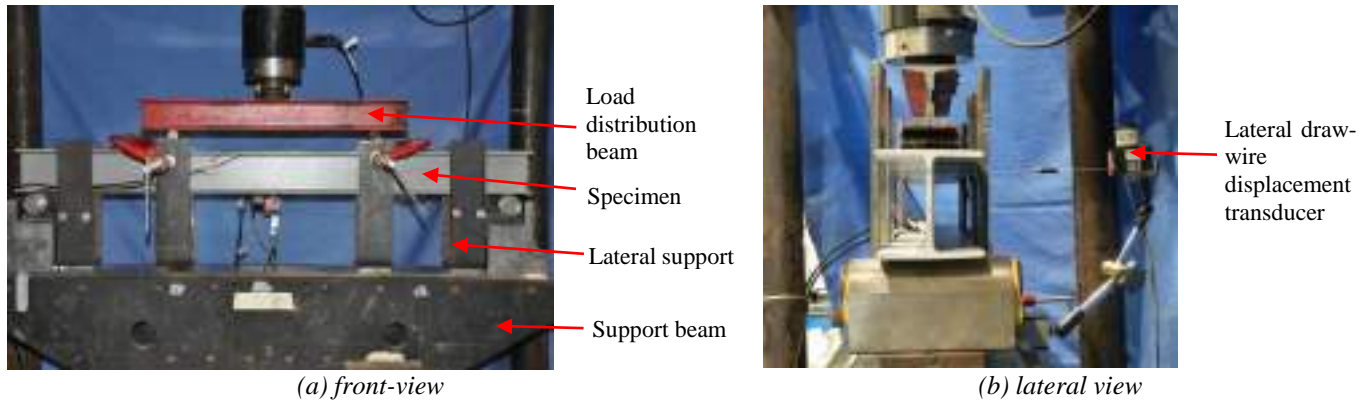


Figure 3: Set-up for pGRFP flexural tests.

FINITE ELEMENT METHOD (FEM)

In order to predict the local buckling critical moment, linear eigenvalue FEM analysis was carried out using Abaqus 6.13.1 (2013) software. The model was discretized with shell elements S8R5 and average experimental mechanical properties were used. To represent the rotational stiffness at the junction, flange and web were joined using connector-type elements with rotational spring about axis Z defined according to the experiments. To simulate the lateral supports, the displacements in X direction were restrained at both flanges. Translations in vertical direction (Y) were restrained at both ends whereas translation at Z direction was included in one of the ends. Figure 4 shows the model of the beam with their boundary conditions. Figure 5 illustrates the first buckling mode obtained from FEM analysis.

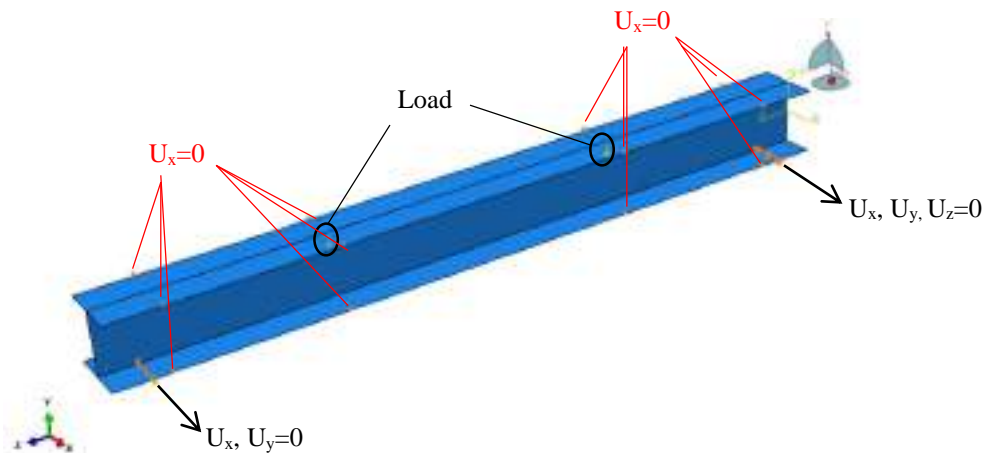


Figure 4: Boundary conditions of the beam implemented in FEM

RESULTS AND DISCUSSIONS

Representative experimental moment vs vertical and moment vs lateral deflections are reproduced in Figure 6a and 6b, respectively. All the tests exhibited negligible lateral motions prior to local buckling. After the formation of local buckling waves, lateral deflections resulting from loss of stiffness can be observed. Failure finally results from an interaction between FLB and LTb, leading to premature failure and unnoticeable post-buckling reserve of strength. This phenomenon can be clearly observed from moment-lateral deflection shown in Figure 6b as well as from the differences in non-dimensional curvature, Φ (equal to strain at top minus strain at bottom of flange), obtained for the pairs of strain-gages for each side of the flange presented in moment vs non-dimensional curvature shown in Figure 6c, which suggests a greater compression stress in one side of the flange and a relief on the opposite side. Larger amplitude on the more compressed side could also be observed during tests, as shown in the typical buckling mode illustrated in Figure 7. All beams tested exhibited flange-to-web tearing failure.

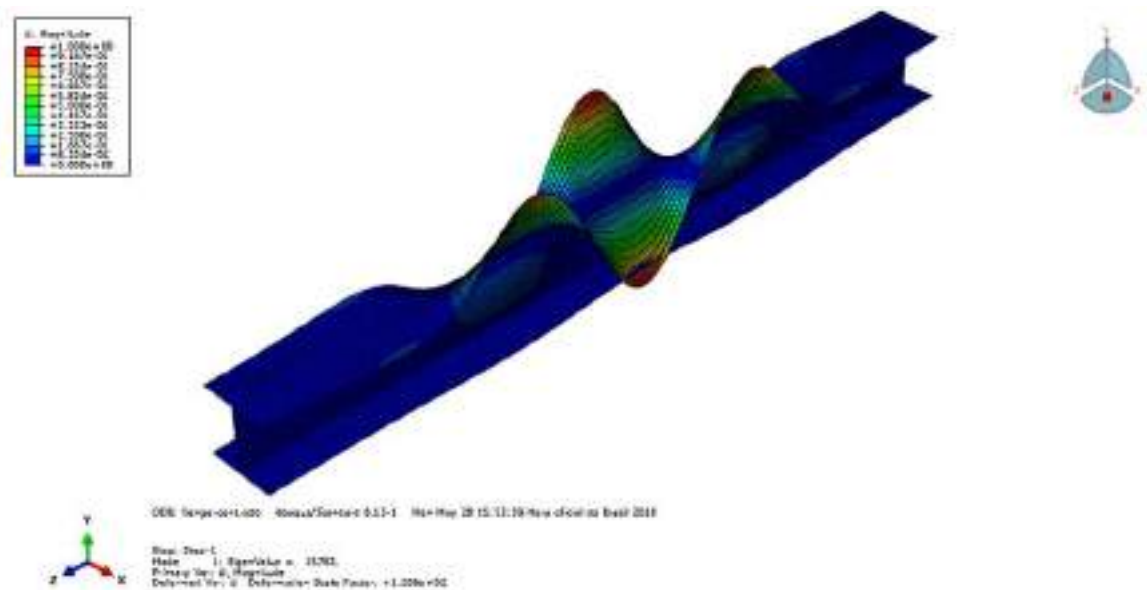


Figure 5: buckling mode of four-point bending FE model

The experimental critical FLB moments obtained using Southwell and Koiter techniques and the results obtained from analytical and computational analyses (FEM) are present in Table 2. In all analyses, nominal section dimensions were used. It is important to mention that Koiter's approach take into account the post-buckling behavior whereas Southwell is usually valid for columns with hyperbolic buckling behavior. A good agreement was achieved between experimental results and those obtained with ASCE Pre-standard, Cardoso and Vieira (2017) and with Finite Element Method (FEM), whereas significant lower critical stress was obtained using EUR 27666 (2016). It is important to note that a closer prediction was expected using FEM model and differences may be explained by a low rotational stiffness and/or shear modulus adopted in the model, suggesting that more characterization tests are necessary to obtain reliable properties. It can also be highlighted that the method proposed by Cardoso and Vieira (2017) is based on energy approach and assumes full compatibility of rotation between flange and web, therefore resulting in greatest prediction among all methods, although relatively close to the experimental results.

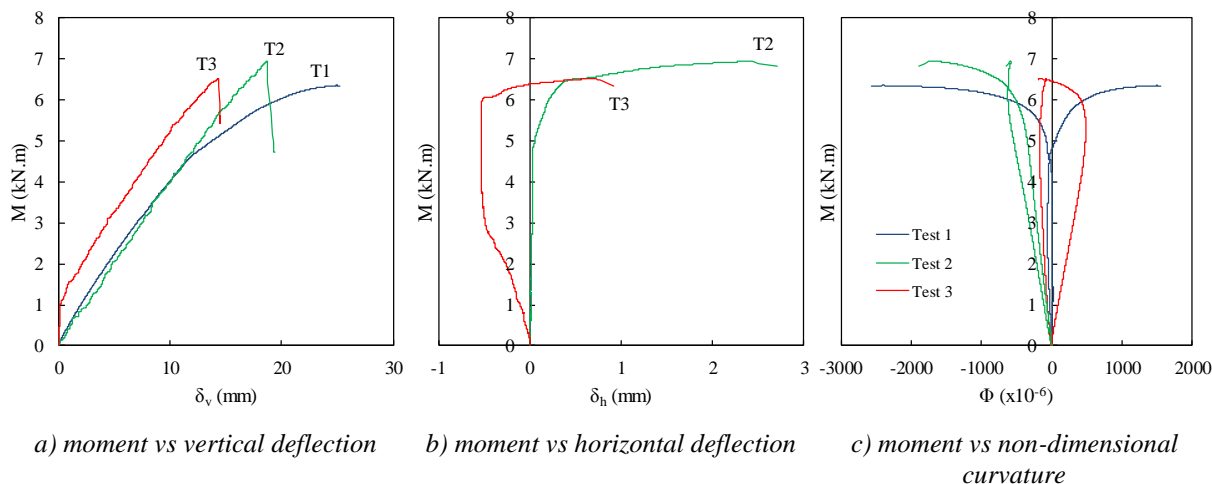


Figure 6: Experimental results.

Table 2: Critical moments in N.m for various analyses.

Experimental (COV)		FEM		Cardoso and Vieira (2017)		EUR 27666 (2016)		ASCE (2010)	
Southwell	Koiter	M_{cr}	pred./exp.	M_{cr}	pred./exp.	M_{cr}	pred./exp.	M_{cr}	pred./exp.



5502 (0.069)	5509 (0.12)	4894 0.81-0.96	5754 0.96-1.13	4424 0.74-0.87	5523 0.92-1.09
-----------------	----------------	-------------------	-------------------	-------------------	-------------------



a) Flange local buckling at constant region moment



b) Differences in the amplitude of half-waves for both sides of compression flange.



c) Web-junction tearing failure



d) Compression flange rotation

Figure 7: Local flange buckling observed in the experimental tests

CONCLUSIONS

This paper presented the results of an ongoing experimental work with the objective to evaluate the local buckling behaviour of GFRP I-beams subject to four-point bending tests. The experimental program included mechanical characterization tests and a simple nonstandard test to obtain the rotational spring constant was proposed.

The beam tests showed that the rotational stiffness of web-to-flange junction influences critical moment and buckling behaviour. A FEM model of the beam was implemented with the rotational spring constant and a good correlation was observed, although FEM results in lower critical stress, which may be attributed to inherent variations of material properties. More characterization tests must be carried out to obtain reliable properties and, therefore, a closer agreement between FEM and experiments.

The equations proposed by ASCE (2010) and by Cardoso and Vieira (2017) presented good agreement with the experimental results. On the other hand, the critical stress obtained using the equation proposed in the EUR 27666 (2016) underestimates significantly the experimental results. It is important to mention that all theoretical approaches studied neglect the rotational stiffness of the web-to-flange junction and more tests are necessary to validate the methods for general conditions.

The failure modes were similar in all tests with rupture in web-flange junction. This type of failure is expected since it can be affected by presence of the resin-rich zone which interfere in the arrangements of the fibers and local imperfections due to the pultrusion process.

ACKNOWLEDGMENTS



The first author thanks to CAPES (Coordenação de Aperfeiçoamento de Pessoal de Nível Superior) for financial support. All authors wish to thanks Stratus Compostos Estruturais Ltda for supplying the GFRP profiles used in this work.

REFERENCES

- ABAQUS (2013). Software Documentation. Version 6.13.1 by SIMULIA.
- ASCE – American Society of Civil Engineers (2010). “Pre-standard for load and resistance factor design (LRFD) of pultruded fiber reinforced polymer (FRP) structures”. ASCE, Reston, VA, USA.
- Ascione, L., Berardi, V. P., Giordano, A., and Spadea, S. (2013). “Local buckling behavior of FRP thin-walled beams: a mechanical model”. *Composite Structures*, 98, 111-120.
- Ascione, F., Feo, L., Lamberti, M., Minghini, F., and Tullini, N. (2016). “A closed-form equation for the local buckling moment of pultruded FRP I-beams in major-axis bending”. *Composites Part B: Engineering*, 97, 292-299.
- Ascione, L. et al. (2016). “Prospect for new guidance in the design of FRP: Support to the implementation and further development of the eurocode”. Publications Office of the European Union, Brussels, Belgium, Report EUR 27666.
- Bank, L., Nadipelli, M., Gentry, T. (1994). “Local buckling and failure of pultruded fiber-reinforced plastic beams”. *Journal of Engineering Materials and Technology*, 116(2), 233-237.
- Bank, L., Yin, J., and Nadipelli, M. (1995). “Local buckling of pultruded beams—Nonlinearity, anisotropy and inhomogeneity”. *Construction and Building Materials*, 9(6), 325-331.
- Barbero, E., Fu, S., and Raftoyiannis, I. (1991). “Ultimate bending strength of composite beams”. *Journal of Materials in Civil Engineering*, 3(4), 292-306.
- Cardoso D., Harries K. and Batista E. (2015). “Compressive local buckling of pultruded GFRP I-sections: development and numerical/experimental evaluation of an explicit equation”. *ASCE Journal of Composites for Construction*, 19(2), 04014042.
- Cardoso, D. C., and Vieira, J. D. (2017). “Comprehensive local buckling equations for FRP I-sections in pure bending or compression”. *Composite Structures*, 182, 301-310.
- Kollár, L. P. (2003). “Local buckling of fiber reinforced plastic composite structural members with open and closed cross sections”. *Journal of Structural Engineering*, 129(11), 1503-1513.
- Kubiak, T., Kolakowski, Z., Swiniarski, J., Urbaniak, M., and Gliszczynski, A. (2016). “Local buckling and post-buckling of composite channel-section beams—Numerical and experimental investigations”. *Composites Part B: Engineering*, 91, 176-188.
- Mottram, J. T. (2004). “Determination of critical load for flange buckling in concentrically loaded pultruded columns”. *Composites Part B: Engineering*, 35(1), 35-47.
- Tomblin, J. and Barbero, E. (1994). “Local buckling experiments on FRP columns”. *Thin-walled structures*, 18(2), 97-116.
- Turvey, G. and Zhang, Y. (2006a). “A computational and experimental analysis of the buckling, postbuckling and initial failure of pultruded GRP columns”. *Computers and Structures*, 84(22), 1527-1537.
- Turvey, G., and Zhang, Y. (2006b). “Characterization of the rotational stiffness and strength of web-flange junctions of pultruded GRP WF-sections via web bending tests”. *Composites Part A: applied science and manufacturing*, 37(2), 152-164.



Vieira, J., Liu, T., and Harries, K. (2017). "Flexural stability of pultruded glass fibre-reinforced polymer I-sections". *Proceedings of the Institution of Civil Engineers - Structures and Buildings*, 1-12.



ADAPTIVE REUSE OF FRP COMPOSITE WIND TURBINE BLADES FOR CIVIL INFRASTRUCTURE CONSTRUCTION

R. Gentry 1, L. Bank 2, J. F. Chen 3, F. Arias 2, and T. Al-Haddad 1

¹ Georgia Institute of Technology, School of Architecture, Atlanta, GA 30332 USA

Email: russell.gentry@arch.gatech.edu

² City College of New York, New York, NY, USA

³ Queen's University Belfast, Northern Ireland, UK

ABSTRACT

The rapid growth in wind energy technology has led to an increase in the amount of thermosetting FRP composite materials used in wind turbine blades that will need to be recycled or disposed of in the near future. Calculations show that 16.8 million tons of waste from wind blades will need to be managed globally by 2030, increasing to 39.8 million tons by 2050. Three waste management routes are possible: disposal, recycling or reusing. Currently, most FRP composites taken out of service are disposed of in landfills or are incinerated. Recycling options consist of reclamation of the constituent fibers or the resins by thermo-chemical methods or recycling of small pieces of granular FRP material as filler material by cutting, shredding or grinding. Reuse options consist of reusing the entire FRP blade or large parts of the blade in new structural applications.

This paper reports on the potential for reusing parts of wind turbine blades in new or retrofitted architectural and civil infrastructure projects. The paper introduces the geometry, materials, and laminates typically used in wind blades and provides a snapshot of the sizes of wind blades likely to be available from the inventory of active turbines. Because the materials and manufacturing of commercial wind blades are proprietary, generic blade geometries and materials are discussed. These come from the Sandia National Laboratory and National Renewable Energy Laboratory, in the United States, and from OPTIMAT in the European Union. The paper presents an example of the geometry and material properties of structural elements cut from wind blades, using the Numerical Manufacturing and Design Tool (NUMAD), published by the Sandia National Laboratory.

KEYWORDS

Recycling of FRP Composites, Adaptive Reuse, Design of FRP Structures, Composite Wind Turbine Blades

INTRODUCTION

Wind turbine blades, also known simply as blades or rotors, are propeller-shaped cantilevering structures that convert the movement of air into rotation to drive wind turbines. The typical horizontal-axis wind turbine uses three of these blades arrayed around a central hub to spin a generator. The material properties of FRP composites: high strength-to-weight and stiffness-to-weight ratios, proven environmental durability, and ability to be manufactured in complex shapes, make them an ideal material for wind turbine blades. The 100 kW wind turbines produced in the 1980's in United States used an 8-meter blade constructed of hand-laid glass-fiber composite with a polyester resin (Johnson 1985). The largest wind turbines available currently are rated for around eight MW and use 80-meter blades, constructed with glass and carbon fibers, typically with an epoxy resin (Marsh 2011). The FRP blades in new wind turbines are designed for a 20-year service life. Many existing operators are opting to 'repower' their wind farms with new turbines (often prior to the 20 years of operation) in order to take advantage of technical innovations to improve energy yield and reliability. In the next two decades, the on-shore repowering market is expected to grow in the mature wind energy markets of Europe and North America, while new off-shore farms are constructed (DOE 2015; SEAI 2015). The repowering and subsequent decommissioning of older on-shore wind farms will begin in earnest in about 2025 and continue to 2050, whereas decommissioning of off-shore wind farms will only begin in earnest after 2045 (SEAI, 2015).

Discussion of the key issues related to the end of life of wind turbines (blades as well as all other parts) can be found in Cherrington et al. (2012) and Ortegon et al. (2013). A typical 2.0 MW turbine with three 50 m blades contains approximately 20 tonnes of FRP material and an 8 MW turbine has approximately 80 tonnes of FRP



material that will need to be disposed of when its end of life is reached (1 MW equals approximately 10 tonnes of FRP composites). Calculations show that a global total of wind blades of 16.8 million tonnes to be disposed of by 2030 and 39.8 million tonnes by 2050 (Bank et al. 2018). These estimates are based on wind power growth rates from 2000–2015, which are likely to be conservative.

In recent years there has been an increased interest in the end of life and recycling of FRP composites (Yang et al. 2012; Job 2013; Bank and Yazdanbakhsh 2014; Oliveux et al. 2015). Two options to dispose of FRP composites at the end of life are used at the present – disposal in landfills and incineration (with or without energy recovery and subsequent disposal of the residual ash or reuse as a precursor for cement production in a cement kiln). Recycling options consist of reclamation of the constituent fibers or the resins by thermo–chemical methods (Oliveux et al. 2015) or recycling of small pieces of granular FRP material as filler material in concrete or other composites by cutting, shredding or grinding (Yazdanbakhsh and Bank 2016; Ribeiro et al. 2016)). Efforts to commercialize shredding and grinding of GFRPs for the filler market or for use in cement-kilns have not been commercially successful (Job et al. 2016).

This paper introduces a recently initiated project to develop load-bearing structural systems and materials from decommissioned wind blades – either whole blades or large sections cut from blades. In the first section, the paper discusses the geometry and materials used in windblades. The paper goes on to introduce a methodology to create sub-structure geometric and finite element models from windblades, as a first step in designing potential applications for use of composite materials cut from the blades. The paper uses the prototype 100 m blade designed as part of the NUMAD initiative completed at the Sandia National Laboratory and identified as SNL-100-00 (Griffith et al. 2012). The NUMAD program provides a means to generate geometric and structural analysis models from airfoil cross-sections and composite laminate data (Berg and Resor 2012). As the project progresses, it is expected that models will be generated for a wide range of blades that are nearing the end of their service life. These models will be used as the basis for the design of structures built from the repurposed wind blades.

GEOMETRY AND LOAD BEARING STRUCTURES IN WIND BLADES

Though wind blades vary widely in terms of material and manufacturing techniques, they all have roughly the same geometry. Blades are hollow, closed-sections and at most, cross-sections have one or more webs that span across the outer skins. The general configuration of wind blades is depicted in Fig. 1. Specific details of the geometry are taken from the SNL-100-00 blade. At the root of the blade, where the blade connects with the hub of the wind turbine, the cross-section of the blade is circular and the skins are made of thick, solid composites. An array of steel bolts, made integrally with the FRP composite, join the blade to the hub at the root. Moving away from the hub, the shape of the blade transitions rapidly from round to an airfoil shape. These airfoil shapes vary along the length of the blade, with the maximum chord dimension occurring at around 20% of the overall blade length and tapering continuously to the blade top (see Fig. 2).

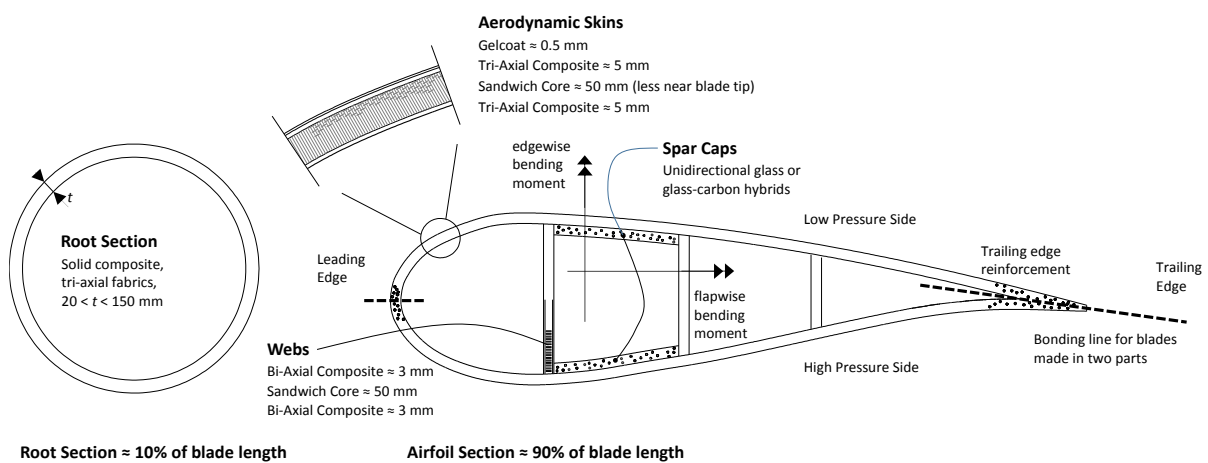


Figure 1: Cross-sections of wind blades showing internal structures and composite materials.

At the root of the blade, the aerodynamic flexural bending is carried in the outer skins of the root, and the skins are thus quite thick. For the SNL-100-00 blade, the root skins are 160 mm at the hub tapering to zero over the first 15 m of the blade (see Fig. 2). As the blade begins to transition into an airfoil shape, the flapwise (weak axis) bending moments begin to be carried by the spar caps and this load bearing element increases in thickness as you move away from the hub. The flapwise bending moments produce the largest normal stresses due to the relatively low section modulus of the airfoil about this axis. For blades longer than 30 meters, longitudinal forces and edgewise (strong axis) bending moments, induced by inertial actions on the blades, become quite significant, leading to the need for additional strengthening about the edgewise axis (Schubel and Crossley 2012).

One or more webs are generally used to carry shear in the blade and to provide stability to the relatively thin blade skins. The webs are constructed of sandwich composites (materials described below). The webs are discontinued near the root and tip of the blade. It is uncommon for blades to have three webs as shown in Fig. 1 for the SNL-100-00 blade. For small and mid-size blades, a single web is generally sufficient.

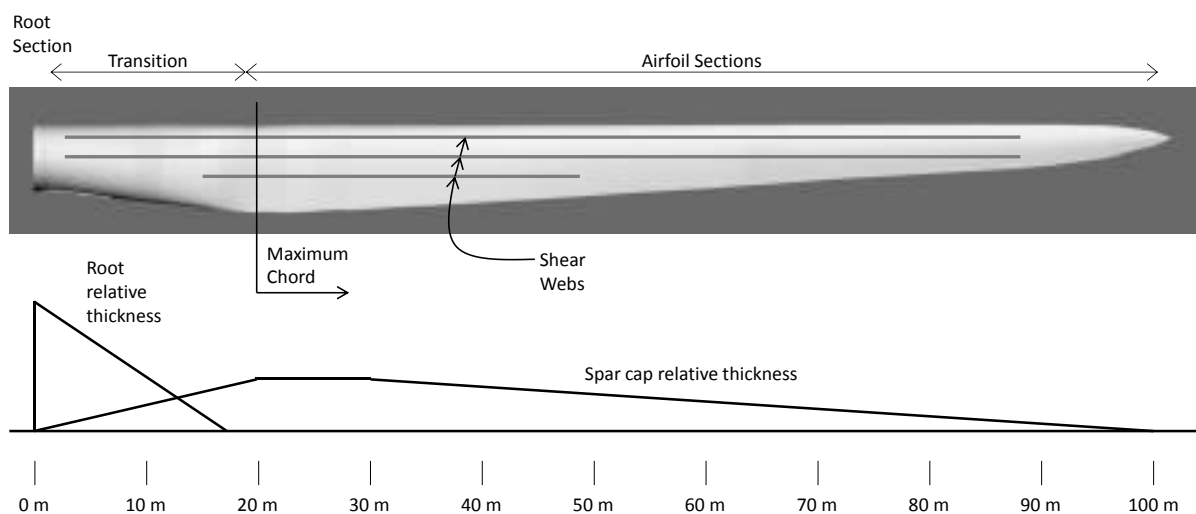


Figure 2: Planform of the SNL-100-00, 100 m wind blade and location of load bearing structures.

Two outer skins, known as the high and low pressure skins due to the differential aerodynamic pressures applied to them, form the load bearing surface of the wind blades. These skins wrap the entire surface of the blades, encapsulating the spar caps and webs. The aerodynamic skins are typically sandwich constructions, but gradually become solid composites in the transition region and into the root.

MATERIALS IN WIND BLADES

Early wind blades were made primarily of glass fiber composites, with polyester resins. These blades were produced by hand-layup in open molds. Most blades today are produced using resin infusion technologies, typically VARTM, with fiber volume fractions around 55%. A few manufacturers use prepreg techniques to manufacture blades and some use filament winding to produce the longitudinal spars. These filament wound sub-structures, which encompass both the spar caps and webs (Fig. 1) are then bonded into the aerodynamic skins.

The spar caps are made from unidirectional laminates, thickest near the root with decreased thickness (and laminate ply drops) toward the tip of the blade (Brondsted and Mikkelsen 2012). In the SNL-100-00 blade, for example, the spar cap thickness ranges from 50 mm near the maximum chord down to 2 mm at the blade tip (Griffith et al. 2012). About one-half of the weight of the given blade will be unidirectional composites, most of these in the spar cap. Consequently, the spar cap is a focus of structural optimization and material substitution, and many of the large wind blades use a glass/carbon hybrid spar cap for weight reduction and increased stiffness.

Because of the proprietary nature of commercial wind blades, the fiber architectures of blades are not generally public information. The OPTIMAT program in Europe designated two standard materials, which are representative of the materials used in blades. The OPTIMAT unidirectional material was a stitched mat, supplied by PPG, with



an areal density of 1250 g/m², constructed of PPG 2002 rovings. Material properties for the unidirectional material were assessed on a [0°]⁴ laminate with a thickness of 3.6 mm and a fiber volume fraction of 54% (Nijssen 2006).

The root section and aerodynamic skins bear a more complex set of stresses compared to the spar cap, and are typically constructed of tri-axial fabrics (see Fig. 1). The root section is solid composite and the aerodynamic skins are sandwich structures. The OPTIMAT tri-axial material consists of N layers of a $\pm 45^\circ$ stitched bi-directional fabric, with an areal weight of 810 g/m², alternating with $(N - 1)$ layers of the 1250 g/m² zero-degree fabric. Material properties of the OPTIMAT tri-axial material were assessed based on a [$\pm 45^\circ, 0^\circ$]⁴ laminate, with a thickness of 6.5 mm and a fiber volume fraction of 54% (Nijssen 2006).

The webs of wind blades do not carry significant forces, as their role in the overall structure is to provide stability to the blade cross sections and thus prevent buckling of the aerodynamic skins. The webs are also sandwich constructions, with relatively thin skins that do not vary in thickness along the length of the blade. Following the spirit of the OPTIMAT material examples provided above, a 0/90° or $\pm 45^\circ$ bi-directional fabric, with an areal weight of 810 g/m² would be appropriate for the skins of the webs. Note that the web laminate is not described in Nijssen (2006) but appears in a later work by Nijssen et al. (2007). For the 3 mm thick skins used in the SNL-100-00 blade, three or four layers of this fabric would be required to create the skins.

The material properties from the three OPTIMAT laminates are provided in Table 1 as taken from Nijssen et al. (2007). The significant figures in the table are exactly as taken from the reference and represent mean property data extracted from the OPTIDAT database.

Table 1: Representative material properties from the OPTIDAT database (after Nijssen et al. 2007)

Material	E ₁₁ MPa	E ₂₂ MPa	G ₁₂ MPa	ν_{12}	ρ Kg/m ³	F _t ⁰ MPa	F _c ⁰ MPa
Uni-axial	38,887	9,000	3,600	0.249	1,869	810	507
Tri-Axial	24,800	11,500	4,861	0.416	1,826	436	349
Bi-Axial	11,700	11,700	9,770	0.501	1,782	180	144

Sandwich Core Materials

The potential for reuse of the web and aerodynamic skins of blades will depend on the properties of the sandwich composites that make up these structures – and the core materials used can have substantial impact on the stiffness and durability of these elements. For sandwich structures that were designed for uniform out-of-plane loading from wind, the performance under concentrated transverse or edgewise loadings in a repurposing application will depend to a great degree on the performance of the core. From the blade design perspective, the primary core property of interest is the shear modulus (Brondsted and Toftegaard 2009). In regions with low shear stiffness demand, PVC foams with a density of around 60 kg/m³ and a shear modulus of around 21 MPa is commonly used. In regions with higher stiffness demands, “wind grade” end-grain balsa with an average density of 130 kg/m³ and a shear modulus of around 160 MPa is used. A number of competing core materials are becoming available for blades, including low-density foams with 3D woven fiberforms. The foam limits the volume of resin infused into the core, but the fiberforms are the primary means of shear transfer.

GEOMETRIC MODELING OF WINDBLADES FOR REUSE DESIGN AND ANALYSIS

The NUMAD model for the SNL-100-00 blade uses a series of 25 cross sections to describe the shape of the blade. Each cross section describes the outer geometry of the blade, but does not capture the material thicknesses or internal structures (e.g., spar caps, webs). At the root, the cross section is a circle and at the tip, the cross section is a point. In the transition region, the intermediate cross sections morph from circular to elliptical to vaguely airfoil shaped (Fig. 2). In the airfoil region, which makes up 80% of the blade, the cross sections reference industry standard airfoil data, which are extracted from libraries of airfoil shapes. Between the cross-sections the blade geometry is linearly interpolated.

To provide 3D CAD geometry for designers, the same approach applied in NUMAD has been implemented in the Rhinoceros program. Figure 3 shows the 25 cross sections and the 24 segments generated for the SNL-100-00 blade. At the current stage of the research, the blade geometry has been modeled manually. As the project

progresses, we anticipate building a library of blade models using design automation tools similar to those described by Charalampous et al. (2015), using Grasshopper, a design scripting tool integrated with Rhinoceros.

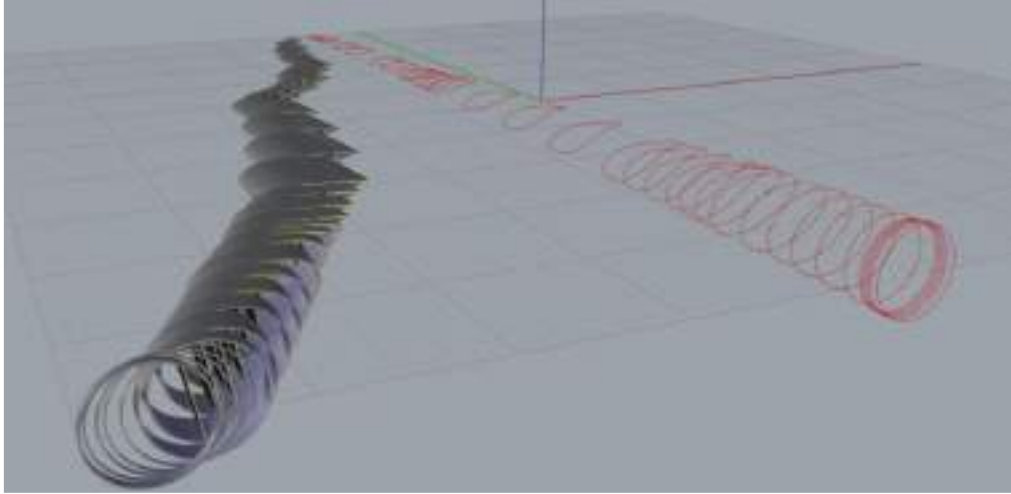


Figure 3: SNL-100-00 cross sections and segments in Rhinoceros.

CAD models often provide surface geometry, but often neglect material thickness and makeup. For comprehensive structural design, it is necessary that both overall and local geometries are captured. To this end the process used to model the windblades has mapped the laminates and sandwich data from the NUMAD database file into the Rhinoceros model (Fig. 4).

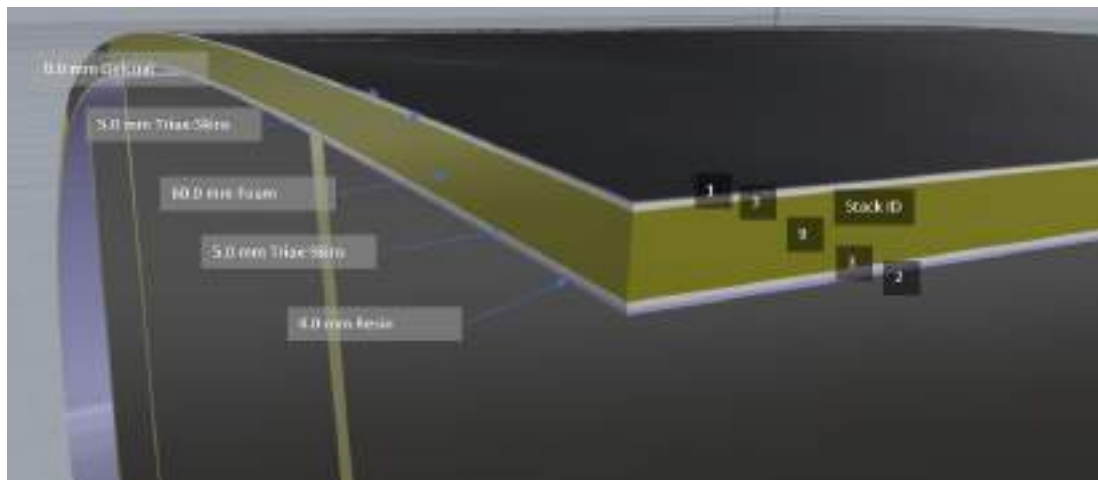


Figure 4: Section of SNL-100-00 from Rhinoceros.

EXAMPLE APPLICATION

An example of a housing application, serving as a roof for a small house typical of that found in the Yucatan Peninsula, Mexico, and composed of a section of the SNL-100-00 wind blade, is shown in Fig. 5. In this case the spar cap and trailing edge of the low pressure skin is cut from the blade, near the point of the maximum chord (see Fig. 2). One-half of the three webs remain in the section, and each web act as a deep beam, spanning approximately 5 meters between load bearing concrete masonry walls.

The example represents a proposal for a structural application. The adequacy of the proposition must be assessed through structural analysis, and design of additional reinforcements necessary for local conditions, connections, etc. For this example the following conditions have been identified for structural analysis and subsequent detailed design (see keynotes in Fig. 5):

1. In-plane flexure of the webs carrying the self-weight and superimposed roof loads.
2. Bearing of the webs at six locations on the masonry walls.
3. Continuous connection to the trailing edge to the roof along one masonry wall.
4. Stability of the web-to-skin interface and ability to resist inadvertent bending at this interface.
5. Concentrated loading on the roof causing out-of-plane bending of the sandwich panel

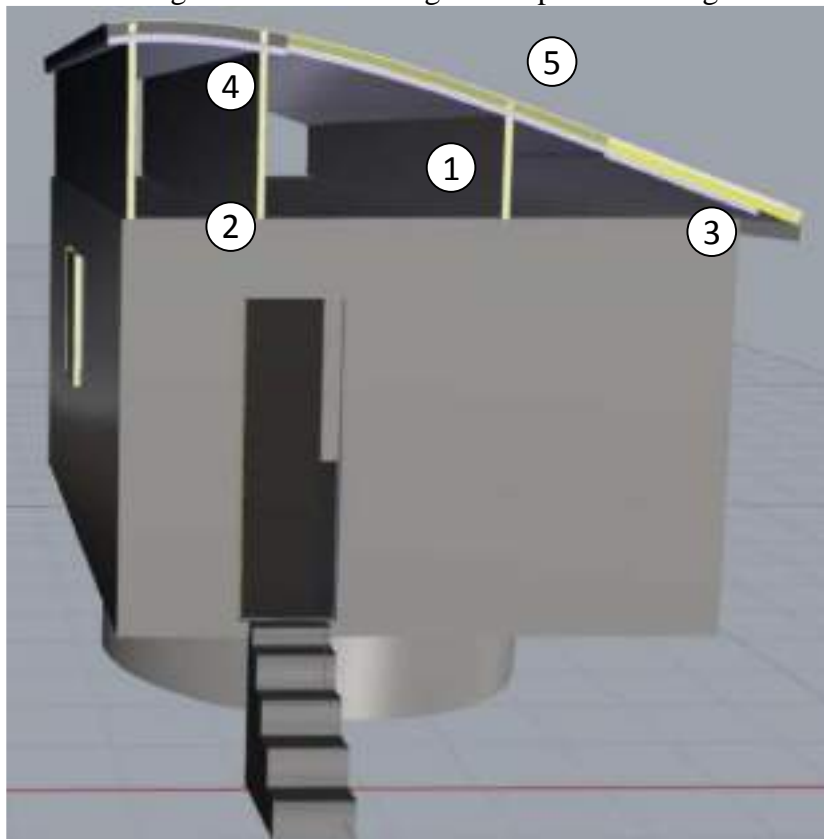


Figure 5: Housing roof concept using blade section from the SNL-100-00 blade (after Bank et al. 2018).

Future work on this project is expected to generate a large number of similar reuse proposals along with a methodology to analyze, assess, and design the retrofits.

CONCLUSIONS

The advantages of FRP composite materials are widely recognized, but at this point no economically-viable methods for recycling FRP materials have been developed. Most decommissioned FRP materials end up in landfills or incinerators. Wind blades show a tremendous potential for reuse applications because of the high quality of the composite materials used in blades. The complex geometry of blades hinders the design of potential reuse applications. Future work by the research team will develop a library of 3D blade geometries, available for architects and structural engineers, as a starting point for design explorations with decommissioned blades. Additional work on the residual properties of composite materials, taking into account the fatigue history of the composite materials, is expected to extend the work and provide design stress allowables for the reuse design process.

ACKNOWLEDGEMENTS

This material is based upon work supported by the U.S. National Science Foundation under Grants Nos. 1701413 and 1701694. Support for co-authors of this paper and research collaborators in the Republic of Ireland and in



Northern Ireland is provided by the National Science Foundation of the Republic of Ireland and InvestNI/Department for the Economy (DfE) respectively. Any opinions, findings, and conclusions or recommendations expressed in this material are those of the authors and do not necessarily reflect the views of the funding agencies.

REFERENCES

- L. C. Bank, F. R. Arias, T. R. Gentry, T. Al-Haddad, J. F. Chen, R. Morrow (2018) "Concepts for Reusing Composite Materials from Decommissioned Wind Turbine Blades in Affordable Housing", *Recycling*, 3(1), 3.
- L.C. Bank, A. Yazdanbakhsh (2014). "Reuse of glass thermoset FRP composites in the construction industry - A growing opportunity." 7th International Conference on FRP Composites in Civil Engineering, CICE 2014, August 20, 22, 2014, Vancouver, BC, Canada.
- J. C. Berg, J. C. Resor (2013). "Numerical Manufacturing and Design Tool (NuMAD v2.0) for Wind Turbine Blades: User's Guide", Report No. SAND2012-7028, Sandia National Laboratory.
- P. Brondsted, L. P. Mikkelsen (2012). "Challenges Testing Composite Materials for Wind Turbine Blades" Indo-Danish Workshop on Future Composites Technologies for Wind Turbine Blades, 8-9 October 2012, Delhi, India.
- P. Brondsted, H. Toftegaard (2009). "Methods for Qualification of the Mechanical Properties of Sandwich Core Materials for Wind Turbine Blades", ICCM-17 17th International Conference on Composite Materials, 27-31 July 2009, Edinburgh, United Kingdom.
- K. G. Charaampous, G. A. Strofylas, G. I. Mazanakis, I. K. Nikolos (2015). "Wind Turbine Blades Parametric Design using Grasshopper" 8th GRACM International Congress on Computational Mechanics.
- R. Cherrington, V. Goodship, J. Meredith, B. M. Wood, S. R. Coles, A. Vuillaume, A. Feito-Boirac, F. Spee, K. Kirwan (2012). "Producer responsibility: Defining the incentive for recycling composite wind turbine blades in Europe" *Energy Policy* 47(Supplement C): 13-21.
- DOE. (2015). "Wind Vision: A New Era for Wind Power in the United States." United States Department of Energy.
- D. T. Griffith, T. D. Ashwill, B. R. Resor (2012). "Large Offshore Rotor Development: Design and Analysis of the Sandia 100-meter Wind Turbine Blade" 53rd AIAA/ASME/ASCE/AHS/ASC Structures, Structural Dynamics and Materials Conference, 23-26 April 2012, Honolulu, Hawaii, USA.
- S. Job, (2013). "Recycling glass fibre reinforced composites – history and progress." *Reinforced Plastics* 57(5): 19-23.
- G. L. Johnson (1985). *Wind Energy Systems*, Prentice Hall.
- G. Marsh (2011). "All set for era of big blades: Part one: the new-generation of wind turbines require very large rotors" *Renewable Energy Focus* 12(5): 66-68.
- R. P. L. Nijssen (2006). "Fatigue Life Prediction and Strength Degradation of Wind Turbine Rotor Blade Composites", Report No. SAND2006-7810P, Sandia National Laboratory.
- R. Nijssen, G. D. deWinkel, J. M. Peeringa (2007). "WMC5MW laminate lay-out of reference blade for WP 3", Knowledge Centre Wind turbine Materials and Constructions.
- G. Oliveux, L. O. Dandy, G. A. Leeke (2015). "Current status of recycling of fibre reinforced polymers: Review of technologies, reuse and resulting properties" *Progress in Materials Science* 72 (Supplement C): 61-99.
- K. Ortegon, L. Nies, J. Sutherland (2013). "Preparing for end of service life of wind turbines", *Journal of Cleaner Production*, 39:191-199.
- M. Ribeiro, A. Fiuza, A. Ferreira, M. Dinis, A. Castro, J. Meixedo, M. Alvim (2016). "Recycling Approach towards Sustainability Advance of Composite Materials' Industry", *Recycling*. 1:178-193.
- P. J. Schubel, R. J. Crossley (2012). "Wind Turbine Blade Design", *Energies*, 5:3425-3449.
- SEAI (2015). "Wind Energy Roadmap." Sustainable Energy Authority of Ireland.
- A. Yazdanbakhsh, L. C. Bank, C. Chen (2016). "Use of recycled FRP reinforcing bar in concrete as coarse aggregate and its impact on the mechanical properties of concrete." *Construction and Building Materials*, 121: 278-284.



DESCRIPTION & MATERIAL FACTOR OF FRP IN THE STANDARD SPECIFICATION FOR HYBRID STRUCTURES 2014 BY JSCE

I. Nishizaki¹, H. Nakamura², Y. Kitane³, T. Matsumoto⁴, K. Hashimoto⁵ and A. Kobayashi⁶

¹ *Public Works Research Institute, iMaRRC, Tsukuba, Japan, Email: nishizaki@pwri.go.jp*

² *Tokyo Metropolitan University, Department of Civil & Environmental Engineering, Tokyo, Japan;*

³ *Nagoya University, Department of Civil & Environmental Engineering, Nagoya, Japan;*

⁴ *Hokkaido University, Faculty of Engineering, Sapporo, Japan;*

⁵ *Kobe University, Department of Civil & Environmental Engineering, Kobe, Japan;*

⁶ *Nippon Steel & Sumikin Materials Co., Ltd, Tokyo, Japan*

ABSTRACT

Japan Society of Civil Engineers (JSCE) has published the standard specifications for hybrid structures in 2014 as its second revised edition. In the revised edition in 2014, FRP members and hybrid structures with FRP and steel/concrete were also introduced as main structural types. In order to describe the standard methods of design, construction and maintenance of structural FRP in the standard specifications, standard methods for the design, construction and maintenance of FRP structures and FRP hybrid structures, and reliability and performance evaluation methods of FRP members were studied by JSCE. The standard material factor was considered based on the study on changes and dispersion of the mechanical properties of FRP materials. This paper introduces the main description of FRP in the standard specifications of hybrid structures 2014, including the results of the study on the changes of the performance of FRP members.

KEYWORDS

hybrid structures, standard specification, FRP, material factor, design, construction, maintenance

INTRODUCTION

The first version of the standard specifications for hybrid structures was published in 2009 by the Committee of Hybrid Structures of Japan Society of Civil Engineers (JSCE) [Tanaka (2010)]. The standard specifications treated hybrid structures made of only steel and concrete. However hybrid structures have wide possibilities to adopt new structural materials other than steel and concrete, and fiber reinforced polymers (FRP) were considered as one of the main candidate for the new structural materials. Under these circumstances and understanding, JSCE proceeded with the study on standard methods for the design, construction and maintenance of FRP and FRP hybrid structures, and in the revised edition in 2014, FRP members and hybrid structures with FRP and steel/concrete were also treated as main structural types. In this paper, the description of FRP part in the standard specifications is introduced including the main results of the study carried out by JSCE.

OUTLINES OF STANDARD SPECIFICATIONS FOR HYBRID STRUCTURES 2014 (JSCE)

Previous research activities on the structural use of FRP by JSCE

After the first all-FRP bridge in Japan was constructed in 2000, more than ten FRP bridges have been constructed in Japan. Moreover, other FRP applications such as inspection passages and FRP hydraulic gates are also spreading in Japan. With the increasing of FRP applications, standard methods for design, construction, and maintenance are required.

On the other hand, the Committee of Hybrid Structures of JSCE has launched several task committees for the study and investigation of FRP and FRP hybrid structures. These task committees include H204 (for hybrid bridges), H205 (for strengthening of steel and hybrid structures with FRP), H102 (for the guidelines for the design and construction of FRP footbridges), H180 (for the guidelines for the design and construction of FRP hydraulic gates), H208 (for FRP hybrid structures), H209 (for strengthening of concrete structure with FRP), and H211 (for the connection methods for FRP and steel) committees, and studied the wide range of matters related to the structural applications of FRP. As the results of these task committees, two guidelines: the guidelines for the design and construction of FRP footbridges, and the guidelines for the design and construction of FRP hydraulic gates have been published [Nakamura et al. (2012)]. Several research reports have also been published from JSCE. Based on these activities as the preparations, the Committee for Hybrid Structures and the task committee for the standard specifications of hybrid structures (H101 committee, chair: Prof. A. Nakajima) decided to describe FRP as a



structural material and to add FRP and FRP hybrid structures in the standard specifications for hybrid structures at the opportunity of the revision in 2014.

Overall outlines of the standard specifications for hybrid structures 2014

Figure 1 shows the structures of the standard specifications for hybrid structures. The standard specifications adopted performance-based verification method, and consists of four parts: Basic principle, Design, Construction and Maintenance, which correspond to the different steps to form hybrid structures. The each part of Design, Construction, or Maintenance is divided into Standards part that shows the principle of design, construction, and maintenance of hybrid structures, and Specifications part that shows the practical methods that can be suggested by JSCE from the various completed structures.

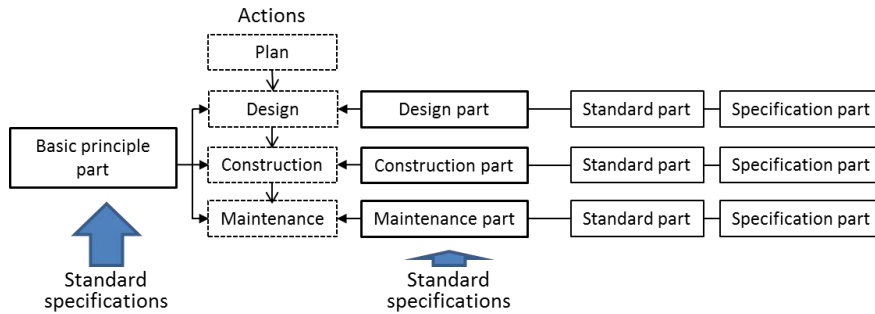
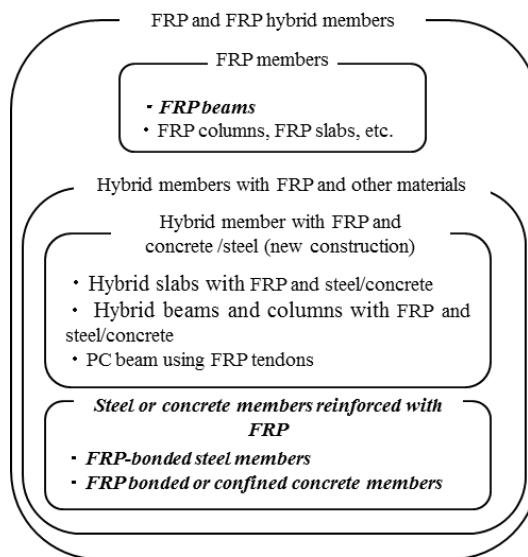


Figure 1: Action of construction and the Standard specifications of hybrid structures

DESCRIPTIONS OF FRP IN THE STANDARD SPECIFICATIONS FOR HYBRID STRUCTURES 2014

Scope and coverage of FRP structures

Figure 2 shows the classification of FRP and FRP hybrid structures. FRP members mean basically all-FRP members including beams, columns and slabs. In these FRP members, FRP beams were selected as the coverage in the standard specifications 2014 and FRP columns and slabs were not included. As regards with the FRP hybrid members, only steel or concrete members strengthened with FRP were covered in the standard specifications, but FRP hybrid members for the new construction were not described. These decisions were made due to the limitations of time and staff with intensions to incorporate them in the next revision.



Note: Coverage of FRP and FRP hybrid member described the 2014 version are shown by *italic characters*



Figure 2: Classification of FRP and FRP hybrid members and the coverage in the specifications 2014

Design Part

Flow of the verification and safety factors

Figure 3 shows the flow of verification in the design of hybrid structures including FRP structures. There are no large differences in the design flow from the first version of standard specification 2009. Five partial safety factors are used in the design: material factor γ_m , member factor γ_b , action factor γ_f , structural analysis factor γ_a , structure factor γ_i . Equation (1) is used in the verification.

$$\gamma_i \frac{S_d}{R_d} \leq 1.0 \tag{1}$$

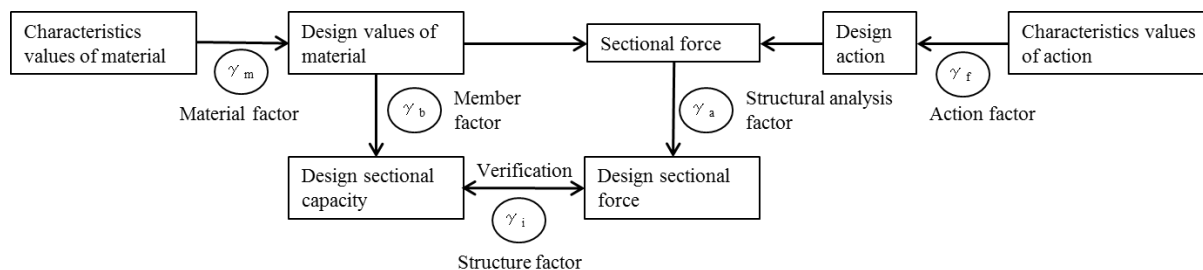


Figure 3: Design flow and partial safety factors

Partial safety factors for structural FRP

Table 1 shows the uncertainties which are considered in the partial safety factors. These uncertainties are common for steel, concrete and FRP. Table 2 shows the standard values of safety factors. Different values are used for material factors because of the difference in conditions depending on the manufacturing method of the materials. FRP should also have a material factor that reflects its conditions properly. The member factor for FRP member should be also considered to have an appropriate value of FRP condition.

Table 1: Considered uncertainties in the safety factors

Considered contents		Corresponding values or factors
Sectional capacity	1. Dispersion of material strength (1) The estimative part from the test results (2) The unestimative part from the test results (lack of data or bias, grade of quality control, difference of structure and specimen, changes over time, etc.)	} Characteristic values } Materials factor
	2. Degree of influence to the limit state 3. Uncertainty of calculation of sectional capacity, Dispersion of size, Importance of the member, Mode of the fracture	
	Sectional force	1. Dispersion of action (1) The estimative part from the statistics data (2) The unestimative part from the statistics data (lack of statistics data of action or bias, change during the service term, uncertainty of the calculation method of action, etc.)
2. Degree of influence to the limit state 3. Uncertainty of structural analysis in the calculation of sectional force		} Structure analysis factor
Importance of the structure, Social and economic influence in case of the limit states		} Structure factor

Design values of structural FRP

Characteristic values of FRP material strength is basically decided by the test in the standard specifications of 2014. Characteristic values are determined as a strength value where the probability of occurrence of lower strength is less than 5%. The materials factor for FRP is set to 1.3 as a standard value in the standard specifications. The



standard value of material factors was confirmed by the H208 task committee (chair: Prof. K. Sugiura) through the experiment on the change and dispersion of the mechanical properties of FRP members. In order to obtain the proper FRP, test methods for the resistance against water, alkali and weathering conditions were also described in the standard specifications. In order to specify the requirements for the structural FRP, “the draft of quality standards for structural FRP in construction” was also included in the appendix of the standard specifications of hybrid structures 2014. In the quality standards for structural FRP in construction, types of FRP, shapes, and tolerances, standard mechanical test methods including the specimens extraction methods, and test methods for the environmental resistance are described.

Table 2: The standard values of safety factors

Safety factors	Material factor γ_m				Member factor γ_b	Structural analysis factor γ_a	Action factor γ_f	Structure factor γ_i
	concrete	rebar	structural steel	FRP				
Requirements (limit state)								
Safety (Sectional fracture) ^{*1}	1.3	1.0	1.05	1.3	1.1~1.3	1.0	1.0~1.2	1.0~1.2
Safety (Sectional fracture) ^{*2}	1.0	1.0	1.0	1.0	—	1.0~1.2	1.0~1.2	1.0~1.2
Recoverability ^{*2}	1.3	1.0	1.05	1.3	1.0, 1.1~1.3	—	—	
Safety (Fatigue) ^{*1}	1.3	1.05	set properly	set properly	1.0~1.1	1.0	1.0	1.0~1.1
Serviceability ^{*1} Recoverability ^{*1}	1.0	1.0	1.05	1.0	1.0	1.0	1.0	1.0

Note: *1: In case of linear analysis, *2: In case of nonlinear analysis

Consideration on the material factor for structural FRP

In order to confirm the standard values of material factors, experimental studies on the changes and dispersions of mechanical properties of structural FRP were carried out. Table 3 shows the results of full scale tensile test of pultrude FRP channel member. Figure 4 shows the cross section of the tested specimens. The results of full scale test was compared with the results of tensile tests using cut out coupons. Table 3 also shows the maximum tensile force estimated by results of the coupon tests. The result of full scale test was 1/1.16 of the coupon test in this case. The H208 committee accumulated these data in order to confirm the material factor of structural FRP. The committee also found the standard value should be reexamined in case of severe conditions where FRPs are used in water, or in concrete, etc.

Table 3: The results of full scaled specimens and the comparison with the coupon test

Full scaled specimens no.	Maximum tensile force P_{max} (kN)	Maximum tensile strength σ_{max} (MPa)
1	334.2	412.6
2	289.5	357.4
3	276.0	340.7
4	306.0	377.8
Average	301.4	372.1
Standard deviation	25.1	30.9
Coefficient of variation	0.08	0.08
Based on the coupon test result	348.7	430.5
Coupon test / Full scale test	1.16	--

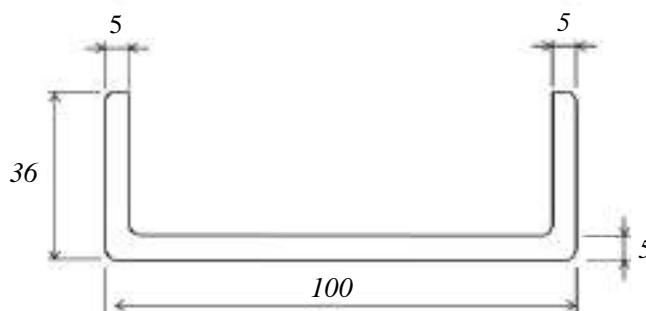


Figure 4: Cross section of the tested specimens of pultruded FRP

Construction Part

Standard Part

Standard part of construction part describes the principles of matters that should be considered and carried out in the construction of hybrid structures including FRP and FRP hybrid structures.

Specification Part

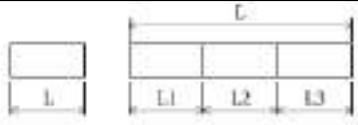
Specification part of construction part is dividedly written into the types of hybrid structures including FRP and FRP hybrid structures. In this part, specifications of construction in each step are described. Table 4 and 5 show the example of the tolerance of FRP members and the assembly accuracy of FRP beams. The practical information on the surface coating of FRP is also prepared in this part.

Table 4: Tolerance of the outer size of FRP products

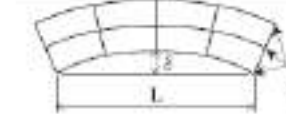
Outer size (mm)	General shape		Pipes	
	Tolerance			
	Difference	Maximum value	Difference	Maximum value
less than 10	±6%	±0.4	±6%	±0.4
10 to 50	±4%	±1.5	±4%	±1.5
50 to 200	±3%	±2.5	±3%	±2.5
more than 200	±1.5%	±3.0	±1.5%	±3.0

Note: Maximum values for hand lay-up FRP is ±0.8mm.

Table 5: The assembly accuracy of FRP beam

Measured values	Tolerance (mm)	Measurement points	Measurement part
Total length L(m) Span length Ln(m)	±(20 + L/5) ±(20 + Ln/5)	Measure all the girder	
			Single span Multi span



Linearity δ (mm)	$\pm(10 + 2L/5)$	L: Span length of main girder: (mm)	 Main girder
Warp δ (mm)	$\pm(25 + L/2)$	Measure all the main girder L: Span length of main girder (mm)	

Maintenance Part

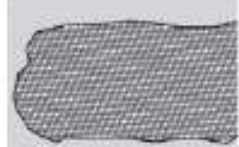
Standard Part

Standard part is written without limiting the type of structures, and describes the principles and standards of maintenance of hybrid structures including its flow, inspection, evaluation, countermeasure and record.

Specification Part

Specification part of the maintenance part is also dividedly written into the types of hybrid structures including FRP and FRP hybrid structures. In this part, evaluation methods of structural performance based on the appearance changes are proposed. Table 6 shows an example of relation between the level of structural performance and the grade of appearance changes for an FRP member. Three appearance grades were set based on the degrees of deterioration found from the appearance of FRP. The evaluation is basically intended not to evaluate the deterioration of the materials but to evaluate the structural performance.

Table 7: Example of relation between the level of structural performance and the grade of appearance change of FRP (FRP beam, general part).

Requirement	Limit state	Grade of appearance change		
		Appearance grade I (slight damage)	Appearance grade II (middle damage)	Appearance grade III (severe damage)
		 <p>Example of slight exposure of the fiber</p> <p>Deterioration remains in the surface coating layer. Deterioration is not reached to the structural fibers.</p> <ul style="list-style-type: none"> - Yellowing, - Flaking of top coat - Slight exposure of the fiber 	 <p>Example of deterioration of coating that reaches to expose the structural fibers.</p> <p>Deterioration begins to reach the structural fibers.</p> <ul style="list-style-type: none"> - Clear exposure of fibers - Deterioration of surface coating that reaches to expose the structural fibers. 	 <p>Example of remarkable exposure of fibers</p> <p>Fracture of structural fibers. Deterioration of adhering between fibers and resin. Influence occurred to the strength.</p> <ul style="list-style-type: none"> - Remarkable exposure of fibers. - Crack that reach the fibers - Damage with the fracture of structural fibers.
Safety	Sectional fracture	1	1	2
	Fatigue fracture	1	1	2
	Limit of structural stability	-	-	-
	Limit of driving performance	1	1	2
	Limit of influence to outsiders	1	2	3
Serviceability	Limit of driving /working performance	1	1	2



FIBER MODEL ANALYSIS ON THE FLEXURAL BEHAVIORS OF CFRP BOX BEAMS

T. Matsumoto¹ and M. Nasu²

¹ Hokkaido University, Faculty of Engineering, Sapporo, Japan, Email: takashim@eng.hokudai.ac.jp

² Hokkaido University, Graduate School of Engineering, Sapporo, Japan

ABSTRACT

Carbon Fiber Reinforced Polymer, CFRP, is a promising structural material for the application to civil structures. However, as CFRP beams show nonlinear and brittle behaviors at the ultimate state, it is necessary to develop a method to obtain the deflection of CFRP beams by considering both the bending and shear deflection component. This study aims to develop a fiber model analysis method to reproduce the behaviors of CFRP box beams that have been tested in earlier experiments, and to verify the effectiveness of the method. CFRP box beams are examined with two laminate structures, quasi-isotropic and cross-ply, and under four-point bending with three different shear span cases. The bending deflection component is obtained by moment-area method, and the shear deflection component is calculated based on Timoshenko's beam theory. The shear strain of quasi-isotropic CFRP is regarded as linear, whereas that of cross-ply CFRP as nonlinear, following the experimental observations. Analytical results reproduce sufficiently the load-deflection relationships, showing the validity and the effectiveness of the current analysis method developed.

KEYWORDS

CFRP, laminate structure, fiber model, nonlinear flexural behavior.

INTRODUCTION

Carbon Fiber Reinforced Polymer, CFRP, is a light and strong composite material with non-corrosive nature. Because of these characteristics, CFRP is expected to be a primary member such as a bridge girder from the view point of increased durability and reduced maintenance cost. In order to design a CFRP member, it is necessary to consider the failure load and deflection of the laminated composite member.

Previous studies reported that, based on the laminas' material properties, the method of estimating the failure load was developed, and that the deflection was estimated by regarding a laminated composite as an elastic material (Sakuraba et al. 2011; Nasu and Matsumoto 2016).

However, actual CFRP is not a fully elastic material. Previous studies reported that, due to the failure of individual laminas, CFRP shows nonlinearity in the direction of normal strain. Moreover, shear stiffness is low due to epoxy resin matrix, and CFRP shows a nonlinear behavior quite early in the direction of shear strain. Because of these reasons, it is necessary to use the method of obtaining the deflection of CFRP beams by considering both the bending and shear deflection component.

This study aims to verify the effectiveness of a fiber model by the analysis of previous experimental results. Fiber model analysis is a method to calculate section moment through nonlinear normal stress-strain relation in partitioned cross section and then to obtain beam deflection. This is a simple method that gives consideration to a nonlinear behavior in normal strain direction on the effect of bending component, and that this method is further expanded to include a nonlinear behavior in shear strain direction.

EXPERIMENTAL METHOD

Specimens for Bending Tests

All specimens have a square box cross section with 100 mm height, 100 mm width, 5 mm thickness, and have a length of 1000 mm. Dimensions of the specimens and loading conditions are shown in Figure 1. Specimens are fabricated with Vacuum assisted Resin Transfer Molding method. The specimens consist of laminates which are thin carbon fiber sheets impregnated with thermoset resin. Two laminate structures were employed to examine the effect of different laminate structures. Three specimens were prepared for each laminate structure.

Material properties of carbon fiber and epoxy resin are shown in Table 1. The two laminate structures are named QI (Quasi-Isotropic) and CP (Cross-Ply), respectively, and shown in Table 2. For example, $[0/90]_5/[90/0]_5$, each number means the fiber orientation angle of the corresponding layer. The subscript, five, indicates that five $[0/90]$ sets are stacked. The two laminate structures are symmetric about the mid-plane. The ratio of longitudinal and transverse to diagonal carbon fibers is 1:1:2 in QI, and it is 1:1:0 in CP.

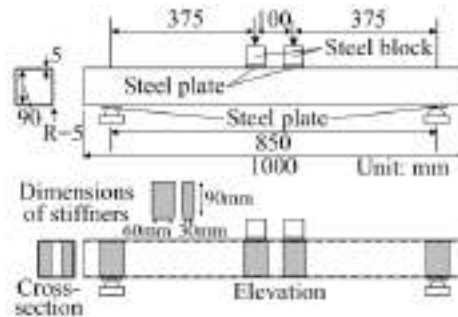


Figure 1: Specimen dimensions and loading conditions

Table 1: Properties of carbon fiber and epoxy resin

	Property	Value	Remarks
Carbon fiber	Elastic modulus E_f (GPa)	240	
	Poisson's ratio ν_f	0.20	Assumed value [8]
	Shear modulus G_f (GPa)	100	$G_f = E_f / 2(1 + \nu_f)$
Epoxy resin	Elastic modulus E_m (GPa)	4.20	Assumed value [6]
	Poisson's ratio ν_m	0.38	Assumed value
	Shear modulus G_m (GPa)	1.52	$G_m = E_m / 2(1 + \nu_m)$

Table 2: Laminate structures of specimens for bending tests

Name	Laminate structure
QI	$[0/45/-45/90]_5/[90/-45/45/0]_5$
CP	$[0/90]_5/[90/0]_5$

Loading Condition and Configuration of Instruments

The specimens were tested under four point bending and under load control. The total span, shear span, and flexural span were 850 mm, 375 mm, and 100 mm, respectively, in QI. The span was 850 mm, shear spans were 375 mm, 285 mm, and 185 mm, and flexural spans were 100 mm, 280 mm, 480 mm, respectively, in CP. They are named CP375, CP285, CP185, respectively. Loading condition and the location of stiffeners are shown in Figure 1.

Stiffeners made of wood are placed inside the box beams at loading points and supports in order to prevent a premature failure at the corner of flange and web. A preliminary test showed that the premature damage will not happen up to the flexural strengths of CP and QI if the stiffeners are installed.

Displacements and strains were measured at nine points and 17 points, respectively, as shown in Figure 2. White arrows show displacement gauges (No.1 to No.9), and black arrows show loading points. Rosette gauges (No.1s to No.4s, No.5s, No.6s, No.9s, No.10s) and uniaxial gauges (No.7s, No.8s, No.11s to No.17s) are also illustrated in the figure. Load was applied under load control, and it was posed at every 5 kN in order to measure the displacements and strains.

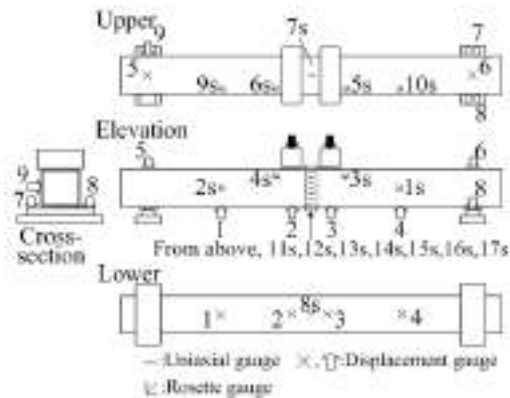


Figure 2: Locations of instruments

Test Results

The three beams of QI showed the load capacity of 97.0 kN, 98.2 kN, 92.9 kN, respectively, and the average was 96.0 kN. The beams of CP375 showed the load capacity of 74.4 kN, 78.5 kN, 82.4 kN, respectively, and the average was 78.4 kN. The beams of CP285 showed the load capacity of 103.1 kN, 98.2 kN, 100.1 kN, respectively, and the average was 100.47 kN. Finally, the beams of CP185 showed the load capacity of 126.2 kN, 127.4 kN, respectively, and the average was 126.8 kN. Only for CP185, two specimens were tested. Brittle failure occurred near a loading point, namely upper flange and web were fractured on the shear span side of the loading plate.

FIBER MODEL ANALYSIS

Deflection due to Bending at the Loading Point

To obtain the deflection by bending moment, moment-area method is applied. The deflection of a beam is obtained by dividing the beam into 10 horizontal elements and 20 vertical elements.

In the analysis, the compressive strain is given to the section, and strain distribution is obtained by assuming a linear distribution. The neutral axis is defined by the equilibrium of sectional force, then the bending moment, M , is calculated. The compressive strain is gradually increased, and $M-\Phi$ equation is obtained by repeating calculations. Φ given by

$$\frac{1}{\rho} = \Phi = \frac{d\theta}{dx} = \frac{\varepsilon - \varepsilon'}{h} \quad (1)$$

where ρ is radius of curvature, h is height of section. $\Phi-x$ diagram is obtained by using $M-\Phi$ relative equation and $M-x$ relative equation. $\Phi-x$ diagram is differentiated by x , and $\theta-x$ diagram is then obtained. The deflection of each horizontal element is calculated by using the moment-area method.

Deflection due to Shear at the Loading Point

Deflection due to shear is calculated based on Timoshenko's beam theory, and is given by

$$y_s = \frac{Pa}{2GA_w} \quad (2)$$

where y_s is shear deflection at the loading point, P is load, and G is shear modulus, A_w is cross sectional area of web, and a is shear span.

In the case of QI, the decrease of shear stiffness hardly occurs with the increase of load, whereas in the case of CP, shear stiffness gradually decreases with the increase of load. This is due to diagonal laminas of QI which enhance shear modulus. Therefore, in CP, the relationship between shear stress and in-plane shear strain at the mid-span of web is approximated by a cubic equation, and shear deflection considering a nonlinear behavior is calculated. Shear stress, τ , at the mid-height (rosette gauges No.1s and No.2s) is given by



$$\tau = \frac{P}{2I} \left(\frac{BH}{4} + \frac{H^2}{8} \right) \quad (3)$$

where I is moment of inertia, B is width of the flange, and H is height of the beam. The relationship between load and shear strain in the experiment is approximated by a cubic equation as

$$\begin{aligned} \gamma(P) &= 0.0536P^3 - 3.2271P^2 + 181.1P \text{ (CP375)} \\ \gamma(P) &= 0.0265P^3 - 1.4055P^2 + 157.28P \text{ (CP285)} \\ \gamma(P) &= 0.0277P^3 - 2.3758P^2 + 199.27P \text{ (CP185)} \end{aligned} \quad (4)$$

where $\gamma(P)$ is in-plane shear strain and P is load (kN). By using equation (2) and (3), the relationship between shear stress and in-plane shear strain is approximated by a polynomial equation as

$$\begin{aligned} \tau(\gamma) &= 3.81 \times 10^8 \gamma^5 - 8.50 \times 10^7 \gamma^4 + 6.99 \times 10^6 \gamma^3 - 2.73 \times 10^5 \gamma^2 + 5.84 \times 10^3 \gamma \text{ (CP375)} \\ \tau(\gamma) &= -6.55 \times 10^8 \gamma^5 + 3.67 \times 10^7 \gamma^4 + 1.67 \times 10^6 \gamma^3 - 1.70 \times 10^5 \gamma^2 + 5.36 \times 10^3 \gamma \text{ (CP285)} \\ \tau(\gamma) &= -2.74 \times 10^9 \gamma^5 + 2.97 \times 10^8 \gamma^4 - 9.74 \times 10^6 \gamma^3 + 3.07 \times 10^4 \gamma^2 + 4.39 \times 10^3 \gamma \text{ (CP185)} \end{aligned} \quad (5)$$

Relationships between shear stress and shear strain for the average of No.1s and No.2s (Figure 2) in CP375-1, 285-1, and 185-1 are shown in Figure 3. A relationship obtained by a material element experiment is also shown. This shows a little higher stiffness, but quickly plateaus out, compared to the relationships obtained from the beam experiments. By using these relations, shear modulus, G , can be obtained by calculating the tangential value at each point.

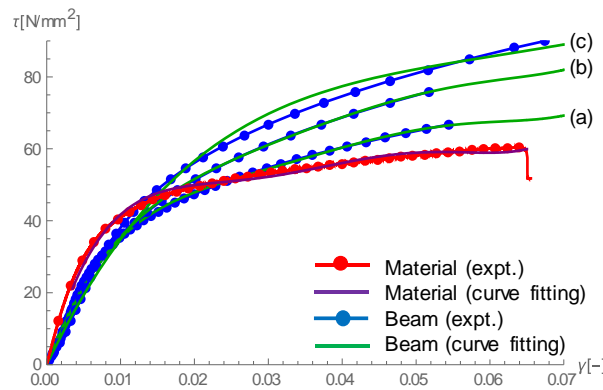


Figure 3: Shear stress-shear strain relationship from beam experiment (a) CP375, (b) CP285, (c) CP185 and material experiment

RESULTS OF ANALYSIS

The bending deflection component that is obtained by moment-area method and the shear deflection component that is obtained by Timoshenko beam theory are shown together with the experimental results in Figure 4. Also, the failure loads of lamina at 90, 45 and 0 degrees are shown. Buckling is not considered in the current analysis.

Figure 4(a) shows a comparison between analytical and experimental results for QI-1 to 3. The failure loads of three specimens, QI-1 to 3, are 97.0, 98.2, 92.9 kN, respectively, and the average of these values is 96.0 kN. In this case, the deflections at loading point of QI-1 to 3 are 10.79, 11.08, 10.97 mm, respectively, and the average of these values is 10.94 mm. Analytical result is 10.40 mm at the average of three failure loads, 96.0 kN. The comparison between analysis and experiment shows that the shape of graph is similar, especially up to the load of 40 kN.

Figure 4(b) shows a comparison between analytical and experimental results for CP375-1 to 3. The failure loads of three specimens, CP375-1 to 3, are 74.4, 78.5, 82.4 kN, respectively, and the average of these values is 78.4 kN. In this case, the deflection at loading point of CP375-1 to 3 are 10.67, 11.76, 12.65 mm, respectively, and the



average of these values is 11.69 mm. Analytical result is 10.63 mm at the average of three failure loads, 78.4 kN. Analysis based on the shear modulus obtained from beams shows a good agreement.

Figure 4(c) shows a comparison between analytical and experimental results for CP285-1 to 3. The failure loads of three specimens, CP285-1 to 3, are 103.1, 98.2, 100.1 kN, respectively, and the average of these values is 100.47 kN. In this case, the deflection at loading point of CP285-1 to 3 are 11.21, 10.89, 10.90 mm, respectively, and the average of these values is 11.00 mm. Up to 50 kN, two analytical results show a good agreement, however they deviate from the experimental results for the load above 50 kN.

Figure 4(d) shows a comparison between analytical and experimental results for CP185-1 and 2. The failure loads of two specimens, CP185-1 and 2, are 126.2, 127.4 kN, respectively, and the average of these values is 126.8 kN. In this case, the deflection at loading point of CP185-1 and 2 are 10.35, 9.65 mm, respectively, and the average of these values is 10.02 mm. Analytical result is 11.71 mm at the average of two failure loads, 126.8 kN. The analytical result based on the shear modulus obtained from beams shows a similar trend with smaller stiffness. On the other hand, the analytical result from materials shows a good agreement up to 60 kN, and later it deviates from the experimental result.

In general, the shape of graph is similar in the comparisons between analysis and experiment. Analytical results based on the shear modulus from beams reproduce correctly the load-deflection relationships, showing the validity and the effectiveness of the current fiber model analysis developed. On the other hand, analytical results based on the shear modulus from material element experiments show an agreement only in the early load level and deviate in the later load level. This is given by the shape of the shear stress - shear strain relation in Figure 3. It is possible that, due to the rectangle shape of specimens, fibers on some layers are not continuous, yielding the shape of this shear stress - shear strain relation.

The failure loads estimated by first ply failure theory are close to the experimental loads for CP375 and CP285, while the failure load is above and below the experimental load for QI and CP185, respectively. The discrepancies might be due to the assumption that all plies with the same angle fail at the same time as soon as the failure criterion is met. In reality, ply failures are progressive and stress redistributions take place.

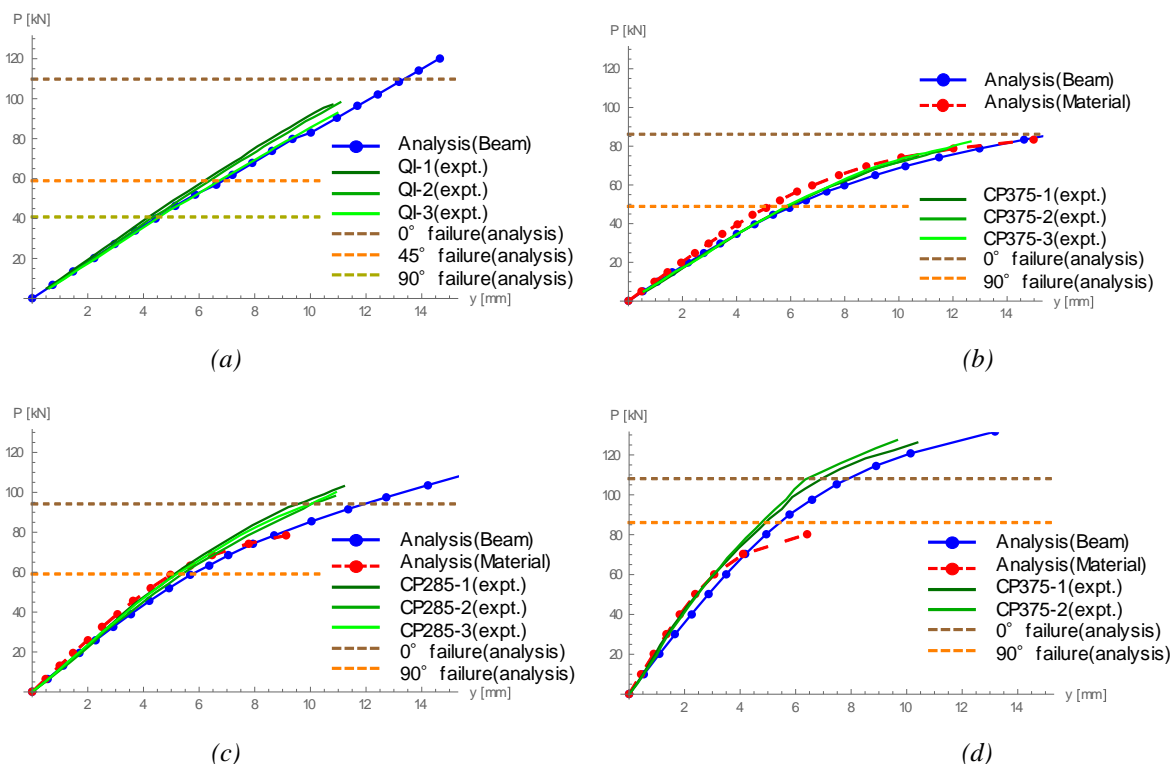


Figure 4: Load-deflection relationship (a) QI; (b) CP375; (c) CP285; (d) CP185



CONCLUSIONS

This paper presented a fiber model analysis on nonlinear bending behaviors of CFRP box beams with two laminate structures, quasi-isotropic and cross-ply, and under three shear spans. These CFRP box beams were tested under four-point bending.

The bending deflection component is obtained by moment-area method, and the shear deflection component is calculated based on Timoshenko's beam theory. The shear of QI is regarded as linear, whereas that of CP regarded as nonlinear, following the experimental observations. Analytical results reproduce correctly the load-deflection relationships, showing the validity and the effectiveness of the current fiber model analysis method developed.

ACKNOWLEDGEMENTS

This work was supported by JSPS Grant-in-Aid for Scientific Research (B) Grant Number 15H04028.

REFERENCES

- H. Sakuraba, T. Matsumoto, and T. Hayashikawa (2011). "A study on the flexural behavior of CFRP box beams with different laminate structures", *Keynote Lectures and Extended Abstracts of the Twelfth East Asia-Pacific Conferences on Structural Engineering and Construction (EASEC-12)*, EASEC12-38, 539-540.
- M. Nasu and T. Matsumoto (2016). "Analysis on nonlinear bending behaviors of CFRP beams by section partition method", *The 3rd International Conference on Sustainable Civil Engineering Structures and Construction Materials*, SCS018.

PREDICTION OF THE WEB CRUSHING CAPACITY OF PULTRUDED GFRP I SECTIONS UNDER TRANSVERSE LOADING

Xi-Dong Wu 1, Chao Wu 1, *

¹ School of Transportation Science and Engineering, Beihang University, 37 Xueyuan Road, Beijing 100191, China, Corresponding author : wuchao@buaa.edu.cn

ABSTRACT

Pultruded glass fiber reinforced polymer (GFRP) sections are prone to web crippling failure under concentrated loading in the transverse direction to the pultrusion axis due to their low elastic and strength properties. This paper reports an analytical and numerical study on the web crushing mechanism of pultruded GFRP I sections. Firstly, finite element (FE) analysis was conducted using Abaqus. FE models were constructed using shell elements. Tsai-Hill failure criterion was adopted to simulate the crushing failure of the I sections. Two transverse loading conditions including interior two flanges (ITF) and end two flanges (ETF) were selected. The length of the bearing plate and the height of the I section were varied to study their effects on the web crushing failure mechanism. The results showed that the web crushing capacity was a linear function of the bearing length. It is also approximately linearly correlated with the height of the section. Finally, an empirical equation for predicting the web crushing capacity of the pultruded GFRP I section was proposed which agreed well with the existing experimental results in the literature. This work contributes to a better understanding of the web crushing failure mechanism of pultruded GFRP I section under transverse loading.

KEYWORDS

Web crushing; Transverse loading; FRP; Pultruded sections; Finite element analysis; Prediction.

INTRODUCTION

Pultruded glass fiber reinforced polymer (GFRP) composites have seen increasing applications in structural engineering (Keller 2002). Compared with traditional construction materials, GFRP profiles have important advantages of high strength, low self-weight, chemical resistance and electromagnetic transparency (Hollaway 2009; Gururaja and Ramulu 2009). However, because the pultruded GFRP sections have fibers aligned in the pultrusion direction, when loaded in the transverse direction, premature failure occurs before the GFRP section could achieve the full capacity. Unfortunately, the transverse loading is inevitable (Zhang and Chen 2016). Therefore, it is necessary to study the behavior of the pultruded GFRP sections under transverse loading.

When subjected to the transverse loading, the pultruded GFRP sections fail by web crippling, including web crushing and web buckling. These failure mechanisms have been thoroughly studied in metallic sections (CEN 2010; AISI 2007). However, there has been limited research in the literature focusing on the pultruded GFRP sections subjected to transverse loading. Additionally, a lack of well-established design codes has become a major obstacle to the applications of the pultruded GFRP profiles in structural engineering (Correia et al. 2010).

In the study of steel sections, four transverse loading conditions were widely considered including (i) end one flange (EOF), (ii) interior one flange (IOF), (iii) end two flanges (ETF), and (iv) interior two flanges (ITF), as illustrated in Figure 1.

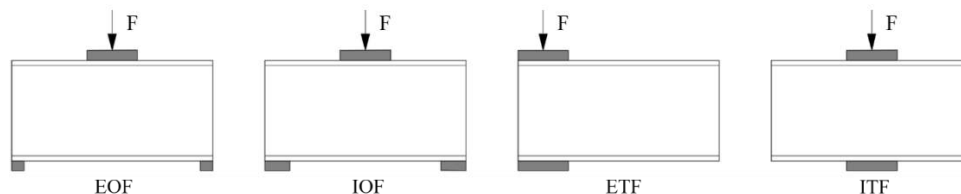


Figure 1: Side view schematics of the four main transverse loading conditions

Recently, a few studies have been conducted on the pultruded GFRP sections under transverse loading conditions. Qiao et al. (2003) conducted an analytical and experimental study on the pultruded FRP I sections. Although the cantilever loading condition can be treated as EOF in Figure 1, this study focused on the global buckling behavior without any statement on the web crippling behavior of the I sections. Borowicz and Bank (2011, 2013) investigated the mechanical behavior of pultruded GFRP wide-flange (WF) sections under three-point bending



condition. Based on the experimental results, a design equation was proposed to predict the load carrying capacity which was conservative. Wu and Bai (2014) presented the first study in the literature focusing on the behavior of pultruded GFRP square hollow sections under transverse loading conditions. The term “web crippling” was used for the first time to describe the failure modes of the pultruded GFRP square sections under transverse loading. Fernandes et al. (2014, 2015) presented a study on pultruded GFRP I sections under ETF and ITF conditions. More recently, Chen and Wang (2015) presented an experimental and numerical research on web crippling behavior of pultruded GFRP I sections under ITF, ETF, EG and IG loading configurations. Four design formulas were proposed according to the four loading conditions. However, all these predictions were too conservative compared with the experimental results. Nunes et al. (2016) developed a FE model using Hashin failure criterion to study the web crippling behavior of pultruded GFRP sections and showed Tsai-Hill criterion was more conservative.

Although there have been a few studies reported in the literature, the web crippling behavior of the pultruded GFRP sections have not been thoroughly understood yet. As studies mentioned above, most of the pultruded GFRP sections failed by web crushing. Therefore, this paper presents an analytical study on the web crushing mechanism of pultruded GFRP I section under two loading conditions of ITF and ETF. FE models were built using shell elements, and Tsai-Hill failure criterion was adopted to simulate the failure initiation of the sections. The variables included the length of the bearing plate as well as the height of the I section. An empirical equation was proposed based on the FE analysis for the prediction of web crushing capacity of the pultruded GFRP I sections. The predictions agreed well with the existing experimental results in the literature.

EXPERIMENTAL RESULTS OF THE PULTRUDED GFRP I SECTIONS

Fernandes et al. (2014) tested four different pultruded GFRP I sections (I100, I120, I200, and I400) under two loading conditions of ETF and ITF. Three lengths of the bearing plate were selected (15 50 and 100 mm). Table 1 lists the main dimensions of each I section, namely the height (*h*), width (*b*), flange thickness (*t_f*), web thickness (*t_w*), and radius at the web-flange junction (*r*). The length of the specimen was twice of the height of section. The steel bearing plates were 20 mm thick and significantly wider than the width of the I sections. A total of 20 specimens were tested, of which 16 specimens failed by web crushing. The web crushing capacities of the specimens are listed in Table 2, where *f_{cu,T}* is the transverse compressive strength of the web and *F_{u,exp}* is the ultimate load. More information can be found in Fernandes et al. (2014)

Table 1: Dimensions of the pultruded GFRP I sections adopted in the experimental study (Fernandes et al. 2014)

Section	<i>h</i> (mm)	<i>b</i> (mm)	<i>t_f</i> (mm)	<i>t_w</i> (mm)	<i>r</i> (mm)
I100	100	50	8	8	2
I120	120	60	6	6	7.5
I200	200	100	10	10	10
I400	400	200	15	15	10

ANALYSIS OF THE EXPERIMENTAL RESULTS

According to the experimental results (Fernandes et al. 2014) in Table 2, it could be concluded that the main factors affecting the load carrying capacity of the GFRP profiles include the loading configurations (ITF or ETF), geometric parameters, the bearing length, and the material properties of the sections. Similarly, in the design of the web yielding capacity of the steel sections under transverse loading (AS 1998), the section capacity is a function of the length of bearing plate, the web thickness and the yielding strength. Therefore, it is necessary to find out the relationships between the capacity and the above mentioned factors.

Figure 2 presents the relationship between the ratio $F_{u,exp}/(t_w \cdot f_{cu,T})$ and the bearing length for both ETF and ITF loading conditions. Similarly, the relationship between the ratio $F_{u,exp}/(t_w \cdot f_{cu,T})$ and the height of the section is plotted in Figure 3 for both ETF and ITF conditions. It is interesting to notice that the ratio $F_{u,exp}/(t_w \cdot f_{cu,T})$ is a linear function of the bearing length and the height of the section. This linear relationship is very important for the development of a model to predict the web crushing capacity of pultruded GFRP I sections. However, the available experimental data are insufficient to support the linear relationships presented in Figure 2-3. Finite element (FE) simulations are then resorted to provide more numerical results to justify these linear relationships.



Table 2: Summary of the web crushing results for the ITF and ETF loading conditions (Fernandes et al. 2014) and comparison of the predicted web crushing capacities with the experimental results

Profile	$f_{cu,T}$ (MPa)	Loading condition	Bearing length (mm)	$F_{u,exp}$ (kN) avg. \pm std. dev	$F_{u,exp}/(t_w f_{cu,T})$ (N/(m \cdot Pa))	F_{pre} (kN)	Ratio		
I100	73.2 ± 12.8	ETF	15	16.77 ± 3.19	0.028	17.33	1.03		
			50	38.24 ± 8.59	0.065	29.87	0.78		
			100	45.48 ± 3.75	0.078	47.79	1.05		
		ITF	15	29.81 ± 1.68	0.051	27.80	0.93		
			50	41.11 ± 3.12	0.070	40.57	0.99		
			100	56.50 ± 6.88	0.097	58.81	1.04		
I120	121.0 ± 8.1	ETF	15	19.66 ± 0.20	0.027	18.81	0.96		
			15	32.17 ± 1.23	0.044	32.96	1.02		
		ITF	50	51.96 ± 1.81	0.072	50.70	0.98		
			100	76.97 ± 5.69	0.106	76.03	0.99		
		I200	106.1 ± 28.5	ETF	15	37.15 ± 2.83	0.035	39.89	1.07
					50	78.17 ± 0.59	0.074	73.98	0.95
100	115.33 ± 17.78				0.109	122.68	1.06		
ITF	15			67.83 ± 3.78	0.064	71.13	1.05		
	50			109.09 ± 3.74	0.103	108.19	0.99		
	100			161.34 ± 1.71	0.152	161.13	1.00		
Average							0.99		
St. dev.							0.07		
CoV							7.1%		

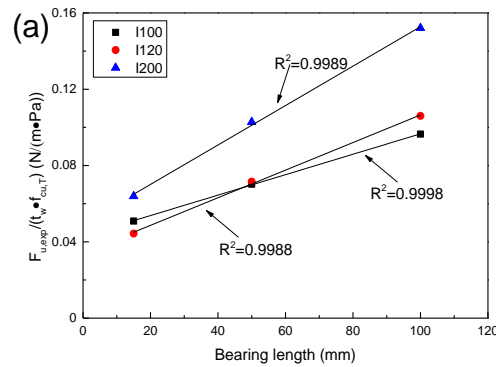


Figure 2: Relationship between the ratio $F_{u,exp}/(t_w f_{cu,T})$ and the bearing length under (a) ITF and (b) ETF loading conditions

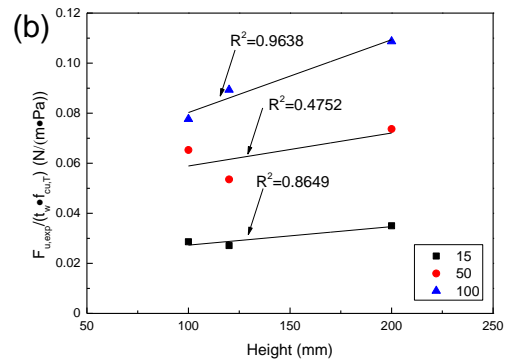
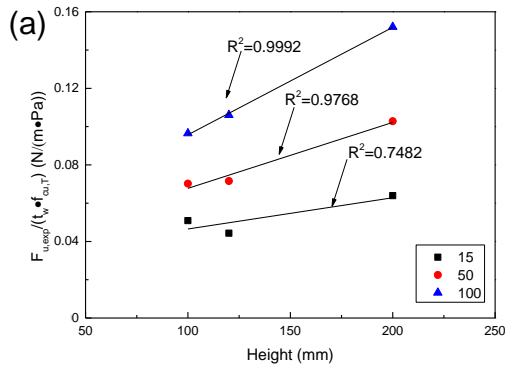


Figure 3: Relationship between the ratio $F_{u,exp}/(t_w \cdot f_{cu,T})$ and the height of the I section under (a) ITF and (b) ETF loading conditions

NUMERICAL STUDY

Objective

FE simulations in this section aims to provide more data to develop the relationship between the ratio $F_{u,exp}/(t_w \cdot f_{cu,T})$ and two parameters including the bearing length and the height of the section. A total of 22 FE models were built using the commercial software Abaqus. In the following discussions, each FE model is identified using a label which consists of three parts. The first part (B or H) means the target parameter to be investigated using this model. B means the bearing length and H stands for the height of the section. The second part (ETF or ITF) means the loading condition. The third part is a number which denotes the bearing length.

Description of the FE models

The material of the pultruded GFRP I section is assumed to be linear elastic in the FE models. The material properties were characterized in experimental study (Fernandes et al. 2014) and listed in Table 3. The parameters in the longitudinal and transverse directions are denoted by labels 1 and 2 respectively. E , G and ν are the elastic Young's modulus, shear modulus, and Poisson's ratio respectively. $S_{1,t}$, $S_{1,c}$, $S_{2,t}$ and $S_{2,c}$ present the tensile strength in the longitudinal direction, compressive strength in the transverse direction, tensile strength in the longitudinal direction and compressive strength in the transverse direction respectively, and the shear strengths are represented by S in Table 3. In addition, steel bearing plates were considered to be linear elastic with a Young's modulus of 210 GPa, a Poisson's ratio of 0.3 and a thickness of 20mm.

Table 3: Material properties of pultruded GFRP I section adopted in the FE models (Fernandes et al. 2014)

Plate	E_1 (GPa)	E_2 (GPa)	G_{12} (GPa)	G_{23} (GPa)	ν	$S_{1,t}$ (MPa)	$S_{1,c}$ (MPa)	$S_{2,t}$ (MPa)	$S_{2,c}$ (MPa)	S (MPa)
Web	26.7	7.7	3.7	1.6	0.266	385.3	464.4	29.1	106.1	27.5
Flange	33.9	5.9	3.7	1.6	0.266	414.2	388.6	29.1	70.4	27.5

Four-node shell elements with reduced integration (S4R) were used to simulate the pultruded GFRP I sections, in which thickness was considered, while eight-node solid elements with reduced integration (C3D8R) were used for the steel bearing plate. The I sections were meshed 40 elements along the height of the web. The bearing plate was meshed with a maximum dimension of 5 mm. A typical FE model of the I section under ITF loading condition is shown in Figure 4. As for the boundary conditions, the lower surface of the bottom bearing plate was restrained in all directions, while the top surface of the upper bearing plate was only allowed to move along the vertical direction. The transverse loading was incrementally applied on the top surface of the upper bearing plate in the form of a pressure. The interface between the pultruded GFRP I section and the steel bearing plates was defined using the surface-to-surface contact. The normal direction of the contact was set as "hard" contact without penetration and the tangential interaction of the contact was considered to be friction with a coefficient of 0.4 (Fernandes 2014). Additionally, the geometrically non-linear effect was considered.

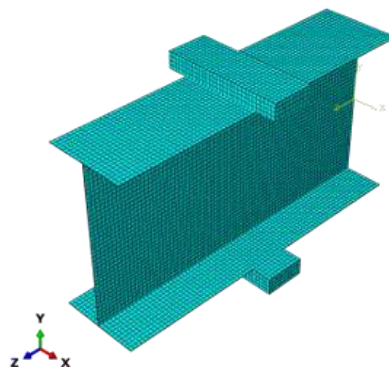


Figure 4: A typical FE model of the pultruded GFRP I section under ITF loading condition

There are two build-in failure criteria for composite materials in Abaqus, including Tsai-Hill and Hashin failure criteria (ABAQUS 6.13). Based on comparison between two criteria in Tunes et al. (2016), it can be concluded that Tsai-Hill failure criterion gave a more conservative and reliable estimation of the load carrying capacity than Hashin criterion. Thus, in this paper, Tsai-Hill failure criterion was used. In the FE simulation, Tsai-Hill failure criterion is represented by I_F . When the I_F of any location of the I section reached 1.0, the analysis was stopped and the load on the bearing plate was extracted as the material failure initiates (Fernandes et al. 2015).

Effect of the Bearing Length on the Web Crushing Capacity F_{in}

In order to study the effect of the bearing length, the other parameters were kept constant. The cross section of B200 was selected with a dimension of $200 \times 100 \times 10 \times 400$ mm (height \times flange width \times section thickness \times length). And 5 lengths of bearing plate were selected including 15 mm, 50 mm, 100 mm, 150 mm and 200 mm. The width of the bearing plate was 150 mm which was larger than the width of the flange of the I section (100mm). The distributions of the Tsai-Hill index of the FE models with various bearing length are presented in Figure 5 for ETF and ITF conditions. The web crushing capacities of the FE models considering various bearing lengths are listed in Table 4.

Table 4: Capacities of the pultruded GFRP I sections considering various bearing lengths using FE simulations

Bearing length (mm)		15	50	100	150	200
F_{in} (kN)	ITF	24.1	41.3	61.3	81.6	102.7
	ETF	17.6	32.6	53.7	75.6	98.3
Area of index distribution (mm ²)	ITF	11115	18531	26535	35101	44130
	ETF	20500	29378	37252	45999	54953

The FE predicted capacities F_{in} in Table 4 are plotted against the bearing lengths in Figure 6(a). It is obvious that the capacity is linearly related to the bearing length for both ETF and ITF loading conditions. The trend is similar to that presented by the experimental results in Figure 2. This linear relationship can be qualitatively explained by the Tsai-Hill index distributions in Figure 5. As can be seen in Figure 5, only the materials within a certain area of the web under the bearing plates respond to the transverse loading. With the increase of the bearing length, the area increases indicating that more materials start engaging in the load carrying mechanism, resulting in higher capacity of the section. This statement is supported by the linear relationship between the area of the distribution of Tsai-Hill index and bearing length in Figure 7(a).

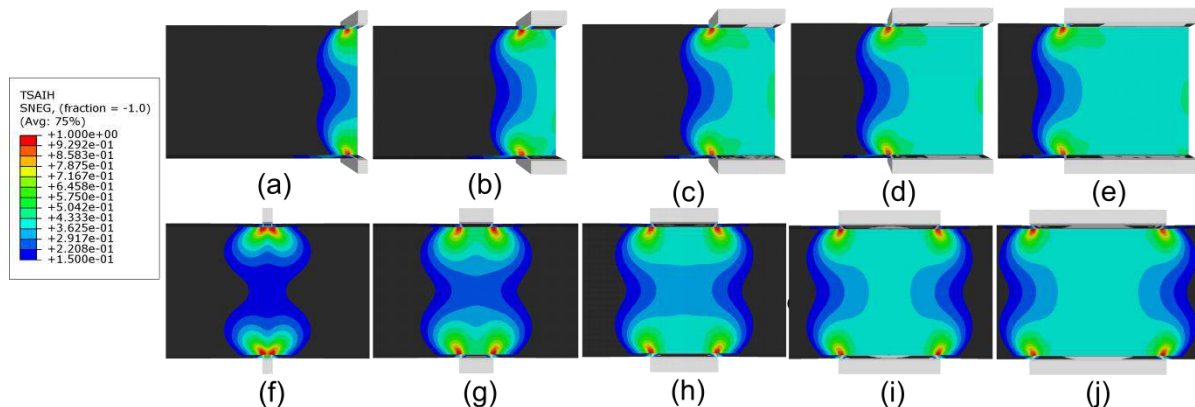


Figure 5: Distributions of the Tsai-Hill index of the FE models under ETF with a bearing length of (a) 15 mm, (b) 50 mm, (c) 100mm, (d) 150 mm, (e) 200 mm and distributions of the Tsai-Hill index of the FE models under ITF with a bearing length of (f) 15 mm, (g) 50 mm, (h) 100mm, (i) 150 mm and (j) 200 mm

Effect of the Height of the Section on the Web Crushing Capacity F_{in}

For the FE simulations, in addition to the four GFRP I sections used in the experiments (Fernandes et al. 2014), another two I sections are adopted. The six I sections used in the FE simulations are listed in Table 5. It should be noted that the thicknesses of all sections were set to 10mm. The bearing length of 15 mm was the same for all FE models because in the experiments all specimens under 15mm bearing length failed by web crushing.

The predicted capacities by the FE simulations (F_{in}) are plotted against the heights of the section (h) in Figure 6(b). It can be seen in Figure 6(b) that, for both ETF and ITF, F_{in} linearly increases with h up to 200 mm. When h is



larger than 200 mm, the increasing rate reduces and F_{in} tends to become constant. For example, F_{in} is 26.9kN/18.5 kN when h is 400 mm for ITF/ETF respectively. It indicates that there exists an effective height of the section beyond which the height has little effect on the web crushing capacity.

Table 5: Selected I sections for the FE simulations to study the effect of the height of section on the web crushing capacity

Section	h (mm)	b (mm)	t_f (mm)	t_w (mm)	F_{in} (kN)		Area of index distribution (mm ²)	
					ITF	ETF	ITF	ETF
H100	100	50	10	10	22.1	14.3	7923	4121
H120	120	60	10	10	23.4	15.1	10592	5463
H150	150	75	10	10	24.8	16.1	14879	7400
H200	200	100	10	10	26.3	17.9	22762	11962
H400	400	200	10	10	26.9	18.5	35198	29087
H1000	1000	500	10	10	27.12	18.8	52382	35379

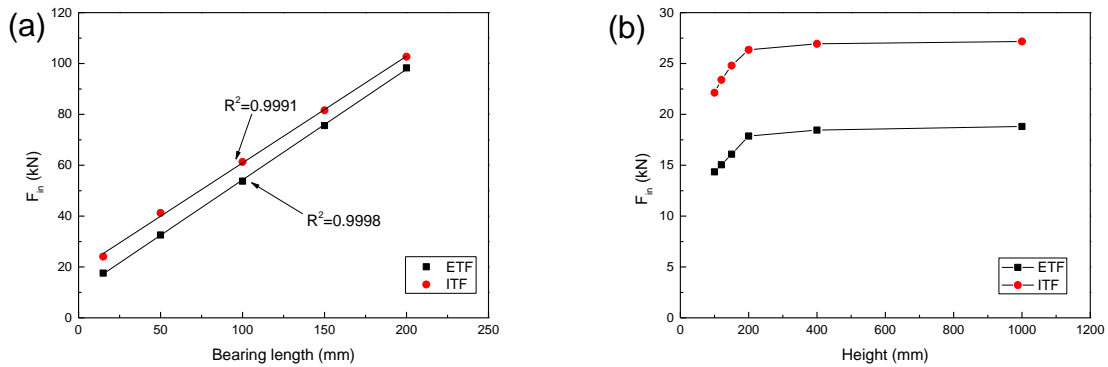


Figure 6: Effect of the (a) bearing length or (b) height on the capacity of the pultruded GFRP I section under ETF and ITF loading conditions

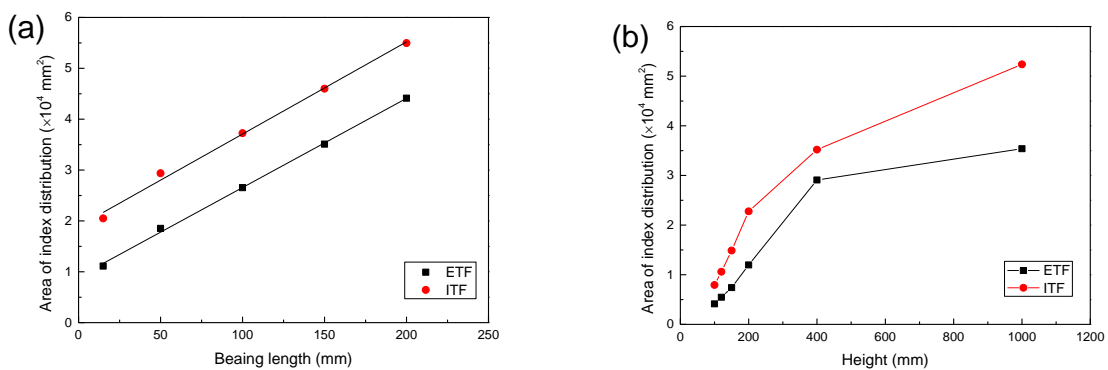


Figure 7: The relationship between the area of distribution of Tsai-Hill index and (a) bearing length or (b) height

The distributions of the Tsai-Hill index of the FE models under ETF and ITF are presented in Figure 8. As mentioned previously, the index distribution represents the range of materials in the I section which engages in the load carrying mechanism. It can be seen in Figure 8 that, the upper half of the web is affected by the top bearing load and the lower half of the web is affected by the bottom bearing load. Because of the symmetry to the neutral axis, the patterns of the upper and lower affected regions of the web are the same. When the height of web is small (i.e. no larger than 200 mm), the upper and lower affected regions of the web may merge showing that the whole height of the web engages in the load carrying mechanism. Therefore, it is reasonable to assume that with the

increase of the height up to 200 mm, the capacity of the section will also increase accordingly. When the height increases to 400 mm, the upper and lower affected regions of the web tend to separate as can be seen in Figure 8(e) and Figure 8(k). It is expected that when the height is large enough, the upper and lower affected regions of the web will eventually separate from each other.

Since the size of the affected upper and lower regions of the web maintain constant due to the failure criterion, the total amount of materials engaging in load carrying mechanism will not change in the case of very large section height as shown in Figure 8(f) and Figure 8(l). This leads to a constant web crushing capacity independent of the height of the section. This relationship between the area of distribution of Tsai-Hill index and the height of section is shown in Figure 7(b). This trend supports the observation in Figure 6(b).

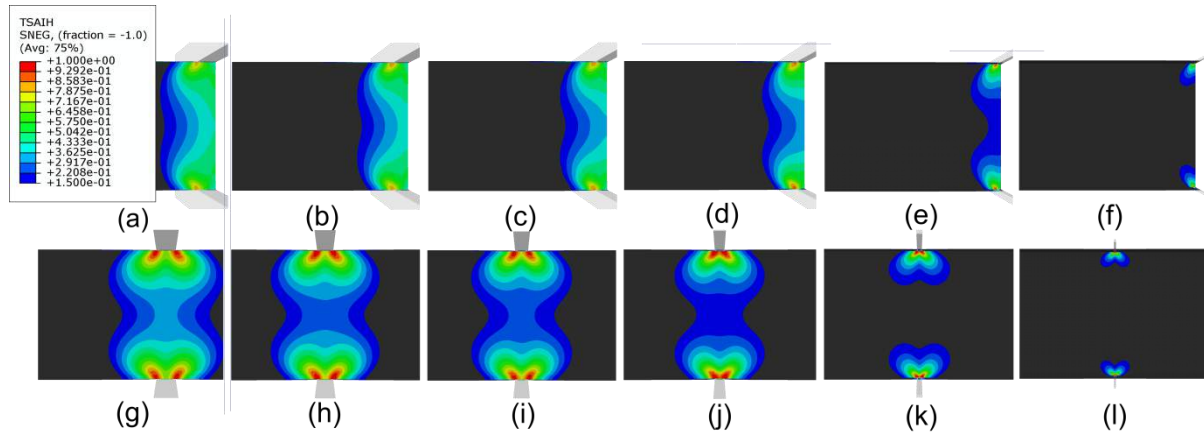


Figure 8: Distributions of the Tsai-Hill index of the FE models under ETF with a section height of (a) 100 mm, (b) 120 mm, (c) 150mm, (d) 200 mm, (e) 400 mm, d (f) 1000 mm and distributions of the Tsai-Hill index of the FE models under ITF with a section height of (g) 100 mm, (h) 120 mm, (i) 150mm, (j) 200 mm, (k) 400 mm and (l) 1000 mm

MODEL FOR THE PREDICTION OF THE WEB CRUSHING CAPACITY OF THE PULTRUDED GFRP I SECTION UNDER TRANSVERSE LOADING

As discussed previously, four parameters may affect the web crushing capacity of the pultruded GFRP I section under transverse loading. Considering the experimental results and discussions of the FE simulations, the following empirical equation is proposed for the prediction of the web crushing capacity of the pultruded GFRP I section under transverse loading:

$$F_{pre} = \alpha f_{cu,T} t_w (C_1 - C_2 \sqrt{\frac{r}{t_w}} + l) \quad (1)$$

$$\alpha = (C_3 h + C_4) \quad (2)$$

Where F_{pre} is the predicted web crushing capacity; h is height of section; t_w is the web thickness; $f_{cu,T}$ is the web compressive strength in the transverse direction; r is the radius at the web-flange junction and l is the bearing length. The coefficients C_1 , C_2 , C_3 and C_4 are calibrated using the experimental results, and the values are listed in Table 6 for ETF and ITF conditions. As for the coefficient α , it is associated with height, and it will be a constant when height is larger than the effective height of section.

The predictions of the web crushing capacities of the pultruded GFRP I sections under transverse loading are listed in Table 2, which generally agree well with the experimental results. The standard deviation of the ratio between the predictions and experimental results is around 0.99 with a CoV of 7.1%.

Table 6: Values of coefficients calibrated using the experimental results in Fernandes et al. (2014)

Load configuration	C_1 (m)	C_2 (m)	C_3	C_4
ETF	0.0358	0.0099	0.00306	0.306
ITF	0.0702	0.0180	0.00375	0.248



CONCLUSIONS

This paper presents a numerical study of the web crushing mechanism of the pultruded GFRP I section under transverse loading. Four parameters were considered having effect on the web crushing capacity including the length of the bearing plate, the height of section, the thickness of the web and the web compressive strength in the transverse direction. A linear relationship was observed between the web crushing capacity and the above mentioned four parameters considering the experimental results. This observation was further supported by the FE simulations. An empirical equation was finally proposed for the prediction of the web crushing capacity of the pultruded GFRP I section based on the experimental observations and FE simulations. The predictions using the proposed equation agreed well with the experimental results. The following conclusions can be drawn:

- (1) Tsai-Hill failure criterion can be used to simulate the pultruded GFRP sections with reasonable accuracy for the predictions of the web crushing capacity under transverse loading;
- (2) The web crushing capacity of the pultruded GFRP I section is linearly related to the bearing length for both ETF and ITF conditions according to both the experimental results and FE simulations;
- (3) There exists an effective height of the pultruded GFRP I section, beyond which the web crushing capacity is independent of the height of the section. When the height is lower than this effective value, the web crushing capacity is a linear function of the height of the section;
- (4) The proposed empirical equation predicted the web crushing capacities with a reasonable accuracy. Considering the ratio between the predictions and the experimental results, the proposed equation yielded a standard deviation of 0.99 with a CoV of 7.1%.

ACKNOWLEDGMENTS

The authors gratefully acknowledge the financial support provided by the Thousand Talents Plan (Young Professionals) in China. This work was also funded by the National Natural Science Foundation of China (Grant Number 51608020).

REFERENCES

- T. Keller (2002). "Overview of Fibre-Reinforced Polymers in Bridge Construction", *Structural Engineering International*, 12, 66-70.
- L.C. Hollaway (2009). "Polymer composites in construction: a brief history", *Engineering & Computational Mechanics*, 162, 107-118.
- S. Gururaja, M. Ramulu (2009). "Failure Analysis of a Fibrous Composite Half-Space Subjected to Uniform Surface Line Load", *Journal of Engineering Materials and Technology*, 131, 77-87.
- W. Zhang, Y. Chen (2016). "Tests on GFRP Pultruded Profiles with Channel Section Subjected to Web Crippling", *Applied Composite Materials*, 24, 849-862.
- CEN (European Committee for Standardization) (2010). "Design of steel structures". Eurocode 3, Brussels, Belgium.
- AISI (American Iron and Steel Institute) (2007). "North American cold-formed steel specification", Washington, DC.
- J.R. Correia, F. Branco, J. Gonilha, N. Silva, D. Camotim, (2010). "GFRP pultruded flexural members: assessment of existing design methods", *Structural Engineering International*, 20, 362-369.
- P. Qiao, G. Zou, J.F. Davalos (2003). "Flexural - torsional buckling of fiber-reinforced plastic composite cantilever I-beams", *Composite Structures*, 60, 205-217.
- D.T. Borowicz, L.C. Bank (2011). "Behavior of Pultruded Fiber-Reinforced Polymer Beams Subjected to Concentrated Loads in the Plane of the Web", *Journal of Composites for Construction*, 15, 229-238.
- D.T. Borowicz, L.C. Bank (2013). "Effect of web reinforcement on the behavior of pultruded fiber-reinforced polymer beams subjected to concentrated loads", *Construction and Building Materials*, 47, 347-357.
- C. Wu, Y. Bai (2014). "Web crippling behaviour of pultruded glass fibre reinforced polymer sections", *Composite Structures*, 108, 789-800.
- L.A. Fernandes, J. Gonilha, J.R. Correia, N. Silvestre, F. Nunes (2014). "Web-crippling of GFRP pultruded profiles. Part 1: Experimental study", *Composite Structures*, 120, 565-577.



L.A. Fernandes, F. Nunes., N. Silvestre, J.R. Correia, J. Gonilha (2015). “Web-crippling of GFRP pultruded profiles. Part 2: Numerical analysis and design”, *Composite Structures*, 120, 578-590.

Y. Chen, C. Wang (2015). “Test on pultruded GFRP I-section under web crippling”, *Composites Part B Engineering*, 77, 27-37.

F. Nunes, N. Silvestre, J.R. Correia (2016). “Progressive Damage Analysis of Web Crippling of GFRP Pultruded I-Sections”, *Journal of Composites for Construction*, 21, 04016104.

AS (Standards Australia) (1998). “Steel structures”, Standards Australia, Sydney.

L.A. Fernandes (2014). “Structural behaviour of GFRP beams subjected to concentrated loads: experimental tests, numerical modeling and analytical study”, *MSc dissertation in Civil Engineering, Instituto Superior Técnico, Lisbon, Portugal*.

ABAQUS (2013). Standard user’ s manual”, Hibbitt, Karlsson and Sorensen, USA, Version 6.13.



FLEXURAL BEHAVIOR OF PRE-CRACKED FRP BEAMS STRENGTHENED WITH CARBON FIBER LAMINATES

Himanshu Chawla¹ and Shamsheer Bahadur Singh²

^{1&2} Birla Institute of Technology and Science, Pilani, Civil Engineering Department, Pilani and India
(corresponding author: himanshuchawla11@gmail.com)

KEYWORDS

Carbon fiber laminates, Cracked beam, Experimental study, Strengthening and repair.

ABSTRACT

This paper presents the experimental investigation on the cracked pultruded beams strengthened with carbon fiber reinforced polymer (CFRP) laminates. Flexural responses were determined for CFRP strengthened beams having length-to-depth (L/d) ratios 3 and 7. Beams had the crack length of 75 mm on the compression web-flange junction at the mid-span of the beam. The length of carbon fiber layers were provided 175, 225 and 275 mm. Flexural responses of beams was determined under three-point bending test. It is observed that the beam having L/d ratio 7 and carbon fiber layers of length 175 mm, failed by debonding of the carbon fiber layers, while other beams of L/d ratio 7 and bonded lengths 225 and 275 mm failed by local failure of compression flange. Moreover, beam having L/d ratio 3 and strengthened with carbon fiber layer throughout the length of beam has strength and stiffness equivalent to the un-cracked beam.

1. INTRODUCTION

Fiber reinforced polymer beams have been widely accepted by construction industries and it has many applications in buildings, bridges and industrial structures. These beams are used as main load carrying member in structures; therefore, there is a need to generate guidelines for strengthening of deteriorated pultruded beams. Carbon fiber reinforced polymer (CFRP) laminates are widely used in external strengthening of civil engineering structural elements such as reinforced concrete (RC) and masonry beams, columns, slabs and steel beams. In comparison to conventional strengthening system, CFRP laminate has various superior properties such as lightweight, high strength-to-weight ratio, non-corrosive, long durability and most important property is chemical and moisture resistant. It is highly civil efficient in improving the flexural, compressive and shear properties of engineering structures. Currently, no study has been carried out on strengthening of deteriorated FRP I-beams.

State-of-the-art reviews of flexural strengthening of RC beams proves that strength, stiffness and ductility of the structures increases, while the crack width decreases (Grace et al. 1999, Ross et al. 1999, Smith & Teng 2002; Aiello & Ombres, 2004). Strengthening of RCC beams under flexural is done by bonding the plate or fixing the layer of carbon fiber, i.e., carbon wrap under the beam (Chen & Teng 2003). It is observed that beam strengthened under flexural fails by shear due to delamination of plate from concrete surface or rupture of the FRP laminate (Chen & Teng 2003, Arduini et al. 1994, Sato et al. 1994, Sato et al. 1997, Triantafillou 1997, Uji 1992). Shear strength of the beams can be enhanced by side bonding, U-jacketing and wrapping of CFRP at the sides of beam. Flexural and shear strengthening of beams usually fails in three different failure modes such as tensile failure of laminate, delamination of laminate and peeling failure of concrete cover (Ashour et al. 2004). With increasing the number of CFRP layers, failure modes of the beams also changes from rupture to the debonding of laminate (Maghsoudi and Bengar 2009). CFRP laminates are also effective in increasing the strength of positive and negative region of continuous beams (Akbarzadeh & Maghsoudi 2010, Kadhim 2011).

Retrofitting of pultruded beams with FRP is similar to retrofitting of steel structures. Debonding of CFRP laminate from beams is the common failure in strengthening of steel sections. Lot of research has been performed on characterizing the bond strength of steel-CFRP specimens. It is observed that in RC beams effective bond length of CFRP laminate is very important (Chen and Teng 2001). The term "effective bond length" means the after a particular length ultimate strength of the CFRP strengthened beams does not increase. Although, strength does not increase by keeping the length of CFRP laminate more than effective bond length, but the risk of debonding of laminate decreases (Deng & Lee 2007 & Narmashiri et al. 2012).

From the above literature review, it is concluded that CFRP laminate is proved to be effective in enhancing the strength of RC and steel beams. Thus, there lies a vast scope of research on strengthening of any structure using CFRP laminate. Although, a lot of research has been carried out on strengthening of masonry, RC and steel beams and columns, and RC slabs and footings. But till date no work has been carried out on strengthening of pultruded beams. The main objective of this study is to investigate the enhancement in the strength and stiffness of the

cracked pultruded I-beam stiffened with CFRP layers. Structural response is evaluated by strengthening the cracked portion at the compression and tension flange-web junction of the beam. Flexural behavior of the strengthened beams is also determined for different L/d ratios. Furthermore, the effect of different bonding lengths of carbon fiber layers on the flexural behaviour is predicted.

2. MATERIALS

This study was performed on pultruded glass fiber reinforced polymer (GFRP) I-beams. The size of the beam was 150 x 75 x 6.5 mm (height x width x thickness). The layup of the beam was determined by burning of specimens of beam as per ASTM D2584 standard and is shown in Figure 1. The materials properties of beams are presented in Table 1. Three-point bending tests were performed on beams having length-to-depth ratios (L/d) ratios 3 and 7, in which depth was kept constant, i.e., 150 mm. All the beams had cracks at the mid-span, therefore before testing beams were strengthened with carbon fiber layers at the cracked portion. Crack length in each beam was 75 mm and it was produced from the three-point bending test of beam without bearing stiffeners. Hence, beams failed by crushing of compression web-flange junction under loading as shown in Figure 2(a). The failure of the beam at junction was due to longitudinal cracking and delamination of layers as depicted in Figure 2(b). Beams were strengthened with two carbon fiber layers (0/90) on each side of the beam. Orientation of the first layer on the surface of the beam was 90°, i.e., transverse to the longitudinal direction and another layer was oriented along the longitudinal direction of the beam.

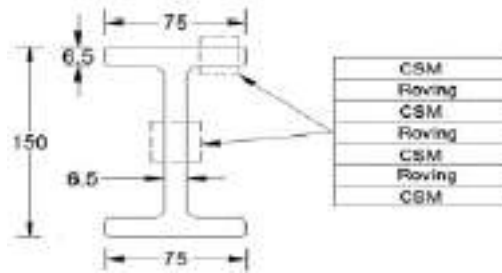


Figure 1: Layup of FRP I-beam (Singh & Chawla, 2018).
Table 1: Mechanical properties of beams and CFRP laminate.

Properties	Beam	CFRP laminate
Longitudinal modulus, E_1 (GPa)	22.77	41
Transverse modulus, E_2 (GPa)	5.60	6.13
Shear modulus, G_{12} (GPa)	1.97	3.52
Poisson's ratio, ν_{12}	0.28	0.27
Longitudinal compressive strength, (MPa)	253	653
Transverse compressive strength (MPa)	46	109
Shear strength, (MPa)	48	71



Figure 2: (a) Cracked beam; (b) Cracked and delaminated region of the beam.

3. STRENGTHENING OF BEAMS

Surface preparation is essential for increasing the bonding (interfacial shear stress) between the carbon fiber layer and beam. It resists the debonding of strengthening element and it is a primary challenge for a designer to avoid debonding in beams. Surface preparation includes making surface abrasive, then cleaning fine abrasive dust.



Hollway and Cadei (2012) recommended that dust should not be removed only by any solvent such as acetone. It is because wiping a wet cloth of acetone spreads the dust uniformly on the surface and after sometimes acetone evaporates, only dust particles left over the surface. Therefore, firstly dust should be cleaned by dry cloth or brush and then acetone should be applied to remove the fine particles. In this investigation, initially external delaminated layer of glass fibers was removed (see Figure 2(b)) and then scratches were made on the surface for proper bonding of carbon fiber layer. The dust of fiber and matrix was removed by cloth first and later surface was cleaned by acetone to remove the fine particles. Mixture (Adhesive) of epoxy resin (grade 691) and hardener (grade reactive polyamide 140) was prepared, having concentration 80% and 20% by weight. Adhesive was poured on the delaminated fiber layers of beam and kept for 15 minutes, so that adhesive flow inside the cracks. It helps in filling the cracks as well as bonding the cracked fiber layers together. As it is manifested in literature, (Deng & Lee 2007 & Narmashiri et al. 2012) bond length is very important in strengthening of a structure. Therefore, debonding strength of the carbon fiber layers is checked for bonding length of 175, 225 and 275 mm.

EXPERIMENTAL SETUP

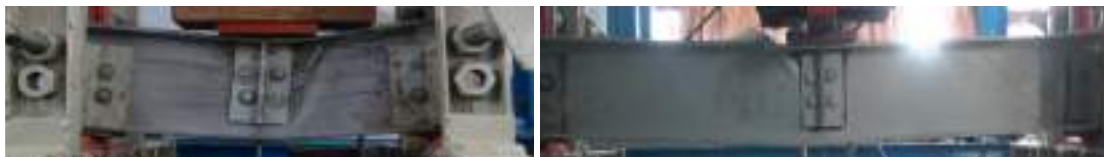
Strengthened pultruded I-beams were tested under three-point loading on a loading frame of capacity 1000 kN and loading actuator of capacity 200 kN. Tests were performed in displacement control mode, with rate of displacement of 0.05 mm/min. A steel bearing plate of size 150 x 125 x 6 mm, i.e., length x width (along the length of beam) x thickness was provided under the loading point, which distributed the load over larger area and avoided the stress concentration at loading point. Simply supported boundary conditions including torsional restraints were provided at the ends of the beam, to prevent the torsion and lateral displacement of ends of the beam at supports as shown in the Figure 3.

RESULTS AND DISCUSSIONS

FRP I-section without bearing stiffener fails by tearing failure of web-flange junction under the loading, while beams with bearing stiffener fails by local failure near to the bearing plate. It is noted that beam with or without bearing stiffeners has weak joint under or near the loading. Therefore, it is important to study the effectiveness of CFRP strengthening on enhancing the strength and stiffness of beams having cracks under the loading. Flexural responses of the un-cracked and cracked beams with strengthening is presented in the following sections:

Un-cracked beam

In order to determine the effectiveness of strengthening technique on regaining the strength of cracked beams, firstly flexural response of un-cracked beams with bearing stiffeners is determined. Later, its load-deflection response and failure mode are compared with CFRP strengthened beams. Beams having L/d ratio 3 and 7 were tested with bearing stiffeners under loading and over supports. It is observed that beam having L/d ratio 3, failed by crushing of web under the bearing stresses produced from load bearing plate as well as cracks produced at holes of bolted connection of bearing stiffener as shown in Figure 3(a). In the beam of L/d ratio 3, high shear stresses produces at supports and bolted connection, which make the section weaker, therefore cracks generated from the holes and propagated towards the mid-span of the beam. It is stated that the beams having L/d ratio 3 with bearing stiffeners are need to be strengthened at ends to avoid the shear failure due to hole of bolted connection. Figure 4(a) shows failure of the beam is brittle and load-deflection curve is linear till the failure. The beam having L/d ratio 7, failed due to local buckling of compression flange (see Figure 3(b)). The load-deflection curve of the beam in Figure 4(a) shows the linear behaviour till failure, it means no any ply failed before local buckling of compression flange. Further, local buckling of compression flange led to delamination and beam lost its strength suddenly.



(a)

(b)

Figure 3. Flexural deformation of beams under three-point loading: (a) beam having L/d ratio 3; (b) beam having L/d ratio 7.

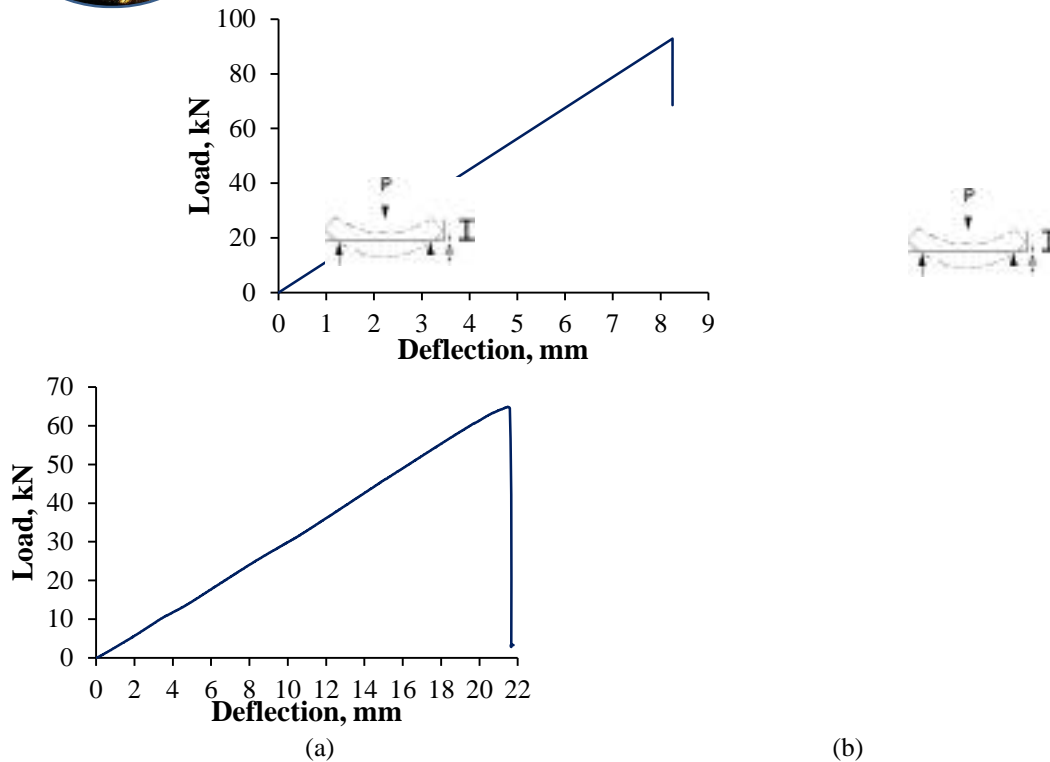


Figure 4. Load vs deflection response of un-cracked beam: (a) beam having L/d ratio 3; (b) beam having L/d ratio 7.

Cracked beam

The main objective of this study is to examine the flexural response of beams strengthened with CFRP laminate at the web-flange junction. Strengthened beams were connected with bearing stiffeners at the location under the loading and over supports. Strength and stiffness of strengthened beams were evaluated for different bonding length of carbon fiber layers and different L/d ratios (3 & 7). The detailed investigation on the flexural behaviour of strengthened beams of different L/d ratios is explained next.

Beams having L/d ratio 7

The flexural responses of beams having L/d ratio 7 are determined for crack length of 75 mm. Length of carbon fiber layers provided on different beams was 175, 225 and 275 mm on each side of crack and these beams are represented by 7L-175, 7L-225 and 7L-275, respectively. From Figure 5, it is noted that the beam which is stiffened by carbon fiber layers of length 175 mm failed by debonding of layers, which led to tearing of compression flange-web junction of I-beam. From the visual inspection, it was observed that cracks started from the mid-section and propagated towards the end of the beam. Debonding attributed to the complete failure of the beam. The load versus deflection responses of beams with different lengths of carbon fiber layers is plotted in Figure 6(a). It is shown that the slope of load-deflection curve of beam 7L-175 is less than the un-cracked beam (7L-UC), while stiffness of other beams (7L-225 and 7L-275) is equivalent to beam 7L-UC. The length of the carbon fiber layer provided in beam 7L-175 is lesser than beams 7L-225 and 7L-275, therefore strength and stiffness of the beam 7L-175 is lesser than other strengthened beams. Beam 7L-225 failed by rupture of compression flange near to the bearing plate and the beam 7L-275 failed by local buckling of compression flange. Load-vs-deflection responses of these beams show that failure of all beams is very brittle. It is worth noting that strength of the cracked beam can be regained by strengthening the cracked portion with two carbon fiber layers of stacking sequence (0/90) on each side of the cracked web-flange junction of I-beam.



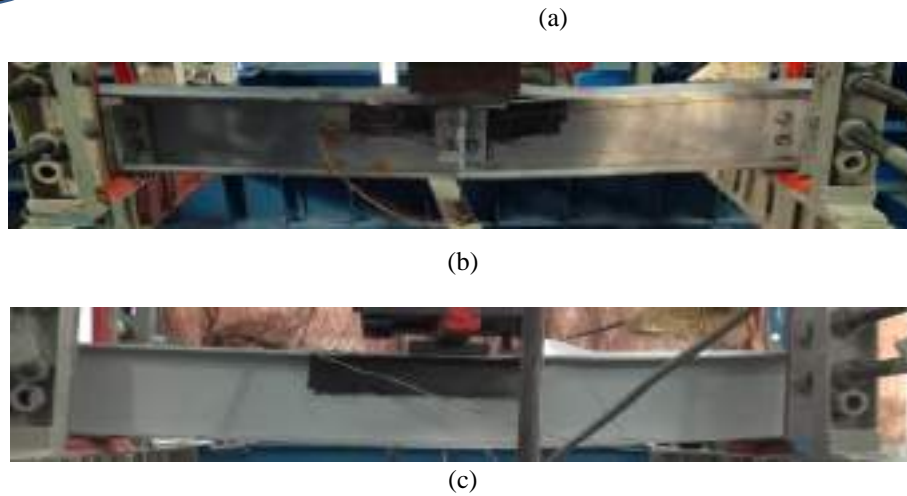


Figure 5. Beam strengthened at junction of compression flange-web: (a) 7L-175; (b) 7L-225 & (c) 7L-275.

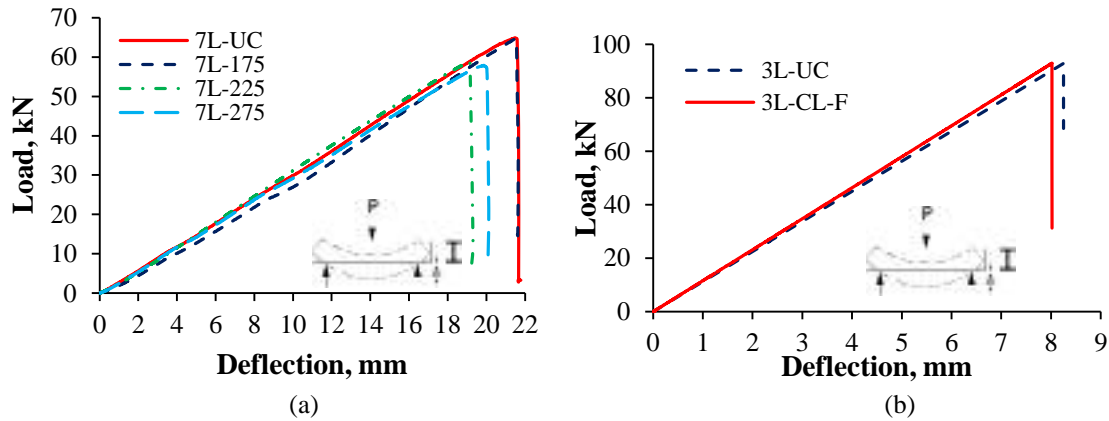


Figure 6. Load-vs-deflection curves of strengthened beam having L/d ratio 7: (a) strengthened at compression flange-web junction; (b) strengthened at both tension and compression web-flange junction.

Further the flexural strength of strengthened beam was evaluated for beam having cracks on the compression and tension web-flange junction. This beam is represented by 7L225-150, numeric terms '225' and '150' denote the bonding length of CFRP laminate over compression and over tension flange-web junction, respectively. The load-deflection responses of beams is shown in Figure 6(b). It is observed that due to cracks in junction of tension flange-web and compression flange-web, beam offered low stiffness and strength than uncracked beam. Beam failed by the crushing of compression flange and there was no debonding of carbon fiber layers (see Figure 7).



Figure 7. Strengthened at top and bottom web-flange junction.

Beams having L/d ratio 3

The CFRP strengthened beam having L/d ratio 3, has depth 150 mm and length 450 mm and it is denoted by 3L-225. This beam had crack length of 75 mm and extra 75 mm length of carbon fiber was kept on each end of the crack, i.e., total length of the carbon fiber provided was 225 mm. While testing of beams of L/d ratio 7, it was observed that debonding failure of carbon fiber was not seen in beams 7L-225 and 7L-275, therefore beam of L/d ratio 3 was strengthened with carbon fiber of length 225 mm under the loading. The comparison of flexural responses of un-cracked beam (3L-UC) and cracked beam with strengthening (3L-225) is presented in Figure 8(a). The stiffness of the beam is equivalent to the stiffness of the uncracked beam but the strength is 28% lower than

uncracked beam. Figure 9(a) show that beam failed by debonding of carbon layer as well as crushing of web due to diagonal bearing stresses. During testing, cracks were also produced from the holes of bolted connection of bearing stiffener. Hence, it is concluded that strengthening of the beam with carbon layers of length 225 mm is not workable as well as bolted connection of the stiffener make the section weaker. Therefore, further study was conducted on the strengthening of the beam with carbon layers throughout the length of the beam (3L-CL-F) and bearing stiffeners were not provided to avoid the shear failure of the web of I-beam. The failure mode of the beam 3L-CL-F was crushing of web-flange junction over the supports as shown in the Figure 9(b). Delamination of the carbon fiber layers and crushing of web was not observed under loading, but crushing of the web was observed over the supports. From Figure 8(b), it is noted that flexural strength of the beam 3L-CL-F is equals to the un-cracked beam and the stiffness is little more than the un-cracked beam. Hence, it is concluded that for beams having L/d ratio 3, strengthening of the beam with carbon fiber layers throughout the length is better technique than strengthening only the cracked portion. Moreover, shear failure of the web can also be avoided with this stiffening technique.

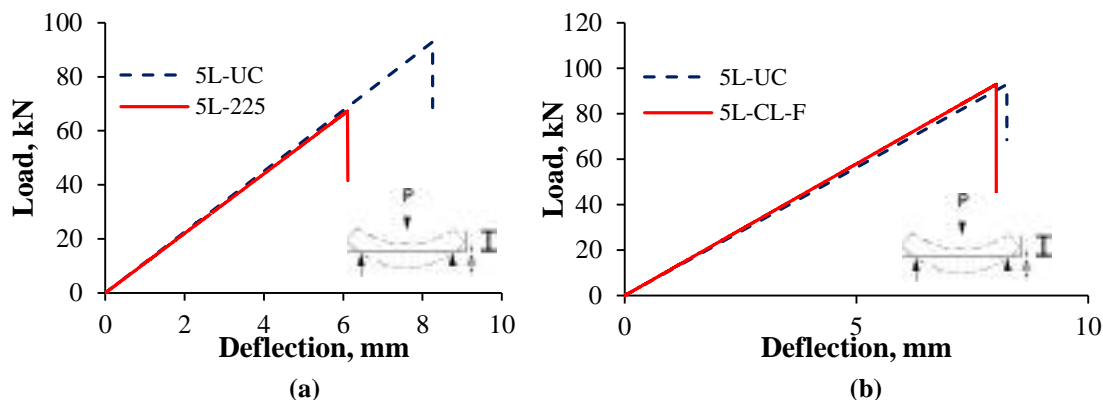


Figure 8. Load-vs-deflection curves of strengthened beam having L/d ratio 3: (a) strengthened at compression flange-web junction; (b) strengthened web both side and flanges internally.



Figure 9. Three-point bending test of beams having L/d ratio 3: (a) 3L-225; (b) 3L-CL-F.

CONCLUSIONS

The key contribution of this paper is to determine the flexural strength of CFRP laminate strengthened FRP I-beam having cracks at the junction of web-flange of beams. Flexural response is evaluated for beams having different bonding length of carbon fiber and different L/d ratios, i.e., 3 and 7. From this study, the following concluding remarks can be made:

1. Strength and stiffness of the cracked FRP I-beam can be regained by strengthening the cracked portion with two layers of carbon fibers having stacking sequence (0/90) on each side of the cracked web-flange junction.
2. For beam having L/d ratio 7, carbon fiber layers of bond length 225 mm is sufficient to the enhanced the stiffness and strength of the cracked beam equivalent to uncracked beam.
3. Strengthened beam of L/d ratio 7 having cracks on both top and bottom web-flange junction at mid span, has lower stiffness than uncracked beam.
4. The mode of failure of the strengthened beam of L/d ratio 3 is shear failure of the web at bolted connection as well as the strength of the beam is lower than uncracked beam, hence this stiffening technique is not recommended.



5. The strength and stiffness of the beam (L/d ratio 3) strengthened with carbon fiber layers throughout the length on the both sides of web and internally on flanges has stiffness and strength equivalent to uncracked beam.

ACKNOWLEDGMENT

The authors are thankful to CSIR, New Delhi (22(0631)/13/EMR-II) for financial assistance provided for the effective execution of the research work.

REFERENCES

- M.A. Aiello, L. Ombres (2004). "Cracking and deformability analysis of reinforced concrete beams strengthened with externally bonded carbon fiber reinforced polymer sheet", *Journal of Materials in Civil Engineering*, 16, 292-399.
- H. Akbarzadeh, A.A. Maghsoudi (2010). "Experimental and analytical investigation of reinforced high strength concrete continuous beams strengthened with fiber reinforced polymer", *Materials and Design*, 31, 1130-1147.
- A.F. Ashour, S.A. El-Refaie, S.W. Garrity (2003). "Flexural strengthening of RC continuous beams using CFRP laminates", *Cement and Concrete Composites*, 26, 765-775.
- ASTM D 2584. (2008). Standard test method for ignition loss of cured reinforced resins. *American society of testing and materials*. Philadelphia, USA.
- M. Arduini, A. D'Ambrisi, A.D. Tommaso (1994). "Shear failure of concrete beams reinforced with FRP plates Proceedings, Infrastructure: New Materials and Methods of Repair", *Proc. Materials Engineering Conference*, ASCE, New York, 804, 123-130.
- J.F. Chen, J.G. Teng (2003). "Shear capacity of FRP-strengthened RC beams: FRP debonding", *Construction and Building Materials*, 17(1), 27-41.
- J.F. Chen, J.G. Teng (2003). "Shear capacity of FRP-strengthened RC beams: FRP rupture", *Journal of Structural Engineering*, 129(5), 615-625.
- J Deng, M.M.K. Lee (2007). "Behaviour under static loading of metallic beams reinforced with a bonded CFRP plate", *Composite Structures*, 78(2), 232-242.
- N.F. Grace, G.A. Sayed, A.K. Soliman, K.R. Saleh (1999). "Strengthening reinforced concrete beams using fiber reinforced (FRP) laminates", *ACI Structural Journal*, 96(5), 865-875.
- L.C. Hollaway, J. Cadei (2002). "Progress in the technique of upgrading metallic structures with advanced polymer composites", *Progress in Structural Engineering Materials*, 4(2): 131-148.
- M.M.A. Kadhim (2012). "Effect of CFRP Sheet Length on the Behavior of HSC Continuous Beam", *Journal of Thermoplastic composite materials*, 25(1), 33-44.
- A.A. Maghsoudi, H. Bengar, (2009). Moment redistribution and ductility of RHSC continuous beams strengthened with CFRP, *Turkish Journal of Engineering and Environmental Sciences*, 33, 45-59.
- K. Narmashiri, R.N.H. Sulong, M.Z. Jumaat, (2012). Failure analysis and structural behaviour of CFRP strengthened steel I-beams. *Construction and Building Materials*, 30, 1-9.
- C.A. Ross, D.M. Jerome, J.W. Tedesco, M.L. Hughes (1999). "Strengthening of reinforced concrete beams with externally bonded composite laminates", *ACI Structural Journal*, 96(2), 65-71.
- Y. Sato, T. Ueda, Y. Kakuta, T. Tanaka (1996). "Shear reinforcing effect of carbon fibre sheet attached to side of reinforced concrete beams", *Proc. Advanced Composite Materials in Bridges and Structures*, 2, 621-627.
- Y. Sato, T. Ueda, Y. Kakuta, S. Ono. (1997). "Ultimate shear capacity of reinforced concrete beams with carbon fibre sheet. Non-Metallic (FRP) Reinforcement for Concrete Structures", *Proc. Third Symposium*, Japan, 1: 499-505.
- S.B. Singh, H. Chawla (2018) "An investigation of material characterization of pultruded FRP H- and I-beams. *Mechanics of Advanced Materials and Structures*", 25(2), 124-142.
- S.T. Smith, J.G. Teng (2001). "Debonding failures in FRP-plated RC Beams with or without U strip end anchorage. *Proc. FRP Composites in Civil Engineering*, Hong Kong, 1, 607-615.
- S.T. Smith, J.G. Teng (2002). "FRP-strengthened RC beams I: Review of debonding strength models. *Engineering Structures*, 24(4), 385-395.
- T.C. Triantafillou (1998). "Shear strengthening of reinforced concrete beams using epoxy-bonded FRP composites", *ACI Structural Engineering*, 95(2), 107-115.
- K. Uji (1992). "Improving shear capacity of existing reinforced concrete members by applying carbon fibresheets", *Transaction of Japanese Concrete Institute*, 14, 253-266.



EXPERIMENTAL STUDY ON THE WEB CRIPPLING BEHAVIOR OF PULTRUDED GFRP CHANNEL SECTIONS

Li-Teng Zhang¹, Xi-Dong Wu¹ and Chao Wu^{1,*}

¹*School of Transportation Science and Engineering, Beihang University, 37 Xueyuan Road, Beijing 100191, China*

Corresponding author : wuchao@buaa.edu.cn

ABSTRACT

Pultruded glass fibre reinforced polymer (GFRP) sections see increasing applications in civil constructions. However, due to their inherent pultrusion manufacturing process, the pultruded GFRP sections are susceptible to web crippling failure under concentrated transverse loading. This paper presents a preliminary experimental investigation on the web crippling behaviour of pultruded GFRP channel sections. Three channel sections were tested under two transverse loading conditions, namely end-two-flange (ETF) and interior-two-flange (ITF). Two failure modes were observed including web buckling and failure at web-flange junction. It was found that the web crippling capacities were not affected by the loading conditions when the failure was at the web-flange junction. When the failure was web buckling, the web crippling capacities were more related to the web slenderness. This paper contributes to enrich the experimental database of web crippling of pultruded GFRP channel sections.

KEYWORDS

Web crippling; Pultruded; Glass fiber reinforced polymer; Channel section; Transverse loading

INTRODUCTION

Pultruded glass fiber reinforced polymer (GFRP) sections have been widely used in civil engineering due to their excellent physical and mechanical properties, like low weight, high strength and durability in harsh environmental conditions (Bank, 2006; Pendhari et al. 2008). However, web crippling behaviour has been a major problem that hinders the widespread of pultruded GFRP sections due to their inherent orthotropic properties (Bai et al. 2013; Borowicz & Bank, 2013; Luciano Feo et al. 2013; Muttashar et al. 2015). The first reported study which specially focused on the web crippling behaviour of pultruded GFRP rectangular hollow sections (RHSs) was conducted by Wu & Bai since 2014 (Chen & Wang, 2015b; Wu & Bai, 2014). Four loading conditions were used including end-two-flange (ETF), interior-two-flange (ITF), end ground (EG) and interior ground (IG) to simulate the loading conditions of floor joist members. Based on the out-of-plane displacement obtained from progressive failure process, design equations were proposed to estimate the web crippling capacities of GFRP RHSs. Similarly, several studies were also conducted on the web crippling of pultruded GFRP I sections with concentrated load applied through different sizes of bearing plates (Borowicz & Bank, 2014; Chen & Wang, 2015a; Feo et al. 2012; Fernandes et al. 2014; Fernandes et al. 2015; Nunes et al. 2016). The experimental results confirmed that the web crippling capacity and initial stiffness were affected by the width of bearing plates and loading conditions. And the I sections with slender webs were more prone to web buckling failure. Several equations were proposed to predict the web crippling capacities of pultruded GFRP sections based the experimental result.

Existing studies mostly focused on the symmetric GFRP sections, such as RHS and I sections. There is no report on the web crippling behaviour of asymmetric GFRP sections like channel sections, which are also widely used in structures and may be subjected to concentrated transverse loading. This study presents an experimental study on the web crippling behaviour of pultruded GFRP channel sections. Three GFRP channel sections of different dimensions were selected and tested under two loading conditions, namely interior two flanges (ITF) and end two flanges (ETF). The transverse loading was applied through bearing plates of 100 mm width. Two failure modes of web buckling and failure at web-flange junction were observed in all tested specimens. Load-displacement curves and web crippling capacities were reported. The strain distributions of the webs were measured and analysed using digital image correlation (DIC) method, in order to investigate the failure mechanism of the channel sections under concentrated transverse loading.

EXPERIMENTAL PROGRAM

Three different pultruded GFRP channel sections were selected in the study. The measured dimensions of the channel sections are presented in Table 1. Burn-off tests were conducted according to ASTM D 3171 (ASTM

D3171) in order to measure the fibre content and the fibre architecture. 30×30mm plates were cut from three locations including the web, flange and web-flange junction (WFJ) of each channel section for the burn-off tests. At least three burn-off tests were repeated for the same location of each section. It was found that the fibre contents at the three locations of each section were very similar. The measured fibre content of each section is presented in Table 1. The detailed fibre components of the channel section after the burn-off test is shown in Fig 1. All the three channel sections had the same fibre architecture of SCUFUCS, where S is the glass fiber surface veil (Fig 1a), C represents the glass fiber combination mat (Fig 1b), U is unidirectional fiber bundles (Fig 1c) and F means glass fiber fabric (Fig 1d). The tensile properties of the channel sections were measured according to ASTM D 3039 (ASTM, 2008). The properties of the GFRP channel sections provided by the manufacturer are presented in Table 2.

Table 1: Dimensions and fibre contents of three pultruded GFRP channel sections

Section	Width b (mm)	Depth h (mm)	Flange thickness t_f (mm)	Fiber content (%)
C1	29	102	6.4	69.0
C2	35	102	4.8	68.8
C3	56	152	6.4	68.7

Table 2: Mechanical properties of three pultruded GFRP channel sections

Item	Tensile strength		Tensile modulus		Interlaminar shear strength τ (MPa)
	Longitudinal $f_{t,L}$ (MPa)	Transverse $f_{t,t}$ (MPa)	Longitudinal $E_{t,L}$ (GPa)	Transverse $E_{t,T}$ (GPa)	
Value	321.4	56.5	25.2	8.6	27.8

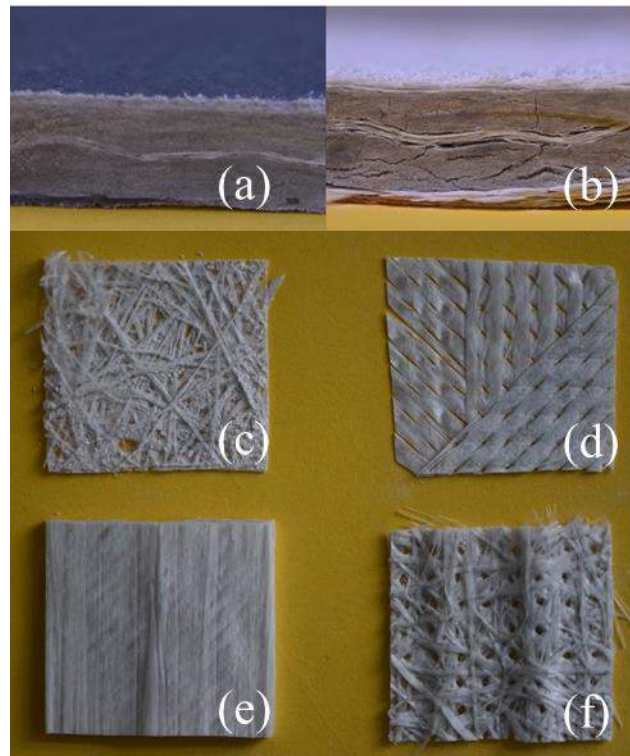


Figure 1: (a) cross section before and (b) after the burn-off test, and the components of GFRP sections including (c) surface veil; (d) combination mat; (e) unidirectional fiber bundle; (f) fabric

A total of twelve channel specimens were tested under transverse loading as listed in Table 3. The length of each specimen was twice of the height of the section. This was to satisfy the requirement specified in ASCE Specifications (ASCE, 1991) in order to avoid the effect of specimen length on the web crippling behaviour. The specimen ID in Table 3 consists of three parts. The first part is the section ID in Table 1, i.e. C1, C2 and C3. The second part represents the loading condition of ETF or ITF. The third part means the repeating times of each test.

The loading conditions of ETF and ITF are presented in Fig 2. The experimental setup is shown in Fig 3. All web crippling tests were conducted using a SANS universal testing machine with a capacity of 100 kN. The load was applied using displacement control at a speed of 1 mm/min. The concentrated transverse loading was applied through two 100 mm wide bearing plates. The channel sections were carefully positioned inbetween the two bearing plates to make sure the transverse loading was applied through the centreline of the web (see Fig 2c). Two LVDTs were symmetrically installed to measure the vertical displacement of the specimen. The specimens were painted with a speckle pattern on the surface for DIC analysis, produced by a thin coating of white paint followed by a uniformly distributed black dots using spray paint. A Nikon camera was equipped to record the progressive failure process. The photos taken by the camera were also used to analyse and measure the strain distribution of the web using the DIC technique through a Ncorr software using MATLAB. The details of the DIC analysis using this software can be referred to (Ghiassi et al. 2013).

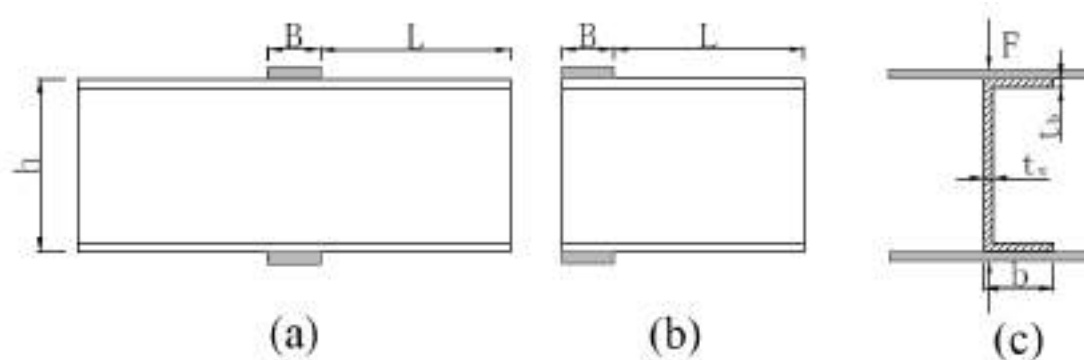


Figure 2: Loading conditions of (a) ITF; (b) ETF and (c) side view of the channel section under loading

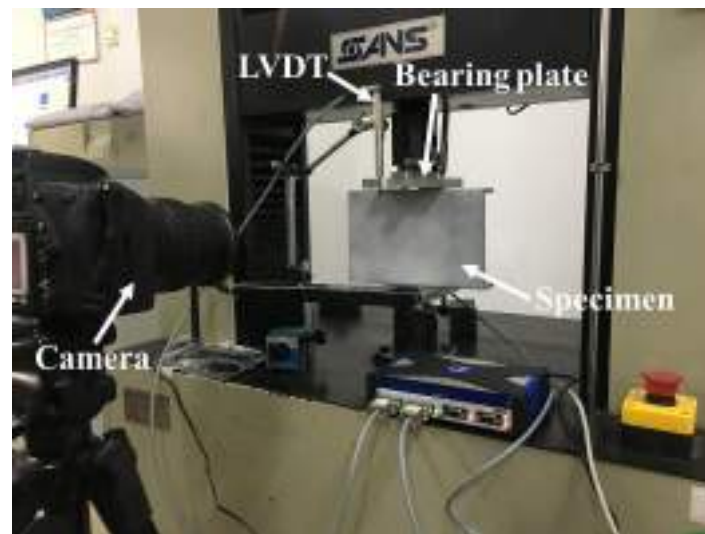


Figure 3: Experimental setup and instrumentations

Table 3: Experimental results of all specimens

Specimen	Capacity (kN)	Failure mode
C1-ITF-1	40.0	Web crushing
C1-ITF-2	39.9	Web crushing
C1-ETF-1	36.4	Web crushing
C1-ETF-2	36.9	Web crushing
C2-ITF-1	27.1	Web crushing
C2-ITF-2	27.9	Web crushing
C2-ETF-1	26.1	Web crushing
C2-ETF-2	26.5	Web crushing
C3-ITF-1	40.1	Web crushing

C3-ITF-2	37.7	Web crushing
C3-ETF-1	22.3	Web crushing
C3-ETF-2	24.4	Web buckling

RESULTS AND DISCUSSIONS

Failure Modes

The typical failure modes are shown in Figs 4-6 for channel sections of C1, C2 and C3, respectively. It was observed that, under both ETF and ITF, C1 sections failed at the web-flange junction as shown in Fig 4(a), with the flange separated from the web with the increase of loading. It was interesting to see that the damages at the web-flange junction only occurred within a certain region underneath the loading point, while the other parts away from the loading point remained intact. It indicated that the length of specimen was sufficient to sustain the transverse loading. Following the initial cracking at the web-flange junction, the transverse loading was transferred to the web which could exhibit cracking in the mid height of the web as shown in Fig 4(b).

The failure modes of C2 specimens are presented in Fig 5. Similarly, the initial failure occurred at the web-flange junction for both ETF and ITF. Then the crack longitudinally extended to both ends of the specimen causing the flange separated from the web with the continuous pressing of the bearing plates. The web buckled and cracked in the mid height subsequently.

For C3 section, web-flange junction failure was only observed under ITF condition as shown in Fig 6(a). On the other hand, C3 failed due to web buckling under ETF condition as shown in Fig 6(b). The web buckling firstly caused a longitudinal bending cracking at the mid-height of the web. With the increase of loading, the extensive out-of-plane deformation caused subsequent cracking at the web-flange junctions. It seems that the C3 with a slender web was more sensitive to web buckling failure under ETF condition.

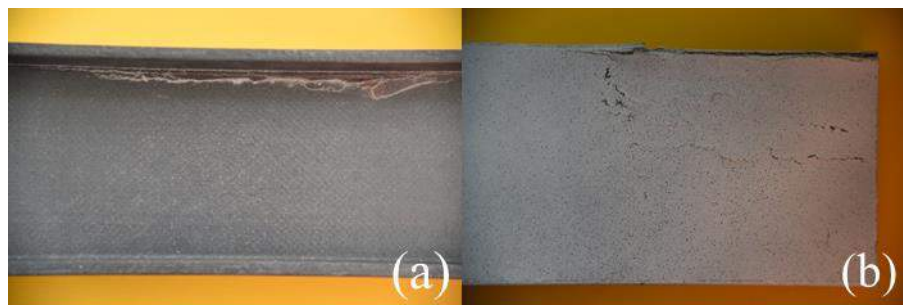


Figure 4: Failure modes of C1 section under (a) ITF and (b) ETF conditions

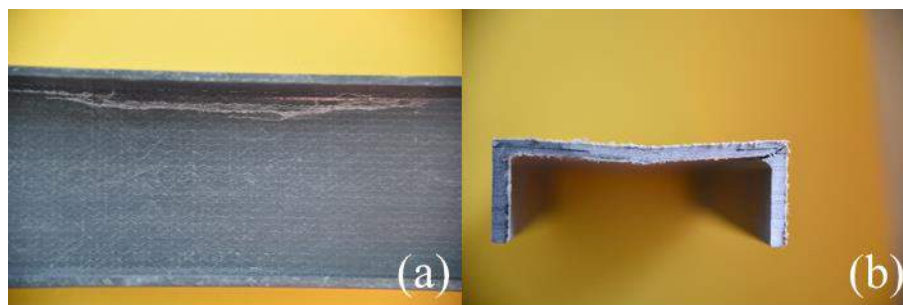


Figure 5: Failure modes of C2 section under (a) ITF and (b) ETF conditions

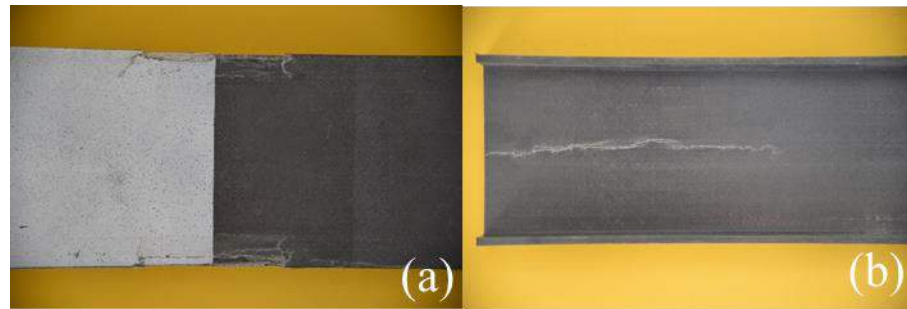


Figure 6: Failure modes of C3 section under (a) ITF and (b) ETF conditions

Load-Displacement Curves and Web Crippling Capacities

The load-displacement curves of the GFRP channel sections under ETF and ITF loading conditions are presented in Fig 7. It was found that, all curves firstly exhibited an elastic linear stage after the load was applied. A peak was reached at the end of the elastic linear stage after which the load dropped suddenly. According to the failure modes, the peak loads corresponded to the failure initiation at the web-flange junction for all specimens, except for C3 under ETF which buckled and also showed a sudden drop of the load. The subsequent load-displacement curve after the peak represented the response of the web after the web-flange junction failure. The peak load of the load-displacement curve is defined as the “web crippling capacity” of the corresponding channel section.

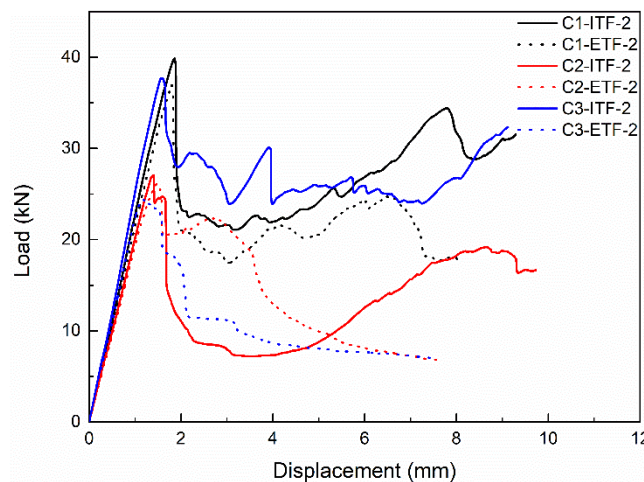


Figure 7: Load-displacement curves of all GFRP channel sections under ETF and ITF conditions

The web crippling capacities of all specimens are listed in Table 3. The average web crippling capacities of the three channel sections under ETF and ITF conditions are compared in Fig 8. It seems that, for the same section, the web crippling capacity was not greatly affected by the loading conditions of ETF and ITF, except for section C3. The web crippling capacity increased by only 9.1% and 4.6% for C1 and C2 sections respectively, when the loading condition changed from ETF to ITF. On the other hand, the web crippling capacity of C3 section under ITF is higher by 66.9% than that under ETF. This is because C1 and C2 specimens failed at web-flange junction under both ETF and ITF conditions. On the other hand, the failure mode of C3 changed from web buckling under ETF to web-flange junction failure under ITF, causing a considerable increase in its web crippling capacity.

The effect of web slenderness on the web crippling capacity can also be identified in Fig 8. It can be seen that, under ITF condition, the web slenderness has little effect on the web crippling capacity. For example, the heights of C1 and C3 were 102 mm and 152 mm respectively, while they had the same web thickness of 6.4 mm. Therefore the slenderness of C3 increases by 50% than that of C1. However, the web crippling capacities of C1 (40.0 kN) and C3 (38.9 kN) were almost the same. It seems that the web thickness has more effect on the web crippling capacities of C1 and C3 sections. This is because the two sections failed by web-flange junction separation under ITF which is not related to the web slenderness. Similarly, under ETF, the capacity of C2 is lower by 28.3% than that of C1, which was proportional to the ratio of their web thicknesses. Under ETF condition, C3 had a much lower capacity due to the web buckling failure, whose failure mode is more related to the web slenderness.

However, since there were no other sections failed by web buckling, it is impossible to compare C3 with other sections under ETF condition.

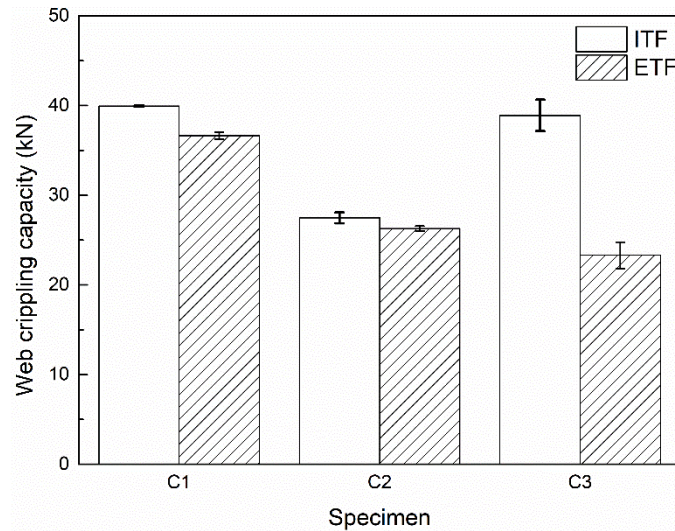


Figure 8: Comparison of the web crippling capacities of all GFRP channel sections under ETF and ITF conditions

Figs 9-11 show the 2D full field strain distributions of the webs of all sections in the transverse direction obtained by the DIC analysis of the web images captured by the camera. It should be noted that the images in Fig 9-11 present the strain distributions at the moment of failure initiation. It is obvious that for all specimens, only certain regions (blue areas) engaged in the load carrying mechanism, while other regions (red areas) showed little response under transverse loading. For ITF condition, all the three sections, C1, C2 and C3, had the same length of blue region at the web-flange junction. Therefore, this is an indication that they had similar capacities because they all failed at the web-flange junction. However, it seems that the two failure modes, failure at web-flange junction and web buckling, can not be distinguished with the help of DIC images. The strain distribution of C3 under ETF (Fig 9b, failed by web buckling) is similar to that of C1 under the same loading condition (Fig 11b, failed at web-flange junction).

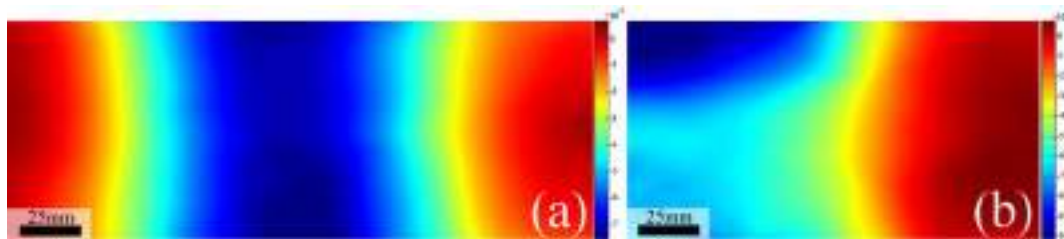


Figure 9: Strain distributions of C1 section under (a) ITF and (b) ETF conditions

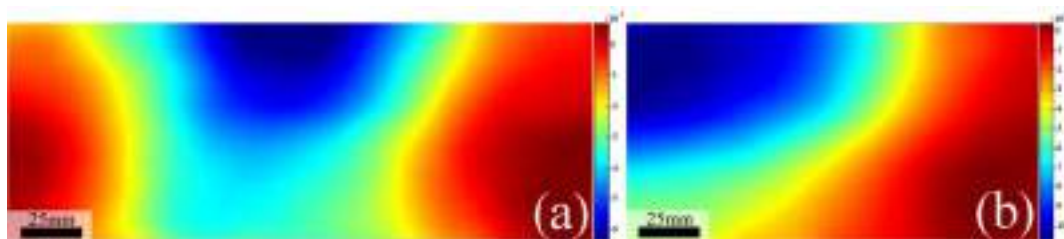


Figure 10: Strain distributions of C2 section under (a) ITF and (b) ETF conditions

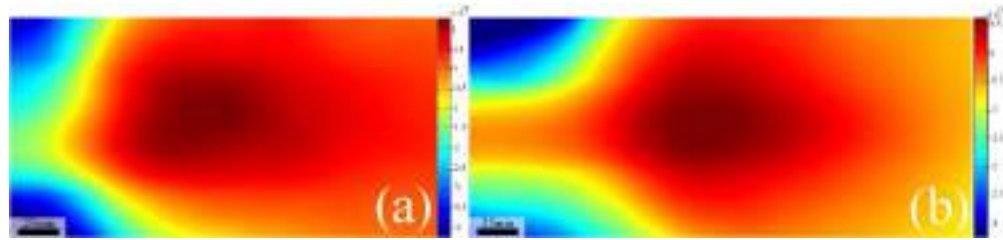


Figure 11: Strain distributions of C3 section under (a) ITF and (b) ETF conditions

CONCLUSIONS

This paper presents a preliminary experimental study on the web crippling behavior of pultruded GFRP channel sections under concentrated loading in the transverse direction. Three channel sections of different dimensions were tested under ETF and ITF conditions. A total of twelve tests were conducted and the failure modes, load-displacement curves were reported. Based on the experimental results, the following conclusions can be drawn:

- (1) Two typical failure modes were observed for all channel sections under ETF and ITF conditions, including the failure at web-flange junction and web buckling;
- (2) When the failure occurred at the web-flange junction, the loading condition had little effect on the web crippling capacities of the channel sections, while the web thickness showed a more dominant effect;
- (3) When web buckling occurred, the web crippling capacities of the channel sections were more related to the web slenderness;
- (4) The strain distribution by DIC analysis indicated that only a certain length of the channel section engaged in the load carrying mechanism given sufficient specimen length.

ACKNOWLEDGMENTS

The authors gratefully acknowledge the financial support provided by the National Science Foundation of China (51608020). This work was also funded by the Thousand Talents Plan (Young Professionals) in China.

REFERENCES

- ASCE (1991). Specification for the Design of Cold-Formed Stainless Steel Structural Members. *SEI, EI/ASCE-8-02*.
- ASTM (2006). Standard Test Method for Short-Beam Strength of Polymer Matrix Composite Materials and Their Laminates. *American Society for Testing and Materials, ASTM D2344/D2344M-00*.
- ASTM (2008). Standard Test Method for Tensile Properties of Polymer Matrix Composite Materials. *American Society for Testing and Materials, ASTM D3039/D3039M-08*.
- Bai, Y, Keller, T, Wu, C (2013). Pre-buckling and post-buckling failure at web-flange junction of pultruded GFRP beams. *Materials and Structures, 46(7)*, 1143-1154.
- Bank L. C (2006). Composites for construction: Structural design with FRP materials. *Design*.
- Borowicz D. T, Bank L. C (2013). Effect of web reinforcement on the behavior of pultruded fiber-reinforced polymer beams subjected to concentrated loads. *Construction & Building Materials, 47*, 347-357.
- Borowicz D. T, Bank L. C (2014). Web Buckling in Pultruded Fiber-Reinforced Polymer Deep Beams Subjected to Concentrated Loads. *Journal of Composites for Construction, 18(3)*, A4013014.
- Chen, Y, Wang, C (2015a). Test on pultruded GFRP I-section under web crippling. *Composites Part B Engineering, 77*, 27-37.
- Chen, Y, Wang, C (2015b). Web crippling behavior of pultruded GFRP rectangular hollow sections. *Composites Part B Engineering, 77*, 112-121.
- Feo, L, Mosallam A. S, Penna, R (2012). Preliminary results of an experimental and computational analysis on the behavior of web-flange junctions of GFRP pultruded profiles subjected to concentrated loads.
- Feo, L, Mosallam A. S, Penna, R (2013). Mechanical behavior of web-flange junctions of thin-walled pultruded I-profiles: An experimental and numerical evaluation. *Composites Part B Engineering, 48*, 18-39.
- Fernandes L. A, Gonilha, J, Correia J. R, Silvestre, N, Nunes, F (2014). Web-crippling of GFRP pultruded profiles. Part 1: Experimental study. *Composite Structures, 120*, 565-577.
- Fernandes L. A, Nunes, F, Silvestre, N, Correia J. R, Gonilha, J (2015). Web-crippling of GFRP pultruded profiles. Part 2: Numerical analysis and design. *Composite Structures, 120*, 578-590.



- Ghiassi. B, Xavier. J, Oliveira D. V, Lourenço P. B (2013). Application of digital image correlation in investigating the bond between FRP and masonry. *Composite Structures*, 106(12), 340-349.
- Mcdonough W. G, Dunkers J. P, Flynn K. M, Hunston D. L (2004). A Test Method to Determine the Fiber and Void Contents of Carbon/Glass Hybrid Composites. *Journal of Astm International*, 1(3), 15.
- Muttashar. M, Karunasena. W, Manalo. A, Lokuge. W. (2015). *The effect of shear span to depth on the failure mode and strength of pultruded GFRP beams*. Paper presented at the The International Symposium on Fiber Reinforced Polymers for Reinforced Concrete Structures.
- Nunes. F, Silvestre. N, Correia J. R (2016). Progressive Damage Analysis of Web Crippling of GFRP Pultruded I-Sections. *Journal of Composites for Construction*, 21(3), 04016104.
- Pendhari S. S, Kant. T, Desai Y. M (2008). Application of polymer composites in civil construction: A general review. *Composite Structures*, 84(2), 114-124.
- Wu. C, Bai. Y (2014). Web crippling behaviour of pultruded glass fibre reinforced polymer sections. *Composite Structures*, 108(1), 789-800



SHAKING TABLE TEST ON CFRP CABLE DOME STRUCTURE

W. H. Qin^{1,2}, Z. Xi^{1,2}, Y.J. Li¹, Z. C. Zhang¹ and X. Zhang¹

¹ Key Laboratory of Concrete and Prestressed Concrete Structures of the Ministry of Education, Southeast University, Nanjing, China, Email: 101005205@seu.edu.cn

² National Prestress Engineering Research Center, Southeast University, Nanjing, China.

ABSTRACT

Cable dome is a kind of whole prestressed structure whose struts are in compression and the other components are in tension. In this article, a 5.4 meter diameter cable dome model, whose cables and struts was made of CFRP bars and CFRP pipes respectively, was fabricated and prestressed. By this way, the advantages of high-strength and lightweight of the CFRP material was combined with advantage of the high proficiency of cable dome structure. So that the anti-seismic performance of this kind of cable dome can be greatly improved. Shaking table experiment of the above-mentioned model was prosecuted with multiple load cases. The time history numerical analysis on the test model was executed and good agreement of the results can be concluded by comparing with the results of the tested ones. Several principles about the dynamic response of this structure under the action of different seismic waves and different maximum acceleration are drawn. Good seismic performance of CFRP cable dome structures can be demonstrated by the research results about this paper.

KEYWORDS

CRFP, cable dome, shaking table experiment, anti-seismic.

INTRODUCTION

Shaking table experiment is capable of reproduce the earthquake process. By analyzing relevant parameters which acquired from shaking table test can reflect the response process and dynamic performance of the structure in earthquake. Through the phenomenon in shaking table test, the accuracy of numerical analysis model can be estimated and evaluated.

Gasparini, et al. (1989) studied the static and dynamic behaviour of a cable dome by testing a 1/50 scale model. Three different pretension levels were considered. The frequency range over which the response is unstable decreases with increasing pretension force. The dynamic to static strain ratio decreased from 20% to 2.3% as pretension increased from the lowest to the highest value. Luo et al. (2005) analyzed numerically the modal of a Geiger cable dome whose diameter is 120m and acquired the influence curve of different parameters on the natural frequencies. By time history analysis, the law how earthquake traveling wave effect influences nodal displacement and strut force have been investigated, the difference of the response between multidimensional earthquake and unidirectional earthquake have also been compared. Song (2008) conducted time history analysis on Geiger, Levy and Kiewitt cable domes which under the action of frequent earthquakes and rare earthquakes. The dynamic response of the cable dome under different wave direction and different earthquake intensity was contrasted and the failure mechanism of cable dome under strong earthquake was discussed.

Nevertheless, up till now, researches mainly focus on dynamic performance by numerical time history analysis of cable dome structures, shaking table test on CFRP cable dome has not been found in references. Therefore, shaking table test on a CFRP cable dome model whose diameter is 5.4m was conducted in this article.

EXPERIMENT DETAILS

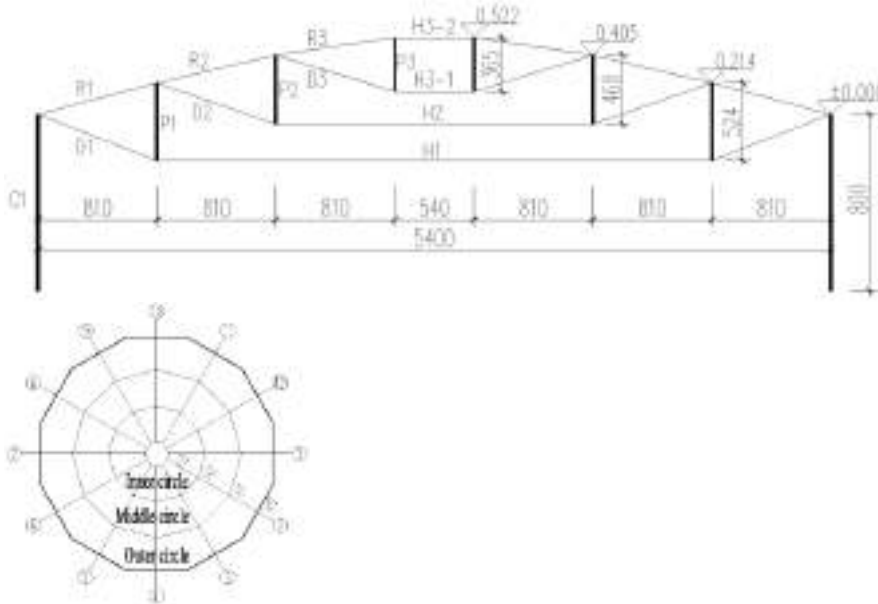
Similarity of the Model

Considering the dimension limitation of shaking table and the convenience of experiment, the geometric similarity ratio of model and original structure is 1/22. The time interval of acceleration of seismic wave is too small if 1/22 is applied, therefore 1/10 is taken as the time similarity.

Components and Connections

Components design

The profile and the plan view of the CFRP cable dome model is shown in Figure 1. The Sections of the cables and struts were designed according to the similarity scale. The CFRP cables were all ϕ 5mm CFRP bars, except that the middle hoop was ϕ 7mm CFRP bars. The dimension of struts were ϕ 24 \times 2 CFRP pipes. Each ridge cable was a continuous CFRP bar which has no tension device. One end of each diagonal cable has tension device (Figure 2) while the other has not. Especially, each of 4 outer diagonal cables and 4 middle diagonal cables and 2 inner diagonal cables is installed with a force sensor (Figure 3) at the end which has tension device. To reduce the problem of uneven distribution of the internal force in hoop cables and to make construction more convenience, middle hoop cable is divided into 2 segments and the outer hoop cable is divided into 3 segments.



(a) Profile

(b) Plan view

Note: R1: Outer ridge; R2: Middle ridge; R3: Inner ridge; D1: Outer diagonal; D2: Middle diagonal; D3: Inner diagonal; H0: Exterior ring beam; H1: Outer hoop; H2: Middle hoop; H3-1: Upper inner hoop; H3-2: Lower inner hoop; P1: Outer strut; P2: Middle strut; P3: Inner strut; C1: Column.

Figure 1. Profile and plan view of the CFRP cable dome model (unit:mm)

Because diagonal cables had a tension end and a fixed end, and some tension ends had force sensors, the anchorages of the two ends of the diagonal cable were different. The anchorages of ordinary tension end were made of steel tube (shown in Figure 2), while the anchorage of the tension end installed with a force sensor had a tapered hole tube (shown in Figure 3). The tapered hole were filled with epoxy glue and small steel balls.

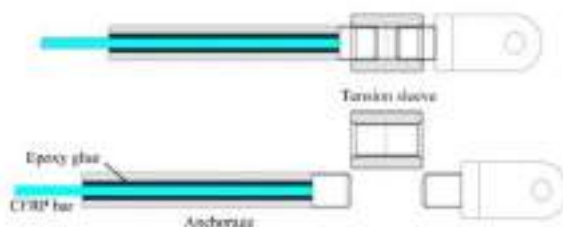


Figure 2. Ordinary tensioning set

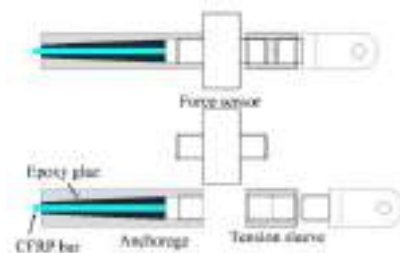


Figure 3. Tensioning set with force sensor

Tensioning device

Steel hexagon stretch sleeves were utilized in all tensioning devices. The plus thread and left-hand thread were tapped internally on the two ends of the hexagon stretch sleeve, and the same direction of exterior thread were

tapped on anchorages of the two sides of the sleeve. The tensioning devices of diagonal cable are shown in Figure 2 and Figure 3.

Connection design

Because of the distinction between CFRP and steel strand, the connections of CFRP cable domes should be different from that of steel domes. The upper and lower connections used in CFRP cable dome are shown as Figure 4.

As is well known, the shear strength of FRP bars is fairly weak comparing with their tension strength. A shallow groove, which was used to place a steering sleeve, was made in the middle of lower connection. The bended steering sleeve can lead the CFRP hoop cables to go through the lower connections without tuning abruptly, in order to prevent the cables from shear failure.

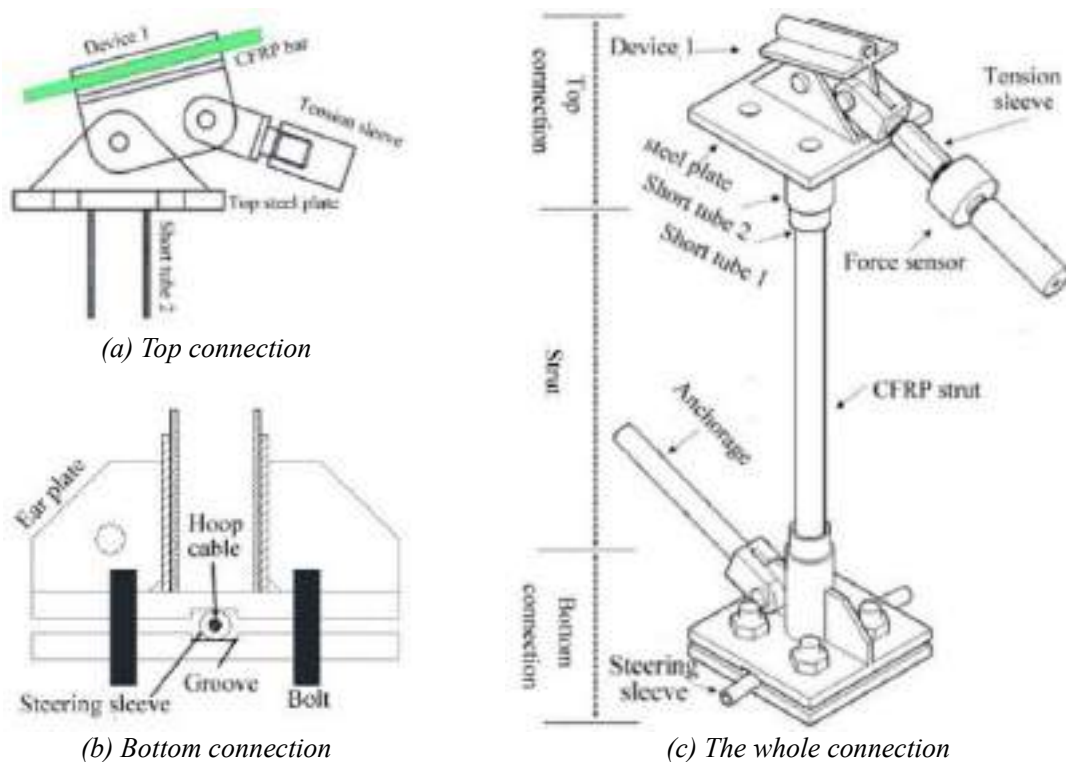


Figure 4. The top and bottom connections

Experiment Equipment and Measurement Layout

In this experiment, piezoelectric acceleration sensors whose range is $-50g \sim +50g$ and sensitivity is 5% were utilized. It is hard to measure the relative displacement because of the limitation of measurement equipment and the narrow space of the model. Therefore only absolute displacements were measured. The range of the displacement meters were 500mm and 300mm.

Seismic waves for test

Different kinds of seismic waves were chosen for shaking table test, including Near-field seismic waves, Long duration time seismic waves, Reference wave and artificial waves. Information about these waves are shown in Table 1.

Table 1: Categories of seismic waves for experiment

Category of seismic wave	Name of seismic	Abbreviation	Year	Earthquake magnitude	Maximum acceleration	Arias strength (m/s)	Duration time of 5-	Duration time of 5-95%
	ChiChi	C	1999	7.62	0.3576g	2.9	5.7	16.7

Near-field	Kobe	K	1995	6.9	0.6177g	8.7	6	11.3
Long duration	Taft	T	1952	7.36	0.1803g	0.6	10.7	30.3
time seismic	Pasadena	P	1952	7.36	0.0478g	0.1	16.6	29.5
waves	Mexico	M	2010	7.2	0.2809g	1.9	10.1	25.3
Reference wave	EI	E	1940	6.95	0.2808g	1.6	17.7	24.2
Artificial waves	H1	H1			0.0713g			
	H2	H2			0.0713g			

Measurement layout

According to the channels of the measurement equipment, there were 16 acceleration sensors, 8 strain gages and 2 displacement meters. Codes and location of each measurement point are shown as Table 2, Figure 5 and 6. In these pictures, the outermost serial numbers which are 1, 4, 7, 10 refer to axial numbers that numbered counterclockwise. The arrows shown in Figure 5 refer to the direction of acceleration sensors, points with no arrows means Z direction of acceleration sensors. The arrows shown in Figure 6 refer to the direction of the top of displacement meters.

Table 2: Locations and numbering of measurements

acceleration	locations	acceleration	locations	strain	Location of strain
A1	1-OE-X	A9	5-OT-XY	OHSG1	Outer hoop cable
A2	1-OT-Z	A10	7-MT-Z	OHSG2	
A3	1-IB-Z	A11	9-MB-Z	MHSG1	Middle hoop cable
A4	4-OE-Y	A12	10-MB-X	MHSG2	
A5	4-OT-X	A13	10-MT-X	ODSG1	Outer diagonal cable
A6	4-MT-X	A14	10-OT-X	ODSG2	
A7	4-MB-X	A15	11-OB-Z	MDSG1	Middle diagonal cable
A8	3-MT-XY	A16	12-OT-XY	MDSG2	

Note: 1: Meanings of the measurements: 1) the number means the axial number (shown in Figure 5); 2) O means outer loop; 3) M means Middle loop; 4) E means External steel beam; 5) T means Top; 6) B means Bottom; 7) X, Y, Z means acceleration direction. Thus, A6 (4-MT-X) in the table means X direction acceleration of Middle hoop Top joint of 4 axis.

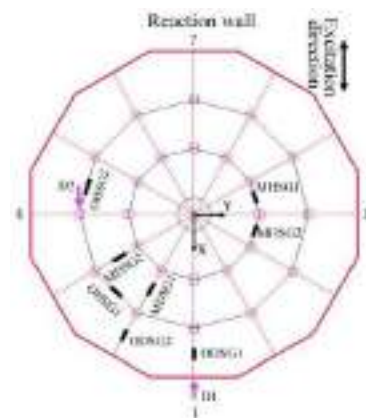
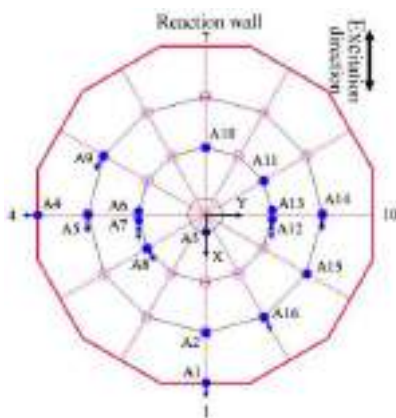


Figure 5. Layout of acceleration sensors

Figure 6. Strain gauges and displacement meters

The additional weight has been placed on the top (6kg) and bottom (4kg) connections before the implementation of shaking table test. The cable dome structure were prestressed successfully. The internal force of the members and the level of the connections of CFRP cable dome model after the formation and prestressing is shown in Table 3. Good agreement can be concluded through the comparison between the experimental results and the numerical simulation ones.



EXPERIMENT RESULTS AND ANALYSIS

Dynamic Characteristics

It is effective to acquire the natural frequencies of a structure when the white noise excitation method is applied. The tested natural frequencies of the model by the white noise method and the ones by the numerical calculation are listed and compared in Table 4. From Table 4, we can learn the following three information. 1) The first three frequencies can be clearly separated from each other. 2) Satisfactory accuracy of the tested first three frequencies and vibration modes can be shown by the comparison with the calculated ones. 3) However, it is hard to acquire accurately the natural frequencies of the high orders vibration modes whose frequencies are close with the adjacent ones, so the accordance of the tested high order natural frequencies are not as satisfactory as the low frequencies, revealing the less measurement accuracy for higher frequencies by this method.

The numerical model is built in Ansys to analysis, whose basic information is shown in Table 5. The first 3 modes of vibration are shown in Figure 7. The first two modes of vibration are twist modes in which all the connections of the dome move circumferentially. The difference between mode 1 and mode 2 is that: in mode 1, the top and bottom connections of outer hoop move in opposite direction, leaving all the middle and inner connections twist in the same direction; in mode 2, the top and bottom connections of outer and middle hoop move in opposite direction, leaving all the inner connections twist in the same direction; The third mode of vibration is a transverse mode in which all connections move along X direction. The fourth mode of vibration is another transverse mode in which the all connections move along Y direction. From the fact that the first 2 modes are all twist modes we can learn that the out-of-plane stiffness of a truss in Geiger dome is weak because of the lack of circumferential linkage between the top joints.

Table 3: Prestress forces in the cables

members	Experiment	Simulation	Error
Outer diagonal cable	2508	2774	-9.6%
Middle diagonal cable	1058	1388	-23.8%
Inner diagonal cable	472	425	11.1%
Outer ridge cable	1954	2386	-18.1%
Middle ridge cable	944	1021	-7.5%
Inner ridge cable	-	594	-
Outer hoop cable	4283	5004	-14.4%
Middle hoop cable	2097	2537	-17.4%

Table 4: Comparison of the natural frequencies between white noise method and the numerical calculation

Order	Simulation frequency/Hz	Experiment frequency/Hz	Error	Order	Simulation frequency/Hz	Experiment frequency/Hz	Error
1	1.159	1.28	10.44%	18	3.160	3.29	4.11%
2	1.826	1.62	11.28%	19	3.338	3.36	0.66%
3	2.050	1.97	3.90%	20	3.344	3.51	4.96%
4	2.052	2.03	1.07%	21	3.973	3.70	6.87%
5	2.200	2.26	2.73%	22	4.077	3.84	5.81%
9	2.230	2.31	3.59%	31	4.270	5.15	20.61%
10	2.238	2.41	7.69%	37	5.102	5.73	12.31%
12	2.244	2.56	14.08%	50	6.442	7.14	10.84%
14	2.472	2.99	20.95%	54	11.623	12.34	6.17%

Table 5: Basic information of the model

Members	Elastic modulus/GPa	Simulation Element	Dimesion/mm
Outer and inner steel beam	206	Beam 188	14#a
Middle hoop cable	178	Link 10	Φ5
Inner strut	206	Link 8	Φ24×2

Other struts	96	Link 8	Φ7
Other cables	213	Link 10	Φ7

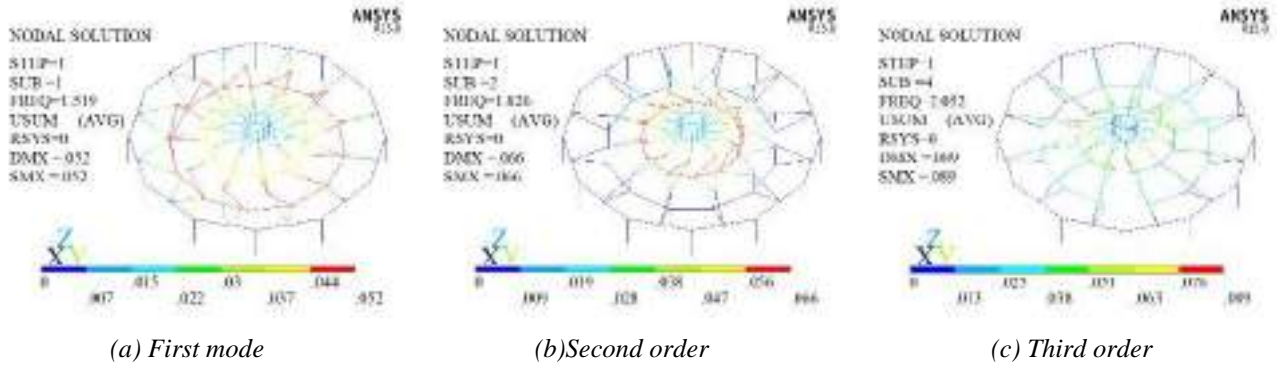


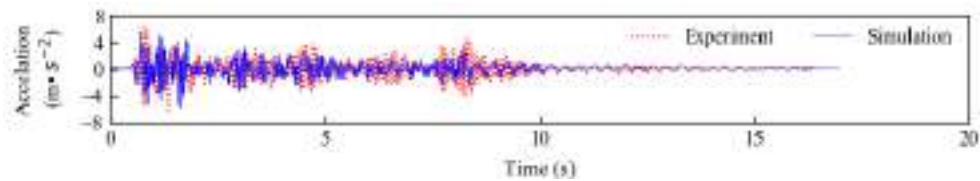
Figure 7. The first three vibration Modes of the model

Results of Shaking Table Test

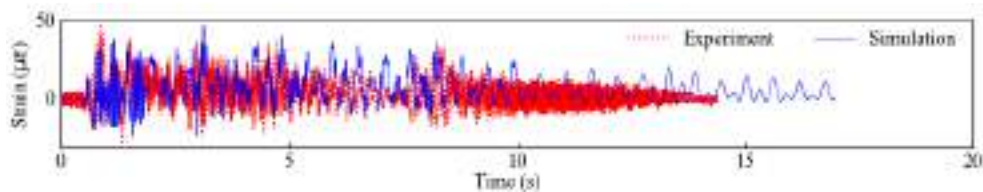
Results of under different kinds of seismic waves

All the seismic waves are excited along X-direction of the model. Under earthquake wave load cases of E300、K300、M300 whose peak value are 300gal, the time history response of the measurement points are shown in Figure 8 - 10. From these figures good agreements can be seen based on comparison of the experimental records and the simulation ones.

Because the members of the cable dome structure have high initial stress and strain before the shaking table test, the additional stress and strain (dynamic stress and dynamic strain we call here) above the initial ones are more important than the total values. The dynamic strain in Figure 8 (b) and the dynamic stress in the following Table 6 refer to the additional ones.



(a) Acceleration response time history curve of 4-MB-X



(b) experiment dynamic strain (ODSG2) and the simulation dynamic value

Figure 8. Contrast between experiment and simulation value under E300 case

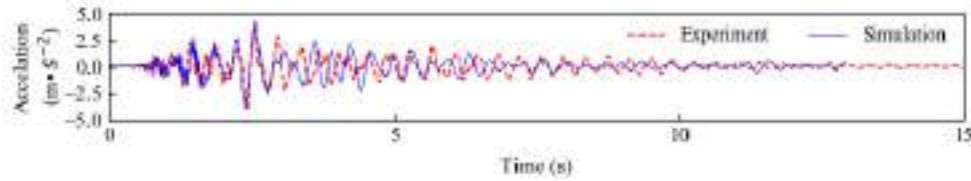


Figure 9. Time history curve of acceleration of point 1-OT-Z under K300 case

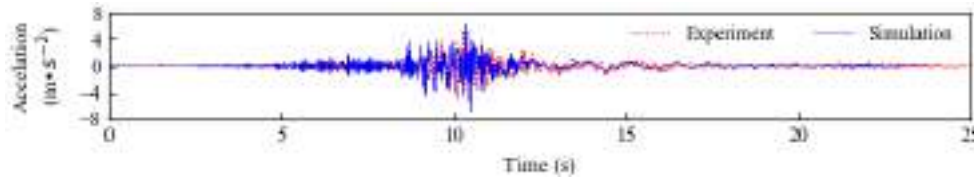


Figure 10. Time history curve of acceleration of point 10-MB-X under M300 case

The acceleration response peaks of different measure points are listed in Table 6, the amplification factor in the table refers to the ratio of peak acceleration response to the peak acceleration of the seismic waves.

Some rules can be summarized from Table 6: (1) Under load case E300, by contrasting the experiment value of measurement points between 4-MT-X and 4-MB-X, 10-MT-X and 10-MB-X, we can learn that the X-direction acceleration responses at bottom connections are slightly larger than those at top connections. The same conclusions can be got from the numerical values. (2) The Z-direction acceleration responses shows that acceleration responses of the middle connections are larger than that of outer connections. (3) the same conclusions as the above 2 rules can be got from the results of load case K300 and M300, but the errors between measurements and numerical results are obviously greater. (4) The sequence for amplification factors among different load cases accords to the following law: $K300 > E300 > M300$.

Table 6: Peak responses of the acceleration

Case	E300				K300				M300			
	Simulation (m/s ²)	Experiment (m/s ²)	Error (%)	Amplification factor	Simulation (m/s ²)	Experiment (m/s ²)	Error (%)	Amplification factor	Simulation (m/s ²)	Experiment (m/s ²)	Error (%)	Amplification factor
1-W-X	6.81	5.45	-	1.8	4.51	5.67	25.9	1.9	5.2	4.05	-22.3	1.4
1-OT-Z	2.63	2.74	4.2	0.9	4.21	3.87	-8.1	1.3	2.92	3.22	10.4	1.1
1-WX-Z	1.88	1.76	-6.4	0.6	3.4	2.69	-20.9	0.9	1.99	1.36	-31.7	0.5
4-OT-X	7.16	4.15	-	1.4	6.12	5.16	-15.7	1.7	7.35	4.42	-39.9	1.5
4-MT-X	6.79	7.23	6.5	2.4	10.31	8.83	-14.3	2.9	8.19	7.74	-5.5	2.6
4-MB-X	8.46	7.78	-8.1	2.6	5.16	7.01	35.8	2.3	6.94	5.85	-15.7	1.9
3-MT-	6.66	5.78	-	1.9	9.43	-	-	-	7.75	7.53	-2.9	2.5
5-OT-	7.17	5.97	-	2	5.29	5.63	6.5	1.9	6.91	7.16	3.5	2.4
7-MT-Z	2.65	3.25	22.6	1.1	4.99	3.87	-22.4	1.3	2.5	3.28	31.0	1.1
10-MB-	8.46	6.23	-	2.1	5.16	7.13	38.2	2.4	6.94	5.22	-24.7	1.7
10-MT-	6.63	5.21	-	1.7	10.28	7.5	-27.0	2.5	8.14	7.2	-11.5	2.4
12-OT-	7.82	6.27	-	2.1	5.38	6.98	29.7	2.3	6.01	4.24	-29.5	1.4

During the experiment, it was hard to arrange displacement meters to measure the absolute displacement between the structure and the ground (not the relative displacement between the structure and she shaking table), so only one absolute displacement was measured. Considering good agreement of numerical displacements with the experimental ones, numerical displacements and numerical dynamic stress response are shown in Table 6.

As shown in Table 7 among load case K300, E300 and M300, the displacement response and dynamic stress response under K300 case are the biggest, where Peak dynamic stress response, which is 33Mpa, occurs at outer hoop cable. The peak stress is 0.353 times higher than the initial stress (the stress after the prestress and all the applied weight), however it is smaller than the strength of corresponding components. This means all the components worked in safety during the shaking wave.



From Table 7, the maximum displacement, which occurs along the same direction as the seismic wave, reaches up to 61.0mm. However the structure members still work safely. The displacement response and dynamic stress response under E300 case and M300 case are about 50% of those under K300 case.

Therefore, it can be concluded that CFRP cable dome posses good anti-seismic performance. CFRP cable dome can survive even under severe near-field strong earthquake.

Table 7: Peak displacements and dynamic stress

Cases	X	Y	Z	Peak stress(MPa)	Maximum ratio of dynamic stress to initial prestress
	Displacement(mm)				
E300	29.4	18.5	18.7	10	0.140
K300	61.0	29.0	34.9	33	0.353
M300	34.1	20.8	20.8	12	0.183

Response of the structure under seismic waves with different intensities

Peek acceleration response under three kinds of seismic waves with different peak accelerations respectively are shown in Figure 11. What can be concluded from Figure 11 is that the acceleration responses vary approximately linearly with the wave intensity, with the exception that when under K wave whose peak acceleration range changes from 300gal to 500gal.

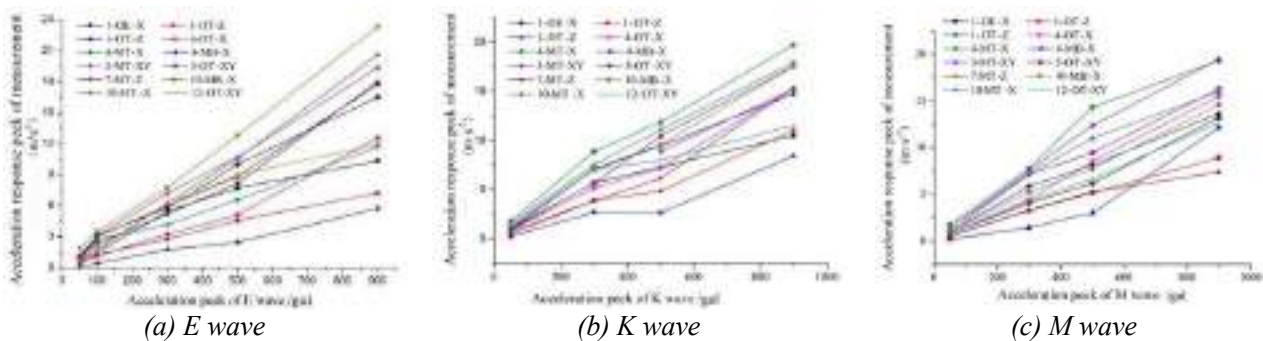


Figure 11. Peaks acceleration response under different seismic wave intensities

RESULTS AND DISCUSSIONS

In the article, multiple kinds of seismic waves are applied to shaking table test on a CFRP cable dome. The following conclusions can be drawn:

- (1) In generally, dynamic responses of CRFP cable dome in experiment agree well with simulation ones. Results of experiment can reflect the response rules of the structure. Though there are some errors depending on different locations of measurement points



- (2) The maximum dynamic responses occur under K wave and the minimum dynamic responses occur under M wave when the applied waves have the same 300gal peak acceleration.
- (3) X-direction acceleration responses of lower connections are larger than those of upper connections. X-direction acceleration responses of middle upper connections are larger than those of outer upper connections.
- (4) CFRP cable dome structure possesses good anti-seismic performance. It can maintain safety even under severe near-field strong earthquake.

ACKNOWLEDGMENTS

The authors would like to acknowledge the financial support of the National Natural Science Foundation of China (51378108, 51678137).

REFERENCES

- Bel Hadj Ali, N., Smith, I.F.C (2010). "Dynamic behavior and vibration control of a tensegrity structure", *International Journal of Solids and Structures*, 47(9), 1285-1296.
- Gasparini, D.A., Perdikaris, P.C., Kanj, N (1989). "Dynamic and static behavior of cable dome model", *Journal of structural engineering New York, N.Y.*, 115(2), 363-381.
- Geiger D H, Stefaniuk A (1986). "The design and construction of two cable domes for the Korean Olympics", *Proc of the IASS Symposium on Shells, Membranes and Space Frames*, 265-272.
- I. Tatemichi, T. Hatato, Y. Anma and S. Fujiwara, V (1997). "Vibration tests on a full-size suspen-dome structure", *Int. J. Space Struct*, 12(3&4), 217-224.
- Lazzari M, Vitaliani R V, Majowiecki M, et al (2003). "Dynamic behavior of a tensegrity system subjected to follower wind loading", *Computers & structures*, 81(22), 2199-2217.
- Luo Yaozhi, Wang Rong (2005). "Study On Dynamic Characteristics and Behavior of Cable Dome Subjected to Multi-Dimensional and Multi-Point Seismic Excitations". *Journal of Zhejiang University (Engineering Science)*, 39(1), 39-45. (In Chinese)
- Zhang, Limei; Chen, Wujun; Dong, Shilin (2014). "Natural vibration and wind-induced response analysis of the non-fully symmetric Geiger cable dome", *Journal of Vibroengineering*, 16(1), 31-41.
- Zhang, Zhi-Hong; Tamura, Yukio (2007). "Wind tunnel test on cable dome of geiger type", *Journal of Computational and Nonlinear Dynamics*, 2(3), 218-224.



SPLICE CONNECTION FOR TUBULAR FRP COLUMN MEMBERS

C. Qiu¹, Y. Bai²

¹ *Department of Civil Engineering, Monash University, Australia*

² *Department of Civil Engineering, Monash University, Australia, Email: yu.bai@monash.edu*

ABSTRACT

Pultruded fibre reinforced polymer (FRP) members are increasingly favoured in civil engineering as they are lightweight and corrosion-resistant. However, their application is limited by the challenge to connect them, especially tubular members, i.e. with closed sections. A splice connection is developed in this paper for tubular FRP members and its mechanical performance under axial and flexural loadings is investigated. The developed splice connection entails two tubular steel-FRP bonded sleeve joints (BSJs) and a steel bolted flange joint (BFJ) in between. Experimental tests were conducted on the splice connections of varied bond lengths and bolt configurations; results are reported and discussed regarding failure mode, load-displacement behaviour and strain response. The experimental investigation revealed that an effective bond length exists for the BSJs under axial loading, and that an eight-bolt configuration for the BFJ is more effective compared to a four-bolt one in terms of tensile and rotational stiffness and strength. Besides, it is concluded that the splice connection can be designed to fail in a ductile manner under both axial and flexural loadings.

KEYWORDS

Fibre reinforced polymer (FRP), tubular member, splice connection, experimental study, axial loading, flexural loading.

INTRODUCTION

Fibre reinforced polymer (FRP) structural members manufactured from the pultrusion process are credited with high strength-to-weight ratio, excellent corrosion resistance, and availability in various section shapes (Bank 2006). However, connecting FRP structural members into assembly is challenging, especially for tubular members, due to the closed section shape and the brittle and anisotropic nature of the materials. Early efforts to connect pultruded FRP I-sections into frame structure adopted bolted flange and web seated angles made of FRP (Bank et al. 1994). Steel seated angles were later proposed to prevent local failure in the connectors (Mottram and Zheng 1996). Utilising the steel flange seated angles and also bolted-through web-gusset plates, FRP tubular members were joined into beam-column assembly (Smith et al. 1999). Tubular FRP-steel bolted sleeve joints were proposed for assembly of space lattice structures and studied under axial loadings (Luo et al. 2015). It was found that bolt fastening caused stress concentration and exposed the weak in-plane shear strength of the FRP composites. To achieve more uniform stress transfer through adhesive bonding, bonded sleeve connections for joining circular FRP truss members into space frames using nodal joints were proposed and examined by Yang et al. (2016). In an experimental investigation by Wu et al. (2016), the bonded sleeve connection was applied in a tubular FRP beam-to-steel column assembly, exhibiting significant improvement in both rotational strength and stiffness over steel angle connections and bolted sleeve connections.

Despite the aforementioned works, research into developing a splice connection for FRP tubular members in column applications is still limited. Inspired by the previous success of the FRP-steel bonded sleeve connection concept, this paper proposes a splice connection for tubular glass FRP (GFRP) members and investigates experimentally its performance under axial and flexural loadings. Figure 1 illustrates the proposed splice connection and provides reference dimensions for this study. The proposed connection consists of a bonded sleeve joint (BSJ) coupling steel and GFRP tubes adhesively, and a bolted flange joint (BFJ) connecting two steel tubes with flange plates by bolts. When used as a column splice, the connection would be subjected to axial or flexural loadings or a combination of both. In this paper, the axial behaviour of the splice connection is investigated by testing the BSJ and the BFJ individually; while the flexural behaviour is studied by subjecting the connection to pure moment loading.

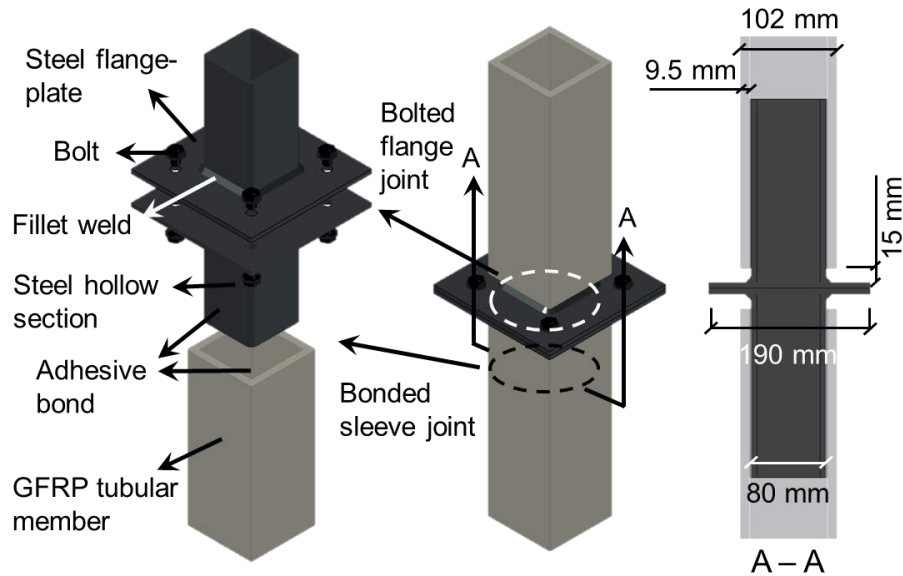


Figure 1: Proposed splice connection for tubular FRP members

EXPERIMENT PROGRAM

Specimens and material properties

All the specimens for axial and flexural loadings are indexed as in Table 1, where the first letter refers to the loading type ('A' for axial and 'B' for bending). Only compression tests were conducted on the A-BSJ (bonded sleeve joint for axial loading) specimens, as theoretical and numerical studies revealed that, considering cohesive failure as the failure mode of interest, tensile and compressive loadings would induce identical adhesive shear stress distribution along the bond length and thus identical joint behaviour (Qiu et al. 2017). For the A-BFJs, compressive failure would be preceded by member failure of the connected steel hollow section member, therefore only the tensile behaviour of the A-BFJs (bolted flange joint for axial loading) was investigated.

Each of the A-BSJ specimens, with geometries illustrated in Figure 2 (a), was assembled by coupling a pultruded GFRP square tube ($102 \times 102 \times 9.5$ mm) and a steel square hollow section (SHS, $80 \times 80 \times 6$ mm) with Sikadur-30, a two-component epoxy-based adhesive; four different bond lengths were covered as listed in Table 1. Although an adhesive layer around 0.5 mm in thickness is recommended for strong and reliable binding (Arenas et al. 2010), a 1.5 mm-layer thickness is selected in this study to provide tolerance for geometric imperfection of the cross sections and practical fabrication. Shown in Figure 2 (b), the A-BFJ specimens were fabricated by bolting (high strength M12 bolts) two 6 mm-thick steel flange-plates each of which was welded to a steel SHS (same as those in A-BSJs); a gusset plate was also slot-welded into the steel SHS for application of tensile loading. Figure 2 (c) presents the two bolt configurations adopted in the A-BFJ and the bending specimens. Two specimens, namely B-170-4 and B-120-8, were prepared for flexural loading, with their configurations and geometries described in Table 1 and Figure 2 (d). In the bending specimens, the steel flange-plates and the SHSs are the same as those used in the A-BSJs and A-BFJs, so is the cross-section geometries of the GFRP tubes; while the GFRPs were sourced from another supplier and a less viscous adhesive (Sikadur-330) was adopted for easier fabrication of the specimens. Material properties of the components used in the aforementioned specimens were summarised in Table 2.

Table 1: Specimens for axial and flexural loading

Specimen index*	Loading	Bond length (mm)	NO. of bolts	GFRP	Adhesive
A-BSJ-50-1, 2	Axial compression	50	-	White	Sikadur-30
A-BSJ-100-1, 2		100	-		
A-BSJ-140-1, 2		140	-		
A-BSJ-180-1, 2		180	-		
A-BFJ-4-1, 2	Axial tension	-	4	-	-
A-BFJ-8-1, 2		-	8	-	-
B-170-4	Four-point bending	170	4	Grey	Sikadur-330
B-120-8		120	8		

* Beside the bending specimens B-170-4 and B-120-8, two repeating specimens were prepared, indicated by the last number in the specimen index.

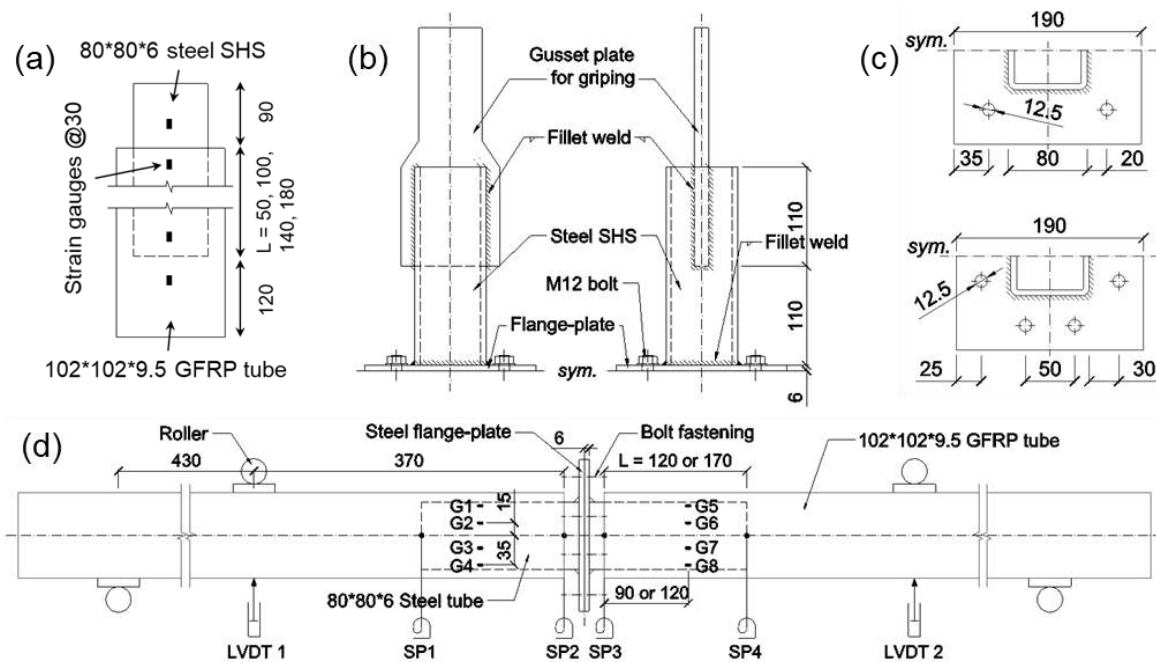


Figure 2: Geometries (all units in mm) and instrumentations (a) A-BSJ specimens; (b) A-BFJ specimens; (c) steel flange-plates for A-BFJ and bending specimens; (d) bending specimens B-170-4 or B-120-8

Table 2: Material properties

Material	Modulus ¹ (GPa)	Strength ² (MPa)	Poisson's ratio
Steel flange	200.6	313.6	0.277
Steel SHS	209.5	420.1	0.277
GFRP tube-white	30.2/5.5/3.5	306.5/-/26.7	-
GFRP tube-grey	25.2/6.2/3.0	330.6/88.5/31.2	0.280
Sikadur-30	11.2	22.4	0.310
Sikadur-330	4.2	32.8	0.280

¹: Young's modulus for steels and adhesives; longitudinal tensile/transverse tensile/shear modulus for GFRPs

²: Yiled strength for steels; longitudinal tensile/transverse tensile/shear strength for GFRPs; tensile strength for adhesives

Setup and instrumentation

Compressive loading on the A-BSJ specimens was implemented by a 500 kN Amsler machine at 0.4 mm/min loading rate (Figure 3 (a)). Axial shortening of the specimens was measured by two linear variable differential transducers (LVDT). As shown in Figure 2 (a), strain gauges were installed on the surface of the steel SHS and

the GFRPs at 30 mm intervals. Tensile loading on the A-BFJ specimens was applied by a 500 kN Baldwin machine at 0.5 mm/min loading rate (Figure 3 (b)). A laser extensometer was used to gauge axial elongation of the specimens. As depicted in Figure 2 (d) and Figure 3 (c), the bending specimens were loaded in a four-point bending setup to subject the splice connection to pure moment loading. Via a 200 kN Amsler machine, the bending action was applied by locking the two upper rollers while lifting the two lower ones at 1.5 mm/min. Strain gauges G1 to G8 were installed on the side surface of the GFRP-steel combined section as described in Figure 2 (d). Two LVDTs and four string pots (SPs) were deployed to measure deflection of the specimens.

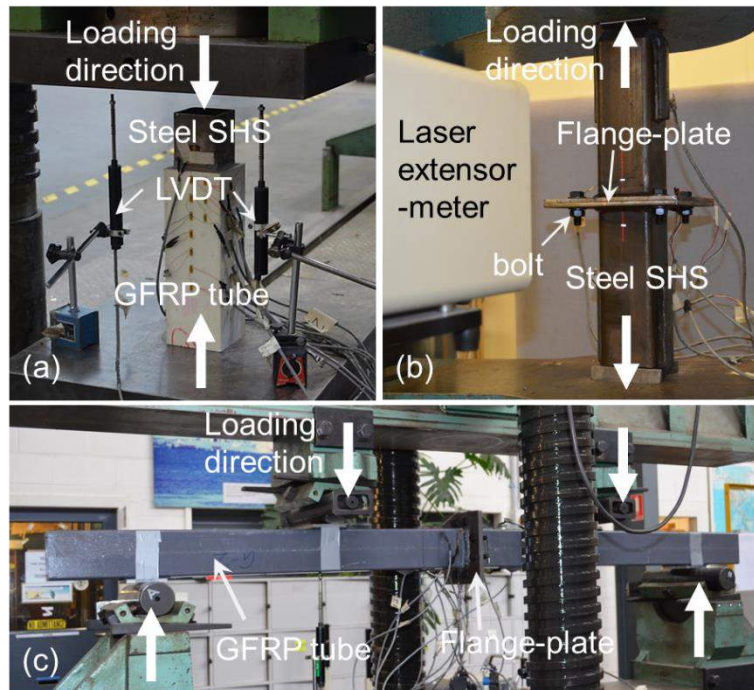


Figure 3: Experimental setup (a) A-BSJ specimens under compression; (b) A-BFJ specimens under tension; (c) bending specimens under four-point bending

RESULTS AND DISCUSSIONS

Load-deflection behaviours and failure modes

For all the A-BSJ specimens, experiments revealed a brittle cohesive failure within the adhesive layer. Upon failure, cracking in the adhesive layer occurred as shown in Figure 4 (a). Figure 4 (b), representative of all the A-BSJs, shows the separated adherends and the crack surface where bond failure occurred; the attachment of adhesive to both the steel and GFRP indicates cohesive failure located within the adhesive layer. Figure 4 (c) shows the typical load-displacement curves, characterised by linear increase before brittle failure. Post-failure residual strength, due to the friction between the fracture surfaces, was recorded between 10 to 45 kN among the specimens. Joint capacities of the A-BSJs (P_u) are plotted versus the bond lengths (L) in Figure 4 (d). The joint capacity P_u increases almost linearly with L up to $L = 100$ mm; while from $L = 100$ mm to 180mm the improvement of P_u slows down dramatically, by a mere 18 % (from an average of 284.5 kN to 336.0 kN), which indicates the existence of an effective bond length around 100 mm.

All the A-BFJ specimens failed by steel yielding of the flange-plates. As shown in Figure 5 (a), elongation of A-BFJ-4 (i.e. A-BFJ with four bolts) resulted in opening gaps between the two flange-plates in the region away from the bolts; while in A-BFJ-8, the flange-plates were bent outwards in the regions between the bolts and the SHS (Figure 5 (b)). Figure 5 (c) presents the tensile load-displacement curves of the A-BFJs. After steel yielding, the curves kept increasing gradually at near constant slopes until the loading process was ceased at 9 mm-elongation for the A-BFJ-4s or at 8 mm for the A-BFJ-8s. Defined as the intersection point of the elastic and hardening tangent line, an average yield load is obtained as 104.2 kN for A-BFJ-4 and 183.8 kN for A-BFJ-8. The average initial stiffness of A-BFJ-4 and A-BFJ-8 is 104 kN/mm and 346 kN/mm respectively. It can be found that the

eight-bolt configuration results in an increase of 77 % in yield load and 233 % in initial stiffness when compared to the four-bolt configuration.

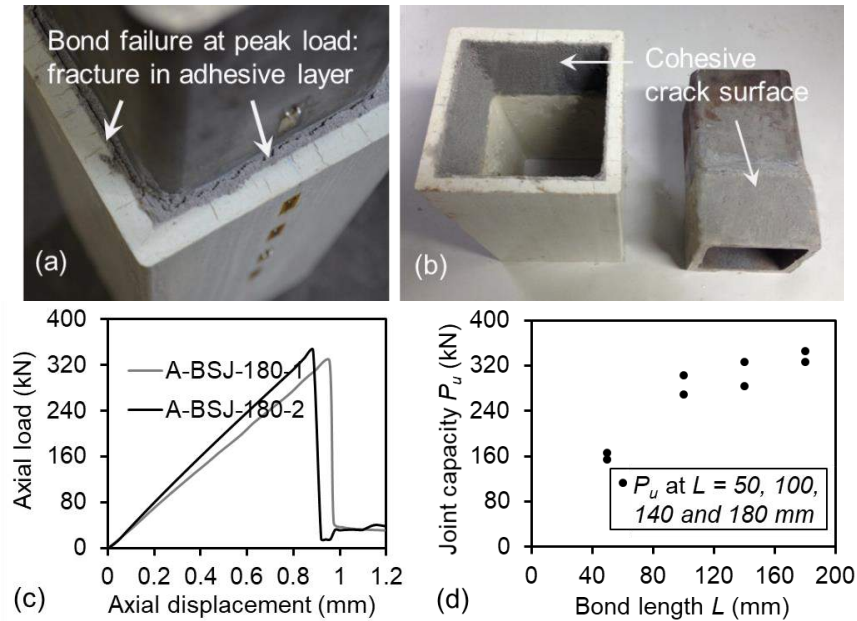


Figure 4: The A-BSJ specimens (a) Adhesive failure at peak load; (b) Bond failure surface; (c) Typical compression-displacement curves of A-BSJs; (d) Joint capacity versus bond length

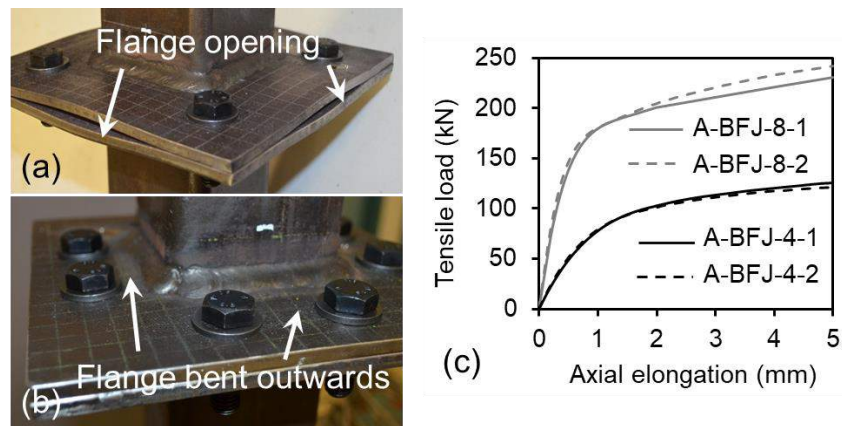


Figure 5: Deformed shape of (a) A-BFJ-4s, (b) A-BFJ-8s and (c) Tension-displacement curves of A-BFJs

The behaviour of the A-BSJ and A-BFJ specimens reported above illuminates the behaviour of the proposed splice connection (integrating the BSJ and the BFJ) under axial loadings. Under compressive loading, the behaviour of the splice connection is governed by the BSJ component: the load-displacement curve would be linear up to brittle failure in the BSJ, and an effective bond length would exist for the joint capacity as found with the A-BSJ specimens. Under tensile loading, the load-displacement behaviour of the splice connection would be linear before brittle bond failure in the BSJ, if the joint capacity of the BSJ is attained before yielding of the BFJ component. It is recommended that a sufficient bond length is designed such that the capacity of the BSJ is above the yield load of the BFJ to achieve a ductile failure. For example, in the case of a suggested specimen A-180-8 (integrating A-BSJ-180 and A-BFJ-8) under tensile loading, substantial energy would be dissipated through yielding of the steel flange-plate before adhesive failure in the BSJ. It should be noted that the bond failure in the BSJ may be preceded by failure in the GFRP, as buckling under compression or tensile failure, depending on the geometries and material properties of the GFRP and also the adhesive. In such cases, under compressive loading, connection failure would be shifted to member failure of the GFRP; under tensile loading, ductility of the BFJ should be utilized before brittle tensile failure of the GFRP.

Figure 6 presents the moment-rotation curves of the bending specimens B-170-4 and B-120-8, where the rotation angle α between the connected GFRP members is illustrated in Figure 7 (a) and calculated by Equation (1) shown below. The moment-rotation curve of B-170-4 starts to show nonlinearity at around 3.9 kNm, caused by yielding of the steel flange-plates. Loading of the specimen was continued until the displacement limit of the loading machine, where the bending moment barely increased (around 8.4 kNm as shown in Figure 6). Figure 7 (a) shows the final overall deformation of B-170-4, no failure in the GFRP and the bonded region was observed. The final deformed shape of the flange-plates is indicated in Figure 7 (b), marked by the opening gaps at the sides and the bottom. For B-120-8, yielding of the steel flange-plates starts at around 7.8 kNm; the bending moment continues to increase at reduced rotational stiffness until a peak bending moment of 13.9 kNm where moment resistance of the specimen drops suddenly (Figure 6). Figure 7 (c) shows the final flange deformation of B-120-8; although not readily visible, the steel flanges were bent outwards between the steel SHS and the bolts at the tensile region. The final failure of B-120-8 was caused by cracking of the upper web-flange junctions of one of the GFRP tubes as indicated in Figure 7 (d); at the same time the GFRP was separated from the steel SHS at the bottom and sides due to cracking in the adhesive. From B-170-4 to B-120-8, the initial rotational stiffness does not see a notable increase (from 233 kNm/rad to 345 kNm/rad), while the yield moment (intersection point of the elastic and hardening tangent line) experiences a remarkable improvement by 86 %, from 5.6 kNm to 10.4 kNm.

$$\alpha = \frac{d_{SP1} - d_{LVDT1}}{L_{1,1}} + \frac{d_{SP4} - d_{LVDT2}}{L_{4,2}} \quad (1)$$

where d is the displacement measured by a LVDT or SP, $L_{x,y}$ is the horizontal distance between SP x and LVDT y (positions of LVDTs and SPs indicated in Figure 2 (d))

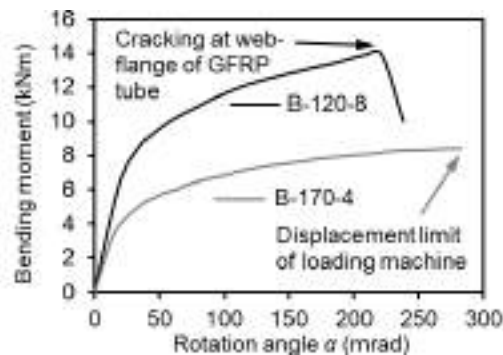


Figure 6: Moment-rotation curves of the bending specimens

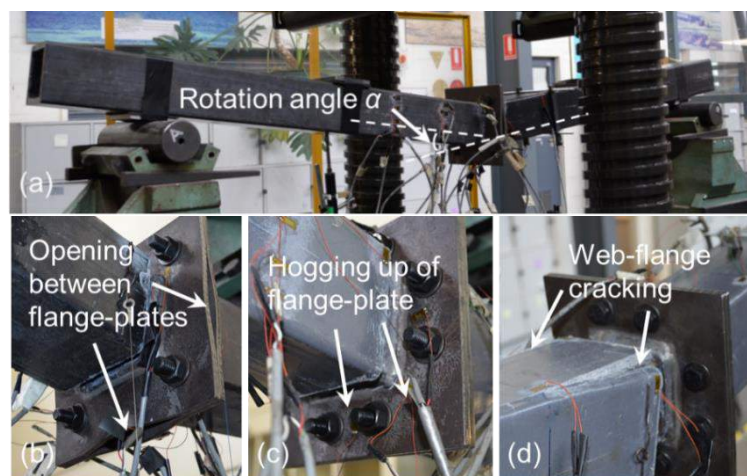


Figure 7: (a) Overall deformation B-170-4; (b) Final flange deformation of B-170-4; (c) Final flange deformation of B-120-8; (d) Web-flange cracking in the GFRP of B-120-8

Strain response

For the A-BSJ specimens, output from the strain gauges on the steel SHS and the GFRP tube indicated both the adherends within elastic range. From the specimen A-BSJ-180-2, axial strains on the outer surface of the GFRP, at four different load levels, are plotted along the centre bond line in Figure 8. It is found that the axial strain distribution at mid-portion of the bond length features a flatter gradient, revealing lower level of adhesive shear stress in this region than at the ends of the bond length. In general, the axial strain distribution near the GFRP end of the bond length ($x = 180 \text{ mm}$) exhibits a steeper gradient than near the steel end ($x = 0 \text{ mm}$). This is consistent with theory that greater shear slip between the adherends would be incurred near the more flexible adherend (GFRP in this case). Also noteworthy is that at 100% P_u , the strain distribution flattens near the GFRP end, indicating a drop of the adhesive shear stress. This can be caused by softening of the Sikadur-30 adhesive, which was discovered, by a single lap pull-off test configuration, with an elastic-softening bond-slip behaviour (Yu et al. 2012).

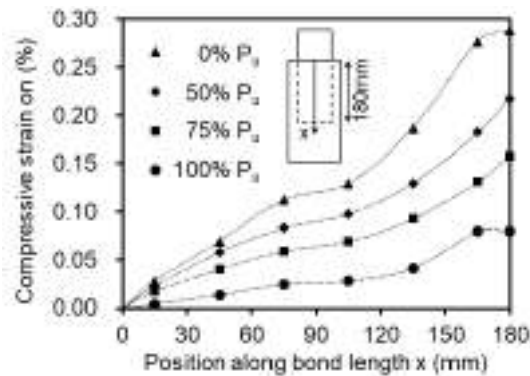
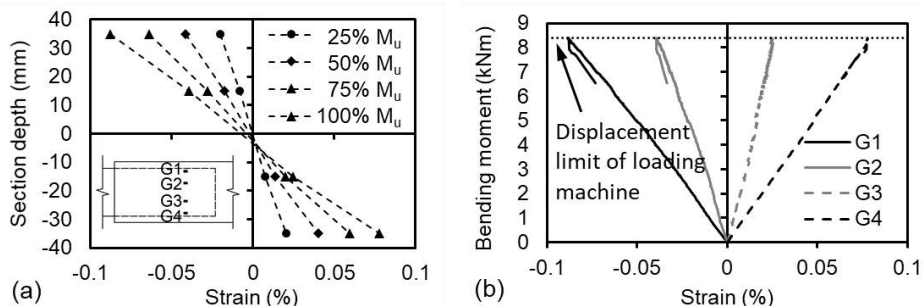


Figure 8: Axial strains on the GFRP along centre bond line (A-BSJ-180-2) at different load levels

For the bending specimens, the axial strain distribution on the side surface of the GFRP-steel composite section is plotted along the section depth in Figure 9. Corresponding to the specimen B-170-4 which failed due to excessive yielding of the steel flange-plates, Figure 9 (b) shows linear distribution of the axial strain along the section depth, revealing that composite action between the GFRP tube and the steel SHS was maintained from start to the ultimate bending moment (M_u). From the same strain gauges, the linear load-strain response presented in Figure 9 (b) indicates the BSJ components of the connection remained intact during the loading process.

Figure 9 (c) shows the axial strain distribution along section depth of B-120-8 which failed ultimately at the web-flange junction of the GFRP (Figure 7 (d)). Strain gauges G5 to G8 on the failed GFRP tube (instead of G1 to G4 on the intact GFRP tube) were selected to output the strain distribution. It is observed from Figure 9 (c) that the strain distribution is almost linear up to 75% M_u , but deviates from linearity at 100% M_u . This strain data is plotted as load-strain curves shown in Figure 9 (d). It is revealed that except for the G7 curve which maintains linear, the other load-strain curves develop in decreasing slope after around a bending moment of 8.5 kNm. This implies an incomplete stress transfer between the steel SHS and the GFRP, possibly caused by softening or cracking of the adhesive.



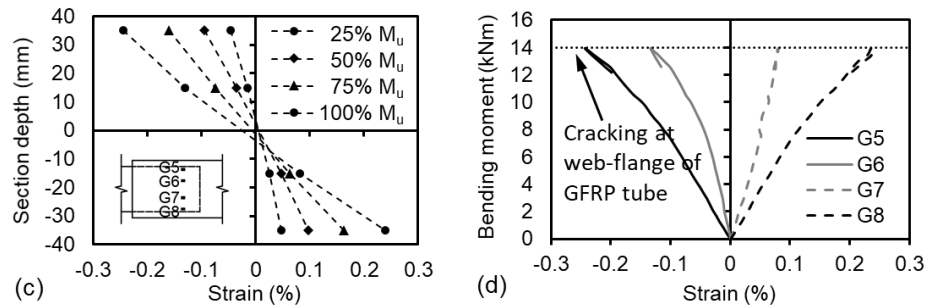


Figure 9: Strain response on the side surface of the steel-GFRP composite section (a) Axial strain distribution along section depth B-170-4; (b) Load-strain response B-170-4; (c) Axial strain distribution along section depth B-120-8; (d) Load-strain response B-120-8

CONCLUSIONS

In this paper a splice connection is introduced for joining FRP tubular column members. It is comprised of two tubular FRP-steel bonded sleeve joints (BSJ) and a steel SHS bolted flange joint (BFJ) in between. Experiments were conducted to investigate the mechanical performance of the connections under axial and flexural loadings. Based on the experimental results from specimens of varied bond lengths and two bolt configurations, the following conclusions can be drawn:

- Under axial loading the BSJs failed brittlely in the adhesive layer, and an effective bond length was found around 100 mm for the section geometries and the adhesive in this study. Strain distribution on the GFRP surface indicated softening of the adhesive near the GFRP end as the load increased. Failure of the BFJs under tensile loading was ductile through yielding of the steel flange-plates. The eight-bolt configuration (A-BFJ-4), compared to the four-bolt one (A-BFJ-4), improved the initial stiffness by 225% and the yield load by 82%. Integrating the BSJ and the BFJ, the splice connection can be designed with the 180 mm bond length and the eight-bolt configuration in this study, such that under tensile loading ductile failure would occur in the BFJ component before brittle failure in the BSJ.

- Under flexural loading the splice connection specimens experienced substantial yielding in the steel flange-plates. The B-170-4 specimen (with 170 mm bond length and the four-bolt configuration) remained intact in the BSJ component, while B-120-8 failed ultimately in the web-flange junction of the GFRP tube. With yielding of both the specimens governed by the BFJ component, the eight-bolt configuration was found to enhance the yield moment by 86 %, compared to the four-bolt one. Strain results indicated that full composite action in the BSJ was maintained in B-170-4, while softening or cracking of the adhesive might have occurred in B-120-8.

ACKNOWLEDGMENTS

The authors acknowledge the support from the Australian Research Council through the Discovery scheme (DP180102208). Thanks are also given to the staffs in the Civil Engineering Laboratory of Monash University for their technical supports.

REFERENCES

- Arenas, J. M., Narbon, J. J., and Alía, C. (2010). "Optimum adhesive thickness in structural adhesives joints using statistical techniques based on Weibull distribution." *International Journal of Adhesion and Adhesives*, 30(3), 160-165.
- Bank, L. C. (2006). *Composites for construction: structural design with FRP materials*, John Wiley & Sons.
- Bank, L. C., Mosallam, A. S., and McCoy, G. T. (1994). "Design and performance of connections for pultruded frame structures." *Journal of reinforced plastics and composites*, 13(3), 199-212.
- Luo, F. J., Bai, Y., Yang, X., and Lu, Y. (2015). "Bolted Sleeve Joints for Connecting Pultruded FRP Tubular Components." *Journal of Composites for Construction*, 04015024.
- Mottram, J., and Zheng, Y. (1996). "State-of-the-art review on the design of beam-to-column connections for pultruded frames." *Composite structures*, 35(4), 387-401.



- Qiu, C., Feng, P., Yang, Y., Zhu, L., and Bai, Y. (2017). "Joint capacity of bonded sleeve connections for tubular fibre reinforced polymer members." *Composite Structures*, 163, 267-279.
- Smith, S., Parsons, I., and Hjelmstad, K. (1999). "Experimental comparisons of connections for GFRP pultruded frames." *Journal of Composites for Construction*, 3(1), 20-26.
- Wu, C., Zhang, Z., and Bai, Y. (2016). "Connections of tubular GFRP wall studs to steel beams for building construction." *Composites Part B: Engineering*, 95, 64-75.
- Yang, X., Bai, Y., Luo, F. J., Zhao, X.-L., and He, X.-h. (2016). "Fiber-Reinforced Polymer Composite Members with Adhesive Bonded Sleeve Joints for Space Frame Structures." *Journal of Materials in Civil Engineering*, 04016208.
- Yu, T., Fernando, D., Teng, J., and Zhao, X. (2012). "Experimental study on CFRP-to-steel bonded interfaces." *Composites Part B: Engineering*, 43(5), 2279-2289.



Bridge Paradis Norway: Design and engineering of a 42m span full FRP footbridge

Liesbeth Tromp¹, Kees van IJselmuiden², Stian Persson³

¹ Liesbeth.Tromp@RHDHV.com, Royal HaskoningDHV, Infrastructure, Rotterdam, The Netherlands;

² Royal HaskoningDHV, Infrastructure, Amsterdam, The Netherlands; ³ Norwegian Public Roads Administration-Statens vegvesen, Bridge Department Region West, Bergen, Norway;

Keywords : All FRP and smart FRP structures; Case studies ; Codes, standards and design guidelines; Durability, long-term performance

Mini-Symposium: "Full FRP system: design and standard"

ABSTRACT:

This paper presents the engineering story behind the bridge Paradis, Bergen, Norway. It is a full Fiber Reinforced Polymer (FRP) tender design, prepared by Royal HaskongDHV. The material and detailing have been optimised for the application in the Norwegian wet and cold climate. Statens vegvesen requires a low maintenance solution to minimise life cycle costs and hindrance for traffic on road and rail. The choice for FRP was made to prevent durability issues due to thermal fatigue and salting in winter times.

With its free span of 42m, this bridge is one of the longest spans for bridges in full FRP worldwide. A team of architects and engineers of RoyalHaskoningDHV prepared the design in close cooperation with a multi disciplinary team of the Client, Statens vegvesen. This way of work contributed to the confidence in FRP design and developing design and engineering protocols for FRP structures in Norway. In the design use was made of the latest insights in FRP design, safety concepts and material safety factors. Structural challenges involved connections, stability of FRP members and behaviour of FRP material and connections under sustained loading. This paper presents the interaction of design, material and manufacturing process from an engineering perspective. It describes the results of the structural analysis and highlights the principle of the solutions for reliable and easy to assemble connections.



Figure 80. Bridge Paradis, Bergen, Norway

INTRODUCTION

THE DESIGN OF THE FRP BRIDGE AT PARADIS AIMS TO REALISE AN AESTHETICALLY PLEASING FRP STRUCTURE, THAT IS OPTIMISED TO BE COST EFFECTIVE AND MAXIMISES DURABILITY BY CHOICE OF MATERIAL, MINIMISING THE NUMBER OF CONNECTIONS AND CLEVER DETAILING. THE MAIN MOTIVATION FOR STATENS VEGVESEN TO LOOK INTO FRP STRUCTURES IS THE POLICY EMPHASISING DURABLE INFRASTRUCTURE CROSSING HIGH TRAFFIC ROADS AND RAILWAYS THAT MINIMISES DEMAND FOR PERIODIC MAINTENANCE.

FOR LIGHTWEIGHT LONG SPAN BRIDGES HUMAN INDUCED VIBRATIONS ARE ONE OF THE MAIN DESIGN GOVERNING PARAMETERS. DYNAMIC ANALYSES FORMED AN



IMPORTANT PART OF THE ENGINEERING, TO DETERMINE THE LEVEL OF COMFORT THE PEDESTRIANS WILL EXPERIENCE ON THE BRIDGE. FOR THIS DESIGN ALSO BUCKLING IS GOVERNING, AS THE DESIGN HAS SOME LONG SLENDER MEMBERS LOADED IN COMPRESSION.

FINITE ELEMENT ANALYSES HAVE BEEN CARRIED OUT TO DETERMINE THE DIMENSIONS AND THE BEHAVIOUR UNDER AMONG OTHERS TRAFFIC LOADS AND WIND LOADS, BASED ON ANALYSES INCLUDING EIGENFREQUENCY ANALYSES AND GLOBAL BUCKLING ANALYSES. IN THIS PAPER THE TENDER DESIGN OF THE BRIDGE PARADIS IS DESCRIBED AND DESIGN CHOICES ARE EXPLAINED, RELATING TO ASPECTS OF THE ARCHITECTURE, STRUCTURE, MATERIAL AND MANUFACTURING PROCESS.

ARCHITECTURE SKETCH

The structure has been designed by RoyalHaskoningDHV architect Joris Smits. Several concepts have been developed, see *Figure 2*. The abutment is located on rocks, which provides an opportunity for clamped supports. However, Statens vegvesen does not prefer clamped supports in this situation, due to the uncertainty in the capacity of the rocks combined with a new type of material.



Figure 81. Architecture sketch Bridge Paradis

Concept 3 was preferred and selected by Statens vegvesen. This structural concept is a faceted arch structure and reminds slightly of the stainless steel truss bridge, which was considered in an earlier design study.

Design for durability

The design is based on Fibre Reinforced Polymer (FRP). Durability is further maximised by the following design measures:

- Selection of vinylester resin, a high grade chemically resistant resin type.
- Application of conservative design factors (conversion factors for wet conditions)
- Design based on high grade manufacturing technique such as vacuum infusion.
- Minimising the number of connections.
- Detailing to minimise moisture or dirt ingress.

The design consists of a profile based upper structure and an integrated monocoque deck. The fiber reinforcement used in the tender design is E-glass. Carbon Fiber reinforcement has been considered in case additional stiffness

was needed, but it was found that sufficient stiffness and strength could be realised using standard glass fiber reinforced polymer (GFRP). The design makes use of stainless steel connectors. The foundation is made out of concrete.

Structural principle

The structure acts as an arch structure and has stays supporting the deck. The upper beams are loaded in compression. The stays are FRP tubes and loaded in tension, see Figure 82.

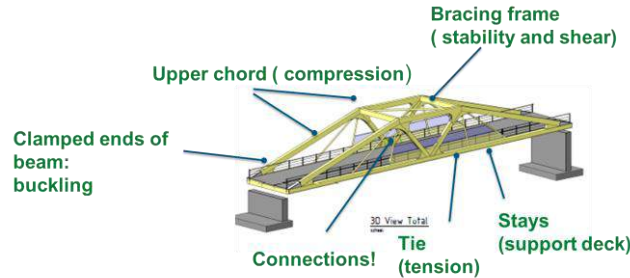


Figure 82. Structural members bridge Paradis

The diagonal beams and transverse beams of the superstructure form a stabilising portal for the top chords, from which the bridge deck is supported.

Dimensions

The global dimensions of the bridge are depicted in Figure 83. Initial calculations on a simplified structure were used to determine the global dimensions. In the materialisation phase the height and cross section of the beams were further adjusted to fit the structural and functional needs.

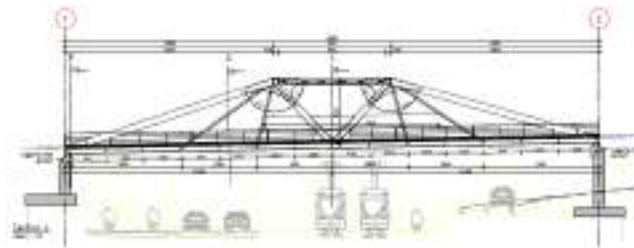


Figure 83. Global dimensions bridge Paradis

The height of the superstructure is 5.5 m. Typical dimensions of the beams of the superstructure are around 0.55 m * 0.50 m.

Connections

The constituting members and connections are seen in Figure 84. The lower chord that functions as the tie has been designed as a continuous member.

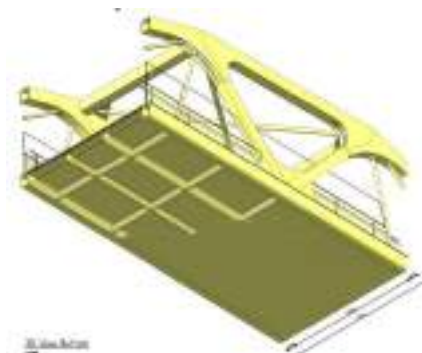


Figure 84. Principle of the connections

Connections of the profiles

The connection of profiles to profiles and the stays to the lower chord have been designed as hybrid bolted and adhesive connections. The adhesive prevents moisture ingress in the bolt holes. Due to the high forces at the location of the bolted connections, the thickness of the laminate must be increased locally. Compressive forces are also transmitted by contact, requiring close tolerances.

In the nodes stainless steel inserts have been applied for ease of assembly and create high strength load transfer in x,y and z-directions, see *Figure 85*. To connect the top chord beams, a stainless steel insert is used. The connection insert consists of a stainless steel web plate welded to tube profiles, see *Figure 85*. Stainless steel is the preferred material for the connectors, because in FRP the connection of the web to the tube is complicated and the strength for an FRP connector will be lower.

The length of the stainless profiles depends on the number of bolts required to transfer the forces. The connection will be a combined adhesive and bolted connection, where each connection type individually will have 100% of the required capacity.

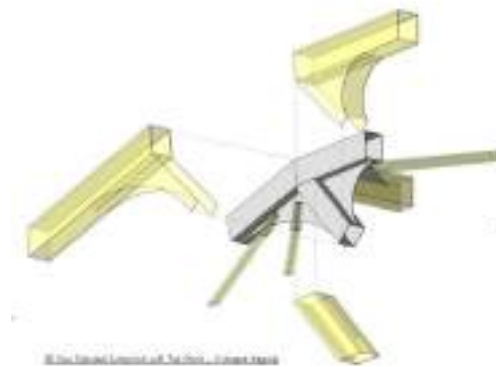


Figure 85. Principle of profile connection

Connections of the deck

The deck sections are built up using prefabricated FRP integrally produced or laminated parts using adhesive and laminated connections. At strategic locations bolted connections and shear studs may be introduced as a structural back up and for reasons of assembly.

Design Standards

The design is elaborated in accordance with the Eurocodes and the Norwegian National annexes. The specific requirements for this design phase have been captured in an AIP (Approval In Principle), which included the Client specific requirements by Statens vegvesen. For the FRP structures use has been made of the CUR96 [1] and Eurocomp Design Code [2]. These codes provide among others FRP specific partial material factors and guidance for the design of connections. Use has been made of latest insights from design guidance development (revision of CUR96, CUR96;2017) and discussions on European level (CEN-TC250 WG4).

Structural analysis

Finite Element software SOFiSTiK version 14.10-30 is used for the analysis of the FRP bridge Paradis structures and the concrete foundation. The software is used for the analysis of the stresses and stability (ULS) and deformations (SLS) of the bridge structure. The design choices are agreed with the technical experts of Statens vegvesen.

FE Model

The model of the bridge structure uses 2D shell elements for the deck structure and 1D beam elements for the superstructure and stays, see *Figure 86*.



Figure 86. FE model bridge Paradis

The bearings are modelled as springs with an infinite stiffness. The spring is connected to a node. Per spring axis a separate spring element has been created. This element is later on used to get the spring force. For the expansion joint a node at deck level is inserted. The translations and movements for this node are used as input for the expansion joint design.

Materials

The materials used In the FE analysis are of type anisotropic GFRP55, a balanced, symmetric lay up of glass fiber reinforced vinylester with fibers distribution of [55%/15%/15%/15%] in orientations [0°/90°/45°/-45°] and quasi-isotropic GFRP with distribution of [25%/25%/25%/25%] in orientations [0°/90°/45°/-45°]. The strongest and stiffest direction of the anisotropic material is in line with the local x-axis of the members. The material properties are given in Table 34.

Table 34. Material properties GFRPQI and GFRP55

Property		GFRP QI	GFRP 55
		GFRP Quasi isotropic	GFRP anisotropic
		[0°/90°/45°/-45°]	[0°/90°/45°/-45°]
		[25%/25%/25%/25%]s	[55%/15%/15%/15%]s
Fiber volume fraction	V_f	50%	50%
Young's modulus in x- direction	E_x [N/mm ²]	18600	25800
Young's modulus in y- direction	E_y [N/mm ²]	18600	15900
In plane shear modulus in xy- direction	G_{xy} [N/mm ²]	7000	5600
Density	ρ [kg/m ³]	1850	1850
Axial strength x- direction	$f_{x,Rk}$ [N/mm ²]	223	310
Axial strength y- direction	$f_{y,Rk}$ [N/mm ²]	223	191
In plane Shear strength xy-direction	$\tau_{xy,Rk}$ [N/mm ²]	112	90
Inter laminar shear strength	$\tau_{ILSS,Rk}$ [N/mm ²]	20	20
Thermal expansion coefficient in x-direction	α_x [mm/(mm·K)]	1.3E-005	1.07 E-005

In the next design phase, further optimisation of the material lay ups is possible. Where more axial stiffness or strength is needed, i.e. in the main members of the superstructure, the percentage of unidirectional fibres can be further increased, or even carbon fibres can be applied in combination with glass fiber reinforcement.

Deformations

The deformations of the bridge under full pedestrian load (5 kN/m^2) are seen in Figure 84.

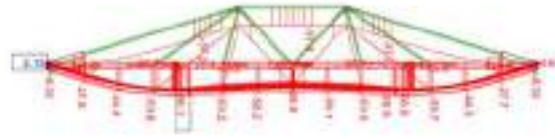


Figure 87. Global deformation [mm]; load 5 kN/m^2

The bridge displacement at quarter of the span is larger than at the mid span. The reason for this is that at mid span a stiff V-shaped frame is present and the fact that the outer stay is a less rigid support due to its angle and its slenderness. The deformations are within the opposed limit of $L/350$ under frequent loading conditions (75%), taking into account the applied conversion factors for effects of temperature and moisture effects.

Permanent loads

An important design requirement for Norwegian infrastructure is the ability to resist spike tyres and snow plows, as they are frequently used in winter season. For that reason in the calculations an asphalt layer with an average thickness of app. 50 mm is taken into account. This implies quite high permanent loads, and as FRP is a creep sensitive material the permanent loads are to be considered with the required attention for both deformations as well as strength evaluations. Methods from [1], [2] and [5] were compared and the most conservative factor has been applied in this preliminary stage.

The self weight of the FRP structure is app. 42 tonnes. The estimated weight of asphalt, steel connectors, handrails, etcetera is 45 tonnes! Due to the weight issues in relation to creep and stability, alternative solutions to the asphalt layer will be looked into in the next design phase.

The deformation under permanent load is approximately 44 mm. The forces in the super structure under permanent loads are app. 700 kN (Figure 88). These forces are used for the assessment of the connections. The resulting stresses in the global structure are very low (around 11 MPa) and not critical for the global design.

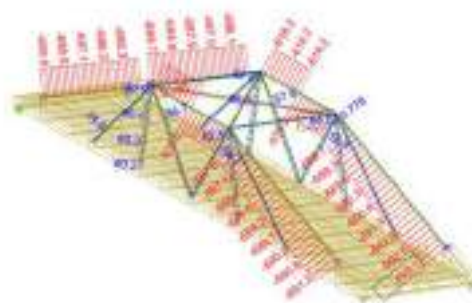


Figure 88. Forces under permanent loads [kN]

Eigenfrequency

For long span footbridges the high strength over stiffness ratio of GFRP means that comfort of the footbridge is an important design criterion. The Eurocode refers to the JRC-technical report on human induced vibrations for footbridges [3], which provides detailed criteria and methods for the analysis. The design requirement prescribes Comfort Class 2 for Traffic Class 3, which implies maximum accelerations of between $0.7 - 1.0 \text{ m/s}^2$ for a pedestrian density of 0.5 person/m^2 .

An important imposed additional requirement, from CUR96, prescribes that between 2.1 Hz – 2.5 Hz the reduction factor Ψ , that takes into account the chances of the occurrence of interlocking, see [3], cannot be taken lower than 0.25, see red line in Figure 89. This restrictive requirement has been added because the accuracy of prediction of eigenfrequency, mass, and changes of mechanical properties over time does not justify the exclusion of interlocking over such a narrow range.

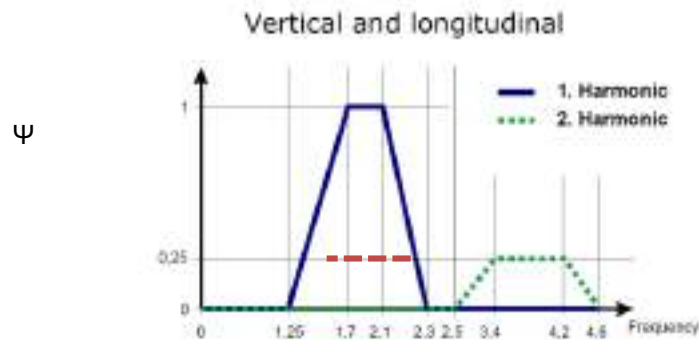


Figure 89. Reduction factor Ψ , [3], with suggested additional restriction (red dashed line)

The first mode for the tender design is a lateral mode: 1.9 Hz. This value is $> 1.2\text{Hz}$ and therefore outside of the critical range for lateral excitation. The first vertical mode including ageing occurs at 2.5 Hz, see Figure 90.

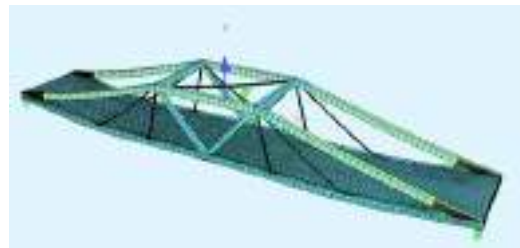


Figure 90. Modal shape of 1st vertical eigenmode

This mode is within the critical range, so a more detailed analysis was performed. Assuming a damping of 1%, the associated maximum vertical acceleration was determined to be $0,2\text{ m/s}^2$. Including the conservatively assumed effects of ageing, the eigenfrequency reduces to 2.1 Hz, and the associated vertical acceleration was determined to be $0,7\text{ m/s}^2$, and thus just within the set acceptable limits. The accelerations are relatively low because of the relatively high modal mass of the vibration mode, with a modal mass factor of 0.8 instead of 0.5. This high modal mass can also be recognised from Figure 87.

The low eigenfrequency is partly due to the contribution of the asphalt. It is recommended to further optimise the design and increase the eigenfrequency. This can be achieved either by reduction of the dead weight, for example by investigating the application of an alternative lighter wear surface, or by increasing the stiffness of the FRP-material.

Stresses

The capacity of FRP for the preliminary design is based on a simplified strain failure criterion with axial failure strain of 1.2% and a shear failure strain of 1.6%. The maximum stress in the global structure is $< 47\text{ N/mm}^2$, and the unity-checks on the stresses are low, < 0.6 . It is concluded that material strength is not governing for the design for the global structure.

Stability

Looking at the structure it can be seen that the long diagonal beams of the super structure are loaded in compression and must be evaluated for stability. Using the FE-model, the resistance against buckling was determined for the structure including buckling. A unity check based on this Eulerian capacity of 0,53 was found for the structure, see Figure 91.



Figure 91. Modal shape of the 1st buckling mode around local y-axis



This includes the conservative reductions to take into account the effect of the climate and ageing, but not the effect of geometric imperfections. To include this effect the reduction factors as described in the revision of [1] have been applied. This method uses the research done on buckling of pultruded profiles [4]. For the interaction between compression and bending moment the formulae according to EN1993-1-1 are used. The resulting unity check of 0.93 proves that the capacity of the structure is sufficient. Because of the limited experience of the applied reduction factors and the importance of stability of the structure, strong recommendations are made for the evaluation of stability in the next design phase as well as during the realisation phase and the health monitoring of the structure.

IT IS RECOMMENDED TO INCREASE THE RESISTANCE OF THE STRUCTURE AGAINST BUCKLING, ESPECIALLY SINCE THESE MEASURES WILL AFFECT BOTH THE COMFORT AND THE LOAD BEARING CAPACITY POSITIVELY. IN ADDITION IT IS RECOMMENDED TO PERFORM A GEOMETRICALLY NON LINEAR BUCKLING ANALYSIS WITH CLEARLY DEFINED AND QUANTIFIED MARGINS ON TOLERANCES FOR MISALIGNMENTS AND OTHER RELEVANT IMPERFECTIONS. THIS ANALYSIS WILL GIVE THE ALLOWABLE LIMITS FOR GEOMETRIC IMPERFECTIONS IN THE REALISATION PHASE. IN ADDITION TO INITIAL IMPERFECTIONS ALSO CREEP DEFORMATIONS MUST BE INCLUDED. BECAUSE BUCKLING IS THE DESIGN GOVERNING FAILURE MODE, THESE GEOMETRICAL TOLERANCES MUST BE VERIFIED WITH GREAT ATTENTION, AND MUST BE ADDRESSED WITH THE REQUIRED PRIORITY IN QUALITY CONTROL PROCEDURES.

CONCLUSIONS

In close cooperation with Statens vegvesen the structural design of the bridge at Paradis was developed to meet the architectural design. As a final statement, a 3D printed model was prepared, see Figure 92.

The technical performance of the tender design has been demonstrated to meet all requirements as specified by the Eurocodes and Statens vegvesen. It has therefore been demonstrated that a 42 m footbridge can be realised with a full FRP structure based on glass fiber reinforcement.

Based on the tender design, the design opportunities and aspects that require special attention have been identified. The FRP technical specifications will be prepared in cooperation with the technical specialists of Statens vegvesen. The bridge is put to tender in 2018. When this bridge is built, it will be the first FRP bridge built by the Norwegian Public Roads Administration.



Figure 92. 3D printed model bridge Paradis

REFERENCES

- [6] CUR96, (2003), CUR aanbeveling 96 "Vezelversterkte kunststoffen in bouwkundige en civieltechnische draagconstructies", eerste herziene uitgave.
- [7] Clarke J. L., (1996), "Structural Design of Polymer Composites"; Eurocomp Design Code and Handbook, E&FN Spon.
- [8] JRC, EUR 23984 EN, (2009) "Design of Lightweight Footbridges for Human Induced Vibrations".
- [9] Trumpf H., (2006), "Stabilitätsverhalten ebener Tragwerke aus pultrudierten faserverstärkten Polymerprofilen", Stuttgart, Shaker Verlag, Aachen.
- [10] BÜV-Empfehlung (2010), "Tragende Kunststoffbauteile im Bauwesen [TKB]".



FALCON – A MULTI-DISCIPLINARY EFFORT TO PROMOTE FRP BRIDGES IN SWEDEN

Reza Haghani¹, Erik Olsson^{1,2}

¹ Chalmers University of Technology, Department of Architecture and Civil Engineering, Gothenburg, Sweden;

² ELU Consultants, Gothenburg, Sweden (corresponding author: reza.haghani@chalmers.se).

ABSTRACT

Sweden has a long history in using fiber reinforced polymer (FRP) composites in marine, transportation and energy sectors. However, when it comes to application of composite materials to build bridge structures, it somewhat falls behind.

Despite several advantages that FRP composites offer, such as high specific strength and stiffness, corrosion resistance and light-weight, their infrastructural applications in Sweden have not been fully understood and yet to be realized. The first efforts to use FRP composites for construction of pedestrian bridges started in 2011, however, due to lack of knowledge about the materials and design of composite structures among engineers, they were halted.

To identify the existing gaps and hindrances, a joint effort project called “Falcon” was realized. The main goal of the project was to realize the first FRP pedestrian bridge and pave the way towards widespread infrastructural application of composites. This paper, presents some findings of the project and a brief description of a few pilot projects realized in the country.

KEYWORDS

FRP bridge, design guidelines, procurements.

INTRODUCTION

At the present, sustainable development is an important aspect in many engineering fields. Construction is, of course, not an exception. Aging and overloading of infrastructure in conjunction with lack of proper maintenance have led to “global infrastructure crisis”. Therefore, finding innovative materials and technical solutions to construct infrastructure with longer service life and lower life cycle cost, has been a priority for many bridge authorities and infrastructure owners in European countries, as presented in Mara et al. (2013). In addition, advanced industrialized production as an approach to reduce production cost, is gaining a great deal of interest among industrial communities and engineers. In this respect, off-site manufacturing and on-site assembly is of great importance in bridge construction.

Emerge of fiber reinforced polymer (FRP) composites in construction industry in mid-1970’s, opened up new horizons towards achieving abovementioned goals. FRPs are classified as composite materials and are basically composed of two constituents: reinforcing fibers and a polymeric matrix. Depending on the expected mechanical and durability characteristics, different types of fibers and matrices can be combined. Common FRPs used in construction include carbon, E-glass and aramid fibers. Matrix is often a thermosetting resin such as epoxy or polyester. Lately, natural fibers and bio-based resins have been researched, but due to concerns regarding the long-term performance, and often inferior mechanical properties of bio-based composites, they have not been realized in commercial projects.

The possibility of combining different types of fibers and matrices offers the great advantage of “tailor-ability” in the sense that the “right” constituents can be mixed to get the “right” properties. FRP composites have superior mechanical properties such as very high specific strength and stiffness and very good durability characteristics. The light weight of FRPs is very attractive when it comes to prefabrication, as it provides the possibility for off-site manufacturing and on-site assembly. When compared to other European countries such as UK and Netherlands, infrastructural application of FRPs in Sweden somewhat falls behind.

This paper, presents results of a research project carried with the aim to identify technical and management problems towards widespread application of FRPs as well as activities to facilitate the acceptance of FRP composites as a reliable and cost-effective alternative to traditional building materials such as steel and concrete. Sweden has a long history in using fiber reinforced polymer composites in marine, transportation and energy sectors. Despite the advantages offered by FRPs, the experience and the knowledge among different industries



about design and manufacturing of FRP components, FRPs have not yet found their place in Swedish construction sector yet.

PREVIOUS EFFORTS

Structural engineers in Sweden are generally not educated about FRP as a construction material so it is not surprising that there has not been a pull from the construction industry to explore the possibilities provided by FRPs as a building material. The initial efforts were made by the composite industry (especially manufacturers and material providers), searching for new market areas in 2010. Architects also found new opportunities in using the material to create complex geometries and tried to “promote” such solutions. The problem, however, was the lack of knowledge among architects about the material which created unrealistic expectations without considering the technical and practical limitations. The idea of using FRP for building pedestrian bridges in Sweden, initiated in 2013. Two examples of these ideas were Kaponjär bridge (Figure 1) proposed by Ramböll consultants and Architect bridge (Figure 2) by ELU consultants. Even though the concepts were very attractive from architectural point of view, the complexity involved in the design and manufacturing of these concepts, halted both projects. A learned lesson from these failures was that it was the lack of knowledge about the FRP materials in the engineering community and among clients which did not allow the realization of these projects.



Figure 93. Concept of Kaponjär FRP bridge over Rosenlundskanal in Gothenburg. Picture courtesy of Ramböll

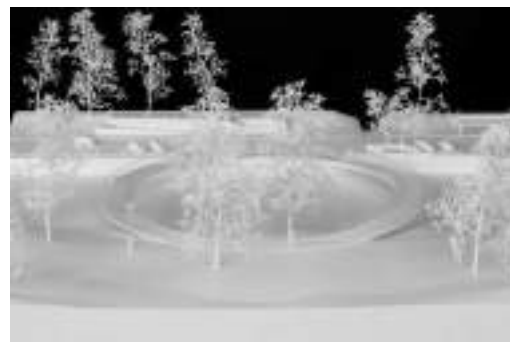


Figure 94. Concept of Architect bridge in Haga area in Gothenburg. Picture courtesy of Erik Andersson Architects

THE FALCON PROJECT: A MULTIDISCIPLINARY EFFORT

It was soon realized that to create the foundation for application of FRPs in bridges, a comprehensive and multidisciplinary work with contribution of all players was needed. In this context, Falcon, “future advanced lightweight construction (2016-2018)”, a joint effort project with total budget of 640 k Euro funded by VINNOVA and co-funded by industrial consortium partners. It is coordinated by Swerea Sicom (a leading Swedish research institute in FRP composites) and was initiated to identify the hindrances towards the infrastructural application of FRP composites and facilitate the acceptance of FRP solutions by paving the way towards realization of the first FRP bridge in Sweden. The project consortium consists of 14 partners from universities, research institutes, bridge designers, manufacturers, material suppliers and clients.

The main objective of the project was to implement the best practice for design and procurement of FRP bridges. In this regard, a draft of “technical client demands” along with a background document were prepared in accordance with Swedish national regulation for design and procurement of bridges. The main aim of these documents was to establish a framework for clients to process innovative technical solutions not covered by Eurocodes within the existing legal boundaries.

THE WAY TOWARDS WIDESPREAD APPLICATION OF FRPS IN SWEDEN

FRP Deck for the bascule road bridge 261

Bridge 261 located in the city of Malmö, is a two-lane bascule steel bridge composed of two supporting side trusses and a steel decking system built in 1953. The orthotropic steel deck in the bridge had dimensions of 8.9m x 32.9m and was degraded due to corrosion over time. Visual inspections also revealed multiple cracks in the asphalt layer, a typical problem due to local bending of the top plate in orthotropic decks, which added to maintenance cost of the bridge, see Figure 3. Therefore, the refurbishment of the bridge was necessary. The client

needed a fast assembly solution as the bridge was located on one of the main roads in the city and considerable traffic disruption would have taken place if the bridge had been closed for a long time. It was decided to use FRP solution to accelerate the operation and provide a more durable solution compared to a steel alternative. Circumstances of the project necessitated using tailor-made FRP sandwich panels. To keep the cost low, glass fibers and polyester matrix were chosen. The design and manufacturing of the deck panels was carried out by the Dutch supplier FiberCore Europe.



Figure 95. Wear of the surface and transverse cracks in the orthotropic steel deck, Photo courtesy of Per Andersson



Figure 96. Cross section of the sandwich panel used as new decking system



Figure 97. Removal of the old steel deck and preparation of the stringers for installation of FRP panels, Photo courtesy of Per Andersson



Figure 98. Installation of FRP deck panels, Photo courtesy of Per Andersson

The deck panels in this project had a height of 105 mm with face sheet thickness of 19mm on the top and 17mm in the bottom, see Figure 4. To avoid on-site joints in the perpendicular to the length direction, two longitudinal panels were manufactured with dimensions of 32.9m x 4.44m with total areas of 292m². The old steel deck was firstly removed from the bridge (Figure 5). In the next step, the holes on the steel girders were prepared by slightly enlarging them. The panels were then placed on the girders and connection were made using hollo-bolts. The project was completed in summer 2016.

FRP deck for rehabilitation of the university bridge

The university bridge in Malmö is a two-span asymmetrical cable-stayed swing bridge with a main span of 25 m and a 15 m long back stay span. The total length of the bridge is ca. 76 m including approach spans. The width of



the bridge is 16 m, including 2 lanes of carriageway and 2 lanes for pedestrians and cyclists. The bridge was built in 2004. Already in 2015, signs of deterioration in wooden planks covering the pedestrian lines were observed. Deformation of the planks had caused uneven surface of the walkway and was a potential threat for the users, see Figure 7.



Figure 99. Deterioration of the wooden planks on sidewalks of the university bridge, Photo courtesy of Per Andersson



Figure 100. FRP panels installed on sidewalks, Photo courtesy of Per Andersson

The municipality of Malmö decided to replace the wooden planks with a more durable alternative. At the same time, there was a need for a lightweight solution not to disturb the balance of the spans as modifying the counterweight was not an option in this project. FRP deck panels with thickness of 65 mm produced by FiberCore Europe were installed on steel stringers spacing at 1.12m. 6 deck panels with width of 3 m were put alongside each other to cover the whole length of the bridge, see Figure 8. The project was completed in 2017.

Pedestrian bridge 254 – The first FRP pedestrian bridge in Sweden

The original bridge 254 in Malmö was a pedestrian timber bridge built in 1981. The bridge had undergone a considerable degradation and was classified as not safe for use. In 2016, the municipality of Malmö decided to replace the bridge. Different alternatives, including full concrete slab and concrete slab on steel girders were studied.



Figure 101. Proof loading of the composite beams during manufacturing, Photo courtesy of Composite Design



Figure 102. Installation of the bridge, Photo courtesy of Composite Design

The results from life cycle cost analyses on different concepts demonstrated that an FRP bridge would be the least expensive choice for this project. Composite Design, a Swedish FRP manufacturing company, took over the



project. The superstructure of this bridge consists of seven sandwich beams glued together creating an FRP composite deck. Each beam consists of four smaller beams, laminated together to form a longer beam. The beams were created using lightweight concrete (Siporex) core wrapped with prepreg carbon fibre fabrics. Each beam was 505 mm wide and 420 mm high and had 11 layers of carbon fiber on the top and bottom with thickness of ca. 0.95 mm for each layer (total skin thickness of ca. 10.5 mm) and 3 layers of carbon fiber on the sides, ca. 2.3 mm.

The FRP bridge is 3.5 m wide, 17.62 m long and has area of 62 m². Each beam was loaded with 4.2 tons at the workshop to check if they fulfill the requirement for stiffness and deformation, see Figure 9. The bridge was installed in March 2017 and the mounting operation took only one hour, Figure 10.

Neptuni Bridge

Neptuni Pedestrian bridge shall be the next FRP bridge project to be started in the beginning of 2018 in city of Malmö, Figure 11. It will have a span of 15 m with variable width from 4.6m in the widest part to 2.4m in the narrowest section, see Figure 12. The main incentive for choosing FRP was the lower life cycle cost of this concept in comparison to steel and concrete alternatives.



Figure 103. Concept of the Neptuni bridge in Malmö, Photo courtesy of municipality of Malmö

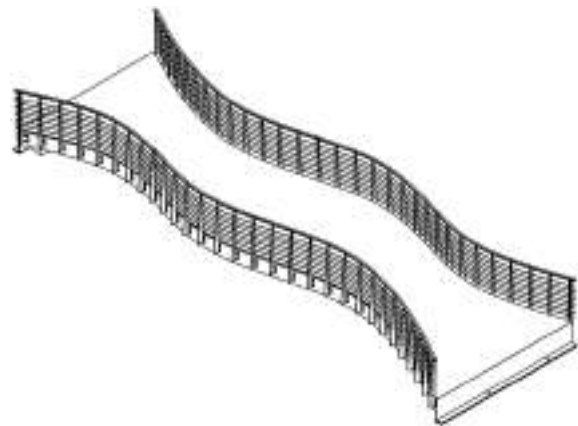


Figure 104. 3D illustration of the Neptuni bridge

SUMMARY AND CONCLUSIONS

FRP composites provide several benefits in bridge construction including: (i) flexibility in geometry and material choice (which of course come at a greater design effort, time and cost), (ii) lightweight, which offers smaller substructure, easier transport, faster installation and, all in all, off-site manufacturing and on-site assembly in addition to better quality, (iii) high specific strength and stiffness as well as good durability leading to resilient structures with large safety margins and low maintenance cost.

This paper presents the latest efforts in Sweden to increase the acceptance of FRP composites as a reliable, cost effective and sustainable building materials by authorities and infrastructure owners. At the present, according to investigations made in Falcon project, a good deal of interest at Swedish Transport Administration and local municipalities to use FRP composites in future bridge projects exists. The main reason is found to be the pressure on infrastructure owners, due to deterioration and consequent large maintenance costs of their assets. Dissemination activities such as demonstrations and workshops arranged in Falcon project, have led to an increased awareness about FRP technology for infrastructural use. Based on the learnings from the outcomes of the project, three main areas for improvement can be speculated:

- **Engineering education:** As mentioned earlier, bridge designers in Sweden, generally have very limited knowledge regarding FRP materials. In authors' view, it is the structural designer's knowledge which determines suitability of FRP for a certain project with specific circumstances in the first place. Providing teaching materials, design examples, coordinated



workshops shall be an essential step towards creating the culture of using FRP in infrastructure in Sweden.

- **Lack of design codes and guidelines:** Lack of codes and regulations on design of FRP bridges adds to the difficulty associated with acceptance of FRP as a construction materials by major clients such as Swedish Transport Administration. Public procurement is strictly governed by laws and regulations so, in that sense, there is no difference between procuring a concrete bridge and an FRP bridge. The difficulty lies in technical questions such as reliability, accuracy of design models, durability and maintainability. It is believed that upon release of the “Technical Specifications” for FRP structures, which is under preparation by WG4 in CEN Technical Committee 250 - Structural Eurocodes in 2020, Ascione et al. (2017), a large part of technical and legal issues with acceptance of FRP solutions will be eliminated and new market opportunities for FRP constructions in Sweden will be arisen.
- **Integrated industrial manufacturing:** The level of interest from FRP manufacturers in other engineering disciplines has a direct relationship with the infrastructure market potential and attractiveness. However, FRPs are fundamentally innovative materials. They have not been resulted from improvement or modification of traditional construction materials. The supply chain of FRP structures is completely separated from those being used in civil engineering projects. At the present, there is a good potential interest among FRP manufacturers, especially from marine related, to enter FRP bridge market. However, the relationship between the FRP manufacturers and bridge design offices has not yet been realized. It of great importance for FRP manufacturing industry to comprehend the specific technical demands put by designers for bridge structures as the nature of bridge structures is completely different from types of products they use to deal with. This is mainly due to more serious consequences of failures and stringent legal issues. Manufacturing tolerances, defect sensitivity and transportation handling are three main areas of consideration which need to be improved. This is where the authors believe the role of universities and knowledge-based SMEs to connect the design offices to manufacturers will be pronounced.

Finally, Falcon is evaluated to be a great step forward and, as almost all the pilot FRP projects in Sweden, were initiated, procured and conducted with direct or indirect support of the expert team in the consortium. This support will continue for future projects as the great potential for FRP materials is realized in Sweden by all involved stake holders. A potential that can lead to considerable cost saving, less impact on the environment and creating new job opportunities.

ACKNOWLEDGMENTS

The authors acknowledge Vinnova (Sweden’s government agency for innovation) for financing and Swerea Sicomp for coordinating the Falcon project. We would like thank Mrs. Cecilia Ramberg, the coordinator of the LIGHTer program and Mr. Abbas Khayyami from municipality of Malmö for their interest and continuous support of the project.

REFERENCES

Mara, V., Haghani, R., Sagemo, A., Storck, L., Nilsson, D., 2013, Comparative Study of Different bridge concepts based on life-cycle cost analysis and life-cycle assessment, Asia Pacific Conference on FRP in Structures (APFIS 2013), Dec 2013, Melbourne, Australia.

Ascione, L. et al. (2017). “Prospect for New Guidance in the Design of FRP”, *Support to the implementation, harmonization and further developments of the Eurocodes*.



TOWARDS A STRUCTURAL EUROCODE FOR FRP STRUCTURES: THE ROLE OF CEN/TC 250

L. Ascione ¹

¹ Dept. of Civil Engineering, University of Salerno, Italy, Email: lascione@unisa.it

ABSTRACT

Over the past twenty years, several innovative solutions have confirmed the usefulness of composite structures made of FRPs (Fibre Reinforced Polymer or Plastics), both within and outside Europe. The use of FRP profiles, shell structures and sandwich structures is particularly advantageous for applications in the Civil Engineering field. FRP bearing structures are therefore widely used for the construction of buildings for industrial or residential purposes. FRP usage has also become increasingly widespread for civil engineering works. Applications range from lock gates, to entire bridges or bridge decks both for pedestrian and vehicular traffic. Due to their steadily increasing market volume and given the complexity of selection from available materials for FRP structures, it became obvious that it would be necessary to develop a standardization document for both the production of FRP structural elements and practical rules for the design and verification of structures to be used for buildings and civil engineering works. CEN Technical Committee 250 (CEN/TC250) has taken the initiative to prepare a document addressing the purpose and justification for new European technical rules and associated standards for the design and verification of composite structures made of FRPs. CEN/TC250 formed a Working Group, WG4, to develop the work item. The convenor is the author of this paper. The work item is motivated by the need to both ensure adequate reliability of the applications, as well as promote a broader market for these materials and ensure a circulation of these materials between EU countries conforming to well-defined standards. The aim of this paper is to summarize and diffuse the activity already developed by CEN/TC 250, as well as highlight the further procedures to be followed on the road towards the publication of a structural Eurocode dedicated to FRP structures.

KEYWORDS

Full composite structures, Design rules, Standardization

INTRODUCTION

Over the past twenty years, several innovative solutions have confirmed the usefulness of composite structures made of FRPs (Fibre Reinforced Polymer or Plastic), both within and outside Europe. The use of FRP profiles, shell structures and sandwich structures is particularly advantageous for applications in the Civil Engineering field. FRP bearing structures are therefore widely used for the construction of buildings for industrial or residential purposes. FRP usage is also increasingly widespread for civil engineering works. Applications range from lock gates, to entire bridges or bridge decks both for pedestrian and vehicular traffic. Because of their steadily increasing market volume and given the complexity of selection from available materials for FRP structures, it became obvious that it is necessary to develop a standardization document for both the production of FRP structural elements and practical rules for the design and verification of structures to be used for buildings and civil engineering works.

In May 2010, the European Commission - DG Enterprise and Industry issued the Programming Mandate M/466 EN to CEN concerning the future work on the Structural Eurocodes. The purpose of the Mandate was to initiate the process of further development of the Eurocode system. M/466 requested CEN to provide a programme for standardisation covering:

- Development of new standards or new parts of existing standards, e.g. a new construction material and corresponding design methods or a new calculation procedure;
- Incorporation of new performance requirements and design methods to achieve further harmonisation of the implementation of the existing standards.

The works of the future generation of Eurocodes has to be carried out in several steps:

- Step 1: Preparation and publication of a "Science and Policy Report", subject to agreement of CEN/TC250.



- Step 2: After agreement of CEN/TC250, preparation and publication of CEN Technical Specifications (TS, previously known as ENV).
- Step 3: After a period for trial use and commenting, CEN/TC250 will decide whether the CEN Technical Specifications should be converted into Eurocode Parts.

The end of the program has been scheduled by 2020. Within this Mandate, CEN/TC250 took the initiative to prepare a document addressing the purpose and justification for new European technical rules and associated standards for the design and verification of composite structures realized with FRPs. CEN/TC250 formed a CEN Working Group WG4 to develop the work item. It was motivated by the need to both ensure adequate reliability of the applications, as well as to promote a broader market for FRPs and ensure a circulation of these materials between EU countries conforming to well-defined standards. The author of this paper is the convener of WG4. The broad interest in the development of a European-wide harmonized and acknowledged coherent set of technical specifications or Eurocode parts for the design and verification of composite structures realized with FRPs is demonstrated by the impressive number of almost 50 highly motivated members in CEN/TC250/WG4 bringing their specific expertise. The Association of the European Composites Industry (EuCIA) also participates in the activities and meetings of WG4.

Several countries have contributed to the development of currently available guidelines (1996-2010), among which it may be appropriate to mention those listed in the References.

After about three years of activity and many meetings, WG4 drew up a proposal of Scientific and Technical Report (2016), whose title is *Prospect for new guidance in design of FRP*. From January 2016 to July 2016, the Report was subjected to public inquiry by the National Standardizations Bodies of EU. At the end of the inquiry, the Report was revised and resubmitted to CEN/TC 250, which, in July 2017, took the decision to start the adaptation into a CEN Technical Specification (Step 2). The revised version of the Prospect is in press by EuCIA.

The Technical Specification will apply to the design of constructions realized with Fibre Reinforced Polymers (FRP). It will comply with the principles and requirements for the safety and serviceability of structures as given in EN 1990-Basis of structural design. The operational rules for the basis of design, supplementary provisions for determination of action effects, robustness requirement and guidance for material-oriented design of FRP constructions will be clearly given.

In order to achieve this goal, a project team of six members have been entrusted by CEN/TC 250 to help WG4 on the road toward a structural Eurocode (Step 3). These members were selected by public tender. The activities of Step 2 will start at the end of July 2018.

MAIN FEATURES OF THE PROSPECT

The goal of the Prospect (Figure 1) is to stimulate the debate about future guidelines and rules for the structural analysis and design of Fibre Reinforced Polymer (FRP) used in load-bearing structures, for buildings and civil engineering works. The topics taken into account address the FRP parts with a fibre volume fraction of at least 15%, i.e. the ratio of fibre volume to total volume. The FRP composite has to be made up of glass fibres (E- glass fibres, R-glass fibres), carbon fibres of type HS, HT, IM or HM and aramid fibres with a thermoset matrix of unsaturated polyester, vinylester and epoxy resins.



(a)



(b)



Figure 1: (a) Cover of the Prospect; (b) Cover of the revised Prospect.

The Prospect applies to FRP structures made of:

- beams
- laminated plates and shells
- sandwich structures.

It does not include:

- structures in which micro-cracks are not permissible
- reinforcing rods, cables or external reinforcement to existing structures using FRP.

The structural elements taken into account are realized by means of the main manufacturing processes as prepregging, pultrusion, compression moulding, resin transfer moulding, filament winding and hand lay-up.

It is well-known how FRP materials have a temperature-dependent behaviour due to the polymeric nature of their matrix. The following temperature ranges are considered for the service conditions:

- ambient temperature: from -40 °C to +40 °C;
- elevated temperature: up to the maximum service temperature (dependent on the glass transition temperature);
- service temperature: temperature range indicating minimum and maximum temperatures for short-term and long-term usage in dry as well as wet conditions, under which a given material or FRP system can be used without altering structural and durability properties more than for the effects taken into account by the applied conversion factors. It shall be defined by the designer, based on environmental data and local conditions.

The topics included in the document are listed in Table 1.

Table 1: Index of the Prospect.

	Preface
Chapter 1	General
Chapter 2	Basis of Design (Partial Factors Method)
Chapter 3	Materials
Chapter 4	Durability (UV Radiation; Temperature; Humidity; Static Charge; Fire)
Chapter 5	Basis of Structural Design (Modeling of FRP; Behaviour in the case of Fire; Design assisted by Testing)
Chapter 6	Ultimate Limit States (Profiles; Plates and Shells; Sandwich Panels)
Chapter 7	Serviceability Limit States (Deformations; Vibration and Comfort; Damage)
Chapter 8	Connections (Bolted and Adhesive Joints)
Chapter 9	Production, Realization, Management and Maintenance
Annex A	About the conversion factor for creep effects
Annex B	Indicative values of Fibres, Resins, Ply and Laminate Properties
Annex C	Elastic Buckling of Columns with Double Symmetric Profiles and Angle, Cruciform and T Profiles
Annex D	Elastic Buckling Formulas for Beams with Double Symmetric Profiles (under Major-Axis Bending)
Annex E	Local Buckling of Double Symmetric Profiles
Annex F	Instability of Plates and Shells
Annex G	Simplified Constitutive Interface Laws
Annex H	Fatigue Testing
(for a total of about 170 pages)	

All the chapters and Annexes include extensive and updated references.

ASPECTS TO BE DEVELOPED IN STEP 2

As a result of the public inquiry, the main aspects to be developed in further detail in Step 2 relate to sandwich panels and adhesively bonded joints.



This need has oriented the selection of some members of the project team, particularly expert in such fields.

Furthermore, each chapter of the Technical Specification will be enriched with examples in order to make using the provisions given clearer.

Sandwich panels

Regarding sandwich panels (Figure 2), the present Prospect only focuses on predictive formulae relative to the main Ultimate Limit States. Nevertheless, many comments, sent during the public inquiry, highlighted the need for further provisions on other aspects, also relevant for the design. Consequently, WG4 has planned to reorganize the chapter dealing with sandwich panels by including the following topics.

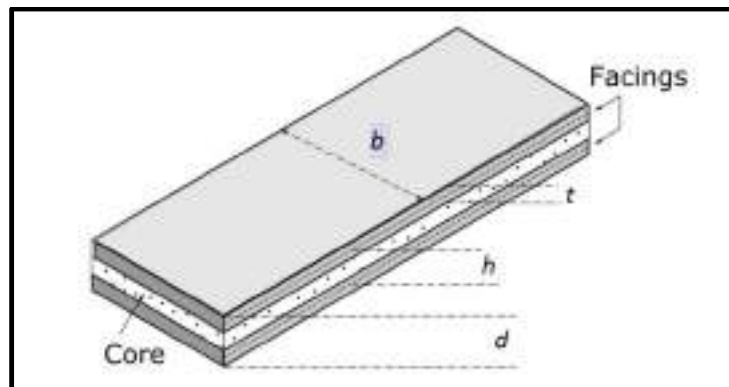


Figure 2: Sandwich panel scheme.

- General
 - Sandwich concept.
 - Timoshenko beam theory. Flexural rigidity. Shear stiffness.
 - Types considered:
 - thin, thick face sheets
 - weak-core, rigid-core, web-core
 - flat, curved, constant/variable thickness
- Materials
 - Facing materials:
 - Indicative mechanical and physical properties
 - How to obtain the mechanical and physical properties
 - Core materials:
 - Indicative mechanical and physical properties
 - How to obtain the mechanical and physical properties
 - Adhesives (e.g. for core joints, panel-to-panel connections)
 - How to obtain the mechanical and physical properties
- Conceptual design of sandwich panels
 - Facings:
 - Requirements (e.g. high stiffness and strength, impact resistance, surface finish, environmental wearing resistance, finishing/appearance, temperature, water tightness)
 - Minimum dimensions (thickness, overlaps)
 - Thickness changes
 - Deviation and curving of facing laminates (non-flat and curved sandwich panels)
 - Core:



- Requirements (e.g. density, shear modulus, shear strength, stiffness \perp facings, thermal insulation, acoustic insulation, temperature)
 - Minimum density
 - Anisotropy
 - Complex cores, inserts
 - Core creep
- Load introduction and supports
- Joints between sandwich elements
 - Joint classification: primary, secondary, non-structural
 - Design requirements: redundancy / back-up acc. to classification
 - Facing joints: symmetry, minimum overlapping, thickness variation (eccentricities), lap, scarf, adhesively-bonded, infused joints.
 - Core joints: butt/inclined joints; adhesively-bonded, mechanical joints.
 - Tolerances
- Structural analysis
 - Generalities / hypotheses:
 - Material hypothesis: linear/nonlinear face sheets/core materials behavior
 - Shear in core material; shear deformation
 - Core anisotropy
 - Boundary conditions
 - Out-of-plane stresses to be considered (curved panels)
 - Local facing bending and core shear at facing discontinuities or core material changes
 - Creep and temperature
 - Homogenization of the structure (material level)
 - Imperfections
 - Geometrical imperfections
 - Pre-existing defects
 - Calculation methods
 - Analytical calculation: Simplified beam / panel analysis
 - FE Analysis
- Ultimate Limit States
 - Partial / conversion factors
 - Strength
 - Facing failure
 - Core shear failure and punching
 - Web shear failure (web-core sandwiches)
 - Core indentation
 - Flexural crushing of core
 - Facing/core delamination
 - Stability verifications
 - Local instability of facing (wrinkling)
 - Intracellular buckling (facing dimpling)
 - Local instability of webs (web-core sandwiches)
 - Global buckling
 - Joints

- Strength verification, experiments

- Inserts
 - Insert verification: stress concentrations; insert/sandwich adherence (structural inserts), core capacity
- Impact damage
- Serviceability Limit States
 - Partial /conversion factors
 - Deformations (bending + shear, short + long term)
 - Vibrations
 - Strain limits
 - Prevent damage: thermal compatibility of materials, blistering due to temperature variations, etc.

Adhesively bonded joints

Regarding the adhesively bonded joints, the present version of the Prospect takes into account the configurations shown in Figure 3.

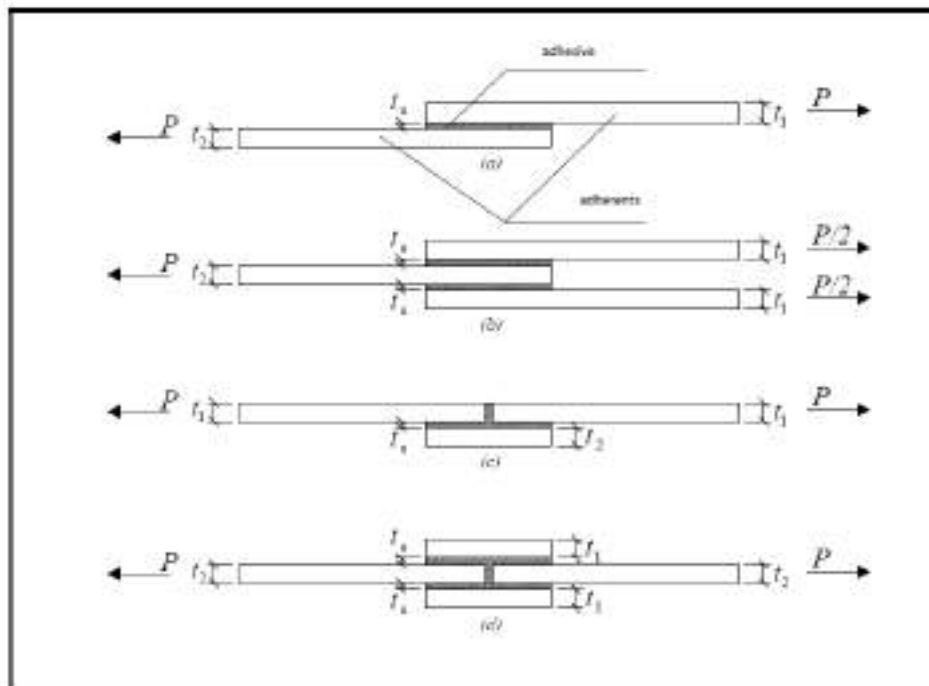


Figure 3: Configurations of adhesively bonded joints.

The structural verifications are addressed through an approach based on fracture mechanics by using interfacial constitutive laws of the type shown in Figure 4.

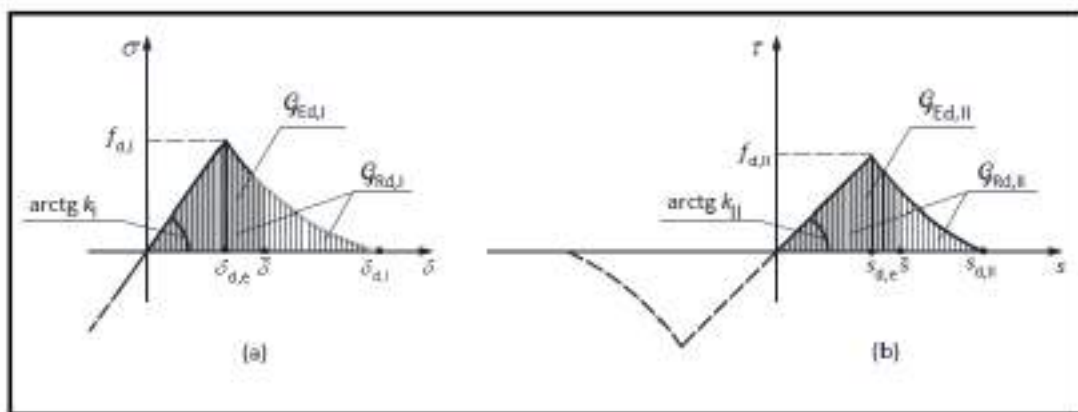


Figure 4: Constitutive interfacial laws.

The subtended areas of the two diagrams are equal to the fracture energies for mode I (diagram $\sigma(\delta)$) and mode II (diagram $\tau(s)$), respectively. The symbols σ and τ denote the orthogonal or tangential stress at the interface, respectively. The symbols δ and s denote the relative displacements between adhesive and adherent for which the previous stresses work. More details can be found in the Prospect.

In Step 2, the purpose is to give provisions for both the cohesive failure, as well as the adhesive-adherent interface failure, the last one already analyzed in the Prospect. Another aim is to provide a simplified approach, to be used as an alternative to the aforementioned one, for applications of limited relevance.

CONCLUSIONS

In this paper, the activity developed by CEN/TC 250 during the last years on the subject of full composite structures made of FRP were summarized.

It was addressed to:

- ensure adequate reliability of such structures,
- promote a broader market for FRPs, and
- assure their circulation between the EU countries, conforming to well-defined standards.

Furthermore, the additional activities planned by CEN/TC 250, in order to develop a structural Eurocode dedicated to these structures, were also highlighted.

ACKNOWLEDGMENTS

The economic support of the *European National Composite Industry Association (EuCIA)* is gratefully acknowledged.

REFERENCES



**9th International Conference on Fibre-Reinforced Polymer (FRP)
Composites
in Civil Engineering (CICE 2018), PARIS 17-19 JULY 2018**

PROSPECT FOR NEW GUIDANCE IN DESIGN OF FRP, JRC Science and Policy report, ISSN 1018-5593 (January 2016).

CUR 96, Fibre Reinforced Polymers in Civil Load Bearing Structures (Dutch Recommendation, 2003).

EUROCOMP, Structural Design of Polymer Composites (Design Code and Handbook, 1996).

BD90/05, Design of FRP Bridges and Highway Structures (The Highways Agency, Scottish Executive, Welsh Assembly Government, the Department for Regional Development Northern Ireland, May 2005).

DIBt, DIBt – Medienliste 40 für Behälter, Auffangvorrichtungen und Rohre aus Kunststoff, Berlin (In German, May 2005).

CNR-DT 205/2007, Guide for the Design and Construction of Structures made of Pultruded FRP elements (Italian National Research Council, October 2008).

ACMA, Pre-Standard for Load and Resistance Factor Design of Pultruded Fiber Polymer Structures (American Composites Manufacturer Association, November 2010) under review by ASCE.

DIN 13121, Structural Polymer Components for Building and Construction (August 2010).

BÜV, Tragende Kunststoffbauteile im Bauwesen [TKB] – Richtlinie für Entwurf, Bemessung und Konstruktion (in German, 2014).

ELASTIC GRIDSHELL IN COMPOSITE MATERIALS: SOME RECENT DEVELOPMENTS

Jean-François Caron, Olivier Baverel, Lionel du Peloux, Cyril Douthe, Pierre Cuveilliers, R.Leroy
Navier Laboratory, Université Paris-Est, ENPC/IFSTAR/CNRS
Ecole des Ponts ParisTech, 6-8 Ave Blaise Pascal
77455 France
caron@enpc.fr

ABSTRACT

This article shows how composite materials might be an original and profitable solution for lightweight structures called gridshells. In this paper the principal characteristics of gridshells are recalled first and a demonstration that glass fibres reinforced polymers (GFRP) are suitable for these structures is shown.

The purpose of the proposed article focuses on the last realization in France, a temporary church in Creteil near Paris, and on some other developments, including a mixed solution with concrete for roofing the gridshell.

KEYWORDS

Gridshell, Composite Materials, GFRP, Concrete.

INTRODUCTION

Composite materials entered definitely the construction game, and not only for reinforcement and strengthening of existing structures. Numerous applications for all-composite applications are already proposed and tested all around the world. Few of them can be quoted, for example Eyecatcher a residential/office building in Basel (fiberline), a bus station in St. Nazaire (France, architects Tetrarc), the train station roof in Saudi-Arabia (arch. Foster + Partners – Saudi Oge and Mecca engineering) or the Orthodox Church domes in Paris, (arch. Wilmotte – Multiplast).

It seems possible however to explore more innovative ways, where composite materials don't only replace traditional materials in traditional structural concepts, but where composites propose disruptive systems. An attempt is presented here, concerning elastic bending systems, and a focus is made on elastic gridshells. Composite materials might definitely be an original and profitable solution for these lightweight complex structures permitting freeforms and new answers to architectural purposes. In this paper, what is an elastic gridshell is recalled, why composite materials are perfectly adapted, and a focus is made on the last realization, located in France, a temporary church in Creteil near Paris. The Ephemeral Cathedral of Créteil, build in 2013, is always in place, and cover 300m² (figure1). It represents the only composite gridshell in the world, and the most



accomplished.

Figure 1: Cathédrale Ephémère de Creteil, T/E/S/S engineering, Navier laboratory (2013)

The topics of numerical simulation, construction, details, reliability and robustness are addressed in several published papers [Douthe et al 2006; baverel et al 2012, Tayeb et al 2013, du Peloux et al 2017 ...], and are not really reminded in this communication. The simulation and construction of elastic gridshells in composite materials is nowadays a technique that one can consider mastered. The bracing of the grid in its final form remains

however a time consuming step with a lot of handiwork. The lack of alternative to membrane covering is also an important limit to the development of such technology. To tackle both issues, a novel concept of hybrid structural skin made of an elastic gridshell braced with a concrete envelope is proposed.

The idea is to use the gridshell as formwork for the concrete and to insure a connection between the thin concrete skin and the main grid, so that concrete assures the bracing of the grid and that the thickness of the concrete is reduced to a minimum. To demonstrate the feasibility and interest of this structural concept, a 10 m² prototype has been built. The authors present here the main aspects of the design and of the realization of the prototype, detailed may be found in [Cuvilliers et al, 2017].

In a first part of this paper, what is an elastic gridshell and why glassfibers profiles are so interesting are reminded briefly. Then two focus on the temporary church in Creteil, and finally, on the mixed solution involving concrete skin are made.

WHAT IS AN ELASTIC GRIDSHELL

The name gridshell commonly describes a structure with the shape and strength of a double-curvature shell, but made of a grid instead of a continuous surface. These structures can be made of any kind of material - steel, aluminum, wood... Generally, the metallic structures are made of short straight elements defining a cladding made of planar triangular or quadrangular elements. The complexity of this geometry requires the development of many clever and expensive assemblies. In order to avoid these complex joints, a very specific erection process was developed using the bending capability of slender components [Douthe et al, 2006]: two layers of long continuous beams are first pinned together on the ground (fig.2 left).

The resulting grid has no shear rigidity, allowing large deformations in space. The grid is then elastically deformed by bending until the desired form is obtained (fig.2 right) and finally stiffened, for example with a third bracing layer of beams (fig.4 right). Only few gridshells were built using this active bending method, among which the most famous are: the Mannheim Bundesgartenschau (arch: Mutschler and Partner and Frei Otto, Str. Eng: Arup, 1975) [Otto et al 1974] [Happold et al 1975], the carpenter hall of the Weald and Downland Museum (arch. E. Cullinan, Str. Eng. Buro Happold, 2002) and the Japanese pavilion for the Hanover 2000 Exhibition (arch: Shigeru Ban, Str. Eng. Buro Happold) [Ban et al 2006].

In addition, the Navier research unit has already participated to the construction of four gridshells in glass fiber reinforced polymer (GFRP), increasingly large. The gridshell for the "Cathédrale Ephémère de Creteil" has been built to replace the Creteil cathedral during its renovation which should last two years [du Pelloux 2016].



Figure 2: Cathédrale Ephémère de Creteil, flat grid (left) and elastically deformed (right) to be attached to boundary conditions.

WHY COMPOSITE MATERIALS SO SUITABLE FOR ELASTIC GRIDSHELLS

Most of the gridshell structures have been made of wood because it is the only traditional building material that can be elastically bent with large deformations without breaking. This flexibility generates curved shapes offering structural stiffness. However looking at other industrial fields (sport and leisure, nautical), it can be noticed that

every time high strength and high deformability are required, composite materials have replaced wood (ship masts, skis, rackets) since more performant. To study accurately the question of the best material for gridshells, the authors adopted the method proposed by M. Ashby [Ashby 1999] and the most valuable alternative to wood is hence glass fiber reinforced polymers (GFRP) (Figure 3). They have higher elastic limit strain (1.5 % at best for GFRP and 0.5 % for wood) so large curvatures, synonymous of interesting free-forms, are possible. Their Young's moduli also are higher (25-30 GPa against 10 GPa for wood). This is an advantage to make a stiff structure, and, assuming that for a given geometry, the buckling load of a gridshell is linearly dependent on the Young's modulus, the expected buckling load of a gridshell in composite materials may be 2.5 to 3 times higher than one made of wood. Moreover, as composites are industrially produced, the reliability of their mechanical properties is much higher than that of natural materials like wood. Finally, while wood beams have to be made of several pieces of wood stuck together, GFRP profiles can be made continuously, and the length limited by the length that can be transported.

Concerning costs, taking into account that the mechanical properties and the ability of composites to be formed into efficient sections like tubes, GFRPs become very interesting challengers, especially if pultrusion production is used. Indeed, hollow and/or complex sections make possible the use of light beams optimized for each application (stiffness and curvature). Moreover, the polymer chosen for the GFRP may be designed to resist to corrosion, UV and other environmental attacks, whereas wood materials need maintenance.

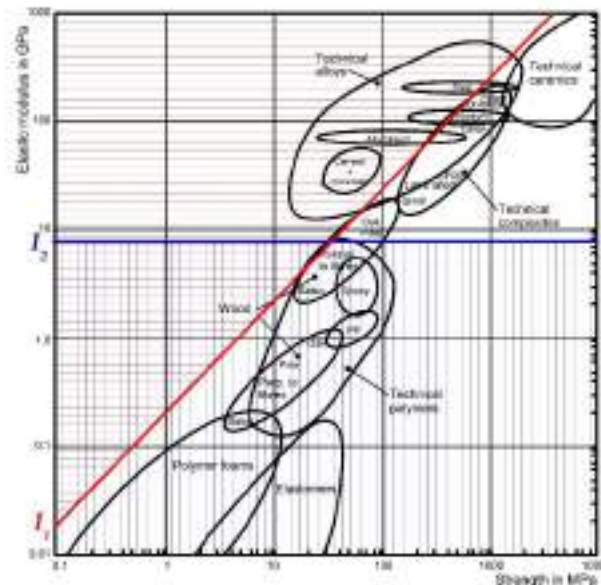


Figure 3: Ashby diagram [Ashby 1999], showing that FRPs are both resistant and flexible.

EPHEMERAL CATHEDRAL OF CRÉTEIL

To demonstrate the feasibility of composite gridshells, four full scale prototypes of composite material gridshells have been built by Navier laboratory. The two first ones were built on the campus of Ecole des Ponts ParisTech. The first prototype was a purely experimental structure which was tested under several loading conditions in order to investigate the behavior of gridshell structures and to compare it with the numerical models. Detailed results of these tests can be found in [Douthe et al 2006]. The behavior of the prototype is very close to numerically performed simulations (dynamic relaxation algorithm presented also in [Douthe et al 2006]).

After that, two gridshells built to house people have been recently made. The first one for the Solidays festival (June 2011, fig.5 right) and the last one [du Peloux 2016] built to temporarily replace the Creteil Cathedral (February 2013 for at least 2 years of use, and always in place in 2017). Both of them were built in collaboration with the engineering company T/E/S/S and have to obtain a clearance from the authorities to house people for a

specified period. The dimensions of these structures are quite similar: around 7 m high, 25 m long and 15 m wide. 2 kilometres of pultruded unidirectional tubes from Topglass (polyester resin from DSM + Owens Corning glass fibres + surface veils and UV protection) are used with a Young's modulus of 32.7 ± 1 GPa and a limit stress of $458 \text{ MPa} \pm 7 \text{ MPa}$ (from our own bending tests). The available length and diameter of the tubes are respectively 13.4 m and 41.7 mm; the wall thickness of the tubes is 3.5 mm.

The coordinates of the extremities were picked up and precisely reported by surveyors on site and stakes were positioned. Then, the grid was assembled flat on the ground: tubes were cut to the right dimensions with hacksaws and connected to the others with standard swivel scaffolding elements (figure 4, left) allowing rotation around their axis (low cost due to industrial production).

Then the grid was deformed and shifted by two cranes that hook up the grid in several places (figure 2). The final form was reached when the extremities of the beams were fixed on the anchorages.

The following step was the bracing. This step is essential as, before bracing, the grid still holds its shear degree of freedom (see figures 4 center). Once the bracing is installed (fig.4 right), the gridshell gets its full mechanical properties and its stiffness becomes about twenty times the stiffness of the grid before bracing.



Figure 4: Left: Joint detail. Centre: Mesh before bracing. Right: Mesh after bracing

The PVC coated membrane was pulled then above the gridshell (figure 5, left). In order to fix the canvas, a girder following the contour of the gridshell was set up 10 cm above the soil, and a rope is installed to tense the canvas (fig.5 center). For the Créteil gridshell, this girder was a pultruded rod able to support a large amount of shear stress as well as high curvatures (here hollow cross-sections are not suited and the outer radius has to be smaller than for structural beams). This step was supposed to be critical as polypropylene-PVC coated canvas is almost not stretchable, and was manufactured according to the geometry of the numerical model. As the gridshells were accurately set up, the canvas fitted to their shape. No wrinkle was observed (figure 5 right, figure 1).

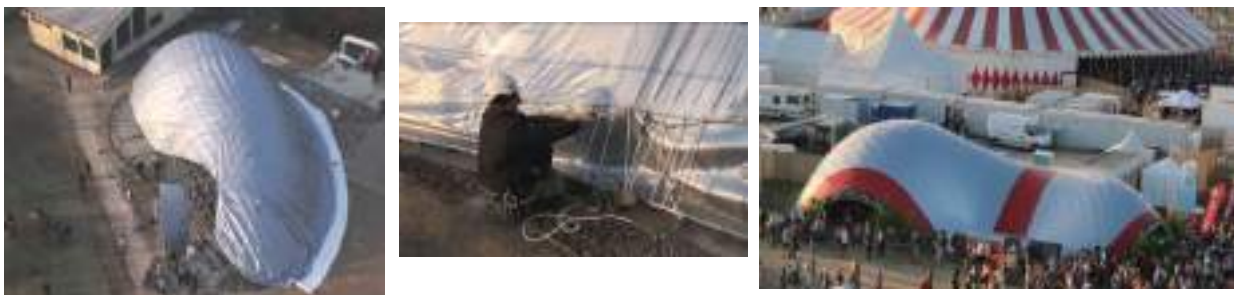


Figure 5: PVC coated membrane without wrinkle for Créteil (left and center) and Solidays (right) gridshells.

The reference construction guide - named Eurocomp, for composite materials – guided the construction and in addition, a robustness study has been performed on the Solidays gridshell [Tayeb et al, 2013]. This study showed that the gridshell can undergo accidental situation such as vandalism without risking collapse. Indeed, thanks to redundancy, the stress from a break would spread largely and the stress in the neighboring beams would not get too high. 71 beams among the 1,357 constituting the structure were broken without triggering dramatic instabilities, but visible deflections. At the same time, large displacements of broken beams would be visible and the evacuation could be launched. This kind of pseudo-ductility is a very positive point.



Figure 6: Connections devised jointly by the Navier laboratory and the company T/E/S/S. Left: Pin anchorage for beams. Right: Assembly used to join two beams

Some connections were also designed and successfully mechanically tested. For example, articulate pin anchorage connections (fig.6 left), or a coupler for connecting several composite pipes to make long beam elements from initially short piece of tubes is shown on figure 6 (right): a steel system that sets up mechanical continuity between two adjacent composite pipes for both traction-compression and bending. It is made of three parts: two connectors linked by a threaded rod.

AN HYBRID CONCEPT: GRIDSELL WITH A CONCRETE ENVELOP

After being braced, and as shown above, gridshell structures need generally to be covered to become buildings and not solely a structure. This operation supposes finding a material and a technique that will be able to adapt to the complex shape of the gridshell. Common covering solutions can be separated into two categories, based on the local surface bending stiffness of the finished product: soft and hard covers. Again, hard covers are desirable but difficult to design. It will thus be interesting to investigate a covering method for elastic gridshells that combines the ease of design and construction of a soft cover with the resistance of a hard cover. Recently, there was a renewal of interest in research on thin concrete shells cast on soft formworks, mostly fabric and cable nets [Abdelgader et al 2008, Veenendaal et al 2014]. It was shown to be a cost-efficient and labour-saving method to build concrete shells of complex forms. Using an elastic gridshell to support a fabric formwork could interestingly build on this idea of a lightweight scaffolding spanning from edge to edge. It would also enable the realization of forms of both positive and negative Gaussian curvature, something that is not possible in the cable-net and fabric formwork of [Veenendaal et al 2014]. However, removing the gridshell after pouring the concrete seems both complicated and unneeded. Create a collaboration, a composite action between the two materials is surely more profitable. The gridshell as a formwork for a concrete shell and a rigid cover is an interesting research directions on its own, but it seems that a hybrid structural skin could beneficially combine all advantages. By applying a skin of concrete on top of an elastic gridshell and connecting it mechanically to the main grid, a rigid, continuous and curved envelop that improves the structural capabilities of the gridshell is created. The intention is indeed that the composite action of the grid and the concrete skin insures bracing of the grid, redistribution of stresses under concentrated load and reduction of local buckling. The feasibility of this concept is demonstrated below and more detailed in [Cuvilliers et al 2017].

Geometry and concept

Based on this preamble, a prototype of an elastic gridshell braced by a rigid concrete envelope was designed. The shape of the structure results from two different sets of constraints: fabrication constraints on the shape of the elastic gridshell and funicularity constraints under the weight of the wet concrete. The final shape and axonometric view of the prototype are presented in Figure 7.

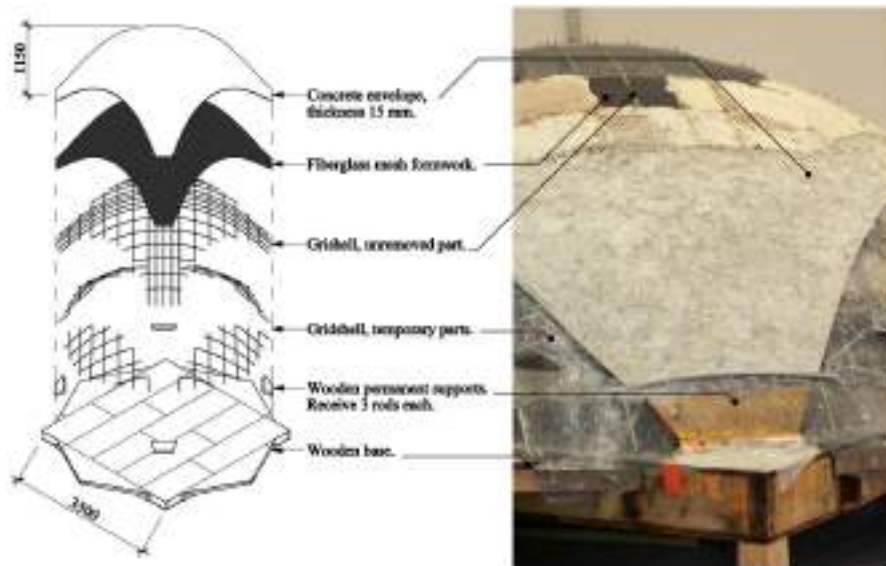


Figure 7: Axonometric view and photograph showing the successive layers in the prototype.

Two components are of particular importance: the fiberglass mesh fabric that provides the formwork for the concrete, and the screw connector that binds the concrete and the gridshell layer, which can be seen in the typical detail section of Figure 8.

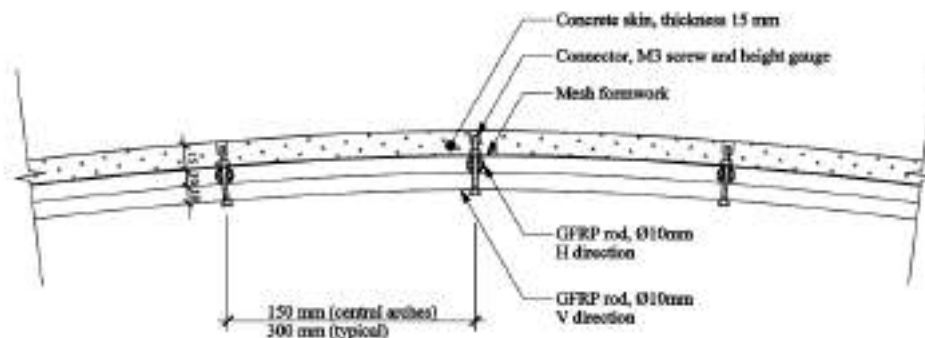


Figure 8: Section cut, typical.

Figure 7 shows also the succession of layers of the structure. On a wooden support structure, an elastic gridshell is shaped, initially with no openings: the whole boundary of the gridshells attached to the ground. The gridshell is made of Glass Fibre Reinforced Polymer, namely Round Triglass by Topglass. This support structure is temporarily partially triangulated with cables (not shown on the drawings). A fiberglass mesh is laid on the gridshell on the area that will receive the concrete. This mesh is a woven fabric of relatively thick fiberglass threads, similar to what is used for insect screens on windows. The concrete is introduced last; it does not cover the whole gridshell so that the structure does not remain as a complete dome in the end. When it has cured, the parts of the gridshell that are not covered by concrete are removed, creating four openings. The structure is 1.15 m high with openings 0.7 m high. The structure spans 3 m from support to support. Those four supports are placed at each corner of the gridshell. The developed area of the concrete layer is 9.55 m² and the structure covers. Figure 9 shows some views of the elaboration, and figure 10 the final structure and one of the case loading! More complete tests can be found in [Cuvilliers 2017] with displacement measurements results.



1. Gridshell preparation



2. Mesh formwork preparation



3. Gridshell erection and bracing



4. Quick-setting cement placing



5. Concrete placing



6. Finished structure, temporary parts removed

Figure 9: Steps of the construction process





Figure 10: The structure loaded with two 0.7 kN point loads.

CONCLUSION

Recent advanced concerning elastic composite gridshells are detailed in this paper, showing that several realisations have been successfully constructed, with progressive improvements. A major remaining difficulty concern the roofing of these discrete structures. A membrane has to be simulated, prefabricated and precisely adapted to the obtained shape. Moreover it doesn't provide to the structure a lot of acoustic, thermal or safety performances. The mixed composite/concrete prototype proposed here proved the feasibility of this innovative technique and the economic data provided shows that it has good potential for application to larger scales. For medium scale, say for cupolas between 10 m² and 50 m², the proposed technique can be also directly adapted and implemented by local craftsmen (like for the Pishwanton gridshell construction [Sassi 2006]). The diameter of the gridshell members and of the connectors (which for the built prototype were slightly undersized) will have to be increased, but the size of the grid and its mass will remain low (about a hundred kilos) so that no extraordinary equipment will be needed for the forming of the grid. No cutting pattern is required for the fabric formwork which is flat, as is the grid: its manufacturing will remain simple, even if the material must be adapted to the scaling and changed into a more technical textile.

ACKNOWLEDGMENTS

The authors acknowledge T/E/S/S engineering and Viry construction, partners for the scale:1 gridshell constructions (Creteil and Solidays), and SaintGobain who provided the *FibraFlex* steel fibers for the concrete skin of the hybrid concept.

REFERENCES

- du Peloux, L., Tayeb, F., Baverel, O., and Caron, J.-F., Construction of a Large Composite Gridshell Structure: A Lightweight Structure Made with Pultruded Glass Fibre Reinforced Polymer Tubes, *Struct. Eng. Int.*, 2016, 26 (2), pp.160-167(8).
- Baverel, O., Caron, J.-F., Tayeb, F., and du Peloux, L., Gridshells in composite materials: Construction of a 300 m² forum for the Solidays' festival in Paris, *Struct. Eng. Int.*, Vol. 22, No. 3, Aug. 2012, pp. 408–414.
- Douthe, C., Baverel, O., Caron, J.-F., Formfinding of a grid shell in composite materials, *J. IASS.*, Vol. 47, No. 150, 2006, pp. 53–62
- Cuvilliers P., Douthe C, du Peloux L., Le Roy R., Hybrid structural skin: prototype of a GFRP elastic gridshell braced by a fiber-reinforced concrete envelope, *Journal of the International Association of Shells and Spatial Structures* (2017), vol 58 n°191, p 65-78.
- Tayeb F, Caron J-F, Baverel O, Du Peloux L. Stability and robustness of a 300 m² composite gridshell structure - *Construction and Building Materials*, Volume 49, December 2013, Pages 926–938
- Otto, F., Hennicke, J., Matsushita, K., Gitterschalen Gridshells, *Institut für Leichte Flächentragwerke*, IL 10, 1974, pp. 340
- Happold, E., Lidell, W. I., Timber lattice roof for the Mannheim Bundesgarten-schau, *The structural engineer*, Volume 53 No. 3, 1975, pp. 99-135.
- Ban, S., The Japanese pavilion, in Shigeru Ban, editor McQuaid M, ed Phaedon, 2006, pp. 8-11.
- Ashby, M., *Materials selection in mechanical design*, eds Reed Educ. & Prof. Pub. 1999.
- Abdelgader, H., West, M., and Górski, J., State-of-the-art report on fabric formwork, in *Proceedings of the International Conference on Construction and Building Technology*, 2008, pp. 93–105.
- Veenendaal, D. and Block, P., Design process for prototype concrete shells using a hybrid cablenet and fabric formwork, *Eng. Struct.*, Vol. 75, 2014, pp. 39–50.



RC structures internally reinforced by FRP bars

IMPROVEMENT OF MECHANICAL SHEAR RESISTANCE OF HIGH MODULUS CFRP ROD WITH GFRP RIBS

Hiroaki Hasegawa ¹, Nobuhiro Hisabe ¹, Yoshiki Onari ² and Isamu Yoshitake ²

¹Mitsubishi Chemical Infratec Co.,Ltd., Tokyo, Japan

²Yamaguchi University, Department of Civil and Environmental Engineering, Ube, Yamaguchi, Japan

Email: yositake@yamaguchi-u.ac.jp (Isamu Yoshitake)

ABSTRACT

This study focuses on the strengthening method for upper-side of cantilevered bridge deck slabs subjected to negative bending moment. A general strengthening method in Japan, RC overlay method, is to place reinforcing bars and concrete on existing deck slabs. For prevention of reinforcement corrosion, thick concrete cover (100 mm or thicker) is required in the method. Such system induces the increase of dead load, and it may negatively influence on bridge girders and substructures. Near-surface-mounted (NSM) method using FRP rods/strips can decrease the thickness of strengthening layer compared to the RC overlay method. In particular, NSM using CFRP rod/strip of high modulus has several advantages, such as high strengthening-effect and low deformation. The high modulus CFRP rod/strip are manufactured by PULTRUSION method, so the surface of the composite materials is smooth without ribs like rebars. Hence, the most concern of the reinforcing material is low bond performance. In this study, GFRP ribs were attached to CFRP rods to improve the bond strength. The study prepared various CFRP ribs and conducted fundamental tests. Pull-out test of the CFRP rod having GFRP ribs was conducted to examine the bond performance. Flexural loading test using RC beam embedding these CFRP rods was carried out to confirm the strengthening effect. The pull-out test confirmed that even CFRP rod attached with GFRP ribs of 3.0 mm thick indicated adequate bond strength. The experimental investigation confirmed that the load-bearing capacity of the strengthened beams were higher than the designed load.

KEYWORDS

Strengthening, Bond strength, Interfacial stresses, CFRP rod internal reinforcement, Cantilevered slab, NSM.

INTRODUCTION

Due to the installation of sound insulation walls, widening of road width, and renovation of wheel guard, strengthening of the upper surface of the cantilevered RC slab is often necessary. In the strengthening of the upper surface of slab, the general method is "RC overlay method" which the upper surface of the deck slab is covered with rebars and additional concrete. In the RC overlay method, the road elevation of bridge vicinity should be reconstructed because thickness of the bridge deck is increased (approximately 100 mm). Furthermore, the burden of the main girder and substructure also increases in addition to the dead load increase.

Near-surface-mounted (NSM) method using carbon fibre-reinforced polymer (CFRP) has been investigated in previous studies (Firas et al. 2009; Teng et al. 2001; Lam et al. 2001; Yoshitake et al. 2010). Figure 1 demonstrates a schematic of CFRP NSM applicable in upper deck slabs. Note is that the asperity of the CFRP surface is small. It may be difficult to ensure the bonding capacity of CFRP to concrete.

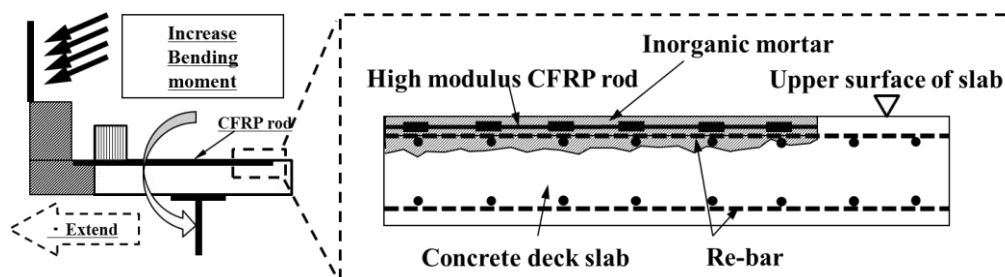


Figure 1: Overview of NSM method for cantilevered bridge deck slab

The authors developed a NSM method in which CFRP rods having ribs to improve bond performance are embedded in inorganic high-strength mortar (Hasegawa et al. 2016; Kuroda et al. 2016). In the present study,

bond performance and flexural behaviour of the NSM strengthened beam were examined to confirm the applicability.

MATERIALS

To improve the bond performance of CFRP rods, glass fibre-reinforced polymer (GFRP) ribs (3.0, 4.5, 6.0 mm thick) were attached to CFRP rod (Figure 2). As the element experiment, the bond performance of CFRP rod with GFRP rib was evaluated by pulling out CFRP rod with one GFRP rib embedded in the mortar. In addition, the flexural performance was evaluated by flexural loading test of RC beams strengthened with the CFRP rods. Properties of concrete, mortar, rebars, CFRP rods used in the study are shown in Tables 1 and 2.



Figure 2: CFRP rod attached with GFRP rib

Table 1: Properties of rebar and CFRP rod

		Rebar	CFRP rod
Diameter	mm	6.0	8.0
Yielding strength	MPa	371	N/A
Tensile strength	MPa	571	1310
Young's modulus	GPa	206	468

Table 2: Properties of concrete and mortar

		Concrete	Mortar
Compressive strength	MPa	32.1	42.5
Young's modulus	GPa	33.5	28.0

ELEMENT EXPERIMENT (PULL-OUT TEST)

Specimens and Test Method

The dimensions of the cylindrical mortar specimen for the pull-out test are 55 mm diameter and 160 mm long. A 8-mm diameter CFRP rod with a GFRP rib was embedded at the centre of cylinder diameter (Figures 3). Referring to JSCE 539-1999, the pull-out test was conducted as shown in Figure 4. The CFRP rod has high elastic modulus of 468 GPa. The GFRP rib attached to the CFRP rod had 50 mm long. The thickness of GFRP rib were 3.0 mm, 4.5 mm, and 6.0 mm thick, respectively. The GFRP ribs for HM8-GD3.0 and HM8-GD-4.5 specimens were made by directly wrapping CFRP rod. The GFRP rib for HM8-GS6.0 specimen was made by filling expansive mortar into the gap between CFRP rod and GFRP hollow sleeve of 3.0 mm thick. For comparison, a control specimen

embedding deformed rebar (nominal diameter of 10 mm) was prepared. The embedment length of CFRP rod in the mortar was 160 mm including the unbonded length of 50 mm (Figure 3).

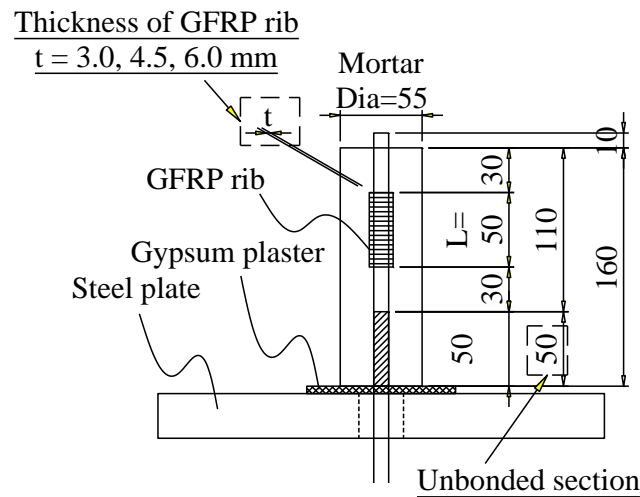


Figure 3: Schematic of pull-off test



Figure 4: Pull-off test

Test Results

As for the failure modes of all test specimens, bond failure between GFRP sleeve and CFRP rod occurred due to pull-off loading. Figure 5 illustrates the bond-slip failure of CFRP rod.

Table 3 summarizes the test results. The maximum stress, i.e. the nominal bond strength, was determined by using Eq.1. The bond strength of control specimen (No. 1) embedding rebar was 9.57 N/mm^2 , whereas the specimens containing CFRP rod with GFRP ribs (No.2-4) indicated the bond strength of $9.83 - 10.49 \text{ N/mm}^2$. It was revealed that by providing a rib of over 3.0 mm thick, the same degree of bonding strength as the reinforcing bars can be obtained.

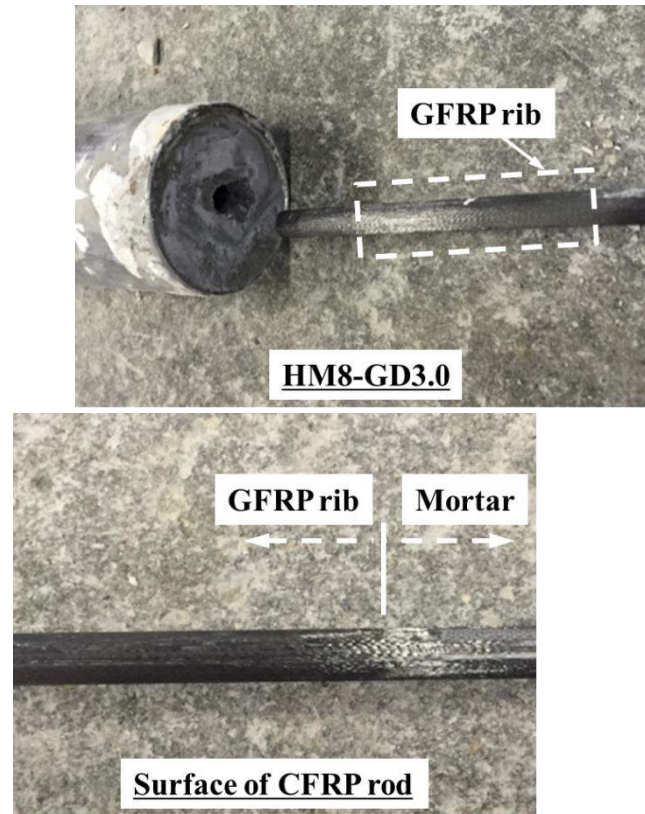


Figure 5: Typical failure mode (slip)

Table 3: Test result of element experiment

Specimen I.D.	Reinforcement	Diameter (mm)	Thickness of GFRP rib (mm)	P_{max} (kN)	Bond strength τ_{cf} (MPa)	Failure mode
Control	Rebar	10.0	N/A	33.06	9.57	Slip
HM8-GD3.0	CFRP	8.0	3.0	29.01	10.49	Slip
HM8-GD4.5	CFRP	8.0	4.5	27.18	9.83	Slip
HM8-GS6.0	CFRP	8.0	6.0	28.42	10.28	Slip

$$\tau_{cf} = P_{max} / (D \times \pi \times L) \quad (1)$$

where τ_{cf} : Bond strength
 D : Diameter of CFRP rod (rebar) P_{max} : Maximum load
 L : Bond length (= 110 mm)

FLEXURAL LOADING TEST

Beam Specimens

Figure 6 shows the schematic of the beam specimen, and Table 4 shows the list of beam specimens. The control specimen is a non-strengthening beam. HM8-GD3.0-200, HM8-GD4.5-200, HM8-GS6.0-200 are specimen I.D. Each specimen I.D. shows the beam strengthened with CFRP rods having GFRP ribs of 3.0 mm thick, 4.5mm thick and 6.0 mm thick, respectively. In addition, HM8 shows a beam specimen strengthened by CFRP rod without GFRP ribs. It should be noted that the rib length is 50 mm, and the rib interval is 200 mm. D6 steel bars (SD345) and D10 steel bars (SD345) were used as tensile reinforcement and shear reinforcement, respectively.

Table 4: Slab specimens

No.	Specimen I.D.	Reinforcements		Thickness of GFRP rib
		Rebar	CFRP	
1	Control	2 x D6	N/A	N/A
2	HM8-GD3.0-200	2 x D6	2 x HM8	3.0 mm
3	HM8-GD4.5-200	2 x D6	2 x HM8	4.5 mm
4	HM8-GS6.0-200	2 x D6	2 x HM8	6.0 mm
5	HM8	2 x D6	2 x HM8	N/A

HM8: High modulus CFRP rod of 8-mm diameter; D6: deformed reinforcing bar (nominal diameter of 6-mm)

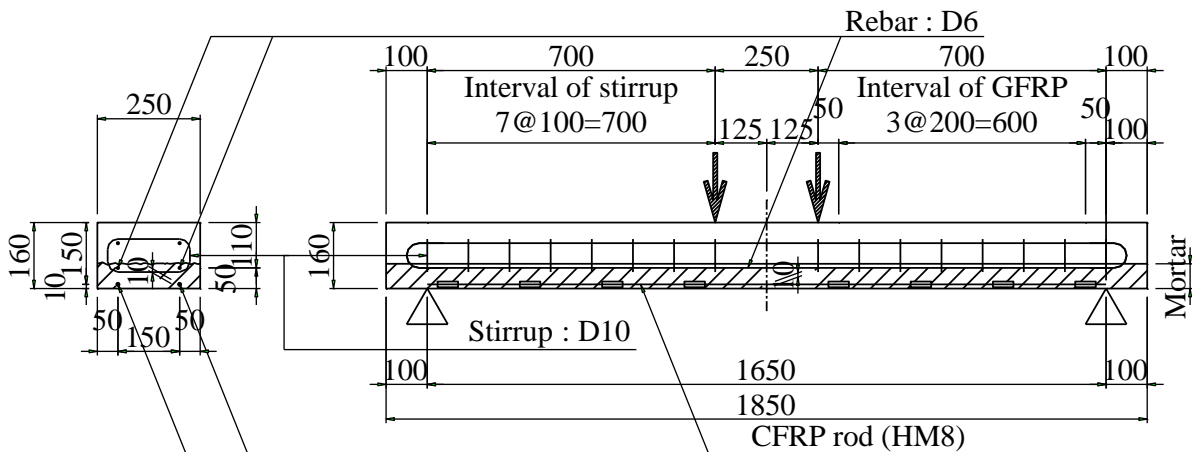
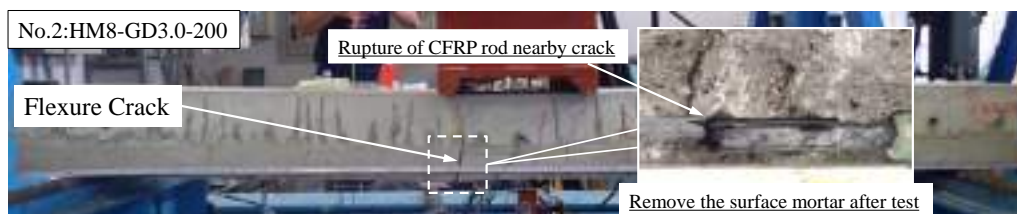


Figure 6: Schematic of beam specimen

Test Results and Discussion

Failure mode

Figure 7(a) shows bending failure of beam specimen No.2 (HM8-GD3.0-200). As well, Figure 7(b) illustrates shear failure of specimen No.5 (HM8). With respect to test specimens (No.2, 3, 4) containing CFRP rods with GFRP ribs, flexural cracks developed in the pure bending section progressed in accordance with deformation. The load decreased significantly after the rupture of the CFRP rod (the failure). Table 5 summarizes the failure mode.



(a) flexural failure (HM8-GD3.0-200)



(b) shear failure (HM8)

Figure 7: Typical failure mode of beam specimen

Load-deformation responses and maximum load

Figure 8 shows the load-deflection responses. As for specimens (No. 2-5) strengthened with the CFRP rod, it can be seen that the deflection properties have improved as compared with specimen No.1 (Control). Regarding specimens (No. 2, 3, 4) containing GFRP ribs, the deflection linearly increased up to the maximum load. However, with regard to specimen No.5 (HM8) not having GFRP rib, the deflection gradient has changed near the maximum load. The observation implies the slipping of the CFRP rod from the concrete.

Table 5 summarizes the maximum load (P_{max}), the deflection (δ), the reinforcement strain, and the CFRP rod strain at the maximum loading. In the table, P_{ycal} represents the calculated load at the yielding of reinforcing bar. The result confirms that the maximum loads of test specimens (No. 2, 3, 4) were higher than the calculated yielding load (P_{ycal}). In addition, it was confirmed that the observed strains were greater than the yielding strain of rebar (approximately 1700×10^{-6}) and CFRP rod fracture strain (approximately 2800×10^{-6}). It should be noted that the fracture strain is calculated by using tensile strength of CFRP rod (1310 N/mm^2) and Young's modulus of CFRP rod (468 kN/mm^2). Of interest is that the specimen (No. 5) containing CFRP rods without GFRP ribs failed at approximately 91% of P_{ycal} . The observation implies that the CFRP rod slipped from concrete before rebar-yielding. Hence, the deformation of the beam specimen significantly increased and the rod broke at the lower load of the calculated load (P_{ycal}).

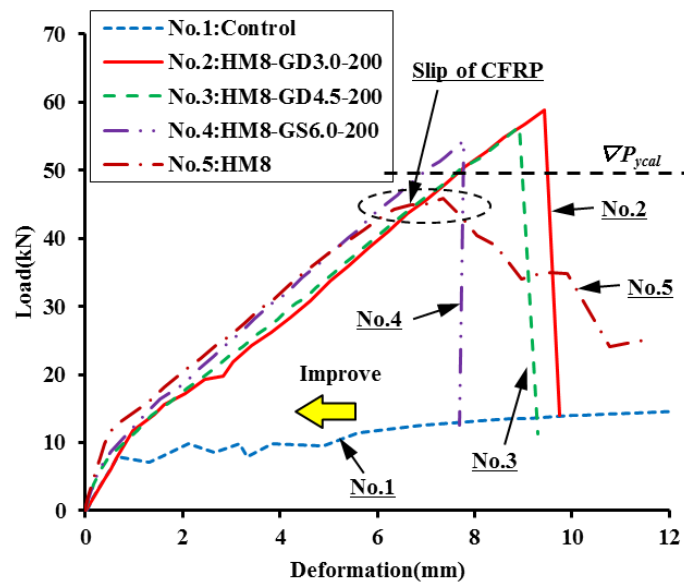


Figure 8: Load-deformation responses

Table 5: Maximum load, deflection, strain and failure mode

No.	Specimen I.D.	P_{max} (kN)	P_{ycal} (kN)	δ (mm)	Maximum strain ($\times 10^{-6}$)		Failure mode
					Rebar	CFRP	
1	Control	15.99	6.52	20.5	1042	N/A	Flexure
2	HM8-GD3.0-200	58.81	49.98	9.4	2278	3094	Flexure
3	HM8-GD4.5-200	56.48		8.9	2297	3005	Flexure
4	HM8-GS6.0-200	54.31		7.8	1904	2852	Flexure
5	HM8	45.82		7.4	1586	2231	Shear

Strain of CFRP rod

Figure 9 shows the strain measurement system. Figure 10 shows the strain of CFRP rods of specimens No. 2 (HM8-GS3.0-200). Figure 10 shows that the gradient of the strain (St2-CF St3-CF St4-CF) in the shear span changes at load of 20 kN, 30 kN and 45 kN, respectively. The changed strain gradients imply the occurrence of new cracks in the shear span. With regard to behaviour after the change in the strain gradient, the CFRP rod strain increased linearly up to the maximum strain at the ultimate load.

Figure 11 shows the strain of CFRP rods (without GFRP ribs) of specimen No. 5 (HM8). The result indicated that strain (St3-CF St4-CF) in the shear span significantly increased before the ultimate load. The shear cracks ultimately induced the shear failure of the beam before the reinforcing bar yield load.

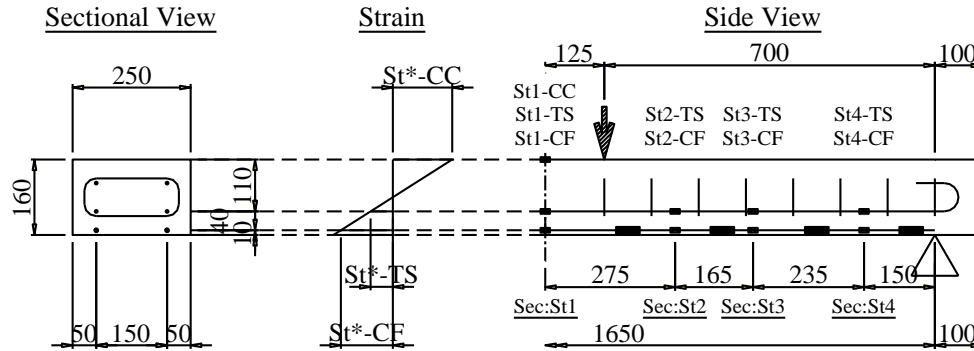


Figure 9 Strain measurement system

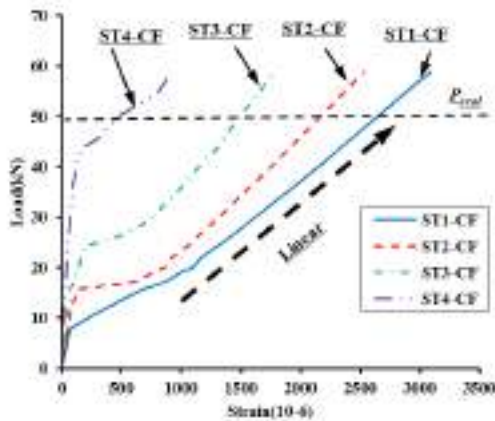


Figure 10 Load-CFRP strain (HM8-GD3.0-200)

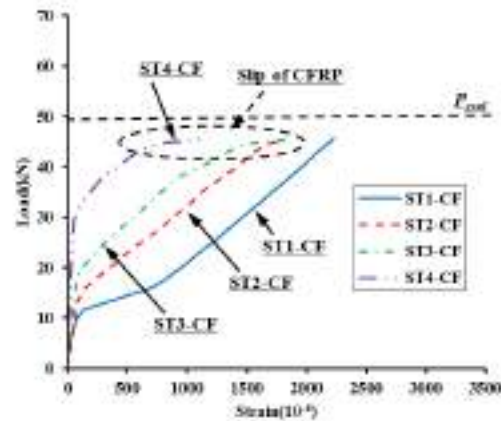
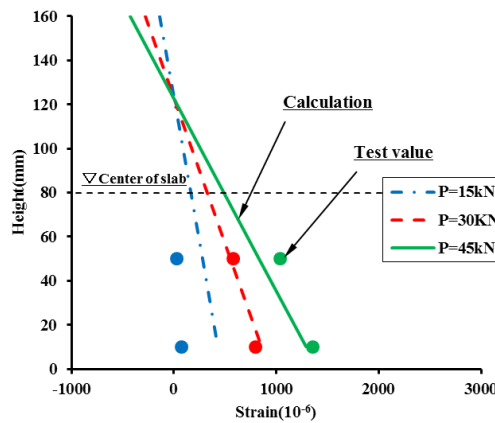
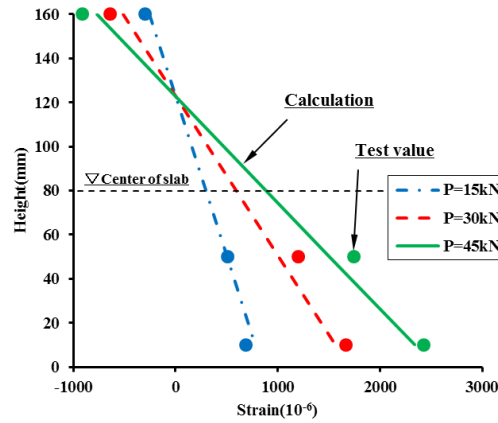


Figure 11 Load-CFRP strain (HM8)

Strain profiles

Figure 12 shows strain profiles of HM8-GD3.0-200 specimen in Sec-St1 (midspan) and Sec-St3 (nearly center of shear span). As well, Figure 13 shows strain profiles of HM8 specimen in Sec-St1 and Sec-St3. The solid and dashed lines in these figures show calculation based on the flexural theory.

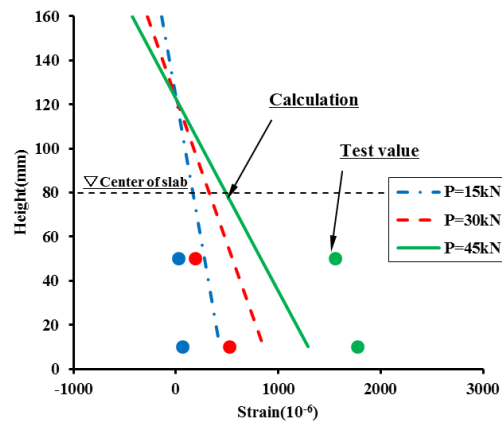
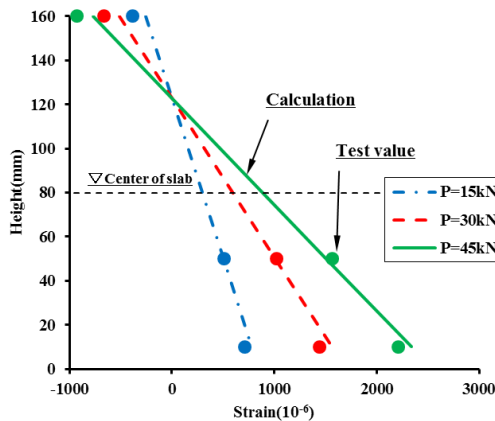
Both test results of strain profiles in Sec-St1 agreed well with calculation value until 45 kN. Meanwhile in Sec-St3, the test result of HM8-GD3.0-200 was almost coincident with calculation value, but the test value in HM8 specimen obviously differed from the calculation value. That is, linear strain profile like “Bernoulli-Euler theory” was not observed in the specimen HM8. The observation confirms the slip of CFRP rod at the shear span.



(a) *St1-TS/CF(HM8-GD3.0-200)*

(b) *St3-TS/CF(HM8-GD3.0-200)*

Figure 12: Strain profiles (HM8-GD3.0-200)



(a) *St1-TS/CF(HM8)*

(b) *St3-TS/CF(HM8)*

Figure 13 Strain profiles (HM8)

CONCLUSIONS

To examine the effect of CFRP rod with ribs, the experimental study conducted pull-out test of CFRP rod and flexural test of NSM CFRP rods RC beam. The conclusions of this study are summarized below:

- (1) The pull-off test of bond-improved CFRP rod confirmed that the bond failure between GFRP sleeve (over 3.0 mm thick and 50 mm long) and CFRP rod is dominant. The bond strengths of the CFRP rod were higher than the strength of deformed rebar which has larger diameter.



- (2) The load-bearing capacity of beam was improved by embedding CFRP rods. The beam specimen embedding CFRP rods without GFRP ribs indicated shear failure due to the slip of the CFRP rod in shear span.
- (3) All beam specimens strengthened with CFRP rods having GFRP ribs showed higher load-bearing capacity than the yielding load of rebars (approximately 1700×10^{-6}) and the fracture strain of CFRP rod (approximately 2800×10^{-6}).
- (4) The strain of CFRP rod with GFRP ribs increased linearly up to the ultimate load, it was greater than the fracture strain of CFRP rod. Based on the test results, sufficient bond capacity of the CFRP rod with GFRP ribs (over 3.0 mm thick) was confirmed.
- (5) The strain profiles at midspan agreed well with the calculation value based on the flexural theory. The strain of CFRP rod without ribs at shear span differed from the calculation though the strain of bond-improved CFRP rod also agreed well with the calculated strain even at shear span.

ACKNOWLEDGMENTS

The authors wish to gratefully acknowledge the support of Mr. Y. Kuroda (OBAYASHI Corporation).

REFERENCES

- A. Firas, C. Arnaud, F. Raoul and T. Christian (2009), "Strengthening of RC members with near-surface mounted CFRP rods", *Composite Structure*, 91, 138-147.
- H. Hasegawa, N. Hisabe, Y. Kuroda and I. Yoshitake (2016), "Flexural behavior of a cantilevered slab strengthened with NSM CFRP rods", *7th International Conference on Advanced Composite Materials in Bridges and Structures*.
- Y. Kuroda, H. Hasegawa, N. Hisabe and I. Yoshitake (2016), "Strengthening effect of a CFRP rod having ribs for a cantilevered slab", *6th International Conference on GEOMATE*.
- L. Lam and J.G. Teng (2001), "Strength of RC cantilever slabs bonded with GFRP strips", *Journal of Composites for Construction*, 5(4), 221-227.
- J.G. Teng, S.Y. Cao and L. Lam (2001), "Behavior of GFRP-strengthened RC cantilever slabs", *Construction and Building Materials*, 15(7), 339-349.
- I. Yoshitake, Y.J. Kim, K. Yumikura and S. Hamada (2010), "Moving-wheel fatigue for bridge decks strengthened with CFRP strips subject to negative bending", *Journal of Composites for Construction*, 14(6), 84-790.



SERVICEABILITY AND MOMENT REDISTRIBUTION OF CONTINUOUS CONCRETE ELEMENTS REINFORCED WITH STEEL-BASALT BARS

M. Akiel¹, T. El-Maaddawy² and A. El Refai³

¹ McGill University, Montreal, Canada

² UAE University, Al Ain, UAE, Email: tamer.maaddawy@uaeu.ac.ae

³ Laval University, Quebec City, Canada.

ABSTRACT

The serviceability and moment redistribution of continuous concrete flexural elements internally-reinforced with either basalt fiber-reinforced polymer (BFRP) bars or a combination of steel and BFRP bars are evaluated in this paper. Six two-span concrete specimens were constructed and tested. The specimens were 200 mm deep, 500 mm wide, and 5000 mm long. Each span had a length of 2400 mm. Three specimens were reinforced with BFRP bars only whereas the remaining three specimens were reinforced with hybrid steel-BFRP bars. The specimens had different hogging-to-sagging reinforcement ratios. Specimens reinforced with hybrid steel-BFRP bars were designed in a way to have nominal sagging and hogging moment capacities similar to those of their counterparts reinforced with BFRP bars only. The use of hybrid steel-BFRP reinforcing bars rather than BFRP bars only improved the serviceability performance of continuous concrete elements without compromising their deformational capacity. Specimens reinforced with hybrid steel-BFRP bars exhibited less deflections and smaller crack widths at service load than those of their counterparts reinforced with BFRP bars only. Hybrid-reinforced specimens reached their ultimate loads at deflection values comparable to those of their counterparts reinforced with BFRP bars only. The behavior of the specimens reinforced with BFRP bars only deviated from the elastic response, which resulted in a considerable moment redistribution between the sagging and hogging regions. Specimens reinforced with hybrid steel-BFRP bars exhibited less deviation from the elastic response and lower moment redistribution ratios compared with those of their counterparts reinforced with BFRP bars only.

KEYWORDS

BFRP, concrete, continuous, hybrid; serviceability, moment redistribution.

INTRODUCTION

Fiber-reinforced polymer (FRP) bars have a great potential to replace steel reinforcement and eliminate corrosion problems in reinforced concrete structures. BFRP bars have recently emerged as a promising addition to the existing FRP family. BFRP bars have become the focus of several studies that were devoted to determining their short- and long-term properties (El Refai 2013; Elgabbas et al. 2015). However, very few studies focused on the feasibility of using such bars as internal reinforcement for concrete structures (Mahroug et al. 2013; Ge et al. 2015). Concrete elements internally-reinforced with FRP fail either by rupture of FRP bars or concrete crushing. Rupture of FRP is considered more brittle than the concrete crushing mode of failure because it leads to a sudden release of energy and immediate loss of strength (Bank 2006; Al-Sunna et al. 2012; Nanni et al. 2014; ACI 440.1R-15 2015). Therefore, the ACI 440.1R-15 (2015) recommends a minimum FRP reinforcement ratio of $1.4\rho_{fb}$, where ρ_{fb} is the balanced FRP reinforcement ratio, to ensure that concrete crushing would take place prior to the rupture of the FRP at ultimate load. Concrete elements internally-reinforced with FRP bars exhibit larger deflections and higher crack widths than those reinforced with conventional steel bars (Bank 2006; Al-Sunna et al. 2012; Nanni et al. 2014; ACI 440.1R-15 2015). Therefore, some researchers recommended the use of hybrid reinforcement (i.e. a combination of FRP and steel reinforcing bars) to improve the serviceability of FRP-reinforced concrete elements (Qu et al. 2009; Safan 2013; Mahroug et al. 2013; El Refai et al. 2015; Ge et al. 2015). Few investigations focused on studying the nonlinear behavior of continuous concrete elements internally-reinforced with FRP bars (Habeeb and Ashour 2008; El-Mogy et al. 2010; El-Mogy et al. 2011; Mahroug et al. 2013; Mahroug et al. 2014). These studies showed that moment redistribution could occur in continuous beams reinforced with adequate FRP reinforcement in the sagging regions without compromising the beam serviceability. Nevertheless, due to the lack of experimental evidence, most design guidelines and standards do not allow moment redistribution in continuous concrete structures internally-reinforced with FRP bars (fib 2007; CAN/CSA-S806 2012; ACI 440.1R-15 2015). This research examines the nonlinear behavior of continuous concrete elements internally-reinforced with BFRP bars only or a combination of steel and BFRP bars. The serviceability and moment redistribution of continuous concrete specimens reinforced with hybrid steel-BFRP bars are studied and compared to those of similar specimens reinforced with BFRP bars only.

EXPERIMENTAL PROGRAM

Test Matrix

The experimental study comprised testing of six two-span concrete specimens. The test matrix is given in Table 1. Specimens of group [A] were reinforced with BFRP bars only whereas those of group [C] were reinforced with hybrid steel and BFRP bars. All specimens were over-reinforced. The sagging reinforcement ratio in all specimens of group [A] corresponded to $3.2\rho_b$. Three hogging-to-sagging reinforcement ratios, namely 0.5, 0.75, and 1, were adopted in specimens of group [A] which corresponded to hogging-to-sagging nominal moment strength ratios of 0.75, 0.85, and 1, respectively. The nominal moment strengths of the sagging and hogging sections in the hybrid-reinforced specimens of group [C] were almost equal to those of their counterparts of group [A] reinforced with BFRP bars only.

Table 1: Test matrix

Group	Specimen	BFRP reinforcement		Steel reinforcement		H-to-S strength ratio ¹
		Hogging	Sagging	Hogging	Sagging	
[A] BFRP-reinforced specimens	A1	1 Φ 10 + 2 Φ 12	2 Φ 10 + 4 Φ 12	-	-	0.75
	A2	2 Φ 8 + 3 Φ 12	2 Φ 10 + 4 Φ 12	-	-	0.85
	A3	2 Φ 10 + 4 Φ 12	2 Φ 10 + 4 Φ 12	-	-	1.00
[C] Hybrid-reinforced specimens	C1	2 Φ 8 + 1 Φ 10	1 Φ 10 + 3 Φ 12	2 Φ 12	2 Φ 12	0.75
	C2	2 Φ 8 + 2 Φ 10	1 Φ 10 + 3 Φ 12	2 Φ 12	2 Φ 12	0.85
	C3	1 Φ 10 + 3 Φ 12	1 Φ 10 + 3 Φ 12	2 Φ 12	2 Φ 12	1.00

¹ H-to-S = Hogging-to-sagging

Materials

The cylinder strength of the concrete used in this study was 43 MPa whereas the splitting cylinder strength was 4.0 MPa. Sand-coated BFRP bars with nominal diameters of 8, 10, and 12 mm, were used with measured ultimate tensile strengths of 1235, 1227, and 1230 MPa, and moduli of elasticity of 48, 46, and 46 GPa, respectively. The steel reinforcement used was 12 mm diameter deformed bars with measured yield and ultimate strengths of 584 and 661 MPa, respectively.

Specimens

Test specimens had a width of 500 mm, depth of 200 mm, and total length of 5000 mm long. The specimens had two equal spans. Each span had a length of 2400 mm. Figure 1 shows a layout of a typical test specimen. The hogging reinforcement in all specimens had a length of 1600 mm and placed symmetrically about the central support. The hogging reinforcement extended inside each span for a distance of $L/3$, where L is the span length. The sagging reinforcing bars were 2395 mm long. They were placed at a distance 15 mm away from the edge of the specimen and 90 mm away from the middle support. The specimens were heavily reinforced in shear to ensure that a flexural mode of failure would dominate. The shear reinforcement in all specimens consisted of 8 mm diameter double-leg deformed steel stirrups spaced at 50 mm. Cross sections of the tested specimens are shown in Figure 2.

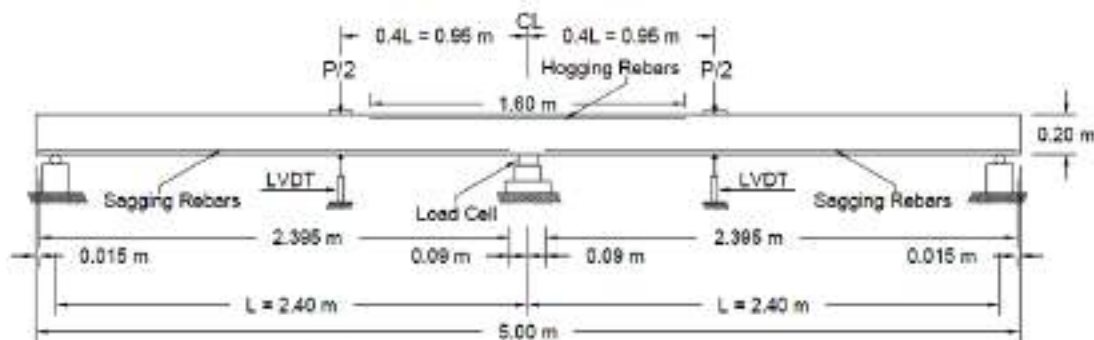


Figure 1: A Typical test specimen

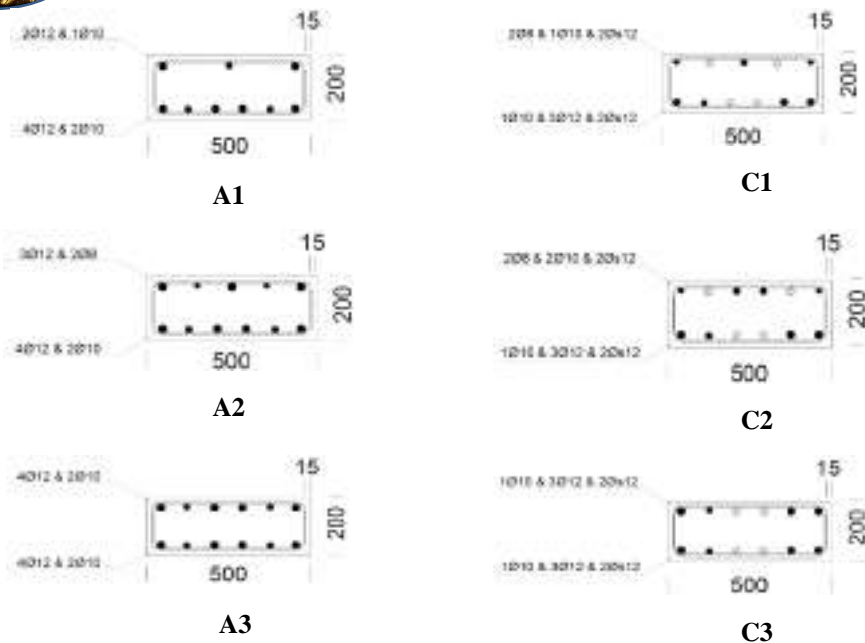


Figure 2: Cross sections of the tested specimens (all dimensions are in mm)

Test Set-up

All specimens were tested to failure under displacement control at a rate of 1.5 mm/min. The specimens were subjected to two point loads; each was located at a distance of $0.4L$ from the middle support. The load was applied using a 500kN-MTS actuator placed at the midpoint of the specimen. A rigid spreader steel beam was used to distribute the load equally to the two point loads. A load cell was placed between the actuator and the spreader beam to record the total applied load. Another load cell was placed between the middle support and the soffit of the specimen to record the middle support reactions. Two linear variable differential transducers (LVDTs) were used to record the deflections under the load points. All specimens were initially loaded until the initiation of the first visible flexural cracks in both sagging and hogging regions took place. The specimens were then unloaded to allow the installation of crack clip transducers at the extreme tension fiber of concrete in the sagging and hogging regions at locations of the first visible flexural cracks. Following the installation of crack clip transducers, the specimens were loaded back to failure.

RESULTS AND DISCUSSION

Failure Mode

Failure of specimens of group [A] was initiated by crushing of concrete in the hogging region at a load value in the range of 83% to 93% of the ultimate load. As the load progressed, concrete crushing initiated in the sagging region(s). All specimens of group [C] failed by concrete crushing after formation of several flexure cracks in both sagging and hogging regions. Initiation of concrete crushing occurred after yielding of the steel reinforcement in both hogging and sagging regions. All specimens of group [C] exhibited concrete crushing in the hogging region prior to sagging regions. In specimens of both groups, final failure took place due to widening and penetration of an inclined flexural-shear crack into the compression zone of the section located at the middle support and/or at one of the sagging regions. Figure 3 shows a photo of specimen A1 at failure.



Figure 3: Specimen A1 at failure



Load Capacity

Load values of the tested specimens are given in Table 2. Flexural cracks initiated earlier in the specimens reinforced with BFRP bars only than in those reinforced with hybrid steel-BFRP bars. This occurred because of the axial stiffness of the hybrid-reinforced reinforcement that was higher than that of the BFRP reinforcement. Yielding of steel in the hybrid-reinforced specimens occurred first in the hogging region then in the sagging region(s). In specimens of both groups, increasing the hogging-to-sagging reinforcement ratio tended to increase the ultimate load. It is interesting to notice that the ultimate loads of the counterpart specimens of both groups were insignificantly different as planned in design. The ultimate loads of specimens A1, A2, and A3 were approximately 0.83, 1.03, and 0.94 of those of their counterparts C1, C2, and C3, respectively.

Table 2: Load values

Group	Specimen	Cracking load (kN)		Yield load (kN)		Ultimate load (kN)
		Sagging	Hogging	Sagging	Hogging	
[A] BFRP-reinforced specimens	A1	67	67	-	-	318
	A2	80	84	-	-	394
	A3	80	82	-	-	375
[C] Hybrid-reinforced specimens	C1	69	82	200	150	363
	C2	92	92	200	175	384
	C3	88	94	225	175	398

Deflection Response

The load-deflection relationships of the tested specimens are plotted in Figure 4. At a given values of load, specimens of group [C] experienced less deflections than those of their counterparts from group [A]. This occurred because the axial stiffness of the hybrid reinforcement (steel + BFRP) was higher than that of the BFRP bars solely. The post-cracking stiffness tended to increase by increasing the hogging-to-sagging reinforcement ratio. Deflection values of the tested specimens at service and ultimate loads are summarized in Table 3. The inclusion of steel bars in the hybrid reinforcement of specimens of group [C] reduced their deflections at service load compared to those of their counterparts from group [A]. The deflections of the hybrid-reinforced specimens at service load were approximately 52% of those of their counterparts reinforced with BFRP bars only. Nevertheless, the deflections at ultimate load of the hybrid- and BFRP-reinforced counterpart specimens were insignificantly different. This indicated that although the use of hybrid reinforcement improved the serviceability of the hybrid-reinforced specimens by improving their stiffness and reducing their deflection at service load, it did not reduce the deflection capacity of the tested specimens (i.e. deflection at ultimate load was not reduced).

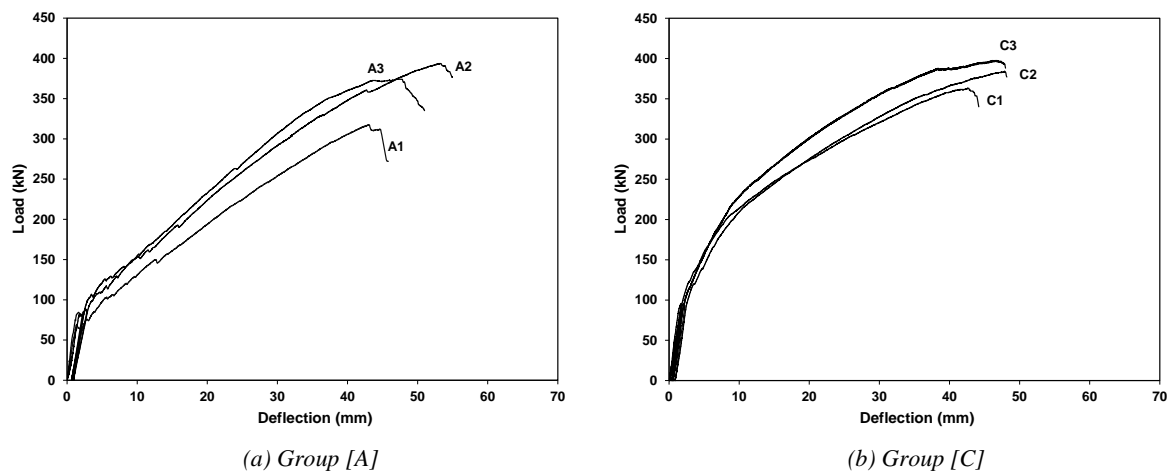


Figure 4: Load-deflection relationships

Table 3: Deflection values

Group	Specimen	Service ¹		Ultimate	
		Load (kN)	Deflection (mm)	Load (kN)	Deflection (mm)
[A] BFRP-reinforced specimens	A1	127	9.4	318	43.1
	A2	157	11.0	394	53.3
	A3	150	9.5	375	47.2
[C] Hybrid-reinforced specimens	C1	145	4.7	363	42.8
	C2	154	5.6	384	47.9
	C3	159	5.2	398	46.9

¹ At 40% of the ultimate load

Crack Width

Figure 5 shows the load-crack width relationships of the tested specimens. Varying the hogging-to-sagging reinforcement ratio had an almost no noticeable effect on the crack width in the sagging region. This occurred because specimens of each group had identical reinforcement in the sagging regions. In contrast, the crack width in the hogging region was affected by varying the hogging-to-sagging reinforcement ratio. The crack width in the hogging regions of specimens of both groups at service and ultimate loads are compared in Figure 6. The crack width in the hogging region of specimens of group [A] at both service and ultimate loads typically decreased by increasing the hogging reinforcement ratio. Increasing the hogging reinforcement ratio tended to decrease the crack width in the hogging region of specimens of group [C] at ultimate load but had no noticeable effect on the crack width at service load. The crack widths in the hogging regions at service load for specimens of group [C] were on average 57% smaller than those of specimens of group [A]. This indicated that the use of hybrid reinforcement rather than BFRP reinforcement solely improved the serviceability performance of the tested specimens.

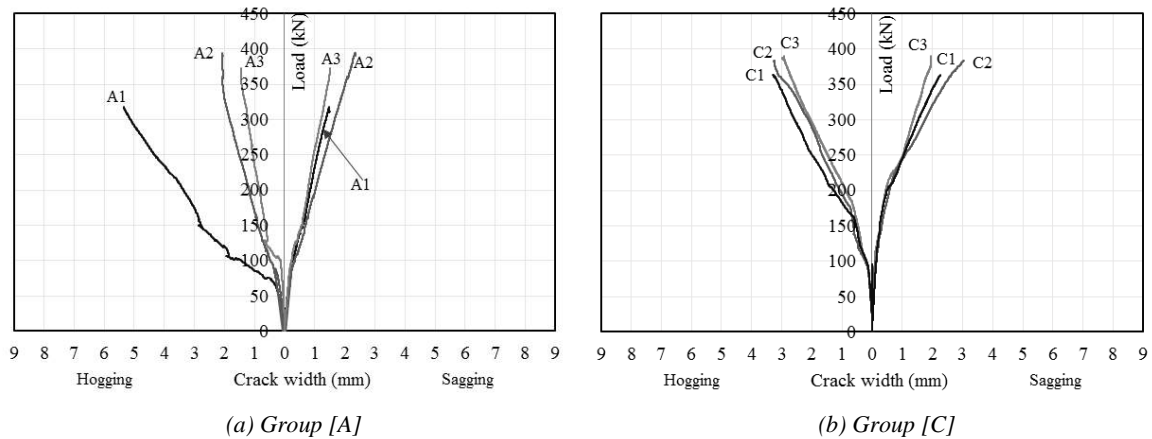


Figure 5: Load-crack width relationships

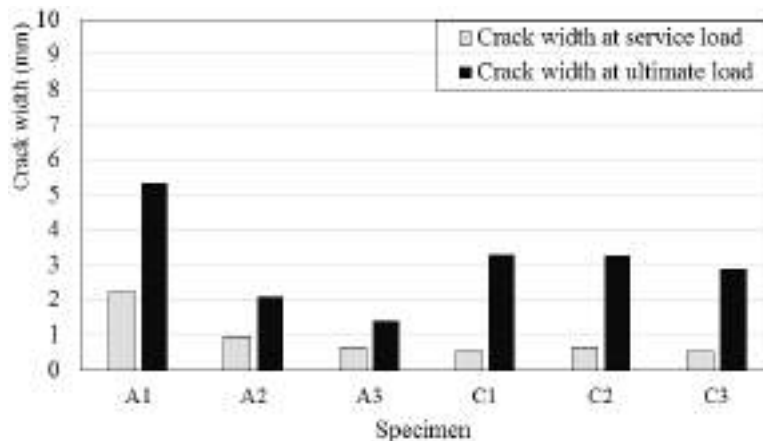


Figure 6: Crack width values in the hogging region at service and ultimate loads

Load-Moment Relationship

The load-moment relationships of the tested specimens are plotted in Figure 7. Among specimens of group [A], specimen A1 exhibited the greatest deviation from the elastic response until the initiation of concrete crushing took place in the hogging region. This occurred because specimen A1 had the smallest hogging-to-sagging reinforcement ratio. The hogging moment in specimen A1 deviated further from the elastic response at a load value of approximately 285 kN, where concrete crushing initiated in the hogging region, then it plateaued. The corresponding sagging moment continued, however, to increase up to failure. Crushing of concrete in the hogging regions of specimens A2 and A3, that took place at a load value of approximately 325 kN, resulted in a significant reduction in the hogging moment and an increase in the corresponding sagging moment. The hogging moment in specimen A2 became constant at a load value of approximately 350 kN, possibly due to initiation of concrete crushing in the sagging region. Specimen A1 failed shortly after the first concrete crushing initiated in the hogging region. In contrast, and due to the increased amount of BFRP reinforcement in the hogging regions of specimens A2 and A3 compared to that of A1, specimens A2 and A3 were able to sustain additional deformation without collapse after initiation of concrete crushing in the hogging region, which resulted in a greater moment redistribution at ultimate load. The response of specimens of group [C] initially coincided with the elastic response until yielding of the steel bars took place in the hogging region at a load value of approximately 150 kN for specimen C1 and 175 kN for specimens C2 and C3. Following yielding, the response deviated from the elastic behavior. Concrete crushing occurred in the hogging regions of specimens C2 and C3 at load values of approximately 375 kN and 385 kN, respectively, which resulted in a sudden reduction in the hogging moment and a corresponding increase in the sagging moment just prior to failure.

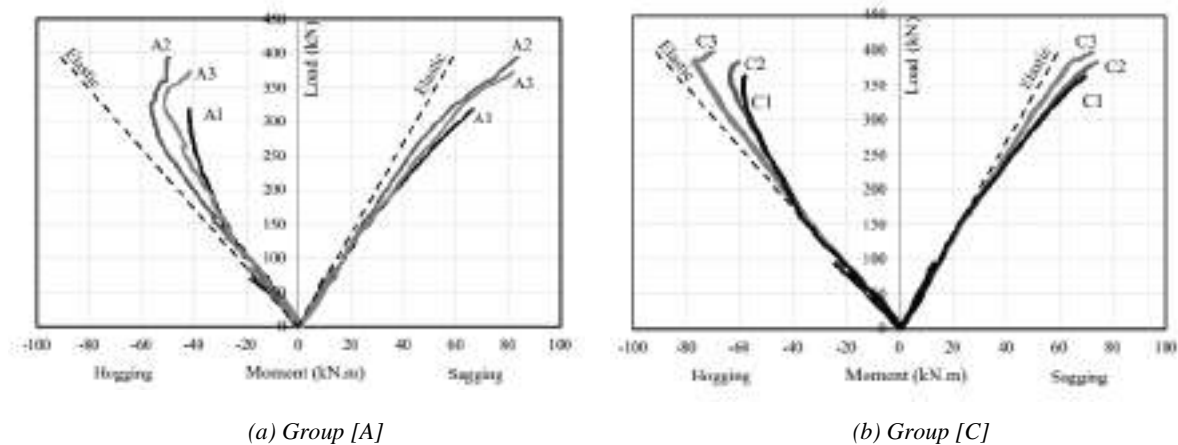


Figure 7: Load-moment relationships

Moment Redistribution

The moment redistribution ratio, β , was calculated using Equation (1), where M_{exp} is the bending moment obtained from the test and M_e is the bending moment obtained from an elastic analysis. Table 4 gives the moment redistribution ratios calculated at the first concrete crushing, which occurred in the hogging region, and also at the ultimate load.

$$\beta\% = \frac{M_{exp} - M_e}{M_e} \times 100\% \quad (1)$$

From Table 4, it can be seen that the hogging regions had negative values for the moment redistribution ratios indicating that they lost moments whereas the sagging regions had positive values indicating that they gained moment. This occurred because of the increased amount of reinforcement in the sagging regions compared to that of the hogging regions. The specimens exhibited considerable moment redistribution between the sagging and hogging regions. The moment redistribution ratios of specimens of group [C] were typically lower than those of their counterparts from group [A]. This can be ascribed to the presence of steel reinforcement, which restricted the growth of cracks in the hogging region prior to yielding, and hence, reduced the moment redistribution between the sagging and hogging regions. At the first concrete crushing, specimen A1 exhibited the highest moment redistribution ratio compared to those of specimens A2 and A3. Following the occurrence of the first concrete crushing in the hogging region of specimens A2 and A3, a significant reduction in the hogging moment took place,



which caused a significant deviation from the elastic response. This in turn increased the moment redistribution ratios at ultimate loads for specimens A2 and A3 to a level higher than that of specimen A1, which failed shortly after the first concrete crushing took place. For specimens of group [C], the moment redistribution ratio typically decreased by increasing the hogging-to-sagging reinforcement ratio. Specimen C3 having same amount of reinforcement in both the sagging and hogging regions exhibited the lowest moment redistribution ratio at first concrete crushing and also at ultimate load.

Table 4: Moment redistribution ratios

Group	Specimen	At first concrete crushing		At ultimate load	
		Sagging	Hogging	Sagging	Hogging
[A] BFRP-reinforced specimens	A1	+35	-38	+40	-43
	A2	+23	-25	+42	-46
	A3	+29	-32	+48	-52
[C] Hybrid-reinforced specimens	C1	+26	-28	+28	-31
	C2	+25	-28	+29	-32
	C3	+13	-14	+22	-24

CONCLUSIONS

The specimens reinforced with hybrid steel-BFRP bars exhibited less deflections and smaller crack widths at service load than those of their counterparts reinforced with BFRP bars only. The deflections at service load for the hybrid-reinforced specimens were approximately 50% of those of their BFRP-reinforced counterparts.. The crack widths in the hogging regions of the hybrid-reinforced specimens were 57% smaller than those of their counterparts reinforced with BFRP bars only. Although the use of hybrid reinforcement rather than BFRP bars only improved specimens' serviceability, the hybrid-reinforced specimens reached their ultimate loads at deflection values comparable to those of their counterparts reinforced with BFRP bars only. The specimens reinforced with BFRP bars only exhibited considerable moment redistribution ratios due to a non-uniform distribution and growth of cracks between the sagging and hogging regions. The deviation from the elastic response decreased by increasing the hogging-to-sagging reinforcement ratio. The inclusion of steel bars in the hybrid-reinforced specimens restricted the growth of cracks prior to yielding and reduced the difference in flexural rigidity between the sagging and hogging regions. Accordingly, the hybrid-reinforced specimens tended to exhibit lower moment redistribution ratios than those of their counterparts reinforced with BFRP bars only.

ACKNOWLEDGMENTS

The authors would like to express their gratitude to the UAE University for financing this project under grant No. 31N232.

REFERENCES

- ACI 440.1R-15 (2015). "Guide for the design and construction of concrete reinforced with FRP bars", American Concrete Institute, Farmington Hills, MI.
- A. El Refai (2013). "Durability and fatigue of basalt fiber-reinforced polymer bars gripped with steel wedge anchors", *Journal of Composites for Construction*, 17(6), 04013006.
- A. El Refai, F. Abed, F., A. Al-Rahmani (2015). "Structural performance and serviceability of concrete beams reinforced with hybrid (GFRP and steel) bars", *Construction and Building Materials*, 96, 518-529.
- A. Nanni, A. De Luca, H. Zadeh, H. (2014). "Reinforced concrete with FRP bars: mechanics and design", CRC Press, Taylor & Francis, Boca Raton, FL.
- CAN/CSA S806 (2012). "Design and construction of building components with fiber-reinforced polymers", Mississauga, ON, Canada.
- F. Elgabbas, E., Ahmed, B. Benmokrane (2015). "Physical and mechanical characteristics of new basalt-FRP bars for reinforcing concrete structures", *Construction and Building Materials*, 95, 623-635.
- fib Bulletin No. 40 (2007). "FRP reinforcement in RC structures", fib-Task Group (TG) 9.3, Lausanne, Switzerland.



- L. Bank (2006). "Composites for construction: structural design with FRP material", John Wiley & Sons, Hoboken, NJ.
- M. El-Mogy, A. El-Ragaby, E. El-Salakawy (2010). "Flexural behavior of continuous FRP-reinforced concrete beams", *Journal of Composites for Construction*, 14(6), 669-680.
- M. El-Mogy, A. El-Ragaby, E. El-Salakawy (2011). "Effect of transverse reinforcement on the flexural behavior of continuous concrete beams reinforced with FRP", *Journal of Composites for Construction*, 15(5), 672-681.
- M. Habeeb, A. Ashour (2008). "Flexural behavior of continuous GFRP reinforced concrete beams", *Journal of Composites for Construction*, 12(2), 115-124.
- M. Mahroug, A. Ashour, D. Lam. (2013). "Experimental response and code modelling of continuous concrete slabs reinforced with BFRP bars", *Composite Structures*, 107, 664-674.
- M. Mahroug, A. Ashour, D. Lam. (2014). "Tests of continuous concrete slabs reinforced with carbon fibre reinforced polymer bars", *Composites Part B: Engineering*, 66, 348-357.
- M. Safan. (2013). "Flexural behavior and design of steel-GFRP reinforced concrete beams", *ACI Materials Journal*, 110(6), 677-686.
- R. Al-Sunna, K. Pilakoutas, I. Hajirasouliha, M. Guadagnini (2012). "Deflection behaviour of FRP reinforced concrete beams and slabs: An experimental investigation", *Composites Part B: Engineering*, 43(5), 2125-2134.
- W. Ge, J. Zhang, D. Cao, Y. Tu. (2015). "Flexural behaviors of hybrid concrete beams reinforced with BFRP bars and steel bars", *Construction and Building Materials*, 87, 28-37.
- W. Qu, X. Zhang, H. Huang. (2009). "Flexural behavior of concrete beams reinforced with hybrid (GFRP and steel) bars", *Journal of Composites for Construction*, 13(5), 350-359.



NUMERICAL MODELING OF THE INTERACTION BETWEEN GFRP REINFORCEMENT AND HIGH STRENGTH CONCRETE DURING HYDRATION PROCESS

S. Kammoun 1,2, A. Sdiri 1 and A. Daoud 1,3

¹ *Université de Tunis El Manar, National Engineering School of Tunis, Civil Engineering Laboratory, Tunisia,
Email: slim.kammoun@enig.rnu.tn*

² *Université de Gabès, National Engineering School of Gabès, Tunisia.*

³ *Université de Sfax, National Engineering School of Sfax, Tunisia.*

ABSTRACT

Numerical study has been conducted to simulate the behavior of the early-age high strength concrete (HSC) reinforced with Glass Fiber Reinforced Polymer (GFRP) rebars. During hydration, HSC is subjected to both thermal and autogenous deformations. Once restrained, these deformations might entail early-age cracking. To model this early-age behavior, a numerical chemo-thermo-mechanical scheme has been developed and implemented in ABAQUS finite element software via various user subroutines. Internal heat generation due to hydration reactions is modeled based on Arrhenius's law and introduced via HETVAL subroutine. Autogenous shrinkage strain is assumed to evolve nonlinearly within the hydration degree, however thermal strain is considered to evolve only as function of temperature. Both thermal and autogenous deformations are implemented in UEXPAN subroutine. Neither basic nor drying strains are accounted for in this paper. To account for damage in HSC, the well known Mazars's elastic-damageable model is adopted. Within this model, Young's modulus, Poisson's coefficient and damage parameters are assumed to evolve depending on the hydration degree. Mazars's constitutive law is implemented via UMAT subroutine. GFRP rebars are considered to be elastic and transversally isotropic. Interface between GFRP rebars and HSC is assumed to be perfect. In a first attempt, an extensive validation of the concrete model is performed against experimental data from literature. They are selected for both plain and steel reinforced early-age HSC, with various thermal and mechanical boundary conditions. In a second attempt, steel rebars are substituted by GFRP ones while keeping the same reinforcement percentages and configurations. Numerical predictions of GFRP reinforcement are compared against those of steel reinforcement.

KEYWORDS

High-strength concrete; Hydration process; Thermal expansion; Autogenous shrinkage; GFRP reinforcement; Early-age cracking.

INTRODUCTION

At early age, concrete undergoes a complex thermo-chemical process, which takes place in different stages and periods. This phenomenon is referred to as hydration. The chemical reactions occurring during this phase are responsible for the release of heat causing variations in volume, the increase of the concrete strength and the growth of porosity inside. This hydration is accompanied by different types of shrinkage, mainly, autogenous and heat ones. Generally, these deformations are internally restrained by reinforcements that can either be made of steel or other materials. There has been a tendency, in recent decades, to substitute steel rebars by others made of Glass Fiber Reinforced Polymers (GFRP). The main advantage of this alternative is to overcome corrosion problems that enhance structures sustainability. However, several points, about this technology, still to be investigated. Among them the influence of thermal expansion of these rebars on their bond strength with concrete. Indeed, GFRP rebars have, in the glass-fibers' direction, a coefficient of thermal expansion (CTE) similar to that of the concrete. Nevertheless, in the radial direction, they have a large CTE that ranges from 2 to 5 times that of the concrete. This decreases the GFRP/concrete bond strength and could entail the collapse of the structure. The interaction between GFRP reinforcement and early-age concrete is not yet well investigated. Few studies have been taken place such as Ghatfar et al. (2015) and Chen and Choi (2015). In this contribution we try to focus on this problem by modeling the main aspects of the early-age concrete behavior by coupling, in a weak form, the hydration evolution to the thermo-mechanical properties including damage. For reasons of simplicity, no bond model is introduced at the reinforcement concrete interface and only damage variable is used to evaluate rebars/concrete bond strength evolution. In the following sections, we firstly highlight the theoretical aspects of the thermo-chemical early-age concrete model. Secondly, details about time discretization and implementation via "ABAQUS" finite element software are given. Finally, numerical simulation tests are presented and compared against experimental data and results are discussed.



EARLY-AGE CONCRETE MODEL

Thermo-chemical modeling of concrete hydration

The hydration of concrete has an exothermic character. The evolution of the hydration reaction of the material over time is characterized by a degree of hydration (ξ) which is a fundamental variable for evaluating the behavior of the concrete during its hardening. The evolution of the temperature is obtained from the heat equation which includes a term characterizing the evolution of heat during the hydration.

$$k\nabla(\nabla T) + r(t) = \rho c \dot{T} \quad (1)$$

With $r(t) = \rho Q_\xi \dot{\xi}$: the hydration heat flux, Q_ξ : latent heat and $\dot{\xi}$: hydration degree rate. \dot{T} : Temperature rate, k : thermal conductivity and c : specific heat.

The thermo-chemical model studied is based on the macroscopic approach proposed by Ulm and Coussy 1998. In their model two constitutive laws that describe hydration while studying the problem from a thermodynamic viewpoint. The result of these two laws is written as follows:

$$\tilde{A} = \eta A \quad (2)$$

With A is the chemical affinity $A(\xi)$ is the normalized chemical affinity. This normalized chemical affinity characterizes the macroscopic evolution of each hydration reaction of concrete at young age. is the permeability directly related to the microcirculation of water in the hydrates formed. Since the hydration reaction is thermally activated, its evolution is described by the Arrhenius law:

$$\dot{\xi}(\xi, T) = \tilde{A}(\xi) \exp\left(-\frac{E_a}{RT}\right) \quad (3)$$

Where $\tilde{A}(\xi)$ the chemical affinity is E_a is the activation energy and R is the universal gas constant equals 8.314J.mol⁻¹.K⁻¹.

The expression of $\tilde{A}(\xi)$ decreases when degree of hydration increases. It is written in the following form:

$$\tilde{A}(\xi) = \frac{k_0}{n_0} \left(\frac{A_0}{k_0 \xi_\infty} + \xi \right) (\xi_\infty - \xi) \exp\left(-\frac{\bar{n}}{\xi_\infty} \xi\right) \quad (4)$$

where k_0, n_0, A_0 and \bar{n} are material constants and (ξ_0, ξ_∞) are the mechanical percolation threshold and the final value of the hydration degree, respectively.

Mechanical properties evolution during concrete hardening

According to De Schutter, the Young's modulus E , the compressive/tensile strength of concrete $f_{c,t}$ and the fracture energy G_f depend on the degree of hydration according to the following formulas:

$$E(\xi) = E^\infty \left(\frac{\xi - \xi_0}{\xi_\infty - \xi_0} \right)^e \quad (5a)$$

$$f_{c,t}(\xi) = f_{c,t}^\infty \left(\frac{\xi - \xi_0}{\xi_\infty - \xi_0} \right)^f \quad (5b)$$

$$G_f(\xi) = G_f^\infty \left(\frac{\xi - \xi_0}{\xi_\infty - \xi_0} \right)^g \quad (5c)$$

ξ_0 is the mechanical percolation threshold ($\xi_0 = 0.15$) [6] and (e, f and g) are material constants. Poisson's ratio is written as a function of the degree of hydration as follows:

$$\nu(\xi) = 0.18 \sin\left(\frac{\pi \xi}{2}\right) + 0.5 \exp(-10\xi) \quad (6)$$

Thermal and autogenous strain

In the case of unrestrained plain concrete specimen, the total strain is the sum of two strain types: thermal ($\underline{\epsilon}_{th}$) and autogenous shrinkage ($\underline{\epsilon}_{sh}$) due to cement hydration: $\underline{\epsilon}_{TS} = \underline{\epsilon}_{th} + \underline{\epsilon}_{sh}$. $\underline{\epsilon}_{TS}$ is the so-called eigenstrain. Thermal strain rate is a linear function of the temperature variation:

$$\dot{\underline{\epsilon}}_{th} = \alpha \dot{T} \underline{I} \quad (7)$$



α is the coefficient of thermal expansion which is considered to be independent of ξ and \underline{I} is the identity tensor.

Based on experimental observations, (Sule 2003), proposed the following function that governs autogenous shrinkage rate:

$$\dot{\underline{\varepsilon}}_{sh}(\xi, T) = (-a\dot{\xi} + b\dot{T})\underline{I} \quad (8)$$

Where a and b are two material constants.

Damage model

To model concrete damage, the elastic damageable Mazars's model is used (Mazars 1986). The stress-strain relation is governed by:

$$\underline{\sigma} = (1-d)\underline{C} : \underline{\varepsilon}_e \quad (9)$$

where d is the damage variable scalar, \underline{C} is the elastic stiffness tensor and $\underline{\varepsilon}_e$ is the elastic strain tensor computed as follows:

$$\underline{\varepsilon}_e = \underline{\varepsilon} - (\underline{\varepsilon}_{th} + \underline{\varepsilon}_{sh}) \quad (10)$$

where $\underline{\varepsilon}$ is the total strain.

Damage evolution is based on the so called "equivalent strain" ($\tilde{\varepsilon}$) defined by:

$$\tilde{\varepsilon} = \sqrt{\langle \underline{\varepsilon}_e^I \rangle_+^2 + \langle \underline{\varepsilon}_e^{II} \rangle_+^2 + \langle \underline{\varepsilon}_e^{III} \rangle_+^2} \quad (11)$$

where $\langle \underline{\varepsilon}_e^I \rangle_+$, $\langle \underline{\varepsilon}_e^{II} \rangle_+$ and $\langle \underline{\varepsilon}_e^{III} \rangle_+$ are positive part of the elastic strain eigenvalues. The damage variable used

here is the enhanced version (Fichant et al. 1999) which controls the fracture energy G_f :

$$d = 1 - \frac{\varepsilon_{d0}}{\tilde{\varepsilon}} \exp\left(\frac{l_c f_t}{G_f} (\varepsilon_{d0} - \tilde{\varepsilon})\right) \quad (12)$$

with $\varepsilon_{d0}(\xi) = \frac{f_t(\xi)}{E(\xi)}$ is the damage threshold.

NUMERICAL IMPLEMENTATION

Time discretization

All variables are discretized implicitly over a time interval $[t_n, t_{n+1}]$ using backward Euler rule. Only mechanical properties Eqs.(5-6) are computed using explicit hydration degree ξ_n . The time discretization of the derivatives

takes the form: $(\dot{\bullet}) = \frac{\Delta(\bullet)}{\Delta t}$. The symbol Δ designates an increment over a typical time interval $[t_n, t_{n+1}]$:

$$\Delta(\bullet) \equiv (\bullet)_{n+1} - (\bullet)_n.$$

Model implementation via ABAQUS

The model has been implemented via three ABAQUS subroutines which are HETVAL, UEXPAN and UMAT user-material. In HETVAL subroutine, the internal hydration heat flux $r(t_{n+1})$ is modeled. The hydration degree

ξ_{n+1} is obtained for the current temperature T_{n+1} by solving the nonlinear equation (3) (in the discretized form) using Newton-Raphson scheme as follows:

$$\xi_{n+1} - \xi_n - \Delta t \left(\frac{k_0}{n_0} \left(\frac{A_0}{k_0 \xi_\infty} + \xi_{n+1} \right) (\xi_\infty - \xi_{n+1}) \exp\left(-\frac{\bar{n}}{\xi_\infty} \xi_{n+1}\right) \right) \exp\left(-\frac{E_a}{RT_{n+1}}\right) = 0 \quad (13)$$

The derivative of the hydration heat flux with respect to temperature $\frac{\partial r(t_{n+1})}{\partial T_{n+1}}$ is also computed.

In UEXPAN subroutine, both thermal and shrinkage deformation increments ($\Delta \underline{\varepsilon}_{th}$ and $\Delta \underline{\varepsilon}_{sh}$) are computed (Eqs. 7-8). The eigenstrain increment $\Delta \underline{\varepsilon}_{TS}$ is then computed. The derivative $\frac{\partial \Delta \underline{\varepsilon}_{TS}}{\partial \Delta T}$ is also computed to be used in the thermomechanical Jacobean matrix. Once eigenstrain increment is obtained, both the mechanical strain increment $\Delta \underline{\varepsilon}_e$ and current mechanical strain $\underline{\varepsilon}_e^{n+1}$ are deduced and used as inputs in the UMAT user-material. In this latter, mechanical properties (Eqs. 5-6) are computed using explicit degree of hydration ξ_n .

This choice is adopted in the aim of simplifying the stress-strain tangent operator: $\frac{\partial \Delta \underline{\sigma}}{\partial \Delta \underline{\varepsilon}_e}$. Damage variable (Eq.12) is calculated depending on the equivalent strain (Eq.11) and the mechanical properties. Figure 1 gives an illustration of the model implementation.

NUMERICAL SIMULATIONS

Experimental data

In this contribution, all experimental data, used to validate the numerical model, are taken from (Sule 2003; Sule and van Breugel 2004). Only results obtained from Autogenous Deformation Testing Machine (ADTM) are used in this paper. Tested specimens have prismatic geometry and made of high strength concrete (HSC). Three different steel reinforcement percentages (0.76%, 1.34% and ~3.2 %) were provided. Each percentage is realized with two different configurations of rebars (4 Φ 6 or 1 Φ 12, 4 Φ 8 or 1 Φ 16 and 4 Φ 12 or 1 Φ 25), respectively. Dimensions of these specimens and reinforcement configurations are depicted in Figure 2. Experimental results for GFRP rebars are not available. We only present numerical predictions of GFRP rebars in the same percentages and configurations of steel rebars and compare them against Sule's experimental data. Rebars are assumed to be perfectly bonded to concrete for both reinforcement materials.

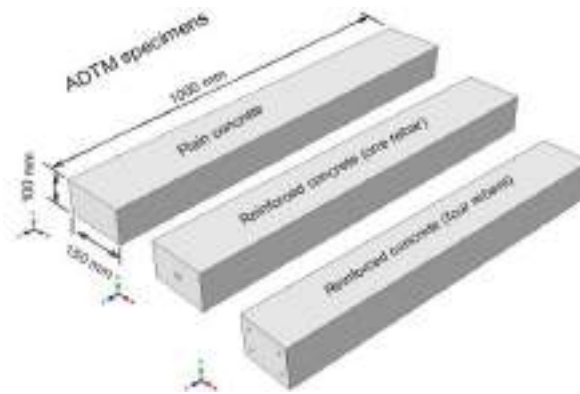


Figure 2: Autogenous Deformation Testing Machine (ADTM) specimens. Dimensions and reinforcement configurations. (Sule 2003; Sule and van Breugel 2004).

Mesh and Boundary conditions

C3D8T coupled temperature-displacement elements are used for both concrete and reinforcements materials. Various thermal conditions are applied for simulating specimens: isothermal (20°C) condition and semi-adiabatic condition (with a convection exchange coefficient equals $0.94 \text{ w m}^{-2} \text{ }^\circ\text{K}^{-1}$). Mechanical boundary conditions are applied as follows. $u_x=0$ imposed at nodes within face ($x=0$), $u_y=0$ imposed at nodes within face ($y=0$) and $u_z=0$ imposed at nodes within face ($z=0$).

Model parameters

Steel and GFRP material parameters are shown in Table 1. Most of GFRP properties are taken from COMBAR@ technical report and missing ones are approximated using Halpin-Tsai relationships, Halpin and Kardos 1976.



Hydration model parameters are presented in Table 2. Identification of these parameters is done using reverse engineering method applied on time-degree of hydration ($\xi(t)$) curves in isothermal conditions. High strength concrete properties are taken from Sule 2003 and shown in Table 3.

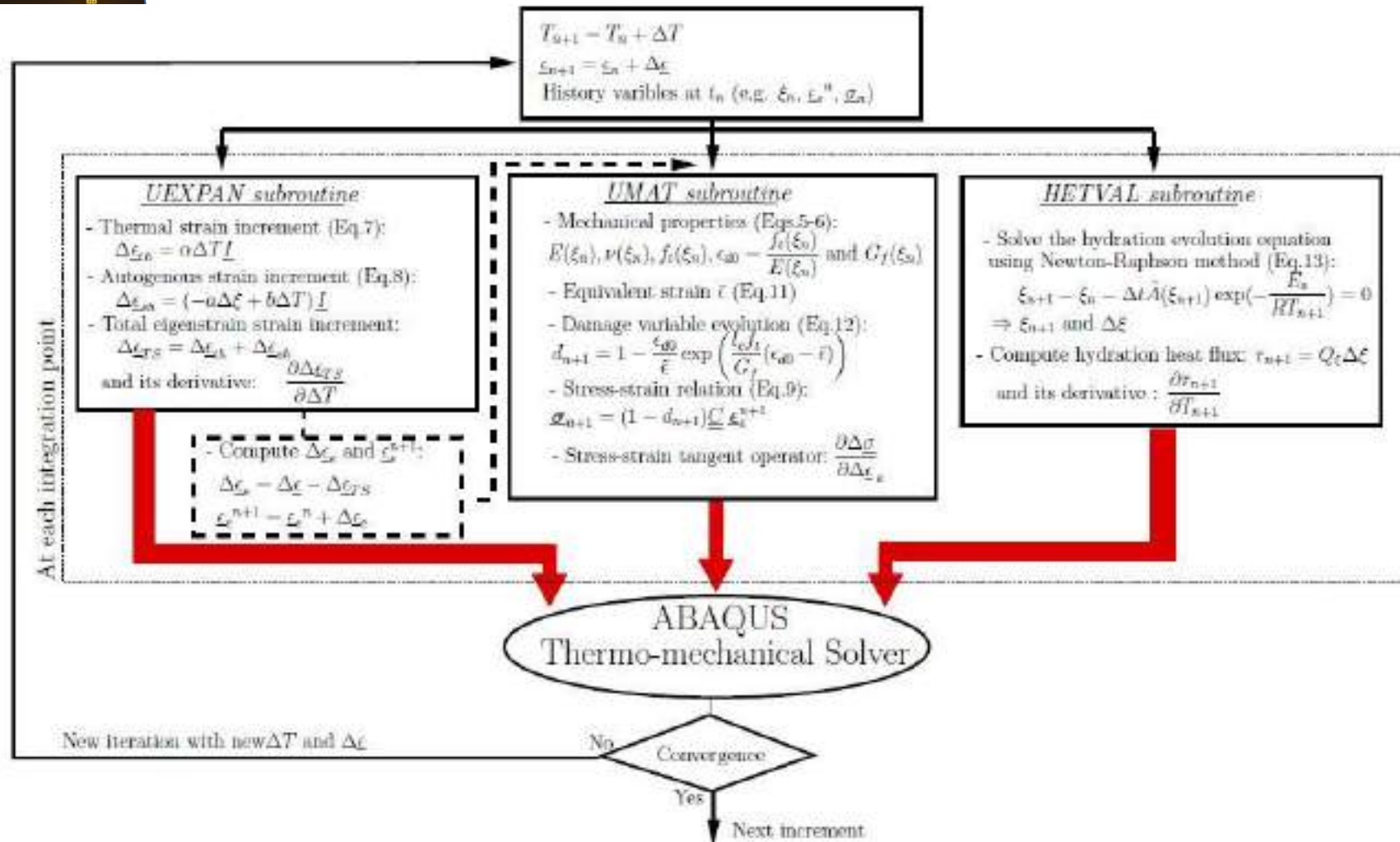


Figure 1: Illustration of the numerical implementation of the model.

Table 1: Thermo-elastic properties of rebars.

	E_R GPa	E_A GPa	G GPa	ν_R -	ν_A -	α_R $10^{-5}/^{\circ}K$	α_A $10^{-5}/^{\circ}K$	k w/m/ $^{\circ}K$	c J/kg/ $^{\circ}K$	ρ 10^3 kg/m ³
Steel	210	210	81	0.3	0.3	1.0	1.0	50	450	7.8
GFRP	15.8	60	$G_A=9$	0.3	0.22	2.2	0.6	0.5	1310	2.2

(\bullet)_R : Radial property / (\bullet)_A : Axial property

Table 2: Hydration model parameters.

ξ_0	ξ_{∞}	$\frac{k_0}{n_0}$	$\frac{A_0}{n_0}$	\bar{n}	$\frac{E_a}{R}$ $^{\circ}K$	Q_{ξ} J / mm ³
-	-	-	-	-	$^{\circ}K$	J / mm ³
0.15	0.651	1.05×10^7	0.014	3.39	5000	0.23

Table 3: Thermo-mechanical parameters of the early age concrete model.

ρ 10^3 kg/m ³	E^{∞} GPa	G_f^{∞} N/m	f_t^{∞} MPa	e -	$f = g$ -	k w/m/ $^{\circ}K$	c J/kg/ $^{\circ}K$	α $10^{-5}/^{\circ}K$	a $\times 10^{-4}$	b $\times 10^{-6}$
2.4	40.6	210	6.65	0.4	0.921	1.3	970.	1.0	3.3	3.75

RESULTS AND DISCUSSIONS

Figure 3 (a) describes the temperature-time evolution in semi adiabatic conditions from experimental data and the proposed model. And figure 3 (b) gives the strain-Time evolution of plain concrete specimens in Semi-Adiabatic and isothermal -20°C- conditions. The validation of concrete model against experiment can be noted.

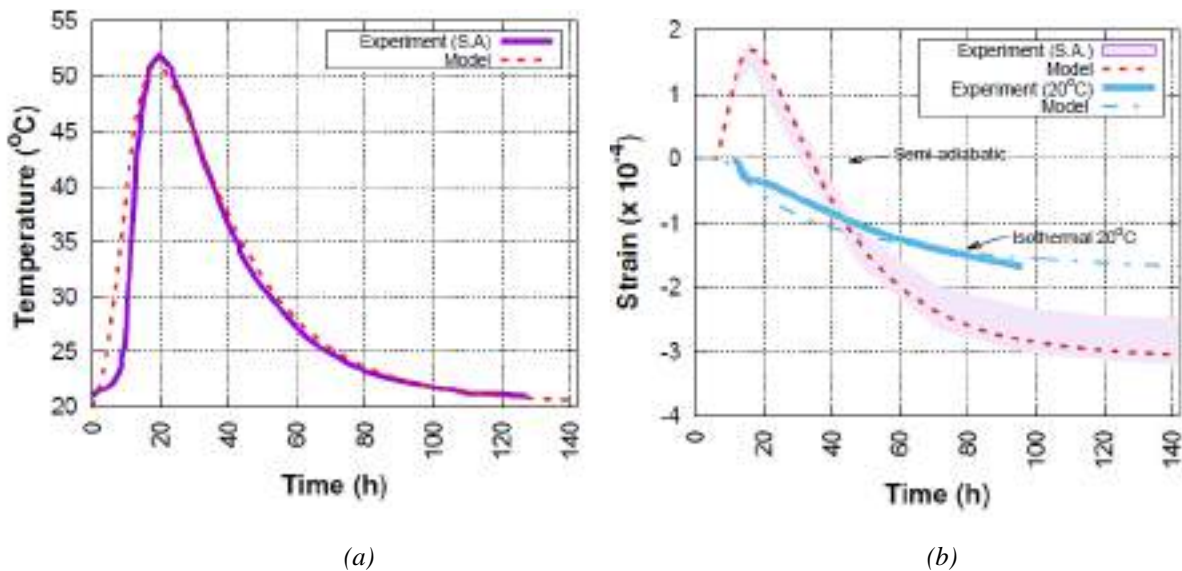


Figure 3: Validation of the concrete model against experimental data. (a) Temperature-Time evolution in Semi-Adiabatic condition (b) Strain-Time evolution of plain concrete specimens in Semi-Adiabatic and isothermal -20°C- conditions.

Figure 4 describes the strain-time evolution of reinforced concrete specimens within Semi-Adiabatic condition for steel and GFRP reinforcement. The curves for the steel and GFRP rebar are similar. The evolution is subdivided into two phases, a first phase where dilation of the specimen is observed, in this phase the reinforcements have no effect and a second phase where a shortening of the specimen is observed, in this phase the larger the diameter of the bar, the more the deformation decreases. However, the reinforcement ratio effect seems to be more pronounced for the steel rebar. This can be attributed to the low Young's modulus of the GFRP bar. For both steel and GFRP rebar the reinforcement configuration has no effect on the strain evolution.

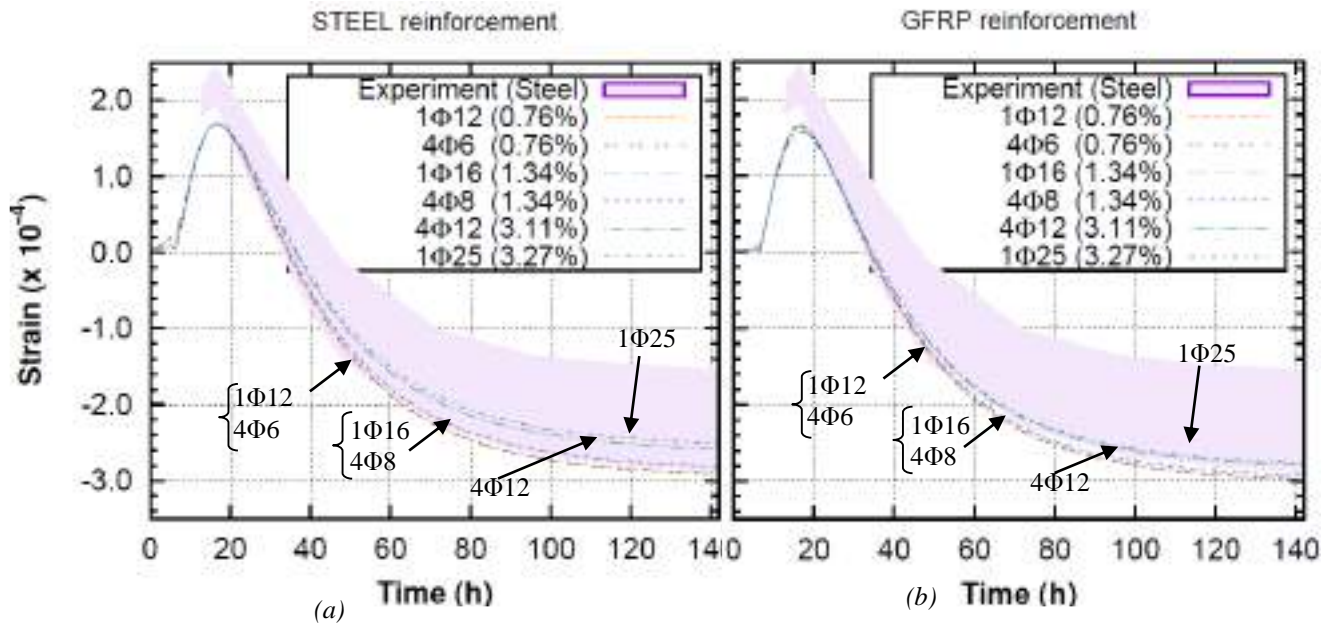


Figure 4: Strain-Time evolution of reinforced concrete specimens within Semi-Adiabatic condition. (a) Steel rebar reinforcement. (b) GFRP rebar reinforcement.

Figure 5 gives the damage contours at 140h in cross sections and longitudinal cuts for two reinforcement configurations: 1Φ12 and 4Φ6 for Steel and GFRP rebar. The damaged zone around the GFRP rebar is larger than the one around the steel rebar for the two configurations. This can be attributed to the higher coefficient of thermal expansion (CTE) of the GFRP rebar. In fact, the GFRP reinforcement produces a pressure resulting from the significant thermal expansion following the increase of the temperature during the hydration process.

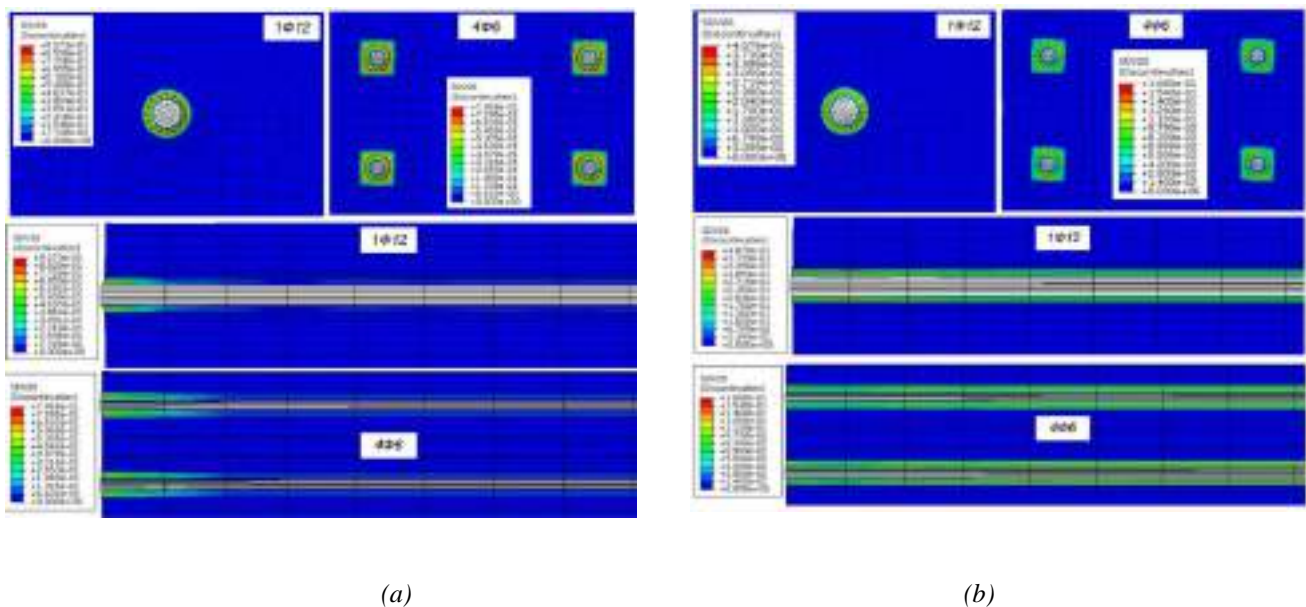




Figure 5: Damage contours at 140h in cross sections and longitudinal cuts for two reinforcement configurations: 1 Φ 12 and 4 Φ 6. (a) Steel rebars (b) GFRP rebars.

CONCLUSIONS

Numerical study has been conducted to simulate the behavior of the early-age high strength concrete (HSC) reinforced with Glass Fiber Reinforced Polymer (GFRP) rebars. To model this early-age behavior, a numerical chemo-thermo-mechanical scheme has been developed and implemented in ABAQUS finite element software. Autogenous shrinkage strain is assumed to evolve nonlinearly within the hydration degree, however thermal strain is considered to evolve only as function of temperature. To account for damage in HSC and even at the reinforcement/concrete interface, the well known Mazars's elastic-damageable model is adopted. Within this model, Young's modulus, Poisson's coefficient and damage parameters are assumed to evolve depending on the hydration degree.

The following conclusions can be drawn from this study:

- The evolutions of the strain with time of reinforced concrete specimens within Semi-Adiabatic condition for the steel and GFRP rebar are similar;
- The reinforcement ratio effect seems to be more pronounced for the Steel rebar. This can be attributed to the low Young's modulus of the GFRP bar;
- For both steel and GFRP rebar the reinforcement configuration has no effect on the strain evolution;
- The damaged zone around the GFRP rebar is larger than the one around the Steel rebar for all the configurations. This can be attributed to the higher coefficient of thermal expansion (CTE) of the GFRP rebar;
- In order to enhance the prediction accuracy at the vicinity of GFRP rebars, it is important to develop and integrate a bond model. This can be the object of a future work.

REFERENCES

- A. Ghatefar, E. El-Salakawy, M.T. Bassuoni (2015), "Early-Age Restrained Shrinkage Cracking Of GFRP-Rc Bridge Deck Slabs: Effect Of Environmental Conditions", *Cement and Concrete Composites* 64, 62-73.
- J-H. Choi and H-L. R. Chen (2015), "Design of GFRP reinforced CRCP and its behavior sensitivity to material property variations", *Construction and Building Materials* 79, 420-432.
- F-J. Ulm, O. Coussy (1998), "Couplings in early-age concrete: From material modeling to structural design", *International Journal of Solids and Structures* 35, 4295-4311.
- M. Sule (2003). "Effect of reinforcement on early-age cracking in high strength concrete", *PhD thesis, Delft University Press, ISBN 90-407-2391-5*.
- M. Sule, K. van Breugel (2004). "The effect of reinforcement on early-age cracking due to autogenous shrinkage and thermal effects", *Cement & Concrete Composites* 26, 581-587.
- J. Mazars (1986), "A description of micro- and macroscale damage of concrete structures", *Eng Fract Mech* 25,729-37.
- S. Fichant, C. La Borderie, G. Pijaudier-Cabot (1999). "Isotropic and anisotropic descriptions of damage in concrete structures", *Mech Cohes-Frict Mater* 4, 339-359.
- Schöck-ComBAR (2015), "Technical informations", www.schoeck-combar.com
- S. JC Halpin, J.L. Kardos (1976), "The Halpin-Tsai equations: A review", *Polymer Engineering. Science* Vol. 16(5), pp. 344-352.



PARAMETRIC STUDY ON BOND OF GFRP BARS IN ALKALI ACTIVATED CEMENT CONCRETE

B. H. Tekle *, A. Khennane * and O. Kayali *

* School of Engineering and Information Technology, UNSW Canberra, Campbell, Australia

ABSTRACT

Bond behaviour plays an important role in the design and performance of reinforced concrete structures. In this study, a beam-end specimen finite element model is used to perform a parametric study. The bond between the GFRP bar and Alkali Activated Cement (AAC) concrete is modelled by surface-based cohesive behaviour. The accuracy of the model is validated by comparing different predictions with experimental results. The effect of concrete cover, bar diameter, concrete compressive strength, lead length (unbonded length at loaded end), embedment length and elastic modulus of GFRP bars on bond behaviour is investigated. Each of these parameters is varied on a range of applicable values to study its influence on bond behaviour. The parametric study showed that the bond behaviour is mainly affected by concrete cover, bar diameter, embedment length and compressive strength of the concrete. The effect of elastic modulus of GFRP bar is not as pronounced as that of the other parameters while the influence of lead length can be avoided by providing enough unbonded length at the loaded end. The parametric study is further used to calibrate a well-known bond equation and develop a new regression equation for predicting the maximum bond stress. The predicted results from these equations showed a good agreement with the experimental as well as with the finite element results.

KEYWORDS

Alkali activated cement concrete, GFRP bars, Bond properties, Parametric study

INTRODUCTION

The high environmental footprint of reinforced concrete and its durability issues have inspired scientists and engineers to search for alternatives for both ordinary Portland cement (OPC) concrete and steel reinforcement for more sustainable construction. Fibre reinforced polymer (FRP) composites and alkali activated cement (AAC) concrete stand out as ideal replacements for steel and OPC, respectively. Due to their better corrosion resistance capacity, FRP reinforcing bars have become a preferable alternative to steel reinforcing bars particularly in areas where durability is a major concern. They are characterised by high tensile strength, high durability, lightweight, and electromagnetic permeability and are available in different surface textures. AAC is produced by reacting alkali liquids with silica (SiO_2) and alumina (Al_2O_3) rich natural materials, like metakaolin or industrial by-products, such as Fly Ash (FA), Silica Fume (SF) or Slag (Hardjito and Rangan, 2005). In addition to the low carbon footprint, the utilization of industry by-product materials such as fly ash, which otherwise would be disposed of, saves a great deal of virgin materials that would otherwise be used for concrete production. Thus, owing to the desirable characteristics of both FRP bars and AAC concretes, it is clear that a great deal of benefits can be acquired by using them together in reinforced concrete structures. However, if these materials are to be used as alternatives for steel reinforcement and OPC concrete, they need to display similar, or better, physical and mechanical characteristics. High ranking among these are bond properties.

AAC concrete is chemically different from OPC concrete, thus the bond properties of GFRP reinforced AAC concrete may be different from that of GFRP reinforced OPC concrete, and thus it may not be permissible to use codes and standards developed for GFRP bars such as ACI 440.1R (2015). It is therefore necessary to study the bond properties between GFRP bars and AAC concrete in order to assess their potential as constituent materials for reinforced concrete structures. In this paper, these properties are investigated by using a parametric study based on a numerical model developed by Tekle et al. (2017a).

EXPERIMENTAL RESULTS

Tekle et al. (2017a) investigated the bond behaviour of GFRP reinforcement in AAC concrete by using beam-end specimens prepared according to ASTM A944 (2010) recommendations. The experimental program consisted of eight AAC concrete specimens and four control OPC concrete specimens. Two bar diameters, two embedment lengths and one concrete strength were used in the study. The experimental results are summarized in Table 1. The specimens are identified by the type of concrete used (A for AAC concrete and O for OPC concrete), the diameter of the bar used, the embedment length as a multiple of rebar diameter, and specimen number.



Table 1: Summary of experimental results (Tekle et al. 2017a)

Specimen	f'_c (MPa)	Load P max (kN)	Average bond stress τ (MPa)	Free end slip (mm)	Loaded end slip (mm)	Failure mode
A16-6d1	36.8	67.9	14.2	265	498	S
A16-6d2	38.4	75.8	15.8	355	636	S
A16-9d1	32.0	81.3	11.3	580	824	T
A16-9d2	38.1	82.1	11.4	474	765	T
A16-9d3	42.6	88.6	12.2	448	562	T
A16-9d4	37.1	99.9*	13.9	143	674	-
A13-9d1	40.1	69.1	14.8	410	856	P
A13-9d2	39.1	79.5	17.0	435	984	P
O16-9d1	38.0	99.9*	13.9	51	546	-
O16-9d2	30.4	78.0	10.8	252	750	T
O16-9d3	37.8	80.3	11.1	268	802	T
O16-9d4	38.7	99.9*	13.9	56	538	-

*Tested only up to 99.9 kN, P = Pullout failure, S = splitting failure; T = splitting of the concrete in the transverse direction

NUMERICAL MODELLING

Tekle et al. (2017a) developed a finite element model to simulate the bond between GFRP bars and AAC concrete. In this model, the GFRP bar and the concrete are modelled using 8-node linear brick element, the shear and flexural steel reinforcements are modelled as a two-node linear 3-D truss element embedded in the concrete. The GFRP bar is modelled as a linear elastic material whereas the steel reinforcements are modelled as elasto-plastic materials with yield strength of 500 MPa and elastic modulus of 200 GPa. Further details of the model such as the concrete properties and GFRP/AAC concrete interface bond behaviour can be found on Tekle et al. (2017a). The model was validated by comparing it to the experimental results and was used to investigate the tensile and bond stress distributions along the embedment length. The model is used in the present to perform a parametric study on the factors affecting bond behaviour.

Parametric study

The embedment or splice length of a bar into concrete is mainly dependant on the strength of the bond, which in turn depends on various factors. ACI 408R (2003) divides these factors into three main categories: structural characteristics, bar properties, and concrete properties. Spacing between reinforcement, concrete cover, embedment length, confinement provided around the main reinforcement are classified under structural characteristics. The surface behaviour of the bar, its diameter and its tensile strength and modulus of elasticity are factors coming from the bar properties. In a similar manner, concrete properties that affect bond are compressive strength, modulus of elasticity, type of aggregate, concrete type, workability and degree of consolidation. The verified beam-end model is used to analyse some of these parameters, which include concrete cover, bar diameter, compressive strength of concrete, lead length, embedment length, and elastic modulus of the GFRP bar. Each of these parameters is varied on a range of applicable values to study how it affects bond behaviour in GFRP reinforced AAC concrete. Table lists a summary of all the parameters studied and their range of variations. A16-6d model from Tekle et al. (2017a) is used as a reference.

Table 2 List of parameters and corresponding range of variations

Parameter	Range of variations	Model ID
Clear concrete cover	As a multiple of bar diameter (ϕ 16 mm): from 1d to 5d at 1d increment	Cover_1d to Cover_5d
Bar diameter	Standard GFRP bar diameters: 9.5, 12.7, 15.9, 19.05, 22.2 and 25.4 mm	Diam_10, Diam_13, Diam_19, Diam_22 and Diam_25
Concrete compressive strength	20 MPa to 80 MPa at 10 MPa increment	Comp_20 to Comp_80
Lead length	25, 50, 75, 100, 150 and 200 mm	Lead_25, Lead_75, Lead_100, Lead_150 and Lead_200
Elastic modulus (GFRP)	42 GPa, 50 GPa and 63 GPa	Modulus_42 and Modulus_50
Embedment length	From 3.0d to 12.0d at 1.5d interval	Embed_3d to Embed_12d

RESULT AND DISCUSSION

Concrete cover analysis

The critical clear concrete cover is the smallest possible concrete cover around the reinforcement. In the beam-end specimen shown in Figure 1, c_x is the clear concrete cover along the width of the beam and c_y along its height. The width of the beam-end specimen is 220 mm, for a 16 mm diameter bar placed at the center, it gives a clear cover of 102 mm, which is kept constant. In the experimental specimens, c_y is the controlling cover. In order to investigate its effect, this cover is varied from 1.0d (one time the bar diameter which is 16 mm) to 5.0d at 1.0d increment.

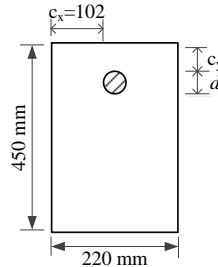


Figure 1: Concrete covers in the beam-end specimen

The bond stress-slip curves for all the models used for the parametric study of the concrete cover are as shown in Figure 2. As can be seen in the figure, all the models show a similar bond stress slip characteristics in terms of shape, however, they showed a significant difference in terms of maximum bond stress. This shows the strong influence of concrete cover on bond behaviour.

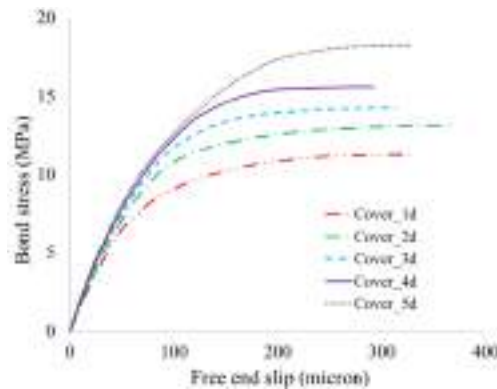


Figure 2: Bond slip curves for concrete cover parametric study

As can be seen in Figure 3, the bond stress increased almost linearly with the concrete cover. Various other researcher also observed a similar behaviour (Ehsani et al., 1997, ACI 408R, 2003, Tefers, 1979). Ehsani et al. (1997) observed that for a given embedment length, the ultimate bond stresses in specimens with a clear concrete cover equal to twice the bar diameter were higher than those for specimens with clear cover of one bar diameter.

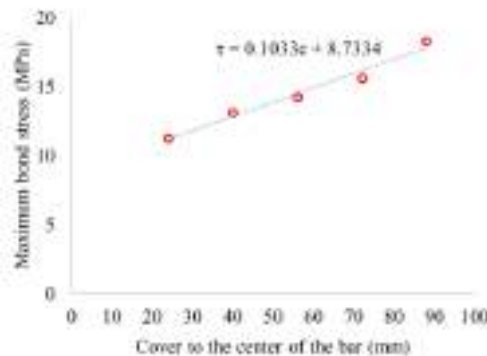


Figure 3: Influence of concrete cover on bond stress



Bar diameter

Different standard GFRP bar diameters were used to investigate the effect of bar diameter on bond behaviour. The elastic modulus of the bars were assumed constant with change of diameter. The influence of bar diameter on bond behaviour is as shown in Figure 4. The bond stress decreases with the increase of bar diameter. This is believed to be caused by the Poisson's effect. During the application of tensile stress on a reinforcing bar, the diameter of the bar reduces due to Poisson's effect. This reduction in diameter is more pronounced for bigger bar diameters, thus reducing frictional and mechanical resistance and ultimately lowering the bond stress.

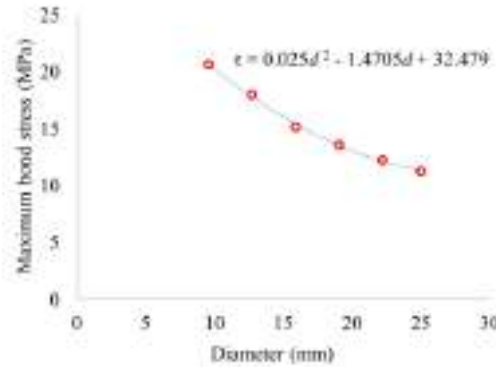


Figure 4: Influence of diameter on bond stress

Concrete compressive strength

The concrete compressive strength was varied from low strength concrete (20 MPa) to high strength concrete (80 MPa) at 10 MPa increment. As there are no experimental results for the elastic modulus of these concrete strengths, it is estimated by using Eq. 1, which is derived by modifying the ACI 363R (1992) equation based on available experimental results (Tekle, 2017b).

$$E_c = 3360\sqrt{f'_c} - 3500 \tag{1}$$

As can be observed from Figure 5, up to a compressive strength of 60 MPa, the bond stress increases with the increase in concrete compressive strength. However, after 60 MPa, not much change is observed on the bond stress with the increase of compressive strength. This is because the concrete is much stronger and is no longer the cause of failure. Karlsson (1997) observed that for low compressive strengths, failure was due to the rupture of the surrounding concrete, while for higher compressive strengths, the damage on the surrounding concrete was negligible. They defined high compressive strength to be greater than 55 MPa, which is very close to what is found in this numerical study, i.e. 60 MPa. The analysis of the failure mode on the models also showed that, models with 60 MPa compressive strength and higher failed by pullout, whereas those with less than 60 MPa failed by splitting and transverse cracking. This can be observed by comparing the failure modes of Comp_40 and Comp_60 in Figure 6, where the tensile damage values at maximum load are plotted for the longitudinal cross-section of the beam-end model. Comp_60 showed a relatively low damage on the concrete, and these damages were not able to make it to the surface of the concrete, thus resulting in a pullout failure mode. Comp_40 showed a relatively higher damage, and the damage progressed to the concrete surface, resulting in a combined splitting and transverse tensile cracking of the concrete. Thus, for high strength concretes, the interface and bar properties are more critical than the concrete property, and failure depends on them.

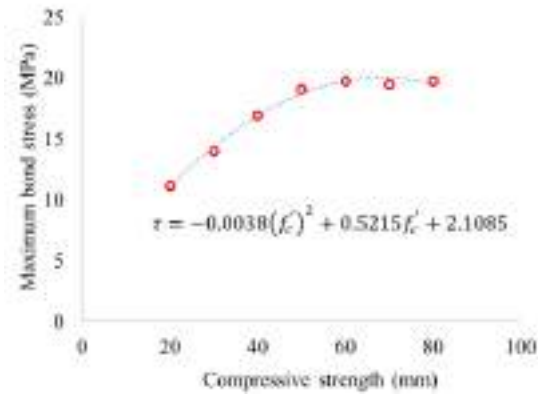


Figure 5: Influence of concrete strength on bond stress

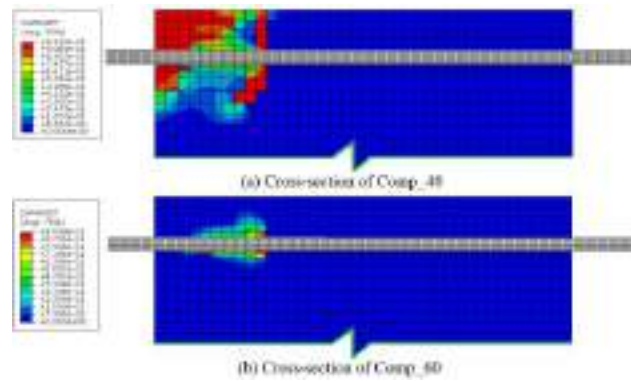


Figure 6: Tensile damage at the longitudinal cross-section of beam-end models

Lead length

Different lead lengths (this is the unbonded length provided at the loaded end of the bar) were investigated to check if they have significant influence on the bond behaviour of the specimens. Lead lengths are used to prevent cone-type pullout failure at the surface of the concrete. ASTM A944 (2010) states that an increase in lead length generally results in an increase of bond strength. As can be seen in Figure 7, a similar behaviour is observed up to 75 mm lead length, where the bond stress increased linearly with the lead length. However, after 75 mm the bond stress remain constant despite the increase of lead length. This indicates that, in such a specimen a lead length of 75 mm is sufficient to prevent cone-type failure.

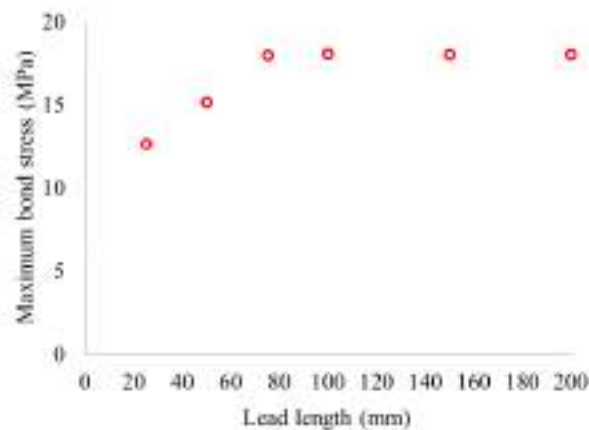


Figure 7: Influence of lead length on bond stress

Elastic modulus of GFRP bar

ACI 440.1R (2015) reports that bond is influenced by the elastic modulus of FRP bars. Three grades of GFRP bars were considered to study the effect of the elastic modulus on bond behaviour. These are, low modulus GFRP bars, 42 GPa, standard GFRP bar, 50 GPa, and high modulus, 63 GPa, (these grades are based on V-ROD GFRP bar classes). A small increment of average bond stress with the increase of elastic modulus was observed. For an increase of about 21 GPa elastic modulus, i.e. from 42 GPa to 63 GPa, about 0.94 MPa average bond stress increase was observed. Thus, elastic modulus influences the average bond stress, but its influence is not as pronounced as the other parameters such as the compressive strength and bar diameter.

Embedment length

The embedment length of the bar was varied from 3.0d to 12.0d at 1.5d intervals. As can be observed from Figure 8, the bond stress decreased linearly with the increase in the embedment length. This is a common phenomenon attributed to the nonlinear bond stress distribution along the embedment length.

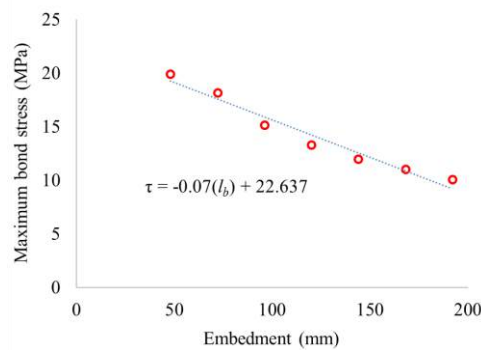


Figure 8: Influence of embedment length on bond stress

Equation of bond stress

The results from the previous parametric studies are used to generate an equation, which can predict maximum bond stress by taking into account concrete cover, bar diameter, concrete strength and embedment length. The effect of GFRP bar elastic modulus is not considered as it is not significant. Effect of lead length is also neglected as it can be avoided by providing sufficient lead length as discussed. The resulting expression obtained from regression analysis is as shown in Eq. 2. Furthermore, the well-known equation for bond originally developed by Orangun et al. (1977) for steel bars and later calibrated and adopted for FRP bars in OPC concrete, is calibrated for FRP reinforced AAC concrete by using the results from the parametric study. The resulting equation is as shown in Eq. 3.

$$\tau = 0.026c + 0.0062d^2 - 0.37d - 0.00095(f'_c)^2 + 0.13f'_c - 0.017l_b + 16.5 \quad (2)$$

$$\tau = 0.083\sqrt{f'_c} \left[0.2 + 5.3 \left(\frac{c}{d} \right) + 57.5 \left(\frac{d}{l_b} \right) \right] \quad (3)$$

where c is the minimum concrete cover to the center of the bar (mm), f'_c is the compressive strength of concrete (MPa), d is the diameter of the bar and l_b is the embedment length.

The experimental results from the beam-end specimens of Tekle et al. (2017a) and pullout specimens of Tekle et al. (2016) are then compared with the predicted value of maximum bond stress using Eq. 2 and Eq. 3. The results are presented in Table 3. Both prediction methods showed a good agreement with the experimental bond stresses for both the beam-end and pullout specimens. For instance, the mean value of the ratio of Eq. 3 prediction to experimental results is 1.02 and 0.98, for beam-end and pullout tests, respectively. The ratios also displayed a low variation with standard deviation (SD) of 0.06 and 0.11, respectively for beam-end and pullout tests.

Table 3: Comparison of experimental and predicted maximum bond stresses

Specimen	c (mm)	d (mm)	f'_c (MPa)	l_b (mm)	τ_{exp} (MPa)	τ_{cO} (MPa)	τ_r (MPa)	τ_{cO} / τ_{exp}	τ_r / τ_{exp}
Beam-end									



A16-6d	58	15.9	37.5	96	15.00	14.73	15.60	0.98	1.04
A16-9d	58	15.9	37.5	144	11.95	13.11	14.78	1.10	1.24
A13-9d	58	12.7	37.5	117	15.90	15.52	15.86	0.98	1.00
							Average	1.02	1.09
							Standard deviation	0.06	0.10
Pullout									
AG13-6d1	50	12.7	24.7	78	10.91	12.51	15.40	1.15	1.41
AG13-6d2	50	12.7	42.6	78	16.72	16.44	16.59	0.98	0.99
AG16-3d2	50	15.9	34.2	48	17.04	17.41	16.01	1.02	0.94
AG16-9d2	50	15.9	34.2	144	13.67	11.24	14.37	0.82	1.05
AG16-3d3	50	15.9	49.3	48	18.84	20.90	16.77	1.11	0.89
AG16-6d3	50	15.9	49.3	96	17.73	15.34	15.95	0.87	0.90
AG16-9d3	50	15.9	49.3	144	15.00	13.49	15.14	0.90	1.01
							Average	0.98	1.03
							Standard deviation	0.11	0.17

τ_{exp} = experimental bond stress, τ_{cO} = bond stress from the calibrated Orangun equation, τ_r = bond stress from the regression equation

The maximum bond stress results from the model are also compared with the predicted maximum bond stress results as shown in Table 4. Here also both Eq. 2 and Eq. 3 predicted the maximum bond stress satisfactorily with an average prediction to FEA model ratio of 1.05 and 1.01, respectively.

Table 4: Comparison of model and predicted maximum bond stress

FEA Model	c (mm)	d (mm)	f'_c (MPa)	l_b (mm)	τ_m (MPa)	τ_{cO} (MPa)	τ_r (MPa)	τ_{cO} / τ_m	τ_r / τ_m
Cover_1d	24	15.9	37.5	96	11.27	8.99	14.72	0.80	1.31
Cover_2d	40	15.9	37.5	96	13.15	11.69	15.13	0.89	1.15
Cover_3d	56	15.9	37.5	96	14.25	14.39	15.55	1.01	1.09
Cover_4d	72	15.9	37.5	96	15.62	17.09	15.96	1.09	1.02
Cover_5d	88	15.9	37.5	96	18.29	19.79	16.38	1.08	0.90
Diam_10	58	9.53	37.5	96	20.68	19.33	16.95	0.93	0.82
Diam_13	58	12.7	37.5	96	18.04	16.22	16.22	0.90	0.90
Diam_19	58	19.05	37.5	96	13.56	14.07	15.12	1.04	1.11
Diam_25	58	25.4	37.5	96	11.26	13.96	14.52	1.24	1.29
Diam_16	58	15.9	37.5	96	15.16	14.73	15.60	0.97	1.03
Diam_22	58	22.2	37.5	96	12.29	13.87	14.76	1.13	1.20
Comp_20	58	15.9	20.0	96	11.14	10.76	14.28	0.97	1.28
Comp_30	58	15.9	30.0	96	14.01	13.17	15.11	0.94	1.08
Comp_40	58	15.9	40.0	96	16.95	15.21	15.74	0.90	0.93
Comp_50	58	15.9	50.0	96	19.08	17.01	16.19	0.89	0.85
Comp_60	58	15.9	60.0	96	19.79	18.63	16.44	0.94	0.83
Comp_70	58	15.9	70.0	96	19.54	20.12	16.51	1.03	0.84
Comp_80	58	15.9	80.0	96	19.79	21.51	16.38	1.09	0.83
Embed_3d	58	15.9	37.5	48	19.91	19.57	16.42	0.98	0.82
Embed_4.5d	58	15.9	37.5	72	18.19	16.34	16.01	0.90	0.88
Embed_6d	58	15.9	37.5	96	15.16	14.73	15.60	0.97	1.03
Embed_7.5d	58	15.9	37.5	120	13.31	13.76	15.19	1.03	1.14
Embed_9d	58	15.9	37.5	144	11.96	13.11	14.78	1.10	1.24
Embed_10.5d	58	15.9	37.5	168	11.03	12.65	14.38	1.15	1.30
Embed_12d	58	15.9	37.5	192	10.06	12.31	13.97	1.22	1.39
							Average	1.01	1.05
							Standard deviation	0.11	0.18

τ_m = maximum bond stress from the model

All the ratios for predicted to model and predicted to experimental bond stress are summarised in Figure 9 for both calibrated Orangun and the regression analysis equations. Comparing these prediction methods shows that, the calibrated Orangun equations provides a better result. This can be observed from both Table 3 and Table 4,



where the calibrated Orangun equation results in a lower standard deviation and better mean value (close to 1.0) in most of the cases. This is also evident from Figure 9, where the calibrated Orangun equation shows a lower scatter.

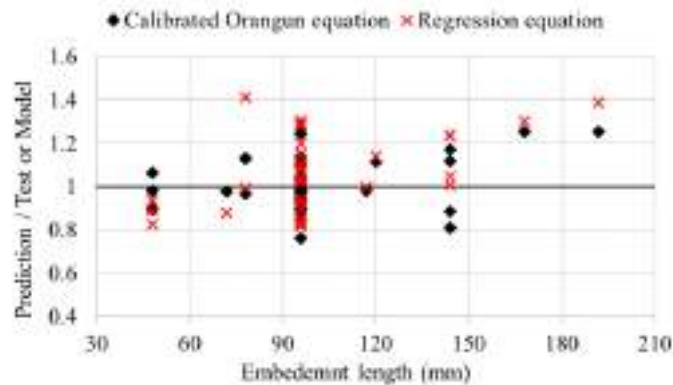


Figure 9: Predicted to test (FEA model) bond stress ratios versus embedment length

CONCLUSION

The parametric study on the beam-end model showed that the bond behavior of GFRP reinforced AAC concrete is mainly affected by concrete cover, bar diameter, embedment length and compressive strength of the concrete. The effect of GFRP bar elastic modulus is not as pronounced as that of the other parameters. Influence of lead length can be avoided by providing enough unbonded length at the loaded end. The parametric study helped to develop equations for predicting maximum bond stress. The predicted results from these equations showed a good agreement with the experimental as well as FE modelling results.

ACKNOWLEDGMENTS

The scholarship support to the first author from UNSW Canberra is greatly acknowledged.

REFERENCES

- ACI 363R (1992). "State-of-the-Art Report on High-Strength Concrete", Farmington Hill, MI, American Concrete Institute.
- ACI 408R (2003). "Bond and development of straight reinforcing bars in tension", Farmington Hills MI, American Concrete Institute.
- ACI 440.1R (2015). "Guide for the Design and Construction of Structural Concrete Reinforced with Fiber-Reinforced Polymer (FRP) Bars", Farmington Hills, MI, American Concrete Institute.
- ASTM A944 (2010). "Standard Test Method for Comparing Bond Strength of Steel Reinforcing Bars to Concrete Using Beam-End Specimens" West Conshohocken, PA, ASTM International.
- B. H. Tekle, A. Khennane, O. Kayali (2016). "Bond properties of sand-coated GFRP bars with fly ash based geopolymer concrete." *Journal of Composites for Construction*, 20(5).
- B. H. Tekle, A. Khennane, O. Kayali (2017a). "Bond behaviour of GFRP reinforcement in alkali activated cement concrete", *Construction and Building Materials*, 154, 972-982.
- B. H. Tekle (2017b). "Bond behavior of GFRP bars embedded in alkali activated cement concrete", PhD thesis, UNSW Canberra.
- C. O. Orangun, J. O. Jirsa, J. E. Breen (1977). "A Reevaluation of Test Data on Development Length and Splices", *ACI Journal*, 12(9), 114-122.
- D. Hardjito, and B. V. Rangan (2005). "Development and Properties of Low Calcium Fly Ash-Based Geopolymer Concrete", *Research Report GC 1*, Curtin University of Technology, Perth, Australia



M. Karlsson (1997). "Bond between C-Bar FRP reinforcement and concrete", Graduation thesis, Chalmers University of Technology.

M. R. Ehsani, H. Saadatmanesh, S. Tao, (1997). "Bond behaviour of deformed GFRP rebars", *Journal of composite materials*, 31, 1413-1430.

R. Tepfers, (1979). "Cracking of concrete cover along anchored deformed reinforcing bars", *Magazine of Concrete Research*, 31, 3-12.



BOND STRENGTH OF POST-INSTALLED GFRP BARS IN BEAM-COLUMN CONNECTIONS

Muhammad Shahraiz Bajwa^{1,3}, Benjamin Z. Dymond¹, Rania Al-Hammoud²

1 1405 University Drive, University of Minnesota Duluth, Department of Civil Engineering, Duluth, Minnesota, 55812, USA; 2 University of Waterloo, Department of Civil and Environmental Engineering, Waterloo, Ontario, Canada; 3 Email: bajwa016@d.umn.edu

ABSTRACT

Post-installed reinforcement in concrete is used to connect a new concrete member to an existing concrete structure. Design using post-installed reinforcing bars is gaining acceptance due to design flexibility, formwork simplification and the ability to have horizontal, vertical, and overhead applications. Research has been conducted on the efficacy of post-installed steel reinforcement in concrete structures. However, steel corrodes in aggressive environments resulting in a loss of bond strength and serviceability. Alternatively, glass fiber-reinforced polymer (GFRP) bars can be used as post-installed reinforcement. GFRP bars are gaining acceptance in the structural field due to their corrosion resistance and high strength to weight ratio. This research presents an experimental study with GFRP bars from three manufacturers, which were post-installed using an epoxy-based adhesive. Eight specimens were constructed and tested monotonically to failure. A specimen was composed of two identical vertical elements, which were anchored into the base of the structure using post-installed GFRP bars. The specimens were designed to simulate a rigid connection of two cantilever beams to a column. The concrete compressive strength for all the specimens was 3 ksi (20.68 MPa) and the size of all the post-installed and cast-in-place bars was #4 (#13). The specimens were tested with bars installed at 6 and 11.5 in. embedment depths (15.24 and 29.21 cm). The results from the specimens with bars installed at a longer embedment depth indicated an increase in the loading capacity and the ductility compared to the specimens with bars installed at a shorter embedment depth. The evaluation of bond strength was done by comparing the type of failure and load capacity of the post-installed GFRP bars with the cast-in-place steel and GFRP bars. The specimens with cast-in GFRP bars exhibited a bond-slip failure, whereas the specimens with post-installed GFRP bars had a splitting failure (concrete cone breakout), indicating a stronger bond of the post-installed GFRP bars with concrete.

KEYWORDS

Post-installing, Glass fiber-reinforced polymers, Strengthening and repair, Bond behavior.

INTRODUCTION AND BACKGROUND

A post-installed reinforcing bar is defined as “a reinforcing bar embedded in a drilled hole with an adhesive and designed in accordance with ACI-318 rules for cast-in-place reinforcing bar development and splices” (ICC, 2016). Post-installed reinforcement in concrete is used to connect an existing concrete element with a new concrete element (i.e., new beam to an existing column). Post-installed reinforcing bars are gaining acceptance due to design flexibility, formwork simplification and the ability to have horizontal, vertical, and overhead applications (Hilti, 2016). Example applications of post-installed reinforcement include: diaphragm walls, slab connections, misplaced bars, vertical and horizontal connections, wall strengthening, new slab constructions, joint strengthening, cantilevers/balconies, slab widening, structural upgrades, slab strengthening and sidewalk upgrades (Hilti, 2011). Steel rebar, widely used as reinforcement in post-installed applications, is known to corrode in reinforced concrete structures (Perenchio, 1994). Corrosion of steel reinforcement can lead to a loss of bond strength and serviceability (Bilcik and Holly, 2013). Glass fiber-reinforced polymers (GFRP) bars can be used as an alternative to avoid this problem in concrete structures. GFRP reinforcing bars are gaining acceptance in structural field due to their corrosion resistance and high strength to weight ratio (ACI 440.1R, 2006).

The bond strength of post-installed GFRP reinforcement is dependent on the mechanical properties of GFRP bars, embedment depth, bar size and concrete compressive strength. Yilmaz et al. (2013) noted that smaller diameter anchors in post-installed applications improve the flexural strength of low strength concrete elements compared to larger diameter anchors. The failure mode of post-installed reinforcement, which is an indicator of bond behavior, depends on the embedment depth of the post-installed reinforcement and is independent of the type of chemical



adhesive used. Concrete cone breakout or bond failure are common modes of failure for post-installed rebar because the bars are often sufficiently developed, which prevents concrete splitting (Charney et al., 2013). Ahmed et al. (2008) stated that the failure mode of post-installed GFRP bars is similar when either epoxy or cement based chemical adhesives are used and that an increase in embedment depth may change the failure mode from bond failure to bar rupture due to the improvement of bond strength. Abolghasem (2013) found that the failure modes of post-installed GFRP bars were independent of the type of GFRP bar surface (silica coated and ribbed) regardless of bar size and embedment depth. The presence of reinforcement in the existing base material may improve the bond strength of post-installed GFRP bars due to confinement provided by the reinforcement (Abolghasem, 2013). Post-installed reinforcing bars must be spaced at or beyond the minimum spacing specified by the adhesive manufacturer. Post-installed GFRP bars spaced close to each other resulted in a loss of bond strength due to an overlap of the conic stress distribution (Abolghasem, 2013). Pullout tests performed by Ahmed et al. (2008) on post-installed GFRP bars showed that the bond strength of GFRP bars was equivalent to or higher than the bond strength of post-installed steel bars. These preliminary studies provide initial evidence on the efficacy of GFRP bars as post-installed reinforcement.

RESEARCH OBJECTIVE

The behavior of GFRP as post-installed reinforcement in a beam-column joint is less understood compared to the behavior of cast-in-place GFRP reinforcement or steel as post-installed reinforcement. Previous studies on post-installed GFRP bars were limited to pullout testing and lacked experimental research replicating reinforced concrete connections. This study aimed to bridge the knowledge gap and involved testing full-scale specimens to evaluate the bond strength of the post-installed GFRP bars at two embedment depths. The post-installed GFRP bars were simultaneously subjected to shear and flexure, which replicated the load in beam-column connections. The realistic loading scenario was used to determine the suitability of GFRP as post-installed reinforcement.

EXPERIMENTAL PROGRAM

The experimental program included testing eight specimens. Five specimens had post-installed GFRP bars and three specimens had cast-in-place GFRP reinforcement. This study involved three types of GFRP bars, each having different surface texture, including: silica coated with wraps (SCW), silica coated with no wraps (SC) and ribbed (R). The variation in surface texture is shown in Figure 1.



Figure 1: Varying surface textures of three different GFRP bars

The adhesive used for post-installing the GFRP bars was epoxy based and had a moderate curing time of 4 to 72 hours (Hilti, 2011). The post-installed and cast-in-place reinforcement consisted of straight GFRP bars with embedment depths of 6 and 11.5 in. (15.24 and 29.21 cm). All of the specimens had a nominal 28-day concrete compressive strength of 3 ksi (20.68 MPa) and contained #4 (#13) post-installed GFRP bars. Results obtained from the testing of specimens with post-installed GFRP reinforcement were compared to the results of previously tested specimens by Hamad et al. (2006), which contained cast-in-place and post-installed steel reinforcement.

Materials

The GFRP bar properties provided by manufacturers are listed in Table 1. The concrete mix was non-air entrained and contained Type I Portland cement. The coarse aggregate was quartzite and the fine aggregate was natural sand.

The maximum size of coarse aggregate was 0.75 in. (1.91 cm). The slump of the concrete mixture was 3.25 in. (8.25 cm).

Table 1: Properties of GFRP bars provided by the manufacturer

	GFRP (SCW)	GFRP (SC)	GFRP (R)
Modulus of Elasticity, ksi (MPa)	7,037 (48,518)	9,090 (62,673)	6,000 (41,369)
Tensile Strength, ksi (MPa)	134 (924)	199 (1,372)	116 (800)

Specimens Details

The specimen geometry was adopted from Hamad et al. (2006). The test specimens consisted of two identical vertical elements, which were anchored into the base element of the specimen. The specimens were designed to simulate a connection of two cantilever beams to a column. The layout of a typical test specimen and a cross section of the vertical elements is shown in Figure 2. The dimensions of the base element were 14 x 68 in. (35 x 170 cm). Two layers of seven #6 (1.9 cm) bars were used as longitudinal reinforcement and two layers of ten #4 bars were used as horizontal reinforcement in the base element. The dimensions of the vertical element were 12 x 28 in. (30 x 70 cm). The rebar for the outer face of the vertical element was seven #4 (#13) cast-in-place steel for all the specimens. The inner face vertical element reinforcement was seven #4 (#13) GFRP for all the specimens (either cast-in-place or post-installed reinforcement). Three #3 (0.94 cm) bars at a spacing of 3.5 in. (8.89 cm) were used as transverse reinforcement in the vertical elements to prevent shear failure during testing. The minimum clear cover of all the bars was 1.5 in. (3.81 cm) in all the specimens.

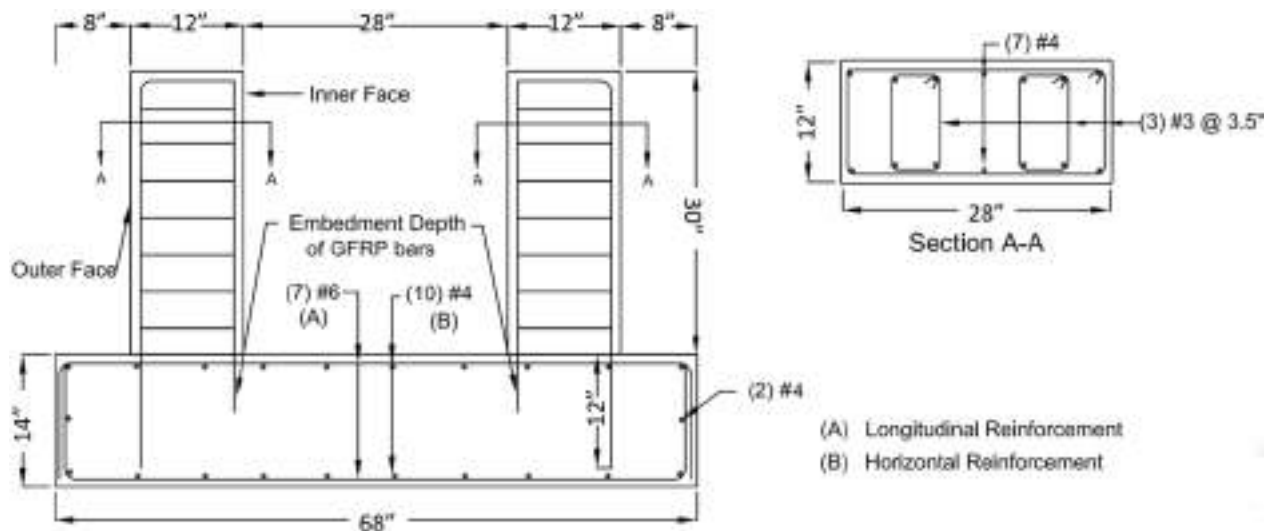


Figure 2: Specimen details and vertical element cross section

Construction of Specimens

Fabrication of the specimens was done in three steps: 1) casting of the base elements, 2) installation of the post-installed GFRP bars, and 3) casting of the vertical elements. Installation of the post-installed GFRP bars was performed seven days after the casting of the base element. Holes with a 0.625 in. (1.59 cm) diameter were hammer-drilled in the base element and cleaned according to the manufacturer's guidelines. The chemical adhesives were injected into the hole and the GFRP bars were pushed in with a twisting motion to ensure uniform coating of the chemical adhesive and to prevent air void formation. The top surface of the base element was roughened at the vertical element joint to ensure proper bond between the base and the vertical element as shown in Figure 3. After the adhesives were cured, stirrups were tied around the post-installed GFRP bars to avoid a shear failure during testing. Finally, the vertical element concrete was placed and allowed to cure. Standard concrete cylinders were made at the time of casting the base and vertical elements to determine the concrete compressive strength on test days, which were all more than 28 days from the time of vertical element concrete placement.



Figure 3: Roughened base element top surface at the post-installed GFRP bars

TESTING METHOD

Two equal point loads were simultaneously applied by hydraulic rams, mounted on built-up steel beams to ensure a distributed load was applied to the vertical element, at a distance of 6 in. (15.24 cm) from the tips of the vertical elements. The distributed load subjected the vertical elements to combined flexure and shear. Force was applied with a hydraulic hand pump, which subjected the GFRP bars at the inner face of the vertical elements to tension. An in-line pressure transducer recorded the hydraulic pump pressure. Specimen deflection at each loading stage was recorded using linear variable displacement transducers (LVDTs). The deflections were measured at the top of each vertical and middle of the base element as shown in Figure 4. The pressure transducer and the LVDTs were connected to a data acquisition system that continuously recorded the load-deflection history of the specimens. Load was applied in increments of 2.25 kips (10.01 kN) until the hydraulic ram stroke was maximized. The crack patterns were marked and photos were taken at each loading stage.



Figure 4: Test setup and instrumentation

RESULTS

Failure Modes

Initial cracking in specimens with cast-in-place GFRP bars began in the base element parallel to the bars. The depth of the initial vertical cracks was similar to the embedment depth of the GFRP bars installed in the base elements. At the conclusion of testing, the failure modes were noted. A bond-slip failure was observed at the interface of the vertical and base element in the specimen with a 6 in. (15.24 cm) embedment depth as shown in Figure 5a. The bond failure mode indicated a weak bond between the reinforcement and the surrounding concrete. When the embedment depth was increased to 11.5 in. (29.21 cm), the failure mode was a combination of bond-slip and concrete cone breakout as shown in Figure 5b. The bond-slip failures were expected because the provided embedment depths were less than the depth required to fully develop GFRP bars based on the development length

calculations. The required development length of the SCW and SC GFRP bars was 35.55 in. (90.17 cm) and 47.59 in. (120.88 cm), respectively.

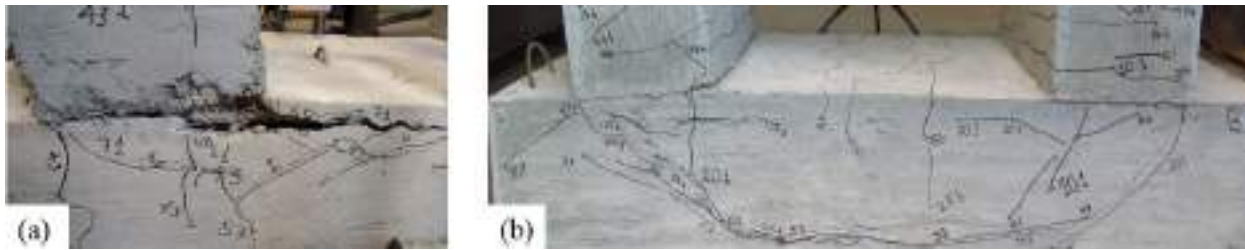


Figure 5: Failure modes of cast-in-place specimens at (a) 6 in. (15.24 cm) embedment depth and (b) 11.5 in. (29.21 cm) embedment depth

In specimens with post-installed GFRP bars embedded 6 in. (15.24 cm), cracking began at the interface of the vertical and base element and propagated downward, parallel to the post-installed reinforcement. The cracks began to form a cone as the applied load was increased. The depth of concrete cone breakout was approximately equal to the embedment depth of the post-installed GFRP bars. The cone-shaped cracks developed below both vertical elements and were connected by a longitudinal crack that formed along the top length of the base element (Figure 6a). The concrete cone breakout was not localized beneath each vertical element in specimens with post-installed GFRP at an embedment depth of 11.5 in. (29.21 cm). In these elements, the concrete cone breakout crack ran along the bottom length of the base element between the exterior edges of vertical elements with a maximum depth of about 11.5 in. (29.21 cm) at the middle of the base element as shown in Figure 6b. Concrete cone breakout failure in the specimens with post-installed GFRP bars indicated a strong connection between the GFRP bars and the surrounding concrete, which was due to the presence of a chemical adhesive not used in the cast-in-place specimens. The failure mode in all the specimens with post-installed GFRP bars was concrete cone breakout, regardless of the surface texture of GFRP bars. Hamad et al. (2006) also reported that the failure mode for specimens with post-installed steel reinforcement was concrete cone breakout.



Figure 6: Failure modes of post-installed specimens at (a) 6 in. (15.24 cm) embedment depth and (b) 11.5 in. (29.21 cm) embedment depth

Bond Strengths and Bond Ratios

Test data were normalized to a concrete compressive strength of 3 ksi (20.68 MPa) to account for variation in compressive strength and allow comparison of results between specimens. The adjustment was made by multiplying the peak loads with a factor, which consisted of the square root of the normalized concrete strength (3 ksi) divided by the concrete strength at the day of testing $[(3 \text{ ksi} / f'_c)^{1/2}]$, as previously done by Hamad et al. (2006). The bond strength of GFRP bars at the inner face of the vertical elements anchored into the base element was calculated using cracked section analysis. The calculated bond strength of the GFRP bars in all of the specimens was lower than the ultimate strength of GFRP bars. The results indicated an increase of approximately 100% in the bond strength due to the increase in embedment depth from 6 to 11.5 in. (15.24 to 29.21 cm). For example, the specimen with post-installed GFRP (SC) bars had bond strength of 22.04 ksi (151.96 MPa) at the embedment depth of 6 in. (15.24 cm), whereas the bond strength of a similar specimen increased to 47.03 (326.33 MPa) at the embedment depth of 11.5 in. (29.21 cm). As seen in Table 2, none of the bond ratios for both post-installed and cast-in-place GFRP bars were greater than 1.0 (i.e., the bond strength of the GFRP bars was equivalent to or less than the bond strength of cast-in-place steel bars). Post-installed GFRP bars with a SCW surface attained the highest bond strength at an embedment depth of 6 in. (15.24 cm) compared to post-installed GFRP bars with the



SC or R surface. Post-installed GFRP bars with a SC surface exhibited higher bond strength compared to post-installed GFRP bars with SCW surface at embedment depth of 11.5 in. (29.21 cm). At an embedment depth of 11.5 in. (29.21 cm), the specimen with post-installed GFRP SCW bars exhibited the lowest bond strength due to improper hammer-drilling technique in the base specimen. Bond ratios were computed by dividing the bond strength of each specimen by the bond strength of a reference specimen. Data collected by Hamad et al. (2006) for specimens with cast-in-place steel rebar were used as the reference data for both embedment depths. Bond ratios indicated that the bond strength of post-installed steel bars at both embedment depths was greater than the bond strength of all GFRP bars investigated in this study. For example, the bond ratio of the specimen with post-installed steel embedded 6 in. (15.24 cm) is 39 percent greater than the reference specimen. The bond ratio of the post-installed steel specimen embedded 11.5 in. (29.21 cm) is 24 percent greater than the reference specimen, whereas all specimens with post-installed GFRP had bond ratios lower than the reference specimen at both embedment depths. Results of all the specimens from this study are listed in Table 2.

Table 2: Test parameters and results

Bar Type	l_e in. (cm)	Anchorag e Method	Concrete Strength at day of Testing, f_c ksi (MPa)	Measured Ultimate Load P_{max} kips (kN)	Deflection of Vertical Elements Δ_{max} in. (cm)	Data Normalized to $(f_c)^{1/2}$		
						Maximum Load P_{max} kips (kN)	Bond Strength f_s and f_f ksi (MPa)	Bond Ratio
Steel (Hamad et al., 2006)	6.00 (15.24)	Cast-in- place	3.76 (25.92)	15.21 (67.66)	0.23 (0.58)	13.36 (15.43)	24.77 (170.78)	1.00
		Post- installed	4.71 (32.47)	23.64 (105.16)	0.72 (1.83)	18.54 (82.50)	34.36 (236.90)	1.39
GFRP (SCW)	6.00 (15.24)	Cast-in- place	3.97 (27.37)	14.26 (63.43)	0.65 (1.65)	12.39 (55.11)	21.57 (148.72)	0.87
GFRP (SCW)		Post- installed	3.97 (27.37)	15.14 (67.35)	0.50 (1.28)	13.16 (58.54)	22.90 (157.89)	0.92
GFRP (SC)		Post- installed	4.84 (33.37)	14.21 (63.21)	0.32 (0.81)	12.71 (56.54)	22.04 (151.96)	0.89
GFRP (R)		Post- installed	3.97 (27.37)	14.62 (65.03)	0.73 (1.85)	11.19 (49.76)	19.59 (135.06)	0.79
Steel (Hamad et al., 2006)	11.50 (29.21)	Cast-in- place	4.20 (28.96)	31.42 (139.76)	0.67 (1.70)	26.59 (118.28)	48.44 (334.00)	1.00
		Post- installed	3.80 (26.20)	36.92 (164.23)	1.31 (3.33)	32.85 (146.12)	59.89 (412.93)	1.24
GFRP (SCW)	11.50 (29.21)	Cast-in- place	4.20 (28.96)	33.16 (147.50)	1.17 (2.97)	28.00 (124.55)	48.74 (336.05)	1.01
GFRP (SC)		Cast-in- place	4.05 (27.92)	32.10 (142.79)	1.19 (3.02)	27.64 (122.95)	48.41 (333.78)	1.00
GFRP (SCW)		Post- installed	4.40 (30.34)	27.80 (123.66)	1.37 (3.48)	23.03 (102.44)	40.08 (276.34)	0.83
GFRP (SC)		Post- installed	4.40 (30.34)	32.63 (145.15)	1.02 (2.59)	27.03 (120.24)	47.33 (326.33)	0.98

Load-Displacement Behavior

Load-displacement curves for all specimens were generated from the applied load and LVDT data collected from the vertical element with maximum displacement. The load-displacement data for specimens with similar embedment depths were plotted together to compare the results. In the load-displacement plots, the specimens with cast-in-place bars are labeled as CIP and the specimens with post-installed bars are labeled as PI. Figures 7a and 7b show the load-displacement curves for all the specimens with an embedment depth of 6 in. (15.24 cm) and 11.5 in. (29.21 cm), respectively.

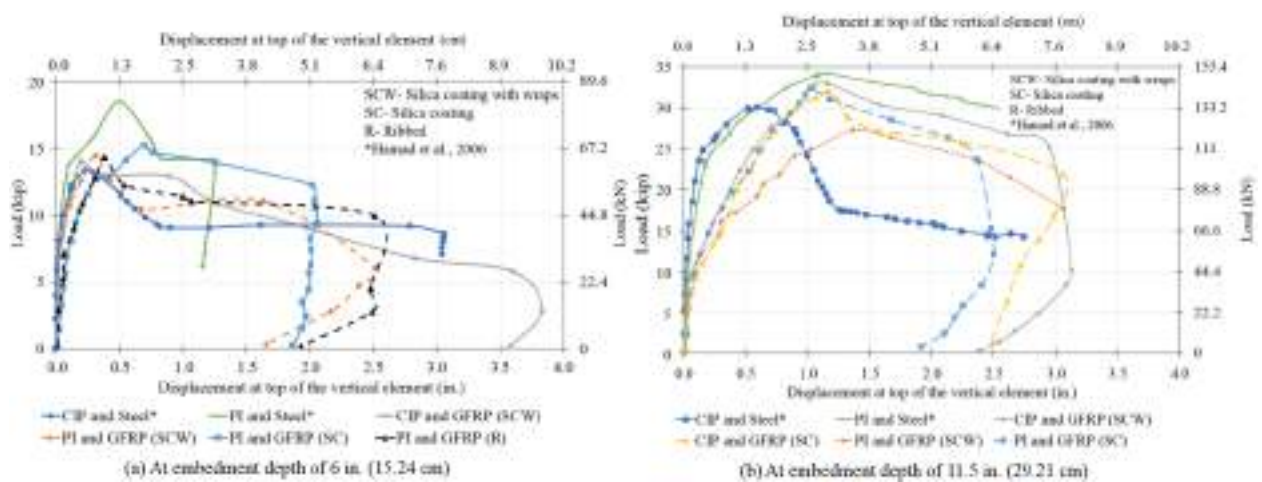


Figure 7: Load-displacement curves

Load-displacement curves allowed for the comparison of ductility and peak applied load of all GFRP specimens with data from cast-in-place steel specimens collected by Hamad et al. (2006). Maximum vertical element displacement at the peak applied load was the indicator of ductility. The ductility and peak load of specimens with CIP and PI GFRP bars at 6 in. (15.24 cm) embedment depth was usually less than the reference CIP steel specimen. The ductility and peak load of specimens with PI and CIP GFRP was frequently more than the CIP steel specimen at the embedment depth of 11.5 in. (29.21 cm). The peak load in all specimens with post-installed GFRP was lower than the reference specimens. A summary of the load-displacement results are presented in Table 3.

Table 3: Load-displacement behavior of all GFRP specimens with respect to cast-in-place steel specimen

Specimen	At embedment depth of 6 in. (15.24 cm)		At embedment depth of 11.5 in. (29.21 cm)	
	Ductility	Peak Load (%)	Ductility	Peak Load (%)
CIP and Steel (Hamad et al, 2006)	–	–	–	–
PI and Steel (Hamad et al, 2006)	Less	+38	More	+23.5
CIP and GFRP (SCW)	Less	-7.3	More	+5.3
CIP and GFRP (SC)	Not available	Not available	More	+3.9
PI and GFRP (SCW)	Less	-1.5	More	-13.4
PI and GFRP (SC)	Less	-4.8	More	+1.6
PI and GFRP (R)	Less	-16.2	Not available	Not available



SUMMARY AND CONCLUSIONS

The purpose of this research was to evaluate the bond behavior of post-installed GFRP reinforcement in beam-column connections and compare the GFRP results to results from cast-in-place and post-installed steel reinforcement. In this study, eight specimens were fabricated with either post-installed or cast-in-place GFRP bars at embedment depths of 6 and 11.5 in. (15.24 and 29.21 cm). The nominal 28-day concrete compressive strength of all the specimens was 3 ksi (20.68 MPa), and the size of the GFRP bars was #4 (#13). The specimens were subjected to static loading and the results indicated the following:

- The specimens with post-installed GFRP bars exhibited concrete cone breakout failure at both embedment depths, whereas the specimens with cast-in-place GFRP bars showed bond failure at 6 in. (15.24 cm) embedment depth and a combination of concrete cone breakout and bond-slip failure at 11.5 in. (29.21 cm) embedment depth. Concrete cone breakout indicated stronger bond between post-installed bars and the surrounding concrete.
- The increase in embedment depth from 6 to 11.5 in. (15.24 to 29.21 cm) resulted in a more than 100% increase of bond strength among most of the GFRP specimens. For the same increase in embedment depth, the increase in bond strength was less than 100% for both PI and CIP steel specimens (Hamad et al., 2006).
- At each embedment depth, the specimens with GFRP bars had similar peak loads regardless of the anchorage method. On the contrary, Hamad et al. (2006) reported significant gain in peak loads among specimens with post-installed steel compared to specimens with cast-in-place steel.
- At the embedment depth of 6 in. (15.24 cm), the specimens with post-installed GFRP bars demonstrated lower ductility compared to the specimen with cast-in-place GFRP bars. Furthermore, the ductility of specimens with cast-in-place steel (Hamad et al., 2006) was found to be greater than the ductility of specimens with cast-in-place GFRP.
- At the embedment depth of 11.5 in. (29.21 cm), the specimens with post-installed GFRP bars demonstrated greater ductility compared to the cast-in-place steel specimen (Hamad et al., 2006), but lower ductility than the specimen with cast-in-place GFRP bars.

In post-installed applications, with variation in the parameters discussed in this study, specimens with steel reinforcement exhibited better peak loads and ductility compared to specimens with GFRP reinforcement due to the surface conditions and ductile nature of the steel bars. GFRP bars are beneficial due to their ability to resist corrosion, which leads to minimal maintenance and rehabilitation costs in GFRP reinforced concrete structures compared to structures with traditional steel bars. Additional research including variation in concrete strength and bar size is warranted to understand the bond behavior of post-installed GFRP bars in more detail.

ACKNOWLEDGEMENTS

The authors are grateful to Hilti Inc., Hughes Brother Inc., Pultrall Canada, and Marshall Composite Technologies for materials used in this research. Assistance provided by undergraduate research assistants Jonas Bauer and Matthew McDermott during this research project is also appreciated.

REFERENCES

- A. Abolghasem, (2013). "Experimental investigation on pull-out strength of pre- and post-Installed GFRP bars for bridge barrier construction", MS Thesis, Ryerson University, Toronto, Ontario.
- ACI Committee 440, 2006, "Guide for the design and construction of structural concrete reinforced with FRP bars", ACI 440-1R-06, American Concrete Institute, Farmington Hills, MI.
- A.F Charney, K. Pal, J. Silva (2013). "Recommended procedures for development and splicing of post-installed bonded reinforcing bars in concrete structures", ACI Structural Journal, 110, 437-446.
- B.S Hamad, R. Al-Hammoud, J. Kunz (2006). "Evaluation of bond strength of bonded-in or post-installed reinforcement", ACI Structural Journal, 103, 207- 218.



E.A Ahmed, E.F El-Salakawy, B. Benmokrane (2008). "Tensile capacity of GFRP post-installed adhesive anchors in concrete", ASCE Journal of Composites for Construction, 12, 596-607.

Hilti Inc. (2016). "Post-installed reinforcing bar guide", 2016, Tulsa, OK.

Hilti Inc. (2011). "Technical manual for post-installed rebar connections", 10th edition, Zollikofen, Switzerland.

ICC Evaluation Service, LLC (2016). "Acceptance criteria for post-installed adhesive anchor systems in concrete elements", AC-308, Plano, TX.

J. Bilcik, I. Holly (2013). "Effect of reinforcement corrosion on bond behavior", Procedia Engineering, 65, 248-253.

S. Yilmaz, M.A Ozen, Y. Yardim (2013). "Tensile behavior of post-installed chemical anchors embedded to low strength concrete", Construction and Building Materials, 47, 861-866.

W.F Perenchio (1994). "Corrosion of reinforcing steel", ASTM STP 169C, 164-172.



EXPERIMENTAL INVESTIGATION OF GEOPOLYMER CONCRETE BEAMS WITH RECTANGULAR GFRP SPIRAL REINFORCEMENT

G.B. Maranan 1, A.C. Manalo 2, T.W. Krishna 2 and B. Benmokrane 3

¹ Faculty of Science and Engineering, University of Waikato, New Zealand, Email: gmaranan@waikato.ac.nz

² School of Civil Engineering and Surveying, University of Southern Queensland, Australia

³ Department of Civil Engineering, University of Sherbrooke, Canada.

ABSTRACT

The combination of glass-fibre-reinforced polymer (GFRP) rebars and geopolymer concrete is an innovative construction technique for the development of civil infrastructures with high durability and high sustainability and with adequate strength and structural integrity. However, few studies have dealt with this system particularly on the use of GFRP spirals as shear reinforcement for geopolymer concrete beams. In this study, the shear behaviour of geopolymer concrete beams transversely reinforced with continuous rectangular GFRP spirals was investigated using the four-point static bending test. Five full-scale beams were designed, prepared, and tested up to failure: one control beam without transverse reinforcement, three spirally-reinforced beams with varying spiral pitch (i.e. 75 mm, 100 mm, and 150 mm), and one beam with conventional GFRP stirrups spaced at 100 mm on-centres. As can be expected, the shear performance of the beam increases as the spiral pitch decreases because the closely spaced spirals enhanced both the shear strength contribution of the confined concrete core and the longitudinal reinforcement dowel action, effectively controlled the widening of shear cracks, and distributed the pressure uniformly along the shear span. The shear load-bearing and deflection capacities of the control beam were 63 kN and 12.7 mm, respectively. With the use of GFRP spirals, the shear strength and deflection capacity increased by as much as 220% and 410%, respectively. The shear strength and deflection capacity of the spirally-reinforced beam were 19 % and 116 % higher than that of the conventionally-reinforced beam, respectively. It can be deduced, therefore, that the GFRP spiral is a viable alternative to the traditional closed GFRP stirrups because, aside from improving the beams' overall performance, it can also reduce the material expenditures and the time and cost of installation.

KEYWORDS

Glass-fibre-reinforced polymer rebars; geopolymer concrete beams; innovative construction technique; shear reinforcement; GFRP spirals; GFRP stirrups; shear

INTRODUCTION

Geopolymer concrete reinforced with glass-fibre-reinforced polymer (GFRP) bars, herein called GFRP-reinforced geopolymer concrete (GFRP-RGC) system, is new and innovative construction technology that mainly addresses the steel corrosion-induced durability problems and cement sustainability issues of the conventional reinforced concrete (RC) system. Aside from being corrosion-resistant, GFRP bars are lightweight, electromagnetic neutral, and have high tensile strength. Geopolymer concrete, on the other hand, is a "green concrete" because its binder – the geopolymer – can be manufactured using alkali-activated industrial waste materials such as fly ash and slags. The use of geopolymer concrete is currently attracting increasingly widespread attention in the construction industry because its manufacture reduces the CO₂ emission by 80-90% compared to those of ordinary portland cement (OPC)-based concrete (Duxson et al. 2007). Furthermore, this material has highly desirable properties that can lead to significant cost savings in many structural members (Lloyd and Rangan 2010). The GFRP-RGC system, therefore, can be anticipated to produce civil infrastructures with high durability and high sustainability and with adequate strength and structural integrity. Scholastic research works focusing on the shear performance of GFRP-RGC beams transversely reinforced with rectangular GFRP stirrups (Maranan et al. 2017) and on the compression behaviour of GFRP-RGC columns with GFRP spirals (Maranan et al. 2016) are available in the literature. No study, however, has been done on the behaviour of GFRP-RGC beams transversely reinforced with continuous rectangular GFRP spirals and this is the key motivation of this undertaking.

The results of the series of tests conducted by Karayannis et al. (2005) and Karayannis and Chalioris (2013) showed that the continuous rectangular spiral steel reinforcement improved both the load-bearing capacity and shear performance of the shear-critical beams. The beam with spiral reinforcement spaced at 120 mm and 80 mm on-centre yielded shear capacities that were 14.9 % and 14.7 % higher than their counterpart beams with conventional stirrups, respectively. Similarly, Shatarat et al. (2016) stated that the beams with rectangular spiral reinforcement yielded better shear strength and ductility than the beams with traditional rectangular stirrups. De Corte and Boel (2013), on the other hand, concluded that the current RC design codes are applicable in designing



beams with spiral-type stirrups. Aside from improving the shear performance of the beams, another advantage of the spiral-type reinforcement over the conventional stirrups is that they can be quickly installed owing to their “accordion” nature when extended (Karayannis and Chalioris 2013), thereby significantly reducing the installation time and labour expenditures. Furthermore, the material cost can be reduced since the extra amount of material needed to fabricate two hooks for a single stirrups are excluded. Clearly, these previous studies showed that the spiral-type shear reinforcement is a viable alternative to the conventional closed stirrups; however, these studies are focused on steel spirals as transverse reinforcement for RC beams.

In this study, the shear performance of geopolymer concrete beams transversely reinforced with continuous rectangular GFRP spirals was experimentally investigated using the four-point static bending test. The main test parameters include the spiral pitch and the web reinforcement configuration (spiral-type versus rectangular-shape stirrups). The failure mode, shear load-deflection response, shear strength, deflection capacity and strains in the shear and flexural reinforcements were carefully evaluated to understand the shear resistance mechanism of GFRP-RGC beams with GFRP spirals.

MATERIALS AND METHODS

GFRP Reinforcement and Geopolymer Concrete

The GFRP spirals and closed stirrups adopted in the study (Figure 1) were manufactured using the pultrusion process wherein the E-glass fibres are pulled through a thermosetting modified vinyl ester resin and into a heated die, where the resin undergoes polymerization. The nominal diameter (\emptyset_f), width (b_s), height (b_i), and internal bend radius (r_{sb}) of the transverse reinforcement were 9.5 mm, 150 mm, 240 mm, and 38.5 mm, respectively. GFRP bars with \emptyset_f of 12.7 mm and 15.9 mm were used as top and bottom longitudinal reinforcement, respectively. The nominal area (A_{fb}), guaranteed tensile strength of straight (f_{fu}) and bent bars (f_{fb}), elastic modulus (E_f), and glass content-by-weight (W), as specified by the manufacturer, are presented in Table 1.

A ready-mix geopolymer concrete (Figure 2) with a commercial mix design – supplied locally in Toowoomba, Australia – was used in the study. It is composed of a blend of fly ash (FA) and ground-granulated blast furnace slag (GGBFS), gravel, sand and water with a proprietary chemical hardener solution. The average compressive strength (f_c') and elastic modulus (E_c) of the geopolymer concrete, determined in accordance with ASTM C39/C39M-04a (2004), were 31 MPa and 35 GPa, respectively.

Five (5) geopolymer concrete beams were prepared and tested up to failure: one control beam without shear reinforcement (CB); three (3) beams transversely reinforced with GFRP spirals with centre-to-centre spiral pitch of 75 mm (S75), 100 mm (S100), and 150 (S150) mm, collectively called as S#; and one beam reinforced with conventional closed GFRP stirrups spaced at 100 mm on-centres (C100). The width (b), height (h), and total length (L_t) of the beams were 200 mm, 300 mm, and 1840 mm, respectively. Figure 1 shows the typical reinforcement cage configuration of the beams.

Four-Point Static Bending Test

Four-point static bending tests (Figure 3) were employed in the study. Two concentrated loads, 200 mm apart, were applied at the midspan of each beam having a clear span (L) of 1640 mm, thereby yielding a shear span (a) of 720 mm. The loads were applied using an electric hydraulic pump and were measured using the 2500 kN capacity load cell. The deflections at midspan were measured using the laser displacement sensor (LDS), positioned at the bottom of the beam, while electrical strain gauges were attached at the mid-length of tensile reinforcement and at the mid-height of the shear reinforcement where the major inclined shear crack was anticipated to transpire. The applied loads, deflections, and strains captured using the System 5000 data logger.

Table 1: Mechanical properties of the GFRP reinforcements

\emptyset_f , mm	A_{fb} , mm ²	f_{fu} , MPa	f_{fb} , MPa	E_f , GPa	W , %
9.5 (#3)	81.6	1029	463	50	77.6
12.7 (#4)	126.7	1312	-	65.6±2.5	84.1
15.9 (#5)	197.9	1184	-	62.6±2.5	84.1



(a) continuous GFRP spirals



(b) closed GFRP stirrups

Figure 1: GFRP reinforcement cages



Figure 2: Geopolymer concrete



Figure 3: Four-point static bending test

RESULTS AND DISCUSSIONS

Failure Mode

Figure 4 shows the final failure configuration of the tested beams. Based on the figure, the beams exhibited a pure brittle shear failure. The failure of CB (Figure 4a) can be categorized as a shear-tension (ST) failure, characterised by the formation of one major diagonal shear crack followed by a bond failure caused by the concrete splitting action along the tension reinforcement at the support. Upon providing GFRP spirals in the shear spans, the mode of failure changed. S75, S100, and S150 (Figure 4b) undergone a shear-compression (SC) failure typified by the crushing of diagonal concrete strut near the loading plate due to the combined compressive and shear stresses in the compression zone. Rupturing of GFRP spirals, specifically at the bent portion, transpired in S100 and S150. The severity of failure, in general, increases as the spiral pitch increases. C100 (Figure 4c) also exhibited a SC failure but, the closed stirrup undergone a lap splice failure at its corner.

Shear Load-Midspan Deflection Relationship

Figure 5 shows the relationships between the shear load (V), one-half of the applied load ($P/2$), and the midspan deflection (Δ) of the tested beams. Based on the figure, CB exhibited a linear elastic V - Δ behaviour up until its peak. S75, S100, and S150, on the other hand, produced a three-segment V - Δ curve. The first segment represents the linear elastic response of the beams, which was similar to that of CB. The second segment embodies the non-linear behaviour up to peak due to the initiation and proliferation of diagonal shear cracks and widening of main inclined crack followed by the crushing of the concrete above the neutral axis. The non-linear segment tend to be more pronounced as the spiral pitch decreases, suggesting that the beams can undergo larger deformation with closely spaced spirals. The third segment typifies the softening behaviour characterised by a gradually decreasing load. C100 produced V - Δ curve composed of linear segment, analogous to that of CB and S#, and a short nonlinear segment prior to peak.

Interestingly, all the beams exhibited similar initial linear stiffness because at this stage, the flexural reinforcement and the geopolymer concrete in the compression zone mainly influenced the behaviour of the beam. Interestingly, this finding corroborates with the previous studies (Karayannis and Chalioris 2013; De Corte and Boel 2013) for beams reinforced with steel web reinforcement, wherein it was generalised that the behaviour of the beams was independent of the amount and configuration of the transverse reinforcement.

Shear Load and Deflection Capacities

Table 2 summarises the maximum shear load capacity (V_u) and the corresponding midspan deflection at peak (Δ_u) of the tested beams. Based on the table, the V_u and Δ_u of CB were equivalent to 63 kN and 12.7, respectively. The V_u of S75, S100, and S150 were equivalent to 202 kN, 187 kN, and 150 kN, which were 3.2, 3.0, and 2.4 times

that of CB, respectively. On the other hand, the Δ_u were 65.1 mm, 59.5 mm, and 31.1 mm for S75, S100, and S150, respectively, which were 5.1, 4.7, and 2.5 times that of CB, respectively.

The provision of GFRP spirals enhanced both V_u and Δ_u of the control beam. The confinement effect of the spirals enhanced the contribution of the geopolymer concrete and controlled the widening of diagonal cracks, which consequently maintained the shear contribution coming from the aggregate interlock. Furthermore, the spirals also enhanced the dowel action of the longitudinal GFRP bars and the geopolymer concrete-reinforcement bond, as evidenced by the absence of splitting action along the longitudinal reinforcement.

It was obvious from the results that V_u and Δ_u increase as the spiral pitch decreases. This trend was consistent with the previous findings (Karayannis, Chalioris, and Mavroeidis 2005; Yang, Kim, and Yang 2011; Karayannis and Chalioris 2013) for ordinary concrete beams with spiral steel bars. In addition to the increased shear strength contribution due to higher number of spiral links, the closely spaced spirals improved the shear contribution of the confined concrete core and of the longitudinal-reinforcement dowel action. Furthermore, the stresses were distributed more evenly along the shear span and the widening of shear cracks were more effectively controlled.

C100 produced V_u (156 kN) and Δ_u (27.6 mm) that were 20 % and 120 % lower than that of S100, respectively. Again, these results are consistent with the conclusions stated by the authors (Karayannis, Chalioris, and Mavroeidis 2005; Karayannis and Chalioris 2013; Yang, Kim, and Yang 2011; Shatarat, Katkhuda, and Alqam 2016) in ordinary concrete beams, wherein the continuous steel spiral produced higher load resistance and deflection capacity than those with the conventional closed steel stirrups. This could be attributed to the favourable inclination of the spiral links being approximately normal to the cracking direction and the continuous nature of the spirals that effectively controlled the widening of main diagonal crack and the distribution of diagonal cracks.

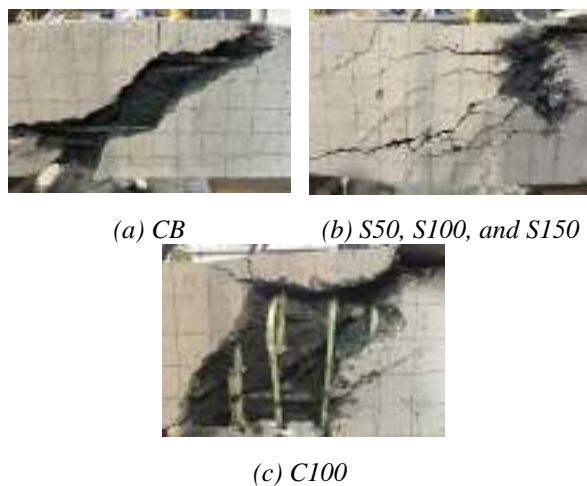


Figure 4: Failure mode of the tested beams

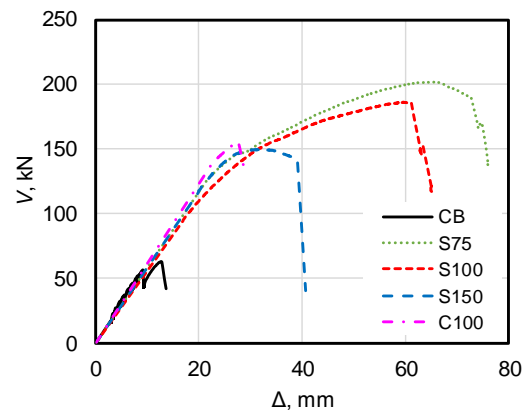


Figure 5: Shear load-midspan deflection relationship of the tested beams

Table 1: Shear load capacity, deflection capacity, and failure mode of the tested beams

Beam	$V_{cr,f}$, kN	V_{cr} , kN	V_u , kN	Δ_u , mm	ϵ_{fu} , $\mu\epsilon$	$\epsilon_{f_{vu}}$, $\mu\epsilon$	Failure Mode [^]
CB	12	-	63	12.7	3649	-	ST
S75	16	25	202	65.1	15915	5754	SC
S100	16	50	187	59.5	14787	3108	SC
S150	17	50	150	31.1	11101	1387	SC
C100	12	20	156	27.6	10208	3062	SC

[^]ST = shear-tension failure; SC = shear-compression failure

Longitudinal and Shear reinforcement Strains

Figure 6 presents the relationships between the shear load (V) and the tensile reinforcement strain (ϵ_f) of the tested beams. Based on the figure, the V - ϵ_f behaviour was not significantly affected by the spacing or pitch of the GFRP spirals. The same trend was also reported by Ahmed *et al.* (2010), but for rectangular concrete beams with closed

GFRP shear reinforcement. Furthermore, it can be observed from the figure that the transverse reinforcement configuration have no direct influence on the development of ε_f .

Figure 7, on the other hand, shows the relationships between the shear load (V) and the shear reinforcement strain (ε_{fv}) of the tested beams. For similar amount of applied loads, S150 yielded the lowest ε_{fv} , followed by S100 and S75, respectively. This could be attributed to the favourable orientation of the straight legs S150 with respect to the cracking direction that made it more effective in resisting shear deformations. Shatarat *et al.* (2016) reported that the ideal angle of inclination for continuous rectangular spirals was 80° . Interestingly, this orientation was relatively analogous to that of S150 (79°).

Table 3 summarises the maximum tensile and shear strains at failure (ε_{fu} and ε_{fvs} , respectively). The beams produced ε_{fu} ranging from $10208 \mu\varepsilon$ to $15915 \mu\varepsilon$, which were 54% to 84% of the ultimate tensile strain capacity of the longitudinal GFRP reinforcement. These results further support the previous findings that the beams failed due to a shear-dominated failure. S75, S100, and S150 yielded ε_{fu} that were 330%, 300%, and 200% larger than that of the control beam, respectively, which tend to decrease as the spiral pitch increases. S100 produced ε_{fu} that was comparable to that of C100. Nevertheless, these results suggest that the use of spirals will allow the effective utilisation of the longitudinal reinforcement. Interestingly, Maranan *et al.* (2017) reported analogous ε_{fu} values for geopolymer concrete beams reinforced with similar type of GFRP bars.

The ε_{fvs} , on the other hand, tend to increase as the spiral pitch decreases. S75 ($5754 \mu\varepsilon$) yielded the largest ε_{fvs} trailed by S100 ($3108 \mu\varepsilon$) and S150 ($1387 \mu\varepsilon$), respectively. This could be explained by the failure mode of these beams, As reported earlier, the spirals did not rupture in S75 and hence the spirals were effectively utilised whereas S100 and S150 failed due to premature rupture of the spiral bent links. Furthermore, the GFRP spiral bents, the weakest segment, further weaken when the spirals are stretched to achieve wider spacing.

The suggested maximum transverse reinforcement strain to limit the crack width were $2500 \mu\varepsilon$ and $5000 \mu\varepsilon$ in accordance with the CSA S6-06 (2006) and the CSA S806-12 (2012), respectively (Razaqpur and Spadea 2015). The ε_{fvs} of the tested beams, except S150, generally surpassed the $2500 \mu\varepsilon$ limit while only S75 exceeded the $5000 \mu\varepsilon$ limit. This observation tend to suggest that the $2500 \mu\varepsilon$ limit should be adopted for beams with continuous rectangular GFRP spirals.

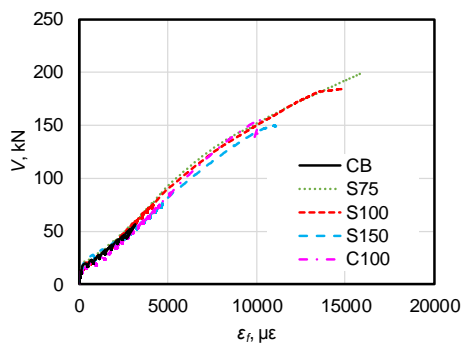


Figure 6: Shear load-bottom longitudinal reinforcement strain relationship of the tested beams

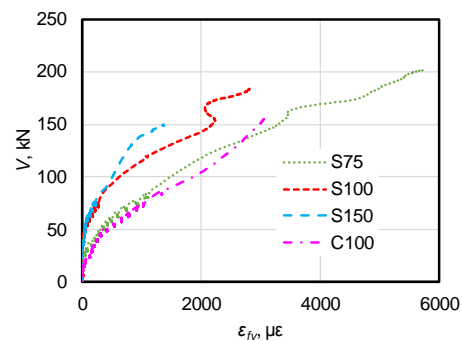


Figure 7: Shear load-transverse reinforcement strain relationship of the tested beams

CONCLUSIONS

This paper presents the investigation of the shear performance of geopolymer concrete beams transversely reinforced with continuous rectangular GFRP spirals. Based on the experimental results, the following conclusions were found:

1. The GFRP spirals improved the overall shear performance, except the stiffness, of the control beam or the beam without transverse reinforcement by maintaining the shear contribution of the aggregate interlock and by enhancing the dowel action of the longitudinal GFRP bars and the GFRP-geopolymer concrete bond.



2. The shear strength and deflection capacity of the beam increase when the spiral pitch decreases. The beam with GFRP spirals spaced at 75 mm, 100 mm, and 150 mm on-centres yielded shear strengths that were 220 %, 200 % and 140 % higher than that of the control beam. Similarly, the deflection capacity increased by 410 %, 370 %, and 150%, respectively. The closer the spiral pitch, the better the shear resistance mechanism of the confined concrete core and the longitudinal reinforcement dowel action, the narrower the shear cracks, and the more even the stress distribution along the shear span.
3. The shear strength and deflection capacity of the geopolymer concrete beam with GFRP spirals were 1.2 and 2.2 times larger than that of the beam with conventional closed GFRP stirrups. These enhancements could be attributed to the favourable inclination of the spiral links, approximately normal to the cracking direction, and the continuous nature of the spirals that effectively resisted the shear stresses and controlled the development of the shear cracks.
4. The 2500 $\mu\epsilon$ limit is proposed for the safe design of GFRP spiral reinforcement. More studies, however, are recommended to support this claim.
5. In general, the continuous GFRP spirals is a viable alternative to the conventional GFRP stirrups. Further experimental works are suggested to verify this generalisation.

ACKNOWLEDGMENTS

The authors would like to express their special thanks to V-ROD® Australia for providing the materials, the Natural Science and Engineering Research Council of Canada (NSERC), and the technical staff of the Centre of Excellence in Engineered Fibre Composites (CEEFC) at University of Southern Queensland.

REFERENCES

- E. A. Ahmed, E. F. El-Salakawy, and B. Benmokrane (2010). "Performance Evaluation of Glass Fiber-Reinforced Polymer Shear Reinforcement for Concrete Beams", *ACI Structural Journal*, 107: 53-61.
- ASTM (2004). "Standard test method for compressive strength of cylindrical concrete specimens (ASTM C39/C39M-04)." In. West Conshohocken, Pennsylvania, USA: American Society for Testing and Materials.
- CSA (2006). "Canadian highway bridge design code (CSA S6-06)." In. Rexdale, Ontario, Canada: Canadian Standards Association.
- CSA (2012). "Design and construction of building components with fiber-reinforced polymers (CSA S806-12)." In. Rexdale, Ontario, Canada: Canadian Standards Association.
- W. De Corte, and V. Boel (2013). "Effectiveness of spirally shaped stirrups in reinforced concrete beams", *Engineering Structures*, 52: 667-75.
- P. Duxson, J. L. Provis, G. C. Lukey, and J. S. J. Van Deventer (2007). "The role of inorganic polymer technology in the development of 'green concrete'", *Cement and Concrete Research*, 37: 1590-97.
- C. G. Karayannis, and C. E. Chalioris (2013). "Shear tests of reinforced concrete beams with continuous rectangular spiral reinforcement", *Construction and Building Materials*, 46: 86-97.
- C. G. Karayannis, C. E. Chalioris, and P. D. Mavroeidis (2005). "Shear capacity of RC rectangular beams with continuous spiral transversal reinforcement", *WIT Transactions on Modelling and Simulation*, 41.
- N. A. Lloyd, and B. V. Rangan (2010). "Geopolymer concrete: A review of development and opportunities." In *35th Conference on Our World in Concrete and Structures (OWICs 2010)*, 317-14. Singapore.
- G. B. Maranan, A. C. Manalo, B. Benmokrane, W. M. Karunasena, and P. A. Mendis (2016). "Behavior of concentrically loaded geopolymer-concrete circular columns reinforced longitudinally and transversely with GFRP bars", *Engineering Structures*, 117: 422-36.



- G. B. Maranan, A. C. Manalo, B. Benmokrane, W. M. Karunasena, and P. A. Mendis (2017). "Shear behavior of geopolymer concrete beams reinforced with glass fiber-reinforced polymer bars", *ACI Structural Journal*, 114: 337-48.
- A. G. Razaqpur, and S. Spadea (2015). "Shear strength of FRP reinforced concrete members with stirrups", *Journal of Composites for Construction*, 19: 04014025.
- N. Shatarat, H. Katkhuda, and M. Alqam (2016). "Experimental investigation of reinforced concrete beams with spiral reinforcement in shear", *Construction and Building Materials*, 125: 585-94.
- K.-H. Yang, G.-H. Kim, and H.-S. Yang (2011). "Shear behavior of continuous reinforced concrete T-beams using wire rope as internal shear reinforcement", *Construction and Building Materials*, 25: 911-18.



BEHAVIOUR OF CONCRETE DEEP BEAMS REINFORCED WITH GFRP HEADED-END BARS

A.M. Mohamed¹ and E. F. El-Salakawy²

¹ University of Manitoba, Winnipeg, MB, Canada R3T 5V6

² University of Manitoba, Winnipeg, MB, Canada R3T 5V6, Email: ehab.el-salakawy@umanitoba.ca

ABSTRACT:

Reinforced concrete (RC) deep beams are commonly used as transfer girders in high rise buildings and bridges, as they have the capability to sustain higher loads compared to slender beams. Deep beams are characterized by their relatively small shear span-to-depth ratio. The use of fibre-reinforced polymer (FRP) bars, as an alternative to steel bars, is now a recognized solution to mitigate the deleterious effect of steel corrosion. Among FRP types, glass (G) FRP reinforcement is of particular interest to the construction industry because of its lower cost and large deformation at failure. However, due to the relatively low modulus of elasticity of GFRP with respect to steel, GFRP-RC deep beams will be susceptible to deeper and wider cracks, which will in turn adversely affect the shear capacity. Also, GFRP has a different bar surface and bond characteristics than that of steel, which require a longer development length. In addition, very little experimental data exist for FRP-RC deep beams. This paper reports on an experimental study designed to investigate the shear behavior of concrete deep beams internally reinforced with GFRP and containing no distributed web reinforcement. In this study, three large-scale simply supported RC deep beams reinforced with headed-end GFRP bars were constructed and tested up to failure under three-point loading system. The specimens have a rectangular-section of 590-mm height by 250 mm width, while the length of the specimens are 2100, 2600, and 3100 mm. The main variable is the shear span-to-depth ratio, which varied between 1.0, 1.5 and 2.0. The test results are presented in terms of ultimate strength, cracking, deflection and strains in reinforcement. The test results confirmed the formation of the strut-and-tie model. Also, it showed that increasing the shear span-to-depth ratio led to decreasing the load capacity of the beam significantly.

KEYWORDS:

Deep beams, glass fibre-reinforced polymers, headed-end bars, shear span-to-depth ratio, shear strength.

INTRODUCTION

In general, deep beams are widely used in many structures like bridges and high-rise buildings as transfer girders and pile caps because of their higher load capacity compared to slender beams. Deep beams are defined as structural members with shear span-to-depth ratio (a/d) less than or equal 2.5 (MacGregor 1997). The small a/d ratio makes the behaviour of such beams more dominated by shear failure (Oh and Shin 2001). Such type of failure is undesirable in concrete structures, as it is sudden and brittle. Strut-and-Tie Model (STM) is the load transfer mechanism in deep beams. In other words, deep beams cannot be designed using linear analysis like slender beams. The design using STM is based on the lower-bound theorem, which assumes that the reinforcement will yield before the failure of any other element in the STM (Tuchscherer et al. 2011).

On the other hand, steel-reinforced concrete (RC) structures which are exposed to harsh environments, especially in North America, are susceptible to corrosion issues. Such a problem will result in decreasing the life span of structures and requires extensive maintenance operations. Currently, the non-corrodible fibre-reinforced polymers (FRP) bars is a recognized solution for this issue. However, compared to steel, FRP bars have a lower modulus of elasticity, lower transverse strength, lower strain at failure, and different bonding characteristics that result in a different shear behaviour for FRP-RC structures. In addition, as mentioned before, the low a/d of deep beams makes shear failure the main mode of failure in such beams, which in turns will not allow reaching the maximum tensile capacity of FRP bars. However, using FRP will affect the behaviour and strength of deep beams. In other words, due to the lower modulus of elasticity of FRP with respect to steel, FRP-RC structures normally exhibit wider and deeper cracks, which will decrease the shear capacity of such members. Moreover, the high and constant tensile stresses developed in reinforcement (Tie) after the formation of STM, will make the deep beam vulnerable to end anchorage failure. Such type of failure is undesirable as it does not represent the failure of the main element (Strut) in the STM. Therefore, a longer development length is required, or the reinforcement must be anchored by hooks or mechanical anchors (headed-end bars). Recent research studies have demonstrated the advantages of headed-end GFRP bars (Benmokrane et al. 2016, Mahmoud et al. 2017). These studies reported that using headed-end GFRP bars improved the mechanical interlock to the bar surface due to its geometry and interface configuration, which resulted in 90% more pull out capacity compared to straight-end bars. In addition, the stress



developed in the headed GFRP bars was more than twice the design values. Thus, the headed-end GFRP bars were introduced in this study to investigate the feasibility of using them in such beams. This paper aims to study the effect of a/d ratio on the behaviour of FRP-RC deep beams with headed-end bars without web reinforcement.

EXPERIMENTAL PROGRAM

Test Specimens

Three large scale concrete deep beams reinforced with Glass (G) FRP headed-end bars were constructed and tested to failure in the W. R. McQuade Structures Laboratory at the University of Manitoba. All specimens had a rectangular cross section (250 mm wide x 590 mm high) and an overhang length of 280 mm. The flexural (longitudinal) reinforcement ratio, ρ , was 1.0%. The test parameter of this study was the shear span-to-depth ratio which varied between 1.0, 1.5, and 2.0. Therefore, the overall length of the specimens varied between 2100, 2600, and 3100 mm. The test specimens were labeled based on the shear span-to-depth ratio. For example, Specimen B1.5 is the beam specimen that has $ald = 1.5$. The details of the specimens are listed in Table 40-Details of test specimens.

Table 40-Details of test specimens

Beam ID	d^* (mm)	a^{**} (mm)	f_c' (MPa)	a/d	Reinforcement ratio, ρ (%)
B1.0	509	520	43	1.0	1.0
B1.5	509	770	46	1.5	1.0
B2.0	509	1020	45	2.0	1.0

* d is the effective depth

** a is the clear shear span

Material Properties

Table 41 shows the properties of the GFRP reinforcing bars. All specimens were constructed using normal-weight ready-mix concrete. The concrete compressive and tensile strengths were determined at the day of testing according to ASTM C39 (ASTM 2012a) and ASTM C 496 (ASTM 2017). The concrete strengths are listed in Table 40.

The headed-ends of the GFRP bars are made of thermoplastic matrix reinforced with short glass fibre, cast at the end of bars at elevated temperature. The end of bars is well developed with rounded grooves on the surface to increase mechanical interlock with the head as shown in Figure 143-a. The head is approximately 100 mm in length with a maximum outer diameter of 50 mm at the end as shown in Figure 143-b.

Table 41- Mechanical properties of GFRP bars

Bar No.	Diameter (mm)	Area (mm ²)	Tensile Strength (MPa)	Modulus of Elasticity (GPa)	Ultimate Strain (%)
15 M	15.9 (19.2)*	198 (291)*	1184	62.6	1.89
19 M	19 (22.4)*	285 (394)*	1105	63.7	1.73

* Effective diameter and cross-sectional area including sand coating.



a)

Bar ended with rounded grooves

b) Configuration of the heads

Figure 143: Details and overview of the bar-head

Test Setup and Instrumentations

Three specimens were tested under a monotonic load acting at the mid-span. All specimens were loaded using a MTS loading machine with a capacity of 5,000 kN. Bearing plates were 150×250×500 mm and 200×250×150 mm at supports and loading point, respectively.

To capture the strain profile in the reinforcement, seven strain gauges were attached to the reinforcement. Also, five linear variable displacement transducers (LVDTs) were installed, three to measure the deflection, the other two were installed to report any slippage between the FRP bars and the heads. In addition, three PI-gauges were installed to capture the propagation and widening of cracks. All instrumentation were connected to a data acquisition system (DAQ) to record the readings during the test. Figure 144 shows a schematic drawing of the test setup.

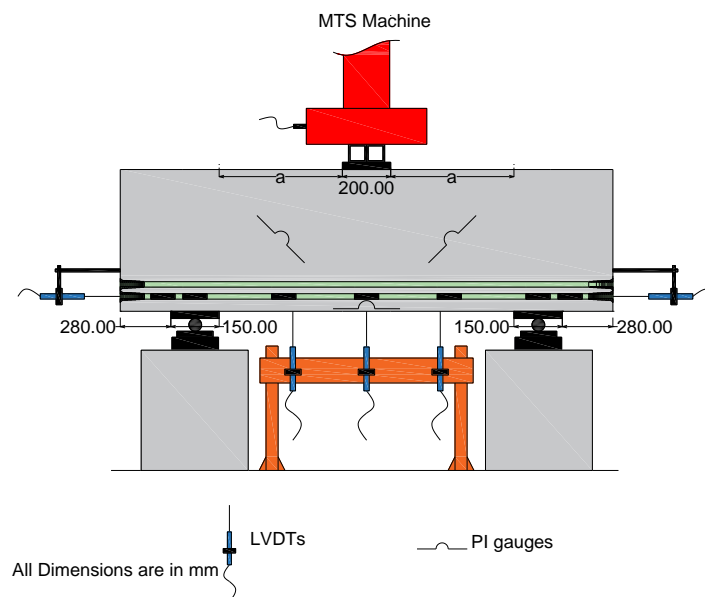


Figure 144: Test setup and instrumentation

TEST RESULTS AND DISCUSSION

Crack Pattern and Failure Mechanism

At early stages of loading, 18-33% of ultimate load, flexural cracks were observed near the mid-span section. The cracks propagated vertically upward to the proximity of mid-height of beam. As loading continues, reaching 38-60% of ultimate load, flexural cracks started to propagate in the shear span, then they became diagonal; parallel to the compression strut aiming at the loading point. At a load of approximately 65-77 % of ultimate load, no more flexural cracks were observed and the rate of widening of flexural cracks decreased after the formation of the diagonal shear crack. With further increase in the load, the width of the diagonal crack increased until failure of specimen. Cracks patterns for the three specimens are provided in Figure 145.

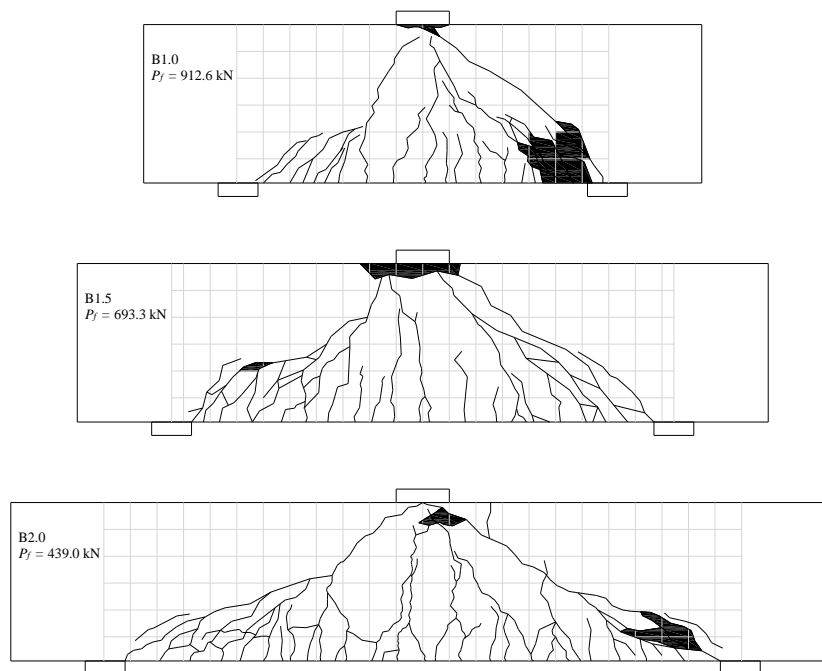


Figure 145: Schematic drawing for crack pattern near failure of test beams

- It was observed that by decreasing the a/d , the shear failure becomes more brittle. No premature failure due to anchorage failure of the tension reinforcement or due to bearing failure at the supports was observed. Three different types of failure occurred in this study. Failure of diagonal compression strut in the region between the loading and supporting plates occurred in specimen B1.0 as shown in

Figure 146-a. This type of failure occurred in a violent and brittle manner. Shear compression failure occurred in specimen B1.5 (

Figure 146-b). Shear compression failure was characterized by crushing of concrete at the tip of the diagonal crack in the flexural compression zone. The diagonal crack extended from the internal edges of the loading and supporting plates. A concrete diagonal tension failure occurred in specimen B2.0, as shown in

Figure 146-c. In this mode of failure, a S-shaped diagonal crack was formed between the inside edges of the loading and supporting plates. A vertical crack developed at the top of the concrete in the shear span and intersected with the diagonal crack leading to a drop in the load-carrying capacity. Similar modes of failure were reported in a previous study by Andermatt and Lubell (2013) for specimens with a/d ranging between 1.07 and 2.08.



Figure 146: Failure mechanisms



Load-Deflection Behaviour

The total applied load versus deflection plots for the three specimens is shown in Figure 147. For all specimens, the load-deflection relationship was approximately bilinear, except specimen B1.0 due to the formation of cracks near the support along with the second diagonal crack that formed the strut resulted in crushing of concrete at the interior edge of the support which allowed more rotation. The behaviour of the specimens were approximately similar before the formation of the flexural cracks where the deflection was of very small values. After cracking, a reduction in the flexural stiffness of the specimens was observed but with different tendencies, which is attributed to the different a/d of each specimen. Decreasing the a/d results in increase in the post-cracking stiffness of beams. In other words, the influence of changing a/d on the load-deflection curve is that the specimen with lowest $a/d = 1.0$ exhibited the steepest curve followed by the specimen with $a/d = 1.5$, then the specimen with $a/d = 2.0$. Similar behaviour was noted in previous studies (Omeman et al. (2008), El-Sayed et al. (2012), Farghaly and Benmokrane (2013), Andermatt and Lubell (2013) and Khaled et al. (2017)).

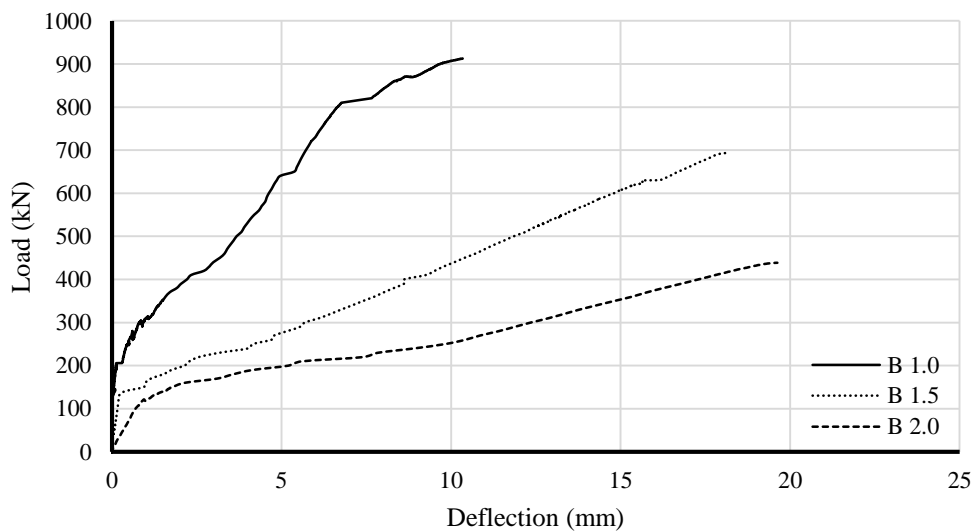


Figure 147: Load-deflection relationship for test beams

Shear Capacity

This study shows that decreasing the a/d has a significant influence on the shear capacity of deep beams reinforced with GFRP bars without web reinforcement as shown in Figure 148. Test results show that increasing a/d from 1.0 to 1.5 resulted in decreasing in the shear capacity by 24%, similarly, a reduction of 37% of the shear capacity was observed with increasing a/d from 1.5 to 2.0. Previous studies (El-Sayed et al. (2012), Andermatt and Lubell (2013)) noted a similar behaviour. The reduction of the shear capacity is attributed to the decrease in the angle of inclination of the strut which adversely affects the efficiency of the compression strut which, in turn, resulted in a decrease in the effect of the arch action. Table 42 shows the load carrying capacity and cracking loads for each specimen.

Table 42: Load carrying capacity

Specimen	Flexural crack (kN)	Flexural shear cracks (kN)	Diagonal crack (kN)	Failure load (kN)
B1.0	160	350	700	912.6
B1.5	90	250	450	693.3
B2.0	90	200	300	439.0

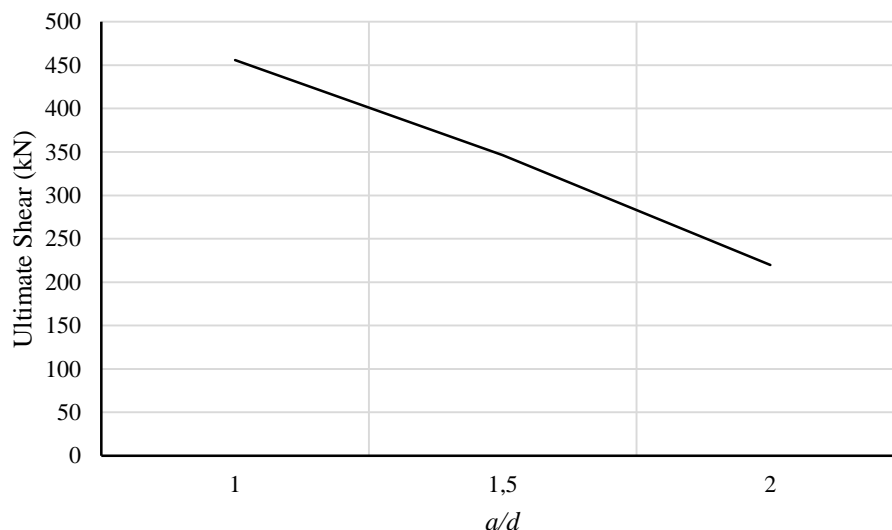


Figure 148: Shear capacity versus shear span to depth ratio

Strains in Reinforcement

For all specimens, the strains in the reinforcement was insignificant until the formation of the first flexural crack. A rapid increase in the strains in the vicinity of the flexural cracks resembling the bending moment diagram. As loading progressed, additional cracks propagated in the shear spans resulted in increasing the strains of the reinforcement near supports. After formation of the diagonal shear crack, a significant increase in the strains over the support occurred, as the strains tend to be similar along the entire length between supports after the development of the tied arch action. The distribution of the reinforcement strain is an indicator of whether a tied arch action is developed in the specimen and to what extent. It is expected to have a fully developed arch action when the strains in the region between supports are approximately similar. Figure shows the reinforcement strain distribution for the specimens B1.5.

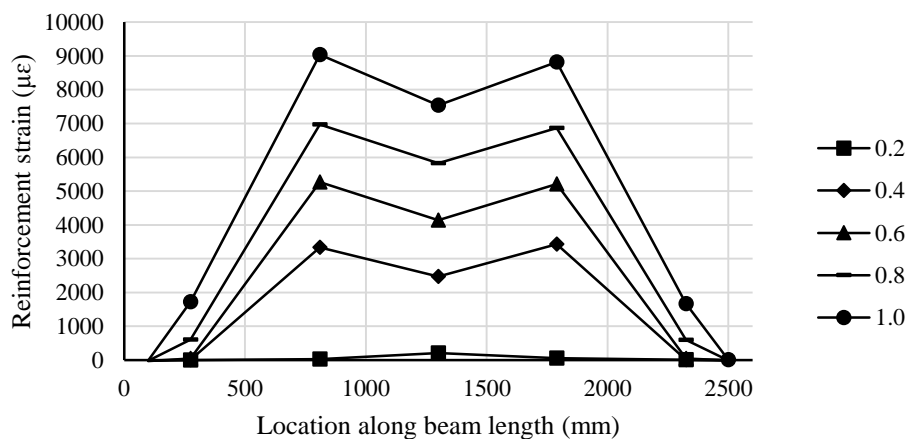


Figure 7: Strain profiles of specimen B1.5

Headed-End Bars

As mentioned previously, the development of the STM in deep beams is confirmed by cracks propagation and the high tensile strains over the supports. These strains indicate that tensile stresses developed in the tie between the two nodes at supports. A longer development length is required after supports than in the case of slender beams such that reinforcement can develop the needed stresses. In previous studies, the development length ranged from 400 to 1000 mm for deep beams with height ranging between 400 to 1200 mm (El-Sayed et al. 2012, Farghaly and Benmokrane 2013 and Mohamed et al. 2017). Andermatt and Lubell (2013) provided overhang length ranging



from 400 mm to 800 mm for specimens with height of 600 mm to prevent the occurrence of the end anchorage failure, as it does not indicate the actual capacity of deep beams. In this study, the required development lengths of each specimen were calculated based on the Canadian standards (CSA/S806 2012) and it ranged between 330 mm to 430 mm. However, only 280 mm was provided as a development length to study the efficiency of the headed-end bars in developing the required tensile stresses in a shorter overhang length. It is worth mentioning that no slippage was observed from the spring LVDTs.

CONCLUSIONS

Based on the presented discussions, the following can be concluded:

With the exception of Specimen B2.0, failure of the specimens was brittle. The majority of the specimens failed after the formation of a major diagonal shear crack extending from the inside edge of the support plate toward the loading plate.

An arch mechanism formed in all specimens. This was confirmed by the crack orientations and measured strains in the longitudinal reinforcement.

The post-cracking stiffness of the FRP-reinforced deep beam specimens decreased as the a/d increased.

The shear strength of the specimens decreased as the a/d ratio increased.

No slippage of reinforcement or signs of end-anchorage failure.

ACKNOWLEDGMENT

The authors wish to express their sincere gratitude to the Natural Sciences and Engineering Council of Canada (NSERC) through the Canada Research Chairs Program. The assistance received from the technical staff of the McQuade Structures Laboratory is acknowledged.

REFERENCES

- Andermatt, M. F., and Lubell, A. S. (2013a). "Behavior of Concrete Deep Beams Reinforced with Internal Fiber-Reinforced Polymer-Experimental Study." *ACI Structural Journal*, 110(4): 585–594.
- ASTM. (2012a). "Standard test method for compressive strength of cylindrical concrete specimens." ASTM C39-12, West Conshohocken, PA.
- ASTM. (2017). "Standard Test Method for Splitting Tensile Strength of Cylindrical Concrete Specimens." ASTM C469-17, West Conshohocken, PA.
- Benmokrane, B., Mohamed, H.M., Manalo, A., and Cousin, P. (2016). "Evaluation of Physical and Durability Characteristics of New Headed Glass Fiber-Reinforced Polymer Bars for Concrete Structures." *ASCE, Journal of Composites for Construction*, 21(2):1-12.
- CSA, "Design and Construction of Building Structures with Fibre Reinforced Polymers (CAN/CSA S806-12)", Canadian Standards Association, Ontario, Canada, 2012, 187 p.
- CSA, "Design and Construction of Building Structures with Fibre Reinforced Polymers (CAN/CSA S806-02)", Canadian Standards Association, Ontario, Canada, 2002, 177 p.
- El-Sayed, A. K., El-Salakawy, E. F., and Benmokrane, B. (2012). "Shear Strength of Fibre-Reinforced Polymer Reinforced Concrete Deep Beams without Web Reinforcement." *Canadian Journal of Civil Engineering*, 39(5): 546–555.
- Farghaly, A., and Benmokrane, B. (2013). "Shear Behavior of Large Reinforced Concrete Beams without Web Reinforcement." *ASCE, Journal of Composites for Construction*, 17(6): 1–10.
- MacGregor, J. G. (1997). *Reinforced concrete: Mechanics and design*, 3rd Ed., Prentice Hall, Upper Saddle River, NJ.
- Mahmoud, k., Ghazy, A., Bassuoni, M.T., El-Salakawy, E. (2017). "Properties of Nanomodified Fiber-Reinforced Cementitious Composites." *ASCE, Journal of Materials in Civil Engineering*, 29(10):1-12.
- Mohamed, K., Farghaly, A. S., and Benmokrane, B. (2017). "Effect of Vertical and Horizontal Web Reinforcement on the Strength and Deformation of Concrete Deep Beams Reinforced with Glass-FRP Bars," *ASCE, Journal of Structural Engineering*, 143(8):1-14.
- Omeman, Z., Nehdi, M., El-Chabib, H. (2008). "Experimental study on shear behavior of carbonfiber-reinforced polymer reinforced concrete short beams without web reinforcement," *Canadian Journal of Civil Engineering*, 35, pp. 1-10.
- Oh, J. K., and Shin, S. W. (2001). "Shear Strength of Reinforced High-Strength Concrete Deep Beams." *ACI Structural Journal*, 98(2): 164–173.
- Tuchscherer, R., Birrcher, D., Huizinga, M., and Bayrak, O. (2011). "Distribution of Stirrups Across Web of Deep Beams." *ACI Structural Journal*, 108(6): 108–115.



INFLUENCE OF DIFFERENT APPROACHES ON DESIGN, DESIGN VALUES AND GENERAL SAFETY FOR INTERNAL FRP REINFORCEMENT

André Weber¹, Faustin Gauffillet,²

*1 Schoeck Bauteile GmbH, R&D, Baden-Baden Germany; 2 Schoeck SARL, Entzheim, France
(corresponding author: andre.weber@schoeck.de)*

KEYWORDS :

Fields applications and case studies; Material ; Codes, standards and design guidelines; FRP internal reinforcement Standards , Design concept

ABSTRACT:

Assuming the physics as well as materials are the same all over the world it seems to be strange, that we have so different design results for FRP reinforced structures, while the design for steel reinforced concrete structures seem to be much more similar.

Especially the question of over- or under-reinforced structures with internal FRP reinforcement has to be posed here again. How the different failure mode has to be taken into account?

How the resistance of FRP is determined. The same bar has different resistance in different regions.

Is there a clear definition of short term loading: Is this 1h, 10h, 100h, 1 year or 10 years. Is there a clear and logical definition of sustained load?

Another question is the size/diameter of reinforcement. While engineers design with required reinforcement areas and can distribute a different number of bars into a structure, some Standards fix local historical sizes known from the steel industry for FRP.

For structures like diaphragm walls, where we have overlap between steel and FRP we need to follow the same design approach for steel as for FRP reinforced parts of the structure. This starts for the partial factors for actions as well as them for different materials.

This paper analyses the different design approaches taking some practical examples from 20 years of experience in this field.

INTRODUCTION

Since more than 20 years there is a growing interest in internal FRP reinforcement. In this time a couple of interesting applications have been developed. It is interesting, that in different regions different applications are in the focus. While in Northern America corrosion applications like bridge decks and barriers are the field of attention in Europe there are temporary and electrical non-conductive applications in the main focus. For these different application groups different design and verification approaches had been followed

FIRST ISSUE: UNDERREINFORCED – OVERREINFORCED

The design distinguishes between two different cases in the design of reinforced concrete. A distinction is made between whether the reinforcement material or concrete limits the capacity. As a common rule, (steel)-reinforced concrete has to be under-reinforced. The reasons for this are the ductility of the reinforcement material and the saving of reinforcement material. We have more than hundred years of experience with this material combination and its design.



When combining two brittle materials such as GRP reinforcement and concrete, the question arose again as to whether such constructions should rather be over-reinforced due to the somewhat greater ductility/deformability of concrete. Shall the safety margins be designed differently depending on whether the cross-sections are over-reinforced or under-reinforced. The cross sections thus determined contain so much reinforcement that the concrete ruptures earlier than the reinforcement.

Such cross-sections are not very deformable. GRP reinforcement sometimes loses a considerable percentage of strength over decades of use. This is not taken into account in the analysis. It is therefore possible that a cross-section is initially overestimated in a design as well as in a short-term test. Over the years, if the material changes the cross-section is under-reinforced.

In contrast to over-reinforced structures the under-reinforced structure shows much more deformability, but the resistance of the FRP has to be predicted correctly.

EXAMPLE

Take the example of a concrete cross-section with a balanced reinforcement cross-section: In order to increase the load capacity, the question arises as to whether we should increase the concrete proportion/cross-section or concrete strength or whether we should increase the amount of reinforcement. For a material that is more than 200 times more expensive than the concrete and has a rated strength of only about 20 times that of the concrete, unless there are other constraints, the logical solution is to increase the static height.

Since reinforced concretes usually have high dead load ratios and therefore a high proportion of permanent loads is usually present, the question of long-term strength arises. Since strength – if short term or long term - is an ultimate limit state, it is necessary to determine not only the level of long term strength but also the probability of failure and a material factor. Information on the exact determination of this strength as well as alternative methods how such a statement can be made from existing time to failure tests are given in Weber14 and fib07 or Keller17

Proposal: There is no strict reason to design over-reinforced or under-reinforced. Therefore both designs should be allowed if the resistances are known and described correctly and safe according a probabilistic safety concept.

SECOND EXAMPLE: NEW MATERIAL WITH INCREDIBLE PROPERTIES:

From time to time new materials come on the market claiming incredible properties. These come from Eastern Europe or Asia and claiming 2.5 times stronger than reinforcing steel and a quarter of the weight. So they claim only one tenth of the material is needed and the construction is cheaper than with reinforcing steel.

Is this verifiable by a bending design?

Modulus of elasticity of this material is 1/4 as B500 and strength 2.5 times as high.

So the elongation of the material is 10 times that of reinforcing steel.

This section according this approach is extremely under-reinforced.

If we want to design a cross-section with such a quantity of reinforcement in practice, we have to check:

What is the remaining concrete compression section?

Is the concrete in the compression section possibly overloaded?

What is the long-term strength of the material?

Other questions are:

What is the crack width?

What is the distance between the cracks?

How big is the deflection?



If realistic assumptions and specifications are applied to the design, it can be noted that only in very few cases a smaller reinforcement cross-section than reinforcement steel can be expected. As soon as the deflection or the crack width has to be limited, usually higher cross-sections have to be chosen with lower modulus reinforcement.

THIRD EXAMPLE: LOCAL STANDARDIZATION WITHOUT PHYSICAL REASONS.

Several decades ago most countries of the world have decided to accept the international unit system to simplify exchange of technical documentation and goods. There has been no official ratification in the Myanmar, Liberia and the U.S. But SI-Units are accepted units in the US since a decree of the government in 1894.

Steel rebars are on the market in different sizes and qualities worldwide. There are product and material standards for steel rebars all over the world in national and international versions. Now the composite rebar industry is dealing with the same wishes in different countries. Canada which is a “metric” country has chosen a compromise by introducing so called “soft metric” sizes which have more or less the same sectional areas like the traditional American rebar sizes. In many specifications the size and the number of bars are taken into account. As the metrical 12mm is different to the American half inch or the Canadian 13mm, metrical sizes are not accepted in different applications.

At the end the engineer has a limited local choice only.

This is even worse as not only sizes differ but also design approaches. The scientific world should here make an appeal to the different national Standardization bodies to prevent such developments

EXAMPLE: BASICS FOR DESIGN AND PERFORMANCE BASED COMPARISON OF MATERIALS

The application of bars made of glassfiber reinforced polymer (gfrp) is widely known from a perspective of the application on site, especially in launching and reception situations for tunnels driven by tunnel boring machines (TBM) which are commonly used for major constructions. Currently there is no common standard in place in terms of product properties or design procedures for gfrp reinforcement bars.

This section aims at giving basic information about design concepts for structural members with gfrp reinforcement bars, the influence of physical properties and also outlines the crucial points for an optimal choice of materials.

GFRP reinforcement for structural applications

Some basics for different application fields of GFRP rebar have been addressed in “Tunnels et Espace Souterrain”. This article focuses on the application of GFRP rebar as structural reinforcement.

How can these properties be applied in structural calculations and detailing to achieve a consistent design concept on the basis of existing codes?

Currently no common standard for material properties or for required tests for glass fibre rebar is available. Properties of all the different materials on the market differ greatly. This is strongly influenced by the application the producers have aimed at when developing their product.

The range of glass fibre bars stretches widely. Examples are:

- a. Materials for the stabilisation of the working face in tunnelling that will be out of function after only some weeks,
- b. Temporary anchors for construction pits with lifetimes of up to several months,
- c. Penetration areas of shaft walls for tunnelling with usually planned lifetimes of two to five years to cover uncertainties during the process of tunnel construction to
- d. Long term applications as foundations for transformers or permanent structures with up to 120 years of design life.

Lifetime under sustained loads is a crucial factor to choose the optimal glass fibre rebar type/1,3,4,8/.

Glass shows linear elastic behaviour and brittle failure – a perfect example of Hooke’s law without yielding as known for steel. With a Young’s modulus of about 70 GPa to 90 GPa, pure glass is significantly softer than steel (about 200 GPa). Comparing same sections of steel and glass under the same force, the strain will differ according to the ratio of the Young’s modulus of the two materials.

Different glass fibre rebar materials will also show different behaviour under tensile stresses: The type of glass fibre will control the Young’s modulus of the fibres. The ratio of glass fibres in the cross section will lead to the combined Young’s modulus of the products.

The typical range of Young’s modulus of GFRP rebar products on the market is from 36 GPa to more than 60 GPa.

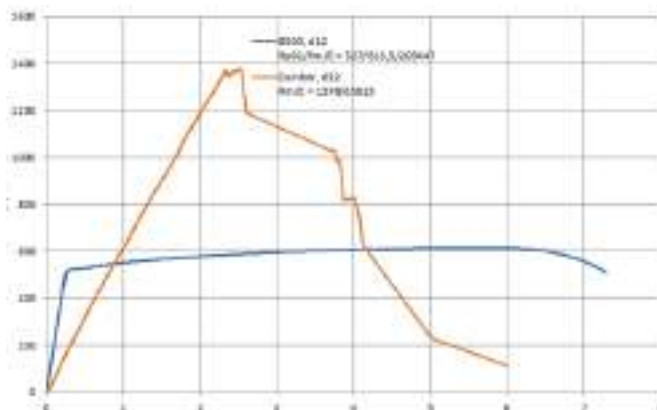


Figure 1: “Stress-strain diagram comparing different materials”

Interaction of glass fibre rebar with concrete

For a first design idea of reinforced concrete a simple framework model can be considered. A beam made of concrete with reinforcement offering different stiffness will show different stress distribution.

In Figure 1 the influence of different materials is shown. For the less stiff rebar material, the strain under same loads is higher. This leads to a concentration of the concrete compression zone. The stress distribution is depending on the stiffness of the rebar material and the concrete grade. For a similar stress distribution in the concrete member, more cross-section of a less stiff product is required.

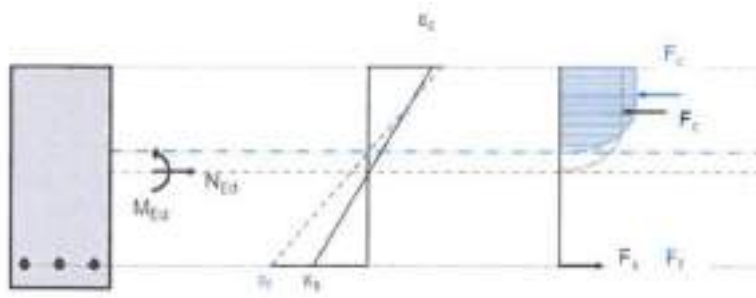


Figure 2: “Stress-distribution in beam for materials with different Young’s modulus but same cross-section of reinforcement”

In figure 2 is to be seen that higher stress in the concrete is the consequence of high strain reinforcing materials. Glass fibre rebars offer lower Young’s modulus and higher strength compared to reinforcing steel. So the concrete compression zone will often be controlling the total flexural capacity of a concrete member. Increasing of the flexural capacity requires for either higher concrete grades or stiffer reinforcement materials to reduce strain in the reinforcement and increase the height of the concrete compression zone.

TIME DEPENDENT BEHAVIOUR UNDER SUSTAINED STRESSES



According to all international guidelines for the design of glass fibre rebar an effect called “creep rupture” needs special attention for the design with glass fibre rebar. Environmental conditions such as moisture, ultraviolet radiation, high alkaline environments and elevated temperature influence the endurance time of glass fibre materials/9,11,13/. For 100 years this is certified in an approval /10/.

The latest issues of the guidelines as ACI 440.1 R15/3/ and FIB TG 9.3 Bulletin 40/5/ refer to a linear relationship of sustained stresses and the logarithm of time. Taking this phenomenon into account and a starting point at 100 hrs, one year (8760 hrs) is nearly half way down the effects at 100 years. So even for short lifetimes the endurance time needs to be considered in design for glass fibre materials. FIB TG 9.3 describes in Bulletin 40 that the slope for extrapolation shall be determined in material specific long term tests under realistic conditions. – The level of stress that may be used for design is controlled by the material quality, production process and blend of components.

DESIGN APPROACHES

Currently EC2 does not cover alternative reinforcement materials to steel. The design concepts or guidelines for glass fibre rebar available on the market do, however, refer to specific codes.

Two main concepts are currently used: One is the approach on basis of the ACI 318 (United States) together with the ACI guideline 440.1 R15. There is also an Italian Guideline by CNR/14/ under which refers to quite similar ideas as the ACI concept but offers the option to enter into a Euro code design. A fully EC based concept has been developed by the FIB (Fédération Internationale du Béton) in Lausanne, Switzerland – The institute that produces the model code as predecessor of the Euro code concepts.

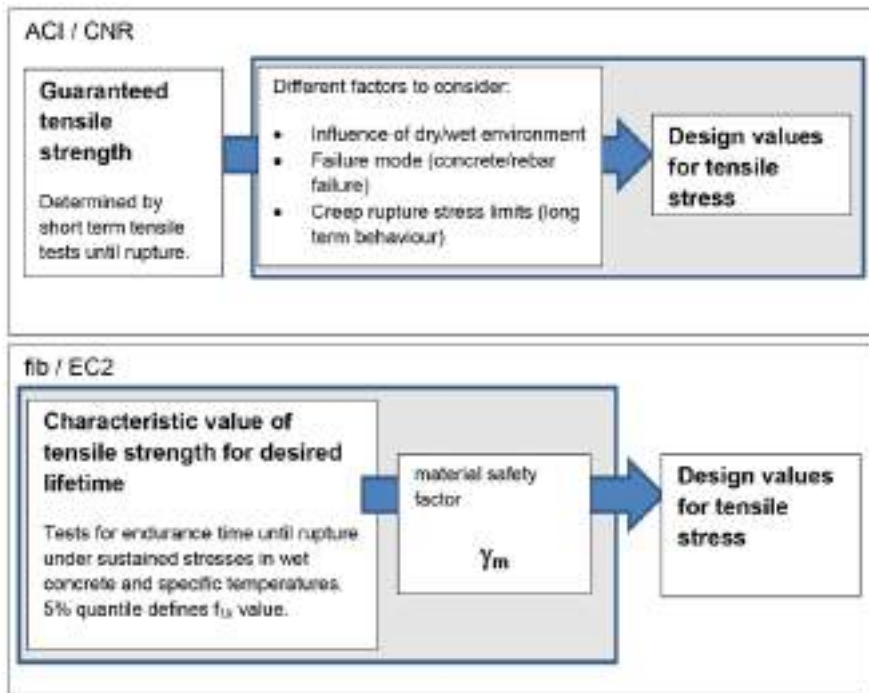


Figure 3: Schema for determination of design values according to different code and guideline concepts

Both of these concepts, the American approach and the Euro Code approach follow each their own individual logical concept of the two codes for steel reinforced concrete and cannot be mixed.

Lifetime considerations according to different concepts

All guidelines report about the creep rupture phenomenon and its need for consideration for the design. The main differences of these concepts for tensile strength are shown in figure 3 (simplified).



According to ACI 440.1 R15 /3/ the stresses under sustained loads shall be limited to a certain level to cope with long term effects. This means that environmental factors and long term considerations are combined and subject to an additional SLS check for creep rupture. The ACI concept (as well as the CNR) uses very basic and easy-to-test mechanical short term properties and pre-defined factors as a basis for design values. Product specific behaviour in terms of lifetime is not considered with regard to the large range of different materials available.

FIB TG9.3 Bulletin 40 /7/ suggests product specific tests under realistic conditions over a period of at least 1000 hours to determine characteristic values for the specific material (5% quantile). From there design values can be achieved by application of a material safety factor as for all materials in the EC concepts.

The biggest difference of these two concepts is that ACI 440.1 R15 /3/ applies global, not material-specific safety factors and FIB takes product specific quality into account. Already in the introduction of this article different aims for the development of different glassfiber bar products have been mentioned.

It is strongly recommended not to mix different code concepts as the safety levels of different concepts vary. Furthermore a material specific lifetime approach as in the FIB concept will lead to more economical design of GFRP reinforced concrete members.

Optimal choice of products and comparison of glass fibre materials

All materials on the market offer very different properties. Acting as electrical isolation or easily being cut by TBM is a common material quality of many available products.

All products have their specific application field for which they are developed. Only there they will offer their full performance in terms of their specific material properties. Tests methods are given in /2,4/, Different performance is shown in /6,11,13/

Codes / Guideline concepts and consideration of lifetimes under sustained load also strongly influence the choice of economical material use in concrete.

Factors influencing the optimal choice are:

- Code / guideline concept (together with material specific considerations and safety concept)
- Applicable design tensile strength for the desired lifetime
- Stiffness of the material for optimal stress distribution in total concrete member
- System specific considerations: Geometry, concrete grade, level of bending moments and shear loads. – Indicating if stresses in reinforcement or concrete failure will be controlling total capacity
- Total reinforcement quantity (enough space in tension zone to include all the required cross section? Still sufficient space for proper flow of concrete?)

Based on these factors, a comparison of different glass fibre materials needs to be made on the basis of material performance. Comparing on the basis of price per ton will ignore the effect that for the same performance a different amount of rebar of different types is required.

An example is the Station “Clamart” on the Grand Paris railway scheme, France: The required lifetime for tunnelling shafts has been defined to 5 years to cope with possible obstacles during construction process. Two different materials have been taken into account by the contractor. The result was a difference in required cross-section of more than 250% in this specific project on the basis of the different performance of the products as long-term reduction was taken into account as stated in the guideline /14/.



Picture 4: Installation of a diaphragm wall cage at the future station of Clamart on the Grand Paris scheme end of 2016

CONCLUSION AND OUTLOOK:

GFRP rebar offers options as a reinforcement material where steel reaches its limits.

No common code is in place for the design of this type of reinforcement material. Current guidelines offer a good basis to design with glass fibre reinforcement on a technically safe basis. Chosen codes and linked guidelines shall be followed thoroughly and not mixed.

Quality of materials differs greatly, so only performance based comparison of materials can lead to reliable results. Comparing on a basis of price per ton ignores the different properties of products and may lead to either unsafe or over-engineered solutions.

In the upcoming generation of Euro Code 2 /5/ it is also planned to include also design concepts for alternative reinforcement materials such as glass fibre rebar.

REFERENCES

- Weber A, Advanced reinforcement technology with GFRP Rebar. Proc. 2nd International fib congress. Naples 2006
- ACI 440.3R04 Guide Test Methods for Fiber-Reinforced Polymers (FRPs) for Reinforcing or Strengthening Concrete Structures, American Concrete Institute, Farmington Hills, Mich.2004,
- ACI 440.1R15 Guide for the Design and Construction of Structural Concrete Reinforced with FRP Bars American Concrete Institute, Farmington Hills, Mich. 2015,
- CSA-S806-10 Canadian Standards Association 2010. Design and Construction of Building Components with Fibre-Reinforced Polymers, CSA, Mississauga, Canada, 2010.
- CEN/TC 250/SC 2/WG 1/TG 1 PT1prEN 1992-1-1:2017-10 Eurocode 2: Design of concrete structures – Part 1- General rules, rules for buildings, bridges and civil engineering structures
- CHAMBERS J J, BURGOYNE C J An experimental investigation of the stress-rupture behavior of parallel-lay aramid rope Journal of Material Science 25 (1990) 3723-3730
- FIB Federation internationale de beton fib 2007. Bulletin 40. FRP reinforcement in RC structures, fib, Lausanne, Switzerland 2007.
- GREENWOOD, M. 2001. Durability: A Key Value. Composites 2001 Convention and Trade Show, Composites Fabricators Association, Tampa, Florida, USA.



WEBER A., WITT C. Representative Application-based Temperatures for Durability Testing in Green M. Proceedings ACMBBS-VI Kingston ON 2012
Z-1.6-238 abZ Bewehrungsstab Schöck Combar aus glasfaserverstärktem Kunststoff Berlin 2008, 2014
WEBER A., VOLKWEIN A. Durability based approach for design values of FRP bars, Proceedings FRPRCS 8, Patras, Greece, 2007
WEBER A. From National Approval to an European Standard - Ways to a Safer and Wider Application of FRP Rebars Proceedings FRPRCS-11 Joaquim Barros & José Sena-Cruz (Eds), Guimarães, 2013
Keller M.L., Pahn, M. Long-term-performance of Loaded GFRP Bars in Alkaline Environment in ACIC Proceedings Sheffield 2017
CNR DT203 Guide for the Design and Construction of Concrete Structures Reinforced with Fiber-Reinforced Polymer Bars - National Research Council Italy 2006



CONTRIBUTION OF SHEAR TRANSFER MECHANISMS AND STRENGTH OF GFRP REINFORCED CONCRETE BEAMS

D. D. E. Pacheco 1, D. C. T. Cardoso 1 and M. Noël 2

¹ Pontifical Catholic University of Rio de Janeiro (PUC-Rio), Department of Civil and Environmental
Engineering, Brazil, E-mail: dctcardoso@puc-rio.br

² University of Ottawa, Department of Civil Engineering, Canada

ABSTRACT

This paper aims to discuss the shear behavior and strength of concrete beams internally reinforced with glass-fiber reinforced polymer (GFRP) longitudinal bars, with and without stirrups. The partial results of an ongoing experimental program intending to investigate the crack kinematics and contribution of different shear transfer mechanisms to the final strength are presented. The test results for two dowel specimens and six beams subjected to four-point bending are reported. Digital image correlation (DIC) was used to gather information about crack opening and sliding throughout the tests and the measured kinematics were used as inputs in theoretical models. The approach was validated with the experimental results and was used to quantify the participation of each shear mechanism. It is shown that the contribution of aggregate interlock gradually reduces as the crack opens, whereas participation of stirrups linearly increases up to failure.

KEYWORDS

GFRP reinforced concrete, Shear transfer mechanisms, Shear strength, Digital image correlation.

INTRODUCTION

Shear problems in reinforced concrete (RC) beams have been investigated for more than a century, but the complexity involved in the phenomenon still draws the attention of researchers interested in understanding how each load transfer mechanism contributes to the final strength. The recent works of Yang (2014), Ruiz *et al.* (2015) and Huber *et al.* (2016), for example, studied the problem from a different perspective, considering participation of shear mechanisms in an attempt to develop a comprehensive mechanical approach to strength.

The use of GFRP RC members has increased in the last years, especially due to superior corrosion resistance, electromagnetic transparency and high strength to weight ratio of the reinforcement. However, its relatively low modulus of elasticity if compared to conventional reinforcing steel results in a greater flexibility and the formation of wider cracks. A considerable number of studies in GFRP RC beams have been carried out for about 20 years and some of the remarks made by researchers who dedicated efforts to the problem on the shear behavior are: i) in beams with stirrups, failure is governed by rupture of stirrups near the bent corner; ii) larger crack widths; iii) small compression block; iv) reduced dowel action; and v) significant influence of reinforcement stiffness (e.g. Alkhrdaji *et al.*, 2001, Yost *et al.*, 2001, El-Sayed *et al.*, 2006). However, most of the studies have been dedicated to validation of design equations.

This work is part of an ongoing research program intending to investigate the kinematics of cracking and contribution of different shear transfer mechanisms to the final strength of GFRP RC beams. The experimental test results for dowel specimens and beams with shear span to effective depth (a/d) ratio of 1.7 are reported and the procedure adopted to gather information about crack opening and sliding using digital image correlation (DIC) is described. The measured kinematics are then used as input for theoretical models, allowing quantification of the participation of each shear transfer mechanism to the beam strength. The used approach consists of a simplified adaptation of the method adopted by Huber *et al.* (2016).

MECHANICAL MODELS FOR SHEAR MECHANISMS

Aggregate Interlock

Many models accounting for crack dilatancy have been proposed in literature to correlate shear (τ_{ag}) and normal (σ_{ag}) stresses with the crack opening (w) and sliding (s). In this work, the so-called contact density model proposed by Li and Maekawa (1987) is used, which has been successfully adopted in literature for comparisons with experimental results (e.g. Soetens and Matthys, 2017). The basis of the model consists in assuming that a crack plane is comprised of contact areas with inclinations, θ , ranging from $-\pi/2$ to $\pi/2$. A contact density probability



function, $\rho(\theta)$, is proposed to describe the distribution of contact angles throughout the crack and the effective stresses are obtained after integrating the fundamental mechanical equations for the interval of θ considered. Assuming $\rho(\theta)$ using a trigonometric function, the authors were able to obtain simple equations for $\tau_{ag}(w,s)$ and $\sigma_{ag}(w,s)$, as follows:

$$\tau_{ag} = k \frac{s^2}{w^2 + s^2} \quad (1)$$

$$\sigma_{ag} = k \left[\frac{\pi}{2} - \tan^{-1} \left(\frac{w}{s} \right) \frac{ws}{w^2 + s^2} \right] \quad (2)$$

in which $k = 3.83f_c^{1/3}$ (in MPa) is a constant depending on the concrete compressive strength, f_c . To account for the reduction in the area of contact due to crack opening, Li and Maekawa suggested an effective area coefficient $K = (1 - 2w/d_g)$, where d_g is the average aggregate size. It is also important to note that Eqs. 1 and 2 were developed for normal concrete exhibiting rough crack surface and a different contact density function must be used for mortars and concretes having small coarse aggregate (Bujadham *et al.*, 1992). To take into account a flatter crack, Model Code (2010) suggests stresses to be multiplied by an aggregate effectiveness factor $C_f = 0.35$. For a beam, τ_{ag} and σ_{ag} vary along crack length, ℓ_c , and the shear contribution due to aggregate interlock, V_{ag} , can be computed as:

$$V_{ag} = C_f b \int_0^{\ell_c} K(\tau_{ag} \sin \alpha - \sigma_{ag} \cos \alpha) ds \quad (3)$$

where b is the beam width, and α is the crack angle with respect to the beam longitudinal axis.

Dowel Action

To model the dowel action, the equations proposed by Baumann and Rüschi (1970) are still widely adopted in studies related to this effect. The approach, as many others available in literature, consists in considering the longitudinal reinforcement as a beam on elastic foundation. The cracking load due to dowel action is obtained assuming a rectangular stress distribution and is given by the following simple equation:

$$V_d = f_t b_n \ell \quad (4)$$

where f_t is the concrete tensile strength, b_n is the effective width of concrete in tension between reinforcement and ℓ is the length of the rectangular stress block. Baumann and Rüschi proposed an empirical formula for ℓ , based on regression of experimental results, observing that it increases with the reinforcing bar diameter, ϕ . In the presence of stirrups, after the formation of the longitudinal splitting crack, the deflection of bars due to dowel action are elastically restrained by the transverse reinforcement. This effect was also studied by Baumann and Rüschi, who proposed an empirical load-deflection curve for members reinforced with conventional steel. In this work, it is simply considered that the stirrup carries all the load when intercepted by the longitudinal splitting crack and, therefore, its contribution can be determined similarly to other stirrups.

When the crack is located near the lower branch of the stirrup, stresses are high at this fragile zone and premature failure may occur at the bent corner (e.g. Alkhrdaji *et al.*, 2001). Ahmed *et al.* (2009) developed specific experimental tests to quantify the capacity of stirrups or bent bars governed by this rupture mode and concluded that the strength can be as low as 30-45% of that corresponding to a straight bar.

Uncracked Concrete

A portion of the shear force can be transferred through the uncracked compression zone of the beam. It is therefore influenced by the depth of this zone, which is also associated to the shape of the critical shear crack (Huber *et al.*, 2016). This effect is neglected in the present work, since all tested beams exhibited very narrow or imperceptible uncracked zones.

Stirrups

When a shear crack intercepts stirrups, besides tension forces associated to crack dilatancy, additional flexure, shear and kinking of reinforcement occurs. To account for this effect, shear friction models for GFRP RC have been proposed in literature to estimate stresses as a function of crack motions (e.g. Connor and Kim, 2016). However, these secondary effects may be ignored if the bending stiffness of the transverse reinforcement is low.



The contribution of each stirrup intercepted by the crack depends on the bond-slip relationship (τ - δ) between stirrup and concrete, which in this case is assumed to be described by a bilinear function, as follows:

$$\tau = K_y \delta \quad \text{for } \delta \leq \delta_y \quad (5a)$$

$$\tau = \tau_y \quad \text{for } \delta_u \geq \delta > \delta_y \quad (5b)$$

where K_y is the bond-slip initial stiffness, δ_y and δ_u are the critical and pullout slip, respectively, and τ_y is the maximum bond stress developed. These parameters vary according to concrete properties, confinement and bar roughness and can be adjusted to pullout tests reported in literature (e.g. Baena *et al.*, 2009). As an approximation, the following values have been assumed in the present work: $K_y = 10$ MPa/mm, $\tau_y = 8$ MPa, $\delta_y = 0.8$ mm and $\delta_u = 3$ mm. The stirrup load at the cracked section vs sliding at the loaded end relationship (V_s - δ) can, then, be determined by solving the differential equations for the pullout of bar with a certain embedment length (e.g. Yankelevsky, 1985). For $\delta < 2$ mm, the relationship can also be approximated by a bilinear function:

$$V_s = K_{sw} \delta \quad \text{for } \delta \leq \delta_y \quad (6a)$$

$$V_s = K_{sw} \delta_y + K_2 (\delta - \delta_y) \quad \text{for } \delta > \delta_y \quad (6b)$$

where K_{sw} and K_2 are respectively the force-slip initial and post-critical stiffnesses. In the present work, for the bond-slip relationship assumed and a 200 mm long bar having diameter of 8 mm, $K_{sw} = 400$ MPa/mm and $K_2 = 50$ MPa/mm. It is important to highlight that crack opening at the stirrup position, w_s , is the sum of slides for both sides of the crack. For example, if the crack intercepts the middle of a stirrup, $w_s = 2\delta$.

EXPERIMENTAL STUDY

The experimental program was divided into 3 parts: i) material characterization; ii) dowel action tests; and iii) beam tests. The testing matrix is summarized in Table 1.

Table 1: Testing matrix

Test	Number of specimens	Longitudinal Reinforcement (Bottom)	Longitudinal Reinforcement (Top)	Transverse Reinforcement
Dowel 2L	1	2 ϕ 12.5 mm	-	-
Dowel 3L	1	3 ϕ 12.5 mm	-	-
Beam 3L-NS (A to C)	3	3 ϕ 12.5 mm	-	-
Beam 3L-S (D to F)	3	3 ϕ 12.5 mm	2 ϕ 10 mm	ϕ 8 @ 150 mm

All concrete specimens were fabricated using normal weight concrete for a target compressive strength of 30 MPa at 28 days. The adopted design mix is presented in Table 2. Portland Cement with 6-10% limestone filler and coarse aggregates with average size of 4.8 mm and maximum size of 9.5 mm were adopted. Tests using larger aggregate particle sizes are underway to study the influence of aggregate interlock. After casting, specimens were moist cured for 2 days followed by 26 days of air curing, for a total of 28 days.

Table 1: Concrete design mix (kg/m³)

Beam	BR
Cement	361
Dry artificial sand	853
Coarse aggregate (< 9.5 mm)	916
Water	191
Superplasticizer	5.4 (1.5%)

Helically wrapped GFRP bars supplied by a single manufacturer were adopted in the study, as shown in Figure 1. For the longitudinal reinforcement, 13 mm diameter bars were used, whereas bars with 8 mm diameter were used for the stirrups.

Material Characterization

To obtain the actual properties of materials adopted in the study, mechanical characterization tests were performed. Five specimens extracted from GFRP longitudinal bars were tested in tension according to recommendations of



ASTM D7205M – 06 (2016). Ten 100x200 mm cylinder specimens cast along with each concrete beam were also produced. Compression tests were carried out to determine stress-strain behavior and cylinder splitting tests were conducted to obtain the tensile strength.

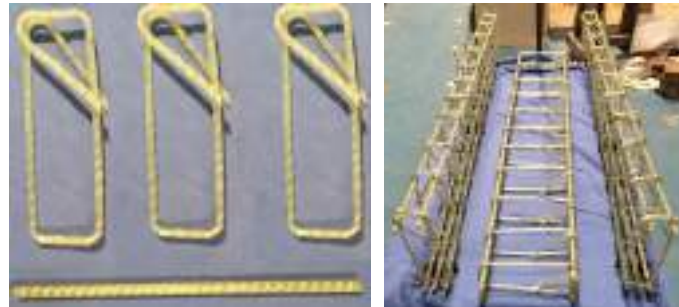


Figure 1 – GFRP bar and stirrups

Dowel Action Tests

Two specimens with dimensions of 150 mm wide 250 mm deep and 1550 mm long internally reinforced with single layer of two and three longitudinal bars were tested in bending using a setup configuration similar to the one proposed by Krefeld and Thurston (1962). No stirrups were adopted in order to determine the minimum dowel action resistance of the longitudinal GFRP bars. To ensure load transfer exclusively by dowel action, expanded polystyrene was used between the surface of the internal loading block and the rest of the beam. Pairs of displacement transducers were positioned at the center of the loading block and at the edges of the gap between the concrete beam and the internal block, i.e. near the points of application of dowel force, for a total of six transducers. The load was applied to the top of the centered internal block using a steel fixture and testing was conducted in displacement control at a rate of 0.3 mm/min. Figure 2 illustrates the test setup.

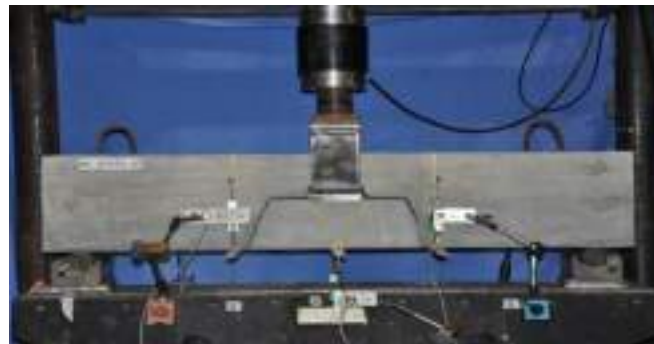


Figure 2 : Setup for dowel action test

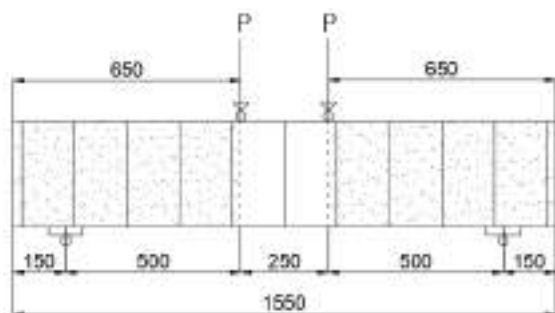
Beam Tests

To investigate the shear behavior, a total of six concrete beams with cross-section dimensions of 120x300 mm were tested in a four-point bending configuration, with total and shear spans respectively of 1250 and 500 mm. All beams were reinforced longitudinally with three bars of 13 mm at the bottom side, leading to a reinforcing ratio of approximately 1.1%. For three beams, transverse reinforcement using 8 mm diameter stirrups every 150 mm was adopted along with two longitudinal bars of 10 mm at the top, for cage assembly purposes. A scheme of the test performed is illustrated in Figure 3a.

To gather information about crack kinematics, digital image correlation (DIC) technique was adopted. This optical non-contact method can be used to find the motions of chosen targets in a series of digital images relative to an initial undeformed state (Dutton, 2012). Prior to testing, the beam surface was prepared with white paint before application of a random speckle pattern with a black spray. A light source providing diffuse light was used to mitigate glare/reflections and images were recorded every minute during the test using two cameras with resolution greater than 3.0 megapixels. The specimens were loaded in displacement control at a rate of 0.3 mm/min up to failure. An overview of the testing setup is presented in Figure 3b.

RESULTS AND DISCUSSIONS

The results obtained in the material characterization tests were satisfactory and are reproduced in Table 3. It can be concluded that the compressive strength of the concrete was between 30 and 40 MPa while the splitting tensile strength was between 2.0 and 3.0 MPa. For the GFRP bar, an average tensile modulus and strength respectively of 46.3 GPa and a 630 MPa were obtained.



(a) Testing scheme (dimensions in mm)



(b) Overview of test setup

Figure 3: Beam test configuration

For the dowel action tests, maximum shear forces of 10.6 and 10.3 kN were obtained for members reinforced with 2 and 3 bars, respectively. While the use of more bars is associated to a reduction in the concrete effective area subject to tension, the bending stiffness increases, mobilizing a longer length subject to tensile stresses. Although only one test of each was performed, it seems reasonable to say that, in the cases studied, these two effects canceled and the peak loads are similar. On the other hand, the relative displacement corresponding to peak load is lower for the specimen with 3 bars, which is related to greater stiffness. After the bottom portion of the beam started detaching, a growth in displacement could be observed under an approximately constant load. Details of the test can be seen in Table 3 and in the load-displacement curves presented in Figure 4a.

All beam specimens exhibited flexural cracks in the constant moment region prior to cracking in the shear span. Maximum loads and corresponding displacements are summarized in Table 3 and load-displacement curves for all specimens are presented in Figure 4b. Typical failure modes are reproduced in Figures 5a and 5b.

For the beams without stirrups, the peak load coincided with the formation of the critical shear crack. After cracking, the load gradually reduces as deflection increases, resulting from the loss of aggregate interlock as the crack opens. At this stage, dowel action apparently provides a significant contribution to the strength and pronounced longitudinal splitting can be observed. The crack shape exhibited a slope with respect to the longitudinal direction ranging from approximately 25-30° near the loading point to 50-60° at the bottom.

For beams with stirrups, steeper cracks developed within the spacing between stirrups and shorter or indistinguishable longitudinal splitting at the level of reinforcement was observed. For all specimens, critical shear crack formed at loads around 25-30 kN but, after this, a combination of aggregate interlock and dowel action contributed to the strength. It is important to note that stirrups were only intercepted at the top and bottom of the crack. Abrupt failure was observed due to rupture of the stirrup at the bent corner, as shown in Figure 5c. Although a greater dispersion of results could be observed, the shear strength for beams with stirrups was up to 3 times greater than that for beams without stirrups.

Table 3: Summary of results

Specimen	f_c' (MPa)	$f_{t,sp}$ (MPa)	V_{max} (kN)	δ (mm)
Dowel 2L	44.0 ± 0.3	-	10.6	0.38 ¹
Dowel 3L			10.3	0.25 ¹

Beam 3L-NS A			28.7	4.45 ²
Beam 3L-NS B	37.8 ± 0.2	2.66 ± 0.59	29.3	6.00 ²
Beam 3L-NS C			33.0	5.70 ²
Beam 3L-S D			79.1	19.4 ²
Beam 3L-S E	32.3 ± 0.8	2.57 ± 0.06	59.0	11.3 ²
Beam 3L-S F			92.7	18.9 ²

¹ relative displacement, corresponding to initiation of longitudinal splitting

² absolute, corresponding to peak load

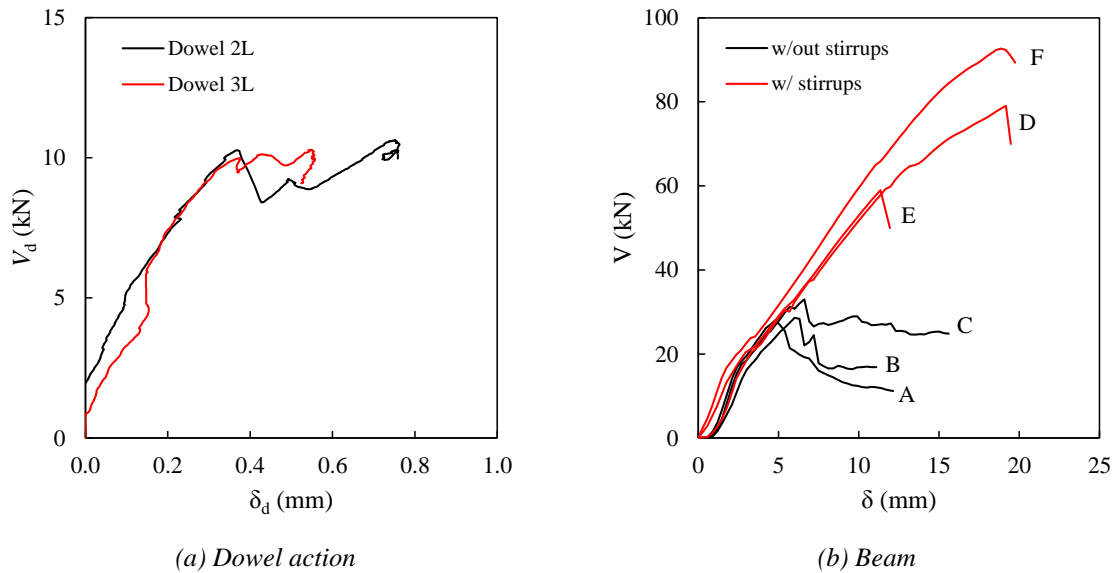


Figure 4: Load-displacement curves

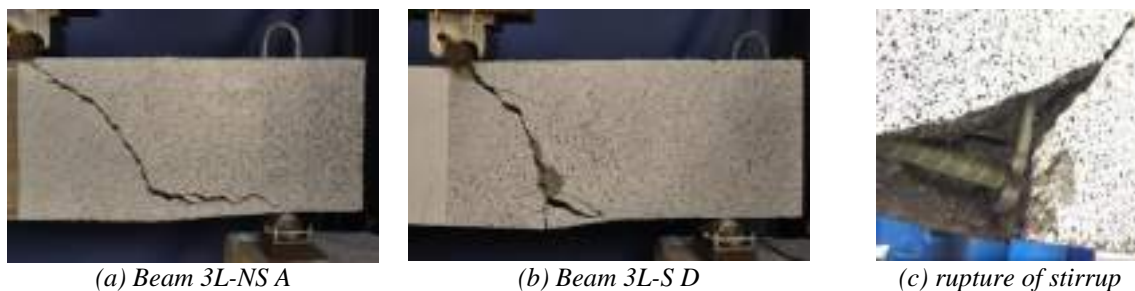


Figure 5: Typical failure modes of tested beams

To study the contribution of shear transfer mechanisms, DIC software GOM Correlate (GOM, 2009) was used to capture crack kinematics. To carry out a simplified analysis, crack shape was divided into two straight segments and their length and slope angles were measured. At the middle of each segment, a pair of points perpendicular to the crack was selected, as shown in Figure 6. Moreover, for beams with stirrups, a pair of points parallel to each stirrup was selected. Displacements were measured for each of the point and crack openings and slidings were determined trigonometrically. Finally, theoretical models described previously were used to determine the resulting forces associated with each shear mechanism. In Figure 7, illustrative load-deflection curves for beams A and D are presented. Predictions using theoretical models corresponding to some conditions are plotted along with the experimental results, showing a good agreement. Contribution of each shear transfer mechanism is also presented in the graphs. It can be seen that, for beams without stirrups, after shear crack formation, strength is provided by a combination of aggregate interlock and dowel action and gradually reduces as the crack opens (loss of interlock). For beam D, only stirrups at the top and bottom of the crack were intercepted. At the end of the elastic limit, strength is provided by 'left' stirrup, aggregate interlock and combined action of longitudinal bar and 'right' stirrup. It can be noted that aggregate interlock reduces whereas contribution of stirrups increases up to

failure. Differences between experiments and theory can be explained mainly by an underestimate prediction of aggregate interlock.

CONCLUSIONS

This paper presented a brief review on the mechanical models for shear transfer mechanisms for reinforced concrete beams. Six tests were conducted on GFRP RC beams to investigate the shear behavior of beams with and without stirrups. In addition, dowel action tests were carried out in order to evaluate the contribution of longitudinal GFRP bars to the shear transfer through cracked zones. Based on the results provided throughout the paper, the following conclusions are drawn:

- beams with stirrups showed steeper cracks and shear strength up to 3 times greater than that for beams without stirrups. Failure was governed by rupture of stirrup at the bent corner;
- DIC seemed to be an easy and adequate technique to gather information about opening and sliding of cracks with loading;
- comparing shear loads obtained experimentally and using theoretical models with actual measured crack kinematics, good agreement was achieved. After validation, participation of each shear transfer mechanism on the strength could be obtained and the clear reduction of aggregate interlock as crack opens can be observed;

Beam tests using different types of aggregate particle sizes and types of bars are underway to validate the approach for other conditions and push-off and pullout tests are being carried out to obtain actual aggregate interlock and bond-slip relationships.

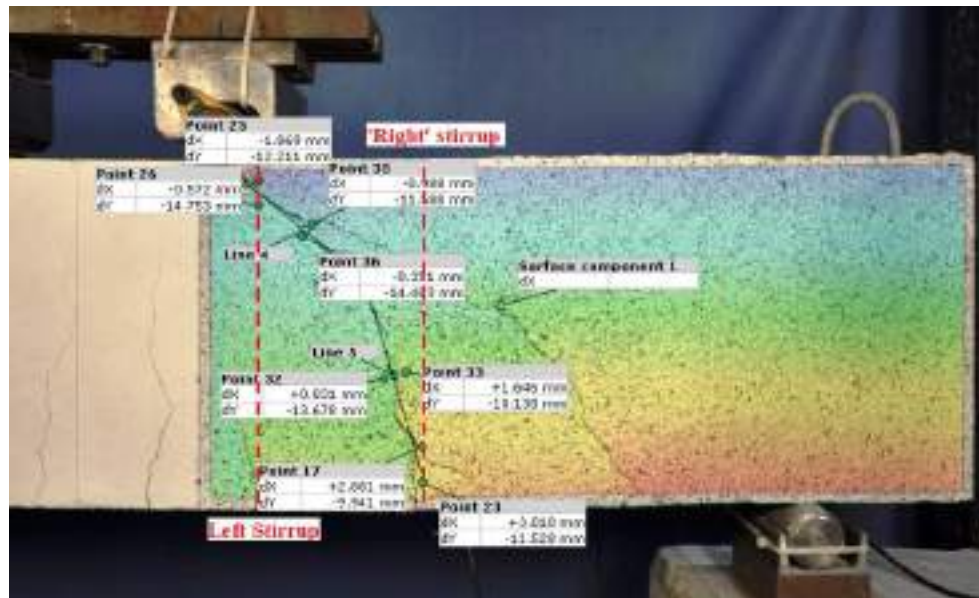


Figure 6: Selection of crack segments and points for analysis using DIC.

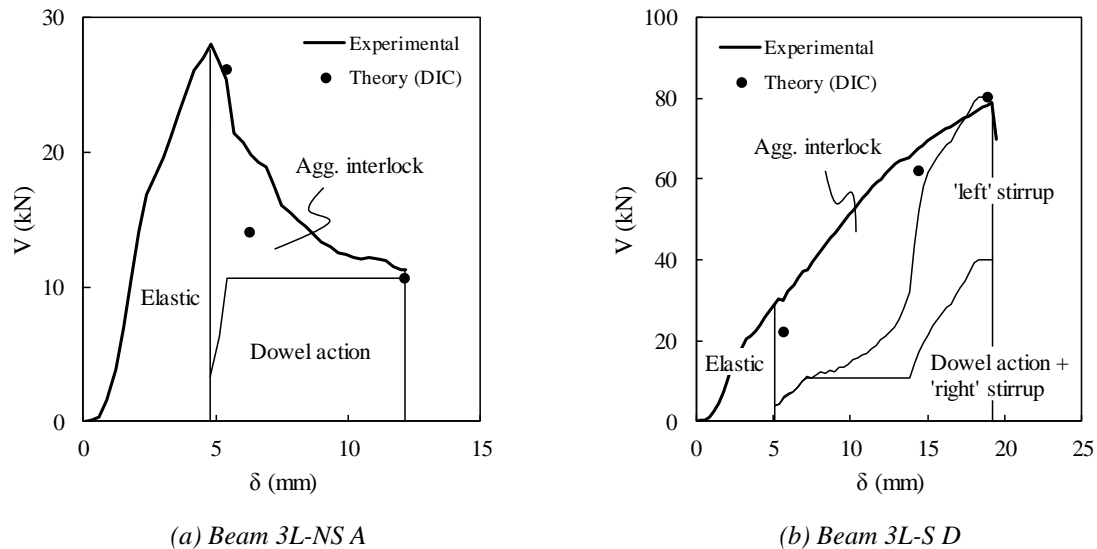


Figure 7: Contribution of shear transfer mechanisms

ACKNOWLEDGMENTS

The first author acknowledges CAPES for the financial support. The authors would like to express their gratitude to STRATUS FRP and IBRATA for supplying the material used in the study.

REFERENCES

- Ahmed, E.A., El-Sayed, A.K., El-Salakawy, E., Benmokrane, B. (2009). "Bend strength of FRP stirrups: Comparison and evaluation of testing methods", *Journal of Composites for Construction*, 14(1), 3-10.
- Alkhrdaji, T., Wideman, M., Belarbi, A., Nanni, A. (2001). "Shear strength of GFRP RC beams and slabs", In: *Proceedings of the International Conference of Composites in Construction*, 409-414.
- Baena, M., Torres, L., Turon, A., Barris, C. (2009). "Experimental study of bond behaviour between concrete and FRP bars using a pull-out test". *Composites Part B: Engineering*, 40(8), 784-797.
- Baumann, T., Rüschi, H. (1970). "Tests for the analysis of dowel action of flexural reinforcement of reinforced concrete beams", *Deutscher Ausschuss für Stahlbeton*, 210, 43-83. Berlin, Germany, Ernst & Sohn (in German).
- Bujadham, B., Maekawa, K. (1992). "The universal model for stress transfer across cracks in concrete". *Proceedings of JSCE*, 451(17), 277-287.
- Connor, A. B., Kim, Y. H. (2016). "Shear-Transfer Mechanisms for Glass Fiber-Reinforced Polymer Reinforcing Bars", *ACI Structural Journal*, 113(6), 1369.
- Dutton, M. (2012). "Digital Image Correlation for Evaluating Structural Engineering Materials", Master Thesis, Queen's University, Ontario, Canada.
- El-Sayed, A. K., El-Salakawy, E. F., Benmokrane, B. (2006). "Shear strength of FRP-reinforced concrete beams without transverse reinforcement", *ACI Structural Journal*, 103(2), 235-243.
- GOM (2009). ARAMIS 3.1 und höher, manual.
- Huber, P., Huber, T., Kollegger, J. (2016). "Investigation of the shear behavior of RC beams on the basis of measured crack kinematics", *Engineering Structures*, 113, 41-58.
- Krefeld, W. J., Thurston, C. W. (1966). "Contribution of longitudinal steel to shear resistance of reinforced concrete beams", *Journal of the American Concrete Institute*, 63(3), 325-344.
- Li, B., Maekawa, K. (1987). "Contact density model for cracks in concrete", In: *IABSE Colloquium*, Delft, 51-62).



Ruiz, M. F., Muttoni, A., Sagaseta, J. (2015). "Shear strength of concrete members without transverse reinforcement: A mechanical approach to consistently account for size and strain effects", *Engineering Structures*, 99, 360-372.

Soetens, T., Matthys, S. (2017). "Shear-stress transfer across a crack in steel fibre-reinforced concrete", *Cement and Concrete Composites*, 82, 1-13.

Yang, Y. (2014). "Shear Behaviour of Reinforced Concrete Members without Shear Reinforcement: A New Look at an Old Problem", PhD Thesis, TU Delft.

Yankelevsky, D. Z. (1985). "Analytical model for bond-slip behavior under monotonic loading". *Building and Environment*, 20(3), 163-168.

Yost, J. R., Gross, S. P., Dinehart, D. W. (2001). "Shear strength of normal strength concrete beams reinforced with deformed GFRP bars", *Journal of Composites for Construction*, 5(4), 268-275.



A REVIEW ON EXPERIMENTAL DEFLECTIONS IN FRP RC FLEXURAL MEMBERS

C. Barris¹, A. Bover², J. Gómez² and L. Torres²

¹ AMADE, University of Girona, Spain, e-mail : cristina.barris@udg.edu

² AMADE, University of Girona, Spain

ABSTRACT

It is commonly acknowledged that serviceability limit states may govern the design of concrete structures reinforced with fibre reinforced polymer (FRP) bars, mainly due to the lower modulus of elasticity of FRPs compared to that of steel. FRP bars present a wide range of rebar surfaces that can have an effect on the deformational behaviour of FRP reinforced concrete (RC) flexural members. In the last three decades, many experimental studies providing results on deflections of FRP RC beams have appeared, and several approaches for adjusting expressions initially developed for steel RC beams have been published.

This paper aims at studying the experimental deflection of FRP RC beams, by analysing the results available in the literature of 171 beam specimens tested under 4-point bending load. The theoretical deflection is calculated according to an equivalent moment of inertia based on interpolation of deflection, and it is compared to the experimental value. A deflection ratio (*DR*) is defined as the predicted/experimental deflection. The influence of the level of loading, the surface coating and the main parameters affecting the tension stiffening effect (*np* and *d/h* ratio) is analysed and conclusions are drawn. It is observed that *DR* increases with the load level. Moment ratios close to the cracking moment provide higher scatter of results, whilst high moment ratios give *DR* lower than the unity. Specimens reinforced with sand coated FRP yield to marginally lower values of *DR* compared to wrapped or ribbed coating. Finally, the effect of *np* or *d/h* ratio on *DR* was not clearly observed in this work due to the scatter of results found in the analysis.

KEYWORDS

Experimental study ; FRP internal reinforcement; Codes, standards and design guidelines

INTRODUCTION

Corrosion in steel reinforced concrete (RC) structures under aggressive environments can cause severe deterioration of the structural performance. In order to avoid such pathologies, the use of fibre reinforced polymer (FRP) rebars as a longitudinal reinforcement has been proposed as an adequate alternative. However, the usual lower modulus of elasticity of the FRP reinforcement compared to that of steel yields to larger deflections, and therefore, their design is often governed by the limit state of serviceability. Along the last three decades, an important number of expressions have been published with the purpose of adjusting existing formulations to calculate the deflection of FRP RC beams.

Deflections in RC elements can be evaluated from geometrical considerations by the basic relationship between curvature (κ) and the deflection (δ):

$$\kappa = \frac{d^2\delta}{dx^2} \quad (1)$$

The discrete nature of concrete cracking leads to a non-uniform stiffness along the flexural member. Due to the bond stresses between reinforcement and concrete, the portions of concrete between cracks contribute to the global stiffness of the element. This phenomenon, usually referred as tension stiffening effect, can contribute significantly to the member deflection.

A simplified, common and accepted methodology to estimate deflections for steel RC beams is Branson equation (Branson 1977), where deflection is calculated using usual elastic theory equations with an equivalent moment of inertia (I_e):

$$I_e = \left(\frac{M_{cr}}{M_a}\right)^3 I_g + \left(1 - \left(\frac{M_{cr}}{M_a}\right)^3\right) I_{cr} \leq I_g \quad (2)$$

where M_a is the service moment at the critical section of the member at the stage at which the deflection is being computed, M_{cr} is the moment at first cracking, I_{cr} is the moment of inertia of the cracked section and I_g is the gross



moment of inertia. This methodology was adapted for the case of FRP RC flexural elements by a number of researchers that adjusted Eq. (2) to experimental results (Faza and GangaRao 1992, Benmokrane et al. 1996, Masmoudi et al. 1996). Other approaches involving integration of curvature along the length of the beam were also proposed for FRP RC beams (Abdalla 2002, Barris et al. 2009, Bischoff and Gross 2011a).

Several experimental databases on deflection of FRP RC beams have been already published (Mota et al 2006, Bischoff and Gross 2011b). Nevertheless, due to the relevant importance of correctly determining deflections in the design of FRP RC, and the continuous publication of new experimental data, it is necessary to re-assess the goodness of fit of the different rational methods to calculate deflection of FRP RC flexural members.

This paper deals with the deflection behaviour of FRP RC beams. The experimental results from an updated database are compared with theoretical predictions given by formulation based on an equivalent moment of inertia calculated from interpolation of deflection. A deflection ratio is defined and it is evaluated at different moment stages within the serviceability range. Special emphasis is placed on the results of the influence of surface coating of the reinforcement on the deflection response. This parameter together with other factors affecting tension stiffening effect are evaluated and discussed.

EQUIVALENT MOMENT OF INERTIA BASED ON INTERPOLATION OF DEFLECTION

It is well accepted that the flexural deflection of a RC member can be calculated from interpolation between a cracked and an uncracked state (CEN 2004):

$$\alpha = \zeta \alpha_{II} + (1 - \zeta) \alpha_I \quad (3a)$$

$$\zeta = 1 - \beta \left(\frac{\sigma_{cr}}{\sigma_r} \right)^2 \quad (3b)$$

where α is the deformational parameter, I and II refer to the uncracked and cracked states respectively, ζ is the distribution coefficient allowing for tensioning stiffening at a given section, σ_r is the stress in the tension reinforcement calculated on the basis of a cracked section, σ_{cr} is the stress in the tension reinforcement calculated on the basis of a cracked section under the loading conditions causing first cracking and β is a coefficient taking into account duration of loading and repeated loading. For the sake of simplicity, the deformational parameter is commonly considered as the deflection value by itself.

From this expression, an equivalent stiffness $(EI)_{eff}$ can be deduced for direct simplified calculation of deflections (fib 2013):

$$(EI)_{eff} = \frac{(EI)_I \cdot (EI)_{II}}{\zeta \cdot (EI)_I + (1 - \zeta) \cdot (EI)_{II}} \quad (4)$$

The same concept was proposed by Bischoff (2005) in the form of an equivalent moment of inertia,

$$I_e = \frac{I_{cr}}{1 - \eta (M_{cr}/M_a)^2} \leq I_g \quad (5a)$$

$$\eta = 1 - I_{cr}/I_g \quad (5b)$$

firstly developed for axial tension members and later extended to flexural members.

Later on, Bischoff and co-workers (Bischoff et al. 2009, Bischoff and Gross 2011a, b) proposed a modification by including an additional factor γ to account for the variation in stiffness along the member length, which depends on the loading arrangement and boundary conditions:

$$I_e = \frac{I_{cr}}{1 - \gamma \eta (M_{cr}/M_a)^2} \leq I_g \quad (6)$$

This last approach was adopted in the ACI 440.1R-15 design guideline.

EXPERIMENTAL DATABASE

Deflection methods described in the previous section were analysed using a database consisting of 171 beams tested under static four-point bending test taken from 31 studies involving test of FRP RC beams (Faza and GangaRao 1992, Larralde and Silva 1992, Benmokrane et al. 1995, Benmokrane et al. 1996, Cosenza et al. 1997, Duranovic et al. 1997, Alsayed 1998, Masmoudi et al. 1998, Pecce et al. 1998, Thériault and Benmokrane 1998, Yost et al. 2001, Abdalla 2002, Bogdanovic 2002, Toutanji and Deng 2003, Ashour 2006, Wang and Berlabi 2005, Rafi et al. 2008, Barris et al. 2009, Barris et al. 2013, Kalpana et al. 2011, Al-Sunna et al. 2012, Miàs et al. 2013, Yang et al. 2012, Adam et al. 2015, Zhang et al. 2014, Acciai et al. 2016, Confrère et al. 2016, Elgabass et al. 2016, Goldston et al. 2016, Goldston et al. 2017). Comparison was restricted to test reporting the experimental



load-deflection curve to be able to compare the experimental value with the predicted. 126 Glass-FRP (GFRP), 31 Carbon-FRP (CFRP), 10 Aramid-FRP (AFRP) and 4 Basalt-FRP (BFRP) RC beams were considered in the analysis. Three different types of FRP surface treatment were distinguished in this study to evaluate their influence on the deflection response: sand coated, wrapped and ribbed surface. Even though some investigations did not specify the type of surface, 31 elements with sand coated surface reinforcement, 53 elements with wrapped surface reinforcement and 44 elements with ribbed surface reinforcement were differentiated.

The amount of specimens considered in this database represent a wide range of properties and beam configurations. All specimens had a rectangular cross section with dimensions varying from 1500 to 125000 mm². The total span ranged between 1500 and 4000 mm. The concrete compressive strength was between 15.5 and 117 MPa, and the elastic modulus of elasticity of the reinforcing bars ranged between 30 and 146.2 GPa.

The main parameters considered in this study that may affect the tension stiffening and deformational behaviour are: i) the $n\rho$ ratio, where n is the modular ratio (E_f/E_c , being E_f the modulus of elasticity of the FRP reinforcement and E_c that of concrete) and ρ is the reinforcement ratio, and ii) the effective depth-to-height ratio, d/h . In this study, the $n\rho$ ratio ranges between 0.002 and 0.069, and the d/h ratio lies between 0.72 and 0.94.

ANALYSIS OF RESULTS

To verify the proposed method, a deflection ratio (DR) was defined as the ratio between the predicted deflection ($\delta_{predicted}$), which was obtained using the proposed method, and the experimental deflection ($\delta_{experimental}$), as:

$$DR = \frac{\delta_{predicted}}{\delta_{experimental}} \quad (7)$$

For the theoretical prediction, the interpolation of deflections (CEN 2004) was adopted. DR was evaluated at four different stages of loading considered to cover the serviceability range: $M=1.5M_{cr}$, $M=2.25M_{cr}$, $M=3M_{cr}$ and $M=4.5M_{cr}$. Due to the disparity of criteria adopted by the different authors when assuming the tensile behaviour of concrete to calculate the cracking moment (M_{cr}), in this work M_{cr} was directly adjusted from the experimental load-deflection response.

The statistical parameters of DR value are represented in Table 1 at the different stages of loading.

Table 1: Statistical analysis on DR at different moment levels.

M/M_{cr}	Mean	Median	Min	Max	St. Dev.	<1	>1	>0.7 & <1.3
1.5	1.07	1.01	0.57	2.46	0.34	46%	54%	69%
2.25	0.99	0.99	0.62	1.58	0.19	56%	44%	92%
3.0	0.96	0.96	0.60	1.39	0.16	62%	38%	92%
4.5	0.91	0.90	0.57	1.61	0.16	76%	24%	90%

As observed in Table 1, DR parameter generally decreases with the increase of load, in terms of mean and median value, which reveals that the experimental deflection becomes higher than the predicted one. The best fit between experimental and predicted values is found at a moment of $2.25M_{cr}$, with a mean and median values of 0.99. The lowest moment ratio ($M=1.5M_{cr}$) provides the highest values of DR . At that moment stage, the influence of the adjusted cracking moment and the behaviour of the first cracks opening is of utmost importance. For that reason, the scatter of results (measured as the standard deviation from the mean value in Table 1) is significantly higher and the percentage of samples with DR ranging between 0.7 and 1.3 is substantially lower at $1.5M_{cr}$. Mean moment ratios ($M=2.25\div 3M_{cr}$) present the highest percentage of samples with DR between 0.7 and 1.3 (92%), the closest mean and median values of DR to 1 and a relatively low disparity of results (standard deviation of 0.16 to 0.19). Hence, at that moment ratios, the methodology analysed in this paper provides a good fit to the results of the experimental database. At the highest moment ratio ($M=4.5M_{cr}$), the experimental deflection is about 10% higher than the predicted one. This finding has been previously identified in several studies when the load surpasses the serviceability range (Barris et al. 2009, Al-Sunna et al. 2012), and it was attributed to other effects that might occur at high loads, due to the high degree of deformability of FRP RC beams, such as the influence of shear cracks or the non-linear behaviour of concrete on the total deflection.

Further analysis on the influence of the reinforcement surface coating on the deflection behaviour can be found in Table 2, where the same statistical results shown in Table 1 are separated depending on the surface treatment,

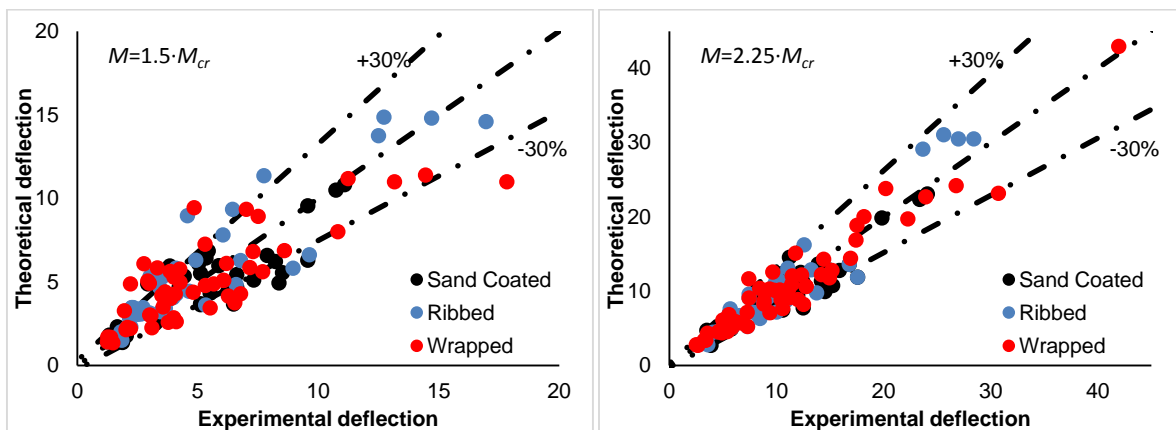


and in Figure 1, where the theoretical deflection is plotted versus its experimental value. Three different surface treatments were identified: sand coated, helical wrapping and grooved (ribbed) surface. In those cases where helically wrapping was accompanied with sand coating, the specimens were considered simply wrapped for simplification purposes. In Table 2, only specimens with clear identification of the surface treatment were used.

Table 2: Statistical analysis on DR at different moment levels considering surface coatings.

M/M_{cr}	Surface	Mean	Median	Min	Max	St. Dev.	<1	>1	>0.7 & <1.3
1.5	Sand Coated	0.96	0.93	0.57	1.67	0.29	57%	43%	72%
	Wrapped	1.10	1.01	0.57	2.21	0.42	52%	48%	62%
	Ribbed	1.16	1.11	0.65	1.96	0.28	25%	75%	77%
2.25	Sand Coated	0.92	0.90	0.62	1.35	0.18	76%	24%	84%
	Wrapped	0.98	0.98	0.66	1.31	0.16	66%	34%	94%
	Ribbed	1.03	1.04	0.68	1.35	0.19	38%	62%	95%
3.0	Sand Coated	0.90	0.91	0.65	1.23	0.14	81%	19%	90%
	Wrapped	0.94	0.94	0.65	1.25	0.14	70%	30%	96%
	Ribbed	0.98	0.99	0.69	1.28	0.15	50%	50%	97%
4.5	Sand Coated	0.88	0.88	0.61	1.17	0.15	83%	17%	83%
	Wrapped	0.90	0.90	0.68	1.19	0.12	80%	20%	93%
	Ribbed	0.93	0.91	0.63	1.61	0.17	79%	21%	91%

As shown in Table 2, the general trends observed in Table 1 are repeated when specimens are separated according to the surface coating of the reinforcement: DR decreases with load increase, the scatter of results is higher at the lowest moment ratio, and the highest number of specimens with DR between 0.7 and 1.3 is at the mean moment ratios.



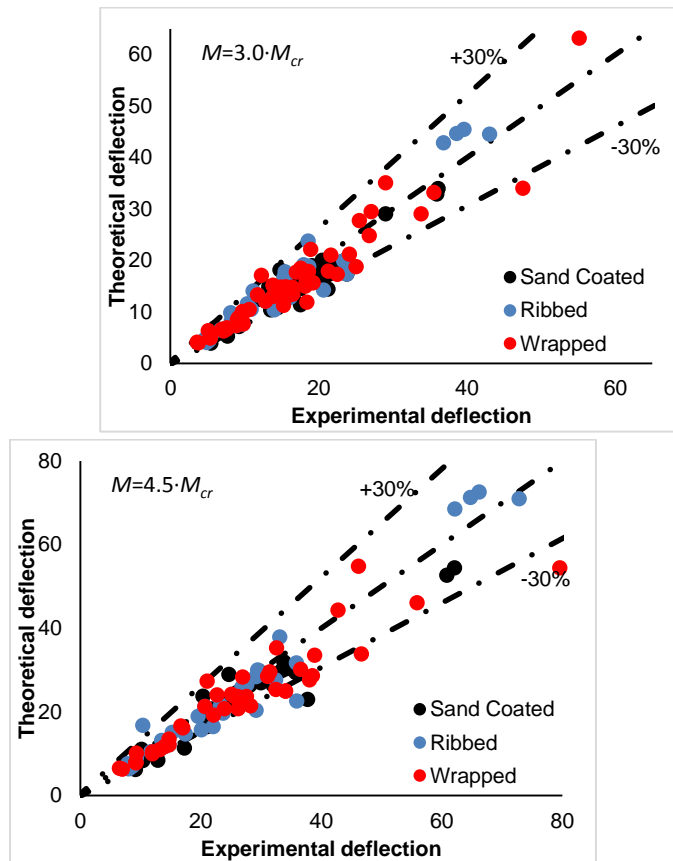


Figure 149: Experimental vs. theoretical deflection at different moment ratios.

As observed in Table 2 and Figure 1, the sand coated treatment consistently provides the lowest value of DR parameter, regardless of the loading stage. In these cases, the load transfer from the reinforcing bar to concrete is expected to occur mainly due to chemical bond and friction between both surfaces (Baena et al 2009). Conversely, the ribbed surface gives the highest values of DR , and for the highest moment ratios, the best fit to the unity. In this case, bond stresses are transmitted mainly by the interaction between the rib and the concrete (Baena et al 2009). The wrapped coating, which presents a surface with a variable rib height, provides values in between those with sand coated surface and ribbed surface.

At the service load, the deformational behaviour due to flexural stresses is highly influenced by the tension stiffening effect. Torres et al. (2015) performed a parametric study to identify the theoretical parameters affecting tension stiffening of bending RC elements, including steel and FRP as reinforcing material. For usual values, the most significant parameters were the $n\rho$ ratio, and the d/h ratio (with higher influence of the first). In Figures 2 and 3, the effect of these two parameters is shown on DR at a moment stage $M=2.25 \cdot M_{cr}$.

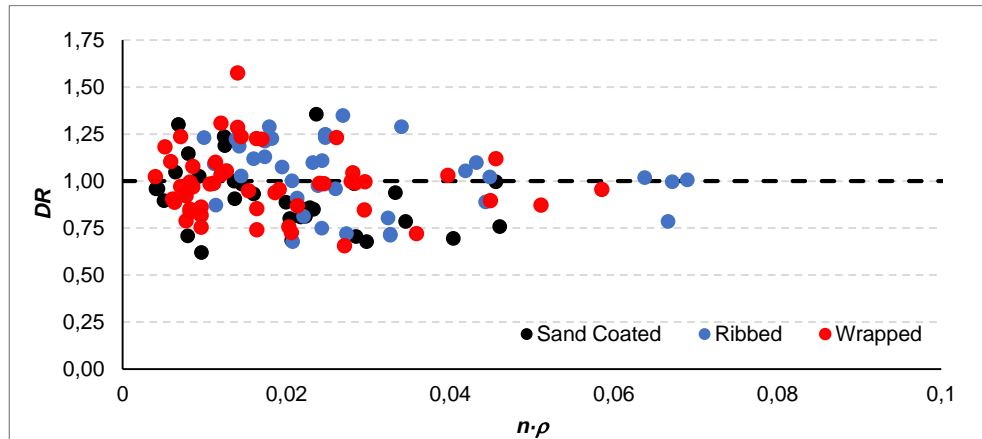


Figure 150: DR versus $n\rho$ at $2.25M_{cr}$.

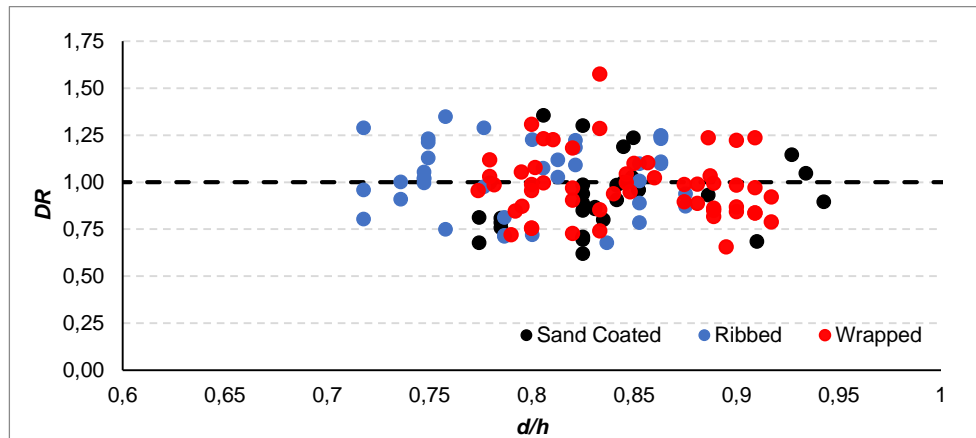


Figure 151: DR versus d/h at $2.25M_{cr}$.

In general, an important scatter of results is found in Figure 2. However, this scatter seems to reduce with the increase of the $n\rho$ ratio. At the same time, DR approaches to the unity at high $n\rho$ ratios, indicating that the deflection behavior of over-reinforced beams is easier to predict than that of RC beams lightly reinforced. In the case of Figure 3, the general trend shows an evenly distributed scatter of results, meaning that the effect of d/h on the deflection could not be identified in this study. It should be noted, however, that values of DR in Figure 2 do not present a constant d/h ratio, and the same comment applies in Figure 3, where the $n\rho$ is neither constant. That could mask the influence of both factors on DR . A coefficient that combines the effect of both parameters on tension stiffening can be taken from Torres et al. (2015), in which the tension stiffening was computed by considering an equivalent modulus of elasticity of the reinforcement ($E_{f,eq}$):

$$\frac{E_{f,eq}}{E_f} = \frac{1}{1-a\mu^2} \quad (8a)$$

$$\mu = \frac{M_{cr}}{M} \quad (8b)$$

where a is a dimensionless parameter that was found to be:

$$a = 10n\rho \cdot (1 - 1.5 d/h) + 1 \quad (9)$$

Looking at Equation (8a) it is seen that when a increases, $E_{f,eq}$ also increases as well as the tension stiffening effect. The effect of parameter a on the DR ratio was investigated at the different load levels and it is represented in Figure 4 for $M=2.25M_{cr}$, although similar trends were observed at other moment ratios.

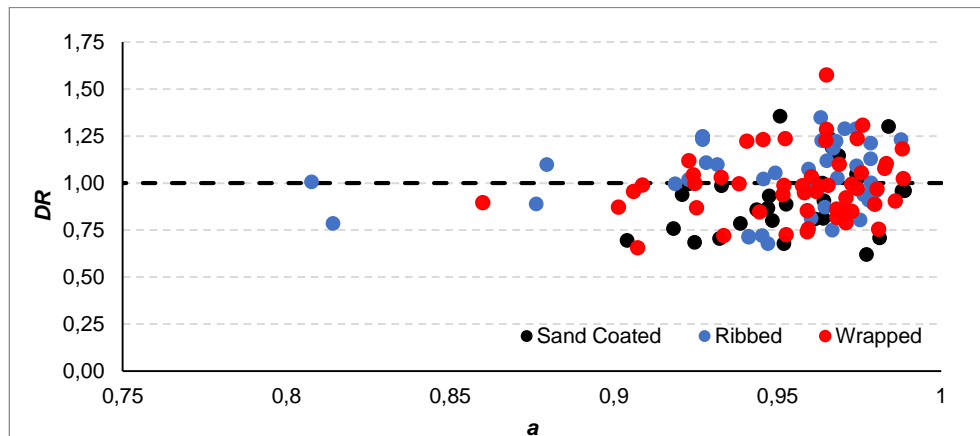


Figure 152: DR versus a at $2.25M_{cr}$.

In that case, it was generally observed that the scatter of results tends to increase with the increase of a , meaning that deflection of beams with relatively low values of tension stiffening (high $n\rho$ and d/h ratios) may result easier to predict.

CONCLUSIONS

This paper presents a parametric study based on a new experimental database of deflection behavior of FRP RC flexural elements. The theoretical deflection is calculated according to the equivalent moment of inertia based on interpolation of deflection, and it is compared to the experimental value at different stages of the test. The paper includes a statistical study where different parameters are studied and evaluated. A deflection ratio, DR , is defined as the predicted/experimental deflection. Evaluation of DR variation allows analyzing the effect that the studied parameters may have in the practical control of deflections. The main conclusions are:

- In general, DR decreases with the increase of load. The best fit between the experimental and predicted deflection is found at a moment of $2.25M_{cr}$. Lower moment ratios provide higher scatter of results, due to the influence of the cracking moment on its result. Higher moment ratios yield values of DR lower than the unity, meaning that the experimental deflection is under-predicted by the proposed formulation, which is based on linear behaviour of materials and only considers flexural effects.
- Surface coating of the FRP reinforcement shows an effect on DR . Specimens with sand coated reinforcement give marginally lower values of DR than wrapped and ribbed surface, regardless of the moment ratio. Contrarily, those specimens reinforced with ribbed FRP reinforcement provided the highest DR values. This trend is in accordance with studies dealing with bond behaviour in FRP RC elements.
- DR parameter does not show a dependency on $n\rho$ or d/h ratios. However a tendency to lower scatter of results is found for higher $n\rho$ values and when the combination of both parameters tends to provide lower values of tension stiffening.

ACKNOWLEDGMENTS

The authors acknowledge the support provided by the Spanish Government (MINECO), Project Ref. BIA2017-84975-C2-2-P.

REFERENCES

H. A. Abdalla (2002). "Evaluation of deflection in concrete members reinforced with fibre reinforced polymer (FRP) bars", *Composite Structures*, 56(1), 63–71.



- A. Acciai, A. D'Ambrisi, M. De Stefano, L. Feo, F. Focacci, R. Nudo (2016). "Experimental response of FRP reinforced members without transverse reinforcement: Failure modes and design issues", *Composites Part B: Engineering*, 89, 397–407.
- ACI Committee 440. ACI 440.1R-15 (2015) "Guide for the design and construction of structural concrete Reinforced with FRP bars", *American Concrete Institute*, Farmington Hill, MI, 83p.
- M. A. Adam, M. Said, A. A. Mahmoud, A. S. Shanour (2015) "Analytical and experimental flexural behavior of concrete beams reinforced with glass fiber reinforced polymers bars", *Construction and Building Materials*, 84, 354–366.
- S. H. Alsayed (1998). "Flexural behaviour of concrete beams reinforced with GFRP bars", *Cement & Concrete Composites*, 20(1), 1–11.
- R. Al-Sunna, K. Pilakoutas, I. Hajirasouliha, M. Guadagnini (2012). "Deflection behaviour of FRP reinforced concrete beams and slabs: An experimental investigation", *Composites Part B: Engineering*, 43, 2125-2134.
- A. F. Ashour (2006). "Flexural and shear capacities of concrete beams reinforced with GFRP bars", *Construction and Building Materials*, 20(10), 1005–1015.
- M. Baena, L. Torres, A. Turon, C. Barris (2009). "Experimental study of bond behaviour between concrete and FRP bars using a pull-out test", *Composites: Part B*, 40, 784-797.
- C. Barris, L. Torres, A. Turon, M. Baena, A. Catalan (2009). "An experimental study of the flexural behaviour of GFRP RC beams and comparison with prediction models", *Composite Structures*, 91, 286-295.
- C. Barris, L. Torres, J. Comas, C. Miàs (2013). "Cracking and deflections in GFRP RC beams: An experimental study", *Composites Part B: Engineering*, 55, 580-590.
- B. Benmokrane, O. Chaallal, R. Masmoudi (1995). "Glass fibre reinforced plastic (GFRP) rebars for concrete structures", *Construction and Building Materials*, 9(6), 353–364.
- B. Benmokrane, O. Chaallal, R. Masmoudi (1996). "Flexural response of concrete beams reinforced with FRP reinforcing bars", *ACI Structural Journal*, 93(1), 46–55.
- B. Bogdanovic (2002). "Deflection calculations of FRP-reinforced concrete beams", Technical report, The Univ. of Manitoba, 23p.
- P.H. Bischoff (2005). "Reevaluation of deflection prediction for concrete beams reinforced with steel and fiber reinforced polymer bars", *Journal of Structural Engineering*, 131(5), 752-762.
- P.H. Bischoff, S.P. Gross, C.E. Ospina (2009). "The story behind proposed changes to ACI 440 deflection requirements for FRP-reinforced concrete", *ACI Special Publication SP-264-4*, 53-76.
- P.H. Bischoff, S.P. Gross (2011a). "Design approach for calculating deflection of FRP-reinforced concrete", *Journal of Composites for Construction*, 15(4), 490-499.
- P.H. Bischoff, S.P. Gross (2011b). "Equivalent moment of inertia based on integration of curvature", *Journal of Composites for Construction*, 15(3), 263-273.
- D. E. Branson (1977). "Deformation of concrete structures".
- CEN (2004). "Eurocode 2: Design of concrete structures - Part 1.1: General rules and rules for buildings (EN 1992-1-1:2004)." Comité Européen De Normalisation, Brussels, 225 pp.
- A. Confrère, L. Michel, E. Ferrier, G. Chanvillard (2016). "Experimental behaviour and deflection of low-strength concrete beams reinforced with FRP bars", *Structural Concrete*, 17(5), 858–874.
- E. Cosenza, C. Greco, G. Manfredi, M. Pecce (1997). "Flexural behaviour of concrete beams reinforced with fiber reinforced plastic (FRP) bars", *Proceedings of the 3rd International Symposium on Non-Metallic (FRP) Reinforcement for Concrete Structures*, 2, 463–470.
- N. Duranovic, K. Pilakoutas, P. Waldron (1997). "Tests on concrete beams reinforced with glass fibre reinforced plastic bars", *Proceedings of the 3rd International Symposium on Non-Metallic (FRP) Reinforcement for Concrete Structures*, 2, 479–486.
- F. Elgabbas, P. Vincent, E. A. Ahmed, B. Benmokrane (2016). "Experimental testing of basalt-fiber-reinforced polymer bars in concrete beams", *Composites Part B: Engineering*, 91, 205–218.



- M. Goldston, A. Remennikov, M. N. Sheikh (2016). "Experimental investigation of the behaviour of concrete beams reinforced with GFRP bars under static and impact loading", *Engineering Structures*, 113, 220–232.
- M. W. Goldston, A. Remennikov, M. N. Sheikh (2017). "Flexural behaviour of GFRP reinforced high strength and ultra high strength concrete beams", *Construction and Building Materials*, 131, 606–617.
- S. S. Faza, H. V. S. GangaRao (1992). "Pre- and post-cracking deflection behaviour of concrete beams reinforced with fibre-reinforced plastic rebars", *Advanced Composite Materials in Bridges and Structures*, 151–160.
- fib (2013). "Model code for concrete structures 2010", *fédération internationale du béton*, 436 pp.
- V. Kalpana, K. Subramanian (2011). "Behavior of concrete beams reinforced with GFRP bars", *Journal of Reinforced Plastics and Composites*, 30(23), 1915–1922.
- C. Kassem, A. S. Farghaly, B. Benmokrane (2011). "Evaluation of Flexural Behavior and Serviceability Performance of Concrete Beams Reinforced with FRP Bars", *Journal of Composites for Construction*, 15(5), 682–695.
- J. Larralde, R. Silva-Rodriguez (1992). "Nuevo tipo de refuerzo para hormigón", *Rev. obras públicas* 3315, 67–72.
- R. Masmoudi, M. Thériault, B. Benmokrane (1998). "Flexural behavior of concrete beams reinforced with deformed fiber reinforced plastic reinforcing rods", *ACI Structural Journal*, 95(6), 665–676.
- C. Miàs, L. Torres, A. Turon, C. Barris (2013). "Experimental study of immediate and time-dependent deflections of GFRP reinforced concrete beams", *Composite Structures*, 96, 279–285.
- C. Mota, S. Aminar, D. Svecova (2006). "Critical review of deflection formulas for FRP-RC members", *Journal of Composites for Construction*, 10(3), 183–194.
- M. Pecce, G. Manfredi, E. Cosenza (1998). "Experimental behaviour of concrete beams reinforced with glass FRP bars", *Proceeding of the 8th European Conference on Composite Materials*, 227–234.
- M. M. Rafi, A. Nadjai, F. Ali, D. Talamona (2008). "Aspects of behaviour of CFRP reinforced concrete beams in bending", *Construction and Building Materials*, 22(3), 277–285.
- M. Thériault, B. Benmokrane (1998). "Effects of FRP reinforcement ratio and concrete strength on flexural behavior of concrete beams", *Journal of Composites for Construction*, 2(1), 7–15.
- L. Torres, C. Barris, G. Kaklauskas, V. Gribniak (2015). "Modelling of tension-stiffening in bending RC elements based on equivalent stiffness of the rebar", *Structural Engineering and Mechanics*, 53(5), 997–1016.
- H. Toutanji, Y. Deng (2003). "Deflection and crack-width prediction of concrete beams reinforced with glass FRP rods", *Construction and Building Materials*, 17(1), 69–74.
- H. Wang, A. Belarbi (2005). "Flexural behavior of fiber-reinforced-concrete beams reinforced with FRP rebars", *Proceedings of the 7rd International Symposium on Non-Metallic (FRP) Reinforcement for Concrete Structures*, 895–914.
- J. M. Yang, K. H. Min, H. O. Shin, Y. S. Yoon (2012). "Effect of steel and synthetic fibers on flexural behavior of high-strength concrete beams reinforced with FRP bars", *Composites Part B: Engineering*, 43(3), 1077–1086.
- J. Yost, C. Goodspeed, E. Schmeckpeper, (2001). "Flexural performance of concrete beams reinforced with FRP grids", *Journal of Composites for Construction*, 5(1), 18–25.
- L. Zhang, Y. Sun, W. Xiong (2014). "Experimental study on the flexural deflections of concrete beam reinforced with Basalt FRP bars", *Materials and Structures*, 2015, 3279–3293.



NUMERICAL SIMULATION OF SHEAR FAILURE IN SCALED GFRP REINFORCED CONCRETE BEAMS WITHOUT STIRRUPS

S. Khodaie 1 and F. Matta 2

¹ University of South Carolina, Dept. of Civil and Environmental Engineering, USA

² University of South Carolina, Dept. of Civil and Environmental Engineering, USA, Email: fmatta@sc.edu

ABSTRACT

Evidence from load tests on concrete beams reinforced with glass fiber-reinforced polymer (GFRP) bars without stirrups highlights a decrease in the shear stress at failure at increasing effective depths. The physical explanation of this size effect remains controversial, and existing nominal shear strength algorithms may not consistently capture this phenomenon. This paper reports on the validation of a computational model based on a concrete Lattice Discrete Particle Model (LDPM) vis-à-vis actual four-point bending test data for slender GFRP RC beams having an effective depth in the range 292-883 mm. The concrete LDPM approximates the physical heterogeneity of concrete, and incorporates constitutive laws that are important to simulate shear transfer mechanisms. The numerical simulations yielded accurate predictions of load-deflection response, strength, and diagonal-tension failure mode. These preliminary results are relevant since, for the first time, they demonstrate the successful use of numerical simulations to accurately predict the shear behavior of scaled GFRP RC beams without stirrups, whereas existing nominal strength algorithms may not consistently yield accurate predictions.

KEYWORDS

Concrete, discrete model, fracture, GFRP bar, numerical simulation, shear, size effect.

INTRODUCTION

Experimental evidence from load tests on scaled slender concrete (RC) beams internally reinforced with glass fiber-reinforced polymer (GFRP) bars, and without stirrups, shows a significant decrease in the sectional shear stress at failure at increasing effective depths (Bentz et al. 2010; Matta et al. 2013). An important practical implication of this phenomenon known as size effect (Collins and Kuchma 1999) is that extrapolating strength values from typical laboratory-scaled experiments to design larger members may be misleading. For the case of GFRP RC structures, representative examples include slab bridges, retaining walls, and seawalls (Matta 2008).

In RC beams without stirrups, shear forces are transferred through the uncracked concrete above the neutral axis, aggregate interlock and tensile cohesive stresses along diagonal cracks, and dowel action provided by the flexural reinforcement (Wight 2015). The physical explanation of size effect and the role of specific shear resisting mechanisms remain controversial. In fact, fundamentally different nominal shear strength algorithms are available for designing GFRP RC structures. For example, in the case of the ACI 440.1R-15 design guidelines (ACI 2015), also reflected in the AASHTO LRFD specifications (AASHTO 2009), it is assumed that shear forces are resisted primarily by the uncracked concrete above the neutral axis. A conservative algorithm is recommended for the estimation of the shear strength of beams without stirrups, which carries the benefit of offsetting shear strength decreases due to size effect (Matta et al. 2013). ACI committee 446 proposed a fracture mechanics-based algorithm for steel RC beams (Bažant et al. 2007). This algorithm was adapted to GFRP RC to account for the lower axial stiffness of GFRP bars, providing more accurate results of the source ACI 440 algorithm irrespective of beam size and reinforcement ratio (Matta et al. 2013). Instead, the nominal shear strength algorithm for steel and GFRP RC beams specified in the Canadian Highway Bridge Design Code (CSA 2014) attributes the size effect to the reduced contribution of aggregate interlock associated with the formation of wider cracks in deeper beams. The different physical explanations of size effect in design algorithms reflects the difficulty of accurately accounting for the contribution of different shear transfer mechanisms, which largely depend on concrete fracture and friction behavior.

Numerical modeling tools can aid with clarifying the underlying physics of shear resisting mechanisms. To this end, it is desirable that candidate tools account for concrete heterogeneity (i.e., role of aggregates and surrounding mortar), and incorporate constitutive laws that are relevant to simulate shear resisting mechanisms. This paper presents preliminary results on the validation of a calibrated concrete Lattice Discrete Particle Model (LDPM) for the case of slender GFRP RC beams without stirrups with effective depth up to 0.9 m. The LDPM is a meso-scale

concrete model that accounts for the concrete heterogeneity, and incorporates constitutive laws for tension-softening as well as shear-compression fracture behavior (Cusatis et al. 2011a, 2011b), which are important to realistically simulate different shear resisting mechanisms, and the associated size effect. The LDPM-based numerical modeling of GFRP RC beams without stirrups is based on: (1) a calibrated LDPM model for concrete with appropriate fracture properties; (2) orthotropic GFRP bar elements with a suitable shear-tension failure criterion; and (3) a nonlinear bond-slip law for GFRP bar-concrete interface. Recent research has demonstrated proof of concept for LDPM-based models to accurately simulate the shear behavior of GFRP RC beams without stirrups having effective depth in the range 146-292 mm, which is significant for size effect (Khodaie et al. 2017). Here, LDPM-based numerical models are deployed to simulate the load-midspan displacement response, crack pattern, shear strength and associated size effect for GFRP RC beams without stirrups having effective depth in the range 292-883 mm, and load-tested using four-point bending setups. The simulation results are successfully compared vis-à-vis previously published experimental results (Matta et al. 2013).

LOAD TESTS

The four-point bending load test setup and the cross section of the GFRP RC beam specimens are illustrated in Figure 1. These beams include companion specimens S3-0.12-1A and S3-0.12-2A, having an effective depth $d = 292$ mm, and companion specimens S1-0.12-1A and S1-0.12-2B, having $d = 883$ mm (Matta et al. 2013). All beams had a similar effective reinforcement ratio, $\rho_{eff} = 0.12\%$. The shear span-to-depth ratio, s/d , was kept at a value of 3.1 to yield lower-bound shear strength values (Kani 1967). Table 1 summarizes salient information including: beam width, b_w ; shear span-to-depth ratio, s/d ; concrete cylinder compressive strength, f_c ; average longitudinal elastic modulus, E_f , and average tensile strength, f_{fu} , of the GFRP bars as determined via uniaxial tension tests; experimental shear force at failure, V_e ; normalized shear strength, $V_e/(b_w d f_c^{0.5})$; theoretical shear force associated with flexural failure, V_b ; nominal shear capacity, V_n , based on the algorithms in ACI 440 (2015), modified ACI 446 (Matta et al. 2013), and CSA (2014); and numerically-simulated shear capacity, V_{LDPM} .

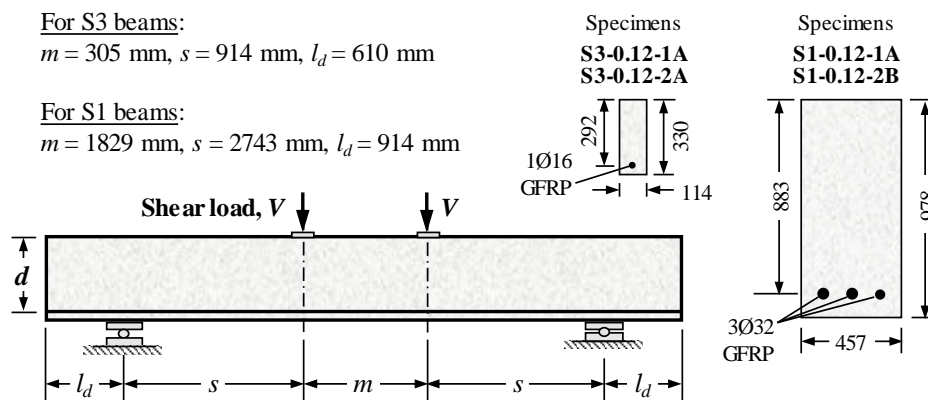


Figure 1: Load tests: schematic of four-point bending load test setup, and cross section with reinforcement of GFRP RC beam specimens without stirrups (Dimensions in mm.)

Table 1: Test matrix and salient specimen parameters, and results of tests and LDPM-based simulations

Specimen	d [mm]	b_w [mm]	$\frac{s}{d}$	f_c [MPa]	E_f [GPa]	f_{fu} [MPa]	V_e [kN]	$\frac{V_e}{b_w d \sqrt{f_c}}$ [$\sqrt{\text{MPa}}$]	V_b [kN]	V_n [kN]			V_{LDPM} [kN]
										ACI 440	ACI 446	CSA 2014	
S3-0.12-1A	292	114	3.1	32.1	43.2	849	19.2	0.102	48.5	10.1	16.1	13.7	20.4
S3-0.12-2A				32.1	43.2	849	17.9	0.095	48.5	10.1	16.1	13.7	
S1-0.12-1A	883	457	3.1	29.5	41.0	483	154	0.070	348	117	132	130	167
S1-0.12-2B				29.6	41.0	483	151	0.069	353	117	133	130	

From Table 1, it is noted that the strength predictions based on existing algorithms in North American guidelines, codes, and proposals are overly conservative for the S3 beams, and tend to be closer to the experimental results

as the beam size increases (Matta et al. 2013). This evidence attests to the difficulty of accounting for different shear resisting mechanisms and their interaction, thereby accurately predicting strength irrespective of size.

COMPUTATIONAL MODELING AND SIMULATION

Lattice Discrete Particle Model

The LDPM is a meso-scale concrete model that describes the displacement and interaction of randomly distributed aggregate particles through discrete formulation and rigid body kinematics (Cusatis et al. 2011a, 2011b). The mechanical interaction of adjacent aggregates is simulated using polyhedral cells that interact along triangular facets. Material behavior is governed by vectorial constitutive laws that are defined at the centroid of each facet. The LDPM constitutive laws for concrete fracture are based on the crack band model (Bažant and Oh 1983), which accounts for the transfer of tensile cohesive stresses along diagonal cracks where tension and shear stresses are produced. In addition, based on the LDPM frictional constitutive laws, the presence of compressive stresses increases the concrete shear strength. These nonlinear mechanics features are important to realistically simulate the shear resisting mechanisms. Together with the aforementioned LDPM constitutive laws, the geometric definition of the potential failure planes (facets), which dictates the propagation path of the discrete cracks to be around the interacting aggregate particles (in lieu of passing through them), enable one to numerically simulate aggregate interlocking along the cracks through which shear (frictional) forces are transferred. Figure 2a illustrates the polyhedral cells surrounding the aggregates and the interacting facets where a discrete shear crack forms. As the shear force increases, the relative sliding of the crack fronts closes the crack opening between the angled facets. This allows the shear force component, V_{ag} , to be locally transferred through the simulated aggregate interlock mechanism.

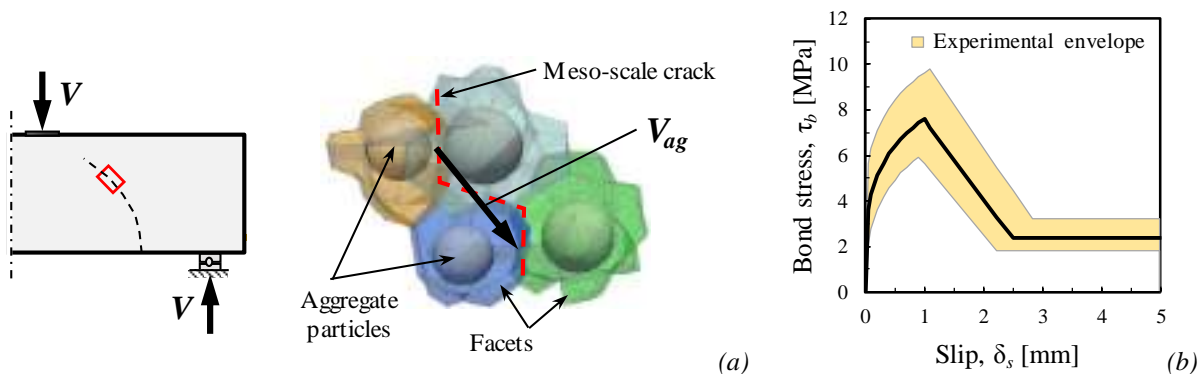


Figure 2: Computational modeling: (a) shear crack in GFRP RC beam and aggregate interlock with transfer of shear force, V_{ag} , in concrete LDPM; and (b) empirical bond stress-slip nonlinear model and envelope

Two sets of parameters characterize the concrete LDPM. The first set includes six geometric parameters that define the number and size distribution of the aggregate particles within a given volume. Information on the actual mixture design of concrete from the load tests (Matta et al. 2013) are used to determine the geometric parameters. The second set includes 15 meso-scale material parameters that describe the concrete elastic and inelastic behavior, and are determined based on uniaxial compression test results and a literature database of concrete properties (Khodaie et al. 2016).

The elastic behavior of concrete is described using the following meso-scale parameters: (1) normal modulus, E_0 ; and (2) shear-normal coupling parameter, α . E_0 and α determine the macroscopic Young's modulus of concrete, E_c , and Poisson's ratio, ν (Cusatis et al. 2011b). For example, the elastic portion of the stress-strain curve obtained through uniaxial compression tests on concrete cylinders provides the necessary information for calibrating these parameters.

The concrete fracture and frictional response are described primarily using the following meso-scale parameters: (1) tensile strength, σ_t ; (2) tensile characteristic length, l_t ; (3) shear strength ratio, σ_s / σ_t ; and (4) initial friction coefficient, μ_0 . Under pure tension, the maximum tensile stress and tensile softening modulus of the facets are described by σ_t and l_t , respectively. These parameters influence significant macroscopic properties including the fracture energy, G_F , where the initiation and propagation of cracks associated with mode I fracture occurs prior to



specimen failure in fracture tests, such as three-point bending tests (RILEM 1985). The resultant G_F for normal strength concrete (i.e., $f_c < 50$ MPa) is expected to lie within the range 80-100 J/m² (Bažant and Becq-Giraudon 2002; Rosselló et al. 2006). Therefore, these parameters can be calibrated also based on the results of numerically simulated fracture tests. The parameter σ_s/σ_t defines the ratio of the shear strength to the tensile strength of the facets. Under mixed-mode (I and II) concrete fracture in tension and shear, the strength limit of the facets is heavily influenced by the ratio σ_s/σ_t . As unconfined concrete undergoes mixed-mode fracture under uniaxial compressive forces, the ratio σ_s/σ_t controls the cylinder compressive strength, f_c . The initial friction coefficient, μ_0 , is the coefficient that is multiplied to the normal compressive stresses, which the product enhances the shear strength of the facets. It affects the frictional response of concrete in phenomena such as aggregate interlocking, by increasing the shear transfer along the diagonal cracks due to the generated compressive stresses as the crack fronts slide on one another. A more detailed example of calibration and validation of concrete LDPM meso-scale parameters is presented in Khodaie et al. (2016).

The salient geometric and material parameters of the concrete LDPM used for the S3 beams (Model A) and the S1 beams (Model B) are summarized in Table 2.

Table 2: Concrete LDPM meso-scale parameters for S3 beams (Model A) and S1 beams (Model B)

Geometric parameter	Models A and B	Material parameter	Model A	Model B
Cement mass content, c [kg/m ³]	389	Normal modulus, E_0 [GPa]	36	36
Water-to-cement ratio, w/c	0.45	Shear-normal coupling parameter, α	0.24	0.24
Aggregate-to-cement ratio, a/c	5.2	Tensile strength, σ_t [MPa]	3.1	2.8
Maximum aggregate size, d_a [mm]	19	Shear strength ratio, σ_s/σ_t	4.1	4.7
Fuller coefficient, η_F	0.45	Tensile characteristic length, l_t [mm]	180	170
Minimum aggregate size, d_0 [mm]	11	Initial friction, μ_0	0.2	0.2

The concrete used for the S3 and S1 beams had a nominal maximum aggregate size $d_a = 19$ mm, and an average cylinder compressive strength, f_c , of 32.1 MPa and 29.6 MPa, respectively (Matta et al. 2013). The meso-scale parameters for LDPM Model A and Model B were calibrated to attain these strength values. The numerical simulations of notched-beam fracture tests (RILEM 1985) using concrete Model A and Model B resulted in $G_F = 89$ J/m² and $G_F = 86$ J/m², respectively. Since these simulations produced realistic estimates for relevant macroscale properties (i.e., f_c and G_F), it was concluded that the suitable LDPM meso-scale parameters had been selected for Model A and Model B (Table 2). From this point, no further parameter calibration was performed, and the calibrated concrete LDPM models were implemented into their respective GFRP RC beam models.

GFRP bar model

Pultruded GFRP bars were used as longitudinal reinforcement in the beam specimens subject to load tests (Matta et al. 2013). These bars are made of an orthotropic GFRP material that exhibits a linear elastic behavior in uniaxial tension up to failure. While GFRP bars generally exhibit a higher tensile strength than conventional Grade 60 steel bars, their longitudinal elastic modulus, E , and shear modulus, G , are significantly lower (e.g., $G_{GFRP} \approx 0.1 G_{steel}$). To model these properties, the GFRP bar elements were formulated based on the Mindlin-Reissner plate theory (Reissner 1945), and the orthotropic shear modulus was obtained as the product of the isotropic shear modulus and a stiffness multiplier equal to 0.36. The Tsai-Hill failure criterion (Kaw 2005) was used for the GFRP bars under combined tensile-shear stresses.

Bond-slip model for GFRP-concrete interface

In the computational model, the interaction of the GFRP bars with the concrete is defined by connecting the GFRP bar nodes to adjacent LDPM tetrahedrons by means of nonlinear springs. The behavior of the nonlinear springs reflects the bond-slip law resulting from pull-out tests and beam tests for GFRP bars embedded in concrete. In this case, the modified Bertero-Popov-Eligehausen (BPE) model was implemented to describe the bond-slip law (Cosenza et al. 1997) in the LDPM-based numerical simulations. This shear (bond) stress-slip model consists of an ascending branch associated with chemo-mechanical bonding followed by a descending branch associated with frictional residual strength. This model is suitable to evaluate the bond-slip response at the GFRP bar-concrete interface (Lin and Zhang 2014). Figure 2b shows the nonlinear bond-slip law that was implemented in the LDPM-

based beam models. This model was defined by averaging numerous experimental data available in the literature (Benmokrane et al. 1996; Cosenza et al. 1997; Focacci et al. 2000).

Numerical simulation of load tests

The computational model for the numerical simulation of the load tests presented (Matta et al. 2013) was assembled using the concrete LDPM, the GFRP bar model, and the GFRP bar-concrete interface model. The model was implemented into a commercially available code that is capable of running LDPM-based simulations (ES3 2017). An explicit dynamic simulation was used, in which the loading plate moved at the constant rate of 4 cm/s, indicating a displacement control procedure. Such simulations are considered quasi-static since the kinetic energy due to dynamic load effects was found to be less than 1% of the internal work. Convergence was achieved using a maximum time step of 0.001 ms. The OpenMP parallel simulations were executed on a high-performance computing node with 12 threads (2.4 GHz Intel Xeon CPU, and 24 GB RAM).

RESULTS AND DISCUSSION

Structural response

Figure 3 presents the comparison of the load-midspan deflection response, crack patterns at failure from the experiments and the numerical simulations, and the maximum principal stress contour at peak load for the S3 beams. Here, the LDPM-based simulations accurately estimated the load-midspan deflection response as well as the crack patterns and the peak shear load (Figure 3a). Similar diagonal tension failures were attained in the experiments (Matta et al. 2013) and in the numerical simulation (Figure 3b), as the peak load was reached once the critical shear (diagonal) crack (Muttoni and Ruiz 2008) propagated in the shear span and into the compression strut.

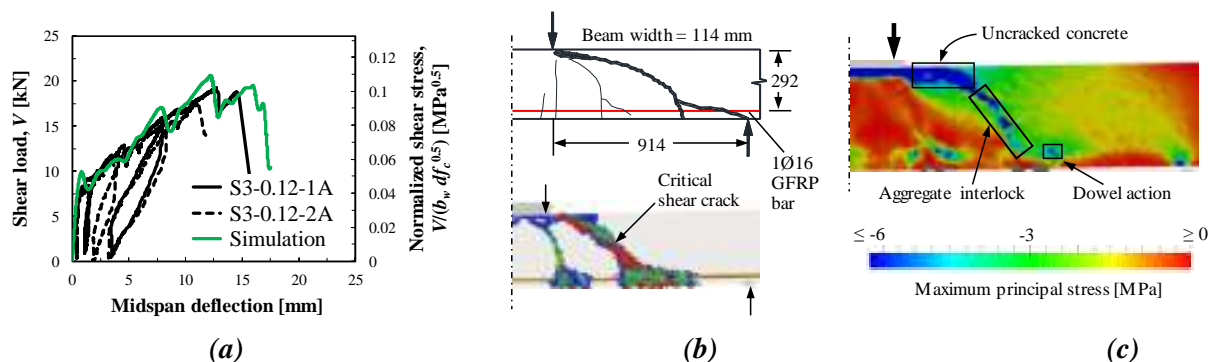


Figure 3: Results for medium-size S3 beams ($d = 292$ mm): (a) load-midspan deflection; (b) crack pattern at failure from experiments (top) and LDPM-based simulations (bottom); and (c) maximum principal stress contour at peak load. Dimensions in mm

For the S1 beams, the computational simulations produced fairly accurate estimates of pre- and post-cracking shear load-midspan deflection as well as crack pattern at failure, as illustrated in Figure 4a-b. In the simulations, the critical shear crack formed at the peak shear load and instantly propagated towards the loading plate, resulting in brittle failure at a sectional shear stress 30% smaller than for the S3 beams. As summarized in Table 1, these preliminary results are significant since they show, for the first time, that computational simulations hold potential to: (a) accurately predict the shear response of slender GFRP RC beams without shear reinforcement up to failure, irrespective of size, thereby overcoming a limitation of existing nominal strength algorithms; and (b) investigate the role of different shear transfer mechanisms at different loading stages.

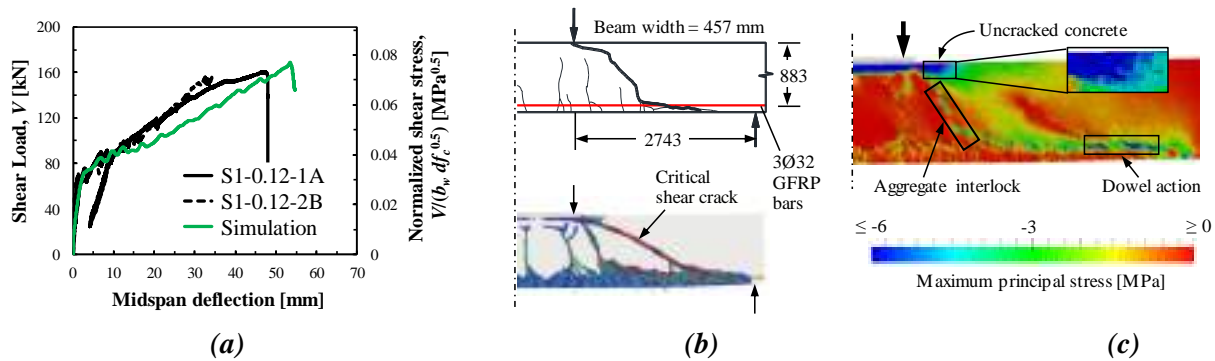


Figure 4: Results for large-size S1 beams ($d = 883$ mm): (a) load-midspan deflection; (b) crack pattern at failure from experiments (top) and LDPM-based simulations (bottom); and (c) maximum principal stress contour at peak load. Dimensions in mm

The contribution of these mechanisms as a function of beam size is discussed in the following section.

Shear force resisting mechanisms

The maximum principal stress contours in Figure 3c and Figure 4c highlight different shear transfer mechanisms in the S3 and S1 beams, respectively. Here, compressive (negative) principal stresses identify areas where shear forces are resisted, including the uncracked concrete above the neutral axis, the diagonal crack fronts where aggregate interlocking develops, and the GFRP bar around the cracked concrete where dowel action develops.

Table 3 summarizes the contribution of each major shear transfer mechanism to the shear capacity of the beams for the LDPM-based modeling approach reported herein. Shear forces are resisted primarily by the uncracked concrete subject to combined compression and shear stresses above the critical shear crack. Here, 68% and 86% of the shear capacity in the S3 and S1 beam model, respectively, is transmitted by means of inclined compressive stresses through the uncracked concrete ligament above the critical shear crack. However, the contribution of said mechanism to the normalized shear strength decreased by $0.008 \text{ MPa}^{0.5}$ (11%) as the effective depth increased from 292 mm (S3 beams) to 883 mm (S1 beams). This result may be attributed to size effect in shear-compression fracture of the concrete above the critical shear crack (Bažant and Yu 2005). Since the concrete used for all beams has a similar compressive strength ($f_c \approx 30 \text{ MPa}$) and maximum aggregate size ($d_a = 19 \text{ mm}$), the effective width of the microcracking ('fracture process') zone (FPZ), $w_c \approx 3d_a$ (Bažant and Oh 1983), is negligibly affected by the size of the beam. Therefore, increasing the effective depth, d , results in a proportionally deeper uncracked concrete ligament, wherein the constant FPZ width results in a less uniform compressive stress profile for the S1 beams (Figure 4c) compared to the S3 beams (Figure 3c), as originally demonstrated by Bažant and Yu (2005) through numerical simulations.

Table 3: Contribution of shear transfer mechanisms at peak shear load

Specimen	Uncracked concrete		Aggregate interlock		Dowel action	
	Portion of shear capacity [%]	Contribution to $\frac{V_e}{b_w d \sqrt{f_c}}$	Portion of shear capacity [%]	Contribution to $\frac{V_e}{b_w d \sqrt{f_c}}$	Portion of shear capacity [%]	Contribution to $\frac{V_e}{b_w d \sqrt{f_c}}$



		[$\sqrt{\text{MPa}}$]		[$\sqrt{\text{MPa}}$]		[$\sqrt{\text{MPa}}$]
S3 beams ($d = 292$ mm)	68	0.073	29	0.031	3	0.003
S1 beams ($d = 883$ mm)	86	0.065	10	0.008	4	0.003

It is of particular interest to note that the contribution of the aggregate interlocking mechanism drastically decreased from 29% to 10% of the shear capacity as the effective depth increased from 292 mm (S3 beams) to 883 mm (S1 beams). This decrease is reasonably attributed to the proportionally wider cracks in the S1 beams, which hindered the transfer of shear forces (Bentz et al. 2010). By the same token, the normalized shear strength contribution of aggregate interlock decreased by $0.023 \text{ MPa}^{0.5}$ (74%) in the S1 beams compared to the S3 beams. Instead, dowel action provides a similarly negligible contribution to shear strength, also due to the relatively small shear stiffness of the longitudinal GFRP bars. Based on these results, and limited to the cases presented in this paper, aggregate interlocking along the critical shear crack appears to be the dominant mechanism contributing to size effect on the shear strength of GFRP RC beams without stirrups.

CONCLUSIONS

Numerical models of GFRP RC beams without stirrups, and with effective depth ranging from 292 mm to 883 mm, were built using a calibrated and validated concrete LDPM, an orthotropic GFRP bar model, and a nonlinear bond-slip law for GFRP bar-concrete interfaces. For the case of beams subject to four-point bending loading reported in the literature (Matta et al. 2013), for which existing nominal strength algorithms may yield overconservative estimates, the results of the numerical simulation accurately described damage progression, failure load, and failure mode, irrespective of the beam size.

In addition, these results indicate that the proposed computational modeling approach holds potential to realistically simulate salient load-resisting mechanisms, and investigate their contribution to size effect. For the scaled beams and loading conditions discussed herein, it was found that: (1) the major contributing mechanisms to shear strength are the shear-compression resistance provided by the uncracked concrete above the critical (diagonal) shear crack, and aggregate interlocking along said crack; and (2) the latter mechanism is the major contributor to size effect.

ACKNOWLEDGMENTS

The authors gratefully acknowledge the support of the University of South Carolina, Columbia (USC). Special thanks are extended to Engineering and Software System Solutions (ES3), Inc., and USC Research Cyberinfrastructure (Division of Information Technology), for technical assistance with the computational software MARS.

REFERENCES

- AASHTO (2009). "AASHTO LRFD bridge design guide specifications for GFRP-reinforced concrete bridge decks and traffic railings", 1st edition, American Association of State Highway and Transportation Officials, Washington, D.C., USA.
- ACI Committee 440 (2015). "Guide for the design and construction of structural concrete reinforced with Fiber-Reinforced Polymer (FRP) Bars", *ACI 440.1R-15*, American Concrete Institute, Farmington Hills, MI, USA.
- Z.P. Bažant, E. Becq-Giraudon (2002). "Statistical prediction of fracture parameters of concrete and implications for choice of testing standard", *Cement and Concrete Research*, 32(4), 529-556.
- Z.P. Bažant, B. Oh (1983). "Crack band theory for fracture of concrete", *Materials and Structures*, 16, 155-177.
- Z.P. Bažant, Q. Yu (2005). "Designing against size effect on shear strength of reinforced concrete beams without stirrups: II. verification and calibration", *Journal of Structural Engineering*, 131(12), 1886-1897.
- Z.P. Bažant, Q. Yu, W. Gerstle, J. Hanson, J.W. Ju (2007). "Justification of ACI 446 code provisions for shear design of reinforced concrete beams", *ACI Structural Journal*, 104(5), 601-610.



- B. Benmokrane, B. Tighiouart, O. Chaallal (1996). "Bond strength and load distribution of composite GFRP reinforcing bars in concrete", *ACI Materials Journal*, 93(3), 246-253.
- E.C. Bentz, L. Massam, M.P. Collins (2010). "Shear strength of large concrete members with FRP reinforcement", *Journal of Composites for Construction*, 14(6), 637-646.
- M.P. Collins, D. Kuchma (1999). "How safe are our large, lightly RC beams, slabs, and footings?", *ACI Structural Journal*, 96(4), 482-490.
- E. Cosenza, G. Manfredi, R. Realfonzo (1997). "Behavior and modeling of bond of FRP rebars to concrete", *Journal of Composites for Construction*, 1(2), 40-51.
- CAN/CSA-S6-14 (2014). "Canadian highway bridge design code", *Canadian Standards Association*, Mississauga, ON, Canada.
- G. Cusatis, A. Mencarelli, D. Pelessone, J. Baylot (2011a). "Lattice discrete particle model (LDPM) for failure behavior of concrete. II: Calibration and validation", *Cement and Concrete Composites*, 33(9), 891-905.
- G. Cusatis, D. Pelessone, A. Mencarelli (2011b). "Lattice discrete particle model (LDPM) for failure behavior of concrete. I: Theory", *Cement and Concrete Composites*, 33(9), 881-890.
- ES3 (2017). "MARS manual", v. 2017.06.27, Engineering and Software System Solutions, Inc., Clearfield UT.
- F. Focacci, A. Nanni, C. Bakis (2000). "Local bond-slip relationship for FRP reinforcement in concrete", *Journal of Composites for Construction*, 4(1), 24-31.
- G.N. Kani (1967). "How safe are our large reinforced concrete beams", *ACI Journal Proceedings*, 64(3), 128-141.
- A.K. Kaw (2005). "Mechanics of composite materials", 2nd edition, CRC Press, Boca Raton, FL.
- S. Khodaie, F. Matta, M. Alnaggar (2016). "Lattice discrete particle modeling of shear failure in scaled GFRP reinforced concrete beams without stirrups", *Proc. 9th International Conference on Fracture Mechanics of Concrete and Concrete Structures (FraMCoS-9)*, Berkeley, CA, USA, V. Saouma, J. Bolander and E. Landis (Eds.), 12 p.
- S. Khodaie, F. Matta, M. Alnaggar (2017). "Numerical simulation of shear behavior of scaled GFRP reinforced concrete beams without stirrups using lattice discrete particle model", *Proc. 6th Asia-Pacific Conference on FRP in Structures (APFIS 2017)*, Singapore, Paper #55.
- X. Lin, Y.X. Zhang (2014). "Evaluation of bond stress-slip models for FRP reinforcing bars in concrete", *Composite Structures*, 107(1), 131-141.
- F. Matta (2008). "Industry/university cooperative research on advanced composite reinforcement for concrete: translating innovation into sustainable engineering practice." *Proc. US National Science Foundation International Workshop on the Use of Fiber Reinforced Polymers for Sustainable Structures*, Cairo, Egypt, S.H. Rizkalla and A.-H. Hosny (Eds.), CD-ROM, 13 p.
- F. Matta, A.K. El-Sayed, A. Nanni, B. Benmokrane (2013). "Size effect on concrete shear strength in beams reinforced with fiber-reinforced polymer bars", *ACI Structural Journal*, 110(4), 617-628.
- A. Muttoni, M.F. Ruiz (2008). "Shear strength of members without transverse reinforcement as function of critical shear crack width", *ACI Structural Journal*, 105(2), 163-172.
- E. Reissner (1945). "The effect of transverse shear deformation on the bending of elastic plates", *Journal of Applied Mechanics*, 12, 69-77.



**9th International Conference on Fibre-Reinforced Polymer (FRP)
Composites
in Civil Engineering (CICE 2018), PARIS 17-19 JULY 2018**

RILEM (1985). "Determination of the fracture energy of mortar and concrete by means of three-point bend tests on notched beams", *Materials and Structures*, 18(106), 285-290.

C. Rosselló, M. Elices, G.V. Guinea (2006). "Fracture of model concrete: 2. Fracture energy and characteristic length", *Cement and Concrete Research*, 36(7), 1345-1353.

J.K. Wight (2015). "Reinforced concrete mechanics and design", 7th edition, Pearson, New York, NY, USA.



EFFECT OF HIGH TEMPERATURES ON THE BOND PERFORMANCE OF GFRP BARS TO CONCRETE

Inês C. Rosa¹, João P. Firmo^{1,2}, Luís Granadeiro¹, João R. Correia¹

¹ CERIS, Instituto Superior Técnico, University of Lisbon, Portugal

² Corresponding author, Email : joao.firmo@tecnico.ulisboa.pt

ABSTRACT

Glass fibre reinforced polymer (GFRP) bars have been successfully used during the last decade to reinforce concrete structures subjected to aggressive environments, especially due to their corrosion resistance and increasingly competitive costs when compared to stainless steel reinforcement. However, it is well known that the strength, stiffness and bond properties of GFRP rebars are severely reduced with increasing temperatures, particularly when approaching the glass transition temperature (T_g) of the polymer matrix (typically in the range of 65-150 °C). This paper presents results of an experimental investigation on the bond between concrete and sand-coated GFRP bars at moderately elevated temperatures. Pull-out tests on GFRP bars embedded in concrete cylinders were performed up to 140 °C; in these tests two bond lengths of the GFRP bars were considered, corresponding to 5 and 9 times the diameter of the rebars. Specimens were first heated up to the predefined temperature (20, 40, 60, 80, 100 or 140 °C) and then loaded up to failure. The applied load and the slip of the bars at both loaded and free ends were measured; the results obtained confirmed that the stiffness and strength of the GFRP-concrete interface suffers significant reductions with temperature, especially when the T_g of the GFRP rebars is approached. Bond vs. slip relations of the GFRP-concrete interface are proposed for each tested temperature; these relations were derived based on a fitting procedure of the experimental data to a bond vs. slip model available in the literature for FRP bars in concrete, originally developed for ambient temperature.

KEYWORDS

Experimental study; temperature; FRP internal reinforcement; bond and interfacial stresses.

INTRODUCTION AND RESEARCH SIGNIFICANCE

Glass fibre reinforced polymer (GFRP) rebars have been emerging as a non-corrodible alternative to ordinary steel reinforcement, especially in highly corrosive environments where the durability of constructions is an issue. GFRP rebars present other advantages, such as low weight, high tensile strength and electromagnetic transparency, making them suitable for applications in both new construction and rehabilitation of existing degraded reinforced concrete (RC) structures (*e.g.*, as a replacement for steel corroded rebars).

In spite of such potential, there are serious concerns about the behaviour of GFRP rebars at elevated temperature and under fire exposure, since their mechanical properties (namely, the tensile strength and the E-modulus) experience significant reductions, especially when approaching the glass transition temperature (T_g) of the polymeric matrix (usually between 65-150 °C). Despite its relevance, the fire performance of GFRP materials and especially of GFRP-RC structures is still not well understood in the literature, which partly explains why a great majority of existing design guidelines do not recommend the use of GFRP rebars in structures where the fire action has to be considered at design (*i.e.*, in buildings).

Moreover, elevated temperature has been referred to play an important role on the deterioration of the bond capacity of GFRP rebars to concrete (Katz *et al.* 1999). This is particularly worrying, even for moderately elevated temperatures, since several authors (*e.g.*, Abbasi and Hogg 2006) have reported premature structural collapses of GFRP-RC slabs exposed to fire, due to the rebar's debonding in the lap-slices. Despite its importance, few studies have been developed about this topic.

Katz *et al.* (1999) performed pull-out tests in steel and GFRP rebars with different superficial finishes. The T_g of the GFRP rebars ranged from 60 °C to 124 °C (test method not reported). The steel/GFRP-concrete specimens, with an embedment length in concrete of 5 diameters, were heated up from room temperature (20 °C) up to 250 °C (measured at the centre of the specimens). The following conclusions were obtained: (i) for GFRP bars most part of the bond strength reduction occurred for temperatures below 180-200 °C; (ii) at 200 °C, the GFRP bond strength was reduced at least 80% (compared to that measured at room temperature), while in the steel rebars the bond



losses, at that temperature, were only of 38%; (iii) above 200 °C, the bond strength did not exhibit significant further reductions with temperature.

Further studies conducted by Katz and Berman (2000) validated the results obtained in the previous study, and allowed concluding that the bond strength depends firstly and mostly on parameters associated with the surface properties and geometry of the rebars. The authors identified the following parameters as being the most relevant to the GFRP-concrete bond degradation with temperature: (i) the bond strength at room temperature (provided by the surface finishing and roughness of the reinforcement); (ii) the T_g of the material at the surface of the rebar; (iii) the residual bond strength, *i.e.*, the bond strength at a high temperature where no further reductions occurs; (iv) the degree of crosslinking of the polymer matrix (as the number of crosslinks increase, the nature of the polymer is expected to change, reducing the degradation rate of the material as temperature increases).

McIntyre *et al.* (2014) studied the GFRP-concrete bond performance for temperatures that varied roughly between 25 °C and 150 °C, using GFRP rebars with two types of surface finishing: (i) a thin sand coating associated with a double helical fibre wrap (BPG rebar); and (ii) a coarse sand coating (PTG rebar). The T_g of the rebars were 86 °C and 84 °C, respectively (based on the onset of the storage modulus curve). The embedment length of the rebars in concrete was approximately 4 times the diameter of the rebars. A steep reduction of the bond strength occurred for temperatures up to the T_g of the rebars: at that temperature, strength retentions were about 54 and 44% (compared to the bond strength at 25 °C), for the BPG and PTG rebars, respectively. At 150 °C, bond strength retentions were 37% for the BPG rebar and only 18% for the PTG rebar. However, it should be noted that the vast majority of the specimens exhibited splitting failure, instead of (the desired) pull-out failure.

In light of the brief literature review presented above, a set of aspects arise as issues of great importance. Firstly, the number of studies about the reduction of the GFRP bond properties with temperature is very limited. Therefore, additional and more comprehensive investigations are required to fully understand the degradation mechanisms that take place at the GFRP-concrete interface, and their influence on the structural performance of GFRP-RC structures exposed to elevated temperature and fire conditions. Secondly, additional experimental studies are needed to further evaluate the temperature dependence of a set of parameters expected to affect the bond properties of the rebars at elevated temperature, namely: surface finishing, diameter, geometry and embedment length in concrete. Finally, bond *vs.* slip models that describe the GFRP-concrete bond constitutive relation as a function of temperature are also not available in the literature.

This paper presents experimental investigations on the effects of moderately elevated temperatures on the bond between GFRP rebars and concrete. In this regard, pull-out tests were performed in sand coated GFRP rebars, embedded in concrete cylinders, from room temperature up to 140 °C. The influence of two different bond lengths (5 and 9 times the diameter of the rebars) in the bond properties at elevated temperature was investigated. In the final part of this paper simplified bond *vs.* slip relations of the GFRP-concrete interface are proposed for each tested temperature; these relations were derived based on a fitting procedure of the experimental data to a bond *vs.* slip model available in the literature for FRP bars in concrete developed for ambient temperature.

DESCRIPTION OF THE EXPERIMENTAL INVESTIGATION

Test programme

The experimental campaign comprised pull-out tests on sand coated GFRP rebars, embedded in concrete cylinders, at the following temperatures: 20, 40, 60, 80, 100 and 140 °C. Two series of pull-out tests were carried out, corresponding to two different embedment lengths (L_b) of the GFRP rebars in concrete: 5 and 9 times the diameter (d_b) of the rebars - 50 and 90 mm, respectively.

Materials

Sand coated GFRP rebars with a vinylester matrix and external helically wound fibres were used in this study. The rebars were 10 mm in diameter and were supplied by Hughes Brothers (model Aslan 100). Dynamic mechanical analyses (DMA) were performed as defined in ASTM E1640 and allowed defining a T_g of 98 °C based on the onset of the storage modulus curve (average value between three curves). The inorganic content in mass (*i.e.*, the fibre content, determined from burn-off-tests) of the rebars was 75%.

Previous tensile tests at elevated temperatures (from room temperature up to 300 °C) on these rebars were performed by Santos (2016). The results (*cf.* Figure 1 a) showed that the tensile strength decreased significantly when the T_g was exceeded, presenting average reductions of 40% and 43%, at 150 °C and 300 °C, respectively,

when compared to the strength at room temperature. The elasticity modulus was substantially less reduced at 300 °C, exhibiting an average reduction of 13% compared to that measured at room temperature.

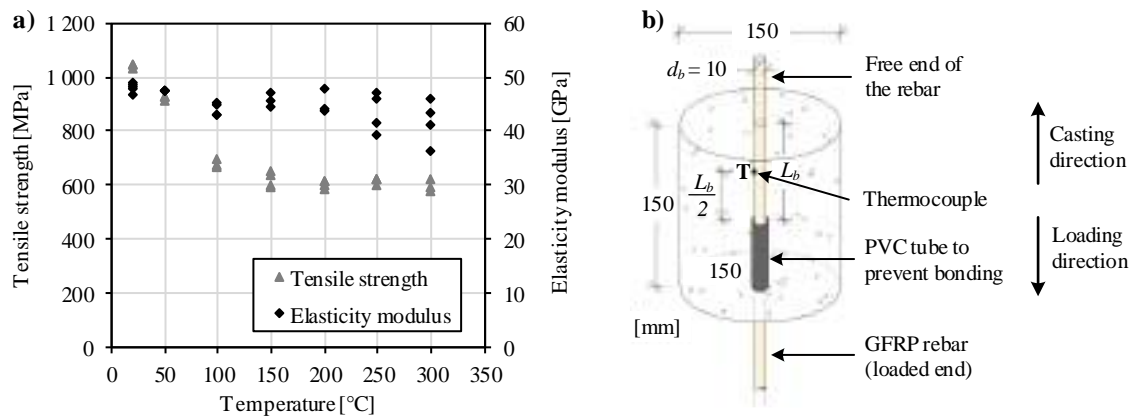


Figure 1: a) Tensile properties of GFRP rebars as a function of temperature; b) Pull-out test specimen geometry and thermocouples placement.

Concrete class C25/30 with cement type CEM II/A-L 42.5R and limestone aggregates was used to produce the specimens for the pull-out tests. The concrete's compressive and tensile properties were determined at the age of 111 days (age of testing). During that period, the test specimens, as well as the cylinders and cubes used to characterize the concrete's properties, were cured in the laboratory facilities at room temperature and relative humidity (indoor, but not controlled). The compressive and splitting tensile strength tests were performed, providing the following average values: cube compressive strength of 43.3 MPa and splitting tensile strength of 3.1 MPa.

Geometry of specimens

The test specimens consisted of concrete cylinders (height of 150 mm, diameter of 150 mm) with a single GFRP rebar (total length of 745 mm) embedded vertically along the central axis of the cylinder (*cf.* Figure 1b). The unbonded length of the rebars was set using a bond breaker made of a PVC tube, as shown in Figure 1b. At the free end, the rebars were slightly protruded from the concrete cylinder, thus allowing to read the slip between that end of the rebar and the top surface of the concrete (with a video extensometer, as explained in the next section). The loaded end of the rebars was protected using stainless steel tubes (diameter of 22 mm, 0.7 mm thick, *cf.* Figure 2a) to prevent premature tensile failure at the grip of the universal testing machine.

Test setup and instrumentation

The test setup used in the pull-out test is illustrated in Figure 2. The concrete specimens were placed on a metal frame composed by two metal plates, connected with steel rods, which acted as a reaction device. The frame was installed inside a *Tinius Olsen* thermal chamber (Figure 2b) and coupled to an *Instron* universal testing machine (load capacity of 250 kN).

The specimens' temperature was measured with type K thermocouples (external diameter of 1 mm), positioned at mid-height of the embedment length at the rebars-concrete interface, as illustrated in Figure 1b. An additional thermocouple was used to control the temperature inside the thermal chamber. The slip of the rebars was measured at both free and loaded ends using a video extensometer (Figure 2c); the equipment consists of a high definition video camera (*Sony*, model *XCG 5005E*, with *Fujinon* lens - model *Fujifilm HF50SA 1*), placed on a tripod. As Figure 2a illustrates, target dots were marked on the GFRP rebar (free and loaded ends) and on angle brackets (fixed to the concrete's surface and to the bottom metal plate, respectively), allowing to measure the relative displacement (*i.e.*, the slip) between the rebar and the concrete at both free and loaded ends.

Test procedure

The experimental procedure consisted of two different stages; in the first stage of the test, the specimens were heated up to a predefined temperature, at an average heating rate of the air inside the thermal chamber of 10.5 °C/min; the second stage, during which the specimens' temperature was kept constant at the target value, consisted of loading the specimen (*i.e.*, pulling the GFRP rebar) until failure; the load was applied under

displacement control, at an approximate speed of 1 mm/min (test speed defined according to the limits set in ASTM D7913). During this stage, the applied load, the cross-head displacement of the test machine and the position of the target dots were monitored. The tests were carried out until the target dots were no longer traceable (by the video extensometer) or the maximum displacement of the testing machine was reached. For each temperature and bond length, at least three specimens were tested.

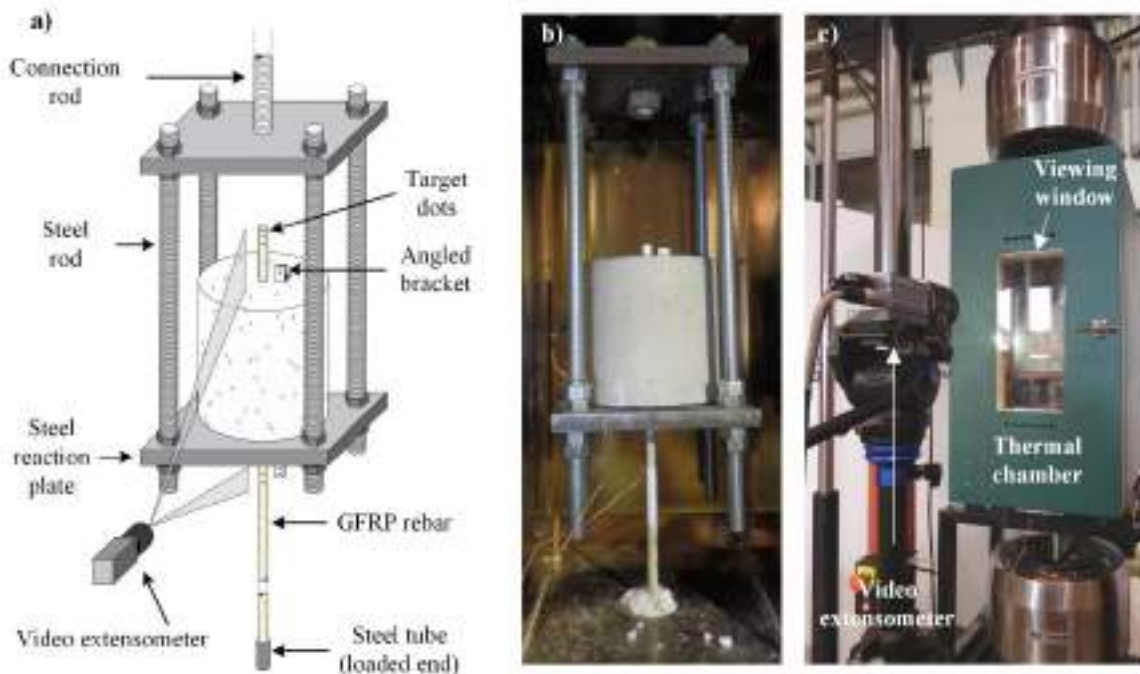


Figure 2: a) Pull-out test setup; b) general view of specimen in the thermal chamber; c) external view of thermal chamber and video extensometer.

EXPERIMENTAL RESULTS AND DISCUSSION

Average bond stress vs. slip curves

Figure 3 presents the average bond stress vs. slip curves, at both loaded (Figure 3a) and free (Figure 3b) ends of the rebars, for representative specimens of each series. It is worth mentioning that the curves for each series and target temperatures were not necessarily obtained from the same specimen, which explains the slight differences of the peak values between curves from Figures 3a and 3b.

Figure 3a shows that regardless of the bond length, the curves reflected an approximately linear behaviour until the maximum average bond stress was attained, which was followed by a stress drop (with exception of the specimens tested at 100 °C, where such drop did not occur); this drop was followed by a progressive stress reduction (presenting almost a plateau for higher slips). This final stage of the curves extended up to the end of the tests, which were interrupted before the complete pull-out of the rebars (this issue is further addressed in the next section). The specimens tested at 100 °C presented a different post-peak behaviour compared to the remaining specimens: (i) after the maximum bond stress was attained, the stress values presented a significantly less expressive drop; and (ii) the maximum bond stress was attained for considerably higher slip values. A possible explanation to this difference may be related to the fact that this temperature virtually matches the glass transition temperature of the rebars (98 °C), for which the viscoelasticity of the material is maximum.

The representative curves plotted in Figure 3a also show that (i) for a certain temperature, as expected, the specimens with shorter bond length ($5d_b$ series) were able to attain higher average bond stresses and (ii) the maximum bond stress values were progressively reduced as the testing temperature increased. The effect of elevated temperature was also noticeable in the reduction of the bond stiffness (corresponding to the slope of the initial linear branch); this result was also expected, since for elevated temperatures the stiffness and strength of the constituent materials and especially of the GFRP-concrete interface are reduced.

Figure 3b shows that, overall, the average bond stress vs. free end slip curves exhibited a similar behaviour to the those plotted in Figure 3a; however, as expected, for specimens tested at lower temperatures (*i.e.* 20 and 40 °C), the initial branch of the curves is almost vertical (*i.e.*, the slip at the free end is practically zero); as the test temperatures increased, the initial slope of the curves decreased, mainly due to the degradation of the rebar-concrete interface, as mentioned above.

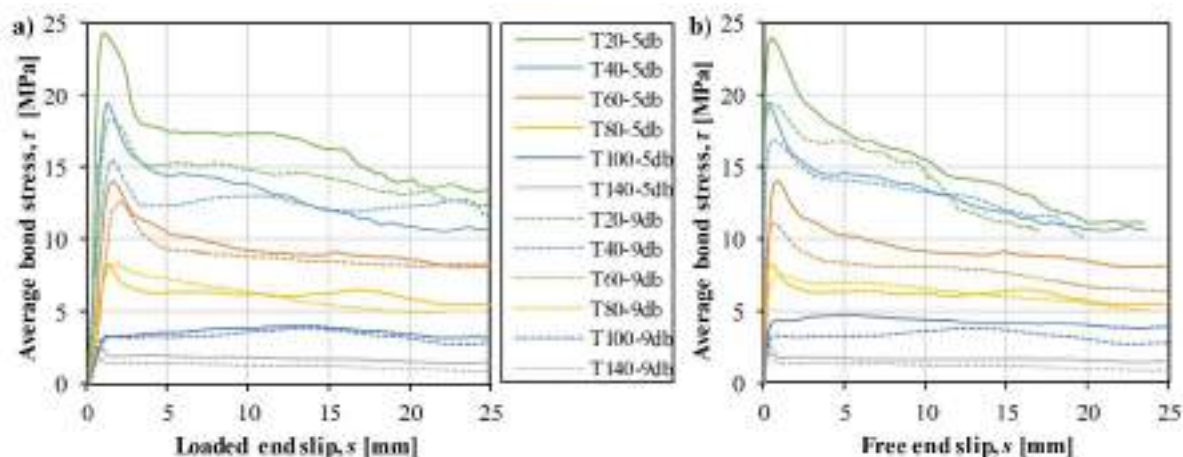


Figure 3: Average bond stress vs. a) loaded end and b) free end slips for representative specimens of all tested temperatures (note: the curves for each series and target temperatures were not necessarily obtained from the same specimen).

Failure modes

The expected failure mode of the specimens consisted of the pull-out of the GFRP rebars. Although the tests were interrupted before the complete pull-out of the rebars (because the video extensometer dots were no longer trackable, or the stroke of the test machine was attained), no splitting failure was observed. The experimental results (described in the previous section) and the visual observations of the specimens throughout the tests (*e.g.*, Figure 4a and b) validated the expected failure mode of the specimens by pull-out.

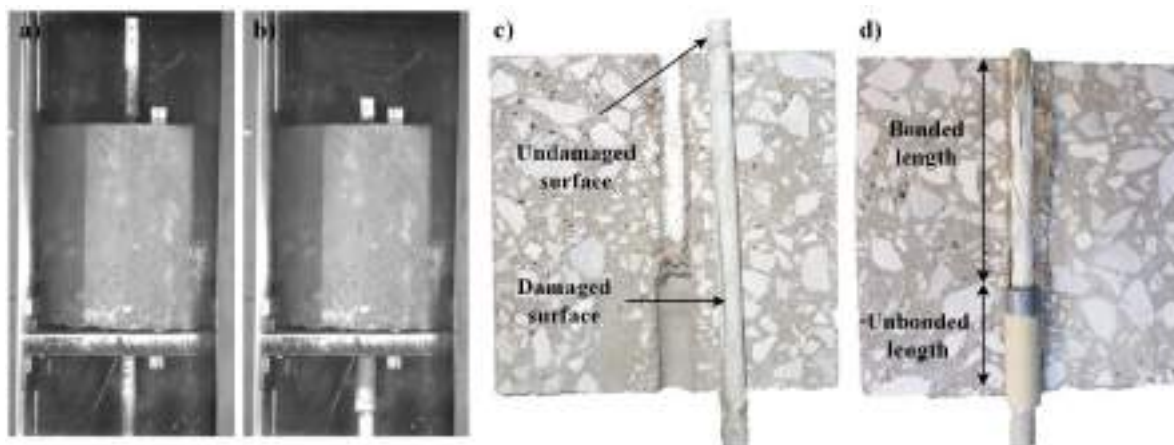


Figure 4: Slip of the rebar (free end) at a) the beginning and b) end of the test; GFRP-concrete specimens tested at c) elevated temperature and d) at room temperature.

After the tests, all concrete cylinders were saw cut into two pieces to confirm the failure modes and evaluate the damage underwent by the materials and the GFRP-interface. As shown in Figure 4c, the external layer of the GFRP rebars in the specimens tested at elevated temperatures was significantly abraded; in particular, the wound fibres were ripped and the sand coated superficial layer was peeled; residues of crushed resin and broken glass fibres were attached to the concrete (along the embedment length of the rebar). No damage on the core of the rebar was observed. However, in some specimens tested at room temperature (Figure 4d) the abrasion introduced to the rebar was more severe: the superficial layer of sand and the wound fibres were completely removed, the core of the rebar was exposed, and a substantial amount of longitudinal fibres were broken and stripped from the core.



A possible explanation for the plateau of the load-displacement curves plotted in Figure 3 is the entrance of the free end length of the rebar into the concrete cylinder. When in contact with the concrete's surface, this undamaged portion of the rebar might have enhanced the GFRP-concrete friction, compared to the one provided by the damaged (and initially embedded) length of the rebar, thus providing an additional contribution to the overall resistance against slip.

Bond strength

Figure 5 presents the variation of the normalized average bond strength with temperature, as well as the tensile properties (strength and modulus) and the storage modulus (from DMA tests) of the rebars. This figure shows that the bond strength was significantly reduced with temperature, even for temperatures well below the glass transition temperature of the GFRP rebars (98 °C). As shown in Table 1, for a temperature as low as 60 °C (that can be attained in outdoor applications), bond strength retentions were about 60-70% of that at room temperature (20 °C), while for 100 °C and 140 °C retentions were only of 20% and 10%, respectively. Moreover, the results highlighted that: (i) the bond strength exhibited a similar decrease with temperature for the two test series (*i.e.*, for the two different bond lengths); (ii) the reduction of the GFRP-concrete bond strength occurred for much lower temperatures than the mechanical degradation at the material level (as measured in the tensile tests and in the DMA tests).

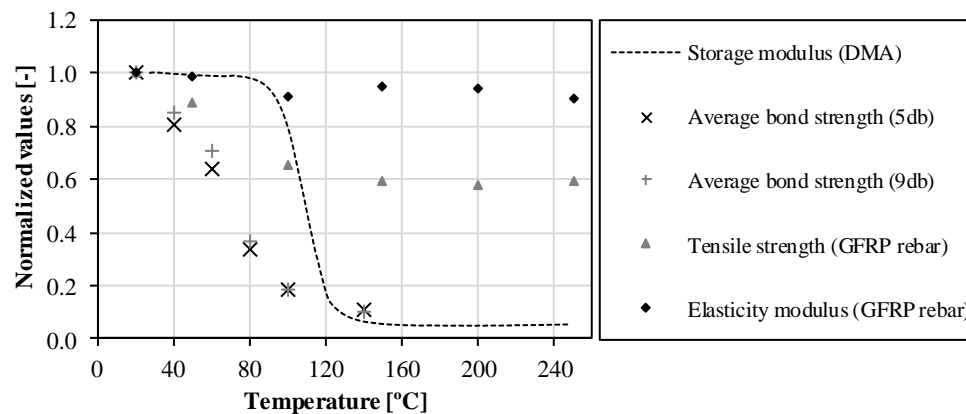


Figure 5: Normalized average values of bond strength, tensile strength, elasticity and storage modulus of the GFRP rebars, all as a function of temperature.

Table 1: Results obtained in terms of maximum load, average bond strength and normalized maximum load (average \pm standard deviation).

Temperature [°C]	Bond length to concrete = 5.d _b			Bond length to concrete = 9.d _b		
	Maximum load [kN]	Average bond strength [MPa]	Normalized bond strength [-]	Maximum load [kN]	Average bond strength [MPa]	Normalized bond strength [-]
20 \pm 2	35.9 \pm 3.4	22.8 \pm 2.2	1.00 \pm 0.09	54.6 \pm 3.1	19.3 \pm 1.1	1.00 \pm 0.06
40 \pm 2	29.4 \pm 2.0	18.7 \pm 1.3	0.82 \pm 0.06	46.5 \pm 2.0	16.4 \pm 0.7	0.85 \pm 0.04
60 \pm 2	23.3 \pm 1.3	14.8 \pm 0.8	0.65 \pm 0.04	38.8 \pm 5.5	13.7 \pm 2.0	0.71 \pm 0.10
80 \pm 2	12.3 \pm 1.0	7.8 \pm 0.6	0.34 \pm 0.03	20.1 \pm 3.2	7.1 \pm 1.1	0.37 \pm 0.06
100 \pm 2	6.8 \pm 1.3	4.3 \pm 0.8	0.19 \pm 0.04	10.1 \pm 2.7	3.6 \pm 1.0	0.18 \pm 0.05
140 \pm 2	4.0 \pm 0.3	2.5 \pm 0.2	0.11 \pm 0.01	5.5 \pm 0.4	1.9 \pm 0.2	0.10 \pm 0.01

Simplified bond vs. slip curves

The bond behaviour between reinforcing bars and concrete is usually described through bond stress vs. slip relations/models; however, for GFRP rebars there is still no unified model to reproduce their bond behaviour to concrete. A recent state of the art review by Yan *et al.* (2016) about this topic summarized the bond models that

have been used in the literature for GFRP rebars; additionally, the accuracy of these bond models in reproducing GFRP-concrete bond at ambient temperature was also assessed; it was concluded that a modified version of the BPE model (originally developed for steel rebars) proposed by Cosenza *et al.* (1997) (*cf.* Figure 6a) is able to accurately simulate the GFRP-concrete bond, provided that its defining parameters are properly fitted to experimental data. This model is characterized by three stages (*cf.* Figure 6a): (i) a nonlinear ascending stage (equation 1); (ii) a linear descending branch (equation 2); and (iii) a final plateau.

In the present paper, a slightly different version of the BPE modified model is proposed, in which the final plateau is replaced by an additional linear descending branch (equation 3), in agreement with the behaviour observed in the experimental data (*cf.* Figure 3). The parameters involved in equations (1) to (3) (defined in Figure 6a) were obtained for all tested temperatures and based on a fitting procedure that minimizes the mean square error to the experimental bond *vs.* slip curves obtained in the specimens from series 5 *db*, as for relatively short embedded lengths the shear stress along the rebar-concrete interface is usually assumed as uniform.

$$\tau(s) = \tau_{max} \left(\frac{s}{s_1} \right)^\alpha \quad (1)$$

$$\tau(s) = \tau_{max} - \tau_{max} p_1 \left(\frac{s}{s_1} - 1 \right) \quad (2)$$

$$\tau(s) = \tau_f - \tau_f p_2 \left(\frac{s}{s_2} - 1 \right) \quad (3)$$

Table 2 lists the parameters obtained for the different temperatures and Figure 6b plots the corresponding bond *vs.* slip curves. As expected, the curves present a similar overall behaviour when compared to the experimental ones (*cf.* Figure 3); this good agreement is attested by the relatively low values of the absolute mean percentage error (AMPE). It is worth mentioning that the bond *vs.* slip curves proposed herein are valid for the specific GFRP rebars used in the tests. In the future, the authors will assess and eventually revise these simplified models to consider the influence of the surface finishing of the rebars; an alternative procedure to derive the bond *vs.* slip relations (assuming a non-uniform distribution of the shear stress along the rebars-concrete interface) will also be used.

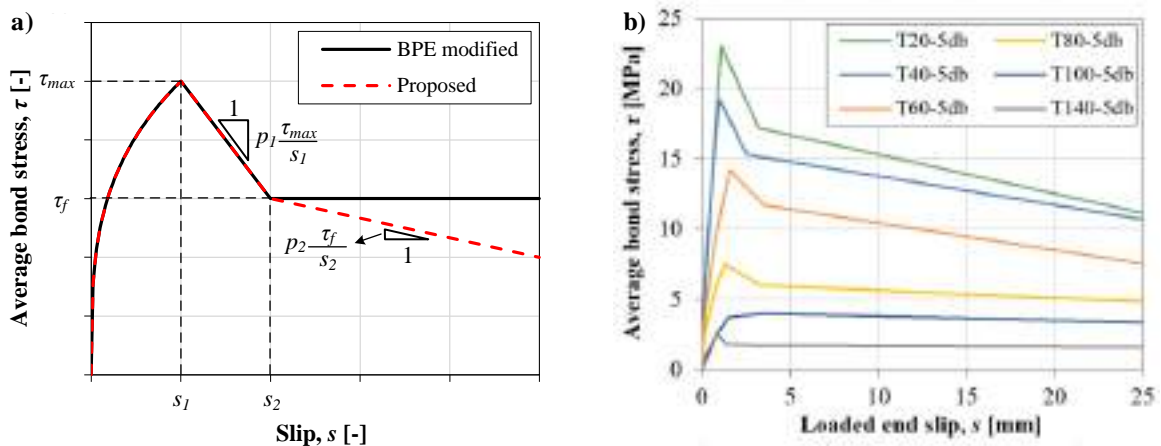


Figure 6: a) BPE modified model and proposed model; b) calibrated bond *vs.* slip relations.

Table 2: Parameters of the calibrated bond *vs.* slip relations (see equations (1) to (3)) for all tested temperatures and both bond lengths; absolute mean percentage errors (AMPE).

Temperature	20 °C	40 °C	60 °C	80 °C	100 °C	140 °C
τ_{max} [MPa]	23.0	19.2	14.2	7.5	3.7	2.5
s_1 [mm]	1.1	1.0	1.6	1.3	1.50	0.83
α [-]	0.783	0.640	0.590	0.538	0.728	1.081
p_1 [-]	0.131	0.130	0.147	0.131	-0.055	0.420
τ_f [MPa]	17.2	15.3	11.7	6.0	4.0	1.8
p_2 [-]	0.052	0.033	0.058	0.030	0.026	0.006
s_2 [mm]	3.2	2.5	3.5	3.3	3.5	1.44



AMPE [%]	8.7	3.7	7.5	16.1	13.8	5.8
----------	-----	-----	-----	------	------	-----

CONCLUSIONS

This paper presented experimental investigations about the bond behaviour between GFRP rebars (sand coated with external helically wound fibres) and concrete from room temperature up to 140 °C. From the results obtained, the following main conclusions can be drawn:

- As expected, the strength and stiffness of the GFRP-concrete interface are significantly affected with increasing temperatures. The average bond strength is severely reduced at elevated temperature, for temperatures well below the glass transition temperature of the GFRP rebars (98 °C), presenting retentions of about 60-70% and of only 10% at respectively 60 °C and 140 °C, compared to the bond strength at room temperature.
- For the materials, test setup and procedure used in the present investigations and for the range of temperatures tested, similar bond strength reductions with temperature were obtained for both bond lengths (5 and 9 times the diameter of the rebars).
- Visual observations of the specimens after the tests allowed concluding that the damage undergone by the GFRP rebars was limited mostly to their surface, with the superficial layer of sand being completely stripped from the rebars' core.
- An alternative version of the BPE modified model was proposed to describe the bond behaviour of the GFRP bars to concrete at different temperatures; this model, which presents a linear descending branch in the final stage of the bond vs. slip constitutive relation, presented a good agreement with the bond vs. slip curves experimentally obtained.

ACKNOWLEDGMENTS

The authors wish to acknowledge FCT (project PTDC/ECM-EST/1882/2014) and CERIS for funding the research, Secil/Unibetão for supplying the concrete and Hughes Brothers for supplying the GFRP rebars. The first and second authors also wish to thank the financial support of FCT through scholarships SFRH/BD/129681/2017 and SFRH/BDP/108319/2015, respectively.

REFERENCES

- A. Abbasi, P.J. Hogg (2006). "Fire testing of concrete beams with fibre reinforced plastic rebar", *Composites Part A: Applied Science and Manufacturing*, 37 (8), 1142–1150.
- A. Katz, N. Berman, L.C. Bank (1999). "Effect of high temperature on bond strength of FRP rebars", *Journal of Composites for Construction*, 3 (4), 153–160.
- A. Katz, N. Berman (2000). "Modeling the effect of high temperature on the bond of FRP reinforcing bars to concrete", *Cement & Concrete Composites*, 22 (6), 433–443.
- ASTM D7913/D7913M (2014). "Standard test method for bond strength of fiber-reinforced polymer matrix composite bars to concrete by pullout testing", *American Society for Testing and Materials*, West Conshohocken, USA, 9 p.
- ASTM E1640 (1999), "Standard test method for assignment of the glass transition temperature by dynamic mechanical analysis", *American Society for Testing and Materials*, West Conshohocken, USA, 5 p.
- E. Cosenza, G. Manfredi, R. Realfonzo (1997). "Behavior and Modeling of Bond of FRP Rebars to Concrete", *Journal of Composites for Construction*, 1 (2), 40–51.



E. McIntyre, L.A Bisby, T. Stratford (2014). “Bond strength of FRP reinforcement in concrete at elevated temperature”, *Proceedings of the 7th International Conference on FRP Composites in Civil Engineering (CICE 2014)*, Vancouver, Canada.

F. Yan, Z. Lin, M. Yang (2016). “Bond mechanism and bond strength of GFRP bars to concrete: A review”, *Composites Part B*, 98, 56–69.

P. Santos (2016). “Fire behaviour of GFRP reinforced concrete slabs” (in Portuguese), *MSc dissertation in Civil Engineering*, Instituto Superior Técnico, Lisboa, Portugal.



SHEAR TESTS ON GFRP REINFORCED CONCRETE BEAMS USING DIGITAL IMAGE CORRELATION SYSTEM

M. Kaszubska 1, R. Kotynia 1, D. Szczech1, M. Urbaniak2

¹ Lodz University of Technology, Faculty of Civil Engineering, Architecture and Environmental Engineering,
Łódź, Poland, Email: monika.kaszubska@p.lodz.pl

² Lodz University of Technology, Faculty of Mechanical Engineering, Łódź, Poland

ABSTRACT

The paper presents results of experimental test carried out on T-shaped concrete beams reinforced with glass fiber reinforced polymer (GFRP) bars without stirrups. The beams varied mainly with longitudinal reinforcement ratio (ρ_l) corresponding to about: 1.0%, 1.4% and 1.8%, a number of bars, their diameter and a number of reinforcement layers (1 or 2 layers). Beams failed due to gradual development of diagonal cracks. Beneficial influence of two reinforcement layers was confirmed especially for the high longitudinal reinforcement ratio equal of 1.8%, while for the low reinforcement ratio about 1.0%, no difference in the shear capacity due to number of layers was observed. Strain and displacement measured during the test are very important parameters used in analysis of the test results. Most researchers still use conventional techniques, e.g. strain gauges or linear displacement transducer (LVDTs), but recently digital image correlation system (DIC) shows increasing popularity especially in the complex stress state like shear. DIC is an innovative non-contact optical technique for the study of crack propagation and material deformation. The paper presents comparison test results registered by LVDT and DIC system. The main aim of the research was to investigate the shear strength and crack propagation until failure.

KEYWORDS

All FRP and smart FRP structures, Experimental study, FRP internal reinforcement, DIC system

INTRODUCTION

Concrete structures reinforced with FRP (fiber reinforced polymer) systems are not susceptible to corrosion, therefore can be more durable and less susceptible to repair and maintenance than those reinforced with traditional steel bars. However, the FRP bars present a linear-elastic behaviour with brittle tensile failure mode, which arouse concerns in terms of ductility. The modulus of elasticity of FRP reinforcement varies between 32 GPa to 148 GPa, depending on the type of fibers: GFRP – 32÷52 GPa, carbon fiber reinforced polymer 105÷148 GPa (CFRP), aramid fiber reinforced polymer (AFRP) – 47÷81 GPa). This lower modulus of elasticity than that of the steel bars and inferior bond performance to cement based materials, place extra challenges in terms of accomplishing the performance requisites for serviceability limit state conditions, mainly in the crack width and deflection.

Generally, the shear strength of RC elements without transverse reinforcement is affected by several shear mechanisms including: un-cracked concrete compressive zone, friction forces (named aggregate interlock action) developing along a diagonal shear crack length and the shear dowel action of longitudinal reinforcement. The contribution of each shear component changes and depends on the load level and a crack pattern. In the beams without stirrups the problem to be investigated is the influence of a dowel effect on the shear capacity of FRP reinforced beams, particularly due to the FRP reinforcement in opposite to steel is an anisotropic material.

The most valuable research investigated the effect of the longitudinal FRP reinforcement ratio (ρ_l) and its stiffness on the shear strength. While Yost *et al.* (Yost *et al.*, 2001) indicated that the GFRP longitudinal reinforcement ratio did not affect the shear capacity, Alkhrdaji *et al.* (2001), El-Sayed *et al.* (2006, 2012), Matta *et al.* (2013), Tureyen and Frosch (2002), and Razaqpur *et al.* (2004) demonstrated that the shear strength of the GFRP and CFRP reinforced beams was proportional to the ρ_l . Based on the tests collected in the data base (DB) of concrete beams reinforced exclusively with FRP bars (Kotynia & Kaszubska, 2016), the influence on the failure mechanisms and beam's shear capacity of the following parameters was investigated: concrete compressive strength, shear span to depth ratio, ρ_l , and axial stiffness of the longitudinal reinforcement. The increase in the axial stiffness of the flexural reinforcement ($\rho_l E_l$) makes the increase in the shear strength. Moreover, the increase in the compressive concrete strength causes the increase in the normalized shear stress ($V_{max} / (\sqrt{f_c} b_w d_{eq})$) (Kotynia & Kaszubska, 2016).

Recently not only new materials are used but also new measuring technique are developed. Most researchers still use conventional techniques, e.g. strain gauges or linear displacement transducer (LVDTs), but recently digital image correlation system (DIC) shows increasing popularity especially in the complex stress state like shear. DIC



is an innovative non-contact optical technique for the study of crack propagation and material deformation. The system has two (or more) of high-resolution digital cameras and specialized software that processes the data in order to quantify the displacements and deformations. The procedure to calculate displacements is based on comparing two digital images of the sample surface captured at two different stages during the test.

EXPERIMENTAL PROGRAM

An experimental program included seven single span, T-cross-section beams ($b_{eff}=400$ mm, $b_w=150$ mm, $h_f=60$ mm, $h_{tot}= 400$ mm) with a clear span of 1800 mm. The GFRP reinforced beams without transverse reinforcement is only a part of a wider shear research on the beams GFRP/or steel reinforced beams without stirrups. The thickness of concrete cover of the flexural reinforcement was 15 mm. All the bars of the bottom reinforcement were straight, so taking into account the relative small length of the beam between its extremities and the closest support, the proper anchored conditions were ensured by embedding the bars into a steel box filled with an epoxy resin. The GFRP bars of three diameters: 12, 16 and 18 mm, were used for the longitudinal tensile reinforcement (Table 1). The relevant tensile properties of the adopted GFRP reinforcement were determined from experimental tests carried out with 15 specimens according to ISO Standard 10406-1 (2015). The average modulus of elasticity and the tensile strength registered in the tests were 50.5 GPa (COV=1.6%) and 1091 MPa (COV=10.7%), respectively. The GFRP bars were arranged in 1 or 2 layers, with an equivalent depth of the tensile reinforcement (d_{eq}), ranged between 367 mm and 379 mm. The beams varied mainly with the flexural reinforcement ratio (ρ_l) corresponding to about: 1.0%, 1.4% and 1.8%, while a number of bars and their diameter varied to finally obtain the assumed reinforcement ratio (see Table 1). For the designation of the beams of the present experimental program the following acronym was adopted, G-X ϕ -Y-Z, where G means the flexural bars of GFRP type, X is the number of bars of ϕ diameter (in mm), Y represents the target average compressive strength for the concrete (in this series it is considered constant and equal about to 30 MPa), and Z is the cover thickness, that in the present program, as already indicated, is constant and equal to 15 mm. In the beams with two layers of flexural reinforcement, the beam’s identification is G-X₁ ϕ ₁/X₂ ϕ ₂-Y-Z, where X_i and ϕ_i represents the number and diameter of the ith layer (1 or 2).

Table 43. Details of tested beams

Beams	Number of	Type of reinforcement	Reinforcement depth, d_{eq}	a/d_{eq} [-]	A [mm ²]	Reinforcement ratio, ρ_l [%]	ρE [GPa]
G-512-30-15	1	5#12	379	2.90	565	0.99	0.50
G-316-30-15		3#16	377	2.92	603	1.07	0.53
G-318-30-15		3#18	376	2.93	763	1.35	0.68
G-416-30-15		4#16	377	2.92	804	1.42	0.71
G-418-30-15		4#18	376	2.93	1018	1.80	0.90
G-312/212-	2	3#12+2#12	368	2.99	565	1.02	0.51
G-318/118-		3#18+1#18	367	3.00	1018	1.85	0.92

$\rho = A/b_w d_{eq}$; A- cross section of reinforcement, d_{eq} – equivalent depth of reinforcement; $d_{eq} = (A_1 * d_1 + A_2 * d_2) / A$; d_1, d_2 – depth of first and second reinforcement layer, A_1, A_2 – the cross section of first and second reinforcement layer

The top longitudinal reinforcement consisted of two straight longitudinal GFRP bars of 10 mm diameter and short bars of 6 mm diameter at a spacing 210 mm as the flange reinforcement. There were no stirrups along the tested shear span, while in the opposite non-tested shear span was reinforced with transverse steel stirrups of 8 mm diameter at 150 or 130 mm spacing and bent rods of 14 mm diameter applied in all beams in order to avoid the shear failure in the non-tested support region. In order to avoid arch effect, in the experimental test program the ratio between shear span (a) and the internal arm of the flexural reinforcement (d_{eq}) was between 2.9 and 3.0 (Imam et al., 1997; Kim & Park, 1996). The concept of equivalent internal arm of the flexural reinforcement (d_{eq}) is used in this work in order to attend the beams where two layers of GFRP bars were applied.

The beams were made of concrete strength class C25/30, including sand (0-2 mm), crushed stone aggregate (2-8 mm), cement CEM I 42.5, plasticizer. The concrete mix was delivered from a local concrete plant. The strength properties of concrete were determined according to EN 206-1 standard (2013). The average cylinder concrete compressive strength (obtained on 16 specimens) was 31.7 MPa (COV=8%), the average modulus of elasticity was 26.7 GPa (COV=6%), while the average splitting tensile strength was 2.9 MPa (COV=8%).

TEST SET-UP

The beams were simply supported on two steel supports with the movable (rotation and beam's axial displacement free movements) one in the monitored shear span, and the other with only free rotation movement (Figure 1). The load was applied under displacement control at $10\mu\text{m/s}$ by using T cross section steel profile to distribute the applied load along the width of the flange (contacted area $10\text{ mm} \times 400\text{ mm}$). Concrete axial strains were evaluated by using displacement transducers (LVDTs) disposed in the middle depth of one of the lateral faces of the beam's flange (number 1 to 4), and LVDTs positioned 30 mm above the bottom beam's surface (number 5 to 8). For estimating the shear deformation in the tested shear span, three sets of LVDTs were disposed in a triangle configuration (delta rosettes) with a LVDT per each edge of the triangle (number 9 to 21). Vertical displacements were registered by eight LVDTs of 20 mm stroke and 0.1 mm accuracy (number 22 to 29) mounted on an independent steel frame (Figure 1, Figure 2).

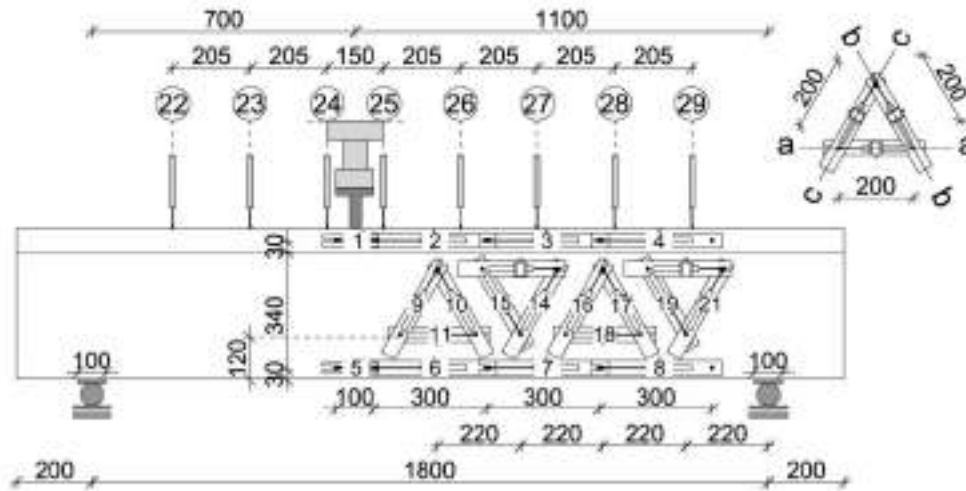


Figure 153: Test set up: static scheme and LVDT gauges and rosette's direction (dimensions in mm)

The digital image correlation system was used to provide complementary information to the displacement measurements from LVDTs, and to help on the interpretation of the cracking process of the tested beams. The information from DIC is obtained by comparing digital photographs of a component or test piece at different stages of deformation. By tracking blocks of pixels, the system can measure surface displacement and build up the full 2D and 3D deformation vector fields and maps of concrete strain.



Figure 154: The side monitored by system DIC (on the left) and LVDTs (on the right)

The photogrammetric technique used in this research was prepared for 3D measurements using two cameras with a focal length of 50 mm and a resolution of 4 megapixels. The registered area of concrete was 500 mm wide and 340 mm high (depth of the web of the beam's cross section) located in the mid-span of the shear region (Figure 4a). Pictures were taken at 1 Hz frequency, while images were analyzed using the VIC3D software (DIC).



TEST RESULTS

All beams failed due to diagonal shear cracking occurred in the test shear span of the beams at different load levels (Table 2). The concept of average shear stress ($\tau = V / (b_w d_{eq})$, where V is the shear force in the monitored span and b_w is the width of the beam's web) was adopted in order to take into account the different flexural reinforcement depth on the shear capacity of the beam.

Table 44. Summary of test results

Beam	f_{cm} [MPa]	$f_{c,cube}$ [MPa]	f_{ct} [MPa]	E_c [GPa]	V_{max} [kN]	τ_{max} [MPa]	θ [°]
G-512-30-15	30.2	31.4	2.75	25.60	34.26	0.60	35
G-316-30-15	28.8	33.2	2.95	27.30	31.73	0.56	25
G-318-30-15	28.8	33.2	2.95	27.30	38.57	0.68	45
G-416-30-15	30.5	30.7	2.70	26.10	34.77	0.61	41
G-418-30-15	28.8	33.2	2.95	27.30	38.15	0.68	51
G-312/212-30-15	31.7	31.4	2.75	25.60	34.78	0.63	27
G-318/118-30-15	31.7	33.2	2.95	27.30	47.72	0.87	47

GFRP reinforced beams, with one reinforcement layer, were less susceptible to changes of the reinforcement ratio than the beams reinforced with two layers (Figure 3). Almost twice increase in the reinforcement ratio caused an increase in the normalized shear strength only 14% for a one reinforcement layer and 38% increase for two layers of the reinforcement. Application of two reinforcement layers instead of one layer in beams G-318/118-30-15 and G-418-30-15 (with reinforcement ratio of 1.8% and 1.85%, respectively) indicated an increase in the normalized shear strength of about 28%. This configuration was more effective than one reinforcement layer in terms of the shear strength mainly due to higher tension stiffening effect provided by the flexural reinforcement in the beams with two reinforcement layers. Moreover, two reinforcement layers tied the shear crack and developed the existing shear cracks along the tensile reinforcement in the support direction. In fact, the shear crack opening decreased with d_{eq} (size effect), which enhanced the aggregate interlock effect. By disposing the flexural reinforcement in two layers, a larger volume of concrete, surrounding these bars, was resisting to the tensile force, which not only led the higher resistance to the opening of the shear cracks (improving the aggregate interlock effect), but also let the sliding of these cracks (due to dowel effect).

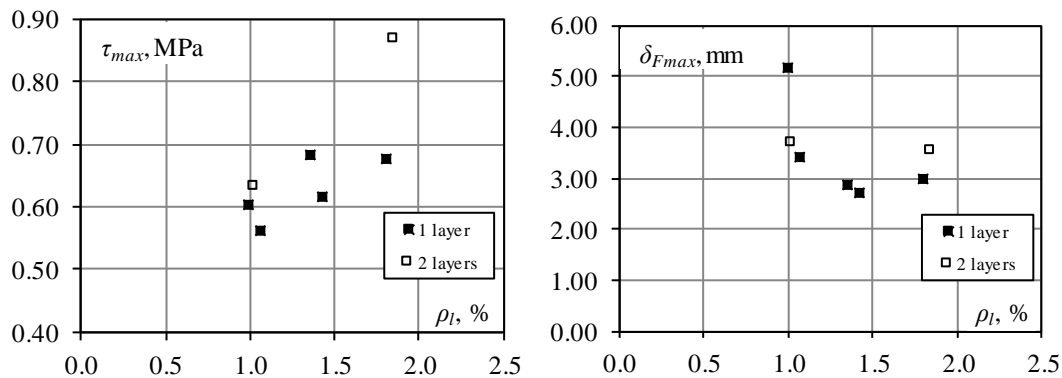


Figure 155: Response of ultimate shear stress and mean deflection corresponding maximum load vs. reinforcement ratio

As it was expected, an increase in the reinforcement ratio caused decrease in the deflection corresponding to the maximum load (δ_{rmax} is a mean deflection from LVDTs no 24 and 25. Figure 1, Figure 3). Moreover, beam G-312/212-30-15 with two reinforcement layers gained a smaller deflection than the beam G-512-30-15 with the similar reinforcement ratio but reinforced in one layer.

The comparison of the deflections registered by LVDT no 27 and gained from DIC for corresponding point on the beam's web of beam for all tested beams is shown in Figure 5. The main rule of choice the point on the web in DIC was location on the vertical line corresponding LVDT no 27, because the horizontal line had a very small influence on the results (Figure 4).

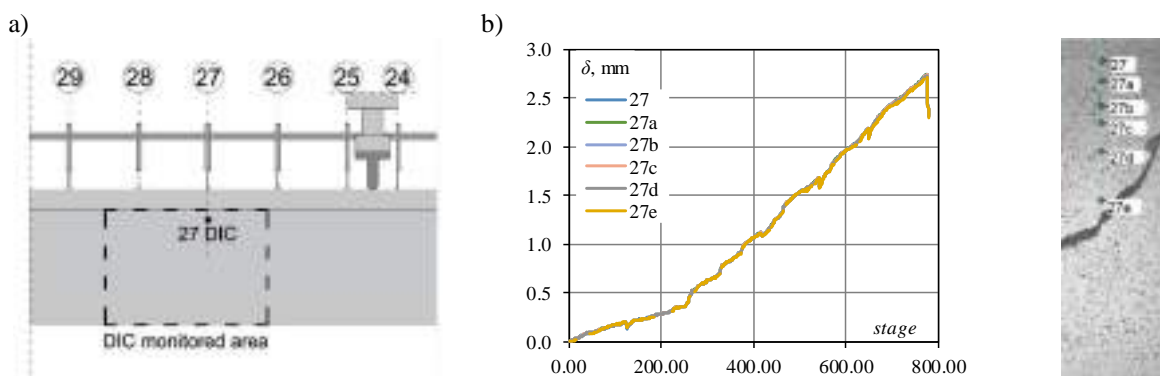
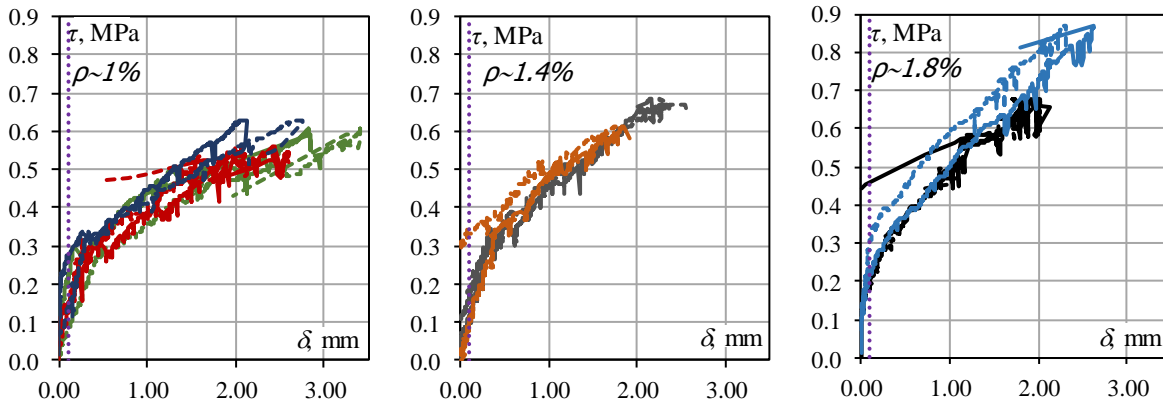


Figure 156: a) Location of point to analyze deflection in DIC, b) Comparison results for deflection in different horizontal location in beam G-312/212-30-15

Generally, the deflection curves based on LVDT and DIC methods had similar tendency. In both cases differences in the curve's inclination appeared after diagonal cracking. The best agreement between LVDT (continuous line, Figure 5) and DIC (dashed line, Figure 5) occurred for the beam G-418-30-15, while the highest difference was registered in the beam G-512-30-15 (the mean difference in deflection was 0.072mm and 0.416mm, respectively for the beam G-418-30-15 and G-512-30-15). In all beams the highest discrepancy between DIC and LVDT displacements occurred after diagonal cracking and before the maximum crack width.

In beams with the low flexural reinforcement ratio $\sim 1\%$ the differences between LVDT and DIC curves increased with the increase in shear stress. Moreover, the DIC system was more susceptible to the deflection (no 27) changes than LVDT gauge (vertical dotted line in Figure 5 shows 0.1mm accuracy of the LVDT gauge).



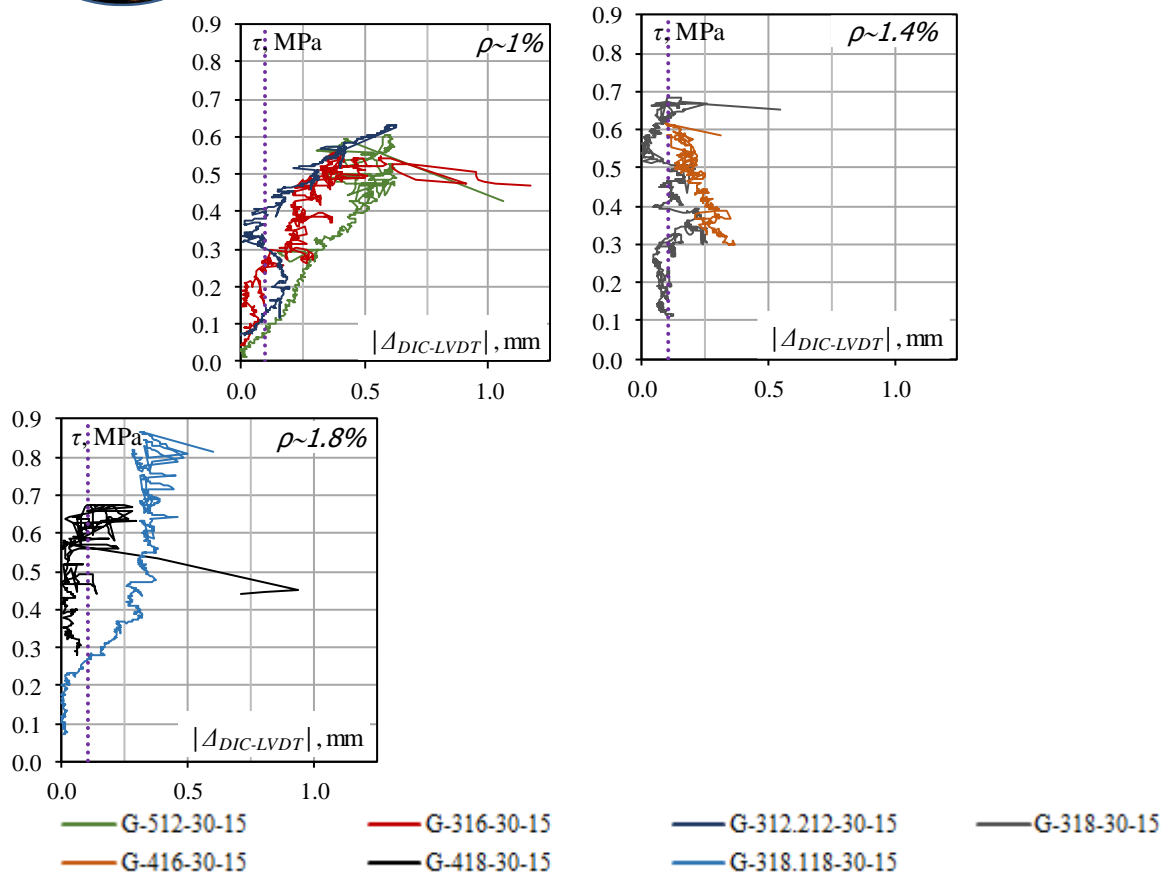


Figure 157: Comparison of vertical displacement (δ) and differences in displacements no 27 between DIC and LVDT ($|\Delta_{DIC-LVDT}|$)

According to the theoretical analysis conducted by Pan et al. (2010) the standard deviation of measured displacement is a function of the sum of square of subset intensity gradient (SSSIG). Therefore, the SSSIG was be used as an effective local parameter for assessing the local speckle pattern quality within a specified subset. Based on the SSSIG method, a novel global parameter, called mean intensity gradient (MIG) of speckle pattern (δ_f), was defined to evaluate the quality of the entire speckle pattern according to the formula:

$$\delta_f = \frac{W}{H} \sum_{i=1}^W \sum_{j=1}^H |\nabla f(x_{ij})| / (W \times H) \quad (1)$$

where W and H (in unit of pixels) are image width and height, $|\nabla f(x_{ij})| = \sqrt{f_x(x_{ij})^2 + f_y(x_{ij})^2}$ is the modulus of local intensity gradient vector with $f_x(x_{ij})$, $f_y(x_{ij})$ are the x - and y -directional intensity derivatives at pixel (x_{ij}) , which were computed using central difference algorithm gradient operator.

The uncertainty associated with displacement measurements is closely related to the quality of the speckle pattern, so the mean intensity gradient (MIG) was evaluated for the tested beams according to the formula (1). The calculated MIG values for the tested beams were good (in the range 19,8-23,8, except for the beam G-418-30-15, with the MIG equal of 35,1) comparing with the main outcomes by Pan et al. (2010) and Di Benedetti et al. (2015). Good preparation of the speckle pattern area on the beam's surface were confirmed by photos showed in Table 3 (only the beam G-418-30-15 had a slight discontinuity on the area monitored by DIC system).

Table 45. Crack pattern development registered by the DIC system



	F=70kN/ V=27.22kN	F=80kN/ V=31.11kN	F=90kN/ V=35.00kN	F_{max}/V_{max} [kN]	Visible wide crack
G-512-30-15				 88.12/34.26	 62.54/24.32
G-312/212-30-15				 89.44/34.78	 15.63/6.08
G-316-30-15				 81.63/31.73	 78.73/28.60
G-318-30-15				 99.17/38.57	 94.39/36.71
G-416-30-15				 89.41/34.77	 84.76/32.96
G-418-30-15				 98.08/38.15	 84.95/33.04
G-318/118-30-15				 122.72/47.72	 26.75/10.40

All beams started to crack in flexure, these primary cracks appeared close to the loaded section (in the highest bending moment region). By increasing the applied load, secondary flexural cracks formed between the previous ones, in the zone close to the flexural reinforcement, in consequence of the bond stress transfer between this reinforcement and surrounding concrete. Then the cracks propagated towards the flexural cracks connected and formed the critical shear crack. With the load increasing the opening of the shear crack increased with its length extension to both the top and the bottom edge of the beam. Almost all flexural cracks extended into the entire height of the web. As it was expected in the beams with the reinforcement ratio about 1.0% the flexural cracks appeared earlier than in the beams with the reinforcement ratio about ρ_l about 1.4% and 1.8%.

Some small horizontal cracks near the support were registered, confirming the bond loss of the bars to the concrete. It seems that when the aggregate interlock was lost, due to the opening of the inclined crack, the dowel action in the longitudinal reinforcement increased to maintain the forces equilibrium. A sudden increase in the dowel action

could lead to the splitting failure along the plane of the reinforcement. These splitting cracks did not pass beyond the support that confirmed a suitable anchorage of the tensile reinforcement.

The critical shear crack inclination θ (Table 2) was determined for the line connecting two points of the intersection of the critical shear crack with the middle depth of the beam's cross section and the flexural reinforcement. Test results indicated that inclination of the shear crack had the tendency of increasing with the increase in the flexural longitudinal reinforcement ratio (from an average value of 30° for $\rho_l \sim 1.0\%$, 43° for $\rho_l \sim 1.4\%$ and 51° for $\rho_l \sim 1.8\%$), due to the decrease of the maximum crack opening that promoted the favourable effect of the concrete aggregate interlock, as well as due to the dowel effect of the flexural reinforcement.

DIC system made it possible to measure the crack width in the full range of loading. A representative width of the shear crack was measured in the horizontal direction located at $z/2$ ($z=0,9d_{eq}$) level above the flexural reinforcement (see Figure 6a). A comparison of shear stress-crack width curves ($\tau-w_x$) for all tested beams is shown in Figure 6b.

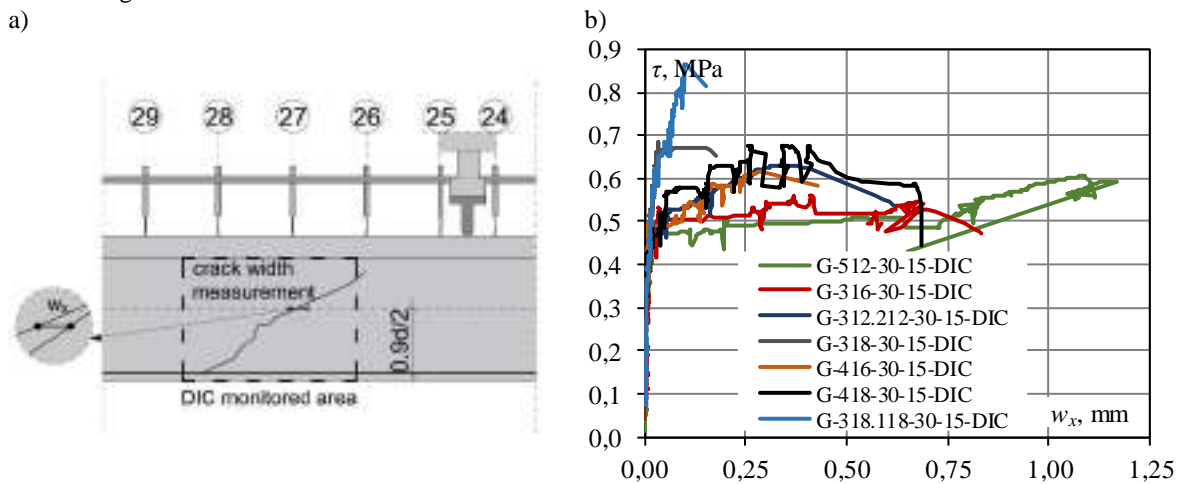


Figure 158: a) Location of virtual strain base; b) comparison of shear stress-crack width curves

It was observed a decrease in the crack width w_x with an increase in the reinforcement ratio. The beams reinforced with the lowest reinforced ratio ($\rho_l \sim 0.01\%$) indicated a very rapid width crack increase with only slight stress increase (G-512-30-15 and G-316-30-15), while the beams with the higher flexural reinforcement ratio indicated gradual increase in the crack width with increase in the shear stress. However, a very limited crack width increase occurred in beams G-318-30-15 and G-318/118-30-15 (with reinforcement ratio about 1.8% and 1.4%) due to the favorable effect of the concrete aggregate interlock, as well as due to the dowel effect of the flexural reinforcement.

CONCLUSIONS

The paper presents shear test results of concrete beams reinforced with GFRP longitudinal reinforcement without stirrups. From the experimental tests the following conclusions can be drawn:

- application of GFRP longitudinal reinforcement in two layers (for $\rho_l \geq 1.8\%$) delayed diagonal shear failure and increased the shear strength by near 28%;
- application of two reinforcement layers is more effective than one reinforcement layer in terms of the shear strength mainly due to higher tension stiffening effect provided by the flexural reinforcement (one or two layers);
- the inclination of the shear failure crack has a tendency of increasing with the flexural reinforcement ratio (average value of 30° for $\rho_l \sim 1.0\%$, 43° for $\rho_l \sim 1.4\%$ and 51° for $\rho_l \sim 1.8\%$);
- by increasing the flexural reinforcement ratio, the beam's load carrying capacity and the stiffness increased due to the decrease in the maximum crack opening, which has mobilized more effectively the favorable effects of the concrete aggregate interlock and dowel shear stress mechanisms;
- twice increase in the flexural reinforcement ρ_l from 0.99% to 1.8% caused an increase in the beam's shear capacity of 11% when the flexural reinforcement was disposed in one layer, while the increase was 25% when arranged in two layers; the beams presented a similar linear behavior before cracking, but after cracking the stiffness increased with ρ_l , leading to a decrease in the deflection at the maximum load;



- relatively high flexural reinforcement located in only one layer promotes a premature propagation of the shear failure crack along the top surface of the flexural reinforcement due to the abrupt transition of the beam's stiffness in this zone;
- the digital image correlation system, based on photogrammetric techniques at high frequencies, is a very useful tool in the interpretation of the cracking process up to the failure of the beams.

ACKNOWLEDGEMENTS:

The authors gratefully acknowledge the ComRebars Company who supplied the GFRP reinforcement for the experimental tests.

REFERENCES

- Alkhrdaji T., Wideman A., Belarbi A., Nanni A.: Shear Strength of GFRP RC Beams and Slabs. Proc., CCC 2001.
- El-Sayed A.K., El-Salakawy E.F., Benmokrane B.: "Shear capacity of high-strength concrete beams reinforced with FRP bars", *ACI Structural Journal*, 103(3), 2006.
- El-Sayed A.K., El-Salakawy E.F., Benmokrane B.: Shear strength of fibre-reinforced polymer reinforced concrete deep beams without web reinforcement. "Canadian Journal of Civil Engineering", 39, 2012.
- European Committee for Standardization (CEN). EN 206 2013. Concrete — Specification, performance, production and conformity, European Standard, 2013.
- Imam, M., Vandewalle, L., Mortelmans, F., & Van Gemert, D. "Shear domain of fibre-reinforced high-strength concrete beams", *Engineering Structures*, 19(9), 1997.
- Kim, J.-K., & Park, Y.-D. "Prediction of Shear Strength of Reinforced Concrete Beams without Web Reinforcement", *ACI Materials Journal*, 93(3), 1996.
- Kotynia R, Kaszubska M: "Analysis of Concrete Contribution in the Shear Strength of Beams Reinforced With FRP / Steel Bars Without Stirrups", *fib Symposium 2016, Performance-Based Approaches for Concrete Structures, Proceedings*. University of Cape Town, Cape Town, South Africa, 21–23 November 2016, Editor: Hans Beushausen
- Matta F., El-Sayed A.K., Nanni A., Benmokrane B.: "Size Effect on Concrete Shear Strength in Beams reinforced with Fiber-reinforced polymer bars", *ACI Structural Journal*, 110, 2013.
- Pan, B., L. Zixing, and X. Huimin.: Mean intensity gradient: "An effective global parameter for quality assessment of the speckle patterns used in digital image correlation", *Optics and Lasers in Engineering*, 48, 2010
- Tureyen A.K., Forsch R.J.: "Shear tests of FRP-reinforced concrete beams without stirrups", *ACI Structural Journal*, 99, 2002.
- Yost J.R., Gross S.P., Dinehart D.W. and Associate Members.ASCE: "Shear Strength Of Normal Strength Concrete Beam_s Reinforced With Deformed GFRP Bars", *Journal of Composites for Construction*", 5(4), 2001



TESTS ON GFRP REINFORCED CONCRETE CLOSING JOINTS

Nader Sleiman 1 and Maria Anna Polak 2

¹ MAsc. Civil Engineering, Department of Civil & Environmental Engineering, University of Waterloo, Canada

² Professor, Department of Civil & Environmental Engineering, University of Waterloo, Canada

ABSTRACT

The use of GFRP as main reinforcement in concrete structures is an appealing option for structures in aggressive environments. Using GFRP reinforcement in frame corner joints may be problematic considering the weak link at the reinforcement bend; the GFRP bars are much weaker at the bent portions of the bars due to non-standardized manufacturing processes. The behaviour of GFRP reinforced corner frame joints has not been previously studied. In the presented research, eight full-scale GFRP reinforced knee-joint specimens were prepared and tested under monotonic closing loads. These specimens consist of beam-column joints where the beam and column terminate at the joint. The presented experimental program was designed to study the effect of reinforcement ratio, confinement stirrups, and corner geometry on the behaviour of the joint. The failure mode was altered from bar rupture to failure of diagonal strut by increasing the reinforcement ratio of bent bars going through the joint; however this had minimal effect on ultimate strength. The addition of confinement stirrups to the joint reinforcement resulted in a substantial increase in ultimate strength and maximum deflection. Joints with altered geometry by including interior chamfers performed better than joints without chamfers; their load capacity was increased marginally but the joints failed in a non-brittle manner.

KEYWORDS

Reinforced concrete, GFRP, knee joints, frame corners, negative moments.

INTRODUCTION

Reinforced concrete knee joints, also known as frame corners, are joints found at the intersection of beams and columns. In this type of joint both members terminate at the joint. Examples of such joints include rooftops of buildings, bridges, as well as joints in concrete box culverts.

Typically, reinforced concrete is reinforced with steel. However, structures exposed to aggressive chloride rich environments are highly susceptible to corrosion, which may lead to loss of load carrying capacity of the structure. In such cases, GFRP reinforcement presents an appealing replacement to steel.

The behaviour of steel reinforced knee joints has been studied since the 1960s. Kemp & Mukherjee (1968) found a direct relationship between the reinforcement ratio and the risk of brittle premature failure within the joint. The sudden failure was controlled by limiting the reinforcement ratio to a maximum, which when exceeded, caused the formation of a splitting crack along the centre of the diagonal strut. High reinforcement ratio specimens tested by Swann (1969), Luo et al. (1994), and Johansson (2001) confirmed this finding. The tensile steel always yielded in specimens with relatively small reinforcement ratios and the experimental strength exceeded the designed specimen strength.

GFRP reinforced frame joints have not yet been studied and this research is the first one showing of the behaviour of such joints. GFRP is a brittle material and, in the closing frame joint where it is directly subjected to tension, it may present a challenge to obtain the ductile or deformable failure. The analogy with steel reinforced joints, which rely on yielding of corner bars at failure to show ductile behaviour, is not possible. Design methodologies for FRP reinforcement aim for a concrete crushing failure; which has been found to show more ductile behaviour than failure by bar rupture. The goal of this research is to investigate the behaviour of knee-joints reinforced with GFRP.

EXPERIMENTAL PROGRAM

The experimental program consists of eight knee-joint specimens with dimensions and details shown in Figure 159 Figure 160. Adjoining member design was performed according to the Canadian Highway Bridge Design Code (CHBDC, 2014). The column height was chosen to minimize sway during testing and sufficient beam length was provided to eliminate the risk of shear failure within the beam.

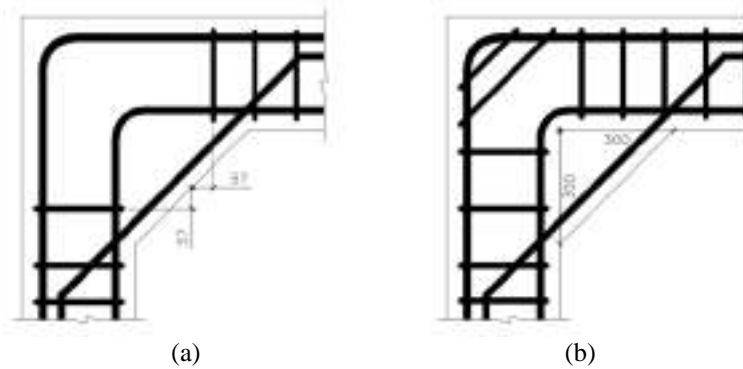


Figure 160: Reinforcement details of (a) unconfined and (b) confined type B geometry

The three variables studied were the effect of reinforcement ratio, the effect of confinement in the joint, and the effect of corner geometry. The specimens can be split into two main groups, unconfined and confined specimens. In the former group, four specimens were designed by varying the size and number of tensile reinforcement bars. In the latter group, two specimens were included by varying the number of tensile reinforcement bars. In each group, an additional specimen was included with type B reinforcement. Confinement was provided in the form of two stirrups installed perpendicular to the anticipated crack formation. The test matrix showing a summary of specimen details is shown in Table 46.

Table 46: Test matrix showing a summary of all specimens

Joint	Notation	Reinforcement	Geometry	Reinforcement Ratio	f'_c *
Unconfined	UA-2-4	2 – No. 4	Regular	Over-reinforced	48
	UA-2-6	2 – No. 6	Regular	Over-reinforced	55
	UA-3-6	3 – No. 6	Regular	Over-reinforced	
	UA-4-6	4 – No. 6	Regular	Over-reinforced	
	UB-3-6	3 – No. 6	Chamfered	Over-reinforced	
Confined	CA-2-6	2 – No. 6	Regular	Over-reinforced	48
	CA-3-6	3 – No. 6	Regular	Over-reinforced	
	CB-3-6	3 – No. 6	Chamfered	Over-reinforced	

* Concrete strength determined on day of testing.

The specimen naming convention used in Table 46 is in the following format: $XY - \# - \#$. Where, X specifies if the specimen joint is Unconfined or Confined, Y indicates the joint geometry (A and B for regular and chamfered corners, respectively), *the first number* shows the number of reinforcing bars and *the second number* indicates the size of bars used. For example $UB-2-4$ is a specimen with unconfined joint, type B geometry, and is reinforced with two No. 4 bars.

The strength of the specimens, M_{design} , was taken to be the moment resistance of the adjoining member as calculated according to the CHBDC. M_{design} was calculated by considering strain compatibility between the concrete stress block and the tensile reinforcement. The ultimate strain at the extreme concrete compression fibre was taken as 0.0035.

Experimental Test Setup

All specimens were fixed at the base of the column to the laboratory floor and loaded at the free end of the beam, shown in Figure 161. Strain readings were measured using electrical resistance strain gauges affixed on the surface of the GFRP. Deflection of the beam under the load application, sway, and angle closing were measured using string potentiometers accurate to the nearest tenth of a millimeter.

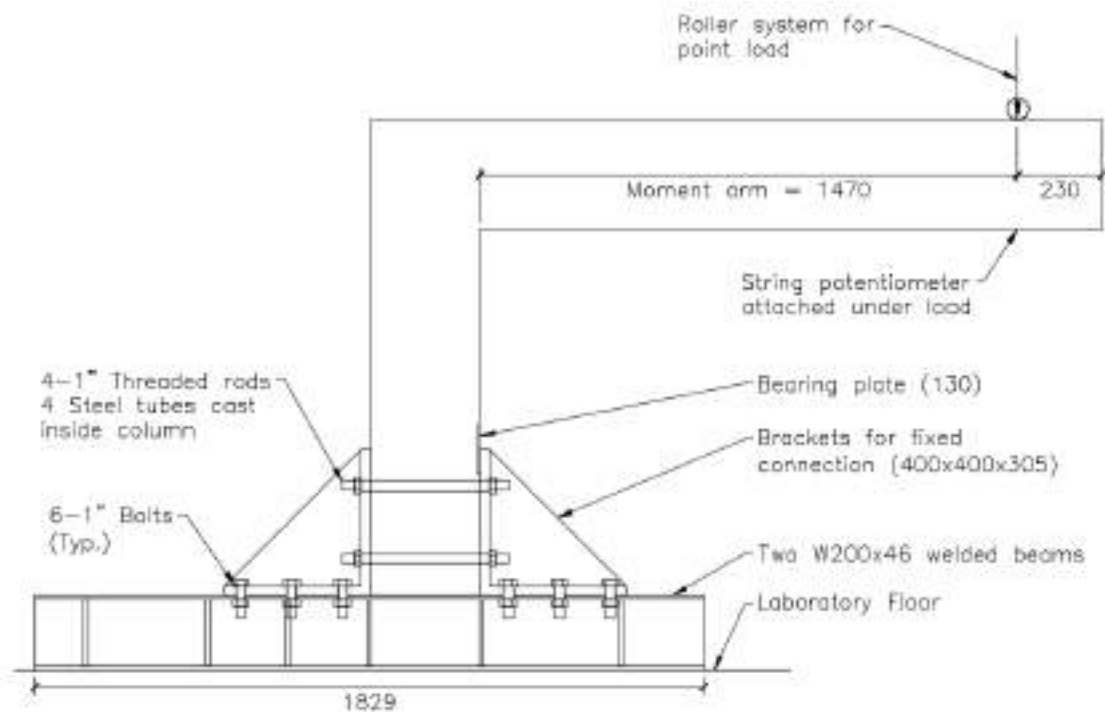


Figure 161: Experimental test setup details, all dimensions in mm unless noted otherwise

Loading was applied using a servo hydraulic load actuator. A static closing load was applied using displacement control; initially at a rate of 0.010 mm/second then increased to 0.017 mm/second after reaching 25 kN load reading.

Material Properties

The concrete strength was 55 MPa and 48 MPa for the unconfined and confined groups, respectively. The difference is attributed due to concrete pours on different days. The maximum aggregate size is 12.7 mm. The concrete strengths were measured by conducting cylinder compression tests at the day of testing. Specimens were at least 150 days old at the time of testing.



A summary of all GFRP material properties is shown in Table 47. The ultimate straight and bend tensile strengths as well as moduli of elasticity were determined by the manufacturer according to CAN/CSA S806 (Canadian Standards Association, 2012).

Table 47: GFRP material properties

Bar Designation	Diameter, mm	Area, mm ²	f _u , MPa	f _{u,bend} , MPa	Elastic Modulus, MPa
No. 4	12.7	127	1287	635	53942
No. 5	15.87	198	1413	655	53838
No. 6	19.05	285	1293	655	53808

RESULTS AND DISCUSSION

The five specimens in the unconfined specimens group failed with strength efficiencies less than 100%. For the confined group, two of three specimens exceeded a 100% strength efficiency, while the third specimen (CA-2-6) failed prematurely through anchorage failure. Table 48 presents a summary of all test results.

Table 48: Summary of test results

Specimen	ρ	Peak Load (kN)	Peak Moment, M _{test} (kN.m)	$\frac{M_{test}}{M_{design}}$	Mode of failure
UA-2-4	0.38%	28.5	39.2	58.8%	Bar rupture
UA-2-6	0.86%	45.0	62.1	64.3%	Bar rupture
UA-3-6	1.29%	53.7	75.2	66.2%	Diagonal strut failure
UA-4-6	1.72%	70.9	98.6	77.7%	Diagonal strut failure
UB-3-6	1.29%	61.0	85.4	72.4%	Crushing of interior corner
CA-2-6	0.86%	55.0	75.0	80.8%	Column bar anchorage
CA-3-6	1.29%	84.9	115.2	106.8%	Crushing of interior corner*
CB-3-6	1.29%	88.8	119.9	110%	Crushing of interior corner

*Failure initiated by crushing of interior corner, but experienced explosive failure at ultimate.

Failure Modes

Three failure modes were observed in the unconfined group: failure by bar rupture, diagonal strut failure, and crushing of the interior corner. The specimens designed with relatively low reinforcement ratios (UA-2-4, UA-2-6) failed by bar rupture at the onset of bend on the beam side of the joint. The failure of the higher reinforcement ratio specimens (UA-3-6, UA-4-6) occurred by diagonal strut failure. This failure was marked by the formation of a diagonal splitting crack in line with the diagonal compression strut in the joint. The concrete in the joint region was ejected in all directions at ultimate and was accompanied by a loud bang. The failure of the specimen with type B geometry, UB-3-6, occurred by crushing of the interior corner. Crushing was observed at the compression side of the column/joint interface. Unlike other specimens of type A geometry, this failure was not explosive.

The failure of specimen CA-2-6 occurred by anchorage failure at the base of the column. A crack formed at the column base and increased in width with increasing load. Loading was stopped after the load decreased with increasing displacement. The failure of specimen CA-3-6 was initiated by crushing of the interior corner. Signs of crushing were observed at 87% of peak load; however at peak load, a sudden brittle failure occurred similar to specimens UA-3-6 and UA-4-6. Bar rupture occurred at the onset of bend of the middle bar at the beam end of the joint. The other two bars shifted laterally and experienced a relative slip towards the adjoining members. Failure of the type B specimen, CB-3-6, occurred by crushing of the interior corner; similar to the failure observed in UB-3-6. At 87% of peak load, the loading essentially plateaued with increasing displacement.

Effect of Reinforcement Ratio

The reinforcement ratio was varied between 0.38% and 1.72%. The moment displacement response of the specimens UA-2-4 and UA-3-6 are shown in Figure 162. As the reinforcement ratio increased, the failure mode

shifted from failure by bar rupture (UA-2-4) to diagonal strut failure (UA-3-6). It is obvious that an increase in ultimate capacity will accompany the increased reinforcement ratio. However, an increase in strength efficiency was observed, from 59% for UA-2-4 to 77% for UA-4-6.

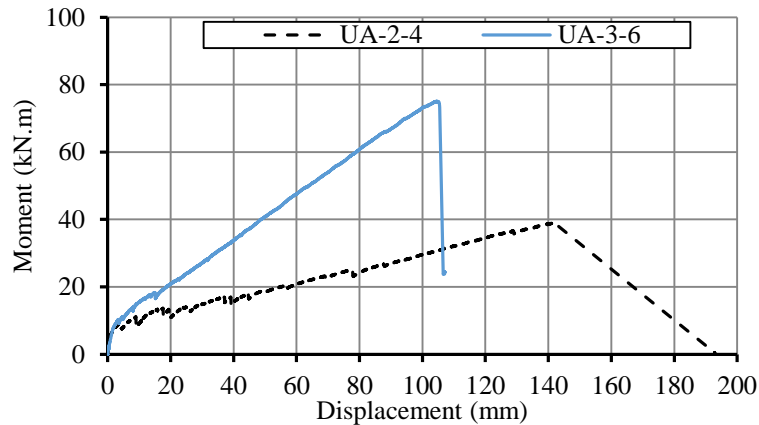


Figure 162: Moment deflection response comparing reinforcement ratio

An increase in specimen stiffness can be observed with increasing reinforcement ratio. In the lower reinforced specimens, specimen UA-2-4 displayed a larger displacement at failure and is attributed to the lower stiffness. Figure 163 (a) and (b) show the typical failure exhibited by the lower and higher reinforcement ratios, respectively. A lack of diagonal crack was noted in the joint region of specimens UA-2-4 which failed by bar rupture. Spalling of concrete occurred only on one side of this specimen. In specimen UA-3-6 a clear splitting crack can be seen in the diagonal region of the joint. Also observed is the exposed bars after the expulsion of concrete at failure.

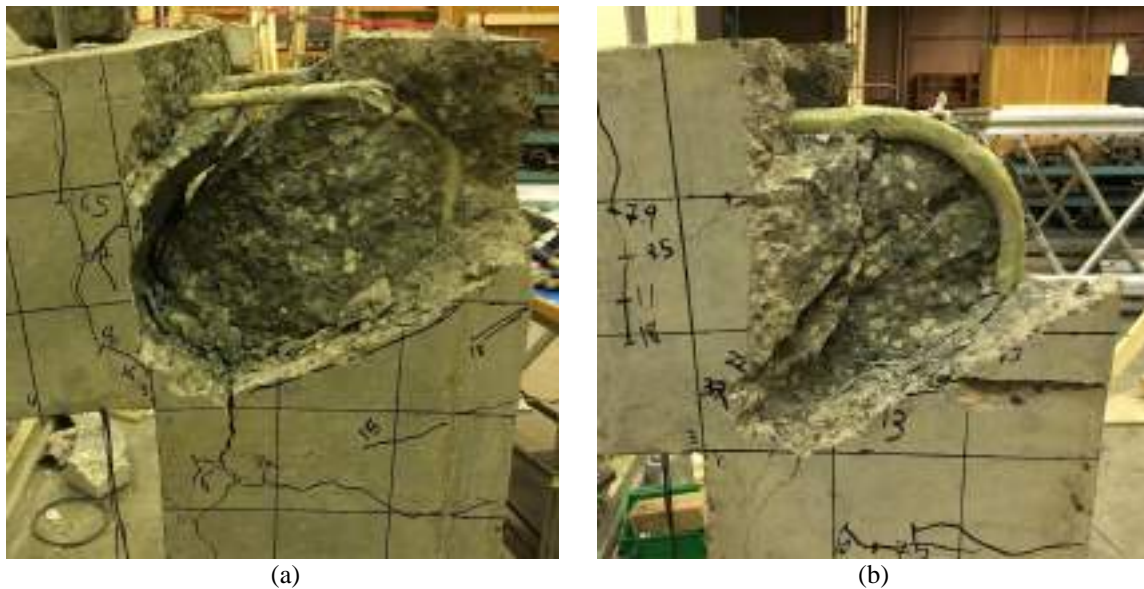


Figure 163: Failed joints (a) UA-2-4 and (b) UA-3-6

EFFECT OF CORNER GEOMETRY

Utilizing a joint with an interior chamfer (type B) slightly increases the strength efficiency. The overall stiffness during the test was larger than the specimen with type A geometry, as shown in Figure 164(a). Specimen UB-3-6 experienced a nonexplosive failure, compared to the sudden brittle failure of UA-3-6.

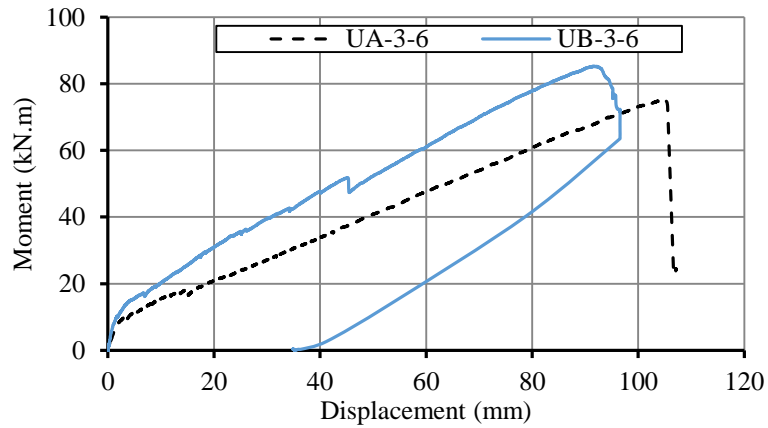


Figure 164: Moment deflection response comparing corner geometry

Cracking behaviour started from the joint/adjoining member interface and then formed within the joint at higher loads. The joint region remained uncracked until 33% of peak load. At 57% of peak load, cracking formed around the diagonal strut region, as shown in Figure 165. As loads increased, the diagonal crack on the column side showed significant widths, up to 5 mm.

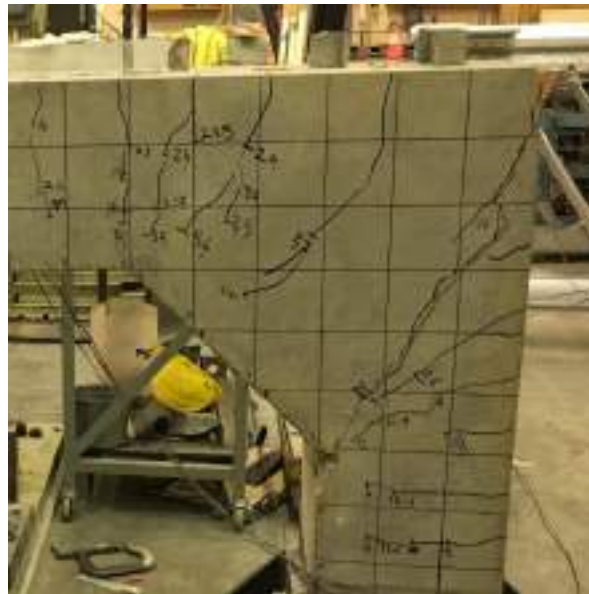


Figure 165: Specimen UB-3-6 at failure

Effect of Confinement Stirrups

The moment displacement response of specimens comparing the effect of confinement stirrups is shown in Figure 166. In both geometry types, the addition of confinement stirrups allowed the specimens to exceed the designed capacity. The confined specimens showed an identical stiffness to the unconfined specimens. The confined specimens showed significantly larger displacements at ultimate compared to the unconfined specimens.

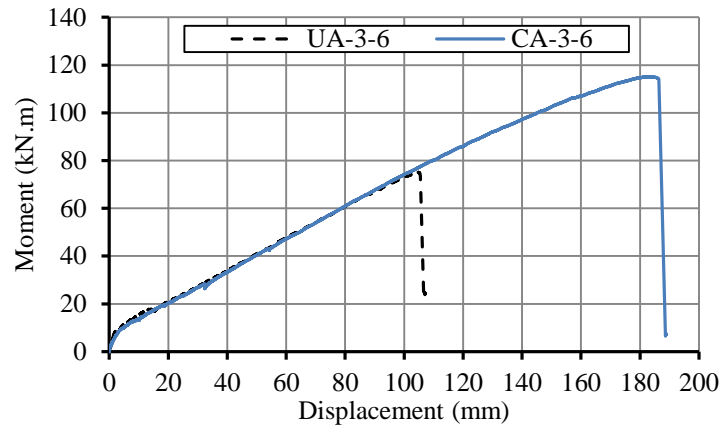


Figure 166: Moment displacement response comparing specimens with and without confinement stirrups

In the unconfined specimen UA-3-6, cracks formed adjacent to the diagonal strut at relatively low load levels when compared to the confined specimen CA-3-6. At approximately 65% of peak load, a crack formed along the centre of the diagonal strut in specimen UA-3-6, signalling the failure of the strut. No cracks within the diagonal strut were observed throughout the test in CA-3-6. Cracking was noted along the diagonal strut after the explosive failure occurred. Figure 167 shows specimen CA-3-6 after failure. The concrete within the joint region was contained by the confinement stirrups. At failure, the concrete in the diagonal strut was held by the stirrups, unlike that shown by the unconfined specimen.

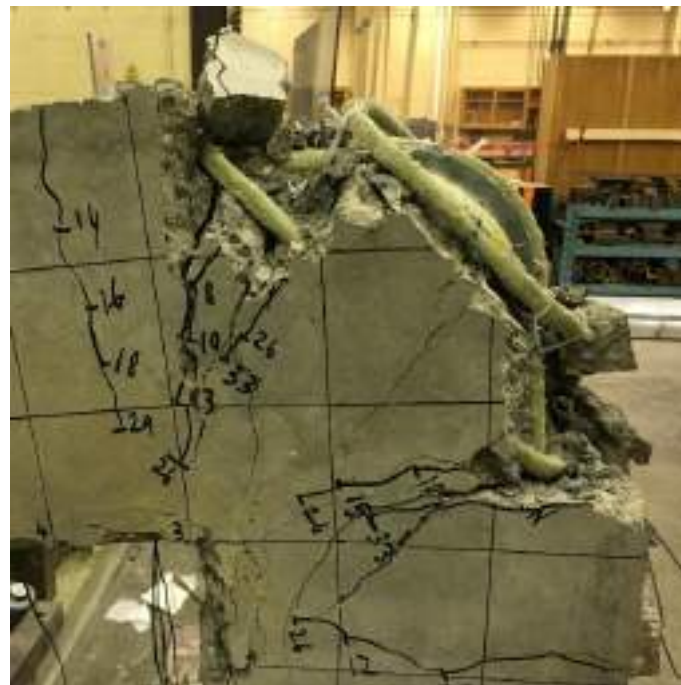


Figure 167: Specimen CA-3-6 after failure

The cracking pattern of CB-3-6 was identical to its unconfined counterpart. Similar to UB-3-6, specimen CB-3-6 formed a diagonal crack on the column side of the joint. The crack width steadily increased with increasing loads.



CONCLUSIONS

The paper presents an experimental program and results on the behaviour of GFRP reinforced concrete corner knee joints. The investigation included the effects of reinforcement ratio, confinement stirrups, and joint geometry on the joint behaviour and efficiency. Eight specimens were tested by loading the knee joint at the free end and fixing the column base.

Based on the presented test the following conclusions can be offered.

1. The unconfined specimens with type A geometry failed in a brittle fashion. Specimen with low reinforcement ratio UA-2-4 failed by rupture of the bars. Other specimens failed by diagonal cracking through the diagonal strut
2. The confined specimen of type A (CA-4-6) failed by crushing of concrete at the interior corner, followed by explosive general failure.
3. All specimens of type B geometry had nonexplosive failures. Unconfined specimens failed at strengths less than the strengths of adjoining members while the confined specimens attained greater than 100% strength efficiency.
4. Increasing the reinforcement ratio caused a marginal increase in strength efficiency. However, the failure mode was altered from bar rupture to diagonal strut failure.
5. The use of type B geometry resulted in a small increase in strength efficiency. Moreover it prevented the brittle failure observed in type A specimens.
6. The addition of confinement stirrups allowed the specimens to achieve full potential by containing the concrete in the joint region and controlling the cracks. However, the explosive behaviour at failure of type A specimens was not prevented by the confinement stirrups.

ACKNOWLEDGMENTS

The authors would like to acknowledge the Ontario Ministry of Transportation (MTO) for their financial support. They also want to thank Pultrall Inc. for donation of the GFRP reinforcement bars.

REFERENCES

- Canadian Standards Association. (2012). "Design and construction of building structures with fibre-reinforced polymers". CAN/CSA S806-12. Mississauga, Ontario, Canada: CSA Group.
- Canadian Standards Association. (2014). "Canadian Highway Bridge Design Code (CHBDC)". CAN/CSA S6-14. Mississauga, Ontario, Canada: CSA Group.
- Johansson, M. (2001). "Reinforcement Detailing in Concrete Frame Corners". ACI Structural Journal, 98(1), 105-115.
- Kemp, E., & Mukherjee, P. (1968). "Inelastic Behaviour of Concrete Knee Joints". The Consulting Engineer, 44-48.
- Luo, Y. H., Durrani, A. J., Bai, S., & Yuan, J. (1994). "Study of Reinforcing Detail of Tension Bars in Frame Corner Connections". ACI Structural Journal, 91(4), 486-496.
- Mayfield, B., Kong, F.-k., Bennison, A., & Davies, J. C. (1971). "Corner Joint Details in Structural Lightweight Concrete". ACI Journal, 68(5), 366-372.
- Sleiman, N. (2017). "Tests on GFRP Reinforced Concrete Knee-Joints Subjected to Negative Moments". Masters' Thesis. Waterloo, Ontario, Canada: University of Waterloo.



EFFECT OF SURFACE TREATMENT AND TEST CONFIGURATION ON BOND BEHAVIOUR OF GFRP REBARS

Ondrej Janus¹, Frantisek Girgile², Vojtech Kostiha², Petr Stepanek²

*1 Brno University of Technology, Faculty of Civil Engineering, Brno, Czech Republic,
Email: janus.o@fce.vutbr.cz*

2 Brno University of Technology, Faculty of Civil Engineering, Brno, Czech Republic

ABSTRACT

This paper deals with the determination of the effect of surface treatment and test configuration on the bond behaviour of GFRP reinforcement embedded in concrete. Several types of tests were performed, such as centric pull-out tests, modified pull-out tests, and beam tests to obtain the bond properties of bars with different surface treatments. The sand-coated bars exhibited different bond behaviour compared to the ribbed ones due to different forces transferred from the reinforcement to the concrete. This paper also focuses on the determination of the effect of alkaline environment degradation on the efficiency of sand-coated bars. It is well-known that test configuration affects bond behaviour, however, this effect was not sufficiently quantified until now. A modified beam-bending test to assess the bond performance is presented in this study. The results of an experimental study comparing the bond performance of GFRP bars with different surface treatments obtained from the beam tests and centric and modified pull-out tests are presented.

KEYWORDS

Reinforcement, Bond strength, Pull-out test, Beam test, Degradation.

INTRODUCTION

One of the basic assumptions of the reliability of reinforced concrete structures is the strain compatibility between the concrete and the reinforcement, which is ensured by the bond of the two materials. The use of composite reinforcement requires modification of the design approach commonly used with steel ribbed reinforcement, however, as the force transfer mechanism from the reinforcement to the surrounding concrete is different.

The study of the bond strength of FRP reinforcement with concrete has been performed by many authors (e.g. Achillides 2004; Aiello 2007; Nanni 1995; S6lyom 2015a). The published results showed a significant influence of the mechanical properties of the reinforcement and, in particular, its surface treatment on the resulting bond behaviour. Due to the considerable amount of surface treatments and properties of the FRP rebars available on the market, without experimental verification it is not possible to reliably determine the force transfer mechanism, the bond strength, and its effect on the behaviour of the FRP reinforced element (i.e. the effect on the deformation behaviour of the reinforced concrete element as well as width and distance of cracks).

Several types of tests are commonly used to determine the bond strength between the reinforcement and the concrete, e.g. pull-out tests (with central or eccentrically placed bars), ring pull-out tests, splice tests, and beam tests. Pull-out tests are used due to their simplicity and ability to isolate individual parameters and are commonly used to determine the bond strength between the reinforcement and the concrete. Eccentric pull-out tests, unlike the standard test configuration, allows for the determination of the effect of the concrete edge on the bond strength. These tests cannot reliably describe the state of stress expected in real constructions, however.

Even though they more accurately describe the behaviour of real structures, the use of beam tests to determine the bond strength of FRP reinforcement with concrete is becoming less frequent and the number of available relevant results is limited. Tighiouart et al. (1998) described the bond behaviour of two types of GFRP reinforcement: a) the surface layer consisting of a significant helical winding together with sand-coating, and b) bars with strand wrapping only, and made a comparison with steel reinforcement for a total of 64 beam tests. The configuration of the test was considered according to RILEM specifications, see FIP-CEB (1973). The tested GFRP bars showed lower bond strength than the steel ones. Seven beam tests were carried out by Pecce et al. (2001) on ribbed bars. The change in the bond length of the bars was tested. For specimens with a $5d_b$ bond length, the bond failure was caused by the pull-out of the reinforcement, when the separation of the ribs from the bar core was evident. Rupture of the bars occurred when $> 10d_b$. Xue et al. (2016) conducted 30 beam tests according to the RILEM configuration (FIP-CEB, 1973), 48 Losberg pull-out tests, and six standard pull-out tests on sand-coated bars. The strength of the concrete, the bond length, the diameter of the bar, and the test configuration were verified during the tests. For the beam tests, the increase in compressive strength of concrete from approximately 30MPa to 63MPa resulted in



increased bond strength. The gradual increase in the bond length resulted in a change of the failure mechanism, from the pull-out of the bar (bond length $2,5d_b$) to the failure caused by concrete cover splitting (bond length $\geq 5d_b$). Only a small difference in the bond strength was observed when comparing the results obtained according to the above-mentioned methods.

Kotynia et al. (2017) carried out 12 beam tests to determine the effect of the reinforcement diameter and the thickness of the concrete cover on the bond strength of ribbed GFRP rebars. By reducing the thickness of the cover layer, the bond strength was reduced, and the failure became more brittle. Mazaheripour et al. (2016) determined the effect of the diameter of the reinforcement, the bond length, the thickness of the cover layer, and the surface treatment of the GFRP reinforcement on 36 beam tests. The bond failure of sand-coated bars occurred by shearing of the surface treatment of the reinforcement. In the case of ribbed bars with a small concrete cover thickness, a combined failure was observed with scratched ribs on the top surface of the bar and shear failure of the concrete at the bottom part of the bar. These studies concluded that bond strength decreases with the increasing diameter of the bar and with an increase in bond length.

An important factor potentially affecting the long-term reliability of the interaction of both materials is the alkaline environment of the concrete, which reduces the mechanical characteristics of the GFRP reinforcement (see Girgle et al. 2018). Conclusions from degradation of bond strength experiments between GFRP reinforcement and concrete when exposed to the alkaline environment did not determine clearly the degree of degradation. The tested samples were often exposed to the degradation medium for only a short time, however. Zhou et al. (2012) did not notice a loss of bond strength on specimens that had been placed in an alkaline solution at 20 °C for 90 days after being encased in concrete.

Bakis et al. (1998) also drew the same conclusion. Reduction of the bond strength in samples that were placed bare in the alkaline solution for 28 days at 80 °C and then encased in concrete was not observed. The mechanical properties of the reinforcement (tensile strength) were affected, however.

EXPERIMENTAL PROGRAMME

The aim of the proposed experimental programme was to verify the influence of the surface treatment and the type of exposure on the bond strength. The bond strength of six types of GFRP reinforcement with sand-coated treatment using silica sand and one type with milled ribs was tested. The overview of the tested samples is shown in Table 1. The mechanical properties of the reinforcements used were experimentally determined before the tests (see Table 2).

All tested sand-coated bars came from the same manufacturer established in the Czech Republic. The ribbed bars were shipped from a manufacturer operating all over Europe. Surface treatment of samples GFRP.E.EP.N.14 was made in low quality. On the surface of the bars, there were bare spots or areas with a higher sand-coating thickness (shown in Figure 1b). For types GFRP.E.EP.K.14 and GFRP.E.EP.N.14, the winding did not create protrusions on the surface of the bar. The GFRP.E.VE.L.10 samples with the vinyl ester matrix were provided with a linen winding, which formed small protrusions on the surface of the samples. The ribs on sample GFRP.R.12 were created by milling a groove with a depth of 0.7 mm.

To determine the effect of the alkaline environment on the degradation of the surface treatment of the sand-coated bars, GFRP.E.EP.K.10.d180, GFRP.E.VE.L.10.d650, and GFRP.AR.VE.L.10.d650 samples were placed into the alkaline solution for a predefined time. The alkaline solution was prepared according to CSA S806-12 (2012) and consisted of 118.5 g of Ca(OH)_2 , 0.9 g of NaOH, and 4.2 g of KOH in 1 litre of deionised water. According to CSA S806-12 (2012), this solution simulates the concrete environment. To increase the rate of degradation, the solution was tempered to 60 °C. The pH values for all monitored samples were between 12.66 and 12.97. For details on an experimental programme of degradation of GFRP reinforcement by an alkaline environment, see Girgle et al. (2018).

The samples of GFRP.E.EP.K.10.d180 were taken out of the bath after 180 days. After this short time interval, the surface layer was already almost completely lost. In addition, the Kevlar winding had been breached in several places (see Figure 1e). The samples of GFRP.E.VE.L.10.d650 and GFRP.AR.VE.L.10.d650 were exposed to the alkaline environment for 650 days. During this time, there was no significant disturbance of the siliceous sand surface layer with the reinforcement core. Even after cleaning, a precipitated layer of calcium hydroxide and calcium carbonate was still clearly visible (see Figure 1f)

Table 1: Used GFRP reinforcement

Bars	Glass fibre type	Matrix type	Surface treatment	Note	Degradation
GFRP.E.EP.K.14 (8 samples)	E	EP	Sand-coating + Kevlar winding		-
GFRP.E.EP.N.14 (3 samples)	E	EP	Sand-coating + nylon winding	Low quality sand-coating	-
GFRP.E.VE.L.10 (4 samples)	E	VE	Sand-coating + linen winding		-
GFRP.R.12 (6 samples)	E-CR	VE	Milled ribs		-
GFRP.E.EP.K.10.d180 (4 samples)	E	EP	Sand-coating + Kevlar winding	Sand-coating loss	180 days degradation at 60 °C
GFRP.E.VE.L.10.d650 (3 samples)	E	VE	Sand-coating + linen winding		650 days degradation at 60 °C
GFRP.AR.VE.L.10.d650 (5 samples)	AR	VE	Sand-coating + linen winding		650 days degradation at 60 °C

EP (epoxy), VE (vinyl ester)

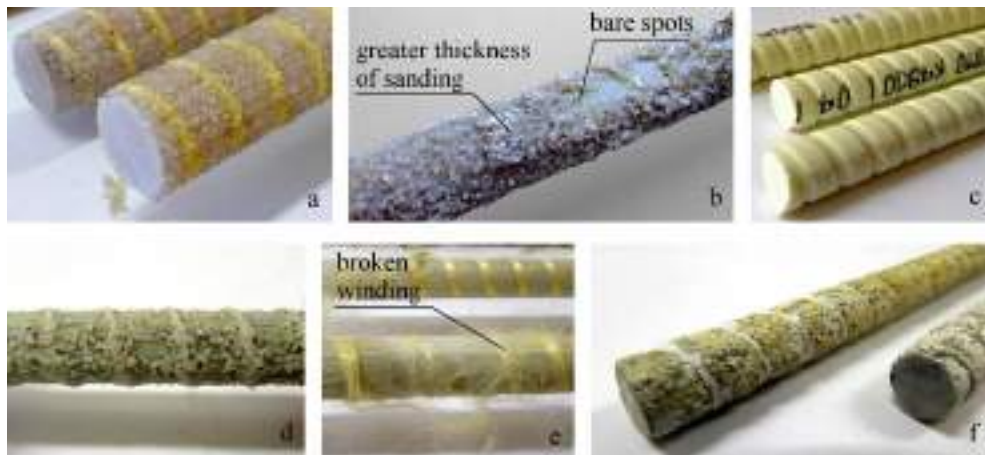


Figure 1: Tested samples: a) GFRP.E.EP.K.14, b) GFRP.E.EP.N.14, c) GFRP.R.12, d) GFRP.E.VE.L.10, e) GFRP.E.EP.K.10.d180, f) GFRP.AR.VE.L.10.d650

Table 2: Mechanical properties of used reinforcement

Bars	Diameter of bar core [mm]	Diameter of bar including surface treatment [mm]	Average tensile strength [MPa] \pm standard deviation	Average elastic modulus [GPa] \pm standard deviation	Ultimate strain [%]
GFRP.E.EP.K.14	14	15.23	980 \pm 9.6	52.1 \pm 1.6	1.88
GFRP.E.EP.N.14	14	15.02	654 \pm 14.6	46.1 \pm 0.8	1.41
GFRP.E.VE.L.10	10	10.87	818 \pm 8.6	48.9 \pm 2.2	1.67
GFRP.R.12	12	13.43	1445 \pm 72.1	59.9 \pm 0.4	2.41
GFRP.E.EP.K.10.d180	10	10.40	795 \pm 51.8	46.0 \pm 0.8	1.73
GFRP.E.VE.L.10.d650	10	10.78	590 \pm 42.8	50.3 \pm 1.1	1.17
GFRP.AR.VE.L.10.d650	10	11.08	453 \pm 19.4	42.9 \pm 1.1	1.06
Steel.14	14	-	*574 \pm 3.5	199.1 \pm 7.7	-

*yield strength of steel reinforcement

As shown in Table 3, a total of 37 samples were prepared. 31 centric pull-out tests were designed to determine the efficiency of each surface treatment. Each type of surface treatment was tested in a set of three to five samples. The effect of the thickness of the concrete cover was verified on the GFRP.E.EP.K.14 samples using an eccentric pull-out test (four samples). For the most accurate determination of the bond strength of the real structures, a beam test was proposed. Only two samples of the first set have been tested up until now, but the experimental programme continues.

Centric and eccentric pull-out tests

Centric pull-out tests were performed according to ACI 440.3R (2012). The bars were encased in a 200 mm cube made of concrete with an average compressive strength of 55 MPa. The length at which the bond is assured is considered to be five times the bar diameter; the remaining part is separated. The specimens were cast in a vertical position while ensuring good concrete compaction. For the eccentric pull-out tests, the concrete cover was equal to the diameter of the bar and the bond length was the same as for the centric pull-out test. The test arrangement eliminated unwanted cube rotation (see Figure 2). The relative displacement of the reinforcement was measured by LVDT sensors. Two LVDTs were used to measure the displacement of the loaded end and one to measure the free end.

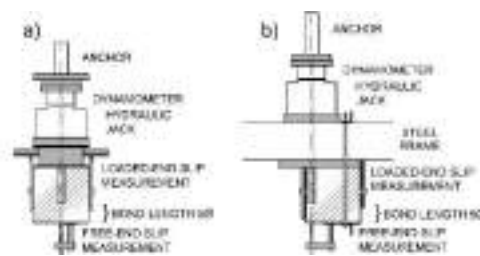


Figure 2: Test configuration: a) centric pull-out, b) eccentric pull-out

Modified beam bending tests

The modified beam tests were based on the RILEM FIP-CEB (1973) steel reinforcement bond test, with most of its dimensions preserved. Modifications were made with respect to FRP reinforcement specifications and for possible cyclic loading, however. Bond length was due to the lower modulus of elasticity of FRP reinforcement compared to the steel ones reduced from ten times the diameter of reinforcement to five times. A value five times the diameter seemed appropriate for evaluating a stress-slip diagram assuming a uniform stress distribution (see Aiello et al. 2007). The steel hinge was also modified and was firmly anchored to the individual segments of the beam. The beam was loaded directly onto this hinge. The average compressive strength of the concrete was 64 MPa.

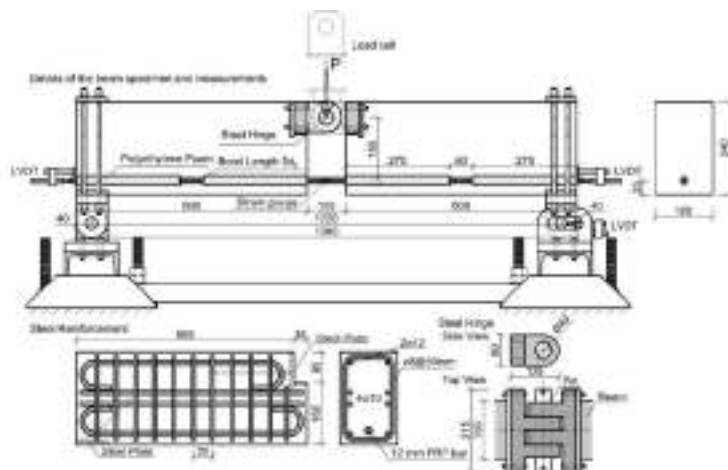


Figure 3: Beam specimen geometry and details

During loading, the horizontal displacement of the roller support and the free-end slip on both sides of the bar were recorded by LVDT sensors (see Figure 3). Measurements of the immediate vicinity of the loaded end of bonded length were not directly realised. To ensure that the real force in the reinforcement was read, a strain gauge was placed in the middle of the free reinforcement length. The force determined by the strain gauge was then compared with the force calculated from the force equilibrium.

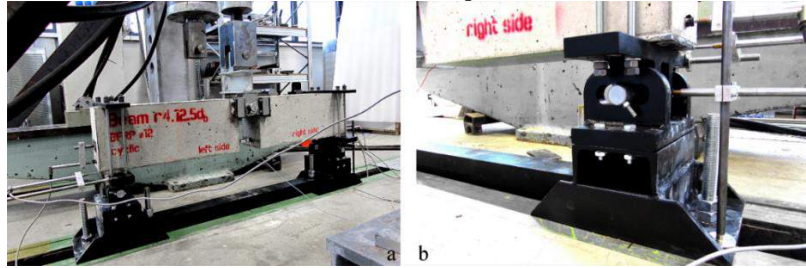


Figure 4: Beam test setup: a) setup, b) roller support

RESULTS AND DISCUSSION

The obtained results are summarised in Table 3. The maximum bond stress τ_{max} was calculated with the assumption of constant stress distribution on the bond length.

Table 3: Summary of experimental results

Test	Designation	Bond length	Bond stress τ_{max} [MPa]		Free-end slip S_f [mm]		Loaded-end slip S_l [mm]		Failure mode
Centric pull-out	GFRP.E.EP.K.14	5d _b	18.98	19.74 ± 2.10	0.143	0.176 ± 0.023	1.406	1.496 ± 0.129	P
		5d _b	22.22		0.197		1.653		P
		5d _b	17.30		0.182		1.377		P
		5d _b	20.47		0.181		1.546		P
	GFRP.E.EP.N.14	5d _b	15.76	16.80	0.336	0.251	2.107	2.148	P
		5d _b	16.83	±	0.248	±	2.176	±	P
		5d _b	17.82	1.03	0.169	0.084	2.162	0.037	P
	GFRP.E.EP.K.10.d180	5d _b	14.14	11.72 ± 2.75	2.114	2.424 ± 0.266	3.147	3.391 ± 0.249	P
		5d _b	8.39		2.465		3.210		P
		5d _b	13.81		2.462		3.644		P
		5d _b	10.53		2.657		3.563		P
	GFRP.E.VE.L.10	5d _b	18.93	19.40 ± 1.50	0.328	0.352 ± 0.118	1.436	1.572 ± 0.142	P
		5d _b	18.06		0.517		1.619		P
		5d _b	21.56		0.323		1.750		P
		5d _b	19.05		0.238		1.481		P
	GFRP.E.VE.L.10.d650	5d _b	22.78	18.14	0.092	0.109	1.434	1.299	P
		5d _b	15.29	±	0.092	±	1.149	±	P
		5d _b	16.36	4.05	0.144	0.030	1.316	0.143	P
	GFRP.AR.VE.L.10.d650	5d _b	10.38	10.86 ± 1.37	0.144	0.118 ± 0.018	1.092	0.996 ± 0.060	P
		5d _b	9.58		0.106		0.995		P
		5d _b	9.68		0.101		0.957		P
		5d _b	12.37		0.107		0.936		P
		5d _b	12.27		0.129		1.000		P
	GFRP.R.12	5d _b	19.98	19.41 ± 0.65	0.415	0.450 ± 0.083	1.666	1.535 ± 0.087	P
		5d _b	18.49		0.442		1.495		P
		5d _b	18.83		0.375		1.482		P
		5d _b	18.87		0.568		1.499		P
	Steel	5d _b	22.24	22.36 ± 1.01	0.831	0.710 ± 0.154	1.373	1.234 ± 0.102	P
		5d _b	23.16		0.884		1.228		P
		5d _b	21.29		0.766		1.197		P
		5d _b	23.56		0.534		1.131		P



Eccentric pull-out	GFRP.E.EP.K.14	5d _b	12.82	14.93 ± 2.10	0.092	0.122 ± 0.026	0.940	0.843 ± 0.126	P + S
		5d _b	14.57		0.129		0.657		P + S
		5d _b	17.84		0.113		0.886		P + S
		5d _b	14.47		0.154		0.888		P + S
Beam test	GFRP.R.12	5d _b	23.37	22.84	0.297	0.307	-	-	P
		5d _b	22.31		0.316		-		P

(P) pull-out, (S) concrete cover layer splitting

Effect of surface treatment

To determine the effect of the surface treatment on bond strength, centric pull-out tests were carried out. Stress-slip diagrams of the free end and the loaded end are shown in Figure 5. For comparison, the behaviour of the steel reinforcement with a diameter of 14 mm was also noted in the graph. After the tests were performed, the samples were cut to analyse the failure mode.

A typical failure of the sand-coated bars is shown in Figure 7. The thin surface layer of the reinforcement was entirely separated from the core. In some cases, a combination of shear failure of concrete and partial separation of the sand-coating from the bar core was observed. For the ribbed bars, a shear failure of concrete occurred at the rib level (a failure mode similar to steel reinforcement). The assumption (e.g. fib Bulletin No. 40, 2007) that the bond strength of FRP reinforcement only increases to a concrete strength of 30 MPa was not confirmed (due to the average strength of the concrete samples).

The achieved bond strength was approximately the same for all types of surface treatments tested without degradation and reached approximately 20 MPa. It should be emphasised, however, that the results were not obtained on bars of the same diameter (see Tables 1 and 2). Lowering the reinforcement diameter generally results in an increase in bond strength, e.g. Achillides et al. (2004). For the GFRP.R.12 samples, the maximum bond strength was achieved at the higher free-end slip than in the case of sand-coated bars.

During the experiment, the conclusion of the Achillides (2004) study was confirmed. This study stated that if bond strength failure is caused by the separation of the surface treatment and the surrounding concrete remains intact (in the case of the current study this applies to all sand-coated bars), it is not appropriate to describe the descending branch based on the stress-slip diagrams. When the bar slips, part of the reinforcement with the intact surface treatment moves to the bonded area and thus increases (overstates) the residual bond.

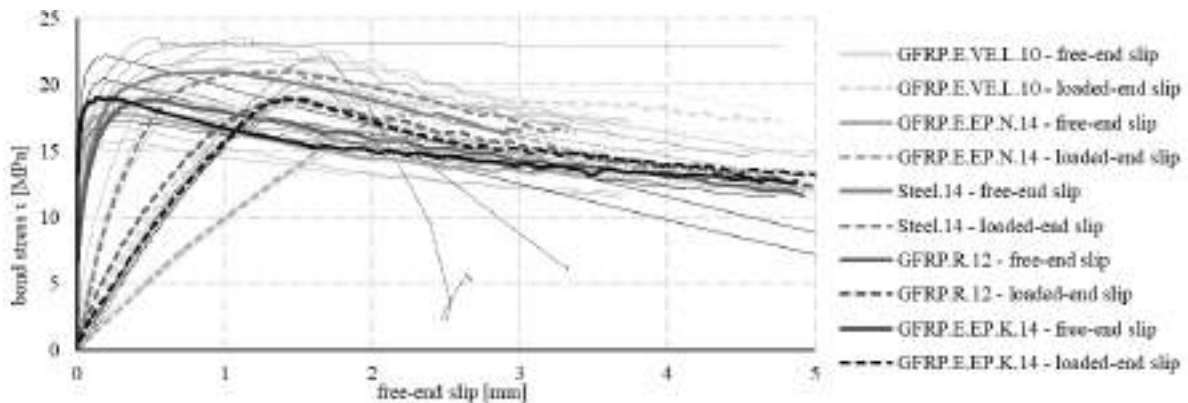


Figure 5: Stress-slip diagrams from centric pull-out tests

Effect of test configuration

Centric/eccentric pull-out

The effect of concrete cover thickness was studied using the GFRP.E.EP.K.14 samples. The bond failure in the centric pull-out test samples occurred, as expected, due to the separation of the thin surface treatment from the core of the bar (Figure 7). There were no concrete cracks observed in the area with the secured bond. For the eccentric pull-out test, a longitudinal crack (Figure 6) was formed during loading in the secured bond area. Pull-out of the sample usually occurred when a complete concrete cover layer was damaged. For bars placed near the edge, not only was the bond strength reduced (compared to the centric placed bar), but the maximum bond stress was also achieved at a lower slip of the reinforcement (see Table 3).



Figure 6: Concrete cover splitting



Figure 7: Separation of the sand-coating

Centric pull-out/beam bending test

The effect of the state of stress in the bond area was studied using the GFRP.R.12 samples. For this purpose, centric pull-out tests and a modified beam tests were performed. In pull-out tests (with centric placement of the bar in concrete cube), sufficient concrete confinement is achieved, and it is generally assumed that the highest bond strength value is reached. As noted above, for the centric pull-out tests, the bond failure of the GFRP.R.12 samples was caused by pulling out the reinforcement and the limiting factor was the shear strength of the concrete at the level of the reinforcement ribs. Only a few abrasions from sharp edges of the aggregate were found on the sample surface. Undesirable splitting of the concrete cube did not occur in any tested samples.

In the beam test, splitting of the concrete cover layer was prevented by a densely spaced transverse reinforcement. Also, in this configuration of the test, none of the samples failed due to the concrete cover splitting and bond failure was achieved by pulling out the reinforcement.

In the beam tests, a slightly different bond failure mechanism was observed after the samples were cut. On the bottom side of the bar (near the concrete surface), a shear failure of the concrete occurred (same as in the case of pull-out tests), but on the upper side of the reinforcement, facing away from the concrete surface, several ribs were scratched. When the beam is deformed (in the middle of the span) during loading, the upper side of the bar is pushed against the concrete, which may have led to the described scratching of the ribs. Bond strength during the beam test was, contrary to expectations, slightly higher than in the pull-out tests. The increase of bond strength during the beam test compared to the pull-out test was 17%, with a drop of free-end slip of about 32%. These data were obtained from a small number of samples, however. This increase in bond strength was probably due to a change of the failure mechanism and to a lesser extent, also by a higher compressive strength of the concrete during the beam test.

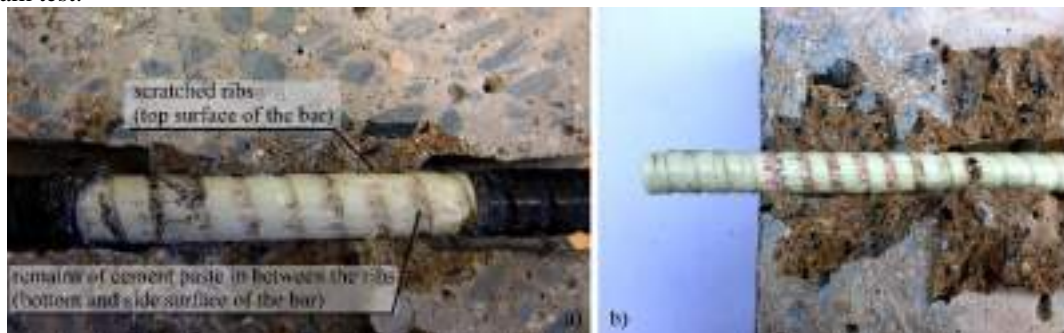


Figure 8: Bond failure: a) beam test, b) pull-out test

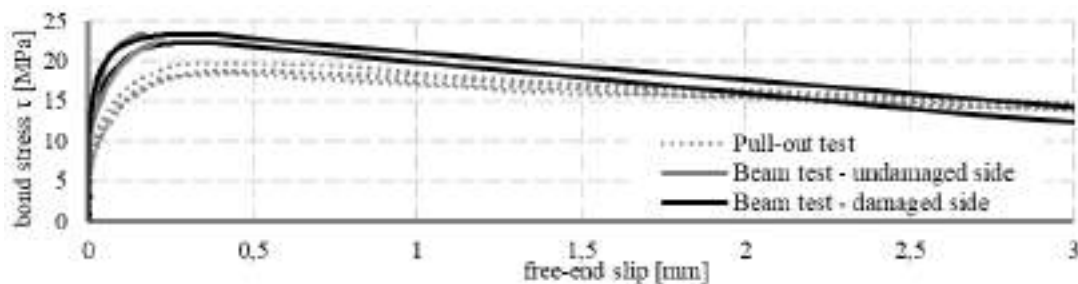


Figure 9: Comparing pull-out test to beam test

Effect of degradation by alkaline environment

Figure 10a shows a comparison of the behaviour of the degraded GFRP.E.P.K.10.d180 samples and the reference samples of GFRP.E.P.K.14 with the epoxy matrix. There is an obvious difference in the force transfer between the reinforcement and concrete. The contact of the GFRP.E.P.K.10.d180 sample with lost sand-coating transmits the acting force after the loss of the adhesion only by friction. With the legitimate assumption that samples of smaller diameters achieve higher bond strength, it can be stated that the bond reduction is more than 40%. In view of the obtained results, the reinforcement will be further analysed, especially to determine the glass transition temperature as a low T_g value could indicate a susceptibility to the higher temperatures used to accelerate the degradation by alkaline environment.

The second type of tested GFRP reinforcement was the samples with the vinyl ester matrix and linen winding, which were exposed to degradation for 650 days. The influence of the alkalinity of the environment was determined on two types of reinforcement with the same surface treatment and matrix, but with a different type of fibres used. Although the visual inspection of the samples after removal from the bath did not indicate a different degradation, there was a different degree of degradation impact. The bond reduction of the GFRP.E.VE.L.10.d650 samples with E-glass fibres was less than 10% (see Figure 10b). For the GFRP.AR.VE.L.10.d650 samples with AR-glass fibres, however, there was a reduction of bond strength of more than 40%. For the AR-glass samples, a different type of failure occurred, not only was there a separation of the surface treatment from the core, but there was also visible damage occurring in the core of the reinforcement. Together with the surface treatment, some of the outer fibres were separated as well. The observed mechanism of the failure is unusual and a clear conclusion should be supported by more detailed examination.

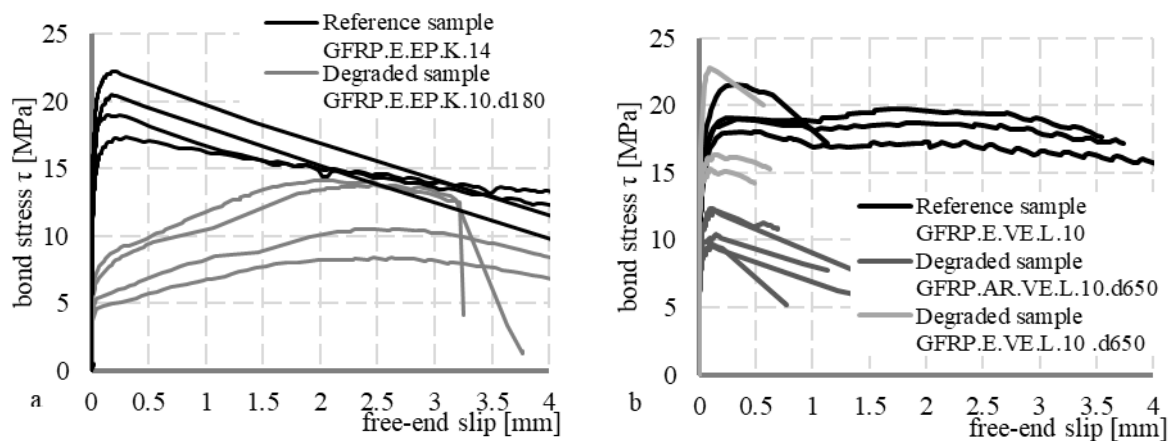


Figure 10: Stress-slip diagrams for sand-coated bars with a) epoxy resin, b) vinyl ester resin

CONCLUSIONS

This paper presents partial results from an ongoing experimental programme that deals with the bond strength of GFRP reinforcement with concrete, especially with regards to the effect of the surface treatment of the bars and test configuration on bond strength. The effect of degradation by contact with the alkaline environment of concrete is also investigated. From the results acquired so far, the following conclusions can be made:

1. The sand-coated and ribbed GFRP bars show a comparable bond strength (approximately 20 MPa). The ribbed bars reach a bond strength with a larger slip of the reinforcement, however. The bond strength of used GFRP rebars is slightly lower compared to conventional steel ribbed bars.
2. The difference between the loaded-end slip and the free-end slip of the reinforcement is directly dependent on the modulus of the elasticity of the reinforcement.
3. The thickness of the concrete cover has a significant effect on the bond behaviour of the reinforcement. With a minimal concrete cover layer, there is a significant reduction in bond strength and corresponding slippage.
4. The introduced modified beam test can isolate the individual test parameters.



5. The bond strength is 17% higher during the beam test (in case of ribbed bars) than for the pull-out test. For the tested ribbed GFRP bars, pull-out tests resulted in shear failure of concrete at the ribs level. In the beam test, however, a combined bond failure occurs: shear failure of concrete along with scratching of ribs. An increase in the compressive strength of concrete would probably result in a further increase in bond strength.
6. The degradation of the reinforcement by the alkaline environment has a considerable influence on bond strength of the tested reinforcement. For the GFRP.E.EP.K.10.d180 samples, the overall loss of the surface treatment resulted in a reduction of bond strength of more than 40%. Experiments have also highlighted the fact that the type of glass fibres influences the level of bond strength reduction. Samples with E-glass show a reduction of less than 10%, whereas the bond strength of the samples with AR-glass fibres decreased by more than 40%. The failure of AR-glass samples occurs differently, i.e. in the core of the reinforcement where the outer fibres are separated along with the surface treatment. This failure mechanism is probably due to the manufacturing process and the chemical composition of the matrix. Samples with AR-glass fibres will be further analysed.

ACKNOWLEDGMENTS

The presented results were obtained with the financial support of Ministry of Education, Youth and Sports under the “National Sustainability Programme I” project LO1408 “AdMaS UP - Advanced Materials, Structures and Technologies” and with the financial support of the Technology Agency of Czech Republic project TH03020067 “FRP reinforcement with increased reliability and durability against fatigue loads”.

REFERENCES

- ACI (2012). “Guide test methods for fiber-reinforced polymers (FRPs) for reinforcing or strengthening concrete structures, 440.3R-12”, Farmington Hills, Michigan.
- Z. Achillides, K. Pilakoutas (2004). “Bond Behavior of Fiber Reinforced Polymer Bars under Direct Pullout Conditions”, *Journal of Composites for Construction*, 8(2), 173-181.
- M. Aiello, M. Leone, M. Pecce (2007). “Bond Performances of FRP Rebars-Reinforced Concrete”, *Journal of Materials in Civil Engineering*, 19, 205-213.
- C.E. Bakis, A. J. Freimanis, D. Gremel, A. Nanni (1998). “Effect of Resin Material on Bond and Tensile Properties of Unconditioned and Conditioned FRP Reinforcement Rods”, *First international conference on durability of fiber reinforced polymer (FRP) composites for construction*, 525–535.
- CSA S806-12 (2012). “Design and construction of building structures with fibre-reinforced polymers”, Canadian Standards Association (CSA).
- fib (2007). “FRP reinforcement in RC structures”, Technical report, Bulletin 40, fib - International Federation for Structural Concrete, Lausanne.
- F. Girgle, L. Bodnarova, O. Janus, V. Kostiha, (2018). “Influence of Alkalinity and Ambient Temperature on Long-Term Properties of GFRP Reinforcement”, *Key Engineering Materials*, 760, 213-218.
- R. Kotynia, D. Szczech, M. Kaszubska (2017). “Bond Behavior of GRFP Bars to Concrete in Beam Test”, *Procedia Engineering*, 193, 401-408.
- H. Mazaheripour, J.A.O. Barros, J.M. Sena-Cruz, M. Pepe, E. Martinelli (2013). Experimental study on bond performance of GFRP bars in self compacting steel fiber reinforced concrete, *Composite Structure*, 95, 202-212.
- A. Nanni, M. Al-Zaharani, S. Al-Dulaijen, T. Boothby (1995). “Bond of FRP reinforcement to concrete - Experimental results”, *Non-Metallic (FRP) Reinforcement for Concrete Structures*, 137-145.
- M. Pecce, G. Manfredi, R. Realfonzo, E. Cosenza (2001). “Experimental and analytical evaluation of bond properties of GFRP bars”, *Journal of Materials in Civil Engineering*, 13(4), 282-290.



RILEM, FIP-CEB (1973). "Tentative recommendations, recommendations for reinforcing steel, bond test for reinforcing steel: 1—Beam test (7-ii-28 d) 2—Pull-out test (7-ii-128)", *Materials and Structures*, 6(2), 79–118.

S. Sólyom, G.L. Balázs, A. Borosnyói (2015a). "Bond behaviour of FRP rebars – parameter study", *SMAR 2015 - Third Conference on Smart Monitoring, Assessment and Rehabilitation of Structures*, 1-8.

S. Sólyom, G.L. Balázs, A. Borosnyói (2015b). "Material characteristics and bond tests for FRP rebars", *Concrete Structures*, 16, 38-44.

B. Tighiouart, B. Benmokrane, D. Gao (1998). "Investigation of bond in concrete member with fibre reinforced polymer (FRP) bars", *Construction and Building Materials*, 12, 453-462.

W. Xue, Y. Yang, Q. Zheng, Z. Fang (2016). "Modeling of Bond of Sand-coated Deformed Glass Fibre-reinforced Polymer Rebars in Concrete". *Polymers & Polymer Composites*, 24(1), 45-56.

J. Zhou, X. Chen, S. Chen (2012). "Effect of Different Environments on Bond Strength of Glass Fiber-Reinforced Polymer and Steel Reinforcing Bars", *KSCE Journal of Civil Engineering*, 16(6), 994-1002.



PERFORMANCE STUDY OF A POST-TENSIONED CONCRETE SLAB STRENGTHENED WITH CFRP USING 24 HR AND CYCLIC LOAD TESTING

Thanongsak Imjai 1, Surin Sutthiprapa 1 Burachat Chatveera 2 and Udomvit Chaisakulkiet 3

¹ Dept. of Civil Engineering, Rajamangala University of Technology Tawan-Ok, Bangkok, Thailand,

Email: thanongsak_im@rmutto.ac.th

² Dept. of Civil Engineering, Thammasat University, Bangkok, Thailand

³ Dept. of Civil Engineering, Rajamangala University of Technology Rattanakosin, Bangkok, Thailand

ABSTRACT

This article presents the showcase on a performance study of post-tensioned concrete slabs using externally bonded carbon fibre reinforced composites (CFRP). The concrete slabs are part of a full-scale 17 storey building located in Thailand. The original building (completed in 2000) is currently used as the residential building. Design verifications based on ACI 318 indicated that the flexural capacity of the original post-tensioned slab was insufficient to resist the new superimposed loads from three water tanks with capacity of 1000 litres that is planned to install on the roof top floor. Conversely, flexural, shear and torsional capacity of the existing RC beam and column sections were sufficient to resist the superimposed loads by up to 120% (under the roof top level). As part of the retrofitting programme, the concrete slab was strengthened with Carbon FRP (CFRP) laminates using a manual lay-up application. The load capacity and deflection of the FRP-strengthened slab was then re-assessed according to the 24 hours (ACI-318) and cyclic load (ACI-437) test protocols. Based on the floor load test results, it was found that the proposed strengthening solution was adequate to sustain the increased load demand imposed by the water tanks.

KEYWORDS

Strengthening and repair, Structural assessment, Externally bonded FRP, Load testing, Post-tensioned slab.

INTRODUCTION

Many existing reinforced concrete (RC) structures change their use/function during their lifespan. In many cases, such structures require structural strengthening due new loading conditions which often impose higher loads than those considered in the original design. In the last decades, the use of Externally Bonded Fibre Reinforced Polymers (EBR FRP) has proven a cost-effective solution to strengthen existing structures. Moreover, EBR FRP can extend the lifespan of concrete structures and reduce the need of future maintenance or repair interventions (Bakis et al. 2002; Imjai et al. 2017; Nanni 2004). While structural upgrades with EBR FRP are carried out regularly in developed countries, such interventions are less common in the developing world. Consequently, it is necessary to highlight successful case studies in the latter countries so as to promote the wider use of FRP.

This paper describes the in-situ strengthening of RC slabs of an existing building using EBR FRP. The original 17 storey RC structure was designed as a residential building. In 2018, as part of rehabilitation of the building, three water tanks with a capacity of 1000 litres are planned to install in the roof top floor. Therefore, the original design document for the building was reviewed in detail to assess the capacity of the existing structural elements. An in-situ structural inspection was also performed to assess the structural capacity of the slabs using 24 hr floor load testing protocol according to ACI 318 (2005). Several strengthening solutions were then proposed, such as externally bonded steel plates (EBS), section enlargement or EBR FRP. Based on the test results and numerical analysis, the concrete slab was eventually strengthened with Carbon FRP (CFRP) laminates using a manual lay-up application as described in this paper. After the installation of EBR CFRP strengthening system, the performance study of the post-strengthening concrete slab was re-assessed using 24 hr (ACI-318, 2005) and cyclic load (ACI-437, 2003) test protocols. This study contributes towards promoting the use of EBR FRP as a strengthening solution in South East Asia by showing a successful practical case study.

Project facts

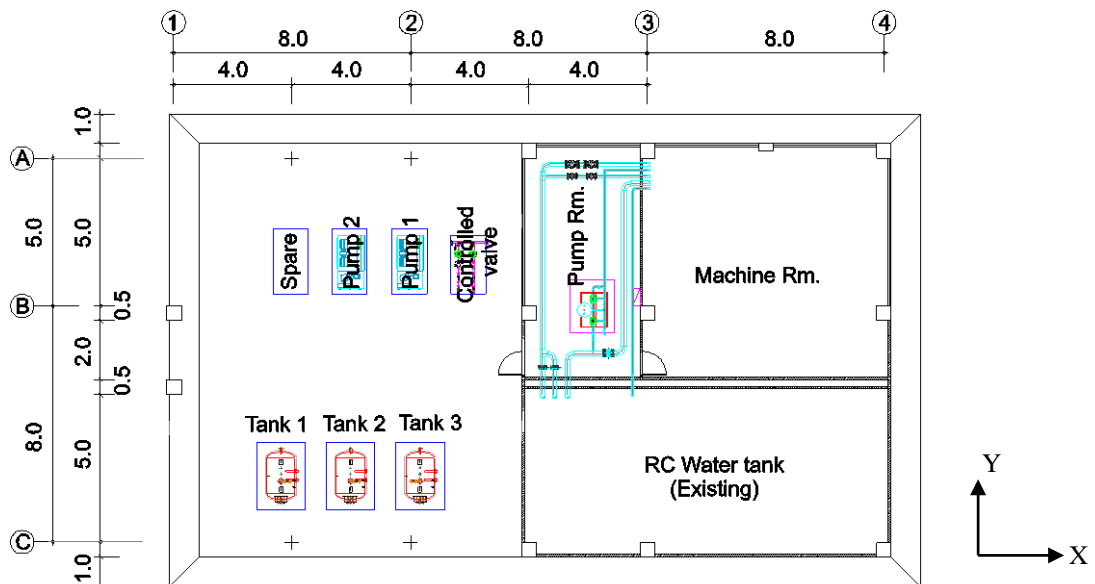
The Jazzotel building is the residential building located in the centre of Bangkok, the capital of Thailand. The building consists of a 17 storey RC structure with 25 mm thick post-tensioned concrete slabs supported on beams. As part of rehabilitation of the building, three water tanks (no. 1-3 in Figure 1a) with a capacity of 1000 litres are planned to install in the roof top floor (see Figure 1b). The building has 3 bays in X and 2 bays in Y directions with typical spans of 8 m (see Figure 1c). The building was built in 2000 and is owned by Poonwaraluck Co. Ltd.

The study of the construction drawings was followed by a walk-through visual inspection and non-destructive material tests. Visual inspection of the roof top floor was carried out and shrinkage cracks on the concrete slab concrete spalls were found as shown in Figure 1b. Before performing the load test, no material data were available and the concrete compressive strength were obtained from NDT test as $f'_c = 24$ MPa and steel yield strength, $f_y = 294$ MPa. With such a limit information from the construction drawings, detailed engineering assessment (DEA) was subsequently performed by the design team to re-check structural capacity of the as-built concrete members.



(a) Overview of 17 stories residence building

(b) Top roof floor



(c) Key plan for three water tanks and pumps on the top roof floor

Figure 1: Overview of the 17-stories building and top roof key plan

SLAB STRENGTHENING USING EXTERNALLY BONDED CFRP

The original live loads used to design the floor ranged from 1.5 to 2.0 kN/m², whereas the new superimposed loads on the roof top floor increased to 2 tons due to new water tanks (up by +120%). Externally bonded CFRP

was proposed as one of the options to enhance the capacity of the slabs, which was accepted by the project manager and client.

Design consideration

A preliminary structural assessment and detailed engineering analysis of the RC building according to ACI 318 (2005) indicated that the flexural capacity of the existing post-tensioned concrete slab was insufficient to sustain the new ultimate bending moment to be imposed on the top roof floor. The design of the original RC slab required that the design flexural strength exceeded the required factored moment (i.e. $\phi M_n > M_u$). However, the unstrengthened concrete slab should have sufficient strength (although without risk of collapse) to resist a certain level of load in case the EBR CFRP system fails. Such sufficient strength (R_n) is given by Eq. (1) (fib 14, 2001).

$$(\phi R_n)_{\text{existing}} \geq (1.1DL + 0.75LL)_{\text{new}} \quad (1)$$

where DL is the dead load, and LL is the imposed load.

EBR CFRP Strengthening system

The increase on demand made necessary a strengthening intervention on the top roof floor slab by the design team using ADAPT computer software. Consequently, one unidirectional CFRP sheet was applied beneath the location where three tanks are to be installed which allows the slab flexural capacity by 120%. A CFRP sheet (TORAYCA™ T300: $b_f=250$ mm, $t_f=0.167$ mm, $E_f=130$ GPa, Poisson's ratio=0.29, $f_{fu}=1760$ MPa, $\epsilon_{fu}=0.013$) was fixed using two-parts epoxy adhesive bonding (NIBICHI-A43: $E_m=3.5$ GPa, $f_m=60$ MPa, Poisson's ratio=0.35). Figure 2 shows the EBR CFRP strengthening typical detail of the post-tensioned concrete slab (roof top floor). The construction details of the FRP strengthening were carried out according to fib Bulletin 14 (2001). A Class 1 ASTM E84 flame and smoke coating was used as fire protection system.

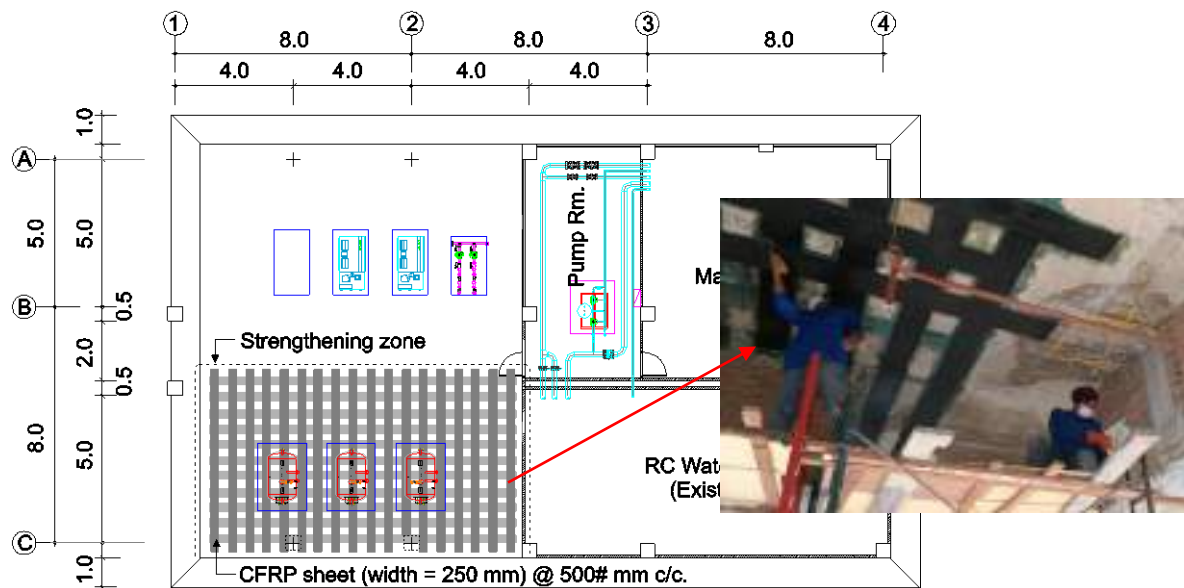


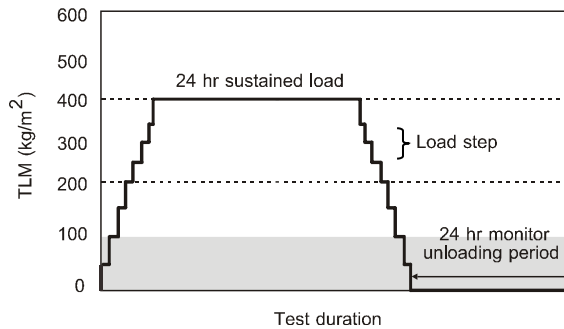
Figure 2: CFRP strengthening layout under the post-tensioned concrete slab

IN-SITU FLOOR LOAD TESTING

ACI 318: 24 hour load testing

To assess the performance of the strengthened concrete slab, in-situ load testing according to ACI 318 (2005) was performed using total load magnitude (TLM) at 85% of the total factored load i.e. $TLM = 0.85[1.4D+1.7L] = 400$ kg/m². The pre-specified load magnitude consists in the monotonic loading of four increments. ACI 318-05, Chapter 20 prescribes that the load must be arranged to maximize the deflections and stress in the critical regions of the structural elements under investigation, but does not specifically indicate what load distribution should be used. In phase 1, the distributed load of 400 kg/m² from water was used and was sustained for the a time period

of 24 hours (i.e. see Figure 2). Maximum deflection due to TLM at the centre of the slab was measured using one Linear Variable Differential Transducers (LVDT) with a measurement range of ± 50 mm (measured under tank 2, see Figure 3b). Five waterproof strain sensors with measurement range $\pm 4000 \mu\epsilon$ (see Figure 3b) measured strains on the concrete elements (gauges no. 5003, 5005, under tank 2 and gauges no. 5004 and 5006 under tank 3 in Figure 3c) and on the concrete column gridline B/2 (gauge no. 5002). After 24 hours, the load was removed from the floor. The slab was then left without load for another 24 hr and the residual deflection was recorded. The maximum and residual deflections of the tested slab can be compared to the ACI 318-05 criteria which indicates an allowable maximum deflection, $\Delta_{max} = L^2/20000h$ and allowable residual deflection, $\Delta_r = \Delta_{max}/4$ (L =span length in inches and h = slab thickness in inches).



(A) Load configuration for 24 hr load test

(B) Sustained load by water

Figure 2: Test setup and instrumentation at the bottom face of the slab



(A) Overview of the floor under the roof top

(B) Installation of strain sensors in X-X and Y-Y direction under the roof top floor



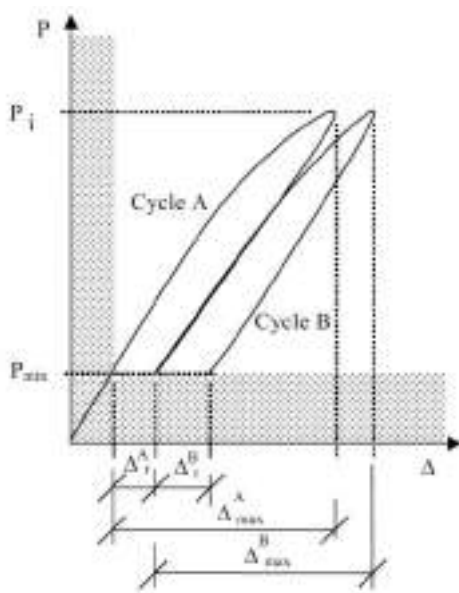
(C) Installation of LVDT for deflection measurement

(D) Real-time monitoring via personal computer

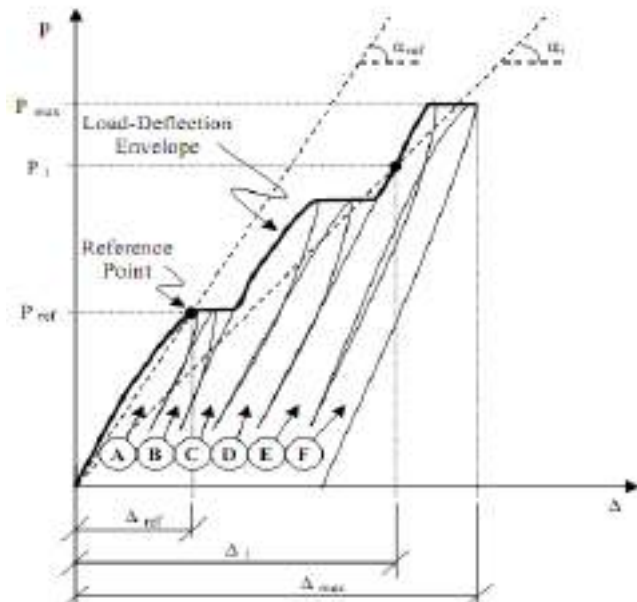
Figure 3: Test setup and instrumentation at the bottom face of the slab

ACI 437: Cyclic load testing

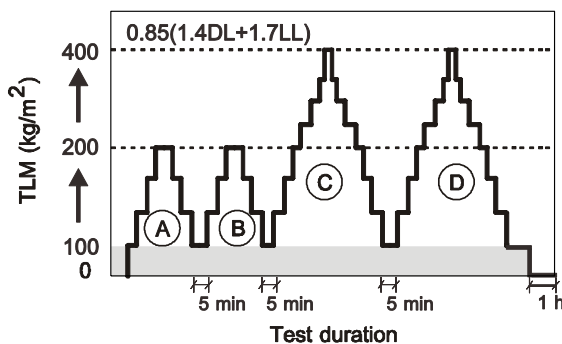
The procedure of ACI 437 (2003) cyclic load test consists of the application of patch loads in a quasi-static manner (i.e., sufficiently slow to avoid any strain rate effect) to the structural member, similar to the 24 hr load test protocol but performing in at least four loading/unloading cycles. Figure 5a shows the cycle characteristics: the load, expressed as a percentage of the maximum applied value is plotted versus the cumulative time. Any load cycle should consist in a sequence of at least four loading steps followed by four unloading steps. For this minimum test protocol, the total load test duration can be minimised with each loading/unloading cycle lasting about 20 minutes. ACI 437 used three distinct acceptance indices for the cyclic load test method, these are 1) repeatability, 2) permanency and 3) deviation from linearity, as expressed in Figure 5b,d. These three indices may be related to any structural responses (e.g. deformation, rotation, strain). However, deformation in term of deflection appears to be the most convenient to describe in the criteria (CIAS 2000).



(A) A couple of twin cycles



(B) Load-deflection curve for deviation from linearly calculation



(C) Load cycles performed in the project

$$I_R = \text{Repeatability Index} = \frac{\Delta_{\max}^B - \Delta_r^B}{\Delta_{\max}^A - \Delta_r^A} \times 100\%$$

$$I_p = \text{Permanency Index} = \frac{\Delta_r^B}{\Delta_{\max}^B} \times 100\%$$

$$\text{Linearity}_i = \frac{\tan(\alpha_i)}{\tan(\alpha_{ref})} \times 100\%$$

$$I_{DL} = 100\% - \text{Linearity}_i$$

(D) Acceptance criteria per ACI 437R-03

Figure 5: Test setup and instrumentation at the bottom face of the slab

PERFORMANCE OF STRENGTHENED POST-TENSIONED SLAB BY LOAD TESTING

The acceptance criteria previously described from ACI 318 and ACI 437 were calculated for 24 hr and cyclic load test protocols, respectively. According to the criteria, the test has to be considered failed if the deflections and indices are not satisfied. Table 1-left shows the Load deflection and strains measurements from the test. The load-

deflection curve at the mid-span of slab (under tank 2) was shown. For 24 hr load test, the maximum deflection and residual deflection were found to be 0.92 mm and 0.34 mm, which indicates that the structure passed the test. Measured strains were also recorded and presented in Table 1-right, it shows that strain value measured in X-X direction exhibit higher than Y-Y direction. This is due to a longer span in X-X direction compared to Y-Y direction. The maximum strain (ϵ_{max}) in X-X is 9.86 $\mu\epsilon$ with the residual strain (ϵ_{res}) of 5.92 $\mu\epsilon$. And for the Y-Y direction, the maximum strain in X-X is 57.89 $\mu\epsilon$ with the residual strain of 13.09 $\mu\epsilon$. The compressive strain of 22.25 $\mu\epsilon$ with residual strain of 14.08 $\mu\epsilon$ was also recorded in the column. Residual strain indicated that the structure behaves non-linear manner when unloading. This is due to the deterioration of material such as creep effect, shrinkage crack, loss in section from concrete spalls or corrosion in steel reinforcement.

Table 1: Load deflection and strains measurements

Strain Ref.	Location	ϵ_{max} ($\mu\epsilon$)	ϵ_{res} ($\mu\epsilon$)
B5002	column	-22.25	-14.08
B5003	slab X-X	9.86	0.75
B5004	slab X-X	9.22	5.92
B5005	slab Y-Y	57.89	11.39
B5006	slab Y-Y	26.41	13.09

Table 2 summarizes the structural responses from both 24 hr and cyclic load tests. In Table 2, it also is shown that the structural slab passed the criteria from both ACI 318 and ACI 437. In the rehabilitation programme, the 24 hr load test was performed as part of DEA task along with an advanced structural analysis. Although the deflection in asterisk showed the structure passed the test, the analysis result proved that the post-tensioned concrete slab was not sufficient to resist new water tanks and required to increase the flexural capacity by up to 120% of the original design. Therefore, EBR CFRP strengthening scheme was chosen and performance study of the post-strengthening of EBR was re-assessed using 24 hr and cyclic load test protocols. In case of cycles load test, results from four cycles are reported and three indices were calculated as per ACI 437. As seen in Table 3, three indices calculated from four load cycles were indicated that the structural slab passed the test.

Table 2: Load test results from phase 2

Type	Load cycles	Load level	Δ_{max} (< 5.00 mm)	Δ_{rmax} (< 1.25 mm)	Remark
24 hrs (ACI 318-05)	-	400	3.15*, 0.92	-	Satisfactory
	After removal of tested load		-	1.03*, 0.34	Satisfactory
Cyclic load (ACI 437-03))	A	200	0.36	-	Satisfactory
	B	200	0.38	-	Satisfactory
	C	400	0.88	-	Satisfactory
	D	400	0.92	-	Satisfactory
	After removal of tested load		-	-	0.34

Note: * is the deflection measurement in the load test phase 1 (prior to EBR CFRP strengthening)

Table 3: Acceptance criteria evaluation according to ACI 437R-03

Cycle	Repeatability, I_R (<95%)	Permanency, I_P (<10%)	Deviation from Linearity, I_{DL} (<25%)	Performance
A-B	94.69	7.76	10.97	Satisfactory



C-D	90.05	0.79	11.50	Satisfactory
-----	-------	------	-------	--------------

CONCLUDING REMARKS

This article presents a case study of the post-assessment of the EBR CFRP strengthening on post-tensioned concrete slab. The project consists of two phases; in phase 1, the 24 hr load test was performed as part of DEA task along with an advanced structural analysis. Design verifications based on ACI 318 showed that the flexural capacity of the original RC slab was insufficient to resist new water tanks and required to increase the flexural capacity by up to 120% of the original design. Therefore, EBR CFRP strengthening scheme was chosen and performance study of the post-strengthening of EBR was re-assessed using 24 hr and cyclic load test protocols with a real-time testing of a structure (Phase 2). Based on the case study discussed in this paper, the following conclusions can be drawn:

- Design verifications based on ACI 318 showed that the flexural capacity of the original post-tensioned concrete slab was insufficient due to an increase of superimposed loads from three water tank at the roof top floor. Conversely, flexural, shear and torsional capacity of the existing RC beam and column sections were sufficient to resist superimposed loads of up to 150% under the roof top floor.
- Externally bonded CFRP systems was successfully to increase the total flexural capacity of original post-tensioned concrete slabs by up to 120% compared to their original design capacity.
- The strengthening was implemented adding minimum weight to the structure (150 kg of CFRP plates) and at a modest cost (USD 3,500).
- Live load mid-span slab deflections from field measurement were lower than the allowable values specified by ACI 318-05. Therefore, the CFRP-strengthened post-tensioned concrete slabs were deemed sufficient to resist the new imposed live load a 2 kN/m².
- For 24 hr load test, the maximum deflection and residual deflection were found to be 0.92 mm and 0.34 mm, which indicates that the structure passed the test.
- For cyclic load test, three distinct acceptance indices; 1) repeatability, 2) permanency and 3) deviation from linearity passed the acceptance criteria as per ACI 437-03, indicating the structure passed the test.
- Measured strains in X-X direction exhibit higher than Y-Y direction. This is due to a longer span in X-X direction compared to Y-Y direction. The maximum strain in X-X is 9.86 me with the residual strain of 5.92 me. For the Y-Y direction, the maximum strain in X-X is 57.89 me with the residual strain of 13.09 me.
- Comparison between two load testing protocols, it was evident that the both testing protocols can be used to assess strengthening performance of EBR CFRP on the post-tensioned concrete slab and cyclic load test method from ACI-437 could minimise the time consumption compared to 24 hour load method according to ACI-318.

ACKNOWLEDGMENT

The first author thankfully acknowledge the financial support from the Rajamangala University of Technology Tawan-Ok and Poonwaraluck Co. Ltd for permission to access the test data. The second author is thankfully the financial support offered by Thammasat University. The third author would like to acknowledge the financial support offered by Rajamangala University of Technology Rattanakosin.

REFERENCES

C.E. Bakis, L.C. Bank, V.L. Brown, E. Cosenza, J.F. Davalos, J.J. Lesko, A. Machida, S.H. Riskalla, T.C. Triantafillou, “Fiber-reinforced polymer composites for construction – State-of-the-art review”, *Journal of Composites for Construction*. 6 (2), May, pp. 73-87, 2002.

T. Imjai, J. Phumkesorn, P. Anchaoen and R. Garcia, “structural assessment of a RC slab strengthened with CFRP composite using in-situ load testing” in APFIS2017 - 6th Asia-Pacific Conference on FRP in Structures Singapore, 19-21st July, 2017.

A. Nanni, “Fiber reinforced polymer composites for infrastructure strengthening - From research to practice”, VII AIMAT Congress, Ancona, Italy, June 29 - July 2, Keynote Paper KP2, pp. 10, 2004.



ACI Committee 318, “Building Code Requirements for Structural concrete and Commentary”, B.M Johnson and A.H. Wilson, Terminology of Building Conservation Industry, Division of Building Research, NRC Canada, 2005.

ACI Committee 437, “Strength Evaluation of Existing Concrete Buildings”, American Concrete Institute, Farmington Hills, Michigan, 2003.

fib Bulletin 14, “Externally Bonded FRP Reinforcement for RC Structures”, fib Task Group 9.3, Lausanne, pp. 1–138, 2001.

CIAS, “Guidelines for the Rapid Load Testing of Concrete Structural Members, Concrete Innovation Appraisal Service”, CIAS Report 00-1, ACI International, Farmington Hills, MI, 2000.



SHRINKAGE BEHAVIOUR OF FIBRE REINFORCED POLYMER GRID REINFORCED INFRA-LIGHTWEIGHT CONCRETE

Y. Liu¹, A. Goldack¹, M. Schlaich¹ and A. Hückler¹

¹ Chair of Conceptual and Structural Design,

Technische Universität Berlin, Germany. Email: yue.liu@mailbox.tu-berlin.de

ABSTRACT

Infra-lightweight concrete (ILC) is a type of lightweight concrete (LC) with a dry density less than 800 kg/m³. ILC has not only extremely low self-weight and excellent heat insulating capacity but also enough structural strength for buildings. However, the shrinkage of ILC is relatively large, which may cause wide concrete cracks and steel reinforcement corrosion. Noncorroding is a main advantage of fibre reinforced polymer (FRP) reinforcement, which makes it suitable to substitute steel reinforcement in ILC. This paper presents the investigation on the shrinkage of ILC reinforced with a FRP grid. Shrinkage experiments on the ILCs of different dry densities and with different FRP grids were conducted. As expected, the shrinkage strains of FRP grid reinforced ILC prisms are significantly smaller than that of plain ILC prisms, which allows to control the shrinkage of ILC. Furthermore, the CFRP (carbon fibre reinforced polymer) grid has a higher efficiency to reduce the ILC shrinkage compared with the GFRP (glass fibre reinforced polymer) grid if the reinforcement ratios are kept the same. Moreover, the higher the reinforcement ratio is, the greater the rate of shrinkage decline will be, if the grid materials remain identical.

KEYWORDS

New composite materials, systems and strengthening techniques, Experimental study, FRP internal reinforcement.

INTRODUCTION

After its emergence in the middle of the nineteenth century, the reinforced concrete quickly became a commonly used building material (Simonnet 1992). For a long time, steel is almost the only reinforcing material. It has high strength and a ductile behaviour, which just counteracts the deficiency of the concrete. The steel reinforced concrete has been applied to various fields, including buildings, bridges, roads, dams, and industrial structures. However, the steel is inherently susceptible to corrosion. The crack of the concrete and the absorbed moisture may cause severe corrosion of the steel reinforcement, which can considerably decrease the structural load bearing capacity as well as the structural durability (Liu and Weyers 1998).

In view of this, some experts proposed using fibre reinforced polymer (FRP) reinforcement in concrete, after the invention of FRP in the 1950s (Bakis *et al.* 2002). The FRP, as its name suggests, is composed of fibres as the reinforcement embedded in a polymer resin as the matrix (Bhargava 2002). It is an advanced composite material with high strength, light weight and no corrosion, which make it suitable to replace the steel as the concrete reinforcement in many cases, especially in strong corrosive environments. Now, there are also a considerable number of researches on the FRP reinforced concrete. Malvar researched the bond characteristics of FRP reinforcements in the concrete (Malvar 1994). Abdalla investigated the flexural behaviour of FRP reinforced concrete members (Abdalla 2002). Zhang and Ou studied the mechanical properties of FRP reinforced concrete columns (Zhang and Ou 2006). ACI Committee published the guide for the design and construction of FRP reinforced concrete (ACI 2001). A review of applications of FRP reinforcements for concrete structures can be found in (Hensher 2016).

However, the existing researches are mainly about the normal-weight concrete (NC) reinforced with FRP, while the researches on the FRP reinforced lightweight concrete (LC), especially infra-lightweight concrete (ILC), are still very rare. Moreover, there is also a shortage of researches on the shrinkage of FRP reinforced concrete. Therefore, the authors investigated the shrinkage behaviour of FRP grid reinforced ILC and presents the work in this paper. This research could provide useful references for designers to choose suitable reinforcement of ILC.

INFRA-LIGHTWEIGHT CONCRETE

Properties and Mixes

According to the Eurocode (EN 206 2014), concretes can be classified into three main types based on their dry densities, i.e. normal-weight, heavyweight and lightweight (see Fig. 1a). The lightweight concrete (LC for short) is defined as the concrete with dry density in the range of 800 kg/m³ to 2000 kg/m³ (EN 206 2014). Therefore, the infra-lightweight concrete (ILC for short) can be defined as the concrete whose dry density is below 800 kg/m³, where “infra” means “below” (see Fig. 1a) (Schlaich and El Zareef 2008). The cross-section of an ILC using expanded clay as aggregate is shown in Fig. 1b (Schlaich and Hückler 2012).

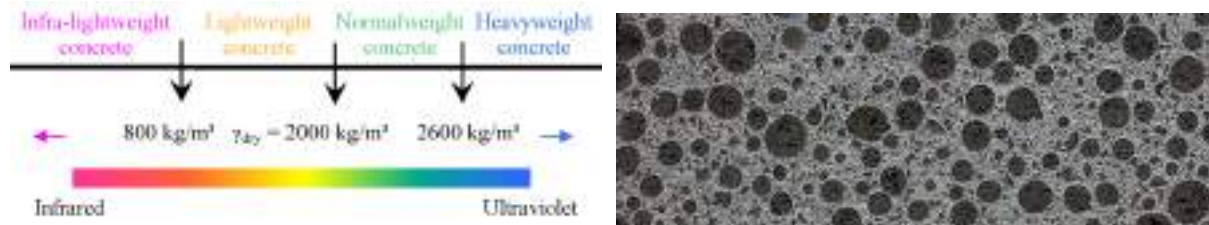


Figure 1 (a) Classification of concretes (b) cross-section of ILC (Schlaich and El Zareef 2008)

Except for the extremely low self-weight, the ILC has also excellent heat insulating property as well as enough strength as a structural material. The mechanical and thermal properties as well as concrete mixes of three typical ILCs (ILC 600, ILC 700 and ILC 800, which are named after their dry densities) (Hückler 2016) are listed in Table 1 and Table 2, compared with that of a commonly used normal-weight concrete (NC, grade C30/37) (Neroth and Vollenschaar 2011).

Table 1 Mechanical and thermal properties of three ILCs (Hückler 2016) and a typical NC (Neroth and Vollenschaar 2011)

	ILC 600	ILC 700	ILC 800	NC (C30/37)
Dry density [g/cm ³]	600	700	800	2188
Cylinder compressive strength [MPa]	5.30	9.41	12.96	30.20
Tensile strength [MPa]	0.65	0.76	0.87	2.91
Elastic modulus [MPa]	2300	3100	3900	31900
Thermal conductivity coefficient [W/(mK)]	0.141	0.166	0.193	1.40

Table 2 Mixes of three ILCs and a typical NC

	ILC 600		ILC 700		ILC 800		NC (C30/37)		
	V [dm ³]	M (kg)							
Light sand	7	19	17	46	26	73	Sand	340	883
Liapor 1/4	118	117	108	108	98	114	Gravel 2/8	322	837
Liapor 2/6	325	197	282	173	240	147			
CEM III-A	62	188	85	260	109	333	CEM III-A	128	391
Water	214	214	234	234	255	255	Water	195	195
Silica fume	31	73	30	70	28	66			
Plasticizer	2.65	2.86	2.95	3.19	3.26	3.52			
Stabilizer	0.30	0.27	0.50	0.45	0.70	0.63	Air	15	0
Air	240	0	240	0	240	0			
Sum	1000	811	1000	895	1000	992			

As can be seen, the dry densities and strengths of ILCs are considerably smaller than that of NC, and their thermal conductivity coefficients are also much smaller, which means their insulation capacities are much better. Furthermore, the strengths of ILCs rise with the dry densities incline, and so do their thermal conductivity



coefficients. This indicates that the ILCs' thermal insulation capacities are inversely proportional to their strengths as well as their dry densities. Furthermore, a prominent feature of ILCs' mixes is that the water consumption is relatively great, while the amount of cement and fine aggregate is relatively low, i.e. their water cement ratios are much larger than that of NC. Moreover, the air void ratio of ILCs is also considerably greater than that of NC.

Shrinkage Behaviour of ILC

Shrinkage of concrete is the decrease in the concrete volume in process of hardening with respect to time (Neville 1995). This decrease is due to change in the moisture content and physical-chemical change of the concrete. Knowledge of the concrete shrinkage is a necessary starting point in the design of concrete structures. There are already a lot of researches on this topic. As early as 1935, Carlson has explained the mechanism of concrete shrinkage and illustrated the factors that can affect the concrete shrinkage (Carlson 1935). Hansen and Nielsen investigated the influences of aggregate and cement paste on the concrete shrinkage (Hansen and Nielsen 1965). Acker and Ulm summarised the physical origins and practical measurements of the concrete shrinkage (Acker and Ulm, 2001). Bazant reviewed the existing research works on the shrinkage of concrete in (Bažant 2001). Furthermore, a quite number of prediction models were also established to estimate the shrinkage values of concrete (CEB-FIP 1990) (ACI 1992) (RILEM 1995). Among them, the RILEM B3 model is regarded as a model that considers various influence factors and has good accuracy (Bažant 2000), although it is more complex than many other models like the CEB-FIP 90 model (CEB-FIP 1990).

Applying the RILEM B3 shrinkage model (RILEM 1995) to the concrete grades in Table 1 and Table 2, the shrinkage strains of ILCs and NC prism (160 mm × 40 mm × 40 mm) in the environment of 20 °C temperature and 65 % humidity could be calculated for a concrete age up to 100 days. The calculation results are depicted and compared in Fig. 2.

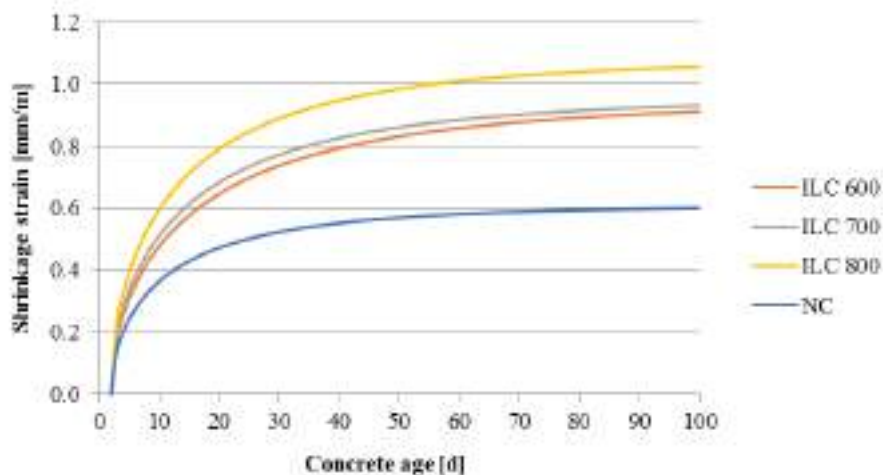


Figure 2 Shrinkage strains of ILCs and NC calculated by RILEM B3 model

It can be seen from Fig. 2, the shrinkage strains of ILCs are significantly greater than that of NC. The increases of ILCs' final shrinkages are more than 50% compared to that of NC. Most of the shrinkage of concretes, except for some high-performance concretes whose cement assumptions are considerably high, is drying shrinkage, which is due to the loss of water (Müller and Kvitsel 2002). It can be inferred that the great shrinkage of ILC is probably caused by the great water consumptions during mixing and the subsequent loss of water during drying. This great shrinkage may cause severe cracks of concrete and thus decreasing the serviceability and durability of concrete structure. Therefore, it should be properly controlled.

CONTROL OF ILC SHRINKAGE WITH FRP REINFORCEMENT

In order to investigate the restriction effect of FRP reinforcement on the ILC shrinkage, three different ILCs reinforced with four different FRP grids were experimentally studied. Their shrinkage strains were not only compared with each other but also compared to that of the corresponding ILCs without any reinforcement.

Experimental Setup

The shrinkage experiment was performed according to the Eurocode (EN 12617 2002). The dimensions of the concrete prism for shrinkage measurement are illustrated in Fig. 3a. Three ILCs with different dry densities, i.e. ILC 600, ILC 700 and ILC 800, were investigated. Moreover, four types of FRP grids with different fibre materials and different dimensions produced by solidian GmbH were used, which are introduced in Fig. 3b and Table 3 (Solidian 2016). The dimensions of the FRP grids are listed in Table 3.

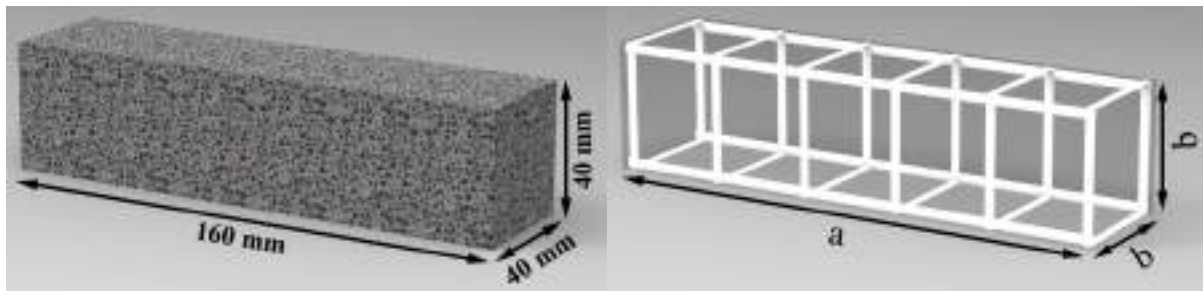


Figure 3 (a) Diagram of concrete prism (b) diagram of FRP grid

Table 3 Properties of four FRP grids used

Name	Fibre material	Length of one grid [mm]	cross section per unit length [mm ² /m]*	Strength [MPa]	Elastic modulus [GPa]	a [mm]	b [mm]
GFRP-21	Glass fibre	21	87	1100	60	150	21
GFRP-25	Glass fibre	25	145	1100	60	150	25
CFRP-21	Carbon fibre	21	85	2300	120	150	21
CFRP-25	Carbon fibre	25	142	2300	120	150	25

* Cross-sectional area of reinforcement per unit length in the both directions of the grid

Two types of FRPs grids were used, one with glass fibres (GFRP) and the other one with carbon fibres (CFRP) as shown in Table 3. The elastic modulus of CFRP is twice of GFRP. The grids used differ also in their grid length, which is the distance between two rovings. Furthermore, the grids with 25 mm grid length have much greater cross section per unit length than the grids with 21 mm grid length. The total cross section of the longitudinal reinforcement of the specimen with the CFRP-21 grid calculates to $85\text{mm}^2/\text{m} \times 21\text{ mm} \times 4 / 1000\text{ mm}/\text{m} = 7.15\text{ mm}^2$. The specimen reinforced with this grid has a reinforcement ratio of $7.14 / (40 \times 40) = 0,4\%$ only. For every type of concrete prism, three specimens were manufactured and kept in the climate room with 20 °C and 65% humidity. Their shrinkage strains were measured with the micrometre length compactor in 2, 3, 7, 14, 28, 50, 100 days of concrete age (EN 12617 2002).

Results and Discussion

After 100 days of test, the shrinkage strain of every specimen was recorded. The results of mean values (three specimen each test) are shown in Fig. 4 and Fig. 5.

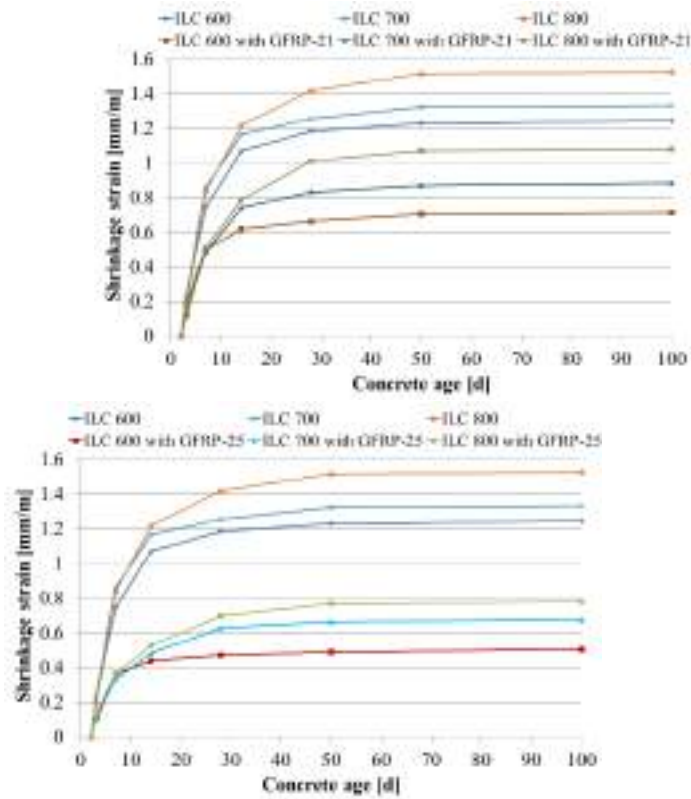


Figure 4 (a) Shrinkage strains of ILC compared to reinforced ILC with GFRP-21 or (b) GFRP-25

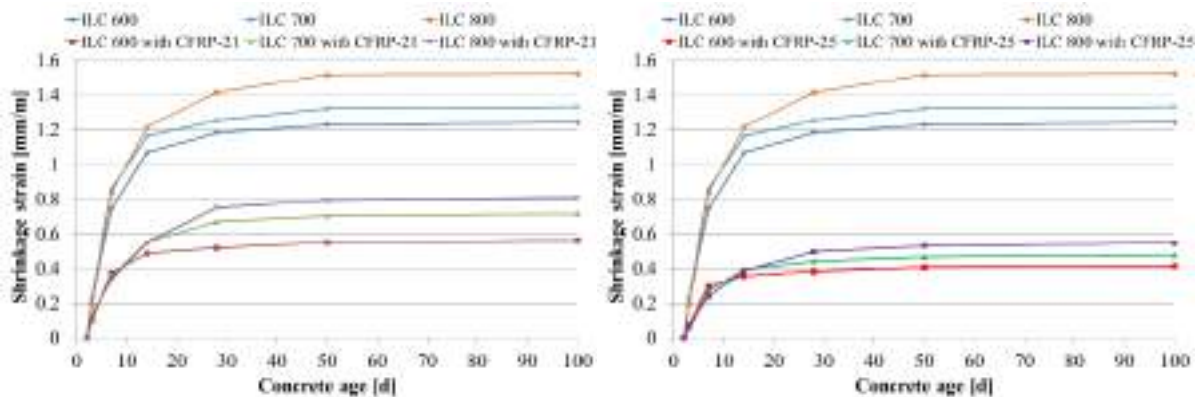


Figure 5 (a) Shrinkage strains of ILC compared to reinforced ILC with CFRP-21 or (b) CFRP-25

Obviously, the reduction of the ILC shrinkage by the FRP grid reinforcement can be identified. The biggest decline of final shrinkage strain reaches 64% (from ILC 800 to ILC 800 reinforced with CFRP 25), while the smallest is also more than 40% (from ILC 600 to ILC 600 reinforced with GFRP 21). Furthermore, the shrinkage strains of ILC 800 are greater than that of ILC 700, and the shrinkage strains of ILC 700 are greater than that of ILC 600. This tendency is the same as the calculation result of RILEM B3 model (see Fig. 2). The experimental results depicted according to the type of ILC are shown in Fig. 6, Fig. 7 and Fig. 8, respectively.

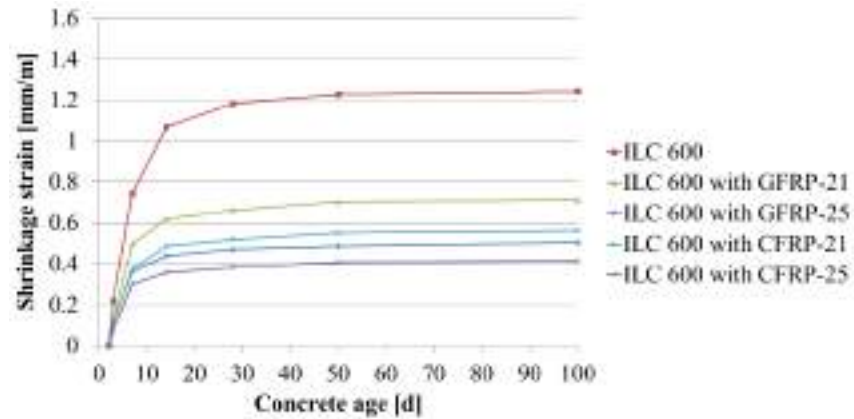


Figure 6 Shrinkage strains of ILC 600 with/without FRP grids

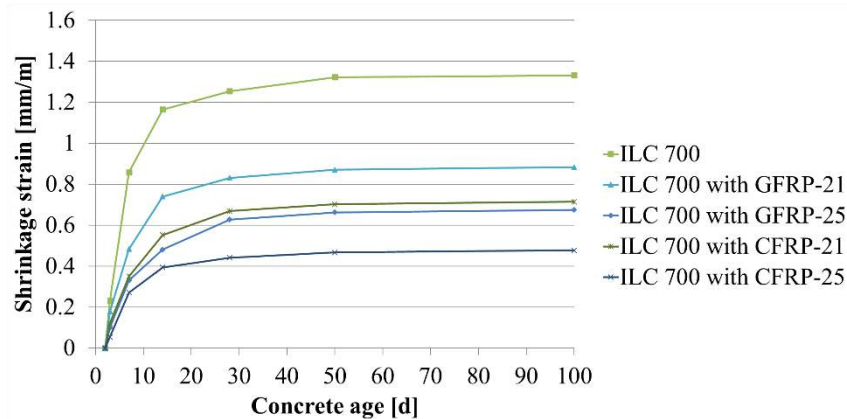


Figure 7 Shrinkage strains of ILC 700 with/without FRP grids

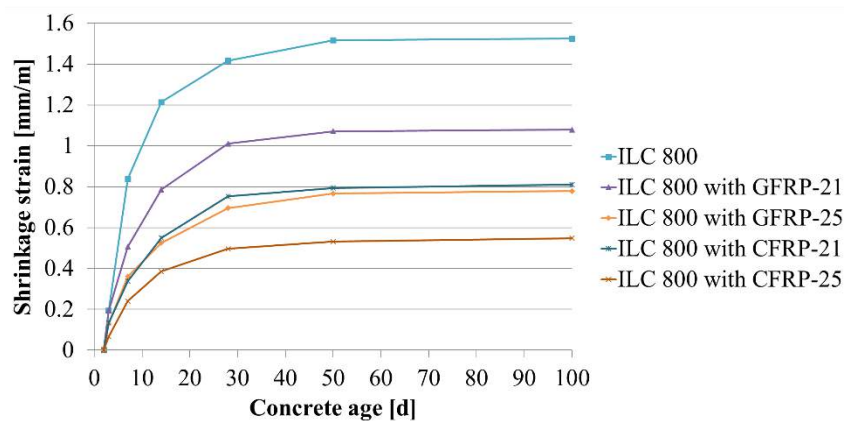


Figure 8 Shrinkage strains of ILC 800 with/without FRP grids

From the above three figures, it can be more clearly seen that the shrinkage control efficiency of CFRP-25 grid is always the highest, while that of GFRP-21 grid is always the lowest. Moreover, the shrinkage control efficiency of CFRP-21 is always approximately equal to that of GFRP-21 for all three types of ILCs. It is primarily because, if the concrete type is determined, the shrinkage control efficiency is positive correlation to the extensional stiffness (EA/L), i.e. the product of elastic modulus and cross-sectional area of the FRP reinforcement divided by the length. The EA/L of the four FRP grids can be easily calculated. The EA/L of the CFRP-25 equals to $120 \text{ GPa} \times 14.2 \text{ mm}^2 \div 150 \text{ mm} = 11.36 \text{ kN/mm}$, which is the most stiff; while the EA/L of the GFRP-21, equals to $60 \text{ GPa} \times 7.31 \text{ mm}^2 \div 150 \text{ mm} = 2.92 \text{ kN/mm}$, is the smallest. The EA/L of the CFRP-21 ($120 \text{ GPa} \times 7.14 \text{ mm}^2 \div 150 \text{ mm}$



= 5.71 kN/mm) is slightly smaller than the EA/L of the GFRP-25 ($60 \text{ GPa} \times 14.5 \text{ mm} = 5.8 \text{ kN/mm}$), which makes the shrinkage control efficiency of CFRP-21 slightly lower than that of GFRP-25.

CONCLUSION AND PROSPECTATION

This paper mainly presents the experimental study on the shrinkage behaviours of ILCs and FRP grid reinforced ILCs. Besides, the shrinkages of ILCs are also calculated and compared to that of NC using empirical formulas, i.e. RILEM B3 model. The results show that the shrinkage strains of ILCs are significantly greater than that of NC, and the higher the dry density of ILC is, the greater the shrinkage strain will be. Using FRP grid reinforcements can effectively reduce the shrinkages of ILCs and their shrinkage control efficiencies are: CFRP-25 > GFRP-25 \approx CFRP-21 > GFRP-21, which infers that the higher value of EA of FRP reinforcement brings the better effect of restriction of concrete shrinkage. More researches still need to be done on this topic. Comparing the ILC shrinkage results from the experiment with that from the prediction model, it can be found that the consistency is not good enough, which means a new prediction model or a special modification of existing model for the shrinkage of ILC is needed. Furthermore, the accurate correlation between the ILC shrinkage and the stiffness of FRP reinforcement should also be found out in the future.

ACKNOWLEDGMENTS

The authors thank Carbon Concrete Composite e.V. for funding the research project.

REFERENCES

- Abdalla, H. A. (2002). Evaluation of Deflection in Concrete Members Reinforced with Fibre Reinforced Polymer (FRP) Bars. *Composite Structures*, 56(1), 63-71.
- ACI Committee (1992). *Prediction of Creep, Shrinkage, and Temperature Effects in Concrete Structures*. American Concrete Institute: Farmington Hills, USA.
- ACI Committee (2001). *Guide for the Design and Construction of Concrete Reinforced with FRP Bars*. American Concrete Institute: Farmington Hills, USA.
- Acker, P., & Ulm, F. J. (2001). Creep and Shrinkage of Concrete: Physical Origins and Practical Measurements. *Nuclear Engineering and Design*, 203(2), 143-158.
- Bakis, C. E., Bank, L. C., Brown, V., Cosenza, E., Davalos, J. F., Lesko, J. J., & Triantafillou, T. C. (2002). Fiber-Reinforced Polymer Composites for Construction—State-of-the-Art Review. *Journal of composites for construction*, 6(2), 73-87.
- Bazant, Z. P. (2000). Criteria for Rational Prediction of Creep and Shrinkage of Concrete. *ACI Special Publications*, 194, 237-260.
- Bazant, Z. P. (2001). Prediction of Concrete Creep and Shrinkage: Past, Present and Future. *Nuclear Engineering and Design*, 203(1), 27-38.
- Bhargava, A. K. (2012). *Engineering materials: Polymers, Ceramics and Composites*. PHI Pvt. Ltd.: New Delhi, India.
- Carlson, R. W. (1935). The Chemistry and Physics of Concrete Shrinkage. In *Proceedings of American Society for Testing Materials* 35, 370-379.
- CEB-FIP Committee (1990). *CEB FIP Model Code 1990*. Thomas Telford: London, UK.
- Hansen, T. C., & Nielsen, K. E. (1965). Influence of Aggregate Properties on Concrete Shrinkage. *Journal Proceedings*, 62(7), 783-794.
- Hensher, D. A. (2016). *Fiber-Reinforced-Plastic (FRP) Reinforcement for Concrete Structures: Properties and Applications*. Elsevier: Amsterdam, Netherland.
- Hückler, A. (2016). *Trag- und Verformungsverhalten von biegebeanspruchten Bauteilen aus Infralichtbeton (ILC)*. Sierke Verlag: Berlin, Germany.



- Liu, Y., & Weyers, R. E. (1998). Modeling the Time-To-Corrosion Cracking in Chloride Contaminated Reinforced Concrete Structures. *Materials Journal*, 95(6), 675-680.
- Malvar, L. J. (1994). *Technical Report: Bond Stress-Slip Characteristics of FRP Rebars*. Naval Facilities Engineering Service Center: Port Hueneme, USA.
- Müller, H. S., & Kvitsel, V. (2002). Kriechen und schwinden von beton. *Beton - und Stahlbetonbau*, 97(1), 8-19.
- Neroth, G., & Vollenschaar, D. (2011). *Wendehorst Baustoffkunde, Grundlagen–Baustoffe–Oberflächenschutz*. Vieweg+ Teubner Verlag: Wiesbaden, Germany.
- Neville, A. M. (1995). *Properties of concrete (Vol. 4)*. Longman: London, UK.
- RILEM Committee (1995). Creep and Shrinkage Prediction Model for Analysis and Design of Concrete Structures - Model B3. *Materials and Structures*, 28, 357-365.
- Schlaich, M., & El Zareef, M. (2008). Infra-lightweight Concrete. In *International fib Symposium, Amsterdam, Netherlands*.
- Schlaich, M., & Hueckler, A. (2012). Infra-Lightweight Concrete 2.0. *BETON-UND STAHLBETONBAU*, 107(11), 757-765.
- Simonnet, C. (1992). *Le béton Coignet: stratégie commerciale et déconvenue architecturale*. OpenBibArt: Paris, France.
- Solidian (2016). *Technical Data Sheet*. Solidian GmbH: Albstadt, Germany.
- Zhang, Y., & Ou, J (2006). Experimental Study on Compressive Behaviour of FRP Reinforced Concrete Short Columns. *Journal of Xi'an University of Architecture and Technology*, 38(4), 467-472



BOND EVALUATION OF GFRP REINFORCING BARS EMBEDDED IN CONCRETE UNDER AGGRESSIVE ENVIRONMENTS

A. Ruiz Empananza ¹, F. De Caso Y Basalo ², R. Kampmann ³ and A. Nanni ⁴

¹ University of Miami, Department of Civil, Architectural and Environmental Engineering, USA, Email:
axr1489@miami.edu

^{2,4} University of Miami, Department of Civil, Architectural and Environmental Engineering, USA

³ Florida State University, Department of Civil and Environmental Engineering, USA.

ABSTRACT

Technologies developed over the last three decades have facilitated the use of glass fiber reinforced polymer (GFRP) composites as internal reinforcement bars (rebars) for concrete structures, which have proven to be an alternative to traditional steel reinforcement due to significant advantages, such as magnetic transparency and, most importantly, corrosion resistance. GFRP rebar manufacturers have developed different GFRP rebar types, where the surface enhancement to create the bond with concrete varies. However, a knowledge gap exists related to adequate durability of the surface enhancement in composite rebars, needed to achieve a proper bond to concrete. Thus, the durability of the bond enhancement of GFRP rebars to concrete must be addressed. This study evaluates the mechanical and bond to concrete properties of GFRP rebars subjected to accelerated conditioning. To this end, specimens were exposed to circulating seawater chambers, at different temperatures (23°C, 40°C and 60°C) for different periods of time (60 and 120 days). The selected GFRP rebars were made from the same glass fibers, but different manufacturing methods and more importantly bond enhancements: i) sand-coated with helical wrap, ii) ribbed/external deformations and iii) external cross fibers. Bond tests after exposure were performed according to ASTM D7913. Preliminary results show that the different surface enhancements for the same nominal size GFRP rebars, result in different bond to concrete strength slip relationships. However, the durability for the different types of surface enhancements for the selected GFRP rebars did not exhibit a significant change in bond to concrete strength over the exposed period of time.

KEYWORDS

Aging, bond strength, concrete, composite rebars, pullout, seawater and surface enhancement.

Introduction

The use of GFRP rebars in reinforced concrete structures is a growing alternative technology, and is becoming a viable substitute to replace traditional steel rebars (Ruiz Empananza et al. 2017a) The primary reason for this growth is related to the inherent durability of the material, due to its corrosion-free nature, which sets it apart from ferrous-based products. In addition, the material has a high tensile strength (2-3 times higher than steel), it is lightweight (1/4 of the weight of steel), and it is transparent to magnetic fields, features that made the material an attractive reinforcement solution for many civil engineering structures (Micelli and Nanni 2004). The Florida Department of Transportation (FDOT), among other organizations and entities, currently puts significant efforts into a full implementation of composite rebars for structural applications to avoid the costly maintenance of deteriorating steel reinforced concrete components exposed to coastal environments, such as bridges, seawalls, etc., with the ultimate goal to extend the service life of such structures (Nolan et al. 2018).

GFRP rebars are composite materials made from continuous longitudinal glass fibers embedded in a resin matrix, which can be Epoxy or Vinyl Ester. These type of rebars are produced globally using the 'pultrusion' process. The composite rebar market, however, to-date is dispersed with manufacturers providing products with very different characteristics: large variety of cross-sectional shapes (round, oval, flat-shape...), sizes, fiber types, and surface enhancements (sand coating, helical wrap, ribbed/external deformation, etc.) (Ruiz Empananza et al. 2017b). This last feature is responsible for ensuring a proper bond between the GFRP rebars and the concrete. Bond, and its behavior over time, is critical for the performance of structural components, because the GFRP reinforcement bars and the concrete matrix must act as a unified composite system for an efficient load transfer. However, to the authors' knowledge, no literature about the durability of the bond-to-concrete property for GFRP rebars exists; the aim of this work is to bridge this knowledge gap.

problem statement and research significance

The design of every structure targets a specific design life defined by existing design code, which means that the designed elements have to be fully functional throughout the corresponding service life, typically a minimum of 50 years. Nonetheless, the demand of the service life of structures is increasing, and therefore, the resilience of



structures is a major concern. This also applies to GFRP reinforced concrete structures. Many research studies have focused on the durability of each component (concrete or GFRP rebars) independently (Khatibmasjedi and Nanni 2017; Robert and Benmokrane 2013; Suraneni et al. 2016) but the authors are not aware of any study related to the aged bond properties between both materials over time; a fundamental property to ensure the long-term behavior of these type of structures.

The aim of this research study is two-fold: i) to identify differences in the bond behavior of different GFRP rebar types and ii) to evaluate the durability of the bond-to-concrete property over time under accelerated aggressive seawater conditions. The results of this study will add necessary information about the long-term performance of GFRP reinforced concrete structures, and thus, provide guidance or additional data for more reliable designs in the future.

Methodology

The bond to concrete behavior of three different commercially available GFRP rebars was tested via the ‘pullout’ test procedure specified in ASTM D7913 “Bond Strength of Fiber-Reinforced Polymer Matrix Composite Bars to Concrete by Pullout Testing” (ASTM International 2014). To study the bond strength behavior with a focus on durability, all three GFRP rebar types were separated into control and test groups; control group specimens were tested in the virgin state, while test group specimens were tested after they were conditioned. The accelerated condition protocols included saltwater exposure at three different temperatures and two aging periods, as described in more detail below.

Materials

The GFRP diameter and tensile strength were experimentally determined according to ASTM D792 (ASTM International 2013) and ASTM D7205 (ASTM International 2011), respectively, as well as the concrete compressive properties as specified in ASTM C39 (ASTM International 2016), prior to the evaluation of the bond strength. The concrete used for the preparation of the bond specimens was the standard FDOT ‘Type II 4500 Bridge deck, with a 28 day compressive strength of 37.20 MPa (Standard deviation of 0.67 MPa and coefficient of variation of 1.8%). Three different GFRP rebar types with various surface enhancements were tested in this study, and their geometric features are presented in Figure 1: Rebar type A, B, and C (from left to right). The selected rebar size was a nominal #3 bar (10mm), for each rebar type. Table 1 summarizes the main properties and surface characteristics of the different rebars analyzed in this study. It should be noted that the three rebar types were made from the same fiber type (same supplier), but the manufacturing pultrusion process and resin constituents.



Figure 1: Rebar type A, B, and C (from left to right)

Table 1: Properties of evaluated GFRP rebars

Rebar type	Exp. Diameter	Surface Enhancement	Tensile Strength	Elastic Modulus
------------	---------------	---------------------	------------------	-----------------

	mm		MPa	GPa
A	10.17	Sand-coated with helical wrap	826.00	45.37
B	10.45	External cross fibers	550.20	50.68
C	9.58	Ribbed/external deformations	804.62	51.37

Specimen preparation

A total of 63 specimens were tested using the the ‘pullout’ test procedure specified in ASTM D7913 (ASTM International 2014). Both sides of the 63 analyzed GFRP rebar were conditioned: at the end where the load was applied (loaded end), the rebar was protected with a 300 mm long steel pipe to shield the rebar from the grips (due to the low load bearing capacity of the FRP rebars in the transverse direction). The other end (free-end) was embedded in a 200 x 200 x 200 mm concrete cube. Out of the 200 mm of embedded length, only a distance of 5 times the diameter of the bar (50 mm in this case) was meant to be in contact with concrete, and the remaining 150 mm of the bar (inside the concrete cube) was protected to break the bond between the rebar and the concrete, as seen in Figure 2. The samples were casted using individual plywood molds as seen in Figure 2 (left). Fresh concrete was placed in the molds in two layers (each layer was compacted with a vibrator), the samples were demolded after 2 days, and left to cure at ambient conditions for 28 days before the samples were tested or exposed to the aging environments.



Figure 2: Concrete casting (left) and grip installation (right)

Aging Exposure

The bond samples were exposed to seawater at different temperatures to accelerate the potential degradation of the bond between the rebar and the concrete. Nine samples (three per specimen type) of the total 63 were tested in their unaged condition to provide benchmark values, while the other 54 were submerged and exposed in environmental chambers filled with circulating seawater as seen in Figure 3. The bond samples were aged at three different temperatures: 18 samples (six per rebar type) were submerged in sea water at 23°C, another 18 at 40°C and the final 18 at 60°C. For each rebar type and conditioning temperature, three specimens were tested after 60 days, and the remaining three specimens were tested after 120 days of exposure.



Figure 3: Exposure process of bond samples

Testing procedure

The bond tests were performed according to the ASTM D7913 (ASTM International 2014). The tests were conducted using a Baldwin universal testing frame. All experiments were performed in displacement control mode at a rate of 0.5 mm/min to properly register and evaluate the behavior after the peak load was exceeded. The load was monitored and recorded using a load cell integrated in the testing frame, while the displacement measurements were logged through three linear variable displacement transducers (LVDT); two LVDTs at the loaded end and one at the free-end of the bar, as seen in Figure 4. Both the load and the displacements (loaded and free-end) were recorded using an automatic data acquisition system.

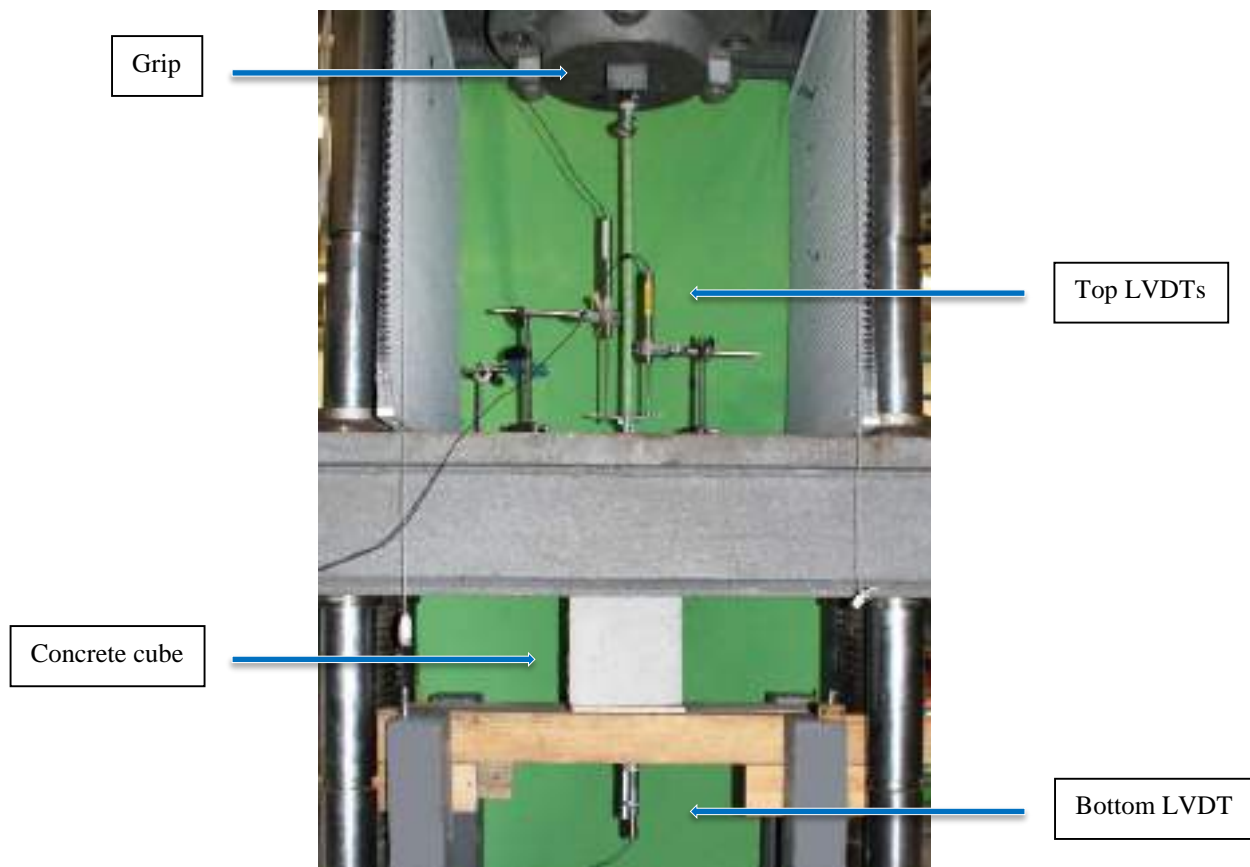


Figure 4: 'Pull-out test' configuration per ASTM D793

RESULTS AND DISCUSSIONS

The bond-slip relationship of the 64 tested specimens was recorded and analyzed. The calculations for the bond strengths were carried out according to the formula provided in ASTM D7913 (ASTM International 2014):

$$\tau = \frac{F}{C_b l}$$

where ‘ τ ’ is the average bond strength (MPa), ‘ F ’ is the tensile force (N), ‘ l ’ is the bonded length (mm) and ‘ C_b ’ is the effective circumference calculated as $3.1416 \cdot d_b$ (mm), being d_b the experimental diameter (see Table 1).

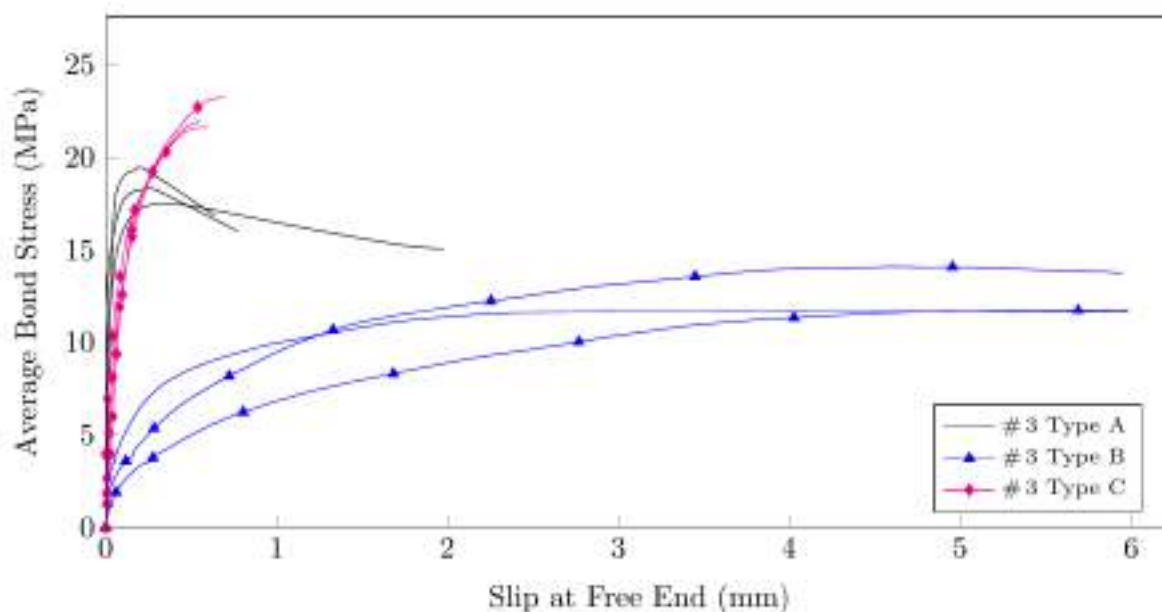


Figure 5. Bond-slip (free-end) behavior of unaged samples

Before the aged bond properties of the GFRP rebars were analyzed, the unaged bond specimens were evaluated. As mentioned before, the rebar types were differently produced and specifically the surface enhancements were a distinguishing feature. Figure 5 shows the significantly different bond strength vs. slip behavior of each of the tested unaged composite rebars. The bond-to-concrete behavior of each rebar type was different, as seen from the bond-slip initial slope, descending branches and peak stress and slip values. The maximum bond strength was recorded for the ribbed rebars (type C) with a value of approximately 22.5 MPa; these were followed by the sand coated bars (type A) with about 18 MPa, and the rebars with external cross fibers (type B) measured values around 12.5 MPa. For type A rebars, the peak bond strength was reached at about 0.25 mm, and after the peak, the bond strength presented a relatively linear decrease. For rebars type B, the slippage at the free-end corresponding to the maximum bond strength, was about 20 times higher (with approximately 5 mm) than the one for type A rebars. Moreover, after the peak bond was reached, the strength decreased gradually. Though the bond development before and after the bond peak was uniform for rebar types A and B, type C rebars showed a dissimilar performance. As soon as the maximum bond strength was attained (at about 0.7 mm), a sudden failure of the bond surface occurred.

It should be noted that although the peak bond strength for the different evaluated rebars differs in magnitude; a relative high bond strength may not be desirable since it can potentially result in tensile stresses in concrete, especially as the rebar increases in nominal size. The authors acknowledge that further research is needed to evaluate the acceptable range of bond to concrete provided by composite rebars.

After the bond behavior of the unaged rebars was evaluated, the aged specimens were analyzed. Four different points of the bond-slip curve were taken into account for the analysis: the bond strength relative to a bond slippage of 0.05 mm, 0.10 mm, 0.25 mm, and the slippage value that occurred at the maximum bond stress (bond strength), as illustrated in Figure 6. For the purposes of assessing bond durability, only slippage at the free end is discussed here.

To visualize the bond-to-concrete durability properties of the three different rebars, nine graphs are presented: the first three (first row), illustrate the bond deterioration for type A composite rebars at 23°C, 40°C and 60°C. The data sets include the unaged properties (as benchmark values) without exposure to the saline bath (horizontal solid lines), the average bond stresses after 60 days of exposure to the saltwater bath (cross hatched bars), and the average bond stresses after an exposure of 120 days to the saltwater bath (bars with diagonal lines). Similarly, the following three graphs display the results for the listed conditions for rebar type B, and the last row shows the measurements for rebar type C.

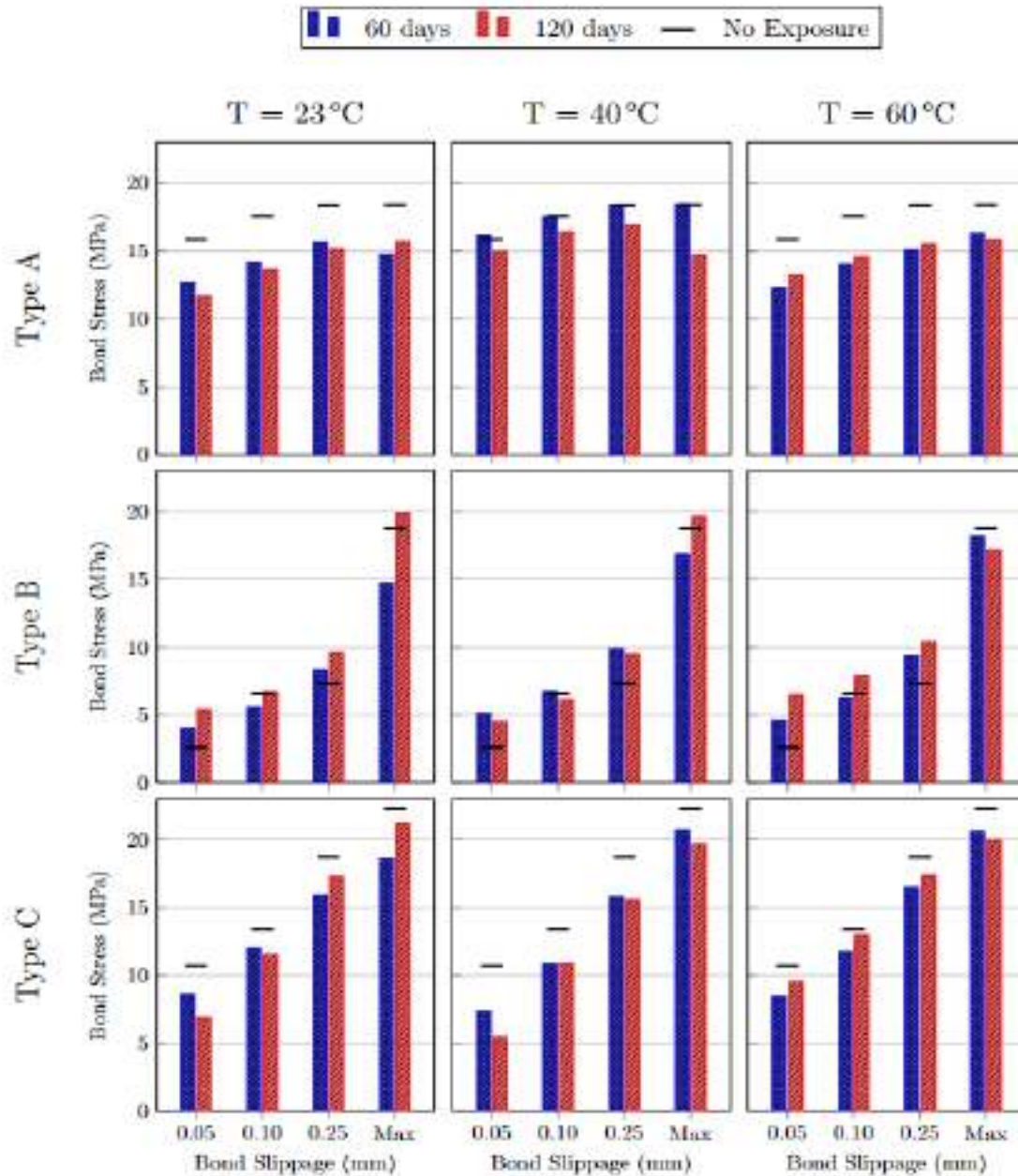


Figure 6: Relative and maximum bond strength deterioration

From the graphs presented in Figure 6, it can be inferred that the bond behavior is relatively invariant for both exposure condition. In all cases, type A rebars (sand coated) measured the highest bond strength values consistency at low levels of slip, followed by type C (ribbed), and type B (external cross fibers) with the least strength development at low levels of slip. The deterioration of the bond between the rebar and the concrete was in all cases lower than about 15% relative to the unaged case (for all the bond stresses at the measured relative slippages – 0.05, 0.10, 0.25 mm –, as well as for the maximum bond values), and in some cases an improvement of bond



strength was measured (mainly for type B rebars). It can also be seen that the degradation was constant at each of the critical points defined by ASTM D7913 (ASTM International 2014). The only exception was the degradation at the slippage of 0.05 mm where differences of 40-50% were observed; which may be attributed to the large variance of the experimental methodology used at relatively small slippage levels.

CONCLUSIONS

GFRP rebar pullout tests were conducted on specimens exposed to various temperature and aging conditions to study the durability performance of the concrete-to-rebar bond characteristics. The test results showed that different GFRP rebars with dissimilar surface features exhibit distinctive bond-slip behaviors. Within the scope of the tested materials, GFRP ribbed rebars (type C) offer the highest bond strength (22.5 MPa), followed by sand coated (type A) rebars (18 MPa), and rebars with external cross fibers (type B) (12.5 MPa); the later ones may lead to 45% weaker bond strengths as compared to the ribbed GFRP rebars. The bond stress development varies as well, based on the selected rebar types: type A rebars (sand coated) form the stiffest bond with concrete as exhibited by a rapid activation of the bond stresses at relatively small displacement measurements. Type C rebars (ribbed) lead to the next stiffer bond behavior, while the highest slippage can be expected for Type B GFRP rebars (external cross fibers); type B rebars may slip about 20 times more than type A. The bond failure mode for sand coated rebars (type A) and rebars with external cross fibers (type B) follows a gradual, continuous slippage behavior, while ribbed bars (type C) lead to a sudden-slip failure.

The potential bond deterioration over time in harsh environments was also analyzed after the specimens were exposed to seawater at 23°C, 40°C, and 60°C for 60 and 120 days. The results show that slight deterioration (maximum around 15%) occurs for all rebar types and exposure condition. This deterioration seems consistent throughout the whole bond-slip curve (for the free-end). Additional test data under long-term exposure are necessary to confirm these initial findings.

ACKNOWLEDGMENTS

The authors acknowledge the financial support of the Florida Department of Transportation (FDOT) and the guidance provided by its staff Chase C. Knight, Ph.D. and Steven Nolan, P.E.

References

- ASTM International. (2011). *ASTM D7205 - Standard Test Method for Tensile Properties of Fiber Reinforced Polymer Matrix Composite Bars*.
- ASTM International. (2013). *ASTM D792 - Standard Test Methods for Density and Specific Gravity (Relative Density) of Plastics by Displacement*.
- ASTM International. (2014). "ASTM D7913 - Standard Test Method for Bond Strength of Fiber-Reinforced Polymer Matrix Composite Bars to Concrete by Pullout Testing." ASTM-International, West Conshohocken, PA.
- ASTM International. (2016). *ASTM C39 - Standard Test Method for Compressive Strength of Cylindrical Concrete Specimens*.
- Khatibmasjedi, S., and Nanni, A. (2017). "Durability of GFRP reinforcement in SEACON." *CDCC 2017 - The Fifth International Conference on Durability of Fiber Reinforced Polymer (FRP) Composites for Construction and Rehabilitation of Structures, At Sherbrooke, Quebec, CANADA*.
- Micelli, F., and Nanni, A. (2004). "Durability of FRP rods for concrete structures." *Construction and Building Materials*, 18, 491–503.
- Nolan, S., Rossini, M., and Nanni, A. (2018). "Seawalls, SEACON and Sustainability in the Sunshine State." *Transportation Research Board 97th Annual Meeting. Washington, DC.*, 123–129.
- Robert, M., and Benmokrane, B. (2013). "Combined effects of saline solution and moist concrete on long-term durability of GFRP reinforcing bars." *Construction and Building Materials*, 38.
- Ruiz Empananza, A., Kampmann, R., and De Caso y Basalo, F. (2017a). "State-of-the-practice of FRP rebar global manufacturing." *CAMX: The Composite And Advanced Materials Expo*, Orlando, FL.
- Ruiz Empananza, A., Kampmann, R., and De Caso Y Basalo, F. (2017b). "State-of-the-Practice of Global Manufacturing of FRP Rebar and Specifications." *ACI Fall Convention*, Anaheim, CA.
- Suraneni, P., Jafari Azad, V., Isgor, O. B., and Weiss, W. J. (2016). "Deicing salts and durability of concrete pavement and joints." *Concrete International*, 38(4), 48–54.

EXPERIMENTAL STUDY OF CONCRETE BEAMS REINFORCED WITH HYBRID (SFCB AND BFRP) BARS

Yang yang¹, and Gang Wu²

¹Doctor, College of civil Science and Engineering, Yangzhou Univ., Yangzhou, China. Email: y.yang@yzu.edu.cn

²Professor, Key Laboratory of Concrete and Prestressed Concrete Structures of the Ministry of Education, Southeast Univ., Nanjing, China. Email: g.wu@seu.edu.cn

ABSTRACT

A combination of steel and fiber-reinforced polymer (FRP) bars can be used to afford favorable strength, serviceability, and durability in the concrete structures. However, the traditional hybrid reinforcements (by placing FRP bars near the outer surface of the tensile zone, and steel bars at the upper levels of the tensile zone) often lead to the decrease of the structural design point (approaching the yielding point). In addition, the corrosion of inner steel reinforcements may still occur after concrete cracking. In this paper, new hybrid reinforcements using steel fiber-reinforced polymer composites bar (SFCB) and basalt fiber-reinforced polymer (BFRP) bar were proposed and investigated. All six concrete beams reinforced with a combination of SFCB, BFRP bars, and steel bars in different hybrid ways were conducted and tested. The result shows that: (1) The hybrid reinforcement (SFCB and BFRP) beams can reduce the crack width and crack spacing, and also increase the ultimate capacity, compared to the traditional hybrid reinforcement (BFRP and steel). (2) With the same the FRP/steel ratio, the SFCB beam almost has the better performance in crack behavior and capacity compared to the traditional hybrid reinforcement (BFRP and steel). (3) The shear failure mode was observed as the FRP/steel ratio increased.

KEYWORDS

Flexural behavior; Steel fiber-reinforced polymer composites bar (SFCB); Basalt fiber-reinforced polymer (BFRP); Hybrid bars

INTRODUCTION

Fiber reinforced polymer bars (FRP) reinforced concrete beam can improve the structural strength and durability, due to light weight, high strength and durability of FRP. And the structural rigidity and ductility can be improved by using the high modulus and elastic-plastic constitutive structure of traditional steel reinforcement

Therefore, hybrid reinforcement reinforced concrete beam, combined with the advantages of FRP bar and steel bar, can obtain high strength, stiffness and ductility, reduce cost and improve durability (Aiello 2002, Leung 2003, Tan 1997, Tefers 1998, Qu 2009).

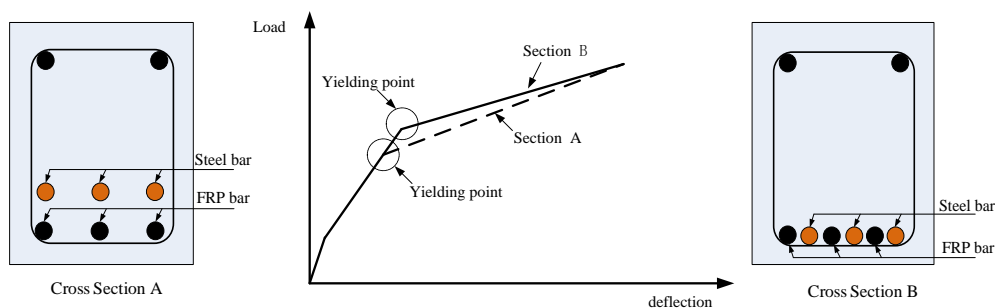


Figure.1 Traditional hybrid reinforcement arrangement

However, the disadvantages of these arrangements often appear as follows:

- FRP bar and steel bar were arranged in the outer and inner tensile area (double layer arrangement, cross section A), respectively, as shown in Fig. 1. Although it can make full use of the durability and high strength of FRP, it leads to reduced structure design (close to the yield point) (Aiello 2002, Qu 2009, Safan 2013)
- The double layer arrangement often leads to the increase of the crack width of the structure, and affect the durability of the structure. its bond correction coefficient 1.4 is proposed by ACI 2006.
- The FRP bar and steel bar were arranged in the same layer in the tension zone (single layer arrangement, cross section B), as shown in Fig.1. Although it can improve the yield point of concrete structure, the spacing of reinforcement is so small that concrete aggregate size need to be reduced. In addition, once the crack occurs, the durability of the reinforcement is not guaranteed.



Steel-fiber-reinforced polymer composite bars (SFCBs) consist of a combination of steel bars and FRP produced using a complex integrated pultrusion technique. Its main characteristics: the stability of the secondary stiffness (elastic-plastic constitutive), high elastic modulus, good bonding properties (Sun 2012, Yang 2015, Sun 2017), in addition, the outer FRP ensure the inner steel from corrosion; Besides, basalt fiber reinforced polymer bar (BFRP) has high performance, such as high strength , excellent durability and high price/performance ratio (Sun 2012, Yang 2015).

EXPERIMENTAL PROGRAM

Materials

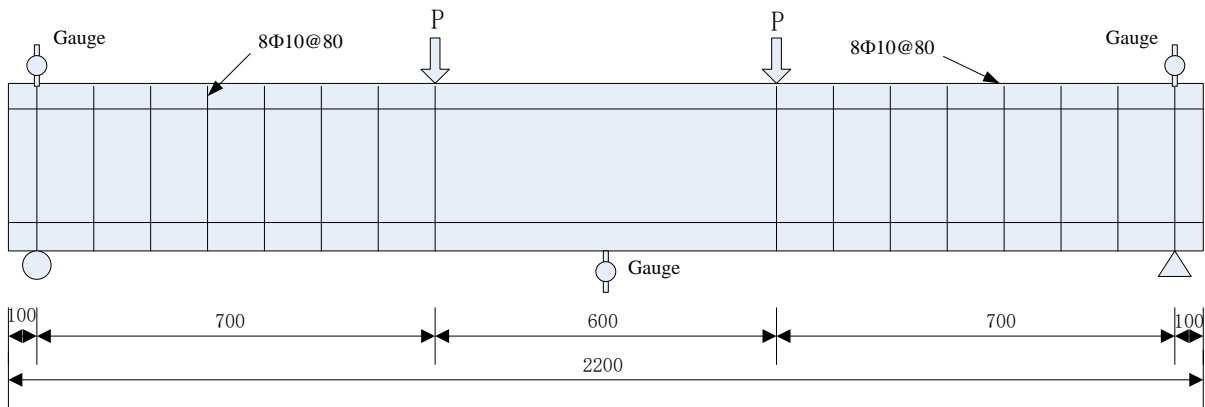
The average cubic compressive strength of three concrete testing cubes with dimensions of 150 mm × 150 mm × 150 mm was 43.3MPa after 28 days, according to the Chinese National Standard GB 50010 (2010). Four types of reinforcements were used in this investigation: BFRP bar, S10B49, S10B85, and No.12 steel bars. The BFRP bar and SFCB were made of continuous basalt fibers and vinyl ester resin (the fiber content was 70% by weight) using pultrusion technology. The BFRP bar was manufactured using 49 bundles of 2,400-tex basalt fiber. The S10B49 and S10B85 were both produced by a No. 10 inner steel bar, and compounded with 49 and 85 of bundles 4,800-tex basalt fibers, respectively, where ‘tex’ is the weight (g) per kilometer of one fiber bundle. The mechanical properties of the reinforcement used in this study are presented in Table 1, where *d* is measured diameter of the reinforcement, respectively. *A* is the measured area of the reinforcement, *E_I* is the modulus of elasticity before yielding, *E_{II}* is the post-yield modulus of elasticity, *f_y* is the yield strength and *f_u* is the ultimate tensile strength. The tensile properties of the FRP bars were determined by testing five specimens according to ACI 440.3R-04 (2004). The measured diameter and area were also derived from the average, which were used for stress calculations in this study.

Table 1. Mechanical properties of the reinforcements

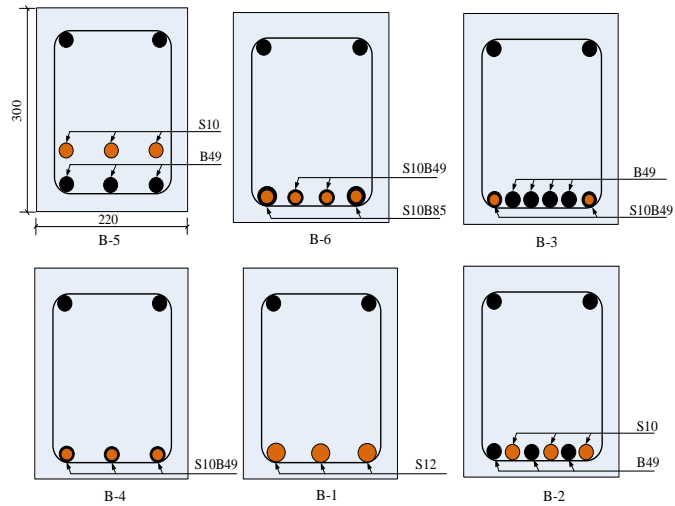
Bar type	<i>d</i> (mm)	<i>A</i> (mm ²)	<i>E_I</i> (GPa)	<i>E_IA</i> (kN)	<i>E_{II}</i> (GPa)	<i>f_y</i> (MPa)	<i>f_u</i> (MPa)	Ultimate strain(%)
B49	10	78.5	47.6	3736.6	—	—	1141	2.7
S10B49	15	176.6	108.8	19214.1	21	256.2	672.6	2.7
S10B85	18	254.3	94.6	24056.8	31	189.2	544.1	2.7
Steel	12	113	200	22600	—	400	529.6	21
Steel	10	78.5	200	15700	—	450	621	21

Specimen design

Six beams with identical dimensions of 2,200 mm long × 220 mm wide × 300 mm deep were tested under cyclic loading, as shown in Fig. 2. One control beam B-1 was reinforced with 3 No. 12 steel bars; two beams (B-5 and B-2) were reinforced with 3 No. 10 steel bars and 3 B49s, however, with double layer and single layer arrangement, respectively. One beam B-4 was reinforced with 3 S10B49s; One beam B-3 was reinforced with 2 S10B49s and 4 B49s; One beam B-6 was reinforced with 2 S10B49s and 2B10B85s; Note that B-1, B-2, B-3, B-4, and B-5 were designed to have the same initial cross sectional stiffness, i.e., *E_sA_s* = *E_{sf}A_{sf}*. In addition, 8@80 No.10 steel bars were used as stirrups to resist the shear failure. Where *E_s* and *A_s* are the modulus of elasticity and the sectional area of the No. 8 steel bars, respectively. *E_{sf}* and *A_{sf}* are the moduli of elasticity and the section areas, respectively, of both the BFRP and SFCB.



(a) setup of specimens



(b) cross section of specimens

Figure.2 Design of specimens

TEST RESULT

Failure mode



Figure.3 Failure mode of specimens

Figure 3 presents the failure modes of each beam. There are two failure modes observed in the test: (1) concrete crushing after ordinary steel bars or inner steel bar yielded (B-1, B-2, B-3, B-4, B-5); and (2) shear failure of concrete beams after inner steel bars yielded (B-6).

For control beam B-1, the first flexural crack occurs when the load is approximately 20 kN. A total of six cracks appear in the pure flexural region after steel bar yield, when the deformation increases to 73.5mm, the load almost remains 63.2kN. For beam B-2, six cracks observed in the pure flexural region, which is nearly same as that in B-1. However, eight cracks were observed in B-5, which use the same reinforcements as B-2. Note that the arrangements of reinforcement were double layer in B-2 and single layer in B-5. For beam B-4, only five cracks were observed, after the inner steel bar of the SFCB yields, the sound of gradual rupture of the outer FRP of the SFCB could be heard. For beam B-3, the crack load is approximately 21 kN, seven flexural cracks appear when the load reaches 50 kN. For beam B-6, only five cracks were observed, and the shear crack development near the right loading point developed quickly, which results in the flexural shear failure.

Load-deflection curves

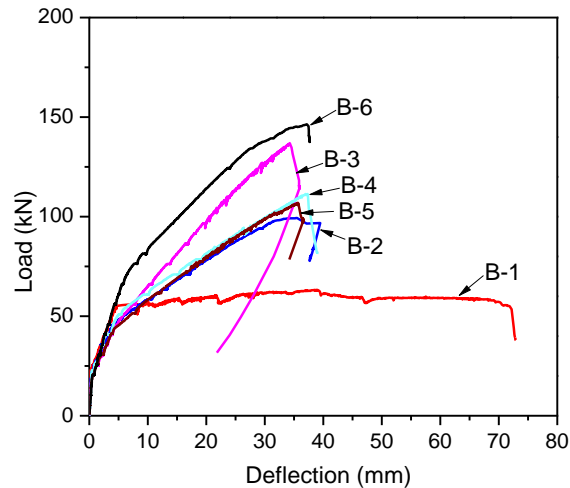


Figure.4 Load-deflection curves

The load-deflection curves for each beam are illustrated in Figure 4. There are three key points in the curves: cracking, yielding, and concrete crushing. These three points divide the loading process into three stages: elastic stage before cracking, service stage after cracking, and post-yield stage concrete crushing.

Before cracking, the curve slopes of the six beams are similar to each other as designed. The cracking moments M_{cr} of all beams are approximately 14 kN·m, as shown in Table 2. The yielding moments M_y and ultimate moments M_u of each beam are also listed in Table along with the corresponding failure modes. For beams B-2, B-4, and B-5, the slopes of post-yield stiffness are similar to each other contributed to the same FRP/steel ratio; and the deviation of ultimate loads did not exceed 10% due to same reinforcement ratio. However, the yielding load of B-5 was almost 83.3% of B-4 resulting from reduced length of arm force (the double layer of reinforcement). For beam B-3, although it had smaller reinforcement ratio than beams B-2, B-4, and B-5, it behaved the greater secondary stiffness and capacity. The ultimate load was almost 1.3 times of the other three beams contributed to high FRP/steel ratio (B-3 was almost 3 times of B-2, B-4, and B-5). For beam B-6, two types of SFCB were used, the yielding moment and ultimate moment increased due to increased reinforcement ratio and FRP/steel ratio. It can be seen that the reinforcement ratio and FRP/steel ratio were the key parameter in beams reinforced with hybrid SFCBs and BFRP bars.

Table 2. Tested values of concrete beams

Slab number	FRP/steel ($E_f A_f / E_s A_s$)	ρ^* (%)	$E_1 A$ (kN)	M_{cr} (kN·m)	Δ_y (mm)	M_y (kN·m)	Δ_u (mm)	M_u (kN·m)	Failure mode
B-1	—	0.5	67800	14	4.56	38.01	73.5	44.24	a
B-2	0.238	0.47	58309.8	15.4	4.46	32.97	39.4	69.43	a
B-3	0.774	0.45	53374.6	14.7	5.42	34.93	34.25	95.86	a
B-4	0.298	0.5	57642.3	12.6	5.03	35.84	36.06	76.73	a
B-5	0.238	0.47	58309.8	14	4.09	29.82	35.1	74.41	a
B-6	0.416	0.72	86541.8	15.4	6.15	47.95	37.2	102.41	b

Note: a = concrete crushing after steel bars yielded; b = flexural shear;

* means equivalent reinforcements ratio, $\rho = A_f E_f / b h_0 E_s$.

Load-Crack width curves

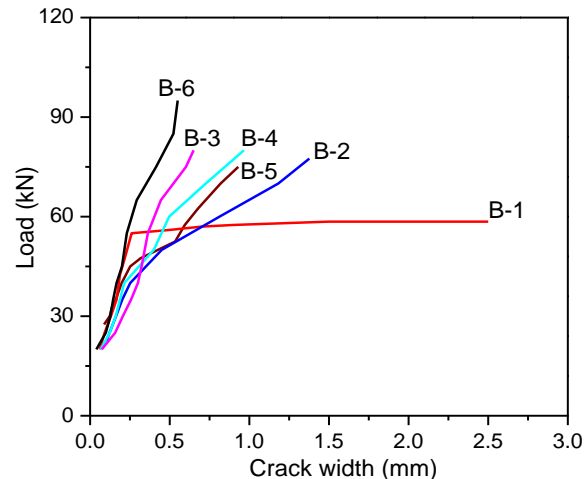


Figure.5 Load-crack width curves

Load-crack width curves are shown in Figure 5. For beam B-1, crack width increased dramatically after yielding when the loading could not increase, which is similar to the development of mid-span deflection.

For the beams B-2, B-4 and B-5 although the crack curves were similar before yielding, the difference was observed after yielding. For beams B-5, the crack width develops from 0.35 mm to approximately 0.96 mm, comparing with beam B-2 from 0.38 to 1.38 mm due to possible poor bonding behavior of the reinforcements to the surrounding concrete (amount of reinforcements was six). However, the smaller crack width can be observed for B-4 due to stable secondary stiffness. The crack width development of B-3 is slower than that of beams B-2, B-4 and B-5, which is caused by greater FRP/steel ratio. The crack was nearly half of B-2 as load applied to 80kN. For beam B-6, the crack is only 0.5 mm, approximately 77% of that in B-3 due to higher reinforcement ratio.

The allowable width of internal cracks and external cracks for RC beams are 0.4 mm and 0.33 mm in ACI 318. The allowable width of internal cracks and external cracks for FRP-reinforced beams are 0.5 mm and 0.7 mm in ACI code (2006). For hybrid (BFRP and SFCB) beams, because of the good corrosion resistance of the outer FRP, the maximum crack width limits can be slightly larger than that of hybrid (steel and BFRP) beam.

CONCLUSION

Four point loading test on six concrete beams reinforced by different hybrid types of composite bars were conducted. The failure modes, load-midspan deflection, crack development was studied in detail. The study found the follow points:

The hybrid reinforced (BFRP and SFCB) beam could behave stable post-yield stiffness, high capacity, and small crack width when using reasonable FRP/steel ratio. SFCB beams showed relatively better flexural performance than regular hybrid (BFRP and steel bars) in capacity and crack width. The reinforcement ratio and FRP/steel ratio were the key parameters for hybrid reinforcement, which decide the failure mode and crack behavior.

ACKNOWLEDGMENTS

The authors would like to acknowledge financial support from the National Natural Science Foundation of China (Grant No: 51528802) and the National Natural Science Foundation of China (Grant No: 51525801).

REFERENCES

- ACI 440.3R-04. Guide test methods for fiber-reinforced polymers (FRPs) for reinforcing or strengthening concrete structures. Farmington Hills, MI: American Concrete Institute Committee 440:2004.
- ACI 440.1R-06. Guide for the design and construction of concrete reinforced with FRP bars. Farmington Hills (MI): American Concrete Institute; 2006.
- Aiello, Maria Antonietta, and Luciano Ombres. Structural performances of concrete beams with hybrid (fiber-reinforced polymer-steel) reinforcements. *Journal of Composites for Construction* 2002, 133-140.
- Leung, H. Y., and Balendran, R. V.. Flexural behaviour of concrete beams internally reinforced with GFRP rods and steel rebars. *Struct Surv.*, 2003,21(4), 146–157.
- GB 50010-2010. Code for design of concrete structures. Beijing, China Building Industry Press, 2010. (in Chinese).



Qu, Wenjun, Xiaoliang Zhang, and Haiqun Huang. Flexural behavior of concrete beams reinforced with hybrid (GFRP and steel) bars. *Journal of Composites for construction* 13.5 2009, 350-359.

Safan, Mohamed A. Flexural Behavior and Design of Steel-GFRP Reinforced Concrete Beams. *ACI Materials Journal*, 2013.

Sun Z Y, Yang Y, Qin W H, Ren S T, Gang Wu. Experimental study on flexural behavior of concrete beams reinforced by steel-fiber reinforced polymer composite bars[J]. *Journal of Reinforced Plastics and Composites*. 31(24), 53-61, 2012.

Tan, K. H. 1997. Behaviour of hybrid FRP-steel reinforced concretebeams. Proc., 3rd Int. Symp. on Non-Metallic (FRP) Reinforcement for Concrete Structures (FRPRCS-3), Japan Concrete Institute, Sapporo,487–494.

Tepfers, R., Apinis, A., Modniks, J., and Tamuzs, V. Ductility of hybrid fiber composite reinforcement FRP for concrete. Proc.,ECCM-8, European Conf. on Composite Materials, 1998,89–96.

Yang Yang, Gang Wu, Zhi-Shen Wu, Jian-Biao Jiang, Xue-Bin Wang. Structural performance of ballastless track slabs reinforced with BFRP and SFCB [J]. *Composites Part B: Engineering*, 71, 103–112, 2015.

Zeyang Sun, Yang Yang, and Gang Wu. Moment Curvature Behavior of Concrete Beam Singly Reinforced by Steel-FRP Composite Bar. *Advances in Civil Engineering*. 2017, DOI: 10.1155/2017/1309629



BEHAVIOUR OF PRECAST SEGMENTAL CONCRETE BEAMS PRESTRESSED WITH CFRP TENDONS

T. M. Pham*, T. D. Le and H. Hao

Center for Infrastructural Monitoring and Protection, School of Civil and Mechanical Engineering, Curtin University, Kent Street, Bentley, WA 6102, Australia. * Corresponding author: thong.pham@curtin.edu.au

ABSTRACT

This paper presents a part of an ongoing research project on precast segmental concrete beam prestressed with fibre reinforced polymer (FRP) tendons which are currently being conducted at Curtin University. Precast segmental prestressed concrete bridge beams (PSBs) have gained rapid acceptance as they not only allow speeding up the construction process, but also improving the quality control. Corrosion of steel tendons at joint locations, however, causes deterioration or even collapse of the structures. This study aims at investigation of the use of CFRP tendons in replacement of traditional prestressing steel tendons for PSBs to deal with corrosion-related issues. Three precast segmental T-section concrete beams of 400 mm height and 3900 mm length which included a control specimen with unbonded steel tendons were cast and tested. Both epoxied and dry shear-keyed joints were used. Tested results indicate that CFRP tendons can be well used to replace the steel tendons on PSBs as the beams with CFRP tendons exhibited both high strength and high ductility as compared to the beam with steel tendons. However, the stresses in the unbonded CFRP tendons at ultimate of the tested beams were low, ranging from only about 69% to 72% of the nominal breaking tensile strength. The type of joints greatly affects the initial stiffness of the beams but has no effect on the opening of joints at ultimate. In addition, the codes examined in this study predicted well the stress at the ultimate of the beam with unbonded steel tendons, however, the accuracy significantly reduced in the case of the beams with CFRP tendons.

KEYWORDS

Precast concrete, segmental beams, CFRP tendons, unbonded tendons, cyclic loads, bending, and joints.

INTRODUCTION

The use of precast segmental concrete girders (PSBs) in bridge construction has presently become popular. Increased speed of construction, improved concrete quality, mitigated disturbances to the environment are among advantages of PSBs. To date, prestressing steel tendons have been the only mean to connect single segments to form completed bridge spans. Steel tendons can be bonded or unbonded to the concrete and positioned inside or outside of the beam cross-section, so-called internal or external tendons. However, corrosion of steel tendons at joint locations caused deterioration or even completed collapse of the whole structures (Woodward and Williams 1988; Wouters et al. 1999; Concrete Society Technical Report 2002).

FRP tendons have been proved as a promising solution to replace steel tendons to tackle the corrosion issue. In the literature, the use of FRP tendons has only been applied to monolithic concrete beams. When internal bonded tendons are used, FRP and steel tendons prestressed beams showed different behaviour after cracking of concrete (Dolan and Swanson 2002; ACI 440.4R 2004). At the beginning, both beams with FRP and beams with steel tendons deform linearly until concrete cracking. After cracking, however, beams prestressed with steel tendons show nonlinear relationship between load and deflection up to failure by concrete crushing or tendon rupture. Whereas, FRP-prestressed beams continue to deform approximately linearly with the increase in the applied load until failure.

In contrast, similar behaviour was observed for beams with FRP or steel tendons when the tendons are unbonded to the concrete (Pisani 1998; Tan and Tjandra 2007; Lou et al. 2012). The only difference is that FRP tendons showed linear behaviour up to the ultimate load and have lower elastic modulus in comparison with steel tendons. Pisani (1998) carried out a numerical study on beams prestressed with unbonded GFRP or steel tendons and concluded that the beams with unbonded GFRP tendons displayed non-linear behaviour between load and deflection relationship up to ultimate, which was very similar to that of the beams with unbonded steel tendons. Lou et al. (2012) reported similar observations for beams externally prestressed with FRP tendons. Tan and Tjandra (2007) tested continuous beams and concluded that the use of external CFRP tendons produce insignificant differences regarding the ultimate loads, tendon stresses, and deflections as compared to conventional steel tendons.

Stress concentration due to harping effect is another factor need due care with FRP tendons. The localized curvature generated by the deviation will cause a high stress concentration in the tendons which adversely prevents the tendons to fully achieve its breaking capacity. The deviator curvature, harped angle, and tendon size are main factors affecting the increase in the CFRP tendons concerning the harping effect (Mutsuyoshi and Machida 1993; Grace and Abdel-Sayed 1998; Wang et al. 2015; Quayle 2016). Wang et al. (2015) recommended a bending angle less than 3° to avoid the strength reduction percentage beyond 10% based on their finite element analysis on beams with Basalt FRP tendons.

Segmental beams have joints between segments, which may cause further stress concentration in the tendon at joint locations resulted by the joint opening and segment sliding. FRP tendon is made of an anisotropic material, it has low transverse modulus and strength than those in the longitudinal direction. This, in turn, raises up a question, is FRP tendon a good prestressing solution for PSBs though it owns advanced mechanical properties? Since the CFRP tendons may suffer from premature failure due to stress concentration at joint locations. Therefore, this study investigates the performance of PSBs prestressed with CFRP tendons. As far as the authors are aware, this is the first time CFRP tendons are applied for precast segmental concrete beams. The effect of tendon types and joint types on the failure modes, load-deflection relations and increase in the tendon stress of segmental concrete beams will be addressed.

EXPERIMENTAL PROGRAM

Specimen design

In order to investigate the use of CFRP tendons on segmental concrete beams, three precast segmental concrete beams with either unbonded CFRP tendons or steel tendons were cast and tested under cyclic loads in this study. All the beams were made of reinforced concrete and were designed in accordance with the requirements of AASHTO (1999) code for segmental concrete beams and ACI 440.4R (2004) code for FRP tendon-prestressed beams. The beams had T-shape cross-section of 400 mm height and 3.9 m length. Each beam consisted of four separated segments which were connected together by two steel or CFRP tendons using the posttensioning technique. For easier reference, each specimen was labelled by three parts as follows: the first part specifies the type of tendons used in the specimen, ("S" for steel tendons, "C" for CFRP tendons); the following two letters represent the bonding condition of the tendons, ("IU" for internal unbonded tendons); and the last letter indicates the type of joints, ("D" for dry joints, "E" for epoxied joints) as presented in Table 49. The dimensions and design detailed of the tested beams are shown Figure 168.

Table 49: Configuration of specimens

Specimen	Tendon type	Joint type	Concrete strength	Effective tendon stress		Tendon force
			f'_c , MPa	f_{pe} (MPa)	f_{pe}/f_{pu}	F_{pe} (kN)
S-IU-D	2 steel tendons	Dry	44	1280	0.64	119
C-IU-D	2 CFRP tendons	Dry	44	818	0.35	108
C-IU-E	2 CFRP tendons	Epoxied	44	661	0.27	83

The shear stress distribution in the multiple shear-keyed joints, which are widely used in practice, is more uniform than in the single keyed joints (Zhou et al. 2005; Li et al. 2013; Jiang et al. 2015). Hence, multiple shear-keyed joints were accepted in this study. These shear keys were of the same cross-section size but different lengths on the flange and on the web of the specimens (Figure 169). 12 mm diameter and 10 mm diameter deformed bars were used for the bottom and top longitudinal reinforcements, respectively. These steel bars were discontinuous at joint locations. 10 mm diameter deformed bars were also used for transverse reinforcements spacing at 100 mm for the two inner segments and at 75 mm for the two end segments to prevent beams fail in shear (Figure 168).

Materials

Pre-mixed concrete was used in the specimens and was supplied by a local supplier. The average compressive strength of concrete cylinders on the testing day was 44 MPa. Two 7-wire steel tendons of 12.7 mm diameter were used in Beam S-IU-D. The area, ultimate strength and elastic modulus of the tendons are 113 mm², 1860 MPa and 195 GPa, respectively. Two CFRP tendons of 12.9 mm diameter, single strand were used in Beams C-IU-D and C-IU-E. The CFRP tendons are of 126.7 mm² area, 2450 MPa ultimate tensile strength, and 145 GPa elastic modulus and were supplied by Dextra Building Products (GuangDong) CO., LTD (Dextra Group). Ordinary steel rebars of 12 mm and 10 mm diameter were used for longitudinal and transverse steel reinforcements. The average tensile strength and elastic modulus of 12 mm rebars were 587 MPa and 200 GPa, respectively. The corresponding numbers for 10 mm rebars were 538 MPa and 200 GPa, respectively.

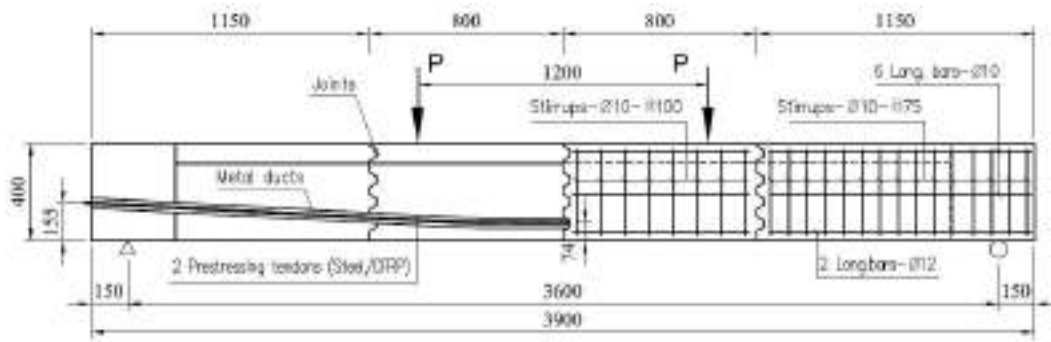


Figure 168: Detailed dimensions of specimens

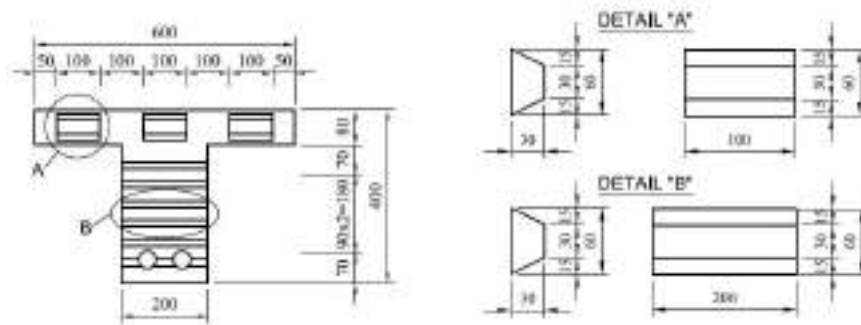


Figure 169: Details of shear keys

Casting of specimens

Steel reinforcements were manufactured and placed in a wooden formwork. 40 mm diameter corrugated metal ducts were also mounted into the steel cages to create holes for installing tendons. Separation plates of T-shape timber were positioned in the formwork at designed distances to separate segments during pouring concrete. Foam blocks of shear-keyed shapes were glued onto the separation plates to form the shear keys.



Figure 170: Casting of specimens

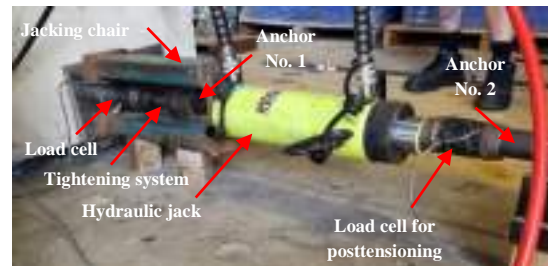


Figure 4: Apparatus for post-tensioning

Match-casting method was employed to cast all segments in which the first and third segments were cast in the first concrete batch, and then they were used as a formwork in the second batch to make the second and fourth segments. Thereby, the male and female keys between two adjacent segments were guaranteed to fit perfectly. Cylinders of 100 mm diameter and 200 mm height were also made to ascertain the concrete properties. A typical segment at completion is shown in Figure 170.

Post-tensioning

A typical set up of post-tensioning is shown in Figure 171. Steel couplers were used to connect CFRP tendons to a steel tendon of 1.5 m length. Consequently, the stressing procedure for the CFRP tendons was done in the same way to the steel tendons. The stressing force was generated by a hydraulic jack placing on a jacking chair. Two sets of anchor including wedges and barrels were used in the stressing end, in which one was placed after the hydraulic jack so-called post-tensioning anchor No.2 and one placed before the jack so-called working anchor No.1. Tightening system (hollow bolts and nuts) was installed inside the jacking chair just before the working anchor No.1 for tightening and releasing the force during stressing. Load cells were used to monitor the tensioning force produced by the jack and to measure the force in the tendons after transfer.

For Beam C-IU-E with epoxied joints, the concrete surfaces of the keys were carefully cleaned, then thoroughly rinsed with water and left to dry for at least 2 hours before applying the adhesive. A thin layer of Sikadur-30 (Sika Australia) was applied to the joint surfaces of the segments using a painting brush. After posttensioning, the epoxied beam was left for curing of the adhesive for 3 days.

At first, the tendons were tensioned by an initial force of approximately 10% of the maximum stressing force in order to close the gaps between segments and to remove the slack. The maximum stressing force F_s was calculated from the control stress in the tendons, which were taken as $0.75 f_{pu}$ for steel tendons (AASHTO 1999) and $0.4 f_{pu}$ for CFRP tendons (ACI 440.4R 2004) in which f_{pu} is the nominal tensile strength of the tendons. Each tendon was then stressed by following steps at $0.2F_s$, $0.6F_s$ and $1.0F_s$ till completion. The stress in the tendons during stressing was monitored and measured by load cells and strain gauges attached in the tendons. Table 49 presents the effective tendon stresses and corresponding force in the tendons after transfer.

Test set up and loading

The applied load was produced by two vertical hydraulic jacks, which were placed equally at one-third span. Two horizontal I-steel beams were used to uniformly transfer the vertical loads from the jacks to the beams. Load cells were used to monitor the applied load generated by the hydraulic jacks. Linear variable differential transformers (LVDTs) were used to measure the vertical displacement and opening of joints. Strain in the ordinary steel bars and prestressing tendons were measured by strain gauges and load cells attached at the end of the beams. All the beams were tested under cyclic loads up to failure in which two loading cycles form a load level. The load increment in each load level was 20 kN. In each cycle, the applied load was increased gradually to the maximum value of that load level then was reduced to about 5 kN before starting next cycles, excluding the first loading cycle when the applied load was started from 0. All the tests were conducted under the load control at a rate of approximately 3 to 5 kN/min.

RESULTS AND DISCUSSIONS

Table 50 gives the tested results of all the specimens in which P_u , $\delta_{mid,u}$, $\Delta_{j,u}$ are the applied load, midspan deflection, and opening of the middle joint of the beams at ultimate, respectively. Beam S-IU-D gained 96 kN in the applied load at ultimate with the midspan deflection and joint opening of 89.4 mm and 30.44 mm, respectively. Those for Beam C-IU-D were 113 kN, 94.7 mm and 27.7 mm, respectively. Beam C-IU-E with epoxied joints, obtained higher applied load and midspan deflection at ultimate as compared to Beam S-IU-D at 123 kN and 101.1 mm, respectively.

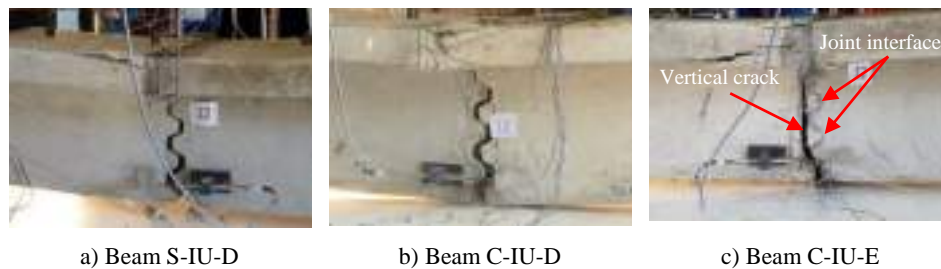


Figure 172: Failure modes of the tested beams

Failure modes

The failure of all the beams is shown in Figure 172. The failure of all the tested beams initiated by crushing of concrete on the top fibre at the middle joint and subsequently yielding of the steel tendons for Beam S-IU-D or rupturing of CFRP tendons in case of beams prestressed with CFRP tendons, which also occurred at the midspan of the specimens. All the beams in the present study were under-reinforced with reference to counterpart beams with bonded tendons and the consequent failure would theoretically be governed by tension controlled. However, the use of unbonded tendons shifted the failure mode of the under-reinforced counterparts from tension controlled to compression controlled. The reason is due to the fact that the strain in the unbonded tendons depends on the whole beam behaviour which enable the beam to attain larger deflection resulting higher compression strain in the concrete on the compression zone (Naaman and Alkhairi 1991).

Table 50: Testing results for specimens

Specimen	P_u	$\delta_{mid,u}$	$\Delta_{J,u}$	Failure mode
S-IU-D	96	89.4	30.44	Compression failure and yielding of tendons
C-IU-D	113	94.7	27.70	Compression failure and rupture of CFRP tendons
C-IU-E	123	101.1	30.02	Compression failure and rupture of CFRP tendons

Load and deflection curves

Figure 173 shows the load and deflection curves for all the beams under cyclic loads. The envelop curves of these relations are also displayed in

Figure 174. When dry joints were used, Beam C-IU-D with CFRP tendons showed very similar behaviour to Beam S-IU-D with steel tendons. In both cases, the load and deflection curves were divided into two parts by a transition zone. Initially, both beams deformed linearly with the applied load and the beams showed high stiffness. In the second stage, the beams' stiffness decreased sharply and the beams showed nonlinear relationship between the applied load and the deflection up to failure. The transition from the first stage to the second stage was resulted by the opening of the middle joint under the applied load. This behaviour is very similar to the segmental beams prestressed with external steel tendons reported in several studies (Li et al. 2013; Saibabu et al. 2013). It is worth mentioning that in all the beams only the middle joints J2 opened while the other joints almost remained closed during testing and the magnitude of the opening in each beam at ultimate was closely equal regardless the types of joint used (Table 50).

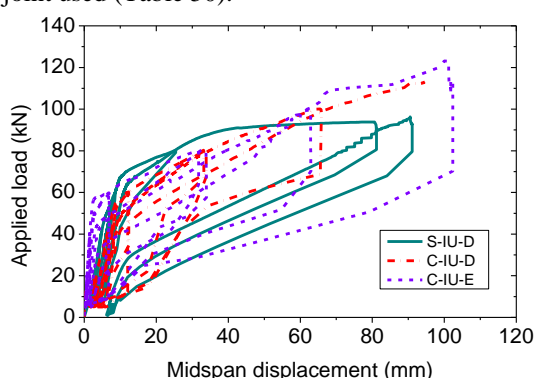


Figure 173: Load and deflection curves

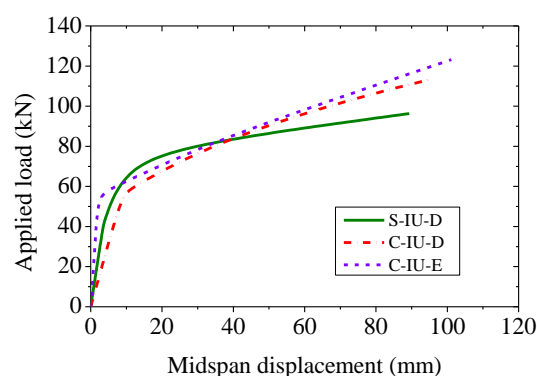


Figure 174: Envelop curves of load and deflection

The load and deflection curve of Beam C-IU-E also displays two stages. In the second stage, however, the beam still showed almost linear behaviour between the applied load and deflection until the tendons ruptured. It is noted that the transition from the first stage to the second stage is the result of concrete cracking at bottom fibre at approximately 44.7 kN. The tensile crack was formed by one vertical crack which cut off all the shear-key bases of joint J2 when the tensile stress caused by the applied load exceeded the tensile strength of the concrete (Figure 172c).

The initial stiffness of the beams was greatly affected by type of joints as shown in

Figure 174. Beam C-IU-E with epoxied joints had a higher initial stiffness in comparison with Beam C-IU-D with dry joints. This variation is owing to the different moment of inertia of the two beams to which Beam C-IU-E with epoxied joint had the moment of inertia much higher than that of Beam C-IU-E with dry joints. Meanwhile, Beam S-IU-D had a higher initial stiffness than Beam C-IU-D since Beam S-IU-D had a higher effective prestressing stress.

Stress in the unbonded tendons

The envelop curves of the tendon stress and the applied load are shown in Figure 175. The effective stresses in the tendon of beams S-IU-D, C-IU-D, and C-IU-E were 1280 MPa, 818 MPa and 661 MPa, respectively. It can be seen from the figure that the tendon stress in all the beams started to increase from the beginning of the test but at a very low rate. After joint opened, the beams deformed at a much faster rate under the applied load resulting in a much higher rate in the increase in the tendon stress (Figure 176). The total increment in the tendon stress in Beam S-IU-D was 468 MPa, which means 25% of the nominal tensile strength of the steel tendons. Those in Beams C-IU-D and C-IU-E were 956 MPa and 1026 MPa, which equal 33% and 27% of the nominal tensile strength of the CFRP tendons, respectively (Table 51).

The increase in the tendon stress was due to the increase in the deflection of the beam under the applied load. Hence, the curves of the applied load and the tendon stress are very similar to the curves of the applied load and deflection. It is also seen from Figure 175 that the applied load and tendon stress of Beams C-IU-D and C-IU-E

with CFRP tendons shows a bilinear relationship but not for Beam S-IU-D with steel tendons. Beam S-IU-D exhibited a highly non-linear relationship between the tendon stress and the applied load. It means the stress in the CFRP tendons increased almost linearly to the applied load, but with different rates before and after joint opening.

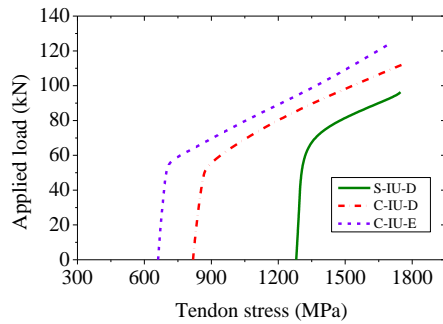


Figure 175: Envelop curves of applied load vs tendon stress

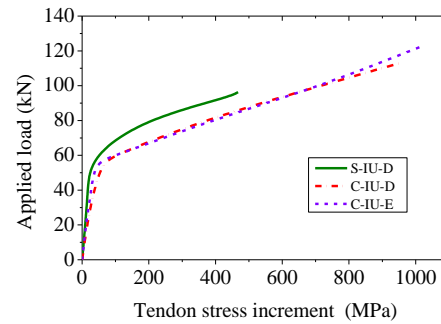


Figure 176: Envelop curves of applied load vs tendon stress increment

The tendon stress at ultimate in Beam S-IU-D was 1748 MPa, which equals 94% of the nominal tensile strength of the steel tendons (1860 MPa). It is noted that the test of Beam S-IU-D was stopped for safety when large physical damage was observed in the concrete on the top fibre of the beam. At that point, the steel tendons already yielded but had not ruptured yet, the beam still recovered to a certain level due to the effect of prestressing after the applied load was removed. In cases of Beams C-IU-D and C-IU-E, the CFRP tendons ruptured at the ultimate stage at approximately 1774 MPa and 1687 MPa, respectively. These stress values were far below the nominal breaking strength of the CFRP tendon as they were only equal to 72% and 69% of the breaking strength of the tendons which was 2450 MPa as reported by the manufacturer. This tensile strength reduction in the CFRP tendons was influenced by the effects of bending loading, harping angle, and the opening of joint. Harped angle significantly prevents the tendon stress increment as indicated in previous studies (Mutsuyoshi and Machida 1993; Grace and Abdel-Sayed 1998; Wang et al. 2015; Quayle 2016). A harping angle of 3° was used in this study, to avoid the strength reduction exceeding 10% as recommended by Wang et al. (2015). Thus, the opening of joint is responsible for low stress increment in the CFRP tendons and it requires further investigation.

THEORETICAL CONSIDERATIONS

This section presents the design procedures and code equations recommended for the computation of the unbonded tendon stress at ultimate. Three codes are examined including AASHTO (1999), ACI 440.4R (2004), and ACI 318-14 (2015). It is noted that none of these codes addresses precast segmental beams with CFRP tendons. These code equations are only valid for beams prestressed with steel tendons, except for ACI-440.4R which was developed for monolithic beams with CFRP tendons. AASTHO-1999 code is used for segmental beams prestressed with steel tendons. For convenience, symbolics for the same parameters in different codes are modified to be identical.

AASHTO (1999) recommended the following equation to calculate the stress in the unbonded tendons in precast segmental concrete beams:

$$f_{ps} = f_{pe} + 6200 \left(\frac{d_{ps} - c}{l_e} \right), MPa \quad (11)$$

where f_{ps} is the effective tendon stress, d_{ps} is the distance from extreme fibre to centroid of prestressing tendons, $l_e = L/(1+[N/2])$; L is the length of the tendon between anchorages, and N is the number of support hinges required to form a mechanism crossed by the tendon. Up to date, there has been no recommendation by AASHTO (1999) for PSBs prestressed with FRP tendons.

ACI 440.4R (2004) adopted the following equation to compute the stress in the CFRP tendons:

$$f_{ps} = f_{pe} + \Omega_u E_{ps} \varepsilon_{cu} \left(\frac{d_{ps}}{c_u} - 1 \right) \quad (12)$$

where E_{ps} is the tendon modulus of elasticity; ε_{cu} is the ultimate concrete compression strain which was taken as 0.003; c_u is the neutral axis depth at ultimate; and Ω_u is a strain reduction coefficient; $\Omega_u = 3/(L/d_{ps})$ for uniform or third-point loading, with L_b is length of span. Eq. 2 was also used to calculate the stress in the unbonded steel tendons since it was originally developed for beams with steel tendons (ACI 440.4R 2004).

ACI 318-14 (2015) recommended the following equation to calculate the stress in the unbonded tendons:

$$f_{ps} = f_{pe} + 69 + \frac{f'_c}{100\rho_{ps}}, MPa \quad (13)$$

where ρ_{ps} is the prestressing reinforcement ratio. This equation is applied for beams with $L/d_{ps} \leq 35$.

Table 51 presents the theoretical and experimental results of the tendon stress and ultimate load of all the tested beams. It is seen from the table that, except for ACI 440.4R, both AASHTO-1999 and ACI 318-14 predicted well the ultimate stress in the unbonded steel tendons for Beam S-IU-D. The experimental results of Beam S-IU-D was close to the theoretical results predicted by AASHTO-1999 and ACI 318-14 equations.

Table 51: Theoretical calculation of the three codes

Specimen	f_{pe} (MPa)	Δf_{ps} (MPa)			P_u (kN)		
		Theo	Expt	Theo/ Expt	Theo	Expt	Theo /Expt
AASHTO (1999)							
S-IU-D	1280	531	468	1.13	97	96	1.01
C-IU-D	818	539	956	0.56	93	113	0.82
C-IU-E	661	543	1026	0.53	83	123	0.67
ACI 440.4R (2004)							
S-IU-D	1280	294	468	0.63	84	96	0.88
C-IU-D	818	1276	956	1.33	141	113	1.25
C-IU-E	661	1345	1026	1.31	136	123	1.10
ACI 318-14 (2015)							
S-IU-D	1280	505	468	1.08	96	96	0.99
C-IU-D	818	413	956	0.43	84	113	0.74
C-IU-E	661	413	1026	0.40	74	123	0.60

However, the accuracy the theoretical predictions significantly decreased in cases of Beams C-IU-D and C-IU-E since these codes are not specified for segmental beams with CFRP tendons. AASHTO-1999 underestimated the ultimate stress in the tendon 24% for Beam C-IU-D with dry joints and 29% for Beam C-IU-E with epoxied joint in comparison with the experimental results, respectively. On the contrary, ACI-440.4R overestimated f_{ps} for both Beams C-IU-D and C-IU-E. This is not common for a code equation since a code generally yields conservative results. This significant difference may be resulted by the ratio L/d_{ps} . ACI-440.4R restricts the use of Eq. 2 for beams with CFRP tendons where the unbonded length of the tendons should not be smaller than 15 times the beam's depth. The unbonded length of the tendon used in this study was equal to the ratio L/d_{ps} , which was 10.9. ACI 318-14 returned the most conservative predictions at 31% and 36% lower than the experimental results for Beams C-IU-D and C-IU-E, respectively.

Accordingly, with the exception of ACI-440.4R, AASHTO-1999 and ACI 318-14 predicted well P_u for Beam S-IU-D with steel tendons but their estimation become less accurate for beams with CFRP tendons. AASHTO-1999 predicted P_u 18% lower than the experimental result for Beam C-IU-D, while that for Beam C-IU-E was even worse at 33%. ACI-440.4R highly overestimates P_u due to the L/d_{ps} used in this study was lower than the code's recommendation. ACI-318-14 underestimates P_u 26% in case of dry joint and 40% in case of epoxied joints, respectively.

CONCLUSIONS

In order to evaluate the use of CFRP tendons on precast segmental concrete beams, three T-shape segmental concrete beams with either unbonded CFRP tendons or steel tendons were tested under cyclic loads. Several conclusions can be made as follows:

- CFRP tendons can be well used to replace steel tendons for precast segmental concrete beams. The tested beams in this study have demonstrated both good strength and ductility capacities.
- The use of unbonded tendons can shift the failure mode of under-reinforced beams from tension controlled to compression controlled. This change in the failure mode may prevent the beams fail in a brittle manner caused by the rupture of CFRP tendons.
- Type of joints significantly affects the overall behaviour of the beams. Beams with dry joints show similar behaviour up to ultimate regardless of the type of tendons used, while the

CFRP prestressed beam with epoxied joints still deformed almost linearly until failure after cracking.

- The ultimate stress in the unbonded CFRP tendons for the beams with dry joints and epoxied joints was only 72 % and 69% of the nominal tensile strength, respectively. The reduction in the tendon stress at ultimate was attributed by the loading type, harping effect and joint opening which requires further investigation.
- All the examined codes predicted well the ultimate stress in the unbonded steel tendon, but much less accuracy in cases of beams with CFRP tendons. AASHTO 1999 and ACI 318-14 highly underestimated the stress in the unbonded CFRP tendons, while ACI 440.4R-04 overestimated f_{ps} .

REFERENCES

- AASHTO (1999). "Guide Specifications for Design and Construction of Segmental Concrete Bridges, 2nd Ed with 2003 Interim Revis." Washington, DC, *American Association of State Highway and Transportation Officials*.
- ACI 318-14 (2015). "Building code requirements for structural concrete and commentary." *American Concrete Institute. International Organization for Standardization*.
- ACI 440.4R (2004). "Prestressing concrete structures with FRP tendons." Farmington Hills, USA, *American Concrete Institute*.
- Concrete Society Technical Report (2002). "Durable post-tensioned concrete structures." *TR 72*,.
- Dextra Group <https://www.dextragroup.com/offices/dextra-building-products-limited>.
- C.W. Dolan, D. Swanson (2002). "Development of flexural capacity of a FRP prestressed beam with vertically distributed tendons." *Composites Part B: Engineering*, 33, 1, 1-6.
- N.F. Grace, G. Abdel-Sayed (1998). "Behavior of externally draped CFRP tendons in prestressed concrete bridges." *PCI journal*, 43, 5, 88-101.
- H. Jiang, L. Chen, Z.J. Ma, W. Feng (2015). "Shear Behavior of Dry Joints with Castellated Keys in Precast Concrete Segmental Bridges." *Journal of Bridge Engineering*, 20, 2, 04014062.
- G. Li, D. Yang, Y. Lei (2013). "Combined shear and bending behavior of joints in precast concrete segmental beams with external tendons." *Journal of Bridge Engineering*, 18, 10, 1042-1052.
- T. Lou, S.M.R. Lopes, A.V. Lopes (2012). "Numerical analysis of behaviour of concrete beams with external FRP tendons." *Construction and Building Materials*, 35, 970-978.
- H. Mutsuyoshi, A. Machida (1993). "Behavior of Prestressed Concrete Beams Using FRP as External Cable." *Special Publication*, 138, 401-418.
- A.E. Naaman, F. Alkhairi (1991). "Stress at ultimate in unbonded prestressing tendons: Part 2—Proposed Methodology." *ACI Structural Journal*, 88, 6, 683-692.
- M.A. Pisani (1998). "A numerical survey on the behaviour of beams pre-stressed with FRP cables." *Construction and Building Materials*, 12, 4, 221-232.
- T.G. Quayle (2016). Tensile-flexural Behaviour of Carbon-fibre Reinforced Polymer (CFRP) Prestressing Tendons Subjected to Harped Profiles, MS thesis. Univ. Waterloo.
- S. Saibabu, V. Srinivas, S. Sasmal, N. Lakshmanan, N.R. Iyer (2013). "Performance evaluation of dry and epoxy jointed segmental prestressed box girders under monotonic and cyclic loading." *Construction and Building Materials*, 38, 931-940.
- Sika Australia <https://aus.sika.com/en/group.html>.
- K.H. Tan, R.A. Tjandra (2007). "Strengthening of RC continuous beams by external prestressing." *Journal of Structural Engineering*, 133, 2, 195-204.
- X. Wang, J. Shi, G. Wu, L. Yang, Z. Wu (2015). "Effectiveness of basalt FRP tendons for strengthening of RC beams through the external prestressing technique." *Engineering Structures*, 101, 34-44.

- R. Woodward, F. Williams (1988). "COLLAPSE OF YNS-Y-GWAS BRIDGE, GLAMORGAN." *Proceedings of the Institution of Civil Engineers*, 84, 4, 635-669.
- J. Wouters, K. Kesner, R. Poston (1999). "Tendon corrosion in precast segmental bridges." *Transportation Research Record: Journal of the Transportation Research Board*, 1654, 128-132.
- X. Zhou, N. Mickleborough, Z. Li (2005). "Shear strength of joints in precast concrete segmental bridges." *ACI Structural Journal*, 102, 1, 3.



STUDIES ON DESIGN AND CONSTRUCTION MONITORING OF PRECAST CONCRETE MUNICIPAL TUNNEL REINFORCED WITH GFRP BARS

X. Hu¹, W.C. Xue¹, F. Peng¹ and T. Liu¹

¹ *Tongji University, College of Civil Engineering, Shanghai China, Email: xuewc@tongji.edu.cn*

ABSTRACT

Municipal tunnel (MT) is a joint-use underground structure that houses several types of power, water, sewerage, communications, gas, and other statutory services. Structural types of MT include cast-in-site and precast, and precast concrete MT (PCMT) would widespread use because of cost effectiveness, high quality, and faster construction. Corrosion of steel reinforcement in PCMT structures is one of the major challenges for structural durability because the structures are exposed to the underground aggressive environments. Substitution of steel bars with glass fiber reinforced plastics (GFRP) bars is an alternative solution to improve the durability of PCMT structures. The design method of PCMT structures reinforced with GFRP bars is firstly investigated in this paper. The improved design equation for flexural capacity of GFRP reinforced concrete members is proposed, and that for crack width in ACI 440.1R-06 and GB 50608-2010 were summarized. Then, a PCMT structure located in the park of 2010 Shanghai World Expo was designed according to the method presented here, and subsequently, the structural safety of the GFRP reinforced PCMT structure is verified according to the results of construction monitoring.

KEYWORDS

Municipal tunnel; Precast concrete, GFRP bars; Flexural capacity; Crack width; Design procedure; Construction monitoring.

INTRODUCTION

A municipal tunnel (MT) is a kind of underground structure that accommodates various utilities as power, water, sewerage, communications, gas, and other statutory services, and also provides enough head-room to allow maintenance personnel to walk through and to perform maintenance tasks. The MTs are linear structures for the cut-and-cover method of installation (see [Figure 1](#)), and they became significant not only for preventing the need to dig up streets for statutory services, but also for the efficient use of the valuable subsurface space under streets ([Curiel-Esparza et al., 2005](#)). Therefore, MTs have been widely constructed throughout the world after it first appeared in Paris in 1851 ([Chen et al., 2012](#)). In general, structural types of MT include cast-in-place and precast. Moreover, the cost effectiveness, high quality, and faster construction of precast concrete municipal tunnel (PCMT) have resulted its relatively more widespread use.

The safety and durability of MTs is of great importance for modern city since they contain pipelines of city's lifeline system. Corrosion of steel reinforcement in PCMT structures is one of the major challenges for structural durability because the structures are perennially exposed to the underground aggressive environments. Substitution of steel bars with glass fiber reinforced plastics (GFRP) bars is an alternative solution to improve the durability of PCMT structures ([Nanni et al., 2014](#)).

In 2007, a PCMT reinforced with GFRP bars was constructed in the park of 2010 Shanghai World Expo. It may be the first GFRP reinforced PCMT structure in the world. In order to construct the GFRP reinforced PCMT, a design method, including design equations for flexural capacity and crack width, was firstly studied. Then, the PCMT structure located in the park of 2010 Shanghai World Expo was designed according to the method presented here. Finally, the structural safety of the GFRP reinforced PCMT structure was verified according to the results of construction monitoring.



Figure 1: Typical in-site photo of PCMT

DESIGN EQUATION FOR FLEXURAL BEHAVIOR OF GFRP REINFORCED CONCRET MEMBERS

Flexural capacity

The flexural capacity of a GFRP reinforced concrete (RC) member is dependent on whether the failure is governed by concrete crushing or GFRP rupture. Existing design guidelines for FRP, such as the ACI-440.1R-06 (2006) and ISIS (2007), distinguish between concrete crushing and FRP rupture through the balanced reinforcement ratio, ρ_{fb} , where strains in concrete and GFRP bars simultaneously reach their maximum values. Theoretically, if GFRP reinforcement ratio ρ_f is less than the balanced ratio ($\rho_f < \rho_{fb}$), GFRP rupture failure mode governs. Otherwise, concrete crushing failure mode governs ($\rho_f > \rho_{fb}$). By considering equilibrium of internal forces and linear strain distribution assumption, the balanced reinforcement ratio can be expressed as Eq. (1)

$$\rho_{fb} = \frac{0.85\beta_1 f'_c}{f_{fu}} \frac{\varepsilon_{cu} E_f}{f_{fu} + \varepsilon_{cu} E_f} \quad (1)$$

where β_1 = ratio of depth of equivalent rectangular stress block to depth of neutral axis; E_f = elastic modulus for GFRP; f_{fu} = ultimate tensile strength of GFRP; f'_c = cylinder compressive strength of concrete; and ε_{cu} = ultimate compressive strain of concrete, which is assumed to be 0.003 according to ACI 440.1R-06 (2006).

Although theoretical delineation of the concrete crushing failure mode of flexural concrete members is possible, the actual member may not fail as predicted. That is, there is a transition region where compression failure mode and tension failure mode are possible. This mainly attributes to the uncertainties of material strengths, assumptions made in analysis, and variations in locations of reinforcements and dimensions of concrete sections.

Based on the analysis results of 173 GFRP RC flexural members by comparing the test results and predictions via Eq. (1), it was found that the upper bound of reinforcement ratio for beams in the transition region ρ^* should be taken as $1.5\rho_{fb}$ (Xue et al., 2016).

From the above discussions, the design equations for flexural capacity of GFRP RC members can be computed by Eq. (2)

$$M_n = \rho_f f_f j b d^2 \quad (2)$$

where f_f = stress in GFRP reinforcement at failure, given by

$$f_f = \begin{cases} f_{fu} & (\rho_{f \min} \leq \rho_f < \rho_{fb}) \\ [1 - 0.23(\rho_f / \rho_{fb} - 1)^{0.2}] f_{fu} & (\rho_{fb} \leq \rho_f \leq 1.5\rho_{fb}) \\ (\rho_f / \rho_{fb})^{-0.55} f_{fu} & (1.5\rho_{fb} < \rho_f) \end{cases} \quad (3)$$

j = coefficient of the lever arm of the couple force, given by

$$j = \begin{cases} 1 - \frac{0.07}{1 + 400\varepsilon_{fu}} - 0.5 \frac{\rho_f f_f}{f'_c} & (\rho_{f \min} \leq \rho_f < \rho_{fb}) \\ 1 - 0.59 \frac{\rho_f f_f}{f'_c} & (\rho_f \geq \rho_{fb}) \end{cases} \quad (4)$$

b = width of GFRP RC member; and d = effective depth of GFRP RC member.

Crack width

The ACI 440 Committee recommended the Frosch equation for calculating the crack width of concrete beams reinforced with FRP bars (ACI 440.1R-06). The Frosch equation was derived based on a physical model, rather than being empirically derived (Frosch, 1999). With considering the different bond behavior of FRP reinforcements compared with steel reinforcements, a corrective coefficient for the bond quality was introduced by ACI 440.1R-06. For predicting the maximum side face cracks in concrete beams reinforced with FRP bars, the equation is given as follows:

$$w = 2 \frac{f_f}{E_f} \beta k_b \sqrt{d_c^2 + \left(\frac{s}{2}\right)^2} \quad (5)$$

where w = maximum crack width; f_f = reinforcing stress; E_f = reinforcement modulus of elasticity; β = ratio of distances to neutral axis from extreme tension fiber and from centroid of FRP reinforcements; d_c = bottom cover measured from center of lowest bar; and s = bar spacing. The k_b term is a coefficient that accounts for the degree of bond between FRP bar and surrounding concrete. For FRP bars having bond behavior similar to uncoated steel bars, the bond coefficient k_b is assumed equal to 1.

In the Chinese code GB 50608-2010 (2010), the crack width can be calculated by Eq. (6)

$$w = 2.1 \psi \frac{\sigma_{fk}}{E_f} \left(1.9c + 0.08 \frac{d_{eq}}{\rho_{te}} \right) \quad (6)$$

where Ψ = non-uniformity coefficient for strain of longitudinal tensile GFRP reinforcements between cracks; σ_{fk} = stress of longitudinal GFRP reinforcement calculated in consideration of characteristic combination for effects of loads; E_f = elastic modulus of GFRP reinforcement; c = distance from the outer edge of tensile GFRP reinforcements in the outmost layer to the bottom edge of tension zone; d_{eq} = equivalent diameter of longitudinal GFRP reinforcement in tension zone; ρ_{te} = ratio of GFRP reinforcement for tensile GFRP reinforcements calculated according to effective tension sectional area of concrete.

DESIGN PROCEDURE OF GFRP REINFORCED PCMT

The GFRP reinforced PCMT structure, which was monitoring in this paper, was located in the park of 2010 Shanghai World Expo and assembled by monolithic segments with bolted connections (see Figure 2). As a result, the PCMT could be designed based on the mechanical model shown in Figure 3. In this model, the mechanical property of PCMT structure was assumed to be uniform in the longitudinal direction.



Figure 2: PCMT in the park of 2010 Shanghai World Expo

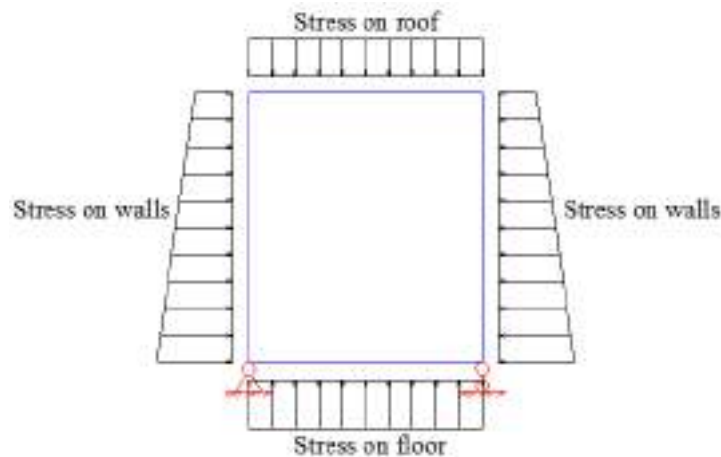


Figure 3: Mechanical model of PCMT in the park of 2010 Shanghai World Expo

According to the requirements of utility, the dimension of cross-section of the GFRP reinforced PCMT was designed as shown in Figure 4. The GFRP reinforced PCMT was located 6m under the ground. The characteristic value and design value of applied loads on the GFRP reinforced PCMT were shown in Figure 5(a) and Figure 6(a). The corresponding bending moment, shown in Figure 5(b) and Figure 6(b), could be calculated based on closed frame model.

The GFRP reinforcements of the municipal tunnel structure can be designed according to the Eq. (1) ~ (4). On this basis, the crack width can be predicted according to Eq. (5) in ACI 440.1R-06 and Eq. (6) in GB 50608-2010 respectively. The details of GFRP reinforcements are shown in Fig. 4, and predictions of crack width are listed in Table 1. The limit values of crack width in ACI 440.1R-06 and GB 50608-2010 are 0.7mm and 0.5mm respectively. It means that the crack width could satisfied the requirements well. The details of GFRP reinforcements were shown in Figure 7.

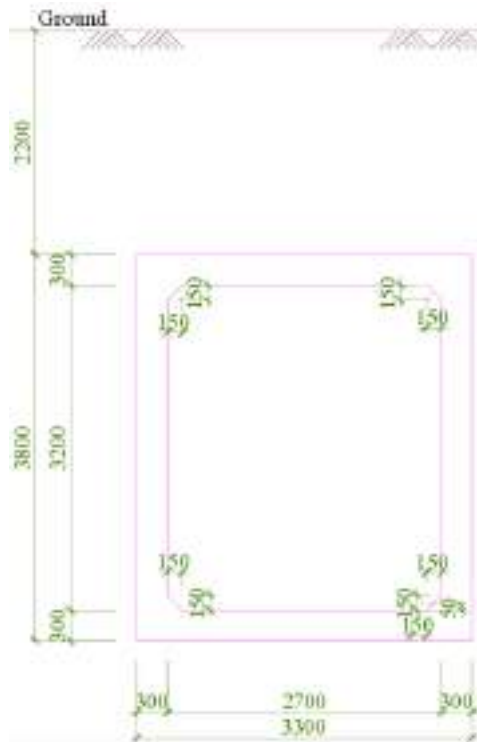


Figure 4: Cross-section of GFRP reinforced PCMT in the park of 2010 Shanghai World Expo

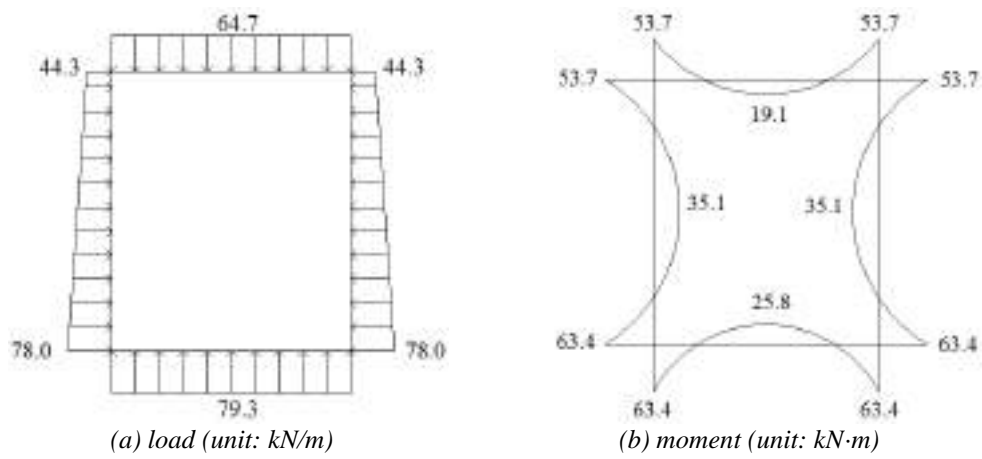


Figure 5: Characteristic values of load and moment of per unit length in longitudinal direction

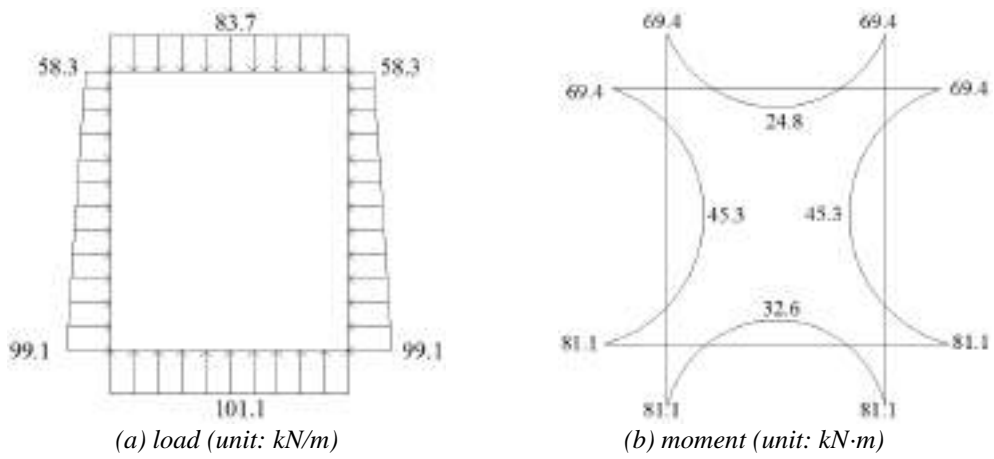


Figure 6: Design values of load and moment of per unit length in longitudinal direction

Table 1: Prediction of crack width

Section		M_k (kN·m)	w (mm)	
			ACI 440.1	GB 50608
Roof	Mid-span	19.1	0.43	0.29
	End	53.7	0.43	0.24
Wall	Mid-span	35.1	0.57	0.38
	End	63.4	0.51	0.32
Floor	Mid-span	25.8	0.57	0.39
	End	63.4	0.51	0.32

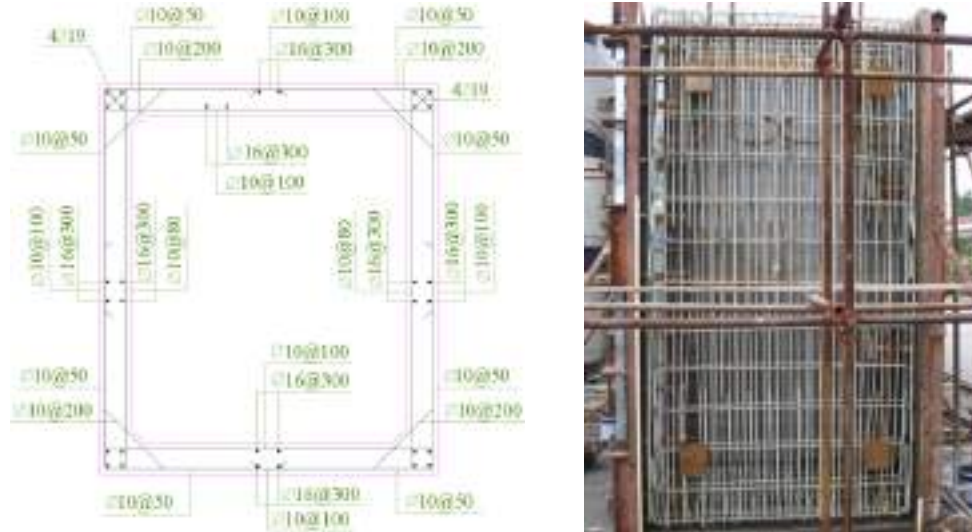


Figure 7: Details of GFRP reinforcements

CONSTRUCTION MONITORING OF GFRP REINFORCED PCMT

Monitoring cases and items

In order to verify structural safety of the GFRP reinforced PCMT, structural monitoring was conducted during the whole construction procedure, including lifting, assembling and filling. Furthermore, the stage of filling was divided into several monitoring cases (see Figure 8) to investigate the mechanical behaviour of the GFRP reinforced PCMT structure under different loading condition of soil pressure.

The monitoring items include: a) strain of GFRP reinforcements and concrete in critical section, b) relative deformation of roof, walls and floor, c) width of gap between two segments, and d) strain of connecting bolts. Arrangement of the monitoring items was shown in Figure 9, and the monitoring cases and the corresponding monitoring items were listed in Table 2.

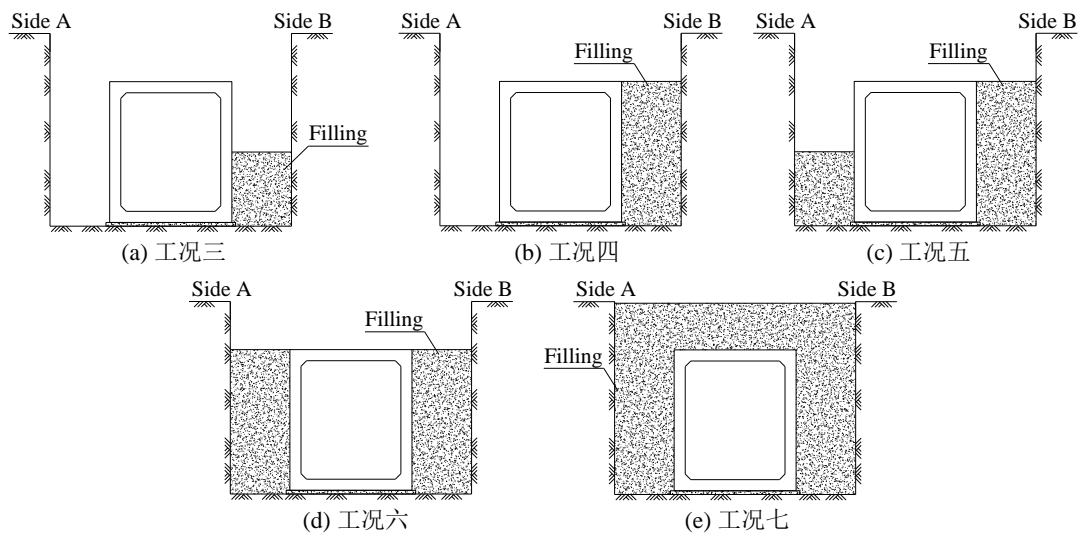
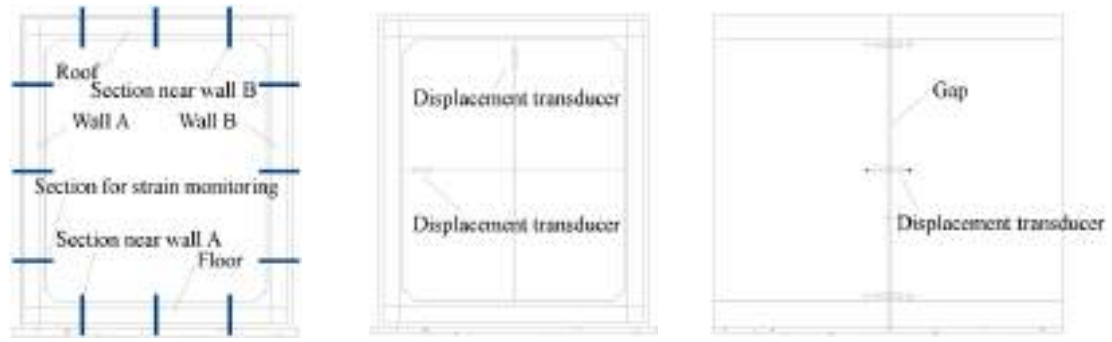


Figure 8: Diagram of monitoring cases in the stage of filling



(a) Strain of GFRP reinforcements and concrete (b) Relative deformation (c) Width of gap between two segments

Figure 9: Arrangement of monitoring items

Table 2: Monitoring cases and the corresponding monitoring items

No. of cases	Name	Monitoring items
Case 1	Lifting	a & b
Case 2	Assembling	c & d
Case 3	Half filling on side B	a & b
Case 4	Fully filling on side B	a & b
Filling Case 5	Fully filling on side B & half filling on side A	a & b
Case 6	Fully filling on side A and B	a & b
Case 7	Fully filling on side A and B & top filling 1.25m	a & b

Monitoring results and analysis

In the stage of lifting, the deflections of roof and floor was nearly null, and the maximum strain of GFRP reinforcements and concrete was both $12\mu\epsilon$. Additionally, there was no crack observed on the tunnel. It meant that the tunnel structure was early in elastic stage.

In the stage of assembling, the municipal tunnel segments were firstly lifted at the position, and then connected by fastening bolts. Strain of connecting bolts and width of gap between two segments were monitored. After assembling, the average strain of connecting bolts was $1000\mu\epsilon$ (about 200MPa), and the gap between two segments was obviously decreased. It could be seen that the assembling construction satisfied the design requirements.

The strain of GFRP reinforcements and concrete, and the relative deformation of roof, walls and floor were monitored during the construction procedure of filling. Table 3 listed the monitoring results of relative deformation in different filling cases. As shown in the table, the maximum relative deformation between two walls was 4.85mm which was about 1/722 of height of the wall, and the maximum relative deformation between roof and floor was 2.81mm which was about 1/1065 of span. The monitoring results also showed that the maximum strain of GFRP reinforcements and concrete was $31\mu\epsilon$ and $20\mu\epsilon$, while the minimum strain was $-106\mu\epsilon$ and $-111\mu\epsilon$, respectively. It could be concluded that the internal force and deformation of the municipal tunnel were both small during the whole construction procedure, and the tunnel structure was kept in elastic stage without any crack.

After filling, raining was continued for several days, and there was no leakage observed in the tunnel, which revealed good waterproof performance of the precast GFRP reinforced PCMT.

Table 3: Monitoring cases and the corresponding monitoring items

	Walls A and B		Roof and floor	
	Relative deformation(mm)	Deformation to span	Relative deformation(mm)	Deformation to span
Case 3	4.477	1/782	0.487	1/6160
Case 4	4.477	1/782	0.487	1/6160
Case 5	4.550	1/769	0.487	1/6160
Case 6	4.610	1/759	0.487	1/6160
Case 7	4.847	1/722	2.817	1/1065

CONCLUSIONS

This paper presents the studies on design and construction monitoring results of GFRP reinforced PCMT located in the park of 2010 Shanghai World Expo which may be the first PCMT reinforced with GFRP bars in the world. The followings and be concluded:

1. Design method of GFRP reinforced PCMT, including equations for flexural capacity and crack width, is proposed. Therein, design equation for flexural capacity of GFRP reinforced concrete members is improved in terms of revising the upper bound of reinforcement ratio to $1.5\rho_{fb}$ in the transition region.
2. According to the aforementioned method, the GFRP reinforced PCMT structure located in the park of 2010 Shanghai World Expo is designed and constructed.
3. Construction monitoring is conducted during the whole construction procedure. The strain of GFRP reinforcements and concrete and relative deformation of the structure are always little. Safety of the GFRP reinforced PCMT can be verified from the monitoring results, and the design method proposed in this paper is demonstrated to be valid.

The works presented in this paper could promote the application of PCMT reinforced with GFRP bars.

ACKNOWLEDGMENTS

The authors gratefully acknowledge the financial support provided by the “National Key Research and Development Program of China (No. 2017YFC0703000)” and “Research and Development Program of MOHURD of China (No. 2016-K4-025)”.

REFERENCES

- American Concrete Institute (ACI) (2006). “Guide for the design and construction of concrete reinforced with FRP bars”, *ACI 440.1R-06*, Farmington Hills, MI.
- A. Nanni, D. A. Luca, H. J. Zadeh (2014). “Reinforced concrete with FRP bars: Mechanics and Design”, *CRC Press*, New York.
- Chinese Standard (2010). “Technical code for infrastructure application of FRP composites (GB 50608-2010),” *Chinese Building Press*, Beijing, China, 19-21. (in Chinese)
- Intelligent Sensing for Innovative Structures, Canadian Network of Excellence (ISIS Canada) (2007). “Reinforcing concrete structures with fibre reinforced polymers, Design manual No. 3”, Winnipeg, Canada.
- J. Curiel-Esparza, J. Canto-Perello (2005). “Indoor atmosphere hazard identification in person entry urban utility tunnels”, *Tunnelling and Underground Space Technology*, 20, 426–34.
- J. Chen, L. Z. Jiang, J. Li, X. J. Shi (2012). “Numerical Simulation of Shaking Table Test on Utility Tunnel under Non-Uniform Earthquake Excitation”, *Tunnelling and Underground Space Technology*, 30, 205–16.
- R. J. FROSCHE (1999). “Another Look at Cracking and Crack Control in Reinforced Concrete”, *ACI Structural Journal*, 96, 437-42.
- W. C. Xue, F. Peng, and Q. W. Zheng (2016). “Design Equations for Flexural Capacity of Concrete Beams Reinforced with Glass Fiber-Reinforced Polymer Bars”, *Journal of Composites for Construction*. 20, 11-21.



EXPERIMENTAL STUDY ON THE BOND BEHAVIOR BETWEEN FRP REBARS AND CONCRETE

A. Rolland 1, K. Benzarti 2, M. Quiertant 3, P. Argoul 3, S. Chataigner 4 and A. Khadour 5

¹ Cerema, Haubourdin, France. e-mail: arnaud.rolland@cerema.fr

² Université Paris-Est, Laboratoire Navier (UMR 8205), Marne-la-Vallée, France.

³ Université Paris-Est, IFSTTAR, Département Matériaux et Structures, Marne-la-Vallée, France.

⁴ IFSTTAR, Département Matériaux et Structures, Bouguenais, France.

⁵ Université Paris-Est, IFSTTAR, Département Composants et Systèmes, Marne-la-Vallée, France.

ABSTRACT

This study focuses on the experimental characterization of the bond behavior between concrete and Fiber Reinforced Polymer (FRP) reinforcing bars (rebars). Pull-out tests were performed on glass, carbon, and aramid FRP rebars, as well as on deformed steel rebars. The influence of various parameters on the bond behavior was studied, such as the type of fibers, the diameter of the FRP bars and their surface geometry. Scanning-electron-microscope observations were performed to study the sand coating. A main originality of the work relied on the instrumentation of pull-out samples using distributed optical fiber sensing instrumentation that provided access to the longitudinal strain distribution along the rebar near the rebar-concrete interface, and then made it possible to determine the effective development length of the various types of rebars considered in this study.

KEYWORDS

Composites, FRP bars, Bond, Pull-out tests, Distributed optical fiber sensors, Development length.

INTRODUCTION

Corrosion of steel reinforcing bars (rebars) is the main cause of degradation of Reinforced Concrete (RC) structures, and has large incidence on maintenance / repair expenses. To prevent such degradations, the use of corrosion-free reinforcements, such as Fiber-Reinforced Polymer (FRP) rebars is gaining interest in new construction projects. Main available products are made of Glass (GFRP), Carbon (CFRP), Aramid (AFRP) or Basalt (BFRP) fiber reinforced polymers. In these materials, polymer matrices are usually based on thermosetting resins, such as vinylester or epoxy systems. Compared to steel reinforcement, FRP rebars are lighter, stronger in tension, corrosion resistant, and electromagnetically neutral (with the exception of CFRP bars).

A key point controlling the performances of FRP RC structures is the bond behavior between the rebar and concrete. In current design practices, bond properties govern serviceability, ductility and ultimate capacity of RC structures. However, designing FRP RC structures is not trivial as the bond behavior of FRP rebars with concrete is affected by many factors, such as rebar constitutive materials, volume ratio of fibers, surface geometry and coating. At the structural scale, FRP/concrete bond properties play a very important role with respect to in-service deformations (deflections), but also to cracking of the concrete cover.

Described in ACI 440.3R-04 (2004), RILEM (1983), and ISO 10406-1 (2015), the direct pull-out test has been applied in many previous studies dedicated to the bond performance of FRP bars embedded in concrete (Larralde 1993, Bank 1998, Achillides 2004, Robert 2010). During bond tests, measured quantities are typically the maximum applied load and the overall slippage of the FRP reinforcement. However, these measures cannot provide local information regarding the interfacial behavior.

Besides, Distributed Optical Fiber Sensor (DOFS) technologies are gaining interest in civil engineering applications (Henault 2012). They allow continuous strain measurement along the Optical Fiber (OF) attached to the host structures, with a sub-centimeter spatial resolution, while being only little intrusive. Such an instrumentation method has already been implemented for pull-out tests (Quiertant 2012, Khadour 2013, Marchand 2016), but to the authors' knowledge, it has never been explored in the case of FRP reinforced samples. The present study investigates the local bond behavior of FRP rebars embedded in concrete using pull-out tests carried out on RC specimens equipped with DOFS instrumentation. A special attention was paid to the influence of the nature of the fibers, the internal microstructure (presence of flaws, fiber arrangement), the surface characteristics (geometry and sand coating), or the rebar diameter, on the interfacial mechanical behavior. In addition, an analysis of the strain profiles recorded by the DOFS system made it possible to evaluate the effective development lengths for the various FRP bars under consideration.

EXPERIMENTAL PROGRAM

Materials

Various rebars available on the international market were selected, based on glass, aramid or carbon fibers. Corresponding series are named GLASS, CARBO and ARA, respectively. These FRPs are manufactured by pultrusion process, with the exception of ARA rebars, which are produced from Kevlar® braided ropes. The main characteristics of all studied rebars are detailed in Table 1. Typical aspects of these rebars are shown in Figure 1. For each series, the FRP materials were supplied with different surface finishes, either sand coated or plain (smooth, without additional surface coating). Corresponding sub-series are labelled xxx-S and xxx-NS respectively. Various rebar diameters were considered, which are also specified in the samples designation. For the sake of comparison, conventional deformed steel rebars (named STEEL-D-12) were also considered. It is to note that ARA rebars present a specific surface geometry made of concavo-convex shapes due to the braiding process, which is supposed to improve their bond capacity with concrete. With regard to CARBO series, one can notice the presence of a white multifilament yarn helically wrapped around the bar which creates an additional surface relief. This feature is observed both on uncoated (CARBO-NS) and sand coated (CARBO-S) rebars.

Table 1: Designations and main characteristics of the rebars under study

Series	Commercial brand	Type of fibers / matrix	Rebar designation	Surface finish	Nominal diameter (mm)	Elastic Modulus (GPa) *
GLASS	V.Rod® (Pultrall®, Canada)	E-glass / vinylester	GLASS-S-9.5	Sanded	9.5	53
			GLASS-S-12.7	Sanded	12.7	
			GLASS-S-15.9	Sanded	15.9	
			GLASS-NS-12.7	Non-sanded	12.7	
CARBO	Carbopree® (Sireg®, Italia)	Carbon / vinylester	CARBO-S-10	Sanded + helically wrapped yarn	10	139
			CARBO-NS-10	Non-sanded + helically wrapped yarn	10	
ARA	Fibra® (Fibex®, Japan)	Kevlar 49® Aramid / epoxy	ARA-S-9	Braided and sanded	9	80
			ARA-S-15	Braided and sanded	15	
STEEL-D-12				Deformed	12	198

* Values obtained by tensile tests (Rolland 2015, 2018)



Figure 1: Visual aspect of the selected FRP rebars and the reference steel rebar

Test Setup for Characterizing Concrete/Rebar Interface Behavior

The bond behavior between the rebars and concrete has been characterized by direct pull-out tests, according to ACI 440.3R-04 (2004). Pull-out tests were performed on RC specimens made with the various rebars listed in

Table 1. For each type of reinforcement (same material, diameter and surface treatment), four RC specimens were tested, among which two were instrumented by OF bonded to the surface of the FRP rebar (Figure 2.a).

The test setup and loading conditions are depicted in Figure 2. RC specimens consist of a 1.20 meter-long straight rebar partially embedded, with centric placement, in a normal strength concrete cylinder (16 cm-diameter and 20 cm-height). Concrete was cast while the rebar was set in the vertical position. A plastic tube, called bond breaker, is placed between the rebar and concrete near the loaded side of the concrete block, in order to prevent edge effects induced by the reaction support. For each RC specimen, the length of the bond breaker is chosen so that the embedment length of the bar in concrete is equal to six bar diameters (Figure 2.c). Such a condition is supposed to favour a preferential failure by slippage of the rebar (Achillides 2004). The compressive strength of the concrete after 37 days of curing (out of water) was 28 MPa (Rolland 2015, 2018).

The RC specimens were put on the drilled horizontal crosshead beam of a universal testing machine, with the rebar passing through the beam hole (Figure 2.b). The test is controlled by the grip displacement at a constant speed of 1.2 mm/min. During the test, the free end slip of the rebar is monitored with a non-contact laser displacement sensor located at an initial distance of 40 mm from the end of the bar.

The OF sensors previously installed on RC specimens were connected to a commercially available Optical Rayleigh Frequency-Domain Reflectometer (OFDR) that allows distributed measurement of the longitudinal strain of the rebar with a gauge length less than 5 mm, while remaining less intrusive than electrical strain gauges (Froggatt 1998, Soller 2005, Henault 2012). Prior to concrete casting, the rebars were grooved over a length of 300 mm, with a width of 1 mm and a depth of 2 mm (Fig 3). The fiber was then sealed into the U-groove using a two-part fast curing methyl methacrylate-based adhesive. During the pull-out tests, DOFS measurements were recorded at different loading stages. The applied load was kept constant during these stages to allow the acquisition of the strain profile.

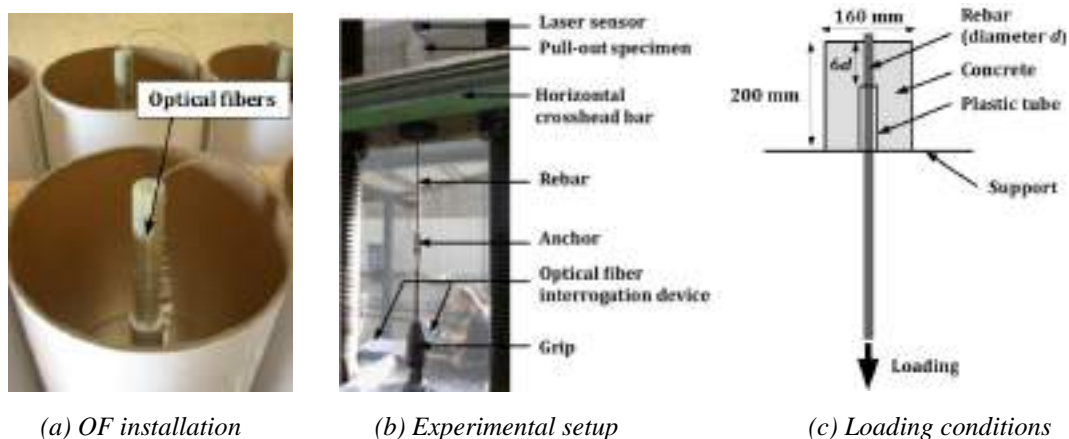


Figure 2: Pull-out tests

RESULTS AND DISCUSSIONS

Preliminary Microstructural Observations by Scanning Electron Microscopy

Micrographic observations were performed on polished cross sections of the various rebars, using a Scanning Electron Microscope (SEM) operating in secondary electron mode, with a picture resolution in the order of one μm . The aim of these observations was to qualitatively evaluate fiber arrangement, size and shape of the sand particles of the surface coating, and to detect the possible presence of manufacturing defects (debonding, voids). In Figure 3 showing SEM micrographs at low magnification, the particle size appears to be higher for GLASS and ARA series (diameter in the range 0.5 to 1.0 mm) than for CARBO series (in the range 0.1 - 0.5 mm). In addition, sand particles of the ARA series are found to exhibit a smoother and less angular shape. SEM pictures at higher magnification (Figure 4) facilitate the visualization of the fiber arrangement and the possible presence of defects. Globally, the fiber distribution is found rather compact and homogeneous for GLASS and ARA series. Differently, numerous voids can be observed on CARBO rebars (Figures 3 and 4).

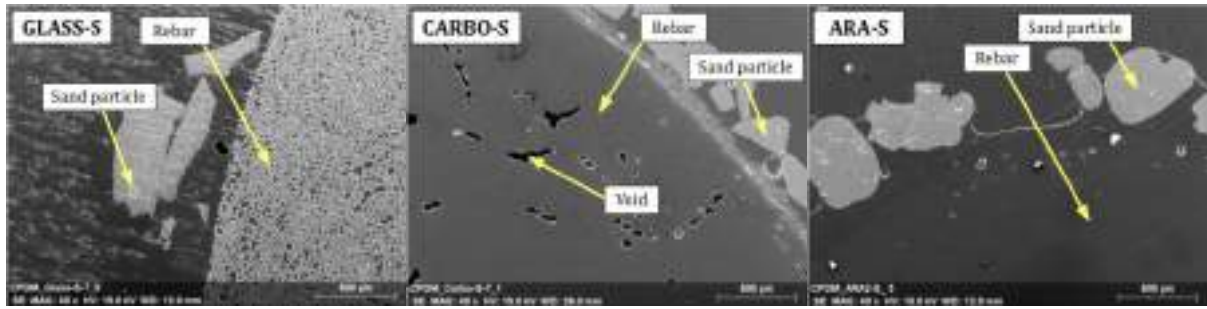


Figure 3: SEM micrographs of cross sections of sand coated FRP bars at low magnification

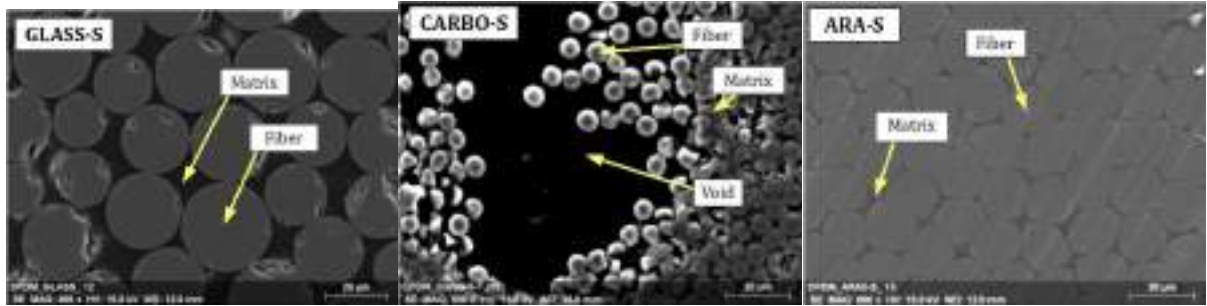


Figure 4: SEM micrographs of cross sections of sand coated FRP bars at high magnification

Characterization of the Bond-Slip Behavior by Pull-Out Test

Failure modes

Failure of the specimens occurred by slippage of the rebar out of the concrete, which was the expected pull-out failure mode. A thin layer of concrete remains attached to all extracted sand-coated FRP-rebars (GLASS-S, CARBO-S and ARA-S series) and to the ribs of STEEL-D rebars as well. Differently, such a layer was not observed for non-sanded FRP rebars (GLASS-NS and CARBO-NS series). In the GLASS-S series, a mixed failure mode was observed, with a partial peeling off of the sand coated layer along the extracted part of the bar.

Bond-slip behavior

Main experimental results are listed in Table 2 and Figure 5 provides typical bond-slip curves. For each type of rebar, the four RC specimens are labelled name-1 and name-2 for the non-instrumented specimens, and name-3-OF and name-4-OF for the specimens instrumented with OF. The average shear stress at any stage of the loading τ_m , is calculated as the ratio of the force F applied at the loaded end, to the bonded area of the rebar with concrete:

$$\tau_m = \frac{F}{\pi d L_E} \quad (1)$$

where d is the diameter of the rebar and L_E is the embedded length ($L_E = 6d$). The bond strength is defined as the maximum value of the average shear stress recorded during the test.

Table 2: Results of pull-out tests

Specimen	Ultimate capacity F_l (kN)	Bond strength τ_l (MPa)	Tensile stress* σ_l (MPa)
Mean of GLASS-S-9.5 series	13.7 ± 1.3	8.0 ± 0.8	193 ± 19
Mean of GLASS-S-12.7 series	31.2 ± 2.2	10.3 ± 0.7	246 ± 17
Mean of GLASS-S-15.9 series	52.8 ± 4.0	11.1 ± 0.8	266 ± 20
Mean of GLASS-NS-12.7 series	5.3 ± 0.5	1.7 ± 0.2	42 ± 4
Mean of CARBO-S-10 series	12.7 ± 1.5	6.7 ± 0.8	161 ± 19
Mean of CARBO-NS-10 series	11.0 ± 1.5	5.8 ± 0.8	140 ± 19
Mean of ARA-S-9 series	10.1 ± 0.4	6.6 ± 0.2	159 ± 6
Mean of ARA-S-15 series	38.7 ± 4.4	9.1 ± 1.0	219 ± 25
Mean of STEEL-D 12 series	26.1 ± 3.0	9.6 ± 1.1	231 ± 26

* Tensile stress in the loaded part of the rebar at bond failure

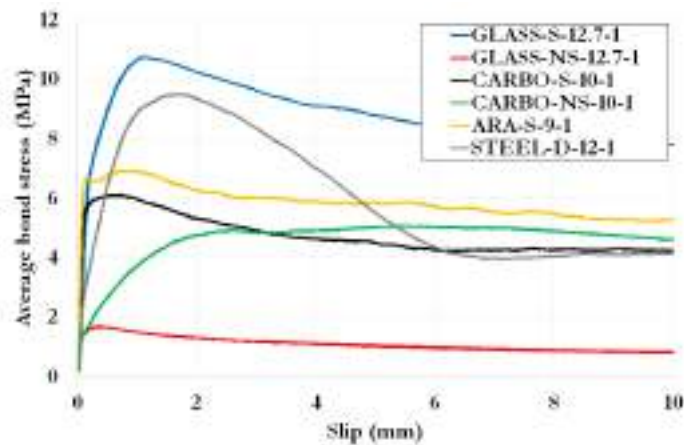


Figure 5: Comparison of typical bond-slip curves for the various types of bars

Specimens of the GLASS-S series exhibit the highest bond strengths. Furthermore, it is interesting to note that GLASS-S-12.7 rebars present slightly higher bond strength compared to STEEL-D-12 rebars, for a quasi-equivalent diameter of the bar (12.7 mm and 12 mm). Most of the time, the literature reports that bond strength of GFRP rebars do not exceed that of steel reinforcement (Larralde 1993, Okelo 2005) in the case of a conventional pull-out failure mode. However, results obtained in the present study with the GLASS-S series show opposite trend and are thus considered very promising for future use of FRP bars as internal reinforcement for concrete. In addition, it is to note that the bond strength of GLASS-S-12.7 rebars is six times higher than that of uncoated GLASS-NS-12.7 rebars. As previously underlined, the latter uncoated rebars present a very smooth surface, which obviously reduces dramatically the bond properties with concrete. In practice, only sand coated rebars of the GLASS-S type are commercialized for construction applications.

Regarding pull-out tests performed on specimens of the CARBO series, and particularly on those with CARBO-NS-10 and CARBO-S-10 rebars, it appears that sand coating has, this time, a more limited effect on the bond strength value. A possible explanation is that the size of sand particles (hence the surface roughness of the coated rebar) is significantly smaller in the case of CARBO-S rebars compared to GLASS-S rebars, as previously shown by SEM observations (Figure 3). Thus, the contribution of the sand particles to interfacial adherence by a mechanical anchoring phenomenon or by friction appears to be lower. In addition, both sand coated and uncoated CARBO rebars present a periodic surface relief due to the helically wrapped white yarn. Such a relief may contribute to interfacial adherence independently of the sand coating, hence providing another explanation for the similar bond strength values obtained for specimens with CARBO-NS-10 and CARBO-S-10 rebars. Nevertheless, a closer comparison of the bond-slip curves of these specimens reveals that sand coating still plays an important role in the initial interface stiffness. Such a trend was already reported in the literature (Cosenza 1997, Achillides 2004, Okelo 2005).

With regard to sand coated aramid FRP rebars, it is found that ARA-S-9 samples present a lower bond strength compared to GLASS-S-9.5 and CARBO-S-10 rebars, despite their braided geometry (note that the comparison is made at nearly equivalent bar diameter). One possible explanation relies in the fact that sand particles of the surface coating are smoother and less angular for rebars of the ARA series, as shown in Figure 5.

When focusing on the effect of the bar diameter, and in view of results of the GLASS-S subseries (3 different diameters in the range 9.5-15.9 mm) and ARA-S subseries (2 different diameters, 9 and 15 mm), it can be concluded that the bond strength globally increases with the bar diameter, although the inverse trend is usually reported in the literature (Tighiouart 1998, Achillides 2004, Okelo 2005, Bank 2006, Sayed Ahmad 2011). Note, however, that for present pull-out tests, all rebars were embedded over a length corresponding to six times their diameter. A constant ratio between diameter and embedded length (here a ratio of six) for all specimen was chosen to facilitate the comparison of bond characteristics, as it produces also a constant ratio between the applied tensile stress (σ) in the free part of the rebars at bond failure ($\sigma = 4F_1 / \pi d^2$, if F_1 is the ultimate load) and the bond strength ($\tau_1 = F_1 / 6\pi d^2$). In these conditions the ratio $\sigma / \tau_1 = 24$ is independent of the rebar diameter. However, as a direct consequence, the embedment length varies with the bar diameter.

Previous results show globally a complex interface behavior, depending not only on the nature of the constituent materials and the surface characteristics of the considered rebar, but also on its diameter (as this latter implies a modulation of the embedded length). To perform a deeper analysis, it was therefore decided to study the interface mechanisms at a more local level, using strain profiles recorded during pull-out tests on specimens instrumented over their entire embedded length by OF sensors.

Analysis of the Local Bond Behavior Using DOFS Instrumentation

Strain distribution along the embedded length

In the following, the “embedded length” refers to the length along which the rebar is in contact with concrete (six times the diameter of the rebar), while the “development length” is the part of the embedded length over which the rebar actually transfers the applied longitudinal force to the surrounding concrete.

As an example of recorded results, some longitudinal strain distributions measured along GLASS-S-9.5-4-OF during pull-out tests are presented in Figure 6.a for several load levels. For a comparison purpose, strain profiles recorded for STEEL-D-12-3-OF rebars are also presented in Figure 6.b. On these curves, the two ends of the embedded length are indicated by two vertical black dotted lines.

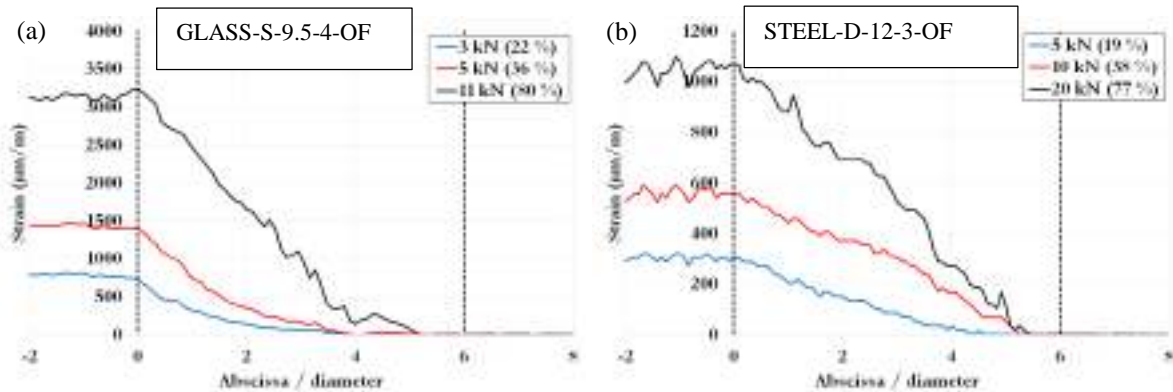


Figure 6: Strain distribution along (a) the GLASS-S-9.5-4-OF and (b) STEEL-D-12-3-OF rebars

Assessment of the development length

Strain profiles recorded during pull-out tests made it possible to assess the development lengths of the various rebars. In order to use an objective quantification method, the definition of the development length proposed by Yuan (2005) was adopted. This author defined the development length as the length L_D necessary to transfer 97 % of the force applied to the rebar. The development length L_D is then calculated considering the following criteria:

$$\varepsilon_{xx}(L_D) = 0.03\varepsilon_{xx}(0) \quad (2)$$

Based on the proposed approach, values of the development lengths were estimated for each type of rebar, considering strain measurements recorded at the lowest recorded load level (around of 20 % of the ultimate load). This load level ensures that the interface remain undamaged and the bond behavior remain, reflecting the service conditions of a structural element. Calculated values of the development length are listed in Table 3. Results point out an increase in the development length as a function of the bar diameter, for a given series of rebars. This trend is consistent with the literature (Newman 2010, CSA 2012, ACI 2015).

With regard to the effect of sand coating, the uncoated rebars GLASS-NS-12.7-OF present a much lower development length than the sand coated rebars GLASS-S-12.7-OF. The opposite trend is observed for rebars of the CARBO series (slightly lower development length obtained for the sand-coated rebars), but this latter result should be taken with circumspection, as the DOFS instrumentation was observed to affect significantly the pull-out response of CARBO-S-10-OF specimens.

Moreover, no clear trend can be established regarding the effect of the nature of the fibers on the development length. Globally, all these results attest to the complexity of interfacial mechanisms between the FRP reinforcements and surrounding concrete.

Table 3: Development lengths calculated for the various rebars

Specimen	Development length L_D (mm)	L_D / d
Mean of GLASS-S-9.5 series	36.5 ± 3.5	3.8 ± 0.4
Mean of GLASS-S-12.7 series	57 ± 6	4.5 ± 0.5
Mean of GLASS-S-15.9 series	71.5 ± 1.5	4.5 ± 0.1
Mean of GLASS-NS-12.7 series	27.5 ± 4.5	2.2 ± 0.4
Mean of CARBO-S-10 series	33	3.3
Mean of CARBO-NS-10 series	38 ± 0	3.8 ± 0.0
Mean of ARA-S-9 series	30	3.3
Mean of ARA-S-15 series	61	4.1
Mean of STEEL-D-12	52	4.3

CONCLUSIONS

Various FRP composite rebars were first observed by SEM. These preliminary observations revealed substantial differences in the size and shape of particles from the sand coatings.

The bond-slip behavior of the various rebars embedded in concrete cylinders was then determined by pull-out tests. Following this experimental campaign, it has been globally noted that characteristics of the sand coating play a major role in the load transfer mechanism at the interface (rigidity of the interface, bond strength and post-peak stress plateau related to friction). Efficiency of the sand coating tends to increase with the size and angularity of the sand particles. The sand coating of GLASS-S was found to provide higher bond performances compared to that of CARBO-S series or ARA-S series, although these latter rebars exhibit additional surface relief due to the braiding process. For equivalent bar diameters, pull-out specimens with GLASS-S-12.7 rebars exhibited slightly higher bond strength values compared to specimens with reference deformed steel rebars (STEEL-D-12), which is quite encouraging. In addition, experimental results showed an increase in bond strength versus the bar diameter, although an inverse trend is usually reported in the literature.

An original aspect of this experimental work relies on the instrumentation of specimens by distributed optical fiber sensors attached to the rebar surface. This DOFS device provided access to local information related to interfacial load transfer mechanisms, such as the longitudinal strain distribution along the embedded length of the rebar. Interpretation of strain profiles recorded by DOFS instrumentation made it possible to estimate the development length of each bar. This latter is an essential criterion in the design of the anchorage. Results revealed an increase in the development length with the bar diameter, but no clear effect of the elastic modulus of rebars (which is closely related to the nature/stiffness of fibers).

More generally, the diversity of strain profiles highlighted the complex distribution of shear stresses and the multiple phenomena involved in the load transfer mechanisms between concrete and its FRP reinforcement. Such a complexity may originate from the high variability in the FRP characteristics, depending on many factors, such as the nature and relative contents of constituent materials (fibers and polymer matrix), the type of surface coating and geometry, or the manufacturing process.

Additional studies are needed to investigate further the bond behavior of FRP rebars with concrete at the local level. This knowledge is essential for establishment of suitable design standards and for further optimization of FRP rebar characteristics (surface coating, manufacturing process...).

ACKNOWLEDGMENTS

The authors wish to acknowledge Pultrall ®, B, Sireg ® and Fibex ® companies for supplying FRP rebars.

REFERENCES

- Z. Achillides, P. Pilakoutas (2004). "Bond behavior of fiber reinforced polymer bars under direct pull-out conditions", *J. Compos. Constr.*, 8 (2), 173-181.
- ACI 440.1R-15 (2015). "Guide for the design and construction of structural concrete reinforced with fiber-reinforced polymer bars", *American Concrete Institute (ACI)*, Farmington Hills, MI, USA.
- ACI 440.3R-04 (2004). "Guide test methods for fiber-reinforced polymers (FRPs) for reinforcing or strengthening concrete structures", *American Concrete Institute (ACI)*, Farmington Hills, MI, USA.
- L.C. Bank, M. Puterman, A. Katz (1998), "The effect of material degradation on bond properties of fiber reinforced plastic reinforcing bars in concrete", *ACI Materials Journal*, 95 (3), 232-243.

- L.C. Bank (2006). “Composites for construction: structural design with FRP materials”, John Wiley and Sons, Inc., Hoboken, New Jersey.
- E. Cosenza, G. Manfredi, R. Realfonzo (1997). “Behavior and modeling of bond of FRP rebars to concrete”, *Journal of Composites for Construction*, 1 (2), 40-51.
- CSA S806-12 (2012). “Design and construction of building structures with fibre-reinforced polymers”, *Canadian Standards Association (CSA)*, Mississauga, ON, Canada.
- EN 1992-1-1 (2004). “Eurocode 2 – Design of concrete structures – Part 1-1: General rules and rules for buildings”, *Comité Européen de Normalisation (CEN)*, Brussels, Belgium.
- M. Froggatt, J. Moore (1998). “High-spatial-resolution distributed strain measurement in optical fiber with Rayleigh scatter”, *Appl. Opt.*, 37, 1735-1740.
- J. M. Henault, M. Quiertant, S. Delepine-Lesoille, J. Salin, G. Moreau, F. Taillade, K. Benzarti (2012). “Quantitative strain measurement and crack detection in RC structures using a truly distributed fiber optic sensing system”, *Construction and Building Materials*, 37 (1), 916-923.
- L.C. Hollaway (2008). “Advanced fibre polymer composite structural systems used in bridge engineering”, *ICE Manual of Bridge Engineering*, 503-529.
- ISO 10406-1 (2015). “Fibre-reinforced polymer (FRP) reinforcement of concrete – Test methods – Part 1: FRP bars and grids”, International Organization for Standardization (ISO), Geneva, Switzerland.
- A. Khadour, F. Baby, A. Herrera, F. Taillade, P. Marchand, P. Rivillon, A. Simon, M. Quiertant, F. Toutlemonde (2013). “Distributed strain monitoring of reinforcement bars using optical fibers for SHM”, *7th International Conference on Concrete under Severe Conditions (CONSEC13) – Environment and Loading*, Nanjing, China, 1620-1629.
- J. Larralde, R. Silva-Rodriguez (1993). “Bond and slip of FRP rebars in concrete”, *Journal of Materials in Civil Engineering*, 5 (1), 30-40.
- P. Marchand, F. Baby, A. Khadour, T. Battesti, P. Rivillon, M. Quiertant, H. H. Nguyen, G. Génereux, J. P. Deveaud, A. Simon, F. Toutlemonde (2016). “Bond behaviour of reinforcing bars in UHPFRC”, *Materials and Structures*, 49 (5), 1979-1995.
- N. Newman, A. Ayoub, A. Belarbi (2010). “Development length of straight FRP composite bars embedded in concrete”, *Journal of Reinforced Plastics and Composites*, 29 (4), 571-589.
- R. Okelo, R. L. Yuan (2005). “Bond strength of fiber reinforced polymer rebars in normal strength concrete”, *Journal of Composites for Construction*, 9 (3), 203-213.
- M. Quiertant, F. Baby, A. Khadour, P. Marchand, P. Rivillon, J. Billo, R. Lapeyrere, F. Toutlemonde, A. Simon, J. Cordier, J. C. Renaud (2012). “Deformation monitoring of reinforcement bars with a distributed fiber optic sensor for the SHM of reinforced concrete structures”, *9th International Conference on NDE in Relation to Structural Integrity for Nuclear and Pressurized Components*, Seattle, Washington, USA.
- RILEM (1983). “RC 6 Bond test for reinforcement steel – Part 2: Pull-out test”, *RILEM Recommendations for the Testing and Use of Constructions Materials*, 218-220.
- M. Robert, B. Benmokrane (2010). “Effect of aging on bond of GFRP bars embedded in concrete”, *Cement & Concrete Composites*, 32 (1), 461-467.
- A. Rolland (2015). “Comportement mécanique et durabilité de structures en béton renforcées par des armatures composites internes”, *PhD thesis manuscript*, Université Paris-Est, France, 235 pages (in French). <https://tel.archives-ouvertes.fr/tel-01223307/document>
- A. Rolland (2018). “Experimental investigations on the bond behavior between concrete and FRP reinforcing bars”, *Construction and Building Materials*, 173, 136-148.
- B. Soller, D. Gifford, M. Wolfe, M. Froggatt (2005). “High resolution optical frequency domain reflectometry for characterization of components and assemblies”, *Opt Express*, 13, 666-674.
- B. Tighiouart, B. Benmokrane, D. Gao (1998). “Investigation of bond in concrete member with fibre reinforced polymer (FRP) bars”, *Construction and Building Materials*, 12 (8), 453-462.
- H. Yuan (2005). “Improved theoretical solutions of FRP-to-concrete interfaces”, *Proceedings of the International Symposium on Bond Behaviour of FRP in Structures (BBFS)*, Hong Kong, China, 97-102.



FLEXURAL BEHAVIOUR OF BFRP REINFORCED BEAMS WITH PRESTRESSED REINFORCEMENT

M. Mirshekari¹, T. Donchev¹ and D. Petkova¹

¹ Faculty of Science, Engineering and Computing, Kingston University, London, UK, Email: m.mirshekari@hotmail.com

ABSTRACT:

Non-corrosive nature and high strength of fibre reinforced polymer (FRP) reinforcement makes it attractive for use in concrete applications. The main problem for using FRP reinforcement is the higher deformability especially in cases of glass and basalt FRP. One of possible approaches for reducing of the deformations is via prestressing of the reinforcement. This research is continuation of previous investigation and presents experimental results of six large scale concrete beams reinforced with different types of reinforcement. Five of the beams are reinforced with Basalt FRP (BFRP) 6mm diameter bars pretensioned with differing degree of pre-stressing and one beam is steel reinforced. The aim of the paper is to present the experimental results reflecting the behaviour of BFRP reinforced beams with different level of prestressing and to compare them with the deformability of steel reinforced beam. Test results showed that the prestressing of BFRP reinforced beams is resulting in reducing of their deformability. The ultimate deflection at mid-span for BFRP beam with 40% of prestressing have 88% lower than the steel reinforced beam at ultimate load for the steel reinforced sample.

KEYWORDS

Large scale samples, RC beams, BFRP reinforcement, Prestressing, Pre-tensioning.

INTRODUCTION

The loadbearing capacity of reinforced-concrete (RC) structures may be reduced due to the deterioration, chemical damage and corrosion of steel reinforcement. New materials, such as FRPs, which are non-corrodible by nature, chemically stable and possessing high strength, can be used as a good alternative to traditional steel reinforcement for RC elements, especially in aggressive environmental conditions. The use of carbon, glass and aramid fibre reinforced polymer (CFRP, GFRP and AFRP) has been extensively investigated and used in concrete structures. Basalt fibre reinforced polymer (BFRP) bars are a relatively recent type of FRP reinforcement. They have low modulus of elasticity and high tensile strength. Due to their low elastic modulus, deflections and cracking in BFRP RC beams are larger than these found in steel RC beams at the same level of loading (Mirshekari et al. 2016), which can be controlled by prestressing the BFRP reinforcement.

The current design codes and guidelines such as ACI 440.1R-15 (2015), 440.4R-04 (2011) and CSA S06-06 (2006) allow the use of CFRP, AFRP and GFRP as the main reinforcement in concrete elements. However, that no sufficient design codes and specifications for prestressing and reinforcing concrete elements with BFRP bars has been established yet.

The investigation and development of FRP reinforcement can be traced to be the period after World War II in the late 1940s when the aerospace industry had recognised the advantages of using composite materials. However, these materials were seriously considered for use as reinforcement in concrete elements after 1960s (ACI 440.1R-15 (2015)). The Japan had the most dramatic increasing of structural applications of FRP reinforcement at about mid-1990s. In the 2000s, china becomes one of the main users of FRPs materials for new construction applications (Ye et al. 2003). The first application of internal FRP reinforcement in Europe began in Germany with the construction of a prestressed CFRP highway bridge in 1986 (Meier, 1992). Series of investigations mainly about post-tensioning with FRP have been conducted by Burgoyne with CFRP and AFRP reinforcement.

Yue-lin et al. (2004) studying the strengthening of RC beams using prestressed GFRP (PGFRP), they indicated that beams with GFRP sheets increased load capacity by 55% while same samples with PGFRP sheets could increase load capacity by 100% also the same beams with GFRP sheets have larger deflections than with PGFRP sheets. Recently investigation on the performance of RC beams prestressed with Near Surface Mounted NSM-CFRP laminates by Costa et al. (2014) showed the deflections in the beams decreased with increase of the applied prestressed level from 20% to 50% of their ultimate nominal strain.

Thorhallsson and Jonsson (2012) investigated prestressed concrete beams with BFRP tendons. They pointed out that Serviceability Limit State (SLS) bearing capacity of the prestressed beams was three times higher than unprestressed beam. Thorhallsson and Gudmundsson (2013) tested four beams prestressed with two 10 mm diameter BFRP tendons, they mentioned that to utilize BFRP tendons high strength and in order to prevent concrete cracking it is necessary to prestress them. Furthermore, the experimental results showed BFRP prestressed beams without shear reinforcement are vulnerable to transvers loading. Crossett et al. (2015) experimental research on the flexural behaviour of self-compacting concrete (SCC) beams pre-stressed with BFRP indicated that the beams with 12 mm diameter BFRP failed by concrete crushing rather than rupture of the bar. In addition, by applying a pre-stress force the capacity of the BFRP beams increased by 85%. In comparison, the capacity of the beams using steel increased by 18%.

Numerous research studies on fibre reinforcement polymer (FRP) have been conducted at The Kingston University London. The main findings are that prestressing with FRP bar is promising for economical design of reinforcing concrete members. In an experimental research by Pearson et al. (2013), seven post tensioned BFRP beams were investigated, some were grouted and some ungrouted. They found that a higher level of prestressing significantly reduces the deformability of BFRP reinforced beams in the case of grouted reinforcement. In addition, the effect of higher levels of prestressing from ungrouted beams is not so significant. Mirshekari et al. (2015) investigated influence of the degree of prestressing on the behaviour of BFRP reinforced beams with low concrete strength C20/25. They stated that the prestressing of 6 mm diameter BFRP bars does not contribute significantly to the ultimate capacity of the beams. However, the effect of prestressing has a significant effect on the deformability of the beams as the increasing level of prestress leads to a delay in the development of the initial cracks. More recently Mirshekari et al. (2016) studied the deformability of pretensioned PC beams with 10 mm diameter BFRP reinforcement. This research showed the ultimate capacity of all BFRP reinforced beams is higher than the capacity of steel reinforced beam and slightly increasing with level of prestressing due to change of model of failure. Therefore, prestressing at and above 30% of ultimate tensile load (UTL) for BFRP reinforcement results in similar or smaller deformation capacity of BFRP reinforced beam in comparison with steel reinforced for all levels of loading.

This paper is mainly focused on investigating the flexural behaviour of BFRP reinforced beams with prestressed reinforcement on large scale RC beams. It presents a third phase of a larger research project.

METHODOLOGY

Four pretensioned BFRP RC beams and one pretensioned hybrid BFRP RC beam were tested in flexure. Five of the samples had BFRP reinforcement with a different degree of prestressing as percentage of the design ultimate capacity of the BFRP reinforcement. In addition, a steel RC beam with the same dimensions and diameter of reinforcement was tested for comparison purposes. All beams were 125 mm in width and 200 mm in depth. Dimensions of each specimen and test arrangement are shown in Figure 1 and Table 1. The beams had a span of 2000 mm and supported at 200 mm distance from the specimens' ends. A load spreader beam allowed the application of loads at two points separated by a distance of 600 mm.

Table 52: Test arrangements of specimens

Beam	Bottom BFRP reinforcement bar size (mm)	Tensioning force (kN per bar)	Reinforcement method	Degree of prestressing (%)
S0	6	0	Reinforced	0%
B0	6	0	Reinforced	0%
B20	6	5.5	Pretensioned	20%
B30	6	11	Pretensioned	30%
B30+1	6	11	Pretensioned	30%
B40	6	17	Pretensioned	40%

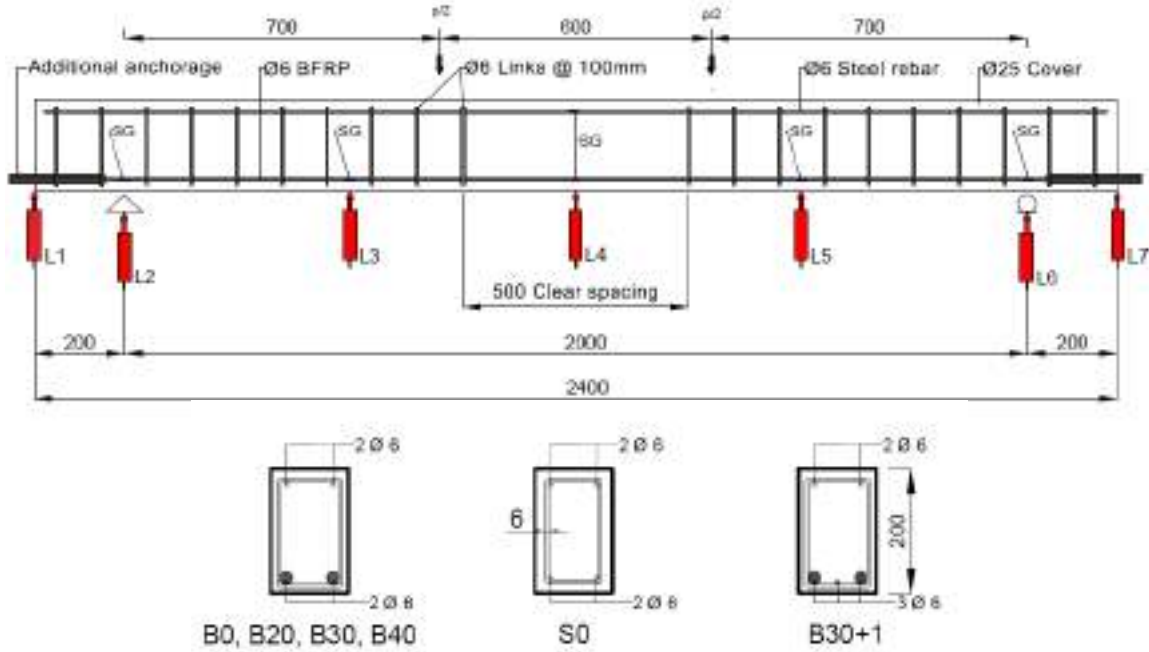


Figure 1: Dimensions of specimens and test set-up (in mm).

Sand, gravel coarse aggregate (10 mm maximum size) and ordinary Portland cement were used to produce concrete with a target compressive strength of C35/45 N/mm² at 28 days. The diameter of BFRP reinforcement was 6mm for all beams and it was supplied by Magma Tech Ltd. The high yield steel was 6 mm in diameter used in steel control beam and as top reinforcement for all beams. To prevent shear failure 6 mm diameter mild steel links were placed at 100 mm intervals in shear spans of the beams. A 25 mm top, bottom and side cover for main longitudinal reinforcement was provided. Steel tubes attached to the ends of the BFRP bars were used for prestressing (Figure 2) and were left to act as additional anchorage throughout the testing to prevent premature anchorage failure.

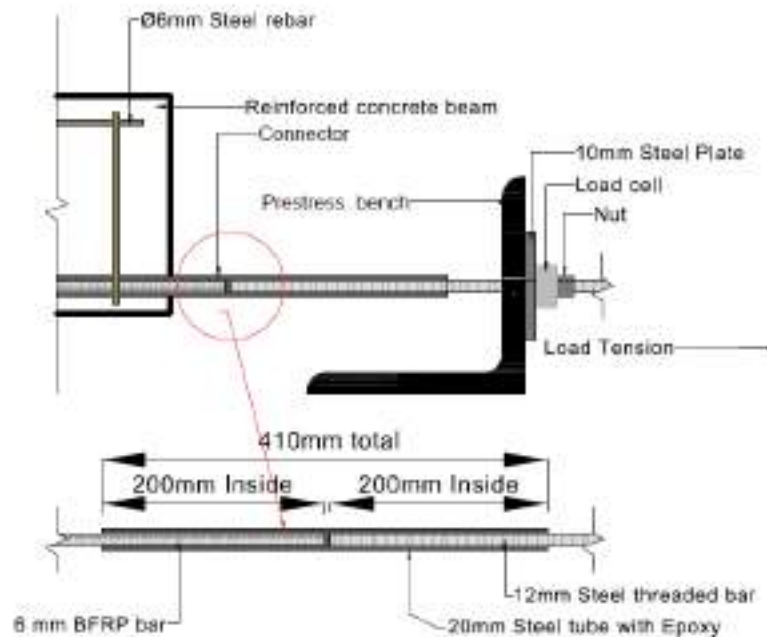


Figure 2: Connection of the reinforcing BFRP bars to the threaded bars for prestressing

The prestressing force was applied via a pre-tensioning method with prestressing equipment as shown in Figure 2. The level of prestress before and during the process of casting and the development of internal stresses during the process of loading were monitored and measured via load cells (Novatech F207–100 kN) and strain gauges for each of the bars during the whole process of prestressing and testing. Deflections were measured by positioning of linear variable differential transformers (LVDTs) at the mid-span, quarter spans and edge ends of beams. Additional LVDTs were located at the two supports of each of the beams to assess any settlement that might take place during the loading process, which could affect the other deflection readings. Loading was applied via two equal point loads at 2 kN load steps as total load with rate of application of 2 kN/m and keeping constant load for 5 minutes at load step. Failure of the beams was considered when the beam under testing could not uphold any additional applied load.

RESULTS AND DISCUSSIONS

The experimental results for all beams are summarized in Table 2. This includes the cracking load, the ultimate load, the deflection at cracking load, the ultimate deflection, and the failure mode. Figure 2 shows the load deflection curves at mid-span for the six beams. For the beam S0, the primary cracks occurred at a load of 8 kN. In beam B0, the two BFRP bars ruptured simultaneously at maximum load of 31kN and displacement of 62 mm. The ultimate load for S0 was 48.7% lower than of beam B0 and was reached at 12.5 mm displacement. In beam B20, B30 and B40 the behaviour of failure mode at the time of rupture was similar to that in beam B0. The ultimate deflection at mid-span for beam B20 was 22%, B30 27% and B40 61% lower than that of beam B0. The behavior of hybrid beam B30+1, was similar to that of beam B40. The maximum load was 62% higher than that of beam B40 and the deformation at ultimate deflections was similar to the B20 and B30.

Table 53: Test results

Beam	Cracking Load (kN)	Ultimate Load (kN)	Ultimate deflection at mid-span (mm)	Failure mode
S0	8	16	12.5	Yielding of steel reinforcement
B0	8	31	61.7	Bar rupture
B20	14	30	48.1	Bar rupture
B30	14	30	45.1	Bar rupture
B30+1	16	42	49.9	Bar rupture
B40	18	26	24.2	Bar rupture

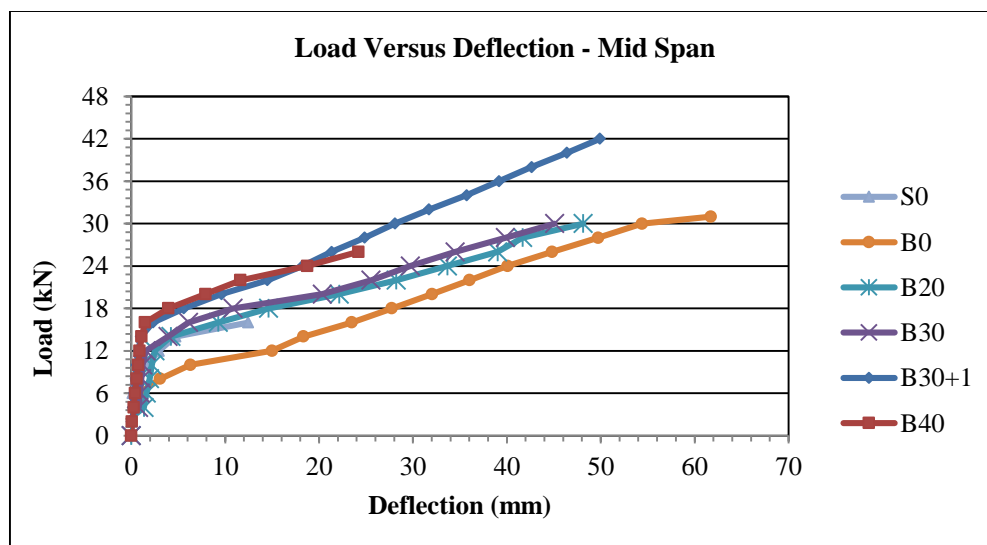


Figure 3: Load-deflection relationship at mid-span

Typical load versus deflection curves at mid-span are shown in Figure 3. The deformations in different samples are depending on the degree of prestressing as indicated earlier in Mirshekari et al. (2015) and Mirshekari et al. (2016). In this specific case properly due to variations of the properties of concrete the results for B20 and B30 are quite close. On similar way, but due to increased amount of reinforcement for B30+1, the results about deformability of B40 and B30+1 are similar. B40 having similar ultimate strength as B0, B20 and B30 as expected. The ultimate capacity of B30+1 is significantly higher than other BFRP reinforced beams due to usage of three BFRP bars as bottom reinforcement.

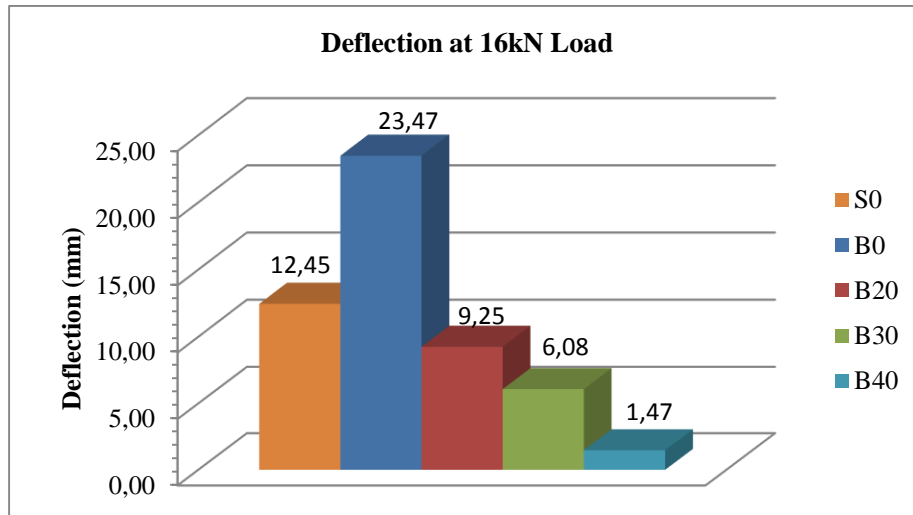


Figure 4: Deflection at ultimate load for steel reinforced beam

Comparison of the deflections at mid-span is conducted for load of 16kN as it is the ultimate load for the steel reinforced sample (Figure 4). Unprestressed BFRP beam (B0) is having higher deformations than S0 as expected. All other samples at this level of loading are less deformable than S0.

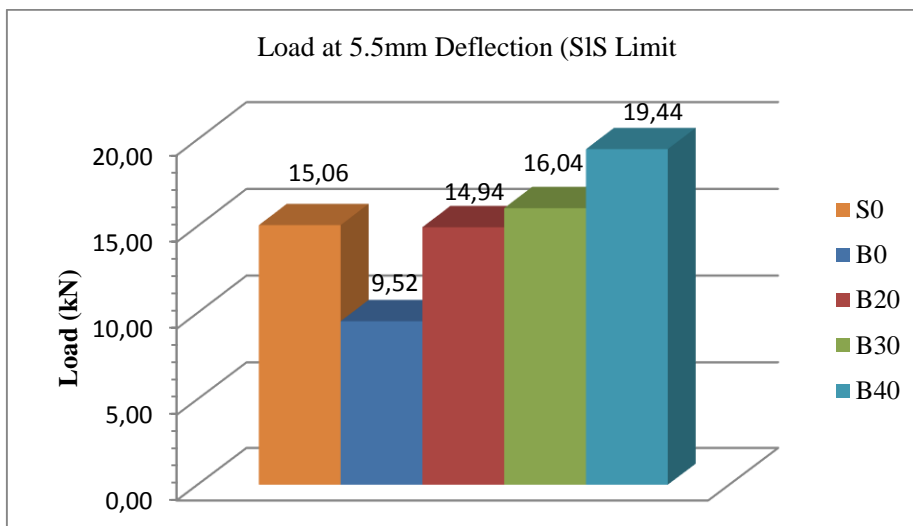


Figure 5: Load at 5.5mm deflection (SLS limit)

Figure 5 shows another comparison between obtained results and conducted on basis of achieving limiting defamation according to SLS requirement on basis of span divided by 360 according to UK national annex (BSI, 2005). This limit of deformations the corresponding load for S0 is 15.06 kN and B30 and B40 are having higher load than steel reinforced beam.

CONCLUSIONS

Based upon the findings of the experimental work the following conclusions were made:

- The prestressing of BFRP reinforced beams is resulting in reducing of their deformability.
- Prestressing equal or higher than 30% of ultimate load for the bars is sufficient to ensure higher stiffness of BFRP reinforced beams in comparison with steel reinforced beam.
- Increasing the amount of the tensile reinforcement with 50% (B30+1 sample) results in increase of the ultimate capacity and decrease of the deformability.

ACKNOWLEDGMENTS

The authors would like to express their gratitude to Magmatech UK for sponsoring this investigation with BFRP reinforcement and to the technical staff in Kingston University for their support during the experiments.

REFERENCES

- ACI 440.1R-15 (2015), *Guide for the Design and Construction of Structural Concrete Reinforced with Fiber-Reinforced Polymer (FRP) Bars*, American Concrete Institute, Farmington Hills, MI, USA.
- ACI 440.4R-04. (2011), *Prestressing Concrete Structures with FRP Tendons, Reported by ACI Committee 440*, American Concrete Institute, Farmington Hills, MI, USA.
- British Standards Institution (BSI), (2005). NA to BS EN 1993-1-1:2005, 7.2.1(1)B". *UK National Annex to Eurocode 3: Design of steel structures, Part 1-1: General rules and rules for buildings*. London: BSI, 2005.
- CAN/CSA-S06-06, (2006), *Canadian Highway Bridge Design Code*, Canadian Standard Association, Toronto, Ontario, Canada.
- C.J. Burgoyne (1992), *Aramid fibres for civil engineering applications, in Construction Materials*, Reference Book, ed. D.K.Doran, Butterworths.
- E. Ferrier, O. Rabinovitch, L. Michel (2016). "Mechanical behavior of concrete–resin/adhesive–FRP structural assemblies under low and high temperatures", *Construction and Building Materials*, 127, 1017-1028.
- E.R. Thorhallsson, B.S. Jonsson, (2012), "Test of prestressed concrete beams with BFRP tendons". *Proceedings of the Sixth International Conference on FRP Composites in Civil Engineering (CICE 2012)*, Rome, June 13–15. Rome, Italy
- E.R. Thorhallsson, S.H. Gudmundsson, (2013) "Test of prestressed basalt FRP concrete beams with and without external stirrups" *In proceedings of Fib symposium Engineering a Concrete future: Technology, modelling & Construction*, At Tel Aviv. Israel
- L.P. Ye, P. Feng, K. Zhang, L. Lin, W.H. Hong, Q.R. Yue, N. Zhang, T. Yang (2003) "FRP in Civil Engineering in China: Research and Applications", *Proceedings of the Sixth International Symposium in FRP Reinforcement for Concrete Structure (FRPRCS-6)*, K. H. Tan., Singapore, 1401 pp.
- M. Lahouar, J.F. Caron, N. Pinoteau, G. Forêt, K. Benzarti (2017). "Mechanical behavior of adhesive anchors under high temperature exposure: Experimental investigation", *International Journal of adhesion and adhesives*, 78, 200-211.
- M. Mirshekari, T. Donchev, D. Petkova, M. Limbachiya, (2015), "Influence of the Degree of Prestressing on the Behaviour of BFRP Reinforced Beams", *The 12th International Symposium on Fiber Reinforced Polymers for Reinforced Concrete Structures (FRPRCS-12)*, Nanjing, China.
- M. Mirshekari, T. Donchev, D. Petkova, M. Limbachiya, (2016), "Deformability of Pretensioned PC Beams with BFRP Reinforcement" *8th International Conference on Fibre-Reinforced Polymer (FRP) Composites in Civil Engineering (CICE 2016)*, 14-16 December 2016, Hong Kong, China
- M. Pearson, T. Donchev, (2013) "Experimental Study on the Behavior of Prestressed Concrete Beams with Internal BFRP Reinforcement", *Conference, 11th International Symposium On Fiber Reinforced Polymers For Reinforced Concrete Structures (FRPRCS-11)*, Guimarães, Portugal
- P. Crossett, S. Taylor, T. Robinson, M. Sonebi, E. Garcia-Taengua, P. Deegan, L. Ferrara, (2015) "The flexural behaviour of SCC beams pre-stressed with BFRP", *In Proceedings of the 7th Biennial Conference on Advanced Composites In Construction. Advanced Composites in Construction (ACIC 2015)*, 09-11 Sep 2015, Cambridge. NetComposites Limited , pp. 62-67.
- U. Meier (1992) "Carbon Fiber Reinforced Polymer: Modern Materials in Bridge Engineering", *Journal of the International Association for Bridge and Structural Engineering*, V. 2, No. 1, pp. 7-12, doi: 10.2749/101686692780617020



EXPERIMENTAL INVESTIGATION ON FLEXURAL BEHAVIOR OF UHPC PANELS REINFORCED WITH FRP BARS

Jiaxing Chen¹, Zhi Fang^{1,2}

¹ College of Civil Engineering, Hunan University, Changsha and China;

² College of Civil Engineering, Hunan University, Changsha and China;

KEYWORDS:

FRP; UHPC ; Panel; Flexural capacity; Equation

ABSTRACT:

The Fiber-Reinforced Polymer (FRP) has many advantages, such as high tensile strength, low self-weight and excellent corrosion resistance, and its application has been growing to solve the problem caused by corrosion of conventional steel reinforcement. However, the FRP bar can be seen as a type of liner-elastic material and has an extremely low ductility, which may lead to a brittle failure of concrete structure. Moreover, the FRP has a low Young's modulus, reducing the flexural stiffness of concrete slab and causing the increase of the crack width. The applications of Ultra-High Performance Concrete (UHPC) are beneficial to improve the flexure capacity and ductility of concrete structures reinforced with FRP bars due to its high strength and compressive strain. This paper presented the experimental results of 8 simply supported panels and studied the effect of reinforcement ratio, type of FRP bar and girder dimension on flexural performance of UHPC panels reinforced with FRP. Experimental results indicated that no obvious improvement of flexural capacity was obtained by increasing reinforcement ratio under concrete crushing failure pattern. The ultimate load increased only by 14.5%, but the reinforcement ratio increased by 39%. Failure mode show that the number of cracks increases and crack spacing decrease with reduce of girder dimension. Based on reasonable assumptions, a predicted equation for flexural capacity of UHPC panels reinforced with FRP bars was derived. Moreover, the results from this set of experimental tests and others literature were compared with the predicted results. Comparison results indicate that the equation can accurately predict the ultimate load of FRP reinforced UHPC panels.

INTRODUCTION:

The corrosion of steel reinforcement is the main problem in concrete structure. The use of FRP (fiber-reinforced-polymer) with high tension strength and resistance to corrosion has been growing to overcome the common problem caused by corrosion of steel reinforcement [1]. However, the low compression strength and strain of NC (normal concrete) restrict the development of excellent mechanical properties of FRP bars. Moreover, FRP reinforced NC member has low cracking load, influencing the serviceability performance of structure. As a solution, the application of UHPC (Ultra-High-Performance Concrete) can significantly solve above problems. The UHPC is a type of very homogenous and dense material with superior characteristics such as high strength in compression and tension, ductility, and durability [2, 3], which is different from the conventional concrete. Due to its pronounced brittleness, the incorporation of fibers is required [4].

In recently decades, many studies have been carried out to research the flexural behavior of concrete panel reinforced with FRP bars. In 2016, Weina M et al. [5] studied the effect of the layer number of glass fiber-reinforced-polymer (GFRP) girds reinforcement on flexural performance of UHPC panels in three-point bending test. The experimental results indicated that the flexural capacity and energy dissipation can be enhanced by GFRP girds. In 2011, flexural performance and serviceability property of 24 full-scale beams reinforced with carbon-, glass-, and aramid- fiber-reinforced-polymer bars were investigated in four-point bending test by Kassem C et al. [1]. Test results shown that FRP reinforced concrete beam have high degree of deformability before failure and CSA S806-02 (CSA 2002) [6] can accurately predict deflection of the type of beams at the service-load levels. In 2016, Doo-Yeol Y et al. [7] researched the effect of reinforcement ratio on flexural manner of ultra-high-performance fiber-reinforced concrete (UHPFRC) reinforced with GFRP bars under three-point static loading. The study revealed that the post-cracking stiffness, flexural bending capacity and deformability increased with the improvement of reinforcement ratio. In 2017, M.W. Goldston et al. [8] researched the influence of reinforced ratio and concrete strength on the flexural behavior of high strength concrete (HSC) and ultra-high strength concrete (UHSC) reinforced with GFRP bars in three-point loading. Experimental results shown that over-reinforced GFRP

bar concrete beam has better ductility than under-reinforced beam, while the energy absorption improved with the increase of concrete strength.

This paper presents the experimental results of three-point bending test of UHPC panels reinforced with GFRP, CFRP and BFRP bars or girds. Three parameters in terms of type, gird dimension and reinforcement ratio were investigated. Based on reasonable assumptions, an equation was derived to calculate the flexural capacity of UHPC panels, and its accuracy was verified by the comparison between test values and predicted values.

EXPERIMENTAL PROGRAM

Specimen Fabrication and Test Setup

All specimens were designed to have same dimensions and concrete strength. The proportion of mix was presented in Table 1. Order to achieve a high strength as rapidly as possible and ensure minimal shrinkage of the UHPC matrix, all specimens, cubes and prisms were covered with plastic sheets to cure under room temperature for two days, then steam-cured for 3 days after removing the molds in a curing room (the temperature was maintained at 90°C and the relative humidity was above 95%). In addition, the temperature was dropped with a speed of 12°C per hour before removing the specimens from the curing room. Three parameters researched were the type of FRP bars, reinforcement ratio and gird dimension respectively. The meaning of specimen code was explained in Fig 1. Fig 2(a) and Table 2 illustrated the details of the UHPC panels.

Table 1 Mix proportions

W/B (%)	Material (kg/m ³)						
	Cement	Silica Fume	Fine Sand	Ground Quartz	Water Reducer	Steer Fibers	Water
19	745	186.3	819.5	275.7	17.9	157.2	149

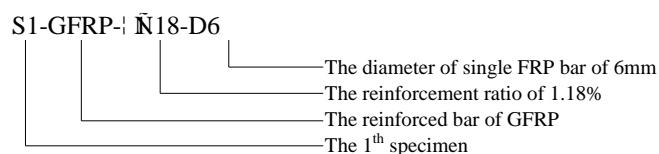


Fig.1 The meaning of specimen code

After 5 days of curing, the specimens were tested in flexural by using a three-point flexural test. Two steel piers supply the simply support system. The loading device obtains a hydraulic jack with a capacity of 1000 kN and a load cell with a capacity of 50 kN. The panels were loaded at a speed of 0.25 kN per three minutes in the stage prior to cracking, while a speed of 0.5 kN per five minutes in the post cracking stage. The mid-span deflection and the settlements of the two roller supports were recorded with three dial gauges installed along the length of specimen. On the load-applied board, the test was performed with a highly elastic rubber board over it in order to avoid the stress concentration. Fig 2(b) shows the three-point bending test setup.

Table 2 Specimen details

Specimen Code	H (mm)	$f_{cu,k}$ (MPa)	E_c (GPa)	f_{tu} (MPa)	E_f (GPa)	ρ_f (%)	Gird dimension (mm)
RS	60	156.5	46.7	--	--	--	--
S1-GFRP-p1.18-D6	60	149.9	46.1	920	48	1.18	--
S2-CFRP-p1.18-D8	60	149.9	46.1	2242	158	1.18	--
S3-CFRP-p1.64-D8	60	149.9	46.1	2242	158	1.64	--
S4-BFRP-p2.11-D4	60	152.5	46.4	980	45	2.11	25×25
S5-BFRP-p2.11-D3	60	152.5	46.4	980	45	2.11	50×50
S6-BFRP-p2.11-D12	60	152.5	46.4	1030	70	2.11	100×100

Note: H = the slab height; $f_{cu,k}$ = the compressive strength; E_c = the Young's modulus of UHPC; f_{tu} = the ultimate tension strength of FRP bar; E_f = the Young's modulus of FRP; ρ_f = the reinforcement ratio.

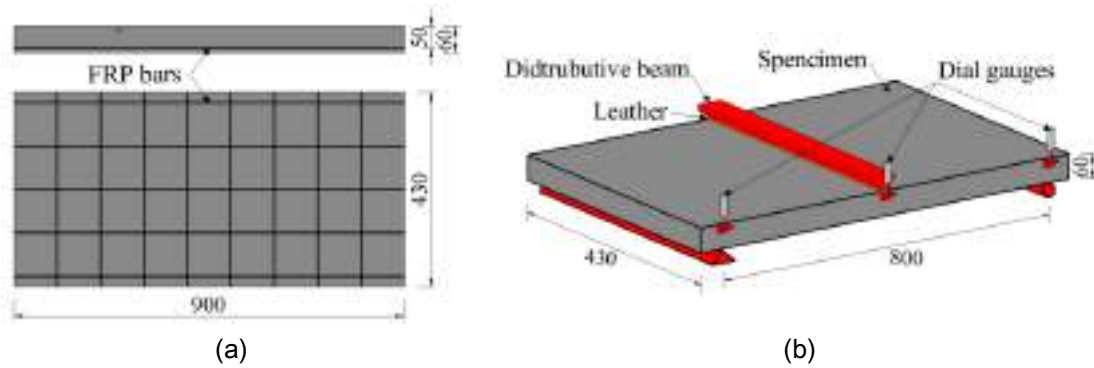


Fig.2 Slab specimen: (a) details (b) flexural test setup

Results and Discussion

The UHPC slab with no FRP reinforcement was coded as RS and designated as the reference specimen. Specimen S1-GFRP- ρ 1.18%-D6 and S2-CFRP- ρ 1.18%-D8 reinforced with single-layer GFRP bar and single-layer CFRP bar respectively research the effect of the type of FRP bar on flexural performance. The influence of the reinforcement ratio was studied on S2 and S3-CFRP- ρ 1.64%-D8 reinforced with single-layer CFRP bar. The effect of the gird dimension was studied on three slabs (both S4-BFRP- ρ 2.11%-D4 and S6-BFRP- ρ 2.11%-D12 reinforced with single-layer BFRP gird, S5-BFRP- ρ 2.11%-D3 reinforced with dual-layer BFRP girds). The slabs show excellent ductile manner because of the bridging behavior of the steel fiber in UHPC. Fig 3(a) shows the load-deflection curve of RS that deflection continue to increasing in the post cracking stage, which is different from normal concrete (NC) panel.

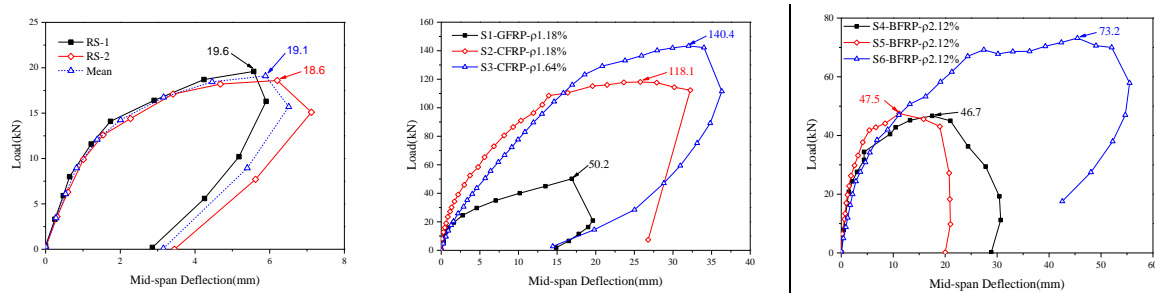


Fig.3 The load-deflection curves

Table 3 presents the average values of the flexural test results. The Flexural performance of UHPC slabs were estimated according to the peak load and the deflection at peak load. The percentage values were calculated as ratios of a given response to that of the reference slab. All specimens have almost same cracking load except RS, which indicates the type of FRP and reinforcement ratio have no effect on P_{ck} . The load-deflection relationships of the tested slab were shown in Fig 2, a, b, c. It was obviously that the ultimate capacity and the area under the load-deflection curve of slabs reinforced with FRP were bigger than reference specimen, which indicates that the UHPC panel reinforced with FRP can be thicker than NC slab and have better energy dissipation capacity. Fig 2(b) presents the influence of reinforcement ratio and the type of FRP bar. The peak load of specimen S3 was increased by 14.5%, but an increase of 39% in reinforcement ratio, respectively compared with S2, which means that the improved reinforcement ratio cannot distinctly increase the panel's flexural capacity because the failure modes of S2 and S3 were compression failure. Meanwhile, the peak load of S2 gained significantly promotion compared with S1 because of higher tension strength of CFRP.

Table 3 The summary of test results

Specimen code	P_{ck} (kN)	Δ_{ck} (mm)	P_{cu} (kN)	Percentage	Δ_{cu} (mm)	Percentage	Failure mode
RS	12.6	1.542	19.1	0	6.204	0	--
S1-GFRP- ρ 1.18-D6	15.9	0.907	50.2	162.8	16.902	172.4	TF
S2-CFRP- ρ 1.18-D8	16.0	0.461	118.1	515.5	19.595	215.8	CF
S3-CFRP- ρ 1.64-D8	15.2	0.419	135.1	607.3	32.03	258.3	CF
S4-BFRP- ρ 2.11-D4	15.4	0.752	47.5	148.7	18.968	205.7	CF

S5-BFRP- ρ 2.11-D3	16.8	1.123	46.7	144.5	21.009	238.6	CF
S6-BFRP- ρ 2.11-D12	16.3	1.733	73.2	283.2	45.461	632.8	CF

Note: P_{ck} = the cracking load; Δ_{ck} = the deflection at P_{ck} ; P_{cu} = the ultimate flexural capacity; Δ_{cu} = the deflection at P_{cu} ; T_F = the tension failure; C_F = the compression failure.

The experimental on material properties of BFRP gird illustrate that the BFRP with a diameter of 12mm has higher tension strength and Young's modulus than other types. And thus, the ultimate load of S6 has remark improvement. The specimen S4 and S5 have similar flexural capacity resulting from same reinforcement ratio and S4 has bigger deflection than S5 at the same one load level because of lower stiffness of S4.

Besides, the UHPC slab reinforced with CFRP has better serviceability. In the post cracking stage, the UHPC panel can resist greater load until CFRP fracture. Moreover, the combination of two types of ultra-high-performance materials can distinctly relieve the influence of environment on mechanical behavior. A reason for these manners is that the CFRP and UHPC have excellent mechanical properties and high corrosion resistance.

Failure pattern

All UHPC slabs were uncracked initially. Initial crack appeared when the cracking load was reached in mid-span. And these cracks were transverse and perpendicular to the direction of the bending stress in mid-span. Moreover, more cracks appeared and extended along the span length of slab. When a load level corresponding to about 65% of the ultimate moment M_u , no crack continued to appearing, and the width of the existing cracks increased with the increase of load. Fig 4 shows the failure patterns of the tested specimens in terms of bottom view and elevation view. The low tension strength of GFRP bars (approximately corresponding to 33% that of the CFRP) lead to the rupture of bars prevented the extension of crack. Thus, specimen S1 has lower crack depth. Fig 4(b) and (c) indicates that S3 has more the number of cracks and lower crack depth than S2, which demonstrates that reduced bars spacing increase the number of cracks and increased reinforcement ratio improve energy dissipation. It was, while, obviously from Fig 4(d) to (f) that reduced gird dimension can increase the number of cracks and decrease the crack spacing, and then improved the energy dissipation.

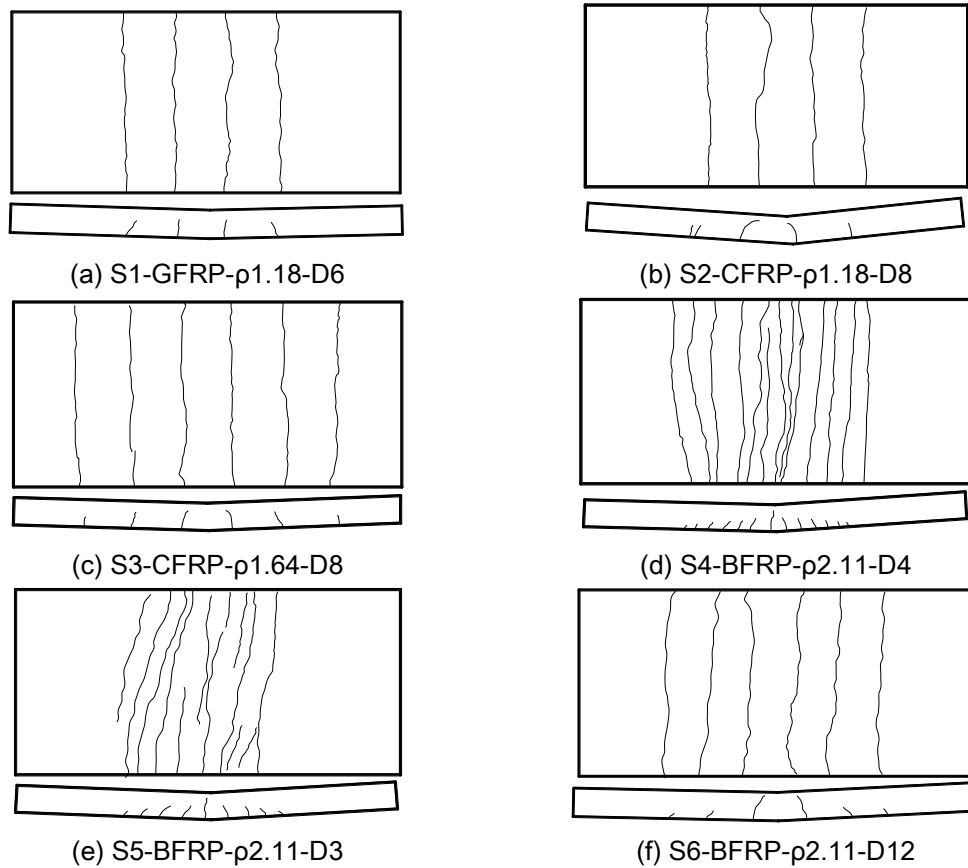


Fig.4 The failure patterns of specimens

PREDICTED EQUATION

Order to predict the flexural capacity of UHPC panels reinforced with FRP, the equations in terms of three failure patterns were conducted with the application of the following basic assumptions:

Under flexural load, the slab cross-section should be in accordance with the plane section assumption.

The Stress-strain relationship of concrete compressive was expressed as Eq. (1).

Ignoring the tensile strength of UHPC.

The debonding at the FRP-UHPC interface will not occur.

The FRP is a type of linear elastic material.

$$\sigma_c = f_c \left[1 - \left(1 - \frac{\varepsilon_c}{\varepsilon_0} \right)^n \right] \quad (\varepsilon_c < \varepsilon_0) \quad (1-1)$$

$$\sigma_c = f_c \quad (\varepsilon_0 \leq \varepsilon_c \leq \varepsilon_{cu}) \quad (1-2)$$

$$n = 1.2 - 0.001(f_{cu,k} - 100) \quad (1-3)$$

$$\varepsilon_0 = 0.0025 + (f_{cu,k} - 100) \times 10^{-5} \quad (1-4)$$

$$\varepsilon_{cu} = 0.0041 + (f_{cu,k} - 100) \times 10^{-5} \quad (1-5)$$

$$f_c = 0.7 f_{cu,k} \quad (1-6)$$

where: σ_c = the concrete strain at ε_c ; f_c = the prismatic strength; $f_{cu,k}$ = the compressive strength; ε_0 = the compressive strain at f_c ; ε_{cu} = the ultimate compressive strain.

Referring the China Code (GB 50010-2010) [9], equivalent rectangular stress block replaced the actual stress layout, as shown in Fig 5. The strength and depth of rectangular stress block are $\alpha_1 f_c$ and $\beta_1 x_c$, respectively, where α_1 and β_1 are the rectangular stress block equivalent coefficient.

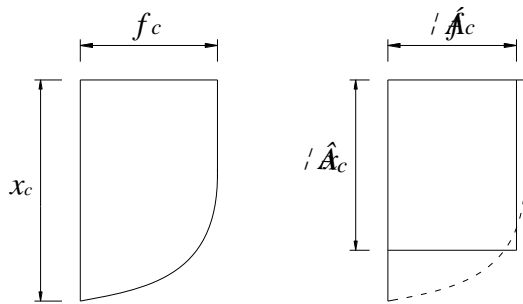


Fig.5 Equivalent rectangular stress block

In according to the equivalence principle, the value of α_1 and β_1 is calculated through the equation as:

$$\alpha_1 = \frac{k_1}{\beta_1} = \frac{k_1}{2(1-k_2)} \quad (2-1)$$

$$\beta_1 = 2(1-k_2) \quad (2-2)$$

$$k_1 = \frac{\int_0^{\varepsilon_{cu}} \sigma_c(\varepsilon) d\varepsilon}{f_c \varepsilon_{cu}} \quad (2-3)$$

$$k_2 = \frac{\int_0^{\varepsilon_{cu}} \sigma_c(\varepsilon) \varepsilon d\varepsilon}{k_1 f_c \varepsilon_{cu}^2} \quad (2-4)$$

Limitation failure

The limitation failure means that the stress of FRP bars reach the ultimate value when the concrete in compressive zone occur crush failure. The failure mode is a kind of critical state which distinguish FRP fracture failure and concrete crush failure. As shown in Fig. 6(a), the limitation compressive depth x_c and reinforcement ratio ρ_{fb} can be calculated as:

$$\alpha_1 f_c b \beta_1 x_c = \rho_{fb} b h_0 f_{fu} \quad (3-1)$$

$$\frac{x_c}{x_t - \alpha_s} = \frac{\varepsilon_{cu}}{\varepsilon_{fu}} \quad (3-2)$$

$$x_t = h - x_c \quad (3-3)$$

$$\varepsilon_{fu} = \frac{f_{fu}}{E_f} \quad (3-4)$$

Combining equation (3-1) to (3-4), x_c , ξ_b and ρ_{fb} can be obtained by the following equation:

$$x_c = \frac{\varepsilon_{cu} (h - \alpha_s)}{\frac{f_{fu}}{E_f} + \varepsilon_{cu}} \quad (3-5)$$

$$\xi_b = \frac{\beta_1}{1 + \frac{f_{fu}}{E_f \varepsilon_{cu}}} \quad (3-6)$$

$$\rho_{fb} = \frac{\alpha_1 f_c}{f_{cu}} \times \frac{\beta_1}{1 + f_{fu}/E_f \varepsilon_{cu}} \quad (3-7)$$

Thus, the calculate equation of flexural bearing capacity can be expressed as:

$$M_u = \rho_{fb} b h_0 f_{fu} \left(h_0 - \frac{\beta_1 x_c}{2} \right) \quad (4)$$

where: b = the width of section; h, h_0 = the depth and the effective depth, respectively; α_s = the distance between action point of FRP bars' tension resultant force and the edge of tension zone; f_{fu} = the ultimate tension strength of FRP bars; x_c = the depth of compressive zone; E_f = the Young's modulus of FRP bars; ξ_b = the relative limitation compressive depth ($\beta_1 x_c/h_0$); ρ_{fb} = the limitation reinforcement ratio; M_u = the ultimate flexural bearing capacity.

Compression failure

The compression failure means that the concrete in compressive zone occur crush failure when the stresses of FRP bars don't attain the ultimate value. As shown in Fig. 6(b), the x_c and the ultimate flexural bearing M_u can be obtained as:

$$\alpha_1 f_c b \beta_1 x_c = \rho_f b h_0 E_f \varepsilon_f \quad (5-1)$$

$$\frac{x_c}{x_t - \alpha_s} = \frac{\varepsilon_{cu}}{\varepsilon_f} \quad (5-2)$$

$$x_t = h - x_c \quad (5-3)$$

Combining equation (5-1) to (5-3), x_c and ε_f can be calculated as:

$$x_c = \frac{2h_0}{1 + \sqrt{1 + \frac{4\alpha_1 \beta_1 f_c}{\rho_f E_f \varepsilon_{cu}}}} \quad (5-4)$$

$$\varepsilon_f = 2\varepsilon_{cu} \left(\sqrt{1 + \frac{4\alpha_1 \beta_1 f_c}{\rho_f E_f \varepsilon_{cu}}} - 1 \right) \quad (5-5)$$

The calculate equation of ultimate capacity M_u can be expressed as:

$$M_u = \alpha_1 \beta_1 b f_c x_c \left(h_0 - \frac{\beta_1 x_c}{2} \right) \quad (6)$$

where: ρ_f = the reinforcement ratio; ε_f = the strain of FRP bars.

Tension failure

The tension failure means that the FRP bars rupture while the strains of concrete in compressive zone don't attain ultimate value. So, equivalent rectangular stress block can't be used. As shown in Fig. 6(c), the x_c and the ultimate flexural bearing M_u can be obtained as:

$$b \int_0^{x_c} \sigma_c(\varepsilon) dx = \rho_f b h_0 f_{fu} \quad (\varepsilon < \varepsilon_{cu}) \quad (7-1)$$

$$\frac{x}{x_c} = \frac{\varepsilon}{\varepsilon_c} \quad (0 \leq x \leq x_c) \quad (7-2)$$

$$\frac{x_c}{x_t - \alpha_s} = \frac{\varepsilon_c}{\varepsilon_{fu}} \quad (7-3)$$

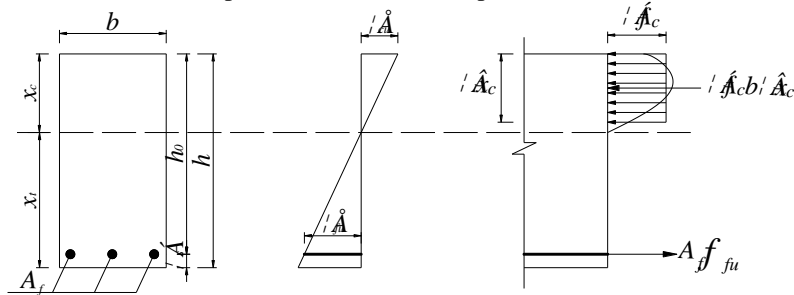
$$x_t = h - x_c \quad (7-4)$$

According to Eq.7, x_c and ε_c can be calculated, while the x_0 and M_u can be expressed as:

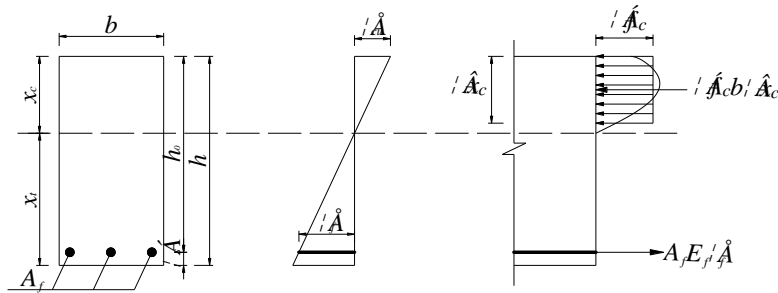
$$b \int_0^{x_c} \sigma_c(\varepsilon) x dx = x_0 b \int_0^{x_c} \sigma_c(\varepsilon) dx \quad (8-1)$$

$$M_u = \rho_f b h_0 f_{fu} (h_0 - x_c + x_0) \quad (8-2)$$

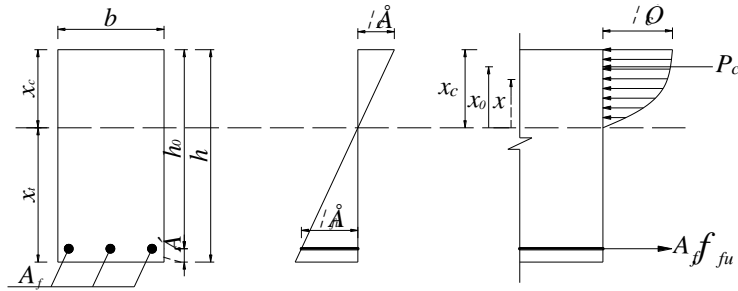
where: x = the distance between any point in compressive zone and the neutral axis; ε = the concrete strain at x ; x_0 = the distance between action point of concretes' compression resultant force and the neutral axis.



(a)



(b)



(c)

Fig.6 The calculation of flexural bearing capacity

THE COMPARISONS BETWEEN THE TEST RESULTS AND PREDICTED VALUES

In this section, the test results obtained in this experimental and other collected from reference literature were compared with the predicted values of derived equations. Table 4 presents the obtained results from the comparisons.

Table 4 The summary of predicted and tested values

Specimen	$f_{cu,k}$ (MPa)	ϵ_{cu} ($\mu\epsilon$)	P_{exp} (kN)	P_{pre} (kN)	P_{exp}/P_{pre}	Failure mode
S1-GFRP-p1.18-D6	149.9	4598	50.2	45.2	1.11	FRP rupture
S2-CFRP-p1.18-D8	149.9	4598	118.1	106.9	1.10	Compression
S3-CFRP-p1.64-D8	149.9	4598	135.1	120.7	1.12	Compression
S4-BFRP-p2.11-D4	152.5	4625	47.5	43.3	1.10	Compression
S5-BFRP-p2.11-D3	152.5	4625	46.7	43.3	1.08	Compression
S6-BFRP-p2.11-D12	152.5	4625	73.2	65.5	1.12	Compression
Weina Meng [5]						
U1G	127.5	4370	24.2	21.8	1.11	Compression
U2G	127.5	4370	24.9	22.4	1.11	Compression
Doo-Yeol Yoo [7]						
UH-G2	193.4	5034	164.1	150.2	1.09	FRP rupture
UH-G6	193.4	5034	253.6	229.9	1.10	Compression

Note: P_{exp} = the experimental results; P_{pre} = the predicted values.

Fig 7 shows the ratio of experimental-to-predicted flexural capacity. The data indicate that the equation underestimated the ultimate load under failure condition because of ignorance of tension strength of UHPC, while, the deviation was controlled at approximately 10%. Thus, it is reasonable to consider that the predicted equation can estimate the flexural capacity of UHPC panels reinforced FRP bars.

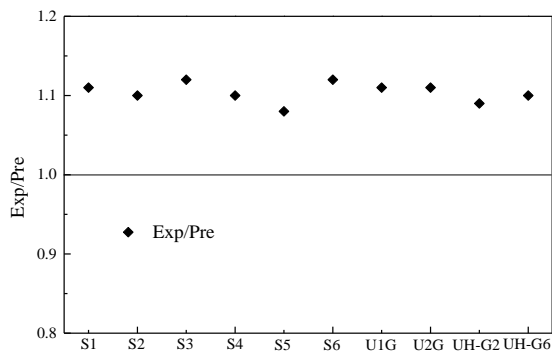


Fig.7 The ratio of experimental-to-predicted values

CONCLUSIONS

This paper researched the flexural performance of UHPC panels reinforced with FRP bars by three-point bending test, and the predicted equation for flexural capacity was proposed. The conclusions can be expressed as followings:

1. Two typical flexural failure modes of UHPC panel reinforced with FRP bars were observed, including FRP rupture and concrete crushing. Load-deflection curves show linear behavior until cracking, and almost linearly after cracking until failure with a greatly reduced slope.
2. No obvious improvement of flexural capacity was obtained by increasing reinforcement ratio under concrete crushing failure pattern. The ultimate load increased only by 14.5%, but the reinforcement ratio increased by 39%.
3. The number of cracks increase and crack spacing decrease with reduce of gird dimension.
4. An equation with ignorance of tension strength of UHPC for flexural capacity of UHPC panels reinforced with FRP bars was derived. The data shows that it is accurate to the predict equation the flexural capacity.

ACKNOWLEDGMENTS

This research is supported by The National Key Research and Development Program of China (Grant No.2017YFC0703008-01).

REFERENCE

- [1] Kassem C, Farghaly A S, Benmokrane B. Evaluation of Flexural Behavior and Serviceability Performance of Concrete Beams Reinforced with FRP Bars[J]. *Journal of Composites for Construction*, 2011, 15(5):682-695.
- [2] Shafieifar M, Farzad M, Azizinamini A. Experimental and numerical study on mechanical properties of Ultra High Performance Concrete (UHPC)[J]. *Construction & Building Materials*, 2017, 156:402-411.
- [3] Graybeal, B. Material Property Characterization of Ultra-High Performance Concrete. FHWA-HRT-06-103. FHWA, U.S. Department of Transportation, 2006.
- [4] Richard, P., Cheyrezy, M., *Composition of Reactive Powder Concretes*, Cement and Concrete Research, Vol. 25, No. 7, 1995, pp. 1501-1511.
- [5] Meng, Weina, and K. H. Khayat. Experimental and Numerical Studies on Flexural Behavior of Ultra-High-Performance Concrete Panels Reinforced with Embedded Glass Fiber-Reinforced Polymer Grids. *Transportation Research Record Journal of the Transportation Research Board* 2592(2016):38-44.
- [6] Canadian Standards Association (CSA) (2002). "Design and construction of building components reinforced with fiber-reinforced polymers." CSA S806-02, Mississauga, ON, Canada.
- [7] Yoo D Y, Banthia N, Yoon Y S. Flexural behavior of ultra-high-performance fiber-reinforced concrete beams reinforced with GFRP and steel rebars[J]. *Engineering Structures*, 2016, 111:246-262.
- [8] Goldston M W, Remennikov A, Sheikh M N. Flexural Behavior of GFRP Reinforced High Strength and Ultra High Strength Concrete Beams[J]. *Construction & Building Materials*, 2017, 131:606-617.
- [9] Chinese Concrete Standard: GB 50010-2010. Code for design of concrete structures; August 2010.



AXIAL PERFORMANCE CAPACITY OF HOLLOW CONCRETE COLUMNS REINFORCED WITH GFRP BARS

Omar S. AlAjarmeh¹, Allan Manalo¹, Warna Karunasena¹, Brahim Benmokrane²

¹ Centre of Future Materials CFM, Faculty of Health, Engineering and Science, University of Southern Toowoomba 4350, Queensland, Australia. (Corresponding author: omar.alajarmeh@usq.edu.au)

² Department of Civil Engineering, University de Sherbrooke, Sherbrooke, Quebec J1K 2R1, Canada.

ABSTRACT:

Hollow concrete sections are widely used in bridge piers, electrical poles, and piles, owing to reduced material usage and high strength-to-weight ratio. However, environmental conditions can be the main reason that affect the performance of concrete elements reinforced with conventional steel by corrosion and rusting the internal reinforcements. In fact, repairing and rehabilitating structural deficient elements experiencing corrosion of steel reinforcements have cost many countries billions of dollars. To address this issue, the potential of hollow concrete sections reinforced with non-corrosive glass fibre reinforced polymer (GFRP) bars should be explored. In this study, four 250 mm diameter and 1000 mm high concrete columns longitudinally reinforced with 6 – 16 mm diameter GFRP bars and 10 mm diameter spirals spaced at 100 mm on centres were cast and tested under concentric compressive load. The effect of the inner-to-diameter ratio on the axial strength capacity and the overall behavior was investigated. This was achieved changing the inside hollow size from 40mm (HG40) and 65mm (HG65) to 100mm (HG100), in addition to a solid column (SG). Hollow concrete columns were tested concentrically until failure. The results showed that the stiffness was approximately same for all concrete columns, i.e. 180 kN/mm. However, the strength enhancement and confinement efficiency was more noticeable for columns with high than low inner-to-outer diameter ratio especially after the post peak stage. Similarly, the ductility factor was ascending as the inner-to-outer diameter ratio is increasing. The average contribution of GFRP bars in carrying the load was 12.2% and with the compressive strength of the GFRP bars around 51% of the tensile strength capacity at the maximum load.

Keywords: Hollow columns; concrete; GFRP bars; spirals; inner-to-outer diameter ratio; compressive behavior.

1. INTRODUCTION

Steel-reinforced hollow concrete columns (HCC) have higher structural efficiency due to their high strength-to-mass and stiffness-to-mass ratios than solid columns with the same area, therefore, it is widely utilized in piers, poles and piles. In contrast, many primary parameters can demonstrate the overall behavior of HCC such as: inner-to-outer diameter ratio, reinforcement ratio, volumetric ratio, and axial load ratio (Liang, et al., 2015, Mo and Nien, 2002, Zahn, et al., 1990). However, steel corrosion can affect this system since HCC is highly corrosion affected not only from the outer face but also from the inner face as well. Accordingly, corrosion can reduce the axial load capacity and damage the lateral confinement (Pantelides, et al., 2013). Therefore, the use of non-corroding reinforcement in hollow concrete columns is suggested to mitigate steel-corrosion problems and to understand the fundamental behavior of such columns under the applied loads.

Glass-fiber-reinforced-polymer (GFRP) composite bars as internal reinforcement in concrete structures has a worldwide acceptance due to some superior characteristics and increased durability performance (Nkurunziza, et al., 2005). Nowadays, it is been implementing in vast applications as beams, slabs, column, and walls due to its high strength and almost similar moduli of elasticity to that of concrete (Manalo, et al., 2014). Specifically, concrete columns has been widely experienced with GFRP reinforcement (Hadi, et al., 2016, Tobbi, et al., 2014). Correspondingly, similar behavior was concluded between RC columns reinforced with GFRP and steel reinforcements. However, GFRP-reinforced columns showed better post peak stability and ability to resist more lateral and cyclic loads than steel-reinforced concrete columns due to the high strain capacity and high confined strength provided by GFRP stirrups (Afifi, et al., 2013, Pantelides, et al., 2013). These results were also captures for GFRP-reinforced shear walls (Mohamed, et al., 2013).

Therefore, this paper aimed at investigating the axial performance of hollow concrete columns reinforced with GFRP bars and spirals as a first step in understanding the structural performance of this construction system. It focused on assessing the influence of the inner-to-outer diameter ratio and comparing between solid and hollow concrete columns reinforced with GFRP reinforcements.

2. MATERIALS AND SAMPLES DETAILS

Grade III #5 GFRP bars with a nominal diameter of 15.9 mm were used as longitudinal reinforcement in the circular hollow concrete columns. The transverse reinforcement was Grade III #3 GFRP spirals with a nominal diameter of 9.5 mm. The GFRP reinforcement was manufactured by pultruding glass fibers impregnated with modified vinyl-ester resin and had a sand-coated surface. Table 1 provides the mechanical properties of the GFRP bars as reported by Benmokrane, et al. (2017). On the other hand, column samples were cast with ready-mix concrete. The coarse aggregate had a maximum size of 10 mm and a slump of 105 mm, the average concrete compressive strength at 28 days was around 31.8 MPa, with a standard deviation of 3.54 MPa.

Five concrete columns 250 mm in diameter and 1 m in height were cast and tested. The spirals had an inner diameter of 180 mm. Four columns were fully reinforced with GFRP bars and spirals. All four columns contained six longitudinal reinforcing bars and GFRP spirals spaced 100 mm on centers along 500mm at mid-height, and at 50 mm along 250mm at the top and bottom of the columns to avoid premature failure due to stress concentration. The inner-to-outer diameter ratios of the hollow columns were achieved by placing a PVC pipe at the center of the specimens during concrete casting. The PVC pipes had outer diameters of 40 mm, 65 mm, and 90 mm, and a wall thickness of 1 mm. These diameters were based on the commercially available PVC pipes. A solid concrete column was also prepared and tested as a reference specimen. Figure 1 shows the cross sections of the tested columns, Table 2 provides the details of the various specimens and gives the reinforcement ratios and volumetric ratios of the columns. The specimens were designated as being either solid (S) or hollow (H), followed by the type of longitudinal reinforcement (G) regarding GFRP bars and the diameter in mm of the hollow core at the column center. For example, specimen HG65 is a hollow column reinforced with GFRP bars and has an inner core diameter of 65 mm.

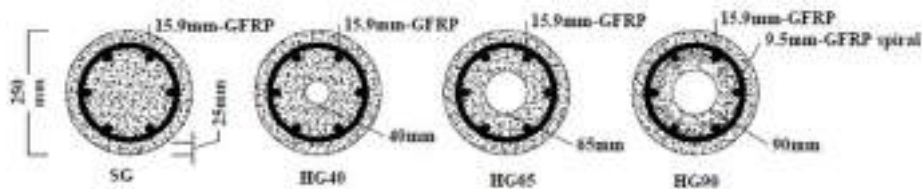


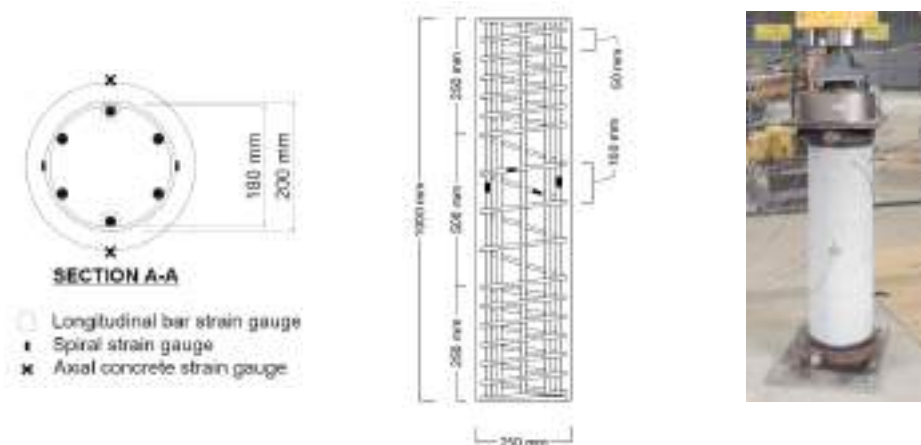
Figure 177: Cross section details

Table 54: Mechanical properties of the GFRP reinforcements

Bar	Bar diameter, Φ_b (mm)	Bar area A_b (mm ²)	Ultimate tensile strength, f_u (MPa)	Modulus of elasticity, E_{GFRP} (GPa)	Ultimate strain capacity, ϵ_u (%)
No.5- GFRP	15.9	198.5	1237.4	60.0	2.1
No.3- GFRP	9.5	70.8	1315.3	62.5	2.3

Table 55: Samples matrix and reinforcement details

	Inner core diameter (mm)	Inner-to-outer diameter ratio (D_i/D_o)	Inner concrete-wall thickness (mm)	Reinforcement ratio (%)	Volumetric ratio (%)
SG	0	0	-	2.41	1.49
HG40	40	0.16	70	2.47	1.56
HG65	65	0.26	57.5	2.59	1.69
HG90	90	0.36	45	2.78	1.92



(a) Location of strain gauges

(b) Test setup

Figure 178: Test setup

TEST RESULTS

Failure mode

Figure 3 shows the tested concrete columns after failure. Failure in all the tested samples initiated with the development of vertical and inclined hairline cracks at column mid-height. With increasing load, more hairline cracks developed, widened, and propagated along column height. This was followed by spalling of the concrete cover, rupturing or buckling of the longitudinal and transverse spiral reinforcement, and crushing of the confined concrete core. The mechanism and extent of rupture of the longitudinal and transverse GFRP reinforcement varied among the tested columns. SG, HG40, and HG65 exhibited almost the same failure behavior: the lateral spirals fractured first, followed by longitudinal-bar failure, and concrete crushing. Figure 3(a) shows the buckled and ruptured longitudinal and spiral GFRP reinforcement in SG. Figure 3(b) shows HG40 experienced more severe rupture of longitudinal GFRP bars than SG. This could be due to the premature concrete cracks observed at the bottom of HG40 extending to the cracks at column mid-height. Figure 3(c) shows rupture in all of the longitudinal GFRP bars and spirals in HG65. Figure 3(d) shows the rupture of the longitudinal GFRP reinforcement in HG90. Interestingly, while HG90 evidenced no rupture of GFRP spirals, its concrete cover spalled along almost the entire column height. There was also concrete crushing observed at the inner concrete wall, as shown in Figure 4(c). Figure 6 gives a more detailed photo of the failure behavior in the test region. Figure 4(a) clearly shows the reinforcement failure in SG and HG40. Figures 4(b), and 4(c), respectively, depict the reinforcement failure in HG65, and HG90. Moreover, once failure occurred, inclined shear-failure planes were observed in the crushed zone of the failed columns. The inclined failure plane was defined by the failure test zone, as seen in Figure 3.

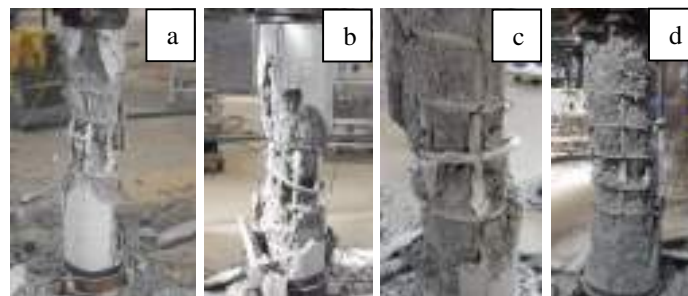


Figure 179: Failure mechanism of samples

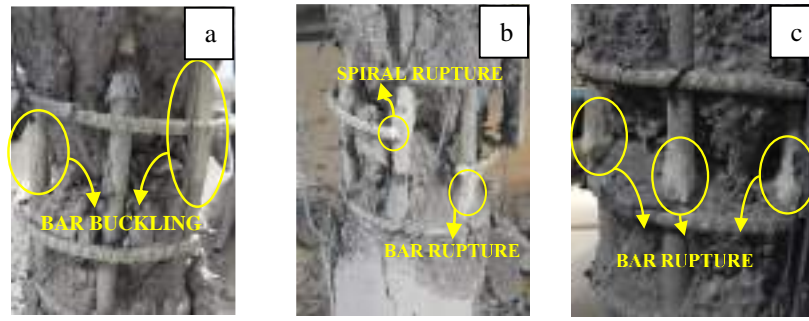


Figure 180: Reinforcement failure

Load-deformation

Figure 5 shows the actual load and deformation behavior of all the tested columns. Firstly, SG exhibited almost linear load–deformation behavior up to an applied load of 1500 kN and axial deformation of 10 mm. Brief nonlinear behavior was then observed until the maximum load of 1588 kN was reached at a deformation of 11.4 mm. This nonlinear load–deformation behavior is due to the development and propagation of cracks in the concrete cover. The concrete cover then spalled, at which point the load capacity dropped to 1306 kN and the deformation was 13 mm. Afterward, the load increased linearly to 1368 kN and deformation of 15.7 mm. This increase in load can be attributed to the transverse GFRP spirals confining the concrete core. The longitudinal and spiral GFRP reinforcement then ruptured, resulting in final column failure, as shown in Figure 4.

The load and deformation behavior of HG40, HG65, and HG90 were similar to that of SG up to the maximum applied load. The maximum load achieved for columns HG40, HG65, and HG90 was 1408 kN, 1559 kN, and 1411 kN, respectively. After the maximum load was reached, the concrete cover of all columns was removed, which decreased the load capacity. The load dropped to 1260 kN, 1251 kN, and 1267 kN for HG40, HG65, and HG90, respectively. It is interesting to note that the capacity of all the columns was almost the same just after the spalling of the concrete cover, despite the different effective cross-sectional areas. This could be due to the confinement efficiency of the spiral reinforcement, as will be discussed in the next section. HG40 and HG90 almost reached load capacity with increasing deformation before final failure. In contrast, the load capacity of HG65 increased to 1458 kN with a deformation of 19.4 mm before the longitudinal and spiral GFRP reinforcement ruptured. Table 4 shows the test results for the four concrete columns, including peak loads, deformations, and GFRP-bar contribution.

Table 56: Test results

Column	P_{n1} (kN)	P_{n2} (kN)	f'_{cc} (MPa)	f'_{cc}/f'_{co}	Δ_1 (mm)	Δ_2 (mm)	Ductility factor	$\epsilon_{u,bar}$ ($\mu\epsilon$)	P_{bars} (kN)	Spiral strain ($\mu\epsilon$)
SG	1588	1368	43.2	1.6	11.41	15.64	1.37	2630	187.4	-
HG40	1408	1295	43.0	1.59	10.94	14.95	1.37	2520	179.6	9091
HG65	1559	1458	51.9	1.92	10.51	19.42	1.85	2710	193.2	12104
HG90	1411	1304	52.1	1.93	10.41	23.89	2.30	2320	165.4	12733

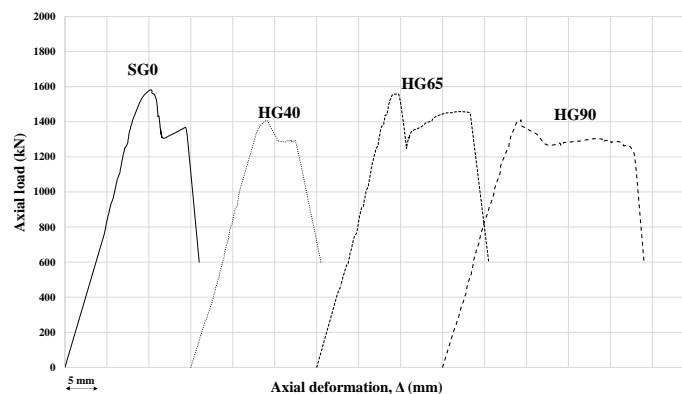


Figure 181: Load-deformation behaviour

Ductility and confined strength

Ductility was examined of GFRP-reinforced hollow concrete columns to be compared with the latter were found to have brittle or limited ductile behavior (Lignola, et al., 2007, Yazici, 2012). In this study, the ductility factor (DF) μ_{Δ} was calculated (Eq.1) as the ratio of axial deformation Δ_2 at 85% of the first peak load (P_{n1}) or maximum axial deformation to the axial deformation Δ_1 at the first peak load (P_{n1}), as described in Figure 6(a).

$$\mu_{\Delta} = \frac{\Delta_2}{\Delta_1} \quad (\text{Equation 1})$$

Δ_2 is considered to be the axial deformation at the failure point for columns that showed stability or increasing in load–deformation behavior at the post-peak stage. Furthermore, it is considered as the axial deformation at the point 85% of P_{n1} for columns that showed descending load–deformation behavior at the post-peak stage. This approach was implemented by Lignola, et al. (2007) to calculate the ductility factor for circular and square hollow and solid concrete columns with and without FRP reinforcement. According to Table 4, HS65 exhibited limited and low ductility. Interestingly, using GFRP reinforcement in hollow concrete columns leads to enhance the ductile behavior for the steel-reinforced hollow concrete columns (Hoshikuma and Priestley, 2000), and shows approximately the same ductility as in hollow concrete columns reinforced with steel bars and wrapped in CFRP material (Lignola, et al., 2007).

On the other hand, Table 3 shows the confined strength (f'_{cc}) and confinement efficiency of the tested concrete columns after concrete cover spalling. These values indicate how effective the spiral reinforcement was in confining the concrete core, as illustrated in Figure 6(b). After reaching the peak stress at point P_{n1} , the columns started to lose the concrete cover, and the confinement process was activated by the transverse GFRP spirals until reaching the maximum confined compressive strength (f'_{cc}) at the failure point P_{n2} . Confinement efficiency was then calculated as f'_{cc} / f'_{co} , wherein f'_{cc} is the confined concrete compressive strength (point P_{n2}) and f'_{co} is the unconfined concrete compressive strength (85% of P_{n1} , when the outer surface was free of cracks), similarly, this approach was implemented by Tobbi, et al. (2014). Based on the test results, a higher confined concrete compressive strength was noticed by increasing the (Di/Do) ratio. Interestingly, the behavior of the steel-reinforced hollow concrete column is consistent with this findings by Yazici (2012), who found that once the steel reinforcement had yielded, it did not confine the concrete core anymore. This can be attributable to high axial strain capacity of the GFRP reinforcements.

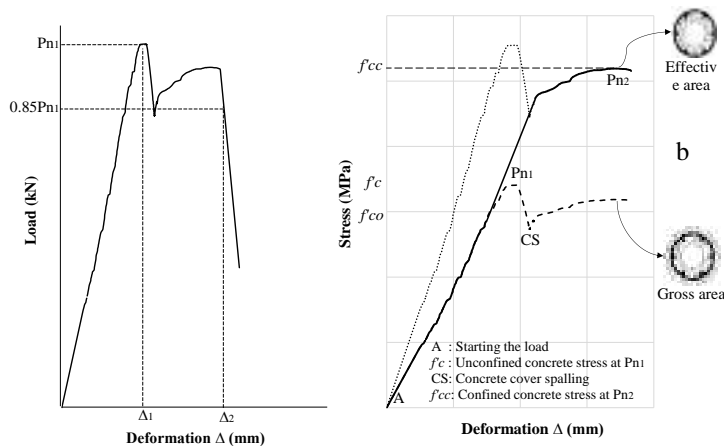


Figure 182: (a) Ductility (b) Confined strength

Influence of Hollowness

The hollow concrete columns reinforced with GFRP bars and spirals (HG90) exhibited some notable behavior compared to the solid column (SG). As expected, SG had the highest failure load owing to it having the largest concrete area. Its failure behavior was brittle, however, due to the lateral and longitudinal reinforcement rupturing. In contrast, HG90 exhibited a pseudo-ductile failure behavior, evidenced as partial crushing of the concrete, followed by bar rupture. The ultimate concrete strain in the solid column reached $1858 \mu\epsilon$, which is 15% less than the concrete strain in HG90, indicating that the concrete cover contributed more to the hollow columns than the

solid column before cracking. Furthermore, the longitudinal GFRP bars' contribution in the hollow columns was almost similar to that of the solid column by an average of 12.2% of P_{n1} . The GFRP-bar contribution was calculated by multiplying the average axial strain by the elastic modulus and the total area of the longitudinal GFRP bars, divided by P_{n1} . Interestingly, the GFRP bars in the solid and hollow columns showed a compressive-strength capacity at failure of around 51% of their tensile strength. It was also observed that the concrete core was confined more effectively in the hollow columns than the solid one, as represented by their higher deformation capacity and higher confinement efficiency as shown in Table 3. This table shows that the confinement efficiency of the concrete core in HG90 was 21% higher than that of SG. Similarly, HG90's ductility was 68% higher than that of SG due to higher volumetric and reinforcement ratio, even though, they are reinforced with the same number of bars and spirals. In addition, low effect of lateral concrete dilation in hollow columns regarding absence of the inner concrete core was clear by increasing the confined strength in hollow columns rather than solid column, especially after concrete-cover spalling.

Influence of Inner-to-Outer Diameter (Di/Do) Ratio

Table 3 and Figure 5 show the behavior and results for the hollow columns with different Di/Do. As expected, decreasing failure load was observed in the hollow columns with increasing Di/Do, although the failure behavior changed from brittle to ductile with increasing Di/Do. This is due to the initiation of crushing failure of the concrete core with the longitudinal and spiral reinforcement still intact. Furthermore, increasing the Di/Do led to an increased confined compressive strength of the inner concrete core. Accordingly, the actual concrete compressive strength of the hollow columns approached the compressive strength obtained from testing standard concrete cylinders. In fact, the columns with Di/Do of 0.36 and 0.26 achieved almost 94% of f'_c , while the column with a Di/Do of 0.16 achieved only 83% of f'_c before concrete spalling occurred. This behavior is due to the increasing axial stiffness of the longitudinal GFRP reinforcement attributable to the increased Di/Do, which was emphasized by the spalling pattern in Figure 7.



Figure 183: Concrete-cover spalling through the tested columns

After P_{n1} , the increase in the Di/Do from 0.16 to 0.36 led to a 21% increase in the confined concrete compressive strength regarding arch effect. In that case, the thinner inner concrete wall led to the increase in circumferential stresses in the inner concrete wall exerted by radial stresses provided by the GFRP spirals. Accordingly, the radial stress is caused by the high Poisson's ratio and increased GFRP-bar stiffness. After concrete spalling occurred, the effective reinforcement ratio in the hollow columns increased, which led to the longitudinal GFRP bars providing high stiffness and withstanding high axial stresses, which resulted in the bars pushing the GFRP spirals outward. In return, the GFRP spirals resisted the deformation of the longitudinal bars and created inward circumferential stress. The concrete-core wall thickness of HG40 and HG65 was adequate to withstand the circumferential stresses resulting in failure to initiate in the longitudinal reinforcement and spirals. Conversely, the failure was initiated in the inner concrete wall when the circumferential stress provided by the GFRP spirals was higher than the radial stresses by the concrete core. This point represents the maximum confined stress of the inner concrete wall. Interestingly, HG65 and HG90 showed almost the same concrete compressive strength before spalling and confined compressive strength after spalling. Their deformation capacity, however, increased with increasing Di/Do. This could be explained by the increase in the effective reinforcement ratio when the concrete cover spalled, resulting in the contribution of the GFRP bars in the overall stiffness increasing as compared to the remaining inner concrete, i.e., the reinforcement ratio increased from 2.47% to 3.78%, and from 2.78% to 4.74% for the columns with Di/Do of 0.16 and 0.36, respectively. Furthermore, the column with a Di/Do of 0.36 exhibited 68% higher deformation capacity compared to the column with a Di/Do of 0.16.

CONCLUSION

This study investigated the axial behavior of hollow concrete columns reinforced with glass-fiber-reinforced-polymer (GFRP) bars and spirals with different inner-to-outer diameter ratios. In addition, the applicability of existing design equations for solid concrete columns was assessed for hollow concrete columns reinforced with GFRP bars. Based on the results of this study, the following conclusions can be drawn:

- The hollow columns failed at a lower load than the solid column due to the reduced effective area. Nevertheless, the hollow columns yielded higher concrete compressive strength at peak load than the solid column. The concrete compressive strength of the hollow columns was up to 94% of the average compressive strength of the concrete cylinders.
- The concrete core can be more effectively confined in hollow columns than in solid columns. Up to 68% higher deformation capacity and 21% higher strength confinement efficiency was exhibited by the hollow columns compared to the solid column.
- Increasing the inner-to-outer diameter ratio (D_i/D_o) in the hollow columns changed the failure behavior from brittle to pseudo-ductile. After spalling of concrete cover, the failure in the hollow columns with a D_i/D_o of 0.16 and 0.26 was initiated by the longitudinal and spiral GFRP reinforcement, while the failure of columns with a D_i/D_o of 0.36 was initiated by crushing of the hollow concrete core.
- The hollow columns with high D_i/D_o showed better deformation capacity than those with low D_i/D_o . This is due to the increased axial stiffness of the GFRP bars to overall column stiffness and strength after spalling of the concrete cover.

ACKNOWLEDGMENTS

The authors are grateful to Inconmat V-Rod Australia for providing the GFRP bars and spirals. The assistance of the postgraduate students and technical staff at the Centre of Future Materials (CFM) is also acknowledged.

REFERENCES

- Afifi, M. Z., Mohamed, H. M., and Benmokrane, B. (2013). "Axial capacity of circular concrete columns reinforced with GFRP bars and spirals." *Journal of Composites for Construction*, 18(1), 04013017.
- Benmokrane, B., Manalo, A., Bouhet, J.-C., Mohamed, K., and Robert, M. (2017). "Effects of Diameter on the Durability of Glass Fiber-Reinforced Polymer Bars Conditioned in Alkaline Solution." *Journal of Composites for Construction*, 21(5), 04017040.
- Hadi, M. N., Karim, H., and Sheikh, M. N. (2016). "Experimental investigations on circular concrete columns reinforced with GFRP bars and helices under different loading conditions." *Journal of Composites for Construction*, 20(4), 04016009.
- Hoshikuma, J.-i., and Priestley, M. (2000). "Flexural behavior of circular hollow columns with a single layer of reinforcement under seismic loading." *SSRP*, 13.
- Liang, X., Beck, R., and Sritharan, S. (2015). "Understanding the Confined Concrete Behavior on the Response of Hollow Bridge Columns."
- Lignola, G. P., Prota, A., Manfredi, G., and Cosenza, E. (2007). "Deformability of reinforced concrete hollow columns confined with CFRP." *ACI Structural Journal*, 104(5), 629.
- Lignola, G. P., Prota, A., Manfredi, G., and Cosenza, E. (2007). "Experimental performance of RC hollow columns confined with CFRP." *Journal of Composites for Construction*, 11(1), 42-49.
- Manalo, A., Benmokrane, B., Park, K.-T., and Lutze, D. (2014). "Recent developments on FRP bars as internal reinforcement in concrete structures." *Concrete in Australia*, 40(2), 46-56.
- Mo, Y., and Nien, I. (2002). "Seismic performance of hollow high-strength concrete bridge columns." *Journal of Bridge Engineering*, 7(6), 338-349.
- Mohamed, N., Farghaly, A. S., Benmokrane, B., and Neale, K. W. (2013). "Experimental investigation of concrete shear walls reinforced with glass fiber-reinforced bars under lateral cyclic loading." *Journal of Composites for Construction*, 18(3), A4014001.
- Nkurunziza, G., Debaiky, A., Cousin, P., and Benmokrane, B. (2005). "Durability of GFRP bars: a critical review of the literature." *Progress in structural engineering and materials*, 7(4), 194-209.
- Pantelides, C. P., Gibbons, M. E., and Reaveley, L. D. (2013). "Axial load behavior of concrete columns confined with GFRP spirals." *Journal of Composites for Construction*, 17(3), 305-313.
- Tobbi, H., Farghaly, A. S., and Benmokrane, B. (2014). "Behavior of concentrically loaded fiber-reinforced polymer reinforced concrete columns with varying reinforcement types and ratios." *ACI Structural Journal*, 111(2), 375.
- Yazici, V. (2012). "Strengthening hollow reinforced concrete columns with fibre reinforced polymers."
- Zahn, F., Park, R., and Priestley, M. (1990). "Flexural strength and ductility of circular hollow reinforced concrete columns without confinement on inside face." *Structural Journal*, 87(2), 156-166.



PERFORMANCE OF GFRP IN BALCONY SLAB THERMAL BREAKS

Sarah Boila¹, David Kuhn², Kevin Knight³, John Wells⁴, Dagmar Svecova¹

¹ University of Manitoba, Civil Engineering, Winnipeg, Canada, Email: unboilas@myumanitoba.ca

² University of Manitoba, Mechanical Engineering, Winnipeg, Canada; ³ Red River College, Building Envelope and Technology Centre, Winnipeg, Canada; ⁴ Crosier Kilgour & Partners Ltd., Winnipeg, Canada

ABSTRACT

In an effort to reduce our collective consumption of natural resources and greenhouse gas emissions, the building industry has recently focused on improving the insulation of the building envelope, thus lowering heating and cooling loads. However, thermal bridges occurring at locations such as the interface of concrete balconies and wall systems continue to compromise the integrity of the building envelope for the entire structure. The objective of this project is to design a practical and cost-effective thermal break system for concrete balconies to improve the sustainability and cost efficiency of modern buildings and enhance the health, safety and comfort of the building occupants. The performance of a glass fibre reinforced polymer (GFRP) reinforced thermal break is compared to that of both steel and stainless steel reinforced systems. Experimental testing is performed on representative sample sizes containing each type of reinforcement both with and without a thermal break, and the results are compared to those obtained from three-dimensional thermal modeling. The introduction of the thermal break is found to effectively increase interior floor temperatures and reduce overall heat flow through the balcony. The GFRP reinforced thermal break significantly outperforms those reinforced with steel and stainless steel, providing the possibility of a new and more effective solution for the building construction industry.

KEYWORDS

New composite materials, systems and strengthening techniques; Experimental study; FRP internal reinforcement; Characterization of FRP and FRC materials/systems; Characterization of FRP reinforced thermal break system; Thermal conductivity

INTRODUCTION

In modern day society there exists a growing public consciousness regarding the need to reduce our consumption of natural resources and greenhouse gas emissions. This will continue to play an increasing role in the industry's approach to creating sustainable and economic buildings, particularly through improving the insulation of building envelope design and thus lowering heating and cooling loads for a building. While wall panels can be insulated fairly easily and the thermal resistance of glass windows is steadily improving, thermal bridging occurring at locations such as the interface of concrete balconies and wall systems may compromise the integrity of the building envelope for the entire structure. In a study performed by Ge et al. (2013) it was found that up to 30% of a residential building's heating energy may be lost through thermal bridges. In a country such as Canada, where space heating of residential buildings accounts for 10% of the total national energy use (Natural Resources Canada, 2010), these heat losses amount to a considerable sum.

After considering windows and doors, balconies are responsible for the second greatest source of thermal bridging and heat loss in multi-story residential buildings (RDH Building Engineering Ltd. , 2013). The concrete and reinforcing steel of a balcony act as excellent thermal conductors to transfer heat from the interior of a building to the exterior in cold winter months. This heat loss then has to be accommodated by mechanical systems, resulting in higher heating loads and higher building operational costs for the owner and/or occupant. In addition to increasing heating loads, thermal bridges may reduce the interior surface temperatures. If the interior surface temperature falls below the dew point, condensation will occur, eventually leading to mold growth. Condensation and mold growth may deteriorate the structural components of the building, and will reduce the interior air quality for its occupants. Exposure to mold growth and its airborne spores has been shown to increase the risk of respiratory symptoms, respiratory infections, and to aggravate symptoms produced by asthma (Adan & Samson, 2011).

The most effective currently available method of reducing heat loss through a balcony is to install a thermal break, in which an insulating material is installed in place of the concrete, in line with the surrounding assembly's insulation. Structural capacity is provided across the thermal break by rebar passing through the insulating material, connecting the cantilevered balcony to the interior floor slab. In most European countries, where the linear or point thermal transmittances of thermal bridges is limited by energy performance regulations, premanufactured

balcony thermal break units are installed more regularly. However in North America, where building codes provide comparatively relaxed regulations regarding thermal bridging, it is often up to the discretion of the designer to include them in design. Combining the high initial cost of premanufactured balcony thermal breaks and the lack of guidelines dictating that thermal bridges must be remedied, designers more often than not forgo the option of installing these units.

The objective of this paper is to evaluate the thermal performance of a GFRP reinforced built-in-place balcony thermal break system. The system differs from pre-existing solutions not only by its reinforcement type, but also in that the insulation and reinforcement are to be installed separately on-site, reducing the initial cost of construction and providing a solution for the North American building construction industry.

METHOD OF SOLUTION

Tested Materials

The thermal performance of a GFRP reinforced thermal break is compared to that of both a steel and stainless steel reinforced system. The performance of GFRP as reinforcement in a thermal break is particularly of interest because it has a thermal conductivity at least 90% lower than that of conventional carbon steel. The thermal break material selected for testing is Armatherm™ 500, a high strength polyurethane material developed by Armadillo from the United States. Each type of reinforcement is tested both with and without a thermal break so that the effects of including the thermal break can be observed, as well as the effects of varying the reinforcement type. Table 1 provides a summary of the materials and their thermal conductivities, obtained from ISO TC 163, the international standard containing tabulated design values for hygrothermal properties.

Table 1: Thermal Conductivities of Tested Materials

Material	Thermal Conductivity [W/mK]
Carbon Steel Rebar	50
Stainless Steel Rebar	25
GFRP Rebar	1-5
Armatherm 500	0.0742
Concrete	2

System Design

Structural designs for a one meter wide section balcony slab with each reinforcement type were developed based on the load requirements of the 2010 National Building Code of Canada for a typical 6 foot cantilevered balcony with a slab thickness of 190 mm. By selecting the reinforcement densities according to one common design load, we are able to compare the effects of each reinforcement type as they would be used in the same application in industry. Preliminary thermal modelling was used to select a thermal break width of 25 mm, providing sufficient thermal separation between interior and exterior environments while minimizing the effect on structural performance.

Available manufactured thermal breaks typically use inclined shear bars to provide shear capacity across the break. This increases the amount of reinforcement traversing the break, which in turn increases the overall thermal conductivity of the system. In order to optimize thermal performance, shear bars were eliminated from the designs. Instead, the connection is designed to provide shear capacity through shear friction of the longitudinal reinforcement. The resulting thermal break design is thus very simple, consisting of an insulating block with longitudinal reinforcement passing through holes drilled into the block. The selected rebar size and spacing for each reinforcement type is provided in Table 2.

Table 2: Thermal Break Reinforcement Design

Material	Bar Diameter [mm]	Bar Spacing [mm]	Reinforcement Density [mm ² /m]
Carbon Steel Rebar	16	167	1200
Stainless Steel Rebar	16	250	800
GFRP Rebar	25	250	1960

Experimental Thermal Testing

Representative sample sizes of each configuration were built in order to experimentally observe their thermal performance. Six samples were therefore tested for this phase of the project, testing each of the three reinforcement types both with and without the thermal break. Each sample measures 0.5 m in width by 1.6 m in length and 0.19 m in depth. The thermal break is placed directly midway along the length of the sample, and the length of the reinforcement needed to develop the required strength at the location of the joint is provided to either side, thus dictating the minimum total length of the samples of 1.6 m. Figure 1 shows the configuration of the GFRP reinforced sample.

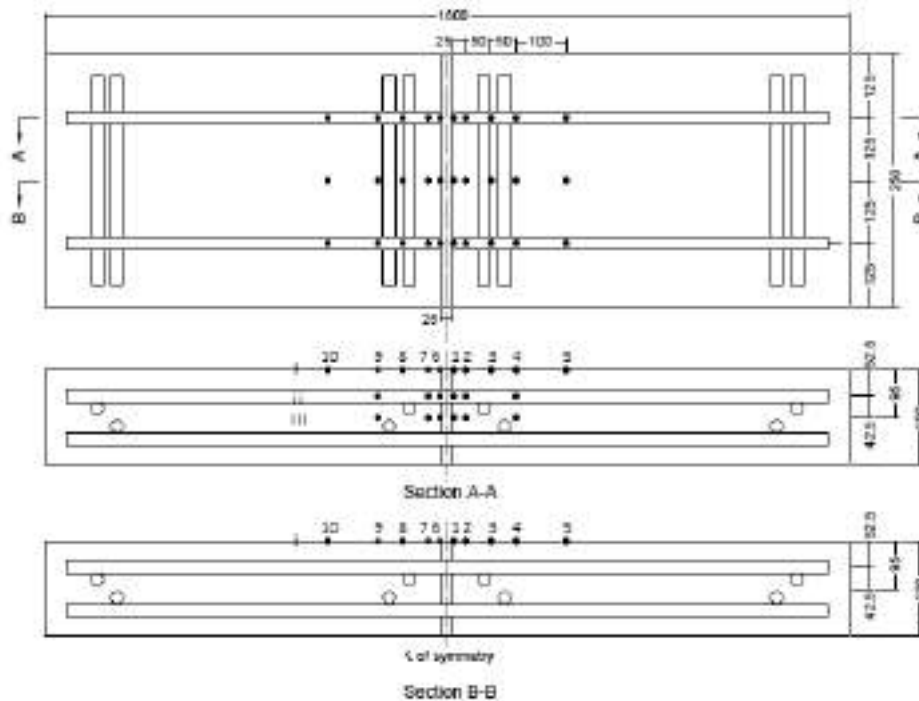


Figure 1: GFRP reinforced samples with thermal sensor layout and labelling system, dimensions in mm.

Thermal testing is carried out using facilities located at Red River College in Winnipeg, Canada. A dual-sided thermal chamber is used to simulate the conditions of a balcony in service, being exposed to warm interior temperatures on one side and cold exterior temperatures on the other. This therefore simulates the highest heat transfer scenario, which would occur in cold winter months. The interior design temperature is selected as 21°C, and the exterior design temperature for Winnipeg of -31°C is used.

The test samples are installed within the thermal chambers and a wall of 100 mm wide rigid extruded polystyrene insulation, with an R-value of 20, is installed around the samples to separate the two thermal environments. The thermal break is aligned with the cold chamber, as shown in Figure 2, to simulate the alignment of the thermal break when installed in an externally insulated building. An approximately 25 mm gap is left between the sample and surrounding insulation wall, which is filled with a polyurethane spray foam sealant to provide insulation directly against the samples. Caulking sealant is applied at all edges between the spray foam, samples, and insulation wall to ensure airtightness between the two thermal environments.

In order to simulate the primarily longitudinal heat flow which would occur in an installed balcony with a width significantly larger than its cantilevered length, the sides of the 0.5 m wide test samples are insulated. Sections of 100 mm thick rigid insulation are adhered using construction adhesive to the sides of the test samples, and caulking is applied around the edges of this insulation to ensure it is sealed directly against the samples, eliminating any possibility of airflow between the insulation and the sample. Two samples are tested at once within the chamber, side by side, with one section of 100 mm wide rigid insulation installed between them.

The temperature within each environmental chamber is regulated by a fan positioned on the rear wall, which blows air of the required temperature into the chamber. Because of this there is a pronounced effect of uneven airflow within each chamber and along the surfaces of the samples when they are left unsheltered, resulting in uneven

convective conditions. To eliminate this convection and provide consistent exposure conditions along all surfaces, a shelter built from plywood is installed around the samples within each environmental chamber. This allows the temperature of air in contact with the samples to reach the design temperatures while eliminating the air flow.

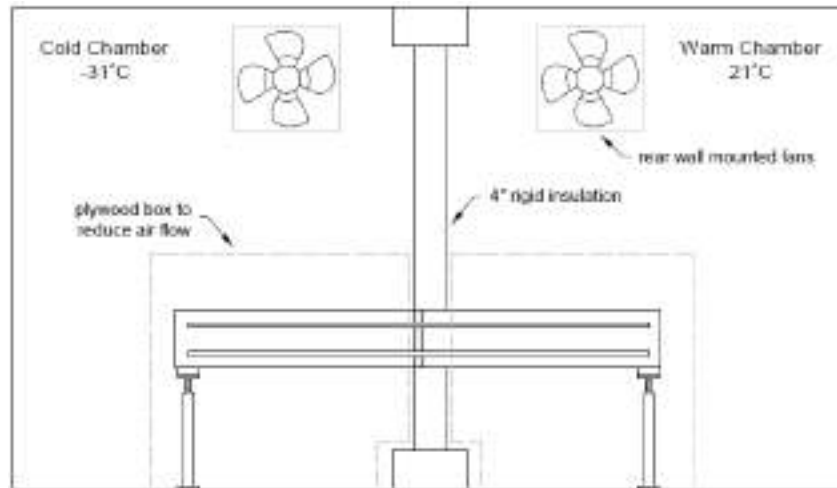


Figure 2: Thermal chamber test setup

In order to record the temperature profiles of the samples, 10K ohm thermistors with a tolerance of $\pm 0.2^{\circ}\text{C}$ are installed on their surface and embedded within the concrete. The thermistor layout for the GFRP reinforced samples is provided in Figure 1. The thermistor layouts for the steel and stainless steel reinforced samples follow the same system, with the cross-sectional layout A-A installed in the locations of the reinforcing bars.

3D Heat Transfer Analysis using Heat3

Steady state thermal modelling was performed using Heat3 8.02, a three-dimensional finite element heat transfer program developed by BLOCON (2017). The models are built according to ISO 10211 (2007), the international standard for modelling thermal bridges in building construction. Each reinforcement type is modelled with and without a thermal break, to allow for a comparison between the temperature profiles obtained through experimental testing with those found in modelling. The purpose of thermal modelling is to simulate the conditions occurring within the experimental testing chambers in order to validate the results and further quantify the physical properties of the different thermal breaks.

Several simplifications are made between the experimental test samples and the models. Due to their minimal effect on longitudinal heat transfer, transverse reinforcing bars are not included in the models. As well, the program is limited to drawing straight line segments, therefore the circular reinforcing bars are each drawn as a square cross-section with an area equal to that of the original circular cross-section, as seen in Figure 4c. According to ISO 10211, the surrounding insulating wall is extended a length of 1m above and below the modelled sample.

The interior boundary condition is specified as 21°C and the exterior boundary condition as -31°C , as per the Winnipeg design temperature. Both boundary conditions are assigned a surface resistance of $0.1 \text{ m}^2\text{K/W}$ to simulate the low airflow occurring within the plywood shelters of the experimental setup. The boundary conditions are assigned to surfaces as shown in Figure 4b. All surfaces in the y-z plane, as well as the uppermost and lowermost rigid insulation wall surfaces in the x-y plane, are assigned the adiabatic boundary condition.

Material thermal conductivities are assigned according to the values found in literature listed in Table 1. Since the value of thermal conductivity for FRP materials found in literature varies, due to the varying properties of each individual FRP product, an analysis is performed by varying the thermal conductivity of GFRP in the model until the sum of differences in temperature between the experimental results and thermal modelling is minimized. The obtained thermal conductivity for GFRP is 1.5 W/mK .

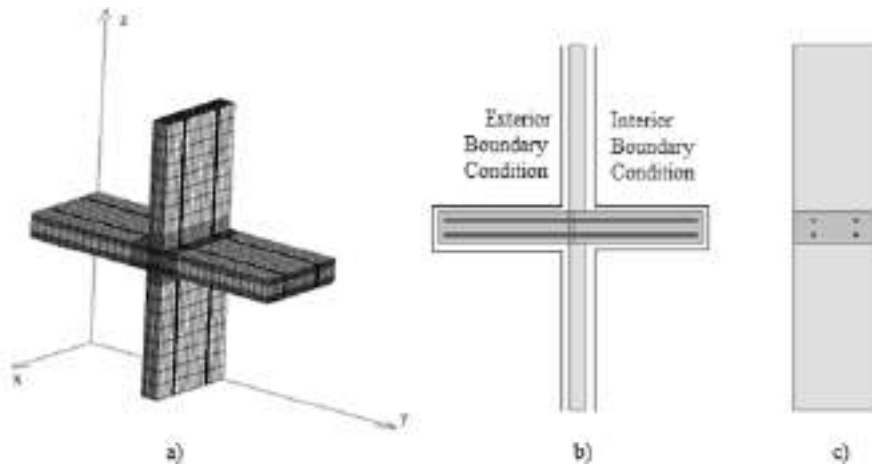


Figure 4: a) 3D Image of model showing materials and numerical mesh. b) Cross-section of materials in y-z plane with boundary condition placement c) Cross-Section of materials in x-z plane

Figure 4a provides a 3D image of the model overlaid with the numerical mesh. The density of the numerical mesh is modified from the program derived numerical mesh, focusing on increasing the density of the mesh as distance from the thermal break decreases. A minimum computational distance of 5.5 mm, 8 mm, and 10 mm are provided around the thermal break in the x, y, and z directions, respectively. This provides a refined temperature profile, allowing for interpolation within the model data to obtain precise temperatures at the locations of the thermal sensors used in experimental testing.

RESULTS AND DISCUSSIONS

Experimental Test Results

Figure 5 below provides an image of two GFRP reinforced samples during thermal testing, one with a thermal break and one without. The infrared image to the right clearly demonstrates the decrease in slab surface temperature observed for the sample without a thermal break, and the improvement provided by including the thermal break.

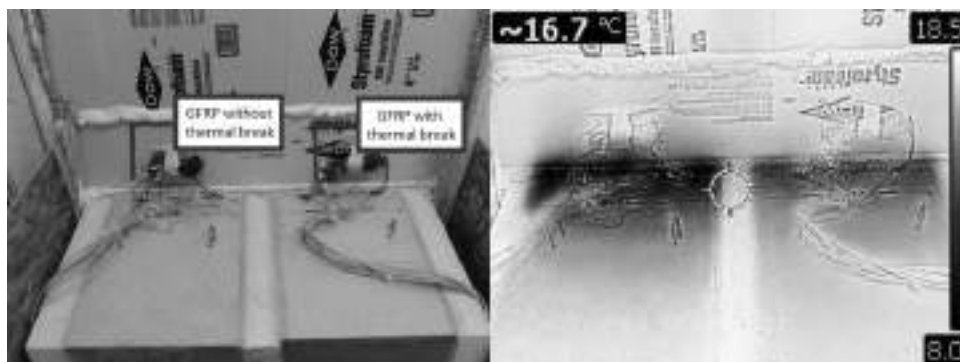


Figure 5: Photograph (left) and infrared image (right) of GFRP reinforced slabs tested in thermal chambers, taken from the warm chamber.

Figure 6 provides the experimentally obtained cross-sectional temperature profiles for the GFRP reinforced samples both with and without a thermal break. Missing data points are due to defective thermistors, which were likely damaged during casting of the concrete. The shaded rectangle in Figure 6a demonstrates where the thermal break is located, whereas the blank rectangle in Figure 6b demonstrates where the break would be located, however it is continuous concrete for this sample since it is constructed without the break.

Of immediate notice is the separation of positive and negative temperatures to either side of the thermal break in Figure 6a. This indicates the effectiveness of the thermal break in shifting and condensing the temperature gradient across the thermal break, reducing the penetration of cold temperatures to the interior of the building. Comparatively in Figure 6b, without the thermal break, temperatures as low as -7.7°C are found to the interior of the break.

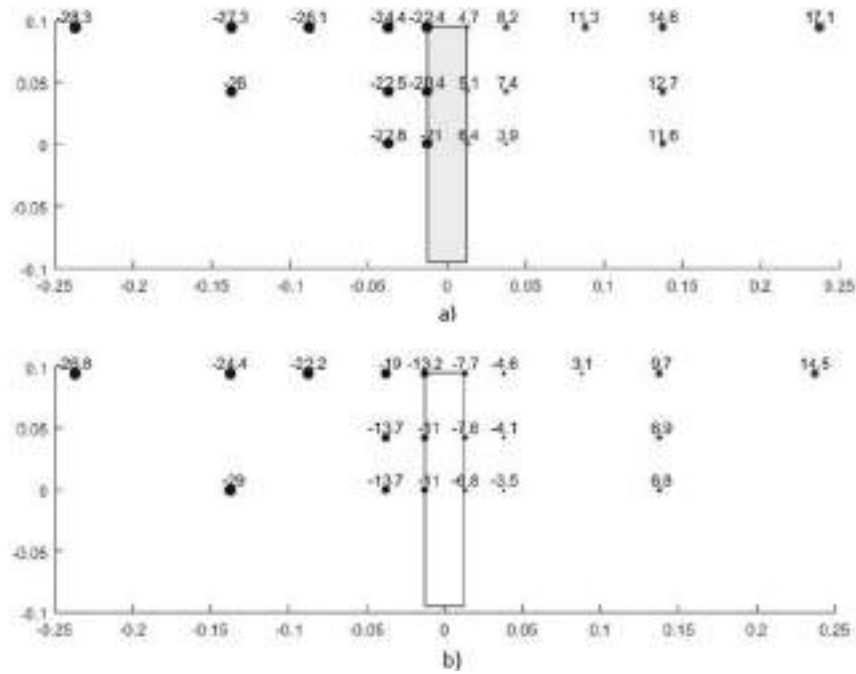


Figure 6: Experimentally obtained temperature profiles for a) test sample with thermal break and b) test sample without thermal break, all temperatures in °C.

Table 3 provides a summary of temperatures located at the surface of the slabs 0 mm and 125 mm from the thermal break on the interior side for all samples. The addition of the thermal break increases the temperatures located 0 mm from the thermal break by 12.4°C, 13.7°C, and 9.5°C for GFRP, stainless steel, and carbon steel reinforced samples, respectively. When observing the difference in temperatures 125 mm from the thermal break, the improvement provided by stainless steel and GFRP reinforced sections are comparable. Although stainless steel has a higher thermal conductivity than GFRP, a significantly higher reinforcement density is required for the GFRP section, which accounts for their comparable performance in increasing temperatures within the interior floor slab.

Table 3: Experimental temperature profile data

Sample Description	0 mm From Break [°C]	125 mm From Break [°C]
Thermal Break	GFRP	4.7
	Stainless Steel	6.1
	Carbon Steel	2.6
No Thermal Break	GFRP	-7.7
	Stainless Steel	-7.6
	Carbon Steel	-6.9

The increase in overall temperature within the interior floor slab observed when including a thermal break is promising for preventing condensation in areas near a balcony which would have dropped below the dew point without a thermal break. Even in applications where condensation is not a risk, the increase in temperature is likely to provide benefits in terms of occupant comfort.

Heat3 Thermal Analysis

Figure 7 provides a comparison of the temperature profiles for GFRP reinforced samples with a thermal break obtained from experimental testing and thermal modelling. Considering all data points, an average temperature difference of 1.7°C and maximum temperature difference of 6.2 °C are present. It is notable that several temperature points closest to the thermal break on the interior side, sensors i1, ii1, iii1, and iii2, provide a higher discrepancy between the experimental and modelled results. Excluding these four data points, the average temperature difference is reduced to 1.2°C and the maximum to 4.9°C.

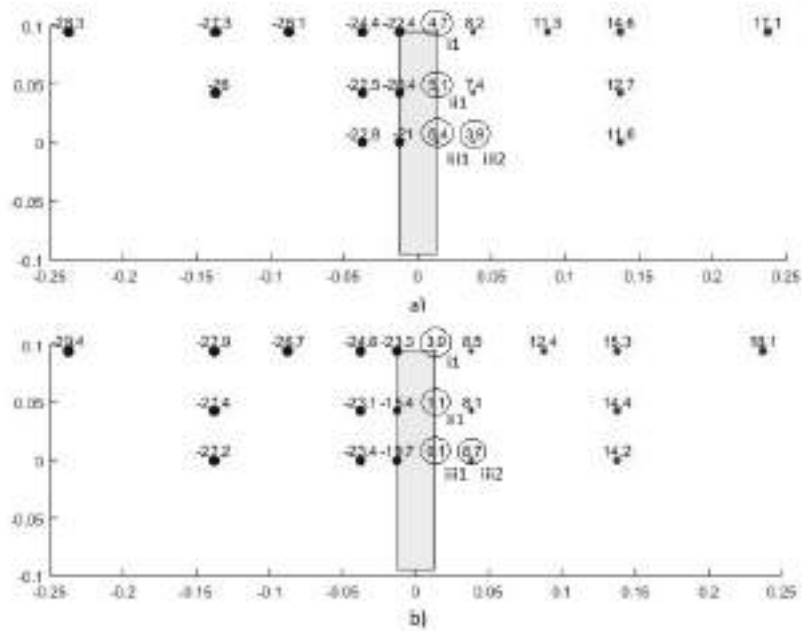


Figure 7: GFRP cross-section temperature profiles a) obtained through experimental testing and b) modelled using Heat3, all temperatures in °C

Table 4 provides a summary of the average and maximum temperature differences between experimental results and thermal modelling for all sample types. In general, when observing the average difference, the samples without the thermal break are predicted more accurately than those with the break. Of interest is the location at which the maximum temperature difference occurs. For all samples with the thermal break, the maximum difference occurs along the vertical line 1, as shown in Figure 6, at the junction of the thermal break and concrete on the interior side. Although the model predicts the general behavior of the system quite well, there remains this discrepancy between the concrete and thermal break material. Conversely, for samples without the thermal break, the largest temperature differences occur in different locations for each reinforcement type. Although there are local discrepancies within the temperature profiles of the modelled systems, the overall behavior of the system predicts quite well the behavior of the experimentally observed results and can therefore be used as a predictor for the relative heat flow through each type of sample.

Table 4: Temperature difference between experimental and modelled cross-sections

		Average Difference [°C]	Maximum Difference [°C]	Location of Maximum
Thermal Break	GFRP	1.7	6.2	iii1
	Stainless Steel	2.1	5.3	i1
	Carbon Steel	1.2	3.5	i1
No Thermal Break	GFRP	1.1	6.9	i9
	Stainless Steel	1.1	2.5	i8
	Carbon Steel	1.3	3.5	i6

Table 5 provides a summary of heat flow through each modelled system in Heat3, taken as the heat flow through the exposed concrete surfaces on the exterior side of the balcony. The greatest improvement from including the thermal break is observed for the GFRP reinforced sample with a 58.6% reduction in heat loss through the slab when compared to the GFRP reinforced sample without a break. This indicates that the addition of a thermal break is most effective when used in combination with reinforcing materials of a lower thermal conductivity.

If we consider the sample reinforced with carbon steel and without a thermal break as a representation of conventionally built balconies, replacing the steel with GFRP alone only provides a 15% reduction in heat loss, whereas including the thermal break increases this reduction to 65%. The stainless steel reinforced section also performs well in comparison to a conventional balcony, reducing heat loss by 52%, but is still out-performed by the GFRP reinforced section regardless of the GFRP section having a significantly higher reinforcement density.

Table 5: Heat3 modelled heat flow

Reinforcement Type	No Break [W]	With Break [W]	% Reduction
GFRP	24.6	10.178	58.6
Stainless Steel	26.09	13.925	46.6
Carbon Steel	28.89	19.742	31.7

CONCLUSIONS

The performance of balcony thermal breaks using GFRP, stainless steel, and carbon steel reinforcement are evaluated through an experimental program. The analyses include experimental testing of samples in a dual-sided thermal chamber to simulate exposure conditions of a balcony, and three-dimensional heat transfer modelling using Heat3 for each type of reinforcement both with and without a thermal break.

The benefits of installing the thermal break are clearly shown through the results. A significant increase in interior floor slab temperature is seen when a thermal break is installed, regardless of the reinforcement type. This reduces the potential for condensation due to thermal bridging near balconies and increases the thermal comfort level for occupants.

Thermal modelling in Heat3 provides a method to validate the heat flow through each system. Through this analysis the improvement in the balcony thermal break performance provided by including GFRP reinforcement is evident. An overall heat loss reduction of 65% is observed when comparing a GFRP reinforced thermal break with a conventional carbon steel reinforced balcony. The GFRP reinforced break outperforms one reinforced with stainless steel, providing 13% further reduction when comparing both to the conventional balcony. GFRP reinforcement is thus an ideal material to be used in balcony thermal breaks to reduce the overall heat flow through the system, providing an effectively green solution for the construction industry.

ACKNOWLEDGMENTS

The authors would like to thank the Natural Sciences and Engineering Research Council of Canada (NSERC) and the Structural Innovation and Monitoring Technologies Resource Center (SIMTReC) for their financial support. The authors are also grateful to Crosier Kilgour & Partners Ltd. for their financial contributions and technical support, and to Armadillo NV, and Pultrall Inc for in kind support of the research. A great thanks is extended to the staff of the University of Manitoba McQuade Structures Laboratory and Red River College's Center for Applied Research in Sustainable Infrastructure for their help in running the experimental program.

REFERENCES

- H. Ge, V. R. McClung, S. Zhang (2013). "Impact of balcony thermal bridges on the overall thermal performance of multi-unit residential buildings: A case study", *Energy and Buildings*, 60, 163-173.
- O. C. G. Adan, R. A. Samson (2011). "Fundamentals of mold growth in indoor environments and strategies for healthy living", *Published by Wageningen Academic Publishers*, 2011.
- (2010) "Energy Use Data Handbook", *Natural Resources Canada*, 2010.
- RDH Building Engineering Ltd (2013). "Report #1: Impact of Slab Thermal Breaks on Effective R-Values and Energy Code Compliance", *The Importance of Slab Edge & Balcony Thermal Bridges*.
- (2007) "Thermal Bridges in building construction – Heat flows and surface temperatures – Detailed calculates", *International Standard*, 2013.
- (2007) "Building materials and products – Hygrothermal properties – Tabulated design values and procedures for determining declared and design thermal values", *International Standard*, 2007.



LOAD DEFLECTION BEHAVIOUR OF SELF-CONSOLIDATING CONCRETE BEAMS PRESTRESSED WITH CFRP BARS

S. Krem 1, K. Soudki 2

¹University of Waterloo, Canada, Email: skrem@uwaterloo.ca

²University of Waterloo, Canada, (was a professor at University of Waterloo 1997-2013)

ABSTRACT

Self-consolidating concrete (SCC) offers a number of potential benefits that derive from its unique flow characteristics: improved productivity and quality of concrete construction. The current ACI 440 design guidelines does not account for SCC in flexural deflection prediction of beams reinforced or prestressed FRP bars. This paper presents measurements from four beams (150 × 250 × 3600 mm) prestressed with 12.7 mm CFRP bars: two beams made from SCC and two beams made from normal vibrated concrete (NVC). All beams were tested under a four-point static bending load under displacement control at a rate of 1.0 mm/minute. Measurements of load, midspan deflection, strain in FRP bars, and strain in the concrete were collected using a data acquisition system. Results was compared to two methods for flexural deflection predictions: Simplified method (ACI 440.4R-04), and detailed analytical method from literature. The simplified method was based on effective moment of inertia approximation while the detailed method was based on effective moment of inertia and effective centroid calculations. Prediction of the midspan deflection based on the simplified method for SCC beams was unconservative after cracking (service loads). The predicted of midspan deflection based on simplified method at failure load differ by more than 30% of the experimental results for SCC beams prestressed to 30 and 60%. The detailed method correlated well with experimental results at higher loads range for both types of concrete at both prestressing levels.

KEYWORDS

Self-Consolidating Concrete, CFRP, Prestressed, flexural, deflection.

INTRODUCTION

Self-consolidating concrete (SCC) has the same ingredient components that are found in NVC: cement, aggregate, and water. However, to increase the flowability and reduce segregation, SCC requires a greater content of fine particles, and superplastizer, and possibly a viscosity-modifying admixture as a lubricant for the coarse aggregate, (ACI 237, 2007). A successful SCC mix must ensure a good balance between two parameters (deformability and stability) and prevent the blockage of concrete flow (Khayat 1999). Deformability is the ability of the mix to deform and change its shape under its own weight, while stability refers to the ability of the mix to resist segregation during all phases of the construction process. These characteristics often require a lower w/c ratio compared to NVC, which is the key component in determining the concrete compressive strength and modulus of elasticity. Other factors such as the sand-to-total-aggregate ratio (s/a) and type and dosage of chemical admixtures can significantly affect the mechanical properties of SCC.

The modulus of elasticity (E_c) is a crucial factor in calculating the stiffness and therefore deflection of reinforced concrete members. As stiffness of a flexural member is increased the deformation of the member decreases. In prestressed concrete application, the E_c plays an important role in reducing the prestress losses. Modulus of elasticity depends on several factors, including the concrete compressive strength, coarse aggregate characteristics and content. Where a low maximum aggregate size and high fines content are used, SCC is anticipated to have a lower E_c than that of NVC by 10 – 15 % (ACI 237, 2007); however, some studies indicate that for a comparable concrete compressive strength, the E_c of SCC is similar to that of NVC, Schindler et al. 2007. ACI 237 allows using the expression given by ACI 318-08 clause 8.5.1 (Eq. 1) to calculate the E_c of normal density concrete to estimate the E_c of SCC mixtures, where f'_c is the concrete compressive strength in MPa.

$$E_c = 4700 \sqrt{f'_c} \quad (1)$$

Schindler et al. (2007) reported that at early ages, and for comparable compressive strength, SCC exhibits a lower E_c than does NVC; however, at later ages, E_c values of SCC mixtures were very similar to those of NVC. A database collected by Holschemacher and Klug (2002) and Domone P. L. (2007) indicated that the modulus of

elasticity of SCC can be 20-40% lower than NVC's at low concrete compressive strength, but the differences decrease to about 5% when the concrete compressive strength approaches 60.0MPa.

Extensive research has been conducted on SCC material. However, the structural properties and assessment of the applicability of the current design equations for SCC members becoming increasingly important. The bond and flexural behaviour of SCC reinforced or prestressed members are main concerns among designers and practice (Schindler et al. 2007, Khayat & Mitchell 2009). This paper focuses on load-deflection performance of SCC beams prestressed with carbon FRP (CFRP) bars.

EXPERIMENTAL PROGRAM

Four prestressed beam specimens were constructed and tested. All beams were 150 mm × 250 mm in cross section and 3600 mm long and were prestressed with a single CFRP bar (12.7 mm in diameter) in the tension zone. Figure 1 shows typical beam reinforcement. Two beams prestressed to 30% and two to 60% of the guaranteed tensile strength of the CFRP bars. The shear reinforcement was kept uniform along the length of the span: 10M closed stirrups spaced at 100 mm. The concrete cover was constant at $3d_b$ (38.1 mm), for all beams.

The CFRP bars used in this study were developed and manufactured from continuous longitudinal fibers impregnated in a thermosetting vinyl ester resin with 73 % fiber content by volume. The bars were sand coated during the curing process. The tensile stress and modulus of elasticity were determined from tensile tests carried out by Soudki (2010) on identical bars at the same lab. Experimental test results showed that the ultimate tensile stress of these bars ranged from 1570 MPa to 2080 MPa, with an average of 1760 MPa, and that the modulus of elasticity was 142 GPa. Deformed steel bars 11.3 mm in diameter with a yield stress of 414 MPa were used as the top steel bars and shear reinforcement.

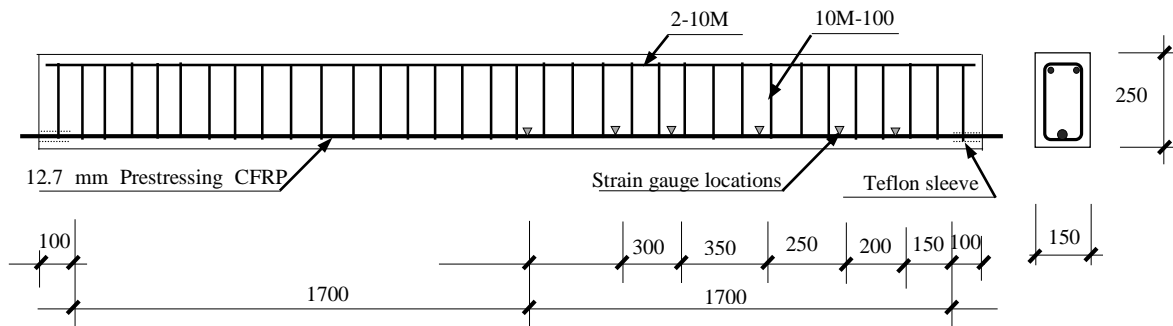


Figure 1 Typical beam geometry and instrumentation arrangements

All four mixes were ready mix concrete from an industrial concrete plant. SCC suppliers use a combination approach to producing the SCC mixes: increased fines and the use of a viscosity-modifying admixture (VMA) to achieve the required degree of mix stability and segregation resistance. A high-range water-reducing admixture (HRWRA) was used in all of the SCC mixtures. The maximum aggregate size for the SCC was 14 mm and for the NVC was 25 mm. All specimens were subjected to similar wet curing at room temperature for three days.

A self-reacting steel frame was fabricated and used as a prestressing bed. Wedge-type anchors that were developed at the University of Waterloo were used to grip the prestressing CFRP bars. At the live end, each anchorage barrel was affixed to a steel coupler with an extended threaded steel rod passing through the steel frame and a 30 T single-acting hollow cylinder. The prestressing force was applied gradually by means of an electrical hydraulic pump. A load cell with a 240 kN capacity was installed at the dead end of each beam to monitor the prestressing load. When the target load was achieved, a locking nut on the steel rod was fastened to the steel frame to maintain the load mechanically. All beams were cast on the next day. At the fourth day, the prestressing force was gradually released. Load cells and strain gauge readings were recorded continuously during the prestressing and up to the completion of the releasing process.

All beams were tested under a four-point static bending regime using a universal testing frame with a 330 kN capacity under displacement control at a rate of 1.0 mm/minute. A National Instrumentation Data Acquisition System connected to a lab computer was used in order to collect measurements of load, midspan deflection, bar slip at the beam ends, strain in the CFRP bar, and strain in the concrete.

ANALYTICAL MODELING AND ANALYSIS

Sectional Analysis

All of the prestressed beams tested in this program has reinforcement ratios less than the balanced reinforcement ratio. Therefore, the failure mode is expected to be due to rupture of the prestressed CFRP bar. Analysis of the internal forces and prediction of moment resistance is based on tension failure mode as given by ISIS Canada design manual (ISIS M5 - 2008). The analysis is based on strain compatibility and force equilibrium. In this analysis, the tensile stress in the concrete after cracking is considered. A schematic of the model is shown in Figure 2 and the analysis is governed by the following equations.

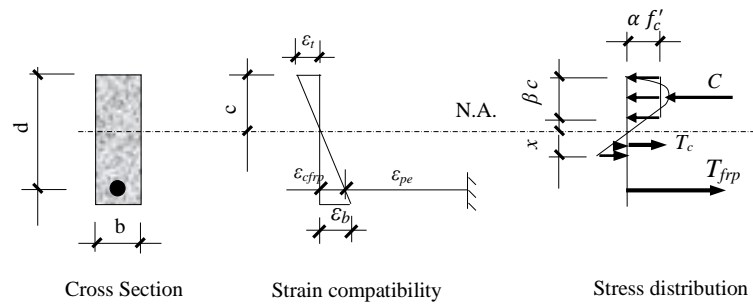


Figure 2 Section analysis model

The equilibrium of forces ($C = T_{frp} + T_c$) must be satisfied:

$$\alpha \phi_c f'_c \beta c b = A_{cfrp} \phi_{cfrp} \varepsilon_{cfrp} E_{cfrp} + \frac{1}{2} \phi_c \varepsilon_c E_c x b \quad (2)$$

The strain compatibility in the cross section as give in Eqn. (3)

$$\frac{c}{d} = \frac{\varepsilon_t}{\varepsilon_t + (\varepsilon_{cfrp} - \varepsilon_{pe})} \quad (3)$$

Where: A_{frp} is the cross-sectional area of the FRP bar; b is the width of the compression face of the member; C is the compressive force in the concrete in the compression region; c is the depth of neutral axis; d is the depth from the concrete top fibre to the centroid of the prestressing CFRP bar; f'_c is the specified compressive strength of concrete; f_{frp} is the tensile stress in the CFRP bar; T is the tensile force in the FRP bar; x is the distance from the neutral axis to where the strain in concrete equal to the rupture concrete strain ($\varepsilon_t = f_r/E_c$); α is the stress factor to calculate the intensity of the compressive stress in concrete; β is the stress-block factor for concrete; ε_{cfrp} is the total strain in the CFRP (effective pre-strain and flexural strain); ε_{pe} is the effective strain in the CFRP bar; ε_t is the compressive strain at the extreme compression fibre of concrete; ϕ_c is the strength reduction factor for concrete taken to be 1.0 in this analysis; and ϕ_{frp} is the strength reduction factor for FRP bar taken to be 1.0 in this analysis.

Using an iterative procedure, a solution can be obtained for the two unknowns, c and ε_{cfrp} . A spreadsheet was used to implement the iterative procedure of the model. Then the moment resistance can be calculated using Eq. 4.

$$M_r = T \left(d - \frac{\beta c}{2} \right) + T_c \left(\frac{2}{3} x + c - \beta \frac{c}{2} \right) \quad (4)$$

Moment Deflection Response

Two methods are used to calculate the midspan deflection in the CFRP prestressed concrete beams. The first method is a simplified method given in ACI440.4 (2004). The deflection is calculated based on the average effective moment of inertia along the beam span. The second method considers two additional parameters not considered in the simplified method. The first parameter is the change in the neutral axis depth in calculating the cracked transformed moment of inertia. As load increases, the neutral axis shifts to the compression side of the cross section, and thus the cracked transformed moment of inertia decreases. The effective moment of inertia used in the detailed model is a function of the cracked transformed moment of inertia. The second parameter reflects the change in the eccentricity in the prestress force as the applied moment increases as proposed by Abdelrahman and Rizkalla (1998). Results of the midspan deflection prediction based on this method had good agreement with

independent experimental measurements for NVC beams and prestressed with CFRP bars (Abdelrahman and Rizkalla 1998). The two methods are presented below.

Simplified method for deflection prediction

The midspan deflection is calculated based on the transformed moment of inertia before the concrete is cracked. Basic elastic analysis is used to obtain the midspan deflection at a given applied moment. After cracking, the midspan deflection is calculated based on the effective moment of inertia (I_e) of the beam. The effective moment of inertia is empirically derived for FRP prestressed concrete flexural members based on the assumption of a uniform moment of inertia along the beam span (ACI 440.4 2004).

$$I_e = \left(\frac{M_{cr}}{M_a}\right)^3 \beta_d I_g + \left(1 - \left(\frac{M_{cr}}{M_a}\right)^3\right) I_{cr} \leq I_g \quad (5)$$

Where: I_{cr} is the moment of inertia of the cracked section; I_t is the moment of inertia of the uncracked transformed section; M_a is the applied moment; M_{cr} is the cracked moment; β_d is a factor that depend on E_{frp} and E_s .

The midspan deflections of a symmetrically simply supported CFRP prestressed beam under four-point flexural loading can be calculated based on the basic elastic beam analysis (Eq. 6).

$$\Delta = \frac{P a}{24 E_c I_e} (3 l^2 - 4 a^2) \quad (6)$$

Where: a is the shear span; l is the total beam span; and P is applied load.

Detailed method for deflection prediction

Abdelrahman and Rizkalla (1998) proposed a model to calculate the effective centroid (y_e) of the transformed cracked section. This model was based on experimental results of beams prestressed with CFRP bars with measurements taken at various load levels. In this model, the calculated deflection accounts not only for the change in the effective moment of inertia but also the change in the eccentricity ($d_p - y_e$) of the effective prestress force (P_e) after cracking. The procedure is given by the following equations. A sectional analysis is necessary to determine the depth of the neutral axis required for calculation of the I_{cr} .

$$I_e = \Psi^3 I_g + (1 - \Psi^3) I_{cr} \leq I_g \quad (7)$$

$$\Psi = \left(\frac{M_{cr} - M_{dc}}{M_a - M_{dc}}\right), \quad M_s > M_{cr} \quad (8)$$

Where: Ψ is a factor that accounts for the applied moment (M_a), cracking moment (M_{cr}) and decompression moment (M_{dc})

The midspan deflection, including the effect of change in the eccentricity of the prestressing force, of beams prestressed with CFRP bars subjected to four-point flexural loading can be calculated as given in Eq. 9.

$$\Delta = -\frac{1}{8} \frac{P_e (d_p - y_e) L^2}{E_c I_e} + \frac{P a}{24 E_c I_e} (3 l^2 - 4 a^2) \quad (9)$$

$$y_e = \Psi^2 y_g + (1 - \Psi^2) y_{cr} \leq y_g \quad (10)$$

Where: Δ is the midspan deflection of, mm; P_e is the effective prestressing force, kN; a is the shear span, mm; L is the total clear span, mm.

RESULTS AND DISCUSSION

Fresh and Hardened Concrete Properties

Three SCC mixes and one NVC mix were used in this program. Table 1 gives the fresh and mechanical properties of all mixes. Beams presented in this paper were cast from only SCC-2 and NVC. Slump flow, J-ring and visual

segregation index for SCC mixes and slump measurements for NVC mix were measured on the fresh concrete. Concrete compressive strength development, modulus of elasticity and cylinder splitting tests were carried out on cylinder specimens of 100mm (4 inches) diameter by 200mm (8 inches) height. The slump flow and confined flow for the SCC mixes were between 650 mm and 720 mm. The confined flow J-ring test results for the SCC mix were between 625 mm and 690 mm. SCC mix-1 and SCC mix-2 had a Visual Stability Index (VSI) of 1.5 and 1.0, respectively. These results are within the definition of the SCC fresh properties as prescribed by ACI 237 (2007). However, SCC mix-1 was susceptible to segregation risk since it was on the border of the acceptance limit.

Table 1 Concrete properties testing results

Test	Concrete mixture			
	SCC-1	SCC-2	SCC-3	NVC
Slump flow, mm	720	680	650	150
Confined flow J-ring, mm	690	625	640	-
Segregation VI	1.5	1.0	0.0	-
Average compressive strength at beam testing, MPa	62.1	49.6	70.9	64.5
Average tensile strength (cylinder split test), MPa	6.31	5.63	6.94	7.07
Modulus of elasticity, GPa	27.8	22.7	30.6	37.4

The concrete compressive strengths of SCC-1, SCC-2, SCC-3 and NVC were 62.1 MPa, 49.6 MPa, 70.9 MPa and 64.5 MPa, respectively. The average experimental values of the modulus of elasticity of SCC mixes ranged from 0.67 to 0.82 of that predicted by the ACI 318 design code. The modulus of elasticity of SCC mix-1, which had a concrete compressive strength similar to that of the NVC mix, was about 75 % of that of the NVC. Vilanova et al. (2012) showed that SCC has a modulus of elasticity of ± 24 % of the ACI 318 predictions. This result agrees with those found in the literature (Schindler et al. 2007). Based on ACI 237 (2007), the modulus of elasticity of the SCC is expected to be, on average, 15 % less than code predictions. NVC modulus of elasticity, slightly, exceeded the ACI prediction. The tensile test results revealed lower tensile stress values for the SCC than for the NVC. The ratio of tensile stress to the square root of the concrete compressive strength of the SCC mixes ranged from 0.70 to 0.85, with an average of 0.79; for NVC, the range was from 0.86 to 0.90, with an average of 0.88. The SCC mixes thus had about 12 % less tensile strength to $\sqrt{f'_c}$ ratio than the NVC. A possible explanation for this finding could be related to the larger maximum size of the aggregate in the NVC mix compared to the SCC mixes. The coarse aggregate content in the NVC mix was also greater than in the SCC mixes. Although the concrete compressive strength of the SCC mixes was typically higher than that of the NVC mix due to the inherently low w/c ratio, the tensile strength was not correspondingly greater, Krem (2013).

Flexural Test Results

Table 2 gives a summary of the prestressing data and the flexural test results. It should be noted that the deflection values do not include camber due to prestressing force. Also, the moment values does not include moment due to beams own weight. The moment-deflection response of all beams showed a bilinear behaviour with an increased smooth transition between the two segments as the initial prestressing level increased. The initial linear part of the curve had a steep slope, which corresponds to the uncracked stiffness. In the second part, the beam stiffness decreased as a result of flexural cracking. As the loading increases, the flexural cracks propagate upward slowly due to the prestressing effect. All the four beams presented in this paper failed by bar rupture; however, Beam SC60, showed local slip failure, which reported by internal strain gauge readings. The local debonding resulted in increased deflection rate (reduced beam stiffness). At applied moment of (33.2 kN.m), the beam start to loose stiffness rapidly. No concrete crushing failure or shear failure recorded in the four beams.

Analytical Analysis Results

Prediction results of the sectional analysis and midspan deflection of Beam SC30 are given in Table 3. The predicted total strain in the prestressed CFRP bar at the midspan at failure was $10040\mu\epsilon$, while the measured value was $12530\mu\epsilon$. The measured CFRP strain was about 20% higher than the predicted value possibly due to the location of the strain gauge with respect to the flexural cracks. The measured compression strain in the concrete at failure was $2160\mu\epsilon$ as compared to the predicted value of $2300\mu\epsilon$; however, the measured compression strain in the concrete did not include the pretension strain in concrete due to prestressing force.

Table 2 Flexural test results

Concrete mix	Beam label	Prestressing, MPa		Shear span, mm	Cracking		Failure	
		Initial	Effective		Moment, kN.m	Deflection, mm	moment, kN.m	Deflection, mm
SCC-1	SC30	645	626	1350	10.1	3.1	33.9	50.4
	SC60	1005	974	1700	17.2	6.3	33.2	22.3
NVC	NC30	582	563	1350	10.5	4.2	42.3	68.8
	NC60	1101	1053	1500	17.9	3.9	43.7	49.4

Table 3 Analytical sectional analysis and deflection predictions for Beam SC30

Beam condition	ε_t	$\varepsilon_{cfpr}^{(1)}$	C mm	Curvature 10^{-6} rad/mm	Moment kN.m	Midspan deflection, mm	
						(2)	(3)
					0.0	0.0	0.0
					4.0	1.0	1.0
Zero curvature				0.0	6.2	1.6	1.6
					9.0	2.3	2.3
Bottom concrete crack					10.1	2.6	2.6
	-400	4349	149.7	2.7	14.2	8.5	6.5
	-500	4519	125.4	4.0	15.1	10.0	8.6
	-1000	5872	76.9	13.0	19.6	17.9	19.9
	-1500	7437	65.1	23.0	25.1	27.7	33.0
	-2000	9057	60.0	33.4	30.8	37.1	44.8
CFRP bar rupture	-2300	10040	58.1	39.6	34.3	42.4	53.1

⁽¹⁾ strain in CFRP bar (including effective prestress strain); (2) simplified method and (3) detailed method

Figure 3 (a) shows a graphical comparison of the midspan deflection of Beam SC30. Since the measured experimental deflection did not include the camber due to prestressing, the camber was removed from the predicted values. Prediction of midspan deflection based on the simplified method had a good agreement with the experimental values at lower load levels; however, the predictions diverged from the measured values as the load increased. At the failure moment (33.9 kN.m), the predicted deflection was 42.4mm as compared to the measured value of 50.4mm. Prediction using the detailed method had better agreements with the experimental results at all load levels. At failure moment, the predicted deflection based on this method was 53.1mm versus the measured value of 50.4mm. On average, the detailed method provided closer predictions (less than $\pm 10\%$) for this beam.

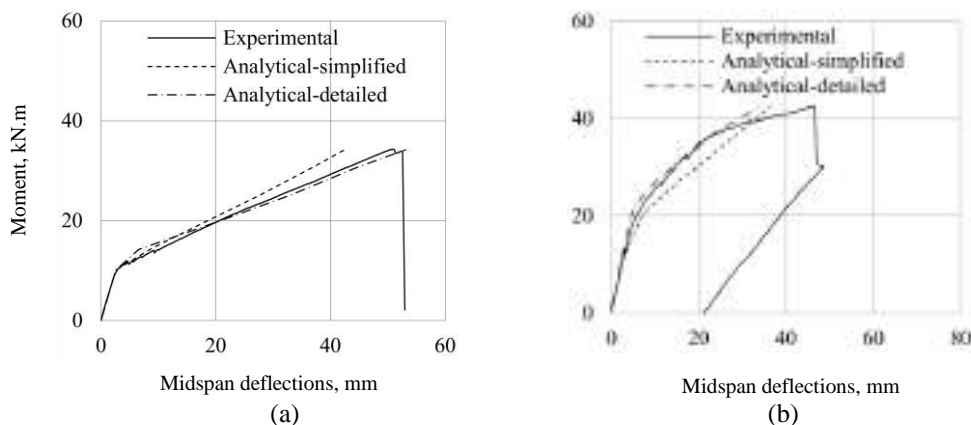


Figure 3 Experimental and predicted moment versus midspan deflection for Beam SC30 (a), and Beam SC60 (b). Similarly, the predicted versus measured moment-deflection responses of Beam SC60, Figure 3 (b), the midspan deflection based on the simplified method was unconservative by about 20% throughout the beam response after cracking. Prediction using the detailed method provided better correlation with the measured values. There was a slight underestimation of the midspan deflection after cracking and up to about 60% of the failure moment. This beam experienced stiffness loss as the applied moment exceeded 36.0kN.m. This softening is possibly due to local slip in the CFRP bar within the transfer zone.

Prediction results of sectional analysis and midspan deflection of Beam NC30 are given in Table 4. Beam NC30 had a failure moment of 43.6kN.m, a measured total strain in the prestressed CFRP bar of 14100 $\mu\epsilon$ and a strain in concrete of -3086 $\mu\epsilon$ (without the pretension strain). The predicted total strain in the prestressed CFRP bar was 12612.0 $\mu\epsilon$ (corresponding to a tensile stress of 1816.0MPa), which was 11% lower than the measured value. The predicted compression strain in the concrete was -2680 $\mu\epsilon$, which was 13% less than the measured value.

Table 4 Analytical sectional analysis and deflection predictions for Beam NC30

Beam condition	ϵ_t	$\epsilon_{cfpr}^{(1)}$	C mm	Curvature 10^{-6} rad/mm	Moment kN.m	Midspan deflection, mm	
						(2)	(3)
					0	0	0
					4.0	0.70	0.7
Zero curvature					5.7	1.0	1.0
					9.0	1.5	1.5
Bottom concrete crack					10.5	1.8	1.8
	-400.0	4258	109.9	3.6	14.2	6.1	4.8
	-500.0	4506	93.8	5.3	15.3	7.5	6.2
	-550.0	4659	87.0	6.3	15.8	8.2	6.9
	-750.0	5322	71.3	10.5	18.0	11.7	11.0
	-1000	6218	62.1	16.1	21.2	16.9	17.5
	-1500	8091	54.3	27.6	27.8	28.0	31.9
Beam failed	-2000	10000	50.8	39.4	34.5	38.5	45.1
	-2500	11926	48.9	51.2	41.2	48.5	60.7
	-2680	12612	48.4	55.4	43.6	51.8	65.7

⁽¹⁾ strain in CFRP bar (including effective prestress strain); (2) simplified method and (3) detailed method

Figure 4 (a) shows the prediction of the midspan deflection based on the simplified method and detailed method as compared to experimental results for Beam NC30. The predicted midspan deflection at the failure moment was 51.8mm, and the measured value was 68.1mm or 31% higher than the prediction value. The predicted midspan deflection based on the detailed method had less unconservative predictions with about 10% at the low load levels, and the difference between predicted and measured values decreased to less than 5% at the failure moment. The possible explanation of this trend in the detailed method could be related to the change in the effective centroid of the cracked transformed section. This specimen had a relatively higher stiffness (E_c of 37.4 GPa) than the SCC specimens. The difference between predicted and measured deflections was less in SCC specimens with small unconservative predictions at low load levels. With a higher modulus of elasticity in the NVC specimens, the difference between the prediction and the measured values increased.

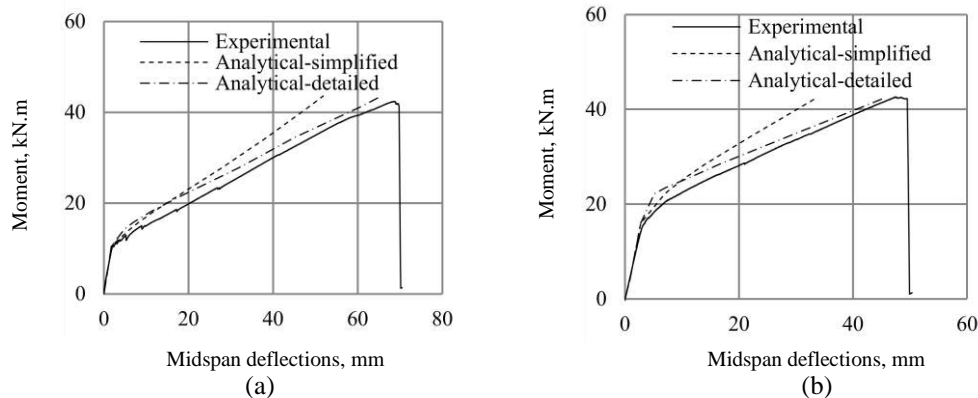


Figure 4 Experimental versus predicted moment-midspan deflection for Beam NC30 (a), and Beam NC60 (b) Prediction of the midspan deflection based on the simplified method for Beam NC60, Figure 4 (b), was unconservative after cracking. The predicted midspan deflection at the failure moment (42.3kN.m) was 33.3 mm, and the measured value was 47.6mm; thus the prediction was 30% lower than the measured value. The prediction of midspan deflection based on the detailed method was also unconservative at low load levels. At an applied moment of 22.0kN.m, for example, the predicted midspan deflection was 5.1mm, and the measured value was 8.2mm (unconservative by more than 50%). The difference between the predicted and measured midspan

deflection decreased as the applied moment increased. At the failure moment (42.3kN.m), the predicted midspan deflection was 45.2mm and the measured was 47.5mm, i.e. the predicted/ measured ratio was 0.95.

CONCLUSIONS

Experimental testing and analytical analysis of load-deflection for NVC and SCC beams prestressed with CFRP bars were completed and presented. Both predictions methods results correlated well with the experimental measurements of midspan deflection at low loading levels (approximate service load conditions). However, the predicted midspan deflection curve based on simplified method start to diverge from the experimental measurement as loading increased: at the failure moment differ by more than 30% of the experimental results. On the other hand, the detailed methods correlated well with the experimental results at higher loads range for both types of concrete.

REFERENCES

- Abdelrahman A. and Rizkalla S. (1998), "Deflection Control of Concrete Beams Pretensioned by CFRP Reinforcements," *Journal of Composites for Constructions*, ASCE, Vol. 3 No. 2, pp. 55-62.
- ACI Committee 237 (2007), "Self-Consolidating Concrete," *ACI 237R-07*, American Concrete Institute, Farmington Hills, MI, USA.
- ACI Committee 318 (2014), "Building Code Requirements for Structural Concrete (ACI 318M-14) and Commentary," American Concrete Institute, Farmington Hills, MI. 48331, USA.
- ACI Committee 440 (2004), "Pre-stressing Concrete Structures with FRP Tendons," *ACI 440.4R-04*, American Concrete Institute, Farmington Hills, MI.
- Anton K. Schindler, A. K., Barnes, R. W., Roberts, J. B., and Rodriguez, S. (2007). "Properties of Self-Consolidating Concrete for Prestressed members." *ACI Material Journal*, 104(1), 53-61.
- Domone, Peter, "A review of hardened mechanical properties of self-compacting concrete", *Cement & Concrete Composites*, Vol. 29, No. 1, January 2007, pp. 1-12.
- Holschemacher Klaus, Klug, Yvette, "A Database for the Evaluation of Hardened Properties of SCC", *LACER*, No. 7, 2002, pp. 123-134.
- ISIS Canada (2008). "Prestressing Concrete Structures with Fiber Reinforced Polymers." Design Manual No. 5, Winnipeg, Manitoba, Canada.
- Khayat, K., and Mitchell, D., (2009). "Self-Consolidating Concrete for Precast, Prestressed Concrete Bridge Elements." NCHRP report 628, Transportation Research Board, Washington, D.C. USA.
- Khayat, Kamal, "Workability, Testing, and Performance of Self-Consolidating Concrete", *ACI Materials Journal*, Vol. 96, No. 3, May 1999, pp. 346-353.
- Krem, Slamah, (2013) "Bond and flexural behaviour of self-consolidating concrete beams reinforced and prestressed with FRP bars", *Doctoral dissertation, University of Waterloo*
- Soudki, K. (2010). "Tensile Capacity of CFRP V-Rod Bars." Technical Report, University of Waterloo, Waterloo, Ontario, (May 3rd 2010).
- Vilanova, A., Fernández-Gómez, J., and Landsberger G., (2012), "Mechanical Properties of Self-Consolidating Concrete Using Conventional Concrete Models," *ACT Str. J.*, 109(6) 587-596.



BOND BEHAVIOUR BETWEEN GFRP RODS AND CONCRETE PRODUCED WITH SEAWATER: AN EXPERIMENTAL RESEARCH

José Sena-Cruz 1, Eduardo Pereira 1, Néelson Freitas 1, Emanuel Pereira 1 and Sérgio Soares 1
¹ *ISISE, Department of Civil Engineering, University of Minho, Portugal (corresponding author:*
jsena@civil.uminho.pt)

ABSTRACT

It is unquestionable that water is an indispensable natural resource for the existence of life on planet Earth, holding enormous environmental, economic and social value. Today, with the increase of the population and consequent increase in pollution, drinkable water is an increasingly sought-after and scarce resource. In this context, the need to explore the potential of the direct use of seawater in the production of reinforced concrete (RC) structures becomes evident. On the other hand, since the earliest times of universal history the sea constitutes the most important space in world economic development, to which onshore and offshore structures are associated. Structures when exposed to marine environments (e.g. ports, offshore structures, buildings located by the sea) are subjected to the simultaneous action of several physical and chemical deterioration processes that accelerate their degradation and greatly reduce their service life. With the advent of fibre reinforced polymers (FRP), the construction industry has experienced a revolution due to the countless advantages that these materials present, among which stands out their resistance to corrosion. Therefore, the use of these new materials in RC structures exposed to marine environments may prevent the main damages that aggressive agents typically originate in conventional RC, as well as to allow seawater to be directly used in the design of concrete, thus avoiding the use of drinkable water.

In this work the possibility of using seawater in the design of RC structures, in combination to the use of glass FRP (GFRP) rods, is explored. The research carried out included two phases: (i) the development of concrete compositions including seawater and (ii) the assessment of the bond behaviour between GFRP rods and the developed concrete. The present part is mainly devoted to the second phase where the influence of type of water (tap water or seawater), the GFRP diameter and anchorage length on the bond between GFRP rods and concrete were investigated. The main results obtained have shown that the use of seawater in the concrete composition had no severe effects on the mechanical properties of the concrete and on the bond behaviour between the GFRP rods and the concrete.

KEYWORDS

Bond behaviour, GFRP rods, concrete produced with seawater, direct pullout tests.

INTRODUCTION

The drinkable water is an increasingly scarce resource. The oceans constitute about 80% of the earth's surface which means that about 98% of the water on the planet is salty. The use of tap water in concrete production is not sustainable, considering that in many latitudes it is considered as a rare resource. In this context, the possibility to use seawater directly in the design of reinforced concrete structures (RC) is of great potential. However, RC structures in marine environments are subjected to the simultaneous action of several physical and chemical deterioration processes that accelerate their degradation and greatly reduce their service life. Among many others, corrosion of conventional steel reinforcement and degradation of the concrete cover layer are the most catastrophic effects that result from the exposure to the typically high chlorides concentrations (Ragab et al. 2016; Pradelle et al. 2017). Nevertheless, the emergence of fibre reinforced polymers (FRP) and the replacement of conventional steel by these new materials can lead to the use of seawater in the concrete structures design, due their resistance to corrosion. Furthermore, FRP materials have other advantages such as the high tensile strength, low weight, low thermal conductivity and good fatigue behaviour (Goldston et al. 2017). Therefore, the use of composite materials in reinforced concrete structures design may be combined with the use of seawater, avoiding the consumption of tap water and contributing to more sustainable construction approaches. This topic requires dedicated studies to understand the consequences of using seawater in the concrete production. Till now, scientific knowledge in this area is still limited. Existing studies (Li et al. 2016; Xiao et al. 2017) have shown that the use of seawater may have a significant effect on chloride-induced steel corrosion but has a negligible effect on the carbonation process of concrete. Furthermore, the results showed that the use of seawater increased concrete's compressive strength at early age, reduced setting time and improved mechanical properties. On the other hand, structural behaviour of reinforced concrete elements using composite materials (FRP) has been extensively

studied, mainly focusing the bond characterization between FRP and concrete, as well as the flexural and shear behaviour in full-scale reinforced concrete beams. Typically, GFRP (Glass FRP) rods have been used to reinforce concrete elements, e.g. Mazaheripour et al. (2013) and Barris et al. (2017). Some research has been carried out on the study of the long-term behaviour and durability of RC elements with FRP rods, particularly when exposed to alkaline environments, chlorides action, seawater immersion, high temperatures, moisture, thermal cycles and freeze-thaw cycles, e.g. Dong et al. (2016). According to the studies carried out, the use of FRP rods in RC structures exposed to marine environments shows to be very promising not only due to the resulting structural performance but also for the contribution to promoting environmental sustainability.

An ongoing research work by the authors of the present paper is exploring the use of seawater in the concrete production, when the conventional steel reinforcement is replaced by GFRP rods. The research work includes two phases. In the first phase concrete compositions were developed through an optimization algorithm to obtain specific properties at fresh and hardened states. The second phase included experimental investigation on the bond behaviour between GFRP rods and concrete through direct pullout tests. As a result, the influence of the type of water (seawater and tap water) in the concrete mixture, as well as the GFRP rod diameter and anchorage length on the bond behaviour between GRFP and concrete, were assessed.

EXPERIMENTAL PROGRAM

Concrete composition

In this section, the procedure used to determine the concrete composition is briefly described. This composition was used in the production of the concrete pullout test specimens. The objective was to find out the best dosages to produce a concrete with mechanical properties required in special projects requiring higher strengths, particularly in maritime environments. The requirements included: (i) good workability at the fresh state and (ii) high mechanical strength at the hardened state. The concrete composition is mainly influenced by two parameters: (i) water/cement (w/c) ratio and (ii) particle size distribution of the aggregates. The concrete compositions were established based on the work carried out by Pereira (2016), using modifications proposed by Andreasen and Andersen (A&A). The aggregates were carefully selected and previously washed. According to the standard NP EN 933-1:2000, the sieve analysis was performed. Once the solids composition was defined, the next step was the analysis of the water/cement (w/c) ratio influence. In order to do so, several mixtures were produced with different w/c ratios. The iterative process included characterization tests in the fresh and hardened state. The composition selected had a w/c ratio of 0.26. Based on the results of the optimization of solids composition, as well as on concrete characterization in the fresh and hardened state, the final composition was: (i) cement CEM I 42.5R according to European standard NP EN 197-1:2001 (480 kg/m³), (ii) class-f fly ash (124.5 kg/m³), (iii) sand (1271 kg/m³), (iv) gravel 4-8 (192 kg/m³), (v) gravel 8-16 (76.7 kg/m³), (vi) superplasticizer *Sika® ViscoCrete® 3002 HE* (5.1 kg/m³) and (vii) viscosity modifying agent *Sika® VPI* (4.8 kg/m³). The required water to saturate the aggregates was determined for each mixture according to ASTM C566-97:2013.

Direct pullout tests: geometry, experimental set-up, instrumentation and materials characterization

The program was composed of 24 direct pullout tests divided into 8 series. Studied parameters were (i) type of water used in the concrete composition (SW- seawater or TP- tap water), (ii) GFRP rods diameter ($\emptyset 8$ or $\emptyset 12$) and (iii) anchorage length ($5\emptyset$ or $10\emptyset$). The SW used in the concrete production was extracted directly from the sea - in Esposende (north coastal area of Portugal). According to laboratory analyses carried out by *APA-ARH Norte* (Portuguese Environment Agency), the water quality was rated as excellent, without chemical pollutants. The salinity of SW, i.e. salt concentration per unit mass of water is about 3.5 % (Antonov et al. 2006). The experimental program is shown in Table 1. The designation of each series was defined as follows: (i) “ \emptyset ” is the GFRP nominal diameter in millimeters, (ii) “LbX \emptyset ” is the anchorage length where X is the multiple of GFRP nominal diameter (5 or 10) and (iii) “TW” or “SW” states the type of water used in concrete composition (tap water or seawater, respectively). In each test series, 3 tests were performed under the same conditions.

Figure 1 depicts the test set-up adopted for the present experimental program. Concrete cubic blocks with 200 mm of edge were used. The applied force was measured with a load cell of 200 kN (0.05% F.S.) maximum capacity. The relative displacement between the GFRP and the concrete (slip) at the loaded end section was assessed by the average of displacements measured by LVDTs 1, 2 and 3, positioned at 120° around the GFRP rebar. Free end slip was assessed by the use of LVDT 4. LVDTs 1 and 2 had a stroke of ± 10 mm (0.25% F.S.). LVDTs 3 and 4 had a stroke of ± 5 mm (0.25% F.S.). Tests were performed under displacement control at a velocity of 0.021 mm/s.

Table 1: Direct pullout tests – experimental program.

Age of concrete [days]	Water type	GFRP rod diameter [mm]	Anchorage length [mm]	Designation*
28	TW	8	40	Ø8_Lb5Ø_TW_i
			80	Ø8_Lb10Ø_TW_i
		12	60	Ø12_Lb5Ø_TW_i
			120	Ø12_Lb10Ø_TW_i
	SW	8	40	Ø8_Lb5Ø_SW_i
			80	Ø8_Lb10Ø_SW_i
		12	60	Ø12_Lb5Ø_SW_i
			120	Ø12_Lb10Ø_SW_i

* "i" represents the specimen 1, 2 or 3.

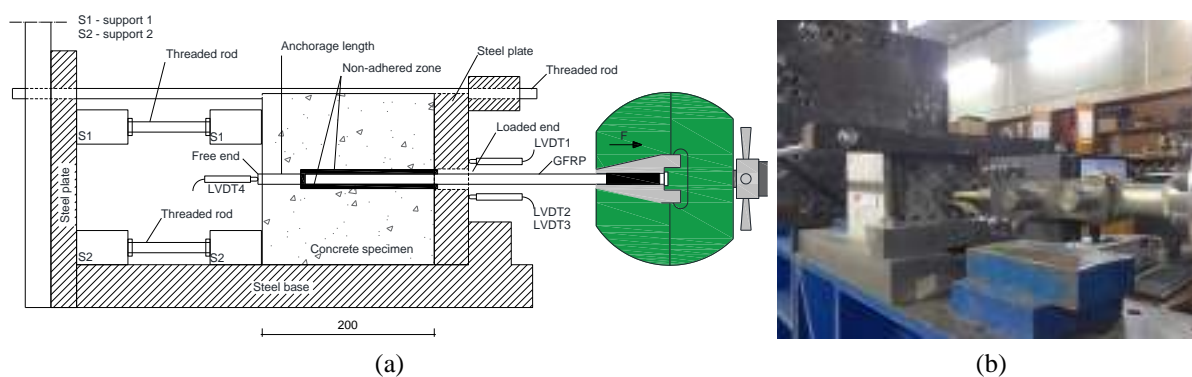


Figure 1 – Pullout tests: (a) scheme; (b) photo. Note: dimensions in millimeters.

Before carrying out the direct pullout tests, the constituting materials were characterized: (i) concrete (with SW and TW) and (ii) GFRP rods.

Concrete was characterized in two different phases: (i) fresh state and (ii) hardened state. To characterize the concrete properties in the fresh state, slump-flow tests were carried out and the T_{500} parameter was measured, according to the standard BS EN 12350-8:2010. This test allows the evaluation of the deformability of the concrete through the deformation velocity and slump flow diameter imposed by the action of self-weight. The T_{500} parameter allows to indirectly assess the concrete viscosity. To produce the concrete for the pullout test specimens, four concrete castings were carried out (two with SW and the others with TW). Each concrete casting was composed of two batches. To characterize the concrete properties in the hardened state, compression tests were carried out with concrete cylindrical specimens. The cylinders had a diameter of 150 mm and a height of 300 mm. Compression tests were carried out 28 days after casting, in order to obtain compressive strength (f_c) and modulus of elasticity (E_c), according NP EN 12390-3:2011 and LNEC E397:1993. In total, eight cylindrical specimens were tested: four with concrete made of seawater and the remaining ones with the concrete made of tap water. All concrete specimens (cylinders for concrete characterization tests and cubes for pullout tests) were cured in a wet environment, fully submerged in a water tank at a temperature of 22 ± 2 °C until the testing day (28 days of age). The type of water (SW or TW) used to submerge the test specimens corresponded to the type of water used in the respective concrete composition. Test results of concrete characterization and corresponding analysis are included in the next section.

ComBAR® GFRP ribbed round rods produced by the company Schöck were used. As stated previously, two distinct diameters were studied: 8 and 12 mm. These rods present a deformed external surface with ribs of a constant height of 6% of bar diameter and a spacing of about 8.5 mm. The tensile mechanical properties of these rods were assessed according to the ASTM D7205/D7205M:2006 by conducting uniaxial tensile tests. From six GFRP rods with 8 mm of diameter (Ø8) tested, an average modulus of elasticity of $E_f=69$ GPa (CoV=3.6%), an average tensile strength of $f_{ult}=1527.9$ (CoV=4.5%) and an average ultimate strain of $\epsilon_f=1.8\%$ (CoV=0.1%), were obtained. From the six samples of GFRP Ø12 rods tested, the following mechanical properties were obtained: $E_f=70.1$ GPa (CoV=3.1%), $f_{ult}=1447.1$ (CoV=6.5%) and $\epsilon_f=1.8\%$ (CoV=1.0%).

RESULTS AND DISCUSSION

Concrete characterization

Table 2 presents the results of the concrete characterization tests in the fresh state. The results show that when seawater was used in the mixture, the concrete exhibited a more cohesive, viscous and compact behaviour compared to the mixture where tap water was used. Consequently, the concrete with seawater presented worse workability than the concrete with tap water, and for that reason it was not possible to obtain the T_{500} parameter (concrete casting 2 and 3) because the fluid concrete did not reach a flow diameter of 500 mm. All concrete mixtures did not show any sign of segregation. Additionally, the results suggest that the use of seawater in the mixture may have reduced concrete setting time and led to the faster development of its mechanical properties (Freitas 2017). Similar conclusions were obtained in other research studies, e.g. Etxeberria et al. (2016).

Table 2: Fresh state concrete properties.

Concrete casting	Concrete casting 1		Concrete casting 2		Concrete casting 3		Concrete casting 4	
	1 st batch	2 nd batch	1 st batch	2 nd batch	1 st batch	2 nd batch	1 st batch	2 nd batch
Water	TW	TW	SW	SW	SW	SW	TW	TW
Slump flow [mm]	625.0	612.5	420.5	447.5	330.0	400.0	400.0	485.0
T_{500} [s]	13	15	*	*	*	*	16	15
Photos								

*invalid results.

Table 3 presents the results of concrete mechanical characterization by compression tests in hardened state (28 days of age). In general, the concrete produced with tap water presented better mechanical properties than the concrete with seawater. Seawater contains several mineral and biological elements that can interact with concrete components and consequently influence their properties. The results show that when seawater was used in the mixture, a lower mean compressive strength (f_{cm}) was obtained (≈ 58 MPa) comparatively to the use of tap water (≈ 66 MPa). A similar trend was observed in terms of modulus of elasticity: when seawater was used in the concrete mixture, a mean modulus of elasticity (E_{cm}) of 33.7 GPa was obtained whereas the use of tap water has resulted in a mean modulus of elasticity of 36.2 GPa. According to EN 1992-1-1:2010, the concrete with seawater complies with the strength class C50/60; while the concrete with tap water in its composition complies with the strength class C55/67.

Bond behaviour

Average results obtained in each series of the direct pullout tests are presented in Table 4 through several parameters that characterize the bond behaviour between GFRP and concrete. The parameters included are the (i) maximum pullout force (F_{max}), (ii) loaded end slip at F_{max} (s_{lmax}), (iii) free end slip at F_{max} (s_{fmax}), (iv) average shear strength (τ_{max}) assuming a constant shear stress along the anchorage length (ratio between F_{max} and contact area between the GFRP and concrete), (v) residual pullout force corresponding to a s_l of 10 mm (F_r), (vi) fracture energy during debonding process up to 10 mm of s_l (G_f), (vii) F_r/F_{max} ratio and (viii) failure mode observed.

Table 3: Hardened state concrete properties.

Compressive Strength (f_c) and Modulus of Elasticity (E_c)	Tap water (TW)	Seawater (SW)
	65.7	61.9
	66.6	57.9
	67.3	54.7
	66.3	57.7
f_{cm} [MPa]	66.5 (0.9%)	58.0 (4.4%)
$E_{c,28d}$ [GPa]	36.8	32.3
	36.7	34.4
	37.1	33.0
	34.7	33.7
E_{cm} [GPa]	36.2 (2.6%)	33.7 (2.3%)

The values in parentheses are coefficients of variation (CoV).

Table 4: Average results obtained from the direct pullout tests.

Serie	F_{max} [kN]	s_{lmax} [mm]	s_{fmax} [mm]	τ_{max} [MPa]	F_r [kN]	G_r [kN.mm]	F_r/F_{max} [%]	Failure Mode*
Ø8_Lb5Ø_TW	19.8 (4.7%)	2.01 (4.2%)	0.39 (25.7%)	13.1 (5.1%)	8.3 (44.0%)	133.0 (22.4%)	41.7 (43.0%)	PF ^{1,2} TF ³
Ø8_Lb10Ø_TW	33.7 (2.2%)	3.15 (3.4%)	0.31 (24.1%)	11.2 (2.1%)	34.3 (4.5%)	341.9 (20.5%)	102.0 (6.0%)	TF ^{1,2,3}
Ø12_Lb5Ø_TW	48.9 (5.8%)	2.06 (7.9%)	0.24 (31.9%)	21.6 (5.7%)	27.7 (28.8%)	317.7 (11.2%)	57.6 (32.6%)	D ¹ TF ^{2,3}
Ø12_Lb10Ø_TW	81.8 (2.5%)	3.25 (3.0%)	0.32 (10.2%)	18.1 (2.5%)	39.4 (18.4%)	494.3 (8.4%)	48.1 (16.6%)	D ^{1,2,3}
Ø8_Lb5Ø_SW	13.7 (2.4%)	1.37 (1.2%)	0.25 (4.9%)	9.0 (2.6%)	3.2 (24.3%)	60.5 (15.7%)	23.4 (22.3%)	D ^{1,2,3}
Ø8_Lb10Ø_SW	25.6 (3.3%)	2.34 (5.0%)	0.29 (8.2%)	8.5 (3.3%)	10.6 (10.1%)	151.7 (9.4%)	41.2 (9.4%)	D ^{1,2,3}
Ø12_Lb5Ø_SW	45.1 (2.3%)	1.89 (2.0%)	0.33 (15.6%)	20.0 (2.3%)	11.6 (11.8%)	210.6 (4.0%)	25.9 (13.4%)	D ^{1,2,3}
Ø12_Lb10Ø_SW	68.7 (6.9%)	2.60 (7.1%)	0.32 (5.8%)	15.2 (6.9%)	23.3 (8.6%)	354.4 (3.1%)	33.9 (5.7%)	D ^{1,2,3}

*Failure modes: (TF)-debonding failure at the interface GFRP/concrete + total failure of GFRP ribs; (PF)-debonding failure at the interface GFRP/concrete + partial failure of GFRP ribs; (D)-debonding failure; 1,2,3 is the specimen number; The values in parentheses are coefficients of variation (CoV).

Figure 2 shows the relation between the pullout force (F) and loaded end slip (s_l) obtained in the direct pullout tests. In general, two distinct phases can be identified in the $F-s_l$ curves. The first phase (pre-peak) is characterized by an approximately linear relationship between the applied force and the slip. At this phase, the bond adherence provided by the chemical adhesion between the involving materials is responsible for the bond strength. Debonding process starts soon after the linear branch where a loss of adhesion and stiffness is observed close to F_{max} . The second phase (post-peak) is characterized by a markedly non-linear bond behaviour. Immediately after the F_{max} has been reached, a downward curve branch with a significant slope is observed, followed by a softer slope in more advanced stages. This last stage is mainly governed by friction between the involved materials.

The bond response observed in the $F-s_l$ curves is directly related to the bond mechanisms and consequent failure modes. Three different failure modes were observed (Figure 3): (i) debonding failure at the GFRP/concrete interface + total failure of GFRP ribs (TF), (ii) debonding failure at the GFRP/concrete interface + partial failure of GFRP ribs (PF) and (iii) debonding failure at the GFRP/concrete interface (D). The latter failure mode was the most frequently observed. However, in some tests (e.g. Ø8_Lb5Ø_TW_3; Ø8_Lb10Ø_TW_1,2,3; Ø12_Lb5Ø_TW_2,3), probably due to better mechanical properties of the concrete and consequently better bond conditions, the resisting mechanisms involved the frictional component and also the mechanical resistance of the GFRP ribs. In the $F-s_l$ curves corresponding to these specimens (Figure 2), the post-peak branch has a low slope and, in some cases, there is an increase in the pullout force with the progressive increase of the loaded end slip. The later behaviour may be related to the additional friction and interlocking caused by the ribs that were destroyed.

Figure 4 shows the influence of studied parameters, mainly the GFRP diameter, anchorage length and water type on the bond behaviour. Before proceeding to the discussion of these results, it is important to highlight that F_r/F_{max} ratio (see Table 4) was strongly influenced by the failure mode observed. On average, when total failure of GFRP ribs was observed, F_r/F_{max} ratio increased from 23% to 102% (Figure 4(e)). Regarding the efficiency of the reinforcement system (F_{max}/F_{ult} ratio), in the best case, only 51% of GFRP rod tensile strength was attained (series $\text{Ø}12_Lb10\text{Ø_TW}$).

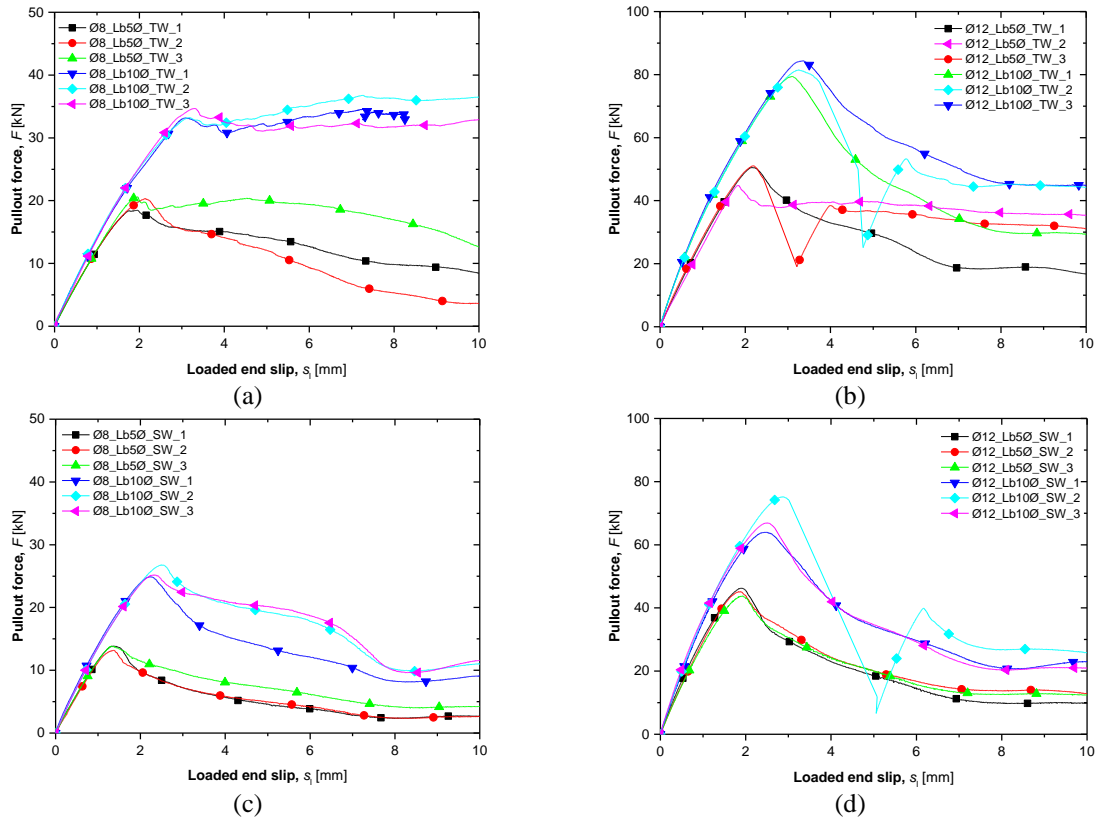


Figure 2 – Pullout force versus loaded end slip curves: (a) $\text{Ø}8_TW$; (b) $\text{Ø}12_TW$; (c) $\text{Ø}8_SW$; (d) $\text{Ø}12_SW$.

Influence of the GFRP diameter

Regarding the GFRP diameter, in spite of the GFRP cross section area (or the external surface in contact with concrete) of the rod $\text{Ø}12$ being 125% larger than the one of rod $\text{Ø}8$, it is found that F_{max} and τ_{max} has increased about 172% and 82%, respectively, when $\text{Ø}12$ was used instead of $\text{Ø}8$ (Figure 4(a) and Figure 4(c)). Thus, it can be concluded that the bond strength tends to increase with the increase of the rod diameter (at least from $\text{Ø}8$ to $\text{Ø}12$). Similar trend was also observed by Mazaheripour et al. (2013) and can be justified by the fact that $\text{Ø}12$ rods show larger ribs, thus promoting better bond conditions than rods $\text{Ø}8$. Consequently, higher values were obtained for the s_{lmax} and s_{fmax} (Table 4). In terms of G_f , a considerable increase was observed (on average about 141%) when $\text{Ø}12$ was used instead of $\text{Ø}8$ (Figure 4(f)).

Influence of the anchorage length

As expected, results demonstrated that by increasing L_b the bond strength has increased, since the adopted lengths are relatively small (lower than effective anchorage length). On average, it is found that F_{max} has increased about 69% when $L_b=10\text{Ø}$ was used instead of $L_b=5\text{Ø}$. On the other hand, by increasing L_b , a larger contact surface between reinforcing material and concrete was mobilized and consequently lower τ_{max} values were obtained, due to the non-linear distribution of bond stresses along the anchorage length. According to the results, it is found that the τ_{max} has increased about 19% when a $L_b=5\text{Ø}$ was adopted instead of $L_b=10\text{Ø}$. Furthermore, s_{lmax} also increased with L_b . In terms of G_f , a considerable increase was observed (on average about 108%) when $L_b=10\text{Ø}$ was used instead of $L_b=5\text{Ø}$ (Figure 4(f)).

Influence of the water type

In general, the analysis of results suggests that the use of TW provided higher bond strength, compared with the use of SW in concrete mixture. On an average, the use of TW instead of SW provided an increase of 26% on the F_{max} and τ_{max} (Figure 4(b) and Figure 4(d), respectively). This can be explained by the presence of mineral,

biological and chemical components on the SW, which may have negative effects on the concrete mechanical properties. Similar observations had been made in the concrete characterization tests at 28 days of age which means that the bond behaviour between GFRP and concrete is influenced by the concrete mechanical strength. Regarding F_r/F_{max} ratio, an increase was verified (on average about 98%) when TW was used instead of SW (Figure 4(e)). In terms of G_f , an increase was observed (on average about 84%) when TW was used instead of SW (Figure 4(f)). However, in general it can be considered that the use of SW in the concrete mixture had a minimal and no severe effects on the interface behaviour between GFRP and concrete.

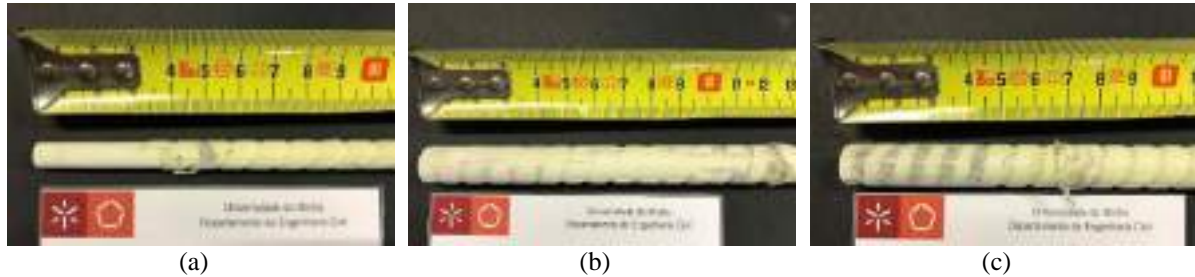


Figure 3 – Failure modes: (a) TF - debonding failure + total failure of GFRP ribs; (b) PF - debonding failure + partial failure of GFRP ribs; (c) D - debonding failure.

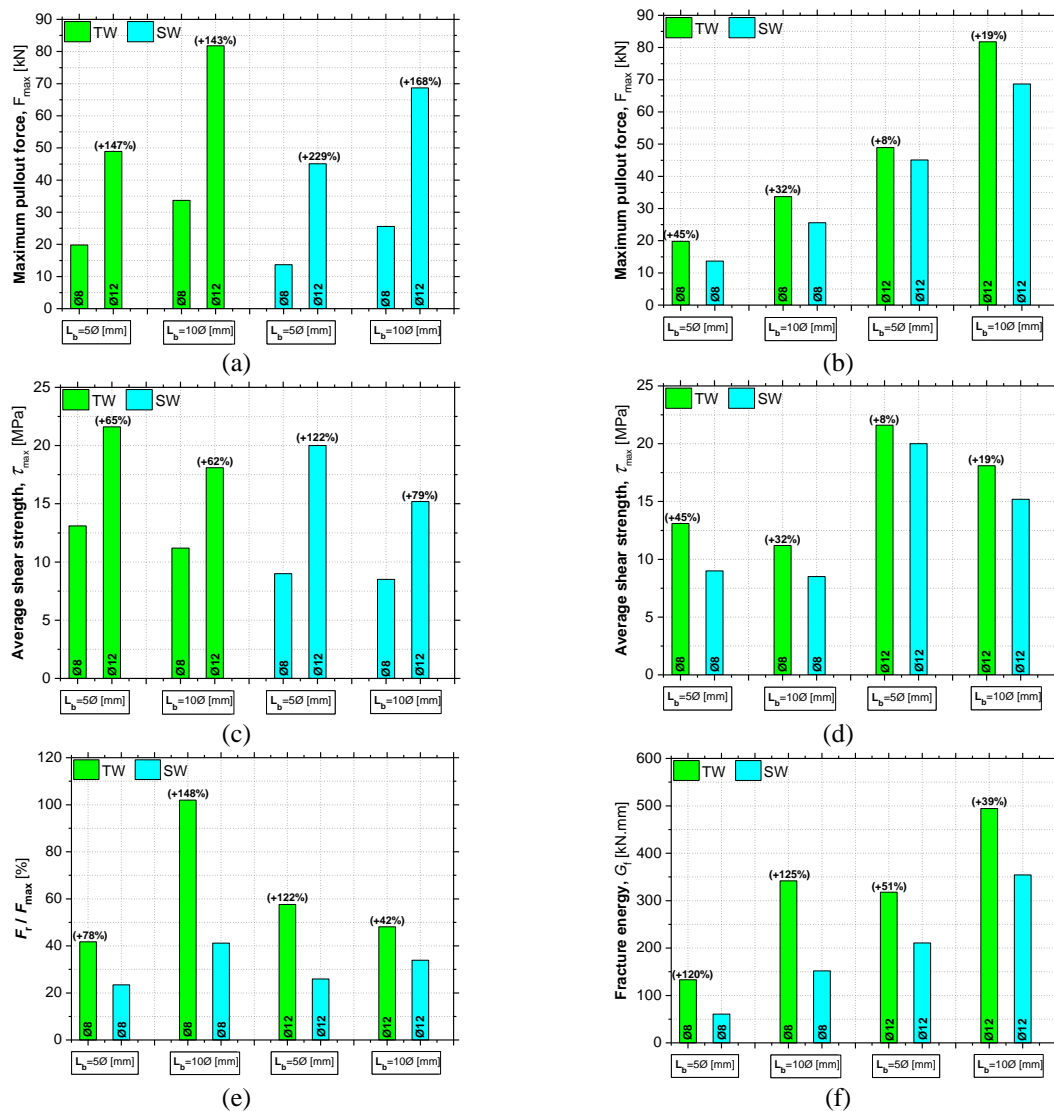


Figure 4: Bond behaviour characterization: influence of GFRP rod diameter, anchorage length and water type on the maximum pullout force (a-b), the average shear strength (c-d), F_r/F_{max} (e) and fracture energy (f).

CONCLUSIONS

An ongoing research work intends to appraise the sustainability of RC structures in marine environment when using SW in concrete combined with the replacement of conventional steel reinforcement by GFRP rods. An experimental program was carried out in two phases: (i) the development of a concrete mixture (including SW) of high strength, including characterization tests at fresh and hardened state and (ii) assessment of bond behaviour between concrete and GFRP rods through direct pullout tests. In both phases the effect of the use of SW instead TW in the concrete mixture was studied. By carrying out pullout tests the influence of parameters such as GFRP rod diameter and anchorage length were also assessed.

From concrete characterization tests it was concluded that the (i) the SW provided a higher cohesion, viscosity and compactness to the fresh concrete. Results have indicated also that SW may have reduced the concrete setting time and led to a faster development of its mechanical properties; (ii) compression tests performed at 28 days of age showed that the concrete which included TW presented a higher value of compressive strength ($\approx +15\%$) and modulus of elasticity ($\approx +7\%$).

From the direct pullout test results, the following conclusions can be highlighted: (i) three different failure modes were observed, mainly debonding failure with total, partial or without failure of GFRP ribs; (ii) the larger GFRP rod diameter provided the higher values of F_{\max} and τ_{\max} . Additionally, higher values of s_1 and G_f were also obtained; (iii) the longer L_b provided an increase in F_{\max} . On the other hand, by increasing the anchorage length, a larger contact surface between GFRP and concrete was mobilized and consequently lower τ_{\max} were obtained, due to the non-linear distribution of the bond stresses along the anchorage length. Additionally, higher values of s_1 and G_f were obtained; (iv) The use of SW instead of TW on the concrete mixture had influence on the interface behaviour between GFRP and concrete. In the specimens where SW was included, lower F_{\max} and τ_{\max} values were obtained. These reductions are directly related to the observed reductions in the concrete mechanical strength at 28 days of age when SW was used. Nevertheless, it can be concluded that the use of SW had no severe effects on the bond behaviour at 28 days after casting.

REFERENCES

- Antonov, J.I., Locarnini, R.A., Boyer, T.P., Mishonov, A.V., & Garcia, H.E. (2006). "World Ocean Atlas 2005, Volume 2: Salinity" S. Levitus, Ed. NOAA Atlas NESDIS 62, U.S. Government Printing Office, Washington, D.C., 182 pp.
- Barris, C., Torres, L., Vilanova, I., Miàs, C., & Llorens, M. (2017). "Experimental study on crack width and crack spacing for Glass-FRP reinforced concrete beams", *Engineering Structures*, 131, 231-242.
- Dong, Z., Wu, G., Xu, B., Wang, X., & Taerwe, L. (2016). "Bond durability of BFRP bars embedded in concrete under seawater conditions and the long-term bond strength prediction", *Materials & Design*, 92, 552-562.
- Etxeberria, M., Gonzalez-Corominas, A., & Pardo, P. (2016). "Influence of seawater and blast furnace cement employment on recycled aggregate concretes' properties", *Construction and Building Materials*, 115, 496-505.
- Freitas, N. E. D. (2017). "Sustentabilidade de Estruturas de Betão em Ambiente Marítimo com Recurso a FRP", *Master Thesis*, University of Minho.
- Goldston, M., Remennikov, A., & Sheikh, M. N. (2017). "Flexural behaviour of GFRP reinforced high strength and ultra high strength concrete beams", *Construction and Building Materials*, 131, 606-617.
- Li, Y. L., Zhao, X. L., Singh, R. K. R., & Al-Saadi, S. (2016). "Experimental study on seawater and sea sand concrete filled GFRP and stainless steel tubular stub columns", *Thin-Walled Structures*, 106, 390-406.
- Mazaheripour, H., Barros, J. A., Sena-Cruz, J., Pepe, M., & Martinelli, E. (2013). "Experimental study on bond performance of GFRP bars in self-compacting steel fiber reinforced concrete", *Composite Structures*, 95, 202-212.
- Pereira, J.E.M., (2016). "Estruturas de Betão Reforçadas com Materiais Compósitos em Ambiente Marítimo e Concebidas com Água do Mar", *Master Thesis*, University of Minho.
- Pradelle, S., Thiéry, M., & Baroghel-Bouny, V. (2017). "Sensitivity analysis of chloride ingress models: Case of concretes immersed in seawater", *Construction and Building Materials*, 136, 44-56.
- Ragab, A. M., Elgammal, M. A., Hodhod, O. A., & Ahmed, T. E. (2016). "Evaluation of field concrete deterioration under real conditions of seawater attack", *Construction and Building Materials*, 119, 130-144.
- Xiao, J., Qiang, C., Nanni, A., & Zhang, K. (2017). "Use of sea-sand and seawater in concrete construction: Current status and future opportunities", *Construction and Building Materials*, 155, 1101-1111.



FLEXURAL BEHAVIOR OF PULTRUDED GLASS FIBER-REINFORCED POLYMER DISTRIBUTION POLES

Omar I. Abdelkarim¹, Jose Manuel Guerrero², Hamdy M. Mohamed³, Brahim Benmokrane⁴

1 Department of Civil Engineering, University of Sherbrooke, Quebec, Canada, J1K2R1.

Abdelkarim.Omar@Usherbrooke.ca

2 Global PoleTrusion Group Corporation, Longueuil, QC, Canada J4N 1R2.

joseg@poletrusion.com

3 Department of Civil Engineering, University of Sherbrooke, Quebec, Canada, J1K2R1.

Hamdy.Mohamed@Usherbrooke.ca

4 Department of Civil Engineering, University of Sherbrooke, Quebec, Canada, J1K2R1.

Brahim.Benmokrane@Usherbrooke.ca

ABSTRACT

This paper presents the behavior of pultruded GFRP distribution poles under flexural loading. Electrical and telecommunication utility infrastructures, including poles, H-frames, and towers, are typically made of wood, concrete, or steel. Each of these materials has several shortcomings due to their performances under the environmental conditions and the difficulty of transportation. In addition, a significant number of the electrical infrastructures in North America needs renewal in the coming few years because of their environmental deterioration. Currently, the industry of the utility poles trends to build new infrastructures to be more reliable, cost-effective, and sustainable. Glass fiber reinforced polymer (GFRP) composites for the utility infrastructures represent a viable alternative to the traditional materials. However, the lack in the theoretical and experimental data on the GFRP composite utility infrastructures delays their implementation. In this study, two identical full-scale GFRP distribution poles Class C5 were tested under flexural loading. Also, the effect of the fiber volume ratio on the load capacity of GFRP poles was investigated using finite element analyses. The tested poles had a height of 10.5 m, a diameter of 254 mm, a thickness of 6.35 mm, and a fiber volume ratio of 0.40. The tested poles exceeded the required strength as per the American National Standards Institute. A finite element (FE) model was developed for the poles using MSC Nastran software. The FE validation showed a very good agreement with the experimental results with accuracies of 98% and 95% for the prediction of the load capacity and maximum displacement, respectively. The FE analyses showed that the moment capacity of the GFRP poles increased almost linearly with increasing the fiber volume ratio.

KEYWORDS

Utility poles; FRP; Composites; Fiber volume ratio; Finite element analysis.

INTRODUCTION

Many electrical and telecommunication infrastructures in Canada are about to reach the end of their life expectancy, resulting in much of these infrastructures being in need of renewing. The Conference Board of Canada stated that approximately \$350 billion dollars will be required by 2030 just to maintain existing capacity of the electricity (Coad et al. 2010), while most of Canada's non-hydro assets will need renewal or replacement by 2050. Also, there are about 600 million electrical poles in the United States are subjected to the same condition of those in Canada, which represents billions dollar of business. Therefore, it is important to build the new infrastructures to be reliable, cost-effective, and sustainable. Most of the electrical and telecommunication towers, poles, and H-frames are made of steel, concrete, or wood materials. Unfortunately, these traditional materials have several shortcomings under the environmental conditions. Wooden utility poles are susceptible to deteriorate because of the insects, leaching, rot, woodpeckers, and fire. They must be treated frequently with toxic chemicals to reduce the significant deterioration. Although, the concrete poles are more durable than the wooden, their weight increases the transportation and erection costs, especially in the case of rough terrains. In addition, the reinforcements of the concrete poles are subjected to corrode due to the environmental conditions which affect the poles' strength. The towers and H-frames made of steel are the most common for transmission lines in North America because of their strength and relatively low weight. However, they are very expensive comparable to the

concrete and wooden infrastructures. Also, they must be painted or galvanized for corrosion protection, while it is not guaranteed for a long-term protection.

The usage of fiber reinforced polymer (FRP) composites, especially the type of glass, in civil engineering structures continues to grow at an impressive rate due to their low weight-to-strength ratio and high durability under severe environmental conditions (e.g., Benmokrane et al. 2006; Abdelkarim et al. 2016). Recently, the research on FRP utility poles has been rising the academic interests. Theoretical and experimental studies have been developed in conjunction with finite element analyses to better understand the behavior of these composite poles (McClure et al. 1992; Polyzois et al. 1999; Ibrahim et al. 2000; Metiche and Masmoudi 2007; Mohamed, and Masmoudi 2009; Selvaraj et al. 2012; Hernández-Corona and Ramírez-Vázquez 2015). However, many points of research are still in need for such utility composite poles to increase implementing this technology in the field. While several studies have been conducted on the FRP poles manufactured using filament winding, very few studies were conducted on the FRP poles manufactured using pultrusion technique. The manufacturing technique is expected to have remarkable effects on the performance of the FRP structures.

The current industry of the FRP structures commonly uses the filament winding process to produce the FRP structural tubular elements which involves winding the filaments under tension over a rotating mandrel where the fibers are laying down in the desired angle, commonly $\pm 45^{\circ}$ - 55° . The main benefit of using fiber composite materials is arranging the fibers in the load direction for optimization. Therefore, arranging the fibers in the vertical (longitudinal) direction for the utility poles makes them much stronger and more efficient to resist the wind loads than the case of filament winding. In the pultrusion process, all the fibers enter a mold following the direction of the effort as shown in Figures 1 and 2. Also, per the American Society of Civil Engineering (ASCE) manual of practice-104, the GFRP poles must meet the same specified bending performance criteria applied to the poles made of other materials (e.g., wood). Therefore, the pultrusion process would be a good solution to produce thinner and lighter GFRP elements than that manufactured using the filament winding to meet the strength and serviceability requirements.



Figure 1: Arrangement of the Fiber rovings behind the mold at Global PoleTrusion Group Corporation



Figure 2: Producing the pultruded poles at Global PoleTrusion Group Corporation

EXPERIMENTAL WORK

Design of the utility poles is categorized into different classes based on the horizontal load capacity as listed by the standard American National Standards Institute (ANSI) 05.1. Two identical full-scale poles were manufactured by the Global PoleTrusion Group Corporation with a diameter of 254 mm, a thickness of 6.35 mm, a height of 10.5 m, and fiber volume ratio of 0.40, for a class C5. Six longitudinal coupons were cut from extra part of each pole and prepared for tension and compression tests. Three coupons were tested under tension loading according to the American Society for Testing and Materials (ASTM) D3039 and three coupons were tested under compression loading according to the ASTM D3410. The displacement loading rate was 1 mm/min for the both types of testing. The average tensile elastic modulus and strength of the coupon specimens were 31.5 GPa and 510 MPa and the average compressive elastic modulus and strength of the coupon specimens were 9.5 GPa and 351 MPa.

The poles were tested under flexural loading according to the ASTM D4923-01 at the University of Sherbrooke to identify the horizontal load capacity. Figures 3 illustrates the general configuration of the tested poles and the test setup. Each pole was setup horizontally on the floor and fixed using two opposite fixed supports at 0.0 and 1.65 m from the first end. The fixed part of the pole (1.65 m) represented the embedded depth of the pole into ground soil which is commonly calculated as (10% of the pole length + 600 mm). Two string potentiometers were installed at the two supports to confirm the fixation by monitoring the movement, if any. The pole was subjected to vertical loading at 0.6 m from the second end using winch and steel rope as shown in Figure 3. Another string potentiometer was attached to the pole at the loading point to measure the displacement. Figure 4 illustrates the pole during the load application.

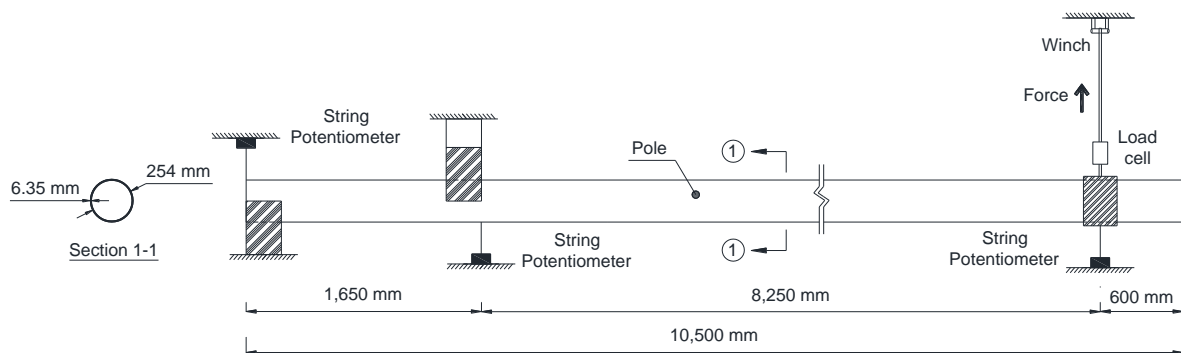


Figure 3: General arrangement and test setup of the tested poles



Figure 4: Loading the pole

EXPERIMENTAL RESULTS

Figure 5 illustrates the average displacement-load relation of the two tested poles. The load increased almost linearly with increasing the displacement until the failure of the pole. The average load and moment capacities of the tested poles were 9.4 kN and 77.6 kN.m, respectively. The average maximum displacement and drift (displacement over the shear span) at the point of load application were 1.92 m and 23%, respectively. The poles failed in compression as shown in Figure 6. The standard required load capacity of the poles Class C5 according to the ANSI 05.1 is 8.45 kN. The average load capacity of the tested poles was approximately 11% higher than the required strength. So, the design of the pole can be adjusted with a lower fiber volume ratio to achieve a load capacity closer to the required strength.

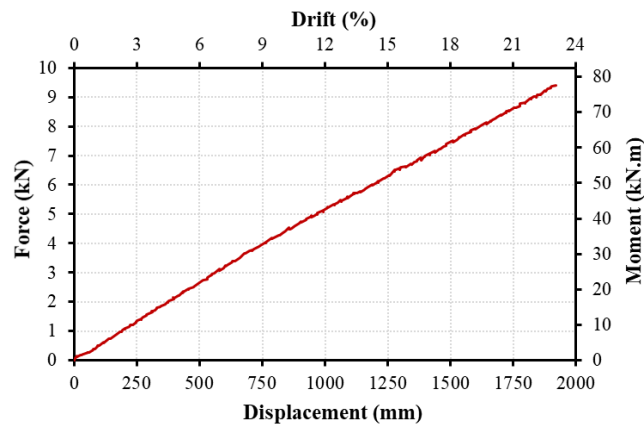


Figure 5: Experimental displacement-load relation of the tested poles



Figure 6: Compression mode of failure

FINITE ELEMENT ANALYSES

Model Validation

Finite element (FE) analyses were conducted to determine the effect of the fiber volume ratio on the GFRP pole load capacity. FE model was developed simulating the tested pole for validation. The FE model was developed using MSC Nastran software. Shell elements were used to simulate the poles with assigning a composite material. The material properties used in this model was collected from the results of the coupons' tests. The simulated pole was subjected to a ramp up horizontal load at 0.60 m from the top end until the pole failed in tension or in compression which means failed by buckling or reaching the compressive strength.

Figure 7 shows the developed FE model and the output results. The pole failed numerically in compression due to buckling as the experimental results. The load-displacement relation from the FE results compared well with the experimental results as illustrated in Figure 8. The average load and moment capacities of the simulated pole were 9.25 kN and 76.3 kN.m, respectively. The average maximum displacement and drift at the point of load application were 1.81 m and 22%, respectively. The accuracies of the finite element analysis for the flexural strength and displacement was 98% and 95%, respectively.

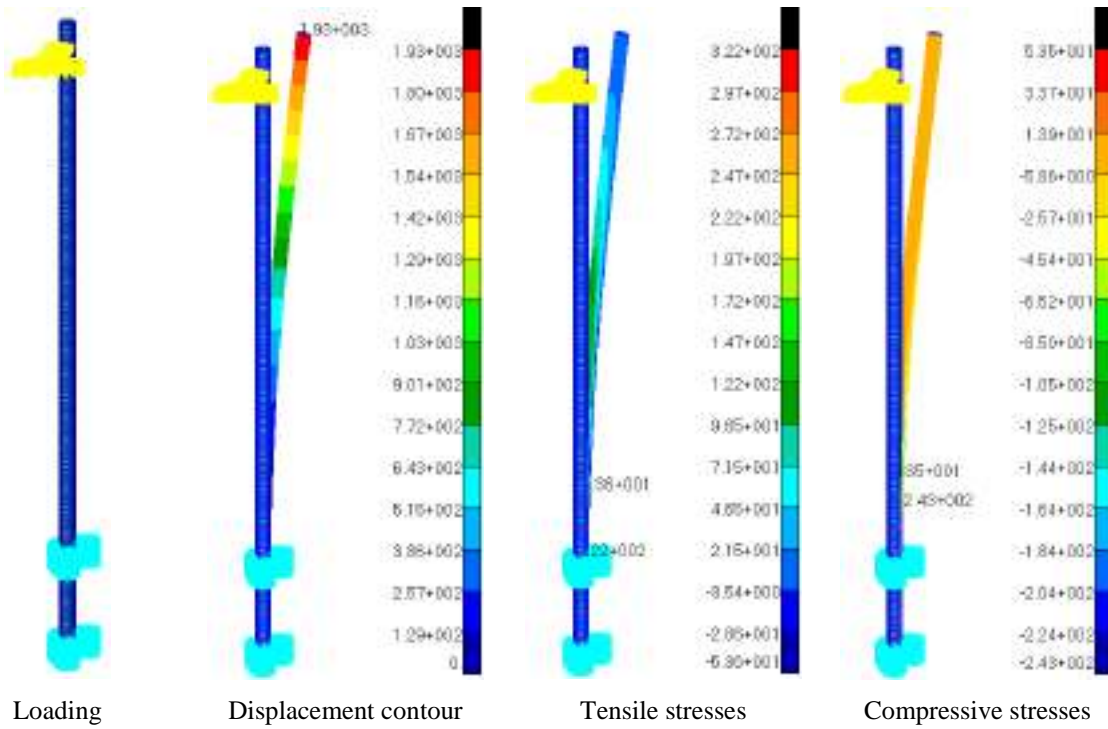


Figure 7: FE results of the validated finite element model of the tested poles

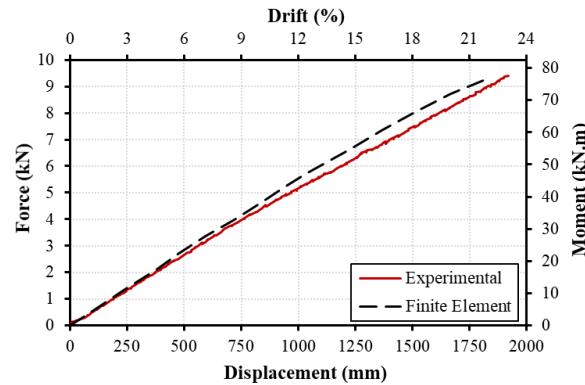


Figure 8: FE versus experimental displacement-load relations

Effect of the fiber volume ratio

The effect of the fiber volume ratio (V_f) on the pole's load capacity was examined. The validated model was examined with four different V_f ratios of 0.10, 0.24, 0.34, and 0.40. Equations 1 to 4 were used to determine the material properties using the rule of mixtures for the elastic moduli and other common equations for shear moduli (Kachlakev et al. 2001). The calculated properties from the Equations 1 to 4 with a V_f ratio of 0.4, as the tested pole, were found very close to the determined properties from the experimental coupons' results. The tensile and compressive strengths were determined by multiplying the elastic tensile and compressive moduli by the designed maximum tensile and compressive strains, respectively. The maximum tensile and compressive strains are 1.6% and 3.5%, respectively, as per the manufacturers' data sheets of the fiber roving and resin material. Figure 9 illustrates the relation between the V_f and the moment capacity of the simulated poles. The moment capacity increased almost linearly with increasing the V_f . The figure shows that the pole with V_f of 0.34 had a maximum load of 8.7 kN which is more suitable for the Class C5 than the pole with V_f of 0.40.

$$E_{11} = E_f V_f + E_m (1 - V_f) \quad (1)$$

$$E_{22} = \left[\frac{V_f}{E_f} + \frac{(1 - V_f)}{E_m} \right]^{-1} \quad (2)$$

$$G_{12} = \frac{E_{11} E_{22}}{E_{11} + E_{22} + 2 \nu_{12} E_{11}} \quad (3)$$

$$G_{23} = \frac{E_{22}}{2(1 + \nu_{23})} \quad (4)$$

where E_{11} is the elastic modulus of the FRP pole in the vertical direction, E_{22} is elastic modulus of the FRP pole in the hoop direction, G_{12} is the major shear modulus, G_{23} is the minor shear modulus, E_f is the elastic modulus of the glass fibers = 78 GPa, E_m is the elastic modulus of the resin material = 3.2 GPa, V_f is the fiber volume ratio (varied for each pole type), ν_{23} and ν_{12} are the Poisson's ratios, were assumed to 0.3.

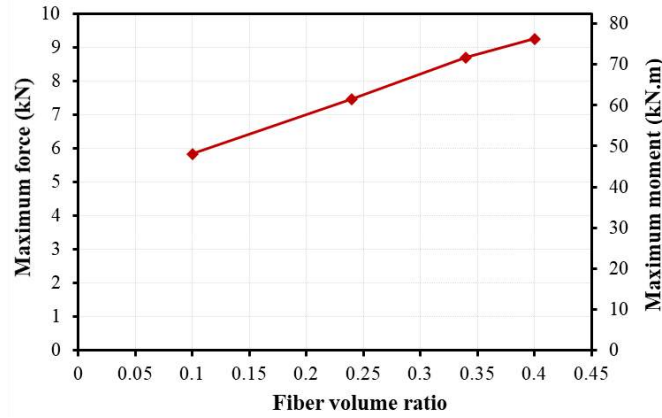


Figure 9: Fiber volume ratio versus the maximum moment and force of the GFRP poles

CONCLUSIONS

Two identical tested poles with a height of 10.5 m, a diameter of 254 mm, a thickness of 6.35 mm, and a fiber volume ratio of 0.40 were tested under flexural loading. Finite element analyses were conducted to examine the effect of the fiber volume ratio on the load capacity of the GFRP poles. A validated FE model was used for this study which showed a good agreement with the experimental results with accuracies of 98% and 95% for the prediction of the load capacity and maximum displacement, respectively. This study revealed that the lightweight pultruded GFRP composite poles were stiff enough to sustain the lateral wind loads. The poles achieved a higher strength than the requirement of the American National Standards Institute for Class C5 by 11%. The finite element study showed that the load capacity increased almost linearly with increasing the fiber volume ratio.

ACKNOWLEDGMENTS

This research was supported by the Government of Canada's Ministry of the Economy, Science, and Innovation (MESI), MITACS organization, and Global PoleTrusion Group Corporation. However, any opinions, findings, conclusions, and recommendations presented in this paper are those of the authors and do not necessarily reflect the views of the sponsors.

REFERENCES

- Abdelkarim, O. I., ElGawady, M. A., Ghani, A., Anumolu, S., and Abdulazeez, M. (2016). "Seismic Performance of Innovative Hollow-Core FRP-Concrete-Steel Bridge Columns." *ASCE journal of Bridge Engineering*, 10.1061/(ASCE)BE.1943-5592.0000985 , 04016120.
- ANSI 05.1 (2008). "American National Standards for Wood Poles and Wood Products." American National Standards Institute, Inc., Specifications & Dimensions.

ASCE manual of practice 104 (2003). "Recommended Practice for Fiber-Reinforced Polymer Products for Overhead Utility Line Structures." American Society of Civil Engineering (ASCE) Manuals and Reports on Engineering Practice, USA, pp. 88.

ASTM D4923-01, Standard Specification for Reinforced Thermosetting Plastic Poles, ASTM International, West Conshohocken, PA, 2001.

ASTM D3039 / D3039M-14, Standard Test Method for Tensile Properties of Polymer Matrix Composite Materials, ASTM International, West Conshohocken, PA, 2014.

ASTM D3410 / D3410M-16, Standard Test Method for Compressive Properties of Polymer Matrix Composite Materials with Unsupported Gage Section by Shear Loading, ASTM International, West Conshohocken, PA, 2016.

Benmokrane, B., El-Salakawy, E., El-Ragaby, A., and Lackey, T. (2006). "Designing and testing of concrete bridge decks reinforced with glass FRP bars." *Journal of Bridge Engineering*, 11(2): 217–229.

Coad, L., Crawford, T., and MacDonald, A. (2010). Shedding light on the economic impact of investing in electricity infrastructure. In Conference Board of Canada.

Hernández-Corona, R. and Ramírez-Vázquez, I. (2015). "Structural Performance of Polymeric Composite Members in a Transmission Line Tower." Proceedings of the 2015 COMSOL Conference, Boston.

Ibrahim, S., Polyzois, D., and Hassan, K. (2000). "Development of glass fiber reinforced plastic poles for transmission and distribution lines", *Can. J. Civil Eng.*, vol. 27, pp. 850-858.

Kachlakev, D.I., Miller, T., Yim, S., Chansawat, K., and Potisuk, T. (2001). "Finite Element Modeling of Reinforced Concrete Structures Strengthened with FRP Laminates." California Polytechnic State University, San Luis Obispo, CA and Oregon State University.

McClure, G., Boire, L., and Carrière, G. C. (1992). "Applications of advanced composite materials in overhead power lines and telecommunications structures", in *advanced composite materials in bridges and structures: 1st International Conference*. Canadian Society for Civil Engineering, pp. 543-549.

Metiche, S., and Masmoudi, R. (2007). "Full-scale flexural testing on fiber-reinforced polymer (FRP) poles." *Open Civil Engineering Journal*, 1, 37-50.

Mohamed, H. and Masmoudi, R. (2009). Design optimization of GFRP pole structures using finite element analysis. In *Proceeding of the ACMA 2009 Conference*, Tampa, Florida, USA, January.

Polyzois, D., Ibrahim, S., Burachynsky, V., and Hassan, S. K. (1999). "Glass Fiber-Reinforced Plastic Poles for Transmission and Distribution Lines: An Experimental Investigation." In *Proceedings of the 12th International Conference on Composite Materials, ICCM (Vol. 12)*.

Selvaraj, M., Kulkarni, S. M., & Babu, R. R. (2012). "Structural evaluation of FRP Pultruded Sections in overhead transmission line Towers." *International Journal of Civil and Structural Engineering*, 2(3), 934.



TECHNICAL STANDARDS FOR DEBONDING IN FRP-CONCRETE SYSTEMS: AN EXPERIMENTAL CONTRIBUTION FOR BASALT-FRP

Elisabetta Monaldo 1, Francesca Nerilli 1 and Giuseppe Vairo 2

¹ *Università degli Studi Niccolò Cusano, Department of Engineering, 00166 Rome, Italy,*
Email: elisabettamonaldo@unicusano.it

² *Università degli Studi di Roma 'Tor Vergata', Department of Civil Engineering and Computer Science (DICII), 00133 Rome, Italy*

ABSTRACT

Fiber-reinforced polymers (FRPs) are widely used in civil-engineering field for strengthening and retrofitting existing concrete structures. In the context of strengthened RC beams subjected to bending loads, a critical issue is the FRP debonding, mainly consisting in a brittle failure mechanism.

In this paper, analytical relationships proposed by different technical standards and guidelines, are consistently summarized and compared. In particular, a wide database of experimental results obtained from debonding tests, and available in the recent literature, is reported and discussed.

Moreover, experimental results obtained via 42 double shear tests on basalt-based FRP (BFRP) sheets attached on concrete supports are presented. In this light, soundness and effectiveness of available technical relationships, mainly proposed for FRP-concrete systems, based on carbon, glass and aramid fibers, are critically discussed with reference to the use of BFRP.

KEYWORDS

Standards and design guidelines, Experimental study, Basalt-FRP.

INTRODUCTION

Strengthening and retrofitting techniques of existing concrete structures based on the use of fiber-reinforced polymers (FRPs) are an innovative and sustainable alternative to traditional solutions. Nevertheless, the application of externally bonded FRP composites to concrete adds potential failure modes including free-end-debonding, intermediate flexural crack-induced interfacial debonding, diagonal crack-induced interfacial debonding, and detachment due to unevenness developed on the concrete surface (Carpinteri et al. 2009).

Failure mechanisms associated to FRP-concrete have been addressed in several experimental (Ali-Ahmad et al. 2006, Bilotta et al. 2011, Cao et al. 2007, Carloni et al. 2012, Chataigner et al. 2011, Dai et al. 2005, Pellegrino et al. 2008, Toutanji et al. 2007), analytical (Colombi et al. 2014, Diab et al. 2014, De Lorenzis et al. 2001, Wu et al. 2013) and numerical studies (Pham et al. 2007), resulting in a number of theoretical and empirical formulations attempting to assess the FRP-concrete bond strength. In detail, some of these studies resulted in analytical relationships for predicting the maximum debonding force, leading to the definition of design codes, recommendations and guidelines, likewise CNR-DT 200 R1/2013, Fib Bulletin 14/2011, TR55/2000 (Arya et al. 2002), SIA166/2004 and JCI 2003 (Serbescu et al. 2013). On the other hand, available indications are mainly based on traditional FRPs (based on carbon, glass and aramid fibers), and their effectiveness when applied to different fiber-reinforced polymers (such as basalt-based ones) can be considered as an open issue.

In this framework, this paper aims discussing and comparing some available technical relationships and their applicability to different fiber reinforcements. In particular, referring to the maximum debonding force, Carbon-FRP-concrete systems, whose use is widely established, and Basalt-FRP-concrete systems are compared and discussed. For this purpose, a wide experimental database of debonding tests is collected from available scientific literature. Moreover, due to the lack of experimental studies regarding structural retrofitting via BFRP, an experimental investigation is also conducted, carrying out forty-two push-pull double shear tests BFRP-concrete systems.

TECHNICAL STANDARDS

Analytical relationships for evaluating the maximum debonding load P , provided by different guidelines/recommendations, are herein summarized. As a notation rule, b and b_f are the concrete and FRP width, respectively; t_f is the FRP thickness; L_b is the FRP-concrete bond length; E_f is the FRP longitudinal elastic

modulus; f_{ctm} and f_{cm} are the concrete tensile and compressive strength, respectively; L_{eff} denotes the effective bond length (Toutanji et al. 2007).

CNR-DT 200 R1/2013

The Italian technical guidelines CNR-DT 200 R1/2013 defines a fracture-mechanics-based bond strength model, deriving the maximum debonding load as:

$$P = b_f \sqrt{2 E_f t_f G_f} \quad (1)$$

where G_f is the specific fracture energy:

$$G_f = k_b k_g \sqrt{f_{ctm} f_{cm}} \quad (2)$$

k_b being a dimensionless geometrical parameter defined as

$$k_b = \sqrt{\frac{2 - \frac{b_f}{b}}{2 + \frac{b_f}{b}}} \geq 1, \text{ if } \frac{b_f}{b} \geq 0.25, \quad k_b = 1.18, \quad \text{if } \frac{b_f}{b} \leq 0.25, \quad (3)$$

k_g being a corrective factor calibrated on the basis of experimental data and suggested equal to 0.063 mm for preformed FRP and 0.077 mm for cured in situ FRP. The guidelines also report indications for k_g associated to the 5% fractiles (0.023 mm and 0.037 for preformed FRP and cured in situ FRP, respectively).

Fib Bulletin 14/2001

The expression of the maximum debonding load results from a modified form of the Holzenkämpfer's model, furnished by Neubauer and Rostàsý (Fib Bulletin 14/2001):

$$P = \alpha c_1 k_c k_b b_f \sqrt{E_f t_f f_{ctm}} \quad (4)$$

where α is a reduction factor accounting for the effects of inclined cracks, k_c is a concrete-compaction factor, and c_1 is an experimental corrective factor based on calibration process associated to CFRP strips bonded to concrete. The technical report suggests $\alpha = 0.9$, $k_c = 1$ and $c_1 = 0.64$. Finally, similarly to the indications provided by the technical document CNR-DT 200 R1/2013, k_b is a geometrical factor equal to:

$$k_b = 1.06 \sqrt{\frac{2 - \frac{b_f}{b}}{2 + \frac{b_f}{400}}} \geq 1, \text{ with } \frac{b_f}{b} \geq 0.33. \quad (5)$$

Relationship (4) applies for $L_b \geq L_{eff}$, whereas when the bond length L_b is lower than the effective bond length L_{eff} the maximum debonding force is:

$$P = \alpha c_1 k_c k_b b_f \sqrt{E_f t_f f_{ctm}} \frac{L_b}{L_{eff}} \left(2 - \frac{L_b}{L_{eff}}\right) \quad (6)$$

where L_{eff} has to be determined as

$$L_{eff} = \sqrt{\frac{E_f t_f}{c_2 f_{ctm}}}, \text{ with } c_2 = 2. \quad (7)$$

TR 55/2000

The British report TR55/2000 indicates the maximum debonding load for $L_b \geq L_{eff}$ as equal to:

$$P = 0.5 k_b b_f \sqrt{E_f t_f f_{ctm}} \quad (8)$$

where k_b is given by Eq. (5). If $L_b < L_{eff}$, the maximum debonding load should be computed as

$$P = 0.5 k_b b_f \sqrt{E_f t_f f_{ctm}} \frac{L_b}{L_{eff}} \left(2 - \frac{L_b}{L_{eff}}\right) \quad (9)$$

where L_{eff} is given by Eq. (5).

SIA166/2004

According to the Swiss code SIA166/2004, the maximum debonding load is expressed as

$$P = 0.5b_f\sqrt{E_f t_f f_{cth}} \quad (10)$$

where f_{cth} is the concrete surface tensile strength (generally assumed equal to f_{ctm}).

JCI 2003

The Japanese Concrete Institute assumes that the maximum debonding load depends on the average bond stress at failure $\tau_a = 0.93f_{cm}^{0.44}$ and on the effective bond length $L_{eff} = 0.125(E_f t_f)^{0.57}$:

$$P = \tau_a b_f L_{eff}, \text{ where } L_{eff} = L_b \text{ if } L_b < L_{eff}. \quad (11)$$

EXPERIMENTAL INVESTIGATION

In order to furnish some insight in debonding mechanisms occurring in FRP-concrete systems when basalt-based composites are considered, an experimental campaign has been carried out at the Laboratory of Structures and Materials of the University of Rome "Tor Vergata". Forty-two push-pull double shear tests have been performed on Basalt-FRP (BFRP) sheets bonded to prismatic concrete specimens by means of in situ application. Some results of this campaign are briefly summarized in the following, whereas details and complete data can be found in Nerilli and Vairo (2018).

Specimen geometry and preparation

Concrete prisms with dimensions 200x150x400 mm (hereinafter referred to as S2) and 300x150x600 mm (S3) have been considered. BFRP sheets with different values of bond length L_b (namely, 200, 250, 300, 350 mm), different values of width b_f (50, 75, 100, 200 mm), and single or double sheet configurations (corresponding to 0.14 and 0.28 mm thick, respectively) have been designed. For the sake of notation, BFRP-concrete specimens are labeled as Sa_bf_Lb_nf, where Sa identifies the concrete sample configuration (S2 or S3) and nf is the number of BFRP sheets.

The bond surface of the concrete blocks, obtained from concrete casting in wooden structures, has been smoothed and cleaned with a mechanical brushing and a compressed air jet, so to ensure a suitable adhesion with the BFRP sheet. The primer resin coating has been followed by the application of a layer of epoxy resin, in turn followed by the application of the basalt sheets, and finally of another layer of epoxy resin. A non-attached zone between BFRP sheets and concrete, 50 mm long, has been considered to avoid critical local failure near the concrete corner.

Materials properties and test set-up

Preliminary tests on concrete blocks and basalt-based sheets have been executed to verify the mechanical properties provided by the manufacturer. Concrete samples, tested after 28 days from the casting, showed a cubic compressive strength of 38.48 MPa and a tensile strength of 3.23 MPa. The unidirectional basalt-based sheets (FIDBASALT UNIDIR 400 C95) showed an along-the-fiber elastic modulus of 95 MPa and a tensile strength of 1900 MPa.

Push-pull tests have been conducted in displacement control with loading rate of 0.1 mm/min. The theoretical static scheme of the double shear test has been realized by considering the concrete block positioned on a rigid frame with two steel plates. Moreover, BFRP sheets have been applied to the concrete samples by adopting a U-shaped configuration, leading to an eyelet wherein a steel cylinder has been inserted. Accordingly, the cylinder constrains the BFRP sheet and it indirectly applies the pulling load. As better clarified in Nerilli and Vairo (2018), the adopted loading scheme allows to prevent any eccentricity in the applied load with respect to the BFRP plane, allowing to address specifically a mode-II debonding failure.

Results

As expected, most of the BFRP-concrete specimens revealed a typical mode-II debonding failure characterized by the detachment of a thin layer of concrete. Only six specimens exhibited fracture of the BFRP sheet, due to possible unevenness at the BFRP-concrete interface.

The debonding load P has been evaluated as the half of the maximum value of the push-pull force registered during the tests and inducing the complete debonding failure. The debonding load ranged from 7.20 kN to 38.04

kN depending on the specimen configuration. Table 1 collects geometrical properties and experimental results. The latter are expressed in terms of both debonding load (P) obtained for the tested specimens that experienced a debonding failure mode, and the average debonding load (\bar{P}) computed on the class of specimens having the same geometrical configuration.

Table 1: Geometrical parameters of BFRP-concrete specimens and corresponding experimental results. N : number of the tested specimens per type; n_d : number of specimens that experienced debonding failure; P : debonding load; \bar{P} : mean value of P for each specimen class.

Specimen	N (n_d)	b_f [mm]	b_f/b	L_b [mm]	t_f [mm]	P [kN]	\bar{P} [kN]
S2_5_25_1	3 (2)	50	0.250	250	0.14	8.11 12.21	10.16
S2_5_30_1	2 (2)	50	0.250	300	0.14	9.29 7.92	8.61
S2_5_35_1	4 (3)	50	0.250	350	0.14	8.12 7.20 9.37	8.23
S2_5_30_2	3 (2)	50	0.250	300	0.28	12.40 16.41	14.40
S2_5_35_2	1 (1)	50	0.250	350	0.28	14.34	14.34
S2_7.5_35_1	2 (2)	75	0.375	350	0.14	11.68 10.84	11.26
S2_10_25_1	3 (3)	100	0.500	250	0.14	17.75 19.62 16.18	17.85
S2_10_30_1	6 (6)	100	0.500	300	0.14	21.08 18.86 16.79 20.87 21.06 16.57	19.21
S2_10_35_1	9 (6)	100	0.500	350	0.14	16.94 16.72 18.77 18.46 18.39 16.72	17.67
S2_10_30_2	3 (3)	100	0.500	300	0.28	33.73 28.20 28.91	30.28
S2_10_35_2	3 (3)	100	0.500	350	0.28	35.10 24.48 28.00	29.19
S3_20_20_1	3 (3)	200	0.670	200	0.14	32.02 38.04 29.80	33.30

COMPARISON OF EXPERIMENTAL DATA WITH TECHNICAL INDICATIONS

For comparison purposes, aiming to assess soundness and effectiveness of previously-introduced technical indications, in addition to BFRP-based experimental tests herein conducted, several experimental results available in recent literature are collected. Accordingly, a database has been built up, consisting in 229 debonding test results, published in 13 experimental studies (Ali-Ahmad et al. 2006, Bilotta et al. 2011, Cao et al. 2007, Carloni et al. 2012, Chataigner et al. 2011, Colombi et al. 2014, Dai et al. 2005, De Lorenzis et al. 2001, Diab et al. 2014, Pellegrino et al. 2008, Pham et al. 2007, Toutanji et al. 2007, Wu et al. 2013), and relevant to Carbon-FRP concrete and Basalt-FRP concrete specimens prepared through in situ application of FRP reinforcement. Data refer to different test setups, including single and double shear tests, as well as bending tests. The case of FRP-reinforcement characterized by fiber aligned with the loading direction is considered. An outline of geometrical and material properties associated to results collected in such a database is provided in Table 2.

Table 2: Outline of geometrical and material properties associated to results collected in experimental database built from available literature. $N-F$: number of the tested specimens-fiber reinforcement type (C: Carbon FRP; B: Basalt FRP).

Ref.	$N-F$	b [mm]	b_f [mm]	L_b [mm]	t_f [mm]	E_f [GPa]	f_{cm} [MPa]
Ali-Ahmad (2006)	5-C	125	46	150	0.167	200	38
Bilotta (2011)	15-C	150	100	50-400	0.166	230-241	21.5-26
Cao (2007)	13-C	150	80	80-150	0.110	165-235	19.2-57
Carloni (2012)	3-C	125	25	152	0.167	230	35
Chataigner (2011)	3-C	200	80	240	0.430-1.200	62-80	33
Colombi (2014)	13-C	150	80-100	100-500	0.160-0.220	239-410	15.2-26
Dai (2005)	15-C	400	100	330	0.110-0.330	230	35
De Lorenzis (2001)	18-C	254	51	102-305	0.352-0.587	227	24.5-47.3
Diab (2014)	9-B	100	50	-	0.170-0.510	91	40
Pellegrino (2008)	34-C	100	50	200-280	0.165-0.990	230-390	58-63
Pham (2007)	24-C	140	70-100	60-220	0.334-1.002	209	53.7
Toutanji (2007)	12-C	200	50	100	0.495-0.990	110	17-61.5
Wu (2013)	65-C	150	50	30-400	0.167-0.501	238.1-248.3	25.3-59

Collected experimental data, also including experimental results herein obtained for BFRP reinforcement, are critically compared in order to verify the predictive effectiveness of previously-introduced technical indications, in terms of debonding load. In Figures 1-5 values of the experimental debonding load P_{exp} are depicted versus the theoretical ones P_{th} . In particular, the available data are divided by distinguishing the fiber (namely, carbon or basalt). Graph bisectors, corresponding to $P_{exp} = P_{th}$, are also shown, allowing for the identification of safe results (i.e., $P_{exp} \leq P_{th}$) with respect to the adopted technical guidelines.

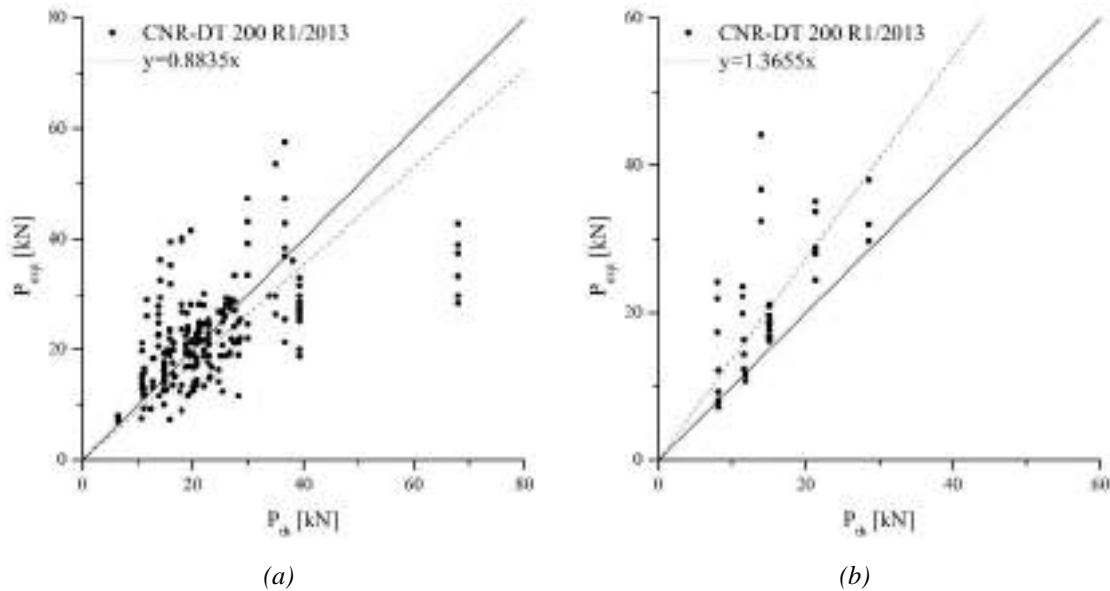


Figure 1: Technical indications in CNR-DT 200 R1/2013. Experimental debonding force versus the theoretical one for (a) CFRP-concrete specimens and for (b) BFRP-concrete specimens.

Through a linear regression-based model (Monti et al. 2009), the least-square fine-tuning parameter, namely the slope of the regression line, is computed by distinguishing the fiber type. In order to guarantee meaningful results, the least-square fine-tuning line is constrained to intercept the origin. The computed regression lines and the corresponding equations are also reported in Figures 1-5.

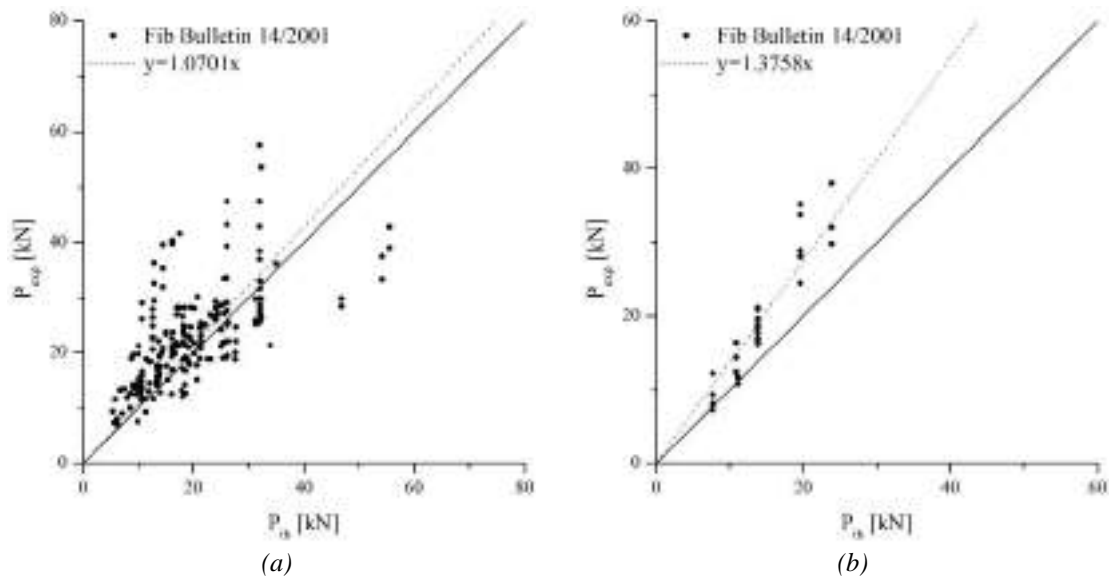


Figure 2: Technical indications in Fib Bulletin 14/2001. Experimental debonding force versus the theoretical one for (a) CFRP-concrete specimens and for (b) BFRP-concrete specimens.

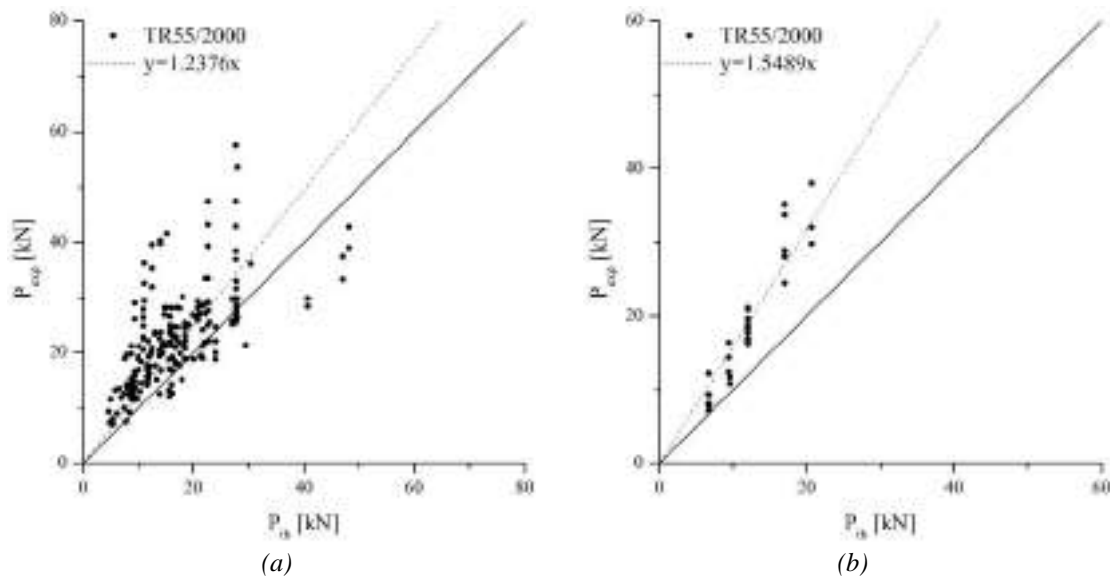


Figure 3: Technical indications in TR55/2000. Experimental debonding force versus the theoretical one for (a) CFRP-concrete specimens and for (b) BFRP-concrete specimens.

Proposed results clearly highlight that all considered technical guidelines seem to furnish conservative indications except the Japanese one. Fib Bulletin and the Italian standards revealed much more accurate for reproducing experimental values of debonding load than the other technical rules (TR55/2000, SIA166/2004 and JCI 2003) both in the case of Carbon-based and Basalt-based reinforcements. Nevertheless, theoretical values of debonding load agree better for CFRP-concrete systems than BFRP-based ones.

CONCLUSIONS

A critical review of existing bond strength models proposed by different technical standards is presented. To evaluate the predictive capacity of these latter, CFRP-concrete systems, whose use is firmly established, and Basalt-FRP-concrete systems are addressed. Due to the lack of available data regarding BFRP-concrete systems, an experimental campaign is conducted, by referring to double shear tests on concrete specimens reinforced with

BFRP sheets. Experienced results have contributed to define an experimental database consisting in data from more than 270 debonding tests, accounting for evidence collected from other 13 published experimental studies. As a result, proposed comparisons suggest that a revision of corrective coefficients defining technical relationships would be considered, by accounting for the influence of fiber stiffness, that is by distinguishing the type of the fibers constituting the FRP layer. To this aim, further experimental results, including not only CFRP-concrete and BFRP-concrete systems but also associated to the use of FRP based on other fibers type (e.g., Glass, Aramid) should be considered and analyzed.

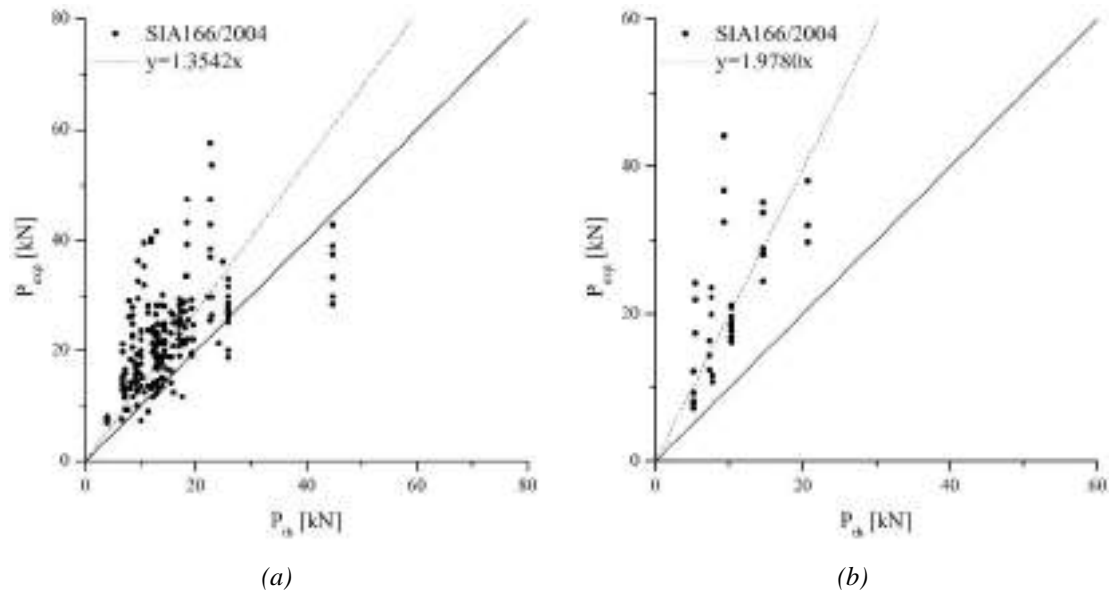


Figure 4: Technical indications in SIA166/2004. Experimental debonding force versus the theoretical one for (a) CFRP-concrete specimens and for (b) BFRP-concrete specimens.

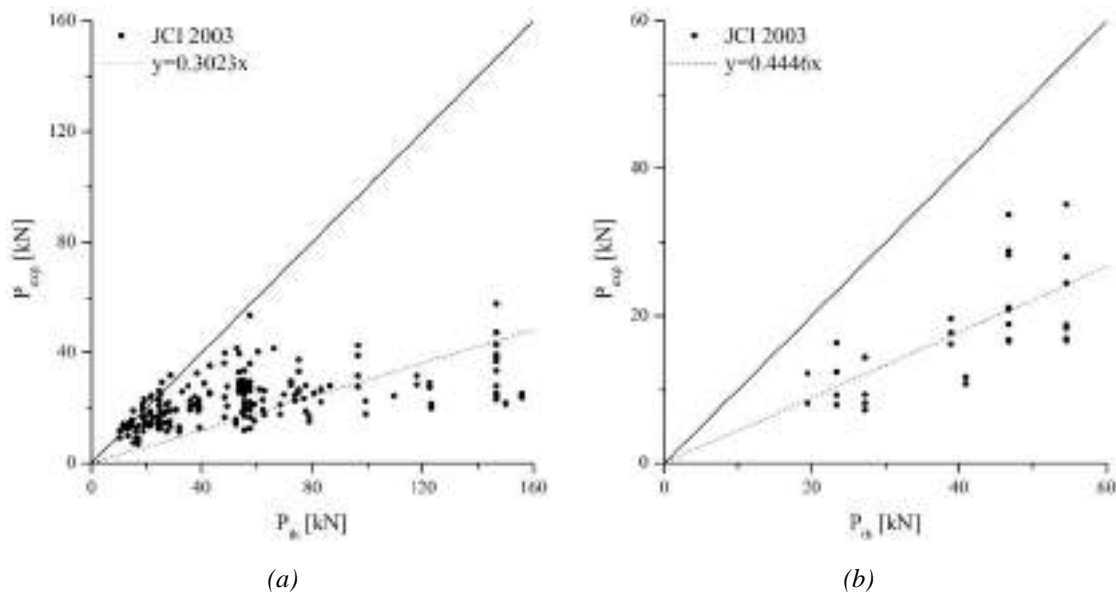


Figure 5: Technical indications in JCI 2003. Experimental debonding force versus the theoretical one for (a) CFRP-concrete specimens and for (b) BFRP-concrete specimens.

ACKNOWLEDGMENTS

This work was partially supported by the Italian Civil Protection Department. [RELUIS-DPC 2014-18, CUP: E82F17000870001].

REFERENCES

- M. Ali-Ahmad, K. Subramaniam, M. Ghosn (2006). "Experimental investigation and fracture analysis of debonding between concrete and FRP sheets". *Journal of Engineering Mechanics*, 132(9), 914-923.
- C. Arya, et al. (2002). "TR 55: Design guidance for strengthening concrete structures using fibre composite materials: a review. *Engineering Structures*", 24(7), 889-900.
- A. Bilotta, C. Faella, E. Martinelli, E. Nigro (2011). "Indirect identification method of bilinear interface laws for FRP bonded on a concrete substrate", *Journal of Composites for Construction*, 16(2), 171-184.
- S.Y. Cao, J.F. Chen, J.W. Pan, N. Sun (2007). "ESPI measurement of bond-slip relationships of FRP-concrete interface", *Journal of Composites for Construction*, 11(2), 149-160.
- C. Carloni, K.V. Subramaniam, M. Savoia, C. Mazzotti (2012). "Experimental determination of FRP-concrete cohesive interface properties under fatigue loading", *Composite Structures*, 94(4), 1288-1296.
- A. Carpinteri, P. Cornetti, G. Lacidogna, M. Paggi (2009). "Towards a unified approach for the analysis of failure modes in FRP-retrofitted concrete beams", *Advances in Structural Engineering*, 12(5), 715-729.
- S. Chataigner, J.F. Caron, K. Benzarti, M. Quiertant, C. Aubagnac (2011). "Use of a single lap shear test to characterize composite-to-concrete or composite-to steel bonded interfaces", *Construction and Building Materials*, 25(2), 468-478.
- CNR, DT. 200/R1 (2013) "Guide for the design and construction of externally bonded FRP systems for strengthening existing structures", *Advisory committee on technical recommendation for construction of national research council*, Rome, Italy.
- P. Colombi, G. Fava, C. Poggi (2014). "End debonding of CFRP wraps and strips for the strengthening of concrete structures", *Composite Structures*, 111(1), 510-521.
- J. Dai, T. Ueda, Y. Sato (2005). "Development of the nonlinear bond stress-slip model of fiber reinforced plastics sheet-concrete interfaces with a simple method", *Journal of Composites for Construction*, 9(1), 52-62.
- L. De Lorenzis, B. Miller, A. Nanni (2001). "Bond of FRP laminates to concrete", *ACI Materials Journal*, 98(3), 256-264.
- H.M. Diab, O.A. Farghal (2014). "Bond strength and effective bond length of FRP sheets/plates bonded to concrete considering the type of adhesive layer", *Composites Part B: Engineering*, 58, 618-624.
- Fib Bulletin No.14. (2001) "Externally bonded FRP reinforcement for RC structures".
- G. Monti, S. Alessandri, S. Santini (2009). "Design by testing: a procedure for the statistical determination of capacity models", *Journal of Construction and Building Materials*, 23(4), 1487-1494.
- F. Nerilli, G. Vairo (2018). "Experimental investigation on the debonding failure mode of basalt-based FRP sheets from concrete", to appear.
- C. Pellegrino, D. Tinazzi, C. Modena (2008). "Experimental study on bond behavior between concrete and FRP reinforcement", *Journal of Composites for Construction*, 12, 180-189.
- H.B. Pham, R. Al-Mahaidi (2007). "Modelling of CFRP-concrete shear-lap tests. *Construction and Building Materials*", 21(4), 727-735.
- A. Serbescu, M. Guadagnini, K. Pilakoutas (2013). "Standardised double-shear test for determining bond of FRP to concrete and corresponding model development", *Composites Part B: Engineering*, 55, 277-297.
- H. Toutanji, P. Saxena, L. Zhao, T. Ooi (2007). "Prediction of interfacial bond failure of FRP-concrete surface", *Journal of Composites for Construction*, 11(4), 427-436.
- Y.F. Wu, C. Jiang (2013). "Quantification of bond-slip relationship for externally bonded FRP-to-concrete joints", *Journal of Composites for Construction*, 17(5), 673-686.



GFRP STRAND PROTOTYPE: EXPERIMENTAL INVESTIGATION AND TECHNOLOGY READINESS

Marco Rossini 1,*, Pedro Jalles 1, Gabriele Balconi 2 and Antonio Nanni 1

¹ CAE, University of Miami, Florida, USA. * email: mxr1465@miami.edu

² Sireg Geotech, Arcore, Italy

ABSTRACT

Employment of corrosion-resistant reinforcement represents a widely-recognized effective strategy to ensure long-term durability of Reinforced Concrete (RC) and prestressed concrete (PC) structures. Fiber-Reinforced Polymer (FRP) composites are a reliable non-metallic solution, able to ensure both the required mechanical properties and corrosion resistance. Among composites, Carbon FRP (CFRP) has historically been the preferred solution for prestressed concrete applications. Nevertheless, the high cost of carbon fiber, along with some technological drawbacks, may prevent the widespread use of this technology.

This study lays within a comprehensive research effort investigating the application of Glass FRP (GFRP) to mild-prestressed concrete elements (MPC). Glass fiber is an economical alternative to carbon fiber in applications that do not require high level of concrete pre-compression. Limiting the level of initial prestress would allow to overcome some constructability issues noticed with CFRP tendons, while the reduced cost of glass would make it a competitive and durable alternative to standard steel strands.

This study focuses on the experimental investigation of GFRP strand prototypes anchored to the cross-heads of the testing frame with conventional steel prestressing chucks. The aim is to verify prototype compatibility with construction techniques traditionally applied to steel-PC. Both instantaneous pull tests and sustained pull tests are presented. The prototypical nature of the strands is accounted for in the data handling. The technology readiness level in association with possible field implementations (i.e. mild-prestressed concrete sheet piles) is discussed. Comparison with traditional materials and corrosion-resistant alternatives is considered.

KEYWORDS

GFRP strands; mild prestress; prototype technology; bridge substructure; technology readiness.

RESEARCH SIGNIFICANCE

Corrosion of steel reinforcement is the primary cause of durability problems in aged reinforced and prestressed concrete (RC and PC) structures. The legacy of extensive development and expansion of the transportation infrastructure, in combination with aggressive environments, represents a critical maintenance, rehabilitation and replacement (MRR) liability at the international scale (Nolan & Nanni, 2017). RC corrosion is ubiquitous, but greatly exacerbated by aggressive sub-tropical environments (Nolan et al., 2018) as well exposure to de-icing agent's aggression and carbonation in cold-weathered regions (Ahmad, 2003). Figure 184a show the effects of corrosion on a marine structure in service conditions in southern Italy, while Figure 184b shows corroded strands exposed after the collapse of a PC structure in the aftermath of Hurricane Irma in Miami (FL).

In the case of transportation infrastructure in coastal areas, the immediate corrosion problems are experienced by bridge substructures, sheet pile bulkheads and seawalls. For the latter structures, typically made with PC elements, the preference for non-corrosive reinforcement is explicitly stated by governing agencies, e.g. the Florida Department of Transportation (FDOT, 2016a; FDOT, 2016b). In the State of Florida alone, about 3,600 coastal miles are armored with aging sheet piles (Nolan et al., 2018) for an estimated \$21B MRR liability.

The construction industry has only partially answered the rising demand for corrosion-resistant technologies, offering expensive, complex and sometimes ineffective solutions. A limited number of manufacturers are active in the market, further stressing the need for cost-effective alternatives (FDOT, 2016c). The research presented contributes to a comprehensive effort aiming to develop a corrosion-resistant tendon for PC application that, in addition to durability and mechanical performance, exhibits favorable constructability and cost characteristics. The University of Miami leads the effort, with the collaboration of international research partners, governing agencies, and representative of the industrial sector.



Figure 184 – Corrosion in a marine structure (a), and corroded steel strands (b).

CORROSION RESISTANT REINFORCEMENT FOR PC

An overview of the corrosion resistant reinforcement alternatives for PC applications do follow to give context. In terms of cost comparison, \$3.30/m (\$1.00/ft) represents the reference value for conventional carbon steel strands as estimated by FDOT (FDOT, 2016c).

High Strength Stainless Steel (HSSS) strands are a possible solution (Paul et al., 2017). Leveraging HSSS application in the construction industry is eased by the perceived similarity with High Strength Carbon Steel (HSCS). However critical differences exist. HSSS drawbacks include relative brittleness (1.2% elongation at failure), and high material cost, estimated as \$13.10/m (\$4.00/ft) for 0.6” strands (FDOT, 2016c). Potential long-term corrosion remains an unaddressed issue.

On the composite side, carbon is the preferred fiber for prestress applications (Spadea et al., 2018). Carbon Fiber Reinforced Polymer (CFRP) strands are immune to corrosion and characterized by high strength. However, the high material cost, estimated in \$12.50/m (\$3.80/ft) for 0.6” strands (FDOT, 2016c), demands for extreme stressing and coupling, lead to safety concerns during tensioning, and introduce the need for complex anchoring devices. Relative brittleness (1.5% elongation at failure) remains an unaddressed concern. Figure 185 compares the system of sleeves and large anchors required for CFRP tensioning to standard chucks traditionally used for HSCS.

Glass FRP (GFRP) prestress applications were first explored in the early 90s (Sippe, 1992) for material systems made with polyester and E glass fibers. The limited creep-rupture performances of the bundle segregated GFRP to RC applications at that time (Schwartz, 1997). Decades of research resulted in better performing material systems, coupling vinylester and E-CR glass fibers (Diwanji, 2011). The technology upgrade is reflected in updated material specifications (ASTM, 2017), and call for a rethinking of the limits traditionally set on GFRP exploitation (Rossini et al., 2017).

A number of recent studies prove GFRP bars to be mechanically suited for prestress applications (Noel & Soudki, 2013; Atutis et al., 2015; Mazaheripour, 2015; Zawam et al., 2017), along with a limited number of field deployments in geotechnical engineering (Hong et al., 2016; Natoli et al., 2017). A strand-like GFRP product has never been developed for commercial applications, even if it is envisioned in some international standards (CSA, 2017), and considered in a limited set of numerical studies (Husan et al., 2015).

Traditional GFRP solid rebars, typically used in RC construction, are not suited for prestressing due to their inability to be coiled, while a GFRP strand-like product is currently not available in the marketplace (Ruiz et al., 2017). In the presented project, the focus is a GFRP prototype strand, that retains immunity to corrosion and maintains a material cost comparable to traditional carbon steel reinforcement, estimated in \$3.80/m (\$1.15/ft), while showing higher strain at failure (1.8% ultimate elongation).



Figure 185 – Tensioning apparatus for CFRP (a) (b) versus standard steel chucks for HSCS, and GFRP (c).

GFRP MILD PRESTRESS CONCRETE

The idea of limiting the level of prestress on CFRP tendons to prevent viscous phenomena, creep rupture issues, and limit safety concerns during tensioning was explored in the early 2000s (Fico et al., 2005). However, the cost

of carbon material, its mechanical properties, and the peculiarity of the application chosen, prevented one from taking full advantage, and envision the implications.

The concept of GFRP mild prestress concrete (GFRP-MPC) was never formalized. Recent industry upgrade allowed to develop a GFRP product tailored for PC application, answering market demand for corrosion-resistant reinforcement, and calling the need to frame technology implications on both PC design and construction process. The lower creep-rupture endurance limit exhibited by GFRP compared to CFRP and HSSS does not allow designing for the same level of prestress. However, mild-prestress presents a number of intrinsic advantageous features. Glass fiber is an effective alternative to carbon fiber in applications that do not require high levels of concrete prestress such as sheet piles for seawalls, substructure bearing piles, noise panels and retaining walls. In these types of structural elements, the level of concrete pre-compression can be typically set to 4.8 MPa (700 psi) and is more of a requirement during installation than during the service life (FDOT, 2016a; FDOT, 2016b).

The major issue faced when pulling composite materials, is their relative transversal softness with respect to steel chucks and wedges. The issue called for the development of a number of variously effective anchoring solutions (Nanni et al., 1996), targeting the highest possible level of prestress, to minimize material consumption and balance the high cost of carbon fibers. Any variation on the construction process adds complexity, and limits deployment. Limiting initial prestress naturally addresses the constructability issues observed with CFRP, guaranteeing compatibility with standard steel chucks and conventional tensioning techniques. At the same moment, the reduced cost of glass fiber makes the GFRP strand a competitive and durable alternative to standard low-relaxation high-strength carbon steel. Figure 185 shows the complex sleeves and wedges system required to pull CFRP strands at high level of prestress, compared to standard steel chucks to be coupled with GFRP.

Mild prestress presents the additional advantage to lower stresses on concrete, thus reducing elastic deformation at strands release, and creep during service life of PC structures. GFRP relatively low modulus of elasticity (nominal 46 000 MPa) synergistically contribute to reduce the effects such deformations have in terms of prestress losses. The latter is also an advantageous feature during construction, resulting in larger and more controllable displacement at prestressing. At the same time, the mild level of applied prestress significantly reduces safety concerns, both in terms of chances of strand failure, sometime experienced with CFRP (Rambo & Gartman, 2017) (Figure 186a and b), and in terms of consequences such failures may have. Finally, CFRP strands have showed a tendency to relatively severe transversal expansion at releasing, resulting in significant transversal cracking (Figure 186c and d). The phenomenon can be made negligible limiting the initial prestress.



Figure 186 – CFRP strand failed during tensioning (a) (b), and cracking following strands release (c) (d).

GFRP STRAND PROTOTYPE AND EXPERIMENTAL PROGRAM

The technology under investigation implements state-of-the-practice E-CR glass fibers and vinyl ester resin, along with a twisted 7-wire geometry optimized for prestress (Figure 187). The strand-like geometry is engineered to reduce shear lag, retain an optimal amount of sustained load, and guarantee adequate creep-rupture strength. Furthermore, it allows the material system to be coiled, easing shipping and deployment on site. The novelty of the material system demands for specific characterization. A complete set of material tests is currently undergoing at the University of Miami, while the results of the exploratory study are presented in the following, summarized in Table 57, and visualized in Figure 188, Figure 189, and Figure 190.

The prototypical nature of the product limited the material available for testing at that time of concept exploration, and priorities had to be set. The fundamental question to answer was whether the GFRP prototype could be coupled with standard steel chucks (Figure 191), and effectively pulled. Assessed the instantaneous capacity of the system, sustained load tests were carried out to verify the creep-rupture capacity over a 24-hour time span, taken as double the typical curing period for PC elements in South Florida (Spadea et al., 2018). Finally, a limited number of material characterization tests was carried out to confirm nominal properties as suggested by the manufacturer, in the form of nominal guaranteed tensile strength ($f_{tu}^* = 800$ MPa), and nominal tensile modulus ($E_f = 46\,000$ MPa). Other nominal properties in Table 57 are defined on the basis of experimental data, as specified in the following. Guaranteed values are computed as the average minus three standard deviations (ACI, 2015).

Different geometrical configurations were tested, at varying twisting per meter. The influence of the parameter will be better discussed in the following, but its effects can generally be considered of secondary importance in reading the results. For stress computation purposes, an average measured area of 128 mm² is adopted for all the specimens. Cross sectional area was also measured per ASTM D7205 (ASTM, 2016), and a coefficient of variation equal to 1.75% was recorded. Both instantaneous and sustained pull tests were performed on 1.2 m long specimens with chucked ends and a free length of 0.9 m. The tensile test was performed per ASTM D7205 (ASTM, 2016), but over a reducer free length of 0.45 m (30 nominal diameters).

In carrying out the test matrix discussed, a limited number of specimens had to be discarded because of the presence of defects expected to hinder their mechanical performances. Such samples cannot be considered representative of the properties of the material system itself. Their presence in the batch can be reconducted to the prototypical nature of the product, coming from a pultrusion line sensibly shorter than a standard production lot. In this sense, the results reported in the following shall be considered indicative of the potential of this technology, expected to improve once quality control procedures are implemented, yet not to be suggested for field implementation until a statistically significant batch is tested.



Figure 187 – GFRP strand prototype cross section (a), and compared to a CFRP alternative (b).

Table 57 – Experimental matrix, test results, and nominal values for the GFRP prototype strand (TM = Tensile Material test, T = Tensile pull test, CR = Creep Rupture pull test, C = Creep pull test).

Specimen ID	twist/m	Failure mode	$F_{f,u}$	$f_{f,u}$	E_f	$F_{f,pull}$	$f_{f,pull}$	$F_{f,sust}$	$f_{f,sust}$	$t_{failure}$
			kN	MPa	MPa	kN	MPa	kN	MPa	hours
SIR #1.50-TM	1.50	Global	109	852	45 644	-	-	-	-	-
SIR #4.50-T	4.50	Global	-	-	-	65.1	510	-	-	-
SIR #1.75-T	1.75	Global	-	-	-	70.8	554	-	-	-
SIR #1.50-T1	1.50	Global	-	-	-	67.4	528	-	-	-
SIR #1.50-T2	1.50	Slipping	-	-	-	61.7	483	-	-	-
SIR #1.25-T1	1.25	Local	-	-	-	67.9	532	-	-	-
SIR #1.25-T2	1.25	Local	-	-	-	67.8	532	-	-	-
SIR #1.25-T3	1.25	Slipping	-	-	-	66.1	518	-	-	-
SIR #1.75-CR	1.75	Local	-	-	-	-	-	57.0	447	0.13
SIR #1.50-CR	1.50	Global	-	-	-	-	-	53.2	417	3.18
SIR #4.50-C	4.50	n/a	-	-	-	-	-	44.5	350	> 24
SIR #1.75-C	1.75	n/a	-	-	-	-	-	44.5	350	> 24
SIR #1.50-C	1.50	n/a	-	-	-	-	-	44.5	350	> 24
SIR #1.25-C	1.25	n/a	-	-	-	-	-	44.5	350	> 24
Mean	-	-	-	-	-	66.7	522	-	-	-
C.O.V.	-	-	-	-	-	3.9 %	3.9 %	-	-	-
Guaranteed	-	-	-	-	-	58.8	461	-	-	-
Nominal	-	-	102	800	46 000	58.8	461	44.5	350	24

EXPERIMENTAL RESULTS

A total of 7 tensile pull tests were carried out, experiencing various failure modes. Slipping failures are localized at the chucks location and do not result in damages over the free length of the strands. Global failures of the whole strand, and local failures of a single cables, happening at about 50% of the strand capacity, are triggered by stress concentrations at chucks location. All the samples exhibit a hardening behavior, as shown in Figure 188a, with

the wedges securing grip at progressive load. Strand localized damaging is a consequence of the gripping process at levels of stress close to failure, as shown in Figure 191b. Conversely, Figure 191c shows the limited scratching experienced by strands pulled at level stress expected on the construction site. In the second case the mechanical properties of the strand are not hindered by the jacking process and the results of the visual inspection are in line with CFRP performances. The end portions of the strand are to be cut after concrete pouring, as per PC standard practice, and will not be included in the final element.

The pull test data gathered allow to compute an experimental guaranteed pull strength of 461 MPa ($0.58 f_{ju}^*$). The value is taken as nominal pull strength for the prototype GFRP strand. The value can be considered constant at varying twisting, with a slight decreasing trend, as shown in Figure 188b. Displacement monitoring during sustained pull tests also showed the viscous behavior to be almost invariant with strand geometry, as shown in Figure 189a. A regression curve over two failure points and four non-failure points is traced in Figure 189b, confirming 350 MPa ($0.44 f_{ju}^*$) as sustained pull strength over 12 hours. This value is not backed by a statistical definition, given the lack of failure points, but is confirmed on four tested specimens and thus taken as nominal sustained pull strength for the prototype GFRP strand.

Figure 190a presents the results of a tensile test, confirming the nominal guaranteed strength and nominal elastic modulus suggested by the manufacturer. In Figure 190b cross sectional area measurements are plotted as a function of the strand geometry in terms of twist per meter. The area tends to slightly increase at increasing twisting. At increasing area, the transversal stiffness of the system is expected to increase accordingly, thus reducing coilability. Furthermore, at increasing cable twisting, the skew angle increases, thus reducing the contribution of each component in the longitudinal direction. These considerations deserve further testing to be confirmed, and shall be intended as notes for future research.

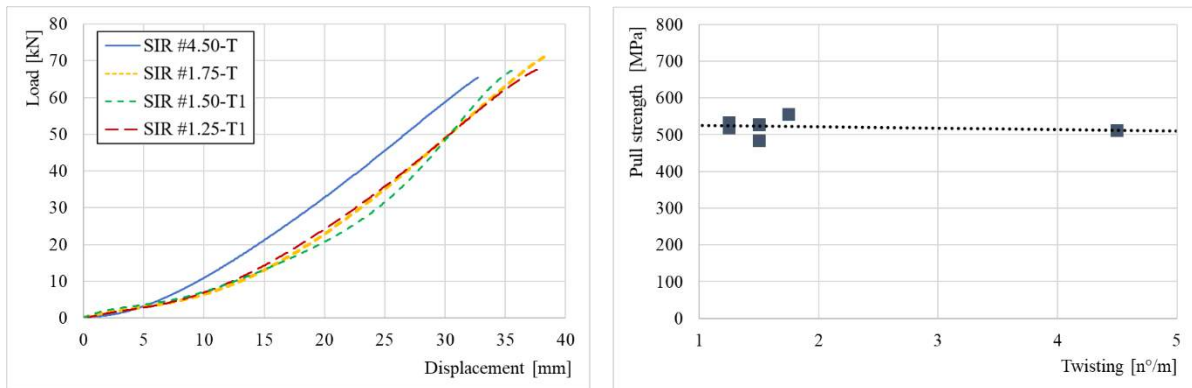


Figure 188 – Pull test load-displacement diagrams (a), and pull strength at varying twist per meter (b).

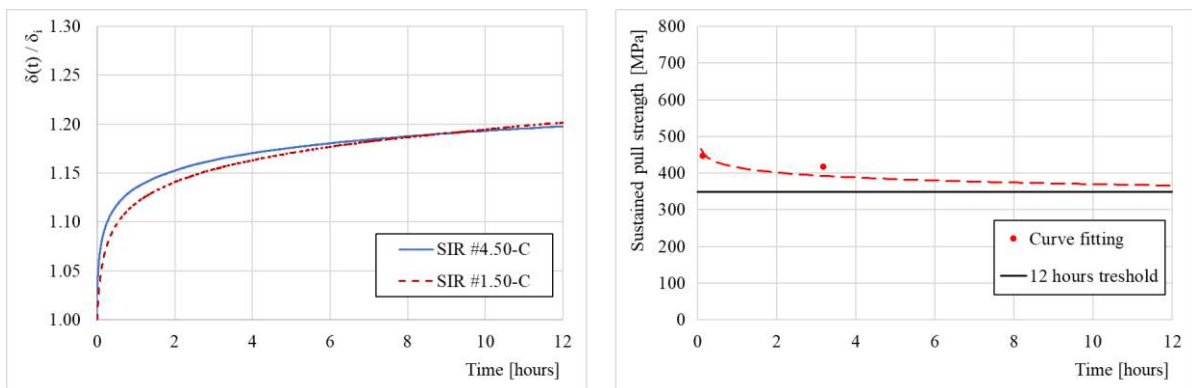


Figure 189 – Creep displacement over initial value (a), and creep rupture logarithmic regression (b).

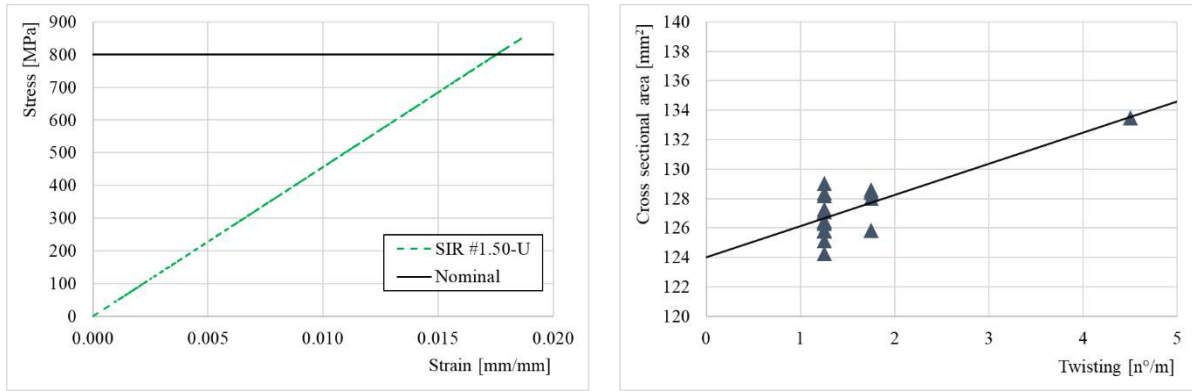


Figure 190 – Tensile test stress-strain diagram (a), and cross-sectional area at varying twist per meter (b).

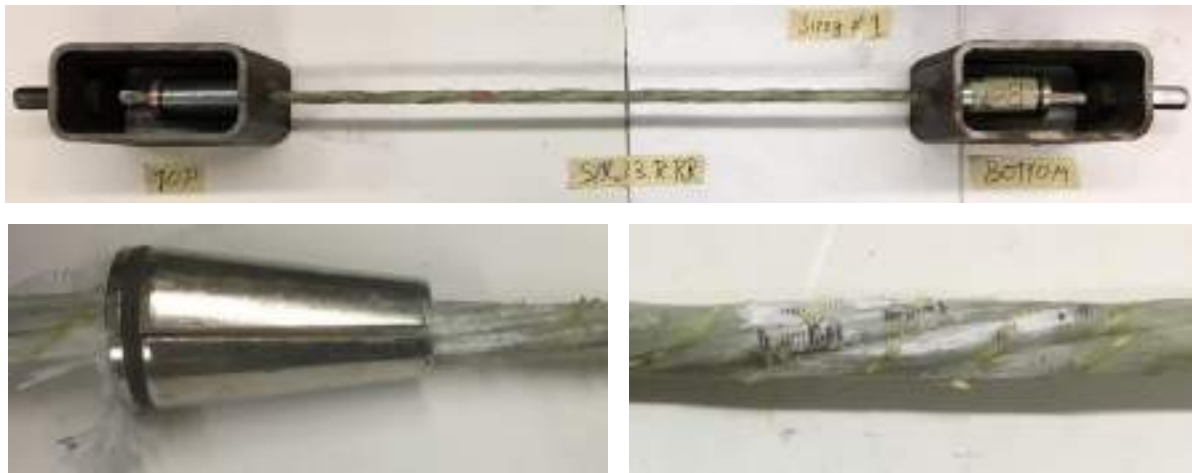


Figure 191 – GFRP strand ready for pull test (a), and details after tensile pull test (b), and sustained pull test (c).

DESIGN EXAMPLE AND TECHNOLOGY READINESS

Experimental results allow to define a minimum set of nominal values to be applied in the design of a concrete element prestress with prototype GFRP strands. The element considered is a 200 mm (8 in.) deep sheet pile, with a gross concrete cross section of $139 \times 10^3 \text{ mm}^2$. The design is compared to equivalent members prestressed with HSCS, HSSS, and CFRP. Material properties are referred to material systems approved by the Florida Department of Transportation for field implementation (FDOT, 2016c).

Results are summarized in Table 58. In the case of GFRP, the reduced level of prestress in combination with the relatively low elastic modulus resulted in reduced losses, and a more efficient exploitation of the material. A total of 8 strands was considered for the case of HSCS, HSSS, and CFP. A total of 18 strands was considered in the case of GFRP. The reduced cost of the material counterbalances the higher number, resulting in a fraction of the total material cost associated to HSSS and CFRP alternatives. The prototype GFRP strand proved able to match FDOT requirements for a minimum prestress of 4.8 MPa (700 psi) on concrete (FDOT, 2016a). The lack of specific data called for assumptions in the definition of long term losses on HSSS, CFRP, and GFRP. The approach is in line with Spadea et al. (2018), and assumed to be on the safe side.

The nominal properties defined in this study, hindered by the prototypical nature of the material tested, are enough performing to allow the design of cost-effective corrosion-resistant PC substructures. In comparing the alternative costs in Table 58, it shall be considered how savings in terms of labor and reduced complexity, coming with GFRP strands and standard steel chucks, are not accounted for. Such results shall be intended as spur for further research, and not as endorsement for field implementation at the current stage, until a complete investigation is conducted to certify strand's mechanical properties over a statistically representative data set. Such a program is currently undergoing at the University of Miami. Among the parameters to be investigated, it is worth mentioning relaxation over the long term, creep rupture strength, and bond performances.

Table 58 – GFRP-PC sheet pile design compared to HSCS, HSSS, and CFRP alternatives.

<i>Material system</i>	<i>Strands cost</i> \$/m	$f_{j,pull}$ -	P_{pull} kN	Δ_e %	P_i kN	$\sigma_{c,i}$ MPa	Δ_{75y} %	P_{75y} kN	$\sigma_{c,75y}$ MPa
HSCS (1x7, 15.2mm)	26	$0.75 f_{su}$	1 673	9.5%	1,513	10.9	29.0%	1,187	8.5
HSSS (1x7, 12.7mm)	105	$0.75 f_{su}$	1 078	6.7%	1,005	7.2	22.5%	836	6.0
CFRP (1x7, 15.2mm)	100	$0.58 f_{fu}^*$	1 264	7.4%	1,170	8.4	23.9%	961	6.9
GFRP (1x7, 15.2mm)	68	$0.44 f_{fu}^*$	804	5.5%	760	5.5	14.7%	686	4.9

CONCLUSIONS

In this study, the need for effective and cost-efficient non-corrosive PC technologies is discussed, and a possible solution is proposed in terms of GFRP mild prestress (GFRP-MPC). The concept of GFRP-MPC is framed, and implications on design, construction, and deployment of non-corrosive PC elements are discussed. Particular attention is devoted to bridge sub structures and marine applications. The mechanical properties of an existing GFRP prototype strand are investigated. The material system, coupled with traditional steel chucks and wedges, proved able to sustain a 44.5 kN pull ($0.44 f_{fu}^*$) allowing the design of 200mm-deep sheet piles. The relatively low modulus of elasticity of GFRP, resulted in losses estimated to be half the value associated with steel strands (15% versus 29% at 75 years). The GFRP prototype tested proved to be a viable and competitive alternative to traditional (HSCS) and innovative (HSSS, CFRP) PC technologies. Some relevant design parameters are left aside, given the limited amount of material available at the time of testing and writing. Thus, field deployment of this technology shall await further investigation, currently undergoing at the University of Miami.

ACKNOWLEDGEMENTS

The authors gratefully acknowledge the financial support from: (1) "I/UCRC Center for the Integration of Composites into Infrastructure (CICI)," NSF, 1439543. (2) Zegna Foundation for supporting the first author's research activity in the field of composite materials for infrastructural applications. (3) Sireg Group for providing the GFRP material required for this investigation.

REFERENCES

- ACI Committee 440. (2015). *Guide for the Design and Construction of Structural Concrete Reinforced with Fiber-Reinforced Polymers (FRP) Bars (ACI 440.1R)*. Farmington Hills, MI. American Concrete Institute.
- Ahmad, S. (2003). Reinforcement Corrosion in Concrete Structures, its Monitoring and Service Life Prediction - A Review. *Cement & Concrete Composites*, 25(4-5 SPEC), 459-471.
- ASTM. (2016). *Standard Test Method for Tensile Properties of Fiber Reinforced Polymer Matrix Composite Bars (D7205/D7205M)*. West Conshohocken, PA. ASTM International.
- ASTM. (2017). *Standard Specification for Solid Round Glass Fiber Reinforced Polymer Bars for Concrete Reinforcement (D7957/D7957M)*. West Conshohocken, PA. ASTM International.
- Atutis, M., Valivonis, J., & Atutis, E. (2015). Analysis of Serviceability Limit State of GFRP Prestressed Concrete Beams. *Composite Structures*, 134, 450-459.
- CSA. (2017). *Design and Construction of Building Components with Fibre-Reinforced Polymers (S806)*. Toronto, ON. CSA Group.
- Diwanji, A. (2011). *Glass Fiber Reinforcement Chemical Resistance Guide, Edition 1A, March*. Toledo, OH. Owens Corning.
- FDOT. (2016a). *Index 22440. Precast Concrete CFRP/GFRP & HSSS/GFRP Sheet Pile Wall*. Tallahassee, FL. Florida Department of Transportation.
- FDOT. (2016b). *Index 22600. Series Square CFRP & SS Prestressed Concrete Piles*. Tallahassee, FL. Florida Department of Transportation.
- FDOT. (2016c). *Design Standards Development Report for Corrosion Resistant Prestress Concrete Piles*. Tallahassee, FL. Florida Department of Transportation.
- Fico, R., Galati, N., Prota, A., & Nanni, A. (2005). Design and Construction of a Bridge Deck using Mild and Post-Tensioned FRP Bars. *ACI Special Publications* (pp. 1121-1138). American Concrete Institute.
- Hong, C., Yin, J., & Zhang, Y. (2016). Deformation Monitoring of Long GFRP Bar Soil Nails Using Distributed Optical Fiber Sensing Technology. *Smart Materials and Structures*, 25, 085044(1-8).
- Husain, M., Fawzy, K., & Nada, A. (2015). Performance of Prestressed Concrete Beam with FRP Tendons. *International Journal of Engineering and Innovative Technology*, 5(2), 22-29.

Mazaheripour, H. (2015). *Structural Behavior of Hybrid GFRP and Steel Reinforced FRC Prestressed Beams*. Braga, PT. Universidade do Minho.

Nanni, A., Bakis, C. E., O'Neil, E. F., & Dixon, T. O. (1996). Performance of FRP Tendon-Anchor Systems for Prestressed Concrete Structures. *PCI Journal*, 41(1), 34-44.

Natoli, E., Admiraal, B., de Wit, D., & Yahyaoui, A. (2017). River Embankment Strengthening by Non-Metallic Nails. Overview on a Permanent Soil Nailing for Flood Protection. *Innovative Infrastructural Solutions*, 2.53, 1-10.

Noel, M., & Soudku, K. (2013). Effect of Prestressing on the Performance of GFRP-Reinforced Concrete Slab Bridge Strips. *ASCE Journal of Composites for Construction*, 17(2), 188-196.

Nolan, S., & Nanni, A. (2017). Deployment of Composite Reinforcing - Part 1. Impetus for more Widespread Application in Transportation Infrastructure. *Concrete International*, May, 40-46.

Nolan, S., Rossini, M., & Nanni, A. (2018). Seawalls, SEACON and Sustainability in the Sunshine State. *Transportation Research Board 97th Annual Meeting*. Washington, DC.

Paul, A., Loritz, G. B., & Lawrence, K. F. (2017, May-June). Transfer and Development Length of High-Strength Duplex Stainless Steel Strand in Prestressed Concrete Piles. *PCI Journal*, 59-71.

Rambo-Roddenberry, M., & Gartman, M. (2017). *Research Progress Report 2nd Quarter - Inspection and Monitoring of Fabrication and Construction for the West Halls River Road Bridge Replacement*. Tallahassee, FL. Florida Department of Transportations.

Rossini, M., Bruschi, E., Matta, F., Poggi, C., & Nanni, A. (2017). Case-Specific Parametric Analysis as Research-Directing Tool for Analysis and Design of GFRP-RC Structures. *The 13th International Symposium on Fiber-Reinforced Polymer Reinforcement for Concrete Structures*. Anaheim, CA. American Concrete Institute.

Ruiz Emparanza, A., Kampmann, R., & De Caso y Basalo, F. (2017). State-of-the-Practice of Global Manufacturing of FRP Rebar and Specifications. *The 13th International Symposium on Fiber-Reinforced Polymer Reinforcement for Concrete Structures*. Anaheim, CA. American Concrete Institute.

Shwartz, M. M. (1997). *Composite Materials, Volume I. Properties, Nondestructive Testing, and Repair*. Upper Saddle River, NJ. Prentice Hall PTR.

Sippe, T. M. (1992). Design, Testing and Loading of an Anchorage System for Resin Bonded Fiberglass Rods Used as Prestressing Tendons. *Advanced Composite Materials in Bridges and Structures - 1st International Conference* (pp. 363-372). Sherbrooke, QC. Canadian Society for Civil Engineering.

Spadea, S., Rossini, M., & Nanni, A. (2018). Design Analysis and Experimental Behavior of Precast Double-Tee Girders with CFRP Strands. *PCI Journal*, January-February.

Zawam, M., Soudki, K., & West, J. S. (2017). Effect of Prestressing Level on the Time-Dependent Behavior of GFRP Prestressed Concrete Beams. *ASCE Journal of Composites in Construction*, 21(4), 04017001-(1-10).



BEHAVIOR OF GFRP REINFORCED CONCRETE UNDER FLEXION: EXPERIMENTAL TESTS ON REAL SCALE SLABS

M. Arduini ¹ and G. Balconi ²

¹ FRC LAB, CEO, Milano, Italy

² Sireg Geotech, Research & Development, Arcore (MB), Italy, Email: g.balconi@sireg.it

ABSTRACT

Glass Fibre Reinforced Polymers (“GFRP”) are currently widely used for reinforcing concrete structures. Reinforcement designs and rebar diameters used in the field for this application vary significantly, lacking mandatory material qualifications or limitations in the existing guidelines. In order to understand the differences in performance of diverse GFRP reinforcement designs, flexion tests were carried out on six real dimension concrete slabs. All reinforcements were designed for very similar flexural capacity but significantly different GFRP-concrete adhesion area. In order to simulate an extreme case of potential material deterioration, the GFRP bars employed had been aged outside for three years. Experimental results confirmed that, for reinforcements with similar flexural capacity, an increase in the shape ratio implies a reduction in the maximum load capacity and the occurrence of slip phenomena. A reinforcement with a high shape ratio may not guarantee a perfect bond between concrete and GFRP, and experience premature slip phenomena.

KEYWORDS

Field applications and case studies, Experimental study, FRP internal reinforcement, Bond and interfacial stresses, GFRP, Reinforced concrete.

INTRODUCTION

The use of Glass Fibre Reinforced Polymers (“GFRP”) cages as reinforcements for concrete diaphragms and piles dates back to two decades ago. The initial reason for substituting traditional steel reinforcements with GFRP bars was the need for having sections of the supporting structures in tunnel construction that the boring machine could easily excavate through. For such application, the solicitations in play are significant and the conventional steel reinforcement project design is usually optimized for the balanced failure of both the compressed and the tensed (steel) sections. In many cases, the substitution of steel with GFRP led to concrete crushing before the reinforcement’s ultimate strain was attained. In these cases, an increase in concrete’s compressive resistance is recommended in order to reach a balanced failure mode. Such solution, required for a few GFRP reinforced diaphragm walls, is not very feasible in a large tunnelling worksite where most of the supporting structures remain reinforced in steel. Therefore, in order to achieve the balanced failure mode, it was necessary to compensate by increasing the reinforcement area, which often led to the use of large diameter bars. As a result, GFRP rebars used for concrete reinforcement rapidly passed from the originally employed 20 to 32 mm diameter bars to those of 32 to 40 mm, or even larger, diameters.

It is indeed very common to find GFRP cages built with large diameter rebars. However, this approach needs to consider that the increase in bar diameter implies three disadvantages:

- It is extremely difficult to perform tensile tests on a full section of a large diameter rebar. The need for samples longer than 3 meters and non-standard horizontal tensile testing equipment, as well as premature breakage of the superficial filaments close to gripping, make obtaining real data almost impossible.
- The larger is the rebar’s diameter, the higher is its maximum load to interfacing area ratio (the same occurs with the rebar’s comprehensive area to interfacing area). As a result, tangential bond stress considerably increases, incrementing the risks of concrete cracking and premature debonding.
- Larger diameter rebars require a larger spacing between bars in order to guarantee the required clear space for aggregates to flow through the cage.

Unfortunately, material qualification requirements are not yet mandatory. IBC Acceptance Criteria AC454 (2016) limits bar diameter to the 6 mm to 32 mm range, but its adoption is not officially regulated. Additionally, the existing international guidelines ACI 440, CNR-DT 203, and Model Code 2010 do not impose a maximum diameter limit to the reinforcing bars.

In order to understand the effect of design and bar diameter of GFRP cages in the behaviour of reinforced concrete slabs while bending, an experimental test program was carried out.

THE EXPERIMENTAL PROGRAM

Three Reinforcement Designs

Three GFRP reinforcing cages were designed with different configurations. All cages were designed for a similar flexural capacity of the reinforced element (M_{rd}) and, therefore, similar FRP reinforcement area. Table 1 summarizes the main characteristics of the three cage configurations. As reported, the larger is the bar diameter in the design, the higher is the shape ratio of the reinforcing cage. Consequently, for the same flexural capacity, the increase in bar diameter implies a reduction in the interfacing area of the longitudinal FRP reinforcements. This translates into a reduction in the reinforcements' overall bonding capacity that causes potential premature GFRP-concrete debonding.

Table 1: GFRP reinforcing cage designs

Cage design	Number of GFRP bars	Bar diameter* Mm	A_f sq. mm	Shape ratio ϕ_s	M_{rd} kN*m
1	25	12	2,826	3	109.3
2	16 (bundled in 4 groups)	16	3,215	4	103.9
3	4	32	3,215	8	102.0

Note:

A_f : comprehensive area of GFRP reinforcement (in tension)

ϕ_s : comprehensive area of GFRP reinforcement / interfacing area of GFRP reinforcement

* Top and bottom bar diameter



Figure 1: GFRP cage design 1 (left) and 3(right) ready for casting

To conduct the tests, six cages, two of each design, were built using glass fiber and polyester resin rebars. Cage designs 1 and 3 are shown in Figure 1. Table 2 shows the mechanical properties of the bars.

Table 2: Mechanical properties of GFRP bars

Diameter Mm	Guaranteed tensile strength (f_{rk}^*) MPa	Elasticity modulus (E_f^{**}) GPa
12	850	46
16	800	46
32	580	46

Note:

* Characteristic value based on ASTM D7205.

** Mean of 5 samples based on ASTM D7205.

The Testing Program

The testing program involved two sets of tests carried out on concrete slabs reinforced with each cage design:

- Bending (test B), to test for loads applied on the slab's middle section
- Shear (test S), to test for loads applied on the two sides of the slab

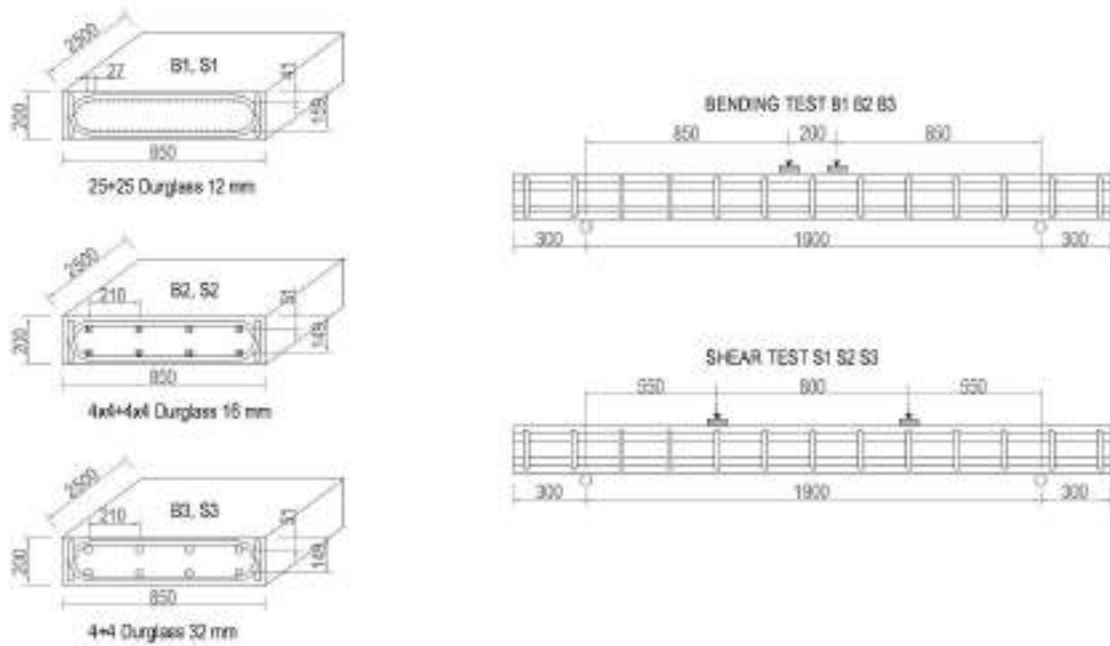


Figure 2: Reinforcing cage designs (left) and flexure test configurations (right)

Figure 2 shows the slabs reinforced with the three different cage designs, and the two flexion test configurations to be performed on each slab type.

In order to account for potential material deterioration caused by the elements or by handling, the rebars used to build the reinforcements for the testing program had been let age outside for about 3 years. In fact, the rebars had been exposed to sun, rain, and very cold weather, simulating an extreme case of material deterioration that could affect the reinforcement's bonding capacity.

The concrete casts were executed contemporarily with the same cement mix, sand and aggregates (maximum diameter 14 mm), and let age for 40 days. After casting, the concrete slabs measured 0.85m x 0.20m x 2.50m.

A non-destructive verification, using the SONREB methodology (hammer test + ultrasonic test), was performed the day before the tests. For each concrete cast, 4 different positions were analyzed, and the Di Leo Pascale (Arduini et al. (1997)) regression formula applied.

The tests were conducted in a monotonic mode, with only one initial adjustment cycle up to about 10% of the breaking load. During the tests, the following data were observed and registered:

- The applied load $2F$
- The mid span deflection
- Concrete's extrados center deformation through LVDT over a measurable base of about 20 cm.

ANALISIS OF EXPERIMENTAL RESULTS

Test observations

Table 3 below summarizes the data observed during the tests. The slabs' concrete cubic compressive strength (f_c) and dynamic elasticity modulus (E_c) (assuming a typical density of 2300 kg/m³ and a Poisson coefficient $\nu=0.15$) show that the resistance values of the concrete slabs during testing registered a minimum difference of +/-1 MPa with respect to their mean.

Before breaking, but after having abundantly exceeded design limits, the crisis formation mechanisms were defined. Deflection and deformation measuring instruments were removed. As a result, the maximum breaking load $2F_{max}$ reached is slightly over the load applied continuously as reported below.

Table 3: Test results

Slab	Load test	f_c MPa	E_c GPa	$2F_s$ kN	$2F^*$ kN	Mid span deflect.* Mm	Concrete strain* $\mu\epsilon$	$2F_{max}$ kN	$2F_{ULS}$ (Mrd) kN	Failure mode
B1	Bending	35.9	38.7	179	246	21.0	1593	262.9	257.2	Crushing
B2	Bending	35.5	38.6	159	246	20.5	1929	319.4	244.5	Crushing
B3	Bending	35.9	39.0	140	246	23.9	2485	278.9	240.0	Crushing
S1	Shear	35.5	36.1	215	339	22.9	1265	385.1	397.5	Shear
S2	Shear	34.9	38.1	213	339	20.5	1450	421.6	377.8	Shear
S3	Shear	36.3	39.3	186	339	19.8	1201	388.4	370.9	Shear
Mean		35.7	38.3							

Note:

f_c : concrete's cubic compressive strength

E_c : concrete's modulus of elasticity

$2F_s$: load at the formation of a 0.6 mm width crack

$2F$: applied load

$2F_{max}$: maximum breaking load

$2F_{ULS}$: ultimate breaking load

*Last observed data before removing the instruments

Slabs B1 and S1, reinforced with cage design 1 and having 12% less comprehensive area of GFRP reinforcement than cage design 3, would allow for a higher service load, equivalent to 1.28 and 1.15 times those of slabs B3 and S3, respectively, based on the load observed at the formation of a 0.6 mm width crack ($2F_s$). With regards to the maximum breaking load ($2F_{max}$) slabs B2 and S2 registered loads equivalent to 1.14 and 1.08 times those registered by slabs B3 and S3, respectively, simply by reducing the reinforcement's shape ratio.



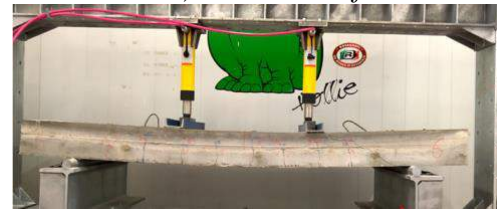
a) Slab B1 at failure



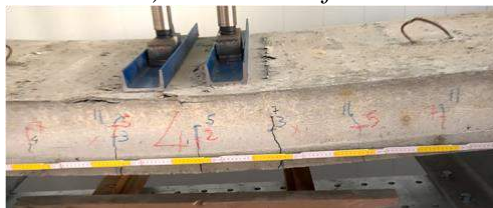
d) Slab S1 at failure



b) Slab B2 at failure



e) Slab S2 at failure



c) Slab B3 at failure



f) Slab S3 at failure

Figure 3 – Failure mechanisms observed during testing

Some images of the slabs at failure are reported on Figure 3. The failure mechanisms observed in the slabs were: concrete crushing in the mid span for slabs B1, B2 and B3, and shear failure near the load points for slabs S1, S2, and S3.

The mid span deflection and the concrete top strain levels experienced by the GFRP reinforced concrete slabs during the bending and shear tests are shown in the following graphs.

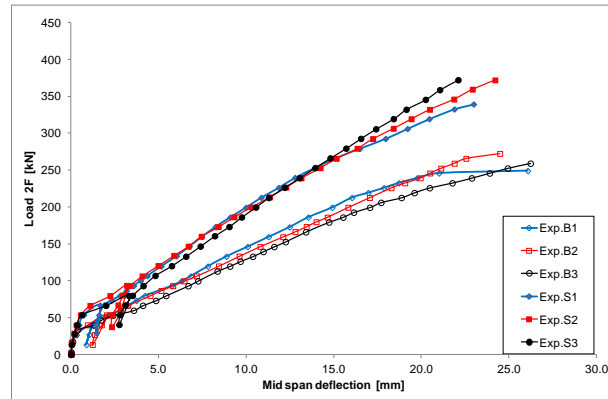


Figure 4: Load-mid span deflection behavior

The relationship between applied load to mid span deflection measured on all reinforced slabs, up to the moment when all instruments were removed, is reported in Figure 4. During the bending tests (B), slab B1 reinforced with the GFRP cage with small diameter (12 mm) bars experienced the smallest mid span deflection for the same applied load, up to an applied load of approximately 225 kN. The higher stiffness provided by Cage 1 revealed highly important in determining the maximum service load value when limiting the crack width to 0.6 mm ($2F_s$). As shown in Table 3 above: slab B1's service load is 179 kN, 28% higher than that of B3. The results shown in Figure 4 are consistent with these observations. Also up to an applied load of 225 kN, slab B3 reinforced with 32 mm diameter bars showed the largest mid span deflection for the same applied load. When the applied load exceeded 225 kN the comparative performance of the three slabs changed. On the other hand, when comparing mid span deflections experienced during the shear tests (S), the three reinforced slabs behaved similarly up to an applied load of approximately 250 kN. Only when exceeding such load level, S1 showed a mid span deflection larger than the others.

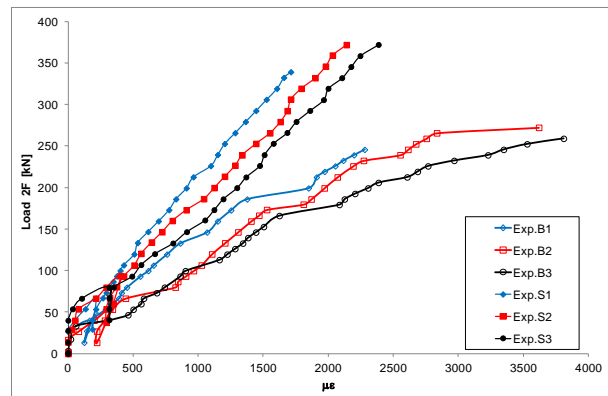


Figure 5: Load-concrete top strain behavior

Figure 5 shows the relationship between applied load and concrete's top strain measured on all tests, up to the moment when the strain gauges were removed. The graph clearly shows that concrete slabs reinforced with GFRP cage design 1 (B1 and S1) registered the lowest concrete top strain for the same applied load during both the bending and the shear tests.

It is worth mentioning that although the three cage designs have similar reinforcing capacity, in reality the longitudinal reinforcement area of slabs B1 and S1 is 12% smaller than that of slabs reinforced with cage designs 2 and 3, implying a 12% material cost savings. Therefore, cage configuration 1 with the smallest bar diameter is able to compensate for a smaller GFRP comprehensive area with GFRP-concrete bonding capacity.

Comparison of test results with "perfect adhesion" model simulations

The GFRP cages used in the tests were designed to sustain the same flexural capacity. However, both the load-deflection responses and the load-deformation responses registered during experimental testing by slabs reinforced with different cage configurations varied significantly. Essentially, variations in observed behaviour were caused by differences in the GFRP-concrete bonding capacity of the reinforcing structures. Slipping becomes more evident as the relationship between the reinforcements' comprehensive area to interfacing area (value of ϕ_s) increases.

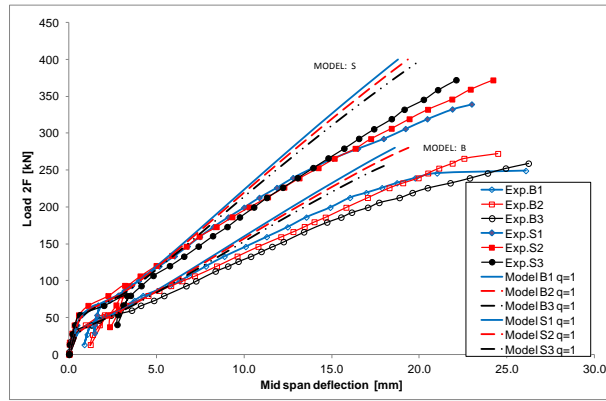
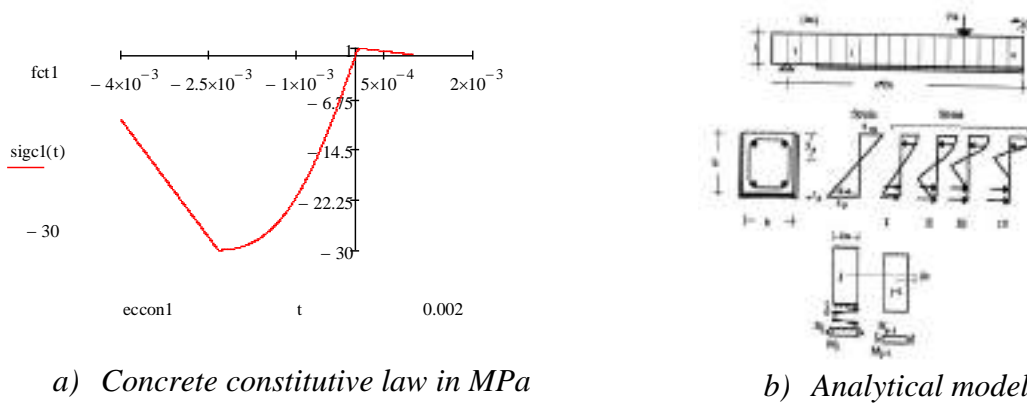


Figure 6: Comparison of mid span deflections observed during testing and numerical model simulations assuming perfect adhesion ($q=1$).



a) Concrete constitutive law in MPa

b) Analytical model

Figure 7: Analytical model used for simulation

Figure 6 reports a comparison between the experimental results and a numerical model already used in Arduini et al. (1997). The analytical model subdivides a GFRP reinforced concrete slab in 25 mm segments and assumes perfect adhesion between GFRP and concrete. Based on the mechanic properties reported in Tables 2 and 3, the load-deflection behaviour is obtained as the integral of each segment's curvature (concrete's initial static modulus of elasticity is assumed equal to $E_s = 2/3 E_d$, the constitutive law is reported in Figure 7). The load-mid span deflection analytical curve is stopped when concrete strength reaches $\epsilon=0.004$ in compression. Using the numerical model, the three reinforced slab configurations generate theoretical load-deflection diagrams basically identical to those obtained during the experimental tests given that the effective reinforcement ratios (ρ_f) are very similar. However, the model's simulations are all stiffer than reality.

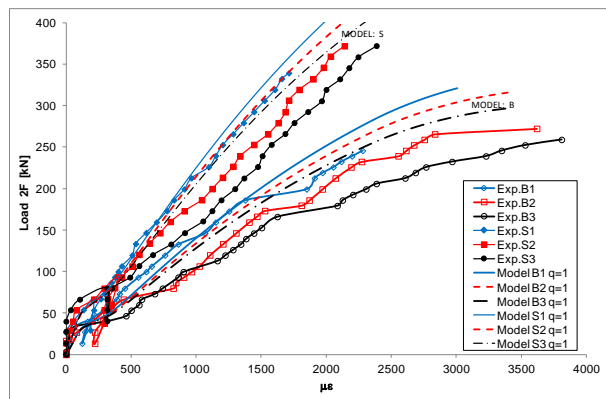


Figure 8: Comparison between concrete strain levels observed during testing and numerical model simulations assuming perfect adhesion ($q=1$).

The comparison between the extrados concrete deformations observed during the experimental tests and those obtained through the perfect adherence model reported in Figure 8 confirms that the simulations are stiffer than their corresponding experimental behaviours. This difference is explained by the presence of slipping phenomena between the GFRP reinforcements and concrete.

Contribution of bent bars to shear resistance

During the shear tests (S), the slab breakages observed were essentially due to shear failure. In fact, the flexion resistance levels reached in the bending tests (B) would have allowed the slabs with the same reinforcing cage design to reach loads about 20% higher than those effectively reached when breakage occurred.

The value of the ultimate shear resistance of concrete only (without stirrups) is calculated as follows (CNR-DT 203):

$$V_{Rd,ct} = 1.3 * (E_f/E_s)^{1/2} * 0.25 f_{ctd} * k * (1.2 + 40\rho_1) * b * d$$

Where:

E_f : modulus of elasticity of GFRP bars

E_s : modulus of elasticity of steel bars

f_{ctd} : design tensile strength of concrete

k : coefficient set $k=1$ if over 50% of bottom reinforcement is interrupted, otherwise $k = (1.6-d) >= 1$

ρ_1 : flexural GFRP reinforcement ratio

b : section width

d : distance from extreme compression fiber to centroid of tension reinforcement

In our case, $f_{ctd} = 2/1.5 = 1.33$ MPa and $k = 1.44$. Table 4 shows the slabs' shear resistance for the given ρ_1 values.

Table 4: Shear capacity of reinforced slabs

Concrete slab	ρ_1	$V_{Rd,ct}$ kN	$V_{Rd,f}^*$ kN	V_{Rd}
S1	0.0206	81.3	47.0	128.3
S2	0.0235	93.0	47.5	140.5
S3	0.0236	93.4	36.0	129.4

Note: * Estimated calculating backwards assuming a safety coefficient of 1.5.

The shear breaking load levels of the GFRP reinforced slabs observed during testing significantly exceeded their concrete ultimate shear resistance. These results are explained by the presence of C shaped GFRP stirrups with 20 cm spacing. Though the C-shape stirrups were used only for assembling purposes (the objective of the test program is to measure the flexural capacity of the longitudinal reinforcements), the bent bars have contributed to the structure's overall resistance by activating Morsch's trellis.

Since proper rectangular shaped stirrups have not been used, the stirrups' contribution to the structure's overall resistance cannot be directly calculated. An estimation is obtained in table 4 by calculating backwards and assuming a safety coefficient of 1.5.

Bond reduction factor

Overestimating adherence capacity can have notable consequences in the verifications of service loads of a GFRP reinforced concrete structure. It is therefore necessary to modify the perfect adherence assumption through a bond coefficient that depends upon both the concrete strength and the reinforcement's surface.

A simplified way to achieve a more accurate estimation of adherence capacity would be by reducing the reinforcement's modulus of elasticity from a theoretical value to an "effective" value $E_{eff} = d E_{nom}$. However, this approach distributes continuously what in reality is a localized phenomena. Figure 9 reports, for slabs B3 and S3 (reinforcing cage design 3), three different load-deflection and load-deformation behaviours obtained for values of $q = 1, 0.8$ and 0.6 . The experimentally observed behaviour for cage 3 can be accurately simulated by assuming $q=0.8$. It can be deduced that assumed values of $q=0.8$ and $q=0.9$ accurately simulate the test results for cage designs 2 and 1, respectively. However, this simplified model underestimates resistance to small loads, since the reduction in modulus of elasticity affects the reinforcements' initial elastic response, response on which perfect adherence is still valid.

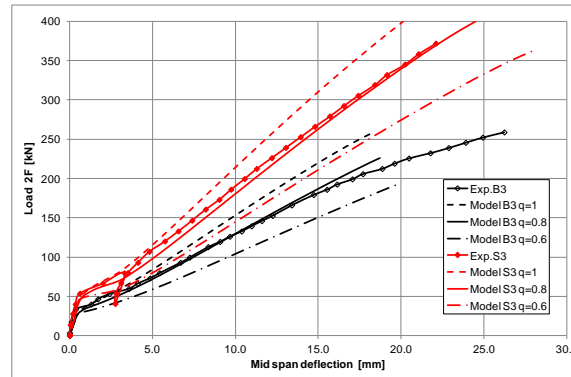


Figure 9: Influence of the bond reduction factor on concrete's behaviour under flexure

A more accurate way to model actual performance would be by modifying the GFRP bars' constitutive bond in such a way that slipping starts occurring at a determined stress level. In this model, the reinforcements' effective modulus of elasticity decreases as the working stress, or GFRP-concrete interfacing stress, increases. This model simulates more accurately how premature debonding affects the response of reinforced concrete slabs when load is applied.

CONCLUSIONS

The objective of this study is to understand the bending behaviour of concrete slabs reinforced with GFRP cages designed for similar flexural and shear capacity (according to guidelines ACI 440, CNR-DT 203 and Model Code 2010), but built with different rebar configurations. The experimental program performed confirmed that bar diameter and configuration affect the overall performance of the reinforced slabs. The shape ratios (rebar total area to concrete interfacing area) of the reinforcing cages tested ranged from 3 to 8. The use of small rebars seem to benefit the service conditions, reducing crack width and concrete's strain. Bundle configuration seems to benefit ultimate capacity. The authors of this paper deem that the observed differences in behaviour among the slabs are the result of diverse tangential adhesion tensions between GFRP reinforcement and concrete. Reinforcing cages built with large diameter bars and smaller concrete interfacing area transfer higher stress to the surrounding concrete. These results confirm the need to introduce in the existing guidelines limitations to the maximum rebar diameter and the maximum distance between bars for GFRP concrete reinforcements, as is the case for steel reinforcements. Alternatively, the design model for GFRP reinforced concrete structures should include a bond reduction coefficient to account for premature slipping phenomena that increases the crack width and reduces the maximum bending capacity at service level.

REFERENCES

- M. Arduini, A. Di Tommaso, A. Nanni (1997). "Brittle failure in FRP plate and sheet bonded beams", *ACI Structural Journal*, vol. 94, n.4. July/August.
- M. Arduini, A. Nanni (1997). "Behavior of precracked RC beams strengthened with carbon FRP sheets", *ASCE Journal of Composites for Construction*, May vol. 1, n 2.
- American Concrete Institute (2008). "Guide for the Design and Construction of Externally Bonded FRP Systems for Strengthening Concrete Structures", *ACI 440*.
- Consiglio Nazionale delle Ricerche (2006). "Guide for the Design and Construction of Concrete Structures Reinforced with Fiber-Reinforced Polymer Bars", *CNR-DT 203*.
- International Federation for Structural Concrete (2010). *Fib Model Code 2010*.
- The International Building Code (IBC) (2016). "Acceptance Criteria for Glass Fibre-Reinforced Polymer Bars for Internal Reinforcement of Concrete Members", *AC454*



A CONSISTENT DESIGN CONCEPT FOR BOLTED CONNECTIONS AND APPLICATION TO INDUSTRIAL STRUCTURES

Matthias Oppe¹, J Toby Mottram², Jan Knippers^{1,3}

¹ Knippers Helbig GmbH, Stuttgart (Germany); ² Warwick University, School of Engineering, Coventry (England); ³ Stuttgart University - Institute of Building Structures and Structural Design, Stuttgart (Germany)

ABSTRACT

Presented in this paper is an introduction to the development of structural design clauses for bolted connections (and joints) towards the preparation of a future Eurocode for fibre reinforced polymer materials. The impetus and drive, from within the composite community, for this code writing has been, for example, the increasing annual number of applications of pultruded shapes and mould components of glass fibre reinforced polymer (FRP) in bridge and industrial structures. Since detachable structural joints with mechanical fasteners remain the most reliable and controllable method for connecting structural members in FRP structures there is a need for a consistent design concept for bolted connections, which is presented in Ascione *et al.* (2016). The first part of this paper gives historical context to, and introduces the content of Chapter 8 for Connections in this Joint Research Centre Science and Policy report. In the second part of the paper we present an application of mechanically fastened bolted connections for cooling tower structures at an electricity-generating power plant in Egypt.

KEYWORDS

All FRP structures, material, codes, standards and design guidelines, case studies.

INTRODUCTION

We start this paper by providing a historical perspective on the preparation and implementation of national or international codified design standards in Europe for structures having components that are of FRP shapes and systems (Bank 2006). New-build structures can be either of all-FRP or in the form of hybrid combinations with components of traditional structural materials. The latter are to be designed using their specific standards, such as available in the Eurocode suite. This paper does not scope standards for the developed applications of FRPs to retrofitting or strengthening of existing non-FRP structures or as non-metallic reinforcement in concretes (Bank 2006).

The historical context for code writing in Europe was founded in independent national projects with publications from: UK (Clarke 1996); Italy (Anonymous 2008); Germany (BÜV-Empfehlung 2014). Thoughts towards the European community preparing a structural Eurocode were voiced more than a decade ago, and from a Joint Research Council (JRC in Ispra, Italy) initiative there is a position publication in 2007 (Gutiérrez, Dimova and Pinto 2007). To quote from this publication “*In view of the importance of the construction industry in the European market, this proposal examines the potential benefits of the new Eurocode, or conversely, the detriments were it not to be implemented. Moreover, given the number of construction works currently using FRP materials without the availability of a standard design code, this proposal considers the urgency with which it is required*”. Moreover, this JRC report provided us with a tentative proposal for the consultation, feasibility analysis and initiation strategies for an FRP structural Eurocode.

In 2009 Professor L. Ascione of the University of Salerno (Italy) was appointed to be the convenor to Working Group 4 (WG4) for *Fibre Reinforced Polymers* in the Structural Eurocode Committee CEN/TC250. After he set-up its membership, now having 56 members from 20 EU countries, work commenced to write an JRC Science and Policy Report, which was published in 2016 (Ascione *et al.* 2016). CEN is the Comité Européen de Normalisation or the European Committee for Standardization,

which is a public standards organization whose mission is to foster the economy of the European Union in global trading. The 2016 JRC report scopes FRP laminates made by a number of processing methods, and thereby, along with pultruded shapes, involves free-form shells, with or without sandwich construction. The report has the same format and style as the materials' Part 1-1 for concrete, steel, composite steel and concrete, timber, masonry and aluminium in the existing Eurocode suite.

It is relevant next to introduce the various sources of design guidance that could be used by the code drafters in WG4 (of CEN/TC250) to inform them of the content in the JRC report. Its preparation draws on knowledge and understanding from the earlier projects to develop design specifications, procedures and formulae (Anonymous 1984; Clarke 1996; EN 13706 2002; CUR Commission C124 2003; Anonymous 2008; Anonymous 2010; Anonymous 2012; BÜV-Empfehlung 2014). The world-first source of guidance is the EUROCOMP Design Code and Handbook (Clarke 1996), which is not a recognized design code, and scopes structural elements made by four composite processing methods. Only the German output (Anonymous 2014) is recognised as a national standard, and along with the Italian guide (which is not recognized) (Anonymous 2008) is restricted to FRP components made by the pultrusion composite processing method. From 2010 there has been a significant national project in The Netherlands to update CUR 96 (2003).

After a pan-European consultation review of Ascione (2016) during 2016, nearly 800 feedback comments have been addressed by WG4 for a major revision of the JRC report, and this version is to be published by JRC before the proceedings of conference CICE 2018. This '2017' report was an item of business at the CEN/TC250 meeting at Naples on 10-11 May 2017. Then the committee gave its approval to proceed to the next stage of three for there to be an Eurocode standard for FRP materials. Stage 2 is to prepare an CEN Technical Specification, which for those knowing the history to the development of the existing Eurocodes was known as an ENV. This stage of standard writing is expected to be completed in 2020.

Prior to the commencement of the WG4 project to prepare a structural FRP Eurocode the only EN standard for construction composites is EN 13706:2002, which is specific to the specification of FRP shapes made by the pultrusion composite processing method.

It is noteworthy and important to understand that the JRC report has the following preamble, this report *“presents scientific and technical proposals intended to serve as a starting point for further work to achieve a harmonized European view on the design and verification of composite structures realized with FRPs. Its fundamental purpose is to stimulate debate. To enable this objective to be fulfilled, it contains preliminary proposals for technical provisions and identifies key issues requiring further discussion. It is emphasised, however, that it is not intended for use in practice at this stage”*.

The next part to this paper is for an introduction to the content of Chapter 8 for Connections (Ascione *et al.* 2016). This chapter scopes the methods of connection by adhesive bonded and mechanical fasteners (i.e. bolting) and it is the latter which the paper reports. It scopes various criteria, including, for example, geometrical limitations that have to be satisfied when designing bolted connections. Verification of joint resistance from the effects of actions subjected to Ultimate Limit State loading cases has to be carried out by taking into account failure modes for action effects in the plane and out-of-plane that consider the material's orthotropic strength properties. Bolted connections are not only subjected to independent shear or tension forces, but to an interaction combination of both.

The third, and final, part to the paper is for a summary report for an application of mechanically fastened bolted connections for cooling tower structures at an electricity-generating power plant in Egypt.

CHAPTER 8 CONNECTIONS

To follow what is reported next, the reader needs to consult the JRC report, which is freely available using the internet link at the end of the reference for Ascione *et al.* (2016); will now be the 2017 version, which was not published when this paper was written. Chapter 8 in the JRC report scopes connections

and joints where the methods of connection is by mechanical fasteners (i.e. steel or stainless steel bolting) or adhesive bonding, and by a hybrid combination method of mechanical and adhesive bonding. Herein we are going to introduce the design philosophy and clauses for the design of bolted connections and joints. It is limited to FRP materials from the pultrusion processing method and to balanced symmetrical cross-ply laminates made using composite processing methods scoped in Section 3, such as resin infusion (Bank 2006).

In Eurocode terminology, a connection is a location at which two or more elements meet. For design purposes it is the assembly of the basic components required to represent the behaviour during the transfer of the relevant internal forces and moments at the connection. The Eurocode definition of a joint is a zone where two or more members are interconnected. For design purposes it is the assembly of all the basic components required to represent the behaviour during the transfer of the relevant internal forces and moments between the connected members.

Chapter 8, for bolted connections, has three sections to cover the following topics: General (8.1); Design Criteria (8.2); Bolted Joints (8.3).

General clauses are needed to provide a robust framework for the design of the resistances of bolted joints (actually connections in Eurocode terminology), when two or more thin-walled members are connected together and one of the members are of FRP material. Design information for the FRP materials is covered in Section 3 of Ascione *et al.* (2016). Because the design clauses might not cover all connection or joint details, it is relevant that one approach is for design by testing, to which Annex D in EN 1990:2002 provides clauses for application of this, often, pragmatic engineering approach.

Design Criteria section sets out how the internal forces and moments are to be established using static equilibrium, definition of configurations in bolted connections or joints and requirement to account for actions due to eccentricities in geometry.

The resistance models for bolted joints are presented in Section 8.3 and this section has five sub-sections.

Sub-section 8.3.1 is for General design requirements, which are for: acceptable type of steel bolts; the requirement for one diameter of bolt per connection; a limit on bolt diameter to 1.5 times of the thickness of the thinnest connected FRP element; the bolt holes to be drilled and with clearance hole (dimension specified in Table 8.1); the presence of stainless steel washers (ISO 7093) of diameter greater than two times the bolt diameter; using information in Table 8.1 to establish bolt spacings and edge distances in a connection; neglecting any benefit to connection resistance from bolt tightening and a requirement to prevent over tightening; a new formula that determines the maximum tightening torque, by knowing the through-thickness compression strength of the FRP material.

Sub-Section 8.3.2 sets the Design Criteria, for enhancement to those clauses in Section 8.2, with an acknowledgement that the recognized distinct failure modes of the FRP bolted connection element to be designed for are: net-tension; pin-bearing; shear-out. The line drawings in Figure 1 illustrate these three modes, and for labelling has the notation: w is element width; e_1 is end distance, d_0 is hole diameter; θ is the orientation of the principal direction of the (FRP) laminate to the direction of V_{Ed} , which is the connection design force at the bolt determined from the effects of the actions that are to be designed for. For the steel or stainless bolts themselves there is to be a resistance check for bolt-shear. There is a recognition that the mode of failure of the FRP element may not be one of these distinct modes when the number of bolt rows is two or higher or for a single row where bolt 'bearing' force is not aligned to a principal axis of the laminate (as shown in Figure 1). Moreover, when the bolt configuration is for a multi-row connection the mode of failure in the FRP material can be that of block shear failure.

Sub-sections 8.3.3 for bolted joints subjected to in-plane actions is further sub-divided in five sub-sections that have clauses for determination of the connection resistances for the five modes of failure just introduced.

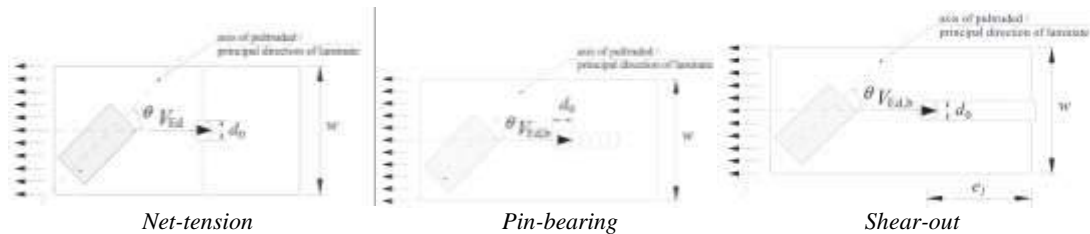


Figure 1: Typical failure modes for bolted joints subjected to in-plane actions (Ascione *et al.* 2016)

To commence the design approach there are clauses on how the design force is distributed to the bolts to establish the bolting's V_{Ed} s using Table 8.2, which has its provenance in Clarke (1996).

The expressions for calculating FRP element strengths are simple in form and are based on connection geometry and an FRP strength (see Section 3.0) that are for each of the distinct modes of failure. Where applicable there are two formulae for the situations when the connection force to be resisted (V_{Ed}) is either in the principal direction of the FRP material (i.e. $\theta = 0^\circ$) or acting in the perpendicular direction (i.e. $\theta = 90^\circ$), for both pultruded and balanced symmetrical cross-ply laminates. The net-tension design approach is not based on the Hart-Smith methods, which is explained in Mottram (2010) and is a design method only for pultruded materials in Anonymous (2010), via an appendix; it is not mandatory. The approach chosen in the JRC report is based on a stress concentration factor of 3.75 for connection load either oriented to or oriented perpendicular to the principal direction of a pultruded material. For the minimum hole spacing of four bolt diameters the net-tension resistance in Ascione *et al.* (2016) is 0.2 of the gross section tension strength, and this is the lowest connection efficiency when applying the Hart-Smith method, as reported by Mottram (2013) for a comprehensive evaluation of the strength predictions from the Hart-Smith formulae to the full range of bolt geometries allowed in Anonymous (2010). The specification of the stress concentration factor at 3.75 is likely to be conservative in determining the connection net-tension resistance. In the JRC report there is a minor amendment to allow the two net-tension resistance formulae just introduced to be used with balanced symmetrical cross-ply laminates. The strength formulae for shear-out and block shear are the same as in Anonymous (2010), whereas for the pin-bearing mode of failure the formula now has a reduction factor based on the square of the non-dimensional ratio for bolt diameter divided by the hole diameter, as initially introduced in Oppe (2009).

The resistance checking in Sub-section 8.3.3.5, for bolt-shear failure, is for the steel or stainless steel bolts and is to be in accordance with the appropriate clauses in Eurocode standards EN 1993-1-8:2005 and EN 1993-1-4:2006.

Sub-section 8.3.4 is for bolted joints subjected to out-of-plane actions and for the composite element there is a strength formula for pull-out resistance. Figure 2 shows that the design force is now N_{Ed} and that the failure plane (dashed line through thickness of FRP material) is based on the perimeter of the steel washer having diameter d_r . For a steel or stainless steel bolt subjected to tensile force N_{Ed} design is in accordance with the clauses in EN 1993-1-8:2005 and EN 1993-1-4:2006.

Sub-section 8.3.5 is for design of bolted connections and joints where the bolted joint is subjected to in-plane and out-of-plane actions at the same time. In the presence of combined shear (V_{Ed}) and tensile (N_{Ed}) actions our consistent design concept has the resistance checked using a linear interaction failure criterion, this is not given in Anonymous (2010).

In Section 8 the strength formulae are without their material partial factor. These are presented in Sub-section 2.3.4 with, for connected FRP elements, the γ_{MS} at Ultimate Limit State determined from a product of a partial factor for the uncertainty in determining the material properties and a partial factor for the uncertainty of material properties due to the nature of the constituent parts. This second partial factor depends on the composite material production method and is given in Table 2.1 (Ascione *et al.* (2016)). It is to be observed that partial factors from the Stage 1 deliverable are the same for all FRP

modes of failure and so there is no differentiation for the type of failure mode and the consequence the failure has on the connection, joint or structure.

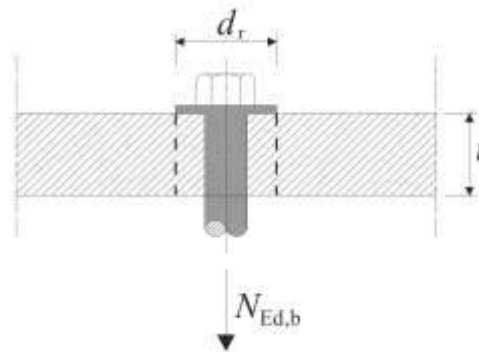


Figure 2: Pull-out failure caused by through thickness tension action (Ascione et al. 2016)

To take account that different application sites will have different environmental conditions, Sub-section 2.3.5 introduces a number of conversion factors that can take account of operational temperature and humidity, and creep response and fatigue from long-term effects of actions due to known design load cases.

The final sub-section 8.3.6 is for 21 primary publication sources giving results of academic research projects to understand various aspects of the structural performance of steel bolted connections with composite materials; predominantly the studies have worked with materials made by the pultrusion composite processing method (Bank 2006).

It is noteworthy now to give a brief summary on what type of revisions are required for us having the Stage 2 CEN Technical Specification, which is expected to be finalised in 2020. It can be observed from the reporting in this paper that for WG4 to progress the drafting, which is towards design practice, furtherwork is needed to enable the clauses and design procedures to be robust, reliable, relevant and having an acceptable risk against failure over the range of bolted connection/joint details that designers will require of the FRP materials, which are within the scope of Chapter 8.

In particular, work is needed to identify, and to integrate into Chapter 8 design clauses to cover all possible/practical connection and joint modes and failures. Moreover, the code drafters will want to consider the need (or otherwise) to differentiate the values of partial factors (in Sub-section 2.3.4) to the various failure modes based on risk analysis and by using relevant and reliable physical test results, from the literature, to calibrated and verify the partial factors using the analysis methodology set out in EN 1990:2002.

Because connection and joint design for resistance requires knowing specific material characteristic strengths (and knowledge of how they change with time; linked to the conversion factors in Sub-section 2.3.5) there is a need, in parallel, to work on having standards to specify the FRP materials and their processing methods, and for the characterization of characteristic strengths by coupon test methods, noting that these standards have to integrate fully with the clauses in the Stage 2 report. It is expected that this report will transform the 2017 JRC report to the next level for progressing the WG4 CEN/TC250 project towards the publication of an FRP structural Eurocode.

CASE STUDY

In June 2015, Siemens was awarded a contract for the expansion of the Egyptian power supply, with the effort to boost Egypt's power generation capacity by 45 percent upon final completion of three new power plants, called Beni Suef, Burullus and New Capital. These power plants are powered by 24 Siemens H-Class gas turbines, selected for their high generation output and efficiency. The size of the

megaproject is enormous, with more than 20k workers engaged on construction sites during civil engineering works and over 1.6 million tons of material being handled.

Part of the power-plant at Beni Suef has 64 cell cooling tower units made of pultruded FRP shapes, FRP sheets for cladding, stainless steel elements for fasteners and other hardware elements. Figure 3 shows, under construction, one of these cooling tower units. Pultruded FRP cooling towers typically consist of ‘stick’ structures having braced frame design. These structures are connected to the ground by steel angles and base plates anchored and grouted to the basin.

Some connection details are presented now to highlight that steel bolted connections are frequently used to join structural FRP elements in industrial applications.

Acting on the client’s request the structural design of the cell cooling towers was performed by Knippers Helbig GmbH in accordance with US-Codes and Standards. This set of codes is not complete, since there is no official US-Standard for this form of FRP structures. Anonymous (2010) is a pre-standard for the design of such pultruded frame structures, which is currently being progressed by an American Society of Civil Engineers/ Structural Engineering Institute Standards Committee to a national standard. As a consequence, it was decided that structural design will be carried out based on two publications from the Cooling Technology Institute (CTI) in the USA, namely, The CTI-Guideline ESG-152 (2013) for the Structural Design of FRP Components and the CTI-Bulletin STD-137 (2013) for FRP Products used in Cooling Towers. Nevertheless, information regarding the design of connections is very limited in these two CTI documents. Design rules or procedures scoping the distinct failure modes for detachable bolted connections summarized in Ascione *et al.* (2016) were therefore applied by the structural engineering designers. Since these non-mandatory rules are based on the European design concept, they had to adjusted to meet the US-Codes concept accordingly.



Figure 3: FRP cooling tower at Beni Suef in Egypt (courtesy of Siemens)

The superstructure of a cell cooling tower unit consists of detachable mechanically fastened connections using stainless steel bolts and nuts, and is similar in design detailing to the form of joints typically found in load-bearing structural steel structures. In order to minimize erection time all bolted connections are pre-fabricated off-site.

Figure 4 shows, in three parts, what measures were applied to locally strengthen bolted connections to satisfy the JRC report resistance clauses. In order to increase the load-bearing capacity in box elements, the bolt holes in the pultruded elements are reinforced with ‘hard’ PVC tubular inserts, where the design calculations required their introduction. The utilization of the PVC tubular inserts that will improve transfer of V_{Ed} into the pultruded FRP material is shown in Figure 4(a). This detailing increased hole diameter in the FRP box-section and consequently the bearing stresses at the interface are decreased. At other bolted connections, the web in a C-shaped element is strengthened either by adhesively bonding on an FRP-plate, this is shown in Figure 4(b), or, when either V_{Ed} was too large or the length of the connection geometry too limited, a stainless steel plate was bolted to the web. In the latter detailing situation, a set of bolts are used to connect the stainless steel plate to the FRP material to realise a monolithic section, while the function of a second set of bolts is to transfer the design forces from one pultruded shape to another pultruded shape. The line drawing in Figure 4(c) is for a square hollow pultruded box (of 60 mm side lengths), that under an exceptional design load case requires a stainless steel tube to be inserted to adequately strengthen the joint so that its design will be fit for purpose over the design working life of the cell cooling tower unit.

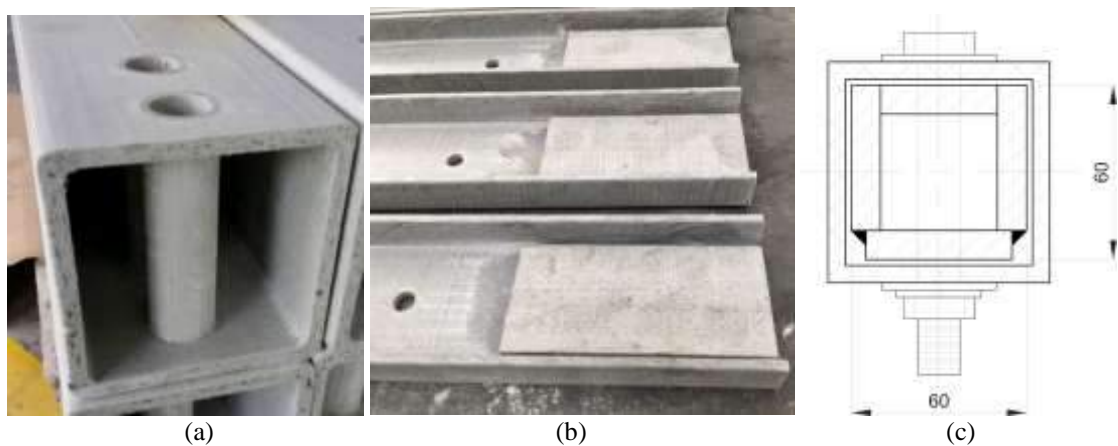


Figure 4: Measures for local strengthening of bolted connection: (a) tubular PVC-insert ;(b) glued FRP- plate; (c) stainless steel tube insert (Siemens / Knippers Helbig)

CONCLUSIONS

Over the last decade, a project with Working Group 4 (WG4 for Fibre Reinforced Polymers (FRPs)) in the Structural Eurocode Committee CEN/TC250 has delivered a Stage 1 consultation JRC report (Ascione *et al.* 2016) that is the starting deliverable for a future FRP structural Eurocode. This paper gives a summary of the consistent approach that the drafters in WG4 have taken to be able to prepare the chapter for the design of structural connections. In particular, this paper focuses on the sections and sub-sections that are for the design of connections and joints where the method of connection is by stainless or structural steel bolting. The main conclusion from the reporting is that a framework has been prepared in this Stage 1, and that, to progress the drafting to Stage 2, which is towards design practice, furtherwork is required to ensure the clauses are going to be robust, reliable, relevant and having an acceptable risk against failure for the range of bolted connection/joint details that structural engineering designers require of the FRP materials, which are within the scope of Chapter 8 (and Ascione *et al.* (2016)).

Using a recent civil engineering project having 64 pultruded FRP cooling tower units at a power plant in Egypt the paper explains why the non-mandatory design rules in the JRC report (Ascione *et al.* 2016) where applied by Knippers Helbig GmbH to carry out the structural design calculations. Introduced are three measures for local strengthening of bolted connection that are required to enable the JRC report clauses and design procedures to be satisfied.

REFERENCES

- Anonymous (1984). "Structural Plastics Design Manual," American Society of Civil Engineers Manuals and Reports on Engineering Practice, No. 63, American Society of Civil Engineers, New York, New York.
- Anonymous. (2008). "Guide for the Design and Construction of Structures made of FRP Pultruded Elements," Advisory Committee on Technical Recommendations for Construction, National Research of Italy, CNR-DT 2005/2007, Rome, CNR. (English Version)
http://www.cnr.it/documenti/norme/IstruzioniCNR_DT205_2007_eng.pdf (08 December 2017)
- Anonymous. (2010). "Pre-Standard for Load and Resistance Factor Design (LRFD) of Pultruded Fiber Reinforced Polymer (FRP) Structures," American Society of Civil Engineers, Reston, VA.
- Anonymous. (2012). "Code of Standard Practice for Fabrication and Installation of Pultruded FRP Structures," ANSI standard, American Composites Manufacturers Association, 1st Edition, Arlington, VA (2012).
- L. Ascione, J-F. Caron, P. Godonou, K. van IJselmuiden, J. Knippers, T. Mottram, M. Oppe, M., Gantriis Sorensen, J. Taby L. Tromp (2016). Editors: L. Ascione, E. Gutierrez, S. Dimova, A. Pinto, S. Denton. "Prospect for New Guidance in the Design of FRP," Support to the implementation and further development of the Eurocodes, JRC Science and Policy Report, Policy Framework Existing Regulations and Standards, Prospect for CEN Guidance, European Commission, Joint Research Centre Institute for the Protection and Security of the Citizen, JRC99714, EUR 27666 EN, European Union, Luxembourg, 2016, p 171.
<http://eurocodes.jrc.ec.europa.eu/showpublication.php?id=539> (08 December 2017)
- L.C Bank (2006). "Composites for Construction - Structural Design with FRP Materials", John Wiley and Sons, New Jersey.
- BÜV-Empfehlung (2014). "Tragende Kunststoffbauteile im Bauwesen [TKB] – Entwurf, Bemessung und Konstruktion", Springer, Wiesbaden. (in German)
- J.L Clarke (Ed.) (1996). "Structural Design of Polymer Composites - EUROCOMP Design Code and Handbook", E. & F.N. Spon, London.
- CTI-Guideline ESG-152 (2013). "Structural Design of FRP Components," (May 2013).
- CTI-Bulletin STD-137 (2013). "Fiberglass Pultruded Structural Products for Use in Cooling Towers," (March 2013).
- CUR Commission C124. (2003). "Recommendation 96 Fibre-Reinforced Polymers in Civil Load Bearing Structures", CUR Gouda, The Netherlands.
- EN 1990: 2002. "Eurocode 0 - Basis of Structural Design," CEN, European Committee for Standardization, Brussels.
- EN 1993-1-8: 2005. "Eurocode 3: Design of Steel Structures - Part 1-8: Design of Joints," CEN, European Committee for Standardization, Brussels.
- EN 1993-1-4: 2006+A1:2015. "Eurocode 3. Design of Steel Structures. General Rules. Supplementary Rules for Stainless Steels," CEN, European Committee for Standardization, Brussels.
- EN 13706: 2002. "Reinforced Plastic Composites - Specification for Pultruded Profiles," CEN, European Committee for Standardization, Brussels.
- E. Gutiérrez, S. Dimova, A. Pinto (2007). "Purpose and Justification for New Codes and Standards Regarding the use of Fibre-Reinforced Polymer Composites in Civil Engineering," Support to the implementation, harmonization and further development of the Eurocodes, EUR 22864 EN, JRC European Commission.
<http://eurocodes.jrc.ec.europa.eu/doc/EUR22864EN> (08 December 2017)
- J.T. Mottram (2010). "Prediction of Net-tension Strength for Multi-row Bolted Connections of Pultruded Material using the Hart-Smith Semi-empirical Modeling Approach," Journal of Composites for Construction, 14 1, 105-114.
- J.T. Mottram (2013). "Rationale for Simplifying the Strength Formulae for the Design of Multi-row Bolted Connections Failing in Net-tension," Proceedings 6th International Conference on Advanced Composites in Construction (ACIC 2013), (Queen's Belfast), 10-12 September 2013, NetComposites Ltd., Chesterfield, UK, 383-392.

M. Oppe (2009). "Zur Bemessung geschraubter Verbindungen von pultrudierten faserverstärkten Polymerprofile," Dissertation, Schriftenreihe Stahlbau, Heft 66, Shaker-Verlag Aachen, ISBN: 978-3-8322-8247-9.



REACTIVE ORGANOCLAY AND OTHER NANOFILLERS AS A MEAN TO IMPROVE POLYMER ADHESIVE OR MATRIX FORMULATIONS

Mohamed M. Chehimi¹, Beata Strzemieska², Karim Benzarti^{3,*}

¹ ICMPE, CNRS, 94320 Thiais, France

² Poznan University of Technology, 60-965 Poznań, Poland

³ Laboratoire Navier, Champs sur Marne, F-77447 Marne la Vallée, Cedex 2, Franc.

ABSTRACT

This paper summarizes handpicked strategies of surface and interface chemical organo-modification of layered silicates and silica nanofillers. Using silanes and onium salts, one can attach functional groups to the filler for compatibilization or reaction with polymer matrices. The level of modification is molecular or macromolecular in nature. Polymer-modified fillers have unique reinforcing properties due to multiple reactive groups towards polymer matrices. Herein, we report case studies to illustrate the role of surface chemical modification of fillers using silanes, ammonium salts and diazonium compounds. We demonstrate that fine control over the surface chemical composition of fillers has profound effect on mechanical, thermal, viscoelastic and electrical properties of end polymer composites.

KEYWORDS

Reactive Nanofillers, Organoclay, Silica, Silane, Onium Salts, Polymer composites.

INTRODUCTION

Mechanical properties of polymer composites depend to a very large extent on the filler-polymer matrix interactions (Rong et al. 2006). Indeed, mechanical stress applied to the composite is transferred to the interface/interphase region which will either resist or fail depending primarily on the molecular interactions between the filler and the polymer. For example, strong molecular interactions at polymer-filler interface (e.g. covalent bonding) results in effective stress transfer from the polymer matrix to nanofillers (Mousa et al. 2016). One key issue is to chemically modify fillers with appropriate coupling agents that interact covalently or non-covalently with the fillers. Whilst silanes are known to readily react with silica and other ceramics, onium salts are routinely used to intercalate layered silicates (clays) to make organophilic fillers and thus compatible with organic polymer matrices. In the last 5 years, we have introduced diazonium compounds as intercalating agents and/or reactive compounds to design, in an original way, organo-fillers such as clays and silicas (Salmi et al. 2013; Jlassi et al. 2014; Sandomierski et al. 2016).

In this paper we will review our strategies for making organo-fillers using traditional and modern coupling agents, and the use of the said modified fillers to prepare high performance polymer composites. The general strategy of modifying the fillers will be first introduced then case studies will be presented and discussed to illustrate the importance of surface organo-modification of fillers, at the molecular and macromolecular level, on the properties of the final composites.

GENERAL STRATEGY FOR MAKING ORGANO-FILLERS

Figure 1 displays examples of reactive fillers we have designed. Clays can be intercalated with ammonium (Figure 1b) or diazonium cations (Figure 1c). If the onium salts bears a reactive group or an initiator or an ethylenic end, one can obtain by *grafting onto* or *grafting from* procedure a highly intercalated or exfoliated clay/polymer nanocomposite to serve as filler. In this respect, clay/PGMA nanocomposite fillers present the advantages to be highly exfoliated on the one hand, and reactive towards aminated hardener of epoxy resins, on the other hand. The final epoxy composites are transparent and robust. Silica grafted with para-hydroxybenzyl groups readily react with phenolic resins; this is an important issue since the process avoids the use of toxic crosslinkers such as hexamethylenetetramine.

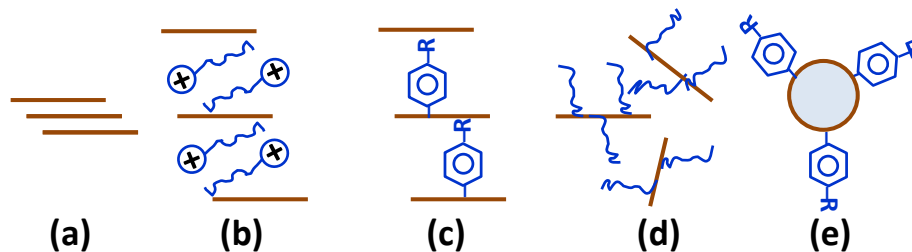


Figure 1. Examples of clay and silica nanofillers: (a) pristine clay; (b) ammonium-exchanged clay; (c) diazonium-modified clay; (d) clay-polymer composite nanofiller via silane or onium chemistries; (e) diazonium-modified silica nanoparticles.

To understand the effect of organofillers on the mechanical properties of the end polymer composites, it is important to employ a range of complementary tools to track chemical modification of fillers. X-ray photoelectron spectroscopy (XPS) and time of flight-secondary ion mass spectroscopy (ToF-SIMS) are surface sensitive techniques tracking changes within a 1-5 nm depth, while Fourier transform infrared spectroscopy (FTIR) characterizes functional groups at the surface of fillers. To these analytical tools, thermogravimetric analysis permits to determine the mass loading of organic matter to the fillers, while nitrogen adsorption measurements provides Brunauer, Emmett and Teller (BET) specific surface area of the fillers. Finally, high resolution transmission electron microscopy (HRTEM) permits to directly image the surface organic layer and determine its thickness, or to measure the interlayer spacing in clays upon intercalation or exfoliation. Organic modification of crystalline fillers results in an amorphous layer easily distinguishable from that of the filler.

In the following, we will tackle case studies of preparation, characterization and use of organo-modified fillers for polymer composites. The mechanical properties were determined for composites in terms of *e.g.* flexural strength, fracture toughness, storage and loss moduli. Epoxy composite curing could also be monitored by measuring viscosity of the composite formulation.

CASE STUDIES OF ORGANO-CLAYS

Figure 2 shows milestones of clay intercalation using a large variety of compounds (Jlassi et al. 2017). Clearly, the modification of clays is getting more and more tricky and much is done to finely tune the properties of these layered fillers.

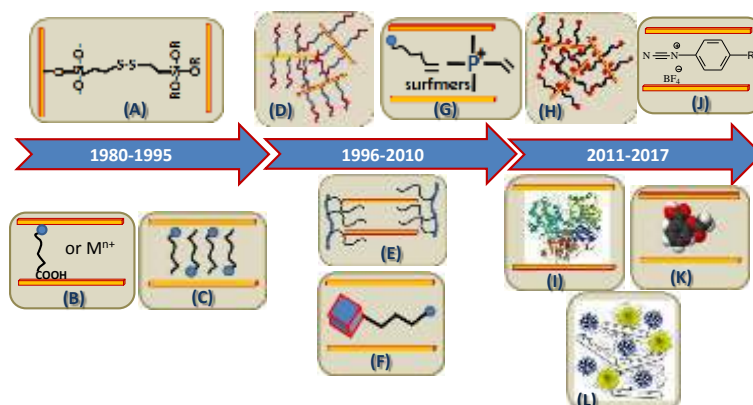


Figure 2. Milestones of clay intercalation strategies. Intercalation or grafting with (A): bifunctional silane; (B) Carboxylic acid functionalized alkylammonium or metal ions; (C) alkyl ammonium; (D) block copolymers; (E) comb copolymers; (F): POSS-functionalized alkyl ammonium; (G): ammonium and phosphonium surfmers; (H) in situ generated carbon nanotubes; (I) enzymes; (J) diazonium salts; (K): drug; (L): dendrimer/TiO₂ NP mixtures. Reproduced with permission of Elsevier from Jlassi et al. 2017. POSS: polysilsesquioxane, NP: nanoparticles.

Modification with silanes

Most of studies using silanes concern aminopropylsilane (APS) given the reactivity of the terminal aminogroup. Other speciality silanes have also been employed to intercalate clays. In this respect, clickable silanes permitted to attach photoinitiator (Tasdelen et al. 2008) while for catalytic applications pyrrole silane was employed to make organophilic clay for the in situ photopolymerization of pyrrole using AgNO_3 as photosensitizer (Jlassi et al. 2013). As far as fillers are concerned, APS permitted to modify montmorillonite (MMT) and MMT-APS organoclay was further reacted to anchor atom transfer radical polymerization (ATRP) initiator (Djouani et al. 2010). In this way, exfoliated MMT/poly(glycidyl methacrylate) (MMT/PGMA) nanocomposite filler was designed with a PGMA mass loading of 65 wt% and a PGMA-rich surface as probed by XPS (Figure 3).

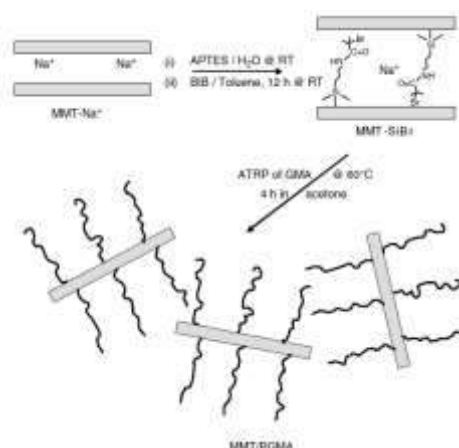


Figure 3. Preparation of layered ATRP macroinitiator (MMT-SiBr) followed by synthesis of MMT/PGMA nanocomposites. Si-Br: bromine-terminated silane.

Similar fillers were designed using mercaptosilane (MPS) as intercalant and PGMA (up to 81 wt%) was prepared by radical photopolymerization using 2,2'-azobis(2-methylpropionitrile) (AIBN) as type I photoinitiator (Jlassi et al. 2015b) or dimethylaminopropyl silane as Type II radical photoinitiator using benzophenone as photosensitizer (Jlassi et al, 2015a). The MMT-MPS/PGMA nanocomposite served to reinforce epoxy matrix hardened with (4,4'-diaminodiphenylsulfone) (DDS) at 220 °C. Robust transparent epoxy composites were obtained. The storage modulus increases in the case of nanocomposite filling compared to neat epoxy with an onset of segmental relaxation shift to high temperature (182 instead of 169 °C). $\tan\delta$ spectrum experiences a shift of 50 °C on going from neat to MMT-MPS/PGMA-filled epoxy.

Modification with ammonium salts

Ammonium salt with ATRP initiator group at the terminus of the alkyl chain was synthesized. As described above, MMT functionalized with bromine-terminated silane (MMT-Br) was prepared to serve as macroinitiator in the in situ graft polymerization of glycidyl methacrylate (GMA) (Djouani et al. 2011). Highly soluble, exfoliated MMT/PGMA nanocomposite filler was obtained and employed to reinforce epoxy using diethylene triamine (DETA) as hardener. The system cures at RT which is necessary for outdoor civil engineering applications. Interestingly, the PGMA chains from the nanocomposite filler react with DETA which in turn crosslinks epoxy (Figure 4).

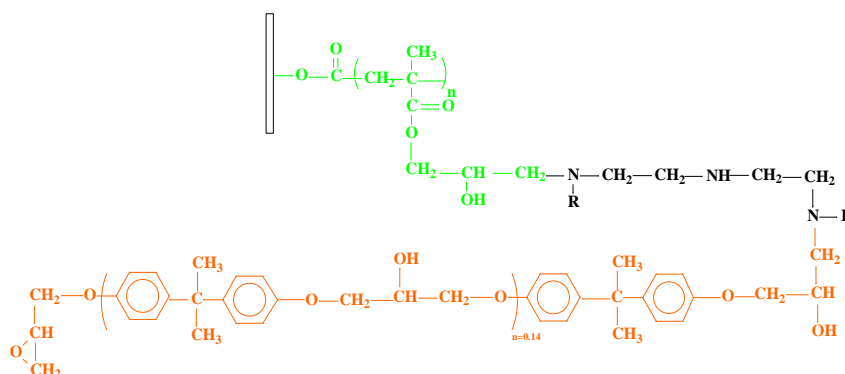


Figure 4. Molecular level of the interface in ternary MMT/PGMA-epoxy-DETA systems.

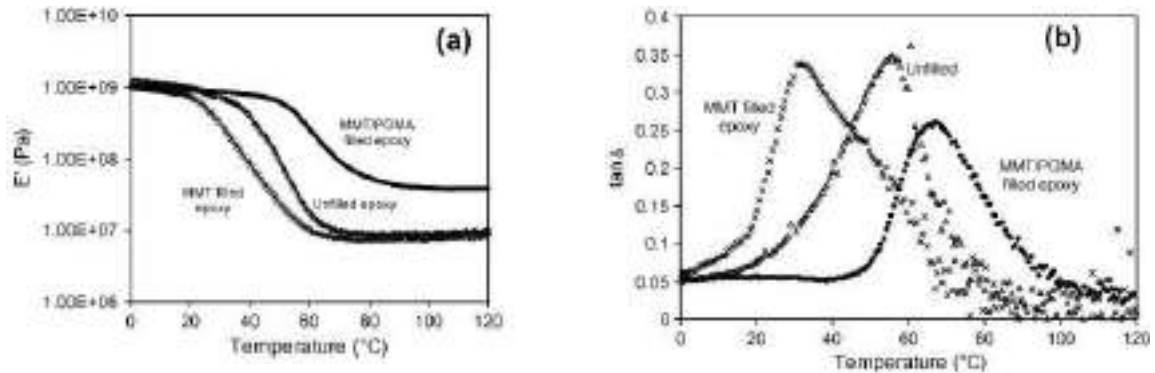


Figure 5. Storage modulus (a) and $\tan \delta$ (b) spectra for the unfilled and filled epoxy adhesives recorded at 1 Hz.

Figure 5 displays E' and $\tan \delta$ spectra recorded in 0-120 °C range for unfilled, MMT-filled and MMT/PGMA-filled epoxy matrices. Figure 5b indicates that the main relaxation peak of the MMT/PGMA filled matrix is centred at 67 °C, higher than for neat epoxy (56 °C) with a decrease in the amplitude. Using MMT/PGMA nanocomposite filler induces large increase in the storage modulus, particularly in the rubbery region (Figure 5a).

Modification with aryldiazonium salts

Diazonium salts are unique alternatives to the traditional silanes and ammonium salts. They easily intercalate clays by exchange mechanism followed by the formation of diazoether linkages: $\text{Si-O-N=N-C}_6\text{H}_4\text{-R}$ which dediazonize at 60 °C. The choice of the radical R depends on the selected type of polymer and the polymerization method. R = $\text{N}(\text{CH}_3)_2$ (DMA), $\text{O=C-C}_6\text{H}_5$ (BP), $\text{NH-C}_6\text{H}_5$ (DPA), and $\text{CH}_2\text{SCSN}(\text{C}_2\text{H}_5)_2$ (iniferter).

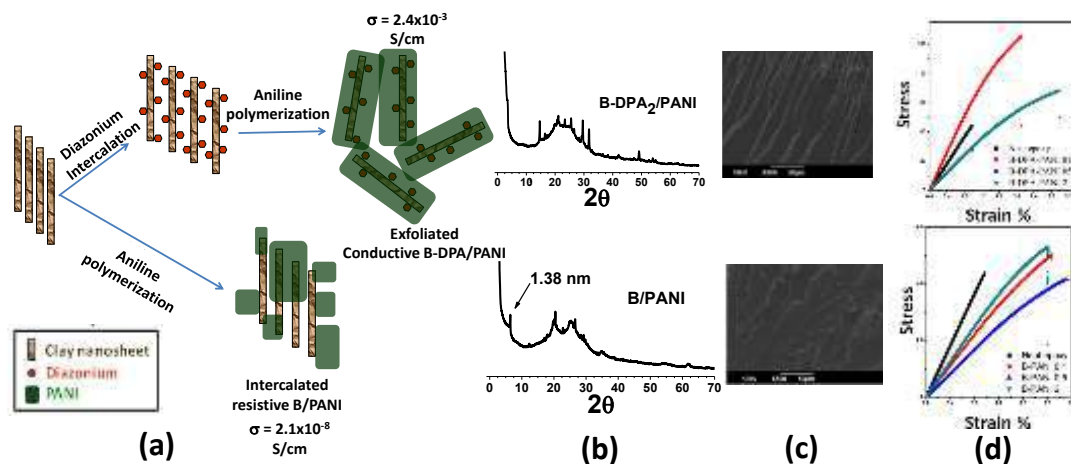


Figure 6. Upper row : oxidative in situ polymerization of polyaniline in presence of DPA diazonium salt-modified bentonite (B-DPA). Lower row : oxidative in situ polymerization of polyaniline in presence of pure bentonite B. (a) synthesis of hybrid fillers with (upper) and without diazonium (lower) ; (b) : SAX patterns ; (c) SEM image of fracture surface of epoxy matrix filled with B-DPA/PANI (upper row) and B/PANI (lower row) ; (d) Fracture toughness of epoxy reinforced with B-DPA/PANI and B/PANI (•: neat epoxy, ♦: B-PANI 0.1 wt% , ▲: B-PANI 0.5 wt%, ▼: B-PANI 2 wt%). (b) Reproduced with permission of RSC from Jlassi et al. (2014) and other images reproduced with permission of ACS from Jlassi et al. (2016).

The N,N-dimethylaminoaniline (DMA) diazonium requires free benzophenone (BP) as photosensitizer (for UV photopolymerization), and BP diazonium necessitates free N,N-dimethylaniline in solution. The DMA diazonium is way better intercalated compared to BP diazonium, and an exfoliated photochemically prepared clay/PGMA nanocomposite could be synthesized using clay intercalated with DMA diazonium (Salmi et al. 2013). The iniferter diazonium is too bulky and intercalation required high initial concentration of diazonium (Salmi-Mani et al. 2016). Finally, the diphenylamine (DPA) diazonium-intercalated bentonite was employed for the in situ oxidative

polymerization of aniline thus providing highly exfoliated bentonite-DPA/PANI as conductive nanocomposite filler (Jlassi et al. 2014). It is possible to synthesize clay/PANI without any diazonium intercalation but the filler is an intercalated composite (as judged from XRD measurements) and the conductivity was 2×10^{-8} S/cm, 5 orders of magnitude lower than the clay-DPA/PANI filler prepared using diazonium salt. After reaction with the epoxy resin and DDS hardener, the clay-DPA/PANI/epoxy final composite exhibited improved fracture toughness by 210–220% much higher than 20–30% in the case of the B/PANI (B: bentonite) filler prepared with any diazonium salt (Jlassi et al. 2016). The fracture surfaces of clay-DPA/PANI/epoxy and clay/PANI/epoxy differ markedly; the former has a very particular fibrillar structure indicating ductile failure mode, whereas the clay/PANI filler induces a smooth fracture surface which accounts for brittle failure mode. Figure 6 compares the effects of diazonium salts on the properties the nanocomposite filler and the properties of the final corresponding epoxy composites.

DIAZONIUM MODIFICATION OF NANOSILICAS

Phenolic resins are used as binders for several purposes such as abrasive materials (Gardziella et al. 2000). Two types of phenolic resins are mostly used for abrasive tools production: novolac and resole (Strzemiecka et al. 2014). Whereas resole is thermosetting polymer that crosslinks at 180 °C without necessity of any crosslinking agent addition novolac is thermoplastic polymer and in order to crosslink it the addition of crosslinking agent is essential. The crosslinking agent for novolac is most often urotropine, additional portion of formaldehyde or paraformaldehyde. All aforementioned crosslinking agents are hazardous compounds. Thus, some efforts are made to exchange these crosslinkers with more eco-friendly ones.

Sandomierski et al. (2016) prepared diazonium-modified silicas to serve as the active fillers of phenolic resins (used e.g. as binders in abrasive products) at 10 - 25 wt. % (Figure 7) that can act as crosslinking agent. The diazonium-modified silica nanoparticles with surface bound $-\text{CH}_2\text{-OH}$ groups react with phenolic resins causing its crosslinking (hardening) and change their viscosity so that the flow distance is shorter than that measured for neat resin. After annealing at 180 °C, the diazonium-modified silica/phenolic resin composites were found to be mechanically robust and the three-point flexural test indicated 35 % increase in the flexural strength compared to pristine Syloid type silica or other standard fillers for phenolic resins.

Diazonium-modified silica with surface bound $-\text{CH}_2\text{-OH}$ groups are thus ideal reactive filler for phenolic resins. Such filler ensures interfacial chemical reactions with the matrix and imparts robust mechanical properties to the final composites.

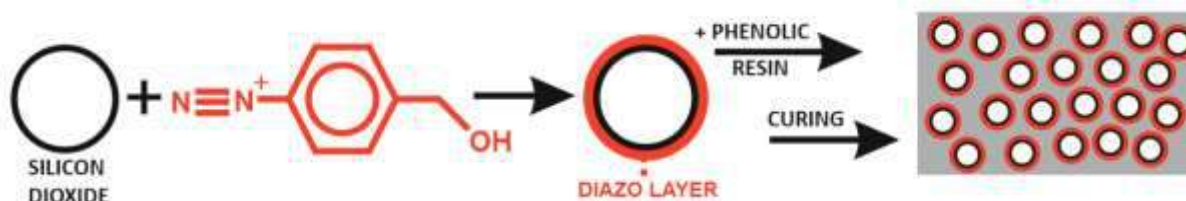


Figure 7. Three-step making cured phenolic resin filled with diazonium-modified silica nanoparticles. Reproduced with permission of ACS.

CONCLUSION

In summary, surface chemical modification of nanofillers is of paramount importance to improve the mechanical properties of polymer composites materials (e.g. fracture toughness, flexural strengths, storage modulus). Clearly, diazonium salts should be included in the composite chemist tool box as they provide efficient modification of the nanofillers and chemical reactivity towards the polymer matrices under test. Moreover, initiator-containing diazonium compounds permit to design filler/polymer hybrid fillers and broaden this way the possibilities offered to the materials scientists to design specialty fillers.

ACKNOWLEDGMENTS

This work has benefited from a French government grant by ANR within the frame of the national program Investments for the Future ANR-11-LABX-022-01 (LabEx MMCD project).

REFERENCES

- F. Djouani, F. Herbst, M. M. Chehimi, K. Benzarti (2010). «Preparation of exfoliated clay/polymer nanocomposites via organosilane grafting and in situ ATRP of glycidyl methacrylate», *Surface Interface Analysis* 42, 1019–1024.
- F. Djouani, F. Herbst, M. M. Chehimi, K. Benzarti (2011). « Synthesis, characterization and reinforcing properties of novel, reactive clay/poly(glycidyl methacrylate) nanocomposites», *Construction and Building Materials*, 25, 424–431.
- A. Gardziella, L.A. Pilato, A. Knop, Phenolic Resins: Chemistry, Applications, Standardization, Safety and Ecology, Springer, Berlin, 2000.
- K. Jlassi, A. Singh, D. K. Aswal, R. Losno, M. Benna-Zayani, M. M. Chehimi (2013), “Novel, ternary clay/polypyrrole/silver hybrid materials through in situ photopolymerization”, *Colloids and Surfaces A* 439, 193–199.
- K. Jlassi, A. Mekki, M. Benna-Zayani, A. Singh, D. K. Aswal, M. M. Chehimi (2014), “Exfoliated clay/polyaniline nanocomposites through tandem diazonium cation exchange reactions and in situ oxidative polymerization of aniline”. *RSC Advances*, 4, 65213-65222.
- K. Jlassi, M. Benna-Zayani, M. M. Chehimi, Y. Yagci (2015a), « Efficient photoinduced in situ preparation of clay/poly(glycidyl methacrylate) nanocomposites using hydrogen-donor silane», *Journal of Polymer Science A*, 53, 800–808.
- K. Jlassi, S. Chandran, M. Mičušík, M. Benna-Zayani, Y. Yagci, S. Thomas, M. M. Chehimi (2015b), «Poly(glycidyl methacrylate)-grafted clay nanofiller for highly transparent and mechanically robust epoxy composites», *European Polymer Journal*, 72, 89–101.
- K. Jlassi, S. Chandran, M. A Poothanari, M. Benna-Zayani, S. Thomas, M. M. Chehimi (2016), “Clay/polyaniline hybrid through diazonium chemistry: conductive nanofiller with unusual effects on interfacial properties of epoxy nanocomposites », *Langmuir*, 32, 3514–3524.
- K. Jlassi, I. Krupa, M. M. Chehimi (2017), “Overview: Clay Preparation, Properties, Modification”, in K. Jlassi, M. M. Chehimi and S. Thomas (Eds.) *Clay-Polymer nanocomposites*, Elsevier, 2017.
- M. H. Mousa, Y. Dong, I. J. Davies (2016), “Recent advances in bionanocomposites: Preparation, properties, and applications”, *International Journal of Polymeric Materials and Polymeric Biomaterials*, 65, 225–254.
- M. Z. Rong, M. Q. Zhang, W. H. Ruan (2006), “Surface modification of nanoscale fillers for improving properties of polymer nanocomposites: a review”, *Materials Science and Technology*, 22, 787-796.
- Z. Salmi, K. Benzarti, M. M. Chehimi (2013), “Diazonium cation-exchanged clay: an efficient, unfrequented route for making clay/polymer nanocomposites”, *Langmuir*, 29, 13323–13328.
- H. Salmi-Mani, Z. Ait-Touchente, A. Lamouri, B. Carbonnier, J.-F. Caron, K. Benzarti, M. M. Chehimi (2016), “Diazonium salt-based photoiniferter as a new efficient pathway to clay–polymer nanocomposites”, *RSC Advances*, 6, 88126- 88134.
- M. Sandomierski, B. Strzemiecka, M. M. Chehimi, A. Voelkel, “Reactive diazonium-modified silica fillers for high-performance polymers”, *Langmuir*, 32, 11646–11654.
- B. Strzemiecka, A. Voelkel, J. Zięba-Palus, T. Lachowicz (2014), “Assessment of the chemical changes during storage of phenol-formaldehyde resins pyrolysis gas chromatography mass spectrometry, inverse gas chromatography and Fourier transform infrared methods”, *Journal of Chromatography A*, 1359, 255–261.
- M. A. Tasdelen, W. van Camp, E. Goethals, P. Dubois, F. Du Prez, Y. Yagci (2008). « Polytetrahydrofuran/Clay Nanocomposites by In Situ Polymerization and Click Chemistry Processes”, *Macromolecules*, 41, 6035–6040.